NO
PAPER
RIGHTS

REIMPRESSION
INTERDITE

micromedia
a division of IHS Canada

20 Victoria Street
Toronto, Ontario M5C 2N8
Tel.: (416) 362-5211
Toll Free: 1-800-387-2689
Fax: (416) 362-6161
Email: info@micromedia.on.ca

VOLUME

VOLUME

1

micromedia
a division of IHS Canada

20 Victoria Street
Toronto, Ontario M5C 2N8
Tel.: (416) 362-5211
Toll Free: 1-800-387-2689
Fax: (416) 362-6161
Email: info@micromedia.on.ca

ICOTOM–12
MONTREAL
1999

Proceedings of the Twelfth International Conference on Textures of Materials

Volume 1

Edited by
Jerzy A. Szpunar

J.A. SZPUNAR, a professor of Physical Metallurgy at McGill University, Montréal, was educated in Poland and received his Ph.D. and D.Sci. degrees from the Academy of Mining and Metallurgy in Cracow. He has held various visiting positions at Sussex and Durham Universities in England, worked in laboratories of the Finnish Academy of Science, Risø National Laboratory and served as an advisor to the National Atomic Agency Research Centre in Bandung, Indonesia.

His research interests span various areas of texture-related investigations. In particular, he is interested in deformation and recrystallization processes in metals, structure and properties of thin films, high temperature oxidation and corrosion, application of x-ray and neutron diffraction, and structure of grain boundaries as related to intergranular fracture, superplasti-city and special properties of nanocrystalline materials.

His group is also very active in the area of computer simulation of texture development during annealing and deformation processes and electrodeposition. This simulation based research is done on various levels: atomistic, microscopic and macroscopic; techniques of Molecular Dynamics - EAM, and Monte-Carlo are used to predict macroscopic properties of materials and to understand various processes that transform textures and properties.

Professor J.A. Szpunar is the author and co-author of over 300 research papers.

ISBN 0-660-17789-7
9 780660 177892

101-03653/

TWELFTH INTERNATIONAL CONFERENCE ON TEXTURES OF MATERIALS

Volume 1 of 2 Volumes

LIST OF SPONSORS

- Canadian Institute of Mining, Metallurgy and Petroleum
- National Research Council of Canada
- Canadian Steel Industry Research Association
- Alcan Research Division, Kingston
- TexSem Laboratories Inc.
- Blake Industry Inc.
- ASM International

ICOTOM-12

PROCEEDINGS OF THE TWELFTH INTERNATIONAL CONFERENCE ON TEXTURES OF MATERIALS

Volume 1 of 2 Volumes

McGill University, Montreal, Canada
August 9–13, 1999

Edited by
Jerzy A. Szpunar

Department of Metallurgical Engineering
McGill University
3610 University Street
Montreal, Quebec, Canada H3A 2B2

NRC·CNRC
NRC Research Press
Ottawa 1999

© 1999 National Research Council of Canada

All rights reserved. No part of this publication may be reproduced in a retrieval system, or transmitted by any means, electronic, mechanical, photocopying, recording or otherwise, without the prior written permission of the National Research Council of Canada, Ottawa, Ontario, Canada K1A 0R6.

ISBN 0-660-17789-7
NRC No. 42844

Canadian Cataloguing In Publication Data

International Conference on Textures of Materials (12th : 1999 : Montreal, Canada)

Proceedings of the Twelfth International Conference on Textures of Materials:
August 9–13, 1999, McGill University, Montreal, Canada

Volume 1 of 2 volumes.
At head of title : ICOTOM-12.
Issued by the National Research Council of Canada.
ISBN 0-660-17789-7 (v.1)
ISBN 0-660-17790-0 (v.2)

1. Materials — Texture — Congresses.
2. Metals — Texture — Congresses.
3. Texture (Crystallography) — Congresses.
I. Szpunar, Jerzy A.
II. National Research Council Canada.
III. Title.

TA418.5I57 1999 620.1'292 C99-980228-3

Inquiries: Proceedings Program, NRC Research Press, National Research Council of Canada,
Building M-55, Ottawa, ON K1A 0R6, Canada.

Correct citation for this publication: Szpunar, J.A. (*Editor*). 1999. Proceedings of the Twelfth International Conference on Textures of Materials (ICOTOM-12). August 9–13, 1999, Montreal, Quebec, Canada. NRC Research Press, Ottawa, Ontario, Canada. Volume 1, pp. 1–802.

Contents

VOLUME 1

Preface xxi
Conference Committees xxii

Plenary Lecture Session

From crystal orientations to material properties: micro–macro linkage illustrated with deformation in the earth.
H.-R. Wenk and P.R. Dawson 3
Texture design for new applications.
J.A. Szpunar 6
Extraction of grain boundary energies from triple junction geometry.
B.L. Adams, C.L. Bauer, D. Casasent, B. El-Dasher, D. Kinderlehrer, I. Livshits, F. Manolache, D. Mason, A. Morawiec, W.W. Mullins, S. Ozdemir, H. Rogan, G. Rohrer, A.D. Rollett, D. Saylor, S. Ta'asan, A. Talukder, C-T. Wu, C-C. Yang, W. Yang 9

Texture and Microstructure Description and Analysis

Development and application of a disorientation correlation function.
P.S. Lee, A.D. Rollett, and B.L. Adams 21
Spatial statistics for individual orientation measurements.
K.G. van den Boogaart 29
On the determination of textures from discrete orientation measurements.
W.B. Hutchinson, E. Lindh, and P. Bate 34
Using sets of individual orientations for ODF determination.
S. Matthies and F. Wagner 40
Reproducibility of experimental texture measurement.
D.J. Jensen and M.T. Lyttle 46
Advancements of ACOM and applications to orientation stereology.
R.A. Schwarzer 52
Reliability of automatic orientation determination from Kikuchi patterns.
A. Morawiec 62
Influence of number and arrangement of single orientation measurements on their statistical relevance.
O. Engler, J. Jura, and S. Matthies 68
Determination of microtexture by EBSD at high spatial resolution in a FEGSEM.
F.J. Humphreys 74
Development of the three dimensional X-ray diffraction microscope.
R.M. Suter and K. Kosack 80

Non-destructive characterization of tube segments by means of neutron diffraction.
H.-G. Brokmeier 86
A method of misorientation distribution calculation using ODF data.
W. Mao, G. Zhu, and Y. Yu 92
Determination of heterogeneous textures by X-ray diffraction.
K. El Ghazouli, J.J. Heizmann, B. Bolle, L. Jolly, and C. Valot 98
Quantification of recrystallized fraction from orientation imaging scans.
S.I. Wright 104
Phase analysis and grazing incidence stress measurements in ZrO_2 films.
M.G. Glavicic and J.A. Szpunar 110
Texture analysis of complex earth materials from neutron diffraction spectra.
L. Lutterotti 116
Polychromatic microbeam diffraction, mesotexture and crack deflection in Al-Li 2090 T8E41.
J.D. Haase, R. Morano, T. Watt, and S.R. Stock 123
"HIPPO", a new high intensity neutron diffractometer for characterization of bulk materials.
K. Bennett, R.B. Von Dreele, and H.-R. Wenk 129
Residual strain measurement of {111} in rolled aluminum as function on in-situ annealing.
G. Langelaan, H. Jin, J. Hu, J. Cooley, and S. Saimoto 135
New development in texture and microstructure analysis of PA11.
L. Jolly, J.J. Heizmann, and A. Tidu 141
Use of a method based on a correlation function to reconstruct the parent textures from the inherited textures in phase transformation.
M. Humbert and N. Gey 147
False patterns of preferred orientation by erroneous background-correction.
H. Schaeben, H. Siemes, and J.-J. Fundenberger 153
Dual forms of texture analysis.
H. Schaeben and D.I. Nikolayev 156
Statistics for individual orientation measurements.
K.G. van den Boogaart 162
Determination of average orientation distribution function in thickness direction.
H. Inoue and N. Inakazu 168
Comparison of experimental techniques for characterization of through-thickness texture variations.
O.V. Mishin, E.M. Lauridsen, N.C. Krieger Lassen, H.F. Poulsen, D.J. Jensen, G. Brückner, and B. Bay 174
Modifications in the grain boundary character distribution in FCC materials through thermomechanical processing.
M. Kumar, A.J. Schwartz, and W.E. King 180
Accurate texture measurements on thin films using a powder x-ray diffractometer.
M.D. Vaudin 186
Adaptive orientation imaging microscopy.
W. Yang, B.L. Adams, and M. De Graef 192

Registry between sections in precision sectioning of polycrystalline materials.
A. Morawiec and D. Saylor 198
Mapping of lattice strain and texture distributions with an x-ray scanning apparatus.
R.A. Schwarzer and A.H. Fischer 204
X-ray and neutron diffraction measurement of textures of two-phase materials.
R.E. Bolmaro and H.-G. Brokmeier 211
Comparison of texture data measured by EBSD and conventional x-ray diffraction.
K. Mehnert, H.S. Ubhi, and A.P. Day 217
Experimental setting for indexing TEM Kikuchi diagrams.
J.J. Fundenberger, E. Bouzy, and J.S. Lecomte 223
Orientations measurements by TEM using spots, Kossel and LACBED patterns.
E. Bouzy, J.J. Fundenberger, J.S. Lecomte, and C. Esling 229
Texture analysis with a digital SEM–EBSD system.
H.-R. Wenk, J.J. Donovan, Y. Xie, G.C. Johnson, and E. Toker 235
X'pert texture: Overview of a software package for quantitative texture analysis
D.I. Nikolayev, V. Luzin, T. Lychagina, A.A. Dzjuba, V.A. Kogen, and J. Te Nijenhuis 241

Modeling of Texture Development

Influence of texture evolution on finite element simulation of forming processes.
E. Hoferlin, A. Van Bael, and P. Van Houtte 249
Monte-Carlo simulation of texture transformation in Ni-045%Fe nanocrystalline electrodeposits.
N. Rajmohan and J.A. Szpunar 255
Why we cannot simulate deformation textures.
T. Leffers 261
Analysis of inhomogeneous rolling texture of FCC metal sheets.
H.T. Jeong, K.K. Um, and D.N. Lee 267
Finite-element simulation of texture development in polycrystalline metals.
A. Bertram and M. Kraska 273
3-D animation of rotation of FCC crystals during various types of deformation.
H. Masui 279
Texture effects on steel sheet behaviour under large strain simulations.
L. Duchene, A. Godinas, and A.M. Habraken 286
Simulation of textural evolution during primary static recrystalization.
R. Sebald and G. Gottstein 292
Relationship between deposition and recrystalization textures of electrodeposits.
J.H. Choi, S.Y. Kang, D.N. Lee, and J. Yang 298
Recrystalization texture of aluminum bicrystals with S orientations deformed by channel die compression.
D.N. Lee and H.T. Jeong 304
A new analytic approach of crystal plasticity and its applications in polycrystal modeling.
L.S. Tóth and T. Hariz 310

Critical stress identification in textured materials using selfconsistent polycrystalline inverse model.
J.A. Signorelli, A. Fourty, R. Lebensohn, and R.E. Bolmaro 316
A discrete orientation model for the FCC-to-BCC phase transformation.
A.M. Lopes and C.S. Da Costa Viana 322
Predictions of recrystalization textures with Monte Carlo Model using deformation characteristics.
J. Tarasiuk, K. Wierzbanowski, B. Bacroix, and A. Miroux 328
Residual strains in Al–Mg powder composites. Simulations by self-consistent models.
A. Fourty, J.A. Signorelli, M.A. Bertinetti, R.E. Bolmaro, H.-G. Brokmeier, and H.-G. Priesmeyer 334
Parameterisation of cold-rolling and annealing textures in cublic metals based on the crystallographic fibres.
L. Delannay, A. Van Bael, and P. Van Houtte 340
Sensitivity of simulated anisotropy to initial texture definitions.
C.T. Necker, C.N. Tomé, F. Jean-Prost, and D.A. Korzekwa 346
Mesoscale modeling of cube texture evolution during hot deformation.
B. Radhakrishnan, G.B. Sarma, and T. Zacharia 352
Short range misorientation correlation and its evolution influence over texture development.
R.E. Bolmaro, A. Roatta, A. Fourty, C.T. Necker, and J. Bingert 358
Modeling of dynamic recrystalization in minerals.
H.-R. Wenk 364
Texture and strain localization prediction using a N-site self-consistent polycrystal model.
D.E. Solas and C.N. Tomé 369
FEM-micromechanics simulation of texture development of Cu–Fe powder composites.
J.A. Signorelli, A. Fourty, R.E. Bolmaro, and H.-G. Brokmeier 375
Simulative model and mechanism for deformation texture formation in FCC metal.
H. Masui 381
Coupling textural and microstructural evolution.
G. Winther 387
Modeling of the recrystalization textures of Al-alloys after hot deformation.
O. Englar and H.E. Vatne 393
Revision of the concept of 1-site models.
G. Winther, T. Leffers, and B. Clausen 399
3-D visualization of BCC iron crystals rotated during cold rolling.
H. Masui, H. Ukaji, O. Tsukamoto, T. Asami, and H. Katoh 405
Analysis of texture evolution of cubic metals by full constraint and two self-consistent viscoplastic models.
K.H. Oh 411
The role of Taylor factor in strain hardening.
L.S. Tóth, H.P. Stüwe, M. Zehetbauer, and I. Kopacz 417

A generalization of Taylor–Bishop–Hill theories and rate-dependent slip model in crystal plasticity.
K. Sekine 423

Texture and Anisotrophy

Modeling texture development during plastic deformation in cubic metals.
U.F. Kocks 431
Texture and anisotropy in low symmetry aggregates: elastic and plastic study of olivine.
C.N. Tomé 433
Finite element simulation with explicit use of polycrystal plasticity theory.
A.J. Beaudoin and P.R. Dawson 435
Crystallographic and morphological anisotropy in γ–TiAl.
H. Mecking 437
Diffractive determination of thermo-elastic single crystal constants using polycrystalline samples.
S. Matthies and H.-G. Priesmeyer 439
Texture and *r*-values of clad metals for button-type batteries.
M. Ishio, M. Umeda, H. Inoue, and K. Morii 445
Texture effects on the evolution of high temperature mechanical properties in zirconium alloys.
P. Sanchez, A.A. Pochettino, and R. Lebensohn 451
Levitation force to texture correlation in bulk Y-Ba-Cu-O.
D. Chateigner, J. Ricote, X. Chaud, P. Gautier-Picard, E. Beaugnon, J.-L. Soubeyroux, C. Leblond, and I. Monot 457
Texture effect on stress corrosion cracking of zirconium alloys in iodine environment.
S.B. Goryachev, A.R. Gritsuk, and M.G. Snegirev 463
Effect of texture on etching property and formability in invar shadow mask.
N.J. Park, M.H. Oh, S.M. Kim, and K.R. Kim 469
Texture measurement in steel industry practice.
C. Klinkenberg, H.-P. Schmitz, and H. Tamler 475
Textures in strip-cast AA3105 alloy and their ultrasonic characterization.
Y. Liu, X-M. Cheng, J.G. Morris, C-S. Man, and M. Huang 481
On-line plasticity prediction in textured steel and aluminum products.
P. Blandford and J.A. Szpunar 487
On-line measurement of texture and plastic strain ratio on steel sheets using laser-ultrasonics.
A. Moreau, D. Lévesque, M. Lord, M. Dubois, J.-P. Monchalin, C. Padioleau, and J.F. Bussière 493
Texture and residual stresses influence on the thermomechanical behaviour of Zircaloy-4 Tubes.
R. Brenner, J.L. Bechade, and B. Bacroix 499
Intercrystalline stresses in metal polycrystals: comparing simulations to diffraction experiments.
P.R. Dawson, D. Boyce, S. MacEwen, and R. Rogge 505

Relationship between texture, magnetic induction and maximum magnetic permeability of Si steels.
W. Mao, N. Chen, and Y. Yu 511
Strain effects and texture at in-plane shearing of Cu alloys.
J. Kusnierz and E.F. Rauch 517
Tilting of c-axise and twist around the c-axes in melt-textured YBaCuO cylinder.
V. Jung, H.-G. Brokmeier, E.M. Jansen, and R. Schnieber 523
The effect of texture on microyielding in near-gamma Ti–Al alloys.
B.A. Simkin, T.R. Bieler, and M.A. Crimp 529
On the evolution of anisotropic elastic properties during metal forming.
A. Bertram and T. Böhlke 535
Practical aspects of calculating elastic properties of textured hexagonal polycrystals.
T.A. Lychagina and H.-G. Brokmeier 541
Consideration of lattice incompatibility in the evolution of hardening.
A. Acharya and A.J. Beaudoin 547
Analysis of orientation-dependent stress heterogeneity.
Y.D. Wang, R.L. Peng, and R. McGreevy 553
Modelling texture influence on the magnetic properties of nanocrystalline nickel and iron.
B. Szpunar, M.J. Aus, E. Renaud, U. Erb, F. Czerwinski, and J.A. Szpunar 560

Deformation Textures

Macroscopic anisotropy in cold rolled AA5XXX sheet.
S.-H. Choi, J.C. Brem, F. Barlat, and K.H. Oh 569
Texture development during equal channel angular forging of BCC metals.
S.R. Agnew 575
The influence of tranverse rolling on texture and microstructure.
J. Pospiech, Z. Jasieński, A. Litwora, A. Piątkowski, and J. Gryziecki 581
Effect of texture on uniaxial tension in AA3003 sheet with inhomogeneous texture.
J.-H. Cho, S.-J. Park, S.-H. Choi, and K.H. Oh 587
Strain hardening effects on texture formation in zirconium alloys.
A.A. Pochettino and P. Sanchez 593
Unsymmetrical deformation texture transition during annealing of Cu–Al alloys.
W. Ratuszek, A. Bunsch, and K. Chruściel 599
Textures of AA3104 deformed by plane strain compression at multiple temperatures.
M.T. Lyttle and D.J. Jensen 605
Effects of reductions in area and of the heat treatments on the phase transformations and the volume fractions of equiatomic TiNi shape memory alloys in wires.
F. Baghdouche and A. Vadon 611
Texture stability during high temperature plane strain compression of a commercial Al–Mg alloy.
R.D. Knutsen, F.J. Humphreys, P.S. Bate, and S. Court 617

Assessment of the Lamel model used for prediction of rolling textures of FCC and BCC metals.
P. Van Houtte and L. Delannay 623

Rolling texture and mechanical twinning in B2 ordered CuZn alloy.
G.H. Zhu, W. Mao, Y. Yu, and G. Brückner 629

Effect of thermomechanical processing parameters on texture development in an X-80 linepipe steel.
G.J. Baczynski and J.J. Jonas 635

Effect of processing variables on texture formation in a two phase Ti$_3$Al-base alloy.
S. Suwas and R.K. Ray 641

Topological aspects of the ridging phenomenon in ferritic stainless steel.
K. Sztwiertnia, J. Pospiech, and T. Rostek 647

Cube texture formation in pure aluminum as influenced by impurities and rolling temperatures.
K. Ito and A. Fukushima 653

Mechanical properties and texture formation during the compression of tantalum.
R.J. De Angelis and J.W. House 659

Texture and microstructure development during plastic deformation of magnesium.
R. Gehrmann and G. Gottstein 665

EBSD analysis of shear banding in α-Brass.
C.S. Da Costa Viana, J.C. Paredes, A.L. Pinto, and A.M. Lopes 671

Effect of texture on internal strains in Mg-7.7at.%Al.
M.A. Gharghouri, C.N. Tomé, and J. Root 677

Texture, microstructure and properties in mechanically alloyed and extruded FeAl.
S. Lenhard, F. Wagner, T. Grosdidier, S. Revol, and R. Baccino 683

Effect of thermohydrogen pretreatment on texture and deformability of BCC titanium alloy.
T.A. Sokolova, L.I. Anisimova, B.K. Sokolov, I.V. Gervasyeva, and L.R. Vladimirov 689

Texture and microstructure development during processing of ultra fine grained copper by equal channel angular extrusion.
A. Tidu, F. Wagner, T. Grosdidier, W.H. Huang, P.W. Kao, and C.P. Chang 694

The texture evolution of torsion-reverse torsion.
S.-J. Park, J.-H. Cho, and K.H. Oh 700

The formation of the Fibre Textures in BCC metals by deformation banding.
B.J. Duggan and G.L. Liu 706

Plastic deformation of a Ti-6%Al-04%V alloy at intermediate and high temperatures.
J.-S. Lecomte 712

Effect of homogenization practice and %Mn on texture in AA3104 during hot rolling.
M.A. Wells, D.J. Lloyd, and J. Kadilak 718

Spatial correlations of orientation, orientation clustering and the variance of the orientation distribution function.
B.L. Adams, P.S. Lee, and A.D. Rollett 724
On the texture change in extruded NiAl.
W. Skrotzki, R. Tamm, and C.-G. Oertel 730
Description of deformation geometry by effective slips in BCC materials.
Y.B. Park, B.I. Kim, and L. Kestens 736
Corrugation of metal at the deformation zone as a cause of the local texture inhomogeneity.
V.V. Gubernatorov, B.K. Sokolov, I.V. Gervasyeva, L.R. Vladimirov, and I.N. Stepanova 742
Microstructure and texture in chromium processed by severe plastic deformation.
N.A. Krasilnikov, A.P. Zhilyaev, R.Z. Valiev, V. Provenzano, and D.G. Rickerby 748
The deformation textures and Lankford values of asymmetrically rolled aluminum alloy sheets.
K-H. Kim, D.N. Lee, and C-H. Choi 755
Predicting the transformation texture of a axisymmetrically compressed Fe-30%Ni using a dislocation reaction model.
M. Sum, J.J. Jonas, and J. Root 761
Heterogeneity of addition elements distribution and texture gradient in rolled zinc–copper–titanium alloys.
M. Diot, J.J. Fundenberger, J. Wégria, and C. Esling 767
Microstructure and microtexture of a copper shaped-charge slug.
A.L. Pinto and C.S. Da Costa Viana 773
Effect of roll bite geometry on shear deformation in ferritic rolling of IF-steel sheets.
K.K. Um, H.T. Jeong, J.K. An, and D.N. Lee 779
The texture of drawing high-carbon steel wire.
K.K. Um, H.T. Jeong, J.K. An, and D.N. Lee 785
Texture evolution of aluminum single crystals during asymmetrical rolling.
C.H. Choi, K.H. Oh, G. Gottstein, and D.N. Lee 791
Texture and microstructure in mechanically alloyed and extruded Al-Al$_3$Ti alloys.
T. Grosdidier, S. Lenhard, K. Helming, C.P. Chang, and F. Wagner 797

VOLUME 2

Recrystallization Textures

A geometrical theory for {111}<hkl> recrystalization texture formation in cold rolled IF steel.
B.J. Duggan, Y.Y. Tse, and G.L. Liu 805
Investigation of steel sheet recrystallisation textures with a new parameter model for texture description.
L. Delannay, A. Van Bael, P. Van Houtte, L. Kestens, and Y. Houbaert 811

Recrystallization texture development in cold rolled super duplex stainless steel.
J. Keichel, M. Crumbach, P. Schraven, G. Gottstein, and J. Foct 817

Textural and structural changes during annealing of a heavily cold deformed $Ni_3Al(B,Zr)$ alloy.
B. Bhattacharya and R.K. Ray 824

Formation of the cube band and its evolution during recrystalization.
Y.B. Park, Y.H. Kim, and B.I. Kim 830

Textures in dynamic recovery and recrystallization.
H.J. McQueen 836

Recrystallization textures in copper–manganese alloys.
O. Engler, K. Lücke, and C. Pithan 842

Effect of Mg content on the development of rolling and recrystallization textures in Al–Mg alloys.
M. Koizumi, T. Saitou, H. Inagaki, and S. Kohara 848

Automatic recognition of recrystallized grains in partly recrystallized samples from crystal orientation maps.
N.C. Krieger Lassen and D.J. Jensen 854

Influence of Fe content on recrystallization, grain growth and recrystallization textures in Al–Mg alloys.
M. Koizumi, H. Okudaira, and H. Inagaki 860

Relationship between primary recrystallization grain size and its texture in 3%Si steels.
S.K. Chang, B.D. Hong, and K.S. Han 866

Texture development in high strength IF steel containing P.
W. Mao, Z. Zhao, and Y. Yu 872

Microtextures in copper undergoing dynamic recrystallization (DRX) in torsion.
L. Gavard, F. Montheillet, and H.J. McQueen 878

Modeling of microstructural evolution and texture development during the secondary recrystallization.
Y. Takayama, M. Inoue, T. Tozawa, H. Kato, and M. Kobayashi 884

Growth substructure formed under recrystallization in textured matrix, its features and origin.
V.V. Gubernatorov, B.K. Sokolov, I.V. Gervasyeva, and L.R. Vladimirov 890

Last stage of recrystallization in Ti sheets.
O. Van Landuyt, T. Grosdidier, and F. Wagner 895

A method for predicting the crystallographic texture from the polycrystalline mechanical strength as a function of heat treatment for a precipitation hardened aluminum alloy.
J.M. Fragomeni 901

The effect of cold rolling reduction on planar anisotropy of interstitial free steels.
L. Kestens, Y. Houbaert, L. Delannay, P. Van Houtte, M. Barnett, and J.J. Jonas 910

Thermal stability of basal texture in Ti_3Al-base alloy.
S. Suwas and R.K. Ray 916

Texture of welded joints of 316L stainless steel.
J.L. Bechade, G. Bouche, M.H. Mathon, and T. Baudin 922

Texture of palladium and palladium–silver alloys after cold rolling and annealing.
Y. Cao, J.A. Szpunar, and W. Shmayda 928

A suggestion concerning the generation of recrystallization nuclei during plastic deformation.
U.F. Kocks and J.D. Embury ... 934
Influence of grain size and retained atoms on the recrystallization texture in deep drawing steel.
H. Ren, D. Tang, Z. Sun, and W. Mao ... 938
Recrystallized cold rolled nickel and nickel-alloys with a strong cube texture.
B. de Boer, N. Reger, R. Opitz, J. Eickemeyer, B. Holzapfel, and L. Schultz ... 944
The evolution of deformation and recrystallization textures of cross rolled sheets.
S-H. Hong, N-J. Park, and D.N. Lee ... 950
Initial and recrystallization textures and microstructures of Zn electrodeposits.
I. Kim and S.C. Hong ... 956
Analysis nanocrystalline Ni-45% Fe electrodeposits for predicting texture transformation during annealing.
N. Rajmohan, J.A. Szpunar, and U. Erb ... 961
Texture development during grain growth in strongly textured materials.
V.Y. Novikov ... 967
Study of recrystallization mechanisms in ingot cast and strip cast Fe-36%Ni alloy
F. Julliard, T. Baudin, and R. Pennelle ... 973

Texture in Steel and Aluminum

Effect of primary recrystallization texture on Goss secondary recrystallization texture in Fe-3%Si alloy.
Y. Ushigami, T. Kubota, and K. Murakami ... 981
Influence of heating rate on recrystallization in low and ultra-low carbon steels.
M. Ferry, D. Muljono, and D.P. Dunne ... 991
Optimisation of galvanisation process parameters to improve the cracking resistance in zinc coatings.
S. Gaignard, C. Esling J. Wégria, and M. Dubois, ... 997
Effect of finishing deformation temperature on texture development of ultra low carbon steel.
D. Yu, M. Ferry, and T. Chandra ... 1003
Grain boundary character distribution in a primary recrystallized grain-oriented silicon steel.
J. Harasse, R. Shimizu, J. Kim, and J.S. Woo ... 1009
Textures and microstructures of strip cast stainless and low-carbon steels.
D. Raabe, H. Krause, A.D. Rollett, and A. Teicher ... 1015
Torsional behavior of pearlitic wires according to their crystallographic texture.
A. Tidu, B. Bolle, Y. Liu, J.J. Heizmann, and L. Zuo ... 1025
Transformation textures and texture memory in low carbon steels.
L. Ryde, D. Artymowicz, and W.B. Hutchinson ... 1031
Influence of precipitates on texture evolution of Ti–IF steels in batch annealing.
J. Shi, Z. Li, and X. Wang ... 1037
Effects of composition on the ansiotropy and texture of continuously annealed low carbon steel sheets.
S.C. Baik, O. Kwon, J. Cho, and K.H. Oh ... 1043

The role of in-plane dislocation reactions during the transformation of hot rolled austenite.
J.J. Jonas and N.J. Wittridge 1049

Through-thickness texture variation in primary recrystallized 3%Si–Fe and its effect on the sharpness of (110)<001> Goss texture.
K.S. Han, J.S. Woo, J.K. Kim, and C.S. Kim 1059

Microstructure and crystallographic texture of strip-cast 4.3wt%Si steel sheet.
J.Y. Park, K.H. Oh, and H.Y. Ra 1065

Texture development in cold-rolled austenitic-ferritic duplex steel.
W. Ratuszek, J. Ryś, and K. Chruściel 1071

Rotated cube texture in semifinished electrical steel: processing and mechanisms of texture formation.
B. de Boer, J. Wieting, and L. Schultz 1077

The texture evolution of non-oriented silicon steel.
C.S. Lee 1083

Application of the dislocation reaction model for variant selection to the transformation of an Fe-30%Ni alloy deformed in extension.
N.J. Wittridge, J.J. Jonas, J.H. Root 1089

Initial orientation dependence of texture evolution in ferritic stainless steels.
S.-H. Park, K.-Y. Kim, Y.D. Lee, and C.G. Park 1095

Relation between grain boundary mobility and grain boundary character in Fe-3%Si.
Y. Hayakawa, T. Takamiya, and M. Kurosawa 1101

Macrostructure-related fatigue crack closure in Al-Li 2090 studied by x-ray microtomography.
R. Morano, G.R. Davis, S.R. Stock, and J.C. Elliott 1106

Predicting recrystallization of aluminum by applying a probablistic cellular automaton to finite element data.
D. Raabe and R.C. Becker 1112

Orientation dependent stored energy in cold rolled can-body aluminum alloy.
N. Rajmohan and J.A. Szpunar 1118

Randomization of the annealing texture in aluminum 5182 sheet.
M.Y. Huh, Y.H. Kim, and O. Engler 1124

The effect of strain path on texture development in aluminum.
R.L. Higginson 1130

Texture evolution during continuous recrystallization of aluminum alloys.
J. Li, H. Jin, F. Seki, and S. Saimoto 1136

Shear texture control and improvement of Lankford value in aluminum alloy sheet by single-roll drive warm rolling.
T. Sakai, H. Inagaki, and Y. Saito 1142

Texture and microstructure in DC cast and SC aluminum alloys.
Y. Liu, Y.L. Liu, G. Liao, and J.G. Morris 1148

The effect of rolling draughts on texture and microstructure in aluminum.
O.V. Mishin, D.J. Jensen, and B. Bay 1154

Deformation banding and texture development during cold drawing of unidirectionally solidified polycrystalline aluminum.
Y. Kaneno, H. Inoue, and N. Inakazu 1160

Influence of strain path on the forming limit curve and texture of aluminum sheet.
S. Kohara 1166

Texture investigation in the system Al-Nb during phase transition.
R. Schnieber, H.J. Bunge, and H.-G. Brokmeier 1172

Selectivity of Goss grains during abnormal grain growth in Fe-Si electrical steels.
N. Rajmohan and J.A. Szpunar 1178

Texture inheritance in HSLA grades subjected to compact strip production.
E. Bouzy, B. Cardiola, C. Esling, M. Humbert, G. Flemming, and K.E. Hensger 1184

Formation of oriented lamellae in TiAl alloys by diffusional reaction.
H. Fukutomi, M. Ueno, M. Nakamura, T. Suzuki, and S. Kikuchi 1190

Texture and multiple twinning in copper.
V. Randle, P. Davies, and H. Davies 1196

Microtexture development in high strength interstitial free steels.
I.J. Cross, V. Randle, and S.R. Daniel 1202

Effect of hot band annealing on the formation of sharp {110) <001> Goss texture in conventional grain oriented electrical steels.
K.S. Han, J.S. Woo, G.S. Choi, and S.K. Chang 1208

Temper rolling effects of low-C cold rolled steels on texture development and stretcher strain phenomena.
Y.H. Koh, J.H. Choi, N.J. Park, and Jeong Ho Choi 1214

Texture evolution during hot plane strain compression of a hot deformed AA5182 Al–Mg alloy.
P. Ratchev, B. Verlinden, P. Van Houtte, R. Van den Broeck, and M.R. van der Winden 1224

Through-thickness inhomogeneity of the texture developed in high strength linepipe.
G.J. Baczynski, J.J. Jonas, and L.E. Collins 1230

Texture development during cold rolling and annealing in two 304 austenitic stainless steel cast strips.
S. Teraoka, G.J. Baczynski, and J.J. Jonas 1236

Comparison of cast and hot strip textures and microstructures in three 304 austenitic stainless steels.
S. Teraoka, J.G. Baczynski, and J.J. Jonas 1242

Experimental approach to continuum dislocation fields in <100> polycrystalline columnar aluminum.
B.S. El-Dasher, W. Yang, and B.L. Adams 1248

Effect of through thickness inhomogeneity of texture on edge cracking during planetary hot rolling of austenitic stainless steel.
J.Y. Cho, H.T. Jeong, and J.A. Szpunar 1254

Residual stress analysis of ridged ferritic stainless steel.
A.P. Clarke, W.D. MacDonald, and S. Saimoto 1260

Study of texture of ULC sheet steel rolled in ferrite region.
K. Zhao, X.C. Mi, and SH.H. Jiao 1266

Characterizing and representing texture gradients in thick aluminum plate.
M.P. Miller, T.J. Turner, and J. Sutliff 1272

Microtexture inhomogeneity in hot rolled two-phase steel.
J. Jura, J. Pospiech, J. Bonarski, T. Baudin, C. Quesne, and R. Penelle 1278

Texture in Films, Coatings and Oxides

Crystallographic texture in 1G DRAM reactive ion etched vs. damascene Al–Cu lines.
K.P. Rodbell, L.M. Gignac, J.L. Hurd, Y.-Y. Wang, L.A. Clevenger,
R.C. Iggulden, R.F. Schnabel, and S. Weber 1287

Influence of processing parameters on the texture of pure zinc electrodeposited coatings on steel.
K. De Blauwe, A. De Broeck, J. Bollen, and W. Timmermans 1293

Microstructures and textures of copper electrodeposits on the WN diffusion barrier.
I. Kim and S.C. Hong 1299

Simulation of texture formation in ZrO$_2$ film grown on Zr-2.5%Nb.
H. Li, M.G. Glavicic, and J.A. Szpunar 1303

Texture evolution in Cu damascene lines.
D.P. Field 1309

Texture of thin layers and nanowires of electrodeposited thermoelectric materials such as Bi$_{1-x}$Sb$_x$ alloys.
F. Besse, C. Boulanger, J.M. Lecuire, B. Bolle, and J.J. Heizmann 1315

Biaxially aligned MgO buffer layers by ion-beam assisted pulsed laser deposition.
R. Hühne, C.-G. Oertel, W. Skrotzki, B. Holzapfel, and L. Schultz 1321

Quantative texture of ferroelectric modified lead titanate thin films.
J. Ricote, D. Chateigner, G. Ripault, L. Pardo, M. Algueró, J. Mendiola,
and M.L. Calzada 1327

Residual stress determination in highly textured titanium nitride coatings.
A. Saerens, P. Van Houtte, and C. Quaeyhaegens 1333

Internal stress in textured molybdenum thin films.
C.S. Shin, J-H. Cho, and K.H. Oh 1339

Texturation in duced by the addition of surfactant during the synthesis of V$_2$O$_5$ thin films.
F. Ansart, S. Mege, A. Rousset, and J.M. Savariault 1345

Texture transforamtion in Ni electrodeposits applied for CD-ROM stampers.
F. Czerwinski, A. Zielinska-Lipiec, and J.A. Szpunar 1351

Affect of localized texture on the sputter performance of tantalum.
C.A. Michaluk, D.B. Smathers, and D.P. Field 1357

Singular value decomposition of the ODF–PDF projection operator.
K.G. van den Boogaart and S. Schaeben 1363

A role of texture and orientation clustering in electromigration failure of aluminum interconnects.
H.T. Jeong, J.A. Szpunar, K.T. Lee, and D.P. Field 1369

Al texture on <001> W, Ti$_x$W$_{1-x}$ and TiN barrier layers.
L.D. Madsen, E.B. Svedberg, D.B. Bergstrom, C.-S. Shin,
I. Petrov, and J.E. Greene 1375

Microstructures and textures of copper electrodeposits on the TiN.
I. Kim and S.C. Hong 1381

Computer simulation of the effect of impurities on diffusion at oxide boundaries.
D.J. Harris and J.H. Harding 1385

A model of NiO texture formation on single crystal substrate.
H. Li, F. Czerwinski, and J.A. Szpunar 1391
The surface texturing of nickel for high temperature oxidation prevention.
F. Czerwinski and J.A. Szpunar 1397
On the calculation of grain boundary character distribution in textured nickel oxide layers.
A.P. Zhilyaev, F. Czerwinski, and J.A. Szpunar 1403
The role of oxide texture in the protection of Zr-2.5%Nb alloys pressure tubes against hydrogen ingress.
M.G. Glavicic, J.A. Szpunar, and Y.P. Lin 1409
The influence of texture on the oxidation kinetics of copper.
K.T. Lee and J.A. Szpunar 1415
The influence of deposition parameters on texture in electrogalvanized zinc coatings.
H. Park and J.A. Szpunar 1421
Influence of heating rate on texture changes in nanocrystalline nickel during annealing.
B.-K. Kim, H.T. Jeong, and J.A. Szpunar 1427
Development of textures and microstructures in Fe–Ni alloy thin films.
C.S. Ha, S.S. Kim, B.I. Kim, and Y.B. Park 1433
Examination of the stress and phase composition in textured zirconium oxide films.
J. Lin and J.A. Szpunar 1439
Texture development during the electrocrystallization of nickel.
Y. Cao, F. Czerwinski, and J.A. Szpunar 1445

Texture in Ceramics, Composites and Polymers

Orientation evolution of textured piezoelectric ceramics under electric fields.
S. Wan and K.J. Bowman 1453
Anisotropy in layered and gadient ceramics.
R. Moon, W. Blanton, F.R. Cichocki, J. Brehm, K.P. Trumble, and K.J. Bowman 1460
Texture development, recrystallization, and transference of texture between ceramic multilayers, epitaxially grown on rolling assisted biaxially textured substrates (RABiTS).
A. Goyal, R. Freenstra, E.D. Specht, D.M. Kroeger, D.F. Lee, M. Parathaman, F.A. List, and D.K. Christen 1466
Particle orientation and texture formation in tape cast ceramic materials.
P.M. Raj, F. Cosandey, W.R. Cannon, and P. Mainwaring 1476
Texture of ceramic reinforced Magnesium composites.
E.M. Jansen, H.-G. Brokmeier, and K.U. Kainer 1482
Contribution of the orientation textures in the amorphous and crystalline phases on the plastic deformation of polymers.
C. G'Sell, C. Cabot, A. Dahoun, M.J. Philippe, and J. Grenet 1488

Application of electron backscattered diffraction (EBSD) and atomic force microscopy (AFM) to determine texture, mesotexture, and grain boundary energies in ceramics.
S.J. Glass, V.R. Vedula, D.M. Saylor, and G.S. Rohrer 1489

Quantitative characterisation of mollusc shell textures.
D. Chateigner, C. Hedegaard, and H.-R. Wenk 1495

Microstructure and mechanical properties of textured alumina.
D. Kovar and P.W. Hall 1501

Predicting microstructural-level residual stresses and crack paths in ceramics.
V.R. Vedula, S.J. Glass, D.M. Saylor, G.S. Rohrer, and W.C. Carter 1509

Texture in Geological Research

Significance of domainal crystallographic fabrics in naturally deformed rocks.
J. Hippertt 1515

Texture development in amphibole: oriented growth versus passive rotation.
T. Takeshita 1522

Constrasting *C*-axis fabric patterns in layers of different proportion of quartz and iron oxide.
L. Lagoeiro 1528

Comparison of natural and simulated quartz shear texture.
T. Takeshita, H.-R. Wenk, and R. Lebensohn 1534

Neutron diffraction strain investigation of sandstones undergoing applied stresses.
Ch. Scheffzük, A. Frischbutter, and K. Walther 1540

Stress-strain distribution in deformed olivine aggregates: inference from microstructural observations and implications for texture development.
S. Karato and K.-H. Lee 1546

Texture and microstructure of halite at a halite-basalt contact
Ch. Scheffzük 1556

QTA and polarised EXAFS correlation in self-supporting films of nontronites.
D. Chateigner, A. Manceau, M. Schlegel, and M. Pernet 1562

Texture development of $CaTiO_3FeO$ composites at high-temperature.
Z-C. Wang, S. Ji, and R. Wirth 1568

Quantitative texture analysis of experimentally sheared anhydrite and albite aggregates.
F. Heidelbach 1574

Texture-related elastic (seismic) anisotropy in crustal and mantle rocks.
H.M. Kern 1580

Textures and elastic anisotropies of amphibolites from the Kola borehole.
T.I. Ivankina, A.N. Nikitin, T. Lokajicek, Z. Pros, K. Klima, and K. Ullemeyer 1587

Applying EBSD techniques to microtextures and mesotextures in rocks.
D.J. Prior, M. Bartozzi, A. Boyle, A. Day, D. Paden, D. Halliday, and M. Tye 1593

MAUD (Materials Analysis Using Diffraction): a user friendly Java program for Ritveld Texture Analysis and more.
L. Lutterotti, S. Matthies, and H.-R. Wenk 1599

A pressure device for strain measurements of geomaterials at the neutron diffractometer EPSILON.
K. Walther, A. Frischbutter, R. Lieckefett, and C. Scheffzük ... 1605

Grain Boundaries and Misorientation Distribution

Characteristics of $\Sigma 3$ boundaries in strongly textured copper.
O.V. Mishin and X. Huang ... 1613
Grain boundary influence on texture evolution during deformation and recrystallisation.
S.J. Lillywhite, M. Aindow, and P.S. Bate ... 1619
The role of triple junctions during normal grain growth under high pressure in 2-D strips of polycrystalline aluminum.
V. Sursaeva, S. Protasova, and W. Lojkowski ... 1625
The orientation distribution of interface determined according to the maximum-entropy principle.
Y.D. Wang, R.L. Peng, R. McGreevy, B. Bolle, A. Vadon, and J.J. Heizmann ... 1631
Determining surface energy anisotropy from measurements of thermal groove geometry.
D.M. Saylor, G.S. Rohrer, and D.E. Mason ... 1637
Multiscale reconstruction og grain boundary energy from microstructure.
D. Kinderlehrer, I. Livshits, S. Ta'asan, and D.E. Mason ... 1643
Correlation of grain boundary character with wetting behaviour.
M. Takashima, A.D. Rollett, P. Wynblatt, and B.L. Adams ... 1649
Calculation of intracrystalline lattice misorientations in face centered cubic polycrystals.
D. Mika and P.R. Dawson ... 1655
Ordinary grain boundaries and recrystallization textures.
D.B. Titorov ... 1661
Computer simulation of diffusion process in polycrystalline material.
H. Li and J.A. Szpunar ... 1667
Atomistic modelling of intergranular fracture in Ni_3Al.
J. Lu and J.A. Szpunar ... 1673
Singularity og grain boundary character distribution in zirconia film grown on Zr-2.5%Nb substrate.
A.P. Zhilyaev, V.Y. Gertsman, and J.A. Szpunar ... 1678
Mobility of mechanical twin grain boundaries in Zinc.
V.G. Sursaeva, A.U. Tuflin, and U. Czubayko ... 1684
Determining relative grain boundary energies from measurements of thermal groove geometry.
D.M. Saylor and G.S. Rohrer ... 1690
Simulation of recrystalization from EBSD or TEM orientation data.
T. Baudin and R. Penelle ... 1696

Author Index ... A1

Preface

ICOTOM Conferences are held every 3 years and are traditionally the most important events for the community of researchers working on various texture-related projects. The present definition of texture incorporates not only the crystallographic texture, as defined by the orientation distribution function, but also the grain misorientation distribution which is related to various aspects of grain boundary engineering. The grain shape, mean size and type of alignment of fibres, rocks, surface deposits and crystals in polymers fall into a broader definition of texture. ICOTOM is a meeting place for all researchers investigating polycrystalline materials, in particular: metallurgists, geologists, mineralogists, those working with polymers, ceramics, thin films and coatings.

The ICOTOM 12 Conference will be held in Montréal August 9–13, 1999. These proceedings will be handed to the participants at the Conference. There were about 400 abstracts submitted for presentation at the conference, however, the number of papers published in the Proceedings is only 279. The papers are divided according to the most important topics that represent various texture related problems. There is some emphasis on new emerging areas of texture research in thin films and modelling and simulation of texture development. Texture research contributes to the development of engineering materials with new or improved properties, optimization of various industrial processes and better understanding of geological phenomena. Traditional areas of research for steel and aluminum industries are also very well represented in these proceedings.

The organizers strongly believe that the ICOTOM12 meeting will contribute to a better understanding of engineering materials and processes and will facilitate scientific exchange and contacts between participants from the industry and academia.

On behalf of the organizers I would like to acknowledge the special contribution of Professor R. Wenk, who organized the session on Geological Applications of Texture, Professor B. Adams for his contribution to organizing the session on Special Correlations of Orientation Measurements and Professor A. Rollett and Dr. F. Kocks for helping to finalize the program on Mechanical Properties and Texture and Simulation of Texture. I would also like to thank all the members of the International and Program Committees for their support as well as acknowledge the successful funding efforts of Dr. J. Root and Dr. J. Savoie, and to thank Professor J. Jonas for all the good advice.

I would also like to express my gratitude to the Canadian Institute of Mining, Metallurgy and Petroleum and Y. Jacques, Executive Director of CIM for agreeing to help organize the ICOTOM12 and working hard to make it a successful event. In particular, I would like to thank S. Major and J. Gaydos for their efforts and expert help.

My thanks to all the sponsors of the conference. Their generosity allowed many more young people to participate and, I believe, make this conference a memorable event.

Finally, I would like to express my thanks to my colleagues and students who often asked me the question "do you need help?", and since my answer was always affirmative, helped me a lot. Particularly I would like to thank Dr. Hyo Tae Jeong and Barbara Hanley for their great efforts in organizing the conference program and proceedings. Thanks to Dr. F. Czerwinski, N. Rajmohan, Dr. V. Gertsman, Jae-Young Cho, Bae Kyun Kim, Slavek Poplawski and other members of our texture group for their support and help.

JERZY A. SZPUNAR

INTERNATIONAL COMMITTEE

Brent L. Adams
Hans-Joachim Bunge
Brian Duggan
Günter Gottstein
John Humphreys
Bevis Hutchinson
Hirosuke Inagaki
Dorte Juul-Jensen
Richard Penelle
Ranjit Ray
Jerzy A. Szpunar
Paul Van Houtte

LOCAL ORGANIZING COMMITTEE

Jerzy A. Szpunar (McGill University)
General Meeting Chairman
Jean F. Bussière (NRC)
Frank Czerwinski (McGill University)
Abdel El-Sherik (Dofasco)
Val Gertsman (McGill University)
Hyo Tae Jeong (McGill University)
John Jonas (McGill University)
John Root (ACL – Chalk River)
Jean Savoie (Alcan)

PROGRAM COMMITTEE

Jerzy A. Szpunar (Canada)
General Meeting Chairman
Brent L. Adams (USA)
Keith Bowman (USA)
Hans J. Bunge (Germany)
Frank Czerwinski (Canada)
Günter Gottstein (Germany)
Christian G'Sell (France)
John Jonas (Canada)
Frank Kajzar (France)
Hyo Tae Jeong (Korea)
Gino Palumbo (Canada)
Yong Bum Park (Korea)
Alberto Pochetino (Argentina)
Jan Pospiech (Poland)
Dierk Raabe (USA)
Ken Rodbell (USA)
Anthony D. Rollet (USA)
John Root (Canada)
Jean Savoie (Canada)
Boris K. Sokolov (Russia)
Yoshyuki Ushigami (Japan)
Hasso Weiland (USA)
Rudi Wenk (USA)

Plenary Lecture Session

FROM CRYSTAL ORIENTATIONS TO MATERIAL PROPERTIES: MICRO-MACRO LINKAGE ILLUSTRATED WITH DEFORMATION IN THE EARTH

H.-R. WENK
Department of Geology and Geophysics, University of California, Berkeley CA 94720
P.R. DAWSON
Sibley School of Mechanical and Aerospace Engineering, Cornell University, Ithaca NY 14853

Abstract

An animated video illustrates the relationship between microscopic processes at the atomic scale and anisotropic macroscopic properties relying on polycrystal plasticity. During convection in the Earth's mantle, deformation produces preferred orientation of olivine that is the primary cause for seismic anisotropy. The development of texture is a highly dynamic process.

Key words: Texture, anisotropy, mantle convection, olivine

Summary

Microscopic processes occurring within crystals are responsible for macroscopic anisotropic properties of materials and these relationships have been quantified and comprise the core of modern texture analysis [Kocks et al. 1998]. A consistent micro-macro linkage approach proved to be highly successful in the simulation of metal forming. It can also be applied to much larger systems that are of geophysical interest. At the large scale of the Earth seismologists documented a directional dependence in the propagation of waves generated by earthquakes [Hess, 1964, Silver, 1996]. Waves travel about 10% more rapidly perpendicular to ocean ridges than parallel to them over distances comparable to dimensions of continents [Morris et al., 1969, Nishimura and Forsythe, 1989]. Anisotropy on such a large scale originates in the directional properties of the rock-forming minerals and the corresponding deformations that induce texture.

The Earth is a very heterogeneous and dynamic system at all scales. Deformation occurs at the large macroscopic level at the scale of continents down to the atomic structure within crystals. Due to this complexity there is limited utility in modeling deformation using approaches that are restricted to the macroscopic scale wherein the mantle is treated as a continuum. Instead, we use an approach that combines models from two scales. At the macroscopic level the finite element method is ideally suited to deal with the heterogeneous deformation patterns present over the dimensions of continents, and to resolve gradients in the flow field associated with deformation [Sarma and Dawson, 1996]. At the microscopic level, polycrystal plasticity theory simulates deformation processes within crystals [Beaudoin et al. 1994, Wenk, 1999]. These processes intimately link the properties of rock's constituent minerals with the Earth's structural formations. Rocks are polyphasic, and comprised of minerals that individually are often strongly anisotropic and may differ substantially in strength. The deformation by intracrystalline slip, often accompanied by dynamic recrystallization, are the single most important factor in establishing the crystallographic texture. The rotation of crystal lattices accompanies deformation by slip, owing to the limited number of discrete slip systems (on rational slip planes and in rational slip directions). The link between the crystal properties and features of a geological formation is evident: anisotropy in the mechanical properties of rocks influences their deformations, and the deformations themselves induce the texture that is the source of anisotropy in the properties. The mechanical anisotropy from texture is one source of direction dependence observed in the seismic wave propagation.

We apply these concepts to model deformation in the solid upper mantle of the Earth. The upper mantle is largely composed of the orthorhombic magnesium silicate mineral olivine and deforms by convection, driven by temperature gradients. There is upwelling of buoyant material along ridges and downwelling of dense material in subduction zones. Finite element simulations indicate that during convection, crystals indeed reorient into characteristic textures that cause anisotropic physical properties [Chastel et al. 1993, Dawson and Wenk, 1999]. These patterns are highly heterogeneous over the span of the convection cell and depend on the specific straining history along individual streamlines of the cell. The rotations that reorient crystal lattices are due to activation of slip systems in deforming single crystals as well as the macroscopic rotation of material progressing along a streamline. Both of these are most intense during upwelling at ridges and during subduction. Thus, texture changes are particularly strong in these regions which is best illustrated in an animated video [Wenk et al. 1999].

Using the crystallographic texture throughout the convection cell and the physical properties of single crystals, seismic velocity averages over mantle sectors can be computed and the directional dependence of wave propagation was determined. The predicted azimuthal variation of p-wave anisotropy of 5-10% in the model agrees well with actual observed values [Morris et al. 1969].

From such models it is evident that the mantle is not a structureless viscous medium but shares many properties with a single crystal which displays internal structure and anisotropy. There are compositional and structural variations both laterally and with depth. The approach described links processes that occur within crystals on an atomic scale to macroscopic dimensions of the size of continents. The results from these studies have raised significant interest from seismologists, geodynamicists and structural geologists who recognize the importance of anisotropy and recent applications to flow at mid-ocean ridges help to distinguish between passive and buoyancy-enhanced upwelling [Blackman et al. 1996]. By including polycrystal plasticity, geophysical deformation modeling is entering a new state of refinement and is an excellent example for quantitative texture analysis.

References

Beaudoin, A.J., Mathur, K.K., Dawson, P.R., Kocks, U.F. & Korzekwa, D.A. (1994). Application of polycrystal plasticity to sheet forming. *Computer Methods in Applied Mechanics and Engineering*, 117, 49-70.

Blackman, D.K., Kendall, J.M., Dawson, P.R., Wenk, H.R., Boyce, D. & Morgan, J.P. (1996). Teleseismic imaging of subaxial flow at mid-ocean ridges: traveltime effects of anisotropic mineral texture in the mantle. *Geoph. J. Int.* 127, 415-426.

Chastel Y.B., Dawson P.R., Wenk H.-R. & Bennett K. (1993). Anisotropic convection with implications for the upper mantle. *J. Geophys. Res.* B98, 17757-17771.

Dawson P.R. & Wenk H.-R. (1999). Texturing of the upper mantle during convection. *Phil. Mag.* (in press).

Hess, H.H. (1964). Seismic anisotropy of the uppermost mantle under oceans, *Nature*, 203, 629.

Kocks U.F., Tomé C.N. & Wenk H-R (1998). *Texture and Anisotropy. Preferred Orientation in Polycrystals and their Effect on Material Properties*. Cambridge Univ. Press.

Morris, G. B., Raitt, R. W. & Shor, G. G. (1969). Velocity anisotropy and delay time maps of the mantle near Hawaii. *J. Geophys. Res.*, 74, 4300-4316.

Nishimura, C. & Forsyth, D. (1989). The anisotropic structure of the upper mantle in the Pacific. *Geophys J.* 96, 203-229.

Sarma, G.B. & Dawson, P.R. (1996). Effects of interaction among crystals on the inhomogeneous deformations of polycrystals. *Acta mater.* 44, 1937-1953.

Silver P.G. (1996). Seismic anisotropy beneath the continents: Probing the depths of geology. *Ann. Rev. Earth Planet. Sci.* 24, 385-432.

Wenk, H.-R., Dawson, P.R. , Pelkie, C. & Chastel, Y. (1999). *Texturing of Rocks in the Earth's Mantle. A Convection Model Based on Polycrystal Plasticity*. Video, AGU (in press).

Wenk, H.-R. (1999). A voyage through the deformed Earth with the self-consistent model. *Model. and Simul. Mat. Sci. Engin.* (in press)

TEXTURE DESIGN FOR NEW APPLICATIONS

J.A. SZPUNAR
Department of Mining and Metallurgical Engineering, McGill University, Montréal, Canada H3A 2B2

Abstract

Optimization of properties of polycrystalline materials through texture control contributed already to improvement of various mechanical and magnetic properties. In this presentation new areas of optimization of materials properties, that emerged more recently, are discussed and techniques and physical models developed to simulate a role that texture plays are presented. In particular, a role of texture in improving a high temperature oxidation resistance, corrosion resistance, time to failure of electronic interconnects, reduction of hydrogen ingress in zirconium alloys are discussed. Examples are chosen to illustrate a role of grain boundary character distribution in controlling the intergranular fracture.

Keywords: Texture, corrosion, high temperature oxidation, electromigration failure, hydrogen transport.

Summary of Presented Applications

Scientists and engineers are continuously working to improve materials and tools made of them. Texture optimization was, and is used extensively to control important properties of metals such as mechanical parameters of steels and aluminum products and magnetic properties of soft and hard magnets. There are, however, new applications for texture design, that may also be explored to develop materials that are more resistant to high temperature oxidation and corrosion, resistant to intergranular cracking, hydrogen ingress and electromigration failure. Some examples from our research will be discussed briefly.

- **Texture and High Temperature Oxidation Resistance**

It is already well known that in Nickel and some Nickel-based alloys different crystallographic planes oxidized at different rates. These anisotropic properties of single crystal have been explored to develop materials that are more resistant to high temperature corrosion [Czerwinski and Szpunar 1999]. In addition it was demonstrated that texture of oxide formed on substrates of different orientation may be very strong and that twin boundaries play an important role in controlling an outward transport of Nickel atoms and therefore the oxidation mechanism is slowed down. Texture design may become in this case an important tool for improvement of high temperature oxidation resistance.

- **Corrosion of Automobile Steel Coatings**

Other mechanisms of corrosion are also sensitive to texture of the surface layer. That application is well illustrated by studying the corrosion protection by Zn, Zn-Fe and Zn-Ni electrogalvanized coatings [Park and Szpunar 1998]. It is illustrated there that the corrosion resistance is a rather complex function of texture, morphology and stress state in the coating. Effective methods for control of the corrosion rate through texture design are proposed. A computer model of texture development is proposed to study influence the processing parameters on electrodeposit texture.

- **Hydrogen Ingress in Zn-Nb Pressure Tubes**

Another example where texture is important is hydrogen ingress through textured Zn-Nb oxides. Hydrogen ingress in Zn-Nb tubes and the subsequent formation of hydrides is a serious problem because the pressure tubes become prone to failure. Monoclinic oxide texture grows by inward diffusion of oxygen in the substrate and may become a barrier against the hydrogen ingress [Zhilyaev and Szpunar 1998]. Examples of such textures and associated grain boundary character distribution that are effective in blocking the hydrogen transport are presented. Also a model of formation of oxide texture based on Monte Carlo simulation of intergranular transport of oxygen is presented [H. Li and J.A. Szpunar 1999].

- **Texture and Electromigration Failure in Al-Cu Interconnects**

A role of texture in controlling the electromigration failure in Al-Cu interconnects is already well acknowledged. A mechanism of relationship between electromigration failure and texture is however not entirely clear. Formation of hillocks and voids is clearly related to the strength of texture in Al-Cu lines, grain boundary character distribution, mesotexture of grain boundaries and existing local stresses [Lee, Szpunar and Knor, 1996]. A role of local texturing seems to be very important and will be illustrated by several examples.

- **Intergranular Fracture in Ni_3Al**

The fracture behavior in brittle polycrystalline materials has been investigated using embedded-atom method, molecular dynamics and Markov chain fracture models by [Lu and Szpunar, 1996]. It has been found from the simulation that fracture resistance greatly depends on the grain boundary structure. That means that grain boundary character distribution and meso-texture plays an important role in controlling the crack path, crack arrest distance and fracture toughness. The improvement of fracture toughness of Ni_3Al brittle polycrystal is due to a high frequency of low energy grain boundaries. Grain boundaries and texture design and control achieved by manipulation of GBCD are important to improvement of toughness of the brittle polycrystalline materials.

References

Czewinski, F. and Szpunar, J.A. (1999) Controlling the Surface Texture of Nickel for High Temperature Oxidation Inhibition. *Corrosion Science*, Vol. 41 pp. 729-740.

Park, H. and Szpunar, J.A. (1998) The Role of Texture and Morphology in Optimizing the Corrosion Resistance of Zinc-based Electrogalvanized Coatings, *Corrosion Science*, Vol. 40, pp. 525-545.

Zhilyaev, A. and Szpunar, J.A., Influence of Stress Developed due to Oxide Layer Formation on the Oxidation Kinetics of Zn 2.5% Nb Alloy, *Journal of Nuclear Materials*, Vol. 264, pp. 327-332.

Li, H. and Szpunar, J.A., Model of Texture Formation in ZnO_2 Films, *Acta Materialia* (Submitted)

Lee, K.T., Szpunar, J.A., and Knorr, D.B., (1996), The Influence of Texture on the Reliability of Aluminum Based Thin Films, *Mat. Sci.Forum*, Vol. 204, pp. 423-427.

Gertsman, V.Y., Zhilyaev, A.P. and Szpunar, J.A., (1997) Grain Boundary Misorientation Distribution in Monoclinic Zirconia, *Simul. Mater. Sci. Eng.* pp. 35-52.

Lu, J. and Szpunar, J.A. (1996) Microstructural Model of Intergranular Fracture During Tensile Tests, Vol. 60, pp. 305-310.

EXTRACTION OF GRAIN BOUNDARY ENERGIES FROM TRIPLE JUNCTION GEOMETRY

B. L. ADAMS, C. L. BAUER, D. CASASENT, B. EL-DASHER, D. KINDERLEHRER, I. LIVSHITS, F. MANOLACHE, D. MASON, A. MORAWIEC, W. W. MULLINS, S. OZDEMIR, H. ROGAN, G. ROHRER, A. D. ROLLETT, D. SAYLOR, S. TA'ASAN, A. TALUKDER, C-T. WU, C-C. YANG, W. YANG
Materials Research Science and Engineering Center, Carnegie Mellon University, Pittsburgh, Pennsylvania, USA

Abstract

From geometrical and crystallographic data obtained from well-annealed polycrystalline samples, it is now possible to extract estimates of the free-energy function for grain boundaries. Grain boundary energy is considered to depend upon the five parameters of lattice misorientation and interface inclination. The method applied requires the precision characterization of large numbers of triple junctions. For this purpose, automated microscopy has been developed which extends the familiar approach known as orientation imaging microscopy to include precision characterization of the salient geometrical features. At each triple junction it is assumed that conditions of local equilibrium are satisfied (i.e., Herring's relations are assumed to be valid). Reconstruction of the misorientation dependence of the energy function is illustrated from a data set consisting of >1,500 triple junctions in MgO. The reconstruction indicates that coincidence site lattice (CSL) boundaries up to $\Sigma 9$ have reduced energies relative to general boundaries. Other boundary types, not immediately associated with the CSL model, have also been identified with reduced free energy.

Keywords: Grain boundaries, misorientation, free energy, orientation imaging microscopy

1 Introduction

The local physico-chemical characteristics of grain boundaries are known to depend strongly upon the crystallographic and thermodynamic variables (Lejcek and Hofmann 1995; Gottstein and Schwarzer 1992). The corresponding anisotropy is distributed through the network of grain boundaries in a way that influences many important macroscopic properties such as the propagation of corrosion and fracture (Pan et al. 1996). It is also a key factor in the evolution of microstructures through a complex interplay of the thermodynamic driving forces and kinetic responses which determine the motions of grain boundaries. Hence the importance of a knowledge of the orientation dependent properties of grain boundaries.

This paper describes the extraction, from measurements of a polycrystal, of the relative excess free energy of the grain boundaries as a function of the crystallographic type (five degrees of freedom) and relevant thermodynamic variables. We require the simultaneous measurement of both the geometry and the crystallography of a large number of grain boundary intersections. The geometrical and crystallographic information may be obtained from an extension of orientation imaging microscopy (OIM) (Adams et al. 1993). For simplicity, the intersections will be assumed to be triple junctions (three intersecting boundaries). The energies are obtained as ratios to respective a standard state that must be determined independently.

The recovery of grain boundary energies is based on the assumption of local equilibrium at the triple junctions; thus each triple junction is assumed to obey the well-known Herring equilibrium equations (Herring 1952). This assumption can be checked from consistency of the data.

A novel new mathematical method for extracting the grain boundary free energy as a function of its crystallographic type from a vast number of these equations was described in previous publications (Adams et al., 1998). This method has been called the statistical/multiscale method. The problem is not trivial because, in general, the equation for any given triple junction connects the free energies (and their derivatives) at widely separated values of the independent variables. Straightforward consecutive solution of these equations can result in large instabilities.

In the present work we demonstrate a simplified approach to the extraction problem. The free energy function is expressed as a series of generalized spherical harmonics that carry the crystallographic symmetries associated with cubic-cubic misorientation. The method employed retains some features of the statistical/multiscale with standard least squares methods. The latter are commonly employed in modern texture analysis.

In section 2, we review Herring's equation relating the grain boundary energies at a triple junction to the intersection angles. Section 3 describes the series method is introduced, using the simplifying assumption that the energy is independent of the grain boundary inclination. Boundary conditions are also introduced. Section 4 briefly describes the experimental methods. The results obtained for MgO are described in section 5.

2. Equilibrium Thermodynamics of Triple Junctions

Triple junctions are presumed to be in local equilibrium so that they obey the Herring equations which may be written for the triple junction depicted in Fig. 1 as

$$\sum_{j=1}^{3}\left\{\sigma_j\hat{b}_j+\left(\partial\sigma_j/\partial\phi_j\right)\hat{n}_j\right\}=\vec{0} \qquad (1)$$

Here σ_j is the excess free energy of the jth boundary, $\hat{n}_j$ is the unit boundary normal of the jth boundary, $\hat{b}_j$ is a unit vector lying in the jth boundary and perpendicular to the triple line $\hat{l}=\hat{n}_j\otimes\hat{b}_j$ which is common to all three adjacent boundaries, and ϕ_j is defined to be the right-handed angle of rotation (inclination) about $\hat{l}$ of the jth boundary from a reference direction. If any boundary is in an energy cusp orientation, special care must be taken in defining the corresponding torque term in Eq. (1) (Herring 1952, Mullins 1963).

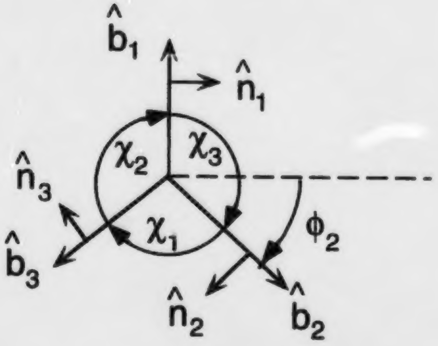

Fig. 1: Definition of geometric parameters associated with boundaries adjoining a triple junction. (Only one inclination parameter, ϕ_j, is shown for clarity.)

In the absence of torques (inclination dependence in the energy function) relation (1) reduces to

$$\sum_{j=1}^{3}\sigma_j\hat{b}_j=\vec{0} \qquad (2)$$

In the present work insufficient data are available to consider the inclination (torque) dependence of the Herring relations; thus, equation (2) will be applied. Equations (2) are also known as the Young's relations.

3 The Fourier Series Solution to the Herring Relations

The misorientation dependence of the energy function is expressed as a series of generalized spherical harmonic functions (cf. Bunge, 1982) according to the expression:

$$\sigma(\Delta g) = \sum_{l=0}^{\infty} \sum_{\mu=1}^{M(l)} \sum_{\nu=1}^{M(l)} S_l^{\mu\nu} \ddot{\ddot{T}}_l^{\mu\nu}(\Delta g) \qquad (3)$$

Here the functions carry the symmetries associated with the crystalline grain boundary which demands that

$$\ddot{\ddot{T}}_l^{\mu\nu}(\Delta g) = \ddot{\ddot{T}}_l^{\mu\nu}(\gamma \Delta g \gamma') \qquad (4)$$

In relations (3) and (4) Δg denotes the lattice misorientation at the grain boundary and γ, γ' are elements of the symmetry subgroup of the crystalline phase.

3.1 Boundary Conditions

The crystallographic symmetry of grain boundaries, which must also be present in the free energy function, is enforced by the symmetry of the generalized spherical harmonic functions. One additional boundary condition must be applied. In the limit that the misorientation between adjacent grains goes to zero, the (excess) free energy function must tend to zero. Thus,

$$\sum_{l=0}^{\infty} \sum_{\mu=1}^{M(l)} \sum_{\nu=1}^{M(l)} S_l^{\mu\nu} \ddot{\ddot{T}}_l^{\mu\nu}(I) = 0 \qquad (5)$$

Here I is the identity misorientation. Further, the grain boundary energy function was normalized so that the average energy was equal to one.

$$\bar{\sigma}(\Delta g) = 1 \qquad (6)$$

With these boundary conditions, the grain boundary energy function is:

$$\sigma(\Delta g) = [1 - \ddot{\ddot{T}}_4^{11}(\Delta g)] + \sum_{\ell=6}^{\infty} \sum_{\mu=1}^{M(\ell)} \sum_{\nu=1}^{M(\ell)} S_l^{\mu\nu} [\ddot{\ddot{T}}_\ell^{\mu\nu}(\Delta g) - \ddot{\ddot{T}}_\ell^{\mu\nu}(I) \ddot{\ddot{T}}_4^{11}(\Delta g)] \qquad (7)$$

3.2 Application of the Series Method

Equations (3,5,7) are truncated at finite levels of the index l (L ≥ l) to obtain a finite approximation for the free energy function. Let N represent the total number of coefficients associated with a truncation level of L in relation (3). Relation (5) provides one additional constraint upon the coefficients. Thus, there are N-1 independent coefficients in the finite series representation of the energy function.

Each triple junction in the data set provides one set of three equations according to relation (2), but only two of these are independent. It follows that if a minimum of (N-1)/2 triple junctions have been characterized, a solution for the approximate free energy function can be retrieved by standard methods. In practice, a much larger number of triple junctions will be characterized. The solution thus represents an average (best fit) for the energy function.

4 Experimental Methods

Ordinary methods of orientation imaging microscopy (OIM) are not suitable for the simultaneous rapid determination of lattice orientation and the geometry of triple junctions. In the usual method (Adams, et. al., 1993) the electron beam is used in the spot mode to scan over a systematic array of points on polished surfaces. Orientations are obtained by indexing algorithms at each point of the array, and a graphical picture of the underlying microstructure is obtained by comparing the orientations of neighboring points on the array. Graphical elements are introduced in the computer image when orientation differences between neighboring points suggest the presence of a grain boundary. The resolution of the geometry of the grain boundaries and triple junctions is thus fixed by the scale of the scanning array. The number of points at which EBSPs must be obtained increases as the inverse of the square of the mesh size of the array. Since it is desirable to resolve dihedral angles to ~2°, the mesh size must be on the order of $D/180$ (D is the grain size) in well annealed materials. Estimating the number of triple junctions in a section to be $2A / D^2$ (A is the measurement area), it is evident that the number of EBSPs required to adequately resolve the geometry of triple junctions using OIM is a multiple of approximately 16,200 times the number of triple junctions which need to be determined. When it is envisioned that many thousands of triple junctions must be characterized to fully resolve the five-parameter energy function, and that sufficient signal-to-noise ratios in EBSPs cannot be obtained in less than ~0.1 second, it becomes very evident that conventional OIM is not suitable for the problem at hand.

For the purposes of interest here, an advanced system of microscopy has been developed. This system is known as the Mesoscale Interface Mapping System (MIMS). The central idea is to use other methods of grain boundary contrast, such as backscattering or secondary electron contrast, to quickly form an image of the geometry of grain boundaries and triple junctions over a field of view that contains a number of triple junctions. A brief description of MIMS follows, with an emphasis on those aspects of the method that differ from conventional OIM.

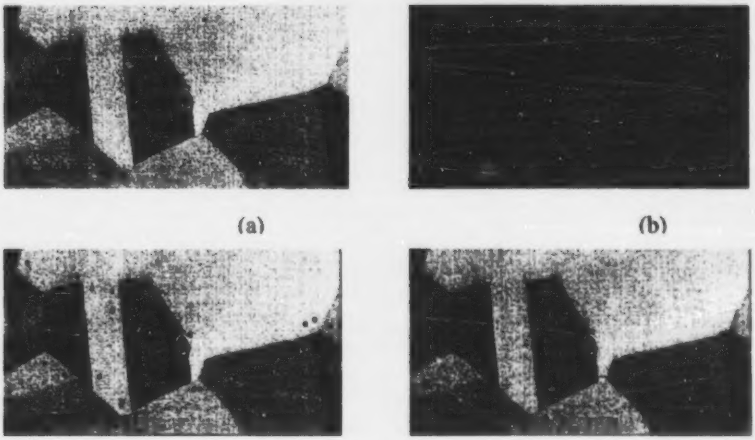

(a) (b)

(c) (d)

Figure 3. Sequence illustrating MIMS: (a) typical backscattering contrast image, (b) image obtained by edge detection and skeletonization, (c) locations of points determined for positioning of electron beam for orientation determination, (d) estimation of (apparent) dihedral angles from skeletonized image.

An example of such an image, obtained by a solid state backscattering detector, is shown in Figure 3a. Using conventional edge detection methods and further processing of the image, a skeletonized image of the grain boundary geometry is obtained. An example is shown in Figure 3b. From the geometry of the skeletonized representation an algorithm has been constructed which locates the triple junctions and determines the locations of selected points (three near each triple junction) where the electron probe can be placed in order to determine the lattice orientations for the adjacent grains. The results are shown in Figure 3c. The digital microscope is then changed from the scanning to spot mode, the beam is directed to each required point, an EBSP is obtained and analyzed for each such point, and thus, complete crystallographic data for several triple junctions are obtained. From the skeletonized image the (apparent) dihedral angles and in-plane curvatures of the grain boundaries can be directly obtained. Figure 3d illustrates this by superimposing tangent lines to each participating grain boundary. This process is repeated many times until sufficient data is obtained. With the present system the in-plane geometry and crystallography of triple junctions is obtained at rates of approximately 20s/triple junction.

The apparent geometry of triple junctions, obtained by 2-D image analysis as just described, must be extended to recover the true dihedral angles of the triple junctions. The method employed here involves precision serial sectioning using polishing and electropolishing. The parallelism between adjacent section planes, and the precision with which the removal thickness is measured, are factors of paramount importance. Adjacent sections are then brought into 3-D registration by considering the relative positions of external and/or internal markers. External markers might include micro-hardness indentations or drill holes. These are generally quite coarse, and provide only limited spatial resolution. Internal markers include triple junctions and grain boundaries. Internal markers must be used in conjunction with an algorithm for minimizing the positioning errors between corresponding markers since the inclination of the marker will not be known. Such an algorithm depends upon additional assumptions about the angular distribution of the markers in the microstructure. Details of the registration method have been described elsewhere (Morawiec and Saylor 1999).

5 Recovery of the Energy Function for MgO

The parameterized expression for the boundary energy, equation (7), was substituted into equation (2) and a standard linear least squares procedure was used to determine the best fit values of the coefficients, $S_l^{\mu\nu}$. Data obtained by MIMS were collected for 1,555 triple junctions. The quality of the fit was assessed by the ratio (ρ) of the sum of the squares of the residuals to the difference between the number of observations and the number of free parameters. Additional terms were added to the series until ρ ceased to decrease; this occurred at $l = 12$, where $\rho = 0.122$.

Figure 3 shows the best-fit grain boundary energy function in Rodrigues-Frank space. In this figure, the values of the function are computed only at observed disorientations and the shading corresponds to the relative energy. Note that the lowest relative energies are near the origin (smallest disorientations) and that the boundary energy increases as the disorientation angle increases.

In Figure 4, the variation in the energy is shown as a function of disorientation angle along the <100>, <110>, <111>, and <321> axes. Several features of the data are noteworthy. For example, as one would expect from a Read-Shockley model, the grain boundary energy increases from zero at zero misorientation to a plateau value as the disorientation angle increases (Read and Shockley, 1950). There are also several local minima where the energy falls below the average of 1.0; a number of these disorientations can be correlated with the positions of CSL boundaries. For example, the energy (in arbitrary units) at the $\Sigma 3$ disorientation is 0.7, at $\Sigma 5$ it is 0.71, at $\Sigma 7$ it is 0.98, and at it $\Sigma 9$ is 0.9.

There are other positions of relatively low grain boundary energy that are not near low-Σ CSL disorientations. For example, in the region between R3= 0.074 and R3=).148 slices of Rodrigues-Frank space, a relatively low energy region can be identified near the right hand side of the cell. This is near the end of the <321> axis. A plot of the grain boundary energy v. rotation about this axis, shown in Fig. 4, shows that the energy drops to 0.5 at this point. The lowest-Σ boundary near this region is the Σ39b at a rotation of 50.13° and it seems unlikely that this broad region of lower energy can be entirely associated with Σ39b. With the exception of the disorientations within 15 ° of Σ1, this point represents an energy minimum.

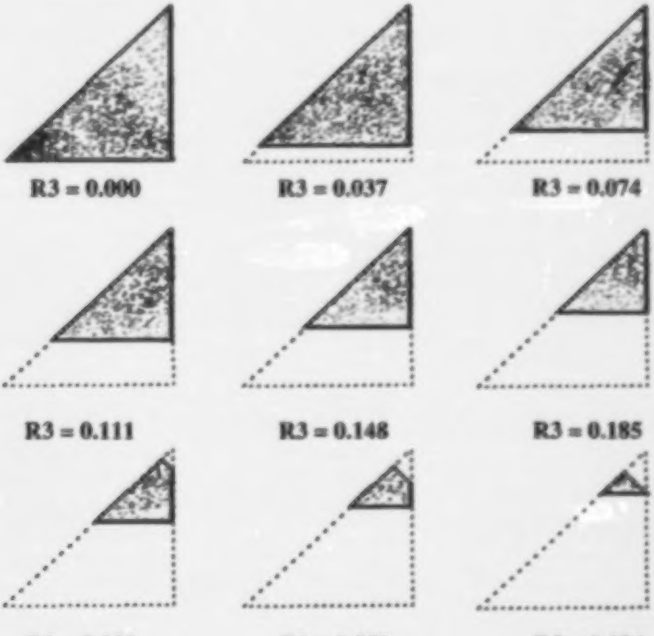

Figure 3. The values of the best-fit function for the grain boundary energy, at each of the observed disorientations, in Rodrigues-Frank space. Each observation is shaded according to its relative energy, with the darkest point being 0 and the lightest equal to 1.24.

6 Concluding Remarks

An earlier study of symmetric tilt boundaries in the isostructural compound, NiO, showed features similar to the current results (Dhalenne et al., 1983). For example, the energy increased from zero disorientation to a plateau region at approximately 30° rotation about the <110> axis and local minima were found at disorientations corresponding to low Σ CSL boundaries. The Σ3 boundary was found to have one third the energy of the highest energy symmetric <110> tilt boundary.

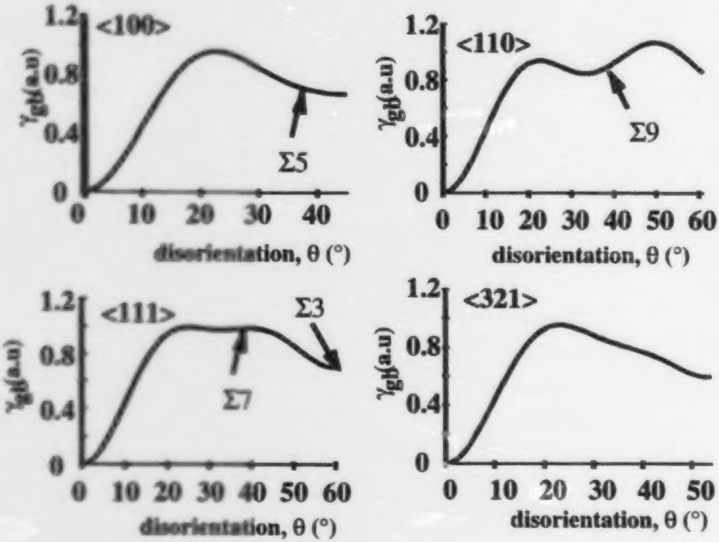

Figure 4. Axis-angle plots showing the grain boundary energy (in arbitrary units) as a function of the rotation angle.

In the current study, the energy of the Σ3 disorientation is approximately half of the highest energy general boundary. However, our fitting procedure makes it unlikely that we will accurately represent the minimum energy if it occurs at a sharp cusp. Because the series representation was truncated at $l = 12$, the function will not reproduce modulations smaller than 7.5°. Taking the width of any cusp to be $15°(\Sigma)^{-1/2}$, we expect most of the cusps associated with CSLs to be smoothed (Brandon, 1966). Furthermore, closely spaced cusps associated with special boundaries are likely to appear as broad minima.

Another likely artifact of the procedure appears at the origin. Instead of having a finite slope at zero disorientation, the slope of the best-fit energy function is zero; this is an unavoidable consequence of parameterizing the energy using a lattice harmonic series of finite order.

Comparisons of the present Fourier series method with the statistical/multiscale method (Adams et al. 1998) are in progress, but have not yet been completed. It is anticipated, however, that some of the aforementioned defects of the present approach may be reduced or eliminated within the statistical/multiscale framework (Kinderlehrer et al. 1999). The strength of the series method is the ease with which it is implemented, and the natural way in which the symmetries and boundary conditions of the problem can be introduced.

6 Acknowledgement

This work was primarily supported by the MRSEC Program of the National Science Foundation under Award Number DMR-9632556.

7 References

Adams, B. L., Wright, S. I. And Kunze, K. (1993) *Metallurgical Transactions,* Vol. 24A, pp. 819-831.

Adams, B. L., Kinderlehrer, D., Mullins, W. W., Rollett, A. D. and Ta'asan, S. (1998) *Scripta materialia,* Vol. 38, pp. 531-536.

Brandon, D.G. (1966) *Acta Met.*, Vol. 14 , pp. 1479-84.

Bunge, H.-J. (1982) *Texture Analysis in Materials Science,* Butterworths, London, pp. 351-401.

Dhalenne, G., Dechamps, M., and Revcolevschi, A. (1983) Advances in Ceramics, Vol. 6, *Character of Grain Boundaries*, American Ceramic Society, Columbus, OH, pp. 139-50.

Gottstein, G. and Schwarzer, F. (1992) *Materials Science Forum,* Vol. 94-96, pp. 187-208.

Herring, C. (1952) *Structure and Properties of Solid Surfaces,* eds. Gomer, R. and Smith, C. S., University of Chicago Press, Chicago.

Kinderlehrer, D., Livshits, I., Mason, D. and Ta'asan, S. (1999) *Proceedings of ICOTOM12,* ed. Szpunar, J.

Lejcek, P. and Hofmann, S. (1995) *CRC Critical Reviews in Solid State and Materials Science*, Vol. 20, p. 1.

Morawiec, A. and Saylor, D. (1999) *Proceedings of ICOTOM12,* ed. Szpunar, J.

Mullins, W. W. (1963) *Metal Surfaces: Structure, Energetics and Kinetics,* eds. Robertson, W. D. and Gjostein, N. A., The American Society for Metals, Ohio, pp. 17-66.

Pan, Y., Adams, B. L. and Olson, T. (1996) *Acta materialia,* Vol. 44, pp. 4685-4695.

Read, W. and Shockley, W. (1950) *Phys. Rev.* Vol. 8, p 275.

Texture and Microstructure
Description and Analysis

DEVELOPMENT AND APPLICATION OF A DISORIENTATION CORRELATION FUNCTION

P. S. LEE, A. D. ROLLETT and B. L. ADAMS
Carnegie Mellon University, Pittsburgh, U. S. A.

Abstract

The correlation of orientation over large distances has rarely been investigated since long-range orientation correlation has been considered to be weak, if present at all. A new description of the spatial correlation of orientation over large distances was developed and named the Disorientation Correlation Function (DCF). This function quantifies the average misorientation angle between two material points separated by the vector r. The DCF has been explored as a function of strain level for samples of 6022 T4 aluminum, deformed under plane strain conditions. The results indicate the presence of long-range orientation correlations. Substantial changes in the DCF are observed as a function of strain level. The implications of these observations for strain localization are explored.

Keywords: Disorientation correlation function, strain inhomogeneity

1 Introduction

Traditionally, the measurement of microstructure in polycrystalline solids is the first and the most fundamental step in analyzing material behavior. Microstructure can be separated into two distinct categories - morphological and orientational. Since the advent of the automated orientation measurement technique (Wright 1992) called orientation imaging microscopy (OIM), microstructural data have been successfully incorporated into models for prediction of thermal, magnetic, elastic and plastic anisotropy requiring both morphological and orientational microstructures together. With the help of OIM, efforts have been directed at quantifying the orientation distribution, the misorientation distribution and their correlation at various length scales. (Wright 1992, Adams et al. 1987, Wang 1990) The misorientation distribution function (MDF) gives the probability density for the occurrence of specific intercrystalline misorientations between adjacent grains (correlated misorientation) as well as between grains taken pairwise throughout the microstructure (uncorrelated misorientation). Some recent studies combined the morphological distribution of microstructure with misorientation distribution, and attempted to visualize the uncorrelated misorientation to a limited degree (Wright 1992), but the spatial distribution of uncorrelated misorientations is never accomplished.

This paper introduces a method for combining spatial information with the misorientation distribution. A disorientation correlation function (DCF) is defined. This function gives the normalized average disorientation of two-point pairs separated by a fixed distance and direction. It is particularly useful in describing orientation clustering or ordering over distances larger than the grain size. Exemplary calculations are shown for 6022 T4 aluminum alloys, which illustrate the presence of particular spatial disorientation distributions through the thickness of the samples at various strain levels.

2 Background

As an effort to reduce weight and increase fuel efficiency of the automobile, new aluminum alloys have been developed and are gradually being used more widely in automobile applications. For automotive body panel applications, 6000 series aluminum alloys such as 6022, 6016 and 6111 have been developed. Many technical issues have been reported for these newly developed aluminum alloys, including surface finish (Lee et al. 1999) and formability (Jarvis 1998, Langerak & Kragtwijk 1998).

In the previous work (Lee et al. 1999), 6111 and 6022 sheet materials were deformed in plane strain tension and a cross-section near the fracture surface was characterized using OIM. Orientation clustering over the through-thickness deformation bands was observed which suggests correlations between orientation clustering and through-thickness deformation bands and between orientation clustering and surface roughness. So in the current work, the DCF was applied to OIM data of cross-sections of deformed 6022 T4 alloys near the fracture surface. Four samples with initial thickness variation were deformed in plane strain tension. The initial thicknesses of the four samples were 880, 760, 620 and 565 microns. Before deformation, the four samples were polished and electro-polished to mirror finish on both free surfaces. The thickness was controlled by the polishing time with rough polishing paper (100 grit).

3 Definition of Disorientation Correlation Function (DCF)

The orientation of a grain is usually defined by three consecutive passive rotations from a reference frame, and the three rotation angles are called Euler angles. When we are interested in the relative orientations of two grains, the orientation difference is described by misorientation. The misorientation obtainable from a pair of grains has as many equivalent forms as there are crystal symmetry elements. Among all the symmetrically equivalent misorientations, the smallest in magnitude is called the disorientation (Δg), which is taken to be the physically meaningful misorientation angle and can be expressed as follows.

$$\left|\Delta g_{AB}\right| = \min\left\{\cos^{-1}\left[\frac{1}{2}\cdot\left\langle trace\left(g_B\cdot\left(S\cdot g_A\right)^{-1}\right)-1\right\rangle\right]\right\} \tag{1}$$

where S is a crystal symmetry operator, g_A is the lattice orientation in matrix form associated with the point A at (x,y), and g_B is the lattice orientation associated with the point B at (x+a,y+b). The disorientation correlation function describes the general dependence of the orientation of one position with the orientation at another position. It provides information about the spatial relation and dependence of the orientation data, hence it is related to the Auto-Correlation Function (ACF) or Areal Auto-Correlation Function (AACF) described for analyzing surface topographic data (Stout et al. 1993).

Intensity in the DCF is the average minimum misorientation of two-point pairs separated by a given vector, (a,b). In calculating the minimum misorientation or disorientation, crystal symmetry operators as well as sample symmetry (optional) were used and compared to find the disorientation. See the Eq. 1. We truncate the low average misorientation region in the center of the map, because when the vector (a,b) is small, most of the misorientations are obtained from within the same grain and the 2-D profile has a deep well around the origin. See Fig. 1.

The well structure at the center is detrimental for visualizing the profiles in the high misorientation region. Therefore, the basic disorientation correlation, f(G), is truncated as defined below, Eq. (2). In Eq. (2), p is the minimum average misorientation angle that is chosen to be included in the output and G is the average disorientation of two-points separated by a fixed vector (a,b). Therefore, the choice of p is governed by intensity of texture, degree of texture clustering and the resolution of DCF profile (See Eq. (4)), and G is given by Eq. (3), where N and M are the number of pixels in an input OIM data file.

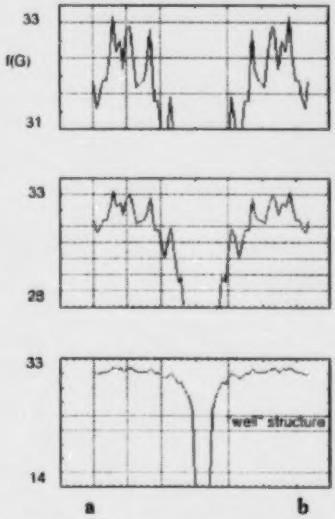

Fig. 1: Line profiles with different truncation disorientations. From the top profile, the truncation disorientation, or the minimum disorientation shown along y-axis, was (a) 31, (b) 28 and (c) 14 degrees, respectively. Maximum disorientation was 33 degrees with sample symmetry operation turned on.

$$f(G)=\begin{cases} p & \text{if} \quad G<p \\ G & \text{if} \quad G\geq p \end{cases} \tag{2}$$

$$G=\frac{\sum_{x}^{N}\sum_{y}^{M}\left(\left|\Delta g_{AB}\right|\right)}{M\times N} \tag{3}$$

p=*f* (clustering, resolution, texture) (4)

The slope of the sides of the well is related to the grain shape and size distribution; a data set with uniform grain size will give a steeper slope than one with a wide range of grain sizes. With a low truncation disorientation angle (p), the dark area at the center of the DCF is related to the average grain size and shape, where grains are defined by local misorientation of that truncation angle.

Eq. 5, e($\sqrt{a^2+b^2}$), is the optional normalization function to make the amplitude fluctuation uniform. The amplitude tend to increase with the increase of vector (a,b) for statistical reason.

$$e\left(\sqrt{a^2+b^2}\right)=\cos\left(\frac{\sqrt{a^2+b^2}}{\sqrt{P^2+Q^2}}\times 25^\circ\right) \tag{5}$$

where P = max(a) = N/2, Q = max(b) = M/2. P and Q are adjustable parameters depending on how large an area is of interest, while N and M are the number of pixels in input OIM data file.

Considering Eqs. 1 to 5, the intensity in the DCF, I(a,b), is defined below. Since OIM data sets contain texture information on a discrete lattice, the equations are formulated in discrete form.

$$I(a,b)=\left\{f(G)-\left\langle\left|\Delta g_{AB}\right|\right\rangle\right\}\times e\left(\sqrt{a^2+b^2}\right)+\left\langle\left|\Delta g_{AB}\right|\right\rangle \tag{6}$$

where (a,b) are the coordinates of a point in DCF space and also define a vector that separates a pair of points in an OIM map with the origin of the DCF space at the tail of the vector, $\left\langle\left|\Delta g_{AB}\right|\right\rangle$ is the average disorientation over the whole DCF space, $e\left(\sqrt{a^2+b^2}\right)$ is the normalization factor defined by Eq. 5 and f(G) is the truncated disorientation average, Eq. 2. $\left\langle\left|\Delta g_{AB}\right|\right\rangle$ can be also understood as $\langle G\rangle$ after the truncation of the center well.

3.1 Filtering of Disorientation Correlation Function

Using disorientation correlation function (DCF), orientation clustering or orientation ordering can be visualized in 2-D space. Orientation filtering of DCF has been also developed to separate the systematic behavior of specific orientations. The orientation filter was designed so that an orientation pair is heavily weighted if one of the orientations is close to the orientation of interest (filtering orientation). If both of the orientations are close to the filtering orientation, then the weighting factor will be near the maximum, but low disorientation will suppress the weighted disorientation.

The weighting factor is applied when the disorientation of two points is calculated.

$$|\Delta g_{AB}|_{\Omega} = \min\left\{\cos^{-1}\left[\frac{1}{2}\cdot trace\left(g_B\left(S\cdot g_A\right)^{-1}\right)-1\right]\right\} * \left(1-\frac{\Delta g_{A\Omega}+\Delta g_{B\Omega}}{C}\right) \tag{7}$$

where Ω is the filtering orientation and C=110, is a scaling coefficient in degrees. Unlike the regular DCF, disorientation should be calculated with sample symmetry operation included. Otherwise, two different sample variants of an orientation will cause highly weighted disorientation. As a result, the average G will be also weighted by the filtering orientation. Then filtered DCF can be calculated with Eq. 6 with orientation filtered G.

4 Results

Four 6022 T4 samples were deformed in plane strain tension mode to fracture. A small piece was cut out near the center of each sample, and then the cross-section was mechanically polished and electro-polished to a mirror finish for OIM analysis. A few OIM sections were used to calculate separate DCF maps. The DCF maps were calculated with and without the sample symmetry operation. Without the sample symmetry operation, average disorientation was shifted upwards by approximately 10

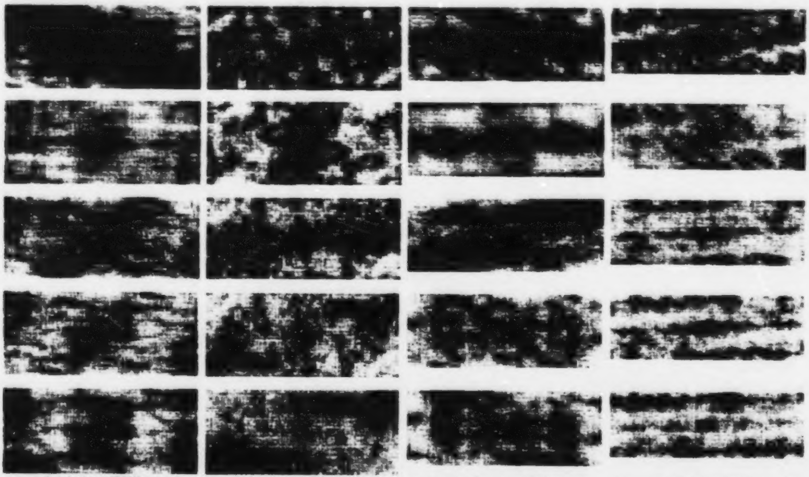

sample 1 (t_0=880 μm) sample 2(t_0=760 μm) sample 3 (t_0=620 μm) sample 4 (t_0=565 μm)

Fig. 2: DCF and Filtered DCF maps obtained from cross-sections of 4 samples near the fracture surface. From the top row to bottom, regular DCF, Cube-filtered, Brass-filtered, S-filtered, Taylor-filtered DCF maps were listed. Average disorientation is linearly scaled with gray shading.

degrees, but the patterns in the DCF maps were very close to the DCF maps calculated with the sample symmetry operations.

The DCF maps and Filtered DCF maps were shown in Fig. 2. The maps shown in Fig. 2 were obtained from the OIM data sets right near the fracture surfaces of the 4 samples with different initial thickness. The strain level of the four sections in Fig. 2 varies due to the initial thickness variation, but it was, in general, just above 0.2 along the major strain direction (extension direction). All the DCF maps are from ND-TD sections since the samples were extended along TD and OIM data sets were obtained from the cross-sections (ND-TD sections). The height of each map in Fig. 2 is the thickness of each sample near the fracture surface, and the width of each map is about 1.1 mm since the dimensions of DCF map are the same as those of the input OIM data set. Diagonal ordering of similar orientation was found on sample 1, 2, and 3. For the two thin samples (sample 3 & 4), horizontal banding was also observed. The wavelengths of diagonal bands are measured in DCF space and listed in Table 1.

By comparing regular DCFs (1st row in Fig.2) and filtered DCFs (2nd to 5th rows in Fig.2), it is apparent that all the texture components contribute in varying degrees to the band structure in the regular DCF. At this high strain level, there exist some dominant orientations such as Brass and Cube for sample 1, but the band structure does not mean that the Brass or Cube components are themselves clustered or ordered. The separate filtered maps exhibit features that are generally unrelated to the bands in the regular DCF. Cross-correlation and auto-correlation were also performed for these texture components and did not show any evidence of banding. The band structure observed in the regular DCF appears to be formed by all the orientations in the observation window.

In general, Brass filtered DCFs have some diagonal bands, while Taylor filtered DCFs have two minima at a long range, i.e. orientations are correlated over as much as 500 μm in certain directions. Brass oriented grains can be qualitatively said to align along a diagonal direction. Even though the initially thinnest sample did not show clear diagonal band structure because of the dominating horizontal band, it also contains some diagonal clustering tendency as shown in cube-filtered DCF.

In order to investigate the correlation of through-thickness orientation ordering and surface waviness at high strain level, surface roughness was also measured on free surface near the fracture surface. Two-dimensional Fourier transformation was used to calculate the wavelength of dominant surface features, and the results are listed in the following Table 1.

Table 1: Comparison of initial thickness, wavelength of orientation ordering, and wavelength of surface roughness obtained from four plane strain tension samples.

Sample #	Initial thickness (μm)	Wavelength of bands measured in DCF (μm)	Wavelength of surface roughness (μm)
1	880	254	980
2	760	199	820
3	620	127	688
4	565	N/A	487

5 Discussion

With these four samples, interactions with preexisting surface defects could be excluded since the surface was mirror-finished before plane strain deformation. From the DCF analysis of consecutive sections from fracture surface, it is shown that orientation clustering is more intense at higher strains in plane-strain deformation.

The initial thickness of the sample and the measured wavelength from the surface profile are of the same order. The wavelengths measured in the DCF maps are smaller than the wavelengths of surface profiles and initial thickness, but there seems to be a simple quasi-linear relation between them. Wavelengths in surface profiles are about 4 times the wavelengths in DCF. The wavelength of diagonal band structure appeared in the Cube-filtered DCF for the thinnest sample (t_0=565 μm), follows the above trend also.

On the cross-section of the sample of which the initial thickness was 880 μm, micro-hardness and Taylor factor were obtained. Taylor factors were obtained by subdividing the OIM data set and calculating <M> for areas 230 μm by thickness in order to detect spatial variation. The size of subsection(~230 μm) was chosen to be very close to the wavelength measured in the DCF for this sample. The results show a fluctuation in <M> near the fracture surface. The amplitude was about 5 % of the overall average Taylor factor.

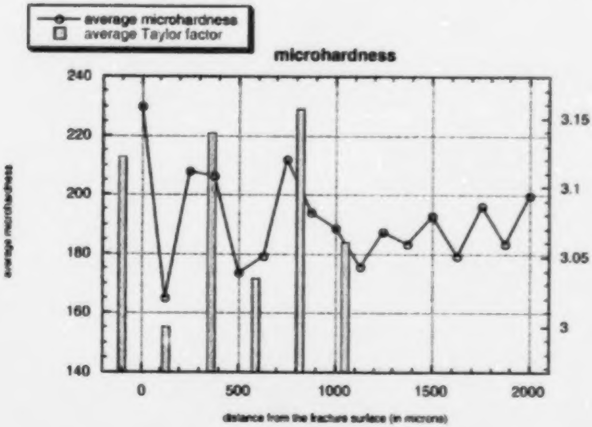

Fig. 3: Trends of average micro-hardness and average Taylor factor near the fracture surface

Over the same area, a series of Vickers micro-hardness tests were made. Starting from the fracture surface, micro-hardness indents were placed every 125 μm, and average micro-hardness was compared to the average Taylor factor (See Fig. 3.) Average size of micro-indents was 50x50 μm^2 and each data point is the average of 2-3 data points through the thickness. The trends of micro-hardness and average Taylor factor were in good agreement, demonstrating that the orientation clustering present in the deformed material results in measurable heterogeneity in mechanical properties.

6 Summary

A disorientation correlation function is defined which represents a logical extension of the successful misorientation distribution function to include both disorientational and positional information. Extension of the DCF technique to the measurement of average grain size, shape and grain size distribution is feasible by analyzing the center "well" structure.

In an example of plane-strain extended 6022 T4 aluminum alloy sheets, a well-defined through-thickness diagonal pattern was found to exist in DCF at high strain level. It was also found that the orientation ordering is highly correlated to the surface roughness behavior as well as to the mechanical properties such as hardness and Taylor factor.

This current work is significant in the sense that it is the first time that the existence of long-range orientation correlation in more than one dimension has been visualized, demonstrated and correlated to mechanical properties.

ACKNOWLEDGEMENTS: The authors acknowledge support of this work by the Department of Energy under grant DE-FG02-96ER45601. The 6022 T4 aluminum alloy was kindly provided by ALCOA Technical Center (ATC) through G. Jarvis. We thank D. Raabe for technical support and R. Becker at ATC and Prof. Piehler for many helpful suggestions.

7 References

Adams, B. L. et al. (1987), Description of Orientation Coherence in Polycrystalline Materials, *Acta metall.* Vol. 35, No. 12, pp. 2935-2946

Barlat, F. (1989), Forming Limit Diagrams-Prediction Based on Some Microstructural Aspects of *Materials, Forming Limit Diagrams* edited by R. H. Wagoner, pp. 275-301

Jarvis, G. (1998), *Ph.D. Thesis*, Carnegie Mellon University

Langerak, N. A. J. & S. P. Kragtwijk October 1998, Lightweight Car Body Design, *Automotive Engineering International*, pp. 106-110

Lee, P. S. et al. In press, Observation of Through-Thickness Deformation Bands in an Al 6111 Alloys Deformed in Plane Strain Tension, submitted for *1999 TMS Spring Proceedings*.

Stout, K. J., et al. (1993), The development of methods for the characterisation of roughness in three dimensions, Commission of the european communities, University of Birmingham, Tech. Report, EUR15178EN, EC Brussels

Wang, T. T. et al. (1990), Development of Orientation Coherence in Plane-Strain Deformation, *Met. Trans.* A, Vol. 21A, pp. 2223-2235

Wright, S. I. 1992, Individual Orientation Measurements Development and Application of a Fully Automatic Technique, *Ph.D. Thesis*, Yale University

SPATIAL STATISTICS FOR INDIVIDUAL ORIENTATION MEASUREMENTS

K.G.v.d.BOOGAART,
Graduate College "Spatial Statistics", University of Mining and Technology
Freiberg, Germany

Abstract

Individual orientation measurements do not only provide crystal orientations but also their spatial locations. This information can be used to analyse and describe the interaction of the orientated grains. This paper gives an outline of a statistical framework, in which processes of dependent crystal orientation can be modelled, simulated, and analysed. This contains a distribution model derived from the theory of Markov random fields and the theory of conditionally specified distributions. Pitfalls and possibilities of the simpler approach by the method of moments are discussed briefly.

Keywords: statistics, spatial statistics, individual orientation measurements, measurement error, texture models

1 Motivation

In many cases the orientation of an individual crystal grain is not independent of the orientation of its neighbours. This dependence actually effects any inference on these type of data in at least three ways. First, this behaviour violates the implicit assumption of independence, which is essential for all statistical inference on the measured data. Thus, adjusted statistical procedures for textures with dependent grain orientations are required. Secondly, this interdependence is an interesting phenomenon by itself, which should be incorporated into the representation of the texture. Thirdly, simulated textures should incorporate this dependence, too.

2 Distributions for spatial orientation processes

A large class of distributions for spatial stochastic processes representing regionalized crystal orientations can be derived from the theory of Markov random field (Cressie 1993) and conditionally specified exponential families (Arnold et al. 1991). This class is based on the class of distributions $ExpRot[L, \overset{L}{G}, \dot{G}; (\theta_\tau)_{\tau \in \overset{L}{I}(L)}]$ defined by a degree L of a series expansion, the crystal symmetry group $\overset{L}{G}$, the sample symmetry group $\dot{G}$, and a set of real valued parameters θ_τ, $\tau \in \overset{L}{I}(L)$, by its distributional density:

$$f_\theta(g) = A(\theta) \exp\left(- \sum_{l=1}^{L} \sum_{\mu=1}^{M(l)} \sum_{\nu=0}^{N(l)} \theta_l^{\mu\nu} \overset{L}{T}{}_l^{\mu\nu}(g) \right) = A(\theta) \exp\left(- \sum_{\tau \in \overset{L}{I}(L)} \theta_\tau \overset{L}{T}_\tau(g) \right)$$

Details on this family are given in the paper "Statistics for individual orientation measurements".

The central idea of the spatial model is that the conditional distribution of the crystallographic orientation of every grain given the orientation of the neighbouring grains has this distributional form. In mathematical terms, with M the set of grains:

$$P(g_i | g_j, j \in M \setminus \{i\}) = ExpRot[L, \overset{L}{G}, \dot{G}; \theta(g_j, j \in M \setminus \{i\})] \tag{1}$$

For simplification we may assume pairwise interaction only. Then it follows by the theory of conditionally specified exponential families given in (Arnold et al. 1991) that the joint distribution density for the crystallographic orientations of all grains is:

$$\begin{aligned} f(g_i, i \in M) &= A(\alpha, \beta) \bullet \\ &\bullet \exp\left(\sum_{i \in M} \sum_{\tau \in \overset{L}{I}(L)} \alpha_{\tau i} \overset{L}{T}_\tau(g_i) + \sum_{\{i,j\} \subset M} \sum_{\tau \in \overset{L}{I}(L)} \sum_{\sigma \in \overset{L}{I}(L)} \beta_{ij\tau\sigma} \overset{L}{T}_\tau(g_i) \overset{L}{T}_\sigma(g_j) \right) \end{aligned} \tag{2}$$

The parameters α_i and β_{ij} should be modelled as linear combinations of entities depending on the grain's shape and the relative position of the two grains i, j. Then the entire model is again an exponential family, and we can use methods known from the theory of exponential families. This could be the maximum likelihood estimation using a Metropolis like stochastic gradient algorithm proposed by L. Younes (Guyon 1995 p.221), and the likelihood ratio tests (under some additional assumptions) for the comparison of two models. Given a specified microstructure in form of a set of grains and known parameters α, β the texture can be simulated by a Metropolis algorithm (Guyon 1995). The details of estimation, test and simulation procedures are far beyond the scope of a six page introductory contribution. Generalisations to more complex dependence structures in various ways are available using the more general results of (Arnold et al. 1991), and using curved exponential families (Kass 1989).

Modelling of a simple dependence structure is exemplified by the following settings:

$$\alpha_{i\tau} = \theta_\tau^{(0)} * \text{"size of grain } i\text{"} * \theta_\tau^{(1)} \tag{3}$$

$$\beta_{ij\tau\sigma} = \theta^{(3)} * \text{"size of common boundary of grain } i \text{ and grain } j\text{"} * \gamma_{\tau\sigma} \tag{4}$$

with a γ such that:

$$\sum_\sigma \sum_\tau \gamma_{\tau\sigma} \dot{T}_\sigma(g_1) \dot{T}_\tau(g_2) \approx \begin{cases} 1, & g_1 \approx g_2 \; mod \, \dot{G} \\ 0, & else \end{cases} \tag{5}$$

representing a texture with preferred orientation ($\theta^{(0)}$) which depends on the grain size ($\theta^{(1)}$), and is affected by excessive small angle grain boundaries ($\theta^{(3)}$).

Similar to the effect of the grain size other characteristics of the grain could be incorporated into the model. These could be a Minkowski measure of the shape or an aspect of the location of the grain in the sample in case of inhomogeneous material.

3 Canonical statistics

For every exponential family model, there exists a set of associated canonical minimal sufficient statistics, which are unique up to affine linear transformation. These statistics contain as much information of the result of the experiment as required for parameter estimation or tests within the model. It is very interesting what these statistics are in the spatial model proposed here:

As an example we will us the model given by the equations (2),(3), and a more general model for the interaction term β:

$$\beta_{ij\tau\sigma} = \theta_{\tau\sigma}^{(3)} * \text{"size of common boundary of grain } i \text{ and grain } j\text{"} * \gamma_{\tau\sigma} \tag{6}$$

The canonical statistics associated with the parameters $\theta_\tau^{(0)}$ are the empirical means of low order harmonics:

$$\dot{C}_\tau = \dot{C}_l^{\mu\nu} = \sum_{i=1}^{n} \dot{T}_l^{\mu\nu}(g_i) \tag{7}$$

The canonical statistics associated with the parameters $\theta_\tau^{(1)}$ are the empirical means of low order harmonics weighted with the grain size:

$$\dot{C}_\tau = \dot{C}_l^{\mu\nu} = \sum_{i=1}^{n} (\dot{T}_l^{\mu\nu}(g_i) * \text{"size of grain } i\text{"}) \tag{8}$$

The canonical statistics associated with the interaction terms $\theta_{\tau\sigma}^{(3)}$ are some weighted non centered moments:

$$K_{\tau\sigma} = \sum_{i=1}^{n} \sum_{j \neq i} \overset{\therefore}{T}_{\tau}(g_i)\, \overset{\therefore}{T}_{\sigma}(g_j) * \text{"size of boundary } i, j\text{"} \tag{9}$$

Because of a stereological argument for the measurement the volume of the grain can be replaced by it's visible area, and the area of the common boundaries can be replaced by their visible length.

4 Method of moments

4.1 Standard errors for harmonic coefficients

The model-driven approaches mentioned in the beginning of this contribution yield standard errors for the experimental harmonic coefficients of the ODF. An alternative approach could be to use the sample variance of the $\overset{\therefore}{T}_l^{\mu\nu}(g_i)$, and divide it by n as usual:

$$\widehat{Var}(\hat{C}_l^{\mu\nu}) \overset{?}{=} \frac{1}{n(n-1)} \sum_{i=0}^{n} (\overset{\therefore}{T}_l^{\mu\nu}(g_i) - \hat{C}_l^{\mu\nu})^2 \tag{10}$$

However, that is not too splendid an idea, because this estimator is heavily biased and not consistent, if the orientation of grains is correlated. This problem has been discussed in depth in the context of regionalized random variables and kriging for univariate measurements cf. (Cressie 1993).

4.2 Simple inference with multiple samples

A simple workaround for this problem is to take multiple samples of equal size sufficiently far from each other that they can be assumed independent. Then we can replace the individual observed $\overset{\therefore}{T}_l^{\mu\nu}(g_i)$ with the means of this statistic in each of the individual samples. Then we estimate the variance of the sample means. The overall mean is given by the mean of the sample means.

$$\hat{C}_l^{\mu\nu} = \frac{1}{n} \sum_{i=1}^{n} \frac{1}{N(i)} \sum_{j=1} N(i)\, \overset{\therefore}{T}_l^{\mu\nu}(g_{ij}) \tag{11}$$

Here g_{ij} denotes the orientation of the grain j in sample i. The estimated variance of the overall mean can be calculated from the empirical variance of the sample means.

$$\widehat{Var}\hat{C}_l^{\mu\nu} = \frac{1}{n(n-1)} \sum_{i=1}^{n} \left(\frac{1}{N(i)} \sum_{j=1} N(i)\, \overset{\therefore}{T}_l^{\mu\nu}(g_{ij}) - \hat{C}_l^{\mu\nu} \right)^2 \tag{12}$$

Since these sample means are mean values, they are distributed approximately normal. Therefore statistical methods assuming multivariate normality such as cluster analysis, discriminant analysis, and MANOVA apply. The first two may have interesting applications in geology, where we may want to classify the unknown process from the observed texture. MANOVA or more general linear models may have interesting applications in materials sciences where we want to model the texture depending on the generating process described by a set of independent variables. Within the context of MANOVA random effects may be used to model the variation between different specimen, while fixed effects could be applied to model the influence of process parameters; MANOVA interaction terms may be used to model the interaction of the effects of process parameters.

Especially the question whether the textures of two objects are equal or not can be formulated as a test problem in the MANOVA context, since two textures, compatible with the same model M, are equal if and only if the sample means of the minimal sufficient statistics of M have the same mean in both objects. This is a multi-response heteroscedastic MANOVA model for the sample means of the minimal sufficient statistics of M as dependent variables and with a single dichotomic variable representing the object as independent variable.

5 Conclusion

Application of spatial statistics to individual orientation measurement data is possible and offers a broad variety of statistical procedures useful to answer many different questions about the observed texture of the investigated material. Only very few of them have been mentioned; many more can be developed in analogy to statistical procedures known for other localised data. There are many different tools for many different purposes available – what kind of purposes are we most interested in?

6 References

Arnold, B.C., E. Castillo, J.-M. Sarabia (1991) *Conditionally Specified Distributions*, Lecture Notes in Statistics 73, Springer-Verlag, New York

Beran, R. (1979) Exponential families for directional data, *The Ann. Statis.* 7, 1162-1178.

Cressie, Noel (1993) *Statistics for spatial data*, Wiley Series in probability and mathematical statistics, revised edition, Wiley, New York

Guyon, X. (1995) *Random Fields on a Network, Modeling, Statistics and Application*, Probability and it's Applications, Springer-Verlag, New York

Johansen, S. (1979) *Introduction to the Theory of Regular Exponential Families*, Institute of Mathematical Statistics University of Copenhagen, Lecture Notes 3, Copenhagen

Kass, R.E. (1989) The geometry of asymptotic inference, *Statistical Science* Vol. 4, No.3, p.188-234

MacCullagh, P. and J.A. Nelder (1983) *Generalized linear models*, Chapman and Hall, London.

Witting, H., U. Müller-Funk (1995) *Mathematische Statistik II, Asymptotische Statistik: Parametrische Modelle und nichtparametrische Funktionale*, Teubner, Stuttgart

ON THE DETERMINATION OF TEXTURES FROM DISCRETE ORIENTATION MEASUREMENTS

W.B. HUTCHINSON and E. LINDH
Swedish Institute for Metals Research, Stockholm, Sweden
P. BATE
Doncasters plc, Melbourne, UK

Abstract

Sources of potential error in conventional x-ray and EBSP determinations are discussed and it is shown that discrete measurements are capable of leading to a more correct measure of the texture provided that the data are sufficiently prolific. In this case there is no lower bound to the sharpness of the gaussian functions that may be employed for generating ODFs.

Keywords: Textures, ODF, EBSP, x-ray diffraction

1 Introduction

Traditionally, textures have been measured by x-ray diffraction as pole figures and orientation distributions have been deduced mathematically from these. More recently, techniques such as electron back-scattering patterns (EBSP) have permitted individual grain orientations to be measured rapidly, and so statistically valid distributions of orientations can be determined directly. There is still a tendency to believe that texture should properly be measured by the traditional x-ray method but the superiority and, indeed, the higher speed of the EBSP technique are becoming ever more apparent. This may well become the standard approach before long, at least for materials from which back-scattering patterns can be reliably obtained. Two questions, however, have not yet been answered satisfactorily: what is the number of measurements required to accurately represent a given texture, and how should the discrete measurements be converted into a continuous density representation or function? A further question concerns the equivalence of textures determined by x-rays and discrete measurements. In fact, all these questions are inter-related.

A number of previous publications (e.g. Wagner et al. 1981, Wright and Adams 1990, Baudin and Penelle 1993) have been concerned with these questions and comparisons have been made between x-ray and EBSP texture determinations. Implicit in these has been the assumption that that x-ray ODF (ghost-corrected) is the touchstone by which others are to be judged. This assumption needs also to be proved.

The procedure most often used within the framework of the harmonic method (Bunge 1982) is to replace the point orientations measured by EBSP by symmetrical 3-dimensional gaussian functions which are then summed to produce the texture ODF. It may be recalled that the uncertainty in an individual EBSP orientation measurement is typically <0.5° and such a value may be considered as its 'instrumental broadening'. By using the gaussian representation, however, this spread may be considerably increased. Typical values applied to data in the literature vary from 5° to 15°. Although such a treatment quite evidently leads to a smearing or flattening of the true texture, there seems to be an aversion to using gaussian functions of higher resolution. Wagner et al. (1981) have stated that the applied gaussian function must be capable of being described by the series expansion and so for very sharp functions this would require a much larger number of terms than is generally used in texture analysis. We will return to this question below.

It is frequently overlooked that x-ray textures also suffer from instrumental broadening which causes the measurements to be less sharp than the true texture. Recent developments can reduce this effect (Bunge 1996) but conventional goniometers typically have a full-width–half-maximum (FWHM) breadth of about 3°. Figure 1 shows the shape of a (200) diffraction peak from a single crystal of iron using a standard commercial goniometer. The intrinsic resolution of the method is considerably less (by a factor of about 6) than that of an EBSP measurement.

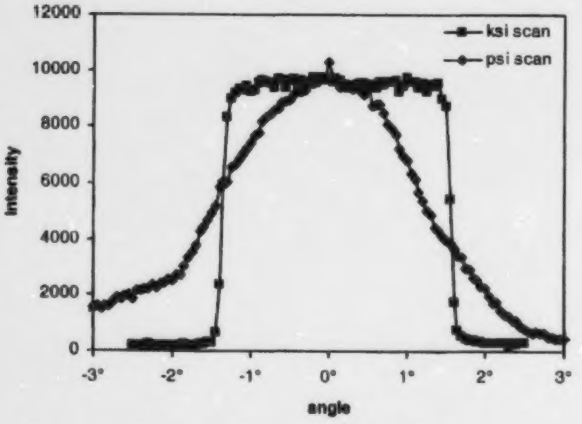

Fig. 1: (200) diffraction peak from a single crystal of iron indicating the resolution of the x-ray goniometer.

2 A thought experiment

There is a widely held viewpoint that errors are introduced into ODFs derived from discrete orientations unless these are sufficiently smoothed (gaussian spread). Oscillations in density and meaningless negative values may result. On the other hand, an increase in the applied gaussian spread must inevitably distort the true texture so it is important to gain some clarity concerning this question. Is it necessary to utilise the very high series truncations to describe the narrow gaussians necessary for high resolution, as was claimed by Wagner et al.?

Let us consider a material having a texture of typical severity which can properly be described by a limited number of terms (e.g. $L_{max}=22$) in the standard manner. All the texture coefficients for $L>22$ must then be equal to zero. This texture is to be generated without loss of sharpness from a large number of discrete orientation measurements on single grains. To ensure this high degree of resolution we will employ narrow gaussians - say with a spread of only 1° - and we shall expand these as harmonic series with a large number of terms (e.g. $L_{max}>100$). These series are then summed and averaged to produce the texture of the material. Clearly, the resulting coefficients for $L>22$ must be zero since this is true for the total texture. Furthermore, the orthogonality of the spherical harmonics means that the inclusion of higher order terms ($L>22$) does not affect the values of the preceding terms and therefore the higher order terms can in fact be omitted with no change to the result. In other words, nothing is achieved by describing the individual gaussians with a longer series expansion than that necessary for the texture of the material as a whole. The angle of spread may therefore be reduced, even to zero, without introducing any error, while at the same time eliminating distortion caused by the smoothing.

If oscillations or negative density values result from the calculations, these must imply that the number of measurements is too small. A proper statistical sample has not been reached and *inter alia* the higher order terms ($L>22$) have not yet cancelled to zero.

3 Numerical simulation

The above reasoning leads to the conclusion that the most correct texture description will always be achieved when the applied gaussian spread is reduced to a minimum (zero) provided that the number of measurements is sufficiently great. The optimum conditions of synthesis from smaller samples of data are not intuitively obvious, however. To map the effects of different parameters the following numerical simulation has been carried out.

A model texture comprising four variants of the aluminium S-texture was generated as gauss distributions having different assumed breadths (Ψ=10°, 15°, 20° and random) centred on the ideal S-orientation. It was confirmed that these could all be well described by series expansions having $L_{max}=22$. For the sharpest of these textures with a 10° spread the largest negative value of the ODF was –0.2 and the errors for the smoother textures were correspondingly smaller. A 'Monte-Carlo' approach was then applied to discretise the model textures into differently sized populations (representing the number of measurements that might be made in an EBSP texture determination). These discrete orientation values were assigned individual gaussian spreads (Φ) in the range 0° to 15° and the texture was then re-calculated by summation of these. Finally, the root mean square error was calculated from the differences between the original orientation densities and those re-calculated from the discrete orientation data.

Figure 2 (a)-(d) summarises results of the model calculation for four different sharpnesses of the starting texture. The first observation that can be made from these results is their confirmation that the error will always be least when the smallest gaussian spread is applied, provided that the number of measurements is sufficiently large. As the measurements become fewer the minimum error follows a locus where the optimum conditions move to higher values of the gaussian spread. If this spread is too small, oscillating densities arise associated with individual points that are not fully smoothed in the texture. This problem is most severe when the texture is weak. On the other hand, if the gaussian spread is too large, the texture becomes flattened and the errors then become most serious when the texture is sharp.

On the basis of these findings it is obviously not possible to make any universal recommendation regarding the ideal procedure to adopt when calculating an ODF from discrete orientation data. The more measurements the better and with this comes the possibility of improving the resolution of the technique. An approximate rule-of-thumb for typical commercial sheet products of cubic metals having well defined textures and assuming about 1000 grain orientation measurements suggests that the optimum gaussian spread value should lie in the range of 2-3 degrees.

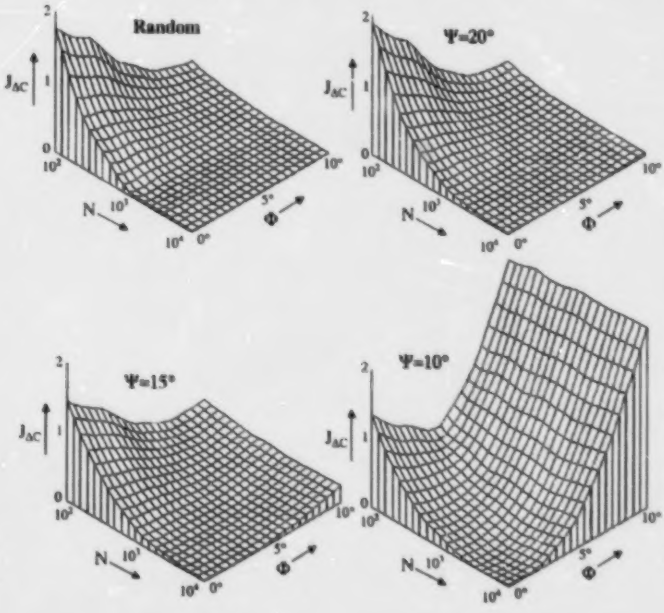

Fig. 2: Isometric plots showing the mean square error, J_{AC} of textures generated from N randomly distributed points using a Gaussian spread of Φ.

4 Comparison of experimental x-ray and EBSP textures

The authors have now several years' experience of measuring textures by EBSP as well as much longer acquaintance of the x-ray goniometer method. The latter has been adequately treated in the literature and we only recall here that there are many potential sources of experimental error and corrections which must be carefully controlled for the results to be accurate. A recent round-robin exercise revealed surprisingly large variations from the same specimens examined in different laboratories (Vatne et al. 1996). The variations were found to originate almost entirely from the x-ray diffraction measurements and not from the calculation of ODFs from pole figures.

The potential sources of error in EBSP measurements are much fewer. Most important here is to achieve a 'hit rate' as close to 100% as possible. False solutions of any EBSPs will naturally induce serious errors but so will the systematic omission of orientations giving weaker patterns or ones less easily solved by the software. For example, the sampling strategy has to handle objectively situations where the electron beam lands on a boundary between two grains without favouring some orientations more than others. It also requires the location of measurements (on an OIM grid, for example) to be representative of the texture of the material as a whole. In order to ensure that a sufficient number of grains are sampled in our work we have chosen the step length to be larger than the grain size of the material.

The example given here is that of a recrystallised IF steel containing a sharp <111>/ND fibre texture (γ-fibre). The same electropolished surface was used for x-ray measurements of {110}, {200} and {211} pole figures using CoKα radiation as for EBSP determinations based on more than 600 point measurements. ODFs were calculated with a value of $L_{max}=22$ with both even and odd texture coefficients. In the EBSP case, the value of the gaussian spread applied in the calculations was varied in the range 0° to 10°. Examples of $\phi_2=45°$ ODF sections according to the two methods are compared in Fig.3 (a) and (b) where the agreement is seen to be good. Notice also here the continuous form of the distribution of orientation density in Fig.3 (b) despite the fact that the calculations were based on 0° gaussian spreads (Dirac functions) of the measured EBSP data.

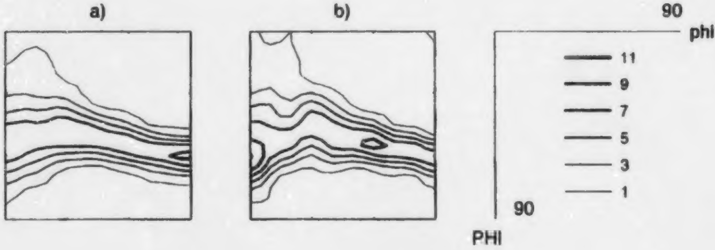

Fig. 3: ODF sections, $\varphi_2=45°$, showing texture determined with a) x-ray and b) EBSP using a Gaussian width of 0°.

Increasing the gaussian spread has a very evident effect on the sharpness of the resulting texture in this case. Plots of orientation density with varying Euler angle Φ ($\phi_1=0^\circ$, $\phi_2=45^\circ$) in Fig.4 show clearly how the texture becomes progressively flattened with loss of angular resolution. It is interesting (although perhaps fortuitous) that the curve for the x-ray diffraction measurements coincides quite closely with the EBSP results for a gaussian spread of about 4°. As remarked in section 1, this is close to the value of instrumental broadening inherent in the x-ray goniometer. It is therefore logical that the results should correspond to those of EBSP measurements when the same degree of instrumental broadening (gaussian spread) is applied to these data.

5 Conclusions

Traditional x-ray methods as well as newer discrete orientation techniques for determining textures introduce errors into the measurements. The closest approach to the true texture of a material should be via a technique such as EBSP provided that systematic errors are avoided and a sufficiently large number of grains are sampled. There is no lower limit to the sharpness which may be assigned to the individual orientations when synthesising the ODF.

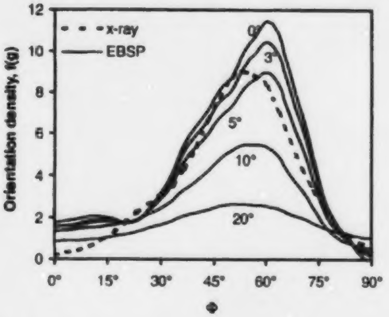

Fig. 4: Orientation density of texture determined with x-ray and with EBSP using different gaussian spreads around the individual orientations.

6 References

Baudin, T. and Penelle, R. (1993) Determination of the total texture function from individual orientation measurements by electron backscattering pattern. *Met. Trans.*, Vol. 24A, pp.2299-2311.

Bunge, H-J. (1982), *Texture Analysis in Materials Science*, Butterworths, London.

Bunge, H-J. (1996), Advanced experimental techniques for texture analysis materials in complex materials. Proc. ICOTOM 11, Ed. Z. Liang , Xi'an, China, pp.3-12.

Vatne, H-E., Oscarsson, A.,Engler, O., Weiland, H.., Reeves, A.., Bate, P., Van Houtte, P., Zeng, X.H., Johnson, C., Fundenburger, J.J., Zhou,Y., Fillit, R., Cerri, E. and Bunge, H-J. (1996), Results from a round robin test on textures measured by x-ray diffraction Proc.ICOTOM 11, Ed. Z. Liang, Xi'an, China, 1996, p.191.

Wagner, F., Wenk, H.R., Esling, C. and Bunge, H-J. (1981) Importance of odd coefficients in texture calculations for trigonal-triclinic symmetries. *Phys. Status Sol.* Vol. 67A, pp. 269-285.

Wright, S.I. and Adams, B. (1990) An evaluation of the single orientation method for Texture determination in materials of moderate texture strength. *Textures and Microstructures*. Vol. 12, pp. 65-64.

USING SETS OF INDIVIDUAL ORIENTATIONS FOR ODF DETERMINATION

S. MATTHIES and F. WAGNER
Laboratoire d'Etude des Textures at Application aux Materiaux, Universite' de Metz, Metz, France

Abstract

The exact linear 1/n dependence of the mean texture index is analytically proved for ODFs derived from n individual grain orientations. The practical application of this law, and terms like resolution power, reliability of ODFs, smoothing width, critical minimum number n_c a.o. are discussed and demonstrated.

Keywords : Individual orientations, ODF, minimum critical number, resolution power

1 Introduction

Applying the ODF f(g) to any problems in texture analysis it is tacitly assumed that this density of probability describes an infinite (or very large - sample representative) ensemble of grains. However, in practice ODF-related experimental data (pole figure or individual orientation measurements) represent only a limited number n of grains*.

The number n affects the statistical reliability of an ODF in any way derived from experimental data. The reliability is closely related to the real resolution power of the ODF, simply understanding resolution as a limit (given by an orientation distance) below which it makes no sense to consider any ODF details. The steps of a working grid in direct algorithms restrict the formally attainable best resolution Ω_{wg}. l-series truncations at l = L in the harmonic method lead to equivalent effects. The real resolution Ω that follows from a finite data set will as a rule be worse ($\Omega > \Omega_{wg}$).

A reasonable estimation of n, able to guarantee an asked resolution Ω was suggested by one of us (F.W.) already in the eighties. Dividing the volume of the orientation space 'G' ($8\pi^2$) by the volume of a sphere with radius $\Omega/2$ it follows $2\pi/[\Omega - 2\sin\Omega/2]$

---

* Below n always means grains of equal size. In case of a grain size spectrum each grain can be weighted by its relative volume in comparison with a grain of mean size. If N individual orientation data are used as experimental INPUT (got by a fine systematic measuring grid, with steps remarkably lower than the mean size of grains) n is to be interpreted as N/N_0 ,with N_0 - the order of measuring points per grain of mean size.

$\approx 48\pi/\Omega^3$ (for $\Omega<<\pi$) as a number of cells in G with equal volume. The required n_Ω will be in this order in case of random texture, supposing all cells will be occupied by one grain. It holds $\Omega(n_\Omega)$: 360°(1), 180°(6), 90°(40), 45°(314), 22.5°(2495), 10°(28374), and 5°(226930). Crystal symmetry (N_B - order of the rotation group G_B) and supposing a sample symmetry ($G_A \rightarrow N_A$) lowers the nonredundant 'elementary' region of the G-space, and n_Ω respectively by the factor $N_{AB} = N_A N_B$.

A strong texture can roughly be imagined as if the G-space consists of two parts, with volumes $V_0+V_1 = 8\pi^2$ and $f(g \subseteq G_0)=0$, $f(g \subseteq G_1)= 8\pi^2/ V_1$. Because there are not any grains within G_0, due to $V_1 \leq 8\pi^2$ the effective n_Ω will be lower than for the random case by the factor $1/(1+ V_0 / V_1)$. Also, if there is a great isotropic background 'phon' (e.g. min $f(g) = 0.5$) this part will remarkably influence n_Ω, despite the concrete texture character of the remaining half of the crystallites of the sample.

The above questions have been considered during the last years by many authors using numerical investigations with working grids and model distributions of certain texture type, or by sophisticated probabilistic approaches in order to get n_Ω, $\Omega(n)$ or reliability estimations, to verify estimating formulas, and to optimize experimental or calculating schemes. Cf. the proceedings of the last four ICOTOMs and of the texture conference in Clausthal 1997. All they confirm our simple, qualitative discussion.

2 The problem

The lack of such estimating formulas for practical application is, that they suppose at least some knowledge on the type of the required ODF. In the opposite case the sure estimation for random texture may lead to a too great n for the given sample. But commonly we are interested in a minimum of expensive single orientation measurements. I.e. the question is: when can we stop measuring an unknown sample?

Moreover, all estimating formulas describe the statistical mean behaviour of a great or infinite number of experiments with n grains. But in practice we have as a rule only one (!) try to determine (or for the inverse problem - to model) the ODF with a fixed quality by n single orientations. Like in Monte Carlo for a concrete experiment, the path through single events with a stochastic character, up to a sufficient result may need sometimes a remarkably lower or greater n than the mean n_Ω.

And at last, there is obviously a minimum number of grains, below that an ensemble of grains is not able to represent a given sample at all, even with a very bad resolution. How to detect the moment when this critical minimum number n_c is reached in a running experiment with an unknown texture? Obviously the answer must come from the individual experiment itself.

First published attempts to resolve this somewhat unorthodox situation have been done by the Aachen-Krakow collaboration [Pospiech et al. 1994]. It was suggested to consider the n-dependence of the squared difference between a known ODF $f_0(g)$ and its approximation $f_n(g)$ by n single orientation data

$$\rho_0(n) = 100\% \int_G (f_0(g)-f_n(g))^2 \, dg \Big/ \int_G f_n(g)^2 \, dg \qquad (1)$$

For increasing n by constant n-steps Δn ($n = n' + \Delta n$) $\rho_0(n)$ first rapidly decreases and then goes over into a plateau. This behaviour can be used to define a n_c-criterion. For an unknown sample $f_0(g)$ can be replaced by $f_{n'}(g)$ in (1) leading to a $\rho_{n'}(n)$ with similar properties. However, without going into details, from the results given below it can be deduced, that the statistically significant properties of $\rho_0\,(n)$ and $\rho_{n'}\,(n)$ will be seen only in a representation with always increasing n-steps.

In order to formulate a well-founded n_c-criterion, a sufficiently sensitive global characterization of an ODF has first to be found. As it turned out [Matthies and Wagner 1996] the well-known texture index 'F_2' can serve for this purpose. Considering its dependence on n, the open questions from above can be managed in an unexpectedly constructive way for practice. However, the analytic proof of the '1/n' key relation has not yet been published.

3 The linear 1/n dependence of the mean texture index

Introducing a working grid of M G-space cells at g_i,with $8\pi^2$-reduced volumes v_i, and correspondingly ODFs in form of staircase functions, we have (with $\Theta(g,gi) = 0$ for g outside the i-th cell and = 1 inside):

$$\underline{dg} = dg / 8\pi^2\,,\;\; v_i = \int_G \Theta(g,gi)\,\underline{dg}\;,\;\; \sum_{i=1}^{M} v_i = 1\,,\;\; f(g) \to \sum_{i=1}^{M} \Theta(g,gi)\,f_i\,, \tag{2}$$

$$\int_G f(g)\,\underline{dg} = 1 = \sum_{i=1}^{M} f_i\; v_i\,,\; F_m \equiv \int_G f^m(g)\,\underline{dg} = \sum_{i=1}^{M} \int_G \Theta(g,gi)\,(f_i)^m\,\underline{dg} = \sum_{i=1}^{M} (f_i)^m\; v_i \tag{3}$$

Representing n single orientations of equal weight (derived in an experiment with number k) in form of such an ODF, we will have ${}^k h_i$ 'hits' into the i-th cell and get:

$$\sum_{i=1}^{M} {}^k h_i = n \;\to\; \sum_{i=1}^{M} [{}^k h_i / (v_i\, n)]\; v_i = 1 \;\to\; {}^k f_i = {}^k h_i \;/ (v_i\; n) \tag{4}$$

$${}^k F_m = \sum_{i=1}^{M} ({}^k f_i)^m\; v_i = \sum_{i=1}^{M} ({}^k h_i)^m / (v_i^{m-1}\; n^m) \tag{5}$$

The ${}^k h_i$ and the value of the corresponding texture index ${}^k F_2$ are statistic quantities. Because n and M are finite numbers, the number $K_0 = M^n$ of all different possibilities k (to put n numbered marbles into M numbered boxes) is finite too. Therefore the mean value of F_2 and its variance can be given in an exact form by averaging (5) over all k, i.e. over all K_0 possible $(h_1, h_2, \ldots, h_M)$-sets

$$\overline{F_2} = \overline{\{{}^k F_2\}}^{K_0} \;\;;\;\; \sigma^2 = \overline{\{({}^k F_2)^2\}}^{K_0} - (\overline{F_2})^2 \tag{6}$$

Supposing an 'attracting power' $w_i = f_i\; v_i$ of the i-th cell the probability to get a set with h_i hits is described by (C - multinomial coefficients: $n! / [h_1!\; h_2! \ldots h_M!]$)

$$P(n; h_1,h_2, \ldots, h_M; w_1,w_2,\ldots,w_M) = C(n; h_1, h_2, \ldots, h_M)\; w_1^{\,h_1}\; w_2^{\,h_2} \ldots w_M^{\,h_M}\,, \text{ with} \tag{7}$$

$$\overline{\{1\}}^{K_0} = \sum_{h_1,h_2,\ldots,h_M=1}^{n} P(n; h_1,h_2, \ldots, h_M; w_1,w_2,\ldots,w_M) \cdot 1 = (\sum_{i=1}^{M} w_i)^n = 1^n = 1 \tag{8}$$

Substituting in (8) w_l by $(w_l\;\; y_l)$ and using the identity $h_l \equiv y_l \dfrac{\partial}{\partial y_l} (y_l)^{h_l} \,\Big|_{y_l=1}$ the mean for any polynomial terms like $h_l^{\,r}$, $h_l^{\,r}\; h_{l'}^{\,r'}$ ... arising in (6) or in expressions of higher order can be calculated.

Finally we have: $$\overline{F_2} \equiv F_2 + \frac{1}{M}(\underline{f} - F_2)\,[M/n] \qquad (\underline{z} \equiv \sum_{i=1}^{M} z_i) \qquad (9)$$

$$\sigma^2 = 4[F_3-(F_2)^2]/n+2[3\underline{f}^2-2F_2\,\underline{f}-6F_3+5(F_2)^2]/n^2+[\,\underline{f/v}-(\underline{f})^2-6\underline{f}^2+4F_2\,\underline{f}+8F_3-6(F_2)^2\,]/n^3 \quad (10)$$

Introducing the variable $x \equiv M/n$ the mean texture index $\overline{F_2}$ shows a linear dependence on x, with a slope that depends on the true ('unknown') texture and the structure of the working grid. For the random case ($F_2 = f_i = 1$) this slope $[1-1/M]$ is v_i-independent, but the variance σ^2 depends on the grid structure. Of course, for M=1 $\overline{F_2}=1$ and $\sigma^2=0$ follow. The expressions (9), (10) and the properties of higher moments ($m > 2$, cf. (3)) as well can be analysed in more detail. But for our purpose the most valuable point is the exact 1/n dependence of $\overline{F_2}$, i.e. the statistical ${}^kF_2(x)$ will show a linear decreasing tendency with decreasing x (increasing n).

Obviously it makes sense to represent a set of individual orientations in form of an ODF (even with a very poor resolution) only if such a comprehensive characterization of the ODF like the texture index has a meaning at all: i.e. if ${}^kF_2(x)$ does not fluctuate too strong in the actual x region and shows a relatively stable linear dependence with decreasing x . Once in the running experiment, with unknown texture, this region is reached, thus the n_c question ($n_c = M/x_c$) is answered*.

For $n \geq n_c$ from the asymptotic linear behaviour of ${}^kF_2(x)$ the true F_2 can now be approximated by F_2^{asy} - the value of the least square fitted ${}^kF_2(x)$-line at x=0 ($n \to \infty$). After F_2 is approximately known, the last open quantity of practical interest can be determined - the ODF resolution $\Omega(n)$ we have got in the running experiment with n grain orientations. Using for smoothing of ${}^kf(n;g)$ a bell-like curve $B(b;\omega)$, with halfwidth b, $\Omega(n)$ follows as the b that obeys the condition $F_2^{asy}(n) = {}^kF_2^{smooth}(b,n)$. Remaining fluctuations in ${}^kf^{smooth}(b,n;g)$ can subjectively be removed by 'filtering' operations as explained in [Matthies and Wagner 1996, Wagner et al. 1998], always keeping the texture index of the resulting ODF equal to F_2^{asy} .

4 Examples

The efficiency of applying the '1/n-law' as well as the correctness of the expressions (9) and (10) have been proved for model calculations and numerous EBSD data. Below some typical examples are given.

Fig. 1 shows the ${}^kF_2(x)$-path for two statistic sequences in the case of random texture. $F_2^{asy}(x)$ is based on the last ten ${}^kF_2(x)$-values for the fit of the 1/n-line. The 'normal' k_1-sequence lies inside the frame of 2 standard deviations ($S=\sigma$) with a slope close to 1. A sure detection of the random texture ($F_2^{asy} \approx 1$) will be able for $x \leq 5$, i.e. for $n \geq n_c = 15132/5 \approx 3000$ grains. Although the k_2-path lies beyond the 2S-boarder $F_2^{asy} \approx 1$ is stable already for 3 times less grains. Fig. 2 corresponds to a cubic/triclinic model texture with 3 Gaussian components in the $\varphi_1=0°$ section and a relatively high phon (0.4) that determines $x_c \approx 6$ in spite of the sharp components.

---

* **Remark**: for decreasing x by constant Δx steps, the number n of single orientations increases with always greater Δn steps. Also, if there are crystal or sample symmetries ($N_{AB} > 1$), for a correct use of equs. (9,10) M means the number of cells of the working grid in an elementary G-space region, with N_{AB} times greater v_i in the i-sums than for the asymmetric case ($N_{AB}=1$).

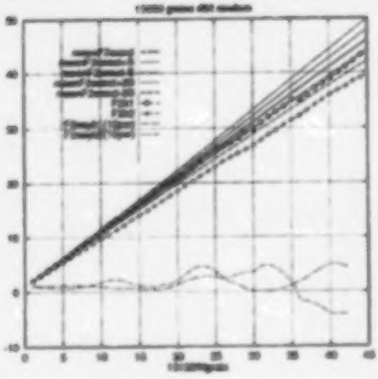

Fig. 1: $F_2(x)$ - random texture; $G_B=D_6$

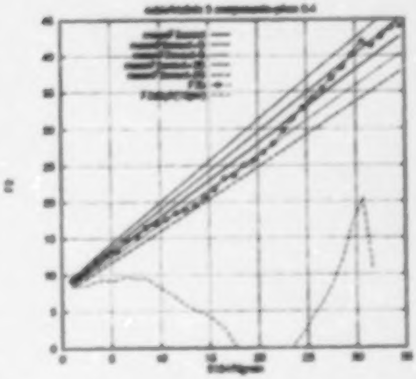

Fig. 2: $F_2(x)$ - 3 cubic components+phon

Compare slope and S with those in Fig. 1. Two φ_1 sections of the true ODF (Fig. 3a) as well as of ODFs calculated from single orientations under different conditions (Fig. 3b-d) are shown hereafter. From Fig. 2 $F_2 \approx 8$ is evaluated. Fig. 3b results from a calculation with n=16432 (x=0.31) and filtering; Fig. 3c is obtained by n=822 (x=6) and filtering, whereas Fig. 3d corresponds to the n=822 'hit-ODF' without filtering. The 'artifacts' seen in the $\varphi_1=25°$ sections in Fig. 3b,c result from accidental close hits in the phon region; c.f. the hit-ODF. For greater n their role decreases. If an ODF is approximately known artifacts can be lowered too using G-space region depending, variable smoothing widths, discussed by [Schaeben,1994] and [Schaefer, 1998].

Fig. 4 (Ti-sheet, $G_B=D_6$) is typical for a sharp texture without isotropic background. In this case n_c is in the order of 10000/25=400, much smaller than n_c=1000 or 3000 for the case of random texture in Fig. 1, with the same hexagonal crystal symmetry.

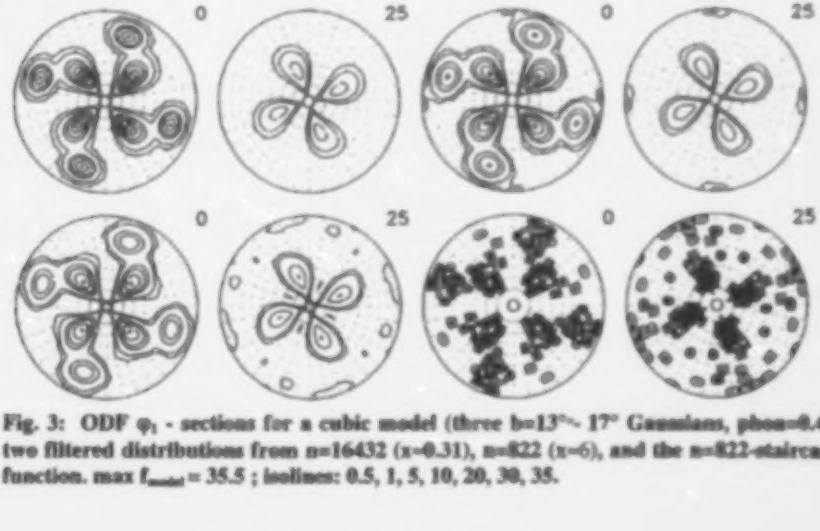

Fig. 3: ODF φ_1 - sections for a cubic model (three b=13°- 17° Gaussians, phon=0.4), two filtered distributions from n=16432 (x=0.31), n=822 (x=6), and the n=822-staircase function. max f_{model} = 35.5 ; isolines: 0.5, 1, 5, 10, 20, 30, 35.

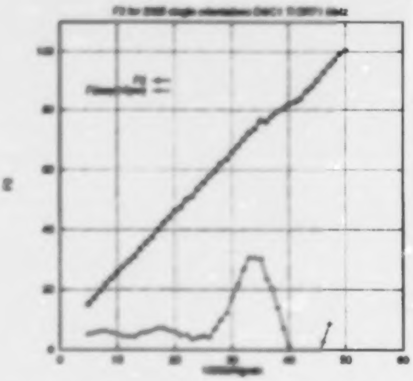

Fig. 4: $F_2(x)$ - sharp texture; $G_B=D_6$

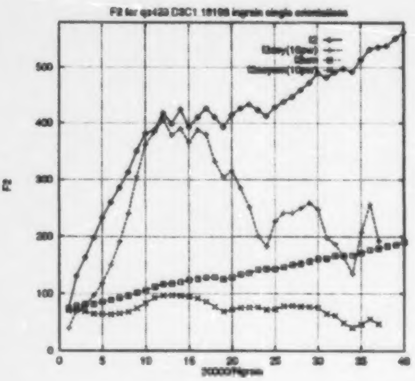

Fig. 5: $F_2(x)$ - grid steps lower grain sizes

Fig. 5 (quartz sample with a strong texture and less than 1000 covered grains) demonstrates a situation for fine, systematic grid data (cf. the Introduction-footnote). For correlated data (many consecutive measured points belong to one grain) the statistic conformities are disturbed, as seen in the two upper curves. Many times randomly rearranging the order of the given 18198 single orientaton data an other equivalent data set (cf. the equal f2 and f2um values at n=18198) was created. For it the lower curves indicate an F_2^{exp}-convergence for already about thirty times less orientation data. This situation would appear for a coarser measuring grid or by a stochastic scanning of the same sample area.

Summarizing it can be stated, that the presented 1/n-law can be an usefull tool for the inspection of the quality of modeling ODFs by single orientations, for the determination as well the analysis of individual orientation data in form of ODFs, and for the optimization of their measurement.

5 References

Matthies, S. and Wagner, F. (1996) On a 1/n law in texture related single orientation analysis. *physica status solidi (b)* Vol. 196, pp. K11-15.

Pospiech, J., Jura, J. and Gottstein, G. (1994) Statistical analysis of single grain orientation data generated from model textures. *Materials Science Forum* Vol. 157-62, pp. 407-12.

Schaeben, H. (1994) Exploratory orientation data analysis: Kernel density estimation and clustering. *Materials Science Forum* Vol. 157-62, pp. 431-38.

Schaefer, B. (1998) Sampling error of texture approximation by individual orientation measurements. *Materials Science Forum* Vol. 273-75, pp. 99-106.

Wagner, F., Matthies, S. and Van Landuyt, O. (1998) Processing individual orientation data to calculate ODFs. *Materials Science Forum* Vol. 273-75, pp. 89-98.

Reproducibility of Experimental Texture Measurement

D. JUUL JENSEN and M.T. LYTTLE

Materials Research Department, Risø National Laboratory, DK-4000 Roskilde, Denmark

Abstract

The reproducibility of neutron texture measurements at Risø is reported. The texture of a rolled aluminium sample has been determined repeatedly over both a short time interval - 24 hours - and over a long time period - 5 years. Five different typical texture representation methods are used for data analysis. Deviations smaller than 1% are found over the short time interval whereas larger deviations are found over the 5 year time period. Depending on the applied texture representation methods these long time deviations are in the range 1-13%. Effects of applying the different representation methods are discussed.

Keywords: Reproducibility, neutron diffraction, volume fraction, peak intensity, integrated intensity, M-factor

1. Introduction

In several round robin tests it is found that there can be large variations in the measured textures, see for example previous ICOTOM proceedings (Wenk et al, 1988a and Vatne et al 1996). Origins for such variations may be classified into 3 types relating to:

1) Different analysis methods: For ODF calculations, for example, ambiguity of up to 30% is typical (Wenk et al 1988b). Corrections for negativity may improve this, but there is no general agreement on how this is best performed. Also for calculations of volume fractions of given texture components, a variety of methods exist which give significantly different results.

2) Different experimental techniques: Different laboratories typically use different texture measuring procedures and different diffraction sources (e.g. neutron, x-rays). Also different data corrections (e.g. defocusing, background and absorption corrections) may contribute to the difference in results.

3) In-house scatter: Even repeated measurements in one laboratory may show scatter due to simple counting statistics and to smaller variations in experimental set up between measurements (for example, change of alignment or change of x-ray anode).

The focus has generally been on the first 2 types. However, type 3 variations can also be quite significant and should of course be considered when effects of type 1 and 2 variations are discussed in round robin tests.
For x-ray texture measurements, it is stated that the accuracy of pole figure measurements is ± 10% (Engler et al 1993). In the present paper the reproducibility of neutron diffraction texture measurements at Risø is reported - i.e. the "in-house scatter" (type 3 above) is documented. Results for multiple measurements of two different samples are given. Data obtained from repeated measurements (over a period of 24 hours) and data obtained over a 5 year period are given. No sample change or instrument realignment are done during the 24 hour period, whereas the sample, of course, has been remounted several times during the 5 year experiment. The obtained accuracy for five different data representation methods are discussed.

2. Experimental

2.1. Set-up

The experimental set-up is sketched in Fig 1. It is a fairly typical set-up for neutron texture measurements except for the detector which is a linear position sensitive detector. The detector is placed with its axis vertical to record diffracted intensities along a Debye Scherrer ring. For a thorough description of the instrument see (Juul Jensen and Kjems 1983). The demand for performing texture measurements at Risø does not justify having a neutron beam line dedicated to texture. The texture instrument is therefore assembled and installed on the beam line only when there is a need for texture measurements which is typically about 3 months per year. In the remaining 9 months the beam line is used for other types of experiments. In practice this means that before each series of texture measurements, the graphite monocromator crystal (see Fig. 1) has to be mounted, the Euler goniometer has to be attached to the sample-column and the detector in its shielding has to be coupled to sample-column. After that, alignment and calibration are performed. Alltogether this may introduce some extra experimental uncertainty compared to a permanent instrument.

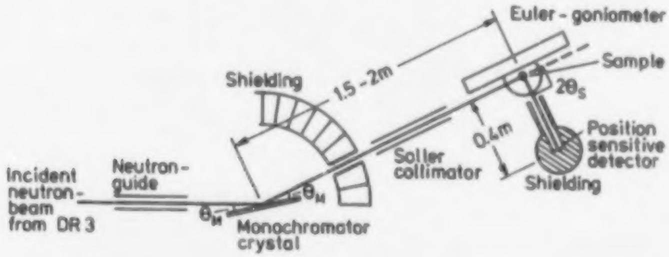

Fig. 1: Sketch of the experimental set-up in the horizontal plane (Juul Jensen and Kjems 1983).

2.2 Samples

For the calibration of the instrument, two samples have been used for more than 10 years. One sample is 90% cold rolled aluminium (AA1050) which has a typical medium strong rolling texture. The other one is an annealed copper sample, which has a very peculiar texture with many local maxima. The Al sample in used for a full texture analysis whereas only the (200) pole figure is measured for the Cu sample to check if the peak positions are correct. During the last 5 years a μ-VAX system has been used for data collection and the calibration data has been stored. So for the present work a long term evaluation of experimental accuracy is possible based on the Al data.
For evaluation of short term (24h) accuracy the Al sample described above is used together with another aluminium (AA1050) sample. The latter sample is recrystallized and has a nearly random texture. This allows an evaluation of accuracy also for very weak textures.

2.3 Data representation

When textures are reported in literature, many different representations are used, for example pole figures, ODFs, skeleton lines, C coefficients and volume fractions of main texture components. To get detailed information about how the experimental accuracy affects the texture, five different representations are used in the present work: Two relating to pole figures: i) normalized intensities at a point in the pole figure and ii) integrated normalized intensities over a selected region in the pole figure. Two relating to ODFs: i) peak intensity in a selected point on the skeleton line and ii) volume fraction of the S {123}<634> component). Finally, M factors are calculated which in a way represents the accuracy in the C coefficients.
The M-factors are calculated based on the Taylor deformation model assuming minimum deformation work for tensile deformation. The M-factor is calculated for 2 directions; along the rolling and the transverse directions. For further details see e.g. (Juul Jensen and Hansen 1990).
The volume fraction of the S component is calculated simply by integration over 15° around the S position in the ODF. The peak intensity in the ODF is taken at the Cu {112}<110> end of the skeleton line at $\varphi_2 = 45°$ and near $\varphi_1 = 90°$, $\phi = 35°$.
In the pole figure it is chosen to integrate over an area near the cube {100}<001> orientation in the (111) pole figure for α and β in the range 35-55°. The intensity at a point is the (111) pole figure is taken at $\alpha = 25°$ and $\beta = 0°$. This is near the Cu {112}<110> orientation.

3. Results and discussion.

In total, the texture of the 90% cold rolled aluminum sample has been measured 17 times during the time period from October 1994 to April 1999. During the 24 h experiment the texture of this sample was measured 12 times without remounting the sample or touching the experimental set-up. This latter experiment was also done for the aluminum sample with an almost random texture.
For each series of measurements and for each data representation method, the mean value and the standard deviation was calculated:

$$S = \sqrt{\frac{\Sigma(xi - \bar{x})^2}{n - 1}}$$

where xi are the i individual measurements, $\bar{x}$ is the mean value and n is the number of measurements (17 or 12 for the long and short time experiment, respectively).

3.1. 5 years' measuring period

The experiment results are shown in Figs. 2-4 and the calculated standard deviations are given in Table 1. As expected, the largest deviation is found for the normalized intensity taken at a point in the pole figure (Fig 2a). Here the average value is 4.7 and the standard deviation is 0.6. This type of data representation is very sensitive to sample alignment. Standardly the samples are mounted with the normal direction (ND) vertical and the rolling direction (RD) towards the detector. Whereas it is straight forward to set ND correctly as the sample is just fixed with the rolling plane to a flat surface sample holder, it is more problematic to align RD as precisely. A misalignment of x degrees of RD simply means that the measured pole figures are rotated x degrees around ND. By using the symmetries of standard pole figures this is easily corrected for, however, in the present analysis no correction of such a possible RD misalignment is done. If the correction was done the observed standard deviation would be reduced.

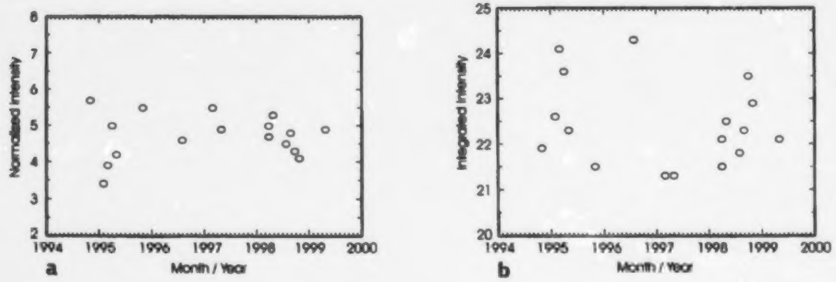

Fig. 2: Reproducibility over a 5 year period of normalized intensities in the (111) pole figure. a) normalized intensities at α=25° and β=0°, b) integrated normalized intensities over the range 35-55° for both α and β.

TABLE 1. Standard deviations (in brachets reported in % of the mean values) for the different types of texture representations for the 5 year and the 24 hour measuring periods. The second line for the 24 h experiment reports results for the almost random texture sample.

Exp.	No. of measure-ments	Pole figure		ODF		M-factor
		Peak	Integrated	Peak	Integrated	
5 years	17	0.6 (13%)	0.9 (4%)	0.7 (7%)	1.2 (2%)	0.01 (<1%)
24 h	12	0.07 (1%)	0.3 (1%)	<0.1 (<1%)	<0.5 (<1%)	<0.005 (<1%)
	12	0.04 (6%)	0.2 (1%)	<0.1 (<1%)	<0.5 (<1%)	<0.005 (<1%)

The smallest deviation is for the M-factors. Here average values are found to be 3.097 and 3.218 along RD and TD, respectively, and the standard deviations are 0.013 and 0.008. The M-factors are calculated based on the C- coefficients and it is obvious that these coefficients give a good and precise description of the texture.

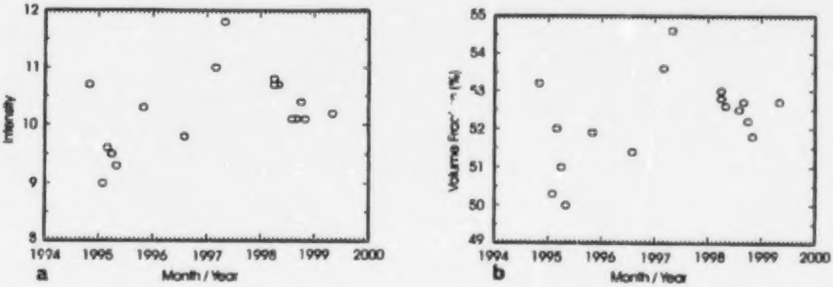

Fig. 3: Reproducibility over 5 year period of intensities in the ODF. a) peak intensities at the Cu {112}<110> end of the skeleton line. b) volume fractions of the S {123}<634> component.

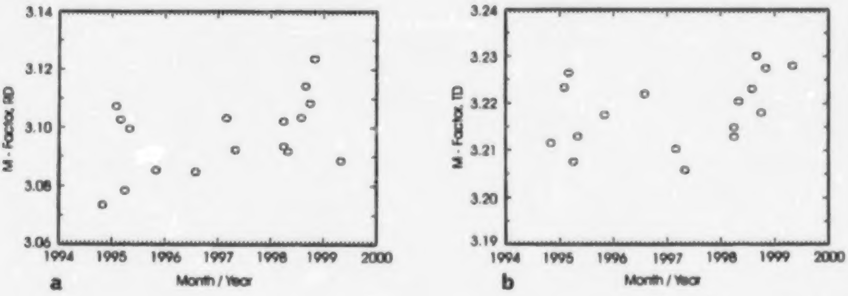

Fig. 4: Reproducibility over a 5 year period of Taylor M-factor. a) along RD. b) along TD.

3.2. 24 hour measuring period.

The experimental results for the pole figure data representations are given in Fig 5 and in Table 1. For both samples – the one with the medium strong rolling texture and the one with the very weak almost random texture - it is found that there are practically no variations between the measurements. This is the case even for the most sensitive data representations methods: a single point in the polefigure (see Fig 5a). For the sample with an almost random texture, the standard deviation of the pole figure intensity is 0.04. As the average intensity for this sample is low (0.725) the standard deviation expressed in percent of average value may seem somewhat large (6%). However a standard deviation of 0.04 in normalized intensity in a pole figure must be considered to be very precise.

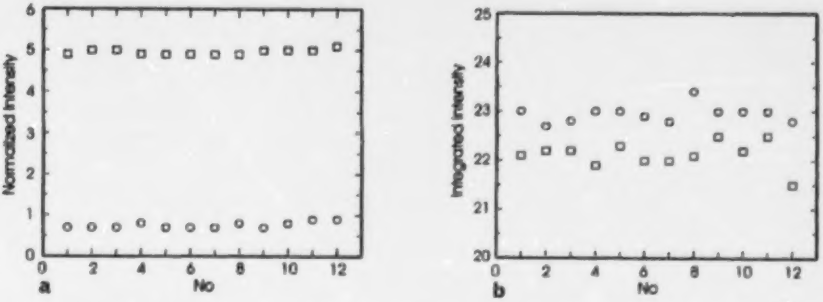

Fig. 5: Reproducibility over a 24 hour period. The square and circular symbols are for the sample with a rolling texture and a nearly random texture respectively. a) norma-lized intensities at $\alpha = 25°$ and $\beta = 0°$, b) integrated normalized intensities over the range 35 - 55° for both α and β.

4. Conclusions and recommendations

Repeated measurements of the texture of *one* sample in *one* laboratory do reveal variations which, depending on the data representation form, can be significant.
Neutron diffraction texture measurements of a cold rolled aluminium sample at Risø show that repeated measurements without interruption, sample remounting or instrument changes give very reproducible results with deviations of 1% or less. For repeated measurements over a 5 year period larger deviations are, however, observed. The standard deviations are here found to be in the range 1-13% for the selected texture representation methods. It is recommended that each texture laboratory performs a reproducibility analysis, and that the observed in-house variations are considered in round-robin tests between different laboratories or between different measuring techniques. Among the selected texture representation methods, the Taylor M-factors calculated based on the C-coefficients are observed to have the least variation. The C coefficients can be a good choice to use when textures are to be exchanged or compared between laboratories.

References

Engler, O., Palacios, J., Schäfer, W., Jansen, E., Lücke, K. and Will, G. (1993), *Textures and Microstructures* Vol. 21, pp. 195-206.

Juul Jensen, D. and Kjems, J.K. (1983), *Texture and Microstructures* Vol. 5, pp. 239 251.

Juul Jensen, D. and Hansen, N. (1990), *Acta mater.* Vol. 8, pp. 1369-1380.

Vatne, H.E., Oscarsson, A., Engler, O., Weiland, H., Reeves, A., Bate, P.S., Houtte, P.V., Zeng, X.-H., Johnson, C., Fundenberger, J.J., Zhou, Y., Fillit, R., Cerri, E. and Bunge, H.-J. (1996), Proc. ICOTOM 11, (eds. Z. Liang et al) Int Acad. Publ., pp. 191-196.

Wenk, H.-R., Kern, H., Pannetier, J., Höfler, S., Schäfer, W., Will, G. and Brokmeier, H.-G. (1988a), Proc. ICOTOM 8, (eds. J.S. Kallend et al.) TMS, pp. 229-234.

Wenk, H.-R., Bunge, H.J., Kallend, J.S., Lücke, K., Matthies, S., Pospiech, J. and van Houtte, P. (1988 b), Proc ICOTOM 8, (eds. J.S. Kallend et al.) TMS, pp. 17-28.

ADVANCEMENTS OF ACOM AND APPLICATIONS TO ORIENTATION STEREOLOGY

R.A. SCHWARZER

TU Clausthal, D-38678 Clausthal-Z., Germany

Abstract

A noticeable advancement in spatially resolved diffraction analysis has been made by the development of *A*utomated *C*rystal *O*rientation *M*easurement (*ACOM*) from *K*ikuchi *P*atterns (B*KP* in the SEM, also named EBSP, and T*KP* in the TEM). Stereological as well as orientation data, as sensitive indicators of the production process and use of a material, are readily available at the same time from crystal orientation maps. The principal objectives are a quantitative representation of the microstructure on a grain-specific level by the determination of crystal orientations, misorientations, the character of grain boundaries, or derived entities. They are commonly depicted in pseudo-colors on the scanning grid to form crystal orientation maps or "images" of the microstructure.

At present 25,000 grain orientations or more are acquired per hour with the ORKID program on an SEM JSM 6400 with digital beam scan. The reliability of orientation measurement depends sensitively on the number and accurate position of the extracted bands used for indexing, the knowledge of the pattern center and the beam spot-to-screen distance. For digital beam scan, dynamic focusing of the SEM as well as dynamic pattern calibration are indispensable. If intragranular structure is not considered, mesh refinement may be used to speed up measurement. The limitations of video-based acquisition of diffraction patterns are discussed.

Keywords: Backscatter Kikuchi diffraction (BKD), Electron BackScatter diffraction (EBSD), ACOM, orientation stereology

---

Authors' address:
Prof. Dr. Robert Schwarzer, AG Textur, TU Clausthal, D-38678 Clausthal-Zellerfeld
Email: schwarzer@tu-clausthal.de

1. Introduction

Modern electron diffraction methods enable local texture and point-to-point orientation correlations to be determined routinely. *B*ackscatter *K*ikuchi *D*iffraction (BKD) in the SEM is the most common technique because of the wide availability of SEM and simple preparation of bulk specimens. For an overview the reader is referred to (Randle 1992; Schwarzer 1997a). *A*utomated *C*rystal *O*rientation *M*easurement/*M*apping (ACOM) with digital beam scan in particular has evolved as a convenient alternative to x-ray pole figure measurement. ACOM in the SEM enables, as major benefits, a fast study of selected small areas of any shape and the construction of the complete ODF (Bunge 1982) without suffering from ghost problems, defocusing effects or inconsistent x-ray diffraction data as a consequence of specimen tilts through large angles when acquiring pole figures. ACOM is, however, limited to materials with grain sizes larger than a tenth of a micron, low to medium local strain, high electrical conductivity and a rather plane surface which has to be free from foreign layers. *T*ransmission *K*ikuchi *D*iffraction (TKD) is not subject to these limitations. With a medium voltage TEM the cumbersome preparation of transparent samples is much alleviated because materials more than one micron thick can be studied with Kikuchi diffraction (Schwarzer 1997b).

2. The fully automated acquisition and interpretation of Kikuchi patterns

The geometry of Kikuchi patterns is unique for a particular crystal structure and crystal lattice orientation. It is sufficient for indexing to know the positions of some bands rather than their accurate intensities. In present ACOM systems the automated extraction of band positions from digitized Kikuchi patterns has replaced interactive measurement by the operator except for system calibration or superimposed patterns. Radon transforms $R(\rho, \varepsilon)$ (Natterer 1986) are applied to the digital, background-corrected gray-tone pattern $f(x,y)$

$$R(\rho,\varepsilon) = \iint_{-\infty}^{\infty} f(x,y)\,\delta(\rho - x\cos\varepsilon - y\sin\varepsilon)\,dx\,dy$$

which transform all points (x_i, y_i) on a Kikuchi line into a single point (ρ_i, ε_i) in Cartesian Radon space. ρ is the distance of the line from the origin, and ε is the angle between the x axis and the perpendicular to the line from the origin. The number of image points of the standard video frame is usually reduced by binning, in order to save computation time. The positions of bright and dark Kikuchi lines, respectively the band edges, are detected separately as bright peaks in an R^+ and cusps in an R^- Radon space, respectively (Schwarzer and Sukkau 1998). The binary version of the Radon transform for straight lines is also known as Hough transform. A modification for BKD has been developed in a thorough investigation by (Krieger Lassen 1994). Band profile analysis may be performed, as an additional option, in the original pattern with high pixel resolution along a small strip enclosing the particular band. Its spacing, the band width, yields the Bragg angle, and the center line of the band corresponds to the (imaginary) section line of the diffracting lattice planes with the screen. The so located bands are sorted according to their intensities and widths. Indexing is based on the comparison of measured interplanar angles (which correspond to the angles between the Kikuchi bands) and interplanar spacings (which are reflected by the band widths) with theoretical values calculated for the actual crystal structure.

Typically the positions of the 5 to 10 smallest and most intense bands are passed to the indexing routine. Consideration of the first 3 to 4 families of {hkl} planes is usually sufficient for indexing a backscatter Kikuchi pattern uniquely thanks to its large angular range. Reference directions in the specimen space (e.g. specimen normal direction, transverse direction in the specimen surface) are finally indexed, and the crystallographic orientation of the grain is described either in (hkl)[uvw] notation, by three Euler angles, (φ_1, Φ, φ_2), or the rotation matrix, **g**, which transform the specimen coordinate system under consideration into the crystal-fixed coordinate system. A simulated Kikuchi pattern to this solution is finally displayed on the monitor for comparison.

3. Automated crystal orientation measurement (ACOM)

An ACOM system requires unattended pattern acquisition point by point on a predefined raster grid across the specimen surface, indexing and storage of orientation data. Scanning can be performed either by translating the specimen in x and y direction with a computer-controlled high-precision specimen stage with respect to the stationary primary beam (Adams et al. 1993), or by moving the primary beam spot, step by step under digital computer-control, across the stationary specimen surface in a similar way as in conventional scanning electron microscopy (Kunze et al. 1994). The measured spots may constitute some clusters of individual points, a dotted line or a raster field on the specimen surface. Advantages of mechanical specimen translation are the accommodation of large measured fields and the stationary diffraction geometry and hence a less elaborated software. Digital beam scan, on the other hand, enables an extremely high speed as well as precision in locating the measured place. It is cost-effective and not susceptible to trouble. Since the beam spot is traveling across the specimen surface, the diffraction geometry is changing from place to place as does the pattern center on the screen. Therefore the system has to be calibrated automatically from spot to spot ("*autocalibration*" in the ORKID system (Schwarzer 1997a)), otherwise errors in calculated grain orientations may exceed several degrees, or indexing may fail on the whole, in particular at low magnifications. A simple test on accuracy can be made by measuring across a large field on a single crystal and checking the uniformity of orientation data.

Two more difficulties with digital beam scan have to be solved by the software: As a consequence of the steep forward scattering of electrons, the specimen surface has to be steeply inclined at typically about 20° to the primary beam in backscatter diffraction in order to generate a Kikuchi pattern of sufficient intensity. When scanning down the specimen line after line the primary beam spot runs out of focus such that spatial resolution is severely decreased. This holds true for low as well as high magnifications since the requirements of high resolution scale, needless to say, with useful magnification. *Dynamic focusing under computer-control* has been implemented in the ORKID program (Schwarzer 1997a) since some SEM hardware appliances for dynamic focusing do not accommodate steep sample tilts nor video cameras placed away from looking on the standard stage tilt. Secondly, conventional SEM images and crystal orientation maps are markedly foreshortened due to the steep specimen tilt. Spatial resolution is reduced in that direction to the same extent. Therefore allowance has to be made for this image distortion in quantitative stereology either by using different length scales for x and y or by stretching out the foreshortened image.

Digital beam scan in our system is performed by applying the scanning signal to the built-in deflection coils through a 12 Bit digital-to-analog converter. The fine raster grid consisting of 4,096 by 4,096 image points enables a very precise positioning of the measured spots on the tilted specimen surface. Since image resolution depends on the size of the beam spot rather than on the actual magnification, a high spatial resolution is enabled, irrespective of low magnification, such that two distant surface regions may be imaged in a sequence without having to translate the sample. In addition to beam scan, the ORKID software controls the mode of SEM operation (imaging or spot mode), final lens current settings ("dynamic focus"), magnification, accelerating voltage, and pattern acquisition (Figure 1).

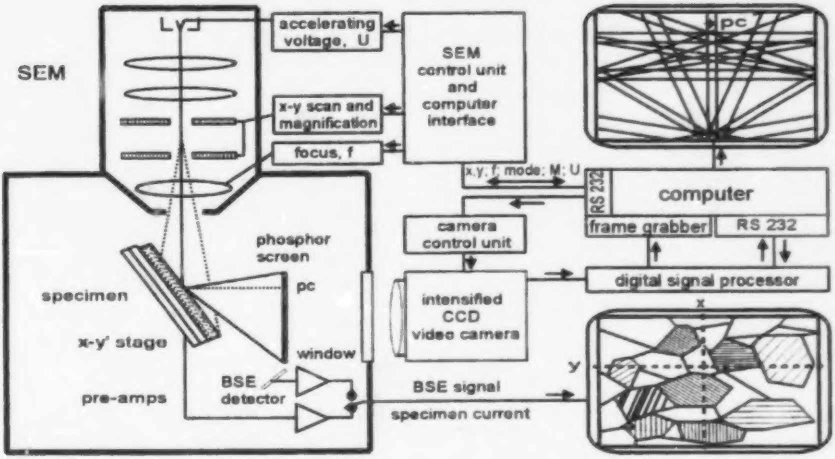
SEM
accelerating voltage, U
SEM control unit and computer interface
x-y scan and magnification
focus, f
x,y; f; mode; M; U
RS 232
computer
frame grabber
RS 232
pc
camera control unit
phosphor screen
pc
specimen
x-y' stage
window
intensified CCD video camera
digital signal processor
x
y
BSE detector
pre-amps
BSE signal
specimen current

Figure 1 The schematics of a modern ACOM system.

A high speed of measurement is not only a value by itself in that the cycling time of the SEM is improved, but is indispensable for dynamic experiments (e.g. *in situ* tensile and bending test or hot stage experiments). For this purpose a set of individual spots, such as in the vicinity of triple points, rather than a regular raster field on the specimen can be selected for repeated measurement. A short time of measurement will also alleviate some difficulties with long-term stability of the SEM. At present more than 25,000 orientations are acquired unattendedly under favorite specimen conditions (e.g. a low-deformed Cu or Ni specimen at 20 keV accelerating voltage) with a Pentium II 400 MHz PC. About 10,000 orientations more were feasible if synchronization delays of the CCD camera and the frame grabber had been solved. In addition mesh refinement has been implemented in ORKID: In a first step a coarse raster grid is scanned. If intragranular structure is of no concern, it is in principle sufficient to measure the orientation of each grain only once. Hence a refined mesh is overlaid in a second and third run, and only those grid positions are measured where orientations between coarse nodal points differ more than a chosen value. Hence the refined mesh measurements in the following passes are concentrated along grain boundaries.

4. Improved ACOM hardware

The digital image is the only source of information for pattern recognition. Software can correct for poor image quality or distortions only to some extent. Hence important consideration has to be spent on the appropriate choice of optics. Almost all current ACOM systems have moved to video cameras with solid-state sensors, either to integrating or to intensified CCD cameras. They are economic, and the sensor geometry is fixed without producing undue distortions nor "blooming" or burn-in of bright spots as has been the case with former vacuum tube sensors. Video standards (RS-170 in USA, respectively CCIR in Europe), however, have been developed for broadcast television and surveillance applications to provide pleasing pictures rather than images for precision measurement. Interlaced scanning, transmission of the lines as analog signals and finally the resampling of each line into digital pixels by the frame grabber require precise synchronized timing of the camera and the frame grabber. Image quality is degraded markedly by these operations, in particular as a consequence of the limited bandwidth of video transmittance, unnecessary DA and AD conversions, noise pick-up, pixel jitter and camera anamorphism. Some of these problems may be overcome by a synchronous analog system, but digital cameras with pixel synchronous transmission only will provide optimum pattern quality. A high performance image acquisition system is in particular a prerequisite for high-speed ACOM. Standard video systems are based on 30 Hz frame rate (respectively 50 Hz in Europe). ACOM at video speed, however, seems not yet feasible in near future, although a single image frame is often sufficient for orientation measurement with a well-designed system. There is still some delay by synchronizing the frame grabber on the camera and waiting for completion of a running frame. Cameras with built-in image store and read-out of the pattern on demand will meet this requirement. Peltier-cooling of the sensor chip or the photocathode of the image intensifier, in order to reduce noise, is ineffective at these short exposures. Some emphasis has to be laid on the light optics. A high-quality macro lens with a small f/number (large aperture, "fast lens") is a good choice. Bright phosphors and reduction of light losses by absorption or spurious reflections are essential. Sensitivity of the acquisition system can be almost doubled, at the extent of high costs and practical inconvenience, by coupling the CCD sensor with a (tapered) fiber optics to the phosphor screen. The highest efficiency is expected from on-chip deposition of the phosphor or direct exposure of the sensor chip to the pattern forming electrons.

High spatial resolution requires an intense primary beam spot as well as a small interaction volume of the primary electrons beneath the specimen surface. The latter can be reached only by lowering the accelerating voltage considerably from about 20 kV as in present systems with a tungsten filament to less than 5 kV. A high beam current in small spots at low accelerating voltages is the domain of field emission SEM. Drawbacks are the liability to magnetic stray fields (hence a small working distance is mandatory which may conflict with the design of current pattern acquisition systems) and the low efficiency of present phosphor screens at low electron energies. An LaB_6 emitter is a good compromise for spots down to about 0.05 µm diameter.

A great challenge of ACOM is the study of low-conductive surfaces such as minerals, geological samples, hard coatings, integrated circuits with dielectric layers, specimens with non-metallic inclusions, or embedded samples. There are several experimental techniques available which either intend to reduce the resistance of the specimen, to reduce the probe current density, to increase the secondary electron emission coefficient or to compensate for the surface charge (Schwarzer 1994). Charging problems are alleviated to some extent by the steep inclination of the specimen surface to the beam. A conductive coating with carbon - not to say gold or heavy metals - as in conventional SEM surface imaging, however, is prohibitive since any foreign layer degrades pattern quality significantly, as a consequence of the low information depth in backscatter Kikuchi diffraction. Low-vacuum SEM (LV SEM) is a convenient means to suppress specimen charging. Excessive scattering of the pattern forming electrons on their path to the phosphor screen, however, is an effect of low-vacuum adverse to backscatter Kikuchi diffraction since a blurred pattern may result. Hence the shortest possible specimen-to-screen distance and a high accelerating voltage are mandatory to reduce undue scattering of the pattern forming electrons in LV SEM. With decreasing specimen-to-screen distance, a larger angular section of the Kikuchi pattern is captured such that the travel of the pattern center with digital beam scan results in a larger deviation of the reference direction from the screen center position. Hence continuous pattern center calibration, as in the ORKID program, becomes indispensable for correct orientation measurement. ACOM measurements have been performed routinely up to 50 Pa pressure with a Hitachi S-3500N, but a pressure of a few Pa is already sufficient for most specimens (Rohde 1999).

5. The evaluation of grain orientation data

The meso- and microstructure of a polycrystal is described by the distributions of size, shape, arrangement, orientation and defects of its constituent grains and phases in three-dimensional space. A mathematical quantification of this state is given by the microstructure function (also named aggregate function)

$$G(x) = \begin{cases} i(x) & \text{phases} \\ \mathbf{g}(x) & \text{orientations} \\ S(x) & \text{defects} \end{cases}$$

which specifies the phases i, the crystal orientations **g** and the lattice defects S in the volume elements at positions x in the specimen (Bunge 1994, 1999). $x = \{x_1, x_2, x_3\}$ are the spatial coordinates, $\mathbf{g} = \{\varphi_1, \Phi, \varphi_2\}$ the orientation parameters, $S = \{s_1, s_2, \ldots, s_n\}$ the substructure parameters, and $i = \{ i_1, i_2, \ldots, i_n\}$ the phases which are characterized by their crystal lattice and element composition. It is a unique feature of ACOM that this technique enables the acquisition of the microstructure function at a high spatial resolution with reasonable effort. Scanning across the specimen surface in a raster grid yields two spatial coordinates $\{x_1, x_2\}$ of the measured site. The third dimensional coordinate $\{x_3\}$ can be obtained in principle by consecutive sectioning. The grain orientation, **g**, is the prime objective of ACOM and readily available along with $\{x_1, x_2\}$. Phases are described by their crystal lattice. The ORKID system enables the discrimination of six crystal lattices for each pattern in one pass. Additional information about the local element composition, e.g. from a simultaneous EDS analysis, may be helpful to rule out less likely phases in advance. The diffuseness of a pattern is a (qualitative) measure of local dislocation density and lattice strain.

In the simplest case, that is a single phase material without considering the grain substructure, the microstructure function G(x) still depends on six coordinates that are the three spatial and the three orientation parameters. They make up a six-dimensional space which is almost beyond imagination. So a split was made in traditional materials science by either emphasizing the morphology of microstructure or the density of grain orientations. Two branches of science developed almost without mutual interaction:

- *Stereology* or *Quantitative Metallography* which is based on microscopy techniques to reveal the morphology and phases with omission of the grain orientations.
- *Crystal Texture Analysis* which until recently was based on pole-figure measurement by diffraction methods without considering the spatial coordinates.

With the availability of ACOM the route is now open to a comprehensive "orientation stereology" by merging both aspects of microstructure (Bunge 1994).

Depending on the application at issue, several special functions may be derived from the universal microstructure function G(x) which are either sections through the six-dimensional space or integrals of it (Bunge 1999). The grain orientation database from ACOM (which constitutes the raw material of the microstructure function G(x)) is used in supplementary programs (Schäfer 1998) for the calculation of the orientation density function (ODF), $f(\mathbf{g})$, pole figures, misorientation distribution function (MODF), orientation correlation functions, texture fields and tensorial materials properties (Bunge 1982). A clear graphical representation of the microstructure is obtained by constructing *C*rystal *O*rientation *M*aps (COM) (Gerth and Schwarzer 1993; Springer 1998). Hereby the measured grid points are stained by colors specific for the crystal lattice orientations or misorientations thus revealing the grain morphology or grain boundaries, respectively. Orientation parameters in crystal orientation maps may be two crystallographic directions (hkl)[uvw] for two sample reference directions, the Euler angles (φ_1, Φ, φ_2), or the Rodrigues vector $\mathbf{R}$. Grain boundaries are commonly marked by the Rodrigues vector, $\mathbf{R}$, the axis-angle parameters of the misorientation, $\Delta\mathbf{g}$, or the Σ character according to the CSL model. Other local properties or parameters can be represented graphically by color maps, such as dislocation density, the predominant glide systems or twin systems in the grains, the Schmid factor or the residual deformation energy in the individual grains (Schwarzer 1997b).

It is worth noting that ACOM discriminates all grains and phases unambiguously by their crystal orientation and lattice structure, whilst conventional light microscopy or scanning microscopy images may display abutting grains by the same color or gray shade. Therefore Quantitative Metallography may fail when deriving grain size distributions or other statistical parameters from microscopy images. Since crystal orientation maps are available in digital form by their way of construction, the derivation of statistical parameters such as the distributions of grain size, length of grain boundaries, grain size as a function of grain orientation, and fraction of Σ grain boundaries is simply reduced to pixel counting.

6. Examples of application

Specimen preparation for BKD study is generally straight-forward, but high-resistance and sensitive materials require a special treatment. Heavy plastic strain and foreign layers on the surface have to be excluded. The preparation of metal specimens may be difficult, since unwanted plastic deformation or artifacts in the surface layer can hardly be avoided during the preparation of ductile materials. Backscatter Kikuchi patterns then appear diffuse. Chemical-mechanical polishing and a final chemical etch are recommended in order to remove deformed layers from the surface.

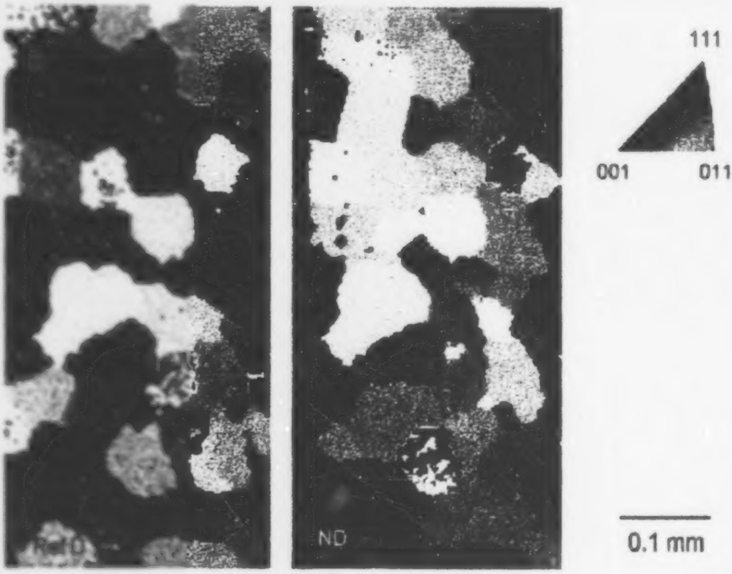
Ref D
ND
111
001
011
0.1 mm

Figure 2 Crystal orientation map of a chemically polished lead specimen at 20 kV.

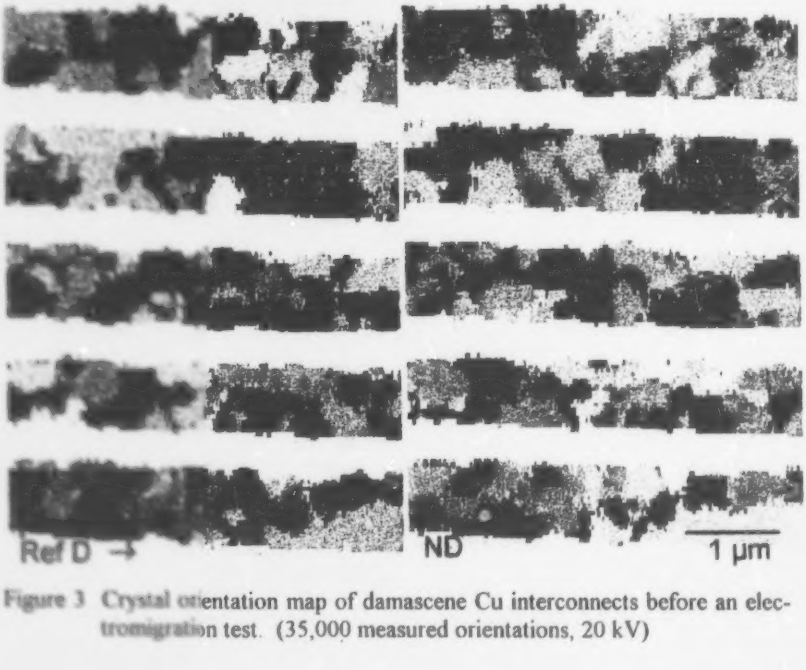

Figure 3 Crystal orientation map of damascene Cu interconnects before an electromigration test. (35,000 measured orientations, 20 kV)

Grain boundary engineering is supposed to be a means for improving the performance of lead acid batteries (Palumbo et. al. 1998). Lead, however, is difficult to prepare for ACOM since it is extremely soft and tends to be rapidly coated by an oxide layer. A careful chemical-mechanical polishing, followed by electrolytic polishing in a perchloric electrolyte immediately before SEM investigation is appropriate. The crystal orientation map reveals a clear microstructure (Figure 2). The ACOM data have been further used for a quantitative characterization of the grain boundaries.

Metal lines fabricated by electrodeposition of copper into narrow damascene trenches are the most promising candidate for future ULSI device interconnections (AMC 1998). The reliability of copper interconnects is expected to depend on the microstructure as well as on the texture of the copper films. ACOM is an ideal means to study both. Mesostructure in the trenches is clearly revealed (Figure 3). As a consequence of the intense scattering and the excellent quality of Kikuchi patterns due to the self-annealing of thin copper layers at ambient temperatures, a high spatial resolution of significantly better than 0.1 µm is achieved with a standard tungsten cathode at 20 kV accelerating voltage. A central seam, caused by the growth of grains from the trench walls with almost the same speed, is found in several sections of this test specimen. Grain boundaries along the line, however, have to be strictly avoided since they may supply a path of high diffusion for electromigration.

Acknowledgment

Financial support by the German Research Foundation (DFG Forschergruppe "Textur und Anisotropie kristalliner Stoffe" and "Elektromigrations-Projekt") is gratefully acknowledged.

The copper interconnect test specimen has been supplied by Dr. A. Fischer, Infineon Technologies, Munich.

References

Adams, B.L., Wright, S.I. and Kunze, K. (1993) Orientation imaging: The emergence of a new microscopy. *Metallurgical Transactions*, Vol. 24A, pp. 819-831.

AMC (1998) *Advanced Metallization Conference*, Conference Program and Abstracts. Colorado Springs, October 6-8, 1998. University of California, Berkeley.

Bunge, H.J. (1982) *Texture Analysis in Materials Science*. Butterworths Publ., London, 2nd Ed. Cuvillier Verlag, Göttingen, 1993.

Bunge, H.J. (1994) Statistical crystallography of the polycrystal. *Materials Science Forum*, Vol. 157-162, pp. 13-30.

Bunge, H.J. (1999) Texture, microstructure and properties of polycrystalline materials. In: Ray, R.K. and Singh, A.K. (eds.) *Textures in Materials Research*. Oxford & IBH Publishing Co., New Delhi and Calcutta, pp. 3-44.

Gerth, D. and Schwarzer, R.A. (1993) Graphical representation of grain and hillock orientations in annealed Al-1% Si films. *Textures and Microstructures*, Vol. 21, pp. 177-193.

Krieger Lassen, N.C. (1994) *Automated determination of crystal orientations from electron backscattering patterns*. PhD Thesis, Danmarks Tekniske Universitet, Lyngby.

Kunze, K., Zaefferer, S. and Schwarzer, R. (1994) Orientierungsmapping mit dem Raster-Elektronenmikroskop. *Beitr. Elektronenmikroskop. Direktabb. Oberfl.*, Vol. 27, pp. 169-176.

Natterer, F. (1986) *The mathematics of computerized tomography*. B.G. Teubner Verlag, Stuttgart.

Palumbo, G., Lehockey, E.M. and Lin, P. (1998) Applications for grain boundary engineered materials. *Journal of Metals (JOM)*, Vol. 50, pp. 40-43.

Randle, V. (1992) *Microtexture determination and its applications*. Institue of Materials, London.

Rohde, D. (1999) NORAN INSTRUMENTS Inc. *private communication*

Schäfer, B. (1998) ODF computer program for high-resolution texture analysis of low-symmetry materials. *Materials Science Forum*, Vol. 273-275, pp.113-118

Schwarzer, R.A. (1994) Preparation of high-resistance or sensitive samples for grain orientation measurement with electron microscopes. *Materials Science Forum*, Vol. 157-162, pp. 201-206.

Schwarzer, R.A. (1997a) Automated crystal lattice orientation mapping using a computer-controlled SEM. *Micron*, Vol. 28, pp. 249-265.

Schwarzer, R.A. (1997b) Advances in crystal orientation mapping with the SEM and TEM. *Ultramicroscopy*, Vol. 67, pp. 19-24.

Schwarzer, R.A. and Sukkau, J. (1998) Automated crystal orientation mapping (ACOM) with a computer-controlled TEM by interpreting transmission Kikuchi patterns. *Materials Science Forum*, Vol. 273-275, pp. 215-222.

Springer, F. (1998) Recent developments in Automated Crystal Orientation Mapping (ACOM) – Evaluation and graphical representation of individual grain orientation data. *Materials Science Forum*, Vol. 273-275, pp. 191-200.

RELIABILITY OF AUTOMATIC ORIENTATION DETERMINATION FROM KIKUCHI PATTERNS

A.MORAWIEC[1]

Department of Materials Science and Engineering, Carnegie Mellon University, Pittsburgh, USA

Abstract

Formal aspects of crystal orientation determination from TEM Kikuchi patterns are discussed with emphasis on ambiguities and on sensitivity of the results to experimental errors. There are two main factors to the reliability of the final orientation. The first one is the reliability of indexing. Assuming correct indexing, the second factor is the accuracy with which the orientation can be calculated. We analyze the quality of the results by recalculating orientations from computer generated patterns and by comparing the initial and recalculated orientations. This method is used to test the sensitivity of the results to errors of basic measurement parameters, including systematic errors in camera length and pattern center, and random errors in location of lines. Moreover, the influence of the number of detected lines on the quality of results and the impact of spurious lines on indexing are investigated.

Keywords: diffraction patterns, indexing, Kikuchi patterns, orientation determination, TEM

1. Introduction

Kikuchi patterns provide one of the most accurate and efficient techniques of crystallite orientation determination. Especially useful in investigating polycrystalline materials is the orientation mapping technique. (For accounts on automatic EBSP based method see, e.g., Wright (1993), Lassen (1995) or Dingley and Field (1997); automatic analysis of TEM Kikuchi pattern is described by Zaefferer and Schwarzer (1994).) However, the mapping requires lots of orientations, thus a fast method of orientation determination is needed. Fully automatic indexing guarantees speed but a question of reliability arises. The pattern analysis is also automatic, and the input data for indexing may be of relatively poor quality. Therfore, the crucial factor for the quality of the indexing procedure is robustness. Because of the combinatorial nature of indexing, the result is either fully correct or completely wrong. Finally, the generality of the program is important for those who want to go beyond the simplest crystal structures. In this account we concentrate on the results for TEM. Results concerning SEM backscattered Kikuchi patterns are given elsewhere (Morawiec, 1999).

---

[1] On leave from Instytut Metalurgii i Inżynierii Materiałowej PAN, Kraków, Poland.

2. Diffraction geometry

The crystallites' orientation is a proper rotation transforming a Cartesian crystal coordinate system into a Cartesian sample coordinate system. Diffraction experiments allow orientations to be determined by matching reciprocal lattice vectors acquired from the experiment with vectors calculated from crystallographic parameters. In the case of Kikuchi patterns, the diffraction geometry can be considered in a way independent of the experimental set-up and crystal symmetry. First, let us express the Cartesian crystal coordinates (h_1, h_2, h_3) of the normal $\mathbf{h}$ to a reflecting plane by integer Miller indices $(h\ k\ l) = (h_1^*\ h_2^*\ h_3^*)$ of the plane. The relation between them is

$$h_i = (A^{-1})_{ij} h_j^* \ , \tag{1}$$

where the matrix A is defined by the following: the element A_{ij} of A equals the j-th coordinate of the i-th basis vector of the direct lattice in the Cartesian crystal coordinate system.

The same normal can be expressed in the sample coordinate system. (It is denoted by $\mathbf{g}$.) This can be done by using the Laue equation $\pm\mathbf{g} = \mathbf{k} - \mathbf{k}_0$, where $\mathbf{k}\cdot\mathbf{k} = 1/\lambda^2 = \mathbf{k}_0\cdot\mathbf{k}_0$, the constant λ is radiation wavelength, and the wave vectors $\mathbf{k}_0$ and $\mathbf{k}$ indicate directions of the incident and reflected beams, respectively. The incident beam is convergent, so the direction of $\mathbf{k}_0$ is arbitrary. Laue equation leads to the condition on possible directions of $\mathbf{k}$ (Ryder and Pitsch, 1968)

$$\pm\mathbf{k}\cdot\mathbf{g} = g^2/2 \ . \tag{2}$$

For a given $\mathbf{g}$, the directions of $\mathbf{k}$ satisfying eq.(2) determine two cones composed of reflected rays. The intersection of the cones (2) with the plane of the detector gives two conics contributing to the pattern of Kikuchi "lines". The equation of the planar detector is given by $\mathbf{n}\cdot\mathbf{x} = L > 0$, where $\mathbf{x}$ represents points of the detector's plane, $\mathbf{n}$ is a unit vector normal to the plane, and L is the effective camera length. The pattern center is defined as the point $\mathbf{x}^0 = L\mathbf{n}$ on the detector. Let $\mathbf{x}^-$ and $\mathbf{x}^+$ be vectors to points closest to the pattern center on each of the two lines of the Kikuchi pair. Because these points lie on the diffraction cones, the vectors $\mathbf{k}^\pm = \mathbf{x}^\pm/(\lambda(\mathbf{x}^\pm\cdot\mathbf{x}^\pm)^{1/2})$ satisfy $\pm\mathbf{k}^\pm\cdot\mathbf{g} = g^2/2$. On the other hand, $\mathbf{k}^+$, $\mathbf{k}^-$ and $\mathbf{g}$ are coplanar, i.e., $(\mathbf{k}^+\times\mathbf{k}^-)\cdot\mathbf{g} = 0$. Hence, the vector $\mathbf{g}$ is given by (Morawiec, 1999)

$$\mathbf{g} = \pm(\mathbf{k}^+ - \mathbf{k}^-) \ . \tag{3}$$

Data needed for the calculation of $\mathbf{h}$ and $\mathbf{g}$ vectors are Miller indices of reflecting planes, coordinates of three independent direct-lattice vectors in the Cartesian crystal coordinate system (A), camera length and pattern center ($\mathbf{x}^0$), and locations of Kikuchi pairs in terms of $\mathbf{x}^\pm$.

3. Indexing

It is assumed here that the structure of the material is known, as well as which reflections can be expected to show up in the pattern. Therefore, the indexing is limited to determination of the assignment of indices to Kikuchi pairs. Eq.(1) applied to the indices of the possible reflectors gives coordinates of the normals $\mathbf{h}$; the normals will be denoted by $\mathbf{h}_m$, with $m = 1, ..., M$. On the other hand, a pattern of N Kikuchi pairs provides (via eq.(3)) the coordinates of N normals $\mathbf{g}_n$, $(n = 1, ..., N)$ in the sample coordinate system. Each

Kikuchi pair results from the diffraction on a crystal plane, thus each $\mathbf{g}_n$ corresponds to a certain $\mathbf{h}_m$. The task is to fit the figure of $\mathbf{g}_n$ vectors to a congruent figure of a subset of $\mathbf{h}_m$ vectors. In other words, indexing is the procedure of determining the mapping $\pi : \{1,...,N\} \rightarrow \{1,...,M\}$ which assigns subscripts of $\mathbf{h}_m$ vectors to subscripts of $\mathbf{g}_n$ vectors.

Apart from experimental errors, there exist an assignment π and a rotation (orthogonal matrix) O such that $\mathbf{h}_{\pi(n)} = O\mathbf{g}_n$ for each $n = 1,...,N$. This relation is only approximate because of experimental errors. The assignment and orientation can be obtained by minimizing the residue $\psi = \sum_{n=1}^{N}(\mathbf{h}_{\pi(n)} - O\mathbf{g}_n)^2$. The assignment π and the matrix O, corresponding to the global minimum of ψ, are solutions to the indexing problem and the orientation determination problem, respectively. The diffraction pattern corresponds to the crystal's Laue group, so the orientation is given by either O, if $\det(O) = +1$, or by IO, if $\det(O) = -1$. (I denotes inversion.)

With known assignment π, there is a standard method of determining O. The orthogonal matrix leading to a global minimum of ψ is given as the orthogonal factor of the polar decomposition of a certain matrix constructed of $\mathbf{g}_n$ and $\mathbf{h}_{\pi(n)}$ vectors. (See, e.g., Wahba, Farrell and Stuelpnagel, 1966.) The problem is that in automatic measurements the assignment π is unknown. One can enumerate all possible assignments and check the values of ψ to find the one corresponding to the minimum. However, for large M and N this leads to combinatorial explosion (prohibitive number of trials), and the direct approach cannot be used. The number of possible assignments can be reduced by eliminating some of them. Because scalar products of vectors are invariants of rotations, the products between $\mathbf{g}_n$ vectors and the products between the matching $\mathbf{h}_{\pi(n)}$ vectors must agree to within the limits of experimental error. The maximal errors of the scalar products between $\mathbf{g}_n$ vectors are calculated from maximal errors of $\mathbf{x}^0$ and $\mathbf{x}^{\pm}$ using the linearized form of (3). The scalar products of vectors are compared for all combinations of i-tuples of not yet eliminated $\mathbf{h}_m$ vectors, with $i = 1, 2, ..., N$; a given $\mathbf{h}_m$ vector can be eliminated if it does not fit into any of the configurations built of other vectors. If a vector is eliminated, the whole procedure is repeated because other vectors may have lost their partner and may be unable to fit into any configuration.

Generally, the result of elimination is ambiguous, i.e., within specified error brackets a number of non-equivalent assignments exist. The ambiguities are resolved by estimating ψ. On the other hand, no match can be found for certain vectors if the pattern contains spurious lines. In these cases, the elimination process must be executed for various subsets of detected Kikuchi pairs.

4. Ambiguities and errors

Besides obvious errors (e.g., in positioning the sample), the resulting orientations are influenced by inaccuracies in camera length and pattern center, and in determination of location of lines. Indexing is also affected by presence of spurious lines. Additionally, even in the absence of experimental errors, one faces geometrical ambiguities in indexing. The most obvious one comes from Friedel's law; in the case of crystals without an inversion center the solution is ambiguous. (For crystals with improper symmetries but without an inversion center, two non-equivalent orientations lead to identical patterns. For crystals without improper symmetry operations, there is no distinction between patterns coming from the right and left enantiomorphic forms.) Generally, "diffraction enhancement of symmetry" (see e.g. Sadanaga and Ohsumi, 1979) causes ambiguities of this type.

Coplanar reciprocal vectors (planes of one zone axis) do not provide a unique solution unless the axis is a twofold symmetry axis. Ambiguous solutions are also possible even if the reciprocal vectors are not coplanar. In general, this occurs if two non-equivalent sets of reciprocal vectors constitute congruent configurations.

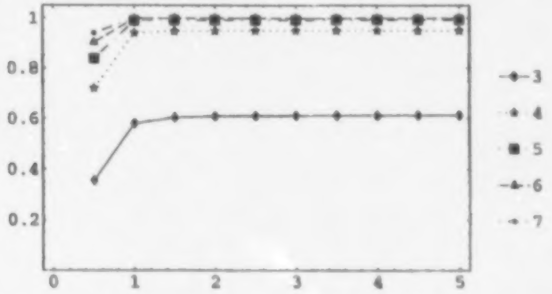

Figure 1. Distribution of deviations of recalculated orientations from correct orientations for various *number of 'detected' Kikuchi pairs*. Values on abscissa are given in degrees. A given value on ordinate, say 0.6 for 3, means that 60% of recalculated orientations were within 3° from the correct orientations. The distance of a line from the center ρ and the inclination of its normal to a fixed direction θ were used to parameterize the location of lines. The parameters (ρ, θ) of all lines were disturbed by random errors with uniform distribution; the maximal error of ρ was $\pm 0.04\rho_{max}$ and the maximal error of θ was ±1.5°. There were no spurious lines.

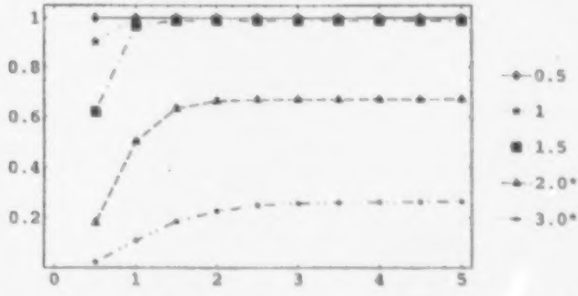

Figure 2. Distribution of deviations of recalculated orientations from correct orientations for various *levels of random errors* in location of Kikuchi lines. The parameters (ρ, θ) of all lines were disturbed by random errors with uniform distribution; the maximal error of ρ was $c \times 0.04\rho_{max}$ and the maximal error of the angle was $c \times 1.5°$. The value of c was 0.5, 1, 1.5, 2.0 and 3.0 for particular graphs of the Figure. Six pairs of lines were used in the calculation.

The quality of final results is determined by the reliability of the indexing and by accuracy of calculating the orientation from an indexed pattern. The first of these two factors corresponds to the percentage of correctly indexed patterns, and the second corresponds to the spread of recalculated orientations around the correct results. The influence of ambiguities and some experimental aspects of line detection on the quality of results can be tested by using simulated patterns (i.e., with known "true" crystal orientation). Those aspects include: the number of detected Kikuchi pairs, presence of spurious reflections, errors in the camera length, errors in pattern center, and random errors in the location of lines. Results of such tests for conditions corresponding to TEM measurements are contained in figures. They were obtained by generating 10^4 Kikuchi patterns corresponding to random orientations of hcp crystals. The pattern center was located at the center of the circular detector of radius $\rho_{max} = 0.25L$. Twenty families of reflectors of hcp structure with growing Bragg angle were taken into account. Pairs of lines used in recalculating orientations were randomly chosen from each pattern. Unit cell parameters were $a = 2.6649$Å and $c/a = 1.8563$, and the wavelength was $\lambda = 0.05$Å. Shapes of the graphs are similar to those corresponding to SEM measurements (Morawiec, 1999) but there are considerable differences in numerical values. The results given here are specific to the program we used, and it is not claimed that it achieves the best possible performance.

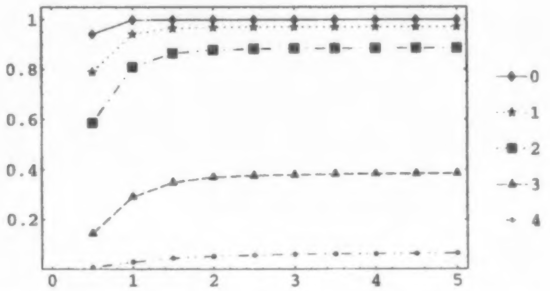

Figure 3. Distribution of deviations of recalculated orientations from correct orientations for various *number of spurious Kikuchi pairs*. The total number of pairs used in calculation was 7. In each pattern exactly 0,1,2,3 or 4 pairs were replaced by spurious pairs. Random errors in the locations of lines are of the same magnitude as in Figure 1.

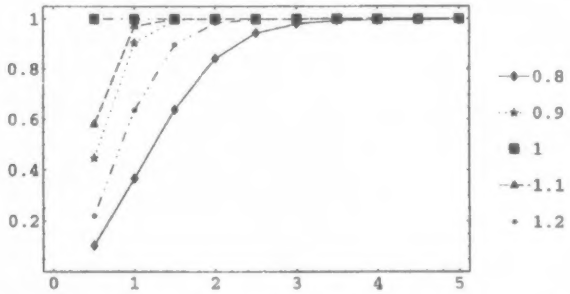

Figure 4. Distribution of deviations of recalculated orientations from correct orientations for various *errors of the effective camera length*. Before recalculating the orientations, the original camera length used for generating the patterns was modified to 0.80, 0.90, ... , 1.20 of its original value. Six pairs of lines were used in the calculation. There were no spurious lines and no random errors in the locations of lines.

Using a sufficiently large number of line pairs for indexing is important for its reliability. Results for some particular conditions are given in Figure 1. Due to geometrical ambiguities, the indexing of just 3 pairs is unreliable. Generally, the number of *legitimate* pairs shouldn't be smaller than 5. Random errors of the line parameters affect indexing, but they also influence the accuracy of the determined orientation from correctly indexed patterns. Some results for various levels of random errors are shown in Figure 2. As for spurious lines, it is worth noticing that the negative influence of n spurious reflections among N pairs is larger than the reduction of the number of reflections from N to $N-n$. This follows from the comparing of Figs 1 and 3. Thus, it is safer not to use doubtful pairs. One must also remember that even a legitimate reflection will be treated as spurious if it is not represented in list of $\mathbf{h}_m$ vectors. The effect of systematic errors in camera length and pattern center on the quality of orientation determination is shown in Figures 4 and 5, respectively. An incorrect pattern center gives systematic error in orientation. The order of the error in radians is the same as the ratio of the deviation from the correct location of the center to the camera length.

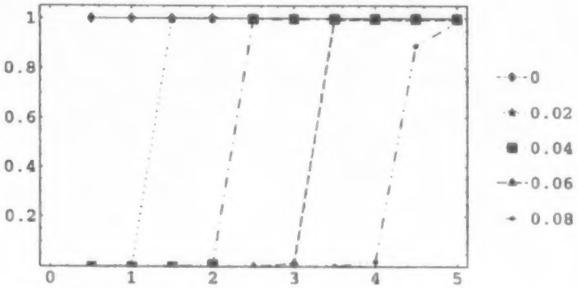

Figure 5. Distribution of deviations of recalculated orientations from correct orientations for various magnitudes of *the shift of the pattern center*. The original pattern center at the center of the screen used for generating the patterns was shifted by 0.00, 0.02,..., 0.08 of the camera length. Six pairs of lines were used in the calculation. There were no spurious lines and no random errors in the locations of lines.

Acknowledgments

Work supported by the MRSEC Program of the National Science Foundation under Award Number DMR-9632556.

References

Dingley,D.J. and Field,D.P. (1997). *Mat.Sci.Technol.* **13**, 69–78.
Lassen,N.C.K. (1995). in *Proc. 16th Riso Int. Symposium on Materials Science.* Ed. by N.Hansen, D.Juul Jensen, Y.L.Liu and B.Ralph. Riso Nat.Lab., Denmark, pp. 405–411.
Morawiec, A. (1999). to appear in *J.Appl.Cryst.*
Ryder,P.L. and Pitsch,W. (1968). *Phil. Mag.* **18**, 807–816.
Sadanaga,R. and Ohsumi,K. (1979). *Acta Cryst. A* **35**, 115–122.
Wahba,G., Farrell,J.L. and Stuelpnagel,J.C. (1966). *SIAM Rev.* **8**, 384–386.
Wright, S.I. (1993). *J.Computer-Assisted Microsc.* **5**, 207–221.
Zaefferer,S. and Schwarzer, R.A. (1994). *Z.Metallkd.* **85**, 585–591.

INFLUENCE OF NUMBER AND ARRANGEMENT OF SINGLE ORIENTATION MEASUREMENTS ON THEIR STATISTICAL RELEVANCE

O. ENGLER
Los Alamos National Laboratory, Center for Materials Science, Mail Stop K765, Los Alamos, NM 87545, USA
J. JURA
Institute for Metal Research, Polish Academy of Sciences, Krakow, Poland
S. MATTHIES
Research Center Geesthacht, Institute for Materials Research, Geesthacht, Germany

Abstract

This paper compares two quantitative measures to derive the minimum number of single orientation measurements required to adequately represent the texture of a given sample or local volume and so to asses the statistical significance of the microtexture data. Both procedures are applied to several test cases with different texture sharpness. The impact of the measurement procedure is explored by analyzing samples rastered by means of orientation imaging microscopy with different step widths.

Keywords: single orientation measurements, statistical relevance, ρ-parameter, F_2 vs. $(1/N)$ analysis

1. Introduction

Despite the relatively large number of orientation data, which can nowadays be obtained by the various techniques for single orientation measurements – in particular by electron back scatter diffraction (EBSD) in an SEM – the number of grains encountered is still small compared to the number of grains contributing to X-ray or neutron pole figure measurements. Even in the case of fully automated EBSD-measurements usually less than 10000 grains are recorded, which raises the question of the statistical relevance of the data with regard to the description of the orientation distribution of the volume of interest.

In several studies on this subject the texture of a given sample was determined from 100, 200, 300... N individual orientations and compared with the corresponding X-ray macrotextures (Wright and Adams, 1990; Baudin and Penelle, 1993; Engler et al., 1994). It turned out that for cubic materials the ODFs derived from only 100 orientations already comprised the main characteristics of the textures, but a statistically sound representation of the textures required 500–750 orientations. The number of orientation measurements necessary to represent adequately a texture strongly depends on sample and crystal symmetry and, in particular, on the texture sharpness (e.g. Jura et al., 1996). Therefore, it is necessary to develop a quantitative measure for the minimum or critical number of single orientation measurements N_c which is required to represent adequately the texture of a given sample. Although in most experimental investigations on this problem so far the texture as derived from the single grain orientation data has been compared with X-ray macrotextures, such a criterion must as well hold for the reproduction of a microtexture of a given part of the microstructure.

In the present paper two different methods to derive numerical data for N_c will be applied to various test cases which are characterized by different textures, in particular by different texture sharpness. The statistical relevance of microtexture results does not solely depend on the number of measurements, but it may also be affected by the measurement procedure, which is of some importance with view to the fully automated EBSD measurements performed in orientation imaging microscopy (Adams et al., 1993). To analyze this, the behavior of the statistical parameters was analyzed for samples that were scanned with different step widths.

2. Experimental Procedure

In the present study three different samples with strongly differing texture sharpness were selected.

(i) As an example for a sharp texture, a sample of high purity Cu was cold rolled to 95% thickness reduction and subsequently recrystallization annealed for 20min at 300°C. After complete recrystallization, a homogeneous microstructure with very small grains (grain size ~10μm) and some recrystallization twins was obtained. The recrystallization texture consisted of a very sharp cube component {001}<100> with an intensity as high as $f(g)\approx 120$ (Fig. 1a). Furthermore, weaker intensities of the first generation twin of the cube-orientation {122}<212> were observed.

(ii) Medium texture sharpness was obtained in a sample of supersaturated Al-1.3wt%Mn after 92% cold rolling and annealing for 10s at 450°C, leading to a rather fine grained recrystallized microstructure (grain size ~30μm). The texture comprised a quite weak cube component ($f(g)\approx 9$) with strong scatter (volume fraction ~30%) and a high fraction (~70%) of randomly oriented grains (Fig. 1b).

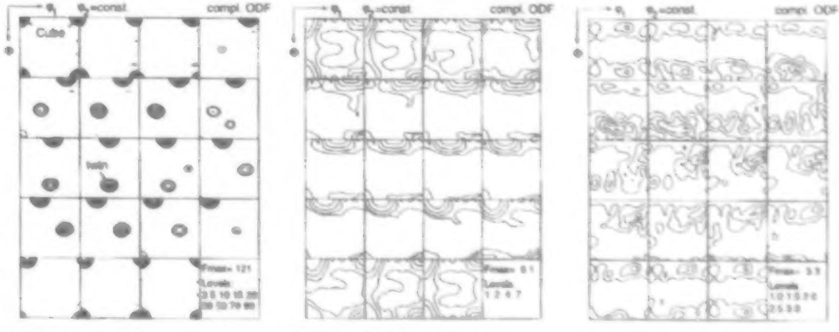

(a) Cu (l_{max}=34) (b) Al-1.3%Mn (l_{max}=22) (c) Ni_3Al (l_{max}=22)

Fig. 1: X-ray macrotextures of the three samples investigated.

(iii) A very weak recrystallization texture was obtained in a sheet of boron-doped Ni_3Al (IC15) which was 60% cold rolled and then annealed for 90min at 1050°C. Microstructural investigation yielded a recrystallized grain size of ~40µm and the occurrence of some recrystallization twins. This material depicted a very weak texture with a maximum intensity of only $f(g) \approx 3$ (Fig. 1c), corresponding to a random fraction exceeding 85%. In all samples investigated the textures were proved to be uniform, i.e. the samples depicted no texture gradients.

To characterize the macrotexture of these three samples, pole figures were measured by standard X-ray diffraction techniques; orientation distribution functions (ODF) $f(g)$ were computed by the series expansion method. Local orientations were determined by EBSD in an SEM JEOL 6100 (Engler et al., 1996). For the Al-Mn alloy, the orientations of 1000 grains were evaluated by a semi-automatic, interactive procedure. To secure statistical homogeneity the grains were measured at various locations in the sheet. The orientations in the Cu and Ni_3Al-samples were scanned by means of a completely automated set-up. The samples were moved with a computer-controlled sample stage in constant steps and for each point the orientation was determined by EBSD. In both cases a rather large step width was chosen (Cu: 50µm, Ni_3Al: 80µm), which was distinctively larger than the average grain size in the corresponding microstructure. By this a comparable stochastic sampling procedure as in case of the manually scanned Al-Mn was realized. In order to analyze the impact of the scanning procedure on the statistical relevance of microtexture data, the Ni_3Al sample was scanned again with a much smaller step width of 4µm.

3. Statistical Relevance of Single Orientation Measurements

3.1 The ρ-parameter analysis

Pospiech et al. (1994) proposed to analyze the convergence of the statistical parameter, ρ, which represents the relative mean square deviation between two textures. ODFs are computed for an increasing number N of single grain orientation measurements, e.g. in successive steps of say 100 orientations. The critical number of measurements N_C is obtained when the evolution of ρ with N approaches saturation. The parameter $\rho_{0,N}$ comparing the intensity values f_N of the ODF as computed from N orientations with the values f_0 of a reference ODF, e.g. the macrotexture, is calculated according to:

$$\rho_{0,N} = \oint (f_0 - f_N)^2 \, dg \Big/ \oint f_N^{\,2} \, dg \cdot 100\% \qquad (1)$$

Single orientation measurements are used more frequently to determine local microtextures rather than bulk textures, so that no data of a reference texture f_0 may be available. In such cases, a parameter $\rho_{N',N}$ can be calculated from the ODF-values $f_{N'}$ and f_N for two consecutive stages of the single grain orientation measurement procedure, e.g. for N'=300 and N=400. The parameter $\rho_{N',N}$ has in general much lower values than $\rho_{0,N}$, because potential measuring errors would show up in all data sets in an equal manner.

In Fig. 2 the evolution of both $\rho_{0,N}$ and $\rho_{N',N}$ is shown for the three samples of this study. For the Al-Mn sample, 100 orientations yielded already a fairly well reproduction of the macrotexture, and with 600 orientations a statistically reliable texture could be derived. The very sharp cube-texture of the Cu-sample is reproduced with statistically sufficient accuracy already from 100 or 200 orientations. For the weaker twin-orientations larger N is required, however, which is reflected in the rather slow convergence of $\rho_{0,N}$ and $\rho_{N',N}$. In contrast, for an adequate reproduction of the much weaker texture of the Ni_3Al (Fig. 1c) obviously many more orientations are required ($N_C \approx 4000$).

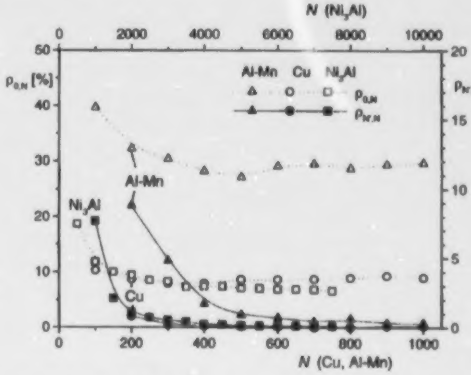

Fig. 2: Evolution of $\rho_{0,N}$ and $\rho_{N',N}$ with N for the three textures with different sharpness.

3.2 The F_2 vs. $1/N$ analysis

Using a discrete structure of the orientation space (e.g. M 5°x5°x5° cells at g_i with volume v_i), N measured single orientations can be sorted into these cells. From the resulting 'hit-numbers' h_i formally a 'hit-ODF' $f_N(g)$ can be constructed as a staircase function:

$$F_m(N) = \int_G \left[f_N(g)\right]^m dg = \sum_{i=1}^{M} \left[h_i/(v_i N)\right]^m v_i \ , \quad \text{with} \ \sum_{i=1}^{M} v_i = 1 \ \text{and} \ \sum_{i=1}^{M} h_i = N \qquad (2)$$

Laws of statistics prescribe a mean linear dependence of the texture index F_2 on $1/N$. Only if this tendency is reached for N greater than the critical number N_C, it makes sense to represent the N orientations in form of an ODF. From the extrapolation of the asymptote of the least-square fitted $F_2(1/N)$-line to $1/N=0$ (i.e. $N=\infty$) the unknown 'true' F_2 of the sample can be determined, yielding the value $F_2^{asy}(N)$ (Matthies and Wagner, 1996). N_C depends on the chosen grid, the crystal/sample symmetry and on the texture of the sample. Sharp textures with a small isotropic background are equivalent to a lower number of cells that can be hit at all. This means the linear dependency of F_2 on $1/N$ will be reached for lower N than in the case of weak textures.

Fig. 3 a–c shows the $F_2(1/N)$ curves as well as the F_2^{asy}-values as derived from the fitted asymptotic $F_2(1/N)$-line for the three different test cases. The fit always considers the last 10 $F_2(1/N)$-points to the right. A second smoothing over the last 10 $F_2^{asy}(1/N)$-values yields the $F_2^{asas}(1/N)$. For the Al-Mn sample, Fig. 3a displays a clean $1/N$ tendency with a stable F_2^{asy} of about 4. Here, $N=5000/20=250$ grain orientations would already be sufficient for a qualitative ODF representation. For the Cu-sample, Fig. 3b shows a not very well established $F_2^{asy}(1/N)$-plateau, which is typical for a sharp texture containing some weak components as the twins in the present case. It is assumed that the true texture index of this sample will be of the order of 300. This means that although with $N=5000/70\approx70$ orientation, the general texture features may be reproduced, a much larger N would be necessary to quantitatively reproduce minor

ODF-details, especially the twin orientations. Fig. 3c (Ni_3Al) is a 'textbook'-example of the 1/*N*-law. $F_2^{exp} = 1.3$ can be deduced from *N*=50000/40=1250 grain orientations.

3.3 *Influence of the measuring procedure*

As already mentioned above, the statistical relevance of microtexture results does not depend solely on the number of measurements, but it may also be affected by the measurement procedure itself, which becomes particularly important in the light of fully automated EBSD measurements, i.e. orientation imaging microscopy. To illustrate this, the Ni_3Al sample was scanned again, but this time with a much smaller step size of 4µm.

Since the grain size of the Ni_3Al was about 40µm, in the first scan – performed with a step size of 80µm – virtually all measured points belonged to different, mostly not even adjacent, grains. Of course, this procedure is not suited for generation of an orientation map or computation of misorientation parameters, but it gives a good *statistical* representation of the orientation distribution. In the second scan the step width was much smaller than the grain size, so that each grain was covered by a large number of measurements. A step width of 4µm results in about 100 measurement points per grain, so that despite the quite large number of measurement points (11000) the number of *grains* was only of the order of 100. Whereas this scan gave a satisfactory orientation map, the statistical relevance of the measurements is much poorer than in the first scan. This resulted in a much slower convergence of the parameter $\rho_{N',N}$ (N_C=7000; Fig. 4a), the parameter $\rho_{0,N}$ showed no convergence at all. Likewise, from the F_2 vs. (1/*N*) analysis not even the order of F_2 (1.3, Fig. 3c) could be determined (Fig. 4b), which means that an ODF-related interpretation of these data is meaningless.

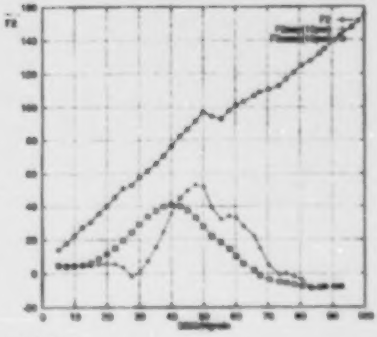

(a) Al-Mn

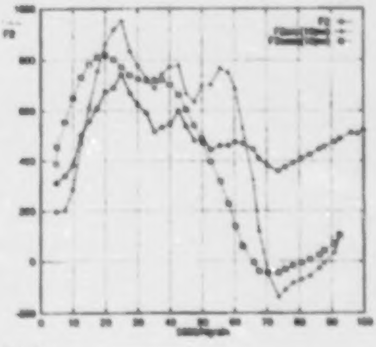

(b) Cu

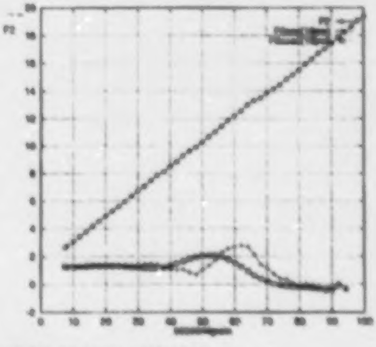

(c) Ni_3Al (step width 80µm)

Fig. 3: Evolution of F_2 as a function of 1/*N* for the three materials with different texture sharpness investigated in the present study.

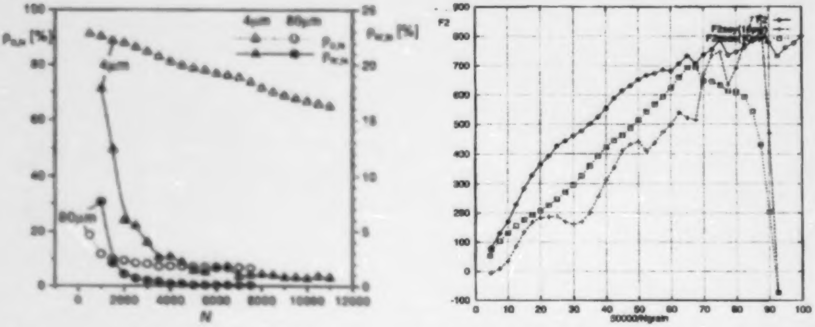

(a) ρ-parameter analysis (Ni$_3$Al)

(b) F_2 vs. $1/N$ analysis (Ni$_3$Al, step width 4µm)

Fig. 4: Influence of the measuring procedure.

4. Conclusions

To asses the statistical relevance of microtexture data the behavior of the statistical parameters $\rho_{0,N}$ and $\rho_{N',N}$ with increasing number of single orientation measurements N and of the texture index F_2 as a function of the inverse $1/N$ were analyzed. The parameters $\rho_{0,N}$ comparing the ODF as computed from N single orientations with a reference texture – typically the X-ray macrotexture of the sample – turned out to be most rigid in the sense that it yielded the largest values of N_C. Qualitatively, however, the evolution of $\rho_{N',N}$ and the F_2 vs. $1/N$ analysis give very similar results, so that analysis of either parameter yields valuable information on the statistical relevance of single orientation data.

In practical applications the number of single orientation measurements N is to be understood as number of measured *grains*. Therefore, too fine and/or systematic sets of measuring points substantially lower the number of actually described grains and thus reduce the stochastic character of the experiment. This leads to much poorer statistical relevance of the data with regard to a quantitative description of the texture.

In conclusion, it is strongly suggested to implement one of the present procedures as a mandatory step in order to asses the statistical significance of microtexture data.

References

Adams, B.L., Wright, S.I. and Kunze, K. (1993). *Met. Trans.*, vol 24A, pp. 819-831.

Baudin, T. and Penelle, R. (1993). *Met. Trans.*, vol. 24A, pp. 2299-2311.

Engler, O., Yang, P., Gottstein, G., Jura, J. and Pospiech, J. (1994). *Mat. Sci. Forum,* vol. 157-162, pp. 933-938.

Engler, O., Escher, C. and Gottstein, G. (1996). *Textures & Microstructures,* vol. 26-27, pp. 337-359.

Jura, J., Pospiech, J. and Gottstein, G. (1996). *Z. Metallk.*, vol. 87, pp. 476-480.

Matthies, S. and Wagner, F. (1996). *Phys. stat. sol. (b),* vol. 196, pp. K11-K15.

Pospiech, J., Jura, J. and Gottstein, G. (1994). *Mat. Sci. Forum*, vol. 157-162, pp. 407-412.

Wright, S.I. and Adams, B.L. (1990). *Textures & Microstructures,* vol. 12, pp. 65-76.

DETERMINATION OF MICROTEXTURE BY EBSD AT HIGH SPATIAL RESOLUTION IN A FEGSEM

F.J. HUMPHREYS
Manchester Materials Science Centre, UMIST, Manchester, England

Abstract

It is shown that that the effective spatial resolution for EBSD using a Field Emission Gun Scanning Electron Microscope (FEGSEM) may typically be some four times better than in a standard W-filament SEM, making the microstructural characterization of materials with very small subgrain or grain structures possible. The application of high resolution EBSD to the determination of microtextures in a number of aluminium projects is demonstrated, and examples include the characterization of submicron-grained alloys, correlation of texture, subgrain size and misorientation in deformed alloys and determination of local textures in the vicinity of large second-phase particles.

Keywords: EBSD, microtexture, FEGSEM, resolution, grains, subgrains

1 Introduction

Electron backscattered diffraction (EBSD) in the scanning electron microscope (SEM) has been one of the most important advances in methods of texture analysis in recent years, and after a period of rapid development, the technique has matured to the stage where it is now regarded as a standard technique for materials investigation. In addition to the many applications requiring correlation of local texture with microstructure, EBSD is now being used as a routine laboratory tool for the quantitative characterization of materials, including quantitative metallography (type, size and distribution of phases, grains and subgrains) (Humphreys 1999) and also the determination of bulk texture.

EBSD has a number of advantages over the transmission electron microscope (TEM) for the investigation of fine-scale microstructures, and these include the larger specimen areas available from bulk samples, and the speed of diffraction pattern solution. The spatial resolution of EBSD normally limits its application to grain, subgrain or phase structures which are larger than ~1μm. However, the use of a thermal field emission gun SEM (FEGSEM) for EBSD, results in a significant improvement in spatial resolution, and this paper discusses the performance, optimization and applications of such an instrument.

A standard commercial EBSD system, comprising a low-light CCD camera (Nordif), ARGUS 20 image processor (Hamamatsu) and CHANNEL acquisition software (HKL Technology) has been interfaced to a Philips XL30 FEGSEM, and the spatial and angular resolutions of EBSD have been compared with those of a conventional W-filament JEOL 6300 SEM equipped with a similar EBSD system. In addition to the results discussed below, a significant advantage of using a FEGSEM instrument for EBSD is the stable and reproducible beam current obtainable from a thermal field emission gun, which is invaluable if large orientation maps are to be acquired over a period of several hours. Our experiments have mainly been carried out with aluminium alloy samples because these are of particular importance in our research, although as discussed below, better EBSD performance is obtained with materials of high atomic number. It should be emphasized that this paper is concerned with the use of EBSD for the rapid accumulation (typically 2-5 patterns/second) by automated acquisition systems, of the large amounts of data required for linescans or orientation maps. Improvements in EBSD performance which may be obtained by the use of film recording or the use of slow-scan cameras are not considered here. Unless stated otherwise, orientations have been determined from patterns averaged for 4 video frames.

2. Spatial resolution

When analyzing a sample with small grains or subgrains, overlapping diffraction patterns are obtained in the vicinity of the boundaries, and the **effective spatial resolution** (L) can be defined as the distance across a boundary over which the patterns cannot be solved. The sample is typically tilted to 70° for EBSD, and the resolution in the direction parallel to the specimen tilt axis (L_A) is then some three times lower than in the direction perpendicular to the axis (L_P). The resolution may be determined by small-step scanning across a boundary and noting the number of non-indexed patterns at the boundary (Farstad et al 1998). However, the resolution may be more conveniently determined by measuring the fraction of patterns (N_S) which are solved during a raster scan of the sample, and for grains of mean size D_A and D_P parallel and perpendicular to the tilt axis, provided that the scan covers a large number of grains, and that all non-indexed patterns are associated with boundaries, the N_S is given approximately (Humphreys et al 1999) by

$$N_S = \frac{(D_A - L_A)(D_P - L_P)}{D_A D_P} \tag{1}$$

For an equiaxed microstructure of grains ($\overline{D}$) and taking $L_P=3L_A$, which is typically found for a 70° tilted sample (Humphreys et al 1999), then when $L_A \ll \overline{D}$

$$L_A = \overline{D}(1 - N_S)/4 \tag{2}$$

Figure 1 is a plot of N_S against D^{-1} for aluminium samples under optimum operating conditions, and it is seen that the spatial resolution for EBSD in the FEGSEM, which is obtained from the slope of the line, is some 3 times better than in the W-filament SEM. As expected, better spatial resolution is obtained for materials of high atomic number, and data for α-brass in figure 1 shows the resolution in the FEGSEM to be ~9nm, which compares to ~25nm in the W-filament SEM (Humphreys et al 1999).

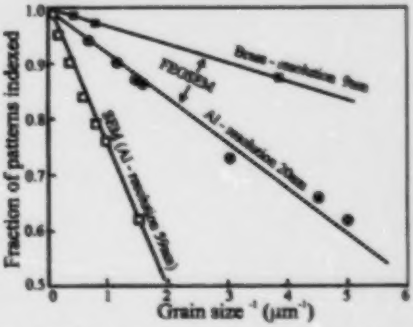

Fig.1: The effect of grain size on the fraction of diffraction patterns indexed at 20kev in a FEGSEM and W-filament SEM.

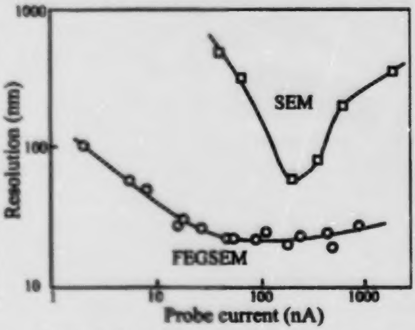

Fig.2: The effect of probe current on the effective spatial resolution in aluminium at 20 keV..

The effect of beam current on L_A is shown in figure 2. For the W-filament SEM, L_A is a strong function of the probe current (Humphreys et al 1999). For small probe currents, the pattern-solving algorithms have difficulty deconvoluting and solving overlapping diffraction patterns of poor quality, whereas at large probe currents the resolution is limited by the large beam size. Thus the optimum resolution is obtained at intermediate probe currents. It is significant that the resolution of the FEGSEM is much less sensitive to the probe current than the W-filament SEM. This arises because the beam size in a W-filament microscope is a much stronger function of probe current than for a field emission gun (Goldstein et al 1992). It was found that the size of the objective aperture had little direct effect on the spatial resolution, apart from its affect on the probe current.

The accelerating voltage and the number of frames over which a diffraction pattern is integrated also affect EBSD performance. A higher voltage results in a larger specimen interaction volume (Goldstein et al 1992), and may lead to worse spatial resolution. Pattern quality is improved because of noise reduction if multiple video frames are integrated before analyzing the pattern. The effects of these parameters on spatial resolution in aluminium are shown in figure 3, all results being obtained at similar probe currents (~150nA). It is seen that integration of up to 32 frames improves the effective resolution by ~20% although this is balanced by the longer data acquisition time and may be counteracted by the effects of specimen contamination as discussed below. There is an improvement in resolution as the voltage is lowered to 15keV, but there is no further improvement at 10keV, and this may be due to a reduction in the efficiency of the transmission phosphor at low voltages. In practice, it may not be possible to make full use of the improved resolution because if a map is acquired with a very fine data grid, carbon contamination may lead to progressive pattern degradation as the data are accumulated, and although we have not investigated the phenomena in detail, we typically find the usable minimum step size for a map to be ~50nm.

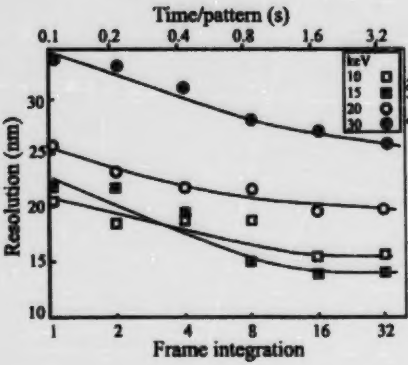

Fig.3: The effect of accelerating voltage and frame integration on the effective spatial resolution for Al at a beam current of ~150nA.

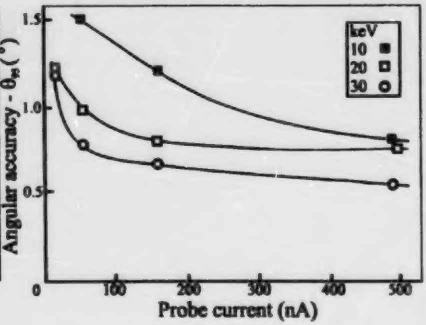

Fig. 4: The effect of probe current on the angular accuracy in the FEGSEM. For large-grained aluminium.

2 Angular accuracy

When characterizing microstructures containing low angle grain boundaries, the accuracy with which the **relative orientation** between successive adjacent data points can be determined is of great importance, and this is related to the precision with which the orientations of data points within the same crystallite can be measured. If diffraction patterns are obtained from a small area of a single crystal or a large-grained polycrystal, then although their analysis should result in identical orientations, this is not usually the case, and a range of orientations or "orientation noise" results. Several of the factors which determine the orientation noise, including the number of pixels in the CCD camera, the resolution of the digitized pattern and the accuracy of the pattern solving algorithms, are beyond the direct control of the microscopist. However, it has been shown that the relative angular resolution is affected by the microscope operating conditions (Humphreys et al 1999), and this effect has been measured for the FEGSEM. Grids of 50 x 50 data points at a spacing of 0.1μm were collected from a silicon crystal (4 frame integration) and the apparent misorientations between adjacent data points determined. The misorientations typically have a gaussian spread about zero (Humphreys 1999).

There are a number of methods of expressing the angular resolution, and it is found that the *misorientation spread encompassing 95% of the data* (θ_{95}) is a convenient parameter. However, the mean value of the data spread ($\bar{\theta}$) may also be used and our results indicate that θ_{95}~2O. Figure 4 shows the effect of probe current on θ_{95} for single grains in aluminium, and it is seen that the angular resolution deteriorates significantly at low probe currents. This is due to the lower pattern quality, which results in less accurate determination of the Kikuchi band positions (Krieger Lassen 1996). With increasing probe current, the angular resolution decreases to a constant value which is the limit imposed by the data acquisition system. It is seen that the angular resolution improves at higher accelerating voltages and this is thought to be because the positions of the narrower Kikichi bands can be determined more accurately. The direct effect of pattern quality on angular resolution may be determined by analyzing the data from a single large orientation map from a polycrystalline sample. The pattern quality varies slightly from grain to grain and is significantly worse close to grain boundaries because of pattern overlap The resulting data show that in a given map (or data set), throughout which the operating and acquisition conditions are identical, the angular resolution is strongly dependent on pattern quality (Humphreys and Brough 1999). Comparison of FEGSEM and W-filament microscopes suggests that there is no significant intrinsic improvement in angular resolution in the FEGSEM, although practical benefits arise because the larger beam currents necessary to achieve optimum angular precision can be used with less degradation of the spatial resolution in the FEGSEM.

4 Applications of high resolution EBSD

The improved spatial resolution of a FEGSEM EBSD system allows good quality diffraction patterns to be obtained from even highly deformed structures and also allows detailed characterization of sub-micron grain and subgrain structures. Fig.5 shows an example of an aluminium alloy in which an 0.2 x 0.35μm grain size has been produced by large strain deformation The microstructure and boundary character distribution can readily be measured by EBSD in the FEGSEM

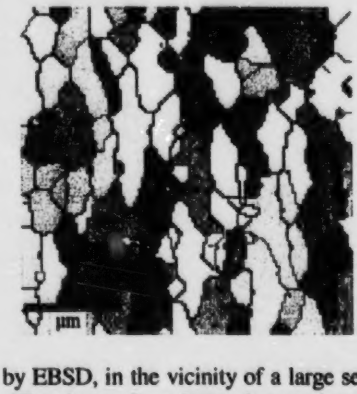

Figure 5. Orientation map of a 98% cold-rolled AA8014 sample (ND-RD section)

Fig.6 shows the grain structure as determined by EBSD, in the vicinity of a large second-phase particle in a deformed aluminium alloy. The change from large elongated grains to smaller equiaxed grains close to the particle can clearly be seen, and analysis of the orientations shows how the strong rolling texture (fig 6b) becomes more random close to the particle (fig 6c). Previously, this type of investigation could only have been carried out with difficulty using the TEM (e.g. Humphreys 1979).

Quantification of such sub-micron structures readily produces detailed and accurate statistical data which was not previously obtainable and which is invaluable in microstructural modelling. This includes the size, shape and misorientation distributions of subgrains, and in addition, correlations between subgrain orientation, size, shape and misorientation.

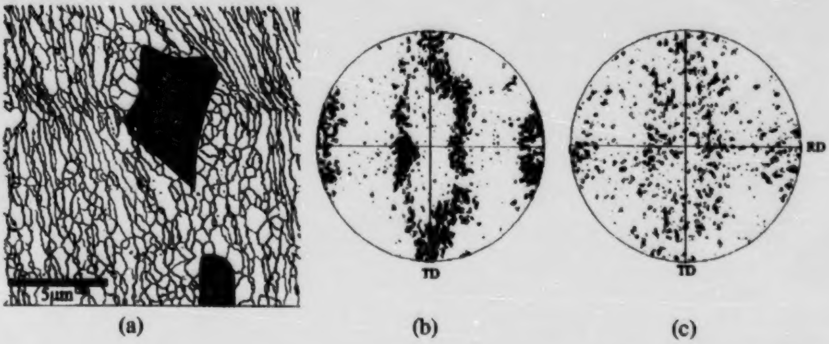

(a) (b) (c)

Fig. 6. EBSD of particle-containing region of 97% cold-rolled AA8014 (ND-RD section). a) Boundary microstructure, b) 111 pole figure far from particle, c) 111 pole figure close to the particle

5 Acknowledgements

The financial support of the EPSRC for this project and the enthusiastic support of Ian Brough and the Light Alloy Processing Group in Manchester, are gratefully acknowledged.

6 References

Farstad, O.; Johanssen, K. and Hjelen, J. (1998). Spatial resolution of EBSP using fully automatic pattern indexing. Proc ICEM 14, Cancun, Mexico, v3 753-754.

Goldstein, J.I., Joy, D.C.; Romig, A.D., Lyman, C.E., Fiori, C and Lifshin, E. Scanning electron microscopy & x-ray microanalysis. Plenum, N. York, (1992).

Humphreys, F.J. (1979). Local rotations at particles in deformed metals. Acta Met. v27, 1801-15

Humphreys, F.J. (1999), Quantitative metallography by electron backscattered diffraction". J. Microscopy (in press).

Humphreys, F.J. and Brough, I (1999). High resolution EBSD with a FEGSEM. J. Microscopy. (in press).

Humphreys, F.J.; Huang, Y.; Brough, I and Harris, C. (1999). EBSD of grain and subgrain structures – resolution considerations. J. Microscopy. (in press).

Krieger Lassen, N.C. (1996). Relative precision of crystal orientations measured from electron backscattered patterns. J. Microscopy. v181, 72-81.

DEVELOPMENT OF THE THREE DIMENSIONAL X-RAY DIFFRACTION MICROSCOPE

R. M. SUTER and K. KOSACK
Department of Physics, Carnegie Mellon University, Pittsburgh, PA 15217

Abstract

We review progress on aspects of the development of the Three-Dimensional X-Ray Diffraction Microscope. This is a tool which promises access for the first time to the internal microstructure of bulk polycrystalline materials. It is a non-destructive probe which is compatible with real-time measurements of microstructure evolution under a wide variety of sample conditions. High energy (~100 keV) x-rays are used because they can penetrate bulk samples. This paper describes several of the technical challenges to full implementation of a robotically controlled measurement system. We describe a two-dimensional silicon pixel detector with threshold based readout appropriate for the expected sparse exposures. The detector can be expanded by tiling the wafers. The 1mm thick wafers will transmit a significant fraction of the x-rays allowing two detectors to be placed in series. This configuration will allow triangulation to determine the position of origin of each Bragg peak. Software data analysis and control algorithms are described for sorting through observed Bragg peaks to determine the set of peaks originating from a central grain of interest. Methods for determining the grain boundary network are described.

Keywords: High energy x-rays, microstructure, synchrotron radiation, x-ray diffraction

1 Introduction

In this paper we review the hardware and software design of an instrument for using small beams of ~100keV x-rays to probe microstructure in bulk polycrystalline materials. Since the small beam intersects a reduced number of grains at any single sample position and orientation, one can imagine isolating the Bragg diffraction from a single grain. We are developing both hardware and software which will make such isolation feasible and allow the nondestructive study of grain boundary networks and dynamics.

The development of a technique to probe internal microstructure is well timed to coincide with the development of computer algorithms, together with the requisite speed, which span the many lengths scales necessary to simulate microstructure (Phillips 1998, Wolf 1998). While the algorithms may start from first principles, it is necessary to check the relevance of their results against real materials. For example, it is well known that trace amounts of impurities which segregate to boundaries may dramatically alter the behavior of a subset of grain boundary types (Wynblatt 1999) and thus the properties of materials. In fact, it may be quite impractical or even undesirable to avoid such effects in industrially relevant materials. We look forward to a close interaction between work on simulations and the measurement techniques we are developing.

X-ray microscope measurements will also be complementary to advanced orientation imaging microscopy (OIM). While OIM is capable of measuring huge numbers of grains and grain boundaries, it is inevitably a destructive technique and one which has an anisotropic resolution of grain boundary orientations (Adams 1999). The 3DXDM should have an isotropic resolution but will be too slow to measure large numbers of grain boundaries. While a statistical treatment of evolution under processing is possible with OIM, the 3DXDM will allow the tracking of specific microstructural features as processing takes place. We expect a close interplay between these experimental techniques.

2 Hardware considerations

Construction of the high energy 3DXDM entails several technological challenges. The Riso/ESRF group has addressed several of these hurdles (Lienert 1998, Lienert 1999). Below, we briefly describe the major challenges and we dwell on those on which we are actively working.

Figure 1 shows a schematic of an apparatus. The front end optics generate a monochromatic beam with small cross-section. The high energy x-rays are able to penetrate the bulk sample (dimensions from a millimeter to a centimeter) allowing for transmission measurement of Bragg diffracted beams. The sample is rotated about an axis passing through and normal to the incident beam. With the translation stage placed on top of the rotation stage, the grain or grains lying in the beam can be varied while the rotation axis is fixed relative to the beam. A two-dimensional detector monitors the scattering as the sample is rotated and translated. Due to the small Bragg angles at high energy, the detector covers a significant portion of the sample's reciprocal space. To a good approximation, $Q(\mathrm{nm}^{-1}) = 10\,E(\mathrm{keV})\sin\theta$, where Q is the magnitude of the scattering vector, E is the photon energy, and θ is the Bragg angle; at 100keV, $Q = 50\mathrm{nm}^{-1}$ appears at $\theta = 2.9$ degrees. A single rotation axis suffices to satisfy the Bragg condition for almost all low and moderate order Bragg peaks. The only omitted peaks are those which lie in a cone centered on the rotation axis and having opening angle $\sin^{-1}(G/2k)$, where G is the Bragg scattering vector and k is the photon wavenumber.

The goal of the 3DXDM is to have as small a *gauge volume* as possible.

Here, gauge volume refers to the sample volume to which the measurement is sensitive and hence to the spatial resolution of the microscope. This volume should lie at the intersection of the sample rotation axis, ω, and the incident beam. The small beam cross-section limits the gauge volume in two dimensions. A major design challenge is to limit the length of the gauge volume along the direction of the incident beam. A variety of post-sample optical elements are being pursued, including use of a conical slit system or diffractive optics (Lienert 1999). This approach attempts to limit the hardware gauge volume (HGV). We are exploring two additional avenues: triangulation by a pair of detectors in series and software algorithms which determine grain dimensions by tomography. We discuss detectors here and postpone software until the following section.

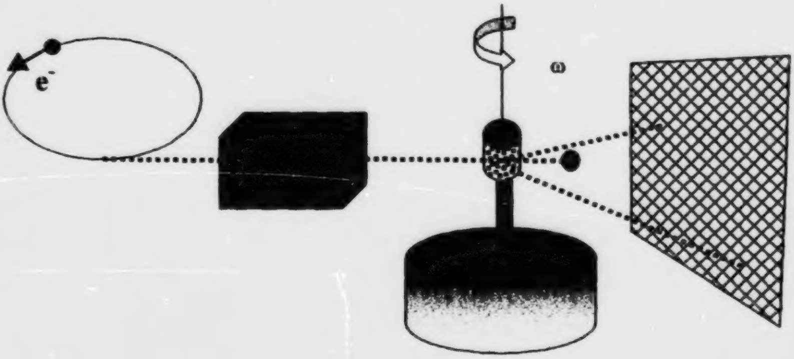

Fig. 1: A schematic diagram of a high energy three dimensional x-ray diffraction microscope. The synchrotron source is at left. The extracted beam first enters the monochromator / optics box. The conditioned beam then strikes the sample which sits on the ω rotation stage which, in turn, is mounted on an XYZ translation stage. A two dimensional pixel detector is represented at right along with a protective beam stop.

Detector development. The 3DXDM puts stringent requirements on the detector system. Coverage of a five degree cone around the incident beam extends to $Q = 44\text{nm}^{-1}$ at $E = 100\text{keV}$ or roughly to {220} Bragg peaks from a crystal with lattice constant $a = 0.4\text{nm}$. Gaining sufficient resolution to observe strain effects requires on the order of 10^7 pixels over this angular region. Furthermore, the measurement requires rapid and efficient data transfer due to the multitude of read cycles involved. The good news is that counting rates should be high so that short exposure times can be used. We expect the overall time limiting factor to be the mechanical motions of the sample stage.

To meet the above detector requirements, we are developing a new silicon based pixel detector system. The system allows selected pixel readout based on a threshold charge level which is preset for each pixel. The readout is performed by a special purpose integrated circuit which was developed for high energy physics particle tracking systems and has been employed in silicon strip detectors (Mathew 1998). Since only pixels with significant exposure are read out, software elimination of irrelevant data is greatly reduced compared to a CCD type detector. Effective data transfer rates are increased by orders of magnitude for sparse exposures. The device layout allows for tiling together many wafers to build a large detector. Furthermore, the silicon detector chip is only ~1mm thick. 100keV photons have significant transmission and one can place two detectors in series. This arrangement allows rapid triangulation to determine the intersection of the diffracted beam with the incident beam and, thus, the grain of origin of observed Bragg peaks. Such a scheme may eliminate the need for post-sample optical elements. We expect to begin testing hardware during the summer of 1999. Various layout schemes will be tested by ray tracing Monte Carlo simulations to determine their ability to localize and restrict the gauge volume.

It should be noted that any triangulation scheme is difficult because of the small Bragg angles at high energy. The length of the hardware defined gauge volume (HGV) determined this way scales as $S/\sin(2\theta)$, where S is an effective slit size. It may be possible to limit S to 10 μm. Even at the outer edge of a 5° cone, one obtains 11S, while at 20°, this is reduced to about 3S. An annular ring of detectors covering relatively large angles may be desirable.

3 Algorithms and software

The measurement of a grain boundary network requires an iterative two-step process; we refer to these steps as *orientation determination* and *boundary determination*. The goal of orientation determination is actually two-fold: to determine a grain's crystallographic orientation and to reduce the gauge volume dimensions to roughly a sphere with a diameter equal to the cross-sectional size of the incident beam. We call this the minimum gauge volume (MGV). We assume that the incident beam cross-section is small compared to the grain size so the HGV is a long cylinder or ellipse. In this case, as the sample is rotated a central grain remains in the incident beam while other grains transit across the HGV. After rotation through a large angle, the central grain has had a large volume of it's reciprocal space probed whereas other grains have had only a smaller region. The software goal is to identify those Bragg peaks which belong to a mutually consistent family associated with the central grain. Given the different angles of incidence for the different Bragg peaks, the grain is localized to the MGV (the MGV is thus a volume defined in the sample frame of reference whereas the HGV is fixed in the laboratory frame). The grain orientation is over determined so an optimized orientation matrix can be evaluated.

Once a central grain's orientation is known, it's boundaries must be determined. We have considered both the case in which the HGV is small compared to the grain size in all directions and the case of a long HGV. For the first case, we have developed an "edge tracking" algorithm which traces a half intensity contour in three dimensions. Boundary points are then stored in a reference frame fixed to the sample. Using simulated data, we have been able to map several neighboring grains and find their common boundaries. We are currently working on mathematical representations of the grain boundary network which will allow optimization of boundary position and topography with respect to multiple data sets obtained from different grains and from different Bragg peaks from the same grain.

In the case of an elongated HGV, one can use both the shape of diffracted beams (Gastaldi 1988) (subject, however, to the $1/\sin(2\theta)$ problem) and the integrated intensities to determine grain size and shape. In either case, one must raster over the entire grain from at least two incident beam orientations (i.e., using two different Bragg peaks).

In order for the 3DXDM to operate at reasonable speed, on-line data analysis must inform the system and step through the entire sequence of orientation determination, grain shape measurement, boundary storage, and sequencing to a neighboring grain. Below we describe several of the robotic control issues.

3.1 Peak tracking

The first task is to take detector output on a pixel-by-pixel basis and track possible Bragg peaks. We assume that a Bragg peak may extend over several pixels in a given exposure and *will* extend over more than one ω setting (i.e., the ω step size should be less than the resolution width). We set a threshold charge level below which pixels are ignored. For pixels with above threshold charge, we accumulate the three dimensional center-of-mass position of a peak by performing a charge-weighted sum over all pixels within a pre-set resolution volume extending in detector coordinates, (y_d, z_d), and in angle, ω. Illuminated pixels outside the resolution volume of a peak being tracked are considered to be distinct peaks. When it is determined that a given tracked peak is no longer present on the detector the center-of-mass coordinates are returned for processing.

3.2 Identification of central grain Bragg peaks

When the (x_d, y_d, ω) coordinates of a peak are determined, the scattering vector, $\mathbf{G}_{lab}$, is calculated in the laboratory frame of reference by simple geometry. This vector is then rotated by ω into the sample frame to give **G**. Peaks are identified by type ({111}, {200}, etc.) from the magnitude of **G**. Peaks which are not within a pre-set resolution width of an allowed magnitude are discarded as spurious.

We next identify families of mutually consistent Bragg peaks. These are groups of peaks whose angular relations are within a pre-set tolerance of valid angles for the relevant peak types and crystal structure. Each new peak, G_j, is tested for compatibility with each existing family. When compatibility with a non-co-linear pair of peaks in a given family is found, G_j is added to this family. Testing continues to see if the peak is compatible with other families. In addition to being added to any compatible families, the peak becomes the sole member of a new family so that it will be tested against all peaks found after it.

After the rotation process is completed, we must determine which family of peaks is most likely to come from the centered grain. The simplest assumption is that this is the family with the most members. This assumption is checked by generating an orientation matrix for the family and checking that all scattered beams which should have reached the detector were, in fact, observed. Runner-up families are likely to originate from grains close to the rotation axis.

4 Conclusions

While the challenges involved in building a fully functional and automated 3DXDM are substantial, the system appears to be feasible. As the technology evolves, the measurement can be scaled to smaller dimensions without changing algorithms and procedures. For large grained materials (grain dimensions of a few hundred microns), these non-destructive measurements will begin very soon. Over the next year, we expect to make significant advances in detectors and software. Precision sample rotation stages with robotic correction of the sphere of confusion are being developed. Ultimate resolution should be at the micron scale allowing measurement of grains with dimensions of a few tens of microns.

The system described here is complementary to other mesoscale texture measurement techniques. While this system may be slow compared to lower energy white beam x-ray techniques, it is the only method for looking deep inside truly three dimensional microstructures. The high energy 3DXDM will not measure the large numbers of grains accessible to modern OIM systems (Adams 1999), but will be able to measure real-time dynamics in the presence of driving. Information from the OIM will be useful in planning interesting 3DXDM measurements.

Acknowledgements. We would like to acknowledge helpful conversations with Brent Adams, Tony Rollett and Adam Moraviec and technical assistance from Chris Raymond and Lou Chomas. This work was supported primarily by the MRSEC program of the National Science Foundation under Award Number DMR-9632556.

5 References

Wu, C.-T., et al (1999) Mapping the mesoscale interface structure in polycrystalline materials, to be submitted to Ultramicroscopy.

Gastaldi et al. (1988) "In-situ" determination of grain boundary migration rates by synchrotron white beam x-ray topography, Phys. Stat. Sol. (a), Vol. 109, p. 403.

Keblinski, P., Wolf, D., Gleiter, H. (1998) Molecular-dynamics simulation of grain-boundary diffusion creep. Interface Science, Vol. 6, p. 205.

Lienert, U. et al. (1998) Focusing optics for high energy x-ray diffraction, J. Synchr. Rad., Vol. 5, p. 226.

Lienert, U., et al. (1999) X-ray optics for the local structural characterization of materials with synchrotron radiation, J. Synchr. Rad., submitted.

Mathew, P., *Construction and evaluation of a high resolution silicon microstrip tracking detector and utilization to determine interaction vertices*, Ph.D. Thesis, Carnegie Mellon University, 1997.

Phillips, R (1998) Multiscale modelling of the mechanics of materials, Curr. Opinions in Solid State and Mat. Sci., Vol 3, p. 526.

Takashima, M., Wynblatt, P. and Adams, B.L. (1999) Correlation of grain boundary character with wetting behavior. *Proceedings of the 12th International Conference on the Texture of Materials*, this volume.

NON-DESTRUCTIVE CHARACTERIZATION OF TUBE SEGMENTS BY MEANS OF NEUTRON DIFFRACTION

H.-G. BROKMEIER
Institut für Werkstoffkunde und -technik der Technischen Universität Clausthal, c/o GKSS-Forschungszentrum, Geesthacht, Germany

Abstract

A method has been tested based on neutron diffraction to investigate the average texture over the thickness of Al, Cu and Nb tubes. The scanning routine follows the reflection technique after Schultz to measure the non-uniform samples in a non-destructive way. A sufficient agreement between a non-destructive tube measurement and a measurement carried out on a cut tube specimen was obtained to verify the method. The results of three examples an Al tube of 90mm in diameter, a Cu tube of 35mm in diameter and a Nb tube of 84 mm in diameter will be presented.

Keywords: Tube texture, neutron diffraction, non-destructive measurement, Nb, Al, Cu

1 Introduction

The motivation of this project was to produce highly symmetrical cavities from a tube to build a new accelerator. Moreover, these cavities must have an excellent surface. One of the preferred materials is very pure niobium with RRR-values of 300 or better. In order to produce such cavities around the perimeter of the tube, which fulfill such high requirements a homogeneous texture around the perimeter is necessary. A texture type for an excellent deep drawing behavior, which should be homogeneous over the wall thickness, has to be settled not to produce a rough surface. Among other topics of this project first a method has to be tested to measure local textures of tube segments with about 100 – 150 mm in length. According to a good correlation between texture result and cavity formation and also according to the expensive production of these highly pure niobium tubes the measurement must be non-destructive.

Neutron diffraction is well known as standard method to measure bulk textures of some cm^3 (Bunge 1989, Brokmeier 1994). Moreover, it was shown first by Choi et al. (1979) and recently applied by Tarasiuk et al. (1998) that neutron diffraction can be used to measure local textures. To verify the method on non-destructive tube measurements three different tubes are tested.

2 Sample description

In addition to a niobium tube a commercial Cu tube and a commercial Al tube (stock material) were studied. Table 1 gives the dimensions of theses three tubes. Beside the tube segments described in table 1 a ring of 10mm in thickness was cut from the Cu tube as well as form the Al tube. Thereafter, the two rings were divided into small sections of 6x6x1.5 cm^3 for the Cu tube and 6x6x5.0 cm^3 for the Al tube. It should be noticed that the tube segments and the rings have identical orientations and that the small sections can be directly compared with a local area on the tube. The present texture was not for interest but how to reproduce the measured texture of the sections by measuring the local tube texture. Therefor, the texture present at the tubes as well as the materials characteristic was not discussed.

Table 1: Specification of the investigated tubes.

Material	Diameter (mm)	Length (mm)	Thickness (mm)
Aluminium	90	120	5.0
Copper	35	100	1.5
Niobium	84	140	3.0

3 Neutron measurements

The texture measurements were carried out at TEX-2, the neutron texture diffractometer located at the 5MW reactor of the GKSS Research Center Geesthacht, Germany. According to the low sample volume the Al sections and the Cu sections were measured by the spherical sample method (Tobisch and Bunge 1972). Using a beam of 12mm in diameter the whole sample takes part on the scattering and the average crystallographic texture of each peace results. In the case of tube samples the reflection method after Schulz (1949) was used. A nearly parallel beam (horizontal divergence = 0.6°; vertical divergence = 1.4°) was guided to the sample by a Cd-slit of 6mm in diameter. In order to fix a defined local sample volume the outgoing scattered beam was also guided by a Cd-slit of 6mm in diameter. Depending on the differences in the tube thickness the gauge volume is different. It should be pointed out that for texture analysis a precise sample volume is less important than for strain measurements. Figure 1 shows the niobium tube mounted on an Eulerian cradle type Huber 512 having 400mm in diameter.

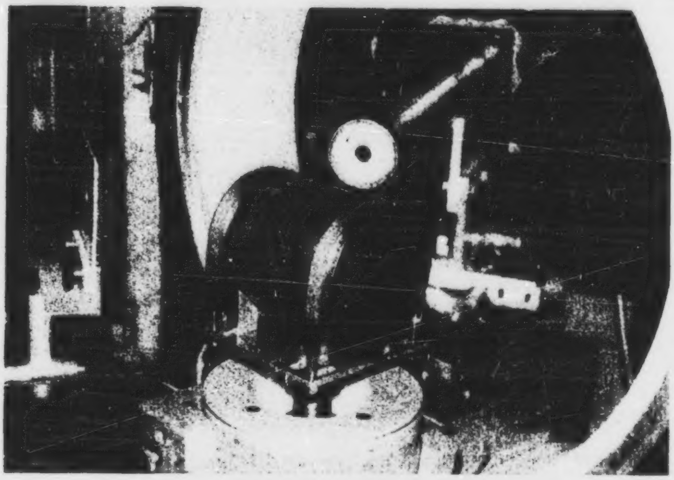

Fig. 1: Nb tube of 140mm in length mounted at TEX-2 (GKSS)

In all cases three pole figures were measured (Al 111, 200, 220; Cu 111, 200, 220; Nb 110, 200, 211). The scanning routine to measure 679 pole figure points by an equal area grid was identical for tubes and sections. To give an impression of the measurements Table 2 collects the main important values a pole figure measurement by neutron diffraction for the Cu-samples describing the peak to background ratio and the statistical relation between the highest and lowest intensity within each pole figure. Together with the reactor statistics during the complete measurement an estimation of the error in counting statistic of each pole figure point can be given. A much bigger error would be expected by the non-uniform sample size of a tube compared to an ideal spherical sample. Stepwise sample rotation around the tube axes after each complete texture measurement allows the documentation of the texture homogeneity along the perimeter. In the case of the Cu and the Al tube two local areas with 30° rotation were measured and in the case of Nb every 30° of rotation the crystallographic texture was determined. Figs 2a- 2d show the complete raw data pole figure for Al 111 and Cu 111 sections and tubes, respectively.

Table 2: Measurements statistics of the Cu-tube and the Cu-section with identical sample orientation

Sample	Reflection	Intensity (counts)		
		Maximum	Minimum	Background
Cu-tube	111	12577	200	200
	200	2965	171	171
	220	2398	121	121
Cu-peace	111	22631	326	326
	200	6066	294	290
	220	4825	246	246

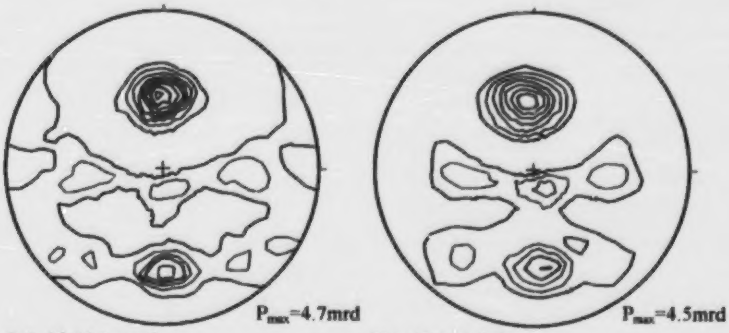

2a) Al 111 section 2b) Al 111 tube

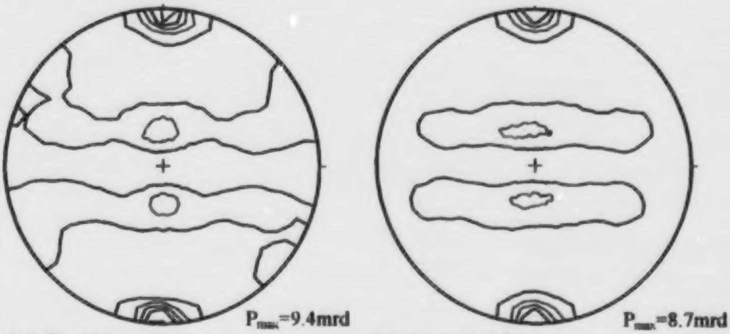

2c) Cu 111 section 2d) Cu 111 tube

Fig. 2: Raw data pole figures of Al 111 and Cu 111 for the tubes and the equivalent sections.

It can be seen clearly that there is a high similarity between the pole figure of tubes and of sections. But it is also visible that the outer part of the tube pole figures is influenced. According to the high penetration of neutrons absorption can be neglected analyzing the peace samples. On the other hand the pole figures obtained for the tube samples has to be corrected for absorption. A partly loss of information at the outer rings of the pole figure leads to a decrease of the texture sharpness, which has been tested by different ODF program systems (ISEM, BEARTEX and popLA).

4 Results

Quantitative texture was obtained by using the iterative series expansion method (Dahms and Bunge 1989). Figs 3 – 5 collect one section of the ODF's for Al, Cu and Nb comparing the results obtained:

- first for the peaces,
- second for the tube samples only with a background correction,
- third for the tube samples with an additionally correction of the outer part of the

pole figures (estimation of the influence of absorption)
- fourth for the tube samples using only the pole figure data up to 70° tilting.

In all three cases (Al, Cu and Nb) it was possible to determine the texture types independent of the sample shape, peace or tube, and also independent of the data evaluation. Looking on the sharpness of the orientation distribution it was found that the peace textures were always stronger. It may result first by an insufficient correction of the background, second by a necessity to improve the absorption

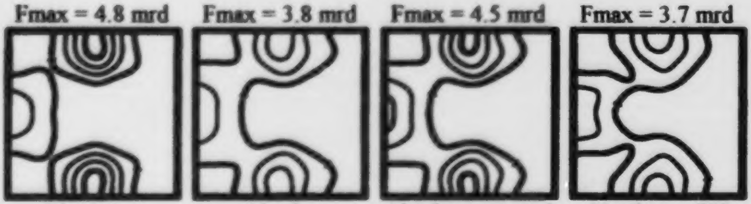

Al-section Al-tube Al-tube corrected Al-tube 70°

Fig. 3: ODF sections PHI/phi1 for phi2 = 0 of Al (levels 1.0, 2.0, 3.0. 4.0 mrd)

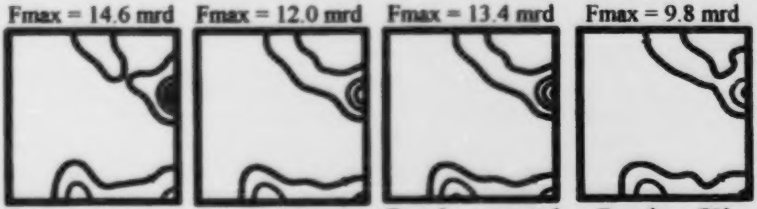

Cu-section Cu-tube Cu-tube corrected Cu-tube 70°

Fig. 4: ODF sections PHI/phi1 for phi2 = 0 of Cu (levels 1.0, 5.0, 9.0., 13.0 mrd)

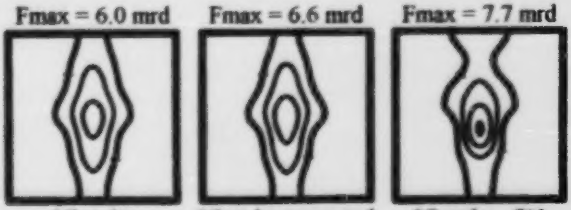

Nb-tube Nb-tube corrected Nb-tube 70°

Fig. 5: ODF sections PHI/phi2 for phi1 = 0 of Nb (levels 1.0, 3.0, 5.0, 7.0 mrd)

In all three cases (Al, Cu and Nb) it was possible to determine the texture types independent of the sample shape, peace or tube, and also independent of the data evaluation. Looking on the sharpness of the orientation distribution it was found that the peace textures were always stronger. It may result first by an insufficient

correction of the background, second by a necessity to improve the absorption correction and third by the normalization of the data. Nevertheless, it can be pointed out that the results of the tube measurements are very close to the comparable investigation of identical sections cut from the tube.

Comparing the texture for different local areas at the tubes it was found that in the case of the Al tube the texture was very homogeneous. Cu shows a variation of the texture sharpness along the perimeter and in the case of the Nb tube an inhomogeneous texture was measured. This would give rise to an inhomogeneous deformation forming cavities.

5 Conclusion

The current paper shows that neutron diffraction is suitable to be applied for tube texture measurements on different materials. Limiting factors of this application are on hand a high counting time if small local areas are necessary and on the other hand the geometrical limits of the used instrument. TEX-2 for example has a limit in the tube dimension, which can be measured, given by the dimension of the Eulerian cradle. There are still improvements thinkable to forward neutron diffraction analysis in the non-destructive texture analysis of non-uniform samples. Nevertheless, compared to other neutron diffraction application the necessity to measure a relatively high number of pole figure points texture analysis needs high counting times. Improvements in the instrumentation as well as in modifications of the scanning routine can combined with new evaluation in front of an ODF analyses to think on much more complicated sample geometry's.

Thanks are due to Dr. V. Singer and Dr. H. Kaiser, for an intense discussion of the niobium tube project initiated this work. The German Ministry for Research and Foundation (BMBF) has been supported the neutron diffraction experiments at TEX-2 under the contract number 03BR4CLA7. The author would like to thank the GKSS-Research Center Geesthacht for opportunity to use the neutron facilities at the FRG-1.

6 References

Brokmeier, H.-G. (1994) *Mat. Sci. Forum* Vol. 157-162, pp. 59-70.

Bunge, H.J. (1989) *Textures Microstruc.* Vol.10, pp. 265-308.

Choi, C.S., Prask, H.J. and Trevino, S.F. (1979) *J. Appl. Cryst.* Vol.12,pp. 327-331.

Dahms, M. and Bunge, H.J. (1989) *J. Appl. Cryst.* Vol. 22, pp. 439-447

Schulz, L.G. (1949) *J. Appl. Phys.* Vol. 20, pp. 1033-1036.

Tarasiuk, J., Wierzbanowski K. and Baczmánski, A. (1998) *Mat. Sci. Forum* Vol. 273-275, pp. 283-288.

Tobisch J. and Bunge H.J. (1972) *Texture* Vol.1, pp. 125-127.

A METHOD OF MISORIENTATION DISTRIBUTION CALCULATION USING ODF DATA

W. MAO, G. ZHU and Y. YU
Department of Materials Science and Engineering
University of Science and Technology Beijing, Beijing, China

Abstract

A new method of misorientation distribution calculation was proposed by using the orientation distribution function data, which could give a very good statistic description of misorientation distribution in polycrystalline materials. The basis assumption is that the contact probability of one grain to an other is proportional to their orientation densities. According to this assumption the statistic misorientation distribution can be calculated using the ODF data. Based on the method the misorientation distribution during a physical metallurgical process, e.g. phase transformation or recrystallization could also be calculated by using the two ODFs before and after the process. The calculation method was described in details, and calculation examples were also given.

Keywords: Misorientation calculation, misorientation distribution, ODF application

1 Introduction

The misorientation between neighboring grains has significant influence on the boundary characteristic and its physical metallurgical behavior (Hughes and Hansen 1993; Raabe et al. 1996). Based on the group theory and random orientation distribution MacKenzie (1958, 1964) and Morawiec (1995) calculated the distribution of misorientation angles of polycrystalline aggregates with cubic or other crystalline symmetry. However many polycrystalline aggregates do not have a random orientation distribution, and their true misorientation distributions could only be determined by the EBSD technique, with which a statistic measurement is extremely vast and numerous. The misorientation distribution in textured materials is very frequently needed by the material scientists, therefore a method of misorientation distribution calculation based on the ODF data is proposed to obtain a statistic misorientation distribution without too much experimental measurement.

2 Basic assumptions and principle calculation process

It is known that the orientation density in the ODF is related to the volume fraction of the correspondingly oriented grains, therefore the calculation is based on following two assumptions:

1. Grains in a polycrystalline aggregate have the possibility to be neighbored with all other kinds of grains, of which the orientations vary in the whole orientation space.
2. The possibility level of the two kinds of differently oriented neighboring grains is proportional to the multiplication of their orientation density.

Based on these assumptions the calculation will be more suitable for the polycrystalline materials with fine grained and homogenous microstructure because of its better statistic background for the calculation.

According to Bunge (1981) an orientation g can be written as:

$$[g]=$$

$$\begin{bmatrix} \cos\varphi_1\cos\varphi_2-\sin\varphi_1\sin\varphi_2\cos\Phi & \sin\varphi_1\cos\varphi_2+\cos\varphi_1\sin\varphi_2\cos\Phi & \sin\varphi_2\sin\Phi \\ -\cos\varphi_1\sin\varphi_2-\sin\varphi_1\cos\varphi_2\cos\Phi & -\sin\varphi_1\sin\varphi_2+\cos\varphi_1\cos\varphi_2\cos\Phi & \cos\varphi_2\sin\Phi \\ \sin\varphi_1\sin\Phi & -\cos\varphi_1\sin\Phi & \cos\Phi \end{bmatrix} \tag{1}$$

and the orientation difference Δg of orientation g_1 and g_2 can be expressed as:

$$\Delta g=[g_2]\cdot[g_1]^{-1}=\begin{bmatrix}\Delta g_{11} & \Delta g_{12} & \Delta g_{13}\\ \Delta g_{21} & \Delta g_{22} & \Delta g_{23}\\ \Delta g_{31} & \Delta g_{32} & \Delta g_{33}\end{bmatrix} \tag{2}$$

where $[g_1]^{-1}$ is the inverse matrix of $[g_1]$. The misorientation angle γ between the two orientations g_1 and g_2 is:

$$\gamma=\mathrm{acos}\left(\frac{\Delta g_{11}+\Delta g_{22}+\Delta g_{33}-1}{2}\right) \tag{3}$$

For the cubic crystalline materials there are 24 identical crystalline rotation operations related to the point group 432 and the minimum rotation angle $\gamma_{min}=\delta$ should be chosen as the real misorientation angle.

If an ODF is known the volume element dv around an orientation g is defined as (Bunge 1981):

$$dv = f(\varphi_1,\Phi,\varphi_2)dg = f(\varphi_1,\Phi,\varphi_2)\frac{1}{8\pi^2}\sin\Phi d\varphi_1 d\Phi d\varphi_2 \tag{4}$$

Hence a relative possibility p_i that two differently oriented grains are neighbored can be written as:

$$p_i=dv_1\times dv_2 \tag{5}$$

which is correspondingly related to a misorientation angle δ_i.

If the range of misorientation angle $[0, \delta_{max}]$ is divided into N equal intervals with the span $\Delta\delta$, the relative frequency f_k (k=1, 2, ……, N) that indicates the misorientation possibility in the interval $[(k-1)\Delta\delta, k\Delta\delta]$ can be expressed as:

$$f_k = \frac{\sum_{(k-1)\Delta\delta}^{k\Delta\delta} p_i\Delta\delta}{\sum_0^{\delta_{max}} p_i\Delta\delta} \tag{6}$$

which can establish the misorientation distribution. The $\sum_{(k-1)\Delta\delta}^{k\Delta\delta} p_i\Delta\delta$ here means the summation of all the relative possibilities p_i, of which their misorientation angles δ_i fall into the interval $[(k-1)\Delta\delta, k\Delta\delta]$.

3 Calculation of misorientation distribution

For the calculation the orientation space is homogeneously divided into 936 small space elements with the equal volume size, and 936 representative orientations were chosen in the corresponding small element respectively (Hirsch and Lücke 1988), after which the δ and p_i can be calculated according to equation 1-3 and 4-5 respectively. For the rolling samples the sample coordinate symmetry is generally included in the ODF, which should be considered in the misorientation calculation. In this case an orientation is considered to be identical to its sample symmetrical orientation and could however lead to different misorientation angles. Therefore there should be actually 936×4=3744 space elements, in which the other 936×3 orientations were obtained by rotation of first 936 orientations around RD, TD and ND for 180° respectively. Hence equation 4 and 5 are written as (m, n=1, 2, 3, ……3744)

$$dv_m = f(\varphi_{m1},\Phi_m,\varphi_{m2})\frac{1}{3744}, \qquad dv_n = f(\varphi_{n1},\Phi_n,\varphi_{n2})\frac{1}{3744} \tag{7}$$

$$p_i = dv_m\cdot dv_n \tag{8}$$

For the random orientation distribution there is $f(\varphi_1,\Phi,\varphi_2)\equiv1$, and the calculation result is shown in figure 1. Together with the calculation the statistic measurement on Al-2.8%Ag-1%Ge alloy conducted by Hirth and Gottstein (1996) is also shown in figure 1. The calculation result is identical with the calculation according to

MacKenzie (1958, 1964). There should be a weak texture in the Al-2.8%Ag-1%Ge alloy since a slight deviation towards lower angle is observed compared with the calculated random distribution, and the textured grains will produce a misorientation distribution concentrated at lower angle area.

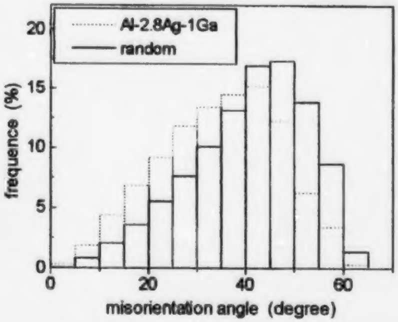

Fig. 1 calculated misorientation distribution for random ODF.

4 Analysis of misorientation distribution in textured aluminum sheet

A high purity aluminum sample (>99.99% Al) is taken, which was 95% cold rolled and then annealed at 300 °C for about 50 minutes. The incomplete pole figures {111}, {200} {220} and {113} were measured in the center layers of the rolling samples and the ODFs were calculated (Bunge 1981). Figure 2 gives the ODF sections of the high purity aluminum sheet before and after annealing, which demonstrates the typical rolling and recrystallization texture in Al sheets.

It was supposed that dv_m and dv_n in equation 8 are the volume elements of the rolling and annealing samples respectively. The misorientation distribution in-between can be calculated, which could indicate the misorientation distribution between deformed grains and recrystallization grains during the recrystallization process. Figure 3 gives the calculated misorientation distribution. Compared with the random distribution no drastic differences can be observed except the distribution is moved a little bit towards the area with higher misorientation angle (fig. 3a), indicating that more high angle boundaries between recrystallization grains and deformed matrix were presented during the annealing. Trying to divide the misorientation distribution into two parts, i.e. a random part and a characterized part, it was found that 67% of the distribution density should belong to the random part. If the random part is reduced from the whole distribution a characterized distribution can be obtained (black area in fig. 3b), which demonstrates that the misorientation distribution is concentrated around the area 45°~50°. The characterized part should be the real misorientation distribution during annealing, which proves the theory that the recrystallization process is completed generally by means of the migration of high angle boundaries.

The great random part might be induced by the too much simplified initial assumptions. Perhaps a third assumption should be added, that the random part should be removed from the calculated distribution since in many cases the first assumption that leads to the great random part is not valid, i.e. grains in a polycrystalline aggregate do not have the possibility to be neighbored with all other possible grains. However the calculation would become impossible without the first assumption. The more details should be investigated further.

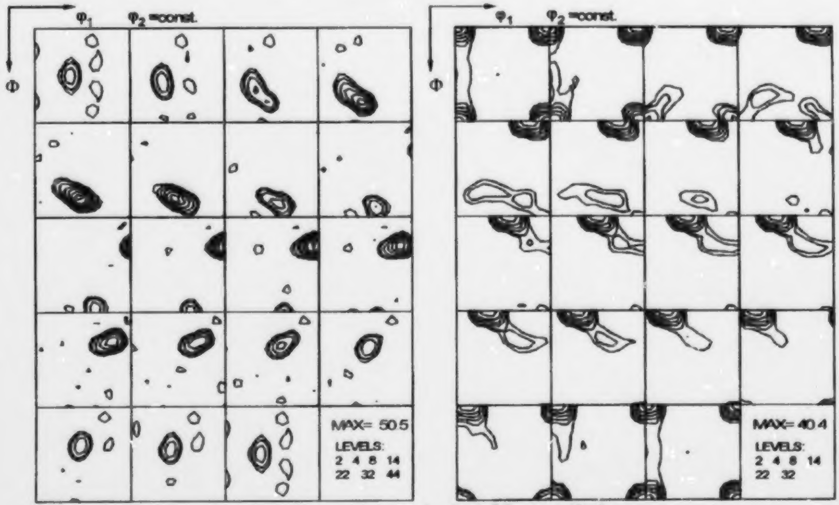

a. 95% rolled b. 300 °C annealed

Fig. 2 ODF sections of the high purity aluminum sheet.

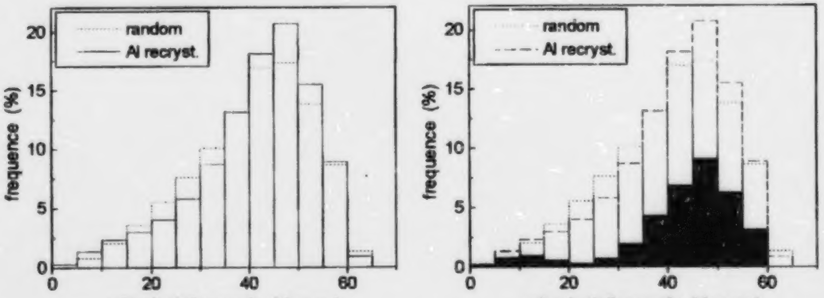

a. general distribution b. characterized distribution

Fig. 3 Analysis of the misorientation distribution of the high purity aluminum.

5 Summary

Using the ODF data the misorientation distribution of the polycrystalline aggregate can be calculated in a statistic view, especially for the textured materials. Based on the method the calculated misorientation distribution can be divided into two parts, i.e. a random part and a characterized part. It might be reasonable to removed the random part from the calculation result because of the incorrect and inevitable simplified assumption. The calculation can be used to analyze any physical metallurgical processes involving boundary migration. The further modification of the calculation still needs to be done.

6 Acknowledgment

The authors would like to acknowledge the National Nature Science Foundation of China for the financial support.

7 References

Bunge, H.J. (1981) General outline and series expansion method, in *Quantitative Texture Analysis*, (ed. H.J. Bunge and C. Esling), DGM-Informationsgesellschaft, Oberursel, pp. 1-72.

Hirsch, J. and Lücke, K. (1988) Mechanism of deformation and development of rolling textures in polycrystalline f.c.c metals-II., *Acta Metall.*, Vol. 36, No. 11. pp. 2883-2904.

Hirth, S. and Gottstein, G. (1996) Microtexture of discontinuous precipitation in an Al-2.8at%Ag-Ga alloy, Proc. 11th. Inter. Conf. on Texture of Materials, (ed. Z. Liang et al.), Inter. Acad. Publisher, Xi'an, Vol. 2, pp. 1339-1344.

Hughes, D.A. and Hansen, N. (1993) Microstructural evolution in nickel during rolling from intermediate to large strains, *Metall. Trans. A*, Vol. 24, No. 9. pp. 2021-2037.

MacKenzie, J.K. (1958) Second paper on statistic associated with the random disorientation of cubes, *Biometrica*, Vol. 5, June. pp. 229-240.

MacKenzie, J.K. (1964) The distribution of rotation axes in a random aggregate of cubic crystals, *Acta Metall.* Vol. 12, No. 2. pp. 223-225.

Morawiec, A. J. (1995) Misorientation-angle distribution of randomly oriented symmetric objects, *J. Appl. Cryt.*, Vol. 28, March. pp. 289-293.

Raabe, D., Fischer-Bühner, J., Ball, J. and Gottstein, G. (1996) Texture in intermetallic compounds-experiments and simulations, Proc. 11th. Inter. Conf. on Texture of Materials, (ed. Z. Liang et al.), Inter. Acad. Publisher, Xi'an, Vol. 2, pp. 941-950.

DETERMINATION OF HETEROGENEOUS TEXTURES BY X-RAY DIFFRACTION

K. EL GHAZOULI, J. J. HEIZMANN, B. BOLLE and L. JOLLY
Laboratoire d'Etude des Textures et Application aux Matériaux LETAM CNRS URA 2090 ISGMP, Université de METZ Ile de Saulcy, 57045 METZ Cedex 01 FRANCE
Ch. VALOT
Laboratoire de Recherches sur la Réactivité de Solides LRRS CNRS UMR 5613, Université de BOURGOGNE Faculté des Sciences Mirande B.P. 400, 21011 DIJON Cedex FRANCE

Abstract

A method using different strategies of measurement which combines the Shulz method and the small incidence one, or measurement with a constant depth penetration of X-ray is described to determine the texture gradients in thin films. This method which only uses one diffraction line (hkl) is tested on samples having an artificial texture gradient. This method is also applied to know the real texture gradient in a thin film of zircon. Quantitative texture analysis results made with the vector method are presented.

1 Introduction:

Heterogeneous textures are very often present in thin films. There is usually a great texture variation between the outside surface and the interface with the substrate. It seems impossible to know this variation because one does not know from where the diffracted beams are coming. Recently, several authors try to solve this problem by using techniques able to give information from different thicknesses, which depend on the depth of X-rays (or neutrons) penetration. All of these studies, as the one presented here, assume that the whole layer is divided into few sub-layers having an homogeneous texture. Choi (Choi et al. 1979) used successive neutrons diffraction orders with the Shulz geometry but this technique is not suitable for X-rays because the diffracted intensities drops a lot when the order increases. Morawiec (Morawiec 1990, 1992) and Tarasiuk (Tarasiuk et al. 1993, 1994) based on their measurement with several different poles figures (PF) in Shulz geometry, so different depths of penetration can be reached ; they have then to solve a system in which there are more unknowns than equations by an iterative process to approach a solution. In the present paper the layer is also divided in homogeneous sub-layers, and PF's of only one set of lattice planes are measured in different geometric conditions. This leads to a system of linear equations equal to the number of unknowns to obtain the PF of each sub-layer.

2 Principle of the method

To study the texture of a sample, a four circles goniometer is regularly used with : ψ (tilt angle), φ (azimuth), ω and 2θ. Several strategies of movements of the sample can be used to get a PF. The Shulz method (ω = 0 with a ψ, φ scanning). The low or great incidence method (ω≠0 with a ψ, φ scanning). The Player method (Player et al. 1992) in which the sample turns around the incident beam. The constant thickness method (Jolly et al. 1996) for which a ω, ψ, φ scanning is needed to obtain a PF which intensities come from the same thickness of the sample.

Whatever the method could be, the diffracted intensity by an elementary volume dV is written as follows : $dI_{\psi_g\varphi_g\omega_g} = iK_{\psi_m\varphi_m} e^{-\mu(X_1+X_2)}dV$

Where : ψ_g φ_g ω_g are the angles of the goniometer and ψ_m φ_m the angles of the diffracting planes in the reference bounded to the sample, i the intensity diffracted by a unit volume without absorption, μ the linear absorption coefficient, X_1, X_2 the paths of the incident and diffracted beams in the sample and K the texture coefficient of the volume dV. The relationships between the angles ψ_g φ_g ω_g and ψ_m φ_m are known (Heizmann and Laruelle 1986).

When the texture is homogeneous, for a given position of the goniometer, the texture coefficients $K(\psi_m\ \varphi_m)$ can easily be determined after correction.

$$I_{\psi_g,\varphi_g,\omega_g} = iK_{\psi_m\varphi_m}\int_V e^{-\mu(X_1+X_2)}dV = iK_{\psi_m\varphi_m}V_d$$

When the texture changes with the depth the layer is divided into several sub-layers, each of them with an homogeneous texture. Let us consider two sub-layers with respectively thickness t_1, t_2 and texture coefficients K^1, K^2. The diffracted intensity at the position: ψ_g φ_g ω_g of the goniometer is the following :

$$I_{\psi_g\varphi_g\omega_g} = i(K^1_{\psi_m\varphi_m}V^1_d + K^2_{\psi_m\varphi_m}V^2_d F^1)$$

Where V^1_d, V^2_d are the diffracting volume of the two sub-layers and F^1 the filter effect induced by the upper sub-layer. In order to know the texture variation, we use PF's of the same lattice plane measured with different geometry ; in fact these measurements give ratios of intensities between the two sub-layers which are different because the absorption is not the same.

So for instance with two measurements made with two different strategies : ψ_g φ_g ω_g and ψ'_g φ'_g ω'_g one obtains two sets of equations each of them having two unknowns. In fact these measurements give two PF's which are distorted.

$$\begin{cases} I_{\psi_g\varphi_g\omega_g} = i(K^1_{\psi_m\varphi_m}V^1_d + K^2_{\psi_m\varphi_m}V^2_d F^1) \\ I'_{\psi'_g\varphi'_g\omega'_g} = i(K^1_{\psi'_m\varphi'_m}V'^1_d + K^2_{\psi'_m\varphi'_m}V'^2_d F'^1) \end{cases}$$

In order to reduce the number of unknowns the previous PF's are transformed into "virtual" PF's i.e. PF's which would have been measured with the Shulz method and which preserve the intensities of each strategy (localisation correction). So these two "virtual" PF's which are in the same reference can be compared directly. The previous equations become :

$$\begin{cases} I_{\psi_m\varphi_m} = i(K^1_{\psi_m\varphi_m}V^1_d + K^2_{\psi_m\varphi_m}V^2_d F^1) \\ I'_{\psi_m\varphi_m} = i(K^1_{\psi_m\varphi_m}V'^1_d + K^2_{\psi_m\varphi_m}V'^2_d F'^1) \end{cases}$$

3 Experimental test

In order to test the method an artificial sample made of two aluminium foils stacked together with a β angle between their rolling directions is prepared. The top layer is 3 µm thick the other is 6 µm thick.

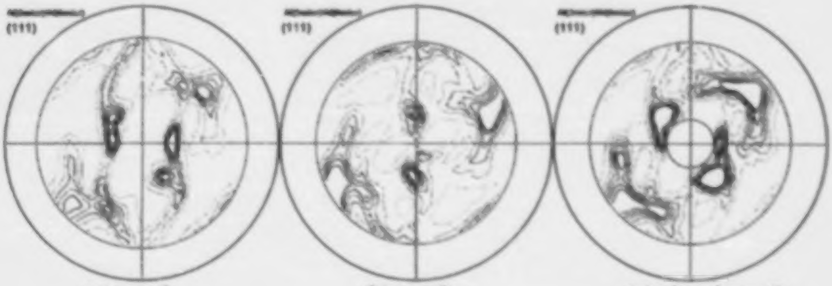

(a) ωg=0 (b) ωg≠0 (c) virtual ωg=0

Fig. 1 : (a) and (b) (111) PF of the whole Al layer measured with two different strategies, (c) virtual PF after localization correction of the PF (b)

Two PF's (111) have been measured with Fe K_α radiation : the first one in Shulz conditions (ω_g=0°) Fig. 1a, the other one with a great incidence angle (ω_g=20°) Fig. 1b. The "virtual" PF is shown on Fig. 1c. The analysis of the intensities from the Fig. 1a and 1c gives after separation the texture of each sub-layer : Fig. 2a and 2b.

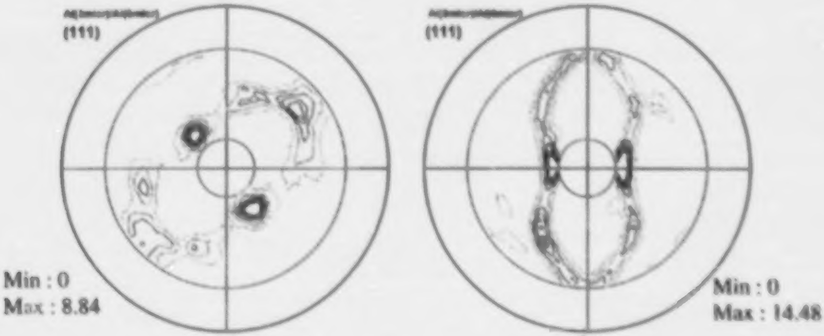

(a) (b)

Fig. 2 : normalized (111) PF after separation of the (a) 3µm thick Al layer and (b) 6µm thick Al layer, deduced from PF 1a and 1c

These two PF's can be compared to those measured on each foil alone: Fig. 3a and 3b. There is a good agreement with the PF obtained after separation except the maximum level of the 6µm sub-layer (19.6 instead of 14.5). This difference comes mainly from the blind areas where the information is not taken into account during the normalisation procedure.

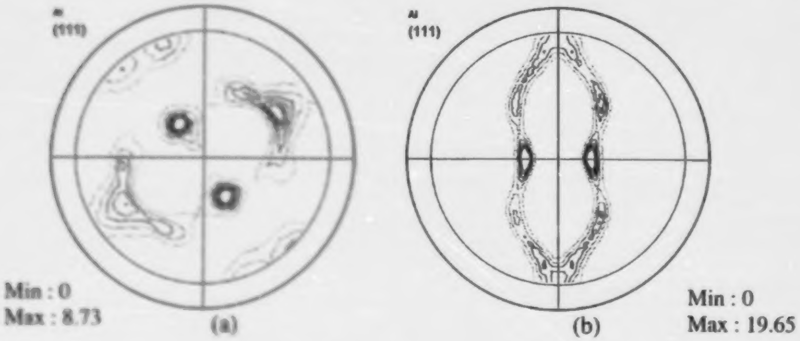

Fig. 3 : normalized experimental (111) PF corrected from the diffracting volume of each layer measured separately, (a) 3μm thick Al layer (b) 6μm thick Al layer

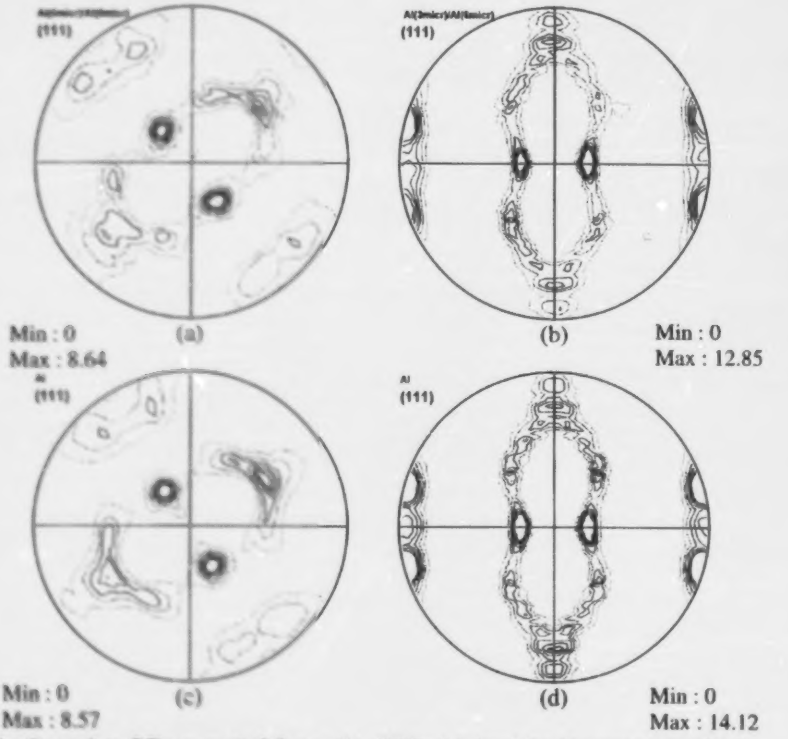

Fig. 4 : Complete PF computed from the ODF obtained by the vector method analysis. (a) and (b) PF of the two layers obtained after separation. (c) and (d) PF of each layer measured alone

The data of the previous PF's and those coming from the (200) PF's are analysed with the vector method and the complete PF's are calculated ; the results are shown Fig. 4a to 4d. There is now a very good agreement between the PF's obtained after separation and those measured on the separate foils. It is pointed out that this method gives a unique solution which accuracy strongly depends on the choice of the measurement strategy. The results are as much precise as the ratio of the diffracted intensities, coming from the two layers of each strategy, is the most different possible. In other words for the previous example when the ω_g is as great as possible i.e. close to the θ angle. Nevertheless as the ω_g angle is also the radius of the central blind area on the PF, there is a loss of information which can be harmful for the precision.

4 Application

This method is applied to know the texture variation through a thin layer 7µm thick of monoclinic zirconium oxide ZrO_2 obtained by oxidation of a zirconium sheet (Valot, 1995). Two PF's (-111) are measured : the first one with ω_g=0 (Shulz) the other with ω_g=-10° (Fig. 5). From these two PF's it is clear that a texture gradient exists in the oxide layer. To get more information on the change in texture, the 7µm oxide layer is divided into two sub-layers and the boundary between them is located at different depths (1µm, 2µm and 3µm). The separation procedure gives PF's of the two sub-layers for each position of the boundary. The evolution of position of the maximum named A or B according to thickness of the sub-layers is drawn on the Fig. 6. It seems that the change of texture across the oxide layer could be explained by rotations around the normal of sample and around the rolling direction. Other experiments must be done to confirm these observations.

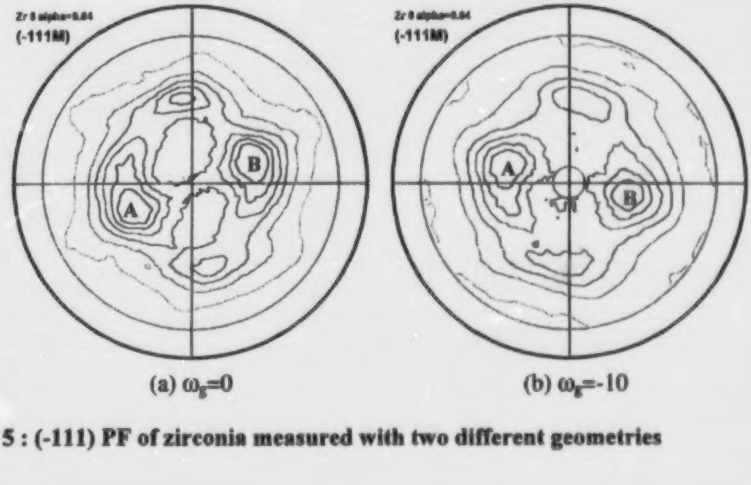

(a) ω_g=0 (b) ω_g=-10

Fig. 5 : (-111) PF of zirconia measured with two different geometries

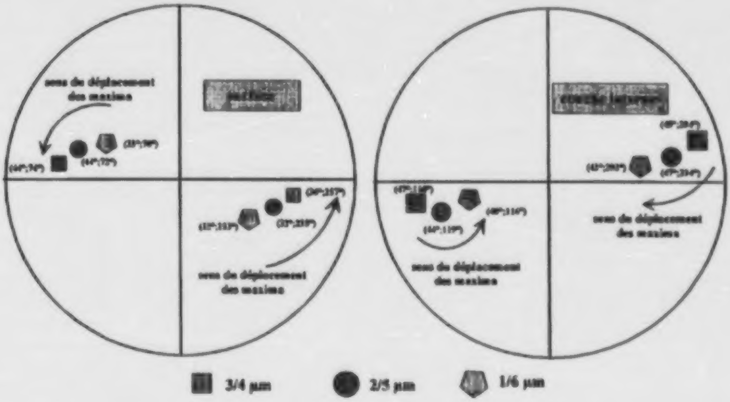
sens de déplacement des maxima
sens de déplacement des maxima
couche inférieure
sens de déplacement des maxima
sens de déplacement des maxima
3/4 µm
2/5 µm
1/6 µm

Fig. 6 : position of the maximum according to thickness of the sub layers

5 Conclusion

This X-ray diffraction method can be used on thin films which thickness is lower than t =1/µ (absorption coefficient). It works with only one diffraction line and it is possible to choose the best geometric conditions of measurement to minimise errors. The results either on artificial or real texture gradients show a promising method. This method could theoretically work with several sub-layers by using at least as many different geometric conditions as the number of sub-layers. Nevertheless it will be unrealistic to use more than three sub-layers to preserve the sensitivity of intensities variations between the different observation conditions of the film. It will be better to move the boundary between the sub-layers rather than to increase their number.

6 References

Choi C. S., Prask H. J. and Trevino S.F. (1979) *J. Appl. Cryst.*, Vol. 12, pp. 327

Heizmann J.J. and Laruelle C. (1986) *J. Appl. Cryst.*, Vol. 19, pp. 467-472

Jolly L., Bolle B., Laruelle C., Valot C. and Heizmann J.J. (1996) *ICOTOM 11*, (ed. by Z. Liang, L. Zuo & Y. Chu) International Academic Publishers, Vol. 1, pp. 116-121

Morawiec A. (1990) *Archives of Metallurgy*, Vol.35, pp. 395-400

Morawiec A. (1992) *J. Phys. Condens. Matter*, Vol. 4, pp. 339-349

Player M.A., Marr G.V., Gu E., Savaloni H. and Öncan N. (1992), *J. Appl. Crys.*, Vol. 25, pp. 770-777

Tarasiuk J., Wierzbanowski K., Baczmanski A. and Helmholdt (1993), *Archives of Metallurgy*, Vol. 38, pp. 339-352

Tarasiuk J., Wierzbanowski K. and Baczmanski A. (1994) *Materials Science Forum*, Vol. 157-162, pp. 213-220

Valot Ch. (1995) PhD thesis, University of Bourgogne, France

QUANTIFICATION OF RECRYSTALLIZED FRACTION FROM ORIENTATION IMAGING SCANS

S.I. WRIGHT
TexSEM Laboratories, Draper, Utah, USA

Abstract

Two methods have been proposed for distinguishing recrystallized structure from deformed structure in a polycrystalline material using electron backscatter diffraction (EBSD) in the scanning electron microscope. One based on the quality of the diffraction images and another based on misorientations. With the wide acceptance of automated orientation measurement techniques based on EBSD, a method is needed for differentiating recrystallized and deformed material based on the data obtained from these automatic techniques. Adaptation of the proposed methods for distinguishing recrystallized and deformed into the framework of the automated orientation measurement techniques is presented. Results obtained from the orientation scanning technique are compared to results obtained using conventional metallography in partially recrystallized low carbon steel. Differences between the proposed method and the conventional technique are discussed and the influence of various parameters on these differences analyzed.

Keywords: electron backscatter diffraction, partial recrystallization

1 Introduction

Orientation imaging microscopy (OIM) (Wright 1993; Adams et al. 1993) has become a widely used technique for making spatially specific orientation measurements in polycrystalline materials. The technique is based on automatic indexing of electron backscatter diffraction (EBSD) patterns in the scanning electron microscope (SEM). By controlling the beam (or translation stage) of the microscope the crystallographic orientations can be mapped out across a sample. While several commercial systems are available, we describe results obtained using the system produced by TexSEM Laboratories. In this system, the data recorded at each point in the scan consists of the crystallographic orientation, position within the scan grid, a parameter describing the quality of the corresponding diffraction pattern, a confidence index describing the success of the indexing algorithm, the phase identified by OIM from a list of candidate phases and the intensity from the secondary or backscatter detector. If the technique can be modified to use this data to decide whether the diffracting crystal volume is deformed or recrystallized then the texture of the recrystallized material can be separated from the texture of the deformed material.

Two methods have been proposed for differentiating deformed material from recrystallized material using EBSD patterns. The first is based on the quality of the diffraction pattern. Any distortion in the crystal lattice leads to a more diffuse diffraction pattern. The OIM techniques use varying techniques for quantifying the quality of the diffraction pattern at each point in a scan. Krieger Lassen et al. (1994) have proposed a method for using such information to differentiate patterns from deformed material from patterns from recrystallized material. This method uses a scalar measure based on the Fourier transform of the diffraction image to describe the quality of the image or IQ. By examining the distribution of this measure for all the measurements in an orientation scan Krieger Lassen et al. were able to select a tolerance value for the scalar such that points with IQ values greater than this tolerance value were considered to represent recrystallized material.

A second approach proposed by Field (1995) is based on the difference between diffraction patterns from successive points in a line scan. This method is based on the fact that deformed material consists of dislocation pile-ups and tangles leading to curvature in the lattice planes. This results in adjacent points within the same grain having small difference in orientation. Field found that the orientation of adjacent point need not be directly measured but diffraction patterns obtained from adjacent points can be compared on a pixel-by-pixel basis. Once again a tolerance value is selected such that adjacent points having image differences less than the tolerance value are considered to come from recrystallized material whereas adjacent points with larger image difference are considered to come from deformed material. An upper bound is also set. Adjacent points with image difference greater than this upper bound are considered to represent points spanning a grain boundary.

Both of these approaches are applied to data obtained from three samples of partially recrystallized low carbon steel; hereafter, denoted samples A, B, and. Measurements of the degree of recrystallization in these samples were using an image analysis system (IBAS from Kontron). Sample A was found to be 20% recrystallized, sample B 60%, and sample C 85%.

OIM scans were performed on all four samples. The scans were done on a hexagonal grid with dimensions of 150×150 microns. The grid spacing was 0.75 microns.

Adaptations of both the image quality and image difference approaches were made using the OIM data obtained on all four samples. In addition, a method based on a combination of both approaches was used to attempt to extract the fraction of recovered material from the data for sample B. To facilitate the description of these adaptations it is helpful to describe the grain grouping algorithm employed by the OIM software. In OIM, a grain is defined by a set of points with similar orientation. The points are grouped into "grains" so that neighboring points within the grain do not exceed some tolerance value. However, it is important to note that the misorientation between non-neighboring points in the "grain" may exceed this value. Calculations were also done at 2.5°, 5°, 10° and 15°. However, 7.5° appeared to be the optimal value and was used for the results presented.

2 Image Quality Approach

Most commercial OIM systems use the Hough transform to detect the bands in the patterns (Krieger Lassen 1992). For the OIM system used in this study, the image quality is defined as the average height of the detected peaks in the Hough transform. The distribution of the IQ parameter for each sample is shown in figure 1a. In this plot the horizontal axis is the normalized image quality - 0 represents the minimum IQ in the scan and 1 is the maximum IQ.

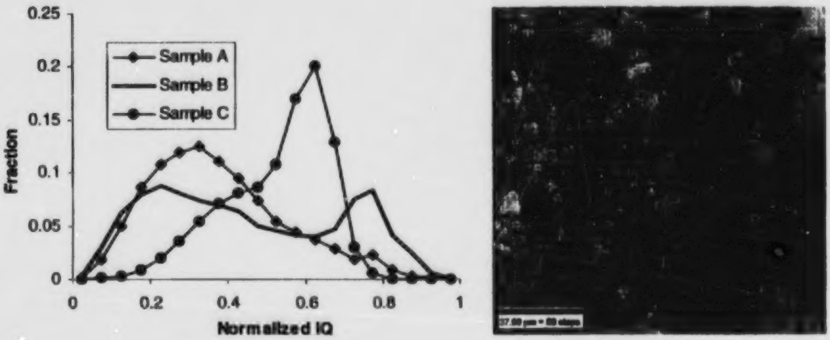

Fig. 1: **(a)** IQ distribution for all samples. **(b)** IQ map for sample B

According to the method proposed by Krieger Lassen et al. (1994) a bimodal distribution is expected – one peak for the deformed grains and a second peak at a higher IQ value for the recrystallized grains. Unfortunately, only sample B shows a bimodal distribution. This may be due to differences in the definition of the IQ parameter between the OIM software and that defined by Krieger Lassen et al. (1994). The IQ parameter defined in the OIM software is dependent on the bands detected and various parameters set by the user to enhance the detection of the diffraction bands in the pattern and is therefore not as generic. In addition, since the average peak height is used, a pattern with many bands detected may produce a lower image quality than a similar pattern with less bands detected. However, both IQ measures may have some orientation dependence. If the majority of band line length in a particular pattern are from crystallographic planes with high structure factors then such a pattern may produce a higher IQ than a pattern from a grain oriented such that the detected bands have relatively lower structure factors. One feature that should be noted in the plot is the IQ distributions are increasingly skewed towards the right with increasing recrystallization fraction as would be expected.

An image can be formed by mapping the IQ parameter at each data point to a gray scale. Such an image is shown in figure 1b. Two features should be noted in this map. The first is that the boundaries are delineated by the darker shades indicating that patterns collected from points near grain boundaries tend to have low IQ values. This occurs since essentially two crystal lattices exist in the diffracting volume. The patterns become more diffuse with the superposition of the patterns from the neighboring crystals. This causes problems in the distribution as these boundary points are difficult to distinguish from points in deformed material based solely on the quality of the associated diffraction patterns. The second feature of note is that the deformed areas are clearly visible in the IQ map. While these grains tend to have an overall lower IQ they are also distinguished by their mottled appearance. This suggests that the deviation of the IQ parameter (as defined in the OIM software) within a grain may be more relevant. However, results obtained for the deviation in IQ within individual grains were no more satisfactory than the results obtained for the point based IQ parameters. In fact, using the average IQ for each individual grain produced somewhat better results.

3 Image Difference Approach

Since the individual diffraction patterns are not saved during an OIM scan the approach proposed by Field (1995) was implemented by comparing the orientation between points in the scan. First the points were grouped into "grains" using the grain grouping algorithm already described. Within a single grain the overall spread in orientation was calculated by averaging the misorientation between all possible pairs of data points making up the grain. This distribution is shown in figure 2a. Figure 2b shows the distribution of the orientation spread calculated by averaging the misorientation between pairs of adjacent points in the grain.

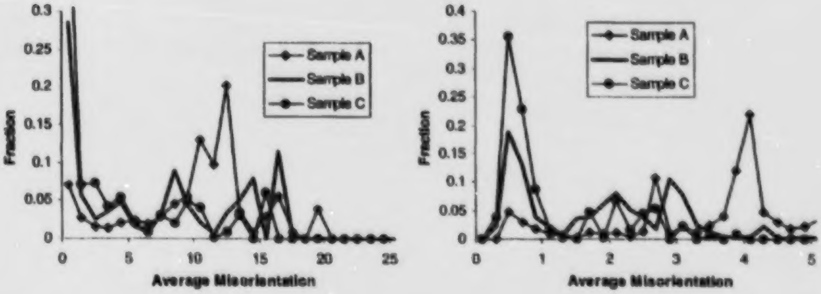

Fig. 2: **(a)** Average grain misorientation distribution, **(b)** average nearest neighbour misorientation distribution.

Average misorientations of 6.8°, 8.7° and 9.6° produce recrystallized fractions matching the conventional results for figure 2a and 2.6°, 2.0° and 2.2° for figure 2b. Neither of the calculation techniques produce clear bimodal distributions. The resolution of the scan grid can impact these results – especially in the nearest neighbor case. For second, third and fourth nearest neighbors values of 3.1, 4.3 and 5.3° are required to produce results matching the conventional ones for sample C.

4 Discussion and Conclusions.

Neither method produces distributions where a tolerance value can be easily identified. Nonetheless, the deformed regions are fairly obvious in the image quality maps. Thus, a tolerance value can be selected by visual inspection. Those points satisfying the tolerance criterion can be highlighted in the IQ map. The map can then be visually inspected to see if the tolerance value chosen results in the visually obvious deformed areas being correctly identified in the map and the tolerance criterion iteratively adjusted to produce the best visual fit. Figure 3a shows the results of such an approach being performed for sample C using the average overall misorientation per grain as the tolerance criterion. A tolerance value of 3.5° was used to generate the map. Comparing figure 3a with figure 1b, it is apparent that some of the recrystallized grains neighboring the deformed regions have been incorrectly identified by the software as deformed grains. This likely occurs because there exists a small angle misorientation between the recrystallized grain and the neighboring deformed material. Thus, the grain grouping algorithm causes these two regions to be combined into the same grain. This is one of the weaknesses of using the averaging approaches. When a small tolerance value is used then the deformed grains tend to be broken up into smaller grains leading to reduced spreads. When large tolerance values are used then the deformed grains and neighboring recrystallized grains can be combined into a single grain.

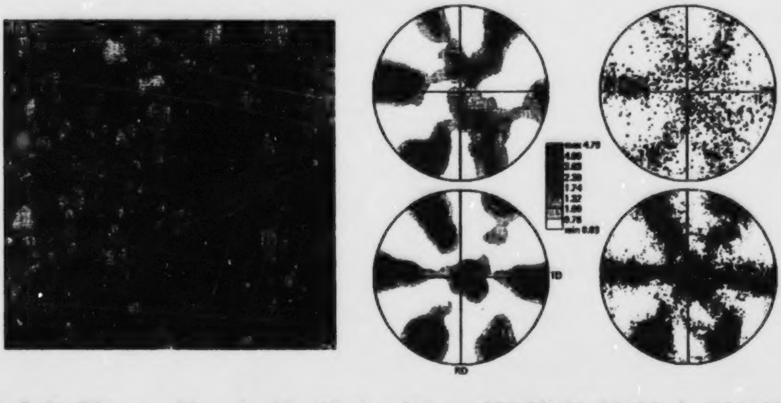

Fig. 3: (a) IQ map with grains identified as deformed highlighted in black, **(b)** (111) pole figures for the recrystallized (top) and deformed (bottom) regions.

If these pattern quality and orientation spread approaches are combined then it may also be possible to distinguish recovered material. Recovered grains would tend to show an orientation spread similar to that observed for the deformed grains but should exhibit higher average IQ's. Of course there is a resolution effect as well. Since the subgrains tend to be small the beam may interact with more than one subgrain at a time. This would result in diffuse patterns similar to those seen in the deformed material. However, a more robust measure of the image quality may make such measurements more feasible. Preliminary results obtained using the IQ parameter suggested by Krieger Lassen et al. (1994) suggest that this IQ measure is more robust.

5 Conclusions

The IQ parameter provided by the commercial version is not adequate to distinguish deformed material from recrystallized material. However, more sophisticated investigations based on the average IQ and spread in orientation show that the OIM data can interrogated to extract the recrystallization fraction and to separate the texture of the recrystallized material from the deformed material. However, a better definition of the image quality may lead to both more accurate results as well as providing information on the fraction of recovered material.

Acknowledgements

The author thanks E. Zimmermann of Thyssen Krupp Steel for supplying the samples and conventional recrystallization fraction measurements and R. Witt of TexSEM for running the OIM scans. Helpful discussions with D. P. Field are also gratefully acknowledged.

References

Adams, B.L., Wright, S.I. and Kunze, K. (1993) Orientation Imaging: The emergence of a new microscopy. *Metallurgical Transactions A*, Vol. 24, No. 4, pp 819-831.

Field, D.P. (1995) Quantification of partially recrystallized polycrystals using electron backscatter diffraction. *Materials Science and Engineering A*, Vol. 190, pp. 241-246.

Krieger Lassen, N.C., Juul Jensen, D. and Conradsen, K. (1994) Image processing procedures for analysis of electron backscattering patterns. *Scanning Microscopy*, Vol. 6, pp. 115-122.

Krieger Lassen, N.C., Conradsen, K. and Juul Jensen, D. (1992) Automatic recognition of deformed and recrystallized regions in partly recrystallized samples using electron back scattering patterns. *Materials Science Forum*, Vol. 157-162, pp. 149-158.

Wright, S.I. (1993) A Review of Automated Orientation Imaging Microscopy (OIM). *Journal of Computer-Assisted Microscopy*. Vol. 5, No. 3, pp. 207-221.

PHASE ANALYSIS AND GRAZING INCIDENCE STRESS MEASUREMENT IN ZrO_2 FILMS

M.G. GLAVICIC[1,2] and J.A. SZPUNAR[2]
[1]Lambda Research, Cincinnati, Ohio, USA
[2]Dept. of Metallurgical Engineering, McGill University, Canada

Abstract

A method to measure the stress in ZrO2 films has been developed using a Grazing Incidence X-ray Scattering (GIXS) geometry. This method allows the average stress present in oxides formed on Zirconium coupons to be determined. The method developed in this study was then used in conjunction with a technique[1] developed for the determination of the volume fraction of the meta-stable tetragonal phase in textured ZrO2 films. The results of this study have shown that the stress present at the oxide growth front governs the volume fraction of the tetragonal phase present in the oxide. More over, this method can be used to measure the stress gradient in the oxide if successive measurements on the same sample are taken at different X-ray glancing angles.

Keywords: Phase Analysis, ZrO2, Stress, Texture, Grazing Incidence,

Introduction

Zr-2.5%Nb pressure tubes form an integral part in the heat transport system of the CANDU reactor design. During the final manufacturing stage of the pressure tubes a protective oxide is grown on the surfaces of the tubes in a 400 C steam environment. This oxide is a two phase material consisting of, at room temperature and atmospheric pressure, a stable monoclinic phase and a metastable tetragonal phase. In a previous study[1], a method to determine the relative amount of these two textured phases present was developed with the aid of pole figure data. The results of this study[1] showed that as the thickness of an oxide formed in steam at 400 C increased, the volume fraction of the metastable tetragonal phase decreased. Several factors are believed to stabilize the metastable tetragonal phase; crystallite size, chemical impurities and stress.

In order to address the question of whether the volume fraction of the tetragonal phase is truely linked to the existence of compressive stress in the oxide a systematic study was performed on two sets of samples which had been oxidized in air and steam at 400 C for various periods of time. An x-ray diffraction method was developed to measure the average stress in the oxides grown using a constant grazing incidence angle. In addition the texture of the specimens was also determined and the relative abundances of the two phases was then determined using a technique previously developed and described elsewhere[1]. The evolution of the volume fractions of the tetragonal phase and compressive stresses in these test sets as a function of oxide thickness were then determined in order to fully address this question.

Theory

The measurement of stresses present in polycrystaline materials using x-rays is a standard non-destructive method used on a wide variety of materials. When a material is under either compressive or tensile stress the interplanar spacings in the material deviate from their unstressed spacings. This deviation manifests itself in a shift in position of the diffraction peak from its unstressed position. In an oxide which adheres to a metal substrate the stress field can be considered to be two dimensional or planar. This stress comes about due to a mismatch in the unit cell volume of the oxide and the underlying metal substrate to which the oxide is adherent. In a bi-axial stress field two orthogonal stress axis lay in the stress plane. For a bi-axial stress field the lattice spacing measured $d_{\phi\psi}$ as a function of tilt angle ψ at some angle ϕ within the sample reference frame is given by;

$$d_{\phi\psi} = [(\frac{1+\nu}{E}\sigma_{\phi} d_{o} \sin^{2}\psi) + d_{o}(1 - \frac{\nu}{E}(\sigma_{1} + \sigma_{2})] \qquad (1)$$

where υ is the Poisson's ratio, E is the modulus of elasticity, d_0 is the unstressed lattice spacing in the material, σ_1 and σ_2 are the principle stresses, and σ_ϕ is the stress component measured.

In the case of ZrO_2 grown on Zr-2.5%Nb coupons a measurement configuration is employed where the incident angle of the incoming radiation with respect to the specimens surface is controlled. This technique is called Grazing Incidence X-ray Scattering (GIXS) and has been used in the past to measure the texture of ZrO_2 films grown on Zr-2.5%Nb pressure tube coupons[2,3]. A technique employing the same geometry has been developed previously to measure the stress in thin textured Ni coatings[4]. In this method[4], the coefficients of a series expansion of spherical harmonics used to describe the Orientation Distribution Function (ODF) of the thin textured film are required. These coefficients are then used in conjunction with the symmetrized elastic compliance tensor of the material to take texture into account. Due to the limited number of pole figures that it has been possible to measure for ZrO_2 films grown on Zr-2.5%Nb coupons[1,2,3] and the low crystallographic symmetry of the monoclinic oxide phase, such and approach is not presently possible. For this reason a simplistic derivative of this method has been developed.

In the past Szpunar et al.[5] have shown that it is possible to maintain a fixed incident angle during pole figure measurements on a four circle goniometer as long as the following condition is satisfied during sample rotation

$$\sin(\alpha + i) = \frac{\sin(i)}{\cos(\beta)} \qquad (2)$$

where i is the incident angle of the x-rays relative to the surface of the sample, α is the angle of rotation about an axis normal to the plane defined by the incident and diffracted x-rays and β is the angle of rotation about an axis in the plane defined by the incident and diffracted x-rays. This condition can also be exploited for the measurement of stress in a grazing incidence geometry with the restriction that the minimum and maximum specimen tilts ψ_{min} and ψ_{max} respectively that are accessible for stress measurements are given by

$$\psi_{min} = \theta_{hkl} - i \qquad (3)$$

$$\psi_{max} = \cos^{-1}\left(\frac{\sin(i)}{2\sin(\theta_{Bl})}\right) \quad (4)$$

where θ_{Bl} is the lowest bragg angle and θ_{Bh} is the highest bragg angle to be scanned in the θ vs. 2θ scan. In addition for this method to be consistent with equation 1 the specimen must be tilted and rotated so that the projection of the scattering vector **S** at minimum and maximum tilt angles, ψ_{min} and ψ_{max} follows a straight line in the samples reference frame. This enables the experimenter to measure the stress σ_ϕ in a chosen direction ϕ.

De Buyser et al.[4], who also used a grazing incidence geometry, found that even a slight error in the alignment of the goniometer had a pronounced effect on the measured data. For this reason a random powder sample which is stress free was measured under exactly the same conditions as the oxide sample. In order to correct for misalignment of the goniometer each lattice spacing calculated for a particular ψ tilt on the oxide was then corrected by subtracting the lattice spacing measurement made on the random sample. This procedure changes the y-intercepts of the measurements recorded but not the slope which is related to the stress level of the specimen. The corrected data along with its cumulative error is then fit by another program to the following equation

$$d^{corr}_{\phi\psi} = d_{\phi\psi} - d_{random} = [(\frac{1+\nu}{E}\sigma_\phi d_o \sin^2\psi) + B \quad (5)$$

where upon the stress level in the sample σ_o, and its corresponding error is calculated.

Experiment

A series of specimens were cut from as received pressure tubes such that the radial direction of the pressure tube was parallel to the sample normal. The samples were then polished down to a 600 grit paper finish where upon two separate sample sets were created. The first set of samples, type I, were created by polishing a portion of the 600 grit mechanically polished samples with 9 µm diamond paste. Ammonium Dichromate powder with a 0.5% HF solution was then used to give the sample their final finish. The second set of specimens, type II, were obtained by polishing the remaining 600 grit mechanically polished samples with 1 µm Al_2O_3 suspended in H_2O with solution of nitric (HNO_3) and hydrofluoric (HF) acids to give the samples their final appearance. The first set of samples were oxidized in steam at 673 K for periods up to 168 hours, while the second set were oxidized in air at 673 K for periods up to 103.3 hours.

The specimens texture was measured using CuKα radiation on a Siemens D500 texture goniometer. The stress measurements were performed on a Thin Film Texture Apparatus employing a 10 degree incident angle. A 12 kW rotating anode source (Rigaku Rotaflex) with $CuK\alpha_1$ radiation that had been monochromated with a (400) cut germanium single crystal was used for these measurements. The method employed for volume fraction analysis was the same as that employed previously[1].

Results

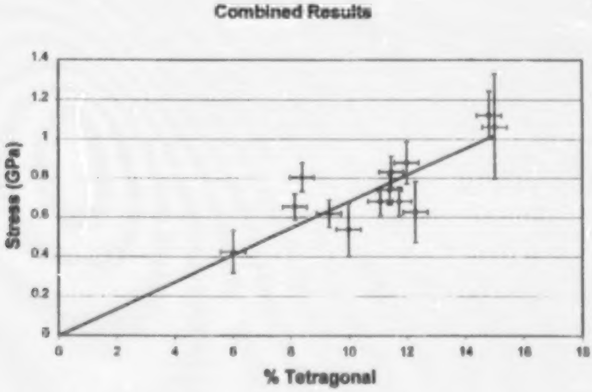

The figure shown above is a combined plot of the average stress measured versus the volume fraction of tetragonal phase measured for both air and steam formed samples. A linear fit to the data is shown by the straight line drawn through the data. Upon examination a clear correlation between the volume fraction of the tetragonal phase present and the stress field present in the samples is observed. This implies that the stress field, as suspected, does control the volume fraction of the meta-stable tetragonal phase present in the oxide. It also implies that if one measures one quantity in a series of test samples one knows semi quantitatively how the other is changing. A decrease in the volume fraction as a function of oxide thickness is to be expected if the tetragonal phase is nucleated at the oxide growth front and then transforms to the room temperature and atmospheric pressure stable monoclinic phase as time progresses and the oxide thickens.

Discussion

In previously performed studies where the temporal characteristics for the tetragonal phase were investigated, the effects of stress on the actual tetragonal content measured were either not studied[6] or could not be directly linked[7,8,9].

Garzarolli et al.[9] examined the stress present in Zircalloy-4 specimens by grinding a single side of a specimen and based upon the resulting curvature of the specimen, deduce a stress level. The maximum stress level measured using this technique was 6.2 MPa. Godlewski et al.[7,8] worked on a series of Zircalloy-4 samples and examined the stress present in the substrates of the specimens using XRD methods. The stress level was determined to be of the order of 1 to 1.3 GPa at the metal oxide interface. Changes in the Fe/Cr atomic ratio distributions were found in different layers of the oxide. These changes in Fe/Cr atomic ratio distributions in the oxide were then attributed the oxidation of the precipitates included in the oxide. For this reason it was proposed that the tetragonal phase at the metal/oxide interface is stabilized by stresses created by the Pilling Bedworth ratio of the metal and oxide. The presence of the tetragonal phase away from the metal oxide interface was attributed to the formation of stress during the oxidation of the inter-metallic precipitates present in the oxide.

In the Zr-2.5%Nb system, the main impurity is the alloying element Nb. Traces of O, N, and Fe in the order of ppm are typically found. Analysis of the β-phase containing a high concentration of Niobium suggests that a sub-oxide is first formed followed by the formation of an amorphous oxide as oxidation becomes complete[10]. In this regard, the same type of argument used by Godlewski[7] can be used to explain the presence of stress stabilised tetragonal phase away from the metal oxide interface. This stress stabilised phase would likely occur only in regions surrounding the sub-oxide where incomplete oxidation has occurred. Due to the incomplete oxidation, a stress field sufficient to stabilise the tetragonal phase may then occur. TEM studies performed thus far on Zr-2.5%Nb coupons have yet to produce a consistent set of results showing the presence of the tetragonal phase. This is likely due to the fact that if the tetragonal phase is stress stabilised, the tetragonal phase present at the metal oxide interface will transform to the monoclinic phase when the metal substrate is ion milled away in the production of a TEM foil. The remaining tetragonal phase which is presumably stabilised by the sub-oxide layer can then be thought of as the remaining source of tetragonal phase present for possible TEM observation. Unfortunately since the β-*Zr* phase, which is the source for a sub-oxide region, transforms to the α-*Zr* phase during the operational lifetime of the tube, the likelihood of observing tetragonal grains away from the metal oxide interface diminishes as the oxide becomes more mature. This likely explains the lack of TEM observations of the tetragonal phase. More over, the results presented indicate that the metal oxide interface is the main source of tetragonal phase stabilisation in mature pressure tubes. Therefore, in mature tubes the tetragonal phase will only be stabilized close to the metal oxide interface where the stress field is sufficient to do so. As the oxide thickens the oxide growth front moves away and the stress field that stabilizes the tetragonal phase diminishes until the tetragonal phase transforms into the monoclinic phase.

The values computed for the average stress in the oxide film in the present work are also consistent with what would be expected for the stress stabilisation of the tetragonal phase. In a pressure-temperature phase diagrams for the ZrO2 system produced by Whitney[11], it was indicated that at room temperature a compressive stress in the order of 4.5 GPa would be required to stabilise the tetragonal phase. The oxides grown on Zirconium alloys are well known for the appearance of cracks and pores visible on the surface[12-16]. Studies in which the effective thickness of the non-porous layer adjacent to the metal oxide interface have also been performed in the past[9]. Since the upper layer of the oxide is known to be porous and presumably stress free and the method described in this paper probes the whole of the oxide, both the porous and non-porous regions contribute to the measured value of stress. The measured stress is therefore an average value of the stress present in the oxide and it is to be expected that the measured value for the oxide as a whole is substantially less than what is present at the metal oxide interface. Therefore the results presented in this paper are sufficiently large for a stabilising stress in the order of 4.5 GPa or greater to appear in regions close to the metal oxide interface and allow the tetragonal phase to be stress stabilised.

Conclusion

A method for the measurement of stress in ZrO_2 has been developed. The method developed allows the stress present in thin oxides to be characterized in a non destructive fashion. Measurements of the volume fractions of the tetragonal phase present in each of the specimens by a previously developed method[1] coupled with the stress measurements presented in this paper have shown that stress is the main factor in determining the relative abundance of the metastable tetragonal phase. In addition, the results presented suggest that the level of stress at the metal oxide interface is sufficient to stabilize the tetragonal phase and that the metal oxide interface is a region where a high tetragonal content is to be expected.

Acknowledgements

The authors of this paper would like to thank Y.P. Lin and N. Ramasubramanian of Ontario Hydro Technologies for their participation and assistance in this work.

References

[1] M.G. Glavicic, J.A. Szpunar, Y.P. Lin J. Nucl, Mater. 245, 147 (1997)

[2] M.G. Glavicic, J.A. Szpunar, P. Blandford, "The Eleventh Internation Conference on the Texture of Materials:ICOTOM 11", 1137 (1996)

[3] M.G. Glavicic, Y.P. Lin, J.A. Szpunar, J. Nucl. Mater. (to be published)

[4] L. De Buyser, P. Van Houtte, E. Aernoudt, Textures and Microstructures 14, 73 (1991)

[5] J.A. Szpunar, S. Ahlroos, Ph. Tavernier, J. Mat. Sci. 28, 2366 (1993)

[6] Barberis J. Nucl. Mater 226, 34 (1995)

[7] J. Godlewski, 'Zirconium in the Nuclear Industry: Tenth International Symposium' ASTM STP 1245, pp.663-686 (1994)

[8] J. Godlewski, J.P. Gros, M. Lambertin, J.F. Wadier, H. Weidinger, "Zirconium in the Nuclear Industry: Ninth International Symposium" ASTM STP 1132, 416 (1991)

[9] F. Garzarolli, H. Seidel, R. Tricot, J.P. Gross, "Zirconim in the Nuclear Industry: Ninth International Symposium", ASTM STP 1132, 395 (1991)

[10] Y.P. Lin, "Third International Conference on Microscopy of Oxidation", Cambridge, England September 1996

[11] E.D. Whitney, J. Electrochem. Soc. 112, 91 (1965)

[12] Y. Ding, D.O. Northwood, Journal of Alloys and Compounds, 179, 207 (1992)

[13] Y. Ding, D.O. Northwood, Journal of Alloys and Compounds, 187, 317 (1992)

[14] Y. Ding, D.O. Northwood, Journal of Alloys and Compounds, 202, 180 (1993)

[15] B.Cox, Y.Yamaguchi, J. Nucl. Mater., 210, 303 (1994)

[16] B.Cox, C. Wu, J. Nucl. Mater., 199, 272 (1993)

TEXTURE ANALYSIS OF COMPLEX EARTH MATERIALS FROM NEUTRON DIFFRACTION SPECTRA

LUCA LUTTEROTTI
Dipartimento di Ingegneria dei Materiali, Università degli Studi di Trento, Italy.

Abstract

Neutron diffraction is a very powerful technique to analyze texture and other structural-microstructural characteristics of complex phases in applications ranging from earth to material sciences. Some of the main challenges are to obtain the orientation distribution in the case of low symmetry compounds and to analyze the crystal structure in the presence of a strong texture. Obviously, obtaining both informations at the same time is essential for many research projects dealing with polycristalline materials. This goal can be achieved with the so-called Rietveld Texture Analysis [1, 2] in which the texture analysis is combined with the Rietveld method normally adopted by crystallographers to obtain structural quantities from powder patterns. The methodology was enhanced by integrating also some line-broadening theories on the aim to obtain microstructural details about dimension and shape of the grains along with line and planar defect probabilities.

The technique has been proved successful in analyzing some deformed rocks composed of calcite, olivine and quartz and examples will be presented. Several neutron spectra (TOF) where collected on the samples at different tilt angles and the diffraction data have been analyzed using the proposed methodology obtaining the orientation distribution function, crystal structure parameters and microstructural features simultaneously. This has permitted a more complete reconstruction of the deformation history of rocks.

As a further example of the practical use of this analysis some applications to multiphase materials will be shown in which in addition to the texture also a very accurate quantitative phase analysis has been obtained. The simultaneous study of more material characteristics at the same time, with solid constraints provided by the RTA methodology, allows the researchers to obtain useful information about a system even if experimental data are of deficient quality or some data corrections are unknown due to the over-determination of the mathematical problem.

Keywords: Texture, earth materials, neutron, limestone, olivine, quartzite.

1 Introduction

The RiTA method was developed starting in 1991 to overcome the classical problem of reflection overlapping that in the case of multiphase samples and/or low symmetry compound greatly reduce the number of pole figures available for a traditional quantitative texture analysis. The procedure makes use of spectra collected at different tilting angles instead of pole figures. One spectrum contains more reflections, so it is possible to obtain the same information using only part of the pole figure coverage. The method will greatly benefit of the last generation machines available that are equipped with position sensitive detectors or energy dispersive spectrometers thus collecting full spectra in a relatively short time. So it is easier to collect entire spectra in few sample directions than entire pole figures for few reflections. In this work we will show the potentialities of the technique to analyze complex earth materials. The procedure gives information not only on the texture but also on the crystal structure and microstructure.

2 Theory and procedures

The RiTA method consists of a fitting procedure based on the so-called Rietveld method, developed by Rietveld in 1967 to refine the crystal structure using powder diffraction experiments. The entire procedure starts with the collection of several spectra at different measuring angles in order to cover the entire or part of a polar figure. Subsequently, by simultaneous least squares fitting of these spectra using the WIMV method for the texture determination the procedure permits to obtain the OD (Orientation Distribution), the crystal structure, the microstructure and phase quantity for nearly any kind of samples, symmetry and complexity. Multiphase materials can be analyzed and some examples are reported in Lutterotti et al., this book. For further details on the procedure we remind to the literature and in particular to Wenk et. al (1994) and Lutterotti et al. (1997).

3 Experimental

3.1 The limestone standard

A deformed limestone, 0.8x0.8x0.8 cm^3 $CaCO_3$, used previously also for a "round robin" on reliability of neutron pole figures determination, was used as a first sample for testing the methodology and the effectiveness of texture and structure analysis on low symmetry compounds by spectra fitting. 19 diffraction spectra were collected on the general purpose powder diffractometer (GPPD) at the Intense Pulsed Neutron Source (IPNS) of Argonne using only one detector. The 19th different sample orientations were chosen to cover a quarter of a pole figure up to 51 following an hexagonal grid of 10 in order to minimize the measurement time under the hypothesis of orthorhombic texture symmetry. The TOF spectra were covering the d-spacing range from 0.5 to 6.0 Angstrom.

3.2 Quartzite sample

A cylindrical metamorphic sample of quartzite was extracted from a metaconglomerate in Wildrose Canyon (Death Valley National Park, California). A typical texture of quartzite deformed at relatively low metamorphic grade resulted from optical measurements on the c-axis. The 2 cm long and wide cylinder was measured at the neutron TOF source of JINR-Dubna (pulsed reactor IBR-2). 650 spectra were collected on a regular grid of 7.2 with a counting time of 15 min each over the entire pole figure. 7 different detectors have been used for the measurements and this required a different intensity correction and calibration performed directly during the computing analysis.

3.3 Olivine sample

One sample containing olivine was chosen to test the methodology on a more complex case. The sample is actually a mixture of an olivine 70%Mg-30%Fe and a pyroxene. The spectra necessary for the texture analysis were collected on the new SKAT texture diffractometer at the pulsed reactor IBR-2 at Dubna (Ullemeyer et al. 1998). The new configuration permits to cover all the necessary angles of the pole figure using only one rotation of the sample around one axis. All the detectors are positioned at an equivalent θ diffraction angle, so the only necessary corrections are concerning the different efficiency of the detectors and the energy or spectral calibration that is equivalent for all. The spectra were collected on a number of 1368 covering with a regular grid of 5 the entire pole figure. The usable d-spacing range is from 0.6 to 5.4 angstrom in which thousand of olivine reflections are present.

4 Results and discussion

4.1 Limestone analysis

The analysis of the limestone measurements was performed selecting different ranges of the TOF data in order to test the ability of the method to deal with peak overlapping and superposition. For any range the first step was dedicated to refine the instrumental related quantities like background, beam intensity and detector related correction for intensity and peak positions. This was done assuming a random texture of the sample. Subsequently we refined trough the program also the texture, microstructure and crystal structure. The texture and crystal structure effects on reflection intensity proved to be highly uncorrelated and a separation of the two occurred just after the first refinement cycle. The refinement of the texture and crystal structure was completed after three cycles. Figure 1 shows some of the spectra fitted by the RiTA method. It is possible to recognize that the intensity is reproduced quite well using the OD determined by the procedure. Figure 2 reports instead the extracted experimental pole figures compared with the reconstructed ones and with the experimental pole figures obtained by the best measurement during the “round robin” at ILL (Grenoble). It is possible to recognize that also the analysis performed using the very overlapped range in the 0.9-1.8 Angstrom region is sufficient to extract the fundamental features of the OD.

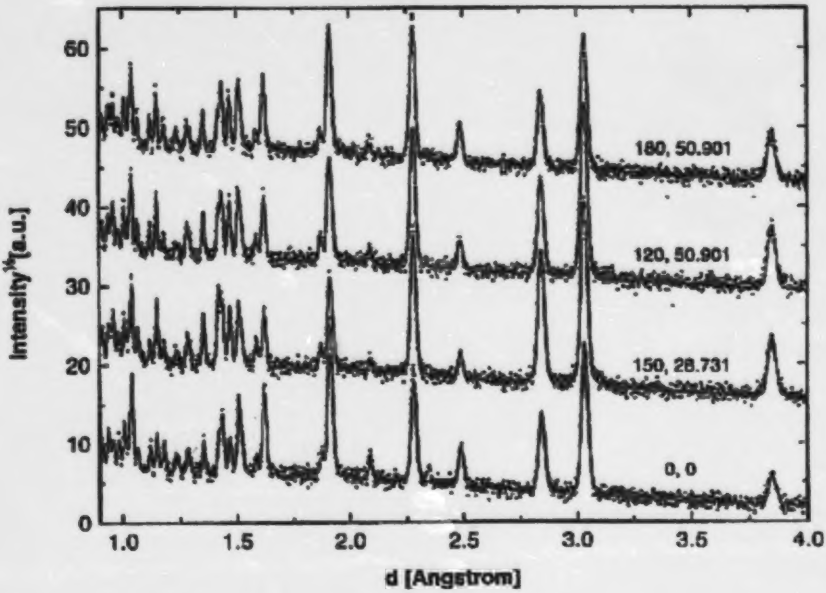

Fig. 1: Some of the TOF spectra for limestone fitted by the RiTA method.

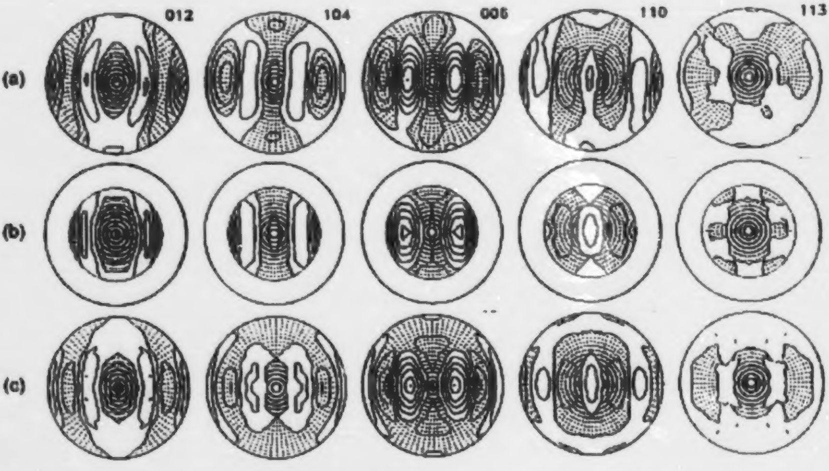

Fig. 2: Pole figures from the analysis of limestone sample. (a) ILL experimental ; (b) RiTA extracted experimental PFs; (c) reconstructed for d-ranges: 0.9-4.0 Å.

1.1 Quartzite

The RiTA analysis was conducted in a similar way to the limestone apart the fact that only one range from 0.5 to 3.5 Angstrom was used for the computing. In that region 527 reflection were used for the fitting but only the more intense were selected for the texture computation by WIMV. These correspond to 37 peaks for which the polar angle up to 40 was used instead of the entire region to speed up the analysis. Figure 3 is showing some of the spectra for the quartzite as fitted by the program. The reconstructed and smoothed pole figures for the significant reflections are available in figure 4. It is possible to distinguish the distinctive features of a deformed quartzite at low metamorphic grade. In table 1 the crystal structure of the quartzite, as refined by the combined procedure, is reported showing the effectiveness of a simultaneous structure and texture refinement.

1.2 Olivine

The method was successful also to analyze the olivine sample. In that case was necessary to cut some data to reduce the computing effort and necessary memory to the program to run. It was not a problem because the number of data was in excess of the necessary one. In particular, a special routine was constructed to use only the spectra sticking on an hexagonal grid and up to 45 of the polar angle. One of the advantages of the RiTA procedure is that, using more reflection, a smaller coverage of the polar figure is necessary. In this case, in addition to the texture and crystal structure, it was possible to refine the Mg and Fe occupancy in the olivine. The results are in progress to refine the pyroxene phase quantity.

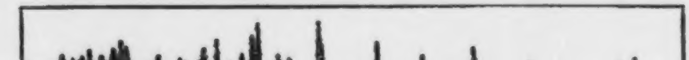

Fig. 3: Some of the TOF spectra for the quartzite fitted by the RiTA procedure.

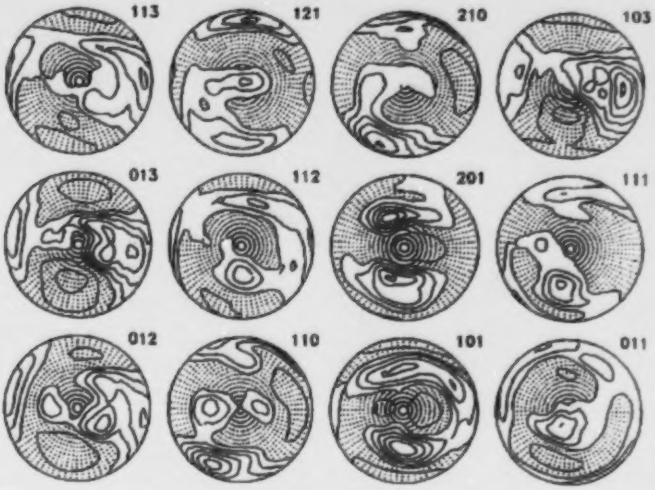

Fig. 4: Smoothed pole figures for the quartzite reconstructed from the OD as determined by the RiTA fitting procedure.

Space Group		$P3_221$
a [Angstrom]		4.91393(5)
c [Angstrom]		5.40394(9)
Si (x,x,0)	x	0.46323(7)
	B [Angstrom^2]	0.4(2)
O (x,y,z)	x	0.41047(5)
	y	0.26474(5)
	z	0.78471(3)
	B [Angstrom^2]	0.7(1)

Table 1: Refined crystal structure values for the quartzite. Errors in parentheses refer to the last digit.

2 References

H.-R. Wenk, S. Matthies and L. Lutterotti, Mater. Sci. Forum 157-162, 473 (1994).

L. Lutterotti, S. Matthies, H.-R. Wenk, A. S. Schultz and J. W. Richardson, Jr, J. Appl. Phys., 81(2), 594-600, (1997).

Ullemeyer, K., Spalthoff, P., Heinitz, J., Isakov, N. N., Nikitin, A.N. and Weber, K. (1998) The SKAT texture diffractometer at the pulsed reactor IBR-2 at Dubna: experimental layout and first measurements, *Nucl. Inst. Meth. Phys. Res.*, A412, pp. 80-88.

POLYCHROMATIC MICROBEAM DIFFRACTION, MESOTEXTURE AND CRACK DEFLECTION IN Al-Li 2090 T8E41

J.D. Haase, R. Morano, T. Watt and S.R. Stock

School of Materials Science & Engineering and Mechanical Properties Research Laboratory, Georgia Institute of Technology, Atlanta, Georgia 30332-0245 USA

Abstract

The geometry of asperities formed by fatigue cracks in the center of plates of Al-Li 2090 T8E41 correlates with macrotexture, but little work has focused on whether or how the variation in grains' orientations determines how the crack will deflect. This report describes synchrotron polychromatic x-ray microbeam diffraction mapping of the three-dimensional microtexture in samples of Al-Li 2090, in other words, microbeam transmission Laue mapping of polycrystalline samples. In particular, the focus is on samples from the center of 12.5 mm thick plates, where effects of crack closure on fatigue are held to be particularly prominent. Groups of adjacent pancake-shaped grains are found to have very similar orientations, with these near single-crystal volumes of ~ 0.3 mm x 0.5 mm x 1mm, and this type of mesotexture appears to underlie the unusual fatigue crack propagation in Al-Li 2090 T8E41.

Keywords: aluminum, fatigue crack growth, microbeam x-ray diffraction, mesotexture, Laue patterns

1. Introduction

In Al-Li 2090 T8E41, fatigue crack growth rates along certain plate orientations are unusually low compared to those of other Al alloys (e.g., Venkateswara Rao et al.1988). This is related to a characteristic macrotexture (i.e., the texture averaged over a large number of grains) in the center of the plates which produces a rough, asperity dominated crack face, significant crack deflection and fatigue crack closure effects. Yoder et al. (1989) have shown that the orientations of the faces of the asperities are related to this macrotexture. Synchrotron polychromatic x-ray microbeam diffraction mapping of the three-dimensional microtexture in samples of Al-Li 2090, in other words, microbeam transmission Laue mapping of polycrystalline samples, has recently shown that groups of five or more adjacent pancake-shaped grains had very similar orientations, with these near single-crystal volumes approaching 0.3 mm x 0.5 mm x 1mm (Haase, 1998; Haase et al. 1998; Haase et al. 1999). This type of mesotexture comprised about forty percent of the samples' volumes and appeared to underlie the unusual crack growth rates and geometry in Al-Li 2090 T8E41. Further, all large asperities studied contained grains with a specific near single-crystal orientation corresponding to one of the more important components of the macrotexture.

Given that the morphology of the crack surface relates to the macrotexture present, the question remains: whether asperities in the center of plates of Al-Li 2090 form at random within the volume of material through which the crack is constrained to grow (by the notch) or whether spatial distribution and character of near single-crystal volumes dictates where large asperities or significant crack deflection develop. In other words, does the crack choose its path to avoid grains or groups of grains with certain orientations or to grow through individual grains, groups of grains or specific orientations of grain boundaries.

Three-dimensional, non-destructive measurement of microtexture within samples have been developed to address this question (Stock et al. 1995; Piotrowski, 1996; Piotrowski et al. 1996; Haase, 1998; Haase et al. 1998; Haase et al. 1999). The approach described below uses synchrotron polychromatic x-ray microbeam diffraction to record transmission Laue patterns from polycrystalline samples. Along with the complication of indexing the Laue pattern of a single grain, an additional challenge exists: multiple grains at multiple depths are irradiated simultaneously. Current results are presented below which address the question of how a fatigue crack chooses a particular path through a sample of Al-Li 2090 T8E41.

2. Experimental Methods

The sample for which microbeam diffraction mapping is reported below is from the center ~2.7 mm of a 12.7 mm thick plate of Al-Li 2090 T8E41. Loading was along the plate's rolling direction (L), the fatigue crack in the compact tension sample was propagated along the plate transverse direction (T) and the sample's thickness, i.e., its smallest dimension, was along the short transverse direction (S). The volume of material adjacent to the crack was cut from the compact tension specimen so that it could be examined with an x-ray beam parallel to L. A 0.01 mm diameter pinhole collimator was used to define the area contributing to each transmission Laue pattern, and 2.7 mm x 4.5 mm was covered using 0.2 mm translation increments: emphasis was on long-range variation of mesotexture rather than the details of each near single-crystal volume. Polychromatic synchrotron x-radiation from Beamline 2-2 of the Stanford Synchrotron Radiation Laboratory (SSRL) and Fuji image storage plates were used to record the Laue patterns. Exposure times were on the order of five minutes, and reading each exposed image plate required about the same time. The diffraction streaks' hkl indices were identified using absorption edge filter techniques (Stock et al., 1993). More complete experimental information appears elsewhere (Haase, 1998; Haase et al. 1998; Haase et al. 1999).

3. Results and Discussion

Figure 1 shows the array of Laue patterns in the correct positions for sample CT-35b; note that the array spans the two facing pages. These patterns were recorded on a 0.2 mm grid of positions covering the 2.7 mm from one face of the compact tension sample to the other and the first 4.2 mm of the crack to grow from the notch. The Laue patterns are quite reduced in size but show the features essential to tracing the mesotexture within this sample. The plate orientations are indicated below the patterns, on the left.

In Fig. 1, the darker pixels (picture elements) represent greater diffracted intensity, and the image of the beam stop is the white square at the center of each Laue pattern. The diffraction streaks in the patterns are from either 111, 200 or 220 reflections; this is a product primarily of the range of wavelengths able to produce reasonable diffracted intensities in this transmission geometry. Column 1 is closest and 23 is farthest from the notch; and the letters identify the rows of images.

The streaks closest to and immediately to the left of the beam stop run nearly parallel to the T direction between positions E1 and E10 and between positions D1 and D8; these are 111 streaks which have been linked with asperity volumes in work cited above. It is not surprising that five or more adjacent patterns along the T-direction (e.g., E16 through E20) are identical because the pancake-shaped grains dimensions can be 2 mm x 0.5-1 mm x 0.04-0.05 mm along the L, T and S directions, respectively. Examining patterns from the area inciuding rows C through F and columns 1 through 10 reveals that the near-single crystal volumes extend, along the S direction, up to 0.4 mm. Data has been collected from the volumes surrounding both faces of the crack, and maps superimposing the three-dimensional crack surface on the array of Laue patterns are currently being studied for links between crack deflection and characteristic transitions between mesotexture components (i.e., differently oriented near single-crystal volumes or randomly oriented and near single-crystal volumes).

Given Al-Li alloys' strong tendency to fracture on {111}, one expects that the near single-crystal volumes, one type of mesotexture, produce large asperities in some cases and large crack deflections with strong mixed mode surface character in others. The relatively large dimensions of the near single-crystal volumes allow the crystallographic characteristics to be expressed. In the absence of this mesotexture, one expects a negligible effect in terms of crack deflection or formation of large asperities: different grains would fracture on different{111}depending on their orientation, the fraction of grains with a specific orientation being dictated by the macrotexture, but the random spatial correlation of orientations between neighboring grains would rarely produce significant deviation from the plane defined by the notch.

4. Conclusions

Microbeam diffraction using synchrotron polychromatic x-radiation showed near single-crystal mesotexture was present throughout the volume of Al-Li 2090 T8E41 through which a fatigue crack could have chosen to grow. Much remains to be learned from the transitions between different mesotexture components and the path of fatigue cracks.

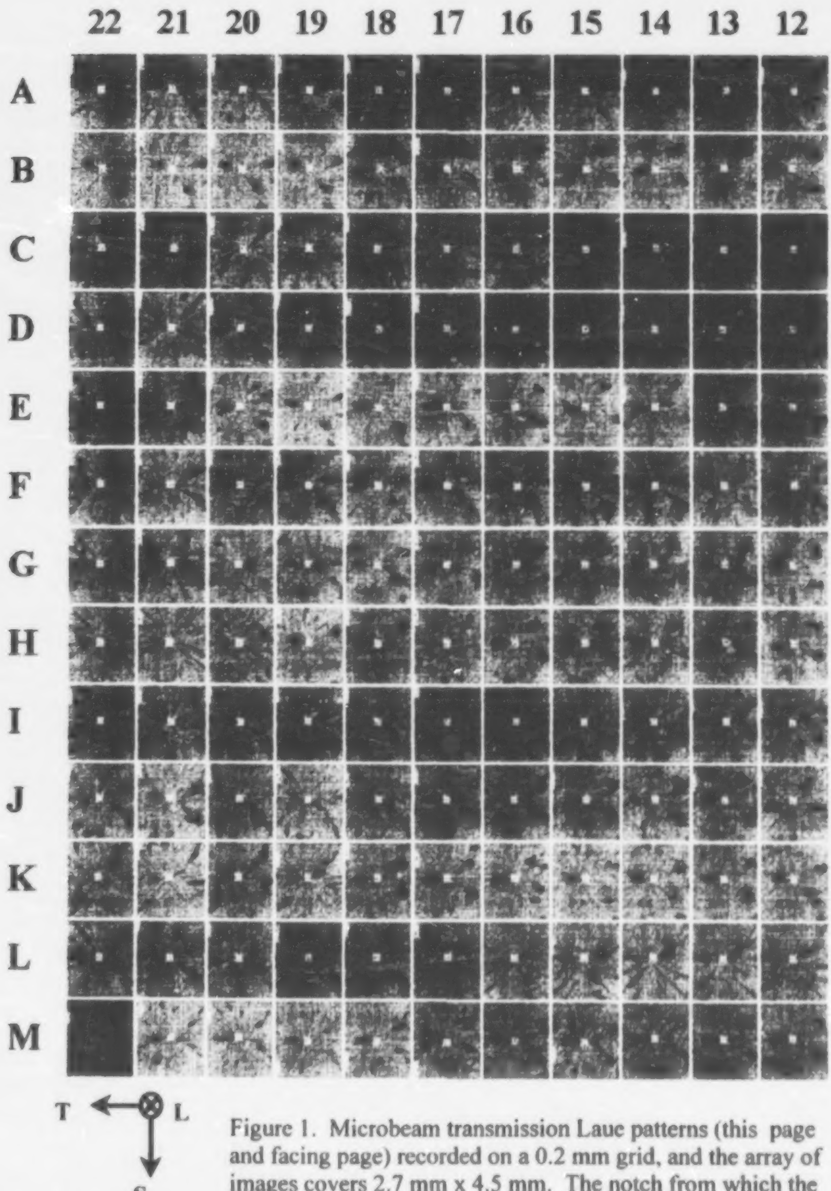
22
21
20
19
18
17
16
15
14
13
12
A
B
C
D
E
F
G
H
I
J
K
L
M
T
L
S

Figure 1. Microbeam transmission Laue patterns (this page and facing page) recorded on a 0.2 mm grid, and the array of images covers 2.7 mm x 4.5 mm. The notch from which the crack initiated is just to the right of column 1.

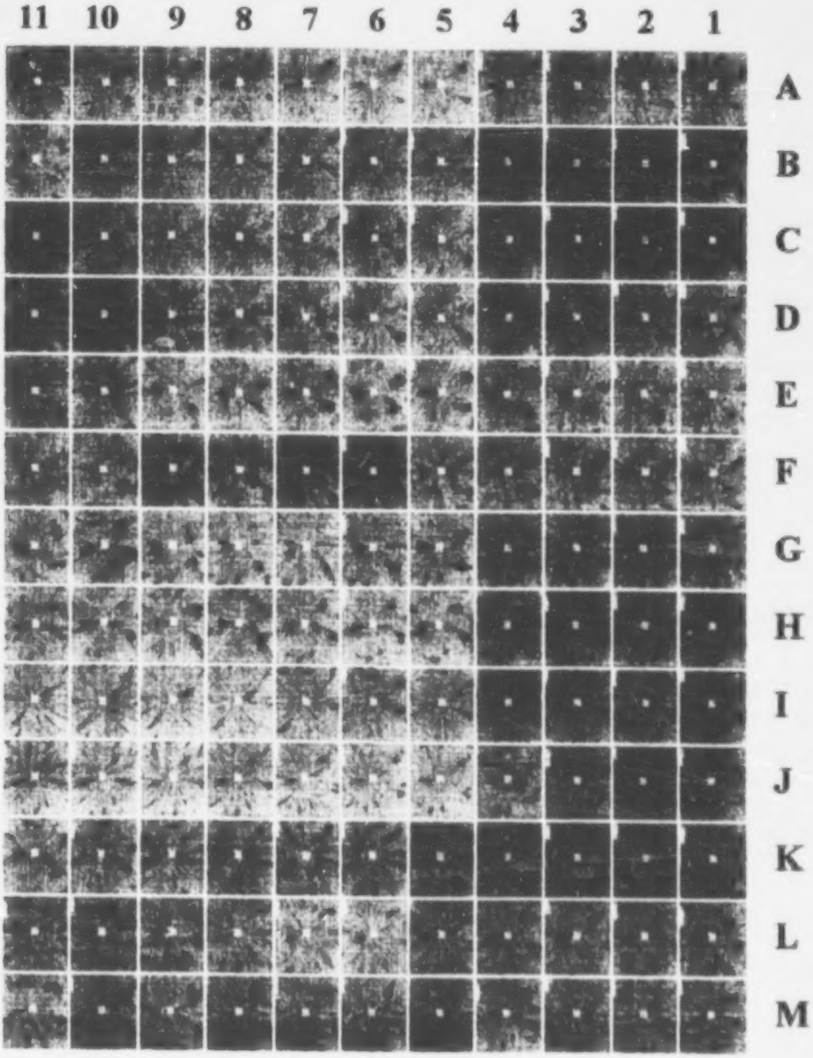
11
10
9
8
7
6
5
4
3
2
1
A
B
C
D
E
F
G
H
I
J
K
L
M

5. Acknowledgments

We gratefully acknowledge the support of the Office of Naval Research and the encouragement of Dr. George Yoder of that office. Experiments were performed at SSRL, which is operated by the Department of Energy, Office of Basic Energy Sciences. We thank Dr. Zofia Rek of SSRL for her invaluable assistance with the microbeam experiments and Mr. R Brown for his help with fatigue crack propagation.

6. References

Haase, J.D. (1998) *Microbeam Diffraction Mapping of Microtexture in Al-Li 2090 T8E41*, MS Thesis, Georgia Institute of Technology.

Haase, J.D., Guvenilir, A., Witt, J.R., and Stock, S.R., (1998) X-ray microbeam mapping of microtexture related to fatigue crack asperities in Al-Li 2090, *Acta Mater* Vol. 46, pp.4791-4799.

Haase, Jake D., Guvenilir, Abbas, Witt, Jason R., Langøy, Morten A. and Stock, Stuart R. (1999) Microtexture, asperities and crack deflection in Al-Li 2090 T8E41,", in press in *Mixed-Mode Crack Behavior* ASTM STP 1359.

Piotrowski, D.P. (1996) *Synchrotron Polychromatic X-ray Diffraction Tomography of Large Grained Polycrystalline Samples*, MS Thesis, Georgia Institute of Technology.

Piotrowski, D.P., Stock, S.R., Guvenilir, A., Haase, J.D. and Rek, Z.U. (1996) High-resolution synchrotron x-ray diffraction tomography of large-grained samples, in *Appl. Synchrotron Rad. Tech. Mater. Sci. III*, MRS Proc. Vol. 437, pp. 125-128.

Stock, S.R., Guvenilir, A., Piotrowski, D.P. and Rek, Z.U. (1995) High resolution synchrotron x-ray diffraction tomography of polycrystalline samples, in *Appl. Synchrotron Rad. Tech. to Mater. Sci. II*, MRS Proc. Vol. 375, pp. 275-280.

Stock, S.R., Rek, Z.U., Chung, Y.H., Huang, P.C., and Ditchek, B.M. (1993) characterization of Si-$TaSi_2$ in-situ composites by synchrotron white beam topography and by double axis diffractometry, J. Appl. Phys. Vol. 73, pp.1737-1742.

Venkateswara Rao, K.T., Yu, W., and Ritchie, R.O. (1988) Fatigue crack propagation in aluminum-lithium alloy 2090: Part I. Long crack behavior and Part 2. Small crack behavior, *Met Trans*. Vol. 19A, pp. 549-569.

Yoder, G.R., Pao, P.S., Imam, M.A., and Cooley, L.A. (1989) Mechanisms of fatigue fracture in Al-Li alloy 2090, in *Proc. Fifth Int. Aluminum-Lithium Conf.*, T.H. Sanders, Jr. and E.A Starke, Jr., Eds, Mat. & Comp. Eng. Publ., Birmingham, UK, pp. 1033-1041.

"HIPPO", A NEW HIGH INTENSITY NEUTRON DIFFRACTOMETER FOR CHARACTERIZATION OF BULK MATERIALS

K. BENNETT and R.B. VON DREELE
Lujan Center, Los Alamos National Laboratory, Los Alamos, NM 87545, USA
H.-R. WENK
Department of Geology and Geophysics, University of California,
Berkeley, CA 94720, USA

Abstract

A consortium of University of California faculty and National Laboratory researchers, representing a broad range of disciplines, is building a new time-of-flight (TOF) neutron diffractometer, "HIPPO", for materials studies at the Los Alamos Neutron Science Center (LANSCE) under the auspices of the United States Department of Energy. The instrument, which will become available in fall 2000, has the extremely high count-rates necessary to study time-dependent processes and materials under a wide variety of environmental conditions (10-2000K, 0-20GPa) in small ($1mm^3$) and large samples (2cm diameter). The 3D arrangement of detectors covering $4.6m^2$ area allows direct measurements of crystal orientation distributions in polycrystalline materials. The analysis of TOF diffraction patterns with versatile Rietveld codes provides simultaneous information on crystal structure, texture, microstructure and phase proportions. [Search for "UCMRD" on the world wide web for more information].

Introduction

During the past decade, however, important new applications of neutron diffraction have emerged in both applied and fundamental research on condensed matter. A major advantage of neutrons *vis-à-vis* X-rays is the low absorption by most elements. This makes it possible to study bulk properties, to utilize sophisticated sample environments for studies at high or low temperatures and pressures, and to investigate orientation distributions and internal stresses in polycrystals. Due to the high spectral resolution that is available, refinements of crystal structures, phase proportions, textures and strains can all be performed simultaneously, e.g. with the Rietveld method [Von Dreele, 1997, Lutterotti, et al., 1997]. For those not yet familiar with neutron diffraction, it is recommended to consult an introductory text such as Bacon [1975].

The new High Pressure Preferred Orientation (HIPPO) Diffractometer will be housed at the Manuel Lujan Jr. Neutron Scattering Center as part of an over $25 M, facility wide upgrade project for the Los Alamos Neutron Science Center (LANSCE) sponsored by the US Department of Energy (DOE). LANSCE is a unique spallation (70 μA proton beam at 20 Hz with upgrade to 30 Hz) source that produces intense burst of polychromatic neutrons that can be captured in time-of flight (TOF) for fundamental condensed matter research. The HIPPO diffractometer is part of a synergistic effort by both the UC campuses and National laboratories to (1) attain scientific excellence and (2) to advance our present knowledge of condensed matter (3) make neutron diffraction an available tool for younger generation scientists. Chosen by the DOE for accelerated construction, the HIPPO diffractometer is anticipated to become available for testing in fall 1999 with a user program initiated in fall 2000.

A major limitation of neutrons has been the weak intensity. With the new diffractometer we can overcome this problem, taking advantage of the improved neutron source at LANSCE, a short flight path (flux at the sample: 10^8 n $cm^{-2}s^{-1}$) and a novel three-dimensional arrangement of detector banks with 1400 He-tubes, on conical rings. The usual data collection time will be reduced from hours to minutes, enabling us to study time-dependent processes in bulk samples with anisotropic properties. A flexible sample environment (large 75 cm diameter sample well) accommodates ancillary equipment such as goniometers, furnaces, cryostats, straining stages, high-pressure cells, magnets etc. Because LANSCE produces

The HIPPO time-of-flight (TOF) neutron diffractometer is designed to study properties of polycrystalline materials and liquids. Of particular interest is the investigation of small (1mm^3) and large (2cm^3) sample volumes at high (<2000K) and low (>10K) temperatures, at high pressure (<20GPa), and in different atmospheres. The diffractometer which we are building will be highly visible in the fields of phase transformations, high pressure research, polycrystal anisotropy (texture-strain-stress) and complex materials crystallography. It will be possible to study the dynamics of reactions, recrystallization and deformation of bulk anisotropic samples at a wide range of temperature and pressure conditions. No existing instrument, world-wide, has this capability. To learn more about LANSCE or the Short Pulse Spallation Upgrade project at LANL please see the web site http://lansce.lanl.gov/overview/index_over.htm.

HIPPO Technical Description

For a detailed description of the diffractometer and the project visit the HIPPO website http://www.seismo.berkeley.edu/~wenk/hippo.htm or search for UCMRD.

The HIPPO Diffractometer features a short initial flight path of 9m at Flight Path 4 of the Lujan Center and an array of 1400 10atm ^{3}He detector tubes covering nearly 4.6m^2 with five detector banks at scattering angles ranging from backscattering (nominally 150°) to low forward scattering (nominally 10°). The characteristics of each detector array are listed in Table 1 and their placement is shown in Figure 1. The detector panels are tilted relative to the scattered neutron paths to give a more constant resolution across their surfaces. The tilt compensates the change in resolution due to the angular range for each panel with a corresponding change in the sample-to-detector flight path. A T_0 chopper removes the fast neutron prompt pulse. The collimation views a 12cm diameter round portion of a high intensity ambient water moderator, and converges to a maximum round beam size of 2cm diameter at the sample position. For most applications samples ought to be fully immersed in the neutron beam and should not exceed this size. Smaller beam sizes at the sample position can be produced with adjustable collimation. A number of sample environments (cryostat, furnace, texture goniometer, high- pressure cells, sample changer) are accommodated within the sample chamber. It is anticipated that the count rate for some experiments will be approximately 20-60 times what is currently obtained on the present High Intensity Powder Diffractometer (HIPD) on Flight Path 3 at the Lujan Center, and will enable measurements in as little as 5-10s. The data acquisition will be based on current VME technology and make use of web-based visualization and control software. Experiments can be controlled remotely, e.g. from the laboratory of the user. Figure 1 shows an exploded view of the HIPPO diffractometer.

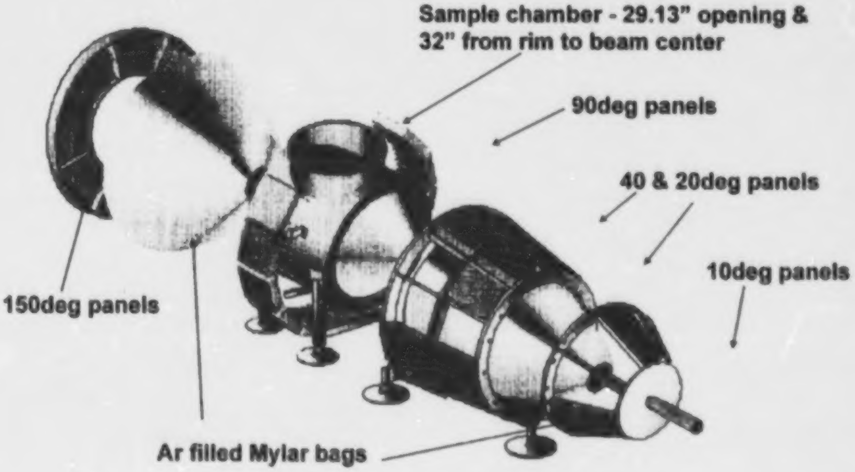

Figure 1. Exploded view of HIPPO diffractometer showing sample chamber surrounded by 5 conical rings of 3D detector tubes. Incident beam travels from left to right of figure, beginning at 150 deg panels. Argon filled Mylar bags are used to reduce incoherent scattering in secondary flight paths.

Table 1. Detector layout for HIPPO. The d and Q ranges are for 0.5-9 Å wavelength range. The resolution is full width at half maximum over position (100% ΔT/T).

Nominal angle	angular range	L_2,m	d-range, Å	Q range, $Å^{-1}$	ΔT/T
150	143°54'-155°48'	1.25	0.12-4.80	1.31-52.4	0.37%
90	76°46'-103°15'	0.75	0.17-6.90	0.91-37.0	0.75%
40	33°29'-47°35'	1.00	0.35-13.9	0.45-18.0	1.5%
20	18°17'-25°47'	1.50	0.65-26.1	0.24-9.67	2.6%
10	7°17'-12°45'	2.00	1.19-47.5	0.13-5.28	5.0%

Research Applications

The HIPPO will significantly advance three principal areas of research, which are all-interdependent and involve properties that can be measured simultaneously; high pressure, texture and magnetic properties. In all three cases, neutron diffraction can contribute crucial data that are presently lacking. These research areas require that the diffractometer have high intensity and moderate to high (though not ultrahigh) resolution and HIPPO has been designed with these features in mind. The HIPPO diffractometer can be applied in a wide variety of disciplines such as materials science and engineering, earth sciences, physics and chemistry. Examples of research include kinetics of reactions, high pressure investigations of complex systems with large sample volumes, texture evolution in polycrystals during deformation, recrystallization and phase transformations, texture and anisotropy of rocks (e.g. granite-mylonite, mantle peridotites), crystal structure of zeolites (Al-Si distribution, water), structure of liquids and melts (including Al-Si melts and glasses). It will be possible to perform real-time experiments on bulk anisotropic samples at a wide range of temperature and pressure conditions. No existing instrument, worldwide, has this capability. Texture information that can only be obtained with this instrument is a prerequisite to interpreting, for example, high-resolution residual stress data.

Time-of-flight neutron diffraction offers some unique advantages in characterizing texture. For most materials, absorption is negligible and large samples can therefore be examined. Because the diffraction signal averages over large volumes rather than surfaces, grain statistics are far better determined than with other methods. Also, intensity corrections are generally unnecessary, thereby allowing a high level of accuracy as demonstrated by a round robin standardization project [Wenk, 1991]. Because of the low absorption, environmental stages (high temperature, low temperature, and bulk stress/strain) can be used for *in situ* observation of texture changes [Bennett, et al. 1995; 1997]. For pulsed polychromatic neutrons, a whole range of wavelengths is available and continuous spectra are recorded at high resolution. They are therefore especially adaptive to problems of low crystal symmetry and composites with many diffraction peaks, as is typical for modern materials and for many environmental problems [Wenk, 1993]. The texture of such materials can not be satisfactorily characterized by X-ray diffraction. New crystallographic methods can be used to analyze these spectra and obtain simultaneous information on crystal structure, orientation distribution and phase proportions (from intensities), internal elastic strains (from peak locations) and microstructure (from peak shapes) [Wenk, et al. 1994; Lutterotti, et al. 1997; Von Dreele, 1997]. We foresee important new developments in theories relating textures and internal strains.

One (or more) texture goniometers will be provided for use on HIPPO. The azimuthal array of detector panels allows texture measurements to be done with very few sample orientations. In Figure 2 we show how a single sample setting gives considerable coverage of the orientation space; resulting in 20-32 points on a pole figure simultaneously from the 150, 90 and 40 deg. detector banks.

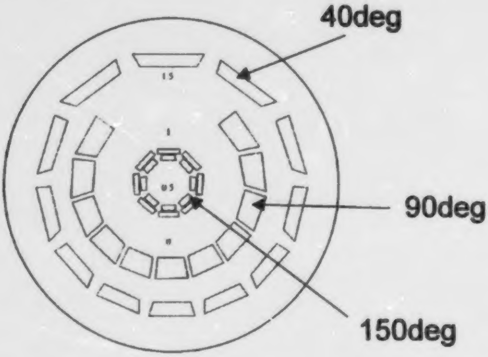

Figure 2 A stereographic projection of the 150, 90 and 40 deg. sets of detector panels on a pole figure for one sample orientation. Incident beam direction is along the projection axis. The gap in one set of detector panel images arises from the gap in the 90deg bank where the sample chamber access port is located. The detector panel images for the 150 and 40 deg. banks have no gaps.

A conventional 3-axis goniometer using Kappa geometry will be used for standard texture measurements. Its operation will be optimized to produce complete coverage of the orientation space taking into account the fact that the goniometer would inevitably obscure some detector panels. Because modern data analysis techniques utilizing Rietveld techniques [Von Dreele, 1997, Lutterotti et al. 1997] can accommodate any set of sample orientation angles, there is no requirement that the pole figures be sampled on a uniform grid as used in classical pole figure measurements. A 32-sample texture changer will allow quick texture analysis of multiple samples in 5-15 minutes if necessary which is important for larger systematic investigations. A future development for texture studies will include a texture goniometer equipped with a computer controlled X,Y,Z stage and 90deg radial collimators; this will permit the determination of position dependent texture within the dimensions of an extended sample. The collimation should be sufficient to determine a $2x2x2mm^3$ gauge volume with a sample positioning precision of 0.1mm or less. Each goniometer requires only modest angular precision for the setting angles; 0.1deg is more than adequate. In addition, H. Mecking (TU Hamburg) is collaborating in the design of a rotatable stress rig. It will be used for the simultaneous determination of texture and strain evolution with applied unidirectional stress.

User Program and Conclusion

The HIPPO diffractometer will be used for investigations of scientific relevance, and be accessible for a wide, multidisciplinary range of experiments in physics, chemistry, materials science, engineering and earth sciences. Experiments at this diffractometer will enhance our knowledge of condensed matter, particularly dynamic changes in bulk materials as opposed to single crystals and powders that have been the emphasis of conventional diffraction research. It will be possible to study simultaneously phase transformations, the evolution of microstructure and anisotropy in polycrystals at high pressure and temperature, in magnetic fields and during deformation.

It is planned to perform 150-250 experiments each year during an 8-month run cycle, making neutron diffraction not only a method for a few dedicated neutron specialists, but also a viable resource for the 'mainstream' materials and earth science communities. By providing easy and sustained access we can open neutron diffraction to graduate student thesis research which can not wait for a year until a proposal for a single experiment is approved. Prior to the operations phase two formal workshops are planned: In fall 1999 a first workshop will be held at the UC Davis Campus (funded through LANL-UCDRD), in spring 2000 a second workshop is planned at Los Alamos (funded through LANL-IGPP), and a paper will appear in August in the ICTOM99- Montreal proceedings to promote the HIPPO diffractometer and the UCMRD user program.

References

Bacon, G.E. (1975). *Neutron Diffraction.* Oxford, Clarendon Press, 436.

Bennett K., H.-R. Wenk, W.B. Durham and C.S. Choi (1994). Texture analysis of high-pressure low-temperature ice polycrystals: a study by neutron diffraction, In: *Textures in Geological Materials,* H.J. Bunge, S. Siegesmund, W. Skrotzki and K. Weber (eds.). Deutsch. Gesell. Metallkunde, Oberursel, Germany, 251-160.

Bennett K., H.-R. Wenk, W.B. Durham, L.A. Stern and S.H. Kirby (1997). Preferred crystallographic orientation in the ice I-II transformation and the flow of ice II, *Phil. Mag. A.*, **76**, 413-435.

Lutterotti L., S. Matthies, H.-R. Wenk, A.J. Schultz and J.W. Richardson (1997). Combined texture and structure analysis of deformed limestone from time-of-flight neutron diffraction spectra, *J. Appl. Phys.* **81**, 594-600.

Von Dreele, R.B. (1997). Quantitative texture analysis by Rietveld refinement, *J. Appl. Cryst.* **30**, 577-587.

Wenk H.-R. (1991). Standard project for pole figure determination by neutron diffraction, *J. Appl. Cryst.* **24**, 920-927.

Wenk H.-R. (1993). Texture analysis with TOF neutrons, In: *Time-of-Flight Diffraction at Pulsed Neutron Sources,* J.D. Jorgensen and A.J. Schultz. (eds.), *Trans. Am. Cryst. Ass.* **29**, 95-108.

Wenk H.-R., S. Matthies and L. Lutterotti (1994). Texture analysis from diffraction spectra, *Proc. ICOTOM 10, Mater. Sci. Forum* **157-162**, 473-479.

Acknowledgements

We thankfully acknowledge the United States Department of Energy, Office of Basic Energy Sciences-Materials Science, under contract number W-7405-ENG-36 with the University of California. We are gratefully for the continued support of the UCMRD Board and those who helped us succeed with this project.J.D. Embury, Dept. Mat. Sci. and Engin., McMaster Univ., Hamilton ON, Canada, S. Gialanella, Dip. Ingegneria dei Materiali, Univ. Trento, Italy, P.R. Gray, Dean of Engineering, UC Berkeley CA L. Lutterotti, Dip. Ingegneria dei Materiali, Univ. Trento, Italy, H. Mecking, Arbeitsbereich Werkstoffphysik, TU Hamburg-Harburg, Germany, D.M. Parkin, CMS, LANL, Los Alamos NM, P.B. Price, Dean of Physical Sciences, UC Berkeley CA, R. Raj, Dept. Mechanical Engineering, Univ. Colorado, Boulder CO , J. Roberts, Lujan Center, LANL Los Alamos, NM, A.P. Sattelberger, STB-DSTBP, LANL Los Alamos NM, R.N. Shelton, Vice Provost for Research, Office of UC President, Oakland CA, S. Sterbenz, SBSS Program, LANL, Los Alamos NM, P. Van Houtte, Dept. Metaalkunde, Katholieke Universiteit, Leuven, Belgium

RESIDUAL STRAIN MEASUREMENT OF {111} IN ROLLED ALUMINUM AS FUNCTION OF IN-SITU ANNEALING

G. LANGELAAN, H. JIN, J. HU, J. COOLEY and S. SAIMOTO
Materials and Metallurgical Engineering, Queen's University, Kingston, ON.,
K7L3N6 CANADA

Abstract

The residual strains in as-rolled electrical conductor grade aluminum were measured by determining the lattice spacing of the most intense X-ray peaks in the (111) pole figure. Direct measurements were made possible by a specially designed holder which permitted in-situ annealing without expansion of the reference reflection plane. The decrease of the lattice parameter with anneal times at 220 °C showed that the measured lattice spacing were in tension. After continuous recrystallization with 2 μm grain size, residual strains of the order of 10^{-4} were observed. The possible genesis of the micro-strains is illustrated.

Keyword: Al, continuous recrystallization, residual strains, in-situ X-ray hot stage

1 Introduction

The evolution of the micro-texture in deformed structures is very complex and recent meticulous transmission electron microscopic studies by Hughes and Hansen (1997) illustrates this. Although their study shows the break-up of a crystallite into a micro-textured fabric which conforms to the global or macro-texture, the method is incapable of depicting the micro-strains within these cellular structures with high angle boundaries. Supplementary methods which have been championed by other workers (Perlovich et al, 1998; Fischer and Schwarzer, 1998) are high resolution X-ray diffraction techniques now available due to recent advances in instrumentation. Perlovich et al (1998) point out that the information ideally possible from pole figure type determinations are not only integral intensity (for texture pole figures) but also those that involve line broadening and peak position. The line broadening analysis is very involved and requires a very low divergent primary beam (Ungar et al, 1984). On the other hand peak position which measures changes in the lattice spacing are comparatively easier and residual stress measurements have been performed for many decades (Noyan and Cohen, 1987). The new aspect to traditional residual stress measurements is the use of low {hkl} diffraction peaks with much increased intensity but with the same precision as with high angle reflections if the beam and diffracting surface alignment are precise (Clarke, Saimoto and Ho, 1993). This precise alignment procedure has now been augmented with a non-expansion specimen holder such that upon in-situ annealing corrections due to the movement of the surface are eliminated (Langelaan and Saimoto, 1999).

In the present work, the d spacing of the {111} in the region of maximum intensity is determined using this expansion-free hot stage before and after in-situ annealing of the rolled specimen. The maximum integral intensity positions are, of course, those of the major texture components.

2 Experimental Design and Procedures

The sample selected was as-rolled electrical conductor grade aluminum (EC Al) which manifests continuous recrystallization (CREX) after a few minutes at 220 °C (Jin, Li and Saimoto, 1998). The resultant structure is a very fine grained (less than 2 μm) such that the conditions necessary for equilibration of micro-stresses within the diffraction volume can be satisfied. The uniqueness of the prior processing was to precipitate out the Fe as Al_6Fe such that starting with a nominal composition in atomic ppm of 2060Fe-306Cu-165Ga-90B-39V-31Zn , the matrix Fe content was reduced to 0.310. Thus upon cold rolling 81% to 0.76 mm, CREX occurred upon annealing for 3 min. at 220 °C. Figure 1a shows the hardness changes with anneal times without any noticeable abrupt drop in the measured Vickers hardness (25 gm). To assess this phenomenon, the residual line broadening of (311) peak was measured as a function of anneal times (Fig. 1b). The method of Hu and Goodman (1970) was used in which an arbitrary parameter $B=(I_{min}-I_b)/(I_{max}-I_b)$ is defined, whereby I_{min} is the intensity minimum between $K_{\alpha 1}$ and $K_{\alpha 2}$ using Cu radiation, I_{max} is the intensity of the $K_{\alpha 1}$ peak and I_b is the background counts. The fraction residual line broadening, F_B, is defined as $(B_T-B_{REX})/(B_{CR}-B_{REX})$ where the subscripts T refers to the microstructure after anneal times at temperature T, REX to the completely recrystallized (annealed) state and CR to the cold rolled one. The residual line broadening parameter unlike that of hardness drops abruptly upon CREX after 3 min at 220 °C and remains relatively constant until the inception of discontinuous grain growth (DGG).

To more quantitatively assess this effect, the change in lattice spacing (d) as function of anneal times were undertaken using our low heat capacity in-situ hot stage which is free from thermal expansion effects. The details of our φ 4-circle diffractometer are reported elsewhere (Langelaan and Saimoto, 1999) in which an angular resolution of better than 0.01° in 2θ and specimen offsets less than 5 μm could be assured. The radiation source was a Rigaku RU-200B rotating anode with a Cr target. The diffracted beam was measured using a sealed gas position sensitive detector, a TEC 205 PSPC with an angular resolution of 0.004° 2θ per channel. The peak position was determined by fitting two Pearson VII functions to the K_α doublet after background subtraction. Suffice to state that using this method the coefficient of expansion of aluminum was measured with a precision comparable to previous workers. In the present tests, the counting times of 60 s for each peak was used to yield good precision.

The design of experiment was to mount in the in-situ hot stage an as-rolled specimen which had been ground to the centre of the sheet and electropolished to remove the damaged layer. Since the specimen was heated and cooled in-situ in the diffractometer with a focussed infra-red heater without large temperature changes in the holder, the instrumental errors before and after the heat treatment were near identical. With the spot welding of a thermocouple to the specimen, the programmable temperature controller imposed the desired heating/cooling rates and the isothermal temperature could be maintained at ±1.5 °C. For these preliminary tests, the optimum procedure was to maintain the θ angle constant at 29.3° and rock the φ using the + and - angles for that specimen which was measured and annealed for 9 and 30 min at 220 °C. The shortest anneal time used was 9 min., since in-situ annealing heating rate was 20 °C/min. with a faster cooling rate.

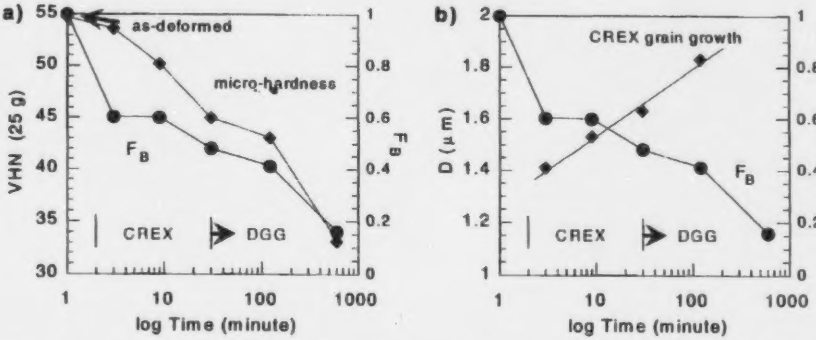

Fig. 1. **a)** Vickers hardness and fraction residual line broadening, F_B, versus anneal time at 220 °C. **b)** Grain size and F_B versus anneal time at 220 °C indicating the occurrence of CREX and initial DGG.

3 Results and Discussion

Figure 2 shows the φ versus 2θ plot over the ranges where the integral intensity is a maximum over the indicated φ angles. In Fig. 3, these values are averaged and plotted as function of anneal times and compared to the unstressed value, a_0 , at the reference ambient temperature of 29 °C derived from Langelaan and Saimoto (1999). First note that the residual stress decreases with anneal times as expected. Second the values at + and - φ are different. Third , the most unexpected result is that the residual stress on the most probable slip planes are in tension and do not reduce to zero for the fine CREX grains. The strains in the as-deformed state is less than 4×10^{-4} but even after 30 min. at 220 °C for this high purity matrix it is about 10^{-4} or higher depending on the peak location. The differences in the measured residual stresses between the possibly two variants of the texture component have been previously observed (Perlovich et al., 1998). These authors comment that "since mutually equilibrated elastic micro-stresses of opposite signs are located in different texture components, it follows that crystalline blocks corresponding to these components are mixed in the studied volume". This conclusion of fine inter-dispersion of cellular orientations is affirmed by the detailed studies of Hughes and Hansen (1997). In the present results, the measured components are both in tension suggesting that the compressive stresses appear to be located in the neighbouring blocks of different texture components, the volume fraction of any specific one is much lower than the measured one. Furthermore the two measured ones are not adjacent spatially.

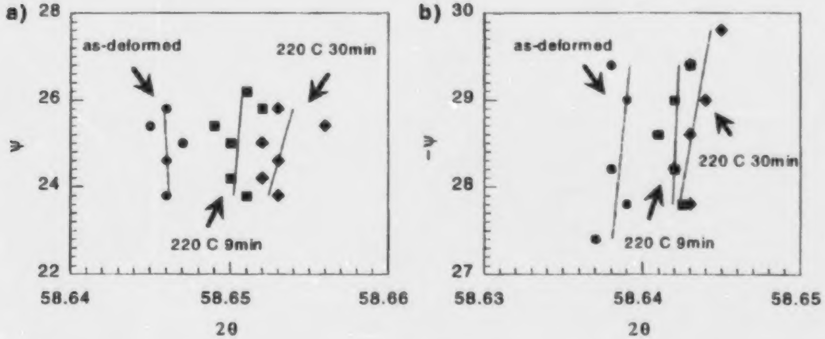

Fig. 2. ψ versus 2θ plot over the maximum intensity region for (111) with θ = 29.3°, a) + ψ and b) - ψ.

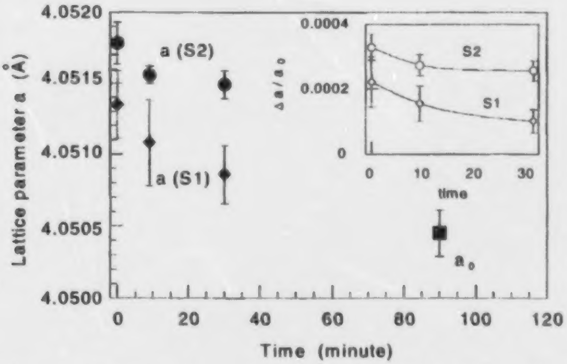

Fig. 3. Derived lattice parameter from Fig. 2 versus anneal time at 220 °C.

The evolution of the tensile stresses perpendicular to the {111} of the major texture component can be assessed as follows. Consider the schematic diagram in Fig. 4 where the ideal texture component crystallite is surrounded by other orientations as illustrated and RD, TD and RPN have their usual meaning. The former cell is labeled R_L whereas the latter ones are designated by R_S. During plane strain deformation, the R_L cell because of its inherent orientation can easily comply to the imposed deformation whereas its neighbours are much more resistant. This illustration becomes clear if R is taken to be the R-value measure and L stands for large and S, for small.

Thus in the plane of the sheet R_L cell suffers an in-plane compression. However in the plane normal to the TD in Fig. 4b, the result is an effective shear stress which resists the flow in the RD, that is a back-stress develops to prevent the R_L cell from deforming incompatibly with its neighbours. A situation similar to the one in Fig. 4 has been observed whereby the areal change of each crystallite is dependent on its orientation and the measured crystallite strains vary considerably from the imposed average (Li, Saimoto and Sang, 1993).

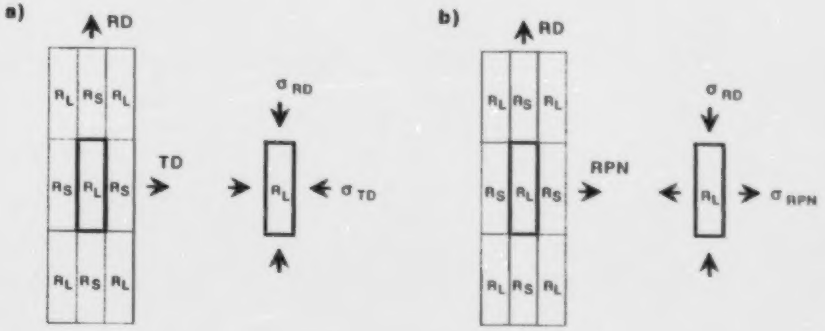

Fig. 4. Schematic illustration of cellular grains when R_L and R_S indicate grains with large and small R-value respectively.

The micro-strains measured in these experiments, however, developed upon unloading the sheet. Re-examination of Fig. 4a under elastic unloading suggests that the unloading strains in the R_S cells should be larger since the flow stresses attained by them are larger than those in R_L due to the greater storage of dislocations demanded by the complex slip modes for these orientations. Moreover the pancaking of the R_L cell is expected be to larger than the others and hence give rise to the tensile forces in the <111> directions which were measured. The observation of reasonably large strains of 10^{-4} even after CREX and uniform grain growth suggests that the outbreak of DGG as indicated in Fig. 1b is related to this stored elastic energy. Since the predominant orientation of the so-called large grains are (001)[100] which would require the least strain energy for the same amount of strain, the driving force for the growth of cube texture component during DGG may be due to the presence of inherent micro-stresses upon unloading.

For the comparison of F_B with the direct measurement of residual stress, differences in geometry must be examined. For the F_B tests using the (311) peak, the φ angle was kept at zero with the RD parallel to the θ axis such that lattice planes parallel to the sheet surface were irradiated. Since {311}<hkl> is not a recognized rolled sheet texture, the contributions could come from many components both in tension and compression because the depth of X-ray penetration is over 10 layering of the cells. Under this geometry, the initial drop of F_B is expected to be larger than that in one set of (111) planes of the same d spacing. Moreover the relative constancy of F_B during uniform grain growth followed by a dramatic drop upon DGG supports the present results of the presence of residual stresses in the fine grained CREX structure.

4 Conclusion

The residual strains in the slip plane of the major texture component where the integral intensity is a maximum were measured and found to be less then 4 × 10^{-4} in the as-rolled sheet. After CREX, this value reduced by about 1 × 10^{-4} . The measured strains were found to be in tension across the {111}, the most prominent slip planes for the rolled aluminum texture. The origin of the micro-strains are attributed to different degrees of strain hardening in the micro-cellular structure which evolves during deformation. The retention of the micro-strains in the fine recrystallized grains may be the driving force for grain growth of cube oriented grains.

5 Acknowledgements

The authors thank the Natural Science and Engineering Council of Canada, Material Manufacturing Ontario and Alcan International Ltd. for the support of this program.

6 References

Hughes, D.A., Hansen, N. (1997) High angle boundaries formed by grain subdivision mechanisms. Acta mater. 45, pp. 3871-3886.

Fischer, A.H. and Schwarzer, R.A.(1998) Mapping of local residual strain with an X-ray scanning apparatus. Mater. Sci. Forum, 273-275 pp. 673-678.

Hu, H. and Goodman, S.R. (1970) Effect of Mn on the annealing texture and strain ratio of low-carbon steels, Met. Trans. 1 pp. 3057-3064.

Jin, H., Li, J. and Saimoto, S. (1998) Thermal-mechanical processing of EC Al to induce continuous recrystallization, in Al Alloys: Their Physical and Mechanical Properties, eds. Sato, T. et al., Japan Inst. Light Metals,pp.1197-1202.

Langelaan, G. and Saimoto, S. (1999) Thermal expansion measurement of pure Al using a very low thermal expansion heating stage for X-ray diffraction experiments. Review Sci. Instruments, in press.

Li, J., Saimoto, S. and Sang, H. (1994) Examination of texture discontinuity at sheet surface due to cold rolling, Mater. Sci. 157-162 pp. 795-800.

Noyan, I.C. and Cohen, J.B. (1987) Residual stress: Measurement by diffraction and Interpretation, Springer-Verlag: New York, NY.

Perlovich, Yu., Bunge, H.J., Isaenkova, M. and Fesenko, V. (1998) The distribution of elastic deformation in textured materials as revealed by peak position pole figures. Mater. Sci. Forum, 273-275 pp. 655-666.

Ungar, T., Mughrabi, H., Ronnpagel, D. and Wilkens, M. (19984) X-ray line broadening of the dislocation cell structure in deformed [001]-oriented copper single crystals. Acta metall. 32 pp. 333-341.

NEW DEVELOPMENT IN TEXTURE AND MICROSTRUCTURE ANALYSIS OF PA11

L. JOLLY and J. J. HEIZMANN
Laboratoire d'Étude des Textures et Application aux Matériaux, Institut Supérieur de Génie Mécanique et Productique, Université de Metz, France
A. TIDU
Laboratoire d'Étude des Textures et Application aux Matériaux, Institut Supérieur de Génie Mécanique et Productique, École Nationale d'Ingénieurs de Metz, France

Abstract

X-Ray Diffraction method is applied to describe amorphous and ordered structures of PA11. The δ' smectic form presence is shown in PA11 samples moulded by compression. Texture and microstructure evolution is followed during an uniaxial deformation until 25%. Evolution of the characteristics values of the fitted peaks allows to characterise the different chains orientation of α form, δ' form and amorphous part during drawing. Spherulites lamellae are made up of α crystalline form and oriented towards drawing direction. Whereas the δ' smectic phase is enclosed in amorphous part. Macromolecules of both last phases tend also to turn towards the drawing direction. The description of α phase texture assumes that this structure is subjected to a twinning mechanism.

Keywords : polyamid 11, polymer deformation, Wide Angle X-Ray Scattering, semicrystalline polymer

1 Introduction

In order to understand some semicrystalline polymers properties, texture and microstructure are important to know. This study shows that the Wide Angle X-Ray Diffraction is an adequate method to describe structure, even if information on X-Ray patterns are overlapped and must be analysed by fitting procedure. This technique is applied to the polyamid 11. In this paper are presented : first, the polymer and the principle of analysis, then as an application the PA11 microstructure and its evolution during drawing.

2 Material and Analysis

2.1 PA11 Polymorphism and Preparation

Polyamid 11 is a semicrystalline polymer, with about 80% of amorphous phase. Its ordered phase polymorphism was studied by several authors. In spite of a lot of disagreements on crystal structure parameters, everyone agrees on five types of ordered structures. They include :

- *α crystalline form*, resulting from annealing of a quenched PA11 or from crystallisation of the melted polymer (Slichter 1959) or from casting of a *m*-cresol solution (Kim 1985),
- *δ form*, resulting from thermal crystal transformation of α form (Kim 1985),
- *δ' smectic form*, arising from melt quenched (Chen 1985; Mathias 1990),
- *γ crystalline form*, appearing by crystallisation in different solutions (Sasaki 1965; Kawaguchi 1981).

The α form is triclinic, with parameters close to the Slichter's theoretical triclinic unit cell. Chains are located in (100), (010) and (110) planes, and hydrogen bonds in the (010) plane (Slichter 1959). The other forms (δ, δ' and γ) are pseudohexagonal.

For our study, PA11, named Rilsan B®, is provided by Elf-Atochem. Plaques of 1mm-thick were obtained by compression moulding from melt (240°C) in *Institut Français du Pétrole* (IFP, Paris). The samples are punched out.

2.2 Measurements and Analysis

Wide Angle X-Ray Diffraction in transmission geometry with Fe Kα radiation is used to measure patterns of samples. The texture goniometer is equipped with a curved position sensitive detector.

All X-ray patterns of our samples, as one of them presented on Fig. 1, show several overlapped halos and lines between 13° and 40° (2θ). The main part of information is located in this area. In order to describe each line or halo, at first, the pattern is corrected from absorption, then each line and halo is fitted by Gauss function.

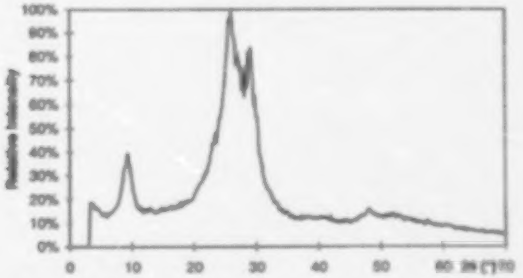

Fig. 1 : uncorrected X-Ray diffraction pattern of the initial PA11

Several patterns are obtained for chosen directions of measurement (ϕ,ψ). For each pattern, the characteristic values of Gauss functions, as area, position and width, are analysed to obtain the texture and microstructure evolution of the polymer.

3 Polymorphism of the PA11 Samples

Chen et al suggested that samples crystallised under pressure lower than 3 Kbar contain both δ' and α structures (Chen 1985). In order to obtain a physically acceptable fit, different PA11 samples, prepared with different cooling rates, are studied to know the real polymorphism of our samples.

To verify the presence of δ' form in the initial samples, new samples are prepared from melt (240°C) with different cooling rates. All the corresponding patterns are fitted with 4 peaks in the 13° - 40° (2θ) area : the α (100) and {(010),(110)} doublet lines, the amorphous diffuse halo and the characteristic δ' line (Fig. 2).

These new results give further information with regard to our first analysis (Jolly 1996), for which only 3 peaks were used to describe the microstructure of the polymer : the two α lines and the amorphous diffuse halo. These new results are sharpened in the description of the non-crystalline part which is, in this paper, splitted in two parts : the amorphous one and the smectic one.

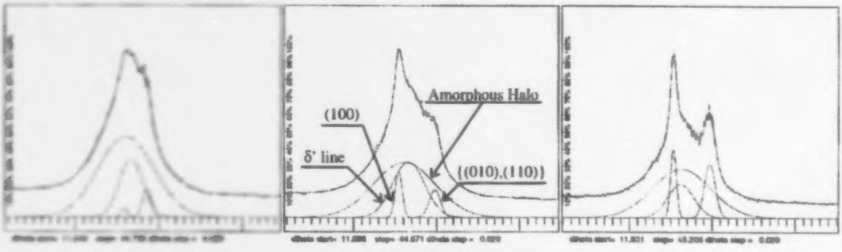

(a) (b) (c)

Fig. 2 : Fitted patterns of PA11 with a cooling speed $v_a > v_b > v_c$, relative intensity versus 2θ

Table 1 shows the different peak areas of these samples. Theses areas are mainly function of the different phases quantities. The previous Fig. 1 showing the initial PA11 sample points out a shape of the global peak, in-between (b) and (c) samples. So the initial PA11 samples can be described by the presence of α, δ' and amorphous phases. The Fig. 3 shows that the four peaks belonging to these phases perfectly describe the shape of the 13°- 40° area.

In the following we will always use all these phases to describe the microstructure evolution of our PA11 samples which are moulded by compression. Therefore the fitting procedure will use four Gauss functions.

Table 1 : Relative area values of fitted patterns peaks

area	cooled samples from melt			
(Arbitrary unit)	(a)	(b)	(c)	Fig. 3
α (100)	0.3	1.9	2.9	1.1
α {(010),(110)}	1.2	1.8	4.2	3.3
δ' line	6.9	10.3	6.3	4.1
Amorphous Halo	22.5	19.7	20.2	22.1

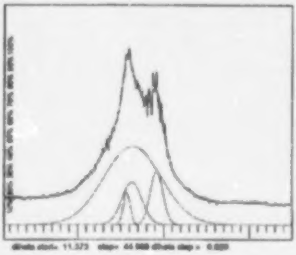

Fig. 3 : Fitted pattern of the initial sample presented on Fig. 1

4 Uniaxial deformation results

To define deformation mechanisms, measurements are carried out before and after uniaxial loading (from 2% to 25% deformation).

The analysis of initial samples shows a texture close to the isotropic one.

Samples remained loaded during the measurement by using a special device. During drawing and measurements, the sample temperature remained lower than the glass transition temperature (Tg = 40°C). A previous study on uniaxial strength deformed samples showed that the texture was close to a fibre texture whose axis is the loading direction. Only one Wulf meridian was measured and represented.

The imposed uniaxial deformations are 2%, 5%, 10%, 15%, 20% and 25%. The areas results are shown on Fig. 4. From these peaks areas evolutions, which are function of deformation, the macromolecules behaviour of each part of the PA11 can be described. Position and width peaks evolutions give some information about the interchain length and the chains packing evolution during loading :

1. *α crystalline part* : According to area evolution, the most of macromolecules of α part achieve to turn perpendicularly to the drawing direction. This tendency becomes stabilised after 10% deformation. Areas evolution show that fibre texture axis is <100>*. From the α peaks positions, one can say that only the chains which are perpendicular to drawing axis have their average hydrogen interchain bonds weakly lengthening.
2. *amorphous part* : A little part of chains of the amorphous phase turns towards the drawing direction. A combined study of the width and position of the halo shows that amorphous chains packing remains constant during loading.
3. *δ' smectic part* : Approximately half of macromolecules tends to turn towards the drawing axis as it is seen for the amorphous phase. Unlike it is seen in the crystalline part, all types of interchain bonds, instead of hydrogen bonds only, get longer when the chains are perpendicular to the drawing axis. The δ' line width is in-between the amorphous and crystalline ones, so it could assumed either that δ' phase is made of small crystallites or that it is disordered. The comparison of width and position peaks evolution indicates a behaviour of δ' phase close to the

amorphous one. So one can suppose that the smectic δ' is enclosed in the amorphous phase.

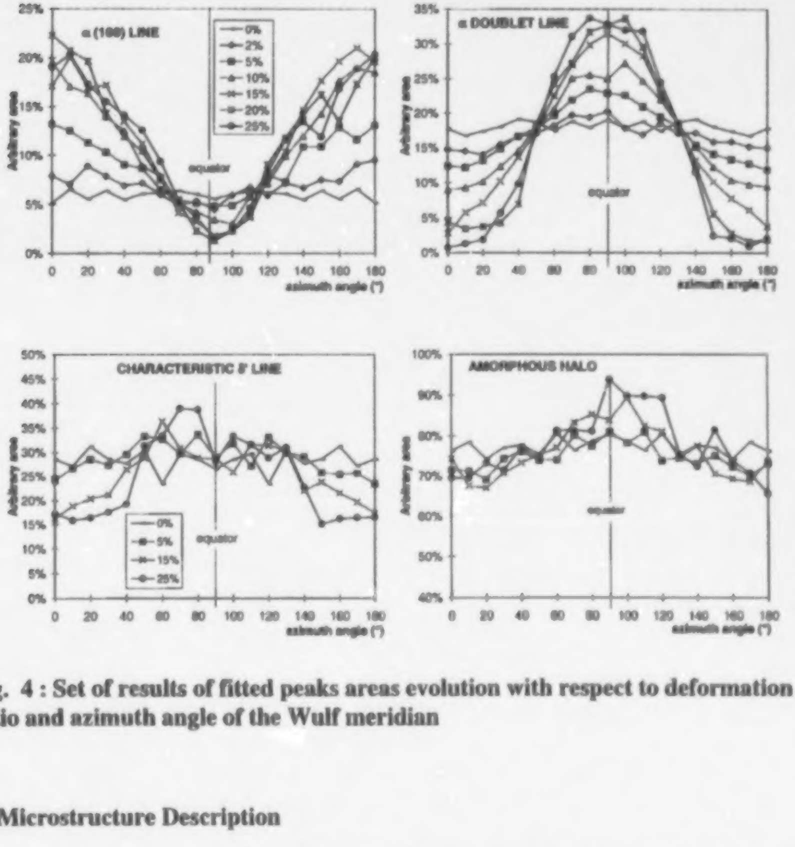

Fig. 4 : Set of results of fitted peaks areas evolution with respect to deformation ratio and azimuth angle of the Wulf meridian

5 Microstructure Description

According to the constitution of the polymer and the behaviour of chains of the crystalline and smectic parts, α form makes up spherulite lamellae and δ' form is enclosed in the amorphous part. Deformation mechanisms can be presented for PA11 plaques moulded by compression. During the drawing, chains of the amorphous and smectic parts tend to turn towards the drawing axis, whereas α form chains move perpendicularly to the drawing direction. This also means that lamellae moves towards the drawing direction. A supplementary study using Small Angle X-Ray Scattering confirmed this assumption (Barré 1996). According to Magill 1969, only spherulites with lamellae growing along the <010>* direction are observed in PA11 crystallised from melt, non deformed samples. On the other hand in our present study, the orientation of the lamellae and the texture of α phase indicate that the lamellae direction is <100>* after drawing. These two observations seem to be contradictory, but could be explained by a twinning mechanism during the drawing. Such on effect has been seen in PA6,6 spherulites (Hay and Keller 1970) and supposed in PA11 spherulites (Autran 1990). The effect of this twinning mechanism is to shift hydrogen bonds planes parallel to the drawing direction.

6 Conclusion

Fitting procedure is adequate to analyse X-ray patterns in order to describe the microstructure in semicrystalline polymers. This PA11 study shows the difficulty in obtaining the α crystalline structure alone by moulding by compression, even if cooling during samples moulding is slow.

During drawing, the chains of the amorphous and δ' form parts achieve their orientation towards the drawing direction, it is the same for Spherulites lamellae. After loading, the α (100) plane orientation could indicate that crystalline lamellae structure is subject to a twinning mechanism.

7 Acknowledgements

Authors thank I.F.P. (Institut Français du Pétrole, Paris) for its financial support, and Dr. Dal Maso, Barré, Meimon and Jarrin for their helpful discussions.

8 References

Autran (1990) Structure, Deformation Behaviour and Properties in Nylon 11 and HDPE Subjected to Planar. *Ph. D. University of Massachusetts*

Barré and Dal Maso (1996) personal communication, *I.F.P., Paris*

Chen, Newman, Scheinbeim, Pae (1985) High pressure melting and crystallization of Nylon-11, *Journal of Materials Science*, Vol. 20, pp.1753-1762

Hay, Keller (1970) Mechanically induced twinning and phase transformation., *Journal of Polymer Science : Part C*, Vol. 30, pp.289-296

Jolly, Tidu, Heizmann (1996) Texture Characterization of the linear Semicrystalline Polymer PolyAmide 11 under low uniaxial Deformation., *Proceeding of 11th ICOTOM* (Ed. By Liang, Zuo and Chu) Xi'an, China, Vol. 2, pp.1269-1274

Kawaguchi, Ikawa, Fujiwara (1981) Polymorphism in Lamellar Single Crystal of Nylon 11, *Journal of Macromolecules Science: Physics*, Vol. B20, No. 1, pp.1-20

Kim, Newman, Scheinbeim (1985) Temperature Dependence of the Crystal Structures of Nylon 11, *Journal of Polymer Science: Polymer Physics Edition*, Vol. 23, pp.2477-2482

Magill (1969) Formation of Spherulites in Polyamids. IV, *Journal of Polymer Science : Part A-2*, Vol. 7, pp.123-142

Mathias, Powell, Autran, Porter (1990) ^{15}N NMR Characterisation of Multiple Crystal Forms and Phase Transitions in Nylon 11, *Macromolecules*, Vol. 23, pp.963-967

Sasaki (1965) Notes on the polymorphism in Nylon 11., *Polymer Letters*, Vol. 3, pp.557-560

Slichter (1959) Crystal Structures in Polyamids Made from ω-Amino Acids, *Journal of Polymer Science*, Vol. 36, pp.259-266

USE OF A METHOD BASED ON A CORRELATION FUNCTION TO RECONSTRUCT THE PARENT TEXTURES FROM THE INHERITED TEXTURES IN PHASE TRANSFORMATION.

M. HUMBERT AND N. GEY
Laboratoire d'Etude des Textures et Application aux Matériaux, Letam
CNRS URA 2090, ISGMP, Université de Metz, 57045 Metz Cedex 01 France.

Abstract

When no variant selection occurs, we reconstruct the ODF of the parent phase from the ODF of the phase, inherited by phase transformation provided that the lattice symmetry of the parent phase is higher than that of the inherited one and that the orientation relation between both phases is known. In the cases of variant selections, information about the ODF of the parent phase can be obtained by considering specific functions and notably function R(g) which is an upper bound of the parent ODF.

Keywords : Phase transformations, Variant selection, Texture.

1 Introduction

In the studies of phase transformation, the knowledge of the ODFs of the parent phases is of importance in the comprehension of transformation mechanisms. In many cases, the direct measurement of the corresponding textures is not an easy task because the parent phases are often of high temperature, which requires very specific measurement attachments. Another possibility to obtain the parent ODFs consists in using indirect determination methods based on the correlation of single orientations within the inherited grains (Humbert et al 1994). In this contribution, we detail another method, which can be used in specific cases. As a matter of fact, the analysis of the cubic to hexagonal or the cubic to cubic phase transformations, occurring without variant selection allowed us to develop a method to calculate the ODFs of the parent cubic phase from the ODFs of the inherited phase. This method requires the existence of orientation relations between lattices (Kurdjumov-Sachs KS, Nishiyama-Wassermann NW, Burgers B). When a variant selection occurs, it is nevertheless possible to deduce the main characteristics of the parent ODF [$f_I(g)$] by using a specific correlation function we named R(g).

2 Theoretical aspects

After complete phase transformation without variant selection, the ODF $f_2(g)$ of the inherited phase can be related to the parent ODF $f_1(g)$ by the convolution integral :

$$f_2(g) = \int W(g_1) \cdot f_1(g_1^{-1} \cdot g) \cdot dg_1 \qquad (1)$$

where $W(g_1)$ is the orientation transformation function taking into account the mutual orientation relation between lattices Δg_0. When Δg_0 is a strict orientation relation, $W(g_1)$ corresponds to a sum of Dirac functions.

Developing each function of relation (1) into series expansion leads to sets of linear equations which link the coefficients $C_\ell^{\mu n}(2)$ of the inherited texture to the coefficients $C_\ell^{\mu' n}(1)$ of the parent texture by the coefficients $W_\ell^{\mu\mu'}(\Delta g_0)$ of the orientation transformation function for l and n fixed (Bunge 1969, 1982) :

$$C_\ell^{\mu n}(2) = \frac{1}{2\ell+1} \sum_{\mu'=1}^{M(l)} W_\ell^{\mu\mu'}(\Delta g_0) C_\ell^{\mu' n}(1) \qquad (2)$$

The coefficients $W_\ell^{\mu\mu'}(\Delta g_0)$ depend on the misorientation Δg_0 between the parent and the inherited lattices and on the dispersion around Δg_0. For the sake of simplicity, each equation set (2) (for l and n given) is now symbolically written :

$$C(2) = WC(1) \qquad (3)$$

where W is a matrix whose dimensions are defined by the μ' and μ integers. When the symmetry of the inherited phase is smaller or equal to that of the parent phase, μ' is higher or equal to μ. Thus, relation (3) corresponds to an overestimated system of linear equations which can be inverted. Hence, coefficients C(1) of the parent phase can be calculated from the coefficients C(2) of the inherited phase by a classical inversion scheme for overestimated systems of equations (Humbert and Gey 1998) :

$$C(1) = ({}^{t}WW)^{-1}({}^{t}W)C(2) = UC(2) \qquad (4)$$

where ${}^{t}W$ is the transposed matrix of W. This solution corresponds to the minimisation of $\|C(2) - WC(1)\|^2$.

It can be outlined that the parent ODF $f_1(g)$ can be calculated from the inherited ODF $f_2(g)$ provided that :

1) no variant occurred during the transformation.
2) the misorientation relation between both lattices is known.
3) the symmetry of the inherited phase is smaller or equal to that of the parent phase.

The third condition is fulfilled for the cubic to hexagonal transformations as well as for the cubic to cubic transformations.

General case
Using relations (3) and (4) shows that the C coefficients of the inherited phase must theoretically fulfil the relation:

$$(I - W({}^tWW)^{-1}({}^tW))C(2) = (I - WU)C(2) = 0 \qquad (5)$$

if no variant selection occurs.

Specific case of the hexagonal symmetry
In the specific case of the cubic to hexagonal transformation, additional relations can be used to check condition (1) (Humbert and Gey 1999). As a matter of fact, certain coefficients of the hexagonal phase (inherited without variant selection) must be null :

$$C_2^{1n}(2) = C_7^{1n}(2) = C_{11}^{1n}(2) = 0 \qquad (6)$$

because the coefficients of rank l equal to 2, 7, 11 in the parent cubic phase do not exist.

In practice, even if no variant selection occurs, relations (5) and (6) are rarely equal to zero because of inevitable experimental errors in the ODF determinations, but must be close to zero. The sensitivity of this method requires that the experimental errors in the determination of the inherited ODF must be the lowest possible.

3 Variant Selection

When a weak selection occurred during the transformation, experience shows that the ODF $f_1(g)$ of the parent phase can be qualitatively evaluated from the inherited ODF $f_2(g)$ with the scheme proposed in the previous section.

For a strong variant selection, using this scheme leads to a recalculated function $f_1(g)$ which presents negative values. It is no more a density function, for $f_1(g)$ must be equal to or greater than zero. The importance of calculated negative values of this function indicates the degree of the variant selection.

Besides, in the case of a cubic to hexagonal transformation, relations (5) and (6) significantly deviate from zero. Using relations (5) and (6), several indexes, sensitive to check the variant selection can be formed (Humbert and Gey 1998) :

$$J_2 = \tfrac{1}{5}\sum_{n=-2}^{n=+2}\left\|C_2^{1n}(2)\right\|^2 \; ; \; J_7 = \tfrac{1}{15}\sum_{n=-7}^{n=+7}\left\|C_7^{1n}(2)\right\|^2 \; ; J_{11} = \tfrac{1}{23}\sum_{n=-11}^{n=+11}\left\|C_{11}^{1n}(2)\right\|^2 \qquad (7)$$

$$Js = \oint \Delta f_3{}^2(g)dg$$

The deviations from zero of these indexes indicate the importance of the variant selection. Experience shows that, if these differences are important, function $f_1(g)$ cannot be accurately calculated according to the previous scheme. Nevertheless, it is possible to obtain some information about the parent texture with the help of an additional function calculated from the inherited ODF.

In the case of a transformation with a strict orientation relation, the relation between $f_1(g)$ and $f_2(g)$ can be written (Humbert et al 1988) :

$$f_2(g) = \frac{1}{|H|}\sum_{j=1}^{|H|} v\left(\Delta g_0^{-1} H_j g\right) f_1\left(\Delta g_0^{-1} H_j g\right) \tag{8}$$

with the following notations :

S_i : one of the $\|S\|$ rotational elements of the parent symmetry group.

H_j : one of the $\|H\|$ rotational elements of the inherited symmetry group.

Δg_0 : rotation leading the co-ordinate system of the parent lattice to the co-ordinate of the inherited lattice.

V : the variant selection function which has the following property :

$\sum_{i=1}^{|S|} v(S_i g) = \|S\|$.

Let us assume that the inherited phase obtained by a β to α transformation is transformed again by a α to β transformation without variant selection. The ODF $f_3(g)$ of the new phase (with the same lattice as that of the parent phase) is linked to $f_2(g)$ by :

$$f_3(g) = \frac{1}{|S|}\sum_{i=1}^{|S|} f_2\left(\Delta g_0 S_i^1 g\right) \tag{9}$$

and by taking into account (8) :

$$f_3(g) = \frac{1}{|S|}\frac{1}{|H|}\sum_{j=1}^{|H|}\sum_{i=1}^{|S|} v\left(\Delta g_0^{-1} H_j \Delta g_0 S_i\, g\right) f_1\left(\Delta g_0^{-1} H_j \Delta g_0 S_i\, g\right) \tag{10}$$

$f_3(g)$ is nothing else that function R(g), calculated according to another principle in a previous work. By taking the symmetries of the parent and inherited phases into account, the following property can be demonstrated (Humbert and Gey 1999) :

$$R(g) = f_3(g) \geq \tfrac{1}{K} f_1(g\ ) \geq 0 \tag{11}$$

(K=24 for KS, K=12 for NW, K=6 for B).

Thus, $f_3(g)$, named from now on R(g) gives the upper limits of the sought function $f_1(g)$.

4 Application

A Ti-64 sheet underwent a thermal treatment in the β field, followed by cooling. The inherited ODF $f_2(g)$ of the α phase, resulting from the phase transformation has been determined from 2777 individual orientations of α plates, measured by EBSD with random localisations. The plates had roughly the same volume. Consequently the same weight was assigned to each Gaussian function with a spread of 8° for Φ_0 according to the symmetry and the sharpness of the texture (Wagner et al 1981). Figure 1 shows the sections of the α ODF at constant Phi1.

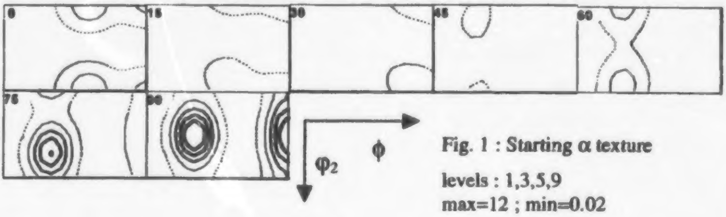

Fig. 1 : Starting α texture

levels : 1,3,5,9
max=12 ; min=0.02

According to the fact that indexes J_2, J_7, J_{11} and J_s are not equal to zero (J_2 = 0.07, $J_2 + J_7 + J_{11}$ = 0.116, and J_s = 0.434) but remain low as in theoretical results presented in another paper (Humbert and Gey 1998), the parent β ODF $f_1(g)$ was calculated (fig. 2). It presents some limited negative values, but the integral of the negative values remains small (-0.6).

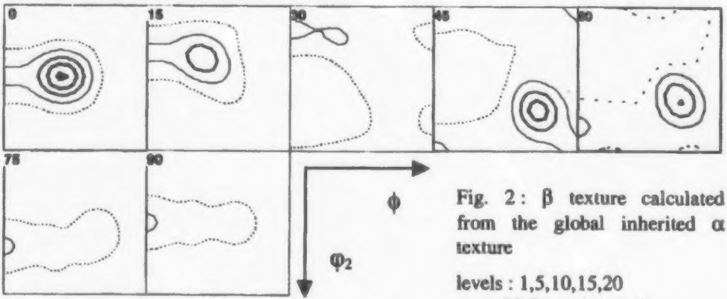

Fig. 2: β texture calculated from the global inherited α texture

levels : 1,5,10,15,20
max=20.74 ; min=-3.51

The corresponding correlation function R(g) (fig. 3) was calculated from the inherited ODF $f_2(g)$. It delimits the domains of the Euler space where the parent ODF $f_1(g)$ can be higher than zero (relation (11)). In this case, one observes that recalculated $f_1(g)$ and R(g) match very well. The analysis of recalculated $f_1(g)$ by using $R(g)$ makes it possible to qualitatively evaluate the main orientations of the parent texture.

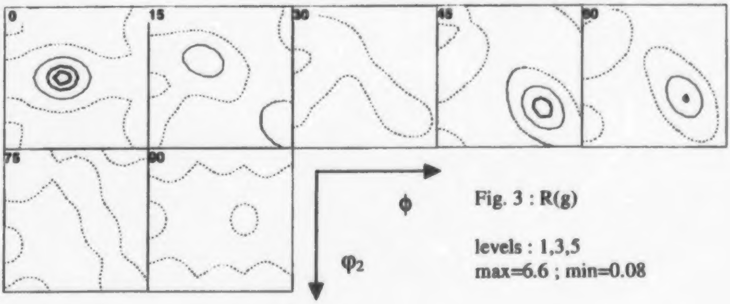

Fig. 3 : R(g)

levels : 1,3,5
max=6.6 ; min=0.08

Moreover the recalculated ODF $f_1(g)$ is in good agreement with the texture of the parent phase (fig. 4) of the same material but determined by a method detailed elsewhere (Humbert et al. 1994).

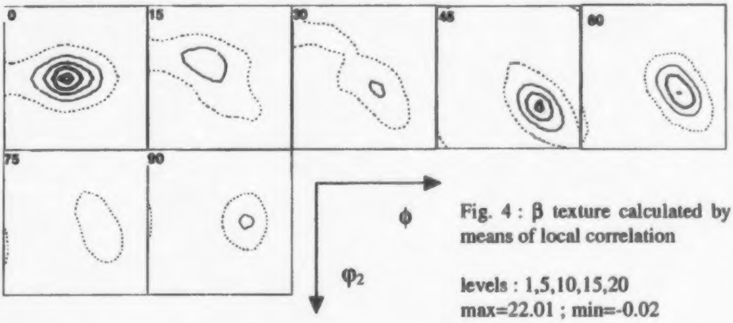

Fig. 4 : β texture calculated by means of local correlation

levels : 1,5,10,15,20
max=22.01 ; min=-0.02

5 References

Bunge H.J. (1969) : Mathematische Methoden der Texturanalyse, Berlin, Akademie Verlag.
Bunge H.J. (1982) : Texture Analysis in Materials Science, London, Butterworths.
Humbert M., Wagner F., Liu W.P., Esling C. and Bunge H. J.(1988), Proc of the 8th ICOTOM edited by J.S. Kallend and G. Gottstein, Met. Soc Warrendale.
Humbert M., Moustahfid H., Wagner and Philippe M.J. (1994).: Scr. Met. 30, 377-382.
Humbert M. and Gey N. (1998). Material Science Forum, 273-275, pp.163-168.
Humbert M. and Gey N. (1999). J. Appl. Cryst. 32, pp.21-26.
Wagner F., Wenk H.R., Esling C. and Bunge H.J. (1981). Physica Status Solidi. 67A, pp. 269-272.

FALSE PATTERNS OF PREFERRED ORIENTATION BY ERRONEOUS BACKGROUND–CORRECTION

H. SCHAEBEN
Geomathematics and Geoinformatics
Freiberg University of Technology and Mining, Germany
H. SIEMES
Department of Mineralogy, RWTH Aachen, Germany
J.-J. FUNDENBERGER
LETAM–ISGMP, University of Metz, France

Abstract

The pdf-odf reconstruction problem considered here was initialized by a case study of preferred orientation in aluminum oxide, where an orientation and corresponding pole density functions were calculated which did not match crystal–geometrically with the experimental ones, independently of the method used for the calculations. Eventually, by modeling with standard functions an erroneous “background–correction” was identified to cause a false pattern of preferred orientation.

Keywords: background–correction, crystal–geometry, standard functions

1 A practical problem

In a practical application of texture analysis the pattern of preferred orientation in a sample of aluminum oxide had to be determined from experimental x–ray diffraction intensity data of the three incompletely measured crystallographic forms (113), (116), and (214). Applying alternatively the harmonic method (Bunge 1982) and the maximum entropy method *MENTEX* (Schaeben and Siemes 1996) the corresponding orientation density functions as well as pole density functions of the three measured reflections (113), (116), (214), and of two additional reflections (110), (001) were calculated. Independently of the method used for the calculations, a pattern of preferred orientation was observed in both the orientation density function and pole density functions which did not match crystal–geometrically with the pattern of the experimental pole figures. In particular, the pole figure of the (110) reflection displayed a maximum in its center which did not match, and it was concluded that the calculated pattern of preferred orientation was false. Since the experimental data did apparently not reveal any irregularities, they did initially not provide any idea leading to an understanding of the problem.

2 Mathematical modeling with standard functions

Applying standard functions (Matthies et al, 1982; Schaeben, 1996, 1997) an orientation density function and corresponding complete and incomplete pole density functions of the crystallographic forms (113), (116), (214), (110), and (001) were mathematically modeled and numerically generated according to the mixture

$$f(g) = 0.25\, u(g) + 0.75\, f_{\mathrm{vMF}}(g; id, 35) \qquad \textbf{(1)}$$

of a uniform distribution u with weight 0.25 and a correspondingly weighted rotationally invariant von Mises–Fisher matrix ("standard Gaussian") distribution f_{vMF} with location parameter $g_0 = (0,0,0)$ denoting the identical rotation and dispersion parameter $b = 35$ degrees halfwidth. Using the first three of them as input to calculate an orientation density function and corresponding pole density functions with the harmonic or the *MENTEX* method all five of them were sufficiently well recalculated.

In a series of numerical experiments to model an erroneous "background correction" the uniform portion of the first three pole density functions was numerically changed in such a way that a different weight was assigned to it for each of them, e.g. more specifically

$$\begin{aligned}
\tilde{P}_{(113)}(\mathbf{r}) &= \tilde{\mathcal{P}}_{(113)}[0.35\, u(g) + 0.65\, f_{\mathrm{vMF}}(g; id, 35)](\mathbf{r}) \\
\tilde{P}_{(116)}(\mathbf{r}) &= \tilde{\mathcal{P}}_{(116)}[0.45\, u(g) + 0.55\, f_{\mathrm{vMF}}(g; id, 35)](\mathbf{r}) \\
\tilde{P}_{(214)}(\mathbf{r}) &= \tilde{\mathcal{P}}_{(214)}[0.25\, u(g) + 0.75\, f_{\mathrm{vMF}}(g; id, 35)](\mathbf{r}) \qquad \textbf{(2)}
\end{aligned}$$

This kind of inconsistency of the uniform portion yields an incompatibility of the pole density functions which is hard to detect in the usual pole figure plots as the geometric relationships imposed by crystallographic symmetries are apparently satisfied.

However, the orientation density function calculated from these three disordered pole density functions with either method significantly deviates in the same way from the mathematically given initial orientation density functions, and the recalculated/calculated pole density functions, especially the one of the (110) reflection, obviously display a false pattern of preferred orientation and do not match with the mathematically given initial pole density functions in terms of the crystallographically imposed geometrical constraints. In fact, they display the same false pattern that was encountered when analyzing the experimental aluminum oxide data.

3 Conclusion

Thus, these numerical experiments verify that an erroneous "background correction" may introduce an incompatibility into the input intensity data that will change and largely falsify the texture to be recovered.

4 References

Bunge, H.J. (trans. P.R. Morris) (1982) *Texture Analysis in Materials Science*, Butterworths, London

Matthies, S., Vinel, G.W., and Helming, K. (1987) *Standard Distributions in Texture Analysis I*, Akademie Verlag, Berlin

Schaeben, H. (1996) Texture approximation or texture modeling with components represented by the von Mises - Fisher matrix distribution on $SO(3)$ and the Bingham distribution on S^4_+, *J. Appl. Cryst.* **29**, 516-525

Schaeben, H. (1997) A simple standard orientation density function: The hyperspherical de la Vallée Poussin kernel, *phys. stat. sol. (b)*, **200**, 367-376

Schaeben, H. and Siemes, H. (1996) Determination and interpretation of preferred orientation with texture goniometry: An application of indicators to maximum entropy pole- to orientation density inversion, *Math. Geol.* **28**, 169-201

DUAL FORMS OF TEXTURE ANALYSIS

H. SCHAEBEN
Geomathematics and Geoinformatics
Freiberg University of Technology and Mining, Germany
D.I. NIKOLAYEV
Joint Institute for Nuclear Research, Dubna, Moscow region, Russia

Abstract

In this contribution we define a hyperspherical x-ray transform, characterize the range of this transform in terms of an ultrahyperbolic differential equation which is derived here without referring to spherical harmonics, and provide its general solution both in terms of its characteristics or spherical harmonics. These results will aid in the solution of the inverse tomographic problem of texture goniometry.

Keywords: hyperspherical x-ray transform, projective spaces, Laplace-Beltrami operator, ultrahyperbolic differential equation, spherical harmonics, characterictics

1 A hyperspherical x-ray transform

Definition: Let $f \in C^2(SO(3))$ be a twice differentiable function defined on the group of proper rotations. Let $\mathbf{h}, \mathbf{r} \in S^2 \subset I\!R^3$, then the integral operator $\mathcal{P}_{\mathbf{h}} : C^2(SO(3)) \mapsto C^2(S^2 \times S^2)$ is defined as

$$(\mathcal{P}_{\mathbf{h}} f)(\mathbf{r}) = \frac{1}{2\pi} \int_{\{g \in SO(3) \,|\, \mathbf{h} = g\mathbf{r}\}} f(g) d\nu(g) = P(\mathbf{h}, \mathbf{r}) \tag{1}$$

In mathematics the function $P(\mathbf{h}, \mathbf{r})$ for a given $\mathbf{h} \in S^2$ is referred to as hyperspherical x-ray transform of f with respect to $\mathbf{h}$. Geometrically, the path of integration $\{g \in SO(3) \,|\, \mathbf{h} = g\mathbf{r}\}$ in eq. (1) is a great circle of $S^3_+ \subset I\!R^4$, or equivalently a line in the projective space H^3.

For reasons originating in crystallography and Friedel's law, the basic crystallographic x-ray transform $\tilde{\mathcal{P}}_{\mathbf{h}} : C^2(SO(3)) \mapsto C^2(S^2_+ \times S^2_+)$ is defined as

$$(\tilde{\mathcal{P}}_{\mathbf{h}} f)(\mathbf{r}) = \frac{1}{2}\Big(P(\mathbf{h}, \mathbf{r}) + P(-\mathbf{h}, \mathbf{r})\Big) = \tilde{P}(\mathbf{h}, \mathbf{r}) \tag{2}$$

where S_+^2 denotes the upper unit hemisphere in $I\!R^3$, or equivalently the projective plane $I\!P^2$. Now, obviously,

$$\tilde{P}(\mathbf{h},\mathbf{r}) = \tilde{P}(-\mathbf{h},\mathbf{r}) = \tilde{P}(\mathbf{h},-\mathbf{r}) \tag{3}$$

that is, $\tilde{P}$ is an even function in both arguments $\mathbf{h},\mathbf{r} \in S^2$, and therefore the operator $\tilde{\mathcal{P}}_{\mathbf{h}}$ maps essentially onto $C^2(S_+^2 \times S_+^2)$.

2 The differential equation governing the spherical x-ray transform

The conventional notation $\tilde{P}_h(\mathbf{r})$ of texture analysis was dropped in favor of $\tilde{P}(\mathbf{h},\mathbf{r})$ to emphasize its features of a general axis distribution

Let Δ denote the Laplace-Beltrami operator, and assume $f \in C^2(SO(3))$. Then

$$\Delta_{\mathbf{h}} \tilde{P}(\mathbf{h},\mathbf{r}) = \Delta_{\mathbf{r}} \tilde{P}(\mathbf{h},\mathbf{r}) \tag{4}$$

where equality is obtained by simultaneously substituting $\mathbf{h},\mathbf{r},g$ by $\mathbf{r},\mathbf{h},g^{-1}$.

Thus, the hyperspherical x-ray transform and hence crystallographic pole density functions satisfy the differential equation $(\Delta_{\mathbf{h}} - \Delta_{\mathbf{r}})P(\mathbf{h},\mathbf{r}) = 0$ which is referred to as ultrahyperbolic differential equation in mathematical physics.

3 Solving the differential equation of texture goniometry

In complete analogy to (i) Fourier's harmonic method and (ii) d'Alembert's method of characteristics to solve an ordinary hyperbolic differential equation we shall derive the general solution of the ultrahyperbolic differential equation for hyperspherical x-ray transforms both in terms of spherical harmonics as well as its characteristics.

3.1 The general solution in terms of spherical harmonics

Theorem 1: The general solution of $(\Delta_{\mathbf{h}} - \Delta_{\mathbf{r}})P(\mathbf{h},\mathbf{r}) = 0$ for $P \in C^2(S^2 \times S^2)$ is

$$P(\mathbf{h},\mathbf{r}) = \sum_{l=0}^{\infty} \sum_{m=-l}^{l} \sum_{m'=-l}^{l} C_l^{mm'} (Y_l^m)^*(\mathbf{h}) Y_l^{m'}(\mathbf{r}) \tag{5}$$

Proof: Any function $u \in C^2(S^2 \times S^2)$ can be represented by its tensor product expansion into spherical harmonics

$$u(\mathbf{h},\mathbf{r}) = \sum_{l=0}^{\infty} \sum_{m=-l}^{l} \sum_{l'=0}^{\infty} \sum_{m'=-l'}^{l'} \lambda_{lm,l'm'} (Y_l^m)^*(\mathbf{h}) Y_{l'}^{m'}(\mathbf{r}) \tag{6}$$

which simplifies for functions $u(\mathbf{h},\mathbf{r})$ satisfying eq. (4) to

$$u(\mathbf{h},\mathbf{r}) = \sum_{l=0}^{\infty} \sum_{m=-l}^{l} \sum_{m'=-l}^{l} \lambda_l^{mm'} (Y_l^m)^*(\mathbf{h}) Y_l^{m'}(\mathbf{r}) \tag{7}$$

which is the form of (5) as the other terms drop out because the eigenvalues of Δ are different for different l.

Physical requirements like non-negativity, evenness, crystallographic or sample symmetries impose additional constraints on the system (5) and lead to special solutions.

Theorem 2: For any function $u \in C^2(S^2 \times S^2)$ satisfying the differential equation (4) there exists a unique function $f \in C^2(SO(3))$ such that $\mathcal{P}_\mathbf{h} f = u$.

Proof: The function $f \in C^2(SO(3))$ given by

$$f(g) = \sum_{l=0}^{\infty} \sum_{m=-l}^{l} \sum_{m'=-l}^{l} \lambda_l^{mm'} D_l^{mm'}(g) \tag{8}$$

with the generalized spherical harmonics $D_l^{mm'}(g)$ defined as usual possesses the x-ray transforms (7).

The same result that the operator of eq. (1) is invertible follows from generalizations of Funk's original work that an even function $f \in C(S^3)$ is uniquely determined by the values of the integrals over all great-spheres.

Thus, the coefficients of the general solution of the ultrahyperbolic equation for spherical x-ray transforms in terms of harmonics are the harmonic coefficients of the function being transformed, i.e. the solution of the ultrahyperbolic equation provides the solution of the inverse x-ray transform problem. This possibility to solve a differential equation instead of an inverse Radon- type problem has already been known for Euclidean spaces.

With respect to texture gionometry, approaching solutions of the differential equation governing pole density functions in this generalized way of Fourier's method is in complete analogy to the harmonic method to solve the inverse tomographic problem starting from the integral equation (1). If it is possible to determine the even part $\tilde{f}$ of an orientation density function conforming with given crystallographic pole density functions of some crystal forms, then it is possible to determine directly the pole density function of any other crystal form, and vice versa.

However, this duality may be exploited to improve on the conventional harmonic solution, e.g. by removing inconsistencies in the intensity data, by completing experimental pole density functions sampled on a subset of S_+^2 only, i.e. generally refining the data, or extending it to different sets of experimental intensity data.

3.2 The general solution in terms of characteristics

Any function $u(\mathbf{h},\mathbf{r}) \in C^2(S^2 \times S^2)$ which depends on $\mathbf{h}\cdot\mathbf{r} = \cos\eta$ only satisfies the differential equation (4). Furthermore, an appropriate linear transformation of $\mathbf{h}$ or $\mathbf{r}$, respectively, with constant coefficients should not change this situation.

Theorem 3: The characteristics of the ultrahyperbolic differential equation are the fibres $(\mathbf{h} \cdot g\mathbf{r}) = \mathrm{const}$, where g is an arbitrary proper rotation. The proof is rather technical and omitted here.

Thus, the general solution of the ultrahyperbolic differential equation can be represented as a sum

$$u(\mathbf{h},\mathbf{r}) = \sum_{l}\sum_{k} u_l(x_{g_k}) \quad \text{with} \quad x_{g_k} = (\mathbf{h}\cdot g_k\mathbf{r}) \tag{9}$$

where $g_k \in SO(3)$ is an arbitrary rotation and $u_l \in C^2(I\!R^1)$ are some real twice differentiable functions.

Proposition: Let $u : S^2 \times S^2 \mapsto I\!R$ be a twice continuously differentiable function, $u \in C^2(S^2 \times S^2)$, satisfying $(\Delta_{\mathbf{h}} - \Delta_{\mathbf{r}})u(\mathbf{h},\mathbf{r}) = 0$. If u reduces to a function of $\mathbf{h}\cdot g_0\mathbf{r}$ for some arbitrary fixed $g_0 \in SO(3)$, then u is uniquely determined provided for some given $\mathbf{h}_0 \in S^2$ it is known for all $g_0\mathbf{r}$ on a great circle containing $\mathbf{h}_0$.

Proof: Any solution of the differential equation must be of the form (9) which according to the assumptions reduces to $u(\mathbf{h},\mathbf{r}) = u(\mathbf{h}\cdot g_0\mathbf{r})$. For a given $\mathbf{h}_0$, and $g_0\mathbf{r}$ covering a great circle containing $\mathbf{h}_0$, $t = \mathbf{h}_0\cdot g_0\mathbf{r}$ covers the interval $[-1,1]$, and u is assumed known, i.e. $u(\mathbf{h}_0\cdot g_0\mathbf{r}) = v(t)$ for all $\mathbf{r}$ on that great circle. Eventually, $u(\mathbf{h},\mathbf{r}) = u(\mathbf{h}\cdot g_0\mathbf{r}) = v(t)$.

Considering the same assumptions with respect to spherical harmonics, the general solution (7) simplifies to

$$u(\mathbf{h},\mathbf{r}) = \sum_{l=0}^{\infty} \lambda_l P_l(\mathbf{h}\cdot g_0\mathbf{r}) \tag{10}$$

Generally, a specific solution is constructed analogously to d'Alembert's method of characteristics by choosing distinguished functions p_l for the functions u_l and fitting them to the initially given pole density functions by

$$P(\mathbf{h}_i,\mathbf{r}) = \sum_{l} p_l((\mathbf{h}_i\cdot g\mathbf{r})) \tag{11}$$

where the p_l belong to some specific dense subset of $C^2(I\!R^1)$, e.g. the set of polynomials.

Below it will be generally shown that a decomposition with an appropriate choice of functions p_l is equivalent to the series expansion into spherical harmonics. Moreover, if the initially given pole density functions are expanded into such a series the solution of the ultrahyperbolic differential equation specified by them is determined. With respect to the crucial problems of existence and uniqueness of a special solution we provide some preliminary formulas.

3.3 Equivalent expansions of functions on the sphere

Any continuously differentiable function on the sphere S^2 can be expanded into an absolutely convergent series of spherical harmonics. It turns out that there exists an equivalent decomposition, which is derived by combination of specified spherical harmonics, but the argument of these functions is the scalar (dot) product of $\mathbf{h}$ and $\mathbf{r}$. This equivalent decomposition provides the means to represent any pole density function in the form (11).

Any function $P \in C^2(S^2)$ can be expanded into a series of spherical harmonics

$$P(\mathbf{r}) = \sum_{l=0}^{\infty} \sum_{m=-l}^{l} F_l^m Y_l^m(\mathbf{r}) \quad \text{with } F_l^m = \int_{S^2} P(\mathbf{r}')(Y_l^m)^*(\mathbf{r}')d\mathbf{r}' \tag{12}$$

where $\mathbf{r}$ and $\mathbf{r}'$ are unit vectors of the sphere S^2 with spherical coordinates (φ, ϑ) and (φ', ϑ'), respectively.

The series

$$P(\mathbf{r}) = \sum_{l=0}^{\infty} \sum_{m=-l}^{l} \Phi_l^m P_l(\cos \nu_m). \tag{13}$$

with $\cos \nu_m = (\mathbf{r} \cdot \mathbf{r}_m) = \cos \vartheta \cos \vartheta_m + \sin \vartheta \sin \vartheta_m \cos(\varphi - \varphi_m)$ provides an equivalent expansion by virtue of

$$\sum_{k=-l}^{l} \Phi_l^k Y_l^m(\mathbf{r}_k) = F_l^m \tag{14}$$

or

$$\sum_{k=-l}^{l} \Phi_l^k P_l((\mathbf{r}_k \cdot \mathbf{r}_m)) = f_l^m = \sum_{m=-l}^{l} F_l^m (Y_l^m)^*(\mathbf{r}_m) \tag{15}$$

Thus, if the coefficients Φ_l^k and directions $\mathbf{r}_k$ are known, eq. (14) allows to find the coefficients F_l^m of the series expansion (12). In turn, suppose the directions $\mathbf{r}_k$ are given; then (14) is a system of linear algebraic equations for Φ_l^k, with matrix $\{Y_l^m(\mathbf{r}_k)\}$.

There is a theorem stating that for each $l \in I\!N$ there exist $2l + 1$ directions $\{\mathbf{r}_k\}$ such that matrix $P_l((\mathbf{r}_k \cdot \mathbf{r}_m))$ of eq. (15) is not degenerate.

However, the choice of the set $\{\mathbf{r}_k\}$ is not unique. Freedom in that choice allows to exploit additional knowledge of the function to be expanded. A preferential choice could be one that turns the matrix of eq. (15) into a special form. For example, choose $\mathbf{r}_k = (\vartheta_0, \varphi_k)$ with $\varphi_k = \frac{2\pi k}{2l+1}$, $k = 0, ..., 2l$, and an arbitrary angle ϑ_0. Then the matrix of eq. (15) becomes of Toeplitz form. The same result will be accomplished if we choose $\mathbf{r}_k = (\vartheta_k, \varphi_0)$ with $\vartheta_k = \frac{\pi k}{2l+1}$, $k = 0, ..., 2l$, and an arbitrary angle φ_0.

3.4 Algorithm to solve the ultrahyperbolic differential equation

According to $(\mathbf{h}' \cdot g\mathbf{r}) = ((g^t\mathbf{h})^t \cdot \mathbf{r})$, we may interpret $(\mathbf{r} \cdot \mathbf{r}_k)$ as $((g_k^t\mathbf{h})^t \cdot \mathbf{r})$. Then, it is possible to summarize any method of solution as follows.

- Choice of the set of orientations $\{g_k\}$.

That step seems hardest to formalize. The set $\{g_k\}$ could be chosen to diminish the required computational efforts. From this point of view, a choice to obtain a Toeplitz matrix looks promising. Alternatively, if it is possible to see peak or axial texture components in the pole density functions, a more natural choice of the set $\{g_k\}$ could be one exploiting this additional information. Such a choice could be done interactively with a computer.

- Determination of the set $\{\mathbf{r}_k\}$ as induced by the set $\{g_k\}$.
- Series expansion of the pole density functions into symmetrized polynomials.

- The resulting coefficients are the coefficients of the required solution.

A specific and successful choice of the set $\{g_k\}$ is expected to depend on the specific problem, particularly on assumptions which are reasonable with respect to this problem; at this time it does not seem possible to give general rules.

4 Applications

Before discussing the existence and uniqueness of the solution of the ultrahyperbolic differential equation it seems worthwhile to give an outlook of potential applications. The most interesting for the practice of texture analysis include

- defining a minimum set of experimentally accessible pole density functions required;
- defining an appropriate set of experimentally accessible pole density functions with respect to (i) numerical stability of the system, and (ii) experimental errors which depend on the crystal form
- completing incomplete pole density functions to normalize them;
- checking the compatibility of experimental pole density functions corresponding to different crystal forms
- calculating additional pole density functions of special crystal forms which cannot be measured in diffraction experiments directly from the experimentally given ones;
- calculating the even portion of an orientation density function explaining the given pole density functions.

The solutions of these particular problems will become straightforward once the existence and uniqueness of a solution for given experimental intensity data $\tilde{P}(\mathbf{h}_q, \mathbf{r}_p)$, $\mathbf{r}_p \in D \subset S^2$, representing initial (or boundary) conditions is guaranteed, that is, once it has been clarified that the given data can be uniquely represented in the form (11).

5 Conclusions

In this contribution we have shown that the central mathematical relationship of texture goniometry can be equivalently formulated in terms of the conventional integral equation representing a hyperspherical analogue of the x-ray transform, and in terms of an ultrahyperbolic differential equation which characterizes the range of the transform. Its characteristics have been determined and geometrically interpreted as the familiar fibres of texture analysis. Thus, the mathematical grounds for methods to solve the differential equation numerically are prepared and new approaches to solve actual problems of quantitative texture analysis are opened.

STATISTICS FOR INDIVIDUAL ORIENTATION MEASUREMENTS

K.G.v.d.BOOGAART,
Graduate College "Spatial Statistics", University of Mining and Technology
Freiberg, Germany

Abstract

A new class of distributions for data from crystal orientation measurements is introduced. This class characterizes its distributions by their low order harmonics up to arbitrary order, and adds harmonic functions of higher order according to the assumption of maximum entropy. This yields a strictly positive distribution density function, which can easily be handled by powerful statistical procedures well known from other sciences. This framework provides solutions to various tasks: Does the ODF follow a given distribution model? Are two sample textures similar? What are the statistical errors of experimental harmonic coefficients? How to simulate from a sample ODF? It also provides models for regression of textures: The variation of texture according to the variation of a controlling parameter.

Keywords: measurement error, OIM, statistics, texture regression models

1 A distributional model for orientations

The ODF is a density of a distribution on the group SO_3 of orientations. We introduce a family of distributions $ExpRot[L, \overset{:}{G}, \dot{G}; (\theta_\tau)_{\tau \in \overset{:\cdot}{I}(L)}]$ defined by a degree L of a series expansion, the crystal symmetry group $\overset{:}{G}$, the sample symmetry group $\dot{G}$, and a set of real valued parameters θ_τ, $\tau \in \overset{:\cdot}{I}(L)$, by its distribution density:

$$f_\theta(g) = A(\theta) \exp\left(- \sum_{l=1}^{L} \sum_{\mu=1}^{M(l)} \sum_{\nu=0}^{N(l)} \theta_l^{\mu\nu} \overset{:\cdot}{T}_l^{\mu\nu}(g) \right) = A(\theta) \exp\left(- \sum_{\tau \in \overset{:\cdot}{I}(L)} \theta_\tau \overset{:\cdot}{T}_\tau(g) \right)$$

(Beran 1979) introduced a similar family for the distributions of directions. This family has some interesting properties:

- These are the distributions of maximum entropy given a series expansion up to order L.[1] The coefficients

  $$C_l^{\mu\nu} = E[\overset{\therefore}{T}{}_l^{\mu\nu}(g)] = \oint f_\theta(g)\,\overset{\therefore}{T}{}_l^{\mu\nu}(g)dg,\ l = 1, \ldots, L$$

  characterize a distribution in $ExpRot[L, \overset{:}{G}, \dot{G}; (\theta_\tau)_{\tau \in \dot{I}(L)}]$ uniquely.
- All distributions in $ExpRot[\ldots]$have strictly positive distribution densities.
- The maximum likelihood estimation factorizes over the empirical harmonic components $\hat{C}_l^{\mu\nu}$ given later in the text.
- Given the harmonic components of the density up to a given degree L, harmonic components of higher order will be added such that we get a positive distribution density which maximizes the entropy of the distribution.
- If the energy $Q(g)$ of a grain with orientation g is given by a function in terms of low order harmonics:

  $$Q(g) = \sum_{l=1}^{L} \sum_{\mu=1}^{M(l)} \sum_{\nu=0}^{N(l)} \tilde{\theta}_l^{\mu\nu}\, \overset{\therefore}{T}{}_l^{\mu\nu}(g)$$

  and the probability of a specific rotation g is governed by Gibbs dynamics, then the correct distribution would be: $ExpRot[L, \overset{:}{G}, \dot{G}; \tilde{\theta}]$.
- In the case of no sample symmetry ($\dot{G} = \{1\}$) the model is rotationally invariant for all L.
- The model $ExpRot[L, \overset{:}{G}, \dot{G}; \cdot]$ is a strict sub-model of the related models $ExpRot[L', \overset{:}{G}, \dot{G}; \cdot]$ and $ExpRot[L, \overset{:}{G}, \dot{G}'; \cdot]$, where $L < L'$ and $\dot{G} \subset \dot{G}'$.
- The models $ExpRot[L, \overset{:}{G}, \dot{G}; \cdot]$, $L \in \mathbb{N}$, are dense in the space of all continuous distribution on SO_3 with the symmetry properties described by $\overset{:}{G}$ and $\dot{G}$, i.e. we can approximate any distribution arbitrarily well, if we only choose L large enough.
- For all $\theta_l^{\mu\nu} \in \mathbb{R}$ there exists an $A(\theta)$ such that $ExpRot[\ldots; \theta]$ yields a valid probability density.
- There is a one to one relation between the parameters θ and the harmonic components $C_l^{\mu\nu}$ of the density. $C_l^{\mu\nu}$ is the expected value of $\overset{\therefore}{T}{}_l^{\mu\nu}(g)$ under the parameter θ, and $\hat{\theta} = \theta$ is the ML-estimation of the parameter θ under observed $\hat{C}_l^{\mu\nu} = C_l^{\mu\nu}$.
- Since this distribution density has no negative parts, it represents a true distribution. Orientations with this distribution can be simulated.
- The Fisher-matrix-distribution is equal to $ExpRot[1, \{1\}, \{1\}, \theta]$.

---

[1] Assuming a nonstandard normalisation: $\oint \overset{\therefore}{T}{}_l^{\mu\nu}(g)^2 = 1$

2 Maximum Likelihood Estimation

Because these families are special cases of regular exponential families some powerful statistical tools are available (assuming you have a fast computer). The maximum likelihood estimator $\hat{\theta}$ of θ is given by the equation:

$$E_{\hat{\theta}}(\ddot{T}_l^{\mu\nu}(g)) = \hat{C}_l^{\mu\nu}, \text{ where} \tag{1}$$

$$\hat{C}_l^{\mu\nu} := \frac{1}{n}\sum_{i=1}^{n} \ddot{T}_l^{\mu\nu}(g_i), \quad g_i = \text{orientation of grain } i$$

is the sample mean of the harmonic functions. The derivative of the $E_\theta[\ddot{T}_l^{\mu\nu}(g)]$ is given by:

$$\frac{d(E_\theta(\ddot{T}_l^{\mu\nu}(g)))_{l\mu\nu}}{d\theta} = Var_\theta\left((\ddot{T}_l^{\mu\nu}(g))_{l\mu\nu}\right)$$

$E_\theta(\ldots)$ and $Var_\theta(\ldots)$ can be calculated for every θ by numerical integration:

$$Q(g) := \sum_{l=1}^{L}\sum_{\mu=1}^{M(l)}\sum_{\nu=0}^{N(l)} \theta_l^{\mu\nu}\, \ddot{T}_l^{\mu\nu}(g) \tag{2}$$

$$A(\theta) := \left(\oint_{SO_3} \exp\left(-Q(g)\right) dg\right)^{-1} \tag{3}$$

$$E_\theta(\ddot{T}) = A(\theta) \oint_{SO_3} \ddot{T}(g) \exp\left(-Q(g)\right) dg \tag{4}$$

$$Var_\theta(\ddot{T}) = A(\theta) \oint_{SO_3} \ddot{T}(g)\, \ddot{T}(g)^t \exp\left(-Q(g)\right) dg - E_\theta(\ddot{T}) E_\theta(\ddot{T})^t \tag{5}$$

where $\ddot{T}(g) = (\ddot{T}_l^{\mu\nu}(g))_{l\mu\nu}$ is used as a vector valued function. The maximum likelihood estimator $\hat{\theta}$ can then be calculated by solving the equation (1) using the Newton algorithm. The maximized likelihood is given by:

$$\mathrm{L}(\hat{C}_l^{\mu\nu}; \hat{\theta}) = A(\hat{\theta})^n \exp\left(-n \sum_{l=1}^{L}\sum_{\mu=1}^{M(l)}\sum_{\nu=0}^{N(l)} \hat{\theta}_l^{\mu\nu} \hat{C}_l^{\mu\nu}\right) \tag{6}$$

The solution is unique, as the continuously differentiable function $E_\theta[\ddot{T}]$ is strictly convex. Therefore, Newton's algorithm will converge to the proper solution. The estimated asymptotic estimation variances of the estimated coefficients θ and C are given by:

$$\widehat{Var}(\hat{\theta}) = \frac{1}{n} Var_{\hat{\theta}}(\overset{\therefore}{T})^{-1}, \quad \widehat{Var}(\hat{C}) = \frac{1}{n} Var_{\hat{\theta}}(\overset{\therefore}{T}) \tag{7}$$

where n is the number of measured crystal grains. Thus our model provides standard estimation errors for the harmonic coefficients. The maximum likelihood estimator exists if and only if $\hat{C}$ is in the interior of the convex hull of the possible values for $\overset{\therefore}{T}$.(Johansen 1979) This holds with probability one if more grains are measured than parameters are in the model.

3 Models and Tests

The model is a full distributional model. Therefore we can test, if the data, which we have, is compatible with a given distribution model. Further we can ask how strong the departure from the model is and how exact we can estimate this departure and we can give confidence regions for models. Only some basic test will be outlined here.

The general theory of exponential families provides a construction scheme of a powerful test for the comparison of a model M_0 with a supermodel $M_1 \supset M_0$ (Witting 1995). This test is called likelihood ratio test. For the test problem

$$H_0 : ODF \in M_0 \quad vs. \quad H_1 : ODF \in M_1$$

the test statistic

$$D := 2 \ln \frac{L_1(\hat{C}; \hat{\theta}^{(1)})}{L_0(\hat{C}; \hat{\theta}^{(0)})} \tag{8}$$

is asymptotically distributed χ^2_d, where d represents the number of parameters added from model M_0 to model M_1. $\hat{\theta}^{(i)}$ denotes the maximum likelihood estimator for model M_i, $i = 0, 1$. L_i denotes the likelihood function for model M_i, $i = 0, 1$. The test does not reject the hypothesis H_0, if the test statistic D is lower than the 0.95-quantile of the χ^2_d-distribution. This test is valid only for a big size of n $(> 30 * \mid \overset{\therefore}{I}(L') \mid)$, because the χ^2-approximation is valid only for large n.

3.1 Testing for the necessary degree L

In the most simple case we assume to know that the data stems from a distribution of this type but with high degree L'. Thus we want to test whether the data is sufficiently well represented by harmonic coefficients up to order L and the additional information that the data is compatible with the model $ExpRot[L, G, \overset{\therefore}{G}; \cdot]$, against the alternative that we have to use more harmonic coefficients. Thus we get the test problem:

$$H_0 : ODF \in ExpRot[L, G, \overset{\therefore}{G}; \cdot] \; vs. \; H_1 : ODF \in ExpRot[L', G, \overset{\therefore}{G}; \cdot], L' > L$$

Since the alternative is an exponential superfamily of the hypothesis, we can use the likelihood ratio test.

3.2 Testing for sample symmetry

Another question could be, whether the data satisfy a specific sample symmetry $\dot{G}$ or only a lower sample symmetry $\dot{G}' \subset \dot{G}$. Thus we get the test problem:

$$H_0 : ODF \in ExpRot[L, \overset{\vdots}{G}, \dot{G}; \cdot] \quad vs. \quad H_1 : ODF \in ExpRot[L, \overset{\vdots}{G}, \dot{G}'; \cdot]$$

As before the likelihood ratio test can be used, because the hypothesis H_0 is a true sub-model of the alternative H_1.

3.3 Testing for specific potential functions

If we presume that in a specific sample the distribution of crystal orientations is governed by an energy function depending linearly on a single or several anisotropic physical properties $f_i(g)$, which are functions of low order harmonics, we can test for compatibility of the data with this hypothesis against a full $ExpRot[L, \overset{\vdots}{G}, \dot{G}; \cdot]$ family.

$$f_i(g) = \sum_{\tau \in I(L)} \theta_\tau^{(i)} \, \overset{\therefore}{T}_\tau(g) \tag{9}$$

The likelihood ratio test is appropriate for the resulting test problem:

$$\begin{aligned} &H_0 : ODF \in \left\{ ExpRot[L, \overset{\vdots}{G}, \dot{G}; \theta] : \theta = \textstyle\sum_i \alpha_i \theta^{(i)} \right\} \quad vs. \\ &H_1 : ODF \in ExpRot[L, \overset{\vdots}{G}, \dot{G}; \cdot] \end{aligned}$$

4 Regression for orientations

Up to now we have generally assumed that all observed orientations came from the same generating distribution. But more relevant are statistics for comparison of different textures. This can be a two sample experiment, after which we want to compare the textures under two different treatments. Or in case of multiple samples it could be interesting how texture depends on a process parameter. Possible models and tests for both situations are given here derived from a multivariate generalisation of the theory of generalized linear models with canonical link functions (MacCullagh & Nelder 1983).

4.1 The full regression model

In the most simple regression situation we deal with one real valued process parameter x. For each value of x the process will produce a certain texture. The most simple model for the influence of x on the texture is that x influences the parameter θ of the ODF linear:

$$\begin{aligned} &H_0 : ODF_x = ExpRot[L, \overset{\vdots}{G}, \dot{G}; \theta_0], \ \theta_0 \in \mathbb{R}^{I(L)} \quad vs. \\ &H_1 : ODF_x = ExpRot[L, \overset{\vdots}{G}, \dot{G}; \theta_0 + x\theta_x], \ \theta_0, \theta_x \in \mathbb{R}^{I(L)} \end{aligned}$$

Here ODF_x denotes the ODF generated under condition x. Other more sophisticated kinds of influence are possible. As long as the relation is a linear combination of θ, the joint distribution of all results of the experiments is a regular exponential family, and therefore the maximum likelihood estimator and the likelihood ratio test can be used as usual.

4.2 Two sample tests

As a special case of the regression model we can ask the question, whether two samples are equal or not, and if they are not equal how strong their departure is. We just have to introduce an artifical regression variable x taking the value 0 for one sample and the value 1 for the other sample. H_0 from the regression model is the hypothesis that both samples are equal, and H_1 is the alternative that both samples are not equal. The estimate of θ_1 tells something about the type and strength of departure.

5 ODF by grains and by volume

The procedures in this paper are concerned with the orientation distribution of the typical grain. Therefore the estimators in this paper say something about the ODF of the grains and not about the ODF of the typical bit of volume. Under the assumption that the texture does not depend on the size of the grain, both definitions of the ODF are equal and the grain-wise estimators are more precise, because they are not disturbed by the variation of grain size. If the probability for a grain to belong to the sample is proportional to its size, we observe a sample of grains which have the volume ODF as underlying distribution and therefore we can use the procedures in this paper for the volume ODF. This happens, if we measure the orientations on a sparse grid, such that we do not hit any grain twice and all measured grains have independent orientations. If our grid is sufficiently fine to measure the area of grains, and we want to model the dependence of the texture on the grain size we have to use spatial models as introduced in "Spatial Statistics for individual orientation measurements". If we presume dependence but do not want to model it, we should use some modified procedures, which are not given here.

6 References

Beran, R. (1979) Exponential families for directional data, *The Ann. Statis.* 7, 1162-1178.

Johansen, S. (1979) *Introduction to the Theory of Regular Exponential Families*, Inst. of Mathematical Statistics University of Copenhagen, Lecture Notes 3

MacCullagh, P. and J.A. Nelder (1983) *Generalized linear models*, Chapman and Hall, London.

Witting, H., U. Müller-Funk (1995) *Mathematische Statistik II. Asymptotische Statistik: Parametrische Modelle und nichtparametrische Funktionale*, Teubner, Stuttgart

DETERMINATION OF AVERAGE ORIENTATION DISTRIBUTION FUNCTION IN THICKNESS DIRECTION

H. INOUE and N. INAKAZU
Department of Metallurgy and Materials Science, College of Engineering,
Osaka Prefecture University, Sakai, Japan

Abstract

In predicting the physical and mechanical anisotropy of rolled sheets, an over-all texture in the thickness direction must be taken into account, particularly for specimens with inhomogeneous texture. To know an average texture over the whole of a sheet, an orientation distribution function (ODF) on the RD-basis was calculated from incomplete pole figures measured by X-ray diffraction in the RD-section perpendicular to the rolling direction, and subsequently transformed into that on the ND-basis with orthorhombic sample symmetry. The calculated results in some samples with inhomogeneous texture were in good agreement with the average of ordinary ODFs determined at various locations in the thickness direction. Therefore, the present method appears to be very suitable for evaluating exactly the average ODF of sheet materials.

Keywords: incomplete pole figure, inhomogeneous texture, orientation distribution function, RD-section, rolled sheet, texture transformation, X-ray diffraction

1 Introduction

The texture of a rolled sheet often changes depending on the location in the thickness direction, especially in the vicinity of the surface. Such inhomogeneous texture is unfavourable for predicting the anisotropy of physical and mechanical properties by a crystallite orientation distribution function (ODF) obtained from conventional pole figures, which are measured by X-ray diffraction in a plane parallel to the sheet surface, namely perpendicular to the normal direction. In this case, it is first necessary to analyse an average texture over the whole of a sheet. The specimen of stacked sheets that were cut at an oblique plane (Lopata and Kula 1962) may be

F3

used for measuring the average texture in the thickness direction. However, the preparation of such a specimen is not so easy. In addition, this method requires the interpolation to usual pole figure data expressed at equiangular spacing, in order to use a conventional ODF program. In the present paper, we propose a method for determining the average texture in the thickness direction by utilising ODF, and apply it to some materials showing texture gradient.

2 Experimental and analytic procedures

2.1 Pole figure measurement

A number of sheet specimens 5 mm in the rolling direction and 30 mm in the transverse direction were cut out from a rolled sheet. They were stacked with an adhesive and embedded in resin, to prepare a sample for pole figure measurement with an area of 30 × 30 mm using the cross section perpendicular to the rolling direction, which is hereinafter called "RD-section". The longitudinal section perpendicular to the transverse direction (TD-section) will be probably unsuitable for measurement of an average texture in the thickness direction, because rolled metal generally shows much larger grain size in length for the TD-section than for the RD-section. For comparison with pole figures of the RD-section, conventional samples parallel to the rolling plane were also prepared from various locations of the thickness direction. With these samples polished mechanically and chemically, incomplete pole figures were measured up to a maximal tilt angle of 75 degrees by the Schulz back-reflection method using MoKα radiation for iron and CuKα radiation for other metals. Intensity of pole figures was corrected with a randomly oriented sample.

2.2 ODF calculation

A flow diagram for calculating ODF from incomplete pole figures measured in the RD-section (RD pole figures) is shown in Fig. 1. In this work, complete ODFs, including odd terms for ghost correction, were determined up to an order of l=22 by the iterative series expansion method using positivity conditions in pole figures and ODF (Dahms and Bunge 1989; Inoue and Inakazu 1994).

At the beginning, the measured incomplete pole figures $\hat{P}_{h_i}(y)$ are quasi-normalised by a simple way (Kern and Bergmann 1978):

$$\tilde{N}_i = 4\pi(1-\cos\Phi_{\mathrm{R}})\Big/\int_0^{\Phi_{\mathrm{R}}} \hat{P}_{h_i}(y)\,\mathrm{d}y \quad (1)$$

where $\tilde{N}_i$ is the normalisation factors and Φ_{R} is a maximal tilt angle in the back-reflection method. Therefore pole density within the unmeasured ranges is set to 1, namely to the value of random orientation. From such false complete pole figures, even coefficients

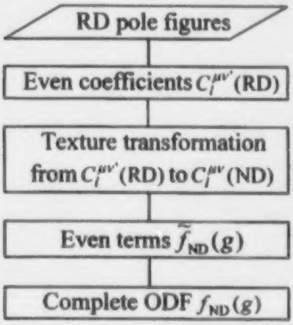
RD pole figures
Even coefficients $C_l^{\mu\nu'}$(RD)
Texture transformation from $C_l^{\mu\nu'}$(RD) to $C_l^{\mu\nu}$(ND)
Even terms $\tilde{f}_{\mathrm{ND}}(g)$
Complete ODF $f_{\mathrm{ND}}(g)$

Fig. 1 Method for calculating an average ODF in the thickness direction.

$C_l^{\mu\nu}$ of ODF can be determined through an iterative calculation under the positivity condition in pole figures. In the case of RD pole figures, the determined even coefficients $C_l^{\mu\nu'}(\text{RD})$ can be related to the even coefficients $C_l^{\mu\nu}(\text{ND})$ obtained from usual ND pole figures by means of texture transformation (Bunge 1982).

$$C_l^{\mu\nu}(\text{ND}) = \sum_{\nu'=1}^{N(l)} \dot{\dot{T}}_l^{*\nu\nu'}(\Delta g)\cdot C_l^{\mu\nu'}(\text{RD}) \qquad (2)$$

When considering the orthorhombic sample symmetry such as rolled sheets, an Euler rotation Δg is equal to φ_1=90°, Φ=90° and φ_2=90°. Even terms of ODF on the ND-basis, $\tilde{f}_{\text{ND}}(g)$, are determined from the coefficients on the RD-basis, $C_l^{\mu\nu'}(\text{RD})$, in this manner. Finally, the calculation of odd coefficients by the positivity method is carried out, to obtain a complete ODF on the ND-basis. As a threshold value for defining the "negativity function" (Dahms and Bunge 1989), an appropriate positive value not more than 0.5, leading to a better result, was in practice used instead of zero.

3 Results and discussion

3.1 Texture transformation

Figure 2 shows complete ODFs on the RD- and ND-bases calculated from four incomplete pole figures for the RD-section of a cold rolled ultra-low carbon steel sheet having a fairly homogeneous texture in the thickness direction. Before texture transformation from the RD-basis to the ND-basis, an ODF similar to the α- and β-fibres in *fcc* metals is observed seemingly. This means that rolling texture of *bcc* metals can be roughly expressed by inverting the indexes of rolling plane and direction in that of *fcc* metals. Such an inverse relation suggests the existence of a

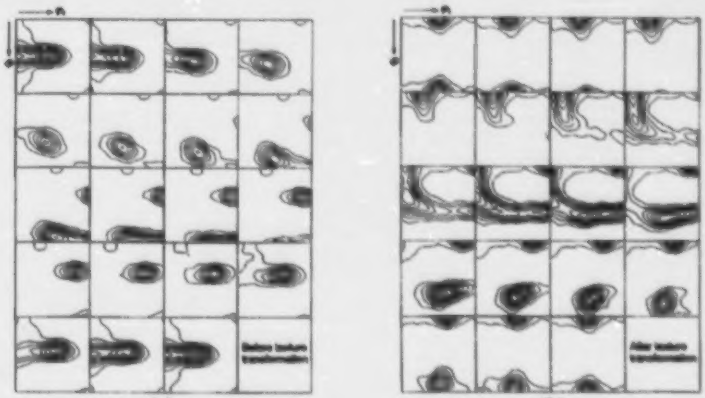
(a) (b)

Fig. 2 φ_2 sections of ODFs on (a) the RD-basis and (b) the ND-basis calculated from incomplete pole figures in the RD-section for an 80% cold rolled ultra-low carbon steel sheet. Contour levels: 1, 2, 3, 4, 5, 6, 7, 8.

fibre from {112}<110> to {111}<112>, which is termed the "β-fibre", rather than the γ-fibre of <111>//ND in addition to the α-fibre of <110>//RD for this steel. After texture transformation into the ND-basis, a familiar ODF consisting of the above fibres is obtained, and it naturally agrees well with an ordinary ODF determined from ND pole figures.

3.2 Samples with texture gradient

Comparisons between ODFs calculated from ND and RD pole figures are shown in Figs. 3 and 4. To indicate a relative location in the thickness direction of a sheet, we define the value *R* as a ratio of depth to thickness. Accordingly *R*=0 and 0.5 represent the surface and centre of the sheet, respectively.

Recrystallisation texture of an ultra-low carbon steel sheet cold rolled and annealed after hot rolling in the α field, consists mainly of the γ-fibre of <111>//ND, but includes a weak {001} component near the surface (*see* Fig. 3 (a) and (b)). Such a tendency is reflected quantitatively in an ODF determined by the RD-section. In the case of the RD-section, the orientation density of the γ-fibre is appreciably lower than that in the centre (*R*=0.5) because of a weak γ-fibre in the vicinity of the surface.

Warm rolling texture of an Al-Mg alloy sheet rolled at a starting temperature of 623 K consists of the β-fibre in the central part and of the <110>//RD partial fibre from {001}<110> to {111}<110> in the range between the surface and a quarter of the thickness (Fig. 4). The latter fibre similar to the α-fibre of *bcc* metals is considered to be attributable to shear stress caused by the friction with rolls. Figure 5 shows the change in orientation density as a function of *R*. A transition from "shear type rolling texture" to copper type rolling texture occurs at about *R*=0.3. To confirm the validity of the method using the RD-section, the orientation density obtained by this method has been compared with the average value of orientation densities at six locations shown in Fig. 5. The result is shown in Fig. 6. The extent of the agreement between them is very good for any orientation. This result proves that a true average ODF over the whole of a sample can be exactly determined by the present method.

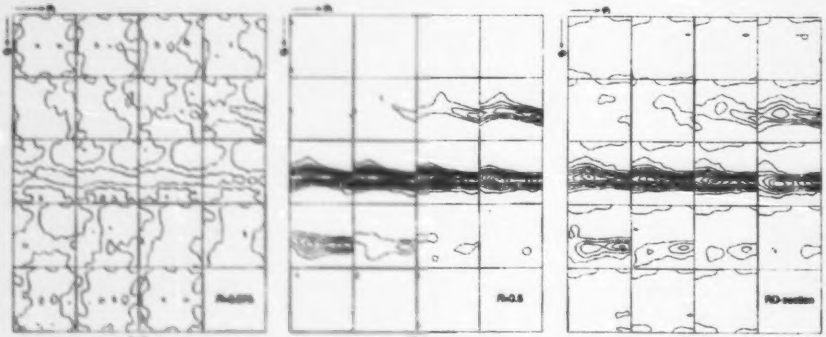

(a) (b) (c)

Fig. 3 ODFs at locations of (a) *R*=0.075 and (b) *R*=0.5 in the thickness direction and (c) an ODF determined by the RD-section for an ultra-low carbon steel sheet cold rolled to 80% reduction and annealed at 1093 K for 180 s. The value of *R* shows a ratio of depth to thickness. Contour levels: 1, 2, 3, 4, 5, 6, 7, 8, 9, 10, 11, 12.

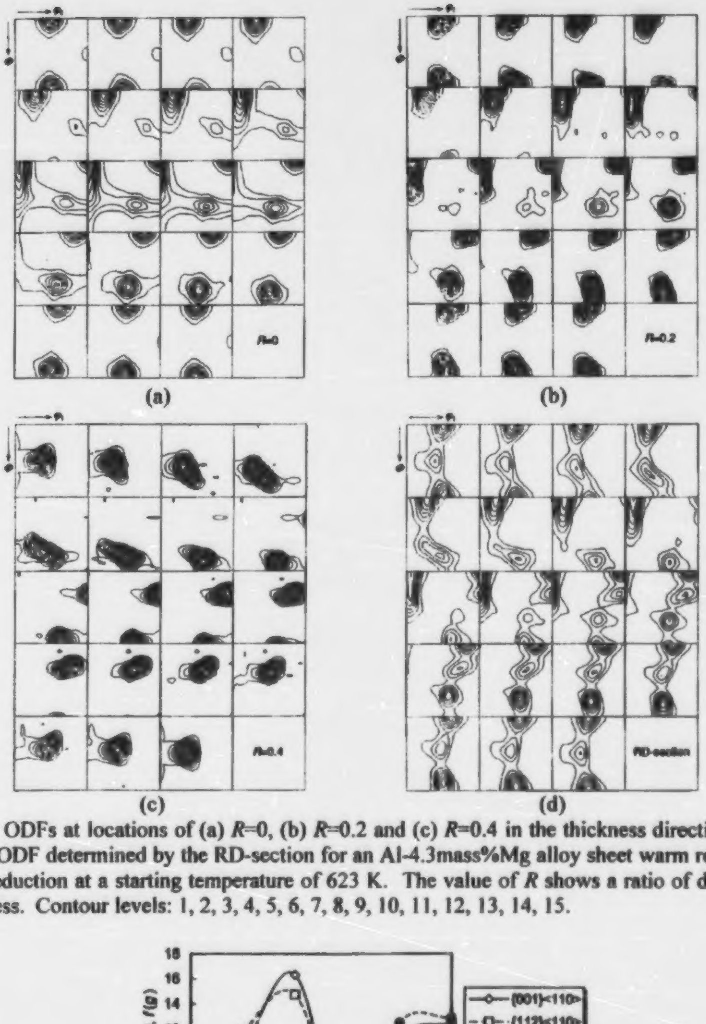

(a) (b)

(c) (d)

Fig. 4 ODFs at locations of (a) R=0, (b) R=0.2 and (c) R=0.4 in the thickness direction and (d) an ODF determined by the RD-section for an Al-4.3mass%Mg alloy sheet warm rolled to 87% reduction at a starting temperature of 623 K. The value of R shows a ratio of depth to thickness. Contour levels: 1, 2, 3, 4, 5, 6, 7, 8, 9, 10, 11, 12, 13, 14, 15.

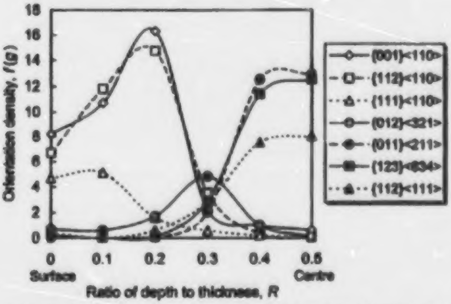

Fig. 5 Changes of orientation density in the thickness direction for some preferred orientations observed in a warm rolled Al-Mg alloy sheet.

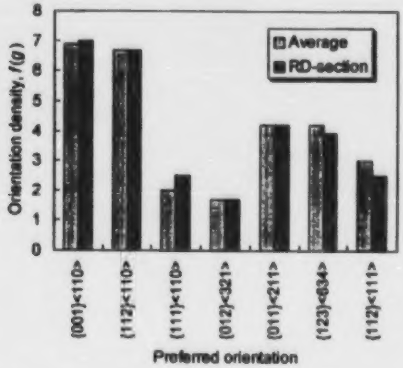

Fig. 6 Comparisons between the orientation density in ODF determined by the RD-section and the average value of orientation densities at six locations shown in Fig. 5.

4 Conclusions

A method for determining an average ODF in the thickness direction from RD pole figures, which were measured in the RD-section by X-ray diffraction, has been proposed, and its validity has been checked for some metals having inhomogeneous texture. Since this method is based on a texture transformation from the RD-basis to the ND-basis for orthorhombic sample symmetry, the texture on the RD-basis as well as the ND-basis was analysed. Consequently, additional information that the "β-fibre" from {112}<110> to {111}<112> existed in cold rolled ultra-low carbon steel was obtained. From comparisons with usual ODFs determined at various locations in the thickness direction, it is concluded that the calculated results by this method express exactly an over-all texture of the sheet, irrespective of the extent of inhomogeneity in texture.

5 References

Bunge, H. J. (1982) *Texture Analysis in Materials Science*, Butterworths, London, pp. 188-93.

Dahms, M. and Bunge, H.J. (1989) The iterative series-expansion method for quantitative texture analysis. I. General outline. *J. Appl. Cryst.*, Vol. 22, pp. 439-47.

Inoue, H. and Inakazu, N. (1994) Determination of orientation distribution functions from incomplete pole figures by iterative series expansion method. *J. Japan Inst. Metals*, Vol. 58, No. 8, pp. 892-8. (in Japanese)

Kern, R. and Bergmann, H.W. (1978) A simple way for calculation ODF from incomplete pole figures. *Proc. of 5th Int. Conf. on Textures of Materials*, (ed. G. Gottstein and K. Lücke), Springer-Verlag, Berlin, Vol. I, pp. 139-47.

Lopata, S.L. and Kula, E.B. (1962) A reflection method for pole-figure determination. *Trans. Metal. Soc. AIME*, Vol. 224, August, pp. 865-866.

COMPARISON OF EXPERIMENTAL TECHNIQUES FOR CHARACTERIZATION OF THROUGH-THICKNESS TEXTURE VARIATIONS

O.V. MISHIN, E.M. LAURIDSEN, N.C. KRIEGER LASSEN, H.F. POULSEN and D. JUUL JENSEN

Materials Research Department, Risø National Laboratory, Roskilde, Denmark

G. BRÜCKNER

Institut für Metallkunde und Metallphysik, RWTH Aachen, Aachen, Germany

B. BAY

Institute for Applied Engineering Design and Production, Technical University of Denmark, Lyngby, Denmark

Abstract

For the investigation of through-thickness texture gradients, a number of layers in rolled plates and sheets are inspected. Crystallographic textures in different layers can be characterized using several techniques. In the present work, traditional low-energy X-ray diffraction, the electron backscattering pattern technique in the scanning electron microscope and a novel technique which involves high energy synchrotron radiation are used for characterization of through-thickness texture variations in commercial purity cold-rolled aluminium. Important experimental aspects of these three techniques are described. The results from the three techniques are compared and their potentials for characterization of through-thickness texture variations are considered.

Keywords: EBSP technique, high-energy synchrotron radiation, X-ray diffraction

1. Introduction

It is known that textures in rolled materials may be inhomogeneous through the thickness (Dillamore and Roberts 1963-64; Hansen and Mecking 1975; Truszkowski et al. 1980). To find locations and intensities of inhomogeneities, texture must be inspected in different depths of the rolled product. Several experimental techniques can be used for characterization of through-thickness texture variations.

Traditionally laboratory based X-ray diffraction equipment is used for the inspection of through-thickness texture gradients. Measurements are performed in the reflection mode, so only a thin layer at the specimen surface is probed. Therefore, sectioning of the sample must be performed to measure texture at a certain depth. Obviously, this procedure becomes rather laborious when many layers are to be inspected.

The electron backscattering pattern (EBSP) technique has become a powerful tool for investigation of textures in annealed or deformed materials with low to moderate dislocation densities (Venables and Harland 1973). Kikuchi-patterns from the polished surface of the sample are obtained in the scanning electron microscope. Recent advances in hardware and software have made fast and fully automatic collection of reliable orientation data possible (Krieger Lassen 1998).

A new alternative approach is suggested by the use of high-energy radiation from synchrotron sources (Poulsen et al. 1997; Fisker et al. 1998). Hard X-rays have a penetration depth in the range of a centimeter, which facilitates transmission studies. At the same time, the synchrotron source is very intense, implying that layers of a micron size thickness can be investigated. It allows texture measurement in any selected depth of the specimen cut out of the test plate.

In this paper, we report the first results of a comparative study, where the three experimental techniques are employed for characterization of through-thickness texture variations in a cold-rolled aluminium plate. Small draught rolling was selected to produce through-thickness texture inhomogeneities at a moderate strain level.

2. Experimental

Commercial purity aluminium AA1050 (99.5% purity) was used in this experiment. A plate was 60% cold-rolled and annealed at 673K for 1 hour. This treatment resulted in a fully recrystallized microstructure. The rolling plane revealed regions with relatively large grain size (up to 200 μm) alternating with regions containing very small (30-40 μm) recrystallized grains. The mean grain size in the rolling plane was estimated to be ~100 μm. In the longitudinal plane, grains appeared to be flattened. The mean grain size in the normal direction was smaller than that in the rolling direction by a factor of 1.7.

This plate was rolled on a laboratory mill with a roll diameter of 75 mm, alternating the top and bottom sides between passes. Rolling was performed at room temperature using kerosene as a lubricant. The l/h ratio is defined as $2\sqrt{r(d-d_0)}/(d+d_0)$, where r is the radius of rolls, d and d_0 are the exit thickness and entrance thickness of the plate. The l/h ratio varied from 0.31 to 0.44 for different passes. To characterize the position of the layer, the parameter $S=2\Delta t/t_0$, where Δt is the distance from the center and t_0 is the plate thickness, is used here.

Co Kα radiation and a fully automated X-ray goniometer were used for texture studies in the rolling plane. The specimens were typically 22 mm in the transverse direction and 13 mm in the rolling direction. During measurements the specimens were oscillated along the transverse direction to cover a larger specimen area. One of the specimens was measured twice to estimate the accuracy of pole figure measurements.

Local orientations (microtextures) were measured in the longitudinal section using the EBSP technique coupled to a JSM-840 microscope. Orientations were investigated in several selected layers parallel to the rolling plane with a step size of 25 μm along a selected layer automatically changing the sample position under the beam. Additionally the top surface in the rolling plane was inspected after removing the oxidized layer by gentle electropolishing with no prior mechanical polishing. Orientations with a low confidence index were considered as incorrectly solved and were excluded from the data set. The final data set consisted of 3200-4500 collected orientations.

Synchrotron experiments were performed at the high-energy beam-line BW5 at HASYLAB using 100 keV X-rays. A Si/Ge gradient crystal was used as the monochromator. The incoming beam was defined by a 50 μm vertical aperture. A cylindrical (Ø15mm) specimen was mounted on a horizontal ω-rotation stage with the normal direction (the cylinder axis) aligned with the ω-rotation axis. During exposures the specimen was moved along the horizontal line to cover larger specimen areas. The diffraction patterns (Debye-Scherrer cones) were registered by a CCD-camera. For each depth, {111}, {200} and {220} pole figures were recorded from exposures at equidistant ω-settings between 0° and 180° with a step of 5°. Each exposure took 10 seconds. The principles of image acquisition and data analysis has been described elsewhere (Fisker et al. 1998). Intensity values on the pole figures were calculated as sums of weights assigned to each measured point on the pole sphere. The weights were identified using the Watson distribution, which can be regarded as the "normal" distribution for axial data (Fischer et al. 1987). The degree of smoothing is controlled by the concentration parameter of this distribution, which was set to give a standard deviation on the rotation angle of 2.5°.

3. Results

Textures in terms of the {111} pole figures produced by the three techniques are shown in Fig.1 for three different layers, where S=1 corresponds to the surface, S=0.5 is the quarter thickness and S=0 is the center of the plate. Volume fractions of different texture components calculated from the EBSP data are given separately (Mishin et al. 1999). Fig.1a gives normalized pole figures obtained by the traditional low-energy X-ray technique. The intensity levels are indicated by contour lines. Local orientations measured using the EBSP technique are shown in Fig.1b. Here each single orientation is represented as a set of four points. The highest concentration of points corresponds to the maximum intensity. Pole figures produced from the synchrotron experiment data are presented in Fig.1c. The intensities of grey levels correspond to the pole densities in the pole figures.

It is obvious that the three applied techniques give fairly similar pole figures at similar depths. A pronounced shear texture is developed near the quarter thickness layer, while a rolling texture is formed in the center and near the surface of the plate. Fig.2 displays the profile of pole densities along the dashed line L in the pole figure for textures measured in or near the quarter thickness of the plate. The distance from the center of the pole figure was calculated as $\sin\alpha/(1+\cos\alpha)$, where α is the radial angle. Local orientations were transformed into intensity levels by integrating over a 2.5° area. Intensity values for the EBSP data were calculated using the same mathematical procedure applied to the data from the synchrotron experiment, i.e. as a sum of weights assigned to each of the measured points. The "EBSP" curve consists of 100 equidistant points within the pole figure. Other curves are produced from experimental points measured at different radial angles with a step of 5°.

The maximum intensities along the RD are in almost exactly the same locations for all pole figures, while the intensity levels are somewhat different for different pole figures (Figs 1,2). Two measurements (runs <1> and <2>) on the same S=0.53 specimen give minor differences in intensities (see Fig.2).

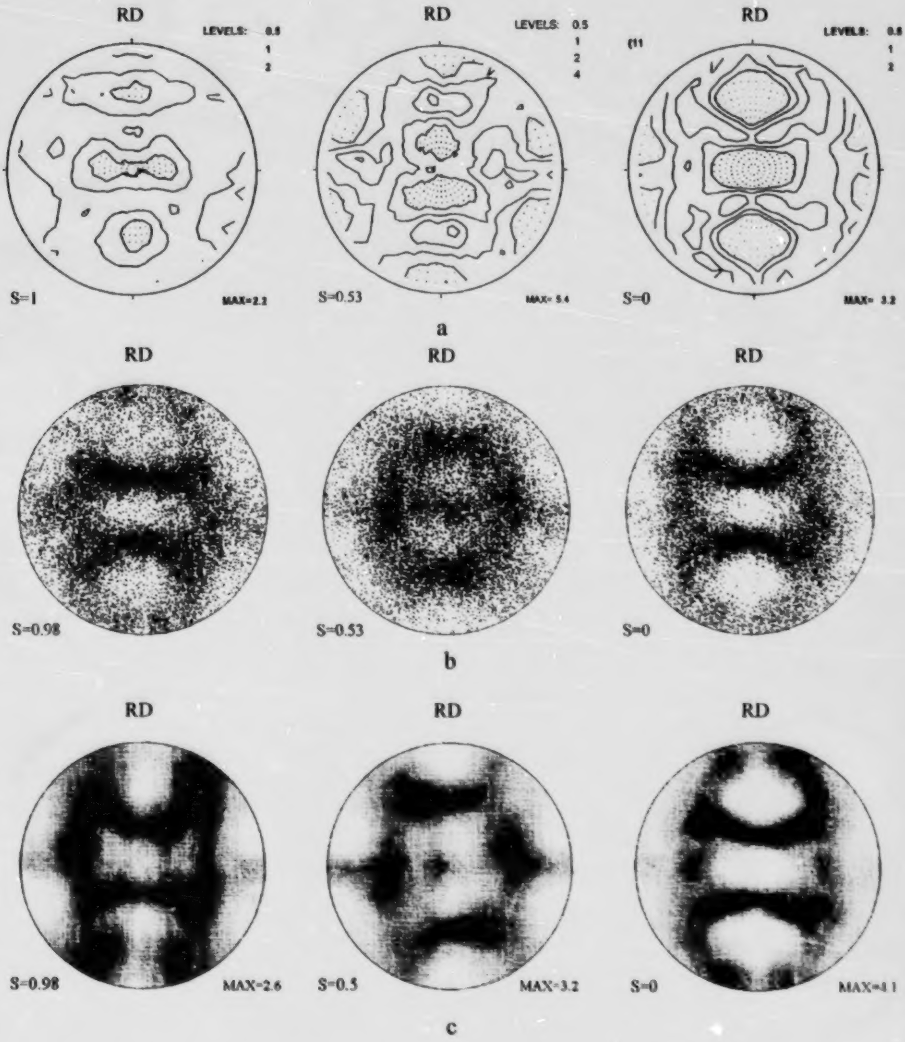

Fig. 1: The {111} pole figures obtained using the traditional low-energy X-ray technique (a), the EBSP technique (b) and high-energy synchrotron radiation (c) in different layers of the plate. S corresponds to the relative distance from the center.

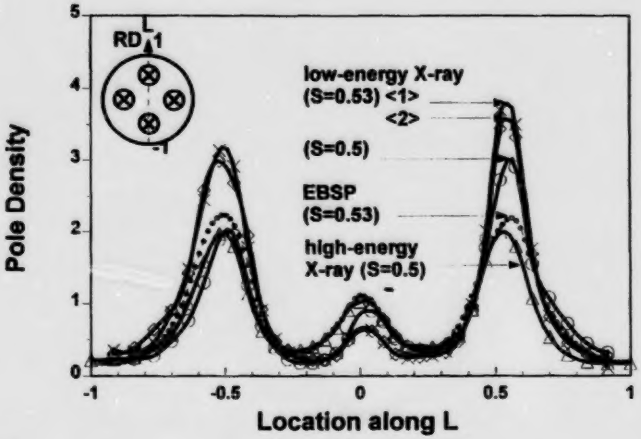

Fig.2: Pole densities along the dashed line L in the {111} pole figures measured near the quarter thickness using different techniques.

4. Potential of different techniques

A good qualitative agreement between the compared techniques is evident, but the peak positions in the pole figures and their intensities are not identical. Moreover, there are slight differences in intensities even for the same specimen repeatedly measured using the same technique. This may be related to the accuracy of texture measurements which is generally accepted to be 10% (Engler et al. 1993). Another reason is that the same specimen was not used for each experimental technique, but multiple specimens were cut out of the different regions in the plate. Since the undeformed microstructure revealed considerable region-to-region variations, it is not surprising that textures after rolling may be somewhat different in different regions even in the same depth. In this regard, it is important that a reasonably large number of grains is inspected by each technique.

Unless the grain size is extremely large, a relatively large specimen combined with its oscillating movement during measurements ensures a large number of grains are sampled by the traditional X-ray technique. The size of the SEM specimens depends on the specimen chamber and the holder. However, if even small specimens have to be used, large sample areas may be covered by the EBSP technique since any large number of specimens can be successively mounted in the SEM. In the transmission synchrotron experiment, the diameter of the cylindrical specimen is limited by the penetration depth of X-rays. For aluminium, the penetration depth of X-rays at 100 keV is around 22 mm. Again for increasing statistics on the number of investigated grains in materials with large grain sizes averaging over several specimens must be applied.

While the analysis of data obtained using high-energy synchrotron radiation is not as trivial as in other "standard" methods, this new technique has important advantages over traditional low-energy X-ray and the EBSP techniques. In contrast to the traditional

X-ray technique, the synchrotron experiment avoids removing layers to get texture information from a selected layer. Texture gradients can be measured in any number of layers in the same specimen once mounted. The inspected depth is changed by moving the position of the specimen in respect to the beam. In this context, it resembles EBSP measurements in the longitudinal or transverse section of the rolled plate. However, the advantage of the synchrotron approach over the EBSP technique is its applicability to heavily deformed materials with excessive dislocation densities. Also, recording macrotextures is much faster than measuring single orientations in the SEM. Measuring textures in the transmission mode results in the unique possibility to perform *in-situ* measurements of texture gradients in bulk samples.

5. Summary

The applicability of high-energy synchrotron radiation is demonstrated for the characterization of through-thickness texture gradients in rolled materials. Pole figures produced using the analysis of Debye-Scherrer cones recorded in the synchrotron experiment agree qualitatively with pole figures obtained through traditional low-energy X-ray diffraction and the EBSP technique. Through-thickness texture gradients can be quickly and successfully studied using transmission synchrotron radiation both in annealed and deformed materials including materials with excessive dislocation densities.

Acknowledgements

This work was supported by the Danish Research Councils: SNF (via Dansync) and STVF. Mr P.Olesen and Dr T.Tschentscher are acknowledged for their assistance during synchrotron experiments.

References

Dillamore, I.L. and Roberts, W.T. (1963-64) *J. Inst. Metals*, Vol.92, pp.193-199.

Engler, O., Palacios, J., Schäfer, W., Jansen, E., Lücke, K. and Will, G. (1993) *Textures and Microstructures* Vol. 21, pp.195-206.

Fischer, N.I., Lewis, T. and Embleton, B.J.J. (1987), *Statistical Analysis of Spherical Data.* Cambridge Univ. Press.

Fisker, R., Schou J., Carstensen, J.M., Poulsen, H.F. and Garbe, S. (1998). *J. Appl. Cryst.*, Vol.31, pp.647-653.

Hansen, J. and Mecking, H., (1975) *Proc. ICOTOM 4*, (eds G.J. Davies, I.L. Dillamore, R.C. Hudd and J.S. Kallend), The Metals Society, Cambridge, pp.34-46.

Krieger Lassen, N.C. (1998) *J. Microscopy*, Vol.190, pp.375-391.

Mishin, O.V., Bay, B. and Juul Jensen, D. (1999) *Proc. ICOTOM 12* (this book of proceedings).

Poulsen, H.F., Garbe, S., Lorentsen, T., Juul Jensen, D., Poulsen, F.W., Andersen, N.H., Frello, T., Feidenhaus R. and Graafsma, H. (1998) *J.Sync.Rad.*, Vol.4,pp.147-154.

Truszkowski, W., Krol, J. and Major, B. (1980) *Metal. Trans.*, Vol.11A, pp.749-758.

Venables, J.A. and Harland, C.J. (1973) *Phil. Mag.* Vol.27, pp.1193-1200.

MODIFICATIONS IN THE GRAIN BOUNDARY CHARACTER DISTRIBUTION IN FCC MATERIALS THROUGH THERMOMECHANICAL PROCESSING

M. KUMAR, A.J. SCHWARTZ, and W.E. KING
Lawrence Livermore National Laboratory, Livermore, CA 94550, U.S.A.

ABSTRACT

Recently, a body of work has emerged that indicates the potential to improve certain materials' properties through thermomechanical processing (TMP) solely by controlling grain misorientations. The grain boundary character distribution (GBCD) is defined as a microstructural property that describes the proportions of "special" and "random" boundaries with reference to the coincident site lattice model. Most of the "optimization" treatments reported in the literature have been performed on f.c.c. metals and alloys with medium to low stacking fault energies and have resulted in microstructures with high fractions of $\Sigma3$, $\Sigma9$, and $\Sigma27$ boundaries, or $\Sigma3^n$ type boundaries. It could be interpreted that only an increased incidence of annealing twinning is required to improve the GBCD. However, it also appears imperative that the formation of annealing twins disrupt the connectivity of the random boundary network, thus implying that $\Sigma3^n$ reactions and resultant triple junctions are critical. Experiments to modify the GBCD in model materials like oxygen–free electronic Cu and Inconel 600 are presented and the efficacy of the processing routes is assessed in terms of the random boundary network and evolution of texture in the processed microstructures.

Keywords: grain boundary character distribution, special boundaries, annealing twinning, random boundaries

1. INTRODUCTION

Intercrystalline defects, such as grain boundaries and triple lines or junctions, are known to exert influence over several key materials parameters. Therefore the ability to manipulate the population of grain boundary types in the microstructure allows tailoring of properties for specific applications in a manner similar to modifications of the microstructure through solid-state phase transformations.

The concept of "grain boundary design and control" [1] has evolved into "grain boundary engineering." Efforts to engineer grain boundaries have primarily concentrated on changing the misorientation distribution function (MDF) through TMP or through thin film deposition and solidification techniques. The effect is to increase the fraction of grain boundaries in the microstructure that exhibit specific disorientations described by the coincident site lattice (CSL) model [2].

When the appropriate processing conditions are obtained, grain boundary engineering appears to produce materials where the grain size gets refined, the fraction of special boundaries increases, and the deviations from exact CSL misorientations decrease. Despite these changes to the microstructure, there is no significant increase in the observed texture; in fact, the texture strength may actually be reduced.

Two fundamentally different paths have been reported thus far in the literature. One approach has been to strain the material to small to moderate levels on the order of 6-8%, followed by annealing that causes rotations of grain boundaries towards lower energy configurations, *i.e.*, low Σ boundaries [3-6]. This approach, however, requires very lengthy annealing times and leads to considerable grain growth [7,8]. It has been shown, however, that this "fine tuning" approach reduces the deviation, as set by the Brandon criterion [9], of the grain boundaries from the exact CSL disorientation.

The second approach resorts to a multi-cycle treatment of moderate strain levels followed by annealing treatments at relatively high temperatures but for very short times. An important aspect of this approach is the total forming reduction being broken up into several cycles of deformation and recrystallization.

Advances in the engineering of grain boundaries in materials have been facilitated in recent years by the commercialization of Orientation Imaging Microscopy (OIM) [10-12]. This SEM-based technique has superceded other experimental techniques, such as TEM and electron channeling patterns in SEM, for the determination of the GBCD due to the relatively straightforward specimen preparation and the large number of orientation measurements attainable in a relatively short period of time. Thus, advances in engineering of grain boundaries can be ascribed due to the following factors: (1) recognition that grain boundaries play an important role in a number of materials properties, (2) recent evidence that thermomechanical processing can alter the GBCD, and (3) ease of characterization of the GBCD by the OIM technique.

This paper describes the different approaches to the engineering of grain boundaries in low and medium stacking fault energy (SFE) f.c.c. materials that are part of an on-going research program investigating face-centered and body-centered metals and alloys.

2. EXPERIMENTAL METHODOLOGY

Bars of oxygen free electronic (99.99%) Cu and nominal purity Inconel 600 alloy were used for the sequential strain-recrystallization (SR) processing series of experiments described below. Strain-recrystallization refers to the application of moderate levels of deformations (between 20 and 30%) followed by intermediate or high temperature anneals.

Table I. Process sequence for ofe-Cu strain-recrystallization treatments.

	Sample/Process Number		
Process	OFE-AR	SR-N-350	SR-N-400
Strain	As-received	~30%	~30%
Heat Treatment	None	350°C/10 min	400°C/10 min
Grain Size	125 μm	27 μm	35 μm

The ofe-Cu bar, initially in the semi-hard condition, was further deformed 30% in compression. Specimen disks were then annealed in an argon sand bath at temperatures between 350° and 400°C for 10 minutes, as described in Table I.

After water quenching, the specimens were prepared for optical metallography and OIM. This process was repeated for three strain-recrystallization cycles.

The Inconel 600 alloy was chosen in order to examine an alloy with the f.c.c. crystal structure, but with a lower SFE. The series of optimization treatments induced a thickness reduction of 20% per rolling sequence. The bar was annealed at 1000°C for 15 minutes in air followed by water quenching. OIM observations were made after step number 1, 3, 4, and 5 and 7 for a total of six observations including the as-received condition.

Samples were observed in a Hitachi S2700 SEM with an automated OIM attachment (TSL, Inc.) [13]. Typically, OIM scans were carried out in a hexagonal grid using 1.5 to 5 μm step sizes over areas approximately 200 × 200 to 500 × 500 μm^2 in dimensions. Plots were produced of confidence index as a function of position and overlaid with boundaries in the range of 2°–15° (low-angle) and 15°–180° (high-angle). The Brandon criterion [9] was applied to identify those boundaries that were special ($1 \leq \Sigma \leq 49$) in nature. The GBCD is reported by number fraction or frequency of occurrence as opposed to the boundary length fraction reported by the TSL, Inc. analysis software. (Note that the Σ1 boundaries were not included in the GBCD for the as-received condition since these materials were in the semi-hard state with a high dislocation density.)

3. RESULTS AND DISCUSSION

The starting material for the strain-recrystallization study was ofe-Cu in the semi-hard condition with a grain size on the order of ~125 μm, but with a few individual grains larger than 500 μm. Therefore, a very high fraction of Σ1 boundaries was observed and hence omitted from the special fraction for better comparison with the processed microstructures. The very low fraction of Σ3 boundaries, as shown in Fig. 1 is rather surprising in light of the low stacking fault energy (~60-70 mJ/m^2) in copper. The first strain-recrystallization treatment provided a large increase in the Σ3 boundaries with a steep drop in the Σ1 boundaries. Fig. 1 demonstrates how the special fraction increases with successive processing using the SR-N-400 strain-recrystallization treatment as an example. The processing successfully increased the number of Σ3 boundaries, the number of $\Sigma 3^n$ boundaries, as well as the total special fraction to approximately 65%.

The 30% compression deformation induced complete recrystallization at 400°C. This was accompanied by a dramatic reduction in the number of Σ1 boundaries in the microstructure. At the same time, the grain size decreased to below 50 μm. Subsequent treatments at this temperature also induced full recrystallization but only insignificant reductions in grain size.

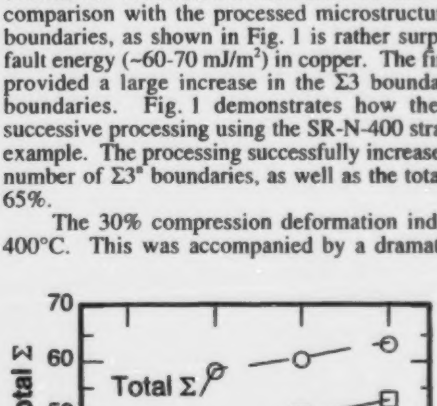

Fig. 1: Distribution of special boundaries with processing sequence in ofe-Cu.

A gradual increase in the fraction of Σ3 boundaries and a dramatic rise in the fraction of Σ9 and Σ27 boundaries was observed, and this can be seen in Fig. 1. The increasing ratio of Σ9 and Σ27 boundaries to twin boundaries is indicative of multiple twinning or twin intersection events, as these $\Sigma 3^n$ boundaries arise from the geometrical necessity of connecting Σ3 boundaries in the grain boundary network. Pole figures from the as-received and processed ofe-Cu bar are shown in Fig. 2. They indicate a factor of more than two reduction in texture that results from multiple twinning events, as shown by the simulations of Gottstein [14].

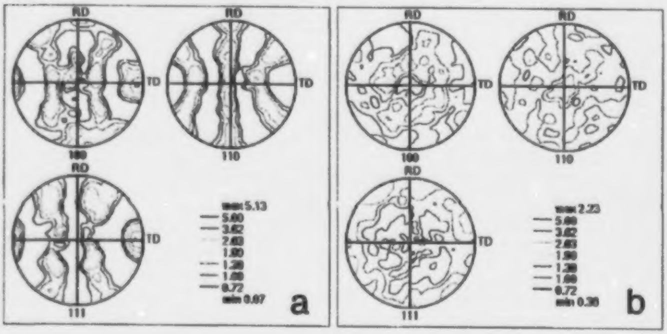

Fig. 2: Pole figures extracted from a) the as-received ofe-Cu bar and b) Cu bar that had been processed to enhance the special fraction, as shown in fig. 1.

The analysis of the Inconel 600 processed samples revealed similar trends (Fig. 3) to those seen for ofe-Cu even though the annealing temperature normalized with respect to the melting temperature was much higher ($0.8T_m$ *vs.* $0.5T_m$ for Cu) in this case. The most notable difference is a slight drop in the fraction of higher order $\Sigma3^n$ boundaries, even though the fraction of Σ3 boundaries is roughly the same. The reason for this apparent decrease could very well be statistical in nature. The striking point is that in all cases the frequency of Σ3 boundaries levels off at approximately 35-40% of the total number of boundaries, with the ratio of Σ3 boundaries to Σ9 and Σ27 boundaries also peaking at about 3:2. The microstructures do not compare favorably with the ideal twin-limited microstructure [15], as evidenced by the fact that the ratio of Σ3 to other $\Sigma3^n$ boundaries levels off very early on in the TMP cycle and never approaches the distribution specified by an ideal twin-limited microstructure [15]. The results, however, are in good agreement with the data reported in the literature on GBCD optimization of Ni-base alloys and austenitic stainless steels [16,17].

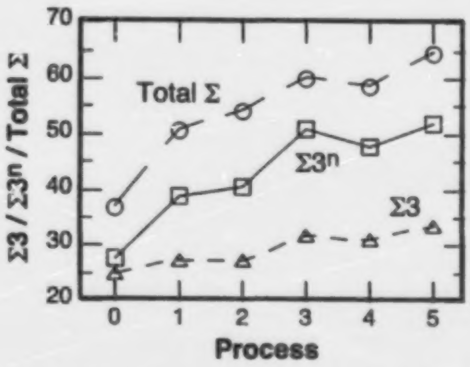

Fig. 3: Distribution of special boundaries with TMP sequence in Inconel 600.

Similar trends were observed [7,8] when the special fractions were considered in terms of the total length of boundaries rather than by their frequency. However, the fraction of Σ3 boundaries was as high as 50–60% compared with 35–40% when the measurement is by frequency of occurrence. This is a clear indication of a lower energy state being achieved by an increase in the length of low-energy Σ3 boundaries at the expense of relatively higher energy boundaries rather than an increase in their relative fraction of the total number of boundaries in the microstructure. It is interesting to note in this context that the fraction of Σ9 and Σ27 boundaries decreases considerably when measured by length. This concurs with the suggestion [5] that Σ9 and Σ27 boundaries appear in the microstructure as a necessity of geometrical considerations, such as the Σ3 + Σ3 = Σ9 reaction, and not because of a reduction in total energy of the grain boundary network.

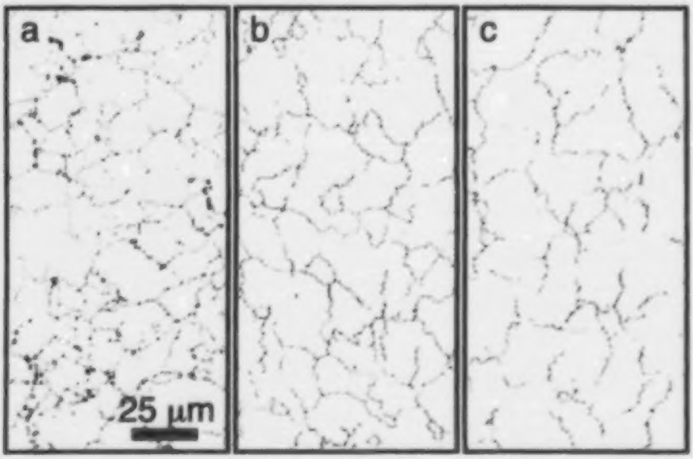

Fig. 4: Reduced OIM scans highlighting only the interconnectivity of random boundaries in the microstructure of Inconel 600 in the following conditions; a) as-received condition, b) after 3 processing cycles, and c) after 5 processing cycles. Note the reduced path length evident after 5 sequential strain and recrystallization cycles.

The idea of grain boundary design has primarily meant the engineering of polycrystalline materials properties through alteration of the GBCD. However, modifications in the GBCD are a necessary, but not sufficient, condition to impact properties such as fracture or corrosion characteristics that are primarily dependent on the spatial distribution and interconnectivity of the boundaries prone to crack propagation. This aspect is qualitatively examined by considering only the random boundaries in the microstructure, as in Fig. 4. From these "reduced" OIM maps it is evident that the network of random boundaries is dramatically altered by the appearance of $\Sigma3^n$ variant boundaries. Thus there is a strong argument to believe that the continuous path length of undesirable boundaries is severely truncated, as the material is sequentially strain-recrystallized. The problem then remains of finding an appropriate function that describes a critical value for an assembly of random boundaries, and is the subject of on-going investigations.

CONCLUSIONS

It has been demonstrated that the fraction of special boundaries in ofe-Cu and Inconel 600 can be increased through thermomechanical processing. Using commercially practical processing methods, it is possible to increase special fractions to about 70%, while the grain size decreases and no significant texture develops or is randomized. It is shown that the new microstructure is composed of a network of random boundaries interrupted by special boundaries through the process of multiple twinning and formation of $\Sigma 3^n$ variants.

ACKNOWLEDGEMENTS

This work was performed under the auspices of the U.S. Department of Energy and Lawrence Livermore National Laboratory (University of California) under contract no. W-7405-Eng-48. The help of L. Nguyen in the metallographic sample preparation and OIM investigations is gratefully acknowledged.

REFERENCES

1. T. Watanabe, *Res. Mech.*, **11**, p. 47 (1984).
2. H. Grimmer, W. Bollmann, and D. H. Warrington, *Acta Cryst.*, **A30**, p. 197 (1974); D. H. Warrington and M. Boon, *Acta Metall.*, **23**, p. 599 (1975).
3. L. C. Lim and R. Raj, *Acta Metall.*, **32**, p. 117 (1984).
4. V. Randle and A. Brown, *Philos. Mag.*, **A59**, p. 1075(1989).
5. C. B. Thomson and V. Randle, *Acta Mater.*, **45**, p. 4909 (1997).
6. V. Randle, P. Davies, and B. Hulm, *Philos Mag.*, **A79**, p. 305 (1999).
7. W. E. King and A. J. Schwartz, *Mater. Res. Soc. Symp. Proc.*, **458**, p. 53 (1997).
8. W. E. King and A. J. Schwartz, *Scripta Mater.*, **38**, p. 449 (1998).
9. D. G. Brandon, *Acta Metall.*, **14**, p. 1479 (1966).
10. R. D. Doherty, I. Samajdar, and K. Kunze, *Scripta Metall. Mater.*, **27**, p. 1459 (1992).
11. B. L. Adams, *Mater. Sci. Engg.*, **A166**, p. 59 (1993).
12. B. L. Adams, S. I. Wright, and K. Kunze, *Metall. Trans.*, **A24**, p. 819 (1993).
13. TSL, Inc. Orientation Imaging Microscopy Software Version 2.5 User Manual (Draper, UT: TSL, Inc. (1997).
14. G. Gottstein, *Acta Metall.*, **32**, p. 1117 (1984).
15. G. Palumbo, K. T. Aust, U. Erb, P. J. King, A. M. Brennenstuhl, and P. C. Lichtenberger, *Phys. Stat. Sol.* (a), **131**, p. 425 (1992).
16. P. Lin, G. Palumbo, and K. T. Aust, *Scripta Mater.*, **36**, p. 1145 (1997).
17. V. Y. Gertsman and J. A. Szpunar, *Scripta Mater.*, **38**, p. 1399 (1998).

ACCURATE TEXTURE MEASUREMENTS ON THIN FILMS USING A POWDER X-RAY DIFFRACTOMETER

MARK D. VAUDIN
NIST, Gaithersburg, MD, USA.

Abstract

A fast and accurate method that uses a conventional powder x-ray diffractometer has been developed for measuring crystalline texture. A θ-2θ scan of a Bragg peak from the textured planes is collected and also a θ scan, or rocking curve, using the same Bragg peak. The method has important advantages over other techniques: a large x-ray footprint can be used, thus obtaining significantly higher intensity which is particularly significant for thin films; no randomly textured specimen is required. The large footprint leads to considerable tilt-induced defocussing during the θ scan – the scattering angle varies along the iradiated length of the specimen as it is tilted out of the symmetric position. To obtain an accurate texture profile from the θ scan, corrections for defocussing and absorption must be applied, and the θ-2θ scan of the Bragg peak, which gives the variation of scattered intensity with angle, is used for the defocussing correction. First principles calculations are used to correct for absorption, with the film thickness and x-ray absorption coefficient as parameters. The technique has been applied to several classes of technologically important materials used in thin film form, such as films of electroplated copper for advanced metallization, and also BST films down to 26 nm thick, which are candidates for DRAM applications.

Keywords: accurate texture; thin films; powder x-ray diffractometer; defocussing

1 Introduction

Crystallographic texture in thin films, i.e. the preferred orientation of particular crystal planes relative to the film substrate, is a common and frequently useful phenomenon. Important materials properties, such as remanent polarization, dielectric constant and elastic moduli, are typically anisotropic, and the most effective use of anisotropic materials in thin film applications often involves controlling the texture of the film. For example, the use of $PbZr_{1-x}Ti_xO_3$ (PZT) in non-volatile ferroelectric random access memories (NVFRAM) requires optimization of the film texture to best utilize the remanent polarization of PZT while satisfying other processing requirements (Hadnagy 1997).

In a typical laboratory or industrial setting, texture is measured using x-ray diffraction. There are certain problems peculiar to the measurement of texture in thin films, the most significant of which is that the intensity of diffracted x-rays that can be obtained from a thin film is frequently so small that intensity measurements are of low accuracy. Thin films deposited on planar substrates typically display fiber (axisymmetric) texture with the substrate normal as the fiber axis. Substrates patterned with surface features such as trenches for conduction vias may display more complex, three dimensional texture (Lingk et al. 1998). In previous work (Vaudin et al. 1998), a technique was described that measures fiber texture using a conventional x-ray powder diffractometer. The technique required the recording of two scans from the sample: a high resolution θ-2θ scan of a Bragg peak whose diffracting planes are normal to the preferred orientation direction; and a θ scan obtained using this peak. The θ scan gives the variation of scattered intensity with specimen orientation and contains the required texture information, but it must be corrected for defocussing and absorption to obtain the texture profile. In a pole figure measurement, this is typically achieved by measuring a specimen of the same phase composition but with no preferred orientation (i.e. a random specimen) and dividing the intensity from the textured specimen by that from the random specimen, thus obtaining multiples of a random distribution (MRD) as a function of specimen orientation. In the technique of Vaudin et al., the θ scan that would be obtained from a random specimen is calculated from the θ-2θ scan of the Bragg peak, taking into account defocussing and absorption, and the texture profile is determined by dividing the experimental θ scan by the calculated random θ scan. In this way, the shape of the texture profile is determined, but the scaling is arbitrary. The technique has been extensively applied to textured bulk alumina (Seabaugh et al., in preparation).

2 Theory

Axisymmetric thin film texture implies the preferential alignment of a particular set of crystal planes parallel to the substrate. The data collected from the specimen are the two x-ray scans described above, $I_{pk}(2\theta)$, a θ-2θ scan of a Bragg peak (Bragg angle θ_B) from the aligned planes, and a θ scan, $I_{rc}(\omega)$, where the specimen orientation is tilted away from the symmetric orientation through ω about an axis in the specimen surface normal to the diffraction plane, while the scattering angle remains fixed at $2\theta_B$. (In Vaudin et al., α was used for the tilt angle instead of ω.) The θ scan for a randomly oriented specimen of the same material, $I_{rand}(\omega)$, is calculated from $I_{pk}(2\theta)$ by correcting for defocussing and absorption, and the texture profile, $T(\omega) = I_{rc}(\omega)/I_{rand}(\omega)$, is calculated. As the specimen is tilted away from the symmetric orientation in either direction, the x-ray scattering angle, 2θ, varies along the irradiated length of the specimen. The central assumption of the theory is that the intensity of a ray scattered by the specimen through 2θ is proportional to the θ-2θ scan intensity at angle 2θ. Thus, the θ scan intensity at angle ω is proportional to the integral of the Bragg peak intensity, as illustrated in Fig. 1; the scattering angle variation is indicated: $2\theta_- < 2\theta < 2\theta_+$.

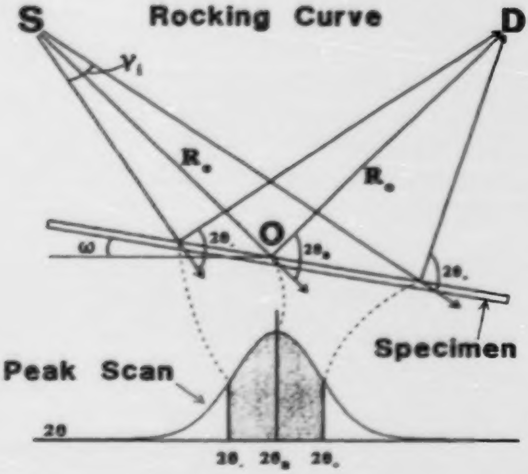

Figure 1: Schematic of x-ray source, specimen and detector showing relation between defocus during θ scan and peak scan intensity

The integral is carried out as a function of γ between $-\gamma_i/2$ and $\gamma_i/2$:

$$I_{rand}(\omega) \propto \frac{1}{\gamma_i}\int_{-\gamma_i/2}^{\gamma_i/2} I_{pk}(2\theta(\omega,\gamma))\,d\gamma \tag{1}$$

where γ_i is the divergence of the incident beam and γ is the angle between the ray and line SO in Fig. 1, i.e. the divergence from the central ray. The factor that determines the constant of proportionality in eqn.(1) is absorption. From simple geometry, an x-ray striking the specimen surface at angle ϕ, penetrating to depth z in the specimen, scattering through 2θ and returning to the surface is attenuated by $K(z, \phi, 2\theta)$:

$$K(z,\phi,2\theta)=\exp\left\{-\mu z\left(\frac{1}{\sin\phi}+\frac{1}{\sin(2\theta-\phi)}\right)\right\}=\exp\{-\mu D(2\theta,\phi)z\} \tag{2}$$

where μ is the linear coefficient of x-ray absorption, $D(2\theta, \phi)$ is defined implicitly, and ϕ is the angle of incidence of the ray on the specimen surface: $\phi = \theta_B + \omega - \gamma$. For a ray at γ to SO incident on a film of thickness t, the total effect of x-ray absorption on the recorded intensity, $A(\omega, \gamma)$, is found by integrating through the thickness of the film:

$$A(\omega,\gamma) = \int_0^t K(z,\phi(\omega,\gamma),2\theta(\omega,\gamma))\,dz$$

$$= \frac{1-\exp\{-\mu D(2\theta,\varphi)t\}}{\mu D(2\theta,\varphi)} \tag{3}$$

To relate I_{pk}, the intensity measured at zero tilt, to the intensity that would be measured during a θ scan when the specimen tilt varies, the I_{pk} values are first divided by $A(0, \gamma)$ and then multiplied by $A(\omega, \gamma)$, giving the correction factor, $F(\omega, \gamma) = A(\omega, \gamma) / A(0, \gamma)$, and thus we obtain:

$$I_{rand}(\omega) = \frac{1}{\gamma_i}\int_{-\gamma_i/2}^{\gamma_i/2} F(\omega,\gamma) I_{pk}(2\theta(\omega,\gamma))\, d\gamma \qquad (4)$$

Thus, measuring I_{pk} and I_{rc} allows the texture profile T(ω) to be calculated. When $I_{pk}(2\theta_B)$ and $I_{rc}(0)$ are measured, the diffractometer is in the same configuration, and therefore the measured intensities should be equal within experimental error. Agreement between them is a good check on the reliability of the data.

The units of T(ω) can be found by considering that when $\omega = 0$, 2θ varies very little with γ (only by the flat specimen correction), and therefore from eqn. (4), $I_{rand}(0) = I_{pk}(2\theta_B)$ to a very good approximation. Since, within experimental error, $I_{pk}(2\theta_B) = I_{rc}(0)$, it can be seen that within experimental error T(0) should equal 1. As ω increases, T(ω) decreases from 1 for positively textured samples. If T(ω) were known over all orientation space, the profile could be scaled to be in MRD by multiplying by the MRD value at $\omega = 0$, MRD_0, which can be found from the normalization condition:

$$\int_0^{\pi/2} MRD_0 T(\omega) \sin\omega\, d\omega = 1 \qquad (5)$$

With this rocking curve technique, ω is limited to a range: $0 < \omega < \theta_B$. However, eqn.(5) can still be used in those cases where the texture profile of a material is narrow enough that it decays to zero within the observed orientation range and can be assumed to be zero in the unobserved orientation range.

3 Experimental

The technique has been designed to be used with a conventional divergent beam powder x-ray diffractometer. The two x-ray scans collected, the θ-2θ and θ scans, were collected under identical conditions; in particular, the incident and receiving slits were the same. In addition, no anti-scatter slits were used; Soller slits could have been used but were not in this case. For both scans, the dwell time was set by experience to be long enough to produce data of an adequately high signal to noise ratio. The angular steps of the θ-2θ and θ scans were at most one tenth of the full width at half maximum of their respective peaks. The θ-2θ and θ scan intensity data were processed using software called Texture^{ref}, which requires the thickness and x-ray absorption coefficient of the film, the beam divergence, the diffractometer radius and $2\theta_B$ for the θ scan as additional input data.

4 Results and Discussion

Fig. 2(a) shows a log scale plot of a θ-2θ scan from a 1.6 μm copper film electrodeposited on a TaN / SiO_2 / Si (001) substrate. In addition to peaks attributed to the substrate from TaN, Si and a weak, unidentified peak at 81°, all the fcc Cu peaks are present, but relative to their random integrated intensities (Powder Diffraction File 1996), the 111 and 222 peaks are over an order of magnitude larger than the 200, 220 and 311 peaks, indicating significant (111) texture, and also the likelihood of a random fraction. This is confirmed by Fig. 2(b) where the (111) texture profile measured using both 111 and 222 peaks is plotted, arbitrarily scaled to a maximum of 1000. The raw data have been corrected using thicknesses of 0.8, 1.6 and 3.2 μm; the texture plots show that

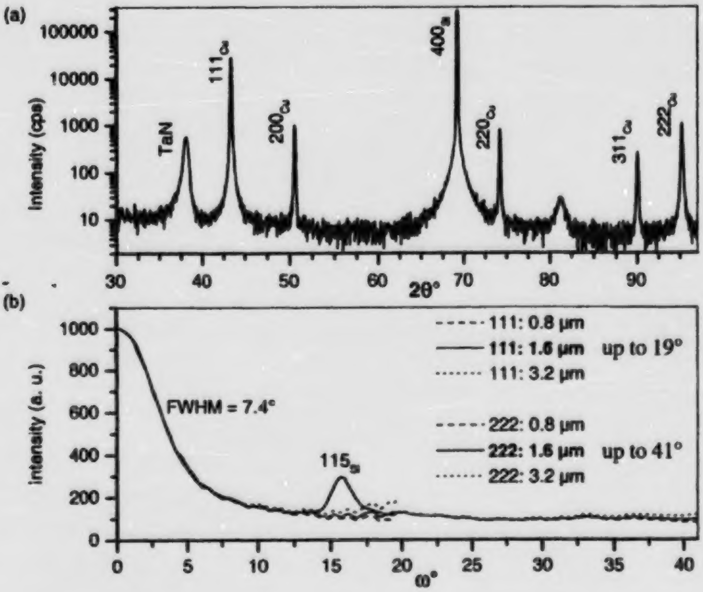

Fig. 2: (a) θ-2θ scan and (b) texture profile from 1.6 µm electroplated Cu film

the best match between the 111 and 222 plots occurs for the 1.6 µm correction. Comparing the FWHM value of 7.4° for the texture profiles with the 6.1° value for the raw θ scans shows that the defocusing and absorption corrections had a significant effect on the profiles. The presence of a significant random fraction is clear from the constant texture level from $15° < \omega < 40°$. When testing the technique on bulk specimens, Vaudin et al showed that a texture profile of constant value was obtained from material that had been shown by other methods to be untextured, indicating that the corrections were correctly formulated. The agreement between 111 and 222 texture in Fig. 2(b) is clearly better when corrected for the true film thickness than double or half the value, which shows the method works well in this case. However, this is not a full validation of the thin film correction, which would require a set of thin film specimens with known textures, not currently available.

Fig. 3(a) shows a θ-2θ scan from a $Ba_{0.7}Sr_{0.3}TiO_3$ (BST) thin film deposited on a thin film of Pt on Si. The position of the 111_{BST} peak is indicated, and, despite the strong overlap with the 111_{Pt} peak, it is clear that the 111_{BST} peak is very weak or absent. This suggests that the film contains very little or no randomly oriented material but consists of two populations of grains with (001) and (110) texture, respectively. Texture profiles collected using the 001, 110 and 002 peaks are shown in Fig. 3(b) and indicate that the two populations are both highly textured with full widths at half maximum (FWHM) values from 2.8° to 3.4°; the agreement between the 001 and 002 FWHM values is good (the FWHM values are accurate to ±0.1°). If the texture profiles (corrected data) are compared with the θ scans (uncorrected data), the raw and corrected data are

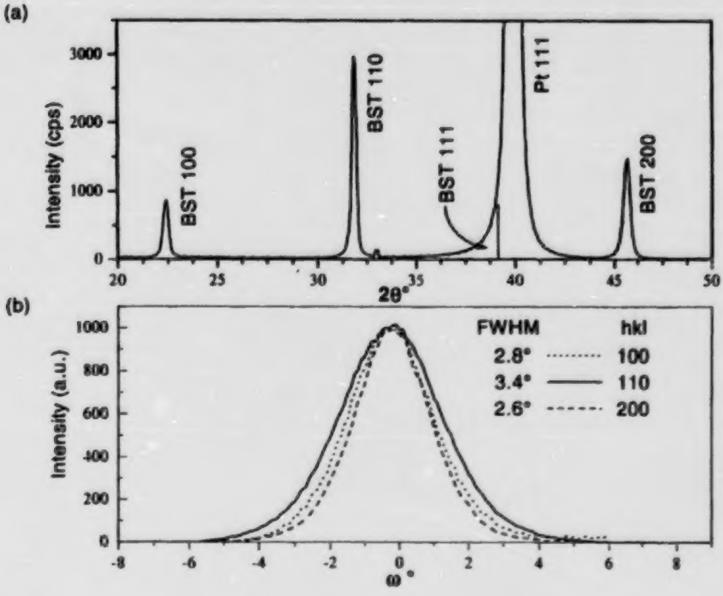

Fig. 3: (a) XRD scan and (b) texture profiles from 36 nm BST film

the same within experimental error, indicating that for highly textured materials, the uncorrected 'rocking curve' data are an accurate measure of texture. However, this would not be known without the analysis methods described in this paper.

5 References

Hadnagy, T.D. (1997) Materials and Production Characterization Requirements for the Production of FRAM Memory Products, Integrated Ferroelectrics, vol. 18, No. 1.

Lingk, C., Gross, M.E. and Brown, W.L.(1999) Applied Physics Letters, vol 74, no. 5, pp. 682-685.

Powder Diffraction File (1996) #4-836, International Center for Diffraction Data, Newtown Square, PA.

Seabaugh, M.M., Vaudin, M.D., Cline, J. P. and Messing, G.L. (in preparation) A Comparison of Texture Analysis Techniques for Highly Oriented α-Al_2O_3.

Texture (1999) available from www.ceramics.nist.gov/staff/vaudin.htm.

Vaudin, M.D., Rupich, M.W., Jowett, M., Riley, G.N. and Bingert, J.F. (1998) A Method for Crystallographic Texture Investigations Using Standard X-ray Equipment, Journal of Materials Research, Vol. 13, No. 10, pp. 2910-2919.

ADAPTIVE ORIENTATION IMAGING MICROSCOPY

W. YANG, B. L. ADAMS, and M. DE GRAEF

Department of Materials Science and Engineering, Carnegie Mellon University,
Pittsburgh, PA 15213, USA

Abstract

The purpose of this paper is to describe a new form of orientation imaging microscopy (OIM): *Adaptive Orientation Imaging Microscopy* or AOIM. For the standard OIM system, one normally employs an equidistant grid of acquisition points to sample the microstructure of a region of interest on the specimen surface. This means that the standard OIM is inefficient when only grain boundary information is desired. The AOIM technique described here minimizes the time spent in the interior of the grain, and rapidly focuses data acquisition on the grain boundary areas, decreasing the overall acquisition time by a factor of 5~50 for a comparable scan area. The scan step size is varied from a coarse initial size to a finer size, depending on the orientation information for the boundary points of the scan. We present AOIM results from several different materials in this paper.

Keywords: grain boundary, misorientation angle, mesoscale, orientation imaging

1. Introduction

In standard OIM experiments the local orientation of the crystal lattice is determined with respect to a suitable reference frame by acquiring and indexing electron back-scattering patterns (EBSPs) on a square or hexagonal grid of sampling points. The spacing of the grid points must be selected prior to the acquisition, and typically remains unchanged for the duration of the experiment. With the development of fast computers and SIT or CCD camera systems in the past few years, the OIM can now acquire and index of the order of 18,000 EBSPs per hour.

There have been many applications of OIM to materials problems since its introduction (Adams *et al.*, 1993). An increasingly important application of OIM has been the characterization of grain boundary networks and the area adjacent to the grain boundary (Lehockey and Palumbo, 1997; Goyal *et al.* 1997; Pan *et al.*, 1996; Adams *et al.*, 1999). In some applications, the distribution of grain boundaries by type or character is most important; in other applications, the connectivity of grain boundaries, for instance at triple junctions, is the main focus. For these applications, the OIM is rather inefficient since only scan points adjacent to the grain boundaries are used to determine the grain boundary character. Furthermore, the spacing of grid points must be optimized for the average grain size of the sample, which typically means that several test runs must be carried out. While this increases the total acquisition time, the sample may also suffer from a buildup of surface contamination, which will decrease the quality of the EBSPs acquired in a later step.

In this paper, we present our new approach, *adaptive orientation imaging microscopy* (AOIM), to overcome the two main obstacles to the mesoscale characterization of an interfacial network. In the next section, we will briefly discuss our approach. In section 3, experimental results obtained by the new AOIM system will be presented and discussed. A summary will be given in the last section.

2. Method

The AOIM system uses the same two components as the standard OIM: a digital scanning electron microscope (SEM) and an external computer to control the microscope during the data acquisition process. The SEM used in the present work is a Philips XL-40 field emission SEM. Sample stage motion and electron beam position are controlled via calls to SEM library routines. Once the EBSP forms on the phosphor screen, it is captured, then Hough-transformed to locate the Kikuchi band positions. These are then used in conjunction with an indexing algorithm to determine the local crystallographic orientation. This is the conventional OIM routine: the computer scans one point after another on a predefined grid with an equidistant step size. For the new AOIM system, this procedure is carried out at varying grid step sizes to obtain the data set relevant to the grain boundaries in the sample.

We start from a coarse step size scan, which rapidly covers the whole area of interest. Then we compare the misorientation angle of adjacent grid points to determine new scan points with a step size equal to half of the previous step size. Two kinds of grids are considered in this paper:

- For the square grid case shown in Figure 1(a), we scan the points A, B, C and D (labeled as solid circles) with a coarse step size S_1. When the entire region of interest has been examined with step size S_1, we calculate Θ_{AB} (the misorientation between points A and B, taking the symmetry of structure into consideration), Θ_{AC}, and Θ_{AD} for each pair of node points. When there is no grain boundary across the area ABCD (i.e., all three misorientation angles Θ_{AB}, Θ_{AC}, and Θ_{AD} are less than the minimum misorientation threshold Θ_c), no additional scan points are required. If there is at least one boundary across the area ABCD, i.e., at least one of the angles Θ_{AB}, Θ_{AC}, and Θ_{AD} is larger than Θ_c, then the next loop at half the original step size scans one or more of the points b, c, or d (labeled as open circles in Figure 1(a)). This procedure is repeated until the step size is smaller than a preset value.

- For the hexagonal grid case shown in Fig. 1(b), the first step is identical to that for the square grid, but with a rectangular grid with an aspect ratio of √3. When the grid is sufficiently refined, one additional procedure is required: the orientations for the points labeled by crosses are obtained either from a scan of the sample at those locations, or, if no grain boundary is present in the corresponding rectangle, by copying the orientation from the point to its upper left.

In order to stop the scan automatically, we introduce a loop-stop parameter ρ_n defined as $\rho_n = f(n)/f(n-1)$, with $f(n)=N_{n+1}/N_n$. Here N_n is the total number of boundary points in the *n*-th scan. Since $f(n)$ is a monotonically decreasing function (see Fig. 2), and also

$$\lim_{n\to\infty} f(n) = const,$$

we have

$$\lim_{n\to\infty} \rho_n = 1.$$

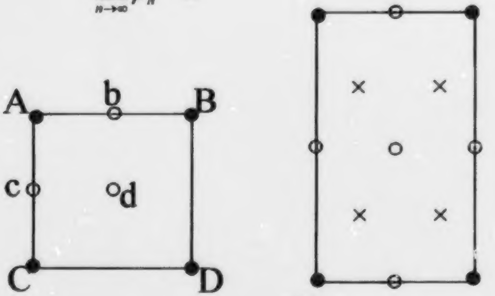

(a) (b)

Figure 1. Scanning point positions in different loop (a) for square grid, (b) for hexagonal grid. For a detaild explanation, see the text.

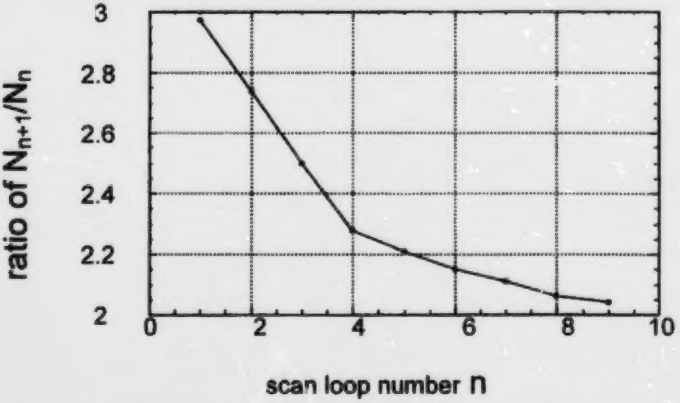

Figure 2. The ratio of the number of boundary points in subsequent loops vs. the scan loop number. Here N_i is the number of boundary points required to scan the i-th loop with step size $S_1/2^{i-1}$.

The scan step size is then refined until $\rho_n > 1-\varepsilon$, where ε is a small positive number.

3. Results

The above algorithm was tested on a number of different samples. Figure 3 shows the timesaving factor λ versus the final scan step size in a logarithmic scale with base 2. Here λ is defined as the ratio of the total number of points in a grid with the smallest step size to the number of scanned points, and θ is defined as the ratio of the step size to the average grain size. From the figure one can see that the AOIM system can save time by a factor 5-50 depending on the spatial resolution required. The higher the resolution required, the more time savings in comparison with a regular OIM run at the same grid resolution. Figure 4 shows the scan result from a grain boundary engineered sample of a Pb alloy. For this sample, the most interesting part is the types of grain boundary. We set the Θ_c angle as 5.0° and the loop-stop criterion ε as 0.05. The time saving factor for this experiment is 8.5. The different grayscale lines in the figure represent the different kinds of CSL boundary according to Brandon's criterion (Brandon, 1967) and the fine and bold black lines represent the random boundaries with misorientation angle between 5° and 15°, and 15° and 180°, respectively. In Figure 5, we present another result from a cube-oriented Ni substrate. For this sample, the most interesting feature is the texture structure. This time we set the Θ_c angle to 3.0° and the loop-stop criterion ε to 0.05. The timesaving factor for this experiment is 5.1. The grayscale in Figure 5(a) represents the crystallographic plane normal parallel to the sample normal. This is defined in the legend in Figure 5(c). The fine and bold black lines in Figure 5(a) represent the grain boundaries with misorientation angle between 3° and 5°, and 5° and 180°, respectively. A strong cube texture is shown in the pole figure as 5(b).

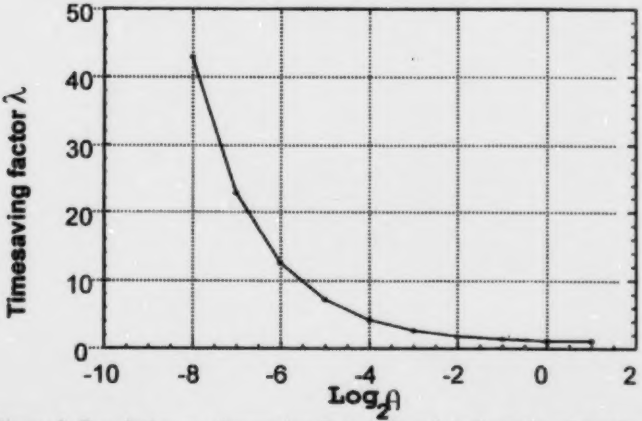

Figure 3. Resolution vs. timesaving factor. Here λ is the ratio of number of total points to the number of scanned points, θ is the ratio of step size to average grain size.

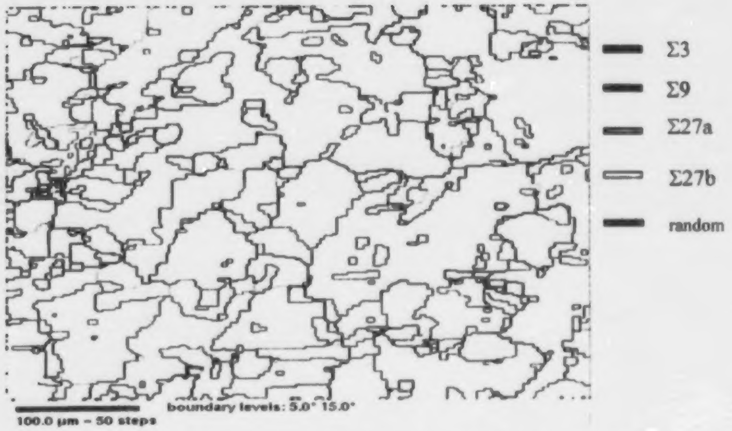

Figure 4. AOIM scan result from grain boundary engineering sample Pb (sample provided by G. Palumbo, Ontario Hydro Technologies). Differently shaded lines represent different kinds of Σ boundaries as indicated by the legend.

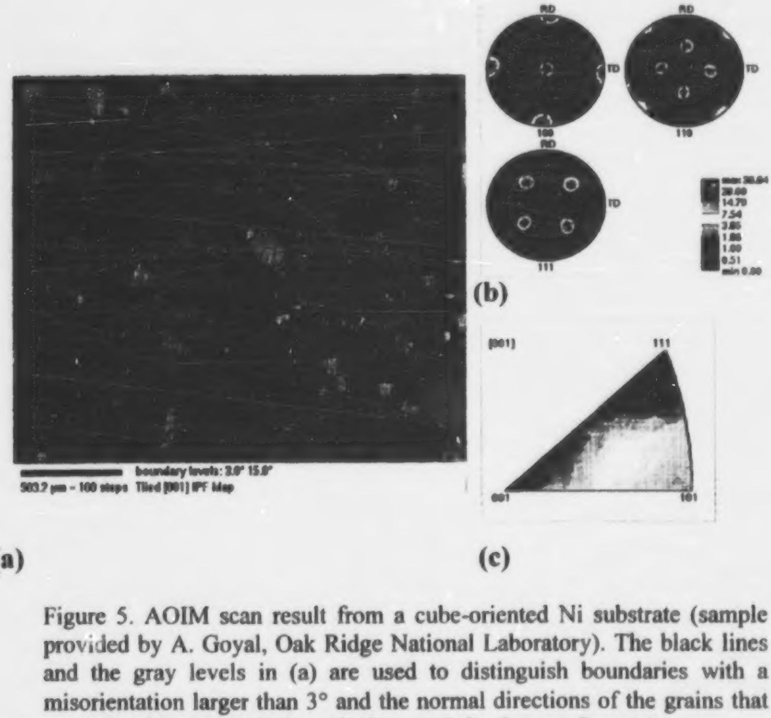

(b)

(a)

(c)

Figure 5. AOIM scan result from a cube-oriented Ni substrate (sample provided by A. Goyal, Oak Ridge National Laboratory). The black lines and the gray levels in (a) are used to distinguish boundaries with a misorientation larger than 3° and the normal directions of the grains that are defined in (c). (b) is the pole figure of the data set from (a).

4. Summary

The AOIM system described above is a powerful tool for the fast and efficient accumulation of data for grain boundaries. The algorithm described above is especially useful for equilibrium grain boundaries, i.e., where the curvature of single boundary does not change too fast locally. For those areas with nonequilibrium grain boundaries, some of the local area will be truncated and the scanned boundary shape will have a zigzag appearance. This illustrates the limitations of the method. By ignoring small intragrain orientation variations, the scan time can be reduced by a factor 5-50. Controlled by the loop-stop parameter ρ, the program can automatically choose the final step size that reliably describes the mesoscale structure statistics.

Acknowledgment:

This work was supported by the MRSEC Program of the NSF under award number DMR-9632556.

References:

Adams, B.L., Wright, S.I., and Kunze, K. (1993) *Metallurgical. Transactions*, 24A, pp. 819-831.

Adams, B.L., El-Dasher, B., Sun, S., and Yang, W., (1999) Proceedings of Plasticity '99.

Brandon, D.G., (1966) *Acta Metall.* 14, pp. 1479-84.

Goyal, A., Specht, E.D., Wang, Z.L., and Kroeger, D.M., (1997) *Ultramicroscopy*, 67,35-57.

Lehockey, E.M., and Palumbo, G., (1997)*Mater. Sci. Engin.* A 237, 168-172.

Pan, Y., Adams, B. L. and Olson, T., (1996) *Acta Materialia*, 44, 4685-95.

REGISTRY BETWEEN SECTIONS IN PRECISION SECTIONING OF POLYCRYSTALLINE MATERIALS

A.MORAWIEC[1] and D.SAYLOR

Department of Materials Science and Engineering, Carnegie Mellon University, Pittsburgh, USA

Abstract

Simple and robust numerical techniques for aligning subsequent sections through polycrystalline materials are presented. Fiducial marks, triple junctions, grain centroids, and grain orientations can be used to determine the best transformation for the alignment of adjacent sections. An application of these techniques to the determination of true dihedral angles between grain boundaries in polycrystalline MgO is also given.

Keywords: dihedral angles, grain boundaries, least squares method, registration, triple junctions

Introduction

It is common to use precision serial sectioning for the determination of microstructural features of polycrystalline materials. In general, two sections are mutually shifted, and one needs to determine the rigid transformation relating coordinates on both sections. Correct alignment (registry) of subsequent sections is crucial for the quality of results. Errors in registry between the sections will cause systematic errors in determination of microstructural features.

One obvious way to deal with registration is to make fiducial marks, e.g. microhardness indentations, visible on both sections. Unfortunately, such external marks are not always available. They can be replaced by microstructural elements recognizable on both sections, such as triple junctions or grain centroids. With additional assumptions concerning their distributions, one can use them in the same way as the external marks.

The transformation of one section with respect to the other consists of planar rotation and translation. When grain orientations are available, the rotational part can be also calculated from the difference in orientations of the same grains on both sections.

In experimental situations, numerous markers and/or numerous orientations may be available but they are influenced by experimental errors. Registry must be based on the best transformation relating the markers and orientations, so in practice, certain optimization procedures must be used. We present some simple and robust methods of registering sections closely related to least-square fitting.

---

[1] On leave from Instytut Metalurgii i Inżynierii Materiałowej PAN, Kraków, Poland

Best rigid transformation relating two sets of points

Let us consider the case with M marks available on each of the two sections. Their locations are assumed to be given in Cartesian coordinate systems assigned to the sections. With vectors (column matrices) x_m and y_m denoting the location of marks on the first and second section, respectively, one has

$$y_m = Ox_m + t \ , \quad (m = 1, ..., M) \ , \tag{1}$$

where O and t are the a rotation matrix and a translation vector. Due to experimental errors the equations (1) for marking points are only approximate. Therefore, the pair (O, t) is calculated by minimization of

$$\psi(O,t) = \sum_m w_m \| y_m - (Ox_m + t) \|^2 \ , \quad \text{subject to} \quad OO^T = I \ , \tag{2}$$

where the norm $\| \cdot \|$ is defined by $\|X\| = (\mathrm{tr}(XX^T))^{1/2}$, superscript T denotes matrix transposition, I denotes unit matrix, and w_m is a non–negative weight assigned to m-th pair of marking points. Without limiting generality, it is assumed that $\sum_m w_m = 1$.

The problem of minimization of ψ is linear. It was discussed numerous times; see e.g., MacKenzie (1957), Schönemann (1966), Wahba, Farrell, and Stuelpnagel (1966), McLachlan (1972, 1982), Kabsch (1976, 1978), Stephens (1979). After differentiating ψ with respect to components of t one obtains the minimum conditions

$$t = y_0 - Ox_0 \ , \tag{3}$$

where $y_0 = \sum_m w_m y_m$ and $x_0 = \sum_m w_m x_m$ denote centroids of the point sets. By substituting t in (2), the residue takes the form $\sum_m w_m \|(y_m - y_0) - O(x_m - x_0)\|^2$. Relocation of the reference points (origins of the coordinate systems) to the centroids corresponds to $(x_m - x_0) \rightarrow x_m$ and $(y_m - y_0) \rightarrow y_m$, and the residue can be rewritten as

$$\psi_0(O) = \sum_m w_m \| y_m - Ox_m \|^2 = \mathrm{const} - 2\mathrm{tr}(PO^T) \ , \tag{4}$$

where $P = \sum_m w_m y_m x_m^T$. To find O minimizing ψ_0 and satisfying the orthogonality conditions $OO^T = I$, the method of Lagrange multipliers can be used. Let Λ denote the symmetric matrix of Lagrange multipliers. By equating derivatives (with respect to O_{ij}) of $\psi_0(O) + \mathrm{tr}\left(\Lambda(OO^T - I)\right)$ to zero one gets the stationarity conditions

$$P = \Lambda O \ . \tag{5}$$

Thus, O is calculated by the polar decomposition of P into the product of a positive semi-definite matrix Λ and an orthogonal matrix O (see, e.g., Halmos, 1958). The solution is unique provided the matrix P is invertible. Because the condition $\det(O) = +1$ was not used, the orthogonal matrix minimizing ψ_0 may have negative determinant. For O satisfying stationarity conditions (5) the value of the residue ψ_0 is const $- 2\mathrm{tr}(\Lambda)$. Thus, it is minimal for Λ with the largest possible trace. Now, if all eigenvalues of Λ are positive and $\det(O) = +1$ the standard polar decomposition gives the sought solution; if $\det(O) = -1$, one has to switch the sign of the smallest eigenvalue of Λ to '$-$' and then calculate O.

In three dimensional space, the above solution can be expressed in the quaternion formalism (Faugeras and Hebert, 1983, Horn, 1987, Diamond, 1988, 1990). In two dimensions, it is reduced to complex numbers. Each 2D vector is represented by a complex number; e.g., for the vector x with components (x^1, x^2) the number is $x = x^1 + ix^2$, where $i^2 = 1$. The residue can be expressed in terms of complex numbers x_m and y_m corresponding to the markers on sections, and t and O representing translation and rotation; let

$$\varphi(O,t) = \sum_m w_m \mid y_m - (Ox_m + t) \mid^2 = \sum_m w_m \left(y_m - (Ox_m + t)\right) \left(y_m - (Ox_m + t)\right)^* ,$$

where star denotes complex conjugation. One can calculate $O = \exp(i\alpha)$ and t by minimizing φ. As before, differentiation with respect to components of t gives $t = y_0 - Ox_0$, where $x_0 = \sum_m w_m x_m$ and $y_0 = \sum_m w_m y_m$ represent centroids. For this t the residue has the form $\sum_m w_m \mid (y_m - y_0) - O(x_m - x_0) \mid^2$. With $x_m - x_0$ and $y_m - y_0$ substituted by x_m and y_m, respectively, one has

$$\varphi_0(\alpha) = \sum_m w_m \mid y_m - \exp(i\alpha) x_m \mid^2 = \text{const} - \left(\exp(i\alpha)\xi^* + \exp(-i\alpha)\xi\right) ,$$

where $\xi = \sum_m w_m y_m x_m^*$. We are looking for α minimizing φ_0. The stationarity condition is $\exp(i\alpha)\xi^* = \exp(-i\alpha)\xi$. Hence, for non-zero ξ one has $\exp(2i\alpha) = \xi^2 / \mid \xi \mid^2$ and

$$\alpha = (1/2)(\arg(\xi^2) + 2\,k\,\pi) = \arg(\xi) + k\,\pi\ , \quad k\ -\ \text{integer}\ .$$

Second order derivative is positive for even k, thus, O minimizing the residue is given by $O = \exp(i\arg(\xi))$.

Rotation from grain orientations

If grain orientations are available, one can calculate the rotational part (O) of the transformation from the difference in orientations of the same grains on both sections. Let X_m $(m = 1, ..., M)$ be 3×3 rotation matrices representing grain orientations on one of the sections, and let Y_m be orientations of the same grains on the second section. In the ideal case they are related by $Y_m = X_m O$. In the presence of experimental errors the rotation matrix O can be calculated by minimizing

$$\phi(O) = \sum_{m=1} w_m \|Y_m - X_m O\|^2 = 6 - 2\text{tr}(RO^T)$$

where $R = \sum_{m=1}^{M} w_m X_m^T Y_m$, subject to orthogonality of O, $OO^T = I$. Formally, the problem is identical to minimization of ψ_0 in (4). Orthogonal matrix O minimizing ϕ is calculated from polar decomposition of R into $R = \Lambda O$. To get the proper orthogonal matrix the sign of the smallest eigenvalue of Λ must be the same as the sign of $\det(R)$.

The problem is that the orientations obtained by current EBSP systems may not be sufficiently accurate. Two main reasons are systematic errors in positioning of the sample and in the determination of the pattern center. The sought planar rotation O is 'part' of the error in positioning the sample; its rotation axis is perpendicular to the surface of the samples. On the other hand, the error caused by the shift of the pattern center corresponds to a rotation with axis in the plane of the samples' surface. Therefore, its influence on determination of O can be assumed to be negligible.

The rotation we look for is about the z axis by the angle α, i.e.,

$$O(\alpha) = \begin{bmatrix} \cos\alpha & -\sin\alpha & 0 \\ \sin\alpha & \cos\alpha & 0 \\ 0 & 0 & 1 \end{bmatrix}$$

Hence, one has

$$\phi(O(\alpha)) = 6 - 2((R_{11} + R_{22})\cos\alpha - (R_{12} - R_{21})\sin\alpha + R_{33}) \ .$$

For non-zero $R_{11} + R_{22}$ stationarity condition $(R_{11} + R_{22})\sin\alpha + (R_{12} - R_{21})\cos\alpha = 0$ gives the rotation angle

$$\alpha = -\arctan((R_{12} - R_{21})/(R_{11} + R_{22})) + k\pi \ , \qquad k \ - \ \text{integer} \ .$$

If $R_{11} + R_{22} = 0$ the minimum corresponds to $\alpha = \pi + \text{sign}(R_{12} - R_{21})\,\pi/2$.[2]

When calculating R, the same orientation can be represented by different rotation matrices due to crystal symmetry. In general, for each m, one has to check the value of the residue for the complete set of matrices symmetrically equivalent to X_m. This may be time-consuming. If the rotation is expected to be small, for a given m, the X_m, of all symmetrically equivalent X_m matrices, closest to Y_m is used. 'Closer' means that the misorientation angle is smaller.

Affine transformation

The transformation between sections may be even more general than the rigid transformation. One may assume that the sections are related by an affine transformation $y_m = Ax_m + t$. The pair (A, t) can be determined by minimizing $\psi(A, t)$, but this time without the orthogonality condition for the first argument. As before, the translation is given by $t = y_0 - Ax_0$, and after shifting the origins of coordinate systems to centroids, the residue can be expressed as $\sum_m w_m \|y_m - Ax_m\|^2$. This residue is stationary for A satisfying $AX = P$, where X is symmetric semi-positive definite matrix given by $X = \sum_m w_m x_m x_m^T$. For non-singular X, the transformation $A = PX^{-1}$ corresponds to a global minimum of the residue. Polar decomposition of A provides the rotational component of the transformation as well as the "stretch" deforming one section with respect to the other.

Application

The registration procedures described above were applied to determine true dihedral angles between grain boundaries in polycrystalline MgO. The ultimate goal is to obtain some insight into the grain boundary free energy by using the dihedral angles and EBSP based orientation mapping; see Adams, Bauer, Casasent, *et al.*, 1999. The registration between parallel sections is required to determine the triple line direction between sections, which is needed for the calculation of true dihedral angles. In EBSP mapping, the sample stage must be tilted. If the tilt angle is not exactly reproduced from one section to the next, a rigid transformation will result in a stretch in the direction perpendicular to the tilt axis. To accommodate for this, one may apply the more generic, affine transformation procedure which will account for the stretch factor.

A polycrystalline MgO sample was imaged using scanning electron microscopy (SEM). SEM contrast images were captured from two parallel sections $6.2\mu m$ apart. The contrast images were used to digitize the locations of 190 triple junctions common to each section. The locations of the junctions then served as markers for the registration. When triple junctions are used as markers, the result is biased by triple lines with long projection on the plane of the section. To reduce that effect, an iteration procedure is applied. In the first step, the transformation is determined with all weights equal. In subsequent steps, the weight (w_m) is related to the length of the projection (d_m): the longer it is, the smaller weight. In this particular application, we have used the formula $w_m \propto (1 + d_m^2/\overline{d^2})^{-1}$, where $\overline{d^2} = \sum d_m^2/M$.

---

[2] If both, $R_{11} + R_{22}$ and $R_{12} - R_{21}$ are equal to zero the function ϕ does not depend on α and this approach cannot be used.

Figure 1(a) shows the registration result when only a rigid transformation was applied to the data. The plot depicts the change in the coordinates of the triple junction locations from the top to the bottom section. It is clear from the plot that the deviations are centered around the origin ($\Delta x_{median} = -0.39\mu m$ and $\Delta y_{median} = 0.74\mu m$)[3]. However, variations in the vertical direction, the direction perpendicular to the tilt axis, are much greater than variations in the horizontal direction. In fact, the standard deviations of Δx and Δy are $5.34\mu m$ and $13.91\mu m$, respectively. The factor of three difference indicates a 'stretch' in the vertical direction. When the more general, affine transformation is applied, the variations in the both directions are now nearly equal. Figure 1(b) shows that the deviations are still centered around the origin ($\Delta x_{median} = -0.95\mu m$ and $\Delta y_{median} = 0.38\mu m$), and the standard deviations of Δx and Δy are $5.21\mu m$ and $4.85\mu m$, respectively.

Using Δx and Δy, along with the distance between sections, the direction of the triple line can be calculated. The direction can be used to determine an inclination angle of the triple line for each of the digitized junctions. The distribution of the inclination angles is shown in Figure 2. The distribution was found to have a mean value of 38.39° and standard deviation of 16.84°.

The triple line directions have been used to calculate true dihedral angles between grain boundaries. The dihedral angles, along with grain boundary misorientations, have been used to extract a distribution of grain boundary energy over misorientation space (Adams, Bauer, Casasent, *et al.*, 1999).

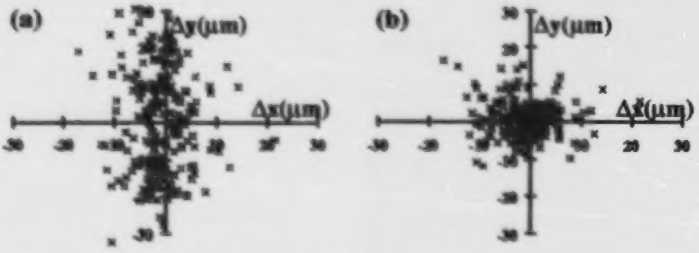

Figure 1. The changes $(\Delta x, \Delta y)$ in the coordinates of the triple junction locations between parallel sections of an MgO polycrystal. (a) The results derived from registration using only a rigid transformation. The standard deviation in Δy is nearly 3 times that of Δx. (b) The results derived from registration using the affine transformation. In this case, the standard deviation in Δy ($4.85\mu m$) is nearly equal to that of Δx ($5.21\mu m$).

---

[3] From now on, the meaning of x and y have changed. Symbols Δx and Δy refer to the horizontal and vertical distance between points on a triple line at the intersection of the top and the bottom sections.

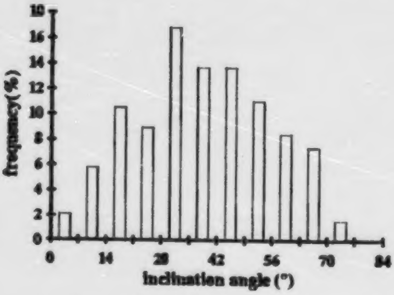

Figure 2. Distribution of triple line inclination angles, i.e., the angles between the triple lines and the direction perpendicular to the sections. The columns represent the percentage of the digitized junctions with inclination angles that fall within each of the 7° bins.

Let us also notice that the boundary surfaces can be used for registry if their shapes are known. This in particular concerns planar boundaries between annealing twins. With a known grain orientation and a trace of a twin boundary, one can calculate the inclination of the boundary with respect to the sample. The inclinations, along with the thickness of the layer between sections, can be used to calculate the expected location of the trace of that boundary on the second section. By minimizing the deviation between expected and actual traces, the transformation (O, t) can be obtained.

Acknowledgments

Work supported by the MRSEC Program of the National Science Foundation under grant number DMR-9632556.

References

Adams,B.L., Bauer,C.L., Casasent,D. *et al.*, (1999). This volume.
Diamond,R. (1988). *Acta Cryst.* **A44**, 211 216.
Diamond,R. (1990). *Acta Cryst.* **A46**, 423.
Faugeras,O.D. and Hebert,M. (1983). *Proc. Eighth Int. Joint Conf. on Artificial Intelligence*, vol.2. Ed. by A.Bundy, pp.996–1002. Los Altos, CA: W.Kaufmann.
Halmos,P.R. (1958). *Finite-dimensional vector spaces*, Princeton, N.Y.: Van Nostrand.
Horn,B.K.P. (1987). *J.Opt.Soc.Am.* **A4**, 629–642.
Kabsch,W. (1976). *Acta Cryst.* **A32**, 922–923.
Kabsch,W. (1978). *Acta Cryst.* **A34**, 827–828.
MacKenzie,J.K. (1957). *Acta Cryst.* **10**, 61–62.
McLachlan,A.D. (1972). *Acta Cryst.* **A28**, 656–657.
McLachlan,A.D. (1982). *Acta Cryst.* **A38**, 871–873.
Schönemann,P.H. (1966). *Psychometrika* **31**, 1–10.
Stephens,M.A. (1979). *Biometrika* **66**, 41–48.
Wahba,G., Farrell,J.L. and Stuelpnagel,J.C. (1966). *SIAM Rev.* **8**, 384–386.

MAPPING OF LATTICE STRAIN AND TEXTURE DISTRIBUTIONS WITH AN X-RAY SCANNING APPARATUS

R.A. SCHWARZER and A.H. FISCHER

TU Clausthal, D-38678 Clausthal-Z., Germany

Abstract

An x-ray scanning apparatus for imaging the spatial distributions of crystal texture, residual lattice strain, and element composition in bulk specimens has been supplemented by the ability to measure pole figures on selected small areas. Equal step, equal area, thinned or incomplete, user-defined angular grids can be generated on the pole sphere. The system is based on a commercial two-circle goniometer and an open Euler cradle (PHILIPS X'Pert MRD goniometer). The specimen is translated with a stepping-motor driven x-y specimen stage step by step across a(n odd-shaped) field up to 100 mm by 100 mm wide in a user defined mesh grid. An annular collimator is used to stop down the "white" primary beam to a narrow spot on the specimen surface. Several texture distribution as well as element composition maps are obtained simultaneously with an energy dispersive solid state spectrometer system as x-ray detector.

Residual lattice strain down to $\Delta a/a = 4 \cdot 10^{-4}$ is analyzed by evaluating the shifts and profiles of diffraction peaks in the spectrum at each image point. Texture is correlated with strain on a mesoscale by constructing maps of the same specimen region. Spatial resolution of pole-figure measurement and residual lattice strain mapping is presently limited to 0.1 mm, whilst resolution of texture and micro x-ray fluorescence element maps is about 0.05 mm, as a consequence of the low intensity of a collimated primary beam.

Keywords: Energy dispersive x-ray diffraction, local strain, local texture, mapping, pole figure measurement, residual stress.

Authors' address:
Prof. Dr. Robert Schwarzer, AG Textur, TU Clausthal, D-38678 Clausthal-Zellerfeld
Email: schwarzer@tu-clausthal.de respectively armin.fischer@infineon.com

1. The x-ray scanning apparatus

Inhomogeneities of morphology and texture in the sub-millimeter range have to be accessed in quantitative microstructural analysis since they are frequently detrimental to reliability and performance of a product. Electron diffraction in the SEM, however, though powerful (Schwarzer 1997) is not a universal technique to meet all requirements of texture measurement. Some examples of limited application are excessive deformation, small grain sizes, or incompatibility of the specimen with vacuum or irradiation by electrons. Some other applications only require the knowledge of the spatial distribution of certain *crystal lattice directions* averaged over small areas (i.e. pole densities) in the specimen surface or cross-sections rather than the full *crystal lattice orientation* of each grain. Spatial resolution of conventional x-ray pole-figure measurement is often insufficient for studying texture gradients. To avoid some limitations specific for electron microscopy as well as conventional x-ray diffraction, an *X*-ray *S*canning *A*pparatus (XSA) based on energy dispersive (ED) x-ray diffraction (Fischer and Schwarzer 1998a) has been further improved and supplemented by the ability to measure spatially resolved pole figures. It enables "images" of the spatial distributions of crystal texture, lattice strain and element composition in bulk samples. Spatial resolution is primarily dependent on the size of the x-ray spot and its elliptical elongation by projection on the tilted surface. A practical limit is presently at 0.1 mm for pole-figure measurement and lattice strain mapping, and 0.05 mm for texture and element mapping, because of the low intensity of the collimated primary beam.

ED x-ray diffraction is based on Bragg diffraction of a collimated "white" primary x-ray beam in dependence on the orientation distribution of the grains in the surface. The energy dispersive separation of *several* diffracted peaks

$$E_{hkl} = n\cdot h\cdot c/(2\cdot d_{hkl}\cdot \sin \vartheta_{hkl}) \qquad (1)$$

at one selected pole-figure point (α, β) in addition to characteristic fluorescent lines is performed simultaneously with a standard EDS detector system. The apparatus is fully controlled by a personal computer. The specimen is translated step by step across a user defined grid pattern with the motor-driven x-y stage. Grid patterns of any shape are possible, e.g. scans along a line, across rectangles or across polygons up to 10 cm by 10 cm wide, in order to match the area to be sampled. In each grid position a spectrum of secondary x-rays is acquired which is composed of broad diffraction peaks and sharp characteristic fluorescence lines superimposed by a low background of scattered primary radiation. Soft x-rays, however, are absorbed in air on the way to the detector such that micro x-ray fluorescent analysis of light elements is not enabled. Windows (Regions of Interest, ROI) are placed on the centers of selected hkl diffraction peaks or fluorescence lines. For a graphical representation of the microstructure, the count rates falling in a selected window are represented pixel by pixel by pseudo-colors or by a gray scale to finally fill in map of spatial texture distribution of pole-density (hkl; α, β) or an element concentration.

Figure 1 shows ED diffraction spectra from a deformed aluminum specimen at two different pole-figure points. The variations of individual peak intensities are clearly visible. A set of diffraction peaks can be identified. The low index peaks are all separated in the spectrum, and no peak overlap occurs for 111, 200, 220 and 400.

Characteristic fluorescence lines from aluminum are not present since soft x-ray radiation is absorbed by air on the path to the detector.

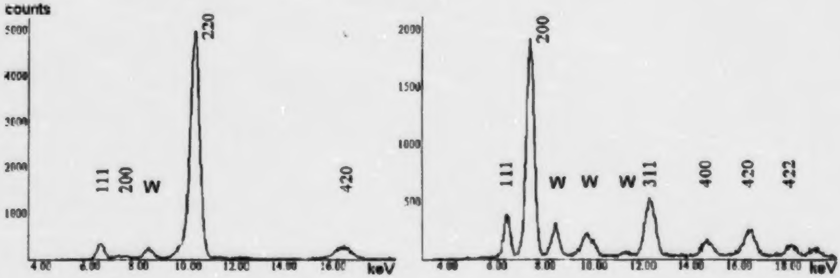

Figure 1 Energy spectra from an aluminum sample at $2\vartheta = 49.5°$.
W marks scattered characteristic radiation from the tungsten tube.

Lattice strain is analyzed and mapped with the same setup, in addition to texture mapping, by evaluating the shift and width of diffraction peaks in the spectrum of each image point (Fischer and Schwarzer 1998b). The shift, $\Delta\vartheta$, of a diffraction peak, ϑ_{hkl}, as compared to the peak position ϑ_0 with a relaxed specimen with lattice spacing d_0 is a measure of long-range residual strain/stress of the first kind. From Bragg's equation follows

$$\Delta\vartheta = \vartheta_{hkl} - \vartheta_0 = - \tan \vartheta_0 \, (d_{hkl} - d_0)/d_0 \qquad (2)$$

or transformed to the scale of photon energy, E, which is more adequate for energy dispersive diffraction:

$$\Delta E = E_{hkl} - E_0 = (d_{hkl} - d_0)/d_0 \qquad (2a)$$

Line profile analysis is performed by Gauss fitting after background correction. More sophisticated quantitative approaches are based on line-profile analysis by Fourier deconvolution or profile matching simulations. The width of a diffraction line reflects the variations of lattice spacing, Δd, respectively residual strain from grain to grain in the diffracting volume, strain gradients across grains or microstructural imperfections in the grains (residual stress of the second and third kind).

Peak broadening due to the finite primary beam and detector apertures, limited spectral resolution and small grain size have to be considered, as well. In the x-ray scanning apparatus the sensitivity and resolution of residual strain measurement are finally limited by the spectral resolution of the solid-state spectrometer system. A standard Si(Li) detector is used with a nominal spectral resolution of 140 eV at 8.4 keV (Mn Kα line). A tradeoff, however, has to be made between intensity and peak width by using rather wide primary beam and detector apertures. At $2\vartheta = 40°$ (corresponding to $E_{hkl} \approx 10$ to 13 keV for low index planes of metals) apertures of 0.35° produce a FWHM between 400 eV and 500 eV which is distributed over about 100 spectral channels. The apertures are adjusted by using appropriate pinhole diaphragms in the primary beam and a sufficient distance of the Si(Li) detector from the specimen. Peak position is not affected by the aperture size in a symmetric goniometer setup ($\vartheta_1 = \vartheta_2$). By a Gauss fit the peak center can so be located to $\Delta E \leq 0.5$ eV. Hence residual strains of the first and second kind are well resolved down to $\Delta a/a \approx 4 \cdot 10^{-4}$. A noticeable improvement is expected from a reduction of the energy interval per spectral channel and a higher energy resolution of the detector system. But a practical limitation still rests on the need of excessively large apertures for gaining peak intensity. Though being very intense, narrow characteristic lines are, unfortunately, inadequate since the primary beam has to supply a sufficiently wide spectrum of primary radiation for ED diffraction. A position sensitive detector with a standard Bragg-Brentano setup and monochromatic radiation is still superior by one order of magnitude or more as far as a high dispersion is concerned for residual strain analysis. This would enable a reliable peak-width analysis and so the mapping of residual strain distributions even of the third kind. The replacement of the ED system, however, is at the expense of simultaneous acquisition of several peaks/maps at the same time, and stringent restrictions would be imposed in addition to satisfy the Rowland focusing condition.

Any specimen reference direction (α, β) can be mapped provided that pole density (i.e. diffracted intensity) is high enough - which of course depends on local texture. It is worth noting that texture as well as residual strain are probed exclusively for those grains which satisfy the Bragg condition for the chosen specimen-fixed reference direction, e.g. the specimen normal direction in case of the symmetric goniometer setup with the specimen not tilted. There is no information acquired on grains at other orientations.

Pole figure measurement has to precede texture mapping on the same specimen area in order to recognize significant texture components. Thinned angular grids, equal area grids or the limitation to relevant sections on the pole sphere is provided to reduce acquisition time. Pole figures are acquired from selected areas of any shape on the specimen by the combination of pole figure measurement with a controlled spatial x-y translation of the specimen. Large tilts, however, may result in inconsistent pole figure data, if texture is not uniform in depth beneath the shallow surface since x-ray diffraction becomes more surface sensitive with increasing incidence angle γ. Information depth decreases linearly with $\cos\gamma = \sin\vartheta \cdot \cos\alpha$. Spatial resolution decreases with angular tilt, as well, since a circular primary x-ray spot is elongated to an ellipse of aspect ratio $1/\cos\gamma$ by oblique projection. The experimental pole figure data can be used for ODF analysis and the calculation of averaged tensorial material properties irrespective of the chosen angular sampling grid and specimen symmetry by using a dedicated ODF program (Schäfer 1998; Klein and Bunge 1999).

2. Example of application

A cross section of a commercial aluminum rivet was carefully polished flat by gentle mechanical grinding and finishing. A final electrochemical polishing was applied in order to remove any mechanical damage introduced during preparation. Before mapping several pole figures have been acquired in steps along lines across the head and the bolt of the rivet to recognize relevant texture components. A strong fiber texture has been found in the bolt region (Figure 2). The 220 diffraction peak P ($\vartheta_1 = \vartheta_2 = 20.1°$, $E_{220} = 12.62$ keV; $\alpha = 35°$ and $\beta = 83°$) has been used for evaluating at the same time the spatial distributions of pole density (texture map) and strain (residual strain map).

Dwell time extended over 240 sec/pixel to yield a sufficient count statistics in view of the low intensity. 2,232 image points at a step width of 120 µm have been acquired.

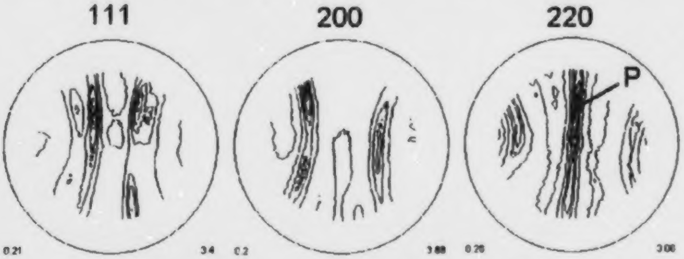

Figure 2 Pole figures acquired across the rivet bolt. The polar specimen direction P ($\alpha = 35°$, $\beta = 83°$) has been used for texture and residual strain mapping (cf. Figure 3).

A clear inhomogeneity is revealed in the texture (Figure 3a) as well as in the strain maps (Figure 3b). Two almost parallel strips of high pole density run along the axis of the bolt with a slight shift to the right hand side. They are supposed to form a tube of about 1/3 of the bolt diameter in the 3-dimensional rivet. The head of the rivet shows a much lower density of this pole. It is worth noting that it forms a butterfly-shaped minimum which might result from punching the head during production.

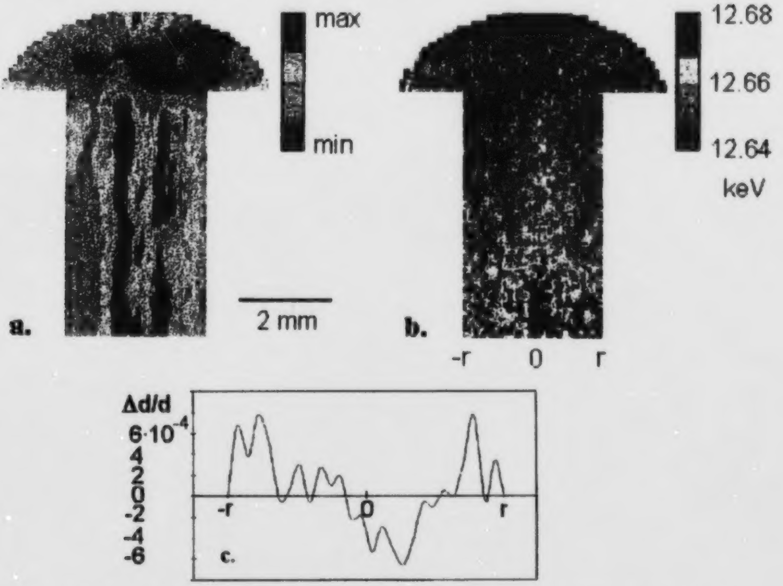

Figure 3 Cross section of an aluminum rivet. Distribution maps (a) of the intensity (pole density, texture) and (b) of the shift (residual strain) of the 220 peak at pole P ($\alpha = 35°$, $\beta = 83°$). (c) The lattice strain $\Delta d/d$ across the bolt.

Dwell time extended over 240 sec/pixel to yield a sufficient count statistics in view of the low intensity. 2,232 image points at a step width of 120 μm have been acquired.

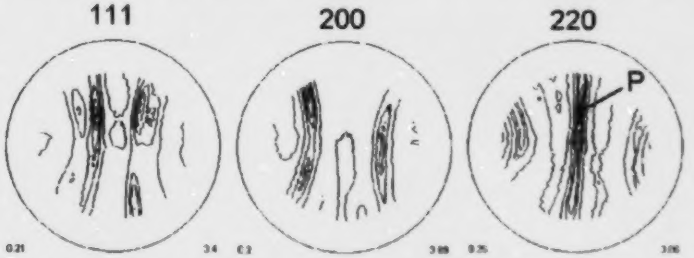

Figure 2 Pole figures acquired across the rivet bolt. The polar specimen direction P ($\alpha = 35°$, $\beta = 83°$) has been used for texture and residual strain mapping (cf. Figure 3).

A clear inhomogeneity is revealed in the texture (Figure 3a) as well as in the strain maps (Figure 3b). Two almost parallel strips of high pole density run along the axis of the bolt with a slight shift to the right hand side. They are supposed to form a tube of about 1/3 of the bolt diameter in the 3-dimensional rivet. The head of the rivet shows a much lower density of this pole. It is worth noting that it forms a butterfly-shaped minimum which might result from punching the head during production.

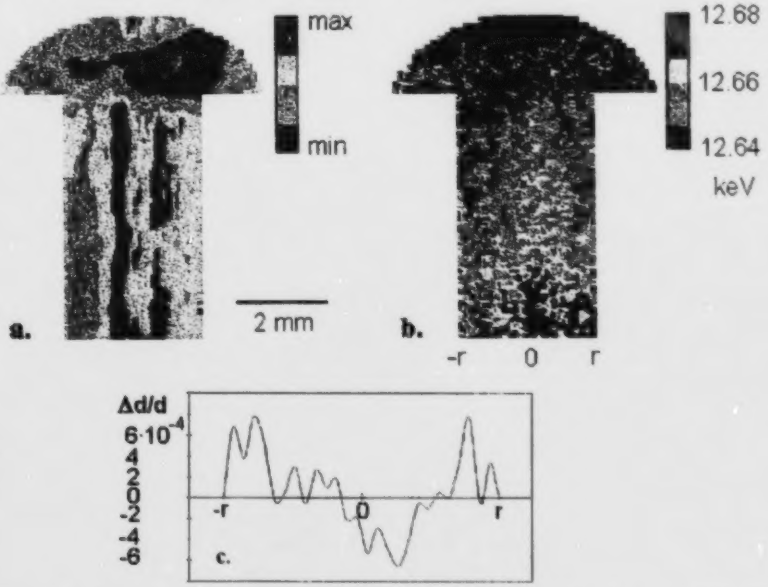

Figure 3 Cross section of an aluminum rivet. Distribution maps (a) of the intensity (pole density, texture) and (b) of the shift (residual strain) of the 220 peak at pole P ($\alpha = 35°$, $\beta = 83°$). (c) The lattice strain $\Delta d/d$ across the bolt.

Along the bolt there is a gradient in compressive residual strain to the head. A dish-shaped maximum of compressive strain (dark) is found in the head which is related to the butterfly-shaped minimum in the 220 texture map. There is an increased compressive residual strain in the interior of the "texture tube" (dark) and a tensile strain (bright) to the bolt surface. Statistics has been improved by averaging the peak shifts along a section of the shaft. So the radial distribution of residual strain across the bolt is clearly seen in the graph line (Figure 3c).

3. Conclusion

An x-ray scanning apparatus (XSA) with an energy dispersive detector system enables a powerful mapping technique to reveal nonuniform distributions of crystal texture, element composition and local lattice strain related to the same specimen area:

- XSA is a gentle technique suited for non-conductive, deformed, fine-grained and rough surfaces.
- XSA is particularly well suited for studying nonuniform texture and composition across large areas up to several cm^2 at a spatial resolution of about 50 µm.
- XSA enables mapping of lattice strain at a spatial resolution of 0.1 mm.
- XSA enables the measurement of pole figures from selected areas down to 0.1 mm.
- The ability to perform both pole figure measurement and texture mapping of selected areas in the same XSA instrument is extremely useful.

Acknowledgment

Financial support by the German Research Foundation (DFG Forschergruppe "Textur und Anisotropie kristalliner Stoffe") is gratefully acknowledged.

4. References

Fischer, A.H. and Schwarzer, R.A. (1998) X-ray pole figure measurement and texture mapping of selected areas using an x-ray scanning apparatus. *Materials Science Forum*, Vol. 273-275, pp. 255-262

Fischer, A.H. and Schwarzer, R.A. (1998) Mapping of local residual strain with an x-ray scanning apparatus. *Materials Science Forum*, Vol. 273-275, pp. 673-677

Klein, H. and Bunge, H.J. (1999) Location resolved texture analysis. *Z. Metallkunde*, Vol. 90, pp. 103-110

Schäfer, B. (1998) ODF computer program for high-resolution texture analysis of low-symmetry materials. *Materials Science Forum*, Vol. 273-275, pp. 113-118

Schwarzer, R.A. (1997) Automated crystal lattice orientation mapping using a computer-controlled SEM. *Micron*, Vol. 28, pp. 249-265

X-RAY AND NEUTRON DIFFRACTION MEASUREMENT OF TEXTURES OF TWO-PHASE MATERIALS

R.E. BOLMARO
Instituto de Física Rosario - Fac. de Ciencias Exactas, Ingeniería y Agrimensura.
Consejo Nacional de Investigaciones Científicas y Técnicas-UNR, Rosario, Argentina.

H.-G. BROKMEIER
Institut für Werkstoffkunde und -technik der Technische Universität Clausthal. GKSS Forschungszentrum Geesthacht, Germany.

Abstract

X-ray and neutron diffraction are the most widely used methods for texture measurements (U.F. Kocks et al. 1998a). The first one is applied mainly for its simplicity and availability and the second one mainly because of its accuracy due to high penetration of neutrons. Comparison between both methods has deserved broad attention in the past (Brokmeier 1989). The current presentation deals with comparissons between X-ray and neutron measurements performed in two-phase co-deformed materials. Ag-Ni powder materials deformed by free compression and rolling and room temperature extruded Al-Mg samples were measured by using both methods. Both composite materials were prepared by powder metallurgy, the starting materials being considered texture free. The textures are compared by using both the direct and inverse pole figures and Orientation Distribution Functions (ODF) calculated by harmonics and WIMV analysis. The influence of volume fraction over texture measurement accuracy is analyzed and the ability of both techniques to judge the severity of different components is also assessed.

Keywords: X-rays, neutrons, Ag-Ni, Al-Mg, textures.

1 Introduction

The two most important methods for measuring bulk textures are definitely X-ray and neutron diffraction. The main advantages and disadvantages of both methods have been extensively discussed in the past. Availability of the technique is notwithstanding the main reason for using one or the other (Kocks et al 1998, Brokmeier 1989a).

It is well known that among the advantages we can summarize the following:

- X-rays: Availability, cheap and reliable sources, easy sample preparation.

- Neutrons: High penetration (allowing measuring coarse grain materials and insensibility to surface sample preparation and shape), constant scattering length (allowing many pole figures to be measured), surface insensitivity.

And among the disadvantages we can list:

- X-rays: low penetration, dependence of the scattering length on the angle 2θ which reduces the number of pole figures, incomplete pole figures and necessity for corrections.
- Neutrons: expensive and difficult to handle neutron sources, large counting times.

Advantages and disadvantages can be used in such way that they can be reversed in character. Low penetration of X-rays can be used to have an idea of surface texture or variation of textures with the distance to certain surface.

The advantages and disadvantages mentioned in the former paragraphs are the kind of differences that can be considered stemming from the physics of both phenomena. Some other rather technical differences are likely more important and difficult to control:

- As a consequence of their different penetration depths they gauge different volume and the inhomogenity of textures can be shown in different measured textures.
- Also the grain statistics is very different and different errors can come out from smoothing techniques.
- Each instrument shows different characteristics giving rise to different results. Pole figure window is qualitative different for neutrons and X-rays. While in neutrons a parallel beam arrangement is usual, in X-rays a focussing beam arrangement is more common. 2θ resolution can be very different in both cases.
- Data corrections are much different in both cases. Defocusing correction is absent in neutrons but background subtraction is necessary in both.
- Each measurement shows a number of experimental errors: sample preparation, mounting, optimization of scanning routine to equipment characteristics, etc..
- Data evaluation is performed by different softwares with its own qualifications and sometimes the hidden assumptions are biased by the technique itself.

The advantages of using neutron diffraction for texture measurement in multi-phase materials have been already emphasized and addressed in a few papers (Brokmeier 1989b). High penetration overcomes the effect known as anisotropic absorption in multi-phase materials (Bunge 1985). Meanwhile constant scattering length allows the measurement of higher [hkl] when the lower indexes are overlapped. Notwithstanding neutron diffraction technique is not always available and X-rays are also utilized. We will present in the current paper, as a byproduct of a wider research in the field of two-phase materials textures, some comparisons between X-ray and neutron diffraction measurements in two-phase composite materials. The same analysis software will be used, whenever possible, to eliminate at least that source of disagreements.

2 Experiments

The experiments were performed mainly in two sets of samples. Some of the neutron and X-ray diffraction results have been extensively shown elsewhere as well as a full description of the preparation procedure (Bolmaro et al. 1993, 1998).

Ag-Ni powder samples were prepared by hot isostatic pressing in the volume fractions 25%Ag-75%Ni, 50%Ag-50%Ni and 75%Ag-25%Ni. Densities were quite close to theoretical densities. The samples were tested in free compression and rolling in steps of different magnitude until we reached a total Von Mises equivalent strain of 1.3 for free compression and 2.6 for rolling. Teflon tape and Molykote lubricant was used to minimize friction effects in free compression. For Al-Mg composites five different volume fractions of both phases (100% Al, 75%Al-25%Mg, 50%Al-50%Mg, 25%Al-75%Mg and 100%Mg) were prepared. They were pre-compacted from Al powder of the size < 41 μm and Mg powder grade 5. They were later extruded until equivalent Von Mises deformations of 2.8.

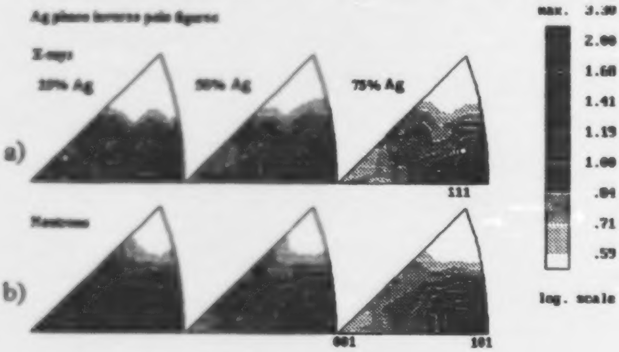

Figs. 1 a) Ag Inverse pole figures Results for Ag-Ni free compressed samples taken by X-rays and b) by neutrons for the three different volume fractions of Ag.

In both cases regular polymeric mounting was performed for X-ray reflection measurements. The samples were mounted on a Scintag texture goniometer, using Cu Kα radiation, in the Center for Materials Science, Los Alamos National Laboratory. The measuring surfaces were metallographic-quality prepared, including grinding up to 4000 grit and light diamond polishing (6, 3 and 1 μm). The samples were etched in a 25 ml NH_4OH - 5 ml H_2O_2(30%) solution to remove the upper mechanically distorted layer. Due to peak overlapping just Ag (111) and (220) and Ni (200) and (311) pole figures were measured. For Al-Mg composites Al (111), (200) and (220) and Mg (100), (002), (101) and (110) pole figures were non-overlapped.

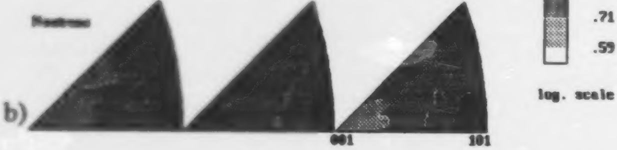

Figs. 2 a) and b) Idem Fig. 1 for Ni.

Neutron measurements were performed in approximately 0.5 cm^3 Ag-Ni samples and 8 cm^3 Al-Mg samples cut for each composition and strain. They were measured in the neutron diffraction goniometer TEX-2, Geesthacht, Germany. Due to the cylindrical symmetry of Ag-Ni free compressed samples and Al-Mg extruded samples, a rotating sample holder was used to optimize counting time. The α-scans, taken every 5^0, were later symmetrized to get whole pole figures in a 5^{0}x5^0 grid. Whole α-β scanning routines were used for Ag-Ni rolled samples.

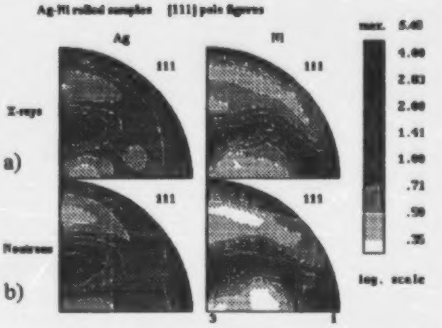

Figs. 3 a) and b) (111) pole figures taken from the normal direction of a rolled 50%Ag-50%Ni sample.

3 Results and conclusions

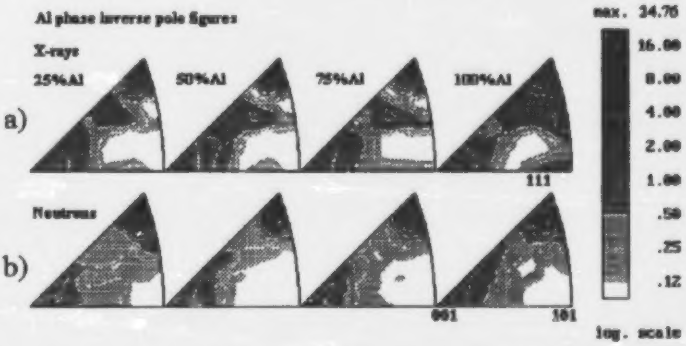

Figs. 4: a) Al inverse pole figures for Al-Mg extruded samples for four different volume fractions of Al, taken by X-rays and b) by neutrons.

Results for Ag-Ni free compressed samples are shown in Figs. 1 and 2. Fig. 1 shows the inverse pole figures taken by X-rays and neutrons for the three different volume fractions of Ag and Fig. 2 the same inverse pole figures for Ni. Fig. 3 shows the (111) pole figures taken from the normal direction of a rolled 50%Ag-50%Ni sample.

Al-Mg extruded samples textures are shown in Figs. 4 and 5. Figs. 4 a) and b) are the inverse pole figures for the four different volume fractions of Al, taken by X-rays and neutrons respectively. The X-rays inverse pole figures were calculated by using both harmonics and WIMV techniques (Kallend 1991). Showed in the figure are the ones calculated by harmonics. Figs 5 a) and b) show the results for the Mg phase. Fig. 6 shows the maxima for each phase and volume fraction by X-rays and neutrons. The X-rays values for Al are shown for the experimental pole figure {111}, harmonics and WIMV calculations.

The first evident and well known result is the smoother appearance of neutron textures due to the averaging capability of neutrons and better statistics The second difference, also well known, is the lower severity of neutron textures. The decrement

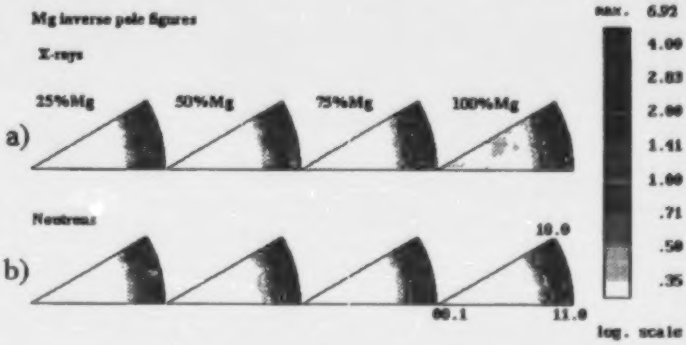

Figs. 5 a) Mg inverse pole figures for Al-Mg extruded samples for four different volume fractions of Mg, taken by X-rays and b) by neutrons.

of the measured maxima by neutron can although stem from different effects. First the lower severity can be consequence of a better statistic because smoother pole figures will show less maxima due to large diffracting crystals. In an inhomogeneously deformed sample the averaging capability of neutrons will give lower intensities mainly due to the process of averaging different local textures. That can help to easily rationalize the high values obtained by X-rays for Al in the extruded Al-Mg samples. It is known that the center of extruded samples develop a stronger texture mainly due to the absence of shearing strains disturbing the texture development. X-ray pole figures are taken mainly from the center of the round extruded samples in an area not easily controllable. {111} poles are aligned with the longitudinal axes and measured mainly in the center of the pole figure with the X-ray spot impinging a small central area of the sample. {200} and {220} poles are mostly out of the center of the pole figure and measured with an elliptical X-ray spot sweeping a larger area of the sample, averaging different texture strengths. In that sense X-rays are used to measure a sort of local texture but without control of the measured area because different pole figures are measured averaging different textures. Even after defocusing background correction the set of three pole figures is not completely compatible and different softwares can give very different severity for recalculated pole figures and inverse pole figures. It is found that WIMV based softwares (popLA and BEARTEX) have a tendency to overestimate the severity of the Al texture providing values higher than the experimental values when trying to compatibilize the pole figure set. Surprisingly, neutron and X-ray texture intensities for Mg are very much alike. High intensities in the center of the Al pole figures are probably difficult to recalculate due to streng sensitivity to defocusing and background correction but Mg textures are not as strong as Al textures and inhomogeneities may be much easy to handle by some kind of smoothing provided by the software.

Inhomogeneity argument can not easily be transferred to the Ag-Ni free compressed samples. They suffered a pretty homogeneous deformation as it could be judged by external shape of the samples. Any inhomogenity should be present at much lower scale. At this point pole figure window differences between X-rays and neutrons should be considered to explain such large decrements of texture severity. Larger neutron pole figure window would average textures to lower values. On the other hand Fig. 3 a) and b) show that texture severities are rather similar, whether coming from X-

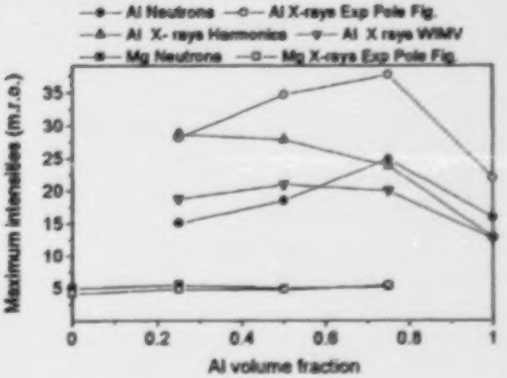

Fig. 6: Texture maxima for each phase and volume fraction measured by X-rays and neutrons.

rays or neutrons, in the case of rolled Ag-Ni. If a larger pole figure window for neutrons (and its concomitant averaging process) is responsible for the diminishing severity of measured textures, that decrement can be partially counterbalanced by the high inhomogeneity of rolling deformation. The central part of the sample has suffered a more homogeneous and "constant strain path" deformation process, developing stronger textures that can be caught by highly penetrating neutrons but not by X-rays measurements in the surface of the plate.

In any case, despite the complementary character of both techniques, the superior capability of neutrons upon X-rays is demonstrated.

4 References

Bolmaro, R.E. Fourty, A. and Brokmeier, H.-G. (1998) Measurement and Simulation of Extrusion Textures in Al-Mg Composites.. Mat. Sci. Forum.. Trans. Tech. Publ.. (Eds. R. Delhez and E.J. Mittemeijer). Accepted for publication.

Bolmaro, R.E., Browning, R.V., Guerra, F. M. and Rollett, A. D. (1993) Texture Development in Ag-Ni Powder Composites. Mat. Sci. and Eng. Vol A175, pp. 113-124.

Brokmeier, H.-G (1989b) Neutron Diffraction Texture Analysis of Multi-Phase Systems. Textures and Microstructures, Vol. 10, pp. 325-346.

Brokmeier, H.-G. (1989a) Advances and Applications of Quantitative Texture Analysis (eds. H.J. Bunge and C. Esling) DGM, Informationgesellschafts, Verlag.

Bunge, H. J. (1985) Texture in Multiphase Alloys. Z. Metall., Vol. 76. P. 92.

Kallend, J.S., Kocks, U.F., Rollet, A.D. and Wenk, H.-R. (1991) Operational Texture Analysis. Mat. Sci. Eng., Vol. A132, pp. 1-11.

Kocks, U.F., Tomé, C.N. and Wenk, H.-R. (1998) Texture and Anisotropy. Cambridge University Press. pp 126-177.

Acknowledgments: This project is partially funded by the German-Argentine Intergovernmental Agreement n° ARG 6 L1A 1A/2 and CONICET-Argentina.

COMPARISON OF TEXTURE DATA MEASURED BY EBSD AND CONVENTIONAL X-RAY DIFFRACTION.

K. MEHNERT[1)], H.S. UBHI[2)], and A.P. DAY[1)]

1) HKL Technology, Hobro, Denmark
2) DERA, Farnborough, UK

Abstract

This paper compares texture measurements based on EBSD and X-ray data from a Zircaloy4 specimen (hexagonal) and a Ni-base superalloy (cubic). The data are displayed as pole figures and orientation distribution functions (ODF). The present studies show that the EBSD technique is not only competitive to the commonly used X-ray method in terms of speed and accuracy, but implies a series of features which make it even more attractive (e.g. complete orientation data, no ghosts, relation to the microstructure, advanced data filtering).

Keywords: EBSP, EBSD, X-ray diffraction, pole figures, ODF, Texture

1 Introduction

1.1 Electron Backscatter Diffraction (EBSD)

Over the last couple of years, electron backscatter diffraction (EBSD) in the SEM has become well established as a powerful tool for microstructural characterization and texture analysis. This technique uses a stationary electron beam (SEM in 'spot mode') that interacts with a highly tilted specimen (typically 70°) to produce an electron backscatter diffraction pattern (EBSP). The information in an EBSP is the result of Bragg diffraction of the backscattered electrons from the atomic planes just underneath the specimen surface, typically within a layer of 50nm. It consists of many intersecting, linear features called Kikuchi bands, brighter than the background, bounded by two edges. Each edge is geometrically attributable to electrons that have been diffracted from a particular plane of atoms within the specimen (Day and Quested, 1999, Wilkinson and Hirsch, 1997)

The challenge for a good EBSD system is to acquire such an EBSP using a suitable detector, to accurately detect the Kikuchi bands, to assign the crystallographic indices to those bands, and finally to determine the crystallographic orientation of the interacting volume in the investigated material. All this should be carried out as fast and as accurately as possible. Furthermore, although often forgotten, such a system should be able to work with all crystal symmetries from triclinic up to cubic.

Increases in acquisition speed due to refined algorithms, improvements in camera technology and more powerful computers now make it possible to obtain over 10.000 local orientation measurements in less than an hour. EBSP scans of large areas of the sample surface (orientation maps) allow the direct comparison of crystallographic and microstructural data.

Although the area from which an EBSD is acquired is typically in the range of 200-500nm, an effective spatial resolution of 50-150nm or better can be obtained (Humphreys, 1999).

1.2 X-Ray Diffraction

X-ray diffraction has, for many years, been the standard technique for texture measurement. It is usually performed on a texture goniometer. In most cases, monochromatic radiation is used, and the pole figures are measured directly by varying the specimen orientation.

X-rays have, compared to EBSD, a considerable penetration depth (about 10-100 µm depending on the average atomic number of the elements and the sample tilt). For anything other than very coarse-grained materials, it is difficult to relate microstructural features to local texture. This is partly due to the relatively low lateral resolution (~0.5mm) of this technique (Bunge *et al.*, 1994). In the literature, texture mapping goniometers are discussed, which may get down to a resolution of 0.1x0.1mm (Schwarzer, 1993, Bunge and Esling, 1981). This is still not fine enough to explore the vast majority of polycrystalline materials.

Due to the setup of the experiment, the measured pole figures are incomplete which causes problems when calculating the orientation distribution function. These reduced pole-figures introduce so-called 'ghost maxima' in the orientation distribution functions (ODFs), which have to be corrected for (Matthies and Wenk, 1985).

2 Experimental

The Zircaloy4 specimen has been taken from a sheet, which was rolled in the β-phase field, then quenched into the α-phase field, where it was subsequently hot rolled and annealed. In order to minimize surface deformation introduced by mechanical polishing, electro-polishing was carried out. The EBSD data was taken on a raster grid 500x250 points with a step size of 2 µm using stage scanning.

The Ni-base superalloy specimen is part of a section through the chill block for a single crystal turbine blade. At the coldest end of the chill block, there is a thin layer of small grains with near random orientation. These grains grow larger, elongate and acquire a strong [100] fiber texture as the chill block is traversed. Following this, there is a spiral selector that allows only one of the strongly textured grains through and it is this that controls the final orientation in the single crystal blade. The part of the specimen where the fiber texture is starting to appear was examined. For this specimen, the EBSD map covered 400x100 data points, again with a step size of 2µm using stage scanning.

The X-ray diffraction experiments were carried out on a *Siemens D500* texture goniometer including the software modules *TEX11/ODF11*. The fully automatic *HKL*

EBSD system (software package *CHANNEL4*), attached to a *CamScan S4* field emission SEM, has been used to perform the EBSD measurements and to post-process the orientation maps.

3 Results

3.1 Zircaloy4

The pole figures determined by EBSD and X-ray diffraction are compared in figure 1. As can be seen, the {0002} pole figures are nearly identical, with respect to position and strength of the maxima. In the case of the {11-20} pole figure, the position of the maxima is the same for both methods, i.e. aligned with the rolling direction. The maximum density, however, differs slightly in this case, which is not surprising, since they lie within the regions where the X-ray pole figures have their biggest uncertainty.

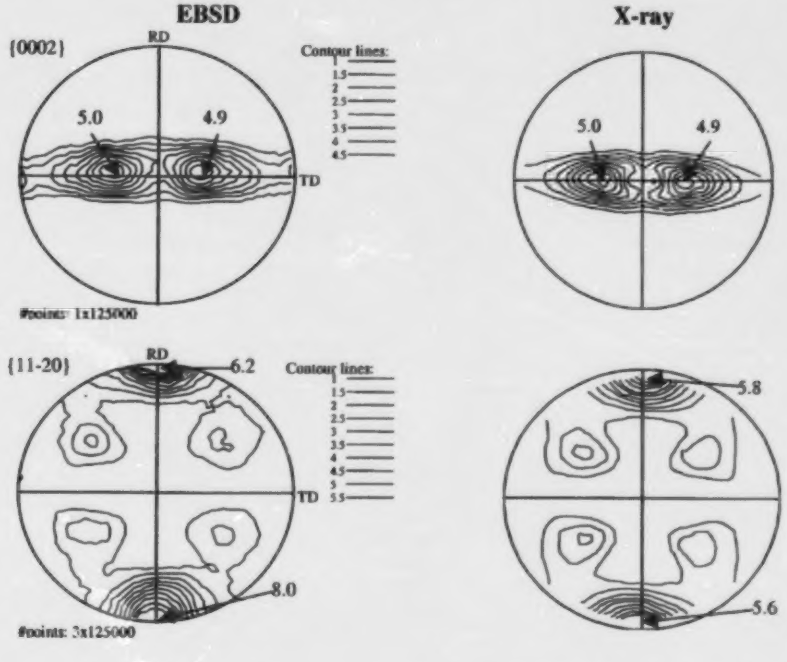

Fig. 1: Comparison pole figures of the Zircaloy4 specimen obtained by X-ray diffraction and EBSD measurements (stereographic projection).

Additionally, the f-factors (Kearns factors) have been determined for both methods, these are often used to quantify the strength of a texture in hexagonal materials via three numbers (Kearns, 1965). They are listed in table 1, and emphasize the excellent agreement between the EBSD and X-ray texture measurements.

Table 1: Comparison of the f-Factors of the Zircaloy4 specimen, obtained by X-ray diffraction and by EBSD measurements.

f-Factors	{0002}		{11-20}	
	EBSD	X-ray	EBSD	X-ray
f_{RD}	0.059	0.077	0.470	0.484
f_{TD}	0.371	0.347	0.315	0.303
f_{ND}	0.570	0.576	0.215	0.213

Table 2: Influence of the number of grains (randomly selected) on the f-Factors of the {0002} pole figure obtained by EBSD measurement.

f-Factors *(grains)*	100% *(11092)*	50% *(5546)*	25% *(2773)*	5% *(555)*	2% *(222)*	1% *(111)*	0.5% *(56)*
f_{RD}	0.059	0.060	0.057	0.061	0.055	0.046	0.084
f_{TD}	0.371	0.367	0.374	0.380	0.358	0.438	0.263
f_{ND}	0.570	0.573	0.569	0.559	0.567	0.515	0.652

In order to test the reliability of the f-factors obtained by the EBSD measurements, the data set was stepwise reduced, by randomly selecting grains from the entity of grains. Therefore, the grains had to be identified, which was done by means of the grain reconstruction facility built into *CHANNEL4*. The critical misorientation angle, which defines a grain boundary, was assumed to be 10°. Table 2 contains the f-factors for the {0002} pole figure for different subset sizes. It can clearly be seen that a couple of hundred grains are enough to get a very good estimate for the f-factor.

3.2 Ni-base Superalloy

The Ni-base superalloy orientation data was also converted into an ODF via the series expansion method. Both the pole figures and ODFs from EBSD and X-ray measurements show consistency (cf. fig. 2 and 4). The [100] fiber is very clear.

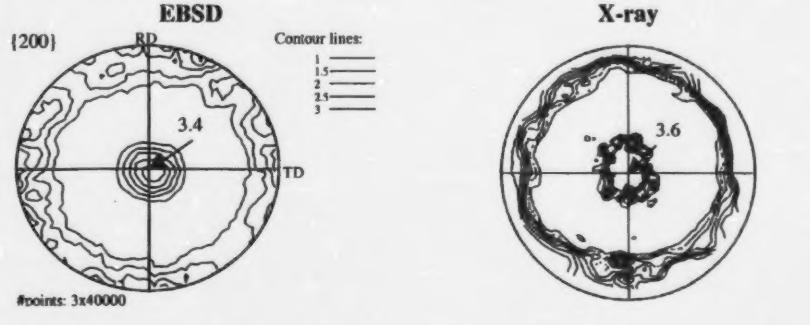

Fig. 2: Comparison of the (200) pole figures of the Ni-base superalloy specimen obtained by EBSD measurements and X-ray diffraction (stereographic projection).

The orientation map for the EBSD measurements is given in figure 3. The deviation of the orientation of the grains away from the [100] fiber texture is illustrated by a continuous gray shading. Additionally, all grain boundaries with a misorientation angle larger than 10° are drawn on top of the orientation image. Based on this misorientation angle, an average grain diameter of 9.4µm (1579 grains) has been determined using *CHANNEL4*'s grain reconstruction facility.

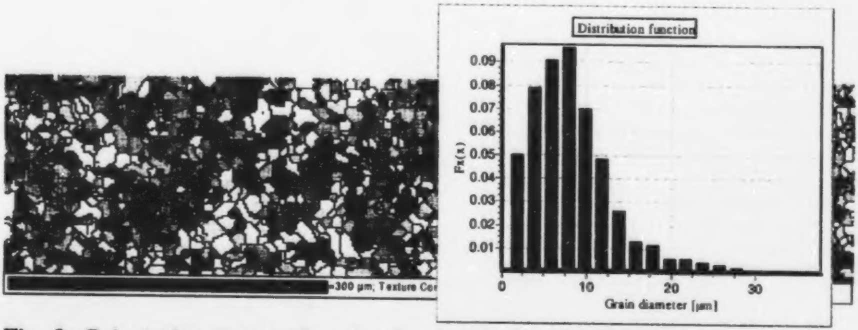

Fig. 3: Orientation map and grain size distribution for the Ni-base superalloy specimen (40.000 data points). The darker the gray-value the closer the orientation to the [100] fiber (white: deviation of >30° from ideal).

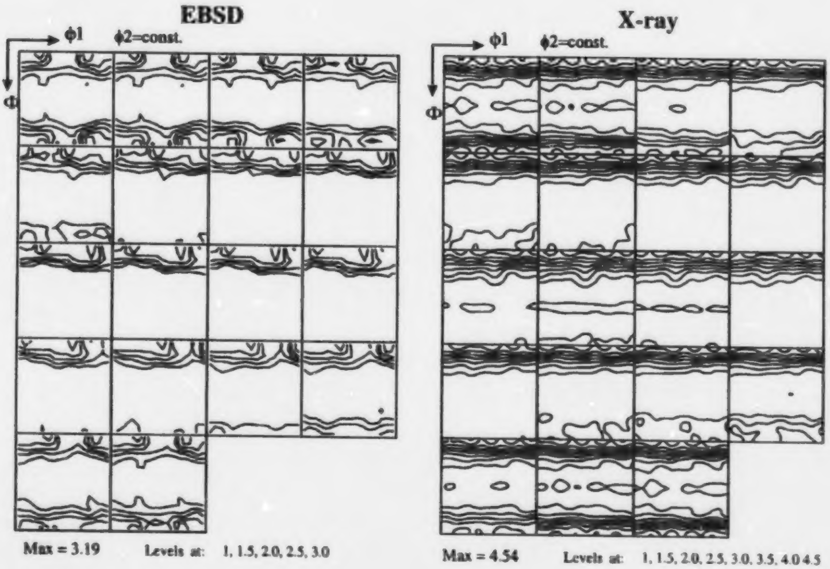

Fig. 4: Comparison of the ODFs of the Ni-base superalloy specimen obtained by EBSD measurements and X-ray diffraction. The ODFs were calculated using the series expansion method with a truncation level of L_{max}=22.

4 Summary

The comparisons in this paper demonstrate that EBSD texture measurements are fully equivalent to those from the well-established X-ray diffraction method.

EBSD can offer extremely rapid data acquisition (500 measurements in about 2-5 minutes) and thus excellent statistics. The ability to directly compare microstructural and local orientation data is a distinct advantage over X-ray measurements.

Also grain reconstruction offers the tantalizing combination of grain size and texture. This would allow complex microstructures and textures to be examined.

5 References

Bunge, H.J. and Esling, C. (1981) Determination of the Odd Part of the Texture Function by Anomalous Scattering. *J. Appl. Cryst.*, Vol. 14, pp. 253-255

Bunge, H.J., Grossterlinden, R., Haase, A., Ortega, R., Szpunar, J.A. and Van Houtte, P. (1994) Advanced Experimental Techniques in X-Ray Texture Analysis. ICOTOM 10, *Mat. Sci. Forum*, Vols. 157-162, pp. 71-96.

Day, A.P. and Quested, T.E. (1999) A Comparison of Grain Imaging and Measurement Using HOCI, COCI, EBSP and Optical Methods. To be published in *Journal of Microscopy*, Vol. 195.

Humphreys, F.J. (1999) Quantitative Metallography by Electron Backscattered Diffraction. To be published in *Journal of Microscopy*, Vol. 195

Kearns, (1965) Thermal Expansion and Preferred Orientation in Zircaloy. WAPD-TM-472, Westinghouse Elec Corp. Pittsburgh, Pa USA.

Matthies, S. and Wenk, H.-R. (1985) ODF Reproduction with Conditional Ghost Correction, *in Preferred Orientation in Deformed Metals and Rocks: An Introduction to Modern Texture Analysis*, (ed. H.-R.Wenk), Academic Press, Inc., Orlando, pp. 139-147

Schwarzer, R.A. (1993) Texture Distributions Imaged by Energy Dispensive X-Ray Diffraction. *Steel Research*, Vol. 64

Wilkinson, A.J. and Hirsch, P.B. (1997) Electron Diffraction Based Techniques in Scanning Electron Microscopy of Bulk Materials. *Micron*, Vol. 28, pp. 279-308.

EXPERIMENTAL SETTING FOR INDEXING TEM KIKUCHI DIAGRAMS

J.J. FUNDENBERGER, E. BOUZY, J.S. LECOMTE
LETAM, CNRS URA 2090, University of Metz, F-57045 Metz, France
jjfund@letam.sciences.univ-metz.fr

Abstract

On-line measurements of single grain orientations by indexing transmission Kikuchi diffraction patterns in the TEM is a very useful technique for fine scale investigations like grain or twin boundary, deformation mechanism or phase transformation. Therefore our attention goes to the development of an interactive indexing computer program the use of which is justified in the case of TEM. The procedure for indexing Kikuchi diagrams is divided into two steps : (i) a first solution is found using at least 3 not concurrent Kikuchi bands chosen by the operator; (ii) if the operator agrees with the proposed solution, other bands can be added and the computer program gives the solution which minimises the angular distance between measured and computed patterns in terms of least-squares. Our aim here is to discuss the relative precision of the crystal orientation versus some experimental settings. The influence of the band's count, the operator's dexterity and some instrumental settings like diffraction focus and calibration will be discussed. An application to twin-matrix interface characterisation in the case of a well-known fcc Σ3 twin boundary is done in order to illustrate the influence of the various parameters.

Keywords : Kikuchi diagrams, TEM, local orientation

1. Introduction

Local crystal orientation studies have a great interest when dealing with recrystallisation, ultra-fine grains, interface characterisation or very fine scale studies. In these cases the local orientation measurements with EBSP are not possible because of the spatial resolution which does not exceed ≈0.5μm in a scanning electron microscope.

The orientation determination using Kikuchi diagrams is well known and has been described by several authors (Ryder and Pitsch 1968, Schwarzer 1989). Recently, fully automated analyses of Kikuchi patterns (Zaefferer and Schwarzer 1994, Krieger Lassen 1995), and also less automated methods (Qing Liu 1995, Van Bakel 1995) have been proposed.

In the present paper we briefly present the method for indexing the Kikuchi diagrams. Then we will discuss the hardware and software settings which seem to be important to us.

2. The method principle

2.1 Hardware

The Kikuchi diagrams are obtained with a Philips CM200 transmission electron microscope operating at 200kV.

Each Kikuchi line can be defined using the deflection coils to shift the diagram and computer control readout of the coils currents allows the diffraction diagrams acquisition without any extra devices. Nevertheless, this method is time consuming and is not adapted in the case of a sample that is sensitive to irradiation damage.

In this work the acquisitions of the Kikuchi diagrams are made thanks to a GATAN 791 slow scan CCD camera. The camera is mounted on the 35mm port above the viewing chamber. In this position, the solid angle which is seen by the CCD detector is as large as possible. The camera has a 14-bit digitalisation depth, which leads to a high dynamic range.

The recorded Kikuchi diagrams have to be corrected for background. The procedure proposed by N.C. Krieger Lassen (1995) has been successfully applied. This background correction consists in calculating the logarithm of each pixel value and then applying a heavy lowpass filter on it. This removes the bright transmitted spot and enhances the contrast of the Kikuchi lines. Even when inserting the beam stop, the central area of the image is much brighter than the border.

We also get quite good results with a simple contraction-expansion procedure in order to correct the image for varying background. This procedure removes the slowly varying background from an image by successive reduction and bilinear interpolation scaling.

Once the Kikuchi diagram is recorded and corrected, the user has to define the pattern centre (transmitted beam) location and select at least 3 bands to start the indexing procedure.

2.2 Software

We give here just a brief recall of the principle and implementation of the method we use.

Once at least 3 non-concurrent bands have been selected and defined by giving the coordinates of 4 points for each band, they have to be indexed, i.e. finding a crystallographic plane (hkl) corresponding to a given band. The first step is to calculate the median and the width of each experimental band. The interplanar spacing value for each band can be derived from its width and location with respect to the pattern centre and the camera length used in the TEM experiment, taking into account for the gnomonic projection. A file containing a list of Miller indexes is read and only those planes which have a structure factor greater than a user defined value (typically 2%) are selected. The calculation of the structure factor needs the knowledge of crystallographic data from the studied material. From the list, we select the crystallographic planes which fit (with a certain tolerance) the interplanar spacing corresponding to the band.

For each band we have now a selection of crystallographic planes based on an interplanar spacing criterion. From the set of selected planes we get out the combinations of (hkl) planes whose interplanar angles fit, with a user-defined tolerance, to the angles between the bands. The calculation of the angles between the experimental bands, has to include the corrections due to the gnomonic projection. All the combinations of (hkl) planes fulfilling the interplanar angle criteria are, at this stage, possible solutions.

For each solution, the first 3 non-concurrent bands are used to calculate the orientation. Removing from the list the crystallographic equivalent solutions according to the rotation subgroup of the crystal space group then reduce the list of solutions. Thereafter only a few solutions are displayed and the user has to select the solution which best fits to the experimental bands. The user can then add bands in order to improve the accuracy of the orientation. In case more than 3 bands are selected to calculate the orientation, a singular value decomposition is used to find the least-squares solution to the overdetermined set of linear equations (Press et al. 1992, Golub and Van Loan, 1989)

3. Experimental.

The above-described method has been applied to partly recrystallized copper. The metallographic observations reveal many twins. Our aim here is to apply the Kikuchi diagrams indexing method to a twin boundary. The figure 1 presents the micrograph of a twin boundary and the Kikuchi diagrams corresponding to the matrix (region M1 and M2) and to the twin (region T). The Kikuchi diagrams were recorded for a camera length of 620mm. As expected, the orientation of the matrix M1 and M2 is the same (Fig. 1a, 1d). The table 1 gives the orientations (expressed in Euler angles) of the matrix and the twin. The misorientation between the matrix and twin can be described by a rotation of 59.73° through an [-56.9 -59.3 56.7] axis. This misorientation is very close to 60° [1 1 1] corresponding to a Σ3 CSL twin boundary.

3.1 Influence of TEM settings on Kikuchi diagrams

We try here to study the influence of some MET settings on the Kikuchi diagrams. The list of parameters is obviously not exhaustive.

For a given crystal orientation, the Kikuchi diagram is independent of the beam direction. Nevertheless, the screen normal going through the pattern centre is taken as a reference and it is parallel to the beam direction if the MET is well aligned. In other words if the beam direction is taken as pattern centre (this is almost always the case), the MET must be well aligned, otherwise the orientation found is not correct.

By increasing the beam convergency and reducing the spot size, Kikuchi diagrams can be obtained even if the sample thickness is small. So even in regions in which the sample is thin, it is possible to obtain diagrams if the density of defects in the crystal is not too high. For a given sample thickness, the spot size gives the spatial resolution. We have to notice here that when the sample is rather thin, often it remains no longer flat and this affects the accuracy of the absolute orientation.

For large camera lengths, the Kikuchi diagrams may contain high index planes, that means that the width of the bands is large (determinable with high accuracy), but the angle between the band median and the pattern centre is small. This leads to an equation system to be inverted in order to get the orientation that can be ill-conditioned. For small camera lengths, the diffraction diagrams may contain low index planes, which produce small bandwidths (determinable with low accuracy). The solid angle subtended by the diagram is large (up to 10°), but some distortions can occur at the border of the diagram, and the pattern centre is located with less precision. An optimum has to be found depending on the application.

Large variations of the diffraction focus show that the Kikuchi diagrams rotate and the lines no longer remain straight lines but become more and more curved. The curvature of the lines affects the precision of the location of the bands. The rotation of the diagram alters the absolute orientation accuracy. The variation of the diffraction focus also directly induces variations in the value of the camera length. As far as the camera length is used for indexing the bands, a wrong setting of the diffraction focus can affect the indexing procedure. Setting the diffraction focus of a Kikuchi diagram is not easy because the contrast in the diagram is low. One can adjust the focus in parallel beam mode (spot pattern) and store the current value in the intermediate diffraction lens. When switching in convergent beam mode to produce Kikuchi diagrams, one can recall the stored value of the current in the lens.

3.2 Influence of software settings on Kikuchi diagrams indexing

In order to run properly, the software for indexing the Kikuchi diagrams needs some TEM related calibration data. For each camera length, the user has to define:

- The rotation angle between the sample holder coordinate system and the camera fixed coordinate system. This rotation is induced by the electron-optical lenses and depends of the camera length.
- The real camera length for the CCD camera port.

These calibration data are stored once in a file.

The evaluation of the operator dexterity for defining the bands is a long work, our aim here is only to give the results of a short test. More complete statistical analysis of crystal orientation determination from Kikuchi patterns can be found in Krieger Lassen et al. 1994, Krieger Lassen 1996. Our test consists in indexing, always with the same bands (bands 1 to 3 in Fig. 1a, 1c), 15 times the Kikuchi diagrams of the matrix and the twin. The results are summarised in table 1. Despite the fact that calculating an average value for each Euler angle has no mathematical meaning, it is convenient for display purpose. We can also notice that the variation width lies in the order of half a degree. The matrix-twin misorientation angle varies within a range from 59.59° to 59.83°.

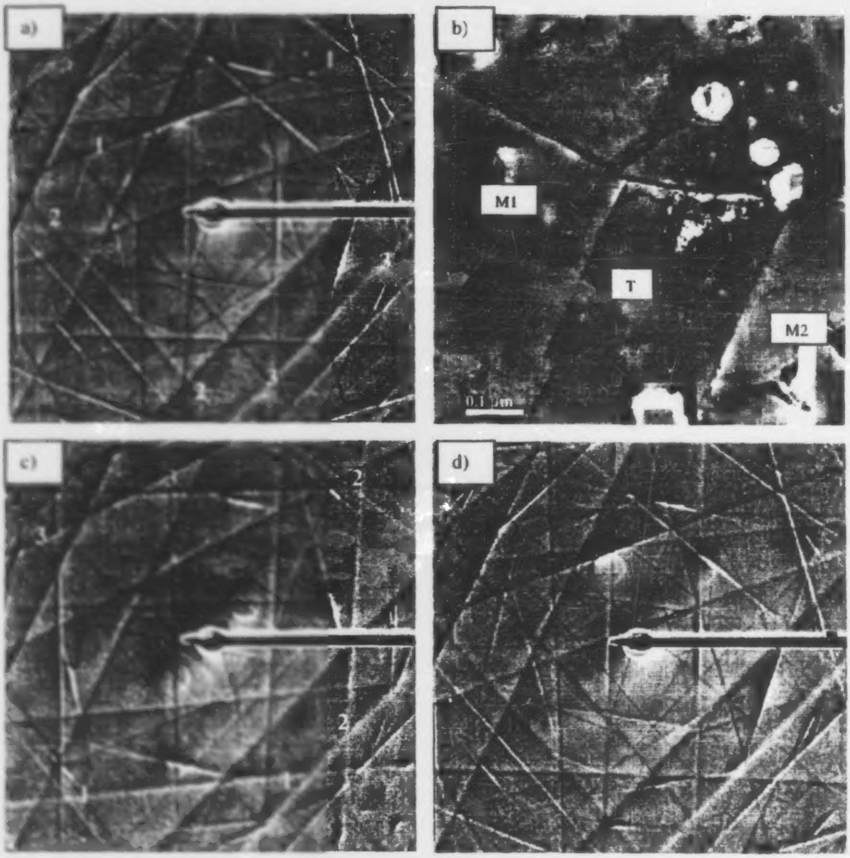

Figure 1 : a) Kikuchi diagram of the matrix M1, b) Micrograph of a twin, c) Kikuchi diagram of the twinned region T, d) Kikuchi diagram of the matrix M2.

Table 1 : The Euler angles for the matrix and the twin. Matrix-Twin misorientation

	Matrix			Twin			Misorientation	
	φ1	Φ	φ2	φ1	Φ	φ2	Θ	[u v w]
Average	50.42°	24.99°	71.86°	-52.00°	48.97°	59.22°	59.73°	[-56.9 -59.3 56.7]
Max. value	50.90°	25.12°	72.13°	-52.74°	49.18°	59.65°	59.83°	
Min. value	50.04°	24.84°	71.62°	-50.28°	48.56°	58.19°	59.59°	

4. Conclusion

The presented partly automated Kikuchi diagrams indexing method can be helpful in many TEM studies of material characterisation, for which the knowledge of the crystal orientation is often of great interest. It seems to us that a fully automated method is not necessary in the case of TEM, since the applications (fine scale studies) need the operator attention and the observable regions are often quite small. It is important to carefully adjust the settings in order to produce faithful Kikuchi diagrams and obtain an accurate and reliable orientation of the crystal.

Acknowledgements

The authors wish to thank Prof. R.A. Schwarzer for fruitful discussions. We would also like to thank Prof. C. Esling for his interest in our work, which helped us to improve the quality of the manuscript.

5. References

Golub, G.H., and Van Loan, C.F. (1989), Matrix Computations, 2nd ed. Baltimore : Johns Hopkins University Press.

Krieger Lassen, N.C. (1995) Computerized Analysis of Kikuchi Patterns. *Proceedings of the 16th Riso International Symposium on Microstructural and Crystallographic Aspects of Recrystallization*. pp. 405-411.

Krieger Lassen, N.C. (1996) The Relative Precision of Crystal Orientations Measured from Electron Backscattering Patterns. *Journal of Microscopy*, Vol. 181, pp 72-81.

Krieger Lassen, N.C., Juul Jensen, D. and Conradsen K. (1994) Automated recognition of deformed and recrystallized regions in partly recrystallized samples using electron backscattering patterns, *Materials Science Forum* Vol. 157-162, pp. 149-158.

Press, W.H., Teukolsky S.A., Vetterling W.T., Flannery B.P. (1992) Numerical Recipes, 2nd ed. Cambridge University Press.

Qing Liu (1995) Applications of a new TEM method for determining local orientations. Proceedings of the Eleventh International Conference on Textures of Materials, Vol. 1, pp 128-133.

Ryder, P.L. and Pitsch W. (1968) On the Accuracy of Orientation Determination by Selected Area Electron Diffraction. Phil. Mag., Vol. 16, pp. 807-816.

Schwarzer R. (1989) Die Bestimmung der lokalen Textur mit dem Elektronenmikroskop, Habilitationsschrift, Technischen Universität Clausthal.

Van Bakel, G.P.E.M. and Seidman D.N. (1995) New method for rapid determination of crystal orientation via Kikuchi patterns. *J. Mater Res.*, Vol. 10, N°12, pp 3026-3036.

Zaefferer S. and Schwarzer R.A. (1994) Automated Measurement of Single Grain Orientation in the TEM. *Zeitschrifft für Metallkunde.*, Vol. 85, pp. 585-591.

ORIENTATIONS MEASUREMENTS BY TEM USING SPOTS, KOSSEL AND LACBED PATTERNS

E. BOUZY, J.J. FUNDENBERGER, J.S. LECOMTE and C.ESLING
LETAM, CNRS URA 2090, University of Metz, F-57045 Metz, France
bouzy@letam.sciences.univ-metz.fr

Abstract

Orientation determination at fine scale using a TEM has a lot of applications in materials sciences (interface characterisation, ultra fine grained materials, etc). The orientation can be derived from a spots diffraction pattern, a Kikuchi, respectively Kossel diffraction pattern or a Large Angle Convergent Beam Electron Diffraction (LACBED) pattern. These two latter techniques have not often been applied although they are known to be very accurate. We will make a comparative study of these methods for a given application of grain boundaries misorientation determination. For each method we will give the drawbacks and advantages in terms of spatial resolution accuracy and ease of application.

Keywords : Kikuchi, Kossel, LACBED, orientation, misorientation

1. Introduction

Local orientation measurement techniques using a Scanning Electron Microscope (SEM)experienced spectacular advances in the recent years, especially the Electron Back Scattering Pattern (EBSP) technique.Automatic mapping of orientations nearly became a routine microstructural characterisation in the material science laboratories with the help of commercial Kikuchi pattern recognition and indexing softwares (Schwarzer 1997). However this technique can be limited by its spatial resolution which is not lower than 0.5µm. For some applications which require ultrafine scale orientation measurements it is necesary to use a TEM. The orientation measurement method by TEM is based on Kikuchi pattern indexing. But there are other methods which allow orientation

measurements. The common point of these methods : Large Angle Convergent Beam Electron Diffraction (LACBED),Kossel Diffraction,etc, is to use a more or less convergent beam.
The aim of the present paper is to compare these different techniques according to spatial resolution, precision and easiness to use in view systematic orientation measurements with an interactive software.

2. Experimental

Our TEM is a CM200 Philips. Like every modern TEM, it has a strong prefield objective lens which allows to select with the electron beam an area which can be lower than 2 nm. The beam convergence semi-angle (controlled by the diameter of the diaphragm of the condenser lens 2) could be up to 5°. This mode is often named nanosonde mode. It is the mode which is used in this study.

The images are recorded on a slowscan CCD camera (Gatan 791). The camera is placed above the viewing chamber. As the maximum diffraction angle in this TEM is about ± 10°, the whole wide-angle view of the pattern can be observed on the camera with a diffraction chamber length of about 300 mm.

We use a Gatan double-tilt cooling holder in order to reduce the thermal diffuse scattering and thus the background intensity. A background subtraction is made on all the Electron Diffraction Patterns (EDP).

The specimen is recrystallized copper which contains many $\Sigma3$ twins.

3. Description of the methods used and characteristics of the corresponding EDP.

We briefly present the various methods used in this study and the main characteristics of the corresponding EDP. For more complete and detailed information, the reader can refer to the very didactic book of J.P.Morniroli (Morniroli 1998) or to Tanaka (Tanaka 1985) and Steeds (Steeds 1992) who are the pioneer of these methods.

By making the beam convergence semi-angle α to vary, different patterns are obtained. As α increases, the EDPs change from a spot pattern when $\alpha << \theta_B$ (θ_B: Bragg Angle) to a Convergent Beam Electron Diffraction pattern (CBED) also named Kossel-Möllenstedt pattern composed of non-overlapping disks when $\alpha < \theta_B$ to a Kossel pattern composed of overlapping disks when $\alpha > \theta_B$.

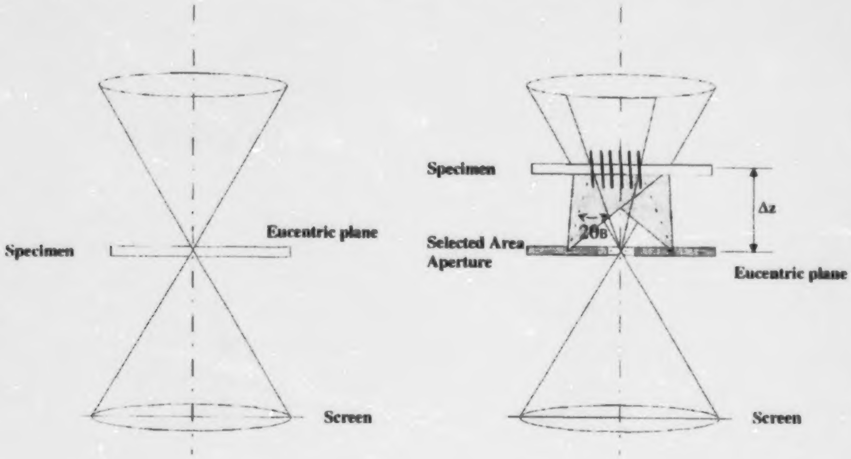

Figure 1 : a) Configuration of the beams for Kossel Patterns acquisition b) Configuration of the beams for LACBED Patterns acquisition

In this study, we use spot patterns, Kossel patterns and LACBED patterns. A Kossel pattern is obtained by focussing a large angle convergent beam on the specimen in the eucentric plane. (see figure 1a)) By raising the specimen to a distance Δz off the eucentric plane, the image of the focussed beam splits to form a small diffraction pattern generated by the Bragg reflections and by selecting the transmitted beam with the area aperture and switching on to the diffraction mode, we obtain a LACBED pattern.(see figure 1b))

The geometry of Kossel and LACBED Patterns is the same as the geometry of Kikuchi Patterns : for each (hkl) plane, the lines form paired, the pairs of lines being parallel to the trace of the plane etc. However, the formation process is different. Kikuchi lines form in two steps : first a divergent beam is formed by inelastically scattering, second the electrons in exact Bragg conditions elastically scatter on the plane (this TEM method is equivalent to the Electron Back Scattering Pattern method in SEM). On the contrary, Kossel lines come in one single step. As α is large, there are already electrons in the beam which are in exact Bragg conditions and thus are elastically scattered by the plane (this TEM method is equivalent to the Electron Chanelling Pattern method in SEM).

4. Indexing Software

As explained previously, the geometry of the Kossel pattern and the LACBED Pattern are the same as the geometry of the Kikuchi pattern. Consequently, the interactive software initially developed for the Kikuchi pattern indexing (Fundenberger et al. 1999) is also able to index Kossel or LACBED Patterns with only minor modifications.

On the other hand, for the orientation determination from spot patterns, the software needs substantial modifications. In order to simulate the spot pattern, the software must take into account the needle like extension of the reciprocal lattice points i.e. the deviation from the exact Bragg condition. As for the Kikuchi, Kossel and LACBED patterns, it is necessary to have at least 3 reflections which do not belong to the same Laue zone, in order to remove the 180° ambiguity in the determination of the orientation. But if it is easy to make such an indexing for any orientation and without tilting the specimen in the case of Kikuchi, Kossel and LACBED patterns, on the contrary in the case of spot patterns it is necessary in practice to tilt the specimen to obtain two different zone axis patterns.

5. Results.

We made several misorientation measurements on Σ3 twin grain boundaries on a recrystallized copper specimen. We find the misorientation 60° <111> with a precision better than 0.1° for the misorientation axis and misorientation angle. We proceed that way : the electron nanoprobe exactly focusses on the grain boundary in order to obtain two Kossel Patterns superimposed on the same pattern. Then the electron probe is focussed on each grain in order to obtain both patterns separately. Finally the indexing of both Kossel Patterns is made on superimposed patterns in order to be sure that it is the misorientation is effectively associated with the grain boundary.

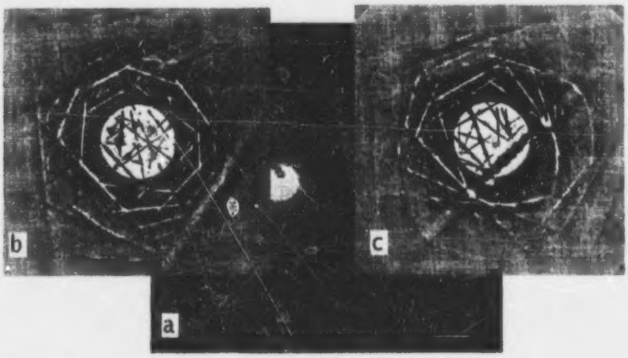

Figure 2 :a) Σ3 twin grain boundary image

Figure 2 shows the image of a Σ3 twin grain boundary and the Kossel pattern of each grain. Both Kikuchi and Kossel lines can be seen in the patterns. The deficient and excess Kikuchi lines (due to inelastic scattering) are reinforced by the deficient and excess lines of the Kossel lines (due to elastic scattering). The Kossel lines pairs are highly contrasted as compared to the Kikuchi lines pairs. For a pair of Kossel lines, we can see the deficient line in the bright central (000) disk and the excess line in the (hkl) diffracted disk.

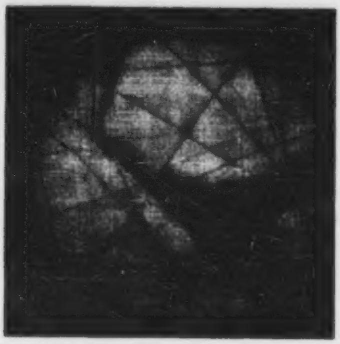

Figure 3 : LACBED pattern of a copper Σ3 twin grain boundary

Figure 3, shows the LACBED pattern of a Σ3 twin grain boundary. We can notice that the EDP and the image are displayed on the same pattern : the image of the grain boundary appears at the discontinuity between the highly contrasted EDP of each grain. The EDPs exhibit large deficient dynamic lines with fringes corresponding to low Miller indices planes and very fine deficient cinematic lines corresponding to high Miller indices planes, often called Holz lines.

6. Discussion

Our aim is to give the drawbacks and advantages of each method and to discuss which method is able to determine the orientations with a good spatial resolution and which method is easy to use with an interactive software.

In LACBED method, the diffracting specimen volume is linked to the Δz removal off the eucentric plane and the beam convergence semi-angle α. The minimal area is about 0.5 μm. Moreover, the quality of LACBED pattern is very poor if the specimen is deformed : the lines become very distorted. However the big advantage of this technique is that both the diffraction pattern and the image are simultaneously displayed on the screen. It is more adapted to the study of defects like, for instance, the complete geometric characterisation (misorientation - grain boundary plane orientation) of a grain boundary.

In spot or Kossel patterns, the specimen diffracting volume is directly linked to the beam size. But unlike Kossel patterns, it is necessary from spot patterns to tilt the specimen in order to determine the orientation . In practice, this results in a drop of the spatial resolution (because there is not any eucentricity for 2 axes of tilt).

For Kossel Patterns, it is better to choose a small beam size : a few nanometers, except if the specimen is sensitive to irradiation damage. As a consequence, the spatial resolution is increased and the quality of the diagram is improved. Indeed, as the beam size decreases, the Koššel and Kikuchi lines which were diffuse or absent, become sharp even if the specimen has either elastic (bending) or plastic (dislocations) strains. Indeed, the smaller the diffracting volume is, the less the orientation is sensitive to the presence of strains. Moreover, it is better to use a large convergent beam in order to improve the contrast of the pattern. Indeed, the Kikuchi lines produced by inelastic scattering are enhanced by the elastic scattering contribution of the Kossel lines which are always present, even if the specimen is very thin (see figure 2).

The comparison between the various techniques for the orientation measurements is summarised in the table below.

Table 1 : Comparison between the various techniques

	spatial resolution	relative precision	ease (not need to tilt)	type of specimen
spots pattern	>>few nm	> 0.1°	no	highly deformed
Kossel pattern	~ few nm	~ 0.1°	yes	all and especially thin specimens
LACBED pattern	> 0.5 µm	~ 0.1°	yes	characterisation of defect

7. Conclusion.

For orientation and misorientation measurements at the scale of the nanometer, Kossel patterns are best adapted.The measurement is easily and quickly made with the help of an interactive software.

Orientation measurements from spot patterns are not so easy to make, they are not much precise and have a poorer spatial resolution. They may be used for highly deformed materials when the previous method fails.

Because of its poor spatial resolution LACBED method is not adapted to fine scale orientation measurements, but could allow the full geometrical characterisation (misorientation + grain boundary plane orientation) of grain boundaries between large grains, provided they are strains free.

Acknowledgements : Thanks to Prof. R . Schwarzer, T U Clausthal (Germany) and Prof. J.P. Morniroli from the E N S de Lille (France) for fruitful discussions.

8. References.

Fundenberger, J.J., Bouzy, E., and Lecomte, J.S. (1999) Experimental Setting for Indexing TEM Kikuchi Diagrams, ICOTOM 12 Proceeding.

Morniroli, J.P. (1998) in Diffraction électronique en faisceau convergent à grand angle (LACBED) (Ed. Société française des microscopies).

Schwarzer, R.A. (1997) Advances in crystal orientation mapping with the SEM and TEM, Ultramicroscopy,67,pp. 19-24

Steeds, J.W., and Morniroli, J.P. (1992) Minerals Reactions at the atomic scale TEM (Ed. P . Buseck)Review in Mineralogy, Vol. 27, pp. 37-84.

Tanaka, M., and Terauchi, M. (1985) Jeol Ltd., Tokyo, Vol. 1.

TEXTURE ANALYSIS WITH A DIGITAL SEM-EBSD SYSTEM

H.-R. WENK, J.J. DONOVAN, Y. XIE
Department of Geology and Geophysics, University of California, Berkeley CA 94720
G.C. JOHNSON
Department of Mechanical Engineering, University of California, Berkeley CA 94720
E. TOKER
MedOptics Corporation, Tucson AZ 85714

Abstract

A purely digital system is described to record electron backscattered diffraction patterns obtained in a scanning electron microscope. The system includes fiber optic image transfer, a 14 bit CCD Peltier-cooled 1 mega pixel CCD camera and PC software to control microscope, camera and data processing in a Windows environment. The system is designed for automatic texture analysis.

Key Words: EBSD, CCD-camera, digital imaging system

1. Introduction

An important feature of polycrystalline materials is the orientation distribution of crystallites also known as crystallographic preferred orientation or texture [Kocks et al. 1998]. Conventionally it is measured by x-ray diffraction, by averaging over sample surfaces. With demands for more quantitative material characterization, both in engineering and earth sciences, new methods have been developed. Of particular importance is orientation imaging, using electron backscattered diffraction patterns (EBSD) in the SEM [Adams et al. 1993, Wright and Adams, 1992, Wright, 1993].

Even for fairly perfect crystals, EBSD images are generally very weak and the small diffraction signal is superposed on a high background. The signal is further attenuated if the surface is damaged, e.g. during polishing, or if the sample contains intrinsic defects such as dislocations. This is particularly severe for minerals and ceramics where chemical and electro polishing are not applicable. In order to have the capability of processing data for such samples, it is imperative to have the largest possible signal and a large dynamic range for the variations in the intensities. Increasing the beam current increases the brightness of the EBSD pattern but introduces surface contamination and charging in non-conducting materials. Ideally one would like to work with low voltage (10kV), low beam current (<2nA) and still obtain interpretable images.

Conventionally EBSD patterns used in texture analysis are transferred from a phosphor screen inside the microscope with a lens system to a silicon intensifier tube (SIT) outside. The standard video analog signal is processed with hardware devices to subtract background. Then the image is converted to a digital array with a frame grabber. Video imaging with standard technologies is limited to 8 bits (256 gray levels). Particularly for noisy and weak signals on an irregular and sloping background, with a signal only a few percent above the noise level, there is little information remaining after the background correction. This digital array is then used by the computer software for interpretation. The procedure is fast and has been very adequate for microtexture analysis of recrystallized and moderately deformed metals but unsatisfactory for many other samples.

In order to overcome some of the limitations and at the same time taking advantage of modern imaging technology, we have developed at Berkeley a purely digital system that controls the microscope and the camera, processes data and produces texture analyses with a micro computer. Some of the functions will be described in this paper.

2. Design of EBSD camera

The system that we have developed is based on advances in high resolution EBSD recording [Michael and Goehner 1993] and biological x-ray imaging [Stanton et al. 1992]. During the last few years great advances have been made in CCD technology and affordable devices have become available which are used in a wide range of industrial applications. For the system we had in mind it was necessary to have a good resolution, high count rate, low noise and a fast readout. Since the microscope which we used (a Leo S430 SEM) is not equipped with a mechanical or electronic shutter (which in any case would be slow and introduce instabilities) a fast frame transfer was required to allow for "smearing" of the image data during the CCD readout.

A schematic drawing of the camera is shown in Figure 1. Instead of using a lens image transfer, a 2.5 cm diameter, 25 cm long 1:1 fiber optics light pipe is employed. The EBSD is recorded on a phosphor coated fiber-optic faceplate attached to the light tube with an optical grease. For a phosphor we chose P-20 red, optimized for 8-20 KeV electrons and the CCD response curve. The phosphor is additionally coated with a film of indium-tin oxide, thin enough to pass 99% of 8 KeV electrons and grounded to the CCD housing to eliminate charging effects from the electron beam.

The light pipe is permanently bonded to the CCD chip with epoxy. The square active imaging area of the CCD chip is completely covered by the light pipe. The light pipe and the CCD camera are mounted on a translation stage, permitting the whole assembly to retract in the microscope in order to change the field of view of the diffraction pattern or to remove the pipe if the microscope is used for other applications. A differentially pumped double Viton static o-ring seal guarantees the integrity of the microscope high vacuum interface.

For a CCD chip we chose the Thomson THX7887A device which is capable of rapid full frame transfer for simultaneous frame readout and image acquisition for shutterless operation. The active imaging area on the chip is 12x12 mm, pixel size <12 µm. There are 1024x1024 image elements and an additional 1024x1024 frame elements. Other characteristics of the chip are a full well depth of >200,000 e^- per pixel, a readout noise of <30 e^- per pixel at 14 bits image depth and a frame transfer speed of <0.05 sec (compared with image recording in the range of 1-5 sec).

The camera was built to our specifications by Med-Optics of Tucson, AZ, incorporating their extensive experience for CCD imaging for medical applications. In order to reduce noise the chip is cooled with a thermo-electric (Peltier) device which is further cooled by recirculated water and provides an operating temperature of –40 to –25°C. The CCD camera is hermetically sealed for vacuum operation. In order to reduce strain on the CCD and to prevent delamination trom the fiber optic pipe, the CCD mount utilizes a "floating head" design that allows the epoxy-bonded chip to move along with the fiber optic throughout repeated thermal cycling.

The electronics have an ADC of 14 bits (4096 grey levels) and a readout speed of 2 mega pixels per second. Without binning, this provides a readout time of < 1 sec. Binning can be adjusted between 1 and 16 pixels in each direction (from 1024x1024 to 64x64). During binning, data in each binned region are summed, providing high counts (at the expense of resolution) and therefore permitting short integration times. For EBSP orientation imaging we typically employ 256x256 arrays. The integration time is controlled with a hardware timer from 0.1 to 1000 sec and an accuracy of better than 0.1%.

3. Software

All functions of data collection, including hardware control of microscope and camera are controlled with an in-house PC software called SEMTEX and written in Microsoft Visual Basic Version 5.0 running under Windows 95.

As far as microscope functions are concerned, we obtained a network DDE interface provided by Leo. They include movement of the xyz-tilt-rotation stage, beam deflection, choice of scanning versus spot mode, recording of voltage, current, magnification, focus and other parameters. For large scans (in excess of 10 µm) the Leo mechanical stage is used that has a reproducibility of +- 1 µm. The stage is Cartesian with respect to the microscope with a tilt and rotation above the stage. Since EBSD measurements require a tilted sample (about 70° from the horizontal), sample surface coordinates on which the scan is performed, need to be converted to stage coordinates. This can be done be simply by applying the tilt angle, or, preferably, by triangulation between three or more points on the focussed sample surface. The latter is particularly important for large scans of bulk samples where the surface is slightly inclined to stage coordinates. The triangulation method ascertains that the surface at each spot is in perfect focus.

The image is first recorded in spot mode. Periodically a background is measured in scan mode. The extent of the scan (determined by magnification) depends on the particular sample. The background is subtracted digitally and the user has several options. One is a straight background subtraction, another one is a flat field correction which is advantageous for edges of the image. We have not observed a significant difference as far as EBSD interpretation is concerned and generally choose simple subtraction. Because the background correction is performed using 16 bit integers, a large dynamic range remains even for a weak signal after a large background subtraction. Figure 2 illustrates a worst case for an EBSD pattern of quartz taken with a damaged phosphor.

The corrected image is then re-normalized to 8 bits for processing with a customized version of the commercial pattern indexing software Channel 3+ [Schmidt and Olesen, 1989]. This is sufficient for most background corrected images.

The procedure is as follows: Initially the imaging conditions are optimized. This includes camera distance, voltage, beam current, magnification, focus, camera resolution and integration time. Subsequently three or more points in the area of interest are focused using a constant focus by adjusting z (axis parallel to beam). Then parameters for Hough transform, camera geometry and crystal structure are determined and refined. Finally a grid in regular sample coordinates is calculated and the automatic procedure begins: drive x,y,z to desired sample coordinates, record image in spot mode, change to scan mode to minimize charging (or to record background image), perform background correction, send corrected image for Hough transform and indexing, receive orientation parameters and so on. At each step, the SEMTEX program periodically checks if the task is finished. One cycle takes between 5 and 15 sec, 2-3 sec to drive motors, 1-5 sec to count, 1-2 sec for image correction and 1-5 sec for indexing with a Pentium 430 MHz processor. This is slower than many SIT cameras but images are superior and there is a lot of flexibility for optimization. In any case, we maintain that for most applications measuring time is not the limiting parameter but the reliability of the system over long periods. For our procedure about 10,000 data points are measured in a bit over a day.

4. Texture Analysis

Sample coordinates, Euler angles, image quality and match parameter are stored on a ASCII file that is used for further processing. The data can be introduced directly into BEARTEX [Wenk et al. 1998] to calculate the orientation distribution and pole figures (for discrete methods INOR enters data into cells and densities are subsequently smoothed, HIOR uses the harmonic method and smoothing occurs by series termination). In the orientation distribution the user may select orientation ranges for mapping. If grain numbers are limited (and grain numbers are different from number of measurements!) a correction for grain statistics may be necessary [Matthies and Wagner, 1995].

For orientation mapping, the in-house developed Visual Basic program MAPTEX is used with the same data file. Different features can be mapped such as Euler angles, image quality, orientations within a defined component. Also misorientations across cell boundaries are mapped with different colors. Figure 3 gives an example for a deformed bi-crystal of aluminum.

Data processing with BEARTEX and MAPTEX are completely independent from data collection and may be performed off-line on any microcomputer running Windows 95, 98 or NT.

5. References

Adams, B.L., Wright S.I. and Kunze, K. (1993). *Metall. Trans.* 24A, 819.

Kocks, U.F., Tome, C. and Wenk, H.-R. (1998). *Texture and Anisotropy*. Cambridge Press.

Matthies, S. and Wagner, F. (1996). *Phys, Stat. Solid.* b196, K11.

Michael, J. and Goehner, R.P. (1993). *MSA Bull.* 23, 168.

Schmidt, N.-H. and Olesen, N.O. (1989). *Canadian Mineral.* 27, 15.

Stanton, M., Philips, W., Li, Y. and Kalata, K. (1992). *J. Appl. Cryst.* 25, 638.

Wenk, H.-R., Matthies, S., Donovan, J. and Chateigner, D. (1998). *J. Appl. Cryst.* 31, 262.

Wright, S.I. and Adams, B.L. (1992). *Metall. Trans.* 23A, 759.

Wright, S.I.(1993). *J. Comp.-Assisted Microsc.* 5, 207.

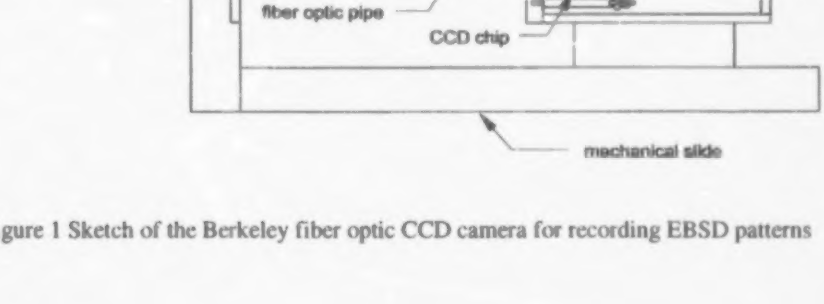
SEM interface
protective metal housing
cooling module
fiber optic face plate
H_2O
fiber optic pipe
CCD chip
mechanical slide

Figure 1 Sketch of the Berkeley fiber optic CCD camera for recording EBSD patterns

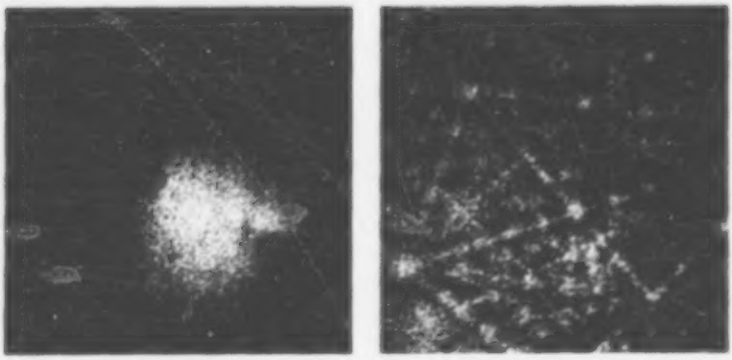

Figure 2. Left: Raw image of quartz EBSD recorded with defective phosphor. Right: Same image after digital background subtraction.

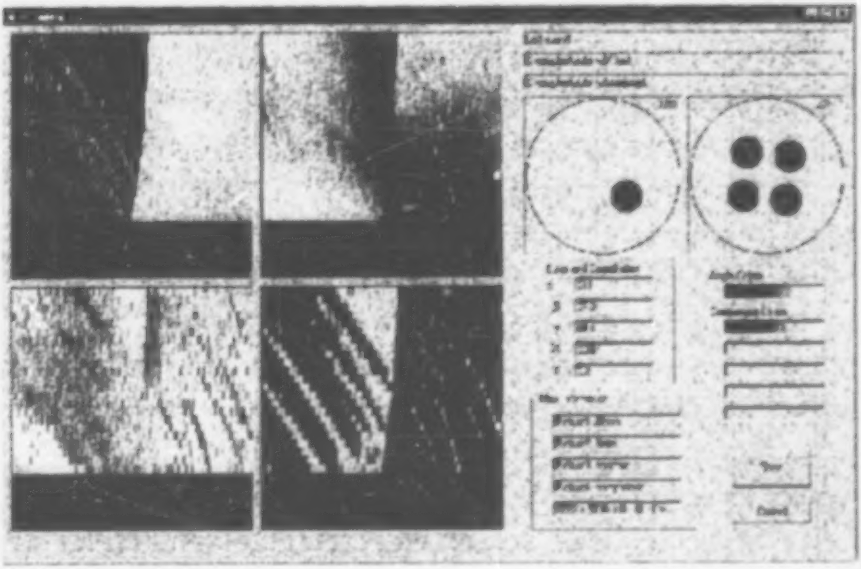

Figure 3. Display of the program MAPTEX illustrating EBSD data for a deformed bi-crystal of aluminum. The maps are Euler angles α and β, image quality and an orientation component.

X'PERT TEXTURE: OVERVIEW OF A SOFTWARE PACKAGE FOR QUANTITATIVE TEXTURE ANALYSIS

D.I. NIKOLAYEV, V. LUZIN and T. LYCHAGINA
Joint Institute for Nuclear Research, Laboratory for Neutron Physics, Dubna, Moscow region, Russia 141980
A.A. DZJUBA, V.A. KOGAN and J. TE NIJENHUIS
Philips Analytical, Lelyweg 1, 7602 EA Almelo, The Netherlands

Abstract

The goal of the present work is to describe and illustrate the main features available in the software package X'Pert Texture. The multiple document user interface of X'Pert Texture is compatible with the Windows®95 and Windows NT™ operating systems. The current version includes corrections of measured pole figures for background intensities and defocusing errors, orientation distribution function (ODF) calculations according to the method of Williams, Imhof, Matthies and Vinel (WIMV) and (re)calculations of arbitrary pole figures as well as inverse pole figures. The graphical facility enables the user to present texture data (pole figures, ODF's and correction curves) in different styles and projections, ranging from one dimensional intensity plots to real 3-dimensional images, clearly presenting the relation between intensities and the orientation of the sample.

Keywords: X'Pert Texture, orientation distribution function calculations, WIMV, graphical facility

1 Introduction

The main idea of the software program X'Pert Texture is based on user requirements for qualitative and quantitative X-ray texture analysis: *i.e.* convenience to visualize and analyze raw texture data, obtained from X-ray diffraction experiments as well as corrected and calculated data. The multiple document user interface is based on Windows®95 and Windows NT™ operating systems.

In the present paper a functional description of X'Pert Texture is given based on a routine workflow through the program. This workflow can be outlined as follows.

The first step is a visual check of the raw data and corrections. The second step comprises ODF computations and visual analysis of the results. The third step comprises additional calculations and analysis of (inverse) pole figures. Each specific step will be considered in detail. This will be illustrated starting with four pole figures measured on a rolled copper specimen using X-ray diffraction

2 Experimental setup

Texture measurements were performed on a rolled copper disc with a diameter of 22 mm and a thickness of 0.8 mm. The sample was mounted on an X'Pert Multi-Purpose Diffractometer (MPD) system equipped with an ATC-3 automatic texture cradle. The pole figures were measured according to the Schulz reflection method (Schulz, 1949). Background intensities were measured next to the diffraction peaks with an offset in 2θ of ±4°. To correct for defocusing errors due to sample tilt, correction curves were measured on a texture free copper "powder" sample under the same experimental conditions as the rolled copper sample. In addition to this, a 2θ - θ scan was measured on the textured sample. From this scan, the Full Width at Half Maximum (FWHM) of the reflections can be obtained. This information is required for calculated defocusing corrections.

3 ODF Projects

In X'Pert Texture, analysis of the experimental data is started by storing all texture data belonging to sample under a single name as an ODF project. In this ODF Project also data, produced as result of calculations such as corrected, calculated and inverse pole figures, ODF data and background and defocusing correction curves are stored.

4 Corrections

The experimental pole figures can be corrected for defocusing errors and background intensities. The defocusing correction can either be applied using correction measurements on a texture-free specimen or according to the formula based on Gale and Griffiths' model (Gale and Griffiths, 1960, Huijser-Gerits and Rieck, 1974). For the latter correction the value for the Full Width at Half Maximum (FWHM) of the reflection at a Psi-tilt of 0° is required. A comparison of the calculated and measured defocusing curve is shown in fig. 1. It is shown that the calculated curve gives a good description of the measurement geometry. The correction for background intensities can be applied from measured data or can be defined by the user.

Fig. 2 shows a 2D representation of (a) the Cu (220) pole figure as measured and (b) as corrected in the Schmidt projection. It is observed that the defocusing correction is especially necessary for the higher Psi-tilt angles.

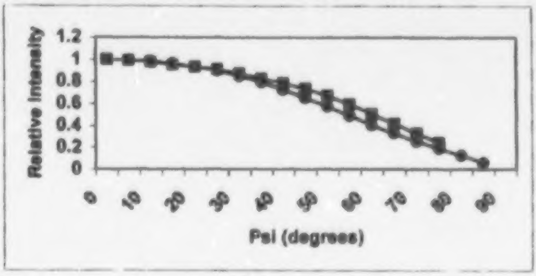

Fig. 1: Measured (squares) and calculated (circles) defocusing corrections for the Cu(220) pole figure.

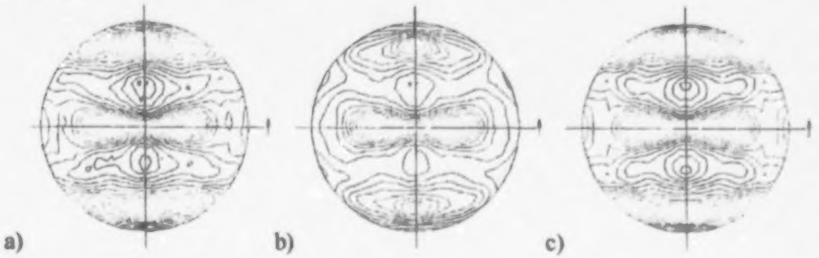

Fig. 2: 2-dimensional (Schmidt) representations of (a) the experimental, (b) corrected and (c) recalculated Cu (220) pole figure. The maximum Psi value is 75°.

5 Displaying pole figures

Besides linear (1D) and standard Schmidt (equal area) and Wulff (stereographic) (2D) projections, the program also provides possibilities to show the data in cylindrical and in spherical projections. In the cylindrical or 2.5D projection the intensity of at a position with coordinates (Phi, Psi) in the base plane is represented by its height in the cylindrical direction. The spherical or 3D representation shows the pole figure intensities at the 'true' Phi and Psi orientation angles. This provides a clear view of the distribution of the diffracting crystallites over the orientation space. Fig. 3 shows an example of the 1D, 2D (Schmidt), 2.5D and 3D representations of the corrected Cu (220) pole figure.

6 ODF calculations and graphical representation

X'Pert Texture calculates the ODF according to the iterative method for ODF reconstruction (Imhof 1981, Matthies and Vinel, 1979). At present, there is no agreement on the question which method for ODF reconstruction is the absolute leader; a detailed discussion on this topic is given by Kocks et al. (Kocks et al., 1998). Reconstructed ODF's can be displayed in a conventional 2D or in a 3D mode. In the 3D representation the three Euler angles (Bunge or Roe notations) are shown in orthonormal space. In Fig. 4 the ODF derived from the rolled copper in a cubic-orthorhombic setting is shown in 2D and 3D representations. The R-value for these calculations was 7.9%.

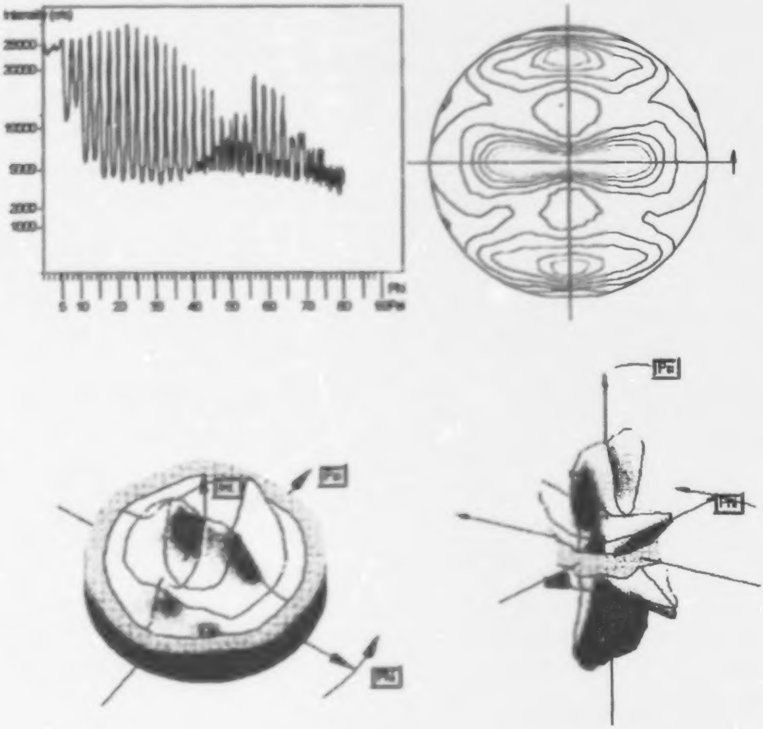

Fig. 3: Cu (220) pole figure as measured in four different representations: a) 1 D, b) 2D, c) 2.5 D and d) 3D.

7 Computation of additional (inverse) pole figures.

When the ODF data are available in the ODF project, pole figures and inverse pole figures can be calculated for any integer set of (*hkl*) values (with *h*, *k* and *l* smaller than 100) and any real set of (*xyz*) co-ordinates (with *x*, *y* and *z* smaller than 100). The user can define the maximum value of Psi to be calculated. Normally, pole figures are calculated up to 90 degrees. Alternatively, the maximum Psi value from the experimental pole figures can be used to simplify comparison between measured (or corrected) and calculated pole figures. In fig. 2c the calculated Cu (220) pole figure is shown. The original pole figure was measured up to a Psi-tilt angle of 75°. To facilitate comparison the Psi-limit for the calculated pole figure was set to 75° as well. The calculated pole figure shows a close resemblance with the corrected one, which confirms the consistent quality of the initial measurements.

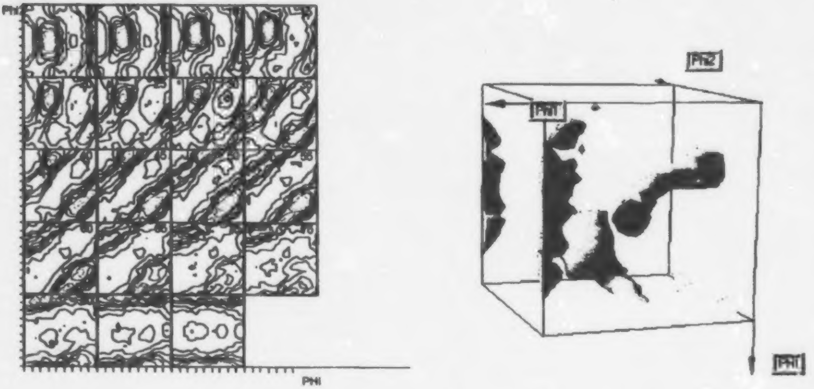

Fig. 4: ODF calculated for the rolled copper sample in the Bunge notation of the Euler angles in two different representations: a) 2D with Phi1 as fixed axis, b) 3D

8 Normalization and K-factors

An additional feature of the program is the evaluation of texture data with the use of K-factors and normalization factors. The K-factor is the ratio of the intensity in a (raw, corrected or calculated) pole figure at Psi=0° to the average intensity over the total pole figure (Kogan and Bethke, 1997). K-factors can be used to convert intensities, which are measured on a textured sample to "random" powder intensities, which would be measured on a texture free sample. With K-factors, you can correct intensities for quantitative phase analysis, Rietveld analysis, etc. To correct the intensities of peaks measured with a 2θ-θ scan on a textured sample; divide the measured intensity by the K-factor. An example of the use of K-factors is given in the table below. In the first three columns the *hkl*-values, the absolute and relative peak intensities as measured from a 2θ-θ scan are given respectively. In the fourth column the K-factors as obtained from corrected pole figures, measured under the same conditions as the 2θ-θ scan are given. These K-factors are used to correct the intensities from the second column for the texture. The results of this are shown after normalization to the strongest intensity in the fifth column. They are in good accordance with the relative intensities as are given on the ICDD reference pattern for copper, PDF No. 04-0836 (last column).

The normalization factor is defined as the total intensity of a pole figure, averaged by area. Normalization factors of a set of pole figures (*hkl*'s) can be compared with the relative intensities present in a "powder pattern" (*e.g.* an ICDD (International Centre for Diffraction Data) reference pattern). For that purpose calculate the relative normalization (normalization factor (%) with the strongest line = 100%). In the table below the absolute and relative normalization factors as derived directly from the corrected pole figures are given in the sixth and seventh columns. It is shown that these factors are also in good accordance with the results from the ICDD pattern as given in the last column.

Table 1: Normalization and K-factors as calculated from the texture measurements on the rolled copper specimen.

hkl	Intensity	Intensity	K-factor	Corr. Int.	Norm. factor	Norm. factor	Ref.*
	(counts)	(%)		(%)		(%)	
111	4926	49	0.2721	100	40994	100	100
200	6196	62	0.8042	42.6	17418	42.5	46
220	9974	100	2.6483	20.8	8336	20.3	20
311	4890	49	1.4680	18.4	7165	17.5	17

*ICDD Reference pattern, PDF No. 04-0836 (Copper)

It should be noticed that the most realistic normalization and K-factors result either from pole figures (re)calculated up to 90 degrees from an ODF or from corrected pole figures, measured up to Psi = 70 or 75 degrees. In the first case, it is sufficient to measure only a few pole figures, and to calculate the ODF and the necessary pole figures subsequently. In the latter case, no ODF calculation is necessary; all pole figures need to be measured.

9 References

Gale, B., and Griffiths, D. (1960) Influence of instrumental aberrations on the Schultz technique for the measurement of pole figures. *British Journal of Applied Physics,* Vol.11, pp. 96-102.

Huijser-Gerits, E.M.C. and Rieck, G.D. (1974) Defocusing effects in the reflexion technique for the determination of preferred orientation. *Journal of Applied Crystallography*, Vol. 7, 286-290.

Imhof, J. (1983) Texture Analysis by Iteration. *Physica Status Solidi (b)* Vol. 119, pp. 693-701.

Kocks, U.F., C.N. Tomé and Wenk, H.-R. (1998) *Texture and Anisotropy*. Cambridge University Press, Cambridge, U.K.

Kogan, V.A., Bethke, J., (1997) Oral contribution at the EPDIC-5

Matthies, S., Vinel, G.W. (1982) On the reproduction of the Orientation Distribution Function of Texturized Samples from Reduced Pole Figures Using the Concept of a Conditional Ghost correction. *Phys. Stat. Sol. (b)* Vol. 112, pp. K111-K114

Schulz, L.G., (1949) *Journal of Applied Physics*, Vol. 20, pp. 1030-1032.

Modeling of Texture Development

INFLUENCE OF TEXTURE EVOLUTION ON FINITE ELEMENT SIMULATION OF FORMING PROCESSES

E. HOFERLIN, A. VAN BAEL and P. VAN HOUTTE
Department of Metallurgy and Materials Engineering, Katholieke Universiteit Leuven, Belgium

Abstract

This paper analyses the usefulness of introducing texture updating into a texture-based constitutive model for Finite Element (FE) simulations of forming processes. The initial crystallographic texture allows the prediction of the anisotropy of the mechanical properties. Nevertheless the crystallographic texture is altered by the forming process itself causing continuous modification of the mechanical properties. The feasibility and the usefulness of taking into account the effect of texture updating during the FE simulation is assessed comparing the results of a deep-drawing simulation performed with and without texture evolution.

Keywords: Anisotropy, texture evolution, finite element

1 Introduction

This paper aims at giving some hints for answering to the question: should we introduce texture updating in FE simulations of deep-drawing of sheet metal? An analysis on this problem is especially relevant since the coupling between texture evolution and FE simulation results in a very computer intensive tool. The method followed for this work consists of performing regularly texture updates during the FE simulation. The so-obtained simulated product is compared with the one which is simulated when texture is assumed to remain constant.

It was decided to study the forming operation of a circular cup because this leads to a typical earing profile at the rim of the cup. This is a clear illustration of anisotropy of mechanical properties due to crystallographic texture and therefore is well suited to study the influence of texture evolution. The deep drawing simulation of a square box would not allow such a study.

2 Anisotropic constitutive model

Elasto-plastic modelling of constitutive material behaviour requires the introduction of a yield surface and an appropriate hardening model describing how the plastic deformations modify the yield locus. The hardening model is usually formulated by describing the history of a set of internal state variables. The latter represent the current material state and can be scalar (e.g. the equivalent plastic strain) or tensorial variables (e.g. the current state of dislocation structures). Note that the crystallographic texture itself should be considered as a state variable since it evolves under plastic deformations. In the present work, an isotropic hardening model is used.

According to the dual potential approach, the yield locus can be derived from the expression of the plastic power dissipation. In our approach, we consider crystallographic slip as the major source of plastic deformation and the plastic dissipation is computed by means of the Taylor model with the Full Constraint (FC) assumption. For BCC phase, the possible slip systems are assumed to be {110}<111> and {112}<111> and the ratio of the critical resolved shear stress of both systems is set equal to 1. The average Taylor factor of the polycrystal then is proportional to the value of the plastic potential.

The Taylor model can be used to obtain the value of the plastic potential for a discrete set of plastic strain rate modes. Such discrete representation is not very suited for FE implementation. Therefore, one introduces a polynomial series expansion (Van Bael 1994, Van Bael et al. 1996) of sixth order to represent to average Taylor factors. The argument of the function is the plastic strain rate mode (5 independent components). The coefficients of the expansion are computed by least square fitting on a set of 70300 average Taylor factors computed for a regular sampling of strain rate modes. The implementation of the procedure is highly optimised and requires only a few seconds on a workstation equipped with a SUN Ultra-2 300 Mhz processor.

A point pertaining to the yield locus in a given stress direction is obtained by solving a fourth order minimisation procedure (Van Houtte et al. 1995). The procedure is fully anisotropic in the sense that it does not assume that the principal strain directions are aligned with the principal stress directions. The efficiency of this procedure is really crucial since it is repeated several thousands of time during the FE simulation. This procedure has recently been speeded up (Hoferlin et al. 1999). Note that, in the derivation of yield locus point from the plastic potential, it is assumed that the critical resolved shear stress is independent of the strain rate.

So far, we have always performed simulations neglecting the evolution of crystallographic texture. When the material undergoes a rigid body rotation, it is obvious that the texture does not change but co-rotates with the material. This means that one has to formulate the current model in material axes and describe how those axes rotate. When the material rotates and deforms, the situation becomes more complex. In that case, the concept of material axes designates the best axes that can be found such that the texture is still correctly approximated by the initial orientation distribution function.

The effects of large rotations are taken into account by using the Jaumann objective rate in the constitutive relation i.e. considering the anti-symmetric part W of the velocity gradient as constitutive spin. By convenience, it is assumed that the material frame also spins at a rate given by W.

3 Material and test geometry

The first material chosen for this study is an ultra-low carbon steel that has been continuously annealed after cold rolling. The crystallographic texture was measured by means of X-ray diffraction and the C-coefficients have been obtained. Fig. 1 shows the φ_2=45° section. It reveals a clear γ-fibre with a maximum on the E-component. The $\bar{r}$ and Δr parameters have been experimentally determined and are equal to 1.52 and 0.97. The material was especially chosen for its high planar anisotropy, and a clear earing profile is expected.

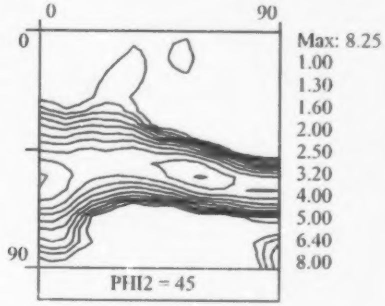

Fig. 1: φ_2=45° section of the initial ODF of the ultra-low carbon steel.

The circular blank has an initial radius equal to 50 mm and a thickness of 0.73 mm. The punch diameter is equal to 50 mm and a clearance of 1.25 mm exists between the punch and the die. The FE mesh has 656 eight-node elements (with one integration point) for the sheet and 1082 triangular elements for the description of the die, the punch and the blankholder. In order to avoid problems of convergence at the end of the simulation, the blankholder is assumed to be fixed whereas experimentally it is loaded by a constant force.

4 Procedure for texture updating

The procedure followed to take the influence of texture updating in the deep-drawing simulation into account is summarised by the flow chart in fig. 2. The initial texture is discretized into 4582 crystallographic orientations. Previous results have demonstrated that this high number guarantees a good reproduction of the texture dependent properties of the materials, while a smaller number (such as 400) does not achieve that.

A new set of C-coefficients corresponding to these 4582 orientations are obtained by assuming Gaussian distributions with a spread of 7 degrees on the 4582 orientations. These C-coefficients are used for determining the plastic potential at the beginning of the FE simulation.

The simulation is started and the punch moves down to 10 mm. It produces a file tracing the plastic strain history experienced in the material frame by each element. At the end of this first phase, the texture of each element is updated with the Taylor model. For each element, the new set of orientations is used to derive new C-coefficients and the corresponding plastic potential. Then, the simulation restarts for the next increment of punch displacement as explained by the flow chart. In this work, texture was updated at 10, 20, 30 and 50 mm punch displacement.

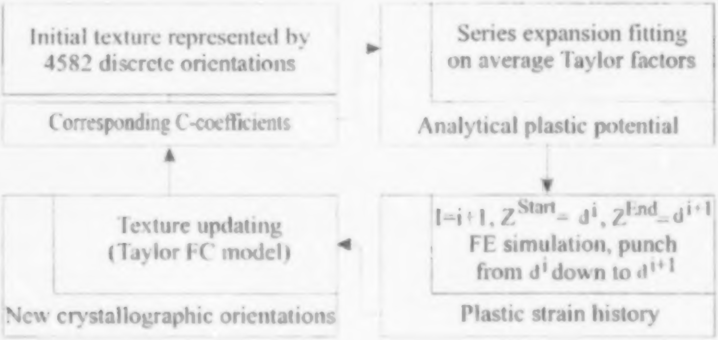
Initial texture represented by 4582 discrete orientations
Corresponding C-coefficients
Series expansion fitting on average Taylor factors
Analytical plastic potential
$I=i+1$, $Z^{Start}=d^i$, $Z^{End}=d^{i+1}$
FE simulation, punch from d^i down to d^{i+1}
Plastic strain history
Texture updating (Taylor FC model)
New crystallographic orientations

Fig. 2: Procedure for texture updating.

A second simulation is performed keeping the initial texture constant in the material axes. A comparison between both simulations is given in the next section.

5 Results

During the simulation, a maximum punch displacement per step of 0.5 mm was allowed. In case of bad convergence, this increment was automatically reduced. The simulation without texture evolution has converged in 120 steps in 3 hours 36 min on a SUN Ultra-2 300 Mhz processor. The 0.5 mm displacement increment was almost always used, confirming the good implementation of the constitutive model. Fig. 3 shows a quarter of the simulated product after 50 mm displacement.

For the simulation with texture update, the evolution of texture has been distributed on 8 CPUs of a network, including 5 Ultrasparc-2 300 Mhz. The update of texture for the 656 elements cost about 6 hours depending on the number of plastic steps.

When texture updating is neglected, the prediction of earing position remains the same but the cup is in average 0.19 mm higher. Finally, an additional simulation with texture updating has been performed for a cold-rolled IF steel for which texture was experimentally measured at position A (see Fig. 3) after deep-drawing (Winters 1996).

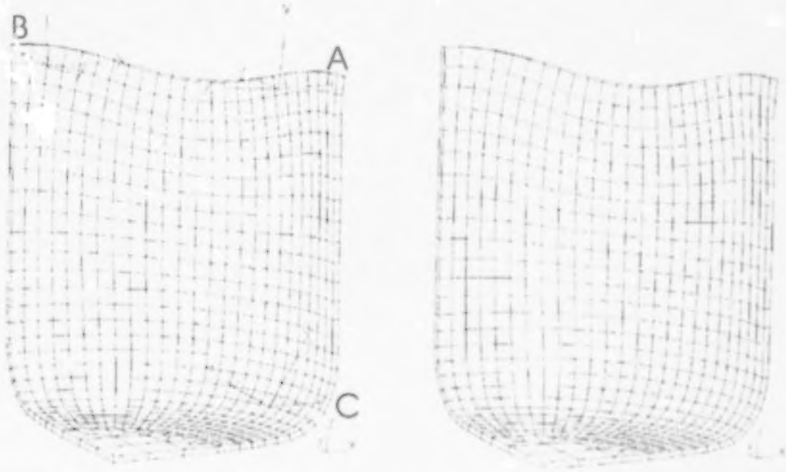

Fig. 3: Simulated cup obtained with (left) and without (right) texture updating. The initial rolling direction corresponds to the X-axis of the global frame. The material frames are also shown for three elements. They were initially aligned on the global frame.

Fig. 4 shows a comparison between the experimental and simulated texture. The γ-fibre which was clearly present in the initial texture has disappeared. A good agreement is found between predicted and experimental texture although the predicted one is more intense. This result is characteristic for the Taylor model.

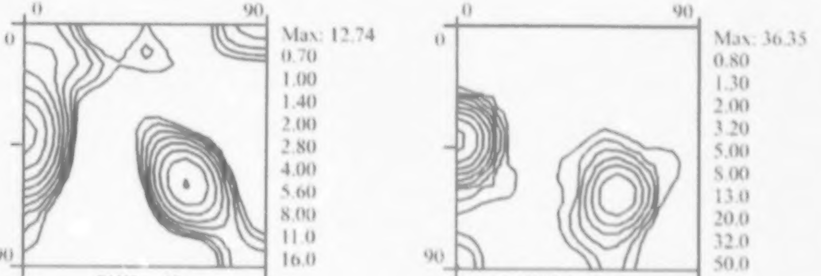

Fig. 4: Comparison between experimental (left) and simulated (right) texture at position A (see Fig. 3) after deep-drawing of an IF-steel.

6 Conclusions

Texture evolution has been coupled with a FE code for anisotropic sheet forming simulations. The constitutive law uses an analytical potential fitted on the average Taylor factors for the description of the yield locus. The method used for the texture updating consists of pausing regularly the FE simulation in order to allow the texture updating by means of the Taylor model. The following conclusions can be drawn:

1. The texture updating and computation of the analytical potential by means of the series expansion method is very computer intensive for a mesh including 656 elements even when parallelizing the work on 8 CPU.
2. A comparison between simulated and experimental texture has been given for one position at the top of the cup. A good agreement is found. The overestimation of the intensity is attributed to the Taylor model that was used.
3. When texture evolution is neglected, the simulated cup is in average 0.19 mm higher when the initial blank radius is 50 mm. This suggests that, for this class of forming processes, texture evolution is not relevant for the accuracy of the shape of the final product.

7 Acknowledgements

This work has been carried out as part of the Brite-EuRam project BE-97-4135 funded by the European Community. The authors would like to thank Professor Cescotto (Université de Liège) for making available a part of the source code of the FE program Lagamine originally developed by his team.

8 References

Hoferlin, E., Van Bael, A. and Van Houtte, P. (1999) Comparison between stress-based and strain-based elasto-plastic finite element models for anisotropic metal, *Proc. of Plasticity'99: the seventh internation symposium on plasticity and its current applications*, (ed. A.S. Khan), Neat Press, pp. 145-148.

Van Bael, A., Winters, J. and Van Houtte, P. (1996) A semi-analytical approach for incorporating crystallographic data into elasto-plastic finite-element formulations, *Proc. ICOTOM 11: the eleventh international conference on textures of materials*, (ed. Z. Liang, L. Zuo, Y. Chu), *Vol. 1*, International Academic Publishers, pp356-361.

Van Bael, A. (1994) Anisotropic yield loci derived from crystallographic data and their application in finite element simulations of plastic forming processes, *Ph.D. thesis*, K.U.Leuven, Belgium.

Van Houtte, P., Van Bael, A. and Winters, J. (1995) The incorporation of texture-based yield loci into elasto-plastic finite element programs, *Textures and microstructures*, Vol. 24, pp. 255-272.

Winters, J. (1996) Implementation of a texture-based yield locus into an elastoplastic finite element code. Application to sheet forming, *Ph.D. thesis*, K.U.Leuven, Belgium.

MONTE-CARLO SIMULATION OF TEXTURE TRANSFORMATION IN Ni-45% Fe NANOCRYSTALLINE ELECTRODEPOSITS

N. RAJMOHAN AND J. A. SZPUNAR
Department of Mining and Metallurgical Engineering, McGill university, Montreal, Canada, H3A 2B2

ABSTRACT

To explain the competition between the (111) and (100)-fiber textures in the Ni-45% Fe nanocrystalline electrodeposits during annealing, a new model is proposed. This model assumes high mobility to the grain boundaries, which are in high non-equilibrium states. The parameter, which specifies the magnitude of deviation of non-equilibrium nanocrystalline grain boundaries from their stable microcrystalline counterparts, defines the mobility. This new model is tested using a Monte-Carlo simulation of grain growth in 3-dimensional computer specimen that describes both texture and microstructure of these electrodeposits. The results of the simulation are compared with experiments.

Keywords: Monte-Carlo simulation, Nanocrystalline materials, Ni-Fe alloy, grain growth

1 Introduction

Thermodynamically, the nanocrystalline materials are in a metastable state because of the excess free energy associated with the intercrystalline components [1]. As grain size decreases, the intercrystalline component increases considerably. In this work, using the texture analysis, a mechanism for the texture and microstructure development in Ni-45% Fe nanocrystalline electrodeposit is proposed. The proposed mechanism is tested using a Monte-Carlo simulation. The results are then compared with the experimental observations and are discussed in detail.

In our previous research paper published in the same volume [2], the analysis based on the textural information has been made. The results suggest that unlike the conventional polycrystalline materials, the boundaries that are deviated from the equilibrium state may have high mobility to achieve the competitive growth of (111)-fiber over (100)-fiber component in nanocrystalline Ni-45% Fe alloys. In practice, (111)-fiber texture component grows much faster than the (100)-fiber. In the case of

Ni-45% Fe, the intensity of (111)-fiber component in the pole figure increases from about 3.5 to 12 when annealed at 673 K [2]. At 673 K, the growth of (111) fiber is stronger than the growth observed at 573K. The texture analysis [2] indicates that (111)-fibers in this nanocrystalline material has a characteristic distribution in which the grain boundaries with misorientation of 45°-63° are high in percentage than the (100)-fibers and average texture components. In this case, the grain boundary misorientation distribution function (GMDF) is computed by calculating misorientation between a pair of orientations generated in accordance with the orientation distribution function (ODF). In the texture analysis [2], the grain boundaries are classified into two types. First, the boundaries with misorientation of 15°-45° is called the middle misorientation type (MM-type) and the remaining boundaries namely, low (<15°) and high misoriented (>45°) boundaries are collectively called the LH-type boundaries. The grain boundary energy is generally high for MM-type boundaries in conventional microcrystalline materials. Unlike the conventional grain boundaries, Wolf and his co-workers [3-4] pointed out that the anisotropy in the grain boundaries of nanocrystalline materials is very little. Based on these arguments, the grain boundaries of the nanocrystalline materials can be regarded as a constant for all misorientation (relative boundary energy is 1). As explained in our previous texture analysis [2], the qualitative description of energy deviation parameter (ΔE_{dev}) is given below

$$\Delta E_{dev} = E_{nano} - E_{micro} \tag{1}$$

Here, E_{nano} and E_{micro} are the grain boundary energies of any misorientation for nanocrystalline and microcrystalline materials, respectively. The ΔE_{dev} can be used as a parameter for deriving mobility conditions for the grain boundaries of any misorientation. According to Gertsman et al [5-6], non-equilibrium grain boundary structure observed in deformed metals results in high mobility. Similarly, one can assume that the boundaries, which deviate from the conventional polycrystalline boundaries, have high mobility. From the above argument, it is evident that LH-type boundaries deviate from the equilibrium states more than the random boundaries; thus, they are assumed to have high mobility. The grain boundaries within the deviation of 5° is not considered for this calculation because at present, the energy values of these boundaries are hard to estimate. The percentage of these boundaries in the matrix is << 1%. Based on the proposed mobility criterion, a simulation method suitable for Monte-Carlo type procedure is discussed in the following section.

2 Simulation Method

The framework of the Monte-Carlo simulation model used in this paper has been described in the research work of Hinz and Szpunar [7]. The 3-dimensional computer specimen consists of nearly half a million sites with a 3-D honeycomb lattice structure [7]. The adjacent lattice sites are grouped into 1500 Voronoi grains with an orientation, which is assigned, according to the orientation distribution function (ODF) [8] using the algorithm developed by Morawiec et al [9]. This algorithm assumes a random correlation between the grains in the matrix. This simulation work has only one important parameter, namely the mobility. The mobility of the boundary is assumed to depend on the energy deviation parameter (ΔE_{dev}) in the following way:

$$\text{Mobility} = 1, \text{ when } \Delta E_{dev} > \Delta E_C$$
$$\text{Mobility} = 0, \text{ when } \Delta E_{dev} < \Delta E_C \qquad (2)$$

The conditions above explains that only those boundaries having energy deviation parameter higher than the critical value ΔE_C can move and all other boundaries are assumed to have zero mobility. The critical energy deviation parameter (ΔE_C) decreases as the simulation progresses according the following equation.

$$\Delta E_C = \Delta E_{max} - MCS\ 10^{-5}/a \qquad (3)$$

Here, ΔE_{max} is the highest energy deviation parameter at the start of the simulation. *MCS* is the number of Monte-Carlo steps [7] and a is a coefficient that describes the rate of decrease of energy deviation parameter during the annealing process of the computer specimen. The equation (2) is similar to the one used for the Monte-Carlo simulation of abnormal growth of Goss grains in microcrystalline high permeability steel by Hayakawa and Szpunar [10]. In their research, the equation relates the grain boundary energy to the number of *MCS*. However, in the present work, the ΔE_{dev} parameter describes the deviation of a particular grain boundary from the equilibrium state and is employed to specify the mobility conditions.

Physically, this assumption can be interpreted as follows: the energy deviation parameter explained in equation (1) qualitatively accounts for the amount of deviation of a particular grain boundary in its nanocrystalline metastable state from the microcrystalline stable state. The higher the deviation, higher is the tendency for the boundary to be more mobile. Thermodynamically, the boundaries with high energy deviation parameter would have a high driving force to reach its equilibrium state. This can be achieved only by grain growth. Thus, as the grains grow, the atoms in the grain boundary region arrange themselves towards a more stable state, thereby reducing its mobility. This explains the higher mobility of grain boundaries in nanocrystalline materials (even at relatively low temperatures) than in microcrystalline materials. Internal stability of the boundaries at low temperatures might come also from the presence of triple lines and vertices. Often, the presence of impurity atoms might stabilize [11,12] the grain boundary migration in the nanocrystalline materials. The equation (2) and (3) collectively states that at any point in time (i.e., MCS) the boundaries, with the energy deviation parameter value above the critical value, ΔE_C, are assumed to be mobile. This means that the boundaries that have enough driving force (high energy deviation parameter) to overcome the resistance offered by the impurities, other intercrystalline defects or even the combination of both, would move and other boundaries would remain pinned in the matrix. As the annealing progresses, the moving boundaries would restructure itself step by step towards the corresponding microcrystalline state. This can be attributed to the increase of the length of the grain boundary segment being considered. As the moving boundary approaches the equilibrium state, the energy deviation parameter and relative mobility would be reduced. Now, the other boundaries with lower values of energy deviation parameter would also have the relative mobility as high as those boundaries that moved first. Thus, as the annealing proceeds, the boundaries with progressively lower ΔE_{dev} would start to move in the simulation. By trials, the values for parameters a and ΔE_{max} are selected as 1 and 0.37, such that the simulations result in abnormal grain growth.

5 Results and Discussion

A series of simulations were carried out using the computer specimen describing the as-electrodeposited texture of Ni-45% Fe. The ϕ_2=0° and 45° sections of orientation distribution function (ODF) for this nanocrystalline electrodeposit is given in Fig. 1. The compiled results of the simulation are shown in Fig.2 in which the grain volume ratio is represented as a function of *MCS*. The Fig. 2 shows that all the 5 simulations carried out for Ni-45% Fe nanocrystalline electrodeposits exhibit abnormal growth of (111)-fiber grains with the volume ratios exceeding 125. Here volume ratio means the ratio between the volume of the grain considered and the average grain volume in the matrix. The results are presented in the plots of fiber intensities of the pole figures (Fig. 3.) calculated from the ODFs obtained from the simulated microstructures. To facilitate a comparison between the materials investigated, the simulated results are presented at the left side of Fig. 3. The experimental observation recorded for two different temperatures, namely 573 K and 673 K, are given on the right side of Fig. 3. Each of the computer specimens has 1500 grains at the beginning of the simulation. For the texture analysis, the simulation results are taken only up to the stage, where the remaining number of grains in the computer specimen is 250 or more. At the end of each simulation, the remaining number of grains is too small to provide accurate values of information about texture. On the other hand, these simulations can be used to compare the general trend observed during the annealing experiments of nanocrystalline electrodeposits. In all these plots, the maximum pole figure intensities of the (111) and (100) fibers are shown as a function of annealing time. Along with these values, the ratio between the (111) and (100)-fiber intensities is also presented. Observation of the simulation results shows that below 15000 *MCS*, no considerable textural change happens. However, beyond 15000 *MCS*, there is considerable texture transformation, which also coincides with the abnormal growth of the fiber grains. In order to verify the model proposed in this work, the texture transformation trend in all these cases is studied by comparing the intensity ratios during the abnormal growth, i.e., beyond 15000 *MCS*. In Ni-45% Fe, the (111)-fiber intensity increases considerably in both the experimental and simulated cases. The intensity of (111) fiber increases and (100)-fiber decreases drastically beyond 15000 *MCS*. As the grain size in the computer specimen increases, the growing grain consumes the entire cluster of random grains and thus, the intensity of the growing grain in the microstructure increases drastically. Because the probability of the (111)-fiber grain is very high growing (111)-fiber grains also consumes the (100)-fiber grains causing the reduction of (100)-fiber intensity significantly.

6 Conclusion

A model to predict the texture transformation in the Ni-45%Fe alloy nanocrystalline electrodeposits is proposed. This model assumes that the grain boundaries that are in high non-equilibrium state have high mobility. As observed in the experiments, this model predicts that there is a higher tendency for the (111)-fiber orientation to grow than for any other orientation in the matrix.

7 Reference

1. C.Suryanarayana, *Int. Mater. Rev.*, **40**, No.2, 41 (1995)
2. N.Rajmohan, J.A.Szpunar and U.Erb, *Int. conf. on texture of Mater. ICOTOM-12*, Montreal, Ed. J. A. Szpunar (1999)
3. S.R.Phillpot and D.Wolf, *Scripta metall. Mater.*, **33**, No.8, 1245 (1995)
4. P.Keblinski, S.R.Phillpot, D.Wolf and H.Gleiter, *Acta Mater.*,**45**, No.3, 987 (1997)
5. R.Z.Valiev, V.Y.Gertsman, and O.A.Kaibyshev, *Scripta metall. Mater.*, 17, 852 (1983)
6. R.Z.Valiev, V.Y.Gertsman, and O.A.Kaibyshev, *Scripta metall. Mater.*, **18**, 639 (1984)
7. D.Hinz, and J.A.Szpunar, *Phys. Rev.*, **B52**, 9900 (1995).
8. Bunge, H.J. in Texture Analysis in Materials Science – Mathematical Methods, Butterworths, London (1982)
9. A.Morawiec, J.A.Szpunar and D.C.Hinz, *Acta metall. mater.*, **41**, No.10, 825 (1993)
10. Y.Hayakawa and J.A.Szpunar, *Acta mater.***45**, No.11, 4713 (1997)
11. K.Boylan, D.Ostrander, U.Erb, G.Palumbo and K.T.Aust, *Scripta Metall. Mater.*, **25**, 2711 (1991)
12. A.M.El-sherik, K.Boylan, U.Erb, G.Palumbo and K.T.Aust, *Mat. Res. Symp. Proc.*, **238**, 727 (1992)

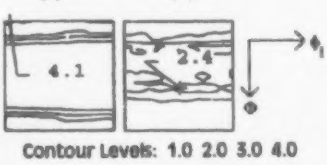

Fig. 1 (a) ϕ_2=0° and (b) ϕ_2=45° sections of the orientation distribution function (ODF) of as-electrodeposited nanocrystalline Ni-45%Fe.

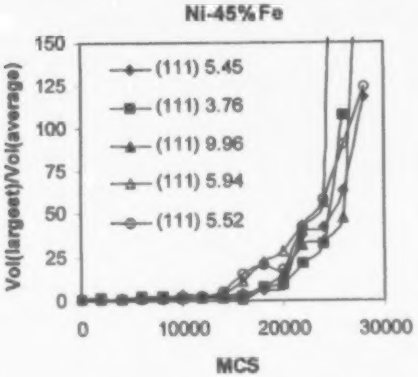

Fig. 2 Growth kinetics of the largest grains observed in various simulations having initial texture of as-electrodeposited Ni-45% Fe. Each curve is specified with type of fiber texture and angle of deviation (in degrees) from that fiber orientation.

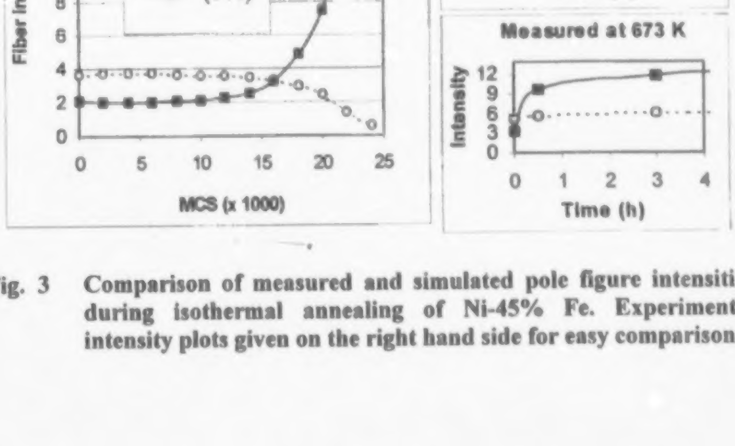

Fig. 3 Comparison of measured and simulated pole figure intensities during isothermal annealing of Ni-45% Fe. Experimental intensity plots given on the right hand side for easy comparison.

WHY WE CANNOT SIMULATE DEFORMATION TEXTURES

T. LEFFERS
Materials Research Department, Risø National Laboratory, Roskilde, Denmark

Abstract

It is demonstrated that the development of deformation texture may be far less regular than we want to believe. The reason is that the actual micromechanics of plastic deformation are far more complex than envisaged in our standard models, which introduces a very significant uncertainty in our texture predictions.

Keywords: Deformation texture, micromechanics, microstructure, simulation

1 Introduction

The title is, obviously, meant as a provocation. We are able to simulate deformation textures - in many cases with a result which comes rather close to the experimental textures.

The standard texture models only include very few microstructural features - normally only the grain shape and, for some materials, mechanical twinning seen as a bulk process (without reference to the actual microstructure of the twins). Of the standard models one may list the Taylor model with full or relaxed constraints (relaxed according to the "lath" or the "pancake" model), various modifications of the Sachs model, self-consistent models with more or less strong interaction with the continuum matrix and a number of other less commonly used models. Many of the models may be used with or without rate sensitivity. All these models are 1-site models in which the grains are considered one by one. Recently Van Houtte et al. (1998) and Lee et al. (1998) have suggested 2-site models (which are mathematically equivalent apart from a difference in the orientation of the grain boundaries separating the two interacting grains).

When looking at the very many attempts to simulate deformation textures in different materials with the above models, one notices the lack of a clear trend: in some cases one model works best, in other cases some other model works best, and there are no physical explanations of these differences, which is a logical consequence of the fact that all the models deal with polycrystals without much further specification. Even when we consider the one parameter which is specified in many models, the grain shape, the results are not necessarily logical: models with relaxed constraints may work well at moderate strains, and models with full constraint may work well at high strains. This is a strong indication that we are not really in control.

The widespread impression that we *are* in control relies heavily on the results of texture simulation for large strains where deviations in the different strain ranges may average out. In section 2 we shall see examples of erratic texture developments which clearly defies any attempt to do texture simulation with our present models.

One notices that there have, so far, been very few references. The reason is that there are so many examples that any attempt to cite a fair selection would overload the paper with references. In the following all statements will be backed up by references according to normal practice.

2 Rolling texture development in fcc materials

Together with Hansen (Leffers and Hansen 1992) the present author has collected data for the texture development in 13 different batches of aluminium and copper as represented by the copper texture component {211}<111>. 10 of the experiments were performed at Risø, and 3 were performed at RWTH in Germany. In the Risø experiments the measurements were made by neutron diffraction. In the RWTH experiments the measurements were made by X-ray diffraction. The results are shown in Fig. 1.

The materials were prepared in different ways (they had different chemical compositions, different grain sizes, different grain-size distributions and different initial textures), and they were rolled in different ways. However, neither of these parameters is of any significance in our standard models - apart from the initial texture which we shall return to. Three of the copper materials, represented by a thick straight line, were prepared in the same way (resulting in almost texture-free starting materials) and rolled in the same way, and they showed very much the same behaviour (the individual curves are shown by Leffers and Hansen). This demonstrates that the results are reproducible for identical conditions - but we do not know why these materials have a particularly regular texture development as compared to the other materials. The broken line represents texture simulation with the lath model (Van Houtte 1981) with random stresses added. This simulation works pretty well for the development of the copper component (the broken line comes quite close to the thick straight line), but it produces an excessively strong cube component (Leffers and Juul Jensen 1992).

It is clear from Fig. 1 that the different materials have different initial textures. For the materials for which the initial texture was known (Cu IV, Al pure, Al A, Al fine, Al coarse) Leffers and Hansen simulated the texture development with the same procedure as used for the broken line in Fig. 1. The use of this procedure should not be seen as implying that it is particularly ingenious, but it works for the three copper materials represented by the thick straight line. The results were approximately straight lines approximately parallel to the broken line. Thus, the difference in initial texture cannot explain the differences between the different materials in Fig. 1. For instance, the texture simulations predict the same texture development for Al coarse and Al fine and a texture development for Cu IV which is slightly faster than for texture-free material (and by implication slightly faster than that represented by the thick straight line).

One notices that even for the final textures after ~90% reduction there is a difference of up to a factor of ~5 between the orientation

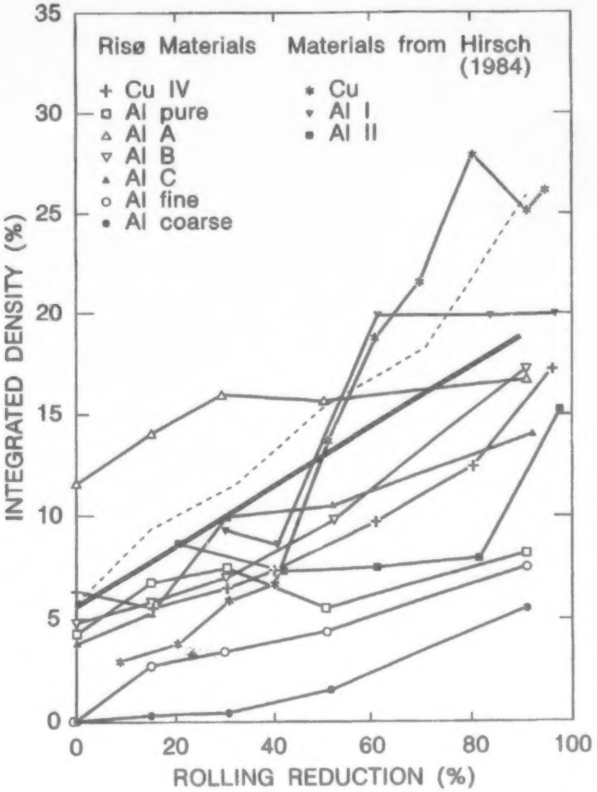

Fig. 1: Texture development in various copper and aluminium materials as represented by the fraction of orientations within 15° from {211}<111>. From Leffers and Hansen (1992) - who quote specific references to the investigations in which the individual materials were used.

densities of the copper component. It should be emphasized that the cases in Fig. 1 were not selected in order to get erratic texture developments. They were the only cases with quantitative data for the texture development known to us at that stage, and they represented, to the best of our knowledge, good and sober experiments.

In the present author's opinion the only possible explanation of the erratic behaviour in Fig. 1 is that the micromechanics of the plastic deformation of polycrystals are far more complex than envisaged in our standard models and that the micromechanics may change with strain for a given material. And that is the reason "why we cannot simulate deformation textures". If we want to come to a situation where we can really simulate deformation textures, we have to come to terms with the proper micromechanics, which requires thorough studies of the microstructure. In section 3 we shall recapitulate various microstructural observations which indicate micromechanics more complex than those envisaged in the standard models.

3 Various complex microstructures

3.1 Rolled aluminium

In aluminium rolled to moderate reductions dense dislocation walls (DDWs) or first-generation microbands subdivide the grains into "cell blocks" which normally have the shape of flat bands (Bay et al. 1989, 1992a; Bay et al. 1992b). The DDWs/first-generation microbands have an orientation approximately parallel to the transverse direction, making an angle of approximately 45° with the rolling plane.

In the following we shall not make any distinction between dense dislocation walls and first-generation microbands; we shall refer to both as DDWs. There is a clear statistical trend for a +/- lattice rotation across consecutive DDWs: if there is a certain positive lattice rotation about a certain rotation axis when passing one DDW, there well be a corresponding negative lattice rotation about the same rotation axis when passing the next DDW.

The present author has interpreted this as follows (Leffers 1998): there are two consecutive families of bands with different slip patterns and different strains, but the average strain corresponds to the macroscopic strain (for moderate strains where full constraint is logical). Formally the mathematics are equivalent to those of Van Houtte et al. (1998) and Lee et al. (1998). The resulting simulated texture agrees better with the experimental textures than the textures simulated with standard models.

Juul Jensen and Hansen (1990) and Winther (1998) have used the DDWs to account for the part of the mechanical anisotropy which cannot be explained by the texture (considering the DDWs as barriers to dislocation motion). Winther (1998) has suggested to take this one step further, letting the DDWs affect the slip pattern and hence the resulting texture.

At high strains the microstructure changes (Bay et al. 1992a). It is now dominated by "lamellae" approximately parallel to the rolling plane. Thus, this appears to be a completely new situation.

3.2 Rolled copper

In copper rolled to moderate strains about 50% of the grains develop a high-wall-density (HWD) structure with two crossing systems of dislocation walls approximately parallel to the transverse direction, making angles of approximately 45° with the rolling plane (Ananthan et al. 1991a). At present we have no micromechanical interpretation of the HWD structure. The interpretation of the DDWs in aluminium suggested by the present author in section 3.1 does not work because there are two systems of DDWs (Leffers 1998).

The other 50% of the grains develop a low-wall-density (LWD) structure with very few DDWs. In these grains one observes a high density of second-generation microbands (Ananthan et al 1991a, 1991b). They are bands parallel to {111} with very high strain. One may speculate whether the second-generation microbands produce glide on one single slip plane in the LWD grains as in the grains with bundles in rolled brass to be described in section 3.3. However, the limited structural stability of the second-generation microbands makes it far more difficult to draw clear conclusions than in the case of the bundled grains in brass.

At higher strains deformation bands are formed in rolled copper (at least in coarse-grained copper) as observed by Lee and Duggan (1993). The predominant orientation of the deformation bands is parallel to the rolling plane. Lee and Duggan incorporated the deformation bands in a texture model based on mathematics similar to those of Leffers (1998), e.g. section 3.1 - with some deviations resulting from the difference in orientation between the deformation bands and the DDWs and some other deviations discussed by Leffers (1994).

At very high strains the microstructure of rolled copper is dominated by dislocation walls parallel to the rolling plane as first observed by Hu (1969). The exact relation between this microstructure and the deformation bands of Lee and Duggan is uncertain.

3.3 Rolled brass

As recently recapitulated by Leffers (1996) (with a more recent addition by Christoffersen and Leffers (1997)) brass rolled to moderate reductions deforms by a composite pattern: about 50% of the grains (those with "bundles" consisting of thin lamellae of deformation twins separated by thin matrix lamellae) deform by predominant glide on one single slip plane, while the other grains deform by multiple glide (thus accounting for strain continuity).

At ~70% reduction shear banding takes over as the predominant deformation mechanism (Duggan et al. 1978) - because a high density of twin lamellae approximately parallel to the rolling plane makes further "normal" deformation impossible as suggested by Duggan et al., or because most grains are filled up with bundles which leaves too few grains to account for strain continuity in the composite pattern as suggested by Leffers. At ~90% reduction shear banding is replaced by a homogeneous deformation pattern as observed by Duggan et al.

Thus, brass is yet another example of a material with a multistage deformation pattern. There are no quantitative micromechanical models considering the actual microstructures for any of the stages. Surprisingly, the simple "modified Sachs model", which does not include any of the specific microstructural features, works fairly well for the whole range of reductions (Leffers 1996), but it does not reproduce the minor texture component with {111} approximately parallel to the rolling plane. The reason for the relatively good performance of the modified Sachs model probably is that it catches one central point: the non-Taylor character of the deformation mechanisms involved.

4 Discussion

The obvious theoretical shortcoming of the standard models is that they are 1-site models, considering the interaction of the individual grains with some kind of continuum matrix - and not with the individual neighbouring grains. The obvious solution is to go to finite-element modelling (FEM), to n-site models. There are several examples of texture simulation with FEM, which are not to be cited here. As expected, the general trend is that the resulting textures, in accordance with experimental observations, are less sharp than those simulated with the standard models.

Recently Mika and Dawson (1999) have used FEM on rolled fcc metals with special emphasis on the theoretically necessary intragranular strain heterogeneities and the derived intragranular variations in lattice orientation. They tried to correlate these variations with the experimentally observed variations in aluminium as described in 3.1 - with limited success. In the present author's opinion one cannot expect that "simple" FEM can simulate the complex micromechanics associated with complex *periodic* microstructures as those described in section 3 - for the simple reason that these micromechanics/microstructures can only be understood in terms of specific dislocation interactions which are not considered in FEM as we know it today. One may imagine more advanced FEM which includes the experimentally observed microstructures without generating them.

5 References

Ananthan, V.S., Leffers, T. and Hansen, N. (1991a) Cell and band structure in cold rolled polycrystalline copper. *Mater. Sci. Techn.*, Vol. 7, pp. 1069-1075.

Ananthan, V.S., Leffers, T. and Hansen, N. (1991b) Characteristics of second generation microbands in cold-rolled copper. *Scripta Metall. Mater.*, Vol. 25, pp. 137-142.

Bay, B., Hansen, N. and Kuhlmann-Wilsdorf, D. (1989) Deformation structures in lightly rolled pure aluminium. *Mater. Sci. Eng.*, Vol. A113, pp. 385-397.

Bay, B., Hansen, N. and Kuhlmann-Wilsdorf, D. (1992a) Microstructural evolution in rolled aluminium. *Mater. Sci. Eng.*, Vol. A158 , pp. 139-146.

Bay, B., Hansen, N., Hughes, D.A. and Kuhlmann-Wilsdorf, D. (1992b) Evolution of f.c.c. deformation structures in polyslip. *Acta Metall. Mater.*, Vol. 40, pp. 205-219.

Christoffersen, H. and Leffers, T. (1997) Microstructure and composite deformation pattern for rolled brass. *Scripta Mater.*, Vol. 37, pp. 1429-1434.

Duggan, B.J., Hatherly, M., Hutchinson, W.B. and Wakefield, P.T. (1978) Deformation structures in cold-rolled 70:30 brass. *Metal Sci.*, Vol. 12, pp. 343-351.

Hu, H. (1969) Reorientation in recrystallization, in *Textures in Research and Practice* (eds. J. Grewen and G. Wassermann), Springer-Verlag, Berlin, pp. 200-226.

Juul Jensen, D. and Hansen, N. (1990) Flow stress anisotropy in aluminium. *Acta Metall. Mater.*, Vol. 38, pp. 1369-1380.

Lee, B.J., Ahzi, S. and Parks, D.M. (1998) Intermediate modeling of polycrystal plasticity, in *Constitutive and Damage Modeling of Inelastic Deformation and Phase Transformation* (ed. A.S. Khan), Neat Press, Fulton, pp. 377-380.

Lee, C.S. and Duggan, B.J. (1993) Deformation banding and copper-type rolling textures. *Acta Metall. Mater.*, Vol. 41, pp. 2691-2699.

Leffers, T. (1994) Variations in the modelling of plastic deformation with grain subdivision, in *Strength of Materials* (eds. H. Oikawa et al.), The Japan Institute of Metals, Tokyo, pp. 235-238.

Leffers, T. (1996) The brass-type texture once again, in *Textures of Materials* (eds. Z. Liang et al.), International Academic Publishers, Beijing, pp. 299-306.

Leffers, T. (1998) Aspects of grain subdivision, in *Constitutive and Damage Modeling of Inelastic Deformation and Phase Transformation* (ed. A.S. Khan), Neat Press, Fulton, pp. 165-168.

Leffers, T. and Hansen, N. (1992) Texture, anisotropy, microstructure and models, in *Modelling of Plastic Deformation and Its Engineering Applications* (eds. S.I. Andersen et al.), Risø National Laboratory, Roskilde, pp. 57-77.

Leffers, T. and Juul Jensen, D. (1992) Quantitative simulation of the copper-type rolling texture, in *ibid*, pp. 323-329.

Mika, D.P. and Dawson, P.R. (1999) Polycrystal plasticity modeling of intracrystalline boundary textures. *Acta Mater.* (in press).

Van Houtte, P. (1981) Adaptation of the Taylor theory to the typical substructure of some cold-rolled metals, in *ICOTOM6* (ed. S. Nagashima), The Iron and Steel Institute of Japan, Tokyo, pp.428-437.

Van Houtte, P., Delannay, L. and Samajdar, I. (1998) Prediction of cold rolling textures and strain heterogeneity of steel sheet by means of the lamel-model, in *Constitutive and Damage Modeling of Inelastic Deformation and Phase Transition* (ed. A.S. Khan), Neat Press, Fulton, pp. 149-152.

Winther, G. (1998) Yield anisotropy caused by interaction between texture and dislocation structure, in *Modelling of Structure and Mechanics of Materials from Microscale to Product* (eds. J.V. Carstensen et al.), Risø National Laboratory, Roskilde, pp. 185-199.

ANALYSIS OF INHOMOGENEOUS ROLLING TEXTURE OF FCC METAL SHEETS

H.T. JEONG
Dept. of Mining & Metall. Eng., McGill University, Montreal, QC Canada H3A 2B2
K.K. UM
School of Eng. & Tech., Deakin University, Geelong VIC. 3217, Australia
D.N. LEE
School of Materials Science Eng., Seoul National University, Seoul 151-742, Korea

Abstract

The shear texture of FCC metals formed by the shear deformation consists mainly of the {001}<110>, {111}<112>, and {111}<110> orientations, but the shear texture varies with material and rolling condition. That is, either only one orientation component or mixtures of the components can develop depending on materials and rolling conditions. The purpose of this study is to analyze the various shear deformation textures.

Keywords: Shear texture, inhomogeneous rolling texture, stable orientation

1 Introduction

Many experimental and theoretical studies have been made of the development of homogeneous rolling textures of FCC metals. The experimental homogeneous rolling texture is known to consist of Cu orientation {112}<111>, S orientation {123}<412>, etc. Simulation using the full or relaxed constraints Taylor-Bishop-Hill model gives rise to D orientation {4 4 11}<11 11 8>, S orientation and Cu orientation. However, real rolling processes give rise to the through-thickness inhomogeneous rolling texture due to the deformation geometry and the friction between the rolls and sheet. The shear texture of FCC metals consists mainly of the {001}<110>, {111}<112>, and {111}<110> orientations, but it varies with material and rolling condition. That is, either only one component or mixtures of the {001}<110>, {111}<112>, and {111}<110> orientations can develop depending on materials and rolling conditions.

The shear texture developed in the surface layer of a rolled sheet is formed by the shear strain developed by friction between the roll and the sheet. The type of shear texture varies with the magnitude of shear strain. The magnitude of shear strain depends on the friction coefficient, the rolling temperature, the rolling speed, and the geometrical parameters such as the size of rolls, the reduction per pass, the total reduction, the initial thickness of the sheet, etc. In this study, the initial thickness of sheet and the reduction per pass were changed and the variation was expressed as a form of l/d parameter.

The variation of the shear deformation texture was measured according to the l/d parameters and simulated according to the sear strain ratio of $d\varepsilon_{13}/d\bar{\varepsilon}$. From the analysis of stable orientation and rotation rate of crystals, it is shown that shear texture formed during rolling varies with the shear strain ratio, $d\varepsilon_{13}/d\bar{\varepsilon}$.

2 Experiments

Commercial purity aluminum sheets were cold rolled using a mill with 127mm diameter rolls. The shear strain in the surface layer of sheet during rolling was controlled by the l/d value, where l and d are the roll-material contact length projected on the rolling direction and the mean value of the sheet thickness before and after rolling. The l/d value was controlled by the initial thickness of sheet and the reduction per pass.

Three different rolling schedules are given in Table 1. The l/d values in each rolling schedule were kept approximately constant. The average l/d values in the rolling schedule A, B and C were 0.55, 2.62 and 4.77, respectively. The (111), (200) and (220) pole figures were measured using the Schulz reflection method up to a tilting angle of 80°.

Figs. 1(a), (b) and (c) show the (111) pole figures obtained at the surface of the specimen rolled by procedures A, B and C in Table 1. Fig. 1(d) was obtained at the surface of an asymmetrically rolled aluminum specimen. The asymmetric rolling gives rise to relatively uniform shear deformation through the sheets thickness.

The texture of specimen A is similar to homogenous rolling texture composed of the {112}<111>, {4 4 11}<11 11 8> and {123}<634> orientations. The texture of specimen B is approximated by the {001}<110> orientation. However, the texture of specimen C is approximated by the {001}<110> and {111}<uvw> orientations. The texture of Fig.1(d) is also approximated by the {001}<110> and {111}<uvw> orientations and the {111}<uvw> texture is stronger in Fig. 1(d) than in Fig. 1(c).

3 Discussion

3.1 Calculation of stable orientation

An arbitrary deformation can be achieved by five active slip systems. The five active slip systems may not be determined uniquely. Many methods have been suggested to solve this problem. In this study, the random choice method (Van Houtte 1981) has been used. However, in this study where the stable orientation is determined by rolling reduction containing shear strains with respect to TD//<110> orientations, the number of active slip systems is four instead of five and uniqueness in the Taylor model is achieved. Therefore, any method yields the same result.

The rotation rate with respect to effective strain may be defined by $d\omega/d\bar{\varepsilon}$ with $d\bar{\varepsilon}$ being the effective strain. Most parts of sheet in rolling are subjected to following strain state: ($d\varepsilon_{11} = -d\varepsilon_{33} \neq 0$, $d\varepsilon_{31} \neq 0$, $d\varepsilon_{22} = d\varepsilon_{23} = d\varepsilon_{12} = 0$). In this case, the effective strain becomes

$$d\bar{\varepsilon} = \frac{2}{\sqrt{3}}\left(d\varepsilon_{11}^2 + d\varepsilon_{31}^2\right)^{1/2} \tag{1}$$

The effective strains of external deformations were set to be $2/\sqrt{3}$ to compare rotation rates for different shear strains. Since the stable orientation can vary with effective strain, the effective strains of deformations should be set equal.

Table 1: Rolling schedules of aluminum sheets.

	Total Reduction	Average l/d	Sheet thickness (mm)
A	80%	0.55	6.3 -(0.15/pass)→ 5.35 -(0.1/pass)→ 3.95 -(0.05/pass)→ 2.95 -(0.025/pass)→ 1.95 -(0.015/pass)→ 1.43 -(0.01/pass)→ 1.26
B	80%	2.62	2.95 → 2.25 → 1.80 → 1.56 → 1.37 → 1.23 → 1.06 → 0.90 → 0.79 → 0.74 → 0.69 → 0.63 → 0.60
C	74%	4.77	3.4 → 1.7 → 0.9

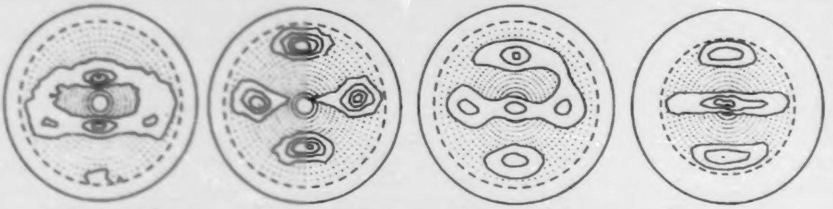

(a) max. 4.1 (b) max. 5.0 (c) max. 3.1 (d) max. 3.8

Fig. 1: (111) pole figures of surface layers of cold rolled aluminum sheets. Specimen (a) A, (b) B, (c) C in Table 1 and (d) asymmetrically rolled sheet.

Therefore, the ratio of shear strain to effective strain, $d\varepsilon_{13}/d\bar{\varepsilon}$, was defined as a measure of shear strain, $d\varepsilon_{13}$. In plane strain deformation without shear strain, $d\varepsilon_{13}/d\bar{\varepsilon} = 0.0$ and in pure shear strain, $d\varepsilon_{13}/d\bar{\varepsilon} = \sqrt{3/4}$.

Fig. 2 shows the rotation rate, $d\omega/d\bar{\varepsilon}$, of crystal orientation as a function of rotation angle for different shear strain ratios. The orientation with the positive rotation rate rotates to positive rotation angle and vice versa. Therefore, the orientations, for which the slope of the curve of the rotation rate against ω is negative at zero rotation rate, is stable and the orientation, for which the slope of the curve is positive at zero rotation rate, is meta-stable. When TD//$[1\bar{1}0]$ and the orientation at a rotation angle, ω, of 0° is $(001)[\bar{1}\bar{1}0]$, the crystal orientation is expressed as follows:

$$g(\omega) = \left(\frac{\sin\omega}{\sqrt{2}} \quad \frac{\sin\omega}{\sqrt{2}} \quad \cos\omega \right) \left[-\frac{\cos\omega}{\sqrt{2}} \quad -\frac{\cos\omega}{\sqrt{2}} \quad \sin\omega \right] \tag{2}$$

D orientation, {4 4 11}<11 11 8>, is calculated to be the stable orientation for plane strain compression. However, The shear strain $d\varepsilon_{13}$ makes the stable orientation rotate from the D orientation about TD//<110> direction. Therefore, the orientations rotated about TD//<110> were calculated to find out the stable orientation as a function of shear strain, $d\varepsilon_{13}$.

The deformation texture was simulated as a function of $d\varepsilon_{13}/d\bar{\varepsilon}$ with randomly distributed 978 single crystals and presented using Gauss type functions of $w_o=10^\circ$. Calculation was performed up to an effective strain of 2.30 without shear strains and up to an effective strain of 3.46 (95% reduction) as a function of $d\varepsilon_{13}/d\bar{\varepsilon}$.

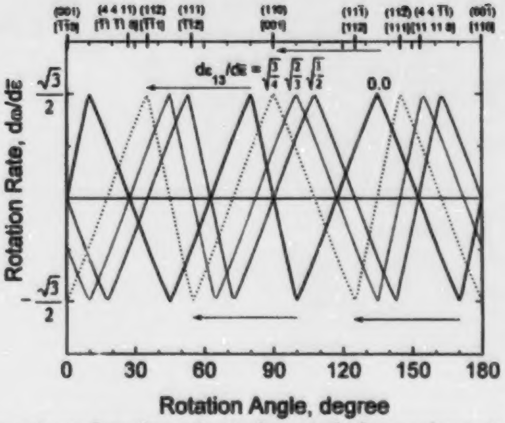

Fig. 2: Rotation rate as function of rotation angle for various $d\varepsilon_{13}/d\bar{\varepsilon}$ values.

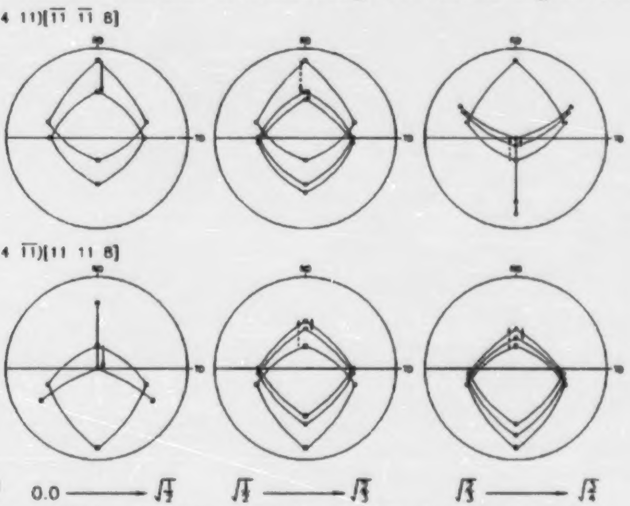
(4 4 11)[$\bar{1}\bar{1}$ $\bar{1}\bar{1}$ 8]
(4 4 $\bar{1}\bar{1}$)[11 11 8]
$\frac{d\varepsilon_{13}}{d\bar{\varepsilon}}$
$0.0 \longrightarrow \sqrt{\frac{1}{2}}$
$\sqrt{\frac{1}{2}} \longrightarrow \sqrt{\frac{2}{3}}$
$\sqrt{\frac{2}{3}} \longrightarrow \sqrt{\frac{3}{4}}$

Fig. 3: (111) pole figures of stable orientation as function of $d\varepsilon_{13}/d\bar{\varepsilon}$.

3.2 Changes of stable orientation according to the shear strain ratio

Fig. 2 shows that the plot of the rotation rate against the rotation angle shifts to the negative rotation angle direction with increasing $d\varepsilon_{13}/d\bar{\varepsilon}$ value and the plot of pure shear deformation shifts by -45° from that of plane strain compression.

The stable orientation in Fig. 2 varies with the $d\varepsilon_{13}/d\bar{\varepsilon}$ value. This change of the stable orientation is shown in the (111) pole figure of Fig. 3. In Fig. 3, two symmetric D orientations of (4411)[$\bar{11}\bar{11}$8] and (44$\bar{11}$)[11118], which are at rotation angles of 27.2° and 152.8° with (001)[$\bar{1}\bar{1}$0], respectively, become asymmetrical stable orientations at some values of $d\varepsilon_{13}/d\bar{\varepsilon}$. For the (4411)[$\bar{11}\bar{11}$8] orientation, the stable orientation moves in the negative angular direction and changed from the $(4\,4\,11)[\overline{11}\,\overline{11}\,8]$ to $(\bar{1}\,\bar{1}\,10)[\overline{5}\,\overline{5}\,\bar{1}]$ orientation as the $d\varepsilon_{13}/d\bar{\varepsilon}$ value or the shear strain ratio increases from 0 to $\sqrt{2/3}$. As the shear strain ratio increases from $\sqrt{2/3}$ to $\sqrt{3/4}$, the stable orientation moves in the positive angular direction and changed from $(111)[\bar{1}\,\bar{1}\,2]$ to $(1\,1\,\sqrt{2})[\bar{1}\,\bar{1}\,\sqrt{2}]$. The sign of rotation angle to stable orientation changes abruptly from negative to positive at the shear strain ratio of $\sqrt{2/3}$.

For the $(4\,4\,\overline{11})[11\,11\,8]$ orientation, the stable orientation moves in the negative angular direction from $(4\,4\,\overline{11})[11\,11\,8]$ to $(1\,1\,\bar{1})[112]$ as the shear strain ratio increases from 0 to $\sqrt{1/2}$. As the shear strain ratio increases from $\sqrt{1/2}$ to $\sqrt{3/4}$, the stable orientation moves in the positive angular direction from $(0\,0\,\bar{1})[110]$ to $(2\,2\,\bar{9})[994]$. The sign of rotation angle to stable orientation was changed abruptly from negative to positive at a shear strain ratio of $\sqrt{1/2}$.

The change of stable orientation depending on shear strain ratio could be classified into three regions in Fig. 3, because the shear strain ratios, at which the sign of rotation angle to stable orientation changed abruptly, were different in two symmetric D orientations, that is, $\sqrt{1/2}$ and $\sqrt{2/3}$. When the shear strain ratio is lower than $\sqrt{1/2}$ or higher than $\sqrt{2/3}$, the {001}<110> and {111}<112> components are stable. When the shear strain ratio is higher than $\sqrt{1/2}$ and lower than $\sqrt{2/3}$, only the {001}<110> component is stable. Therefore, the shear texture of surface layer of rolled specimen may be the {001}<110> orientation, or mixture of the {001}<110> and {111}<112> orientations.

3.3 Shear deformation dependent rolling texture

The deformation textures of aluminum and copper sheets are similar to each other when they are subjected to homogeneous rolling deformation. Whereas, the aluminum and copper sheets, when subjected to rolling deformation including shear deformation, may have different shear textures.

In order to understand the evolution of the textures in Fig.1, the texture simulation has been made using the Taylor-Bishop-Hill full constraints method, in which the initial texture was assumed to be randomly distributed 987 orientations. The simulated results are shown in Fig. 4. Fig. 4(a) shows the simulated (111) pole figure obtained when the initial sheet is subjected to plane strain deformation up to ε_{11} = 2.30 (90% reduction) without shear strain and the 987 orientations is replaced by the Gauss type function with a half width of 10°. It is similar to Fig. 1(a).

Figure 4 (b), (c) and (d) are calculated for a plane strain deformation up to ε_{11} = 3.00 (95% reduction) with $d\varepsilon_{13}/d\bar{\varepsilon}$ being 0.7047, 0.7206, and 0.8187, respectively, after deformation without shear strain. The $d\varepsilon_{13}/d\bar{\varepsilon}$ values of 0.7047 and 0.7206 are slightly smaller and larger than $\sqrt{1/2}$, respectively. The value of 0.8187 is slightly larger than $\sqrt{2/3}$. As already explained, abrupt changes in the rotation angle and direction take place and hence sever texture changes take place at $d\varepsilon_{13}/d\bar{\varepsilon}$ values of $\sqrt{1/2}$ and $\sqrt{2/3}$.

It can be seen that the (001)[110] and $(111)[1\,1\,\bar{2}]$ orientations develop in Fig. 4(b), only the (001)[110] orientation in Fig. 4(c), and the $(1\,1\,10)[5\,5\,\bar{1}]$ and $(344)[\bar{8}\,5\,1]$ orientations in Fig. 4(d).

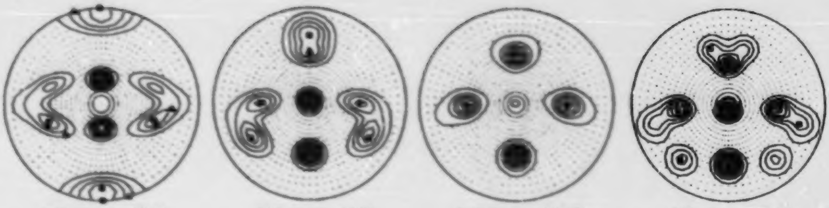

(a) max. 7.6 (b) max. 7.2 (c) max. 13.2 (d) max. 7.7

Fig. 4: (111) pole figures calculated using FC model with $d\varepsilon_{13}/d\bar{\varepsilon}$ value of (a) 0.0, (b) 0.7047, (c) 0.7296, and (d) 0.8187.

4 Conclusions

1. Since the shear deformation does not have the orthorhombic symmetry unlike plane strain compression, the $(4\,4\,11)[\overline{11}\,\overline{11}\,8]$ and $(4\,4\,\overline{11})[11\,11\,8]$ orientations, which are equally stable at plane strain compression, change to other stable orientations, which are asymmetric, for inhomogeneous rolling.

2. As the shear strain increases, the stable orientation rotates about TD//<110> direction in the same sense but the rotating direction changes in the opposite sense when the shear strain ratio reaches a critical value. The critical value is $\sqrt{1/2}$ and $\sqrt{2/3}$ for the $(4\,4\,11)[\overline{11}\,\overline{11}\,8]$ and $(4\,4\,\overline{11})[11\,11\,8]$ orientations, respectively. As a result, the combined orientations of the $(4\,4\,11)[\overline{11}\,\overline{11}\,8]$ and $(4\,4\,\overline{11})[11\,11\,8]$ orientations changes to 3 types of shear textures depending on shear strains.

3. When the $d\varepsilon_{13}/d\bar{\varepsilon}$ value is smaller than $\sqrt{1/2}$ or lager than $\sqrt{2/3}$, the shear texture is approximated by {001}<110>+{111}<112> or {001}<110>+{111}<110> orientations, whereas the {001}<110> is stable for $\sqrt{1/2} < d\varepsilon_{13}/d\bar{\varepsilon} < \sqrt{2/3}$.

5 References

Arminjon, M. (1987) *Acta Metall.*, Vol. 35, p.615

Dillamore, I.L. and Roberts, W.T. (1964) *Acta Metall.*, Vol. 12, p.281

Dillamore, I.L. and Katoh, H. (1974) *Met. Sci.*, Vol. 8, p.21

Gilormini, P. (1989) *Acta Metall.*, Vol. 37, p.2093

Hirsch, J. and Lucke, K. (1988) *Acta metall.*, Vol. 36, p.2863

Holscher, M., Raabe, D. and Lucke, K. (1994) *Acta Metall. Mater.*, Vol. 42, p.879

Jeong, H.T. (1997) *Ph.D. Thesis*, Seoul National University

Major, B. (1992) *Mater. Sci. & Tech.*, Vol. 8, p.510

Raphanel, J.L. and Van Houtte, P. (1985) *Acta Metall.*, Vol. 33, p.1481

Truszkowski, W., Krol, J. and Major, B. (1982) *Metall. Trans.*, Vol. 13A, p.665

Von Schlippenbach, U., Emren, F. and Lucke, K. (1986) *Acta metall.*, Vol. 34, p.1289

Van Houtte, P. (1978) *Acta Metall.*, Vol. 26, p.591

Van Houtte, P. (1981) *Proc. ICOTOM 6*, Tokyo, Vol. 1, p.428

Van Houtte, P. (1988) *Textures and Microstructures*, Vol. 8&9, p.313

FINITE-ELEMENT SIMULATION OF TEXTURE DEVELOPMENT IN POLYCRYSTALLINE METALS

A. BERTRAM

Institute of Mechanics, Otto-von-Guericke-University Magdeburg, Germany

A. KRASKA

CargoLifter, Krausnick, Germany

Abstract

Texture simulations are performed by the Representative Volume Element technique. An aggregate of grains with isotropic initial orientation distribution is subjected to large standard deformations. Within the grains, slip system theory with Voce-type hardening is implemented. The results are compared with experimental data.

Keywords: Finite Inelastic Deformations, Texture Induced Anisotropy

1. Introduction

In Bronkhorst et al. (1992) experimental results of texture development of polycrystalline copper under different standard deformations have been reported, which clearly show the induction of anisotropy into an initially isotropic specimen.

The present simulation of this process has been performed by the Representative Volume Element technique (RVE). For that purpose, a cubic specimen has been implemented with 512 grains, each of them consisting of 5 constant strain tetrahedral elements. In the interior and on the boundaries of the RVE, a displacement split of the deformation into a homogeneous global one and a fluctuation part is assumed, such that the mean deformations equals the global one, and that the fluctuations on the boundaries fullfil periodic boundary conditions. In that way compatibility on the boundaries is gained, whereas equilibrium of the boundary tractions results from the finite element solution of the initial and boundary value problem. The initial ODF, assumed as isotropic, has been generated randomly, selected by a filter technique, and finally optimized by means of an appropriate isotropy measure.

Within the grains, the material is modelled by a slip system model taking into account the 12 octahedral slip systems of an FCC crystal. On each of them, a slightly rate dependent law with Voce-type hardening has been applied. The ration between latent and self hardening has been taken as 1.4.

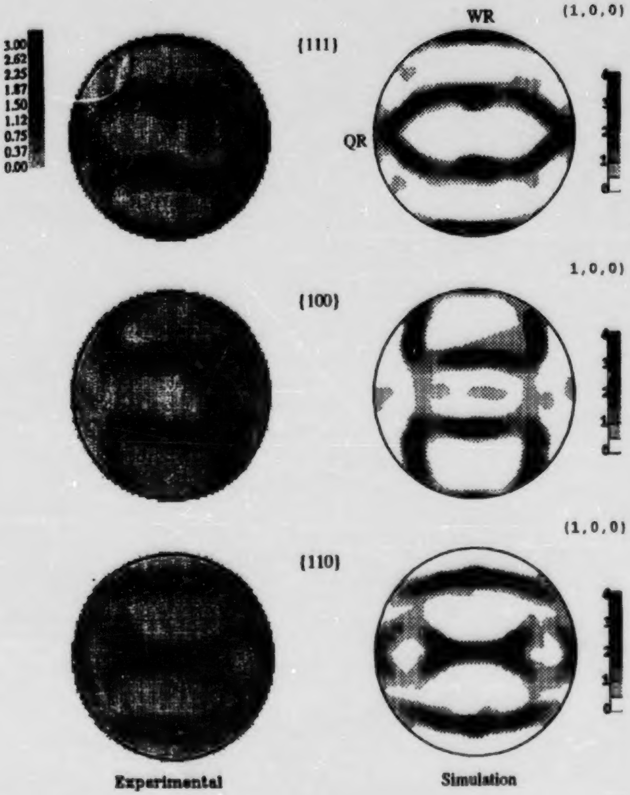

Fig. 1: Rolling texture

The specimen has been submitted to the following standard deformations, (A) uniaxial compression to 21% of the initial length, (B) uniaxial extension to 145%, (C) plane strain compression to 21%, and (D) simple shear up to a shear number of 1.5. All these tests imply large deformations, such that a fully nonlinear analysis had to be applied.

2. Texture

In Fig. 1 and Fig. 2 the resulting pole figures of test (C) and (D) are shown for the {111}, {100}, and {110} orientations. Comparison of the experimental and simulated textures show good agreement in all cases. The analogue results for the other tests are shown in Kraska (1999).

Besides of these results the RVE-technique gives much more information on the resulting material, such that one can consider the RVE as "numerical laboratory" (C. Miehe). Indeed, by the results of the FEM calculation, we can among other

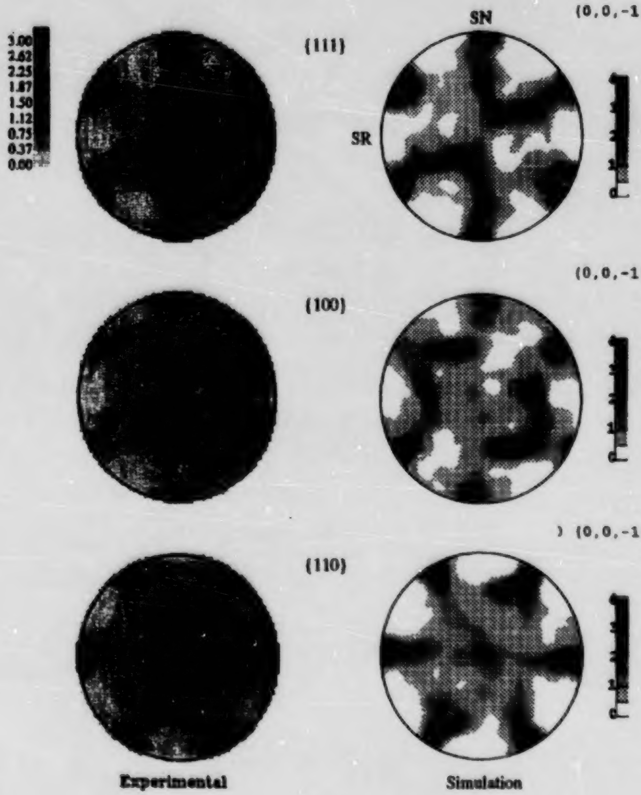

Fig. 2: Shear texture

features determine the induced elastic and inelastic anisotropy.

3. Elastic anisotropy

The induced elastic anisotropy can easily be investigated by the following procedure. By 5 independent shear tests and one compression test the elastic stiffnesses are identified. Their deviation from the initial (isotropic) ones indicates the texture induced anisotropy. The bulk moduli under all deformations remain the same, whereas the shear moduli vary up to 2.3% under compression. For many applications this effect is negligible. However, it is not unexpected and in accordance to experimental findings.

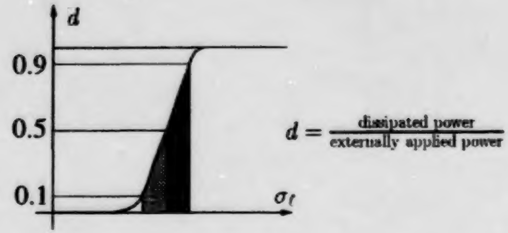

Fig. 3: The energy based yield indicator for different *d*-values

3. Inelastic anisotropy

The induced inelastic anisotropy is much more apparent and important. It can be investigated and demonstrated in different ways. One is to determine the yield loci with respect to different definitions. We are free to apply the usual offset criteria with different offset strains. However, we can also introduce energy based criteria, which can be easily evaluated by our RVE. One of them is the ration *d* of the dissipated energy per unit time over the entire energy supply. In Fig. 3 this has been depicted for three different values of *d*. In Fig. 4 samples of the sheet after test (B) have been (computationally) strained in different directions within the three planes. In the three radiograms, the yield loci for the three *d*-values have been plotted for the three planes. When x indicates the tensile axis, the plots for the x-z-plane are expected to equal those of the x-y-plane. This can be observed, as well as a strong distortion of the yield loci due to texture development.

Another measure for the texture influence on further deformations is the Lankford coefficient or *r*-value. In Fig. 4 it is plotted versus the angle to the rolling direction and compared with experimental results of Fundenberger (1993) for an aluminum sample submitted to the same channel die test. Although these data stem from different materials, the qualitative similarity gives rise for another promising applications of the RVE results.

4. Conclusions

The RVE technique with periodic boundary conditions and FEM solutions is shown to be a "numerical laboratory" for investigations of various aspects and details of texture evolution in polycrystalline materials. Comparison with experimental results give good agreement with the numerical simulation. For further results the reader is referred to Bertram et al. (1999) and Kraska (1999).

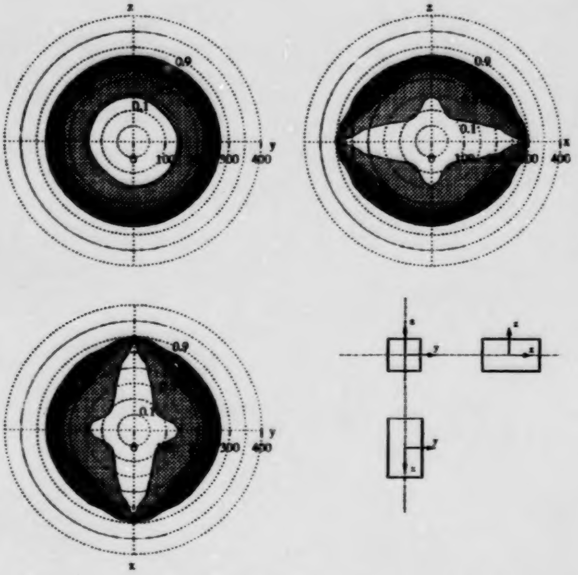

Fig. 4: Yield loci for tensile tests with different inplane directions

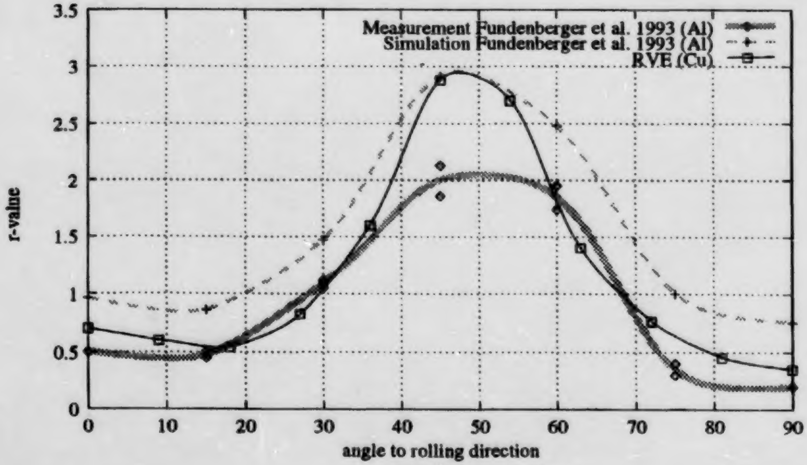

Fig. 5: r-values in simulation and experiment

5. References

Bertram, A., Böhlke, T. and Kraska, K. (1999) Texture development of aluminum polycrystals under finite plastic deformations. *IUTAM-Symposium Micro- and Macrostructural Aspects of Thermoplasticity*, Bruhns, O.T. and Stein, E., Kluwer Academic Publishers, pp. 127–136

Bronkhorst, C.A., Kalidindi, S. R., Anand, L. (1992) Polycrystalline plasticity and the evolution of crystallographic texture in f.c.c. metals. *Phil. Trans. R. Soc. Lond.*, A341, pp. 443-477

Kraska, M. (1999) Textursimulation bei großen inelastischen Verformungen mit der Technik des repräsentativen Volumenelements. *Dissertation* TU Berlin

Fundenberger, M. J., Philippe, M.J., Esling, C., Lequeu, P. and Chenal, B.(1993) Calculation of yield surfaces and determination of forming limit diagrams of aluminium alloys, *Textures Microstruct.*, 21, 93 108

3D-ANIMATION FOR ROTATION OF F.C.C. CRYSTALS DURING VARIOUS TYPES OF DEFORMATION

H.MASUI
Department of Material Science and Engineering, Teikyo University,
Utsunomiya, Japan

Abstract

It has been recognized in another paper by the author in this conference that the model based on pencil glide theory can be also considerably utilized for deformation texture formation of face centered cubic metal. Using the model, 3D-animation by visualization of crystal rotation was tried in rolling deformation, tensile elongation and compression with increasing strain on face centered cubic metal. The 3D-animation simulated a rotation of the crystal visually and intelligibly with increasing strain irrespectively both of initial orientation and of deformation style.

Keywords: Animation,compression,face centered,rolling,texture,visualization

1 Introduction

Crystal rotation during deformation has been usually described on a pole figure method by stereographic projection. The pole figure method, however,is not always easy to comprehend the rotation of crystal intuitively compaired with 3D-visualized information. On the other hand, animation by 3D-visualization during deformation needs elaborate digital data for the rotation of face centered cubic(hereafter,abbreviated to fcc) metal with increasing strain according to both initial orientation and deformation style.

From these backgrounds, 3D-animation of fcc crystal rotation during deformation has been tried using the model based on pencil glide theory for fcc metal. Pencil glide theory had been formerly applied to body centered cubic iron (Dillamore and Katoh 1974; Katoh 1985).

Summary of the present model by pencil glide theory for deformation texture of fcc metal, is as follows. The model divides the 12 glide systems of fcc metal into 3 equivalent groups which are composed of 8 $\{111\}\langle 110\rangle$ glide systems $(dX_i, dY_i; i = 1 \sim 4)$ around the principal axes respectively. The principle of the minimum total amount of shear magnitudes(Taylor 1938; Bishop and Hill 1951)is applied to sum of the 8 glide systems differentiating by rotation $d\ \Phi_j (j = 1 \sim 3)$ and yields two kinds of solutions $\Omega(3)$ and $\Omega(1)$. A group with active glide systems is determined with the aid of the maximum plastic work theory(Bishop and Hill 1951; Ookubo 1968;Kochs 1970).

2 Method

The 3D-animation of fcc crystal rotation during deformation was realized in following steps.

1. ND indicates the direction parallel to compressive or tensile direction and the direction normal to the rolling sheet plane as well. ND uses both α as measured from X([100]) axis on X([100])-Y([010])plane and subsequently β as measured from X([100])-Y([010]) plane toward Z([001]) axis in the position of α. Further, RD indicates rolling direction in the rolling plane and uses θ as measured from the intersecting line of X([100])-Y([010])plane and plane normal to ND, on the rollig plane. Strain tensor components $d\ \varepsilon_{11}, d\ \varepsilon_{12}, \cdots$ are defined by α, β and θ according to deformation style such as rolling,tensile elongation and compression.

2. Firstly, only one group whose value of the plastic work is the greatest among the 3 groups,is chosen in solution $\Omega(3)$ if requirements that four vectorial sums of dX_i and dY_i,i.e., $a \geq 0$,$b \geq 0$, $c \geq 0$ and $d \geq 0$ are satisfied,while, otherwise, there is still a need to look for the minimum total amount of shear magnitudes of the glide systems in solution $\Omega(1)$.

3. Rotation $d\ \Phi_1, d\ \Phi_2$ and $d\ \Phi_3$ around the principal axes X[100],Y[010] and Z[001] respectively are obtained in the chosen group in $\Omega(3)$ or $\Omega(1)$. These change values of angle parameters α, β and θ in every strain steps.

4. Animation by 3D-visualization for the crystal rotation uses the change of the angle parameters. 3D-visualization for the crystal rotation, however, needs also 3D-rotation of the coordinates(x,y,z) according to the change of the angle parameters.

   Thus,animation of fcc crystal rotation is realized on display of computer.

3 Results

3.1 Rolling

Fig.1 shows arrow map between α (alpha) and θ (theta) in case of β=0 in rolling deformation by the model ,where all arrows seem to be attracted to definitely one point of ND,RD:(110)[$\bar{1}$12];(α = 45.0, β = 0.0, θ = 54.74(degree)).

Table 1 shows example of changes of orientation with strain by the model for two fcc cryatals of different initial orientation in Fig.1. Glide modes of two crystals were always $\Omega(3)(Z)$ for crystal A and $\Omega(1)(Z)$ for crystal B respectively.

Fig.2 shows several shots of 3D-animation pictures for fcc crystal A and B. These pictures can be projected from arbitrary direction so that precise difference of angle may be measured.

Table 1: Change of orientation for fcc crystal A and B during rolling.

	Crystal A	Crystal B
Initial state	$(110)[\bar{2}21]$ $\alpha=45.0$, $\beta=0.0$, $\theta=20.0$	$(100)[011]$ $\alpha=0.0$, $\beta=0.0$, $\theta=45.0$
Reduction:59.4%	$(110)[\bar{1}11]$ $\alpha=45.0$, $\beta=0.0$, $\theta=35.6$	$(100)[025]$ $\alpha=0.0$, $\beta=0.0$, $\theta=68.2$
Reduction:93.8%	$(110)[\bar{5}59]$ $\alpha=45.0$, $\beta=0.0$, $\theta=51.8$	$(100)[0\,1\,17]$ $\alpha=0.0$, $\beta=0.0$, $\theta=86.7$
Reduction:98.5%	$(110)[\bar{1}12]$ $\alpha=45.0$, $\beta=0.0$, $\theta=54.1$	$(100)[001]$ $\alpha=0.0$, $\beta=0.0$, $\theta=89.3$

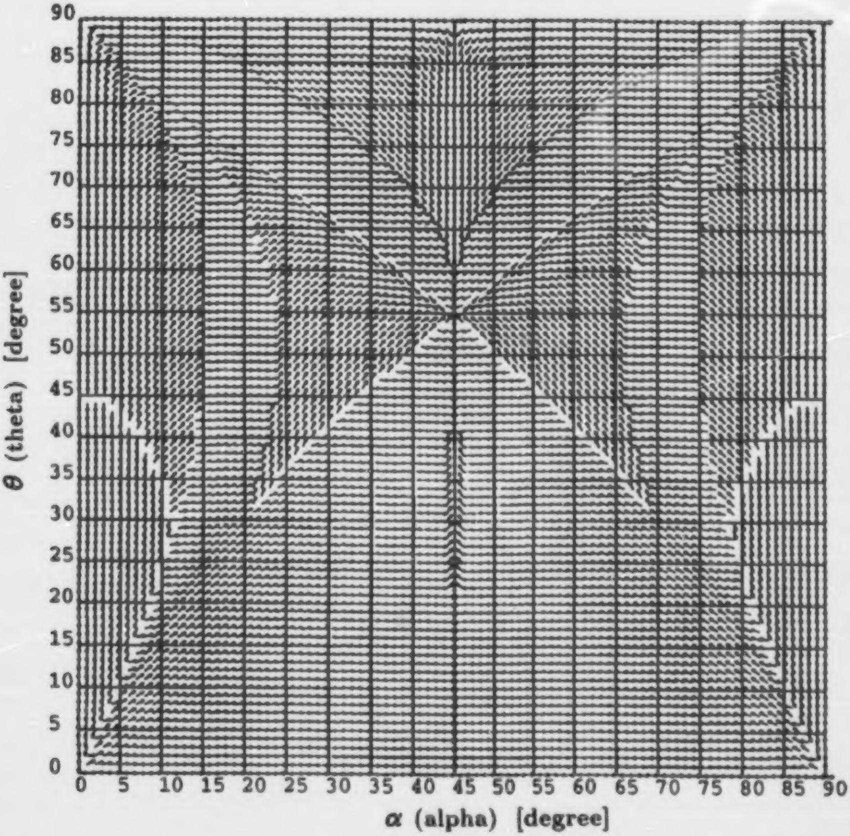

Fig. 1: Crystal rotation arrow map between α and θ in case of $\beta=0$ in rolling deformation of fcc crystal by the pencil glide model.

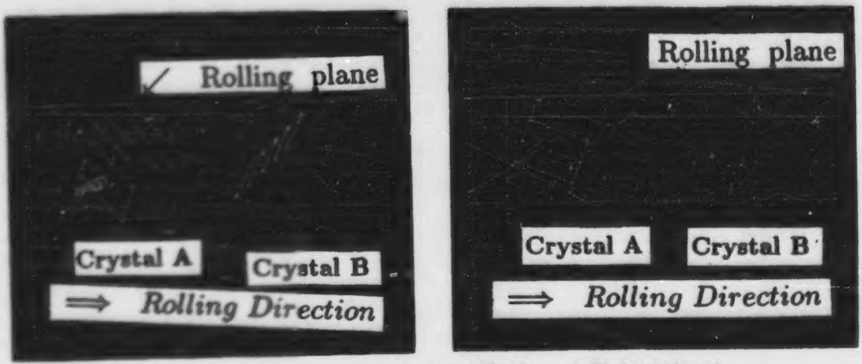
Rolling plane
Crystal A
Crystal B
⟹ Rolling Direction
Rolling plane
Crystal A
Crystal B
⟹ Rolling Direction

2-(1) Initial state of fcc crystal A:(110)$[\bar{2}21]$ and B:(100)[011]

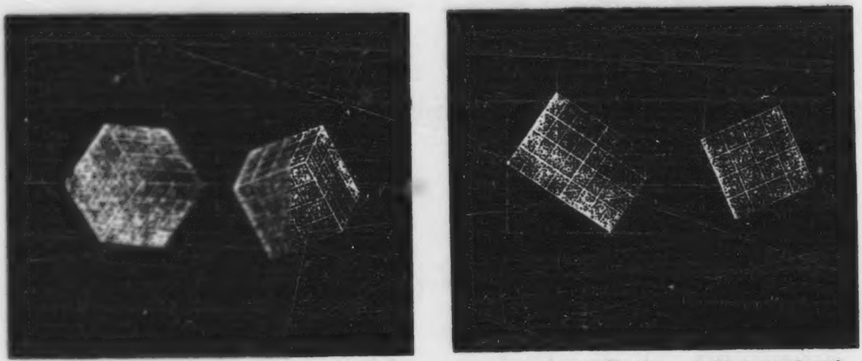

2-(2) Reduction:59.4% state of fcc crystal A:(110)$[\bar{1}11]$ and B:(100)[025]

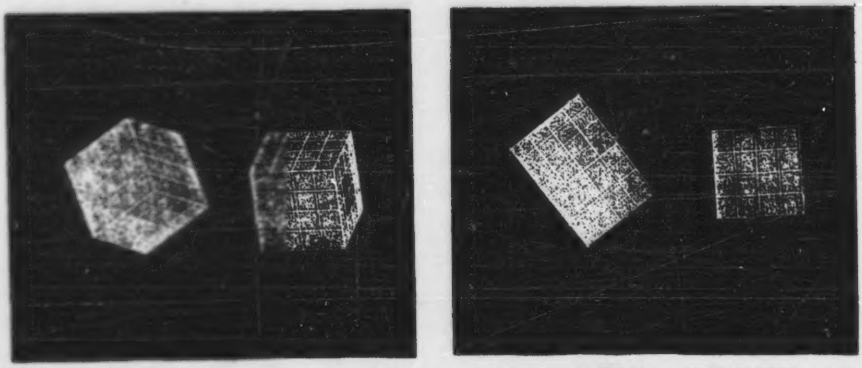

2-(3) Reduction:93.8% state of fcc crystal A:(110)$[\bar{5}59]$ and B:(100)[0 1 17]

Fig. 2: Several shots from 3D-animation pictures of crystal rotation during rolling deformation by the pencil glide model for fcc crystal A and B in Table 1.

3.2 Uni-axial deformation

Uni-axial compression and tensile elongation are easier for the 3D-animation by the model than rolling.

Therefore,it seems rather informative to show example of digital data for changes both of orientation and glide mode with strain in compression in Fig.3.

```
initial               alpha   beta
                      45.00   35.26
 strain  mode(Ω)      alpha   beta           ND
  0.025   1 Z   23    45.00   34.26   0.58 0.58 0.56
  0.050   1 Z   23    45.00   33.26   0.59 0.59 0.55
  0.074   1 Z   23    45.00   32.26   0.60 0.60 0.53
  0.099   1 Z   23    45.00   31.26   0.60 0.60 0.52
  0.124   1 Z   23    45.00   30.26   0.61 0.61 0.50
  0.149   1 Z   23    45.00   29.26   0.62 0.62 0.49
  0.174   1 Z   23    45.00   28.26   0.62 0.62 0.47
  0.199   1 Z   23    45.00   27.26   0.63 0.63 0.46
  0.224   1 Z   23    45.00   26.26   0.63 0.63 0.44
  0.249   1 Z   23    45.00   25.26   0.64 0.64 0.43
  0.274   1 Z   23    45.00   24.26   0.64 0.64 0.41
  0.299   1 Z   23    45.00   23.26   0.65 0.65 0.39
  0.324   1 Z   23    45.00   22.26   0.65 0.65 0.38
  0.350   1 Z   23    45.00   21.26   0.66 0.66 0.36
  0.375   1 Z   23    45.00   20.26   0.66 0.66 0.35
  0.399   1 Z   23    45.00   19.26   0.67 0.67 0.33
  0.424   3 Z         45.00   18.26   0.67 0.67 0.31
  0.450   3 Z         45.00   17.26   0.68 0.68 0.30
  0.477   3 Z         45.00   16.26   0.68 0.68 0.28
  0.505   3 Z         45.00   15.26   0.68 0.68 0.26
  0.535   3 Z         45.00   14.26   0.69 0.69 0.25
  0.566   3 Z         45.00   13.26   0.69 0.69 0.23
  0.598   3 Z         45.00   12.26   0.69 0.69 0.21
  0.634   3 Z         45.00   11.26   0.69 0.69 0.20
  0.671   3 Z         45.00   10.26   0.70 0.70 0.18
  0.713   3 Z         45.00    9.26   0.70 0.70 0.16
  0.758   3 Z         45.00    8.26   0.70 0.70 0.14
  0.808   3 Z         45.00    7.26   0.70 0.70 0.13
  0.865   3 Z         45.00    6.26   0.70 0.70 0.11
  0.930   3 Z         45.00    5.26   0.70 0.70 0.09
  1.007   3 Z         45.00    4.26   0.71 0.71 0.07
  1.102   3 Z         45.00    3.26   0.71 0.71 0.06
  1.226   3 Z         45.00    2.26   0.71 0.71 0.04
  1.405   3 Z         45.00    1.26   0.71 0.71 0.02
  1.724   3 Z         45.00    0.26   0.71 0.71 0.00
```

Fig. 3: Digital output data on crystal rotation in compression for fcc crystal by the pencil glide model.

Orientation of fcc metal with ND:(111)($\alpha = 45.0$, $\beta = 35.26$(degree)) as initial state was changed under uni-axial compression to finally ND:(110)($\alpha = 45.0$, $\beta = 0.26$(degree)), where the glide mode was transited from $\Omega(1)(Z)$ to $\Omega(3)(Z)$ at strain 0.424(34.6% compression). There are still four cases of mathematical analytical solutions $a = 0$(case:1),$b = 0$(case:2), $c = 0$(case:3) and $d = 0$(case:4) in each group in case of $\Omega(1)$. Normally two cases of them are valid due to satisfaction of the requirements of $a \geq 0, b \geq 0$, $c \geq 0$ and $d \geq 0$ in the model and do operate as shown in "2,3" in $\Omega(1)(Z)$ at the mode in Fig.3.

4 Conclusion

3D-animation of fcc crystal rotation by the model based on pencil glide theory was realized irrespectively of initial orientation and of deformation style. The change of fcc crystal orientation conformed considerably to the experimental results(Goeler and Sachs 1927; Barret and Levenson 1940; Calnan and Clews 1950;Zhou et al. 1992) with additional information on the glide modes by pencil glide theory with increasing strain as well.

3D-visualization of fcc crystal rotation made it easy to understand a change of crystal orientation intelligibly and did it possible even to measure a difference of angle precisely as well.

5 References

Barrett,C.S. and Levenson,L.H. (1940) The structure of aluminum after compression. *Trans.AIME*, Vol.137,pp.112-27.

Bishop,J.F.W. and Hill,R. (1951) A theoretical derivation of the plastic properties of a polycrystalline face-centered metal. *Phil.Mag.*, Vol.42,pp.1298-307.

Calnan,E.A. and Clews,C.J.B. (1950) Deformation textures in face-centered cubic metals. *Phil.Mag.*, Vol.41,pp.1085-100.

Dillamore,I.L. and Katoh,H. (1974) A comparison of the observed and predicted deformation textures in cubic metals. *Metal Science*, Vol.8,pp.21-7.

Goeler,F.V. and Sachs,G. (1927) Rolling deformation and recrystallization textures of fcc metal. *Z.Tech.Phys.*, Vol.41,pp.873-88.

Katoh,H. (1985) Deformation texture. *Proc.J.I.M.Seminar on Texture(Japanese)*, pp.15-30.

Kochs,U.F. (1970) The relation between polycrystal deformation and single crystal deformation. *Met.Trans.AIME*, Vol.1,pp.1121-43.

Ookubo,T. (1968) Plasticity of cubic metal under constraint condition. *Plasticity (Japanese)*, Vol.9,pp.681-90.

Taylor,G.I. (1938) Plastic strain in metals. *J.Inst.Metals*, Vol.62,pp.307-24.

Zhou,Y.,Toth,L.S. and Neale,K.W. (1992) On the stability of the ideal orientations of rolling textures for f.c.c.polycrystals. *Acta metall.*, Vol.40,pp.3179-93.

TEXTURE EFFECTS ON STEEL SHEET BEHAVIOUR UNDER LARGE STRAIN SIMULATIONS.

L. DUCHENE, A. GODINAS and A.M. HABRAKEN
Department MSM, Liège University, Belgium

Abstract

This paper presents a constitutive law based on the Taylor model implemented in our non linear finite element code LAGAMINE. The yield locus is only locally described and the interpolation method is described. This local yield locus model uses a discrete representation of the material's texture. A rolling simulation with texture prediction is presented.

Keywords: finite element simulation, rolling, texture evolution, yield locus

1 Introduction

Various constitutive laws based on texture analysis have been implemented in the non linear finite element code LAGAMINE. Our first step in the integration of the texture effects was the use of a 6th order serie yield locus defined by a least square fitting on a large number of points (typically 70300) in the deviatoric stress space (Munhoven et al. 1996). Those points were calculated by a Taylor model based on an assumed constant texture of the material. This method, i.e. a global description of the yield locus, is actually used in the FEM code.

Unfortunately, taking into account the texture evolution effects with this yield locus would imply the computation of the 210 serie coefficients for each integration point, each time a texture updating is necessary. This would require an impressive amount of computation and memory storage (210 coefficients for each integration point) which is only partially useful as generally the stress state remains in a local zone of the yield locus. So, two new approaches, where the whole yield locus is unknown, have been investigated.

In the first case, the interesting part of the yield locus is represented by an hyperplane which is a plane defined in the five-dimensional deviatoric stress space.

As it has been shown (see Duchêne et al. 1999), the yield locus discontinuities bred by this very simple interpolation method give rise to convergence problems in the finite element code. That is the reason why a second method has been developed.

For that second approach, no yield locus is defined and a direct stress-strain interpolation between Taylor points is achieved. In this case, the stress and the plastic strain rate continuity conditions are fulfilled but, as there is no yield locus formulation, a particular stress integration scheme has to be used.

This stress-strain interpolation method and the implementation of the Taylor texture updating model are briefly described; a rolling simulation with texture evolution prediction is presented.

2 Description of the constitutive law

2.1 The stress-strain interpolation model

We use a linear stress-strain interpolation described by Equation 1.

$$\underline{\sigma} = \tau \cdot \underline{\underline{C}} \bullet \underline{u} \tag{1}$$

In this equation, $\underline{\sigma}$ is a 5-D vector containing the deviatoric part of the stress; the hydrostatic part being elastically computed according to Hooke's law. The 5-D vector $\underline{u}$ is the deviatoric plastic strain rate direction; it is a unit vector. The interpolation is included in the matrix C of Equation 1 and is based on the following concepts. We assume 5 directions: $\underline{u}_i$ (i=1…5) advisedly chosen in the deviatoric strain rate space and the associated deviatoric stress: $\underline{\sigma}_i$ (i=1…5) lying on the yield surface according to the Taylor model. These points will define the interpolation domain and will be called stress nodes. Additionally, we compute the contravariants vectors $\underline{ss}_i$ and $\underline{uu}_i$ defined by Equations 2 and 3.

$$\underline{ss_i} \bullet \underline{\sigma_j} = \delta_{ij} \tag{2}$$

$$\underline{uu_i} \bullet \underline{u_j} = \delta_{ij} \tag{3}$$

With the use of those contravariants vectors we define intrinsic co-ordinates in the interpolation domain for any stress vector $\underline{\sigma}^*$ by projection according to Equation 4 and for any plastic strain rate direction $\underline{u}^*$ with Equation 5.

$$\eta_i = \underline{\sigma^*} \bullet \underline{ss_i} \tag{4}$$

$$\eta_i = \underline{u^*} \bullet \underline{uu_i} \tag{5}$$

The most important property of our stress-strain interpolation states that if the stress $\underline{\sigma}^*$ and the plastic strain rate direction $\underline{u}^*$ physically correspond to the same point, then the intrinsic co-ordinates η_i computed for $\underline{\sigma}^*$ (Eqn. 4) or for $\underline{u}^*$ (Eqn. 5) are equal.

The interpolation is achieved with the use of those intrinsic co-ordinates to compute the stress or the strain rate with a common formulation:

$$\underline{\sigma} = \sum_i \eta_i \cdot \underline{\sigma_i} \tag{6}$$

$$\underline{u} = \sum_i \eta_i \cdot \underline{u_i} \tag{7}$$

Putting together Equations 5 and 6, we can compute the stress associated to a plastic strain rate direction and get the expression of the interpolation matrix $\underline{\underline{C}}$ (the hardening is not being taken into account here):

$$\underline{\sigma} = \underbrace{\sum_i \underline{\sigma_i} \cdot \underline{uu_i}}_{=\underline{\underline{C}}} \bullet \underline{u} \tag{8}$$

As long as the interpolation is achieved in the domain delimited by the 5 stress nodes, all the 5 η_i must remain between 0 and 1. When one of the 5 η_i becomes negative, it means that the current stress is out of the domain and an updating of the stress nodes must take place. The classical updating method consists in finding 5 new stress nodes defining a new domain containing the current stress direction. The improved updating method makes use of the adjacent domain. Therefore, only 1 new stress node is computed with the Taylor model and 4 of the 5 old stress nodes are kept for the interpolation.

2.2 Implementation of the texture updating

Our texture updating model is based on the Taylor's assumptions with a full

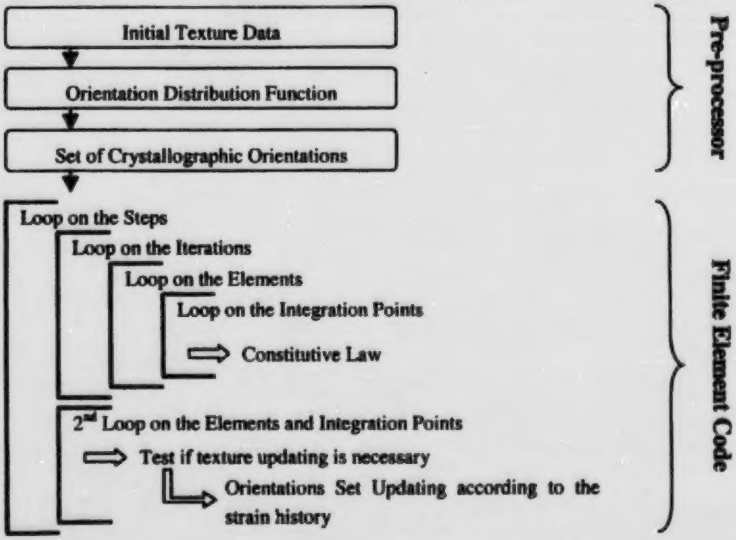
Initial Texture Data
Orientation Distribution Function
Set of Crystallographic Orientations
Loop on the Steps
Loop on the Iterations
Loop on the Elements
Loop on the Integration Points
Constitutive Law
2nd Loop on the Elements and Integration Points
Test if texture updating is necessary
Orientations Set Updating according to the strain history
Pre-processor
Finite Element Code

Fig. 1: Flowchart of the finite element code.

constraint method. The main ideas of the implementation are summarised on Figure 1. It should be noticed that the constitutive law is based on the interpolation method described earlier and on the Taylor model applied on the actual set of crystallographic orientations. These orientations are represented with the help of the Euler angles ranging from 0° to 360° for φ_1 and from 0° to 90° for ϕ and φ_2 so as to take crystal cubic symmetry into account but not the sample symmetry. A second loop on the elements and on the integration points has been added in order to achieve texture updating only on converged time step. The lattice rotation of each crystal is computed with the same Taylor model by subtracting the slip induced rotation from the rigid body rotation included in the strain history.

During a large finite element simulation, it is not possible to achieve a texture updating for each integration point and at the end of each time step. That is the reason why an updating criterion must be used so as to reduce computation time. This is still under investigation; at this stage, an updating occurs after a predefined number of time steps. A criterion based on a maximum cumulated plastic strain will also be examined.

3 Applications

This paper will present the first test of our constitutive law which is the prediction of texture during rolling for b.c.c. metals compared to f.c.c. metals.

3.1 Description of the finite element modelling

The rolling process is very simply represented by only one finite element in plane strain state. A compressive force is applied along the normal axis and will produce an expansion along the rolling direction as the displacements along the transverse direction are fixed.

The kind of metal is chosen by the imposed slip systems. In order to show up the appearance of a rolling texture, we started our simulations with an isotropic (random) texture in both cases. Such a texture was represented by a set of 2000 crystals. Arbitrarily, the hardening behaviour has also been chosen the same for both metals.

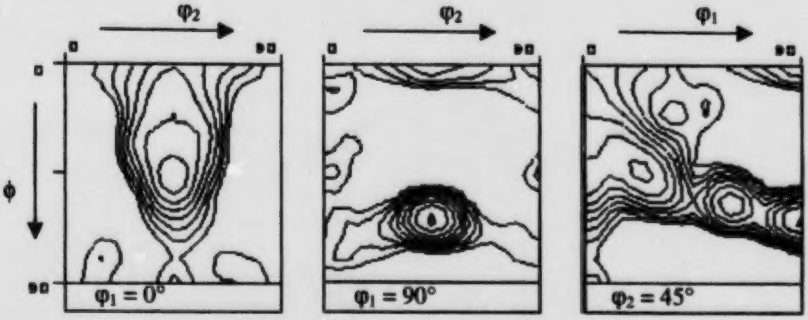

Fig. 2: $\varphi_1 = 0°$, 90° and $\varphi_2 = 45°$ -Sections of the O.D.F. of the b.c.c. metal (curves levels are 0.70 1.00 1.40 2.00 2.80 4.00 5.60 8.00 11.0 and 16.0).

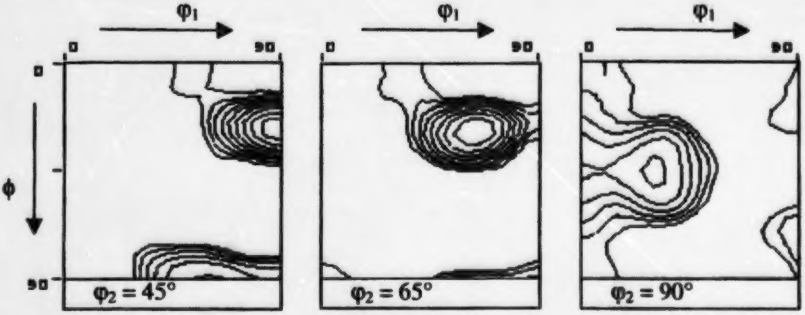

Fig. 3: $\varphi_2 = 45°$, 65° and 90° -Sections of the O.D.F. of the f.c.c. metal (curves levels are 0.70 1.00 1.40 2.00 2.80 4.00 5.60 8.00 11.0 and 16.0).

3.2 Predicted texture

The simulation is achieved until the thickness of the finite element is reduced by a factor 2; this corresponds to a 69% rolling reduction. At the end of the simulation, the updated texture is no more isotropic; some classical sections of the predicted O.D.F. are shown on Figure 2 for the b.c.c. metal and on Figure 3 for the f.c.c. metal.

For the b.c.c. metal, a typical rolling texture can be observed; a strong γ- and an α-fibres are present with the components E and F. The maximum of the O.D.F. is 11.94 times the random texture and is located at $\varphi_1 = 25°$, $\phi = 50°$ and $\varphi_2 = 55°$.

A typical f.c.c. rolling texture is also observed in the second case with an O.D.F. maximum of 14.67 at $\varphi_1 = 40°$, $\phi = 70°$ and $\varphi_2 = 20°$.

3.3 Comparison of the rolling forces

In spite of a common hardening behaviour, a non-negligible influence of the crystal lattice was noticed on the computed rolling forces. The larger stiffness observed for the f.c.c. metals can be related to the lower number of permitted slip systems, which yield a material less able to be easily deformed. On the contrary, although the predicted texture is quite different from the initial random texture, the influence of the texture updating was found to be very small (0.3% for the final force of the b.c.c. metal).

3.4 π-sections of the yield locus

The influence of the texture evolution is more effective when you look at sections of the resulting yield locus. We chose to use the π-section as it is more adapted to the deviatoric stress representation. We have plotted the π-sections of the yield locus for the b.c.c. and f.c.c. metals at the beginning and at the end of the rolling simulation on Figure 4.

The first remark is that the size of the yield locus is clearly larger for the f.c.c. metal than for the b.c.c. one. This fact is directly related to the larger value of the rolling forces observed for the f.c.c. metal. It can also be noticed that the initial yield locus is symmetric in both cases because of the imposed random texture. As the texture evolves strongly, an important evolution of the resulting yield locus occurs. The length of the yield stress changes differently according to the stress direction; the anisotropy already revealed with the O.D.F. sections is then clearly present in the finite

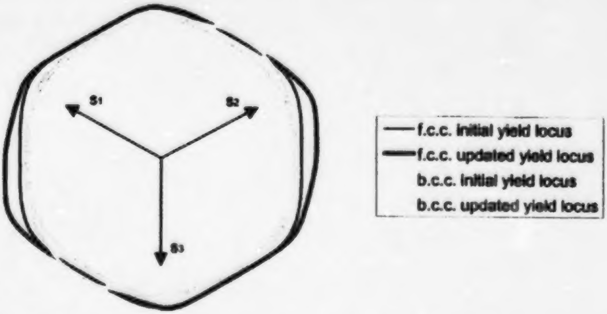

Fig. 4: π-sections of the yield locus (S_1, S_2, S_3 are the 3 principal stresses).

element model of the rolled material.

4 Conclusion

The considerations brought in this paper show that large differences are observed in the results simply when the microscopic slip systems are changed. The predicted textures fit to the experimental ones for b.c.c. as well as for f.c.c. metals.

Taking texture updating into account during finite element simulations is a very important point considering the large evolution of the O.D.F. and of the resulting yield locus. The application presented here did not show a significant influence of the texture updating method on the rolling forces. However, a more complicated simulation would present a complex stress history varying from one finite element to another; so, texture evolution effects would become very important.

Our next step will be the validation of this model on finite element simulations such as forming limit diagram prediction or deep-drawing. We will also investigate the computation time optimisation i.e. reducing the Taylor model calls without reducing the accuracy.

5 Acknowledgements

The Belgian National Scientific Research Fund and the Region Wallone are acknowledged for their support as well as P. Van Houtte for his texture model.

6 References

Duchêne, L., Habraken, A. M., Cescotto, S. (1999), *Elastoplastic anisotropic model based on texture analysis to simulate steel sheet behavior*, Proc. 7th Int. Symp. (Cancun, Mexico).

Munhoven, S., Habraken, A. M., Van Bael, A., Winters, J. (1996), *Anisotropic finite element analysis based on texture*, Proc. 3rd Int. Conf.: NUMISHEET'96, pp.112-119.

SIMULATION OF TEXTURAL EVOLUTION DURING PRIMARY STATIC RECRYSTALLIZATION

R. SEBALD, G. GOTTSTEIN
Institut für Metallkunde und Metallphysik, RWTH Aachen, Germany

Abstract

An analytical model for predicting texture evolution during primary static recrystallization has been developed. Random nucleation and oriented nucleation via subgrain growth were implemented as nucleation models Oriented nucleus growth is simulated through an algorithm that is discrete in time using an Avrami approach for statistical impingement. Due to the time resolved approach it is possible to include processes which occur during nuclei growth. Recrystallization twinning is simulated by a growth accident approach. Recovery is also included in the calculations. Preliminary results show good agreement with experimental data.

Keywords: static recrystallization, texture, modelling, annealing twinning

1 Introduction

Several approaches have been introduced for the simulation of primary static recrystallization. Models like cellular automata and kinetic Potts-type Monte-Carlo methods achieve high spatial resolution in terms of microstructure and recrystallization kinetics. To obtain statistically relevant texture information these models require very large simulated volumes. Hence, if primarily the texture evolution is to be investigated special analytical approaches are more convenient. Some analytical approaches consider nucleation and growth to be two independent events. This precludes processes which occur during nuclei growth. In such case these two step models are not applicable. Recovery, for example, reduces the driving force of grain boundary migration. In extreme cases some components of the deformation texture recover completely and remain in the annealed structure. If such effects have to be accounted for time discrete growth models are required.

2 Outline of the model

The analytical model described in this work is based on both nucleation and nuclei growth. The microstructure is simplified by the assumption of a random spatial distribution of the nuclei. The texture information given by an orientation distribution function (ODF) is represented by a set of 3744 randomly oriented components according to Fortunier and Hirsch (1987). The volume fractions are obtained from the measured ODF with the method of Virnich et al. (1978). The volume fraction of a component with the orientation g is denoted as V(g).

2.1 Nucleation

Although there is no comprehensive theory of nucleation, several nucleation mechanisms are well established in literature. Particle stimulated nucleation ("PSN"), for example, can be quite well simulated by random nucleation where a constant number of nuclei is generated for every orientation. Many nucleation phenomena are based on subgrain growth. A subgrain to develop into a nucleus for recrystallization must build up a mobile (large angle) grain boundary. Hence, it has to develop a misorientation to its neighbouring subgrains of at least 15°. Therefore it is necessary that the investigated grain has an orientation gradient of at least 15°. This orientation gradient is simulated by the comparison of a full constraints Taylor model and a relaxed constraints Taylor model. If the orientation difference reaches the threshold value, nuclei of the corresponding orientation are generated (Raabe 1994). The number is assumed to depend on the stored energy. From these two hypotheses the number $N(g_{rx})$ of nuclei with an orientation g_{rx} is calculated.

In the following we assume the nucleation to be site saturated, i.e. all nuclei are created at $t = 0$. This represents quite well the case for nucleation at deformation inhomgeneities and particles. Of course, it is possible to extend the approach towards other nucleation kinetics.

2.2 Nuclei growth

The growth rate of nuclei corresponds to the grain boundary velocity. The velocity of a grain boundary v_{GB} between a growing nucleus with the orientation g_{rx} and a grain in the deformed matrix with the orientation g_d is given by the product of the grain boundary mobility m and the local driving force p.

The mobility of a grain boundary depends on the misorientation between the two adjacent grains. Low angle grain boundaries are assumed to be hardly mobile. Large angle grain boundaries show finite mobilities. Some special grain boundaries exhibit very high mobilities (i.e. 40°<111> in aluminium). For the simulation the mobility of average large angle grain boundaries is typically set to 20% of the highest mobility. To implement this growth dependence the misorientations of all possible combinations of the 3744 texture components are classified. Low Σ coincidence misorientations are identified according to the Brandon criterion (Brandon 1966).

The driving force of primary static recrystallization is the difference between the specific stored energy of the nucleus and the deformed matrix. The Taylor energy of the deformed matrix components as derived from the simulation of the deformation texture is taken as an approximation for this energy.

If all nuclei could grow independently the difference of the recrystallized volume fraction ΔV_{ex} of nuclei with orientation g_{rx} in the deformed component g_d between two points of time (t_1 and t_2) would be:

$$\Delta V_{ex}(g_d, g_{rx}) = N(g_d, g_{rx}) \cdot \sigma \cdot v_{KG}(g_d, g_{rx})^3 \cdot \left(t_2^3 - t_1^3\right) \qquad (1)$$

N is the number of nuclei and σ is a shape factor describing the growth geometry. In the model growth is assumed to be isotropic but it stops locally whenever two nuclei impinge. Therefore, a growing nucleus can only grow into the non-recrystallized volume fraction (1-X). Avrami (1939) has derived a relation between growth ΔV_{ex} of the recrystallized volume fraction without consideration of impingement (expanded volume fraction) and growth ΔV with impingement for the case of random spatial distribution:

$$\frac{\Delta V}{\Delta V_{ex}} = 1 - X \tag{2}$$

The non-recrystallized volume fraction (1-X) of a deformed component with the orientation g_d is the ratio of the actual volume fraction of the deformed component and its volume fraction before recrystallization. Integration of this equation leads to the well known Johnson-Mehl-Avrami-Kolmogorov equation for recrystallization kinetics:

$$X = 1 - \exp(-X_{ex}) = 1 - \exp\left\{-\left(\frac{t}{t_R}\right)^q\right\} \tag{3}$$

Assuming that every deformation texture component develops the same density and orientation distribution of nuclei the change of the volume fraction of the component g_{rx} which grows into g_d:

$$\Delta V(g_d, g_{rx}) = X_d(g_d) \cdot N(g_{rx}) \cdot \sigma \cdot v_{KG}(g_d, g_{rx})^3 \cdot \left(t_2^3 - t_1^3\right) \tag{4}$$

The volume fraction of the deformed matrix is reduced by this amount ΔV and the recrystallized volume is increased by the same quantity. This volume shift is performed at every time step for all possible combinations of g_d and g_{rx}.

2.3 Recovery

Recovery reduces the driving force during nuclei growth. The following function fits well to measurements of the growth rate $\dot{G}$ of recrystallization nuclei:

$$\dot{G} = C \cdot t^{-r} \tag{5}$$

C is a constant. The measured range of the exponent r is $0 \le r \le 1$. In the computer code this function describes the temporal evolution of the driving force. If the driving force decreases below a threshold level growth ceases. The threshold is influenced by precipitation and alloy composition. In the case of site saturation the Avrami exponent q of equation (3) follows the relation q=3(1-r) (Furu et al. 1990).

2.4 Twinning

Fcc metals with low stacking fault energy commonly develop annealing twins. The atomistic mechanism of twin formation is not fully understood but it is well established that twins can be formed at moving grain boundaries. This can be simulated by transferring a small fraction of every nucleus orientation into its twin orientations at every simulation time step.

3 Recrystallization of CuZn10

Nucleation was simulated with the subgrain growth mechanism. The orientation distribution of the resulting nuclei is very sharp (Fig. 1). The measured texture of a 90% rolled and recrystallized specimen is quite weak (Fig. 2). In (Sebald et al. 1997) it was shown that this recrystallization texture can be simulated with a nucleation texture comprising 90% randomly oriented nuclei and only 10% nuclei generated by subgrain

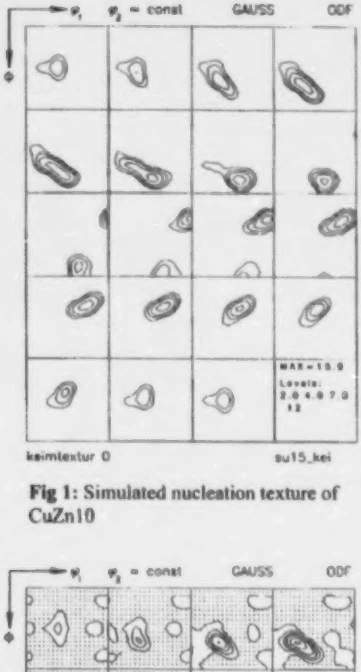

Fig 1: Simulated nucleation texture of CuZn10

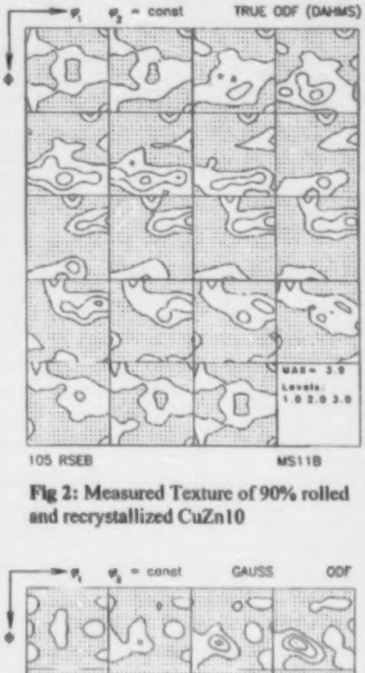

Fig 2: Measured Texture of 90% rolled and recrystallized CuZn10

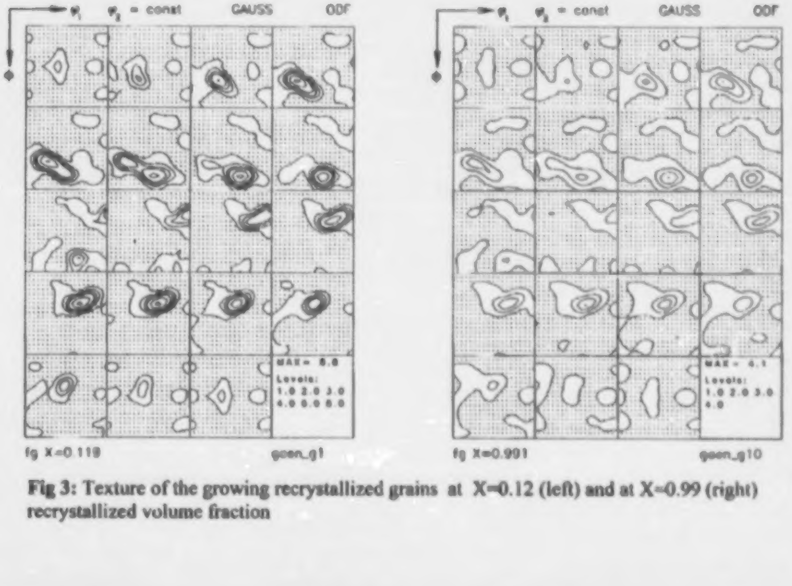

Fig 3: Texture of the growing recrystallized grains at X=0.12 (left) and at X=0.99 (right) recrystallized volume fraction

growth. What can be the origin of this high amount of randomly oriented nuclei. The microstructure of recrystallized brass reveals many annealing twins. Twinning during nuclei growth tends to randomise the orientation distribution (Gottstein 1984). To model this, the sharp nucleation texture of fig. 1 was used. Orientation dependent growth was introduced in such a way that low angle grain boundaries were considered to be immobile, grain boundaries with 40°<111> misorientation were associated with the highest mobility and the mobility of other large angle grain boundaries was taken to be 20% of the maximum mobility. Fig. 3 shows the texture of the growing grains with increasing annealing time. Evidently, the texture heavily weakens due to twinning. The texture at 99% recrystallized volume fraction is in good agreement with the measured texture in fig. 2

4 Recrystallization of warm rolled IF-Steel

Fig. 4 shows the annealing texture of ferritic warm rolled ULC-steel (Sebald et al. 1998). The specimen was rolled at 650°C to 40% thickness reduction in one pass. It was water quenched immediately after exiting the rolls. The measured texture of this sample was used as initial texture for modelling the annealing texture. The rolled sample was annealed for two hours in a salt bath furnace at 650°C. The texture of the annealed sample was characterised by the high amount of α-fibre rolling texture components. The microstructure of this sample contained remains of the deformation structure. It is not possible to obtain a completely recrystallized structure by annealing for longer times or at higher temperatures. This behaviour can be explained by recovery during warm rolling, between rolling and quenching and in the beginning of annealing.

Again, nucleation was simulated by the subgrain growth mechanism. Nuclei growth was simulated assuming that 25°, 30° and 35°<110> grain boundaries had the

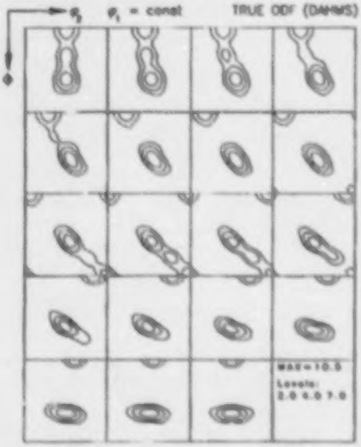

Fig. 4: Annealing texture of ferritic warm rolled ULC-steel

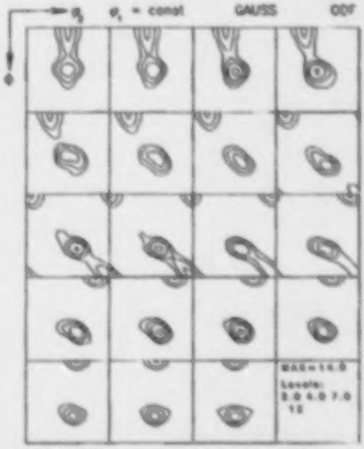

Fig. 5: Simulated annealing texture according to Fig. 4

highest mobility, low angle grain boundaries were considered to be immobile and other large angle grain boundaries moved with 20% of the highest mobility. The texture in fig. 5 was simulated under consideration of recovery. The α-fibre components at low Φ-angles in the simulated annealing texture are stemming from the deformation texture. During the computation their stored energy dropped below the threshold level for growth, hence they were not consumed and remained in the final annealing texture.

5 Summary

We presented a recrystallization model that describes the temporal evolution of texture components. Microstructure is replaced by statistical considerations. Nucleation is assumed to be site saturated. Two nucleation mechanisms are implemented: random nucleation and subgrain growth. Nuclei growth is simulated using an Avrami approach including growth selection. The model is capable of accounting recovery and twinning during nuclei growth.

Partly recrystallized states can be calculated to distinguish recrystallized and deformed texture components. Thus, a subsequent deformation simulation can treat these components separately. Hence, the model is suitable for the simulation of multi pass warm rolling.

6 Acknowledgement

This research project was supported by the Deutsche Forschungsgemeinschaft (DFG) within the Collaborative Research Centre 370 "Integral Material Modelling".

7 References

Avrami, M (1939), J. Chem. Phys., Vol. 7, pp. 1103

Brandon, D.G. (1966), ActaMet., Vol. 14, pp. 1479

Fortunier, R., Hirsch, J. (1987), "Theoretical Methods of Texture Analysis" ed. H.J. Bunge,

Furu, T., Marthinsen, K., Nes, E., (1990), Mats. Sci. and Tech., Vol. 6 pp. 1093

Gottstein, G., (1984), Acta net., Vol. 32, pp 1117

Raabe, D. (1994), phys. stat sol., Vol. 181, pp. 291

Sebald, R., Marx, V., Gottstein, G.,(1997), Proc. EUROMAT 97, pp. 633

Sebald, R., Beckers, B., Gottstein, G., Kim, G., Kwon, O.J., Choi, W., (1998), Proc. „International Symposium: Modern LC and ULC Sheet Steels for Cold Forming" ISBN 3-89653-304-5, , Vol. 2, pp. 363

Virnich, K.H., Pospiech, J.,Flemmer, A., Lücke, K., (1978) Proc. ICOTOM 5, Aachen „Textures of Materias", eds. G. Gottstein, K. Lücke, Springer, Berlin, Vol II, pp.129

RELATIONSHIP BETWEEN DEPOSITION AND RECRYSTALLIZATION TEXTURES OF ELETRODEPOSITS

J. H. CHOI, S. Y. KANG, and D. N. LEE
Division of Materials Science and Engineering, Seoul National University, Seoul, Korea
J. YANG
R&D Team, ILJIN Copper Foil Co., Iksan-Si, Korea

Abstract

Electrodeposits may undergo recrystallization when annealed. The texture of recrystallized deposits may differ from that of as-deposited state. The <100>, <111> and <110> orientations of copper electrodeposits obtained from copper sulfate, copper fluoborate and cyanide baths changed to the <100>, <100> and <$\sqrt{3}$ 10> orientations, respectively. The <111> and <100> orientations of chromium electrodeposits obtained from the standard Sargent bath remained unchanged even after recrystallization. The results are in agreement with the prediction of the strain energy release maximization model, in which the minimum elastic modulus direction of recrystallized grains becomes parallel to the absolute maximum internal stress direction of the original deposits. The absolute maximum internal stress direction can be obtained from the texture of deposits when the driving force for recrystallization is the stored energy due to dislocations generated during electrodeposition.

Keywords: Chromium, copper, electrodeposition, recrystallization, strain energy release maximization model, texture

1 Introduction

Electrodeposits may undergo recrystallization when annealed. The texture of recrystallized deposits may differ from that of as-deposited state. Recently Lee et al. investigated recrystallization textures of copper electrodeposits having a simple texture such as the <100>, <110> or <111> orientation which were obtained from copper sulfate, copper fluoborate (Lee et al. 1995) and cyanide (Yang and Lee) baths. The <100>, <110> and <111> orientations changed to the <100>, <$\sqrt{3}$ 10>, <100> orientations, respectively, after recrystallization. The result was explained based on the strain energy release maximization model in which the recrystallized grains orient themselves so that their minimum elastic modulus directions can be parallel to the absolute maximum internal stress direction of non-recrystallized matrix.

Chromium is an interesting metal because its minimum elastic modulus directions are <111>, whereas most bcc and fcc metals have the minimum elastic modulus directions in the <100> directions. Therefore, the recrystallization textures of chromium may differ from those of other cubic metals.

The objective of this study is to investigate the recrystallization textures of copper and chromium electrodeposits.

2 Experiment

About 35μm thick copper electrodeposits were obtained from copper sulfate baths. Electrodeposition conditions are given in Table 1. A 316L stainless steel sheet and a lead sheet were used as cathode and insoluble anode, respectively. The deposits were peeled off from the cathode. The peeled deposits were annealed in a potasium nitrate salt bath.

Chromium was electrodeposited from a Sargent bath containing 2.5M CrO_3, 0.0255M H_2SO_4. A copper sheet and a lead sheet were used as cathode and insoluble anode, respectively. Chromium electrodeposits obtained under two electrolysis conditions are summerized in Table 2. The copper substrate was dissolved in 30%HNO_3 for 10 min. to obtain the chromium deposit only. The chromium deposits were annealed in vacuum chamber of 10^{-5} torr. The hardness was measured with a Knoop hardness tester under a load of 50 g.

The textures of the deposits were measured using a diffractometer or a pole figure device. The measurement of pole figure was carried out by the Schultz reflection method with Zr filtered Mo Kα radiation. The pole figure data were used to calculate the inverse pole figures (Bunge 1982).

In the case using the diffractometer, the orientation of the deposit was expressed in terms of texture frations, TFs, of the (hkl) plane defined by

$$TF(hkl) = \frac{I(hkl) \,/\, I_0(hkl)}{\Sigma[I(hkl) \,/\, I_0(hkl)]} \qquad (1)$$

Table 1: Copper electrodeposition condition.

Bath	Bath Composition	Temp. (K)	Cathode C.D ($A\cdot m^{-2}$)	Specimen	Annealing
A	1.00M $CuSO_4\cdot 5H_2O$ 0.714M H_2SO_4	303	50	Cu(100)	773K, 5h
B	1.12M $CuSO_4\cdot 5H_2O$ 0.816M H_2SO_4	303	600 800	Cu(110) Cu(111)	673K, 10m 873K, 1h

Table 2: Chromium electrodeposition conditions.

Condition	Bath Temp. (K)	Cathode Current Density ($A.m^{-2}$)	Stirring	Specimen
cond-A	338	2500	Stirred	Cr(111)
cond-B	293	5000	Not stirred	Cr(100)a

3 RESULTS

Fig. 1 shows the texture fractions of the {111} and {100} planes of Specimen Cu(100) before and after annealing at 773K for 5h. Other reflection peaks did not appear in Specimen Cu(100). This indicates that Specimen Cu(100) has the <100> growth orientation, which remained unchanged even after annealing. Fig. 2 shows the inverse pole figures of Specimen Cu(111) before and after annealing at 873K for 1h. Specimen Cu(111) has the <111> growth orientation, which changed to <100> after annealing. Fig. 3 shows the inverse pole figures of Specimen Cu(110) before and after annealing at 673K for 10min. This specimen has the <110> orientation, which changed to the $<\sqrt{3}\,10>$ orientation after annealing.

These results are the same as the previous results, in which the <100>, <111> and <110> deposition textures changed the <100>, <100> and $<\sqrt{3}\,10>$ recrystallization textures (Lee et al. 1995).

Table 3 shows the texture fractions of as-deposited chromium electrodeposits under three electrodeposition conditions. Specimen Cr(111) has a very strong <111> fibre texture and the texture of Specimen Cr(100)a may be approximated by the <100> fibre texture.

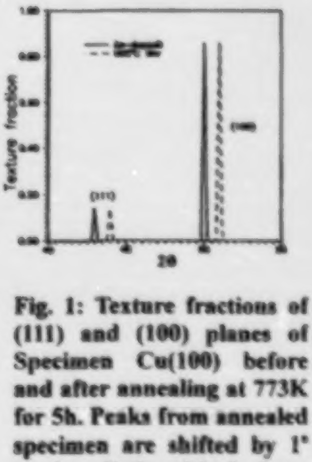

Fig. 1: Texture fractions of (111) and (100) planes of Specimen Cu(100) before and after annealing at 773K for 5h. Peaks from annealed specimen are shifted by 1° to be distinguished from those from as-deposited one.

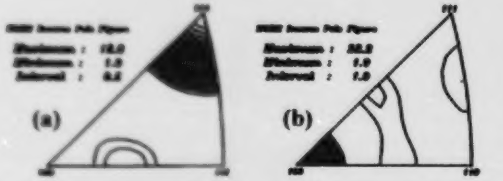

Fig. 2: Inverse pole figures of Specimen Cu(111) (a) before and (b) after annealing at 873K for 1h.

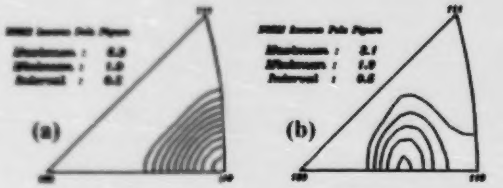

Fig. 3: Inverse pole figures of Specimen Cu(110) (a) before and (b) after annealing at 673K for 10m.

Table 3: Texture fractions of reflection planes of as-deposited chromium electrodeposits.

Specimen	(110)	(200)	(211)	(220)	(310)	(222)	Texture
Cr(111)	0.02	0.05	0	0	0	**0.93**	<111>
Cr(100)a	0.19	**0.47**	0.13	0.05	0.13	0.03	<100>

Figs. 4 shows the optical microstructures of Specimen Cr(111) before and after annealing at 903K and 973K for 1h. The microstructure of the deposit remained unchanged up to 823K. Partial recrystallization of the electrodeposit took place at 903K, and complete recrystallization was observed at temperatures above 973K. Fig. 5 shows the texture fractions of Specimen Cr(111) when annealed at various temperatures for 1 hour. It can be seen that the <111> texture of chromium electrodeposit did not change even after recrystallization.

Fig. 6 shows the optical microstructures of Specimen Cr(100)a before and after annealing at 1173K for 1 hour, which indicate that the annealed specimen was fully recrystallized. The measured (200) pole figures of Specimen Cr(100)a before and after annealing at 1173K for 1 hour are shown in Fig. 7. The chromium electrodeposit having major <100> orientation did not undergo the texture change even after recrystallization.

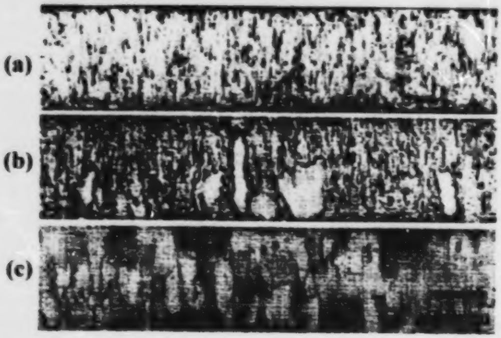

Fig. 4: Optical microstructures of Specimen Cr(111) (a) before and after annealing at (b) 903K and (c) 973K for 1 hour.

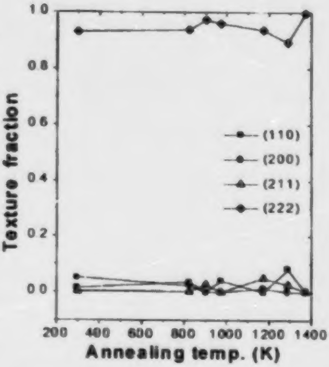

Fig. 5: Texture fraction of Specimen Cr(111) as function of annealing temp. for 1 hour.

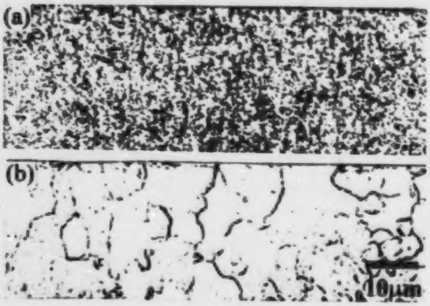

Fig. 6: Optical microstructures of Specimen Cr(100)a (a) before and (b) after annealing at 1173K for 1 hour.

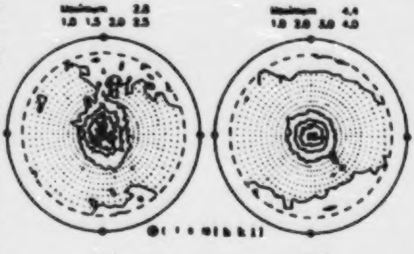

(a) (b)

Fig. 7: Measured (200) pole figures of Specimen Cr(100)a (a) before and (b) after annealing at 1173K for 1 hour.

4 DISCUSSION

One of the present authors (Lee 1995) advanced a model for the evolution of recrystallization texture in which the direction of absolute maximum internal stress due to dislocations in the deformed or fabricated materials becomes parallel to the minimum Young's modulus direction in recrystallized grains, whereby the strain energy release during recrystallization can be maximized.

For electrodeposits, the absolute maximum internal stress direction can be determined by the texture. The density of dislocations whose Burgers vectors are directed away from the growth direction was supposed to be higher than when the Burgers vector is nearly parallel to the growth direction, because dislocations whose Burgers vector is close to the growth direction are easy to glide out from the deposit by the image force during its growth (Lee 1996). This has been experimentally confirmed (Lee and Lee). Therefore, the absolute maximum internal stress direction is the Burgers vector direction which is approximately normal to the growth direction.

It has been well known that copper and chromium have the minimum Young's modulus along <100> and <111> directions, respectively. Once the absolute maximum internal stress directions and the minimum Young's modulus directions are known, we are in position to discuss the recrystallization textures of electrodeposits based on the strain energy release maximization model.

4.1 Cu electrodeposits

The <110> directions of the original copper grains tend to be oriented along the <100> directions of the recrystallized copper grains. There are six equivalent directions in the <110> directions, with opposite directions being taken as the same. The absolute maximum internal stress direction is the Burgers vector direction which is approximately normal to the growth direction. Therefore, for copper deposits, the <110> directions at right angle or near right angle to the thicknesss direction of the deposit become the <100> directions after recrystallization.

For the deposit with the (100) texture, two of the six <110> directions are at right angles; the remaining four are at an angle of 45° to the thickness direction. The two <110> directions will change to the <100> directions after recrystallization. The recrystallized deposit would then have the (100) texture in agreement with the experimental result.

For the (111) texture, three of the six <110> directions are at right angles to the thickness direction; the remaining three <110> directions are at an angle of 35.26° to the thickness direction. The former three <110> directions will be able to change to the <100> directions, after recrystallization, but angles between the <110> directions are 60° and the angle between the <100> directions is 90°. Correspondence between the <110> and <100> directions, therefore, is impossible in a grain. Two of the <110> directions in neighboring grains, that are at right angles, may change to the <100> directions, however, to form nuclei having the (100) texture in grain boundaries, which grow at the expense of a high dislocation region. Thus, the (111) texture will change into the (100) recrystallization texture, in agreement with the experimental result.

For the (110) texture, one <110> direction is normal to the <110> thickness direction; the remaining four <110> directions are at angle of 60° to the <110> thickness direction. The first one of the <110> and the last four <110> directions are assumed to determine the recrystallization texture because the last four are closer to the planar direction than to the thickness direction. Recalling that the <110> directions change to <100> directions after recrystallization, the thickness direction of recrystallized grains should be at angles of 60 and 90° with the <100> directions at the same time. The thickness direction satisfying the condition is $<\sqrt{3}\,10>$, in agreement with the experimental results.

4.2 Cr electrodeposits

There are four equivalent <111> directions in bcc chromium, with opposite directions being taken as the same. In case of <111> fibre texture of chromium, one of four <111> directions is parallel to the thickness direction and the remaining three <111> directions are at an angle of 70.5° to the thickness direction of electrodeposit. The remaining three <111> directions, which are also the Burgers directions and the absolute maximum normal stress directions, will become parallel to the minimum Young's modulus directions of recrystallized grains, according to the strain energy release maximization model. The minimum Young's modulus directions of chromium, the <111> directions, are also the absolute maximum normal stress directions. Therefore, the texture of chromium will not change after recrystallization, in agreement with the experimental result. Similarly, other texture components of deposits are likely to remain unchanged after annealing.

The deposition textures of Specimen Cr(111) and Cr(100)a did not change after recrystallization in agreement with the prediction of the model.

Thus, the experimental texture results can be very well explained based on the strain energy release maximization model.

5 DISCUSSION

The <100>, <111> and <110> deposition texture of copper electrodeposits changed to the <100>, <100> and $<\sqrt{3}\,10>$ recrystallization textures, respectively, when annealed. However, the deposition textures of chromium electrodeposits remained unchanged when recrystallized. The results could be explained by the strain energy release maximization model.

6 References

Bunge, H.J. (1982) in *Texture Analysis in Materials Science*, Butterworths, London.

Lee, D.N. (1995) The Evolution of Recrystallizaion Textures from Deformation Textures. *Scripta Metall. Mater.*, Vol. 32, pp.1689-1694

Lee, D.N. (1996) Maximum Energy Release Theory for Recrystallization Textures. *Metals and Materials,* Vol. 2, No. 3. pp. 121-31.

Lee, D.N., Kang, S. and Yang, J. (1995) Relationship between Initial & Recrystallization Textures of Copper Electrodeposits. *Plat. and Surf. Fin.*, Vol. 82, No. 3. pp. 76-9.

Lee, Y.-S. and Lee, D.N. (unpublished result).

Yang, J. and Lee, D.N. (unpublished result).

RECRYSTALLIZATION TEXTURE OF ALUMINUM BICRYSTALS WITH S ORIENTATIONS DEFORMED BY CHANNEL DIE COMPRESSION

D.N. LEE
Division of Material Sci. & Eng., Seoul National University, Seoul 151-742, Korea
H.T. JEONG
Dept. of Metallurgical Eng., McGill University, Montreal, QC Canada H3A 2B2

Abstract

The texture changes during recrystallization in high-purity aluminum bicrystals with S orientations of $(123)[41\bar{2}]/(123)[\bar{4}\bar{1}2]$ and $(123)[41\bar{2}]/(\bar{1}\bar{2}\bar{3})[41\bar{2}]$, deformed by channel die compression were investigated by Blicharski et al. There was no <111> rotational relationship between the recrystallized and the deformed matrix phases. This result could be explained by the strain energy release maximization model in which the direction of absolute maximum internal stress due to dislocations in the deformed matrix becomes parallel to the minimum Young's modulus direction in recrystallized grains, whereby the energy release during recrystallization can be maximized.

Keywords: Recrystallization texture, aluminium bicrystals, strain energy release maximization model.

1 Introduction

Blicharski et at.(1995) studied the microstructural and texture changes during recovery and recrystallization in high purity aluminum bicrystals with S orientations of $(123)[41\bar{2}]/(123)[\bar{4}\bar{1}2]$ and $(123)[41\bar{2}]/(\bar{1}\bar{2}\bar{3})[41\bar{2}]$, which had been compressed by the 90 to 97.5% reduction in thickness using a channel die. The geometry of deformation for these bicrystals was such that the bicrystal boundary lies parallel to the plane of compression, i.e. {123} and the <412> directions are aligned with the channel, and the die constrains deformation in the <121> direction.

The annealing of the deformed bicrystals was conducted in a fused quartz tube furnace with He+5%H_2 atmosphere. The textures of the fully recrystallized specimens were examined by the {111} and {200} pole figures from sectioned planes at 1/4, 1/2 and 3/4 specimen thickness. The recrystallization texture, together with the EBSP measurements of the partially recrystallized specimens did not seem to be related to the deformation textures of the matrix crystals by specific orientation relationships, such as a [111] rotation of ~40°. The 40° <111> rotational orientation relationship has traditionally been associated with the oriented growth theory. Such a misorientation relationship between a growing recrystallized grain and the surrounding deformation matrix has been reported to have a high mobility (Liebman et al. 1956). The relationship is also claimed to be associated with the oriented nucleation theory (Nes and Vatne 1996). Blicharski et al. concluded that either oriented nucleation or oriented growth alone appeared to be inadequate to explain the recrystallization textures.

Recently, one of the present authors(Lee 1995) advanced a model for the evolution of recrystallization texture in which the direction of absolute maximum internal stress due to dislocations in the deformed material becomes parallel to the minimum Young's modulus direction in recrystallized grains, whereby the energy release during recrystallization can be maximized because material concerned does not change macroscopically its shape and volume during recrystallization, and so the recrystallization is a displacement controlled process. This strain energy release maximization model originates from the presumption that the stored energy due to dislocations is the dominant driving force for recrystallization.

The purpose of this work is to discuss the recrystallization textures of the high purity aluminum bicrystals with S orientations obtained by Blicharski et al.(1995) based on the strain energy release maximization model.

2 Experimental textures

The deformation textures of the two bicrystals, $(123)[41\bar{2}]/(123)[\bar{4}\bar{1}2]$ and $(123)[41\bar{2}]/(\bar{1}\bar{2}\bar{3})[41\bar{2}]$, deformed 90% by channel die compression, are reproduced by the {111} pole figures in Figs. 1(a) and (b), respectively. The central pole figures represent the textures measured at the initial boundary of the bicrystals, hence the deformation textures of both of the component crystals are shown.

The recrystallization textures of bicrystal $(123)[41\bar{2}]/(123)[\bar{4}\bar{1}2]$ were determined from specimens annealed at 125°C for 5 min., and those of bicrystal $(123)[41\bar{2}]/(\bar{1}\bar{2}\bar{3})[41\bar{2}]$, from specimens annealed at 185°C for 5 min. The {111} pole figures of these fully annealed specimens are reproduced in Fig. 4.

3 Strain energy release maximization model

One of the present authors (Lee 1995) advanced a model for the evolution of recrystallization texture. In the model the direction of absolute maximum internal stress due to dislocations in the deformed materials becomes parallel to the minimum Young's modulus direction in recrystallized grains, whereby the strain energy release during recrystallization can be maximized.

The stress fields of the array of an infinite number of edge dislocations can be calculated by superposing the stress fields of isolated dislocations (Sutton and Ballufi 1996). The absolute maximum stress direction is parallel to the Burgers vector or the slip direction. For multiple slip, the shear strains on active slip systems may not be equal. The dislocation density ρ on a slip system is expected to increase with increasing the related shear strain γ, that is, $\rho \propto \gamma^a$. Since the relation between γ and ρ is not known, a is assumed to be unity. It follow that $|\sigma_{11}| \approx |\sigma_{max}| \propto 1/D \propto \rho \propto \gamma$. Therefore, the contribution of each active slip system to the absolute maximum stress direction will be proportional to its shear strain.

When a crystal rotates during deformation, the shear strain increments on slip systems can vary with deformation. In this case the contribution of each slip system to the absolute maximum stress will be proportional to

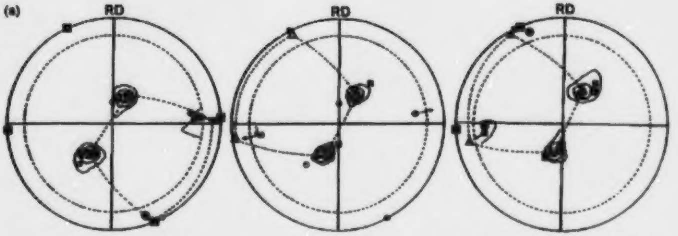

Crystal $(123)[41\bar{2}]$ Boundary Crystal $(123)[\bar{4}\bar{1}2]$

Contour Level : 1, 5, 15, 35

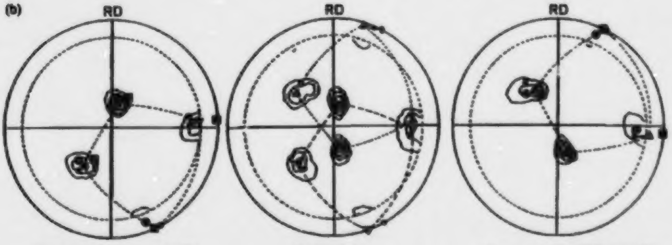

Crystal $(123)[41\bar{2}]$ Boundary Crystal $(\bar{1}\bar{2}\bar{3})[41\bar{2}]$

Fig. 1: (111) pole figures of the bicrystals after 90% reduction by channel die compression. (a) Bicrystal $(123)[41\bar{2}]/(123)[\bar{4}\bar{1}2]$**, (b) Bicrystal** $(123)[41\bar{2}]/(\bar{1}\bar{2}\bar{3})[41\bar{2}]$ **(Blicharski et al. 1995). ● Crystal ~{135}<211>, ■ Crystal ~{011}<522>**

$$k = \int_0^{\varepsilon} |\gamma| \, d\varepsilon \qquad (1)$$

In order for this method to be used, it is necessary to know active slip systems and shear strains on them. They can be obtained from the deformation texture or from a model which can simulate the deformation texture. In the real situation, the stress field is triaxial. However, this simple concept can be a starting point. Another orientation relation between the matrix and recrystallized grain must be known to obtain the recrystallization texture. This relation will be discussed in the next section.

4 Discussion

The slip systems and their shear strain increments can be obtained in the process of simulation of deformation. Fig. 2 shows the orientation change of crystal $(123)[41\bar{2}]$ during the plane strain compression calculated using the full constraints, ε_{31}-relaxed and ε_{31}, ε_{23}-relaxed constraints models, and the strain rate sensitivity models with m=0.01. The measured orientation change during deformation seems to be best simulated by the full constraints strain rate sensitivity model. Therefore, the full constraints strain rate sensitivity model was used to simulate the deformation texture.

The experimental deformation texture is better described by $(135)[21\bar{1}]$ or $(0.1534\ 0.5101\ 0.8463)\ [0.8111\ 0.4242\ \overline{0.4027}]$, which is calculated based on the full constraints strain rate sensitivity model with m=0.01, than $(011)[52\bar{2}]$, which Blicharski et al.(1993) described as shown in Fig. 1.

Fig. 3 shows the calculated shear strain increments on acting slip systems of crystal $(123)[41\bar{2}]$ as a function of true thickness strain when subjected to the plane strain compression. For a true thickness strain of 2.3 or 90% reduction, the k values (eq. (1)) of the slip systems, $(111)[10\bar{1}]$, $(111)[01\bar{1}]$, $(\bar{1}1\bar{1})[110]$, $(1\bar{1}\bar{1})[110]$, $(\bar{1}1\bar{1})[011]$ and $(1\bar{1}\bar{1})[101]$, which are calculated by using the data in Fig. 3, are 2091, 776, 1424, 2938, 76 and 139, respectively. The contributions of slip system, $(\bar{1}1\bar{1})[011]$ and $(1\bar{1}\bar{1})[101]$, are negligible compared with other active slip systems. Therefore, the slip systems, $(111)[10\bar{1}]$, $(111)[01\bar{1}]$, $(\bar{1}1\bar{1})[110]$ and $(1\bar{1}\bar{1})[110]$ are considered in calculating the absolute maximum internal stress direction. It is noted that all the slip directions are designated so that they can be at acute angle one another and the absolute maximum internal stress direction calculated in eq. (2) can be at acute angle with the major extension direction or the rolling direction, $[0.8111\ 0.4242\ \overline{0.4027}]$. The absolute maximum stress direction is calculated as follows:

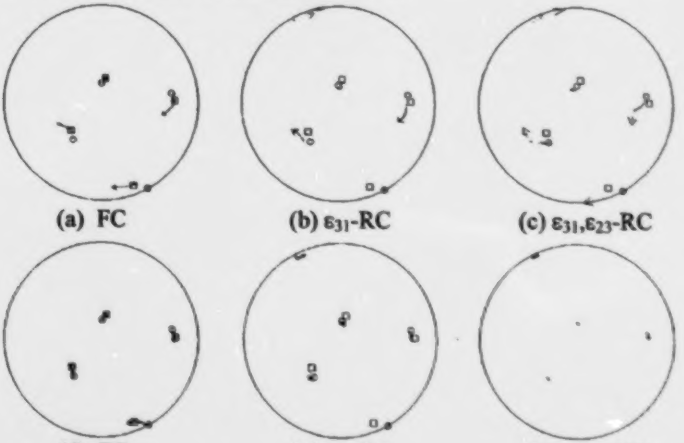
(a) FC (b) ε_{31}-RC (c) ε_{31},ε_{23}-RC

(d) FC (e) ε_{31}-RC (f) ε_{31},ε_{23}-RC

Fig. 2: Orientation changes of crystal $(123)[41\bar{2}]$ during plane strain compression calculated using Taylor-Bishop-Hill (a,b,c) and strain rate sensitivity models (d,e,f). ○: Initial orientation of $(123)[41\bar{2}]$, □: 90% deformed orientation of $(135)[21\bar{1}]$.

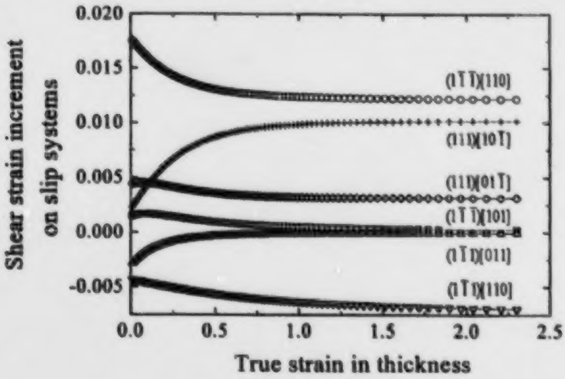

Fig. 3: Calculated shear strain increments on acting slip system of crystal $(123)[41\bar{2}]$

$$2091[10\bar{1}] + 776[01\bar{1}] + 1424 \times 0.577[110] + 2938 \times 0.577[110] = [4608\ 3293\ \overline{2867}] \quad (2)$$

where the factor 0.577 originated from the fact that the duplex slip systems of $(1\bar{1}1)[110]$ and $(\bar{1}11)[110]$ are equivalent to a single slip system with slip direction [110]. The $[4608\ 3293\ \overline{2867}]$ or $[0.7259\ 0.5187\ \overline{0.4516}]$ direction will become parallel to one of the <100> directions, the minimum Young's modulus direction of aluminum, after recrystallization, according to the strain energy release maximization model.

Another orientation relation between the matrix and the recrystallized grain is obtained in the following. If the absolute maximum internal stress direction in the deformed state becomes parallel to one of the <100> directions in the recrystallized state, another <100> direction in the recrystallized state which is normal to the previous one will tend to be parallel to a direction which is at the smallest possible angle with another high stress direction in the deformed state. Possible candidates of the high stress direction must be the [011], [101], and $[1\bar{1}0]$ directions, which are unused in calculation of the maximum internal stress direction among six possible Burgers vector directions. The three direction are at angles of 87.3, 78.8 and 81.6°, respectively, with the absolute maximum internal stress direction. The [011] direction is closest to, but less than the right angle. The direction which is at the smallest possible angle with the [011] direction and normal to the absolute maximum internal stress direction must be on a plane made of the [011] and the absolute maximum internal stress direction. This direction is calculated to be $[\overline{0.0345}\ 0.6833\ 0.7294]$. The third <100> direction in the recrystallized state is obtained to be $[0.6869\ \overline{0.5139}\ 0.5139]$ direction by the vector product of the two directions.

If the $[0.7259\ 0.5187\ \overline{0.4516}]$, $[0.6869\ \overline{0.5139}\ 0.5139]$ and $[\overline{0.0345}\ 0.6833\ 0.7294]$ unit vectors are set to be parallel to [100], [010] and [001] directions after recrystallization, the rolling plane normal direction, $(0.1534\ 0.5101\ 0.8463)$, and the rolling direction, $[0.8111\ 0.4242\ \overline{0.4027}]$, in the deformed crystal can be transformed to the expressions in the recrystallized crystal coordinate system using the following calculations:

$$\begin{pmatrix} 0.7259 & 0.5187 & -0.4516 \\ 0.6869 & -0.5139 & 0.5139 \\ -0.0345 & 0.6833 & 0.7294 \end{pmatrix} \begin{pmatrix} 0.1534 \\ 0.5101 \\ 0.8463 \end{pmatrix} = \begin{pmatrix} -0.0062 \\ 0.2781 \\ 0.9606 \end{pmatrix} \quad (3)$$

$$\begin{pmatrix} 0.7259 & 0.5187 & -0.4516 \\ 0.6869 & -0.5139 & 0.5139 \\ -0.0345 & 0.6833 & 0.7294 \end{pmatrix} \begin{pmatrix} 0.8111 \\ 0.4242 \\ -0.4027 \end{pmatrix} = \begin{pmatrix} 0.9907 \\ 0.1322 \\ -0.0319 \end{pmatrix} \quad (4)$$

The calculated result means that $(0.1534\ 0.5101\ 0.8463)\ [0.8111\ 0.4242\ \overline{0.4027}]$ crystal, which is obtained by the channel die compression of 90% reduction, transforms to the recrystallization texture $(\overline{0.0062}\ 0.2781\ 0.9606)\ [0.9907\ 0.1322\ \overline{0.0319}]$. Similarly, crystals deformed by channel die compression from $(123)[\bar{4}\bar{1}2]$ and $(\bar{1}\bar{2}\bar{3})[41\bar{2}]$ orientations transform to $(\overline{0.0062}\ 0.2781\ 0.9606)\ [\overline{0.9907}\ \overline{0.1322}\ 0.0319]$ and $(0.0062\ \overline{0.2781}\ \overline{0.9606})\ [0.9907\ 0.1322\ \overline{0.0319}]$, respectively, after recrystallization.

The results are plotted in Fig. 4 superimposed on the experimental data. The calculated values are not plotted in the textures of boundaries, because the boundary textures reflect the textures in the top and bottom layers. It can be seen that the calculated recrystallization textures are in good agreement with the measured data.

5 Conclusions

1. The channel die compression by 90% of aluminum bicrystal with $(123)[41\bar{2}]/(123)[\bar{4}\bar{1}2]$ or $(123)[41\bar{2}]/(\bar{1}\bar{2}\bar{3})[41\bar{2}]$ gave rise to a deformation texture which are similar to the original crystal orientations. This result could be well simulated using the full constraints strain rate sensitivity model.

2. Recrystallization textures calculated based on the strain energy release maximization model are in good agreement with the measured data.

6 References

Blicharski, M., Becker, R. and Hu, H. (1993) *Acta metall. mater.* Vol. 41, p.2007.
Blicharski, M., Liu, J. and Hu, H. (1995) *Acta Mater.* Vol. 43, p. 3125.
Lee, D.N. (1995) *Scripta Metall. Mater.* Vol. 32, p.1689.
Lee, D.N. (1996b) *Met. Mater.* Vol. 2, p.121.
Liebman, B., Lücke , K. and Masing, G. (1956) *Z. Metallkd.* Vol. 47, p.57.
Nes, E. and Vatne, H.E. (1996) *Z. Metallkd.* Vol. 87, p.448.
Sutton, A.P. and Ballufi, R.W. (1996) *Interfaces in Crystalline Materials*, Clarendon Press, Oxford, pp.115-120.

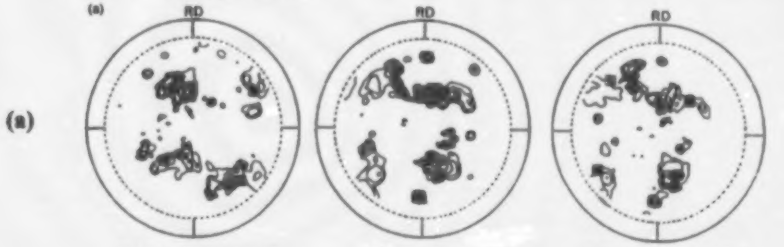

Crystal $(123)[41\bar{2}]$ Boundary Crystal $(123)[\bar{4}\bar{1}2]$

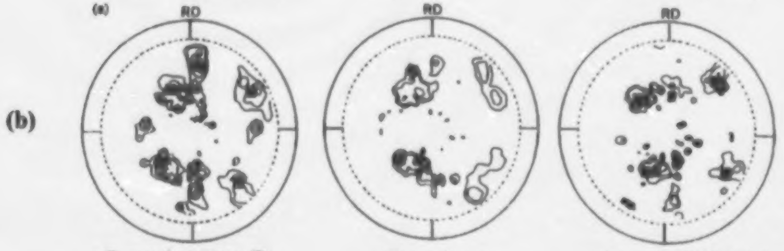

· Crystal $(123)[41\bar{2}]$ Boundary Crystal $(\bar{1}\bar{2}\bar{3})[41\bar{2}]$

Fig. 4: (111) pole figures of bicrystal (a) $(123)[41\bar{2}]/(123)[\bar{4}\bar{1}2]$ annealed at 125°C and (b) $(123)[41\bar{2}]/(\bar{1}\bar{2}\bar{3})[41\bar{2}]$ annealed at 185°C, for 5 min after 90% reduction.

■ $(\overline{0.0062}\ 0.2781\ 0.9606)[0.9907\ 0.1322\ \overline{0.0319}]$, Contour Level : 0.5, 1, 2, 3, 4, 8

A NEW ANALYTIC APPROACH OF CRYSTAL PLASTICITY AND ITS APPLICATIONS IN POLYCRYSTAL MODELING

LÁSZLO S. TOTH and TASSADIT HARIZ
Institut Supérieur de Génie Mécanique et Productique,
Université de Metz – Ecole Nationale d'Ingénieur de Metz, Metz, France

Abstract

Inspired from the expression of plastic potentials for viscoplastic slip (Tóth et al. 1988) and by an earlier proposition concerning the modification of the Schmid law (Arminjon 1991), a new yield surface is formulated in rate independent crystal plasticity and its properties are analyzed. In its limit case, the yield function approaches the classical Bishop and Hill single crystal yield surface but it gives a unique solution for both the stress state and the slip distribution. The new function is then used to obtain an analytic expression for the elastic-plastic modulus which includes also self and latent hardening of the slip systems. The advantage of the analytic modulus is that no iterations are needed to obtain stress or strain increments during deformation, so the numerical code is very much simplified. This elastic-plastic modulus is then implemented into the Taylor-Lin model of polycrystal plasticity. Some examples of the application of the model are shown; the elastic-plastic transition of polycrystals, cyclic tension-compression, finally a modellization of a special experiment, carried out by Hohenemser on steel tubes, in 1931.

Keywords: Crystal plasticity, polycrystal plasticity, yield surface, Taylor-Lin model, elastic-plastic modulus, strain path changes

1. Introduction

During the first period of crystal plasticity studies (up to about 1970), the yield surface of single crystals was based on the Schmid law. Its simplicity permitted to understand several experimental phenomena. It also produced, however, severe ambiguity problems in the selection of the operative slip systems when multiple slip (5 systems) were needed to accommodate the prescribed deformation. This problem was overcome when the strain rate sensitivity of slip was considered (Rice, Hutchinson, 1976, Pan and Rice, 1983). However, the selected power-law which connects the resolved shear strain rate to the resolved shear stress in a slip system permits plastic slip to occur at any small level of stress. For this reason, it was criticized by several authors, who considered it just a mathematical tool for the solution of the ambiguity problems. (The non-existence of the ambiguities is a consequence of the rounded shape of the yield surface in rate sensitive slip (Tóth et al, 1988).)

In the present work, another approach to deal with the single crystal yield surface is examined. It is based on a corrected interpretation of the Schmid law. A similar type of modification was already presented by Arminjon (1991). Here we resume his basic idea and develop it further for the more general elastic-plastic case. Schmid considered that there is only one critical shear stress in a slip system to activate plastic slip. The Schmid law could be accepted for individual dislocations, but for each of them, with different critical stresses. For this reason, when the crystal is loaded, there has to be slip activity in several slip systems simultaneously. From the point of view of theoretical plasticity, it is only possible if the yield surface is rounded. For this reason, the yield surface of single crystals is defined in a general rounded form, following the expression of the yield potential function derived for rate sensitive slip by Tóth et al. (1988). In the present approach, however, slip is not rate sensitive.

In this paper, the elastic-plastic modulus of the single crystal deformation is calculated analytically which is based on the proposed shape of the yield surface. It permits to obtain stress increments in terms of the increments of strain. Hardening is also incorporated at the slip system level. This approach is then implemented into a Taylor type of polycrystal model (the Taylor-Lin model), which includes elasticity. It is verified that the new model can predict the texture evolution as good as earlier Taylor type approaches. Its main advantage, however, resides in the elastic effects which can be readily followed when strain path changes occur.

2. The single crystal yield surface and the elastic-plastic modulus

The following yield function is adopted for single crystals:

$$f\left(\sigma_{ij},\tau_0^s\right) = \sum_{s=1}^{n} \frac{\left|M_{ij}^s \sigma_{ij}\right|^{h+1}}{\left(\tau_0^s\right)^h} - \tau_0 = 0 \ . \tag{1}$$

Here σ_{ij} is the stress tensor, τ_0^s represents the strength of slip system s, and the term $M_{ij}^s \sigma_{ij} = \tau^s$ is the resolved shear stress. The M_{ij}^s quantities describe the orientation of the slip systems defined by the slip plane normal $\vec{n}^s$ and the slip direction $\vec{b}^s$:

$$M_{ij}^s = \frac{1}{2}\left(b_i^s n_j^s + b_j^s n_i^s\right) . \tag{2}$$

Finally, h describes the form of the yield surface in (1), while τ_0 controls its size. It can be shown that f is strictly convex and approaches the Bishop-Hill yield surface when h→ ∞ and when for all s: $\tau_0^s = \tau_0$. For the plastic strain rate $\dot{\varepsilon}_{ij}^p$, the normality rule is used:

$$\dot{\varepsilon}_{ij}^p = \dot{\lambda}\frac{\partial f}{\partial \sigma_{ij}} . \tag{3}$$

Using relations (1-3), a unique solution for the slip rate distribution $\dot{\gamma}^s$ can be obtained:

$$\dot{\gamma}^s = \dot{\lambda}(h+1)r^s, \quad \text{where } r^s = \frac{\tau^s}{\tau_0^s}\left|\frac{\tau^s}{\tau_0^s}\right|^{h-1} . \tag{4-5}$$

$\dot{\lambda}$ still has to be determined, for which purpose the consistency condition: $\dot{f} = 0$ can be used. In the present work, the calculations are carried out by imposing the strain rate $\dot{\varepsilon}_{ij}$, which is the sum of the elastic and plastic strain rates:

$$\dot{\varepsilon}_{ij} = \dot{\varepsilon}_{ij}^e + \dot{\varepsilon}_{ij}^p . \tag{6}$$

For the elastic part, the elastic modulus C_{ijkl} can be used:

$$\dot{\sigma}_{ij} = C_{ijkl}\dot{\varepsilon}_{kl}^e . \tag{7}$$

With the help of the consistency condition, $\dot{\lambda}$ can be expressed as follows:

$$\dot{\lambda} = \frac{1}{H+J}P_{mn}C_{mnpq}\dot{\varepsilon}_{pq} . \tag{8}$$

where H, J and P_{mn} are defined fined as:

$$H = h(h+1)\sum_{s=1}^{n} r^s \frac{\tau^s}{\tau_0^s}\sum_{\beta=1}^{n} H^{s\beta}|r^\beta| , \; J = P_{ij}C_{ijkl}P_{kl} , \; P_{ij} = \frac{\partial f}{\partial \sigma_{ij}} = (h+1)\sum_{s=1}^{n} r^s M_{ij}^s , \tag{9-11}$$

with $H^{s\beta}$ being the hardening matrix which describes the interaction of slip systems through the usual relation:

$$\dot{\tau}_0^s = \sum_{\beta=1}^{n} H^{s\beta}|\dot{\gamma}^\beta| . \tag{12}$$

The above relations permit us to relate the stress evolution directly to the total imposed strain rate in an analytic way:

$$\dot{\sigma}_{ij} = \left[C_{ijkl} - \frac{1}{H+J}C_{ijpq}P_{mn}C_{mnkl}P_{pq}\right]\dot{\varepsilon}_{kl} , \tag{13}$$

where the quantity in parenthesis is called the elastic-plastic modulus:

$$C^{ep}_{ijkl} = C_{ijkl} - \frac{C_{ijpq}P_{pq}P_{mn}C_{mnkl}}{H + P_{ij}C_{ijkl}P_{kl}} . \tag{14}$$

The second member in the expression of C^{ep}_{ijkl} only exists if both of the following plasticity criteria are fulfilled:

$$f=0 \text{ and } d\sigma_{ij}\frac{\partial f}{\partial \sigma_{ij}} \geq 0 . \tag{15}$$

The solution of an elastic–plastic problem of single crystal deformation consists in the integration of eq. (13). However, if the strain increments are sufficiently small, the integration can be avoided by using (13) in an incremental form:

$$d\sigma_{ij} = C^{ep}_{ijkl} d\varepsilon_{kl} . \tag{16}$$

Employing eq. (16) involves the assumption that the orientation factors M^{s}_{ij} stay constant during an increment of strain, which is just an approximation. They are, however, updated after each increment, so their evolution is not disregarded. That is, the orientation changes are calculated; the evolution of the texture is followed.

3. Application of the elastic-plastic modulus in polycrystal deformation

In the present paper, the Taylor model is adopted for the behaviour of polycrystals with extension to the elastic part of the deformation. It means that the macroscopic strain rate is taken to be the same for each grain. This kind of modelling was first proposed by Lin (1957), this is why we call this approach as the Taylor-Lin model of polycrystal plasticity. In this model, only the total strain is imposed; the repartition of it into elastic and plastic parts is found out from the crystal plasticity model presented in the preceding section.

In what follows, the boundary conditions to be applied in the simulation of elastic-plastic deformation of polycrystals will be examined. The case discussed here is compression tension in the direction of axis z of a cylindrical tube. (Other cases can be treated similarly.) In order to approach the experimental conditions, mixed boundary conditions are necessary to realise at the *macroscopic* level. That is, the stress components obtained as the average of the stresses in the grains of the polycrystal $\langle\sigma_{rr}\rangle$ and $\langle\sigma_{\theta\theta}\rangle$ have to be zero, while the strain rate components $\dot{\varepsilon}_{zz}, \dot{\varepsilon}_{r\theta}, \dot{\varepsilon}_{rz}, \dot{\varepsilon}_{\theta z}$ have to be imposed, the shear components having zero values. Two strain rate components are left free; $\dot{\varepsilon}_{rr}$ and $\dot{\varepsilon}_{\theta\theta}$. As the calculation is done in strain control, these two components are the unknowns of the *polycrystal* deformation problem. They can be readily obtained via a Newton-Raphson numerical procedure in which they are varied until the boundary conditions for the stresses ($\langle\sigma_{rr}\rangle = 0$ and

$\langle\sigma_{\infty}\rangle = 0$) are fulfilled. Please note that as the present approach is elastic-plastic, the *true stress* components can be calculated, not only the deviatoric ones (that would be the case in an approach where only plastic deformations are modelled).

4. Examples of applications

Because of space limitations, only some particular cases are examined in the present paper; see below. In what follows, 100 or 500 randomly oriented grains were generated to represent the polycrystalline specimen. In each grain, the average slip resistance (the τ_0^* value) was taken to be the same: 16 MPa.

4.1 The elastic-plastic transition in combined torsion and extension of a non-hardening thin walled tube

The sample was loaded in combined uniaxial tension and torsion with mixed boundary conditions corresponding to the deformation of a thin walled tube. The shape factor of the yield surface was taken to h=20. The crystal structure is fcc. Fig. 1 shows the computed yield surfaces in the axial stress (σ) – shear stress (τ) space for three conditions. The curve marked by the number (1) in Fig. 1 corresponds to the stress states when the first grain of the polycrystal begins to deform plastically. It has a hexagonal shape. The second curve belongs to the condition when all grains (500) become plastic. It displays an irregular form. Finally, the third one is obtained when the stress state is saturated; it is perfectly convex. Please note that there is no hardening in this example and the expansion of the yield surface is due to kinematic hardening which takes place on the individual yield surfaces of the constituent crystals, which is terminated when the loading point reaches a "vertex" in each grain.

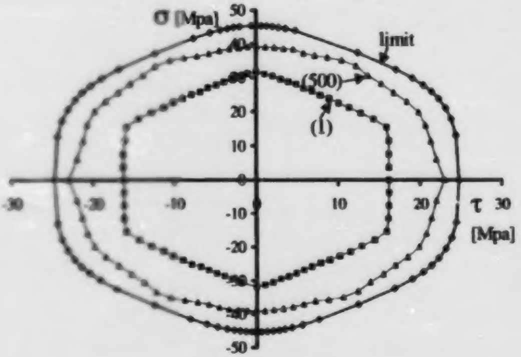

Fig. 1. Predicted subsequent and limiting yield surfaces in combined tension and torsion of a thin walled tube.

4.2. Cyclic deformation

Zouhal et al. (1996) presented the first study of cyclic deformation of polycrystal elasto-viscoplasticity employing also the Taylor-Lin model, however, using the theory of rate sensitive slip (with an m value of 1/81). They deformed a random population of 100 grains (having fcc crystal structure) in tension-compression at an amplitude of ε=0.001 using microscopic hardening. The same case was studied using the present model (with a shape factor of the yield surface of h=81) and the results were compared to the published results of Zouhal et al. For the first 25 cycles of deformation, the cyclic stress-strain curves are also shown here in Fig. 2. The obtained results are practically identical to the rate sensitive case, that is, correctly reproduce the Bauschinger effect (which is also the result of kinematic hardening).

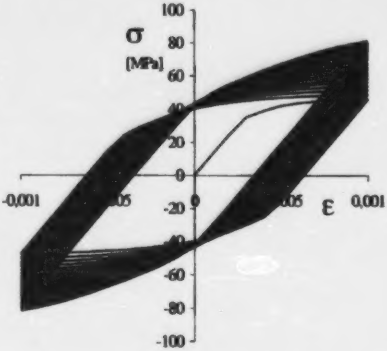

Fig. 2. Cyclic deformation in tension-compression of a polycrystal.

4.3. Elastic effects during strain path changes - Hohenemser's experiment

Hohenemser (1931) observed that the shear stress necessary for plastic deformation gradually vanishes during tensile testing of previously twisted and non-unloaded steel tubes. This experiment has been simulated with the present approach using 500 randomly oriented grains and the {110}<111> as well as the {112}<111> slip systems with equal critical stresses. The h parameter was taken to 20. First, the polycrystal was twisted up to a shear strain of 0.005, then, without unloading, the sample was deformed in uniaxial extension. The evolution of the shear and axial stresses (normalised by their limiting values) during this second test is plotted in Fig. 3. It can be seen that the model reproduces quite well the observations of Hohenemser (represented by the solid points in Fig. 3). Differences can be due to the Taylor assumption in the present modelling, and also from the possible textures present in the specimens of Hohenemser.

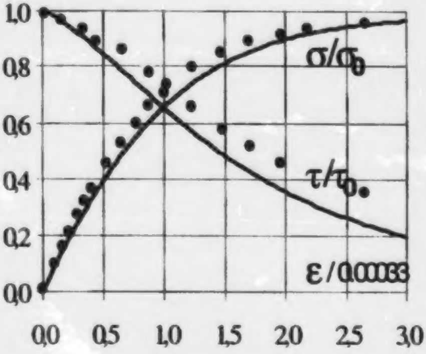

Fig. 3. Predicted evolution of the shear and axial stresses during tension of a previously twisted steel tube. Solid points are from the experiments of Hohenemser (1931).

5. References

Arminjon, M. (1991), *Textures and Microstructures*, Vol. 14-18, pp. 1121-1128.
Tóth, L.S., Gilormini P. and Jonas, J.J. (1988) *Acta Metall.*, Vol. 36, pp. 3077-3091.
Hohenemser, K. (1931) *Zeits. Ang. Math. Mech.*, Vol. 11, p. 15.
Hutchinson, J.W. (1976) *Proc. Roy. Soc. Lond. A.*, Vol. 348, pp. 101-127.
Lin, T.H. (1957) *J. Mech. Phys. Solids*, Vol. 5, 143.
Pan, J. and Rice, J.R. (1983) *Int. J. Solids Structures*, Vol. 19, pp. 973-987.
Zouhal, N., Molinari A. and Tóth, L.S. (1996) *Int. J. Plasticity*, Vol. 12, pp. 343-360.

CRITICAL STRESS IDENTIFICATION IN TEXTURED MATERIALS USING SELFCONSISTENT POLYCRYSTALLINE INVERSE MODEL

J. SIGNORELLI, A. FOURTY, R. LEBENSOHN and R.E. BOLMARO

Instituto de Física Rosario-Fac. Ciencias Exactas, Ingeniería y Agrimensura. CONICET-UNR. Rosario. Argentina. *e-mail: signorel@ifir.ifir.edu.ar*

Abstract

Polycrystalline models have been developed to describe the mechanical behavior of anisotropic textured materials. Particularly, visco-plastic self-consistent (VPSC) models (Molinari et al. 1987, Lebensohn and Tomé 1993) have been widely used to predict texture evolution: Zr alloys (Lebensohn et al. 1996), geological applications (Castelnau et al. 1997) and Ti-Al (Lebensohn et al. 1997) are among the examples. More recently these models have been coupled with Finite Elements Methods codes (FEM) in order to consider the plastic anisotropy (texture induced) in each element (Logé et al. 1998, Maudlin et al. 1998). In all cases it is necessary to known the microscopic constitutive parameters which are not usually available by direct measurement, as it is the case of Critical Resolved Shear Stresses (CRSS). Experimental determination of CRSS in Zr alloys are extremely difficult because of the current impossibility of growing single crystals of those alloys. In this work we present an inverse method for the automatic identification of CRSS values and active deformation modes in the VPSC framework. The solution of an inverse problem consists in finding the set of parameters that minimize a certain objective function, which measures the "distance" between the experimental and predicted results. In our case, the cost function is expressed, in terms of crystallographic textures, as the square difference of the simulated and measured Orientation Distribution Functions (ODF).

Keywords: Texture development simulation, inverse problems, Self-Consistent methods.

1. Introduction

Texture development simulation is performed with a VPSC code (Lebensohn and Tomé 1993). For a more clear description of the inverse formulation we briefly reproduce the main equations of the VPSC model. The viscoplastic constitutive relation between the strain rate in the crystal and the stress state can be written as a sum over all active slip systems:

$$\dot{\varepsilon} = \left\{ \dot{\gamma}_{\circ} \sum_{s} \frac{m^{(s)} \otimes m^{(s)}}{\tau_{c}^{(s)}} \left| \frac{m^{(s)} : \sigma'}{\tau_{c}^{(s)}} \right|^{n-1} \right\} : \sigma' = M^{c\,sec}(\sigma') : \sigma' \tag{1}$$

where $\dot{\gamma}_{\circ}$ is a reference rate, $\tau_{c}^{(s)}$ is the CRSS for each system and n is the inverse of the rate sensitivity, $m^{(s)}$ is the Schmid tensor , σ' is the deviatoric Cauchy stress tensor and $M^{c\,sec}$ is the secant compliance tensor (c = crystal). The stress and strain states in the grains can be different from the corresponding macroscopic ones; the deviations between the local and macroscopic magnitudes are related by the interaction tensor $\tilde{M}$. This tensor is the base of the self-consistent (SC) approach and can be expressed as function of the tangent modulus M^{tg} and the Eshelby tensor S^{esh}. The polycrystal modulus is calculated as a solution of the transcendental equation:

$$M = \left\langle M^{c\,sec} : \left(M^{c\,sec} + \tilde{M}\right)^{-1} : \left(M^{sec} + \tilde{M}\right) \right\rangle \tag{2}$$

In the SC approach the total rotation rate for the grain or orientation can be expressed as:

$$\omega = W + \Pi^{esh} : S^{esh^{-1}} : \left(\dot{\varepsilon} - \dot{E}\right) + \sum_{s} \frac{1}{2} \left(n^{(s)} \otimes b^{(s)} - b^{(s)} \otimes n^{(s)}\right) \dot{\gamma}^{(s)} \tag{3}$$

where W and Π^{esh} are the antisymmetric parts of the macroscopic distortion rate and Eshelby tensor respectively. The evolution from the original to the current orientation is given by:

$$R^{t+dt} = R^{t}\, exp(\omega^{t} \Delta t) \tag{4}$$

2. Model Description

The identification of parameters by inverse analysis is reduced to a minimization problem. We can express that in the classical form :

$$\begin{cases} \text{find } \; \overline{p} / Q\left(C^{cal}(\overline{p}), C^{exp}\right) = \underset{p \in P}{min}\, Q\left(C^{cal}(p), C^{exp}\right) \\ P = \left\{ p / h_{i_{min}} \le h_i(p) \le h_{i_{max}},\ i = 1, \ldots, \mathrm{Npar} \right\} \end{cases} \tag{5}$$

where p={ $p_1, \ldots, p_{Npar}$ } is the parameter vector (Npar: number of parameters to identify). The parameter space P allows to define the admissible set of physical values. C^{exp} = { $C_1^{exp}, \ldots, C_{Nob}^{exp}$ } is the experimental data vector (Nob represents the number of measured points). Feeding the model with parameters representative of experimental conditions, it predicts a similar data vector C^{cal} = { $C_1^{cal}, \ldots, C_{Nob}^{cal}$ }. The cost function is expressed in terms of the difference of squares:

$$Q = \sum_{i} \beta_i \left[C_i^{cal} - C_i^{exp} \right]^2 \tag{6}$$

where C_i^{cal} and C_i^{exp} are the calculated and experimental ODF intensities respectively. The system (5) is solved using an iterative gradient approach, and completed with a line search algorithm to find the optimal descent vector. The sensitivity matrix is evaluated by analytical differentiation of the calculated coefficients.

The evolution of the ODF intensities during the deformation process can be related directly with the evolution of a set of rotation matrices, { R }, which relate the grain orientation with a sample frame using Eulerian scheme to represent the texture evolution. From expression (4), the derivative of R can be calculated by:

$$\frac{\mathrm{dR}^{t+\Delta t}}{\mathrm{dp}}=\frac{\mathrm{dR}^{t}}{\mathrm{dp}}\,exp(\omega^{t}\Delta t)+\mathrm{R}^{t}\,exp(\omega^{t}\Delta t)\frac{\mathrm{d}\omega^{t}}{\mathrm{dp}}\Delta t \tag{7}$$

The eq. (7) is evaluated for each grain, later the derivative of the distortion rate for each grain and for all t increment should be calculated. This derivative is a complex function of the initial model parameters, then it involves the calculation of many intermediate derivatives in the VPSC approach: $\mathrm{d\,M^{(sec)}/dp}$, macroscopic secant modulus; $\mathrm{d\,M^{c^{sec}}/d}$, microscopic secant modulus; $\mathrm{d}\sigma'/\mathrm{dp}$, deviatoric stress tensor; $\mathrm{d}\gamma^{c(s)}/\mathrm{dp}$, single shear in each system; $\mathrm{dS/dp}$ and $\mathrm{d}\Pi/\mathrm{dp}$, symmetric and screw parts of Eshelby tensor. Uncoupled equations result if a Taylor hypothesis is assumed. Next, all derivatives are expressed in terms of the derivatives of the macroscopic compliance tensor (eq. 8) and the derivatives of the stress tensor in each grain (eq. 9). In consequence the goal is to write those two derivatives as functions of the magnitudes calculated on the direct model: $\mathrm{M^c}$, M, Σ, σ, S, n and τ.

$$\frac{\mathrm{dM^{sec}}}{\mathrm{dp}}=\frac{\mathrm{d}\left\langle \mathrm{M}^{c^{sec}}:\mathrm{B}^{c}\right\rangle}{\mathrm{dp}} \tag{8}$$

$$\frac{\mathrm{d}\sigma'}{\mathrm{dp}}=\frac{\mathrm{dB}^{c}}{\mathrm{dp}}:\Sigma+\mathrm{B}^{c}:\frac{\mathrm{d}\Sigma}{\mathrm{dp}} \tag{9}$$

The terms $\frac{\mathrm{dM}^{c^{sec}}}{\mathrm{dp}}\left[\frac{\mathrm{d}\sigma'}{\mathrm{dp}}\right]$ and $\frac{\mathrm{dB}^{c}}{\mathrm{dp}}\left[\frac{\mathrm{dM^{sec}}}{\mathrm{dp}},\frac{\mathrm{d}\sigma'}{\mathrm{dp}},\frac{\mathrm{dS}}{\mathrm{dp}}\right]$ in equation (8) are replaced by their explicit expression to obtain a set of 25 equations with $\mathrm{d}\sigma'/\mathrm{dp}$ and $\mathrm{d\,M^{sec}/dp}$ as unknown; in a similar form the $\mathrm{dB^c/dp}$ and $\mathrm{d}\,\Sigma/\mathrm{dp}$ derivatives are computed analytically and replaced in equation (9) to obtain a set of 5 equations per grain. The precedent equations (8-9) can be expressed in a simple format as a set of linear equations:

$$\mathrm{A}^{c}:\left[\frac{\mathrm{d}\sigma'}{\mathrm{dp}}\right]+\mathrm{B}^{c}:\left[\frac{\mathrm{dM^{sec}}}{\mathrm{dp}}\right]=\mathrm{C}^{c}\qquad \text{no sum over c.} \tag{10}$$

$$D^c:\left[\frac{d\sigma'}{dp}\right]+E\ :\left[\frac{dM^{sec}}{dp}\right]=F \qquad \text{sum over c.}$$

where A^c, B^c, C^c, D^c, E and F are constant tensors which are not function of any derivative magnitude. The Eshelby derivative contribution is taken into account in an iterative form in equation (10). As an initial guess no dependence on p is assumed. Then the system (10) is recalculated with the current dS/dp value. An explicit development of this equations is done in Signorelli et al. 1999.

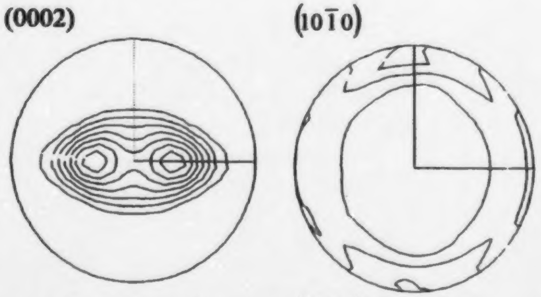

Fig. 1: Experimental (0002) and $(10\bar{1}0)$ initial pole figures for Zircaloy4 rolled sheet. The initial texture is a classical rolling texture with a maximum at 20°-30° tilt in NT plane.

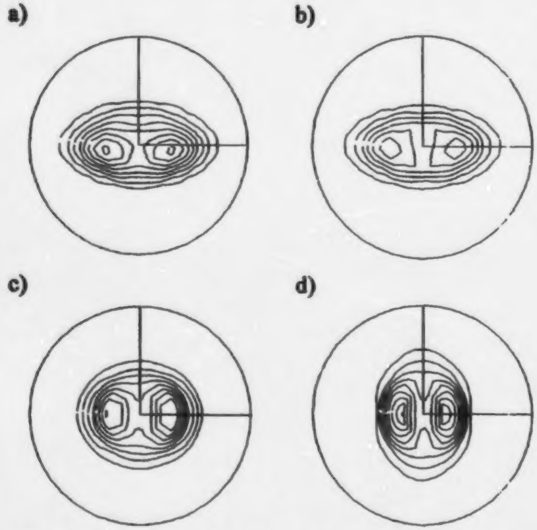

Fig. 2: Experimental (0002) pole figures: a) after 20% rolling reduction in rolling direction. b) idem (a) after 40% reduction. c-d) idem (a-b) in transverse direction.

3. Results

We applied the described method to evaluate the CRSS values for a rolled Zircaloy4 sheet at low temperature. Rolling tests were performed up to 20% and 50% reduction plastic strain on samples with the original rolling direction (R20 and R50) or transversal direction (T20 and T50) as the rolling direction (Signorelli 1997). The initial rolled sheet texture presents a tilting angle of the c-axis of about 20°-25° from the normal direction (ND) to the transverse direction (TD) (Fig 1). The associated Kearns factor are f_n =0.601, f_t =0.267 and f_r =0.132. After 20% and 50% rolling R20 and R50 textures present a weak reorientation of c-axis because the initial texture is already a characteristic rolling texture.

The re-orientation of the c-axis smoothes the texture in the ND-TD plane and the initial maximum is weakened (Fig. 2a-b). Meanwhile the $\{10\bar{1}0\}$ poles tend to get aligned with the rolling direction. A more important reorientation of the $\{0002\}$ poles is observed in the T20 and T50 textures (Fig. 2c-d). In both cases the maxima is more clear and the maximum intensity does not significantly change with deformation. The initial maximum position moves to ND direction. Kearns factor for T20, T50, R20 and R50 samples are

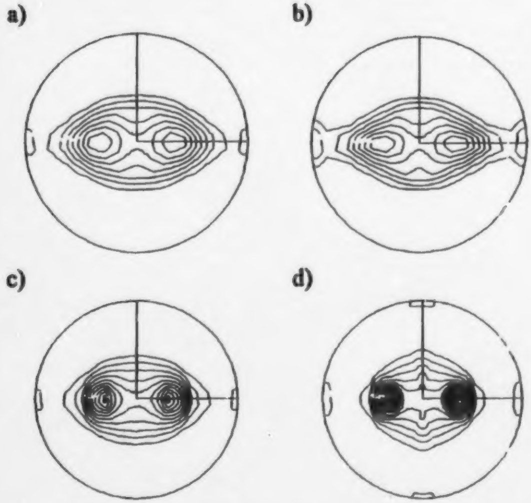

Figure 3: Calculated (0002) pole figures using the identified deformation modes and CRSS values. a) rolling direction 20% reduction, b) idem (a) 40% reduction, c) transverse direction 20% reduction, d) idem (c) 40% reduction. Lines are multiples of random distribution (mrd).

reported on Table 1. Zirconium alloys present more than one active deformation mode; the most active is the $\{10\bar{1}0\}<1\bar{2}10>$ prismatic slip, but many secondary systems can be active: $\{10\bar{1}1\}<1\bar{2}13>$ pyramidal $<c+a>$, $\{10\bar{1}1\}<1\bar{2}10>$ pyramidal <a>, $\{0001\}<1\bar{2}10>$ basal $<a>$, $\{1012\}<1011>$ tensile twinning, or $\{1011\}<1123>$ compressive twinning (Akhtar 1973, Tenckhoff 1988). The activation of twining mechanisms strongly depends on deformation history, chemical composition, heat treatment and grain size, among other factors. Moreover, it is worthy to emphasize the influence of the direction of the applied stress and initial texture over the selection and activation of the secondary deformation modes. In the current case, optical microscopy studies show no active twinning, and we considered prismatic $\{10\bar{1}0\}<1\bar{2}10>$, basal $\{0001\}<1\bar{2}10>$ and pyramidal $\{10\bar{1}1\}<1\bar{2}13>$ systems as potentially active deformation modes. The parameter vector to be optimized $p=\left(\tau^c_{ba<a>}/\tau^c_{pr<a>}, \tau^c_{py<c+a>}/\tau^c_{pr<a>}\right)$ was defined in function of the relative CRSS. The optimization process is initiated assuming $\tau^c_{ba<a>}/\tau^c_{pr<a>}=1, \tau^c_{py<c+a>}/\tau^c_{pr<a>}=1$ for which the objective function value is equal to 2.03. The iterative process converges easily (4 iterations) to Q = 0.933. Such rather high absolute value shows that the model cannot reproduce simultaneously all cases although the four experimental pole figures are in a qualitative agreement. The Kearns factors for the simulated textures obtained with the optimized parameters are shown in Table 1.

Table 1: Experimental and simulated Kearns factors. F_n = ND , F_t = TD and F_l = RD.

Sample	Experiments			Simulations		
	F_n	F_t	F_l	F_n	F_t	F_l
R20	0.600	0.252	0.149	0.600	0.272	0.128
R50	0.535	0.282	0.183	0.583	0.303	0.114
T20	0.623	0.192	0.186	0.606	0.255	0.139
T50	0.578	0.186	0.236	0.592	0.234	0.173

4. Discussion and Conclusions

We have implemented an inverse VPSC model for parameter identification using an analytic computation of the sensitivity matrix. We have optimized the relative CRSS for zircaloy4, in function of experimental textures obtained for different strains and rolling directions. The optimized CRSS assuming prismatic, basal and pyramidal slip systems were $\tau^{c}_{ba<a>} / \tau^{c}_{pr<a>} = 4.1$, $\tau^{c}_{py<c+a>} / \tau^{c}_{pr<a>} = 5.09$. Twining activation did not provide physically acceptable results, in agreement with experimental evidence. Twining activation is justified only in the case of a random orientation initial material, such that $\{1012\}<1011>$twining strongly contributes to reorient c-axis around normal direction. Tensile and compression experimental data would be needed to validate results.

Acknowledgements: The first author wish to thank Dr. Y.Chastel and Dr. R.Logé for fruitful discussions.

5. References

Akhtar, A., (1973) Compression of zirconium single crystals parallel to c-axis", J.Nucl. Mater., Vol. 47,pp. b 79.

Castelnau, O., Canova, G., Lebensohn, R., Duval, P., (1997) Viscoplastic modelling of texture development in polycrystalline ice with a self-consistent approach; comparison with bound estimates", Acta metall. Vol. 45, pp. 4823.

Lebensohn, R. and Tomé C. (1993) A self -consistent anisotropic approach for the simulation of plastic deformation and texture development of polycrystals: application to zirconium alloys", Acta Metall., Vol. 41, pp. 2611.

Lebensohn, R., González, M., Tomé, C., Pochettino, A. (1996) Mesurement and prediction of texture development during a rolling sequence of zircaloy-4 tubes,J. of Nuc. Mat. Vol. 229, pp. 57-64.

Lebensohn, R., Turner, P., Canova, G. (1997) Recent advances in modelling polycrystals with complex microstructures, Comp. Mat. Sci. Vol. 9, pp. 229.

Logé, R., Chastel, Y., Signorelli, J., Lenbensohn, R., Barberis, P. (1998) Finite element simulation of a zircaloy sheet deep drawing using a polycrystalline model, Simulation of Materials Processing: Theory, Method and Applications, Huétlink & Baaijens (eds.) NUMIFORM 98, pp. 329-334.

Maudlin, P., Tomé, C., Kaschner, G., Gray, G. (1998) Introduction of polycrystal constitutive laws in a finite element code with applicatiuons to zirconium forming, Simulation of Materials Processing: Theory, Method and Applications, Huétlink & Baaijens (eds.) NUMIFORM 98, pp. 309-313.

Molinari,A., Canova, G., Ahzi, S., (1987)A self-consistent approach of the large deformation polycrystal viscoplasticity, Acta metall. Vol. 35, pp. 2983.

Signorelli, J. (1997) Optimization des textures de laminage a froid du Zyl4, Rapport DEA. École Nationale Supérieure des Mines de Paris - CEMEF.

Signorelli, J., Lebensohn, R. and Chastel, Y. (1999) Parameter identification method for a polycrystalline viscoplastic selfconsistent model based on analytical derivatives of the direct model equations", Mod. and Simul. Mat. Sci. and Eng., Submitted for publication.

Tenckhoff, E. (1988) Deformation Mechanics, Texture, and Anisotropy in Zirconium and Zircaloy", Philadelphia: ASTM.

A DISCRETE ORIENTATION MODEL FOR THE FCC-TO-BCC PHASE TRANSFORMATION

A.M. LOPES and C.S. DA COSTA VIANA
Department of Mechanical and Materials Engineering, Instituto Militar de Engenharia – IME, Rio de Janeiro, Brazil

Abstract

In the present work a model for the γ-to-α phase transformation, originally tested only on a few individual orientations, is extended for use with real textures. Variant selection based on transformation work and slip activity is used. The texture of the parent γ-phase is here represented by the textures of copper, 70:30 brass and aluminium cold rolled to 40%. These were discretised and transformed, the product orientations being refitted with Gauss functions for comparison and discussion of the model's physical assumptions.

Keywords: γ-to-α transformation, variant selection, model

1 Introduction

In hot rolling and many other metallurgical applications, deformed austenite is frequently transformed to ferrite, bainite or martensite before it recrystallises. This is well known to happen with variant selection and, since the austenite texture cannot be measured experimentally, its prediction based on information from the bcc product texture requires a knowledge of the transformation phenomena. Many models have been developed for the γ-to-α transformation, some purely mathematical (Davies and Bateman 1981), some based on physical assumptions (Miyaji and Furubayashi 1991, Da Costa Viana et al. 1996). The origins of variant selection, however, remain still uncovered. Recently, Butrón-Gullén et al. (1997) developed a crystallographic discrete orientation model for the fcc-to-bcc transformation taking into account the Kurdjumov-Sachs orientation relationship and variant selection rules based on slip activity and a transformation work condition. It was successfully applied to a set of seven components representing the fcc rolling tube. The present work describes the application of the model to whole real rolling textures of copper, brass and aluminium. The main assumptions of the original model are briefly described below. Further detail can be found in the work referred to above.

2 The model

The product orientations are obtained from the discretised orientations of the parent texture via the Kurdjumov-Sachs (1930) orientation relationship, here expressed by a 90^0 rotation about the 24 <112> directions of the fcc system. Variant selection is achieved by means of two rules: (i) the selected variants are those that relieve the residual strain energy left in the parent by the previous rolling pass (different for each crystal), and (ii) nucleation occurs only on the active slip systems of the parent crystal. Parent orientations within 8^0 from {11-2}<111> are treated separately and are transformed to near {1-1 2}<110> product components. The residual strain energy is calculated by the product of the residual plastic stress and the Bain strain, ε_{ij}. The former is defined as the difference between the Bishop-Hill (1951) stresses for rolling the crystal, σ_{ij}, and the parent, S_{ij}. Here, S_{ij} was calculated assuming the parent to be random. The condition for parent strain energy relief and for variant selection is:

$$\Delta w = (\sigma_{ij} - S_{ij}).\varepsilon_{ij} > 0 \qquad (1)$$

Each selected nucleus shares a fraction of the parent orientation volume (intensity) proportional to the slip activity in the system connected to the selected <112> rotation axis. In this work an extra parameter, λ, was introduced which allows choosing, from among the selected nuclei, those originating from systems with slip activities lying within a specified spread (in percent) of the maximum slip activity. The model is comprised by a set of computer programs.

3 Experimental

The textures of 40% cold rolled 70:30 brass, copper and commercial purity aluminium were used to typify the texture of rolled austenite. The ODFs were discretised into approximately 300 Bunge orientations which were individually transformed, the product orientations being refitted by Gauss functions. Figure 1 shows the main orientations in the $\varphi_2 = 45^0$ section of the Bunge ODF.

4 Results and Discussion

Figure 2 shows the textures of the 40% cold rolled brass, copper and aluminium used to represent the austenite texture. The latter, unfortunately, does not display the well known {11-2}<111> typical behaviour of a high stacking fault energy fcc material. In fact, the ODF maximum at the bottom of

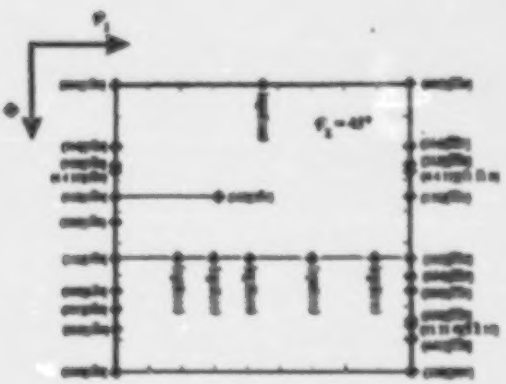

Figure 1: ODF $\varphi_2 = 45^0$ section interpreting diagram in Bunge co-ordinates.

Figure 2c is close to {110}<1-1 1> rather than to {110}<1-1 2>. The maximum intensities for each material are, respectively, 9, 6 and 7.

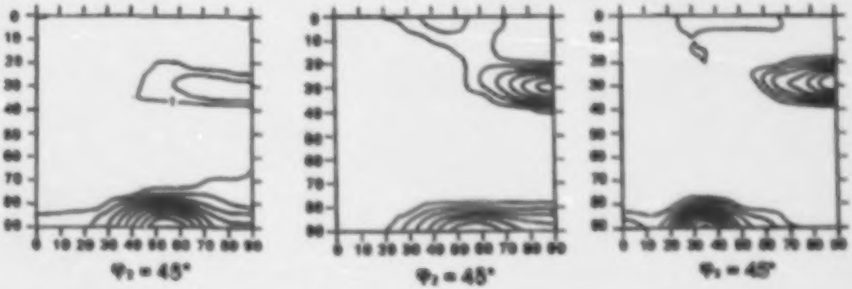

(a) (b) (c)

Figure 2: ODFs of the 40% cold rolled (a) brass, (b) copper and (c) aluminium.

In Figure 3 the product textures predicted for λ = 5% are shown. This is practically restricting nucleation to the system with maximum slip activity only. These textures were produced from 717, 834 and 960 product orientations, respectively (intensities below 0.5 were discarded). It can be seen that the textures for the brass and the copper are similar except for the slightly higher intensity of the former (7.7 and 6.0, respectively) and a small peak near {001} <110> in Figure 3b. The peak maxima occur for the {113}-{112}<1-1 0> and {221}<1 1-2> orientations, the same being valid for the aluminium product texture. The texture predicted from the aluminium texture shows an extension towards the {113}<3 3-2> orientation and a general low intensity (4.8 maximum), mainly near {221}<11-2>. It is important to note the total absence of the {001}<110> component in all the textures predicted for these conditions.

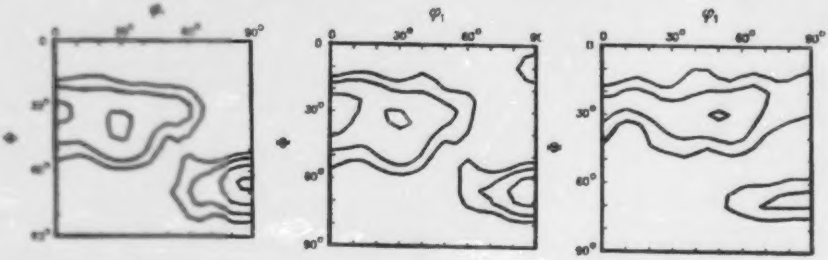

(a) (b) (c)

Figure 3: BCC textures predicted from: (a) brass; (b) copper and (c) aluminium using variants with slip activities within 5% of the maximum.

Figure 4 shows the textures predicted from the brass, copper and aluminium textures using variants with slip activities within 98% of the maximum. In practice this includes all variants with slip activity values different from zero, which satisfy the strain energy condition. The maximum intensities are now practically the same: 6.5, 6.2 and 5.9, respectively, smaller than for the λ = 5% case. It seems that the added variants populate preferentially the lower intensity areas of the texture. The product from the copper texture now displays the {001}<110> component (Figure 4b). The same happens to the aluminium product, though with a smaller intensity (Figure 4c), but not for the brass product texture (Figure 4a). There the {001}<110> component is completely absent.

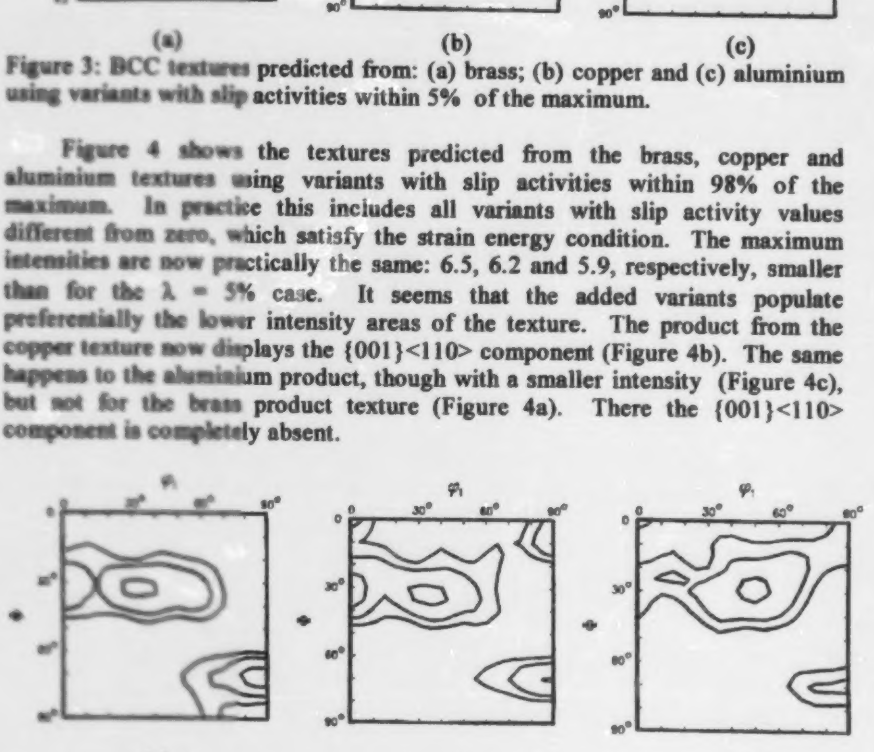

(a) (b) (c)

Figure 4: BCC textures predicted from: (a) brass; (b) copper and (c) aluminium using variants with slip activities within 98% of the maximum.

A common feature of nearly all the predicted textures is the presence of a peak near {112}<1-3 1>. This and the extension of the intensities along the {112}-{113} plane ($\Phi \cong 30^0$) do not seem to be linked to slip activity since their presence is independent of the λ parameter. At the time of writing their origin is still under investigation.

Figure 5 shows typical textures of martensite, bainite and ferrite, obtained from quenched rolled austenite, found in the literature. It can be seen that, apart

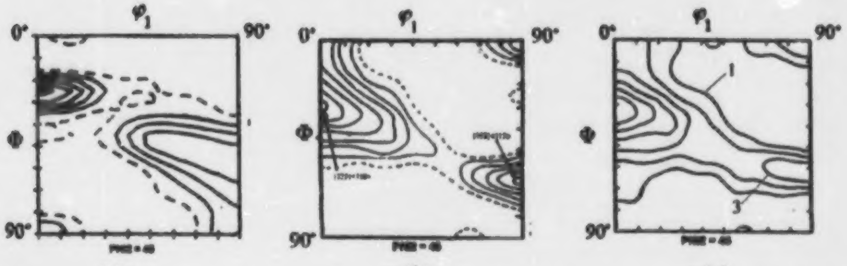

(a) (b) (c)

Figure 5: Experimental ODFs of martensite, bainite and ferrite obtained from quenched rolled austenite.

from what was just pointed out, the model is capable of reproducing the main features present in transformation textures. Further investigation is now required to refine the assumptions concerning the residual strain energy calculation and the effect of the slip activity criterion in order that a better agreement can be obtained.

5 Conclusions

A model for predicting transformation textures originally tested with just a few orientations was applied to real textures. It seems that the assumptions with respect to variant selection can be generalised to textures commonly found in fcc materials. The main features of the transformation textures can be reproduced and the severity of the product textures is compatible with those of the parent. The fact that the model is completely automated by a sequential set of computer programs makes it an adequate tool for further investigation of the influence of variant selection on transformation textures.

6 Acknowledgements

One of the authors is deeply indebted to Professor J.J. Jonas and to Dr. M.P. Butrón-Guillén for their decisive contribution to the development of the original model.

7 References

Davies, G.J. and Bateman, R.M.. (1981). Proceedings of the 6th International Conference on Texture of Materials, Tokyo, vol.1, pp.132-148.
Miyaji, H. and Furubayashi, E..(1991). Texture and Microstructures, vol. 14-18, pp.561-566.

Da Costa Viana, C.S., Butrón-Guillén, M.P. and Jonas, J.J. (1996). Textures and

Microstructures, vol. 8, pp.1-12.
Butrón-Guillén, M.P., Da Costa Viana, C.S. and Jonas, J.J. (1997).Metallurgical and Materials Transactions A, vol. 28, pp. 1755-1768.
Kurdjumov, G. and Sachs, G. (1930). Z. Physik, vol. 64, p. 225.
Bishop, J.F.W. and Hill, R. (1951). Philosophical Magazine, vol. 42, pp. 414-427.

PREDICTIONS OF RECRYSTALLIZATION TEXTURES WITH MONTE CARLO MODEL USING DEFORMATION CHARACTERESTICS

J. TARASIUK, K. WIERZBANOWSKI, B. BACROIX* and A. MIROUX*

Wydział Fizyki i Techniki Jądrowej, Akademia Górniczo-Hutnicza, 30-059 Kraków, Poland
(*) LPMTM, CNRS, Université Paris XIII, Institut Galilée, 93430 Villetaneuse, France

Abstract

The energy stored during plastic deformation is the driving force in the recrystallization process. The goal of the present work is to find the best parameter characterizing this energy (and available from deformation models) and to use it next as the input data in the recrystallization model of the Monte Carlo type.

Keywords: Recrystallization, texture, stored energy, deformation model, Monte Carlo model

1 Deformation models

The energy stored in a material after plastic deformation plays an important role in the recrystallization process. Two quantities characterizing deformed grains were considered to be „candidates" for the stored energy parameter: dislocation density: $\rho \propto <\tau>^2$ (τ - is the critical shear stress for slip) and total plastic work of a grain: $W = \sum_i \int \tau^i \dot{\gamma}^i \, dt$ (i - numbers active slip systems and γ is the slip shear glide).

Three polycrystalline deformation models were used to calculate the above quantities: isotropic elasto-plastic model (EP model, Wierzbanowski al. 1992), viscoplastic self-consistent model (VPSC model, Molinari et al. 1987) and Taylor model (T model, Taylor 1938). The basis of any model is the interaction law. It describes the interaction between a grain and the sample; e.g. for the EP model it has the following form:

$$\dot{\sigma} - \dot{\Sigma} = -L(\dot{\varepsilon} - \dot{E}) \qquad \text{(EP model)} \qquad (1)$$

where: σ and Σ are local and macroscopic stress tensors ($\Sigma = <\sigma>$), ε and **E** are plastic deformation tensors of a grain and of the sample (**E** $= <\varepsilon>$) and **L** is the interaction tensor. In the simplified isotropic EP model the **L** tensor is replaced by a scalar parameter L. Its value was estimated by comparison of predicted and experimental results; the value of L around $10^{-2}\,\mu$ was found (μ is the shear modulus). This gives L abut 1000 MPa for the rolled low carbon steel (considered in this work).

The above models were applied in the case of b.c.c. interstitial free steels; consequently the <111>{110} and <111>{112} slip system families were considered. The linear and saturating hardening laws were applied (Molinari et al. 1987; Wierzbanowski et al. 1999). In both cases the hardening matrix H^{ij} has the following form:

$$H^{ij} = q^{ij} h_o \tag{2}$$

where h_o is the hardening matrix „amplitude" (constant in the linear case and variable in the saturating one) and q^{ij} describes the „structure" of slip systems hardening: $q^{ij}=1$ if i=j and $q^{ij}=q_0$ otherwise. The isotropic hardening occurs if $q_0=1$ and anisotropic one if $q_0>1$. Appropriate glide distribution laws are used (Schmid law - in EP model, minimization of deformation work - in T model and viscoplastic flow law - in VPSC model). The isotropic initial grain orientation distributions (2000-2500 grains) and the same initial critical shear stress were used. Two values of L parameter from the EP model were used: L=1000 MPa and L=400 MPa (strong and weak interactions).

2 Recrystallization Monte Carlo model

The Monte Carlo type model was elaborated (WIERZBANOWSKI et al. 1999), basing on the earlier works (Wimmer et al. 1996; Miroux et al. 1998). This model describes the kinetics of recrystallization process; it predicts also the texture modification and the released heat. The important features of the MC program are listed below.

- MC program contains effectively 2 500 000 sites (points) covering the hypothetical sample surface. Each grain or nucleus contains in general many sites.
- Microstructure of the deformed material is considered. This microstructure is generated taking into account real parameters of the rolled material: grain shapes and crystallographic texture. The texture was composed of 9 model gaussian peaks in the present work.
- The $<\tau>^2$ is used as the stored energy parameter. The criterion of *minimization of total energy* is applied during recrystallization; bulk energy (driving force) and boundary energy are taken into account.
- Highly oriented nucleation is assumed. It means that nuclei are created only within grains with high stored energy (probability of nucleus creation is proportional to the stored energy).
- Recrystallization process simulation (repeated many times for each site having recrystallized environment) contains the following steps: a) sum of stored (volume) and boundary (surface) energy for a grain is calculated (E_1), b) orientation of a site is changed to that of one of neighboring, recrystallized grains, c) stored energy is released, d) grains boundaries and boundary energy are modified, e) new total energy (E_2) is calculated, f)

change of total energy ($\Delta E=E_2-E_1$) is calculated, g) if $\Delta E>0$ - we return to the state before operation., in the opposite case the new state is preserved with the probability proportional to $|\Delta E|$. These operations are continued until the whole material volume is recrystallized.

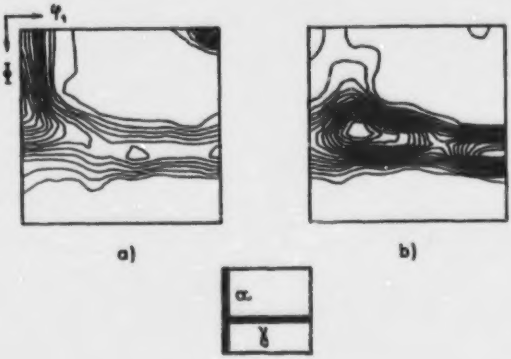

Fig. 1. Modification of deformation texture after recrystallization (titanium interstitial free steel): a) deformation texture (90% rolling reduction), b) recrystallization texture (annealing in 750 °C). The α and γ fibers are also schematically shown.

3 Results for law carbon steel

Exemplary texture transition from deformation to recrystallization type for the interstitial free titanium steel is shown in Fig.1. Two texture fibers are specified in the presented $\varphi_2=45°$ ODF section: α fiber ($\varphi_1=0°$ and γ fiber ($\phi=54.7°$). It may be seen that the intensity of α fiber decreases and that of γ fiber increases during recrystallization. The deformation textures predicted by three models discussed previously are shown in Fig. 2

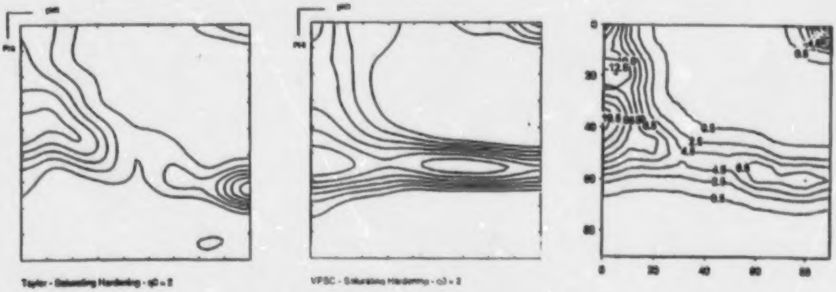

Fig. 2. Deformation textures predicted by deformation models: Taylor (left), viscoplastic (middle) and elasto-plastic with L=1000 MPa (right). Saturating and anisotropic hardening ($q_0=2$) was considered.

(T, VPSC and EP models; $q_0=2$, saturating hardening). The VPSC model reproduces quite well the γ fiber but not good enough - the α fiber. The EP model (with L=1000 MPa) reproduces both fibers. The worst texture prediction is given by T model.

The orientation variation of $<\tau>^2$ predicted by T, VPSC and EP models are shown in $\varphi_2=45°$ section in Fig.3 (the circles visualize the quantity distribution between its minimal and maximal values). It can be seen that the T and VPSC models (Fig. 3 a,b) predict contradictory results: the T model predicts higher dislocation density for grains belonging to γ (distorted) fiber and the VPSC model - for those belonging to α fiber. This contradiction may be partly explained by the results obtained with the EP model: $<\tau>^2$ predicted by this model for the usual L value (L=1000 MPa, Fig. 3c) is distinctly higher in γ fiber than in α one while an inverse result (higher dislocation density in α fiber) is found for much weaker interaction level (L - 400 MPa, Fig. 3d). The experimentally observed transition from deformation to recrystallization texture confirms that γ fiber intensity grows at the expense of α fiber (Fig.1) and, accordingly, one can expect more stored energy in γ fiber than in α one. This is the reason why the distribution of $<\tau>^2$ from Fig. 3c was used in the subsequent Monte Carlo modeling of recrystallization process (plastic work, W, could also be used).

The measured (X-ray diffraction) α and γ fibers for the rolled and recristallized titanium interstitial free steel are shown in Fig. 4. The results for three samples,

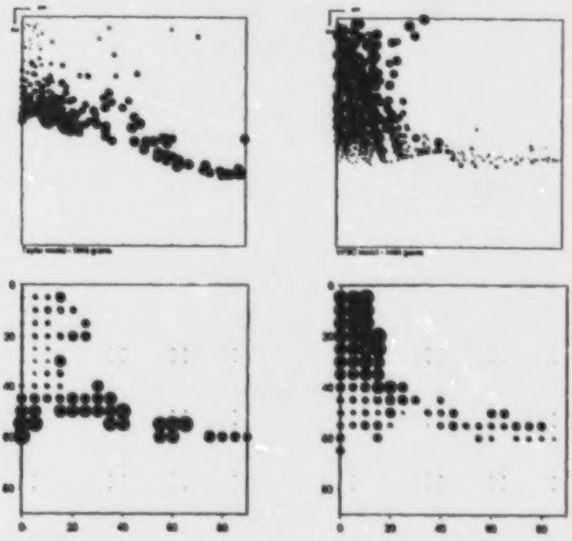

Fig. 3. Predicted distributions of $<\tau>^2$. Upper raw: Taylor model (left) and viscoplastic model (right) - $q_0=2$, saturating hardening. Lower raw: elasto-plastic model with L=1000 MPa (left) and L=400 MPa (right) - $q_0=1$, linear hardening.

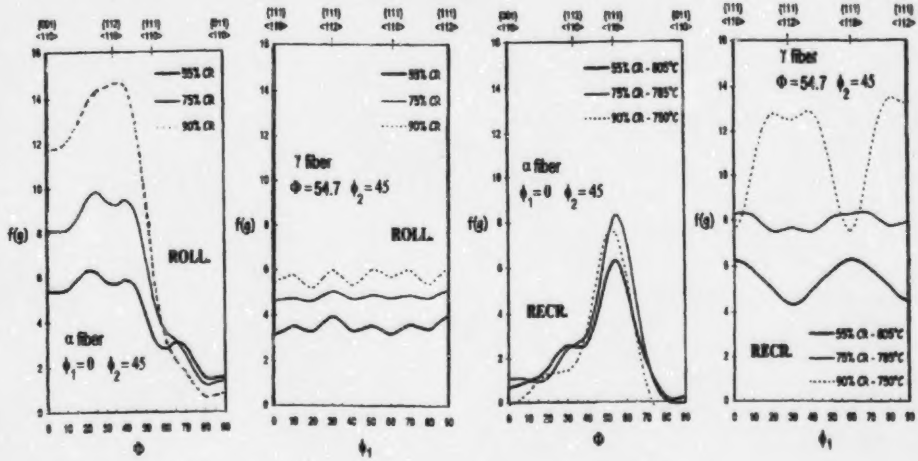

Fig. 4. Experimental texture profiles of the interstitial free titanium steel. Rolling and recrystallization textures are shown; α and γ fibers are presented for three samples (rolling reductions of 55%, 75% and 90% and annealing temperatures of 805°C, 785°C and 750°C).

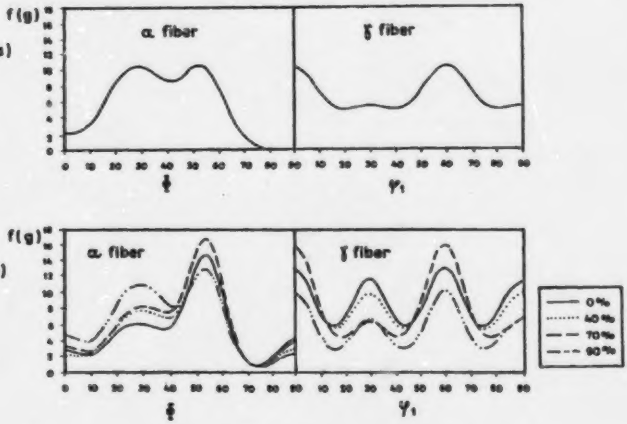

Fig.5.

a) Rolling model texture (input texture for the Monte Carlo model); it was composed of nine gaussian components,

b) Predicted recrystallization textures (Monte Carlo model). Different aspect ratio of grains (expressed as rolling reduction) are indicated.

corresponding to rolling reductions of 55%, 75% and 90% and to annealing temperatures of 805°C, 785°C and 750°C, are shown. The most characteristic change occurs for α fiber: the maximum around the {112}<110> orientation is replaced by a sharp peak located near the {111}<110> orientation. The γ fiber increases its intensity of a factor between 1.5 and 2.

The starting model deformation texture (for the prediction of recrystallization process) was composed of nine appropriate gaussian components; its α and γ fibers are shown in Fig.5a. The recrystallization textures, predicted by Monte Carlo model, are presented in Fig.5b. The dislocation density ($\sim <\tau>^2$) distribution shown in Fig. 3c was used as the stored energy parameter (EP model, q_o=1, linear hardening). The four lines shown in Fig.5b correspond to different initial grain shapes described by the rolling reduction parameter. Highly oriented nucleation was assumed and the total volume of initial nuclei was 0.1% of the material. The predicted recrystallization textures show a correct evolution: the characteristic change of α fiber and a general growth of γ fiber intensity are reproduced.

4 Conclusions

The predicted behavior of recrystallization texture agrees with the experimental one. It confirms that the stored energy parameter ($<\tau>^2$) was correctly selected. Further work has to be done to improve the MC model, especially a higher number of texture components should be used.

5 Acknowledgments

Two of us (J.T. and K.W.) acknowledge a support of the Committee of Scientific Foundation (KBN) and the Université Paris XIII, Institut Galilée.

6 References

Miroux, A., Reglé, H. and Bacroix, B. (1998) Effect of cold rolling level on recrystallization textures in low carbon steel sheets - modeling. *Materials Science Forum*, Vol. 273-275, pp. 433-438

Molinari, A., Canova, G.R., and Ahzi, S. (1987) A self consistent approach of the large deformation polycrystal viscoplasticity. *Acta Metall.*, Vol. 35, pp. 2983-2994

Taylor, G.I. (1938) Plastic strain in metals. *J. Inst. Metals*, Vol 62, pp. 307-325

Wierzbanowski, K., Jura, J., Haije, W.G. and Helmoldt, R.B. (1992) FCC rolling texture transitions in relation to constraint relaxation. *Cryst. Res. Techn.*, Vol 27, pp. 513-522

Wierzbanowski, K., Tarasiuk, J., Bacroix, B., Miroux, A. and Castelnau, O. (1999) Deformation characteristics important for nucleation process. Case of low-carbon steels. *Arch. of Metall.*, Vol 44 - in print

Wimmer, M., Kiaei, M., Bacroix, B., Lanteri, S. and Reglé, H. (1996) Modeling of primary recrystallization textures in BCC steels- comparison with EBSD data. IRSID Report No. MPM96.769, Maizieres -les-Metz, France

RESIDUAL STRAINS IN AL-MG POWDER COMPOSITES. SIMULATIONS BY SELF-CONSISTENT MODELS

A. FOURTY, J.A. SIGNORELLI, M.A. BERTINETTI and R.E. BOLMARO
Instituto de Física Rosario - Fac. de Ciencias Exactas, Ingeniería y Agrimensura.
Consejo Nacional de Investigaciones Científicas y Técnicas, Rosario, Argentina.

H.-G. BROKMEIER
Institut für Werkstoffkunde und -technik der Technische Universität Clausthal. GKSS Forschungszentrum Geesthacht, Germany

H.-G. PRIESMEYER
Christian Albrechts University, Institute for Pure and Applied Nuclear Physics, Kiel, Germany.

Abstract

In the current work we present some simulations of 2nd kind residual strains (RS) performed by Self Consistent models for two-phase materials. The results are compared with experimental results, obtained by Reverse Time Of Flight (RTOF) neutron diffraction, in Al-Mg powder composites deformed by extrusion until Von Mises strains of 2.8. 2nd kind RS calculations should be attainable by micromechanical modeling. The presence of two phases produces a split of the measured 2nd kind RS to values representative of the two populations of grains. Also the texture provides further complexity useful for model assessment. Some information about 3rd kind RS should also be recoverable. 3rd kind RS calculations need the introduction of statistical dislocation modeling which is out of the scope of the current paper, but some hints about its relative importance can be obtained by peak broadening computing.

Keywords: grain interaction, residual strains, self-consistent models, textures.

1 Introduction

Texture development in polycrystalline materials has deserved special attention during the last thirty years and many micromechanical models have been successful in the understanding of such phenomena. Notwithstanding, simulated and measured textures have been always rather in a qualitative agreement, mainly due to some randomization mechanisms that render the experimental textures much weaker than the simulated ones (Lee and Duggan, 1993). A real assessment of the assertion in choosing the micromechanisms active at crystal level is rather difficult because of the statistical nature of such hidden mechanisms. Moreover interaction among first neighbor crystals is one of the unsolved computational quests of micromechanical modeling. The problem has been approached by assuming equal deformation for every crystal (Taylor models), equal stress (Sachs models), a few versions of relaxed constraints and the so called Self-Consistent models (SC) (Kocks et al., 1998). Lately hybrid micromecanics-FEM models have also been introduced (Beaudoin, 1995). In any case the fingertip left by texture development is a rather not very detailed collection of the causes and consequences of the deformation process. It means that texture represents the history of the strain in such compact way that it is almost impossible to recover the information about active slip systems, inhomogeneous strain and stress fields, interaction among crystals, etc.. Extra information has been procured through residual strain measurements (Van Houtte and Buyser 1993). The activity of some slip systems can relax residual stresses by plastic strain and, by using them in theoretical simulations, a better match with experiments can be achieved. Texture simulation provides results sometimes very close to experiments but texture and RS information should be compatible.

Residual strains are usually classified as 1st kind RS, acting at macroscopic sample level and mainly due to uneven heat treatment, macroscopic inhomogeneities or shapes and/or machining; 2nd kind, acting in the range of a few first neighbor crystals and mainly due to short range interaction among them, stemming from phase transformations, differences in thermal coefficients and/or plastic deformation; and 3rd kind, acting at distances of a few microns inside each grain and usually explained and modeled by the accumulation of different dislocation arrangements (Delhez et al. 1982, Butler and McDowell 1998). Worthy is to mention the contribution of grain size and experimental set-up to line broadening.

1st kind RS are detected and calculated by peak shift measurements. On the other hand 2nd and 3rd kind RS are shown through peak broadening although some overlapping between 1st and 2nd kind effects and between 2nd and 3rd kind peak broadening can exist. 1st and 2nd kind RS effects may be overlapped because some differential peak shift may appear if a collective behavior is enforced by some special apportion of crystals like in textured or polyphase materials. The presence of two phases can clearly split the 2nd kind RS in two populations that must counterbalance each other to achieve long range equilibrium. In the case of 3rd kind RS the elastic stresses relax along very short distances, and being the dislocation substructure internal to the grains, the macroscopic effect is detected through peak broadening. But the interaction among a crystal and its closest neighbors can also give rise to peak broadening because of the many possible different misorientations between each set of grains and the surrounding crystals. A valuable information would be the relative proportion of peak broadening due to 2nd and 3rd kind RS. An iterative evaluation of peak broadening is performed considering gradual incorporation of 1 (2-SSC) and 4 (5-SSC) closest neighbors to asses the relative importance of 2nd and 3rd kind RS.

1 Site SC (1-SSC) models consider the interaction of each crystal with an average matrix. Peak broadening would be due to variations of the third crystal orientation angle and small misorientations between crystals that are considered to be oriented in the same direction for experimental purposes (5^0 window in the simulations). 2 Sites SC (2-SSC) models incorporate a privileged interaction of each grain with a closest companion and the misorientation between them, commanded by texture development, together with the matrix interaction can induce some peak broadening that would overlap with the 3rd kind RS peak broadening.

2 Model Briefing

SC calculations were performed by using a Visco-Plastic Self Consistent (VPSC) model. It allows each grain to deform and rotate according to a local velocity gradient that can be different from the macroscopic one. The interaction of each grain with the surroundings can be understood as mediated through interactions with N closest companions and that whole set embedded in a matrix with the properties calculated by an average over all crystals. This N-Site Self-Consistent model is a generalization of the classic SC models and can be used by successively calculating interactions with 0, 1, 2, 3, etc. neighbors.

The macroscopic constitutive equation may be expressed, using the secant form as:

$$\dot{\varepsilon} = M^{c(sec)} : \sigma' \qquad (1)$$

where the local secant compliance of each individual grain (N sites) is defined by:

$$M^{c(sec)}_{(n)} = \dot{\gamma}_0 \sum_s \frac{m^s_{ij}\, m^s_{kl}}{\tau^s_c} \left(\frac{m^s : \sigma'}{\tau^s_c}\right)^{n-1} \qquad (2)$$

where m^s, $\dot{\gamma}^s$, τ^s_c and $\underline{n}$ are the Schmid tensor, the reference shear rate, the Critical Resolved Shear Stress (CRSS) of each slip system (s) and the inverse of the rate sensitivity or stress exponent, respectively. The sum runs over the complete set of active slip systems for each phase.

Strain deviations and eigen-strains are related through

$$[\tilde{\varepsilon}] = [S] : [\varepsilon^*] \qquad (3)$$

$$[S] = \begin{bmatrix} S^{11} & S^{12} & \cdots & S^{1,N} \\ S^{21} & & & \cdots \\ \cdots & & & \\ \cdots & & & S^{N,N} \end{bmatrix} \qquad (4)$$

and S^{ii} are the usual Eshelby tensors for inclusions $\underline{i}$ and S^{ij} are defined as 2-site Eshelby tensors, i.e. coupling factors between eigen-strain in one inclusion and the local deviation in strain of the other one.

3 Experiments

The samples were prepared by pre-compaction of different volume fractions of Al powder of the size < 41 μm and Mg powder grade 5. They were later extruded until area reductions correspondent to Von Mises equivalent deformations of 2.8. The residual strains were measured by the Reverse Time of Flight (RTOF) technique in GKSS (Geesthacht, Germany), with the neutron beam impinging in the direction

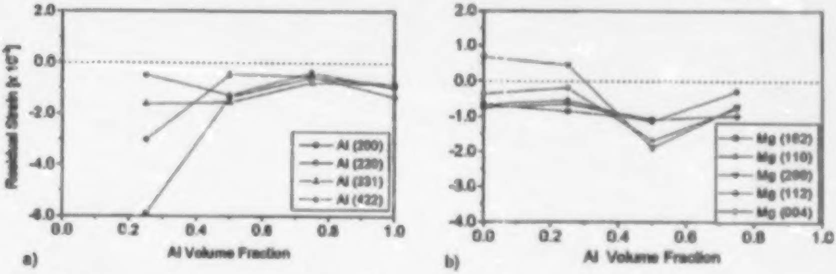

Fig. 1. Experimental Residual strains vs. Al volume fraction

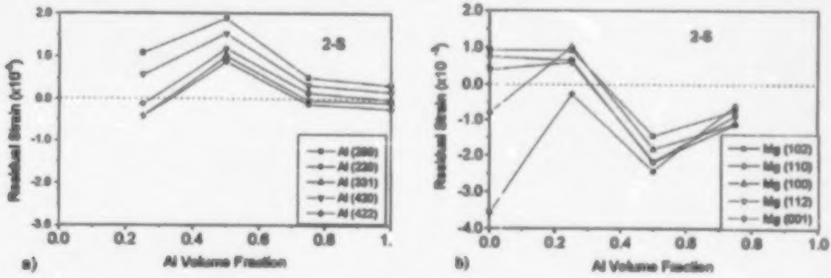

Fig. 2. Simulated residual strains vs. Al volume fraction

perpendicular to the longitudinal axes (Schröder et al. 1994). The diffraction peaks were fitted locally with a relative error of less than 0.01 %. The peak positions and their width were determined for the deformed materials and for the same loose powder used for sample fabrication. Figs. 1 a) and b) show the residual strains calculated for different diffracting planes of Al and Mg vs. volume fraction of both phases. The Al residual strains show a very isotropic behavior and only when mixed with high Mg contents some anisotropy is more evident.

The Half Full Peak Widths (HFPW) were in the interval of a few percents for all orientations and different volume fractions of Al-Mg.

For pure and 75% Mg cases, Mg presents different residual strains for different planes due to its anisotropy. The deformations in the $\{10\bar{1}0\}$ family compensates, both in sign and magnitude, the strains of practically all other planes. The behavior changes for less content of Mg (50% and 25%) and all plane families undergo a compression state. Moreover for 25% Mg the Mg behavior becomes more isotropic.

4 Results

The program was modified to be able to recover in unloading, by calculating hydrostatic stresses and volumetric strains, the residual strains in each grain. We simultaneously adjusted textures and residual strains for one composition (50%Al-50%Mg) in order to get strain values just close to the experimental ones. The usual FCC {111}<110> slip system, to which we assigned a relative CRSS of 1 and an absolute value of 0.020 GPa, was used for Al. For Mg we chose basal $\{0001\} < 11\bar{2}0 >$, prismatic $\{10\bar{1}0\} < 11\bar{2}0 >$, pyramidal $\{10\bar{1}1\} < 11\bar{2}0 >$ and pyramidal $\{10\bar{1}1\}$ $<11\bar{2}\bar{3}>$ slip systems with relative strength of 1.5, 7.5, 45 and 45 with respect to the Al CRSS, respectively.

Hardening law was considered stepwise linear. A new approach for calculating the spin of each crystal was applied. The usual assumption of each grain spinning back to its own hole was replaced by the condition of sharing of spins between two grains that were assumed to be closest neighbors all along the deformation process (Bolmaro et al. 1997). By carefully searching for the best match among experimental and simulated textures we find the best stress exponents for the visco-plastic equation. The residual strains were calculated for all volume fractions for each plane family. The results are shown in Figs 2 a) and b) for Al and Mg vs. volume fraction of both phases. 1-Site and 2-Sites calculations were performed and they look pretty much alike. The model allows both phases to comply with the deformation requirements by activation of a number of slip systems that is related with the strain rate sensitivity but also with the current CRSS after each deformation step, the volume fraction of both phases and the texture development.

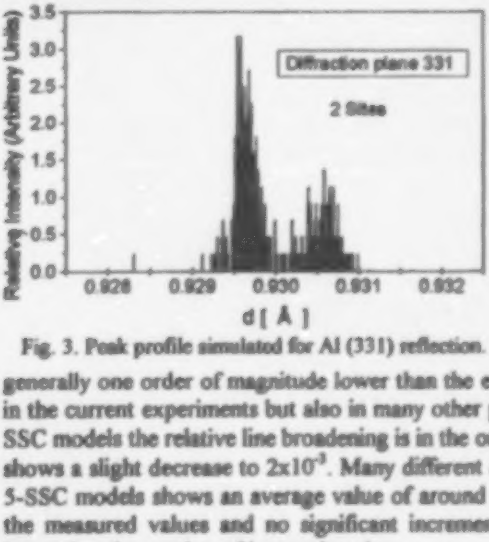

Fig. 3. Peak profile simulated for Al (331) reflection.

Relative intensities, vs. interplanar distance d, were obtained by 1-SSC, 2-SSC and 5-SSC approaches. Fig. 3 shows a 2-Sites simulated profile for the peak Al (331) by considering a beam with a solid angular span of 5° and apportioning the crystals in bins of 0.001 Å. A line split is observable due to the two well developed texture components of Al ([100] and [111]). Peak broadening was minor and generally one order of magnitude lower than the experimental values obtained not only in the current experiments but also in many other plastically deformed samples. For 1-SSC models the relative line broadening is in the order of $4x10^{-3}$ for Al and Mg. 2-SSC shows a slight decrease to $2x10^{-3}$. Many different arrangements of grains performed by 5-SSC models shows an average value of around $4x10^{-3}$. They represent one tenth of the measured values and no significant increment of the peak width is obtained by increasing the number of interacting sites.

5 Discussion and Conclusions

The measured 2nd kind RS are well represented by the simulations except for the Mg basal plane for 100% Mg and a disagreement between experiments and simulations for Al. The Al experimental values are clearly not well determined because they show the Al under compression for all planes for 50%Al and 75%Al and not compensated by Mg RS. Two reasons can be arguable for such experimental inconsistency. The most general difficulty in RS determination is the determination of d_0. Despite the determination was made for loose powder and independently for all planes some experimental error may have given rise to a general shift of all peaks. Some RS could have been present in the powder that were not relaxed by annealing. The measurements were performed for the central 85% volume of the samples and the outer layer can be carrying the balancing stresses.

Misorientation between closest neighbors could give rise to the development of local residual strains due to crystal anisotropy. Slightly differently oriented crystals are prone to originate different residual strains and consequent peak broadening. Consideration of a growing number of those closest neighbors was expected to reveal a larger peak width for each computed interaction. From the results we can reach two main conclusions: a) whichever the contribution of the grain-grain interaction to peak broadening, it is much smaller than the usually measured values b) an increment of the number of first neighbors does not show a related increment in peak width. That result would be rather surprising by considering the residual stresses and strains a consequence of anisotropy and interaction between different crystal orientations. By using a co-rotation scheme, the misorientation among grains would be larger than the misorientation expected between different fragments of the same grain, each one limiting with the others by different dislocation arrangements. The resulting RS contribution to peak broadening should be larger for crystal-crystal interaction than for RS generated between different regions of the same crystal. Notwithstanding not much is known about mechanism for stress generation inside dislocation arrangement regions or its generation.

6. References

Beaudoin, A.J., Dawson, P.R., Mathur, K.K. and Kocks, U.F. (1997) A Hybrid Finite Element Formulation for Polycrystal Plasticity with Consideration of Macrostructural and Microstructural Linking. Int. J. of Plast., Vol. 11, 5, pp. 501-521.

Bolmaro, R.E., Lebensohn, R.A. and Brokmeier, H.-G. (1997) Crystal Spin in Two-Sites Self Consistent Models: From Kinematics to Kinetics. Comp. Mat. Sc., Vol. 9, pp. 237-250.

Butler, G.C. and McDowell, D.L. (1998) Polycrystal Constraint and Grain Subdivision. Int. J. of Plast., Vol 14, 8, pp. 703-717.

Delhez, R., de Keijser, Th. H. and Mittemeijer, E.J. (1982) Determination of Crystallite Size and Lattice Distortions through X-Ray Diffraction Line Profile Analysis. Fresenius Z. Anal. Chem., Vol. 312, pp. 1-16.

Kocks, U.F., Tomé, C.N. and Wenk, H.-R. (1998) Texture and Anisotropy. Cambridge University Press. pp 126-177.

Lee, C.S. and Duggan, B.J. (1993) Studies on the Sharpness of Simulated Deformation Textures. Scripta met. et mat., Vol 28, pp. 121-126.

Schröder, J., Kudryashev, V.A., Keuter, J.M., Priesmeyer, H.G., Larsen, J. and Tiitta, A.(1994) FSS-A Novel RTOF-Diffractometer Optimized for Residual Stress Investigations. J. Neutron Res. Vol. 2, 4, pp. 129-141.

Van Houtte, P. and De Buyser, L. (1993) The Influence of Crystallographic Texture on Diffraction measurements of Residual Stress. Acta metall., Vol. 41, pp. 323-336.

Acknowledgements: This project is partially funded by the German-Argentine Intergovernmental Agreement n° ARG 6 L1A 1A/2 and CONICET-Argentina.

PARAMETERISATION OF COLD-ROLLING AND ANNEALING TEXTURES IN CUBIC METALS BASED ON THE CRYSTALLOGRAPHIC FIBRES

L. DELANNAY, A. VAN BAEL and P. VAN HOUTTE
Department of Metallurgy and Materials Engineering, Katholieke Universiteit Leuven, Belgium

Abstract

It is demonstrated that cold rolling and annealing textures in bcc and fcc metals can efficiently be characterised with less than 30 parameters. The definition of these parameters is based on a quantitative description of three crystallographic fibres in the ODF. The parameters specify the position of the fibre skeleton lines in Euler space, as well as the evolution of the ODF-intensity and of the fibre "thickness" along these skeleton lines. All major crystallographic components of bcc and fcc rolling textures are considered. The parameter set leading to the best reproduction of a given experimental texture is automatically identified using a computer optimisation routine. This is illustrated by applying the model to three experimental cold-rolling textures (two low-carbon steels and one aluminium grade). It is discussed how the model can be applied in systematic sensitivity studies of texture influence on material properties and how it improves three-dimensional visualisation of ODFs.

Keywords: bcc, fcc, crystallographic fibres, quantitative texture analysis

1 Introduction

It is commonly admitted today that the most efficient means of quantitative texture characterisation is the Orientation Distribution Function (ODF) expressed by a truncated series of generalised spherical harmonics (Bunge 1982). Many computer models that predict the influence of texture on material properties take these series expansion coefficients as input. This means that several hundreds of parameters (524 for an orthorhombic ODF truncated at "l_{max}"=32) are used to describe the texture.

The series expansion coefficients are however not convenient at all when different textures must be compared. Indeed it is impossible to select the series expansion coefficients that are most relevant for the comparison, as these coefficients have no physical meaning (they are extracted from a mathematical formula). Three alternative texture characterisation techniques have been proposed: (i) computing crystallographic volume fractions (Cortie 1997), (ii) recording the ODF-intensity along the "skeleton line" of characteristic crystallographic fibres (see for example (Hirsch and Lücke 1987)), (iii) reproducing textures with model functions as reviewed by Eschner (1993).

The parameter model that we propose is a compromise between the second and third techniques. It relies on a quantitative reproduction of the crystallographic fibres observed in bcc and fcc cold-rolling textures. The parameter model has two major advantages compared to the computation of volume fractions: it accounts for possible shifts of the stable texture components relative to their ideal orientation and it is very convenient for the description of crystallographic fibres.

In the following, we first define the parameters of the model (25 for bcc and 28 for fcc textures). We then illustrate the capability of the model to reproduce experimental steel and aluminium cold-rolling ODFs. Finally, we explain how the model can be applied in a systematic study of the sensitivity of material properties on texture and we draw some conclusions.

2 Presentation of the parameter model

Cold rolling textures have two remarkable properties: they are orthorhombic and they are predominantly composed of crystallographic fibres. We will therefore assume that cold rolling ODFs can be fully characterised by only describing the fibres in one symmetrical portion of the Euler space. For a quantitative description of these fibres, one must prescribe

- the "true position of the skeleton line" which is the line of maximum intensity along the fibre (i.e. the fibre central axis),
- the intensity distribution along this skeleton line, and
- the evolution of the "fibre-thickness" along the skeleton line. The "thickness" of a fibre defines how the ODF-intensity decreases from the central axis of the fibre to orientations away in a section perpendicular to the fibre.

The definition of the parameters requires that a set of 10 points be selected along the skeleton lines of the three principal fibres in the ODF. This is illustrated in fig. 1 and fig. 2, for bcc and fcc cold rolling textures respectively. The intensity, the fibre thickness and the orientation of these points are recorded. However, to reduce the number of parameters to a minimum, orientation shifts that are not frequently observed are not taken into account. For example, the α- and θ-fibres in bcc textures and the α-fibre of fcc textures are kept fixed to their ideal position in Euler space. In the same way, the fibre thickness is not measured at some less important orientations. All this results in 25 parameters for bcc metals and 28 for fcc metals. Their definition is summarised in Table 1.

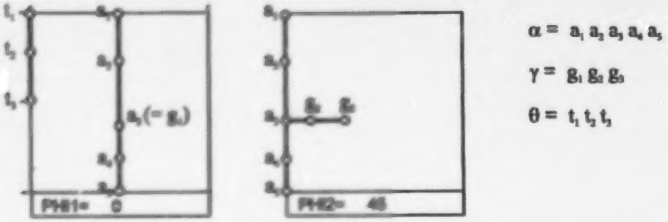
t1
t2
t3
a1
a2
a3(= g1)
a4
a5
PHI1= 0
a1
a2
a3
a4
a5
g2
g3
PHI2= 45
α = a1 a2 a3 a4 a5
γ = g1 g2 g3
θ = t1 t2 t3

Figure 1: bcc crystallographic fibres: α (<110> // RD), γ (<111> // ND), and θ (<100> // RD). Note that α and γ intersect at a_3=g_1 and that t_1 and t_3 correspond respectively to "cube"={100}<001> and "Goss"={110}<001>. (φ_1=0° and φ_2=45° ODF-sections.)

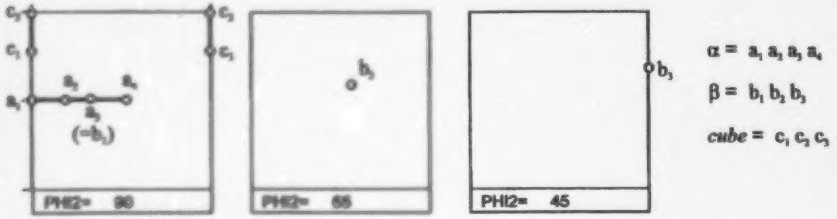
c2
c1
a1
a2
a4
a3
(=b1)
c2
c3
PHI2= 90
b2
PHI2= 65
b3
PHI2= 45
α = a1 a2 a3 a4
β = b1 b2 b3
cube = c1 c2 c3

Figure 2: fcc crystallographic fibres: α (from "Goss" until "brass"={110}<112>); β (from "brass", through "S"={123}<634>, until "copper"={112}<111>); and "cube-fibre" (from "RD-rotated cube", through "cube", until "TD-rotated cube". Note that α and β intersect at a_3=b_1. (φ_2=90°, 65° and 45° ODF-sections).

Table 1: Definition of the parameters for bcc and fcc textures [*].

bcc						
point	**Int**	**T(φ_2)[†]**	**T(φ_1)[†]**	**φ_1**	**Φ**	**φ_2**
a_1	P_1	P_2		0	0	45
a_2	P_3	P_4	P_5	0	P_6	45
a_3=g_1	P_7	P_8		0	P_9	45
a_4	0.5			0	P_{10}	45
a_5	P_{11}	P_{12}		0	90	45
g_2	P_{13}	P_{14}		P_{15}	[‡]	[‡]
g_3	P_{16}	P_{17}		30	P_{18}	P_{19}
t_1	P_{20}			0	0	0
t_2	P_{21}	P_{22}		0	P_{23}	0
t_3	P_{24}	P_{25}		0	45	0

fcc						
point	**Int**	**T(φ_2)[†]**	**T(Φ)[†]**	**φ_1**	**Φ**	**φ_2**
a_1	P_1	P_2		0	45	90
a_2	P_3	P_4		P_5	45	90
a_3=b_1	P_6	P_7		P_8	45	90
a_4	P_9	P_{10}		P_{11}	45	90
b_2	P_{12}	P_{13}	P_{14}	P_{15}	P_{16}	P_{17}
b_3	P_{18}	P_{19}	P_{20}	90	P_{21}	P_{22}
c_1	P_{23}			0	P_{24}	90
c_2	P_{25}	P_{26}		0	0	90
c_3	P_{27}			90	P_{28}	90

[*] Fixed orientations are also indicated.

[†] "T(φ_2)" means "thickness measured along φ_2".

[‡] g_2 is on the straight line between g_1 (=a_3) and g_3.

3 Reproduction of experimental textures

The parameter model presented above as been implemented in a FORTRAN code (Delannay et al. 1999a). The identification of the parameter values that best reproduce an existing experimental texture requires almost no interaction with the operator. The texture reproduction is strictly based on the minimisation of (1).

$$Min_{P_1,\dots,P_{25}}\left(\frac{\oint\limits_{g}\left[f_{P_1,\dots,P_{25}}(g)-f_{\exp}(g)\right]^2 dg}{\oint\limits_{g} f_{\exp}(g)^2\, dg}\right) \tag{1}$$

The code may be used as black box taking on input the series expansion coefficients of the experimental ODF, and yielding as output the value of the 25-28 parameters as well as the series expansion coefficients of the generated ODF. In practice, the reproduced texture is generated as a superposition of spherical gaussian components (Bunge 1982). The orientation, the weight and the spread of these gaussians is found automatically from the values of the 25-28 parameters (Delannay et al. 1999a).

The parameter model has already been successfully applied to more than 20 industrial cold rolling and annealing textures in low-carbon steels. Two examples are shown on fig. 3. The model has only recently been adapted to study fcc cold rolling textures. As an example, the texture of a cold-rolled 1080 aluminium is reproduced in fig. 4. The quality of these reproductions is evaluated by computing the difference between the experimental and the generated ODFs over a 5°-grid in Euler space. The results of the texture reproductions are presented in Table 2.

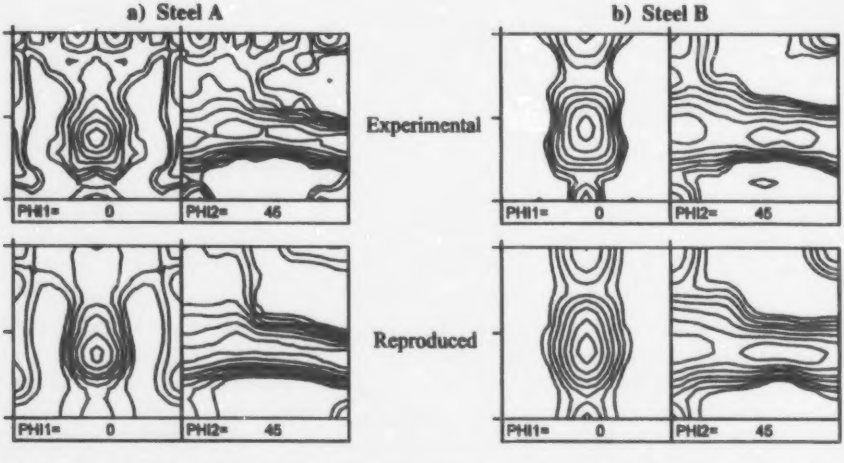

Figure 3: Reproduction of two low-carbon steel sheet textures (φ_1=0° and φ_2=45° ODF sections).

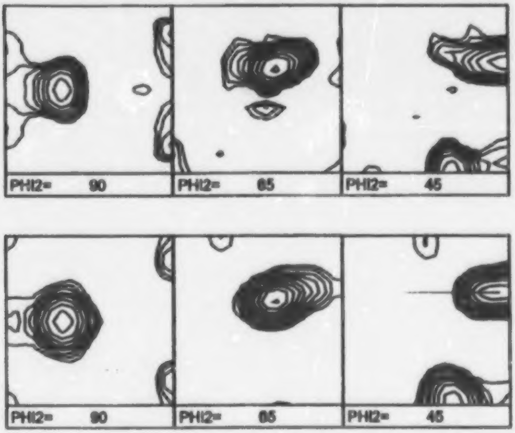

a) Experimental

b) Reproduced

Figure 4: Texture reproduction for a cold rolled 1080 aluminium (φ_2=90°, 65° and 45° ODF-sections).

Table 2: Quality of the texture reproductions.

Texture label	Minimal value for expression (1)	Maximal ODF-intensity	Averaged difference*	Maximum difference*	Orientation of max. differ.(°) (φ_1, Φ, φ_2)
Steel A	0.053	7.91	0.30	1.66	35 0 0
Steel B	0.052	7.09	0.28	0.89	70 50 60
Aluminium	0.054	17.5	0.40	3.04	80 30 40

* Difference between the experimental and the reproduced ODF calculated over a 5°-grid covering the Euler space.

4 Discussion

4.1 Using the parameterisation to compare textures

The parameters of this model are directly linked to visual aspects of the ODF. In this regard, the model facilitates three-dimensional visual interpretation of the ODF. It may therefore be used as a didactic tool to help understand the complicated symmetry rules of the distorted Euler space and the requirement for normality of the ODF.

The model has proved to be an efficient tool for the comparison of cold-rolling and annealing textures in bcc steels (see also in these proceedings (Delannay et al. 1999b)). Further investigations on fcc textures are required to check if the present choice of parameters is the most judicious in this case.

4.2 Investigation of the sensitivity of material properties on texture

A second interesting application of the model is the optimisation of texture with regard to some material properties. Such an optimisation can be performed based on a systematic sensitivity study: (i) the experimental texture is reproduced (i.e. the 25-28 parameter values are identified); (ii) other textures are generated that only differ by the value of one of the parameters; (iii) the influence of each parameter on the material property is evaluated by computing the value of the material property from the series expansion coefficients of the generated textures.

In a recent paper Delannay et al. (1999c) investigated the sensitivity of plastic planar anisotropy on steel sheet texture. The Taylor model was used for r-value predictions.

5 Acknowledgements

D. Vanderschueren from OCAS n.v. (Zelzate, Belgium) is acknowledged for fruitful discussions about the parameterisation of steel sheet textures. One of the authors (LD) acknowledges his grant as “aspirant” of the “Fonds voor Wetenschappelijk Onderzoek - Vlaanderen”. Financial support was also provided by the Federal Government of Belgium (DWTC) through the contract IUAP P4/33.

6 References

Bunge, H.J. (1982) *Texture analysis in Material Science*. Butterworths, London.

Cortie, M.B. (1997) Calculation of texture volume fractions by integration and gaussian fitting. *Textures and Microstructures*, No. 29, pp. 155-183.

Delannay, L., Van Houtte, P. and Van Bael, A. (1999a) New parameter model for texture description in steel sheets. *Textures and Microstructures*, (in press).

Delannay, L., Kestens, L., Van Bael, A., Houbaert, Y. and Van Houtte, P. (1999b) Investigation of steel sheet recrystallisation textures with a new parameter model for texture description. *These proceedings*.

Delannay, L., Van Houtte, P., Van Bael, A. and Vanderschueren, D. (1999c) New parameter model for texture description in steel sheets - Sensitivity of planar anisotropy on texture. *Model. and Simul. in Mat. Sci. Eng.* (in press).

Eschner, Th. (1993) Texture analysis by means of model functions. *Textures and Microstructures*, No. 21, pp. 139-146.

Hirsch, J. and Lücke, K. (1988) Mechanism of deformation and development of rolling textures in polycrystalline F.C.C. metals. *Acta Metall.*, Vol. 36, No. 11, pp. 2863-2882.

SENSITIVITY OF SIMULATED ANISOTROPY TO INITIAL TEXTURE DEFINITIONS

C. T. NECKER, C. N. TOMÉ, F. JEAN-PROST, D. A. KORZEKWA

Los Alamos National Laboratory, Los Alamos, NM, 87545

Abstract

Free compression tests were performed on 0.040 inch thick 5754 aluminum sheet stock producing a slight in-plane anisotropy. A visco-plastic self-consistent (VPSC) deformation modeling code was used to model the mechanical properties and resultant deformation textures. Calculations using a discretized description of the initial texture simulated the deformation texture very closely. Simulation of the mechanical properties were also captured nicely with one exception. The simulated direction of in-plane anisotropy was reversed from the experimental results. Analysis of the impact of various texture components on the anisotropy indicated that the shift of texture toward stronger brass, {110}<112>, and Goss, {110}<001>, components during the simulation led to the reversal of simulated anisotropy. The simulated deformation texture was more intense than the experimental texture in the brass and Goss positions. This result suggests that the more intense simulated texture components may be responsible for the reversal of anisotropy.

Keywords: Aluminum, compression, simulations, texture components

1. Introduction

The formability of metallic sheet product is often best when the amount of in-plane anisotropy is minimized and this is often accomplished by tailoring the texture. During deformation the initial texture evolves often yielding a material which is not mechanically isotropic in-plane. The anisotropy is experimentally measured either by in-plane tensile tests or by compression tests through the thickness of the sheet. In the latter case the anisotropy is measured by the degree of ovality of originally circular samples.

The development of mechanical properties, anisotropy and textures is often studied with the aid of models. Although many models reasonably simulate mechanical properties and textures, anisotropy are not always properly predicted and textures are often too strong and too sharp. Depending on the texture and the method of discretization, experimental textures may not always be as completely or properly described as would be necessary for the deformation model to accurately simulate the deformation process. Minor variations in texture intensities can lead to inaccurate texture evolution (Kocks and Necker 1994).

For this study, through-thickness compression tests were performed on O-temper AA5754 alloy. These results were then compared to those simulated by a VPSC deformation code (Lebensohn and Tomé 1993). The crux of the model is based on the assumption that each discrete orientation, referred to as a grain, can be treated as an inhomogeneity embedded in a homogeneous effective medium (HEM). The HEM represents the polycrystal, the medium surrounding each grain, characterized by a macroscopic stress and strain rate. The stress and strain rate of a grain may then be linearly related to the stress and strain rate of the HEM through an interaction equation. The model provides self-consistency because the iterative process relies on the convergence of the average of the stress and strain rate over all grains to the macroscopic stress and strain rate (Lebensohn and Tomé 1993).

2. Experimental procedure

The aluminum alloy used in this study was AA5754, a magnesium-manganese-iron alloy. The material was DC cast, conventionally processed sheet stock in the O-temper condition. The sheet was 1.47 mm thick.

The compression tests were performed on a screw driven Instron model 1125. All tests were run at a strain rate of 1.0×10^{-3}. The platens were lubricated with Dow Corning Molykote 321R. The compression samples were electrical discharge machined into 6 mm diameter disks and stacked to a 1.4:1 height to diameter ratio. Sample fabrication and stacking was performed without compromising the sheet surface or rolling direction alignment. Following testing, the compression data was corrected for the load frame stiffness and true stresses and true strains were calculated.

The samples for texture analysis of the initial sheet texture were fabricated by cutting and stacking the sheet for through-thickness analysis. Compressed disks were arranged in a metallographic mount with surface and sheet alignment preserved. The samples were ground, polished and etched. The texture was measured by the standard reflection technique on a Scintag 5-axis pole figure goniometer. The raw data was corrected and ODF were calculated using popLA software (Kallend et al. 1991).

The ODF data was discretized into a file of 2916 grain orientations, grouping orientations within 10° cells, and weights, representing the volume fraction of each orientation in the texture. Experimentally determined true stress-true strain data was used to adjust an extended-Voce hardening law at the single crystal level, of the form

$$\tau(\Gamma) = 40 + (65 + 20\,\Gamma)[1-\exp(-450\,\Gamma/65)]\ [\mathrm{MPa}] \qquad (1)$$

where τ is the critical resolve shear stress for (111)<110> slip and Γ is the accumulated shear in the grain. Deformation was imposed in sequential incremental steps along the compressive direction starting from the initial texture and reorienting the grains after each deformation step. In addition, the lateral stress components were enforced to be zero and the evolution of the lateral strains was a consequence of this condition. The simulation was performed on subsets of the initial to determine the impact of these components. The components of interest were cube, {100}<001>, Goss {110}<001>, brass {110}<112>, copper {121}<111> and S {123}<634>, each defined by a 15° maximum misorientation criterion.

3. Results and discussion

The initial texture of the sheet is a combination of the recrystallized cube component and the retained deformation fiber components, S, brass and copper, the cube component being most prominent. This mix of texture components is favorable for aluminum sheet forming because the cube component and the retained deformation fiber components counter each other's in-plane anisotropic tendencies, providing a reasonably isotropic in-plane composite texture, Fig.1. The deformation texture after a compressive strain of 0.5 tends toward the {110} fiber texture with maximum intensity at the brass component and a weaker intensity Goss component. The cube, copper and S components are significantly weaker than in the initial material.

Measurement of the compressed disks shows that the transverse direction (TD) strain is greater than the rolling direction (RD) strain, 0.253 and 0.241 respectively. The anisotropy is repeatable for all disks in each stack of disks as well as over all four stacks of disks. This level of in-plane anisotropy could be related to slight texture variations, grain shape or other factors. Although the direction and magnitude of the anisotropic behavior is repeatable, it is difficult to identify which of these factors is responsible for the rather small degree of anisotropy.

The initial simulation was performed using the entire texture, Fig. 2. However, the simulation predicts the opposite anisotropy, strain in RD greater than strain in TD. Closer inspection of the strain paths shows that the TD initial strains are slightly greater than the RD initial strains. At a compressive strain of 0.3 the two curves cross. The simulated stress-strain curve overlays the experimental curve indicating that the adjustments to the hardening law were proper. Simulated true stress-true strain curves are also plotted in Fig. 2 to show the impact each component has on strain hardening.

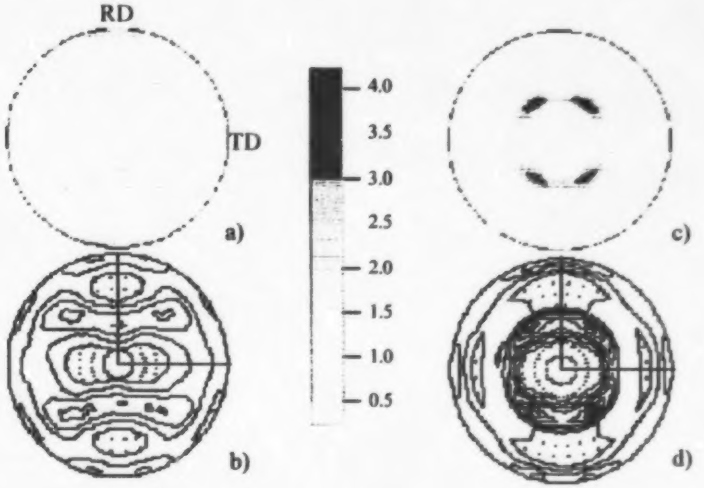

Figure 1 (111) pole figures, times random scale a) initial texture, b) discretized initial texture, c) compression texture, d) simulated compression texture.

The five primary components described above, cube, copper, S, brass and Goss, were separated from the initial texture. Equivalent simulations were performed on a texture which included those components as well as a complementary texture, the texture remaining after the components were removed. The components were defined by a maximum misorientation of 15° from the ideal orientation. The complementary texture exhibited in-plane isotropy whereas the component texture showed a similar trend to that of the entire texture, the TD strain > RD strain up to about a ND strain of 0.4 before the curves cross. These results suggest that one or more of these components is responsible for the predicted anisotropic behavior.

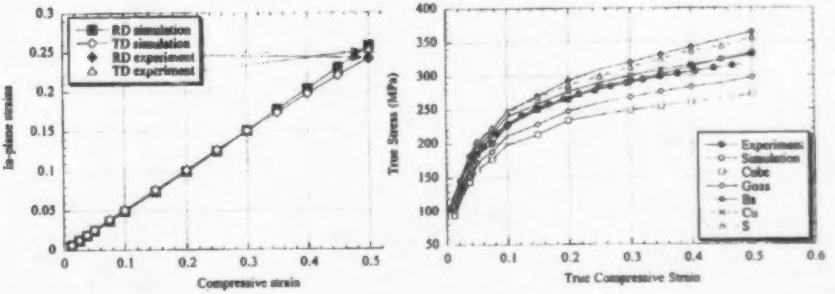

Figure 2 a) RD and TD strains, b) true stress-true strain diagram for experimental and simulated results.

The compressive simulation was performed on each of the component subsets. Table 2 summarizes the in-plane strain bias for the components. Simulation using the ideal components plus all symmetry related ones showed the same strain biases.

Table 2: Simulated in-plane strain bias.

Component	Volume Fraction	Strain Bias
initial texture	100%	RD>TD
component texture	≈35%	RD>TD
complementary texture	≈65%	RD≈TD
cube	19%	RD>TD
Goss	3%	RD>>TD
brass	7%	RD>>TD
copper	9%	TD>RD
S	8%	RD>RD

Obviously this composition of components does not remain stable throughout deformation. During deformation the simulated and experimental textures develop stronger brass and Goss components, a combined 30% of the texture, and significantly weaker cube, S and copper components, a combined 6%.

The enhancement of the brass-Goss combination would bias the anisotropy away from the TD toward the RD. This is exactly what the simulation shows. The cross-over of the TD and RD curves suggests that the texture transition toward a brass-Goss type texture does not occur until ND strains of 0.3 to 0.4. At ND strain of 0.5 the RD strain is 8% greater than the TD strain. The experimental results indicate that the anisotropy should go in the TD direction ≈5%. Comparison of the experimental and simulated deformation textures, Fig. 1, shows that the two textures match very nicely except for the intensity of the primary components, brass and Goss. The experimental data define the brass component at 2.9 times random whereas the simulated data define the brass component at 4.8 times random. Although a weaker component, Goss shows the same trend. Comparison of the brass and Goss component stress-strain curves shows that the Goss component is significantly softer than the brass component, brass falling above the experimental curve while Goss falls much below the experimental curve. The simulated strain bias toward RD for brass is about 2:1 whereas it is 6:1 for Goss. These results suggest that the increased presence of the simulated Goss component has a significant impact on the development of in-plane anisotropy. Additionally, the over-prediction of the volume of Goss and brass components by the simulation most likely result in the in-plane anisotropy reversal seen in simulated RD and TD strains.

Several other criteria employed in the simulation were manipulated to determine if they were responsible for the RD-TD strain cross-over. An initial grain shape criterion was skewed from the equiaxed condition yet the strain cross-over condition persists. The stiffness of the grain-matrix interaction was also analyzed as a possible cause for the bias. A tangent approximation (more compliant) was used. Application of a secant approximation only amplifies the simulated strain bias.

4. Conclusions

Compression of AA5754, O-temper disks resulted in a slight in-plane anisotropy biased toward the transverse direction. Simulation of the compression test resulted in a slightly depressed strain-strain curve and a reversal of the in-plane anisotropy, biased toward the rolling direction. Analysis of the primary texture components in the simulated deformation texture indicated that the brass-Goss components were responsible for this reversal. Based on the softness of the Goss component, it is expected that the presence of the Goss component is primarily responsible for the reversed in-plane strain anisotropy. It is suggested that the reversal found in the simulation, as compared to the experimental data, is due to the over-prediction of the combined brass-Goss components.

5. Acknowledgments

The authors wish to thank Manny Lovato for performing the compression tests and data reduction.

6. References

Kallend, J.S., Kocks, U.F., Rollett, A.D. and Wenk, H.-R. (1991) Operational texture analysis, *Materials Science and Engineering*, A132, pp. 1-11.

Kocks, U.F. and Necker, C.T. (1994) Polycrystal models to fit experiments, *Numerical Predictions of Deformation Processes and the Behaviour of Real Materials*, Proceedings of the 15th Risø International Symposium on Materials Science (ed. S.I. Anderson et al.), Risø National Laboratory, Roskilde, Denmark.

Lebensohn, R.A. and Tomé, C.N. (1993) A self-consistent anisotropic approach for the simulation of plastic deformation and texture development of polycrystals: application to zirconium alloys, *Acta Metallurgica et Materialia*, Vol. 41, No. 9, pp. 2611-2624.

MESOSCALE MODELING OF CUBE TEXTURE EVOLUTION DURING HOT DEFORMATION[*]

B. RADHAKRISHNAN, G.B. SARMA and T. ZACHARIA
Computer Science and Mathematics Division, Oak Ridge National Laboratory, Oak Ridge, Tennessee, USA

Abstract

A coupled finite element-Monte Carlo simulation technique was used to study the hot deformation and recrystallization of fcc grain structures consisting of S+cube, Copper+cube, and S+Copper+cube grains, respectively. The simulations using S+cube grains captured the formation of cube recrystallization nuclei from the deformed cube grains, and the preferential growth of the nuclei into the deformed S-grains. However, for the Copper+cube case, the cube nuclei did not grow into the deformed Copper matrix. In this case, the substructure evolution was dominated by the growth of Copper nuclei within the Copper matrix. When cube grains were present with both Copper and S grains in the initial grain structure, the evolution sequence of the three components became quite complicated. These findings are discussed in the context of modeling cube texture evolution during thermomechanical processing of aluminum alloys.

Keywords: hot deformation, cube texture, mesoscale, Monte Carlo, crystal plasticity

1 Introduction

Optimization of cube texture is one of the key issues in the hot rolling of commercial aluminum alloys for beverage can applications. Subsequent cold rolling of the hot-band provides, in addition to the required mechanical properties of the can stock, an optimum combination of cube and other deformation components that results in the minimization of material waste due to earing. Therefore, considerable effort has been made in the past to understand the texture evolution during thermomechanical processing of aluminum alloys.

---

[*] The submitted manuscript has been authored by a contractor of the U.S. Government under contract No. DE-AC05-96OR22464. Accordingly, the U.S. Government retains a non-exclusive royalty-free license to publish or reproduce the published form of this contribution, or allow others to do so, for U.S. Government purposes.

One of the issues that seem to be still unresolved is the formation and evolution of cube texture from deformation substructures. Early work on cold deformation and recrystallization of fcc materials by Dillamore and Katoh (1974), Ridha and Hutchinson (1982) and Hjelen et al. (1991) indicated that the cube nuclei formed in the transition bands present in the deformation substructure. A similar mechanism was assumed to apply to hot deformation as well. However, more recent work by Daaland and Nes (1996) clearly revealed that the cube orientations (that are invariably present in cubic materials during solidification processing) are metastable during hot deformation. Through careful analysis of the deformation substructures produced by hot deformation using electron back-scattering (EBSP) technique, they demonstrated the stability of the cube orientation during hot deformation, the existence of supercritical subgrains in the cube bands acting as nuclei, and the discontinuous growth of these nuclei into the deformation substructure. Based on analysis of slip traces in hot-deformed aluminum, Maurice and Driver (1993) showed that the stability of cube orientation is due to the operation of non-octahedral slip systems of the type {110}<110>, in addition to the octahedral slip systems of the type {111}<110>. Vatne et al. (1996) carried out a detailed analysis of cube stability, nucleation, and growth in commercial purity aluminum, and showed that the growth of cube nuclei preferentially occurred by consuming the S orientation present in the deformation substructure.

The growth preference of cube into S orientation was attributed to a higher stored energy in S than in Copper. Through analyses of subgrain sizes and misorientations, Vatne et al. (1996) showed that the stored energy per unit volume was 30% higher than average in S, and 10% less than average in Copper. In addition to a higher driving pressure, the cube-S interface also has the potential for forming the 40° <111> special boundary that is believed to have a high mobility and a low boundary energy. However, Samajdar and Doherty (1995) have shown that nuclei of both cube and non-cube orientations were favored when surrounded by S, indicating that the preferential growth into S could be only due to the higher driving pressure. The concept of "oriented growth" requiring such a special boundary at the cube-S interface was also not favored by Hjelen et al. (1991). Another argument against oriented growth is the concept of "orientation pinning" put forth by Juul Jensen (1995). It was shown that a growing cube nucleus will have a lower probability of being pinned by the deformation texture components than nuclei of orientations close to that of the deformation components.

The objectives of the work described here are to quantify the distributions of stored energy within the cube and non-cube orientations during hot deformation, and to understand the influence of the stored energy distributions and neighbor environments on the formation and growth of cube nuclei during recrystallization following hot deformation.

2 Simulation Procedure

The approach is to first model the deformation of a grain structure using a finite element (FE) technique. The grain structure is discretized such that there are a large number of elements per grain. The details of the FEM simulations using crystal plasticity theory are described by Sarma et al. (1998). The simulations capture the heterogeneous distributions of the stored energy of deformation and the crystallographic orientation at the microstructural length scale. The stored energy and orientation distributions obtained from the FE simulations are then mapped to a regular grid. Each grid point is assumed to contain a deformation substructure consisting of subgrains. The development of the deformation substructure and its evolution using a Monte Carlo technique are described by Radhakrishnan et al. (1998). The simulation methodology described above was used to simulate the deformation and recrystallization of the following simple grain configurations:

- S matrix containing approximately 8% cube grains (S+cube)
- Copper matrix containing approximately 8% cube grains (Copper+cube)
- Matrix of roughly equal fractions of S and Copper and 8% cube grains (S+Copper+cube)

Hot deformation was simulated using the 12 octahedral slip systems and 6 {110}<110> non-octahedral slip systems following Maurice and Driver (1993). The initial grain structures were obtained by generating the required configurations in two dimensions (48x48 elements) and extending them in the third direction (6 elements). MC simulations were carried out in two dimensions using a RD-ND section. The simulations were carried out in a square grid, and a neighborhood of 8 sites consisting of the first- and second-nearest neighbors was used in local energy calculations.

3 Results and Discussion

The ability of the FE simulations to capture the non-uniform deformation and stored energy distribution at the microstructural length-scale is illustrated in Fig. 1, which shows the microstructure containing the cube grains in an S matrix after a plane strain deformation of about 33%. The FE mesh in Fig. 1a indicates a band of high shear deformation that runs diagonally across the RD-ND section. Such localized deformation was observed for all three types of grain configurations studied. Non-uniformity of deformation to a lesser extent is also seen in other locations of Fig. 1a. Fig. 1b shows the stored energy distribution along with the location of the cube grains. The stored energy values in the immediate vicinity of the cube grains are both higher and lower than the stored energy values within the cube grains.

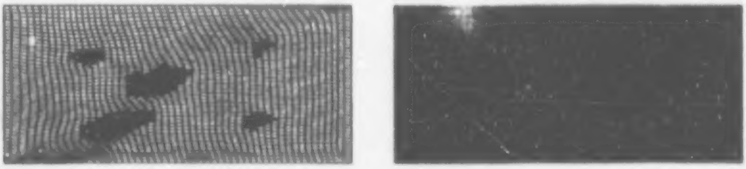

Fig. 1. Deformed FE mesh (left) and stored energy distribution (right) for S+cube case after a plane strain deformation of 33%.

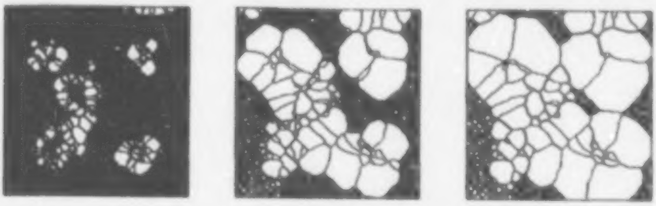

Fig. 2. Temporal evolution of deformation substructure for S+cube case.

Fig. 2 shows the temporal evolution of the deformation substructure. The deformation substructure is obtained by mapping information from the deformed FE mesh to the undeformed geometry. Therefore, the shape change associated with the deformation is not captured. However, it captures the distributions in stored energy and orientation that resulted from the deformation process. Rigorous one-to-one mapping of orientations from the deformed mesh to a regular mesh of the same overall shape is difficult and was not considered in this work for the sake of simplicity. It is significant to note that segments of the high angle grain boundaries (HAGBs) separating the S matrix and cube grains migrate in opposite directions driven by the stored energy differences. While some of the HAGB segments migrate inward and consume the cube grains, other segments that migrate outward become active cube nuclei and consume the S matrix.

Fig. 3 shows the temporal evolution of the substructure obtained by 33% deformation of initial grain structure consisting of cube grains in Copper matrix (Copper+cube). Unlike in the S+cube case, where no HAGBs were produced within the S matrix, a large number of deformation-induced HAGBs are produced within the Copper matrix. The substructure evolution in this case appears to be dominated by the nucleation and growth of Copper subgrains from within the Copper matrix. Rapid subgrain growth in the Copper matrix results in a rapid loss of stored energy, thus inhibiting the growth of cube grains into the Copper matrix.

Fig. 4 shows the growth kinetics of the cube grains into the S matrix for different amounts of prior hot work. The growth kinetics is seen to decrease with increasing prior deformation. This is apparently due to the faster recovery of the S matrix when deformed to 33%. Fig. 4 also shows the evolution of the cube grains in a Copper matrix. The cube fraction appears to be relatively stable, indicating that the cubes are unable to consume the copper matrix.

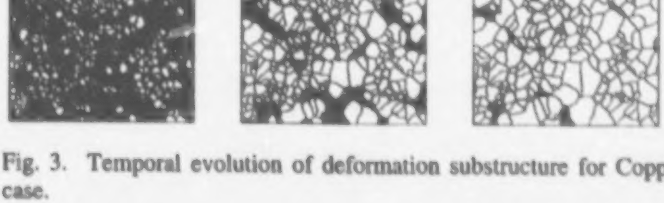

Fig. 3. Temporal evolution of deformation substructure for Copper+cube case.

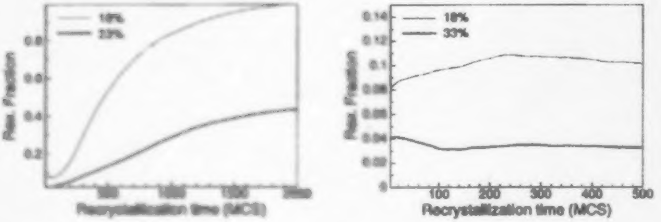

Fig. 4. Growth kinetics of cube grains into S matrix (left) and Copper matrix (right).

Fig. 5 shows the kinetics of evolution of the different components when the matrix is initially composed of approximately equal fractions of S and Copper grains. For 18% deformation, the recrystallization appears to occur essentially by the consumption of S and cube by nucleation fronts in Copper. The fall in the cube fraction indicates a lack of driving force to consume the S grains. This is in contrast to the S+cube case, where the cube nuclei actively grow and consume the S orientations. When the prior deformation is increased to 33%, active cube nuclei begin to form after a brief period, and start consuming the S. However, as in the cube+Copper case, the cube nuclei do not consume the Copper due to the presence of active nucleation fronts within Copper. Instead, the Copper nuclei grow at the expense of S oriented subgrains.

When the prior deformation is increased to about 50%, the recrystallization sequence becomes more complicated. Initially, the cube and Copper subgrains grow at the expense of S as in the 33% deformation case. However, this is followed by another stage where S and cube consume the Copper grains. Examination of the microstructure at the beginning of this stage reveals that recrystallization is not complete, as indicated by the presence of islands of subgrain networks.

In the above simulations, the increase in the surface area of cube bands with deformation is not considered. Hence, the evolution sequence of the cube grains is controlled primarily by the stored energy differences. The presence of a 40° <111> boundary at the cube-S interface is also not considered. The results indicate that under these circumstances, the growth preference of cube into S is primarily due to the absence of deformation induced HAGBs such as in the case of Copper, which promote active recrystallization within Copper.

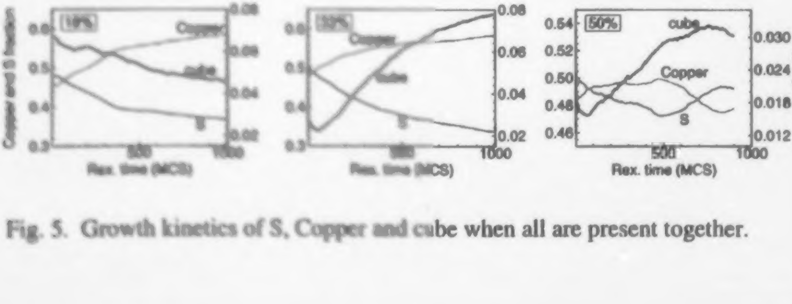

Fig. 5. Growth kinetics of S, Copper and cube when all are present together.

The stored energy difference between the S and cube grains appears to decrease with deformation, thus resulting in a slower growth velocity of cube into S as the prior deformation is increased. The above factor should be considered in analytical models of cube texture evolution. The stored energy difference also appears to depend on the volume fraction of Copper and the spatial distribution of Copper and S with respect to cube.

4 Conclusions

Mesoscale modeling of cube texture evolution during recrystallization after hot deformation indicates that the metastable cube grains provide active cube nuclei that grow by consuming S. The lack of growth into Copper appears to be due to the nucleation and growth of near-Copper orientations within the deformed Copper matrix that prevents the migration of cube fronts. The stored energy difference between cube and S depends on both the amount of deformation and the volume fraction of Copper.

5 Acknowledgments

This research was sponsored by the Division of Materials Science, U.S. Department of Energy, under contract DE-AC05-96OR22464 with Lockheed Martin Energy Research Corporation. The authors acknowledge the use of the Intel PARAGON XP/S 35 computer, located in the Oak Ridge National Laboratory Center for Computational Sciences (CCS), funded by the Department of Energy's Mathematical, Information, and Computational Sciences (MICS) Division of the Office of Computational and Technology Research.

6 References

Daaland, O. and Nes, E. (1996) *Acta mater.*, Vol. 44, No. 4, pp. 1389-411.

Dillamore, I.L. and Katoh. H. (1974) *Metal science*, Vol. 8, pp. 73-83.

Hjelen, J., Ørsund, R. and Nes, E. (1991) *Acta metall. mater.*, Vol. 39, No. 7, pp. 1377-404.

Juul Jensen, D. (1995) *16th Risø International Symposium On Materials Science*, Risø National Lab., Roskilde, Denmark, p.119.

Maurice, Cl. and Driver, J.H. (1993) *Acta metall. mater.*, Vol. 41, No. 6, pp. 1653-64.

Radhakrishnan, B., Sarma, G.B. and Zacharia, T. (1998) *Scripta Materialia*, Vol. 39, No. 12, pp. 1639-45.

Ridha, A.A. and Hutchinson, W.B. (1982) *Acta metall.*, Vol. 30, pp. 1929-39.

Sarma, G.B., Radhakrishnan, B. and Zacharia, T. (1998) *Computational Materials Science*, Vol. 12, pp. 105-23.

Vatne, H.E., Furu, T. and Nes, E. (1996) *Materials Science and Technology*, Vol. 12, No. 3, pp. 201-10.

SHORT RANGE MISORIENTATION CORRELATION AND ITS EVOLUTION INFLUENCE OVER TEXTURE DEVELOPMENT

R.E. BOLMARO, A. ROATTA and A. FOURTY
Instituto de Física Rosario-Fac. Ciencias Exactas, Ingeniería y Agrimensura.
CONICET-UNR. Rosario. Argentina. *e-mail: bolmaro@ifir.ifir.edu.ar*

C.T. NECKER and J. BINGERT
Los Alamos National Laboratory. MST-6. Los Alamos. New Mexico. U.S.A..

Abstract

Texture development in two-phase materials is highly influenced by the elasto-plastic interactions established between phases during the deformation process. Taylor type models neglect such interactions and the reorientation of each crystal is mainly determined by the orientation of the crystal with respect to a laboratory system. In 1-Site Self-Consistent (1-SSC) models such interactions are dependent on the orientation of each crystal with respect to the average of field variables represented by the matrix. 2-Sites SC (2-SSC) models are similar to the 1-site models except they consider interactions functions of the relative orientations of pairs of grains taken as the closest permanent neighbors. In these models the relative orientations of the first neighbors are necessary as input parameters and can also be a possible output of the simulations. The experimental information about short range orientation correlation between phases, either before or after deformation, is not abundant. The current work shows some preliminary results collected from Ag-Ni composites rolled to Von Mises equivalent strains of 2.6 for the starting random material and some intermediate rolling strains. The results show that short range misorientation remains almost unchanged throughout the deformation process. A reorientation model is outlined that can explain some texture development characteristics of two-phase materials.

Keywords: EBSD, EBSP, two-phase materials, crystal misorientations, textures, Self-consistent models.

1. Introduction

The development of deformation textures is described by the evolution of an Orientation Distribution Function (ODF) in the Euler space of orientations (Kocks et al. 1998). The resultant ODF depends on the crystal structure and characteristics of the mechanical test (strain path, strain rate, temperature, etc.). Without considering recrystallization textures and/or phase transformation, deformation texture development has achieved a fairly good level of understanding, at least in its qualitative aspects. Notwithstanding, regarding the quantitative results of simulations and/or predictions, the success of current models is rather poor. The main reason for the quantitative disagreements has been argued to be the inhomogeneities of deformations not properly considered by Taylor or Self Consistent models. A rather high level of sophistication has been achieved by refinements of the Self Consistent theories (Molinari et al. 1987). Notwithstanding, quantitative agreement is still an elusive task and the minor texture components are usually consider not worthy of further simulation efforts.

The deformations are the components of the deformation gradient better understood by the continuum theory as well as through micromechanical models. Due to the symmetry of the stress tensor there is a lack of constitutive equations relating the spin with the applied stresses. At this point what has been called the missing link of the continuum mechanics, the spin or the antisymmetrical component of the velocity gradient, should be studied in detail (Dawson and Marin 1998).. The nature of reorientation of grains has deserved a great deal of dedication by almost every author that has been caught by texture topics (Kocks et al. 1994, Bolmaro 1994, Van der Giessen and Van Houtte 1992). The only agreement that has been reached is: the issue is very complicated, it can be solved only in an approximate way and every kinetic solution comes more from the geometry of the deformation than from the constitutive equations relating strains and stresses.

More detailed studies about the orientation of grains can be performed by using the concept of Misorientation Distribution Functions (MDF) which statistically describe the orientation correlation between each grain and every possible neighbors. The amount of information that can be collected by Electron Back Scattering Diffraction (EBSD) techniques is hardly digestible (Wright et al. 1993), leading to the use of MDF analysis. The aim of the current paper is the comparison of the so called Correlated Misorientation Distribution Function (CMDF) which describes the statistical distribution of first neighboring grains and the plain uncorrelated MDF, which describes the statistical distribution of misorientations between all potential grain pairs. The purpose is the study of the evolution of both functions for a two-phase material vs.

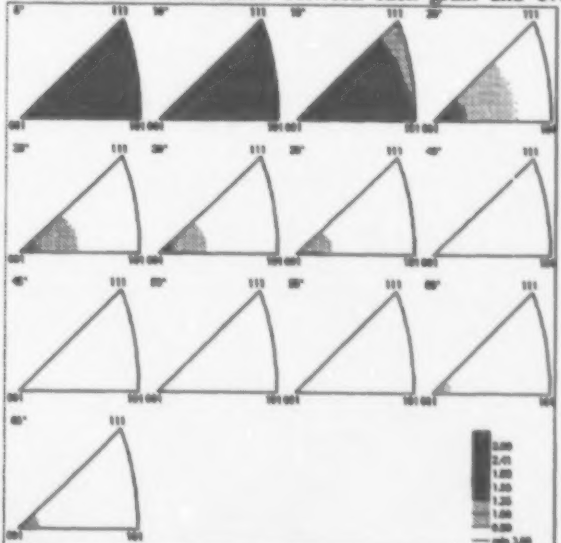

Fig. 1. Ag-Ni Correlated Misorientation Distribution Function for as received samples

plastic strain. Both functions are restricted to the case of measuring the correlation among phases in such a way that each pair of grains of the CMDF is composed of different phases and the uncorrelated MDF is calculated by using the ODF of each individual phase.

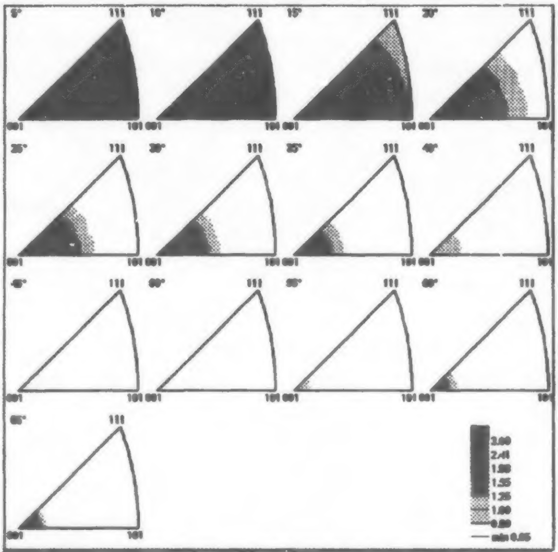

Fig. 2. Ag-Ni Correlated Misorientation Distribution Function for 80% reduction rolled sample.

2. Experiments

Sample preparation details are described elsewhere (Bolmaro et al. 1994). The measurements were performed by electron back-scatter pattern (EBSP) analysis in a SEM. Manual capture of Kikuchi patterns and automatic indexing and analysis was used. We measured CMDF and un-correlated MDF were calculated between one phase with respect to the other for each deformation degree.

Optical discrimination between both phases was easily obtained by polishing and etching but very flat and smooth surfaces were not achievable with the quality needed for automatic capture and analysis of patterns. Both phases present different hardness and chemical reactivity which impedes perfect EBSP quality surfaces. Uneven surfaces resulted in beam shading near phase interfaces because of the sharp sample tilt needed to collect patterns. The best quality patterns were obtained by 30 minutes polishing with 1 μm alumina followed by 30 minutes with 0.3 μm alumina. Even in that case grain boundaries were easily visible between Ag and Ni but not between grains of the same phase. The scanning was performed manually keeping the distance between Ag and Ni orientation determination in approximately 5 μm which is between one half and one tenth of the average grain size. The crystal orientation was automatically calculatedby using OIM-TSL commercial analysis software (TexSEM Laboratories, Inc. 1996). Approximately 500 Ag-Ni pairs were measured for each deformation step. Fig. 1 shows the results in the angle-axes representation for undeformed 50%Ag-50%Ni sample and Fig 2 similar results for a sample deformed by rolling to a Von Mises strain of 2.2.

3. Model Description

In the following paragraphs we will outline a model of reorientation that will be called ReOrientation Domain Model (RODM). Each grain is in contact with many grains that are considered as the closest or first neighbors. Some others, in growing number, are the second, third and so on to the n-th neighbors. The elastoplastic interaction is assumed to be larger among the closest neighbors than among crystals placed far away one from the other. The successful application of Self-Consistent models is assumed to be direct consequence of that space relaxation of the interaction. In very inhomogeneous materials, on the contrary, significant influences at large distances from hard inclusions have been found (Bolmaro et al. 1993).

Many texture development models do not address the mechanisms by which each crystal is allowed to freely rotate in order to fit in the hole that the rest of the grains, regarded as a matrix in the selfconsistent models, have left to it. It is not expected that the grains can free themselves, rotate, and then re-adhere to neighboring grains once the reorientation has finished. It is rather more likely that the grains will try to achieve strain compatibility by going through one of the following mechanisms:

- stretching and spinning together in a larger area comprising more than just a single crystal. Those areas or domains will be larger when the grain boundary mechanisms accommodating the inhomogeneity of the deformation are more energy demanding or too dependent on the grain boundary structure (grain boundary plane and/or grain misorientation).
- fragmenting in such a way that the bordering zone of each grain will experience no reorientation with respect to the first neighbor grain. The orientation change along a grain would be composed of large areas of no change at all and small areas of sudden concentrated change of orientation.

An oversimplified texture could be one described by an ODF with just one, more or less intense, component. Understanding the problem in terms of order and disorder we can address the system as perfectly ordered if all the grains are aligned along the orientation described by such component. In such case long range and short range orders are undistinguishable from each other. A two-phase material with the same characteristic would be represented by two different ODF with one texture component each, both well defined and intense. Two neighboring grains belonging to different phases would be disoriented, statistically speaking, by the same Euler angles no matter how far apart the grains are. In both cases the MDF and CMDF would be absolutely equal (understanding CMDF as the MDF that measures the disorientation probability between different phase first neighbors). In lesser oriented materials some grains, that could be a majority, are oriented in one direction and the rest in some other direction that can constitute a different component or just randomly oriented grains (background). So the task of characterizing the internal order among grains is more difficult now because each grain has to be related with the rest not only by the relative orientation but also by the vector that goes from one grain to the other. Among the many probabilistic functions used to describe order in a polycrystalline material the uncorrelated MDF and the CMDF are the ones that measure the misorientation of grains in two cases: when the coordinates of both grains is immaterial and when both grains are first neighbors. Strictly speaking MDF's are functions of the vector placed between two points and can be considered an almost continuous function if the many internal misorientation effects are considered (Geometrically Necessary Dislocations GNB, Dense Dislocation Walls DDW, Micro Bands MB, Cell Blocks CB, etc.). Notwithstanding the discrete nature of the material will show in sudden discontinuities in the MDF's. One of the questions that can rise from the discussion is whether the

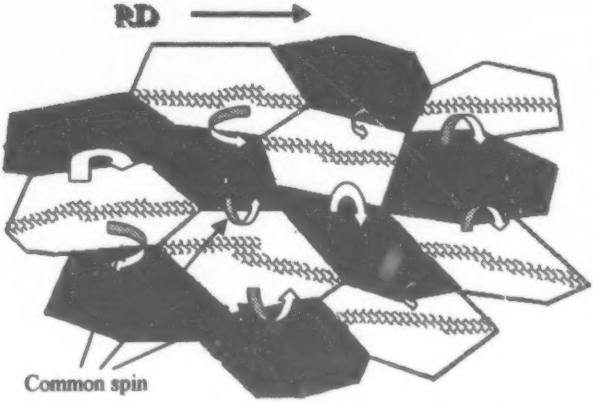

Fig. 3 Schematic representation of fragmented grains sharing spins

misorientation created among first neighbors is mainly due to intra-grain fragmentation mechanisms (misorientation accumulated in the interior of grains) or it is due to grain boundaries misorientation (which would give more validity to the usual assumption made for grain spin calculation).

If the phase boundaries are not able to absorb relative reorientation between phases as fast as they are expected from the usual texture development, the CMDF will show an evolution slower than the MDF. In such case the texture will develop by using one of the following mechanisms or a combination of them: a) fragmentation of grains at the expenses of one or many of the previously described mechanisms or b) collective reorientation mechanisms that can comprise a few grains spinning together taking advantage of a weak ReOrientation Domain Boundary (RODB). The larger the number of grains composing such RODB the lower the intensity of the developed texture. The local disorder among closest neighbors and the need to spin to achieve the macroscopic average texture have to be compatible. But even if the RODB is limited to just a combination of two different phase grains, or portion of them, the need for a different apportionment of spins is evident.

It is always arguable that a FEM calculation at a level of discretization much smaller than the grain size would be able to capture the misorientation between the different intra-grain areas. It is unlikely in any case that such kind of models can finely describe the large variety of dislocation arrays and its concomitant influence over texture intensities.

4. Discussion and Conclusions

We are not taking in account the plane between grains, just misorientations are considered (three angles). The MDF can have many maxima but if the process of deformation is a steady one it is supposed that the intensity of all those maxima increase steadily (but not necessarily linearly) from 0 to a value characteristic of the mechanical process, etc..

We see that the reorientation or spin of the grains is probably consequence of a collective local rotational behavior. There is a short range arrangement that is difficult to change even at medium levels of deformation. Those domains of orientational stability remain with the same relative orientation along large deformation paths. They are probably connected to each other by much weaker interfaces and/or develop inter-domain misorientations by gradually accumulating spins by cell wall misorientations, sub-grain development or any other velocity gradient inhomogeneity. Fig. 3 shows a schematic representation of a collection of grains developing intra-grain misorientation by some dislocation arrays. By this model the spin is better calculated by averaging through two grains regarded as part of the local domain. The larger the domain (the more the grains included in that local array of stable misorientations) the weaker the texture. More freely spinning grains will give rise to stronger textures. The texture severity of some phases in two-phase materials can be explained by the diminishing domain size induced by the weaker interface. In that case single grains are rotating in a matrix that does not preclude the grain from spinning.

The current model becomes a justification of the co-rotation model or spin sharing approach implemented in Self Consistent models by one of the authors (Bolmaro et al. 1997, 1998). The experimental evidence is rather weak and deserves further investigation.

5. References

Bolmaro, R.E., (1994) Grain Axes Coincidence Model: Relaxed Constraints and Finite Strains Revisited, Text. And Microstructures, Vol. 22, pp. 187-198.

Bolmaro, R.E., Guerra, F.M., Kocks, U.F., Browning, R.V., Dawson, P.R., Embury, J.D. and Poole, W.J. (1993) On Plastic Strain Distribution and Texture Development in Fiber Composites. Acta metall. mater., Vol. 41, 6, pp. 1893-1905.

Bolmaro, R.E., Browning, R.V., Guerra, F.M. and Rollet, A.D. (1994) Texture Development in Ag-Ni Powder Composites. Mat. Sci. Eng., Vol 175 A, pp. 113-124.

Bolmaro, R.E., Lebensohn, R.A. and Brokmeier, H.-G. (1997) Crystal Spin in Two-Sites Self-Consistent Models: From Kinematics to Kinetics. Comp. Mat. Science. Vol. 9, pp. 237-250.

Bolmaro, R.E., Fourty, A. and Brokmeier, H.-G. (1998) Measurement and Simulation of Extrusion Textures in Al-Mg Composites. Mat. Sci. Forum.. Trans. Tech. Publ.. Ed. R. Delhez and E.J. Mittemeijer.

Dawson, P.R. and Marin, E. B. (1998) Computational Mechanics for Metal Deformation Processes Using Polycrystal Plasticity. Adv. Appl. Mech.. Vol. 34, pp. 77-169.

Kocks, U.F., Dawson, P.R. and Fressengeas C. (1994) Kinematics of Plasticity Related to the State and Evolution of the Material Microstructure. J. Mech. Behaviour of Mat.. Vol. 5, 2, pp.107-128.

Kocks, U.F., Tomé, C.N. and Wenk, H.-R. (1998) Texture and Anisotropy. Cambridge University Press.

Molinari, A., Canova, G.R. and Ahzi, S. (1987) A Self Consistent Approach of the Large Deformation Polycrystal Viscoplasticity. Acta metall. Vol. 35, pp. 2983-2994.

TexSEM Laboratories, Inc. (1996) Orientation Imaging Microscopy. Software Version 2.0. User Manual.

Van der Giessen, E. and Van Houtte, P. (1992) A 2-D Analytical Multiple Slip Model for Continuum Texture Development and Plastic Spin. Mech. Mater., Vol 13, pp.93-115.

Wright, S. I., Adams, B.L. and Kunze, K. (1993) Application of a New Automatic lattice Orientation Measurement Technique to Polycrystalline Aluminum. Mat. Sci. Eng., Vol. 160 A, pp. 229-240.

Acknowledgments: This work was performed while one of the authors was on leave at Los Alamos National Laboratory (R.E. Bolmaro) funded by the J. W. Fulbright Foreign Scholarship Board.

MODELING OF DYNAMIC RECRYSTALLIZATION IN MINERALS

H.-R. WENK
Dept. Geology and Geophysics, University of California, Berkeley CA 94720

Abstract

The deformation texture of many minerals can be adequately modeled with a viscoplastic self-consistent polycrystal plasticity theory. This model can be expanded to include recrystallization as a balance of boundary migration (growth of relatively undeformed grains at the expense of highly deformed grains) and nucleation (nuclei replacing highly deformed grains). Examples are shown for halite, quartz, olivine and calcite.

Key words: Recrystallization, minerals, texture

1. Introduction

Whereas deformation textures of many minerals and metals can be adequately modeled with polycrystal plasticity theory, the role of dynamic recrystallization in the development of lattice preferred orientation in deformed and recrystallized rocks has remained enigmatic even though it is pervasive. Subgrain rotation recrystallization is important at relatively low strains. At larger strains migration recrystallization becomes dominant and can greatly modify the texture.

An important driving force for grain boundary migration is the difference in the strain energy associated with dislocations between adjacent grains [Humphreys and Hatherly, 1995]. Since the deformation of individual grains is orientation-dependent, the strain energy is also. Therefore polycrystal plasticity models which predict strain energy in differently oriented grains can be used to predict processes during dynamic recrystallization. The viscoplastic self-consistent model can be generalized to include texture development during dynamic recrystallization and a phenomenological model has been successfully applied to several mineral systems.

F5

2. Model

The complex mutual influence of anisotropy, texture, plastic deformation and recrystallization of real polycrystalline materials has been investigated with polycrystal plasticity models [Kocks et al. 1998]. A real polycrystal deforms maintaining local stress equilibrium and strain compatibility which is achieved through the development of intergranular and intragranular heterogeneities (i.e. variation of stress and strain from grain to grain and within grains, respectively). The viscoplastic self-consistent (VPSC) formulation [e.g. Molinari et al., 1987; Lebensohn and Tomé, 1993] captures some aspects of this heterogeneity by allowing stress and strain-rate in the grains to vary, depending on crystal orientation.

Based on the assumption that the stored strain energy provides the driving force for recrystallization, Wenk et al. [1997] proposed a deformation-based recrystallization model for low-symmetry materials, which has been implemented within the VPSC formulation. In the model, highly strained grains are likely to recrystallize by nucleation or to be replaced by grain boundary migration recrystallization of less deformed neighbor grains. The strain energy is calculated, assuming a linear hardening law on slip systems. The dynamic recrystallization texture is due to a balance between nucleation and boundary mobility that makes a grain shrink or grow. In the model nucleation occurs at a rate that is related to the strain energy, after a grain attains the threshold value of strain. It is assumed that the crystallographic orientation of nucleus is the same as that of the host grain. Also, if the stored strain energy of a grain is lower than the average strain energy in the polycrystal, it grows; if it is higher, it shrinks by grain boundary migration. Newly nucleated grains are strain free and have an advantage over old grains, at least in the initial stages of ongoing deformation. The relative grain volume after each strain increment is calculated from the strain energy difference and boundary mobility.

The recrystallization simulations have been in good agreement with previously unexplained texture features observed in experimentally and naturally deformed rocks.

3. Applications

Halite NaCl, cubic

If axial extension of halite with dominant {110}<1-10> slip is modeled with the self-consistent theory, a concentration of highly deformed grains with the fibre direction near [001] is predicted. All other grains are less deformed [Wenk et al. 1989]. Extrusion experiments produced such a texture and the microstructure was indicative of recrystallization [Skrotzki and Welch, 1983]. Such a texture can be predicted with the recrystallization model if nucleation dominates over growth [Wenk et al. 1997].

Quartz SiO_2, trigonal

In quartz deformed in axial compression three different regimes of dynamic recrystallization have been identified: strain-induced grain boundary migration at low

T, subgrain rotation at medium T, and grain boundary migration driven by grain boundary energy at high T [Gleason et al. 1993].

In recrystallized high temperature quartz mylonites, with prismatic slip as a main mechanism, a conspicuous (0001) maximum in the intermediate strain direction (in the foliation plane and perpendicular to the lineation) is often observed. As in halite this corresponds to the most highly deformed grains which nucleate and replace less deformed grains [Wenk et al. 1997].

In a quartzite, naturally deformed in simple shear at low temperature and with basal slip dominant, it was observed that the texture is comprised by two c-axes maxima at high angles to the shear plane. One (A) is displaced against the sense of shear, the second one (B) with the sense of shear. A grains are fairly equant and are not recrystallized, whereas B grains have a high aspect ratio and are highly recrystallized [Takeshita et al. 1999]. In the model initially A grains dominate during deformation but with increasing recrystallization B grains prevail. The final shear texture is largely composed of the "easy slip" component in which the slip plane of the dominant slip system (0001)<11-20> is parallel to the macroscopic shear plane and the slip direction parallel to the shear direction. A similar transition from a deformation to a recrystallization texture was observed in experimentally sheared quartzite [Dell Angelo and Tullis, 1989] and in the quartz analog norcamphor [Herwegh and Handy, 1996].

Olivine Mg_2SiO_4, orthorhombic

Also in olivine with dominant (010)[100] slip simple shear experiments of Zhang and Karato [1996] illustrate a transition from a asymmetric deformation texture to a more highly symmetric "easy slip" recrystallization texture at higher strain. The fine grained microstructure illustrates that recrystallization occurs through nucleation by subgrain formation. Simulations of Wenk and Tomé [1999] can predict the [100] maximum in the shear direction as a texture component that remains stable to large strains.

Calcite $CaCO_3$, rhombohedral

Calcite is the major component of limestones and marbles that are often deformed and recrystallized. Calcite deforms by various mechanisms, including e-twinning and r-slip at low temperature and c-a slip at high temperatures [De Bresser and Spiers, 1997]. Recrystallization of calcite has been investigated experimentally in compression and in simple shear. An enigmatic maximum of compression axes at high angle positive rhombs in inverse pole figures can be explained if the least deformed grains grow [Lebensohn et al. 1998]. Indeed the microstructure displays large grains with triple junctions [Wenk et al. 1973). Of particular interest are high temperature torsion experiments to very large strains [Kunze et al. 1998]. A highly asymmetric deformation texture at low strains transforms to a very strong symmetrical recrystallization texture with the single (10-14)[-12-10] texture component. Both, the deformation and the recrystallization texture can be modeled very well if one assumes that the slip system {10-14}<-12-10> is active at the conditions of the experiment. So far this slip system has not been observed in TEM investigations, even though slip plane and slip direction do occur in different combinations. It would not be the first time that texture information predicts slip systems that were later confirmed.

4. Discussion

The deformation and recrystallization textures in minerals contain information about the strain history and about the microscopic deformation mechanisms that were active during the deformation process. A phenomenological model for dynamic recrystallization that balances growth and nucleation, satisfactorily explains recrystallization textures in several mineral systems. Clearly this model is limited. In the current version it is assumed that the crystallographic orientations of recrystallized (new) grains are same as those of host grains. As a result, the recrystallized fabric is the same as some components of the deformation fabric, but the volume of different components changes due to concurrent grain boundary migration. The predicted textures are very strong whereas experimental and natural textures are often more disperse. This dispersion could be introduced by increasing the number of grains and applying some spreading function during the nucleation event.

The growth velocity may not be simply a function of microstructural hardening due to strain but other factors may play a role. Low mobility of original grain boundaries could result from a low degree of lattice coincidence between adjacent host grains. Once the original grain boundaries are recycled by dynamic recrystallization, a high degree of lattice coincidence may be attained at some of the new grain boundaries leading to an increase in grain boundary mobility. Such considerations could be included in a topologic polycrystal plasticity model if the detailed processes were known [e.g. Solas et al. 1999].

The transition from a deformation to a recrystallization texture is in all model cases very rapid. The model merely reproduces some important changes. There is no absolute time or size scale included and the few parameters which are used, such as onset of recrystallization (step), critical grain deformation to initiate nucleation, nucleation and growth rates, are all arbitrary and only experiments and a physical understanding of the detailed processes could quantify the parameters for a particular system. In other words we should not expect from this model more than it contains.

Calcite is an example for a hard grain dominated growth texture but in most mineral systems, both naturally and experimentally deformed, it appears that the recrystallization texture corresponds to the orientation of the most highly deformed grains. Those grains divide into subgrains with high misorientations and become strain-free nuclei. In the case of simple shear deformation the recrystallization texture consists largely of soft grains with the slip direction of the dominant slip system in the shear direction and the slip plane in the shear plane.

5. References

De Bresser, J.H.P. & Spiers, C.J. (1997). Strength characteristics of the r, f and c slip systems in calcite. Tectonophysics 272, 1-23.

Dell' Angelo, L. N. & Tullis, J. (1989). Fabric development in experimentally sheared quartzites. Tectonophysics 169, 1-21.

Gleason, G. C., Tullis, J. & Heidelbach, F. (1993). The role of dynamic recrystallization in the development of lattice preferred orientations in experimentally deformed quartz aggregates. J. Struct. Geol. 15, 1145-1168.

Herwegh, M. & Handy, M.R. (1996). The evolution of high-temperature mylonitic microfabrics: evidence from simple shearing of a quartz analogue (norcamphor). J. Struct. Geol. 18, 689-710.

Humphreys, F. J. & Hatherly, M. (1995). Recrystallization and Related Annealing Phenomena. Oxford Univ. Press, Oxford.

Kocks, U.F., C. Tomé & H.-R. Wenk (1998). *Texture and Anisotropy. Preferred Orientations in Polycrystals and Their Effect on Materials Properties.* Cambridge University Press

Kunze, K., Pieri, M., Burlini, L. & Wenk, H.-R. (1998). Texture development in calcite during deformation and recrystallization. Interpretation of high strain torsion experiments. EOS, Trans. Am. Geophys. U. 79.

Lebensohn, R. & Tomé, C. (1993). A self-consistent approach for the simulation of plastic deformation and texture development of polycrystals: application to zirconium alloys. Acta metall. mater. 41, 2611-2624.

Lebensohn, R., Wenk, H.-R. & Tomé, C. (1998). Modelling deformation and recrystallization textures in calcite. Acta mater. 46, 2683-2693.

Molinari, A., Canova, G. & Ahzi, S. (1987). A selfconsistent approach of the large deformation polycrystal viscoplasticity. Acta metall. 35, 2983-2994.

Solas, D.E., Tome, C.N., Engler, O. and Wenk, H.-R. (1999). A coupled Monte Carlo and N-site self-consistent approach to static recrystallization. Recrystallization 99 (JIMIS-10).

Skrotzki, W. & Welch, P. (1983), Development of texture and microstructure in extruded ionic polycrystalline aggregates. Tectonophysics 99, 47-62.

Takeshita T., Wenk H.-R. & Lebensohn R. (1998). Development of preferred orientation and microstructure in sheared quartzite: comparison of natural and simulated data. Tectonophysics (submitted).

Wenk, H.-R., Canova, G., Molinari, A. & Mecking, H. (1989). Texture development in halite: Comparison of Taylor model and self-consistent theory. Acta Metall. 37, 2017-2029.

Wenk, H.-R.., Venkitasubramanyan, C.S., Baker, D.W. & Turner, F.J. (1973). Preferred orientation in experimentally deformed limestone. Contrib. Mineral. Petrol. 38, 81-114.

Wenk, H.-R. & Tomé, C.N. (1999). Recrystallization of olivine deformed in simple shear. J. Geophys. Res. (submitted)

Wenk, H.-R. (1999). A voyage through the deformed Earth with the self-consistent model. Model. Mater. Sci. Engin. (in press)

Wenk, H.-R., Canova, G., Bréchet, Y. & Flandin, L. (1997). A deformation-based model for recrystallization of anisotropic materials. Acta mater. 45, 3283-3296.

Zhang, S. & Karato, S.-I. (1995). Lattice preferred orientation of olivine aggregates deformed in simple shear. Nature 375, 774-777.

TEXTURE AND STRAIN LOCALIZATION PREDICTION USING A N-SITE SELF-CONSISTENT POLYCRYSTAL MODEL

D.E. SOLAS and C.N. TOMÉ
MST Division, Los Alamos National Laboratory, Los Alamos, NM 87545 USA

Abstract

A N-site self-consistent polycrystal approach is used to calculate deformation and texture evolution of polycrystalline materials. As this model accounts for local effects, it predicts local deformation and misorientation. This model is used to test some of the assumptions of the classical 1-site polycrystal plasticity approach.

Keywords: intragranular deformation, N-site, misorientation, polycrystal model, self-consistent

1. Introduction

Among the many models proposed to predict the mechanical behavior of polycrystalline materials, the N-site visco-plastic self-consistent model was developed to describe the texture development of two-phase aggregates (Canova et al. 1992). As this model accounts for strain localization and intragranular heterogeneity, it also constitutes an important tool for incorporating recrystallization.

In this work, we present the modeling of texture development in fcc and hcp polycrystals during rolling and emphasize the analyze of topological and localization effects.

2. The N-Site model

Within the N-site model, the polycrystal is represented by a compact arrangement of grains. Each grain is decomposed in cubic cells which deform plastically by slip on crystallographic defined slip systems. In this section we will not describe the visco-plastic self-consistent formulation (Molinari et al. 1987), but we will only give some elements necessary for introducing the 'cluster scheme'. The tangent approach is assumed and we express the local tangent behavior relating deviatoric stress to plastic strain rate as:

$$S(x) = Q(D(x)) : D(x) + S^0(D(x)) \tag{1}$$

where Q is the local tangent stiffness, S^0 is the stress intercept at zero strain rate. A Homogeneous Effective Medium (HEM) is defined so as to provide the same response as the aggregate. Its behavior is assumed to be described by a tangent law:

$$\bar{S} = \bar{Q}(\bar{D}) : \bar{D} + \bar{S}^\circ(\bar{D}) \tag{2}$$

where Q is the overall tangent stiffness of the medium, $\bar{S}$ and $\bar{D}$ are the overall stress and strain rate. A discretization is enforced within each cell domain: the material properties (hardening), the deviatoric stress S^V, and the plastic rate D^V are assumed to be homogeneous in each cell. The hypothesis of discretization introduces discontinuities of stress and displacement across the element boundaries, which means that compatibility and equilibrium are only fulfilled approximately, as in FE methods. As a consequence of this discretization the stress equilibrium equation leads to an interaction equation, which links the stress and strain rate of the cells and the aggregate:

$$D^v = \bar{D} + \sum_{v'} \Gamma^{vv'} : \left(S^{v'} - \bar{S} - Q\left(D^{v'} - \bar{D}\right)\right) \tag{3}$$

where $\Gamma^{vv'}$ is a tensor that mechanically couples the cells v and v'. The first term of the equation corresponds to the Taylor full constraint approach. When the terms where v ≠ v' are omitted in this equation, only the element-matrix interaction remains, leading to the 1-site model. When more terms are taken into account, we obtain the N-site approach. With the N-site model, a shell of neighbors surrounds each element and this cluster is embedded in the HEM. As a consequence, this scheme takes into account neighboring effect. The coupling tensor depends on Q, on the shape of the volume elements v and v', and on their relative separation, but not upon the absolute dimensions and position of the elements. The numerical procedure for solving the integral equation was derived by Canova et al. (1992) for cubic domains. The formulation has been extended to parallelepipedic domains in order to be able to update the element shape with deformation (Solas and Tomé 1999). Such updating is performed only on the average shape of the elements. Equation 3 is a non linear equation function of the stress in each domain. Solving this system requires us to know explicitly the topology of the domain, their spatial correlation and the orientation of the crystallographic structure associated with each domain. The method used to define the microstructure is explained in the next section. The numerical procedure for solving the system is described in Kocks et al. (1998). Once the stress and the strain rate are known in each cell, the state of the material can be updated (crystallographic rotation and hardening). The shape of the cells is also updated according to the average deformation of the aggregate and the mesh remains regular.

As this model takes into account intragranular deformation it gives microstructural information about the evolution of misorientation between cells and local variations in stored energy. As a consequence it provides the information required to study recrystallization processes.

3 Generation of the microstructure

An important issue of the N-site approach is how to generate the initial microstructure. In this application we used a 3D Monte Carlo model, which gives directly the decomposition in cubic cells. Each cube is assigned a number, which represents a numerical (not a crystallographic) orientation and a grain is defined by a connected domain of cells with the same number. Grain boundaries are assumed to exist between cells with different orientation numbers. At the beginning, each cube is assigned a numerical orientation from 1 to N^3, where N^3 corresponds to the number of sites. The reorientation procedure is similar to the one used by Anderson et al. (1985), except that in our case reorientation of a site is allowed only with the orientation of one of its six first neighbors. N^3 reorientation attempts correspond to one Monte Carlo Step (MCS)

The aim of this Monte Carlo Model is to generate the grain microstructure for the N-site model and not to simulate the physical process of grain growth. In our simulations the grain microstructure is composed by a total of 25*25*25 cubes and periodic boundary conditions are assumed. This represent a compromise between CPU time and storage memory on the one hand, and a realistic representation of the microstructure for simulating deformation on the other hand. Eventually, the grain microstructure generated with this Monte Carlo approach is linked the N-site model. Each numerical orientation is assigned a real crystallographic orientation from a set of randomly generated Euler angles

4 Rolling of fcc and hcp aggregates

In this part we present the rolling simulation of fcc and hcp aggregates. The microstructure obtained after 32 MCS was chosen as an input of the N-site model: the number of grains is 189, the grain size distribution resembles the real microstructure, and the average grain size is equal to 82,3 cubes (Fig. 1). The slip systems and their relative strengths are summarized in Table 1 for the fcc and the hcp symmetries. In the case of the hexagonal crystal we do not include twinning and we assume a large plastic anisotropy. In both cases the hardening of the individual systems τ^s is assumed to increase linearly with the accumulated shear strain in the grain Γ: $\Delta\tau^s = h\,\Delta\Gamma$

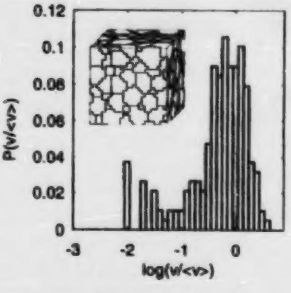

Fig. 1: Initial microstructure and grain size distribution (<v> = 82.3 cubes).

Crystal	Slips systems	τ	h
fcc	$(111)\ <1\bar{1}0>$	2	0.25
hcp	$(10\bar{1}0)<01\bar{2}0>$ (prism.)	1	0.25
	$(10\bar{1}1)<\bar{1}\bar{1}23>$ (pyram.)	4	0.25

Table 1: Slip systems and relative critical shear stress τ, assumed in the deformation modeling

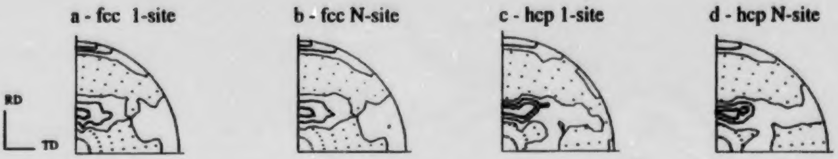
a - fcc 1-site b - fcc N-site c - hcp 1-site d - hcp N-site

Fig. 2: Simulated rolling textures (ε=0.50)

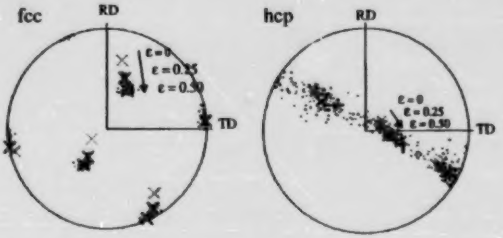

Fig. 3: Spreading of the orientation within a grain

Textures results obtained after rolling (ε_{33} = -0.5) are presented in (111) pole figures for the fcc aggregates and ($10\bar{1}0$) pole figures in the hcp case. The pole figures obtained with the 1-site or the N-site approaches are similar in the fcc case (Fig. 2a and 2b), and the hcp case (Fig. 2c and 2d). The relevance of these results, although they are not specific for a particular system, is that they validate textures calculations done with 1-site models, which rely on the assumption of uniform deformation within the grain domain.

The N-site calculation provides a spread in texture within each grain, which is not present in the 1-site calculation (Fig 3). The large crosses correspond to the orientation of the grain simulated with 1-site model, and the small crosses correspond to the orientation of the cells associated with this grain in the N-site model. The rotations are roughly the same except that we observe a spreading which increases during deformation. As a result of intragranular deformations we observe the development of misorientation between elements which initially have the same orientation.

This difference in local reorientation starts near grain boundaries and propagates inside the grain during deformation (Fig. 4). The thickness of the line between cells depends on the value of the misorientation. The low angle grain boundary distributions for fcc and hcp after 0.25 and 0.50 of plastic deformation are compared (Fig. 5). Here we quantify the misorientation using the angle of rotation around the axis that produces coincidence between the two crystallographic lattices associated with the cells being compared. For the low angle distribution, only the first neighbors to a given element are accounted for in the statistic. It comes out that the misorientations are larger for hcp than for fcc case. This is related to the anisotropy of the crystal, more precisely to the number of active systems during deformation. For the hcp polycrystal the average number of active systems increases during deformation from 2.5 to 3.5, whereas it varies from 3.4 to 3.6 for the fcc case. For the Taylor approach there are 5 independent slip systems, the deformation is homogeneous, and no intragranular misorientations develop.

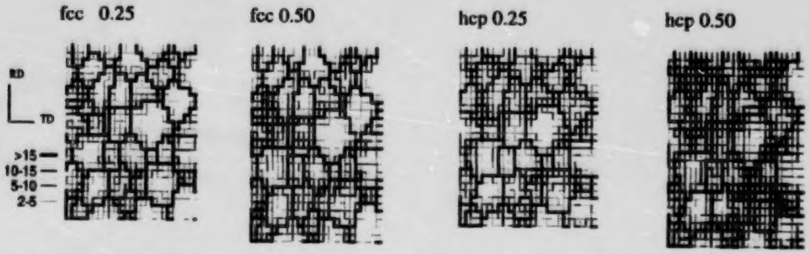

Fig. 4: Misorientations

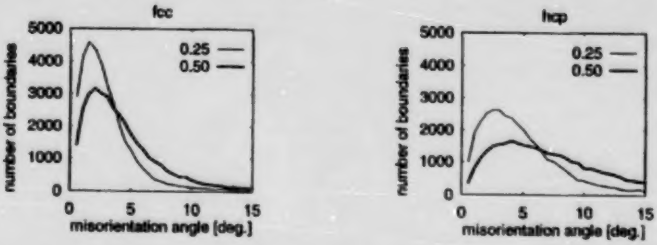

Fig. 5: Low angle boundary distributions

An analogy between these misorientations and the geometrically necessary boundaries (GNB) observed in deformed materials can be made (Bay et al. 1992). In this simulation, the intragranular deformation is accommodated at the boundary between cells, whose position is determined from the beginning of the deformation by the discretization of the microstructure. For real materials, on the other hand the intragranular deformation is accommodated by the development of GNB. The fact that the distribution function of GNB angles and its evolution with deformation measured in aluminum after hot deformation (Fig 4 in Cizek et al.1996) are similar to the results obtained with the N-site model may indicate that the elements can be regarded as sub grains for practical purposes.

In order to verify the assumption of the 1-site model (constant strain inside the grains), we have plotted the different value of the equivalent strain along an axis of the aggregate in the case of the 1-site and the N-site model. Fig. 6 represents the equivalent strain profile along a row of cells in the polycrystal. The equivalent strain is defined as $E_{eq} = (\sum_i \varepsilon_i^2)^{1/2}$.

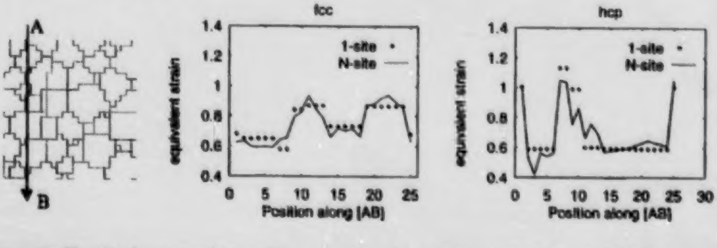

Figure 6: Equivalent strain profiles. Comparison between 1-site and N-site approaches

It turns out that the strain variations within the grain domain are more important in the case of the anisotropic hcp polycrystal, while the N-site approach gives a result closer to the 1-site model for the fcc polycrystal. Overall uniform deformation seems to be a reasonable assumption for the larger grains. It is likely that the number of cells across a grain will play an important role in determining the deformation gradients

5 Conclusions

The prediction of texture deformation obtained with the 1-site and the N-site model are similar. When the crystal is more anisotropic, topological effects become more important, localization, misorientation and non-uniform deformation in the grain domain increase, but the 1-site assumption seems to hold, at least for the prediction of texture development.

It is clear that in what concerns neighbor effects and intragranular deformation, the N-site model can predict interesting results, such as the development of misorientation between cells. These misorientations are in agreement with the misorientation observed in Geometrically Necessary Boundaries. This approach can be used to develop a more physical model for recrystallization than the one based on the 1-site approach (Wenk et al. 1997). Such application is described by Solas et al. (1999).

5 References

Anderson, M.P., Grest, G.S. and Srolovitz D.J. (1985) Grain growth in three dimensions: a lattice model. *Scripta Metallurgica.,* Vol.19, No. 2. pp. 225-30

Bay, B., Hansen, N., Hughes, D.A. and Kuhlman-Wilsdorf, D. (1992) Evolution of fcc deformation structures in polyslip. *Acta metalurgica and materiala*, Vol. 40, No. 2. pp.205-19.

Canova, G.R., Wenk, H.R., and Molinari, A. (1992) Deformation modelling of multi-phase polycrystals: case of quartz mica aggregate. *Acta metallurgica and materiala, Vol.* 40, No. 7. pp. 1519-30

Cizek, P., Wynne, B.P. and Parker, B.A. (1996) The behaviour of incidental dislocation boundaries and geometrically deformation of aluminium. *Scripta Materiala,* Vol. 35, No. 10. pp. 1229-34

Kocks, U.F., Tomé, C.N. and Wenk H.R. (1998) *Texture and Anisotropy*. Cambridge University Press.

Molinari A., Canova, G.R., and Ahzi, S. (1987). A self consistent approach of the large deformations polycrystal viscoplasticity. *Acta metallurgica,* Vol 35, No. 12. pp. 2983-94

Solas, D.E., Tomé, C.N., (1999), Texture and strain localization prediction using a N-site self consistent polycrystal model. Submitted to *International Journal of Plasticity.*

Solas, D.E., Tomé, C.N., Engler, O. ,Wenk, H.R. (1999) A coupled Monte Carlo and N-Site self consistent approach to model static recrystallization. to appear in *proc. of Recrystallization 99*, july 1999, Japan

Wenk, H.-R. ; Canova, G. ; Bréchet, Y. ; Flandin, L. (1997) A deformation-based model for recrystallization of anisotropic materials. *Acta Materiala,* Vol. 45, No. 8. pp. 3283-96

FEM-MICROMECANICS SIMULATION OF TEXTURE DEVELOPMENT OF Cu-Fe POWDER COMPOSITES

J.A. SIGNORELLI, A. FOURTY and R.E. BOLMARO
Instituto de Física Rosario - Fac. de Ciencias Exactas, Ingeniería y Agrimensura. Consejo Nacional de Investigaciones Científicas y Técnicas, Rosario, Argentina.

H.-G. BROKMEIER
Institut für Werkstoffkunde und -technik der Technische Universität Clausthal. GKSS Forschungszentrum Geesthacht, Geesthacht, Germany

Abstract

Polycrystalline models have shown to be powerful tools for prediction of texture developments. When more than one phase is present, it is necessary to take into account their interaction because of their elastic and plastic co-deformation. A first approach is called a 1-Site Viscoplastic Self-Consistent model (1-S VPSC) by which a mean field theory is used to simulate the interaction between each grain and an average matrix. A more realistic approximation is reached applying a 2-Sites VPSC model. This one adds a term to the mean field approximation that depends on the local interaction between closest neighbors. New levels of complexity can be incorporated either by extending the VPSC model to n-Sites or by hybridizing polycrystalline models with finite elements codes to obtain a complete integration between the different scales (microscopic, mesoscopic and piece scale). In this work a 2-S VPSC model is used as a constitutive equation in a fully 3D finite element code. The resulting code is applied to predict cold drawing textures for a two-phase 25%Cu-75%Fe composite. The simulation is performed starting from a well defined microestructural state (morphologic and crystallographic texture). The results are in good qualitative agreement with the experimental ones and some clues about co-deformation and spin sharing can be obtained.

Keywords: FEM, micromechanical models, two-phase materials, inhomogeneous strain.

1 Introduction

Deformation texture development in two-phase materials has been studied by means of Taylor based models as well as 1 Site and 2 Sites Self Consistent (1-SSC and 2-SSC) simulations. The incorporation of elasto-plastic interactions between a crystal and a homogenized average matrix, as SC models do, has improved the results of simulations as well as the interpretation of experiments (Molinari et al. 1987). An utter improvement of the models has been obtained by using first neighbor interaction and partition laws for strain rates and spins (rotation rates) (Lebensohn and Canova 1997, Bolmaro et al. 1997). It is notwithstanding worthwhile to emphasize that mechanical tests, even the best controlled ones, show some intrinsic macroscopic inhomogeneities that can obscure experimental results and its simulation based analysis. The purpose of the current simulation is to show preliminary results of simulations performed by coupling Finite Element Methods (FEM) with micromechanics simulations (Beaudoin et al. 1995, Aukrust et al. 1997). We will present some results of extrusion textures obtained in Cu-Fe powder composites by neutron diffraction. They will be compared with the computed results obtained by using 1 and 2-SSC models. The main purpose is the obtainment of, other than the final average textures, information about different micromechanical parameters and the correct way of dealing with crystal spins. Texture weakening will be assessed to infer in which proportion the weakening is due to microscopic or macroscopic inhomogenities and/or spin partition.

2 Experiments

Experiments have been extensively informed elsewhere and some of them are shown here just for the sake of completeness (Bolmaro et al. 1997). Fig. 1 shows the inverse pole figures of wire drawn 25%Cu-75%Fe powder composites. They were measured after an equivalent Von Mises strain of 3.00. TEX-2 diffractometer at FRG-1 neutron diffraction facility, Geesthacht, Germany, was used. Experimental information was processed by using software packages supported in popLA and Beartex.

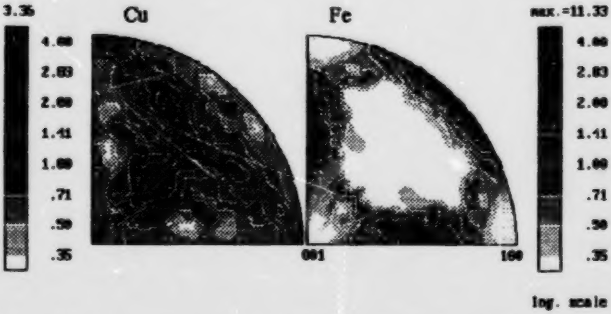

Fig. 1: Experimental inverse pole figures for 25%Cu-75%Fe powder composites. Extruded at Von Mises equivalent strain of 3.0

3 Simulations

Wire drawing process was modeled by using a 3D FEM code coupled with a polycrystalline plasticity code (Beaudoin et al. 1995, Aukrust et al. 1997).

Polycrystalline plasticity codes as constitutive equations are appropriate to consider microstructural material details not well described by a phenomenological equation. The resolution method is based in the weak formulation or velocity-pressure formulation: v,p. It requires the resolution of the following equations:

$$\begin{cases} \forall \mathbf{v}^* \in \vartheta^* & \int\limits_{\Omega} \mathbf{s}:\dot{\varepsilon}^* \, dv - \int\limits_{\Omega} p:\operatorname{div} \mathbf{v}^* \, dv - \int\limits_{\partial\Omega_c} \tau:\mathbf{v}^* \, ds - \int\limits_{\partial\Omega_T} T.\mathbf{v}^* \, ds = 0 \\ \forall p^* \in Q & \int\limits_{\Omega} p:\operatorname{div} \mathbf{v} \, dv = 0 \end{cases} \tag{1}$$

where ϑ^* y Q are the cinematically admissible velocity and pressure fields, $\mathbf{s}$: deviatoric stress tensor, $\dot{\varepsilon}$: strain rate tensor, p: pressure, $\mathbf{v}$: velocity, $T=\sigma.\mathbf{n}$, $\mathbf{n}$: outgoing normal, Ω: volume, Ω_C : contact surface, Ω_T :loaded surface.

The material behavior under a viscoplastic regime is described through the following expression:

$$\mathbf{s} = \mathbf{M}^{-1}[\dot{\varepsilon}]:\dot{\mathbf{e}} \tag{2}$$

where $\dot{\mathbf{e}}$ is the macroscopic deviatoric strain rate tensor and **M** is the material modulus. Currently **M** is calculated by means of a 2-Sites VPSC model (Lebensohn and Canova 1997). The crystal behavior follows a potential law relating the applied stress τ^s in each plane and the CRSS of that system τ_c^s. The total strain rate in each grain is obtained adding the shear strain rates $\dot{\gamma}^s$ of each active slip system and/or twining.

$$\dot{\varepsilon} = \left\{ \dot{\gamma}_o \sum_s \frac{\mathbf{m}^s \otimes \mathbf{m}^s}{\tau_c^s} \left(\frac{\mathbf{m}^s : \mathbf{s}}{\tau_c^s} \right)^{n-1} \right\} \mathbf{s} = \mathbf{M}^{c(sec)}[\mathbf{s}]:\mathbf{s} \tag{3}$$

where $\mathbf{m}^s = \frac{1}{2}\left(\mathbf{n}^s \otimes \mathbf{b}^s + \mathbf{b}^s \otimes \mathbf{n}^s\right)$ is the Schmid tensor describing the geometry of the slip system in the single crystal, $\mathbf{n}^s$ is the slip plane normal, $\mathbf{b}^s$ is the slip direction and $\dot{\gamma}_o$ is reference strain rate velocity. The polycrystalline **M** modulus is calculated through the micro-macro relationship (crystal-polycrystal), function of the individual response of each grain of the polycrystalline aggregate. An implicit relation for **M** is obtained:

$$\mathbf{M}^{sec} = \left\langle \mathbf{M}_{1,2}^{c(sec)} : \mathbf{B}_{1,2}^{c} \right\rangle \tag{4}$$

where , $\mathbf{M}_{1,2}^{c(sec)}$ secant viscoplastic crystal modulus (sites 1 or 2), $\mathbf{B}_{1,2}^{c}$ viscoplastic "accommodation" tensor of the crystal c (site 1 or 2), and $\mathbf{S}$ de Eshelby.

Coupling between polycrystalline models and FEM consist in using in eq. (2) the viscoplastic modulus obtained by means of the polycrystalline model (4), and lately solving the boundary problem defined by (1), using as a constitutive equation the following relationship:

$$\mathbf{s} = \mathbf{M}_{poly}^{-1}[\dot{\varepsilon}]:\dot{\mathbf{e}} \tag{5}$$

The combined scheme allows the calculation of texture development from a texture and morphology defined starting material.

Fig. 2 shows the mesh used to perform 12 successive wire drawing processes of 0.25 equivalent Von Mises deformation each to accumulate a total deformation of 3.00. The velocity gradients were calculated along "stream lines" for each set of elements representative of a fixed proportional radial distance. Figs. 3, 4 and 5 show the inverse pole figures obtained by using the FEM calculated velocity gradients for three different radial distances. Stress exponents of 5 and 35 for Cu and Fe were found to be the best values to achieve good match with experimental textures.

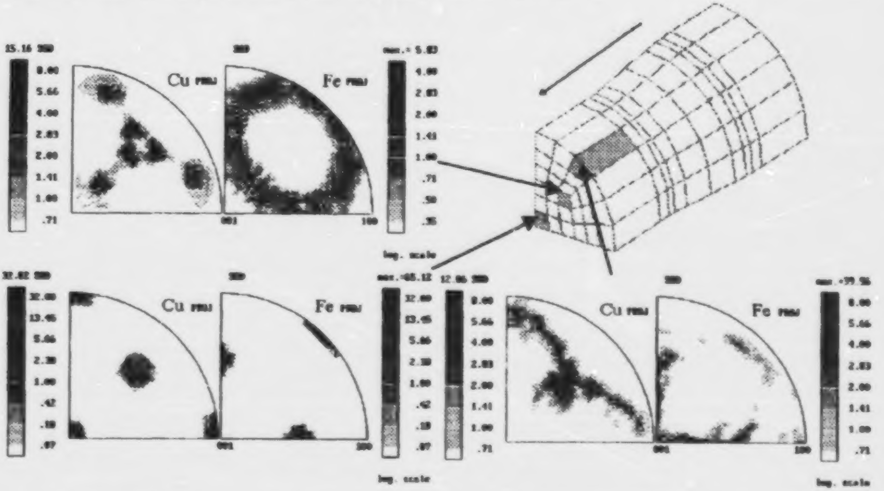

Fig. 2, 3, 4 y 5: FEM mesh and simulated textures for a central, r/2 and border elements respectively.

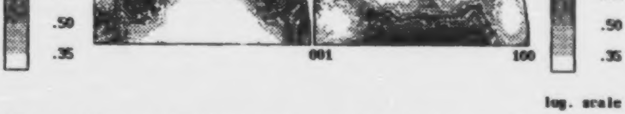

Fig. 6: Average simulated texture. Weighted superposition of the final layer of elements. n-Cu = 5; n-Fe= 35; no spin sharing.

Both sites in the simulation, representative of each phase, were alternatively subject to the independent spin and co-spin schemes described in Bolmaro et al. (1997). Results shown in Figs. 3, 4 and 5 were obtained with the independent spin approach. Texture in the central element (Fig. 3) shows the usual pattern and intensities of a homogeneous extrusion texture, with no shearing strains, at the same equivalent deformation. It is worthy to note that texture severity is higher

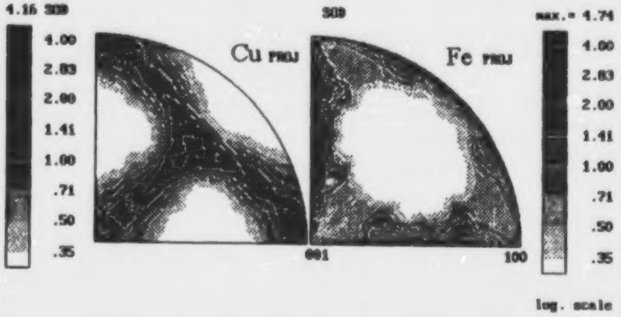

Fig. 7 Average simulated texture. Weighted superposition of the final layer of elements. n-Cu=2; n-Fe= 35; no spin sharing.

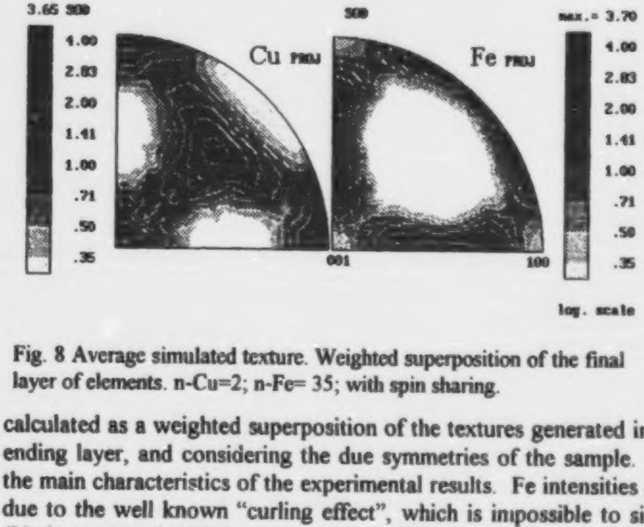

Fig. 8 Average simulated texture. Weighted superposition of the final layer of elements. n-Cu=2; n-Fe= 35; with spin sharing.

than the experimental ones, which is a common characteristic of almost every simulation. Redundant deformation generated by the shearing strain does not represent more than 3% of the total deformation in the outer layer elements and is negligible in the central elements. The outer layer elements undergo through a weakening process due to the combination of texture patterns characteristic of pure radial compression and shearing induced in the die walls. Fig. 6 shows the average texture calculated as a weighted superposition of the textures generated in each element of the ending layer, and considering the due symmetries of the sample. Both textures show the main characteristics of the experimental results. Fe intensities are too low probably due to the well known "curling effect", which is impossible to simulate by the model (Verhoeven et al. 1991).

3 Conclusions

The simulated textures show the expected symmetries and patterns in each case. Intensities are lower in the outer layers because of the strain path change process enforced by the existence of a macroscopic spin. Notwithstanding, the weakening in the average texture is mainly due to the superposition of the different element patterns, consequence of radial variation of velocity gradient. Fig. 7 shows the ending average texture for different stress exponents and the same condition of no sharing of spins. Both maximum intensities have slightly decreased showing better results for Cu and worsening the agreement for Fe texture. The Cu texture is still too strong showing that macroscopic inhomogeneity is not enough to explain low texture severity. By incorporating spin sharing between grains the texture intensities are closer to experimental values for Cu. Both inverse pole figures are shown in Fig. 8 for the same stress exponents and spin sharing. Fe texture reproduces quite well the general pattern but not the intensities. The severity of Fe texture is lower than the experimental values even without considering spin sharing between grains. The sole effect of considering strain ihomogeneity, by FEM modeling, decreases texture intensities to values lower than the experiments. The fact that a spin apportion scheme cannot improve the results should not be taken as evidence that such scheme is not necessary: Macroscopic inhomogeneity is clearly not enough to decrease texture intensities for Cu and too demanding for Fe textures. Some other effect must be present in the co-deformation of Fe that is not considered by simulations. Plane strain deformation rather than axisymmetric elongation is probably the mechanism bestowing Fe with higher deformation than the average, plus curling and folding to accomplish the due macroscopic deformation.

4. References

Aukrust, T., Tjotta, S., Vatne, H.E. and Van Houtte, P. (1997) Coupled FEM and Texture Modeling of Plane Strain Extrusion of an Aluminium Alloy. Int. J. of Plast., Vol. 13, 1-2, pp. 111-125.

Beaudoin, A.J., Dawson, P.R., Mathur, K.K. and Kocks, U.F.. (1995) A Hybrid Finite Element Formulation for Polycrystal Plasticity with Consideration of Macrostructural and Microestructural Linking. Int. J. of Plasticity, Vol. 11, 5, pp. 501-521.

Bolmaro, R.E., Lebensohn, R.A. and Brokmeier, H.-G. (1997) Crystal Spin in Two-Sites Self Consistent Models: From Kinematics to Kinetics. Comp. Mat. Sc., Vol. 9, pp. 237-250.

Lebensohn, R.A. and Canova, G.R. (1997) A Self-Consistent Approach for Modeling Texture Development of Two-Phase Polycrystals: Application to Titanium Alloys. Acta mater., Vol. 45, 9, pp. 3687-3694.

Molinari, A., Canova, G.R. and Ahzi, S. (1987) A Self Consistent Approach of the Large Deformation Polycrystal Viscoplasticity. Acta metall. Vol. 35, pp. 2983-2994.

Verhoeven, J.D., Chumbley, L.S., Laabs, F.C. and Spitzig, W.A. (1991) Measurement of Filament Spacing in Deformation Processed Cu-Nb Alloys. Acta metall. Mater., Vol. 39, 11, pp. 2825-2834.

Acknowledgements: This work has been partially supported by the German-Argentinian Agreement MAT/I/97/OG and CONICET.

SIMULATIVE MODEL AND MECHANISM FOR DEFORMATION TEXTURE FORMATION IN F.C.C.METAL

H.MASUI
Department of Material Science and Engineering, Teikyo University,
Utsunomiya, Japan

Abstract

Pencil glide theory for deformation texture formation of face centered cubic metal was tried. Model is based on an assumption that from the three glide groups indivisually composed of eight {111}⟨110⟩ glide systems around the principal axes X[100], Y[010] and Z[001] , only one group in the glide systems, may operate under the minimum shear magnitude principle. The model,considering the twelve glide systems of the face centered cubic crystal as a whole, demonstrated for example how the crystal rotates toward {110}⟨112⟩ in rolling deformation, indicating a change of modes of glide systems as well with increasing strain.

Keywords: Deformation,face centered,pencil glide,simulation,texture

1 Introduction

Summaries of the deformation textures in the past experimental data for face centered cubic (hereafter,abbreviated to fcc) metals such as Al,Cu,Ni,Au,Ag,Pt, brass,Fe-Ni alloy and austenitic stainless steel, are as follows.

- Final stable rolling texture is {110}⟨112⟩,even if it takes {110}⟨001⟩ etc. as a metastable texture intermediately.
- Stable tensile elongation textures are planes of {111} and {100} normal to tensile direction.
- Stable compression texture is plane of {110} normal to compressive direction,even if it spreads near {311}.

Theories of mechanism for the deformation texture formation in fcc metal, which seem to be closely related to present study, are as follows. Taylor(Taylor 1938) advanced Sachs's theory(Sachs 1928) and proposed the principle of the minimum total amount of shear magnitudes in the 12 glide systems in fcc metal. Bishop & Hill(Bishop and Hill 1951) developed Taylor's theory and led to the principle of the maximum plastic work magnitude by the glide systems against external deformation constraints, i.e.,macroscopic deformation, so that the deformation is generated when the plastic work by the glide systems which was defined as a product of stress and strain,becomes maximum under the condition of not exceeding yield condition in given strain $d\ \varepsilon_{ij}$. In body centered cubic iron, Dillamore & Katoh (Dillamore and Katoh 1974) succeeded in quantitative estimation of texture formation for compressive, tensile and rolling deformation on pencil glide theory under the principle of the minimum total amount of shear magnitudes on 8 glide systems which are composed of four $\{110\}\langle 111\rangle$ glide systems and four $\{112\}\langle 111\rangle$ ones.

2 Model

There is reason that it is believed complex to take the 12 glide systems of fcc metal at once in the calculation. Therefore, the new model divides the 12 glide systems into 3 equivalent groups which are composed of 8 $\{111\}\langle 110\rangle$ glide systems respectively. Fig.1 shows the 8 glide systems of Z group which are represented as 4 pairs of shear magnitudes of $dX_1, dY_1; dX_2, dY_2; dX_3, dY_3$; dX_4, dY_4 of Z group. Similarly, another ones are X group around X([100]) axis with a top of "A" and Y group around Y([010]) axis with a top of "B". If the calculation model takes the 3 groups alternatively and impartially according to the external deformation constraints on arbitrary orientation of crystal, it will succeed to take the 12 glide systems as a whole into consideration due to geometrical symmetry as supposed in Fig.1. It is quite important which of these 3 groups may act against both the external deformation constraints and the orientation of crystal. The calculation method of the model is referred to in detail in case of Z group as an example as follows. Strain tensor $d\ \varepsilon_{X-Y-Z}$ in crystal lattice coordinates of X([100])-Y([010])-Z([001]) is represented in equation (1). In (1),numerical suffix values of 1,2 and 3 coincide with X([100]),Y([010]) and Z([001]),respectively. For example, $d\ \Phi_3$ represents increment of rotation around Z([001]).

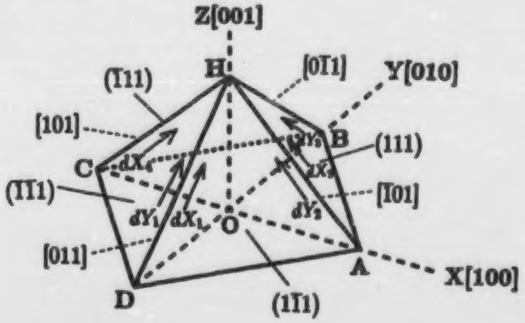

Fig. 1: Illustration of the $\{111\}\langle 110\rangle$ glide systems in Z group and the principal axes in the pencil glide model for fcc crystal.

$$d\,\varepsilon_{X-Y-Z} = \begin{bmatrix} d\,\varepsilon_{11} & d\,\varepsilon_{12} - d\,\Phi_3 & d\,\varepsilon_{13} + d\,\Phi_2 \\ d\,\varepsilon_{12} + d\,\Phi_3 & d\,\varepsilon_{22} & d\,\varepsilon_{23} - d\,\Phi_1 \\ d\,\varepsilon_{13} - d\,\Phi_2 & d\,\varepsilon_{23} + d\,\Phi_1 & d\,\varepsilon_{33} \end{bmatrix} \tag{1}$$

From Fig.1,relations among the 8 shear magnitudes $dX_1, dY_1; dX_2, dY_2; dX_3, dY_3; dX_4, dY_4$ and strain tensor components $d\,\varepsilon_{11}, d\,\varepsilon_{12}, \cdots$ are obtained in following equations (2).

$$\sqrt{6}d\,\varepsilon_{33} = dX_1 + dX_2 + dX_3 + dX_4 + dY_1 + dY_2 + dY_3 + dY_4 \tag{2}$$

....

Simultaneous equations (2) could be solved as follows.

$$(8/\sqrt{6})dX_1 = d\,\varepsilon_{33} - d\,\varepsilon_{22} + d\,\varepsilon_{11} + 2d\,\varepsilon_{12} + 4d\,\varepsilon_{13} + 2d\,\varepsilon_{23} - 2d\,\Phi_3 + 2d\,\Phi_1 \tag{3}$$

....

Simplifying calculation in the model, a is introduced to represent approximately a right-angled vectorial sum of shear magnitudes dX_1 and dY_1 where Θ_1 is tangent angle of them,Θ_1=$\tan^{-1}(dY_1/dX_1)$. Similarly, b and Θ_2 for dX_2 and dY_2, c and Θ_3 for dX_3 and dY_3,and d and Θ_4 for dX_4 and dY_4 are defined as well. Suppose total shear amount, Γ, sum of these indivisual shear magnitudes a,b,c and d, i.e.,4 pairs of glide systems, it may be represented in following equation (4).

$$\Gamma = a + b + c + d = \sqrt{dX_1^2 + dY_1^2} + \sqrt{dX_2^2 + dY_2^2} + \sqrt{dX_3^2 + dY_3^2} + \sqrt{dX_4^2 + dY_4^2} \tag{4}$$

Table 1: Mathematical analytical equations for Z group.

	$\Omega(3)$ (by (5))	$\Omega(1)$ (by (6))
a	$\frac{\sqrt{3}}{2}(-E_2 + \frac{E_3E_5}{E_4})\sqrt{1 + \frac{E_4^2}{E_3^2}}$	0
b	$\frac{\sqrt{3}}{2}(-E_1 - \frac{E_3E_6}{E_4})\sqrt{1 + \frac{E_4^2}{E_3^2}}$	$\frac{\sqrt{3}\sqrt{E_1^2 + E_6^2}}{2}(1 - \frac{E_4 + E_5}{E_6})$
c	$\frac{\sqrt{3}}{2}(-E_2 - \frac{E_3E_5}{E_4})\sqrt{1 + \frac{E_4^2}{E_3^2}}$	$\sqrt{3}\sqrt{E_2^2 + E_5^2}$
d	$\frac{\sqrt{3}}{2}(-E_1 + \frac{E_3E_6}{E_4})\sqrt{1 + \frac{E_4^2}{E_3^2}}$	$\frac{\sqrt{3}\sqrt{E_1^2 + E_6^2}}{2}(1 + \frac{E_4 + E_5}{E_6})$
Γ	$\sqrt{3}\sqrt{E_3^2 + E_4^2}$	$\sqrt{3}\sqrt{E_1^2 + E_6^2} + \sqrt{3}\sqrt{E_2^2 + E_5^2}$
$d\,\Phi_1$	$-\frac{E_6}{2} + \frac{E_3E_5}{E_4}$	$\frac{2E_2 - E_6}{2}$
$d\,\Phi_2$	$\frac{E_5}{2} - \frac{E_3E_6}{E_4}$	$\frac{E_5}{2} + \frac{E_1(E_4 + E_5)}{E_6}$
$d\,\Phi_3$	$\frac{E_4(E_2 - E_1)}{2E_3}$	$\frac{E_4 + 2E_5}{2}$

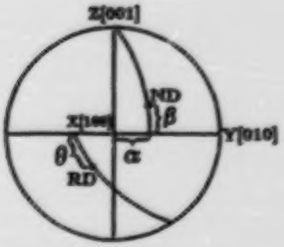

Fig. 2: Definition of α, β and θ in (100) stereographic projection in cubic crystal.

Here,the principle of the minimum total amount of shear magnitudes is applied to (4). Γ in (4) is also a function of $d\,\Phi_1, d\,\Phi_2$ and $d\,\Phi_3$. This means that rotation of fcc crystal is determined by differentiating Γ partially by $d\,\Phi_1, d\,\Phi_2$ and $d\,\Phi_3$ and selecting the least. Important in the model is to derive relations among $\Theta_1, \Theta_2, \Theta_3$ and Θ_4. From (3) and (4) by means of the minimum shear magnitude principle, following relations (5) and (6) could be derived.

$$\text{Solution } \Omega(3) : \Theta_1 = \Theta_3 = \Theta,\ \Theta_2 = \Theta_4 = \Psi\ ;\ \Theta + \Psi = \pi/2 \tag{5}$$

$$\text{Solution } \Omega(1) : \Theta_1 + \Theta_3 = \pi/2,\ \Theta_2 + \Theta_4 = \pi/2 \tag{6}$$

Substituting the relations in (5) and (6) into the equations (2) so as to eliminate $\Theta_1, \Theta_2, \Theta_3$ and Θ_4, mathematical solutions are obtained as listed in Table 1 for Z group as an example where E_1, E_2, E_3, E_4, E_5 and E_6 represent $d\,\varepsilon_{11}, d\,\varepsilon_{22}, d\,\varepsilon_{33}, d\,\varepsilon_{12}, d\,\varepsilon_{13}$ and $d\,\varepsilon_{23}$,respectively. $\Omega(3)$ gives all of the 4 pair glide systems,a,b,c and d completely, while $\Omega(1)$ can be solved under the condition that one of the 4 pair glide systems is zero. The minimum total amount of shear magnitudes of the glide systems of Γ in (4) indicates the maximum plastic work magnitude of the glide systems against external deformation(Bishop and Hill 1951;Ookubo 1968;Kochs 1970;Katoh 1985). Γ takes cyclic equations among the 3 axes of Z, X and Y. This can be an important rule for the glide systems of fcc metal. It is of no doubt that the greatest value of Γ among the 3 groups chooses an initation of the 4 glide systems of the group in solution $\Omega(3)$ where there are completely the 4 glide systems, a,b,c and d, while ,on the other hand, there is still a need to look for the minimum total amount of shear magnitudes of the glide systems in solution $\Omega(1)$. If the group chosen above meets requirements of $a \geq 0, b \geq 0$, $c \geq 0$ and $d \geq 0$, it is valid for generating rotation of the crystal by glide deformation so that deformation texture is formed.

For the calculation, the model uses angle parameters α, β and θ which are defined with stereographic projection as shown in Fig.2. ND is calculated from α, β and indicates the direction parallel to compressive or tensile direction and the direction normal to the rolling sheet plane as well, while RD indicates rolling direction in the rolling plane and uses θ as measured from the intersecting line of X([100])-Y([010])plane and plane normal to ND, on the rollig plane.

3 Results

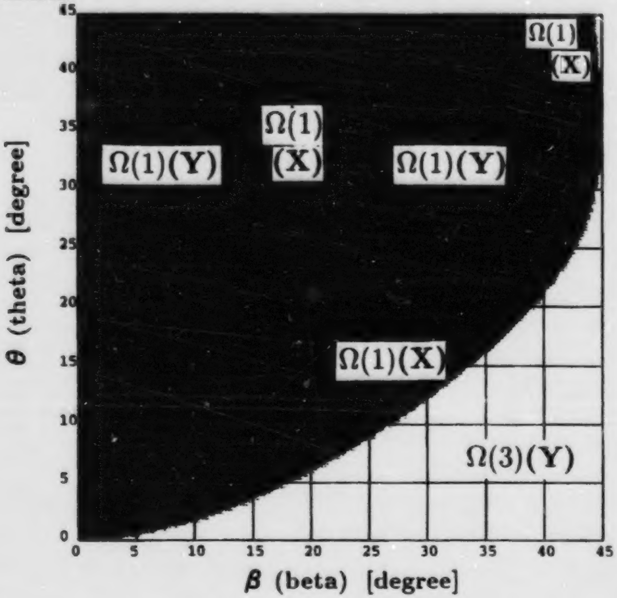

Fig. 3: A map of the glide modes between β and θ in case of $\alpha=0$ in rolling deformation of fcc crystal by the pencil glide model.

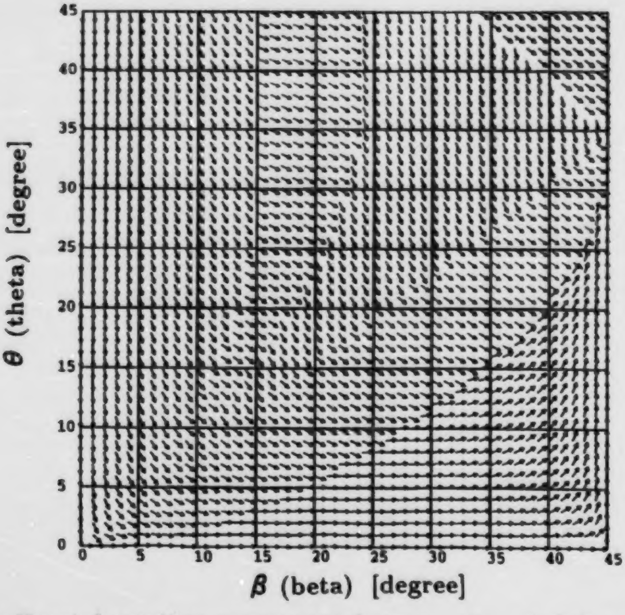

Fig. 4: Crystal rotation arrow map between β and θ in case of $\alpha=0$ in rolling deformation of fcc crystal by the pencil glide model.

Fig.3 shows a map of the glide modes and Fig.4 shows arrow map which indicates crystal rotation between β (beta) and θ (theta) in case of $\alpha=0$ in rolling deformation. The arrows in Fig.4 move from ND,RD:(100)[011] to (100)[010], (100)[010] to (101)[010] and finally (101)[010] to (101)[$\bar{1}$21]. Other orientations as well almost rotate toward ND,RD:(101)[$\bar{1}$21] at last.

More conspicuous arrow map in rolling deformation was one between α (alpha) and θ (theta) in case of $\beta=0$ where all arrows seem to be attracted to definitely one point of ND,RD:(110)[$\bar{1}$12]; (α = 45.0, β = 0.0, θ = 54.74(degree)).

The arrow map in compression where all orientation arrows moved finally toward ND:(110),though intermediatly there was partially another local tendency of arrows toward ND:(722) which is consistent with rather sophisticated glide mode map.

In tensile elongation, arrows of reverse orientations appeared for same glide mode map of compression and moved finally toward both ND:(111) and (100).

4 Conclusion

Pencil glide theory based on the assumption that from three glide groups indivisually composed of eight {111}⟨110⟩ glide systems around the principal axes X[100], Y[010] and Z[001] ,only one group may operate under the minimum shear magnitude principle, was applied to simulative calculation for a deformation texture formation in fcc metal. The model explained namely stable orientation of {110} in compression, {111} and {100} in tensile elongation and {110}⟨112⟩ in rolling deformation.

5 References

Bishop,J.F.W. and Hill,R. (1951) A theoretical derivation of the plastic properties of a polycrystalline face-centered metal. *Phil.Mag.*, Vol.42,pp.1298-307.

Dillamore,I.L. and Katoh,H. (1974) A comparison of the observed and predicted deformation textures in cubic metals. *Metal Science*, Vol.8,pp.21-7.

Katoh,H. (1985) Deformation texture. *Proc.J.I.M.Seminar on Texture(Japanese)*, pp.15 -30.

Kochs,U.F. (1970) The relation between polycrystal deformation and single crystal deformation. *Met.Trans.AIME*, Vol.1,pp.1121-43.

Ookubo,T. (1968) Plasticity of cubic metal under constraint condition. *Plasticity (Japanese)*, Vol.9,pp.681-90.

Sachs,G. (1928) Introduction of the flow stress condition. *Z. Ver.Deut.Ing.*, Vol.72,pp.734 -5.

Taylor,G.I. (1938) Plastic strain in metals. *J.Inst.Metals*, Vol.62,pp.307-24.

COUPLING TEXTURAL AND MICROSTRUCTURAL EVOLUTION

G. Winther
Materials Research Department, Risø National Laboratory, Roskilde, Denmark

Abstract

A new modelling scheme which couples the evolution of texture and dislocation microstructure is presented. One component of this modelling is an extension of standard polycrystal plasticity models which predicts the slip pattern from the crystallographic orientation of a grain and its dislocation microstructure. The other components consist of updating steps of both texture and dislocation structure. The current status of the components in the model are discussed and a realistic implementation is proposed.

Keywords: Polycrystals, microstructure, dislocation boundaries, texture

1 Introduction

Plastic deformation occurs by slip on a number of slip systems in the individual grains in a polycrystal. Slip pattern prediction is therefore the essential element in modelling of polycrystal plasticity. Traditionally, polycrystal plasticity models are used to calculate the slip pattern in individual grains merely from their crystallographic orientation by enforcing various types of boundary conditions concerning strain and stress compatibility between the grains.

Contributions from microstructures within the grains have not been included in the polycrystal plasticity models although there is experimental evidence that both crystallographic precipitates in alloys (Vasudévan et al. 1996) and twins in fcc metals of low stacking fault energy (Leffers 1996) have an effect on texture, which cannot be modelled by the standard polycrystal plasticity models.

In fcc metals of medium to high stacking fault energy, the dominant microstructure consists of long, parallel dislocation boundaries. The fact that the grains are subdivided by these boundaries, which have a spacing of a few micrometers, must influence the slip pattern in the grain and the boundaries must therefore be considered in the models used to predict the slip pattern.

The dislocations in the dislocation boundaries are generated by slip on the active slip systems and the boundary characteristics, e.g. orientation and strength, therefore evolve during deformation. There is thus a coupling between the evolution of texture and microstructure that must be taken into account in the modelling. Neither textural nor microstructural evolution can be treated alone.

This paper presents a modelling scheme for the coupling. The scheme consists of a combination of a) slip pattern prediction taking the current texture and dislocation boundaries into account and b) prediction of the evolution of both texture and dislocation boundaries. Finally, the current state of the various components in the coupling model is discussed and an implementation which can be realised in the near future is proposed.

2 Effect of microstructure on slip pattern

The long parallel dislocation boundaries are geometrically necessary boundaries which separate small volumes of crystallographically misoriented material. The slip pattern in the misoriented material volumes must be different in order to create and increase the misorientation with strain. From geometric reasons alone, the presence of boundaries in the grain must therefore affect the slip pattern and it is basically incorrect to predict only one slip pattern in a grain with dislocation boundaries - although an average slip pattern may be obtainable.

Apart from being associated with slip pattern differences, the boundaries can also directly affect the slip pattern by offering resistance to slip like grain boundaries (Hansen and Juul Jensen 1992), which also separate material with different crystallographic orientations. The resistance may be enhanced by the fact that the boundary spacing is of the order of the slip length. Due to the resistance, slip parallel to the boundaries is easy while slip perpendicular to the boundaries become difficult. In addition to strengthening the material, this effect can be sufficient to activate slip systems that would not be active in the absence of the boundaries.

3 Microstructure, crystallographic grain orientation and slip pattern

There is a strong correlation between the type of dislocation structure developed in a grain and the crystallographic orientation of the grain for fcc metals deformed in both tension (Huang and Hansen 1997; Huang 1998) and rolling (Liu and Hansen 1995; Liu et al. 1998). A recent study of tensile deformed aluminium has shown that the dislocation boundaries form on certain crystallographic planes and that the crystallographic boundary orientation depends on the grain orientation. Based on the crystallographic orientation of the boundaries, the stereographic triangle representing all grain orientations in axisymmetric tension can be divided into six regions. The details of this study will be presented elsewhere.

The correlation between grain orientation and microstructure is explained in terms of the slip pattern. Grains with similar orientations, i.e. grains lying in the same region in the triangle, have similar slip patterns. The active slip systems feed the dislocations to the boundaries and the boundary orientation in grains with similar slip patterns must therefore also be similar.

The subdivision of the triangle into regions with different microstructures is also a subdivision into regions with different slip patterns and microstructural studies can therefore provide new important information on the slip pattern.

The subdivision of the triangle is based on microstructural observations in aluminium deformed to tensile strains between 0.05 and 0.34. In this strain range the boundaries do not change their crystallographic orientation with strain. Still, the dislocations in the boundaries are accumulated over the whole deformation history and a strain effect must also be expected. In rolling, for example, the boundaries in samples deformed to low and high strains have neither the same crystallographic nor macroscopic orientations. At low strains the boundaries are inclined about 45° to the macroscopic rolling direction and at high strains they become roughly parallel to the rolling plane. This macroscopic orientation change cannot be explained by the macroscopic orientation change of boundaries on fixed crystallographic planes due to texture evolution and the crystallographic boundary plane in each grain must therefore change when going from low to high strains.

4 Modelling scheme for coupled textural and microstructural evolution

The coupling between textural and microstructural evolution is caused by the dependence of the slip pattern in an individual grain on both the crystallographic grain orientation and the microstructure combined with the fact that the slip pattern determines the evolution of both texture and microstructure.

Modelling of the coupled evolution of texture and microstructure must therefore follow the scheme outlined in Fig. 1. The scheme consists of three basic steps which are carried out for each grain orientation in the material: 1) prediction of the slip pattern in a grain from its current crystallographic orientation and dislocation microstructure, 2) updating of the grain orientation with a lattice rotation derived from the slip pattern and 3) updating of the dislocation microstructure with new dislocations which have their burgers vectors defined by the active slip systems and are generated in quantities depending on the shear amplitude of each slip system.

As illustrated in Fig. 1 the yield stress also depends on both grain orientation and dislocation structure and the yield stress is directly obtainable from the slip pattern. The coupling of textural and microstructural evolution and calculation of the yield stress at each updating step will therefore give the work hardening.

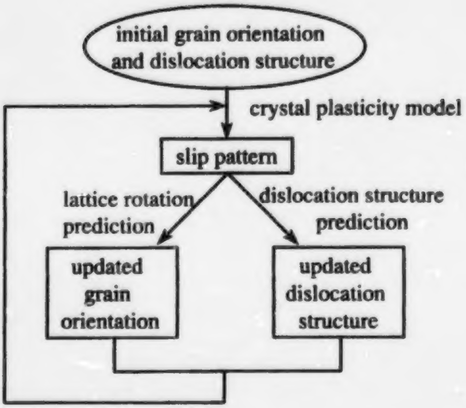
initial grain orientation and dislocation structure
crystal plasticity model
slip pattern
lattice rotation prediction
dislocation structure prediction
updated grain orientation
updated dislocation structure

Fig. 1: Modelling scheme for the coupling between evolution of texture and dislocation microstructure.

5 Current implementation

The status of the three basic components is considered, leading to a currently realistic implementation of the modelling scheme outlined in Fig. 1.

Slip pattern prediction

The framework of the standard polycrystal plasticity models which are widely used for prediction of slip patterns without consideration of the dislocation microstructure has been extended to predict the effect of the dislocation boundaries.

The geometric effect of boundaries causing different slip patterns on the two sides of the boundaries has been modelled from a given boundary orientation assuming that each material volume deforms according to full constraints (Driver and Winther 1997) or relaxed constraints boundary conditions (Leffers 1994).

The resistance to slip offered by the boundaries has been modelled by assigning a critical resolved shear stress given by a Hall-Petch relation to the individual slip systems (Winther et al. 1997). The spacing between the boundaries in the slip plane is taken as the distance parameter in the Hall-Petch relation, and this distance depends on the relative orientation of the slip system and the boundary. So far this model has only been applied to predict the slip pattern in a grain after strain path changes, i.e. prediction of yield anisotropy, but the method is equally applicable to all models that are based on critical resolved shear stresses.

It is therefore concluded that models which take the microstructure into account when predicting the slip pattern are available. The strong correlation between grain orientation and microstructure type can be used in further evaluation of these models. The models must predict similar slip patterns for grain orientations with similar microstructures and different slip patterns for grain orientations with different microstructures.

Updating of grain orientation

Standard derivations of the lattice rotation from the slip pattern assuming that certain planes and directions are kept constant are available (see e.g. (Kocks and Chandra 1982) for a general description). The fact that the two volumes of material with different slip patterns on each side of a boundary must still meet at the boundary plane complicates the calculations but the problem can still be handled within the framework of the standard lattice rotation calculations (Leffers 1994).

Updating of dislocation microstructure

Unfortunately, the current understanding of the formation and evolution of the dislocation microstructure is definitely inadequate to allow formulation of general updating schemes for the dislocation structure based on the slip pattern and the deformation history, i.e. the arrow labelled 'dislocation structure prediction' in Fig. 1 cannot be realised at present.

The on-going microstructural studies are, however, beginning to establish sufficient experimental information on the dislocation microstructure that may serve as a database in which the necessary updating steps can be looked up. This implementation is presented in Fig. 2.

For example, the grain orientation dependence of the microstructure type in tensile deformed aluminium within moderate strain ranges suggests the following updating scheme: It is checked whether the grain has rotated to a new orientation with a different microstructure and if so the old microstructure is replaced with the proper type for the new orientation. To model the evolution over large strains, it is necessary to have several maps of the correlation between grain orientation and microstructure, each giving information on a specific strain range.

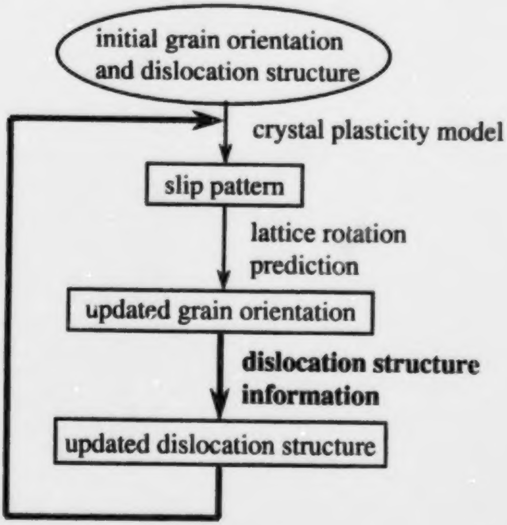
initial grain orientation and dislocation structure
crystal plasticity model
slip pattern
lattice rotation prediction
updated grain orientation
dislocation structure information
updated dislocation structure

Fig. 2: Implementation with the current status of the basic components. Modifications to the modelling scheme in Fig. 1 are marked in bold.

6 Conclusion

A modelling scheme for the coupling of textural and microstructural evolution has been proposed. The model is based on the dependence of the slip pattern on both texture and dislocation microstructure combined with the importance of the slip pattern for the evolution of both texture and microstructure. A full implementation of this model is not possible at present – primarily due to insufficient theoretical understanding of the evolution of the dislocation microstructure. However, this understanding may be substituted by experimental characterisation of the microstructure, which is at a much more advanced state.

7 Acknowledgement

The author wishes to thank Dr. Niels Hansen for inspiring discussions and constructive criticism.

8 References

Vasudévan, A.K., Przystupa, M.A. and Fricke, W.G. (1996) Effect of composition on crystallographic texture in hot-rolled Al-Li-Cu alloys. *Materials Science and Engineering*, Vol. A208, No. pp. 172-180.

Leffers, T. (1996) The Brass-type texture once again. *Proc. of ICOTOM 11*. pp. 299-306.

Hansen, N. and Juul Jensen, D. (1992) Flow stress anisotropy caused by geometrically necessary boundaries. *Acta Metallurgica et Materialia*, Vol. 40, No. 12. pp. 3265-3275.

Huang, X. and Hansen, N. (1997) Grain orientation dependence of microstructure in aluminium deformed in tension. *Scripta Materialia*, Vol. 37, No. 1. pp. 1-7.

Huang, X. (1998) Grain orientation effect on microstructure in tensile strained copper. *Scripta Materialia*, Vol. 38, No. 11. pp. 1697-1703.

Liu, Q. and Hansen, N. (1995) Deformation microstructure and orientation of FCC crystals. *Phys. Stat. Sol. (a)*, Vol. 149, No. pp. 187-199.

Liu, Q., Juul Jensen, D. and Hansen, N. (1998) Effect of grain orientation on deformation structure in cold-rolled polycrystalline aluminium. *Acta Materialia*, Vol. 46, No. 16. pp. 5819-5838.

Driver, J.H. and Winther, G. (1997) Microtextures et hétérogénéités de deformation. *La Revue de Metallurgie-CIT/Science et Genie des Materiaux*, Vol. No. pp. 1021-1028.

Leffers, T. (1994) Lattice rotations during plastic deformation with grain subdivision. *Materials Science Forum*, Vol. 157-162, No. pp. 1815-1820.

Winther, G., Juul-Jensen, D. and Hansen, N. (1997) Modelling flow stress anisotropy caused by deformation induced dislocation boundaries. *Acta Materialia*, Vol. 45, No. 6. pp. 2455-2465.

Kocks, U.F. and Chandra, H. (1982) Slip geometry in partially contrained deformation. *Acta Metallurgica*, Vol. 30, No. pp. 695-709.

MODELING OF THE RECRYSTALLIZATION TEXTURES OF Al-ALLOYS AFTER HOT DEFORMATION

O. ENGLER
Los Alamos National Laboratory, Center for Materials Science,
Mail Stop K765, Los Alamos, NM 87545, USA
H.E. VATNE
Hydro Aluminium, R&D Centre Sunndalsøra, N-6601 Sunndalsøra, Norway

Abstract

The recrystallization textures of rolled Al-alloys can be interpreted in terms of a growth selection of distinct grains out of a limited spectrum of preferentially formed nucleus orientations. Accordingly, recrystallization textures can be modeled by the multiplication of a function $f(g)^{\mathrm{nucl}}$ describing the probability of nucleation of the various orientations with a function $f(g)^{\mathrm{grow}}$ representing their growth probability.

Whereas the growth probability can be accounted for by a 40°<111> transformation of the rolling texture, the nucleation probability of the respective grains is given by the distribution of potential nucleus orientations. The number of nuclei forming at each nucleation site is calculated based on microstructural investigations on the evolution of the various nucleation sites during deformation.

The paper illustrates the model by examples of the recrystallization textures of AA3004 deformed in plane strain compression at a variety of strains, deformation temperatures and strain rates.

Keywords: modeling, recrystallization, AA3004, plane strain compression

1. Introduction

Recently, a new model to simulate the recrystallization textures of Al-alloys has been proposed, which is based on two complementary approaches by the present authors (Vatne et al., 1996a, 1996c; Engler, 1997, 1999; Engler and Vatne, 1998). In the present paper this model is applied to reproduce the recrystallization textures that form in samples of the Al-alloy AA3004 which were deformed in plane strain compression at a variety of strains, strain rates and deformation temperatures so as to demonstrate the predictive power of the model.

2. The model approach

The model is based on the assumption that the recrystallization textures of rolled Al-alloys form by a growth selection of some orientations out of a limited spectrum of preferentially formed nucleus orientations (Engler, 1996). Under such circumstances, the probability of a given orientation to form during recrystallization is given by the probability of its nucleation and the probability of its subsequent growth. With this basic premise, recrystallization textures can be modeled by multiplication of a function $f(g)^{nucl}$ representing the probability of the nucleation of the new grains with their growth probability function $f(g)^{grow}$ (Engler, 1997):

$$f(g)^{sim} = f(g)^{nucl} \cdot f(g)^{grow} \tag{1}$$

The ODF is defined as the function describing the intensity or *probability* with which a given orientation appears in the corresponding texture. Therefore, the probability of nucleation corresponds to the orientation distribution of the potential nuclei. Based on the current understanding on the mechanisms of recrystallization nucleation in Al-alloys, generic nucleus orientation distributions were generated for the most prominent nucleation sites, that are the cube-bands, grain boundaries and second-phase particles (Engler, 1999). In order to take the simultaneous nucleation at different nucleation sites into account, the nucleation distribution function $f(g)^{nucl}$ is derived by weighting the contributions of the different nucleation sites:

$$f(g)^{nucl} = x_{Cube} \cdot f(g)^{nucl}_{Cube} + x_{GB} \cdot f(g)^{nucl}_{GB} + x_{PSN} \cdot f(g)^{nucl}_{PSN} \tag{2}$$

The weight factors x_i denote the probability or efficiency of nucleation at the corresponding nucleation sites. They are derived according to an approach to calculate the number of nuclei N_i forming at each nucleation site, which is based on experimental investigations on the nature and particularly on the evolution of the various nucleation sites during the preceding deformation (Vatne et al., 1996a).

The growth probability function $f(g)^{grow}$ must consider the preference of nuclei with a 40°<111> orientation relationship to the deformed matrix (Engler, 1996). It turned out that a numerical rotation of the corresponding rolling texture by 40° about all possible <111>-axes gives satisfactory results. Finally, the nucleation and the growth probabilities are multiplied to yield the simulated recrystallization texture (Eq. 1), which can then be plotted and compared to the corresponding experimental recrystallization texture.

The present model to simulate recrystallization textures is based on a thorough description of the evolution of the microstructure – especially of the ensuing nucleation sites – during the deformation of the material prior to recrystallization. For that purpose, the processing parameters strain ε, strain rate $\dot{\varepsilon}$ and deformation temperature T_D as well as the texture in the as-deformed state must be known. Furthermore, several parameters to characterize the microstructure prior to the deformation have to be determined, namely the initial grain size D_0, the initial fraction of cube-oriented grains M_0, and two parameters L and N_0 which describe the particle distribution. In the next step, a set of model constants c_{Cube}, c_{GB}, and c_{PSN} describing the efficiency of nucleation at the respective nucleation sites has to be determined in a fitting procedure. As these modeling constants c_i merely depend on the alloy investigated, fitting of one of the experimental recrystallization textures is sufficient, and with this set of modeling constants the model is able to predict recrystallization textures within a given range of experimental parameters. Finally, the model can be run to perform the necessary rolling texture transformations and to derive the weight factors x_i so that eventually the recrystallization textures can be simulated.

3. Application of the Model

In order to study to what extent the model can account for the influence of the processing parameters during hot deformation on the resulting recrystallization textures, samples of the Al-Mn-Mg alloy AA3004 were deformed in plane strain compression (PSC) to different strains ε at different deformation temperatures T_D and strain rates $\dot{\varepsilon}$ (Vatne et al., 1996d). In order to take the opposite effects of T_D and $\dot{\varepsilon}$ into account, the parameters were incorporated into a single parameter, the Zener-Hollomon parameter Z, which is defined as $Z=\dot{\varepsilon}\cdot exp(Q/RT_D)$ (*R*: gas constant) with an activation energy $Q=156kJ/mol$. Subsequently, the samples were recrystallization annealed at the temperature of the preceding deformation to a fully recrystallized condition.

It turned out that both the texture and the microstructure results could be linked to the deformation parameters in form of the Zener-Hollomon parameter. To illustrate this, Fig. 1 shows the recrystallization textures of three samples which were deformed under conditions that gave rise to a wide range of Z. After the recrystallization of the samples that were deformed at low values of $Z<10^{11}s^{-1}$, i.e. high T_D and/or low $\dot{\varepsilon}$, typical fairly sharp cube-textures with pronounced RD-scatter formed (Fig. 1a); the recrystallized grain size exceeded 100µm with the grains being elongated in the rolling direction. Note that the sample shown in Fig. 1a was not completely recrystallized, which resulted in the quite strong intensities of the rolling texture components.

In the samples deformed at high values of $Z>10^{17}s^{-1}$, i.e. low T_D and/or high $\dot{\varepsilon}$, very fine grained equiaxed microstructures (~10µm) and much weaker recrystallization textures were obtained. The recrystallization textures comprised a weak cube-orientation with a characteristic scatter about the ND, furthermore, intensities of the P-orientation {011}<122> could be observed (Fig. 1c).

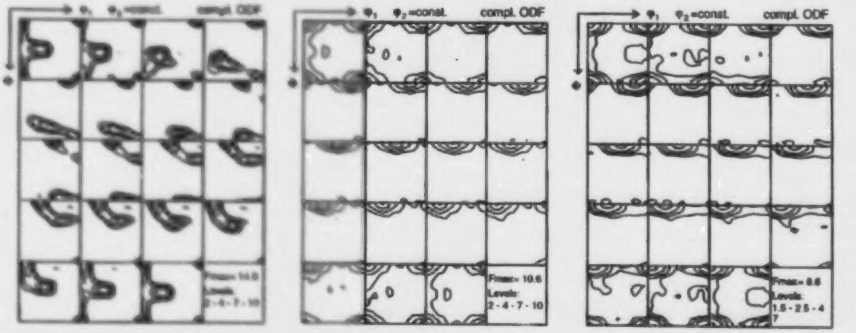

(a) $\varepsilon=2.0$, $\dot{\varepsilon}=0.02s^{-1}$, $T_D=450°C$, $Z=3.8\cdot10^{9}s^{-1}$

(b) $\varepsilon=2.0$, $\dot{\varepsilon}=0.02s^{-1}$, $T_D=250°C$, $Z=7.8\cdot10^{13}s^{-1}$

(c) $\varepsilon=2.0$, $\dot{\varepsilon}=100s^{-1}$, $T_D=250°C$, $Z=3.9\cdot10^{17}s^{-1}$

Fig. 1: Examples of experimental recrystallization textures in dependence on *Z*.

In the intermediate range of Z medium grain sizes and mixed textures were observed, e.g. Fig. 1b. In accordance with earlier investigations, it is concluded that with decreasing Z nucleation at the cube-bands is favored, whereas PSN becomes less effective, so that the cube-oriented grains increasingly dominate the recrystallization textures (Daaland and Nes, 1996; Engler et al., 1996; Vatne et al., 1996b, 1996d).

In order to assess the capability of the present model of accounting for the influence of the processing parameters on the recrystallization, the resulting recrystallization textures were simulated for a variety of strains, strain rates and deformation temperatures. The necessary input data for M^{U}_{Cube} (10%), D_0 (30μm) and the particle size distribution parameters N_0 ($10^{16}\mathrm{m}^{-3}$) and L ($1.3 \cdot 10^{6}\mathrm{m}^{-1}$) as well as the experimental rolling and recrystallization textures were taken from an earlier paper (Vatne et al., 1996a).

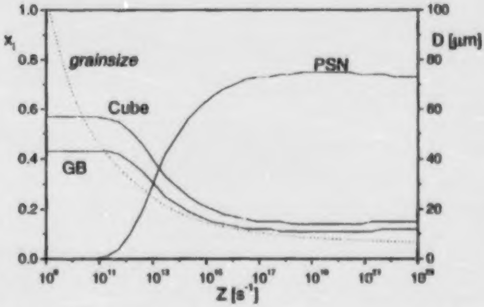

Fig. 2: Evolution of weight factors x_i and grain size D in dependence on Z.

Fig. 2 shows the model predictions in terms of the evolution of the weight factors x_i and the grain size D as functions of the Zener-Hollomon parameter Z, which were obtained with the modeling constants c_{PSN}=1.0, c_{Cube}=0.7 and c_{GB}=0.05. These data were then used to simulate the recrystallization textures. Fig. 3 shows the modeled textures of the three examples presented in Fig. 1, indicating good agreement between both. In order to account for the partial recrystallization of the sample shown in Fig. 1a, the modeled texture was derived by the superposition of the orientation intensities in the simulated recrystallization texture $f(g)^{sim}$ with those in the corresponding rolling texture $f(g)^{def}$ according to $X \cdot f(g)^{sim} + (1-X) \cdot f(g)^{def}$ with a recrystallized volume fraction of X=0.25.

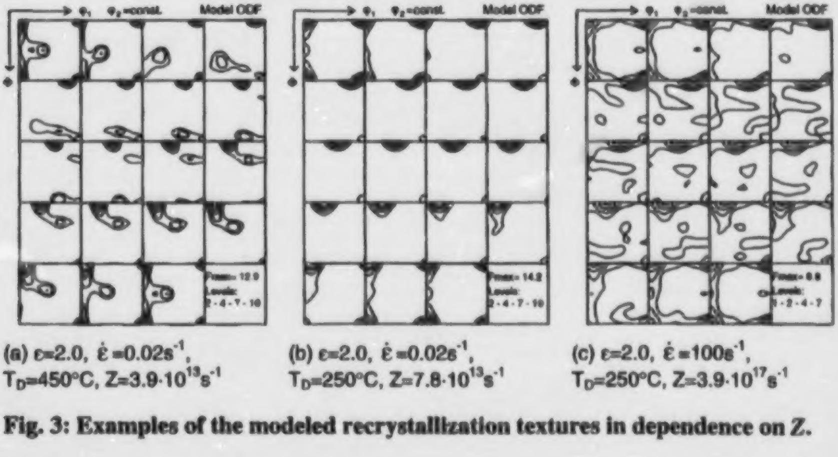

(a) ε=2.0, $\dot{\varepsilon}$=0.02s^{-1}, T_D=450°C, Z=3.9·10^{13}s^{-1}

(b) ε=2.0, $\dot{\varepsilon}$=0.02s^{-1}, T_D=250°C, Z=7.8·10^{13}s^{-1}

(c) ε=2.0, $\dot{\varepsilon}$=100s^{-1}, T_D=250°C, Z=3.9·10^{17}s^{-1}

Fig. 3: Examples of the modeled recrystallization textures in dependence on Z.

To compare simulated and experimental recrystallization textures in more detail, the data were condensed by representing the maximum overall texture intensity *f(g)* as well as the ND-scatter of the cube-orientation (Fig. 4a). For the latter, the angle ψ at which the cube-peak had decayed to 1/*e* (~37%) was determined. It is obvious that the model simulates the main features of the recrystallization textures very satisfactorily by reproducing the shift from the cube-recrystallization texture towards the PSN-texture as well as the simultaneous texture weakening with increasing Z.

It turned out that x_{PSN} strongly increased from about 0 to values exceeding 0.9 with increasing Z (Fig. 2), reflecting the strong dependence of the stored energy of recrystallization on the Zener-Hollomon parameter Z. Accordingly, x_{Cube} and x_{GB} decreased, although the corresponding numbers of nucleation sites, N_{Cube} and N_{GB}, happened to increase slightly. This strong increase in the total number of nucleation sites N_i gave rise to a strong decrease in the final recrystallized grain size D_{RX} with increasing *Z*, which is in very good agreement with the experimental data (Fig. 4b).

Fig. 5 shows the comparison of the experimental and modeled textures for a constant value of the Zener-Holloman parameter, $Z \approx 5 \cdot 10^{17} s^{-1}$, as a function of the applied strain ε. Again, the model predicts the main texture trends fairly satisfactorily. With increasing strain ε the driving force for recrystallization generally increases.

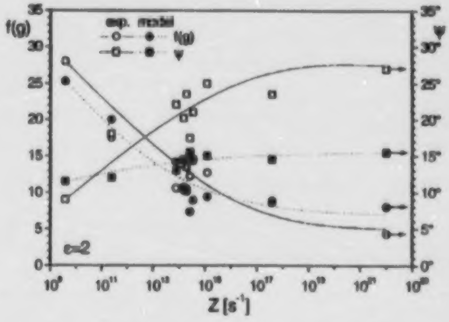

(a) max. texture intensity, *f(g)*, and scatter width, ψ

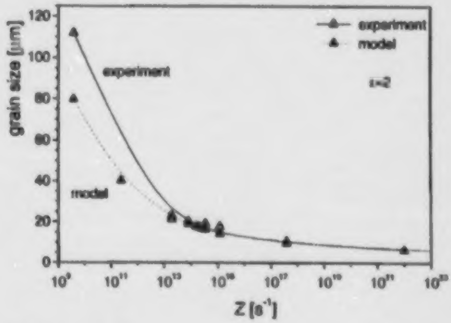

(b) grain size, *D*

Fig. 4: Comparison of model and experimental results in dependence on the Zener-Holloman parameter Z.

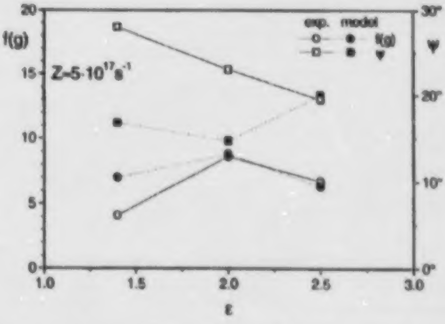

Fig. 5: Comparison of model and experimental results in dependence on strain ε.

Consequently, the numbers N_i of all nucleation sites – cube bands, particles and grain boundaries – increase. Furthermore, the average grain boundary area increases with ε, favoring the nucleation at cube bands and grain boundaries. The volume fraction of the cube-orientation remaining after the deformation – and hence the probability for nucleation of cube-grains – decreases with strain, however. Thus, with regard to the recrystallization texture simulation, the weight factors x_i showed no very pronounced dependencies, but remained more or less constant with increasing ε. This may account for the somewhat unsystematic dependence of the texture attributes $f(g)$ and ψ on ε displayed in Fig. 5.

4. Summary and Conclusions

As an example to demonstrate the predictive power of the present recrystallization model, the recrystallization textures of the Al-alloy AA3004 deformed in plane strain compression at a variety of strains, strain rates and deformation temperatures – i.e. at different values of the Zener-Hollomon parameter Z – were simulated. The model provided a very satisfactory simulation of the corresponding recrystallization textures by reproducing the characteristic shift from a cube-recrystallization texture towards a weak texture as obtained in the case of PSN with increasing Z. Thus, the model is able to simulate the recrystallization textures of Al-alloys for a wide range of microstructural characteristics and processing parameters during the thermomechanical processing of Al-alloys, which can be used to predict and eventually to improve the properties of the final Al-sheet products.

Acknowledgments

The authors are grateful to Dr. U.F. Kocks and Prof. Dr. E. Nes for valuable discussions. The work of OE has been supported by the U.S. Department of Energy and by the Alexander von Humboldt-Foundation through a Feodor Lynen Research Fellowship.

References

Daaland, O. and Nes, E. (1996). *Acta mater.*, vol. 44, pp. 1389-1411.
Engler, O. (1996). *Mat. Sci. Tech.*, vol. 12, pp. 859-872.
Engler, O. (1997). *Textures and Microstructures*, vol. 28, pp. 197-209.
Engler, O. (1999). *Textures and Microstructures*, in the press.
Engler, O. and Vatne, H.E. (1998). *JOM*, vol. 50, (No. 6) p. 23-27.
Engler, O., Mülders, B. and Hirsch, J. (1996). *Z. Metallk.*, vol. 87, pp. 454-464.
Vatne, H.E., Furu, T., Ørsund, R. and Nes, E. (1996a). *Acta mater.*, vol. 44, pp. 4463-4473.
Vatne, H.E., Furu, T. and Nes, E. (1996b). *Mater. Sci. Tech.*, vol. 12, pp. 201-210.
Vatne, H.E., Marthinsen, K., Ørsund, R. and Nes, E. (1996c). *Met. Trans.*, vol. 27A, pp. 4133-4144.
Vatne, H.E., Shahani, R. and Nes, E. (1996d). *Acta mater.*, vol. 44, pp. 4447-4462.

REVISION OF THE CONCEPT OF 1-SITE MODELS

G. WINTHER and T. LEFFERS
Materials Research Department, Risø National Laboratory, Roskilde, Denmark
B. CLAUSEN
LANSCE-12, Los Alamos National Laboratory, Los Alamos, NM, USA

Abstract

Pseudo n-site models or "improper" 1-site models may be alternatives to proper n-site models (finite-element models) for the description of grain-to-grain interaction during plastic deformation of polycrystals and the resulting formation of deformation texture. Pseudo n-site models are 1-site models with some stochastic feature added to simulate grain-to-grain interaction. Recent investigations show that the modified Sachs model (the simple Sachs model with random stresses added in the individual grains) works quite well as a pseudo n-site model for fcc textures. Attempts to add stochastic features (random stresses or random strains in the individual grains) in Taylor-type models are less successful in recreating the experimental texture.

Keywords: Deformation texture, grain-to-grain interaction, 1-site models, n-site models, pseudo n-site models

1 Introduction

A proper 1-site model for the plastic deformation of polycrystals - and hence for the development of deformation texture - is a model where the individual grains interact with some kind of a continuum matrix and *not* with individual neighbouring grains with their specific crystallographic orientations. The great majority of texture models are 1-site models with the common shortcoming that they produce textures which are too sharp - probably because the interaction with the continuum matrix is too "systematic" compared to the interaction with the actual neighbouring grains in real materials.

Recently, various 2-site texture models have been suggested (Leffers 1991, 1998; Lee and Duggan 1993; Lee et al. 1998; Van Houtte et al. 1998). The mathematical basis for these models is quite similar (with certain deviations in the model of

Lee and Duggan as discussed by Leffers (1994)): strain continuity between the two interacting crystallites is maintained with relaxed constraints. The model of Leffers and the model of Lee and Duggan refer to specific microstructural observations, whereas the models of Lee et al. and Van Houtte et al. just aim at coupling the deformation of two crystallites without specific microstructural reference.

The radical solution is to go to n-site models which in practice means finite-element models. This, theoretically attractive, approach has been adopted by several authors, e.g. Kalidindi et al. (1992), Bronkhorst et al. (1992), Dawson et al. (1994), Mika and Dawson (1998). The disadvantages are the complexity of the computer programs and the very heavy demands on computer power.

Even though finite-element models do stand for the ultimate solution within the universe of "simple" texture models, they do not solve all problems with the modelling of deformation texture, e.g. Bate (1999). As for instance pointed out by one of the present authors (Leffers 1999), the finite-element models do not account for the complex micromechanics associated with the complex microstructures encountered during the plastic deformation of polycrystals. Thus, even finite-element models are only approximations to the real textures. Therefore we may make do with simpler solutions to the "simple" problem of grain-to-grain interaction.

2-site models as described above are one possible solution. In the present work we investigate an alternative solution: "improper" 1-site models or pseudo n-site models.

2 Pseudo n-site models

Pseudo n-site models are 1-site models with some feature added to simulate grain-to-grain interaction in a stochastic manner. Thus, they combine the simplicity of 1-site models with some of the attractive features of n-site models. For instance, two grains with identical crystallographic orientations will have different slip patterns.

2.1 The modified Sachs model

The basic philosophy behind the modified Sachs model (mSm) is that grain-to-grain interaction necessarily implies violation of the strictly deterministic multiple slip pattern of the Taylor model (Taylor 1938). It is assumed that only one active slip system in each grain can be taken for granted, that with the highest resolved shear stress as in the simple Sachs model (Sachs 1928). However, this does not imply single glide as in the simple Sachs model. It implies that we only *know* one slip system in the apparently stochastic pattern of multiple slip (stochastic because the crystallographic orientations of the neighbouring grains are unknown). Details about the theory behind the mSm were presented by Pedersen and Leffers (1987) and Leffers (1995). In practice the stochastic multi-slip pattern is produced as follows: a stress pattern consisting of the applied stress plus random stresses, which vary during deformation, selects one slip system in each deformation step, but the many steps combine to a pattern of multiple slip. As discussed by Pedersen and Leffers, the average magnitude of the components of random stress is not just a fitting parameter; it is derived by rational considerations.

Using "plain-strain analysis" (PSA) as the rule for lattice rotation (see below) the mSm simulates the development of the brass-type rolling texture quite well even

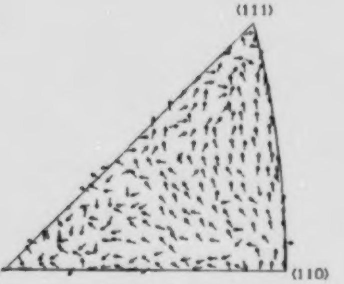

Fig. 1: Lattice rotations during 2% tensile strain of an fcc polycrystal as calculated with the modified Sachs model. The arrows indicate the direction of the rotations, not the magnitude.

though the mSm does not consider the special microstructural conditions in rolled brass, e.g. Leffers (1999). In the present work we shall focus on the use of the mSm to simulate the texture development in fcc materials with higher stacking fault energy, for instance the development of the copper-type rolling texture.

Leffers and Lebensohn (1996) have shown that the rolling textures simulated with Sachs-type models (with large deviations from the Taylor model) depend strongly on the rule used to describe the lattice rotation. The combination of the mSm and the "mathematical analysis" (MA) rotation rule (the rule used routinely in solid mechanics) leads to a simulated fcc texture very close to the experimental copper-type texture - with a realistic sharpness. The simple Sachs model combined with MA leads to a simulated texture with one single dominant orientation, the copper orientation {211}<111>.

So far Sachs-type models have been completely discarded for the simulation of fcc fibre textures (in tension, drawing and extrusion) because they were thought to produce a <211> fibre texture. However, this refers to the use of a single-crystal rotation rule. With MA the modified Sachs model produces a dual <111>/<100> fibre texture as shown in Fig. 1 in accordance with experimental observations for fcc materials with high and intermediate stacking fault energies, whereas simple Sachs with MA leads to a <111> texture with a very weak <100> component (Lorentzen et al. 1998).

Thus, the mSm combined with MA works quite well as a pseudo n-site model in the simulation of fcc "metal" deformation textures (as opposed to "alloy" textures): it scatters the texture without introducing orientations which are not observed experimentally.

It is evident that the rotation rule is very important. Lebensohn and Leffers (1999) have shown that MA is theoretically the correct rule for approximately equiaxed grains whereas PSA is the correct rule for the elongated and flattened grains after substantial rolling reduction. One may therefore ask whether it is theoretically justified to use MA at higher rolling strains. As a possible justification Lebensohn and Leffers suggest that the elongated and flattened grains may be subdivided into approximately equiaxed crystallites - which would be in perfect agreement with the philosophy behind the mSm. Lebensohn and Leffers also suggest that the bundle structure in a large fraction of the grains in rolled Brass (Leffers 1999) may prevent such a subdivision, thus justifying a transition to PSA which, as mentioned earlier and as discussed by Leffers (1999), leads to a brass-type texture.

2.2 Modified Taylor models

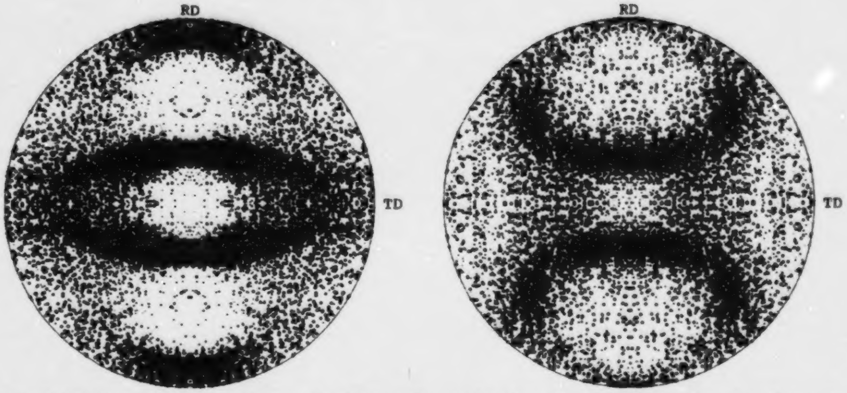

Fig. 2: {111} and {200} pole figures for 50% rolling reduction of an initially texture-free fcc polycrystal as simulated with the Taylor model plus a moderate level of random strains.

The mSm is a pseudo n-site model which is radically different from the Taylor model. As an alternative possibility we may consider models based on the Taylor concept with some added stochastic feature. For instance, Leffers and Juul Jensen (1992) simulated the fcc rolling texture with Taylor models combined with random stresses as those described in 2.1. In practice this means deviation from the minimum-shear criterion of the Taylor model while the strain in the individual grains is kept identical to the macroscopic strain. For the Sachs model as described in 2.1 we cannot imagine any other way of introducing the stochastic feature which makes it a pseudo n-site model than to add random stresses. For the Taylor model (in casu in the full-constraint version for plane strain) we have tested an alternative possibility: the addition of random strains. We let the imposed strain in the individual grain oscillate randomly (within certain limits) around a mean value which is equal to the macroscopic strain. In practice this means that we maintain the minimum-shear criterion while we relax the requirement that the microscopic strain must be identical to the macroscopic strain.

As it turns out, the addition of random strains have approximately the same effect as the addition of random stresses. Fig. 2 shows the {111} and {200} pole figures simulated with the full-constraint Taylor model with a moderate level of random strains. They are almost identical to the pole figures simulated with a moderate level of added random stresses by Leffers and Juul Jensen (1992). In both cases the addition of random strains/stresses leads to a simulated texture which is similar to that without random additions apart from a decrease in texture sharpness - and which differs from the experimental copper-type texture. For instance, there is still, in the {111} pole figure near RD, a distinct maximum in pole density at the Taylor orientation {11 4 4}<8 11 11> which is not observed in the experimental copper-type pole figures (and which is not present in the pole figures simulated with the mSm combined with MA by Leffers and Lebensohn (1996) as described in 2.1). In order to suppress this distinct maximum we must go to a high level of random strains, and this leads to simulated pole figures (Fig. 3) which differ very significantly from the experimental

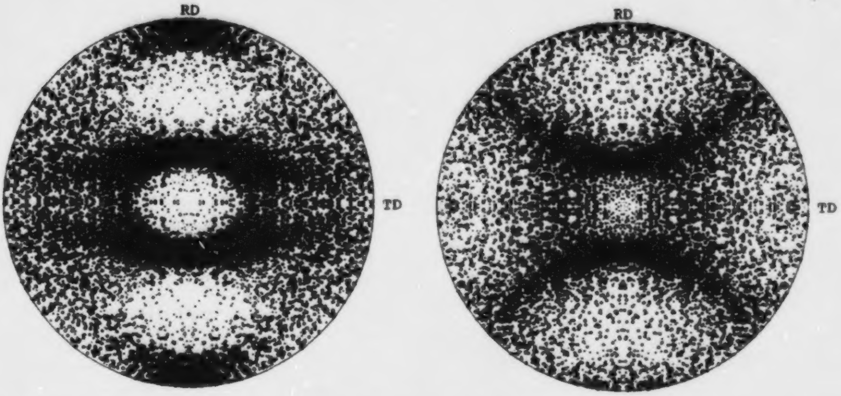

Fig. 3: As Fig. 2 but now with a high level of random strains.

copper-type pole figures (or any experimental fcc pole figures). This is in agreement with unpublished results from the work of Leffers and Juul Jensen (1992). In order to suppress the maximum at the Taylor orientation they had to go to a high level of random stresses which distorts the overall similarity with the experimental copper-type texture.

Thus, the present preliminary results indicate that pseudo n-site models derived from the Taylor model are not particularly successful in reproducing the experimental textures. However, it is encouraging to notice that two modelling schemes which are mathematically different (addition of random strains and addition of random stresses) lead to similar results, i.e. that this type of modelling is rather "robust".

3 Conclusion

Stochastic modelling of grain-to-grain interaction in pseudo n-site models has been demonstrated in more or less radical versions derived from the Sachs model and the Taylor model, respectively. Apparently, the models derived from the Sachs model produce textures closer to the experimental textures than those derived from the Taylor model.

4 References

Bate, P.S. (1999) Modelling deformation microstructures with the crystal plasticity finite element method. *Phil. Trans. R. Soc. Lond. A*, Vol. 357 (in press).

Bronkhorst, C.A., Kalidindi, S.R. and Anand, L. (1992) Polycrystalline plasticity and the evolution of crystallographic texture in fcc metals. *Phil. Trans. R. Soc. Lond. A*, Vol. 341, pp. 443-477.

Dawson, P.R., Beaudoin, A.J. and Mathur, K.K. (1994) Finite element modeling of polycrystalline solids, in *Numerical Predictions of Deformation Processes and* *the Behaviour of Real Materials* (eds. S.I. Andersen et al.), Risø National Laboratory, Roskilde, pp. 33-43.

Kalidindi, S.R., Bronkhorst, C.A. and Anand, L. (1992) Crystallographic texture evolution in bulk deformation processing of fcc metals. *J. Mech. Phys. Solids*, Vol. 40, pp. 537-569.

Lee, B.J., Ahzi, S. and Parks, D.M. (1998) Intermediate modeling of polycrystal plasticity, in *Constitutive and Damage Modeling of Inelastic Deformation and Phase Transformation* (ed. A.S. Khan), Neat Press, Fulton, pp. 377-380.

Lee, C.S. and Duggan, B.J. (1993) Deformation banding and copper-type rolling textures. *Acta Metall. Mater.*, Vol. 41, pp. 2691-2699.

Lebensohn, R.A. and Leffers, T. (1999) The rules for the lattice rotation accompanying slip as derived from a self-consistent model. *Textures and Microstructures* (in press).

Leffers, T. (1991) Modelling of the formation of organized structures and their effect on mechanical properties, in *Strength of Metals and Alloys* (eds. D.G. Brandon et al.), Freund Publishing House, London, pp. 615-622.

Leffers, T. (1994) Variations in the modelling of plastic deformation with grain subdivision, in *Strength of Materials* (eds. H. Oikawa et al.), The Japan Institute of Metals, Tokyo, pp. 235-238.

Leffers, T. (1995) Long range stresses associated with boundaries in deformed materials. *Phys. Stat. Sol. (a)*, Vol. 149, pp. 69-84.

Leffers, T. (1998) Aspects of grain subdivision, in *Constitutive and Damage Modeling of Inelastic Deformation and Phase Transformation* (ed. A.S. Khan), Neat Press, Fulton, pp. 165-168.

Leffers, T. (1999) Why we cannot simulate deformation texture, in *these proceedings*.

Leffers, T. and Juul Jensen, D. (1992) Quantitative simulation of the copper-type rolling texture, in *Modelling of Plastic Deformation and Its Engineering Applications*, (eds. S.I. Andersen et al.), Risø National Laboratory, Roskilde, pp. 323-329.

Leffers, T. and Lebensohn, R.A. (1996) Ambiguities in the calculation of lattice rotations for plane-strain deformation, in *Textures of Materials* (eds. Z. Liang et al), International Academic Publishers, Beijing, pp. 307-314.

Lorentzen, T., Leffers, T. and Clausen, B. (1998) Polycrystal models and intergranular stresses, in *Modelling of Structure and Mechanics of Materials from Microscale to Product* (eds. J.V. Carstensen et al.) Risø National Laboratory, Roskilde, pp. 345-354.

Mika, D.P. and Dawson, P.R. (1998) Effects of grain interaction on deformation in polycrystals. *Mater. Sci. Eng. A*, Vol. 257, pp. 62-76.

Pedersen, O.B. and Leffers, T. (1987) Modelling of plastic heterogeneity in deformation of single-phase materials, in *Constitutive Relations and Their Physical Basis* (eds. S.I. Andersen et al.), Risø National Laboratory, Roskilde, pp. 147-172.

Sachs, G. (1928) Zur Ableitung einer Fliessbedingung. *Z. Verein. deut. Ing.*, Vol. 72, pp. 734-736.

Taylor, G.I. (1938) Plastic strain in metals. *J. Inst. Metals*, Vol. 62, pp. 307-324.

Van Houtte, P., Delannay, L. and Samajdar, I. (1998) Prediction of cold rolling textures and strain heterogeneity of steel sheet by means of the lamel-model, in *Constitutive and Damage Modeling of Inelastic Deformation and Phase Transition* (ed. A.S. Khan), Neat Press, Fulton, pp. 149-152.

3D-VISUALIZATION OF B.C.C. IRON CRYSTALS ROTATED DURING COLD ROLLING

H.MASUI, H.UKAJI, O.TSUKAMOTO and T.ASAMI
Department of Material Science and Engineering, Teikyo University,
Utsunomiya, Japan
H.KATOH
Kurosaki,Ltd., Kitakyuushu,Japan

Abstract

Based on pencil glide theory on body centered cubic iron crystal, 3D-visualization for rotation and deformation of the crystal was tried. 3D-rotation showed,e.g., two crystals of different initial orientations rotated according to both initial orientation and deformation style. Further,deformation of two crystals which includes intermediate region,i.e., grain boundary, was also simulated in 3D-visualization.

Keywords: body centered,grain boundary,pencil glide,texture,visualization

1 Introduction

Summaries of the deformation textures in the past experimental data for bcc iron are as follows.

- Stable uni-axial deformation textures are plane of $\{110\}$ normal to tensile direction and planes of $\{111\}$ and $\{100\}$ normal to compression direction.
- Stable rolling textures are $\{211\}\langle 011\rangle$, $\{100\}\langle 011\rangle$ as one group and $\{111\}\langle 011\rangle$,$\{111\}\langle 112\rangle$ as another one.

Pencil glide theory had been studied on texture formation for compressive, tensile and rolling deformation in body centered cubic(hereafter, abbreviated to bcc) iron by Dillamore & Katoh (Dillamore and Katoh 1974; Katoh 1985).

One of the purposes of the present study is 3D-visualization on a rotation of bcc iron crystal for intuitive comprehension of bcc crystal rotation during deformation. Another of them is to know a deformation behavior of intermediate region sandwiched by two crystals,i.e., grain boundary.

2 Model and methods

2.1 Pencil glide theory

Summaries of pencil glide theory(Dillamore and Katoh 1974; Katoh 1985) are as follows. From 12 glide systems of bcc iron, 8 glide systems which are composed of four $\{110\}\langle 111\rangle$ and four $\{112\}\langle 111\rangle$ are chosen. These are described as dX_1, dX_2, dX_3, dX_4 and dY_1, dY_2, dY_3, dY_4 respectively ,and total amount of shear magnitudes, Γ ,is expressed as equation (1).

$$\Gamma = a + b + c + d = \sqrt{dX_1^2 + dY_1^2} + \sqrt{dX_2^2 + dY_2^2} + \sqrt{dX_3^2 + dY_3^2} + \sqrt{dX_4^2 + dY_4^2} \quad (1)$$

The principle of the minimum total amount of shear magnitudes(Taylor 1938; Bishop and Hill 1951) is applied to Γ differentiating by rotation $d\,\Phi_j (j = 1 \sim 3)$ and yields two kinds of solutions which are indivisually composed of four cases. Only one case with active glide systems is determined with the aid of the maximum plastic work theory(Bishop and Hill 1951; Ookubo 1968;Kochs 1970) under the condition of $a \geq 0, b \geq 0$, $c \geq 0$ and $d \geq 0$. The rotation $d\,\Phi_j$ can be obtained from equation by means of strain tensor $d\,\varepsilon_{11}, d\,\varepsilon_{12}, \cdots$ in the chosen case of the solutions so that deformation textures are formed.

2.2 3D-visualization

Strain tensor $d\,\varepsilon_{X-Y-Z}$ in crystal lattice coordinates of X([100])-Y([010])-Z([001]) is represented in equation (2). In (2),numerical suffix values of 1,2 and 3 coincide with X([100]),Y([010]) and Z([001]),respectively. For example, $d\,\Phi_3$ represents increment of rotation around Z([001]).

$$d\,\varepsilon_{X-Y-Z} = \begin{bmatrix} d\,\varepsilon_{11} & d\,\varepsilon_{12} - d\,\Phi_3 & d\,\varepsilon_{13} + d\,\Phi_2 \\ d\,\varepsilon_{12} + d\,\Phi_3 & d\,\varepsilon_{22} & d\,\varepsilon_{23} - d\,\Phi_1 \\ d\,\varepsilon_{13} - d\,\Phi_2 & d\,\varepsilon_{23} + d\,\Phi_1 & d\,\varepsilon_{33} \end{bmatrix} \quad (2)$$

The 3D-visualization of bcc crystal rotation during deformation and microscopic deformation behaviors of the intermediate region were realized in following steps.

1. ND indicates the direction parallel to compressive or tensile direction and the direction normal to the rolling sheet plane as well. ND uses both α as measured from X([100]) axis on X([100])-Y([010])plane and subsequently β as measured from X([100])-Y([010]) plane toward Z([001]) axis in the position of α. Further, RD indicates rolling direction in the rolling plane and uses θ as measured from the intersecting line of X([100])-Y([010])plane and plane normal to ND, on the rollig plane. Strain tensor components $d\,\varepsilon_{11}, d\,\varepsilon_{12}, \cdots$ are defined by α, β and θ according to deformation style such as rolling,tensile elongation and compression.

2. Rotation $d\,\Phi_1, d\,\Phi_2$ and $d\,\Phi_3$ around the principal axes X[100],Y[010] and Z[001] respectively are obtained in the chosen case. These change values of angle parameters α, β and θ in every strain steps so that deformation textures are formed.

3. 3D-visualization for the crystal rotation uses the change of the angle parameters. 3D-visualization for the crystal rotation, however, needs also 3D-rotation of the coordinates(x,y,z) according to the change of the angle parameters. Thus,visualization of bcc crystal rotation is realized.

4. Deformation of the crystal is described using displacement variables,du, dv and dw in X[100],Y[010] and Z[001] respectively in equation (3).

$$\begin{aligned} du &= d\ \varepsilon_{11}dx + (-d\ \Phi_3 + (1/2)d\ \varepsilon_{12})dy + (d\ \Phi_2 + (1/2)d\ \varepsilon_{13})dz \\ dv &= (d\ \Phi_3 + (1/2)d\ \varepsilon_{12})dx + d\ \varepsilon_{22}dy + (-d\ \Phi_1 + (1/2)d\ \varepsilon_{23})dz \\ dw &= (-d\ \Phi_2 + (1/2)d\ \varepsilon_{13})dx + (d\ \Phi_1 + (1/2)d\ \varepsilon_{23})dy + d\ \varepsilon_{33}dz \end{aligned} \qquad (3)$$

Deformation of single bcc crystal is easily described according to (3). Deformation of an intermediate region between two crystals,i.e.,grain boundary needs a few additional ideas as follows. The midst of the intermediate region(grain boundary) has to have same displacement amount with both crystals in the three directions of the iron specimen. For that,the displacement du, dv and dw of each crystal are transformed by coordination change to displacement dU, dV and dW in the specimen direction by equation (4).

$$\begin{bmatrix} dU \\ dV \\ dW \end{bmatrix} = \begin{bmatrix} \cos\beta\cos\theta & \sin\alpha\cdots & \cos\alpha\cdots \\ \cos\beta\sin\theta & \sin\alpha\cdots & \cos\alpha\cdots \\ -\sin\beta & \sin\alpha\cos\beta & \cos\alpha\cos\beta \end{bmatrix} \begin{bmatrix} du \\ dv \\ dw \end{bmatrix} \qquad (4)$$

Using (4), it is taken in the calculation that both displacement dU, dV and dW and the work done by deformation calculated from each crystal orientation on both side have to approach respectively as near as possible at the midst of the intermediate region.

3 Results

3.1 Rotation

Table 1 shows example of rotation,i.e.,change of orientations with strain during

Table 1: Change of orientation for bcc crystal A and B during rolling.

	Crystal A	Crystal B
Initial state	(665)$[\bar{1}10]$ α=45.0, β=30.0, θ=0.0	(7 7 17)$[\bar{1}10]$ α=45.0, β=60.0, θ=0.0
Reduction:50.0%	(557)$[\bar{1}10]$ α=45.0, β=45.4, θ=0.0	(6 6 13)$[\bar{1}10]$ α=45.0, β=57.5, θ=0.0
Reduction:71.3%	(335)$[\bar{1}10]$ α=45.0, β=50.0, θ=0.0	(8 8 17)$[\bar{1}10]$ α=45.0, β=56.4, θ=0.0
Reduction:93.8%	(112)$[\bar{1}10]$ α=45.0, β=53.8, θ=0.0	(112)$[\bar{1}10]$ α=45.0, β=55.1, θ=0.0

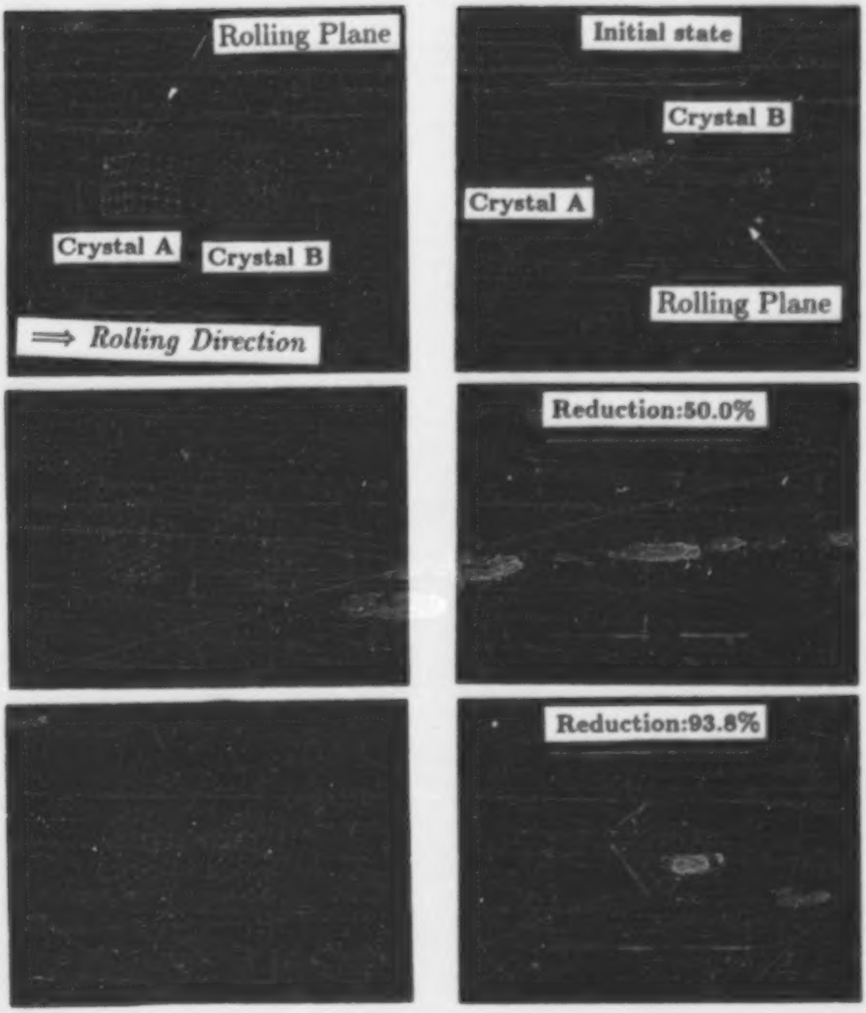
Rolling Plane
Crystal A
Crystal B
⟹ *Rolling Direction*
Initial state
Crystal B
Crystal A
Rolling Plane
Reduction:50.0%
Reduction:93.8%

Fig. 1: 3D-visualization pictures of crystal rotation during rolling deformation by the pencil glide theory for bcc iron crystal A and B in Table 1.

rolling by pencil glide theory for two bcc crystals of different initial orientation A(α = 45.0, β = 30.0, θ = 0.0(degree)) and B(α = 45.0, β = 60.0, θ = 0.0(degree)). Fig.1 shows pictures of 3D-visualization for rotation of bcc iron crystal A and B during rolling in Table 1. These pictures can be projected from arbitrary direction so that precise difference of angle can be measured.
Two crystals of different initial orientation come near to namely stable orientation of $\{112\}\langle110\rangle$ in bcc iron(Dillamore and Katoh 1974; Katoh 1985; Akisue 1996).

3.2 Deformation of the intermediate region

Two iron crystals of different initial orientation C($\alpha = 30.0, \beta = 45.0, \theta = 0.0$(degree)) and D($\alpha = 45.0, \beta = 60.0, \theta = 0.0$(degree)) are joined with the intermediate region.

Table 2 shows change of orientations of C and D during rolling by pencil glide theory which consequently affects also 3D-visualization deformation.

Fig.2 shows pictures of 3D-visualization for bcc iron crystal C and D during rolling in Table 2. 3D-visualization pictures in Fig.2 were,however,a little modified in visualization so as to have same order of thickness for easiness of comparison.

From Table 2 and Fig.2, a few points on deformation were made clear as follows.

- 3D visualization for deformation of bcc crystal is realized according to change

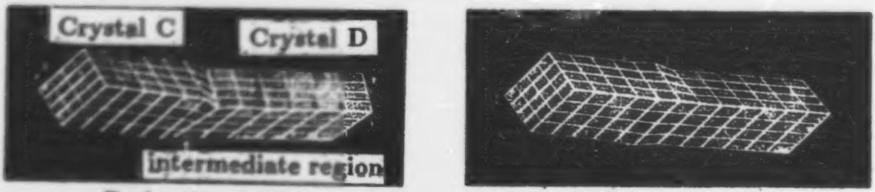

Reduction:6.7%

Reduction:81.1%

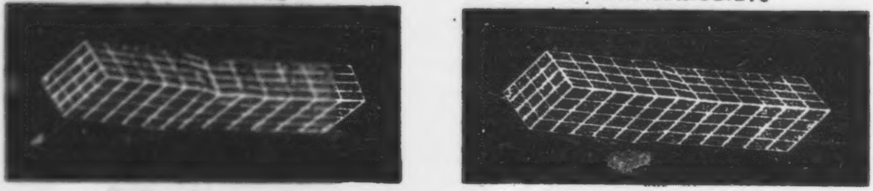

Reduction:13.0%

Reduction:84.6%

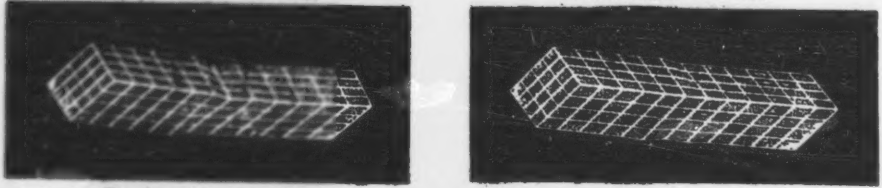

Reduction:18.8%

Reduction:92.3%

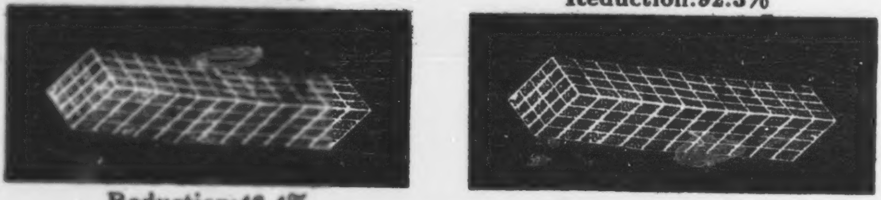

Reduction:48.4%

Reduction:94.6%

Fig. 2: Several shots from 3D-visualization of crystal deformation during rolling deformation by the pencil glide model for bcc iron crystal C, D and the intermediate region in Table 2.

Table 2: Change of orientations for bcc crystal C and D during rolling.

	Crystal C	Crystal D
Initial state	(12 7 14)[10 17 0]	(7 7 17)[110]
Reduction:6.7%	(536)[13 22 0]	(7 7 17)[110]
Reduction:13.0%	(759)[9 14 1]	(337)[110]
Reduction:18.8%	(9 7 12)[14 21 2]	(337)[110]
Reduction:46.4%	(12 11 19)[9 13 2]	(7 7 16)[110]
Reduction:81.1%	(8 7 13)[681]	(8 8 17)[110]
Reduction:84.6%	(8 7 13)[681]	(8 8 17)[110]
Reduction:92.3%	(15 14 26)[10 13 1]	(112)[110]
Reduction:94.6%	(22 21 39)[10 13 1]	(112)[110]

in their orientations and displacements with strain. Deformation of the intermediate region(grain boundary) is affected by orientations of both crystals. The intermediate region seems to be hardly deformed when a difference of orientations in two crystals is large.

- With increasing strain,i.e.,rolling reduction, the bi-crystal including the intermedate region, cooperates to deform uniformly due to the approach in orientations calculated by pencil glide theory in the experimental case.

4 Conclusion

3D-visualization of bcc iron crystal rotation by the model based on pencil glide theory was displayed irrespectively of initial orientation and of deformation style, where the change of bcc crystal orientation conformed considerably to the experimental results.

3D-visualization of deformation of the intermediate region sandwiched by two crystals of different orientations during rolling, was also realized with both pencil glide theory and such physical continuity in the region as macroscopic displacement and work done by deformation.

5 References

Akisue,O. (1996) Summary of Texture of iron and steel. *Proc.J.I.M.Symposium on texture(Japanese)*,pp.33-6.

Bishop,J.F.W. and Hill,R. (1951) A theoretical derivation of the plastic properties of a polycrystalline face-centered metal. *Phil.Mag.*, Vol.42,pp.1298-307.

Dillamore,I.L. and Katoh,H. (1974) A comparison of the observed and predicted deformation textures in cubic metals. *Metal Science*, Vol.8,pp.21-7.

Katoh,H. (1985) Deformation texture. *Proc.J.I.M.Seminar on Texture(Japanese)*, pp.15-30.

Kochs,U.F. (1970) The relation between polycrystal deformation and single crystal deformation. *Met.Trans.AIME*, Vol.1,pp.1121-43.

Ookubo,T. (1968) Plasticity of cubic metal under constraint condition. *Plasticity (Japanese)*, Vol.9,pp.681-90.

Taylor,G.I. (1938) Plastic strain in metals. *J.Inst.Metals*, Vol.62,pp.307-24.

ANALYSIS OF TEXTURE EVOLUTION OF CUBIC METALS BY FULL CONSTRAINT AND TWO SELF-CONSISTENT VISCOPLASTIC MODELS

K. H. OH

School of Materials Science and Engineering, Seoul National University
San 56-1 Shinrim-dong Kwanak-ku Seoul 151-742, Korea and
Research Institute of Advanced Materials

Abstract

The texture evolutions of FCC metals during tension, compression and rolling have been analyzed by full constraint and two self-consistent models with large deformation theory of viscoplastic materials. The final textures predicted from an initial random texture during tension and compression showed similar behaviors in full constraint and two self-consistent models. The final rolling texture of full constraint model was D-type texture, but those of two self-consistent model were Copper type texture due to a lower interaction. The effect of rate sensitivity during rolling was analyzed. The texture evolutions at various rate sensitivities are the same at two self-consistent models due to a high symmetry of octahedral slip system.

Keywords: Full constraint, Self-consistent models, Rate sensitivity, Major component

1 Introduction

In polycrystal plasticity, two extreme points of view have been used, Taylor and Sachs approaches. The Taylor approach requires a complete strain compatibility between single crystals and matrix, which results in a uniform plastic strain condition, called the full constraint model. The Sachs approach requires a stress equilibrium, which results in a uniform stress condition. The self-consistent approach lies between Sachs and Taylor approaches and takes into account both compatibility and equilibrium conditions. The self-consistent condition is intermediate and satisfies a condition that the volumetric averages of stress and strain rate over single crystals are the macroscopic stress and strain rate of polycrystal.

The viscoplastic self-consistent schemes have been formulated. (Molinari and Toth 1994;Lebensohn and Tome 1993) The application of the equilibrium and compatibility equations gives an integral equation, where a single crystal in the polycrystal can be regarded as an inclusion embedded in a homogenous equivalent medium (HEM). The interaction law and the constitutive equation could be solved together by a Newton Raphson method. (Oh 1997)

In this study, the viscoplastic full constraint and two self-consistent schemes were used for the analysis of texture evolution in cubic metals during tension, compression and rolling. The evolution of major component during rolling was examined at various rate sensitivities.

2. Viscoplastic deformation of polycrystal

2.1 Stress-strain relation (Hutchinson 1976)

The rate sensitivity of slip can be described by a power law relation between the shear rate $\dot{\gamma}^s$ and the resolved shear stress τ^s on slip system s. m is the rate sensitivity. $\dot{\gamma}_o^s$ and τ_o^s are the reference shear rate and the reference critical resolved shear stress, respectively. The strain rate tensor **D** can be calculated as follows.

$$\frac{\tau^s}{\tau_o^s} = \mathrm{sgn}(\dot{\gamma}^s)\left|\frac{\dot{\gamma}^s}{\dot{\gamma}_o^s}\right|^m \quad \text{and} \quad \mathbf{D}_{ij} = \sum_s \mathbf{R}_{ij}^s\left(\frac{\mathbf{R}_{kl}^s\sigma'_{kl}}{\tau_o^s}\right)\left|\frac{\mathbf{R}_{kl}^s\sigma'_{kl}}{\tau_o^s}\right|^{\frac{1}{m}-1} \tag{1}$$

where σ' and **R** are the deviatoric Cauchy stress tensor and the Schmid tensor of the slip system s, respectively. A first order Taylor expansion and secant expansion of the stress-strain relation give the following equations (2a) and (2b), respectively.

$$\sigma'_{ij} = \mathbf{A}_{ijkl} : \mathbf{D}_{kl} + \sigma'^{o}_{ij} \quad \text{and} \quad \mathbf{D}_{ij} = \mathbf{M}_{ijkl} : \sigma'_{kl} + \mathbf{D}^{o}_{ij} \tag{2a}$$

$$\sigma'_{ij} = \mathbf{A}^{(s)}_{ijkl} : \mathbf{D}_{kl} \quad \text{and} \quad \mathbf{D}_{ij} = \mathbf{M}^{(s)}_{ijkl} : \sigma'_{kl} \tag{2b}$$

A and M are the tangent stiffness and compliance tensor, respectively. The superscript o and s denote the back extrapolating tensor and the secant tensor, respectively. These formulations are the bases of the self-consistent models and are assumed for the single crystals and for whole polycrystal. The bar over tensor property denotes the macroscopic property over polycrystal.

2.2 Self-consistent model

2.2.1 Isotropic self-consistent model (Molinari and Toth 1994)

Using the equilibrium and compatibility equations can be solved by a Green function method. The proper differentiation and symmetrization of the equations can give the following solution for the strain rate tensor **D**, by ignoring the interaction between single crystals, which is called the 1-site formulation. In plastically isotropic material, the $\overline{\mathbf{A}}^{(s)}$ can be given as follows. I and μ are the fourth order Kroneck delta and the plastic modulus, respectively.

$$\sigma'_{ij} - \overline{\sigma}'_{ij} = \sigma'_{ij} - \overline{\mathbf{A}}^{(s)}_{ijmn} : \overline{\mathbf{D}}_{mn} = \alpha\left(\Gamma^{-1}_{ijkl} + \overline{\mathbf{A}}^{(s)}_{ijkl}\right) : \left(\mathbf{D}_{kl} - \overline{\mathbf{D}}_{kl}\right) \tag{3}$$

$\alpha = 0$: Sachs Model $\quad \alpha = \mathrm{m}$: Tangent Model $\quad \overline{\mathbf{A}}^{(s)}_{ijkl} = \mu \mathbf{I}_{ijkl}$

$\alpha = 1$: Secant Model $\quad \alpha = \infty$: Taylor Model

2.2.2 Anisotropic self-consistent model (Lebensohn and Tome 1993)

At single crystals embedded in HEM, the following equation can be obtained.

$$\tilde{\mathbf{D}}_{ij} - \mathbf{D}^{*}_{ij} = \overline{\mathbf{M}}_{ijkl} : (\sigma'_{kl} - \overline{\sigma}'_{kl}) \tag{4}$$

D^*_{ij} is a fictitious transformation strain rate due to the replacement of the inhomogeneity as an equivalent inclusion. At the uniform strain rate in the inclusion, the solution of the viscoplastic inhomogeneity problem leads to the interaction equation. Using interaction equation, $\overline{M}^{(s)}_{ijkl}$, the secant viscoplastic modulus of polycrystal can be obtained from the following transcendental equation by a numerical way. Using the obtained $\overline{M}^{(s)}$, the stress state of each single crystal can be solved.

$$\overline{M}^{(s)}_{ijkl} = < M^{(s)}_{ijmn} : (M^{(s)}_{mnpq} + \tilde{M}_{mnpq})^{-1} : (\overline{M}^{(s)}_{pqkl} + \tilde{M}_{pqkl}) > \qquad (5)$$

3. Calculation procedure

The rate sensitivity m was set to be 0.05 for tension and compression. The slip system is {111}<110> slip system. Full constraint model was calculated at the scalar parameter of $\alpha = \infty$. Three deformation modes were considered; tension, compression and rolling. The effect of the rate sensitivity on the texture evolution during rolling was examined at various rate sensitivities such as 0.05, 0.1, 0.2 and 0.5. To obtain the ODF value of a component during deformation, single orientations were converted into the ODF by "Gaussian standard function". (Choi et al. 1999)

4. Result and discussion

4.1 Tension

Figs 3 (a), (b) and (c) show the inverse pole figures along tension axis after tensile strain of 1 obtained by full constraint Taylor model and two self-consistent models, respectively. Major component along loading axis is {111} fiber and minor component is {100} fiber. The reported {111} to {100} fiber ratio is about 2 in pure Copper. The {111} to {100} fiber ratio from full constraint, isotropic and anisotropic self-consistent schemes are 2.2, 2.5 and 1.1, respectively. The ratios from full constraint and the isotropic self-consistent model are closer to the experimentally measured ratio than that from the anisotropic self-consistent models.

4.2 Compression

Figs 4 (a), (b) and (c) show the inverse pole figure along compression axis after compression strain of 1 by full constraint Taylor model and two self-consistent models, respectively. The orientations are mainly concentrated at {110} fiber. It is in good agreement with experimental results. The concentration degree of {110} fiber from self-consistent model is larger that that from Taylor model and is in better agreement with experiments. The maximum intensities of the two inverse pole figure from self-consistent models are the same, which represents the same texture evolution of the two self-consistent models.

4.3 Rolling

Figs 3 show the calculated (111) pole figures from the full constraint model after rolling strain of 1. Figs 4 and 5 show the calculated (111) pole figures from the isotropic and anisotropic self-consistent models after rolling strain of 1, respectively. It is well known that Taylor model predicts D-Texture. During the experimental rolling of Copper, Copper component can be obtained at the rolling strain of 1. Two self-consistent models can predict the Copper component at the rolling strain of 1. The Copper component could be obtained due to lower interaction between single crystals and matrix. Gambin *et al.* reported that using lower bound rate sensitivity model, Copper component could also be obtained at rate sensitivity of 0.2.[Gambin]. But 0.2 is unacceptable in Copper and the experimentally acceptable value is 0.05 or less. At the low rate sensitivity of 0.05, the major Copper component {112}<111> and minor Brass component {110}<111> evolved. As shown in Figs 4 and 5, the major Copper and minor Brass components develop at the low rate sensitivity and the intensities of the components decrease with increasing rate sensitivity.

Fig 6 shows the calculated ODF values of Copper and Brass components, respectively, during rolling from the isotropic and anisotropic self-consistent models. The ODF intensities of Copper and Brass components increase almost linearly with increasing rolling strain at the two self-consistent models. The symmetric part of the internal shear strain is equivalent to the applied strain and the anti-symmetric part of the internal strain is equivalent to the lattice rotation rate in case of rolling. In case of rolling, the macroscopic rotation rate and the reorientation of the single crystal are zero, because the antisymmetric part of Eshelby tensor is zero in spherical shape. Thus the linear increase of the applied strain causes the linear increase of the internal shear strain and consequently the linear increase of lattice rotation rate leading to the almost linear development of major Copper component.

The intensities of Copper component at the two self-consistent models are almost same at the same rate sensitivity. The same ODF value shows that the evolution mechanisms of the two self-consistent models are similar. The similar texture evolution in the two models shows that the anisotropy of $\overline{\mathbf{M}}^{(s)}$, is low. The texture evolutions in highly anisotropic materials are different from isotropic behavior, because $\overline{\mathbf{M}}^{(s)}$ is highly anisotropic due to the low symmetry of slip system. But in the cubic metals, the anisotropy is low, because the {111}<110> slip system has the cubic symmetry. The high symmetry of slip system give rise to the high symmetry of $\overline{\mathbf{M}}^{(s)}$, leading to the almost isotropic behavior of texture evolution in fcc metals.(Oh 1997)

5. Conclusions

Full constraint Taylor and two self-consistent models were formulated using rate sensitivity material model with large deformation plasticity. The final texture during tension and compression by two self-consistent model showed better agreement than that by full constraint model. The rolling texture from full constraint Taylor model was D-type, but that from two self-consistent models was Copper component due to the lower interaction between single crystals and matrix. With increasing rate sensitivity, rate of texture evolution decreases. The major Copper component increases linearly with increasing rolling strain. The texture evolutions at various rate sensitivities are the same at both self-consistent models due to high symmetry of slip system.

6. References

Choi S.-H.,Cho J.H., Barlat F., Chung K., Kwon J.W. and Oh K.H. (1999) Prediction of Yield Surfaces of Textured Sheet Metals *Met. Trans.* A Vol 30A pp. 377-386

Gambin and F. Barlat,.(1997)Modeling of Deformation Texture Development based on Rate independent crystal plasticity, *Int. J. Plasticity* Vol 13 pp. 75-85

Hutchinson W. (1976), Bounds and Self-consistent estimates for creep of polycrystalline Material. *Proc. R. Soc.* **A348**, pp. 101-127.

Lebensohn R. and Tome C. (1993), Self-consistent Anisotropic Approach for the

Simulation of Plastic Deformation And Texture Development of Polycrystal : Application to Zirconium Alloys, *Acta metall.* **41**, pp. 2611-2624

Molinari A. and Toth L.S. (1994) Tuning a self consistent viscoplastic model by Finite Element Results. *Acta Metall.* **42**, 2453-2466

Oh K.H. (1997) Analysis of Texture Evolution by Isotropic and Anisotropic Self-consistent models *Metals and Materials* **5**, pp17-23

Acknowledgement

The authors wish to acknowledge the financial support of the Korea Research Foundation made in the program year of (1998)

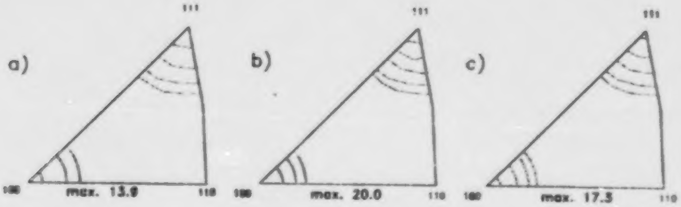

Fig 1. Inverse Pole figure along Tensile axis after tensile strain of 1.
a) Full constraint b) Isotropic Self consistent c) Anisotropic Self-consistent

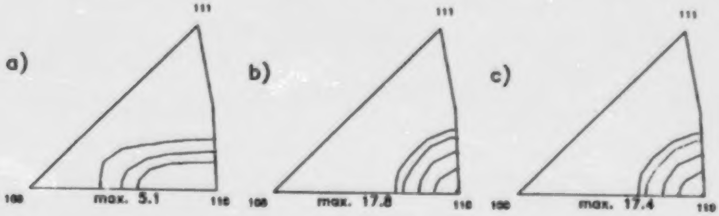

Fig 2. Inverse Pole figure along Compression axis after tensile strain of 1.
a) Full constraint b) Isotropic Self consistent c) Anisotropic Self-consistent

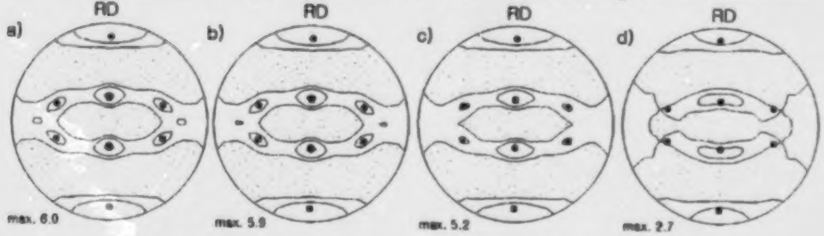

Fig 3. (111) Pole figure calculated by Full constraint model at various rate sensitivities The symbols denote Copper component. a) 0.05 b) 0.1 c) 0.2 d) 0.5

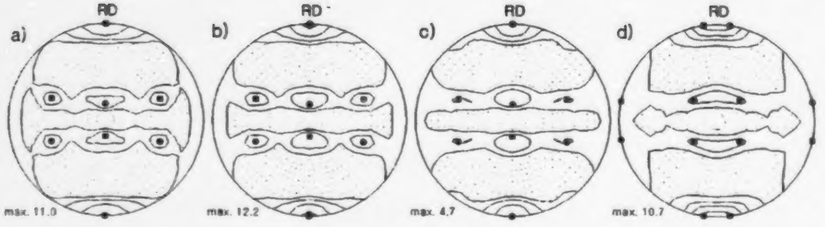
a)
RD
max. 11.0
b)
RD
max. 12.2
c)
RD
max. 4.7
d)
RD
max. 10.7

Fig 4. (111) Pole figure calculated by Isotropic Self-consistent model at various rate Sensitivities. The symbols denote Copper component in a),b),c) and Brass component in d). a) 0.05 b) 0.1 c) 0.2 d) 0.5

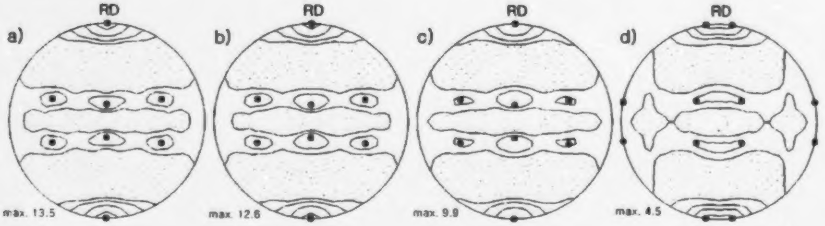
a)
RD
max. 13.5
b)
RD
max. 12.6
c)
RD
max. 9.9
d)
RD
max. 4.5

Fig 5. (111) Pole figure calculated by Anisotropic Self-consistent model at various rate sensitivities The symbols denote Copper component in a),b),c) and Brass component in d). a) 0.05 b) 0.1 c) 0.2 d) 0.5

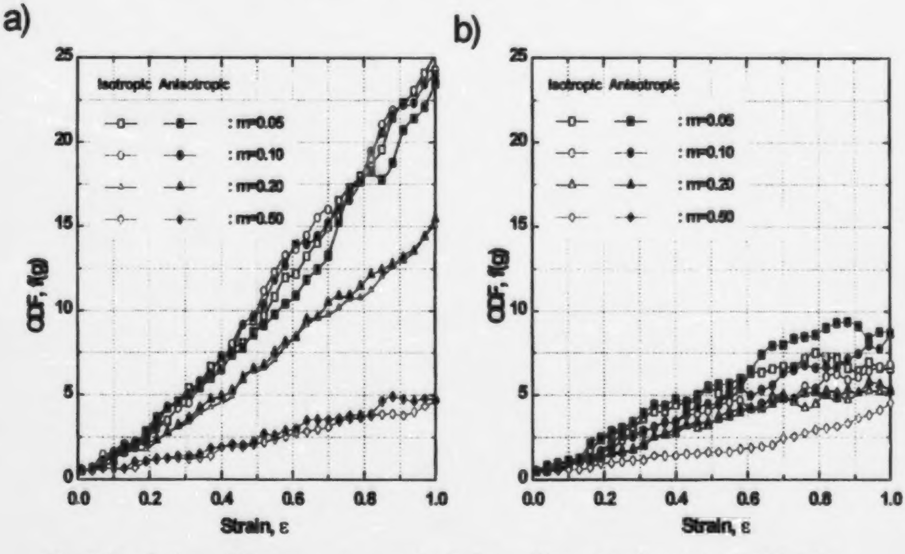

Fig 6. Evolution of Texture components during rolling at various rate sensitivities
a) Copper component b) Brass component

THE ROLE OF TAYLOR FACTOR IN STRAIN HARDENING

L.S. TÓTH*, H.P. STÜWE**, M. ZEHETBAUER*** AND I. KOPACZ***
*Institut Supérieur de Génie Mécanique et Productique,
Université de Metz – Ecole Nationale d'Ingénieur de Metz, Metz, France
**Erich Schmid Institute of Materials Science, Austrian Academy of Sciences, Leoben, Austria
***Institute of Materials Physics, University of Vienna, Austria

Abstract

The Taylor factor is calculated for different strain paths and its role in the macroscopic hardening curves is examined. For the case of single crystals, some analytical formulas are derived, while numerical results are presented for polycrystals using the Taylor and self-consistent viscoplastic models. It is also discussed in the present work how to construct equivalent stress - equivalent strain curves on the basis of crystallographic slip. It is shown that " textural hardening " - which is represented by the Taylor factor - can be either positive or negative and is especially important when intrinsic hardening is low (in easy glide of single crystals, or at late stages of deformation when dislocation hardening is exhausted). Therefore they play a role in plastic deformation instabilities which are examined for both single and polycrystals in the present work.

Keywords: Crystal plasticity, polycrystal plasticity, Taylor factor, strain hardening, equivalent stress-strain curves, plastic instabilities

1. Introduction

The focus of the present paper is on strain hardening which has a twofold origin:

i. intrinsic hardening due to crystallographic slip and the accumulation of defects (mostly dislocations),
ii. geometrical (or "textural") hardening which is a consequence of the rotation of grains during plastic strain.

While the first effect has been studied extensively in the past, little attention was paid to the latter one, believed to be negligible. However, when large strains are involved, individual grains of the polycrystal may rotate to new ideal positions during which they exhibit variations in their plastic behavior. That is, the very same grain can be relatively soft or hard, even in the absence of intrinsic hardening. Such variations can be well represented by the Taylor factor which, for a uniaxial test, can be defined simply as the ratio of the sum of crystallographic slip rates and the prescribed strain rate ($\dot{\varepsilon}$):

$$M = \frac{1}{\dot{\varepsilon}} \sum_{s=1}^{n} |\dot{\gamma}_s| \tag{1}$$

(s: slip system index, n: number of slip systems in the grain). When this relation is used in the equality of external and internal plastic work rates, one obtains for the external stress level σ:

$$\sigma = \tau_c M, \tag{2}$$

where τ_c is the critical resolved shear stress for slip in a slip plane, taken to be equal in all systems. A change in grain orientation affects M and therefore σ so that this is called “geometric” softening or hardening.

The Taylor factor can be also employed in the construction of equivalent stress - equivalent strain curves, when hardening is studied on different strain paths and comparisons are made. This problem is addressed in the present work in order to compare the hardening characteristics in tension, compression, rolling and torsion.

Finally, as M can also *decrease* in certain cases, it can lead to a reduction of strain hardening which may affect the conditions of plastic strain localization. It represents additional terms in a Considère type of analysis which will be carried out here, in an analytic way for tension of single crystals, and numerically for polycrystal deformation.

2. The Taylor factor, equivalent stress and strain for single and polycrystals

These quantities are defined in Kopacz et al. (1999), here only the resulting formulas are recalled.

The rate of resolved shear strain is defined as:

$$\dot{\Gamma}_r = \sum_{s=1}^{n} |\dot{\gamma}_s| \text{ (single crystal)}, \qquad \bar{\dot{\Gamma}}_r = \sum_{i=1}^{N} \left(\sum_{s=1}^{n} |\dot{\gamma}_s^i| \right) V_i \text{ (polycrystal)}, \tag{3}$$

where the i-index signifies grain number i; V_i its volume fraction, and N is the total number of grains. To take into account the multi-component nature of the prescribed (imposed) strain rate, M is defined for the case of single and polycrystal as follows:

$$M = \dot{\Gamma}_r / \dot{\varepsilon}_{eqv} \text{ (single crystal)}, \qquad M = \bar{\dot{\Gamma}}_r / \bar{\dot{\varepsilon}}_{eqv} \text{ (polycrystal)}, \tag{4}$$

where $\dot{\varepsilon}_{eqv}$ and $\bar{\dot{\varepsilon}}_{eqv}$ are the von Mises equivalent strain rates for the single crystal and the polycrystal, respectively. The equivalent stress can be defined with the help of the equality of the external and internal work rates, which yields:

$$\tau_r = \frac{\sigma_{ij}\dot{\varepsilon}_{ij}}{M\dot{\varepsilon}_{eqv}} \text{ (single crystal)}, \qquad \bar{\tau}_r = \frac{\sigma_{ij}\dot{\varepsilon}_{ij}}{\overline{M}\dot{\bar{\varepsilon}}_{eqv}} \text{ (polycrystal)}. \tag{5}$$

The equivalent resolved shear strain can be obtained by integration of M:

$$\Gamma_r = \int M d\varepsilon_{eqv} \text{ (single crystal)}, \qquad \overline{\Gamma}_r = \int \overline{M} d\bar{\varepsilon}_{eqv} \text{ (polycrystal)}. \tag{6}$$

3. 'Semi-experimental' evolution of the Taylor factor during polycrystal deformation

As can be seen from the above definitions, the M-factor can be obtained if the slip distribution is known. The latter can be calculated by suitable crystal plasticity simulations if the orientation distribution of the grains is available. In order to follow the evolution of M, several ODFs were measured successively during large strain deformation of OFHC copper on three strain paths: compression (at 12 strains), rolling (at 11 strains) and torsion (at 4 strains). The ODFs were discretized to several thousand orientations, then the Taylor (FC) and the Self-Consistent (SC) viscoplastic models were employed to obtain the Taylor factors (for the polycrystal model, see Molinari and Tóth (1994)). Here results are shown only for the SC model, see Fig. 1. (For the FC case, the obtained M values were up to 20% higher than for the SC model.) The dots in Fig. 1 denote the M-values at strains where the ODF was measured. The polycrystal simulations were also continued from each of these starting points up to large strains; the results are indicated by the solid lines.

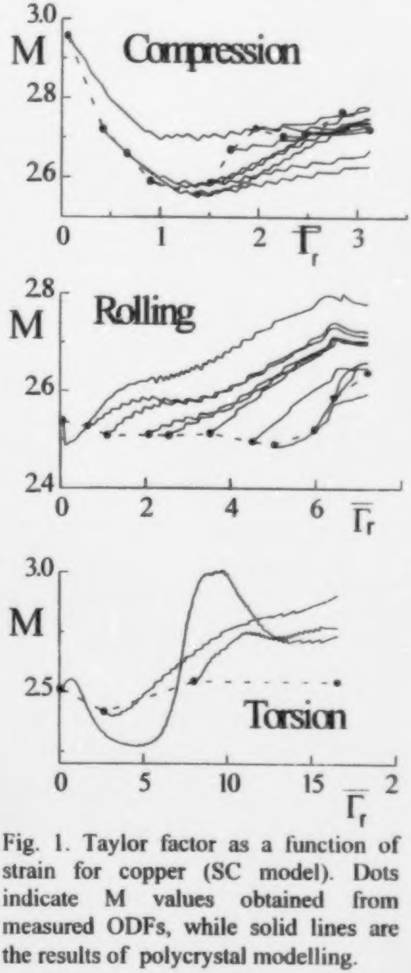

Fig. 1. Taylor factor as a function of strain for copper (SC model). Dots indicate M values obtained from measured ODFs, while solid lines are the results of polycrystal modelling.

It can be seen from Fig. 1 that the polycrystal simulations reproduce the main tendencies of the M-factor evolution (excepting torsion at very large strains) while failing to predict them with precision. Note that for compression there was a strong <111> initial texture – which explains the rapid drop of M at the beginning of deformation – in contrast to all other strain paths studied where the initial textures were almost isotropic.

4. Equivalent stress – equivalent strain curves

Knowing the Taylor factor, eqs. 5 and 6 can be used to construct equivalent stress-equivalent strain curves. Concerning the M-values, the most reliable ones are those which are obtained from the experimental ODFs. As they are only known at discrete points, a polynomial fitting procedure was applied to obtain continuous $M(\Gamma_r)$ functions. They were then used to calculate the equivalent resolved shear stress (from eq. 5) and the equivalent resolved shear strain (from eq. 6 by integration). In this way, the measured hardening curves (see in Fig. 2) could be converted into equivalent stress-strain curves, the latter are displayed in Fig. 3.

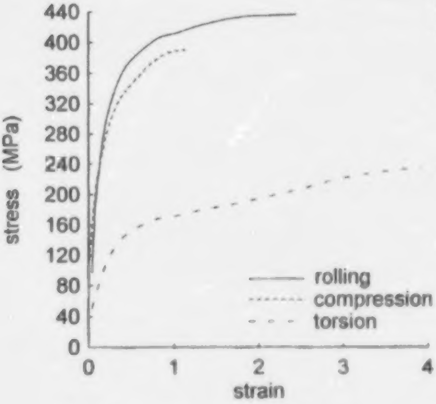

Fig. 2. Strain hardening curves measured for copper in rolling, compression and torsion.

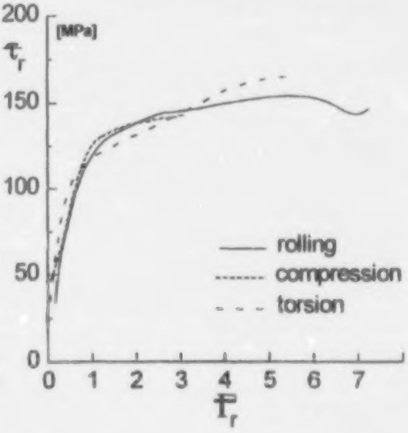

Fig. 3. Equivalent stress-strain curves using semi-experimental Taylor factors.

The obtained equivalent stress-equivalent strain curves in Fig. 3 nearly coincide. This result indicates that a unique hardening rule may exist which can be based on crystallographic slip. The small differences left may arise for two reasons. One is the possible differences in dislocation pattern formations, while the other can be the differences in the strain rates used in the tests (strain rate dependence of hardening (Zehetbauer and Seumer, 1993; Stüwe and Les, 1998)). Both of them influence directly the measured stress levels in Fig. 1 and are not considered in the polycrystal model which was used to obtain the Taylor factor.

5. The role of Taylor factor in the stability of deformation

According to the classical Considère criterion, stability of plastic deformation in a tensile test requires that the stress-normalised hardening rate is larger than unity:

$$\frac{1}{\sigma}\frac{d\sigma}{d\varepsilon} > 1 \ , \qquad (7)$$

where σ is the stress and ε is the tensile strain. In the present analysis, intrinsic and geometrical hardening are distinguished by considering the stress to depend on both the resolved shear stress $\tau_r(\varepsilon)$ and the Taylor factor $M(\varepsilon)$: $\sigma=\sigma(\tau_r(\varepsilon),M(\varepsilon))$. A refined version of the Considère criterion can then be obtained (Stüwe, 1998):

$$\frac{1}{\tau_r}\frac{d\tau_r}{d\varepsilon} + \frac{1}{M}\frac{dM}{d\varepsilon} > 1 \ , \qquad (8)$$

where the first and second terms represent intrinsic and geometrical hardening, respectively. Relation (8) can be rewritten in a form similar to (7):

$$\frac{1}{\tau_r}\frac{d\tau_r}{d\gamma_r} > \frac{1}{M}\left(1-\frac{dM}{d\gamma_r}\right) \ , \qquad (9)$$

where γ_r is the resolved shear strain. Here the left hand side is the stress normalized intrinsic hardening rate while the right hand side is related to the geometrical hardening; they will be denoted as H and S, respectively:

$$H \equiv \frac{1}{\tau_r}\frac{d\tau_r}{d\gamma_r} \ , \qquad S \equiv \frac{1}{M}\left(1-\frac{dM}{d\gamma_r}\right) \ . \qquad (10)$$

S can be adopted as a stability parameter of plastic deformation. It can be obtained from crystal plasticity calculations. In the present work, results are shown for the case of tensile deformation of fcc and hcp single crystals oriented for single slip, as well as for fcc polycrystals.

For single slip, analytical calculations can be carried out to obtain the S parameter. The results are shown in the unit triangle of the stereographic projection; for fcc crystals in Fig. 4, for the hexagonal case in Fig. 5.

With our new notation, the stability criterion reads: H>S. That is, in order to assure stable plastic deformation, the intrinsic hardening H (in the present case, during easy glide) has to be higher than the S values displayed in Figs. 4 and 5.

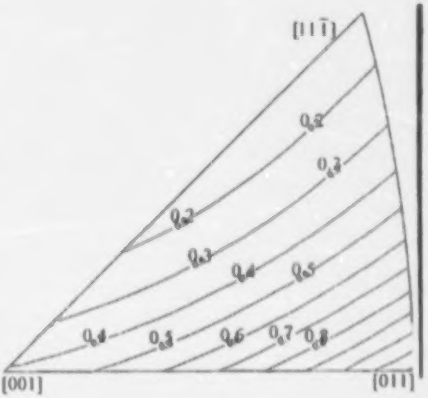

Fig. 4.
Isovalue-map of the S stability parameter in the unit triangle of fcc crystals for tensile deformation in single slip.

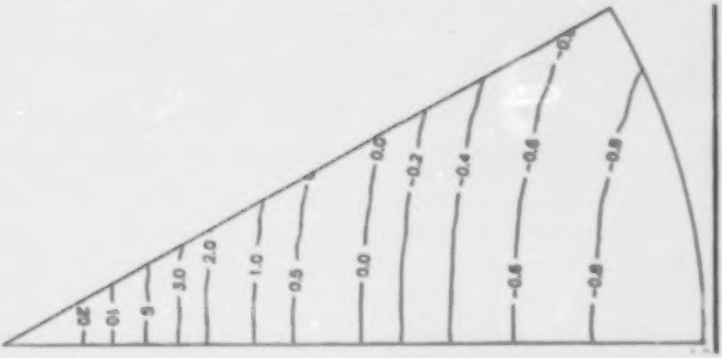

Fig. 5. Isovalue map of the geometrical stability parameter (S) for single slip in the unit stereographic triangle for hexagonal crystals in tension.

We can see that there has to be intrinsic hardening during easy glide for any orientation in fcc crystals, while it is necessary only for a certain domain of orientations in the hexagonal case.

For the polycrystal case, simulations have been carried out for tensile deformation of an isotropic orientation distribution of 500 grains with the Taylor viscoplastic model for fcc crystals. In order to approach the rate insensitive limit, a very low m value was applied for the strain rate sensitivity index (m=0.01). The obtained stability parameter is shown in Fig. 6. It can be seen that texture evolution affects the stability by an amount of about ~10%.

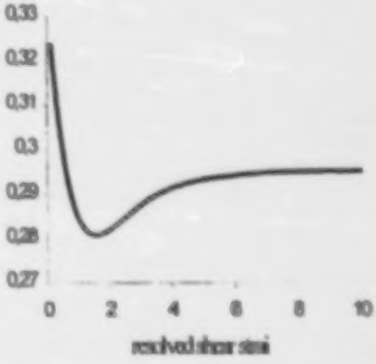

Fig. 6. Evolution of the stability factor during tensile deformation.

A detailed discussion of possible plastic instabilities in view of experimental easy glide hardening data is to be published in due time (Stüwe and Tóth, 1999).

6. References

Kopacz, I., Tóth, L.S., Zehetbauer, M. and Stüwe, H.P. (1999) " Large strain hardening curves corrected for texture development ", *Modelling and Simulation in Materials Science and Engineering*, in press.

Molinari A. and Tóth, L.S. (1994) *Acta Met. Mat.*, Vol. **42**, pp. 2453-2458.

Stüwe, H.P. (1998) "Examples of strain localization", ch.1 in: *Localization & Fracture Phenomena in Inelastic Solids*, ed. P. Perzyna, Springer, p.1.

Stüwe H.P. and Les P. (1998) *Acta Mater.*, Vol. 46, p. 6375.

Zehetbauer M. and Seumer V. (1993) *Acta Metall. Mater.*, Vol. 41, p. 577.

A GENERALIZATION OF TAYLOR-BISHOP-HILL THEORIES AND RATE-DEPENDENT SLIP MODEL IN CRYSTAL PLASTICITY

K. SEKINE
School of Materials Science and Chemical Engineering, Faculty of Engineering,
Yokohama National University, Yokohama, Japan

Abstract

In the Taylor-Bishop-Hill theories of crystal plasticity for the prediction of deformation textures, the problem of determining the shear rate on a slip system is reduced to the optimization procedures under linear constrains. On the other hand, the rate-dependent slip theory which is modeled by a power law relationship between the shear rate and the resolved shear stress on a slip system is formulated as the non-linear simultaneous equations system with respect to the stresses. It has been recognized to date that the Taylor-Bishop-Hill theories are essentially distinct from the rate-dependent slip one. The purpose of this paper is to generalize the Taylor theory as a norm minimization problem in the finite dimensional Banach space in terms of the mathematical programming, and then to demonstrate that the rate dependent slip theory is included in such generalized Taylor-Bishop-Hill crystal plasticity ones. Finally, the mathematical formulation for the extended relaxed constraints model including the rate-dependent slips is comprehensively presented based on · such generalized Taylor-Bishop-Hill theories.

Keywords: Crystal plasticity, deformation texture, optimization problem, Banach space, relaxed constraints model

1 Introduction

When predicting the evolution of deformation texture in crystalline materials caused by large plastic deformation, the Taylor-Bishop-Hill analysis (Taylor 1938 ;Bishop and Hill 1951a,1951b) have been commonly employed. In methods of this kind for rate-independent plasticity, the problem of finding the active slip systems and their shear rates $\dot{\gamma}^{(k)}$ in a particular crystallite is based either on the minimization of the internal work or the maximization of the stress work, and these two procedures have been demonstrated to be equivalent (Chin and Mammel 1969). However, when these methods are applied for calculating the lattice rotations of crystallite, we encounter the non-uniqueness of solution in the determination of shear rates $\dot{\gamma}^{(k)}$(Anand and Kothari 1996). To overcome this limitation of rate-independent crystal plasticity theory, many workers use a simple rate-dependent slip model which is expressed by a following power type law relationship between the shear rate $\dot{\gamma}^{(k)}$ and resolved shear stress $\tau^{(k)}$ on the slip system k (Asaro and Needleman 1985),

$$\tau^{(k)} = \tau_0 sgn \ (\dot{\gamma}^{(k)}) \left| \dot{\gamma}^{(k)} / \dot{\gamma}_0 \right|^m \tag{1}$$

In the above equation, τ_0 and γ_0 are slip system deformation resistance and reference rate of shearing respectively, and the parameter m is corresponding to the material rate sensitivity. The rate-independent limit is $m \to 0$. If we employ this rate dependent model for calculating the deformation texture, the model is formulated as the non-linear simultaneous equation problem with respect to the stresses. And, this predicts uniquely the solution.

It has been most commonly recognized to date that the Taylor-Bishop-Hill theories of the rate independent case are essentially distinct from the rate-dependent slip theory. In this paper, first the problem of determining shear rates on each slip system based on the Taylor theory is regarded as a norm minimization problem in the finite Banach space consisting of the whole sets whose members are the shear rate $\dot{\gamma}^{(k)}$ on slip systems, and then the Taylor-Bishop-Hill theories are re-defined more generally. Next, as a result of generalization of the theories, it is demonstrated that the rate dependent approach of Asaro and Needleman can be included in such generalized Taylor-Bishop-Hill crystal plasticity theories. Furthermore, this paper presents the comprehensive mathematical formulation for the extended version including the rate-dependent slips for the relaxed constraints model (Kocks and Chandra 1982;Van Houtte 1984) based on the generalized Taylor-Bishop-Hill theories.

2 Generalization of the Taylor theory

We first consider N-dimensional linear vector space V^N (real vector space), the points of which are defined by a set of shear rates $\dot{\gamma}^{(k)}$ on all possible slip systems, as denoted by

$$\Gamma = (\dot{\gamma}^{(1)}, \dot{\gamma}^{(2)}, \dot{\gamma}^{(3)}, \cdots\cdots, \dot{\gamma}^{(N)}) \in V^N \tag{2}$$

and the origin of which is described by

$$\Gamma_0 = (0,0,0, \ \cdots\cdots, 0) \in V^N \tag{3}$$

To endow the vector space V^N with the geometrical structure for making it more useful for analysis of physical phenomena, we introduce into V^N the metric notion of distance function $d(\Gamma_1, \Gamma_2)$ or norm $\| \Gamma \|$. This complete real vector space equipped with a distance function or a norm is called "a finite dimensional Banach space".

With this Banach space, the Taylor analysis can be interpreted as a optimization problem for minimizing the distance from the origin Γ_0 to the point Γ under the linear constraints that all the slip rates linearly combined must achieve the given strain rate D_{ij}. We then can state the generalized Taylor theory in the following terms,

$$E'_T(\Gamma)= d(\Gamma_0,\ \Gamma) \quad \rightarrow \quad minimize$$

subject to
$$D_{ij} = \frac{1}{2}\sum_{k=1}^{N}(m_{ij}^{(k)} + m_{ji}^{(k)})\dot{\gamma}^{(k)} \qquad (4)$$

where $m^{(k)}=b^{(k)}\otimes n^{(k)}$ is the Schmid tensor, and $b^{(k)}$ and $n^{(k)}$ denote the unit slip direction and unit slip plane normal of *k*th slip system , respectively.

Since the distance function of $d(\Gamma_0\ ,\Gamma)$ would be equivalent to the norm $\|\ \Gamma\ \|$, the object function in the above optimization problem may be replaced by the norm attached to the point Γ. And, as a general candidate for the norm introduced into the finite dimensional Banach space, we may take the so-called "*p*-norms" defined by

$$\|\Gamma\|_p = \left(\sum_{k=1}^{N}|\dot{\gamma}^{(k)}|^p\right)^{1/p} \qquad (5)$$

where the parameter p is with real values in the range of $1\leq p<\infty$.With the above definition of p - norms in the eq.(5), the Taylor analysis thus can be generalized as a following optimization problem,

$$E_T(\Gamma)=\tau_0\left(\sum_{k=1}^{N}|\dot{\gamma}^{(k)}|^p\right)^{1/p} \rightarrow minimize$$

subject to
$$D_{ij} = \frac{1}{2}\sum_{k=1}^{N}(m_{ij}^{(k)} + m_{ji}^{(k)})\dot{\gamma}^{(k)} \qquad (6)$$

Note that the objective function of this optimization problem implies the internal work rate by multiplying the norm with slip system deformation resistanse τ_0 , and for a special case of $p=1$, this formulation is identical with the strict Taylor one for rate-independent plasticity.

3 Generalized Bishop-Hill analysis and rate-dependent slip model

The dual problem for the above generalized Taylor problem of minimizing $E_T(\Gamma)$ subject to the liner constraints can be derived by the use of duality theorem in the mathematical programming (Mangasarian 1969). According to the duality theorem, the Langrangian function may be written in the form

$$L\left(\dot{\gamma}^{(k)},\sigma_{ij}\right)=E_T\left(\dot{\gamma}^{(k)}\right)+\sigma_{ij}\left\{D_{ij}-\frac{1}{2}\sum_{k=1}^{N}(m_{ij}^{(k)}+m_{ji}^{(k)})\dot{\gamma}^{(k)}\right\} \qquad (7)$$

Thus, the dual problem can be stated as following optimization one,

$$L\,(\dot{\gamma}^{(k)},\sigma_{ij}) \rightarrow \text{maximize}$$

subject to
$$\frac{\partial L}{\partial\dot{\gamma}^{(k)}}=0,\quad \frac{\partial L}{\partial\sigma_{ij}}=0 \qquad (8)$$

where the σ_{ij} are the Lagrange multipliers and they also mean the Cauchy stresses.

In the equations(8), the summation convention over repeated subscripts is implied and we use this in the present paper. For the formulations stated in the equations (8) to be mathematically reasonable, the Lagrangian function L is required to be differentiable for any values of $\dot{\gamma}^{(k)}$. However, in the usual sense, it is not differentiable at $\dot{\gamma}^{(k)}=0$. To remove this singularity, we here introduce into the analysis the notion of derivates in the sense of "distribution", with

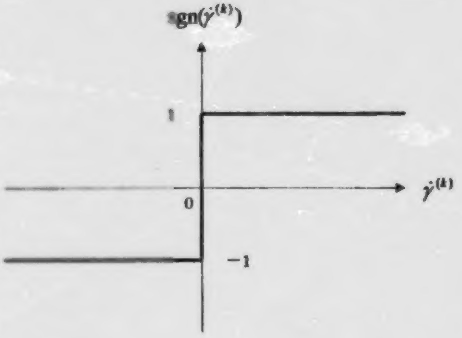

Fig.1: Derivative of $|\dot{\gamma}^{(k)}|$ as a distribution.

$$d|\dot{\gamma}^{(k)}|/d\dot{\gamma}^{(k)}=\mathrm{sgn}(\dot{\gamma}^{(k)}) \tag{9}$$

The distributional function of $sgn(\dot{\gamma}^{(k)})$ defined above can be sketched as shown in Fig.1, in which the $sgn(\dot{\gamma}^{(k)})$ takes +1 for $\dot{\gamma}^{(k)}>0$ and −1 for $\dot{\gamma}^{(k)}<0$ respectively, and it belongs to a closed interval of [-1, 1] at the $\dot{\gamma}^{(k)}=0$.

Referring to the equation (9), the forms of optimization problem stated in the equation (8) can be re-formulated as the generalized Bishop-Hill analysis such that

$$E_{sm}(\sigma_q)=D_q\sigma_q \quad \rightarrow \quad maximize$$

subject to $$\frac{1}{2}\left(m_q{}^{(k)}+m_p{}^{(k)}\right)\sigma_q=\left(\tau^{(k)}\right)=\tau_0/A\; Sgn\left(\dot{\gamma}^{(k)}\right)\left|\dot{\gamma}^{(k)}\right|^{p-1}$$

and $$D_q=\frac{1}{2}\sum_{k=1}^{n}(m_q{}^{(k)}+m_p{}^{(k)})\dot{\gamma}^{(k)} \tag{10}$$

If the power exponent (p-1) is replaced by the rate sensitivity parameter $m(m\geqq 0)$ and the constant A is identified with the equivalent strain rate as expressed by $\dot{\gamma}_0{}^{p-1}$, the first form of constraints becomes to be equivalent to the power type low of rate-dependent theory for $p>1$ $(m=p-1>0)$. In the special case of p=1 (m=0), we can denote the conventional Schmid law expressed just as a equality, not as inequality by

$$\tau^{(k)}=\frac{1}{2}(m_q{}^{(k)}+m_p{}^{(k)})\sigma_q=\tau_c\mathrm{sgn}(\dot{\gamma}^{(k)}) \tag{11}$$

where τ_c means the critical resolved shear stress. This equation confirms from the Fig.1 that the resolved shear stress on slip systems where slip occurs ($\dot{\gamma}^{(k)}>0$, or $\dot{\gamma}^{(k)}<0$) is attaining the value of τ_c , whereas on inactive systems ($\dot{\gamma}^{(k)}=0$),the $\tau^{(k)}$ is not exceeding τ_c.

Upon combining the first form of constraints with the second one of the eqs.(10), we may re-write the generalized Bishop-Hill analysis of the eqs.(10) in terms of variables of stress σ_q as

$$E_{BH}(\sigma_{ij}) = D_{ij}\sigma_{ij} \quad \rightarrow \quad maximize$$

subject to $$D_{ij} = \frac{1}{2}\left(\frac{A}{\tau_0}\right)^{1/(p-1)} \sum_{k=1}^{N} (m_{ij}^{(k)} + m_{ji}^{(k)}) m_{kl}^{(k)} \sigma_{kl} \left| m_{mn}^{(k)} \sigma_{mn} \right|^{(2-p)/(p-1)} \qquad (12)$$

From the above expressions, we remark that the form of constraint is identical to itself the non-linear simultaneous equation system for the conventional rate-dependent model. However, the result of our formulation shows explicitly that the analysis for rate-dependent materials should be exactly considered as a problem of solving the non-linear optimization problem stated in the eqs.(12),but not the non-linear algebraic equations.

4 Formulation for the relaxed constraints model covering the rate-dependent plasticity

Here, we present ,in brief , a new version of relaxed constraints models including the rate-dependent slips based on the generalized Taylor-Bishop-Hill problem formulated in the previous section. For this attempt, we shall now consider the symmetrical part of the "relaxation tensor" as follows (Van Houtte 1996),

$$\rho_{ij}^{s} = D_{ij} - \langle D_{ij} \rangle \qquad (13)$$

where D_{ij} is the microscopic strain rate that is used in the previous section, and $<D_{ij}>$ corresponds to the prescribed macroscopic one as whole polycrystal deformation.

Next, for the analysis the ρ_{ij}^{s} can be implemented by introducing "pseudo-slip rate $\dot{\gamma}_p^{(s)}$" for relaxation, whose slip direction and slip plane normal vectors are denoted by $\boldsymbol{d}^{(s)}$ and $\boldsymbol{s}^{(s)}$ respectively. Let $\boldsymbol{g}^{(s)}$ be defined as $\boldsymbol{g}^{(s)}=\boldsymbol{d}^{(s)} \otimes \boldsymbol{s}^{(s)}$, we thus have

$$\rho_{ij}^{s} = \sum_{s=1}^{M} \frac{1}{2}(g_{ij}^{(s)} + g_{ji}^{(s)})\dot{\gamma}_p^{(s)} \quad \text{(non-negative integer } M \leqq 4) \qquad (14)$$

Since the pseudo-slip rate $\dot{\gamma}_p^{(s)}$ may be interpreted to be the internal variables in crystal plasticity theories as well as the $\dot{\gamma}^{(k)}$ on real slip systems, the extended relaxed Taylor method including rate-dependent slips can be formulated by the same way proposed in the previous section as follows,

$$E_T(\dot{\gamma}^{(k)}, \dot{\gamma}_p^{(s)}) = \tau_0 \left(\sum_{k=1}^{N} \left| \dot{\gamma}^{(k)} \right|^p + \sum_{s=1}^{M} \left| \alpha \dot{\gamma}_p^{(s)} \right|^p \right)^{1/p} \quad \rightarrow \quad minimize \qquad (15)$$

subject to $$< D_{ij} > = \frac{1}{2}\sum_{k=1}^{N}(m_{ij}^{(k)} + m_{ji}^{(k)})\dot{\gamma}^{(k)} - \frac{1}{2}\sum_{s=1}^{M}(g_{ij}^{(s)} + g_{ji}^{(s)})\dot{\gamma}_p^{(s)} \qquad (16)$$

where $\alpha = \tau_p / \tau_0$, and τ_p corresponds to the deformation resistance for the pseudo-slip for relaxation, and also the parameter p is related to the m by $m=p-1$.

Using the same approach as the previous section by the duality theorem of mathematical programming, consequently the dual problem can be stated as the following maximization problem with respect to the Cauchy stresses σ_{ij},

$$E_{BH}(\sigma_{ij}) = < D_{ij} > \sigma_{ij} \quad \rightarrow \quad maximize$$

subject to

$$< D_{ij} >= \frac{\dot{\gamma}_0}{2\tau_0{}^{1/m}}\left[\sum_{k=1}^{N}(m_{ij}{}^{(k)} + m_{ji}{}^{(k)})m_{kl}{}^{(k)}\sigma_{kl}\left|m_{mn}{}^{(k)}\sigma_{mn}\right|^{1/m-1}\right.$$

$$\left. - \frac{1}{\alpha^{1/m}}\sum_{s=1}^{M}(g_{ij}{}^{(s)} + g_{ji}{}^{(s)})g_{kl}{}^{(s)}\sigma_{kl}\left|g_{mn}{}^{(s)}\sigma_{mn}\right|^{1/m-1}\right] \qquad (17)$$

This formulation shows with emphasis on the Bishop-Hill approach more generally defined for the relaxed constraints model for rate-dependent materials.

5 Conclusions

The main concern of this paper is to generalize the Taylor-Bishop-Hill theories for them to cover the rate-dependent slip model. As the result of mathematical treatment of the strict Taylor analysis in the finite dimensional Banach space, this paper presents the generalized forms of the Taylor-Bishop-Hill analysis which include the rate-dependent slip model. Moreover, we have applied the strain relaxation concept to the generalized Taylor-Bishop-Hill theories stated in this paper, and the comprehensive formulations for the relaxed constraints model including rate-dependent slips have been presented.

6 References

Anand, L. and Kothari, M. (1996) A computational procedure for rate-dependent crystal plasticity, *J.Mech.Phys.Solids*, Vol.44, pp.525-558

Asaro, R.J. and Needleman ,A.(1985) Texture development and strain hardening in rate dependent polycrystals, *Acta Metall.*,Vol.33, pp.923-953

Bishop, J.F.W. and Hill, R. (1951a) A theory of the plastic distortion of a polycrystalline aggregate under combined stresses, *Phil. Mag.*, Vol.42, pp.414-427

Bishop, J.F.W. and Hill, R. (1951b) A theoretical Derivation of plastic properties of polycrystalline face-centered cubic metals , *Phil.Mag.*,Vol.42, pp.1298-1307

Chin, G.Y and Mammel, W.L.(1969) Generalization and equivalence of the minimum work(Taylor) and maximum work(Bishop-Hill)principles for crystal plasticity, *Trans. Met.Soc.AIME*, Vol.245, pp.1211-1214

Kocks, U.F. and Chandra, H.(1982) Slip geometry in partially constrained deformation, *Acta Metall.*, Vol.30, pp.695-709

Mangasarian, O.L.(1969) *Nonlinear Programming*, McGraw Hill Inc. New York, pp.280-290

Taylor, G.I.(1938) Plastic strain in metals, *J.Inst.Metals*,Vol.62,pp.307-324

Van Houtte,P.(1984) Some recent developments in the theories for deformation texture prediction, *Proc.7th ICOTOM*,(ed. C.M. Brakman, P. Jongenburger and E.J.Mittemeijer), Netherland Soc.Mat.Sci.,pp.7-23

Van Houtte,P.(1996) Microscopic strain heterogeneity and deformation texture prediction, *Proc.11th ICOTOM* ,(ed.Z.Liang, L.Luo and Y.Chu),Int.Academic Pub.,Beijing,Vol.1,pp.236-247

Texture and Anisotrophy

MODELING TEXTURE DEVELOPMENT DURING PLASTIC DEFORMATION IN CUBIC METALS[†]

U.F. KOCKS
Center for Materials Science, Los Alamos National Laboratory, Los Alamos
NM, USA

Abstract

A number of examples will be given for texture development in various deformation modes: tension, compression, torsion, rolling. The range of possibilities is sometimes quite limited, though they may depend sensitively on the initial orientation distribution (especially the low-intensity areas). The wider the range of possibilities, the greater the dependence on path: both total strain and assumed grain-shape development. Emphasis will be placed on the relation – or absence of a relation – between observed failures in predictions and shortcomings of particular models.

Keywords: deformation modes, difference pole figures, grain shape, polar representation, strain dependence

Summary

In our book on Texture and Anisotropy [1], we have given an exposition of, among other topics, the ingredients appropriate for deformation texture development, as well as the mutual interaction between models and experiments. Much of this work has not otherwise been published. We will highlight some examples and conclusions and, in the process, present our views on appropriate representations of textures (and texture differences).

Example 1: fcc tension, bcc compression. Two components develop (<111> and <001> fibers); the ratio of the resulting volume fractions depends entirely on the initial population of orientations in the two 'drainage volumes' (and on what is included in the chosen measure of a 'component').

[†] Work supported by the U.S. Department of Energy, Basic Energy Sciences.

There is no reason why the Taylor model should not be applicable, and there is no conceivable cause for a material dependence within fcc metals. For bcc, the result is insensitive to pencil glide [1, p. 408].

Example 2: fcc compression, bcc tension. This is a case where the Taylor model fails, and for good reasons: the internal stresses that would develop are just too large. A self-consistent formulation should help – and it does [1, p.485] (but this formulation does *not* predict the tension case correctly [1, p.486]). Taylor simulations should routinely print out the predicted standard deviations of the stresses (both in the straining direction and others).

Example 3: fcc torsion. The range of possibilities, even within the Taylor model, is large, and the strain dependence significant. It predicts the point at which the lack of orthotropic symmetry vanishes (by chance, and approximately) [1, p.402]. The difference between predictions under free- and fixed-end boundary conditions is nicely seen in a difference pole figure [1, p.401]. A comparison between torsion (simple shear) and rolling (pure shear) is best made on a TD-pole figure [1, p. 86].

Example 4: fcc rolling. The change in grain shape should affect the boundary conditions on the grain in all models; assuming flat grains throughout gives a different result: the predictions are *path-dependent*. (This is well seen on a *difference OD* [1, p. 400].) The strain dependence is significant: comparisons at the same strain are misleading. Initial textures can have a long-term effect on the distribution along the fibers. With random initial texture, Taylor simulation leads to a brass component for a significant amount of initial straining, and this appears to correspond to observation in all materials [1, pp. 398-399]. (Fiber analysis can be quite misleading; polar representation is most visual [1, pp. 82-84].) - The spread between different fcc materials that develops at larger strains cannot be explained by the Taylor model *or* any homogeneous effective medium model. Texture patterning seems the only viable possibility [1, pp. 413-417].

Example 4: bcc rolling. The most instructive representation is one in which ND and RD are interchanged with respect to fcc: then, both are identical for bcc {110} glide in the absence of grain shape effects (regardless of model). For a well-characterized case, one needs both pencil glide and increasing grain-shape effects to explain the experiments [1, p. 406].

Overall assessment of models for cubic metals. Valid comparisons can be made only when the initial texture and the strain dependence of experimental textures are known. While the Taylor model is quite successful in general, there are two cases in which it fails. One is predictable: when the local stresses demanded by it vary *too* much from grain to grain; this should be monitored [1, p. 378] and, in this case, a self-consistent approach is appropriate. The other is unexplained: the material dependence (for non-twinning, low-SFE materials); it cannot be resolved by *any* homogeneous effective medium model, including "Sachs" type models [1, pp. 372,366].

References

[1] Kocks, U.F., Tomé, C.N. and Wenk, H.-R., eds. (1998), *Texture and Anisotropy*, Cambridge University Press

TEXTURE AND ANISOTROPY IN LOW SYMMETRY AGGREGATES: ELASTIC AND PLASTIC STUDY OF OLIVINE

C.N. TOMÉ
Los Alamos National Laboratory - MS G755 - Los Alamos NM 87545 - USA

Abstract

The connection between texture and anisotropic mechanical response is the focus of a book that we published recently [1]. Such connection is specially important in the case of highly textured aggregates formed by highly anisotropic crystals. In this work we discuss the formalism of self-consistent models as it applies to elastic and plastic polycrystals. We use the orthorhombic mineral olivine to illustrate the practical applications of the formalism.

Keywords: Self-consistent models, low symmetry, olivine

1 Summary

In practice, mechanic, electric and transport properties of single crystals are always anisotropic. For crystals of low symmetry the anisotropy is usually quite marked. In addition, while the tensors that represent the physical properties are the same for all crystals when expressed in crystal axes, they differ for grains of different orientations when referred to an unique set of axes. As a consequence, aggregates of crystalline grains exhibit local variations of the properties which arise from the distribution of orientations (texture) at the polycrystalline level. Finding the overall properties of polycrystals requires to perform an adequate volume average of the constituent grain's properties.

In most cases, a straightforward average of the single-crystal properties is not correct or consistent. A well known example in this respect is the elastic properties: the average of the elastic stiffness tensor is not consistent with the average of their inverses, the compliances. The former average is known as the Voigt upper bound and relies on the assumption of uniform strain field. The latter average is the Reuss lower bound, and requires the stress field to be uniform. In the case of plastic deformation, imposing uniform strain or stress across the aggregate leads to the well known bounds of Taylor or Sachs, respectively.

Upper and lower bounds estimates do not account for the local perturbations to the stress and strain fields induced by the grain interactions. Such approximation may still be reasonable when simulating single phase cubic aggregates, because the high symmetry of the lattice guarantees a closer to isotropic response. In the case of low symmetry aggregates, though, such assumption is usually not valid and polycrystal models which account for local effects are required. One of such class of models is the self-consistent polycrystal models, which represent each grain as an inclusion embedded in and interacting with a Homogeneous Effective Medium (HEM). The HEM is anisotropic and provides an average environment for the deforming grain.

In this work we briefly discuss the formalism of self-consistent models for the elastic [1, Ch.7] and the plastic [1, Ch.11] regimes. We illustrate the method for the specific case of an olivine aggregate, chosen here for its anisotropy and for its geological importance. The orthorhombic mineral olivine ($MgSiO_4$) is the major constituent of the upper mantle of the Earth and, as a consequence, its mechanical response strongly influences convection, plate tectonics, and seismic wave characteristics [1, pg.587). In what concerns anisotropy, the single crystal elastic moduli can differ by as much as 60% along different directions. In addition, the plastic characteristics are even more anisotropic since only shear parallel to the facets of the orthorhombic cell is feasible. As a consequence, the single crystal yield surface is open and the Taylor model cannot be applied.

Here we simulate texture development of olivine associated with simple shear, which is an approximation to the more complex deformation history associated with convection of the upper mantle of the Earth [1, pgs.307 & 591]. Next, we calculate the overall elastic moduli of the aggregate using the shear textures calculated above [1, pg.306]. Finally, the elastic moduli are introduced in the theory of wave propagation in elastic anisotropic media and seismic wave velocities are computed as a function of the direction of propagation [1, pgs.308 & 590]. The calculations are consistent with measured longitudinal seismic waves in different directions.

2 References

[1] Kocks, U.F., Tomé, C.N. and Wenk, R.-H. eds. (1998) *Texture and Anisotropy*, Cambridge University Press

FINITE ELEMENT SIMULATION WITH EXPLICIT USE OF POLYCRYSTAL PLASTICITY THEORY

A. J. BEAUDOIN

University of Illinois at Urbana-Champaign, Urbana, IL

P. R. DAWSON

Cornell University, Ithaca, NY

Abstract

In this overview, we examine the combined application of polycrystal plasticity theory and the finite element method in examination of metal deformation. Two possible approaches, that of many crystals contained in a finite element or a crystal comprising one or more finite elements, allow for the study of deformation at the macroscale or microscale. A survey is made of simulations for bulk and sheet forming operations using the macroscale approach. Microscale simulations enable study of inhomogeneity developed through grain–to–grain interaction. The deformation history drawn from a macroscale simulation and applied to a microscale simulation provides a link between the two procedures.

Keywords: Finite element, non-uniform deformation, polycrystal plasticity

Summary

The augmentation of polycrystal plasticity theory with finite element analysis generally follows two courses of development [1, Chs. 12 & 13]. Polycrystal plasticity theory may serve as the constitutive basis for the finite element formulation in similar spirit as classic relations used in continuum elastoplasticity. Such application provides for the analysis of non-uniform deformations inherent in specification of the boundary value problem, with material behavior following the physically-motivated theory of polycrystal plasticity. As focus is on non-uniform deformation developed at the macroscale, each element "contains" sufficient number of crystals to represent response of a polycrystal aggregate. In a second approach, finite element analysis is used as a tool to investigate interaction among crystals that, in ensemble, pose the polycrystal aggregate. Here, the inhomogeneity of deformation follows from grain–to–grain interaction; each grain is composed of one or more finite elements. Boundary conditions are typically construed so as to render homogeneous response of the aggregate proper. It is of importance to note that the utility of both implementations follows from the ability to initialize state variables through quantitative texture analysis of experimental data.

We take this overview as an opportunity to survey results from simulations of the "macroscale" and "microscale" – and draw connection between the two. With respect to macroscale simulations:

- gradients inherent in bulk forming operation of rolling highlight the effect of deformation pathway on crystallographic texture evolution, and,
- anisotropy inherent in rolled sheet products exposes the complementary trend of texture on deformation pathway.

Deformation paths characteristic of such processing operations can be used to drive microscale simulations of crystal interaction in the aggregate. Such simulations are useful in studying neighbor interaction, shear deformation within grains, effect of grain aspect ratio, the progression of elasto-viscoplastic transition within the aggregate, and development of lattice curvature.

The macroscale and microscale simulations may be viewed as a whole, offering a tool for exploring the inhomogeneity inherent in plasticity. Polycrystal plasticity offers the means of introducing this inhomogeneity into finite element analysis with firm physical basis. Similarly, finite element techniques offer a means for detailed exposition of the theory itself. The deformation history drawn from a macroscale simulation and applied to a microscale simulation provides a link between the two procedures. Finally, it is of no small significance that this exploration is done in a manner in which results are articulated using representation identical to experiment.

References

[1] Kocks, U. F., Tomé, C. N. and Wenk, H.-R. (1998), *Texture and Anisotropy*. Cambridge University Press, Cambridge.

CRYSTALLOGRAPHICAL AND MORPHOLOGICAL ANISOTROPY IN γ-TIAL

H. Mecking
Materials Science and Technology, Technical University Hamburg-Harburg,
21071 Hamburg, Germany

Abstract

γ-TiAl has a closed packed tetragonal lattice. Slip geometry and evolution of deformation as well as recrystallzation texture exhibit close similarities to the f.c.c. case. The plastic anisotropy, however, is quite different. This is due to ordering requirements which cause considerable differences in the arrangement of atoms along <101] and <110] glide directions and the suppression of 8 twinning modes. In lamellar microstructures, consisting of aggregates of polysynthetically twinned (PST) grains, morphology superimposes on the crystallography. There are again three distinct slip modes but slip geometry and slip resistance are now dominated by the inclination of slip planes and slip directions with respect to the interfaces between the lamellae. Effects on texture evolution and plastic anisotropy are large and distinctively different from those in globular microstructures [1,2].

Keywords: Yield surface, texture, morphology, anisotropy, intermetallics, TiAl

Summary

Globular microstructure: In γ-TiAl with globular structure the grains are regular single crystals where the slip systems are distinguished by crystallography. The slip planes are the close packed {111}-planes with 3 crystallographically different slip directions, so that 3 deformation modes exist: Ordinary dislocation slip of {111}<110]-type, super dislocation slip of {111}<101] type and twinning of {111}<11$\bar{2}$]-type with merely one twin direction per plane which can be activated only unidirectionally in the forward direction while dislocation glide is bidirectional. The topography of the yield surface depends on the relative values of the critical resolved shear stress of the 3 modes [3]. They can not be measured directly since single crystals generally are not available and thus have to be determined indirectly from a comparison of measured and theoretically predicted plastic anisotropy of polycrystals, which is possible with reasonable accuracy in strongly textured material. Hot rolled sheets generally develop a strong cube-type texture with the [001] direction preferentially parallel to the cross direction. They develop a strong anisotropy of plastic flow which can be simulated quite satisfactorily by ascribing a critical resolved shear stress of equal magnitude to the ordinary and twin mode and a 2.5 times higher value to the superdislocation mode [4].

Lamellar microstructures: In lamellar grains of γ–TiAl the lamellar interfaces are generally {111} twin planes (some with a small layer of α_2). Three morphologically different modes can be distinguished: The longitudinal mode consists of slip on planes parallel to the interface. The mixed mode has slip directions also parallel to the interface but the slip planes are inclined. The transversal mode has slip directions and slip planes with transversal components perpendicular to the interfaces. Each of the modes contains several crystallographically identical slip systems which are complex mixtures of ordinary, super and twinning slip.

Polysynthetically twinned crystals can be produced as large samples. They allow to measure the strength of the different modes directly which increases by more than a factor of two in the order longitudinal. mixed and transversal slip. The experimental values can then be used to construct the yield surface of a PST-crystal and to calculate plastic anisotropy of lamellar polycrystals [5].

Typically cast material of γ-TiAl is made up by lamellar grains with a strong morphological texture, since the lamellae are preferentially aligned perpendicular to the direction of solidification. The anisotropy is large and can be calculated rather accurately with the general polycrystal plasticity codes by employing the PST yield surface, as will be demonstrated by comparing experimental results with simulations.

References

[1] H. Mecking in "Texture and Anisotropy" (Ed.: U.F. Kocks, C.N. Tomé and H.R. Wenk, Cambridge University Press, 1998); pp. 1

[2] U.F. Kocks, ibidem, pp. 326

[3] H. Mecking, Ch. Hartig, U.F. Kocks; Acta Mater. 44 (1996), pp. 1309

[4] A. Bartels, H. Uhlenhut; Intermetallics 6 (1995), pp. 685

[5] R.A. Lebensohn, H. Uhlenhut, C. Hartig and H. Mecking; Acta Mater. 46 (1998), pp. 4701

DIFFRACTIVE DETERMINATION OF THERMO-ELASTIC SINGLE CRYSTAL CONSTANTS USING POLYCRYSTALLINE SAMPLES

S. MATTHIES and H.-G. PRIESMEYER

GKSS Forschungszentrum Geesthacht, Institut für Werkstofforschung, Geesthacht, Germany

Abstract

The possibility to determine single crystal thermo-elastic constants using diffractive strain data from polycrystalline samples is discussed and demonstrated for the common case ($f(g) \neq 1$, any crystal symmetries). The necessary high precision of all components of the complex scheme is especially underlined.

Keywords: thermo-elastic constants, polycrystalline sample, high temperatures

1 Introduction

Thermo-elastic single crystal constants ('°') like thermal expansion, described by a second rank tensor α°, and elastic stiffness C° or compliance S° (fourth rank tensors) are typical INPUT data used in applied or modeling calculations of texture analysis. There are well established direct methods for the determination of the elastic constants by acoustic methods using single crystals [Schreiber et al. 1973]. Applying modern dilatometers the determination of thermal expansion parameters is also not a problem if appropriate monocrystalline samples are available. However, difficulties appear if for any reason single crystals with the necessary size, purity and shape precision are not available, and especially if high temperature data of technical interest are asked, and common detector systems may fail. In such cases diffractive methods can be used, that determine temperature or stress induced strains (changed crystal plane spacings d_{hkl}). In analogy with crystal structure analysis it should be possible to extract the required single crystalline parameters from experiments with (well known and/or specially prepared) polycrystalline samples.

Below a short review on some experimental and theoretical developments in this field is given. Especially the high demands to all components of the complex scheme (polycrystalline sample - diffraction experiment - data analysis) will be underlined.

2 Diffractive strain determination

For wave length λ (X-rays or thermal neutrons) a detector D will measure a non-zero diffraction intensity from a single crystal if the Bragg equation

$$\lambda = 2\, d_{hkl} \sin \Theta \tag{1}$$

is obeyed, with Θ - the Bragg angle determined by the incoming and reflected beam. At this the scattering vector **N** (bisector of both beams) must be parallel to the normal of the (hkl)-plane. Its direction described in the crystal coordinate system K_B is denoted by $\mathbf{h}_i$. If the spacing d_{hkl} is changed (e.g. by rising temperature or applied stress) relative to a reference spacing d^0_{hkl} the 'measured' strain follows as

$$\varepsilon^L_{33} = (d_{hkl} - d^0_{hkl}) \,/\, d^0_{hkl} \tag{2}$$

'$_{33}$' indicates the corresponding tensor component in K_L - the 'laboratory' coordinate system, with $Z_L \parallel \mathbf{N}$, and X_L in the plane of incoming and reflected beam, showing to the side of the beam source. The difference $d_{hkl} - d^0_{hkl}$ can be determined using (1) and the corresponding line shift of the hkl-diffraction peak in Θ (for fixed λ) or in λ for fixed Θ. In the polycrystalline case all crystallites in reflecting orientation give their contribution to the detector signal, i.e. to position and form of the diffraction peak. Neighboring crystallites interact, and crystallites, that differ in their orientation by a rotation around **N**, feel a macroscopic stress field in a different way. The resulting experimental $\bar{d}_{hkl}$ is a complicated mean value over individual d, that also includes texture characteristics like the ODF f(g):

$$\bar{d}_{hkl}(\mathbf{y}) = d^0_{hkl}\,(1 + \bar{\varepsilon}^L_{33}(\mathbf{h}_i,\mathbf{y})) \tag{3}$$

y describes the direction of the scattering vector **N** in the sample fixed coordinate system K_A. It depends on the orientation of the sample within the spectrometer (K_L).

3 Direct and inverse problem

In dependence on the sample composition (structure, texture), on the role of the grain interaction for a phenomenon of interest (e.g. thermal expansion) model equations (including simplifying assumptions or approximations) can be derived, that try to describe the 'measured' $\bar{\varepsilon}^L_{33}(\mathbf{h}_i,\mathbf{y})$ by the 'microscopic' (single crystalline) properties 'P^0', by grain system characterizations (e.g. the ODF), and by the driving macroscopic fields 'F', like stress or temperature:

$$\bar{\varepsilon}^L_{33}(\mathbf{h}_i,\mathbf{y}) \equiv \bar{\varepsilon}^L_{33}(\mathbf{h}_i,\mathbf{y};P^0,f(g),F) \tag{4}$$

Using (3) and (4) two kinds of problems can now be treated. The 'direct' problem (cf. residual stress analysis) tries to determine the macroscopic field characteristics F, using the known microscopic parameters P^0 and sample characteristics like f(g).On the other hand, if the model (4) sufficiently well describes the experiment (what can be supported by special choice of the experimental conditions, of the sample, and by its preparation) also the 'inverse' problem can be considered. I.e. we try to extract the microscopic parameters P^0 from (4) using the known data on the applied macroscopic fields and grain system characteristics. Below this will be demonstrated for thermal expansion and elastic properties. But before going into details it is worth to list some moments, necessary for successful considerations of the inverse problem:

- The sample should be simple and well known - preferably one phase, small grains, spherical and of approximately same size, weak or strong texture.
- A sufficiently great irradiated volume is to be used. The number of the involved grains must be able at all statistically well to represent a given texture. This is especially critical in the analytically simplest case of random texture (cf. Matthies and Wagner, 1999). E.g. the averaging over all rotations around **N** that enters (4) must be represented for the whole 360°-region by real crystallites for each measuring point.
- In case of non-random texture try to measure the line shifts at points **y** with great pole figure values $P_{hi}(\mathbf{y})$. 'From there, where are not grains of the asked orientation at all no information can be extracted.'
- To prefer are experimental conditions (cf. point 5, $\mathbf{y}_I$ - REUSS approximation) for that the average (4) by reasonable approximations does not depend on the ODF.
- After formulation of a fit criterion in the common case the resulting expressions from (4) cannot explicitly be resolved for P^0. I.e. the fit will be a blind numerical procedure. Depending on the crystal symmetry and the experimental conditions the measured data may not depend on some P^0-parameters at all or contain only linear depending combinations of them. Therefore a planned experiment is preferably first to test using constructed 'experimental ' data of high numerical quality.
- At the end. The order of the experimental effects determines a threshold of precision, below that any activities will be quite questionable. Typical thermal expansion paramemeters have an order of 10^{-5} [1/K]. I.e. temperature steps of about 100K will lead to strains ε of the order of 10^{-3}. Loading steps of about 100 MPa in uniaxial compression or tensile tests lead to the same order of ε (The Young modulus for Fe: $\approx 10^2$ GPa). I.e. the quality of the line shift measurements, of the loading and texture data as well as of other important sample characteristics for (4) has to guarantee in a reproducible way a precision of about 10^{-4}. The same concerns the reliability of the theoretical models and precision of the numerical calculation - a quite pretentious demand.

4 Thermal expansion

The temperature induced strain in a single crystal (described in K_B; '0' - omitted) is given by

$$\varepsilon^{B}_{mn}(T) = \alpha_{mn}\,dT \quad ; \quad \alpha_{mn} = \alpha_{nm} \quad ; \quad m,n = 1,2,3 \tag{5}$$

Commonly α itself depends on T. In usually sufficient linear approximation we have

$$\alpha_{mn}(T) = \alpha^{(0)}_{mn} + \alpha^{(1)}_{mn}\,T \tag{6}$$

The α_{mn} can be translated into K_L using the rotation $g^{BL} = \{\varphi_i, \vartheta_i, \tilde{\varphi}\}$, with $\mathbf{h}_i = (\varphi_i, \vartheta_i)$ and $0 \le \tilde{\varphi} \le 2\pi$. The grain orientations with $\mathbf{h}_i \parallel \mathbf{y}$ are given by a path through the orientation space well known from pole figure calculations :

$$g_r = \{\varphi_i, \vartheta_i, \tilde{\varphi}\}^{-1}\{\varphi, \vartheta, 0\} = \{\mathbf{h}_i, \tilde{\varphi}\}^{-1}\{\mathbf{y}, 0\} \; ; \; \mathbf{y} = (\varphi, \vartheta) \tag{7}$$

Using the approximation of non-interacting grains from (4) and (5) follows

$$\bar{\alpha}^{L}_{33}(\mathbf{h}_i, \mathbf{y}) = \alpha_{mn} \int_0^{2\pi} g^{BL}_{3m}\, g^{BL}_{3n}\, f(g_r)\, d\tilde{\varphi} \Big/ \int_0^{2\pi} f(g_r)\, d\tilde{\varphi} \tag{8}$$

Because the '3k' matrix elements of g^{BL} do not depend on $\tilde{\varphi}$, in this case of a second rank tensor the ODF and **y** dependence cancels out in (8). With

$$\alpha^{L}_{33}(\mathbf{h}_i, T) = \delta \ln \bar{d}_{hkl}(T) / \delta T \tag{10}$$

the required $\alpha^{(0)}_{mn}$ and $\alpha^{(1)}_{mn}$ can directly be related to the experimental $\bar{d}_{hkl}(T)$. For the TiAl example (tetragonal crystal symmetry) given below only the $\alpha_{11} = \alpha_{22}$ and α_{33} coefficients are different from zero. With $\cos^2\vartheta_i = l^2/[(h^2+k^2)(c/a)^2+l^2]$ it follows

$$\begin{aligned}\ln[\bar{d}_{hkl}(T)/\bar{d}_{hkl}(T_0)] = {} & [\alpha^{(0)}_{11} + (\alpha^{(0)}_{33} - \alpha^{(0)}_{11})\cos^2\vartheta_i]\,(T-T_0) + \\ & [\alpha^{(1)}_{11} + (\alpha^{(1)}_{33} - \alpha^{(1)}_{11})\cos^2\vartheta_i\,](T^2-T_0^2)/2\end{aligned} \tag{11}$$

Fig. 1 shows some typical experimental data and recalculated d_{hkl} curves after fitting the four single crystal parameters $\alpha^{(0)}_{11}$, $\alpha^{(0)}_{33}$, $\alpha^{(1)}_{11}$ and $\alpha^{(1)}_{33}$. Seven hkl-reflection have been considered in the temperature region from 20 up to 600° C. The resolution of the time of flight neutron FOURIER spectrometer at the reactor FRG-1 of the GKSS research center is in the required order of 10^{-4}. The relatively great error bars at the experimental data points follow from the not well adapted coarse grained pilot sample with limited poor grain statistics. Nevertheless, the resulting α coefficients are in good agreement with data for equivalent TiAl materials determined by conventional non-diffractive methods. For more details see [Bittorf et al. 1998].

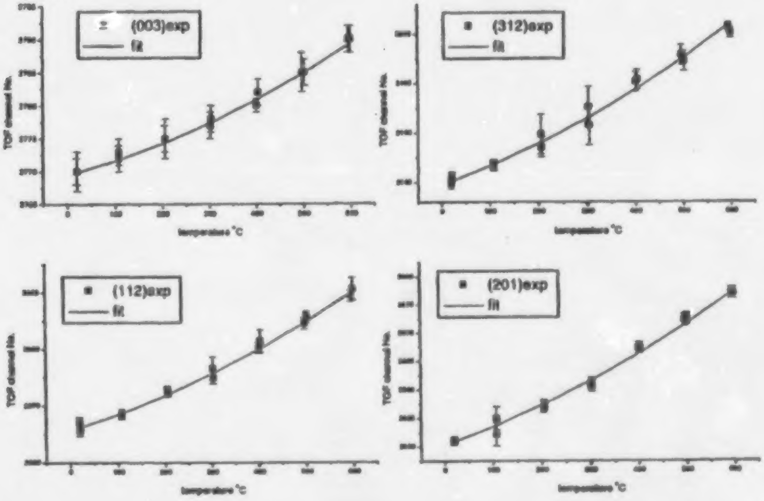

Fig. 1: TiAl - experimental and recalculated reflection line positions (T = 20 - 600° C)

5 Elastic coefficients

Measuring the $\bar{d}_{hkl}(\mathbf{y})$ in an uniaxial tensile or compression test within the elastic region the data points will lie on a straight line, according to (4) and HOOKE's law, that connects the strains with the applied macroscopic stresses σ_{33}^{A} :

$$\bar{\varepsilon}_{33}^{L}(\mathbf{h}_i, \mathbf{y}; \sigma_{33}^{A}) = S_{3333}^{LA}(\mathbf{h}_i, \mathbf{y})\, \sigma_{33}^{A} \ ; \ S_{33mn}^{LA} = S_{33kl}^{L}(\mathbf{h}_i, \mathbf{y})\{\mathbf{y},0\}_{km}\{\mathbf{y},0\}_{ln} \qquad (11)$$

The $S_{33kl}^{L}(\mathbf{h}_i, \mathbf{y})$ are closely connected with the 'XECs' (X-ray elastic constants), well known from residual stress analysis. They depend on the single crystal compliances S_{ijkl}^{0} and texture. For a review on the commonly used micromechanical approximations (VOIGT, REUSS, HILL, self-consistent a.o.) to determine the $S_{33kl}^{L}(\mathbf{h}_i, \mathbf{y})$ see [VanHoutte and DeBuyser,1993]. The ODF enters the corresponding expressions by integrals of the type (8), however with common g_{mn}^{BL}-elements, now depending on $\tilde{\varphi}$.

The possibility to extract the S_{ijkl}^{0} from strain data was already discussed by [Hauk and Kockelmann, 1979], but only special cases (cubic or hexagonal crystal symmetry, and random texture f(g) = 1) have been considered up to now. The application of the 'geometric mean' approximation (that exactly obeys some necessary general properties of the grain system) to stress analysis, and the reduction of the complicated f(g)-related expressions for the S_{33kl}^{L} to a small number of simple integrals ('moment pole figures', cf. [Matthies, 1996]) opened practicable possibilities of the S_{ijkl}^{0} determination for any crystal symmetries and really textured samples: f(g) ≠ 1.

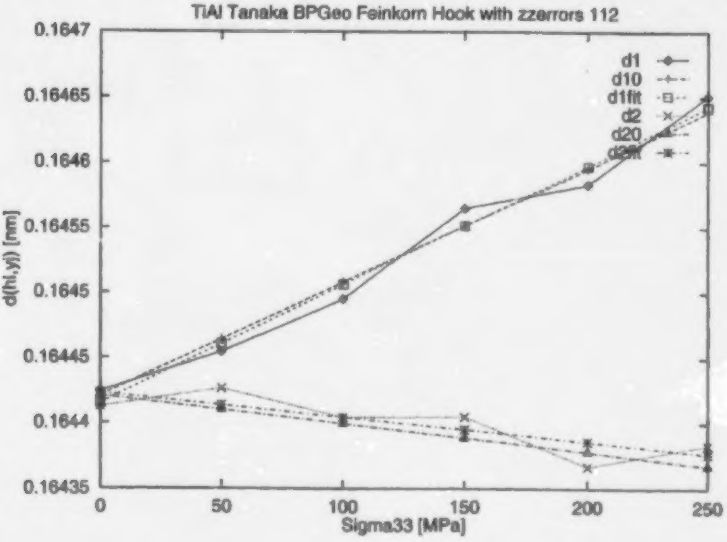

Fig. 2: TiAl - modeled ideal, disturbed and recalculated d_{112} for uniaxial tension

As preparation for the diffractive determination of the single crystal elastic constants of TiAl at high temperatures the corresponding 'experimental' line shift data were simulated by model calculations. The known ODF of a cyclic fibre type ($f(g)_{min} = 0.3$, $f_{max}=2.6$) and S^0_{ijkl}-data from quantum mechanical first principle calculations served as inputs. Fig. 2 shows one of seven modeled hkl-Hooke lines ((201),(112),(003),(221), (310),(203), and (312)) for two detector positions ($\mathbf{y}_1=\mathbf{Z}_A$, $\mathbf{y}_2=\mathbf{X}_A$) in dependence on σ^A_{33} up to 250 MPa (geometric mean approximation). For $\mathbf{y}_1$ and the REUSS approximation S^{LA}_{3333} does not depend on f(g). The ideal (d10, d20) curves have been randomly disturbed then in the order of maximum10 MPa. These data were fitted by straight lines that first leads to a refinement of the lattice parameter a_0 at zero σ^A_{33} (cf. the open d^0_{hkl} in (4)). The slopes of the fitted lines give the $S^{LA}_{3333}(\mathbf{h}_i,\mathbf{y}_1 \text{or } \mathbf{y}_2)$, that have to be explained by the 6 independent (due to tetragonal crystal symmetry) $S^0_{ijkl}\neq 0$.

The comparison of the results with the input data demonstrates the reliability of the scheme, but also the high sensitivity to experimental errors, already underlined above. Remarkable is the right order of the errors estimated by the fit procedure [10^{-5}/MPa]:

S^0_{1111} = 0.83757, Fit 0.76(0.06); S^0_{3333} = 0.76873, Fit 0.66(0.05)
S^0_{2323} = 0.20833, Fit 0.25(0.02); S^0_{1212} = 0.50000, Fit 0.47(0.07)
S^0_{1122} = -0.34719, Fit -0.32(0.09); S^0_{2233} = -0.23453, Fit -0.17(0.04)
a_0 = 0.3975 , Fit 0.3975(0.0002) [nm], c_0/a_0 = 1.02

Model calculations for the simpler case of random texture led to comparable results.

6 Conclusion

The possibility to extract single crystal thermo-elastic data by diffractive strain measurements was discussed and demonstrated. The scheme can be applied to any crystal symmetry and really textured cases as well. However, a high precision of all components of the complex scheme is demanded. The first step of the diffractive method considers thermal expansion and elastic data independently. In a next step these coupled characteristics have to be considered together, additionally including effects of grain interaction.

7 References

Bittorf, Ch., Matthies, S., Priesmeyer, H.G. and Wagner, R. (1998) Diffractive determination of thermo-elastic single crystal constants. *Intermetallics*, Vol. 7, pp. 1-8.

Hauk, V. and Kockelmann, H. (1979) Ermittlung der Einkristallkoeffizienten aus den Elastizitätskonstanten des Vielkristalls, *Z. Metallkde.*, Vol. 70, pp. 500-502.

Matthies, S. (1996) Moment pole figures in residual stress analysis. *Textures and Microstructures*, Vol.25, pp. 229-236.

Matthies, S. and Wagner, F., Using sets of individual orientations for ODF determination. Proceedings of this conference.

Schreiber, E., Anderson, O.L. and Soga, N. (1973) *Elastic Constants and Their Measurement,* McGRAW-HILL, New York.

Tanaka, K. and Koiwa, M. (1996) Single-crystal elastic constants of intermetallic compounds. *Intermetallics* Vol. 4, pp. 529-539.

VanHoutte, P. and DeBuyser, L. (1993) The influence of crystallographic texture on diffraction measurements of residual stress, *Acta metall.mater.*, Vol. 41, pp. 323-336.

TEXTURE AND R-VALUES OF CLAD METALS FOR BUTTON-TYPE BATTERIES

M. ISHIO and M. UMEDA
Sumitomo Special Metals Co., Ltd., Suita, Japan
H. INOUE and K. MORII
College of Engineering, Osaka Prefecture University, Sakai, Japan

Abstract

The texture and r-value were investigated for improving strength and drawability of the Cu/18Cr-8Ni stainless steel (SUS304)/Ni clad metals, which are applied to anode cases of the button-type miniature batteries. It was found that the texture of each layer of the clad metals was different from usual single sheet. The SUS304 in the clad metals has lower Goss orientation density and higher brass orientation density than the SUS304 single sheet under a 25% finish rolled condition after annealing. The texture formation of SUS304 in the clad metals will be brought about by influence of the Cu layer. The clad metals in the 25% finish rolled condition have higher strength and smaller anisotropy, so they are suitable as a material for the button-type battery case. The planar anisotropy of r-values was calculated from the ODF of SUS304 by using the Taylor model, and it agreed qualitatively well with that of the measured r-values.

Keywords: r-value, anisotropy, clad metal, 18Cr-8Ni stainless steel, Copper, button-type battery, orientation distribution function, Taylor theory.

1 Introduction

The spread of the portable electronic equipment increases demand for the micro-batteries. Then, miniaturization and a long life of a battery are technical assignments. For these button type micro-batteries, the Cu/SUS304/Ni clad metals, which had some good properties (strength, deep-drawing property, resistance to corrosion, and low electrical contact resistance), were developed (Ishio 1989,1991). It has been recently proposed that the thickness of the clad metals for anode cases is reduced should be extend the life of the battery due to the expansion of the inside contents. Therefore, the clad metals that have both high strength and excellent drawability (small anisotropy) have been required strongly now. There have been a few studies about mechanical properties, drawability and anisotropy for several clad metals, explained by dynamic composite law (Yamaguchi and Yoshida 1989; Sakamoto 1990; Yoshida 1991; Kondo and Hiraiwa 1991; Yoshida and Hino 1996). It is considered that the properties of the SUS304 core govern those of the clad metals, because the core in the clad metal has higher strength and larger volume than the surface Cu and Ni. Although there are many researches on the textures of austenitic stainless steel (Goodman and Hu 1964, 1965), the difference between single plate and clad metal is not clarified. We studied the processing condition of the clad metals, and established the way of manufacturing the clad metals having high strength and good drawability. Furthermore we reported that the stainless steel core in the clad metals had a different texture from the single sheets of SUS304, because the core material was rolled without direct contact with the rolls (Ishio et al. 1999).

In the present study, the textures of Cu and SUS304 in the clad metals at each manufacturing process have been clarify by comparing with the single sheets of SUS304, and the planar anisotropy of r-values has been calculated from ODF by using the full constraints model.

2 Specimens and Experimental Procedure

The chemical composition and the bonding ratio of each metal are shown in Table 1. The clad specimens having clad layers of copper and nickel bonded to a SUS304 core were made by the cold roll bonding method, and then were cold rolled to an 80% reduction and annealed, finally rolled to a 25% reduction, as shown in Fig.1. Here the symbols CR-60, CR-80 and CR-25 are used to denote the 60%, 80% and 25% rolled conditions. CA is also used to denote annealed condition. As the reference specimens, the SUS304 sheets after removing copper and nickel by etching were prepared under the same condition. Tensile tests were carried out on an Instron-type machine at a strain rate of 1.7×10^{-3} s^{-1}, and the r-values were measured at 5% strain.

Table 1: Bonding ratio and chemical composition of each layer.

Component materials	Bonding ratio (%)	Thickness (μm)	Chemical composition (mass%)												
			C	Si	Mn	P	S	Mg	Al	Ni	Co	Cr	Fe	Cu	Mo
Cu	16	24	–	<0.001	–	<0.001	0.001	–	–	–	–	–	–	99.995	–
SUS304	82	123	0.05	0.59	0.84	0.032	0.002	–	–	8.51	–	18.17	bal.	0.17	0.19
Ni	2	3	0.002	0.03	0.20	<0.001	<0.001	<0.001	0.01	bal.	0.01	–	0.05	–	–

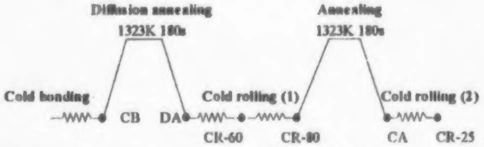

Fig. 1: Procedure for preparing specimens of Cu/SUS304/Ni clad metals and SUS304 sheets. SUS304 sheets were taken from the clad metals of DA condition by removing copper and nickel by etching, and then they were rolled and annealed.

{111}, {100}, {110} and {311} incomplete pole figures of Cu and SUS304 in the clad metals and those of the reference SUS304 single sheets were measured in the surfaces for Cu of the clad metals and for the SUS304 single sheets and in the Cu/SUS304 interface for SUS304 in the clad metals. The ODFs were analyzed from these pole figures (Inoue and Inakazu 1994). The texture of the Ni layer could not be measured, because the thickness of the Ni layer was too thin (only three microns). The planar anisotropy of r-values was calculated from this result by using FC (Full constraints) model based on the Taylor theory (Taylor 1938), and it was compared with the actual measured r-values.

3 Results and Discussion

3.1 Textures

Pole figures of the Cu layer and SUS304 are shown in Fig. 2. A sharp cube texture existed in copper surface of the clad metals after diffusion annealing (DA), and it remained still in this orientation, even if they were rolled to a 60% reduction (CR-60). Moreover, when they reached an 80% reduction by cold rolling (CR-80), the preferred orientations of the Cu layer were not copper type rolling texture, but were {001}<uv0> that turned a cube texture around the normal direction (ND). This orientation in copper are dispersed to random orientation, if they were annealed (CA). When the material with this random texture is rolled, the copper type rolling texture forms even under a comparatively low reduction like 25% (CR-25). The texture formation for Cu layer of the clad metals is different from the generally well-known rolling texture of pure copper, as above mentioned. Namely, the cube texture from diffusion annealing remains after 60% rolling. A rotation around ND occurs when the clad metals are further rolled. It is considered that a crystallographic rotation around ND occurs preferentially by rolling and rotations around TD and RD are suppressed, because the Cu layer is bonded to the SUS304 layer. On the other hand, the formation of an interesting annealing texture of Cu will be attributed to the following reason. The clear copper type rolling texture is developed by cold bonding, and it changes to the sharp cube texture by diffusion annealing (DA) after that. In the final annealing (CA), the texture does not change to the cube texture, but becomes random texture. This may be related to the fact that the {100} rolling texture (CR-80) including the cube orientation is formed before the final annealing.

Next, we compared the texture formation of the SUS304 core in clad metals with that of SUS304 sheets. The texture of SUS304 in clad metal is generally weaker than the texture of SUS304 sheet, and this tendency is especially remarkable in the recrystallization texture (CA). Although the formation of the Goss orientation is observed clearly in SUS304 sheet under the CR-25 condition, that of clad metal is weak. Therefore, the orientation density of this condition was evaluated quantitatively by the ODF analysis, as shown in Fig. 3. When comparing the α-fiber and the β-fiber of the clad metals with those of the SUS304 sheets, the Goss {110}<100> and {112}<111> accumulate highly in the SUS304 sheet, and it is characteristic that {011}<211> is strongly recognized in clad metals. The orientation densities of SUS304 and Cu in the clad metals are qualitatively similar to each other. This suggests that a different texture in the clad metals would be formed through the influence of the Cu layer.

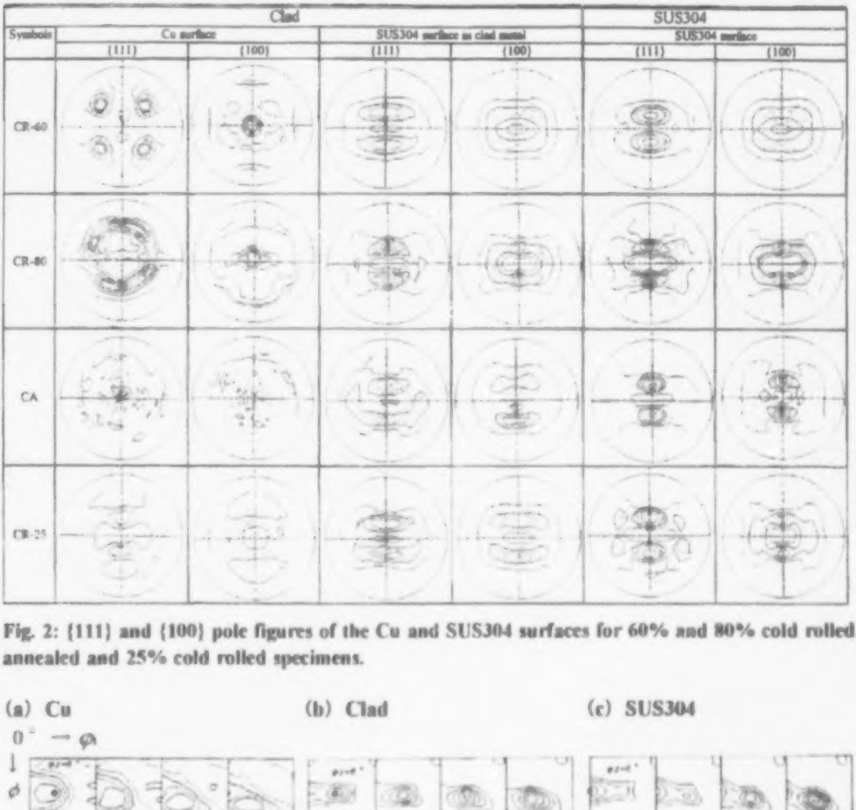

Fig. 2: {111} and {100} pole figures of the Cu and SUS304 surfaces for 60% and 80% cold rolled, annealed and 25% cold rolled specimens.

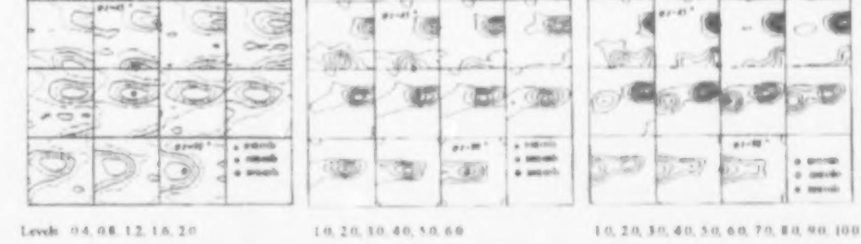

Fig. 3: φ_1 sections of orientation distribution function for 25% finish rolled specimens.
(a) Cu: the surface of Cu layer in the clad metals. (b) Clad: the surface of SUS304 core in the clad metals. (c) SUS304: the surface of SUS304 single plates. ($\varphi_2 = 0°$, $5°$, ···, $90°$)

3.2 r-values and mechanical properties

The measured r-values and mechanical properties of the clad metals and SUS304 single sheets in the annealed and finish rolled condition is shown in Table 2. Although the r-values are higher at 45 degrees to the rolling direction under annealed condition for both samples. The planar anisotropy of r-values of the clad metals decreases (Δr = −0.08, r0−r90 = −0.1), but for the SUS304 sheets, the r-value of 0 degree decreases drastically from 0.9 to 0.68 and that of 90 degrees increases from 0.7 to 1.31 after 25% finish rolling. As an additional experiment, the r-values were measured again by removing Cu and Ni from the clad metals after 25% finish rolling. This result became the same as that of the clad metals, and was different from the result of the SUS304 single sheets. The clad metal has higher strength and good formability by 25% finish rolling after annealing. Tensile strength at 0 degree increases from 675 to 862 MPa, and the Δr-values indicating the planar anisotropy decreases from 0.25 even to 0.08. This clad metal is very suitable as a material for the button-type battery anode case.

Table 2: r-values and mechanical properties in the annealed and finish rolled condition.

Clad metals		r-values					Tensile strength	Yield strength
Angle to rolling direction		0° (r0)	45° (r45)	90° (r90)	Δr=(r0+r90−r45x2)/4	r0−r90	MPa	MPa
Conditions	Annealed	0.95	1.34	0.75	-0.25	0.2	657	324
	25% rolled	1.08	1.29	1.20	-0.08	-0.1	862	781
SUS304 single sheet		r-values					Tensile strength	Yield strength
Angle to rolling direction		0° (r0)	45° (r45)	90° (r90)	Δr=(r0+r90−r45x2)/4	r0−r90	MPa	MPa
Conditions	Annealed	0.9	1.8	0.7	-0.50	0.2	740	380
	25% rolled	0.68	1.3	1.31	-0.15	-0.6	998	897

3.3 Estimation of r-value by calculation

As a prediction model, by using the full constraints (FC) model based on the Taylor theory, r-values were calculated (Bunge 1970,1982) and compared with the measured r-values.

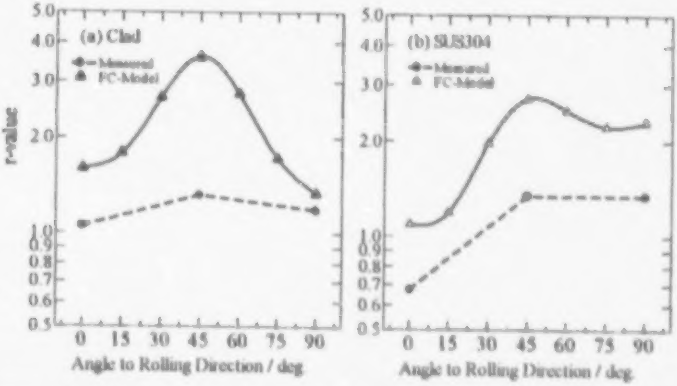

Fig. 4: Planar anisotropy of r-values measured and calculated by {111}<110> slip systems for 25% finish rolled clad metals and SUS304 single sheet.

The r-values calculated using the {111}<110> slip systems are shown in Fig.4. The measured r-values of the clad metals are high at 45 degrees, and low in the same level at 0 and 90 degrees, though the measured r-value at 0 degree direction of SUS304 sheet is remarkably low. The curves of calculated r-values corresponded to those of the measured r-values, but they were higher in all the ranges.

4 Conclusions

The texture of SUS304 in the clad metals has the characteristics that are different from the texture of the SUS304 single sheet in the same processing. It has lower Goss orientation density and higher brass orientation density under the CR-25 condition. The cube texture of the Cu surface of the clad metals caused by annealing is stable very much. It remains after 60 per cent reduction by cold rolling as well, and then it changes to the {001}〈uv0〉 orientation through a rotation around ND after 80 % cold rolling. At the CR-25 condition, the same qualitative tendency of orientation density was observed in each α- and β-fiber of SUS304 and Cu in the clad metals. The Cu layer will bring about the different texture formation of SUS304 in the clad metals. The planar anisotropy of r-values computed by using the FC-model corresponded to the tendency of the measured r-values for both the clad metals and single sheets.

5 References

Bunge, H. J. (1970) Some applications of the Taylor theory of polycrystal plasticity. *Kristall und Technik*, Vol. 5, pp. 145-75.

Bunge, H. J. (1982) *Texture Analysis in Materials Science*, Butterworths, London.

Goodman, S.R. and Hu, H. (1964) Texture transition in austenitic stainless steels. *Trans. Met. Soc. AIME*, Vol. 230, pp. 1413-9.

Goodman, S.R. and Hu, H. (1965) Annealing textures in an 18-8 austenitic stainless steel. *Trans. Met. Soc. AIME*, Vol. 233, pp. 103-10.

Inoue, H. and Inakazu, N. (1994) Determination of orientation distribution functions from incomplete pole figures by iterative series expansion method. *J. Japan Inst. Metals*, Vol. 58, No. 8, pp. 892-8.

Ishio, M. (1989) Manufacturing process and bonding mechanism of clad metals by cold roll welding. *Tetsu-to-Hagane*, Vol. 75, pp. 716-22.

Ishio, M. (1991) *J. Japan Soc. Tech. Plasticity*, Vol. 32, pp. 27-33.

Ishio, M., Umeda, M., Inoue, H. and Morii, K. (1999) Texture and r-values of Cu/18Cr-8Ni-Fe/Ni clad metal. *J. Japan Inst. Metals*, Vol. 63, pp. 305-11.

Kondo, K and Hiraiwa, M. (1991) *J. Japan Soc. Tech. Plasticity*, Vol. 32, pp. 13-9.

Sakamoto, T. (1990) Elasto-plastic models for evaluating r value of clad sheets and dual-phase steels. *Tetsu-to-Hagane*, Vol. 76, pp. 12-20.

Taylor, G. I. (1938) Plastic strain in metals. *J. Inst. Metals*, Vol. 62, pp. 307-24.

Yamaguchi, K. and Yoshida, F. (1989) *J. Soc. Mater. Sci. Japan*, Vol. 38, pp. 92-8.

Yoshida, F. (1991) *J. Japan Soc. Tech. Plasticity*, Vol. 32, pp. 20-6.

Yoshida, F and Hino, R. (1996) *J. Japan Soc. Tech. Plasticity*, Vol. 37, pp. 1125-9.

TEXTURE EFFECTS ON THE EVOLUTION OF HIGH TEMPERATURE MECHANICAL PROPERTIES IN ZIRCONIUM ALLOYS.

P. SANCHEZ and A.A. POCHETTINO
Universidad Nacional de General San Martín, San Martín, Argentina.
Departamento Materiales, Comisión Nacional de Energía Atómica,Buenos Aires, Argentina.
R. LEBENSOHN
Instituto de Física Rosario, Universidad Nacional de Rosario, Rosario, Argentina.

Abstract

In the present work, the validity of extrapolations of hot torsion tests results to describe the mechanical properties associated to Zr alloys undergoing to other hot pre-deformation (rolling, drawing) processes is analyzed. Results concerning texture evolution during hot pre-deformation and its effects on mechanical properties are presented and compared.

Keywords: drawing, high temperature, rolling, texture, torsion, yield surface

1. Introduction

Metallic materials generally undergo hot work processes during their transformation into a final product. These materials can get into service in this hot worked as-deformed state or can be further deformed at room temperature. Either as an intermediate or as a final product, the mechanical properties of such hot deformed materials are markedly influenced by the texture and the microstructure developed during the deformation processes.

Sometimes, results from high temperature torsion tests together with the so-called equivalence principle are used to describe the macroscopic mechanical response of materials during any arbitrary high temperature mechanical transformation (Rossard 1976). The equivalence principle is based on the assumption that texture and microstructure differences do not determine any appreciable variations of the macroscopic mechanical properties. The aim of this work is to assess if hot torsion tests extrapolations can be used to describe the mechanical properties associated to Zr alloys submitted to other hot pre-deformation processes. In doing this, predicted and experimental results concerning texture evolution (for torsion, rolling and drawing predeformations) and their effect on mechanical properties (considering the yield surfaces for hot and room temperature subsequent deformations) are presented and compared.

2. Hot deformation textures

Figures 1.a-b show experimental (0002) pole figures obtained by means of X-Ray diffraction techniques. They correspond to a hot rolling deformation process (Fig. 1.a) and to a hot torsion test (Fig. 1.b), both samples deformed to an Von Mises equivalent strain $\varepsilon=1$. Similarly, figures 2.a-b show the predicted (0002) pole figures for hot rolling (Fig. 2.a) and torsion (Fig. 2.b).

Predictions were obtained using the viscoplastic self-consistent formulation (Lebensohn and Tomé 1993). For high temperatures, a value n=7 (inverse of the rate sensitivity coefficient) was used. The slip systems that allow a good agreement between experimental and predicted results are: <a> prismatic slip {1100}<1120> (pr), <a> basal slip {0001}<1120> (b) and <c+a> pyramidal slip {1011}<1123> (pyr). The associated Critical Resolved Shear Stress (CRSS) for these systems - relative to that corresponding to prismatic slip - are $(\tau_b / \tau_{pr}) = 1.5$; $(\tau_{pyr} / \tau_{pr}) = 4.0$ (Lebensohn et al. 1994, Pochettino et al. 1994).

In the case of hot rolling, it was previously shown that, texture development (particularly the concentration of <c> poles around the normal direction of the sample) is related to the high activity of prismatic and basal slip (Lebensohn et al. 1994). In the case of hot torsion tests, a similar argument can be applied to explain texture development: the activities of prismatic and basal <a> slip systems are of the same order and represent more than 95% of the total activity. Moreover, basal <a> slip explains the (0002) reinforcements placed around the direction of maximum contraction (Fig. 1.b and 2.b). Simulations show that the activity of basal slip produces two texture reinforcements placed near the direction of maximum contraction and the neutral direction (which is coincident with the axial direction of the sample). This last reinforcement is observed experimentally but it becomes less significant as deformation increases. We believe that the effect of dynamic recovery can explain this result since tests were performed at temperatures around 970°K (P. Sanchez et al., to be published).

On the other hand, textures associated to hot drawn processes show, for (0002) pole figures, a quasi-fiber texture, being the axial direction of the sample the fiber direction. In this case, <a> prismatic slip is the most important deformation mode (≈ 80% of the total activity) while <c+a> pyramidal slip is the less active (2-3%).

It is important to assess, at terms of texture, if the results of torsion tests in Zr samples can be extrapolated in order to describe the mechanical properties associated with other hot deformation processes. Considering rolling and torsion processes, the equivalence of the principal deformation axes defined in Table 1 allows to compare both textures. This comparison requires an adequate rotation of the torsion texture (see Fig. 1.a-b). The rotation is composed by a rotation of 45° around the Radial Direction to put the Rolling Direction paralell to the maximun expansion direction (+) and by a second rotation of 90° around the latter. Rotated textures put in evidency a strong concentration of <c> axis around the ND, which can be associated to grains having an initial orientation near the (-) direction (Fig. 1.b), where the <a> basal slip systems have an strong activity during pre-deformation. An distribution <c> poles is

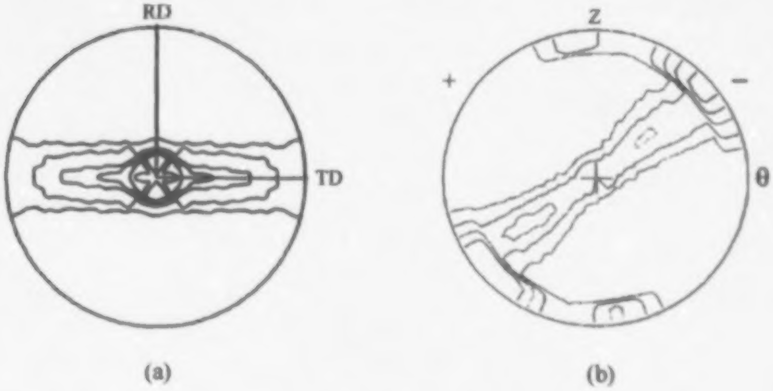

Fig. 1: Experimetal (0002) poles figures (a) Hot rolling (b) Hot torsion. Isodensity values: 1, 2, 3.

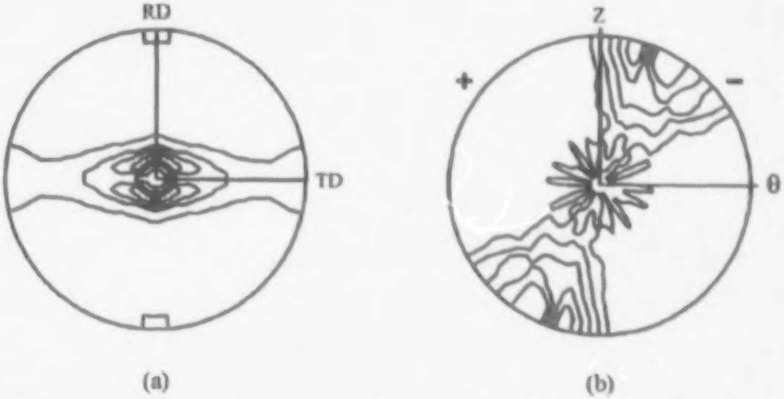

Fig. 2: Calculated (0002) poles figures (a) Hot rolling (b) Hot torsion. Isodensity values: 1, 2, 3.

Table 1: Equivalence of principal deformation directions in order to compare Rolling and Torsion processes.

Rolling	Torsion
Rolling Direction (RD)	Maximum expansion direction (+)
Transverse Direction (TD)	Radial Direction (RD)
Normal Direction (ND)	Maximum contraction direction (-)

also observed in the ND-TD plane. It corresponds to the poles initially placed in the plane defined by (-) and RD.

3. Yield surface calculations

Polycrystal yield surfaces at high and room temperatures were obtained using the viscoplastic selfconsistent model. Textures corresponding to hot pre-deformation processes were used as input for yield surface calculations. The yield surfaces were predicted by proving that the material is tested in different strain directions at high and room temperature (Sanchez et al. 1998). At high temperature, deformation modes and CRSS are the ones used for previous texture development calculations, while for room temperature studies the deformation modes considered were <a> prismatic slip and tensile and compressive twinning (Pochettino et al. 1994). Yield surface projections on the deviatoric π plane are presented in Fig. 3.a-h. These figures can be associated to the following cases:

- Hot rolling pre-deformation (Figs. 3.a-b).
- Hot torsion pre-deformation (Figs. 3.c-d).
- Hot torsion pre-deformation + rotations described above (Figs. 3.e-f)
- Hot-drawn process (Figs. 3.g-h)

Stress and $q = -(\varepsilon_2/\varepsilon_1)$ values at some particulars points of the yield surface are presented in Table 2. They correspond to uniaxial tension along x_1 and x_2 (indicated

Table 2: Stress and $q = -(\varepsilon_2/\varepsilon_1)$ values for significant points of the yield surface. σ^{s}_{eq} values are given in units of τ_{pr}

		High Temp. Yield Surface		Room Temp. Yield Surface	
Textures	Strain- path	σ^{s}_{eq}	Q	σ^{s}_{eq}	q
Hot Rolling	(1)	3.76	0.65	3.31	0.65
	(2)	4.03	0.82	3.55	0.99
	(3)	5.13	-0.53	4.78	-0.54
	(4)	4.85	0.0	4.52	0.0
	(5)	3.67	1.0	3.46	1.0
Hot Torsion	(1)	3.57	0.59	3.79	0.81
	(2)	3.95	0.72	3.96	0.67
	(3)	4.63	-0.53	5.08	-1.00
	(4)	5.32	0.0	4.86	0.0
	(5)	3.68	1.0	3.46	1.0
Rotated Hot Torsion	(1)	3.65	0.81	3.38	0.65
	(2)	3.78	0.85	3.88	0.91
	(3)	4.82	-1.39	4.83	-0.65
	(4)	4.71	0.0	4.37	0.0
	(5)	3.50	1.0	3.66	1.0
Hot-drawn	(1)	3.72	0.50	3.42	0.50
	(2)	4.31	0.50	3.73	0.85
	(3)	4.31	-0.53	4.36	-0.53
	(4)	4.07	0.0	4.10	0.0
	(5)	4.07	1.0	4.02	1.0

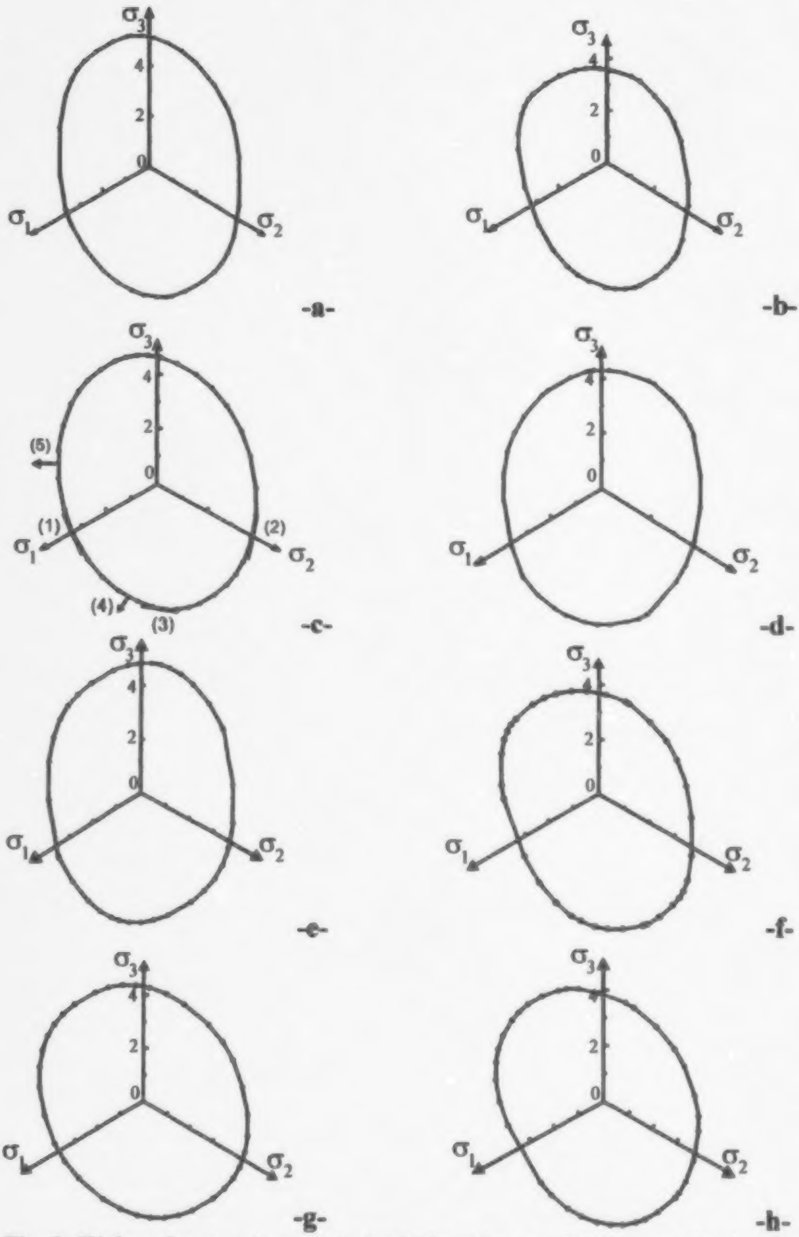

Fig. 3: High and room temperature yield surface projections on the deviatoric π plane. (a-b) Hot rolling, (c-d) torsion, (e-f) torsion + texture rotation and (g-h) drawning predeformations

with labels (1) and (2) respectively), uniaxial compression test along x_3 (label 3) and plane strain deformation with $\varepsilon_2=0$ and $\varepsilon_3=0$ (labels (4) and (5) respectively). Results are normalized to units of τ_{pr}.

In general, the equivalent stress and the q values corresponding to rolling pre-deformation are in good agreement with results corresponding to a hot torsion pre-deformation with a texture rotation

In the case of hot-drawn pre-deformed samples, the high temperature yield surface exhibits the symmetry of the texture. This is a direct consequence of the large activity of prismatic slip systems. In the case of room temperature, twinning activity is become significant and the symmetry of texture is not reflected by the yield surfaces.

4. Conclusions

Results from hot torsion tests can be extrapolated to adjust the material parameters for the description of the mechanical properties associated with hot rolling pre-deformations. It is possible when hot torsion textures are rotated in sucha way that the maximum expansion direction (+) becomes parallel to the rolling direction and the minimum expansion direction (-) becomes parallel to the normal direction of the rolled sample. This extrapolation allows to describe subsequently mechanical tests at room and high temperature.

On the other hand, there is not a clear way of extrapolating torsion tests results for the description of mechanical properties associated with hot drawning.

5. References

Lebensohn, R., Sanchez, P. and Pochettino, A. (1994) Modelling texture development of zirconium alloys at high temperature. *Scripta Metallurgica et Materialia*, Vol. 30, pp. 481-486.

Lebensohn, R. and Tomé, C. (1993) A self-consistent anisotropic approach for the simulation of plastic deformation and texture development of polycrystals: application to Zr alloys. *Acta Metall.*, Vol. 41, No 9, pp. 2611-2624.

Pochettino, A., Sanchez, P., Lebensohn, R. and Tomé, C. (1994) Temperature effects on rolling texture formation in zirconium alloys. *Materials Science Forum*, Vol. 157-162, pp. 835-840.

Rossard, C. (1976) Mise en forme des métaux et alliage, Ed. Du CNRS, Paris.

Sanchez, P., Lebensohn, R. and Pochettino, A. (1998) Influence of microestructural evolution on the macroscopic behavior of Zr alloys predeformed at high temperature in *Proc. of the 19th Risø International Symposium on Materials Science* (eds. J.V. Cartensen et al.) RISØ National Laboratory, Denmark, pp. 455-460.

Sanchez P., Lebensohn, R., Pochettino A. and Bacroix, B., to be published.

LEVITATION FORCE TO TEXTURE CORRELATION IN BULK Y-Ba-Cu-O.

D. CHATEIGNER AND J. RICOTE [#]
Laboratoire de Physique de l'Etat Condensé, Université Du Maine, Le Mans, France
X. CHAUD
Consortium de Recherche pour l'Emergence des Technologies Avancées, Centre National de la Recherche Scientifique, Grenoble, France
P. GAUTIER-PICARD, E. BEAUGNON and J.-L. SOUBEYROUX
Laboratoire de Cristallographie, Centre National de la Recherche Scientifique, Grenoble, France
C. LEBLOND, I. MONOT
Laboratoire Cristallographie et Sciences des Matériaux, Institut des Sciences de la Matière et du Rayonnement, Caen, France.
[#] present address: Instituto de Cienca de Materiales de Madrid, Consejo Superior de Investigaciones Científicas, Madrid, Spain

Abstract

Neutron diffraction Quantitative Texture Analysis is used to show the correlation between magnetic levitation force and texture in large bulk samples of the Y-Ba-Cu-O high-temperature superconducting systems. Samples are elaborated using the top-seeding process, with or without application of a high magnetic field and thermal gradient. The epitaxial-like texture relationships developed between the two main phases are evidenced, for a fraction of the volume.

Keywords: Correlation texture-levitation, full-pattern QTA, superconductors, $YBa_2Cu_3O_7$

1 Introduction

After twelve years of intensive research, the HTSCs are only barely used technologically, mainly because of the difficulties encountered in the elaboration of these complex systems. This has made the relatively easy-to-synthesise phases $YBa_2Cu_3O_{7-\delta}$ the most studied phase among all others. With critical temperatures around 90 K and relatively high critical magnetic fields, the $YBa_2Cu_3O_{7-\delta}$ (or Y123) phase have interest for its capability to be used as magnetic bearings. Large samples are needed in order to provide large magnetic levitation forces. However, several major facts limit the achievement of large bulks with suitable magnetic properties. First, the main superconducting phase (Y123) is stabilised through peritectic reaction, which causes partial formation of Y_2BaCuO_5 (Y211) influencing the properties, and which needs a precise control of the elaboration cycle. Secondly, the Y123 phase is strongly anisotropic, with critical current densities (Jc) about 10 times larger in the **(a,b)** plane than along **c**, which requires the development of strong textures. In levitation devices, the levitation forces are proportional to the product of the field gradient by the magnetisation, which is related to the size of the current loops and to the Jc of the Y123 phase grains. Since grain boundaries are strongly limiting the current flows through the basal (**a**,**b**) planes (Pernet et al., 1994), large grains oriented with **c** along the magnetisation direction, with a strong alignment of the **a** and **b** axes will prevent grain boundary effects. While many methods have been developed in order to produce strong alignment of Y123 crystallites, neither the effect of texture on levitation, nor the textural relationships between phases, has however been reported in the literature of such systems. We are using here neutron diffraction with position sensitive detector (PSD) and full peak analysis. We then quantitatively describe the textures and correlate them to the levitation forces of Y123 samples.

2 Samples

We have chosen combinations of several techniques for the elaboration of our samples. A $SmBa_2Cu_3O_7$ (Sm123) seed is placed at the centre of the surface pellet prior to melt-texturing (Gautier-Picard et al., 1998). One pellet (Y1) has been processed while applying a 8 T magnetic field (**H**), while the other (Y2) not. Both pellets are processed in the presence of a radial thermal gradient because of the furnace geometry. The after-process diameter is 44 mm and the height 17 mm. The surface is covered by one single grain starting from the seed (Figure 1, left). The growth follows a square pattern imposed by the seed and visible as diagonal growth lines. Three 8x8x8 mm^3 cubes were cut on each pellet and analysed (Figure 1, right): one from the centre (a), one from the edge (b) and a last one from the diagonal (along a seed growth line) near the edge (c). A third pellet (Y3) was prepared without measurable radial thermal gradient nor magnetic field. On this latter we only measured the differences between the centre of the pellet (Y3a) and its diagonal (Y3c). Prior to their characterisation, samples were carefully oxygenated to ensure superconducting properties.

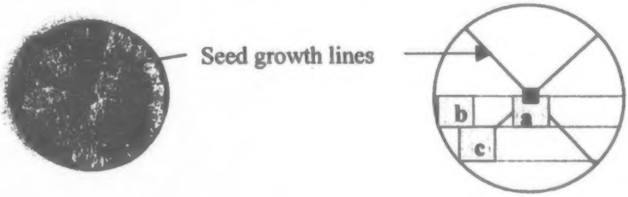

Figure 1: Y2 sample (left) prepared by the top seeded melt-texturing technique without magnetic field, and scheme (right) of the cubic cuts operated on each sample.

3 Experimental

3.1 Levitation measurements

The levitation measurement were performed with a Nd-Fe-B permanent magnet (22 cm diameter, 22 mm high, saturation magnetisation: 0.46 T). The force between the superconductor and the permanent magnet, F, is measured by a strength gage supporting the magnet and is recorded as a function of the distance, z, between the superconductor and the magnet, using a controlled translation table.

3.2 Texture measurements

Neutron diffraction experiments were carried out at the ILL, Grenoble, using the PSD and the Eulerian cradle of the D1B beam line (λ = 2.523 Å). We used a 5°x5° grid measurement with 15 s of measuring time for each diagram, and a neutron incidence angle of ω=30°. The Y123 phase crystallises in the Pmmm space group (a=3.81 Å, b=3.88 Å, c=11.66 Å), while Y211 is stabilised in the Pnma space group (a=12.181 Å, b=5.658 Å, c=7.132 Å), parameters that we used for the refinement of the Orientation Distribution (OD). The chosen ω allows to obtain full coverage of the pole figures for $\{112\}_{Y123}$, and blind areas of 10° in the centre of the $\{101/011\}_{Y123}$ and $\{102/012\}_{Y123}$ pole figures. These three pole figures offer enough orientation space coverage to refine the OD of the Y123 phase. We declared the overlaps as the one of the powder.

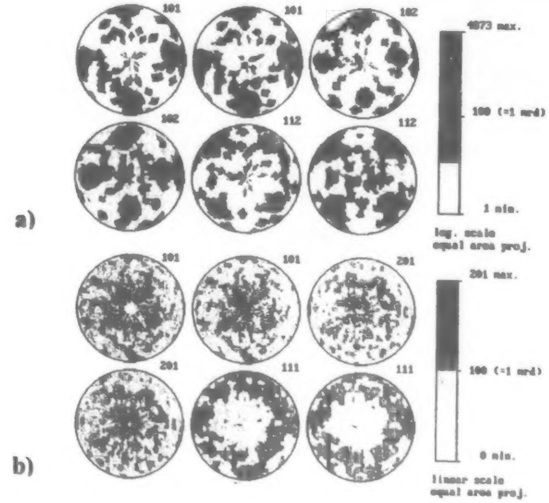

Figure 2: Typical experimental and recalculated pole figures (sample Y1a), to show the reproducibility of the pole figures from the OD refinement for **a)**: the major Y123 and **b)**: secondary Y211 phases.

For the Y211 phase, we choose the {101}, {201} and {111} non overlapped reflections. The detailed procedure for data reduction and correction is explained in a previous work (Chateigner et al., 1997). The OD was refined with the WIMV algorithm (Matthies & Vinel, 1982) of the Berkeley texture package (Wenk et al., 1998). The RP values for the refinements (Table 1) may appear high for the Y123 phase, but very high texture strengths are obtained (see entropy values and maximum OD). Typical reproductions for these phases are satisfactory as shown on Figure 2 for Y1a. We then recalculated the {001} and {100} pole figures to compare the samples.

4 Results and discussion

4.1 Levitation force

Figure 3 shows the results of the levitation measurements for Y1a, Y1b and Y1c. When the sample is brought to Nd-Fe-B, the levitation force increases up to a maximum value, F(z=0), near the contact. A severe decrease of F is observed with the distance to the centre of the pellet. This decrease is more pronounced for sample Y1 prepared with **H** than for Y2 (not shown here). For the centre of each sample the maximum levitation pressure values, P (Table 1) are comparable. The centre of each sample exhibits the largest P, but interestingly, for the edge, the piece cut along the growth lines exhibits larger P values than the one cut between two lines. For Y1, the edge (b) shows very low P, approximately half of the ones for Y2.

4.2 Quantitative Texture Analysis

Figure 4 shows the recalculated {001} and {100} pole figures of all samples for the major Y123 phase. Textures are very strong as denoted by the very low entropies (Table 1). In general, textures are single (0,0,0) component (Roe/Matthies convention) except Y1b which shows two [(0,0,0) and (280,40,75) in equal proportions]. Looking at samples Y2, with comparable textures (similar OD component and weak random component (FON)), there is a clear correlation between texture entropy and P. P is maximum at the centre where textures reach the strongest values (entropy as low as -6.6 and OD_{max} = 9500 m.r.d. for Y2a). The lower P(z=0) of Y2b is explained by the larger dispersion of the c axes denoted by a OD_{max} value of 1240 m.r.d., the lowest observed for the (0,0,0) single-component samples. When two texture components are present (Y1b), with one tilted from the pellet axis, levitation properties are further decreased. Also, the Y3 samples (Fig. 4, last row), which show the lowest FON, exhibit similar texture strengths to Y2a, and comparable P values.

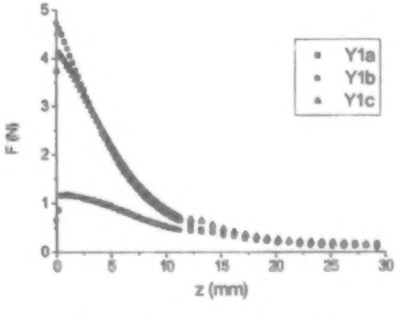

Figure 3: Levitation measurements for Y1 pellet, prepared with a magnetic field.

Comparing Y1 and Y2, we observe a tendency for Y1 to present a larger FON, though weak, than Y2, whatever the location in the pellet (a, b or c). At the same time Y1 shows a lower dispersion of the c axes for the (0,0,0) component. These two tendencies play opposite rules regarding entropy and OD_{max} variations. For instance, Y1a with a narrow dispersion of c axes and a relatively high FON, presents a larger entropy and a lower OD_{max} than Y2a. Globally, the Y1 pellet shows a relatively more disrupted texture than Y2 or Y3, may be as a result of a competition between the effect of the applied magnetic forces and grain growth. Without the application of a magnetic field (top seeding only), the texture looks to improve at the global scale, but the component becomes then more dispersed, only guided by the initial seed. With negligible thermal gradient (Y3), the top seed induces comparable texture on the diagonal (Y3c) than at the centre (Y3a).

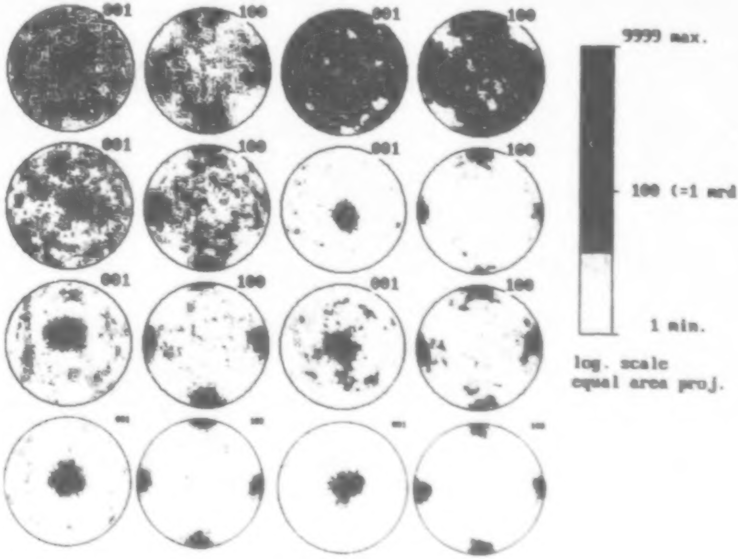

Figure 4: {001} and {100} recalculated pole figures for Y123 in Y1a, Y1b, Y1c, Y2a, Y2b, Y2c, Y3a and Y3c (successive order from top to bottom and left to right).

	P (z=0) (N/cm²)	Entropy		Max. OD (m.r.d.)		RP0 (%)		RP1 (%)	
		Y123	Y211	Y123	Y211	Y123	Y211	Y123	Y211
Y1a	7.9	-4.97	-0.15	1990	12.0	70	3.36	89	3.39
Y1b	2	-3.20	-0.03	429	3.03	54	2.34	50	2.13
Y1c	6.05	-5.16	-0.14	5370	18.4	61	2.93	71	2.65
Y2a	7.7	-6.57	-0.11	9500	5.67	78	2.56	71	2.17
Y2b	4.4	-4.96	-0.06	1240	8.03	58	1.48	44	1.50
Y2c	5.8	-5.01	-0.04	1520	6.64	51	2.08	38	1.94
Y3a	7.4	-6.36	-0.01	5650	1.62	77	1.84	74	1.35
Y3c	7.9	-6.25	-0.01	6240	1.55	66	2.09	58	1.57

Table 1: Maximum levitation pressure P(z=0) and OD-refinement characteristics for all phases of the samples: entropy and maximum in the OD, RP0 and RP1 reliability factors.

Results for the secondary Y211 phase are presented on Figure 5. This phase is also oriented, in a much less degree than Y123, with a maximum of the OD around 18 m.r.d. in Y1c. Remarkably, for the samples having the strongest (0,0,0) orientation component for the Y123 phase, the Y211 phase also presents this component. Also, the $\{010\}_{Y211}$ pole figure in these cases shows in-plane orientations corresponding to the $\{110\}_{Y123}$ positions (and the equivalent $\{013\}_{Y123}$ and $\{103\}_{Y123}$ positions by pseudo-symmetry relationships). We believe that this is due to the very similar $\{010\}_{Y211}$ and $\{110\}_{Y123}$ d-spacing which represents a relative mismatch of only 4%.

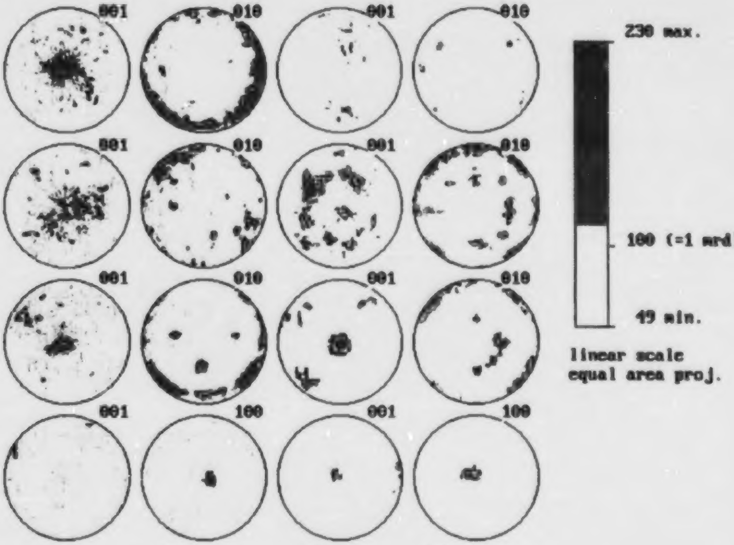

Figure 5: {001} and {010} recalculated pole figures for Y211 in Y1a, Y1b, Y1c, Y2a, Y2b, Y2c, Y3a and Y3c (successive order from top to bottom and left to right).

Without significant thermal gradient (Y3), the Y211 phase is also textured, with a lower strength than in Y1 and Y2, and presents two components, (0,0,0) and (0,90,0), the latter being predominant.

5 References

Chateigner, D., Wenk, H.-R. and Pernet, M. (1997). *J. Appl. Cryst.*, 30, pp 43-48.

Gautier-Picard, P., Chaud, X., Beaugnon, E., Erraud, A. and Tournier. R. (1998), *Mat. Sci. & Eng.*, B53, pp 66-69.

Pernet, M., Chateigner, D., Germi, P., Dubourdieu, C., Thomas, O., Sénateur, J.-P., Chambonnet, D. and Belouet C. (1994). *Physica C*, Vol. 235-240, pp 627-628.

Matthies S. and Vinel G.W. (1982). Phys. Stat. Sol. B 112, K111.

Wenk, H.-R., Matthies, S., Donovan, J. and Chateigner, D. (1998). *J. Appl. Cryst.* 31, pp 262-269.

TEXTURE EFFECT ON STRESS CORROSION CRACKING OF ZIRCONIUM ALLOYS IN IODINE ENVIRONMENT

S.B. GORYACHEV
Laboratory of Physical Metallurgy and Material Engineering, Lille University, Lille, France
A.R. GRITSUK and M.G. SNEGIREV
Moscow Physical Engineering Institute, Moscow, Russia

Abstract

An investigation of texture effect on deformation and fracture of Zr and Zr alloys used as fuel cladding materials has been performed in well-controlled conditions of an uniaxial tension at a constant strain rate in a flowing iodine vapor. As test objects we have used flat specimens, which have been cut out from a textured Zr-1% Nb plate in rolling, transversal, normal directions and by 45° degree to these directions in rolling-transversal, transversal-normal and rolling-normal planes as well as from Zr, Zr-1% Nb, Zry-2 and Zry-4 industrial preflattened claddings in axial and tangential directions. For a qualitative study of the crystallographic textures the X-ray reflection diffractometry method was used and texture parameters f representing the resolved fraction of basal poles in the tension direction have been calculated. By this way we have prepared a set of specimens with f varying over a wide range. The iodine environment influence on deformation and fracture of specimens has been investigated by stress-strain curves analysis and by scanning electronic microscopy observation of specimen surfaces after mechanical tests. We have concluded that the texture is the most important factor of Zr alloys susceptibility to stress corrosion cracking (SCC) in studied conditions. As a consequence Zr and its alloys have an universal dependence of susceptibility to SCC on the texture, which does not depend on alloy compositions. The dependence has a non-monotone, critical character: the susceptibility goes down slowly as f is reduced from 1 to 0.2, then it falls considerably as f decreases from 0.2 to 0.1 and after that it disappears. We have established that the limit state of SCC of Zr alloys in these conditions is a stressed state for which an effective cleavage stress in basal plane reaches a critical value.

Keywords: Zirconium alloys, texture, stress corrosion cracking, iodine

1 Introduction

Zirconium fuel claddings of water cooled reactors are sensitive to SCC in iodine environment, which is released as fission product. SCC presents a complicated phenomenon depending on many factors: chemical composition and physical state of corrosive environment; surface state of cladding; chemical composition and structural state of cladding material, stress-strain state of cladding. The cladding crystallographic texture is a major metallurgical factor defining susceptibility of claddings to SCC (Cox 1990; Goryachev et al. 1992). SCC is increased when orientation of basal planes is becoming more radial as a consequence of crack initiation and propagation along certain crystallographic planes. Though the texture effect on SCC has long been known, it has been never studied for different Zr alloys under the same experimental conditions. So a clear distinguishing of the texture effect on SCC from the other physico-chemical, metallurgical and mechanical factors is very difficult by comparing the results of different laboratories. That is the reason why we have performed this comparative investigation of texture effect on SCC of all industrial Zr alloys in simple, well-controlled conditions of an uniaxial tension at a constant strain rate in a flowing iodine vapor by using as test objects the flat specimens with quite different crystallographic textures.

2 Experimental procedure

Zr and its industrial alloys Zr-1% Nb, Zry-2, Zry-4 have been chosen as a materials for research in the form of industrial cladding tubes, specially rolled thick plates and specially rolled sheets (Table 1). Texture was analyzed by the X-ray diffraction techniques of direct pole figures (0001). All materials have a texture with a preferential distribution of basal poles in the RT-plane and pole intensity maxima arranged in this plane at an angle of about ±30° from N-direction. To describe the texture quantitatively its parameters f_R , f_T and f_N were calculated that indicates the fraction of basal poles in the R, T and N-directions, respectively (Table 1).

Table 1: Materials.

N°	Material	Form	Size(mm)		Texture parameters		
			Thickness	Diameter	f_R	f_T	f_N
1	Zr-1% Nb	Plate	20		0.10	0.30	0.60
2	Zr-1% Nb	Sheet	2		0.05	0.24	0.71
3	Zr-1% Nb	Sheet	1.2		0.10	0.17	0.73
4	Zr-1% Nb	Tube	0.9	13.6	0.05	0.18	0.77
5	Zr-1% Nb	Tube	0.65	9.15	0.05	0.18	0.77
6	Zr	Tube	0.65	9.15	0.06	0.17	0.77
7	Zry-2	Tube	0.72	9.6	0.06	0.18	0.76
8	Zry-4	Tube	0.65	9.55	0.06	0.18	0.76

Rectangular (flat) tension specimens from Zr, Zr-1% Nb, Zry-2 and Zry-4 industrial preflattened cladding tubes have been cut out in axial (R) and tangential (T) directions and by 45° degree to these directions (RT). To extend the texture change range the specimen set has been supplemented with specimens being cut from textured Zr-1% Nb sheets in rolling (R) and transversal (T) directions and by 45° degree to these directions (RT). Sizes of specimen working part were 9 mm x 2 mm x thickness for materials n° 2, 3, 5-8 and 15 mm × 3 mm × thickness for material n° 4 (Table 1). The claddings and the sheets have too small thickness to prepare tension specimens in all orthotropy directions and this decreases drastically the change range of specimen crystallographic textures. That is why a specially rolled thick Zr-1% Nb plate was taken as a basic material for the research. Rectangular specimens have been cut out from the plate in rolling (R), transversal (T), normal (N) directions and by 45° degree to these directions in rolling-transversal (RT), transversal-normal (TN) and rolling-normal (RN) planes. Specimen working part have had the sizes 10 mm × 6 mm × 1 mm for the specimens being cut out along plate thickness and 24 mm × 6 mm × 1 mm for the other ones. To analyze the orientation effect of corrosive contact surface with reference to the texture, the specimens in R-, T- and N-directions have been cut out with their wide face oriented in two possible orthotropy planes. All specimens after fabrication were treated by recrystallization annealing in vacuum for 6 hours at 873°K and then they were etched in solutions of acetic and perchloric acid. In designation of specimens (e.g. 1-N-R or 1-RT-N) the first index gives the material number (Table 1), the second one indicates the direction of specimen tension and the third one gives the direction being perpendicular to the wide specimen face.

Equipment for active tensile tests of zirconium specimens in the argon gaseous atmosphere with iodine was described early (Goryachev et al. 1992). The main parameters of the testing conditions are as follows: deformation rate $1,2 \times 10^{-5} s^{-1}$; temperature 623°K; rate of gas pumping through the test chamber 140 ml/min; iodine partial pressure in the chamber 900 Pa. « Load-elongation » diagrams were recorded and specimen cross-section measurements were made after their fracture. Engineering stress-strain curves were constructed (Fig. 1). The following mechanical characteristics for each group of 8+10 specimens of the same type have been determined: yield strength $s_{0.2}$, tensile strength s_u , critical true stress of corrosion cracking σ_{SCC}, true fracture stress σ_f, strain to fracture ε_f , reduction in area at fracture q and relative value of SCC change of reduction in area at fracture $\eta = (q_{Ar} - q_I)/q_{Ar}$. Critical true stress of corrosion cracking σ_{SCC} was determined as the true stress for the salient point of stress-strain curve corresponding to the intensive SCC beginning.

3 Results and discussion

Typical stress-strain curves obtained under tests in argon environment and argon-iodine environment are shown in Fig. 1. It is clear that iodine does not have any

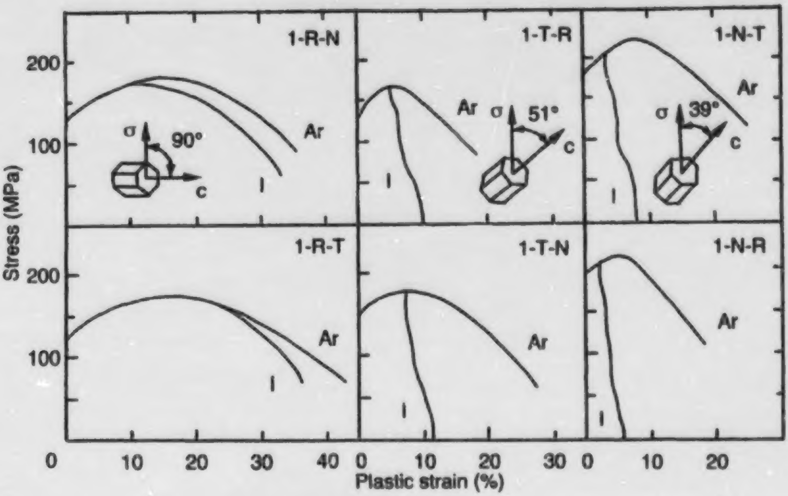

Fig. 1: Stress-strain tension curves of Zr-1% Nb alloy in the argon (Ar) and argon-iodine (I) environments. C -axis orientations with reference to the tensile direction σ are shown approximately.

embrittlement effect on R-specimens (1-R-N and 1-R-T) and the curve for the specimen tested in aggressive environment practically coincides with the curve of the specimen tested in neutral environment. However, the embrittlement for T- (1-T-R and 1-T-N) and N-specimens (1-N-T and 1-N-R) was clearly expressed. The plasticity described by reduction in area at fracture q falls considerably (Table 2).

Optical and scanning electron microscopy have shown that the fracture of all the specimens in neutral environment was ductile, the fracture of R-specimens in aggressive environment was also ductile and the fracture of T- and N-specimens was brittle.

Table 2: Mechanical characteristics of Zr-1% Nb alloy.

Specimen	Environment					
	Argon			Argon-iodine		
	$s_{0.2}$ (MPa)	s_u (MPa)	q (%)	$s_{0.2}$ (MPa)	s_u (MPa)	q (%)
1-R-T	122	169	80.4	123	171	74.8
1-R-N	132	175	73.2	129	170	70.7
1-T-N	144	182	80.0	142	179	12.6
1-T-R	123	178	86,0	120	175	26.6
1-N-T	175	226	71.4	169	207	8.3
1-N-R	176	222	80.9	174	205	3.3

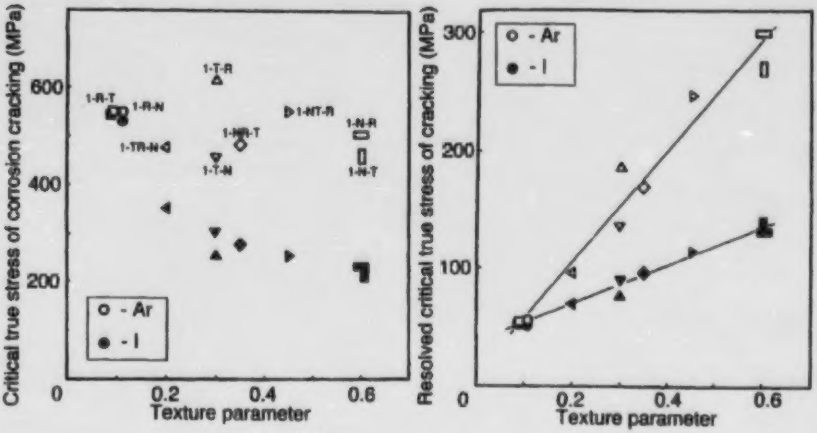

Fig. 2: Critical true stress of corrosion cracking σ_{SCC} and resolved critical true stress of corrosion cracking σ_{SCC} f as functions of texture parameter of Zr-1% Nb alloy in tension direction.

Fig. 2 presents the dependence of critical true stress of corrosion cracking σ_{SCC} on the texture parameter f of Zr-1% Nb alloy in tension direction. The stress σ_{SCC} was determined as the true stress of SCC beginning for the tests in argon-iodine environment and as the true fracture stress σ_f for the tests in argon. As the data of Fig. 2 suggest σ_{SCC} does not practically depend on f in neutral environment, it increases with decreasing of f in aggressive environment and they have the same value for f smaller a critical value f_c=0.1. The resolved critical true stress of corrosion cracking (σ_{SCC} f), which has a sense of normal stress in basal crystallographic plane, changes linearly with f for f >0.1. This dependence may be presented by the relation:

$$\sigma_{SCC} = \sigma_n / f + \sigma_i \ , \qquad (1)$$

where $\sigma_n \approx 37$ MPa is a critical cleavage stress in basal crystallographic plane and $\sigma_i \approx 162$ MPa is an effective internal tension stress. Rewriting Eqn 1 as $(\sigma_{SCC} - \sigma_i)f = \sigma_n$ we can conclude that SCC begins when the effective cleavage stress in basal plane $(\sigma_{SCC} - \sigma_i)f$ reaches its critical value σ_n.

Comparative analysis of mechanical characteristics of Zr-1% Nb alloy, Zr and other Zr alloys shows that SCC essentially depends on the alloy strength. A higher strength of alloys favours SCC and, on the contrary, a lower strength improves SCC resistance (Fig. 3). At the same time relation (1) for critical true stress of corrosion cracking σ_{SCC} still stands. Hence the texture is the most important factor of SCC susceptibility of Zr alloys and the limit state of SCC is the stressed state for which the effective cleavage stress in basal plane reaches the critical value.

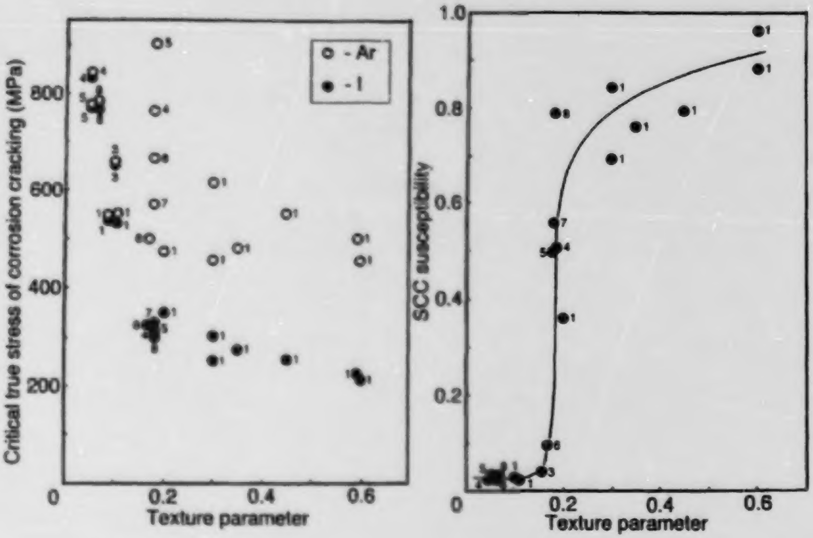

Fig. 3: Critical true stress of corrosion cracking σ_{SCC} and SCC susceptibility η as functions of texture parameter f in tension direction. Each point is related to a group of specimens of the same type. Material numbers are indicated.

Turning back to Fig. 1 we see that under deformation of N-specimens ($f \approx 0.6$) the limit state of SCC is reached for small plastic deformation; under deformation of T-specimens ($f=0.3$) the limit state is reached in necking region of specimen and under deformation of R-specimens ($f=0.1$) the limit state is never reached.

Crucial influence of texture on SCC of Zr alloys and the universal character of SCC susceptibility dependence on texture, whatever the alloy composition, may be also confirmed if we define the susceptibility by the relative value of SCC change of reduction in area at fracture $\eta = (q_{Ar} - q_{I})/q_{Ar}$. The dependence of η on f has a non-monotone, critical character: the susceptibility goes down slowly as f is reduced from 1 to 0.2, then it falls considerably as TP decreases from 0.2 to 0.1 and after that it disappears below critical value $f_c=0.1$ (Fig. 3).

4 References

Cox, B., (1990) Pellet-clad interaction (PCI) failures of zirconium alloy fuel cladding - a review. *Journal of Nuclear Materials*, Vol. 172, pp. 249-292.

Goryachev, S.B., Gritsuk, A.R., Prasolov, P.F., Snegirev, M.G., Shestak, V.E., Novikov, V.V. and Bibilashvili, Yu.K. (1992) Iodine induced SCC of Zr alloys at constant strain rate. *Journal of Nuclear Materials*, Vol. 199, pp. 50-60.

EFFECT OF TEXTURE ON ETCHING PROPERTY AND FORMABILITY IN INVAR SHADOW MASK

N.J. PARK and M.H. OH
Dept. of Mat. Sci. & Eng., Kumoh National Univ. of Tech., Kumi, Rep. of Korea
S.M. KIM and K.R. KIM
Display device research lab., LG Electronics Inc. Kumi, Rep. of Korea

Abstract

In order to make a high quality color cathode ray tube, the influence of the texture on the etching and forming property has been studied by invar shadow mask. New characteristic values such as RD- and FR-value which are calculated with ODF, are suggested to the estimation of properties. The good etching property is obtained when the RD-value is more than 2. For making the shadow mask, the FR-value has to be more than 0.5, which means the low orientation density of {100}<001>-component.

key-words : texture, invar, shadow mask, etching property, formability

1 Introduction

For the high-definition TV or monitor, an excellent quality of color cathode ray tube (CRT) with fine pitched uniform holes in shadow mask is required (Higashinakagawa et al. 1985). In a color CRT as shown in Fig.1, if the video signal is coming, the thermal electrons are emitted from the electron gun. The electrons are accelerated, focused and deflected by several electrodes and deflection coil. The deflected electrons travel toward the front side of the tube. The holes (Fig.2) in the shadow mask allow that the electron-beam run into precisely specific spots on fluorescent screen for colors on the glass-panel and reproduce the video signal. An Al-killed steel has been used as a material for shadow mask. However, because of the large thermal expansion coefficient (11.5 x 10^{-6}/℃), the good reproducing of the colors is hindered. The shadow mask expanded during the operation by heat from collision of the electrons on the shadow mask. This causes the small displacement of the holes and doming which is color dispersion occurring when the electrons run into other spots of the fluorescent screen. In order to prevent the doming, an invar alloy (Fe-36%Ni) with small thermal expansion coefficient (1.5 x 10^{-6}/℃) is used (Saito 1978; Beranger et al. 1996). The high manufacturing accuracy of the electron-beam holes has been achieved by etching a shadow mask plate. However the invar has a bad etching and forming property in comparison with the Al-killed steel (Higashinakagawa et al. 1985; Suzuki et al. 1986). Therefore the control of the etching and formability is very important for the manufacturing of the fine pitched uniform holes. In this study the etching and forming properties are controlled by means of heat-treatment and established new control-values using texture analysis.

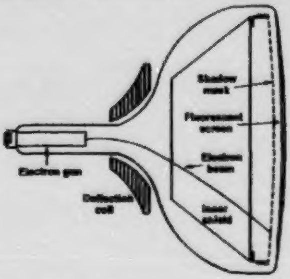

Fig.1: Interior structure of a color cathode ray tube

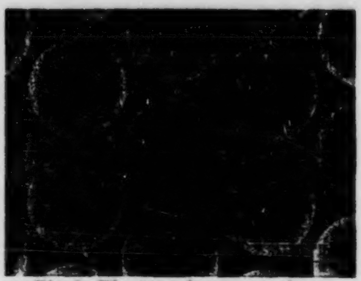

Fig.2: Electron-beam passing hole of shadow mask

2 Concept of the characteristic values

Generally, if many grains with {100} or {111}-lattice planes are clustered parallel to the surface of the invar sheet, the electron-beam holes are formed better by etching. And if the grains with {110}-lattice plane are more in the surface, then elliptical holes will be formed during the etching. This lead to failing to form circular holes with high accuracy. Up to now, the following g- and a-value were used for the control of orientation-distribution of grains.

$$g = \frac{I_{(111)} + I_{(200)}}{I_{(220)}}, \qquad a = \frac{I_{(200)}}{I_{(220)}} \tag{1}$$

Hereby the integral-intensity of X-ray diffraction patterns is used. If the g-value is more than 2 or a-value more than 1, the etching property is good (Higashinakagawa et al. 1988). However, the direct measured diffraction-intensity depends on many factors, such as structure factor, multiplicity factor and Lorenz-polarization factor (Cullity 1978). Therefore, the g-value>2 can not indicate that the more grains with {100} or {111}-lattice planes are clustered parallel to the surface than with {110}-lattice plane. Actually, the calculated g-values are 3.6 and 5.96 with the values of JCPDS-card No. 23-297 or 47-1405 which was measured by powder sample of invar. For that reason, the measured intensity must be corrected with random sample. In the present work, for the decision of the etching property and formability, new characteristic values (RD- and FR-value which are calculated with ODF directly) are proposed. The idea for these values is coming from the manufacturing process of invar sheet. Usually by materials with face-centered cubic structure, the texture after cold-rolling can be characterized mainly with β-fiber component which run from {112}<111> into {123}<634> and {011}<211> orientations (Hirsch and Luecke 1988). And after full recrystallization, the texture can be represented by the ideal orientation {100}<001>-component (Ridha and Hutchinson 1982). If the strong {100}<001>-orientation is developed by invar, the etching property is improved. Therefore, the ratio of these intensities is taken as RD-value for etching property (eq.2). For the shadow mask of CRT, the invar sheet is formed after heat-treatment by means of deep drawing. The formability by shadow mask means therefore the deep-drawing property, which is promoted generally by the γ-fiber(<111> ‖ NR) texture. The FR-value is determined with the intensity-ratio of {100}<001>-component and γ-fiber(eq.3).

$$RD = \frac{f(g)_{\{100\}<001>}}{mean \;\; of \;\; f(g)_{\beta-fiber}} \tag{2}$$

$$FR = \frac{mean \;\; of \;\; f(g)_{\gamma-fiber}}{f(g)_{\{100\}<001>}} \tag{3}$$

3 Experimental

Two invar sheets with 0.12mm thickness (sample-A and B) were delivered from different manufactories. The composition of the impurities was controlled as follows; $C \leq 0.01\%$, $Mn \leq 0.4\%$, $Si \leq 0.05\%$, $Al \leq 0.015\%$, $Cr \leq 0.1\%$. In order to check the property according to the texture-change, heat-treatments were carried out at 750, 800, 850, 880, 900℃ for 30 minutes. Yield strength, elongation and average normal anisotropy $r_m = (r_0+2r_{45}+r_{90})/4$, are measured with tensile test. The texture was determined with {111}, {200}, {220} and {311} incomplete measured pole figures with a maximum series expansion degree $L_{max}=32$. The pole figures were measured on the BRUKER-D5005 automatic texture goniometer using Co Kα-radiation. The complete ODFs were calculated using an iterative positivity method (Bunge 1982; Dahms and Bunge 1989). The etching property was estimated by the etching rate, which is obtained by the ratio of weight before and after etching. The spray etching was carried out with a ferrous chloride solution using a photoresist pattern with holes. The forming property had controlled with drawn depth by stretching and deep-drawing which were carried out with the drawing machine for the mask-forming.

4 Results and discussion

Mechanical property: The properties measured by tensile test are given in table 1. The yield strength of the as-received sample-A is 365MPa, and 468MPa by the sample-B. After heat-treatment the strength is decreased to ca. 200MPa regardless of the temperatures of both samples. The elongation is ca. 30% after heat-treatment by all samples. But before the heat-treatment, sample-A was elongated 9.3% and 1% by sample-B. The average normal anisotropy r_m-value after heat-treatment is 1 by sample-A which is higher than the value 0.9 of sample-B.

Texture: The measured pole figures and complete ODF of the initial sample-A is shown in Fig.3. The sharp {001}<100>-texture with the maximum intensity of 63 x random distribution and a weak β-fiber component was observed. This indicated, the sample-A was mainly recrystallized. The β-fiber is developed not with the same intensity over whole fiber but only near the {123}<634>-component with the maximum density f(g)=10. By the sample-B (Fig.4) the {001}<100>-texture was developed more weakly (f(g)max=21.4) than by the sample-A, and the β-fiber is maintained over whole fiber which means that the sample-B was not fully recrystallized or after hot-rolling the temper-rolling was carried out. This can be understood also from the high value of yield stress and low elongation of the initial sample-B. After heat-treatment, the grains were rearranged nearly randomly by both sample-A, B, which is shown in Fig.5 and 6 by the inverse pole figures for the normal direction.

Table 1. Mechanical properties and characteristic values

	Property and Characteristic value	**As received**	**Temperature of heat-treatment (30min)**				
			750℃	**800℃**	**850℃**	**880℃**	**900℃**
Sample A	Yield strength (MPa)	365	216	211	205	200	199
	Elongation (%)	9.3	28.1	30.7	31.0	29.9	27.9
	R_m-value	-	1.00	0.98	1.02	1.07	1.04
	RD	18.71	3.87	1.07	0.88	0.96	1.09
	FR	0.01	0.28	1.10	1.09	1.08	0.93
Sample B	Yield strength (MPa)	468	215	209	208	207	203
	Elongation (%)	1.0	30.9	31.9	31.6	30.3	28.9
	R_m-value	-	0.90	0.83	0.92	0.90	0.90
	RD	4.90	1.58	1.78	2.06	1.91	1.70
	FR	0.04	0.87	0.82	0.71	0.46	0.83

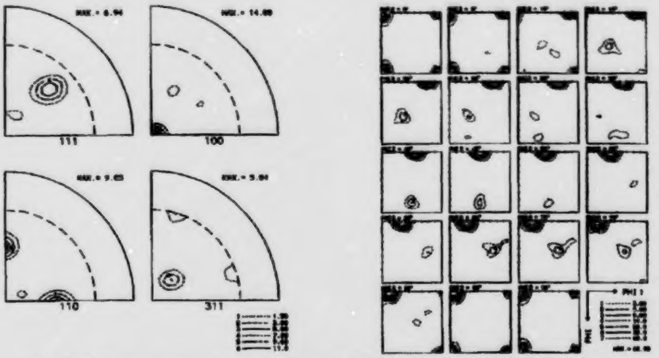

Fig.3: Measured pole figures and ODF of the initial sample-A

Characteristic values: The values which were calculated with eq.(2) and (3), are given in table 1. By the sample-A, the RD-value is very high by the initial sheet which was caused by the sharp texture with {100}<001>-component. After heat-treatment the values were decreased, and above a temperature of 800℃ these are not changed(RD-value is decreased from 18.71 to near 1). This means that the etching property of the as-received sample must be better than the sample after heat-treatment.

FR-values are increased after heat-treatment(above 800℃) from 0.01 to near 1. As a consequence, the formability after heat-treatment must be better. By the sample-B, the RD-value of the initial sheet is 4.9 and after heat-treatment is 1.58~2.06. The RD-values are higher than 1, which indicate the {100}-planes are still more arranged on the surface. The FR-values after heat-treatment are increased to ca. 0.5.

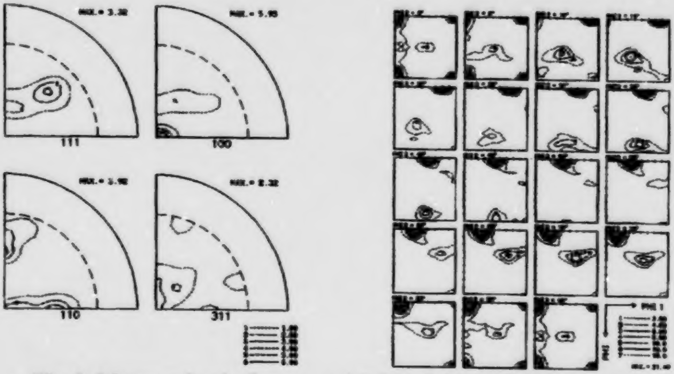

Fig.4: Measured pole figures and ODF of the initial sample-B

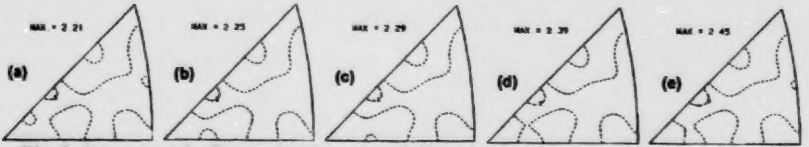

Fig.5: Inverse pole figure for the normal direction of the heat-treated sample-A
(a) 750℃ (b) 800℃, (c) 850℃ (d) 880℃, (e) 900℃

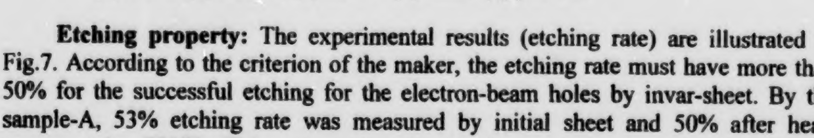

Fig.6: Inverse pole figure for the normal direction of the heat-treated sample-B
(a)750℃ (b) 800℃, (c) 850℃ (d) 880℃, (e) 900℃

Etching property: The experimental results (etching rate) are illustrated in Fig.7. According to the criterion of the maker, the etching rate must have more than 50% for the successful etching for the electron-beam holes by invar-sheet. By the sample-A, 53% etching rate was measured by initial sheet and 50% after heat-treatment by 750℃. This means that the etching property is still good for the formation of the holes. But after heat-treatment above 750℃ the etching rate is decreased to an unfavorable value of 47%. These can be clearly understood with the low RD-values. By the sample-B, the etching rate is measured 52% by the initial sheet, but other samples with heat-treatment have ca.47%. This trend of the etching rate is confirmed by the RD-value.

Formability: Without the heat-treatment by both samples, the deep-drawing test failed. The drawn depth by the heat-treatment samples is given in Fig.8. By increasing the temperature of the heat-treatment, the drawn depth is increased from 16.4mm by 750℃, which is not adequate for the forming of shadow mask, because a good finished mask has to have a drawn depth more than 16.55mm. This value can be achieved with a heat-treatment more than 850℃ by the sample-A and 900℃ by the sample-B. The FR-values (Tab.1) express good this formability of the mask. A FR-value of more than 0.5 recommend for the good formability.

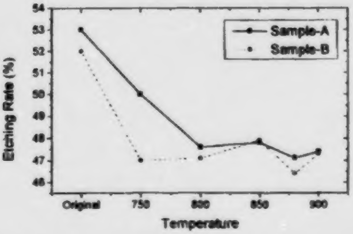

Fig.7: Etching rate(%) after heat-treatments

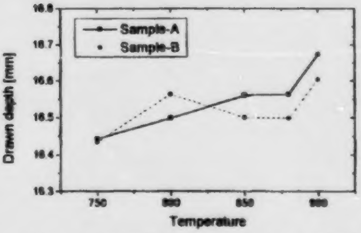

Fig.8: Drawn depth (mm) by forming-test

5 Conclusions

The influence of the texture on the etching and forming property has been studied by shadow mask which is made with invar (Fe-36%Ni) sheet. For the decision of the etching property and formability of invar shadow mask, new characteristic values - RD- and FR-value - are proposed which is calculated with ODF. The good etching property is obtained when the RD-value is more than 2. For the deep drawing property for making the shadow mask, the FR-value has to be more than 0.5, which means the low orientation density of 100<001>-component. This can achieved with a heat-treatment of more than 850℃ or 900℃.

6 References

Beranger, G., Duffaut, F., Morlet, J. and Tiers, J.-F. (1996) *The iron-nikel alloys*, Laboisier Publishing, France

Bunge, H.J. (1982) *Texture Analysis in Materials Science*, Butterworths Pub., London

Cullity, B.D. (1978) *Element of X-ray diffraction*, Addison-Wesley Pub., Massachusetts

Dahms, M. and Bunge, H.J. (1989) J. Appl. Cryst., Vol.22, 439

Higashinakagawa, E., Sato, K., Inaba, M., Ohtake, Y., Kanto, M. and Itoh, M. (1985) US-patent 4,528,246

Higashinakagawa, E., Inaba, M., Ohtake, Y. and Kanto, M. (1988) US-patent 4,771,213

Hirsch, J. and Luecke, K. (1988) Acta Metall., Vol.36, 2863

Ridha, A.A. and Hutchinson, W.B. (1982) Acta Metall., Vol.30, 1929

Saito, H. (1978) *Physis and application of invar alloys*, Maruzen Comp., Tokyo

Suzuki, F., Hujinuma, M., Ohtake, Y. and Inaba, M. (1986) US-patent 4,612,061

TEXTURE MEASUREMENT IN STEEL INDUSTRY PRACTICE

C. KLINKENBERG, H.-P. SCHMITZ and H. TAMLER
Thyssen Krupp Stahl AG

Abstract

From industrial point of view, texture analysis is an interesting tool for the prediction of the anisotropic mechanical behaviour of sheet materials. The r-values calculated from the C-coefficients of the ODF are in good agreement to those achieved by standard mechanical tests and may even be online measured during industrial processing. This contribution points out some possibilities of industrial application of quantitative laboratory and online texture analysis by example of austenitic and ferritic hot rolling and it's influence on the later hot- and cold-rolled strip's properties of low carbon steel.

Keywords: r-values, on-line texture measurement, low carbon steel, ferritic rolling

1 Introduction

Hot strip is either bound for direct use or cold rolled and annealed before further processing. The texture related structural and mechanical properties can be optimised by an appropriate choice of hot rolling conditions as temperature cycle and forming parameters. The newly developed techniques of hot rolling in the ferritic state give rise to more pronounced hot strip texture properties than classical processing in the austenitic range. Texture and mechanical properties of ferritic rolled hot strip match those of cold-rolled steel.

Hot strip texture and microstructure strongly influence the later cold rolling textures and their related anisotropic behaviour. Therefore, the pronounced hot strip textures of ferritic rolled hot strip arise the effective cold rolling degree of the later cold rolled strip.

Texture measurement has become an important tool for the development of new steel grades, quality assurance and process control. Consequently the continuous annealing line of the Thyssen Krupp Stahl AG is equipped with an on-line texture analyser, in order to control the uniformity of the r-value along the entire strip length. This contribution will point out, that specific effects of different hot rolling conditions on the later cold strip's textures can be met by on-line measurement.

2 Experimental investigations

All investigations have been carried out on industrially produced and processed steels.

2.1 Materials

Table 1 contains the chemical compositions of the investigated steels.

Table 1: Chemical compositions [mass %].

Steel	C	Mn	P	S	Al	N	Ti
IF	0.004	0.13	0.006	0.011	0.050	0.004	0.06
LC	0.028	0.16	0.009	0.006	0.025	0,006	-

2.2 Texture measurement

Results from laboratory measurements have been achieved by X-ray back-reflection method in mid-thickness position of the specimen.

Figure 1 gives a schematic set up of the on-line texture measurement. The examined strip is irradiated by the bremsstrahlung radiation of a 100keV X-rax tube in transmission mode. A primary collimator system selects four X-ray beams according to representing positions within the pole figures. The diffracted and transmitted parts of the radiation are measured by four energy-dispersive detectors in fixed positions corresponding to the above mentioned optimal pole positions (Richter and Tamler 1999).

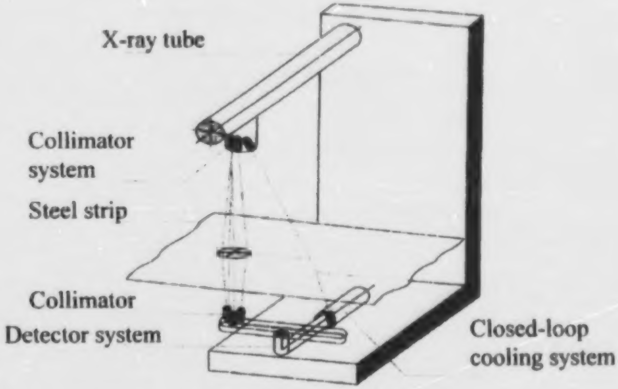

Fig. 1: On-line texture measurement.

2.3 Experimental results

2.3.1 Effect of different hot rolling conditions

Steel textures can generally be described by fibre components, having a common crystallographic axis (Klinkenberg, Raabe and Lücke 1993). As shown in **Figure 2**, austenitic rolled hot strip has a nearly random orientation distribution as a result of the phase transition, whereas ferritic rolled strip has a sharply defined texture with high occurrence of the orientations between Φ = 0 and 40° on the α-fibre, similar to cold rolling textures (Engl, Kawalla, Schmitz, Heckelmann, Friedrich, and Stich 1998).

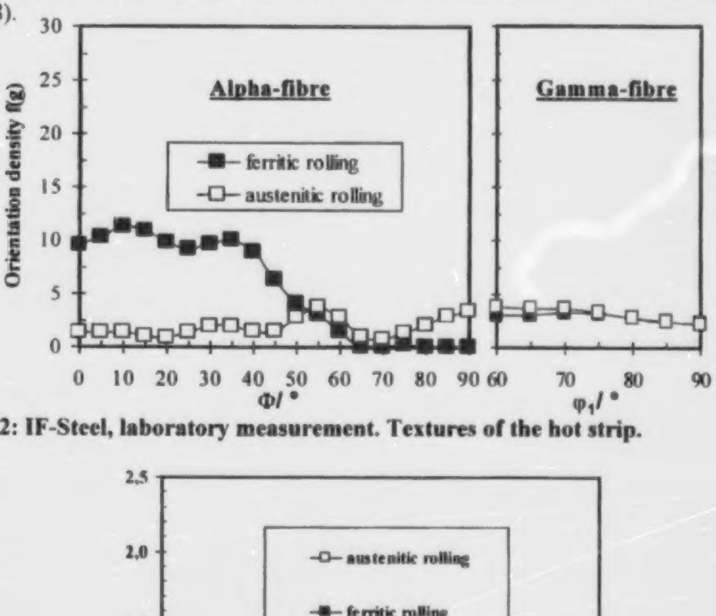

Fig. 2: IF-Steel, laboratory measurement. Textures of the hot strip.

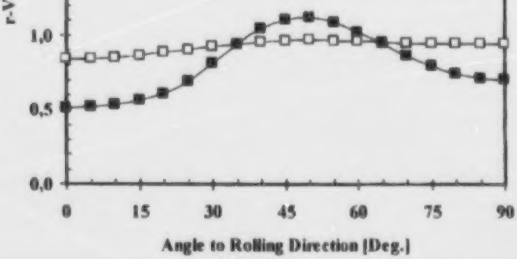

Fig. 3: From textures calculated r-values of austenitic and ferritic hot rolled strip (IF-Steel).

Figure 3 contains the mutual comparison of the r-value curves for austenitic and ferritic rolled hot strip calculated from the C-coefficients. In contrast to the quasi-isotropic austenitic rolled hot strip, the ferritic rolled material has a higher mean r-value r_m but also a greater Δr-value. This behaviour is explained by the texture differences depicted in Figure 2. The dominating α-fibre in ferritic rolled material leads to an increased r-value at 45° with respect to the rolling direction and lower r-values in the rolling and transverse directions.

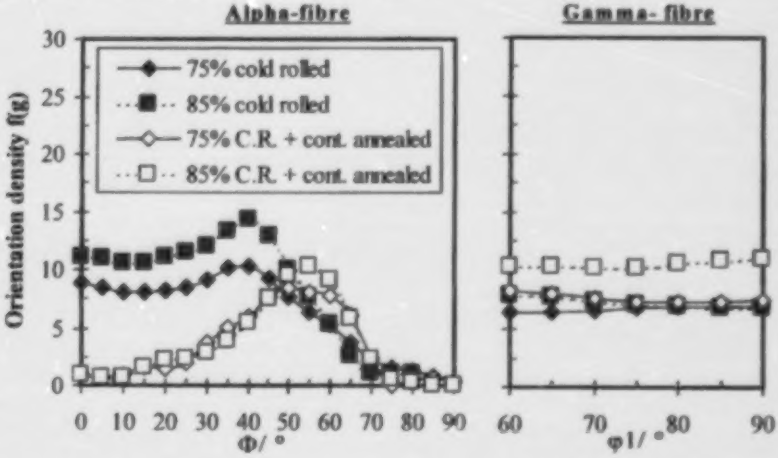

Fig. 4: IF-Steel, laboratory measurement. Textures of cold rolled strip from *austenitic rolled* hot strip.

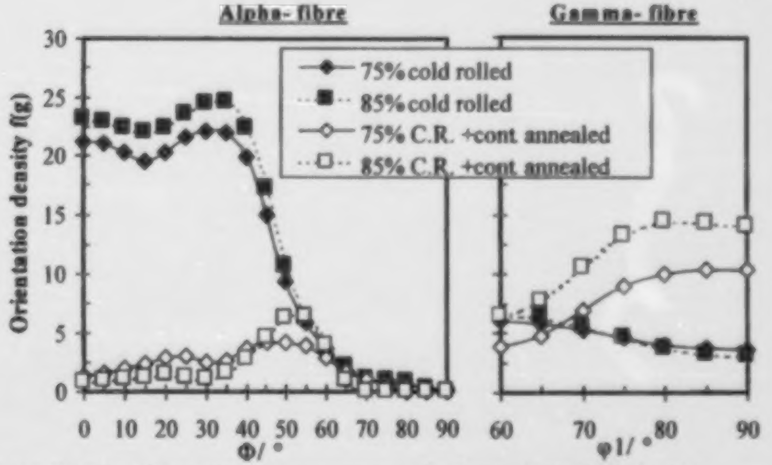

Fig. 5.: IF-Steel, laboratory measurement. Textures of cold rolled strip from *ferritic rolled* hot strip.

Figure 4 and Figure 5 show the textures of cold-rolled and continuous annealed strip from ferritic and austenitic hot-rolled material of the IF-steel. The respective degrees of cold-rolling are 75% and 85%. The chief component of the cold-rolling textures is always an α-fibre with high frequencies of occurrence between Φ = 0 and about 50°. These orientation densities increase with the effective degree of cold-rolling. Therefore the ferritic rolled strips which have already been pre-hardened during hot-rolling manifest greater orientation densities on the α-fibre. The recrystallisation textures of the ferritic hot-rolled strips are characterised by the orientation {111}<112> on the γ-fibre. The density of this orientation increases with the cold-rolling degree. The austenitic hot-rolled 75% cold-rolled and recrystallised annealed strip has a γ-fibre with uniform occupation of all orientations between {111}<110> and {111}<112>. After 85% cold rolling, the orientation {111}<112> becomes the texture-determining component here too.

The r-value curves calculated from the textures for the continuous annealed, 75% cold-rolled strips from austenitic and ferritic hot-rolling are shown in Figure 6. The austenitic rolled strip exhibits the classical r-value distribution of recrystallised cold strip, having a cold-rolling reduction of about 75%. The r-values from ferritic rolled strip show the characteristics of an higher cold reduction degree. This is due to pre-straining, which has been introduced during ferritic rolling.

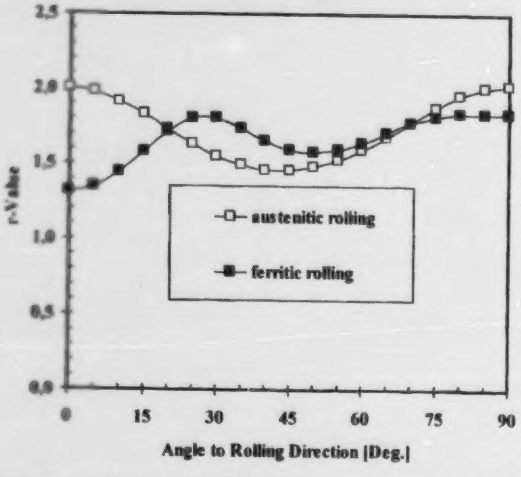

Fig. 6: From textures calculated r-values of recrystallised cold strip from austenitic and ferritic hot rolled strip.

2.3.2 Verification by on-line measurements

The above described effects of austenitic and ferritic hot rolling on the final cold strip's properties are controlled by on-line measurements. Figure 7 gives the comparison of the transverse r-values (r_t) determined from the on-line measurement, with the mechanically achieved r_t-values of the LC-steel. It demonstrates the good agreement of the two methods. Like in Figure 6, the transverse value r_t is higher after austenitic rolling. The more pronounced differences are due to the fact, that finish rolling temperatures of about 850°C means that end rolling takes place in the $\alpha+\gamma$ two-phase region for the low carbon steel (LC) containing about 0.028% carbon, considered here.

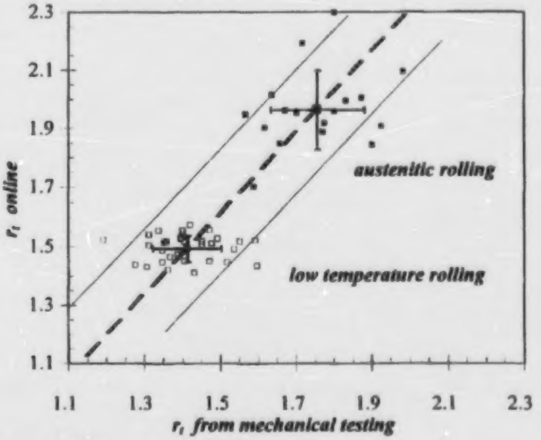

**Fig. 7: LC-steel, on-line measurement.
Comparison of texture-based and mechanical achieved transverse r-values (r_t)**

3 Conclusion

Texture analysis in industrial praxis is a sensitive tool. At the example of different hot-rolling conditions on same steel grades, significant influences on the final cold strip's texture could be found by off-line laboratory as well as on-line texture analysis. These differences are at the origin of different mechanical properties as e.g. r-values.

4 References

Klinkenberg, C., Raabe, D. and Lücke, K. (1993) Influence of intercritical annealing on the texture formation in low carbon steel strips. *Steel research ,No. 5.* pp. 262-66.

Richter, H. and Tamler, H. (1999) Measuring steel textures. *Steel Technology International*, pp. 155-58.

Engl, B., Kawalla, R., Schmitz, H.P., Heckelmann, I., Friedrich, K.-E. and Stich, G. (1998) The influence of hot rolling processing on structure, texture and mechanical properties of Ti alloyed ULC steels. *Proc. of Int. Symposion Aachen on Modern LC and ULC sheet steels for cold forming.*

TEXTURES IN STRIP-CAST AA3105 ALLOY AND THEIR ULTRASONIC CHARACTERIZATION

Y. LIU, X.-M. CHENG and J.G. MORRIS
Light Metals Research Laboratories, Department of Chemical and Materials Engineering, University of Kentucky, Lexington, USA
C.-S. MAN and M. HUANG
Department of Mathematics, University of Kentucky, Lexington, USA

Abstract

Texture measurements were made by X-ray diffraction on specimens of strip-cast AA3105 alloy which had been subjected to various annealing and cold-rolling treatments. Our findings serve as a data base for the textures of this alloy under different conditions, and they show that the ODF coefficient W_{400} varies significantly with each texture condition. We conclude that ultrasonic measurement of W_{400} would provide a possible means for monitoring textures in this alloy. As ultrasonic measurement of W_{400} in aluminum alloys is still an outstanding research problem, we discuss one possible approach in attacking this problem.

Keywords: On-line texture characterization, strip-cast aluminum alloys, textures, ultrasonic measurement

1 Introduction

Ultrasonics with its relatively simple, inexpensive instrumentation offers a promising means for on-line monitoring of textures in sheet metals. For orthorhombic sheets of cubic metals, ultrasonic measurements will at best deliver only the texture coefficients $W_{4m0}\,(m = 0, 2, 4)$ with sufficient accuracy. Such information would not suffice for texture characterization unless the orientation distribution function (ODF) in question should range approximately over a three-dimensional manifold parametrized by W_{400}, W_{420}, and W_{440}. In applications, we shall be concerned only with specific alloys which have undergone thermomechanical processing sequences in some predetermined class. As a result, the possible textures of an alloy might indeed fall in a range that can be characterized by ultrasonics.

Whether this in fact occurs for a specific alloy can only be answered by a detailed cataloging of the textures and the W_{4m0} coefficients of this alloy after it has undergone various processing sequences of interest.

In the present work we focus our attention on strip-cast AA3105 aluminum alloy sheets. First we study the textures in this alloy after various conditions of annealing and cold rolling. While textures in DC-cast aluminum alloys have been the theme of many studies, much less is known about textures in strip-cast aluminum alloys. Indeed it has been found (Liu et al. 1998) that there are major differences between texture evolution in DC-cast and in strip-cast aluminum alloys. This fact renders our cataloging of textures in strip-cast AA3105 all the more necessary.

Our data on the textures in strip-cast AA3105 alloy show that the coefficient W_{400} by itself can be used as an indicator for texture characterization. We shall present this finding in the next section.

2 Results of texture measurements

A commercial hot band of strip-cast AA3105 aluminum alloy was used in this investigation. Samples of the hot band were annealed and cold rolled under various conditions to simulate different situations. Pole figures were determined by X-ray diffraction. The texture coefficients W_{lmn} and the volume fractions of the main texture components of the samples were derived by ODF calculations. Here we present the general trend of our findings through a few typical examples.

Figure 1 depicts the $\varphi = 45°$ section of the ODFs of the hot band cold rolled to different reductions. This ODF section shows most of the main texture components in the samples. The initial hot band has a typical cold rolling texture of FCC metal with relatively strong C-{112}<111>, B-{110}<112> and S-{123}<634> components. The intensities of the C, B and S components increase with thickness reduction. The maximum intensity (i.e. the maximum value of the ODF), which starts from a value of 7.8 for the initial hot band, reaches 19.2 at 80% reduction. The Goss component, which has a relatively high intensity initially, slightly weakens with cold rolling.

Under annealing, the hot band exhibits a texture transition. Figure 2 shows the textures in three samples annealed for one hour at 343 °C, 399 °C, and 454 °C, respectively. At the annealing temperature of 343 °C, the textures in the annealed sample are similar to those of the initial hot band (cf. Figure 1). When the annealing temperature is over 399 °C, the intensities of the C, B and S components decrease, and the Rotated-Cube and Cube components develop. The <111> fiber texture and {110}<111> texture become strong in samples annealed at 454 °C. During annealing the Goss component also shows a decreasing trend with an increase of annealing temperature. Volume fraction calculations reveal that the C, B and S components have approximately the same volume fraction and have a similar trend of change both during cold rolling and annealing: cold rolling tends to increase the volume fractions of these components, while annealing causes them to decrease. Both the Cube and Rotated-Cube textures have a volume fraction of about 2% in the initial hot band. Cold rolling further reduces the volume fractions of these two components. On the other hand, these two components become the dominant textures after the hot band is annealed for an hour at a sufficiently high temperature.

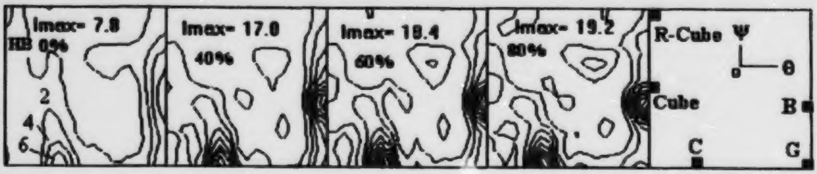

Fig. 1: Plots of the φ=45° section of the ODFs of hot band cold rolled to different reductions. Texture components are marked in the map on the right: B-{110}<112>, C-{112}<111>, G-Goss-{110}<001> , Cube-{001}<100> , and R-Cube-{001}<110>.

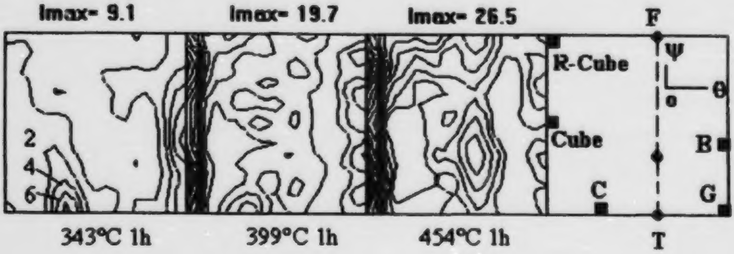

Fig. 2: Plots of the φ=45° section of the ODFs of hot band annealed at different temperatures for an hour. The heat-up rate was 55 °C/h . Samples were kept at 343 °C, 399 °C and 454 °C for one hour and then air cooled to room temperature. The line FT indicates the <111> fiber. The {110}<111> texture can be seen in the sample annealed at 454 °C.

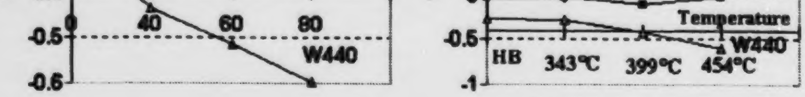

(a)

(b)

Fig. 3: Texture coefficients W_{4m0} of hot band (a) cold rolled to different reductions and (b) annealed at different temperatures for an hour.

The texture coefficients W_{4m0} of the aforementioned cold rolled and annealed samples are plotted in Figure 3. Clearly W_{400} and W_{440} decrease with thickness reduction, while W_{420} is not sensitive to cold rolling. The sample annealed at 343 °C has the same W_{4m0} as those of the initial hot band. For samples annealed at a sufficiently high temperature (e.g., ≥399 °C), W_{400} increases and W_{440} decreases with the increase of annealing temperature, while W_{420} remains almost unchanged.

Cold rolling of the hot band which has previously been annealed at 482 °C for two hours gives a texture distribution shown in Figure 4(a). With increasing thickness reduction, the initially strong Cube and Rotated-Cube textures, the <111> fiber and {110}<111> textures gradually change into the C, B and S components. At 40% reduction, cold rolling has eliminated the initial annealing texture, but the C, S and B components are not well developed. Samples with reductions lower than 40% show features of the initial annealing textures; those with higher reduction have typical cold rolling textures. Volume fraction calculations indicate that the C, B and S components have a similar trend of increase during cold rolling. The intensity of the Goss component increases slowly with increase in reduction. The Cube and Rotated-Cube textures decrease with increase in reduction. The W_{400} coefficient of the annealed samples decreases with thickness reduction under cold rolling.

The results reported above pertain to the surface of each sample. We also made measurements at the midplane of the samples. While the textures at the surface and at the midplane of the samples often have notably different intensities, they show the same trend in evolution under both cold rolling and annealing. We made X-ray texture measurements on specimens over a broad range of annealing and cold-rolling conditions. Figures 3 and 4(b) illustrate our main finding, namely, that the ODF coefficient W_{400} varies significantly with each texture condition. Thus the value of W_{400} gives a good indication of the texture condition of strip-cast AA3105 alloy.

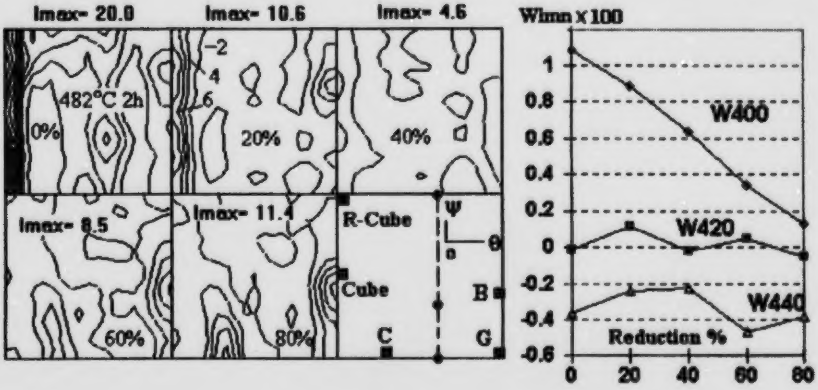

(a) (b)

Fig. 4: Texture evolution (a) and W4m0 variation (b) of annealed hot band (482 °C for two hours) during cold rolling.

3 Discussion

The X-ray work reported above has identified W_{400} as a good indicator for on-line ultrasonic monitoring of textures in strip-cast AA3105 alloy. Unlike the coefficients W_{420} and W_{440}, ultrasonic measurement of W_{400} in aluminum alloys remains an outstanding research problem (cf. Clark et al. 1988; Anderson et al. 1996).

To illustrate the difficulty at issue, let us compare two equations which can be used for ultrasonic measurement of W_{400} and W_{420}, respectively:

$$\frac{V_{33}}{(V_{31}+V_{32})/2}=\sqrt{\frac{\lambda+2\mu}{\mu}}\left(1+\frac{\lambda+4\mu}{\mu(\lambda+2\mu)}\frac{8\sqrt{2}}{35}\pi^2 cW_{400}\right), \tag{1}$$

$$\frac{V_{31}-V_{32}}{(V_{31}+V_{32})/2}=\frac{16\sqrt{5}\pi^2}{35\mu}cW_{420}; \tag{2}$$

here V_{33} is the speed of a longitudinal wave propagating in the normal direction of the sheet; V_{31} and V_{32} are speeds of through-thickness shear waves with polarization in the rolling and transverse directions, respectively; λ and μ are the Lame constants for the isotropic polycrystal, and c is a material constant. The preceding equations were first derived through simple averaging procedures (Voigt, Reuss, Hill), each of which also delivers a different set of formulae that express λ, μ and c in terms of the single-crystal elastic constants (see Hirao et al. 1988 for references). All these averaging procedures lead to the same equations (1) and (2); only the predicted values of λ, μ and c are different. For aluminum, the Voigt, Reuss, and Hill averages of λ, μ and c differ by only a few percent. To use equation (2) for measurement of W_{420}, we may simply use the Hill average values; a small error in the adopted value of μ and of c will not significantly affect the predicted value of W_{420}. In contrast, to compute W_{400} from equation (1), we must first subtract $\sqrt{(\lambda+2\mu)/\mu}$ from the measured velocity ratio. For aluminum alloys, this difference is so small that a tiny error in the estimated $\sqrt{(\lambda+2\mu)/\mu}$ will translate into a huge error in the predicted W_{400}. Indeed, hardly any micromechanical model could be expected to deliver a sufficiently accurate estimate of $\sqrt{(\lambda+2\mu)/\mu}$ for the present purpose.

As it turns out, all wave-speed equations which deliver W_{400} are similar to equation (1) in that this texture coefficient can only be calculated from the small difference between some measured quantity and an expression involving the isotropic elastic constants. Herein lies the main difficulty in ultrasonic measurement of W_{400}.

A recent work of Man (1998) has put equations such as (1) and (2) in a different light. Appealing to basic principles that govern constitutive equations in continuum mechanics, he showed that the constitutive equation which leads to (1) and (2) can be derived by symmetry arguments alone, i.e., without any specific micromechanical modeling. The main assumption he made is that the fourth-order elasticity tensor be a function of the ODF. Equations (1) and (2) are then correct up to terms linear in the texture coefficients W_{lmn}. In this phenomenological theory we should interpret λ, μ and c as macroscopic elastic constants pertaining to the particular (polycrystalline) orthorhombic material in question. In fact, the constants λ, μ and c define the elastic "material", which may acquire different textures from various thermomechanical processing procedures. Differences in alloying elements and in microstructures which significantly affect the values of λ, μ and c lead to different "materials" in the sense here.

If the strip-cast AA3105 alloy can be taken as the same "material" during its processing sequence in the rolling mill, we may tackle the problem of ultrasonic monitoring of textures in this alloy as follows: First we prepare a calibration graph by measuring both $2V_{33}/(V_{31}+V_{32})$ (ultrasonically) and W_{400} (e.g., by X-ray diffraction) for judiciously prepared samples of this alloy. We may simply estimate the slope of this linear plot by using the values of λ, μ and c as obtained from some simple micromechanical model. The intercept $\sqrt{(\lambda+2\mu)/\mu}$, however, must be determined experimentally. With this calibration line in hand, we may measure $2V_{33}/(V_{31}+V_{32})$ on line and then read off the corresponding W_{400}.

Whether and to what extent the parameter $\sqrt{(\lambda+2\mu)/\mu}$ of strip-cast AA3105 alloy remains constant during thermomechanical processing will determine the feasibility of the approach suggested above. A collaborative effort to study the effect of processing history on the parameter $\sqrt{(\lambda+2\mu)/\mu}$ of strip-cast AA3105 alloy is currently underway at the University of Kentucky and at Iowa State University.

Acknowledgement. The research reported here was supported in part by a DoD EPSCoR grant from AFOSR (No. F49620-98-1-0469).

4 References

Anderson, A.J., Thompson, R.B., Bolingbroke, R. and Root, J.H. (1996) Ultrasonic characterization of rolling and recrystallization textures in aluminum. *Textures and Microstructures*, Vol. 26-27, pp. 39-58.

Clark, A.V., Reno, R.C., Thompson, R.B., Smith, J.F., Blessing, G.V., Fields, R.J., Delsanto, P.P. and Mignogna, R.B. (1988) Texture monitoring in aluminum alloys: a comparison of ultrasonic and neutron diffraction measurement. *Ultrasonics*, Vol. 26, pp. 189-197.

Hirao, M., Hara, N. and Fukuoka, H. (1988) Ultrasonic monitoring of texture in cold-rolled steel sheets. *J. Acoust. Soc.* Am., Vol. 84, pp. 667-672.

Liu, Y., Liu, Y.L., Cheng., X.-M. and Morris, J.G.(1998) Texture in hot rolled aluminum alloys. in *Hot Deformation of Aluminum Alloys II* (ed. Bieler,T.R., Lalli, L.A. and MacEwen, S.R.), The Mineal, Metals & Materials Society, Warrendale, Pennsylvania, pp. 73-84.

Man, C.-S. (1998) On the constitutive equations of some weakly-textured materials. *Arch. Rational Mech. Anal.*, Vol. 143, pp. 77-103.

ON-LINE PLASTICITY PREDICTION IN TEXTURED STEEL AND ALUMINUM PRODUCTS

P. BLANDFORD and J.A. SZPUNAR
Department of Mining and Metallurgical Engineering, McGill University
Montréal, Canada

Abstract

Equipment has been built to test x-ray sensor design for texture analysis and plasticity prediction of rolled steel in the production environment. Experimental testing was made on a set of cold-rolled and annealed interstitial-free steels. Tests performed on the steel specimens showed that an optimized design sampling can predict the average r-value, r and the 2-fold anisotropy measure, $(r_{90} - r_0)/2$ with an accuracy σ = 0.1 and 0.03 respectively. An optimized design can predict the same plasticity with an accuracy of $\sigma = 0.18$ and 0.06. As a whole, the work has demonstrated that statistically reliable predictions of plasticity of commercial sheet can be made using specialized sensor design that measure 10-50 pole densities.

Keywords: texture, plastic strain ratio, X-ray, on-line sensor

1 The laboratory test facility

An automated system for testing a range of methods for quantitative texture analysis on-line consists of the following mechanical components: 1) two rotational stages which independently rotate the CPSD and X-ray source about the measurement axis of the test facility, 2) a precision machined arc and cradle, used to tilt the measurement axis in 5 degree increments away from the sheet normal, 3) a mounting table, which serves as a base for the cradle or CPSD/X-ray source assembly, and 4) a specimen oscillator for samples of maximum 30 x 30 cm, by 2 cm thick. A photograph of the laboratory tester is presented in Fig. 1.

The measurement of the laboratory sensor can be optimized for measurement of different metal products. Such an optimization requires specifying the number and locations of all x-ray sources and detector configurations used in the system, as well as the data weights, normalization factor and expansion order used in the ODF calculation.

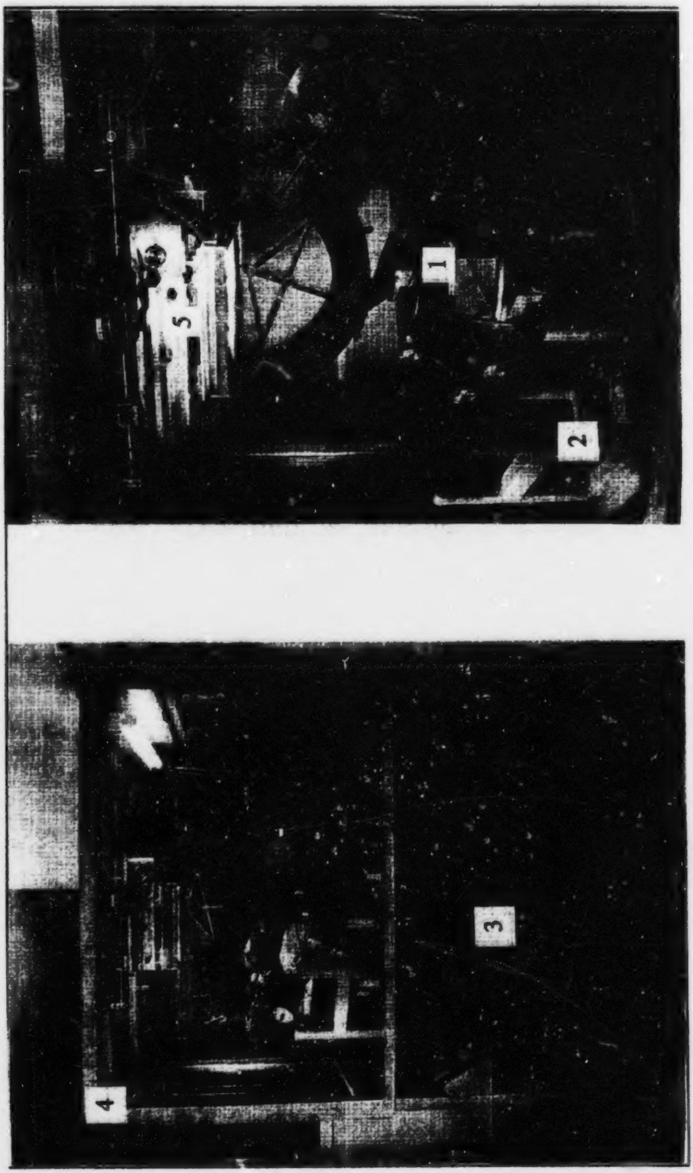

Figure 1. Photographs of the laboratory facility built to test methods for on-line texture analysis

2 Experimental testing of the sensor; correlating the texture and plastic anisotropy

The purpose of this section is to describe the correlations developed between the r-value and standard texture measurements of the steel test set.

The correlations are statistical in nature and presume that the *n*-fold symmetry components of the plasticity are linearly related to the texture coefficients that control the *n*-fold contributions to the ODF (Szpunar and Hinz, 1989); for cubic-orthorhombic symmetry in the ODF, these texture coefficients share a common ν index that is equal to the symmetry component, *n*, in the property. Using this assumption, a model function for the r-value measured in the plane of the sheet, $r(\phi)$, can be constructed as a Fourier series weighted by the texture coefficients, $C_l^{\mu\nu}$. This model function is written as follows:

$$r(\phi) = a_2^0 + \sum_{l=4(2)}^{l_{\max}} \sum_{\mu=1}^{MU(l)} \sum_{\nu=0(2)}^{l} a_l^{\mu\nu} C_l^{\mu\nu} \cos\nu\phi \tag{1}$$

where the Fourier coefficients, $a_l^{\mu\nu}$, determine what proportion of the symmetry components of the texture contribute to the plastic anisotropy. These Fourier-type correlations differ from the statistical correlations often developed between the *n*-fold property measures, r, $(r_{90} - r_0)/2$ and Δr, and the C_4^{10}, C_4^{12}, and C_4^{14}, texture coefficients. These latter correlations allow an extra degree of freedom in fitting each symmetry components that can only be interpreted as an anisotropy affect that is unrelated to texture. In this regard, the Fourier series fit is self-consistent.

Several attempts were made to correlate the experimental r-values and the mid-plane textures of the sheet using the Fourier model. The tests demonstrated that the experimental anisotropy could not be accurately predicted using only the fourth-order texture coefficients of the bulk texture. Upon expanding the fit to include the sixth-order coefficients, the fit improved mainly because the addition of the C_6^{16} coefficients significantly improved the fit of the 2-fold component of the experimental data. The C_6^{16} coefficient controls the 6-fold contributions to the sheet texture, and therefore using it to improve the fit of the 2-fold anisotropy measure is justified. An optimization of the fit showed that the experimental anisotropy of six of the eight sheets can be predicted within error using the C_4^{10}, C_4^{12}, C_4^{14} and C_6^{16} coefficients of the bulk texture; the goodness-of-fit value for the correlation was 0.22, indicating that the four parameters is justified for the fit.

Correlating the bulk plasticity and the surface texture is problematic because the two are strictly related only in as much as the surface texture is related to the texture of the bulk. In general, the surface and bulk texture are related in a complicated way through the inhomogeneity in the sheet chemistry and processing. However, the standard texture measurements presented previously show that the surface and bulk texture share the main feature of a {111}//ND fibre, although the surface textures are much less intense. Therefore, predictions of the bulk properties using these surface coefficients can be justified, because of their strong relation to the bulk texture. Correlating the 2-fold anisotropy would be highly unreliable because the $\nu = 2$ and 6 coefficients of the surface texture are uncorrelated with the bulk texture.

3 The optimized predictions

The main aim of the steel testing is to determine how well the laboratory sensor can predict the 0-, 2- and 4-fold plastic anisotropy measures, r, $(r_{90} - r_0)/2$ and Δr. For this, three separate measurements of the mid-plane and surface texture of each of the eight sheets were made using the optimized sensor designs.

The sensor predictions demonstrate that the average plasticity of the sheet predicted from the optimized designs are generally in good agreement with the experimental values. The predictions of the 2- and 4-fold anisotropy are reasonable, although the sensor error is significant. For these experiments, the sensor error for the mid-plane design can be calculated as 0.15, 0.12 and 0.10 for the r, $(r_{90} - r_0)/2$ and Δr predictions, respectively; the sensor resolution for the measures are: 0.33, 0.80 and 0.97.

The results of the optimized measurements of the surface texture of the sheet are generally in good agreement with the experimental values. The sensor error and resolution for the design are 0.18 and 0.41 respectively, which are very similar to the values obtained from the predictions of r from the bulk texture. This illustrates that the useful predictions of bulk properties can be obtained from measurements of the sheets' surface texture.

These results demonstrate that predicting the average plasticity of the steel test set is possible by measuring a small number of data characterizing the surface or mid-plane texture of the sheet. However, the sensor resolution for the prediction of the 2- and 4-fold anisotropy measures, are poor. For the particular set of steel sheet studied, this weakness in the design can in part be remedied by taking advantage of the strong correlation that exists between the average r-value and the 2-fold anisotropy. For the mid-plane measurements, the correlation is utilized by re-optimizing the sensor to product accurate predictions or r, from which accurate predictions of $(r_{90} - r_0)/2$ can be made. For the surface designs, the correlation is used directly, and enables the 2-fold anisotropy to be predicted whereas, without the specialized correlation, it could not be.

Figure 2 and Figure 3 present the sensor predictions of the average plasticity and 2-fold anisotropy for mid-plane and surface designs optimized to use this specialized correlation. For the mid-plane measurements in figure 2, freeing the optimization reduces the error in the sensor's prediction of 4 and $(r_{90} - r_0)/2$ to 0.10 and 0.03; this corresponds to sensor resolutions of 0.22 and 0.21 respectively. For the surface measurements, the error and resolution of the prediction of the 2-fold anisotropy are 0.06 and 0.41 respectively. Considering that the 4-fold anisotropy measure, Δr, of all eight samples are similar within error, the $r/(r_{90} - r_0)/2$ correlation allows the most significant component of the plastic anisotropy of the test set to be accurately predicted from 20 data measured at either sheet mid-plane or surface.

4 Summary of the sensor testing

The measurements on the steel test set using the standard optimized designs demonstrated that only 20 pole density data from either the bulk or surface texture are required to predict the average r-value of the sheet with an error of $\sigma = 0.10$. The 2-

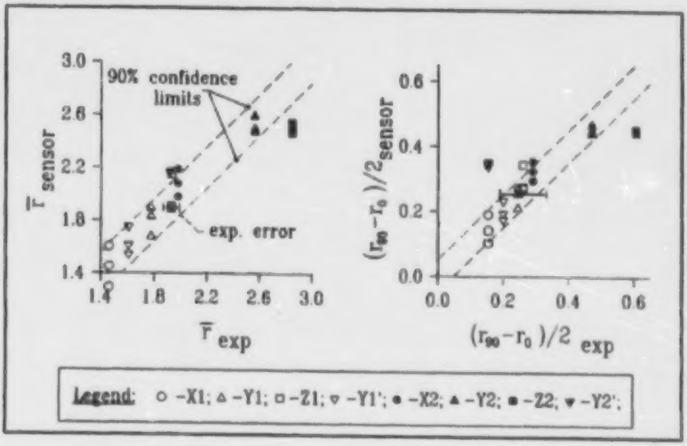

Figure 2. Specialized predictions of the 0- and 2-fold anisotropy of the steel test set from optimized measurements of the mid-plane texture

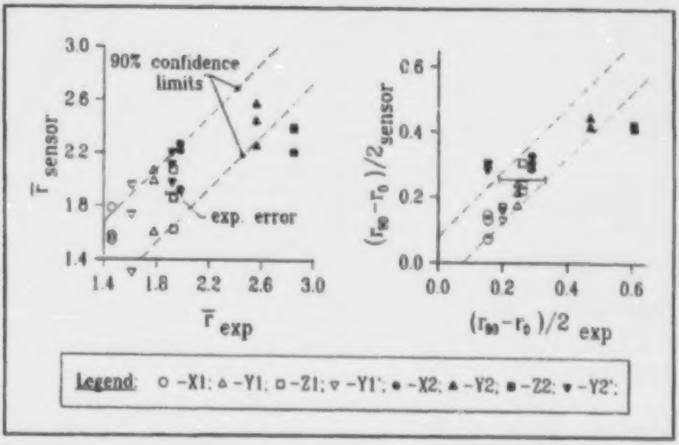

Figure 3. Specialized predictions of the 0- and 2-fold anisotropy of the steel test set from optimized measurements of the surface texture

and 4-fold anisotropy measures $(r_{90} - r_0)/2$ and Δr, can only be predicted from measurements of the bulk texture, and even then, only with a resolution of 0.80 and 1.00. Measurements using alternate designs demonstrated that the resolution for the sensor's predictions of the average and 2-fold plasticity can be reduced to about 0.20 using the correlation that exists between r and $(r_{90} - r_0)/2$ for the IF steel test set.

5 References

J.A. Szpunar and D.C. Hinz (1989), Correlating the Plastic Strain Ratio with
Ultrasonic
Velocities in Textured Materials, vol. 24, p. 1233.

ON-LINE MEASUREMENT OF TEXTURE AND PLASTIC STRAIN RATIO ON STEEL SHEETS USING LASER-ULTRASONICS

A. MOREAU, D. LÉVESQUE, M. LORD, M DUBOIS*, J.-P. MONCHALIN, C. PADIOLEAU, and J. F. BUSSIÈRE
Industrial Materials Institute, National Research Council Canada, Boucherville, Canada

* Now at General Electric Company, Corporate Research & Development, Schenectady, NY, USA

Abstract

Laser-ultrasound resonance spectroscopy, a non-contact ultrasonic technique, was used to determine reliably and rapidly the crystallographic texture, the average plastic strain ratio, and the thickness of sheet metal on the production line. As with laser-ultrasonics, a short laser pulse is used to generate a wideband pulse of ultrasound and a laser interferometer is used for its detection. In this paper, a large number of echoes are collected and analyzed together using Fourier techniques to measure the natural resonance frequencies in the thickness of the sheet. From these frequencies, two texture coefficients, W_{400} and W_{420}, are obtained, as well as a highly accurate measurement of the sheet thickness that is corrected for changes in ultrasonic velocity caused by texture variations. Using these coefficients, the average and in-plane two-fold and four-fold variations of the plastic strain ratio can be evaluated.

Keywords: laser-ultrasonics, plastic strain ratio, texture, formability, spectroscopy

1 Introduction

The processing of metal sheets induces a preferred crystallographic orientation, or texture, that affects the mechanical properties. In particular, texture is the most important factor affecting the formability of metal sheets. Traditionally, texture is measured using x-ray or neutron diffraction techniques. Although these techniques provide very complete information, x-rays only sense a very thin surface layer; and cheap and intense neutron sources are not available for on-line monitoring. Hence, ultrasonic measurement of texture is an attractive alternative because it is comparatively cheap and fast, and because it provides a bulk measurement.

Two ultrasonic approaches have been reported to measure the texture and plastic strain ratio of sheet metal on a production line. Both methods are based on electromagnetic acoustic transducers (EMAT) technology. The first approach is to measure angular variations of plate mode velocities (Thompson et al. 1986). The second approach is the electromagnetic acoustic resonance (EMAR) technique, which involves exciting an EMAT by radio-frequency narrow-band tonebursts while sequentially sweeping through a frequency range (Kawashima et al. 1993). Each toneburst generates forces in all three polarization directions and when the excitation frequency equals the resonant frequency of a specific longitudinal or shear mode, standing waves are set up (Kawashima 1990). A drawback of EMAT sensors is that they must be positioned close to the sheet surface, e.g. 1 mm. Sheet fluttering must be strictly controlled, and special hardware is needed to retract the sensor when surface irregularities pass by the sensor.

An alternative to EMAT sensors is laser-ultrasonics, which is a practical solution for remote sensing at large distances, for inspection of fast moving parts on production lines, and for inspection in hostile environments (Monchalin 1993). Laser-ultrasonics uses a short pulse of laser light (few ns in duration) to generate ultrasound and a long pulse (tens of μs in duration) or a continuous laser coupled to an optical interferometer to detect the ultrasound. In this paper, a laser-ultrasound resonance (LUR) technique is proposed, whereby a large number of echoes are collected and analyzed together using Fourier techniques to measure the resonance frequencies in the thickness of the sheet. In contrast with the EMAR technique, all ultrasonic modes and their harmonics are excited and detected simultaneously.

2 Laser-ultrasound resonance spectroscopy

In a typical laser-ultrasonic signal, large negative peaks are the multiple echoes of the longitudinal wave which is reflected back and forth between the two free surfaces. Between the longitudinal echoes, some shear signal may be observed but cannot be easily interpreted. Because the sheet is essentially floating in space, the signal may be observed for hundreds of echoes. To obtain the various resonances, the signal is windowed and Fourier transformed. The resonance peaks in Fig. 1 are harmonics of the longitudinal wave and of the two shear waves which are polarized in orthogonal directions in the plane of the sheet. The longitudinal resonances are identified as 1L, 2L, and 3L and shear wave resonances are identified as 1S, 2S, 3S, and 6S. In the case illustrated here, the second harmonic, 2L, is selected for the longitudinal wave while for the two shear waves, the 3S harmonics are selected because they are more easily separated than lower order harmonics. The best choice of harmonics depends on material properties as well as sheet thickness. As seen in Fig. 1 however, the signal amplitude for shear harmonics is usually 40 dB lower than that for the longitudinal resonances. Therefore a signal-to-noise ratio of 50 dB or higher is required for single shot experiments in a 15 MHz bandwidth. Signal averaging may be used to improve this further.

Once the resonances have been identified and their center frequency, f_L, f_{S1}, and f_{S2} measured, the sample thickness, e, and two texture coefficients, W_{400} and W_{420}, may be calculated using the following equations:

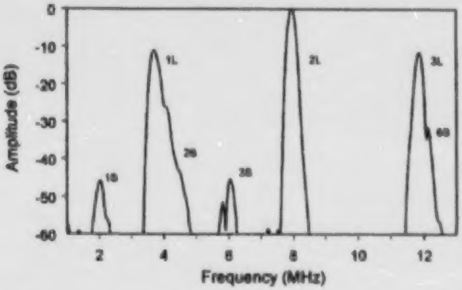

Figure 1: Amplitude spectrum of a time signal comprising hundreds of echoes.

$$
\begin{aligned}
e &= \sqrt{\frac{\lambda_M + 4\mu_M}{4\rho(f_L^2 + f_{S1}^2 + f_{S2}^2)}} \\
W_{400} &= \frac{35\sqrt{2}\left[4\rho e^2 f_L^2 - (\lambda_M + 2\mu_M)\right]}{64\pi^2 c_M} \qquad (1) \\
W_{420} &= \frac{56\sqrt{5}\rho e^2 (f_{S1}^2 - f_{S2}^2)}{64\pi^2 c_M}
\end{aligned}
$$

where ρ is the density of the metal sheet, and λ_M and μ_M are the Lamé elastic constants (using either the Voigt, Reuss or Hill procedure) of an ideal metal sheet having an isotropic crystallographic orientation distribution.

3 Description of the system tested at LTV Steel Company

The system described here was installed at LTV's #1 inspection line in Cleveland. The generation laser was installed on a platform above the line. Typically, we employ 100 to 200 mJ of 248 nm radiation pulse lasting from 3 to 6 ns fwhm and focused on an area about 5 mm in diameter. This high power laser beam was steered with mirrors down to a horizontal rail installed above the line. The beam traveled along the rail up to a movable "generation head" which reflected and weakly focused the beam onto the sheet. If the pulse energy density is large enough, the UV light pulse causes a slight ablation of the surface, or of the dirt and oil present on the surface, and the recoil energy generates an ultrasound pulse in the direction normal to the sheet surface. This ultrasound pulse is broadband in its frequency content, typically between 1 and 40 MHz. The detection laser and interferometer were located remotely from the line. The detection laser was a long pulse, 3 kW peak power, Nd:YAG laser with a variable attenuator to provide a large but stable amount of light for detection. A confocal Fabry-Perot interferometer was used, which has a large light gathering capability and is insensitive to speckles. The detection laser light was carried using an optical fiber to another movable "detection head" located on another rail below the sheet. This detection head weakly focused the detection light onto the sheet and collected the reflected light, which was carried to the interferometer using a second optical fiber. The two sensing heads could be moved together manually to position the sensor anywhere across the sheet and to allow manual scans.

The two sensing heads were positioned about 30 cm from the sheet. Vertical fluttering of the moving sheet has no effect as long as the sheet remains within the depth of focus of the focusing optics (a few cm). Line speeds of up to tens of meters per second, depending on the optical properties of the Fabry-Perot cavity and of the sheet surface, are possible. The goal of the prototype was to demonstrate that the technology could be used online. Therefore, important practical features such as cost, size, and data acquisition rate were not optimized. However, a high level of automation was achieved and included real time data analysis and display, automatic recording of measurement position along the coil, line speed and sheet height (to shut off lasers in case of sheet buckling or other anomalous conditions), and end of coil detection, etc. The measured coils had been oiled with an electrostatic oiler which spreads a thin and uniform layer of oil on the sheet surface. The presence of the oil layer had no effect on the observed resonance peaks. Using this prototype, a large number of test samples were measured with the sensing heads positioned off the line. However, a limited number of coils were also inspected on-line, along their length.

4 Measurement results and applications

Ultrasonics is well established as a means to measure texture coefficients of order up to four for polycrystalline aggregates of cubic and hexagonal metals. Therefore, to show that texture can be measured using Eqs. (1), it is sufficient to show that we can measure the ultrasonic velocity accurately. Here the comparison was made with commercial piezoelectric transducers. The two techniques agreed to within 0.5% (rms residual) for 79 samples of low carbon steel having round trip time delays ranging from 200 to 800 ns. Ultrasonic time-of-flight (TOF) measurements are often used to measure the thickness of objects. However, texture variations caused by common processing methods can significantly affect the ultrasonic velocity and consequently, affect the accuracy of the thickness measurement. In LUR, the texture coefficients that affect the velocity of the three acoustic modes propagating in the thickness direction are measured and the thickness calculated according to Eqs. (1) is corrected for texture variations. Thickness was measured for 100 samples of ultra low carbon (ULC), low carbon (LC) and high-strength low-alloy (HSLA) steels having widely different textures. The thickness estimated using TOF of the longitudinal wave was accurate to ±22 μm, while that using the LUR technique was ±5 μm. Also, the main source of error was that the thickness and LUR measurements were not taken at the same locations.

Crystallographic texture is one of the most important microstructural features that affects the formability of metals and measured plastic strain ratio. Arithmetic combinations of measurements, made in the rolling (0°), transverse (90°), and diagonal (45°) directions, are formed to define the average plastic strain ratio ($\bar{r}$), the four-fold ($\Delta_4 r$) and two-fold ($\Delta_2 r$) in-plane variations of r. The texture coefficients W_{400}, W_{420}, and W_{440}, describe the statistical distribution of orientation of the grain's crystallographic axes. For example, the better the {111} planes are aligned in the plane of the sheet, the more negative is the value of W_{400}, the better is the ability of the steel to flow in its plane without thinning, and the higher is the average plastic strain ratio, $\bar{r}$. Recently, Man (Man 1995) applied the averaged elastic constants of textured materials to Hill's quadratic yield criterion to calculate expressions relating $\bar{r}$ and W_{400} as well as $\Delta_4 r$ and W_{440} in the limit of weak textures. These expressions, including an extension of Man's paper to $\Delta_2 r$ are:

$$\begin{aligned}
\bar{r} &= \left[r(0^\circ) + 2r(45^\circ) + r(90^\circ)\right]/4 = 1 - \frac{8\sqrt{2}\pi^2\beta}{7} W_{400} \\
\Delta_4 r &= \left[r(0^\circ) - 2r(45^\circ) + r(90^\circ)\right]/2 = \frac{32\pi^2\beta}{\sqrt{35}} W_{440} \\
\Delta_2 r &= r(0^\circ) - r(90^\circ) = \frac{64\pi^2\beta}{7\sqrt{5}} W_{420}
\end{aligned} \qquad (2)$$

where β is a positive constant. Fig. 2 shows $\bar{r}$ as a function of W_{400} measured by LUR for 122 samples of ULC, HSLA and LC steels. As predicted in Eqs. (2), HSLA steels samples, which have near zero values of W_{400}, have an $\bar{r}$ value of approximately one. Also, $\bar{r}$ is found to decrease linearly with W_{400}. If only the ULC steel samples are retained, then the rms residual to a linear least squares fit is ±0.08. Fig. 2 also shows $\Delta_2 r$ as a function of W_{420} for the HSLA and ULC samples. As predicted by Eqs. (2), $\Delta_2 r$ appears proportional to W_{420} for the ULC steel samples, and perhaps also for the HSLA steel samples. The two straight lines are linear least squares fits with the intercept forced to zero for the two steel grades. The rms residuals to the correlations are ±0.13 and ±0.06 for the ULC and HSLA steel samples, respectively.

LUR spectroscopy was used to measure a limited number of coils along their length. In one case, five consecutive coils of low carbon steel manufactured for a single client were inspected. Three of these five coils showed identical variations of W_{400} as a function of position, and two of the three coils also showed identical variations in W_{420}. These features included identical absolute values of W_{400} and W_{420}, sudden jumps in W_{400} near 1500 feet, and similar increases of W_{420} along the coil's length. The fact that the prototype can sense similar features on coils produced in similar manners is strong evidence that the observed variations were real.

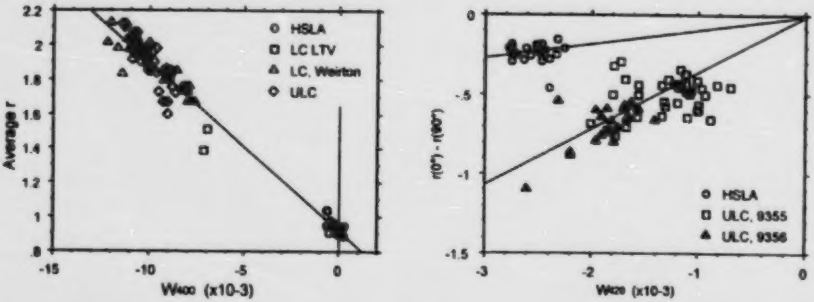

Figure 2: $\bar{r}$ **as a function of the** W_{400} **(left) and** $\Delta_2 r$ **as a function of** W_{420} **(right).**

Also, two of the same five coils showed a regular oscillatory pattern of the W_{400} texture coefficient with an apparent periodicity of 1100 and 1400 feet, respectively. If these patterns were observed in more coils, one might be able to identify the source of the variability in the process and perhaps improve the process itself. If one uses the approximate empirical relation $\bar{r} = 1 - 1000\ W_{400}$ (see Fig. 2), then this coil has a $\bar{r}$ of approximately 1.4 and the peak to peak amplitude of the $\bar{r}$ oscillations is about 0.15 (i.e. 1.4 ± 0.075). These variations are well within the sensing capabilities of the apparatus. In fact, it is clear that the sensor's online $\bar{r}$ measurement repeatability of order ± 0.02 far exceeds the combined accuracy of the mechanical and ultrasonic measurements of ± 0.08 which was determined from Fig. 2.

5 Conclusion

Laser-ultrasound resonance spectroscopy was reported as a non-contact technique to determine reliably and rapidly the crystallographic texture, the average plastic strain ratio, and the thickness of sheet metal on the production line. In addition to evaluating the two texture coefficients W_{400} and W_{420}, the method allows a highly accurate measurement of the sheet thickness that is corrected for the effect of texture variations on the sound velocity. The measured texture coefficients may be used to evaluate the average plastic strain ratio $\bar{r}$, as well as its in-plane two-fold variations. The combined accuracy of the ultrasonic and mechanical measurements for $\bar{r}$ was ±0.08 while the online ultrasonic repeatability was estimated to be of order ±0.02.

Acknowledgments

This work was made for the American Iron and Steel Institute and partial funding of the Department of Energy under Contract No. DE-FC07-93ID130205. The authors also wish to thank Weirton Steel Corporation, as well as LTV Steel Company for providing the necessary support for on-line tests.

References

Kawashima, K., Hyoguchi, T. and Akagi, T. (1993) On-line measurement of plastic strain ratio of steel sheet using resonance mode EMAT. Journal of Nondestructive Evaluation Vol. 12, p. 71-77.

Man, C.-S. (1995) Correlation of earing and texture in weakly orthotropic sheets of cubic metals. Review of Progress in Quantitative Nondestructive Evaluation, Vol. 14. Plenum, NY, p. 1923-1930.

Monchalin, J.-P. (1993) Progress towards the application of laser-ultrasonics in industry. Review of Progress in Quantitative Nondestructive Evaluation, Vol. 12A. Plenum, NY, p. 495-506.

Thompson, R. B., Lee, S. S. and Smith, J. F. (1986) Angular dependence of ultrasonic wave propagation in a stressed orthorhombic continuum. J. Acoust. Soc. Am. Vol. 80, p. 921-931.

TEXTURE AND RESIDUAL STRESSES INFLUENCE ON THE THERMOMECHANICAL BEHAVIOUR OF ZIRCALOY-4 TUBES

R. BRENNER and J-L. BECHADE
Commissariat à l'Energie Atomique, Centre d'Etudes et de Recherche sur les Matériaux, Service de Recherches Métallurgiques Appliquées, Saclay, France
B. BACROIX
Centre National de la Recherche Scientifique, Laboratoire des Propriétés Mécaniques et Thermodynamiques des Matériaux, Villetaneuse, France

Abstract

This paper is dealing with the influence of texture on the thermomechanical behaviour of Zircaloy-4 via a micromechanical approach. Three different types of loading paths (tensile, compression and internal pressure tests) were performed at 20°C. First, using a thermoelastic self-consistent model, the residual stresses induced by cooling are calculated and the minimum stress level is found for the main texture component. Second, with the use of an elastoplastic self-consistent model, we show that a minor effect of residual stresses on the elastoplastic transition is predicted in the case of a forward and reverse pressure test. The experimental results obtained for the tensile and compressive tests seem to indicate the necessity of taking into account the viscous relaxation during the mechanical loading.

1 Introduction

This study has been undertaken in the frame of a work concerning the influence of the structural parameters on the thermomechanical behaviour of Zr alloys (especially thermal creep). Among numerous parameters, we first focused on the influence of the texture which is known to be a preponderant factor on the mechanical response of Zr alloys due to the thermal, plastic and elastic anisotropies of the single crystal. Thus, the influence of the crystallographic texture on the plastic behaviour and on the thermal residual stresses are investigated here. The material studied is a Zircaloy-4 alloy widely used as cladding tubes and guide thimbles in the nuclear industry especially in the Pressurised Water Reactors (PWR).

The influence of thermal residual stresses on the mechanical response of Zr alloys for uniaxial loadings has been extensively investigated (Mc Ewen and Tomé 1987, Turner et al. 1995 and Pang et al. 1999).

Here, the experimental work consists of mechanical tests at room temperature for three types of loading (tension, compression and internal pressure). The modelling associated is made of two parts (both of them are in the frame of the self-consistent schemes). Thermoelastic and elastoplastic calculations are performed to predict respectively the initial residual stress state at room temperature and the plastic behaviour for the three loadings up to a total strain of 2%. Finally, predicted internal and external pressure responses are compared and the pertinence of the modelling is discussed.

2 Material and texture

2.1 Alloy studied

Zircaloy-4 is a zirconium based alloy (Sn : 1.2% - Fe : 2000 pppm - Cr : 1000 ppm - O : 1300 ppm) of hexagonal close-packed structure at room temperature. The alloy studied here was recrystallised at 893 K during two hours after the last cold-rolling operation. The main sources of anisotropy at the single crystal level are the thermal, the plastic and, to a minor degree, the elastic properties. Due to the lack of data on Zy-4 single crystals, we will consider for this study the single crystal properties of zirconium (Fisher and Renken 1964; Goldak et al. 1966). They are listed in Table 1. The thermal behaviour of the single crystal, transversely isotropic with a ratio $\alpha_c / \alpha_a \approx 2$, is responsible for the residual stresses induced during cooling after an annealing treatment. It results in a tensile stress along the <c> axis and a compressive stress across the prismatic planes (Piercy 1968). The main characteristics of the plastic behaviour of h.c.p. metals are the few number of independant "easy" slip systems (two independant prismatic systems for Zr alloys) and the existence of "hard" slip systems as the pyramidal <c+a>, the only slip system able to accomodate a deformation along the <c> axis. Twinning can also be a mode of deformation at low temperatures. In this study, it does not contribute in a significant proportion to the plastic deformation.

These different aspects at the single crystal level will give rise to important "thermal" and plastic incompatibilities. It will lead to high grain-to-grain interactions and residual stresses as it has been shown in different experimental studies (MacEwen and Tomé 1987, Pang et al. 1999).

Thermal expansion coefficients (K^{-1})		Elastic constants (GPa)			
α_1	$5.8.10^{-6}$	c_{11}	143.5	c_{13}	65.4
α_2	$5.8.10^{-6}$	c_{33}	164.9	c_{44}	32.1
α_3	$10.3.10^{-6}$	c_{12}	72.5		

Table 1 : Thermal expansion coefficients and elastic constants of zirconium using the Voigt two-indices notation.

2.2 Texture measurements

At the polycristal level, the material presents an anisotropy of "organization" resulting from the thermomechanical process. It is characterized by the shape of the grains (morphological texture), their orientation with respect to the sample axes (crystallographic texture) and their repartition. Because of the equiaxed shape of the grains and their random repartition, only the crystallographic texture of the polycrystal has to be taken into account

After polishing and chemically etching (to a depth of 0.2 mm) the observed surface of the specimen taken at half thickness in the tube, x-ray diffraction pole figures were obtained in reflexion using the Cu Kα radiation. The Orientation Distribution Function (ODF) analysis was applied for the quantitative evaluation using the spherical harmonics algorithm (Bunge 1982) up to rank l=16 for even l only using (10.0), (00.2), (10.1), (10.2) and (11.0) experimental pole figures measured in the 0-75° range. The reference system is denoted RD (Radial Direction), TD (Tangential Direction) and AD (Axial Direction). As can be seen from (00.2) and (11.0) experimental poles figures and from one section of the ODF in Euler space (with the Bunge notation φ_1, ϕ, φ_2) at

φ_1=0° (ϕ ranging from 0 to 90° and φ_2 from 0 to 60°) (Figure 1) the main peaks lie in the (RD-TD) plane at about 30° from RD. The <11.0> axes are mainly oriented along AD.

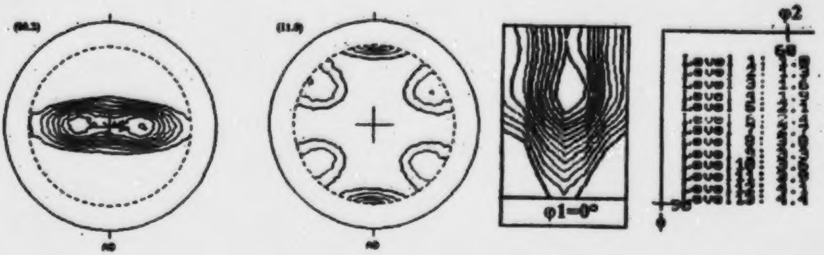

Figure 1 : (00.2) and (11.0) experimental pole figures and section of the ODF at φ_1= 0°

3 Mechanical tests

The mechanical tests were performed on tubular samples (ϕ_{ext} = 9.5 mm- e = 0.6 mm) at room temperature and at a constant strain rate of 2,5 x 10^{-4} s^{-1}. Three different types of loading conditions were investigated : tension and compression along the axial direction and internal pressure.

Because of the strong crystallographic texture, uniaxial loading along the axial direction is expected to involve essentially prismatic slip during the early stage of plastic deformation (Caré 1995). With respect to the texture of the material, an easy way to have a significant contribution of "hard" slip systems is to perform an internal pressure test. With the thick tube hypothesis, we assume for this test a biaxial stress state. Expressed in cylindrical coordinates, we have $\sigma_{TD} = 2.\sigma_{AD}$.

For the uniaxial test, the elastic behaviour had to be corrected after testing because of the elasticity of the machine. Besides, we made abstraction of a small hook at the very beginning of the plastic deformation probably due to interactions between dislocations and solute atoms. We suppose that it does not strongly affect the plastic curve.

4 Self-consistent modeling

The use of the self-consistent scheme is motivated by its accurate description of grains interactions which play a significant role in this material as described above. The Eshelby's solution is used to determine the local fields in each phase.

To describe the initial residual stress state induced by cooling from annealing to room temperature, we use a thermoelastic calculation since it has been shown (Turner and Tomé 1994) that no plastic relaxation takes place in the polycrystal during cooling for this temperature variation.

Following previous studies, we use an incremental elastoplastic self-consistent scheme to simulate the mechanical loading. At each strain (or stress) increment, the non-linear behaviour is approximated by the tangent behaviour. Details can be found in a review of the different self-consistent schemes for constitutive laws relating stress (or stress rate) to strain (or strain rate) (Canova and Lebensohn 1996).

5 Results and confrontation

5.1 Calculated thermal residual stresses

We performed a thermoelastic calculation with a single thermal loading ($\Delta T = -600^{o}K$) to represent the cooling from annealing to room temperature. We used a set of 2160 orientations to represent the experimental texture. The result of the calculation is presented in Figure 2. Due to the transversely isotropic behaviour of the single crystal, we made an average over φ_2 (rotation around the <c> axis) for each orientation. Thus, we have plotted the Von Mises stress and the ODF for an orientation (φ_1, ϕ) with an isodensity representation. The average stress level predicted for the main texture component lies between 60 and 80 MPa. As expected, the main crystallographic orientation presents the weakest stress level. Since it brings the main contribution to the effective properties of the polycrystal, the elastic accomodation field will be less than those of the minor orientations. But, attention must be paid to the spread of the texture. As a matter of fact, the orientations with a low density level (ranging from 1 to 2) present a high stress level (up to 120 MPa) due to their misorientation with the main component. Therefore, the early stage of their plastic behaviour will differ from that of the main component. This result points out the importance of determining experimentally the residual stress field, before and during a mechanical test, taking into account the spread of the main texture to get a better understanding of the strong strain heterogeneities observed experimentally.

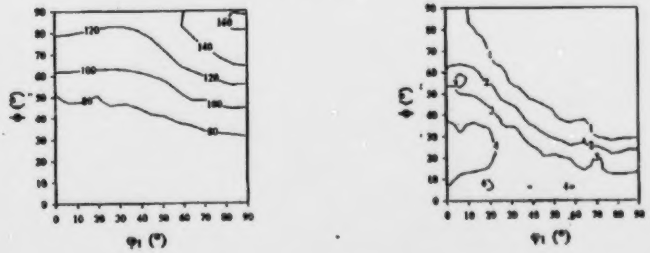

(a) (b)

Figure 2 : Initial residual stress level (Von Mises) (MPa) (a), ODF (random units) averaged over φ_2 (b). φ_1 is ranging from 0 to 90° due to the orthotropy of the sample.

5.2 Mechanical response

We have considered three slip systems families to describe the plastic behaviour of the single crystal : prismatic (pr), first-order pyramidal <c+a>, (pyr<c+a>) and basal (bas). The Critical Resolved Shear Stresses (CRSS) associated with each of them are adjusted to give the best description of the mechanical response. We found : $\tau^{pr} = 155$ MPa, $\tau^{pyr<c+a>} = 242$ MPa and $\tau^{bas} = 320$ MPa. The best agreement is obtained without intracrystalline hardening.

There is quite a good agreement between the experiments and the simulations for the conventional yield stress, defined at 0.2% plastic deformation, for the internal pressure and compression tests (Figure 3). In both cases, we observe a short elastoplastic transition correctly reproduced by the model. For the tension test, the model fails to reproduce the yield stress and the stress evolution in the early stage of plastic deformation. The apparent hardening predicted at the beginning of the plastic deformation is higher than the one observed experimentally. Besides, the yield stress difference between the tension and the compression test predicted is about 70 MPa although experimentally it is only of 40 MPa. Yet, the model exhibits the correct trend since it predicts a lower yield stress in tension than in compression which is experimentally observed. Following these confrontations, we performed a simulation for a reverse biaxial loading (i.e. external pressure). The predicted difference in the elastoplastic transition is much lower between internal and external pressure than between tension and compression (Figure 3).

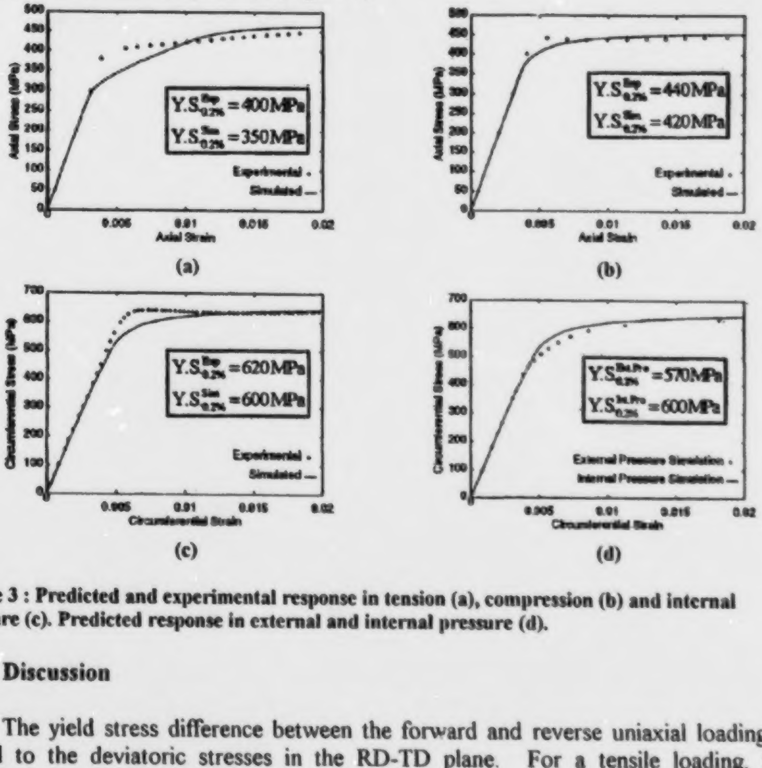

(a) (b) (c) (d)

Figure 3 : Predicted and experimental response in tension (a), compression (b) and internal pressure (c). Predicted response in external and internal pressure (d).

6 Discussion

The yield stress difference between the forward and reverse uniaxial loading is linked to the deviatoric stresses in the RD-TD plane. For a tensile loading, the deviatoric stresses are compressive in the RD-TD plane. They superimpose to the "thermal" compressive stresses across the prismatic planes resulting in an earlier activation of prismatic slip (Turner et al. 1995). Here, the spread of texture in the plane RD-TD has no effect since the deviatoric stresses are compressive in this plane. But as we remarked above, the predicted yield stress difference between the tensile and compressive tests is higher than the experimental one. Besides, a long elastoplastic transition is predicted for the tensile loading although it is not observed experimentally. These two remarks can be related to an underestimation of the residual stresses relaxation by the model. The smaller difference between the yield stresses experimentally observed is consistent with a lower residual stress level. If we suppose a lower residual stress level, it involves an increase of the yield stress in tension since the contribution of the residual compressive stresses will be decreased. Since the initial residual stress level is consistent with experimental values reported (Turner et al. 1995), we can think that the viscous relaxation which is not taken into account in the model, is responsible for the smaller yield stress difference observed experimentally.

The differences observed between the simulations of internal and external pressure can be explained as follow. An external pressure test induces tensile and compressive deviatoric stresses respectively in the RD and TD direction which will consequently give rise to an early elastoplastic transition with respect to the main texture component. But, due to the spread of the texture and the balance of the deviatoric stresses in the RD-TD plane, this effect will be less important than for the uniaxial loadings.

To conclude, with the use of an elastoplastic model, we show that the effect of the thermal residual stresses on the elastoplastic transition is less important in the case of a pressure test than in the case of an uniaxial test. Moreover, compared to previous studies, the experimental results tend to indicate the necessity of taking into account the viscous relaxation during the mechanical loading.

7 References

Bunge, H.J. (1982) Texture analysis in material science. Butterworths Publ. London.

Canova, G.R. and Lebensohn R. (1996) Micro-macro modeling in *Computer Simulation in Materials Science*, Kirchner H.O. et al (Eds), pp. 449-481.

Caré, S. (1995) Plasticité et endommagement du zirconium alpha polycristallin déformé en traction à la température ambiante.Thèse de doctorat de l'Ecole Polytechnique.

Fisher, E.S. and Renken, C.J. (1964) Single crystal elastic moduli and the hcp→ bcc transformation in Ti, Zr and Hf. *Physical Review*, Vol. 135, No. 2A. pp. 482-494.

Goldak, J., Lloyd, L.T. and Barrett, C.S. (1966) Lattice parameters, thermal expansions and Grüneisen coefficients of zirconium, 4.2 to 1130°K. *Physical Review*, Vol. 144, No. 2. pp.478-483.

Mac Ewen, S.R. and Tomé, C.N. (1987) Residual stresses in textured zirconium alloys. *Proceedings of the 7th International Symposium "Zirconium in the Nuclear Industry"*, ASTM STP 939, Adamson, R.B. and Van Swam, L.F.P., eds., American Society for Testing and Materials, pp. 631-652.

Pang, J.W.L., Holden, T.M., Turner, P.A. and Mason, T.E. (1999) Intergranular stresses in Zircaloy-2 with rod texture. *Acta Materialia*, Vol. 47, No. 2. pp. 373-383.

Piercy, G.R. (1968) Mechanisms for the in-reactor creep of zirconium alloys. *Journal of Nuclear Materials*, Vol. 26. pp. 18-50.

Turner, P.A., Christodoulou N. and Tomé C.N. (1995) Modeling the mechanical response of rolled Zircaloy-2. *International Journal of Plasticity*, Vol. 11, No. 3. pp 251-265.

Turner, P.A. and Tomé, C.N. (1994) A study of residual stresses in Zircaloy-2 with rod texture. *Acta Metallurgica et Materialia*, Vol. 42, pp. 4143

Acknowledgements

The authors would like to thank FRAMATOME / Nuclear Fuel (J-P. Mardon) and EDF/DER for their financial support and ZIRCOTUBE for providing the material.

INTERCRYSTALLINE STRESSES IN METAL POLYCRYSTALS: COMPARING SIMULATIONS TO DIFFRACTION EXPERIMENTS

P. DAWSON and D. BOYCE

Cornell University, Ithaca, New York, USA

S. MacEWEN

Alcan International Limited, Kingston, Ontario, Canada

R. ROGGE

National Research Council, Deep River, Ontario, Canada

Abstract

The focus of this paper is on residual stresses at the crystal level in a polycrystalline metal following plastic deformation. Residual stresses exist in polycrystals after unloading as a consequence of the single crystal anisotropy and grain interactions. In this work, tensile specimens were loaded and unloaded *in situ* to progressively larger amounts of plastic strain, and neutron diffraction measurements were taken at the various points in the loading history to determine the elastic lattice strains. The same tensile tests were simulated with a finite element model, in which the lattice strains at the crystal level were computed grain by grain. Detailed comparisons of lattice strains are presented for steel (HY100) and aluminum (Al5182) alloys.

Key words: crystal plasticity, finite elements, neutron diffraction, residual stress.

1. Introduction

Plastic deformation of a polycrystalline metal induces a state of residual stress following removal of the loads acting on it. The single crystal anisotropy implies spatial heterogeneity in mechanical properties, both elastic and plastic, of a polycrystalline material. When deformed, the elastic and plastic contributions to the deformations individually are incompatible. This incompatibility is the source of residual stress once external loads are removed. Finite element simulations of polycrystals offer an avenue to study the occurrence of residual stress following plastic straining, and provide a means to access the interior of the material in a manner that is difficult to achieve experimentally. Of course, confidence in the validity of such simulations comes only with detailed comparison to experiment under closely controlled conditions. In this paper we present a summary of a coordinated set of neutron diffraction experiments and finite element simulations. The investigation was designed to permit a critical assessment of the ability of a finite element formulation to capture important trends in the distributions of residual stress among the constituent grains of a polycrystalline metal.

The experiments consisted of tensile loading of specimens with uniform gage section. The complete loading history was comprised of a number of loading/unloading

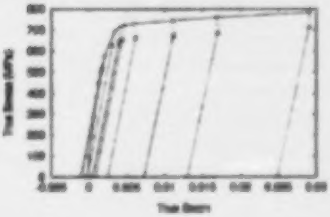

Figure 1: HY100 axial stress response computed from measured loads.

episodes. During each episode, diffraction measurements were taken both while under load and in the unloaded state. Neutrons diffraction permits measuring elastic strains in specific subsets of the crystals in small volumes of metal within the bulk of a specimen. From diffraction measurements, lattice strains were deduced for a number of crystal sets, as determined by specified combinations of scattering vector and lattice plane normal. In the simulations, a section of the specimen was discretized with finite elements, and each element was assigned a lattice orientation based on the measured initial texture. The discretized specimen was then subjected to the same loading history as imposed in the experiment, and lattice strains were recorded for subsequent comparison to the values deduced from the diffraction experiments. The comparisons reveal a number of interesting behaviors, and indicate that the polycrystal model has both strengths and limitations.

2. Experiments

Experiments have been conducted on two alloys, one steel and one aluminum. The steel is HY100, a low alloy steel, which after deformation processing and heat treatment has a BCC structure with finely dispersed carbide particles and nearly equiaxed grain shape. The aluminum is Al5182, which after processing has an FCC matrix with slightly elongated grains and dispersed intermetallic particles. The crystallographic texture has been measured for both. The texture of the steel was quite weak and thus was taken as initially uniform (random). For the aluminum alloy, the texture was characterized as a weak cube texture, and was quantified in terms of an orientation distribution function. Tensile specimens were loaded quasi-statically while in the neutron environment. This permitted diffraction measurements while under load, with these measurements being made during a number of unloading episodes over the course of each test. Each specimen was taken to the maximum deformation prior to failure by diffuse neck. Load-displacement data recorded during the test were reduced to stress-strain data for the full specimen, as shown in Figures 1 and 2.

The diffraction data were collected at three points in every unloading episode. The points correspond to 90% of the load prior to the start of the unloading sequence, to zero load, and again to 90% of the pre-episode stress level during reloading. Data were taken for several crystal sets, corresponding to (400), (220), (222), and (321) or (311) lattice planes. The tests were performed with the scattering vectors in either the lateral and axial directions. In a neutron diffraction test, diffraction data are accumulated as a distributions of neutron counts about a

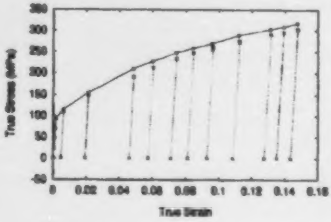

Figure 2: Al5182 axial stress response computed from measured loads.

Table 1: Single crystal parameters

	C_1 GPa	C_2 GPa	C_3 GPa	$\dot{\gamma}_0$ $(\frac{1}{s})$	m $(-)$	h_0 MPa	g_0 MPa	g_s MPa
HY100	228	132	233	1.0	0.02	1000	360	500
Al5182	61.3	57	108.2	1.0	0.02	2376	48.5	120

diffraction peak (MacEwen, Faber Jr., & Turner 1983). Of interest are: the shift of the position of the mean, the changes in the magnitude of the mean, and the width of the distribution. Here we focus only on the first of these. In this case, the reduction of the count distribution data gives changes in the average of the lattice strains from the changes in the distribution mean position.

3. Simulations of the tests

The mechanical response of the tensile specimen to the applied loading was simulated using a finite element formulation that incorporates large strain kinematics (Marin & Dawson 1998). The constitutive behavior within each element is that of a single crystal and is anisotropic for both the elastic and plastic behaviors. The form of the elastic response is determined by cubic crystal symmetry, wherein small elastic strains are assumed. The plastic response is determined by relations for slip on a restricted number of slip systems. The plastic shearing rate on each slip system is a power law function of the ratio of the resolved shear stress and the slip system strength. The strength values for all slip systems within a single crystal harden identically based on a Voce hardening model. The elastic moduli are handbook values. The slip system parameters appearing in the plasticity model were evaluated by choosing values that provided a good match between the measured and computed stress-strain curve for the full specimen. Table 1 contains the elastic moduli and the slip system parameters for the plastic behavior. See (Dawson, Boyce, MacEwen, & Rogge) for parameter definitions.

The finite element formulation employed is quasi-static, and is written to execute on a scalable parallel architecture using a combination of F90 and MPI. All of the simulations reported here were carried out on an IBM SP at Cornell University. The simulations performed on HY100 were obtained using a mesh with approximately 15000 crystals. The crystal lattice orientation for each crystal (one for each element) was assigned from a random sampling of uniform distribution.

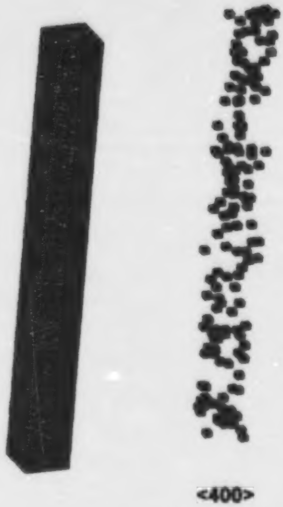

Figure 3: HY100 residual stress state after final unloading Shown are transverse normal components of the lattice strain. White: -0.0015; black: 0.0015; linear scale

The Al5182 specimen was modeled with a mesh of 7000 crystals; in this case the texture could not be assumed to be random, so that it was initialized from an orientation distribution that had been determined by neutron techniques.

4. Comparisons

Presentation of detailed comparisons for every crystal set studied is not possible in the limited space available. Instead, for each material, we present the comparisons between experiment and simulation for a single family of crystals for two scattering vector directions. Each experimental data point represents the average lattice (elastic) strain computed from the shift in the diffraction peak. Each simulation data point represents the average of crystal strains taken over all crystals (elements) having lattice orientation sufficiently close to the nominal value.

For the steel, we present comparisons for the (400) diffraction planes. Figure 3 shows the state of lattice strain after the final unloading for the full mesh (showing only surface crystals) and for those crystals having a (400) lattice plane close to the transverse direction of the specimen. The normal component of strain in the transverse direction is plotted. This component corresponds to the diffraction measurments having a transverse scattering vector. Measured and computed average axial lattice strains are in good agreement for the loaded condition, exhibiting similar magnitudes throughout the test. Figure 4 shows an initial regime of elastic loading, followed by an elastic-plastic transition occurring between strains of 0.2% and 1%. The elastic-plastic transition is characterized by movement of crystal

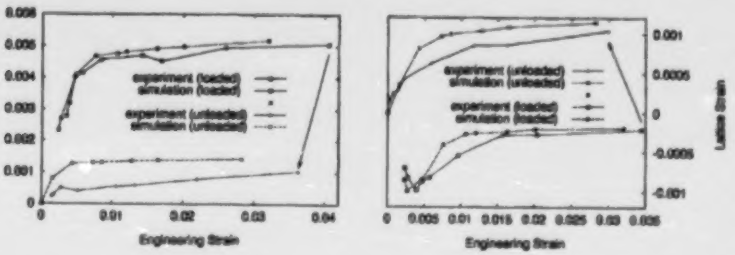

Figure 4: HY100 axial (left) and transverse (right) (400) lattice strains. Arrow connects loaded to unloaded experimental records.

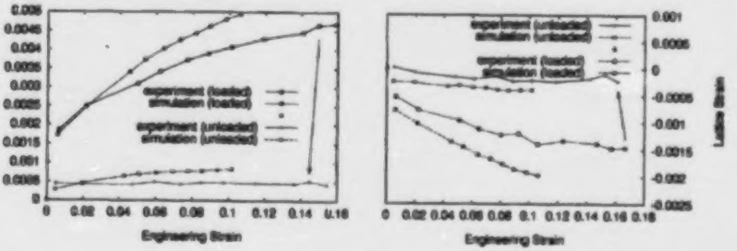

Figure 5: Al5182 axial (left) and transverse (right) (222) lattice strains. Arrow connects loaded to unloaded experimental records.

stresses along facets or edges of the single crystal yield surface toward a vertex of the surface. Subsequent points in the history, those having specimen strain above about 1%, are in a fully plastic regime, with crystal stresses only slowly increasing as the crystals strain harden. While the simulations and experiments show quite similar lattice strains under load, the magnitude of the average axial lattice strain after unloading in the simulation is consistently larger than that measured, especially early in the test. The unloaded values are extensional, on the order of 0.001, and evolve little after completion of elastoplastic transient The lattice strains under load are contractive, and increase as the specimen is loaded for the first time. Once the crystal stresses reach the yield point, however, the lattice strains begin to decrease in magnitude. This trend is clear from the experimental record and is replicated by the simulation. Upon unloading, the average lattice strains are extensional and mimic the transient observed under load, so that the difference between loaded and unloaded lattice strains remains nearly constant. The magnitude is on the order of 0.001, which is appreciably larger that the value under load.

For the aluminum alloy, we present comparisons for the (222) diffraction planes in Figure 5. The specimens extended to over 10% strain, and in contrast to the steel test, the specimen is already strained beyond its elastic limit for the first diffraction data point shown. In the axial direction, the lattice strains increase at a diminishing rate as the material strength increases as a result of strain hardening. Measured residual strain are nearly constant throughout the test. The simulation shows lattice strains under load that are greater than the measured values. The residual values are similar in magnitude to the measured values, but are increasing throughout the deformation of the specimen. In the transverse direction (aligned with the normal direction to the plate stock material), the lattice strains are contractive under load, and compare favorably between experiment and simulation. The residual strains are contractive as well, a trend captured by the simulations.

It should be noted that, in the simulations, all crystals were assumed to be stress-free at the start of the test. The measured data imply that this might not be the case. Consequently, the most relevant aspect of the behaviors for comparison is the change in strain on unloading once the plastic deformations on unloading is fully developed. Here, the comparisons are consistently quite good.

5. Summary

Finite element techniques currently available, together with parallel computing architectures, enable the simulation of the elastoplastic response of large aggregates of crystals. The numbers of crystals that may be modeled are sufficient to study behaviors of polycrystals in light of the variability in responses brought about by the variations in local neighborhood of individual crystals. Here we present the modeling of residual stresses that arise from incompatible elastic and plastic strain distributions following permanent deformation, and make comparisons to measurements obtained from neutron diffraction experiments. The comparisons are good, especially with respect to the magnitudes of the strain changes on unloading for various crystal sets. Further, the changes in texture accompanying straining can be detected in the experiments, as well captured in the simulations.

6. Acknowledgements

Support for this work has been provided by the Office of Naval Research under contract NOOO 14-95-I-0314. Neutron diffraction experiments were performed on a National Research Council (Canada) neutron diffractometer located at the NRU Reactor of AECL (Atomic Energy of Canada Limited). Computing resources were provided by the Cornell Theory Center.

7. References

Dawson, P., D. Boyce, S. MacEwen, & R. Rogge. Residual stresses in hy100 polycrystals: Comparisons of experiment and simulations. in preparation.

MacEwen, S., J. Faber Jr., & A. L. Turner (1983). The use of time-of-flight neutron diffraction to study grain interaction stresses. *Acta Metallurgica 31*, 657 – 676.

Marin, E. B. & P. R. Dawson (1998). On modeling the elastio-viscoplastic response of metals using polycrystal plasticity. *Computer Methods in Applied Mechanics and Engineering 165*, 1– 21.

RELATIONSHIP BETWEEN TEXTURE, MAGNETIC INDUCTION AND MAXIMUM MAGNETIC PERMEABILITY OF SI STEELS

W. MAO, N. CHEN and Y. YU
Department of Materials Science and Engineering
University of Science and Technology Beijing, Beijing, China

Abstract

The magnetic induction (B_{1000}) and maximum magnetic permeability (μ_{max}) of a commercial oriented Si steel were calculated according to its texture and the corresponding magnetic anisotropy energy, in which the contribution to the magnetic properties of differently oriented grains is proportional to their volume fractions. The calculations show good agreement with the measured data.

Keywords: Magnetic induction, maximum magnetic permeability, Si steels

1 Introduction

Texture is usually considered to be the most important factor to determine some magnetic properties of Si steels, which could be calculated using the texture data (Hutchinson and Swift 1972, Szpunar and Ojanen 1975, Chen et al. 1998). It is very important to calculate not only the magnetic properties for the theoretical investigation e.g. the calculation of magnetic torque (Hutchinson and Swift 1972) or anisotropy energy (Szpunar and Ojanen 1975), but also some magnetic properties for the technical purposes, of which the relationship to the crystallographic texture could be therefore better revealed. On the other hand, new kinds of Si steels with strong cube texture or {100} fiber texture (see fig. 1a)(Mao 1998) will be produced using a final continuous annealing technology. Therefore the on-line measurement equipment for r value determination of IF steels could also be used to confirm the commercial magnetic properties of the new Si steel sheets.

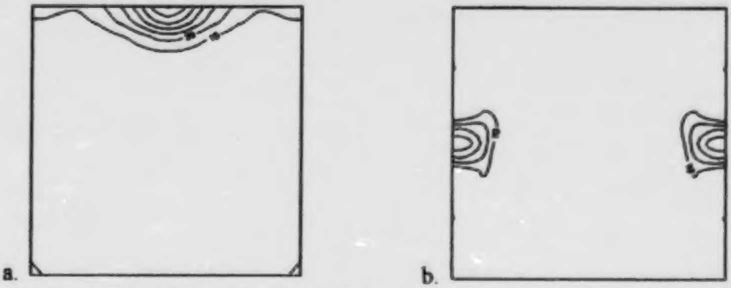

(a: density levels: 10, 20, 30, 40, 50, 60, 70, Max.=71.1, $\varphi_1=0°$ section)
(b: density levels: 10, 15, 20, 25, Max.=29.5, $\varphi_1=0°$ section)

Fig. 1 Oriented Si steel with strong {001}<110> (a) or {110}<001> (b) texture.

2 Calculation of anisotropy energy

According to the phenomenological theory the magnetic anisotropy energy E of a single crystal can be calculated as (Bitter 1937):

$$E = k_4(\alpha_1^2\alpha_2^2 + \alpha_2^2\alpha_3^2 + \alpha_3^2\alpha_1^2) + k_6\alpha_1^2\alpha_2^2\alpha_3^2 + \cdots\cdots \quad (1)$$

where k_4, k_6, are the known constants and α_1, α_2, α_3 are the direction cosines of the magnetization vector in the crystalline coordinate system. If the single crystal or a grain is observed in a sample coordinate system the E can be written as a function of orientation g in the format of series expansion of generalized spherical harmonics i.e. (Bunge 1981a):

$$E(g,\alpha) = \sum_{l=0}^{l_{MAX}} \sum_{m=-l}^{l} \sum_{n=-l}^{l} e_l^{mn} \cdot T_l^{mn}(g,\alpha) \quad (2)$$

where the α is the angle between observed direction and the rolling direction on sheet plane, and e_l^{mn} are the series coefficients that can be calculated in advance (Chen et al. 1998).

The orientation distribution function i.e. the ODF f(g) of a polycrystalline aggregate can be expressed as (Bunge 1981b):

$$f(g) = \sum_{l=0}^{l_{MAX}} \sum_{m=-l}^{l} \sum_{n=-l}^{l} C_l^{mn} \cdot T_l^{mn}(g) \quad (3)$$

and therefore the corresponding average magnetic anisotropy energy $\overline{E}$ can be written as (Bunge 1981a):

$$\overline{E}(\alpha)=\sum_{l=0}^{l_{max}}\sum_{m=-l}^{l}\sum_{n=-l}^{l}\frac{1}{2l+1}e_l^{mn}\cdot C_l^{mn}\cdot\cos n\alpha \tag{4}$$

in which all grains will contribute to the magnetic properties according to their orientations and corresponding volume fractions.

The magnetization curve of a Si steel sheet can be measured, which shows the relationship between magnetic field intensity H and magnetic induction B (fig. 2). The $\overline{E}(\alpha)$ is the integrated area between magnetic induction B axis and magnetization curve. Generally the magnetization curve can only be measured in a limited field intensity range (fig. 2). However the induction $B(\alpha)$ e.g. $B_{1000}(\alpha)$ or the maximum permeability $\mu_{max}(\alpha)$ shown in the magnetization curve are the very useful technical properties, which should be obtained according to the texture data, of which the maximum permeability $\mu_{max}(\alpha)$ is defined as:

$$\mu_{max}(\alpha)=\left(\frac{B(\alpha)}{H\cdot\mu_0}\right)_{max} \tag{5}$$

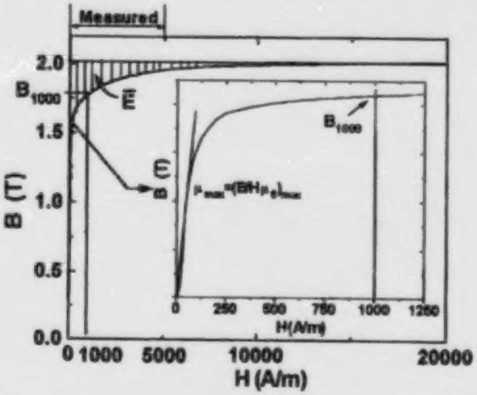

Fig. 2 The sketch of magnetization curve.

3 Experimental results

A conventional oriented Si steel with strong {110}<001> texture was taken. The {110}, {200} and {112} pole figures were measured and the corresponding ODF was calculated (Bunge 1981b), of which the $\varphi_1=0^\circ$ section is shown in fig. 1b.

The magnetization curves of the Si sheet were measured in different α angles(fig. 3). It can be estimated that with increasing α value the $\overline{E}(\alpha)$ becomes larger at $\alpha=0^\circ\sim45^\circ$ and becomes lower at $\alpha=60^\circ\sim90^\circ$(fig. 3). On the other hand, the $\mu_{max}(\alpha)$ is also reduced if the $B(\alpha)$ level becomes lower and (fig. 3). It seems that the $\overline{E}(\alpha)$ is inversely proportional to $B(\alpha)$ and $\mu_{max}(\alpha)$. At the range of measured magnetic field intensity the magnetization curve is approximately parallel each other.

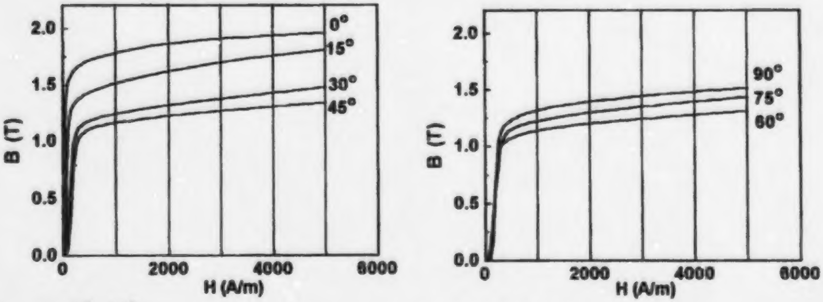

a. at $\alpha=0^\circ\sim45^\circ$

b. at $\alpha=60^\circ\sim90^\circ$

Fig. 3 The measured magnetization curves of the oriented Si steel sheet.

4 Calculation of the magnetic properties

According to equation 4 the average magnetic anisotropy energy of the oriented Si steel sheet can be calculated. Figure 4 gives the result. Supposing that the average magnetic anisotropy energy $\overline{E}(\alpha)$ is inversely proportional to the induction $B(\alpha)$ and the maximum permeability $\mu_{max}(\alpha)$, the $B_{1000}(\alpha)$ and $\mu_{max}(\alpha)$ can be calculated on an empirical basis as:

$$\frac{1}{\mu_{max}(\alpha)} = a\overline{E}(\alpha) + b, \qquad \frac{1}{B_{1000}(\alpha)} = c\overline{E}(\alpha) + d \tag{6}$$

where the a, b, c, d are the constants of the regression calculation. Figure 5 gives the linear relationship of $\overline{E}(\alpha)$ to the $\mu_{max}(\alpha)$ and $B_{1000}(\alpha)$ with really high relation coefficient of 0.9809 and 0.9742 respectively.

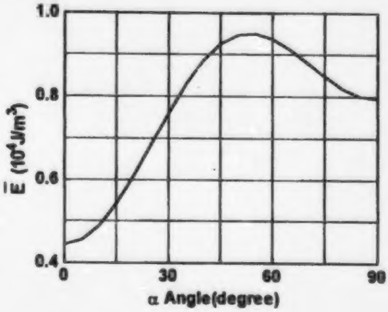

Fig. 4 The calculated average magnetic anisotropy energy of the oriented Si steel sheet.

According to the linear regression equation 6 the function of $\mu_{max}(\alpha)$ and $B_{1000}(\alpha)$ at any α can be calculated. Figure 6 compares the calculation with the measured data and confirms again the linear relationships.

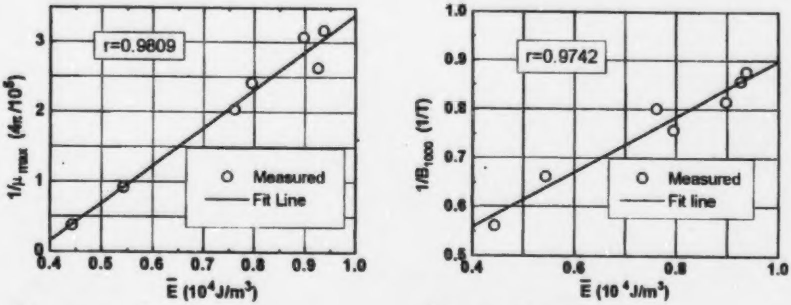

a. $\bar{E}(\alpha)$ vs. $\mu_{max}(\alpha)$ b. $\bar{E}(\alpha)$ vs. $B_{1000}(\alpha)$

Fig. 5 Linear relationship of $\bar{E}(\alpha)$ to the magnetic properties.

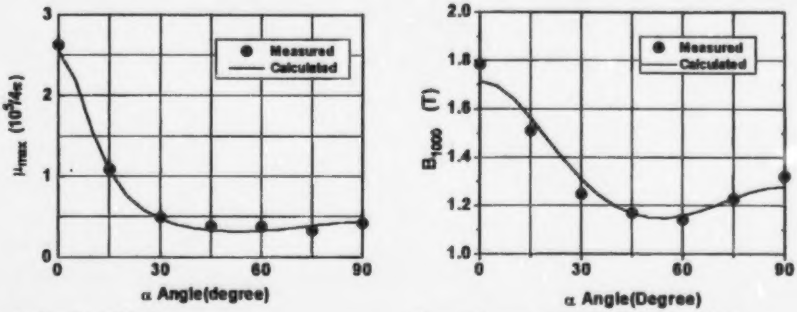

a. induction B(α) b. maximum permeability $\mu_{max}(\alpha)$

Fig. 6 Comparison of the calculation with the measured data.

5 Summary

The technical magnetic properties i.e. the induction and the maximum permeability of Si steels can be calculated using the texture data, however the potential theoretical background of the linear relation should be investigated in details.

6 References

Bitter, F. (1937) *Introduction to ferromagnetism*, Mac Graw-Hill, p. 213.

Bunge, H.J. (1981a) The relation between preferred orientation and the Lankford parameter r of plastic anisotropy, *Arch. Eisenhüttenwes.*, Vol. 52, No. 10. pp. 407-411.

Bunge, H.J. (1981b) General outline and series expansion method, in *Quantitative Texture Analysis*, (ed. H.J. Bunge and C. Esling), DGM-Informationsgesellschaft, Oberursel, pp. 1-72.

Chen, N., Mao, W. and Yu, Y. (1998) Relationship between texture and magnetic properties of non-oriented Si steel, *Advanced Materials and Processing*, PRICM3, conf. proc., (ed. M.A. Imam, et al.), TMS, Vol. 1, pp. 223-228.

Hutchinson, W.B. and Swift, J.G. (1972) Anisotropy in some soft magnetic materials, *Texture*, Vol. 1, pp. 117-123.

Mao, W. (1998) Research and development of anisotropy in iron and steel, *J. Baotou Univ. Iron & Steel Tech.*, Vol. 17, No. 3. pp. 167-172.

Szpunar, J. and Ojanen, M. (1975) Texture and magnetic properties of Fe-Si steel, *Met. Trans.* A, Vol. 6, No. 3. pp. 561-567.

STRAIN EFFECTS AND TEXTURE AT IN-PLANE SHEARING OF Cu ALLOYS.

J. KUSNIERZ
Institute of Metallurgy and Materials Science, Polish Academy of Sciences,
Kraków, Poland
E. F. RAUCH
Génie Physique et Mécanique des Matériaux, Institut National Polytechnique de
Grenoble, France

Abstract

The paper discusses the shearing in the plane of a sheet, performed by means of a shear apparatus. The strain softening effect and shearing at constant shear stress in the case of predeformed copper and brass respectively were observed, while the interruptions of stress-strain dependences in sheared bronze were evidence of local cracking; annealed samples demonstrated regular power law dependences. Texture measurements revealed increasing dispersion of the crystallite orientation around normal to shear plane. TEM observations have shown, in rolled copper, the formation of cellular structure of dislocation elongated in the shear direction, whereas in rolled brass we have noted the shear banding against the background of twin + matrix sets. In recrystallized samples only dislocation arragements distributed on the grain scale have been observed.

Keywords: in-plane shearing, strain effects, shear banding, work softening

1. Introduction

Hardly cold-worked F.C.C. alloys sheets reveal inhomogeneous mode of deformation; the phenomenon is known as shear banding (SB) and observed on micro- and macro-scale.(compare discussion in the paper: Kusnierz (1992) on cold rolling of Cu and CuZn brass sheets). After initial cold working z, depending on the stacking fault energy (SFE), i.e. after z=40% (deformation ε=0.5) in case of CuZn30 brass and after z=70% (ε=1.2) in case of copper, SBs are noted, generally on a macroscopic scale, as the strain localizations in the form of macroscopic shear bands. Because SBs are inherently related to shear deformation, we have been interested in the shearing experiment itself. In a model shear plane test, the shear deformation is acting on the plane of sheet (Rauch (1989)) and recently it was applied to investigate the mild steel (Bacroix(1994)) and copper alloys (Kusnierz (1998)) under shearing. Two characteristics promote this type of test: (i) homogeneity of applied stress in the deformed volume and (ii) facility of shear bands identification as their plan is positioned perpendicularly to the sheet plane.

The main objective of the paper was to investigate the mechanical behaviour and texture evolution in model materials, such as Cu and Cu-based alloys under shearing conditions, and with processed materials in various mechanical states including that with the shear bands preliminary formed by cold rolling to observe the strain effects under shearing.

2. Experimental procedure and results

The experiments were performed on commercial purity bands of copper, CuZn37 brass and CuAl8 bronze, which were prior to shear tests cold-rolled in laboratory up to z=75% reduction of area: copper (C4), brass (M5) and up to z=91.5% in case of bronze (BA), and then annealed at 723K during 0.5h: C4r, M5r and BAr (Kusnierz (1992)). Microstructural investigations were carried out using Philips EM 301 electron microscope with a voltage of 100 kV. The samples were prepared by electrolytic thinning. The measurements of pole figures were performed using Philips X-ray diffractometer and CoK_α characteristic radiation. For characteristic cases there were calculated Orientation Distribution Function (ODF) using the method of ADC (Pawlik (1988)).

2.1 In-Plane Shearing

The shearing was performed in a shear test apparatus by means of a tensile test machine and the experimental part is described elsewhere (Rauch (1989)).

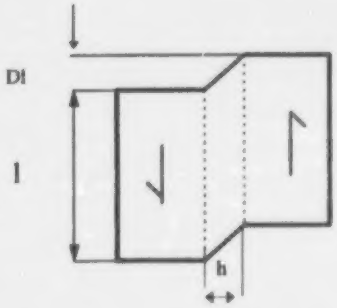

Fig. 1 presents schematically the basic idea of a shear experiment where under the force **F**, the lateral displacement **Dl** of a sheet sample can be performed by means of a tensile test machine. Then, the macroscopic shear deformation **γ=Dl/h,** and the shear stress **τ=F/e/l,** where **h** denotes the width of the shear zone, and **e** -the thickness of the shear zone, and **l** - length of the sheet sample, can be calculated (in our case **l**= 65 mm, **e** = 0,5 mm, **h** = .2 mm).

Fig. 1: Scheme of shearing in a shear plane test. Semi-arrow indicates Shearing Direction (SD).

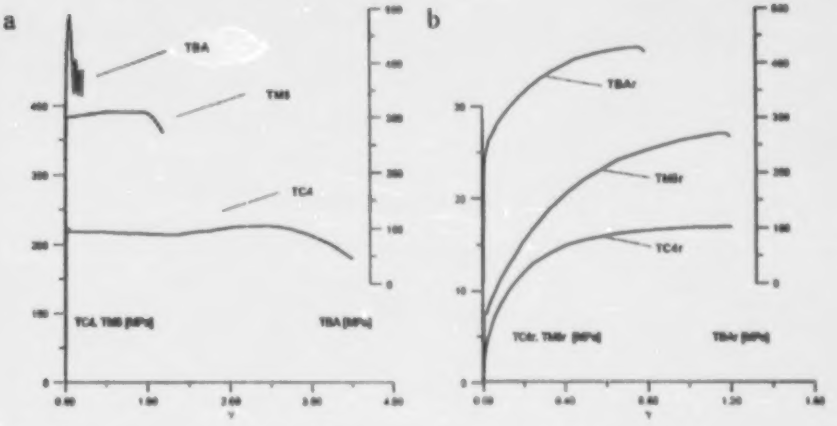

Fig. 2: Shear stress-shear strain (τ-γ) : a) predeformed by rolling, b) annealed.

The experiments with copper and brass, preliminarily rolled to 75% reduction of area and next sheared, have revealed the formation of regular shear zones in the case of copper, whereas to the contrary, non-regular and stepped shear zones were observed in the case of brass (Kusnierz (1998)). In a recrystallized copper sheet (C4r) and two recrystallized: CuZn37 brass (M5r) and CuAl8 bronze (BAr) sheets the formation of shear zones was less evident (Kusnierz(1999)). In Fig. 2b there are presented τ-γ curves of sheet samples in annealed state. They resemble those observed in tensile tests. The curves presented in Fig. 2a correspond to predeformation by cold-rolling. They demonstrate typical effects observed during changing of the deformation path. The behaviour of copper resembles that of mild steel; after initial yield point some strain softening is observed. In case of brass, the shearing is performed under constant shear stress and strain localization is noted. In CuAl8 bronze, high deformation degree of rolling is accompanied by discontinuity of τ-γ curves corresponding to local fracture events (Fig. 2a, TBA curve).

2.2 Texture examination

As it was demostrated in previous experiments on Cu (C4) and CuZn37 brass (M5), predeformed by rolling, the shearing is accompanied by increasing dispersion

Fig. 3: Main components of C4, M5, C4r and M5r sheets (before shearing);
Ct= (112)[1 $\bar{1}$ 0], Bt= (110)[1 $\bar{1}$ 1], Cc= (001)[100, G= (011)[100].

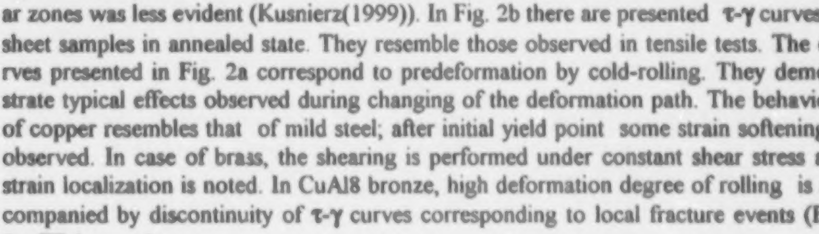

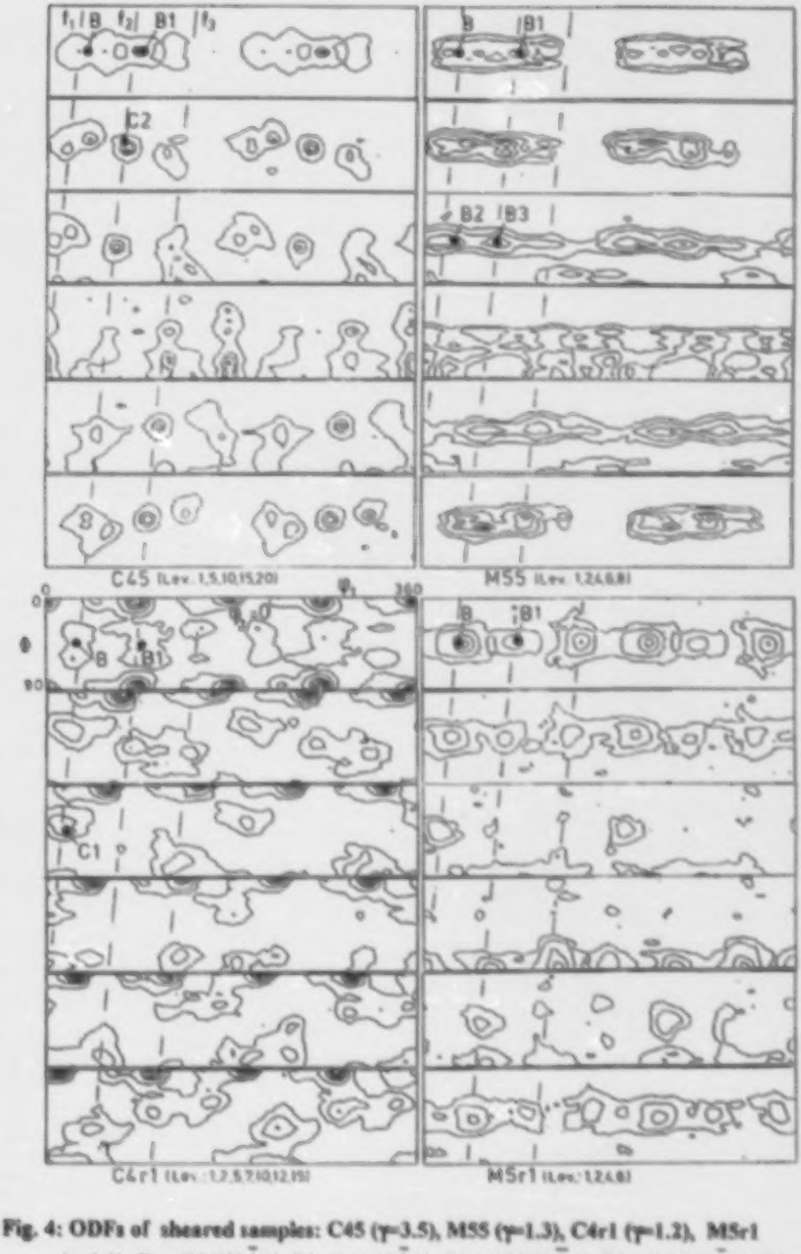

Fig. 4: ODFs of sheared samples: C45 (γ=3.5), M55 (γ=1.3), C4r1 (γ=1.2), M5r1 (γ=1.2); B= $(011)[2\bar{1}1]$, B1=$(011)[0\bar{1}1]$, B2= $(122)[2\bar{2}1]$, B3= $(122)[0\bar{1}1]$, C1= $(123)[5\bar{4}1]$, C2= $(132)[1\bar{3}4]$. Others denotations as in Fig. 3.

about shear direction (SD) and as well as about normal direction (ND).

Fig. 3 presents ODF cross-sections $\varphi2 = 45^\circ$ for Cu (C4) and brass (M5) predeformed and $\varphi2 = 0^\circ$ for annealed state (C4r and M5r, respectively) where typical main ideal components in convention (ND)[SD] are positioned, i.e. Ct= $(112)[1\bar{1}0]$, Bt= $(110)[1\bar{1}1]$, Cc= (001)[100]. Shearing deformation causes the appearence of orientation fibers (Bacroix (1994)), the based parts of which are represented by f1, f2 and f3 in Fig. 4. Certain characteristic components, which were ecountered during crystal rotations analysis under shearing deformation (Kusnierz (1999)), are also shown; particular metals are differenciated by the crystal orientation density distribution along fibers.

3. Discussion of results

Mechanical tests during in-plane shearing reveal some characteristic features of deformed metals. Shear stress - shear strain τ-γ curves of all sheet samples in annealed state (Fig. 2a) resemble those observed in tensile tests; they can be described by power low dependences on shear γ. Predeformation by rolling leads to certain particular behaviour depending on SFE. Copper, which is characterized by medium value of SFE (Kusnierz (1992)), when predeformed 75% by cold rolling, demonstrates during shearing the behaviour similar to that of mild steel (Rauch (1989)) through its yield phenomenon (strain softening), followed by growing strain hardening (C4-5 in Fig. 2a).

The Transmission Electron Microscopy (TEM) photographs present, at the end of the strain softening range, the beginning of the formation of the cellular distribution of dislocation with cells elongated in SD (Fig. 5a); that process seems to be accomplished at the end of shearing, i.e. for γ equal to about 3.5. In case of brass, the shearing is performed under constant shear stress and strain localization is noted. In CuAl8 bronze, high deformation degree of cold-rolling (z=91.5%) is accompanied by discontinuity of τ-γ curves corresponding to local fracture events (TBA in Fig. 2a). TEM photographs of a sheared brass sample demonstrate the localization of deformation in the form of shear bands (Fig. 5b) and, as it was observed in previous experiments, the SBs were activated under constant resolved stress and the failure was observed at the end of shear banding; in bronze that discontinuity of τ-γ dependences is attributed to the latter phenomenon (TBA in Fig. 2a). The lack of shear banding in TEM micrographs (Fig. 5c) of an annealed sheet is not surprising, as was already stressed, among others, by Kusnierz (1992) that SBs appear after certain deformation degree, depending on SFE (in brass beginning from z=40% and in Cu - z=70% by rolling).

To sum up, we can conclude that in case of shearing of annealed metals the strain hardening is governed mainly by a structure sensitive factor resulting from homogeneous interaction of in-bulk distributed dislocations on grain scale (structure strengthening factor). In predeformed sheets the mechanical behaviour is SFE depending. In copper SSE, due to realease of internal stresses by cross slip mechanism this formation is most probable which leads to cellular distribution of dislocation, independently of the constraint condition, as it was observed during the change of the deformation path from rolling to twisting (Kusnierz (1999)). In case of low SFE, like brass and bronze, the strain path change is sensitive additionally to the deformation degree, at high degree of predeformation the shearing is accomplished under constant shear stress (in case of brass, and the local fracture leads to final failure as in case of bronze (Fig. 2a)).

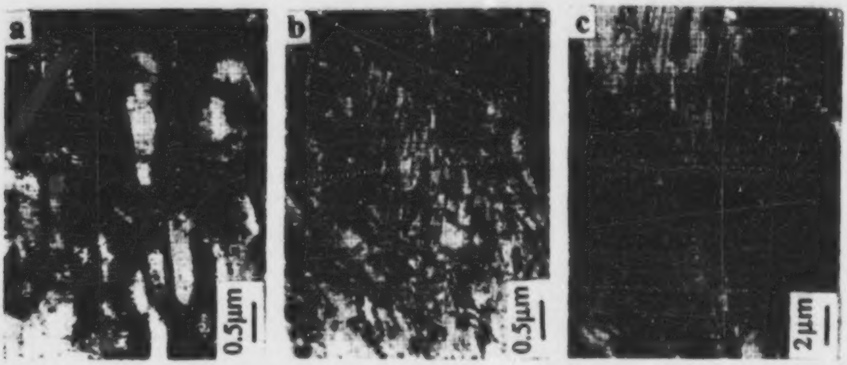

Fig. 5: TEM of sheared sheets: a) C45 (γ=3.5), b) M55 (γ=1.3), c) M5r1 (γ=1.2). Magnification mark indicates SD.

4. Conclusions

Copper, predeformed by rolling up to z=75%, demonstrates, under shearing, the strain softening effect associated with rearrangement of dislocations to form microbands elongated in SD. In an analogous case of CuZn37 brass, the shearing takes place under constant shear stress, and SBs are observed.

The τ-γ curves of investigated metals in annealed state conform to the power law formula and the strengthening results from dislocation interaction on the grain scale.

ODFs of sheared samples indicate the formation of shear fiber orientations; individual metals are differentiated by the distibution of orientations along the fibers corresponding to the realized shear induced rotation.

5. References

Bacroix B. and Hu Z. (1994) Texture evolution induced by strain path change in low carbon steel sheets. Metall. Trans., Vol. A26, pp. 601-613.

Kusnierz J. (1992) Localization of strain and fracture in anisotropic metal sheets with F.C.C. lattice. Archives of Metallurgy, Vol. 37, pp. 203-282.

Kusnierz J. and E. Rauch (1998) Texture and microstructure of Cu and CuZn37 brass under shearing in a planar shear test. Mat. Sci. Forum, Vol.273-275, pp. 339-344.

Kusnierz J., Rauch E., Baudin T., Penelle R. and Jura J. (1999) Microtexture and non-homogeneity of deformation at planar shear tests of Cu and Cu-based alloys. Archives of Metallurgy - in press.

Kusnierz J. and Kurowski M. (1999) Strain softening effects in microstructure of Al rods under torsion. - to be published

Pawlik K., Pospiech J. and Lücke K. (1991) The ODF approximation from pole figures with the aid of the ADC method. Textures Microstructures, Vol. 14-18, pp. 25-30

Rauch E.F. and G'sell C. (1989) Flow localization induced by a change in strain path in mild steel. Materials Sci. Eng., Vol. A111, pp. 71-80.

TILTING OF c-AXES AND TWISTS AROUND THE c-AXES IN A MELT-TEXTURED YBaCuO CYLINDER

V. JUNG
Forschungszentrum Karlsruhe, INFP, P.O.B. 3640, D-76021 Karlsruhe, Germany
H.-G. BROKMEIER, E.M. JANSEN, and R. SCHNIEBER
Institut für Werkstoffkunde und Werkstofftechnik der TU Clausthal, Germany
GKSS-Forschungszentrum, P.O.B. 1160, D-21494 Geesthacht, Germany

Abstract

To investigate the ordering effect of a seed crystal, a melt-textured YBaCuO cylinder of 43 mm diameter and 15 mm depth was cut into 21 pieces. Two of these pieces were cut again, now into three and two pieces, respectively, in the plane normal to the cylinder axis. These pieces were used to measure the distributions of the c-axes of the YBaCuO domains by neutron diffraction using the (005) reflection. The distributions of the a- and b-axes were measured using the (113) reflection. Some initial results show the decreasing influence of the seed crystal in the direction of the boundary region of the YBaCuO cylinder.

Keywords: Magnetic bearing, Texture of YBaCuO

1 Introduction

In superconducting self-stabilizing magnetic bearings, YBaCuO pieces in which the superconducting currents are induced by a permanent magnet must have a very sharply defined texture. The c-axes of the crystalline domains must not deviate by more than 5° ... 10° from the cylinder axis of the melt-textured YBaCuO cylinders produced by an implanted seed crystal. Eight well-textured YBaCuO cylinders were cut to a wedge shape and combined in a ring of superconducting material. A permanent magnet was levitated on this ring, constituting a superconducting magnetic bearing at 77 K.

In a more effective approach, a melt-textured ring will be produced by implanting eight seed crystals into the melt at peritectic temperature. To guarantee a homogeneous texture in the melt-textured ring, the ordering effect of seed crystals as a function of the distance to the seed crystal in the direction of the next seed crystal on the ring and in the direction of the bulk of the ring material must be known.

2 Experimental Method

Measurement of the (005) reflection intensity distributions over the central area of the pole sphere, and measurement of the (113) reflection intensity distribution from one branch of the four [113] directions of the upper half of the pole sphere, allowed both the distribution of c-axis deviation from the cylinder axis of the uncut cylindrical specimen and the distribution of directions of the a- and b-axes, respectively, to be determined in each part of the cut YBaCuO specimen. The measurements were conducted in the TEX 2 neutron texture diffractometer at Geesthacht.

As can be seen from Fig. 1, the YBaCuO cylinder shown was cut into 21 pieces, with the cut planes extending parallel to the axis of the cylinder. The pieces have maximum dimensions of 10 mm x 10 mm x 15 mm and, therefore, can be immersed in a neutron beam. This means that rotation of the specimen by 180° in φ about an axis parallel to the cylinder axis is bound to result in a mirror-image cut through the pole sphere, provided that the angle, χ, is traversed in steps of 1° at constant φ. As always the entire specimen volume is irradiated, and if also the beam intensity is constant over the specimen volume, such mirror-image distributions are to be expected. Minor deviations are attributable to the beam intensity not being constant across the beam cross section, and to textural inhomogeneities within a piece of the specimen.

After preliminary measurements (Jung 1998) with a relatively coarse mesh (1.5° in χ and 2.2° on great circles in φ), the mesh was refined to 1° mesh width each, as is shown in Fig. 2. This fine mesh was necessary up to 10° axial deviation. However, between axial deviations of 10° and 20°, twice the mesh width, i.e. 2°, was sufficient.

To obtain the distribution of axial deviations of the c-axes from the cylinder axis, the measured (005) reflection intensities must be summed up on small circles of the pole sphere. At twice the mesh width, the respective sums must be multiplied by a factor of 2 if values true to scale are to be obtained for the distributions above 10° axial deviation. The sums obtained in this way then represent the individual points of the distribution curve of c-axis deviations from the cylinder axis of the uncut specimen (Bornemann et al. 1996) (Jung et al. 1997, 1998a, 1998b, 1999).

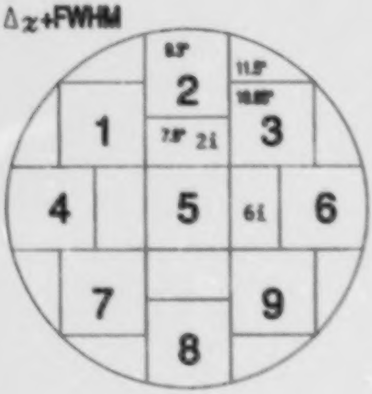

Fig. 1: A bulk YBaCuO cylinder with sufficient texture and with a high magnetic levitation force (95 N) was cut into 21 pieces for investigation of the local texture by neutron diffraction. Diameter of the cylinder = 43 mm, height = 15 mm.

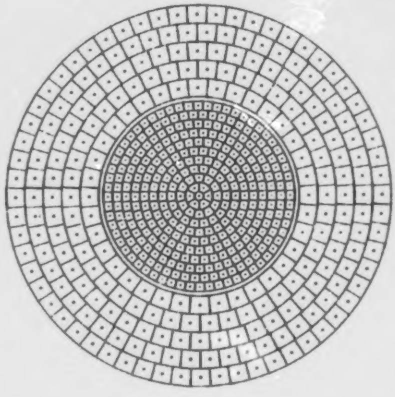

Fig. 2: As the axis of distribution of c-axis deviations from the cylinder axis was close to the cylinder axis of the YBaCuO cylinder, a 1° wide mesh is sufficient up to a deviation of 10° from the cylinder axis. From 10° to 20° deviation, a mesh width of 2° is used. This scan scheme is used for the (005) reflection only.

3 a- and b-axis Distributions, respectively

In a similar way as in the measurements of c-axis distribution, the angular distribution of the a- and b-axes, respectively, can be measured. However, in this case, the summation procedure is conducted not over entire small circle rings of the pole sphere but only, e.g., over 11 χ-values of a 1° mesh in φ and χ. The mesh over φ in this case must have 1° spacing on small circles. The sums over χ represent the values of the distributions over φ. As is evident from Fig. 3, eleven readings over the χ area are fully sufficient in this case. However, also for the three distributions in Fig. 4, with the distributions of pieces 6i, 6, and 5 of the specimen shown in Fig. 1, the angular range of 10° in χ is sufficient for obtaining, from the two-dimensional distribution of the (113) reflection intensities, a one-dimensional distribution by summation over χ. At any rate, the full widths at half maximum of the one-dimensional distributions obtained in this way are clearly apparent in Fig.4.

It is striking to see in Fig. 3 that the distribution width in the upper part of piece 8 is narrower (FWHM = 3.1°) than in the bottom part, 8u (FWHM = 4.0°). Figure 4 reveals a tendency that, obviously, the distribution of the directions of a- and b-axes, respectively, is broader underneath the seeding crystal placed in piece 5 (FWHM = 5.7°), while it is narrowest in the intermediate piece , 6i (FWHM = 4.1°), and broader again at the edge of the specimen shown in Fig. 1 in piece 6 (FWHM = 4.2°).

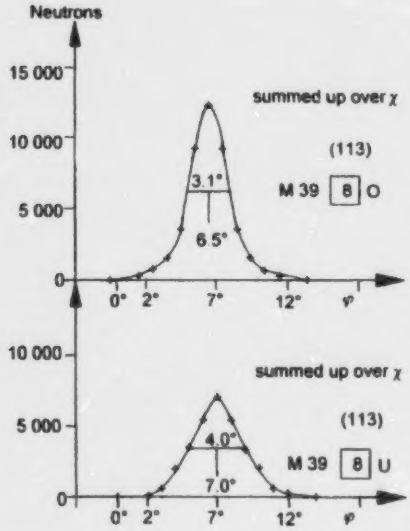

Fig. 3: Angular distributions of the a- and b-axes of the upper part (8o) of piece 8 and the lower part (8u) of piece 8 of the cylinder in Fig. 1. The (113) reflection intensities were summed up over χ. In this way, a large number of neutrons counted were used to calculate the distribution shown.

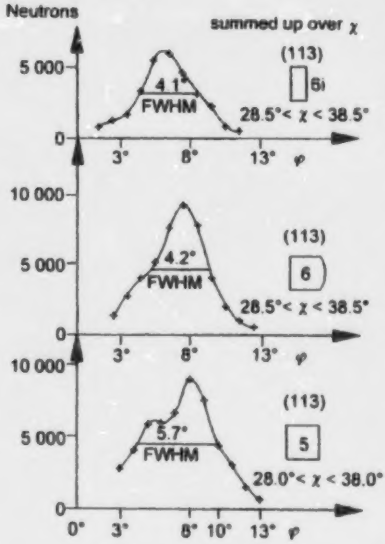

Fig. 4: Angular distributions of the a- and b-axes of pieces 6i, 6, and 5. The numbers of neutrons counted were summed up over χ. In this way, the statistical error became very small.

4 c-axis Distributions

The tendency of the distribution width increasing from the top, where the seed crystal is implanted, towards the bottom is confirmed also by the distributions of c-axis deviations from the cylinder axis for piece 8 cut horizontally into two parts in Fig. 5. However, this applies only to the edge piece, 8.

Figures 6 and 7 show the results of measurements performed in pieces 4, 5, and 6 and, moreover, the results of measurements in piece 4, which was cut further. This piece 4 was further subdivided in a direction normal to the cylinder axis into parts 4o at the top, 4m in the middle, and 4u at the bottom, for studies of the depth effect of the seed crystal implanted into the center piece, 5.

While the full widths at half maximum of the distributions of the c-axis deviations are rather similar in pieces 5 and 6, piece 5 (FWHM = 5.8°), piece 6 (FWHM = 5.7°), the two distributions have tails rather different in length. This is particularly evident in Fig. 7 for the uncut piece 4 situated symmetrical to piece 6 in the cut specimen (see Fig. 1). While the full width at half maximum of the entire piece 4 is quite narrow (FWHM = 3.55°), the tail of the distribution is extremely long in this case. Obviously. the specimen in Fig. 1 grew asymmetrically although the seed crystal had been implanted in the middle of piece 5. This asymmetrical recrystallization growth is evident from measurements in parts 4o, 4m, and 4u of piece 4. The angular error of the cut

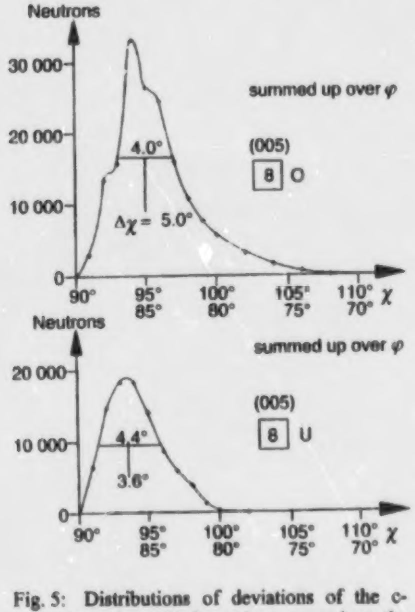

Fig. 5: Distributions of deviations of the c-axes from the cylinder axis measured at the (005) reflection for parts 8o and 8u of piece 8 of the cylinder in Fig. 1. The neutrons counted were summed up over φ on small circles of the pole sphere. The tendency is similar to that in Fig. 3 for a- and b-axis distributions.

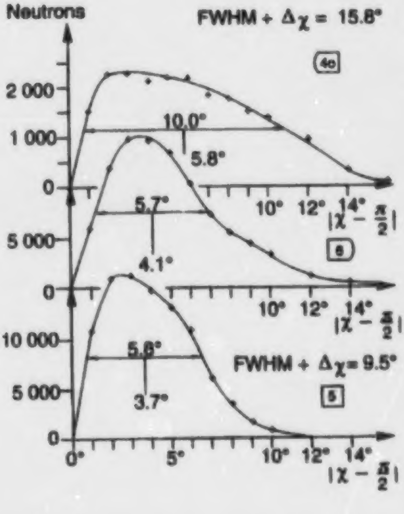

Fig. 6: The distributions of c-axis deviations from the cylinder axis were measured at part 4o of piece 4, at piece 6, and at piece 5 from the (005) reflection as well. The neutrons counted were summed up over φ on small circles of the pole sphere.

planes normal to the cylinder axis did not exceed ± 0.5°. In the upper part, 4o, the full width at half maximum, FWHM = 10.0°, in the center part, 4m (center) FWHM = 2.9°, and in the bottom part, 4u, it is FWHM = 3.7°.

5 Systematic Error

The measurements performed disclose clear tendencies of variation in the c-axis distribution widths within the specimen in Fig. 1. While no systematic error can occur in the distributions of direction of the a- and b-axes, the measurements of distribution widths of the c-axis orientations are caused by two reasons given (1) by the angular error of the cut planes normal to the cylinder axis, and (2) by the angular error produced in bonding the vanadium pin. A magnitude of ± 0.5° must be assumed for both errors. These angular errors can add up to 1°, or compensate to 0°. For this reason, the cuts through the (005) reflection intensity distributions in Fig. 8 are helpful. As explained above, the angular errors referred to above cannot impair the full widths at half maximum of the cuts, but can impair the full widths at half maximum of the distributions, whose individual values were summed up on small circles. In the cuts shown in Fig. 8

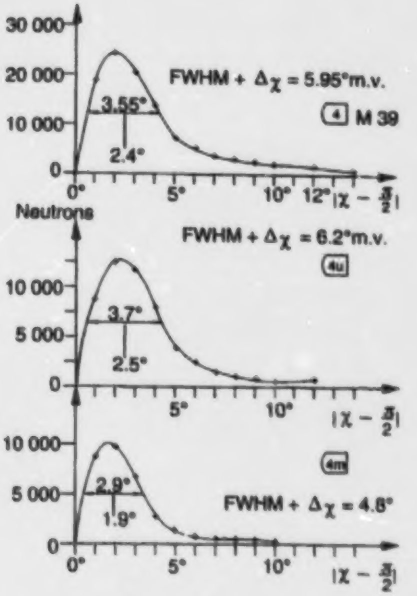

Fig. 7: Piece 4 of the specimen in Fig. 1 was cut into three parts normal to the axis of the YBaCuO cylinder. This measurement shows the local texture to be a function of the distance of the seed crystal. At the top, the distribution of the bulk piece 4; in the middle, the part at the bottom (4u); finally part 4m, which is 3 mm beyond the seed crystal

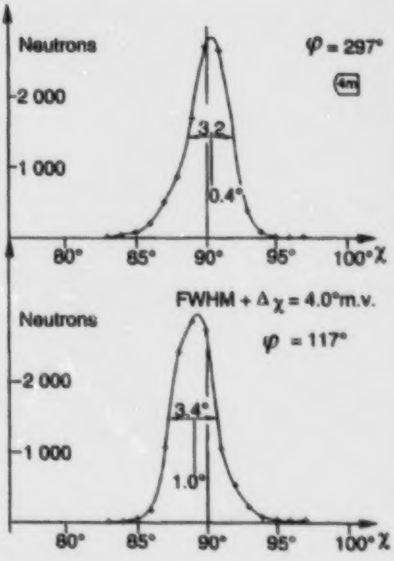

Fig. 8: Cuts through the pole sphere of the (005) pole figure of part 4 m, 3 mm beyond the seed crystal. The cuts at φ and at $\varphi + \pi$ are mirror symmetrical about χ = 89.7°. This small deviation by 0.3° from χ = 90° is caused by the inhomogeneity of the beam intensity over the beam divergence of the neutron beam.

only major or minor misalignments of the distribution axis can occur, while the full widths at half maximum are independent of angular errors of the mechanical cut planes normal to the cylinder axis, and independent of angular errors of the vanadium pin.

Thus, the full width at half maximum in Fig. 8 is 0.3° wider for part 4m than in Fig. 7 for the distribution function of part 4m. The cuts through the pole sphere of part 4o, for instance, exhibit a much more differentiated structure for part 4o than is evident for the distribution function from Fig. 6. The full widths at half maximum are 0.5° narrower for piece 6 than they are in the distribution function in Fig. 6 for piece 6. On the other hand, the full widths at half maximum of the cuts through the pole sphere of part 4u are 1.3° wider than in the distribution function in Fig. 7. In this case, the angular errors of the cut plane and the vanadium pins are the causes of the narrower distribution of part 4u in Fig. 7. However, the differences in the distributions from Fig. 5 to Fig. 7 are so grave as to allow errors of 1° to be tolerated.

6 Outlook

The measurements show that, even in a specimen with excellent magnetic levitation force (95 N), crystal growth from the seed crystal is not symmetrical on both sides and does not produce equally good textures. This condition must be taken into account in the YBaCuO rings with eight seed crystals to be used in the future. Perhaps the number of seed crystals will have to be increased. Texture measurements in an YBaCuO ring of approx. 12 cm outside diameter will then provide information about the boundary region between adjacent seed crystals. This would allow the question as to the optimum number of seed crystals for a melt textured YBaCuO ring to be answered in further texture measurements of such rings.

7 References

Bornemann, H.J. et al. (1996) Neutron Texture Measurement on Solid YBaCuO Specimens with a View to Manufacturing a Superconducting Magnetic Bearing. Textures of Materials, Proc. of the 11th Int. Conf. on Textures of Materials, vol. 2, pp. 951-5. ICOTOM 11, Xi ' an, 1996.

Jung, V. et al.(1997) Texture of Superconducting YBaCuO Cylinders..., FZKA 5961, Forschungszentrum Karlsruhe, June 1997.

Jung, V. et al.(1998a) Local Texture and Magnetic Levitation Force of YBaCuO Cylinders. Int. Conf. on Texture and Anisotropy of Polycrystals, Sept. 22-25, 1997, Clausthal, Germany, Material Science Forum, vol. 273-5, pp. 595-600, 1988.

Jung, V. et al.(1998b) The Influence of a Seed Crystal on the Texture of a Bulk YBaCuO Specimen. FZKA 6072, Forschungszentrum Karlsruhe, February 1998.

Jung, V. et al. (1999) Texture and Magnetic Leviation Force of Melt-Textured YbaCuO Cylinders, Proc. of the Int. Conf. on Neutron Texture and Stress Analysis, Dubna June 23-26, 1997, in print at Textures and Microstructures (1999).

THE EFFECT OF TEXTURE ON MICROYIELDING IN NEAR-GAMMA TiAl ALLOYS

B.A. Simkin, T.R. Bieler, and M.A. Crimp
Department of Materials Science and Mechanics, Michigan State University, East Lansing, MI, USA

Abstract

In an effort to relate aspects of crystallographic texture to the microscale plasticity of gamma-TiAl alloys, Schmid factor analysis based on electron back scattered patterns (EBSP) has been related to deformation defect structures observed using electron channeling contrast imaging (ECCI). The relative activity of dislocation slip and deformation twinning was examined in about 10 neighboring grains near the fracture surface of a four-point bend specimen. In most grains, the relative values of the Schmid factors for ordinary dislocation slip and true twinning appear to correlate with the active deformation mechanisms. However, in some grains, the compliance mismatch with neighboring grains and the resulting strain transfer across grain boundaries appears to have been the controlling factor in activating the observed deformation system.

Keywords: Deformation, dislocations, EBSP, ECCI, TiAl, texture, twins

1 Introduction

Despite low densities and high temperature strengths, gamma titanium-aluminum alloys are limited by relatively low ductility at ambient temperatures. This low ductility can be traced to a limited number of slip systems with high dislocation mobility (Yamaguchi and Umakoshi 1990), which results from the γ-TiAl tetragonal ordered crystal structure ($L1_0$) with alternating layers of Ti and Al atoms along the c axis. The limited ductility that is observed in TiAl can be attributed to its c/a ratio of 1.02, which results in a nearly face centered cubic atomic arrangement. When TiAl based materials have strong texture, as is often the case in wrought materials, elongations up to 7-8 % can be achieved (Kim 1998; Dimiduk et al. 1998; Jin et al. 1997; Maeda et al. 1995). Cast materials do not have such strong textures, and they generally display fracture strains less than 2%. This effect of texture implies that the ease of slip transfer across boundaries is an important, perhaps definitive, criterion for obtaining the ductility necessary for structural applications. Gaining predictive control of the texture and the misorientation between crystals may lead to improvements in ductility of this class of materials.

Using TEM, Luster and Morris (1995) have investigated slip transfer in TiAl deformed at room temperature. They found that the Schmid factor was an effective means to characterize slip activity. (Since there are several deformation systems with different CRSS values, the Taylor factor becomes more difficult to assess.) From statistically valid sample sizes, they found that ordinary dislocations and true twins were observed in grains when their Schmid factor was greater than 0.25. Superdislocations were only observed when they had a Schmid factor greater than 0.35 *and* when slip transfer was efficient across boundaries impinged upon by twins or ordinary dislocations. Seo et al. (1997) calculated Schmid factor maps for TiAl which show that when twinning occurs, the crystal is rotated into a hard orientation in which only superdislocations have a high Schmid factor, a phenomena described as orientational hardening due to twinning. Also, when the Luster and Morris criteria are used for a random population of crystal orientations, only about 19% of the grains have 4 or more ordinary or true twinning systems operative in tension (at orientations near <100]), while 28% of the orientations have 4 or more in compression (away from [110]). Because these grains have less than 4 easy deformation systems, they cannot deform arbitrarily according to the von Mises criteria (1928) (which specifies a minimum of 5 independent slip systems), and neighboring grains will have to absorb more strain in order to prevent crack initiation. Kad et al. (1995) have examined this situation computationally in 2-D representations of fully lamellar TiAl microstructures to identify grain misorientations that lead to large incompatibility stresses and strains.

In the present study, the relationship between grain orientation and deformation activity is examined by correlating orientations measured using electron backscattered patterns (EBSP) with dislocation and twin observations made in the same sample using electron channeling contrast imaging (ECCI). This allows the relationship between global stress-state (and associated Schmid factors) and strain transfer from neighboring grains to be observed in the context of the microtexture of the material.

2 Experimental Procedure

An investment cast plate of Ti-47.9Al-2Cr-2Nb alloy was heat treated at 1093°C for 5h, HIPed at 1205°C for 4h and heat treated at 1205°C for 2 additional hours, followed by rapid cooling. Bend specimens were extracted using EDM such that the long direction was parallel with the upward flow direction into the mold, and the axis of bending was perpendicular to the surface of the cast plate. The final dimensions were 34.0 mm x 4.0 mm x 1.3 mm. The sample was ground to a finish of 600 grit then deformed at room temperature in four-point bending to failure at a stress of 616 MPa (Dowling and Bieler 1999), which produced tensile deformation in the surface examined in the present study. The particular specimen examined here fractured at the highest stress of the group evaluated. To carry out diffraction studies in SEM, the tensile surface was prepared using 1000 grit SiC paper, and then electropolished at -50 °C in a 65% methanol - 30% 1-butanol - 5% perchloric acid solution using a voltage of 30 V.

EBSPs and subsequent orientation images were produced using a Leica 360FE SEM equipped with a TexSEM Laboratories OIM system using Unix based software version 2.6.6. EBSP indexing was based on a TiAl $L1_0$ unit cell. However, it is not clear what fraction of the orientations were correctly indexed with respect to the tetragonality of the crystal structure (c/a = 1.02). Orientation maps were produced by beam scanning in a hexagonal array with a 2 μm spacing over an area of about 400 x 500 μm on the tensile surface near the fracture region at the center of the bar.

ECCI was performed using a CamScan 44FE field emission SEM and a pole piece mounted solid state backscattered electron detector using a low tilt configuration as described elsewhere (Simkin and Crimp 1999). Images were taken using {111} channeling contrast conditions. Twins and dislocations were imaged in the equiaxed grains within the area of the EBSP scan.

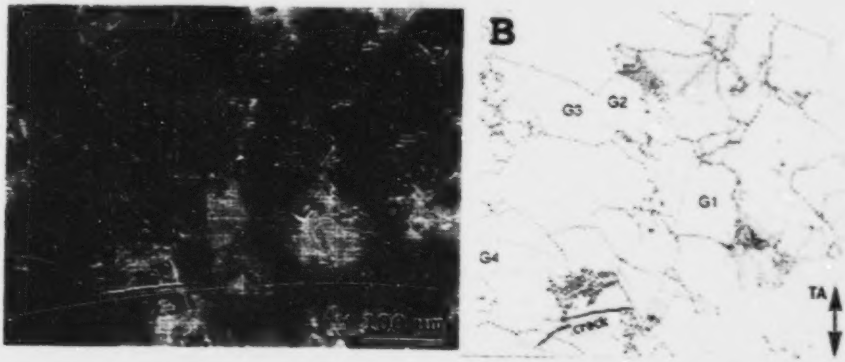

Fig. 1: (a) Backscattered electron image of the region studied. Channeling contrast distinguishes grains; grains G1-G4 are referenced in later Figures. The tensile direction is vertical. (b) EBSP image quality map of the region of interest, which clearly delineates the grain boundaries.

3 Results and discussion

Fig. 1a shows a backscattered electron image of the area of interest. The fracture surface is just above the top of the image. The structure contains relatively large equiaxed γ grains with a low fraction of lamellar regions having relatively coarse Ti_3Al DO_{19} α_2 plates. There is a prominent secondary crack in the lower left corner, and there is a line of small pores to the right and slightly above the more obvious crack. Fig. 1b shows an EBSP image quality map that highlights the grain boundary locations.

From orientation images of the scanned region (not shown), the majority of the crystals show a tendency for the c axes to be within 45° of the specimen normal direction (i.e. closer to the cast plate surface normal and perpendicular to the flow direction). Assuming that the indexing correctly resolved the tetragonality, the Schmid factors were mapped for {111}<110] ordinary dislocations and {111}<112] true twinning deformation systems with reference to the tensile stress direction using the OIM software. Fig. 2 shows the resulting maps of Schmid factors with the numerical Schmid factors superposed for several grains (Schmid factors for other grains can be determined from the gray scales) . Fig. 2a illustrates how most of the grains have orientations that have high Schmid factors for ordinary <110] dislocations. The Schmid factors for <101] superdislocations were generally lower. The grain with a crack bisecting it clearly has a lower Schmid factor for ordinary dislocations than any of its neighboring grains which all have high Schmid factors. Fig. 2b shows the Schmid factor map for {111}<112] true twinning. The Schmid factors for <121] type superdislocations (or pseudo-twins) were lower. The software does not give the sign of the Schmid factor, so the uni-directionality of twinning cannot be properly assessed. There are some grains that have a high Schmid factor for true twinning, but most of them have moderate values.

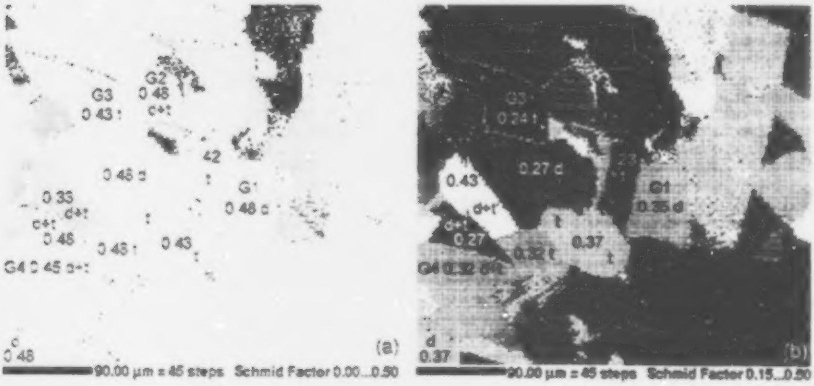

Fig. 2: Schmid factors for (a) ordinary dislocations and (b) true twinning are indicated along with observations of ordinary dislocations "d" or twins "t" using ECCI in selected grains (the values in other grains can be determined from the shade of gray).

The deformation structure in the majority of the equiaxed γ grains within the area studied using EBSP was imaged in detail using ECCI. The state of the microstructure was found to vary significantly from grain to grain. In some grains the deformation structure was dominated by dislocations, whereas in other grains deformation twins prevailed. These observations are summarized in Fig. 2, where "d" or "t" represent the presence of dislocations or twins, respectively. The grain orientations and ECCI observations show that the crystal orientations are favorable for plastic deformation based upon the Luster and Morris criteria, and this is consistent with the fact that this specimen broke at the highest stress (and thus the greatest amount of plastic strain and work hardening) of all the related samples tested in 4-point bending (Dowling et al 1999).

Examples of ECCI images are given in Figs. 3-5. In some cases, dislocations were found to be randomly distributed throughout the grains, as shown in fig. 3a, which is an area from the grain labeled G1 in Figs. 1 and 2. In this case, most of the

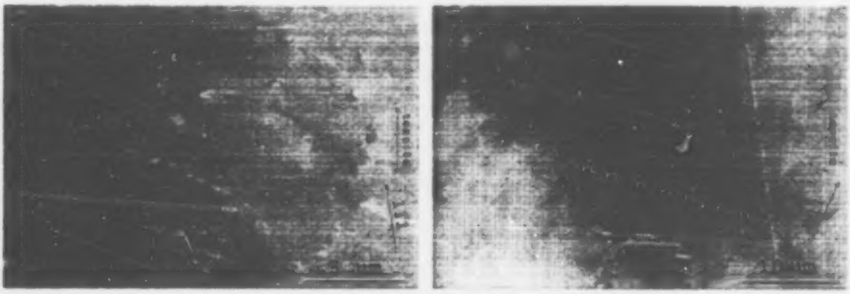

Fig. 3: Channeling contrast images of (a) the dislocation distributions in the dislocation-dominated grain G1 (Schmid factor for d=0.48, t=0.35), and (b) slip bands and twins in grain G2 (Schmid factor for d=0.48, t=0.31).

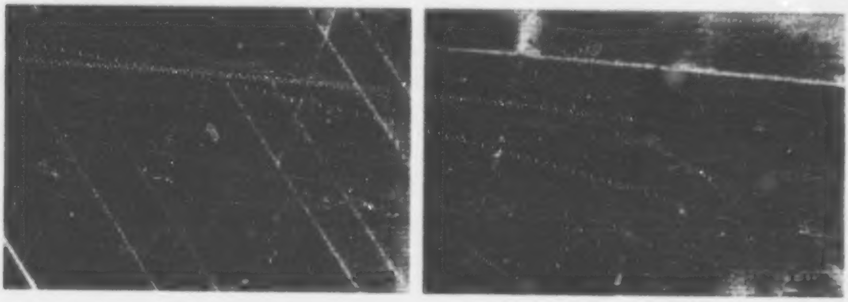

Fig. 4: (a) Channeling contrast of the deformation structure of twin-dominated grain G3 (Schmid factor for d=0.43, t=0.24). (b) Slip transmission through (left) and blockage of dislocation slip (right) by twins in grain G4.

dislocations are inclined to the surface, and they appear as light or dark spots where they exit the crystal. Other dislocations are more parallel to the grain surface and they appear as short lines. In other grains the dislocations are arranged in well defined slip bands (Fig. 3b, from grain G2 in Fig 1).

An example of a grain dominated by twin deformation is shown in Fig. 4a (taken from grain G3 in Fig. 1). An interesting feature within many of the twin dominated grains is that significant numbers of dislocations are observed at the outer edges of the grains, but slip of these dislocations into the centers of the grains appears to have been blocked where the dislocations piled up at the twins (Fig. 4b).

In some places, deformation transfer between grains is apparent. Fig. 5 shows an example where a series of deformation twins have impinged from below upon the horizontal grain boundary. The thicker twins that have produced more local shear at the boundary have driven dislocation slip bands into the upper grain.

Comparison of the presence of twins and dislocations with the Schmid factors in Fig. 2 correlates fairly well with their observed presence, assuming that the observed dislocations are ordinary dislocations. An exception is the observation of only twins in Fig. 4a (grain G3) in which twins have a low Schmid factor of 0.24, and ordinary

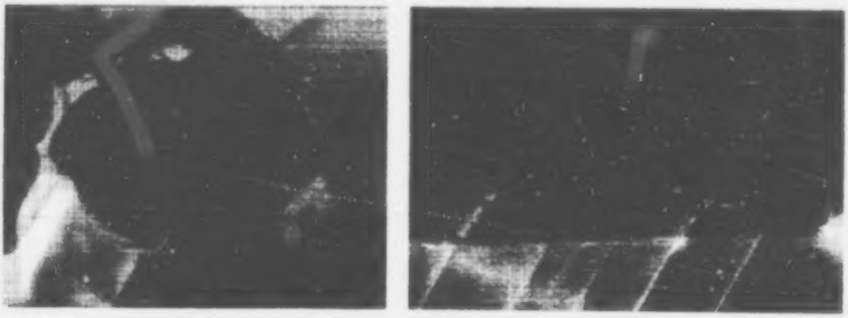

Fig. 5: Strain transfer across grain boundaries. Twins in the lower grain that impinge upon the grain boundary drive the emission of dislocations in slip bands into the upper grain (G2). B is an enlargement of the lower center part of A

dislocations have a higher Schmid factor of 0.43. This could result from an incorrect indexing of this grain orientation, but this grain was also quite close to the fracture location of the specimen, where the local stress state may have been quite different from the global stress state. The fact that twins or dislocations were not always observed when their Schmid factors were high indicates that local neighbor interactions alter the stress state enough to alter the probability of a given system to operate. Further work is needed to quantify the degree that the Schmid law dictates the operation of particular deformation systems, and to assess the effect of stress concentrations arising from elastic strain incompatibilities and grain misorientation that affect deformation transfer from one grain to another.

4 Conclusions

From a preliminary study of the correlation between slip and twinning activity in TiAl and the grain orientations, it is apparent that Schmid's law is roughly followed on the basis of the externally imposed stress state. In some locations, local grain compliance mismatch leads to stress concentrations that alter the local stress state so much that the observations are not consistent with the simple application of the Schmid law.

Acknowledgments

The ECCI portion of the research was supported by the Michigan State University Composite Materials and Structures Center and used the CamScan 44FE purchased using funds from the National Science Foundation, Grant No. DMR 9302040. The EBSP measurements were made at the Air Force Research Labs by TRB while on sabbatical as a visiting scientist in the Materials and Manufacturing Directorate under contract F33615-94-C-5804. The material was provided via Air Force Office of Scientific Research PRET Program F49620-95-1-0359.

References

Adams, B.L., Wright, S.I., Kunze, K. (1993) *Met. Trans.* A, Vol. 24A, pp. 819-31.

Dimiduk, D.M., Hazzledine, P.M., Parthasarathy, T.A., Seshagiri, S., Mendiratta, M.G. (1998) *Metal and Mater. Trans*, Vol. 29A, pp. 37-47.

Dowling, G.T., and Bieler, T.R. (1999) *Int. Sym. on Gamma Titanium Aluminides*,. Kim, Y.W. et al. eds., TMS, Warrendale, PA, in press.

Jin, Z., Gray, G.T., Kim, Y-W. (1997) *Mat. Sci. and Eng. A*, Vol. 239-40, pp. 729-735.

Kad, B.K., Dao, M., Asaro, R.J. (1995) *High Temperature Ordered Intermetallic Alloys VI*, Horton, J.A., et al. eds., MRS Proceedings Vol. 364, Pittsburgh, PA, pp. 169-74.

Kim, Y-W. (1998) *Interstitial and Substitutional Solute Effects in Intermetallics*, I. Baker, et al. eds., TMS, Warrendale, PA, pp. 189-200.

Luster and. Morris, M.A. (1995) *Metall. and Mater. Trans*, Vol. 26A pp. 1745-56.

Maeda, T., Hosomi, M., Okada, M. (1995) *Gamma Titanium Aluminides*, Kim, Y.W. et al. eds., TMS Warrendale, PA, pp. 771-78.

Seo, D.Y., Bieler, T.R., and Larsen, D.E., (1997) *Structural Intermetallics 1997*, TMS, Warrendale, PA, pp. 137-46.

Simkin, B.A., Crimp, M.A. (1999) *Ultramicroscopy*, accepted for publication.

von Mises, R. (1928), *Z. ang. Math. Mech.*, Vol. 8, p. 161.

Yamaguchi, J.M., and Umakoshi, Y. (1990) *Prog. Mater. Sci.*, Vol. 34, pp. 1-148.

ON THE EVOLUTION OF ANISOTROPIC ELASTIC PROPERTIES DURING METAL FORMING

A. BERTRAM and T. BÖHLKE

Institute of Mechanics, Otto-von-Guericke-University Magdeburg, Germany

Abstract

Since single crystalline copper exhibits a significant degree of elastic anisotropy, the polycrystalline elastic properties can be affected by the crystallographic texture in an amount that is relevant for engineering applications. In the present paper the evolution of the elastic properties is studied for different deformation paths.

Keywords: Finite Inelastic Deformations, Texture Induced Elastic Anisotropy

1. Introduction

There is a rapid progress in the capabilities to simulate the evolution of material properties due to macroscopic deformation or loading processes. The evolution of material properties is caused by microstructural changes, like localization phenomena or the formation of morphological and crystallographic textures.

The crystallographic texture evolution of materials with high and intermediate stacking fault energy (e.g. pure copper) can be determined by the Taylor model within a first-order accuracy (Leffers 1993). In the present paper the evolution of the elastic properties of polycrystalline copper undergoing large inelastic deformations is numerically studied for three finite deformation modes using the Taylor-Lin-model (Asaro and Needleman 1985).

The elastic law on the microscale, i.e. within the grains, is derived from the assumption that the elastic behaviour is not affected by inelastic deformations (Bertram 1999). The simulations are restricted to proportional deformation processes, and so, only isotropic hardening models (Harren et al. 1989, Meric et al. 1994) are considered. The hardening parameters are taken from the literature (Wu et al. 1996).

For a given grain orientation distribution there are different methods to determine the elastic properties of a heterogeneous linear elastic material (Kocks et al. 1998). Simple estimations are those suggested by Voigt (1928) and Reuss (1929). The first assumed a constant strain, the latter a constant stress field in the aggregate. Under these assumptions, the effective fourth-order elasticity tensors turn out to be volume averages of the corresponding local fields, and can be derived directly from texture data. The volume averages of the local elastic moduli generally result in more or less anisotropic elasticity tensors if determined from empirical texture data. In order to determine effective properties in the isotropic case, the averaging has to be performed in the orientation space with a constant orientation distribution function. The advantage of these approaches, which represent arithmetic means of the local properties, is that they give bounds for the macroscopic strain energy density (Hill 1952).

Therefore, alternative approaches have been developed in order to obtain more precise information from the texture data. Hill (1952) proposed both an arithmetic and a geometric mean of the isotropic bounds of Voigt and Reuss, which give estimations closer to experimental values. An approach that focusses on an homogenization that guarantees unique effective properties, such that the inverse of the mean compliance is equal to the mean stiffness, was given by Aleksandrov and Aizenberg (1967) and further developed by Matthies and Humbert (1995). Within that approach the geometric mean of the local elastic moduli is used. Beside the uniqueness, the advantage of this method lies in improved predictions of experimental values. The disadvantage is that the physical implications are unclear since any assumption concerning the kinematic or dynamic fields is avoided.

On the macroscopic scale material symmetries determined by experiments or simulations generally exist only in some approximate sense, because the microstructure induces deviations from the behaviour described by classical point-groups. For metals the elastic behaviour can be linearized within elastic ranges. Therefore, a fourth-order tensor is sufficient for the description of the mechanical properties within some elastic range. In order to identify the anisotropy, the fourth-order elasticity tensor given by the homogenization technique can be approximated by fourth-order tensors corresponding to distinct symmetry groups. In this paper an approximation is suggested, which contains the isotropic bounds as special cases if applied to the isotropic bounds by Voigt and Reuss, and which is furthermore applicable to any fourth-order elasticity tensor given by experiments or simulations.

The texture induced elastic anisotropy is investigated by simulating a plane strain compression, a drawing, and a simple shear deformation. The evolving macroscopic elastic properties due to the texture development are approximated by linear elastic laws with the ten traditional, distinct symmetries.

2. Single crystal and polycrystal elasticity

It is assumed that the symmetric stress tensor $\mathbf{T}$ is given as a linear invertible map of the symmetric strain tensor $\mathbf{E}$. The operators of this map - the fourth-order stiffness $\mathbb{C}$ and compliance tensor $\mathbb{S}$ - are specified by the symmetry group $\mathcal{S}$ of the material being a subgroup of the orthogonal group

$$\mathbf{T} = \mathbb{C}[\mathbf{E}], \qquad \mathbf{E} = \mathbb{S}[\mathbf{T}], \qquad \mathbf{H}^{\mathrm{T}}\mathbb{C}[\mathbf{E}]\mathbf{H} = \mathbb{C}[\mathbf{H}^{\mathrm{T}}\mathbf{E}\mathbf{H}], \qquad \forall\, \mathbf{H} \in \mathcal{S}. \tag{1}$$

The elasticity tensors are positive definite and possess the major symmetry in the case of hyperelastic materials. Without loss of generality, the symmetry in the first and last pair of indices is assumed.

Voigt's and Reuss' assumption of constant strain and stress fields, respectively, yield the most simple estimations of the elastic properties of the aggregate. The macroscopic elasticity tensors are then given by the volume averages of the corresponding local fields

$$\mathbf{C}^V = \frac{1}{V}\int_V \mathbf{C}\,\mathrm{d}V, \qquad \mathbf{S}^R = \frac{1}{V}\int_V \mathbf{S}\,\mathrm{d}V \neq \mathbf{C}^{V^{-1}}. \tag{2}$$

An approach that guarantees unique effective properties is given by the geometric mean (Aleksandrov and Aizenberg 1967, Matthies and Humbert 1995)

$$\mathbf{C}^A = \exp\left(\frac{1}{V}\int_V \ln(\mathbf{C})\,\mathrm{d}V\right), \qquad \mathbf{S}^A = \exp\left(\frac{1}{V}\int_V \ln(\mathbf{S})\,\mathrm{d}V\right) \equiv \mathbf{C}^{A^{-1}}. \tag{3}$$

An estimation of the elastic properties with the additional assumption of a uniform orientation distribution follows by transforming the integrals (2) and (3) to the orientation space using $\mathrm{d}V/V = f(g)\,\mathrm{d}g$ and setting the orientation distribution function $f(g)$ equal to one (Bunge 1993)

$$\mathbf{C}^{VI} = \int_g \mathbf{C}(g)\,\mathrm{d}g, \qquad \mathbf{S}^{RI} = \int_g \mathbf{S}(g)\,\mathrm{d}g, \qquad \mathbf{C}^{AI} = \exp\left(\int_g \ln(\mathbf{C}(g))\,\mathrm{d}g\right). \tag{4}$$

If the orientation space is parameterized by Euler angles, the corresponding volume element is given by $\mathrm{d}g = \sin(\Phi)\,\mathrm{d}\Phi\,\mathrm{d}\varphi_1\,\mathrm{d}\varphi_2/8\pi^2$.

In the case of cubic single crystals the difference of the anisotropic and isotropic averages can be brought into the comprehensive form (Böhlke and Bertram 1999)

$$\mathbf{C}^V - \mathbf{C}^{VI} = f^V\mathbf{D}, \qquad \mathbf{S}^R - \mathbf{S}^{RI} = f^R\mathbf{D}, \qquad \ln(\mathbf{C}^A) - \ln(\mathbf{C}^{AI}) = f^A\mathbf{D}, \tag{5}$$

with

$$\mathbf{D} = \frac{\sqrt{30}}{30}\left(\mathbf{I}\otimes\mathbf{I} + 2\mathbf{I}^S - \frac{5}{V}\int_V \mathbf{A}\,\mathrm{d}V\right), \qquad \mathbf{A} = \sum_{i=1}^{3} \mathbf{g}_i\otimes\mathbf{g}_i\otimes\mathbf{g}_i\otimes\mathbf{g}_i, \tag{6}$$

$\mathbf{g}_i$ being the lattice vectors. $\mathbf{I}$ denotes the second-order identity tensor and $\mathbf{I}^S$ the identity on symmetric second-order tensors. The scalar factors in equations $(5)_{1,2,3}$ are given by

$$\begin{aligned} f^V &= \|\mathbf{C} - \mathbf{C}^{VI}\| &&\equiv \sqrt{30/25}\,|\lambda_3 - \lambda_2|, \\ f^R &= \|\mathbf{S} - \mathbf{S}^{RI}\| &&\equiv \sqrt{30/25}\,|1/\lambda_3 - 1/\lambda_2|, \\ f^A &= \|\ln(\mathbf{C}) - \ln(\mathbf{C}^{AI})\| &&\equiv |\ln(\lambda_3) - \ln(\lambda_2)|. \end{aligned} \tag{7}$$

The difference of the averages is influenced on the one hand by the degree of anisotropy of the single crystals through, e.g., $\|\mathbf{C} - \mathbf{C}^{VI}\|$, and on the other hand by the orientation distribution in form of the tensor $\mathbf{D}$. The norm $\|\mathbf{D}\|$ is equal to one for a single orientation, equal to zero for a uniform orientation distribution, and in the interval $(0, 1)$ otherwise.

4. Numerical example

In this paper the texture induced elastic anisotropy is investigated by simulating a plane strain compression (A), a drawing (B), and a simple shear deformation (C). The corresponding deformation gradients are given by

$$\begin{aligned} A:\quad \mathbf{F} &= \kappa\mathbf{e}_1\otimes\mathbf{e}_1 + \kappa^{-1}\mathbf{e}_2\otimes\mathbf{e}_2 + \mathbf{e}_3\otimes\mathbf{e}_3, && \kappa \in [1, 10], \\ B:\quad \mathbf{F} &= \kappa\mathbf{e}_1\otimes\mathbf{e}_1 + \kappa^{-1/2}(\mathbf{e}_2\otimes\mathbf{e}_2 + \mathbf{e}_3\otimes\mathbf{e}_3), && \kappa \in [1, 10], \\ C:\quad \mathbf{F} &= \mathbf{I} + \kappa\mathbf{e}_1\otimes\mathbf{e}_2, && \kappa \in [0, 5]. \end{aligned} \tag{8}$$

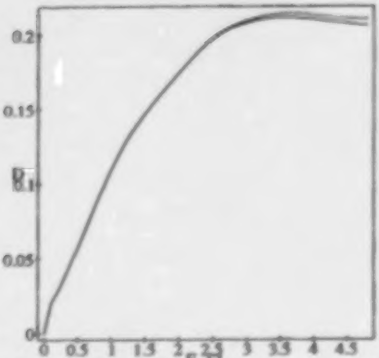

Fig. 1: $D = \| \mathbf{D} \|$ vs F_{12} for simple shear and different hardening laws, H1: (-), H2: (--).

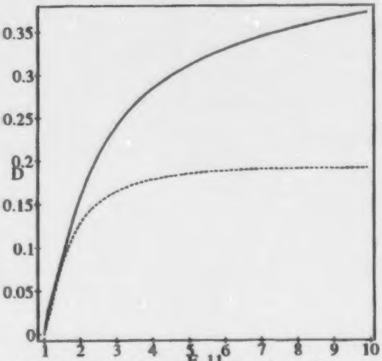

Fig. 2: $D = \| \mathbf{D} \|$ vs F_{11} for plane strain compression (-) and uniaxial drawing (--) based on H1.

In Fig. 1 the norm of $\mathbf{D}$ is shown for the simple shear deformation. H1 and H2 stand for the models used in Harren et al. (1989) and Meric et al. (1994), respectively. The curves determined from a calculation with 1000 modified random orientations (Böhlke and Bertram 1998) and two hardening laws indicate that the predictions of both hardening models are almost the same.

The norm of $\mathbf{D}$ is shown in Fig. 2 for the plane strain compression and the drawing deformation. In the former case no saturation of anisotropy is observed in the range $F_{11} \in [0, 10]$, in the latter the magnitude of $\mathbf{D}$ is almost stationary in the range $F_{11} \in [6, 10]$, and so are the components of $\mathbf{C}^V$.

The approximation $\mathbf{C}^{VA}$ of the elasticity tensor $\mathbf{C}^V$, is determined by the condition that $\mathbf{C}^{VA}$ has a certain symmetry group and minimizes the Frobenius norm of $\triangle\mathbf{C} := \mathbf{C}^V - \mathbf{C}^{VA}$. If there is an exact solution $\| \triangle\mathbf{C} \| = 0$ the identification problem is equivalent to that posed and solved by Cowin and Mehrabadi (1987). In order to solve the optimization problem $\| \triangle\mathbf{C} \| \to \min$ for a given $\mathbf{C}^V$, a direct search polytope algorithm (Gill et al. 1981) has been used. The standard representations of $\mathbf{C}^{VA}$ for different symmetry classes can be easily used, if $\| \triangle\mathbf{C} \|$ is parameterized in form of

$$\| C^V_{ijkl} - Q_{im} Q_{jn} Q_{ko} Q_{lp} \tilde{C}^{VA}_{mnop} \| \to \min,$$

where $\tilde{C}^{VA}_{mnop}$ are the components of $\mathbf{C}^{VA}$ with respect to the symmetry axes of the material. The Q_{ij} represent a proper orthogonal matrix describing the rotation from a reference coordinate system to the above mentioned symmetry axes.

In Fig. 3 the norm of $\triangle\mathbf{C}^* := (\mathbf{C}^V - \mathbf{C}^{VA}) / \| \mathbf{C} - \mathbf{C}^{VI} \|$ is shown for the plane strain compression deformation and approximations $\mathbf{C}^{VA}$ having the following symmetry groups: (-)= isotropy; (- -)= transverse isotropy C_{12} and hexagonal systems $C_{10,11}$; (□)= hexagonal systems $C_{8,9}$; (-)= cubic system $C_{6,7}$; (◇)= tetragonal systems $C_{4,5}$; (○)= rhombic C_3; (+)= monoclinic system C_2 (Gurtin 1972). The approximation with an orthotropic symmetry leads to a significant reduction of $\| \triangle\mathbf{C}^* \|$, which indicates that $\mathbf{C}^V$ possesses an orthotropic symmetry within an acceptable tolerance.

In Fig. 4 the norm of $\triangle \mathbf{C}^*$ is shown for a drawing deformation. In contrast to the rolling deformation, here the approximation with a hexagonal symmetry ($C_{8,9}$) yields better results than the one with a rhombic, i.e. orthotropic, symmetry.

5. References

Asaro, R.J. and Needleman, A. (1985) Texture development and strain hardening in rate dependent polycrystals. Acta Metall. 33, pp.923–953. Aleksandrov, K. and Aizenberg, L. (1967) *Dokl. Akad. Nauk. SSSR*, 167, pp. 1028–1031.

Bertram, A. and Olschewski, J. (1991) Formulation of anisotropic linear viscoelastic constitutive laws by a projection method. In A. Freed and K. Walker, editors, *High temperature constitutive modelling: Theory and Application*, pp. 129–137. ASME. MD-Vol. 26, AMD-Vol. 121.

Bertram, A. (1999) An Alternative Aproach to Finite Plasticity Based on Material Isomorphisms, *Int. J. Plast.* 15(3), pp. 353–374.

Böhlke, T. and Bertram, A. (1998) Simulation of texture development and induced anisotropy of polycrystals. In S. Alturi and P. O'Donoghue, editors, *Proceedings of ICES'98, Modeling and Simulation Based Engineering*, pp. 1390–1395.

T. Böhlke and A. Bertram (1999) An isotropy condition for discrete sets of cubic single crystals. *Z. Angew. Math. Mech.* 79, S447–448

Bunge, H. (1993) *Texture Analysis in Material Science.* Cuviller Verlag Göttingen.

Cowin, S. and Mehrabadi, M. (1987) On the identification of material symmetry for anisotropic elastic materials. *Q. J. Mech. appl. Math.*, 40, pp. 451–476.

Gill, P.E., Murray, W. and Wright, M. (1981), *Practical Optimization*, Academic Press, New York

Harren, S., Lowe, T., Asaro, R., and Needleman, A. (1989) Analysis of large-strain shear in rate-dependent face-centred cubic polycrystals: Correlation of micro- and macro-mechanics. *Phil. Trans. R. Soc. Lond. A*, 328, pp. 443–500.

Gurtin, M.E. (1972) The Linear Theory of Elasticity. In Encyclopedia of Physics, Vol. VIa/2. Editor C. Truesdell. Springer-Verlag.

Hill, R. (1952) The elastic behaviour of a crystalline aggregate. *Proc. Phys. Soc. Lond.*, A 65, pp. 349–354.

Kocks, U., Tomé, C., and Wenk, H. (1998) *Texture and Anisotropy: Preferred Orientations in Polycrystals and Their Effect on Materials Properties.* Cambridge Univ. Pr.

Leffers, L. (1993). Microstructures, textures and deformation patterns at large strains. In S. Teodosiu, Raphanel, editor, *MECAMAT'91*, pp. 73–86.

Matthies, S. and Humbert, M. (1995) On the principle of a geometric mean of even-rank symmetric tensors for textured polycrystals. *J. Appl. Cryst.*, *28*, pp. 254–266.

Méric, L., Cailletaud, G., and Gaspérini, M. (1994) Calculations of copper bicrystal specimens submitted to tension–compression tests. *Acta metall. mater.*, 42(3), pp. 921–935.

Wu, P., Neale, K., and Van der Giessen, E. (1996) Simulation of the behaviour of fcc polycrystals during reversed torsion. *Int. J. Plast.*, 12(9), pp. 1199–1219.

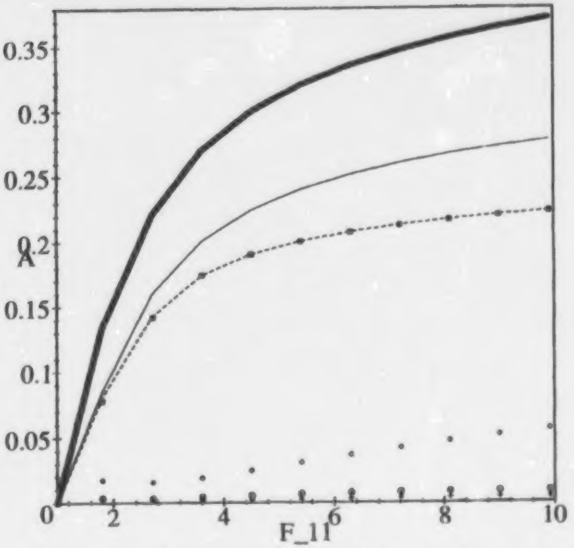

Fig. 3: $A = \| \triangle \mathbf{C}^{*} \|$ vs F_{11} for plane strain compression.

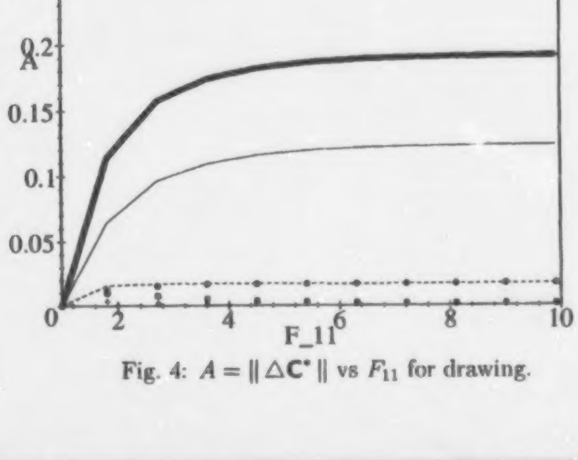

Fig. 4: $A = \| \triangle \mathbf{C}^{*} \|$ vs F_{11} for drawing.

PRACTICAL ASPECTS OF CALCULATING ELASTIC PROPERTIES OF TEXTURED HEXAGONAL POLYCRYSTALS

T.A. LYCHAGINA
Laboratory of Neutron Physics, Joint Institute for Nuclear Research, Dubna, Russia
H.-G. BROKMEIER
Institut für Werkstoffkunde und Werkstofftechnik der Techn. Universität Clausthal
c/o GKSS-Forschungszentrum, Geesthacht, Germany

Abstract

In this paper we consider a textured material with hexagonal crystal symmetry (Zn). The information about texture is obtained from pole figures measured by means of neutron diffraction. The orientation distribution function (ODF) is used as a weighting function for calculating the mean values of the elastic properties according to different approximations (Reuss, Voigt, Hill). ODF is calculated using different methods: iterative series expansion method, texture component method, WIMV method. The conformity between different results is discussed.

Keywords: Elastic properties, ISEM, component method, WIMV method, Zn texture

1 Introduction

The behavior of a polycrystalline material is mostly anisotropic according to the intrinsic properties of single crystals and of the structural parameters characterizing the polycrystalline material. Among these parameters the crystallographic texture appears to be very important to understand macroscopic behavior of the material (Bunge 1982). Therefore, the crystallographic texture is in use to predict and to explain an anisotropy of elastic material properties. From the mathematical point of view a physical property of a polycrystalline sample is the averaging of a correspondent single crystal property with the orientation distribution function (ODF) of the polycrystalline sample. The ODF is calculated using measured pole figures (PF). Several methods were proposed to derive an ODF from PFs. Most frequently the iterative series expansion method (Dahms and Bunge 1989), WIMV (Matthies and Vinel 1982) and the texture component method (Helming 1996; Nikolayev et al.1992) are used. The accuracy of ODF calculations by means of these methods depends on texture type, on texture sharpness and on the handling of experimental errors. In the present work we consider the case of hexagonal crystal symmetry to calculate the elastic properties using the ODF calculated by means of different methods.

2 Fundamentals

By physical property E^* of a material one understands the relation between two quantities: mean value of an external influence $\overline{X}$ and a reaction $\overline{Y}$. E^* can be presented by (Bunge 1982):

$$E^* = \overline{E} + \frac{1}{V}\int_V \Delta E(\bar{r})U(\bar{r})dV\,, \tag{1}$$

where $\overline{E}$ is mean property, $U(\bar{r}) = \frac{\Delta X(\bar{r})}{\overline{X}}$. If the additional quantity in the equation (1) is relatively small in comparison with $\overline{E}$, the approximation $E^* \approx \overline{E}$ is valid. Exact equality $E^* = \overline{E}$ can be reached in case: X = const. This is the well-known Voigt approximation. Another approximation $E^* \approx \left(\overline{E^{-1}}\right)^{-1}$ is valid in the case: Y = const (Reuss approximation). The real E^* value lies between these two extremes, so that the Hill's approximation is frequently in use: $E^* \approx \frac{1}{2}\left[\overline{E} + \left(\overline{E^{-1}}\right)^{-1}\right]$. The elastic property can be described in a crystal coordinate system K_b by the fourth-rank tensor E^b_{ijkl}. Then, the mean polycrystalline property $\overline{E}^a_{ijkl}$ is in a sample coordinate system K_a:

$$\overline{E}^a_{ijkl} = \frac{1}{8\pi^2}\int_{SO(3)} a_{im}(g)a_{jn}(g)a_{kp}(g)a_{lq}(g)E_{mnpq}f(g)dg\,. \tag{2}$$

Here E_{mnpq} is the single crystal property, $f(g)$ is the ODF and a_{mn} are the direction cosines of the crystal axis n with respect to the axis m, which corresponds to the sample coordinate system. In our work we calculated mean values of elastic properties by direct numerical integration of the expression (2).

3 Methods

We used three methods for ODF-calculation from experimental PFs: iterative series expansion (harmonic) method (ISEM), WIMV and texture component method. Below we present a brief description of these methods and the main features.

The main idea of the harmonic method is to present the ODF and PF in the form of series expansion over the symmetrized generalized spherical harmonics and spherical harmonics respectively. The program system we used based on an iterative procedure has some options to depress the effect of negative values and of 'ghosts'. A reduced number of pole figures compared to the standard package of the harmonic method is applicable as well as additional non-measured pole figures. Moreover, the phon concept first described for the WIMV method was included in our program. The complete ODF is given by an infinite series of harmonic functions, but because of the orthogonality between these functions only terms up to the 4th order contribute to the mean-value evaluation. That means, we need only the even ODF coefficients up to $l = 4$ for the calculation of elastic properties. Nevertheless, the ODF calculation was carried out up to $l = 10$ (hexagonal crystal symmetry and triclinic sample symmetry).

The WIMV method uses the discrete form for the integral equation connecting PF and ODF. Continuous ODF values and continuos PF values are substituted by multidimensional vectors. Coordinates of these vectors are connected by the linear equation system. The ODF can be found by an iterative procedure taking into account the main demand $f(g)>0$ and the "principle of the maximum phon". The result of WIMV is an array with a three-dimensional density distribution. Since the ODF is known in terms of discrete density values, physical properties can be calculated directly by weighted averaging of the single crystal properties over ODF array (Wenk et al. 1988).

Texture component method enables to approximate ODF by standard distributions. In our work we used normal distributions satisfy the central limit theorem for the rotation group SO(3) (Savyolova 1984):

$$f(g,g_0,\varepsilon)=\sum_{l=0}^{\infty}(2l+1)exp[-l(l+1)\varepsilon^2]\frac{sin((l+1/2)t)}{sin(t/2)}, \qquad (3)$$

where t is the distance between g and g_0, $t \in [0,\pi]$, $cos\,t=[Tr(g_0 g^{-1})-1]/2$. Function (3) describes only circular dispersion around texture component maximum. So to approximate many texture types (which have non-circular character) we have to sum a number of such distributions with the different "centers" g_0.

4 Results

We have considered the texture of a Zn sheet after two rolling procedures: the first one was rolled at 150°C and the second one was at room temperature. Only two complete PFs (002) and (101) were measured by means of neutron diffraction at the spectrometer TEX-2, GKSS Research Center Geesthacht, Germany (Brokmeier et. al 1998). Experimental PFs are shown in Fig. 1a and compared with recalculated PFs (Fig 1b – Fig 1d). The ODFs calculated by means of three methods (ISEM, WIMV and texture components) are presented in Fig. 2 given in the form of the γ–sections with a grid of 5°. The comparison shows that all three ODFs are qualitatively rather close to each other. Moreover, the results obtained by WIMV and ISEM show an excellent agreement.

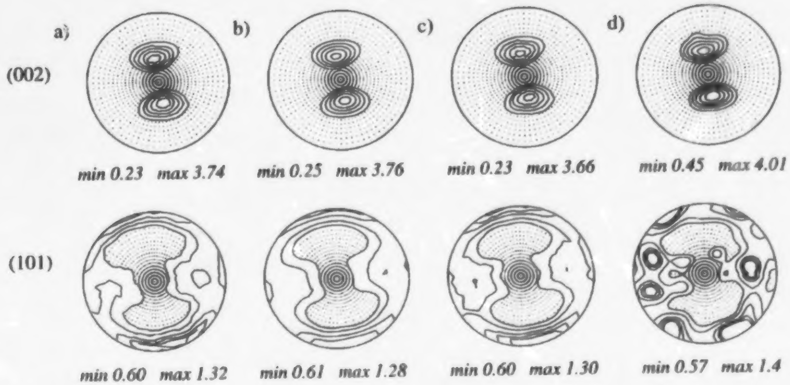

Fig. 1: a) Experimental pole figures of the rolled Zn sheet; pole figures recalculated by b) ISEM, $RP0_{(002)}=4\%$, $RP1_{(002)}=0.96\%$, $RP0_{(101)}=3.4\%$, $RP1_{(101)}=1.3\%$, c) WIMV method, $RP0_{(002)}=0.81\%$, $RP1_{(002)}=1.1\%$, $RP0_{(101)}=4.2\%$, $RP1_{(101)}=3.25\%$, d) texture component method, $RP0_{(002)}=11\%$, $RP0_{(101)}=7\%$. Row 1: pole figures (002), norm=782, contours are 1.5, 2.0, 2.5, 3.0, 3.5 mrd; Row 2: pole figures (101), norm=2735, contours are 1.0, 1.1, 1.2, 1.25, 1.28 mrd.

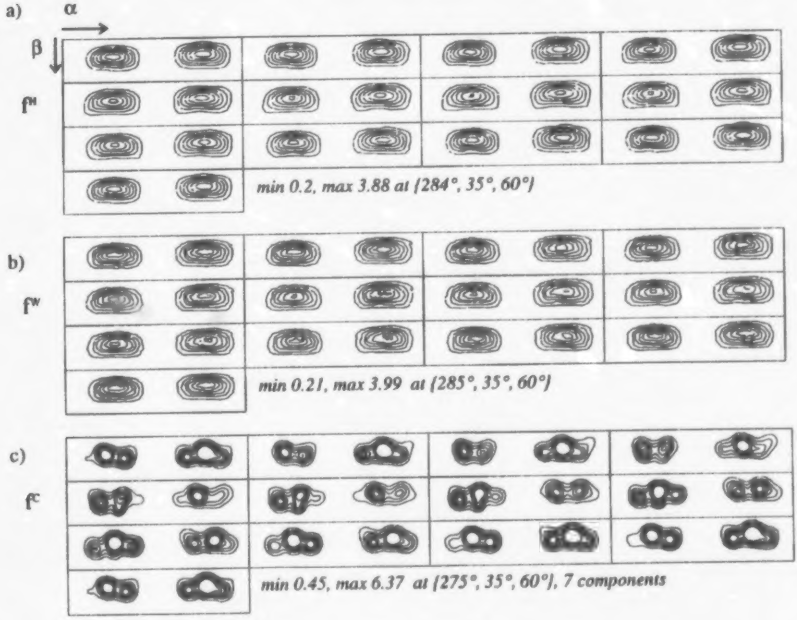

Fig. 2: Complete orientation distribution functions (5°, γ–sections, Matthies's coordinates) for the rolled Zn sheet calculated by a) ISEM, b) WIMV method, c) texture component method. Contours are 1.0, 1.5, 2.0, 2.5, 3.0, 3.5 mrd.

The small difference in the intensity on $f^{H}(g)$ in comparison to $f^{W}(g)$ can be explained by lack of terms in the series expansion used for $f^{H}(g)$ calculation and by a different usage of the phon. RP values are for recalculated PFs by ISEM: $RP0_{(002)}$ = 4%, $RP0_{(101)}$ = 3.4%, by the WIMV method: $RP0_{(002)}$ = 0.81%, $RP0_{(101)}$ = 4.2%. To calculate the ODF by the component method we have to sum seven circular peak components. We had got satisfactory results for the recalculated PFs as well ($RP0_{(002)}$ = 7%, $RP0_{(101)}$ = 11%), while the ODF values are different compared to other two calculations. To describe this texture type it seems to be preferable to use elliptical texture components than circular texture components. Thereafter, we have calculated mean values of elastic properties (Young's modules) for the rolled Zn sheet with the ODF as a weighting function (Fig. 3). Young's modules calculated in Reuss, Voigt and Hill approximations are in between maximum (125 GPa) and minimum (37.7 GPa) values of the single crystal function for Zn. The sections of Young's module surfaces in the rolling plane calculated for the approximation after Reuss, Voigt and Hill using the three different ODFs are given in the Fig. 4. It can be seen clearly that the results are very close to each other even in the case of the component method. That means the anisotropy of the Young's modules depends strongly on the main texture components, which can be described by all of the three ODF-routines sufficiently. Table 1 shows the stiffness constants calculated in the Reuss approximation for the considered Zn sheet. There are no differences between ISEM and WIMV and a difference to the component method not exceed 3%.

Table 1: Elastic constants (stiffness) for the rolled Zn sheet (Reuss approximation)

S_{ij} (10^{-2}, GPa^{-1})	Single crystal	Rolled Zn sheet		
		ISEM	WIMV method	Component method
S_{11}	0.84	0.98	0.98	0.96
S_{12}	-0.35	-0.24	-0.24	-0.24
S_{13}	-0.67	-0.30	-0.30	-0.30
S_{33}	2.65	1.22	1.22	1.24
S_{44}	2.50	3.38	3.38	3.41
S_{66}	1.58	2.57	2.57	2.52
S_{55}	$= S_{44}$	2.67	2.67	2.68
S_{22}	$= S_{11}$	1.07	1.07	1.07
S_{23}	$= S_{13}$	-0.25	-0.25	-0.25

5 Conclusions

Looking on the different approximations (Reuss, Voigt and Hill) the expected differences in the Young's modules can be seen. All of the three used ODF calculations (ISEM,WIMV and texture component method) leads to sufficient results in the description of the Zn sheet. It should be noticed that only two but complete pole figures are contributed for this hexagonal material. The best results are given by ISEM and WIMV. In spite of some deviations in the ODF obtained by the texture component method the calculation of the elastic constants shows only minor differences compared to ISEM and WIMV usage.

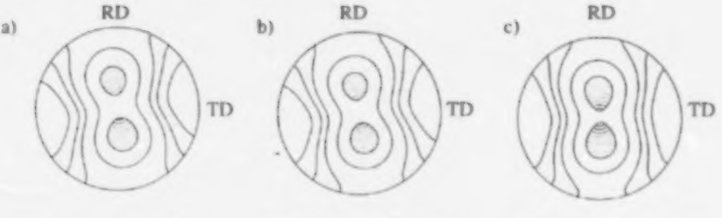

min 87.1 max 112.0 *min 87.4 max 112.0* *min 87.0 max 112.9*

Fig. 3: Stereographic projections of Young's module surfaces (GPa) on the rolling plane for the Zn sheet calculated with Hill approximation using the ODF obtained by a) ISEM, b) WIMVmethod, c) texture component method. Contours are 90.2, 96.5, 102.7, 105.8 108.9 GPa

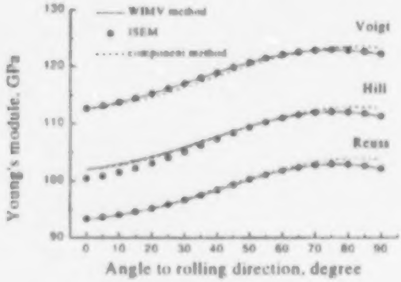

Fig 4: Young's modules in the rolling plane calculated for Reuss, Voigt and Hill approximations with ODFs obtained by ISEM, WIMV and texture component methods.

6 Acknowledgements

The authors would like to thank Dr. S. Matthies for helpful discussions on elastic properties computing. The present work was supported by the GKSS-Research Center Geesthacht GmbH, Germany.

7 References

Brokmeier, H.-G., U. Zink, R. Schnieber, B. Witassek (1998) Materials Science Forum, 273-275, 277.
Bunge, H. J. (1982) Texture Analysis in Material Science, Butterworth, London.
Dahms, M. and Bunge, H.J. (1989) J. Appl. Cryst., 22, 439-447.
Helming, K. (1996) Texturapproximation durch Modellkomponenten, Göttingen.
Matthies, S.and Vinel, G. (1982) Phys. Stat. Sol. (b), 112, K111-K114.
Nikolayev, D.I., Savyolova, T.I., Feldmann, K. (1992) Textur. Microstr., 19, 9-27.
Savyolova, T.I. (1984) Zavodskaya Laboratoriya, 50, 48-52 (Russian).
Wenk, H.R., Johnson, G.C., Matthies, S. (1988) J.Appl.Phys., V. 63, N 8, 2876-2879.

CONSIDERATION OF LATTICE INCOMPATIBILITY IN THE EVOLUTION OF HARDENING

A. ACHARYA & A. J. BEAUDOIN

University of Illinois at Urbana-Champaign, Urbana, IL

Abstract

This model considers 3-D, polycrystalline aggregates of purely viscoplastic crystals. The hardening response of the individual single crystals is considered to be isotropic (Taylor model), but modified to include a physically- motivated measure of lattice incompatibility which is supposed to model, in the continuum setting, the resistance to plastic flow provided by lattice defects. The length-scale in constitutive response that is required on dimensional grounds appears naturally from a widely accepted empirical relationship between the flow strength and the dislocation density. We use such a theory and the finite-element-method to study metallic behavior at moderate strains in the range of 0.02-1.0, in particular, the grain size-effect in FCC polycrystal response and Stage IV hardening in a BCC material.

Keywords: Incompatible lattice curvature, finite element, polycrystal plasticity

1. Introduction

This paper describes recent progress in incorporating a continuum measure of lattice incompatibility, developed solely from the kinematic ingredients of the continuum theory of crystal plasticity (Acharya & Beaudoin 1999; Acharya & Bassani 1998), in the phenomenological description of work hardening proposed by Mecking & Kocks (1981) and Estrin & Mecking (1984). As will be shown, the 'slip plane lattice incompatibility' measure pertaining to individual slip systems can be interpreted as a forest dislocation density in a fairly suggestive way, thus finding a natural place in the evolution equation for the total dislocation density.

The kinematic aspects of our work were strongly motivated by a desire to make a connection between crystal plasticity, the theory of continuous distribution of dislocations and the theory of materially uniform inhomogeneous bodies, initiated in the works of Kondo, Nye, Bilby, Bullough & Smith, and Kröner & Seeger (for references see Acharya & Bassani 1998). These seminal works deal either with a 'static' elastic theory of dislocations where the dislocation density is assumed to be specified *a priori* and the internal stress distribution due to it is calculated (e. g. Kröner 1981), or with purely kinematical connections between dislocation density distributions of specific forms and admissible lattice configurations corresponding to such distributions (e.g. Nye 1953; Bilby 1960). Our point of departure lies in the desire to utilize the lattice incompatibility as an evolving measure in a full continuum theory – a theory that deals with kinematics, stress, strength and, most importantly, work hardening – while defining the lattice deformation and its incompatibility from within.

We find it important to distinguish between 'lattice strain incompatibility' and 'lattice incompatibility'. While an incompatible lattice strain (and consequently long-range internal stress) necessarily implies lattice incompatibility, the converse is not true (Acharya & Bassani 1995). We capitalize on this fact by considering a purely viscoplastic theory and so render lattice deformations characterized by a rotation field (which can be incompatible but whose strain has no incompatibility), thus eliminating the possibility of the existence of internal stress.

The lattice incompatibility measure in a rigidly rotating lattice with rotation $\boldsymbol{R}^e$ is given by

$$\mathbf{\Lambda} := \left(R^e_{ji,k} - R^e_{ki,j}\right) \boldsymbol{e}_i \otimes \boldsymbol{e}_j \otimes \boldsymbol{e}_k. \tag{1}$$

It is obtained by asking for conditions under which the inverse 'elastic' deformation $\boldsymbol{R}^{eT}$ is derivable from a vector valued potential function on the current configuration. If we now consider a closed, continuous lattice circuit C enclosing area A on a slip plane with normal $\boldsymbol{n}^\kappa$ in the current configuration, then

$$\int_C \boldsymbol{R}^{eT} \cdot d\boldsymbol{x} = \int_A \mathbf{\Lambda} : \hat{\boldsymbol{n}}^\kappa \, da, \tag{2}$$

represents the closure failure associated with this circuit in the reference lattice, and can be associated with the net cumulative Burgers vector of all forest dislocations threading the area A. In the above, $\hat{\boldsymbol{n}}^\kappa$ is the unique skew-symmetric tensor defined by $\hat{\boldsymbol{n}}^\kappa \cdot \boldsymbol{a} = \frac{1}{2}\boldsymbol{n} \times \boldsymbol{a}$, for all vectors $\boldsymbol{a}$. Defining

$$\lambda^\kappa := \sqrt{(\mathbf{\Lambda} : \hat{\boldsymbol{n}}^\kappa) \cdot (\mathbf{\Lambda} : \hat{\boldsymbol{n}}^\kappa)}, \tag{3}$$

we note that while $\Lambda \neq 0$ represents the presence of net dislocations threading at least some plane in the body, $\lambda^\kappa \neq 0$ represents the presence of net dislocations threading slip plane κ. Also, λ^κ/b, where b is the Burgers vector of the lattice, may also be interpreted as a measure of the density of such a net dislocation distribution on slip plane κ.

2. An Example

As an exposition of the incompatibility measure, consider the deformed lattice shown in Figure 1. The pointwise rotation field is approximated by

$$\beta(x_1) = -\beta^* \tanh\left(\frac{x_1}{w}\right) \tag{4}$$

where w provides for description of the boundary width. Non-zero components of R^e_{ij} are $R^e_{11} = R^e_{22} = \cos\beta$, $R^e_{21} = -R^e_{12} = \sin\beta$, and $R_{33} = 1$.

Evaluation of (3) follows from the gradient of the rotation field

$$R^e_{ij,1} = \frac{\partial R^e_{ij}}{\partial \beta}\frac{\partial \beta}{\partial x_1} = -\frac{\beta^*}{w}\operatorname{sech}^2\left(\frac{x_1}{w}\right)\frac{\partial R^e_{ij}}{\partial \beta}. \tag{5}$$

Evaluating at $x_1 = 0$, non-zero terms of $\mathbf{\Lambda}$ are $\Lambda_{112} = -\Lambda_{121} = \frac{\beta^*}{w}$. Subsequently, Nye's dislocation tensor $\boldsymbol{\alpha}$, or $\alpha_{ip} = -\frac{1}{2}e_{pjk}\Lambda_{ijk}$, has the non-zero component

$$\alpha_{13} = -\frac{\beta^*}{w}. \tag{6}$$

However, the measure of incompatibility, λ^κ, *is zero for any slip plane with normal n^κ contained in the plane of the paper.* Only lattice planes which are threaded by dislocations in the subboundary of Figure 1 will have a non-zero incompatibility that contributes to the hardening rate, when slip occurs on such planes.

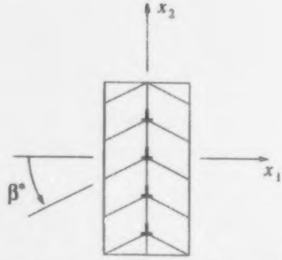

Figure 1: Lattice with subboundary

3. Development

Our model for deformation of the polycrystal follows that posed by Mecking (1981). Interaction between grains leads to regions of incompatible lattice curvature – the vicinity of grain boundaries serves as one (but not the only) example. With plastic deformation on the order of a percent, the bulk of the dislocations in this region will have their stress field 'shielded off' due to polyslip. Hence, geometrically necessary dislocations (Ashby 1970) with long range stress fields are relatively few. In the grain interior, storage of dislocations develops in statistical fashion. On the other hand, the hardening rate will be accentuated in regions of marked incompatible lattice curvature.

With the total dislocation density denoted as ρ, the slip system shearing rate on system κ as $\dot{\gamma}^\kappa$, $\dot{\epsilon}$ as the strain rate and T the temperature, we consider an evolution equation for the dislocation density of the form

$$\dot{\rho} = \sum_\kappa \left\{ \frac{\lambda^\kappa}{b} + k_1\sqrt{\rho} - k_2(\dot{\epsilon}, T)\rho \right\} |\dot{\gamma}^\kappa|, \tag{7}$$

where b is the lattice Burgers vector, and k_1 and k_2 are functions to be determined from observations. The first term provides that an increment of slip on a given system gives rise to an increment in the total dislocation density due to entanglement of dislocations on that system with the forest dislocations, on the corresponding slip plane, as identified by the lattice incompatibility. The second and third terms follow exactly the development of Kocks (1976), Mecking & Kocks (1981), and Estrin & Mecking (1984).

Let $\hat{\tau}$ represent an isotropic measure of single crystal flow strength, and $\hat{\tau}_0$ the initial yield stress. Also, let α be a non-dimensional constant of order unity and μ a suitable elastic shear modulus. On combining (7) with the relationship

$$\hat{\tau} - \hat{\tau}_0 = \alpha\mu b\sqrt{\rho} \tag{8}$$

and differentiating with respect to time, we obtain an expression for isotropic single crystal hardening given by

$$\dot{\hat{\tau}} = \frac{\alpha^2\mu^2 b}{2\left(\hat{\tau} - \hat{\tau}_0\right)}\sum_{\kappa}\lambda^{\kappa}\left|\dot{\gamma}^{\kappa}\right| + \left\{\frac{\alpha\mu b}{2}k_1 - k_2\frac{\hat{\tau} - \hat{\tau}_0}{2}\right\}\sum_{\kappa}\left|\dot{\gamma}^{\kappa}\right|. \tag{9}$$

Defining θ_0 as the strain-hardening rate that prevails at initial yield characterized by flow strength $\hat{\tau}_0$ in the absence of athermal hardening due to geometric effects (and assumed, in this work, to be the well-defined Stage II hardening rate), and $\hat{\tau}_s$ as the strain-rate and temperature dependent saturation stress $\left(\dot{\hat{\tau}}\left(\hat{\tau}_s\right) = 0\right)$ in the absence of geometric effects, the following relations are obtained;

$$k_1 = \frac{2\theta_0}{\alpha\mu b} \quad \text{and} \quad k_2\left(\dot{\epsilon}, T\right) = \frac{2\theta_0}{\hat{\tau}_s\left(\dot{\epsilon}, T\right) - \hat{\tau}_0}. \tag{10}$$

Substituting in (9), an isotropic, single crystal work hardening model is obtained in the form

$$\dot{\hat{\tau}} = \frac{\alpha^2\mu^2 b}{2\left(\hat{\tau} - \hat{\tau}_0\right)}\sum_{\kappa}\lambda^{\kappa}\left|\dot{\gamma}^{\kappa}\right| + \theta_0\left\{\frac{\hat{\tau}_s - \hat{\tau}}{\hat{\tau}_s - \hat{\tau}_0}\right\}\sum_{\kappa}\left|\dot{\gamma}^{\kappa}\right|. \tag{11}$$

The model incorporates hardening effects due to lattice incompatibility and does not require the total dislocation density to be conceptually split into additive geometric and statistical parts. The material length-scale required to include the gradient measure of lattice incompatibility into the constitutive equation for work hardening arises solely from physical considerations of dislocation storage leading to strain-hardening, as represented within the conceptual framework of Mecking & Kocks (1981).

4. Examples

A finite element mesh has been developed to represent a hypothetical polycrystal aggregate. A rectangular mesh geometry is simply perturbed to form Wigner-Seitz cells, with each cell assigned a random orientation from a uniform texture. In the present work, individual cells contain twelve elements; a sample mesh is shown in Figure 2.

To investigate dependence of physical length scale on hardening, the effect of grainsize on stress in pure nickel was studied. Figure 3 provides a comparison of model prediction with data (circles) taken from the experimental study by Narutani & Takamura (1991). Offset and spacing of the predicted curves of Figure 3 follow from manipulation of the terms, $\hat{\tau}_0$ and $\hat{\tau}_s$. The initial value of the mechanical threshold was set to $\hat{\tau}|_{t=0} = \hat{\tau}_0 = 29.0$ MPa and the saturation

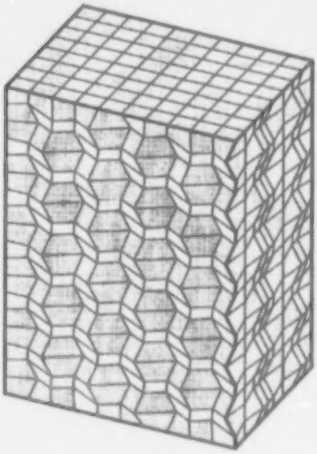

Figure 2: Quadrant of finite element mesh for model polycrystal aggregate

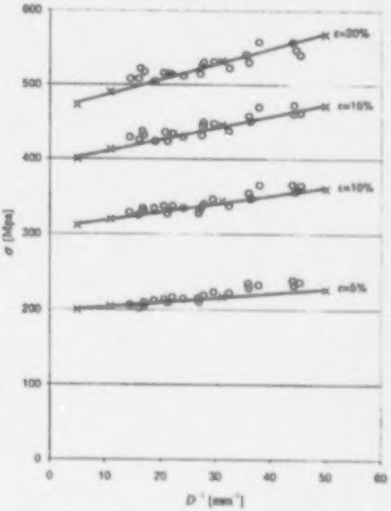

Figure 3: Effect of grainsize on effective stress for nickel at 77K

stress was taken as $\hat{\tau}_s = 250.0$ MPa. Simulations were carried out for grain diameters of 200 μm, 91 μm, 32 μm, and 20 μm by simply scaling the dimensions of the mesh. There is a clear relationship between the effective stress and D^{-1}.[1]

A study for the response of the incompatibility measure at large strains was conducted for a BCC material (intended to be similar to pure iron). Slip system geometry was prescribed for the 12 BCC $\{110\}\ \langle 111 \rangle$ slip systems. The parameters of (11) were taken as $\theta_0 = 388.0$ MPa, $\hat{\tau}_0 = 80.0$ MPa, $\hat{\tau}_s = 190$ MPa, and $\alpha = 0.3$. The hardening rate, $\theta = \frac{d\sigma}{d\epsilon}$, is plotted against stress in Figure 4. After an initial linear decrease in hardening rate (Stage III), there is a transition to a constant rate (Stage IV).

We must emphasize that, in both of the above examples, the hardening parameters are intended to be representative. Current efforts are directed at study of finite element discretization and issues related to mesh convergence.

5. Acknowledgements

We wish to thank Dr. Fred Kocks and Prof. David Parks for fruitful discussions. This work was supported by the Center for Simulation of Advanced Rockets at the University of Illinois at Urbana-Champaign (UIUC) under U.S. Dept. of Energy subcontract B341494 and utilized the Origin2000 computer system at the National Center for Supercomputing Applications, UIUC.

---

[1] The study of grain-size effect of polycrystal response using an approach similar to ours in some respects has also been undertaken by Dai & Parks (1998). They incorporate slip system hardening due to obstacle densities directly into the flow strength. These obstacle densities are inferred from the incompatibility in the plastic deformation tensor.

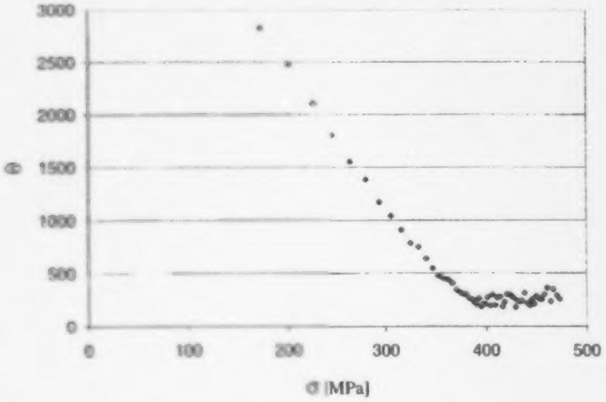

Figure 4: Evolution of hardening rate

6. References

Acharya, A. and Bassani, J. L. (1998) Lattice incompatibility and a gradient theory of crystal plasticity. *submitted for publication.*

Acharya, A. and Bassani, J. L. (1995) Incompatible lattice deformations and crystal plasticity. In *Plastic and Fracture Instabilities in Materials*, ed. N. Ghoniem, AMD-Vol. 200/MD-Vol. 57, pp. 75-80, ASME, New York.

Acharya, A. and Beaudoin, A. J. (1999) Grain-size effect in FCC viscoplastic polycrystals at moderate strains. *submitted for publication.*

Ashby, M. F. (1970) The deformation of plastically non-homogeneous materials. *Philosophical Magazine* 21, 399-424.

Bilby, B. A. (1960) Continuous distributions of dislocations. *Progress in Solid Mechanics* 1, 329-398.

Estrin, Y. and Mecking, H. (1984) A unified phenomenological description of work hardening and creep based on one-parameter models. *Acta Metallurgica* **32**, 57-70.

Kröner, E. (1981) in *Physics of Defects*, ed. R. Balian et al., 216-315, North-Holland Publishing.

Mecking, H. (1981) Low temperature deformation of polycrystals. In *Deformation of polycrystals*, ed. N. Hansen *et al.*, pp. 73-86. Roskilde, Denmark: Riso National Laboratory.

Mecking, H. and Kocks, U. F. (1981) Kinetics of flow and strain-hardening. *Acta Metallurgica* **29**, 1865-1875.

Narutani, T. and Takamura, J. (1991) Grain-size strengthening in terms of dislocation density measured by resistivity. *Acta Metallurgica et Materialia* **39**, 2037-2049.

Nye, J. F. (1953) Some geometrical relations in dislocated crystals. *Acta Metallurgica* 1, 153-162.

ANALYSIS OF ORIENTATION-DEPENDENT STRESS HETEROGENEITY

Y.D. WANG[1], R. LIN PENG[1,2] and R. McGREEVY[1]

[1]Studsvik Neutron Research Laboratory, Uppsala University, Nyköping, Sweden
[2]Dept of Mechanical Engineering, Linköping University, Linköping, Sweden

Abstract

Stress heterogeneity in polycrystalline materials has recently received great attention in the field of materials science and engineering. In the present paper, a stress orientation distribution function (SODF) is defined to describe the orientation-dependent stress anisotropy and a method is proposed for analyzing the stress heterogeneity of textured materials directly from the measured strain distribution. As an example, the stress heterogeneity in a cold rolled austenitic stainless steel is investigated based on strain data obtained by neutron diffraction measurements. The initial results are presented and compared with those obtained from the Reuss model.

Keywords: Stress heterogeneity, anisotropy, stress orientation distribution function

1 Introduction

Non-linear diffraction strain *vs* $\sin^2\psi$ phenomena are frequently observed in residual stress measurement of textured materials. The physical nature of this non-linear strain behavior is attributed to two main factors: the influence of crystal texture on the diffraction elastic constants (Brakman 1983; Brakman and Penning 1988) and the existence of the second kind of residual stress (stress heterogeneity) (Noyan and Schadler 1993). The existence of stress heterogeneity has recently become evident from computer simulations considering both the anisotropy of elastic and plastic deformation behaviors and combining diffraction strain measurements (van Acker et al. 1996). It is usually believed that heterogeneity of stress or strain originates from the difference of stress states in grains with different orientation, which is caused by the elastic and plastic anisotropy of the single crystalite.

Similarly to crystallographic preferred orientation (texture), which is quantitatively described by the crystal orientation distribution function (CODF) (Bunge 1982), the orientation-dependent stress heterogeneity may be described by a function called the stress orientation distribution function (SODF). In fact, the SODF should be attributed to one of the generalized textural quantities proposed by Bunge (1994). This orientation-dependent stress distribution function can be expanded into generalized spherical harmonics and represented using some series coefficients of the second-rank tensor. The crystal and specimen symmetry significantly reduces the number of independent coefficients required for a complete description of the SODF. In this paper, a method is proposed for determining the SODF directly from the strain distributions as measured by diffraction techniques. As an example, the method is applied to study the stress heterogeneity in a cold rolled austenitic stainless steel. The primary results of the SODF analysis of this material, based on strain data obtained by neutron diffraction, are given.

2 Description and representation of SODF

The CODF, $f(\vec{g})$, describes a statistical orientation distribution of grains in a polycrystalline material with regard to a fixed sample coordinate system K_s. This can be expanded into generalized spherical harmonics (Bunge 1965; Roe 1965)

$$f(\vec{g}) = \sum_{l=0}^{L_{max}} \sum_{m=-l}^{l} \sum_{n=-l}^{l} W_{lmn} Z_{lmn}(\cos\theta) \exp(-im\psi) \exp(-in\varphi) \tag{1}$$

where W_{lmn} are the series coefficients of the CODF, $Z_{lmn}(x)$ is the augumented Jacobi function and $\psi\theta\varphi$ are the Euler angles defined by Roe (1965).

In this paper, we use the SODF to describe statistically the orientation-dependent stress distribution of the grains. It should be noticed that the SODF is a three-dimensional function with a second-rank stress tensor. In a fixed sample coordinate frame K_s, the SODF, $\sigma_{ij}(\vec{g})$, may be also expanded into generalized spherical harmonics

$$\sigma_{ij}(\vec{g}) = \sum_{l=0}^{L_{max}} \sum_{m=-l}^{l} \sum_{n=-l}^{l} \Gamma_{lmn}^{ij} Z_{lmn}(\cos\theta) \exp(-im\psi) \exp(-in\varphi) \tag{2}$$

where Γ_{lmn}^{ij} are the series coefficients of the SODF.

There exist two kinds of symmetry in the SODF, crystal symmetry and specimen symmetry. Both crystal and specimen symmetry can significantly reduce the number of independent series coefficients Γ_{lmn}^{ij}. Actually, the crystal symmetry in the SODF is the same as that in the CODF. However, there are some difference between the specimen symmetry in the SODF and the CODF. More detailed discussions about the symmetry groups in SODF will be given in later paper. Another difference between the SODF and the CODF is that some lower order series coefficients are enough to give a complete description of the SODF, wheareas series coefficients up to the maximum order of 22 are usually needed for the CODF.

The average stress $\tilde{\sigma}_{ij}$, in the fixed sample frame, may be written as

$$\tilde{\sigma}_{ij} = \oint_{\Omega} \sigma_{ij}(\bar{g})\, f(\bar{g})\, dg \tag{3}$$

where the integrand range Ω is taken over the whole Euler space. Introducing (1) and (2) into (3) leads to

$$\tilde{\sigma}_{ij} = \sum_{l=0}^{L_{max}} \sum_{m=-l}^{l} \sum_{n=-l}^{l} (-1)^{m+n}\, \Gamma_{lmn}^{ij}\, W_{l\bar{m}\bar{n}} \tag{4}$$

with

$$\sigma_{ij}^{mic}(\bar{g}) = \sigma_{ij}(\bar{g}) - \tilde{\sigma}_{ij} \tag{5}$$

In practice, $\tilde{\sigma}_{ij}$ is traditionally called type I stress (mac-stress) and $\sigma_{ij}^{mic}(\bar{g})$ is called type II stress (mic-stress).

3 Method for determining the SODF

X-ray or neutron diffraction measures the strain, $\tilde{\varepsilon}(\bar{h}, \bar{y})$, of certain (hkl) plane along the direction $\bar{y}$ in the fixed sample coordinate system K_s, i.e.

$$\tilde{\varepsilon}(\bar{h}, \bar{y}) = \frac{\lambda}{2d_0 \sin\theta} - 1 \tag{6}$$

$\bar{h}$ is the normal direction of the (hkl) plane in the fixed crystal coordinate frame K_c, θ is its Bragg angle, λ is the wave length of the incident X-ray or neutron beam and d_0 is the planar distance along $\bar{h}$ under stress-free conditions.

Actually, the measured strain $\tilde{\varepsilon}(\bar{h}, \bar{y})$ of diffraction plane $\bar{h}$ at $\bar{y}$ should correspond to the average value of strains of all grains with the orientation $\bar{g}$, whose $\bar{h}$ is parallel to $\bar{y}$, i.e.

$$\tilde{\varepsilon}(\bar{h}, \bar{y}) = \oint_{\bar{g}\in\bar{y}/\!/\bar{h}} f(\bar{g})\, \varepsilon_{33}^{m}(\bar{h}, \bar{g})\, dg \Bigg/ \oint_{\bar{g}\in\bar{y}/\!/\bar{h}} f(\bar{g})\, dg \tag{7}$$

where $\varepsilon_{ij}^{m}(\bar{h}, \bar{g})$ is a second-rank strain tensor of the grains with the orientation $\bar{g}$ in the fixed measurement coordinate system K_m. $\varepsilon_{ij}^{m}(\bar{h}, \bar{g})$ may be transformed from the strain tensor $\varepsilon_{ij}^{c}(\bar{g})$ in the fixed crystal coordinate system K_c by the following equation

$$\varepsilon_{ij}^{m}\left(\vec{h},\vec{g}\right)=\sum_{k=1}^{3}\sum_{l=1}^{3} a_{ik}a_{jl}\varepsilon_{kl}^{c}\left(\vec{g}\right) \tag{8}$$

where a_{ik} is the direction cosine of $\vec{h}$ in K_c.

Using the generalized Hooke's law, $\varepsilon_{ij}^{c}(\vec{g})$ can be converted into a stress tensor $\sigma_{ij}^{c}(\vec{g})$ in K_c:

$$\varepsilon_{ij}^{c}\left(\vec{g}\right)=\sum_{k=1}^{3}\sum_{l=1}^{3} S_{ijkl}\,\sigma_{kl}^{c}\left(\vec{g}\right) \tag{9}$$

where S_{ijkl} are the elastic constants of the single crystal. On the other hand, $\sigma_{ij}^{c}(\vec{g})$ can be transformed from $\sigma_{ij}(\vec{g})$ by

$$\sigma_{ij}^{C}\left(\vec{g}\right)=\sum_{l=0}^{L_{max}}\sum_{m=-l}^{l}\sum_{n=-l}^{l}\sum_{p=-l}^{l}\Gamma_{lpn}^{ij}\,Z_{lpm}(\cos\beta)\,Z_{lmn}(\cos\theta) \\ \exp(-ip\alpha)\exp(-im(\psi+\gamma))\exp(-in\varphi) \tag{10}$$

where $(\alpha\beta\gamma)$ are the Euler angles which transform K_s into K_c.

Thus, if the strain distributions of a few hkl planes in the range covering the whole spherical surface are measured, the series coefficients of the SODF, Γ_{lmn}^{ij}, may be uniquely determined by the least-squares method. However, if only a number of discrete directions are measured, some extra physical conditions must be used to ensure a unique solution for the SODF. In this paper, we use the condition of minimizing the index of SODF, Π_{index}, which is defined as

$$\Pi_{index}=\sum_{l=1}^{L_{max}}\sum_{m=-l}^{l}\sum_{n=-l}^{l}\left(\Gamma_{lmn}^{ij}\right)^{2} \tag{11}$$

This condition is used in order to minimise the stress anisotropy, which leads to a small extra strain energy caused by different orientations in adjacent grains.

4 Measurement and analysis of stress heterogeneity in stainless steel

A cold rolled austenitic stainless, with nominal chemical composition of 17 Cr and 7 Ni (remainder Fe), is used as an example to illustrate the application of the proposed method in the analysis of stress and strain heterogeneity. Using a neutron beam of wavelength 1.76 Å, the (111), (200), (220) and (311) diffraction peaks were measured in various directions $\vec{y}$ in the fixed sample coordinate frame K_s. For each (hkl) plane, about 30 strain data, distributed between $\chi = 0°$ and $90°$ at $\eta = 0°$ and $\eta = 90°$, respectively, and between $\eta = 0°$ and $\eta = 90°$ at $\chi = 0°$, were measured (χ and η

are the polar and azimuthal angles of $\bar{y}$ in K_s). Each diffraction peak was fitted by a Lorentzian distribution to determine the peak position. The detailed experimental proceedure will be reported elsewhere.

The ODF of the cold rolled stainless steel (Fig. 1) obtained by neutron diffraction measurement shows that textures mainly consist of the components running from {110}<211> (Brass) to {123}<634> (S) and to {112}<111> (Cu), which is typically found in some fcc metals or alloys. Fig. 2 shows the measured strain variations as a function of χ at $\eta = 0°$ for four diffraction planes. A different variation of the strains is found for different (hkl), which indicates a large orientation-dependent stress heterogeneity.

On the Reuss assumption (i.e. assuming a constant stress), macro-stresses were calculated and the results are listed in Table 1. The strain distributions recalculated from the macro-stresses do not fit well to the measured data, as can be see in Fig. 3 which shows the strain distributions for (200) as a function of χ at $\eta = 0°$.

Table 1: Calculated macro-stress $\tilde{\sigma}_{ij}$ (MPa) based on different models

Model	σ_{11}	σ_{22}	σ_{33}	σ_{32}	σ_{31}	σ_{12}
Reuss assumption	-226.3	-146.5	-223.6	89.5	138.6	-7.5
The present model	-146.1	-1.2	21.3	0	0	0

Using the method proposed in the present paper, the SODF has been determined from the measured strain distributions. Fig. 4 shows one of the stress components, $\sigma_{11}(\vec{g})$, in SODF. As can be seen, there is a strong stress anisotropy, with the Brass texture component possessing a large compressive stress. The calculated macro-stress $\tilde{\sigma}_{ij}$ is also listed in Table 1. As $\tilde{\sigma}_{ij}$ is the sum of residual stress over all the grain orientations, they are expected to be zero. The non-zero $\tilde{\sigma}_{ij}$ obtained here could be attributed to the existence of a second phase, deformation induced martensite during cold rolling. Fig. 3 shows that the recalculated strain distribution from the present model agrees well with experiment. Detailed analysis of the stress anisotropy will be given in another paper.

5 Conclusions

(1) The stress orientation distribution function has been defined to describe the orientation-dependent stress heterogeneity.

(2) An method has been proposed for solving the SODF directly from measured strain distributions.

(3) A large strain anisotropy is found in a cold rolled austenitic stainless steel by neutron diffraction measurement using different (hkl) planes.

(4) The primary results from SODF analysis in the cold rolled austenitic stainless steel are given, which shows the existence of strong stress heterogeneity.

6 References

Brakman C.M. (1983) *J. Appl. Cryst.* **16**, 325-340.

Brakman C.M. & Penning P. (1988) *Acta Cryst.* **A44**, 163-167.

Bunge H.J. (1965) *Z. Metall.* **56**, 872-874.

Bunge H.J. (1982) *Texture Analysis in Materials Science*, Butterworths, London.

Bunge H.J. (1994) *Materials Science Forum* **157-162**, 13-29.

Noyan I.C. & Schadler L.S. (1994) *Metallurgical and Materials Transactions* **25A**, 341-347.

Roe R.J. (1965) J. Appl. Phys. Vol.36, pp. 2024-2031.

Van Acker K., Root J., van Houtte P. & Aernoudt E. (1996) *Acta Mater.* **44**, 4039-4049.

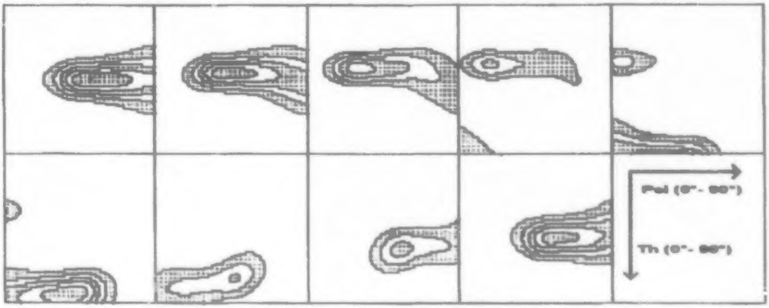

Constant Fi (0°, 10°, 20° ...... 90°) Levels: 1.20, 2.40, 3.61, 4.81, 6.01, 7.21

Fig.1: ODF of cold rolled austenitic stainless steel

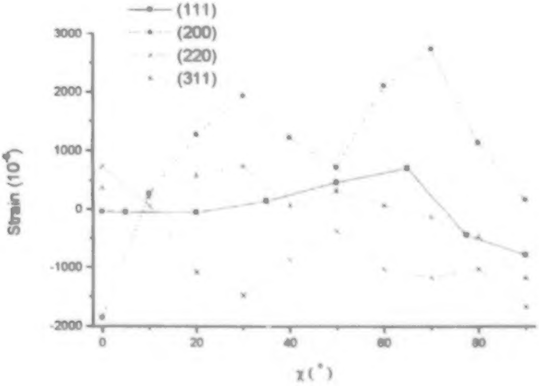

Fig. 2: The strain variation as function of χ at η = 0° for (111), (200), (220) and (311) diffraction peaks

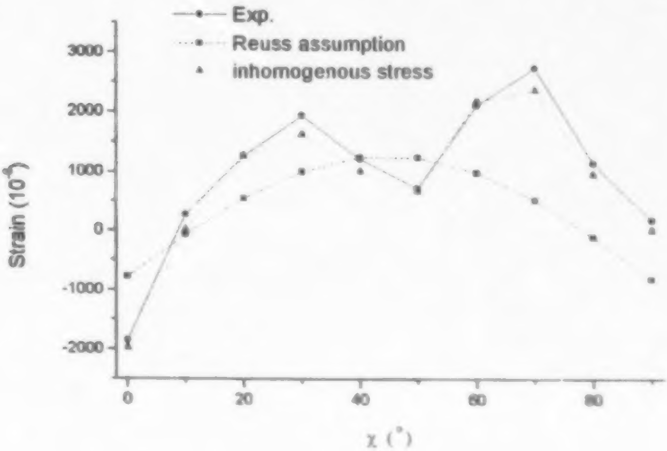

Fig. 3: The measured and recalculated strain distributions for (200) along different χ at η = 0°

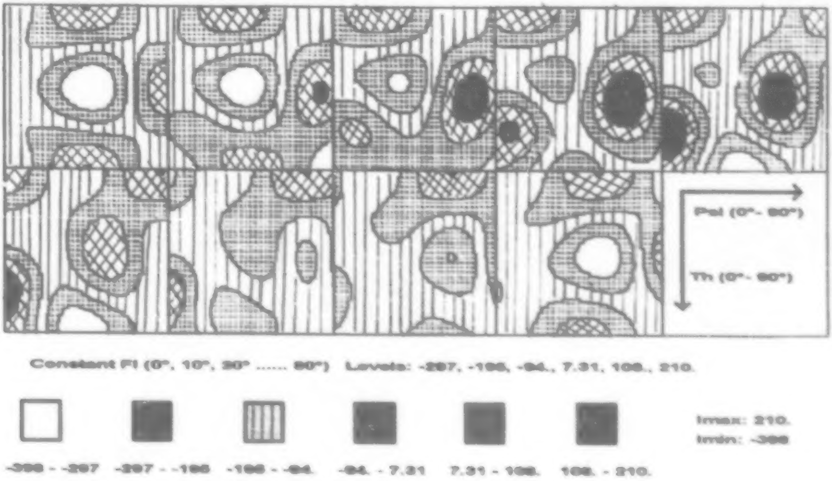

Fig. 4: SODF of cold rolled austenitic stainless steel for $\sigma_{11}(\vec{g})$

MODELLING TEXTURE INFLUENCE ON THE MAGNETIC PROPERTIES OF NANOCRYSTALLINE NICKEL AND IRON

B. SZPUNAR, M.J. AUS, E. RENAUD
Department of Materials and Metallurgical Engineering, Queen's University, Kingston, Ontario, Canada
U. ERB
Department of Metallurgy and Materials Science, University of Toronto, Canada
F. CZERWINSKI and J.A. SZPUNAR
Department of Mining and Metallurgical Engineering, McGill University, Montréal, Québec, Canada

ABSTRACT

Recently developed nanocrystalline materials with the percentage of atoms at grain boundaries as high as 50% are expected to have properties quite different than those of bulk polycrystalline materials. The influence of texture on magnetic properties has been studied for nanocrystalline nickel and iron. The effects of thermal excitations and random anisotropy from coupled grains is also discussed.

Keywords: nanocrystalline materials, electrodeposition, magnetic properties, texture

1. Introduction

In the past, theoretical calculations often neglected the effect of defects such as grain boundaries on the physical properties of materials. Grain boundary contribution is often negligible for physical properties of materials with large grain sizes but cannot be neglected in nanocrystalline materials where the percentage of atoms at grain boundaries can be as high as 50% (Gleiter, 1981; Palumbo et al., 1990). For these materials the effect of structural disorder at interfaces has significant influence on material properties. Magnetic properties are strongly affected. For example, Gleiter (1981) reported a reduction in the saturation magnetization by 40% for iron with 6nm grain size. In contrast to this experimental data, our theoretical calculations (B. Szpunar et al., 1996) showed that the magnetic moment at grain boundaries should not differ more than 20% from bulk magnetic moment. This is in agreement with recent observations (Aust et al., 1992) that the saturation magnetization of nanocrystalline nickel produced by electroplating is not strongly dependent on the grain size. We assume therefore that for pure nanocrystalline material the saturation magnetization is the same as for the bulk.

F7

Nanocrystalline grain should consist of one magnetic domain. If those grains are small enough thermal activation at room temperature would make them superparamagnetic and therefore it would be impossible to study the influence of texture on the magnetic properties. Another complication in studying texture influence arises from exchange interaction between grains which leads to a drastic reduction of the anisotropy due to the effect of averaging of the magnetocrystalline anisotropy within the group of correlated grains (Perez et al., 1995). This effect is difficult to take into account in the simulations since it requires a knowledge of the misorientation between neighboring grains. However, we can assume that at low temperature this effect is not significant and the influence of misorientation on magnetic anisotropy is random.

With this assumption, we should be able to calculate the remanence accurately since the value of the effective anisotropy constant is not important, but the orientation of easy directions is. The initial susceptibility and coercive field are directly related to the value of effective anisotropy constant, which can be altered significantly in nanocrystalline materials (Loffler, 1998). Therefore the correlation between texture and these properties might be difficult to evaluate.

2. Single domain model

Our samples of electrodeposited nickel with an average grain size of 16nm show fiber texture. The magnetic field is applied perpendicularly to the sample surface. The notation used for fiber texture is illustrated in Fig. 1 where θ is the angle between the easy direction and the direction of the magnetic moment, α is the angle between the easy direction and the direction of the applied magnetic field. The <111> is the easy magnetization direction for nickel and <100> for iron.

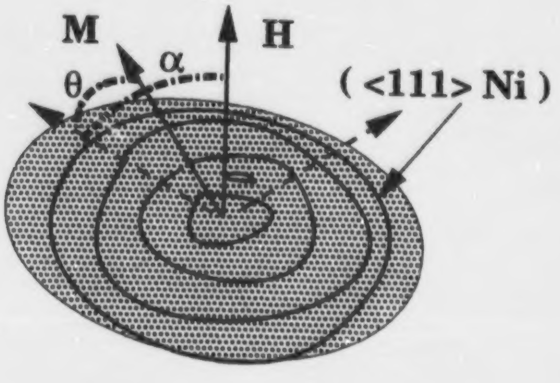

Fig. 1: Schematic representation of notation used for the direction of applied magnetic field (perpendicular to the sample), easy magnetization direction and the direction of the magnetic moment.

To represent the fiber texture the following representation was used:

$$g(\theta) = \sum t_l P_l \; (\cos(\theta)) \qquad (1)$$

where P_l (cos θ) are associated Legendre polynomials.

In case of random distribution only one of the expansion coefficients is not zero:

$$t_o = 1/\sqrt{2}$$

Magnetic properties like the susceptibility, remanence, coercive field can be calculated by minimizing the total energy as it was described in details in a previous paper (Szpunar and Szpunar, 1984).

The remanence is expressed by the following formula

$$M_R/M = N \sum t_l \gamma_l \qquad (2)$$

M is the saturation magnetization and N is a constant equal to one for uniaxial anisotropy, but for the cubic anisotropy with N is expressed by:

$$N = 1/\int_0^{54.7} \sum t_l \, P_l(\cos(\theta)) \sin(\theta) \, d\,\theta \qquad (3)$$

Constants used in the calculations of the influence of the texture on the remanence in crystals with cubic (with <111> and <100> easy directions) and the uniaxial anisotropies are listed in Table 1.

Table 1

	Remanence Constants γ_l	
l	Uniaxial anisotropy	Cubic anisotropy
0	0.707	0.474
2	0.395	0.527
4	-0.088	-0.030
6	0.040	-0.115
8	-0.023	-0.083
10	0.015	0.020
12	-0.010	0.066
14	0.008	0.027
16	-0.006	0.034
18	0.005	0.041
20	-0.004	0.000

In the later case the largest angular distance of the closest easy direction to the direction of the applied magnetic field is 54.7° (in contrast to π/2 for uniaxial anisotropy) and therefore correspondingly larger value of the remanence is observed. Using Table 1 we can calculate the remanence for random texture. The relative remanence for random texture ($t = 1/\sqrt{2}$) equals to 0.77 and 0.5 correspondingly for the <111> or <100> cubic and the uniaxial magnetocrystalline anisotropy.

3. Results and discussion

As an example we presented here the results obtained for iron with random texture and three samples of nickel for which textures were quite different. Fiber texture was found in all our samples and the texture for these samples is presented in Figures 2a, b and c. In Table 2 the calculated remanence values are presented. As it should be expected for cubic system, there is no strong dependence of the magnetic properties on texture as it should be in the case of uniaxial magnetocrystalline anisotropy. The remanence is high and is not dependent on texture. At present we are not able to present low temperature measurements but our results (0.77) for remanence of iron with the random grain orientation are in good agreement with the remanence for nanocrystalline iron at 10K of 0.75 as measured by Perez et al (1995). Our room temperature measurements of the remanence of nanocrystalline nickel are one order of magnitude smaller than calculated and no correlation with our predictions has been found.

Measurements of the coercive force at room temperature using vibrating sample magnetometer were presented in Fig. 3 as a function of the direction of applied field. We notice that coercivity field vary quite a lot from sample to sample and in the same way as a function of the specimen direction. Even though the texture of those samples were quite different (Figures 2a, b, c). The coercivity field is the highest in the direction perpendicular to the sample and the lowest in the direction parallel to the sample. We observe here the effect of shape anisotropy, which manifests itself through elongation of grains in the direction of electroplating.

We can conclude that at room temperature the texture effect on magnetic properties is completely wiped out. Further studies and measurements of magnetic properties at low temperature are planned.

Calculated (in units of M) magnetic properties for the random texture (0) and textures presented in Figure 2a, b and c correspondingly for samples 1, 2, 3.

Table 2

Sample	M_R/M
0	0.77
1	0.77
2	0.72
3	0.76

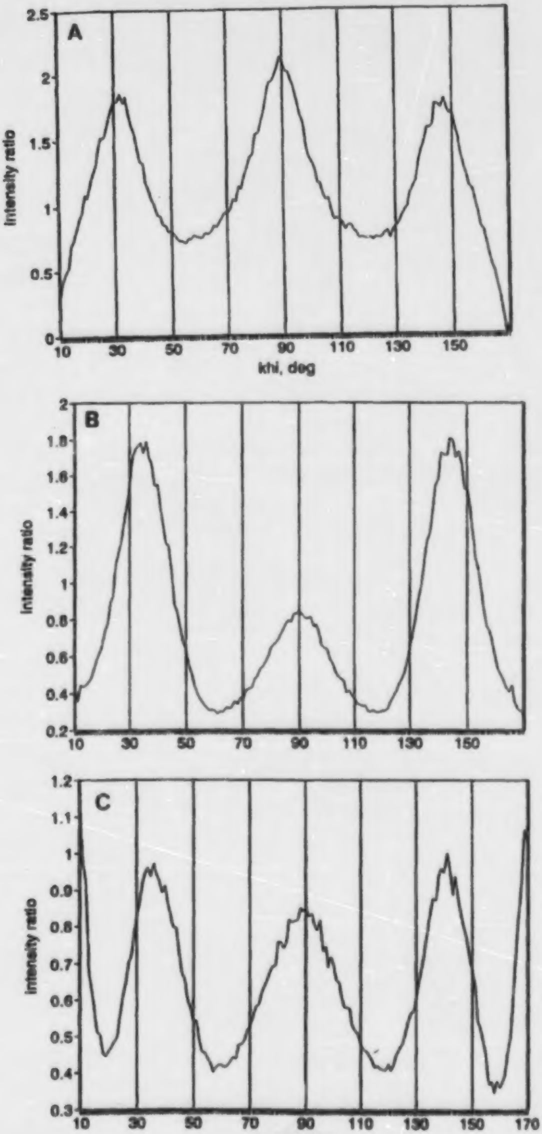

Fig. 2a, b, c: Examples of textures for electroplated nickel. Magnetic field is applied perpendicularly to the samples (90°).

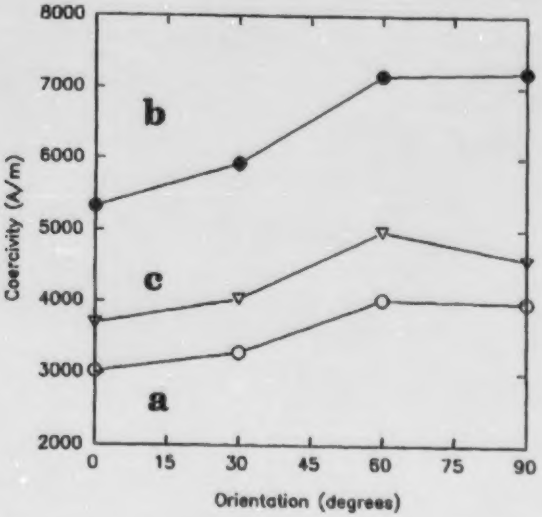

Fig. 3: Coercivity field as a function of the direction of applied field.

4. Conclusion

A simple model is presented which can be used as a guideline in studying the influence of texture on the magnetic properties for textured nanocrystalline materials. In conclusion, for nanocrystalline materials the results obtained at room temperature cannot be correlated with texture.

5. References

Aust, M.J., Szpunar, B., El Sherik, A.M., Erb, U., Palumbo, G. and K.T. Aust (1992) Magnetic Properties of Nanocrystalline Nickel, *Scripta Metall.* Vol. 27, pp. 1639-1643.

Gleiter, H. (1981) Nanocrystalline Materials, *Progr. Mat. Sci.,* Vol. 33, pp. 22.

Löffler, J.F., Meier, J.P., Doudin, B., Ansermet, J.-P. and Wagner, W. (1998) Random and Exchange Anisotropy in Consolidated Nanostructured Fe and Ni, *Phys. Rev.* Vol. B57 pp. 2915-2924.

Palumbo, G., Thorpe, S.J. and Aust, K.T. (1990) On the Contribution of Triple Junctions to the Properties of Nanocrystalline Materials, *Scripta Metall.*, Vol. 23 pp. 1347-1350.

Perez, J.P., Dupuis, V., Tuaillon, J., Perez, A., Paillard, V., Melinin, P., Treilleux, M., Thomas, L. and Bouchet-Fabre, B. (1995) Magnetic Properties of Iron Films Obtained by Low Energy Beam Deposition, *J. Magn. Mag. Mat.* Vol. 145 pp. 74.

Szpunar, B. and Szpunar, J. (1984) Magnetic Properties in Textured Fine-Particles Magnets, *J. Magn. & Magn. Mat.* Vol. 43 pp. 317.

Szpunar, B., Erb, U., Palumbo, G., Aust, K.T. and Lewis, L.J. (1996) Magnetism in Complex Atomic Structures, *Phys. Rev.* Vol. B53 pp.1.

Deformation Textures

MACROSCOPIC ANISOTROPY IN COLD ROLLED AA5XXX SHEET

S.-H. CHOI, J.C. BREM, and F. BARLAT
Alcoa Technical Center, 100 Technical Drive, Alcoa, USA
K.H. OH
School of Material Science and Engineering, Seoul National University,
Seoul 151-742, Korea

Abstract

The anisotropy of mechanical properties in a cold rolled AA5XXX sheet sample was investigated. In order to simultaneously consider the effects of morphological texture and crystallographic texture on macroscopic anisotropy, predictions of plastic properties were carried out using a visco-plastic self-consistent (VPSC) polycrystal model. The predicted r-value (width-to-thickness plastic strain ratio in uniaxial tension) anisotropy was in good agreement with experimental data.

Keywords: macroscopic anisotropy, texture, self-consistent polycrystal model, r-value

1 Introduction

Macroscopic anisotropy of metals has been studied widely due to its importance in process design. Many studies have been conducted to predict anisotropic properties considering crystallographic texture (Choi et al. 1999), precipitates (Barlat and Liu 1998), dislocation structure (Winther et al. 1997) and grain shape (Rollet et al. 1992). In the present work, the effect of crystallographic texture and grain shape on the macroscopic properties of a cold rolled AA5XXX sheet metal was investigated. In order to consider the effect of grain shape, the visco-plastic self-consistent (VPSC) polycrystal model proposed by Molinari et al. (1987) was used.

2 Experimental

The experimental investigation was carried out on a 0.22mm thick AA5XXX sheet sample. Mg and Mn are the main alloying elements in this alloy with approximate contents of 5% and 0.3%, respectively. The final samples were obtained after 90% cold rolling reduction. The grain morphology was investigated by optical microscopy. Pole figure measurements were carried out using a Seifert X-ray diffractometer for as-rolled samples and for those exposed to 93°C (the thermal exposure of tensile test specimens). From the {111} and {200} complete pole figures, the crystallographic orientation distribution function (ODF) was calculated using the series method. Tensile specimens were cut from the sheet at angles of 0°, 15°, 30°, 45°, 60°, 75° and 90° to the rolling direction. Tension tests were conducted at room temperature (RT) and 93°C to measure the yield stresses and plastic strain ratios (r-value). Many of AA5XXX sheets exhibit serrated flow during tensile deformation. This phenomenon leads to difficulties in measuring the plastic strain ratio during tension tests at room temperature. Therefore, in order to overcome this problem, in this work tension tests were conducted at elevated temperature, 93°C, where serrated flow is suppressed.

3 Experimental Results

Fig. 1 shows the microstructure of the RD / ND section of the sheet as observed by optical microscopy. Although grains elongated in the rolling direction of the sheet can be observed, it is difficult to define the grain shape accurately in this heavily deformed sheet sample. In the AA5XXX sheets having high Mg content, shear localization can develop during severe rolling deformation. Grains are probably broken up in many domains (Hughes 1993) which can be assumed to be more equiaxed than the grains. In this work, two types of grain shape were assumed for predicting the macroscopic properties of AA5XXX sheet. If the grains deform homogeneously during cold rolling, the final grains are assumed to be ellipsoidal with a 10-1-0.1 aspect ratio (RD-TD-ND). If equiaxed domains develop within each grain, the final domains are assumed to be spherical. In this case, the domains are assumed to play the role of embedded cells of uniform deformation in a self-consistent polycrystal model.

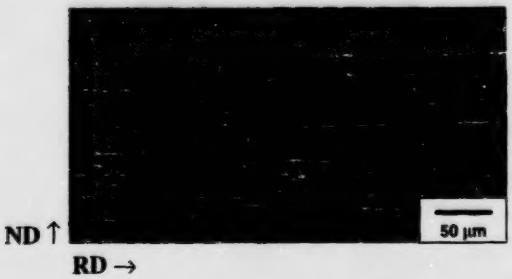

Fig. 1 Optical microscopy of AA5XXX sheet.

The {111} complete pole figure and the orientation density, f(g), on the β-fibre for the cold rolled specimen and the specimen exposed at elevated temperature are shown in Figs.2 and 3, respectively. The characterization of the β-fibre shows that the sharp rolling texture components such as C (Copper) {112}<111>, S (123}<634>, B (brass) {110}<112> are dominant and that almost the same level of texture intensity is observed for both specimens. Therefore, the difference in texture for both materials (RT and exposure at 93°C during tensile testing) can be neglected.

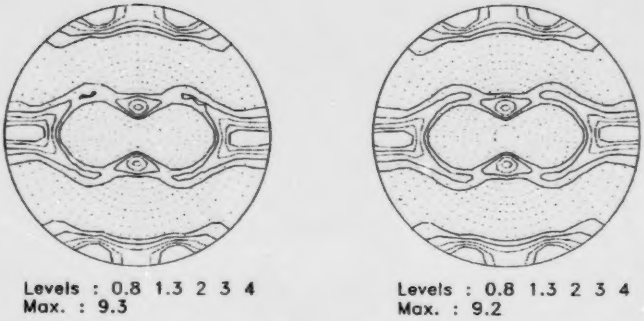

(a) (b)

Fig. 2 {111} pole figure for AA5XXX sheet.
(a) as-rolled (b) exposed at 93°C

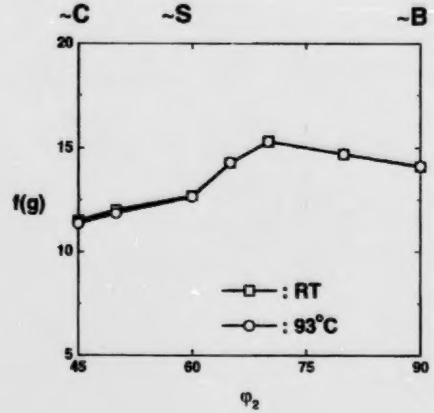

Fig. 3 The orientation density f(g) along the β-fibre.

4 Anisotropy Prediction

In order to predict the macroscopic properties of the polycrystalline aggregates, the Taylor (full constraints) polycrystal model and the VPSC polycrystal model are used. The VPSC polycrystal model is introduced to take into account texture and grain shape in the prediction of macroscopic properties. The shear rate on a given slip system s, $\dot{\gamma}^s$ is related to the resolved shear stress, τ^s, with a viscoplastic power law relation.

$$\frac{\tau^s}{\tau^s_o} = \left(\frac{\dot{\gamma}^s}{\dot{\gamma}^s_o}\right)^m \tag{1}$$

where m is the rate sensitivity parameter. $\dot{\gamma}^s_o$ and τ^s_o are the reference shear rate and reference shear stress, respectively. The microscopic strain rate can be calculated as follows

$$D_{ij} = \dot{\gamma}_o \sum_s R^s_{ij} \left(\frac{R^s_{kl} S_{kl}}{\tau^s_o}\right)^{1/m} \tag{2}$$

where **D** and **S** are the strain rate and the deviatoric stress tensors, respectively. The tensor **R** is associated with the slip system and can be expressed as follows

$$R^s_{ij} = \frac{1}{2}\left(b^s_i n^s_j + b^s_j n^s_i\right) \tag{3}$$

where **b** and **n** are the slip and the slip plane normal direction, respectively.
Using the concept of Homogeneous Equivalent Matrix (HEM) and 1-site approximation, the following interaction law between a grain and the matrix is derived

$$\mathbf{S}^g - \overline{\mathbf{S}} = \left(\Gamma^{gg'^{-1}} + \mathbf{A}_o\right) : \left(\mathbf{D}^g - \overline{\mathbf{D}}\right) \tag{4}$$

where $\overline{\mathbf{S}}$ and $\overline{\mathbf{D}}$ are the deviatoric stress and the strain rate for the matrix. The effect of the grain shape can be taken into account by the interaction tensor Γ between single crystals g and g' whose components only depend on their shape. The tensor Γ can be obtained by integration of the symmetric part of the second derivative of the Green function. For a plastically isotropic material, the interaction tensor A° is given as follows

$$A^o_{ijkl} = \frac{2}{3} m I_{ijkl} \frac{S_{eq}}{D_{eq}} \tag{5}$$

where the S_{eq} and D_{eq} are the von Mises equivalent stress and strain rate, respectively. **I** is the fourth rank identity matrix. The self-consistent model relies on the fact that **A°** is calculated so that

$$\langle \mathbf{S} \rangle = \overline{\mathbf{S}} \quad \text{and} \quad \langle \mathbf{D} \rangle = \overline{\mathbf{D}} \tag{6}$$

where < > means the arithmetic volume average over the polycrystal aggregate.
The r-value anisotropy and yield stress anisotropy were calculated using the full constraints and VPSC polycrystal models. The ODF was used to generate a set of 1016 grain orientations. For uniaxial tension test simulations, plastic strain rates were imposed on all grains in the polycrystal models. Macroscopic deformation states were changed iteratively until the macroscopic stress state converged toward the uniaxial stress state. The predicted r-value and yield stress were determined from the final macroscopic deformation state as the ratio of the width strain rate to the thickness strain rate and final stress state, respectively.

5 Results and Discussion

Fig. 4 shows the r-values calculated with the polycrystalline models in different directions as well as those determined experimentally. The predicted r-values using the Taylor model overestimate the experimental data for most of the tensile directions, whereas the predicted r-values using the VPSC model are in good agreement with the experimental trend. The VPSC calculations assuming both spherical and ellipsoidal grain shapes exhibit good agreement with experimental values within the range of experimental errors. Fig. 5 shows the normalized yield stresses calculated with the polycrystal models as well as those determined experimentally. The Taylor model underestimates the experimental data for loading directions between 0° and 55° to the rolling direction (RD), and overestimates the experimental data for the directions greater than 55° to the RD. The VPSC model underestimates the experimental data for all loading directions. In order to predict the flow stresses of cold rolled specimens, an additional model considering the deformed initial microstructure (such as the dislocation structure) should be considered in this calculation to make the initial critical resolved shear stress dependent on the orientation of the slip system with respect to the sheet sample reference frame (Winther et al. 1997).

6 Conclusions

Macroscopic plastic properties measured in uniaxial tensile tests, i.e. r-value and normalized yield stress for a cold rolled AA5XXX sheet, were experimentally measured in different loading directions with respect to the rolling direction and theoretically predicted using the Taylor and VPSC models. For the r-value, the Taylor model overestimated experimental data particularly for tension around 45° to the RD. The VPSC model resulted in excellent predictions in all directions. For the normalized yield stress, both the Taylor and VPSC models showed deviations compared to experimental results. Grain shape effects predicted using the VPSC model for yield stress directionality were negligible.

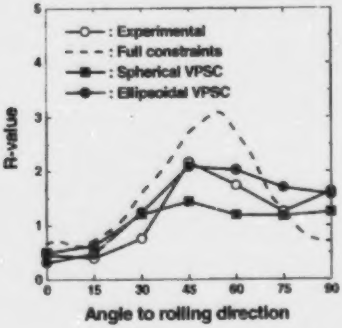

Fig. 4 Measured r-value for AA5XXX sheet with predictions from Taylor and VPSC models.

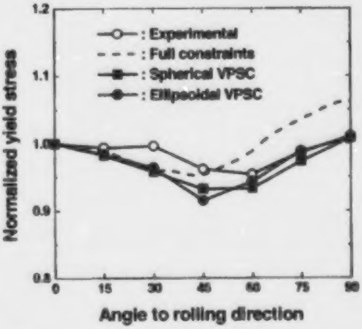

Fig. 5 Measured normalized yield stress for AA5XXX sheet with predictions from Taylor and VPSC models.

7 Acknowledgements

The authors would like to thanks D.J. Lege, P. Baggethun, E. Llewellyn and P.A. Hollinshead for their contribution to this work.

8 References

Choi, S.H., Cho, J.H., Barlat, F., Chung, K., Kwon, J.W. and Oh, K.H. (1999) Prediction of yield surfaces of textured sheet metals. *Metall. Trans.*, Vol. 30A, pp. 377-386.

Barlat, F. and Liu, J. (1998) Precipitate-induced anisotropy in binary Al-Cu alloys. *Mater. Sci. Eng.*, Vol. A257, pp. 47-61.

Winther, G., Juul Jensen, D. and Hansen, N. (1997) Modelling flow stress anisotropy caused by deformation induced dislocation boundaries. *Acta mater.*, Vol. 45, No. 6, pp. 2455-2465.

Rollet, A.D., Juul Jensen, D. and Stout, M.G. (1992) Modelling the effect of microstructure on yield anisotropy. *Proc. Of 13th Riso International Symposium on Materials Science* (edited by S. I. Anderson, et al.), pp. 93-109.

Molinari, A., Canova, G.R. and Ahzi, S. (1987) A self consistent approach of the large deformation polycrystal viscoplasticity. *Acta Metall.* Vol. 35, No. 12, pp. 2983-2994.

Hughes, D. A. (1993) Microstructural evolution in a non-cell forming metal : Al-Mg. *Acta Metall. Mater.* Vol. 41, No. 5, pp. 1421-1430.

TEXTURE DEVELOPMENT DURING EQUAL CHANNEL ANGULAR FORGING OF BCC METALS

S.R. AGNEW
Oak Ridge National Laboratory, Metals and Ceramics Division,
Oak Ridge, TN 37831, USA

Equal channel angular forging (ECAF) has been proposed as a severe plastic deformation technique for processing metals, alloys, and composites [e.g. Segal, 1995] (Fig. 1). The technique offers two capabilities of practical interest: a high degree of strain can be introduced with no change in the cross-sectional dimensions of the work-piece, hence, even greater strains can be introduced by re-inserting the work-piece for further deformation during subsequent passes through the ECAF die. Additionally, the deformation is accomplished by *simple shear* (like torsion of a short tube) on a plane whose orientation, with respect to prior deformations, can be controlled by varying the processing route. There is a nomenclature that has developed in the literature for the typical processing routes: A: no rotations; B_A: 90° CW (clockwise), 90° CCW (counterclockwise), 90°CW, 90° CCW…; B_C: 90° CW, 90° CW, 90° CW…; and C: 180°, 180°.… The impact of processing route on the subsequent microstructure [Ferasse, Segal, Hartwig & Goforth, 1997; Iwahashi, Horita, Nemoto & Langdon, 1996] and texture [Gibbs, Hartwig, Cornwell, Goforth & Payzant, 1998] has been the subject of numerous experimental studies.

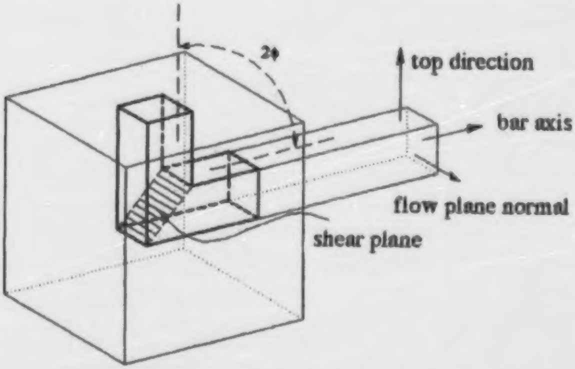

Fig. 1 Schematic of Equal Channel Angular Forging (ECAF) Die, where ϕ is the included channel half-angle. Also shown is the coordinate system referred to throughout this report.

An interesting feature of route C is its similarity to the torsion-reverse-torsion experiment analyzed by Cho, Park and Oh [1998] because the net strain (and rotation) is zero after each even pass. Route B_C is more complicated, however, it is similar in that the net strain is zero after every fourth pass. An important fact elucidated in a previous publication [Agnew, Kocks, Hartwig & Weertman, 1998] is that regardless of the processing route, each subsequent pass through the ECAF die represents a radical strain path change, even route A with no rotations of the work piece (Fig. 2). It was also shown that a viscoplastic self-consistent approach accurately predicted the texture evolution of FCC copper (Cu) during a series of ECAF passes [Agnew *et* al, 1998]. The current report is concerned with the simulation of texture development of BCC metals and comparisons are made with experimental textures of commercial purity iron (Fe).

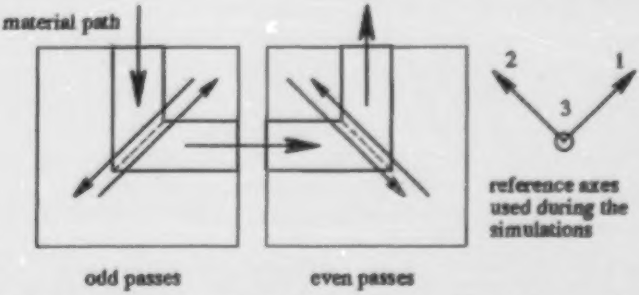

Fig. 2 Schematic of Route A ECAF processing demonstrates that the even with no sample rotations between passes, the shear plane during each subsequent pass through the die crosses that of the previous pass.

The viscoplastic self-consistent (VPSC) formulation of Lebensohn and Tomé [1993] was used to simulate the texture evolution during the ECAF process. The standard rate-sensitive constitutive equation is used:

$$D^c_{ij} = \dot{\varepsilon}_o \sum_s \left| \frac{m^s_{ij}\sigma^c_{ij}}{\tau^s_o} \right|^{n^s} m^s_{ij}\,\mathrm{sgn}(m^s_{ij}\sigma^c_{ij}) .$$

Where D^c and σ^c are the distortion rate and stress imposed on the crystal c, respectively; $\dot{\varepsilon}_o$ is the scalar strain rate; m^s is the Schmid tensor, which resolves the stresses and strains onto the s^{th} slip system; τ^s_o that system's critical resolved shear stress; n^s is the inverse of the rate sensitivity; and sgn(x) is simply the "sign" of x. If it is assumed that the solid is incompressible, this is a set of 5 equations with 10 unknowns (the components of D^c and σ^c.) Unlike the full constraints approach, which provides for 5 of the unknowns (the components of D^c) by assuming that each grain undergoes the same degree of strain, the self-consistent models provide 5 more equations relating the stresses and strains in the grains to those applied to the aggregate. Hence, the strain is distributed throughout the polycrystalline aggregate in a way that explicitly accounts for the anisotropic interaction between the grain and the aggregate at large. For details on the viscoplastic self-consistent approach, the reader is referred to seminal papers by Ahzi, Molinari, and Canova [1987] and Lebensohn and Tomé [1993].

The self-consistent approach may be considered an unnecessary computational burden when simulating texture evolution in cubic metals. Simpler models like the relaxed constraints models [e.g. Mecking, 1981, Van Houtte, 1981] are often sufficient. In the case of noncubic metals, such as hexagonal zirconium, the intrinsic plastic anisotropy of the individual grains demands explicit incorporation in the model [Lebensohn & Tomé, 1993]. In the current case, the grain's shapes become highly anisotropic. Though this also happens during other forms of deformation such as uniaxial tension or plane strain compression, the rigid body rotations associated with simple shear represent an additional factor, which is exacerbated in a multiple pass ECAF process.

The importance of the rigid body rotations which occur during simple shear was emphasized by Bolmaro and Kocks [1992] and provided an explanation of why simple shear textures tend to be weaker than pure shear textures at the same equivalent shear strain. Recall, the crystal rotation, Ω, that produces texture is the difference between the rigid body rotations, Ω^{rb}, that *each individual grain* undergoes, and the rotations induced by crystallographic slip, Ω^{c}. (i.e. $\Omega = \Omega^{rb} - \Omega^{c}$. Note this formula only holds for *differential* rotations or rotation *rates*.) For simple shear the rigid body rotations are monotonic, while those of multiple pass ECAF processing have radical changes in direction between passes.

PROCEDURE

In this study, the ECAF process was modeled as consisting of simple shear on the plane at which the two die channels intersect (Fig. 1). Because the die under consideration has an included angle, $2\phi = 90°$, the shear plane is inclined by 45° to the bar axis and the degree of imposed shear strain, $\gamma = 2$. To model subsequent passes through the ECAF die, the shear plane was simply rotated to the proper orientation, with respect to the sample coordinates (e.g. Fig. 2). For clarity, only the results of the route A simulations are presented. The BCC lattice was incorporated by designating the crystallographic shear directions as <111> and the shear planes as {110} and {112}. It was presumed that Schmid effects dominated (i.e. τ_o^s on the two plane types were assumed equivalent.) The simulations were initiated with a random texture consisting of one thousand discrete orientations. Each strain step corresponded to a von Mises equivalent true strain of 2.5% and the rate sensitivity was fixed at $m = 0.05$.

The simulated textures were compared with experimental data [Gibbs *et* al., 1998] in order to assess the current modeling approach. A complete description of the sample histories can be found in Gibbs *et* al. [1998]. The important figures will be repeated here to clarify the sample orientation. Primarily pole figures from the flow plane (Fig. 1) will be presented. This point of view makes the intrinsic symmetries of the imposed deformation obvious. There is a mirror plane within the flow plane and a two-fold rotation axis about the flow plane normal. In the previous study of Cu [Agnew *et* al., 1998], it was demonstrated that this lower symmetry inherent to simple shear (as compared to pure shear) persisted through the first 4 ECAF passes, though near-orthotropy was observed after 8 passes.

RESULTS

Similar to the results observed for FCC Cu, the texture resulting after one ECAF pass (Fig. 3a) is equivalent to a simple shear, $\gamma = 2$. Both the simulated data of this study (Fig. 3b) and experimental data from specially designed simple shear tests of Fe [Williams, 1962] enforce this conclusion.

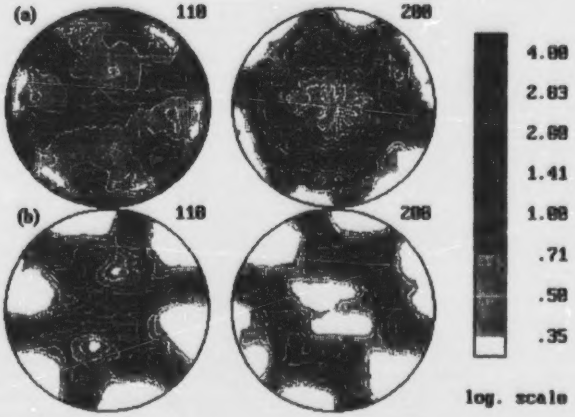

Fig. 3 (a) Experimental pole figure data of Fe after one ECAF pass (full pole figures calculated from harmonic expansion) [Gibbs *et* al., 1998]; and (b) VPSC simulated textures for a BCC material after a simple shear, $\gamma = 2$. In each case the pole figures have been rotated to correspond to ECAF geometry with bar axis right and top direction up.

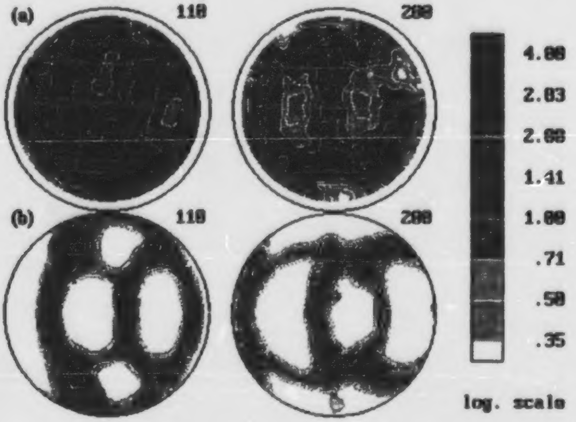

Fig. 4 Experimental [Gibbs *et* al., 1998] and simulated pole figure data after 2 ECAF passes (route A). The lower symmetry complicates calculation of the full pole figures from experimental data. These data are rotated 90° about the bar axis from the other figures in this report. (The bar axis is right and the flow plane normal is down.)

When analyzing route A processing, previous investigators [Gibbs *et* al., 1998] have focused on the top plane (Fig. 1 and 4) and the similarity to rolling textures. However, the deformation geometry only has the one mirror plane (contained by the flow plane) which can be utilized when analyzing the pole figure data from the top plane. After 2 passes the lower symmetry remains in the experimental data (Fig. 4a) and, qualitatively, all of the features in the experimental textures are correctly predicted by the VPSC code (Fig. 4b). For example, the two vertical bands in the {110} pole figures are asymmetrically disposed about the centerline (~20° ahead, ~40° behind) and the simulated data show the same features (Fig. 4). Viewing the simulated data from the flow plane after 2 and 3 passes (Fig. 5) illuminates the 2-fold symmetry referred to above. Interestingly, the location of the high intensity regions becomes essentially stable from this point on, and if viewing the top plane, the lack of orthotropy remains even after 9 passes, despite the fact that the shear plane keeps rotating back-and-forth as shown in Figure 2. At some level of strain, the simulated textures do become significantly sharper than the experimentally measured ones, and it is suggested that dynamic recovery or recrystallization may play an important role in "randomizing" the actual textures.

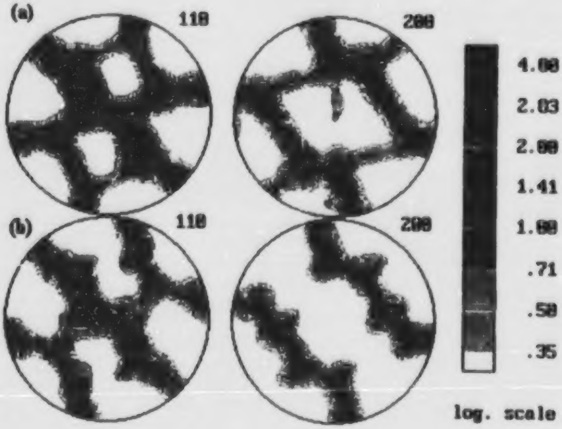

Fig. 5 Simulated textures of (a) 2 and (b) 3 ECAF passes. (Bar axis right, top direction up.)

CONCLUSIONS

This study has extended the earlier results found for FCC Cu to BCC Fe. Based on the similarity in the deformation textures, the ECAF process appears to enforce a simple shear on the plane at which the die channels intersect. Using the viscoplastic self-consistent formulation, it is possible to simulate the evolution of texture during a single ECAF pass (equivalent to torsion, $\gamma = 2$, for an included die angle of 90°). Additionally, by using the simulated results of previous deformations, subsequent ECAF passes can be adequately modeled by appropriately altering the shear plane and direction. This allows prediction of textures after a sequence of ECAF passes by route A or B_A. After a sequence of route A passes, there is some similarity to BCC rolling texture when viewing the top plane, however, after careful consideration of the deformation geometry and comparison with simulated data, a lower symmetry is apparent. Finally, it remains to be demonstrated that existing constitutive models can predict the texture evolution for strain paths after which the net strain is zero. This is the case for routes C (after each even pass) and B_C (after each fourth pass).

ACKNOWLEDGMENTS

The author is grateful for support from the Wigner Fellowship and help with the experimental data provided by E. A. Payzant at Oak Ridge National Laboratory. C. N. Tomé of Los Alamos National Laboratory kindly provided the VPSC code.

REFERENCES

Agnew, S. R., U. F. Kocks, K. T. Hartwig & J. R. Weertman, 1998, "Texture Evolution During Equal Channel Angular Forging and Dislocation Boundary Misorientations After Severe Plastic Deformation", *in Proc. 19th Risφ Inter. Symp. Mater. Sci.*, Eds. J. V. Cartensen *et* al., Risφ Nat. Lab., Roskilde, DK, pp. 201-207.

Ahzi, S., A. Molinari & G. R. Canova, 1987, "A Self-Consistent Approach of the Large Deformation Polycrystal Viscoplasticity", *Acta Metall.*, **35**, 2983-2994.

Bolmaro, R. E. & U. F. Kocks, 1992, "A Comparison of the Texture Development in Pure and Simple Shear and During Path Changes", *Scripta Metall. Mater.*, **27**, 1717-1722.

Cho, J.-H., S.-J. Park & K. H. Oh, 1998, "Analysis of Texture Evolution of Torsion-Reverse Torsion of Copper Rods", *Mat. Sci. Forum*, **273-275**, 649-654.

Ferasse, S., V. M. Segal, K. T. Hartwig & R. Goforth, 1997, "Microstructure and Properties of Copper and Aluminum Alloy 3003 Heavily Worked by Equal Channel Angular Extrusion", *Metall. Mater. Trans.*, **28A**, 1047-1057.

Gibbs, M. A., K. T. Hartwig, L. R. Cornwell, R. E. Goforth & E. A. Payzant, 1998, Texture Formation in Bulk Iron Processed by Simple Shear", *Scripta Mater.*, **39**, 1699-1704.

Iwahashi, Y., Z. Horita, M. Nemoto & T. G. Langdon, 1997, "An Investigation of Microstructural Evolution During Equal Channel Angular Pressing", *Acta Mater.*, **45**, 4733-4741.

Lebensohn, R. A. & C. N. Tomé, 1993 "A Self-Consistent Anisotropic Approach for the Simulation of Plastic Deformation and Texture Development of Polycrystals", *Acta Metall. Mater.*, **41**, 2611-2624.

Mecking, H., 1981, "Computer Simulation of Texture Development", in *ICOTOM 6*, Iron Steel Inst. Japan, Tokyo, pp. 53-66.

Segal, V. M., 1995, "Materials Processing by Simple Shear", *Mat. Sci. Eng.*, **A197**, 157-164.

Van Houtte, P., 1981, "Adaptation of the Taylor Theory to the Typical Substructure of Cold Rolled FCC Metals", in *ICOTOM 6*, Iron Steel Inst. Japan, Tokyo, pp. 428-437.

Williams, R. O., 1962, "Shear Textures in Copper, Brass, Aluminum, Iron, and Zirconium", *Trans. Metall. Soc. AIME*, **224**, 129-139.

THE INFLUENCE OF TRANSVERSE ROLLING ON TEXTURE AND MICROSTRUCTURE

J. POSPIECH, Z. JASIEŃSKI, A. LITWORA, A. PIĄTKOWSKI
Polish Academy of Sciences, Institute of Metallurgy and Material Science, Kraków, Poland
J. GRYZIECKI
Academy of Mining and Metallurgy, Department of Metal Forming, Kraków, Poland

Abstract

Texture and microstructure changes released by a slight (5% or 10%) transverse rolling of a CuGe8 sample unidirectionally rolled are analysed and compared with corresponding textures of unidirectionally and cross rolled materials. The paper refers to earlier studies by Korbel 1992.

Keywords: Recrystallization textures, rolling textures, shear bands, transverse rolling

1 Introduction

A change in the strain path (additional rolling along the transverse direction) leads to destabilization of the substructure formed during earlier unidirectional rolling. The consequence is the unstable plastic flow of the metal which, according to Korbel 1992, may be of catastrophic character. This implies that already a relatively small amount of deformation imposed on the metal along new rolling direction may lead to drastic changes in the substructure, to destabilization of the dislocation configurations and local barriers in the dislocation network. This gives rise to local rearrangement and highly cooperative movements of dislocations resulting in micro and macro shear band formation. From Korbel's investigations on copper it follows that the destabilization of the substructure is accompanied by distinct texture effects.

Taking into account also the microstructures observation it has been found that in the process of the observed texture changes the shear banding is the dominant mode of deformation. The amount of shear in the band and the orientation of the shear system in the sample along with the external constrains are responsible for the texture changes. These texture changes are then considered as the rotation of subgrains around the axis perpendicular to the shear vector and to the normal to the shear plane. The axis of such a rotation would be situated near the direction of the primary unidirectionl rolling.

Destabilization of the substructure caused by deformation along a new rolling direction affects the deformation texture and consequently must also influence the recrystallization texture. The destabilization disturbs the substructure as well as the distribution of recrystallization nuclei induced by conditions of the former deformation mode.

The effect of the change of the strain path on texture has not yet been fully recognized. This refers in particular to metals of small stacking fault energy (SFE). The object of the investigations in the present study are the texture and microstructures of rolled CuGe8 alloy (Gryziecki et al. 1991, Eichelkraut et al. 1984). The considerations will refer to texture changes initiated by transverse rolling with a relatively small amount of 5% or 10% reduction preceded by unidirectional rolling of 65% or 60% reduction respectively. For comparison, also textures of cross rolling will be considered. Some results illustrating the effect of the change of the deformation path (the rolling direction) on the microstructure and texture of the CuGe8 alloy will be shown.

2 Experimental

The examined material was copper alloy with an addition of 8 wt % of germanium, prepared from components of 99.99% purity. Such an alloy is characterized by low SFE amounting to about 4mJ/m^2.

After thermomechanical treatment of the CuGe8 alloy two different kinds of sheets have been obtained:

A- with small mean grain size of 50μm and sheet thickness of 3 mm

B- with large mean grain size of 600μm and sheet thickness of 6 mm

The sheets were next cold rolled in a triple way:

1- both A and B unidirectionally rolled up to 70% reduction,

2- both A and B cross rolled up to 70%,

3- sheet A with a 5% transverse rolling after unidirectional 65% reduction and sheet B with 10% transverse rolling after unidirectional 60% reduction.

One part of sheets A and B from each deformation mode was annealed up to the state of primary recrystallization. For each sample X-ray pole figures have been measured from which texture functions ODFs were calculated using the ADC method. Metallographic observations have been performed for the series B. All ODFs are presented in the same reference system of the unidirectional rolling.

3 Results and discussion

3.1 Microtextures and textures after rolling

Figs 2 a, b, c show the observation results of the rolled sample B in an optical microscope. The observation plane of the microstructure is perpendicular to the transverse direction TD of the final rolling. The symbols used are illustrated by the outline in Fig. 1, which shows the scheme of the geometry of shear bands SB$_1$ formed during unidirectional rolling (Fig. 2a), the shear bands SB$_2$ formed during additional transverse rolling (Fig. 2b), and the shear bands SB$_1$ and SB$_2$ formed during cross rolling (Fig. 2c). Observation of the microstructure in Fig. 2b shows clearly that additional transverse rolling with small reduction induces new shear bands SB_2 (of two intersecting families) visible together with the trace (parallel to RD_2) of old bands SB_1 formed during unidirectional rolling. The traces of the shear band SB_1 and the two families of shear bands SB_2 observed after cross rolling (Fig. 2c) are more distinct than in the former case (Fig. 2b) after additional transverse rolling.

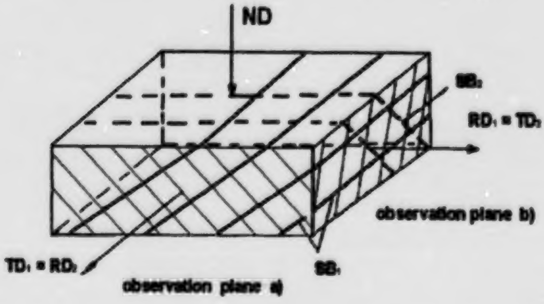

Fig. 1: Scheme of a rolled sample

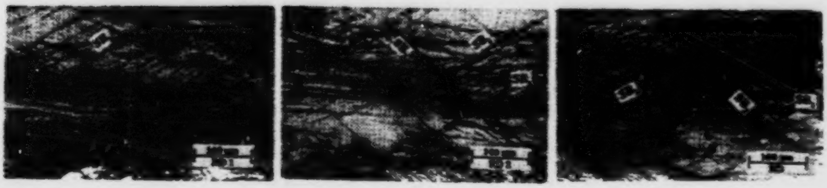

a b c

Fig. 2: Microstructures of CuGe8 samples rolled up to 70% reduction;
a) unidirectionally rolled, b) 60% unidirectionally rolled + 10% transversely rolled, c) cross-rolled

The successive Figures 3a, b, c show the texture functions (ODFs) for the samples of series **A** (small sheet thickness): a) rolled unidirectionally up to 70%, b) rolled unidirectionally up to 60% and additionally 10% transverse rolled, and c) cross-rolled up to 70%. Similarly, the figures 4a, b, c show the corresponding ODFs for the samples of series **B** (greater sheet thickness).

Figures 3a and 4a show typical rolling textures of f.c.c. metals with low SFE in the range of medium reductions. Characteristic are here the twin areas originating from the components C={112}<111> and S={213}<364> around the {111}<uvw> positions, in which the twin planes have become parallel to the rolling plane, and the twins {114}<172> from the Bs={110}<112> component. The twinning is much more advanced in the sample **B** because of its larger grains.

Fig. 3b and Fig. 4b show that the small amount 5% or 10% of transverse rolling reduction introduces disturbing changes in the earlier formed texture, from diminishing of the S position up to complete disappearance in the broad surroundings of the

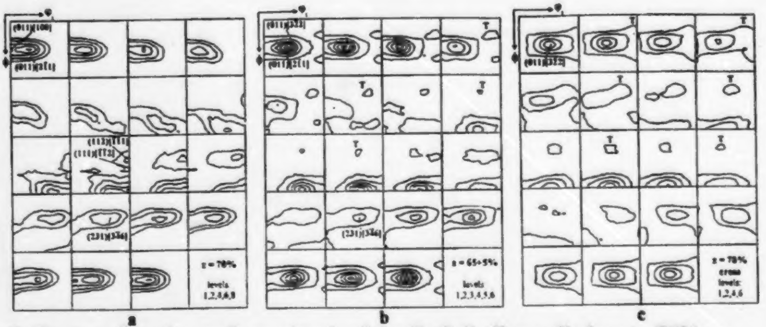

Fig. 3: Texture functions of samples A of the CuGe8 alloy rolled up to 70%.

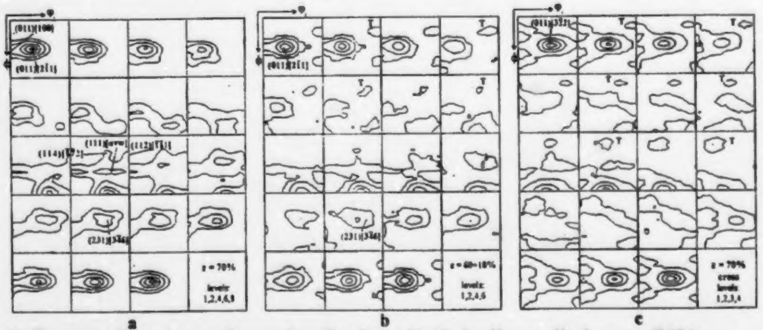

Fig. 4: Texture functions of samples B of the CuGe8 alloy rolled up to 70%;

a) unidirectionally rolled, b) 65% or 60% unidirectionally rolled + 5% or 10% transversely rolled, respectively, c) cross-rolled.

C component. The Goss component {011}<100> disappears and the Bs component shifts towards the symmetric {011}<322> position. Numerous new twin positions T of the Bs component and of its surroundings can be recognized.

It can be seen that cross rolling does not introduce anything significant to the textures (shown in Figs 3c or 4c) in comparison with the textures affected by additional slight transverse rolling (in Fig. 3b or 4b).

The texture effects induced by small additional transverse rolling observed for CuGe8 correspond to those described for copper by Korbel 1992. From among the three components of copper C, S, and Bs only the Bs component remained stable. These destructive texture effects have been accounted to the rotation of the crystallites bounded by shear bands under the constraint imposed by rolling. The new shear bands released by the additional transverse rolling which have been observed in copper are also seen in the microstructure of the CuGe8 sample on Fig. 2b. The above explanation seems to be responsible. It is hardly to assume that the observed great changes in the texture, which are released by relatively small transverse reduction, could be realized by a homogeneous crystallographic slip. On the other hand, however, the alternative deformation mechanism, the homogeneous crystallographic slip cannot be fully excluded. The texture components C, S and Bs of the unidirectional rolling change into unstable {112}<110>, {213}<013> and {011}<111>, respectively after

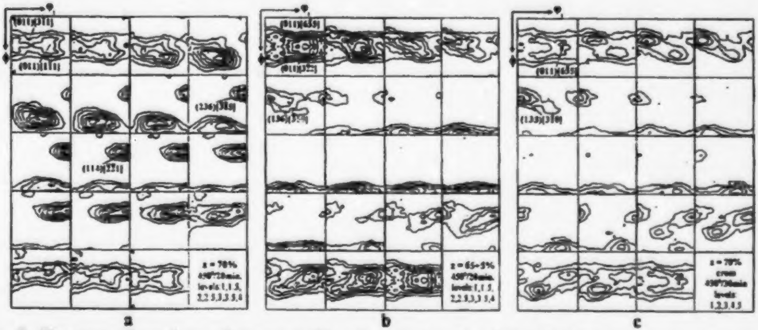
a b c

Fig. 5: Texture function of recrystallized samples A of the CuGe8 alloy

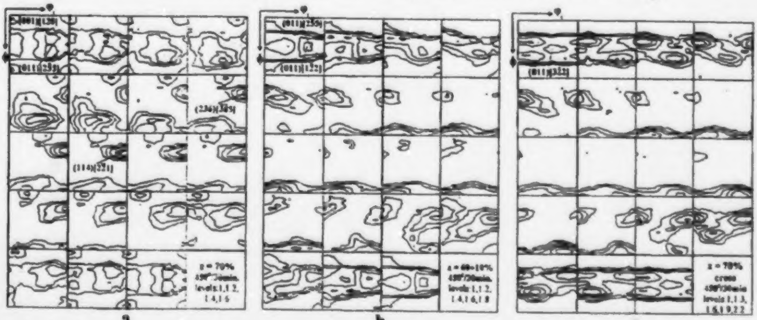
a b c

Fig. 6: Texture functions of recrystallized samples B of the CuGe8 alloy;

a) unidirectionally rolled, b) 65% or 60% unidirectionally rolled + 5% or 10% transverse rolled, respectively, c) cross-rolled

the rotation of the rolling direction. Model calculations (K. Wierzbanowski and Z. Jasieński 1977) have shown that the {112}<110> is very sensitive and shifts towards the position {110}<112> which in the reference system of the unidirectional rolling (in which the ODF is presented) corresponds to the diminishing of the {112}<111> in favour of the {110}<111>. This would be in agreement with the results shown in Fig. 3b and Fig. 4b. It should be added, however, that the calculated texture effects have been achieved not after small but after strong rolling reduction.

3.2 Textures after recrystallization

The recrystallization textures of samples A and B rolled up to 70% (Fig.5a and Fig.6a) are typical. The brass recrystallization component Bs/R = {236}<385> dominates together with the Ts={114}<221> position which is in twin relation to the Goss component. These texture components are much more pronounced in the sample A with the small grain size. The Bs/R component is thought to be a result of combined mechanism of oriented nucleation and oriented growth. The nuclei of the Bs/R component are recrystallization twins to orientations from the area Goss/Bs of the α fibre (Sztwiertnia and Haessner 1994). The nuclei grow according to oriented growth theory which favour the Bs/R orientation.

The recrystallization textures after additional small amount of transverse rolling shown on Fig. 5b and 6b differ essentially from the recrystallization textures of unidirectionally rolling. First of all, the main recrystallization brass component Bs/R and the Ts component which have been dominant in the unidirectionally rolled sample are not observed. This phenomenon is much more pronounced in the thinner sample **B** with smaller grain size and smaller, only 5% additional transverse rolling reduction. A widely scattered orientation concentration around the shifted Bs position dominates which indicates the inheritance mechanism of texture formation. Numerous new twins stemming from orientations around Bs are also observed.

In the deformation textures prior to recrystallization it could be noticed that the small additional transverse rolling leads to disappearance or diminishing of the areas of orientations (between the Goss and the Bs positions) from which the above mentioned main recrystallization components T_s and B_s/R are created by twinning.

4 Conclusions

Destabilization of the substructure caused by slight transverse rolling after unidirectional rolling of CuGe8 leads to significant changes of the earlier formed texture: the elimination of the C component and stabilization of the Bs component shifted toward the symmetric {011}<322> position. This position is achieved during cross rolling. According to Korbel's suggestion it is assumed that the observed texture effects can be due to the shearing in the shear bands released in the action of destabilization.

Drastic changes in the textures are also observed after annealing. The recrystallization texture after additional transverse rolling does not contain the earlier observed main {236}<285> - and also the {114}<221> components. This is explained by the destruction of nuclei and elimination of the Goss component existing in the sample after unidirectional rolling.

5 References

Eichelkraut, H., Hirsch, J. and Lücke, K. (1984) Rolling and recrystallization textures in copper-germanium alloys. *Z. Metallkde*, Vol. 75, pp. 113-123.

Gryziecki, J., Truszkowski, W., Pospiech, J. and Jura, J. (1991) Development of textures and microstructures during rolling of CuGe8 alloy. *Textures and Microstructures*, Vol. 14-18 pp. 1061-1066.

Korbel, A. (1992) Mechanical instability of metal substructure - catastrophic plastic flow in single and polycrystals. *Proc. of the Z.S Basinski Intern. Symp. on Crystal Plasticity*, Kingston, Ontario, pp. 43-86.

Sztwiertnia, K. And Haessner, F. (1994) In situ observation of initial stage of recrystallization of highly rolled phosphorus copper. *Materials Science Forum, Vol. 157-162 pp. 1069-1074.*

Wierzbanowski, K. and Jasieński, Z. (1977) Simulation numérique de la déformation d'un cristallite individuel au cours de laminage. *Bull. de l'Academie Polonaise de Sciences*, Vol. 25, pp. 67-79.

EFFECT OF TEXTURE ON UNIXIAL TENSION IN AA3003 SHEET WITH INHOMOGENEOUS TEXTURE.

J.-H. Cho, S.-J. Park, S.-H. Choi* and K.H. Oh

School of Materials Science and Engineering, Seoul National University
San 56-1 Shinrim-dong, Kwanak-ku, Seoul 151-742, Korea
*Aluminum Company of America, Alcoa Technical Center,
100 Technical Drive, Alcoa Center, PA 15069-0001, U.S.A.

Abstract

The development of texture during tension in Aluminum alloy sheet with inhomogeneous texture through thickness direction is analyzed. In the specimen parallel to RD, initial rotated Goss in the center are weakened after tension and (100) fiber in the surface is changed to cube, copper, brass, P components. In the specimen parallel to TD, cube, rotated copper, {112}<110> and brass increase in the surface and rotated Goss in the center slightly decrease. The variation of width displacement through thickness direction during tension is larger in RD than TD. Using the finite element method (FEM) with a rate-dependent polycrystalline model of crystal plasticity, both texture evolutions and variation of width displacement are predicted and compared with the measured results. The experimental textures are similar to the calculated ones with FEM. The variation of width displacement is related with texture components through thickness direction. The variation of width displacement is well predicted with the crystal plasticity FEM.

Keywords: Finite element, Crystal plasticity, Texture, Tension, Rate sensitivity

1. Introduction

The plastic anisotropy of sheet metals mainly results from the presence of crystallographic texture and it has a large influence on the subsequent forming processes. Various models have been proposed to predict the plastic behavior of the textured materials. Basically, there are two possible approaches to account for the macroscopic behaviors of polycrystalline material in finite element simulation; the phenomenological approach and the micromechanically based approach. The phenomenological approach makes use of phenomenological yield condition, flow rule and work hardening law to describe the material behaviors. The micromechanically based plasticity models can take into account the crystallographic texture and are based on the rate-insensitive materials behavior (Y. Zhou, 1997; Van Bael, 1994). Asaro and Needleman have developed an elastic-plastic, rate-dependent model (R.J. Asaro and

Needleman, 1985). This model differs from the classical rate-independent model in that there is no yield condition. Instead, plastic flow is assumed to occur at all non-zero values of stress. To predict the global behavior of the polycrystal, they follow the Taylor's assumption that all grains have equal volume, and that the deformation gradient within each grain has a uniform value throughout the polycrystalline aggregate. Kalidindi *et al.* include the polycrystalline constitute model of Asaro and Needleman to time-integration procedure in the finite element simulation and calculated the evolution of the crystallographic texture (S. R. Kalidindi *et al.*1992).

The purpose of this paper is to analyze the evolution of texture in Aluminum alloy during tension and the effect of texture on tensile deformation through thickness direction. Using finite element method of crystal plasticity, the texture evolution and the variation of width displacement are calculated and compared with the experimental results.

2. Experimental procedure

Aluminum alloy 3003 sheet of 2.6-mm thickness was used in this study. The tensile specimen was prepared according to the ASTM E8. Pole figures were measured in Seifert D3000 PTS X-ray diffractometer to characterize crystallographic texture along thickness direction. The parameter s, the normalized thickness, in Fig. 1 is given $s = \Delta h / 0.5 t_o$, where Δh is a distance from the center of sheet to interested surface, and t_o is an initial thickness. From the three (111), (200) and (220) incomplete pole figures, the orientation distribution function (ODF) was calculated using the WIMV method with conditional ghost correction. After tensile deformation, the variations of width displacement through thickness direction were measured with the surface roughness measurement machine, SE1100.

3. Constitutive model and finite element calculation

Asaro and Needleman assume that all grains have equal volume, and that the local deformation gradient in each grain is homogeneous and identical to the macroscopic deformation gradient **F** at the continuum material point level. With $\sigma^{(k)}$ denoting the Cauchy stress in the *k*th crystal, these assumptions lead to

$$\bar{\sigma} = \frac{1}{N}\sum_{k=1}^{N}\sigma^{(k)} \tag{1}$$

where $\bar{\sigma}$ is the volume-averaged stress, and N is the total number of grains comprising the material point.

The constitutive equation for the stress in each grain can be taken as

$$\sigma^{*} = C^{E}[E^{*}] \tag{2}$$

where E^{*} is an elastic strain measure, C^{E} is a fourth order elasticity tensor and σ^{*} is the stress measure, which is the elastic work conjugate to the strain measure, $\mathbf{E}^{*}$. The plastic shear rate on the slip system α, $\dot{\gamma}^\alpha$ is given in terms of the resolved shear stress τ^α by using the power law relationship.

$$\dot{\gamma}^\alpha = \dot{\gamma}_0^\alpha \left|\frac{\tau^\alpha}{\tau_0^\alpha}\right|^{\frac{1}{m}} sign(\tau^\alpha) \qquad (3)$$

where γ_0^α, τ_0^α and exponent, m are the reference shear rate, the reference critical resolved shear stress and the strain rate sensitivity, respectively. The detailed calculation procedures are referred to Kalidindi's work (S. R. Kalidindi 1992).

In the finite element calculation, an aggregate of 200 crystals is given to each element to describe the texture of Al alloy sheet. The stress and strain are solved in commerial FEM code, ABAQUS(ABAQUS 1998) by using user subroutine UMAT. The elastic modulus and Poisson ratio are set to be 200GPa and 0.3 respectively. The reference shear rate and the reference critical resolved shear stress are assumed to be constant during calculation. The rate sensitivity, m is given as 0.05

4. Result and discussion

Fig. 1 shows (111) pole figures of the initial AA3003 sheet, which were measured at the five positions through thickness. Fig. 1-a) shows the (111) pole figure at a surface having a weak (100) fiber. Fig. 1-b) shows the (111) pole figure at s=0.75 and c), d), e) are at s=0.5, s=0.25, and s=0.0, respectively. At the center of the sheet, near-Goss component develops. The initial sheet has a texture variation along the thickness direction.

Fig. 2 shows the geometry of the tensile specimen and three dimensional finite element meshes. The tensile specimen has a four-fold symmetry and the quarter section is taken as the calculation domain. The number of FEM meshes along thickness direction is 5 and each element contains the measured texture data which is represented by a set of 200 single crystals calculated from the ODF. The boundary condition and loading directions are given in Fig. 2.

Fig. 3-a), b), c) show the original mesh, the deformed mesh along RD and TD respectively. After tensile deformation along RD, the thickness displacement is uniform along the width direction but the width displacement is not uniform along the thickness direction. The magnitude of width displacement at the center is larger than that at the surface. There is a steep gradient in width displacement in RD. After tensile deformation along TD the thickness displacement is uniform along the width direction. The magnitude of width displacement along the thickness direction at a surface is slightly larger than that at the center.

Fig. 4 shows the measured relative width displacement along thickness direction together with the calculated relative width displacement from FEM. The measured relative displacement is in good agreement with the calculated data. The variation of width displacement is related with plastic strain ratio, R. The large plastic strain ratio gives rise to the large contraction along width direction, i.e. large width strain and displacement. The measured (111) pole figure shows that at the center of AA3003 sheet, rotated Goss component, {110}<011> develops and at the surface weak (100) fiber develops. The rotated Goss component shows the plastic strain ratio of near 10 (Choi 1999) in the rolling direction (RD), which represents the large contraction along width direction during RD tension. The plastic strain ratio of (100) fiber is smaller than that of Goss component. Therefore the tensile deformation along RD gives rise to the large contraction at the center due to the large R-value. But the R-value of rotated Goss component is about 1.0 in the transverse direction (TD) and R-value of (100) fiber is slightly larger than that of Goss component. Thus the tensile deformation along TD gives rise to the slightly large contraction along width direction at the surface.

Fig. 5 shows the (111) pole figures measured after tensile deformation along RD and TD. The rotated Goss component at the center decreases and (100) fiber changes into cube, copper, brass and P after tensile deformation along RD. During tension along TD rotated copper, {112}<110>, cube and brass increase in the surface and the rotated copper, {112}<110>, cube, P and brass increase in the center. The rotated Goss in the center slightly decreases but the quantity is smaller than that of RD. Fig. 6 shows the calculated (111) pole figures from FEM. In the surface and center element indicated in Fig. 3 the calculated texture results are taken. The main components of the calculated pole figure from FEM show a good agreement with those of the measured (111) pole figures.

5. Conclusions

The texture evolution during tension in AA3003 sheet is analyzed. Using the finite element method with a large deformation, elastic-plastic, rate-dependent polycrystalline model of crystal plasticity, texture evolution and variation of width displacement is calculated and compared with the measured results. During tension along RD initial rotated Goss in the center are weakened and (100) fiber in the surface changes into mainly cube and copper component. During tension along TD, rotated copper, {112}<110> and cube, brass increase both in the surface and center. The rotated Goss in the center slightly decreases. The variation of width displacement through thickness direction can be explained by texture component and it is well predicted with finite element method of crystal plasticity.

6. References

ABAQUS standard user manual (1998) Hibbitt, Karlsson & Sorensen.

A.Van Bael. (1994) Anisotropic yield loci derived from crystallographic data and their application in finite-element simulations of plastic forming processes, Ph.D. thesis, K.U.Leuven, Belgium

Choi S.-H.,Cho J.H., Barlat F., Chung K., Kwon J.W. and Oh K.H. (1999) Prediction of Yield Surfaces of Textured Sheet Metals, *Met. Trans. A*, **30A**, pp. 377-386

Choi S.-H., and Oh K.H. (1997) Rate sensitive analysis of texture evolution in fcc Metals *Metals and Materials*, **3**, pp. 252-259.

R. J. Asaro and A. Needleman (1985), Texture development and strain hardening in rate dependent polycrystals, *Acta metall.* **33**, pp. 923-953

S. R. Kalidindi, C. A. Bronkhorst and L. Anand (1992) Crystallographic texture evolution in bulk deformation processing of fcc metals. *J. Mech. Phys. Solids* **40**, pp. 537-569

Y. Zhou, J. J. Jonas, L. Szabó, A. Makinde, M. Jain and S. R. MacEwen, Incorporation of an anisotropic (texture-based) strain-rate potential into three-dimensional finite element simulations.

Acknowledgement

The authors wish to acknowledge the financial support of the Korea Research Foundation made in the program year of (1998)

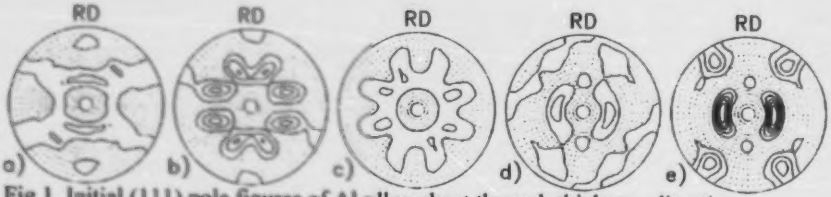

Fig 1. Initial (111) pole figures of Al alloy sheet through thickness direction
a) s=1.0(surface) b) s=0.75 c) s=0.5 d) s=0.25 e) s=0.(center)
Contours: 1, 1.5, 2, 2.5, 3, 3.5.

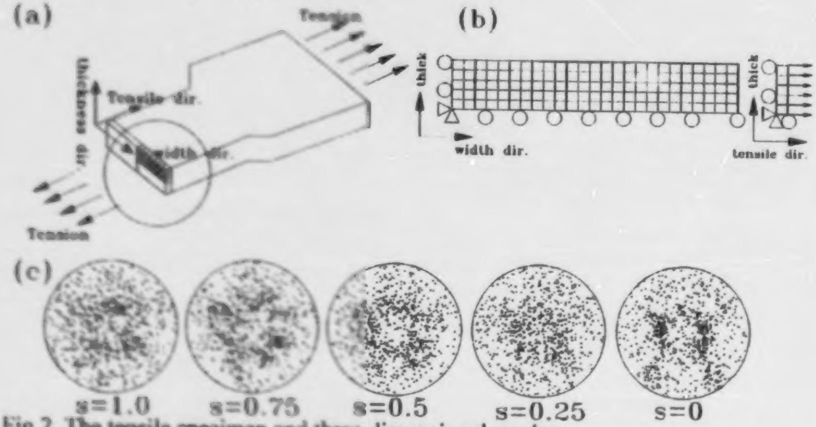
(a)
Tension
thickness dir.
Tensile dir.
width dir.
Tension
(b)
thick
width dir.
thick
tensile dir.
(c)
s=1.0
s=0.75
s=0.5
s=0.25
s=0

Fig 2. The tensile specimen and three dimensional meshes
a) tensile specimen b) Initial meshes and directions
c) 200 single crystals concerned with thickness direction

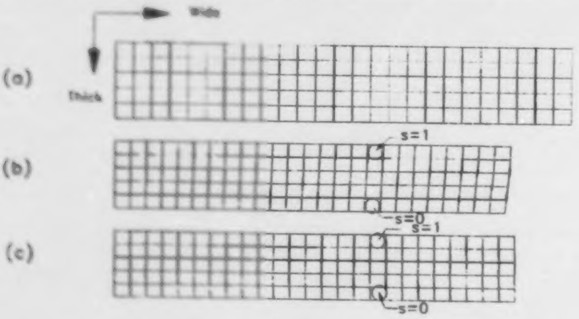
Wide
Thick
(a)
(b)
s=1
s=0
(c)
s=1
s=0

Fig 3. The deformed meshes together with the original ones from FEM
a) initial mesh b) deformed mesh along RD c) deformed mesh along TD

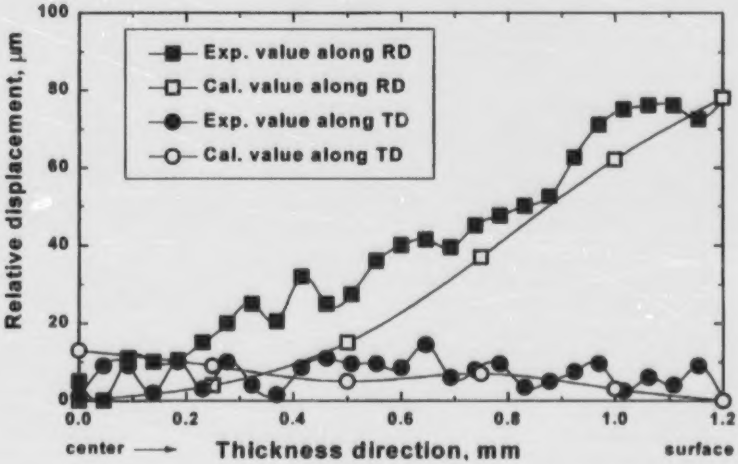

Fig 4. Relative variation of width displacement along thickness direction.

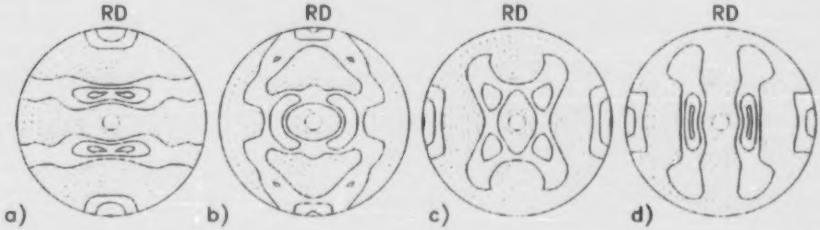

Fig 5. The experimental (111) pole figures during tension along a) RD at s=1.0 b) RD at s=0. c) TD at s=1.0 d) TD s=0. Contours: 1, 1.5, 2, 2.5.

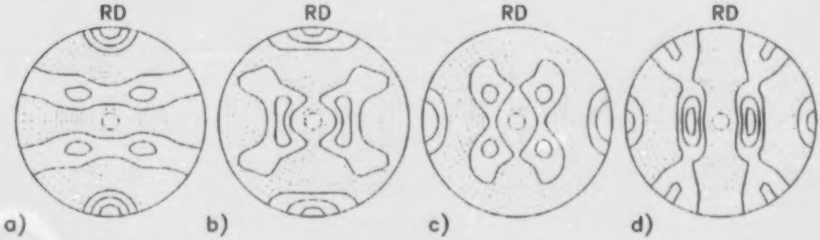

Fig 6. The calculated (111) pole figures from crystal plasticity finite element method a) RD at s=1.0 b) RD at s=0. c) TD at s=1.0 d) TD s=0. Contours: 1, 1.5, 2, 2.5.

STRAIN HARDENING EFFECTS ON TEXTURE FORMATION IN ZIRCONIUM ALLOYS.

A.A. POCHETTINO and P. SANCHEZ
Departamento Materiales, Comisión Nacional de Energía Atómica, Buenos Aires, Argentina
Universidad Nacional de General San Martín, San Martín, Argentina

Abstract

Strain hardening effects on texture generation in Zr alloys are studied considering the hardening mechanisms for different deformation modes in grains and also the topology of the single crystal yield surface, which is associated to the possible active deformation modes. Our results put in evidence that differences in rolling textures (L and T textures) can be related to hardening parameters.

Keywords: Strain hardening, texture, yield surface, Zirconium.

1. Introduction

The description of texture evolution in hexagonal close packed (hcp) materials such as Zirconium alloys, presents more difficulties than in the case of cubic materials (bcc or fcc). In fact, in hcp materials it is necessary to take into account the effect of the different deformation modes which can be activated in grains. In the case of Zr alloys deformed at room temperature, the prismatic <a> or {1100}<1120> slip is the most active deformation mode in grains. Nevertheless, since prismatic slip does not suffice for accommodating an arbitrary imposed strain in grains, other deformation modes must be activated: {1012}<1011> tensile twinning and {1101}<1123> compressive twinning and the pyramidal slip{1011}<1123> (Pochettino et al. 1994).

In hcp materials not only the hardening mechanisms should be considered. In fact, together with hardening description in grains, the Critical Resolved Shear Stress (CRSS) values for different deformation modes must also verify well established relationships defined by the topology of the single crystal yield surface. Tomé and Kocks 1985 have studied and defined topological maps which identify characteristic regions of the single crystal yield surface. Inside these regions, which are associated to a range of CRSS values for deformation modes on Zr, only a given set of deformation modes can be activated.

As in the case of cubic materials, the viscoplastic selfconsistent model was used in order to describe texture generation of Zirconium alloys at room and high temperatures, showing good agreement between predictions and experimental results (Pochettino et al. 1994, Lebensohn et al. 1994). Nevertheless, strain hardening processes and their possible effects on the mechanical properties and the texture generation for hcp materials have not been discussed in hcp materials.

The purpose of this presentation is to contribute to the knowledge of strain hardening effects on texture generation in Zr alloys. The study considers:

- Strain hardening mechanisms for different deformation modes in grains.
- The topology of the single crystal yield surface.

2. Strain hardening mechanisms

The hardening in grains was described using an approach rather similar to that proposed by Bronkhorst et al. 1992 and also used by Toth 1996 to analyze the effect of microscopic hardening in deformation texture development. The proposed hardening law considers self and latent hardening and was modified in order to account the activity of the different deformation modes. The Critical Resolved Shear Stress (CRSS) value for each deformation system active in each grain (τ_0^i) can be written as:

$$\tau_0^i = \Sigma_j h^{ij} |\gamma_j| \qquad i, j = 1,n \tag{1}$$

$$h^{ij} = C^{ij} (\gamma^i)^{\eta - 1} \tag{2}$$

where n is the total number of slip and twinning systems considered in the analysis, h^{ij} is a n x n hardening matrix which describes the interaction between these systems, η the hardening coefficient for each deformation mode in grains and γ^i the amount of slip (or twinning) accumulated by each system. According to the above definitions, the microscopic hardening parameters to be determined are: τ_0^i , η, C^{ij}. They can be considered as physical parameters of the material and, consequently, their values are independent of the macroscopic deformation mode. In this work, the parameters were adjusted from the best fitting of experimental and theoretical predictions of texture development in rolling and tensile tests in textured samples. In order to handle a reduced and comprehensible number of parameters, only self hardening effects were considered in this work.

3. Topology of the single crystal yield surface.

The results of the studies of topological maps performed by Tomé and Kocks 1989 indicate that during room temperature rolling, the active deformation modes are associated to the region 2 of the topological map, Fig. 1. Nevertheless, a detailed study

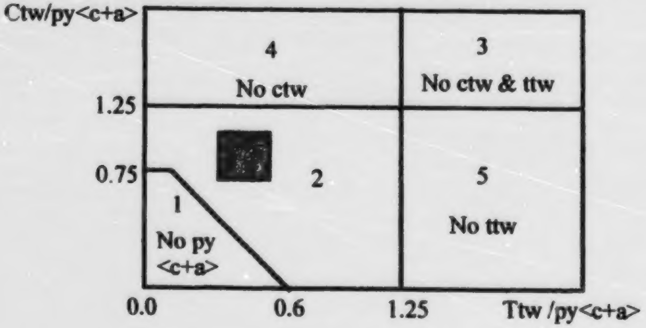

Fig 1: Region 2 of the topological map of the single crystal yield surface. The shaded region corresponds to CRSS values assuring the best agreement between predictions and experiments

of predicted textures using the self consistent model and CRSS values corresponding to this region, allow us to define that the best agreement between predicted and experimental textures is obtained when the CRSS values (τ) used in predictions corresponds to a sub-region defined by the following relationships:

$0.7 < (\tau_{ctw} / \tau_{py}) < 0.9$

$0.3 < (\tau_{ttw} / \tau_{py}) < 0.5$

$(\tau_{py} / \tau_{pr}) > 3$

being pr = prismatic slip, py = pyramidal <c+a> slip, ttw = tensile twinning, ctw = compressive twinning. The CRSS values used in our description of the plastic behavior of Zirconium, including hardening, must verify the above relationships.

4. Results and discussion

4.1. Microscopic hardening coefficients

Microscopic hardening parameters were adjusted in order to assure the best fitting between experiments and simulations of the mechanical behavior of Zr alloys under different solicitations. These experiments were:

- Tensile tests along rolling and transverse direction in textured Zr alloys which present initially the well known "T texture", i.e. the maximum of the (0002) pole density is placed in the Normal Direction (ND)-Transverse Direction (TD) plane at ≈30-35° from the ND (Charquet et al. 1987).
- Tensile tests along rolling and transverse direction in samples having a "(0002) pole central or C texture", i.e. samples presenting a symmetric distribution of (0002) poles around the ND (Charquet et al. 1987).
- Cold Rolling: In this case, we try to assure the correct description of textures after cold rolling process.

In order to assure a correct handling of the coefficients and reduce the number of parameters to be adjusted, some simplifications were done in a first step of the calculations. In fact, self-hardening was assumed for each prismatic slip system (h_{ii} with

i=1,3, η_{pr}) while for pyramidal slip (h_{44}, η_{pyr}) and tensile (h_{55}, η_{ttw}) and compressive twinning (h_{55}, η_{ctw}) a mean value coefficient was assumed for each deformation mode (not for each deformation system). The values associated to these coefficients are presented in Table 1.

Table 1: Coefficients h_{ij} and micro-hardening exponents η for the hardening law given by eq.1

	h_{11}-h_{33}	h_{44}	h_{55}	h_{66}	η_{pr}	η_{pyr}	η_{tt}	η_{ctw}
Case 1	1.31	3.81	1.59	3.06	0.10	0.15	0.15	0.15
Case 2	1.12	3.57	1.60	3.21	0.07	0.07	0.10	0.10

4.2. Rolling texture predictions

The values presented in Table 1 correspond to two different cases. Even if the h_{ij} values do not seem to present significant differences between them, the relationships between the values of the microscopic hardening exponent values η differ essentially. In the first case, the value of η corresponding to the pyramidal <c+a> slip is equal to the exponent corresponding to ttw and ctw modes. In the second case, the value of the hardening coefficient for pyr <c+a> slip is equal to that corresponding to the prismatic slip mode. These two sets of values give quite similar rolling textures, Fig. 2 (a-b), which are in good agreement with experimental results. Nevertheless, a difference between predicted textures can be observed. In fact, in case 2, as a consequence of the lower hardening exponent η presented by the pyr <c+a> slip, the mean activity of this deformation mode is higher than in case 1 (Table 2).

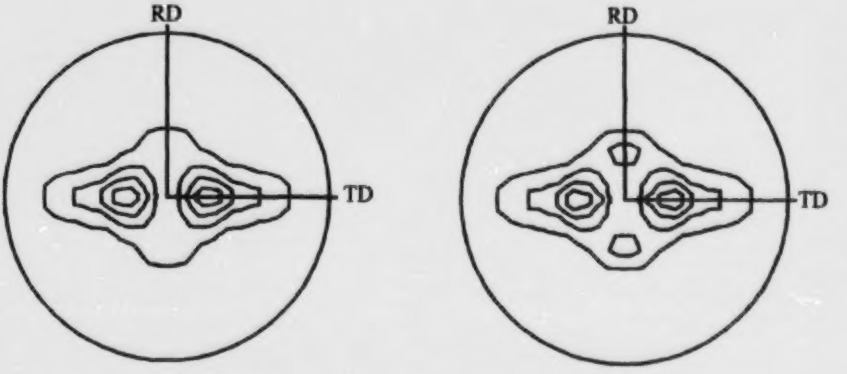

(a) (b)

Fig. 2: Predicted (0002) pole figures, (a) case 1 and (b) case 2

This difference in activities produces a reinforcement - typical of L textures - of the (0002) pole density at ≈10-15 from the ND in the direction defined by ND-RD, Fig. 2-

b. This result is interesting because differences in the microstructure of the material, introduced by the alloy composition or by thermomechanical treatments, could produce differences in the hardening mechanisms and, particularly, in the value of the hardening coefficient η for each deformation mode. This fact could contribute to explain differences in cold rolling textures observed in Zr alloys (L and T textures) (Charquet et al. 1987).

Table 2: Mean values of the activity (in the polycrystalline material) for the different deformation modes during rolling.

	Pr	pyr<c+a>	ttw	ctw
Case 1	59%	7%	15%	19%
Case 2	62%	9%	13%	16%

4.3. Macroscopic hardening

The predicted hardening coefficients describing the macroscopic behavior of the material were obtained from the equivalent stress-strain curves and, in the case of tensile tests, they are compared with experimental values (Table 3).

Table 3: Macroscopic hardening coefficients. Experimental and predicted values from tensile tests along Rolling (RD) and transverse direction (TD) for different textures (P and C textures).

Texture	Test direction	n (exp)	n (pred)
T	RD	0.13	0.11
T	TD	0.102	0.09
C	RD	0.127	0.11
C	TD	0.124	0.11

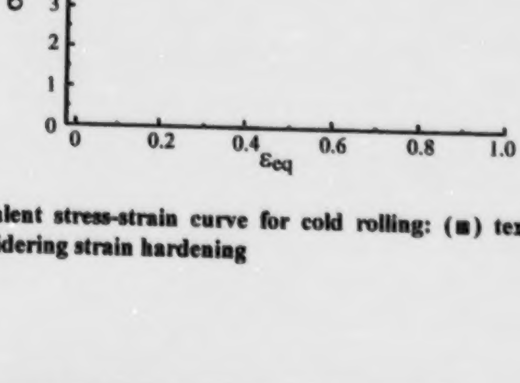

Fig. 3: Equivalent stress-strain curve for cold rolling: (■) textural hardening (n=0), (•) considering strain hardening

It can be observed in Table 3 that the predicted values of the macroscopic hardening coefficients are lower than those determined by experiments. For T textures, the predicted value in the RD is lower than the predicted in the TD, result which agrees whit experiments. In the case of C textures, predicted and experimental results agree with the symmetry around the ND presented by the texture.

Fig. 3 shows the equivalent stress-strain curve for cold rolling considering the possible hardening induced by the texture development (n=0) and the effect of strain hardening (case 1). Stress values are given in units of the CRSS corresponding to prismatic slip (τ_{pr}). It can be observed that textural hardening is practically negligible (σ values change ≈ 10%) and that an important strain hardening effect is introduced.

5. Conclusions

This work is a first approach to the description of hardening during room temperature deformation of hcp materials. The obtained results point out the importance of a good adjustment of micro-hardening parameters and CRSS values (which also must verify relationships defined by the topology of the single crystal yield surface) with experimental results. The proposed description of hardening allows a good description of rolling texture generation in Zr. It also shows that differences in rolling textures (L and T textures) could be related to micro-hardening parameters, especially those describing the behavior of the pyramidal <c+a> slip.

6. References

Bronkhorst, C.A., Kalindi, S.R., and Anand, L. (1992) Polycrystalline plasticity and the evolution of crystallographic texture in FCC metals. *Philosophical Transactions. Roy Soc.* London A. N° 345, pp. 443-477.

Charquet, D. Alheritiere, E. and Blanc, G. (1987) Cold-rolled and annealed textures of zircaloy-4 thin strips in zirconium (ed. R.B. Adamson and L.F.P. Van Swam), *American Society for Testing Materials*, Philadelphia, pp. 663-672.

Lebensohn, R., Sanchez, P. and Pochettino, A. (1994) Modelling texture development of zirconium alloys at high temperatures. *Scripta Met. et Materialia*, pp. 481-486.

Pochettino, A., Sanchez, P., Lebensohn, R. and Tomé, C. (1994) Temperature effects on rolling texture formation in zirconium alloys. *Materials Science Forum*, Vol. 157-169, pp. 835-840.

Tomé, C. and Kocks, U. (1985) The yield surface of hcp crystals, *Acta Metallurgica*, Vol. 33, No 4, pp. 603-621.

Toth, L. (1996) The role of microscopic hardening in deformation texture development. *Proc. of 11 International Conference on Textures of Materials* (ed. Z. Lliang, et al.) International Academic Publishers, China, pp. 347-355.

UNSYMMETRICAL DEFORMATION TEXTURE TRANSITION DURING ANNEALING OF Cu-Al ALLOYS.

W. RATUSZEK, A. BUNSCH, K. CHRUŚCIEL

Faculty of Metallurgy and Materials Science, University of Mining and Metallurgy
Krakow - Poland

Abstract

In the present work the relation between rolling and recrystallization textures in the materials exhibiting unsymmetrical deformation textures was examined. On the base of wide experimental work it was found that asymmetry of the deformation texture is hereditary what means that, recrystallization textures are always unsymmetrical if only deformation texture are not symmetrical. This dependence was found in fine and coarse-grained polycrystals and especially very evident in single crystals.

Keywords: copper-aluminium alloys, deformation, recrystallization, texture

1. Introduction

Most of the works dealing with the problems of deformation texture transition into recrystallization textures were done on materials, which exhibit deformation textures with orthorhombic symmetry *(Lucke, 1981)*. The question appears, whether inheritance of the texture symmetry takes place when deformation textures are transformed during annealing into recrystallization textures. To answer such a question it was necessary to investigate texture transition during recrystallization in materials, which do not posses orthorhombic texture symmetry.

Present work was prepared on the base of wide texture investigations of Cu-Al alloys *(Ratuszek, 1995)*. In this work deformation textures of polycrystals with different grain size and of single crystals were investigated. Both types of materials, with symmetrical and unsymmetrical deformation textures were obtained depending on preparation procedures. These materials were used in presented work for investigation of the texture transition during recrystallization.

2. Materials and experimental procedure

Polycrystalline samples were prepared from the hot rolled Cu-5,6%Al ingots. Starting material was annealed for 5 hours at 200°C or 20 hours at 850°C, resulting in two different average grain sizes namely 25-35μm, and 225-240μm respectively. Single crystals with two different orientations ~$(017)[57\bar{1}]$ and $(253)[\bar{5}20]$ were prepared from Cu-6,5%Al alloy. Polycrystalline materials and single crystals were cold rolled up to 97,5% of deformation, taking small (lower then 10%) reductions per pass. Textures of all deformed samples were measured on the different deformation stages. Specimens of selected reductions (75% and 97,5%%) were subsequently annealed at 450°C and their recrystallization textures were also measured.

Deformation and recrystallization textures were measured by X-ray back-reflection method. For the use in this work textures are presented on pole figures, although they were also carefully studied by ODF calculations. Textures were measured within the centre layer of the specimens using radiation beam which size assured good statistic of the texture measurements for both types of materials fine and coarse-grained.

3. Experimental results and discussion.

The results of the texture measurements are described and presented in this paper first of all in order to discuss their symmetry. So texture are presented on pole figures where their symmetry with reference to rolling (RD), normal (ND) and transverse (TD) directions can be easy analysed – Fig. 1-4.

In the case of both, fine and coarse-grained materials after 75% deformation the main rolling components were $(552)[11\bar{5}]$ and $(332)[11\bar{3}]$ as well as $(774)[22\bar{7}]$ and $(110)[001]$, which belong to the τ-orientation fibre. Orientations heaving $\{111\}$ planes parallel to the rolling plane were also present in this texture - Fig. 1.a.

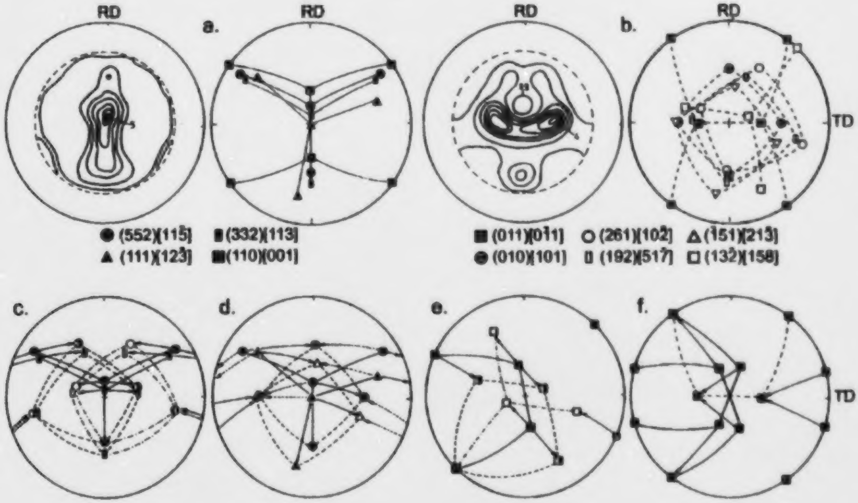

Fig. 1. Deformation (a) and recrystallization (b) unsymmetrical textures of 75% deformed and annealed 450°C/30' polycrystalline samples and relations between ideal orientations describing these textures:

c/. orientations obtained from the deformation one by 36°-40° rotation around <111> axes laying near rolling direction (RD).

d/. orientations obtained from the deformation one by 60° rotation (twining) around <111> axes laying near rolling direction (RD).

e/. orientations obtained from the deformation one by 40° rotation around <111> axes laying near projection circle.

f/. orientations obtained from the deformation one by 60° rotation around <111> axes laying on projection circle and near rolling direction.

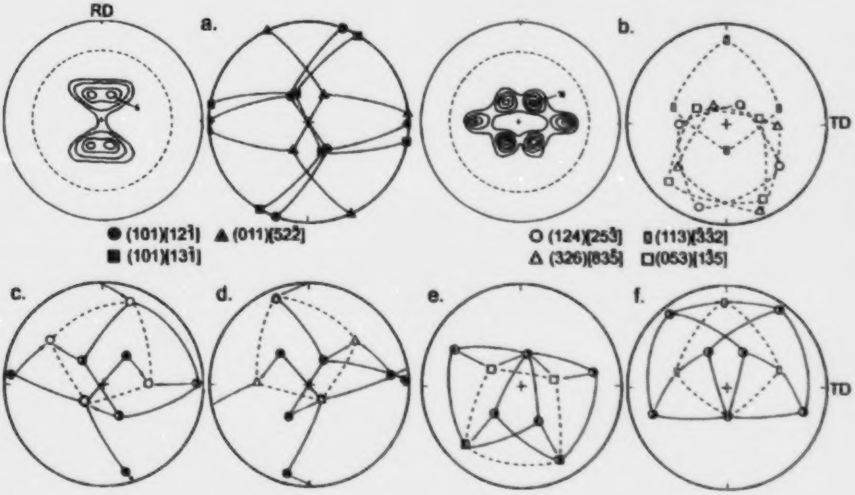

Fig. 2. Deformation (a) and recrystallization (b) symmetrical textures of 97% deformed and annealed 450°C/30' polycrystalline samples and relations between ideal orientations describing these textures:

- c/. one of the {124}<253> orientation obtained from the orientations laying within spread of the deformation texture by rotation around <111> axes laying near rolling (RD) and normal direction (ND).
- d/. one of the {326}<835> orientation obtained from the orientations laying within spread of the deformation texture by 40° rotation around <111> axes laying near rolling (RD) and normal direction (ND) – opposite rotation than on Fig. 2.c.
- e/. one of the {053}<135> orientation obtained from the orientations laying within spread of the deformation texture by 40° rotation around <111> axes laying on projection circle and near (RD)
- f/. one of the {113}<332> orientation obtained from the orientations laying within spread of the deformation texture by 40° rotation around <111> axes laying near normal direction (ND).

After deformation to 97,5% typical alloy type {110}<uvw> texture was formed with the limited α-fibre in which the strongest texture component was {110}<225>. In addition the {146}<211> and {135}<211> orientations as well as {123}<uvw> components were also present in this texture - Fig. 2.a.

Texture of material deformed up to 75% - Fig. 1.a. - does not exhibit symmetry as the texture of the material after 97,5% reduction - Fig. 2.a. Within the texture after 75% of deformation, not all symmetrically equivalent components are present. Texture unsymmetry of the materials deformed to intermediate degrees was observed in both fine and coarse-grained materials. Grain size does not influence the type of the texture although in fine-grained samples the texture was always a little stronger then in coarse-grained.

It can be concluded that texture has orthorhombic symmetry in heavily deformed samples. In materials deformed to intermediate state the textures are not symmetric with reference to transverse direction although they exhibit symmetry with reference to rolling direction.

Materials after deformation were annealed at 450°C. At this temperature recrystallization occurs in reasonable time and with the speed which gives chance to monitor texture changes during their transition. So for the experiment this temperature was chosen and textures were measured in different recrystallization stages.

When samples with unsymmetrical deformation textures (75% deformed) were annealed unsymmetrical recrystallization texture was created. This texture can be described by the components (011)[0$\bar{1}$1], ~(010)[101], (261)[10$\bar{2}$], ~(192)[51$\bar{7}$] and ($\bar{1}$51)[21$\bar{3}$], (13$\bar{2}$)[158] - Fig. 1.b. Unsymmetrical textures were observed on the intermediate stages of the recrystallization as well as after full recrystallization. For the case of the material with symmetrical deformation texture (97% reduction), recrystallization texture after annealing were also symmetrical including the {124}<235>, {236}<358>, {035}<035> and {113}<233> components and all of these symmetrically equivalent texture components were present in these texture - Fig. 2.b.

Deformation and recrystallization textures of the two single crystals are given on Fig. 3 and 4. Both single crystals have either unsymmetrical or symmetrical deformation textures and hence their recrystallization textures have different symmetry.

Single crystal (253)[$\bar{5}$20] after deformation had unsymmetrical texture with one component (101)[010-121]. Unsymmetrical recrystallization textures of this single crystal was created gradually and texture components formation corresponds, on the first recrystallization stage, to the 40° or 60° rotations of the (101)[uvw] orientations around <111> axes laying near rolling direction - Fig. 3.d. The next recrystallization step could be explained by rotation of previously created components of 39-41° around <111> axes, which are near normal direction - Fig. 3.e-f. or by rotation of starting components by 32-34° around <111> axes laying near normal direction - Fig. 3.g.

Single crystal ~(017)[57$\bar{1}$] after deformation had symmetrical texture with two strong components namely {110}<001> and {111}<uvw>. After recrystallization four equivalent texture components of the orientations {572}<234>, {472}<235> and {123}<112> were created.

4. Discussion

The dependence between deformation and annealing textures were analysed by the geometric relation between ideal crystallographic orientations describing these textures. Rotation in range 20-40° around <111> common poles or rotations of 60° (corresponding to the twin relation) were found as the best describing this relation. These relations work in both materials with symmetrical and unsymmetrical textures however, very often do not refer exactly to the orientations describing main rolling texture components, but to the orientations laying within the spread of these textures components - Fig. 1-4.

When the deformation textures are symmetrical, than the recrystallization textures can be described by the components obtained by the mentioned rotation of all (four) symmetrically equivalent components. The axes of rotations, which operate are only some selected from all existing <111> poles. In case of symmetrical textures four equivalents of them works. On the figures in present work only one operating pole is usually presented not to make these pictures too much complicated.

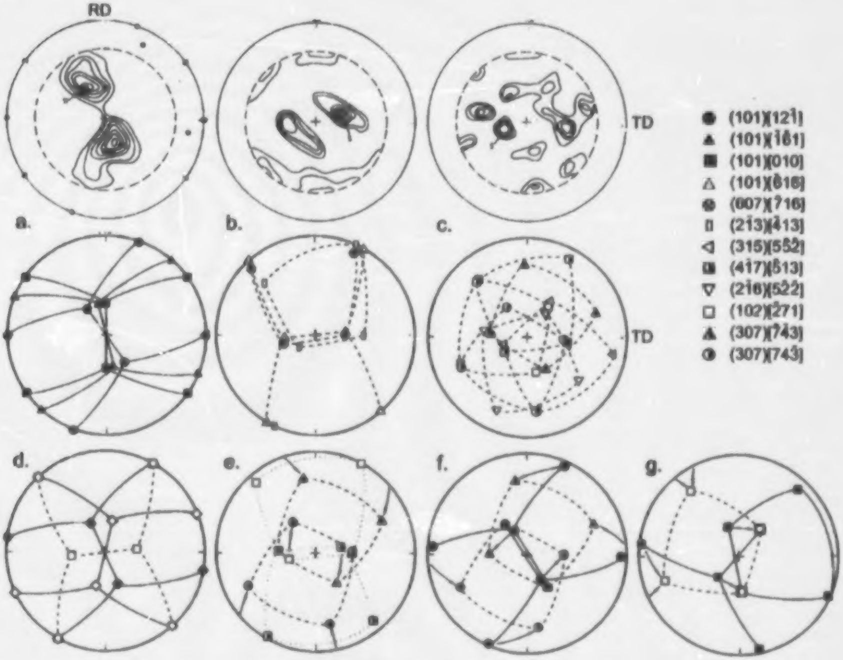
RD
TD
TD
a.
b.
c.
d.
e.
f.
g.
● $(101)[12\bar{1}]$
▲ $(101)[\bar{1}\bar{6}1]$
■ $(101)[010]$
△ $(101)[\bar{6}16]$
● $(607)[\bar{7}16]$
▯ $(2\bar{1}3)[\bar{4}13]$
◁ $(315)[55\bar{2}]$
■ $(4\bar{1}7)[\bar{5}13]$
▽ $(2\bar{1}6)[5\bar{2}\bar{2}]$
□ $(102)[\bar{2}71]$
▲ $(307)[\bar{7}\bar{4}3]$
● $(307)[74\bar{3}]$

Fig. 3. Deformation (a) and recrystallization (b) textures of deformed and annealed 450°C/30' single crystal $(253)[\bar{5}20]$ and relations between orientations describing these textures:

- d/. or. $(101)[\bar{6}16]$ obtained from $(101)[\bar{1}31]$ and $(101)[\bar{1}\bar{6}1]$ by 60° rotation (twinning) around <111> axes laying on projection circle near rolling direction (RD).
- e/. or.$(307)[\bar{7}\bar{4}3]$ and $(307)[74\bar{3}]$ obtained from $(101)[\bar{6}16]$ by 39-41° rotation around two <111> axes laying near normal direction (ND).
- f/. or.$(307)[\bar{7}\bar{4}3]$ and $(307)[74\bar{3}]$ obtained from ~$(101)[12\bar{1}]$ by 41° rotation around <111> axes laying near normal direction (ND).
- g/. or.$(102)[\bar{2}71]$ obtained from ~$(101)[010]$ by 32-34° rotation around <111> axes laying in centre of the projection.

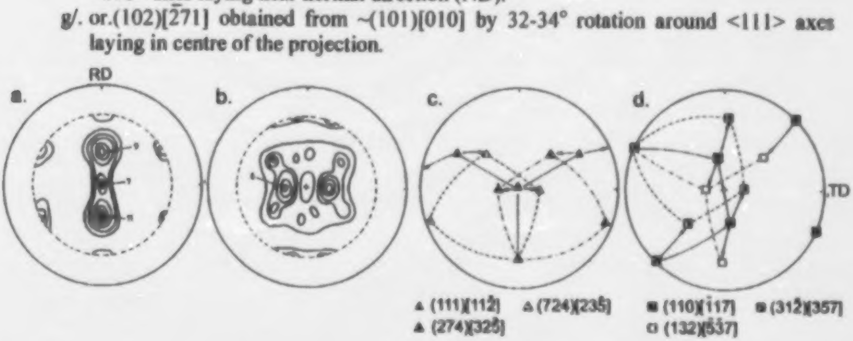
RD
a.
b.
c.
d.
TD
▲ $(111)[11\bar{2}]$
△ $(724)[23\bar{5}]$
▲ $(274)[32\bar{5}]$
■ $(110)[\bar{1}17]$
■ $(31\bar{2})[357]$
□ $(132)[\bar{5}\bar{3}7]$

Fig. 4. Deformation (a) and recrystallization (b) textures of deformed and annealed 450°C/30' single crystal ~$(017)[57\bar{1}]$ and crystallographic relations between ideal orientations describing these textures (c-d).

In materials with unsymmetrical textures such relations were also found - Fig. 1.c and 3.c-g. Assuming that these relations are the basis of recrystallization texture formation and as in deformation textures only selected components are present it could be stated that, only these limited number of components gave their contribution to the recrystallization textures. Because of this, unsymmetrical recrystallization textures are created. Experimental results gave strong evidence supporting this assumption.

Selection of the operating rotation axes (poles) is still not very well understood although on the base of the obtained experimental results and analysis which was done in this work it could be stated that the mutual relation between deformation and recrystallization texture components are very often as follow:

- rotation of the {111}<uvw> orientations of 20-28° around common <111> poles which are laying near rolling direction (RD) - Fig. 4.c.
- rotation of the ~{111}<uvw> orientations of 60° or 36-40° around common <111> pole which are laying near rolling direction (RD) - Fig. 1c, d
- rotation of the {110}<uvw> orientations and orientations from their spreads of 32-42° around common [111] pole which are laying on the projection circle or are close to normal direction (ND) – Fig. 3. e, f, g.
- rotation of the {110}<uvw> orientations and orientations from their spreads of 60° and ~40° around common [111] pole which are laying on the projection circle - Fig. 1. f. and Fig. 3. d.

Obtained results indicate that formation of the recrystallization textures in copper alloys is rather complex. Neither oriented growth *(Beck, 1950)*, nor oriented nucleation theory *(Burgers, 1931)* can explain this process. It is also evident that, as well in polycrystalline materials as in single crystals, 40° rotation around <111> poles *(Liebman, Lucke, 1956)* is not the only one describing relation between deformation and recrystallization texture components. Some preferences of the rotation poles selection indicate that during recrystallization selection of the recrystallization nucleus (orientations) take place and than oriented growth occurs and both give the contribution to the recrystallization texture formation.

Acknowledgements: The authors are grateful for the financial support from Polish Committee of Scientific Research (KBN).

5. References

Beck P.A., Sperry P.K., Hu H. (1950) The Orientation Dependence of the Rate of Grain Boundary Migration *J. Appl. Physics Vol. 21 p. 420-425*

Burgers W.G., Louwerse P.C. (1931) Uber den Zusammenhang zwischen Deformationsvorgang und Recrystallisationstextur bei Aluminium *Z. Physik Vol. 67, p.605-677*

Liebman B., Lucke K. (1956) Untersuchungen Uber die Orientierungsabhangigkeit der Waschstumsgeschwindiigkeit bei der primaren Rekristallisation von Aluminium-Einkristallen. *Z. Metallkunde Vol. 47. p. 57*

Lucke K. (1981) The Formation of Recrystallization Txtures in Metals and Alloys "Verbraak Lecture" *Proc. 7th Conf. Textures of Materials, ICOTOM7, p. 195-210*

Ratuszek W. (1995) Deformation and Annealing Textures of Copper-Base Alloys. *Dissertations and Monographies No. 27*

TEXTURES OF AA3104 DEFORMED BY PLANE STRAIN COMPRESSION AT MULTIPLE TEMPERATURES

Temperature effects on deformation texture

M.T. Lyttle and D. Juul Jensen

Materials Research Department, Risø National Laboratory, Roskilde, Denmark

Abstract

Deformation textures of AA3104 were determined for a wide range of temperatures, strains, and strain rates by neutron diffraction. For each temperature and strain rate, textures were measured at strains of 1.5 and 2.5, and for some conditions, the texture at strains of 0.1 and 0.5 were additionally examined. The scope of temperatures (25°C, 350°C, 430°C, 510°C, and 590°C) and strain rates (0.1 sec^{-1} and 5 sec^{-1}) studied allowed the strength of principal texture components to be observed over a wide range of the Zener-Hollomon parameter. A marked decline in the strength of the deformation texture components (brass + S + copper) was observed with decreasing Zener-Hollomon parameter, i.e. increasing temperature or decreasing strain rate. The strengthening of the deformation texture components with strain occurred at roughly the same rate for all deformation conditions. Recrystallization textures from some deformation conditions are also discussed.

Keywords: aluminium, deformation temperature, plane strain compression, recrystallization texture, strain rate, Zener-Hollomon parameter

1. Introduction

The crystallographic textures that develop during deformation processes have a significant effect on the subsequent mechanical behavior. There are many controllable parameters that can contribute to the resulting deformation texture including deformation temperature, strain rate, and strain state. While the effect of changing a single parameter has been frequently examined, i.e. deforming to a single strain at multiple temperatures, the number of studies that examine a large matrix of specimens while varying several parameters is more limited.

When varying solely a single parameter, e.g. the deformation temperature, it is generally straightforward to assess the effect of that variation on the resultant texture (e.g. Engler, et al.1994). With a large matrix of conditions and multiple varying parameters, it is sometimes difficult to assess the cumulative effect of these variations. The Zener-Hollomon parameter has been seen to be an effective single parameter for the description of the variation in subgrain size and recrystallization grain size due to strain rate and temperature (Nes and Marthinsen 1998). In this study, the applicability of the Zener-Hollomon parameter for the characterization of texture development is investigated.

To enable the identification of any trends in texture development in a single alloy deformed at a wide range of temperatures, strains, and strain rates it is important to minimize other secondary effects on the deformation texture, e.g. roll gap geometry in rolling. It has been seen that deformation produced by plane strain compression is a good proxy for that produced during rolling (Juul Jensen, et al. 1994). Since plane strain compression is performed in one pass and rapid quenching is available, there is greater chance for suppression of any unwanted recovery or recrystallization.

2. Experimental

Specimens of an aluminium alloy, AA3104 (Al-1.25Mg-1.01Mn-0.47Fe-0.21Ti-0.20Si-0.17Cu), were investigated. Two sets of samples were cast similarly and homogenized by different schedules. For the purposes of this paper, the texture differences due to the different homogenizations is insignificant when compared to the effects due to temperature and strain rate. Because of this, for a given strain and strain rate, there are generally two data points each corresponding to a different homogenization. From the cast ingot, specimens were industrially hot-rolled on a reversible mill from a thickness of 385 mm to 12 mm and subjected to an intermediate heat treatment. Specimens were machined from the strip and deformed by plane strain compression to strains of 0.1, 0.5, 1.5, and 2.5 at room temperature and at 350°C, 430°C, 510°C, and 590°C.

Bulk texture measurements were performed using neutron diffraction (Juul Jensen and Kjems 1983). To construct the orientation distribution function (ODF),

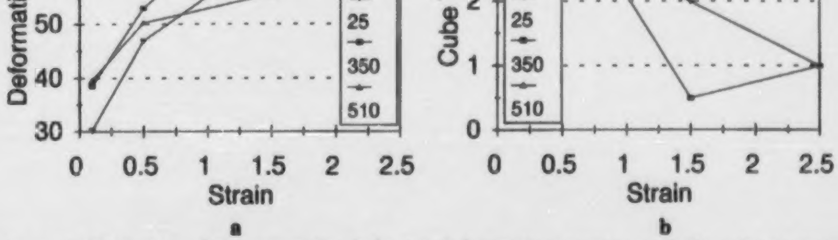

Figure 1. Variation of the strength of the (a) deformation texture and (b) cube texture with strain in AA3104 for three deformation temperatures; 0°C, 350°C, and 510°C.

quarter pole figures were measured from the {111}, {200}, and {220} planes. The volume fraction of specific texture components was determined by discretizing the ODF, and counting the fraction of orientations within 15° of each specific ideal {hkl}<uvw> texture orientation. When an orientation could be ascribed to multiple texture components, it was classified to be of the ideal component with the smallest deviation from that specific orientation. For the discussions in this paper, the deformation texture is described as the summed volume fraction of the brass {110}<112>, copper {112}<111>, and S {123}<634> components.

To enable the comparison of texture results from a large range of deformation temperatures, volume fractions of texture components are plotted versus the Zener-Hollomon parameter, Z, defined as $\dot{\varepsilon}$ ln (Q/RT), where Q is taken as 160 kJ/mol.

3. Results and Discussion

3.1 Deformation Texture

For examination of the texture evolution with strain, component volume fractions resulting from deformation to four strains at a range of temperatures is shown in Figure 1. For all temperatures, a similar evolution of texture is observed. The deformation texture fraction increases from ~35% at a strain of 0.1 to ~75% at a strain of 2.5. The strengthening of the texture occurs at roughly the same rate for the three deformation temperatures showing no systematic effect of temperature. Similarly, the cube fraction decreases from 4% at a strain of 0.1 to ~2% at a strain of 2.5 for all deformation temperatures, although this variation is nearly within the range of experimental scatter.

The volume fractions for the summed deformation and cube texture components are displayed as a function of Z in Figure 2. For the deformed AA3104, each specimen deformed to the higher strain ($\varepsilon = 2.5$) had a stronger deformation texture than the comparable specimen deformed to the lower strain ($\varepsilon = 1.5$) at a given strain rate and deformation temperature. The specimens deformed at 590 °C (ln(Z)

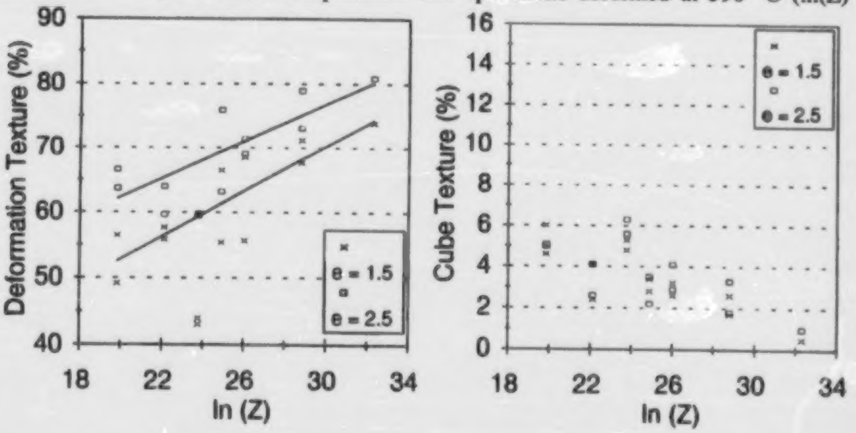

a b

Figure 2. The variation in the strength of the resulting texture due to the deformation of AA3104 to two strains at varying values of the Zener-Hollomon parameter. Volume fraction of (a) the deformation texture components and (b) the cube component.

values of ~20 and ~24 in figures) contain a larger cube component than the samples deformed at lower temperatures. This may be due to some recovery or recrystallization occurring during or immediately after deformation.

Figure 2a reveals a clear trend between an increase in Zener-Hollomon parameter and an increase in the deformation texture component volume fraction, but there is hardly a perfect correlation. Disregarding the ln(Z)≈23 specimens which have likely undergone some recovery/recrystallization, the majority of samples are within ±5% of a linear fit of the deformation texture fraction to ln(Z). This is counter to a previous study of AA1050 in which the deformation texture had no strain rate dependence and there was the opposite effect due to temperature (Juul Jensen 1994).

3.2 Recrystallization Texture

After annealing, only the high strain rate, high deformation temperature samples developed a moderately strong cube texture. Annealing of the other samples produced minor changes of the cube volume fraction compared to the deformation texture. These changes were not similar for all specimens, but did appear to follow a discernible pattern. There was a small decrease in the cube volume fraction of the low Z samples and a small increase in the cube volume fraction of the high Z samples during annealing. The cube volume fraction appears to have little dependence on the amount of strain.

In most of the ODFs from the annealed specimens, a small increase in the contours surrounding the cube component can be observed, but there is little consequent increase in the cube volume fraction. This behavior was also observed in a study of the recrystallization behavior of a cold-rolled AA3104. In both cases, recrystallization caused a small decrease in the rolling texture and only minor changes in the cube component volume fraction.

The annealing of specimens was performed in a tin bath, where the heating rate was ~80 °C/s (or approximately seven seconds of heat-up for the high temperature

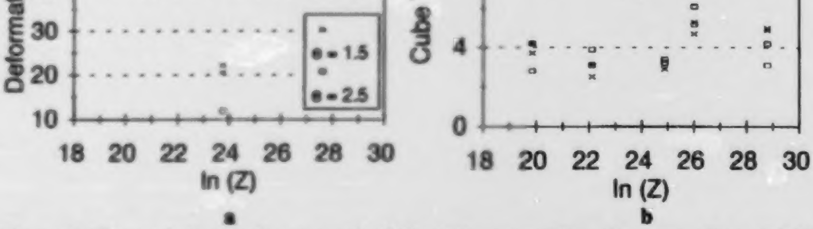

a b

Figure 3. The variation in the strength of the texture resulting after annealing of AA3104 deformed to two strains at varying values of Zener-Hollomon parameter. Volume fraction of (a) the deformation texture components and (b) the cube component.

anneals). It has been suggested that with such a rapid heating rate there is generated an excess of nucleation sites (Hirsch and Engler 1995). This excess serves to limit the development of a standard recrystallization texture and may produce a nearly random texture or a weaker deformation-like texture.

3.3 Recrystallized Grain Size

Recrystallized grain sizes have been measured for the 24 deformation conditions after an anneal of one hour at the deformation temperature. For a given strain rate and temperature, the grain size is larger in the specimens subjected to a lower strain. Figure 4 shows the dependence of recrystallized grain size from specimens of a single homogenization on the Zener-Hollomon parameter. As Z decreases, there appears to be a slight increase in the grain size which is in broad agreement with previous observations (Furu, et al. 1991). The only exception occurs in high strain rate specimens at 590 °C which have a significantly larger grain size. These are additionally the only specimens that display a strong elevated cube fraction.

Additional support for the idea of nucleation-dominated recrystallization is provided by the recrystallized grain size data. The relatively small recrystallized grain sizes, ~15 μm, of the samples deformed at lower temperature is similar to that observed in a cold-rolled AA3104. An earlier kinetics study of the cold-rolled alloy indicated the likelihood of a nucleation-limited grain size (Lyttle and Juul Jensen 1999).

In contrast, there was an observable texture difference in both the deformed and recrystallized textures of the specimens that developed anomalously large grain sizes. In the samples that contained a large recrystallized grain size, there was a larger cube fraction in the deformed and recrystallized textures. These specimens appear to have undergone some recovery/recrystalllization during the deformation process as indicated by their slightly weaker deformation texture. This pre-existing texture and microstructure difference could alter the local distribution of nuclei, allowing any growth advantage of cube-oriented grains to manifest itself.

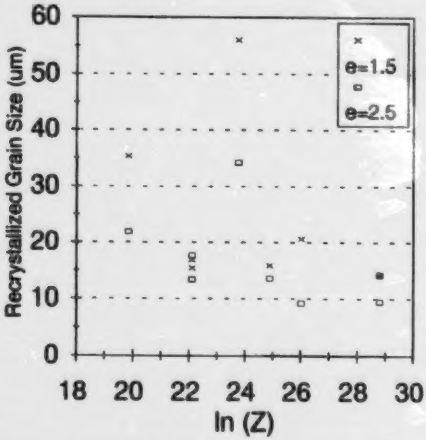

Figure 4. Recrystallized grain size of AA3104 deformed by plane strain compression to two strains at different values of Zener-Hollomon parameter.

4. Conclusions

Similar deformation textures are formed over a wide range of temperatures and strain rates in AA3104 deformed by plane strain compression. The weakest textures developed at low values of Zener-Hollomon parameter and with an increase in Zener-Hollomon parameter, there was a consistent increase in the strength of the resultant deformation texture.

Except for the high temperature, high strain rate specimens, all deformed specimens produced textures upon annealing with a weaker version of the deformation texture and a cube volume fraction indistinct from that of a random texture, ~4%. The lack of a distinct recrystallization texture may be attributable to an excess of nucleation sites. The specimens that developed a conventional cube texture during annealing appeared to undergo some recovery/recrystallization during the deformation process that could affect the development of texture during subsequent annealing.

5. Acknowledgements

The results presented in this paper were obtained during the course of an EC-funded Brite/Euram program under contract BRPR-CT96-0299. The authors would like to thank their partners in this project for helpful discussions.

6. References

Engler, O., Hirsch, J., Karhausen, K., and Gottstein, G. (1994) Influence of the Rolling Temperature on the Texture Gradient in an Al-Mg-Si Alloy. in ICOTOM 10, *Materials Science Forum*, Vols. 157-162, pp. 673-678.

Hirsch, J and Engler, O. (1995) Texture, local orientation and microstructure in industrial Al alloys. in *16th Risø International Symposium* (ed. Hansen, et al.), Risø, Roskilde, pp. 49-62.

Furu, T., Vatne, H.E., Ørsund, R., and Nes, E. (1996) Modelling recrystallization after hot deformation of aluminum. *Acta Materialia*, Vol. 44. pp. 4463-4473.

Juul Jensen, D. and Kjems, J.K. (1983) Apparatus for dynamical texture measurements by neutron diffraction using a position-sensative detector. *Textures and Microstructures*, Vol. 5, pp. 239-251.

Juul Jensen, D., Shi, H., and Bolingbroke, R.K. (1994) Texture development in AA3003 during hot plane strain compression. ICOTOM 10, *Materials Science Forum*, Vols. 157-162, pp. 745-752.

Lyttle, M.T. and Juul Jensen, D. (1999) Recrystallization Kinetics of AA3104 deformed at cold and elevated temperatures. in *Recrystallization '99*.

Nes, E. and Marthinsen, K. (1998) Modelling plastic deformation of aluminium alloys: A microstructural approach. in *Hot Deformation of Aluminum Alloys II* (ed. Bieler, et al.), TMS, Warrendale, pp. 171-184.

EFFECTS OF THE REDUCTION IN AREA AND OF THE HEAT TREATMENT ON THE PHASE TRANSFORMATION TEMPERATURES OF EQUIATOMIC TiNi SHAPE MEMORY ALLOY WIRES

F. BAGHDOUCHE and A. VADON
LETAM; ISGMP. Université de Metz, Ile du Saulcy. F 57045 METZ Cedex 1

ABSTRACT : The influence of the area reduction in wires during wire drawing and of the heat treatment on the phase transformation temperatures of the equiatomic TiNi shape memory alloy (SMA) has been studied. The martensite, the austenite, and the R-phase transformation temperatures were measured on 10% to 40 % area reduced cold worked wires and on the same wires after annealing. The subsequent memory imparting heat treat temperatures ranged from 450°C to 600°C for a time of one hour in vacuum, followed by nitrogen gas quench. A differential scanning calorimeter (DSC) was used to determine the transformation temperatures.

The reduction in area and the heat treatment process have a significant influence on the transformation temperature of the TiNi SMA. Generally, the martensite transformation temperature decrease as the reduction increases and the heat treatment temperature decreases. This general behaviour is not followed at heat treatment temperatures approaching the temperature of fully annealed SMA (571°C). At the heat treat temperatures of 450°C and 510°C, the martensite transformation temperature increases with a reduction over 20%.The austenite peak temperature decreases with an increasing reduction for heat treatment temperature of 450°C, 510°C and 570°C. This behaviour is different for 570°C and a reduction over 20 % ; and for a 600°C heat treat temperature and for all reductions, the austenite peak temperature is the same. The martensite peak temperature ranges from -27.8°C to +30.55°C. The austenite peak temperature ranges from 46°C to 61.66°C. The R-phase transformation temperature increases with reduction and the decreasing heat treatment temperature. The R-phase peak temperature ranges from 32.22°C to 47.5°C.

This decrease in martensite and austenite transformation temperatures and the increase of the R-phase transformation temperature with an increasing reduction and a decreasing heat treatment temperature are attributed to the level of residual stresses within the SMA. The increasing of martensite and austenite transformation temperatures with an increasing reduction at the heat treatment temperature is attributed to the recrystallization process.

1. INTRODUCTION

The transformation temperatures of shape memory alloys (SMA) are known to depend on their chemical composition, their story, the memory imparting heat treatment and the externally applied stresses [1,2,3]. Todoroki et al [3] show the effect of heat treatment on the phase transformations of three TiNi alloys having nearly equiatomic compositions.

In this paper, we will point out the effects of a reduction in area of the wires during wire drawing (Reduction) and of a heat treatment on the phase transformation temperatures of an equiatomic TiNi SMA wire.

2. MATERIAL AND PROCESS

The material used at the start was a set of equiatomic TiNi SMA wires commonly produced by the French Memometal Company in Albertville (France). The final wire diameters were 1.41 mm, 1.34 mm, 1.25 mm and 1.13 mm after respectively 10%, 20%, 30% and 40 % Reductions. The phase transformation temperatures were measured by a differential scanning calorimeter (DSC) for samples weighing 78 mg, 73.5 mg, 63 mg and 49 mg. They underwent a heat treatment in vacuum for 1 hour at the memory imparting temperatures of 450°C, 510°C, 570°C and 600°C, and were quenched with nitrogen gas.

3. RESULTS

The effects of the Reduction and of the memory imparting heat treatment on the phase transformations of this equiatomic TiNi SMA is shown by the DSC graphs.

3.1 Annealing at 600°C.

The DSC graphs in figure 1 show (for wires with 10% and 40% Reductions) only two transformation peaks, a martensitic peak on cooling and an austenite peak on heating, whatever Reduction the wires have undergone.

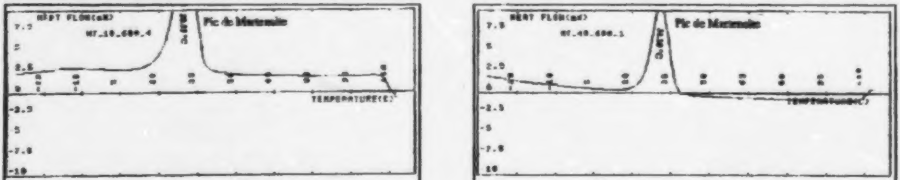

a) fil déformé à 10% et recuit à 600°C c) fil déformé à 40% et recuit à 600°C

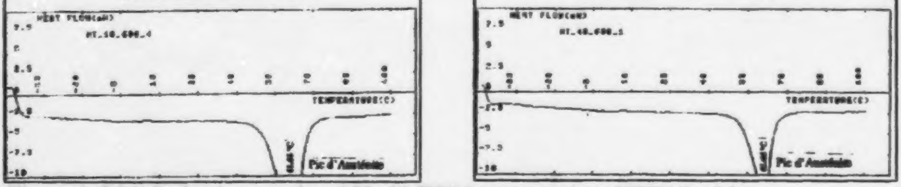

Figure 1. DSC Reduction graphs of 50- 50 TiNi heat treated at 600°C for 1 hour.

3.2 Annealing at 450°C.

The DSC graphs in figure 2 show (for wires with 10% and 30% Reductions) the R-phase prior to the martensite transformation during cooling, and an austenite transformation peak during heating. The separation between the R-phase peak and the martensite peak, as well as the separation between the martensite peak and austenite peak, increase as the Reduction increases.

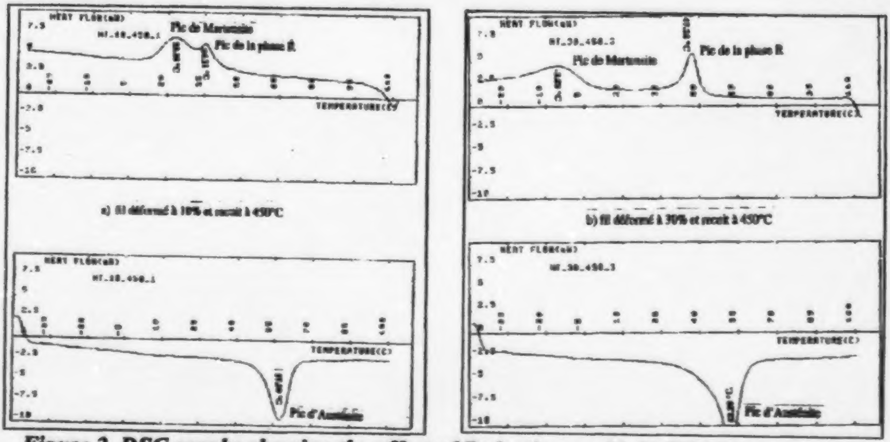

a) fil déformé à 10% et recuit à 450°C

b) fil déformé à 30% et recuit à 450°C

Figure 2. DSC graphs showing the effect of Reduction on 50-50 TiNi heat treated at 450°C for 1 hour.

3.3 Annealing at 510°C

In addition to the Reduction, the memory imparting heat temperature has a significant influence on the SMA transition temperatures. Figure 3 shows the effects of the Reduction and of the heat treatment temperature on the peak temperatures of the martensite, the austenite, and the R-phase transformations.

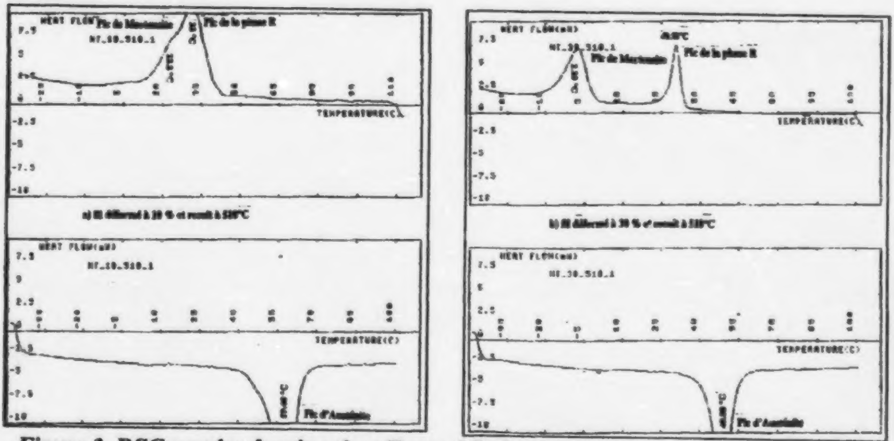

a) fil déformé à 20 % et recuit à 510°C

b) fil déformé à 30 % et recuit à 510°C

Figure 3. DSC graphs showing the effects of Reduction on 50-50 TiNi heat treated at 510°C for 1 hour.

For the 450°C and 510°C heat treatment temperatures, the martensite peak temperature decreases with a Reduction over 20 % (figure 5-A). This behaviour is different for 570°C and 600°C heat treatment temperatures, where the martensite peak temperature is the same for all Reductions. The martensite peak temperature ranges from -27.8°C (40 %

Reduction and 450°C heat treatment temperature) to +30.55°C (10% Reduction and 600°C heat treatment temperature).

The austenite peak temperature decreases as the Reduction increases for heat treatment temperatures of 450°C, 510°C and 570°C (figure 5B). This behaviour is different for 570°C and a Reduction over 20 %. For a 600°C heat treatment temperature and for all Reductions the austenite peak temperature is the same. The austenite peak temperature ranges from 46°C (40 % reduction and 510°C heat treatment temperature) to 61.66°C (10 % reduction and 600°C heat treatment temperature).

Unlike the martensite and austenite peak temperatures, the R-phase peak temperature increases as the Reduction increases and the heat treatment temperature decreases (figure 5-C).

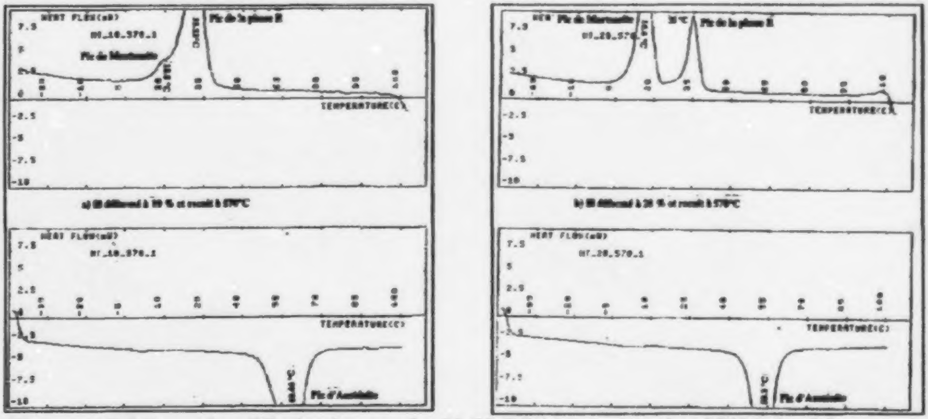

Figure 4. DSC graphs of Reduction on the 50-50 TiNi heat treated at 570°C for 1 hour.

4. COMMENTS ON RESULTS

The increase of internal stresses that occurs during wire drawing when the Reduction increases, is delayed when the alloy undergoes heat treatment at a high temperature because recrystallization also occurs in the alloy. The effects of the Reduction and of the heat treatment on the transformation temperatures of TiNi SMA are associated with the residual internal stresses and the recrystallization process.

The observed decrease in martensite and austenite peak temperatures and increase in the R-phase peak temperature with an increasing Reduction and a decreasing memory imparting temperature are associated with increasing residual internal stresses. The highest amount of internal stresses exists in the material undergoing the biggest Reduction and heat treated at the lowest temperature. The lowest martensite peak temperature is -27.8°C and the highest R-phase peak temperature is 47.5°C. Both transformation temperatures occur in the SMA having a 40 % Reduction and heat treated at 450°C (conditions of highest internal stress).

The increase in the R-phase transition temperature causes the reverse transformation to austenite during heating to occur at a higher temperature. The graph showing the R-phase peak temperature and the austenite peak temperature for 450°C and 510°C heat treatment temperatures (figure 2, 3) shows the convergence to a constant difference of temperatures between the austenite and the R phase peaks for the 450°C heat treatment.

The highest value for both austenite and martensite peak transition temperatures is observed at a 600°C heat treatment temperature regardless of the amount of Reduction. At a temperature of 600°C, the martensite and R-phase peaks are merged. The authors feel that, at heat treatment temperatures higher than 570°C, regardless of the Reduction, the internal stress is minimised and associated with complete recrystallization. At slightly lower temperatures, the recrystallization process is evidenced by an over 20% increase in the martensite and austenite peak temperatures. It is believed that this increase is transition temperatures for martensite and austenite is due to the higher density of recrystallized grains in the material with the biggest Reduction.

The material with a 10 % Reduction has the same martensite peak temperature and austenite peak temperature for all heat treatment temperatures. Also, the R-phase does not develop in the 10 % Reduction specimens. This can be explained by the fact that the 10 % Reduction obtained by wire drawing is completely recoverable when the wire is heated.

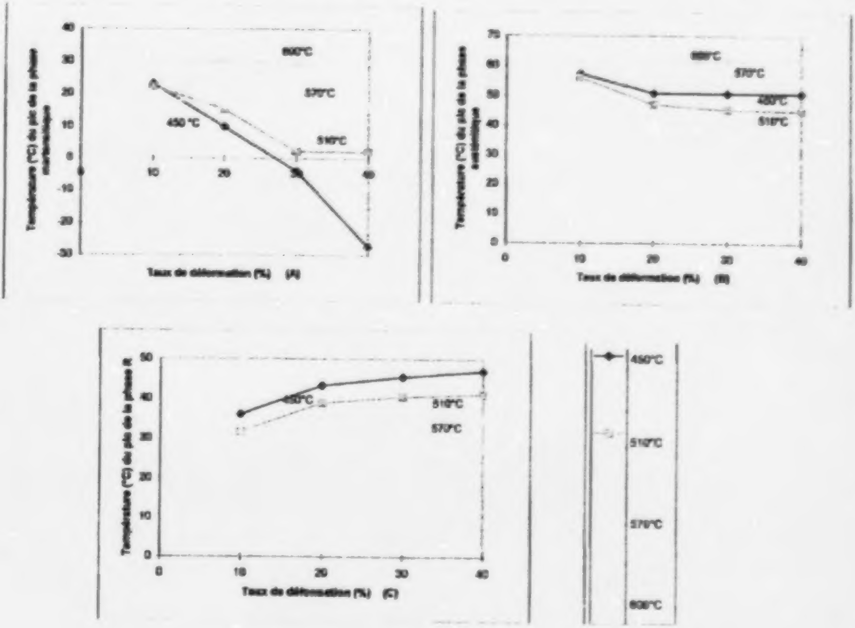

Figure 5 . Effects of Reduction and heat treatment temperature on the martensite, austenite, and R-phase peak transformation temperature of the TiNi SMA.

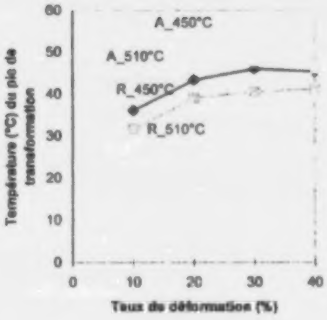

Figure 6 . Convergence to a constant temperature difference between the austenite and the R-phase peaks.

5. CONCLUSION

The results of this study can be summarised as follows :

- The phase transformation temperatures of TiNi SMA are affected by thermal and mechanical processing. The effects of Reduction and heat treatment on the transformation temperatures are associated with the residual internal stress and the recrystallization process.

- As the internal stress increases, the martensite and austenite transformation temperatures decrease and the R-phase transformation temperature increases.

- At a low heat treatment temperature (450°C), the increase of the R-phase transformation temperature causes the reverse transformation to austenite on heating to occur at a higher temperature than when the heat treatment temperature is higher.

- At a high heat treatment temperature (600°C), the internal stress is minimised and associated with complete recrystallization. The highest value for both martensite and austenite transformation temperatures is observed regardless of the Reduction, and the R-phase transformation coincides with the martensite transformation.

REFERENCES

1. Buehler, W.J : U.S. Patent N°. 3, 508, 914, April 28, 1970.
2. Goldstein, D., Kabacoff, L. and Tydings, J. : Journal of Metals, 1987, 39 (3), 19-26.
3. Todoroki, T. and Tamura, H. : Transactions of the Japon Institue of Metals, 1987, 28 (2), 83-94.

TEXTURE STABILITY DURING HIGH TEMPERATURE PLANE STRAIN COMPRESSION OF A COMMERCIAL Al-Mg ALLOY

R.D. KNUTSEN
Department of Materials Engineering, University of Cape Town, South Africa
F.J HUMPHREYS
Manchester Materials Science Centre, University of Manchester and UMIST, UK
P.S. BATE
DONCASTERS plc, Melbourne, Derbyshire, UK
S.A. COURT
Alcan International Limited, Banbury Laboratories, Banbury, England, UK

Abstract

Elevated temperature plane strain compression tests were performed on a commercial Al-3Mg alloy (AA5754) which possessed a strong initial cube texture. Deformation at 475°C and at a strain rate of 1 s^{-1} results in significant fractions of cube texture being retained during deformation. The cube stability increases with strain, and furthermore, the cube fraction increases above the initial level at logarithmic strains approaching 2.0. Although there is no direct indication of dynamic recrystallisation of cube orientations, evidence based on microtexture studies is presented to suggest cube grain boundary migration during the deformation event. These observations are discussed relative to the evolution of deformation texture that can be predicted by the Taylor model approach.

Keywords: Cube texture, aluminium, plane strain compression, texture modelling.

1 Introduction

Texture development during the deformation and subsequent recrystallisation associated with the thermomechanical processing of aluminium alloys has important implications for downstream manufacturing. In particular, preferred orientations which develop during the early stages of thermomechanical processing will strongly influence the texture evolution right up to the final stages of processing, especially where rolled plate and sheet products are concerned. For face centred cubic (FCC) metals, such as aluminium, it is common for the orientations to become concentrated along two fibres in Euler space during the plane strain conditions associated with rolling deformation. These are known as the alpha fibre, running from the Goss orientation {011}<100> to the brass orientation {110}<112>, and the beta fibre which spans the orientations from the brass to copper {112}<111> components. The formation of the aforementioned deformation texture is attributed to slip on the {111}<110> octahedral systems and consequently the cube orientation is unstable during deformation. In this way, initial orientations close to cube will be destroyed during deformation and the amount of cube texture will decrease with increasing strain. Experiments on aluminium alloy AA1050 have shown that this is true even at deformation temperatures up to 500°C (Vernon-Parry et al 1996). The mechanics related to rotations away from cube are quite complicated in a sense that grain fragmentation is considered to account for the retention of cube transition bands, and there are several works that deal with this aspect in detail (for example, Dillamore and Katoh 1974, Akef and Driver 1991). On the other hand, there are numerous accounts that indicate that cube orientations can be stable in aluminium at high temperatures (Maurice and Driver 1993 and 1997, Panchanadeeswaran and Field 1995), to a point where the cube orientation is classified as a deformation component.

In the present work, the stability of the cube texture in a commercial AA5754 alloy is examined during high temperature plane strain compression (PSC). The as deformed microstructures have been investigated using electron backscattered diffraction microtexture analysis, and modelling of the deformation texture has been carried out to establish the possible role of non-octahedral slip in developing the increased cube component.

2 Experimental approach

The composition of the commercial AA5754 alloy is nominally Al-3wt% Mg. The alloy was DC cast and subsequently processed to produce a more or less equiaxed fully recrystallised grain structure, which formed the starting structure for PSC testing. The PSC tests were carried out at 475°C, at a constant strain rate of 1 s^{-1}, and individual tests were performed to strains of 0.5, 1.0 and 2.0. All specimens were quenched within one second of completion of the deformation event.

2.1 Texture analysis

Deformed textures from the half thickness position were quantified by a bulk X-ray technique using Mo K_α radiation. Four incomplete pole figures ((111), (200), (220), and (113)) were measured from which the ODF was derived using the series expansion method up to L=22. The volume fractions of the major crystallographic components were calculated by allowing for a 15° spread around the ideal orientations. Microtexture measurements were performed on both undeformed and deformed specimens by using the *HKL Channel* system attached to a *JEOL6300* scanning electron microscope. In all cases the orientation data were analysed and displayed using a custom written software package called *VMAP*.

2.2 Simulation of deformation texture

Some calculations were performed to assess the possibility of slip other than {111}<110> influencing the stability of cube texture in plane strain deformation. The calculations employed the Taylor model, either fully constrained (FC) or with relaxation of simple shears (RC), and the rate sensitivity was set to zero. The initial texture was obtained from the measured undeformed crystallographic texture, f(g), by representing the texture using 10 000 orientations weighted according to f(g). In defining the slip systems, glide corresponding to perfect dislocations only was considered. The Peierls-Nabarro force, which essentially depends on the Burgers vector magnitude divided by the interplanar spacing, was used as a guide for selecting feasible non-octahedral slip systems. The non-octahedral systems that were evaluated included {200}<110>, {200}<100>, and {220}<110>. Some of these system groups cannot fulfil the von Mises condition for all orientations by themselves, so non-octahedral systems were added to the octahedral ones to test their effects.

3 Results

3.1 Texture analysis

Emphasis is placed on the evolution of the cube orientation during deformation and the texture fraction after each deformation is normalised with respect to the initial cube fraction, which was measured as 0.21. X-ray bulk texture analysis presented in Fig. 1 indicates the trend in cube texture, as function of strain at 475°C. Although the cube fraction decreases slightly at a strain of $\varepsilon=0.5$, the cube fraction at a strain of $\varepsilon=1.0$ is equivalent to the starting fraction, and continues to rise above this level at a strain of $\varepsilon=2.0$. Given this trend in cube texture, a suspicion is raised that recrystallisation may be occurring during the interval between termination of the deformation event and quenching. However, a microtexture orientation map presented in Fig. 2 displays a highly elongated grain structure, which contains a dense subgrain structure (light grey lines).

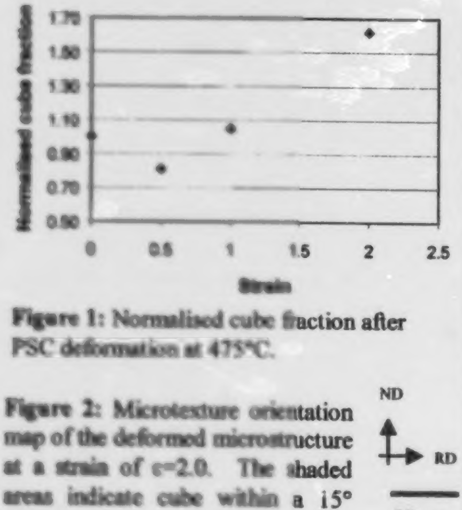

Figure 1: Normalised cube fraction after PSC deformation at 475°C.

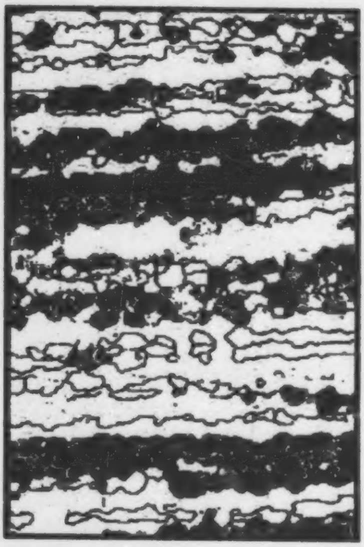

Figure 2: Microtexture orientation map of the deformed microstructure at a strain of $\varepsilon=2.0$. The shaded areas indicate cube within a 15° spread.

3.2 Texture simulation

In the first instance, the Taylor model was employed with full constraint and {111}<110> slip was considered along with the non-octahedral systems described in section 2.2. The results for each slip condition are shown in Fig. 3. Apart from the slip condition that includes {200}<100>, the model predicts a significant decrease in the cube fraction following plane strain deformation. Relaxing the 13 simple shear constraint for the same calculation has a marked effect on cube stability. These results are also shown in Fig. 3 and the cube fraction increases above the initial level for all slip combinations, with the highest fraction being achieved when the non-octahedral {200}<100> system is included. Since one cannot easily allow only one constraint to be relaxed, relaxation of the other simple shear (23) was also included in the calculation. In this case, the cube is destroyed for octahedral slip, but including the {200}<100> systems allows some retention. This situation is not strictly real, since in practice changes in grain geometry would mean that these constraints become progressively relaxed during deformation, with 13 relaxation occurring first. If we allow the constraints to be suddenly relaxed at critical values of the relevant grain aspect ratio, then an approximation to the "real" case can be tested. Figure 4 illustrates the situation where 13 is relaxed after a strain of $\varepsilon=0.8$, and 23 is relaxed after a strain of $\varepsilon=1.6$. The situation is only presented for {111}<110> slip and the case involving the {200}<100> non-octahedral systems, since the latter is the only system that seems to have some positive influence on the cube level.

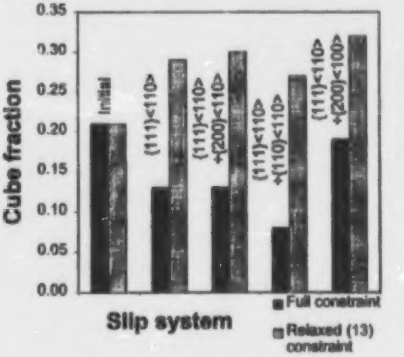

Figure 3: Cube fraction as function of Taylor model constraint and slip system.

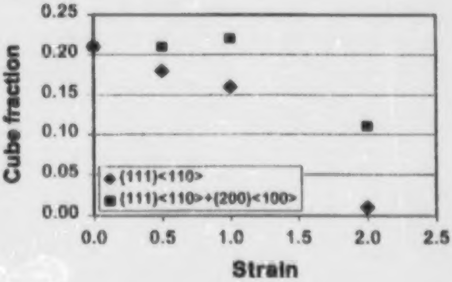

Figure 4: Cube texture evolution when Taylor constraints are progressively relaxed (ε_{13} at $\varepsilon=0.8$, ε_{23} at $\varepsilon=1.6$).

3.3 Microtexture

Microtexture analysis of the deformed specimens provided useful information concerning the thickness (normal direction, ND) of the cube bands relative to the other deformation texture components. The initial average grain dimension (ND) was 57μm, with similar averages for each principal texture component, namely cube, brass, copper, Goss and S. The ND size distribution for the cube orientations was determined from several orientation maps of the undeformed microstructure, and the predicted ND size distribution for a plane strain of $\varepsilon=2.0$ was calculated from these results. This size distribution predicts that about 80% of the deformed cube bands have a thickness of 10μm and less. Measurement of the actual cube band thickness after a strain of $\varepsilon=2.0$ produces an average ND dimension of 15μm. Other orientations, namely brass, copper and S, give average values of 8-10μm, which is more consistent with the values predicted by the plane strain condition. An example of the cube morphology is indicated in the orientation map presented in Fig.2.

4 Discussion

The measurement of the bulk texture of the as deformed specimens by X-ray diffraction has demonstrated that not only is the cube orientation very stable during high temperature deformation, but that the cube fraction can increase significantly during the deformation event. Microtexture analysis has shown that the deformed cube bands are much thicker than anticipated if one were to consider only the survival of the original cube grains during plane strain compression. There are two possible explanations for this situation, although it is likely that neither of these is mutually exclusive. One possibility is that existing cube grains have increased their volume by boundary migration into neighbouring non-cube orientations, thereby creating an average ND grain dimension that is larger than expected. On the other hand, rotation of non-cube grains towards the cube orientation would increase the cube volume fraction, and at the same time coalescence of neighbouring cube grains would increase the grain dimension. The same material, when deformed under much higher Z conditions (T=325°C, strain rate=$100s^{-1}$), results in the cube fraction decreasing significantly with concomitant increase in rolling texture components. Thus the cube stability is not peculiar to the material, but rather is related to the deformation condition.

The results of the texture simulation employed in this study demonstrate that non-octahedral slip, when combined with octahedral slip under full constraint, cannot account for the increase in cube fraction that is observed after a strain of ε=2.0. Only {200}<100> systems seem to have some positive effect. Relaxation of the 13 constraint has a very noticeable effect (Fig. 3), but when relaxation of 13 and 23 are combined at the appropriate grain geometry, inclusion of the {200}<100> systems only provides limited increase in cube stability (Fig. 4). So, even with the extreme case of the non-octahedral systems having the same slip resistance as the octahedral ones, it is highly unlikely that simple deformation effects can explain the increase in cube texture. In fact Kocks et al (1994) have also shown that an increase in cube texture during uniaxial compression of Al-Mg alloys can be predicted only under unreasonable conditions of slip. On the other hand, Maurice and Driver (1997) have proposed that near-cube grains rotate towards cube by slip on {110} planes, and have shown in their results that the cube component in a polycrystal sample actually increases during hot deformation as a consequence of {110} slip. Their analysis of the channel-die compression of an initially cube-oriented single crystal indicates that the crystal is stable at 400°C, but that some degree of transverse direction (TD) spread occurs. Consideration of {110} slip in our simulations does not promote cube stability, and in fact the experimental as deformed cube textures demonstrate a strong RD rotation. The latter disagreement, together with the results of our simulations, suggest that the influence of non-octahedral slip cannot, by itself, be sufficient to account for the experimental results. This does not rule it out as a contributing factor, but it does suggest that dynamic cube grain boundary migration may occur to such an extent that it increases the cube volume. The driving force for the cube boundary migration would be associated with the lower energy cube subgrain structure (Ridha and Hutchinson

1982). This proposal is easily supported by the cube ND grain dimensions, which were recorded from the microtexture assessment.

5 Conclusions

Plane strain compression of a commercial Al-3Mg alloy (AA5754), which possessed a strong initial cube fraction, has demonstrated a high degree of cube stability during high temperature (475°C) deformation. The cube fraction increases above the initial value at a strain of $\varepsilon=2.0$. This increase in cube fraction cannot be explained by employing non-octahedral slip in a relaxed constraint Taylor model. The increase in ND cube dimension suggests that dynamic cube grain boundary migration may contribute towards the increased cube fraction in the as deformed microstructure for a strain of $\varepsilon=2.0$.

6 Acknowledgements

The Foundation for Research Development (RSA) and Alcan International are acknowledged for the provision of financial support. One of the authors (RDK) is grateful for the research facilities provided by the Manchester Materials Science Centre during a recent research visit.

7 References

Akef, A., and Driver, J.H. (1991) Orientation splitting of cube-oriented face-centred cubic crystals in plane strain compression. *Mat. Sci. Eng.*, Vol. A132, pp. 245-255.

Dillamore, I.L., and Katoh, H. (1974) The mechanisms of recrystallisation in cubic metals with particular reference to their orientation-dependence. *Metal Science*, Vol. 8, pp. 73-83.

Kocks, U.F., Chen, S.R., and Dawson, P.R. (1994) Failures to model the development of a cube texture during the high temperature compression of Al-Mg alloys. *Materials Science Forum*, Vol. 157-162, pp. 1797-1802.

Maurice, Cl., and Driver, J.H. (1993) High temperature plane strain compression of cube oriented aluminium crystals. *Acta Metall. Mater.*, Vol. 41, No. 6, pp. 1653-1664.

Maurice, Cl., and Driver, J.H. (1997) Hot rolling textures of f.c.c. metals – part I. Experimental results on Al single and polycrystals. *Acta Mater.*, Vol. 45, No. 11, pp. 4627-4638.

Panchanadeeswaran, S., and Field, D.P. (1995) Texture evolution during plane strain deformation of aluminum. *Acta Metall. Mater.*, Vol. 43, No. 4, pp. 1683-1692.

Ridha, A.A., and Hutchinson, W.B. (1982) Recrystallisation mechanisms and the origin of cube texture in copper. *Acta Metall.*, Vol. 30, pp. 1929-1939.

Vernon-Parry, K.D., Furu, T., Jensen, D.J., and Humphreys, F.J. (1996) Deformation microstructure and texture in hot worked aluminium alloys. *Mat. Sci. Tech.*, Vol. 12, No. 11, pp. 889-896.

ASSESSMENT OF THE LAMEL MODEL USED FOR PREDICTION OF ROLLING TEXTURES OF FCC AND BCC METALS

P. VAN HOUTTE and L. DELANNAY
Department of Metallurgy and Materials Engineering, Katholieke Universiteit Leuven, Belgium

Abstract

The Lamel model, a new model for the prediction of rolling textures is presented. It has been validated by comparing its predictions to experimentally observed cold rolling textures. This has been done for two drawing steels which had been cold rolled to 70% reduction. Their hot rolling and cold rolling textures were measured by X-ray diffraction and converted into ODFs. The cold rolling ODFs are qualitatively and quantitatively compared to the predictions of the new theory as well as to those of three older polycrystal deformation models, namely the full constraints (FC) Taylor model, the "pancake" relaxed constraints models (RCP), and the more complex generalised relaxed constraints model which has a self-consistent scheme. From a quantitative point of view, the recent Lamel model was found to provide better predictions than the other models. However, for an aluminium 5182 alloy, the Lamel model did not lead to satisfactory results, although its results were better than those of older models. It is suggested that grain subdivision should be taken into account in this case.

Keywords: deformation textures, micromechanical model, Taylor theory, relaxed constraints theory, rolling, grain subdivision

1 Introduction

Models for the prediction of deformation textures have been used since many years. They are most often based on the generalised Schmid law and on Taylor's hypothesis of uniform strain throughout the polycrystal, see for example the review paper by Aernoudt et al. (1993). For low carbon steel, which is a bcc metal, the {110}<111> and {112}<111> slip systems are normally considered, whereas for fcc metals, {111}<110> slip systems are used. In the first part of this paper, the performances of four deformation models are compared for the prediction of the cold rolling textures of two industrial steels. A simplification that is common to all four models is that the strain and stress distributions are homogeneous inside each grain. The first and simplest model is the Taylor "full constraints" model (Taylor FC) which assumes homogeneous strain, whereas the second model is the Taylor relaxed constraints pancake model (RCP) in which the components l_{13} and l_{23} components (RD= x_1, TD= x_2, ND= x_3) of the velocity gradient tensor vary freely from grain to grain (see e.g. Aernoudt et al. 1993). Since the internal plastic work is minimised, this also means that the shear stress components σ_{13} and σ_{23} are set to zero in all grains (Van Houtte 1988). The fulfilment of the stress equilibrium among the grains is then improved compared to the Taylor FC model. On the other hand, the discontinuity of l_{ij} at the grain boundary gives rise to geometrical incompatibilities.

Over the years, experience has shown that experimental results often lie between the predictions of the Taylor FC and RCP models. This means that better results would be obtained if the relaxations allowed by Taylor RCP were partially constrained. The last two models considered here introduce the previously missing constraints. The first of these is the "generalised relaxed constraints" model which is a self-consistent model (Van Houtte and Rabet 1997). Finally, the last model is the recently developed "Lamel model" which does not treat the grains one by one, but by pairs. Such pair forms a stack of lamella-shaped grains in which opposite pancake relaxations are allowed (see fig.1) (Van Houtte et al. 1998, 1999). Similarly to the pancake model, the relaxations allowed lead to a misfit between these pairs of grains and their surroundings when the structure is pancaked. However, the supplementary condition in the Lamel model ensures that there is no grain boundary sliding (see fig. 1). The mathematical details of this model have been described elsewhere (Van Houtte et al. 1998, 1999)

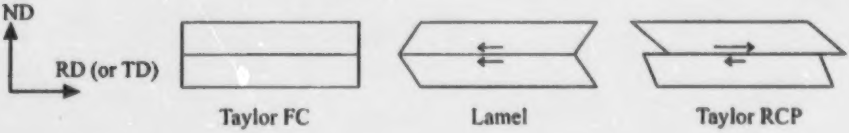

Fig. 1: Illustration of the relaxations allowed by some deformation models simulating cold rolling. The arrows symbolise the relaxations l_{13} or l_{23} (RD= x_1, TD= x_2, ND= x_3).

2 Results (bcc metals)

The textures predicted by above models have been compared to experimentally measured cold rolling textures. Two steels were selected for the validation procedure. The first is a Ultra Low Carbon (ULC) steel with a hot rolling texture that is almost random, the second is an Interstitial Free (IF) steel having, on the contrary, a very pronounced hot rolling texture. The two steels were cold rolled to 70% thickness reduction. Pole figures of the hot- and cold rolled specimens were measured by means of X-ray diffraction. The Orientation Distribution Functions (ODFs) (Bunge 1982) were then mathematically derived including ghost correction. Fig. 2 shows the ODF of the hot and cold rolling textures.

The models described above have then been used to simulate these deformation textures. The hot rolling textures have first been discretised into 2000 orientations using the "statistical method" described by Tóth and Van Houtte (1992). These discrete sets of orientations were then used as initial textures for the simulations. For the Lamel model, the 1000 stacks of two grains were defined by randomly arranging the 2000 grains into 1000 pairs. The cold rolling process was subdivided into 48 increments of equivalent strain of 0.025. After each increment, the slip rates were computed in all grains, and the corresponding stress, strain and rotation increments were derived. The result of the simulation for a given deformation model is a list containing the final orientation of each grain, as well as its stress, strain, and Taylor factor. The ODFs of the simulated deformation textures were then constructed as the sum of 2000 Gaussian distributions lying at the grains' final orientations. The Gaussian scatter-width is by convention set to 7°. The result of the Lamel model is also shown in fig. 2.

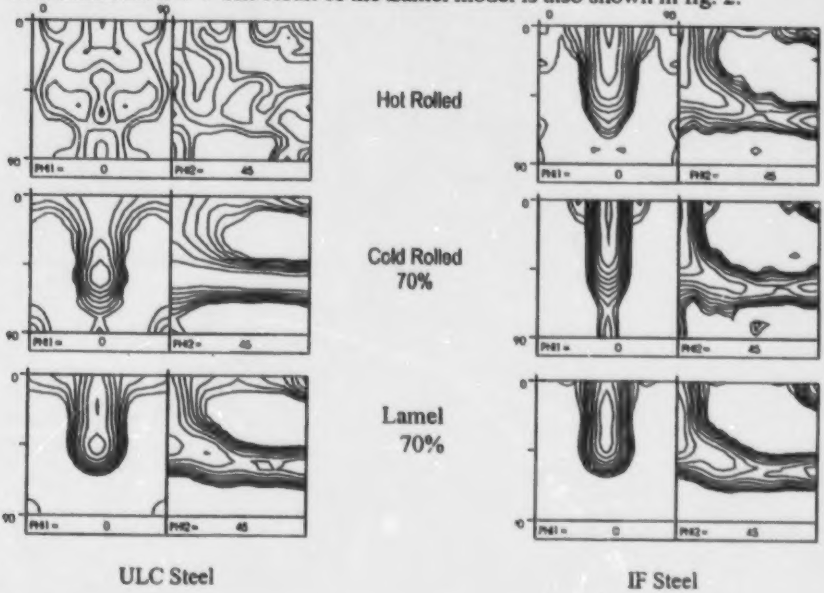

Contour lines:0.70, 1.00, 1.40, 2.00, 2.80, 4.00, 5.60, 8.00, 11.0, 16.0

Fig. 2: ODFs of the two investigated steels before and after cold rolling, and according to the Lamel-model. (φ_1= 0° and φ_2= 45° sections.)

The simulated textures have the same qualitative features as the experimental cold rolling textures. The main components are the classical α (<110> parallel to RD) and γ (<111> parallel to ND) fibres. Other components such as "Goss" and "cube" are absent. The φ_1=0° sections in fig. 2 show the α-fibre, whereas the φ_1=45° sections show both the α-fibre as the γ-fibre. Quantitative comparisons of the ODFs have been carried out by comparing the intensity distributions along the skeleton lines of the α- and γ-fibres. The skeleton line of a fibre is the line of maximum intensity along the fibre (i.e. the central axis of the fibre). The skeleton line is often shifted a few degrees in the Euler space with respect to the ideal position of the fibre. Once the skeleton line is found, the fibre can be characterised in two ways: (i) by the distribution of intensity along the skeleton line, (ii) by the distribution of the intensity spread around the fibre. These two parameters (i.e. intensity and spread) can be combined into one parameter by computing the integral of the ODF in a section perpendicular to the fibre. This is what is presented in figs. 3-4. It is seen that the Lamel model yields the best results .

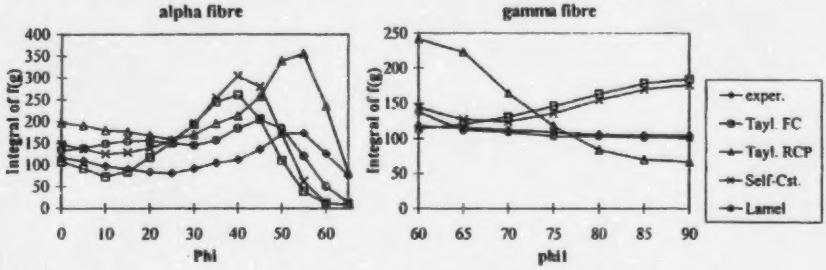

Fig. 3: Skeleton lines of the cold rolling textures of the ULC-steel.

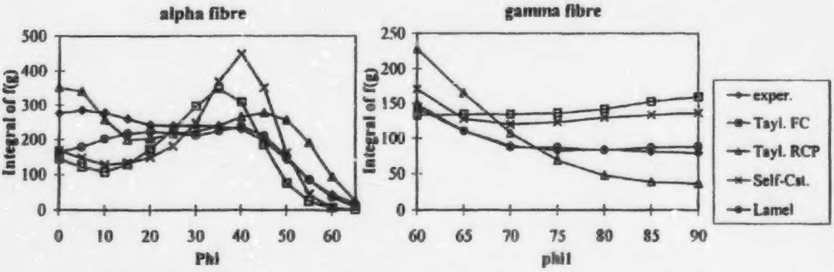

Fig. 4: Skeleton lines of the cold rolling textures of the IF-steel.

3 Results (fcc metals)

Fig. 5a shows results obtained for an aluminium AA5182 alloy sheet. The hot rolling texture consisted mainly of a cube-component with a moderate spread, and some remnants of a β-fibre. The material was then cold rolled from 4 mm until 1.2 mm. The figure shows the maximal intensity of the ODF $f(g)$ for a particular angle φ_2 along the β-fibre of the resulting cold rolling texture, as well as the simulation results using the classical full-constraints Taylor model, the self-consistant method (generalised relaxed constraints model) (Van Houtte and Rabet 1997) and the Lamel model, used in the same way as for bcc metals. It is seen that in this case, the Lamel model yield a result which is intermediate between the result of the Taylor FC and the S.C. model and the experimental texture. None of the models could predict the nice peak at the brass orientation which can be seen in a φ_2=90° section of the experimental ODF (fig. 5b).

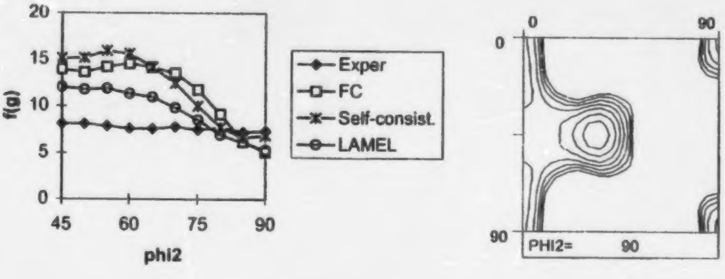

(a) (b)

Fig. 5 (a) Skeleton lines of the cold rolling textures of the AA5182 alloy. (b) φ_2=90° section of the ODF of the experimental rolling texture.

4 Discussion

It has been demonstrated that the Lamel model provides much better predictions of cold rolling textures of typical drawing steels than other deformation models existing at present. This has been verified by quantitative texture analysis. However, the predictions of the Lamel model are excellent as regard to the γ-fibre, but tend to overestimate the intensity of the α-fibre. This is more outspoken for the ULC-steel than for the IF-steel. Perhaps the Lamel model captures an effect due to the typical morphology of grains belonging to the γ-fibre, but not of for those belonging to the α-fibre. This point needs further investigation.

Much more problematic are the predictions of the Lamel model for fcc metals. Although the results are considerably better as those of other models, the new model does not seem to capture the dominant aspect of the local strain heterogeneity as it probably does for bcc metals. In recent years, it has become clear that grain subdivision takes place during the rolling of aluminium alloys (see for example Juul Jensen et al., 1998; Hughes et al., 1998). One aspect of it is the splitting of grains into cell blocks each with a different deformation pattern. It has been suggested by Leffers (1994) that this splitting and the heterogeneous strain pattern associated to it could be the dominant feature which we are looking for. Formally the Lamel model is not so much different from Leffers' model (1994). The following modifications of the Lamel model would allow the treatment of this case. A stack of two bands originally belonging to the same grain would be represented by a pair of grains as those shown in fig. 1. The interface plane should not be taken parallel to the rolling plane, but should form an angle of about 45° with it. This variant of the model will be tested in the near future.

5 Acknowledgment

Financial support for this work has been obtained from the Federal government of Belgium (DWTC) through the contract IUAP P4/33. One of the authors (LD) acknowledges his grant as 'aspirant' of the FWO.

6 References

Aernoudt, E., Van Houtte, P. and Leffers, T. (1993) Deformation and Textures of Metals at Large Strains, in *Materials Science and Technology: A Comprehensive Treatment,* (ed. by R.W. Cahn et al.), VCH, Weinheim, Germany, Vol. 6, pp. 89-136.

Bunge, H.J. (1982) Texture Analysis in Material Science, Butterworth, London.

Hughes, D.A. and Godfrey, A. (1998) Dislocation Structures formed during Hot and Cold Working, in *Hot Deformation of Aluminium Alloys II,* (ed. T. Bieler, L.A. Lalli and S.R. MacEwen), TMS, pp. 23-36.

Juul Jensen, D., Lyttle, M. T. and Hansen, N. (1998) Hot and Cold Deformed Aluminium: Deformation Microstructure and Recrystallisation Behaviour, in *Hot Deformation of Aluminium Alloys II,* (ed. T. Bieler, L.A. Lalli and S.R. MacEwen), TMS, pp. 9-21.

Leffers, T. (1994), Lattice rotations during Plastic Deformation with Grain Subdivision, in *Proc. ICOTOM 10, Mat. Sci. Forum* Vol. 157-162, pp. 1815-1820.

Van Houtte, P. (1988) A Comprehensive Mathematical Formulation of an Extended Taylor-Bishop-Hill Model Featuring Relaxed Constraints, the Renouard-Wintenberger Theory and a Strain Rate Sensitivity Model. *Textures and Microstructure,* Vol. 8-9 pp. 313-350.

Van Houtte, P., Delannay, L. and Samajdar, I. (1998) Prediction of cold rolling textures and strain heterogeneity of steel sheet by means of the LAMEL-model, in *Consititutive and Damage Modeling of Inelastic Deformation and Phase Transformation (Proc. Plasticity '99),* (ed. A. S. Khan), Neat Press, Fulton, Maryland, USA, pp.149-153.

Van Houtte P., Delannay, L. and Samajdar, I. (1999) Quantitative prediction of cold rolling textures in low-carbon steel by means of the Lamel-model, *Textures and Microstructures* (in press).

Van Houtte, P. and Rabet, L. (1997) Generalisation of the relaxed constraints models for the prediction of deformation textures. *Revue de Métallurgie-CIT/Science et Génie des Matériaux,* Vol. 94 pp. 1483-1494.

ROLLING TEXTURE AND MECHANICAL TWINNING IN B2 ORDERED CUZN ALLOY

G.H. ZHU, W. MAO and Y. YU
University of Science and Technology Beijing, P. R. China
G. BRÜCKNER
Institut für Metallkunde und Metallphysik, RWTH, Aachen, Germany

Abstract

The deformation mechanism of mechanical twinning in inverse direction in B2 ordered CuZn was proposed based on the evolution of cold rolling textures. The occurrence of strong {111}<112> texture component could be attributed to a rotation of the {221}<114> component resulting from {001}<110> by the mechanism of the inverse direction twinning on {112}, of which the details have been discussed.

Keywords: B2 structure, deformation, mechanical twinning, inverse twinning

1 Introduction

During deformation, the grains would rotate into some stable orientations which depends on the deformation mechanisms. Texture analysis is a very useful method for investigation of the fundamental principles of the deformation behavior.

The deformation behavior can be divided into two fundamental mechanisms, i.e. dislocation slip and mechanical twinning. Dislocation slip is the most common deformation process, which widely happen during the deformation of crystalline materials. The operation of mechanical twinning depends closely on the crystallographic structure and stacking fault energy in disordered alloys or anti-phase boundary energy in ordered alloys. It is well known that the BCC metals may mechanically twin on {112} planes by a simple a/6<111> shear (Barrett and Massalski 1980). But if the same twinning operation is applied to a B2 ordered material, the B2 ordered structure would be destroyed and extra energy would be induced, which would result in a new crystalline structure and there would be no mirror symmetry between sheared and unsheared regions. As a conclusion in general, the mechanical twinning is very difficult or even impossible in B2 ordered materials. However, an experimental evidence about mechanical twinning in B2 ordered $Ti_{50}Ni_{47}Fe_3$ alloy has been reported using TEM analysis (Goo et al. 1985; Moberly et al. 1990). Although the mechanical twinning in other B2 ordered materials have not been reported and the mechanism of the mechanical twinning should be in argument, the possibility of the mechanical twinning in B2 ordered materials have been confirmed experimentally.

2 Experimental

Two samples with the composition of Cu-45%Zn and Cu-47%Zn (wt.) were prepared. The ingots were melted using high purity Zn and Cu in vacuum and argon atmosphere respectively. By means of X ray analysis, two phases, namely α(FCC) with a volume fraction of about 17.4%, and β′ (ordered B2) were determined in Cu-45%Zn alloy. The Cu-47%Zn alloy consisted of single β′ phase. The Cu-45%Zn sample was forged into 4.5 mm thick sheet and cold rolled to 60%, 70%, 80%, 90% and 95% reduction respectively. The Cu-47%Zn sample was annealed at 400°C after hot rolling (8.7 mm thick), and then cold rolled to 31% and 40% reduction at room temperature. During cold rolling many cracks were observed in the sample. Three incomplete pole figures {110}, {200} and {112} of the rolling samples were measured for Cu-45%Zn and Cu-47%Zn alloys, and the orientation distribution functions (ODFs) were calculated according to the series expansion method (Bunge 1981).

3 Results

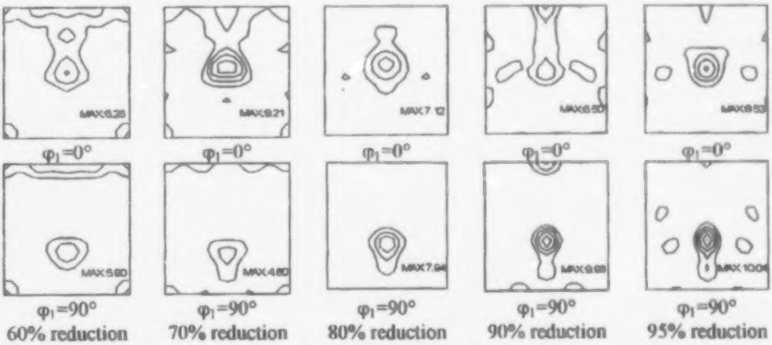

$\varphi_1=0°$ $\varphi_1=0°$ $\varphi_1=0°$ $\varphi_1=0°$ $\varphi_1=0°$

$\varphi_1=90°$ 60% reduction; $\varphi_1=90°$ 70% reduction; $\varphi_1=90°$ 80% reduction; $\varphi_1=90°$ 90% reduction; $\varphi_1=90°$ 95% reduction

Fig. 1: Deformation textures in β′ phase of Cu-45%Zn (level: 2, 4, 6, 8, 10)

Figure 1 represents the evolution of the deformation textures during cold rolling in B2 ordered β′ of Cu-45%Zn alloy at the $\varphi_1=0°$ and $\varphi_1=90°$ ODF sections, which has a rather random initial oriented distribution. With increasing thickness reduction, the orientations of the grains are collected into some dominant texture components at {001}<110>($\varphi_1=0°$, $\Phi=0°$, $\varphi_2=45°$), {557}<110> ($\varphi_1=0°$, $\Phi=45°$, $\varphi_2=45°$) and {111}<112> ($\varphi_1=90°$, $\Phi=55°$, $\varphi_2=45$). However the most important texture characteristic should be the continuous increase of {111}<112> during the rolling. When the reduction was up to 95%, a very strong {111}<112> texture component has been formed and inhomogeneous γ fiber was obtained as shown in figure 2, which is significantly different from that of BCC (Lücke and Hölscher 1991) and other B2 ordered alloys, like FeCo (Zhu et al. 1998b) and Fe-28Al (Mao et al 1999).

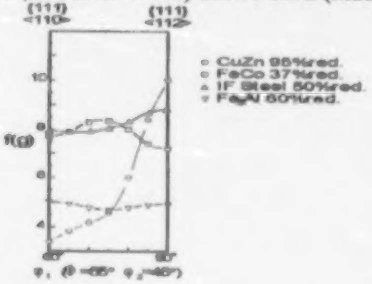

Fig. 2: γ-fiber analysis of different rolling sheets

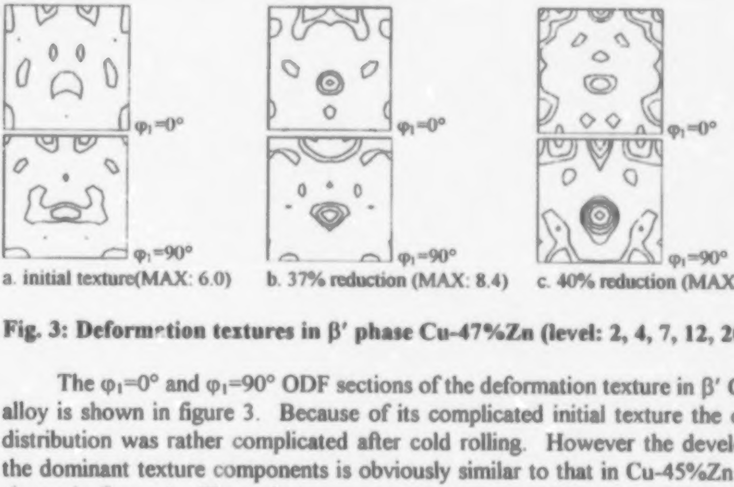

a. initial texture(MAX: 6.0) b. 37% reduction (MAX: 8.4) c. 40% reduction (MAX: 24.5)

Fig. 3: Deformation textures in β′ phase Cu-47%Zn (level: 2, 4, 7, 12, 20)

The φ_1=0° and φ_1=90° ODF sections of the deformation texture in β′ Cu-47%Zn alloy is shown in figure 3. Because of its complicated initial texture the orientation distribution was rather complicated after cold rolling. However the development of the dominant texture components is obviously similar to that in Cu-45%Zn sample as shown in figure 1. The main texture components were located at {001}<110>, near {557}<110> or {111}<110> (φ_1=0°, Φ=55°, φ_2=45°), and around {111}<112> with the maximum density value. As the reduction increased up to 40%, a rather sharp {111}<112> texture component was formed with a density level of 24.5.

A twin-like microstructure embedded in the shear bands (Duggan et al. 1978) can be seen in optical microscopy of Cu-45%Zn alloy at 60% rolling reduction (Zhu 1998a). A microstructure called "strain marking" (Humphreys and Hatherly 1995) of Cu-47% alloy can also be observed in SEM (Zhu 1998b). It should be a possible experimental evidence of mechanical twinning in B2 ordered CuZn.

4 Discussion

The more details of the evolution of deformation textures have been discussed by Zhu et al. (1998a). According to the report of Stoloff and Davies (1966), the active slip system in B2 ordered CuZn was similar to that in B2 ordered FeCo, which is a planar glide on the {110} with Burgers vector <111> at the room temperature up to 470K. But a significant difference of the γ fiber texture between CuZn and FeCo was shown in figure 2. The sharp {111}<112> texture component which is experimentally found here can not obtained by a {110}<111> dislocation slip using computer simulation based on the Taylor model (Raabe et al. 1996). Therefore the evolution of the texture component {111}<112> in B2 ordered CuZn could not be perfectly interpreted just using the dislocation slip mechanism.

However if the twinning mechanism like that in BCC metals appears, the B2 ordered structure would be destroyed which will result in the formation of a new crystal structure accompanied by an increase of extra energy. Furthermore it could not be the real twin mechanism since there is no mirror symmetry between the sheared and unsheared regions, which was called as pseudo-twin (Goo et al. 1985). As a consequence, the mechanical twinning is expected to be difficult or impossible in B2 ordered materials (Laves 1952).

It should be notable that the B2 ordered structure and the mirror symmetry between sheared and unsheared regions would remain if the twinning direction is in the opposite i.e. inverse direction Considering the lower anti-phase boundary energy, the inverse twinning may be a possible mechanism in B2 ordered CuZn.

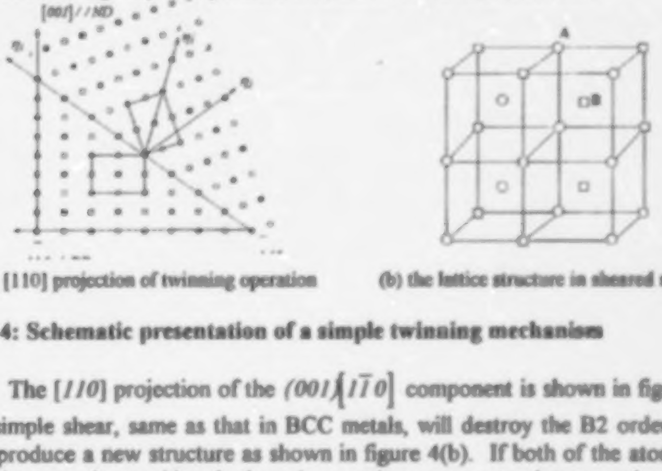

(a) [110] projection of twinning operation (b) the lattice structure in sheared region

Fig. 4: Schematic presentation of a simple twinning mechanism

The [*110*] projection of the $(001)[1\bar{1}0]$ component is shown in figure 4, where the simple shear, same as that in BCC metals, will destroy the B2 ordered structure and produce a new structure as shown in figure 4(b). If both of the atomic sites and atomic types is considered, there is no mirror symmetry between the sheared and unsheared regions. Assuming an ideal rolling situation of σ_{11}//*RD* and σ_{33}//*ND* ($\sigma_{11}=-\sigma_{33}$), the orientation factor for the twinning can be calculated as -0.94, and correspondingly the strain components are(Zhu et al. 1998b):

$$\varepsilon_{ij}=\gamma\begin{pmatrix}-0.47 & 0 & 0.17\\ 0 & 0 & 0\\ 0.17 & 0 & 0.47\end{pmatrix}\quad (i,j=1,2,3;\ 1\text{-}RD,\ 2\text{-}TD,\ 3\text{-}ND) \qquad (1)$$

That indicates a decrease of the length along the RD and an increase of the thickness along ND. This is not in agreement with real rolling process. The same result would be obtained if the twinning plane is $(1\bar{1}2)$. Therefore a simple twinning shown above should be impossible in B2 ordered materials and even if it could be operated, a real twinning symmetry could not be obtained.

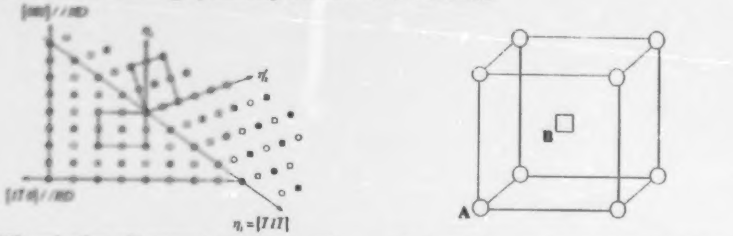

(a) [110] projection of inverse twinning operation (b) the lattice structure in sheared region

Fig. 5: Schematic presentation of a inverse direction twinning

However, because of the lower anti-phase boundary energy in B2 ordered CuZn, mechanical twinning should be possible if the ordered structure would not be destroyed. Considering the twinning shear is twice as large as above and in the inverse direction, as shown in figure 5(a), B2 ordered structure would remain in sheared region and the mirror symmetry required by twins would be obtained. In this case, the orientation factor is 0.94 and the strain can be calculated as (Zhu et al. 1998b):

$$\varepsilon_{ij}=\gamma\begin{pmatrix}0.47 & 0 & 0.17\\ 0 & 0 & 0\\ 0.17 & 0 & -0.47\end{pmatrix}\quad (i,j=1,2,3;\ 1\text{-}RD,\ 2\text{-}TD,\ 3\text{-}ND) \qquad (2)$$

Here an elongation along RD and a compression along ND is obtained. Although the twinning shear inversely is twice as that of the simple twinning shear, it should be possible because it has a very large orientation factor and reasonable strain components. Especially this inverse direction twinning would not result in destroy of the B2 ordered structure and corresponding mirror symmetry.

The orientation rotations, orientation factors and corresponding strain components during the twinning are calculated for 5 dominant deformation texture components based on the crystallography of plastic deformation (Zhu et al. 1998b). The result demonstrated that the most favorable twinning on {112} will transform the {001}<110> to {221}<114>(φ_1=90°, Φ=70°, φ_2=45°) (Zhu et al. 1998b). The unstable {221}<114> orientation would move further to the stable orientation {111}<112>(φ_1=90°, Φ=55°, φ_2=45°) nearby during rolling, and result in a strong {111}<112> texture component (fig. 1-3). The details of the calculation will be described elsewhere (Zhu et al. 1998b).

5 Summary

The strong {111}<112> rolling texture component in B2 ordered CuZn alloy should be initiated by an orientation rotation from {001}<110> to {221}<114> by means of the mechanical twinning, in which the mechanism is different from that in BCC materials. Twinning in inverse direction is proposed for the deformed grains with lower anti-phase boundary energy, very high twinning orientation factor, as well as reasonable strain components in B2 ordered CuZn. Especially the B2 ordered lattice and the mirror symmetry between sheared and unsheared regions would remain after the inverse direction twinning.

6 Acknowledgement

Financial supports given by the National Natural Science Foundation of China and the Deutsche Forschungsgemeinschaft are gratefully acknowledged. The authors are very grateful to Professor G. Gottstein, Dr. W. Hu and Mr. A. Ziemons for the helps they offered.

7 References

Barrett, C.S. and Massalski, T.B. (1980) *Structure of Metals*, 3rd edn., Pergamon Press, Oxford, p. 414.

Bunge, H.J. (1981) General outline and series expansion method, in *Quantitative Texture Analysis*, (ed. H.J. Bunge and C. Esling), DGM-Informationsgesellschaft, Oberursel, pp. 1-72.

Duggan, B., Hutchinson, W. and Hatherly, M. (1978) Recrystallization studies in 70:30 brass using a high voltage electron microscope. *Scripta Met.* , Vol. 12, No 3, pp. 293-295

Goo, E., Duerig, T., Melton, K. and Sinclair R. (1985) Mechanical twinning in $Ti_{50}Ni_{47}Fe_3$ and $Ti_{49}Ni_{51}$ alloys. *Acta metall.*, Vol. 33, No. 9, pp. 1725-1733

Humphreys, F.J. and Hatherly, M. (1995) *Recrystallization and Related Annealing Phenomena*, Elsevier Science Ltd. p. 33

Laves, F., (1952) Über den Einfluß von Ordnung und Unordnung auf mechanische Zwillingsbildung, *Naturwissenschaften*, Vol. 39, pp. 546-546

Lücke, K. and Hölscher, M. (1991) Rolling and recrystallization textures of BCC steels. *Textures and Microstructures*, Vol. 14-18, pp. 585-596

Mao W., Zhu G.H., Zhao Z. and Yu Y. (1999) Influence of B2 ordered structure on deformation texture. *Trans. Non-Ferrous Metals Soc., China.* (accepted)

Moberly, W., Proft, J., Duerig, T. and Sinclair, R. (1990) Deformation, twinning and thermo-mechanical strengthening of $Ti_{50}Ni_{47}Fe_3$. *Acta metall. mater.*, Vol. 38, No. 12, pp. 2601-2612.

Raabe, D., Fischer-Bühner, J., Ball, J. and Gottstein, G. (1996) Texture in intermetallic compounds-experiments and simulations, *Proc. 11th. Inter. Conf. on Texture of Materials*, (ed. Z. Liang et al.), Inter. Acad. Publisher, Xi'an, Vol. 2, pp. 941-950.

Stoloff, N. and Davies, R. (1966) The mechanical properties of ordered alloys. *Progress in Materials Science*, Vol. 13, pp. 3-10

Zhu, G.H., Mao, W., Yu, Y. and Sun, Z. (1998a), Rolling texture development in CuZn ordered alloy. *Advanced Materials and Processing*, PRICM3, conf. proc., (ed. M.A. Imam, et al.), TMS, Vol. 2, pp. 1983-1988.

Zhu, G.H., (1998b) Investigation of recrystallization behaviors in cold deformed B2 order alloys, *Doctoral thesis*, Univ. Sci. & Technol. Beijing, pp. 55-67.

EFFECT OF THERMOMECHANICAL PROCESSING PARAMETERS ON TEXTURE DEVELOPMENT IN AN X-80 LINEPIPE STEEL.

G. J. BACZYNSKI and J. J. JONAS
Department of Metallurgical Engineering, McGill University, Montreal, Canada

Abstract

An X-80 pipeline steel that was finish rolled in the γ phase was selected for examination. Two reheat temperatures (1150°C and 1275°C), three cooling rates (less than 1°C/s, 20°C/s and 40°C/s), and two cooling interruption temperatures (520°C and 620°C) were chosen for evaluation. The textures and microstructures were investigated. Polygonal and acicular ferrite were formed under the present conditions. The textures consisted of the {001}<110>, {113}<110>, {225}<110>, and {112}<110> components located along the <110>//RD fiber, the {332}<113> orientation formed along the <110>//TD fiber, and the {335}<372> component. The textures were qualitatively similar in all the samples, although the maximum intensities and volume fractions of particular components differed. These are associated with the processing conditions and related to the final microstructures developed.

Keywords: Bcc rolling textures, polygonal and acicular ferrite, YS anisotropy

1 Introduction

The effect of thermomechanical processing (TMP) parameters (soaking temperature, finish rolling temperature, cooling rate and cooling interrupt temperature) on the final properties of linepipe steels has been studied extensively during the last ten years Tanaka (1981), Faucher and Dogan (1988). These properties can change significantly when different industrial schedules are employed. For example, the final microstructures can range from entirely polygonal to almost exclusively acicular ferrite by modifying the TMP practice.

Concurrently, improvements have been made to the chemical compositions, which have led to the development of new grades, Okatsu et al. (1997). These trends have been accompanied by a better understanding of microstructural evolution as well as of the anisotropy of mechanical properties. Nevertheless, texture effects have only recently begun to be studied, Baczynski et al. (1999a).

This work was undertaken to analyze the development of crystallographic texture and to relate it to the final microstructure present in the steel. The TMP parameters employed in industrial rolling were varied over a significant experimental range. The microstructures and textures were then determined and analyzed carefully.

2 Experimental material and methods

The chemical composition of the present X-80 steel is given in Table 1. This steel was first produced commercially in North America by Ipsco Inc. in Regina, Canada, in 1994, Kostic, et al. (1998). Standard Ipsco chemistries for this grade were employed in the present work. All steels were continuously cast into 20 cm (8") thick slabs. The finishing passes were performed entirely in the γ phase and a finish rolling temperature of 780°C was used. The ten different TMP schedules that were studied involved two reheat temperatures (1150°C and 1275°C), three cooling rates (less than 1°C/s, 20°C/s and 40°C/s), and two cooling interruption temperatures (520°C and 620°C). (The cooling was interrupted only for the steels that were cooled at rates of 20°C/s and 40°C/s).

The determination of the no-recrystallization (T_{nr}=975°C) and ferrite-start (Ar_3=750°C) temperatures is described elsewhere, Baczynski et al. (1999a). The metallographic observations were recorded using a Neophot 21 optical microscope. The textures were measured on the Siemens D-500 goniometer system at McGill. ODFs were calculated from {110}, {200}, and {211} incomplete pole figures. Further details are available in Baczynski et al. (1999a).

3 Experimental results

The four microstructures formed in the steel that was reheated to 1275°C are shown in Figs. 1a-d. Polygonal ferrite was present in the air cooled sample (cooling rate (CR) less than 1°C/s), see Fig. 1a. When the cooling rate (CR) was increased to 20°C/s and the cooling interruption temperature CIT was 620°C, the volume fraction of polygonal ferrite decreased and an acicular ferrite phase appeared in the steel, see Fig. 1b. The amount of this phase was significantly higher at lower CITs. The sample for which the CIT was 520°C, see Fig. 1c, consisted almost exclusively of acicular ferrite grains. This trend was also observed in the samples reheated to 1150°C.

Table 1. Steel composition (in weight %)

	C	Mn	Si	Nb	Mo	Ti	Al	Cu+Ni+Cr	S	P	N
X-80	0.038	1.84	0.28	0.091	0.25	0.017	0.045	0.61	0.003	0.011	0.009

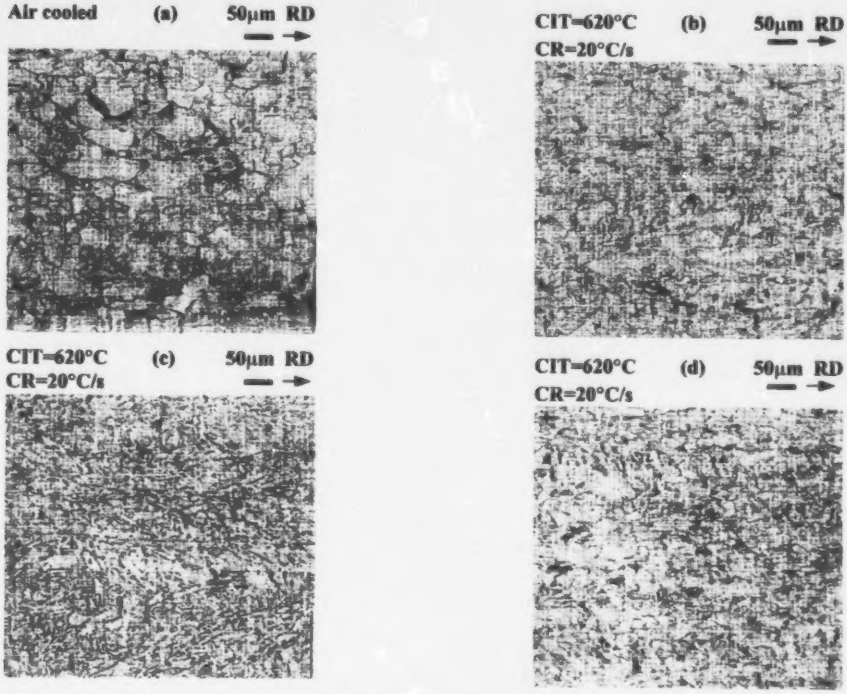

Fig. 1. Microstructures produced in the X-80 steel (RT=1275°C, FRT=780°C).

When the cooling rate was further increased from 20 to 40°C/s, there was a *decrease* in the volume fraction of the acicular phase, see Figs. 1c and d. These observations apply to all the samples (i.e. RT=1150°C, CIT=520°C and 620°C; RT=1275°C, CIT=520°C and 620°C).

Ten experimental textures are displayed in Figs. 3a-j in the usual φ_2=45° Euler space cross section. The processing conditions are described for each texture and the maximum intensities and contour levels are shown as well. All ten textures are qualitatively similar. These can be described as consisting of the {001}<110>, {113}<110>, {225}<110> and {112}<110> components (located along the <110>//RD fiber), the {332}<113> (located along the <110>//TD fiber), and the {335}<372> component (located close to φ_1=25°, ϕ=40°, φ_2=45° in Euler space).

The maximum intensities are shown in Fig. 4. In general, these are higher for the samples reheated at the lower temperature (RT=1150°C), compare the gray and black shaded blocks in Fig. 4. The lower cooling interruption temperature (CIT=520°C) leads to higher densities as well.

The ratios of the volume fractions of the {332}<113> and {225}<110> components are displayed in Fig. 5. For each reheat temperature, the employment of the lower CIT (520°C) led to the higher ratio. The volume fractions of the {332}<113> grains display maxima at a cooling rate of 20°C/s. However, an increase in the cooling rate from 20°C/s to 40°C/s leads to higher volume fractions of the ferrite grains associated with the {225}<110> orientation.

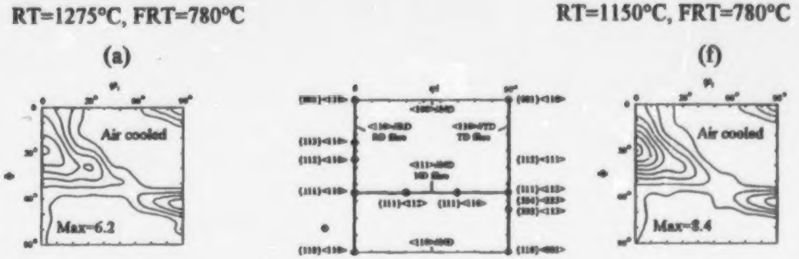

Fig. 3. $\varphi_2 = 45°$ ODF sections of the X-80 plates reheated at 1275 °C and 1150°C and finish rolled at 780 °C. Contour levels: 1, 2, 3, 4, 5, 6, 7, 8, 9, 10.

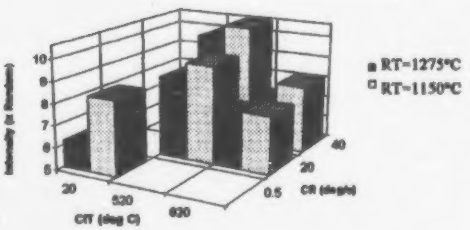

Fig. 4. Maximum texture intensities produced by following the various TMP schedules.

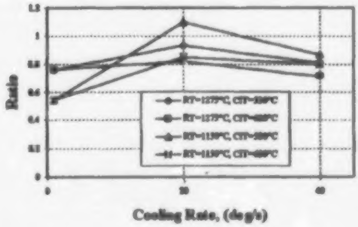

Fig. 5. Ratio of the volume fractions of the {332}<113> and {225}<110> components present after the TMP schedules employed in this work.

4 Discussion

In the present series of experiments, all the steels were finish rolled in the γ austenite phase. The finish rolling temperature was 780°C, which is appreciably higher than the measured ferrite-start (Ar_3=750°C) temperature. The final microstructures and textures therefore resulted from transformation of the pancaked austenite into ferrite. Finer austenite grains (formed when the lower RT=1150°C was used) are associated with finer polygonal ferrite and with more intense textures in the air cooled samples, compare Figs. 3a and f. Such observations are in agreement with those presented in the literature, Tanaka (1981), Ray and Jonas (1990). For instance, it is known that the α grain size correlates with the effective γ interfacial area S_V (grain boundary area plus deformation bands), Tanaka (1981).

It has also been reported that the texture intensities associated with acicular ferrite are appreciably higher than those related to the polygonal phase, Tanaka (1981). This trend can be deduced here by comparing the three microstructures (Figs. 1a, b and c) and the three corresponding textures (Figs. 3a, d and b). The maximum intensity of the air cooled sample is 6.2, while the condition: CIT=620°C and CR=20°C/s leads to an intensity of 7.4 and that of CIT=520°C and CR=20°C/s to 8.7. It is clear that the amount of acicular ferrite increases in the same order as well.

Nevertheless, the increase in texture intensity from 8.7 (Fig. 3b) to 10.0 (Fig. 3c) is associated with a *decrease* in the volume fraction of acicular ferrite, as shown in Figs. 1c and d. This trend was observed in all the samples reheated to 1150°C (see Figs. 3g and h and Figs. 3i and j). It therefore appears that increases in the volume fraction of acicular ferrite are not always related to intensity increases, as claimed in Tanaka (1981).

For the above reasons, it seems to be more accurate to relate the amounts of acicular and polygonal ferrite present in the final microstructure to the volume fractions of particular texture components. This analysis is shown in Fig. 5. The ratios of the volume fractions of the {332}<113> and {225}<110> grains are plotted against cooling rate for all ten processing conditions investigated in this study. Here it can be seen that the decrease in volume fraction of acicular ferrite grains observed in Figs. 1c and d (when the cooling rate was increased from 20°C/s to 40°C/s) corresponds to a decrease in the {332}<113>/{225}<110> ratio, see Fig. 5. This relationship was also observed in all the samples reheated to 1150°C.

It thus appears that the acicular ferrite grains are associated with the {332}<113> orientations while the {225}<110> component is related to the polygonal ferrite grains. This is entirely consistent with earlier observations (Ray and Jonas, 1990) regarding transformation textures. These authors have shown that higher cooling rates increase the intensity of the {332}<113> component, while that of the {225}<110> is relatively insensitive to cooling rate.

5 Conclusions

1. The ten textures investigated were qualitatively similar. These were characterized by the {001}<110>, {113}<110>, {225}<110>, {112}<110> {335}<372>, {332}<113> and {335}<372> orientations. The maximum intensities and the volume fractions of particular components nevertheless depended on the particular rolling schedules employed.
2. The lower reheat temperature (RT=1150°C.), lower cooling interruption temperature (CIT=520°C) and highest cooling rate (40°C/s) led to the strongest texture.
3. The volume fraction of acicular ferrite is linked to a single parameter, namely the volume fraction ratio of {332}<113>/{225}<110> grains. An increase in this ratio is associated with an increase in the volume fraction of the acicular phase.

6 Acknowledgements

The authors are grateful to Ipsco Inc. for supplying the X-80 steels and for financial support.

7 References

Baczynski, G.J., Jonas, J.J. and Collins, L.E. (1999a) The influence of rolling practice on notch toughness and texture development in high strength linepipe. Metall. Trans. A, in press.

Baczynski, G.J., Jonas, J.J. and Collins, L.E. (1999b) Through-thickness inhomogeneity of the texture developed in high strength linepipe. ICOTOM 12, in press.

Faucher, B. and Dogan, B. (1988) Evolution of the fracture toughness of hot-rolled low-alloy Ti-V plate steel. Metall. Trans., vol. 19A, pp. 505-516.

Kostic, M.M., Collins, L.E., Kapoor, A. and O'Hara, R.D. (1998) Development of heavy gauge X-80 linepipe. Proc. International Pipeline Conference, vol. 1, Calgary, June 7 - 11, ASME, New York, N.Y., pp. 665-688.

Okatsu, M., Kawabata, F. and Amano, K. (1997) Metallurgical and mechanical features of X-100 linepipe steel. Proc. OMAE, vol. 3, ASME, New York, USA, pp. 119-124.

Ray, R.K. and Jonas, J.J. (1990) Transformation Textures in Steels. International Materials Reviews, 35, pp. 1-36.

Tanaka, T. (1981) Controlled rolling of steel plate and strip. Int. Metals Reviews, vol. 26, n 4, pp. 185-212.

EFFECT OF PROCESSING VARIABLES ON TEXTURE FORMATION IN A TWO PHASE Ti_3Al-BASE ALLOY

SATYAM SUWAS and R. K. RAY
Department of Materials and Metallurgical Engineering
Indian Institute of Technology, Kanpur-208016 (INDIA)

Abstract

An attempt has been made to explore the effects of processing variables during hot rolling on the evolution of basal texture in a Ti-24Al-11Nb alloy. A range of rolling temperatures (1173 K–1523 K) was selected for this purpose. It has been found that basal texture strengthens in intensity with amount of deformation at 1173 K, assuming the highest intensity after 80% deformation. The texture of transformed (secondary) α_2, which is generally dictated by the texture of parent β-phase, is mostly non-basal when transformation takes place from deformed β, and basal when transformation takes place from recrystallised β.

Key Words: basal texture, hot rolling, secondary α_2, Ti-24Al-11Nb, transformation texture.

Introduction

The two phase (α_2+β) ordered intermetallic alloy Ti-24Al-11Nb is viewed as a candidate material for many aerospace applications [Kumpfert *et al.* 1992]. Texture is likely to be of extreme importance for such applications that require this alloy in sheet form. In spite of the fact that texture affects most of the properties of h.c.p. structured materials, it has not been paid much serious attention [Banerjee 1994]. It is known that significant improvement in ductility, which ultimately decides sheet formability, is obtained in h.c.p. Ti alloys with basal textured α grains. Other than a few preliminary papers by [Knorr and Stoloff 1991, Hon et al 1991 b], the only comprehensive study of texture evolution during thermomechanical processing of the Ti-24Al-11Nb alloy in recent years is due to Suwas [Suwas *et al.* 1999, Suwas 1998]. The present paper is a part of the above study [Suwas 1998], and is aimed at analysing the role of processing parameters on the evolution of basal texture in this alloy.

Experimental Procedure

The starting material used was in the form of a cast pancake having the chemical composition: Al 24.60 (at%), O 650 ppm, N 80 ppm, H 28 ppm and Ti balance. Rectangular pieces from this pancake were used for thermomechanical processing.

Thermomechanical processing involved multipass rolling at temperatures 1173 K, 1293 K, 1373 K and 1523 K followed by water quenching as well as furnace cooling. The rolling deformation varied between 50% and 80%. After each pass the samples were put back into the furnace for 2-3 minutes so that they re-attain the rolling temperature. The above sequence of operation was repeated till the sample acqired the final desired thickness. Rolling was kept strictly unidirectional. Crystallographic texture of the α_2 phase of the processed materials was determined from mid-thickness section of samples by measuring the (0002) pole figure using a Siemens Crystalloflex D-5000 Texture Goniometer with Mok_{α} radiation.

Results

The (0002) pole figure recorded from the cast specimen surface, which is normal to the direction of heat extraction during solidification from the melt, is shown in Fig. 1(a). The basal poles here exhibit {0002}<uvtw> type texture where <uvtw> is the longitudinal direction of the specimen. Heat treatment (24 hrs at 1173 K) of the as-cast material followed by furnace cooling has not been found to cause any perceptible change in the texture (Fig. 1 b).

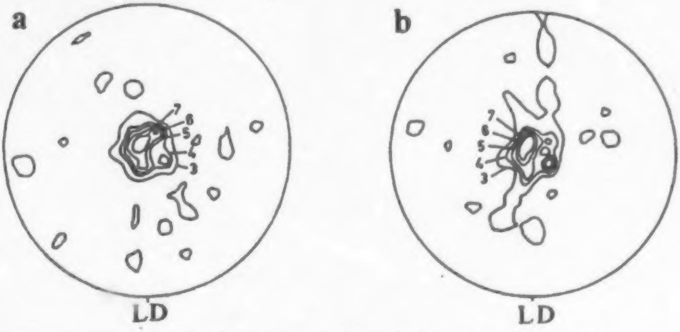

Fig. 1 (0002) pole figures for the (a) as-cast material, and (b) heat treated material

Rolling at 1173 K

As cast, rolled and quenched

The (0002) pole figure for the α_2 phase in the 50% rolled material shows a reasonably strong (~6R) near basal component of texture (Fig. 2a). The pole density at the centre of the pole figure shows splitting along both RD and TD — the splitting along TD being most prominent. After 70% rolling the near basal component maintains its strength and shows splitting along TD only (Fig. 2b). The basal component becomes more perfect after 80% rolling, although there is a slight tendency towards splitting along RD (Fig. 2c). In all the above cases, a host of other weak components of texture is also seen.

Heat treated, rolled and quenched

Figs. 3 (a-c) show the (0002) pole figures of the heat treated material rolled 50%, 70% and 80% respectively. All the three pole figures show reasonably perfect basal texture, the degree of perfection increasing with the amount of rolling reduction. In all of them, in addition to the basal component, some other weak components can also be seen.

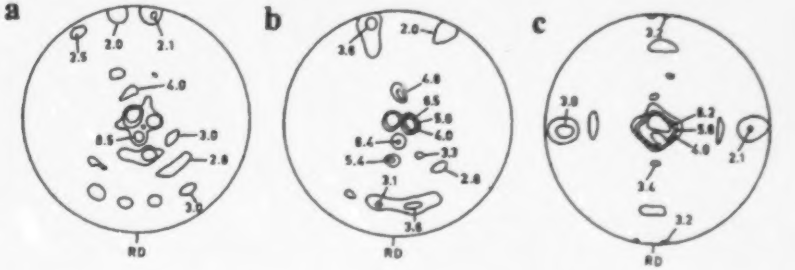

Fig. 2 (0002) pole figures for the as-cast materials rolled at 1173 K to (a) 50%, (b) 70% and (c) 80% rolling reductions (water quenched)

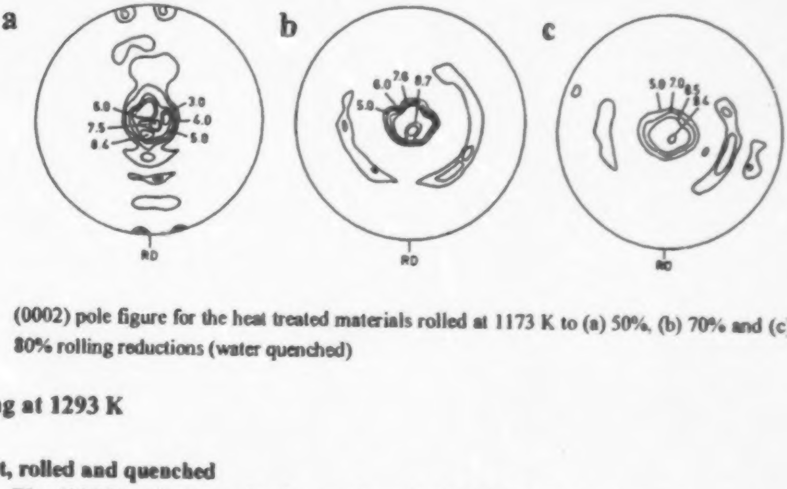

Fig. 3 (0002) pole figure for the heat treated materials rolled at 1173 K to (a) 50%, (b) 70% and (c) 80% rolling reductions (water quenched)

Rolling at 1293 K

As cast, rolled and quenched

The (0002) pole figure for the α_2 phase in the 50% rolled material shows a basal component of texture plus few other components (Fig. 4a). At the higher degree of deformation (80%), the sharpness of the basal texture increases and this also shows a tendency of splitting (Fig. 4b). Some extra orientations do appear in this case also but with lesser intensity.

As cast, rolled and furnace cooled

The (0002) pole figure for the 80% rolled material (Fig. 4 c) shows the presence of a weak texture of mixed character. The basal poles here show a tendency of splitting along both RD and TD.

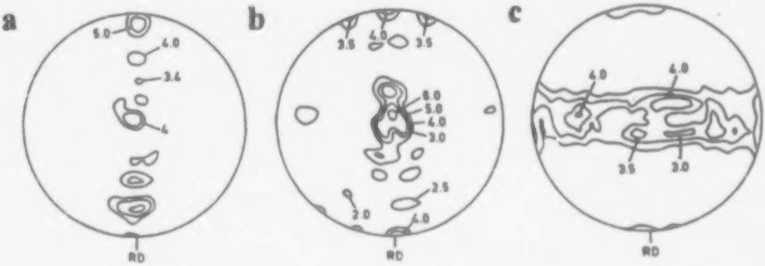

Fig. 4 (0002) pole figures for the 1293K rolled materials; (a)50%, (b)80% (both water quenched) and (c) 80% and furnace cooled

Rolling at 1373 K

As cast, rolled and furnace cooled

The (0002) pole figure for the 80% rolled material represents a completely non-basal texture with (0002) poles located almost 70° off from the centre towards TD (Fig. 5 a).

Rolling at 1523 K

As cast, rolled and furnace cooled

The (0002) pole figure for the 80% rolled material is shown in Fig. 5 (b). In contrast with the pole figure for the 1373 K rolled and furnace cooled material, the pole figure here shows the presence of (0002) poles concentrated at the ND position. In addition the pole figure also indicates the split TD character of the basal texture.

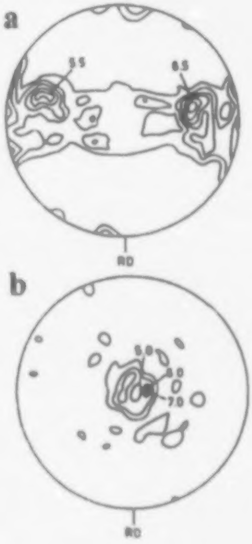

Fig. 5 (0002) pole figures for (a) 1373 K and (b) 1523 K rolled materials

Discussion

The deformation processing of the alloy was carried out (i) in the (α_2+β) phase field at two different temperatures namely at 1173 K and 1293 K, (ii) at near β-transus temperature, which is (1373±10K) in the present case and (iii) in the β phase field, at the temperature of 1523 K. Thus during rolling in the (α_2+β) phase field the material being deformed has different volume fractions of α_2; had almost no α_2 during rolling at near the β-transus temperature, and had literally no α_2 during rolling at the rolling temperature of 1523 K.

The thermomechanically treated materials were examined under two conditions : (a) hot rolled and water quenched and (b) hot rolled and furnace cooled after the last rolling pass. While the objective of examining the material in the first condition was to study texture formation in primary α_2 as a function of rolling temperature and amount of deformation, the second condition was expected to provide an insight into the evolution of texture in a mixture of (primary+secondary)α_2 and in fully secondary α_2 as a function of the processing variables.

Texture of rolled primary α_2

The results of this investigation clearly show that a lower temperature of rolling and a higher degree of rolling deformation favour the evolution of basal (0002) texture with improved intensity. Rolling at higher temperatures, where the content of the β phase is more, can impose additional constraints on the rotation of α_2 grains, thereby lowering the intensity of $(0002)_{\alpha 2}$. These observations broadly tally with those of Hon *et al.* [Hon *et al* 1991 b] for an alloy of similar composition.

Texture of secondary α_2

In the course of the present investigation there have been two cases where texture measurements were performed exclusively on the secondary α_2 phase. These are the materials rolled at 1373 K and 1523 K followed by furnace cooling. Microstructural examination of the 1373 K rolled (80%) and water quenched samples shows β grains with profuse strain markings inside. On the other hand, the 1523 K rolled (80%) and water quenched sample consists of larger β grains, which appear to be rather strain free (no strain markings inside the grains). Therefore, in the former case the secondary α_2 phase results from more or less recrystallised β.

Fredericks [Fredericks 1973] proposed that if the β to α transformation takes place under constraints from the rolling deformation, only one of the six highly textured {110} planes of the β phase is favoured in transforming to the {0002} planes of the product hexagonal phase, as per Burger's relationship. It has also been argued that if the textured β phase is allowed to recrystallise first, before transforming into α phase, all six {110} planes will be equally favoured in transforming to the basal plane giving rise to a strong basal texture. This could be a possible explanation of the textural differences of the secondary α_2 derived from the 1373 K and 1523 K rolled materials.

Texture of primary plus secondary α_2

The samples which were rolled at 1293 K and either water quenched or furnace cooled belong to this category. In the former, the room temperature microstructure consists roughly of 50% primary and 40% secondary α_2, plus some retained β.

The crystallographic texture of α_2 in the primary α_2/β sample (Fig. 4 b) is basal in nature while that in the primary α_2/secondary α_2 sample (Fig. 4 c) is very much non-basal. The difference in the processing between the above two materials was that while the latter stayed after rolling in a high temperature region. For a much longer period of time, the former did not have that opportunity. In other words, the furnace cooled material underwent much more extensive recovery and partial recrystallisation as compared to the quenched material. It therefore appears quite plausible that the tangible decrement of the near basal texture of primary α_2 in the furnace cooled sample has been caused at least partly by the annealing effect. The fact that the secondary α_2 in this sample has been derived from primary strained β will add to the observed effect.

Conclusions

1. Unrestricted rolling of primary α_2 at 1173 K leads to the formation of the sharpest (0001)[*uvtw*] basal texture. Basal texture strengthens in intensity with amount of deformation at 1173K.
2. The texture of transformed (secondary) α_2 is dictated by the texture of parent β-phase. Texture is mostly non-basal when transformation takes place from deformed β, but possess some basal components when transformation takes place from β phase in the annealed state.

Acknowledgements

The authors are grateful to Dr. D. Banerjee, Director, DMRL, Hyderabad for his constant encouragement as well as for providing the texture measurement facility. We also thank Dr. A. K. Singh for his cooperation and Dr. A. K. Gogia and Mr. T. K. Nandy for several useful discussions. The grant-in-aid from AR & DB, Ministry of Defence, Government of India, is duly acknowledged.

References

Banerjee, D. (1994) in Intermetallic Compounds: Vol. 2, Practice, eds. Westbrook, J.H. and Fleischer, R.L., John Wiley & Sons Ltd., p. 91.
Frederick, S.F., AFML-TR-73-265, 1973.
Hon, W.P., Koo, C.H., Wu, S.K., and Chou, T.S., Scripta Metall, 1991, Vol. 25, p. 2171.
Knorr, D.B., and Stoloff, N.S., Mater. Sc. Engg., 1991, Vol. A 123, p. 81.
Kumpfert, J. and Ward, C. H. (1992) in Advanced Aerospace Materials, ed. Buhl, H., Springer Verlag, Heidelberg, p. 73-83.
Suwas, Satyam, Ray, R. K., Singh, A. K. and Bhargava, S. (1999) to be published in Acta Materialia.
Suwas, Satyam (1998) Ph. D. Thesis, I. I. T. Kanpur.

TOPOLOGICAL ASPECTS OF RIDGING PHENOMENON IN FERRITIC STAINLESS STEEL

K. SZTWIERTNIA, J. POSPIECH and T. ROSTEK
Institute of Metallurgy and Materials Science, Polish Academy of Sciences, Kraków, Poland

Abstract

The ridging phenomenon occurring in ferritic stainless steel sheets in the case of elongation or deep drown is here investigated by the SEM-EBSD technique (Electron Backscattering Diffraction in the Scanning Electron Microscope). Orientation topography acquired using this technique shows that the interior of the sheet is composed of two macro-elements of different anisotropy: thin, {001}<110> oriented bands lying parallel to the former rolling direction and the matrix with orientations: {112}<110>, {111}<134>, {111}<110> and {111}<112>, mixed on the local scale. From the analysis of the rope or ripple shaped deterioration results that their geometry is formed by two kinds of superimposed effects, namely the macro-ridging on the millimetre scale and micro-ridging on the micrometer scale. The first of them is directly related to inhomogeneity of the texture and it can be interpreted according to the mechanism proposed by Wright (Wright 1972). Then the micro-ridging can be explained by the anisotropic interaction between sample symmetry related variants of the same component, particularly of the type {112}<110>, which roughly corresponds to the model of Appel-Lücke (Appel 1971).

Keywords: Ferritic stainless steel, orientation topography, ridging phenomenon

1 Introduction

Ferritic stainless steel sheets, after cold rolling and annealing, turn from flat into corrugated when pulled or deep drawn. The resulting deterioration of the surface quality is a severe and a long known problem in industrial processing. It consists in the fact that a transverse section of such an elongated sheet displays (nonperiodic) undulations, with peaks on one side of the sheet coinciding with valleys on the other side without changes of the sheet thickness. The valleys, with a depth of about 10 – 20 μm, extend over the whole, elongated piece of sheet parallel to the former rolling direction, whereas in the transverse direction the distance between the peaks reaches 1 to 2 mm. This characteristic roping morphology (called macro-ridging), observed with the naked eye, is superimposed by other much smaller ripples on a micrometer scale (called micro-ridging).

2 Experimental

The investigated material was a ferritic stainless steel sheet Type 434 (17% Cr, 1% Mo), 80% cold rolled, recrystallized and 7% elongated parallel to the former rolling direction. For this state, using the SEM-EBSD technique, orientation measurements have been performed: in the form of scans along rolling direction and transverse direction and also over rectangular areas with their shorter sides situated parallel to the former rolling direction and the areas arranged one after the other in a series in a defined plane parallel to the sheet plane. Because of the existence of through-sheet microstructure inhomogeneity, the measurements in several layers trough the thickness were required. The measuring point distance was fixed at 10 μm, which corresponds to the mean size of the grain.

3 Results

The ODF plots in Fig. 1a,b show the variation of texture from the surface to the centre of the sample. The orientation distribution in the surface layers (about 20% of the sheet volume) as well as the texture of the sample interior (about 70% of the sheet volume) can be described by the α-fibre with the main components {001}<110>, {112}<110> and {111}<110> and γ-fibre with the main components {111}<112> and {111}<134>. These components comprise respectively ~10%, ~8%, ~10%, ~6% and ~9% of the volume of the surface layers and ~10%, ~11%, ~8%, ~6% and ~8% of the volume of the internal layers. A particular component comprises orientations inside a distance of 15^0. It is noted that texture inhomogeneity through thickness is relatively

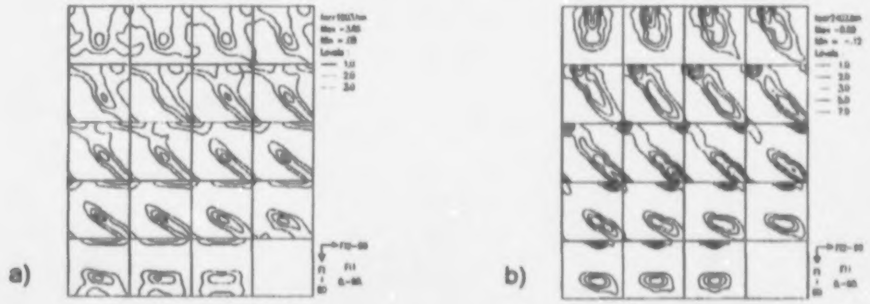

Fig. 1: The ODFs calculated from single orientations measured of cold rolled to 80% ferritic stainless steel sheet: a) surface layer; b) central plane.

weak. A more spectacular disagreement between the microstructure of the surface and the interior of the sample can be observed in the topological arrangement of the particular components. The texture components in the near surface layers of the sample are randomly distributed, while in their interior the same components have a distinct tendency to form thinner or thicker bands lying roughly parallel to the former rolling direction. This tendency refers particularly to the orientation CF (cube-on-face)={001}<110> (Fig. 2). The thickness of the CF oriented bands reaches up to 1mm in the transverse direction and up to 70% of the total sample thickness in the normal direction. Measuring orientation topographies in the rectangular areas lying one after the other along the rolling direction, it could be proved that CF oriented bands extend in this direction for dozens of millimetres. These bands are significantly richer in chromium and molybdenum than the matrix and their geometry corresponds with the arrangement of the macro-ridges (Fig. 3). Thus, the material is composed of two macro-elements of different anisotropy and of different content of the alloying elements.

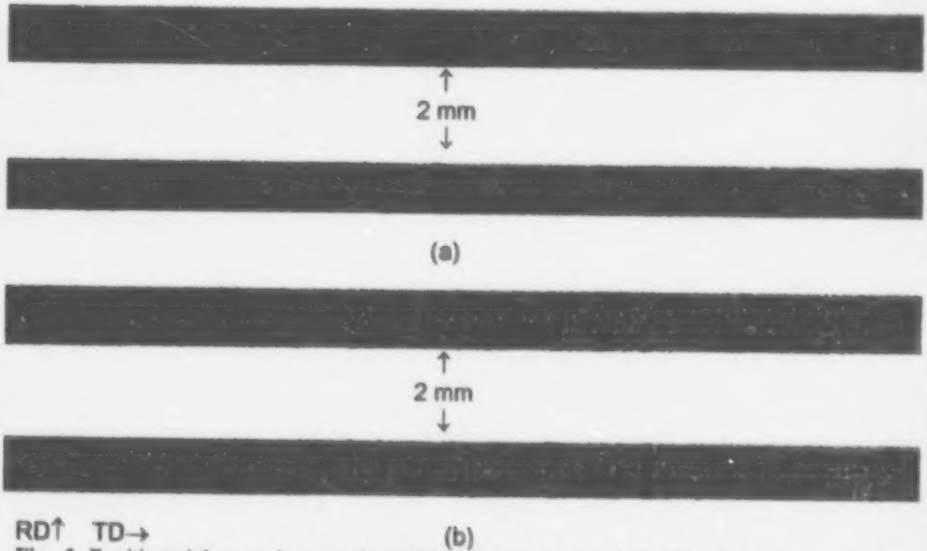

Fig. 2: Ferritic stainless steel, scanned area RDxTD (a) two sets of 40x900 orientations on the surface, (b) two sets of 30x900 orientations in the central plane. In black - the topological arrangement of the orientation CF in the matrix with the mixed orientation arrangement (grey).

The orientation image of the matrix along the transverse direction shows, as a rule, large variations in orientations over a region as small as several dozens of micrometers. The neighbouring, strongly disoriented orientations, belong often to different sample symmetry related variants (SSVs) of the same component (Table 1). Incidentally, as an exception to the above rule, regions (on the millimetre scale), whose orientations belong only to one SSV of some particular component, can be found (Fig. 4). This last observation means that in the sample after 80% cold rolling there exist quite large regions where the statistic orthorhombic symmetry of the sheet is not completely satisfied.

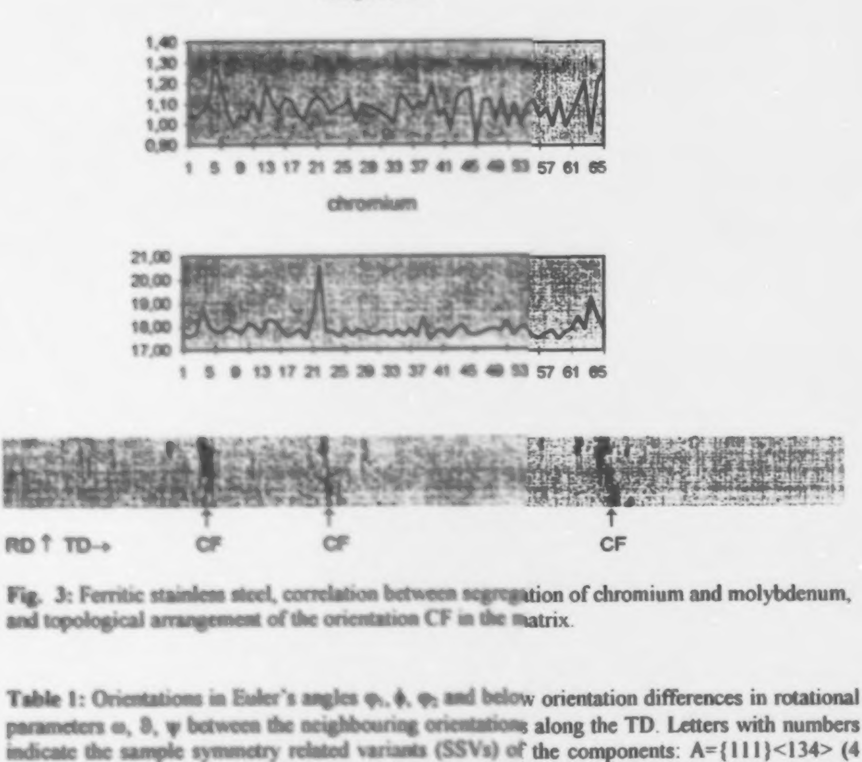

Fig. 3: Ferritic stainless steel, correlation between segregation of chromium and molybdenum, and topological arrangement of the orientation CF in the matrix.

Table 1: Orientations in Euler's angles φ_1, ϕ, φ_2 and below orientation differences in rotational parameters ω, θ, ψ between the neighbouring orientations along the TD. Letters with numbers indicate the sample symmetry related variants (SSVs) of the components: A={111}<134> (4 SSVs), B={111}<112> (2 SSVs), C={112}<110> (2 SSVs) and CF={001}<110> (1 SSVs) nearest to the measured orientation. The numbers in brackets give the smallest modulus of the rotation angle ω to the particular component. a) The matrix: cluster comprising both SSVs of {112}<110> oriented grains can be recognised. b) Section across the CF oriented band.

Nr	φ_1	ϕ	φ_2	SSV ω
365	181.7	43.8	42.9	** C_2(8.9)
	59.5	46.2	45.0	
366	353.0	18.4	52.8	** C_1(16.9)
	57.5	47.7	39.7	
367	176.5	45.3	44.4	** C_2(11.0)
	-57.9	49.2	39.7	
368	355.0	19.8	50.7	** C_1(15.4)
	32.5	25.8	15.1	
369	13.7	50.6	38.6	** A_2(7.9)
	19.0	49.1	40.4	
370	12.7	34.1	48.7	** C_1(15.9)

(a)

Nr	φ_1	ϕ	φ_2	SSV ω
867	154.9	51.6	49.5	** B_2(9.0)
	55.9	41.8	14.7	
868	13.9	12.2	32.3	** CF(12.3)
	15.4	37.7	1.6	
869	127.2	5.7	9.3	** CF(5.9)
	-6.5	12.6	33.9	
870	187.8	7.0	39.8	** CF(7.5)
	13.8	40.6	32.5	
871	333.2	6.5	69.8	** CF(6.8)
	10.9	32.3	40.1	
872	1.8	15.5	45.4	** CF(15.7)

(b)

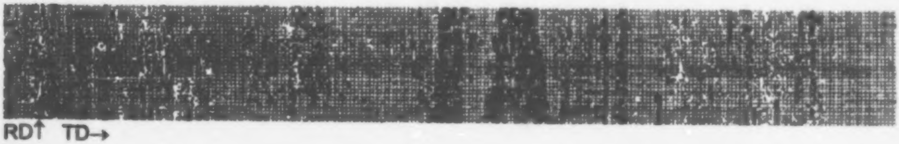

Fig. 4: Ferritic stainless steel, scanned area RDxTD of 50x700 orientations, example of region whose orientations belong mostly to one sample symmetry related variant of the particular component; black= $(112)[1\bar{1}0]$, white= $(11\bar{2})[1\bar{1}0]$

4 Discussion

The morphology of the central rolling plane suggests that in order to explain the origin of the macro-ridging the plastic buckling mechanism of Wright (Wright 1972) can be adopted. The model of Wright assumes, according to our observation, that highly anisotropic thin bands, relatively rich in {001}<110> texture, exist within a matrix of different anisotropy. Such bands contract mostly in the normal direction upon tensile loading in the rolling direction. These bands are surrounded by material relatively rich in near {111}<112> texture (or near {111}<134>), which involves much less contraction in the normal direction, and much more contraction in the transverse direction, when subjected to tensile elongation in the rolling direction. When such a structure is pulled in the rolling direction, the failure of the band to contract in the plane (nearly parallel to the transverse direction) of the sheet will result in the generation of compressive stresses across the band's width and the ultimate buckling of the band.

At present exist other essential concepts like for example Takechi et al. (Takechi et al. 1967) or Appel and Lücke (Appel 1971), associating the ridging phenomenon with the anisotropy of plastic deformation. Each of these concepts is based on the assumption that the SSVs of the same texture component when pulled undergo a shear of the same modulus but of different sign, which leads to characteristic undulation of the sheet. In both models it is assumed that in the material there exist sufficiently large, neighbouring grains or grain clusters of orientations belonging to different SSVs of appropriate component (Takechi {111}<011>, Appel and Lücke {112}<110>). Unfortunately these models cannot be fully correct, because to large factor of about 100 (in general) between the magnitudes of the macro-ridging width and the scale of the matrix orientations changes in the transverse direction [e.g. (Bethke et al. 1997), (Sztwiertnia et al. 1998)]. In the sheet there were incidentally found quite large, band-like, {112}<110> or {111}<011> oriented regions, but of orientations belonging only to the one SSV. Such regions can contribute to the macro-ridging in this sense that after elongation some deflection of the sheet, strengthening the ridges, can originate.

On the other hand, a model such as that of Appel and Lücke may explain the micro-ridging phenomenon. The clusters consisting of both SSVs of the {112}<110> component varying over regions as small as several dozen micrometers along the transverse direction correspond well to the above model (Table 1).

In order to explain the relationship between the band-like distribution of the orientation CF, and the segregation of chromium and molybdenum in the ferritic stainless steel sheet one should analyse the processing sequence for this type of steels.

From such the analysis it follows that the distribution of the CF component in the interior of the sample results from the segregation of the alloying elements in the sheet. The segregation itself is caused by the former processing steps. The most critical is here the hot rolling of dendritically solidificated ingots (Defilippi and Chao 1971; Suzuki and Asami 1984).

5 Conclusions

The analysis of our observations as well as observations of other authors (Appel 1971; Bethke et al. 1993; Brochu et al. 1997; Defilippi and Chao 1971; Wright 1972) allows some important conclusions. First, one should distinguish between the macro-ridging on the millimetre scale and the micro-ridging on a micrometer scale, the origin of which can be quite different. Secondly, the macro-ridging phenomenon is directly related to the different anisotropy of two macro-elements - the CF oriented bands and the matrix - composed structure of the ferritic stainless steel sheet. The origin of the main features of the macro-ridging morphology could be explained by the plastic buckling mechanism of Wright. Then the micro-ridging is probably related to the behaviour of the texture component of the {112}<110> type during elongation of the sheet in the <110> direction. Thirdly, the feature of the sheet structure causing the macro-ridging - the band-like distribution of the CF component - results from the segregation of the alloying elements in the sheet.

5 References

Appel, W H. G. (1971) Thesis, RWTH Aachen.

Bethke, K., Hölscher, M., Lücke, K. (1993) Local orientation investigation on the ridging phenomenon in Fe 17% Cr steel. in *Proc. ICOTOM 10*, (ed. H. J. Bunge), Clausthal, pp. 1137-44.

Bethke, K . (1997) Thesis, RWTH Aachen.

Brochu, M., Yokota T. and Satoh, S. (1997) Analysis of grain colonies in type 430 ferritic stainless steels by electron back scattering diffraction (EBSD). *ISIJ International*, Vol. 37, pp. 872-77.

Defilippi, J. D. and Chao, H-. C. (1971) Effect of chromium and molybdenum segregation on the ridging behaviour of type 434 stainless steel. *Met. Trans.*, Vol. 2, pp. 3209-16.

Suzuki, K., Asami, S. (1984) Microsegregation of chromium and carbon and ridging phenomenon in 18 Cr stainless steel sheets. *Trans. Iron Steel Inst. Jap.*, 1, pp. 1-6.

Sztwiertnia, K., Pospiech, J., Bethke, K. (1998) Ridging phenomenon in ferritic stainless steel. in *Proc. XV Physical Metallurgy and Materials Science Conference on „Advanced Materials & Technologies"*, (eds. J. Kusiński, I. Suliga, S. Kąc), Krynica, pp. 264-67.

Takechi, H., Kato, H. , Sunami, T. , Nakayama, T. (1967) The mechanism of ridging formation in 17% chromium stainless steel sheets. *Trans. Jap. Inst. Metals*, Vol. 8, pp. 233-39.

Wright, R. N. (1972) Anisotropic plastic flow in ferritic stainless steels and the roping phenomenon. *Met. Trans.*, Vol. 3, pp. 83-91.

CUBE TEXTURE FORMATION IN PURE ALUMINIUM AS INFLUENCED BY IMPURITIES AND ROLLING TEMPERATURES

Kunio Ito* and Akihiro Fukushima
Department of Materials Science, The University of Tokyo
* now with Department of Industrial Engineering and Management, College of Industrial Technology, Nihon University, Narashino, 275-8575 Japan

Abstract

With the aim to examine effects of low concentration Fe on formation of cube texture, one commercial alloy for capacitor foil and three laboratory made alloys containing Fe between 2ppm and 80ppm were rolled at -77°C and 85°C, and annealed at 350°C and 500°C. The laboratory alloy develops more cube component than the commercial alloy, even when it contains more Fe than the commercial alloy . The cube component forms more in the higher Fe concentration laboratory alloy than in the lower Fe concentration laboratory alloy. It has been hence concluded that not Fe but rather Si and/or Cu suppresses the formation of cube texture in the commercial alloy. The results are explained by the consideration that only impurities precipitating during recrystallization can critically influence the recrystallization process.

Key words: Cube texture, effect of iron, effect of rolling temperature, pure aluminium

1 Introduction

The solute iron which may precipitate during recrystallization annealing is known to suppress severely formation of cube texture in aluminium sheet(Ito et al. 1983). It is considered to influence a recrystallization process even at a smaller concentration(Li and Saimoto 1998). The effect of smaller amount of Fe seems, however, to be not clarified yet. Aluminium free from solute Fe recrystallizes during rolling at room temperature (Takei et al. 1980 and Seki et al. 1996). In the present report, textures were examined of Al sheets with low contents of Fe rolled at two temperatures.

2 Experimental procedure

The compositions(mass ppm) are given by alloy names. Other not specified impurities are less than 2ppm. Alloy 7Fe7Si50Cu is a commercial alloy for electrolytic condenser foil. A 38mm thick plate was machined from the centre layer of hot rolled 60mm thick plate. Other alloys were cast into permanent mould(200Lx100Wx50T in mm) in laboratory and forged at room temperature to about 100W-> 40mm and machined to 38mm thick plates. The plates were rolled to 20mm at room temperature and annealed; 7Fe7Si50Cu for 1h at 360°C, 2Fe1Si for 2h at 400°C, 35Fe10Si for 2h at 420°C, and 80Fe2Si for 2h at 470°C. The commercial alloy shall be designated as the ternary alloy and the three laboratory alloys shall be called the binary alloys.

The plates were rolled through the same pass schedule either to about 0.35mm, being dipped into an oil bath of 85°C for 2 - 3 min during each pass and after the final pass, or to about 0.55mm, being dipped into an ethanol bath of -77°C for 1 min during each pass. Specimens rolled at -77°C and at 85°C were annealed at 350°C respectively for 20min and 30min in an electric furnace, and at 500°C for 30s in a salt bath.

The Vickers hardness HV(kgf/mm^2) was obtained with a loading of 200gf(specimens rolled at -77°C) or 100gf(specimens rolled at 85°C). Pole figures were measured of layers beneath the sheet surface by about 1/3 – 1/2 of the thickness. The intensity levels(0.5, 1, 2, 4, 6) are referred to a powder specimen. Cube index was calculated from the symmetrized pole figure by the following equation(Ito et al. 1996 and Seki et al. 1996);

Cube index = sum of intensities in the area α=45 to 65°, β=35 to 55° / sum of intensities in the area α =0 to 70°, β=0 to 90°. Structures were observed on the plane containing RD(rolling direction) and ND(sheet plane normal).

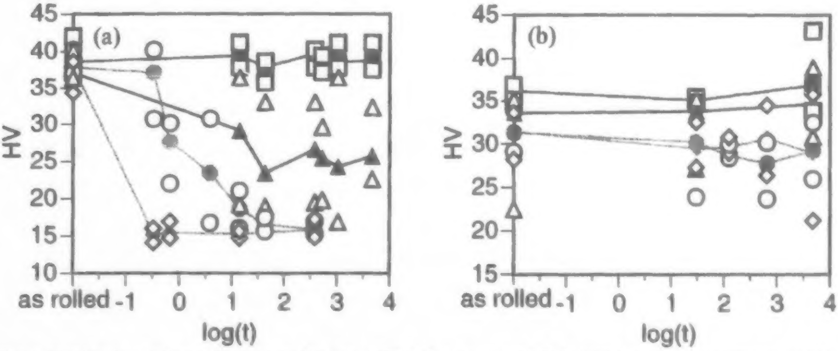

Fig.1 Softening of specimens rolled at -77°C (a) or at 85°C (b) and kept at room temperature for time t(in h). Solid marks present mean values and open marks indicate observed maximum and minimum values. ■:7Fe7Si50Cu, ●:2Fe1Si, ▲:35Fe10Si, ◆:80Fe2Si

3 Experimental results

The binary alloys rolled at -77°C soften quickly at room temperature, especially when Si concentration is low(Fig.1 (a)). The cube component is correspondingly rich(cf. Fig.3 (a) and (b) with Fig.3 (c), see Fig.6 also). When rolled at 85°C, they do not soften at room temperature(Fig.1 (b)). The structure is similar to cold worked ones(Fig.2). Their textures, however, look like annealing textures(Fig.3 (d) , see Fig.6 also).

In the case of specimens rolled at -77°C, the ternary alloy develops more cube component by annealing at 500°C than by annealing at 350°C(Fig.6 (a)). The same trend is a little observed for the binary alloy with higher Si concentration(35Fe10Si in Fig.6 (a)), annealing textures of the other binary alloys show little dependence on the two annealing temperatures(cf. Fig.4 (a) with Fig.5 (c) and Fig4 (c) with Fig.5 (e)). The low Si binary alloys develop more cube component with higher Fe content than with lower Fe content(cf. Fig.4 (a) with Fig4 (c) and Fig.5 (c) with Fig.5 (e), see Fig.6 (a) also).

When rolled at 85°C, annealing textures of the ternary alloy show little dependence on the annealing temperatures(Fig.6 (b)). The dependence is small in the binary alloys too, except for the higher Si alloy, (cf. Fig.4 (b) with Fig5 (d) and Fig.4 (d) with Fig.5 (f), see Fig.6 (b)). The same trend as for the specimens rolled at -77°C, that higher Fe content develops more cube component than lower Fe content, is observed for the low Si binary alloys(cf. Fig.4 (b) with Fig4 (d) and Fig.5 (d) with Fig.5 (f)).

The textures of the ternary alloy annealed at 500°C are not influenced by the rolling temperatures(cf. Fig.5 (a) with Fig.5 (b)). The low temperatur rolling yields more cube component than the high temperature rolling in the low Si binary alloys(Fig.4, Fig.5, and Fig.6). The difference is small in the higher Si binary alloy.

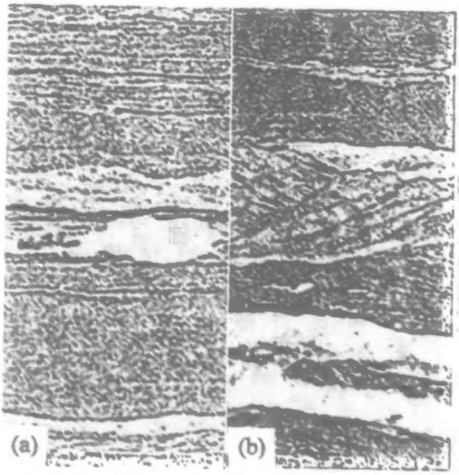

Fig.2 35Fe10Si rolled at -77°C (a) or at 85°C (b). 20μm

4 Discussion

The results have shown that Fe less than 80ppm does not critically influence the recrystallization behaviour of the laboratory made binary alloys, while the bihaviour of the commercial ternary alloy is distinctly different from the binary alloys.

The diffusivity of Fe in Al is quite low and its activation energy is higher compared with the selfdiffusion of Al(Fujikawa 1996). The precipitation of Fe must hence not be able to compete with progress of recrystallization, when Fe content is lower than a critical value(see Fig.7). In the case of such elements as Si and Cu, the diffusivity is high and activation energy is low(Fujikawa 1996). They can hence precipitate at lower temperatures competing with recrystallization. The contents of Si(10ppm) and Cu(50ppm) are reasonably expected to be larger than their solubilities around room temperature.

The dependence of recrystallization behaviour of Al on Fe contents observed in this work and reported earlier(Ito et al. 1983) can be understood by the consideration that only Fe precipitating on recrystallization fronts and/or in recovering matrix can critically influence the progress of recrystallization. The dragging of recrystallization fronts by segregating Fe must not be realized at lower temperatures, because of its too much low diffusivity. The suppression of cube component in the commercial capacitor alloy must be also due to precipitation of Si and/or Cu. The dragging by Si and Cu must be small because of their high diffusivities (and very probably of their low interaction with bound-

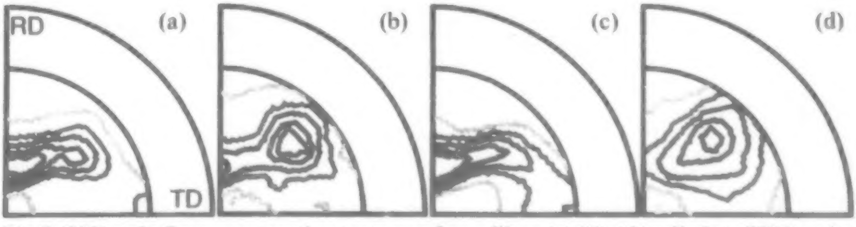

Fig.3 (111) pole figures presenting textures after rolling. (a) 2Fe1Si rolled at -77°C, cube index = 0.19 and HV after pole figure measurement = 34, (b) 80Fe2Si rolled at -77°C, cube index = 0.39 and HV = 19, (c) 7Fe7Si50Cu rolled at 85°C, cube index = 0.15 and HV =36, and (d) 80Fe2Si rolled at 85°C, cube index = 0.37 and HV =31.

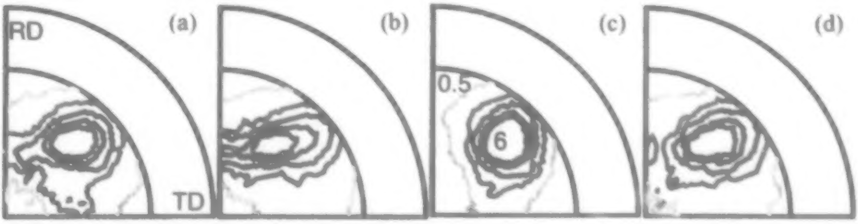

Fig.4 (111) pole figures presenting textures after annealing at 350°C. (a) 2Fe1Si rolled at -77°C, cube index = 0.46, (b) 2Fe1Si rolled at 85°C, cube index = 0.37, (c) 80Fe2Si rolled at -77°C, cube index = 0.62, and (d) 80Fe2Si rolled at 85°C, cube index = 0.49.

aries). Any effects of minor impurities such as Na cannot certainly be excluded.

Extensive recovery and/or recrystallization has yielded the cube component in rolling texture, indicating that the cube oriented regions are formed during rolling process. The formation process of deformation structure in pure Al rolled around room temperature and its effects on recrystallization process are at moment not clear.

5 Summary

Rolling and annealing textures of a commercial electrolytic condenser foil alloy rolled at -77°C and 85°C have been compared with those of laboratory made alloys containing Fe between 2ppm and 80ppm.

Even when the Fe content in the laboratory alloy is higher than that in the commercial alloy, the laboratory alloy recrystallizes more quickly and develops more cube component than the commercial alloy. Among the laboratory alloys, the Fe contents play no critical roles in the recrystallization behaviours.

The conclusion has been drawn that the suppression of cube texture formation in the commercial alloy is not due to Fe but rather due to Si and/or Cu, and explained by the consideration that only impurities precipitating during recrystallization can critically influence the process of recrystallization. Any effects of minor impurities such as Na cannot certainly be excluded.

The annealing textures of the commercial alloy have not been critically influenced by the rolling temperatures, while the lower temperature rolling develops a little more cube component in

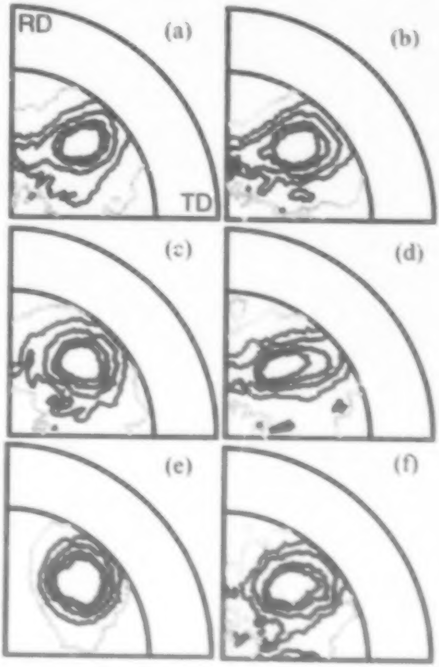

Fig.5 (111) pole figures presenting textures after annealing at 500°C.
(a) 7Fe7Si50Cu rolled at -77°C, cube index = 0.49, (b) 7Fe7Si50Cu rolled at 85°C, cube index = 0.49, (c) 2Fe1Si rolled at -77°C, cube index = 0.50, (d) 2Fe1Si rolled at 85°C, cube index = 0.42, (e) 80Fe2Si rolled at -77°C, cube index = 0.67, and (f) 80Fe2Si rolled at 85°C, cube index = 0.50.

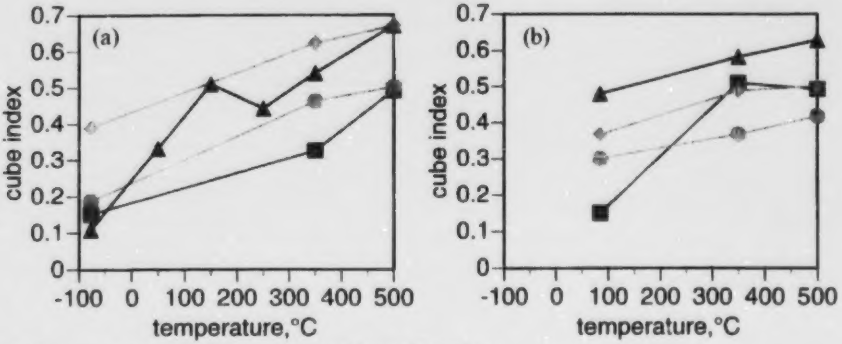

Fig.6 Summary of textures presented by cube index.
(a) specimens rolled at -77°C and annealed, and (b) specimens rolled at 85°C and annealed. ■:7Fe7Si50Cu, ●:2Fe1Si, ▲:35Fe10Si, ◆:80Fe2Si

the annealing textures of the lower Si laboratory made alloys than the higher temperature rolling.

The formation process of cold worked structure in the purest Al and its recrystallization behaviours are not clear.

Acknowledgement

This work was supported by The Light Metal Educational Foundation of Japan. The authors thank the Foundation.

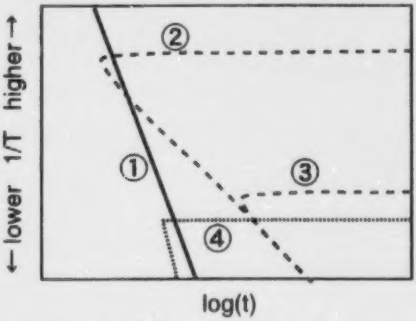

Fig.7 Schematic time-temperature diagramm for relation among progress of recrystallization and precipitation.
① :recrystallization, ② :precipitation of higher concentration Fe,
③ :precipitation of lower concentration Fe, ④ :precipitation of Si or Cu

6 References

Fujikawa, Sh. ,(1996), J.Japan Inst. Light Met., **46**, pp.202-215.

Ito, K., Musick, R. and Lücke, K., (1983), Acta Met., **31**, pp.2137

Ito, K., Sasaki, K., Yang, Jiping and Seki, F., (1996), Textures of Materials(Proc. ICOTOM11), pp.478-483

Li, Jian and Saimoto, S., (1998), Mat.Sci.Forum, **273-275**, pp.459-464

Seki, F., Yang, Jiping, Ueno, N. and Ito, K., (1996), Materials Science Forum (Proc. of ICAA5), **217-222**, pp.499-504

Takei, H., Sato, K. and Yokota, M.:, (1980), J.Japan Inst. Light Met., **30**, pp.626.

F8

MECHANICAL PROPERTIES AND TEXTURE FORMATION DURING THE COMPRESSION OF TANTALUM

R. J. DE ANGELIS
Department of Mechanical Engineering, University of Nebraska-Lincoln, Lincoln, NE
J. W. HOUSE
Air Force Research Laboratory, Eglin Air Force Base, FL

Abstract

The effects of the interstitial content of tantalum on its mechanical response and structural evolution during compression are investigated. Compression specimens were obtained from two tantalum plates; one of fine grain size and high interstitial content produced by the hot isostatic pressing of powder, and the second of large grain size and low interstitial content made by cold forging and rolling of a cast ingot. The compressive strength of specimens from the powder processed plate was twice that of the ingot processed material. During the initial 0.6 compressive strain a relatively strong mixed <111> and <100> wire texture formed. Deformation to strains greater than 0.6 had very little effect on the texture. The differences in the mechanical and crystallographic response of the two materials are directly related to the variations in the grain size and the interstitial content.

Keywords: compression, interstitial content, Tantalum, texture

1 Introduction

In the case of pure body centered cubic (BCC) metals the grain size and interstitial concentration have a great influence on the deformation dynamics. The changes in the texture of a polycrystalline material during plastic deformation are due to grain rotations caused by dislocation dynamics (Barrett 1943). Therefore the interstitial concentration existing in a BCC metal is expected to influence texture evolution.

The main objective of this investigation is to determine the roles of grain size and interstitial content on the mechanical behavior and structural evolution of tantalum during compressive deformation. To accomplish this requires the definition of the relationships existing between the crystallographic texture and the mechanical properties of tantalum.

2 Materials Processing

Approximately 2.04 kg of tantalum powder with a chemistry given in Table 1 and having an average particle size of 13 microns was consolidated by Ceracon , Inc. A 16.5 mm (0.65 inches) thick and 140 mm (5.5 inches) diameter preform was fabricated by cold isostatic pressing at 345 MPa. The preform was wrapped in tantalum foil sealed in a stainless steel container and outgassed for 24 hours at 400 C under a vacuum of 10^{-5} torr. The preform was **Ceracon™** forged into a 150 mm in diameter 13 mm thick plate in 30 seconds at 980 MPa at 1186 C. The average grain size in the as received plate was 38 um.

Table 1: Chemistry of tantalum powder and ingot, by weight.

Tantalum	H	O	Si	Fe	Mo	C	N
Powder Chemistry	28ppm	182	10	<5	5	16	26
Ingot Chemistry	<5ppm	45	<5	<5	<5	15	<10

A 305 mm diameter ingot, with a chemistry given in Table 1, produced by Cabot Corporation by vacuum arc remelting of a three electron beam processed electrode ingot. The ingot was turned to 290 mm diameter and side forged at 200 C to a 100 mm thick slab for rolling. The slab was machined clean, annealed at 1050 C and cold rolled with the rolling direction perpendicular to the ingot axis to an 8 mm thick plate. The plate was annealed at 1050 C for one hour. The average grain size determined from nine locations in the plate was 68 um (Last 1993).

3 Experimental Methods

3.1 Mechanical Testing

Compression specimens 7.6 mm in diameter and length were machined from the plates. Specimens from the Cabot plate had the compression axes in the rolling (RD) and transverse (TD) directions. Specimens from the Ceracon plate had compression axes in thru thickness (CZ) and in radial directions (CR).

Compression tests at an initial strain rate of 0.025/s were performed using an Instron testing machine with a 50,000 load cell. To minimize barreling tests were performed in stages. A stage consisted of an engineering strain of approximately 0.3. After each stage a specimen was withdrawn from further deformation and prepared for structure characterization. Specimens that were subjected to multi-stage compression testing were machined to a circular cross-sections between stages. The load-displacement data from each stage of deformation was transformed to true stress and logarithmic strain.

The compressed specimens were sliced in half transverse to the compression axis and metallographically prepared (Kelly et al. 1995) and utilized for the determination of x-ray pole figures.

3.2 X-Ray Pole Figure Measurements

Crystallographic pole figures were determined on eleven specimens of the Cabot plate material, five of the specimen surfaces had normals parallel to the rolling direction and six surfaces had normals parallel to the transverse direction. X-ray pole figures were determined on eight specimens of the Ceracon plate, four specimen surfaces had normals parallel to the thickness direction and four had normals parallel to the radial direction. X-ray pole figures were determined on a Siemens D5000 diffractometer. The pole figure data were converted to ODFs (Bunge 1982) and inverse pole figures utilizing popLA (Kocks et al.1994).

3.3 Texture Quantification

The texture quantification employed in this investigation was reported recently by (De Angelis 1999). The technique, based on inverse pole figures, was developed by (Hosford 1999). The fraction of grains, $F_{<hkl>}$, contained within 12.5 of the <111>, <100> and <110> orientations were determined from the inverse pole figure.

In the case of an ideally random distribution of grain orientations the $F_{<hkl>}$ values for an angle of 12.5 are 0.0965, 0.0715 and 0.1428 for the <111>, <100> and <110> orientations respectively. These $F_{<hkl>}$ from a random grain distribution are the normalization constants to times random.

4 Results

4.1 Mechanical Properties

Typical compression stress versus strain curves for the three stage specimens CZ-4 and CR-4 (powder processed) are shown in Fig. 1. The mechanical response of these two specimens is almost identical with both showing a yield point in the second stage of deformation; however only CR-4 showed a yield point in the first stage of compression. The sample to sample variations are less than ±10 MPa. The specimens cut from the radial direction demonstrate flow stress that are approximately 20 MPa higher than the specimens compressed in the thru thickness direction. The upper and lower yield and the flow stresses up to strains of 0.3 are given in Table 2.

Typical compression stress versus strain curves for the three stage specimens RD-5 and TD-5 (Cabot processed) are shown in Fig. 1. The mechanical behavior of these two specimens is almost identical with both demonstrating upper and lower yield points. The sample to sample variations in the values of the flow stresses are less than ±6 MPa. The specimens with compression axis in the transverse direction demonstrate flow stress that are approximately 10 MPa higher than the specimens compressed in the rolling direction. The upper and lower yield and the flow stresses up to strains of 0.3 are given in Table 2.

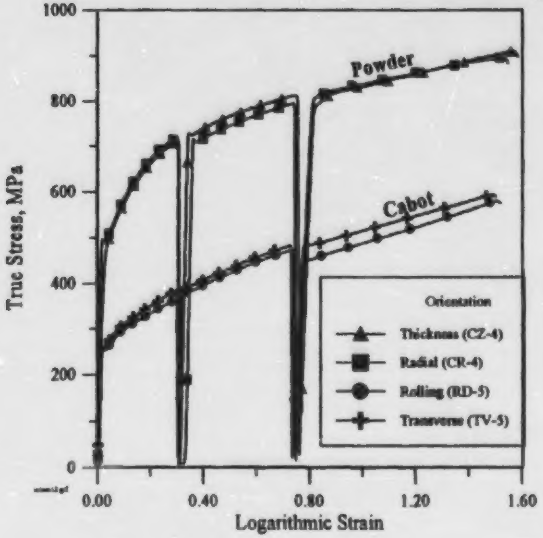

Fig. 1: Stress versus strain behavior of tantalum in three stages of compression.

Table 2: Averages of the yield and flow stresses of tantalum specimens.

Specimen ID	Avg. Upper YP MPa	Avg. Lower YP MPa	Flow Stress Strain = 0.1	Flow Stress Strain = 0.2	Flow Stress Strain = 0.3
CZ	495.6	475.6	569	659.5	704.7
CR	512.6	488.2	587.0	670.0	717.8
RD	265.8	255.0	303.6	340.2	372.3
TD	279.2	261.0	312.7	349.3	381.3

4.2 Texture Quantification

The texture intensity, in times random, for grains within 12.5 of the <111>, <100> and <110> poles in the thickness and radial directions of the **Ceracon™** forged plate as a function of compressive strain are shown in Fig. 2. During compression of a BCC metal the <111> and <100> poles rotate to align with the compression axis. As these poles align the <110> poles rotate away from the compression axis. The data in Fig. 2 indicate that grain rotations occurred during the initial 0.6 compressive strain. At a strain of 0.6 the <111> and <100> texture intensities reach their plateau values.

The texture intensity, in times random, for grains within 12.5 of the <111>, <100> and <110> poles in the rolling and transverse directions of Cabot plate as a

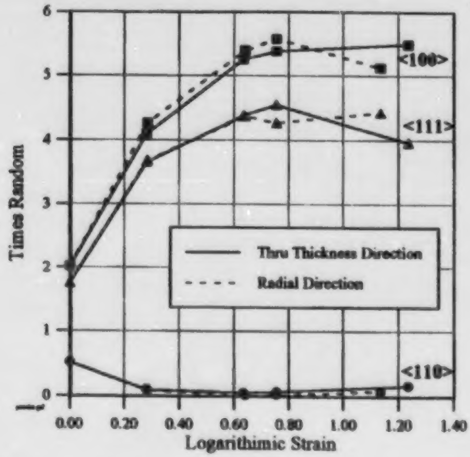

Fig.2: Variations in texture intensities with compressive strain for powder processed tantalum.

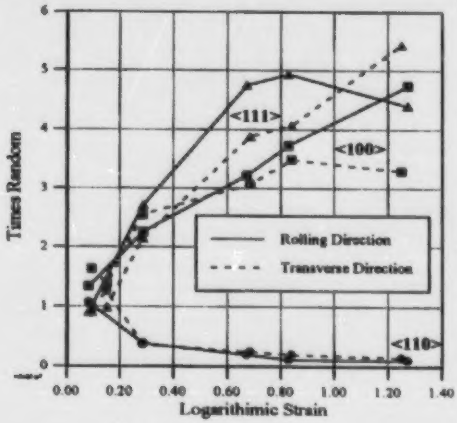

Fig. 3: Variations in texture intensities with compressive strain for Cabot plate tantalum.

function of compressive strain are shown in Fig. 3. These data indicate that normals to the <111> and <100> grains rotate to the compression axis during the initial 0.7 compressive strain. At a strain of 0.7 the <111> texture intensity reaches a plateau value of between four and five. The <100> texture intensity value is 3.3. The texture of the specimens with compression axes in the rolling direction was consistently stronger than the texture in the specimens having compression axes transverse to the rolling direction. The strength of the <111> texture is generally between 4 and 5 times random which is slightly stronger than the <100> texture (between 3 and 4 times random).

5 Discussion

The texture intensity data in Figs. 2 and 3 show the powder plate texture increasing more rapidly with compressive strain. The mechanical property data in Fig. 1 show that rapid changes in texture occur when the strain hardening rate of the powder material is at a maximum, between compressive strains of zero and 0.30. Higher yield strength, higher hardening rate and faster texture evolution are a result of chemistry and the consolidation and processing of the powder material.

The high yield strength results from the higher level of interstitial content and smaller grain size. The increased hardening rate and faster texture development (grain rotation) are a result of the characteristics of the grain boundaries. The initial powder material has on the outer surface of each particle a higher concentration of oxygen in the form of tantalum oxide. When consolidated the residue of this oxide is expected to reside on or near grain boundaries. This layer of material, in combination with the grain shape, generates the increased grain rotation when compared with the Cabot plate material at equal levels of compressive strain.

The consolidated powder has a finer grain size, 38 um versus 68 um. With a finer grain size, the material has an increased amount of grain boundary surface are per unit volume. The increase in grain boundary surface area, the grain shape, the interstitial content, and the oxide distribution at the grain boundaries, each contribute to the increased hardening rate. At higher stains, above 0.3, both materials display similar hardening characteristics. This observation suggests that the initial strain of the powder material has a unique character in-terms of the hardening behavior. As the defect structure develops, the processes for further plastic flow become similar as indicated by the uniformity of the hardening rates at higher values of strain.

6 References

Barrett, C.S. (1943) *Structure of Metals*, McGraw-Hill, New York.

Bunge, H.J. (1982) *Texture Analysis in Materials Science*, Butterworth, London.

De Angelis, R., Snyder, T., House, J. and Hosford, W. (1999) *Quantitative Description of Fiber Textures in Cubic Metals*, Proc. 47th Denver X-Ray Conf., to be published.

Hosford, W., O'Brien, J., House, J. and De Angelis, R. (1999) *Use of ODF Data to Quantitatively Describe Fiber Textures*, Proc. 47th Denver X-Ray Conf., to be published.

Kelly, A.M., Bingert, S.R. and Reiswig, R.D. (1995) *New Metallographic Preparation Techniques for Tantalum and Tantalum Alloys*, LA-UR-95-2631, Los Alamos National Laboratory.

Kocks, U.F., Kallend, J.S., Wenk, H.-R, Rollett, A.D. and Wright, S.I. (1994) *popLA: Preferred Orientation Package - Los Alamos*, LA-CC-98-18, Los Alamos National Laboratory.

Last, H. (1993) *Metallurgical Study of Tantalum Plate for U.S. Air Force*, NSWC Memorandum R31:HRL:hrl, 08 MAR 1993.

TEXTURE AND MICROSTRUCTURE DEVELOPMENT DURING PLASTIC DEFORMATION OF MAGNESIUM

R. GEHRMANN, G. GOTTSTEIN
Institut für Metallkunde und Metallphysik, RWTH Aachen, 52056 Aachen, Germany

Abstract

Plastic deformation of hexagonal metals such as magnesium is strongly determined by the hexagonal crystal structure, and thus, for an understanding of the deformation behaviour of magnesium texture must be taken into account. Plane-strain compression tests on pure magnesium were carried out at 100°C. A special emphasis was laid upon the influence of different starting textures on the deformation characteristics and the development of texture and microstructure. The measured flow curves reveal that plastic deformation of polycrystalline magnesium at this temperature is inhomogeneous and dominated by the appearance of shear bands. Nevertheless, different starting textures affect the plastic deformation and the activity of possible deformation mechanisms in a characteristic way. The analysis of microstructure and the development of texture during deformation additionally support the results obtained from the flow curves and yield information on the deformation mechanisms.

Keywords: Magnesium, hexagonal, channel die deformation, texture, microstructure

1 Introduction

The demand of several industries such as the automobile, the aircraft or the aerospace industry for the reduction of weight makes magnesium a material of high interest. A low density and a high specific strength are reasons for the development of new magnesium alloys with good corrosion resistance and good mechanical properties. In general, magnesium shows a pronounced anisotropy of their mechanical properties after deformation. This anisotropy is mainly due to a pronounced texture which develops during plastic deformation. This behaviour is typical for metals with hexagonal crystal structure.

The aim of this investigation is a more profound understanding of texture development during plastic deformation of magnesium and the mechanisms of texture evolution. Therefore, it is essential to gain more detailed information on microstructure and texture evolution as well as deformation mechanisms such as basal, prismatic and pyramidal glide and potential twinning modes in order to develop models of texture evolution. In the following results of deformation experiments on pure magnesium at 100°C will be presented. In particular, the influence of different starting textures on deformation behaviour and texture development is addressed. Macro-textures determined by X-ray diffraction as well as results of microstructure analysis obtained by means of light-optical microscopy are reported.

2 Experimental methods

In order to realise a state of plane-strain compression at a defined temperature of 100°C channel die experiments were carried out. Specimens of commercially pure magnesium with the dimension of 6 mm (ND) x 10 mm (TD) x 15 mm (RD) were chosen for this kind of compression test. Channel die deformation allows an elongation of the sample only in longitudinal direction, whereas in transversal direction deformation is suppressed. For these compression tests the longitudinal direction of the samples is equivalent to the rolling direction in rolled samples. Push rods with heating elements were used to reach the desired deformation temperature of 100°C. The temperature was measured within each sample with the use of a NiCr/Ni-thermocouple. After reaching the deformation temperature the experiment was started and finished when a fixed thickness reduction of 10%, 30% or 70% was attained. Immediately upon releasing the load the sample and the channel die device were quenched in cold water. According to the chosen crosshead velocity the initial strain rate was $\dot{\varepsilon} = 1.67 \cdot 10^{-2}\ s^{-1}$.

Macro-textures were determined by measuring incomplete pole figures ($5° \leq \alpha \leq 80°$) in the back reflection mode. A set of six pole figures ($\{10\bar{1}0\}$, {0002}, $\{10\bar{1}1\}$, $\{10\bar{1}2\}$, $\{11\bar{2}0\}$ and $\{10\bar{1}3\}$) was used to calculate the orientation distribution function (ODF).

For a characterisation of microstructure longitudinal sections were machined and analysed by means of lightoptical microscopy. For this purpose the samples were electrolytically polished and etched with a solution of 2% HNO_3 in alcohol.

3 Results and discussion

3.1 Initial state

The channel die experiments were carried out on four types of samples with different starting textures. To realise these different initial textures the specimens were taken from a hot rolled and recrystallized plate of pure magnesium (table 1). This plate had a pronounced texture with the {0002}-basal planes parallel to the surface of the plate. The microstructure consists of equiaxed grains of about 20 µm to 300 µm.

According to the choice of the four different initial textures a division into four sample series A, B, C and D was made. The samples of the series A had the same

Table 1: Choice of reference systems for channel die experiments.

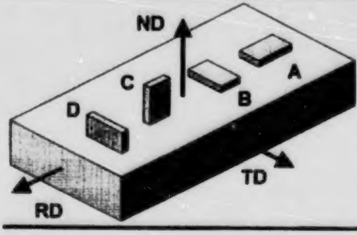

old reference system: *rolling geometry*	new reference system: *sample geometry for channel die experiment*			
	A	B	C	D
ND	ND	ND	RD	TD
RD	RD	TD	TD	ND
TD	TD	RD	ND	RD

Table 2: Initial textures for channel die experiments.

A: initial texture	C: initial texture	D: initial texture
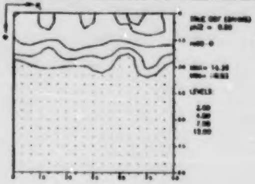 $\varphi_2 = 0°$	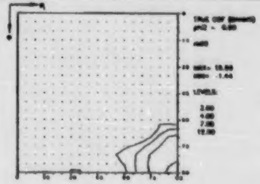 $\varphi_2 = 0°$	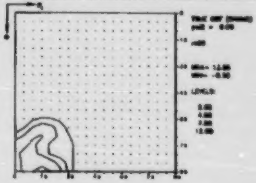 $\varphi_2 = 0°$
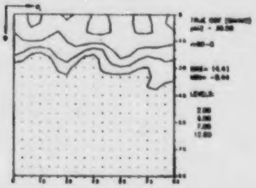 $\varphi_2 = 30°$	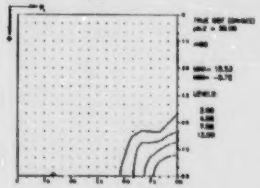 $\varphi_2 = 30°$	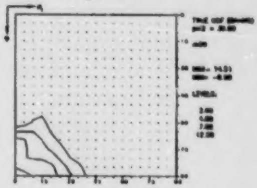 $\varphi_2 = 30°$

reference system as the plate. Rolling direction, transversal direction and normal direction correspond to the sample geometry for the channel die experiment (table 1). Therefore, the texture was characterised by a [0002]-direction parallel to the normal direction (table 2). The φ_2-sections ($\varphi_2 = 0°$, $\varphi_2 = 30°$) for this initial texture showed that no pronounced direction parallel to the rolling direction existed. In comparison to series A the samples of the series B were rotated 90° about the normal direction of the plate. Thus, both starting textures could be described as being identical. The samples of series C were taken in such a way that the crystallographic c-axis ([0002]-direction) was parallel to the longitudinal direction of the channel die experiment. Within the φ_2-sections this kind of [0002]-texture intensities could be found at (90 90 0) and (90 90 30). Similar intensities of both positions prove that no pronounced crystallographic direction was parallel to the normal direction and the transversal direction, respectively. Series D can be described comparably. With regard to the channel die experiment the [0002]-direction was parallel to the transversal direction. Again no pronounced direction was parallel to the rolling direction or the normal direction ((0 90 0) and (0 90 30)).

3.2 Deformation at elevated temperature

The channel die experiments were carried out at a deformation temperature of 100°C. Fig. 1 shows that samples with different initial textures exhibited a different true stress-strain behaviour. But all curves had a special characteristic in common, they all revealed a local maximum of the flow curve accompanied by a drastic drop of strength. In this context the different possible deformation mechanisms are of special importance. As soon as a homogeneous deformation by slip and twinning is not possible any more local inhomogeneities of stress lead to the formation of shear bands. These shear bands carry the further deformation, first on a microscopic scale at grain boundaries and later on on a macroscopic scale. In the latter case a massive deformation is localised in these shear bands. The drop of strength that can be observed in the flow curves is therefore related to this localisation of deformation within the shear bands and the formation of cracks. In correlation with the texture development this inhomogeneous plastic behaviour occurs if the [0002]-directions are aligned parallel to the normal direction of the sample. In this case homogeneous plastic deformation by basal slip $\{0002\}<2\bar{1}\bar{1}0>$ or $\{01\bar{1}2\}$-twinning is only possible in a very limited way. The influence of texture on the shape of the flow curves and the position of the local maximum seems to be typical for polycrystalline magnesium (Kelley 1968). Each starting texture has a characteristic behaviour concerning the activity of deformation mechanisms and the development of texture.

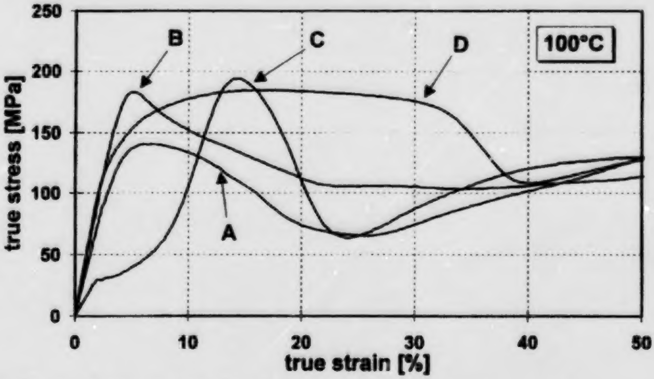

Fig. 1: Flow curves at a deformation temperature of 100°C.

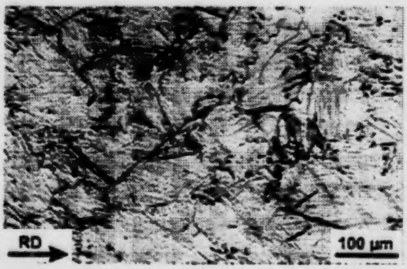

Fig. 2: B, 70% deformation

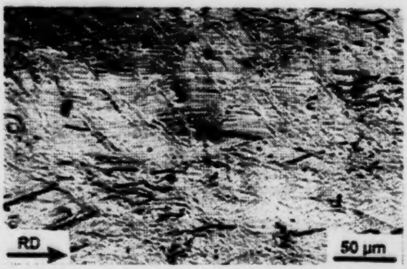

Fig. 3: C, 10% deformation

Table 3: Deformation textures of channel die experiments.

A: 70% deformation	C: 30% deformation	D: 30% deformation
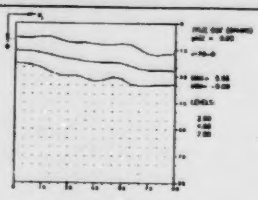 $\varphi_2 = 0°$	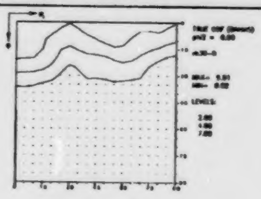 $\varphi_2 = 0°$	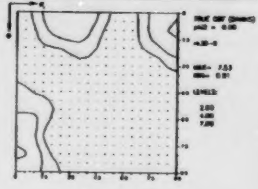 $\varphi_2 = 0°$
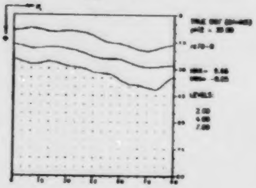 $\varphi_2 = 30°$	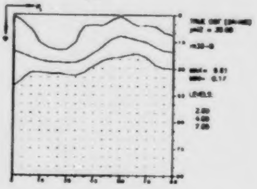 $\varphi_2 = 30°$	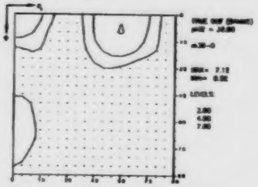 $\varphi_2 = 30°$

The initial texture of the samples of series A and B corresponds to a typical deformation texture of polycrystalline magnesium (Philippe 1994a, Wassermann 1962), thus in both cases the texture shows no basic change during deformation (table 3). With regard to the flow curves series B shows larger values of maximum strength than series A. This difference becomes clear if we start from the assumption that a local accumulation of stress initiates the formation of shear bands. Series A has no possibility for plastic deformation through basal slip or twinning, therefore local peaks of stress cannot be released and the plastic deformation is localised in the shear bands. Series B has no obvious different initial texture in comparison to series A, but the rotation of 90° about the normal direction makes basal slip or twinning possible to a small amount. Thus, a critical peak of stress is reached at higher values of external stress. Microstructure investigations reveal the occurrence of the shear bands (fig. 2). Due to the high local stresses within the shear bands further deformation mechanisms such as prismatic or pyramidal glide could be activated. On samples with the same initial texture as series A and B also cold rolling experiments were carried out. At high deformation degrees the development of a new texture component could be observed, which has not yet been reported as rolling texture component in magnesium: (90 90 30) or $\{10\bar{1}0\}<0001>$. If the texture evolution in zinc is considered (Philippe 1994b) this component results from the activity of prismatic slip $\{11\bar{2}2\}<11\bar{2}3>$ and basal slip or twinning $\{01\bar{1}2\}<01\bar{1}1>$ and basal slip. Analogous to this observation the development of the new component in magnesium can be attributed to the activity of pyramidal slip and twinning within the shear bands. The channel die experiments did not reveal the existence of this component, but it seems obvious that these deformation mechanisms were active in a similar way. The samples of series C showed a completely different deformation behaviour that resulted in a comparably low yield strength and an increasing hardening at low deformation degrees. In agreement with a complete rotation of the crystallographic c-axis parallel to the normal direction the flow curve goes through a local maximum at about 12% thickness reduction. At higher deformation degrees a $\langle 10\bar{1}0\rangle$-direction becomes parallel to the rolling direction (table 3). The initial texture supports a homogeneous deformation by basal slip and twinning, and the increase of hardening occurs due to the intense activity of these deformation mechanisms. Fig. 3 shows the microstructure after 10% deformation. Up to this point shear bands seemed not to be active, and the microstructure is characterised by deformation twins and slip. When reaching the maximum strength a homogeneous deformation is not possible any more and the formation of shear bands is initiated. With regard to the flow curve series D exhibited a very broad stress maximum. At low deformation degrees the microstructure was dominated by intense twinning, and a (30 0 0)-texture component developed. The initial texture of these samples was unfavourable for basal slip, but the twinning activity rotated the c-axis parallel to the normal direction (Wonsiewicz 1967). Twinning is not the only deformation mechanism that is of great importance for this type of samples. Double prismatic slip (Saxl 1974) supports the stability of the component (0 90 0) as a constituent of the initial texture (table 3). Due to these deformation mechanisms the broad stress maximum is achieved, and texture only changes slowly during plastic deformation.

4 Summary

Channel die experiments on samples of different initial textures at a deformation temperature of 100°C showed that texture has an important influence on the deformation behaviour of polycrystalline magnesium. A strong initial basal texture with [0002]-directions parallel to the normal direction reduced the formability dramatically. The deformation became inhomogeneous and was dominated by the formation of shear bands. If the basal planes were aligned parallel to the normal direction further deformation mechanisms enabled a more homogeneous deformation and thus, an increase of formability. Nevertheless, a conventional rolling process leads to a strong basal texture, which results in a general restricted formability at low temperatures.

5 Acknowledgements

The financial support of the Deutsche Forschungsgemeinschaft is gratefully acknowledged.

6 References

Kelley, E.W., Hosford Jr., W.F. (1968), Trans AIME, Vol. 242, pp. 654-660
Philippe, M.J. (1994a), Materials Science Forum, Vol. 157-162, pp. 1337-1350
Philippe, M.J., Wagner, F., Mellab, F.E., Esling,C., Wegria, J. (1994b), Acta metall. mater., Vol. 42, No. 1, pp. 239-250
Saxl, I., Haslingerová, I. (1974), Czech. J. Phys., Vol. B24, pp. 1351-1361
Wassermann, G., Grewen, J. (1962), *Texturen metallischer Werkstoffe*, Springer
Wonsiewicz, B.C., Backofen, W.A. (1967), Trans AIME, Vol. 239, pp. 1422-1431

EBSD ANALYSIS OF SHEAR BANDING IN α- BRASS

C.S. DA COSTA VIANA, J.C. PAREDES, A.L. PINTO and A.M. LOPES
Department of Mechanical and Materials Engineering, Instituto Militar de Engenharia
IME, Rio de Janeiro, Brazil

Abstract

In the present work an investigation of shear banding in 70:30 brass using EBSD is described. Special attention is directed to the microstructural and microtextural features of the 50% cold rolled specimen, in particular to the orientation in the shear band containing grains and the relation between these and the lamellar substructure of microtwins. A tentative rationalisation of the observations is advanced.

Keywords: Shear banding, texture, EBSD analysis

1 Introduction

Shear banding is one of the features of heterogeneously deformed microstructures that has received great attention in recent decades though it had been observed already as early as in 1922 (Adcock 1922). However, its nature, origin and contribution to texture development still need further investigation. Sevillano et al. (1977) studied several materials and observed that shear bands appear at about 50% rolling reduction in low stacking fault energy (SFE) materials but require much higher strains in high SFE metals. Duggan et al. (1978a) studied α-brass and showed that shear bands tend to form at about $\pm 35^0$ to the rolling plane and that, initially confined to a few grains, its volume fraction increases with rolling reduction reaching about 85% by 95% cold reduction. In a further work (Duggan et al. 1978b), they showed that shear bands are made up of highly misoriented fine crystals elongated in the shear direction. They also noted that the bands appear to form in grains that display a lamellar substructure of fine twins oriented nearly parallel to the rolling plane. Dillamore et al. (1979) used a detailed argument of plastic instability to explain the $\pm 35^0$ angle observation. Disregarding both strain hardening and strain rate sensitiveness effects on strain localisation, they showed that the angle was linked to the orientations present in the deformation texture, in particular to the {4 4 11}<11 11 –8> end orientation whose contribution to the attainment of that angle was highlighted. In the present work the EBSD technique is used to investigate the connection between microstructure, microtexture and shear banding in cold rolled α-brass. Attention is concentrated on the analysis of the 50% cold rolled sample since this seems to be a turning point in both microstructural and textural development in α-brass.

2 Experimental

A 7.50mm thick plate of 70:30 commercial brass with initial grain size of 100μm was 10%, 30%, 40%, 50%, 60% and 70% cold rolled. Microstructural observation and texture measurement were carried out on the longitudinal section (plane DN-DL) of the specimens. The individual orientations identified on this surface were rotated by 90^0 about the rolling direction (RD) in order that the pole figures and ODFs could be plotted with reference to the sheet's DL-DT-DN axes. The ODFs were represented in Bunge co-ordinates represented in φ_2 = constant sections.

3 Results and Discussion

Figure 1 shows the microstructures of the 10%, 30%, 40% and 50% cold rolled specimens as observed by MEV. Different types of deformation markings can be seen inside the grains and annealing twins. In general, the observations conform to the description made by Duggan et al. (1978a). In Figure 1d, strain localisation as shear bands can be seen in the central grain. Their characteristic 35^0 angle and the underlying lamellar substructure of deformation twins (Fargette and Whitwham 1976) are easily identified. It is interesting to note that the lamellae are nearly parallel to RD in the central grain (C) but lie at different angles with it in the two neighbouring grains, at the top (T) and bottom (B) of the micrograph. No shear bands were observed in these grains. This was the standard microstructural behaviour observed in this work. The grains in Figure 1d will from now on be referred to as grain C, T and B, respectively. The region shown in Figure 1d is typical of many areas observed in the 50% cold rolled specimen and it will be on its features that the present analysis will be concentrated.

Table 1 shows representative orientations obtained in each grain of Figure 1d. The orientation in grain C is very close to the copper {-211}<111> orientation (less than 7^0 from it) and is different from those in grains B and T. It can be seen, in Figure 2a, that the {111} poles in grain C practically coincide with those of the {112}<111> ideal orientation shown in Figure 2b. From the same Figures it is also clear that the orientation in grain B can be brought into coincidence with the symmetrical of the copper orientation by means of a rotation of about 20^0 about ND. The presence of these near-copper orientations in the microstructure is confirmed by the ODF shown in Figure 2c, which was measured, on a larger area of the same specimen.

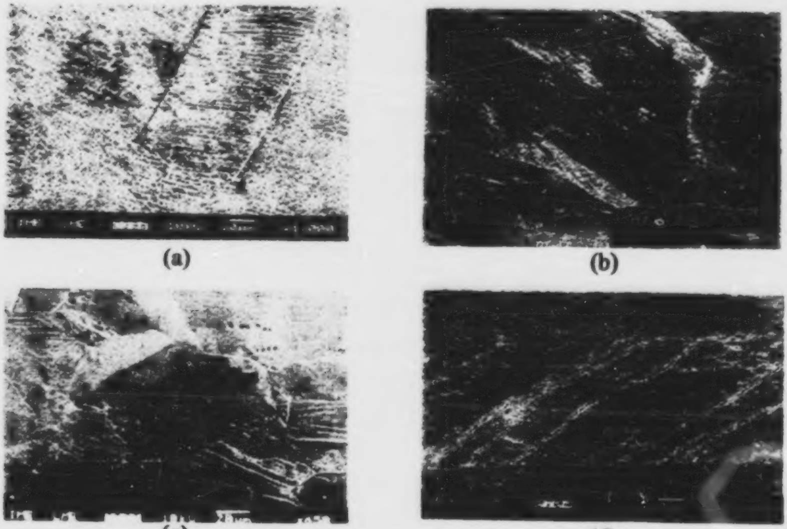

(a) (b)

(c) (d)

Figure 1: Microstructures of samples cold rolled (a) 10%; (b) 30%; (c) 40%; (d) 50%

The connection between the 35^0-shear banding and the near-copper orientations, as theoretically determined by Dillamore et al. (1979) for the {4 4 11}<11 11 –8> orientation, is therefore experimentally confirmed. This connection was observed in many other areas of this and other specimens cold rolled above 50%. Now with respect to the lamellar substructure in the grains. According to Fargette and Whitwham (1976), the lamellae are formed by microtwins and, after about 40%-50% reduction, they tend to rotate until their boundaries are nearly parallel to the rolling plane. This would be the requirement for the formation of shear bands (Duggan et al. 1978b). This rotation has never been properly explained in the literature.

Table 1: Representative orientations observed in the grains of Figure 1d.

Grain	Orientation
C	{-100 56 49}<93 100 75>
B	{80 –100 60}<19 75 100>
T	{-100 35 69}<53 100 26>

Experimentally, by 40% reduction, many grains are observed with lamellae oriented in different directions with respect to the rolling direction and, by 50%, grains containing shear bands appear. In cold rolled brass, deformation twinning takes place in {111}<11-2> systems and becomes a significant alternative to slip after about 40% reduction, when, helped by the low SFE of this material, which hinders cross slip, strain accommodation by slip is already becoming exhausted. Twinning then occurs in the grains best oriented for it such as the C{11-2}<111>. Figure 3i shows the {111} planes for the copper orientation. It can easily be shown that, for the near-copper orientations, both the top and the front {111} planes have very low resolved shear stresses for twinning. However, the parallelism to DL of the lamellar boundaries can be explained if we assume that the material would prefer twinning on the plane with the least amount of accumulated strain during the previous deformation by slip, in this case the top {111} plane referred to above. The trace of this plane with the longitudinal section is at 19.5^0 to RD and this angle can be reduced as the orientation rotates, due to overshooting, towards orientations near {111}<1 1-2> for which the lamellar alignment with RD would be complete (Figure 3ii). This rotation would also explain the progressive decrease of the copper orientation and the build-up of orientations near {111}<uvw>, as indicated by Duggan et al. (1978a). In fact, {111}<110>-<11-2> orientations were found in the lamellar areas of a specimen cold rolled 70% and annealed at 450^{0}C for 1 minute, seen in Figure 4. Note that recrystallisation had just started along the shear bands. The slight annealing aimed at relaxing the excess strain and increasing the quality of the EBSP. By the time the

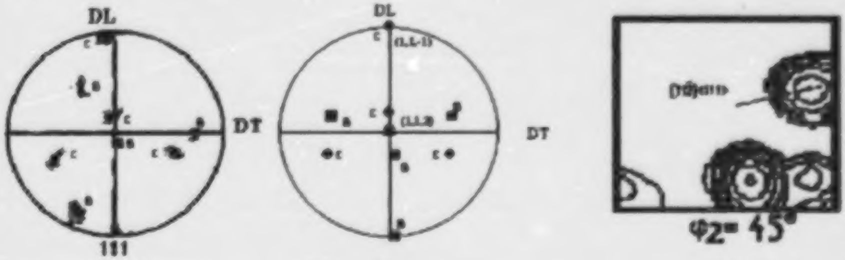

(a) (b) (c)

Figure 2: (a) EBSD {111} pole figure of the orientations in grains C and B; (b) Ideal poles of the Cu {11-2}<111> orientation; (c) EBSD ODF of the 50% cold rolled material.

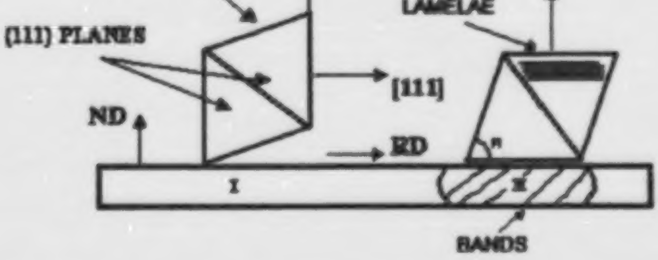

Figure 3: (I) {111} slip and twinning planes for the copper orientation and (II) for the {111}<11-2> orientation; longitudinal section view.

grains reach those orientations, general ductility should have been considerably reduced and, according to Dillamore et al. (1979), the textural conditions for plastic instability should have already been developed. Shear banding then sets in, assisted by highly localised deformation.

The question of the ±35° angle to RD has been dealt with by Dillamore et al. (1979), regarding the bands as a manifestation of plastic instability. Though it is well accepted that shear banding takes place in a way independent of crystallographic considerations, it is tempting to point out that 35.26° is precisely half of the angle A shown in Figure 3ii, which corresponds, in this case, to a plane of the {110} family.

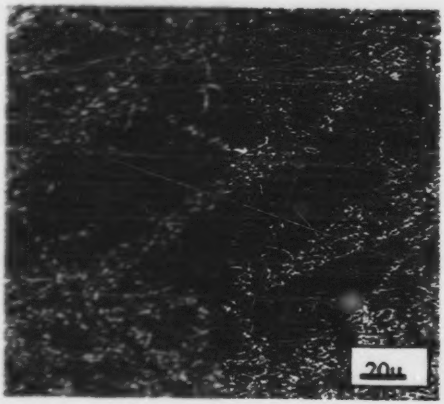

Figure 4: Microstructure of a sample cold rolled 70% and annealed at 450°C for 1 minute. Nucleation of new grains along shear bands and lamellar substructure.

4 Conclusions

Despite the possibilities offered by EBSD, a more detailed investigation is still needed to clarify the nature of shear bands and its relation to texture formation in 70:30 brass. Here, the connection between shear band formation and the existence of an oriented lamellar substructure in the grain was once again verified. It was also confirmed that the orientation in shear banded grains is close to the copper orientation. However, the role of deformation mechanisms and crystal orientation, as well as its interrelation, is not clear yet in determining some of the microstructural features in deformed brass especially referring to shear band development.

5 References

Adcock, F. (1922) Journal of the Institute of Metals, vol. 27, p.73.

Sevillano, J.G., Van Houte, P. and Aerlnoudt, E. (1977) The contribution of macroscopic shear bands to the rolling texture of FCC metals. Scripta Metallurgica, vol. 11, pp.213-218.

Duggan, B.J., Hatherly, M., Hutchinson, W.B. and Wakefield, P.T .(1978a) Deformation structures and textures in cold-rolled 70:30 brass. Metal Science, vol. 12, pp.343-351.

Duggan, B.J., Hutchinson, W.B. and Hatherly, M. (1978b) Recrystallization studies in 70:30 brass using high voltage electron microscopy. Scripta Metallurgica, vol. 12, pp.293-295.

Dillamore, I.L., Roberts, J.G. and Bush, A.C. (1979) Occurrence of shear bands in heavily rolled cubic metals. Metal Science, vol. 13, pp.73-77.

Fargette, B. and Whitwham, D. (1976), Mémoires Scientifique de la Révue de Métallugie, vol. 73, p.197.

EFFECT OF TEXTURE ON INTERNAL STRAINS IN Mg - 7.7at.%Al

M.A. GHARGHOURI
Dept. of Mining and Metallurgical Engineering, DalTech, Halifax, Canada
C.N. TOMÉ
MST-8, MS G755 – Los Alamos National Laboratory, Los Alamos, NM, USA
J. ROOT
National Research Council Canada, Chalk River Laboratories, Chalk River, Canada

Abstract

Current elasto-plastic self-consistent (EPSC) models, which treat twinning as a polar slip mechanism, are unable to account for the stress relaxation and texture evolution associated with twinning. Previous in-situ neutron diffraction experiments on a two-phase extruded Mg-Al alloy have shown that twinning is associated with changes in intensity for certain reflections. In addition, twinning can result in appreciable stress relaxation in certain components of the texture. An EPSC model has been modified to account for these two features. Twinning is treated as a stress-free transformation strain, homogeneous over a given grain, which is applied when a critical resolved shear stress is reached. A prescribed grain volume fraction, of the order of 0.5 to 1%, is associated with each twinning event. This treatment of twinning predicts a level of stress relaxation in broad agreement with that observed experimentally.

Keywords: Elasto-plastic self-consistent, neutron diffraction, magnesium, twinning

1 Introduction

The plastic deformation of polycrystalline magnesium alloys depends strongly on both texture and stress state. Magnesium alloys deform primarily by slip on the basal $(0001)\langle 11\bar{2}0\rangle$ systems. Slip on the $\{10\bar{1}0\}\langle 11\bar{2}0\rangle$ prism and $\{10\bar{1}1\}\langle 11\bar{2}0\rangle$ pyramidal systems has been observed experimentally, but the critical resolved shear stress (CRSS) is orders of magnitude higher than for basal slip (Partridge 1967). None of these slip systems can contribute to plastic strain parallel to the c-axis, which must be accommodated elastically, or by twinning. Only $\{10\bar{1}2\}\langle 10\bar{1}\bar{1}\rangle$ tensile twinning (i.e. which produces elongation in the c-direction) is common in magnesium. Compressive twins have only been found to contribute significantly to plastic deformation in thorium-containing polycrystalline alloys (Couling et al. 1959).

The c/a ratio of magnesium is such that the basal plane is reorientated by 86° by

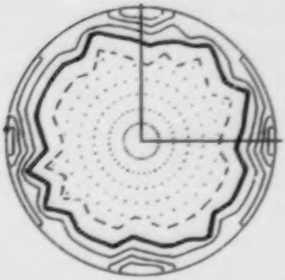

centre = extrusion axis

contour separation = 0.5 × random

Fig. 1: (0002) stereographic pole figure.

$\{10\bar{1}2\}\langle 10\bar{1}\bar{1}\rangle$ twinning. As a consequence of the anisotropic plastic behaviour of magnesium crystals, a non-uniform internal stress field on a length scale of the order of the grain size develops during plastic deformation of polycrystalline material.

The material considered here is an extruded and artificially aged Mg-7.7at.%Al alloy. The texture is axisymmetric, with most grains having the basal pole oriented at greater than about 60° to the extrusion axis (Fig. 1).

Uniaxial tensile and compressive in-situ neutron diffraction tests were performed, in which the lattice strains were measured at 25 MPa intervals in grains having the basal plane oriented normal to, parallel to, and at approximately 60° to the stress axis (Gharghouri et al. 1999). The stresses calculated from the lattice strains obtained by neutron diffraction were consistent with basal slip and $\{10\bar{1}2\}\langle 10\bar{1}\bar{1}\rangle$ twinning, which optical and transmission electron microscopy showed were the predominant plastic deformation modes. The observed $\{10\bar{1}2\}\langle 10\bar{1}\bar{1}\rangle$ deformation twins either engulfed, were impeded by, or bypassed the second phase particles (Gharghouri et al. 1998). Strain plateaux and diffracted peak intensity variations during loading were consistent with $\{10\bar{1}2\}$ twinning.. The stress tensors corresponding to these intensity variations were used to show that a CRSS criterion was applicable for $\{10\bar{1}2\}$ twinning in the alloy, and that the onset of twinning does not correlate with the stress normal to the twin plane.

The objective of the work presented here is to develop a modification to a classical elasto-plastic self consistent (EPSC) model for polycrystal plasticity which takes into account the relaxation associated with twinning.

2 Theoretical

A detailed account of the formulation used here is presented elsewhere (Turner and Tomé 1994). Only the main concepts associated with the model are given here. The EPSC model is based on the Eshelby (1957) solution of the inclusion problem. Each grain *orientation* is modeled as a single ellipsoidal inclusion, weighted in accordance with the specimen texture, embedded in a Homogeneous Effective Medium (HEM). The stress-strain behavior of the HEM is in fact that of the polycrystalline aggregate and depends on the behavior of each individual grain orientation.

The crystal constitutive law is expressed in equations (1) to (3), where $\dot{\sigma}_{ij}$ is the grain stress rate, C_{ijkl} is the single crystal elastic stiffness tensor, $\dot{\varepsilon}_{ij}$ is the total grain strain rate, $\dot{\varepsilon}^{T}_{ij}$ is the strain-free transformation strain rate, $\dot{\gamma}^{s}$ is the shear rate on plastic shear system *s* (slip or twinning), m^{s}_{ij} is the Schmid tensor for plastic shear system *s*, L^{C}_{ij} is the incremental elasto-plastic grain stiffness tensor. $X^{ss'}$ is a square matrix of the same order as the number of active shear systems in the grain which is a function of the linear hardening matrix $h^{ss'}$.

$$\dot{\sigma}_{ij} = C_{ijkl}(\dot{\varepsilon}_{kl} - \dot{\varepsilon}^{T}_{kl} - \sum_{s} m^{s}_{kl}\dot{\gamma}^{s}) = L^{c}_{ijkl}(\dot{\varepsilon}_{kl} - \dot{\varepsilon}^{T}_{kl}) \tag{1}$$

$$L^{c}_{ijkl} = C_{ijpq}(I_{pqkl} - \sum_{s}\sum_{s'} m^{s}_{pq} Y^{ss'} m^{s'}_{mn} C_{mnkl}) \tag{2}$$

$$Y^{ss'} = (X^{ss'})^{-1} = (h^{ss'} + m^{s}_{ij} C_{ijkl} m^{s'}_{kl})^{-1} \tag{3}$$

For a shear system to be considered active, the resolved shear stress in the system must be equal to the CRSS, τ^{s}_{c}. In addition, for the system to remain under load, the rate of change of the resolved shear stress must equal that of the CRSS ($\dot{\tau}^{s}_{c}$) produced by hardening.

The constitutive law for the HEM is given in equation (4), where L_{ijkl} is the polycrystal incremental elasto-plastic stiffness tensor, $\dot{\Sigma}_{ij}$ is the polycrystal stress rate, and $\dot{E}_{ij}$ is the overall strain rate of the polycrystal.

$$\dot{\Sigma}_{ij} = L_{ijkl}\dot{E}_{kl} \tag{4}$$

The polycrystal stress and strain rates are coupled to the equivalent magnitudes in each grain through the interaction equation:

$$(\dot{\sigma} - \dot{\Sigma}) = -L : S^{-1} : (I \ - S\ ) : (\dot{\varepsilon}\ - \dot{E}\ ) = -\widetilde{L}\ : (\dot{\varepsilon}\ - \dot{E}\ ) \tag{5}$$

In equation (5), **S** is the Eshelby tensor, function of **L** and of the inclusion shape and orientation, which is calculated as described by Lebensohn and Tomé (1993). The above equations allow the stress and strain for each grain to be determined once L_{ijkl} is known. However, L_{ijkl} is not known *a priori* as it is itself a function of the behaviour of all the grain orientations. It is thus calculated from the self-consistent condition that the weighted average of the stress (or strain) rates in all the grains must coincide with the imposed polycrystal stress (or strain) rate (equation (6)), which leads to the condition in equation (7).

$$\dot{\Sigma}_{ij} = <\dot{\sigma}_{ij}> \quad \text{or} \quad \dot{E}_{ij} = <\dot{\varepsilon}_{ij}> \tag{6}$$

$$L = <(L^{c} + \widetilde{L})^{-1}>^{-1} : <(L^{c} + \widetilde{L})^{-1} : L^{c}> \tag{7}$$

At the end of a stress or strain increment, σ, ε, **L**, Σ, $\dot{E}$ and the potentially active systems in each grain are known. The same set of systems is assumed to be active in the next increment, which allows L^{c} to be calculated using equation (2). $\dot{\sigma}$ is then calculated from the known $\dot{\Sigma}$. If $\dot{\sigma}$ does not fulfil the conditions for the selected shear modes to be active, a different subset of systems is selected and the previous procedure is repeated. This inner loop is performed for all the grains. The new L^c's are found and L is found by numerical iteration such that equations (6) and (7) are satisfied. The new value of L is then used to verify again whether the loading conditions for the active shear modes are satisfied in each grain. If not, the innermost loop is repeated using the new value of L. Once a satisfactory L is found, the stress and strain are updated incrementally in every grain.

The classical EPSC model just described has been modified to deal with the relaxation associated with twinning as follows. At the end of an increment, the transformation strain, $\dot{\varepsilon}^T_{ij}$, is first reset to zero in all the grains. If the shear ($\dot{\gamma}^{twin}$) contributed by a given active twinning system is greater than a pre-set threshold value ($\dot{\gamma}^{th}$), then a corresponding transformation strain ($\dot{\varepsilon}^T_{ij}$) is calculated as follows:

$$\text{If } \dot{\gamma}^{twin} \geq \dot{\gamma}^{th}, \varepsilon^T_{ij} = V_f^{twin} m_{ij}^{twin} \gamma^S \qquad (8)$$

where V_f^{twin} and γ^S are the volume fraction of the grain assumed to twin (typically 1% at any given incremental step) and the characteristic twinning shear, respectively. This twin transformation induces a relaxation of the shear stress acting on the twinning plane. The amount of such relaxation is controlled by the fraction of the grain that twins (V_f^{twin}) which in our model is an adjustable parameter. The overall value of the transformation strain is thus the sum of the contributions from all of the active twinning modes. Note that the calculated transformation strain does not affect the current increment, but rather the following increment.

3 Results and Discussion

The behaviour of the magnesium alloy in uniaxial tension and compression was modelled using the modified EPSC formulation described above. The results of the simulation for uniaxial tension are shown in Fig. 2. In the figure, 'ax*hkil*' represents axial lattice strains measured parallel to the stress axis using the *hkil* reflection. Similarly 'rad*hkil*' represents radial lattice strains measured normal to the stress axis using the *hkil* reflection. For the experimental results, the data points corresponding to loading are linked by solid lines, whereas those corresponding to unloading are connected by dashed lines. The linear hardening law used describes the evolution of the CRSS in every system in every grain as a function of the accumulated shear in the grain. τ_0 is the initial value of the CRSS in the system and θ_0 is the slope of the CRSS-shear strain graph. τ_0 and θ_0 for the allowed deformation modes are included in the Fig. 2.

In monotonic tension, $\{10\bar{1}2\}$ twinning is favoured in only a small fraction of the grains. The relaxation produced by this twinning is seen in the 'ax0002' and 'rad1010' experimental results, in which strain plateaux are clearly visible. The model predictions correlate well with the relaxations produced by $\{10\bar{1}2\}$ twinning for all of the neutron diffraction results.

In monotonic compression, $\{10\bar{1}2\}$ tensile twinning is favoured in the majority of grains. Compression was modelled using the optimised CRSS and strain hardening parameters determined from the monotonic tension results. In this case,

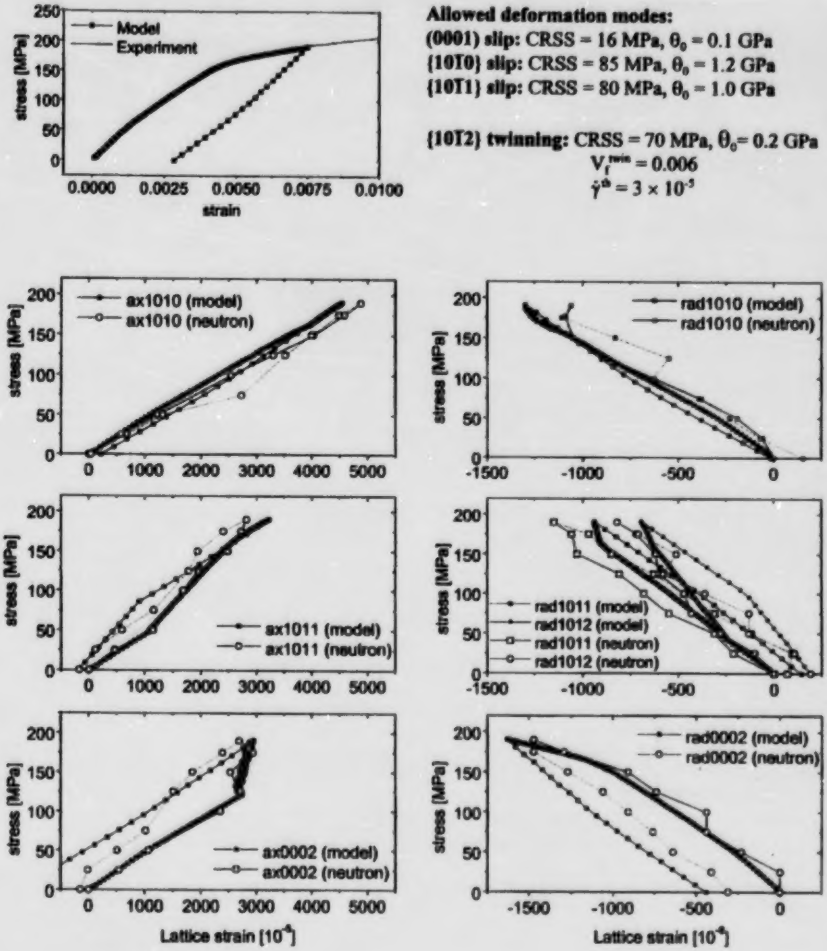

Allowed deformation modes:
(0001) slip: CRSS = 16 MPa, θ_0 = 0.1 GPa
$\{10\bar{1}0\}$ slip: CRSS = 85 MPa, θ_0 = 1.2 GPa
$\{10\bar{1}1\}$ slip: CRSS = 80 MPa, θ_0 = 1.0 GPa

$\{10\bar{1}2\}$ twinning: CRSS = 70 MPa, θ_0= 0.2 GPa
$V_f^{twin} = 0.006$
$\dot{\gamma}^{th} = 3 \times 10^{-5}$

Fig. 2: Analysis of monotonic tension.

the mechanical behaviour is well modelled up to the onset of twinning. However, beyond this point the model underpredicts the amount of $\{10\bar{1}2\}$ twinning observed experimentally. An analysis of the problem revealed that once twinning had started in a grain in a grain, the resulting stress relaxation was such that the internal resolved shear stress retracted from the single crystal yield surface and did not reach it again until much later in the simulation sequence. As a result of this, new twin nucleation and propagation within a grain was too difficult and could not accurately follow the easy propagation observed experimentally. We are presently working on an improved twinning model to overcome this limitation (Gharghouri and Tomé, 1999).

4 References

Couling, S.L., Pashak, J.F., and Sturkey, L. (1959) *Trans. ASM*, Vol. 51, pp. 94-107.

Eshelby, J.D. (1957) The determination of the elastic field of an ellipsoidal inclusion, and other problems. *Proc. R. Soc. Lond. A*, Vol. 241. pp. 376-396.

Gharghouri, M.A., Weatherly, G.C. and Embury, J.D. (1998) The interaction of twins and precipitates in a Mg-7.7at.% Al alloy. *Phil. Mag. A.*, Vol. 78, No. 5. pp. 1137-1149.

Gharghouri, M.A., Weatherly, G.C., Embury, J.D. and Root, J. (1999) Study of the mechanical properties of Mg-7.7at.% Al by in-situ neutron diffraction. *Phil. Mag. A.*, in press.

Gharghouri, M.A. and Tomé, C.N. (1999) to be published.

Hill, R. (1965) Continuum micro-mechanics of elasto-plastic polycrystals. *J. Mech. Phys. Solids*, Vol. 13. pp. 89-101.

Hutchinson, J.W. (1970) Elastic-plastic behaviour of polycrystalline metals and composites. *Proc. Roy. Soc. Lond. A*, Vol. 319. pp. 247-272.

Lebensohn, R.A. and Tomé, C.N. (1993) A self-consistent anisotropic approach for the simulation of plastic deformation and texture development of polycrystals: application to zirconium alloys. *Acta metall. mater.*, Vol. 41, No. 9. pp. 2611-2624.

Partridge, P.G. (1967) The crystallography and deformation modes of hexagonal close-packed metals. *Met. Rev.*, Vol. 12. pp. 169-194.

Turner, P.A. and Tomé, C.N. (1994) A study of residual stresses in Zircaloy-2 with rod texture. *Acta metall. mater.*, Vol. 42, No. 12. pp. 4143-4153.

TEXTURE, MICROSTRUCTURE AND PROPERTIES IN MECHANICALLY ALLOYED AND EXTRUDED FeAl

S. LENHARD, F. WAGNER and T. GROSDIDIER*
Laboratoire d'Etude des Textures et Applications aux Matériaux, Université de Metz, Metz, France
* Now also with Laboratoire d'Etudes et de Recherches sur les Matériaux et Propriétés de Surfaces - UTBM, Belfort, France
S. REVOL and R. BACCINO
CEA/CEREM, Grenoble, France

Abstract

Mechanically alloyed FeAl powders were extruded at 1000 and 1100°C for two different extrusion ratios 14:1 and 28:1 in the shape of bars. The influence of extrusion temperature and extrusion ratio on texture, microstructure and properties of the alloys was investigated. In the range tested, the extrusion temperature had a more important influence on the properties. Extruded bars were subjected to heat treatments and significant evolution in texture and microstructure could only be observed for temperatures above 1200°C. In this case, from the initial <110> texture, abnormal grain growth of <111> oriented grains was observed.

Keywords: Mechanical alloying, texture, microstructure, Young's modulus, secondary recrystallization

1 Introduction

Iron aluminides based on the equiatomic compound FeAl (B2 structure for a composition going from 34 to 48 Al at.%) have an excellent resistance to corrosion until 1000°C, good mechanical properties at high temperature and a relatively low density (≈6g/cm^3) that should make them suitable for high temperature applications. However, the use of such alloys was delayed for two major reasons : their brittleness at room temperature and their low creep resistance. The adjunction of B and Zr, improving the grain boundary resistance, as well as the use of the Mechanical Alloying (M.A.) and extrusion route have permitted to overcome these problems (Baccino et al. 1997). Indeed, the employment of MA improves the resistance to cleavage by reducing the grain size, and increases the creep resistance due to a fine and stable oxide (Y_2O_3 for one) intergranular dispersion. Accordingly, CEA / CEREM has developed a new type of high strength MA alloy labelled FeAl40 Grade 3 (Moret 1995). Table 1 gives a comparison of the mechanical and physical properties of FeAl40 Grade 3 with other industrial alloys.

The drawback of MA in this type of alloys is that it affects the development of the texture during extrusion. Indeed, for atomised and extruded FeAl material the resulting texture is composed of a major <111> fibre and a minor <110> fibre (Stout and Crimp 1992) whereas FeAl40 Grade 3 presents a <110> fibre texture (Pirot et al. 1996; Baccino et al. 1997). This reduces significantly the elastic properties of the material (Moret 1995) as a consequence of the monocrystal anisotropy. The aim of this work was thus to study the influence of processing parameters and additional heat treatments on microstructure, texture and associated properties of mechanically alloyed FeAl extruded bars.

Table 1: Mechanical and physical properties at room temperature of FeAl40 Grade 3 compared to other industrial alloys (From Moret et al. 1995).

	Density	Ultimate tensile strength (MPa)	Young's modulus (GPa)	Specific stiffness $\sqrt{(E/\rho)}$ $(MPa.g^{-1}.cm^{-3})^{1/2}$
FeAl40 Grade 3	6	1147	200	184
Titanium (TA6V)	4.43	930	114	156
Steel (316L)	8	480-620	190-215	154-164
Super alloy IN100	7.75	1010	215	167

2 Experimental Procedure

Powders were atomized and subsequently attrited by CEA / CEREM. The powders were extruded (canned in mild steel) in the form of cylindrical rods at two different temperatures (1000°C and 1100°C) and for two different extrusion ratios (E.R. = 14:1 and 28:1 at 1100°C). The FeAl40 Grade 3 alloy had the following composition (atomic %): Fe-39.78Al-0.054Zr-0.01B-0.2Y_2O_3. The microstructural investigations were carried out by transmission electron microscopy using a Philips CM200 microscope operating at 200 kV. X-ray texture measurements were performed on cross sections of the rods. The pole figures measurements were collected from the (110), (200) and (211) Bragg peaks for the $\lambda_{Co} = 0.1789$ nm wavelength. The ODFs were calculated using the harmonic method. All materials examined in this study possessed a fibre texture so that a single cut of the ODF (for $\varphi 1$ constant) is sufficient to describe the texture of the extruded bars. EBSP measurements were also carried out on transverse sections of the heat treated samples.

The elastic behaviour was calculated by the Voigt - Reuss - Hill modells (Hill 1952) using a software developed in LETAM by M. Humbert. Reuss and Voigt methods involve calculating the average compliance tensor S or stiffness tensor C, respectively, corresponding to a given ODF (Bunge 1969). The values of the elastic constants for FeAl used for the calculations were $C_{11} = 194.1$, $C_{12} = 116.1$, $C_{44} = 133.3$ GPa (Leamy et al. 1967).

3 Results and discussion

3.1 Anisotropy of the elastic properties of FeAl

Using the elastic constants, a simple calculation of the single crystal Young's modulus as a function of the crystallographic orientation gave E values of 107, 209, 305 GPa in the <100>, <110> and <111> directions, respectively. Table 2 shows the results obtained for three different simulated textures and for the three calculation methods.

Table 2: Values of Young's modulus for different simulated textures

Texture	Young's modulus (GPa)		
	Reuss	Voigt	Hill
Isotropic	175	234	200
<111> fibre (10° dispersion)	276	295	285
50% <111> + 50% <110> fibre	234	277	253

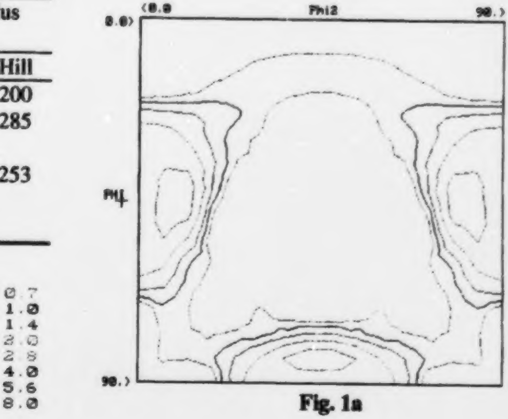

Fig. 1a

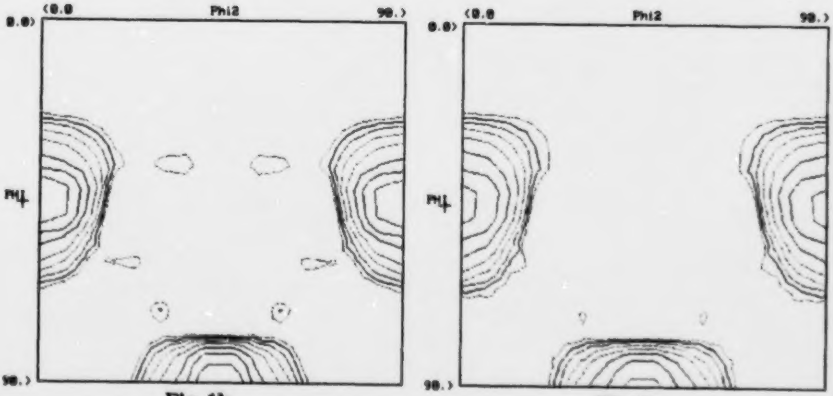

Fig. 1b **Fig. 1c**

Figure 1: ODFs of the samples in the as-extruded state, a) extruded at 1000°C, E.R. = 14:1; b) extruded at 1100°C, E.R. = 14:1; c) extruded at 1100°C, E.R. = 28:1

These results show the large anisotropy and therefore the high potential to modify the material stiffness by texture changes. It can also be seen that, even if the appearance of a <110> texture component reduces the stiffness of the M.A. processed bar, the presence of this <110> component gives better stiffness properties than what would be obtained from an isotropic material.

3.2 Influence of extrusion parameters

Figure 1 shows the ODFs of the three as extruded states that were studied here.

At a given extrusion ratio of 14:1, the texture has evolved from a fibre formed at 5 to 9° from the <110> fibre when the extrusion was carried out at 1000°C to a well defined <110> fibre at 1100°C. This is also associated with an increase in intensity of the fibre going from 3.5 to 11. No significant difference in the ODF, either in the type of texture component nor in its intensity, was noticed when changing the extrusion ratio from 14:1 to 28:1 (figures 1b and 1c).

The microstructure consisted in slightly elongated grains parallel to the extrusion direction pinned by fine oxide precipitates. The apparent grain size range was about 0.5 to 0.8 µm and 0.8 to 1.5 µm for an extrusion performed at 1000°C and 1100°C, respectively. As for the texture, the variation of the extrusion ratio did not modify the microstructure in a significant manner.

Table 3: Influence of the processing parameters on the mechanical properties

Sample		Yield strength $R_{0,2}$ (MPa)	Ultimate tensile strength R_m (MPa)	Elongation A% (%)	Young's modulus (GPa) in the extrusion direction			
Temp. (°C)	E.R.				Experimental values	Computed values		
						Reuss	Voigt	Hill
1000	14 :1	1280	1288	3	186	173	231	198
1100	14:1	888	1150	6,8	201	190	247	215
1100	28:1	891	1157	6,3	197	185	243	210

Tensile test have been carried out on the three samples and their Young's moduli have been computed from the obtained ODFs. The results are reported in table 3. First, it has to be noted that the tendencies in the evolutions of the calculated and the experimental Young's moduli are in rather good agreement. It can also be noted that the mechanical properties are rather strongly affected by an elevation of the extrusion temperature. This is not the case when the extrusion ratio is increased. The higher yield strength measured for the sample extruded at 1000°C can be explained by the finer grain size of this sample compared to the ones extruded at 1100°C. The Young's modulus, is higher for the samples extruded at 1100°C because of the sharper <110> fibre than at 1000°C. The samples extruded at 1100°C with the extrusion ratios 14:1 and 28:1 have a very similar texture and microstructure, and, thus, also have very similar elastic and mechanical properties.

3.3 Influence of heat treatments

To modify the texture, heat treatments were carried out on samples from the bar extruded at 1100°C with an E.R. = 14:1. Up to 1200°C, no significant evolution was observed either in the microstructure nor in the texture even after a heat treatment as long as 1 hour. This is illustrated in figure 2 that shows the ODF of a sample annealed 10 min. at 1200°C. This shows that at this temperature the required activation energy to start recrystallization or for the grain boundaries to overcome the pinning effect of particles seems not to have been reached. This is consistent with results from Morris et al. (1997) who observed significant recrystallization only at temperatures above 1250°C for this type of alloy.

Heat treatments at higher temperatures led to strong texture and microstructure evolutions, even for fairly short annealing times. Figure 3 shows an optical micrograph of such a sample. Few large grains can be easily seen, suggesting abnormal grain growth. Some fine grains inclosed in these large ones could be observed at higher magnification. Texture in this sample was investigated by recording 5265 local orientations on a rectangular frame of about 34 x 42 µm. In the inverse pole figure (figure 4) each point represents a direction parallel to the extrusion direction. Many points near the [111] orientation can be noticed. These points near [111] represent the orientation of the grains who have abnormally grown while the single points in the [101] corner represent the matrix grains who have not been consumed yet in the early stage of secondary recrystallisation.

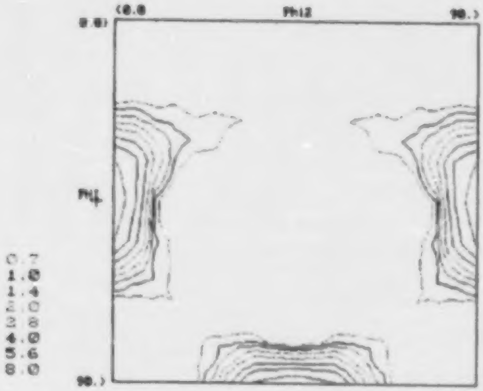

Figure 2: ODF of the sample annealed 10 min. at 1200°C

4 Conclusion

1. Due to the important anisotropy of the Fe40Al monocrystal and to the differents textures obtained, the Young's modulus of extruded bars also presented significant variations.

2. The temperature had a more important influence than the extrusion ratio on the evolution of textures, microstructure and on the associated mechanical and elastic properties.

3. For heat treatments below 1200°C, no significant changes in texture and microstructure were noticed. Secondary recrystallization occured at higher temperature leading to the development of coarse <111> oriented grains.

5 References

Baccino R., Wolski K.,Thevenot F., Le Coze J. and Moret F., (1997) *Ann. Chim. Sci. Mat.*, 22, pp. 423-433.

Bunge H.J., (1969) *Mathematische Methoden der Texturanalyse*, Academie Verlag, Berlin.

Hill R., (1952) *Proc. Phys. Soc.*, A65, pp. 349-354.

Leamy H.J. et al., (1967) *Acta Met.*, 15.

Moret F., Baccino R., Martel P. and Guetaz, L., in *Actes du colloque FeAl*, 14 septembre 1995, CEA / CEREM, ed. F. Moret and R. Baccino.

Morris D.G., Gunther S. and Briguet C. (1997) Scripta Met., Vol. 37, No 1, pp. 71-77.

Pirot V.E., Verlinden B., Delaey L. and Aernoudt E. (1996) *Rev. Met.*, JA96, pp. 220.

Stout J.J. and Crimp M.A., (1992) *Mat. Sci. Engng*, A152, pp. 335-340.

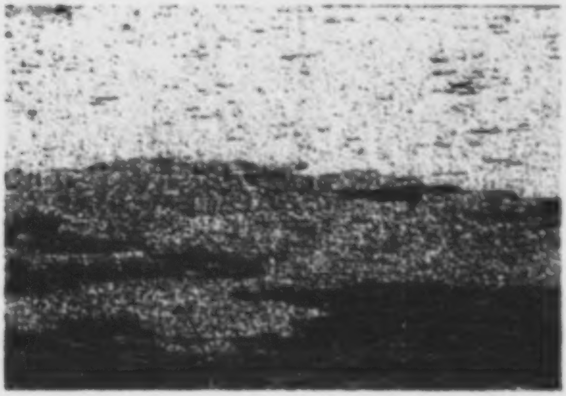

Figure 3: Micrograph of a sample extruded at 1100°C and annealed at high temperature

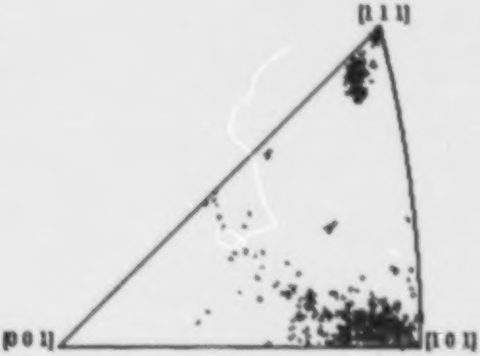

Figure 4: Inverse pole figure of a sample extruded at 1100°C and annealed at high temperature

EFFECT OF THERMOHYDROGEN PRETREATMENT ON TEXTURE AND DEFORMABILITY OF BCC TITANIUM ALLOY

T.A. SOKOLOVA and L.I. ANISIMOVA
Institute of Machines Science, Ural Division, Russian Academy of Sciences,
Ekaterinburg, Russia
B.K. SOKOLOV, I.V. GERVASYEVA and L.R. VLADIMIROV
Institute of Metals Physics, Ural Division, Russian Academy of Sciences,
Ekaterinburg, Russia

Abstract

The results of investigations of the texture, structure, and dimensions of the cold-rolled strips of β- titanium alloy VT35 containing hydrogen of a concentration of up to 0.55% prior to the deformation are reported. Inserting hydrogen of 0.1-0.2 wt.% is shown to increase the alloy plasticity, thereto, the elongation of the strips grows and their widening decreases upon rolling. The texture peculiarities of the alloys with 0.1-0.2 wt.% H consist in increase in the intensity of the {111}<112> component, enhancement of components of the friction texture, and growth of the degree of the texture asymmetry. Possible explanations of the experimental data are presented.

Keywords: Cold-rolling, hydrogen, slipping, texture, titanium alloy, widening.

Researches dealing with the problem of interacting hydrogen with metals usually pay attention to either hydrogen brittleness or plasticizing role of hydrogen. The results obtained and their explanations suggested are diversified and contradictory (Goltsov 1982; Kimura and Matsui 1987). The effect of hydrogen on the formation of a crystallographic texture upon deformation has not virtually been studied though the texture essentially controls mechanical properties of substances.

In most cases, the behavior of a material upon deformation was studied directly in the hydrogen atmosphere. Meanwhile, a thermohydrogen treatment that comprises inserting the required amount of hydrogen into metal workpieces, their deformation and subsequent removing hydrogen by vacuum annealing finds commercial application. To make the best use of the thermohydrogen treatment, it is necessary to gain proper knowledge on the texture.

In the paper presented, the results of investigations of the texture, structure, and behavior of the mechanically stable β-titanium alloy VT35 containing hydrogen upon cold rolling are given.

The alloy had the following chemical content (wt%): Ti-2.7Al-0.55Mo-15.2V-3Cr-0.4Zr-2.8Sn and exhibit single-phase bcc structure. Sheets of the alloy 1.2mm thick were annealed in a vacuum at a temperature of 850C for 2 hours. Then they were hydrogenated at 780C and different holdings. Cooling from 780C to room temperature was performed in air. The hydrogen content in alloys amounted to 0.04-0.55wt%. The specimens were cold-rolled to a reduction ranged from 1 to70%. The thus prepared samples were used to study microstructure and texture in different sections through depth and to determine the changes in dimensions of the strips rolled. The texture was analyzed using X-ray diffraction methods in transmission and reflection geometry. As the texture had an asymmetry, the ODF method was not applied.

In the starting state before deformation samples had an identical structure with a mean grain size of 60-70 mkm and a poor recrystallization texture. The texture analysis of the deformed alloys revealed that upon cold rolling a texture develops that is typical of the high-alloyed bcc compounds.

After rolling to a 30 % reduction there arises a difference in the textures between alloys with various hydrogen concentration. Increasing it to 0.1 - 0.2 wt.% leads to an enhancement of the texture component {112}<110>. Its further growth to 0.3-0.55 wt % results in weakening of the {112}<110> and enhancement of the {111}<112> and {100}<011> components. On increasing reduction to 70 %, in the hydrogen-free alloy, the strong components {111}<110> and {100}<011> are formed (Fig.1a), whereas in the alloy with 0,18 wt %H, these components are much weaker and the main ones are {111}<112> and {112}<110> (Fig.1b).

An important feature of the texture in the alloy with 0.18 wt.% H is its asymmetry. The symmetry center of the pole figure is shifted from the position of the normal to the rolling plane.

Another peculiarity of the texture in the alloy with 0,18 wt.% H is the occurrence of the components such as {110}, mostly {110}<011> and {110}<112>, {531}<112>, and {112}<111> which are not specific to the texture of rolling in bcc alloys.

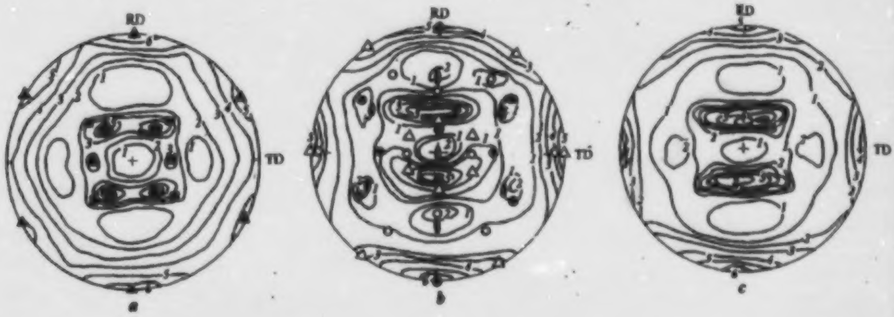

Fig. 1: {110} pole figures of the cold-rolled VT35 alloy ($\varepsilon = 70\%$) with hydrogen concentrations 0 (a), 0.18 (b) and 0.55 wt.% (c): (▲) - {111}<011>, (△) – {111} <112>, (■) – {001}<110>, (⬮) – {110}<112> , (●) – {211}<011>, (○) - {211} <111> orientations.

Intensities are indicated by numbers along the contour lines.

These components were discovered in both the surface layers of the strip rolled and at a depth of one forth of its thickness. They are inherent in the textures of friction that form in the surface and subsurface layers of a strip under contact friction in the course of rolling. As the rolling of all the alloys was carried out under the same conditions, the texture formation can be related to the hydrogen influence on the contact surface of the strips or else, deformability of the material as it is.

The above texture peculiarities didn't manifest themselves in the hydrogen-free alloy and were poorly pronounced in the alloys with high concentrations of hydrogen. Thus, at 0.55 wt.% H, the main texture components proved to be {111}<110>. {111}<112>, and {100}<011> (Fig.1c).

The microstructure investigations of the alloys showed that after cold rolling to a reduction of 10%, in the structure of hydrogen-free samples, the deformation twins are present along with the slip bands. With increasing H content their amount decreases.

Starting from the 30% reduction, in the alloys containing hydrogen there takes place a band structure, which is known as the shear band structure. In different grains, these bands are disposed similarly: in the rolling plane they go across the rolling direction and in the side planes, at an angle of 25-35 to the rolling direction. In the alloys with 0,1-0,2 wt.%H, the shear bands appear in the deformation structure at a smaller reduction than in the alloys with higher H contents, not to mention hydrogen-free alloys. This phenomenon might be caused by both the texture and structure inhomogeneities in the deformed strips that arise at early stages of the cold rolling. In the hydrogen-free samples, the shear bands were observed only after reduction to 60%.

Measurements of the dimensions of the rolled samples showed up their different deformability. Thus, resulted from one rolling run were the 7.5% reduction for the alloys containing 0.1-0.2 wt.%H and 6.8-6.9%, for the specimens with more than 0,3 wt.%H as well as hydrogen-free ones. In the Table, averaged form-changing characteristics are presented that were obtained from the measured dimensions of the strips with different H contents and after cold rolling to a large reduction.

Table: Form-changing characteristics of the test alloys.

Hydrogen concentration, wt. %	Reduction,%	Elongation, %	Widening, %
0.00	58.7	57.3	3.2
0.18	60.0	59.4	1.4
0.38	59.3	58.3	2.9
0.04	68.0	67.3	4.1
0.18	68.6	67.9	1.6
0.38	68.3	67.0	4.5

As is seen from the table, the strips of the specimens with 0.1-0.2 wt.% H are less widened and more elongated in comparison with other alloys. Since in all the experiments the deformation zone had the same parameters, the above behavior of the form-changing characteristics for the alloy with 0.1-0.2 wt.% H is likely to be traceable to changes in mechanical properties of the material, peculiarities of its plastic deformation and texture formation.

As is known, growth of the plasticity of the titanium alloys hydrogenated is related to the development of the phase transformations (Il'in 1994). In single-phase materials, the plasticity growth that was discovered upon dynamic hydrogenation (upon saturating hydrogen during loading) mostly manifests itself in decreasing yield strength. The results reported and their treatment can't serve to explain the plasticizing effect of the deformation of hydrogenated material in the same way as changes in mechanical properties upon dynamic loading.

The above experimental results on changes in the texture, structure, and properties of the hydrogenated alloys upon cold rolling might be related to the hydrogen effect on the mechanism of plastic deformation. Plastic deformation in the alloyed β titanium compounds is considered to mainly proceed by slipping along the {112}<111> systems. Inserting hydrogen can change the type of acting slip systems, which, for instance, was reported in the work (Kimura and Matsui 1987), where upon dynamic loading of iron, slipping along the {112} planes changed to slipping along {110} planes.

The hydrogen influence on the type of active slip planes may be caused by different changes in bonding energy of main atoms in different crystallographic planes. A part of the tetrahedral interstices which are occupied by the hydrogen ions lies in the slip planes {112} and {321}, whereas planes {110} don't contain them. The hydrogen ions are likely to hinder slipping and twinning along the first two systems of planes thus activating slipping along the {110} planes. The changes in the crystallographic type of slip systems (in particular, activating planes of complanar slipping) must manifest itself in changes of the stable orientation type and the texture evolution upon deformation.

Theoretical analysis performed for bcc crystals subject to planar deformation showed that upon compression stable orientation proved to be {112} and {113} for complanar slipping whereas cross slipping leads to the stability of the {111} orientations (Vishnyakov et al. 1979). Upon tensile stresses, complanar slipping serves to preserve orientations <112> <110>, but the cross one, <110> only. Thus, the above changes in the texture might be related to the changeover of the mechanism of the texture formation when under the hydrogen effect, acting slip systems change their type: the cross slipping involving {112} type planes gives way to the complanar one along the {110} planes.

As was shown in the experiments, increasing the hydrogen content to 0.3-0.55 wt.% leads to the alloy strengthening and the formation of the rolling textures close in the concentration of the main constituents to the texture in the hydrogen- free alloys. Besides the hardening of the solid solutions, the reason for the growth in the alloy strength can be found in the hydrogen hindering of the dislocations that becomes stronger on forming pairs of dipoles H-H and hydrogen clusters (Alefeld and Volkl 1978).

Conclusion

1. Inserting 0.1-0.2 wt.% H into bcc titanium alloy VT35 leads to increasing the alloy plasticity upon cold rolling.

2. At a concentration of 0.1-0.2 wt.% H, the mechanism of the plastic deformation and the rolling texture change:

twinning and slipping along the{112}planes are hindered, with slipping along the {110} being activated;

the intensity of the main components of the rolling texture increases;

formation of the shear bands is facilitated;

upon cold rolling, the elongation of the strips increases whereas its widening lowers.

References

Alefeld, G. and Volkl, J. (1978) *Hydrogen in Metals*, Springer-Verlag, Berlin-Heidelberd-New York.

Goltsov, V.A. (1982) The phenomenon of controllable hydrogen phase naklep and the prospects for its use in metal science and engineering. *Proc. Intern. symp. metal-hydrogen systems, Miami Beach, Fla., Apr. 13-15, 1981.* Pergamon press, pp.211-23.

Il'in, A.A. (1994) *Mechanism and kinetics of phase and structural transformation in titanium alloys* Nauka, Moscow.

Kimura, H. And Matsui, H. (1987) Mechanism of hydrogen induced softening and hardening in iron. *Scr. Metall.*, No. 21. pp.319-24.

Vishnyakov, J. D. et al. (1979) *Theory of texture formation in metals and alloys.* Nauka, Moscow.

TEXTURE AND MICROSTRUCTURE DEVELOPMENT DURING PROCESSING OF ULTRA FINE GRAINED COPPER BY EQUAL CHANNEL ANGULAR EXTRUSION

A. TIDU, F. WAGNER, T.GROSDIDIER[+]
Laboratoire d'Etude des Textures et Applications aux Matériaux (LETAM)
URA CNRS 2090, ISGMP, F-57012 Metz Cedex 01, France
+ also with : Laboratoire d'Etude et Recherche sur les Matériaux et Propriétés des Surfaces (LERMPS) - UTBM/ENIBe, B.P. 449, 90010 Belfort Cedex, France.

W.H. HUANG, P.W. KAO, C.P. CHANG
Institute of Material Science and Engineering, Sun Yat-Sen University, Kaohsiung, 80424 Taiwan, R.O.C..

Abstract

This work deals with an X-ray texture and microstructure characterization of copper samples produced by the ECAE (Equal Channel Angular Extrusion) process following the so-called route C. The texture of the ECAE processed samples can be described using a monoclinic sample symmetry. The amount of micro-strain and the size of the coherently diffracting domains depend on which peak of a given family plane is investigated. It is also shown that, whereas the size of the domains decreases rapidly with increasing strain, changing the amount of strain from 6.8 to 10.8 did not change further the domain size that seemed to have reached a minimum value.

Keywords: ECA process, size-strain analysis, texture, UFG copper

1 Introduction

Equal-Channel Angular Extrusion (ECAE) is a recently developed process authorizing the production of Ultra-Fine Grained (UFG) materials by successive extrusion steps of a billet through an angular die that introduce cumulative severe plastic deformation (SPD) without changing its shape.

A number of unusual properties have been reported in UFG materials. Many of them have been attributed to the large amount and non-equilibrium character of the grain boundaries present in these nanocrystalline and sub-microcrystalline materials. Crystallographic texture was also shown to be responsible for significant anisotropy in the elastic behavior of UFG copper produced via ECAE (Agnew and Weertman, 1998).

The effect of increasing the number of ECAE passes and deformation routes on strength, hardness and structural alteration mechanisms of the microstructure has recently been described (Ferrasse et al., 1997; Iwahashi et al., 1998). The development of texture has however not been addressed yet. The aim of this work was therefore to study the influence of cumulative deformation by successive ECAE passes on the microstructure and texture development in copper.

2 Experimental approach and X-Ray method

Recrystallised oxygen-free high conductivity copper (99.99wt%) with a mean grain size of 120 μm was used as the starting material. Billets with a square 12 by 12 mm section were pressed through a die having two channels, equal in cross section, which intersect at an angle of 120°. Shearing occurs as the sample moves through the angle and, for this angle condition, the equivalent strain introduced on each passage is approximately 0.68 (Segal, 1995). Cumulative strain was introduced using the so-called route C: the billet was rotated 180° around its extrusion axis after each pass (Iwahashi et al., 1998).

The X-Ray diffraction experiments were done on the plane perpendicular to the extrusion direction (ED). The specimen coordinates are defined in figure 1 where the extrusion, transverse and height directions are labeled. In the following, the crystallographic orientations will be given by {hkl} perpendicular to (ED) and <uvw> parallel to (HD)

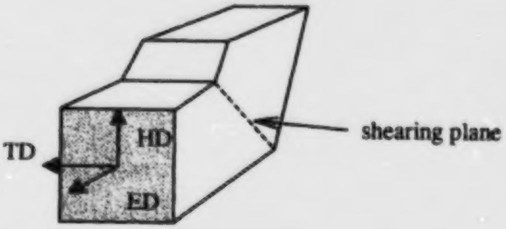

Figure 1 : Geometric description of the sample

For our study, the sample characterization was carried out at each even number of passes ; this is to say, every time the samples was back to its original position. Texture analysis was also carried out by measurements of the (111), (200), (220) and (310) pole figures. X-Ray line shape broadening analysis was also used. In this field, two kinds of effect have to be distinguished : size broadening caused by a finite size of domains in the sample, and strain broadening caused by small displacements of the atoms from their reference positions. Among all existing methods, we used the original two order Warren-Averbach method in order to obtain information about the size of the coherently diffracting domains D_{eff} and the micro-strain $<\varepsilon^2(L)>^{1/2}$ (Warren and Averbach, 1965). The Warren-Averbach theory is based on the splitting of the Fourier coefficients describing the line profile in two components : the size coefficient $A_S(L)$ which is independent of the order of the reflection, and the strain coefficient $A_D(L,l)$ which depends on the order l of the reflection. In these coefficients, L is a distance normal to the reflecting planes of interplanar spacing d_{hkl}. From a practical point of view, a deconvolution is necessary to remove the instrumental broadening part. This deconvolution was achieved by using the Stokes method. The instrumental line profiles were obtained from an annealed copper powder. The Warren-Averbach analysis was performed by measuring accurately the (111) and (222) diffraction lines at given directions of measurement ($\phi\psi$). All the X-Ray line profiles were measured in similar conditions on a curved position sensitive detector using the FeK_{α} line emission of a rotating anode together with a graphite monochromator. The lines were corrected from background, Lorentz-polarisation factor and absorption.

3 Results and discussion

The evolution of texture and microstructure was carried out for increasing amount of strain up to 10.88 (16 passes). This paper will concentrate on the X-Ray investigations for the last stage of the process (10 to 16 passes) where the higher amounts of strain were sustained by the samples (6.8 to 10.88) leading to the finer microstructures.

3.1 Texture

For samples pressed 10 to 16 times through the die, the textures were fairly moderate with maximum at about 3 times random. A quick look at the pole figures revealed features very similar to typical copper-type texture generally obtained in flat rolling with the orientations assembled along the so-called β fiber which runs through the Euler angle space from the C{112}<111> over the S{124}<211> towards the B{011}<211> orientations. Differences in the intensity of the various ideal components were however observed from one sample to the other. This is illustrated in figure 2 that shows the recalculated pole figures obtained on samples passed 14 times ($\varepsilon = 9.52$) and 16 times ($\varepsilon = 10.88$) through the die: C and B components are marked in figure 2a and 2b, respectively. A more careful look at the pole figures revealed however that there is no mirror symmetry about TD in the pole figures. In particular, one of the "central" <111> pole (arrowed) in the upper part of the pole figures has a higher intensity than his corresponding counterpart. These are labeled (H) and (L), referring to Higher and Lower pole in figure 2. This asymmetry in the intensity of the poles was always observed in the ECAE samples that were investigated and is a direct consequence of the processing route. The sample symmetry is thus best described as approximately monoclinic. This is consistent with the symmetry plane of the deformation being defined by the extrusion (ED) and the height (HD) directions (figure 1).

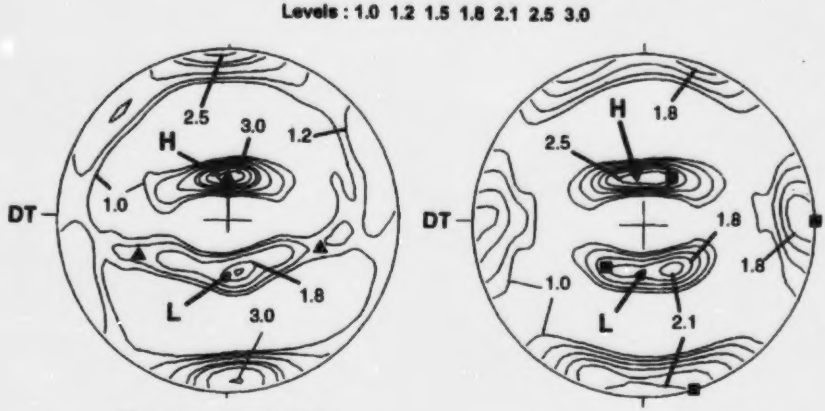

16 passes - route C - 120° C

14 passes - route C - 120° C

Figure 2 : Recalculated (111) pole figures

3.2 Size-strain microstructure

According to the texture observed, this analysis is made for the two directions of measurement ($\phi\psi$) marked H and L in the pole figures in figure 2.

Figure 3 shows the variation of the size of the effective coherently diffracting domains with respect to the number of passes. The sizes of the domains for the two directions of measurement (L) and (H) are initially different and tend to converge to very similar values as the number of passes increases. This evolution also suggests that higher values of macroscopic strain cannot give smaller values of the diffracting domain. The final value can thus be seen as a limit size of the domains that can be reached for this alloy under these extrusion conditions.

Figure 4 presents the variation of the micro-strain $<\varepsilon^2(L)>^{1/2}$ for the particular value L=4.5 nm with respect to the number of passes. Two different behaviors are observed. The micro-strain determined from the high intensity pole remains approximately the same. On the contrary, the micro-strain determined from the low intensity pole increases with the increase in macroscopic strain.

Typical values obtained for rolled copper ($\varepsilon = 0.8$) are : $D_{eff} = 25$ nm and $<\varepsilon^2(L)>^{1/2} = 2.10^{-3}$ for L = 5 nm (Mikkola and Cohen, 1966).

It is clearly seen in figures 2 and 3 that the microstructure is characterized by the small size of the coherently diffracting domains and the high level of micro-distorsion. These results reveal a highly anisotropic microstructure. These differences with respect to the directions of measurement are considered to be due to the deformation process.

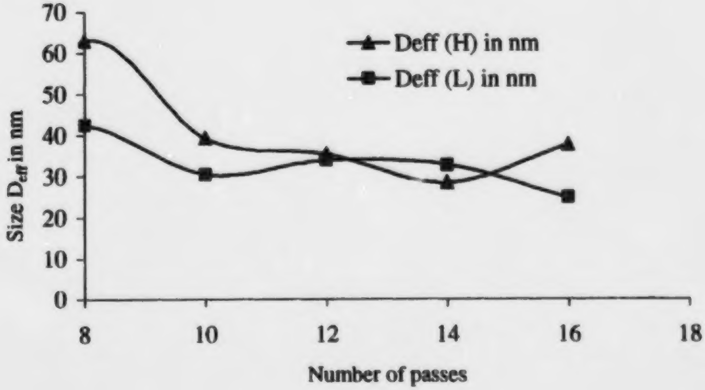

Figure 3: Evolution of the size of the coherently diffracting domain with the number of passes for the (H) and (L) directions of measurement

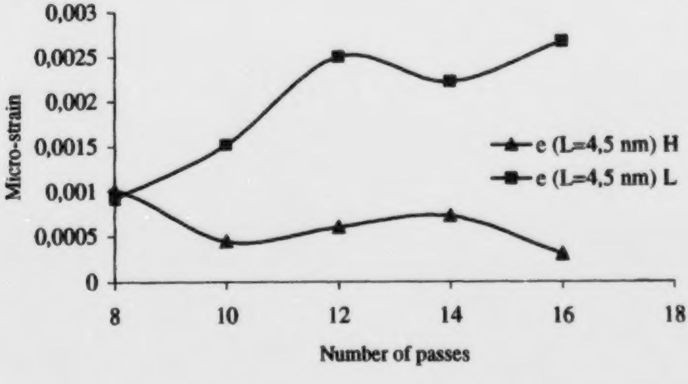

Figure 4: Evolution of the micro-strain for the (H) and (L) directions of measurement with the number of passes.

Our results indicate that all measurements of the size of the coherently diffracting domains and micro-strain must be associated to a given family of plane as well as a given direction of measurement in order to be really meaningful. As a consequence, great care must be taken when comparing earlier XRD results of ECAE processed materials, for which the direction of measurement are never mentioned.

4 Conclusions

1. The textures of samples produced by the ECEA process (120°), where the symmetry plane of deformation is defined by extrusion and height directions, is better described by a monoclinic symmetry: there is a significant asymmetry in the pole figures where a given family type of plane shows higher (H) and lower (L) intensities.
2. The preferred crystallographic orientations of ECAE copper produced at room temperature in the strain range 6.8 to 10.88 - 10 to 16 passes with an extrusion angle of 120° - assembled along the typical copper β-fiber.
3. The amount of micro-strain measured by X-rays were very much dependent on which (H or L) peak of a given plane family was investigated. This reflects again the asymmetry of the deformation associated with the shearing process.
4. Increasing the strain from 6.8 to 10.88 did not change drastically the size of the coherent domains, that seemed to have reached their minimal value, but globally introduced higher amount of internal micro-strains.

REFERENCES

Agnew, S.R. and Weertman, J.R. (1998), Mat. Sci. Eng., A242, 174-180

Ferrasse, S, Segal, V.M., Hartwig, K.T. and Goforth, R.E. (1997); Metal. and Mater. Trans. A, 28A, 1047.

Iwahashi Y., Horita Z., Nemoto M. and Langdon T.G. (1998), Acta Mater., 46, 3317

Mikkola D.E., Cohen J.B.,(1966), in Local Atomic Arrangements Studied by X-Ray Diffraction, Vol. 36, Gordon and Breach Science Publishers

Segal V.M. (1995), Mat. Sci. Eng., A197, 157-164.

Warren B.E., Averbach B.L. (1952), J. Appl. Phys., 23, 497

THE TEXTURE EVOLUTION OF TORSION-REVERSE TORSION

S.-J. PARK, J.-H. CHO, and K.H. OH
Division of Materials Science and Engineering, Seoul National University,
San 56-1, Shinrim Dong, Kwanak-ku, Seoul 151-742, Korea

Abstract

The texture evolution in torsion-reverse torsion of FCC metal is calculated by single crystal plasticity FEM where both equilibrium and compatibility hold. The results are compared with those calculated with a Taylor-type model where holds compatibility only. The calculation of torsion-reverse torsion by FEM shows a residual shear texture at large shear strain and texture close to its initial one at small shear strain as observed in experiments reported previously. On the other hand, the calculation with a Taylor-type model always produce a complete restoration to the initial texture. The residual texture calculated by FEM is due to the grain interaction to satisfy both equilibrium and compatibility during deformation.

Keywords : Torsion-reverse torsion, single crystal plasticity FEM, Taylor-type model, residual shear texture, grain interaction, equilibrium, compatibility

1. Introduction

It has been reported that reversing a torsion test to zero net shear strain does not restore the texture of the material to its initial state (Backofen 1950; Rollet *et al.* 1987). Backofen observed a remained shear texture very similar to a normal torsion texture from torsion-reverse torsion of copper. He also showed that the grain shape was restored to its initial equiaxed character at zero net shear strain. Rollet *et al.* carried out torsion-reverse torsion experiments with Al-Mg alloy. They obtained similar results to those of Backofen, i.e. a residual shear texture and a restored grain shape. They also calculated texture evolution using a code based on the Taylor model and showed that the calculated texture was completely restored. They pointed out the disagreement of experimental results with theoretical calculations of texture development that are based on grain shape change only. The reason for the disagreement could be thought in following two ways. First, grains break up into subgrains with misorientations between them at large strains, therefore, the Taylor type model which does not take the break-up of grain into account is not able to predict the irreversibility of texture evolution. Second, as with the Taylor type model, compatibility is satisfied but equilibrium is violated between grains, the calculated texture is not able to consider interaction between grains. The interaction could cause incomplete grain shape restoration to the initial configuration and consequently the irreversibility of texture evolution.

In the present work, the texture evolution in torsion-reverse torsion of FCC metal is calculated by single crystal plasticity FEM in which equilibrium is also satisfied not only compatibility. The results are compared with those predicted by a Taylor-type model and the effects of grain interaction following the equilibrium condition on texture evolution are investigated.

2. Single crystal plasticity FEM

Asaro and Needleman proposed a finite-strain elastic-plastic rate-dependent constitutive relation of single crystal (Asaro and Needleman 1985). Kalidindi *et al.* proposed an implicit time-integration procedure for a modified form of the constitutive relation of Asaro and Needleman (Kalidindi *et al.* 1992). The constitutive equation for the stress in each grain is taken as

$$\sigma^* = \mathbf{C}^E[\mathbf{E}^*],\ \ \mathbf{E}^* = (1/2)\{\mathbf{F}^{*T}\mathbf{F}^* - 1\} \text{ and } \sigma^* = \mathbf{F}^{*-1}\{(\det \mathbf{F}^*)\sigma\}\mathbf{F}^{*-T} \qquad (1)$$

where $\mathbf{C}^E$, σ and $\mathbf{F}^*$ are a fourth order elasticity tensor, the symmetric Cauchy stress tensor and an elastic deformation gradient, respectively. With use of flow rule, the stress tensor at time $\tau = t + \Delta t$, $\sigma^*(\tau)$, can be approximately expressed by deformation gradient, $\mathbf{F}(\tau)$, and plastic deformation gradient, $\mathbf{F}^p(t)$, that are already known as follows.

$$\sigma^*(\tau) \approx \sigma^{*tr} - \sum_s \Delta\gamma^s \mathbf{D}^s,\ \ \sigma^{*tr} = \mathbf{C}^E\{1/2[\mathbf{F}^{p^{-T}}(t)\mathbf{F}^T(\tau)\mathbf{F}(\tau)\mathbf{F}^{p^{-1}}(t) - \mathbf{I}]\} \text{ and}$$

$$\mathbf{D}^s = \mathbf{C}^E\{1/2[\mathbf{F}^{p^{-T}}(t)\mathbf{F}^T(\tau)\mathbf{F}(\tau)\mathbf{F}^{p^{-1}}(t)\mathbf{R}_0^s + \mathbf{R}_0^s\mathbf{F}^{p^{-T}}(t)\mathbf{F}^T(\tau)\mathbf{F}(\tau)\mathbf{F}^{p^{-1}}(t)]\} \qquad (2)$$

where $\mathbf{R}_0^s$ and $\Delta\gamma^s$ are the Schmid tensor at initial configuration and increment of shear of a slip system s, respectively. The constitutive equation for the shear rate $\dot{\gamma}^s$ of a slip s is taken as

$$\dot{\gamma}^s = \dot{\gamma}_0^s \left|\frac{\tau^s}{\tau_0^s}\right|^{1/m} \operatorname{sign}(\tau^s) \qquad (3)$$

A non-linear problem of equations (2) and (3) could be solved numerically by Newton-Raphson iterative method. The calculation scheme of the present work follows that of Kalidindi *et al.* and has been implemented in the finite element program ABAQUS via the user material subroutine UMAT (ABAQUS, 1997). In typical implicit finite element procedures, the principle of virtual work enforces equilibrium and compatibility conditions in a weak sense.

3. Results and discussion

The rate sensitivity m was set to be 0.05. The slip system is {111}<110> slip system. Hardening on slip system is not considered, i.e. τ_0^s in equation (3) is taken as a constant. In the finite element calculation, an aggregate of 400 crystals is represented by 400 three-dimensional eight-noded C3D8R elements (ABAQUS, 1997). Fig. 1 shows the initial finite element mesh and boundary conditions. The sense of shear is negative at first, then is positive to make zero net shear strain at last. Each element represents one crystal and is assigned an orientation which is randomly picked from the set of 400 grain orientations used to represent the initial texture. The (111) pole figure of an initial random texture is shown in Fig. 2. Fig. 3 (a) shows the deformed mesh to a shear strain of –1. Because of the crystallinity of the material, the deformation of elements is inherently inhomogeneous and both equilibrium and compatibility are satisfied through out the aggregate. Fig. 3 (b) shows the deformed mesh after torsion-reverse torsion to a shear strain of –1, followed by a return to zero. Note that the geometry of elements is not restored to their exact initial square shape after restoration of macroscopic geometry. Though the elements become nearly in equiaxed shape, many of them acquires some amount of positive or negative shear and even rigid body rotation. Fig. 3 (c) shows the deformed mesh after torsion-reverse torsion to a shear strain of –4, followed by a return to zero. It also can be observed that the deformation of elements in macroscopic restored geometry is not homogeneous as in the case of Fig. 3 (b).

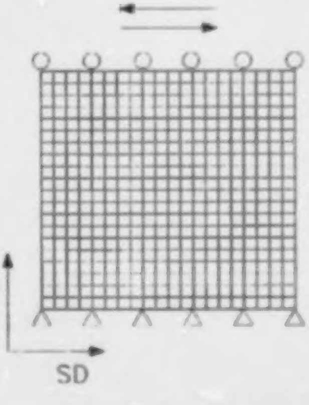

Fig. 1. Initial finite element mesh.

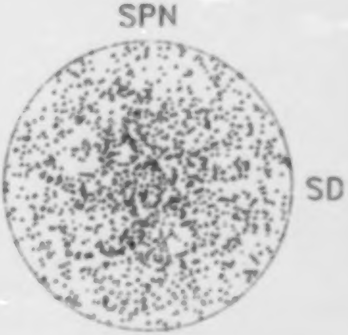

Fig. 2. (111) pole figure of initial random texture with 400 crystals.

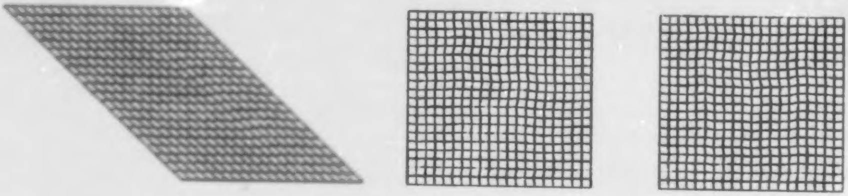

(a) (b) (c)

Fig. 3. Deformed mesh (a) at shear strain of –1, (b) to shear strain of –1 followed by reverse shear to zero net strain and (c) to shear strain of –4 followed by reverse shear to zero net strain.

Figs. 4 (a) and (c) show the (111) pole figures obtained from FEM calculation of the torsion cases in which shear strain is –1 and –4, respectively. It can be seen that the A fiber {1 1 1}<u v w> and B fiber {h k l}<1 1 0> (Tóth *et al.* 1989) which are observed in typical shear texture develop. Figs. 4 (b) and (d) show the (111) pole figures obtained from FEM calculation of the macroscopic restored torsion-reverse torsion cases in which shear strain is –1 and –4, respectively. It could be noted in Fig. 4 (b) that when the amount of shear is small before reverse torsion, the texture almost restores to its initial random texture. The calculated result is similar to the previous experimental result (Cho *et al.* 1998) in that the initial texture almost restores. On the other hand, when the amount of shear is large before reverse torsion, a residual shear texture remains as shown in Fig. 4 (d). This residual texture in calculation is due to the incomplete restoration of element geometry or grain shape that is caused by the interaction between elements or grains to satisfy equilibrium. Beaudoin *et al.* also discussed about the effects of grain interaction on deformation of grains during aluminum sheet forming (Beaudoin *et al.* 1998).

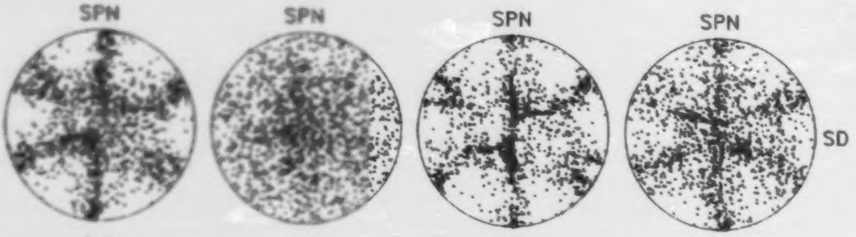

(a) (b) (c) (d)

Fig. 4. (111) pole figures calculated by FEM (a) at shear strain of –1, (b) to shear strain of –1 followed by reverse shear to zero net strain, (c) at shear strain of –4 and (d) to shear strain of –4 followed by reverse shear to zero net strain.

These results could be compared with those calculated with a full-constraint Taylor-type model shown in Figs. 5 (a)-(d). In case of shear amount of –1 and its reversed case, the (111) pole figures shown in Figs. 5 (a) and (b) which are calculated with a Taylor-type model show little difference from those calculated with FEM. However, In case of shear amount of –4 and its reversed case, the (111) pole figures shown in Figs. 5 (c) and (d) which are calculated with a Taylor-type model show differences from those calculated with FEM. The shear deformation texture restores almost completely to its initial random texture as can be seen in Fig. 5 (d). It is also reported that even the use of a Taylor-type relaxed-constraint model results in complete restoration to initial texture after torsion-reverse torsion (Rollet *et al.*). All these complete restoration of texture are caused by the inherent limit of Taylor-type model which ensures compatibility only.

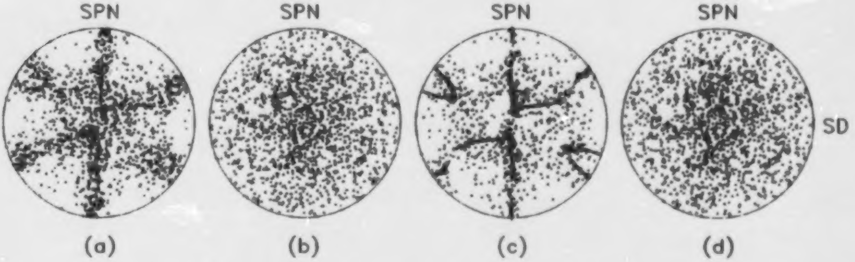

Fig. 5. (111) pole figures calculated by a full-constraint Taylor-type model (a) at shear strain of –1, (b) to shear strain of –1 followed by reverse shear to zero net strain, (c) at shear strain of –4 and (d) to shear strain of –4 followed by reverse shear to zero net strain.

4. Summary

The texture evolution in torsion-reverse torsion of FCC metal is calculated by single crystal plasticity FEM where both equilibrium and compatibility hold. The calculation of torsion-reverse torsion shows a residual shear texture when the amount of shear before reversion is large while it shows a restored texture when the amount of shear before reversion is small. The results are compared with those calculated with a Taylor-type model where holds compatibility only and the calculated texture restored completely in both the cases of large and small amount of shear before reversion. The residual texture calculated by FEM is due to the grain interaction to satisfy both equilibrium and compatibility.

Acknowledgements

The authors wish to acknowledge the financial support of the Korea Research Foundation made in the program year of (1998)

References

ABAQUS (1997) *Reference manuals*, Hibbitt, Karlsson and Sorensen, Inc., Pawtucket, RI.

Asaro R.J. and Needleman A. (1985) Texture development and strain hardening in rate dependent polycrystals. *Acta metall.*, Vol. 33, No. 6, pp. 923-953.

Backofen W.A. (1950) The torsion texture of copper. *Trans. AIME*, Vol. 188, pp. 1454-1459.

Beaudoin A.J., Bryant J.D. and Korzekwa D.A. (1998) Analysis of ridging in aluminum auto body sheet metal. *Metall. Trans. A*, Vol. 29A, pp. 2323-2332.

Cho J.-H., Park S.-J. and Oh K.H. (1998) Analysis of texture evolution of torsion-reverse torsion of copper rods. *Materials Science Forum*, Vols. 273-275, pp. 649-654.

Kalidindi S.R, Bronkhorst C.A and Anand L. (1992) Crystallographic texture evolution in bulk deformation processing of fcc metals. *J. Mech. Phys. Solids*, Vol. 40, No. 3, pp. 537-569.

Rollet A.D., Lowe T., Kocks U.F. and Stout M.G. (1987) The microstructure and texture of torsion-reverse torsion experiments. *ICOTOM-8*, Santa Fe, New Mexico, pp. 473-478.

Tóth L.S., Neale K.W. and Jonas J.J. (1989) Stress response and persistence characteristics of the ideal orientations of shear texture. *Acta metall.*, Vol. 37, No. 8, pp. 2197-2210.

THE FORMATION OF THE FIBRE TEXTURES IN BCC METALS BY DEFORMATION BANDING

B.J. DUGGAN and G.L. LIU
Department of Mechanical Engineering, The University of Hong Kong,
Pokfulam Road, Hong Kong

Abstract

Grain orientation splitting or deformation banding (DB) in BCC metals has been established in rolled low carbon steel by SEM investigation depending partially on etching and partially on channelling contrast imaging. Deformation banding occurs in both longitudinal and rolling planes and develops progressively with increasing strains.

Deformation Banding (DB) model has been incorporated as a deformation mode in texture modelling. A deformation banding criterion (DBC) is used to predict the evolution of BCC rolling texture in a physically meaningful way. The process of grain rotation was traced to demonstrate how the α (<110> // RD) and the γ (<111> // ND) fibres, as well as individual components, develop by deformation banding during computer rolling.

Key Words: Deformation Banding, BCC Rolling Texture, Computer Modelling

1. Introduction

Microstructure and texture influence each other during deformation. In homogenous deformation, texture development is controlled by dislocation slip but the influence of inhomogeneous deformation is also significant. The development of inhomogeneous deformation structures during rolling are now known to be very complex and important in texture development, because different deformation mechanisms cause different crystal rotations. It has been shown that crystals may split into different orientations during deformation because of varying local conditions existing in different zones within one grain, and the term "deformation banding" (DB) has been used to describe such deformation (Barrett, 1940; Chin, 1969). Experimental evidence of deformation banding in FCC metals has been reported by many researchers with different nomenclatures (Lee and Duggan, 1993; Bay *et al.*, 1989) at either SEM or TEM level. Theoretical simulation has also demonstrated the influence of DB on texture development in medium-to-high SFE FCC polycrystals (Lee *et al.*, 1993), but for BCC metals, the case for including deformation banding is not as clear as for FCC materials. Taylor's Full Constraints (FC) theory (Taylor, 1938) has been widely used in texture modelling and the most significant modifications of this model are the "lath" and "pancake" Relaxed Taylor Models (Honneff and Mecking, 1978; Van Houtte, 1981) introduced as major improvements over the classical FC model.

2. Microstructure Development

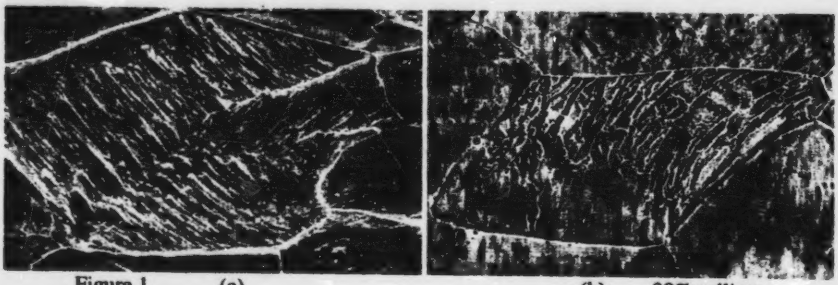

Figure 1 (a) (b) 30% rolling

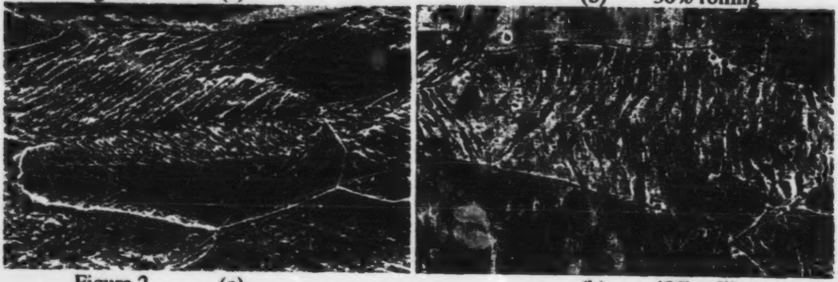

Figure 2 (a) (b) 40% rolling

Figures 1 and 2 Microstructure development of cold rolled low carbon steel with increasing strains (a) longitudinal sections (b) rolling plane sections

A low carbon steel was used in this work as the reference material. The hot band grain size was about 40μm and was rolled at room temperature to different rolling reductions. The development of deformation banding or grain orientation splitting is shown in the longitudinal and rolling planes, figures 1 and 2 for representative strains of 30% and 40%. At these lower deformations, grain subdivision into regions of different orientations, called deformation bands in this paper, can be clearly recognised. It is clear that such deformation banding must have occurred at earlier deformation stages, *i.e.*, less than 30% rolling. However, it becomes impossible to distinguish DB directly by SEM at higher strains (> 70% rolling). A series of EBSP measurements were made to detect sharp orientation changes and these frequencies were compared with the expected high angle boundary frequency to estimate splitting ratios. On average grains split into 2 segments in the longitudinal section and 3 in the rolling plane after 85% rolling.

3. Computer Modelling

Simulation procedures for the DBC modeling are described elsewhere (Duggan *et al.*, 1998; Liu *et al.*, 1999). Different slip system combinations from 110 + 112 are used to accommodate shape change with minimum internal plastic work and their CRSS are assumed to be the same. Two adjustable parameters in the model are L_h and σ. The first, L_h, is a latent hardening term which is multiplied by the CRSS of slip systems which do not belong to the most heavily stressed shear plane. This has the effect of reducing the number of slip systems on average to 2 for each orientation subject to DB, with the self canceling shear strain criterion assumed. It also has the effect of making DB occur in all orientations from the first plastic strain increment. To overcome this shortcoming in the DB–only model, an energy term σ is introduced such that DB will occur only if $E_{DB} > (1 + \sigma) E_{RC}$, otherwise the grain deforms by RC only. The effect of varying values of σ for 110 + 112 slip systems on the number of grains subject to DB is shown in figure 3. For the reminder of the paper L_h is set at 1.2 and σ at 5%. Figure 4 shows the measured and predicted ODFs after a rolling strain of 2.0.

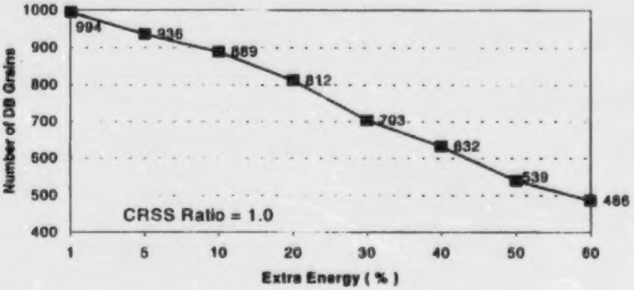

Figure 3 Energy dependency on the deformation banding

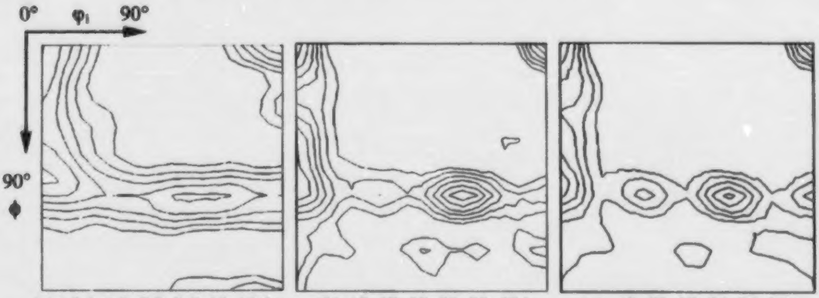

(a) (2.4, 4.8, 7.2, 9.6, 12, 14.4) (b) (5, 10, 15, 20, 25, 30) (c) (5, 10, 15, 20, 25, 30)

Figure 4 (a) 90% cold rolled LC steel, (b) DB only model, (c) DBC model with $\sigma = 5\%$

3.1 Resources for the α and γ fibres in DBC modelling

To investigate the effect of conditional deformation banding on texture evolution, the resources for the α and γ fibres in DBC modelling were picked by tracing back in strain the specific orientations along the α and γ fibres found at 87% rolling when the random initial texture was used. If the final orientation falls into these fibres, its corresponding orientation in the initial array is picked and all such grains are shown in 200 pole figures, figures 5 (a) and (b). It is clear that the γ fibre in the final ODFs result from a spread around the γ fibre, figure 5 (a), while the α fibre source is more complex, figure 5 (b).

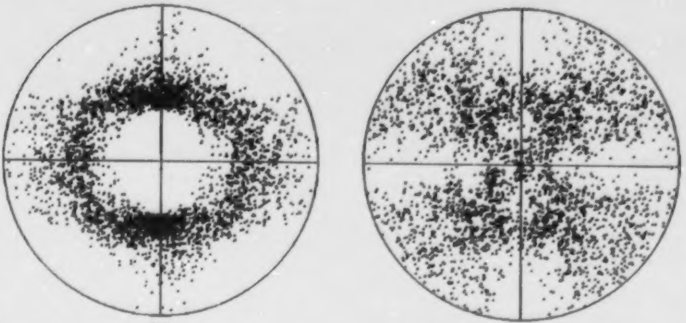
(a) (b)

Figure 5 Initial orientations arriving (a) the γ fibre and (b) the α fibre with DBC model

3.1.1 The α fibre

Figure 6 shows the process of grain rotation in each computer rolling step to the α fibre. The initial orientation is coded "0", and the final orientations are either "1" or "2" depending on whether DB occurred. From these examples, it is seen that {100}<110> is fairly stable after its formation, figure 6 (a) and (b), and sometimes no DB occurs throughout computer rolling, figure 6 (c). {110}<112> may be built by DB accompanied with another orientation, figures 6 (d) and (e). Figure 6 (f) shows that after DB occurs at early deformation, the two resultant orientations move to the same site before the end of 2.0 true strain.

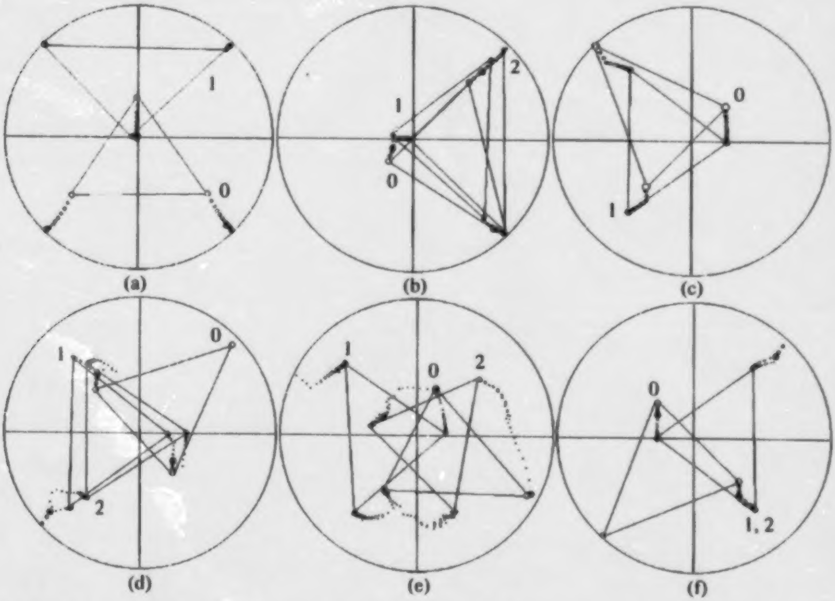

(a) (b) (c)
(d) (e) (f)

Figure 6 Rotation of the specific orientations from initial array to the α fibre

3.1.2 The γ–fibre

Orientations near {111}<110> and {111}<112> are stable, figures 7 (c) and (d). {111}<110> can be strengthened by DB for the original orientations shown in figure 7 (b). Orientation near {111}<112> feed into the γ fibre once DB has occurred, figure 7 (a), but for an orientation already located on the γ fibre, DB does not occur, but rotations around <111> // ND are shown, figure 7 (f). The technologically important {114}<110> ("1") can be generated by one segment following DB, figure 7 (e), while the other ("2") rotates towards the γ fibre.

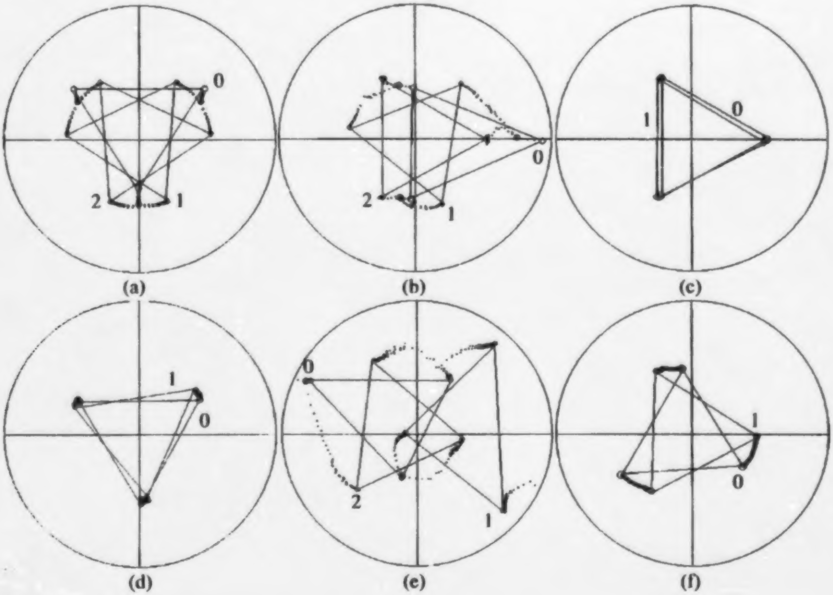

(a) (b) (c)

(d) (e) (f)

Figure 7 **Rotation of the specific orientations from initial array to the γ fibre**

4. Discussion

It is widely accepted that two fibres, the α and γ fibres, characterise measured BCC rolling textures and the main components found in observations belong to these fibres. To obtain predictions comparable with experimental ODFs, the inclusion of the deformation banding process in modelling is very helpful, as is proved by the DB and DBC modelling with 110 + 112 slip systems (Liu *et al.*, 1999). The difference between the DB and DBC models lies in introducing an energy criterion for DB occurrence associated with latent hardening considerations. The DBC model increases the strength of the {111}<112> compared with the DB–only model but the γ fibre is not sufficiently "flat" in both the DB and DBC models due to the concentration at {111}<110>, cf. figures 4 (b) and (c). The reason for the formation of an intense {111}<110> component is considered to arise from the high stability of this component, as well as a strong tendency for crystal rotation to {111}<110>, as found through the progressive tracing of initial orientations, where {111}<110> is formed by either deformation banding, figure 7 (a) and (b), or net rotation from the γ-fibre, figure 7 (f).

It should be noted that the present simulation is only for the case of true strain = 2.0. In fact, experimental investigations (Inagaki and Suda, 1972) have shown that there is a net rotation from {111}<112> to {111}<110> at higher deformations, and DBC modelling has shown similar behaviour, which is indicated for a specific initial orientation in figure 7 (a). Experimental ODFs (Liu *et al.*, 1999) have shown that cold rolling textures have higher {111}<112> at early deformation, and this is probably associated with the occurrence of DB, cf. figures 1 and 2. After this, {111}<110> strengthens associated with the decreasing of {111}<112>. It is thus suggested that {111}<112> is formed partially by DB in early rolling and then its density is reduced due to its rotation to {111}<110>. There is thus a relationship between {111}<110> and {111}<112> in that although both are stable in the model, certain orientation pathways lead through {111}<112> to {111}<110>. Hence {111}<110> is expected to be of higher intensity than {111}<112>.

5. Conclusion

Computer simulation has shown that the α fibre is built from a wide range of orientations. The γ fibre arises from a spread of near γ orientations. {111}<110>, {111}<112> and {100}<110> are stable texture components. Orientations which are subject to DB contribute to all stable orientations, but in complicated ways.

Acknowledgement

The authors would like to thank Croucher Foundation for the research grant supporting the project.

References

Barrett, C. S. and Levenson, L. H. (1940) *Trans. AIME.*, Vol. 137, p.112

Bay, B., Hansen, N., Hughes, D. A. and Kuhlmann-Wilsdorf, D. (1989) *Acta metall.* Vol. 40, p. 205

Chin, G. Y. (1969) *Textures in Research and Practice*, p.236

Duggan, B. J., Liu, G. L. and Zhang, L. X. (1998) *Material Science Forum*, Vols. 273-275, p. 273

Honeff, H. and Mecking, H. (1978) *Proc. ICOTOM 5*, p.265

Inagaki, H. and Suda, T. (1972) *Texture*, Vol.1, p. 129

Lee, C. S. and Duggan, B. J. (1993) *Acta metall.* Vol. 41, p. 2691

Lee, C. S., Duggan, B. J. and Smallman, R. E. (1993) *Acta metall.*, Vol. 41, p. 2265

Lee, C. S., Smallman, R. E. and Duggan, B. J. (1995) *Scripta Metall.*, Vol. 33, p. 727

Liu, G. L., Duggan, B. J. and Zhang, L. X. (1999) *EPD Congress 1999*, p.1019

Taylor, G. I. (1938) *J. Inst. Metals*, Vol. 62, p. 307

Van Houtte, P. (1981) *Proc. ICOTOM 6*, p. 428

PLASTIC DEFORMATION OF A Ti-6%Al-4%V ALLOY AT INTERMEDIATE AND HIGH TEMPERATURES

J.S. LECOMTE
LETAM, CNRS URA 2090, University of Metz, F-57045 Metz, France
lecomte@letam.sciences.univ-metz.fr

Abstract

The deformation of a Ti-6%Al-4%V (90% vol. α phase + 10% vol. β phase) alloy with a strong single component texture(<**c**>-axis of α phase aligned in the transverse direction) was studied in compression and tension at different temperatures in the range from 300 K to 1070 K. Specimens were cut-out at 0°, 45° and 90° according to the rolling direction in order to activate different deformation systems. The deformation systems were investigated by TEM in range of various temperatures ranges. The yield stress of the different specimens decreases with increasing temperature, except for the temperature ranges around 500 and 700 K, where the yield stress stay constant for the specimens at 0° and 45°. This region seems to have a dynamic strain ageing.

At room temperature, TEM observations shows that the alloy obeys at the Schmid Law. But between 500 and 700 K, there is an anomalous activity of the pyramidal <**c+a**> slip in all specimens regardless the cut-angle, this glide system becomes preponderant. For this temperature range, two phenomena are observed : dynamic strain ageing and the critical resolved shear stress (CRSS) for the movement of <**c+a**> dislocations in alloy is directionally asymmetric.

A hard sphere atomic model is used to explain the directional asymmetry of the CRSS. The dynamic strain ageing is explained with a Fleischer-type elastic interaction between dislocations and interstitial solutes, which are very effective strengtheners at temperatures below 700 K.

Keywords : TA6V, Texture, Deformations mechanisms, High temperature

1. Introduction

The Ti-6%Al-4%V (α+β) alloy is the most popular and the best know of all the Ti alloys. Depending on different thermomechanical treatments, it is possible to obtain this alloy with a large variety of microstructures and crystallographic orientations (Weiss et al. 1986). The mechanical properties for commercial Ti (α+β) alloys are strongly anisotropic because of the sharp texture associated with the anisotropic of α phase.

Now, the need is felt for a clear understanding of the mechanisms of texture and microstructure evolution during the processing of hcp metals and their alloys. A good knowledge of the deformation mechanisms (slip and twinning) and their respective critical resolved shear stresses (CRSS) is particularly important to set coherently the parameters used in the plasticity models in order to calculate the texture evolution during rolling and the plastic anisotropy for subsequent forming (Jones and Hutchinson 1981). In present work, a Ti-6%Al-4%V sheet with a strong « edge-type » texture was tested under different stress-strain states. Deformation mechanisms and the local texture were investigated in order to understand, explain and predict the mechanical properties.

2. Experimental procedure

2.1 Material

The material used is a Ti-6%Al-4%V 5 mm thick sheets of made by Cezus (France). The material was in the annealed state (1000K for 1 h) after cold rolling. Previously it had been hot rolled in the $\alpha+\beta$ field. The chemical composition is given in Table 1. The alloy has a nominal O_2 of 1300 ppm (weight) and an equivalent O_2 of 0,35 at.% calculated by Conrad's equation $O_{eq}= O + 2N + 0,75\ C$ (Doner and Conrad 1973). The texture analysis showed that the sheet presents a strong transverse texture with a majority of grains having their <c> axes in transverse direction.

Table 1 : chemical analysis of the Ti-6%Al-4%V alloy (wt. %)

Element	Ti	Al	V	Fe	Si	O	C	N	H
Speci-fication	Balance	5,5 - 6,5	3,5 - 4,5	< 0,4	< 0,04	< 0,2	< 0,01	< 0,05	< 0,015

2.2 Microstructural investigations

Transmission electron microscopy (TEM) techniques were also used to analyse the starting material substructure and to determine the deformation systems. Foil preparation followed the recommendations of Zaefferer (Zaefferer and Schwarzer 1994). The specimens were examined at 300 kV with a Philips EM 430 and at 200 kV with a Philips CM 200 electron microscope.

2.3 Mechanical testing

Tensile tests were conducted between 300 K and 1070 K using a Zwick machine at a cross-head rate of $1 \times 10^{-3}\ s^{-1}$. Compression tests on small cylinders (4 mm diameter and 6 mm high) were performed on a MTS machine at strain $\dot{\varepsilon}=1 \times 10^{-3}\ s^{-1}$. Tensile and compressive tests were systematically repeated at least twice for every direction. Tests were conducted on the differently shaped tensile and compressive test pieces shown in Fig. 1.

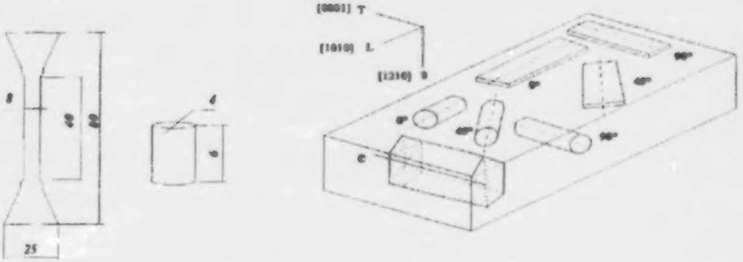

Figure 1 : The orientations of the tensile and compressive test pieces in relation to crystallographic orientations in the Ti-6%Al-4%V.

3. Results

3.1 Metallographic and crystallographic characterization

Metallographic observations revealed an inhomogeneous two-phase structure. The equiaxed α-grains have a mean size of about 15 μm. They are decorated by a dispersion of small β-phase grains. TEM observations showed a heterogeneous α structure only partially recovered and recrystallized. The mean size of the mostly equiaxed β particles is below 1 μm and and the volume fraction is of the order of 10% at 300 K but increases during the test with the temperature (~30% at 1070 K). No twinned areas were observed in the whole temperature range.

3.2 Deformation systems

The investigation of deformation systems was performed with a computer program which makes the on-line determination of Burgers vectors, dislocation line direction, glide planes and twinning systems easier (Zaefferer and Schwarzer 1994). The determination of Burgers vectors and line directions, however, is limited to a deformation degree less than 10%, since individual dislocations must be recognized after successive tilts of the sample about large angles.

3.2.1 Specimens strained at 300 K.

The change in the main slip system is normal and due to the strong <c> transverse texture. Zaefferer (Zaefferer and Schwarzer 1994) showed a correlation between the grain orientation and the degree of local deformation, evaluated through the dislocation density : the closer the crystallites are oriented to $(11\bar{2}0)[10\bar{1}0]$ the more they are deformed, i.e. higher their dislocation density is. Results are listed in Table 2. The dislocations remaining in the foil belong to the $\{10\bar{1}0\}$ slip system and were shown to be of <a> type . They are mainly of screw type, suggesting that here the edge dislocations are more mobile.

Table 2 : deformation systems on the Ti-6%Al-4%V deformed at ε=0,05

		300 K			500 K		
		0°	45°	90°	0°	45°	90°
Main slip system		P<a>	B<a>	π_1<c+a>	π_1<c+a>	π_1<c+a>	π_1<c+a>
Secondary slip	1	π_1<a>	π_1<c+a>	B<a>	B<a>	B<a>	π_2<c+a>
system (in order of	2	π_1<a>	π_1<a>	π_1<a>	π_2<c+a>		
% of occurrence)	3	B<a>		P<a>			

P<a>=$(10\bar{1}0)\langle 11\bar{2}0\rangle$;B<a>=$(0001)\langle 11\bar{2}0\rangle$;Π_1<a>=$(10\bar{1}1)\langle 11\bar{2}0\rangle$;Π_1<c+a>=$(10\bar{1}1)\langle 11\bar{2}3\rangle$; Π_2<c+a>=$(11\bar{2}2)\langle 11\bar{2}3\rangle$

3.2.2 Specimens strained at 500 K.

For the orientations a high activity of <c+a> dislocations was found. Figure 2 shows the dislocation substructure in an α-grain on the $\{11\bar{2}2\}$ planes. The latter plane is unusual in Ti alloys because twinning is commonly activated in this plane.

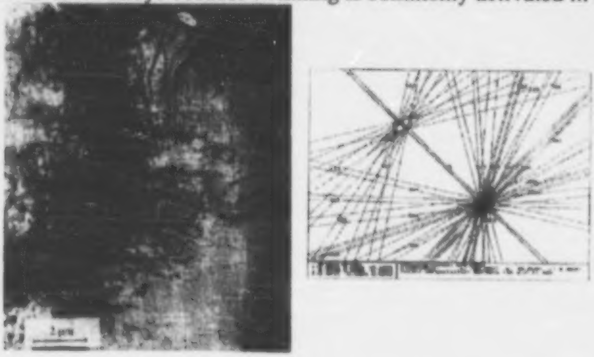

Figure 2 : <c+a> dislocations on the $(2\bar{1}\bar{1}2)$ and $(10\bar{1}\bar{1})$ planes in a specimen compressed along $[0001]$ (foil normal). Beam direction g =$\langle 0002\rangle$.

3.2.3 Specimens strained at 1070 K.

It is quite difficult to find all system because the CRSS are narrow.

3.3 Mechanical properties.

Figure 3 shows flow stresses of the Ti-6%Al-4%V, which decrease normally with temperature for the specimen oriented at 0°, 45° and 90°. For the two first orientations an anomalous behaviour is noticed between 500 K and 700 K. In this range, there is a temperature dependence of the flow stress. Although it has been established that interstitial solutes are responsible for this behaviour, the exact details of the process are not clear yet. For the specimens tested at 90° to Rolling Direction (RD), the decrease is given in discussion (§ 4). In the same way the differences between the yield stress in tension and compression are larger for the specimens tested at 90° to RD.

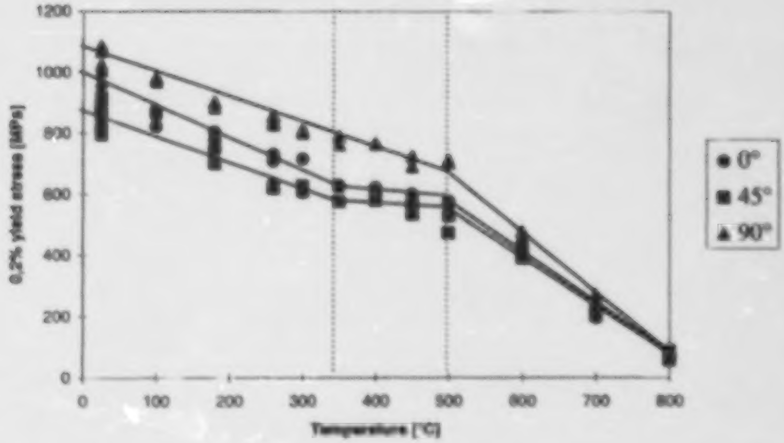

Figure 3 : The variation of the yield stresses with temperature for tensile specimens

4. Discussion

At room temperature, most dislocations were of <a> type on the prismatic planes. Secondary slip system were basal or an pyramidal $\{1\bar{1}01\}$ planes.

In the range from 500 K to 700 K, some of these so called « secondary slip systems » were found to be the most active for dislocation motions : <c+a> dislocation gliding on the pyramidal planes $\{1\bar{1}01\}$ and $\{11\bar{2}2\}$ was prominent.

At higher temperatures the prismatic slip is the common glide but cross-slip is very frequent. All types of slip are found.

Welsch and Bunk (Welsch and Bunk 1982) investigated the influence of the oxygen concentration on the mechanical properties. They found that the room temperature deformation of a Ti-6%Al-4%V alloy containing 0,22 wt.% oxygen produced a predominant planar pyramidal slip only after that the samples had been aged at 500K for an extended period of time. They use the Churchman's model (Churchman 1954) to explain it. The latter study a model on the effect of relatively small concentrations of oxygen and nitrogen (~0,1 wt.%) on the slip systems in a α-Ti has been presented. The model predicts that oxygen (or nitrogen) atoms occupying octahedral positions interfere with $\langle\bar{1}2\bar{1}0\rangle$ type slip more severely on the basal (0001) and the prismatic $\{10\bar{1}0\}$ slip planes than on the $\{10\bar{1}1\}$ pyramidal slip planes.

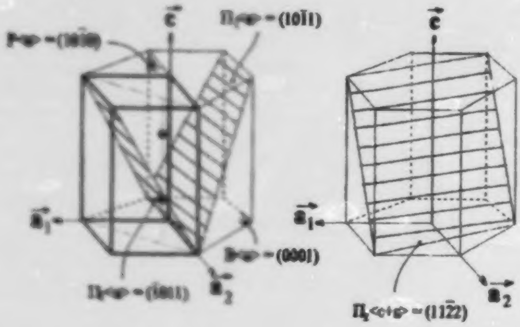

Figure 4 : Possible slip planes of <a> and <c+a> dislocations in α-Ti. The possible interstitial sites within the unit cell formed by a_1 ,a_2 , and c are indicated by •.

Figure 4 illustrates that the interstitial sites are never coplanar neither with the basal plane nor with the prismatic slip planes. However, they can be coplanar with one of the two possible pyramidal slip planes. In the vicinity of this temperature, the respective interstitial solutes will be sufficiently mobile so that they can no longer be considered as stationary obstacles, and plastic deformation will reflect the interaction between mobile dislocations and mobile interstitial solute atoms, resulting in a behaviour known as dynamic strain ageing. Our results in microscopy confirm this possible explanation because in this range of temperature the most common system is the pyramidal <c+a> indicating that the other <a> glides have higher CRSSs.

5. References

Churchman, A.T. (1954) The Slip Modes of Titanium and the effect of purity on their occurrence during tensile deformation of Single Crystals. *Proc. Royal Soc.*, Vol. 226, pp. 216-226.

Doner, M. and Conrad, H. (1973) Deformation mechanisms in commercial Ti-50A at intermediate and high temperatures. Met. Trans., Vol. 4, pp. 2809-2817.

Jones, I.P. and Hutchinson, W.B. (1981) Stress, State dependence of slip in Titanium-6Al-4V and other hcp metals. *Acta. Met.*, Vol. 29, pp. 951-968.

Weiss, I., Froes, F.H., Eylon, D. and Welsch G.E. (1986) Modification of alpha Morphology in Ti-6Al-4V by thermomechanical processing. *Met. Trans. A*, Vol. 17A, pp. 1935-1947

Welsch, G. and Bunk W. (1982) Deformation Modes of the alpha-Phase of TA6V as a function of oxygen Concentration and aging Temperature. *Met. Trans. A*, Vol. 13A, pp. 889-899.

Zaefferer, S. and Schwarzer, R.A. (1994) Determination of a local texture and deformation systems in TA6V and T40. *Materials Science Forum*, Vol. 157-162, pp. 1319-1324.

EFFECT OF HOMOGENIZATION PRACTICE AND %MN ON TEXTURE IN AA3104 DURING HOT ROLLING

M.A. WELLS
Department of Metals and Materials Engineering, UBC, Vancouver, Canada

D.J. LLOYD
Alcan International Ltd., Kingston, Ontario, Canada

J. KADILAK
Alcan Aluminum Corporation, Oswego, New York, USA

Abstract

A statistically designed experiment in an industrial aluminum hot rolling mill was conducted to assess the effect of homogenization cycle (typical cycle and typical cycle with a second stage soak at a lower temperature) as well as %Mn (0.81 and 0.93%) on the microstructure and texture development in AA3104 during hot rolling. Earing behaviour and %Mn in solid solution were measured across the width of the sheet in both slab-gauge material after hot breakdown rolling as well as reroll-gauge material after hot tandem rolling. In addition samples for texture measurement and microstructural characterization were taken for some of the experimental conditions. Results indicated that a variation in earing behaviour and texture existed across the width of the sheet with the edges of the sheet having significantly higher levels of 0-90° earing relative to the centre. It was also found that the level of Mn in the material significantly affected the earing and texture in the hot rolled sheet with the material containing 0.81%Mn exhibiting higher levels of cube texture and 0-90° earing. On the other hand, the modified homogenization cycle, although it did precipitate out more Mn prior to hot rolling had no significant affect on the final texture or earing behaviour of the material.

Keywords: Homogenization, AA3104, %Mn, texture, earing, hot rolling

1 Introduction

There is an ever increasing thrust by can bodystock customers to try to reduce the wall thickness of the can to save both weight and material cost. In order to reduce the body thickness it is necessary to increase the amount of reduction done in the cold mill. This can have an adverse affect on the earing as increasing the level of cold reduction will lead to unacceptably high ears and a substantial yield loss. One means to combat this is to increase the reroll earing so as to reduce the final gauge earing [1].

In an effort to understand what controls the reroll earing and texture development in hot rolled material, a statistically designed trial was conducted, in an industrial aluminum rolling mill, to assess the effect of homogenization practice (usual practice versus usual practice with a cool down to 540°C) as well as %Mn level (0.81 versus 0.92). The reason homogenization practice was investigated was that it can have a large effect on the precipitation and distribution of second phase particles into the matrix which in turn can affect the final texture which develops. Composition (%Mn) can also have a large influence on the particles and dispersoids which form as well as the temperature at which recrystallization will occur [1,2].

2 Experimental

A replicated, 2^2 factorial design (Table 1) was run in the mill during regular production to determine the influence of the thermal profile during homogenization (regular cycle Vs. regular cycle with a second stage soak at a lower temperature) (Figure 1) as well as composition (0.81%Mn Vs. 0.92%Mn) on the microstructure and texture development during hot breakdown and tandem rolling. Samples were taken after breakdown rolling as well as hot tandem rolling and conductivity, texture, and earing behaviour across the width of the sheet were measured.

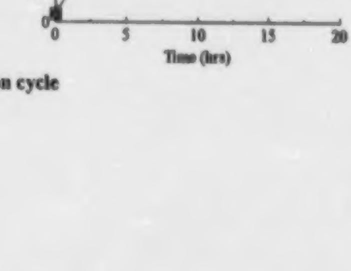

a) Current homogenization cycle

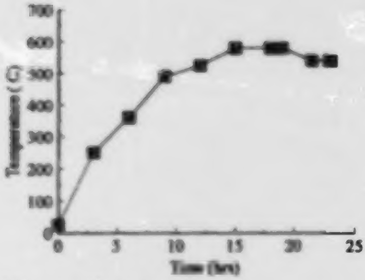

b) Homogenization cycle with a second stage cool

Figure 1: Homogenization cycles used during the trial a) current homogenization cycle (heat to 580°C and soak for two hours) and b) current homogenization cycle with a second stage soak at 540°C for four hours.

3 Results

Composition (%Mn) appeared to have the largest affect on final reroll earing and volume fraction cube texture, with the lower Mn level increasing the reroll earing and cube texture in the reroll gauge material (Figure 2). This was seen for both homogenization practices and concurs with previous research [2,3]. The modified homogenization profile did not have any statistical affect on the final reroll properties or texture, however, conductivity measurements across the width of the sheet indicated that, more precipitation of Mn out of solid solution did occur in the homogenization cycle with the second stage soak at 540°C (Figure 3). This was seen in both the slab-gauge (after hot breakdown rolling) as well as reroll gauge (after hot tandem rolling) material

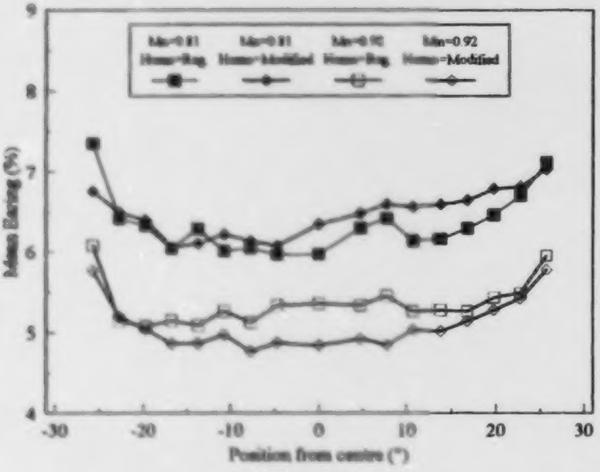

a) final reroll earing

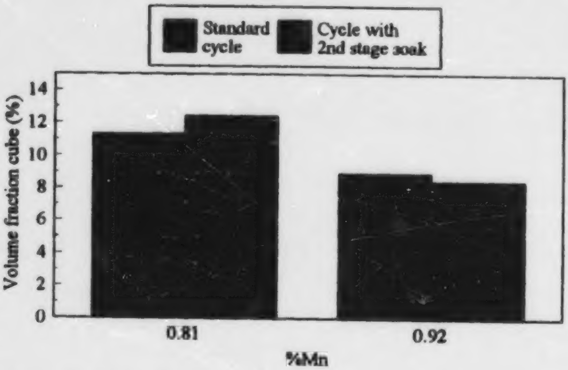

b) Volume fraction cube texture in reroll-gauge material

Figure 2: Effect of homogenization treatment and %Mn on a) final reroll earing and b) volume fraction cube texture in reroll-gauge material

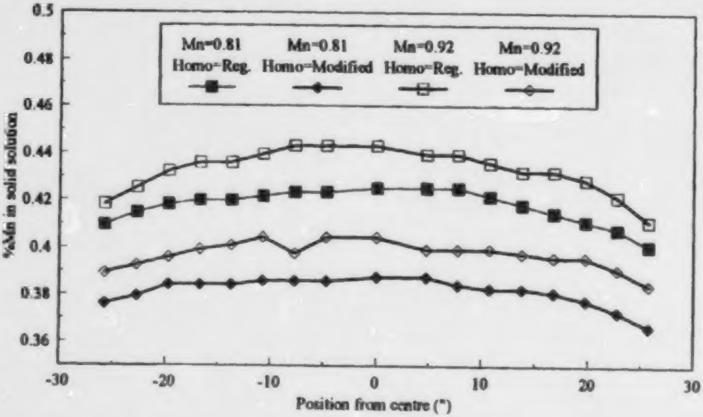

a) Reroll-gauge

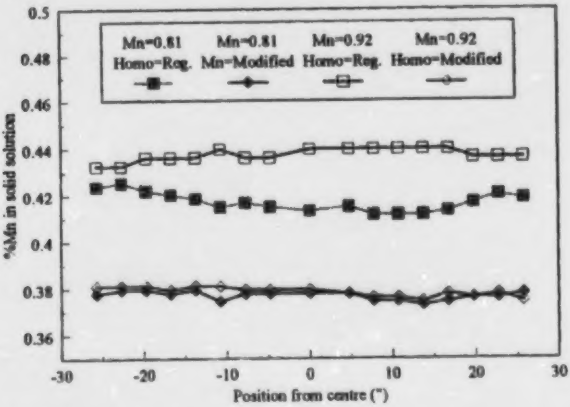

b) slab-gauge material

Figure 3: %Mn in solid solution in both the slab-gauge and reroll gauge material a) reroll-gauge and b) slab-gauge.

In general, as the volume fraction cube in the slab-gauge material increased, the volume fraction of cube and goss in the reroll gauge material increased and the reroll earing increased (Figure 4).

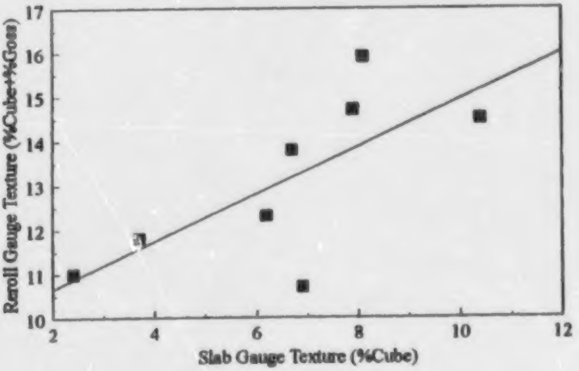

a) Effect of slab-gauge texture on reroll-gauge texture

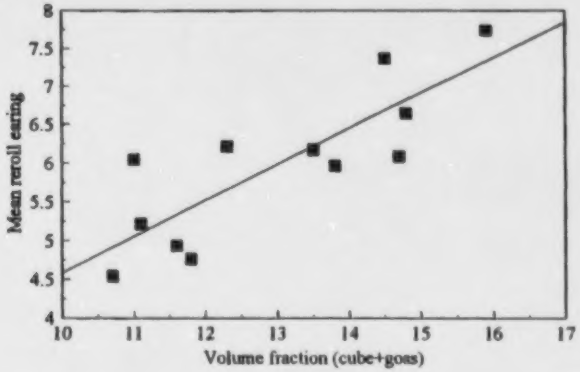

b) Effect of reroll-gauge texture (cube+goss) on reroll earing

Figure 4: Effect of slab-gauge texture on reroll-gauge texture.

4 Conclusions

- The %Mn in AA3104 has a significant effect on the texture and earing bahaviuor ofaluminum sheet after hot tandem rolling, with lower %Mn producing higher levels of cube and goss texture and higher levels of reroll earing

- Although the modified homogenization process with a second stage cool precipitated out more Mn from solid solution this did not have a significant influence on either the texture measured in material after hot breakdown (slab-gauge) or tandem rolling (reroll gauge).

- Higher levels of cube in slab gauge material appear to lead to higher levels of cube and goss in reroll gauge sheet for AA3104 which in turn led to higher levels of reroll earing.

- Higher earing and lower levels of %Mn is solid solution were seen at the edges of the sheet relative to the centre of the sheet for reroll-gauge material.

5 References

1. R.K. Bolingbroke, E. Creed, G.J. Marshall and R.A. Ricks "The Effect of Composition and Microstructure on the Recrystallization of AA3004" Aluminum Alloys for Packaging, eds. J.G. Morris, H.D. Merchant, E.J. Westerman and P.L. Morris, TMS Conference 1992, 215-225.
2. R.G. Kamat, "AA3104 Can-Body Stock Ingot: Characterization and Homogenization", JOM, Vol. 48, No. 6, 1996 34-38

SPATIAL CORRELATIONS OF ORIENTATION, ORIENTATION CLUSTERING AND THE VARIANCE OF THE ORIENTATION DISTRIBUTION FUNCTION

B. L. ADAMS, P. S. LEE and A. D. ROLLETT
Materials Research Science and Engineering Center, Carnegie Mellon University, Pittsburgh, USA

Abstract

The purpose of this paper is to address two related issues that frequently arise in connection with texture analysis. The first concerns the extent to which components of the orientation distribution cluster in the sample. The second has to do with the reliability of the measured orientation distribution when orientation sampling is restricted in its spatial dimensions. It is demonstrated that both issues can be addressed by calculating the variance of the orientation distribution function. Furthermore, it is illustrated that the variance requires the two-point autocorrelation functions of the orientation field.

Keywords: Orientation distribution, variance, clustering, reliability

1 Introduction

Arguably, the most important mesoscale representation of polycrystalline structure, beyond the specification of crystalline phase, is the orientation distribution function (ODF). It is well known, for example, that the ODF substantially controls the anisotropy of defect insensitive properties such as elasticity, and thermal and electrical conductivity (Bunge 1982; Adams and Olson 1998). The ODF also has first-order impact upon some defect-sensitive properties such as the yield strength, although other defect sensitive properties, such as intergranular corrosion and fracture, are much less sensitive to the ODF, and more closely related to the misorientation distribution function (Adams and Olson 1998).

With the advent of orientation imaging microscopy (OIM) (Adams *et al.* 1993), it has become possible to relate the components of the ODF with their spatial arrangement within the microstructure. Of particular interest is the clustering of specified components of the ODF. For example, the clustering of specified components of the ODF has recently been associated with surface roughness in 6xxx aluminum alloys used for auto-body components (Lee *et al.* 1999). Also of interest has been the reliability of finite sets of single orientation measurements in estimating the ODF (cf. Schafer 1998, Wright and Kocks 1996).

In this paper we define the variance of the ODF, Var(γ, ω) as a representation of the clustering of orientation components within a *specified range of spatial observation.* It is suggested that this representation comprises a useful quantification of the heterogeneity of microstructures. It can also be used to evaluate the spatial extent of experimental characterization required for reliable estimation of the ODF.

A definition for Var(γ, ω) in terms of an ensemble of polycrystals is presented in section 2. Section 3 illustrates results obtained for Var(γ, ω) for samples of an aluminum alloy. Some concluding remarks are given in section 4.

2 Definition of Var(γ, ω)

At the mesoscale the polycrystal is modeled as an aggregate of crystallites filling a region, Ω, of the three-dimensional space. These crystallites have finite volume, and each material point, $\mathbf{x}$, belonging to any particular crystallite, carries local structure represented at the mesoscale by a rotation $g(\mathbf{x})$ of the reference crystal. The polycrystal will also contain material points for which this association is not possible, but these are not of interest in that which follows.

With reference to Fig. 1, define two indicator functions, $\Theta(\mathbf{x})$ and $\chi_\gamma(\mathbf{x})$, defined such that:

$$\Theta(\mathbf{x}) = \begin{cases} 1 \text{ if } \mathbf{x} \in \omega(\mathbf{x}_c) \subset \Omega \\ 0 \text{ otherwise} \end{cases} \qquad (1)$$

$$\chi_\gamma(\mathbf{x}) = \begin{cases} 1 \text{ if } \mathbf{x} \text{ associates with } \gamma \subset SO(3)/G \\ 0 \text{ otherwise} \end{cases} \qquad (2)$$

Here $\omega(\mathbf{x}_c)$ is the subregion of the material sample over which the orientation determination is performed. It is centered at $\mathbf{x}_c$. G is the point symmetry subgroup of the crystal lattice and SO(3)/G is the fundamental zone of physically-distinctive lattice types. The symbol γ is used to denote that portion of the fundamental zone that is of interest; thus, Var(γ, ω)

refers to the variance of that component of the mesostructure which associates with orientations belonging to class γ within the observation window defined by ω.

Let $f_{\gamma\omega}$ denote the fraction of the observation window ω that associates with γ in any particular element of the ensemble. Also $< f_{\gamma\omega} >$ will be used to indicate the ensemble average of volume fractions. The (normalized) variance is here defined to be

$$\mathrm{Var}(\gamma,\omega) = \frac{< f_{\gamma\omega}{}^2 > - < f_{\gamma\omega} >^2}{< f_{\gamma\omega} >} \tag{3}$$

It is evident that $f_{\gamma\omega}$ can be defined in terms of the indicator functions by

$$f_{\gamma\omega} = \frac{1}{vol(\omega)} \iiint_{\Omega} \Theta(\mathbf{x})\chi_\gamma(\mathbf{x})d\mathbf{x} \tag{4}$$

Our primary interest lies here, not in representation of particular individual polycrystals, but rather in the representation of ensembles of polycrystals sharing a common thermal-mechanical processing path. Taking the ensemble average of both sides this expression becomes

$$< f_{\gamma\omega} > = \frac{1}{vol(\omega)} \iiint_{\Omega} \Theta(\mathbf{x}) < \chi_\gamma(\mathbf{x}) > d\mathbf{x} \tag{5}$$

If the ensemble exhibits statistical homogeneity, this expression reduces to

$$< f_{\gamma\omega} > \; = \; < \chi_\gamma(\mathbf{x}) > \; = \; \iiint_{\gamma} f_1(g)dg \tag{6}$$

Here $f_1(g)$ is the ODF.

Next consider the quadratic term in relation (3). We proceed directly to the ensemble average:

$$< f_{\gamma\omega}{}^2 > = \frac{1}{vol(\omega)^2} \iiint_{\Omega} \iiint_{\Omega} \Theta(\mathbf{x})\Theta(\mathbf{x}') < \chi_\gamma(\mathbf{x})\chi_\gamma(\mathbf{x}') > d\mathbf{x}d\mathbf{x}' \tag{7}$$

For statistically-homogeneous mesostructure in the ensemble, this expression can be rewritten as

$$< f_{\gamma\omega}{}^2 > = \frac{1}{vol(\omega)^2} \iiint_{R} F_2(\gamma,\gamma \mid \mathbf{r}) \iiint_{\Omega} \Theta(\mathbf{x})\Theta(\mathbf{x}+\mathbf{r})d\mathbf{x}d\mathbf{r} \tag{8}$$

In this expression R is defined to be the set of all vectors **r** that are contained within the probe region ω. The two-point function contained in the integrand is related to the common two-point orientation correlation

$$F_2(\gamma,\gamma \mid \mathbf{r}) = \iiint_{\gamma} \iiint_{\gamma} f_2(g,g' \mid \mathbf{r})\,dg\,dg' \qquad (9)$$

function (Adams et al. 1987), $f_2(g,g'|\mathbf{r})$, by double integration over the range of orientations considered:

Given that the integration of both variables is over γ, $F_2(\gamma,\gamma|\mathbf{r})$ describes the *auto-correlation* of γ at points separated by **r**.

3 Measured Var(γ, ω) in 6022 T4 Aluminum

Var(γ, ω) was calculated for samples of 6022 T4 aluminum that have been investigated in connection with a surface roughness problem in auto-body applications (Lee et al. 1999). The experimental arrangement is shown in Figure 1. The observation window, ω, was taken to be a square 2-dimensional window of 30 microns width. Thus, all vectors $\mathbf{r} = \mathbf{x}'-\mathbf{x}$ that lie within ω belong to set R. In Fig. 1, the gray areas depict the location of grains lie within the range of orientations of interest, γFor each selected orientation, all grains with disorientation lying within 10 degrees were considered to belong to the same orientation class, γ. It was assumed that the mesostructure exhibits statistical homogeneity in region ω.

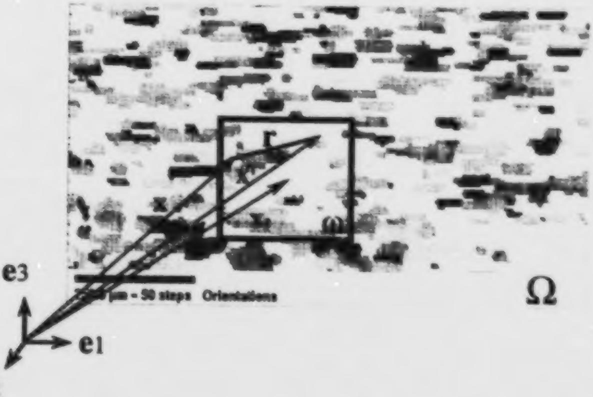

Figure 1. Description of the parameters ω and **r**. ω is centered at $\mathbf{x}_c$.

Figure 2 shows the distribution of Var(γ, ω) obtained over the full range of the fundamental zone. This is to be compared with the ODF for this material, which is shown in Figure 3. (Bunge's euler angles have been used in both of these figures.) That the peak levels of variance of the ODF do not coincide with the same positions in orientation space as the peaks of the ODF is clearly evident from these figures.

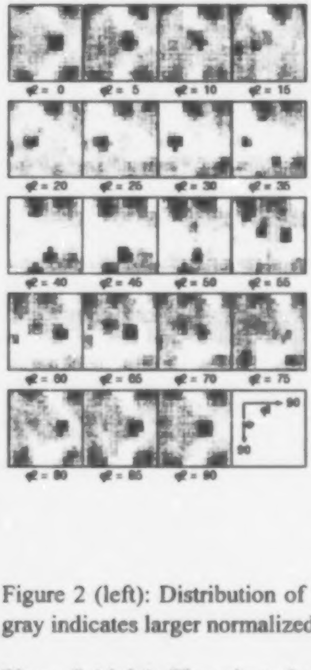

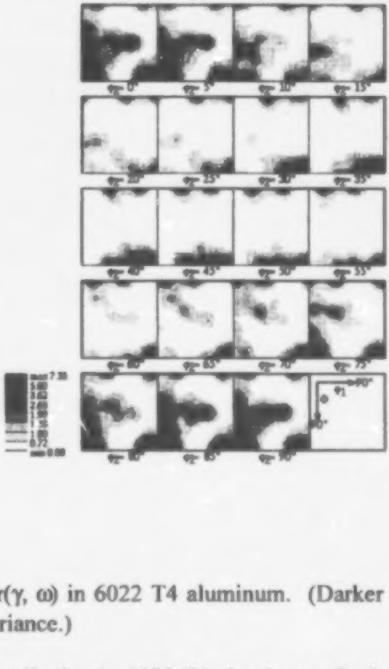

Figure 2 (left): Distribution of Var(γ, ω) in 6022 T4 aluminum. (Darker gray indicates larger normalized variance.)

Figure 3 (right): The orientation distribution in 6022 T4 aluminum. (Peak value ~ 8 times random.)

4 Concluding Remarks

The variance of the ODF, Var(γ, ω), can be used in at least two important ways. First, it can be used to determine the reliability with which inference can be made about the strength of components of the ODF when measurements have been made from a limited spatial window. A second important application is to explore the question of heterogeneity in the mesostructure.

With regard to the reliability of the ODF, it is evident from Figs. 2, 3 that for a given window size and orientation range, ω and γ, the variance is rather varied from one component to another. If a specified component of the ODF must be known with a high degree of certainty, then a larger window size must be utilized. Var(γ, ω) can thus be used as a means to determine an adequate size for the observation window, consistent with the demands applied to the ODF.

With regard to the question of heterogeneity in the mesostructure, high levels of variance, associated with any particular component, can be interpreted as an indication of clustering of that component over the scales (and shapes) associated with the observation window ω. Thus, windows of varying size and shape can be employed as a means to explore mesostructure for clustering.

Finally, although the present 2-dimensional observation window does not require the explicit use of the 2-point orientation correlation functions, extensions of the present work to 3-dimensional windows would demand these functions for the computation of the variance. Thus, relation (8) is of interest mainly in the case of 3-dimensional observation windows.

5 Acknowledgement

This work was primarily supported by the U. S. Department of Energy under award number DE-FG02-96ER45601.

6 References

Adams, B. L. and Olson, T. (1998) *Journal of Progress in Materials Science*, Vol. 43, pp. 1-88.

Adams, B. L., Morris, P. R., Wang, T. T., Willden, K. S. and Wright, S. I. (1987) *Acta metallurgica*, Vol. 35, pp. 2935-2946.

Bunge, H.-J. (1982) *Texture Analysis in Materials Science*, Butterworths, London.

Lee, P. S., Rollett, A. D. and Adams, B. L. (1999) *Proceedings of ICOTOM12*, ed. Szpunar, J.

Schafer, B. (1998) *Materials Science Forum*, Vols. 273-275, pp. 99-106.

Wright, S. I., and Kocks, U. F. (1996) *Textures of Materials: Proceedings of the Eleventh International Conference on Textures of Materials*, eds. Liang, Z., Zuo, L. and Chu, Y., International Academic Publishers, Beijing, pp. 53-62.

ON THE TEXTURE CHANGE IN EXTRUDED NiAl

W. SKROTZKI, R. TAMM and C.-G. OERTEL
Institut für Kristallographie und Festkörperphysik, Technische Universität Dresden,
Dresden, Germany

Abstract

The microstructure and texture of extruded NiAl were investigated as a function of temperature, strain and deformation geometry. Extrusions were made through a round and rectangular die with ratios of 4:1 and 7:1. Small strain between 700 and 1250°C leads to a subgrain structure. Isolated recrystallized grains are only found at the highest temperature. For high strain the samples are almost completely recrystallized with only a few deformed areas left. The texture exhibits changes from a <110> to a <111> fibre (round die) and from a {111}<110> to a {110}<110> component (rectangular die). Recrystallization takes place by a discontinuous mechanism.

Keywords: EBSD, extrusion, NiAl, recrystallization, texture

1 Introduction

NiAl, an ordered B2 intermetallic, is a potential structural material for high-temperature applications because of its high melting point, low density, high thermal conductivity and good oxidation resistance. However, the main problem for its practical use is the low-temperature brittleness. The reason for this may be the strong plastic anisotropy measured in single crystals below the brittle to ductile transition temperature (BDTT), i.e. the critical resolved shear stress (CRSS) for slip on {110}<100> systems is much smaller than for slip on {112}<111> systems. These slip systems yield 3 and 5 independent systems, respectively. Thus, in order to deform a polycrystalline aggregate homogeneously, according to the von Mises criterion the secondary slip systems have to be activated simultaneously, raising the yield stress above the fracture stress. In order to investigate the influence of deformation and recrystallization on the formation of texture and microstructure above the BDTT samples have been extruded under different conditions.

2 Methods

Cast stoichiometric NiAl samples were extruded at different reduction ratios and temperatures through a round and rectangular die. The extrusion parameters are shown in Table 1. The samples were sealed using copper cans for extrusions below 1000°C and steel cans above 1000°C. The indicated temperatures are those of the furnace prior to extrusion, the die container of the extrusion press was preheated up to about 650°C.

The grain structure of the air-cooled extruded rods has been revealed on well-polished surfaces by orientation contrast imaging in the scanning electron microscope. The textures have been measured globally by neutron diffraction and locally by electron back-scattering diffraction (EBSD). Inverse pole figures have been calculated from neutron diffraction (111), (100) and (110) pole figures using a series expansion model (Dahms and Eschner 1996).

Table 1: Extrusion parameters

	reduction ratio = 4:1 strain rate ≈ 0.7 s^{-1}	reduction ratio = 7:1 strain rate ≈ 2 s^{-1}
round die	700 - 1000°C	1100 - 1200°C
rectangular die	950 - 1250°C	1100°C

3 Results and discussion

All samples extruded at a reduction ratio of 4:1 show a subgrain structure with a grain size of about 5 µm (Figs. 1a, b). At high temperature (1250°C) some bigger recrystallized grains can be seen (Fig. 1b), but the volume fraction is less than 1%.

Extrusion at a reduction ratio of 7:1 already at 1100°C leads to recrystallization (Fig. 1c). The recrystallized average grain size is about 100 µm. A few deformed areas still exist with a subgrain size of about 5 µm.

To gain information about the misorientation between neighbouring grains automatic EBSD mappings were carried out. The frequency histogram of misorientation angles for a sample with subgrain structure (rectangular die, reduction ratio 4:1, 950°C) is shown in Fig. 2a. Mainly low angle boundaries occur, indicating a non-recrystallized, but highly recovered structure. A typical distribution for a recrystallized sample (round die, reduction ratio 7:1, 1100°C) is shown in Fig. 2b. A broad maximum at about 30° indicates high angles boundaries between the grains.

At all temperatures used, extrusion through the round and rectangular die at a reduction ratio of 4:1 leads to a <110> fibre texture (Fig. 3a) and a {111}<110> texture component (Fig. 3b), respectively. The axisymmetric textures are represented by inverse pole figures parallel to the extrusion direction, the textures with plane strain symmetry are represented by inverse pole figures parallel to the normal and extrusion direction. Areas below 1 m.r.d are shaded grey.

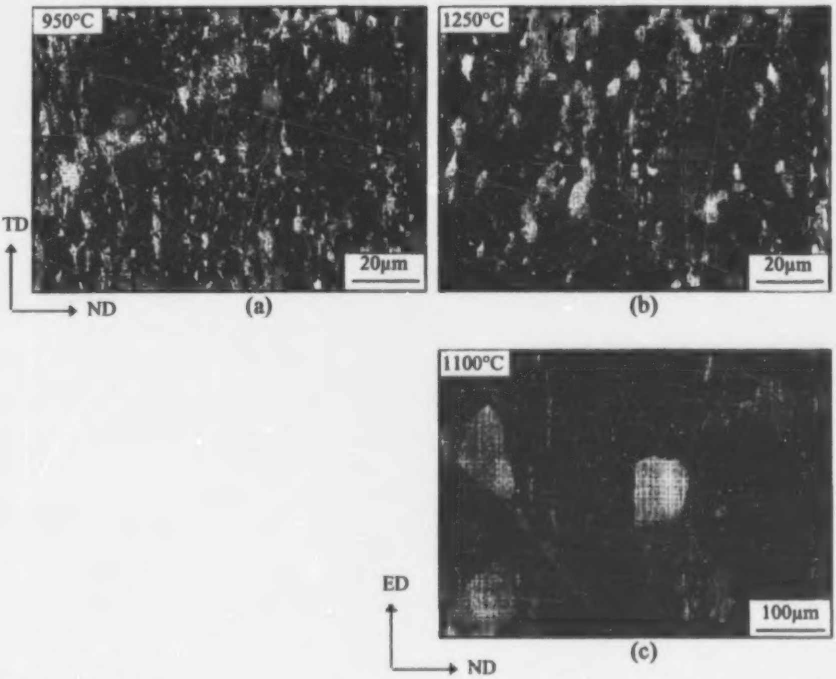
950°C
1250°C
1100°C
20µm
20µm
100µm
TD
ND
ED
ND
(a)
(b)
(c)

Fig. 1: Microstructure of samples extruded through a rectangular die at a reduction ratio of 4:1 (a, b) and 7:1 (c); ED: extrusion direction, ND: normal direction, TD: transverse direction

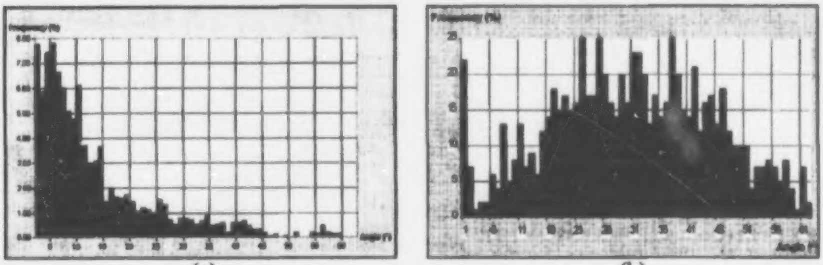

(a) (b)

Fig. 2: Frequency histogram of misorientation angles of neighbouring grains for samples extruded at a reduction ratio of 4:1 (a) and 7:1 (b)

At high strains (reduction ratio 7:1, 1100°C) the texture changes to a predominant <111> fibre (Fig. 4a, round die) and a {110}<110> main component (Fig. 4b, rectangular die), respectively.

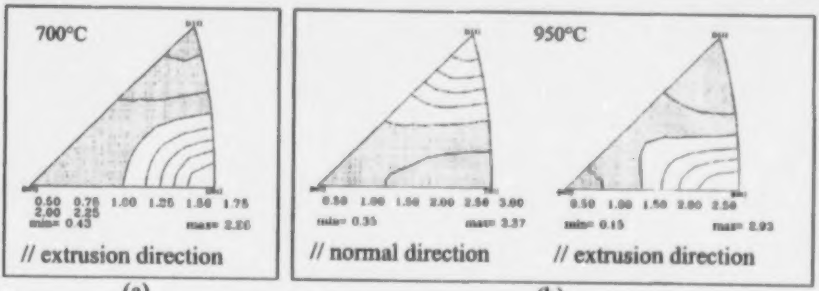

(a) (b)

Fig. 3: Texture of samples extruded at a reduction ratio of 4:1 (a) round die, (b) rectangular die. Inverse pole figures are shown with corresponding extrusion temperatures.

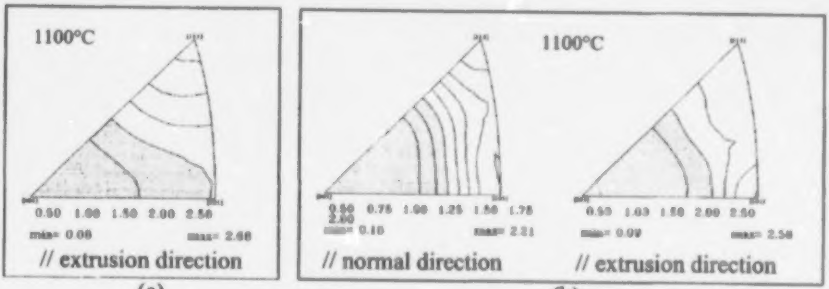

(a) (b)

Fig. 4: Texture of samples extruded at a reduction ratio of 7:1, (a) round die, (b) rectangular die. Inverse pole figures are shown with corresponding extrusion temperatures.

In order to separate the contributions of deformation and recrystallization on texture formation, the orientations of several deformed areas occasionally left in the recrystallized sample (Fig. 1c) have been measured by means of EBSD. There is a tendency for a preferred {111}<110> orientation (Fig. 5) which corresponds to the deformation texture shown in Fig. 3b. Likewise, orientations of isolated recrystallized grains in the sample deformed at low strain and high temperature (see Fig. 1b), have been measured. However, no trend is observed due to a poor statistics.

To investigate the transition between the deformation and recrystallization texture in more detail, low strain extrusions at higher temperatures are planned.

The change from <110> to <111> fibre texture in axisymmetric extrusion correlated with an increase in grain size (onset of recrystallization) has also been reported by other authors. In (Bieler et al. 1992, 1994) and (Margevicius 1993) the change is caused by increasing the extrusion temperature. Dymek et al. (1992) and Dollar et al. (1993) suppressed recrystallization by extruding mechanically alloyed NiAl and revealed a <110> fibre texture at a grain size below 1 μm. Cast material extruded under the same conditions lead to a <111> fibre texture and a grain size of 30 μm. In this study it is especially the strain which affects recrystallization and thus the texture.

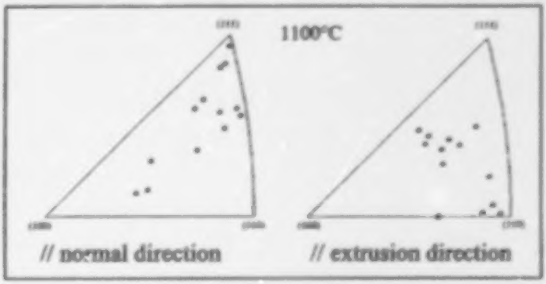

Fig. 5: Orientations of several deformed areas in an almost completely recrystallized sample (rectangular die, reduction ratio 7:1)

4 Conclusions

The reported change in microstructure and the correlated change in texture is much more affected by the reduction ratio than by the extrusion temperature. At low strain the <110> (round die) and {111}<110> (rectangular die) textures are deformation textures. The microstructure is highly recovered. Higher strain leads to discontinuous recrystallization and a change in texture towards <111> (round die) and {110}<110> (rectangular die).

5 Acknowledgements

The authors thank Dr. H.-G. Brokmeier, GKSS Research Center, Geesthacht, and Dr. W. Tirschler, IKMP, TU Dresden, for help in neutron and EBSD texture measurements, respectively. Thanks are also due to Dr. K. B. Müller, Forschungszentrum Strangpressen, TU Berlin, and R. Opitz, IFW Dresden, for carriing out the extrusions.

6 References

Bieler, T.R., Noebe, R.D., Whittenberger, J.D., Luton, M.J. (1992) Extrusion textures in NiAl and reaction milled NiAl/AlN composites. *Mat. Res. Soc. Proc.* Vol. 273, pp.165-170

Bieler, T.R., Noebe, R.D., Hebsur, M., Saminathan, R. (1994) The effects of extrusion parameters on recrystallization kinetics, texture, and corresponding fracture toughness of NiAl. In *Advances in Hot Deformation Textures and Microstructures*, ed. J. J. Jonas, T. R. Bieler, K. J. Bowman, The Minerals, Metals & Materials Society, pp. 519-533

Dahms, M. and Eschner, T. (1996) Quantitative Texturanalyse durch iterative Reihenzerlegung von Beugungspolfiguren. *Software manual*

Dollar, M., Dymek, S., Hwang, S.J., Nash, P. (1993) The Role of Microstructure on Strength and Ductility of Hot-Extruded Mechanically Alloyed NiAl. *Metall. Trans.* Vol. 24A, pp. 1993-2000

Dymek, S., Hwang, S.J., Dollar, M., Kallend, J.S., Nash, P. (1992) Microstructure and texture in hot-extruded NiAl. *Scripta Metall. Mater.* Vol. 27, pp. 161-166

Margevicius, R.W. and Lewandowski, J.J. (1993) Deformation texture of hydrostatically extruded polycrystalline NiAl. *Scripta Metall. Mater.* Vol. 29, pp. 1651-1654

DESCRIPTION OF DEFORMATION GEOMETRY BY EFFECTIVE SLIPS IN BCC MATERIALS

Y.B. PARK and B.I. KIM
Department of Materials Science and Metallurgical Engineering, Sunchon National University, Sunchon, Korea
L. KESTENS
Laboratory for Iron and Steel Making, University of Gent, Gent, Belgium

Abstract

In the present study, effective slip systems were suggested to easily describe a deformation geometry of each grain as well as to realize the development of the microstructures of deformed grains. Although the effective slip systems are, in most cases, not true crystallographic slip systems, they nevertheless represent the occurrence of the actual shears associated with the localized strain. Under the assumption that the shape change of a grain by a set of the active slip systems is the same as that by a set of the effective slip systems, the stabilized orientations of individual grains were described by the latter in steels cold rolled under plane strain conditions.

Keywords: Active slip system, effective slip system, internal stress, shear band

1 Introduction

During plastic deformation, the shape changes of individual grains in a polycrystalline material are produced by the slip systems that are active. A minimum of five independent slip systems must be operated for a completely arbitrary shape change (Taylor 1938). In bcc materials, with <111> pencil glide there are eight variables, namely the amount of slip and the orientation of the slip plane for each of the <111> directions. The requirement of five independent slip variables means that at least three <111> slip directions must be active (Hosford, 1993). However, these multiple slip systems (or directions) are difficult to directly link to the actual deformation geometry of a deformed grain. To avoid this complexity, it is necessary to effectively reduce the number of the active slip systems only if the deformation geometry produced by the latter can be conservative.

In the present study, "effective" slip systems were proposed to visualize the formation of the major texture components which are observed in steels cold rolled under plane strain conditions. The development of the microstructures of a deformed matrix will be discussed in terms of the possible effect of the effective slips on it. In order to calculate the amounts of the shears on each of the active slip systems, a strain rate sensitivity model (Savoie et al., 1994) based on Taylor assumption was employed under the assumption of the activation of the {110}<111> and {112}<111> slip systems (total 24 slip systems).

2 Mathematical description of deformation

A deformation mode is characterized by its displacement gradient tensor *D*.

$$D = \begin{bmatrix} D_{11} & D_{12} & D_{13} \\ D_{21} & D_{22} & D_{23} \\ D_{31} & D_{32} & D_{33} \end{bmatrix} \tag{1}$$

The displacement gradient tensor consists of a symmetric component D_S and an antisymmetric component D_A, namely

$$D = D_S + D_A \tag{2}$$

The symmetric part corresponds to the strain tensor ε whereas the antisymmetric part represents the rigid body rotation.

$$\varepsilon = \begin{bmatrix} \varepsilon_{11} & \varepsilon_{12} & \varepsilon_{13} \\ \varepsilon_{21} & \varepsilon_{22} & \varepsilon_{23} \\ \varepsilon_{31} & \varepsilon_{32} & \varepsilon_{33} \end{bmatrix} \tag{3}$$

Such an arbitrary strain mode can always be represented in a reference system that coincides with its principle axes. Therefore,

$$\varepsilon = \begin{bmatrix} \varepsilon_{I} & 0 & 0 \\ 0 & \varepsilon_{II} & 0 \\ 0 & 0 & \varepsilon_{III} \end{bmatrix} \tag{4}$$

where $\varepsilon_{I} + \varepsilon_{II} + \varepsilon_{III} = 0$. Furthermore, Eqn (4) can be decomposed into two plane strain deformations. This decomposition, however, is not unique, but there exist different possibilities. One example is given by

$$\varepsilon = \begin{bmatrix} \varepsilon_{I} & 0 & 0 \\ 0 & 0 & 0 \\ 0 & 0 & -\varepsilon_{I} \end{bmatrix} + \begin{bmatrix} 0 & 0 & 0 \\ 0 & \varepsilon_{II} & 0 \\ 0 & 0 & -\varepsilon_{II} \end{bmatrix} \tag{5}$$

A plane strain deformation can be expressed by a pure shear mode. For example, by rotating the reference system over 45° around the Y-axis, the first term of the right hand of Eqn (5) transforms into the pure shear γ given by

$$\gamma = \begin{pmatrix} 0 & 0 & \gamma_{13} \\ 0 & 0 & 0 \\ \gamma_{13} & 0 & 0 \end{pmatrix} \tag{6}$$

Thus, an arbitrary deformation mode can be realized by a combination of two pure shear deformations.

3 Determination of the effective slip systems

Contribution of each active slip system to the shape change of a deformed grain is assumed to be proportional to the amount of shear on it. If more than one slip system is activated along a given slip plane, the effective slip direction may be calculated by a vector sum of shears on the active slip systems. For example, when the shears occur on the (101) in the $[\bar{1}\bar{1}1]$ and $[\bar{1}11]$ directions, the effective slip direction is derived by a vector sum as follows.

$$a[\bar{1}\bar{1}1] + b[\bar{1}11] = [uvw] \tag{7}$$

where *a* and *b* denote the relative amounts of shears along the respective slip directions. Therefore, the effective slip system is (101)[uvw], and when $a = b$, it becomes $(101)[\bar{1}01]$. This effective slip system is expected to produce the same shape change as the relevant active slip systems, $(101)[\bar{1}\bar{1}1]$ and $(101)[\bar{1}11]$.

Fig. 1(a) gives another example where two slip systems are activated on the different slip planes; $(112)[\bar{1}\bar{1}1]$ and $(1\bar{1}2)[\bar{1}11]$. Also, the effective slip direction, [uvw], is derived by Eqn (7). However, in this case, the calculated [uvw] effective slip direction can be crystallographically contained neither on the (112) nor $(1\bar{1}2)$ active slip planes. As shown in Fig. 1(b), the (101) plane which contains both the $[\bar{1}\bar{1}1]$ and $[\bar{1}11]$ active slip directions is assumed to be the effective slip plane only if the plane can carry the resolved shear stresses for a given deformation mode. Thus, the effective slip system is proposed to be (101)[uvw]. In comparison of Figs. 1(a) and (b), the deformation geometry by the effective slip system seems to be the same as that by the active slip systems.

In general, a deformed grain can contain more than one effective slip direction, e.g. when more than one slip plane is active. The number of the effective slip systems in a grain of the deformed matrix depends on the crystallographic orientation of the grain for a given strain path. Therefore, when the vector sum of shears on the active slip systems is employed to determine the effective slip systems, the deformation geometry need be taken into account. In the following, this concept will be applied to the observed texture components in bcc steels cold rolled under plane strain conditions.

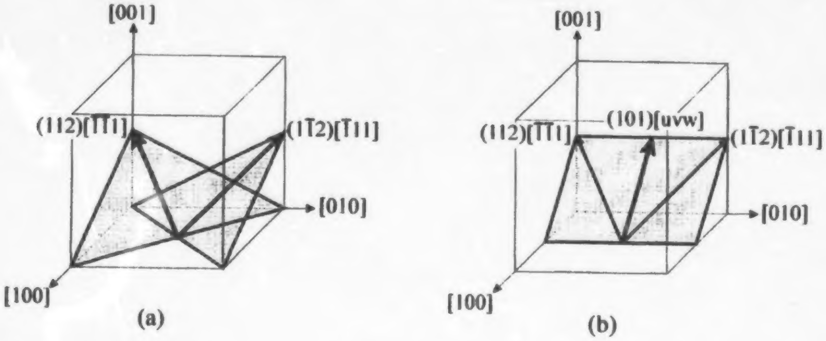
$[001]$
$(112)[\bar{1}\bar{1}1]$
$(1\bar{1}2)[\bar{1}11]$
$[010]$
$[100]$
(a)
$[001]$
$(101)[uvw]$
$(112)[\bar{1}\bar{1}1]$
$(1\bar{1}2)[\bar{1}11]$
$[010]$
$[100]$
(b)

Fig. 1: Derivation of the effective slip system from the active slip systems.

4 Results and discussion

Fig. 2(a) depicts a $(111)[1\bar{2}1]$ oriented grain which appears as one of the major texture components in steel sheets. The $(111)[1\bar{2}1]$ texture component is stabilized during rolling by activation of the major $(101)[1\bar{1}\bar{1}]$, $(101)[\bar{1}\bar{1}1]$, $(121)[\bar{1}1\bar{1}]$ slip systems and the minor slip systems in the grain. Equal shears take place along the $[1\bar{1}\bar{1}]$ and $[\bar{1}\bar{1}1]$ directions on the common (101) plane, resulting in effective slip along the $[0\bar{1}0]$ direction. Thus, the active slip systems in the grain can be reduced to two effective slip systems, namely $(101)[0\bar{1}0]$ and $(121)[\bar{1}1\bar{1}]$. Similarly, the $(1\bar{1}2)[1\bar{1}\bar{1}]$ and $(\bar{1}12)[\bar{1}1\bar{1}]$ effective slip systems are expected to stabilize of the $(001)[\bar{1}10]$ texture components, as shown in Fig. 2(b). In this case, two effective slip systems are symmetrically equivalent. The above method was therefore extended to all the texture components contained in the RD- and ND-fibres; the results obtained in this way are listed in Tables 1 and 2, respectively. For each of the RD-fibre components, there are always two symmetrical effective slip systems. On the other hand, the ND-fibre oriented grains (except for {111}<110>, which also belongs to the RD-fibre) have two *asymmetrical* effective slip systems.

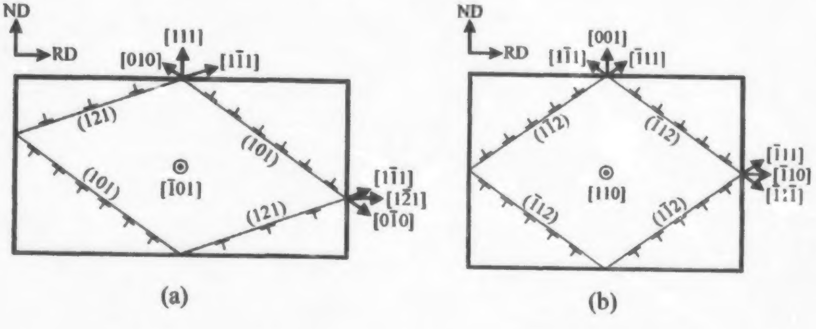
ND
RD
$[111]$
$[010]$
$[1\bar{1}1]$
(121)
(101)
(101)
(121)
$[\bar{1}01]$
$[1\bar{1}1]$
$[1\bar{2}1]$
$[0\bar{1}0]$
(a)
ND
RD
$[001]$
$[1\bar{1}1]$
$[\bar{1}11]$
$(1\bar{1}2)$
$(\bar{1}12)$
$(\bar{1}12)$
$(1\bar{1}2)$
$[110]$
$[\bar{1}11]$
$[\bar{1}10]$
$[1:\bar{1}]$
(b)

Fig. 2: Effective slip systems in (a) $(111)[1\bar{2}1]$ and (b) $(001)[\bar{1}10]$ oriented grains.

Table 1: Effective slip systems for selected cold rolling (CR) texture components belonging to the RD-fibre.

CR Texture Component $(\varphi_1, \phi, \varphi_2)$	Effective slip systems
0, 0, 45	$(1\bar{1}2)[1\bar{1}\bar{1}]$ and $(\bar{1}12)[\bar{1}1\bar{1}]$
0, 5, 45	$(1\bar{1}2)[1\bar{1}\bar{1}]$ and $(\bar{1}12)[\bar{1}1\bar{1}]$
0, 10, 45	$(101)[\overline{17}\ 18\ 17]$ and $(011)[18\ \overline{17}\ 17]$
0, 15, 45	$(101)[\overline{38}\ 43\ 38]$ and $(011)[43\ \overline{38}\ 38]$
0, 20, 45	$(101)[\overline{17}\ 21\ 17]$ and $(011)[21\overline{17}\ 17]$
0, 25, 45	$(101)[\bar{8}\ 11\ 8]$ and $(011)[11\ \bar{8}\ 8]$
0. 30, 45	$(101)[\bar{9}\ 14\ 9]$ and $(011)[14\ \bar{9}\ 9]$
0, 35, 45	$(101)[\bar{5}\ 9\ 5]$ and $(011)[9\ \bar{5}\ 5]$
0, 40, 45	$(101)[\bar{9}\ 19\ 9]$ and $(011)[19\ \bar{9}\ 9]$
0, 45, 45	$(101)[\bar{5}\ 13\ 5]$ and $(011)[13\ \bar{5}\ 5]$
0, 50, 45	$(101)[\bar{9}\ 29\ 9]$ and $(011)[29\ \bar{9}\ 9]$
0, 54.7, 45	$(101)[\overline{19}\ 79\ 19]$ and $(011)[79\ \overline{19}\ 19]$

Table 2: Effective slip systems for selected cold rolling (CR) texture components belonging to the ND-fibre.

CR Texture Component $(\varphi_1, \phi, \varphi_2)$	Effective slip systems
0, 54.7, 45	$(101)[\overline{19}\ 79\ 19]$ and $(011)[79\ \overline{19}\ 19]$
5, 54.7, 45	$(101)[\bar{1}51]$ and $(011)[4\bar{1}1]$
10, 54.7, 45	$(101)[\bar{1}61]$ and $(011)[3\bar{1}1]$
15, 54.7, 45	$(101)[\bar{1}91]$ and $(011)[5\bar{2}2]$
20, 54.7, 45	$(101)[\bar{1}\ 13\ 1]$ and $(011)[17\ \bar{9}\ 9]$
25, 54.7, 45	$(101)[0\ 1\ 0]$ and $(011)[4\bar{3}3]$
30, 54.7, 45	$(101)[0\ 1\ 0]$ and $(121)[1\bar{1}1]$

It is noted that the effective slip directions of the RD-fibre components (Table 1) as well as the ND-fibre components (Table 2) are, in most cases, inclined at angles of 30°-35° with respect to the rolling plane. Barnett and Jonas (1997) reported that in IF steels, in-grain shear bands were observed to be inclined at angles of 30°-35° to the rolling plane and occasionally 17°-20°. According to the present method, in a (111)[1-21] oriented grain, the effective slip directions, [0-10] and [-11-1] are calculated to be inclined at angle of 35.3° and 19.5°, respectively, with respect to the rolling plane. These directions are exactly coincident with those of the in-grain shear bands that Barnett and Jonas (1997) observed in their {111}<112> oriented grains. Therefore, it is apparent that in a deformed grain (or matrix), in-grain shear bands are approximately parallel to the effective slip directions. Shear bands correspond to narrow regions of intense shear that carries significant strains during deformation. The number of shear bands increases rapidly with strain and in the range of $0.8<\varepsilon<2.6$ shear band formation appears to be the major deformation mode (Humphreys and Hatherly, 1995). Although the effective slip directions are not true crystallographic slip directions, they represent schematically the true shear strains occurring during deformation (Park et al, 1998).

5 Conclusions

Under the assumption of the same shape change of a deformed grain, the active slip systems were reduced to the effective slip systems, which were employed to easily describe a deformation geometry of each grain in bcc steels cold rolled under plane strain conditions. It was clarified that the effective slip directions are parallel to the in-grain shear bands of the deformed matrix.

Acknowledgements

The authors are indebted to the Research and Development Center for Automobile Parts and Materials (RRC) of Sunchon National University through the Korea Science and Engineering Foundation (KOSEF) for financial support.

References

Barnett, M.R. and Jonas, J.J. (1997) Influence of ferrite rolling temperature on microstructure and texture in deformed low C and IF steels. *ISIJ* Int., Vol. 37, pp. 697-705.

Hosford, W.F. (1993) *The Mechanics of Crystals and Textured Polycrystals*, Oxford University Press, New York, p. 79.

Humphreys, F.J. and Hatherly, M. (1995) *Recrystallization and Related Annealing Phenomena*, Elsevier Science Ltd., Oxford, p. 35.

Park, Y.B., Kestens, L. and Jonas, J.J. (1998) Effect of internal stresses in deformed bcc metals on the orientations of new grains. in *Grain Growth in Polycrystalline Materials III*, (ed. H. Weiland et al.), TMS, Warrendale, pp. 173-178.

Savoie, J., Ray, R.K., Butrón-Guillén, M.P. and Jonas, J.J. (1994) Comparison between simulated and experimental transformation textures in Nb microalloyed steel. *Acta metall.*, Vol. 42, pp. 2511-2523.

Taylor, G.I. (1938) Plastic strain in metals. *J. Inst. Met.*, Vol. 62, pp. 307-324.

CORRUGATION OF METAL AT THE DEFORMATION ZONE AS A CAUSE OF THE LOCAL TEXTURE INHOMOGENEITY

V.V. GUBERNATOROV, B.K. SOKOLOV, I.V. GERVASYEVA,
L.R. VLADIMIROV and I.N. STEPANOVA
Institute of Metal Physics, Russian Academy of Sciences, Ekaterinburg, Russia

Abstract

A suggestion is discussed that local texture and structure inhomogeneities in the deformed materials are caused by corrugation of metal layers in the deformation zone. Sheet bcc single crystals were used to demonstrate the effect of rolling on the corrugation pitch, associated dispersity of the deformation band structure, and the texture of rolling.

Keywords: Band Structure, BCC Single Crystals, Corrugation, Deformation Zone, Rolling

1 Introduction

Band structures (deformation bands, microbands, transition bands, shear bands) that are formed in materials upon different deforming treatments affect the structure transformations and properties of the materials. They control further development of the deformation and failure processes, changes in the crystallographic texture, texture and structure after annealing. The reasons and mechanisms of the deformation band structure formation remain unclear still, though they have already been studied for some dozens years.

From the viewpoint of the physical mesomechanics of structure-inhomogeneous media, which has lately been developed (Likhachov et al. 1989; Panin et al. 1995), the formation of band structures is caused by the existence in a structure-inhomogeneous material of stress concentrators. There is some evidence (Vladimirov and Romanov 1986) that band structures are formed in structure-homogeneous materials as well, such as plastics, amorphous alloys and so on.

In paper (Gubernatorov et al. 1999) an assumption has been made that the emergence of the band structures results from corrugation of material layers in the deformation zone. Corrugation implies distortions of outer and inner layers of a metal in such a way that a system of regularly alternating ridges and spaces forms. The above approach can serve to explain the band structure formation in structure-homogeneous materials.

Pure single crystals are good subjects for verifying this suggestion. They have a homogeneous structure and allow one to monitor the flow inhomogeneity in the deformation zone and formation of the deformation bands. Bcc single crystals of the Goss orientation are well known to be transformed under rolling into two symmetrical double orientations $(111)[1\bar{1}2]$ and $(1\bar{1}1)[112]$ (Taoka 1967). This transformation is accompanied by the emergence in the structure of the alternating deformation bands. In the adjacent deformation bands, the crystal lattice turns in opposite directions.

Fig.1a,b show a distribution of the deformation increments upon roll forming the strip deformed. Maximal deformation increment Δh is observed in the starting point of the deformation zone. The metal layer S that underwent maximum compression stress under conditions of a hindered deformation might lose its stability similar to the bar system (Backofen 1972). This gives rise to corrugation of the layer and alternation of reversed stresses σ acting at neighboring regions of the metal (see Fig.1c). It is the resulting stresses that cause the reorientation of the adjacent regions of the sample in opposite directions.

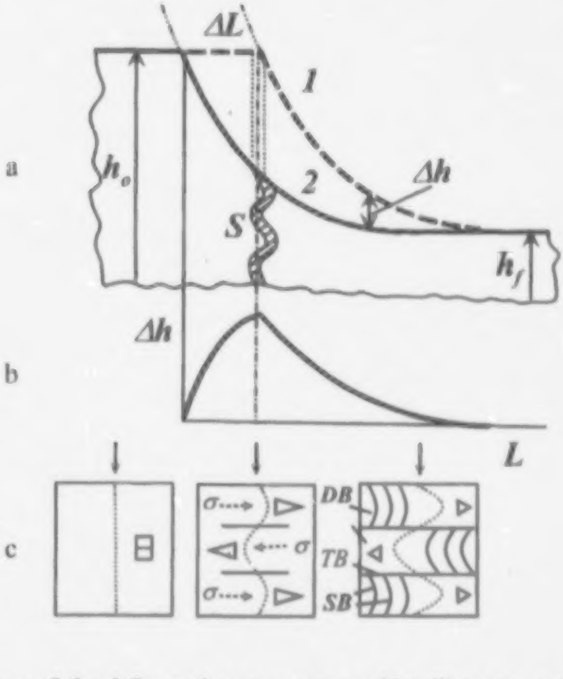

Fig.1: A scheme of the deformation zone upon cold rolling (a), a distribution of deformation increments Δh along the length of the deformation zone L (b), and deformation bands formed as a result of alternating mesostresses σ (c). DB – deformation bands, SB – shear bands, TB – transition bands.

Corrugation of the layer, which is perpendicular to the rolling direction, in depth is controlled by the flow inhomogeneity of the horizontal layers of the material in the deformation zone. Corrugation of the layer across the strip results from the inhomogeneous widening. Maximum widening gradient refers to the starting point of the deformation zone. Its value is affected by the crystal orientations. Tendency to corrugation increases when a crystal is favorably oriented for widening.

Evidently, changes in the rolling conditions – parameters of the deformation zone, rate, and others can influence the tendency to corrugation.

If corrugation in the deformation zone is universal in nature, some signs of band structures formation must manifest themselves in single crystals with stable orientations as well. However the deformation bands in these single crystals are considered to not form upon rolling and their orientation diverges only slightly because of formation of the cellular structure (Hu 1962).

In the paper presented, this suggestion is verified and a part that the rolling parameters take in the band structure formation is clarified.

2 Experimental and Discussion

The bcc alloy Fe – 3 wt.% Si with an impurity content of not more than 0.06% was taken to produce sheet single crystals 0.3 – 0.7 mm thick by recrystallization method. The sheet surfaces of the single crystals coincided with the crystallographic planes of {100}, {110}, and {111} types.

Deformation was performed by cold rolling in the quarto mill with the working rolls 45 or 135 mm in diameter at the room temperature. The rolls surfaces and planes of the single crystals were polished. To study evolution of the deformation structure along the deformation zone, the method of underrolling was used (the rolling process was stopped when the sample still remained in the deformation zone).

The surface relief of the single crystals and the structure in different sections were studied using light metallography techniques. Week local changes in the orientations were observed in the light microscope after creation on the sample surface of small etching figures.

Single crystals {110}<001>, {110}<110>, {111}<110>, {100}<011> were cold-rolled to 65% in the rolls of the same diameters. On their surface there arose a specific corrugation relief (Fig.2).

Fig.2: The surface relief of the single crystals cold-rolled to 65%.

Such relief was observed both along and across the rolling direction.

It should be noted that the relief occurred in the single crystals of both stable and unstable orientations. The corrugation pitch used to match the distance between the bands formed in the structure. Fig.3 shows the structure appearance that was revealed using small etching figures on the surface of a single crystal of a stable orientation {100}<011> deformed to 65%.

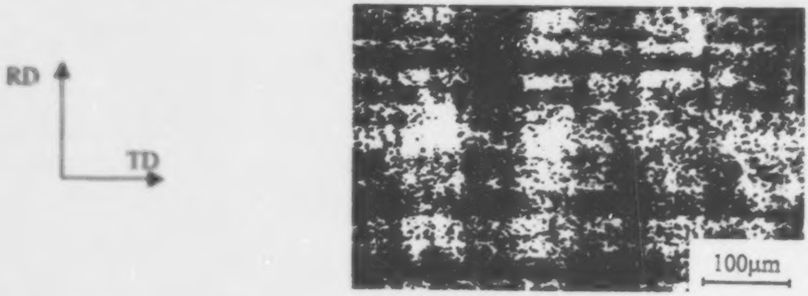

Fig.3: The structure of the cold-rolled single crystal {100}<011> revealed by etching pits.

In the structure, mesoregions are seen to be stretched along the rolling direction, resembling the deformation bands with alternating orientations. Orientations change within the scattering of the main orientation in the deformation texture.

Samples produced from the Goss single crystal 0.48 mm thick and 12 mm wide were rolled to 65% in one pass in the rolls of different diameters. After rolling in the 45-mm rolls, an average width of the deformation bands in the rolling plane made up 75 mkm. The treatment in the 135-mm rolls led to a significant decrease in the average width of the deformation bands which amounted to 15 mkm. Consequently, corrugation on the sample surface was detected to have smaller pitch. The deformation texture observed in both cases was approximately the same (Fig.4a) and consisted of

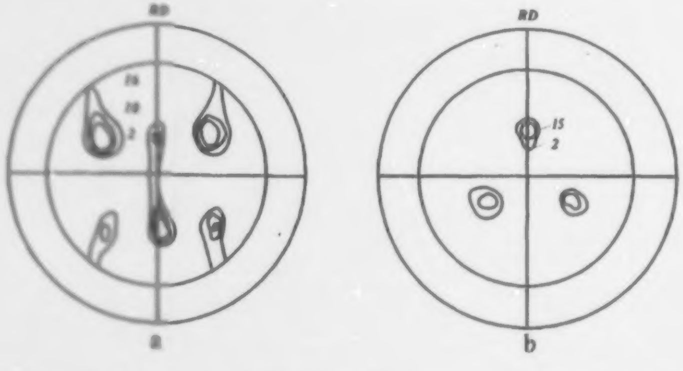

Fig.4: Pole figures {110} after cold rolling of a Goss single crystal to 65%; strip width 12 mm (a), 1.5 mm (b).

two symmetrical components $\{111\}<112>$.

However, a change in the width of the rolled strip can essentially affect the texture. Thus, after rolling a strip of a Goss crystal 1.5 mm wide and 0.48 mm thick, its structure doesn't show up alternating deformation bands and the texture consists of one component $(111)[1\bar{1}2]$ (Fig.4b).

Such single-component texture is produced also in rolling when the total deformation is achieved after a great many passes with a small reductions.

Modifications in the deformation procedure may significantly change the deformation structure and texture. Fig.5 shows the structure of the Goss crystal strip subject to bending by 90° in the starting condition and subsequent rolling to 65%. The surface that underwent a preliminary tension didn't exhibit alternating deformation bands and that one gone through a contraction possessed deformation bands far narrower than in the strip regions that didn't experience a deformation by bending.

3 Conclusion

The relief analysis of the surface as well as of the deformation structure produced by rolling single crystals of silicon iron confirms the suggestion that the band structure is caused by corrugation in the deformation zone.

The band structure is formed both in structure - inhomogeneous and structure-homogeneous materials, including single crystals with an orientation stable against

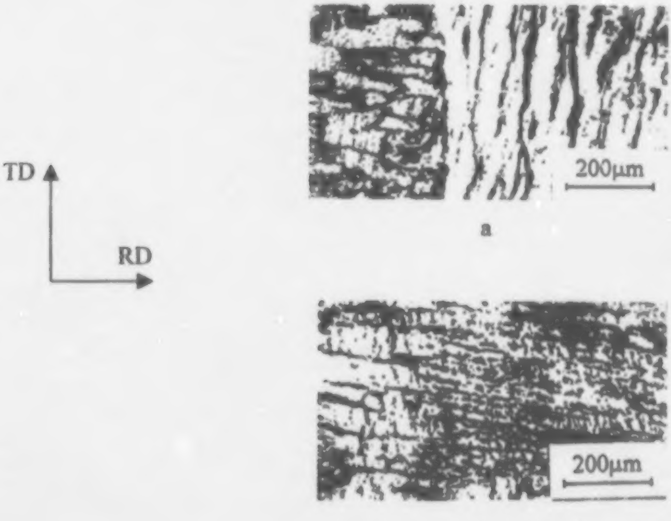

a

b

Fig.5: The structure of a Goss single crystal after bending followed by cold rolling to 65%: a – the strip side suffered a tension under bending; b – the strip side suffered a compression under bending.

deformation.

The rolling conditions and sample shape influence morphology of the band structure and deformation texture. Varying the number of passes when rolling, the width of the samples exposed to rolling, and the deformation routine may modify dimensions and dispersity of the bands and the deformation texture mode. One can achieve the resulting absence of the deformation bands, with the texture becoming a single-component one.

Thus, the deformation band structure, its mode, and arrangement are controlled by the peculiarities of the stressed state resulted from corrugation.

4 References

Backofen, W.A. (1972) *Deformation Processing*, Addison-Wesley Publishing Company, Reading, Massachusetts-Menlo Park, California–London–Don Mills, Ontario.

Gubernatorov, V.V., Sokolov, B.K., Sbitnev, A.K., Vladimirov, L.R. and Gervasyeva, I.V. (1999) Band Structure Formation in Metals under Deformation. *Textures and Microstructures*, in print.

Hu, H. (1962) Annealing of Silicon Iron Single Crystals, in *Recovery and Recrystallization of Metals*, Edited by L.Himmel. Interscience Publishers, Division of John Wiley & Sons, New York-London.

Likhachov, V.A., Panin, V.E., Zasimchuk, E.Z., Vladimirov, V.I., Romanov, A.E.,Gorskii, V.V. et al. (1989) Cooperative Deformation Processes and Deformation Localization. Kiev, Naukova Dumka.

Panin, V.E., Yegorushkin, V.Ye., Makarov, P.V., Grinajev, Y.V., Popov, V.L., Derugin, E.E. et al. (1995) *Physical Mesomechanics and Computer-Aided Design of Materials*. In two volumes, (ed. V.E. Panin), Nauka, Novosibirsk.

Sokolov, B.K., Gubernatorov, V.V., Gervasyeva, I.V., Sbitnev, A.K. and Vladimirov, L.R. (1999) The Deformation and Shear Bands in the Fe-3%Si Alloy. *Textures and Microstructures*, in print.

Taoka, T., Furubayashi, E., Takeuchi, S. (1967) Formation of Cold-rolled Texture and Recrystallization Texture in Single Crystals of 3% Silicon Iron. Part1. Cold-rolled texture. *Trans. Nation. Res. Inst. Metals*, Vol. 9, No 4, pp.155-187.

Vladimirov, V.I. and Romanov, A.E. (1986) *Disclinations in crystals*, Nauka, Leningrad.

MICROSTRUCTURE AND TEXTURE IN CHROMIUM PROCESSED BY SEVERE PLASTIC DEFORMATION

N. A. KRASILNIKOV, A. P. ZHILYAEV AND R Z. VALIEV
Institute for Physics of Advanced Materials, USATU, Ufa, 450000 RUSSIA
V. PROVENZANO
Physical Metallurgy Branch, Code 6320, Naval Research laboratory, Washington DC 20375 USA
D. G. RICKERBY
Institute of Advanced Materials, JRC, I-21020 Ispra (VA), Italy

Abstract

This study presents mechanical property and microstructural results obtained on chromium samples that were subjected to severe plastic deformation processing in order to obtain an ultrafine-grained (UFG) microstructure. After the severe plastic deformation at room temperature, the microstructure of the starting coarse-grained chromium samples was refined to an average grain size of about 100 nm. With respect to starting material, the ultrafine-grained chromium exhibited a much higher microhardness together with some ductility improvement at 200°C. The textured microstructure observed on UFG chromium, is typical of metallic samples that are subjected to severe plastic deformation by torsion straining. For the case of chromium, the texture is characterized by a preferred axial orientation along the (100) direction.

Keywords: Chromium, severe plastic deformation, and ultrafine-grained (UFG) microstructure.

1 Introduction

Chromium and chromium-iron alloys are of scientific and technological interest due to their attractive high temperature properties, such as high melting temperature and strength, high oxidation and corrosion resistance, etc. (Stamm et al. 1997). However, the use of these chromium-based alloys for structural applications has been severely limited by their poor low temperature mechanical properties; namely, low ductility and fracture toughness and an unacceptable high brittle-to-ductile transition (BTDT) temperature. However, past studies have indicated that microstructural refinement in this class of alloys can lead to significant improvements in their mechanical properties, especially: increased low temperature ductility, higher fracture toughness and a lower BTDT temperature. Microstructural refinement through severe plastic deformation processing (SPDP), either by equal-channel angular pressing or by torsion straining, is a very effective method for producing ultrafine-grained microstructure (UFG) with grain sizes less than 1 μm (Valiev et al. 1996).

There are a few ways to improve low temperature ductility of refractory metals and alloys. For example, it is known that phase modification (Kovsh et al. 1973; Igolkina et al. 1986, Trefilov et al. 1986) or the addition of small amounts of VII and VIII groups elements increases the plasticity of chromium alloys. Another way to improve the plasticity of these alloys, without changing their composition, is to produce an ultrafine, ultra-disperse microstructure. In this latter case, the increased plasticity is due to the large number of grain boundaries (GB) that act as obstacles to crack propagation when the crack moves from one grain to next. Recent studies conducted on materials whose microstructure had been refined by severe plastic deformation, resulting in a high number of grain boundaries, have shown improvements in the plasticity of many metals and alloys (Valiev et al. 1996, 1999). In fact, in a number of metals and alloys it has been observed a superplastic behavior at low temperatures and/or high strain rate superplasticity, when their microstructure was refined to nanoscale dimensions. For example, nanocrystalline pure nickel, with an average grain size of 35 nm, exhibited an elongation of about 900% at the relatively low homologous temperature of $0.36 \cdot T_m$ (McFadden et al. 1999).

2 Materials and Experimental Procedure

In this study, pure chromium (99.7%) with coarse-grain microstructure, with an average grain size of 80 μm, was used as the starting material. Using Bridgman anvils, the metal was subjected to torsion straining under high quasi-hydrostatic pressure in order to obtain ultrafine-grained (UFG) microstructure. Two different processing temperatures were used to produce the UFG microstructure: room temperature and 540°C. The samples that were processed at room temperature under a pressure of 6 GPa, were disk-shaped samples with dimensions of 10 mm in diameter and 0.2 mm in thickness, whereas the samples processed at the higher temperature were also disk-shaped with a diameter of 20 mm and the same thickness. The microstructure of the deformed samples was examined by transmission electron microscopy (TEM). The strength property data were obtained by performing bend

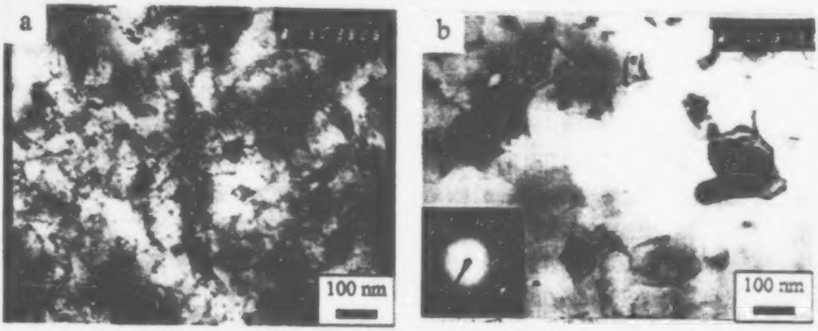

Fig. 1: Microstructure of pure chromium subjected to torsion straining at room temperature (a) and at temperature of 540 ° C (b).

tests by means of cutting edge loading with traverse velocity of 1 mm·min^{-1} in temperature range of 20-200oC. The samples for bend tests were parallelepipeds with dimensions of: 2×0.2×14 mm. The output data, consisting of "load-traverse displacement" curves, was PC controlled and recorded. Subsequently, the data was recalculated and expressed in terms of "stress-bending displacement" curves. Standard x-ray procedure has been used to measure texture in samples under study.

1 Results and discussion

1.1 Transmission electron microscopy (TEM).

TEM analysis showed that the microstructure of Cr samples processed at room temperature consists of highly dispersed fragmented structure, whose fragments have a mean size of 100-150nm (Fig. 1a). The same TEM micrograph shows also that there is high density of lattice dislocations up to 10^{15} m^{-1}. The microstructure was stable during annealing treatments up to 400°C temperature. However, for the samples deformed at 540oC, some structure recovery was observed. As demonstrated by the TEM micrograph shown in Fig. 1b. In this latter case, a well-defined granular-type structure was observed with a mean grain size of 0.3 µm. In addition, numerous spots, arranged in circles showing azimuth spreading, were observed in the SAED patterns. This is characteristic of high angle misorientation between adjacent fragments (grains). The grain boundaries in such microstructure have a high density of dislocations, whereas the grain interiors are almost free of dislocations. Such type of microstructure indicative of recovery processes taking place during intense plastic deformation at the higher processing temperature.

1.2 Microhardness

As stated earlier, in its initial state, pure chromium had an average grain size of about 80 µm and a microhardness of 1.75 GPa. It was found that the microhardness of UFG chromium processed at room temperature is more than 3 times higher (6 GPa) than the coarse-grained counterpart. It is believed that this increase in the microhardness is a direct result of the much finer microstructure of the deformed samples. Further, within the experimental error, the microhardness value across the sample was fairly constant. This is consistent with the uniform microstructure observed in processed material. Fig. 2 shows the microhardness of UFG chromium processed at room temperature as a function of annealing temperature. It should be noted that a relatively high microhardness value was retained up to 600° C temperature. Only for annealing temperatures above 900° C, the microhardness

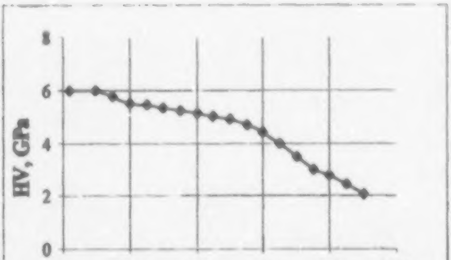

Fig. 2: Microhardness of UFG chromium as a function of annealing temperature.

Table: Results of bending tests for UFG chromium.

Processing Temperature	Number of turns	Temperature of bending test	Stress, MPa			
			σ_Y	σ_U	σ_R	$K=\sigma_U-\sigma_R$
Starting materials		20° C	430	550	530	20
540° C	1		724	1010	1010	0
540° C	5		840	1340	1340	0
Starting materials		100° C	356	517	410	107
540° C	1		560	696	332	364
540° C	5		610	984	508	476
Starting materials		200° C	300	507	386	111
540° C	1		480	760	456	304
540° C	5		600	1100	610	490

Here σ_Y is yield strength; σ_U is ultimate strength; σ_R is fracture stress or stress in unbroken samples bent on the angle of 90°.

approaches the value of starting coarse-grained chromium. Also, at this point it useful to note that UFG chromium samples processed at higher temperature had lower microhardness values than those processed at room temperature.

In fact, the microhardness was about 4 GPa for samples deformed at 470° C and 2.6 GPa for those deformed at 540° C. This latter value, is still about 1.5 times higher than that of the starting materials.

1.3 Mechanical testing

The most reliable method for determining the mechanical properties of brittle materials, such as chromium and chromium-iron alloy, is bending testing (Zolotorevski 1983). Bending tests under the same conditions were also performed on chromium samples processed at 540 oC for 1 or 5 turns whose UFG microstructure had a grain size is in the range of 0.3-0.8 μm. All results are summarized in the above Table. In Fig. 3 Shows "Stress-bending displacement" curves for different test temperatures. Main difference in mechanical behavior of UFG chromium compared to the course-grained counterpart is an absence of significant strengthening of UFG chromium observed at all testing temperatures. At the same time flow stress is much lower in case of coarse-grained chromium. Increasing the testing temperature to 200° C leads to an increase in the plasticity coefficient (Zolotorevski 1983) $K = \sigma_U - \sigma_R$ (see the Table 1 and Fig. 3b). Furthermore, similar behavior has been observed in other UFG and nanocrystalline materials (for example, Mishra et al. 1998). It has been suggested that such a behavior is due to enhanced grain boundary diffusivity in the fine-grained material. In fact, it has been shown that in UFG materials GB diffusion coefficient is higher by 2-3 order of magnitude when compared to the corresponding coarse-grained materials (Kolobov 1998). It has been proposed that the

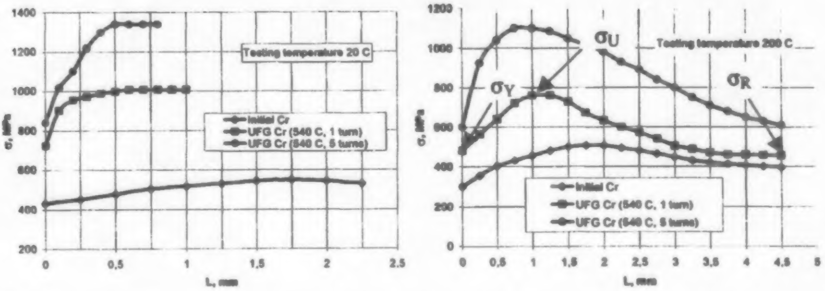

Fig. 3: "Stress- bending displacement" curves for UFG chromium tested at the room temperature and at 200° C.

increased diffusivity results from the fact that the grain boundaries after severe plastic deformation are in highly strained, non-equilibrium state This would explain the relaxation processes starting at relatively low homologous temperatures. Additionally enhanced diffusivity through the triple junctions, which is normally 2-3 orders of magnitude higher than GB diffusivity, may also be contributing to the increased diffusivity.

In Fig. 4 (a) shows the fracture surface of a coarse-grained chromium sample, whereas Fig. 4 (b) shows the fracture surface of a UFG chromium sample processed at 540° C. From this figure, one can see the essential differences in two fracture surfaces corresponding to the two different samples. For coarse-grained chromium, fracture features are "river"-like patterns that is typical for brittle fracture By contrast, the fracture features of the UFG sample are more "cup"-like (Fig. 4b), that is indicative of ductile fracture (Gordeeva and Zhegina 1978).

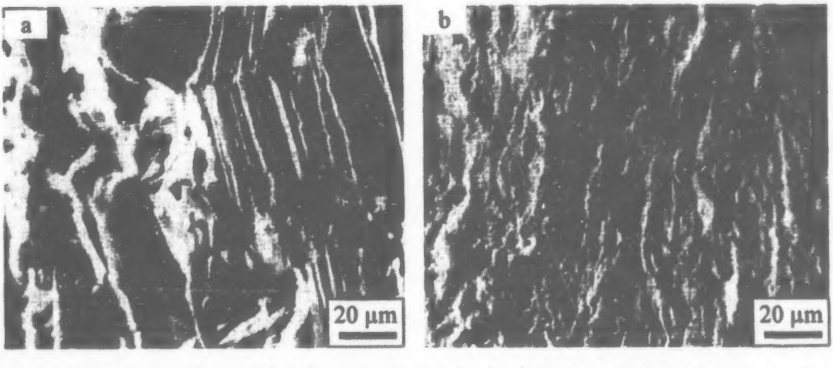

Fig. 4: Fracture surface of the chromium samples broken at room temperature: a – in initial state; b – with ultrafine-grained microstructure.

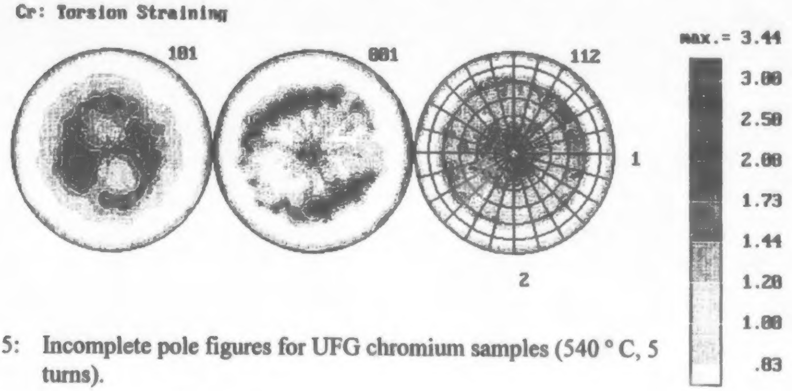

Fig. 5: Incomplete pole figures for UFG chromium samples (540 ° C, 5 turns).

1.1 Texture measurement

Texture measurements were carried out on UFG pure chromium samples processed at 540° C, for 5 turns. The pole figures (PF) of pure chromium are fairly symmetrical with an axial texture pattern. As mentioned before, this typical pole figures for UFG materials after torsion straining show quite strong texture which can affect grain boundary statistics and, as a result, behavior UFG chromium.

2 Concluding remarks

UFG chromium samples have been obtained by using severe plastic torsion straining. The mean grain size was about 100 nm for the samples processed at room temperature. Increasing the processing temperature to 540° C result in chromium samples with an average grain size of 0.3μm. Compared to the starting coarse-grained material, UFG chromium has higher microhardness at room temperature and higher bend strength for test temperatures up to 200°C. Also, the UFG microstructure exhibited a high degree of thermal stability. The study of mechanical behavior during bending tests and the corresponding fracture features observed by SEM have revealed a visible tendency for increasing ductility of the processed UFG chromium, when compared to the coarse-grained counterpart. X-ray study revealed an axial texture that forms during torsion straining, that is typical of many metals with cubic crystal structure.

3 References

Gordeeva T. A., Zhegina I. P. (1978) *Fracture analysis in materials evaluation*. Moscow, Mashinostroenie Publishing, (in Russian).

Igolkina L. S. et al. (1986) Quenching and Aging in Chromium Alloy. *Physics of Metals*, Vol. 8, No 2, pp. 32-37.

Kolobov Yu. R. (1998) *Diffusion-controlled processes on grain boundaries and plasticity of metals*. Novosibirsk, Nauka Publisher, (in Russian).

Kovsh V. et al. (1973) Influence of Cyclic Deformation on Dislocation Structure and Mechanical Behavior of Molybdenum, Chromium and Tungsten. *Problems of Strength*, No 11, pp. 15-20.

S. X. MacFadden et al. (1999) Low-temperature superplasticity in nanstructured nickel and metal alloys. *Nature*, Vol. 398, April, pp. 684-686.

Stamm H. et al. 1997, Thermomechanical Characteristics of Low Activation Chromium and Chromium Alloys, *In Processing of ICFRM-8*, October 26-31, 1997, Sendai, Japan.

Ultrafine grained materials produced by severe plastic deformation (1996) Spesial issue. Ed. by R. Z. Valiev. Annales de Chimie - Science des Materiaux, Vol. 21.

Valiev R. Z., Islamgaliev R. K., Alexandrov I. V. (1999) Bulk nanostructured materials processed by severe plastic deformation. Submitted to *Annual review "Progress in Materials Science*.

Zolotorewski V. S. (1983) *Mechanical properties of metals*. Moscow, Metallurgy Publisher, (in Russian).

THE DEFORMATION TEXTURES AND LANKFORD VALUES OF ASYMMETRICALLY ROLLED ALUMINUM ALLOY SHEETS

KEUN-HWAN KIM and DONG NYUNG LEE
Division of Materials Science and Engineering, Seoul National University, Seoul 151-742, Korea
CHANG-HEE CHOI
Microelectronic materials T/G Research Lab., LG Cable Ltd., Anyang, Korea

Abstract

An asymmetric rolling of aluminum alloy sheets which enhances shear deformation has been theoretically and experimentally studied. The effect of the well developed rolling and cube textures as initial textures on the shear texture were investigated. The variation of stable orientation with shear strain was discussed based on the rate of rotation calculated using the Taylor-Bishop-Hill model. The texture variation along the sheet thickness was much suppressed by the asymmetric rolling and the texture consisted of the {100}<011>, {111}<011> and {111}<112> orientations. The Lankford values of the asymmetrically rolled aluminum alloy sheets were remarkably improved due to the relatively well developed {111} texture.

Keywords: Asymmetric rolling, shear texture, Lankford value, aluminum alloy

1 Introduction

Aluminum alloy sheets are considered as one of the high potential substitutes for steel sheets considering weight reduction of automobiles. However aluminum alloy sheets have drawbacks such as higher prices and inferior formability. The inferior formability is mainly due to low strain hardening exponent, strain rate sensitivity, and plastic strain ratio or Lankford value. The strain hardening exponent and strain rate sensitivity are increased by alloying. But the plastic strain ratios of aluminum alloy sheets are still low, due to the texture developed in conventional process. The cold rolling texture of aluminum alloy sheets under the conventional rolling condition has been characterized by the β-fiber texture, which changes to the cube texture after annealing. However, the shear texture characterized by the {001}<110>, {111}<110>, and {111}<112> orientations have been observed in the surface layer of aluminum sheets rolled with high frictions and a characteristic deformation geometry between sheet and rolls. Recently, the present authors have tried to develop a process called asymmetrical rolling which could impose shear deformation homogeneously through the sheet thickness.

2 Experiment

A schematic diagram of the asymmetric rolling process is shown in Fig. 1 and the ratio of upper roll radius to lower roll radius is designated the roll ratio. The upper roll of 198mm in diameter and the lower roll of 126mm in diameter were used for a roll ratio of 1.5. The deformation texture developed by asymmetric rolling of 99.99pct pure aluminum sheets may be influenced by the initial textures of the material. Therefore, specimens with plane strain rolling and cube textures were prepared. The specimens were asymmetrically rolled by three different schedules with a roll ratio of 1.5 at room temperature according to the rolling schedules given in Table 1.

The asymmetric rolling of the alloy AA5052 was carried out up to 75pct at 450°C. The rolled AA5052 specimen was annealed at 275 $^{\circ}$C for 1hr and 400 $^{\circ}$C for 0.5hr.

The (111) pole figure was acquired using X-ray texture goniometer in the back reflection mode with Fe filtered Co-Kα radiation. The Lankford values were measured for the annealed AA5052 specimens cut along 0°, 45°, and 90° to the rolling direction after homogeneous elongation.

3 Results and discussion

3.1 Effect of rolling parameters on deformation texture

3.1.1 Plane strain rolling initial texture

Fig. 2 shows the measured (111) pole figures of the upper surface layer of 99.99pct pure aluminum sheet asymmetrically rolled by three different schedules given in Table 1, in which rotating paths of initial orientations of $(225)[\bar{5}\bar{5}4]$ and $(22\bar{5})[554]$ are indicated. The rotating path was calculated as a function of reduction suffixes 1 and 3 indicate the rolling and sheet normal directions, respectively. In schedule I, the deformation texture of the specimen can be described as orientations rotated through about 5° from the initial orientations about TD. These orientations are in good agreement with the end orientations of rotating path calculated assuming that

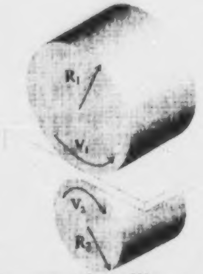

Fig. 1: Schematic diagram of asymmetric rolling process (R_1:R_2 = v_1:v_2).

Table 1: Asymmetric rolling schedules of 99.99pct pure aluminum sheets.

Schedule	Initial thickness (mm)	Number of passes	Rolling depth per pass (mm)	Total reduction (%)	Initial texture
I	2.0	16	0.1	80	β-fiber, Cube
II	2.0	6	0.25	75	β-fiber, Cube
III	2.0	2	1.0, 0.6	80	β-fiber, Cube

α is 1.1. In schedule II, the orientations of deformation texture were rotated through 7-8° about TD from initial orientations. These orientations are in good agreement with the end orientations of rotating path calculated assuming that α is 1.3. In schedule III, well defined shear texture components were obtained. The shear texture of deformed aluminum sheets usually consists of major {001}<110> and minor {111}<110> and {111}<112> components. These orientations are in good agreement with the end orientations of rotating path calculated assuming that α is 10.

The above results indicate that the stable end orientations in the asymmetric rolling texture depend on the α value, which can be controlled by the rolling depth per pass (Table 1). For a given reduction of area, an increase in shear strain increases the rotation of the initial orientations toward the well known shear texture components. In the asymmetric rolling process, the deformation imposed to the rolled specimen is close to simple shear rather than pure shear. This means that the displacement gradient de_{13} is much larger than de_{31}. The rates of rotation were calculated in order to investigate the variation of stable orientation with de_{13} / de_{11} (=α), based on the Taylor-Bishop-Hill model. Fig. 3 shows the rotation rate for fcc crystals undergoing deformation at various α values with zero stain along [1 $\bar{1}$ 0], where the orientations at zero rotation rate with the negative slope of curves are stable. The stable orientation {4 4 11}<11 11 8> in plane strain condition is obtained when de_{13} / de_{11} = α =0. When α is larger than zero, stable orientations rotate about TD and are located between the symmetric components about TD, i.e. {4 4 11}<11 11 8>, {001}<110>, and {111}<112>. This is the reason why the pole figures of asymmetrically rolled sheets are asymmetric as shown in Fig. 2(a) and (b). When α

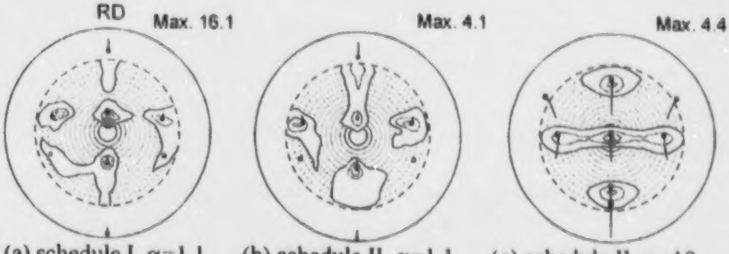

(a) schedule I, α=1.1 (b) schedule II, α=1.1 (c) schedule II, α=10

Fig. 2: Measured (111) pole figures of upper surface layer of 99.99pct aluminum asymmetrically rolled by schedules given in Table 1 and calculated rotating paths of (225)[$\bar{5}\bar{5}4$] and ($22\bar{5}$)[554], (■: end orientation).

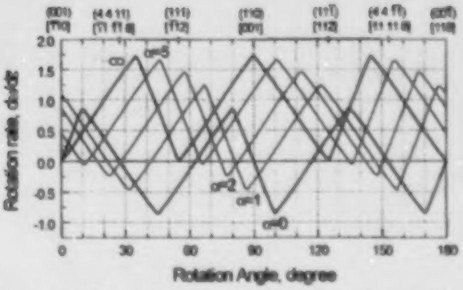

Fig. 3: Rotation rate, $d\omega/d\bar{\varepsilon}$, for fcc crystals undergoing deformation at various $de_{13}/de_{11}(=\alpha)$ values.

approaches to infinity, practically above 10, the stable orientations become {001}<110> and {111}<112> as shown in Fig. 2(c).

3.1.2 Cube initial texture

Fig. 4 shows the measured (111) pole figures of the upper surface layer of 99.99pct pure aluminum sheet asymmetrically rolled by three different schedules and the calculated rotating paths of cube orientation, (001)[100]. In schedule I, the deformation texture of the specimen can be described as orientations rotated mainly about ND towards the rotated cube orientation and rotated about TD and RD at the same time, resulting in non-orthorhombic symmetry. These orientations are in good agreement with the end orientations of rotating paths calculated using an α value of 1.1. In schedule II, the initial cube orientations rotated mainly about ND and TD, and α can be approximated by 1.3. In schedule III, well defined shear texture components were obtained but their intensity was relatively weak in comparison with the texture obtained from initial β-fiber. These orientations are in good agreement with the end orientations of rotating path calculated using α value of 10. This means that cube orientations rotate about ND towards the rotated cube orientation when deformed by shear deformation with very large α values and these rotation paths are considered to yield the diffuse shear textures.

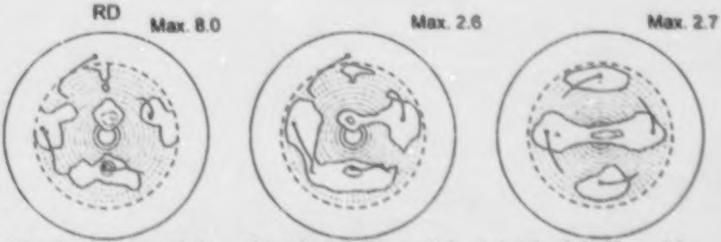

(a) schedule I, α=1.1 (b) schedule II, α=1.1 (c) schedule II, α=10

Fig. 4: Measured (111) pole figures of upper surface layer of 99.99pct aluminum asymmetrically rolled by schedules given in Table 1 and calculated rotating paths of (001)[100], (■: end orientation).

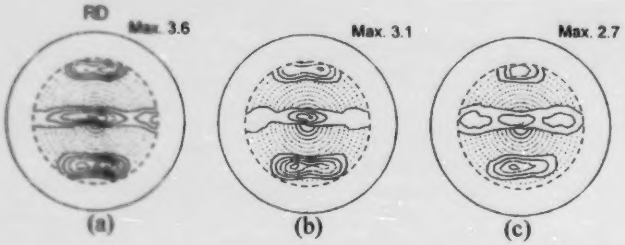

Fig. 5: Measured (111) pole figures of (a) upper surface, (b) center, and (c) lower surface layers of asymmetrically 75pct rolled AA5052.

3.2 Lankford value

3.2.1 Effect of asymmetric rolling on texture evolution

Fig. 5 shows the measured (111) pole figures of upper surface, center, and lower surface layers of an asymmetrically rolled AA5052 sheet. Texture variation through the thickness was much suppressed by asymmetric rolling, and the specimen was composed of shear textures. Here, the shear textures can be described as orientations rotated through 5-10° from the {001}<110> and {111}<110> or {111}<112> components about TD and a high intensity is shown near the {111} components. It is well known that the {111} components give rise to higher Lankford values in cubic metal sheets.

Fig. 6 shows the measured (111) pole figures of upper surface layers of AA5052 annealed at 275°C for 1hr and 400 °C for 0.5hr. The texture of a specimen annealed at 275°C for 1hr is almost the same as the deformation texture in Fig. 5(a), which may indicate that no recrystallization took place during annealing. However, the deformation texture remained unchanged even after annealing at 400 °C for 0.5hr although a little texture spread occurred around the center of pole figure. The cube texture, which is obtained from conventional rolling and subsequent annealing process of aluminum alloys and gives rise to low Lankford values, did not develop.

3.2.2 Lankford value

Table 2 shows the Lankford values of AA5052 aluminum alloy sheets annealed after symmetric rolling and asymmetric rolling measured along 0°, 45°, and 90° to the rolling direction. Asymmetrically rolled sheet shows higher average Lankord values

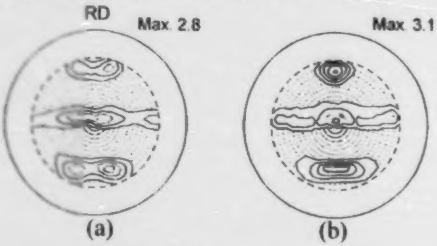

Fig. 6: Measured (111) pole figures of upper surface layer of AA5052 sheet annealed at (a) 275°C for 1hr and (b) 400°C for 0.5hr.

Table 2: Lankford values of AA5052 sheets.

Rolling	**Annealing temperature**	$\mathbf{R_0}$	$\mathbf{R_{45}}$	$\mathbf{R_{90}}$	$\overline{\mathbf{R}}$	$\mathbf{\lvert\Delta R\rvert}$
Symm.	400°C for 0.5hr	0.80	0.86	0.94	0.87	0.01
Asymm.	275°C for 1hr	0.64	2.16	1.04	1.50	1.32
	400°C for 0.5hr	1.04	1.48	0.90	1.22	0.51

($\overline{R}$) in comparison with the symmetrically rolled sheet, with a highest value of 2.16 at 45° to the rolling direction. The average Lankford values ($\overline{R}$) of asymmetrically rolled sheets are approximately 1.4-1.7 times higher than those of symmetrically rolled sheets. However, asymmetrically rolled sheet has a drawback of severe planar anisotropy. The specimen annealed at 400 °C for 0.5hr shows the increased R_0 and decreased R_{45} values in comparison with the specimen annealed at 275 °C for 1hr, giving rise to remarkable decrease in $|\Delta R|$ indicating planar anisotropy, and 19% decrease in average Lankford value ($\overline{R}$).

4 Conclusion

The textures developed due to shear deformation imposed by asymmetric rolling depend on the ratio of the shear strain to the compression strain, which can be controlled by the rolling depth per pass.

Asymmetric rolling of AA5052 sheets much reduced the through thickness texture inhomogeneities, resulting in shear textures with high {111} components. The average Lankford values of asymmetrically rolled sheets are approximately 1.4 to1.7 times higher than those produced by symmetric rolling.

Severe planar anisotropic properties of asymmetrically rolled sheet could be mitigated by subsequent high temperature annealing.

5 References

C.-H. Choi, K.-H. Kim and D.N. Lee, Effect of shear texture development on the formability in rolled aluminum alloy sheets, *Mater. Sci. Forum*, 273-275, (1998) 391-396

C.-H. Choi, K.-H. Kim, S.-Y. Jeong and D. N. Lee, "Analysis of Texture in Aluminum Alloy Sheets Rolled Using Asymmetric Rolls", *J. Korean Inst. Met. Mater.* 35, (1997) 429.

C.-H. Choi, K.-H. Kim and D. N. Lee, "Texture Control of Aluminum Alloy Sheets", *Synthesis/Processing of Lightweight Metallic Materials II* Edited by C. M. Ward-Close, F. H. Froes, D. J. Chelleman and S. S. Cho, TMS(1997) 37-48.

H. O. Asbeck and H. Mecking, "Influence of Friction and Geometry of Deformation on Texture Inhomogeneity during Rolling of Cu Single Crystals as an Example", *Mat. Sci. Eng.* 34, (1978) 111-119.

I. L. Dillamore and W. T. Roberts, "Crystallographic Texture Variation through Rolled Aluminum and Copper Sheet", *J. Int. Metals*, 92, (1963~1964) 193-199.

W. Truszkowski, J. Krol and B. Major, "Inhomogeneity and Rolling Texture in fcc Metals", *Metall. Trans.* 11A, (1980) 749-758.

PREDICTING THE TRANSFORMATION TEXTURE OF AXISYMMETRICALLY COMPRESSED Fe-30%Ni USING A DISLOCATION REACTION MODEL

MAISIE SUM, JOHN J. JONAS and JOHN ROOT*

McGill University, Department of Metallurgical Engineering, 3610 University Street, Montreal, Canada H3A 2B2
** National Research Council (NRC), Chalk River Laboratories (CRL), Chalk River, Canada K0J 1J0*

Abstract

Variant selection takes place upon the transformation to martensite of deformed Fe-30%Ni alloys. Such selection can be predicted using a model based on the Kurdjumov-Sachs relationship and the presence of dislocations on slip planes. The model involves a slip activity criterion, which states that variants are selected when the associated slip activity is positive, so that all variants with "negative" activities are eliminated. In addition to the active slip dislocations, it is possible to form product *(unstressed)* dislocations by the reaction of two active dislocations. These participate in the transformation even though they are not selected by the conventional slip activity rule. These variant selection rules have been used successfully to predict the transformation texture resulting from plane strain rolling. In the current study, the model is tested for a second strain path, that of axisymmetric compression. A cylindrical specimen of Fe-30%Ni was compressed uniaxially, after which the texture was analysed using a neutron diffraction method. The measured textures included those of i) the initial (as-received) material, ii) the parent austenite (after deformation, but before transformation), and iii) the product martensite (following transformation of the compressed specimen). These detailed results have permitted a step-by-step analysis to be carried out. Excellent agreement is demonstrated between the predicted and observed textures.

Keywords: Bishop and Hill, dislocation reactions, Kurdjumov-Sachs, slip activity, transformation textures, variant selection.

1 Introduction

The study of variant selection during the γ-to-α' transformation has been a subject of great interest to researchers for decades [Bateman and Davies, 1981; Ray and Jonas, 1990]. The inheritance of texture is of significant interest to the steel industry because of its critical effect on material properties [Haslam et al., 1973; Jonas, 1998]. Extensive experimental and modeling work has therefore been carried out on the textures that result from these phase transformations [Ray et al., 1990; Butrón-Guillén and Jonas, 1993]. It has been shown that, for *deformed* metals, not all the expected variants are present, whether the Kurdjumov-Sachs (K-S) or Nishiyama-Wassermann (N-W) relationship is used. This indicates that variant selection occurs primarily due to the presence of dislocations.

Several models have been proposed, based on one or another of the transformation laws, i.e. Bain, K-S or N-W, with the aim of predicting transformation textures in the presence of variant selection [Davies and Bateman, 1981; Liu and Bunge, 1991; Da Costa Viana et al., 1996; Butrón-Guillén et al., 1997]. Until recently, no model has been proposed that can describe the phenomenon with accuracy. The present approach employs the K-S transformation law and combines the classical slip activity model of Bishop and Hill with a dislocation reaction criterion [Sum and Jonas, 1999]. It was derived by analysing the experimental results obtained by earlier authors [Liu and Bunge, 1991] for single parent orientations of the present material that had undergone deformation by plane strain.

This particular paper is concerned with predicting transformation textures after deformation along a different strain path, that of axisymmetric compression. In the study, neutron diffraction measurements were made to determine the parent and product textures of the compressed Fe-30%Ni alloy before and after transformation, respectively. Finally, the experimental results are compared with the predictions made using the present variant selection criteria.

2 Methodology

A deformed austenite texture was produced by conducting the compression tests at 300°C. This temperature was chosen to avoid the formation of deformation-induced martensite [Kaufman and Cohen, 1956]. Transformation was subsequently induced by quenching in liquid nitrogen to -196°C. The parent texture after compression and the product texture after transformation were then measured directly. The measured initial orientations that make up the texture prior to transformation were used as the actual inputs for prediction of the transformation texture. The predicted components were then obtained by combining the individual orientations selected from each parent using the present model. Meanwhile, the actual transformation texture of the compressed specimen was determined experimentally by neutron diffraction.

3 Experimental Texture Components

The compression texture, defined as the <110> fibre, was achieved after applying a compressive strain of $\varepsilon = 0.4$, see Figure 1. For simulation purposes, parent orientations were chosen along the [1-10] compression fibre; these are represented here by the following nine components: (001)[1-10], (113)[1-10], (112)[1-10], (223)[1-10], (111)[1-10], (332)[1-10], (221)[1-10], (331)[1-10] and (110)[1-10]. These were all given equal "weights" in the calculations.

The transformation texture inherited from the compressed specimen was determined experimentally by neutron diffraction. The measured inverse pole figure is illustrated in Figure 2. From the figure, it is evident that the product consists of a major <111> component and two minor <112> and <001> components, where the latter are about two or three times less intense than the former.

4 Predicted Texture Components using the Present Model

By using the nine crystallographic orientations as input for the slip activity and K-S rotation programs, the transformation texture of the uniaxially compressed Fe-30%Ni alloy was predicted. The shear rates and list of the twenty-four possible variants generated from each of the starting orientations *in the absence of variant selection* are given elsewhere [Sum, 1998] and are not presented here.

From the classical slip activity rule of the selection criteria, the active Burgers vectors are those associated with "positive" shear (i.e. with slip *parallel to* the resolved shear stress). These correspond to the following eight slip systems, where their associated shears are shown in parentheses: **+aI** (0.31), **-aII** (0.31), **-bI** (0.31), **+bII** (0.31), **-cI** (0.61), **+cII** (0.61), **-dI** (0.61) and **+dII** (0.61). The product components pertaining to each of these Burgers vectors were selected as required by the slip activity rule [10, 11] and used to plot the inverse pole figure shown in Figure 3(a). The highest intensities in this plot pertain to the <111> and <001> components. The "negative" slip components are illustrated in Figure 3(b). (These involve slip in directions *opposed to* the resolved shear stresses.) The strong <001> component evident here does not play a role in the inherited texture, as will be shown in more detail below.

The components obtained from the dislocation reaction criterion are those that correspond to the following eight slip systems produced by the in-plane dislocation reaction of the active Burgers vectors: **±aIII**, **±bIII**, **±cIII** and **±dIII**. Both positive and negative product vectors form due to the equal shear rates of the reactants; thus either sign can be adopted [Sum and Jonas, 1999]. That is, both directions satisfy the necessary parallelism condition of the dislocation lines for the reaction to take place. The product components that result from the dislocation reaction criterion are illustrated in Figure 3(c). Unlike the previous inverse pole figure produced from the first selection criterion, this plot clearly calls for the presence of the <112> component.

5 Comparison of Experimental and Predicted Inverse Pole Figures

The transformation components selected using the i) classical slip activity and ii) dislocation reaction approaches, are illustrated in Figures 3(a) and (c) respectively. Finally, the predicted overall transformation texture (which combines the two sets of orientation components) is shown in Figure 4. By comparing Figures 2 and 3(a), it is clear that, when only the slip activity rule is applied, although the texture bears a resemblance to the experimental one (Figure 2), the <112> component is missing. The variants selected by employing the dislocation reaction approach (Figure 3(c)) reproduce the experimental texture in the vicinity of the <111> and <112> fibre axes very faithfully. Finally, combination of the two approaches, as represented by the two sets of variant selection criteria, leads to an accurate prediction of the measured texture. This is evident when Figures 4 and 2 are compared. The predicted texture is indeed made up of a major <111> component, in excellent agreement with the actual transformation texture, which displays the same principal component. Similar remarks apply to the minor components <112> and <001>. Thus, the present model applies not only to plane strain rolling [11], but also to the axisymmetric compression strain path. Experiments are currently under way to extend this study to axisymmetric extension and to simple shear (torsion) [Wittridge and Jonas, 1999].

6 Conclusions

The transformation texture predictions formulated by applying the present variant selection criteria were compared with measured austenite and martensite textures of a deformed Fe-30%Ni alloy specimen. The following conclusions are drawn from this work:

1. As expected, the parent austenite texture of the deformed Fe-30%Ni alloy revealed a typical <110> compression fibre.
2. The measured martensite texture of the axisymmetrically compressed sample was made up essentially of a strong <111> component and two weak <112> and <001> components.
3. The texture predicted using the first selection criterion, that is, the classical slip activity rule, is somewhat similar to that measured using neutron diffraction. The main texture component is the <111>, with somewhat less intensity at the <001>.
4. The dislocation reaction criterion produces a texture that is closer to the measured one in the vicinity of <111>. The major component in this case is <111>, in agreement with experiment, while the minor one is <112>. The latter leads to a spread around the <111>.
5. When the classical slip activity and dislocation reaction approaches are combined, a texture is predicted that is in excellent agreement with the observations. The products consist of the <111> major component and the <112> and <001> minor orientations.
6. The components associated with negative slip lead to appreciable texture intensities near <001>. These high intensities are not observed and therefore show why it is important to reject the negative (as opposed to positive) slip orientations.

7 Acknowledgements

The authors are indebted to the Natural Sciences and Engineering Research Council (NSERC) of Canada for the financial support of this investigation. They also express their gratitude to Professor Druce Dunne of the University of Wollongong for providing the experimental material and to Dr. Jerzy Baczynski of McGill University for his assistance with the preparation of the inverse pole figures.

8 References

Bateman, R.M. and Davies, G.J. (1981) The inheritance of texture on transformation from austenite to martensite in an Fe-30Ni alloy. *Proc. of the 6th International Conference on Textures of Materials (ICOTOM6), The Iron and Steel Institute of Japan*, vol. 1, p. 690.

Butrón-Guillén, M.P. and Jonas, J.J. (1993) Effect of austenite recrystallisation on ferrite transformation textures. *Materials Science Forum*, vols. 113-115, p. 691.

Butrón-Guillén, M.P., da Costa Viana, C.S. and Jonas, J.J. (1997) A variant selection model for predicting the transformation texture of deformed austenite. *Metallurgical and Materials Transactions*, vol. 28A, p. 1755.

Da Costa Viana, C.S., Butrón-Guillén, M.P. and Jonas, J.J. (1996) A residual stress-based criterion for variant selection during the gamma-to-alpha transformation. *Proc. of ICOTOM11*, vol. 1, p. 604.

Davies, G.J. and Bateman, R.M. (1981) The influence of variant selection in the inheritance of texture during phase transformations. *Proc. of ICOTOM6*, vol. 1, p. 132.

Haslam, K., Coleman, T., Dulieu, D. and Dillamore, I.L. (1973) Deformation and recrystallisation textures in metals and their industrial applications. *Société Française de Métallurgie*, p. 369.

Jonas, J.J. (1998) Effect of processing parameters on texture and anisotropy of high performance steels. *The 7th International Conference in Steel Rolling, Steel Rolling '98, The Iron and Steel Institute of Japan*, p. 524.

Kaufman, L. and Cohen, M. (1956) The martensitic transformation in the iron-nickel system. *Transactions A.I.M.E., Journal of Metals*, p. 1393.

Liu, W.P. and Bunge, H.J. (1991) Variant selection in the martensitic transformation of an Fe-30%Ni alloy with cube texture. *Materials Letters*, vol. 10, no. 7-8, p. 336.

Ray, R.K. and Jonas, J.J. (1990) Transformation textures in steels. *International Materials Reviews*, vol. 35, no. 1, p. 30.

Ray, R.K., Chapellier, Ph, and Jonas, J.J. (1990) Correlation between the rolling textures in fcc Ni-Co alloys and the bcc transformation textures in control rolled steels. *Textures and Microstructures*, vol. 12, p. 141.

Sum, M. and Jonas, J.J. A dislocation reaction model for variant selection during the austenite-to-martensite transformation. *Textures and Microstructures*, in press.

Sum, M. Variant selection during the austenite-to-martensite transformation. M.Eng Thesis, McGill University, 1998.

Wittridge, N. and Jonas, J.J. work in preparation.

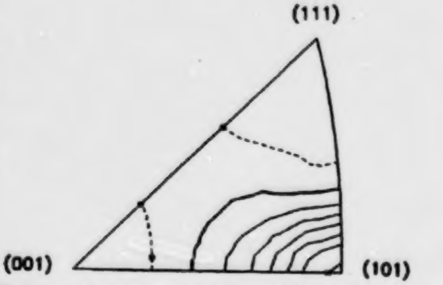

Figure 1. Inverse pole figure of the compression texture. Broken line: 0.5 x random; heavy line: 1 x random; intervals: 0.5.

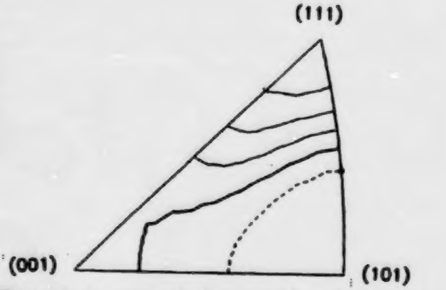

Figure 2. Inverse pole figure of the transformation texture. Contours and intervals as for Figure 1.

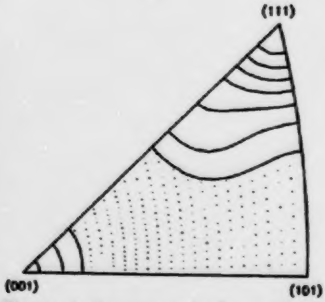

Figure 4. Inverse pole figure illustrating the transformation texture (with 30% random background) predicted using the present variant selection criteria.

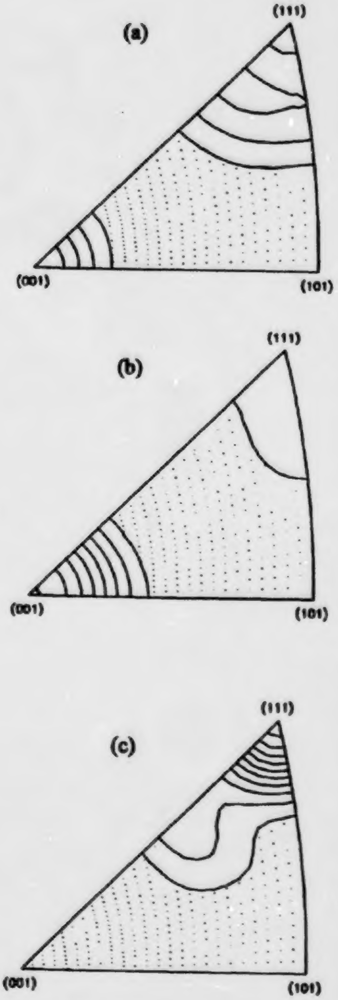

Figure 3. Inverse pole figures obtained from the texture simulations (with 30% random background). Predictions produced using only: a) slip activity, b) negative slip, and c) dislocation reactions. Contour intervals: 0.5, beginning with 1 x random.

HETEROGENEITY OF ADDITION ELEMENTS DISTRIBUTION AND TEXTURE GRADIENT IN ROLLED ZINC-COPPER-TITANIUM ALLOYS

Rolled zinc alloys texture gradient

M. DIOT, J.J. FUNDENBERGER, J. WÉGERIA, AND C. ESLING
Laboratoire d'Etude des Textures et Application aux Matériaux, Institut Supérieur de Génie Mécanique et Productique, University of Metz, France

Abstract

The rolled zinc copper titanium alloys, which are used in the building industry show an important texture gradient. This is to say that the aspect of the computed (00.2) pole figure really differs from the surface to the middle of the sheet. The modelling of the texture evolution can show that the friction is the principal parameter of this texture gradient. Moreover, the heterogeneity of addition element distribution certainly increases the texture inhomogeneity.

Keywords : texture gradient, texture evolution modelling, heterogeneity of addition element distribution

1 Introduction

The bendability of zinc-copper-titanium alloys at low temperature is an important problem for industrial applications as far as the building industry is concerned. Previous studies have shown a clear relationship between the bendability and the sharpness of the texture (Wégria 1984, Philippe et al. 1994). More recently, a texture gradient was shown (Diot 1996, Diot et al. 1998). In fact, the bendability of industrial rolled sheets depends on the surface characteristics of the materials but the various aspects of the industrial production must be taken into account : the rolling process and the real composition of the alloy (Diot et al. 1999).

On one hand, this work aims at correlating the texture gradient with the variation in the distribution of addition elements between the surface and the middle of the sheet.

On the other hand, the texture gradient in the thickness of the sheet is evaluated in order to understand the reason of its development in this kind of alloys.

2 Experimental

The studied sample, supplied by Union Minière (Viviez, France), is a zinc-copper-titanium rolled sheet dynamically recrystallized. It is a ternary zinc alloy which contains 0.165 wt % copper and 0.07 wt % titanium; the distribution of these two elements is well-known (Wégria 1984). Some low content of aluminium is added in this alloy to protect the zinc bath against oxidation. The percentage of microcracks for this sample measured at 0°C is 3.6%. The micrograph shown is obtained with a light optical microscope using the polarised light mode. The Sputtered Neutrals Mass Spectrometry (SNMS) measurements have been made in 'Laboratoire de Métallurgie Physique et de Science des Matériaux' in Nancy, France. The pole figures have been measured on a texture goniometer in the reflection range with a cobalt radiation. The computed pole figures have been obtained using the harmonic method (Bunge 1993).

3 Results

The sample microstructure shows a linear distribution of second phase grains ($TiZn_{15}$ platelets) oriented in the rolling direction. The matrix grains (zinc containing copper) have nearly homogeneous shape and size with an average diameter of 10 µm, as shown in Fig. 1. No microstructure gradient appears in the sample studied.

The SNMS measurements present two different types of profiles. The copper and titanium profiles are constant. The aluminium shows an important peak near the surface of the sheet, which decreases with the analysis depth (Fig. 2). Thus, an aluminium distribution heterogeneity occurs in the zinc copper titanium alloy.

The results of texture can be simpler described using only the maxima of the c axes of the computed (00.2) pole figure as a function of the analysis depth (from the surface to the middle of the sheet) (Fig. 3). Near the surface, only one c axes component can be seen on the (00.2) computed pole figure (Fig. 4). In the course of the in-depth analysis, a second component appears and from 200 µm down to the mid-thickness, the (00.2) pole figure is quasi-symmetric.

Fig. 1 : Microstructure of the studied sample.

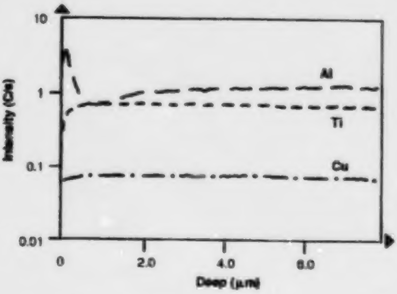

Fig. 2 : SNMS measurement of the studied sample.

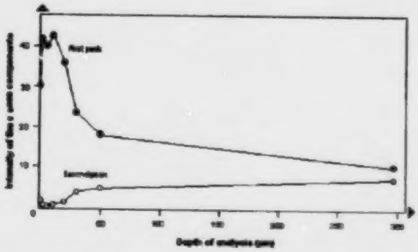

Fig. 3 : Texture gradient of the studied sample.

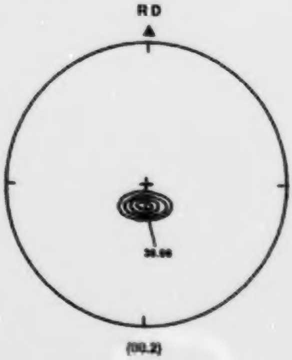

Fig. 4 : Computed (00.2) pole figure of the as-received sample.

4 Modelling of the texture evolution, taking into account asymmetrical strain tensors

The texture gradient evolution of this kind of alloy is principally due to the effect of friction on the surface during the rolling process as it was reported in an earlier paper (Diot et al. 1998).

We have used the Taylor model in the full constrained version developed by Van Houtte (1988) in view of modelling the texture.

The critical shear stresses used for these simulations were determined with results obtained in Transmission Electron Microscopy on the statistical occurrences of the gliding systems. They are defined as follows :

$$\frac{\tau_{prism}}{\tau_{basal}} = 15\,;\ \frac{\tau_{<c+a>}}{\tau_{basal}} = 10\,;\ \frac{\tau_{<a>}}{\tau_{basal}} = 30$$

We have used the same principle as in the work of Duggan and Lee (1991). Indeed, in the subsurface, there is a shear and friction effect modifying the subsurface of the sheet. The displacement gradient tensors E_i and E_o describe the strain at the entry and at the exit of the rolling mills respectively. γ_g and γ_f are the shear and the friction components respectively. They are used in accordance with these authors.

All the modelling conditions can be found in an earlier paper (Diot et al. 1998). In our case, the best result of modelling can be found for high value of γ_f. The displacement gradient tensors used are :

$$E_i = \begin{bmatrix} 0.05 & 0 & \gamma_f = 0.12 \\ 0 & 0 & 0 \\ -\gamma_g = -0.001 & 0 & -0.05 \end{bmatrix} \text{ and } E_o = \begin{bmatrix} 0.05 & 0 & -\gamma_f = -0.12 \\ 0 & 0 & 0 \\ \gamma_g = 0.001 & 0 & -0.05 \end{bmatrix}$$

10 steps 10 steps

In this case, it appears that the c axes of the simulated (00.2) pole figure are tilted to an angle whose value is close to that observed in the experimental (00.2) pole figure and also in the ND / - RD plane, in any case, independently of the γ_g value (Fig. 5).

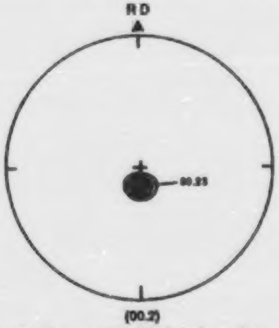

Fig. 5 : Simulated (00.2) pole figure with high value of γ_f.

5 Discussion of the results

SNMS results have shown that the aluminium distribution is heterogeneous from the surface to the middle of the alloy. This heterogeneity appeared from time the slab ended solidifying (Diot et al. 1999). This result can be clearly understood if we use Ellingham-Richardson's diagram. Indeed, the formation enthalpy curve for aluminium oxide is in all cases located below the curve for zinc oxide. Thus, the aluminium oxide is generated before zinc oxide ; this is the reason why a part of aluminium is present at the surface.

The aim of the present work is to model, as a function of γ_f, the texture evolution on the surface of an industrial rolling zinc-copper-titanium alloy which displays an evolution completely different of that measured at sheet mid-thickness as described previously (Philippe et al. 1994). The surface is characterised by a severe asymmetry in the texture components and especially in the c axes distribution. First of all, in the modelling, it is clear that the introduction of friction and shear coefficients has induced an asymmetry in the (00.2) pole figure but only in the case where the values of the coefficients are different. Fig. 6 summarises the tilt variation of the c axes as a function of γ_g and γ_f values. The continuous line describes the variation of the tilt angle as a function of γ_f, ($\gamma_g = 0.001$) whereas the dotted line describes the variation of the tilt angle as a function of γ_g ($\gamma_f = 0.001$). In the both cases, the coefficients vary from 0.03 to 0.15. For γ_f, the c axes tilt decreases from about +30° (in the ND / RD half-plane) to about -16° (in the ND / -RD half-plane) with a flat asymptotic shape. Once more, for γ_g, the c axes tilt also decreases from about +17° (in the ND / RD half-plane) to about -11° (in the ND / -RD half-plane). Thus, using a high value for the friction component, the texture presents a very strong component of the c axes in the ND / -RD half-plane in close agreement with the experimental one. These results are very interesting, because they demonstrate that the effect of the friction coefficient is more important than that of the shear coefficient. Truszkowski et al. (1980) showed that for a high value of the rolling parameter l/h the measured texture was a shear texture in the case of fcc materials. In our case, hcp material, the friction effect is predominant. This could be explained by the different multiplicities of deformation systems in both types of materials.

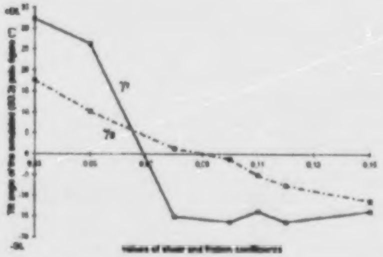

Fig. 6 : Variation of the tilt angle as a function of the shear and friction coefficients

6 Conclusion

On one hand, an heterogeneous distribution in aluminium was shown in the rolled zinc copper titanium alloy studied by the SNMS measurement.

On the other hand, a texture gradient is observed in zinc-copper-titanium cold rolled sheets. This texture gradient is probably due to the shear stress and the friction at the surface induced by the rolling process. We have shown that the introduction of different values of γ_g and γ_f lead to great asymmetries comparatively to the symmetric results obtained with an orthotropic rolling tensor (Philippe et al. 1994). The best modelling results with respect to the experimental results show that industrial rolling introduces high values of friction deformation in the sheet. This is to say that the friction effect is greater than that of the shear. It can be stated that the choice of the lubricant is very important. These results are encouraging, because we succeeded in obtaining an asymmetry in the modelled (00.2) pole figure that is very close to the experimental results.

7 Acknowledgements

The authors acknowledge the support of UNION MINIERE for this work which was carried out while one of them (J. W.) was with U. M. Research (B- Olen).

8 References

Bunge, H. J. (1993) Texture Analysis in Materials Science. (ed. Cuvillier) Göttingen.

Diot, M., (1996) Etude des modifications de composition d'alliages de zinc cuivre titane. Conséquences sur l'aptitude au formage. *Thesis*, Univ. of Metz, France.

Diot, M., Fundenberger, J.J., Philippe, M.J., Wégria, J. and Esling, C. (1998) Texture gradient in rolled zinc sheets. *Scripta Materialia*, Vol. 39, No. 11, pp.1623-1630.

Diot, M., Philippe, M.J., Wégria, J. and Esling, C. (1999) Addition elements and texture gradients in rolled zinc alloys. *Scripta Materialia (in press).*

Duggan, B. J. and Lee, C. S. (1991) A simple theory for the development of inhomogeneous rolling textures. *Metallurgical transactions A*, Vol. 22A, pp. 2637-2643.

Philippe, M.J., Wagner, F., Mellab, F. E., Esling, C. and Wégria, J. (1994) Modelling of texture evolution. *Acta Materialia*, Vol. 42, No. 1, pp. 239-250.

Truszkowski, W., Krol, J. and Major, B. (1980) Inhomogeneity of rolling texture in fcc metals. *Metallurgical Transactions A*, Vol. 11A, pp. 749-758.

Van Houtte, P. (1988) A comprehensive mathematical formulation of an extended Taylor-Bishop-Hill model featuring relaxed constraints, the Renouard-Wintenberger theory and a strain rate sensitivity model. *Textures and Microstrutures*, Vol. 8 & 9, pp. 313-350.

Wégria, J. (1984) Etude de la plasticité des alliages de zinc cuivre titane. Application à l'amélioration de leur aptitude au pliage. *Thesis*, UST Lille, France.

MICROSTRUCTURE AND MICROTEXTURE OF A COPPER SHAPED-CHARGE SLUG

A. L. PINTO and C. S. DA COSTA VIANA

Departament of Mechanical and Materials Engineering, Instituto Militar de Engenharia – IME, Rio de Janeiro, Brazil

Abstract

In this work, the microstructures of copper shaped-charge slugs were analysed with respect to grain size distribution, deformation features and recrystalization, both by optical and Scanning Electron Microscopy (SEM). Detailed Electron Backscattered Pattern (EBSP) analysis was conducted in longitudinally and transversally cut slugs. This kind of microtextural study permitted to verify the existence of orientation gradients in the fiber textures developed in both sections. Spatial distribution of orientations revealed that the microstructure has distinct zones in which the misorientation textures were studied. The presence of this orientation gradient during recrystallization is probably due to strain gradients developed during slug formation.

Keywords: shaped-charge slug, dynamic recrystallization, EBSP, microtexture.

1 Introduction

The collapse of a shaped charge metal liner is a phenomenon which still defies understanding. Since the early works (Birkhoff et al. 1948), much progress has been done such as the introduction of hydrocode simulations for studying the formation of both jet and slug (Zernow and Lowry 1992). The collapse of the liner creates a collision zone where the inner layer flows into the jet and the outer into the slug. The sudden pressurisation leads to temperatures as high as 700°C during collision, which is reduced to less than 500°C during the liner flow to form the jet and slug. The sequence of shock loading, plastic flow (high strain and strain rate) of material towards the apex and the sudden pressurisation and release of the metal flowing in and out of the collision zone produces waviness in the deformation microstructure and temperatures, resulting in radially periodic zones of dynamic recrystallisation (Murr et al. 1993). Recently

(Wright et al.), electron backscattered diffraction (EBSD) was used to obtain point-by-point measurements of the crystalographic orientation of a soft-caught fragment of an OFE copper shaped-charge jet. In that analysis, three distinct zones were described. The first zone had a clear <100> fiber texture, the second showed a mixture of the <100> and <211> fibers, and the third, a weak <100> fiber with some <111>. In the present work the microstructure and microtexture of a slug are analysed and conclusions are drawn with respect to their origin.

2 Experimental Procedures

A slug from an OFE copper shaped charge was characterized by optical and scanning electron microscopy (SEM). The crystallographic orientations of individual grains were obtained from the Kikuchi patterns of EBSD in the SEM. Automated capture and analysis of the patterns were used. The result of such an analysis is an orientation map where each point measured is indexed by its (X, Y) position in the sample and has its orientation associated to the Euler angles provided by the identification of the respective Kikuchi pattern. An "image quality" (IQ) index of the patterns, which is linked to the amount of distortion of the crystalline lattice, is also associated to each point. Several scans were performed in different regions of samples extracted from varying parts of the slug. Both transversal and longitudinal sections were observed to characterise fully the developed microstructures. Each scan had betwen 5,000 and 10,000 point-by-point measurements of the crystallographic orientation. At each measured point, the orientaion was recorded in Bunge angles together with (x,y) coordinates and the IQ parameter.

3 Results

The metallographic observation of the etched transverse and longitudinal sections of the slug revealed the existence of axisymmetric regions with different microstructures. In the center the presence of some voids could be seen. The combination of optical and SEM analyses showed that the microstructure of the slug can be morphologically divided into four different regions, with characteristic features, here referred to from the centre to the border of the slug:
-Region I - small, 4μm average equiaxed grains; faceted voids;
-Region II - grains with curved boundaries, size as above, no voids;
-Region III - larger 6 μm average grains with visible twins;
-Region IV - presence of shear bands at 35° with radial direction;

Figure 1 shows SEM micrographs from the transverse section corresponding to each of the regions mentioned above. In Figure 2a, an IQ map of the OIM scan is presented where regions I, II and III can be noted. Let us call the longitudinal axis of the slug Z, and the other two X and Y. Separated scans were performed on each of the three regions in order to confirm the distribution of orientations among the regions, as it could already be seen from the orientation color maps extracted from Figure 2. Figures 2b to 2d show IQ maps from the scans carried through at each of the three regions seen in Figure 2a. Low angle grain boundaries are marked with thin black lines, high angle

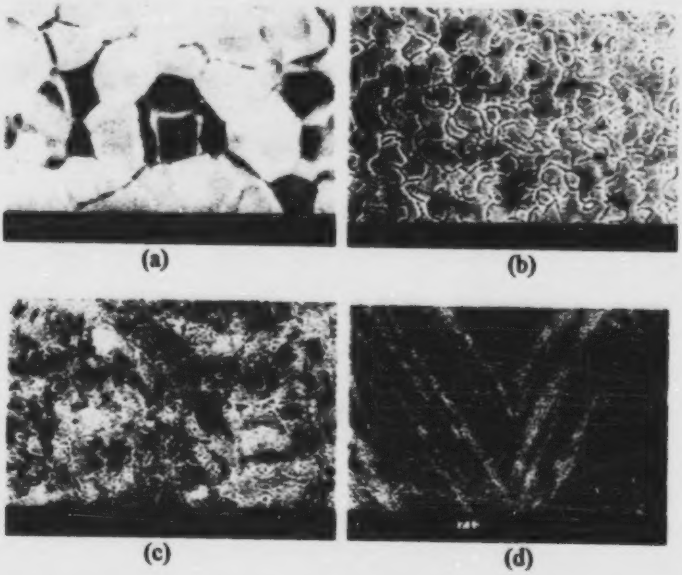

(a) (b)

(c) (d)

Figure 1: SEM micrographs from the transverse section of a slug. (a) center region (region I), (b) 100 μm towards the border (region II), (c) 300μm towards the border (region III) and (d) detail of shear bands near the border (region IV).

grain boundaries are marked with thick black lines and CSL grain boundaries (those that obey the Brandon criterion) are marked with thick white lines. It is interesting to notice the large amount of CSL boundaries (42% of all high angle grain boundaries) in region II, although the amount of twin boundaries (Σ=3) is not so large (<1%). In region III, the CSL boundaries correspond to 49% of all boundaries but twin alone corresponds to 39% of the boundaries observed.

Figure 3 presents the pole figures from each region. Region I showed a random distribution of orientations with no particular strong component. Region II showed a very strong <100> fiber texture component and in region III it is possible to see the presence of a weaker <111> fiber texture.

The distribution of the misorientation in each of the regions was also examined in order to describe local orientation relationships, thus the misorientation distribution function (MDF) was calculated for each case. Aiming at isolating features in the MDF that can be simply attributed to the overall texture, a normalization was used in order to subtract the sample texture of the MDF distribution. In this way, Figure 4 presents the texture reduced MDFs for each region. There is a clear evidence of the presence of twin boundaries in region III, 60° rotation about (111), which is not true for regions I and II.

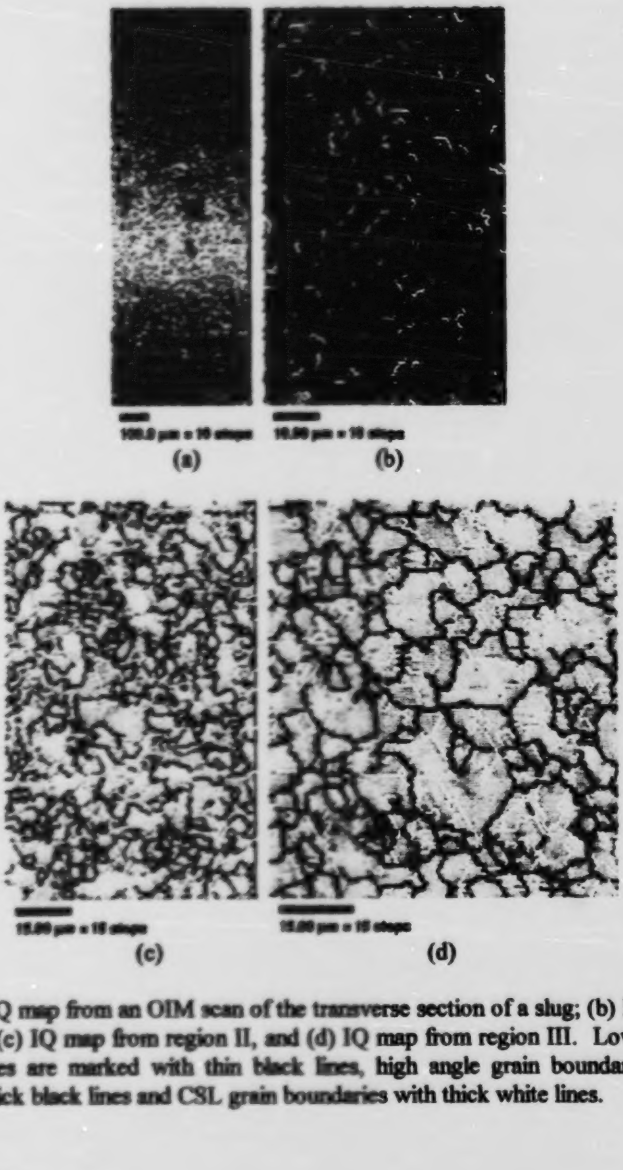

Figure 2: (a) IQ map from an OIM scan of the transverse section of a slug; (b) IQ map from region I; (c) IQ map from region II, and (d) IQ map from region III. Low angle grain boundaries are marked with thin black lines, high angle grain boundaries are marked with thick black lines and CSL grain boundaries with thick white lines.

4 Discussion

The analysis confirmed the presence of concentric regions with different microstructures, texture and misorientation. The small equiaxed grains in (region I) did not show strong texture components or particular misorientation among neighbouring regions. The faceted boundaries constitute a clear evidence of the ocurrence of recrystallization; however, time and temperature should have been small because the average grain size also remained small. Large deformation must have ocurred at this region as random nucleation seems to be responsible for the random orientation observed.

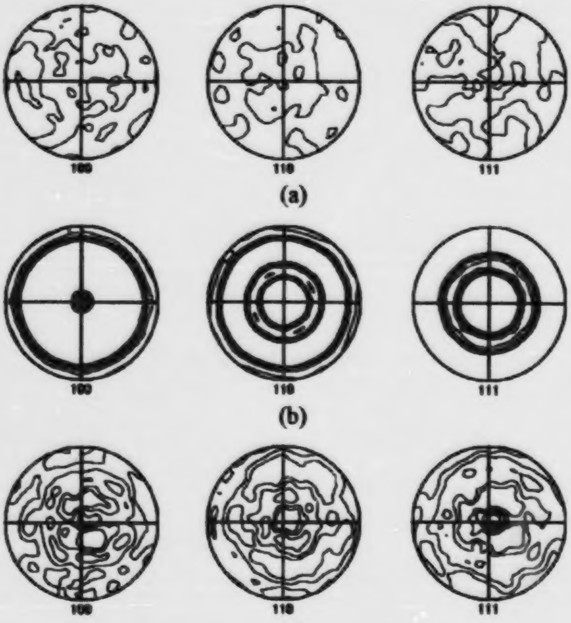

(a)

(b)

(c)

Figure 3: (100), (111) and (110) pole figures from: (a) Region I, (b) Region II and (c) Region III.

In region II, grains presented an average grain size a little larger than in region I. The texture consists of an unique strong <100> fiber component which has been associated to axisymetrically deformed CFC material recrystallized at low temperatures [Humphrey and Hattherly 1995). As grains are not equiaxed anywhere else and there are no signs of other deformation microstructures, it can be suggested that they have been plastically deformed after recrystallization. There is no apparent cause for the large amount of CSL boundaries observed.

A large amount of twin boundaries can be observed in region III, both by microstructural and MDF analyses. The shape of the grains indicate that these twins are due to deformation after recrystallisation. The combination of <111> and <100> fiber components usually corresponds to the texture of CFC round bar stocks (Kocks et al. 1998). The shear bands near the border of the slug seem to be adiabatic, linked to the combined effect of the thermal gradient between the center and the border and the deformation of the slug.

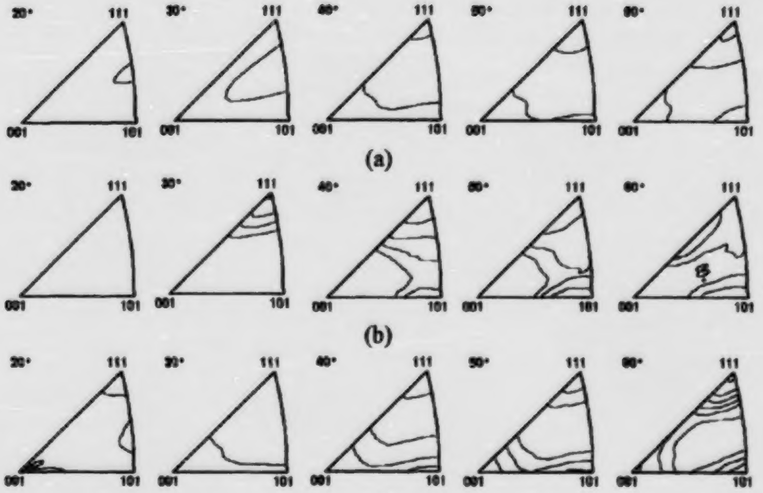

(a)

(b)

(c)

Figure 5: Texture reduced MDFs from region: (a) I, (b) II and (c) III.

5 Conclusion

In this work a slug from a shaped charge metal liner was carefully analysed with respect to its microstructure and microtexture. Four different concentric regions could be observed and information about the orientation of each of these regions was obtained. Yet, there is no clear connection between the observed microstructure and the mechanical process of formation of the slug. The abrupt changes in the texture of the recrystallised regions indicate the existence of great radial strain gradients.

6 References

Birkhoff, G., MacDougall, D. P., Pugh, E. M. and Taylor, G., Journal of Apllied Physics, 19, 563 (1948).

Humphrey, F. J. and Hattherly, M., *Recrystallization and Related Annealing Phenomena*, Ed. Pergamon, 1995.

Kocks, U. F., Tomé, C. N. and Wenk, H. R., *Texture and Anisotropy*, Ed. Cambridge University Press, Cambridge, 1988.

Murr, L. E., Shi, H. K., Niou, C-S and Zernow, L., Scripta Metallurgica et Materialia, 29, 567 (1993).

Wright, S. I., Bingert, J. F. and Zernow, L., "Microstructural development in a copper shaped-charge fragment", unpublished results.

Zernow, L. and Lowry, L., *Shock-Wave and High-Strain Rate Phenomena in Materials*, Meyers, M. A., Murr, L. E. and Staudhammer, K. P., Eds., Marcel Dekker Inc., New York, 1992, p. 521.

EFFECT OF ROLL BITE GEOMETRY ON SHEAR DEFORMATION IN FERRITIC ROLLING OF IF-STEEL SHEETS

K.K. Um[1], H.T. Jeong[2], J.K. An, and D.N. Lee
Div. of Materials Science and Eng., Seoul National University, Seoul 151-742, Korea
[1]School of Eng. & Tech., Deakin University, Geelong, Australia,
[2]Dept. of Met. Eng., McGill University, 3610 University, Montreal, QC Canada

Abstract

The effect of the roll bite geometry on the shear deformation and texture in ferrite rolling of IF steel sheets has been studied. In order to evaluate the shear deformation, the shape of wire inserted into sheet before rolling was observed after rolling and compared with the result simulated by FEM. It was found from the experimental and simulated results that the shear deformation and shear texture decreased with increasing initial sheet thickness and decreasing roll diameter.

Keywords: ferrite rolling, roll bite geometry, shear deformation, Goss texture

1. Introduction

Recently, the ferrite (or warm) rolling has been studied to reduce the production cost of steel sheets[1-3]. In the ferrite rolling, the reheating temperature of slabs is lower than the conventional rolling temperature by 200-300°C and the finish rolling is conducted in the ferrite phase region below the Ar_3 temperature. Therefore, the steel sheets are rolled in the austenite and ferrite phase regions in the same process.

The ferrite rolling has some advantages, such as decreases in the energy consumption, scale loss by oxidation, and cracks at the edges due to a decrease in the reheating temperature[4]. However, the ferrite rolling has a serious problem of lubrication due to the high rolling temperature.

For an alternative method, the processing parameters such as the rolling speed and temperature, front and back tensions, and the roll bite geometry(including roll radius, sheet initial thickness, and reduction per pass) have been studied[5-12]. In this study, we have considered the effect of roll bite geometry on the shear deformation and texture. The roll bite geometry is generally described by the l/d parameter[11], where l is the length of the contact arc projected to the horizontal plane and d is the average sheet thickness.

Hashimoto et al.[12] reported that the r-value of the cold rolled and annealed steel sheets increased with increasing l/d parameter. They increased the parameter by increasing the initial thickness and roll radius. However, Kawade et al.[13] showed that the shear deformation in the ferrite rolling decreased with decreasing l/d parameter, which could be achieved decreasing roll radius.

In order to understand the above results better, the effect of the l/d parameter in the ferrite rolling on the shear deformation and texture has been investigated by

Table 1. Chemical composition of IF steel sheets.

C	N	Mn	P	S	Al	Ti
0.0025	0.0025	0.1	0.01	0.01	0.04	0.04

varying the initial thickness as a processing variable. The deformation behavior was calculated by FEM with the isotropic material model and the texture evolution was analyzed using the Taylor model with the full constraints for a qualitative understanding of the texture evolution. The calculated results were compared with experimental data.

2. Experimental procedure

The chemical composition of IF steel sheets used is given in Table 1. For given roll radius and reduction, the initial sheet thickness is only the variable for the *l/d* parameter. Hot rolled IF steel sheets of 3.4, 12 and 30mm in initial thickness were rolled by a reduction of 50% per one pass using a mill with a roll radius of 155mm, resulting in *l/d* parameters of 2.1, 3.4 and 6.7, respectively. For a given *l/d* parameter, the rolling temperature can affect the deformation of sheets. The rolling temperature ranged from 600 to 800°C and lubrication condition was also varied.

In order to observe the deformation of sheet, the IF-steel wires were inserted in the plane normal direction of the sheets before rolling. The distorted shape of the wires was observed under an optical microscope after rolling. To eliminate possible recrystallization, the sheets were water-quenched immediately after rolling. The pole figures were measured from the surface layer to the mid-thickness(center) layer of the sheet by removing layer by layer. The depth was indicated by the parameter $s(=2r/h_o)$ which is the ratio of the depth of the measured layer(r) to the half of thickness($h_o/2$), that is, s=1.0 and 0.0 indicate the surface and mid-thickness layers, respectively.

3. Experimental results

Photo 1 shows the distorted shapes of the inserted wires in steel sheets rolled at 800°C without lubrication. The slope of wire, which is a measure of shear deformation [14], shows that the shear deformation and its penetration depth decrease with decreasing *l/d* parameter. The rolling temperature did not influence deformation of wires.

For rolling with lubrication, the deformed shapes of the wires are shown in Photo 2. The shear deformation of the sheet decreased in comparison with rolling without lubrication as expected. The slopes of the wires are almost the same regardless of the *l/d* parameter and rolling temperature.

4. Simulation

The texture evolution was analyzed using the Taylor model with the full constraints and strain history obtained by FEM. The rolls and steel sheets were assumed to be rigid and isotropic hardening, respectively. The flow behavior of IF steel sheets was described by the Hollomon relation, $\sigma=K\varepsilon^n$, with K=500.5MPa and

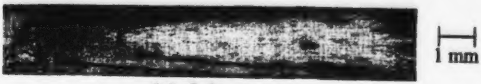

(a) 3.4mm

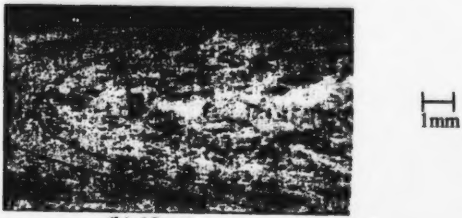

(b) 12mm

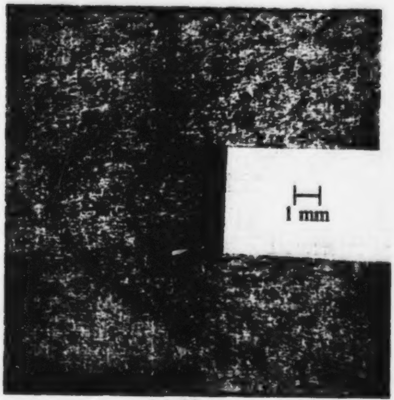

(c) 30mm

Photo 1. Distortion of inserted wire in the initial (a)3.4, (b)12 and (c)30mm IF steel sheet rolled by 50% without lubrication. (Temp.=800°C)

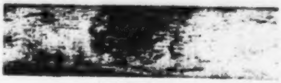

(a) 3.4mm

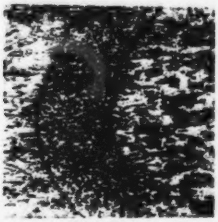

(b) 12mm

Photo 2. Distortion of inserted wire in the initial (a)3.4 and (b)12mm IF steel sheet rolled by 50% with lubrication. (Temp.=800°C)

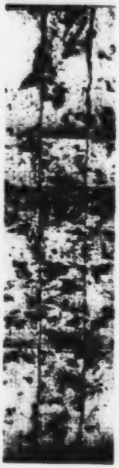

Photo. 3. Distortion of inserted wire in the initial 30mm IF steel sheet rolled by 20% with lubrication. (Temp.=800°C)

n=0.256. The Coulomb friction condition was assumed between the rolls and the sheets.

Fig.1 shows the deformed meshes for the sheets rolled by 50% as functions of *l/d* parameter at friction coefficients of 0.2 and 0.4. The inclined grids are equivalent to the inclined shape of the wires in Photos. The slope of the grids increases with increasing friction coefficient as expected and *l/d* parameter. The calculated effective strains in the surface layer of the rolled sheets are shown in Fig.2. The shear deformation increases with increasing *l/d* parameter and friction coefficient.

5. Discussion

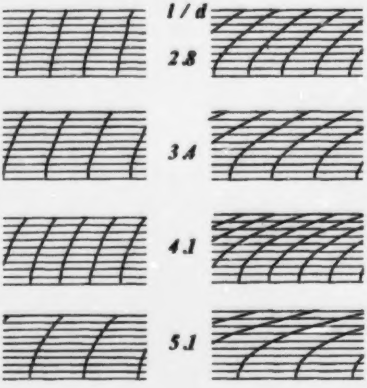

(a) (b)

Fig.1. Meshes deformed by 50% rolling at (a)μ=0.2 and (b)0.4

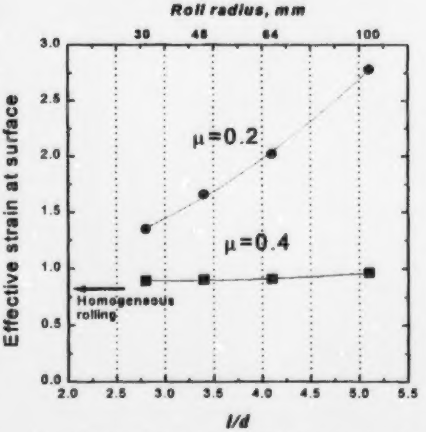

Fig.2. Calculated effective strains in surface layer of 50% rolled sheet.

5.1. Penetration of shear texture

In order to describe the penetration depth of the shear texture, a new variable of the rotated angle, θ, is defined. The typical rolling orientations of bcc metal are the {11 11 8}<4 4 11> Dillamore for the plain strain deformation and the {110}<001> Goss for the shear deformation. The both orientations are on the <110>//TD trace. Therefore, the degree of the shear deformation can be evaluated by the rotated angle,θ, from the Dillamore((11 11 8)[4 4 11],θ=0°) to the Goss((110)[001],θ=27.2°) about the [110]//TD axis.

Fig.3(a) and (b) show the rotated angles obtained from the measured and calculated (110) pole figures. The mid-thickness layers have the Dillamore orientation

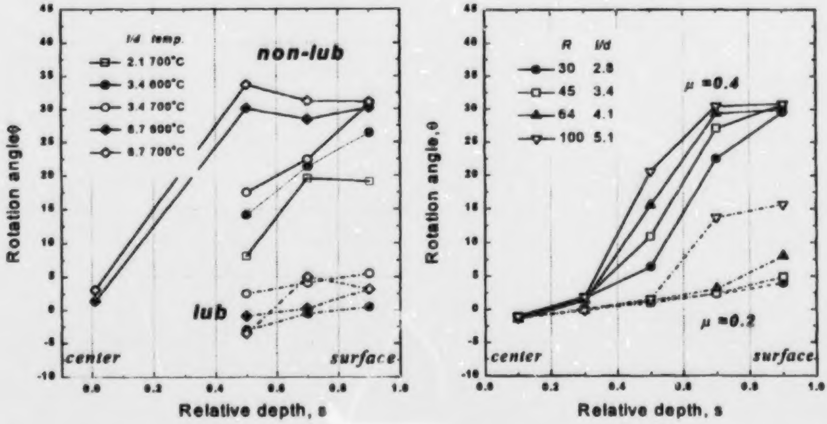

(a) (b)

Fig.3. Positions of major orientations obtained from (a) measured and (b) calculated (110) pole figures.

as expected, where the rotated angle is zero. The rotated angle increases with increasing friction and *l/d* parameter. The measured rotated angles have a trend similar to the simulation. Without lubrication, the rotated angles for the initially thick sheets are smaller than for thin ones, whereas a difference in rotated angle is negligible in the case of lubrication.

5.2. Friction coefficient

Assuming the Coulomb friction law, the minimum frictional coefficient for biting and rolling can be obtained by $\mu \geq \tan\alpha$, where α is the contact angle. This relation can be used to estimate the lower bound friction coefficient. The upper limit of the friction coefficient in the Coulomb friction law is 0.577 for the sticking friction[16]. The friction coefficient calculated for each experimental rolling condition assuming that the friction coefficient is constant regardless of the *l/d* parameter and rolling temperature are given in Table 2. When rolled for a *l/d* value of 2.1 with lubrication, the sheets were not pulled into the roll bite. Therefore, estimated friction coefficients are $0.20 < \mu_{with} < 0.32$ and $\mu_{without} > 0.32$, where μ_{with} and $\mu_{without}$ are the friction coefficients with and without lubrication, respectively.

Another method for evaluation of the friction coefficient is the comparison between the deformed shape of the inserted wires and the distorted grids in FEM. The inclination of the wires for rolling with lubrication is close to the simulation at a friction coefficient of 0.2, whereas, for rolling without lubrication, the inclination is larger than the simulation at a friction coefficient of 0.4. Therefore, the friction coefficients for with and without lubrication are about 0.25 and above 0.4, respectively.

5.3. Rolling by 20% reduction

In the industrial hot or cold rolling process, the reduction per pass is about 15-40%. Therefore, the deformation behavior when the rolling reduction is less than 50% needs to be considered. The effective strains in the surface layer of sheets rolled by 20% reduction were calculated as functions of the *l/d* parameter and friction coefficient. The calculated results are shown in Fig.4. A friction coefficient of 0.1 may be applicable to cold rolling. The effective strain decreases with decreasing friction coefficient as expected. It is interesting to note that the effective strain-*l/d* curves have minimum values. For high frictions, the smaller *l/d* parameter the better, since the *l/d* parameter of 1 is too small for real process. For low frictions as in cold rolling, an increase in the *l/d* parameter tends to increase the homogeneity of deformation. These trends are in good agreement with the reported experimental results[12,13].

Photo 3 shows the deformed shape of wire in an initially 30mm thick sheet rolled by 20% with lubrication at a *l/d* parameter of 1.12. The wire is almost parallel to the

Table 2. Calculated critical friction coefficient as a function of *l/d* parameter.

Initial thickness, mm	3.4	12	30
l/d	6.7	3.4	2.1
Friction coefficient, μ_{cr}	0.11	0.20	0.32

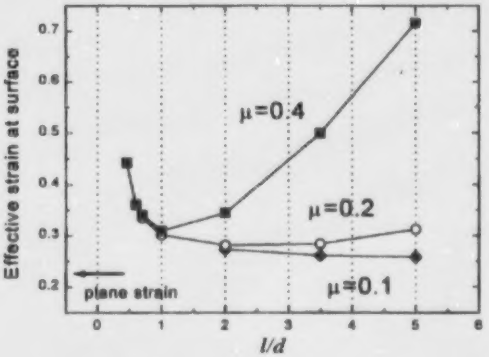

Fig.4. Calculated effective strains of surface layer of 20% rolled sheet.

sheet thickness direction even after rolling, implying that the sheet was rolled under a condition of minimum shear deformation. Since the friction coefficient is approximately 0.2 for rolling with lubrication, a *l/d* parameter of 1.12 is in the optimum region of 1-2.

6. Conclusion

The penetration depth of the shear texture increased with decreasing initial sheet thickness (increasing the *l/d* parameter). The calculated pole figures also showed that the penetration depth of the shear texture increased with increasing friction coefficient and *l/d* parameter in a good agreement with the experimental result. The calculated effective strain in the surface layer of the sheet rolled by 20% showed that a critical *l/d* value existed in which the shear strain was minimized. The critical *l/d* value increased with decreasing friction coefficient.

Acknowledgement

This study has been supported by Pohang Iron and Steel Co., Ltd.

References

1. G.H.Akabari, C.M.Sellars and J.A.Whiteman, Acta Mater., Vol.45, 1997, No.12, p.5047
2. M.R.Barnett and J.J.Jonas, ISIJ International, Vol.37, 1997, No.7, p.697
3. A. Sander, Iron and Steel Making Fev., 1995, p.21
4. W.H.Parks, C.S.Haggerty and T.R.Rock, Iron and Steel Engineer, Oct., 1997, p.35
5. S.Matsuoka, K.Sakata, S.Satoh and T.Kato, Textures and Micorstructures, 1993 Vol.22 p.113
7. Gyosung Kim and Ohjoon Kwon, Bulletin of Korea Institute of Metals and Materials Vol.6 No.1, 1993 p.33
8. S.Matsuoka, M.Morita, O.Furukimi and T.Obara, Tetsu-to-Hagane Vol.83 1997 No.2 p.127
9. W.L.Roberts, Iron and Steel Engineer, July 1974, p.56
10. T.Sakai, Y.Saito and K.Kato, Trans.ISIJ Vol.28 1988 p.1036
11. W.A.Backofen, Deformation Processing, Addison-Wesley Pub.Co.,1972
12. S.Hashimoto, T.Yakushiji and Y.Maeda, Tetsu-to-Hagane 1990 No.1 p.50
13. H.Kawade, S.Matsuoka, O.Furukimi and T.Obara, CAMP-ISIJ Vol.9 1996 p.1333
14. T.Sakai, Y.Saito, K.Hirano and K.Kato, Trans. ISIJ, Vol.28, 1988, p.1028
15. Tselikov and Grishkov, 1970 Tieoriya Prokatki, Metallurgiya, Moskva
16. W.L.Robert, Hot Rolling of Steel, Marcel Dekker, Inc. 1983

THE TEXTURE OF DRAWN HIGH-CARBON STEEL WIRE

K.K. Um[1], H.T. Jeong[2], J.K. An, and D.N. Lee
Division of Mater. Sci. and Eng., Seoul National University, Seoul 151-742, Korea
[1]School of Eng. & Tech., Deakin University, Geelong, Australia,
[2]Dept. of Met. Eng., McGill University, 3610 University, Montreal, QC Canada

Abstract

The texture variation along the radial depth of a heavily drawn high-carbon(0.73%) steel wire has been considered. The ideal <110> fiber and near <110> fiber textures were obtained in the center and surface layers, respectively, while the circular texture of {110}<110> was obtained in the sub-surface layer. This texture variation through the radius has been calculated by the crystal rotation by the Taylor-Bishop-Hill theory and the strain history obtained from FEM simulation of wire drawing. The texture calculation results showed a circular texture of {110}<114> as well as {110}<110> in the sub-surface layer. The stability of the orientation components has also been discussed.

Keywords : wire drawing, circular texture, FEM, strain history, stable orientation

1. Introduction

The high carbon (0.7-1.2 %) pearlitic steel wires are widely used for bridge cables and tire cords because of their ultra-high strength. High-carbon steel wires of 0.15-0.25 mm in diameter are fabricated by wire drawing of hot-rolled 5.5mm dia. wire rod and heat treatments called patenting.

The texture of wire drawn through the converging dies is not homogeneous. The center has a fiber texture, while the sub-surface and surface layers have a circular(or cylindrical) texture [1,2]. In BCC wires, the circular texture in the sub-surface layer is known to have the {110}<110> and {100}<110> components, which indicate that the axial direction is parallel to the <110> direction and the radial direction is parallel to the <110> and <100> directions. The texture of surface layer is known to be approximated by weak {112}<110> or <110> orientation [3]. The inhomogeneous texture in the drawn high-carbon steel wire is often thought to be responsible for delamination phenomena when the wire is subjected to torsion deformation during bunching or stranding process [3]. Heizmann [4] reported that the delamination increased with increasing intensity of the circular texture. Therefore, it is important to understand the development of the inhomogeneous texture.

The circular texture is reported to develop by the shear strain or pressure by die wall during passing through the converging die [5]. Van Houtte [6] obtained the circular texture in surface region of wire by an upper bound solution for deformation and the Taylor theory for calculation of textures. Heizmann [7] also obtained the circular texture in the surface region by adopting two velocity fields proposed by Altan and Avitzur. However, there has been no discussion on the development of the near ideal fiber texture in the surface layer and the circular texture in the sub-surface layer. The objective of this study is to measure and analyze the texture variation of drawn high carbon steel wires along the radial direction with emphasis on the difference in textures of the surface and sub-surface layers.

2. Experimental procedures

The patented and brass coated 1.4mm dia. high-carbon(0.73%) steel wire was drawn to 0.25mm in diameter through 22 dies with a die angle of 12° immersed in liquid lubricant. Thus, the total area reduction of drawing was 96.8%.

In order to measure the texture of wire or rod, it may be machined to the tube shape and flattened to make its aimed layer exposed to X-ray [8]. In the case of fine wires, however, a method proposed by Van Houtte[9] may be more convenient. In this study, the Van Houtte method was used because the wire diameter was 0.25mm. The wires were glued parallel to each other on the flat sample holder. Since the specimen has corrugated surface, its measured pole figure can have geometrical X-ray intensities. The geometrical intensities can be calculated by taking into account the X-ray path length and shadowing by neighboring wires as a function of angular coordinate. The corrected intensities, $I_{corrected}$, are calculated by the following equation.

$$I_{corrected} = I_{measured} \,/\, I_{geometric} \tag{1}$$

In order to measure the textures on different radial positions, the drawn wires were etched to smaller diameters in nitric acid solution. The relative depth is described by a parameter, s ($s = r/r_0$, where r and r_0 are the distance from the center and the radius of wire, respectively) ; s = 1.0 for the surface and s = 0.0 for the center.

3. Simulation of texture evolution

The deformation of wire during the drawing process was calculated by FEM using elasto-plastic material model and updated Lagrangian analysis [10]. In FEM calculations, the tensile behavior of the pearlitic steel was described by Hollomon's relation, $\sigma = K\varepsilon^n$, with K = 1575 MPa and n = 0.188 which were obtained by tensile test. It is difficult that FEM simulation of wire drawing using 22 dies as in the experiment. In this simulation, only five dies were used and total area reduction was set to be 84%. To obtain 84% reduction with the small number of dies, the higher die angle of 24° and the larger area reduction per pass(about 30%) were used. The Coulomb friction law between the wire and die was assumed to hold and the friction coefficient was assumed to be 0.03.

It is noted that the present simulation does not exactly follow the experimental procedures. However, this simulation is good enough to understand the texture formation of wires. The rotations of crystal orientations were calculated based on the Taylor-Bishop-Hill full constraints model. The {110}<111> and {112}<111> slip systems were assumed and active slip systems were calculated by linear programming and random choice [11,12]. Each element was assumed to have randomly distributed 978 single crystals at the initial state. For representation in form of continuous orientation distribution functions(ODFs), series expansion (l_{max} = 22) was used with each orientation being replaced by the Gauss-type scattering with a half-width of 7°.

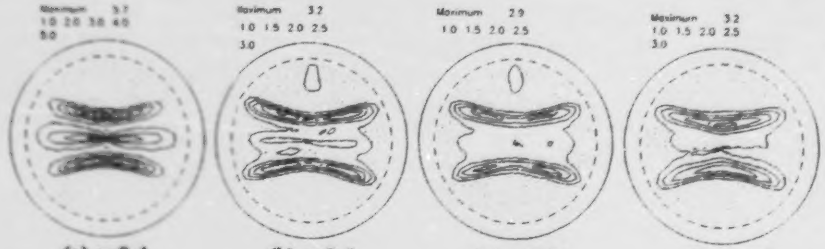

(a) s=0.4 (b) s=0.6 (c) s=0.8 (d) s=1.0

Fig.1. Measured (110) pole figures at various depth of high-carbon steel wire.

4. Results

4.1. Measured texture

Fig.1 shows the measured and geometrical effect corrected (110) pole figures of various layers of the drawn wire. It can be seen that a layer of s = 0.4 has a near fiber texture. As the s value increases or the distance from the center increases, the texture changes from a fiber to a circular one (s = 0.6 - 0.8). The circular components in the sub-surface layer can be approximated by the {110}<110> and {100}<110> orientations. However, the texture of the surface layer (s=1.0) can be approximated by a fiber texture again.

4.2. Simulation

The initial and deformed FEM meshes for a die-angle of 24° are shown in Fig.2. The deformed mesh shows that the distortion and rotation of elements increase to a maximum value and then slightly decrease with increasing distance from the center. The distributions of axial deformation rates (D_{ll}) are in agreement with the results from Eulerian analysis by Mathur and Dawson [13]. Fig.3 shows the shear deformation rates (D_{13}) in different layers. The shear deformation rate near the center (s=0.1) is negligible as expected. It is noted that the surface layer undergoes mainly negative shear deformation rate, while the sub-surface layer (s=0.5-0.7) undergoes a negative shear deformation rate followed by a positive shear deformation rate.

Fig.4 shows the effective strain and hardness as a function of distance from the center of wire. The sub-surface layer undergoes a maximum effective strain and has the maximum hardness. The effective strain distributions calculated by FEM and the hardness distribution showed a similar trend [14]. The calculated (110) pole figures are shown in Fig.5. A circular texture of {110}<110> component develops in the sub-surface layers (s = 0.5-0.7), while the ideal fiber texture develops near the center (s = 0.1), and the surface layer shows an almost ideal fiber texture.

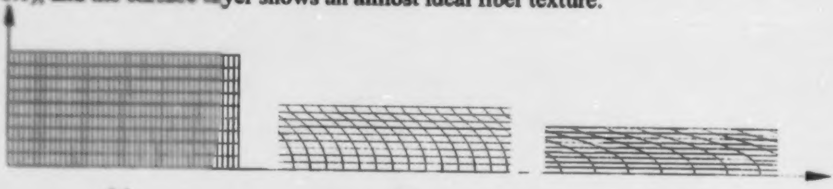

(a) (b) (c)

Fig.2. FEM meshes for (a) initial and after passing (a) 3rd die and (c) 5th die.

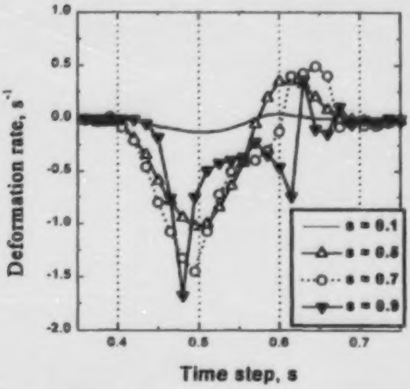

Fig.3. Shear deformation rates in various layers.

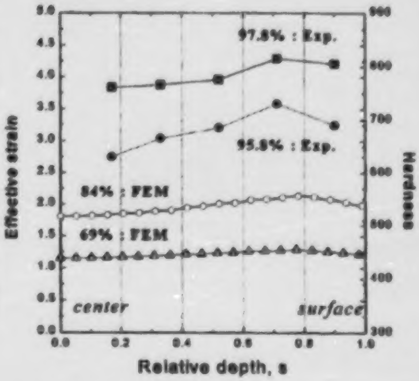

Fig.4. Measured hardness distribution and calculated effective strain.

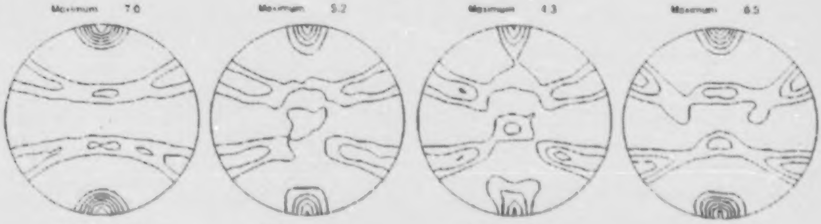

(a) s=0.1 (b) s=0.5 (c) s=0.7 (d) s=0.9

Fig.5. Calculated (110) pole figures at various depths of high-carbon steel wire.

5. Discussion

5.1. Shear strain history

In order to understand the texture variation along the radius direction, the shear strain history of each layer as shown in Fig.6 is considered. The total axial strain achieved by drawing through 3 dies was estimated to be 1.8. The surface layer was assumed to have only the negative shear strain increments, while the sub-surface layer had the negative-positive shear strain increments. For simplicity of calculation, the initial texture was assumed to be the ideal <110> fiber. The calculated pole figures of the surface layer during drawing steps are shown in Fig.7-(a). At the initial period of negative shear strain (Fig.7-(a) A), the ideal <110> fiber texture is rotated to two fibers. When the wire passes through the first die (B), the two fibers are still maintained although the gap between them decreased. The two fibers have a common orientation near {112}<110>. This behavior repeats to the third die (C).

For the sub-surface layer of Fig.7-(b), the texture at A is similar to that of the surface layer, and splits into two fibers. But, the two fibers are merged again at B by the positive shear strain. This makes the texture difference between the surface and sub-surface layers. This difference is strengthened by repetition of drawing passes (C). The final pole figures at C indicate that the near fiber texture develops in the surface, while the circular texture in the sub-surface layer.

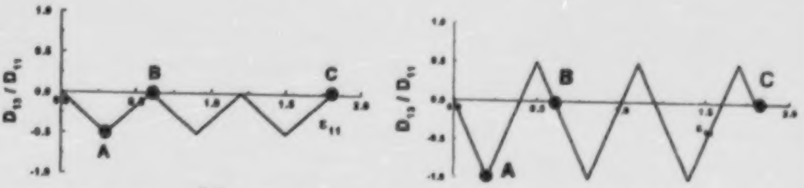

(a) (b)

Fig.6. Modeling strain histories in (a) surface and (b) sub-surface layers

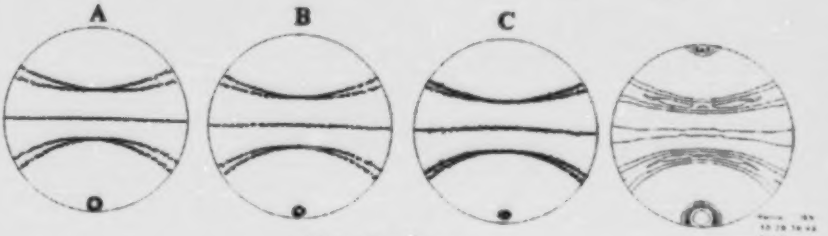

(a) surface layer

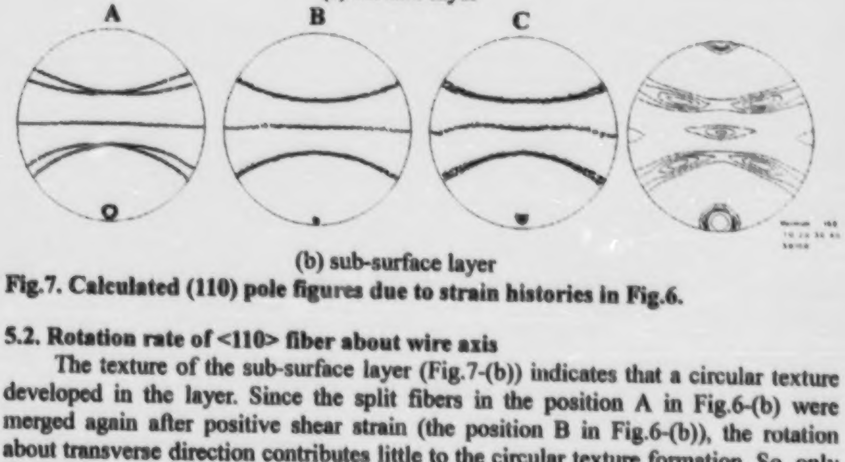

(b) sub-surface layer

Fig.7. Calculated (110) pole figures due to strain histories in Fig.6.

5.2. Rotation rate of <110> fiber about wire axis

The texture of the sub-surface layer (Fig.7-(b)) indicates that a circular texture developed in the layer. Since the split fibers in the position A in Fig.6-(b) were merged again after positive shear strain (the position B in Fig.6-(b)), the rotation about transverse direction contributes little to the circular texture formation. So, only the rotation rate of orientations on the <110> fiber about wire axis is considered. The stable orientation is defined by the condition that the rotation rate, $\delta\omega / \delta\varepsilon_{eff}$, is zero and the slope of the rotation rate-rotation angle curve is negative [15].

The calculated rotation rates of various orientations about the <110> wire axis are shown in Fig.8. Since the <110> fiber is symmetric about TD, the shear strain direction is indistinguishable. For the homogeneous drawing, $\alpha = D_{13}/D_{11} = 0$, the rotation rates about the <110> fiber axis are zero and independent of the rotation angle,θ, as expected. This means every orientation is stable during homogeneous drawing. When α is 1.0, despite the scattering of the rotation rates, the orientations near {110}<110> are stable. The {100}<110> orientation is not stable but meta-stable, because of it's positive slope

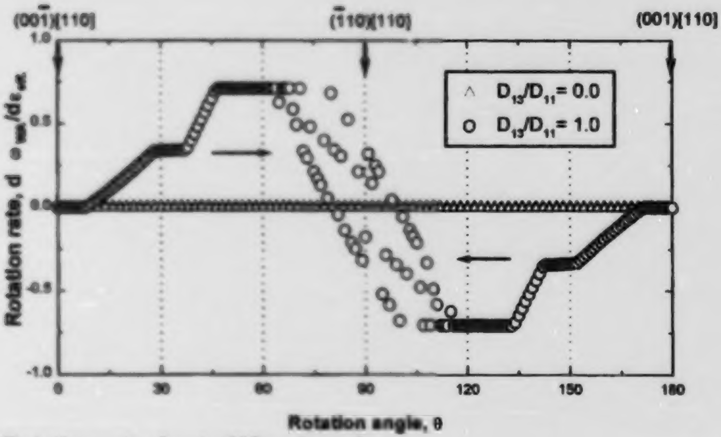

Fig.8. Rotation rate about <110> wire axis.

6. Conclusion

The measured texture of 97% drawn 0.73% carbon steel wire could be approximated by the {100}<110> and {110}<110> components in the sub-surface layer, the near fiber texture having weak {112}<110> component in the surface layer, and the ideal <110>fiber texture in the center layer. The textures simulated using the Taylor-Bishop-Hill theory for the rotation of crystal orientations and FEM method for deformation are in good agreement with the experiments. The difference between the textures of the surface and sub-surface layers is due to the difference of shear strain histories. The calculation of the rotation rate indicates that the {110}<110> orientation is stable and {100}<110> orientation is meta-stable.

References

1. S.Leber, (1961) Trans. ASM. Vol.53, pp.697-713
2. T.Montesin,(1991) Ph.D. Thesis. Universite de Metz
3. Y.Kanetsuki and R.Ogawa, Proc. ICOTOM-6, 1981, p.1127
4. J.J.Heizmann, C.Lauelle, A.Vadon, and A.Abdellaoui. Proc. ICOTOM-11, 1996, p.266
5. H.P.Stuwe, Z.Metallkde, 1961, Vol.52, p.34
6 P.Van Houtte, P.Watte, E.Aernoudt, J.Gil Sevillano, L.Lefever, and W.Van Raemdonck, Material Science Forum Vol. 157-162 (1994) pp. 1881-1886
7. J.J.Heizmann, L.S.Toth, and A.Abdellaoui, Proc. ICOTOM-11, 1996, p.274
8. D.N.Lee, Y.H.Chung, and M.C.Shin, Scripta Metal. Vol.17, pp.339-342, 1983
9. P.Van.Houtte, J.Appl.Cryst.(1989). 22, pp.533-538
10. K.J.Bathe, Finite Element Procedures in Eng. Analysis, Prentice Hall, 1982
11. J.Gil Sevillano, P.Van Houtte, and E.Aernoudt, Prog. in Mater. Sci., Vol.25, pp.69-412,1981
12. K.K.Um, Ph.D. Thesis.1998, Seoul National University
13. K.K.Mathur and P.R.Dawson, Trans.ASME. Vol.112, July, 1990 pp.292-297
14. S.H.Lim, M.S. Thesis. 1997, Pohang University of Sci. and Tech.
15. I.L.Dillamore, E.Butler and D.Green, Metal Science Journal, 2, 161, 1968

TEXTURE EVOLUTION OF ALUMINUM SINGLE CRYSTALS DURING ASYMMETRIC ROLLING

C.H. CHOI, K.H. OH*, G. GOTTSTEIN** AND D.N. LEE*

LG Cable Ltd. Microelectronic Materials T/G, Anyang-shi, Kyungki-do, Korea
*School of Materials Science and Engineering, Seoul National University
Research Institute of Advanced Materials, Seoul , Korea
** Institut für Metallkunde und Metallphysik RWTH Aachen, Germany

Abstract

The texture evolution of aluminum single crystals during asymmetric rolling was investigated using full constraint rate sensitivity analysis and pole figure measurement. The calculated end orientations were Rotated Cube and Y components. The initial orientation could determined the end orientation. The experimentally measured poled figure shows the same trend with model calculation. The formation of substructure can change the measured rotation rate due to an interaction between substructures.

Keywords: Single crystal, Asymmetric rolling, Rate sensitivity, Pole figure.

1 Introduction

Asymmetric Rolling process developed to obtain a high formability sheet of cubic metals. (Choi and Lee 1997) In asymmetric rolling, two rolls of different diameter rotate at a same angular velocity, leading to the different linear velocity of roll surface. During asymmetric rolling, the different linear velocity of roll surface gives rise to a combined deformation of shear and plane strain compression. The combined deformation usually occurred near the surface of rolled sheet during equal diameter rolling and was known to be a main reason of the inhomogeneous texture called the shear texture or the surface texture. The basic idea of the asymmetric rolling is to enhance the combined deformation mode in whole material, because the shear texture component shows the high sheet formability. One of authors, Lee extensively applied asymmetric rolling process to various materials such as aluminum, copper, steel ,etc.

The obtained texture components of asymmetrically rolled aluminum sheet were {111}<112> and {100}<110>.(Choi and Lee 1997) These two components were found to be stable component and the ratio of two components was dependent on various conditions. Oh investigated the effect of initial orientation during asymmetric rolling and showed without experimental evidences that at a given asymmetric rolling condition the initial orientation could determine the final stable component. (Oh 1997)

In this study, to see the effect of initial orientation on stable component, various orientations of aluminum single crystal were asymmetrically rolled and the pole figure was measured. The large deformation viscoplastic full constraint model was used to analyze the texture evolution of various aluminum single crystals during asymmetric rolling.

2. Viscoplastic analysis of aluminum single crystal

The shear rate of a slip system s, $\dot{\gamma}^s$, is related to the resolved shear stress, τ^s, by a power law relation, which is called the viscoplastic law. (Hutchinson 1976)

$$\tau^s = \tau_0 \operatorname{sgn}(\dot{\gamma}_s) \left|\frac{\dot{\gamma}_s}{\dot{\gamma}_0}\right|^m = \tau_0 \frac{\dot{\gamma}_s}{\dot{\gamma}_0} \left|\frac{\dot{\gamma}_s}{\dot{\gamma}_0}\right|^{m-1} \tag{1}$$

m is called the rate sensitivity. τ_0 is a reference shear stress and $\dot{\gamma}_0$ is a reference shear rate. The resolved shear stress τ^s is related to Cauchy stress tensor σ_{ij} of the crystal through the following relation.

$$\tau^s = \mathbf{R}^s_{ij}\sigma_{ij} \quad \text{and} \quad \mathbf{R}^s_{ij} = \frac{1}{2}(b^s_i\, n^s_j + b^s_j\, n^s_i) \tag{2}$$

The unit vector n^s_j is normal to the slip plane and the unit vector b^s_i is parallel to the slip direction of the slip system s. The component of the strain tensor **D** associated with the a given stress tensor σ_{ij} can be obtained as follows.

$$\mathbf{D}_{ij} = \sum_s \mathbf{R}^s_{ij}\, \dot{\gamma}_s = \frac{\dot{\gamma}_0}{\tau_0^{1/m}} \sum_s \mathbf{R}^s_{ij}\, \mathbf{R}^s_{kl}\sigma_{kl} \left| \mathbf{R}^s_{pq}\sigma_{pq} \right|^{\frac{1}{m}-1} \tag{3}$$

It should be noted that the deformation rate can be deduced from a stress potential. The stress potential can be given as follows. (Toth 1988)

$$f(\sigma_{ij}) = \frac{m}{(m+1)} \sum_s \left|\mathbf{R}^s_{ij}\sigma_{ij}\right|^{\frac{1}{m}+1} = \frac{m}{(1+m)} W(\sigma_{ij}) \quad \text{and} \quad \mathbf{D}_{ij} = \frac{\partial f(\sigma_{ij})}{\partial \sigma_{ij}} \tag{4}$$

where W is the rate of plastic work according to the prescribed deformation rate. The stress state which satisfies the above equation at the given deformation rate, can be obtained by a Newton-Raphson method. (Toth 1988; Oh 1997)

The lattice rotation rate Ω_{ij} is the rotation rate of principal interest of texture evolution. The lattice rotation rate can be obtained from the prescribed velocity gradient $\dot{L}_{ij}$ and shear rate $\dot{\gamma}_s$. The Euler angles$(\varphi_1, \Phi, \varphi_2)$ of the deformed materials should be changed according to the lattice rotation rate as follows.

$$\Omega_{ij} = L_{ij} - \sum_s m^s_{ij}\dot{\gamma}_s \quad \text{and} \quad \begin{aligned} \dot{\varphi}_1 &= (\Omega_{23} \sin \varphi_2 + \Omega_{31} \sin \varphi_2)/\sin \Phi \\ \dot{\Phi} &= \Omega_{23} \cos \varphi_2 - \Omega_{31} \sin \varphi_2 \\ \dot{\varphi}_2 &= \Omega_{12} - \dot{\varphi}_1 \cos \Phi \end{aligned} \tag{6}$$

2-3 Numerical Calculation of the Texture Evolution

The rate sensitivity of 0.05 was used in this study. The combined deformation of plane strain compression and simple shear was prescribed as given in equation (7). η is the strain rate increment during plane strain compression and was set to be 0.01 in this study. α and β are ratio of the shear component to the normal strain. The values of α and β are dependent on the process conditions during asymmetric rolling. The actual asymmetrically rolled sheets bent due to the difference of linear roll velocity. The degree of bending is partly represented by α in velocity gradient. To obtain a flat sheet, an unbending operation is required. For example, to measure the pole figure of asymmetrically rolled sheet, bent specimens were flattened and to get the flat rolled sheet, a special tooling is required at the roll exit. The flattening or special tooling include the unbending strain, which is partly represented by β of velocity gradient. The determination of α and β is quite complicated in actual asymmetric rolling. Thus, the same value of α and β as 1.5 was used in this study to simulate the asymmetric rolling. The slip system is {111}<110> slip system.

$$L_{ij} = \eta \begin{vmatrix} 1 & 0 & \alpha \\ 0 & 0 & 0 \\ \beta & 0 & -1 \end{vmatrix} \quad \text{with} \quad \alpha = \frac{L_{13}}{L_{11}} \quad \beta = \frac{L_{31}}{L_{11}} \tag{7}$$

3. Experiments

The aluminum single crystals were made from high purity aluminum by unidirectional solidification. The grown single crystal was cut to obtain the single crystals of various orientations such as {100}<001>, {111}<110>, {123},<634>. The single crystal was rolled to obtain the total 90% reduction. The incomplete (111) pole figures of the asymmetrically rolled single crystals were measured in Seifert D3000 PTS X-ray diffractometer.

4. Result and discussion

Fig 1 shows the map of stable orientation at the condition of total rolling strain 10. During asymmetric rolling, initial orientations in the hatched region and the blank region rotated toward the stable end orientation {100}<011> i.e. Rotated Cube component and {111}<112> i.e. Y component, respectively.(Oh 1996) Fig. 2 shows the rotation path during asymmetric rolling in (111) pole figure at various single crystals, which is typically found in cubic metal sheet. The stable orientation of {100}<001>, {112}<110>, is Rotated Cube component and that of {112}<111>, {110}<001>, {110}<011>, {123}<634> is Y component.

Fig 3 shows the measured (111) pole figures of the initial {100}<001> single crystal during asymmetric rolling. The calculated rotation path is given in Fig. 2-e). With increasing reduction ratio, the measured {111} pole rotated clockwise around normal direction, having near Rotated Cube component at the reduction ratio of 90%. The theoretical calculation showed that the Cube component rotated toward Rotated Cube component. The texture evolution from the measurement and theoretical calculation showed the same trend. The measured rotation rate of {111} pole was slower than that of the calculated data and the measured pole intensity decreased and broadened with increasing reduction ratio. The decrease and broadening of measured intensity is related with the substructure formation of aluminum during asymmetric rolling. As shown in Fig. 3-c), the equivalent (111) pole intensities are different with each other, which represents the asymmetrical substructure formation due to the asymmetric deformation. The substructure formation can give interfaces or subgrain boundaries, which give rise to subgrain interaction. These interaction can change the rotation rate of texture.

Fig 4 shows the measured (111) pole figures of initial {123}<634> single crystal during asymmetric rolling. The calculated rotation path is given in Fig. 2-d). As shown Fig. 4-c), with increasing reduction ratio, the {111} pole rotated clockwise around transverse direction, having near Y component at the reduction ratio of 90%. And a new component was found after 90% reduction. The decrease and broadening of pole intensity and new component formation show the substructure formation, which is similar to the {100}<001> single crystal.

Fig 5 shows the measured (111) pole figures of initial {110}<001> single crystal during asymmetric rolling. The calculated rotation path is given in Fig. 2-b). As shown Fig. 5-c), with increasing reduction ratio, the measured {111} pole of {110}<001> component showed almost no rotation to 90% reduction. The theoretical calculation shows that {110}<001> single crystal rotate around transverse direction. The decrease of pole intensity and new component evolution shows the formation of substructure during deformation.

The rotation rate of single crystal depends on the its orientation and deformation. During deformation of single crystals, the substructure can be formed and the interaction between substructure in the initial single crystal can change the rotation rate.

5. Conclusions

Full constraint model of viscoplastic material was used to analyze the asymmetric rolling of aluminum single crystals. The calculated end orientations were Rotated Cube and Y components. The initial orientation could determined the end orientation. The experimentally measured poled figure showed the same trend with model calculation, but the measured rotation rate was different from the calculated rate, which is related with substructure formation.

References

Choi C.H., Kwon J., Oh K.H. and Lee D.N. (1997) Analysis of Deformation Texture Inhomogeneity and Stability Condition of Shear Components in fcc metals *Acta Metall. 45 pp5119-5128*

Hutchinson W. (1976), Bounds and Self-consistent estimates for creep of polycrystalline Material. *Proc. R. Soc.* **A348**, pp. 101-127.

Oh K.H. (1996) Calculation of Changes in Initial Textures of FCC metals Under a Combined Load of Plane Strain Compression and Shear. *J. of the Korean Inst. of Met. & Mater.* **34** No. 9 pp1145-1151

Oh K.H. (1997) Analysis of Texture Evolution by Isotropic and Anisotropic Self-consistent models *Metals and Materials* **5**, pp17-23

Toth L.S., Gilormini P. and Jonas J.J. (1988) Effect of Rate Sensitivity on the Stability of Torsion Texture *Acta Metall.* **36**, 3077-3091

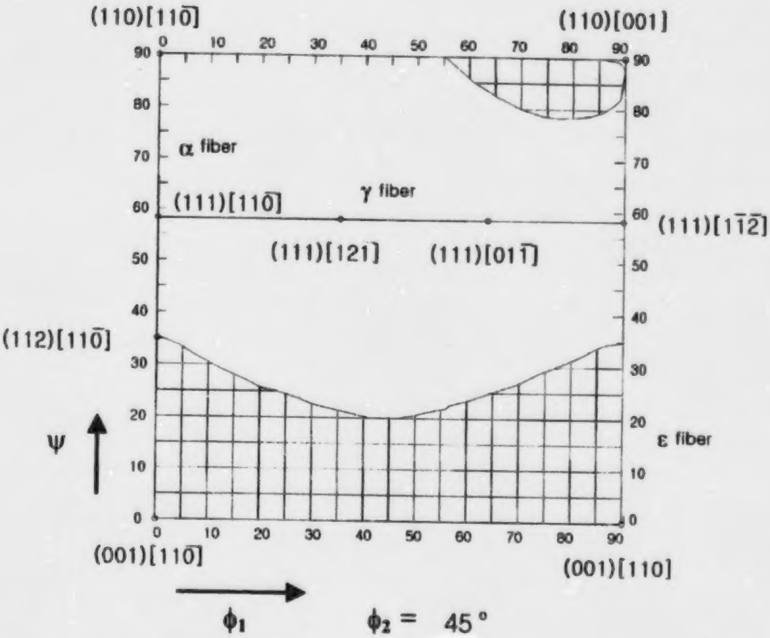

Fig 1. Map of stable orientation at rolling strain of 10. The hatched and blank regions show the final end orientations as Rotated Cube and Y components.

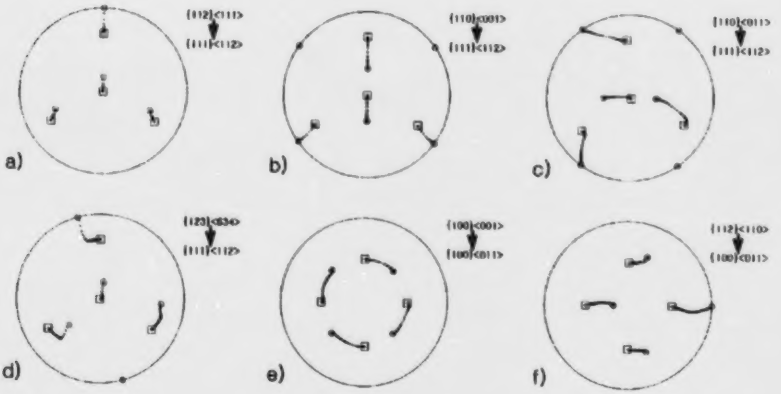

Fig. 2 Rotation Path of various single crystals, plotting in (111) pole figure.

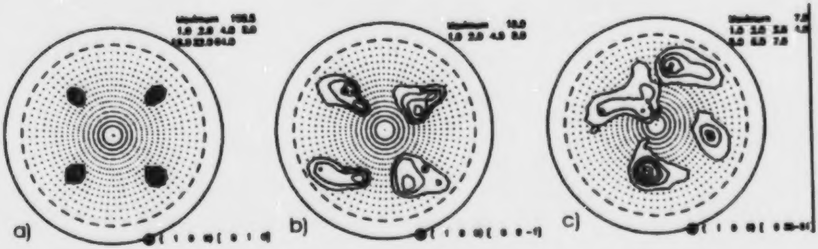

Fig. 3 Measure (111) pole figures of initial {100}<001> single crystal
a) Initial b) 60% reduction c) 90% reduction

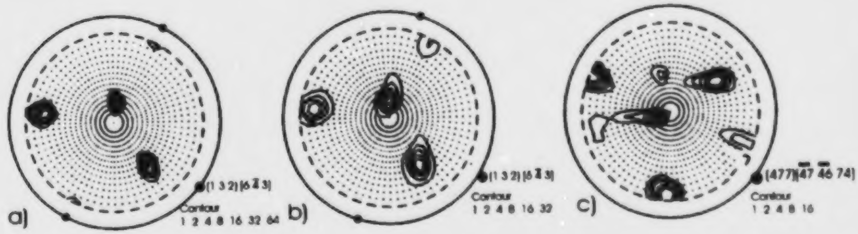

Fig. 4 Measure (111) pole figures of initial {123}<634> single crystal
a) Initial b) 60% reduction c) 90% reduction

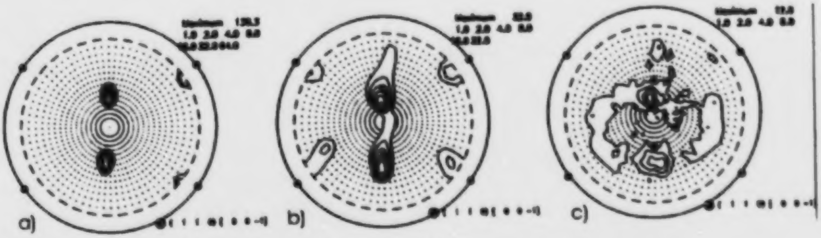

Fig. 5 Measure (111) pole figures of initial {110}<001> single crystal
a) Initial b) 60% reduction c) 80% reduction

TEXTURE AND MICROSTRUCTURE IN MECHANICALLY ALLOYED AND EXTRUDED AL-AL$_3$TI ALLOYS.

T. GROSDIDIER*+, S. LENHARD*, K. HELMING**,
C.P. CHANG*** and F. WAGNER*
* Laboratoire d'Etude des Textures et Applications aux Matériaux (LETAM)
URA CNRS 2090, University of Metz, F-57012 Metz Cedex 01, France.
* * I.M.M., T.U. Clausthal , Großer Bruch 23, D-38678 Clausthal - Zellerfeld, Germany
* * * Institute of Material Science and Engineering, Sun Yat-Sen University, Kaohsiung, 80424 Taiwan, R.O.C..
+ Now also with : Laboratoire d'Etudes et Recherche sur les Materiaux et les Propritetes des Surfaces - UTBM/ENIBe, B.P. 449, F-90010 Belfort Cedex, France

Abstract

This work characterises the influence of increasing volume fractions of Al$_3$Ti on the formation of texture in bars of Al/Al$_3$Ti mixtures obtained from mechanically alloyed powders. At low volume fraction (9%) of Al$_3$Ti, the <111> fiber texture in the matrix is concomitant with a weak and broad <210> texture of the intermetallic reinforcing phase. Increasing the volume fraction of Al$_3$Ti tends to decrease the texture intensity in both phases. A weak $<441>_{Al}$ fiber texture component is created in the MA processed alloy containing a high volume fraction of intermetallic (27%).

Keywords: Mechanical Alloying, Texture, Intermetallic reinforced alloys, Al, Al$_3$Ti

1 Introduction

Alloys strengthened by high melting point intermetallics are finding increasing interest because of improved mechanical properties. These alloys are often produced by the rapid solidification and extrusion route. Mechanical alloying (MA) can also be used before extrusion in order to additionally improve the properties by reducing further the grain size and by introducing a higher amount of finely dispersed intermetallics. These different processing routes were successfully developed on Aluminium based alloys (Jones, 1988) (Benjamin et al., 1981).

Texture has been widely studied in conventional Al alloys which usually contain 5% volume or less of second phase. Although it is well known that texture can significantly influence the properties of the materials, very limited work has concentrated on the influence of high volume fraction of intermetallics phases on the development of texture in aluminium strengthened alloys (Tsukuda et al., 1991) (Grosdidier et al., 1999). In addition, the influence of the MA step on texture has, to the authors knowledge, been studied only for the aluminium 2124 alloy + 5 % SiC particulate composites (Shamsul et al., 1998). Thus, it is the aim of this paper to investigate both the influence of the volume fraction of intermetallics compounds and the influence of the additional step of mechanical alloying on the development of texture in the as-extruded bars of fine grained Al/Al_3Ti mixtures.

2 Experimental procedure

This work was carried out on 3 aluminium alloys containing about 4, 8 and 12 wt% Ti and thus reinforced by increasing volume fractions 9, 18 and 27 vol. % of Al_3Ti intermetallics, respectively. The alloys were obtained following a mechanical alloying and subsequent hot extrusion procedure described in detail elsewhere (Cheng et al., 1996). In this paper, the extruded material will be referred to as A4, A8 and A12 as termed by Wang et al., (1999). The MA process involves the milling of mixtures of Al and Ti powders with 0.5wt% stearic acid used as a process control agent. The MA powders were degassed at 823 K, cold compacted and extruded at about 753 K to a ratio of 22:1. The resulting alloys thus contained about 1.5 vol% fine (Al_4C_3 + Al_2O_3) dispersoids and the various volume fractions of Al_3Ti intermetallics. The chemical compositions of the MA alloys and their main microstructural features are given in Table 1.

Alloy	**Ti**	**C**	**O**	**Al grain size**	**f (Al_3Ti)**	**f (Al_4C_3 + Al_2O_3)**
A4	3.98	0.42	0.07	370 nm	0.088	0.018
A8	7.84	0.39	0.07	360 nm	0.176	0.017
A12	11.70	0.39	0.07	300 nm	0.268	0.017

Table 1 : Main microstructure features of the various bars studied (from Wang et al., 1999). Chemical compositions are in weight %.

The texture of the cubic Al and tetragonal Al_3Ti phases was determined by X-rays goniometry. Because of the two phase mixture, the pole figure measurements were carried out using a position sensitive detector (PSD) which allows to better separate the peaks. The following peaks were measured : Al_3Ti (004), Al (200), Al_3Ti (200), Al (220) + Al_3Ti (006), and Al3Ti (220). Due to the axial symmetry of the deformation pass, fibre textures were observed. The texture analysis was carried out with the component method (Helming et al., 1990) using the Multex computer program (Helming, 1994). Following this method, the texture will be described by Gauss shaped components, in the orientation space, characterised by their relative weight and their half-widths. The maximum of the f(g) value for each fibre determined from the ODF will also be given for both phases.

3 Results

Table 2 shows the results of the texture analysis using the linear detector measurements and the so-called Multex component method. For each phase of each sample, the table gives the main fibers that were used to best described the texture. The weight and half width of the "Gaussian" that have been used to describe the fiber textures are also given in table 2. These two characteristics can be seen respectively as the volume fraction of crystals contained within the described fiber and their spread around the ideal orientation. Figure 1 shows the evolution of the volume fraction of the fibers in both phases with increasing volume fraction of Al_3Ti in the material.

	Al_3Ti				Aluminum matrix			
	Fiber	Half width	Weight	$f_{(g)}$	Fiber	Half width	Weight	$f_{(g)}$
A4	<210>	30.3	41	2.6	<111>	10	13.4	7.1
	iso		59		iso		86.6	
A8	<210>	34.5	36.7	2.1	<111>	12.8	3.3	1.9
					<441>	19.3	2.7	1.1
	iso		63.3		iso		94	
A12	<210>	33.6	33.5	2	<441>	18.7	5.3	1.2
	iso		66.5		iso		94.7	

Table 2 : Preferred orientations, relative weight (volume fraction), half-widths (dispersion) and f(g) max values of the texture components for the Al and Al_3Ti phases. The fraction of isotropic material for each phase is also given.

Increasing the volume fraction of hard Al3Ti globally tends to lower the texture of the Al matrix and there is also a change from a <111> fiber at low volume fractions toward <441> at high volume fractions of intermetallics. It is also interesting to note that there is a wider spread around these ideal components at higher volume fraction of particles.

The texture of condition A4 was a fiber texture with crystallographic directions parallel to the extrusion direction. It consisted of a major <111> fiber component with a maximum close to 7 times random. The presence of this component is consistent with earlier studies of extruded Al (Reed et al., 1968) or reinforced extruded aluminum alloys (Poudens et al., 1995, 1996) (Tsukuda et al., 1991). Increasing the volume fraction of Al_3Ti to 18% (sample A8) tended essentially to lower the intensity of the <111> fiber with a maximum at about 2 times random. Increasing further the Al_3Ti content (sample A12 with 27%) randomized even more the texture. It is interesting to note however that the very weak texture of the aluminum matrix has concentrated toward a new fiber close to <441>.

Although weak, texture effects were seen for the Al_3Ti phase. The analysis suggested a preferred orientation with the planes (210) perpendicular to the extrusion axis and a very large spread around this ideal position. Note that, because of the large half-width of the Gaussien necessary to describe the texture in these samples, the volume fraction of material contained in the <210> fibres is fairly high. It has to be kept in mind that this reflects in fact a fairly weak texture coming from a large volume fraction of material that is widely spread in the orientation space around the ideal <210> direction. Very similar results, in terms of weak texture with a very large spread, were obtained in extruded Al alloys reinforced with high volume fractions (>30 vol%) of coherent intermetallics obtained via atomization and extrusion route (Grosdidier et al., 1999). It is also interesting to note here that increasing the volume fraction of Al_3Ti phase tends to lower the texture of the Al_3Ti phase.

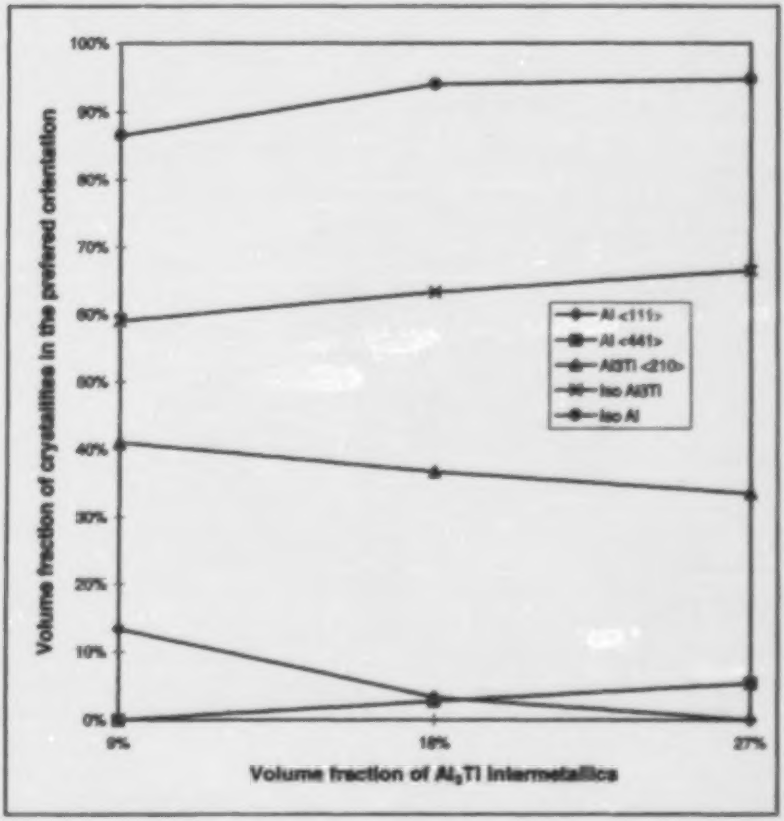

Figure 2 : Evolution of the various fiber intensities for the Al and Al_3Ti phases with increasing the volume fraction of Al3Ti intermetallic.

4 Discussion

Numerous studies on particle reinforced alloys have shown that increasing the volume fractions of hard phases can randomize the matrix texture in cold and warm deformed materials because of the increasing amount of highly rotated deformation zones at the particles (Humphreys and Kalu, 1990) (Bowen et al.,

1991) (Poudens et al., 1995) (Humphreys and Hatherly, 1995). More recently, it was shown in Al-based alloys obtained via atomization and extrusion that the intermetallic reinforcing phase could also be slightly textured. This texture effect was concomitant with the presence of a <111> fiber component of the aluminum matrix. On the contrary, when no noticeable texture effect was seen in the Al matrix, the reinforcing intermetallic phase was also randomly oriented (Grosdidier et al., 1999). This was interpreted by considering that some coherent precipitates within the matrix grains had rotated to follow the matrix grain motion.

At low volume fractions of intermetallics, the results of the texture analysis in MA Al/Al_3Ti reported here are globally consistent with the above description. First, increasing the volume fraction of Al_3Ti phase randomizes the texture of the matrix. Second, the <111> texture in the matrix (sample A4 - 9% Al_3Ti) is concomitant with a weak and broad <210> texture of the intermetallic reinforcing phase. Third, the intermetallic texture decreases, together with the matrix texture, as the volume fraction of intermetallic increases. This suggest that the deformation behaviour of these MA processed materials is very similar to conventional dispersion hardened aluminium alloys at low and moderate volume fraction of intermetallics. This is also consistent with a recent study on MA and conventional powder metallurgy processed Al-extrusions reinforced by 5% SiC where no significant differences in texture was observed (Shamsul et al., 1998). For the higher volume fractions of intermetallics, however, a new texture component arises in the Al matrix whereas the intermetallic phase keeps a very similar, but weaker, distribution of orientation. As suggested by TEM observations, it is unlikely that this change is associated to any type of recrystallisation process which, in addition, are also known to be inhibited by sufficient volume fraction of fine and closely spaced particles. Large scale deformation heterogeneities and large deformation zones at particles are also unlikely to be promoted during hot deformation of sub-micron sized particles containing aluminium alloys (Habiby and Humphreys, 1993) (Humphreys and Hatherly, 1995). It is thus possible that these texture effects reflect more the fine grain nature of these high volume intermetallic MA processed materials. Clearly, further work is needed to improve the understanding of the deformation during consolidation of high volume fraction particles containing MA powders to fully explain these results.

5. Conclusions

The aim of this work was to characterise the influence of increasing volume fraction of Al_3Ti on the formation of texture in bars of Al/Al_3Ti mixtures obtained from mechanically alloyed powders. At low volume fraction of Al_3Ti particles, the results in the MA processed bars are very similar to what is usually obtained in conventionally processed Al reinforced alloys. The matrix has a <111> fiber texture which is concomitant with a weak and broad texture of the intermetallic reinforcing phase. Increasing the volume fraction of Al_3Ti lowers the texture of the matrix and intermetallic phases. A weak <441> fiber texture component arises in the Al matrix of the MA bars containing high volume fractions of intermetallics.

Acknowledgement : The authors wish to thank Dr. J.J. Fundenberger for his fruitful help with some texture computing and calculation.

6 References

Benjamin J.S. and Schelleng R.D.(1981), *Met. Trans. A*, vol. 12A, p. 1827.

Bowen W., Ardakani M. and Humphreys F.J., (1991), 12th Int. RISO Symp., *Metal matrix composites processing*, Roskilde, DK, pp 241 - 246.

Cheng Y.C., Wang S.H., Kao P.W. and Chang C.P. (1996), *Mat. Sci. Forum*, 217 - 222, pp 1891 - 1896.

Grosdidier T., Keramidas P., Fundenberger J.J., Wagner F. and P. Tsakiropoulos (1999), *Mat. Sci. and Eng. A*, Vol. 267/1, p. 71-81.

Helming K. (1994), *Mat. Sci. Forum*, 157 - 162, pp 363 - 368.

Helming K. and Eschner T. (1990), *Cryst. Res. Technol.*, 25, K203.

Habiby F.and Humphreys F.J. (1993), *Texture and Microstructure*, 20, p. 125.

Humphreys F.J. and Kalu P.N. (1990), *Acta Metal.*, 38, p. 917.

Humphreys F.J. and Hatherly M. (1995), *"Recrystallization and related Annealing Phenomena"*, Pergamon Press, Elsevier Science Ltd, Oxford, UK.

Jones H. (1988) in Y.-M. Kim and W. M. Griffith (eds), *Dispersion Strengthened Aluminium Alloys*, TMS-AIME, Warrendale, PA, pp 57 - 76.

Poudens A., Bacroix B. and Bretheau T. (1995), *Mater. Sci. Eng.*, A196, p. 219.

Poudens A. and Bacroix B. (1996), *Scripta. Mater.*, 34, p. 847.

Reed R.E. and McHargue C.J., (1968), *Trans. Met. Soc.* AIME, 242, p. 180.

Shamsul J.B., Hammond C., Cochrane R.F. and Shakesheff (1998), *Material Science and Technology*., 14, p. 949.

Tsukuda I., Nagai S., Fukui K., and Ihakakus N. (1991), *Texture and Microstructure*., 14-18, p. 219.

Wang S.H., Kao P.W. and Chang C.P. (1999), *Scripta. Mater.*, 40, pp. 289-295.

Author Index

Acharya, A., 547
Adams, B.L., 9, 21, 192, 724, 1248, 1649
Agnew, S.R., 575
Aindow, M., 1619
Algueró, M., 1327
An, J.K., 779, 785
Anisimova, L.I., 689
Ansart, F., 1345
Artymowicz, D., 1031
Asami, T., 405
Aus, M.J., 560
Baccino, R., 683
Bacroix, B., 328, 499
Baczynski, G.J., 635, 1230, 1236, 1242
Baghdouche, F., 611
Baik, S.C., 1043
Barlat, F., 569
Barnett, M., 910
Bartozzi, M., 1593
Bate, P.S., 34, 617, 1619
Baudin, T., 922, 973, 1278, 1696
Bauer, C.L., 4
Bay, B., 174, 1154
Beaudoin, A.J., 435, 547
Beaugnon, E., 457
Bechade, J.L., 499, 922
Becker, R.C., 1112
Bennett, K., 129
Bergstrom, D.B., 1375
Bertinetti, M.A., 334
Bertram, A., 273, 535
Besse, F., 1315
Bhattacharya, B., 824
Bieler, T.R., 529
Bingert, J., 358
Blanford, P., 487
Blanton, W., 1460
Böhlke, T., 535
Bolle, B., 98, 1025, 1315, 1631
Bollen, J., 1293
Bolmaro, R.E., 211, 316, 334, 358, 375
Bonarski, J., 1278
Bouche, G., 922
Boulanger, C., 1315
Bouzy, E., 223, 229, 1184
Bowman, K.J., 1453, 1460
Boyce, D., 505
Boyle, A., 1593
Brehm, J., 1460
Brem, J.C., 569
Brenner, R., 499
Brokmeier, H.-G., 86, 211, 334, 375, 523, 541, 1172, 1482
Brückner, G., 174, 629
Bunge, H.J., 1172
Bunsch, A., 599
Bussière, J.F., 493
Cabot, C., 1488
Calzada, M.L., 1327
Cannon, W.R., 1476
Cao, Y., 928, 1445
Cardiola, B., 1184
Carter, W.C., 1509
Casasent, D., 4
Chandra, T., 1003
Chang, S.K., 866, 1208
Chang, C.P., 694, 797
Chateigner, D., 457, 1327, 1495, 1562
Chaud, X., 457
Chen, N., 511
Cheng, X-M., 481
Cho, J., 1043
Cho, J.-H., 587, 700, 1339
Cho, J.Y, 1254
Choi, C-H., 755, 791
Choi, G.S., 1208
Choi, Jang Hyun, 1214
Choi, Jeong Ho, 298,1214
Choi, S.-H., 569, 587
Christen, D.K., 1466
Chruściel, K., 599, 1071
Cichocki, F.R., 1460
Clarke, A.P., 1260
Clausen, B., 399
Clevenger, L.A., 1287
Collins, L.E., 1230
Cooley, J., 135
Cosandey, F., 1476
Court, S., 617
Crimp, M.A., 529
Cross, I.J., 1202
Crumbach, M., 817
Czerwinski, F., 560, 1351, 1391, 1397, 1403, 1445
Czubayko, U., 1684
Da Costa Viana, C.S., 322, 671, 773

Dahoun, A., 1488
Daniel, S.R., 1202
Davies, H., 1196
Davies, P., 1196
Davis, G.R., 1106
Dawson, P.R., 3, 435, 505, 1655
Day, A.P., 217, 1593
de Boer, B., 944, 1077
De Angelis, R.J., 659
De Blauwe, K., 1293
De Broeck, A., 1293
De Graef, M., 192
Delannay, L., 340, 623, 811, 910
Diot, M., 767
Donovan, J.J., 235
Dubois, M., 493, 997
Duchene, L., 286
Duggan, B.J., 706, 805
Dunne, D.P., 991
Dzjuba, A.A., 241
Eickemeyer, J., 944
El Ghazouli, K., 98
El-Dasher, B.S., 9, 1248
Elliott, J.C., 1106
Embury, J.D., 934
Engler, O., 68, 393, 842, 1124
Erb, U., 560, 961
Esling, C., 229, 767, 997, 1184
Ferry, M., 991, 1003
Field, D.P., 1309, 1357, 1369
Fischer, A.H., 204
Flemming, G., 1184
Foct, J., 817
Fourty, A., 316, 334, 358, 375
Fragomeni, J.M., 901
Freenstra, R., 1466
Frischbutter, A., 1540, 1605
Fukushima, A., 653
Fukutomi, H., 1190
Fundenberger, J.J., 153, 223, 229, 769
G'Sell, C., 1488
Gaignard, S., 997
Gautier-Picard, P., 457
Gavard, L., 878
Gehrmann, R., 665
Gertsman, V.Y., 1678
Gervasyeva, I.V., 689, 742, 890
Gey, N., 147
Gharghouri, M.A., 677
Gignac, L.M., 1287
Glass, S.J., 1489, 1509
Glavicic, M.G., 110, 1303, 1409
Godinas, A., 286
Goryachev, S.B., 463
Gottstein, G., 292, 665, 791, 817
Goyal, A., 1466
Greene, J.E., 1375
Grenet, J., 1488
Gritsuk, A.R., 463
Grosdidier, T., 683, 694, 797, 895
Gryziecki, J., 581
Gubernatorov, V.V., 742, 890
Ha, C.S., 1433
Haase, J.D., 123
Habraken, A.M., 286
Hall, P.W., 1501
Halliday, D., 1593
Han, K.S., 866, 1059, 1208
Harasse, J., 1009
Harding, J.H., 1385
Hariz, T., 310
Harris, D.J., 1385
Hayakawa, Y, 1101
Hedegaard, C., 1495
Heidelbach, F., 1574
Heizmann, J.J., 98, 141, 1025, 1315, 1631
Helming, K., 797
Hensger, K.E., 1184
Higginson, R.L., 1130
Hippertt, J., 1515
Hoferlin, E., 249
Holzapfel, B., 944, 1321
Hong, B.D., 866
Hong, S.C., 956, 1299, 1381
Hong, S-H., 950
Houbaert, Y., 811, 910
House, J.W., 659
Hu, J., 135
Huang, H., 1613
Huang, M., 481
Huang, W.H., 694
Huang, X., 1613
Huh, M.Y., 1124
Hühne, R., 1321
Hukushima, A., 653
Humbert, M., 147, 1184
Humphreys, F.J., 74, 617
Hurd, J.L., 1287

Hutchinson, W.B., 34, 1031
Iggulden, R.C., 1287
Inagaki, H., 848, 860, 1142
Inakazu, N., 168, 1160
Inoue, H., 168, 445, 884, 1160
Ishio, M., 445
Ito, K., 653
Ivankina, T.I., 1587
Jansen, E.M., 523, 1482
Jasieński, Z., 581
Jean-Prost, F., 346
Jensen, D.J., 46, 174, 605, 854, 1154
Jeong, H.T., 267, 304, 779, 785, 1254, 1369, 1427
Ji, S., 1568
Jiao, SH.H., 1266
Jin, H., 135, 1136
Johnson, G.C., 235
Jolly, L., 98, 141
Jonas, J.J., 635, 761, 910, 1049, 1089, 1230, 1236, 1242
Julliard, F., 973
Jung, V., 523
Jura, J., 68, 1278
Kadilak, J., 718
Kainer, K.U., 1482
Kaneno, Y., 1160
Kang, S.Y., 298
Kao, P.W., 694
Karato, S., 1546
Kato, H., 884
Katoh, H., 405
Keichel, J., 817
Kern, H.M., 1580
Kestens, L., 736, 811, 910
Kikuchi, S., 1190
Kim, B.I., 736, 830, 1433
Kim, B.-K., 1427
Kim, C.S., 1059
Kim, I., 956, 1299, 1381
Kim, J., 1009
Kim, J.K., 1059
Kim, K-H., 755
Kim, K.-Y., 1095
Kim, K.R., 469
Kim, S.M., 469
Kim, S.S., 1433
Kim, Y.H., 830
Kim, Y.H., 1124
Kinderlehrer, D., 9, 1643
King, W.E., 180
Klima, K., 1587
Klinkenberg, C., 475
Knutsen, R.D., 617
Kobayashi, M., 884
Kocks, U.F., 431, 934
Kogen, V.A., 241
Koh, Y.H., 1214
Kohara, S., 848, 1166
Koizumi, M., 848, 860
Kopacz, I., 417
Korzekwa, D.A., 346
Kosack, K., 80
Kovar, D., 1501
Krasilnikov, N.A., 748
Kraska, M., 273
Krause, H., 1015
Krieger Lassen, N.C., 174, 854
Kroeger, D.M., 1466
Kubota, T., 981
Kumar, M., 180
Kurosawa, M., 1101
Kusnierz, J., 517
Kwon, O., 1043
Lagoeiro, L., 1528
Langelaan, G., 135
Lauridsen, E.M., 174
Lebensohn, R., 316, 451, 1534
Leblond, C., 457
Lecomte, J.S., 223, 229, 712
Lecuire, J.M., 1315
Lee, C.S., 1083
Lee, D.F., 1466
Lee, D.N., 267, 298, 304, 755, 779, 785, 791, 950
Lee, K.-H., 1546
Lee, K.T., 1369, 1415
Lee, P.S., 21, 724
Lee, Y.D., 1095
Leffers, T., 261, 399
Lenhard, S., 683, 797
Lévesque, D., 493
Li, H., 1303, 1391, 1667
Li, J., 1136
Li, Z., 1037
Liao, G., 1148
Lieckefett, R., 1605
Lillywhite, S.J., 1619
Lin, J., 1439
Lin, Y.P., 1409

Lindh, E., 34
List, F.A., 1466
Litwora, A., 581
Liu, G.L., 706, 805
Liu, Y., 481, 1025, 1148
Liu, Y.L., 1148
Livshits, I., 9, 1643
Lloyd, D.J., 718
Lojkowski, W., 1625
Lokajicek, T., 1587
Lopes, A.M., 322, 671
Lord, M., 493
Lu, J., 1673
Lücke, K., 842
Lutterotti, L., 116, 1599
Luzin, V., 241
Lychagina, T., 541, 241
Lyttle, M.T., 46, 605
MacDonald, W.D., 1260
MacEwen, S., 505
Madsen, L.D., 1375
Mainwaring, P., 1476
Man, C-S., 481
Manceau, A., 1562
Manolache, F., 9
Mao, W., 92, 511, 629, 872, 938
Mason, D., 9
Mason, D.E., 1637, 1643
Masui, H., 279, 381, 405
Mathon, M.H., 922
Matthies, S., 40, 68, 439, 1599
McGreevy, R., 553, 1631
McQueen, H.J., 836, 878
Mecking, H. 437
Mege, S., 1345
Mehnert, K., 217
Mendiola, J., 1327
Mi, X.C., 1266
Michaluk, C.A., 1357
Mika, D., 1655
Miller, M.P., 1272
Miroux, A. 328
Mishin, O.V., 174, 1154, 1613
Monchalin, J.-P., 493
Monot, I, 457
Montheillet, F., 878
Moon, R., 1460
Morano, R., 123, 1106
Morawiec, A., 9, 62, 198
Moreau, A., 493
Morii, K., 445
Morris, J.G., 481, 1148
Muljono, D., 991
Mullins, W.W., 9
Murakami, K., 981
Nakamura, M., 1190
Necker, C.T., 346, 358
Nikitin, A.N., 1587
Nikolayev, D.I., 156, 241
Novikov, V.Y., 967
Oertel, C.-G., 730, 1321
Oh, K.H., 411, 569, 587, 700, 791, 1043, 1065, 1339
Oh, M.H., 469
Okudaira, H., 860
Opitz, R., 944
Ozdemir, S., 9
Paden, D., 1593
Padioleau, C., 493
Parathaman, M., 1466
Pardo, L., 1327
Paredes, J.C., 671
Park, C.-G., 1095
Park, H., 1421
Park, J.Y., 1065
Park, N.J., 469, 950, 1214
Park, S.-H., 1095
Park, S.-J., 587, 700
Park, Y.B., 736, 830, 1433
Peng, R.L., 553, 1631
Pennelle, R., 973, 1278, 1696
Pernet, M., 1562
Petrov, I., 1375
Philippe, M.J., 1488
Piątkowski, A., 581
Pinto, A.L., 671, 773
Pithan, C., 842
Pochettino, A.A., 451, 593
Pospiech, J., 581, 647, 1278
Poulsen, H.F., 174
Priesmeyer, H.-G., 334, 439
Prior, D.J., 1593
Pros, Z., 1587
Protasova, S., 1625
Provenzano, V., 748
Quaeyhaegens, C. 1333
Quesne, C., 1278
Ra, H.Y., 1065

Raabe, D., 1015, 1112
Radhadkrishnan, B., 352
Raj, P.M., 1476
Rajmohan, N., 255, 961, 1118, 1178
Randle, V., 1196, 1202
Ratchev, P., 1224
Ratuszek, W., 599, 1071
Rauch, E., 517
Ray, R.K., 641, 824, 916
Reger, N., 944
Ren, H., 938
Renaud, E., 560
Revol, S., 683
Rickerby, D.G., 748
Ricote, J., 457, 1327
Ripault, R., 1327
Roatta, A., 358
Rodbell, K.P., 1287
Rogan, H., 9
Rogge, R., 505
Rohrer, G.S., 9, 1489, 1509, 1637, 1690
Rollett, A.D., 9, 21, 724, 1015, 1649
Root, J., 677, 761, 1089
Rostek, T., 647
Rousset, A., 1345
Ryde, L., 1031
Ryś, J., 1071
Saerens, A., 1333
Saimoto, S., 135, 1136, 1260
Saito, Y., 1142
Saitou, T., 848
Sakai, T., 1142
Sanchez, P., 451, 593
Sarma, G.B., 352
Savariault, J.M., 1345
Saylor, D.M., 9, 198, 1489, 1509, 1637, 1690
Schaeben, H., 153, 156
Schaeben, S., 1363
Scheffzük, Ch., 1540, 1556, 1605
Schlegel, M., 1562
Schmitz, H.-P., 475
Schnabel, R.F., 1287
Schnieber, R., 523, 1172
Schraven, P., 817
Schultz, L., 944, 1077, 1321
Schwartz, A.J., 180
Schwarzer, R.A., 52, 204
Sebald, R., 292
Seki, F., 1136
Sekine, K., 423
Shi, J., 1037
Shimizu, R., 1009
Shin, C.S., 1339
Shin, C.-S., 1375
Shmayda, W., 928
Siemes, H., 153
Signorelli, J.A., 316, 334, 375
Simkin, B.A., 529
Skrotzki, W., 730, 1321
Smathers, D.B., 1357
Snegirev, M.G., 463
Sokolov, B.K., 689, 742, 890
Sokolova, T.A., 689
Solas, D.E., 369
Soubeyroux, J.-L., 457
Specht, E.D., 1466
Stepanova, I.N., 742
Stock, S.R., 123, 1106
Stüwe, H.P., 417
Sum, M., 761
Sumas, S., 641
Sun, Z., 938
Sursaeva, V., 1625
Sursaeva, V.G., 1684
Suter, R.M., 80
Sutliff, J., 1272
Suwas, S., 641, 916
Suzuki, T., 1190
Svedberg, E.B., 1375
Szpunar, B., 560
Szpunar, J.A., 6, 110, 255, 487, 560, 928, 961, 1118, 1178, 1254, 1303, 1351, 1369, 1391, 1397, 1403, 1409, 1415, 1421, 1427, 1439, 1445, 1667, 1673, 1678
Sztwiertnia, K., 647
Ta'asan, S., 9, 1643
Takamiya, T., 1101
Takashima, M., 1649
Takayama, Y., 884
Takeshita, T., 1522, 1534
Talukder, A, 9
Tamler, H., 475
Tamm, R., 730
Tang, D., 938
Tarasiuk, J., 328
Te Nijenhuis, J., 241
Teicher, A., 1015
Teraoka, S., 1236, 1242

Tidu, A., 141, 694, 1025
Timmermans, W., 1293
Titorov, D.B., 1661
Toker, E., 235
Tomé, C.N., 346, 369, 433, 677
Tóth, L.S., 310, 417
Tozawa, T., 884
Trumble, K.P., 1460
Tse, Y.Y., 805
Tsukamoto, O, 405
Tuflin, A.U., 1684
Turner, T.J., 1272
Tye, M., 1593
Ubhi, H.S., 217
Ueno, M., 1190
Ukaji, H., 405
Ullemeyer, K., 1587
Um, K.K., 267, 779, 785
Umeda, M., 445
Ushigami, Y., 981
Vadon, A., 611, 1631
Valiev, R.Z., 748
Valot, C., 98
van den Boogaart, K.G., 29, 162, 1363
van der Winden, M.R., 1224
Van den Broeck, Y., 1224
Van Bael, A., 249, 340, 811
Van Houtte, P., 249, 340, 623, 811, 910, 1224, 1333
Vatne, H.E., 393
Vaudin, M.D., 186
Vedula, V.R., 1489, 1509
Verlinden, B., 1224
Vladimirov, L.R., 689, 742, 890
Von Dreele, R.B., 129
Wagner, F., 40, 683, 694, 797, 895
Walther, K., 1540, 1605
Wan, S., 1453
Wang, X., 1037
Wang, Y.D., 553, 1631
Wang, Y.-Y., 1287
Wang, Z-C., 1568
Watt, T., 123
Weber, S., 1287
Wégria, J., 767, 997
Wells, M.A., 718
Wenk, H.-R., 3, 129, 235, 364, 1495, 1534, 1599
Wierzbanowski, K., 328
Wieting, J., 1077
Winther, G., 387, 399
Wirth, R., 1568
Wittridge, N.J., 1049, 1089
Woo, J.S., 1009, 1059, 1208
Wright, S.I., 104
Wu, C-T., 9
Wynblatt, P., 1649
Xie, Y., 235
Yang, C-C., 9
Yang, J., 298
Yang, W., 9, 192, 1248
Yu, D., 1003
Yu, Y., 92, 511, 629, 872
Zacharia, T., 352
Zao, K., 1266
Zehetbauer, M., 417
Zhao, Z., 872
Zhilyaev, A.P., 748, 1403, 1678
Zhu, G.H., 92, 629
Zielinska-Lipiec, A., 1351
Zuo, L., 1025

VOLUME

VOLUME

2

micromedia
a division of IHS Canada

20 Victoria Street
Toronto, Ontario M5C 2N8
Tel.: (416) 362-5211
Toll Free: 1-800-387-2689
Fax: (416) 362-6161
Email: info@micromedia.on.ca

ICOTOM–12
MONTREAL
1999

Proceedings of the
elfth International Conference
on Textures of Materials

Volume 2

y
A. Szpunar

J.A. SZPUNAR, a professor of Physical Metallurgy at McGill University, Montréal, was educated in Poland and received his Ph.D. and D.Sci. degrees from the Academy of Mining and Metallurgy in Cracow. He has held various visiting positions at Sussex and Durham Universities in England, worked in laboratories of the Finnish Academy of Science, Risø National Laboratory and served as an advisor to the National Atomic Agency Research Centre in Bandung, Indonesia.

His research interests span various areas of texture-related investigations. In particular, he is interested in deformation and recrystallization processes in metals, structure and properties of thin films, high temperature oxidation and corrosion, application of x-ray and neutron diffraction, and structure of grain boundaries as related to intergranular fracture, superplasti-city and special properties of nanocrystalline materials.

His group is also very active in the area of computer simulation of texture development during annealing and deformation processes and electrodeposition. This simulation based research is done on various levels: atomistic, microscopic and macroscopic; techniques of Molecular Dynamics - EAM, and Monte-Carlo are used to predict macroscopic properties of materials and to understand various processes that transform textures and properties.

Professor J.A. Szpunar is the author and co-author of over 300 research papers.

ISBN 0-660-17790-0
9 780660 177908

TWELFTH INTERNATIONAL CONFERENCE ON TEXTURES OF MATERIALS

Volume 2 of 2 Volumes

LIST OF SPONSORS

- Canadian Institute of Mining, Metallurgy and Petroleum
- National Research Council of Canada
- Canadian Steel Industry Research Association
- Alcan Research Division, Kingston
- TexSem Laboratories Inc.
- Blake Industry Inc.
- ASM International

ICOTOM-12

PROCEEDINGS OF THE TWELFTH INTERNATIONAL CONFERENCE ON TEXTURES OF MATERIALS

Volume 2 of 2 Volumes

McGill University, Montreal, Canada
August 9–13, 1999

Edited by
Jerzy A. Szpunar

Department of Metallurgical Engineering
McGill University
3610 University Street
Montreal, Quebec, Canada H3A 2B2

NRC·CNRC
NRC Research Press
Ottawa 1999

© 1999 National Research Council of Canada

All rights reserved. No part of this publication may be reproduced in a retrieval system, or transmitted by any means, electronic, mechanical, photocopying, recording or otherwise, without the prior written permission of the National Research Council of Canada, Ottawa, Ontario, Canada K1A 0R6.

ISBN 0-660-17790-0
NRC No. 43255

Canadian Cataloguing In Publication Data

International Conference on Textures of Materials (12th : 1999 : Montreal, Canada)

Proceedings of the Twelfth International Conference on Textures of Materials:
August 9–13, 1999, McGill University, Montreal, Canada

Volume 2 of 2 volumes.
At head of title : ICOTOM-12.
Issued by the National Research Council of Canada.
ISBN 0-660-17789-7 (v.1)
ISBN 0-660-17790-0 (v.2)

1. Materials — Texture — Congresses.
2. Metals — Texture — Congresses.
3. Texture (Crystallography) — Congresses.
I. Szpunar, Jerzy A.
II. National Research Council Canada.
III. Title.

TA418.5157 1999 620.1'292 C99-980228-3

Inquiries: Proceedings Program, NRC Research Press, National Research Council of Canada,
Building M-55, Ottawa, ON K1A 0R6, Canada.

Correct citation for this publication: Szpunar, J.A. (*Editor*). 1999. Proceedings of the Twelfth International Conference on Textures of Materials (ICOTOM-12). August 9–13, 1999, Montreal, Quebec, Canada. NRC Research Press, Ottawa, Ontario, Canada. Volume 2, pp. 803–1701.

Contents

VOLUME 1

Preface xxi
Conference Committees xxii

Plenary Lecture Session

From crystal orientations to material properties: micro–macro linkage illustrated with deformation in the earth.
H.-R. Wenk and P.R. Dawson 3
Texture design for new applications.
J.A. Szpunar 6
Extraction of grain boundary energies from triple junction geometry.
B.L. Adams, C.L. Bauer, D. Casasent, B. El-Dasher, D. Kinderlehrer, I. Livshits, F. Manolache, D. Mason, A. Morawiec, W.W. Mullins, S. Ozdemir, H. Rogan, G. Rohrer, A.D. Rollett, D. Saylor, S. Ta'asan, A. Talukder, C-T. Wu, C-C. Yang, W. Yang 9

Texture and Microstructure Description and Analysis

Development and application of a disorientation correlation function.
P.S. Lee, A.D. Rollett, and B.L. Adams 21
Spatial statistics for individual orientation measurements.
K.G. van den Boogaart 29
On the determination of textures from discrete orientation measurements.
W.B. Hutchinson, E. Lindh, and P. Bate 34
Using sets of individual orientations for ODF determination.
S. Matthies and F. Wagner 40
Reproducibility of experimental texture measurement.
D.J. Jensen and M.T. Lyttle 46
Advancements of ACOM and applications to orientation stereology.
R.A. Schwarzer 52
Reliability of automatic orientation determination from Kikuchi patterns.
A. Morawiec 62
Influence of number and arrangement of single orientation measurements on their statistical relevance.
O. Engler, J. Jura, and S. Matthies 68
Determination of microtexture by EBSD at high spatial resolution in a FEGSEM.
F.J. Humphreys 74
Development of the three dimensional X-ray diffraction microscope.
R.M. Suter and K. Kosack 80

Non-destructive characterization of tube segments by means of neutron diffraction.
H.-G. Brokmeier 86

A method of misorientation distribution calculation using ODF data.
W. Mao, G. Zhu, and Y. Yu 92

Determination of heterogeneous textures by X-ray diffraction.
K. El Ghazouli, J.J. Heizmann, B. Bolle, L. Jolly, and C. Valot 98

Quantification of recrystallized fraction from orientation imaging scans.
S.I. Wright 104

Phase analysis and grazing incidence stress measurements in ZrO_2 flims.
M.G. Glavicic and J.A. Szpunar 110

Texture analysis of complex earth materials from neutron diffraction spectra.
L. Lutterotti 116

Polychromatic microbeam diffraction, mesotexture and crack deflection in Al-Li 2090 T8E41.
J.D. Haase, R. Morano, T. Watt, and S.R. Stock 123

"HIPPO", a new high intensity neutron diffractometer for characterization of bulk materials.
K. Bennett, R.B. Von Dreele, and H.-R. Wenk 129

Residual strain measurement of {111} in rolled aluminum as function on in-situ annealing.
G. Langelaan, H. Jin, J. Hu, J. Cooley, and S. Saimoto 135

New development in texture and microstructure analysis of PA11.
L. Jolly, J.J. Heizmann, and A. Tidu 141

Use of a method based on a correlation function to reconstruct the parent textures from the inherited textures in phase transformation.
M. Humbert and N. Gey 147

False patterns of preferred orientation by erroneous background-correction.
H. Schaeben, H. Siemes, and J.-J. Fundenberger 153

Dual forms of texture analysis.
H. Schaeben and D.I. Nikolayev 156

Statistics for individual orientation measurements.
K.G. van den Boogaart 162

Determination of average orientation distribution function in thickness direction.
H. Inoue and N. Inakazu 168

Comparison of experimental techniques for characterization of through-thickness texture variations.
O.V. Mishin, E.M. Lauridsen, N.C. Krieger Lassen, H.F. Poulsen, D.J. Jensen, G. Brückner, and B. Bay 174

Modifications in the grain boundary character distribution in FCC materials through thermomechanical processing.
M. Kumar, A.J. Schwartz, and W.E. King 180

Accurate texture measurements on thin films using a powder x-ray diffractometer.
M.D. Vaudin 186

Adaptive orientation imaging microscopy.
W. Yang, B.L. Adams, and M. De Graef 192

Registry between sections in precision sectioning of polycrystalline materials.
A. Morawiec and D. Saylor 198

Mapping of lattice strain and texture distributions with an x-ray scanning apparatus.
R.A. Schwarzer and A.H. Fischer 204

X-ray and neutron diffraction measurement of textures of two-phase materials.
R.E. Bolmaro and H.-G. Brokmeier 211

Comparison of texture data measured by EBSD and conventional x-ray diffraction.
K. Mehnert, H.S. Ubhi, and A.P. Day 217

Experimental setting for indexing TEM Kikuchi diagrams.
J.J. Fundenberger, E. Bouzy, and J.S. Lecomte 223

Orientations measurements by TEM using spots, Kossel and LACBED patterns.
E. Bouzy, J.J. Fundenberger, J.S. Lecomte, and C. Esling 229

Texture analysis with a digital SEM–EBSD system.
H.-R. Wenk, J.J. Donovan, Y. Xie, G.C. Johnson, and E. Toker 235

X'pert texture: Overview of a software package for quantitative texture analysis
D.I. Nikolayev, V. Luzin, T. Lychagina, A.A. Dzjuba, V.A. Kogen, and J. Te Nijenhuis 241

Modeling of Texture Development

Influence of texture evolution on finite element simulation of forming processes.
E. Hoferlin, A. Van Bael, and P. Van Houtte 249

Monte-Carlo simulation of texture transformation in Ni-045%Fe nanocrystalline electrodeposits.
N. Rajmohan and J.A. Szpunar 255

Why we cannot simulate deformation textures.
T. Leffers 261

Analysis of inhomogeneous rolling texture of FCC metal sheets.
H.T. Jeong, K.K. Um, and D.N. Lee 267

Finite-element simulation of texture development in polycrystalline metals.
A. Bertram and M. Kraska 273

3-D animation of rotation of FCC crystals during various types of deformation.
H. Masui 279

Texture effects on steel sheet behaviour under large strain simulations.
L. Duchene, A. Godinas, and A.M. Habraken 286

Simulation of textural evolution during primary static recrystalization.
R. Sebald and G. Gottstein 292

Relationship between deposition and recrystalization textures of electrodeposits.
J.H. Choi, S.Y. Kang, D.N. Lee, and J. Yang 298

Recrystalization texture of aluminum bicrystals with S orientations deformed by channel die compression.
D.N. Lee and H.T. Jeong 304

A new analytic approach of crystal plasticity and its applications in polycrystal modeling.
L.S. Tóth and T. Hariz 310

Critical stress identification in textured materials using selfconsistent polycrystalline inverse model.
J.A. Signorelli, A. Fourty, R. Lebensohn, and R.E. Bolmaro 316
A discrete orientation model for the FCC-to-BCC phase transformation.
A.M. Lopes and C.S. Da Costa Viana 322
Predictions of recrystalization textures with Monte Carlo Model using deformation characteristics.
J. Tarasiuk, K. Wierzbanowski, B. Bacroix, and A. Miroux 328
Residual strains in Al–Mg powder composites. Simulations by self-consistent models.
A. Fourty, J.A. Signorelli, M.A. Bertinetti, R.E. Bolmaro, H.-G. Brokmeier, and H.-G. Priesmeyer 334
Parameterisation of cold-rolling and annealing textures in cubic metals based on the crystallographic fibres.
L. Delannay, A. Van Bael, and P. Van Houtte 340
Sensitivity of simulated anisotropy to initial texture definitions.
C.T. Necker, C.N. Tomé, F. Jean-Prost, and D.A. Korzekwa 346
Mesoscale modeling of cube texture evolution during hot deformation.
B. Radhakrishnan, G.B. Sarma, and T. Zacharia 352
Short range misorientation correlation and its evolution influence over texture development.
R.E. Bolmaro, A. Roatta, A. Fourty, C.T. Necker, and J. Bingert 358
Modeling of dynamic recrystalization in minerals.
H.-R. Wenk 364
Texture and strain localization prediction using a N-site self-consistent polycrystal model.
D.E. Solas and C.N. Tomé 369
FEM-micromechanics simulation of texture development of Cu–Fe powder composites.
J.A. Signorelli, A. Fourty, R.E. Bolmaro, and H.-G. Brokmeier 375
Simulative model and mechanism for deformation texture formation in FCC metal.
H. Masui 381
Coupling textural and microstructural evolution.
G. Winther 387
Modeling of the recrystalization textures of Al-alloys after hot deformation.
O. Englar and H.E. Vatne 393
Revision of the concept of 1-site models.
G. Winther, T. Leffers, and B. Clausen 399
3-D visualization of BCC iron crystals rotated during cold rolling.
H. Masui, H. Ukaji, O. Tsukamoto, T. Asami, and H. Katoh 405
Analysis of texture evolution of cubic metals by full constraint and two self-consistent viscoplastic models.
K.H. Oh 411
The role of Taylor factor in strain hardening.
L.S. Tóth, H.P. Stüwe, M. Zehetbauer, and I. Kopacz 417

A generalization of Taylor–Bishop–Hill theories and rate-dependent slip model in crystal plasticity.
K. Sekine 423

Texture and Anisotrophy

Modeling texture development during plastic deformation in cubic metals.
U.F. Kocks 431

Texture and anisotropy in low symmetry aggregates: elastic and plastic study of olivine.
C.N. Tomé 433

Finite element simulation with explicit use of polycrystal plasticity theory.
A.J. Beaudoin and P.R. Dawson 435

Crystallographic and morphological anisotropy in γ–TiAl.
H. Mecking 437

Diffractive determination of thermo-elastic single crystal constants using polycrystalline samples.
S. Matthies and H.-G. Priesmeyer 439

Texture and *r*-values of clad metals for button-type batteries.
M. Ishio, M. Umeda, H. Inoue, and K. Morii 445

Texture effects on the evolution of high temperature mechanical properties in zirconium alloys.
P. Sanchez, A.A. Pochettino, and R. Lebensohn 451

Levitation force to texture correlation in bulk Y-Ba-Cu-O.
D. Chateigner, J. Ricote, X. Chaud, P. Gautier-Picard, E. Beaugnon, J.-L. Soubeyroux, C. Leblond, and I. Monot 457

Texture effect on stress corrosion cracking of zirconium alloys in iodine environment.
S.B. Goryachev, A.R. Gritsuk, and M.G. Snegirev 463

Effect of texture on etching property and formability in invar shadow mask.
N.J. Park, M.H. Oh, S.M. Kim, and K.R. Kim 469

Texture measurement in steel industry practice.
C. Klinkenberg, H.-P. Schmitz, and H. Tamler 475

Textures in strip-cast AA3105 alloy and their ultrasonic characterization.
Y. Liu, X-M. Cheng, J.G. Morris, C-S. Man, and M. Huang 481

On-line plasticity prediction in textured steel and aluminum products.
P. Blandford and J.A. Szpunar 487

On-line measurement of texture and plastic strain ratio on steel sheets using laser-ultrasonics.
A. Moreau, D. Lévesque, M. Lord, M. Dubois, J.-P. Monchalin, C. Padioleau, and J.F. Bussière 493

Texture and residual stresses influence on the thermomechanical behaviour of Zircaloy-4 Tubes.
R. Brenner, J.L. Bechade, and B. Bacroix 499

Intercrystalline stresses in metal polycrystals: comparing simulations to diffraction experiments.
P.R. Dawson, D. Boyce, S. MacEwen, and R. Rogge 505

Relationship between texture, magnetic induction and maximum magnetic permeability of Si steels.
W. Mao, N. Chen, and Y. Yu 511
Strain effects and texture at in-plane shearing of Cu alloys.
J. Kusnierz and E.F. Rauch 517
Tilting of c-axise and twist around the c-axes in melt-textured YBaCuO cylinder.
V. Jung, H.-G. Brokmeier, E.M. Jansen, and R. Schnieber 523
The effect of texture on microyielding in near-gamma Ti–Al alloys.
B.A. Simkin, T.R. Bieler, and M.A. Crimp 529
On the evolution of ansiotropic elastic properties during metal forming.
A. Bertram and T. Böhlke 535
Practical aspects of calculating elastic properties of textured hexagonal polycrystals.
T.A. Lychagina and H.-G. Brokmeier 541
Consideration of lattice incompatibility in the evolution of hardening.
A. Acharya and A.J. Beaudoin 547
Analysis of orientation-dependent stress heterogeneity.
Y.D. Wang, R.L. Peng, and R. McGreevy 553
Modelling texture influence on the magnetic properties of nanocrystalline nickel and iron.
B. Szpunar, M.J. Aus, E. Renaud, U. Erb, F. Czerwinski, and J.A. Szpunar 560

Deformation Textures

Macroscopic anisotropy in cold rolled AA5XXX sheet.
S.-H. Choi, J.C. Brem, F. Barlat, and K.H. Oh 569
Texture development during equal channel angular forging of BCC metals.
S.R. Agnew 575
The influence of tranverse rolling on texture and microstructure.
J. Pospiech, Z. Jasieński, A. Litwora, A. Piątkowski, and J. Gryziecki 581
Effect of texture on uniaxial tension in AA3003 sheet with inhomogeneous texture.
J.-H. Cho, S.-J. Park, S.-H. Choi, and K.H. Oh 587
Strain hardening effects on texture formation in zirconium alloys.
A.A. Pochettino and P. Sanchez 593
Unsymmetrical deformation texture transition during annealing of Cu–Al alloys.
W. Ratuszek, A. Bunsch, and K. Chruściel 599
Textures of AA3104 deformed by plane strain compression at multiple temperatures.
M.T. Lyttle and D.J. Jensen 605
Effects of reductions in area and of the heat treatments on the phase transformations and the volume fractions of equiatomic TiNi shape memory alloys in wires.
F. Baghdouche and A. Vadon 611
Texture stability during high temperature plane strain compression of a commercial Al–Mg alloy.
R.D. Knutsen, F.J. Humphreys, P.S. Bate, and S. Court 617

Assessment of the Lamel model used for prediction of rolling textures of FCC and BCC metals.
P. Van Houtte and L. Delannay 623
Rolling texture and mechanical twinning in B2 ordered CuZn alloy.
G.H. Zhu, W. Mao, Y. Yu, and G. Brückner 629
Effect of thermomechanical processing parameters on texture development in an X-80 linepipe steel.
G.J. Baczynski and J.J. Jonas 635
Effect of processing variables on texture formation in a two phase Ti_3Al-base alloy.
S. Suwas and R.K. Ray 641
Topological aspects of the ridging phenomenon in ferritic stainless steel.
K. Sztwiertnia, J. Pospiech, and T. Rostek 647
Cube texture formation in pure aluminum as influenced by impurities and rolling temperatures.
K. Ito and A. Fukushima 653
Mechanical properties and texture formation during the compression of tantalum.
R.J. De Angelis and J.W. House 659
Texture and microstructure development during plastic deformation of magnesium.
R. Gehrmann and G. Gottstein 665
EBSD analysis of shear banding in α-Brass.
C.S. Da Costa Viana, J.C. Paredes, A.L. Pinto, and A.M. Lopes 671
Effect of texture on internal strains in Mg-7.7at.%Al.
M.A. Gharghouri, C.N. Tomé, and J. Root 677
Texture, microstructure and properties in mechanically alloyed and extruded FeAl.
S. Lenhard, F. Wagner, T. Grosdidier, S. Revol, and R. Baccino 683
Effect of thermohydrogen pretreatment on texture and deformability of BCC titanium alloy.
T.A. Sokolova, L.I. Anisimova, B.K. Sokolov, I.V. Gervasyeva, and L.R. Vladimirov 689
Texture and microstructure development during processing of ultra fine grained copper by equal channel angular extrusion.
A. Tidu, F. Wagner, T. Grosdidier, W.H. Huang, P.W. Kao, and C.P. Chang 694
The texture evolution of torsion-reverse torsion.
S.-J. Park, J.-H. Cho, and K.H. Oh 700
The formation of the Fibre Textures in BCC metals by deformation banding.
B.J. Duggan and G.L. Liu 706
Plastic deformation of a Ti-6%Al-04%V alloy at intermediate and high temperatures.
J.-S. Lecomte 712
Effect of homogenization practice and %Mn on texture in AA3104 during hot rolling.
M.A. Wells, D.J. Lloyd, and J. Kadilak 718

Spatial correlations of orientation, orientation clustering and the variance of the orientation distribution function.
B.L. Adams, P.S. Lee, and A.D. Rollett 724
On the texture change in extruded NiAl.
W. Skrotzki, R. Tamm, and C.-G. Oertel 730
Description of deformation geometry by effective slips in BCC materials.
Y.B. Park, B.I. Kim, and L. Kestens 736
Corrugation of metal at the deformation zone as a cause of the local texture inhomogeneity.
V.V. Gubernatorov, B.K. Sokolov, I.V. Gervasyeva, L.R. Vladimirov, and I.N. Stepanova 742
Microstructure and texture in chromium processed by severe plastic deformation.
N.A. Krasilnikov, A.P. Zhilyaev, R.Z. Valiev, V. Provenzano, and D.G. Rickerby 748
The deformation textures and Lankford values of asymmetrically rolled aluminum alloy sheets.
K-H. Kim, D.N. Lee, and C-H. Choi 755
Predicting the transformation texture of a axisymmetrically compressed Fe-30%Ni using a dislocation reaction model.
M. Sum, J.J. Jonas, and J. Root 761
Heterogeneity of addition elements distribution and texture gradient in rolled zinc–copper–titanium alloys.
M. Diot, J.J. Fundenberger, J. Wégria, and C. Esling 767
Microstructure and microtexture of a copper shaped-charge slug.
A.L. Pinto and C.S. Da Costa Viana 773
Effect of roll bite geometry on shear deformation in ferritic rolling of IF-steel sheets.
K.K. Um, H.T. Jeong, J.K. An, and D.N. Lee 779
The texture of drawing high-carbon steel wire.
K.K. Um, H.T. Jeong, J.K. An, and D.N. Lee 785
Texture evolution of aluminum single crystals during asymmetrical rolling.
C.H. Choi, K.H. Oh, G. Gottstein, and D.N. Lee 791
Texture and microstructure in mechanically alloyed and extruded Al-Al$_3$Ti alloys.
T. Grosdidier, S. Lenhard, K. Helming, C.P. Chang, and F. Wagner 797

VOLUME 2

Recrystallization Textures

A geometrical theory for {111}<hkl> recrystalization texture formation in cold rolled IF steel.
B.J. Duggan, Y.Y. Tse, and G.L. Liu 805
Investigation of steel sheet recrystallisation textures with a new parameter model for texture description.
L. Delannay, A. Van Bael, P. Van Houtte, L. Kestens, and Y. Houbaert 811

Recrystallization texture development in cold rolled super duplex stainless steel.
J. Keichel, M. Crumbach, P. Schraven, G. Gottstein, and J. Foct 817

Textural and structural changes during annealing of a heavily cold deformed $Ni_3Al(B,Zr)$ alloy.
B. Bhattacharya and R.K. Ray 824

Formation of the cube band and its evolution during recrystalization.
Y.B. Park, Y.H. Kim, and B.I. Kim 830

Textures in dynamic recovery and recrystallization.
H.J. McQueen 836

Recrystallization textures in copper–manganese alloys.
O. Engler, K. Lücke, and C. Pithan 842

Effect of Mg content on the development of rolling and recrystallization textures in Al–Mg alloys.
M. Koizumi, T. Saitou, H. Inagaki, and S. Kohara 848

Automatic recognition of recrystallized grains in partly recrystallized samples from crystal orientation maps.
N.C. Krieger Lassen and D.J. Jensen 854

Influence of Fe content on recrystallization, grain growth and recrystallization textures in Al–Mg alloys.
M. Koizumi, H. Okudaira, and H. Inagaki 860

Relationship between primary recrystallization grain size and its texture in 3%Si steels.
S.K. Chang, B.D. Hong, and K.S. Han 866

Texture development in high strength IF steel containing P.
W. Mao, Z. Zhao, and Y. Yu 872

Microtextures in copper undergoing dynamic recrystallization (DRX) in torsion.
L. Gavard, F. Montheillet, and H.J. McQueen 878

Modeling of microstructural evolution and texture development during the secondary recrystallization.
Y. Takayama, M. Inoue, T. Tozawa, H. Kato, and M. Kobayashi 884

Growth substructure formed under recrystallization in textured matrix, its features and origin.
V.V. Gubernatorov, B.K. Sokolov, I.V. Gervasyeva, and L.R. Vladimirov 890

Last stage of recrystallization in Ti sheets.
O. Van Landuyt, T. Grosdidier, and F. Wagner 895

A method for predicting the crystallographic texture from the polycrystalline mechanical strength as a function of heat treatment for a precipitation hardened aluminum alloy.
J.M. Fragomeni 901

The effect of cold rolling reduction on planar anisotropy of interstitial free steels.
L. Kestens, Y. Houbaert, L. Delannay, P. Van Houtte, M. Barnett, and J.J. Jonas 910

Thermal stability of basal texture in Ti_3Al-base alloy.
S. Suwas and R.K. Ray 916

Texture of welded joints of 316L stainless steel.
J.L. Bechade, G. Bouche, M.H. Mathon, and T. Baudin 922

Texture of palladium and palladium–silver alloys after cold rolling and annealing.
Y. Cao, J.A. Szpunar, and W. Shmayda 928

A suggestion concerning the generation of recrystallization nuclei during plastic deformation.
U.F. Kocks and J.D. Embury 934
Influence of grain size and retained atoms on the recrystallization texture in deep drawing steel.
H. Ren, D. Tang, Z. Sun, and W. Mao 938
Recrystallized cold rolled nickel and nickel-alloys with a strong cube texture.
B. de Boer, N. Reger, R. Opitz, J. Eickemeyer, B. Holzapfel, and L. Schultz 944
The evolution of deformation and recrystallization textures of cross rolled sheets.
S-H. Hong, N-J. Park, and D.N. Lee 950
Initial and recrystallization textures and microstructures of Zn electrodeposits.
I. Kim and S.C. Hong 956
Analysis nanocrystalline Ni-45% Fe electrodeposits for predicting texture transformation during annealing.
N. Rajmohan, J.A. Szpunar, and U. Erb 961
Texture development during grain growth in strongly textured materials.
V.Y. Novikov 967
Study of recrystallization mechanisms in ingot cast and strip cast Fe-36%Ni alloy
F. Julliard, T. Baudin, and R. Pennelle 973

Texture in Steel and Aluminum

Effect of primary recrystallization texture on Goss secondary recrystallization texture in Fe-3%Si alloy.
Y. Ushigami, T. Kubota, and K. Murakami 981
Influence of heating rate on recrystallization in low and ultra-low carbon steels.
M. Ferry, D. Muljono, and D.P. Dunne 991
Optimisation of galvanisation process parameters to improve the cracking resistance in zinc coatings.
S. Gaignard, C. Esling J. Wégria, and M. Dubois, ... 997
Effect of finishing deformation temperature on texture development of ultra low carbon steel.
D. Yu, M. Ferry, and T. Chandra 1003
Grain boundary character distribution in a primary recrystallized grain-oriented silicon steel.
J. Harasse, R. Shimizu, J. Kim, and J.S. Woo 1009
Textures and microstructures of strip cast stainless and low-carbon steels.
D. Raabe, H. Krause, A.D. Rollett, and A. Teicher 1015
Torsional behavior of pearlitic wires according to their crystallographic texture.
A. Tidu, B. Bolle, Y. Liu, J.J. Heizmann, and L. Zuo 1025
Transformation textures and texture memory in low carbon steels.
L. Ryde, D. Artymowicz, and W.B. Hutchinson 1031
Influence of precipitates on texture evolution of Ti–IF steels in batch annealing.
J. Shi, Z. Li, and X. Wang 1037
Effects of composition on the ansiotropy and texture of continuously annealed low carbon steel sheets.
S.C. Baik, O. Kwon, J. Cho, and K.H. Oh 1043

The role of in-plane dislocation reactions during the transformation of hot rolled austenite.
J.J. Jonas and N.J. Wittridge 1049

Through-thickness texture variation in primary recrystallized 3%Si–Fe and its effect on the sharpness of (110)<001> Goss texture.
K.S. Han, J.S. Woo, J.K. Kim, and C.S. Kim 1059

Microstructure and crystallographic texture of strip-cast 4.3wt%Si steel sheet.
J.Y. Park, K.H. Oh, and H.Y. Ra 1065

Texture development in cold-rolled austenitic-ferritic duplex steel.
W. Ratuszek, J. Ryś, and K. Chruściel 1071

Rotated cube texture in semifinished electrical steel: processing and mechanisms of texture formation.
B. de Boer, J. Wieting, and L. Schultz 1077

The texture evolution of non-oriented silicon steel.
C.S. Lee 1083

Application of the dislocation reaction model for variant selection to the transformation of an Fe-30%Ni alloy deformed in extension.
N.J. Wittridge, J.J. Jonas, J.H. Root 1089

Initial orientation dependence of texture evolution in ferritic stainless steels.
S.-H. Park, K.-Y. Kim, Y.D. Lee, and C.G. Park 1095

Relation between grain boundary mobility and grain boundary character in Fe-3%Si.
Y. Hayakawa, T. Takamiya, and M. Kurosawa 1101

Macrostructure-related fatigue crack closure in Al-Li 2090 studied by x-ray microtomography.
R. Morano, G.R. Davis, S.R. Stock, and J.C. Elliott 1106

Predicting recrystallization of aluminum by applying a probablistic cellular automaton to finite element data.
D. Raabe and R.C. Becker 1112

Orientation dependent stored energy in cold rolled can-body aluminum alloy.
N. Rajmohan and J.A. Szpunar 1118

Randomization of the annealing texture in aluminum 5182 sheet.
M.Y. Huh, Y.H. Kim, and O. Engler 1124

The effect of strain path on texture development in aluminum.
R.L. Higginson 1130

Texture evolution during continuous recrystallization of aluminum alloys.
J. Li, H. Jin, F. Seki, and S. Saimoto 1136

Shear texture control and improvement of Lankford value in aluminum alloy sheet by single-roll drive warm rolling.
T. Sakai, H. Inagaki, and Y. Saito 1142

Texture and microstructure in DC cast and SC aluminum alloys.
Y. Liu, Y.L. Liu, G. Liao, and J.G. Morris 1148

The effect of rolling draughts on texture and microstructure in aluminum.
O.V. Mishin, D.J. Jensen, and B. Bay 1154

Deformation banding and texture development during cold drawing of unidirectionally solidified polycrystalline aluminum.
Y. Kaneno, H. Inoue, and N. Inakazu 1160

Influence of strain path on the forming limit curve and texture of aluminum sheet.
S. Kohara 1166

Texture investigation in the system Al-Nb during phase transition.
R. Schnieber, H.J. Bunge, and H.-G. Brokmeier 1172

Selectivity of Goss grains during abnormal grain growth in Fe-Si electrical steels.
N. Rajmohan and J.A. Szpunar 1178

Texture inheritance in HSLA grades subjected to compact strip production.
E. Bouzy, B. Cardiola, C. Esling, M. Humbert, G. Flemming, and K.E. Hensger 1184

Formation of oriented lamellae in TiAl alloys by diffusional reaction.
H. Fukutomi, M. Ueno, M. Nakamura, T. Suzuki, and S. Kikuchi 1190

Texture and multiple twinning in copper.
V. Randle, P. Davies, and H. Davies 1196

Microtexture development in high strength interstitial free steels.
I.J. Cross, V. Randle, and S.R. Daniel 1202

Effect of hot band annealing on the formation of sharp {110} <001> Goss texture in conventional grain oriented electrical steels.
K.S. Han, J.S. Woo, G.S. Choi, and S.K. Chang 1208

Temper rolling effects of low-C cold rolled steels on texture development and stretcher strain phenomena.
Y.H. Koh, J.H. Choi, N.J. Park, and Jeong Ho Choi 1214

Texture evolution during hot plane strain compression of a hot deformed AA5182 Al–Mg alloy.
P. Ratchev, B. Verlinden, P. Van Houtte, R. Van den Broeck,
and M.R. van der Winden 1224

Through-thickness inhomogeneity of the texture developed in high strength linepipe.
G.J. Baczynski, J.J. Jonas, and L.E. Collins 1230

Texture development during cold rolling and annealing in two 304 austenitic stainless steel cast strips.
S. Teraoka, G.J. Baczynski, and J.J. Jonas 1236

Comparison of cast and hot strip textures and microstructures in three 304 austenitic stainless steels.
S. Teraoka, J.G. Baczynski, and J.J. Jonas 1242

Experimental approach to continuum dislocation fields in <100> polycrystalline columnar aluminum.
B.S. El-Dasher, W. Yang, and B.L. Adams 1248

Effect of through thickness inhomogeneity of texture on edge cracking during planetary hot rolling of austenitic stainless steel.
J.Y. Cho, H.T. Jeong, and J.A. Szpunar 1254

Residual stress analysis of ridged ferritic stainless steel.
A.P. Clarke, W.D. MacDonald, and S. Saimoto 1260

Study of texture of ULC sheet steel rolled in ferrite region.
K. Zhao, X.C. Mi, and SH.H. Jiao 1266

Characterizing and representing texture gradients in thick aluminum plate.
M.P. Miller, T.J. Turner, and J. Sutliff 1272

Microtexture inhomogeneity in hot rolled two-phase steel.
J. Jura, J. Pospiech, J. Bonarski, T. Baudin, C. Quesne, and R. Penelle 1278

Texture in Films, Coatings and Oxides

Crystallographic texture in 1G DRAM reactive ion etched vs. damascene Al–Cu lines.
K.P. Rodbell, L.M. Gignac, J.L. Hurd, Y.-Y. Wang, L.A. Clevenger, R.C. Iggulden, R.F. Schnabel, and S. Weber 1287

Influence of processing parameters on the texture of pure zinc electrodeposited coatings on steel.
K. De Blauwe, A. De Broeck, J. Bollen, and W. Timmermans 1293

Microstructures and textures of copper electrodeposits on the WN diffusion barrier.
I. Kim and S.C. Hong 1299

Simulation of texture formation in ZrO_2 film grown on Zr-2.5%Nb.
H. Li, M.G. Glavicic, and J.A. Szpunar 1303

Texture evolution in Cu damascene lines.
D.P. Field 1309

Texture of thin layers and nanowires of electrodeposited thermoelectric materials such as $Bi_{1-x}Sb_x$ alloys.
F. Besse, C. Boulanger, J.M. Lecuire, B. Bolle, and J.J. Heizmann 1315

Biaxially aligned MgO buffer layers by ion-beam assisted pulsed laser deposition.
R. Hühne, C.-G. Oertel, W. Skrotzki, B. Holzapfel, and L. Schultz 1321

Quantative texture of ferroelectric modified lead titanate thin films.
J. Ricote, D. Chateigner, G. Ripault, L. Pardo, M. Algueró, J. Mendiola, and M.L. Calzada 1327

Residual stress determination in highly textured titanium nitride coatings.
A. Saerens, P. Van Houtte, and C. Quaeyhaegens 1333

Internal stress in textured molybdenum thin films.
C.S. Shin, J-H. Cho, and K.H. Oh 1339

Texturation in duced by the addition of surfactant during the synthesis of V_2O_5 thin films.
F. Ansart, S. Mege, A. Rousset, and J.M. Savariault 1345

Texture transformation in Ni electrodeposits applied for CD-ROM stampers.
F. Czerwinski, A. Zielinska-Lipiec, and J.A. Szpunar 1351

Affect of localized texture on the sputter performance of tantalum.
C.A. Michaluk, D.B. Smathers, and D.P. Field 1357

Singular value decomposition of the ODF–PDF projection operator.
K.G. van den Boogaart and S. Schaeben 1363

A role of texture and orientation clustering in electromigration failure of aluminum interconnects.
H.T. Jeong, J.A. Szpunar, K.T. Lee, and D.P. Field 1369

Al texture on <001> W, Ti_xW_{1-x} and TiN barrier layers.
L.D. Madsen, E.B. Svedberg, D.B. Bergstrom, C.-S. Shin, I. Petrov, and J.E. Greene 1375

Microstructures and textures of copper electrodeposits on the TiN.
I. Kim and S.C. Hong 1381

Computer simulation of the effect of impurities on diffusion at oxide boundaries.
D.J. Harris and J.H. Harding 1385

A model of NiO texture formation on single crystal substrate.
H. Li, F. Czerwinski, and J.A. Szpunar 1391
The surface texturing of nickel for high temperature oxidation prevention.
F. Czerwinski and J.A. Szpunar 1397
On the calculation of grain boundary character distribution in textured nickel oxide layers.
A.P. Zhilyaev, F. Czerwinski, and J.A. Szpunar 1403
The role of oxide texture in the protection of Zr-2.5%Nb alloys pressure tubes against hydrogen ingress.
M.G. Glavicic, J.A. Szpunar, and Y.P. Lin 1409
The influence of texture on the oxidation kinetics of copper.
K.T. Lee and J.A. Szpunar 1415
The influence of deposition parameters on texture in electrogalvanized zinc coatings.
H. Park and J.A. Szpunar 1421
Influence of heating rate on texture changes in nanocrystalline nickel during annealing.
B.-K. Kim, H.T. Jeong, and J.A. Szpunar 1427
Development of textures and microstructures in Fe–Ni alloy thin films.
C.S. Ha, S.S. Kim, B.I. Kim, and Y.B. Park 1433
Examination of the stress and phase composition in textured zirconium oxide films.
J. Lin and J.A. Szpunar 1439
Texture development during the electrocrystallization of nickel.
Y. Cao, F. Czerwinski, and J.A. Szpunar 1445

Texture in Ceramics, Composites and Polymers

Orientation evolution of textured piezoelectric ceramics under electric fields.
S. Wan and K.J. Bowman 1453
Anisotropy in layered and gadient ceramics.
R. Moon, W. Blanton, F.R. Cichocki, J. Brehm, K.P. Trumble, and K.J. Bowman 1460
Texture development, recrystallization, and transference of texture between ceramic multilayers, epitaxially grown on rolling assisted biaxially textured substrates (RABiTS).
A. Goyal, R. Freenstra, E.D. Specht, D.M. Kroeger, D.F. Lee, M. Parathaman, F.A. List, and D.K. Christen 1466
Particle orientation and texture formation in tape cast ceramic materials.
P.M. Raj, F. Cosandey, W.R. Cannon, and P. Mainwaring 1476
Texture of ceramic reinforced Magnesium composites.
E.M. Jansen, H.-G. Brokmeier, and K.U. Kainer 1482
Contribution of the orientation textures in the amorphous and crystalline phases on the plastic deformation of polymers.
C. G'Sell, C. Cabot, A. Dahoun, M.J. Philippe, and J. Grenet 1488

Application of electron backscattered diffraction (EBSD) and atomic force microscopy (AFM) to determine texture, mesotexture, and grain boundary energies in ceramics.
S.J. Glass, V.R. Vedula, D.M. Saylor, and G.S. Rohrer 1489

Quantitative characterisation of mollusc shell textures.
D. Chateigner, C. Hedegaard, and H.-R. Wenk 1495

Microstructure and mechanical properties of textured alumina.
D. Kovar and P.W. Hall 1501

Predicting microstructural-level residual stresses and crack paths in ceramics.
V.R. Vedula, S.J. Glass, D.M. Saylor, G.S. Rohrer, and W.C. Carter 1509

Texture in Geological Research

Significance of domainal crystallographic fabrics in naturally deformed rocks.
J. Hippertt 1515

Texture development in amphibole: oriented growth versus passive rotation.
T. Takeshita 1522

Contrasting *C*-axis fabric patterns in layers of different proportion of quartz and iron oxide.
L. Lagoeiro 1528

Comparison of natural and simulated quartz shear texture.
T. Takeshita, H.-R. Wenk, and R. Lebensohn 1534

Neutron diffraction strain investigation of sandstones undergoing applied stresses.
Ch. Scheffzük, A. Frischbutter, and K. Walther 1540

Stress-strain distribution in deformed olivine aggregates: inference from microstructural observations and implications for texture development.
S. Karato and K.-H. Lee 1546

Texture and microstructure of halite at a halite-basalt contact
Ch. Scheffzük 1556

QTA and polarised EXAFS correlation in self-supporting films of nontronites.
D. Chateigner, A. Manceau, M. Schlegel, and M. Pernet 1562

Texture development of $CaTiO_3FeO$ composites at high-temperature.
Z-C. Wang, S. Ji, and R. Wirth 1568

Quantitative texture analysis of experimentally sheared anhydrite and albite aggregates.
F. Heidelbach 1574

Texture-related elastic (seismic) anisotropy in crustal and mantle rocks.
H.M. Kern 1580

Textures and elastic anisotropies of amphibolites from the Kola borehole.
T.I. Ivankina, A.N. Nikitin, T. Lokajicek, Z. Pros, K. Klima, and K. Ullemeyer 1587

Applying EBSD techniques to microtextures and mesotextures in rocks.
D.J. Prior, M. Bartozzi, A. Boyle, A. Day, D. Paden, D. Halliday, and M. Tye 1593

MAUD (Materials Analysis Using Diffraction): a user friendly Java program for Ritveld Texture Analysis and more.
L. Lutterotti, S. Matthies, and H.-R. Wenk 1599

A pressure device for strain measurements of geomaterials at the neutron diffractometer EPSILON.
K. Walther, A. Frischbutter, R. Lieckefett, and C. Scheffzük 1605

Grain Boundaries and Misorientation Distribution

Characteristics of Σ3 boundaries in strongly textured copper.
O.V. Mishin and X. Huang 1613
Grain boundary influence on texture evolution during deformation and recrystallisation.
S.J. Lillywhite, M. Aindow, and P.S. Bate 1619
The role of triple junctions during normal grain growth under high pressure in 2-D strips of polycrystalline aluminum.
V. Sursaeva, S. Protasova, and W. Lojkowski 1625
The orientation distribution of interface determined according to the maximum-entropy principle.
Y.D. Wang, R.L. Peng, R. McGreevy, B. Bolle, A. Vadon, and J.J. Heizmann 1631
Determining surface energy anisotropy from measurements of thermal groove geometry.
D.M. Saylor, G.S. Rohrer, and D.E. Mason 1637
Multiscale reconstruction og grain boundary energy from microstructure.
D. Kinderlehrer, I. Livshits, S. Ta'asan, and D.E. Mason 1643
Correlation of grain boundary character with wetting behaviour.
M. Takashima, A.D. Rollett, P. Wynblatt, and B.L. Adams 1649
Calculation of intracrystalline lattice misorientations in face centered cubic polycrystals.
D. Mika and P.R. Dawson 1655
Ordinary grain boundaries and recrystallization textures.
D.B. Titorov 1661
Computer simulation of diffusion process in polycrystalline material.
H. Li and J.A. Szpunar 1667
Atomistic modelling of intergranular fracture in Ni_3Al.
J. Lu and J.A. Szpunar 1673
Singularity og grain boundary character distribution in zirconia film grown on Zr-2.5%Nb substrate.
A.P. Zhilyaev, V.Y. Gertsman, and J.A. Szpunar 1678
Mobility of mechanical twin grain boundaries in Zinc.
V.G. Sursaeva, A.U. Tuflin, and U. Czubayko 1684
Determining relative grain boundary energies from measurements of thermal groove geometry.
D.M. Saylor and G.S. Rohrer 1690
Simulation of recrystalization from EBSD or TEM orientation data.
T. Baudin and R. Penelle 1696

Author Index A1

Preface

ICOTOM Conferences are held every 3 years and are traditionally the most important events for the community of researchers working on various texture-related projects. The present definition of texture incorporates not only the crystallographic texture, as defined by the orientation distribution function, but also the grain misorientation distribution which is related to various aspects of grain boundary engineering. The grain shape, mean size and type of alignment of fibres, rocks, surface deposits and crystals in polymers fall into a broader definition of texture. ICOTOM is a meeting place for all researchers investigating polycrystalline materials, in particular: metallurgists, geologists, mineralogists, those working with polymers, ceramics, thin films and coatings.

The ICOTOM 12 Conference will be held in Montréal August 9–13, 1999. These proceedings will be handed to the participants at the Conference. There were about 400 abstracts submitted for presentation at the conference, however, the number of papers published in the Proceedings is only 279. The papers are divided according to the most important topics that represent various texture related problems. There is some emphasis on new emerging areas of texture research in thin films and modelling and simulation of texture development. Texture research contributes to the development of engineering materials with new or improved properties, optimization of various industrial processes and better understanding of geological phenomena. Traditional areas of research for steel and aluminum industries are also very well represented in these proceedings.

The organizers strongly believe that the ICOTOM12 meeting will contribute to a better understanding of engineering materials and processes and will facilitate scientific exchange and contacts between participants from the industry and academia.

On behalf of the organizers I would like to acknowledge the special contribution of Professor R. Wenk, who organized the session on Geological Applications of Texture, Professor B. Adams for his contribution to organizing the session on Special Correlations of Orientation Measurements and Professor A. Rollett and Dr. F. Kocks for helping to finalize the program on Mechanical Properties and Texture and Simulation of Texture. I would also like to thank all the members of the International and Program Committees for their support as well as acknowledge the successful funding efforts of Dr. J. Root and Dr. J. Savoie, and to thank Professor J. Jonas for all the good advice.

I would also like to express my gratitude to the Canadian Institute of Mining, Metallurgy and Petroleum and Y. Jacques, Executive Director of CIM for agreeing to help organize the ICOTOM12 and working hard to make it a successful event. In particular, I would like to thank S. Major and J. Gaydos for their efforts and expert help.

My thanks to all the sponsors of the conference. Their generosity allowed many more young people to participate and, I believe, make this conference a memorable event.

Finally, I would like to express my thanks to my colleagues and students who often asked me the question "do you need help?", and since my answer was always affirmative, helped me a lot. Particularly I would like to thank Dr. Hyo Tae Jeong and Barbara Hanley for their great efforts in organizing the conference program and proceedings. Thanks to Dr. F. Czerwinski, N. Rajmohan, Dr. V. Gertsman, Jae-Young Cho, Bae Kyun Kim, Slavek Poplawski and other members of our texture group for their support and help.

JERZY A. SZPUNAR

INTERNATIONAL COMMITTEE

Brent L. Adams
Hans-Joachim Bunge
Brian Duggan
Günter Gottstein
John Humphreys
Bevis Hutchinson
Hirosuke Inagaki
Dorte Juul-Jensen
Richard Penelle
Ranjit Ray
Jerzy A. Szpunar
Paul Van Houtte

LOCAL ORGANIZING COMMITTEE

Jerzy A. Szpunar (McGill University)
General Meeting Chairman
Jean F. Bussière (NRC)
Frank Czerwinski (McGill University)
Abdel El-Sherik (Dofasco)
Val Gertsman (McGill University)
Hyo Tae Jeong (McGill University)
John Jonas (McGill University)
John Root (ACL – Chalk River)
Jean Savoie (Alcan)

PROGRAM COMMITTEE

Jerzy A. Szpunar (Canada)
General Meeting Chairman
Brent L. Adams (USA)
Keith Bowman (USA)
Hans J. Bunge (Germany)
Frank Czerwinski (Canada)
Günter Gottstein (Germany)
Christian G'Sell (France)
John Jonas (Canada)
Frank Kajzar (France)
Hyo Tae Jeong (Korea)
Gino Palumbo (Canada)
Yong Bum Park (Korea)
Alberto Pochetino (Argentina)
Jan Pospiech (Poland)
Dierk Raabe (USA)
Ken Rodbell (USA)
Anthony D. Rollet (USA)
John Root (Canada)
Jean Savoie (Canada)
Boris K. Sokolov (Russia)
Yoshyuki Ushigami (Japan)
Hasso Weiland (USA)
Rudi Wenk (USA)

Recrystallization Textures

A GEOMETRICAL THEORY FOR {111}<hkl> RECRYSTALLISATION TEXTURE FORMATION IN COLD ROLLED IF STEEL

B.J. DUGGAN, Y.Y. TSE and G.L. LIU
Department of Mechanical Engineering, The University of Hong Kong,
Pokfulam Road, Hong Kong

Abstract

The introduction of conditional deformation banding into BCC rolling texture modelling has produced a clue as to the origins of the {111}<hkl> texture as it develops from the γ fibre material. OIM has revealed that deformation bands are present in many deformed γ grains, which therefore produce the geometrical condition for successful nucleation of rotated <111> ND material by either subgrain growth or SIBM. Clearly the roles of solutes and precipitates have to be established in this deformation microstructure.

Key words: IF Steel, Recrystallisation Texture, Deformation Banding, Nucleation Sites

1. Introduction

The introduction of deformation banding (DB) into texture modelling by Lee and Duggan (Lee and Duggan, 1993) for the case of intermediate to high stacking fault energy FCC materials produced significant improvement in modelled textures in the rate insensitive regime. The model was refined and successfully predicted the orientations which split into different orientations on straining (Lee *et al.*, 1995). Further improvement was achieved by introducing a conditional energy term which allowed DB to occur progressively with rolling strain (Duggan *et al.*, 1998). Liu *et al.*(1996, 1998) used the essential ideas of DB due to Lee and applied them to the BCC case, and managed to predict BCC rolling textures quite well. A significant drawback is that although DB is a three dimensional phenomenon in which lath-like elements are free to shear as in the pancake model as well as in the rolling plane, it has proved difficult in mathematical terms, to construct a model which works in this way. Instead, in all the models, relaxation in the pancake mode is allowed in the Relaxed Constraints (RC) formulation, and e_{23} is modelled by DB in a Taylor/Chin framework (Chin, 1969). Thus each orientation in the model becomes two orientations in the sheet plane geometry, either immediately as in the DB case, or with progressive computer straining in the conditional DB (DBC) case. Disregarding DB in longitudinal sections is severe in terms of violation of the observed physics of deformation because DB is obvious in this section at higher strains, and grain fragmentation, its precursor, in the lower strain regime. However, this drawback has lead the authors to different conclusions regarding the origins of {111}<hkl> recrystallisation textures because, in seeking verification of the BCC DB theory, emphasis has been on the orientations formed in the rolling plane and predicted by the model. The results are significant in terms of nucleation theory.

2. Experimental

Commercially supplied hot band of 3–mm thickness, 30μm grain size and composition shown in table 1 was cold rolled 85% in a laboratory mill of 252–mm diameter rolls at 15m/min under homogeneous rolling conditions. The continuous annealing process was simulated with the heating rate in the hundreds of degrees per minute and a furnace temperature of 850°C. Partial annealing experiments were carried out by interrupting the cycle with a rapid quench from the temperature attained. Also, to allow the deformed structure to be examined by channelling contrast and EBSP, a recovery anneal lasting 168 hours at 450°C was done, after which no sign of recrystallisation was detected in either longitudinal or rolling plane sections. Pole figures were determined by X–ray diffraction using the Schulz reflection method and Mo radiation, and conventional processing from 200, 220, 310 and 222 pole figures gave the ODF. OIM was done on a S360 SEM using the HKL software and the ICE program.

Table 1 **Chemical composition of reference material, (mass%)**

C	Si	Mn	P	S	Al	Ti	N
0.0019	0.010	0.13	0.014	0.014	0.041	0.046	0.0026

2.1 Results

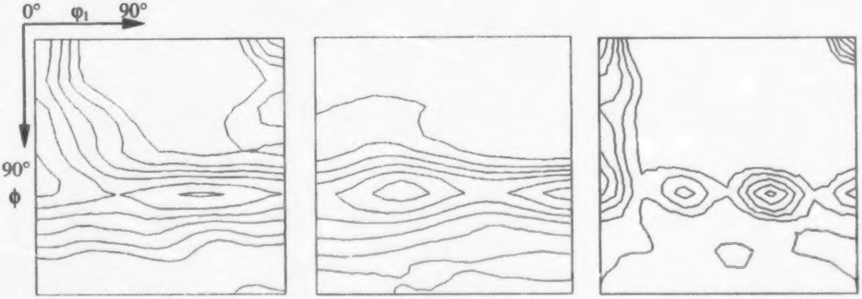

(a) (1, 3, 5, 7, 9, 11) (b) (1, 5, 10, 14.5, 19, 23.5) (c) (5, 10, 15, 20, 25, 30)

Figure 1 **φ_2 = 45° sections of measured and simulated ODFs,**
(a) 85% cold rolled IF steel, (b) annealed at 850°C, (c) predicted with DBC, $\sigma = 5\%$

The ϕ_2 = 45° section of the Bunge Euler space is used to represent the full ODF and figure 1 shows the results after cold rolling 85%(a) after complete recrystallisation (b) and (c) after computer simulated rolling 87% following the procedures outlined by Liu *et al.* (1998). The rolling texture is as expected, showing well populated α and γ fibres, and the recrystallisation texture a strong {111}<hkl>

texture with a peak at {111}<112>. The simulated ODF is of peak type in α and γ fibres after computer rolling 87% and is too strong. The orientations which feed into the α and γ fibres after 87% computer rolling in the model are shown in figure 2. It is clear that the γ fibre is fed from a spread around the γ fibre (figure 2a) while the α fibre source is more complex, figure 2b.

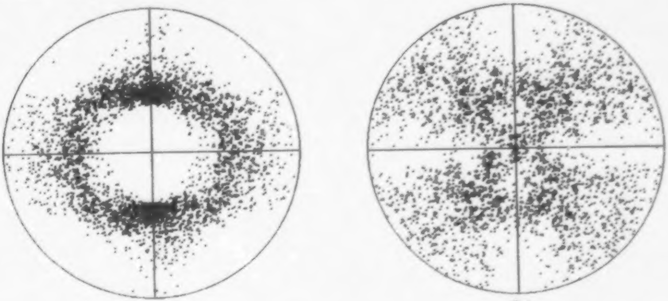

(a) (b)

Figure 2 **Initial orientations arriving (a) the γ–fibre and (b) the α–fibre**

Certain orientations which rotated into the γ fibre were then located and followed by increments of 0.05 strain to 87% reduction. A representative set of three such orientation paths are shown in figure 3. In the first case, figure 3a, the orientation rotates to the γ fibre and then splits into two components to give approximately complementary pairs of {111}<110>. {111}<112> and {111}<110> are predicted to be stable at this level of straining in the computer simulation, but slight rotation about the <111> ND produces rotation towards these stable orientations, the particular one being selected by the particular rolling direction, an example is shown in figure 3b. A third kind of rotation is shown in figure 3c in which one component ("1") rotates towards the γ fibre, the other ("2") rotates away towards an important component {114}<110>.

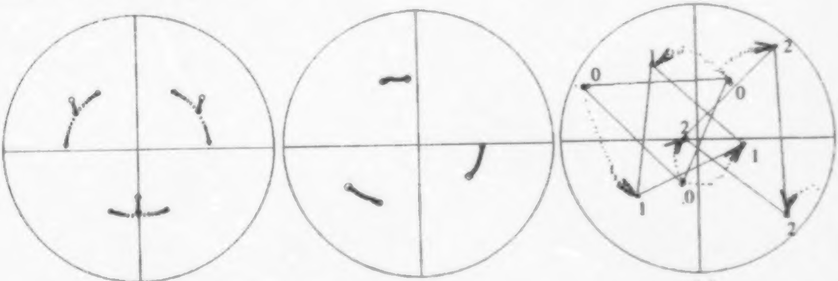

(a) (b) (c)

Figure 3 **Rotation of the specific orientations from initial array to the γ–fibre "0" is the original orientation, "1" and "2" are the DB orientations**

These predicted orientation splittings were then sought in the rolling plane of electro–polished samples by Orientation Imaging Microscopy (OIM) and, perhaps surprisingly given the two adjustable parameters in the modelling, such geometrical configurations were discovered without much difficulty in the 85%, cold rolled IF steel in the recovered state. Figure 4a, taken from reference Duggan *et al.* (1999), shows line scans across two contiguous regions having the γ fibre orientation. It is not clear in this micrograph whether these are one or two grains but such a distinction does not matter given the physics involved in DB which can occur several times in one grain. In figure 4a the spread of orientations is ~ 30° and the material in the central region indicated has the orientation ~ {111}<110> and is surrounded by complementary versions of ~ {111}<112>. These outer regions are those predicted by the model in figure 3a. Presumably the original splitting of orientation occurred at ~ {111}<112> and if some material remained in this orientation this arrangement would resemble precisely that of the transition band described by Hu (1963), and would favour nucleation of recrystallisation. It is unclear which component will dominate in the recrystallisation process, since this depends intimately on several unknown factors to do with the distribution of driving forces. Figure 4c shows a second region divided into two γ fibre components with ~ 15° misorientation.

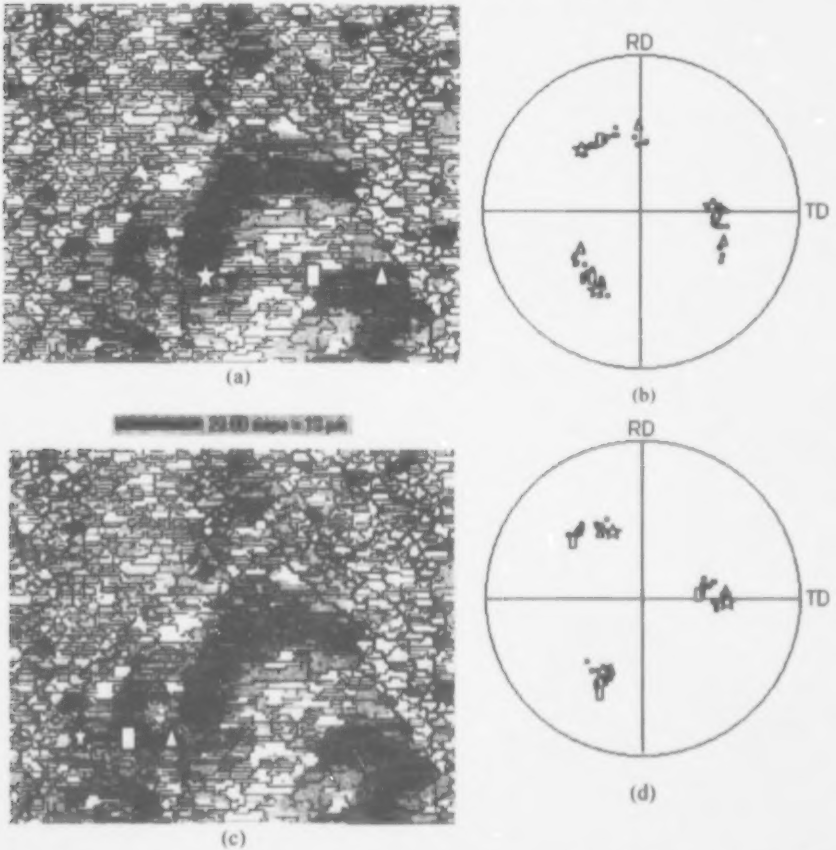

(a) (b) (c) (d)

Figure 4 Lattice curvature in annealed IF steel, 450°C and 168hrs, rolling plane

An electro–polished sample was etched lightly to pick out grain boundaries and hence remove some uncertainties in interpretation. The result might not convince sceptics, but an example is shown in figure 5. The width of the grain (if it is indeed a single grain) is 30μm, precisely the original measured hot band grain size and it can be seen from the channelling contrast image (figure 5a) of the recovered and lightly recrystallised microstructure that a line of subgrains (arrowed) is present curving through the centre of the grain. OIM is shown in figure 5b along with the orientations present in this volume. The orientation are localised into areas, the most prominent being the left side in which a single variant {111}<112> dominates. The right side consists of two components, the complementary {111}<112> to the left side segment, plus volumes spreading from this complement of {111}<112> towards {111}<110>. Such rotations are predicted to occur in DB modelling. Space presents examples of 3c being shown.

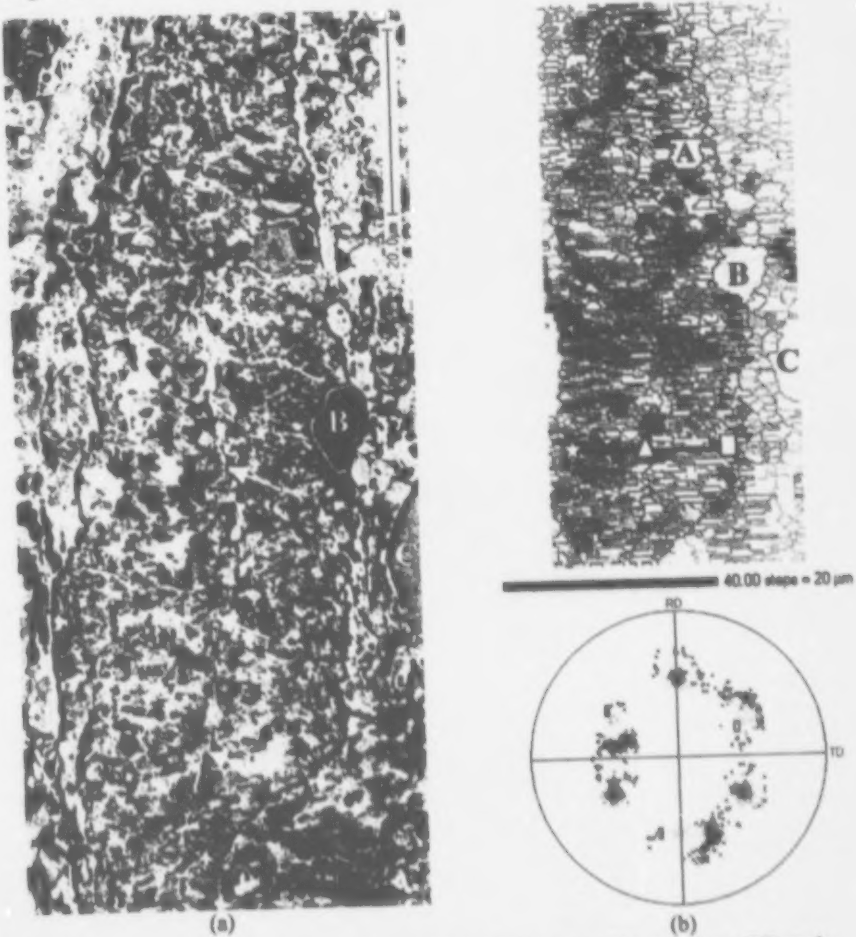

(a) (b)

Figure 5 **Channelling contrast image (a) and OIM image (b) showing a DB grain**

3. Summarising Discussion

It seems that all work attempting to link deformed microstructure to recrystallisation processes has, for good reason, concentrated on longitudinal sections for it is here that geometrically necessary dislocation are seen systematically to be associated with regular microstructures. Such microstructure can be associated with nucleation, which must also be a systematic process given the ubiquity of {111}<hkl> nucleation. Work done here up to quite recently was not able to improve on work done elsewhere and so explanation was suggested in particle solute effects. It is only by considering the deformation banding process in the one dimensional sense modelled here that has lead to surface examination and to the observations reported. Two points can be made: the DB modelling, even in a one dimensional sense, seem to be predictive of the actual orientation splitting that is observed which gives some confidence in the modelling procedure. The second is that the observed orientation splitting in crystals belonging to the γ fibre is capable of providing the necessary geometrical conditions for nucleation. When the gradient is sharp, *i.e.* {111}<hkl> is next to {111}<h'k'l') and the misorientation is ≥15° then nucleation can occur by SIBM. When there is a more gradual orientation gradient, then nucleation is also favoured because subgrain growth need not be too extensive before the necessary misorientation is created for runaway high angle boundary migration. Clearly, this work only provides a geometrical framework for nucleation, neither distribution of driving forces nor the effects of particles or solutes is included and these must also be of critical importance. However, given the three dimensional structure of cold rolled IF steel it is clear that longitudinal sections probably hide more than they reveal, when early recrystallisation processes are being examined either by TEM or SEM.

Acknowledgements

The authors would like to thank the Croucher Foundation and the Research Grants Council (Hong Kong), for the research grants supporting the work.

References

Chin, G. Y. (1969) *Textures in Research and Practice*, p. 236

Duggan, B. J., Liu G. L. and Zhang, L. X. (1998) *Materials Science Forum*, Vols. 273–275, p.291

Duggan, B. J., Liu, G. L. and Tse, Y. Y. (1999) *Recrystallisation '99*, to be published

Hu, H. (1963) *Recovery and Recrystallisation of Metals*, p. 311,

Lee, C. S. and Duggan, B. J. (1993) *Acta metall.* Vol. 41, No. 9, p.2691

Lee, C. S., Duggan, B. J. and Smallman, R. E. (1995) *Scripta Metall.*, Vol. 33, p. 727

Liu, G. L., Duggan, B. J. and Zhang, L. X. (1996) *ICOTOM–11*, p.318

Liu, G. L., Duggan, B. J. and Zhang, L. X. (1999) *EPD Congress 1999*, p.1019

INVESTIGATION OF STEEL SHEET RECRYSTALLISATION TEXTURES WITH A NEW PARAMETER MODEL FOR TEXTURE DESCRIPTION

L. DELANNAY, A. VAN BAEL and P. VAN HOUTTE
Department of Metallurgy and Materials Engineering, Katholieke Universiteit Leuven, Belgium
L. KESTENS and Y. HOUBAERT
Laboratory for Iron and Steelmaking, University of Gent, Belgium

Abstract

The recrystallisation texture of a steel sheet is influenced by the cold-rolling reduction prior to annealing. In order to study this relationship, textures have been characterised using a new parameter model for texture description in steel sheets. It relies on 25 parameters that characterise the intensity, the "thickness" and the true position of three fibres of the ODF: the classical α- and γ-fibres and the θ-fibre which comprises the "Goss" and "cube" components. For the purpose of this sensitivity study, a commercial steel sheet was cold rolled to different reductions varying between 65 and 95% and was annealed afterwards. The experimental ODFs are reproduced using the new parameter model. This allows for an efficient investigation of texture sensitivity based on the 25 relevant parameters. Besides the commonly observed shifts of intensity peaks to more stable crystallographic components, one recognises gradual changes in the position and the "thickness" of the fibres with increasing cold rolling reduction.

Keywords: Quantitative texture analysis, recrystallisation textures, steel sheets

1 Introduction

The crystallographic texture present in a cold-rolled and annealed steel sheet is responsible for the anisotropy of the material properties. For example, very slight changes in the Orientation Distribution Function (ODF) can strongly affect planar anisotropy (Delannay et al. 1999a). The optimisation of the sheet texture with regard to its further applications, requires fine-tuning of the rolling and annealing process conditions.

In the present study, we investigate how the level of cold rolling (CR) modifies the ODF obtained after annealing. For this purpose, six experimental textures corresponding to different CR-reductions are compared. It is expected that an increased CR-reduction lead to higher ODF intensities close to the {554}<225> component (Hutchinson and Ryde 1997). This can be concluded from the computation of crystallographic volume fractions (Bunge 1982).

A more detailed investigation of the sensitivity of texture on CR-reduction requires a quantitative comparison of the crystallographic fibres of the six experimental textures. This is carried out here by relying on a recently developed parameter model for the description of steel sheet textures (Delannay et al. 1999b). The latter model provides a complete description of the ODF based on 25 physical parameters. The value of these parameters is found automatically by the computer, for any experimental ODF. In the present study, it turns out that only few of the 25 parameter values systematically change with CR-reduction. A procedure is proposed to assess whether these parameters fully characterise the texture sensitivity, and to judge whether the texture reproduction is satisfactory.

2 Experimental procedure

The material used for the sensitivity study is a Ti-based Interstitial Free (IF) steel. It was industrially hot rolled with a reheating temperature of 1250°C and a finish rolling temperature of 920°C, that is austenitic rolling.

The sheet was then cold rolled on a laboratory mill with reductions of 65, 75, 80, 85, 90 and 95% respectively. Samples were annealed in a salt bath at 800°C, with 60 sec holding time. Finally, texture measurements were performed by measuring four pole figures on the mid-thickness section of the recrystallised samples. ODFs were calculated from these pole figures employing the software developed by Van Houtte (1995). Four of the six resulting ODFs are plotted in fig. 1a.

3 Texture reproductions

3.1 Presentation of the parameter model

The aim of this model is to provide a simple means of texture description in steel sheets. The model is based on the definition of 25 relevant parameters that are directly linked to visual aspects of the ODF. In this way, the parameter model helps to visualise the ODF in the three dimensions of the Euler space. Details about this model have been given by Delannay et al. (1999b).

The idea behind the model is that cold rolled and annealed steel sheet textures predominantly consist of three crystallographic fibres: α (<110> parallel to RD), γ (<111> parallel to ND), and θ (<100> parallel to RD). The latter θ-fibre comprises the "Goss" and "cube" components. The reader is referred to fig. 1 of another paper in the present volume (Delannay et al. 1999c) in which these three fibres are shown. In the same figure, ten points are defined: a_1-a_5 along α, g_1-g_3 along γ and t_1-t_3 along θ. The 25 parameters of the model define the ODF-intensity, the "fibre thickness" and the crystallographic orientation of these 10 points. The computer automatically finds the parameter values for any experimental texture.

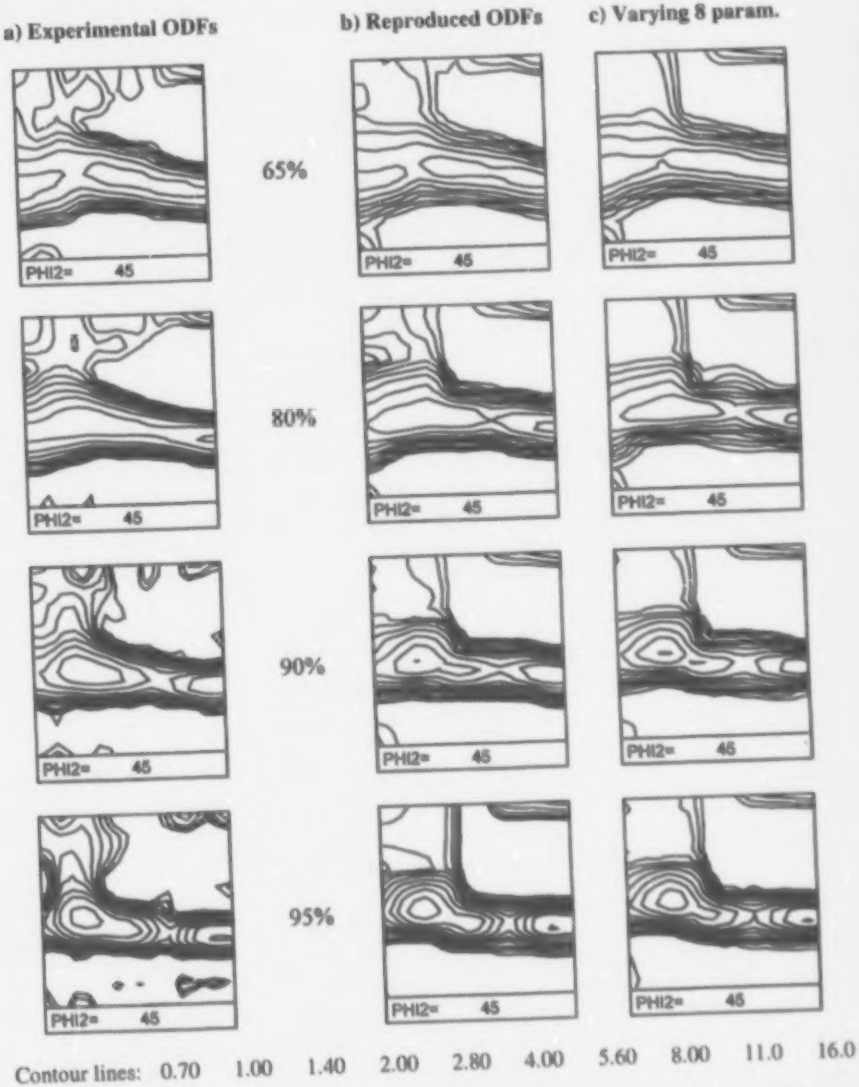

Figure 1: φ_2=45° ODF-sections obtained after various CR-reductions. a) Experimental ODFs; b) ODFs reproduced with the parameter model; c) ODFs generated by varying only 8 of the 25 parameter values.

3.2 Characterisation of the six experimental textures

The experimental textures that are compared have a strong γ-fibre and a weaker α-fibre. The θ-fibre is absent in all cases. Visual inspection of the different ODFs (fig. 1a) suggests that the main changes occur along the γ-fibre.

The computer code for texture reproductions was applied. Four of the six reproduced ODFs are plotted in fig. 1b. The resulting parameter values are presented in Table 1. One observes a gradual change with CR-reduction, of some parameters describing the γ-fibre. The evolution of most parameters characterising the weaker α- and θ-fibres is not so systematic. From this study, one may conclude that, by increasing the CR-reduction,

- the intensity at g_2 is strongly increased,
- the point g_3 of which the intensity is lowest at 65% CR-reduction, is shifted towards lower Φ and φ_2 orientations, (g_2 is thereby implicitly shifted as it must lie on the straight line joining g_1 and g_3),
- the point $g_1=a_3$ which is the intersection of α and γ, is shifted to lower Φ values (i.e. upwards in fig. 1), the same is true for a_4,
- the intensity at a_5 is decreased.

Table 1: Parameter values[*] corresponding to different CR-reductions.

Point		65%	75%	80%	85%	90%	95%
a_1	Intensity	1.83	1.37	2.55	1.31	1.88	3.34
	Thickness	5.46	5.72	4.82	5.62	5.34	5.58
a_2	Intensity	2.20	1.29	0.44	2.44	2.02	1.21
	Thickness	3.29	5.17	10.51	2.75	2.61	3.28
	Φ	30.5	29.5	25.5	30.9	28.5	29.9
a_2^*	Intensity	1.85	1.74	1.79	2.72	1.58	2.15
$a_3=g_1$	Intensity	6.59	10.01	8.32	7.85	7.40	5.59
	Thickness	3.32	2.25	2.46	2.69	2.33	2.47
	Φ	58.7	57.8	56.4	52.3	52.5	50.4
a_4	Φ	78.4	77.0	77.5	77.8	68.3	65.5
a_5	Intensity	1.66	1.08	1.30	0.35	0.90	0.79
	Thickness	4.63	3.48	1.59	3.71	2.83	1.06
$g_2^\dagger$	Intensity	6.73	11.56	10.75	12.44	17.35	23.07
	Thickness	2.55	1.96	1.70	1.78	1.50	1.42
	φ_1	14.9	18.3	12.7	14.9	21.2	18.2
g_3	Intensity	6.53	11.75	12.31	14.14	11.90	13.50
	Thickness	2.70	2.05	1.98	1.68	1.92	2.15
	Φ	53.8	53.6	54.9	55.6	47.7	49.6
	φ_2	51.2	52.0	50.0	49.9	47.2	47.2
t_1	Intensity	0.75	0.60	0.53	0.59	0.26	0.33
t_2	Intensity	0.52	0.43	0.56	0.50	0.37	0.25
	Thickness	5.83	5.65	3.34	3.29	4.00	7.48
	Φ	18.1	20.0	25.6	24.8	24.8	20.7
t_3	Intensity	0.25	0.44	0.24	0.26	0.43	0.42
	Thickness	8.28	2.80	8.66	6.19	3.36	2.90

[*] Refer to (Delannay et al. 1999c) in this volume for the parameter definitions.

[†] At high reductions (90%, 95%), g_2 approximately corresponds to {554}<225>.

3.3 Generation of ODFs by varying 8 parameters

It is stated above that only 8 of the 25 parameters are systematically modified from one texture reproduction to the next. We now assess whether these 8 parameters provide a quantitative description of the sensitivity of texture on CR-reduction:

- We generate a second set of ODFs using the parameter model in which only the 8 relevant parameters are varied. All other parameters are kept fixed to their averaged value of Table 1. The generated ODFs are plotted in fig. 1c.
- Then, we compute the value of a texture sensitive material property. The value is predicted three times: (i) from the experimental ODFs (fig. 1a), (ii) from the reproduced ODFs (fig. 1b), and (iii) from the ODFs generated varying only 8 parameters (fig. 1c). If the predictions are similar, the texture characterisation is judged satisfactory.

An important property of industrial steel sheets is their plastic planar anisotropy which is characterised by the r-value profile. This property can be predicted using the Taylor theory (Schouwenaars et al. 1996; Van Bael et al. 1996). Such predictions have been performed from the three sets of ODFs as illustrated on fig. 2. The r-value profiles predicted from the experimental and the reproduced textures are almost identical. Those predicted from the set of ODFs generated by varying 8 parameters are relatively satisfactory. They follow the same trend but fail to reproduce the exact level of the r-values. (Attempts to reproduce the textures with only 7 relevant parameters yielded much worse predictions of the r-value profiles).

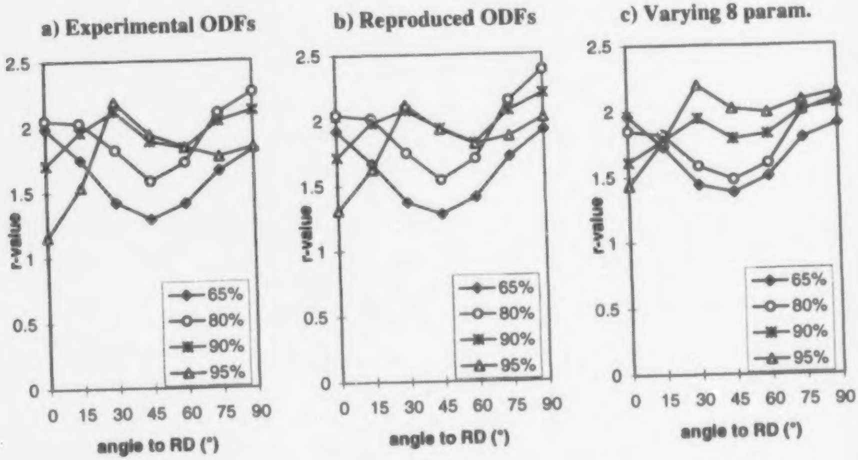

Figure 2: Predicted r-value profiles for a) the experimental ODFs; b) the ODFs reproduced with the parameter model; c) the ODFs generated by varying only 8 of the 25 parameter values.

4 Conclusion

We have quantitatively compared 6 experimental steel sheet textures corresponding to different CR-reductions prior to annealing. The comparison was based on a reproduction of the experimental ODFs using a recently developed parameter model. According to the study, 8 parameters are necessary to fully characterise the experimentally observed transformation of the ODF. Beside the increased intensity at {554}<225>, there is a systematic shift of the γ-fibre relative to its ideal position in Euler space, and a diminution of the intensity at the "bottom" of the α-fibre (point a_5). The relevance of the 8 parameters for this sensitivity study was further confirmed by computing r-value profiles from, respectively, the experimental ODFs, the reproduced ODFs and a set of ODFs generated by varying the 8 relevant parameters only.

5 Acknowledgements

One of the authors (LD) acknowledges his grant as "aspirant" of the "Fonds voor Wetenschappelijk Onderzoek - Vlaanderen". Financial support for this work was provided by the Federal Government of Belgium (DWTC) through the contract IUAP P4/33. D. Vanderschueren from OCAS n.v. (Zelzate, Belgium) is acknowledged for fruitful discussions during the elaboration of the parameter model.

6 References

Bunge, H.J. (1982) *Texture analysis in Material Science*. Butterworths, London.

Delannay, L., Van Houtte P., Van Bael, A. and Vanderschueren D. (1999a) New parameter model for texture description in steel sheets - Sensitivity of planar anisotropy on texture. *Model. and Simul. in Mat. Sci. Eng.*. (In press).

Delannay, L., Van Houtte P. and Van Bael, A. (1999b) New parameter model for texture description in steel sheets. *Textures and Microstructures*, (in press).

Delannay, L., Van Bael, A. and Van Houtte P. (1999c) Parameterisation of cold-rolling and annealing textures in cubic metals based on the crystallographic fibres. *These proceedings*.

Hutchinson, B. and Ryde L. (1997) Proc. Int. Conf. Thermo-Mechanical Processing [TMP]2, Ed. by Hutchinson, B., Andersson, M., Engberg, G., Karlsson, B. and Siwecki, T., pp. 145-161.

Schouwenaars, R., Van Houtte, P., Van Bael, A., Winters, J. and Mols, K. (1996) Analysis and prediction of the earing behaviour of low carbon steel sheet. *Textures and Microstructures*, No. 26-27, pp. 553-570.

Van Bael, A., Van Houtte, P. and Winters, J. (1996) *Proc. 11th ICOTOM*, Liang Z., Zuo L. and Chu Y. Eds., International Academic Publishers (Beijing), vol. 1, pp. 356-361.

Van Houtte P. (1995) *User Manual of the MTM-FHM software, version 2*, Department MTM, K.U.Leuven.

RECRYSTALLISATION TEXTURE DEVELOPMENT IN COLD ROLLED SUPER DUPLEX STAINLESS STEEL

J. KEICHEL, M. CRUMBACH, P. SCHRAVEN and G. GOTTSTEIN
Institut für Metallkunde und Metallphysik, RWTH Aachen, 52056 Aachen, Germany
J. FOCT
Laboratoire de Metallurgie Physique et Genie des Materiaux, UMR CNRS 8517, Université de Lille I, 59655 Villeneuve d'Ascq, France

Abstract

The texture development of three cold rolled and annealed (super) duplex stainless steels is presented for the austenite and ferrite phases and compared with single phase materials. The austenite texture development is related to primary recrystallisation while the ferrite textures reveal mainly recovery accompanied by recrystallisation. Two different heat treatments, one in a salt bath furnace (1100°C) and the other one in a conventional furnace (1050°C), accompanied by transformation and precipitation result in the same textures after all.

Keywords: duplex stainless steel, texture, recrystallisation, microstructure

1 Introduction

Duplex stainless steels (DSS) have been known since the 1930's, but due to an insufficiently accurate chemical analysis and too high residual levels, two important prerequisites for reproducible properties, their successful use in corrosive environments under high mechanical duty is rather recent. Meanwhile it is predicted that duplex stainless steels will reach 5% share of the stainless steels market in 2005 [Mou]. In this class of materials the high nitrogen alloyed grades seem to have the most promising properties and economic qualifications. While the texture development of cold rolled and annealed single phase steels (ferritic and austenitic steels) is well known, the texture evolution in duplex stainless steels has not been systematically investigated and is poorly understood.

2 Experimental methods

The composition of the investigated steels is given in table 1. These duplex and super duplex stainless steel grades - the terms refer to their pitting resistance equivalent

(PRE) - are commercial alloys with different thermomechanical histories. DSS 1 was an extruded and round forged rod material Ø 30 mm, DSS 2 was a hot rolled plate with 6 mm thickness and DSS 3 was available as slab of an ingot. Prior to the recrystallisation experiments all samples were homogeneously unidirectionally cold rolled with the same pass sequence under oil lubrication at room temperature on a laboratory rolling mill up to a thickness reduction of 90%. The annealing treatments were carried out in a salt bath furnace at 1100°C and in a conventional air furnace at 1050°C both with subsequent water quench. While the salt bath annealings allowed softening mechanisms to develop without being influenced by precipitation, the conventionally annealed samples experienced a lower heating rate and slowly passed phase fields where transformations and precipitates like σ-phase, χ-phase and CrN_2-nitrides had time to form. The microstructure was investigated by optical microscopy and TEM. All textures were determined from the normal direction (ND) in the sheet center layer with Co-Kα1 radiation (λ=1.79 Å) by means of incomplete pole figures in the range of the pole distance angle α from 5 to 75°, three [{200}, {220}, {113}] for the austenitic phase and two [{200}, {112}] for the ferritic phase in the back reflection mode on a fully automatic texture goniometer. By use of a position sensitive detector (PSD) it was possible to record and deconvolute the {111} austenite and {110} ferrite pole figures despite of their close interplanar spacing ($d^a_{\{111\}} \approx d^f_{\{110\}}$). Single orientation measurements were carried out by EBSD technique.

Table 1. Composition of the investigated duplex (DSS 1) and super duplex (DSS 1 and 2) alloys.

steel	% N	% Cr	% Ni	% Mo	% Mn	% Cu	% C	% Fe
DSS 1	0.153	24.16	5.48	3.27	1.20	-	0.022	rest
DSS 2	0.25	25.00	6.50	3.50	-	1.50	<0.03	rest
DSS 3	0.62	22.50	2.80	2.52	0.46	0.025	0.025	rest

3 Results

The austenite/ferrite ratio changed with increasing nitrogen content due to its strong austenite stabilising properties from 45/55 for DSS 1 over 50/50 for DSS 2 to 60/40 for DSS 3. In DSS 1 and 2 ferrite represented the matrix phase while in DSS 3 ferrite was the inclusion. Figure 1 shows schematically the microstructure development during annealing without occurrence of precipitation or transformation as obtained for annealings with high heating rates e.g. in a salt bath furnace at 1100°C [Keichel]. First new small grains appeared in the ferritic layers while the other elongated phase sections remained in the as rolled state (Fig. 1 a). Instantly the ferrite formed a kind of bamboo structure with grain boundaries extending perpendicular to

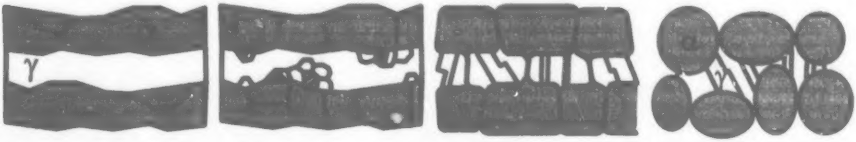

Fig. 1: Schematical microstructure development during annealing (a,b,c,d). Rolling direction →.

the rolling direction through the whole phase (Fig. 1 b). The austenite underwent primary static recrystallisation with nucleation at phase and grain boundaries. Subsequently, grain growth occurred until a bamboo like structure, intersected by many twins, had formed (Fig. 1 b, 1 c). After grain growth and comparably long annealing times the flat phase morphology started to break up by coarsening and a kind of pearl structure developed (Fig. 1 d). The annealing experiments conducted in a conventional furnace at 1050°C of cause required longer annealing times to accomplish softening. Additionally, due to a lower heating rate the samples underwent precipitation, mainly CrN_2 precipitates besides others (DSS 1, DSS 2, DSS 3). Depending on chemical composition and microstructure dimensions ferrite transformed to a greater part to austenite and σ- and/or χ-phase (DSS 2). In the course of annealing both the precipitates and the transformation products dissolved, respectively retransformed, and afterwards the microstructure developed like in the salt bath annealed case, shown in figure 1. Only in the very high nitrogen alloyed DSS 3 precipitates remained stable for even longer annealing times.

Objective of the current investigation was the effect of microstructure on the texture development of both phases during annealing? Despite different initial textures because of their entirely different hot deformation, after 90% cold rolling all austenite textures (fig. 2, 0s) were qualitatively comparable and similar to those of other cold rolled materials with low stacking fault energy (SFE), e.g. brass 30% Zn [Savoie, Engler]. The austenite texture of all three cold rolled steels was dominated by an α–fiber with the typical maximum intensities in the {011}<211> Brass- (B) orientation. In DSS 1 also {011}<100> Goss (G) constituted high intensities. Additionally all steels comprised an incomplete β-fiber with weak intensities from {123}<634> (S) to the B orientation. While DSS 1 and 3 showed nearly the same austenite texture intensities after cold rolling, in DSS 2 the values were about 50% higher. After 80 seconds annealing (fig. 2, 80s) there was only a small intensities loss for DSS 1 and 3, while the texture of DSS 2 sharpened slightly. During this time all austenite textures remained qualitatively nearly unchanged. After 200 seconds the intensities of DSS 2 decreased strongly to about 50% compared to the as cold rolled state and in all steels the β-fiber orientations between S and B started to disappear, while the {11 11 8}<4 4 11> Taylor- (D) orientation developed. While after 5000 seconds furnace time the austenite texture of DSS 3 consisted of only some weak α-fiber remnants and β-fiber compounds between D and S, the texture of DSS 1 and 2 sharpened again with G, B and D orientations as main components (fig. 2, 5000s).

The ferrite textures of DSS 1, 2 and 3 (fig. 3) differed more than the austenitic textures. Apparently the different manufacture of the test material and the different phase distribution had a strong effect on texture. After 90% cold rolling the textures still distinctly differed from each other (fig. 3, 0s). In such cases where the ferrite presented the matrix phase (DSS 1 and 2) the ferrite texture intensities were higher than the austenite texture intensities. In DSS 3 where ferrite was the enclosed phase the intensities were not considerably lower but the austenite (matrix) phase intensities were higher. DSS 1 exhibited a strong γ-fiber with maximum intensities at {111}<110> and a weaker 45° ND rotated cube orientation (RC) with spread along the α-fiber. DSS 2 showed a balanced incomplete α-fiber from RC to the scattered γ-fiber compound {111}<110>. This is similar to single phase ferritic chromium steels

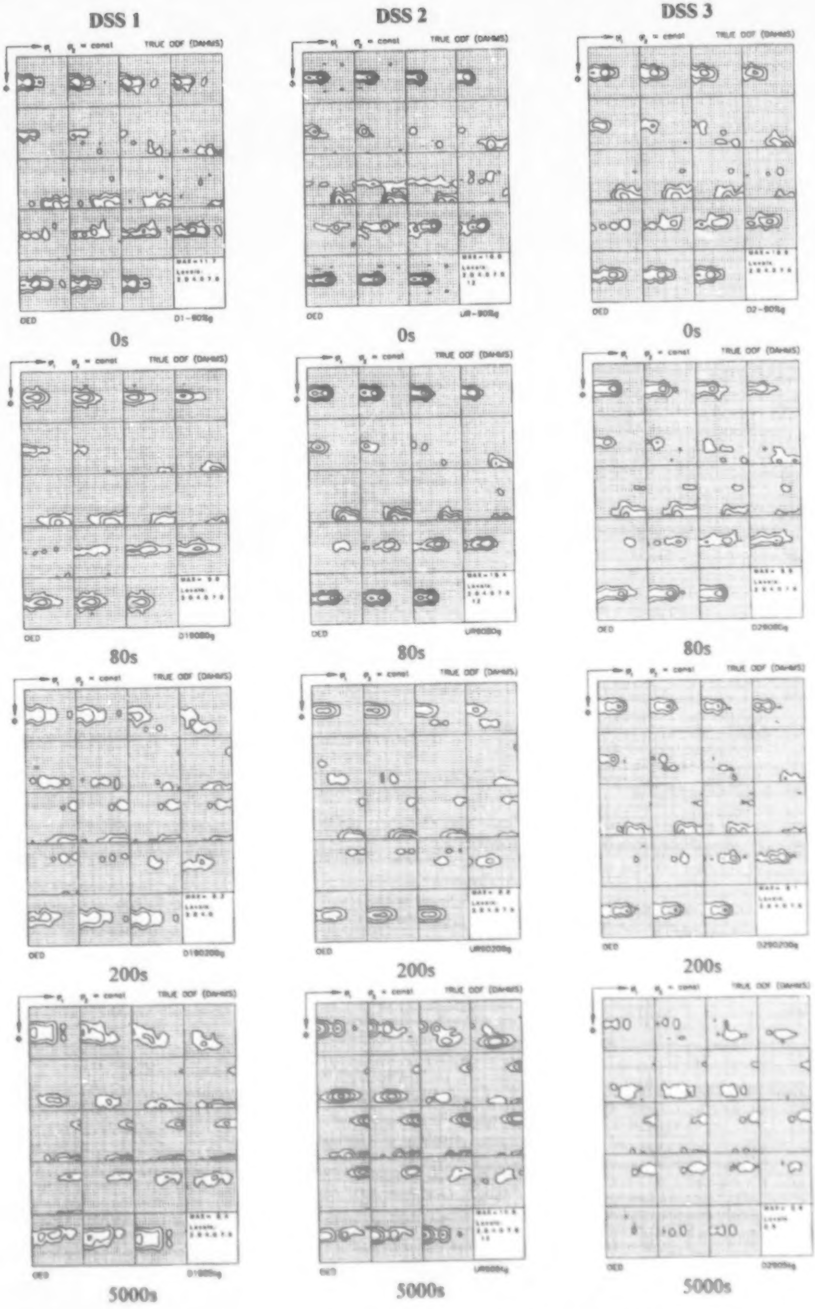

Fig. 2: Austenite texture development of DSS1, DSS2 and DSS 3 during annealing at 1050°C.

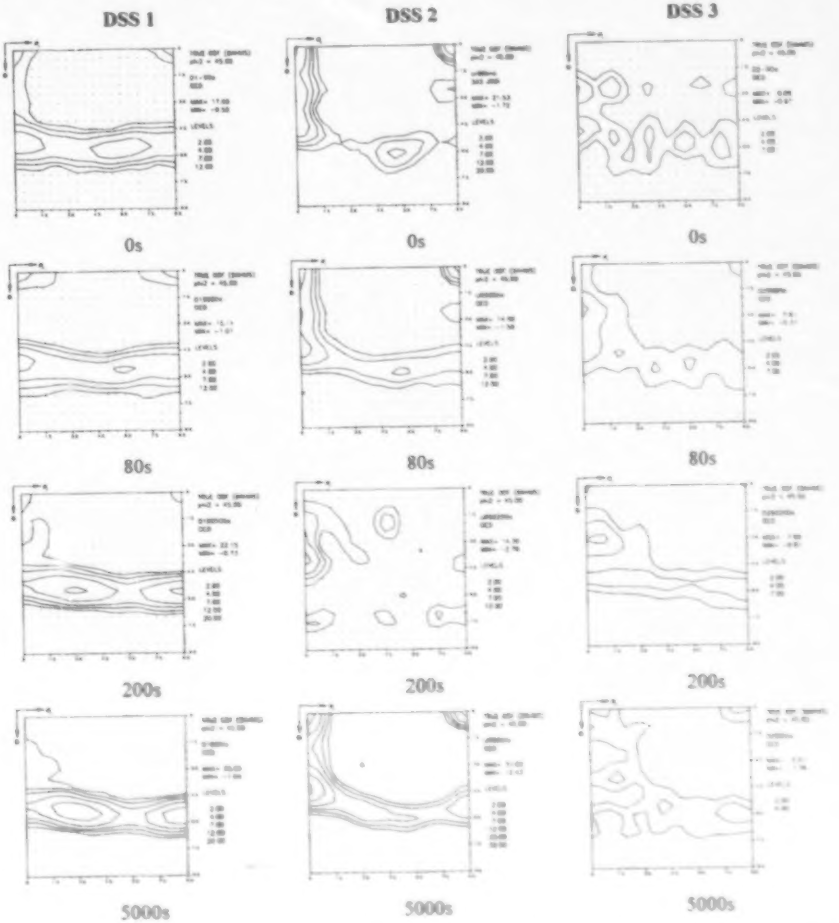

Fig. 3: Ferrite texture development of DSS 1, DSS 2 and DSS 3 during annealing at 1050°C, selected furnace times.

[Raabe]. DSS 3 developed some α- and γ- fiber components during cold rolling. The shown orientation distribution function does not reflect good statistics for the ferrite pole figure measurements in DSS 3 because of the reduced phase content in addition to the large deformation and thus high dislocation density. After 80 seconds annealing the intensities decreased slightly, and the textures of all steels - in particular the γ-fibers - appeared more balanced (fig. 3, 80s). In the annealing period between 100 and 300 seconds precipitates of CrN_2 (DSS 1, 2, 3), and transformation to secondary austenite, σ- and κ-phase took place for a large fraction of the ferritic phase in DSS 2. Due to the transformation the ferrite texture of DSS 2 perished with the exception of {112}<110> orientations after a 200 seconds anneal (fig. 3, 200s). The texture of DSS 3 remained nearly unchanged, respectively slightly sharpened in the case of DSS 1 for this annnealing time. After 5000 seconds the γ-fiber of DSS 1 increased up to as high intensities as 28-times random. The ferrite texture of DSS 2 qualitatively reappeared again after the mentioned transformation and then revealed twice as high intensities at RC and {111}<110> with an absolute maximum of 31.6. For DSS 3 the texture components appear spread out with decreased intensities (fig. 3, 5000s).

TEM microstructure investigations elucidated that after formation of the bamboo structure, nearly the whole ferrite phase consisted of large subgrains inside these bamboo segments. The few observed new ferrite grains, first visible in the beginning of the annealings (fig. 1a), partly remained in the new structure. During single grain orientation investigations inside these grains no pattern shift or rotation was observed i.e. no large misorientations were observed. Mostly stable orientations close to {111}<112> on the γ-fiber or α-fiber orientations were found.

4 Discussion

The austenite microstructure and texture development indicated primary recrystallisation for the austenitic phase. While the rolling texture development, resulting in a typical Brass type texture and qualitatively independent of pre-treatment and phase distribution (matrix or inclusion), was quite similar to other face centred cubic materials with low SFE, the annealing textures did not exhibit the usual recrystallisation texture components. The development of D orientations during recrystallisation accompanied by decreasing {011}<100> α-fiber intensities can be explained by a twinning relation between Goss and D. This is also known from recrystallisation textures in Cu- 1%P where also D instead of {236}<385> (BR) develops [Gottstein]. Since the phosphorus reduces the grain boundary mobility nuclei with usually fast growing orientations, e.g. the BR-orientations [Engler], are not favoured anymore. Because the nuclei consist predominantly of orientations of the deformation microstructure, the texture remains almost unchanged and only the described twinning results in new orientations and thus, texture alteration during recrystallisation. Also CrN_2 nitrides or other precipitates could have acted as obstacles for grain boundary migration in the investigated duplex stainless steels, but recrystallisation in the salt bath furnace, where no precipitates by TEM were found, resulted in the same texture. It seems improbable that the high nitrogen content caused a drag effect on grain boundary motion because the diffusion rate of nitrogen at those annealing temperatures was more than sufficient to allow nitrogen to follow the grain boundaries. The influence of precipitation on the austenite texture development concerns only DSS 3, where precipitates did not dissolve for long annealing times and texture intensities finally did not increase again. In DSS 1 and 2 grain growth and ripening lead to texture sharpening while this was hindered by precipitates in DSS 3.

TEM investigations and texture analyses showed that the ferrite deformation microstructure suffered recovery and subsequent subgrain growth. Due to the different deformation textures, the ferrite annealing texture development was not unique but besides dominant recovery showed certain correspondence. The γ-fiber orientations near {111}<112> grew at the expense of α-fiber orientations near {110}<112>. This is known from the recrystallisation of single phase ferritic chromium steels [Raabe]. The described single grain orientation investigations substantiated that the first energising grains belonged to α-fiber and {111}<112> orientations. After longer

EP

annealing times only some of the γ-fiber grains asserted in the microstructure. These grains were recrystallized rather than recovered since almost no orientation rotation inside these grains was recognizable like in that part of the recovered bamboo structure that consisted of big subgrains. The influence of precipitates energizing and dissolving during the annealing on ferrite texture development is negligible. In DSS 2 the ferrite transformed to austenite and σ-phase but after the retransformation to ferrite the texture appeared almost unchanged. This proves an orientation correspondence during transformation between austenite, σ-, κ-phase and ferrite [Brückner].

5 Conclusions

The texture development during annealing of duplex stainless steels shows some correspondence to single phase austenitic and ferritic materials. But due to the presence of a second phase and possible changes from connected to unconnected phase morphology (depending on chemical composition) there are specific differences. These differences are caused by effect of second phases on the deformation mechanisms during hot and cold deformation. For the austenitic phase typical Brass type rolling textures were found. The microstructure and the annealing textures revealed strong twinning and primary recrystallisation. The ferrite texture development was dominated by recovery followed by primary recrystallisation which intensified the γ-fiber. While the austenite texture seems not to be very sensitive to different thermomechanical treatment, the ferrite texture surely is.

6 Acknowledgements

The financial support by the ECSC Program is gratefully acknowledged.

7 References

Brückner, G., Aretz, W. and Gottstein, G. (1996) In situ measurement of the transformation texture of a microalloyed LC steel. Proc. ICOTOM 11, Vol. 1, p 592.

Engler, O., Hirsch, J. and Lücke, K. (1995) Texture development in dual phase α/β-brass - Part I and Part II. Zeitschrift für Metallkunde, Vol. 86, pp. 465-484.

Gottstein, G. (1984) Rekristallisation metallischer Werkstoffe. DGM Verlag.

Keichel, J., Gottstein, G. and Foct, J. (1999) Recrystallisation in high nitrogen alloyed super duplex stainless steel. Proc. HNS 98.

Mou, M.A., Proc. Duplex Stainless Steels 97 5th World Conference, Maastricht.

Raabe, D. (1992) Texturen kubisch-raumzentrierter Übergangsmetalle. Dissertation RWTH-Aachen.

Savoie, J.F. (1990) Einfluß des Zinkgehaltes und der Korngröße auf die Walz- und Rekristallisationstexturentwicklung in α-Messing. Dissertation RWTH-Aachen.

TEXTURAL AND STRUCTURAL CHANGES DURING ANNEALING OF A HEAVILY COLD DEFORMED $Ni_3Al(B,Zr)$ ALLOY

B. BHATTACHARYA* and R. K. RAY
Department of Materials and Metallurgical Engineering
Indian Institute of Technology, Kanpur-208016 (INDIA)

*CRM Project, TISCO Jamshedpur-831001 (INDIA)

Abstract

The paper describes the changes in texture, microstructure and ordering behaviour of a 73% cold rolled $Ni_3Al(B, Zr)$ alloy after being subjected to recrystallisation annealing. This alloy is made up of two phases, namely, ordered γ' and disordered γ. In the initial stages of annealing the deformed material undergoes both recovery and reordering. The cold rolled material, which has a DO_{22} structure, undergoes a change in order during the recovery stage itself, leading to the formation of the initial (undeformed) $L1_2$ structure. The weak texture at the end of recovery persists even during recrystallisation, leading ultimately to a texture which is not far from the random.

Key words: Annealing texture, $Ni_3Al(B, Zr)$, recovery, recrystallisation, texture transition

Introduction

The two phase Ni_3Al base alloy, commercially known as IC50, contains the phases γ' (ordered $L1_2$) and γ (disordered FCC). This alloy is used as a master alloy for the manufacture of the other multiphase Ni_3Al base alloys meant for advanced engineering applications. The production of these alloys in sheet form may require processing schedules comprising cold work and annealing treatments. This will produce both microstructural and textural changes within the material. Although the evolution of texture and microstructure during thermomechanical processing of the basic $Ni_3Al(B)$ alloy composition has been examined by several workers, very limited amount of work has so far been reported on the IC50 alloy. An attempt has therefore been made in this paper to characterise the textural and structural changes during annealing of a heavily cold deformed $Ni_3Al(B, Zr)$ alloy (IC50). The evolution of crystallographic texture in this alloy during cold deformation has been reported in an earlier publication [Ray et al. 1996].

Experimental

The nominal composition of the alloy was Ni-21.8Al-0.1B-0.34Zr (in atomic percent). The continuously cast alloy sheet (~1 mm thickness) was subjected to homogenisation annealing at 1160°C for 24 hrs to produce a two phase ($\gamma'+\gamma$) microstructure with an average primary grain size (of γ') of 40-45 μm. The volume fraction of the second phase (γ) was about 25 percent.

The alloy was subjected to cold rolling in a 2-high laboratory rolling mill to 73% reduction in thickness. This was then subjected to isochronal annealing for 1 hr, at temperatures ranging from 500°C to 1200°C, with intervals of 100°C. Isothermal annealing treatments were done at five temperatures, namely, 800°C, 900°C, 1000°C, 1100°C and 1200°C, for various lengths of time ranging from 1 min to150 hr.

Texture studies on a number of samples were carried by using ODF (Orientation Distribution Function) method of Bunge while a few selected samples were mechanically thinned, followed by electropolishing for the purpose of TEM (Transmission Electron Microscopy) study.

Results and Discussion

The ODFs of the 73% cold rolled material and of those annealed at 900°C for 4 min, 10 min, 1 hr and 10 hr are presented in Figs 1(a-e). It is clear from these plots that after 4 min anneal, the overall texture intensity decreases only marginally from that of the 73% rolled material, although the nature of the ODF shows a discernible change. From the annealing time of 10 min onwards, the texture intensity reduces drastically and thereafter remains more or less unchanged for longer periods of annealing.

The variation of textural intensity with annealing time can be better illustrated with the help of the β fibre plots (Fig. 2). The corresponding volume fractions of recrystallisation are listed in Table 1.

A close inspection of Fig. 2 and Table 1 reveals that both the Cu and the Bs components decrease in intensity at the very early stage of recrystallisation. A situation close to the equilibrium is reached after 1 hr annealing, beyond which the overall texture does not undergo any significant change.

From the above it becomes clear that sharpness of the deformation texture decreases drastically much before the volume fraction of recrystallisation reaches a significant amount. The texture of the material after 10 min and 1 hr of annealing at 900°C (Fig. 1 c and d) illustrate this point. The volume percent of recrystallisation at these two conditions are found to be 8% and 10% respectively. Therefore any change of the overall texture at these stages can be ascribed to mostly recovery preceding recrystallisation and only marginally to the recrystallisation process. Although the overall intensity of the texture does not practically change after 4 min annealing at 900°C, the β fibre plot (Fig. 2) shows the drastic decrement of the intensities at the Cu {112}<111>, S{123}<634> and Bs/S {168}<211> locations and an increase in the Bs {011}<211> position.

The textural changes, during deformation and recrystallisation, in a $Ni_3Al(B,Zr,Fe)$ alloy were investigated by Gottstein et al. [Gottstein et al. 1989] and Ball et al. [Ball et al. 1995]. They, however, did not attempt measurement of texture

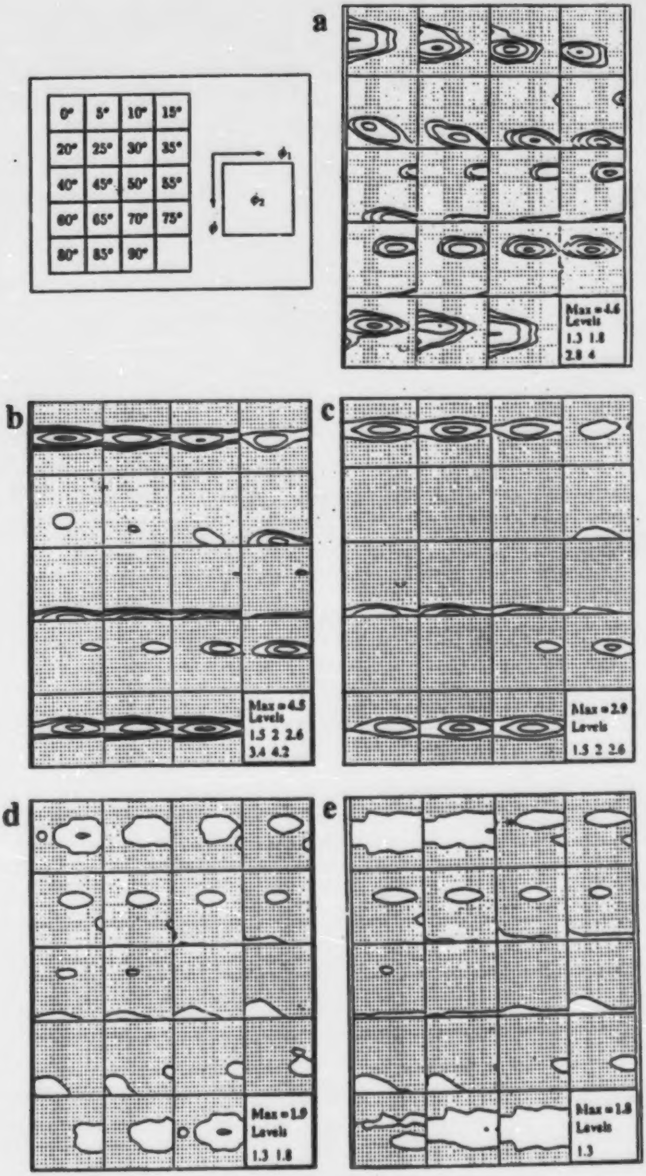

Figs 1 The ODFs of (a) the 73% cold rolled material, and of those annealed at 900°C for (b) 4 min, (c) 10 min, (d) 1 hr and (e) 10 hr

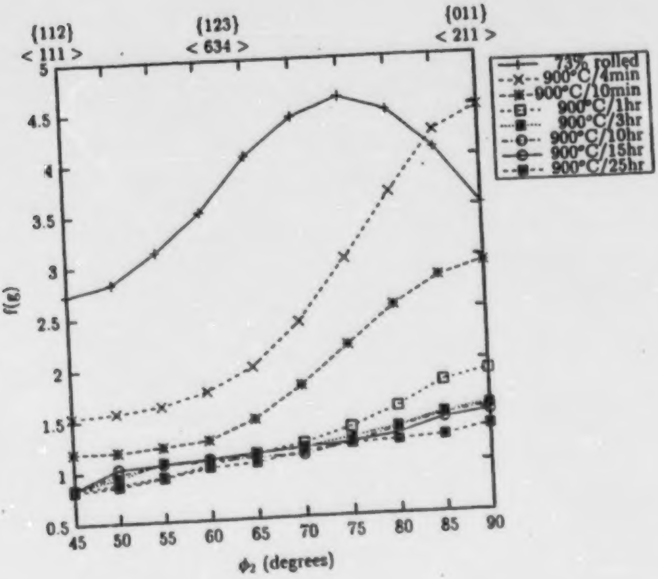

Fig. 2 β-fibre plots for the materials annealed at 900°C for different lengths of time

Table 1 Recrystallised volume fraction with annealing time at 900°C

Time of Annealing	Fraction recrystallised
4 min	4 %
10 min	8 %
1 hr	10%
3 hr	46%
10 hr	94%
15 hr	100%
25 hr	100%

during the recovery stage. Ghosh Chowdhury et al. [Ghosh Chowdhury et al. 1998] who made a systematic study of structural and textural changes during processing of a single phase $Ni_3Al(B)$ alloy, reported a marked weakening and change of the cold rolling texture during the very early stage of annealing prior to recrystallisation. They also showed that during cold rolling there is a gradual but perceptible change from the $L1_2$ structure of the γ′ phase to DO_{22}. Again the DO_{22} structure of the heavily cold rolled γ′ has been found to transform back to the initial $L1_2$ during recrystallisation annealing. This structural transformation is much faster during initial recovery stages [Ghosh Chowdhury et al. 1996].

Thus the drastic weakening of texture during the recovery stage itself can be correlated with changes in order of the material from DO_{22} to $L1_2$. It is now quite clear that before any significant recrystallisation takes place, the material already possesses a weak texture. TEM examinations have revealed that the first recrystallisation nuclei to appear are the ones in the γ region within the shear bands (Fig. 3 a). The final size of the recrystallised grains is rather small and the grain growth has also been found to be quite sluggish. The small size of these grains can be attributed to the high nucleation rate in the shear bands and low grain boundary mobility due to the presence of Zr. As recrystallisation progresses, numerous such grains will appear which will lack any growth selection and as a result the overall texture will be very weak. Many of the earlier formed recrystallised grains are found to contain (cellular) precipitates inside them (Fig. 3 b).

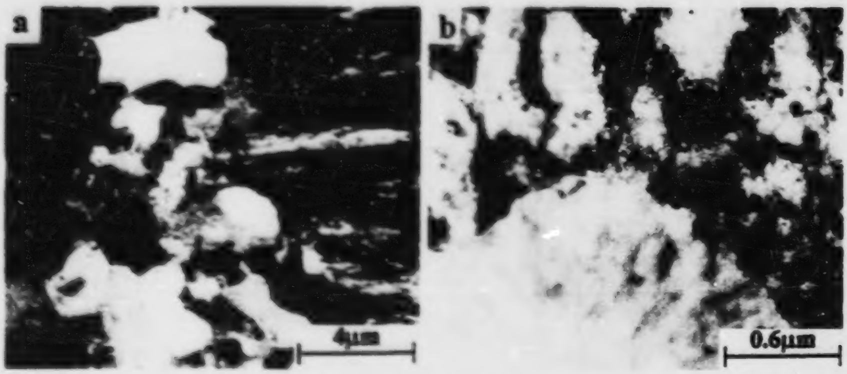

Fig. 3 TEM micrographs of the materials annealed at 700°C showing (a) recrystallisation nuclei within the shear band, and (b) cellular precipitation inside the recrystallised grains

Recrystallisation of the γ' regions will start later after the deformed γ regions are more or less fully recrystallised. The process is expected to be quite sluggish as the mechanism of recrystallisation in the ordered state will involve migration of only low or medium angle boundaries. Finally when all the deformed γ and γ' regions are fully recrystallised, a very weak (nearly random) texture will be produced.

Conclusions

1. Annealing of the 73% cold rolled $Ni_3Al(B, Zr)$ alloy comprises two main stages, recovery and recrystallisation. The recovery stage is accompanied by the reverse structural transformation of the γ' phase from DO_{22} to $L1_2$, whereas the recrystallisation stage is accompanied by a cellular precipitation within γ.

2. The overall texture intensity drastically reduces during the recovery stage and remains so till recrystallisation is complete. This appears to be due to a high density of randomly oriented nuclei at the beginning of recrystallisation. The final recrystallised material has a texture not much different from random.

Acknowledgement

The authors are grateful to Prof. G. Gottstein, Director of the Institut fur Metallkunde, RWTH Aachen, Germany for kindly providing the laboratory facility for texture measurement.

References

Ball, J., Zeumer, B. and Gottstein, G. (1995) Intermetallics, Vol. 3, p.209.
Ghosh Chowdhury, S., Ray, R. K. and Jena, A. K. (1998) Mater. Sci. & Engg., A 246, p. 289.
Ghosh Chowdhury, S., Ray, R. K. and Jena, A. K. (1996) J. Mater. Sci. Letters, Vol. 15, p. 1710.
Gottstein, G., Nagpal, P. and Kim (1989), W., Mater. Sci. & Engg., A 108, p. 209.
Ray, R. K., Bhattacharya, B. and Ghosh Chowdhury, S. (1996) Proc. of ICOTOM-11, Sept. 1996, Vol. 1, p. 336.

FORMATION OF THE CUBE BAND AND ITS EVOLUTION DURING RECRYSTALLIZATION

Y.B. Park, Y.H. Kim and B.I. Kim
Department of Materials Science and Metallurgical Engineering, Sunchon National University, Sunchon, Korea

Abstract

Concept of effective slip system was suggested to visualize deformation geometry of a deformed grain. It was demonstrated that the shear components could be formed in the shear bands inside each grain of fcc metals and alloys deformed under plane strain conditions. A recrystallization model originally proposed for bcc materials was developed to explain the evolution of the cube and rotated cube components dominating recrystallization textures of fcc materials. The model relies on two principles: a strain energy release maximization component and higher boundary mobility. The prediction calculated using the model is in good agreement with the observation in cold rolled and annealed aluminum.

Keywords: Deformation, effective slip, recrystallization, shear band, textures,

1 Introduction

Recrystallization textures of fcc metals and alloys are characterized by a strong development of the cube component, {100}<001>. However, the fundamental mechanism that the cube recrystallization component evolves from the deformed matrix is not yet clarified, and thus, this has provided a matter of dispute in the last decades (Humphreys and Hatherly, 1995). With the aid of advanced analysis equipments, the recent studies on the textures of fcc metals frequently reported that the cube orientation is observed in the deformed matrix (Vatne et al., 1996; Engler et al., 1996). The cube-oriented grains (or volumes) are of band-like structures and always lie parallel to the rolling direction of sheets. For the formation of the cube band, there are two controversial models: (i) the transition band mechanism suggested by Dillamore and Katoh (1974); (ii) the retention of the cube-oriented grains formed in the starting materials (Vatne et al., 1996; Engler et al., 1996).

Both the models commonly claim that the cube component of the recrystallization textures takes place in the cube band of the deformed matrix and grow rapidly into the other components of the deformation texture due to its high boundary mobility. However, this interpretation seems to be ambiguous between the theories of oriented nucleation and oriented growth. Furthermore, fundamental ambiguity appears to originate from the above conventional approaches to explain the formation of the cube band observed in the deformed matrix. Therefore, in order to elucidate the development of the cube recrystallization texture, the origin of the cube band should be necessarily understood.

In the present work, for cold rolled aluminum sheet, concept of "effective slip" has been employed to explain the formation of the cube band (or component)) under the consideration of the active slip systems and deformation geometry. Finally, the evolution of the cube recrystallization component will be discussed in terms of a new recrystallization model (Park et al., 1998). The latter that was originally proposed for bcc materials has been modified for the application to fcc materials.

2 Model description

Consider a plane strain deformation given by Eqn (1).

$$\varepsilon = \begin{bmatrix} \varepsilon & 0 & 0 \\ 0 & 0 & 0 \\ 0 & 0 & -\varepsilon \end{bmatrix} \tag{1}$$

This expression is referred to the principal axes. Such a plane strain deformation transforms into a pure shear state by rotating the reference system over 45° around the Y-axis, namely

$$\gamma = \begin{pmatrix} 0 & 0 & \gamma_{13} \\ 0 & 0 & 0 \\ \gamma_{13} & 0 & 0 \end{pmatrix} \tag{2}$$

Combination of a pure shear deformation and a rigid body rotation results in a simple shear as follows.

$$\begin{pmatrix} 0 & 0 & \gamma_{13} \\ 0 & 0 & 0 \\ \gamma_{13} & 0 & 0 \end{pmatrix} + \begin{pmatrix} 0 & 0 & \gamma_{13} \\ 0 & 0 & 0 \\ -\gamma_{13} & 0 & 0 \end{pmatrix} = \begin{pmatrix} 0 & 0 & 2\gamma_{13} \\ 0 & 0 & 0 \\ 0 & 0 & 0 \end{pmatrix} \tag{3}$$

The rotation expressed by the second term of the left hand of Eqn (3) may occur due to a condition that the plane strain deformation is obstructed during deformation of a body. Therefore, the change of strain path given by Eqn (3), i.e. from pure shear to simple shear, is accompanied by the modification of the slip systems that are active in the corresponding body.

Contribution of each active slip system to the shape change in a deformed grain is assumed to be proportional to the amount of shear on it. Therefore, if more than one slip system is activated along a given slip plane, the effective slip direction may be calculated by a vector sum of shears on the active slip systems. For example, when the shears occur on the (111) plane in the $[01\bar{1}]$ and $[10\bar{1}]$ directions, the effective slip direction is derived by a vector sum as follows.

$$a[01\bar{1}] + b[10\bar{1}] = [\mathrm{uvw}] \tag{4}$$

where a and b denote the relative amounts of shears along the respective slip directions. Therefore, the effective slip system is (111)[uvw], and when $a = b$, it becomes $(111)[11\bar{2}]$. This effective slip system is expected to produce the same shape change as the relevant active slip systems, $(111)[01\bar{1}]$ and $(111)[10\bar{1}]$.

On the other hand, in case of co-directional slip, for example $(\bar{1}11)[110]$ and $(1\bar{1}1)[110]$, contribution of each slip plane to the shape change is assumed to be proportional to the amount of shear along it.

$$c(\bar{1}11) + d(1\bar{1}1) = (\mathrm{hkl}) \tag{5}$$

where c and d denote the relative amounts of shears on the respective slip systems. Therefore, the effective slip system is (hkl)[110], and when $c = d$, it becomes (001)[110]. In the following, this method will be applied to determine the effective slip systems for the texture components dominating the cold rolling texture of fcc metals and alloys. In order to calculate the amounts of the shears on each of the active slip systems, a strain rate sensitivity model based on Taylor assumption was employed under the assumption of the activation of the {111}<110> slip systems (total 12 slip systems).

Figure 1 depicts that a $(112)[11\bar{1}]$ oriented grain is embedded in a polycrystalline specimen cold rolled under plane strain conditions. Visualize, for simplicity, the shape of a deformed grain as an orthorhombic parallelepiped although the morphology of cold rolled grains is frequently observed to be irregularly elongated. Activation of the $(111)[01\bar{1}]$, $(111)[10\bar{1}]$, $(\bar{1}11)[110]$ and $(1\bar{1}1)[110]$ slip systems in the grain results in the stabilization of the $(112)[11\bar{1}]$ texture component. In this case, one set of the active slip systems, $(111)[01\bar{1}]$ and $(111)[10\bar{1}]$, can be reduced to the effective slip system, $(111)[11\bar{2}]$, while the other set of the active slip systems, $(\bar{1}11)[110]$ and $(1\bar{1}1)[110]$, constructs the effective slip system, (001)[110]. These two effective slip systems are illustrated in Fig. 1.

As described above, if the plane strain deformation is obstructed during plastic flow of a material, strain path can be altered from plane strain (and hence, pure shear) to simple shear, *see* Eqn (3). As a result, due to a local lattice rotation, a shear texture component (001)[110], which is, in fact, a well-known shear texture component for fcc metals, can be formed in the $(112)[11\bar{1}]$ oriented grain. Thus, Fig. 1 shows that the ND-rotated cube band (or component) can be formed in the shear band inside the copper (C) deformation texture component.

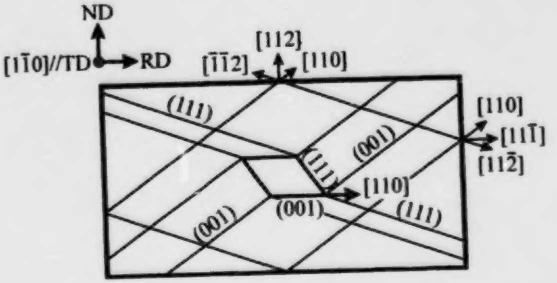

Fig. 1: Occurrence of the (001)[110] shear component in the shear band inside a $(112)[11\bar{1}]$ oriented grain deformed under plane strain conditions.

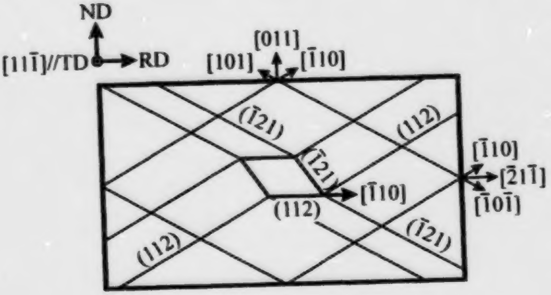

Fig. 2: Occurrence of the $(112)[\bar{1}10]$ shear component in the shear band inside a $(011)[\bar{2}1\bar{1}]$ oriented grain deformed under plane strain conditions.

Now, the model of Park et al. (1998) is employed to predict the corresponding recrystallization texture component. The model relies on two principles: a strain energy release maximization component and higher boundary mobility. In the shear component (001)[110], the effective slip direction is [110], which is parallel to the maximum internal stress direction. To satisfy the first principle of the model, [110] transforms into one of <001>, which is the minimum Young's modulus direction. This orientation change is assumed to occur on the most stressed plane, namely, the shear plane, (001), for the ND-rotated cube component. Therefore, the (001)[100] cube recrystallization texture component is expected to form in the ND-rotated cube component inside the $(112)[11\bar{1}]$ deformed grain. This prediction is in good agreement with the observation of Hjelen et al. (1991) such that the cube-oriented grains nucleate from transition bands inside the C deformation texture component.

Another example is given in Fig. 2, which shows the configuration of the effective slip systems in a $(011)[\bar{2}1\bar{1}]$ oriented grain deformed under plane strain conditions. In this case, the relevant active slip systems are $(111)[01\bar{1}]$, $(111)[\bar{1}01]$, $(\bar{1}11)[110]$ and $(1\bar{1}1)[110]$, and thus, using the current method the effective slip systems are calculated to be $(112)[\bar{1}10]$ and $(\bar{1}21)[\bar{1}0\bar{1}]$. Figure 2 depicts the occurrence of one possible shear component, $(112)[1\bar{1}0]$, inside the shear band of the grain. The effective slip direction (and hence, the maximum internal stress direction) of the shear component is $[1\bar{1}0]$, which changes, in turn, into one of the minimum Young's modulus direction <001> on annealing. Since the latter direction cannot be contained in the shear plane (112), one of the crystallographically possible {kk0} planes replaces it. Therefore, the recrystallization component predicted by the present model is {hk0}<001>, namely the RD-rotated cube component.

3 Experimental procedure

The chemical composition (wt-%) of the commercial purity Aluminum used for the present work is Al-0.127Si-0.48Fe-0.005Cu-0.002Mn-0.013Ti-0.011V. A slab of this material was hot rolled to a thickness of 6.3 mm. The sheet was then reversibly cold rolled using a laboratory rolling mill with a diameter of 127mm in 10 passes to a final thickness of 1.26 mm, corresponding to reduction of 80% or logarithmic strain of $\varepsilon=1.6$. For full recrystallization textures, the strips were annealed at 400°C for 1 hr in H_2 atmosphere.

4 Results and discussion

Figure 3(a) shows the ODF of the deformation texture in the center layer of the 80% cold rolled Al sheet. The development of the C component, {112}<111>, was relatively outstanding among the deformation texture components. As described in Fig. 2, a cube recrystallization component is expected to evolve from a {001}<110> shear component inside a {112}<111> oriented grain. The cube component may grow rapidly into the deformed matrix owing to its high growth rate (Engler et al., 1996) and dominate the deformation texture. As obviously from Fig. 3(b), on annealing the 80% cold rolled Al sheet, the center layer of the specimen revealed a strong intensity of the cube component.

Redundant shear strains caused by friction between the sheet surface and the rolls during cold rolling results in a through-thickness texture gradient of the specimen.

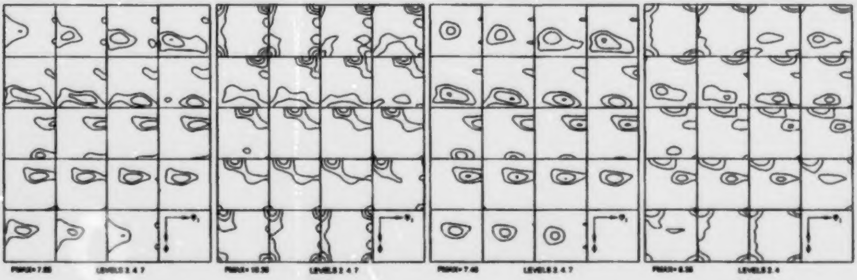
(a) (b) (c) (d)

Fig. 3: ODFs of Al sheet after 80% reduction : (a) Center layer as-rolled, (b) On annealing the specimen of (a), (c) Surface layer as-rolled, (d) On annealing the specimen of (c).

The through-thickness texture inhomogeneity seems to have occurred in the present work. In 80% cold rolled specimen, the brass (Bs) component was dominant in the surface layer (Fig. 3(c)) contrary to the center layer (Fig. 3(a)). As demonstrated in Fig. 2, even under plane strain conditions, a shear component, {112}<110>, can be formed inside the shear band in a {011}<211> oriented grain. The present recrystallization model predicts that the shear component transforms into a RD-rotated cube component, namely {hk0}<001>. This prediction appears to be in reasonably good agreement with the observed recrystallization texture as shown in Fig. 3(d). When compared to the intensity of the cube component, the development of the RD-rotated cube components is apparent.

5 Conclusions

The present work has demonstrated that the shear components may occur in the shear bands inside the each grain of fcc materials deformed under plane strain conditions. A new recrystallization model was employed to explain that the shear components result in the development of the cube and rotated cube components dominating the recrystallization textures in fcc metals and alloys. The prediction calculated in this way is in good agreement with the observation in the cold rolled and annealed aluminum.

Acknowledgements

The authors are indebted to the Research and Development Center for Automobile Parts and Materials (RRC) of Sunchon National University through the Korea Science and Engineering Foundation (KOSEF) for financial support.

References

Hjelen, J., Ørsund, R., and Nes, E. (1991) On the origin of recrystallization textures in Aluminum. *Acta metall. Mater.*, Vol. 39, pp. 1377-1404.

Dillamore, I.L. and Katoh, H. (1974) The mechanisms of recrystallization in cubic metals with particular reference to their orientation-dependence. *Metal. Sci.*, Vol. 8, pp. 73-83.

Vatne, H.E., Shahani, R. and. Nes, E. (1996) Deformation of cube-oriented grains and formation of recrystallized cube grains in a hot deformed commercial AlMgMn aluminum alloy. *Acta mater.*, Vol. 44, pp. 4447-4462.

Engler, O. Yang, P. and Kong, X.W. (1996) On the formation of recrystallization texture in Binary Al-1.3%Mn Investigated by means of local texture analysis. *Acta mater.*, Vol. 44, pp. 3349-3369.

Park, Y.B., Kestens, L. and Jonas, J.J. (1998) Effect of internal stresses in deformed bcc metals on the orientations of new grains. in *Grain Growth in Polycrystalline Materials III*, (ed. H. Weiland et al.), TMS, Warrendale, pp. 173-178.

Humphreys, F.J. and Hatherly, M. (1995) *Recrystallization and Related Annealing Phenomena*, Elsevier Science Ltd., Oxford, p. 359.

TEXTURES IN DYNAMIC RECOVERY AND RECRYSTALLIZATION

H.J. McQueen

Mechanical Engineering, Concordia University, Montreal H3G 1M8
Canada

Abstract

Textures have been measured over the range 20 to 840°C after a series of torsional strains extending as high as ε=60 (von Mises equivalent true strain) in Al, αFe and Cu polycrystals. After the core of a specimen was bored out, the surface of the cylinder was slit and flattened so that texture could be measured by x-ray diffraction. The STEM microtextures were determined by Kikuchi analysis from foils cut from the Al specimens normal to the radius near the surface and found to agree with the macrotexture. The texture of Al (also of αFe) underwent a transition near ε=10 as a result of relaxation of the grain edge constraints; this caused a reduction of the Taylor factor. The Al underwent only dynamic recovery but at high ε the serrated grain boundaries met, thus pinching-off the grains into short segments in the process known as geometric dynamic recrystallization (gDRX). The Cu texture was similar to that of Al until it underwent discontinuous dynamic recrystallization (dDRX), where new components developed without disappearance of the old. It never developed the texture transition observed in Al because the grains remained almost equiaxed. When dDRX takes place, the texture is never intense since the maximum strain in any grain is limited.
Keywords: hot working, dynamic recovery, dynamic recrystallization, microtexture.

1. Introduction

Efforts to distinguish the incidence of dynamic recovery (DRV) and of dynamic recrystallization (DRX) have been made for almost half a century. While elongated or equiaxed grains containing substructures are good criteria (McQueen, Bergerson, 1972), in some instances the texture can aid differentiation. In rolling to high strains (ε = 1-2.7) in one or several passes, Al, Cu or stainless steels with elongated grains exhibit textures similar to Al or Cu at room temperature. In contrast, those with equiaxed grains showed the common cube texture indicating static recrystallization SRX as confirmed by TEM (McQueen and Mecking, 1987). Deformation to high strains in torsion notably in Al alloys and ferritic steels has generated debate regarding interpretation of the microstructure so that micro and macrotexture have been invoked for clarification and lead to the introduction of new mechanisms geometric gDRX or continuous cDRX in distinction from classical discontinuous dDRX (nucleation and growth).

2. Geometric Dynamic Recrystallization (gDRX)

Aluminum with grain sizes of 100 and 2000 μm was deformed in torsion at 400°C 0.2 s^{-1} to strains $\varepsilon = 3, 10, 20, 40$ and 60; the flow curves showed hardening to $\varepsilon = 4$ as commonly observed with DRV and then about 20% softening to a second plateau up to $\varepsilon = 60$ (McQueen et al. 1985, Solberg et al. 1989). Such Taylor softening is due to a new texture developing as was confirmed by torsion, tension and hardness tests at 25°C. In polarized optical micrography (POM), (Fig. 1) the coarse grained specimens exhibited elongated grains with thickness many times the contained subgrain size (d) whereas the fine grained sample exhibited equiaxed crystallites at $\varepsilon > 5$, where the grain thickness became less than about 3 X d. Observation by TEM throughout the entire range revealed equiaxed subgrains with size and regular dislocation walls as at low ε for similar T-$\dot{\varepsilon}$ or σ, consistent with substructure repolygonization (McQueen et al. 1967). In the fine grained a high portion of the cell walls were the original grain boundaries GB which had become highly serrated with half wavelength and amplitude about equal to d; as neighboring GB approach, initially at acute triple junctions and ultimately along the thin elongated grains, serrations touch pinching-off shortened grains. Kassner and McMahon (1987) confirmed this behaviour to strains of 16 with additional evidence that the average subgrain misorientation ψ measured in TEM became stable near 2°; this phenomenon was also observed in Al-5.2Mg alloy by Henschall et al. (1992). The micro and macrotextures will be discussed after a resumé of some creep developments.

As a result of internal stress determinations and observations of SGB migration, disintegration and reformation (Caillard and Martin 1987), Blum and colleagues (1996 ab) turned from the theory relating T-$\dot{\varepsilon}$ or σ to the spacing $\rho_i^{-0.5}$ of dislocations in the subgrains to a model based on all three substructural parameters including spacing of walls (w=d) and dislocation spacing in the walls ($s=b/\psi$, b Burgers vector). These three parameters scale in the same way with modulus reduced stress and the SGB have a role in defining strength as the cell walls do in cold working

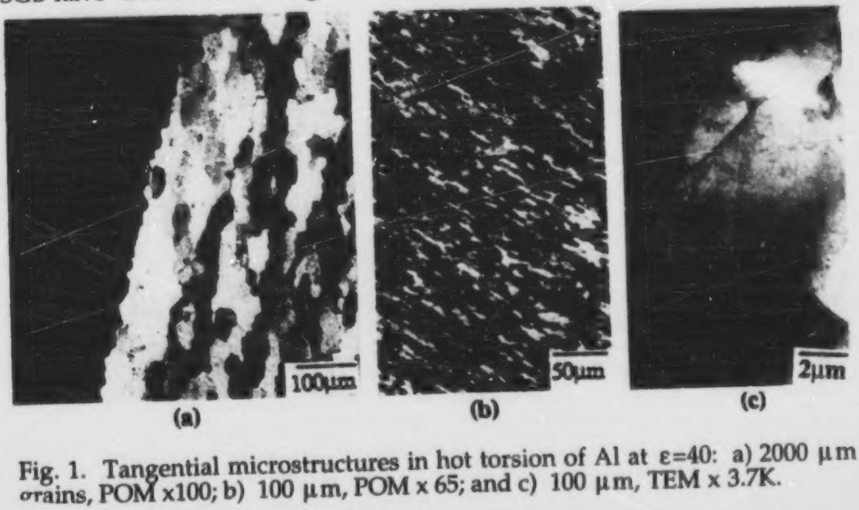

(a) (b) (c)

Fig. 1. Tangential microstructures in hot torsion of Al at ε=40: a) 2000 μm grains, POM x100; b) 100 μm, POM x 65; and c) 100 μm, TEM x 3.7K.

(Kuhlman-Wilsdorf 1977). In a recent torsion study over the range 10^{-3} to 5 s^{-1}, 200 to 550°C and ε 0.2 to 4, which confirmed the creep laws applied to hot working for Al and Al-5Mg, $T-\dot{\varepsilon}$ conditions for gDRX were determined; it occurs at a lower strain as initial grain size is finer and characteristic subgrains larger (i.e. T higher, $\dot{\varepsilon}$ lower). It is important to note that the steady state stress in Blum's composite creep theory depends on the SGB maintaining constant w and s as well as ρ_i. The theory does not take account of widely spaced (50-100 µm) transition boundaries TB developing between deformation bands which initiate at low strains and rotate differently as they follow alternative systems according to Taylor theory (McQueen, Blum 1998). Unlike SGB, the TB are permanent and increase in misorientation having different systems to supply the geometrically necessary dislocations. As a result of repolygonization replacing the substructure at strain intervals equalling the initial transient, there are no blocks of cells defined by dense dislocation walls that originated from microbands due to slip on a new system from that of the existing cell walls, as has been noted in cold working (McQueen,Blum 1997,1998). Since there is continuity of substructure evolution as T declines or $\dot{\varepsilon}$ rises from creep conditions there is a warm level, wDRV in which some higher misorientation walls form.

3. Torsion Textures in DRV and gDRX

In the hot torsion tests above on Al, the initial texture in 100 µm specimens are strong C, medium A and medium B (Fig. 2) from the list (Montheillet at al. 1984):

C $\{001\}\langle 110\rangle$ for fcc
A $\{1\bar{1}\bar{1}\}\langle 110\rangle$ and $\{\bar{1}11\}\langle\bar{1}\bar{1}0\rangle$
A* $\{\bar{1}\bar{1}1\}\langle 112\rangle$ and $\{11\bar{1}\}\langle 112\rangle$
B $\{\bar{1}12\}\langle 110\rangle$ and $\{1\bar{1}\bar{2}\}\langle\bar{1}\bar{1}0\rangle$

F $\{110\}\langle 000\rangle$ for bcc
E $\{01\bar{1}\}\langle 111\rangle$ and $\{01\bar{1}\}\langle 111\rangle$
J $\{0\bar{1}1\}\langle\bar{2}11\rangle$ and $\{1\bar{1}0\}\langle\bar{1}\bar{1}2\rangle$
D $\{11\bar{2}\}\langle 111\rangle$ and $\{\bar{1}\bar{1}2\}\langle 111\rangle$

where each orientation gives first the shear plane (normal to the torsion axis) and the shear direction (normal to the radial direction). As strain

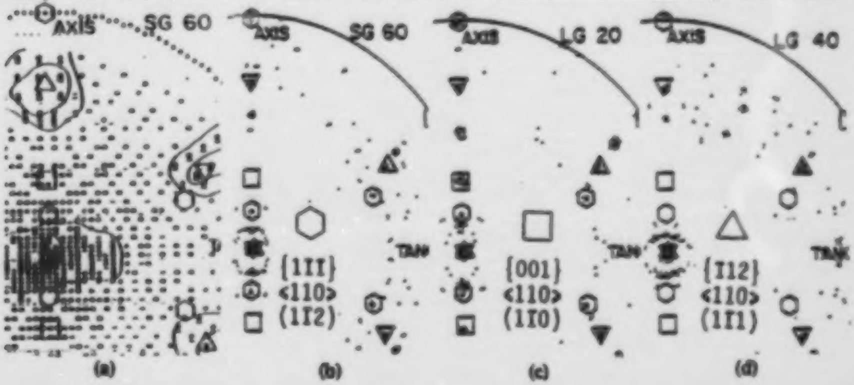

Fig. 2. Comparison of macro and microtextures in hot torsion of Al: a) 100 µm grains, ε=60, x-ray; STEM: b) 100 µm, ε=60; 2000 µm: c) ε=20, d) ε=40.

increased to 10 the C and A diminished and B strengthened so that at 20, 40 and 60, C and A became quite weak and B very strong. The microtextures were also measured from 25 crystallites by STEM and gave exactly the same progression in the intensities of the components. The 2000 μm grained specimen gave approximately the same development of the three components but with some scatter. The similar textures for the two grain sizes is significant since the small one undergoes gDRX at $\varepsilon = 5$ and the large one has not yet done so at $\varepsilon = 60$ (Solberg et al. 1989).

From the STEM measurements of 25 crystallites as ε rose from 3 to 60, the fraction of boundaries below 2° decreased from 35 to 25%, 2-8° decreased from 30 to 25% whereas those with 9-16° and those above 16° increased (Solberg et al 1989). Since the STEM diffraction were located on adjacent areas with well defined Kikuchi patterns without visual observation, the estimated subgrain size was 9 μm compared to 6.5 μm from TEM which means that about half of the very low ψ boundaries were missed and the number of small cells should be increased proportionately, i.e. SGB<2%, altered from 46 to 33% and SGB=2-8° from 25 to 22%. The 9-16° boundaries are transition boundaries (TB) and appear to be about 1 or 2 per grain. The boundaries greater than 16° are considered GB and for the 2000 μm specimen are in agreement with the density expected from the plastic strain. For the 100 μm specimens, GB increase in proportion up to $\varepsilon = 10$ and then become constant due to the effects of gDRX.

4. Discontinuous dDRX and Continuous cDRX

In a study by Montheillet et al. (1984) on Cu at 20°C, the A and weaker A* grow weaker with strain while the C component becomes strongest at $\varepsilon = 4.7$. As T rises the A* and C progressively diminish up to 200°C while the A is increasing and the B is becoming more intense at 200 and 300°C ($\varepsilon = 31$). As discontinuous dDRX took place at 400 and 500°C ($\varepsilon = 31$), the B and A textures remained but became much more diffuse. The newly formed grains have diverse orientations but return towards the matrix texture as they deform. McQueen and Bergerson (1972) (McQueen, 1982) examined Cu torsioned at 800°C, 4 s^{-1} to steady state ($\varepsilon = 30$) by SEM EBS and TEM, observing nuclei of 2 μm among old grains of 10 μm containing cells with ψ=6-8°. At 950°C, the 25 μm grains were easily discerned and contained subgrains of about 3 μm with regular walls. Bocher et al. (1996) observed similar DRX grains and textures in γ stainless steel; the randomization was ascribed to multiple twinning.

In torsion tests on Al at 20°C, some A component at $\varepsilon = 0.62$ and 2.18 has been superseded by C and weak A* components at 4.98. As T and final strain rise to 300°C (ε=10), C and A* diminished while B became the strongest this continued to 350°C (31) and 400°C (31) where B was sole and sharp, in excellent agreement with above. Perdrix et al. (1981) observed equiaxed crystallites and a ψ distribution ranging from a peak for SGB at 0-5°, low density across 5-20° and another peak above that; they proposed that the ψ of SGB continually increased thus creating cDRX (Gourdet et al. 1996). Common SGB cannot increase in ψ unless the neighboring regions are slipping on different systems to provide the geometrically necessary dislocations as for TB. Finally as cDRX affects only 20% of the boundaries near 10-20°, it is considerably different from other manifestations of the mechanism that usually requires strong particle pinning. Continuous cSRX was clarified by Ahlborn et al. (1969) who observed that alloys which contained a high density of fine particles became strongly stabilized resisting both recovery and dSRX during prolonged annealing. However, a large fraction of cell walls underwent a reorganization and conversion to high angle boundaries with almost no cell growth because of the strong pinning. In developing superplasticity of particle stabilized alloys (Hales et al. 1991, McQueen, Blum 1996), after initial thermo-mechanical processing (TMP) to create a high density substructure resistant to dSRX and (during slow straining near 450°C) cDRX produced fine grains with boundaries capable of sliding for superplasticity much more rapidly than in cSRX due to the GB shear stresses.

5. Textures and gDRX in Ferritic Alloys

In hot straining, αFe alloys (notably with Cr or Si) undergo a high level of DRV (Evangelista et al. 1993) and appear to avoid dDRX except for very high purities (Bourell and McQueen, 1987; McQueen et al. 1996). For creep, Straub and Blum (1996) have shown that for αFe alloys d(=w), s and $\rho_i^{-0.5}$ are constant in steady state and scale together in an inverse manner with modulus reduced stress. For high strains, Cizek and Wynne (1997) found that α phase in duplex stainless steel developed low ψ SGB and occasional high ψ TB as distinct from dDRX or cDRX. Such a duplex set of boundaries is consistent with the observations of Lombry et al. (1981). In interstitial free iron at 900°C, Tsuji et al. (1997) observed that as $\dot{\varepsilon}$ was lowered from 10 or 1 s^{-1} (elongated grains) to 10^{-2} or 10^{-3} s^{-1}, the structure became equiaxed crystallites of similar or larger diameter than the expected elongated grains. TEM revealed the presence of subgrains, many with ψ less than 5° but others with ψ 10-15° in addition to the serrated original GB. This is clearly a case of gDRX because of its close similarity to that phenomenon in Al alloys.

In a study of textures in hot torsion of IF steels, Baczynski and Jonas (1997) noted the formation of equiaxed crystallites at 840° replacing the elongated grains at lower T. As T rises, the texture progressed from mixtures of F, E, J and D (in agreement with Montheillet et al. 1984) to D becoming very intense. In modeling the texture, glide processes alone would not lead to such intensity with almost disappearance of the other components. It was thus proposed that regions of D orientation formed and grew as part of cDRX. These regions of lower Taylor factor having lower dislocation density grew into regions with higher Taylor factor. The expansion of low energy regions can be achieved by gDRX; as the apex of serrations move to absorb SGB there can be a net motion into grains of higher energy so that pinching off occurs more frequently in them both at triple junctions and generally. The same reasoning can be applied to Al alloys where the lower Taylor factor B component dominates.

6. Conclusion

In high DRV metals Al and αFe, the torsion texture develops due to the slip systems operating and the degrees of constraint which leads to a new sole intense component at high strains; this may be strengthened by the growth of low Taylor factor regions during occurrence of gDRX. In low DRV Cu, the torsion texture initially develops as above but as DRX occurs, the texture becomes more random due to the newly nucleated grains but the deformation components survive as the DRX grains deform.

7. References

Ahlborn H., E. Hornbogen and U. Koster, (1969) J. Mat.Sci. 4 944-950.

Baczynski J. and J.J. Jonas, (1998) Metal. Mat. Trans. 29A, 447-462.

Blum W. and H.J. McQueen, (1996) Aluminum Alloys, Physical and Mechanical Properties, (ICAA5) J.H. Driver et al., eds. Mat.Sci. Forum 217-222, 31-42.

BlumW., Q. Zhu, R. Merkel and H.J. McQueen, (1996) Z. Metalkde 87, 341-348, Mat. Sci. Eng. A205, 25-30.

Bocher Ph., J. Azar, B.L. Adams, J.J. Jonas, (1997) Proc ITAP R.A. Schwarzer, Clausthal, Germany, pp. 249-254.

Bourell D.L., H.J. McQueen, (1987), J.Mat Shaping Tech. 5, 53-73.

Caillard D. and J.L. Martin, (1987) Rev. Phys. Appl. 22 169-183.

Cizek P. and B.P. Wynne, (1997), Mat. Sci. Eng. A230 88-94.

Evangelista E., P. Mangucci, J. Bowles, H.J. McQueen (1993), High Temp. Mat. Proc. 12, 57-66.

Gourdet S., E.V. Konopleva, H.J. McQueen and F. Montheillet, (1996) Mat. Sci. Forum 217-222 pp. 441-446.

Hales S.J., T.R. McNelley, H.J. McQueen, (1991) Metal. Trans. 22A 1037-1047.

Henshall G.A., M.E. Kassner and H.J. McQueen, (1992) Metal. Trans. 23A, 881-889.

Kassner M.E. and M.E. McMahon, (1987) Met. Trans. 18A, 835-846.

Kuhlman-Wilsdorf D., (1977) Work Hardening in Tension and Fatigue, A.W. Thompson, ed. (AIME, New York), p. 1-44.

Lombry R., C. Rossard, B.J. Thomas (1981) Rev. Metall. CIT, 78, 975-988.

McQueen H.J. (1982), Strength of Metals and Alloys (ICSMA6), R.C. Gifkins, ed., Pergamon Press, Oxford, pp. 517-522.

McQueen H.J. and S. Bergerson, (1972) Met Sci. J. 6 25-29.

McQueen H.J. and W. Blum (1997), Recrystallization and Related Topics (Rex '96), T.R. McNelley ed., Monterey, CA, pp. 123-136.

McQueen H.J. and W. Blum (1998), Aluminum Alloys, Physical and Mech. Properties (ICAA6). T. Sato ed., Japan Inst. Metals, pp. 99-112.

McQueen H.J., O. Knustad, N. Ryum, and J.K., Solberg, (1985) Scripta Met.,19, 73-78.

McQueen H.J. and H. Mecking (1987), Z. Metall. 78, 382-396.

McQueen H.J., N.D. Ryan, R. Zaripova, K. Farkhutdinov, (1996) 37th Mech. Work. Steel Proc. Conf., Vol. 33, pp 883-894.

McQueen H.J., W.A. Wong, J.J. Jonas, (1967) Can. J. Phys. 45, 1225-1239.

Montheillet F., M. Cohen, J.J. Jonas, (1984) Acta Metal. 32, 2077-2089.

Perdrix Ch., M.Y. Perrin and F. Montheillet, (1981) Mem. Et. Sci. Rev. Métal. 78 309-320.

Solberg J.K., H.J. McQueen, N. Ryum and E. Nes, (1989) Phil. Mag. 60 447-471; 473-485.

Straub S. and W. Blum (1996), Hot Workability of Steels and Light Alloys/Composites, H.J. McQueen et al., eds., Met. Soc. CIM, Montreal, pp. 189-204.

Tsuji N., Y. Matsubara and Y. Saito (1997), Scripta Mat. 37, 477-484.

RECRYSTALLIZATION TEXTURES IN COPPER-MANGANESE ALLOYS

O. ENGLER
Los Alamos National Laboratory, Center for Materials Science, Mail Stop K765, Los Alamos, NM 87545, USA
K. LÜCKE
Institut für Metallkunde und Metallphysik, RWTH Aachen, Germany
C. PITHAN
Materials Design Laboratory, University of Tokyo, Japan

Abstract

Mn is the only element that can be dissolved in Cu up to 12% without notably changing the SFE. It was the purpose of the present study to investigate the recrystallization behavior of Cu-Mn alloys. To support the results obtained by conventional X-ray macrotexture analysis and in particular to track the origin of the recrystallization texture orientations, local orientations of the deformed matrix and of individual recrystallized grains were studied by EBSD. The recrystallization textures observed are discussed in terms of a retardation of grain boundary motion by the Mn-atoms in solid solution. Consequently, the growth of the cube-nuclei is impeded and the formation of competitive nuclei at other nucleation sites increasingly dominates the recrystallization textures.

Keywords: recrystallization, Cu-Mn, stacking fault energy, nucleation, EBSD

1. Introduction

The development of the crystallographic textures during rolling and recrystallization of Cu-alloys as function of their composition has been subject of a large number of investigations over the last decades (see, e.g., Hirsch, 1986). With an increasing amount of alloying elements the stacking fault energy (SFE) of the materials generally decreases, causing a continuous transition from the pure metal (copper) to the alloy (brass) type rolling texture (Hirsch and Lücke, 1988). For the recrystallization textures, a much more complicated transition is observed. A decrease in the SFE leads to the profuse formation of shear bands, which upon recrystallization annealing may act as nucleation sites. Solute atoms strongly impede grain boundary motion and thus heavily influence the recrystallization textures as well.

Mn is the only element that can be dissolved in Cu up to 12 at% without significantly changing the SFE (Steffens et al., 1987). It therefore appeared interesting to study the influence of Mn on the rolling and recrystallization textures of Cu-Mn alloys, as this should yield a clear distinction between the effects caused by the changes of the SFE and those by other factors.

2. Experimental

Three Cu-Mn alloys with the nominal composition 4, 8 and 16at% Mn were prepared from high purity Cu and Mn. After homogenization annealing for 72h at 800°C the alloys were subjected to a series of cold deformations and recrystallization annealings so as to achieve a homogeneous fine grained (~30μm) starting material with a virtually random starting texture for all three alloys. These samples were deformed by reversible cold rolling to reduction degrees up to 97.5%. Finally, the samples were annealed for 1000s at 450°C in a salt bath until recrystallization had been completed. Microstructural investigations were carried out by means of optical microscopy and SEM. The recrystallization textures were determined by means of conventional X-ray macrotexture analysis. In addition, local orientations of the new recrystallized grains were determined by means of electron back scattering diffraction (EBSD) in an SEM.

3. Results and Discussion

3.1 Summary of the Rolling Experiments

The rolling textures of the three different Cu-Mn alloys have been presented in a preceding paper (Engler et al., 1994). For low Mn-content (4%) a typical copper-type texture formed in which the orientations were assembled along the so-called β-fiber running from the C-orientation {112}<111> through the S-orientation {123}<634> towards the B-orientation {011}<211> through the Euler angle space (Hirsch and Lücke, 1988). With increasing Mn-content the B-orientation tended to dominate the rolling texture, suggesting a transition from the copper- to the brass-type texture. The microstructural results did not resemble the microstructures of low-SFE materials, however. The samples appeared to deform rather homogeneously, and only a few copper-type grain-scale shear bands were observed, which is in contrast to the massive shear band formation known from low-SFE alloys like brass.

3.2 Recrystallization Textures

Figures 1–3 give examples of the textures obtained after complete recrystallization. Fig. 1 shows the {111}-pole figures of the three alloys for 97.5% rolling reduction and recrystallization annealing, Fig. 2 and 3 the corresponding ODFs for 90% and 97.5% reduction, respectively. Similar as commonly observed in pure Cu, these textures were dominated by a strong cube-orientation {001}<100> and its rotations around the RD. Moreover, strong intensities occurred close to the former rolling texture orientations along the β-fiber which – in analogy to the recrystallization textures of Al-alloys – will be denoted as R-orientation in the following. Finally, intensities of the BR-orientation {236}<385> were observed.

In Cu-4%Mn (Fig. 1a, 2a, 3a) the texture maximum lies in the exact cube-orientation (*i.e.* at $\Phi=0°$). In addition, minor intensities of a widely scattering α-fiber (orientations with {011} parallel ND) were obtained, which with increasing deformation concentrated in the orientation ($\varphi_1,\Phi,\varphi_2\sim 45°,30°,0°$).

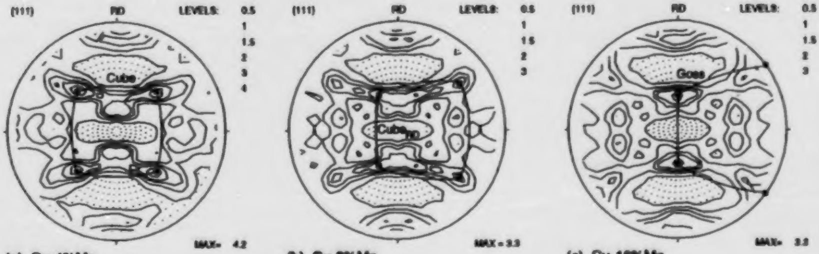

(a) Cu-4%Mn (b) Cu-8%Mn (c) Cu-16%Mn

Fig. 1: {111} pole figures of the three alloys after recrystallization (97.5% red.).

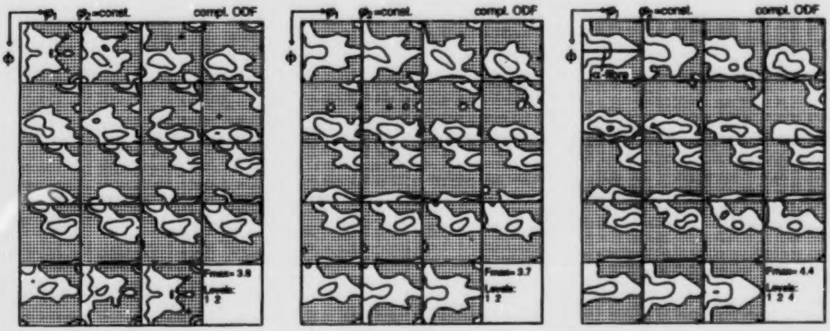

(a) Cu-4%Mn (b) Cu-8%Mn (c) Cu-16%Mn

Fig. 2: ODFs of the three alloys after recrystallization (90% red.).

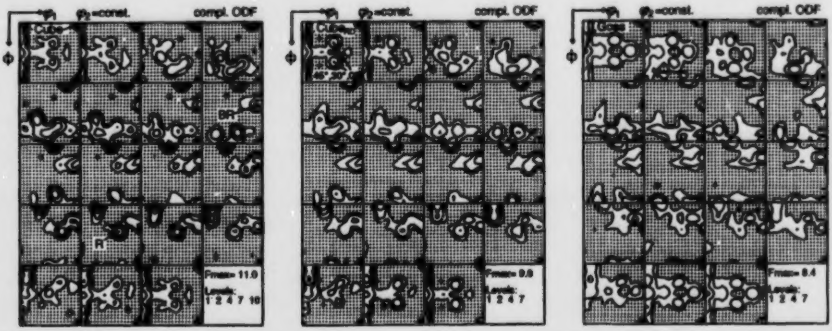

(a) Cu-4%Mn (b) Cu-8%Mn (c) Cu-16%Mn

Fig. 3: ODFs of the three alloys after recrystallization (97.5% red.).

In Cu-8%Mn the texture maximum has shifted from the exact cube-position at $\Phi=0°$ about the RD towards $\Phi\approx 22°$ (Figs. 1b, 2b, 3b). Additionally, as in Cu-4%Mn, the R-, the BR- and some α-fiber orientations formed. The texture intensity was generally weaker than in Cu-4%Mn.

In Cu-16%Mn the texture maximum is situated at $\Phi=45°$, *i.e.* in the Goss-orientation {011}<100> (Figs. 1c, 2c, 3c). In the 97.5% rolled samples the overall texture sharpness was further reduced in comparison to the 4%Mn and 8%Mn alloys, whereas in the 90% rolled samples the intensity remained about constant. With view to the mechanisms of recrystallization nucleation it should be noted that virtually no twins of the cube-orientation (at 27°,48°,27°) have been observed.

3.3 Investigation of the nucleation mechanisms

In order to clarify the mechanisms of recrystallization nucleation operating in the present Cu-Mn alloys, samples in a partially recrystallized state were analyzed by EBSD with respect to the spatial arrangement of the orientations of the recrystallized grains (e.g. Fig. 4a). In accord with the macrotexture results (Figs. 1–3), the orientations of the new grains could roughly be separated into three different groups.

(i) Class "Cube": In many cases, new grains could be attributed to a band-like structure parallel to the rolling direction. The local orientations of such new grains comprised orientations close to the cube-orientation or a cube-orientation being rotated about the RD up to ±35° (Fig. 4b). The cube-texture is the typical recrystallization texture of pure Cu and it is anticipated that in the present Cu-Mn alloys the formation of this orientation proceeds very similar, that is, nucleation of cube and RD-rotated cube-orientations takes place in band-like structures present already in the as-deformed microstructure, the so-called cube-bands (e.g. Duggan et al., 1993). Since cube-oriented subgrains are furthermore capable to rapidly recover, a very good prospect for successful nucleation events is given (Ridha and Hutchinson, 1982).

With increasing Mn-content the volume fraction of the cube-orientations decreased. This is attributed to the increasing initiation of shear bands that are known to intersect through the transition bands and thus to destroy the potential cube nucleation sites (Ridha and Hutchinson, 1982), as well as the successful nucleation of other, competitive orientations (see below). Furthermore, solute atoms are known to strongly affect grain boundary mobility which leads to a strong retardation of the growth of the nuclei and, in turn, favors the orientations forming at other nucleation sites.

(ii) Class "R": Other grains that also nucleate at band-like structures parallel to the rolling direction comprised orientations close to the rolling texture, which were labeled R-orientation above (Fig. 4c). These orientations do not occur in pure Cu, but have been described in Cu-alloys with moderate contents of P (Hutchinson and Ray, 1979; Hirsch, 1986), Ge (Eichelkraut et al., 1984) and Zn (Schmidt and Lücke, 1979). In accordance with investigations in Al-alloys – where the R-orientation may strongly dominate the recrystallization textures – it is assumed that R-oriented nuclei form at the boundaries between the former deformed grains. The R-orientation turned out to prevail at intermediate strains and Mn-concentrations, where the growth of cube-oriented grains is retarded by the solutes (see *(i)*), but shear banding is not yet sufficiently pronounced to give rise to additional nucleation sites (see *(iii)*).

(iii) Class "BR": Finally, new grains were observed to nucleate at shear bands; their number increased with increasing deformation as well as with increasing Mn-content. As shown in Fig. 4d, the orientations of these grains preferentially comprised the BR-orientation and orientations close to the α-fiber including the Goss-orientation, i.e., by orientations that are characteristic of the recrystallization textures of Cu-alloys with a low SFE, as e.g. brass with a Zn-content exceeding 20% (Schmidt and Lücke, 1979; Engler et al., 1995). Therefore, it is concluded that they form by similar mechanisms as in brass, i.e. nucleation in the shear bands and a growth selection into the deformed matrix, which mainly comprises the B-orientation in such samples. Because of the increased tendency to planar slip (Engler et al., 1994), the frequency of forming shear bands increased with rolling degree and Mn-content, so that the nucleation probability of BR-oriented grains is enlarged.

(iv) Phon. It must be emphasized that the recrystallization textures of the present Cu-Mn alloys were rather weak in comparison with other Cu-alloys and, particularly, with pure Cu. At low reductions the random part (phon) of the textures reached values as high as 80% and even after 97.5% rolling it was still ~40%. As already mentioned

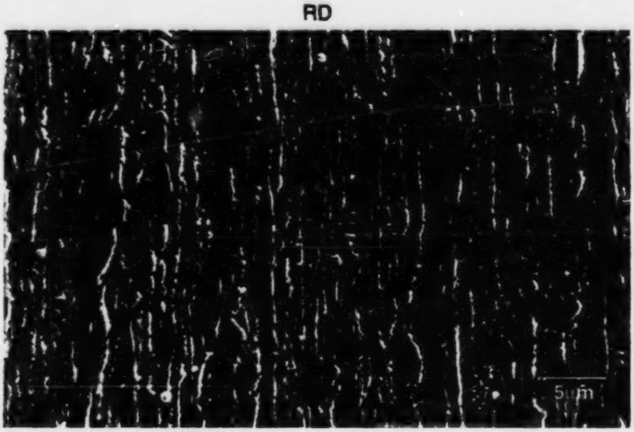

(a) microstructure (SEM)

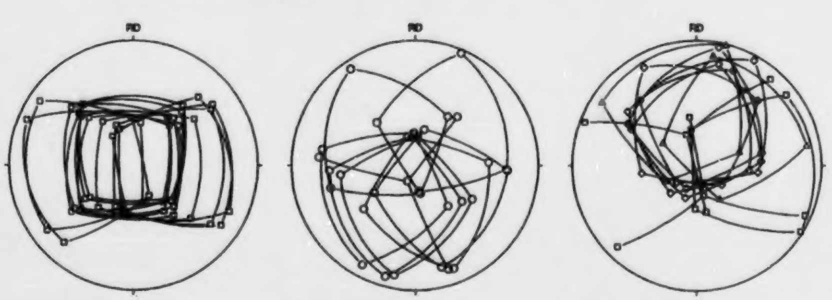

(b) cube-bands (c) grain boundaries (d) shear bands

Fig. 4: EBSD single grain orientation measurements in partially recrystallized Cu-4%Mn (90% red., annealed for 100s at 450°C).

above, the solute Mn strongly affects grain boundary mobility which leads to a strong retardation of the growth of the nuclei. Moreover, in contrast to other Cu-alloys, the SFE remains constant in Cu-Mn, so that recrystallization nucleation by twinning can be ruled out and nucleation at shear bands is not as prevalent as in low SFE materials. Consequently, the randomization effect due to the solved Mn is presumably even more pronounced than that in other Cu-alloys, which would account for the strongly delayed recrystallization kinetics, the small grain sizes and the very weak textures observed in the present study.

4. Summary and Conclusions

Mn is the only element that can be dissolved in Cu up to 12% without notably changing the stacking fault energy (SFE). Nonetheless, the recrystallization textures of three different Cu-Mn alloys (4, 8, 16%Mn) investigated in the present study turned out to substantially depend on the Mn-content. With increasing Mn-content the recrystallization texture deviated from the typical cube-recrystallization texture of pure Cu by a rotation of the exact cube-orientation about the RD towards the Goss-orientation. Simultaneously, the cube texture intensity decreased and, instead, retained rolling texture orientations – denoted R-orientation – prevailed. At highest Mn-content and reduction degrees orientations known from the recrystallization textures of highly alloyed brass, especially the BR-orientation {236}<385>, were observed as well.

By means of EBSD local texture analysis it could be shown that the cube-oriented grains formed at the cube-bands, the rolling texture orientations could be attributed to the former grain boundaries and the BR-orientation formed at the shear bands. The texture transition observed with increasing Mn-content is attributed to the retardation of grain boundary motion by the Mn-atoms in solid solution and by enhanced nucleation activities at competitive nucleation sites. Consequently, the growth of the cube-nuclei is impeded and the formation of other nuclei increasingly dominates the recrystallization textures.

References

Duggan, B.J., Lücke, K., Köhlhoff, G. and Lee, C.S. (1993). *Acta metall. mater.*, vol. 41, pp. 1921-1927.

Eichelkraut, H., Hirsch, J. and Lücke, K. (1984). *Z. Metallk.*, vol. 75, pp. 113-123.

Engler, O., Hirsch, J. and Lücke, K. (1995). *Z. Metallk.*, vol. 86, pp. 475-484.

Engler, O., Pithan, C. and Lücke, K. (1994). *Mat. Sci. Forum*, vol. 157-162, pp. 679-683.

Hirsch, J. (1986). In *Proc. 7th Risø Int. Symp.*, ed. by N. Hansen et al., Risø Nat. Lab., Roskilde, Denmark, pp. 349-360.

Hirsch, J. and Lücke, K. (1988). *Acta metall.*, vol. 36, pp. 2863-2882.

Hutchinson, W.B. and Ray, R.K. (1979). *Metal Sci.*, vol. 13, pp. 125-130.

Ridha, A.A. and Hutchinson, W.B. (1982). *Acta metall.*, vol. 30, pp. 1929-1939.

Schmidt, U. and Lücke, K. (1979). *Texture of Cryst. Solids*, vol. 3, pp. 85-112.

Steffens, T., Schwink, C., Korner, A. and Karnthaler, H.P. (1987). *Phil. Mag. A*, vol. A56, pp. 161-173.

EFFECT OF Mg CONTENT ON THE DEVELOPMENT OF ROLLING AND RECRYSTALLIZATION TEXTURES IN Al-Mg ALLOYS

M. KOIZUMI, T. SAITOU and H. INAGAKI

Shonan Institute of Technology, Fujisawa, Japan

S. KOHARA

Science University of Tokyo, Noda, Japan

Abstract

In order to investigate the effect of Mg in solution on the development of rolling and recrystallization textures, Al-Mg alloys containing Mg up to 9% were solution treated at 450 °C and quenched into water. They were immediately cold rolled 95 % and further isothermally annealed at 325 °C. Orientation distribution function analysis of the cold rolled specimens has revealed that the effect of Mg in solution on the development of the rolling texture is strongly orientation dependent at Mg content below 5%. Above this content, however, such orientation dependence disappear and all main orientations decreased rapidly with increasing Mg content, giving more random rolling textures. Also annealing textures developed in these specimens after complete recrystallization at 325 °C were strongly dependent on Mg content. At Mg content below 3%, {100}<001> was strong and increased with increasing Mg content. At Mg content above 3%, {100}<001> was weak and decreased remarkably with increasing Mg content. All these results could be explained in terms of shear banding and solution hardening due to Mg atom in solution, both of which occur during cold rolling, and in terms of the precipitation of ß phase particles which takes place during recrystallization and grain growth.

Key words: Al, Mg, Rolling Texture, Recrystallization Texture, Shear Band

1. Introduction

Mg is one of the most important alloying elements that significantly affects the development of rolling and recrystallization textures of Al. Although such an effect of Mg has been studied by several investigations (Korbel et al. 1986; Wagner et al. 1991; Engler et al 1994), results obtained in previous studies (Inagaki and Kohara 1997;

Koizumi et al. 1997, 1998) have strongly suggested that this effect is dependent on Mg content. However, such an influence of Mg content has not been studied quantitatively as yet. It was therefore tried in this paper to investigate the effect of Mg content systematically by using Al-Mg alloys containing Mg up to 9 %.

2. Experimental Procedure

The starting materials were 10 mm thick hot bands of Al-Mg alloys containing Mg up to 9 %. They were solution treated at 450 °C and quenched into water. All these specimens were stored in a refrigerator before cold rolling. These specimens were cold rolled 95% under good lubrication. Temperature rise during cold rolling was kept minimum by cooling the specimens at each rolling pass. Cold rolled specimens were chemically thinned down to 0.15 mm thickness by using NaOH solution. By using Rigaku RINT 2200 diffractometer, complete {111}, {220} and {200} pole figures were determined on these specimens. From these pole figures, orientation distribution functions were calculated with the method of Roe (Roe 1965).

3. Results and Discussions

3.1 Rolling textures

In Fig. 1, {111} pole figures observed on specimens cold rolled 95% are illustrated. With increasing Mg content, the rolling textures became significantly weak. This is quite evident in Al-7%Mg and 9%Mg alloys. Orientation densities of {123}<634>,{112}<111> and {110}<112> main rolling texture components obtained

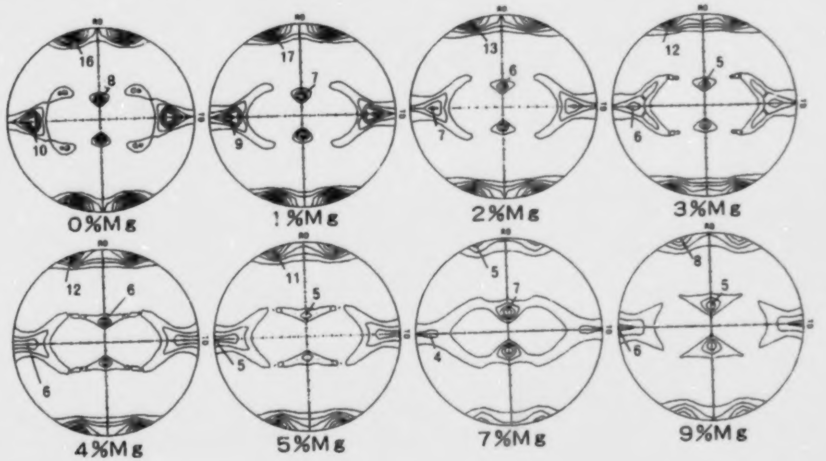

0%Mg 1%Mg 2%Mg 3%Mg

4%Mg 5%Mg 7%Mg 9%Mg

Fig. 1 Effect of Mg content on rolling textures of Al-Mg alloys cold rolled 95%. {111} pole figures.

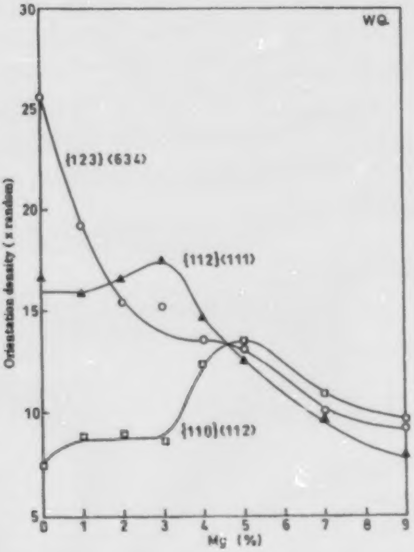

Fig. 2 Effect of Mg content on orientation densities of {123}<634>, {112}<111> and {110}<112> orientations.

by orientation distribution function analysis are plotted in Fig. 2 against Mg content.

Depending upon the Mg content, three different effects of Mg could be observed. (1) Mg content below 3 %: In this range, the effect of Mg was strongly orientation dependent. With increasing Mg content, {123}<634> decreased rapidly, while {112}<111> and {110}<112> increased only slightly. Since shear banding rarely occurred in this range of Mg content (Inagaki and Kohara 1997), such texture changes should be ascribed to orientation dependent solution hardening due to Mg atom. (2) Mg content between 3 and 5%: In this range,{112}<111> became unstable and decreased remarkably with increasing Mg content, whereas {110}<111> increased significantly. It is interesting to note that the decrease in the former correlated quite well with the increase in the latter. Since shear bands are formed in this range of Mg content, and since their densities increase with Mg content (Inagaki and Kohara 1997), these texture changes may be related with shear banding. (3) Mg content above 5%: In this range, all main component of the rolling texture decreased significantly with increasing Mg content, resulting in weak and more random rolling texture. Although shear bands observed in Al-low Mg alloys are for the most part single variant, shear bands formed in these Al-high Mg alloys are multi-variant. Since several variants of shear bands are developed simultaneously in the same grain crossing each other, and since their densities increase with increasing Mg content, the development of the normal rolling texture is suppressed and the rolling texture tends to be more random.

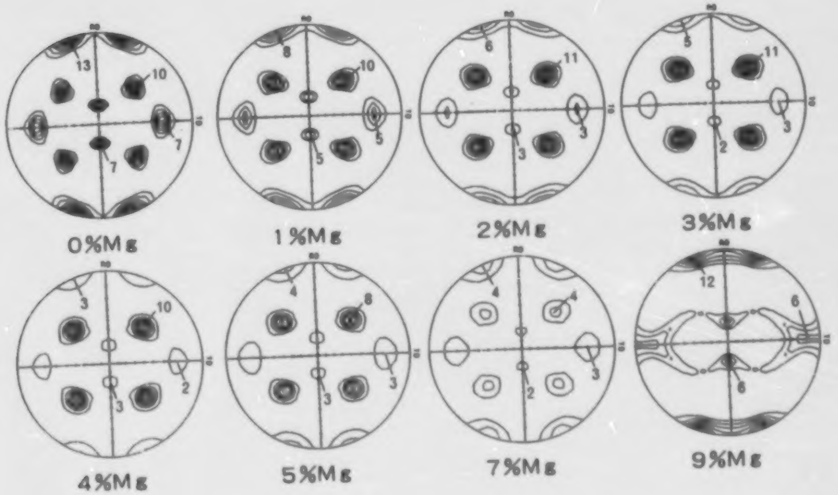

Fig. 3 Effect of Mg content on recrystallization textures of Al-Mg alloys cold rolled 95% and annealed 0.5 h at 325 °C. {111} pole figures.

3.2 Recrystallization textures

{111} pole figures observed in the specimens cold rolled 95% and annealed isothermally at 325 °C for 0.5h are illustrated in Fig.3. At this stage, all specimens were completely recrystallized. It is quite obvious that recrystallization textures became considerably weak with increasing Mg content. This correlates quite well with the observations that rolling textures of these specimens also became weak with increasing Mg content. This is evident, since nucleation was more important process up to this stage. Orientation densities of {100}<001> orientations determined by orientation distribution function analysis are plotted in Fig. 4 against Mg content. With increasing Mg content up to 3%, {100}<001> increased remarkably, although {123}<634> component in the rolling texture which is favorably oriented for the oriented growth of {100}<001> recrystallized grains decreased significantly. Fig. 2. This may be ascribed to the increase in the stored energy, i.e. in the increase in the driving force for recrystallization through solution hardening (Koizumi et al. 1997, 1998). At Mg content above 3%,{100}<001> decreased rapidly with increasing Mg content. This may be related with frequent shear banding which occurred during cold rolling and which suppressed the nucleation of the {100}<001> recrystallized grains (Koizumi et al.1998).

In Fig. 4, results obtained on specimens annealed for 4 and 96 hr at 325 °C are also illustrated. It is interesting to note that, in Al-Mg alloys containing Mg in the range between 2 and 4%, {100}<001> increased much more remarkably than in pure Al. In Al-Mg alloys containing Mg above 5%, {100}<001> did not increase on prolonged annealing at 325 °C. This may be related with the precipitation of ß phase particles which took place in these Al-high Mg alloys during isothermal annealing at 325 °C and

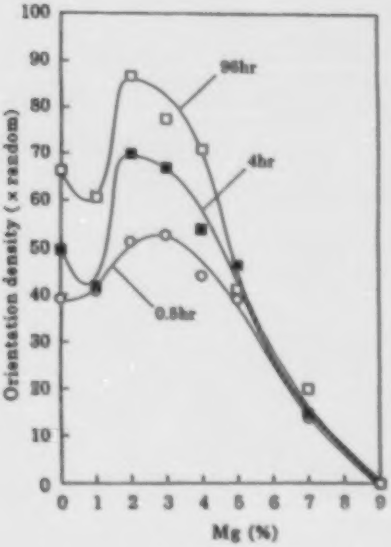

Fig. 4 Effect of Mg content on orientation density of {100}<001> orientation observed in the specimens annealed at 325 °C for 0.5, 4 and 96h.

which inhibited grain growth of grains having this orientation.

4. Conclusions

Mg atom in solution affects the development of rolling and recrystallization textures of Al-Mg alloys through orientation dependent solution hardening and shear banding which occur during cold rolling, and through precipitation as ß phase particles, which takes place during annealing.

5. References

Engler, O., Heckelmann, I., Rickert, T., Hirsch, J. and Lücke, K. (1994) Effect of pretreatment and texture on recovery and recrystallization in Al-4.5%Mg-0.7%Mn alloy. Mater. Science and Technology Vol. 10. No. 9. pp. 771-781.

Inagaki, H. and Kohara, S. (1997) Shear bands in cold rolled Al-Mg alloy polycrystals. Z. Metallkde, Vol. 88, No. 7. pp. 570-575.

Koizumi, M., Kohara, S. and Inagaki, H. (1997) Rolling and recrystallization textures in high purity Al-Mg alloys. Z. Metallkde, Vol. 88, No. 7. pp. 576-

582.

Koizumi, M, Okudaira, H. and Inagaki, H. (1998) Development of annealing textures in Al-Mg alloys. Z. Metallkde, Vol. 89, No. 7. pp. 576-582.

Korbel, A., Embury, J. D., Hartherly, M., Martin, P. L. and Erbsloh, H. W. (1986) Microstructural aspects of strain localization in Al-Mg alloys. Acta metall. Vol. 34, N0. 10. pp. 1999-2009.

Roe, R. J. (1965) Inversion of pole figures for materials having cubic symmetry. J. Appl. Phys. Vol.37, No. 5. Pp. 2069-2072.

Wagner, p., Engler, O. and Lücke, K. (1991) Texture development in Al-3%Mg influenced by shear bands. Textures and Microstructures Vol. 14-18, No. 3. pp. 927-932.

AUTOMATIC RECOGNITION OF RECRYSTALLIZED GRAINS IN PARTLY RECRYSTALLIZED SAMPLES FROM CRYSTAL ORIENTATION MAPS

N.C. KRIEGER LASSEN and D. JUUL JENSEN
Materials Research Department, Risø National Laboratory, Roskilde, Denmark

Abstract

A computationally efficient procedure for identifying grains in 2D crystal orientation maps (COMs) is presented. The procedure is applied to COMs obtained in the scanning electron microscope using electron back-scattering patterns (EBSPs) collected on a rectangular grid. However, it can be used with other techniques for measuring local lattice orientations and may easily be modified for use with other sampling grids.

While the presented grain identification procedure has a broad range of applications for quantitative analysis of COMs, it is applied here specifically for the recognition of grains in partly recrystallized samples. For this particular purpose, the procedure is combined with the use of an EBSP quality measure, which is applied for discarding small grains with an overall low pattern quality. We demonstrate the performance of the procedure by using it for automatic measurements of the area fraction of recrystallized material. A comparison of such measurements with those made by an experienced operator display a good agreement.

Keywords: EBSP, EBSD, image processing, orientation imaging microscopy, orientation mapping, connected components, recrystallization.

1 Introduction

Within the last decade, the electron back-scattering pattern (EBSP) technique has evolved from being a fairly exotic technique used only at a few research laboratories into a mature analytic tool applied all over the world. The primary reason for this development has been the automation of the EBSP technique (Krieger Lassen et al. 1992; Wright 1993) which has made it accessible to the non-specialist and has allowed thousands of crystal orientation measurements to be obtained within hours.

Today, it is customary to collect crystal orientations on a fine, normally rectangular or hexagonal, 2D grid on the surface of the sample under investigation. The result of such measurements is a crystal orientation map (COM) providing an image of the lattice orientations within the sampled area. It is natural to envision the COM as a digital image in which the quantity assigned to each pixel is not an intensity value but an orientation matrix $g(x_i, y_i)$. Indeed, by applying a mapping from orientation space to colour space, the COM is often visualised as a colour image in which points with similar orientation are shown as pixels with similar colour. With the aid of such colour images, it is normally easy for the human eye to identify grains in COMs from fully or partly recrystallized samples. Difficulties in defining a good mapping from orientation space into colour space can, however, present a problem (Gerth and Schwarzer 1993). Alternatively, one can create images, which visualises the disorientation angle between neighbouring points by drawing a line between the corresponding pixels when this angle is larger than some threshold. Often these lines are drawn on top of the colour image to further aid the human eye in identifying orientational differences and grains in the COM. Even though such visualisations can be very useful, the ultimate aim is often to extract quantitative information from the 2D data, which describes the microstructure in a compact fashion. This could, for example, be measures such as the average grain size, grain size distribution, grain morphology parameters, or the area fraction of recrystallized grains in partly recrystallized samples. To extract such information from the COM, a procedure for automatic grain identification is clearly needed. Such a procedure will be described in the following section.

The EBSP technique has proved to be an extremely valuable tool for studies of the recrystallization process (Juul Jensen 1996). In such studies it is often essential to be able to recognise and localise recrystallized grains within the deformed material. This is the case, for example, when growth rates of differently oriented grains are to be determined, when the spatial distribution of grains are of interest, or when the orientational relationship between grains and the surrounding matrix are being examined. Today, the recognition of recrystallized regions in partly recrystallized samples is mostly performed manually by an operator who observes the changes in EBSPs as a linear scan is made across the sample. Recrystallized regions are then recognised by the stability and sharpness of EBSPs within the region. Clearly, this method is tedious and highly time-consuming when statistically sound measurements are required. Furthermore, the recognition of recrystallized material is known to be fairly subjective. The development of an automated technique has therefore been a goal for several years now, see Krieger Lassen et al. (1993) and Field (1995).

2 Identification of grains in crystal orientation maps

Let $G = [\, g(x_i, y_j)\,]$ denote the N×M matrix of crystal orientations which have been measured on a rectangular grid whose grid points are members of the set *S*:

$$S = \left\{(x_i, y_j) \,\middle|\, x_i = x_0 + i\cdot dx,\ y_j = y_0 + j\cdot dy,\ i \in [0, N-1],\ j \in [0, M-1]\right\}.$$

Thus, G is simply a formal description of the COM, our orientation image. In this paper, as in most cases, the sampling intervals in the x- and y-direction are identical, $dx = dy$. For convenience (and in lack of a better word) each sampled orientation $g(x_i, y_j)$ shall frequently be referred to as a *pixel* (picture element) in the following. Furthermore, we shall often write $g(i, j)$ to denote the orientation of the pixel at sample point (x_i, y_j).

In our terminology, a *grain* shall now be defined as a subset of the pixels measured on *S*. This subset will consist of pixels which satisfy some definition of connectivity. Before providing the definition, the concept of neighbours to a pixel must be introduced. The ***4-neighbours*** of pixel (i, j) are the four points (i+1, j), (i-1, j), (i, j+1) and (i, j-1). The set of 4-neighbours to pixel g(i, j) is denoted $N_4(g)$. We now define *4-connectivity* as follows: two pixels g_1 and g_2 are 4-connected if g_2 is in $N_4(g_1)$ and $D(g_1,g_2) \le \theta_{max}$. Here, $D(g_1, g_2)$ is the disorientation angle between the two orientations g_1 and g_2 and θ_{max} is the angle which defines connectivity. If g_1 and g_2 are connected we also say that the two pixels are *adjacent*. Before providing our grain definition, we must introduce the concept of a *path*. A path from the pixel at point (i_0, j_0) to the pixel at (i_N,j_N) is a sequence of distinct pixels at points: $(i_0, j_0), (i_1, j_1), \ldots, (i_N, j_N)$, where (i_n, j_n) is adjacent to (i_{n-1}, j_{n-1}), $1 \le n \le N$. We can now extend the concept of connectivity as follows: two pixels g_r and g_s are *connected* in *S* if there exists a path from g_r to g_s consisting entirely of pixels in *S*. Let g be any given pixel within *S*. A *grain* is defined as the set of pixels which are connected to g in *S*. It is clear that any two pixels within a grain are connected to each other, and that distinct grains are disjoint.

The concepts of connectivity introduced above originate from the literature on digital image processing (Ballard and Brown 1982; Gonzales and Woods 1992) and the problem of identifying grains in G is quite similar to the problem of finding the so-called *connected components* in a digital image. The difference between the problems lie in the way similarity between pixels is defined. In image processing, a connected component is a connected region of pixels having the same pixel value (or values in some interval). In the present problem, a grain is a region characterised by the fact that any given pair of pixels within the grain can be connected by a path (within the grain) along which no disorientations are larger than θ_{max}. It follows from this definition that the disorientation at the borders of the grain will always be larger than θ_{max}. But it is also evident that with this definition, a grain may well include neighbouring pixels that have a disorientation larger than θ_{max} (as long as such pixels are connected along a path which circumvents this boundary). Note also that this definition allows grains to have disorientations from one end to other which are significantly larger than θ_{max}. The grain definition given here may not seem as the most obvious choice, but we believe it agrees fairly well with the "definition" provided by the physical world. Furthermore, the definition allows one to design an efficient algorithm for grain identification.

The task of identifying connected components in digital images is normally referred too as *connected component labeling*. Due to the close relation between connected components in images and grains in COMs, which follows from the definition, it is possible to use the algorithms which are normally used for connected component labeling as the basis for a procedure for grain recognition in COMs. This procedure scans the COM pixel by pixel, from left to right and from top to bottom. Let g denote the pixel at any step in the scanning process and let u and l be the upper and left-hand neighbours of g, respectively. The following four possibilities are then considered: (1) $D(g,u) \le \theta_{max}$ and $D(g,l) > \theta_{max}$, (2) $D(g,u) > \theta_{max}$ and $D(g,l) \le \theta_{max}$, (3) $D(g,u) > \theta_{max}$ and $D(g,l) > \theta_{max}$, and (4) $D(g,u) \le \theta_{max}$ and $D(g,l) \le \theta_{max}$. In the case of situation (1), pixel g will be assigned to the same grain/label as pixel u. In case (2), g is assigned to the label of l, and in case (3), g is assigned to a new label. Finally, in case (4), g can arbitrarily be assigned to any of the labels of u or l, which need not be identical. If this is the case, we make a note that the two labels are actually equivalent, i.e. u and l are connected through g. After completion of the scan, all pixels have been labeled, but several of the labels are likely to be equivalent. All pairs of equivalent labels are then sorted into equivalence classes and new unique labels assigned to each class. Finally, a second scan is made through the image, during which each label is replaced by the label assigned to its equivalence class. For more details on how equivalence classes can be identified, see Ballard and Brown (1982).

3 Identification of recrystallized grains in crystal orientation maps

The procedure presented above can be used for automatic recognition of recrystallized grains in COMs from partly recrystallized samples. Within the recrystallized grains the measured point-to-point disorientations should be no larger than the relative precision of orientation measurements by EBSP, say 0.5–1.0°, whereas the point-to-point disorientations within the deformed microstructure are typically significantly higher. If we therefore apply the grain identification procedure to the COM of a partly recrystallized sample with θ_{max} set to the precision of the orientation measurements, deformed regions of the sample will appear to be made up of very small grains consisting of just a few pixels. Recrystalllized grains can then be recognised simply from their size, which should be at least 2 pixels or – more statistically meaningful – larger than say 4 pixels. The minimum grain size in pixels is denoted N_{min}. With $N_{min} = 2$, we are likely to find many (small) grains within the deformed material, e.g. large subgrains or cell blocks. By increasing the value of N_{min}, we can limit the chance of finding false non-recrystallized grains within the deformed matrix, but at the expense of not being able to identify grains smaller than N_{min}. In this paper we have chosen to use $N_{min} = 5$ pixels and $\theta_{max} = 0.75°$.

The likelihood that an automatically identified grain is not truly a recrystallized grain is clearly larger for the smaller grains. We shall try to minimise the risk of erroneously accepting small detected grains as true recrystallized grains by exploiting the fact that the pattern quality within recrystallized regions is generally higher than within the deformed matrix. The measure of pattern quality Q applied here was defined in Krieger Lassen et al. (1993). A new threshold N_{minx} ($> N_{min}$) for the grain size is defined so that grains larger than this size are regarded as being recrystallized with probability 1. The Q-values for all points within these grains are recorded and the lower α-percentile ($\alpha \in [0,1]$) value Q_α of their distribution is determined and used to separate erroneous from recrystallized grains. Detected grains larger than N_{min} and smaller than N_{minx} are then accepted as recrystallized grains if their average Q-value is larger then Q_α. Obviously, increasing values for α will lead to the rejection of an increasing number of the small grains. The percentile α should be chosen while considering two factors: our general confidence in the small grains (those between N_{min} and N_{minx} in size) and our confidence in the ability of the Q-value to distinguish recrystallized from deformed regions. The limited space does not permit a discussion of how proper values for the parameters N_{min} and α can be chosen. In this study we use $N_{minx} = 10$ and $\alpha = 0.15$.

4 Experiments and results

The procedure for recognition of grains in partly recrystallized samples was tested on three annealed samples of commercially pure aluminium (AA1050). The starting material, with an average grain size of 100μm, was cold rolled to 90% reduction

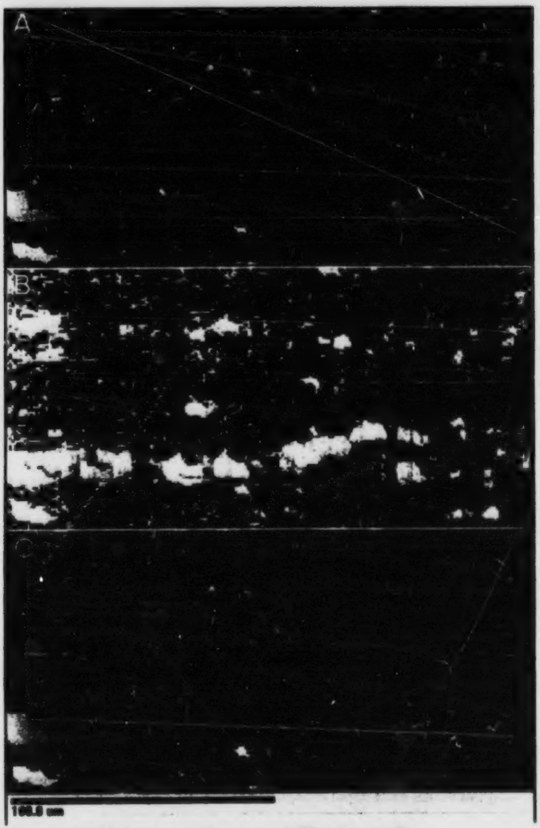

Fig. 1: COM from partly recrystallized sample. (A) Visualisation with black lines indicating disorientations larger than 0.75°. (B) Pattern quality Q shown illustrated with gray tones. (C) Recrystallized grains found automatically. Deformed regions shown in black.

and then annealed isothermally at 250°C for 2000, 11000, and 38000 seconds. The three samples, named A, B, and C, respectively, were polished and prepared for EBSP analysis on the longitudinal plane (the RD-ND plane), and two long perpendicular line scans were made across the samples to manually detect and localise deformed and recrystallized regions. From the recorded data, area fractions of recrystallized material were calculated to allow a quantitative comparison with the data that was later found with the automatic procedure. From each of the three samples, three COMs where collected at positions well spread over the sample surface. For all COMs, the sampling distance was 1µm and the size of the sampling grid 200×100 pixels. Thus, the total area covered on each sample was 0.06mm^2. Fig. 1a shows a COM from sample B (~20 % recrystallized) with black lines drawn where the point-to-point disorientation is larger than 0.75°. The bigger grains are easily recognised from this visualisation of the structure. Fig. 1b shows a picture of the same COM where the pixels have been assigned gray tones according to the value of the pattern quality Q (bright areas correspond to large Q-values). It is evident that recrystallized regions generally have higher Q values. Fig. 1c shows the grains that were identified in the COM by the procedure described in this paper. Q-values have been used here to exclude a fraction of the small grains.

A comparison of the area fractions of recrystallized material found manually and automatically is presented in Table 1. The first column shows the results obtained by an experienced researcher. Each value is obtained as the average of two measurements, one for each of two perpendicular line scans. The second column shows the results obtained by applying the grain identification procedure presented above with the parameters: $\theta_{max} = 0.75°$ and $N_{min} = 5$. Finally, the third column shows the results obtained when a fraction of the small grains have been discarded on the basis of their average pattern quality, as explained above. The parameters used were: $N_{minx} = 10$, and $\alpha = 0.15$.

Table 1: Area fractions determined for three annealed samples by three different methods: Manually by operator, automatically without using Q, and automatically using Q.

	Area Fraction Recrystallized (%)		
Sample	**Manual**	**Automatic**	**Automatic (+Q)**
A	8.6	9.5	7.6
B	21.8	23.5	19.6
C	52.9	55.9	54.7

5 Conclusion

Inspired by the concept of connected components from digital image analysis, a definition of grains in COMs has been given. With this definition it is fairly simple to design an efficient procedure for identifying grains in COMs, as described above. The availability of such a grain identification procedure is of fundamental importance when COMs are to be analysed and described quantitatively. This generally applicable procedure is employed here for the recognition of recrystallized grains in partly recrystallized samples, in which case the grain identification procedure incorporates and exploits the information carried by measurements of the pattern quality.

A comparison of area fractions of recrystallized material determined manually and automatically show a good agreement, considering the limited sampling statistics for both manual and automated measurements. The results obtained without incorporation of the pattern quality are all higher than what was obtained manually, but the small difference could easily be explained by the statistical uncertainty and objectiveness of the operator. With the presented data, it is not possible to judge whether the results obtained by discarding small grain with low pattern quality are more correct than those which were obtained without use of the pattern quality.

References

Ballard, D.H. and Brown, C.M. (1982) *Computer Vision*, Prentice-Hall, Englewood Cliffs, NJ.

Field, D.P. (1995) Quantification of partially recrystallized polycrystals using electron backscatter diffraction. *Mater. Sci. Eng. A*, Vol. 190, pp. 241-246.

Gerth, D. and Schwarzer, R.A. (1993) Graphical representation of grain and hillock orientations in annealed Al–1%Si films. *Textures Microstruct.*, Vol. 21, pp. 177-93.

Gonzales, R.C. and Woods, R.E. (1992) *Digital Image Processing*, Addison-Wesley, New York.

Juul Jensen D. (1996) EBSP studies of growth rates during recrystallization. *Mater. Sci. Forum*, Vol. 204-206, pp. 713-722.

Krieger Lassen N.C., Conradsen, K., and Juul Jensen, D. (1992) Image processing procedures for analysis of electron back scattering patterns. *Scanning Microsc.*, Vol. 6, pp. 115-121.

Krieger Lassen, N.C., Juul Jensen, D., and Conradsen K. (1994) Automatic recognition of deformed and recrystallized regions in partly recrystallized samples using electron back scattering patterns. *Mater. Sci. Forum*, Vol. 157-162, pp. 149-158.

Wright, S.I. (1993) A review of automated orientation imaging microscopy (OIM). *J. Comp.-Assist. Microsc.*, Vol. 5, pp. 207-221.

INFLUENCE OF Fe CONTENT ON RECRYSTALLIZATION, GRAIN GROWTH AND RECRYSTALLIZATION TEXTURES IN Al-Mg ALLOYS

M. KOIZUMI, H. OKUDAIRA and H. INAGAKI

Shonan Institute of Technology, Fujisawa, Japan

Abstract

Recrystallization textures developed in Al-5%Mg alloys are strongly dependent on Fe content. In the case of high purity Al-5%Mg alloy, cube texture is strong already after complete recrystallization. On annealing at higher temperatures, it increases up to 350 °C. Above this critical temperature, it decreases rapidly and annealing texture becomes random. In Al-5%Mg alloys with low Fe content, i.e. between 0.02 and 0.1%, retained rolling texture is obtained after complete recrystallization, indicating that precipitation of Fe has occurred during recrystallization. On annealing at higher temperatures, cube orientation developes in these alloys without showing abrupt decrease above a critical temperature, such as that observed in high purity Al-5%Mg alloy. In Al-5%Mg alloys containing Fe more than 0.1%, textures observed after complete recrystallization are very weak. On annealing at higher temperatures, however, cube texture increases also in this case appreciably. This increase in cube texture is more remarkable in Al-0.10%Fe and 0.20%Fe alloys than in Al-0.40% Fe alloy. This suggests that the optimum distribution of Al_3Fe favors grain growth of cube oriented grains. From these results, it is concluded that, in impure commercial Al-Mg alloys containing significant amount of Fe, the effect of Mg is masked considerably by the effect of Fe.

Keywords: Al, Fe, Mg, Recrystallization Texture

1. Introduction

Rolling and recrystallization textures of high purity Al is strongly influenced by Mg (Koizumi et al. 1997, 1998). Addition of Mg above 3% strongly suppresses the development of the cube recrystallization texture. In applying these results to commercial Al-Mg alloys such as AA5182 and AA5083, influences of other elements such as Fe, Si, Cr, Ti and Mn must be taken into account. It is therefore suggested that the effect of Mg may be reduced or masked by the effect of such third elements. Since Fe is the most popular element contained in commercial Al, the effects of Fe content on the development of recrystallization texture was investigated in detail in Al-5%Mg alloys. Since the effect of Fe may be different depending upon the annealing temperature, it was investigated by varying annealing temperatures.

2. Experimental procedure

Hot bands of Al-5%Mg alloys containing Fe up to 0.4% were solution treated at 400 °C for 0.5h and cooled in air. They were cold rolled 95% reduction in thickness and isothermally annealed at temperatures between 275 and 450 °C. Annealed specimens were chemically thinned down to 0.15 mm thickness by using NaOH solution. By using Rigaku RINT 2200 diffractometer, complete {111}, {220} and {200} pole figures were determined on these specimens. From these pole figures, orientation distribution functions were caluculated. Microstructures of these specimens were revealed with Keller's solution. Grain growth behavior of these specimens was investigated with optical microscopy.

3. Results and discussions

3.1 Recrystallization textures observed after low temperature annealing

Specimens were isothermally annealed either at 275°C or at 300 °C up to complete recrystallization. (Specimens containing Fe more than 0.06% could be readily recrystallized at 275 °C. However, in the specimens containing Fe less than 0.06%, recrystallization did not occur so easily at 275°C, so that they were annealed at 300 °C.) {111} pole figures measured on these specimens are given in Fig. 1. It is evident that {100}<001> was strong in pure Al and Al-0.04%Fe alloy. In Al-0.06%Fe, 0.10%Fe and 0.20%Fe alloys, the textures appear to be retained rolling textures. At higher Fe content, however, these retained rolling textures became weak and the overall texture tended to be random.

Orientation densities of {100}<001> and main rolling texture components, {123}<634>, {112}<111> and {110}<112> observed in these specimens are plotted in Fig. 2 against Fe content. These results show that in specimens with low Fe content, i. e. below 0.04%, cube texture developed remarkably. In the specimen containing Fe in the range 0.06 to 0.1%, it is evident that the formation of cube texture was strongly suppressed during low temperature recrystallization. The resultant recrystallizaition texture was therefore weak and random, Fig. 1, but main components of the rolling texture were clearly retained, suggesting that some precipitation had occurred during annealing. Among the main rolling texture components, {110}<112> was most strongly retained. In the specimens with 0.2 and 0.4% Fe, such retained rolling texture components were weak. Their textures were random.

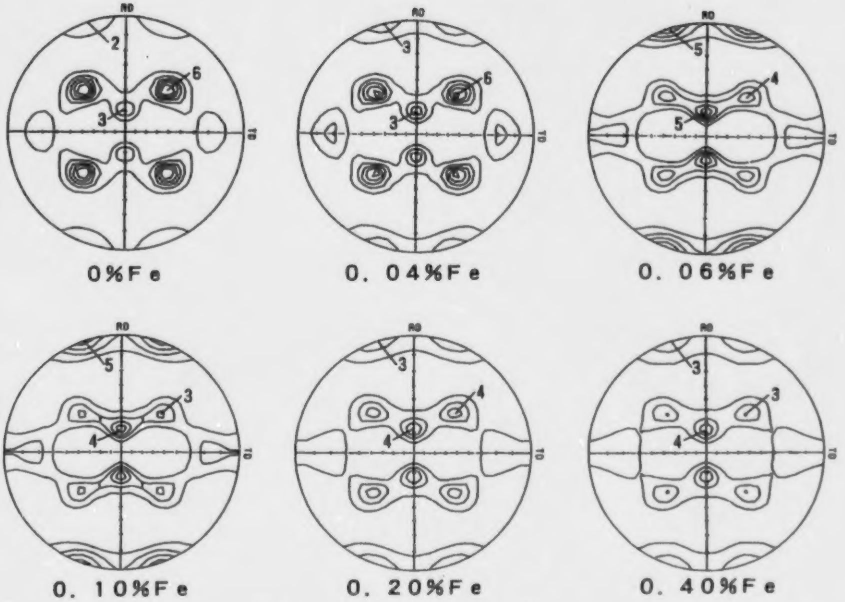

0%Fe 0.04%Fe 0.06%Fe

0.10%Fe 0.20%Fe 0.40%Fe

Fig. 1 {111} pole figures observed on specimens annealed up to complete recrystallization at 275 or 300 °C.

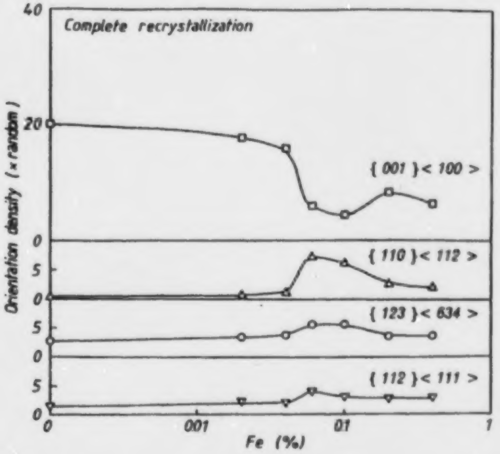

Fig. 2 Effect of Fe content on orientation densities of {100}<001>, {110}<112>, {123}<634> and {112}<111> orientations observed in the specimens annealed up to complete recrystallizatin at 275 or 300 °C.

3.2 Effect of annealing temperature on recrystallization texture

Taking the results described above into account, alloys with 0, 0.1 and 0.4% Fe were selected as representative alloys and they were annealed 0.5h at higher temperatures. Orientation densities of {100}<001> and ND rotated cube, i.e. {100}<012> and {100}<013> are plotted in Fig. 3 as a function of the annealing temperature. In Fig. 4, grain growth behavior observed on these specimens on prolonged isothermal annealing at each annealing temperature is illustrated. In high purity Al-5%Mg alloy, it has been observed (Koizumi et al 1998) that {100}<001> increased with increasing annealing temperature up to 350 °C, and that above this citical

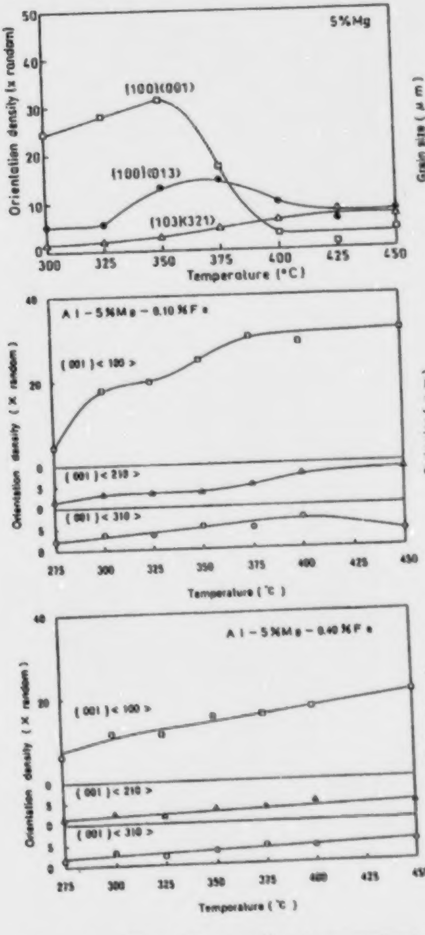

Fig. 3 Effect of annealing temperature on the development of cube and rotated cube recrystallization texture components.

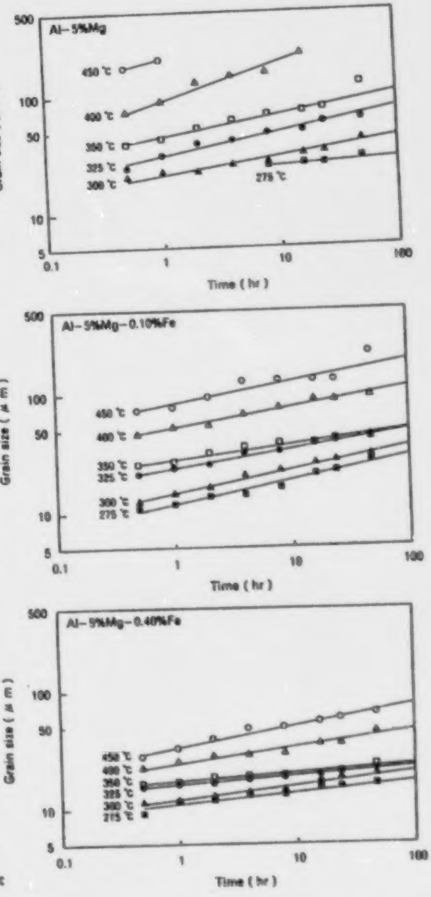

Fig. 4 Isothermal grain growth observed in Al-5%Mg alloys containing 0, 0.10 and 0.40 %Fe.

annealing temperature, it decreased dramatically. This result is also shown in Fig. 3. Such decrease in {100}<001> was not observed in Al-5%Mg alloys with 0.10 and 0.40% Fe, Fig. 3. In the alloy with 0.10%Fe, {100}<001> increased remarkably with increasing annealing temperature up to 300 °C. In the temperature range between 300 and 350 °C, {100}<001> increased only gradually. Above 350 °C, it increased again, saturating at temperatures above 375 °C. Such two step increase in {100}<001> may be related with grain growth behavior given in Fig. 4. Figure 4 indicates that grain growth was abnormal and considerably difficult at temperatures between 300 and 350 °C. It is suggested that precipitation of Fe (Ito et al. 1983) occurred in this alloy at these temperatures. Thus, in contrast with high purity Al-5%Mg alloy, strong {100}<001> recrystallization texture was observed in this alloy even after annealing at 450 °C. In this alloy, ND rotated cube developed at temperatures above 375 °C.

In Al-5%Mg-0.40%Fe alloy, the texture observed after complete recrystallization should be more random, since PSN could occur at larger Al_3Fe particles. This was in fact observed in low temperature annealing, Figs. 1 and 2. This may be true also in the case of short time annealing at high temperatures. Since grain growth in addition occurred very slowly due to pinning by Al_3Fe particles, Fig. 4, {100}<001>increased only gradually with increasing annealing temperatures. Anomalies in grain growth behavior shown in Fig. 4 suggest that, also in this alloy, precipitation of Fe occurred during annealing at temperatures between 325 and 350 °C.

Orientation densities of {100}<001> and main rolling texture components, {123}<634>, {112}<111> and {110}<112> observed in the specimens annealed 0.5h at 450 °C are plotted in Fig. 5 against Fe content. These results show that cube texture showed maximum development in the specimens containing Fe in the range between

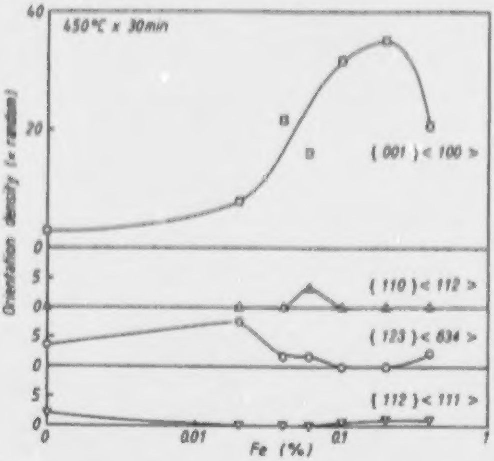

Fig. 5 Effect of Fe content on orientation densities of {100}<001>, {110}<112>, {123}<634> and {112}<111> orientations observed in the specimens annealed 0.5h at 450°C.

0.02 and 0.4%. This is a marked contrast with the results obtained in low temperature annealing. In that case, development of cube texture was strongly suppressed in these specimens, Fig. 2. Since a large amount of Al_3Fe particles is present in these specimens, their optimum distribution seems to have enhanced the development of cube texture in high temperature annealing.

5. Conclusions

Effect of Mg on the texture development of Al is strongly influenced by the purity of the base metal. In high purity Al, addition of Mg above 3% remarkably suppresses the development of the {100}<001> recrystallization texture in high temperature annealing. However, such an effect of Mg is considerably reduced by the addition of Fe above 0.1%.

6. References

Ito, K., Musik, R. and Lücke, K. (1983) The influence of iron content and annealing temperature on the recrystallization textures of high purity Aluminum-iron alloys Acta metall. Vol. 31, No. 12, pp.2137-2149.

Koizumi, M., Kohara, S. and Inagaki, H. (1997) Rolling and recrystallization textures in high purity Al-Mg alloys. Z. Metallkde. Vol. 88, No. 7, pp. 576-582.

Koizumi, K., Okudaira, H. and Inagaki, H. (1998) Development of annealing textures in Al-Mg alloys Z. Metallkde. Vol. 89, No. 6, pp. 424-432.

RELATIONSHIP BETWEEN PRIMARY RECRYSTALLIZATION GRAIN SIZE AND ITS TEXTURE IN 3%SI STEELS

S.K. CHANG, B.D. HONG and K.S. HAN
POSCO Technical Research Laboratories, Pohang, Korea

Abstract

The magnetic properties of 3% Si grain oriented electrical steels are much influenced by the primary recrystallization texture. In this study, the evolution of primary recrystallized texture was investigated in the low temperature slab reheating process. Primary recrystallization annealing was carried out in the atmosphere of 25% H_2 + 75% N_2, 53℃ for 3.5minutes. Texture was analysed by EBSP (Electron Back Scattering Pattern) in the SEM. The relationship between primary texture and grain size is discussed.

Keywords: Grain oriented electrical steels, Low temperature slab reheating, Primary recrystallization, and Secondary recrystallization

1 Introduction

Grain oriented electrical steels are produced in several different ways. Two-stage cold rolling method was developed by ARMCO [1]. With one stage cold rolling method, Hi-B was developed by Nippon Steel [2]. Both methods are based on high temperature slab reheating technology. It is necessary to fully dissolve coarse AlN and MnS particles formed during casting by reheating slab at the temperature higher than 1350℃. However, the extremely high temperature in slab reheating makes the hot rolling process very difficult and reduces its productivity and yields.

Recently, a new fabrication method for grain oriented electrical steels was developed by Nippon Steel with low slab reheating temperature at 1150℃ through nitriding after decarburization annealing to form AlN as an inhibitor in the secondary recrystallization annealing [3,4].

Chemical composition and technology are very similar between Hi-B and new technology. In new technology, AlN particles as an inhibitor are formed in the early stage of secondary recrystallization annealing. Therefore, inhibiting strength is weaker than Hi-B before secondary recrystallization annealing and primary recrystallized grain size is much larger than that of Hi-B. In general, primary grain size of Hi-B is less than 10μm and small grain size is desirable due to strong driving force for secondary recrystallization.

In this paper, the relationship between primary recrystallization grain size and primary recrystallization texture formation in the low temperature slab reheating process.

2 Experimental Procedure

The compositions of materials melted by induction in vacuum were given in Table 1. The 30Kg ingot was heated in an Ar atmosphere at 1200℃ for an hour and hot rolled to thickness of 2.3mm. Hot bands were annealed at 1100℃ for two minutes and quenched to boiling water. They were cold-rolled to 0.29mm thickness and decarburized in a wet atmosphere for three and half minutes (D.P.52℃, 75%N_2+25%H_2). Primary recrystallized specimens in decarburization annealing were secondary recrystallized in high temperature annealing (15℃/hr up to 1200℃, 75%N_2+25%H_2). Nitriding was carried out at the heating stage of high temperature annealing.

Table 1. Chemical Composition of Specimen (wt %)

Si	C	Mn	S	Sol.Al	P	N
3.2	0.055	0.12	0.007	0.025	0.01	0.008

Texture was analyzed by Electron Back Scattering Pattern (EBSP) technology with scanning electron microscope at a quarter depth from surface along thickness direction. EBSP specimens were prepared with electro-polishing (85.7% acetic acid + 14.3% perchloric acid) and scanning interval was 5μm.

3 Results

Fig. 1 shows the relationship between Magnetic flux density of the secondary recrystallized specimens and primary recrystallization temperature. The highest B10 was 1.90Tesla at 900℃. The average primary grain diameter was increased with primary recrystallization temperature.

In order to investigate the relationship between primary recrystallization grain size and texture, orientation measurement was carried out with the two grain size groups, small grains (less than 26μm) and large grains (over 37μm) in the same specimen primary recrystallized at 875℃. Areal fraction of large primary grain over 37μm was 7%, and that of small grain less than 26μm was 71%. Their textures were much different from each other.

Fig. 2 shows the misorientation angle from {110}, {100}, {111}, and {112} plane in the specimens primarily recrystallized at 875℃. Large grains were closer to

{110} plane than small grains. Small grains showed larger fraction of {111} and {100} plane. There was not significant difference in {112} plane.

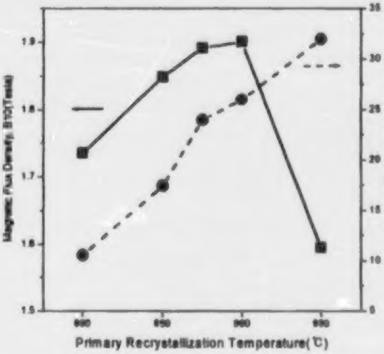

Fig. 1: Effects of Primary Recrystallization Temperature on Magnetic Flux Density and Primary Grain Size.

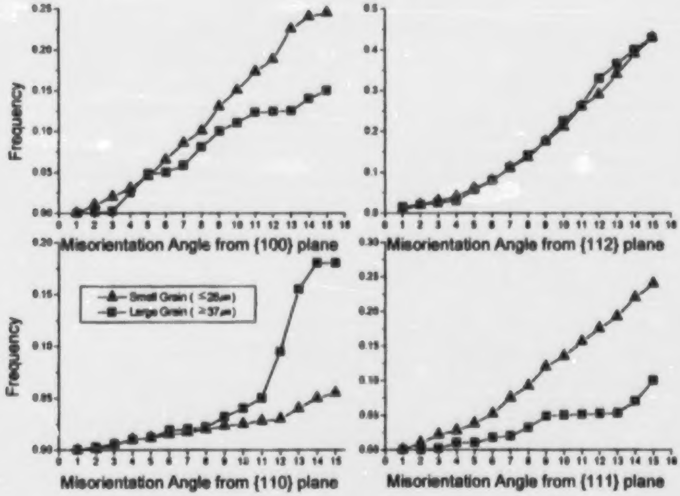

Fig. 2: Misorientation Angle in the Specimen of 1/4t in Primary Rerystallized Grain Oriented Electrical Steels.

Fig. 3 shows the inverse pole figures with grain size. In the inverse pole figure of grains larger than 37μm, <001> and <103> directions parallel to rolling direction show strong intensity. In the transverse direction, <112> direction shows strong intensity. Small grains less than 26μm showed strong intensity of <111> and <001> directions parallel to the ND (normal direction). In other word, there are many grains near {111} and {001} planes. In the rolling direction, it was shown that <102> direction was strong.

Fig. 4 shows the misorientation angle from {111}<112> γ orientation and {110}<001> Goss orientation. The small grain group is close to γ orientation, while the large grain group is far from this orientation. Therefore, from a viewpoint of Goss orientation, large grains are not relevant to γ orientation but to Goss orientation even though the small grains are vice versa.

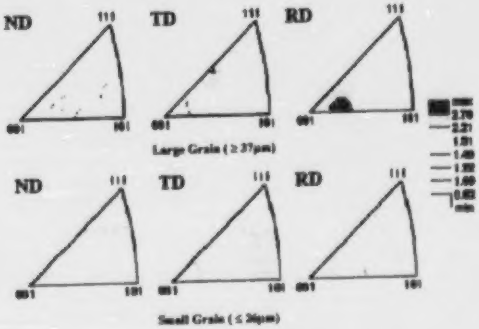

Fig. 3: Inverse Pole Figure of Primary Recrystallized Grain Oriented Electrical Steels at 1/4t thickness.

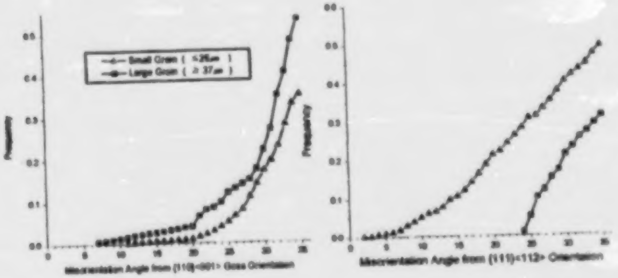

Fig. 4: Misorientation Angle from Goss Orientation in the Specimen of the Primary Rerystallized Grain Oriented Electrical Steels at 1/4t depth from the surface.

4 Discussion

High permeability grain oriented electrical steels like Hi-B [2] and RG-H [4] were produced by high temperature slab reheating temperature. In these cases, fine primary recrystallized grain is preferable to good magnetic properties. In high temperature slab reheating process, fine grain size is helpful for stable secondary recrystallization because of the strong driving force.

However, in low temperature slab reheating technology, optimum primary grain size for better magnetic properties has been reported to be larger than the Hi-B grains having less than 10μm, but the magnetic flux density decreases when it exceeds a certain critical size of 24μm [4]. In the present work, as seen in Fig.1, this critical size was 25μm. In the low slab reheating temperature, the larger primary grain size, the higher secondary recrystallization temperature was known [4,6,7]. The optimum primary grain size is different depending on the inhibiting strength. Therefore, the primary grain size distribution is thought to be related with primary texture and play a different role in contributing to the secondary recrystallization evolution under the different inhibiting strength .

In the process of low slab reheating temperature, large primary grains were closer to {110}<001> Goss orientation than small grains (Figs.2 and 4). Large grains also showed stronger <001> direction intensity parallel to rolling direction (Fig.3). On the other hand, small grains showed the closer relationship with {111}<112>. {110}<001> and {111}<112> have $\Sigma 9$ coincidence site lattice (CSL) relationship and there is $\Sigma 19a$ CSL relationship between {110}<001> and {554}<225> near to {111}<112>. Therefore, Goss grains in the secondary recrystallization annealing can easily consume the primary recrystallized grains around {111}<112>.

The volume of {110}<001> Goss texture is investigated in the primary recrystallized specimens. Despite of the different primary recrystallization temperature and grain size, the volume of Goss grains was similar between 800 and 875℃. In case of primary recrystallized specimen at 875℃, the volume fraction of Goss grains was only 0.1 and 0.8% within 10 and 15 degree tolerance, respectively. The volume fraction of Goss grains were only 0.1 and 0.9% within 10 and 15 degree tolerance, respectively, in the primary recrystallized specimen at 800℃. Therefore, it is thought that there is a nucleation or incubation stage for Goss nuclei to secure the enough size to be able to grow into the large secondary recrystallization grains.

It is considered that each of the grain size groups plays a different role in the secondary recrystallization stage, because they have the different primary texture. It has not been clearly proved yet, however, the large grains in primary recrystallized specimens may be related with securing the size advantage at the early stage of secondary recrystallization and small grains may play a role at the growth stage of secondary recrystallization. Because large primary grains were close to Goss texture and small primary grains were closer to {111}<112>.

5 Conclusion

The effect of the primary recrystallization size on the primary recrystallization textures of 3% Si-Fe grain oriented electrical steels were investigated in low temperature slab reheating process. Large primary recrystallized grains over 37μm showed the primary texture formation close to {110}<001> Goss orientation and strong <001> direction intensity parallel to rolling direction. Small grains less than 25μm showed the primary recrystallization texture close to {111}<112> orientation.

6 References

1. Goss, N.P. (1934) *US Patent* No. 1,965,559
2. Taguchi, S. and Sakakura, A. (1964) *US Patent* No. 3,159,511
3. Takahashi, N. and Harase, J. (1996) *Material Science Forum* Vol. 204-206, p.143.
4. Yoshitomi, Y., Harase J. and Takahashi, N. (1996) *Material Science Forum* Vol. 204-206, pp. 629-634.
5. Goto, I., Matoba, I., Imanaka, T., Gotoh, T. and Kan, T. (1975) *Proc.Soft Magnetic Mater.* vol 2, p262
6. Hong, B.D. and Woo, J.S. (1998) *Journal De Physique* vol 8, pp. Pr2-519 - Pr2-522
7. Woo, J.S., Han, C.H., Hong, B.D. and Harase J. (1998) *Acta Mater.* Vol46, pp 4905-4909

TEXTURE DEVELOPMENT IN HIGH STRENGTH IF STEEL CONTAINING P

W. MAO, Z. ZHAO and Y. YU
Department of Materials Science and Engineering
University of Science and Technology Beijing, Beijing, China

Abstract

The evolution of rolling and recrystallization texture in high strength IF steel sheet strengthened by P and Mn was investigated in comparison with normal IF steel sheet. Starting from very similar rolling textures a dominant {111}<112> texture component was observed in high strength steel, while a relatively homogenous {111} fiber texture was obtained in normal IF steel after recrystallization annealing. According to the analysis of recrystallization process it is believed that the P and Mn atoms in solid solution slowed down the grain boundary migration and reduced the recrystallization driving force, which provides a good condition for grain growth selection based on migration of high angle boundaries, and leads to the strong {111}<112> texture. The precipitation of potential FeTiP phase, which will reduce the {111} fiber texture and the r value, was avoided by reducing the Ti content.

Keywords: High strength steel, IF steel, recrystallization mechanism

1 Introduction

With the development of automotive industry the weight of the car body and therefore the energy consumption should be efficiently reduced. More attention have been paid to the research and development of high strength steel sheets with high r value (Takechi 1994 and Bleck 1995). Compared with other kinds of high strength steel sheets, solid-solution hardened IF steels have higher strength and comparatively lower formability reduction. Therefore the high strength IF steel containing P and Mn becomes one of the most important IF steels for the automotive industry. Due to the addition of solid solution elements, such as Si, Mn and P, certain special precipitate e.g. the FeTiP phase (Kurosawa et al. 1980, Okamoto and Mizui 1990 and Zhao et al. 1999) might occur besides the solid solution atoms in the matrix. In order to improve the deep draw-ability of the high strength IF steels the atoms, effecting as strengthening elements in the matrix or in the precipitates, will influence the texture development as well as the deep draw-ability, which should be therefore investigated.

2 Materials and experimental procedure

Hot rolled plates of Mn and P added high strength IF steel (H-IF) and normal IF steel (N-IF) were used. The chemical compositions are listed in table 1. The steel H-IF belongs to the high strength steel with the tensile strength over 340 MPa.

Table 1 Chemical composition of experimental steels (wt. %).

steel	C	Si	Mn	P	S	Al	Ti	Nb	N	B
H-IF	0.0034	<0.03	0.32	0.043	0.0040	0.036	0.019	0.019	0.0018	added
N-IF	0.0032	<0.03	0.13	0.010	0.0030	0.039	0.033	0.010	0.0023	-

The hot plates were cold rolled down to 55%, 70%, 80%, 86% and 90% of the thickness respectively, after which the rolling samples were annealed at 700°C or 850°C in salt bath, which is comparable to the industrial batch annealing or continuous annealing. The incomplete pole figures, i.e. {110}, {200} and {112} were measured in the center layers of the samples using X-ray diffractometer with Co tube, and the ODFs were calculated (Bunge 1981).

3 Results

Figure 1 gives the φ_2=45° ODF sections of rolling texture in the IF steels. The density levels in all following φ_2=45° ODF sections are 2, 4, 6, 8, 10 ,12, 14 and 16.

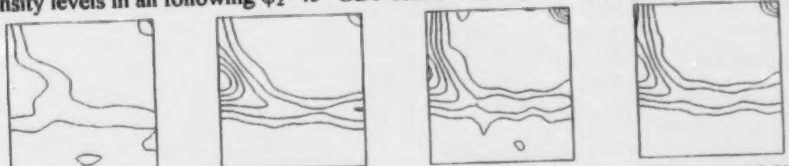

0% (max.: 6.0) 55% (max.: 13.9) 80% (max.: 12.8) 90% (max.: 12.2)

a. H-IF steel

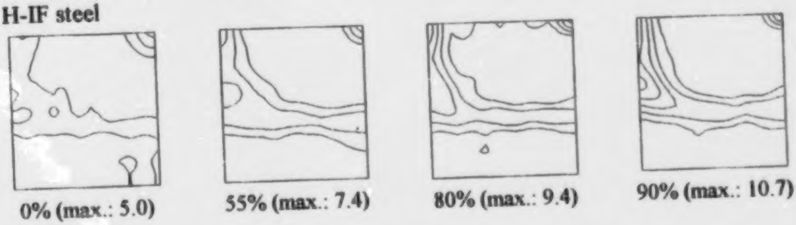

0% (max.: 5.0) 55% (max.: 7.4) 80% (max.: 9.4) 90% (max.: 10.7)

b. N-IF steel

Fig. 1 Rolling texture at different rolling reductions of the IF steels (φ_2=45°)

Figure 2 is the corresponding fiber analysis of the rolling textures which are characterized by the conventional <110>//RD and <111>//ND fiber textures after heavy rolling. No obvious texture difference between H-IF and N-IF steel was observed though more Mn and P had been added in the H-IF steel (table 1).

A dominant {111}<112> texture component in 80% rolled H-IF steel was formed after the annealing at 700 °C and 850 °C (fig. 3). The fiber analysis indicates that the rolling texture component {111}<110> was even reduced during annealing at 700 °C (fig. 4a) or after the annealing at 850 °C (fig. 4b). But a rather homogeneous <111>//ND fiber texture was formed in the 80% rolled N-IF steel after the annealing (fig. 5), in which the {111}<110> texture was drastically increased with the increasing {111} fiber texture (fig. 6). This difference of recrystallization texture between H-IF steel and N-IF steel is confirmed by other heavy rolled and annealed(at 850 °C for 60 sec.) sheets, in which the primary recrystallization was completed (fig. 7).

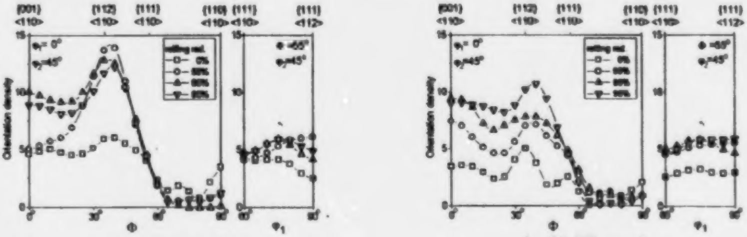

a. H-IF steel b. N-IF steel

Fig. 2 α and γ fiber analysis of the rolling texture.

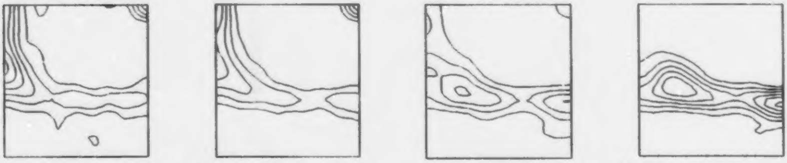

0 min. (max.: 12.8) 15 min. (max.: 10.3) 150 min. (max.: 8.4) 300 min. (max.: 12.8)

a. annealed at 700 °C

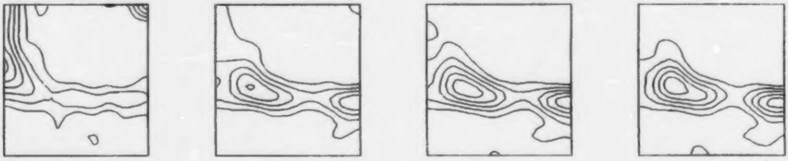

0 sec. (max.: 12.8) 16 sec. (max.: 10.3) 64 sec. (max.: 11.7) 1024 sec. (max.: 11.8)

b. annealed at 850 °C

Fig. 3 Annealing texture evolution of the 80% rolled H-IF steel (φ_2=45°).

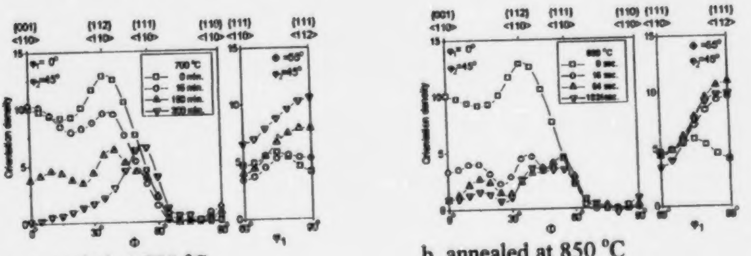

a. annealed at 700 °C

b. annealed at 850 °C

Fig. 4 α and γ fiber analysis of the annealing texture in the H-IF steel.

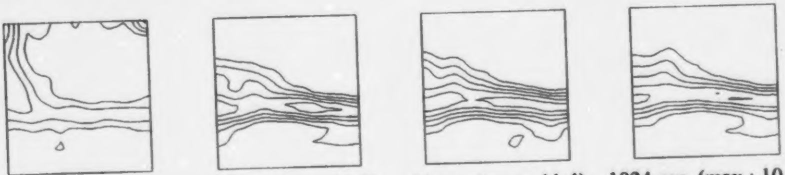

0 sec. (max.: 9.4) 16 sec. (max.: 12.0) 64 sec. (max.: 11.4) 1024 sec. (max.: 10.7)

Fig. 5 Annealing texture evolution of the 80% rolled H-IF steel annealed at 850°C (φ_2=45° sections).

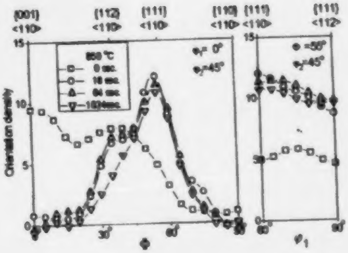

Fig. 6 α and γ fiber analysis of the annealing texture in the N-IF steel.

4 Discussion

According to table 1 it can be seen that the main strengthening elements for the H-IF steel are P and Mn. It is known that in this kind of steels the formation of TiC would be retarded by the P atoms, and the FeTiP phase could precipitate which will destroy the strength and draw-ability (Kurosawa et al. 1980, Okamoto and Mizui 1990 and Zhao et al. 1999). Therefore the H-IF steel used here contains lower Ti and higher Nb (table 1), which could remain the interstitial free matrix and produce no FeTiP phase, since the Ti would combine merely with N atoms and no extra Ti atoms could be left for the FeTiP (Zhao 1999). FeTiP will start to precipitate during the recrystallization at 700 °C or after the recrystallization at 850 °C (Zhao 1999), therefore the batch annealing at 700 °C is not recommended for the high strength steels containing high P. However if the Ti content is reduced properly the FeTiP precipitation could be avoided. Figure 3 and 4 demonstrate that very similar recrystallization texture was formed in the H-IF steel, indicating that no FeTiP precipitates have interrupted the recrystallization process at 700 °C, and P atoms should still keep in the solid solution.

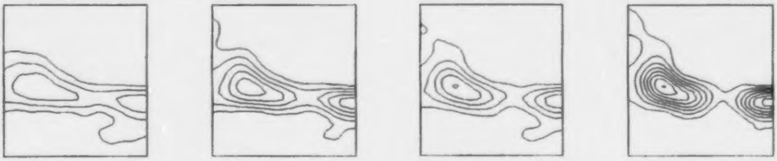

70% (max.: 8.0) 80% (max.: 11.8) 86% (max.: 10.4) 90% (max.: 16.2)

a. H-IF steel rolled over 70% (annealed at 850°C for 60 sec.)

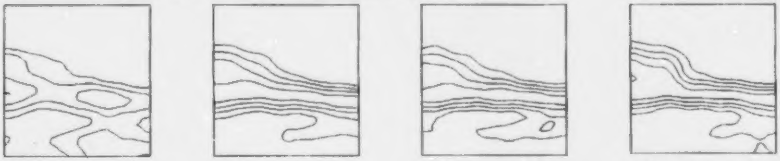

70% (max.: 8.1) 80% (max.: 9.7) 86% (max.: 10.0) 90% (max.: 10.0)

b. N-IF steel rolled over 70% (annealed at 850°C for 60 sec.)

Fig. 7 Annealing texture of the IF steels (φ_2=45° sections).

Figure 1 and 2 indicate that no drastic changes on crystallographic mechanism of the plastic deformation could be observed for the interstitial free matrix containing higher P and Mn atoms though the deformation resistance of the H-IF steel was therefore obviously increased. In this case the strengthening elements in the solid solution do not basically changed the combination of the active slip systems during rolling, so that very similar rolling textures have been obtained.

The {111} fiber texture was drastically increased in the N-IF steel during annealing(fig. 6), while only the {111}<112> texture was increased in the H-IF steel. Observing the changes of {111}<110> component during annealing (fig. 4), it can be seen that the orientation density around {111}<110> was reduced, which indicates that the deformed grains oriented in rolling texture component {111}<110> were swallowed by other recrystallization grains during annealing.

It was observed that the substructure oriented around the <111>//ND in deformed IF steel has advantages to be recovered firstly and grow as the recrystallization nuclei during the annealing processes (Mao et al. 1995). In this case the oriented nucleation will determine the recrystallization texture and a homogeneously strengthened {111} fiber texture would be obtained in N-IF steel (fig. 5, 7b). The growth selection effect in the N-IF steel is not important (Raabe and Lücke 1994) since the basic driving force is high enough to promote the recrystallization. The P and Mn atoms in solid solution of the H-IF steel will impede the migration of grain boundaries, which surely leads to elongation of incubation and strengthening of recovery process before primary recrystallization. Therefore the stored energy for recrystallization in H-IF steel will be reduced as the recrystallization starts. The growth selection effect of the nuclei will become more important comparing with the reduced driving force since the special high angle boundaries with lower growth obstructing are needed for a rapid growth, which has been observed very often in pure aluminum. The grains in {111}<112> component of the H-IF steel have the special orientation relationship to the rolling texture components and could become the dominant recrystallization texture (Raabe and Lücke 1994).

5 Summary

The evolution of rolling and recrystallization texture in high strength and normal IF steel was investigated. Reducing the Ti content could avoid the precipitation of FeTiP and ensure the final formation of {111} fiber texture. The P and Mn atoms in solid solution do not obviously change the crystallographic mechanism of the plastic deformation, i.e. the combination of active slip systems. Solid solution atoms will strengthen the recovery effect and impede the formation of {111} fiber texture produced mainly by the oriented nucleation process, and lead to a dominant {111}<112> texture component by oriented growth of the nuclei during the primary recrystallization.

6 References

Bleck, W., (1995) Anforderungen an Karosseriewerkstoffe, *Stahl u. Eisen*, Vol. 115, No. 4. pp. 55-64.

Bunge, H.J. (1981) General outline and series expansion method, in *Quantitative Texture Analysis*, (ed. H.J. Bunge and C. Esling), DGM-Informationsgesellschaft, Oberursel, pp. 1-72.

Kurosawa, F., Taguchi, I. and Matsumoto, R.,(1980) Observation and analysis of phosphides in steels using a non-aqueous electrolyte-potentiostatic etching method, *J. Jpn. Inst. Met.*, Vol. 44, No. 5. pp. 539-548.

Mao, W., Wang, X., Zhang, S. and Kong, B., (1995) Formation of annealing texture in rolling IF steel sheet, HSLA Steels'95, conf. proc.(ed. G. Liu et al), China Sci. & Tech. Press, Beijing, pp. 175-178.

Okamoto, A. and Mizui, N. (1990) Texture formation in ultra-low-carbon Ti-added cold rolled sheet steels, *Metallurgy of Vacuum-Degassed Steel Products*, (ed. R. Pradhan), the Minerals, Metals & Materials Society, pp. 161-180.

Raabe, D. and Lücke, K. (1994) Rolling and annealing textures of bcc metals, *Mater. Sci. Forum*, 1994, Vol. 157-162, Part 1, pp. 597-610.

Takechi, H., (1994) Metallurgical aspects on interstitial free sheet steel from industrial viewpoints, *ISIJ Inter.*, Vol. 34, No. 1. pp. 1-8.

Zhao, Z., Mao, W. and Yu Y., Precipitation behavior of FeTiP phase in high strength IF steel, (1999) to be published

MICROTEXTURES IN COPPER UNDERGOING DYNAMIC RECRYSTALLIZATION (DRX) IN TORSION

L. GAVARD and F. MONTHEILLET
Ecole Nationale Superieure des Mines de Saint-Etienne, France
H.J. McQUEEN
Mechanical Engineering, Concordia University, Montreal, Canada

Abstract

Copper polycrystal tubes were deformed in torsion in the steady state regime at high temperatures. Typical fine grain DRX microstructures were observed after instantaneous quenching while coarse grain metadynamically recrystallized (MRX) microstructures appeared within 2 seconds after straining. Comparison is made to hot rolled copper specimens which did not undergo DRX but yielded fine grains from static recrystallization (SRX). It is shown that the deformation texture is partially randomised by DRX and almost completely by MRX and SRX in both torsion and rolling.

Keywords: DRX, SEM-EBSD-OIM, hot working, torsion, rolling, microtextures, microstructures, copper

1 Introduction

Copper deformed in torsion into the steady state ($\varepsilon=30$) exhibited discontinuous DRX grains with substructure and few visible twins on quenching in less than 0.5 s, and much larger MRX grains with frequent twins when cooled in 2 s [McQueen and Bergerson 1972; McQueen 1982]. The DRX grains were larger at higher temperatures and contained a more recovered substructure (TEM, SEM channelling contrast) with hardness much above that of MRX and equivalent to 10 to 30% cold work. Nuclei with 1 or 2 subboundaries were observed among mature grains (8 μm). Textures have been previously measured over a range of temperatures both before and after DRX [Montheillet et al. 1984]. In contrast, Cu rolled in a single pass (900-500°C) to $\varepsilon=2.66$ (less than the critical strain for DRX) exhibited a denser substructure (TEM) without DRX or SRX nuclei but SRX ensured in a few seconds [McQueen 1968]. Deformation and rolling textures were determined by X-ray diffraction to be similar to those developed after 20°C and annealing [McQueen and Mecking 1987]. These samples, with structures thoroughly explored by optical microscopy, TEM, SEM-EBSI and X-ray diffraction were subjected to SEM-EBSD-OIM.

2 Experimental procedure

OFHC copper specimens 1, 2 and 3 were deformed in torsion at constant strain rates and temperatures up to strains of 30. Specimen 1 was deformed at 800°C and 3.7 s^{-1}, and specimens 2 and 3 at 950°C and 11.25 s^{-1}. Quenching was achieved with no time delay by injecting water down the axes while stopping the deformation. Specimen 3 was quenched 2 seconds after the deformation stopped. Copper specimens 4, 5 and 6 were hot rolled to a 90% reduction at 20 s^{-1} with roll chilling from 950 to 500°C and quenched within 0.5, 2 and 4 seconds respectively.

For metallographic analysis, specimens were mechanically and electrolytically polished using a H_3PO_4 electrolyte and etched using a $HF\text{-}HNO_3$ solution. The steady state microstructures were investigated by SEM-EBSD. This technique [Dingley and Field 1997, Humphreys and Ferry 1997] allows determination of crystallographic orientations by automatic Kikuchi pattern indexing

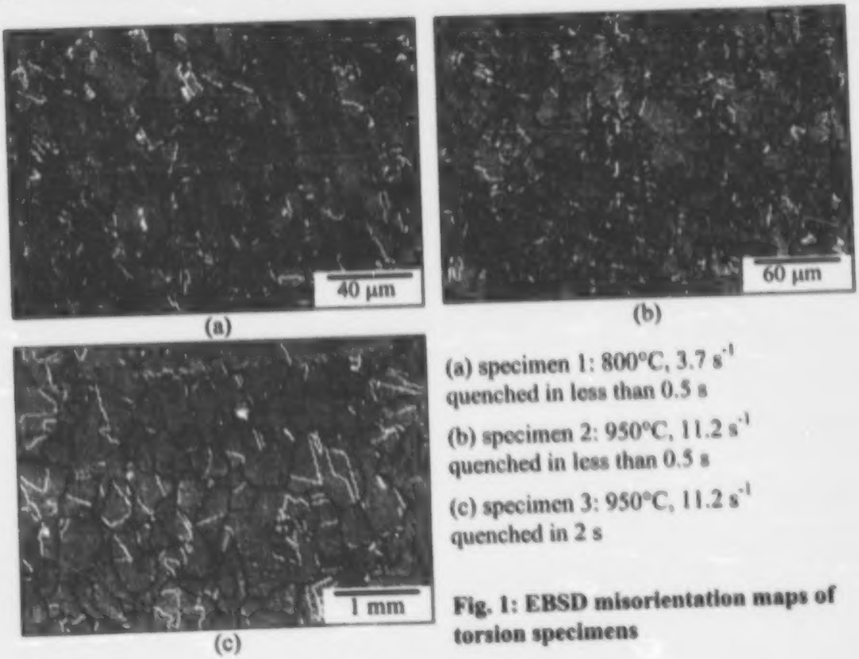

(a) specimen 1: 800°C, 3.7 s^{-1} quenched in less than 0.5 s

(b) specimen 2: 950°C, 11.2 s^{-1} quenched in less than 0.5 s

(c) specimen 3: 950°C, 11.2 s^{-1} quenched in 2 s

Fig. 1: EBSD misorientation maps of torsion specimens

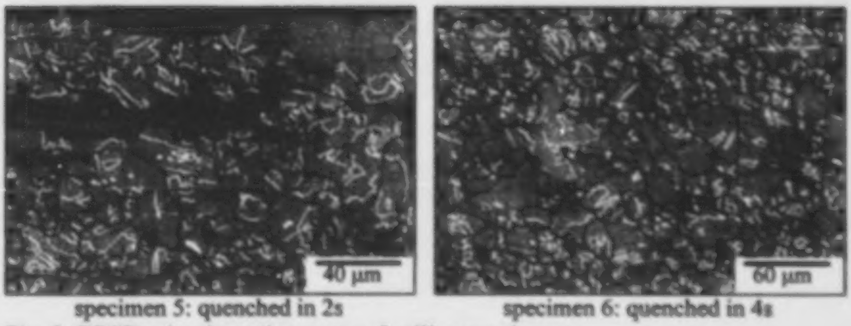

specimen 5: quenched in 2s specimen 6: quenched in 4s

Fig. 2: EBSD misorientation maps of rolling specimens

and calculation of local misorientations. The analysis was performed, using the Channel™ software, in order to investigate up to a 5 mm² area with a spatial resolution of 1 µm and a misorientation detection limit of 0.5°. The misorientation maps display the following microstructural features: grain boundaries (misorientations greater than 15°, shown as black lines), twin boundaries (misorientation of 60° about a <111> axis shown as white lines), subboundaries (misorientations from 5 to 15°, shown as fine dark lines) and smaller misorientations (fine grey lines) which may be associated with substructure, i.e. dislocation walls. A twin boundary length ratio can be calculated from the total interfaces length (i.e. taking into account all the misorientations greater than 5°). Pole figures were also obtained from the EBSD analysis.

3 Results

As can be seen from Figure 1, specimens 1 and 2 exhibit the typical features for steady state microstructures developed during DRX: a wide range of grain sizes uniformly distributed throughout the material, a wide range of dislocation densities within the grains (regardless of their sizes), and a small density of twins as compared to statically recrystallized microstructures [Varin and Kruszynska 1987]. However, specimen 3 exhibits strain free grains with a uniform coarse grain size, and a twin boundary ratio which is twice as much (Table 1).

Table 1: Experimental data

Specimen	Temperature (°C)	Strain rate (s^{-1})	Quenching time (s)	Mean grain size (µm)	Twin ratio (%)
1	800 (0.8 T_m)	3.7	<0.5	7.2	21
2	950 (0.9 T_m)	11.2	<0.5	10.3	16
3	950	11.2	2	215.5	36
4	900 to 500 (0.6 T_m)	20	<0.5	-	-
5	900 to 500	20	2	5.5	39
6	900 to 500	20	4	6.8	42

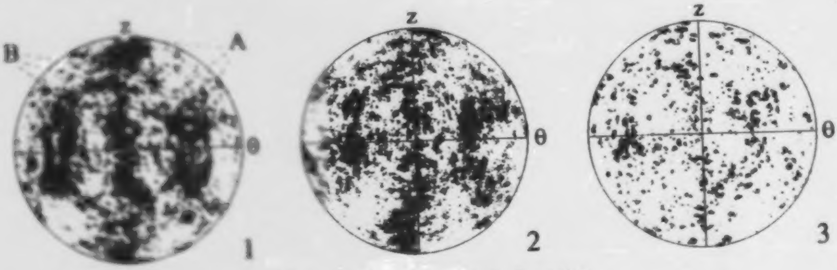

Fig. 3: <111> pole figures of torsion specimens 1, 2 and 3

Figure 2 shows the development of microstructures during rolling. Specimen 4 exhibited very elongated grains but could not be analysed because its DRV substructure is to fine with too high a dislocation density. Specimen 5 exhibits some large heavily strained grains elongated in the rolling direction, surrounded by smaller dislocation free grains. Numerous twin boundaries are detected in the latter grains while no twin can be seen in the deformed grains. No evidence for DRX appears in this microstructure. Specimen 6 is fully statically recrystallized and has a greater twin ratio. Parallel to the rolling direction, successive layers of small and coarse grains can be noticed.

Microtexture measurement results are displayed in Figures 3 and 4, as <111> pole figures. DRX microstructures, i.e. torsion specimens 1 and 2, exhibit a mixture of A {111}<110> and B {112}<110> orientations with slight rotation around the radial direction. Rolling specimens 4 and 5 have a {110}<112> texture. Statically recrystallized specimens 3 and 6 show no obvious texture.

4 Discussion

In DRX, the OIM maps agree with the previous optical and SEM micrographs [McQueen and Bergerson 1972, McQueen 1982]; moreover, small grains could be distinguished as nuclei or remnants as in TEM. The low visual density of twins in the previous microscopy is explained by their severe distortion. Even at these high

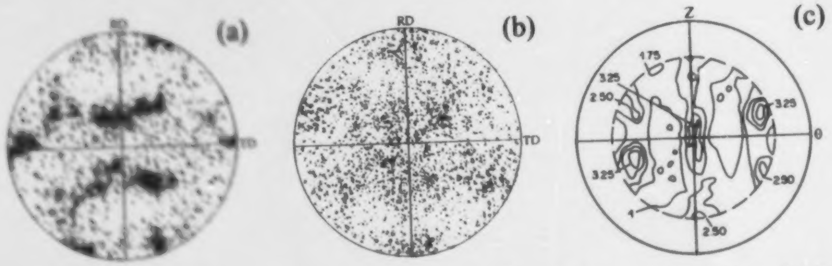

Fig. 4: <111> pole figures. (a) and (b) specimens 5 and 6 (quenched in 2 and 4s); (c) torsion at 400°C and $5\times10^{-2}s^{-1}$ (X-ray) [Montheillet et al. 1984]

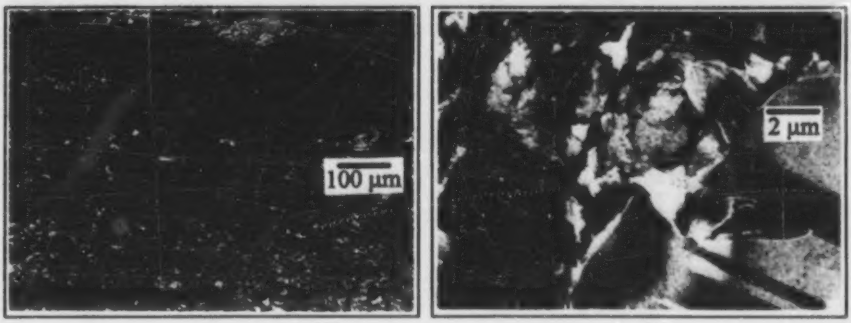

(a) (b)

Fig. 5: Rolling specimens 5. (a) optical (x100), (b) TEM (x4500) [McQueen 1968]

strains, the level of hardening ranges from 10% cold work for 950°C to 40% for 800°C; in consequence the MRX grains are rather large. They form quickly through the continued static growth of only the few DRX nuclei which formed shortly before the end of deformation. In contrast, Al at 400°C (0.72 T_m), $0.2s^{-1}$, in steady state (ε=10-60), exhibits subgrains of about 7 µm with polygonized walls, requires over 100 s for SRX and still has a similar but more intense texture than the Cu [Solberg et al. 1989]. The microtexture of the DRX specimens agrees well with the X-ray texture [Fig. 4(c)], which were similar to those at high strains at lower temperature before DRX: therefore the DRX does not change the principal component but leads to considerable randomness. The MRX texture reflects this phenomenon. Aluminum, in which nucleation of new grains does not occur, exhibits under the same deformation conditions a much stronger texture [Montheillet et al. 1984]. Recent work by Bocher et al. [1996, 1997] shows that the randomisation arises from the multiple twinning that occurs during growth of the nuclei. Of course, the continued straining tends to move the texture towards that previously established.

In the rolled specimens, no nucleus was observed optically or in TEM, in the rapidly quenched material; however, many cells were observed to have high misorientations (in 70Cu-30Zn similarly treated, SRX nuclei were frequently seen) [McQueen 1968]. Rapid growth of the nuclei appears to be responsible for the heterogeneous distribution of grain sizes in the recrystallized material [Fig. 2, 5]. The microtexture agrees with the X-ray texture [McQueen and Mecking 1987] on the centre plane, which was similar to rolling at 25°C although there were distortions due to poor shape control. The random recrystallization texture is a surprise compared to the cube texture determined by X-rays; however the present results may be related to the limited sample. In comparison, Al rolled under equivalent conditions exhibited large subgrains with regular walls and resisted recrystallization up to 1000 s; the deformation and SRX textures were similar to the Cu and to those commonly observed.

The measured twin boundary length ratio are smaller in the case of DRX microstructures than in MRX. First, on opposite sides of a twin boundary, the strain rate may differ, ultimately altering the neighbouring orientations so that they no longer meet the extended twin definition. Of course, new twins form as the grains grow so that an equilibrium is maintained, but the densities of nuclei involved in both recrystallization processes are different. In the case of DRX, at the steady state, every grain will give birth to one nucleus on average before disappearing. MRX proceeds from only a few nuclei which form near the end of deformation. This also explains the huge difference in the MRX and SRX grain sizes. It should be pointed out that the grain size itself does not influence the twin ratio (see specimens 3 and 6).

5 Conclusions

The EBSD maps provide evidence of microstructures closely resembling optical and electron micrographs both fine DRX and coarse MRX grains in torsion and both elongated DRV grains and fine SRX ones in rolling. The OIM shows many curved twin boundaries in DRX which were not recognized microscopically. The density of twins is still much less than in SRX or MRX because the adjoining lattices are distorted beyond the definition limit of twin orientation. The microtextures in DRV and DRX regions agree well with the X-ray macrotextures. The substructure in DRX is much less dense than in DRV rolling, so that MRX provides much larger grains than does SRX.

6 References

Bocher, Ph., Montheillet, F. and Jonas, J.J. (1997) *Proc. ReX-96*, Monterey California, pp. 355-362

Bocher, Ph., Azar, J., Adams B.L. and Jonas, J.J. (1998) *Proc. ITAP*, ed. R.A. Schwarzer, Clausthal Germany, pp. 249-254

Dingley, D.J. and Field, D.P. (1997) *Mater. Sci. and Technol.*, 13, p. 69

Humphreys, F.J. and Ferry, M. (1997) *Mater. Sci. and Technol.*,13, p. 85

McQueen, H.J. (1968) *Trans. Japan Inst. Metals* (ICSMA 1), 9 supp., pp. 170-177

McQueen, H.J. and Bergerson, S. (1972) *Metal Sci. J.*, 6, pp. 25-29

McQueen, H.J. (1982) *Strength of Metals and Alloys* (ICSMA 6), ed. R.C. Gifkins, Pergamon Press Oxford, pp. 517-522

McQueen, H.J. and Mecking, H. (1987) *Z. Metallkunde*, 78, pp. 387-396

Montheillet, F., Cohen, M. and Jonas, J.J. (1984) *Acta Metall.*, 32, pp. 2077-2089

Solberg, J.K., McQueen, H.J., Ryum, N. and Nes, E. (1989) *Phil. Mag. A*, 60, pp. 447-471

Varin, R.A. and Kruszynska, J. (1987) *Acta Metall.*, 35, p. 1767

MODELING OF MICROSTRUCTURAL EVOLUTION AND TEXTURE DEVELOPMENT DURING THE SECONDARY RECRYSTALLIZATION

Y. TAKAYAMA, M. INOUE*, T. TOZAWA, H. KATO and M. KOBAYASHI*
Department of Mechanical Systems Engineering, Utsunomiya University,
Utsunomiya, Japan
*Graduate Student

Keywords: grain boundary energy, misorientation, Potts model, secondary recrystallization, simulation

Abstract

In order to clarify the effect of grain boundary energy on the secondary recrystallization, microstructural evolution resulting in texture development has been investigated using a Potts model simulation. The simulation makes use of dependence of grain boundary energy on crystallographic misorientation, which is expressed as the same ways the Vector method (one of ODF analysis methods). It is confirmed that the size effect is insufficient for the secondary recrystallization to occur. The secondary recrystallization nuclei surrounded by low energy boundaries grows preferentially and drastically. The configuration of evolved grain structure is similar to that of the actual structure after the secondary recrystallization.

1 Introduction

The secondary recrystallization has been studied by numbers of researchers as the significant phenomenon related to the production of the industrial materials, such as silicon steel for transformer cores. Several models have also proposed to explain mainly the texture development. Previous studies emphasized that certain Coincident Site Lattice (CSL) boundaries having low energy play the significant role in the secondary recrystallization process (Harase et al. 1989). Recently, the role of high energy boundaries was stressed (Hayakawa et al. 1998). In the present study, to clarify the effect of grain boundary energy on the secondary recrystallization, microstructural evolution resulting in texture development is investigated using a Potts model simulation.

2 Simulation Method

The present simulation of grain growth preformed by the modified MC technique using the Potts model. The 2-dimentional square lattice of 200×200 sites with a periodic boundary condition was used. The Potts model has integral numbers that corresponds to crystallographic orientation on each site. Then, an aggregate of sites with the same number is regarded as a grain, and there are grain boundaries between sites of the different number. A site and a next orientation number are selected at random. The difference ΔE of grain boundary energy with reorientation is calculated. If ΔE is less than or equal to zero, the re-orientation is accepted. However, If ΔE is grater than zero, the re-orientation is not accepted. The condition of $T \cong 0$ is employed, because a site is fairly larger than an atom. A site is regarded as the cluster consisting of a number of atoms. The unit of time is defined as 1 Monte Carlo step (MCS) per site, which corresponds to N microtrials or re-orientation attempts, where N is the total number of sites in the system. Grain boundary energy of a site depends upon the number of neighbors shell k_s which is a parameter of interactive range. It was reported that for large k_s the grain boundary energy is approximately isotropic (Anderson et al. 1989). In this study, the number of neighbors shell k_s is set as 3 and 4.

2.1 Application of the Vector Method for Orientations

The orientation given to each site is selected by the Vector method, which is one of the ODF analysis methods in order to describe actual microstructures. In the vector method, relation of coordinates based on a sample and grains is expressed with angle parameters ψ, ω and ζ. A stereo spherical surface is divided into 48 stereo triangles T_1 and T_2, which are made up by circles connecting poles of {001}, {011}, and {111}. The stereo triangles were divided into 36 equivalent areas on spherical surface. The angle ζ is divided by every 5° in the actual analysis. Thus, the number of all orientation G is 5184; the division numbers are 36, 72 and 2 for stereo triangular division, the rotation angle ζ, and the type of stereo triangular, respectively.

2.2 Calculation of Grain Boundary Energy

The dependence of grain boundary energy on crystallographic misorientation in various materials has been studied to date. It is well known that the grain boundary energy for low-angle boundaries is smaller than that for random boundaries, and that energy cusps exist at specific misorientations. However, there is insufficient knowledge for energy between grains with random orientation in actual microstructure. In this simulation, the grain boundary energy, J_{GB} is assumed to be a function of misorientation parameters that has low-angle grain boundaries and energy cusp, as shown in **Fig. 1**.

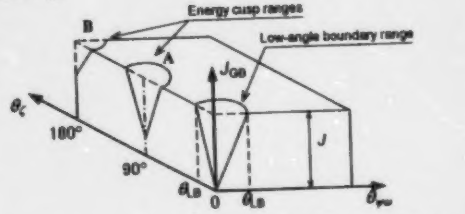

Fig. 1 : Illustration of grain boundary energy J_{GB} defined by crystallographic misorientation parameters θ_ζ and $\theta_{\psi\omega}$.

In the vector method, misorientation is expressed by two parameters; one is a difference in orientation (ψ,ω) on [001] and the other is a difference in rotation angle θ_ζ. Then, the misorientation parameters, $\theta_{\psi\omega}$ on [001] and θ_ζ on rotation angle, are used to describe the difference between orientations of two grains. The angle $\theta_{\psi\omega}$ is changed in the range of 0~54.75° (the maximum is taken in [001], [111]) and the angle θ_ζ is in the range of 0~180°. Next equations are formulated, supposing a distance from J_{GB}-axis is r,

$$\theta_{\psi\omega}^2 + \theta_\zeta^2 = r^2 \tag{1}$$

$$r = \{J_{GB} - 1\} \times \theta_{LB} \tag{2}$$

where, θ_{LB} is a border angle between large-angle boundary and low-angle boundary, and θ_{LB} =15° is adopted because low-angle grain boundary was generally understood to be less than 15°. Therefore, grain boundary energy J_{GB} with dependence on crystallographic misorientation is given by

$$J_{GB} = \sqrt{\theta_{\psi\omega}^2 + \theta_\zeta^2} \,/\, \theta_{LB} + 1. \tag{3}$$

Energy cusp A and B are set at θ_ζ=90° and 180°, as shown in Fig. 1. These cusps are based on symmetry of the cubic lattice. Then, grain boundary energy decreases as well as a low-angle grain boundary, when orientations of two grains have little difference in angles. The orientation difference between two grains is selected as the minimum among possible combinations of T_1 and T_2. Moreover, the depth of the cusps is assumed to be reduced by angles λ between coordinates of sample and crystal, and $\theta_{\psi\omega}$.

2.3 Grain Growth with A Texture

It is understood that the grains with a certain preferential orientation tend to grow *preferentially* because the grains have low-angle and low energy boundaries. In this study, the texture is given by initial fraction $f_{PO.0}$ of preferred orientation, which is a ratio of numbers of preferred orientations to all ones on initial microstructure. This simulation is performed with $f_{PO.0}$=0, 25, 50 and 75(%). The preferred orientations represents an angle less than 15° made by the normal axis of plane on a sheet sample and the [001] axis of grain, and ζ rotation less than 15°. Non-preferred orientations are selected among orientations excluded from the preferred ones.

3 Results and Discussion

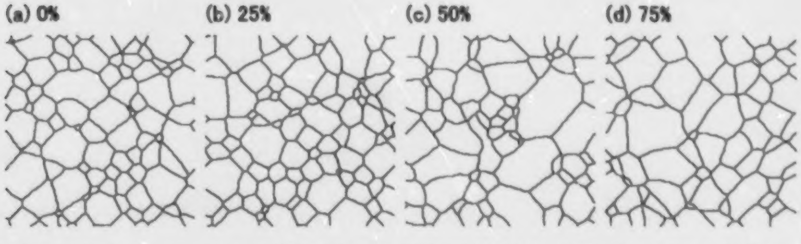

Fig. 2 : Evolved microstructures at 10000MCS for different initial fractions of preferred orientation.

3.1 Effect of Texture

Figure 2 displays evolved microstructures at 10000MCS for different initial fractions, $f_{PO.0}$=0, 25, 50 and 75% of preferred orientation. In the evolved microstructures, irregular grains are observed for $f_{PO.0}$=50% and 75% (Figs. 2(c) and (d)), in contrast to equiaxed ones in $f_{PO.0}$=0% and 25%(Figs. 2(a) and (b)). The grains having preferred orientation form low-energy boundaries for $f_{PO.0}$=50% and 75% because of small misorientations between one and another. As a result, the grains grow preferentially and exhibit the irregular shape with increasing peripheral length. The irregularity for $f_{PO.0}$=75% is smaller than for $f_{PO.0}$=50%. This is attributed to very large fraction of low-energy boundaries resulting from the strengthened texture.

Grain area distributions corresponding to the microstructures in Fig. 2 are shown in Fig. 3. The distributions for the four initial fractions, $f_{PO.0}$ are close to a lognormal one with a positive skew. Difference in shape of the distribution between with and without texture is found distinctly. It is obvious that the spread of distribution is largest for $f_{PO.0}$=50%.

Figure 4 indicates change in grain orientation distribution represented by inverse pole figure, which are expressed in unit stereo triangle divided into 36 areas, for $f_{PO.0}$=25% The distributions concentrates to near (001) as time passes. In brief, it can be summarized that the preferred orientation grains have grown preferentially while the random orientation grains have disappeared during grain growth.

3.2 Growth of a large grain

Figure 5 shows a time evolution of the microstructure including a large circular grain created artificially in its center. The initial circular grain size is 60 sites of diameter, which is a factor of 13.8 of mean size. It is found that although the initial grain

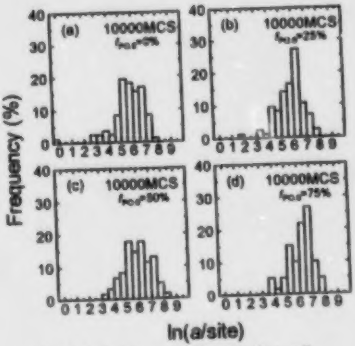

Fig.3 : Grain area distribution of evolved microstructures.

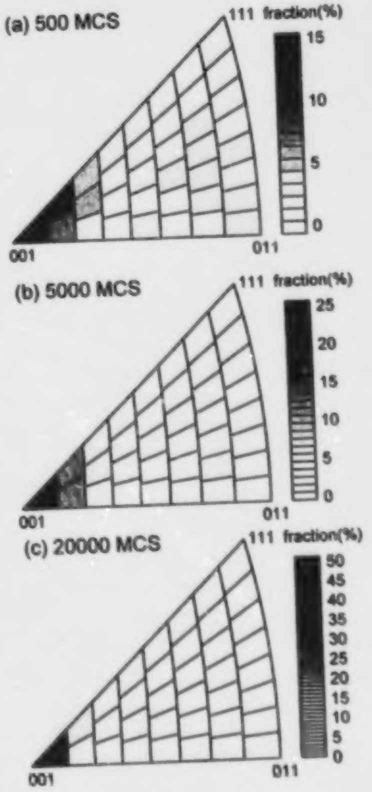

Fig. 4 : Change in grain orientation distribution for a microstructure at $f_{PO.0}$=25%

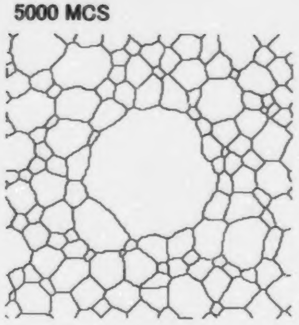

Fig. 5 : The growth of large grain in a microstructure without texture.

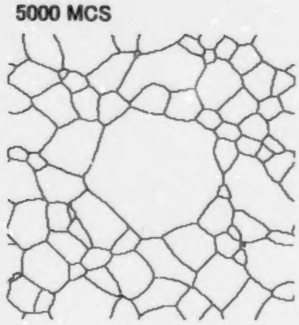

Fig. 6 : The growth of a large grain in a microstructure with texture of $f_{PO,0}$=50%

is much larger than all its neighbors, its growth rate is slower. While an initial ratio of a_0/a is 189.5 at 100MCS, the ratio lowers to 7.42. The initial area of the large grain and the mean grain area excluding the large grain are designated by a_0 and a, respectively. Thus, it is confirmed that the size effect is insufficient for the secondary recrystallization to occur (Srolovitz, 1986).

The evolved microstructure including a large circular grain initially, with texture of $f_{PO,0}$=50% is shown in Fig. 6. Surrounding grains influences the growth rate of the large grain. Some of the surrounding grains grow preferentially, which retards the growth of the large grain. This is understood to indicate the size effect weakened by the preferential growth.

3.3 Effect of low energy boundary

The boundary energy of nuclei influences the secondary recrystallization directly. Figure 7 illustrates evolved microstructures after the nuclei having various levels of boundary energy is created initially with the size of 2 sites. It is obvious that the nuclei of low energy boundary grows preferentially and drastically, as shown in Fig. 7(a). This is consistent with the result of the previous simulation (Srolovitz et al. 1986). Further, as the level of the energy rises, the degree of the preferential growth lowers. All the microstructures reveals characteristic feature of the large secondary

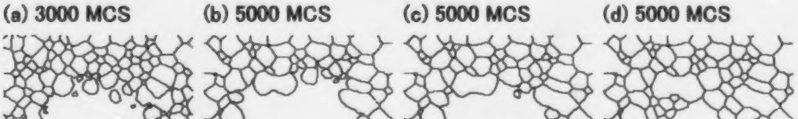

Fig. 7 : Large secondary grains grown preferentially : (a) J_s/J=0.1, (b) J_s/J=0.3, (c) J_s/J=0.4 and (d) J_s/J=0.6.

grain having a concave shape, sometimes including the other orientation grains retained inside during rapid growth. The configuration of evolved grain structure is similar to that of the actual structure after the secondary recrystallization. Moreover, the concave shape of the secondary grain suggests that the triple junction consisting of one high-energy and two low-energy boundaries plays the significant role during secondary recrystallization. It may be implied geometrically that low energy boundaries of such junction involve at least a coincidence one.

4 Summary

In the present study, to clarify the effect of local migration of grain boundaries on the secondary recrystallization, microstructural evolution resulting in texture development has been investigated using a Potts model simulation. It is confirmed that the size effect is insufficient for the secondary recrystallization to occur. The secondary recrystallization nuclei surrounded by low energy boundaries grows preferentially and drastically. Moreover, it is suggested that the triple junction consisting of one high-energy and two low-energy boundaries plays the significant role during secondary recrystallization.

5 References

Anderson, M.P., Grest, G.S. and Srolovitz, D.J. (1989) Computer Simulation of Normal Grain Growth in Three Dimensions. *Philosophical Magazine B,* Vol. 59, No. 3. pp. 293-329.

Harase, J., Shimizu, R., and Dingly, D. (1991) Texture Evolution in the Presence of Precipitates in Fe-3%Si Alloy. *Acta Metallurgica et Materialia,* Vol. 39, No. 5. pp. 763-770.

Hayakawa, Y., Muraki, M., and Szpunar, J.A. (1998) The Change of Grain Boundary Character Distribution During the Secondary Recrystallization of Electrical Steel. *Acta Materialia,* Vol. 46, No. 3. pp. 763-770.

Srolovitz, D.J., Grest, G.S. and Anderson, M.P. (1991) Computer Simulation of Grain Growth – V. Abnormal Grain Growth. *Acta Metallurgica,* Vol. 33, No. 12. pp. 2233-2247.

GROWTH SUBSTRUCTURE FORMED UNDER RECRYSTALLIZATION IN TEXTURED MATRIX, ITS FEATURES AND ORIGIN

V.V.GUBERNATOROV, B.K.SOKOLOV, I.V.GERVASYEVA AND L.R.VLADIMIROV
Institute of Metal Physics, Russian Academy of Sciences, Ekaterinburg, Russia

Abstract

Conditions for arising substructure interlayers in a growing grain upon secondary recrystallization have been studied. Possible mechanizms of their formation are discussed.

Keywords: Growth substructure, Quadruple junction, Secondary recrystallization

It was found (Gubernatorov et al. 1980) that upon secondary crystallization in silicon iron, in growing grains there arose a specific substructure consisting of defective zones in the form of a "bush" of substructure interlayers extended in the direction of the grain growth. Such substructure interlayers are characterized by a high density of subboundaries and individual dislocations.

Fig.1 shows examples of the substructure interlayers revealed by etching a grain surface of Goss orientation {110}<001>. Misorientation between adjacent fragments in the grain separated by a substructure interlayers was determined, using x-ray topography, to be minutes or several dozen minutes, but less than 1 deg. Their width reaches 0.2 mm that is comparable to the size of a dozen small grains of a matrix in which a secondary recrystallized grain grows. The following peculiarities of the substructure interlayers formation have been established (Gubernatorov et al. 1980, 1985).

- The substructure interlayers form at definite rates of growth of a secondary recrystalized grain – 20-50 mm/h. Maximal number of grains with substructure interlayers is produced at heating rates 30-40 mm/h.
- Of great importance is the fact that the substructure interlayers form in a moment when a growing grain envelopes a site which hinders the growth. It was simulated in the situation where a growing grain bent around a hole made in the sample before the recrystallizating annealing.

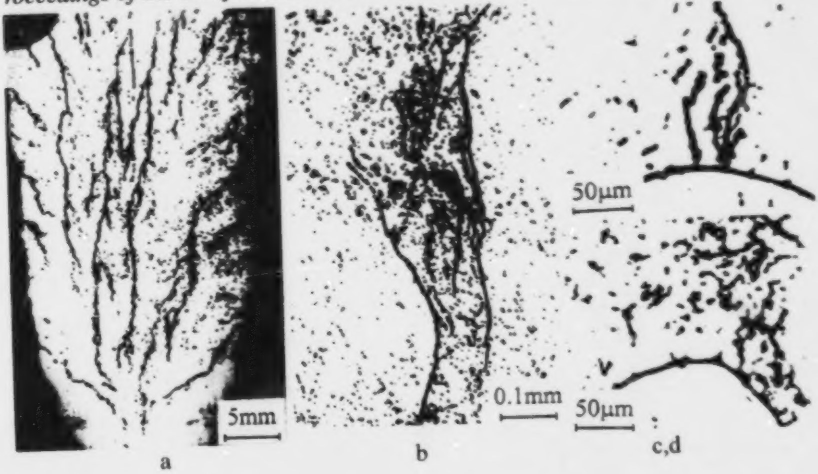

Fig.1: Examples of substructure formation in Goss grains upon secondary recrystallization. A "bush" of substructure interlayers in a secondary recrystallized grain (a); microstructure of a substructure interlayer (b); patterns of substructure interlayers formed in growing grain behind a grain of unfavorable orientation (c,d). The growth direction is upright.

- It's necessary for the substructure interlayers to form that the growing grain enveloping an unfavorable site should have a small misorientation between parts of the grain encountering behind this site. Such misorientation was simulated by locally bending a sample on one side of the hole before recrystallization. This leads to a certain variation of the primary recrystallization texture and a change in the orientation of the growing secondary grain in the course of the subsequent treatment. It has been shown that an essential increase (more than 1 deg.) in misorientation between the separately growing regions of a grain resulted in the emergence after their encounter of a distinct ordinary boundary (subboundary), rather than a wide substructure interlayer.
- The substructure interlayers formed are thermally stable. Long-term high-temperature annealing doesn't result in their failure.
- The substructure interlayers affect magnetic properties of some electrical sheet materials. Thus they can refine magnetic domains and lower magnetic loss in sheets of the Fe-3%Si alloy with a Goss texture.

One more work dealing with the study on similar substructures using synchrotronic x-ray topography has lately been reported (Ushigami et al. 1996). Secondary recrystallized grains with orientations {110} and {100} were examined. Misorientation between individual mosaic blocks reached 0.2 deg. The boundaries between individual fragments are supposed to form because of regrouping crystal defects in the course of the grain growth. However, this suggestion can't serve to explain the reasons for the substructure interlayers to be concentrated in separate configurations which alternate with far- extended substructure-free regions.

Mechanisms of the formation and development of such a substructure remain still unclear, including micromechanism of the substructure interlayers formation, reasons for their thermal stability and the substructure interaction with a moving boundary of a growing grain.

As is seen from Fig.1, when a secondary grain grows, the substructure interlayers extend perpendicular to the growth front. They may arise near small grains that aren't taken up by a growing secondary grain. One can observe early in their formation one or a few subboundaries or else, a wide substructure interlayer appears at once comprising a great number of various defects. When developing, the substructure interlayer follows the boundary of the growing secondary grain and in so doing, its structure suffers different changes, namely, dislocation boundaries move apart or closer together; they can disappear or come into being again. The density of individual dislocations either increases or decreases, which manifests itself in changes in the density of the etched pits. Some cases have been observed when the substructure interlayers development terminated inside a growing secondary grain.

The following mechanisms of the substructure interlayers formation can be taken into consideration.

According to update concepts, the role of the centers of the grain growth upon secondary recrystallization can be played by groups (colonies) of small grains having a slightly different orientations. Such groups can be taken as pseudograins with small-angled boundaries inside. On growing such pseudograin, small-angled boundaries might follow a moving large-angled boundary. However, this assumption doesn't give an explanation to an irregular substructure interlayers configuration, a high density of individual dislocations inside it.

Another mechanism of the substructure interlayers formation can be related to the above mentioned process of grain bending around the structure sites that don't favor the secondary grain growth. Such a grain grows consuming fine-grained matrix and running into an unfavorable for growth site envelopes it. In so doing, the grain regions independently growing acquire the certain misorientation. The possibility for local orientation changes to take place upon growing grains into the fine-grained matrix was experimentally proved in the study (Ketov et al. 1990) where x-ray topography method was used to study misorientation between junctions of winds of a crystallite grown upon secondary recrystallization in the form of a spiral. In this case, the regions of the crystallite which are at different distances from the starting point of its growth are linked up. A subboundary between these regions is clearly seen. An assumption is made that upon growing a crystal, orientations of its microregions change in such a way that favors formation of more moveable boundaries with some matrix regions of which the texture isn't ideally homogeneous.

An encounter of the grain regions with somewhat differing orientations after they overcame an obstacle, may result in the formation of a subboundary. However, since the matrix grains that are consumed have small sizes, such an encounter may happen at different instants, depending on depth, which leads to the formation of several subboundaries. Farther movement of the subboundaries following the secondary grain boundary might take place concurrently with interacting dislocations with subboundaries resulting in their scattering and rearrangement. An unfavorable site may be an individual large grain, inclusion, small grains with such orientations that form low-mobile boundaries with the growing secondary grain etc.

However, employing this mechanism one can't clarify why the interaction between subboundaries occurs later in the process and the resulting substructure interlayers configuration isn't changed by long-term high-temperature annealing.

As it has been pointed out, in most cases, substructure interlayers appear just in contacting parts of the secondary recrystallized grain. Therefore, one more mechanism was suggested which governs interaction between the grain boundary junctions with the formation of quadruple junctions. In this mechanism much importance is attached to enveloping an unfavorable site by the growing grain and a slight misorientation between the encountering regions of the grain.

Fig.2 shows a scheme of the case when a secondary grain grows in a fine-grained matrix of the Fe-3%Si alloy upon the annealing after rolling and primary recrystallization. The matrix grains have the texture with the predominant components {111}<112> and {113}<631> that form boundaries of high mobility with the secondary recrystallized grain {110}<001> (Gervasyeva et al. 1990). At the same time, in the texture there occur grains with the orientation {100}<011> (unfavorable site) that hinder the growth of the grain with a Goss orientation. When growing, the grain of secondary recrystallization runs into such a site and bends around it, forming triple junctions of the boundaries TJ1 and TJ2. As the matrix grains are consumed, these junctions move along the boundary between the growing grain and the unfavorable site till encounter in the point QJ. Interaction between triple junctions, depending on their structure, can result in either anihilation of the junctions (if the orientation of the encountering regions of the growing grain is completely identical) or the formation of the quadruple junctions (QJ) with more complex structure.

Among the factors that control the quadruple junction structure, of great importance is the degree of misorientation of the grains making the junction. Depending on it, the quadruple junctions can have different degree of imperfectness.

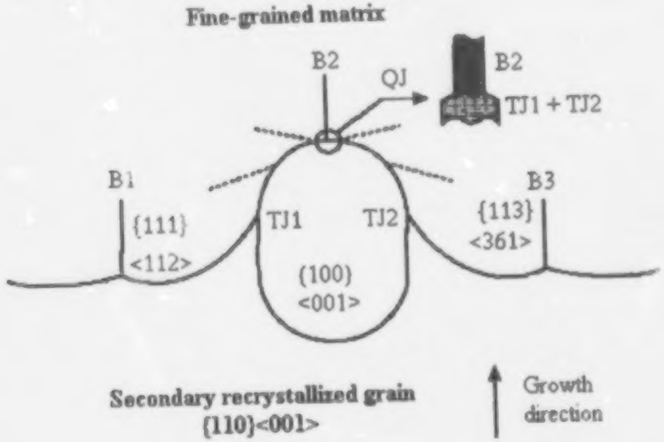

Fig.2: A scheme of Goss {110}<001> grain growth in a fine-grained matrix upon the secondary recrystallization. {100}<001> - a matrix grain of unfavorable orientation; B1, B2, B3 – grain boundaries between matrix grains; TJ1, TJ2 – triple junctions, QJ – quadruple junction.

The cases are possible when, because of a slight imperfectness, the region of quadruple junctions initiates the structure changes in the adjacent regions similar to a recrystalization center after critical degree of deformation. Some evidence is available (Gorelik 1978) that the boundary movement in the course of recrystalization after critical degree of deformation proceeds with a high rate. In our opinion, this peculiarity is related to the opportunity for defects and impurities to sink from the migrating boundary into the defective developing grain. It is a cause of a large density of defects in large grains formed by critical recrystallization in comparison with ordinary recrystalized grains. It's these features that are responsible for growing of the quadruple junction into the relatively wide defective zone (substructure interlayer).

The substructure interlayers formation affects the impurity distribution in the material; impurities accumulated by the boundaries of the growing secondary grain when consuming the matrix grains are released in the course of the substructure interlayers formation and fix its defects, providing an enhanced thermal stability of the substructure.

The mechanism suggested allows explanation of the above peculiarities of the substructure interlayers formation upon secondary recrystallization.

References

Cervasyeva, I.V., Sokolov, B.K., Zhigalin, A.G. and Ketov, S.P. (1990) Quantitative analysis of recrystallization textures in anistropic electrical steel. *Fizika metallov i metallovedeniye*, Vol. 4, pp. 145-151.

Gorelik, S.S. (1978) *Recrystallization of Metals and Alloys*, Metallurgia, Moscow.

Gubernatorov, V.V., Kurlyandskaya, G.V. and Bryshko, N.A. (1985) Subboundaries in secondary recrystallized grains, their formation and using for magnetic properties improving in Fe-3%Si alloy. *Izvestiya AN SSSR, Seriya Physicheskaya* Vol. 49, No. 8, pp. 1624-1628.

Gubernatorov, V.V., Sokolov, B.K., Bryshko, N.A., Gervasyeva, I.V. and Gundyrev, V.M. (1980) Substructure formation in grains during recrystallization. *Dokladi Akademii Nauk SSSR*, Vol. 255, No. 6, pp. 1367-1369.

Ketov, S.P., Gubernatorov, V.V. and Gundyrev, V.M. (1990) Change of the crystal orientation at the growth upon recrystallization. *Dokladi Akademii Nauk SSSR*, Vol. 313, No. 1, pp. 91-94.

Usigami, Y., Kawasaki, K., Murakami, K., Okazaki, Y., Kubota, T. and Chikaura, Y. (1996) Substructure in the secondary recrystallized grain in Fe-3% Si alloy observed by synchrotron x-ray topography, in *Proceedings of the ICOTOM 11, Part 1*, International Academic Publishers, Beijing, pp. 560-565.

LAST STAGE OF RECRYSTALLISATION IN TI SHEETS

O. VAN LANDUYT, T. GROSDIDIER and F. WAGNER
LETAM/ISGMP, University of Metz, Ile du Saulcy, 57045 Metz-Cedex, France

Abstract

Titanium sheets have been cold rolled and partially recrystallized. At the last stage of recrystallization, some grains ('white grains') remain unaffected whereas the rest of the sample is made from smaller already recrystallized grains. The 'white grains' have nearly the same orientation. On the basis of microstructure observations and of plastic deformation calculations it is demonstrated that the prior deformation mechanisms govern this particular recrystallization kinetic.

Keywords: recrystallization texture, Titanium sheets, delayed recristallization

1 Introduction

Modelling the texture evolution during recrystallization requires a detailed understanding of the mechanisms which operate at various stages of this transformation, or at least their effect on the orientation changes. Whereas many studies have brought such information in the case of cubic materials, a much more limited amount of results is available in the case of hexagonal alloys (see for example the review by Doherty et al. 1997). This was the reason why we started a detailed analysis of the several stages of the recrystallization in low alloyed titanium sheets. For this purpose, titanium sheets have been deformed by cold rolling, submitted to various heat treatments and quenched in order to produce specimens at different recrystallization stages. The determination of microstructures and textures was made at several scales by using optical microscopy (OM), scanning and transmission electron microscopy (SEM and TEM) as well as electron back scattering diffraction (EBSD) in SEM and X-ray diffraction (XRD). Some specific effects appear in the beginning of the recrystallization (nucleation and initial growth). In this paper we will focus on the next stage of the recrystallization where a large amount of the material is already recrystallized whereas some deformed grains are still present.

2 Material, deformation and first stage of recrystallization

The starting materials were 3 mm thick sheets of T40 titanium alloy (52ppm C, 237ppm Fe, 3ppm H , 41ppm N, 1062ppm O, <100ppm Si). Room temperature rolling, up to 80% reduction, was applied as the deformation mode. The early stages of deformation (<30%) were characterised by a strong activity of twinning. This is illustrated by the optical micrograph in Figure 1 where many initial grains contain numerous thin twins. TEM revealed that, apart from the deformation twins, the grains contained a large amount of fairly homogeneously distributed dislocations (Van Landuyt 1999). This strong activity of twinning in the early stages of deformation of T40 is consistent with other results from the literature (Philippe et al. 1988, Philippe et al. 1995, Zaefferer et al. 1994). Further deformation led to the formation of microbands. The boundaries of the microbands were somewhat diffused and had a high dislocation content. The inner part of the microbands also contained a high density of dislocation, so that it was very difficult to make good quality imaging with the TEM. An interesting observation however was that some grains did not appear to contain a high amount of twin or microbands, but, comparatively contained only a high density of well distributed dislocations. This heterogeneity in the deformation microstructure was confirmed by optical microscopy where large areas of the microstructure appeared strongly deformed whereas other areas of the specimen remained quite free of strain marking. In the following, these later will be referred as to 'white grains '.

Figure 1 : OM image of a 25% cold rolled Ti sheet showing deformation twins.

This heterogeneity could be imaged in the TEM when the deformed samples were brought up for a few minutes in the temperature range 400 to 500°C, so that numerous dislocations could be annihilated. Figure 2 is a map of TEM micrographs of such a sample showing the heterogeneous microstructure. Figure 3 corresponds to a partially recrystallized specimen and shows some 'white grains' surrounded with small already recrystallized grains (80% cold rolling followed by 160mn at 500°C annealing).

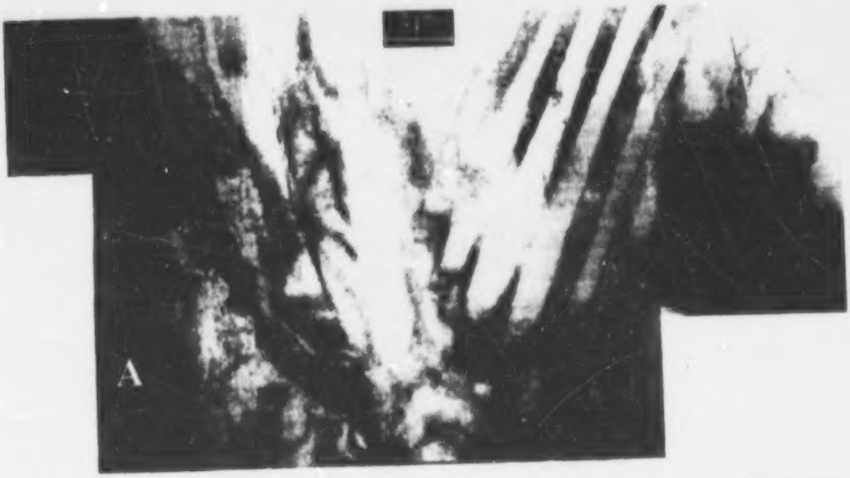

Figure 2 : Map of TEM micrographs showing the heterogeneous microstructure in a 50 % cold rolled T40 sample and then annealed for 2 min at 500°C. Note that the area marked A ('white grain') contains only fairly well distributed dislocations.

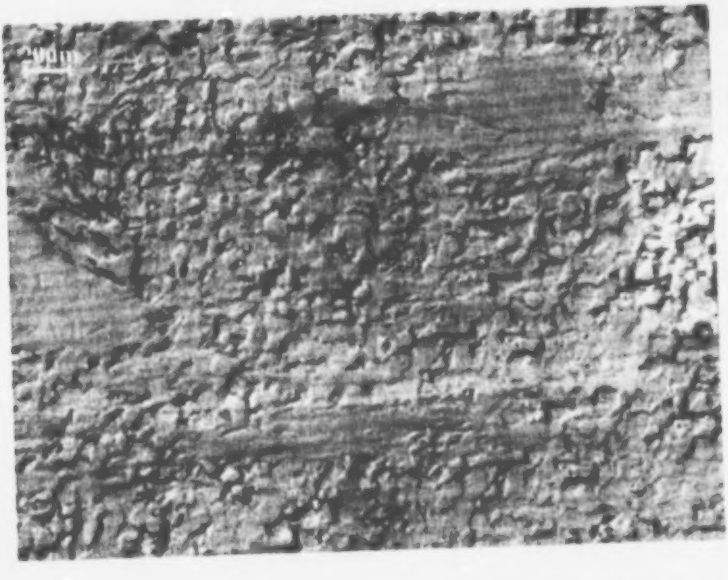

Figure 3 : Optical micrograph showing 'white grains' and their neighbourhood (rolling rate 80% followed by an annealing of 160 mn at 500°C).

3 Specific features of the 'white grains'

These 'white grains' appear in OM or in SEM as pancakes with some 'waves' in the (RD, ND) plane. Their sizes are consistent with the applied rolling ratio. The Kikuchi patterns, produced by EBSD in the SEM, are more diffuse than those of the neighbour recrystallized grains, accounting, in a qualitative way, for a higher dislocation density. Their orientation is very close to {φ1=0°, ϕ=48°, φ2=0°}[*] . In the interior of such grains there is some misorientation (up to 10° in some cases) in the RD. Figure 4a shows only one section of the ODF of the whole specimen as calculated from pole figure measurements. The 'central orientations' around {φ1=0°, ϕ=35°, φ2=30°}are typical for recristallyzed Ti sheets. Figure 4b shows one section of the ODF of the 'white grains' ; in this case the ODF was determined from individual orientations (900 measurements with EBSD corresponding to 300 grains). Although these 'white grains' represent about 15% of the volume their ODF is arbitrarily normalized to 1. It exhibits a strong preferred orientation.

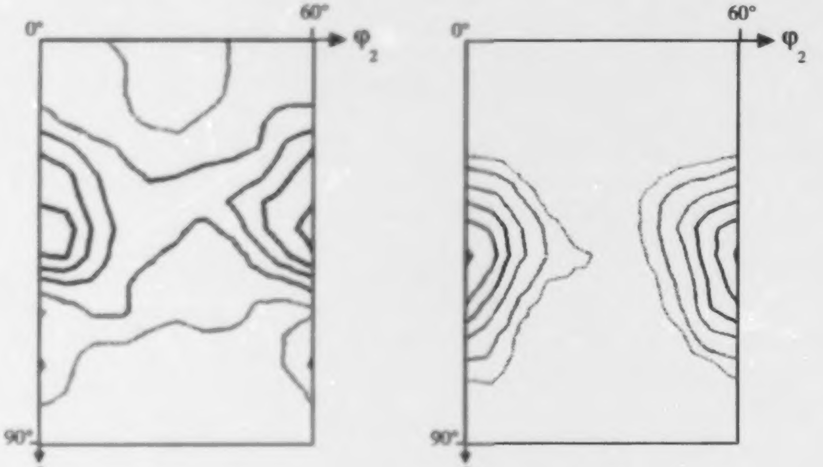

a) b)

Figure 4 : The section φ1=0° of the ODF for a) the whole partially recrystallized specimen (levels : 1., 2.5, 4., 5.5, 7.) b) the subset of 'white grains' (levels : 5., 10., 20., 30., 40., 50.)

4 Discussion

To understand the behaviour of these 'white grains' we have performed some simulations of the cold rolling deformation by using a Taylor model (with relaxation according to a pancake shape of the grains). The Taylor model, together with an adequate choice of the slip and twinning systems and their associated critical resolved shear stresses, has been shown to predict reasonable texture evolution during cold deformation of hexagonal alloys (Philippe et al. 1988, Philippe et al. 1995). The slip systems are the prismatic, pyramidal **a**, pyramidal **c+a** and basal ones and two possible twinning systems are taken into account. The used critical resolved shear stresses are those of the paper of Philippe et al. 1995. From these calculations it appears that the orientation $\{\varphi 1=0^\circ, \phi=45^\circ, \varphi 2=0^\circ\}$ is a stable orientation. We have also checked the distribution of the Taylor factor versus the orientation. The Taylor factor is seen as an indicator of the dislocation density and therefore an indicator of the stored elastic energy. From this point of view no specificity is remarked for this stable orientation, which leads to the conclusion that the difference in behaviour for the recrystallization is not linked with the stored energy. However it is noticeable that the Taylor model predicts that no twinning system is activated for this stable orientation. Figure 5 shows, always for the first section ($\varphi 1=0^\circ$) of the orientation space, the orientation domain for which no twinning system operates. The observed microstructures are in good agreement with this result. We thus understand the influence of the deformation in the following way. The grains which are not in this stable orientation will be deformed partly by twinning at the beginning of the deformation (up to about 30%) which leads to a quite inhomogeneous microstructure in these grains at the end of the deformation. They offer then many nucleation sites and a higher possibility of growth to these nuclei because of the presence of many misoriented subgrains. On the contrary, in the grains whose orientation is close to the stable orientation, a much more homogeneous dislocation microstructure is developed without (or with very few) twinning lamellae leading to less nuclei with a low probability of growth.

---

[*] *We use here the Bunge's 1969 definition for Euler angles with the crystal coordinate system {[10.0], [12.0], [00.1]}.*

The influence of deformation heterogeneities, as shear bands for example, on static recrystallization has been already extensively discussed for fcc alloys. This is also the case in low carbon steels where the grains with orientations belonging to the

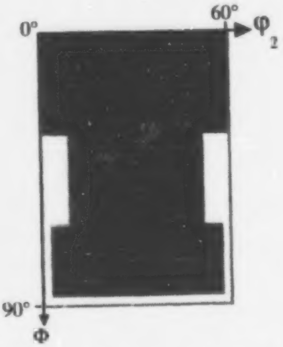

Figure 5 : The section $\varphi 1=0^\circ$ of the orientation space showing orientations for which twinning is one of the activated deformation mechanisms (grey colour) or not activated (white)

α fibre recrystallize with some delay being 'eaten' by the neighbour grains with orientations belonging to the γ fibre (B. Hutchinson et al. 1995, Lefever et al. 1995). In our case the 'white grains' recrystallize at last in two simultaneous ways. Some new recrystallized grains appear along dislocation walls perpendicular to the rolling direction whereas already recrystallized grains, at the vicinity of these 'white grains', progressively invade them.

4 Conclusion

The kinetic of the recrystallization in cold rolled titanium sheets is clearly influenced by the orientation of the grains. From calculations for the plastic deformation as well as from direct observations of the microstructure at several stages of the deformation and of the recrystallization it is concluded that the heterogeneity of the deformation, linked to the orientation of the grains, is the main influencing factor. A much higher heterogeneity, leading to a faster recrystallization response, is present in the grains whose orientations allow the twinning to be activated, at least at the beginning of the deformation. On the contrary, a more homogeneous dislocation distribution is built in the stable orientations ('white grains') which deform mainly by slip, leading to a delayed recrystallization.

6 References

Bunge, H.J. (1969), Mathematische Methoden der Texturanalyse, Akademie Verlag, Berlin

Doherty, R.D., Hughes, D.A., Humphreys, F.J., Jonas, J.J., Juul Jensen, D., Kassner, M.E., King, W.E., Mc Nelley, T.R., Mc Queen, H.J. and Rollett, A.D. (1997), Mat. Science and Eng., Vol A238, pp 219-274

Hutchinson, B. and Ryde, L. (1995), Proceedings of the 16th Risö Int. Symposium on Materials Science, Risö National Laboratory - Denmark -pp 105-117

Lefever, A., Schouwenaars, R., Raabe, L., Ratchev, P., Van Houtte, P. and Aernoudt, E. (1995), Proceedings of the 16th Risö International Symposium on Materials Science, Risö National Laboratory - Denmark - pp 435-440

Philippe, M.J., Wagner F. and Esling, C. (1988), Proceedings of ICOTOM 8, The Metallurgical Society Inc., pp 837-842

Philippe, M.J., Serghat, M., Van Houtte, P. and Esling, C. (1995), Acta metall. Mater., Vol. 43, No. 4, pp 1619-1630

Van Landuyt, O., Phd thesis, in preparation

Zaefferer, S., Gerth, D. and Schwarzer, R.A. (1994), Proceedings of ICOTOM 10, Trans Tech Publication, pp 1319-1324

A METHOD FOR PREDICTING THE CRYSTRALLOGRAPHIC TEXTURE FROM THE POLYCRYSTALLINE MECHANICAL STRENGTH AS A FUNCTION OF HEAT TREATMENT FOR A PRECIPITATION HARDENED ALUMINUM ALLOY

J. M. FRAGOMENI
Assistant Professor, Department of Mechanical Engineering, Ohio University, Russ College of Engineering and Technology, Athens, Ohio.

Abstract

A micromechanics method was developed for predicting the variation in the deformation texture or Taylor factor with heat treatment variables for the precipitation strengthened demonstration alloy. The heat treated alloy which exhibited a strong crystallographic texture was solution heat treated and artificially aged for a range of aging times (0 to 225 hrs.) at different aging temperatures of 185, 193, and 200 °C. The method or approach predicted the Taylor factor based on the mechanical yield strength and microstructure corresponding to the specific aging practice and alloy composition. The method used a total number of only four mechanical tensile tests to perform the analysis. The alloy that was used as a vehicle to demonstrate the method was a precipitation hardened Al-2.6wt.%Li-0.09wt.%Zr alloy that is strengthened from intermetallic δ' (Al_3Li) precipitates which are uniformly distributed throughout the microstructure. The crystallographic texture was predicted in terms of the Taylor grain orientation factor for the different aging temperatures and various aging times along the aging curves. The overall approach for estimating the Taylor factor from the polycrystalline yield strength was based on the dislocation particle interaction strengthening mechanisms, the particle coarsening kinetics, and the overall final microstructure.

1 Introduction

The effect of precipitation hardening on texture-induced anisotropy was determined in an as-extruded and heat treated aluminum alloy containing lithium and a small amount of zirconium. The nature of the preferred grain orientations in the polycrystalline aggregate which depends on the composition, material processing, and heat treatments were studied in relation to the polycrystalline and single-crystal strength. The effect of the intermetallic precipitates that strengthen the alloy and result from the artificial aging heat treatment were examined to determine a correlation with the polycrystalline texture evolution and changes in the plastic anisotropy due to preferential precipitation. A method was developed for predicting the variation in the deformation texture or Taylor factor (M) with heat treatment variables for the precipitation strengthened demonstration alloy. The heat treated alloy which exhibited a strong crystallographic texture was solution heat treated and artificially aged for a range of aging times (0 to 225 hrs.) at different aging temperatures of 185, 193, and 200 °C. The method or approach predicted the Taylor factor based on the mechanical yield strength and microstructure corresponding to the specific aging practice and alloy composition. The method used a total number of only four mechanical tensile tests to perform the analysis. The alloy that was used as a vehicle to demonstrate the method was a precipitation hardened Al-2.6wt.%Li-0.09wt.%Zr alloy that is strengthened from intermetallic δ' (Al_3Li) precipitates which are uniformly distributed throughout the microstructure. The δ' precipitates in the microstructure impede the dislocation glide motion through the order hardening mechanisms where the dislocations will shear the particles, and the Orowan mechanisms where the dislocations bypass and loop the particles. The δ' particle size, spacing, distribution, and morphology can be correlated to the crystallographic texture of the alloy and are a direct consequence of the material processing and composition. The crystallographic texture was predicted in terms of the Taylor grain orientation factor for the different aging temperatures and various aging times along the aging curves. The overall approach for estimating the Taylor factor from the polycrystalline yield strength was based on the dislocation particle interaction strengthening mechanisms, the particle coarsening kinetics, and the overall final microstructure.

2 Experimental Methods and Materials

The aluminum-lithium-zirconium alloy was fabricated/cast by the Aluminum Company of America (ALCOA) and also extruded by the ALCOA, Lafayette Extrusion Works, in the direct extrusion mode to produce both round and rectangular geometry extruded product. Zirconium was added to the aluminum-lithium alloy to act as a grain refiner by inhibiting the recrystallization of the alloy during extrusion. The extruded product was machined into tensile samples and then solution heat treated and water quenched, followed by artificial aging and quenching to determine the aging hardening response in terms of the mechanical strength of the alloy. Standard ASTM (American Society for Testing and Materials) mechanical testing was performed to measure the various mechanical properties such as yield and ultimate strength, and ductility. Transmission electron microscopy, scanning electron microscopy, and optical microscopy were performed on the samples corresponding to various heat treatments to evaluate the microstructure of the alloy as a function of the heat treatments. In addition, particle size measurements of the microstructure were made directly from the TEM negatives to determine the average size, distribution, interparticle spacing, number density, and morphology of the intermetallic strengthening precipitates. This quantitative analysis was done as part of the overall microstructural approach to correlate the internal structure to the mechanical properties via. the texture of the demonstration alloy.

In order to predict the mechanical behavior of a metal or alloy, the particle size distribution must be determined, either by experimental measurements, or theoretical predictions. One way to determine the distribution of particle sizes produced from the coarsening process is through the Wagner (1961) theoretical distribution function. The Lifshitz-Slyozov (1961) and Wagner (1961) theory predicts both the mean particle size and particle size distribution for a given microstructure containing spherical, coherent, deformable, precipitate particles. For example, the Wagner distribution (Wagner 1961) is most accurately obeyed in alloy systems where the precipitates are spherical or regular polyhedra with crystallographically equivalent faces. In general, the distribution of the particles throughout the microstructure of the alloy determines the strength of the alloy by impeding the glide motion of the dislocations. The dislocations must either shear through or bypass via. Looping the individual particles of the size distribution in order to continue their glide motion in the microstructure. The micromechanics method presented in this communication is an analytical approach to predict the crystallographic texture of a particle strengthened alloy utilizing a total of four experimental tensile tests to evaluate the required microstructural constants of the overall model. This method was developed to simplify the very cumbersome task of determining the many different microstructural constants that are necessary to evaluate for predicting the precipitation strengthening response of particle hardened alloys. Some of the critical microstructural constants include for example the antiphase boundary energy, the shear moduli of the matrix and precipitates, Poisson's ratio, the dislocation line tension, Burgers vector, etc., and often vary from one alloy to another even similar alloy, and may not be readily available, and can often be very difficult to experimentally accurately measure. Therefore it was desired and even necessary to develop a procedure to simplify the task of predicting the texture grain orientation factor of some basic particle strengthened alloys that have the classical underaged, peak-aged, and overaged heat-treatment conditions. The method presented is capable of providing relatively good analytical estimates of texture in some basic precipitation hardened alloys that have a uniform distribution of spherical particle sizes. In addition, this method provides prediction of the Taylor factor along the entire classical aging hardening curve based on an evolving distribution of particle sizes from the underaged state to the severely overaged condition.

The material used as the demonstration alloys for this research were precipitation hardened aluminum-lithium alloy. This alloy were utilized as the demonstration materials to relate the strength to the microstructure, heat treatment practice, and composition. The variation in texture with aging time, aging temperature, and composition can be predicted utilizing a number of existing models that describe dislocation mechanics, particle coarsening, thermodynamics, and particle strengthening mechanisms applicable to precipitation hardened alloy systems. These precipitates impede dislocation motion during plastic deformation causing the observed increase in the yield strength. The misfit strain of these precipitates with the matrix is extremely small (~0.1%), so the strengthening contribution is almost entirely due to the ordered structure of the precipitate and is a function of the sheared cross-sectional diameter. The δ' particle size, distribution, and interparticle spacing are closely related to the precipitation strengthening response and are a direct consequence of the aging practice and composition. From detailed study of the strengthening mechanism applicable to the aluminum-lithium system, it is well understood that the order hardening mechanism is responsible for the strengthening where the precipitates were sheared by the dislocations and the Orowan hardening mechanism is responsible for the strengthening response in the overaged condition when the dislocations bypassed and looped the particles. Consequently, the strengthening of these alloys can be directly correlated to the size, distribution, spacing, and volume fraction of the strengthening precipitates based on the active dislocation particle interaction mechanisms.

3 Theoretical Approach

To develop a model for predicting the precipitation hardening response, the particle size distribution for each aging time along the age hardening curve must be determined. The basis for determining the particle size distribution is an accurate prediction of the average particle size, $\bar{r}$. The particle size can be determined from the Lifshitz-Slyozov-Wagner (Wagner 1961; Lifshitz and Slyozov 1961) cubic coarsening theory, which can be expressed by the relation (Wagner 1961; Lifshitz and Slyozov 1961)

$$\bar{r}^3 - r_o^3 = K_c\,(t - t_o) \tag{1}$$

where r_o is the initial particle size (at $t_o = 0$) and can be taken as approximately equal to zero for the Al-Li and Ni-Al demonstration alloys. The growth rate constant K_c is given by the expression (Wagner 1961; Lifshitz and Slyozov 1961; Shercliff and Ashby 1990)

$$K_c = \frac{8\gamma V_m^2 C_{eq} D}{9RT} = \frac{C_k}{T}\exp\left[\frac{-Q_A}{RT}\right] \tag{2}$$

where Q_A is the activation energy, T is the aging temperature, C_k is the kinetic constant, t is the aging time, R is the universal gas constant (8.314 J/mole-K), D is the diffusion coefficient, γ is the interfacial energy, C_{eq} is the equilibrium concentration of the solute in the matrix, and V_m is the molar volume of the precipitate. The cubic coarsening expression can therefore be expressed by the relation (Wagner 1961; Lifshitz and Slyozov 1961; Shercliff and Ashby 1990)

$$\bar{r}^3 - r_o^3 = \frac{8\gamma V_m^2 C_{eq} Dt}{9RT} = \frac{C_k t}{T}\exp\left[\frac{-Q_A}{RT}\right] \tag{3}$$

In the underaged condition where particle shearing dominates the deformation, the total mechanical (yield) strength response with aging practice can be determined from the dislocation particle shearing single crystal critical resolved shear strength. The expression for the yield or proofstrength in the underaged condition can be written as

$$\sigma_y = \Delta\sigma_{sss} + \overline{M}\Delta\tau_{shear} \tag{4}$$

where $\overline{M}$ is the Taylor factor, $\Delta\tau_{shear}$ is the single crystal strength from dislocation particle shearing, and $\Delta\sigma_{sss}$ which is the as-quenched yield strength, consists of the combined solid solution strengthening, intrinsic lattice strength, and grain size strength of the polycrystal. A value for $\Delta\sigma_{sss}$ can be determined by experimentally measuring the strength of a solutionized polycrystalline tensile specimen. The single crystal critical resolved shear strength for dislocation particle shearing with constant volume fraction can be written in terms of the average particle size radius by the expression given by

$$\tau_{shear} = B\bar{r}^{1/2} \tag{5}$$

where B is a constant which includes together constants for the volume fraction of the precipitates, the dislocation line tension, the antiphase boundary energy, and the Burgers vector. Using a value of t=0 (time=0), the value for the parameter $\Delta\sigma_{sss}$ was determined to be 140.6 MPa by mechanically tensile testing a solutionized polycrystalline tensile specimen. Utilizing the Lifshitz-Slyozov-Wagner (Wagner 1961; Lifshitz and Slyozov 1961) coarsening expression with $r_0^3 = 0$ and $t_0 = 0$, and substituting in the value for $\bar{r}$, from equation (3), into the above expression yields an equation for σ_y in terms of aging temperature and aging time given by

$$\sigma_y = \Delta\sigma_{sss} + Ft^{1/6}\left\{\frac{1}{T}\exp\left[\frac{-q}{T}\right]\right\}^{1/6} \tag{6}$$

where F is a constant consisting of E and the kinetic factor and q is a constant equal Q_A/R. Q_A is the activation energy for precipitate growth and coarsening, and R is the universal gas constant (= 8.314 Joules/mole°K).

In the overaged condition where most of the particles are larger than a critical particle size diameter, referred to as the looping diameter d_{loop}, the variation in yield strength with aging practice can be predicted from the Orowan looping model (Orowan 1948). During plastic deformation of an overaged alloy the dislocations will bypass the precipitates in the microstructure often by a dislocation-particle looping mechanism, referred to as the Orowan looping mechanism. The single crystal resolved shear strength can thus be determined from the Orowan equation which can be expressed in its simplest form as

$$\Delta\tau_{loop} = G_t\frac{b}{\lambda} \tag{7}$$

where b is the Burgers vector, G_t is the shear modulus of the material, and λ is the interparticle separation i.e., the particle spacing. The interparticle spacing can be approximated, in terms of the average particle size and volume fraction, as (Martin 1980)

$$\lambda = 1.25\bar{r}\left\{\frac{2\pi}{3f_v}\right\}^{0.5} \tag{8}$$

Equation (8) can be substituted in the expression based on the Orowan model given in equation (7). Thus in the overaged condition for constant volume fraction the critical resolved shear strength can be predicted for the demonstration alloys in terms of the average particle radius from the expression given by

$$\Delta\tau_{loop} = \frac{H}{\bar{r}} = H\bar{r}^{-1} \tag{9}$$

where H is a constant which includes the volume fraction of precipitate, the Burgers vector, and π, r̄ is the average particle size, and $\Delta\tau_{loop}$ is the single crystal critical resolved shear strength for dislocation particle bypassing via. the Orowan looping mechanism. This relation can be substituted in the expression for the yield strength in the overaged condition given by

$$\sigma_y = \Delta\sigma_{sss} + \bar{M}\Delta\tau_{loop} \tag{10}$$

The yield strength in the overaged condition can therefore be written in terms of average particle size radius by substituting equation (9) into equation (10). Using the Lifshitz-Slyozov-Wagner coarsening expression with $r_0^3 = 0$ and $t_0 = 0$, and substituting in the value for r̄ into equation (10) yields an expression for σ_y in terms of aging temperature and aging time in the overaged condition given by

$$\sigma_y = \Delta\sigma_{sss} + Lt^{-1/3}\left\{\frac{1}{T}\exp\left[\frac{-q}{T}\right]\right\}^{-1/3} \tag{11}$$

where L is a constant consisting of the kinetic factor, C_k, and q is equal to Q_A/R.

A total number of four experimental tensile tests were necessary for determining the microstructural calibration constants of the model to predict the precipitation strengthening response. The four experimental yields strength tensile tests that were required included the solution heat-treated (0 hour aging time) condition, 4 hours aging time at 185° C, 4 hours aging time at 193° C, and 225 hours aging time at 185° C. The expressions with the appropriate constants that were determined from the four experimental tests are the yield shearing and looping equations and are given by

$$\sigma_{shear} = 140.6 + 125{,}086t^{1/6}\left\{\frac{1}{T}\exp\left[\frac{-14824.}{T}\right]\right\}^{1/6} \tag{12}$$

$$\sigma_{loop} = 140.6 + 0.0030630t^{-1/3}\left\{\frac{1}{T}\exp\left[\frac{-14824.}{T}\right]\right\}^{-1/3} \tag{13}$$

where σ_{shear} and σ_{loop} is the yield strength in the underaged condition due to particle shearing and the yield strength in the overaged condition due to particle looping respectively. These expressions were used with the Wagner distribution function in determining the precipitation hardening response. Using the results of the equations (4) through (6) for particle shearing, the contribution to the single crystal shear strength for dislocation particle shearing can be written as

$$\overline{M} = \frac{F}{\Delta\tau_{shear}} t^{1/6} \left\{ \frac{1}{T} \exp\left[\frac{-q}{T} \right] \right\}^{1/6} + \frac{\Delta\sigma_{sss}}{\Delta\tau_{loop}} \tag{14}$$

For the Al-Li alloy, substituting in the previously determined values for the constants F and q gives the result

$$\overline{M} = \frac{125{,}086}{\Delta\tau_{shear}} t^{1/6} \left\{ \frac{1}{T} \exp\left[\frac{-14824.}{T} \right] \right\}^{1/6} + \Delta\sigma_{sss}/\Delta\tau_{shear} \tag{15}$$

where T is the aging temperature in degrees Kelvin and t is the aging time in hours. The shearing stress can therefore be determined for a given aging practice.

Using the results of the analysis of equations (7) through (11), the contribution to the crystallographic texture with aging and overaging from dislocation particle bypassing and looping can be expressed as

$$\overline{M} = \frac{L}{\Delta\tau_{loop}} t^{-1/3} \left\{ \frac{1}{T} \exp\left[\frac{-q}{T} \right] \right\}^{-1/3} + \Delta\sigma_{sss}/\Delta\tau_{loop} \tag{16}$$

For the Al-Li alloy, using the values that were previously determined for the constants L and q gives the result

$$\overline{M} = \frac{0.0030630}{\Delta\tau_{loop}} t^{-1/3} \left\{ \frac{1}{T} \exp\left[\frac{-14824.}{T} \right] \right\}^{-1/3} + \Delta\sigma_{sss}/\Delta\tau_{loop} \tag{17}$$

where t is the aging time in hours and T is the aging temperature in degrees Kelvin, and $\Delta\sigma_{sss}$ represents the contribution to the total strengthening from solid solution and grain size strengthening along with the intrinsic lattice strength. Based on the above equations, Table 1 was developed which shows the predicted Taylor factors.

4.0 Final Remarks and Conclusions

The overall method for predicting the crystallographic texture Taylor factor of a particle strengthened alloy required a total number of four experimental tensile tests to determine all of the constants of the overall model. The calibration microstructural constants were evaluated from the underaged hardening condition where dislocation particle shearing controls the plastic deformation, and also from the overaged hardening condition where dislocation particle bypassing dominates the deformation. Also one tensile test was required for the solution-heat treated condition to determine the baseline as-quenched strength of the given alloy. This approach eliminated the need to predetermine the values of various microstructural constants required for predicting the strengthening response of the demonstration alloys. The development of a micromechanical approach to predict the crystallographic texture of particle strengthened alloys hardened by ordered precipitates was validated for the aluminum-lithium demonstration alloys. The Wagner distribution function was utilized with the micromechanical method to determine the particle size distribution as the basis to predict the Taylor factor from a total of four tensile tests to determine the microstructural constants of the overall model. The microstructural constants include the contributions, or combined effects of, the antiphase boundary energy, the shear modulus of the material, the activation energy, Berger vector, texture factor, interfacial energy, volume fraction, dislocation line tension, Poisson's ratio, and the kinetic growth rate constant. This overall approach provides the basis for predicting the variation in texture with age hardening of other similar particle strengthened alloy systems. Using the given demonstration alloy, the overall texture model predicted the variation in the Taylor factor with both artificial aging time and aging temperature, for the underaged, peak-aged, and overaged heat-treatments. The predicted Taylor factors for this alloy, which corresponds to the {111}<100> duplex fiber texture, were found to be in very good agreement with texture Taylor factor values obtained from the literature within the range of approximately 2.5 to 3.3 for aluminum-lithium alloys with similar compositions and heat treatments.

5 Acknowledgements

The Al-Li-Zr material used in this study was cast at the ALCOA Technical Center, Pittsburgh PA, and extruded by the ALCOA Lafayette Extrusion and Tube Division, Lafayette, IN. The composition analysis of the Al-Li research alloy was performed at the ALCOA Lafayette Extrusion and Tube Division. This work was supported by the National Science Foundation under Grant CDR 8803017.

6 References

American Society for Testing and Materials. (1988) *Metals Test Methods and Analytical Procedures*. Annual Book of ASTM Standards. Philadelphia, PA. Vol. 3.01: Section 3.

Lifshitz, I.M., and Slyozov, V.V.(1961) The Kinetics of Precipitation from Supersaturated Solid Solutions. *Journal Physical Chemical Solids*, Vol. 19, pp. 35-50.

Martin, J.W. (1980) *Micromechanisms in Particle-Hardened Alloys*, Cambridge University Press, New York.

Orowan, E.(1948) *Symposium on Internal Stresses in Metals and Alloys*. Session III Discussion, Institute of Metals, London England, p. 451.

Shercliff, H.R., and Ashby, M.F. (1990) A Process Model for Age Hardening of Aluminum Alloys: The Model. *Acta Metallurgica*, Vol. 38, No. 10. pp. 1789-1802.

Wagner, C. (1961) Theories Associated With Age Hardening and Overaging During Ostwald Ripening. *Zeitschrift fur Elekrochemie*, Vol. 37, pp. 581-591.

Table 1. **Comparison between the experimentally measured yield strength and the predicted precipitation hardening response for particle strengthening for the Al-2.6wt.%Li-.09wt.%Zr demonstration alloy aged at 185° C using the Wagner probability distribution function.**

Aging Time t (hours)	Predicted Shearing Stress $\Delta\tau_{shear}$ (MPa)	Predicted Looping Stress $\Delta\tau_{loop}$ (MPa)	Predicted Particle Strengthening $\Delta\tau_{particle}$ (MPa)	Predicted Taylor Factor M (MPa)
0.12	47.9	0.	47.9	3.34
0.25	54.1	0.	54.1	3.38
0.50	60.8	0.	60.8	3.43
1.0	68.2	0.	68.2	3.48
2.0	76.6	0.	76.6	3.54
4.0	85.9	0.	85.9	3.61
8.0	96.5	0.	96.5	3.68
12.0	103.2	0.	103.2	3.73
18.0	110.4	0.	110.4	3.78
24.0	115.8	0.	115.8	3.82
32.0	121.5	120.2	121.5	3.85
40.0	126.1	111.6	121.9	3.79
48.0	130.0	105.0	118.8	3.74
72.0	139.1	91.7	106.6	3.65
96.0	145.9	83.3	96.6	3.59
120.0	151.3	77.4	88.9	3.55
180.0	162.1	67.6	75.9	3.48
225.0	168.2	62.7	69.5	3.44

THE EFFECT OF COLD ROLLING REDUCTION ON PLANAR ANISOTROPY OF INTERSTITIAL FREE STEELS

L. KESTENS and Y. HOUBAERT
Laboratory for Iron and Steelmaking, University of Gent, Belgium

L. DELANNAY and P. VAN HOUTTE
Department of Metallurgy and Materials Engineering, Katholieke Universiteit Leuven, Belgium

M.R. BARNETT
BHP Research, BHP, Australia

J.J. JONAS
Department of Metallurgical Engineering, McGill University, Canada

Abstract

Rolling and annealing experiments were carried out on a Ti-stabilized interstitial free steel with cold rolling levels varying from 75 to 95% reduction. The planar anisotropy was assessed on the basis of calculated r value profiles derived from the experimental annealing textures. It was observed that the planar anisotropy of r value displays a minimum after 85 to 90% reduction. Detailed analysis of the experimental recrystallization textures allows the negative effects of deviations from the perfect deep drawing texture, i.e. the <111>//ND fibre, to be quantified. A small residual intensity of the cube fibre components (particularly after 95% rolling reduction) and a slight shift of the experimental fibre skeleton with respect to the perfect fibre skeleton, are characterized as the dominant features leading to the deterioration of deep drawing quality.

Keywords: Interstitial free steel, planar anisotropy, quantitative texture analysis.

1 Introduction

The drawing properties of single phase ferritic steels are primarily determined by the crystallographic texture of the material. It is well known that the ND fibre texture (<111>//ND) provokes the best deep drawability. By a rather fortunate spell of metallurgical coincidence, this texture arises naturally during the thermomechanical processing of mild steel sheet, i.e. after cold rolling and annealing. A key parameter that can be used to optimize the deep drawing texture is the cold rolling reduction prior to annealing. Conventionally, the rolling reduction is optimized to increase the average normal anisotropy r_m (= $(r_0+r_{90}+2r_{45})/4$). Far less attention is paid, however, to the planar anisotropy, i.e. to the variation of deep drawing properties with respect to the rolling direction.

It is well established (Hutchinson, 1984) that the normal anisotropy displays an optimum as a function of cold reduction, which can vary from 75 to 90%, depending on the steel grade. The question arises as to whether or not such an optimum exists with regard to the planar anisotropy and if these two optima are compatible. It is the objective of this paper to address this question for the present grade of Ti stabilized interstitial free (IF) steel, which is the reference grade for automotive applications.

2 Experimental procedure

A Ti IF steel, of which the composition is mentioned in Table 1, was hot rolled in the austenite range on an industrial mill; a finish rolling temperature of 920°C and a coiling temperature of 730°C were employed. Hot band strips were cold rolled in the laboratory on a two-high reversible mill with reductions of 75, 80, 85, 90 and 95%. Subsequently the cold rolled samples were annealed in a salt bath at 800°C for 60 s. The textures were evaluated in the conventional way by measuring four incomplete pole figures on a Siemens D500 texture goniometer; these were further processed by the ODF software developed by Van Houtte (1995).

3 Results

The annealing textures are presented in Fig. 1. All the ODFs exhibit well developed ND fibre textures which intensify with increasing rolling reduction. At the lower reductions (75 and 80%), the intensity distribution along the skeleton line is relatively homogeneous, whereas at the higher reductions (85, 90 and 95%) an intensity peak develops at the {554}<225> component. Together with this component, a secondary fibre appears, which runs from {001}<225> on the cube fibre (<001>//ND) to {554}<250>, apparently parallel to the RD fibre (<110>//RD) in the $\varphi_2=45$ deg section. Although the orientation selection mechanisms that govern the formation of recrystallization textures are not yet understood in detail, some progress has been reported recently in this field (Barnett and Kestens, 1999, Kestens et al., 1999).

In the present study, the deep drawing properties are characterized by means of simulated r values, which were calculated from the measured ODFs. Although it has been reported (Daniel and Jonas, 1990) that the relaxed constraint pancake model is slightly better for predicting r_m values, Van Bael et al. (1996) have demonstrated that

Table 1: Composition of Ti IF steel (mass%).

C	Mn	Si	P	S	Al	N	Ti
0.0019	0.097	0.007	0.010	0.004	0.047	< 0.002	0.041

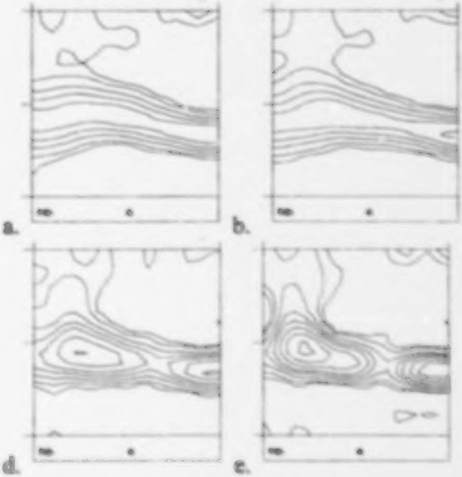

Fig. 1 : Annealing textures obtained after (a) 75, (b) 80, (c) 85, (d) 90 and (e) 95% cold rolling reductions, respectively. Levels: 1-2-4-6-8-11-14-18.

the planar anisotropy after large rolling reductions can only be satisfactorily modelled by the full constraint plasticity model. For this reason, the latter model was employed here, with the aid of the mathematical algorithms that were developed by Van Houtte (1988).

As a first approximation, the r value profiles, represented in Fig. 2, can be interpreted as one quarter of the earing profile that results from a cup drawing test. It is therefore apparent that the r value profile after a rolling reduction of 75%, with maxima at 0 and 90 deg, corresponds to a 4-ear cup drawing profile. When the rolling reduction is gradually increased, the maxima on the r value curve shift towards 30 and 90 deg, respectively, corresponding to a 6-ear profile in a cup drawing test.

Conventionally, the planar anisotropy is characterized by the Δr value ($\Delta r = ((r_0+r_{90}-2r_{45})/2)$. This measure of planar anisotropy is only appropriate, however, when the r value extremes are located at 0, 90 and 45 deg, respectively. Since this condition is not fulfilled at the higher rolling reductions, it is proposed here to consider the r value range ($r_{max}-r_{min}$) as the appropriate parameter for quantification of the planar anisotropy, rather than Δr. Fig. 3 shows the evolution of the normal and planar anisotropy parameters r_m and ($r_{max}-r_{min}$), respectively. It is evident that the normal anisotropy is relatively independent from the rolling reduction, except for a notable decrease at the largest reduction. This is a commonly observed feature of IF steels (Vanderschueren et al., 1996). The planar anisotropy parameter, on the other hand, displays an obvious optimum at

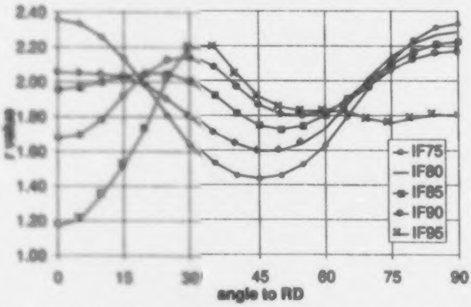

Fig. 2: Planar anisotropy profiles corresponding to the textures of Fig. 1.

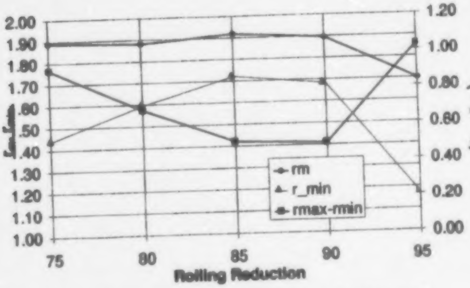

Fig. 3: Evolution of the planar anisotropy parameters vs. cold rolling reduction.

rolling reductions between 85 and 90%. The change that accompanies an increase in the reduction from 90 to 95% is of special interest as it involves a sharp increase in (r_{max}-r_{min}). In some cases, the steel manufacturer intends to optimize the minimum r value r_{min}, rather than the average. It should be noted that r_{min} is more sensitive to the rolling reduction than r_m and reaches a maximum at 85 and 90% reduction, which is coincidentally compatible with the minimum planar anisotropy.

4 Discussion

4.1 Planar Anisotropy After Conventional Rolling Reductions

In order to understand the observed anisotropy profiles it is necessary to analyze the features of the recrystallization textures in detail. Although the textures obtained after moderate rolling reductions (75 and 80%) are characterized by a relatively homogeneous intensity distribution along the fibre skeleton, they display the largest anisotropy. Even when non $\varphi_2 = 45$ deg sections are considered, the ND fibre maintains its homogeneity. A possible reason for the U shaped anisotropy in this case can be the observed curvature of the experimental skeleton line with respect to the perfect ND fibre, at exactly $\Phi = 55$ and φ_2=45 deg.

To examine the effect of this curvature, the experimental texture after 75% reduction (cf. Fig. 1a) was simulated in the following way. First, this texture was discretized into a set of 800 individual orientations. All the ND fibre orientations within a range of 20 deg were removed from this set. The remaining orientations were converted into a continuous ODF, displayed in Fig. 4a, by superimposing Gaussian distributions on the individual components (with a spread of 7 deg). This ODF represents the residual intensity that appears primarily on the cube fibre and near the {110}<110> component. Then, a curved ND fibre, shown in Fig. 4b,

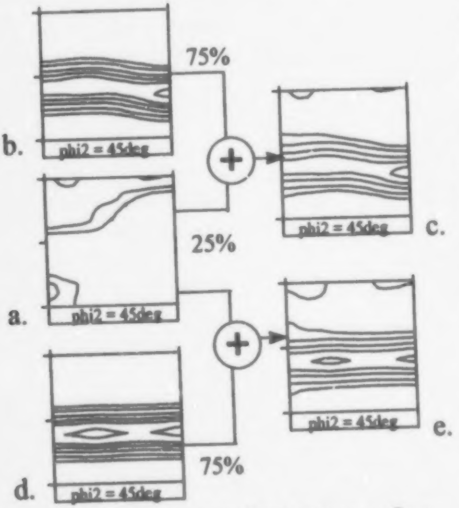

Fig. 4: Modelled annealing textures after 75% rolling reduction. For full explanation cf. Section 4.1. Levels: 1-2-4-6-8-11.

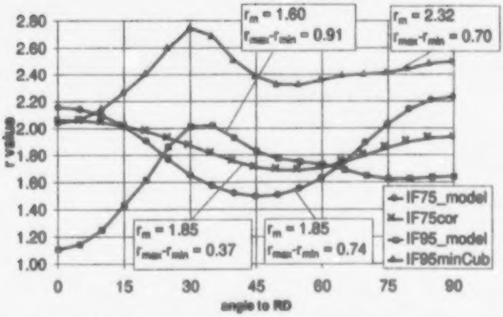

Fig. 5: Planar anisotropy of modelled annealing textures after 75% reduction with and without curvature correction.

was generated by superimposing 30 Gaussian components located on the exact fibre skeleton of the experimental texture (cf. Fig. 1a). The relative weights of these Gaussians are selected in order to reproduce the experimentally observed intensities.

When the ODFs of Figs. 4a and b are added with weight factors of 25 and 75%, respectively, the texture of Fig. 4c is obtained, which can be considered as a model of the experimental texture, cf. Fig. 1a. However, if the partial texture of Fig. 4a is merged, not with the curved fibre of Fig. 4b, but with the *straight* ND fibre located exactly at Φ = 55 deg instead (cf. Fig. 4d), then the texture of Fig. 4e is produced. This texture can be considered as a *straightened* version of the experimental one. The anisotropy profiles of the two textures are compared in Fig. 5. It should be noted that the planar anisotropy has decreased considerably due to the removal of the fibre curvature. The remaining anisotropy in the straightened texture is likely to be caused by the intensity that remains on the non ND fibre components of Fig. 4a and by the small heterogeneity of intensity along the ND fibre.

4.2 Planar Anisotropy After Large Rolling Reductions

Increasing the rolling reduction produces an intense {554}<225> component in the annealing texture and concurrently the 6-ear anisotropy profile appears. This profile resembles the anisotropy curve associated with the {554}<225> component. However, the planar anisotropy initially decreases when the {554}<225> orientation is intensified. Between 85 and 90% rolling reduction, an optimum is attained and beyond 90% reduction a sharp deterioration is observed. The reduction in ND curvature beyond 80% rolling reduction is a possible explanation for the initial improvement in the planar anisotropy. At the highest reduction level, another feature of the recrystallization texture can no longer be neglected, i.e. the increase in the intensity on the {001}<250> component which is the maximum along the cube fibre. Increasing the cold reduction from 90 to 95% produces an increase in the cube fibre maximum ({001}<250>) from 1.6 to 2.5 times random, corresponding to an increase in volume fraction of these components from 9 to 12%.

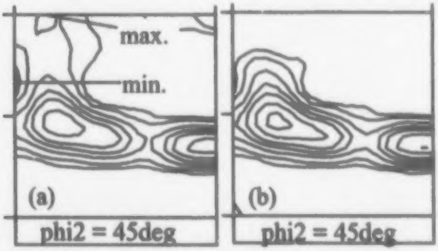

Fig. 6: Modelled annealing textures after 95% rolling reduction:(a) including and (b) excluding cube fibre components. Levels: 1-2-4-6-8-11-14.

In order to assess the disturbing effect of the cube fibre components, the experimental texture obtained after 95% rolling reduction (cf. Fig. 1e) was discretized into a set of 800 individual grains. The ODF of Fig. 6a was then calculated by superimposing Gaussian functions on these discrete orientations with a spread of 4 deg. However, if orientations within 20 deg of the cube fibre, are removed from the discretized set, the texture of Fig. 6b is obtained. The corresponding anisotropy curves are illustrated in Fig. 5. It is evident that removing the cube fibre orientations results in a sharp increase in r_m value, thus explaining the sudden drop in r_m after very large rolling reductions in spite of the intensification of the ND fibre. Additionally, the cube components are responsible for a slight but nevertheless significant part of the planar anisotropy, although the intricate features of the {554}<225> component also contribute to the planar anisotropy.

5 Conclusions

The planar anisotropy parameter (r_{max}-r_{min}) displays a minimum after cold rolling to a reduction of 85 to 90%; this also coincides with the optimum in the average normal anisotropy r_m. The 4-ear anisotropy at the lower rolling reductions (75 and 80%) originates primarily from the slight curvature of the experimental ND fibre skeleton with respect to the theoretical position of the perfect fibre skeleton. At larger rolling reductions (≥ 85%), the {554}<225> component dominates the annealing texture producing 6-ears anisotropy. Although initially (after 85 and 90% reduction) the planar anisotropy decreases as a result of this development, this trend is reversed after a reduction of 95%, which is responsible for the introduction of near cube components in the recrystallization texture. These components affect both the planar and normal anisotropy negatively and are thus responsible for the observed optima.

Acknowledgements

Dr. D. Vanderschueren from N.V. OCAS is gratefully acknowledged for providing the material. Financial support for this research is granted by the Federal Government of Belgium (DWTC) through the contract IUAP P4/33.

References

Barnett, M.R. and Kestens, L. (1999), {111}<110> and {111}<112> Textures in Cold Rolled and Annealed IF Steel Sheet, *ISIJ. Int.*, Vol. 39, in press.
Daniel, D; and Jonas, J.J. (1990), Met. Trans. A, Vol. 21A, pp. 331-343.
Hutchinson, W.B. (1984) *Int. Met. Rev.*, Vol. 29, pp. 25-42.
Kestens, L., Yoshinaga, N, Vanderschueren, D. and De Cooman, B.C, (1999), Texture Change During the Late Stages of Recrystallization of a Cold Rolled and Annealed Ultra Low Carbon Steel et al., *Proc. Recrystallization '99*, in press.
Van Bael, A, Winters, J. and Van Houtte, P. (1996), *Proc. ICOTOM-11*, pp. 356-361.
Van Houtte, P. (1988), *Textures and Microstructures*, Vol. 8-9, pp. 313-350.
Van Houtte, P. (1995), The MTM-FHM Software Version 2, *Users Manual*.
Vanderschueren, D., Bultinck, I. and De Rore, N. (1996) *Proc. ICOTOM-11*, pp. 879.

THERMAL STABILITY OF BASAL TEXTURE IN A Ti_3Al-BASE ALLOY

SATYAM SUWAS and R. K. RAY
Department of Materials and Metallurgical Engineering
Indian Institute of Technology, Kanpur-208016 (INDIA)

Abstract

An attempt has been made to study the stability of basal texture formed in a Ti-24Al-11Nb alloy during hot rolling as a function of both annealing and $\alpha_2 \rightarrow \alpha_2+\beta/\beta \rightarrow \alpha_2$ phase transformation. Results of texture study indicate that the basic characteristics of the rolling texture do not change during isochronal or isothermal annealing. Although the rolling (basal) texture somewhat weakens during recovery, it starts regaining its strength in the recrystallisation stage. The texture starts deteriorating during grain growth. Heat treatment involving $\alpha_2 \rightarrow (\alpha_2+\beta)/\beta \rightarrow \alpha_2$ transformation of sample with a reasonably sharp basal texture seems to impair the basal character of the texture. This could be due to some processes involving variant selection during the forward as well as the reverse transformation from α_2 to β.

Key words: Annealing texture, isochronal annealing, isothermal annealing, Ti-24Al-11Nb, transformation texture, thermal stability.

Introduction

The application of Ti_3Al base alloys in aerospace industry requires the material mostly in sheet form [Banerjee 1994]. The effects of various processing parameters on the evolution of texture during hot rolling of a Ti-24Al-11Nb alloy have been discussed in a previous paper [Suwas *et al.* 1999]. Good ductility and formability of this alloy require a good basal {0002}<uvtw> texture [Hon *et al.* 1991] as well as a suitable microstructure. Microstructural modifications are usually carried out by subjecting the rolled material to further heat treatments, which may in turn affect the texture of the sheet material. Thus it is important to examine the thermal stability of the hot rolling texture during subsequent heat treatments. The heat treatments may involve (i) relaxation processes such as recovery and recrystallisation, or (ii) phase transformation. The effects of both these phenomena on the stability of hot rolled texture of a Ti-24Al-11Nb alloy will be discussed in this paper.

Experimental Procedure

Initially a strong basal texture was produced in the alloy using the processing sequence : as-cast→heat treated for 24 hrs at 1173 K→hot rolled 80% at 1173 K→water quenched. The details have been given in the previous paper. This was chosen as the starting material, which was then isochronally annealed for a period of 1 hour at four different temperatures, 1123 K, 1173 K, 1233K and 1293 K. Further, isothermal annealing was also performed at the temperature of 1173 K for 15 min., 30 min., 1 hr, 2 hrs and 12 hrs.

In the second type of heat treatment, the as-cast alloy was rolled to 80% reduction in thickness at 1173 K and furnace cooled and this formed the starting material. It was then subjected to heat treatment at 1173 K, 1293 K and 1373 K for the periods 24 hrs, 8 hrs and 4 hrs respectively, and finally furnace cooled.

Results

The (0002) pole figures for the starting material and the isochronally annealed samples at 1123 K, 1173K, 1233 K and 1293 K are shown in Figs. 1 (a-e). These pole figures indicate the presence of a sharp basal texture in all the heat treated samples. The intensity of the near basal poles in the 1123 K / 1 hr annealed sample shows a drastic decrement (from 9.4R to 6.0R) from the pole density of the starting material (Fig. 1 a). The basal pole density increases after heat treatment of 1 hr at 1233 K, and decreases once again after isochronal annealing at 1293 K. While the basal poles in the 1173 K / 1 hr sample show a distinct RD split behaviour, those in the 1123 K/ 1hr and 1293 K / 1 hr samples indicate splitting along the TD direction.

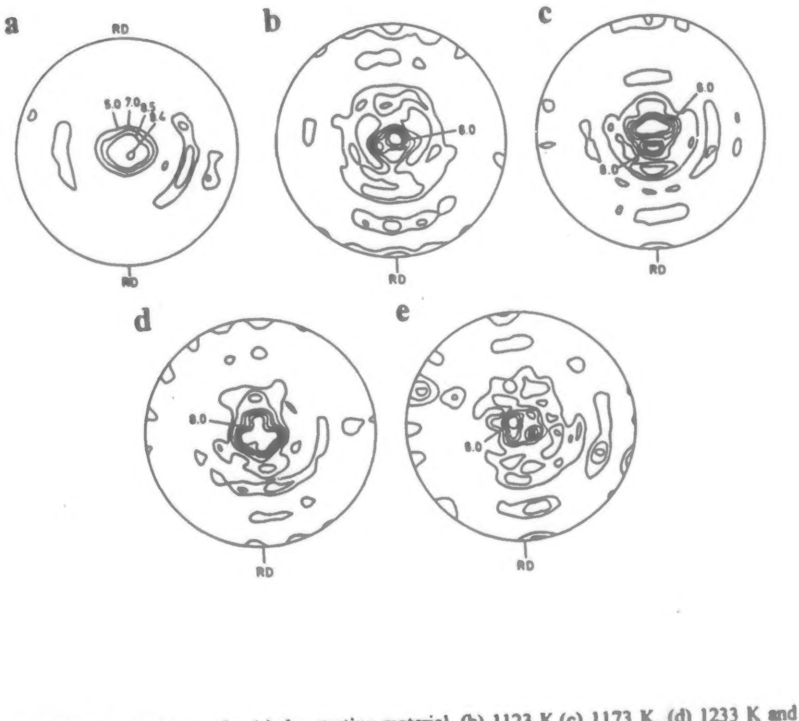

Fig. 1 (0002) pole figures for (a) the starting material, (b) 1123 K,(c) 1173 K, (d) 1233 K and (e) 1293 K annealed materials

The (0002) pole figures for isothermally annealed samples at 1173 K are presented in Figs. 2 (a-d). As can be seen from Fig. 2 (a), the specimen annealed for 15 min shows weakening of the basal texture as compared to the starting material (Fig. 1 a). There are some other weak orientations also in the pole figure. In addition, the basal texture shows a split TD tendency. For the specimen annealed for 30 min, the basal texture begins to get somewhat strengthened. High densities of poles are seen to arrange all around the ND, and the subsidiary orientations become perceptibly weaker at this stage. The texture intensity does not change after 2 hrs annealing; however, it brings about the tendency towards the formation of a split RD basal texture. Further annealing for a period of 12 hrs not only causes a weakening of the basal texture, but at the same time strengthens the non-basal components.

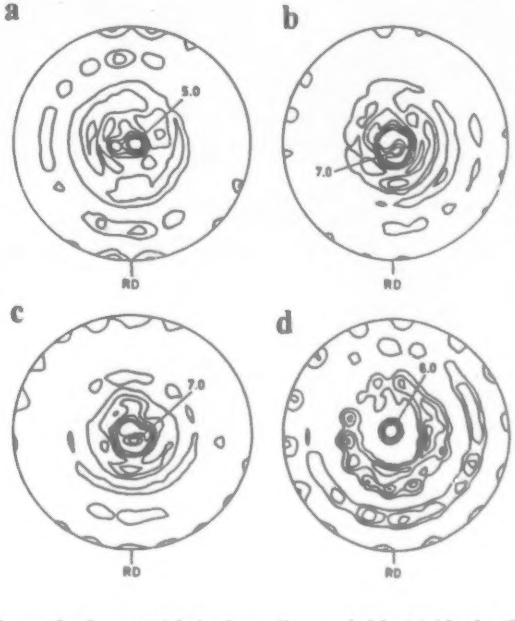

Fig. 2 (0002) pole figures for the materials isothermally annealed for (a) 15 min, (b)30 min, (c) 2 hrs and (d) 12 hrs at 1173 K.

The (0002) pole figures of the starting material along with those for the samples subjected to the second type of heat treatment at 1173 K, 1293 K and 1373 K are shown in Fig.3 (a-d). Heat treatment of this kind appears to cause a degradation of the nearly perfect basal texture of the starting material. Heat treatment at 1173 K causes splitting along TD, while that at the higher temperature of 1293 K causes RD splitting. The 1373 K heat treatment of the material appears to remove most of the basal textured material, with the pole density maxima shifting by about 20/25° from the perfect basal location. Still there is some perceptible intensity in the basal region.

Discussion

The work described above basically deals with the stability of the basal texture formed during hot rolling, as a function of both (i) annealing and (ii) $\alpha_2 \rightarrow (\alpha_2+\beta)/\beta \rightarrow \alpha_2$ phase transformation.

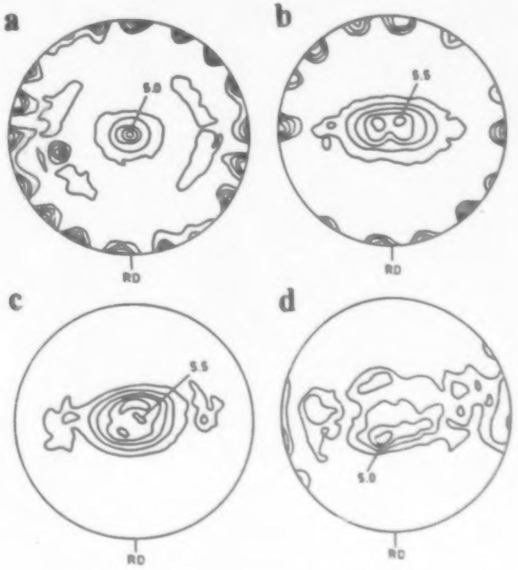

Fig. 3 (0002) pole figures for the (a) starting material, (b) 1173 K heat treated (24 hrs/ FC), (c) 1293 K heat treated (8 hrs/ FC) and (d) 1373 K heat treated (4 hrs/ FC).

The physical processes which accompany annealing are basically recovery, recrystallisation and limited grain growth of the α_2 phase. The temperature of annealing has been purposely kept low and quenching after heat treatment was practised so as to avoid the effect of phase transformation on the original basal texture.

Isochronal annealing of the material for 1 hr at 1123 K shows that the basal pole density decreases perceptibly as compared to the starting material. Recovery of the original warm rolled structure goes on at this stage (Fig. 4 a). Thus any reorientation of the grains, which normally occur during recrystallisation (say), is not possible and therefore the textural change appears to be quite intriguing. Recent works on the effect of annealing on cold rolled ordered $Ni_3Al(B)$ and $Ni_3Al(B, Zr)$ [Ghosh Chowdhury 1995, Bhattacharya 1996] have shown that these intermetallic materials undergo a change in order during cold rolling, and the state of order tries to revert back to the original state during annealing. As a result of this, the texture of the cold worked material decreases in intensity perceptibly during the recovery stage also when the changes in ordering are taking place, although no reorientation of grain due to recrystallisation etc. occurs. Since the α_2 phase in the present alloy is an ordered phase [Banerjee 1994] and since hot rolling of the material at 1173 K can be considered as similar to cold (warm) rolling, at least in this case, a situation similar to the cases of the Nickel aluminides can be envisaged.

SEM microstructures indicated that after isochronal annealing at 1173 K and 1233 K, the materials show distinct signs of recrystallisation of the α_2 phase. This is shown typically in Figs. 4 (a and b). Thus the textures of the materials at these stages can be considered as due to recrystallisation and possibly some concurrent reordering process. When the experimental material is annealed at 1293 K for 1 hr (i.e. within the $\alpha_2+\beta$ phase field) it undergoes rapid grain growth of the α_2 (Fig 4 c) after recrystallisation will occur simultaneously with the $\alpha_2 \rightarrow \beta$ transformation. The textural results after isothermal annealing at 1173 K for different lengths of time are quite similar to those of isochronal annealing. In this case, partial recrystallisation starts after 30 min of annealing (Fig. 5), which corresponds to beginning of the improvement in basal texture over the texture in the recovery stage. The trend continues further till the recrystallisation stage. It thus appears that hot rolling texture remains rather stable during annealing at temperatures within (nearly) single phase α_2 region. Annealing at temperatures in the $(\alpha_2+\beta)$ phase field has the effect of decreasing the basal texture to some extent.

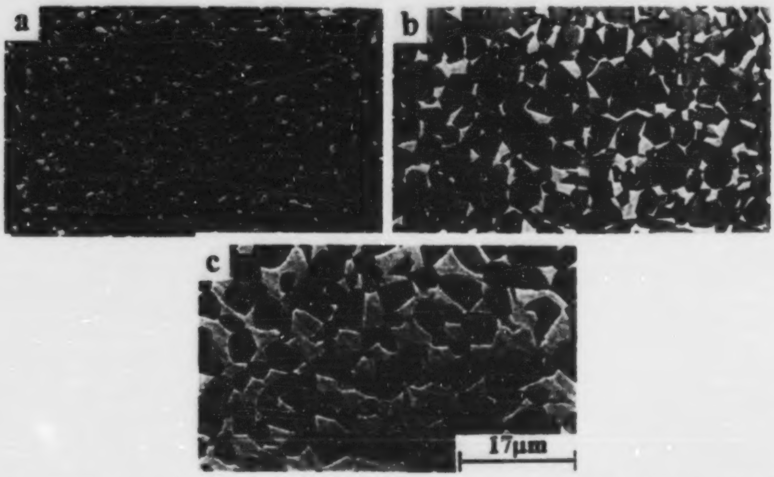

Fig. 4 SEM micrographs for the materials annealed for 1 hr at (a) 1173 K (b) 1233 K and (c) 1293 K

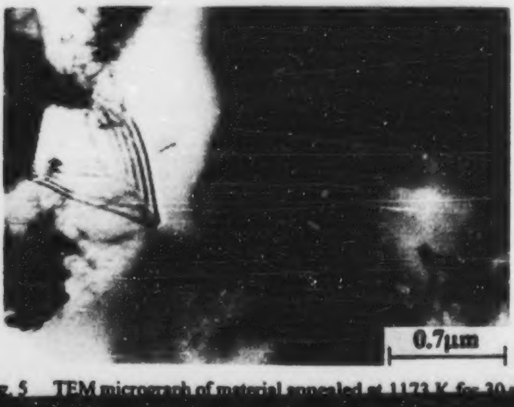

Fig. 5 TEM micrograph of material annealed at 1173 K for 30 min

F 11

The results of the second type of heat treatment clearly show that when the starting material has a reasonably strong basal texture, annealing at the successively higher temperatures of 1173 K, 1293 K and 1373 K appears to gradually degenerate the texture from the perfect basal. In case of the 1173 K rolled and furnace cooled material, where the primary α_2 is in a more or less deformed condition [Suwas and Ray, 1999] and which has a reasonably strong basal texture, heat treatment through the $\alpha_2 \rightarrow \beta \rightarrow \alpha_2$ cycle does not seem to improve the basal texture. Location of high pole density has been found to deviate from the perfect basal component as temperature of annealing increases. The β phase that forms in the material, as it is annealed at 1293 K or at 1373 K, comes about by transformation from deformed primary α_2 mainly. The basal texture shows some perceptible deterioration after the $\alpha_2 \rightarrow \beta \rightarrow \alpha_2$ transformation. It appears that variant selection during the forward and reverse transformation from the α_2 to β phase plays quite an important role in this phenomenon. Further work is needed to clarify this aspect.

Conclusions

1. The basal hot rolling texture remains rather stable during recrystallisation annealing at temperatures within the (nearly) single phase field of α_2. Grain growth after recrystallisation, produces orientations other than the basal. Moreover, annealing in the $(\alpha_2+\beta)$ phase field decreases the intensity of the basal texture to some extent.
2. Heat treating the basal textured material through the $\alpha_2 \rightarrow \beta \rightarrow \alpha_2$ cycle gradually degenerates the basal component in the final α_2.

Acknowledgements

The authors are grateful to Dr. D. Banerjee, Director, DMRL, Hyderabad for his constant encouragement as well as for providing the texture measurement facility. We also thank Dr. A. K. Singh for his cooperation and Dr. A. K. Gogia and Mr. T. K. Nandy for several useful discussions. The grant-in-aid from AR & DB, Ministry of Defence, Government of India, is duly acknowledged.

References

Banerjee, D.(1994), in Intermetallic Compounds: Vol. 2, Practice, eds. Westbrook, J.H., and Fleischer, R.L., John Wiley & Sons Ltd., p. 91.
Suwas, Satyam and Ray, R. K. (1999) previous paper in this proceedings.
Hon, W.P.,, Wu, S.K., and Koo, C. H. (1991) Mater. Sci. Engg., Vol. A 131, p. 85.
Ghosh Chowdhury, S. (1995) Ph. D. Thesis, IIT Kanpur.
Bhattacharya, B. (1996) Ph. D. Thesis, IIT Kanpur.

TEXTURE OF WELDED JOINTS OF 316L STAINLESS STEEL

J.L. BECHADE
Commissariat à l'Energie Atomique - Centre d'Etudes et de Recherche sur les Matériaux, Service de Recherches Métallurgiques Appliquées, Gif-sur-Yvette, France
G. BOUCHE
Ecole des Mines de Paris, Centre des Matériaux, UMR CNRS 7633, Evry, France
M.H. MATHON
Laboratoire Léon Brillouin, CEA-CNRS, Gif-sur-Yvette, France
T. BAUDIN
Université de Paris Sud, Laboratoire de Métallurgie Structurale, URA CNRS 1107, Orsay, France

Abstract

The present work has been undertaken during the study of creep damage in welded joints. The composition of the filler metal used for the welded joints under investigation is a 316L(N) type 19Cr-12Ni-2Mo stainless steel. The complex dual phase microstructure of 316L welds is simulated by manually filling a mould with longitudinally deposited weld beads.

Creep tests show that the damage is located at the different grain interfaces. Columnar grains of austenite constitute a matrix in which thin dendrites of δ-ferrite can be found. In order to obtain information concerning the strength of the interfaces, the texture of the two phases has been investigated by neutron diffraction. This technique gives access not only to the texture of coarse grains of austenite (several millimetres in length and approximately 50 to 100 μm in the cross section) but also to that of δ-ferrite (thin dendrites of 1 μm thick which can be observed inside and between austenite grains) in very small content (5%).

The texture analysis, before and after ageing at 600°C, revealed that the phases are not in a classical reciprocal orientation : austenite and ferrite appeared to be in cube-cube relationship with a fibre texture [010] along the solidification direction with reinforcements such as {001}[100] and {102}[010]. This proves that the solidification has been duplex itself, with a solidification front and the growth of both ferrite and austenite primary phases.

EBSD and TEM analyses performed recently on the same material seem to confirm locally the results obtained on a global scale.

Keywords: Neutron diffraction, ODF, stainless steel, texture, welded joint,

1 Introduction

Stainless steels are largely used in components working at elevated temperature, such as nuclear power plants. These components are usually assembled by welding. Under service conditions, welded joints may be preferential sites of creep damage, as compared to the base material. Creep damage results in the formation of cavities and the development of creep cracks which can lead to the premature failure of a component.

Weld material of type 316L is employed in making the welded joints of fast breeder reactors. The microstructure of as-welded 316L weld deposit consists of two phases : the columnar grains of γ-austenite constitute a matrix where thin dendrites of δ-ferrite can be found. The texture resulting from the solidification process may induce an anisotropy in the creep behaviour which has been experimentally observed and reported elsewhere (Bouche 1998). Greenwood (1998) highlighted the role, with respect to creep, of the microstructural features and of the anisotropy in the material. Metallographic observations performed on polished cross sections of creep tested samples show that creep damage is located at γ–γ grain boundaries (Bouche 1998). The purpose of this paper is to study the texture of the material in order to assess the influence of the crystallographic texture upon creep behaviour and localisation of damage initiation. To minimise the energy involved, these two phases often present in steels misorientation relationships such as those described by Kurdjumov-Sachs (KS) or Nishiyama-Wassermann (NW).

The present paper deals with the texture of both phases which is quite difficult to determine using conventional X-ray analysis. In deed, the γ grains can be as long as 1 cm in the direction of solidification and the δ-ferrite is a second minor phase in very small amount (5 weight %). Therefore global texture measurements were performed using neutron diffraction which is especially suitable in case of coarse grains and is also very sensitive to minor phases. To understand the development of creep cracks and the evolution of anisotropy, it is important to measure the texture of both phases after ageing. Consequently, the texture analysis has been also performed after ageing at 600°C for 2300 hours. In this case, the δ-ferrite is partly transformed into secondary austenite and carbides which are preferential sites for cavitation during creep. Moreover, these results have been recently complemented by more local orientation investigations using Electron Back-Scatter Diffraction (EBSD) and Transmission Electron Microscopy (TEM).

2 Material and microstructure

2.1 Weld metal preparation and composition

The actual welded joints encountered in the elements of a typical nuclear power plant are X section weldments. Since it is difficult to cut specimens from an X weldment, a piece of material was built using the manual filler metal arc technique. Figure 1, which includes the conventional orientations for longitudinal (L), transverse (T) and short transverse (ST) directions and the location of the samples used for the texture analyses reported in this paper, schematically shows a transverse cross section of the mould where several deposited beads can be identified.

The filler metal used for the welded joints is a 316L type 19Cr-12Ni-2Mo stainless steel. The composition of the material is close to that of the fully austenitic base metal, except that the balance between the γ and δ stabilising elements was chosen to result in 5% to 10% ferrite left in the weld to prevent hot liquation during the solidification of the material (Brooks 1991) which is beneficial for creep strength (Thomas 1978).

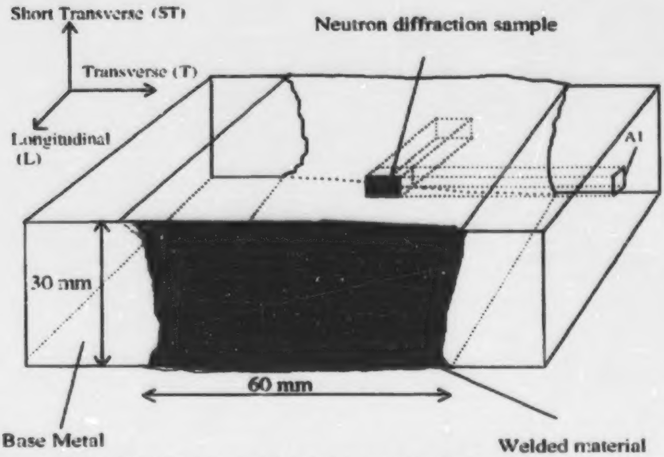

Fig. 1: Schematic sketch of the 316L(N) mould and location of texture samples.

2.2 Microstructure

A scanning electron micrograph of the microstructure, Figure 2, shows the black skeletal bcc ferrite phase while fcc austenite grains appear in grey. The bead deposition results in the formation of a complex two-phase (γ+δ) material in which γ is the dominant phase (94%). The γ phase is organised into columnar grains several millimetres long and approximately 50 to 100 μm across the section. Grains are oriented close to the ST direction by both the thermal solidification gradient and fluid mechanics in the weld-pool during solidification. As will be shown later, the consequence is a strong crystallographic texture. The second phase is residual δ ferrite. The amount of δ, 6% ±0.5%, has been experimentally measured using a magnetic gauge. The presence of ferrite in the present case is due to the rapid solidification of the weld which is equivalent to a quench. Thin dendrites of ferrite, less than 1 μm thick, are observed within the austenite grains. The boundary between two austenite grains is also partially filled by δ ferrite.

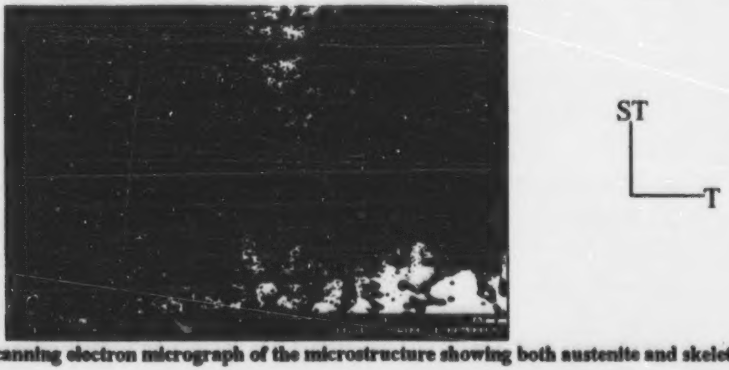

Fig. 2: Scanning electron micrograph of the microstructure showing both austenite and skeletal ferrite

3 Texture analysis

3.1 Experimental procedure

The volumic texture analysis was performed using the neutron diffraction technique. One of its specificities is to measure complete pole figures in transmission mode whereas conventional X-ray pole figures are unreliable for high tilt angles (χ). Other advantages are that no surface preparation is required for the sample and that the analysis is performed for a volume which can be up to 1 cm^3 in comparison with conventional X-ray diffraction methods dealing with a surface (small penetration depth depending on the material and wave length used, generally ~ 10 microns).

The experiments were performed at the Laboratoire Léon Brillouin CEA-CNRS, Saclay, on a four circle diffractometer -6T1- dedicated to pole figure determination. The neutron wavelength was 1.159Å, selected by a Cu (111) monochromator (L.L.B. 1995). The sample was a cube of 1 cm edge. Its position and orientation in the mould are given in Figure 1.

The pole figures which were established were {111}, {200}, {220} and {311} for the austenitic phase, {110}, {200} and {211} for the ferritic phase. The Bragg angles of $\{111\}_\gamma$ and $\{110\}_\delta$ are so close to each other that strong collimations had to be used to assess separately these pole figures. No absorption correction was applied.

Texture is also described quantitatively by a three dimensional function in Euler space (here Euler angles ψ, θ and φ, with the Roe notation), the Orientation Distribution Function (ODF) (Roe 1965, 1966).

The ODF was calculated using the iterative series expansion method up to the rank $l_{max}= 22$, for even l only (Viglin 1960 and Bunge 1965, 1982). The pole figures were then recalculated from the ODF and compared with the experimental ones.

3.2 Results

Experimental pole figures presented in Figure 3 have been tilted to have the growing direction of the grains perpendicular to the pole figure.

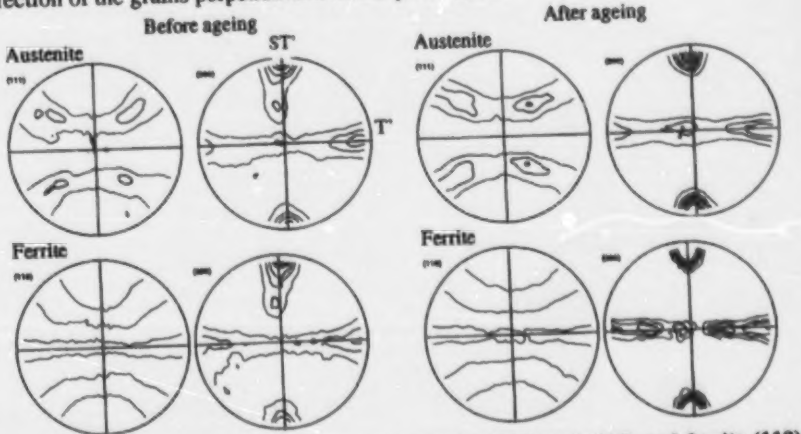

Fig. 3: Experimental tilted pole figures of austenite (111) and (200) and ferrite (110) and (200) before and after ageing (density levels : 1, 3, 5, 8, 10, 12)

This enabled us to calculate the exact angular deviation between the <100> direction of solidification and the ST direction of the mould. This angle is in fact the combination of two rotations : the first one is due to the inclination of the electrode during the welding, β=20° on the ST-T plane and the second one is due to the thermal gradient during the cooling of the mould, ω=10° on the ST-L plane.

The figures obtained after rotations and calculated from the ODF coefficients are those of a fibre-like <100> texture with reinforcements such as {102}[010] and {001}[100], and γ–δ pole figures are very similar. It clearly appears that the growing direction of the grains is of a type <100> parallel to ST' (which is the transformation of ST after β and ω rotations, T' being the transformation of T).

The good agreement obtained between the experimental and calculated pole figures from the ODF allows the ODF to be used to analyse precisely the two phases texture .

The skeleton lines, presented in Figure 4, which gives the values of the ODF along a specifically chosen linear path through the orientation space (here for ψ = 90° and 0°, φ = 0° and θ ranging from 0 to 90°), confirms the similarity between the γ and δ pole figures with small differences before ageing also showing the effect of ageing on residual ferrite (stronger texture).

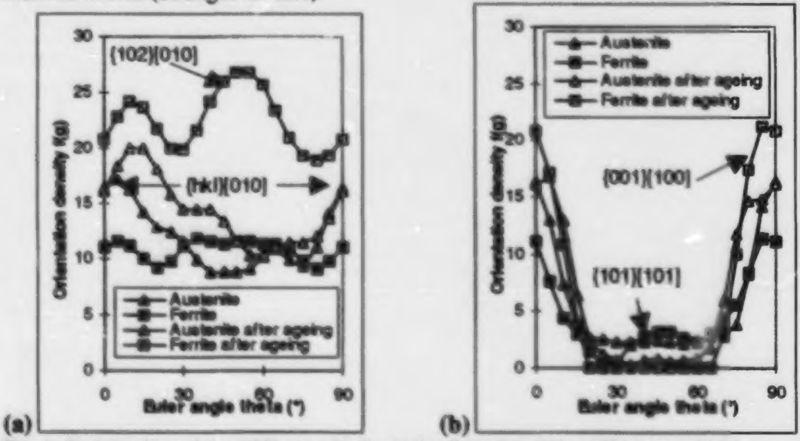

Fig. 4: Skeleton line of the ODF at φ=0°, θ ranging from 0 to 90°, ψ=90° (a), ψ=0° (b).

As a consequence, it comes out that on the macroscopic scale the phases are not in a classical orientation relationship like KS or NW but more in a cube-cube one.

After ageing at 600°C for 2300 hours, the austenite texture is unchanged in opposition to the texture of residual ferrite which is sharper : the <100> fibre texture and the {102}[010] component become stronger than before ageing.

4 Discussion

A fibre-like texture such as the one identified in the present study confirms the results of Takalo (1979) on a similar weld alloy. These authors present X-ray texture determinations on austenite but the texture of δ-ferrite could not be identified due to its low volume fraction. Although the material of the present study contains more ferrite, the success in acquiring pole figures for ferrite was essentially due to the specificity of neutron diffraction compared to X-ray diffraction, as discussed previously. Furthermore, there is no degradation of the signal when χ approaches 75° as it is the case for X-ray diffraction : the pole figure is consequently complete and the ODF more reliable. It is interesting to point out that results of this type on neutron diffraction work on a bcc δ phase in the case of welded joint could not be found in the literature.

The ferrite shows a fibre-like texture with a second component {102}[010] which becomes more pronounced after ageing. The pole figures of both phases are very similar on a global scale. Recent EBSD and TEM studies show that the same conclusions as the ones obtained by neutron diffraction can be drawn on a microscopic scale, thus giving meaningful information about the solidification mechanisms acting during the welding process.

Previous work by Finlan (1987) showed that the solidification mechanism of such stainless steel welds is complex, involving either primary ferrite solidification, or primary austenite solidification, or a simultaneous formation of δ and γ. The present results show that both δ and γ phases bear one common <100> direction which can be thought as the solidification direction. Ageing has only a little effect on γ texture when it makes the residual δ texture sharper and especially increases the <100> fibre texture.

5 References

Bouche, G., Allais, L., Lezaud, V., Piques, R., Pineau, A., Microstructural creep damage in welded joints of 316L stainless steel, *Materials at high temperatures*, 15 (3/4), (1998) 403-408.

Brooks, J.A., Thompson, A.W., Microstructural development and solidification cracking susceptibility of austenitic stainless steel welds, *International Materials Reviews*, 36 (1), (1991) 16-44.

Bunge, H.J., Zur Dorstellung allgemeiner Texturen, Z. *Metalllkd*. 56, (1965) 827-874.

Bunge, H.J., Texture Analysis in Material Science. Butterworths Publ. London (1982).

Finlan, G.T., Lin, Y.P., Steeds, J.W., Microstructure and creep properties of type 316 stainless steel welds. In *Materials for nuclear core applications*, (1987) 147-152, London : BNES.

Greenwood, G.W., An overview of failure mechanisms in creep. In *Proceedings of the 12th European Conference on Fracture*: Fracture from defects, (1998) 3-14.

L.L.B.: Laboratoire Léon Brillouin, *Equipements expérimentaux*, CEA Saclay, (1995) 41-42.

Roe, R.J., Description of crystallite orientation in polycrystalline materials. III General solution to pole figure inversion. *Journal of Applied Physics*, 36, (1965) 2024-2031.

Roe, R.J., Inversion of pole-figures for materials having cubic-crystal symmetry. *Journal of Applied Physics*, 37, (1966) 2069-2072.

Takalo, T., Suutala, N., Moisio, T., Austenitic solidification mode in austenitic stainless steel welds, *Metallurgical Transactions*, 10 A, (1979) 1173-1181.

Thomas, R.G., The effect of δ-ferrite on the Creep Rupture Properties of Austenitic Weld Metals, *Welding Journal Research Supplement*, (1978) 81s-86s.

Viglin, A.S., A quantitative measure of the texture of a polycrystalline material. Texture function. Sov. Phys. Solid State, 2, (1960) 2195-2207.

TEXTURE OF PALLADIUM AND PALLADIUM-SILVER ALLOYS AFTER COLD-ROLLING AND ANNEALING

YANG CAO and J. A. SZPUNAR
Department of Metallurgical engineering, McGill University, Montreal, PQ, H3A 2B2, Canada
W. SHMAYDA
Ontario-Hydro Technologies, Toronto, ON, M8Z 5S4, Canada

Abstract

The cold rolled sheets of palladium and palladium-silver alloys are widely used in the energy and chemical industries. The main method to get thin membrane is cold-rolling with intermediate softening annealing. The cold rolling will produce textures which influence properties of palladium and palladium-silver alloys. In this paper, the texture of cold-rolled Pd and Pd-Ag alloys has been investigated. The orientation distribution function (ODF) analysis shows that palladium has {112}<111> texture with different orientation density at 40%-82% deformation. However, $Pd_{77}Ag_{23}$ alloy has {110}<211> and {123}<111> type textures. An attempt to explain this texture transition is based on analysis of a role of alloying element. After annealed at 850^{0}C, texture of palladium and Pd-Ag alloy have been changed. Also a decrease in sharpness of textures was observed. The rolling texture and recrystallization texture are related to the stacking fault energy.

Keywords: deformation, palladium, palladium-silver alloys, texture

1 Introduction

Palladium is a noble metal in the platinum group. Like other platinum group metals, palladium has high stability, adequate heat resistance, and good deformation characteristics and corrosion resistance in many aggressive media.(1) Palladium-silver system alloys crystallize to form a continuous series of solid solutions. Palladium alloys with 20-30% Ag not only have the highest hardness and strength, but also have good ability for hydrogen permeation.(1,2) Pd-Ag alloys are plastic and easily worked by rolling, drawing and pressing-forming. The cold rolled sheets of palladium and palladium-silver alloys are widely used in the energy and chemical industries.(3) The main method to get a thin membrane is cold-rolling with intermediate softening annealing. The cold rolling will produce textures which influence properties of palladium and palladium-silver alloys. Unfortunately, there is little information about deformation texture in palladium and $Pd_{77}Ag_{23}$ alloys. Thus, the texture of cold-rolling and annealing in Pd and Pd-Ag alloys has been investigated. The transformation from rolling texture to recrystallization texture is analyzed.

2 Experimental Procedures

The materials used in the investigation are palladium and $Pd_{77}Ag_{23}$ alloys. The two alloys were subjected to cold rolling in a rolling mill to different strain levels. The $Pd_{77}Ag_{23}$ alloy foils have been cold rolling with 80% deformation. The palladium samples are subjected to 40%-82% cold rolling. Pd and $Pd_{77}Ag_{23}$ alloys are annealed respectively at 250^0C for 3 hours and 850^0C for 1.5 hours. The textures were examined by X-ray diffraction. The (111), (200), (220) pole figures have been measured. The orientation distribution functions (ODFs) were calculated from those pole figures.

3 Results and Discussion

3.1 Deformation Texture of Palladium and Palladium-Silver Alloys

The (111), (200), (220) pole figures from the sheet surface in deformed state of 82% rolling reduction are shown in Figure 1. After large deformation, the strong texture appears. The (111), (200), (220) pole figures after 40%, and 60% deformation is nearly the same as Figure 1. The rolling textures of palladium at 40%, 60%, 82% deformations are mainly {112}<111> component with additional {124}<112> component. The cold-rolling texture {112}<111> component of palladium developed and sharpened gradually as deformation strain was increased.

The ODFs for all specimens are shown in Fig. 2. According to the ODF, the main component of the rolling texture for palladium is {112}<111>. The summary of texture has been shown in Table 1.

Table 1 Cold-Rolling Texture of Palladium and Pd-Ag alloys after large deformation

Materials	Texture		Stacking fault energy(7,8) mJ/m^2
Palladium	{112}<111>	{124}<112>	180
$Pd_{77}Ag_{23}$	{123}<111>	{011}<112>	125
$Pd_{20}Ag_{80}$(4)	{112}<111>	{011}<112>	30
Silver(5)		{011}<112>	24

The (111), (200), (220) pole figures of $Pd_{77}Ag_{23}$ in deformed state of 80% rolling reduction are shown in Figure 3. The rolling texture of palladium is mainly {011}<112>/{123}<111>. The cold-rolling texture of palladium developed with large deformation strain. From Table 1, we can find that there are some differences between palladium and Pd-Ag alloy as well as silver. The pure palladium has {112}<111> texture and pure silver has {011}<112> texture. $Pd_{77}Ag_{23}$ alloy has {011}<112> and {123}<111> mixture texture. $Pd_{20}Ag_{80}$ has a mixture texture of {011}<112> and {112}<111>. That means that the texture has changed from {112}<111> for palladium to {011}<112> for silver.

The stacking fault energy plays an important role in determining deformation texture in fcc metals at room temperature. There are different stacking fault energy (SFE) values for palladium, silver and Pd-Ag alloy with fcc structure. Since the mean width of separation for extended dislocation has an inverse ratio with the stacking-fault energy, cross-slip for close-packed crystals becomes increasingly difficult as the stacking-fault energy decreases.(6) Stacking fault energy has influences on a deformation mode, and deformation mechanism will control the development of texture. Metals deformation is relative to the active slip systems, whose slip planes and directions will be determined by metals structure. The sheet rolling is an approximation to a biaxial stress system. In fcc metals, the selection of independent shear systems will be made from among twelve {111} <112> twin systems and twelve {111} <110> slip systems. The {111}<112> texture as a result of rotations of the tension and compressive axes caused by slip on the two systems with the highest resolved shear stresses under the bi-axial stress condition of rolling. For palladium and silver, they are fcc structures. Palladium has a high stacking fault energy value, which forms {111}<112> Cu-type texture. The silver has a low stacking fault energy value, which essentially leads towards the {110}<112> brass-type texture. For Pd-Ag alloys, the stacking fault energy will decrease when Ag concentration increase(7,8). It means the deformation mode will change from pure slip to slip with twin. So it should include a set of mixture textures {111}<112>/{110}<112> for Pd-Ag alloys. When it approaches pure silver, there is more component of {110}<112> texture.

3.2 Annealing Texture of Palladium and Palladium-Silver Alloys

After 850^{0}C annealing, the texture of palladium and $Pd_{77}Ag_{23}$ will be changed. The textures of annealing palladium and Pd-Ag alloy were shown in Table 2. The textures of palladium have changed from {121}<111> to {131}<112>. For Pd-Ag alloys, the deformed texture will not change {011}<211>/{123}<111> after low temperature annealing. The textures in annealed (850^{0}C) materials are {113}<110>&<581>. In our research, the annealing temperature (850^{0}C) is higher than the temperature of recrystallization. During annealing, the metals have been subjected to recrystallize. In recrystallization the dislocation density controls the stability of grains and determines which orientations grow at the expense of others. Deformation texture will influence recrystallization texture. Usually, a fcc metal with a low enough stacking fault energy after primary recrystallization produces {326}<835> texture.(10) After annealing at high temperature (600^{0}C), {113}<332> texture will be produced in 70:30 brass with high reduction. Here {113}<110> texture for $Pd_{77}Ag_{23}$ has been observed after 850^{0}C annealing, this texture is near to brass texture. It means that adding silver to palladium will make Pd-Ag alloy texture close to silver texture. But there are still some problems to explain how to form {113}<581> texture after annealing $Pd_{77}Ag_{23}$.

Table 3 Recrystallization Texture of Palladium and Pd-Ag alloys

Materials	Texture
Palladium	{011}<114> {113}<112>
Pd$_{77}$Ag$_{23}$	{113}<110> {113}<581>
Pd$_{20}$Ag$_{80}$ (4)	{011}<112>/{112}<111>/{001}<100>
Silver (9)	{311}<112>

4 Conclusion

- The stacking fault energy has significant influence on deformation texture of Pd-Ag alloys. Pure palladium with a higher stacking fault energy than silver exhibits {111}/<112> texture. When the silver concentration is increased, {110}<112> texture gradually appears and {111}/<112> texture gradually disappears in Pd-Ag alloys. There is a large transition range between pure Pd and pure Ag.

- The recrystallization texture after 850^0C annealing is {113}<112> for palladium and {113}<110>/<581> for Pd$_{77}$Ag$_{23}$ respectively. When the silver concentration is increased, recrystallization texture has been changed.

Acknowledgments

One of the authors(Y. Cao) is grateful to the Natural Sciences and Engineering Research Council of Canada (NSERC) for the financial support in the form of a scholarship.

5 Reference

1. Savitskii, E. M. (1969) *Palladium Alloys*, Primary Sources Publishers, pp1-40
2. Lewis, F. A. (1996) *Int. J. Hydrogen Energy*, **216**, pp461-464
3. Armor, J. N. (1992) *CHEMTECH*, **9**, pp557-563
4. Mirzaev , D. A. et al., (1996) *The Physics of Metals and Metallography*, **82(5)**, pp553-560
5. Hu, H. et al, (1961), *J. Applied Physics*,**32(7)**, pp1392-1399
6. Murr, L. E. (1975) *Interfacical phenomena in metals and alloys*, Addsion-Wesley Publishing Co.,pp346-7
7. Rao, P. R. and Rao, K. K. (1968) *J. Appiled Physics*, **39**, pp4563-4568
8. Harris, I. R. et al, (1968) *Philosophical Magazine*, **14**, pp325-333
9. Schmid, E. and Boas, W. (1950) *Plasticity of Crystals*, pp299-300
10. Schmidt, W. and Lucke, K. (1979) *Texture of Cryst. Solids*, **3**, pp85-112

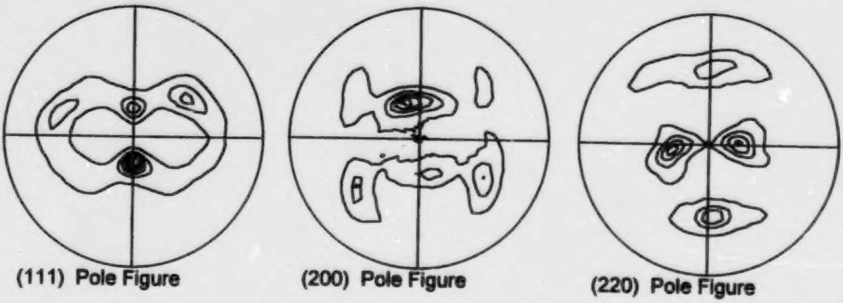
(111) Pole Figure (200) Pole Figure (220) Pole Figure

Contour Levels: 1, 3, 5, 7, 9, 11

Fig. 1 Pole figures of palladium after 82% deformation

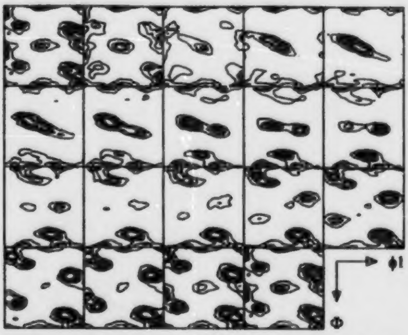

Contour Levels: 1.00 3.00 5.00 7.00 9.00 14.00

(a) 40%

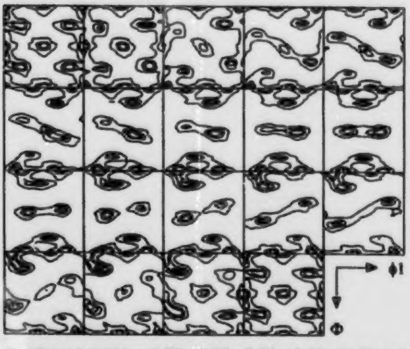

Contour Levels: 1.00 3.00 5.00 9.00 11.00 14.00

(b) 60%

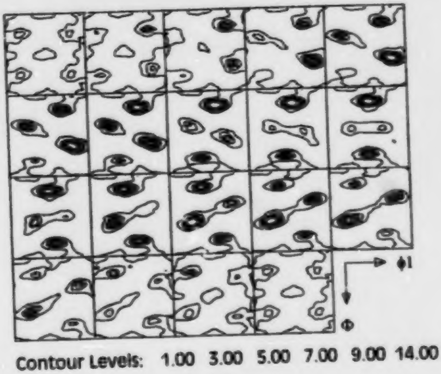

(c) 82%

Fig. 2 ODFs of palladium with different rolling reductions

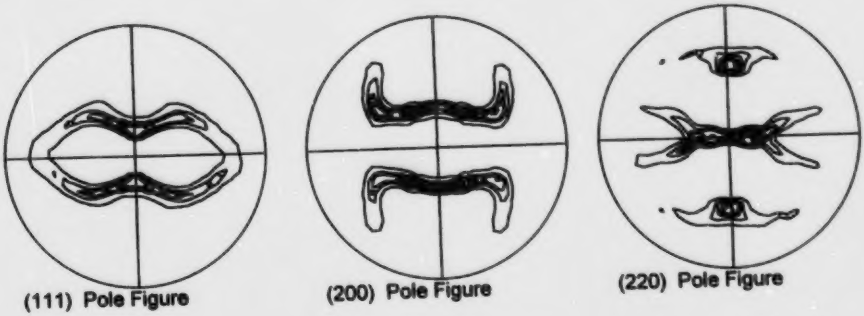

Contour Levels: 1, 3, 5, 7, 9, 11

Fig. 3 Pole figures of $Pd_{77}Ag_{23}$ after 80% deformation

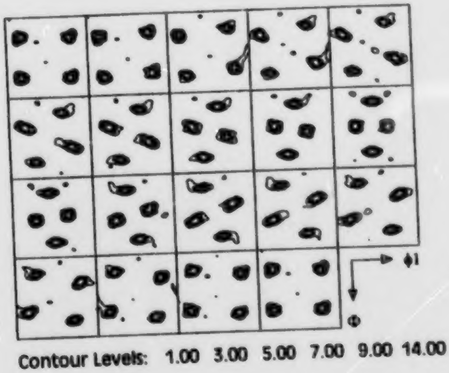

Fig. 4 ODFs of $Pd_{77}Ag_{23}$ after 80% rolling reductions

A SUGGESTION CONCERNING THE GENERATION OF RECRYSTALLIZATION NUCLEI DURING PLASTIC DEFORMATION[†]

U. F. Kocks and J. D. Embury
Center for Materials Science, Los Alamos National Laboratory, Los Alamos, NM, USA

Abstract

Differences in Taylor factor between different grains have been used to rationalize different recrystallization behavior in deformed polycrystals since Dillamore and Katoh. There may be an alternative of some similarity. The rate of orientation change (the 'lattice spin') in a grain is characterized by the anti-symmetric equivalent of the Taylor factor. It too is usually different from grain to grain, and the difference reflects itself in a change in the grain boundary misorientation – *if* the slip dislocations are absorbed into the boundary. Otherwise, a region of the appropriate misorientation will be generated along the boundaries. Such flat regions could, under certain circumstances, serve as nuclei for (dynamic or static) recrystallization.

1 Introduction

It is now widely agreed that nucleation proper (in the thermo-kinetic sense) does not exist in recrystallization; rather, the 'nuclei' that lead to successful growth of recrystallized grains must form during plastic deformation. In many cases, they are associated with shear bands, transition bands, etc. But recrystallization does occur in the absence of such macroscopic heterogeneities, for example, at low strains. The locations of successful beginnings of growth can then be associated with, among others, an advantage in stored-energy gradient or an advantage in misorientation; the former is intimately linked with the driving force for growth, the latter may be associated with an increase in grain boundary *mobility* [Solas et al. 1999],

---

[†] Work supported by the U.S. Department of Energy, Basic Energy Sciences

but it also represents a truly separate phenomenon. Any recovery processes that might precede recrystallization would hurt the former but help the latter in that they can lead to a sharpening of subboundaries and associated cleaning-up of subgrain interiors [Hasegawa and Kocks 1979]. Note that it is established that misorientations are in fact necessary for recrystallization; stored energy alone does not suffice [Martin, Doherty and Cantor 1997].

It has been common since Dillamore and Katoh [1974] to associate the locations of successful nuclei with grains of relatively high Taylor factor. The physical basis for this possible correlation will be reviewed. Then, a complementary principle will be introduced that attempts to locate regions of high misorientation that may be generated during deformation.

2 Stored-Energy Gradients

If the (tensor) strain rate $\dot{\boldsymbol{\varepsilon}}^c$ is prescribed for the grain (or crystal) c — or any region of given orientation — then the stress necessary in that region can be derived from the principle of maximum work [Bishop and Hill 1951] and it can be expressed in terms of the scale factor τ^c of the yield surface (the glide resistance of a reference slip system) by

$$\boldsymbol{\sigma}^c = \mathbf{M}\,\tau^c \tag{1}$$

where M is a tensor equivalent of the Taylor factor [Kocks, Tomé and Wenk 1998]. It follows from the principle of virtual work that the sum of the glide-shear rates in that region is

$$\Gamma = \mathbf{M} : \dot{\boldsymbol{\varepsilon}}^c \tag{2}$$

If now the Taylor hardening rule is applied:

$$\tau = f(\Gamma) \tag{3}$$

where Γ is the time integral of Eq. 2, it is seen that the stored energy, which is (at least to first order) proportional to τ^2, is proportional to M^2 when hardening is linear — and *independent* of M when hardening is saturated (as is approximately true at large strains.

Thus, if the Taylor model of polycrystal deformation is applied and $\dot{\boldsymbol{\varepsilon}}^c = \dot{\boldsymbol{\varepsilon}}$ (the polycrystal *average* strain rate), then indeed the stored energy is higher the higher the Taylor factor (although less so the higher the strain). But if regions that are harder (higher M) deform less than the average, as is often assumed to be somewhat more realistic than an exact Taylor model, then the correlation becomes weaker at the beginning *and may actually reverse at the end* of straining!

To the extent that the energy storage rate is correlated with the Taylor factor (positively or negatively), large driving forces for growth in recrystallization should be correlated with large local differences in Taylor factor.

3 Spin Gradients

The (tensor) Taylor factor **M** is the inverse of the (tensor) Schmid factor

$$\mathbf{m} \equiv \tfrac{1}{2}\,(\mathbf{b}\otimes\mathbf{n} + \mathbf{n}\otimes\mathbf{b}) \tag{4}$$

where **b** and **n** are the slip direction and slip plane normal, respectively, for a particular slip system (and the **m**'s are all the same at the **M**-vertex). Its antisymmetric equivalent

$$\mathbf{q} \equiv \tfrac{1}{2}\,(\mathbf{b}\otimes\mathbf{n} - \mathbf{n}\otimes\mathbf{b}) \tag{5}$$

describes the crystal spin and is (in combination with any 'rigid-body spin') responsible for the orientation change in the region [Kocks et al. 1998]. It is routinely calculated in all polycrystal plasticity simulations.

The suggestion is that local differences in this spin should be kept track of: they characterize the need for the generation of *misorientations* between adjacent regions. If the 'regions' are complete grains and all the dislocations that arrive at a grain boundary are absorbed into it, nothing new happens except a change in the misorientation angle at this (large-angle) grain boundary [Kocks et al. 1998, p.327]. But if the absorption of dislocations into the grain boundary is not perfect — for example, because of a large density of other dislocations in its neighborhood — then a new local misorientation develops. It may be spread over an area, in the manner of a tangled cell wall, but it could become a discrete new subboundary by local (dynamic or static) recovery. This, then, would constitute a mechanism for the generation of new boundaries, or the increase in misorientation of existing ones.

Note that the spin gradient can be perpendicular to the boundary, in which case a plate-like nucleus would develop parallel to the boundary; but it can also be parallel to the boundary, in which case a new boundary may develop perpendicular to the old one. This can even happen when the dislocations are absorbed into the boundary — before they spread out to make a uniform misorientation [Grabski and Korski 1970] — and further, this case may occur in co-deforming two-phase structures [Sinclair 1998].

4 Summary

Our main suggestion is that gradients in orientation change be watched in simulations of polycrystal plasticity and used to study any potential correlation with sites of recrystallization nuclei. In the simplest approximation, this can be done by calculating the total rotation angle per step in each grain and comparing this to the average: a large deviation flags the possibility of a likely nucleation site.. In simulations that include the grain location, one could study local differences in orientation change between neighbors and across particular boundaries. Finally, an overall estimate of nucleation probability can be obtained by merely following the *dispersion* of spins.

Large rotation gradients are expected to occur with preference in the immediate proximity of grain boundaries [Acharya and Beaudoin 1999] and, even more so, grain edges [Larson and Kocks 1963]. Careful experiments by orientation imaging microscopy on large-grained (preferably columnar) specimens could also shed light on the viability of this mechanism.

5 References

Acharya, A. and Beaudoin, A.J. (1999) Grain-size effect in fcc viscoplastic polycrystals at moderate strains. Submitted to *J.Mech.Phys.Sol.*

Bishop, J.F.W., and Hill, R. (1951) A theory of plastic distortion of a polycrystalline aggregate under combined stresses. *Philos. Mag.* Vol. 42, pp. 414-427.

Dillamore, I.L. and Katoh, H. (1974) The mechanisms of recrystallization in cubic metals with particular reference to their orientation dependence. *Metal. Sci.* Vol. 8, pp. 73-83.

Grabski, M.W. and Korski, R. (1970). *Philos. Mag.* Vol. 22, p. 707.

Hasegawa, Y. and Kocks, U.F. (1979) Thermal recovery processes in deformed aluminum. *Acta Metall.* Vol. 27, pp. 1705-1716.

Kocks, U.F., Tomé, C.N. and Wenk, H.-R., eds. (1998) *Texture and Anisotropy*, Cambridge University Press.

Larson, D.C. and Kocks, U.F. (1963) Discussion to "The influence of recovery on recrystallization in aluminum". *Recovery and Recrystallization of Metals*, L. Himmel, ed., Interscience

Martin, J.W., Doherty, R.D. and Cantor, B. (1997) *Stability of microstructure in metallic systems*, Cambridge University Press.

Sinclair, C.W. (1998) *priv. comm.*, McMaster Univ., Hamilton, Ont., Canada.

Solas, D.E., Tomé, C.N., Engler, O. and Wenk, H.-R. (1999) A coupled Monte Carlo and N-site self-consistent approach to model static recrystallization. To appear in Proc. *Recrystallization'99* (Japan).

INFLUENCE OF GRAIN SIZE AND RETAINED ATOMS ON THE RECRYSTALLIZATION TEXTURE IN DEEP DRAWING STEEL

H. REN, D. TANG, Z. SUN and W. MAO
University of Science and Technology Beijing, Beijing, China

Abstract

The influence of grain size and the retained atoms on recrystallization texture in deep drawing steel sheets taken from commercial products was analyzed. The texture evolution is very sensitive to the retained atoms. The {111} fiber texture has been drastically reduced in the steel sheet with higher retained element content. The processing parameters of the deep drawing steel sheets will mainly determine the grain size distribution and corresponding strength level, which will also influence the texture development in certain extent. The behavior of retained atoms and their influence on the texture evolution and mechanical properties are discussed.

Keywords: Deep drawing steel, grain size, recrystallization texture, retained atoms

1 Introduction

It is well known that both the grain size and retained atoms in solid solution could strengthen the steel sheets for deep drawing. However they have different influence on the draw-ability of the steels. It is commonly accepted that the yield strength would be reduced with increasing grain size, but the draw-ability i.e. the Lankford parameter or r value could be improved in certain extent simultaneously before the formation of equiaxial grains (Yang et al. 1995) while the {111} fiber texture becomes stronger during the initial stage of the grain growth process after the primary recrystallization (Mao et al. 1995). On the other hand the retained atoms will impede the formation or strengthening of {111} fiber texture and reduce the r value, therefore for extra deep drawing steels an interstitial free (Takechi 1994) and highly pure matrix is needed (Ushioda et al. 1994). For a common deep drawing steel a balance between strength and draw-ability is often requested without using any special alloy elements. In this case the control of grain size and retained atoms would be very important for the property adjustment.

2 Experiment

Three different deep drawing steel sheets with 0.5 mm thickness were taken from steel market, which are shown here as steel no. 1, 2 and 3. The contents of carbon and main retained atoms were analyzed. The microstructure was observed in the optical microscope and the grain size was statistically counted and calculated. The {110}, {200} and {112} pole figures were measured in the center and surface layers of the sheets and the corresponding ODFs were calculated using the Bunge methods (Bunge 1981). The tensile properties of the sheets were also measured, in which the r values were taken at 10%, 15% and 20% elongation respectively.

3 Results

Table 1 gives the chemical composition of the sheets. It could be seen that with increasing steel number the contents of C, Mn and Si become slightly higher, while the P and S keep roughly the same levels in consideration that the content differences have no obvious influence on the mechanical properties. Though no drastic composition change was observed the mechanical properties of the three steels are quite different (table 2), which are not simply relative to the chemical composition, but also to the microstructure of the sheets.

Table 1 Composition analysis (wt. %)

No.	C	Mn	Si	S	P
1	0.043	0.11	0.010	0.011	0.016
2	0.048	0.12	0.013	0.007	0.016
3	0.056	0.22	0.021	0.012	0.016

Table 2 Mechanical properties

No.	YS (MPa)	TS (MPa)	El (%)	r_0 (10%)	r_0 (15%)	r_0 (20%)
1	271.0	360.7	37.5	1.54	1.53	1.55
2	342.3	402.3	40.4	1.48	1.47	1.48
3	321.0	383.0	37.8	1.16	1.17	1.21

Figure 1 gives the corresponding statistical grain size distributions. The average grain size of steel 1, 2 and 3 is 14.78 μm, 8.66 μm and 11.53 μm respectively.

Figure 2-4 demonstrate the ODF sections of the three steel sheets in the center layer and surface layer. There is no very obvious shear texture in the surface layer. Also no strong texture difference can be observed between surface and center layers. However the general texture characters are quite different in the three steels (fig. 2-4), which can be observed better in the texture fiber analysis (fig. 5-6). Steel 1 has the strongest γ fiber texture, while a relative strong α fiber texture and low orientation density in γ-fiber remain in steel 3, which should have special influence on the r value (Hutchinson 1984).

a. steel no. 1

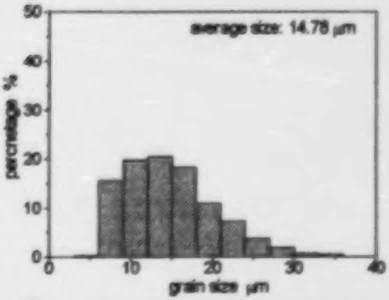

b. steel no. 2

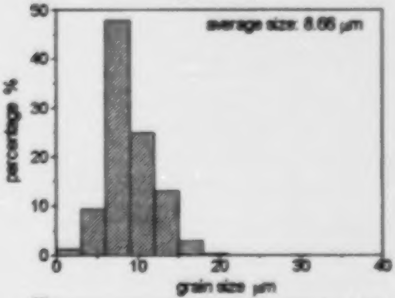

c. steel no. 3

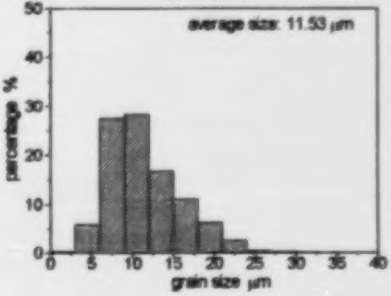

Fig. 1 Grain size distribution

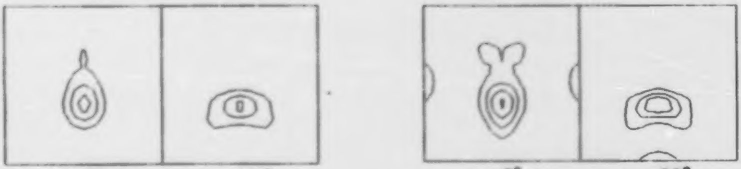

φ_1=0°, φ_1=90°,
a. center texture (Max.=7.0)

φ_1=0°, φ_1=90°,
b. surface texture (Max.=8.9)

Fig. 2 Texture in steel 1 (density levels: 2, 4, 6, 8)

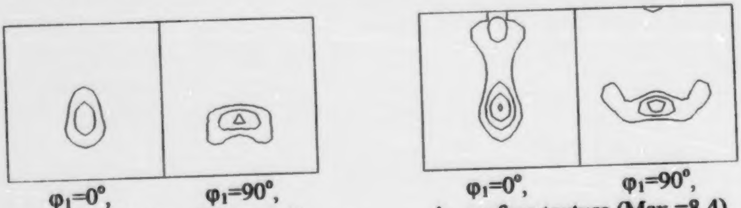

a. center texture (Max.=7.1)

b. surface texture (Max.=8.4)

Fig. 3 Texture in steel 2 (density levels: 2, 4, 6, 8)

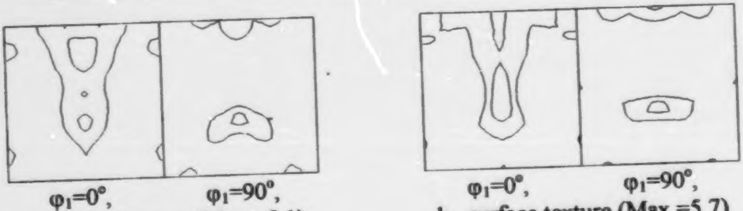

a. center texture (Max.=5.1)

b. surface texture (Max.=5.7)

Fig. 4 Texture in steel 3 (density levels: 2, 4)

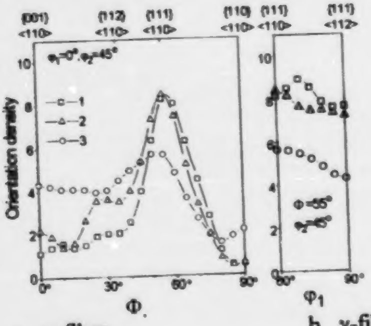

a. α-fiber,

b. γ-fiber

Fig. 5 Surface texture

4 Discussion

According to table 2 and fig. 1, the steel strength is predominantly determined by the grain size. The C, Mn and Si atoms in solid solution should also have certain strengthening effects, but the content differences are so low among the steels(table 1) that the no obvious difference of element strengthening effect can be observed. Therefore the steel 3 do not has the highest strength level in spite of its highest C, Mn and Si content. The relationship can be summarized in fig. 7a, which indicates that the grain refinement is induced not mainly by the retained atoms but by the steel processing technology.

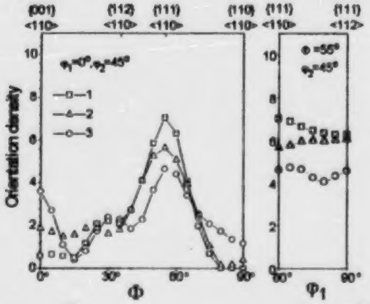

a. α-fiber, b. γ-fiber

Fig. 6 Centure texture

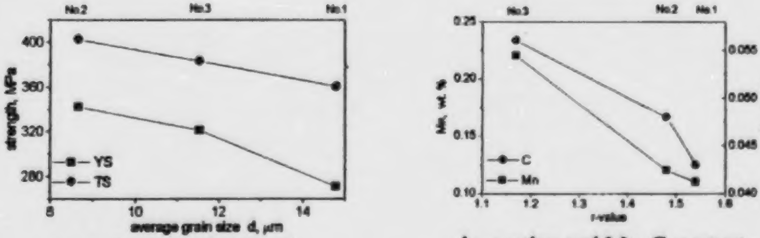

a. grain size and strength b. r value and Mn, C content

Fig. 7 Influence of grain size and retained atoms

However the retained elements can reduced the draw-ability i.e. r value, which is shown in fig. 7b. As interstitial atoms, carbon will impede the formation of {111}//ND fiber texture and therefore reduce the r value (Takechi 1994). The other retained elements e.g. Mn could have the similar effect (Yoda et al. 1994). It was reported (Ushioda et al. 1994), that Mn would retard the primary recrystallization as well as the following grain growth, which tends to result in a finer grained structure after the final industrial annealing treatment. In interstitial free steels the substructure oriented around {111}//ND remains after cold rolling because of the high purity of deformed matrix and the practical stability of its orientation (Kern 1986). This substructure has obvious advantages to be recovered at first and become the recrystallization nuclei during annealing (Mao et al. 1995). Therefore the recrystallization grains oriented around {111}//ND should grow preferably because of their relative larger size, which leads to the strengthening of {111}//ND fiber texture and the increase of r value at initial grain growth stage after primary recrystallization (Yang et al. 1995).

It can be seen in fig. 4 that a texture very similar to rolling texture has been obtained in steel 3 with the highest retained atoms after the recrystallization annealing.

This tendency is drastically reduced in steel 2 (fig. 3), and can not be observed in steel 1 with lowest retained atoms(fig. 2). It is believed that the retained atoms will impede the grain boundary migration and therefore a greater part of the deformed matrix will be recrystallized by means of oriented nucleation or recrystallization in situ.

5 Summary

The strengthening effect of grain size reduction, induced by processing parameter control and retained atoms, is much stronger than the solid solution strengthening of the retained atoms in deep drawing steel sheets. A slight increase of retained element could induce an obvious reduction of {111}//ND texture as well as the r value, since the recrystallization mechanism will be changed, which will impede the formation of {111}//ND fiber texture during rolling and recrystallization.

6 References

Bunge, H.J. (1981) General outline and series expansion method, in *Quantitative Texture Analysis*, (ed. H.J. Bunge and C. Esling), DGM-Informationsgesellschaft, Oberursel, pp. 1-72.

Hutchinson, W.B., (1984) Development and control of annealing texture in low-carbon steels, *Metal Science*, Vol. 29, No. 1. pp. 25-42.

Kern, R., Lee, H.P. and Bunge, H.J., (1986) The rolling texture of iron of different purities, *Steel Research*, Vol. 57, No. 11. pp. 563-571.

Mao, W., Wang, X., Zhang, S. and Kong, B., (1995) Formation of annealing texture in rolling IF steel sheet, HSLA Steels'95, conf. proc.(ed. G. Liu et al), China Sci. & Tech. Press, Beijing, pp.175-178.

Takechi, H., (1994) Metallurgical aspects on interstitial free sheet steel from industrial viewpoints, *ISIJ Inter.*, Vol. 34, No. 1. pp. 1-8.

Ushioda, K., Yoshinaga, N. and Akisue, O., (1994) Influence of Mn on recrystallization behavior and annealing texture formation in ultralow-carbon and low-carbon steels, *ISIJ Inter.*, Vol. 34, No. 1. pp. 85-91.

Yang, D., Wang, X., Mao, W. and Zhang, Z., (1995) Influence of microstructure of extra-deep drawing IF steel sheet on its mechanical properties, *Iron and Steel (Gang-Tie)*, Vol. 30, No. 1. pp. 60-62.

Yoda, R., Tsukatani, I. and Inoue, T., (1994) Effect of chemical composition on recrystallization behavior and r-value in Ti-added ultra low carbon sheet steel, *ISIJ Inter.*, Vol. 34. No. 1, pp. 70-76.

RECRYSTALLISED COLD ROLLED NICKEL AND NICKEL-ALLOYS WITH A STRONG CUBE TEXTURE

B. DE BOER, N. REGER, R. OPITZ, J. EICKEMEYER, B. HOLZAPFEL, and L. SCHULTZ
Institute of Solid State and Materials Research Dresden, Institute of Metallic Materials, Dresden, Germany

Abstract

Cube textured Ni tapes are useful substrates for the epitaxial deposition of long lengths of High Temperature Superconductor (HTS). Such Ni tapes with a thickness of 100µm were produced by rolling and recrystallisation. The texture of the tapes was optimized in order to prevent misoriented grains and high angle grain boundaries, especially at the sheet surface which would reduce the HTS-properties. Disadvantages of Ni as a substrate material for HTS are its ferromagnetism, and its low tensile strength. Both disadvantages were counteracted by alloying. Ni alloys with ferromagnetic Curie temperatures below 77 K and which exhibit an enhanced hardness in comparison to Ni and also form a sharp cube texture after rolling and annealing were found.

Keywords: Cube texture, EBSD, nickel, nickel-alloys, recrystallisation, substrate for HTS

1 Introduction

An interesting approach for the profitable production of long high temperature superconducting $YBa_2Cu_3O_{7-\delta}$ tapes which are suitable for carrying heavy currents in magnetic fields is the Rolling Assisted Biaxially Textured Substrates (RABiTS) method developed at the Oak Ridge National Lab (Goyal et al. 1996). By this method $YBa_2Cu_3O_{7-\delta}$-films are grown epitaxially on cold rolled and recrystallised Ni tapes having a strong cube texture. The texture of the Ni tape plays an important role because the grain boundaries of the substrate are carried into the $YBa_2Cu_3O_{7-\delta}$ film by the epitaxial growth, and the ability of $YBa_2Cu_3O_{7-\delta}$ to carry heavy currents depends strongly on its grain boundaries - high angle grain boundaries act as so called "weak-links" and lead to a reduction in the critical current (Dimos et al. 1990). This means that a tape with a very strong cube textured surface and as few misoriented grains as possible, is required as substrate. For this reason one aim of this contribution is to optimize the cube texture.

The other aim is related to disadvantageous intrinsic properties of the substrate material. The first is the ferromagnetism which leads to magnetization losses in the tape and the second the low tensile strength of Ni which is limits the possibility of producing the very thin foils that are desirable for high technical current densities (current density of the superconductor related to the whole cross-section of the tape). Both disadvantages can be overcome by the use of Ni-based alloyed substrates. On the other hand alloying may prevent the formation of the cube texture. For this reason several Ni-alloys with reduced ferromagnetic Curie temperatures were investigated according to their ability to form a strong cube texture and to their tensile strength that can be estimated by hardness measurements.

2 Experimental

Two preparation methods were employed. Pure Ni and alloyed samples for the texture optimization were first molten in an induction furnace and then cooled in a cylindrically shaped mould having a diameter of 32 mm. The resulting 15 cm long rod was hot rolled at decreasing temperatures between 1100°C and 1000°C into a square shaped rod with 22 mm edges. Afterwards, the damaged and oxidized surfaces were removed to get a smooth surface for regular cold rolling. The cold rolling was performed with several passes by which the thickness was reduced from 20 mm to the final thickness of 0.1 mm. The recrystallisation temperature was varied between 500°C and 1100°C in a mixed atmosphere of N_2 and H_2.

The other preparation method was used in the search for suitable Ni-alloys. In this case 10 g pellets were molten in an arc melting furnace. These pellets were cast into a cylindrical copper mold having a diameter of 4 mm and a length of about 50 mm. Afterwards these small rods were cold rolled to 0.1 mm tapes. Because of the small dimensions, broadening to 10 mm during rolling could not be avoided. These tapes were also recrystallised at different temperatures.

Samples prepared by these methods were investigated both by x-ray texture analysis and by (Electron Back Scattering Diffraction (EBSD) mappings. For the x-ray texture analysis the three pole figures {111}, {200}, and {220} between 0° and 70° were measured to calculate the orientation distribution function (ODF) which is a quantitative measure for the texture. The EBSD mappings give clear evidence of the texture quality – in this case grains with increasing deviation from the exact cube orientation are depicted by a grayscale of decreasing brightness. Furthermore the misorientation distributions were calculated, from which a direct insight into the suitability of the tape's texture is given.

The Vickers microhardness HV 0.2 of 100 µm tapes is measured both to estimate the strength of the tapes and to find the recrystallisation temperature. The load of 200 g for the indentations was chosen because this is the maximum load for which the influence of the sample holder on the result is negligeble.

3 Results

3.1 Texture improvement in Ni tapes

An EBSD map of a Ni tape recrystallised at 550°C is shown in fig. 1a). It shows more than 30% highly misoriented grains, mostly arranged in clusters that are elongated in the rolling direction. The misoriented grains are usually smaller than the cube textured. The fraction of misoriented grains can be reduced either by gently polishing the surface with a velvet coated grinding disk before the recrystallisation or by an annealing treatment that is conducted with a slow heating rate of 5 K/min to 550°C (fig. 1b,c). Both results confirm that misoriented grains nucleate preferably at the sheet surface due to inhomogeneities caused by the surface of the rollers. If the specimen is put into the hot furnace (fast heating rate) a lot of misoriented grains can nucleate at the surface before the cube oriented grains grow into the surface region. By polishing, the nucleation sites at the surface are partly removed.

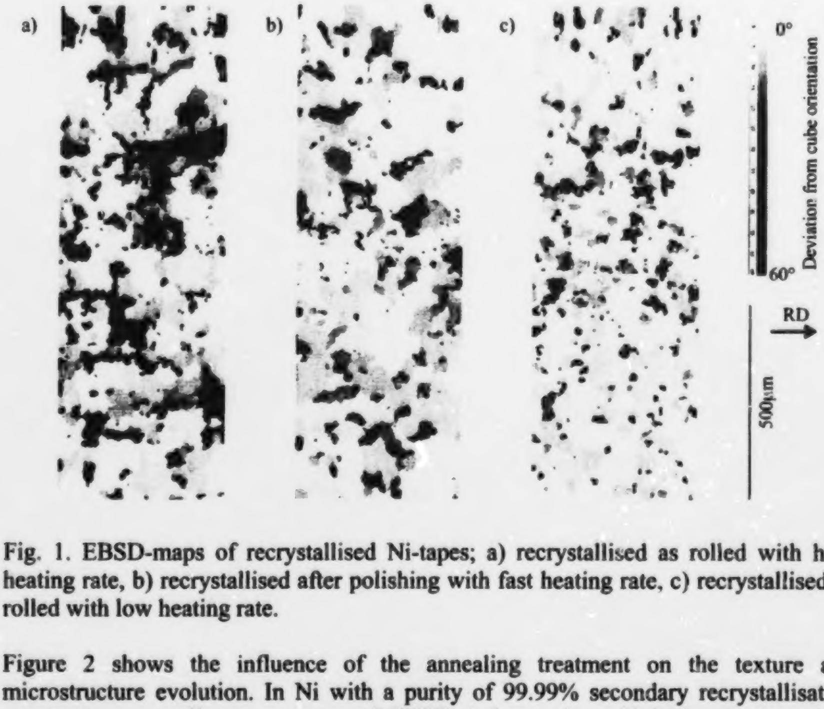

Fig. 1. EBSD-maps of recrystallised Ni-tapes; a) recrystallised as rolled with high heating rate, b) recrystallised after polishing with fast heating rate, c) recrystallised as rolled with low heating rate.

Figure 2 shows the influence of the annealing treatment on the texture and microstructure evolution. In Ni with a purity of 99.99% secondary recrystallisation occurs at an annealing temperature of 600°C. A few grains with high misorientations to the cube textured matrix grow and reach sizes of about 1 mm. These grains are randomly oriented, with no cube orientation. Alloying the same Ni with 0.1 at.% Mo prevents secondary recrystallisation. In this case the misoriented grains disappear due to normal grain growth. All grains remaining after an annealing at 1100°C are misoriented less than 10° from the exact cube orientation (FWHM≤10°). The development of the grain boundary distribution on the misorientation angles shows that the fraction of low angle grain boundaries is increasing and the fraction of high angle grain boundaries (including twin boundaries) is decreasing continually with increasing annealing temperature (fig. 3).

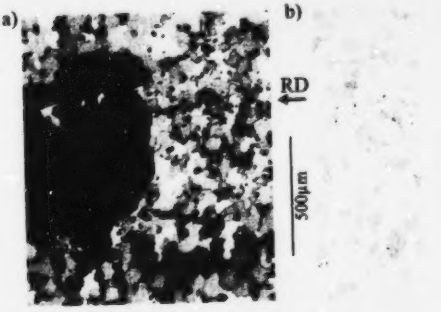

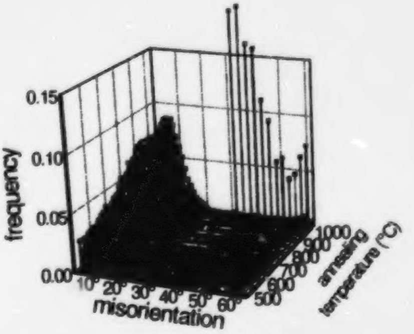

Fig. 2. a) secondary recrystallisation in pure Ni after annealing at 600°C, b) EBSD-mapping of Ni-0.1at.%Mo after annealing at 1100°C

Fig. 3. development of grain boundary misorientations

3.2 Preselection of Ni-alloys

Figure 4 shows the influence of alloying elements on the ferromagnetic Curie temperature. Powerful elements are V, Cr, Si, Al, and Ti within the solubility region, though the solubilities of Ti, Al, and Si are not high enough to reach the Curie temperature of 77 K. Different Ni-alloys with these alloying elements were prepared according to the preparation method of the 10 g pellets. Also Ni-Cu alloys with 33%, 50%, and 67% Cu were prepared because Cu and Ni are completely soluble into each other, the Curie temperature of Ni with more than 55% Cu is lower than 77K, and both Ni and Cu form a strong cube texture. It is expected that the sharpness of the texture is lower compared to the samples prepared by the first procedure because the rolling deformation is worse (the tape broadens) and the degree of deformation is less (97.5% compared to 99.5%), but the differences between the samples as well as the fact if the cube texture is formed in the alloys can be measured.

The results of the x-ray texture analysis are presented in fig. 5. Here the ODF intensity of the cube texture component of each alloy after recrystallisation at 900°C is plotted against the fraction of the alloying element expressed as a percentage of the maximum solubility. It is recognized that in general the intensity of the cube component decreases with increasing alloying. Exceptions are observed in Ni-Cr and the completely soluble system Ni-Cu. According to these results, non magnetic alloys which form the cube texture after recrystallisation are Ni-V, Ni-Cr, and Ni-Cu.

3.3 Texture improvement in alloyed tapes

Tapes of the aforementioned alloys were prepared according to the first preparation method. The annealing temperature was varied between 400°C and 1100°C. Fig. 6 shows the temperature dependence of the Vickers hardness of the non magnetic alloys Ni-13at.%Cr and Ni-9at.%V compared with Ni-0.1at.%Mo. It can be seen that both Ni-13at.%Cr and Ni-9at.%V exhibit the same behaviour. The drop in hardness marks the recrystallisation temperature which is increased from 350°C to 550°C. Furthermore the HV 0.2 value of both alloys is almost twice the value of Ni-0.1at.%Mo. This finding can be attributed to solution hardening.

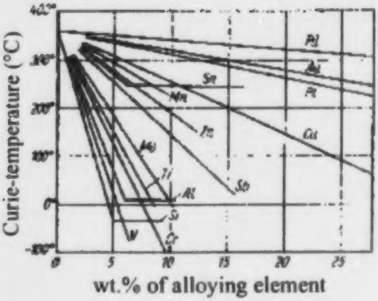

Fig. 4. Dependence of the Curie-temperature on the alloying content of several Ni-alloys (Gmelin 1959)

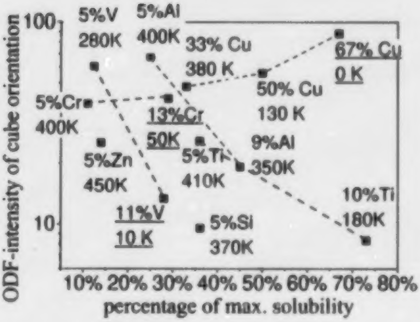

Fig. 5. Influence of the alloying content on the formation of the cube texture.

The x-ray texture measurements on the alloys also reveal strong cube textures. In Ni-Cr the cube intensity reaches its maximum after annealing at 900°C ($ODF_{max}=150$). At higher annealing temperatures, secondary recrystallisation destroys the cube texture. The EBSD-mapping of the microstructure of the 900°C sample is shown in fig. 7a). The dark almost circular grain in the lower part of the microstructure that is clearly larger than the grains of the environment indicates the onset of secondary recrystallisation. In the Ni-V alloy, the strongest cube texture occurs after annealing at the highest temperature (1100°C) because secondary recrystallisation does not take place. Its EBSD-microstructure (fig. 7b) reveals that the texture is comparable with that of the Ni-0.1at.%Mo sample.

The Ni-Cu alloys also develop sharp cube textures comparable to that of Ni-0.1%Mo, although the first, hot deformation at the beginning of the preparation procedure is not feasible due to embrittlement during hot rolling. In this case instead of hot rolling, the homogenisation was performed by cold rolling and subsequent static recrystallisation. The final cold rolling was like that of the other samples. The hardness of these tapes annealed at 900°C is only about 10% higher than that of pure Ni.

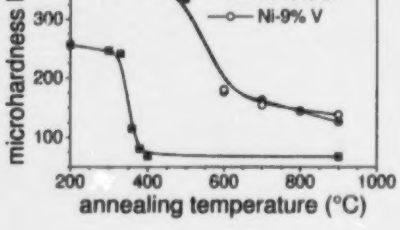

Fig. 6. The hardness of the alloyed tapes after different annealing temperatures compared with pure Ni.

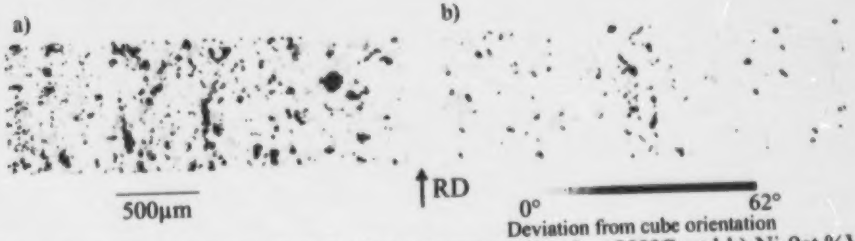

Fig. 7. Orientation maps of a) Ni-13at.%Cr recrystallised at 900°C and b) Ni-9at.%V recrystallised at 1100°C.

4 Summary

Tapes of pure Ni (purity 99.99%) exhibit a strong cube texture after cold rolling and annealing at temperatures up to 550°C. At higher temperatures this texture becomes unstable due to secondary recrystallisation. This can be prevented by alloying Ni with 0.1% Mo. In this case the sharpness of the texture increases with increasing annealing temperatures due to normal grain growth of the cube oriented grains. EBSD mappings reveal that no grains larger than 20° remain in the microstructure after annealing at 1100°C for 1 hour. The fact that almost all adjacent grains are misoriented by less than 15° to each other makes this tape suitable as a substrate for HTS.

Also, non-magnetic Ni-alloys which develop a strong cube texture were found. A necessary condition for the alloying element is a high solubility in Ni. It was found that Ni-9at.%V and Ni-13at.%Cr possess the required properties of a Curie temperature lower than 77K and a significantly increased hardness compared to pure Ni that is important for the preparation of thinner tapes. Especially, the texture of Ni-9at.%V reaches the quality of the Ni-0.1at.%Mo texture. Another non-magnetic alloy is Ni-Cu, but with this alloy, no solution hardening is observed.

Acknowledgement

The authors want to thank the Federal Ministry of Education, Science, Research, and Technology, Germany for financial support.

References

D. Dimos and P. Chaudhari, Phys. Rev. B41 (1990) 4038.
A. Goyal et al., Appl. Phys. Lett. **69** (1996) 1795.
Gmelins Handbuch der anorganischen Chemie, ed. E. J. Meyer, E. H. Pietsch, Verlag Chemie GmbH, Weinheim, 1959, p. 272.

THE EVOLUTION OF DEFORMATION AND RECRYSTALLIZATION TEXTURES OF CROSS ROLLED COPPER SHEETS

S. – H. Hong[1], N. – J. Park[2] and D. N. Lee[1]
[1]Division of Materials Science and Engineering, Seoul National University, San 56-1, Shinrim-dong, Kwanak-gu, Seoul 151-742 Korea
[2]Department of Materials Science and Engineering, Kumoh National University, 188 Shinpyung-dong, Kumi 730-701 Korea

Abstract

A study has been made of the deformation and recrystallization textures of cross rolled copper sheets. Cross rolling of 10 mm thick 99.99 pct. copper sheets was carried out by rotating the rolling direction through 90° about the rolling plane normal with lubrication. The specimen was annealed at 450°C for 1hr in a salt bath after 96 pct. rolling reduction. The {110}<557> orientation developed as a major component in the center layer and the {110}<557> and {001}<100> orientation was found in the surface layer of cross rolled copper sheet. The recrystallization texture components of the center layer of a heavily cross rolled copper sheet was approximated by the $(86\,50\,9)[10\,\overline{34}\,94]$ texture. The evolution of the recrystallization texture was discussed based on the strain energy release maximization theory advanced by one of the present authors (DNL).

Keywords: Cross rolling, strain energy release maximization theory, recrystallization texture

1 Introduction

A subject that has a major dispute for over 50 years has been the origin of the strong recrystallization textures often found after heavy deformation. Recently one of the present authors proposed a model for the evolution of primary recrystallization texture (Lee 1995). In this model, the absolute maximum internal stress direction of a deformed or fabricated material is parallel to the minimum elastic modulus direction of recrystallized grain, whereby the strain energy release can be maximized. This concept originates from the presumption that the stored energy due to dislocations is a major driving force for recrystallization. This energy release maximization theory could explain many well known recrystallization textures (e.g. Hong et al. 1997; Park et al. 1997; Choi et al. 1997).

2 Experiment

A billet forged after melting and casting of electrolytic copper was used as a starting material. A 20 mm thick billet was cut from the billet and annealed at 600°C for 12 hours. The specimen was forged to 10 mm in thickness and annealed at 450°C for 30 minutes in a salt bath. This specimen was cross rolled by a thickness reduction of 96 pct. at room temperature with a laboratory mill having 127mm diameter rolls. The rolling direction was rotated by 90° about the rolling plane normal each pass (RD1→ RD2→ -RD1→ -RD2 in Fig.1). The final rolling direction was always the transverse direction, -RD2. The rolling schedule is listed in Table 1. Chemical etching after mechanical grinding was carried out to measure the center layer of specimen. Data from {111}, {200}, and {220} incomplete pole figures were used to calculate the three dimensional orientation distribution functions (ODFs) using the series expansion method ($l_{max} = 23$) proposed by Bunge (1982).

3 RESULTS and DISCUSSION

3.1 Deformation Textures

The deformation texture of a cross rolled specimen was different from that of a plane strain rolled specimen. The ODFs of the surface and the center layer of cross rolled copper sheet were represented in the Fig. 2. The former can be approximated by the {110}<557> orientation : (ϕ_1, Φ, ϕ_2) = (45, 45, 0). The latter was characterized as the mixtures of {110}<557> as a main component and {001}<100> as a minor one. The early works indicated that the texture of the cross rolled copper specimen was characterized by the {110}<223> orientation as a main component (Merlini and Beck 1953; Suet To et al. 1994) and {001}<100> orientation as a minor component (Öztürk 1988).

The crystal plasticity model adopted in the present work is based on the rate-sensitive slip in the {111}<110> systems of a FCC metal (Canova and Kocks 1984). It is expressed by a power law relationship between the rate sensitive shear rate $\dot{\gamma}_s$, and the resolved shear stress τ_s.

$$\tau_s = \tau_0 (\dot{\gamma}_s / \dot{\gamma}_0) |\dot{\gamma}_s / \dot{\gamma}_0|^{m-1} \qquad (1)$$

Table 1. Rolling schedule

Initial	Final	Reduction/pass
10.00mm	4.00mm	0.30mm/pass
4.00mm	0.80mm	0.20mm/pass
0.80mm	0.40mm	0.10mm/pass

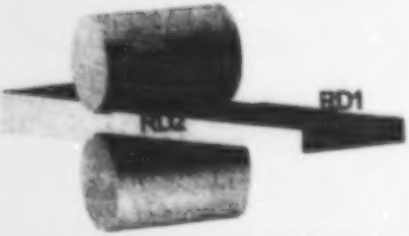

Fig.1 A schematic diagram for cross rolling

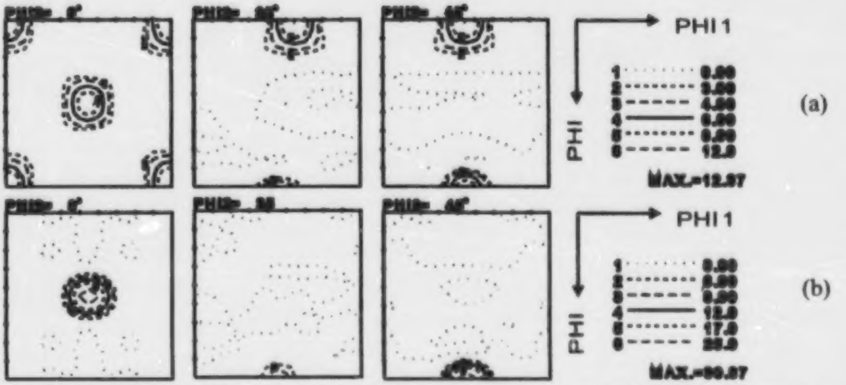

Fig. 2. ODFs of 96 pct. cross rolled copper sheet ($\phi_2 = 0°, 35°, 45°$, respectively) (a) surface layer (b) center layer

where the strain rate sensitivity index m, the reference shear stress τ_0 and the reference shear strain rate $\dot{\gamma}_0$ were assumed to be constant and equal for all slip systems in this simulation. The simulation was carried out with randomly distributed 978 grains as the initial condition. The strain increment of each step was 0.1. Calculation was ended after 32 steps, that is, the total true strain was 3.2. The calculated ODF is shown in the Fig. 3. The {011}<755> component was well predicted, but the cube component of the surface layer could not be predicted on the basis of this method.

3.2 Recrystallization Textures

The recrystallization texture of the 96 pct. cross rolled copper sheet is shown in Fig. 4. The recrystallization texture of the surface layer of cross rolled sheet can be approximated by the $(86\ 50\ 9)[10\ \overline{34}\ 94]$ orientation and the cube orientation (Fig. 4.-(a)), and that of center layer can be approximated by the $(86\ 50\ 9)[10\ \overline{34}\ 94]$ ($\equiv (\phi_1, \Phi, \phi_2) = (70°, 85°, 60°)$) orientation (Fig. 4-(b)). This result is similar to early data in which the main component was {519}<4 11 1> (Merlini and Beck 1953; Suet To et al. 1994) or weak cube component and its twin components (Öztürk 1988).

The present recrystallization texture is discussed based on the strain energy release maximization theory in the following. The active slip systems and the shear strain increments on them during cross rolling of the $(011)[7\bar{5}5]$ crystal were calculated by the strain rate sensitivity model. The results are given in Table 2. If the

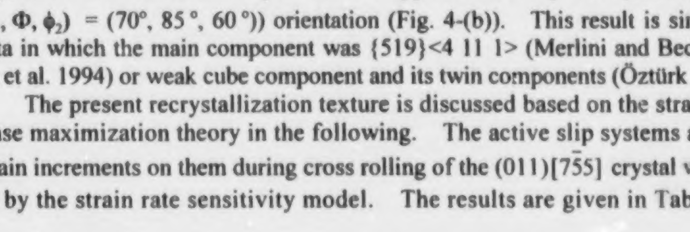

Fig. 3. ODFs of simulated 96 pct. cross rolled copper ($\phi_2 = 0°, 35°, 45°$, respectively)

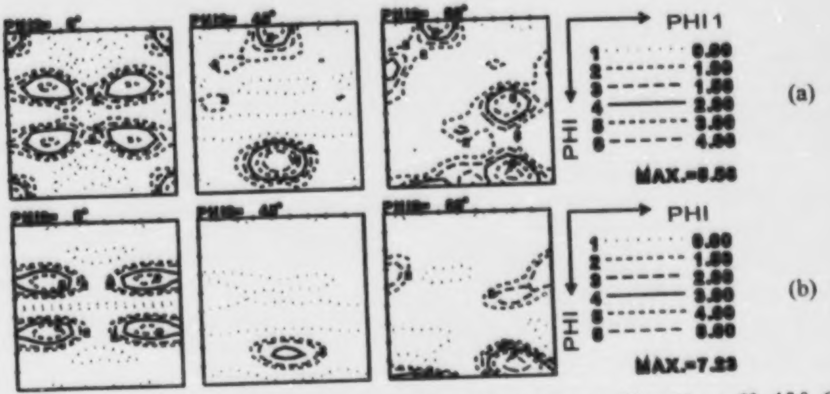

Fig. 4. ODFs of recrystallized copper after 96 pct. cross rolling (ϕ_2 = 0°, 45°, 60°, respectively) (a) surface layer (b) center layer

stored energy is proportional to the shear strain on each slip system, the maximum principal internal stress directions can be calculated by the vector sum of relevant slip directions multiplied by their shear strains. In even–th rolling, the maximum internal stress direction would be [0.121145, 0.179019, 0.057874], which could be calculated by adding the major slip directions of [110] and $[10\bar{1}]$ multiplied by their shear strains considering slip geometry.

The another maximum internal stress direction would be [0.236977, -0.058019, 0.178958], which was calculated for the major slip systems of $[1\bar{1}0]$ and [101] and their shear strains in odd-th pass by the same procedure as in even-th rolling. The two different rolling direction may interact each other. One possible net maximum internal stress direction would be calculated by adding the two maximum internal stress directions, that is, [0.121145, 0.179019, 0.057874] + [0.236977, -0.058019, 0.178958] = [0.358122, 0.121000, 0.236832]. This direction will become parallel to one of the

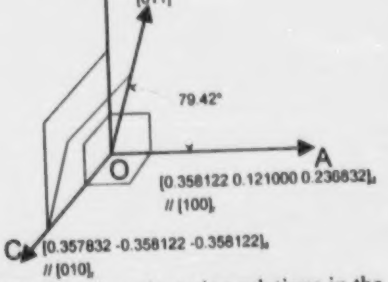
$[-0.041482\ -0.212998\ 0.171549]_d$
$// [001]_r$
B
[011]
79.42°
O
A
$[0.358122\ 0.121000\ 0.236832]_d$
$// [100]_r$
C
$[0.357832\ -0.358122\ -0.358122]_d$
$// [010]_r$

Fig. 5 The orientation relations in the deformed and recrystallized state d: deformed, r:recrystallized state.

Table 2. Active slip systems during cross rolling

Active Slip Systems	Shear strain increments	
	Odd-th	Even-th
$(\bar{1}11)[110]$	-0.003986	-0.118446
$(1\bar{1}1)[110]$	-0.001792	-0.060572
$(111)[1\bar{1}0]$	0.118489	0.004028
$(11\bar{1})[1\bar{1}0]$	-0.060470	-0.001816
$(\bar{1}11)[101]$	-0.118489	-0.004028
$(11\bar{1})[101]$	-0.060470	-0.001816
$(111)[10\bar{1}]$	0.003986	0.118446
$(1\bar{1}1)[10\bar{1}]$	-0.001792	-0.060572

<100> directions, the minimum Young's modulus direction of copper, after recrystallization according to the strain energy release maximization model.

Another orientation relationship between the matrix and recrystallized grain is obtained in the following. If the absolute maximum internal stress direction in the deformed state becomes parallel to one of the <100> directions in the recrystallized state, another <100> direction in the recrystallized state which is normal to the previous <100> will tend to be parallel to a direction which is at the smallest possible angle with another high stress direction in the deformed state. Possible candidates of the high stress direction must be two Burgers vector directions, [011] and $[01\bar{1}]$. The angle between absolute maximum internal stress direction and these directions are 55.44° and 79.42°, respectively. The $[01\bar{1}]$ direction is the closest to but less than the right angle with the maximum internal stress direction. The direction which is at the smallest possible angle with the $[01\bar{1}]$ and normal to the net maximum internal stress direction (OA in Fig. 5) at the same time must be on a plane made of the $[01\bar{1}]$ direction and the direction OA. The direction is shown as OB in Fig. 5. The direction OB must be normal to both the plane normal (OC in Fig. 5) and the direction OA. The direction OC is obtained by the vector product of the $[01\bar{1}]$ and the net maximum internal stress direction. The direction OB is obtained by the vector product of the directions OC and OA. The directions of OC and OB become the [0.357832, -0.358122, -0.358122] and [-0.041482, -0.21299 8, 0.171549] directions, respectively. In summary, the [0.358122, 0.121000, 0.236832], [0.357832, -0.358122, -0.358122] and [-0.041482, -0.21299 8, 0.171549] directions, which are normal to each other, will become parallel to the <100> directions after recrystallization.

If the unit vectors along the [0.358122, 0.121000, 0.236832], [0.357832, -0.358122, -0.358122] and [-0.041482, -0.21299 8, 0.171549] directions are set to parallel to [100], [010] and [001] directions after recrystallization, components of unit vectors are direction cosines relating the deformed and recrystallized crystal coordinate axes. Therefore, the rolling plane normal direction, [011], and the rolling direction, $[7\bar{5}5]$, in the deformed crystal coordinate system can be transformed to the expressions in the recrystallized crystal coordinate system. The calculated result means that crystal (0.000000 0.7107107 0.7107107)[0.703526 –0.502519 0.502519] transforms to the recrystallization texture (0.567228, -0.105953, -0.816717)[0.695303, 0.593084, 0.405962] after recrystallization.

Taking symmetry into account, another $(011)[75\bar{5}]$ orientation is similarly considered. Its calculated recrystallization component was (0.567228, -0.105953, -0.816717)[0.434323, -0.804089, 0.405962]. Thus the net recrystallization texture component was calculated to be (0.567228, -0.10595, -0.81672)[0.802831, -0.14996, 0.577039] by adding the two calculated recrystallization texture components. The calculated recrystallization orientation component superposed with the measured one is shown in Fig. 6.

4 Conclusion

The deformation texture of cross rolled copper was characterized as {110}<557> orientation as a major component and {001}<100> component was found only in the

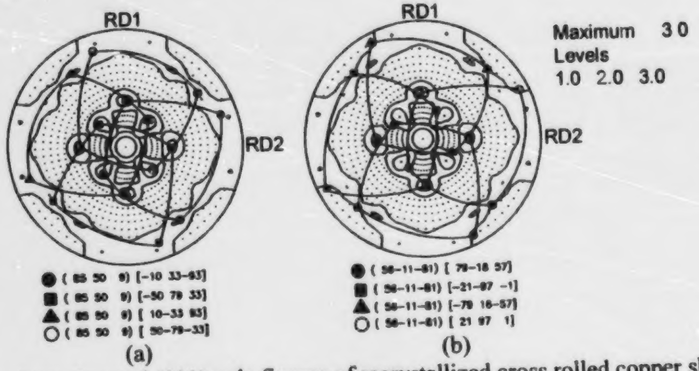

(a) (b)

Fig. 6. Experimental (111) pole figures of recrystallized cross rolled copper sheet. (a) Experimental data, (b) Calculated main orientation component.

surface layer. After annealing, the recrystallization texture developed as $(86\,50\,9)[10\,\overline{34}\,94]$ in the center layer of 96 pct. deformed sample. The recrystallization textures of cross rolled sample was well explained by the strain energy release maximization theory.

5 References

Bunge, H.-J. (1982) in *Texture Analysis in Materials Science* (Butterworths)

Canova, G.R. and Kocks, U.F. (1984) The Development of Deformation and Resulting Properties of FCC Metals. *ICOTOM* 7, pp. 573-579

Choi, C.-H. and Lee, D.N. (1997) Evolution of Recrystallization Texture from Aluminum Sheet Cold Rolled under Unlubricated Condition. *Metall. Mater. Trans.*, Vol. **28A**, pp. 2217-2222

Hong, S.-H, Jeong, H.-T., Choi C.-H. and Lee. D.N. (1997) Deformation and Recrystallization Textures of Surface Layer of Copper Sheet. *Mater. Sci. Eng.*, Vol. **A229**, pp. 174-181

Lee, D.N. (1995) The Evolution of Recrystallizaion Textures from Deformation Textures. *Scripta Metall. Mater.*, Vol. **32**, pp.1689-1694

Merlini, A. and Beck, P.A. (1953) Study on the Origin of the Cube Texture. *Acta Metall.*, Vol. **1**, pp. 598-606

Öztürk, T. (1988) Deformation and Recrystallization Textures in Cross Rolled Sheets of Copper and alpha Brass. *Script. Metall.*, Vol. **22**, pp. 1611-1615

Park, Y.B., Lee, D.N. and Gottstein, G. (1997) Evolution of Recrystallization Textures from Cold Rolling Textures in Interstitial Free Steel. *Mater. Sci. Tech.*, Vol. **13**, pp. 289-298

Suet To, Lee, W.B. and Ralph, B. (1994) Deformation and Recrystallization in Cross Rolled AL-Cu Precipitaion Alloys. *J. Mater. Sci.*, Vol. **29**, pp. 269-275

INITIAL AND RECRYSTALLIZATION TEXTURES AND MICROSTRUCTURES OF ZN ELECTORDEPOSITS

Insoo KIM and Sang Chul HONG
School of Advanced Materials and Systems Engineering, Kum Oh National University of Technology, Kumi, Kyung Buk, Korea, 730-701

Abstract

The textures, microstructures and surface morphologies of electrodeposits are related to deposition conditions. When the electrodeposits annealed, the recrystallization texture may be different from the original deposits texture.
The microstructure and surface morphology of Zn electrodeposits, as-deposited and recrystallized texture varied with deposition conditions are discussed in this study.
The surface morphology and microstructure are varied with the deposits conditions.
The <110> and <002> textures of zinc electrodeposits can be obtained from ammonium chloride, sodium hydroxide and zinc chloride baths. The <110> and <002> textures of zinc electrodeposits did not change even after recrystallization.

Key-words : Electrodeposits, Recrystallization texture, Microstructure, Surface morphology

1 Introduction

The texture, microsturcture, surface morphology and mechanical properties of electrodeposits are known to vary with electrolysis conditions, such as bath composition, overpotential, pH, current density, bath temperature, etc(Rashikov, Stoichev, Tomov, 1972 ; Lee, Chang, 1974 ; Ye, Lee, 1981 ; Lee, Ye, 1981 ; Ye et al., 1992 : Kang, Yang, Lee, 1995 ; Lee, Kang, Yang, 1995).

Electrodeposits are recrystallized when annealed, as in heavily deformed metals. The development of the recrystallization texture in electrodeposits can be related to the deposition texture.

Recently, Lee, Kang and Yang (1995) and Lee (1995) proposed the strain energy release maximization model, in which the absolute maximum internal stress direction of a deformed or fabricated materials becomes parallel to the direction of the minimum elastic modulus of recrystallized grains.

This model can explain the recrystallization of copper electrodeposits (Lee, Kang, Yang, 1995 ; Lee, 1995a ; Lee, 1996b) and deformation texture (Lee, 1995a ; Lee, 1996b).

In this study, zinc deposits with <110> and <002> textures were obtained from zinc chloride and ammonium chloride baths, their initial and recrystallization textures, surface morphologies and microstructures were investigated.

2 Experimental Procedure

An AISI 304 stainless steel plate was polished with 2000-grit emery paper to reduce the possible influence of the texture of the substrate on the nickel deposit when used as a cathode. The surface of the substrate was cleaned by HCl and distilled water before the plating.

A high purity zinc plate was used as an anode. The distance between the anode and cathode was 6 ㎝. The current density ranged from 10 to 30 A/dm^2 and the bath temperature ranged from 20℃ to 30℃. The bath was stirred and controlled to maintain a pH of 3.0.

The annealing of the zinc deposits was carried out at 200℃ for 1 hr. The texture of the deposits was measured by an x-ray diffractometer and a pole figure device. The surface of the electrodeposits was observed under a scanning electron microscope, respectively.

3 Results and discussion

Figure 1 shows the surface morphologies of zinc electrodeposits with <110> texture, which is characterized by ellipsoidal shape. The size of ellipsoidal shape decreased with increasing current density and decreasing temperature.

Figure 2 shows the surface morphologies of zinc electrodeposits with <002> texture, which is characterized by hexagonal shape. The size of hexagonal shape decreased with increasing current density and decreasing temperature.

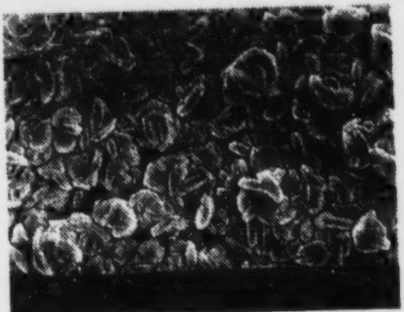

Fig 1. Surface morphology of zinc electrodeposits with <110> texture .

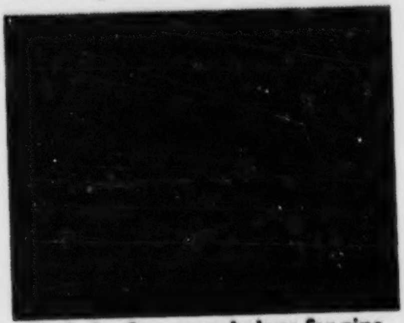

Fig 2. Surface morphology for zinc electrodeposits with <002> texture.

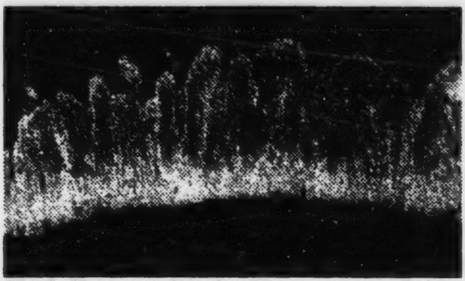

Fig 3. Cross sectional microstructure of zinc electrodeposits having [110] texture.

Figure 3 shows the initial and recrystallized microstructures of the cross section of zinc electrodeposits having <110> texture.

Figure 4 shows the inverse pole figures of zinc electrodeposits having a <110> texture before and after the recrystallization specimens. The <110> texture did not change even after recrystallization.

Figure 5 shows the verse pole figures of zinc ectrodeposits having a <002> texture before and after the recrystallization specimens. The <002> texture did not change even after recrystallization.

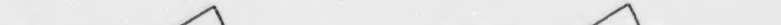

a) **b)**

Fig 4 The inverse pole figures of zinc electrodeposits having <110> texture a) as-deposited b) recrystallized

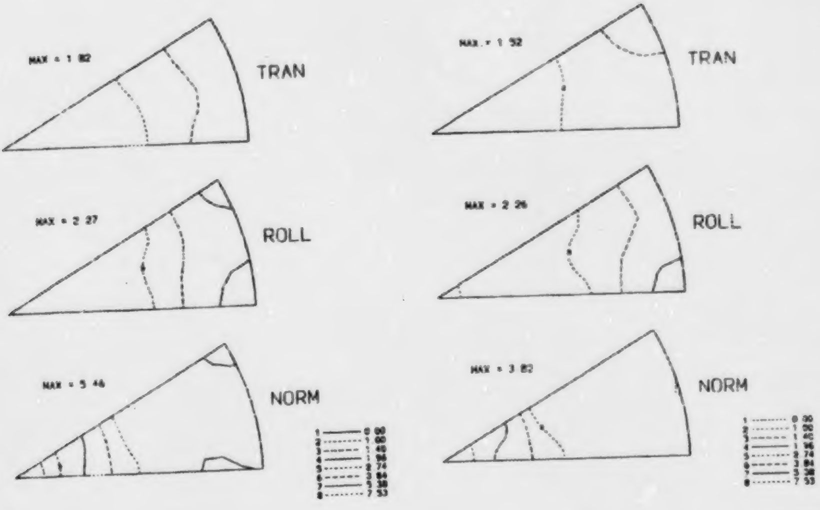

a) b)

Fig 5. The inverse pole figures of zinc electrodeposits having <002> texture
a) as-deposited b) recrystallized

4 Conclusions

1. The <110> and <002> textures of zinc electrodeposits can be obtained from the ammonium chloride, sodium hydroxide and zinc chloride baths.
2. The <110> and <002> textures of zinc electrodeposits did not changed even after annealing.

5 References

Kang, S., Yang, J., and Lee, D. N.,(1995). *Relationship between texture and surface morphology of copper electrodeposits*. Plating and Surface Finishing, 82(10) 67-70

Lee, D. N. and Chang, Y. W.,(1974). *Changes in preferred orientation and structure of copper deposit depending upon electrolysis conditions*. Journal of the Korean Institute of Metals, 12, 243-249

Lee, D. N. and Chang, Ye. G. C.,(1981). *Orientation and microstructure of watts and bright nickel electrodeposits. Plating and Surface Finishing, 68(11), 46-50*

Lee, D. N., Kang, S. and Yang, J.,(1995). *Relationship between initial and recrystallization textures of copper electrodeposits*. Plating and Surface Finishing. 82(3), 76-79

Lee, D. N.,(1995). *The evolution of recrystallization textures from deformation textures*. Scripta Metallurigica and Materialia, 32, 1689-1694

Lee, D. N.,(1996). *Texture and related phenomena of copper electrodeposits*. Materials Research Society Symposium Proceedings, 427, 167-178

Lee, D. N.,(1996). *Maximum energy release theory for recrystallization textures*. Metals and Materials, 2(3), 121-131

Lee, Y. S. and D. N. Lee, (1988). Private communication

Rashikov, S. T., Stoichev, D. S. Stoichev and Tomov, I., (1972), Electrochemica Acta, 17, 1995

Ye, G. C. and Lee, D. N., (1981), *Plating and Surface Finishing*, 68(4), 60

Ye, X., Bonte, M. D., Celis, J. P. and Roos, J. R., (1992), Journal of Electrochem Soc., 139, 1592

ANALYSIS NANOCRYSTALLINE Ni-45% Fe ELECTRODEPOSITS FOR PREDICTING TEXTURE TRANSFORMATION DURING ANNEALING

N. RAJMOHAN AND J. A. SZPUNAR
Department of Mining and Metallurgical Engineering, McGill university, Montreal, Canada, H3A 2B2
U.Erb
Department of Metallurgy and Materials science, University of Toronto, Toronto, Canada, M5S 3E4

Abstract

To understand the competition between the (111) and (100)-fiber textures in Ni-45% Fe nanocrystalline electrodeposits during annealing, a systematic texture analysis is made. This analysis indicates that the high number of grain boundaries that have energy considerably different from their microcrystalline counterparts, surround the (111) fiber grains in the investigated materials. Based on this observation, an explanation is given for the competitive growth of (111)-fiber and (100)-fiber texture.

1 Introduction

Ever since the synthesis of ultrafine-grained polycrystals by consolidation of small clusters formed via gas condensation [1], a couple of decades ago, thermal stability of such nanocrystalline materials has been given much attention in order to preserve their special properties at higher temperatures. The nanometer-sized grains in these materials account for much high volume percentage of intercrystalline regions compared to conventional polycrystalline materials.

1.1 Nanocrystalline grain boundaries

Before attempting to solve the grain growth problem, it is important to know the structure of the grain boundaries that exist in the nanocrystalline materials. There are two different opinions in the literature about the nature of the grain boundaries. In extremely small grained materials up to 50% of the atoms may be situated in the highly distorted and defected environments provided by the high density of grain junctions. Therefore, the non-equilibrium high-energy structure of atoms along the grain boundaries [2,3] in such materials appears plausible. Various other TEM investigations on nanocrystalline materials [4,5] indicate that the grain boundary structures are no different from those observed in conventional coarse-grained polycrystalline materials. In the review about nanocrystalline materials, Suryanarayana [6] raises the concerns regarding the interpretation of results on grain boundary structure by high resolution TEM. First, electron microscopic observation is done under ultrahigh vacuum, making the influence of impurities an important consideration. Second, the influence of high-energy electron beam on the shape and stability of the nanostructures is yet to be defined. Third, since very thin specimens are required for ultrahigh resolution TEM, the 3D crystal arrangement of a bulk nanocrystalline specimen gets transformed into a 2D arrangement. This process might change the boundary structure as it alters the forces due to the energy of the free surface. Though the controversy over the structure of the grain boundaries in nanocrystalline material is still on as far as experimental observations are concerned, molecular-dynamics computer simulation works recently carried out by Wolf and his co-researchers [7,8] support the argument that the grain boundaries are indeed in an very disordered state. As a consequence, the grain boundary energy is considerably more isotropic than in polycrystalline materials and the grain boundary width is rather uniform. Such isotropic energy of grain boundaries may result from a high density of junctions which makes rigid body translations more difficult in the grain boundary plane and therefore, energy of boundaries in nanocrystalline materials is high.

1.2 Grain growth in nanocrystalline electrodeposits

Grain growth occurs in order to decrease the total energy of the system by reducing the interfacial area and thus the energy associated with it. A detailed grain growth study [9] on Ni electrodeposits with the starting grain sizes of 10 and 20 nm shows that the temperature at which the materials tend to become unstable is as low as 353 K. With increasing temperatures an anomalous grain growth takes place forming a dual microstructure consisting of large grains that grow in a nanocrystalline matrix until uniform grain growth of all grains occurs at a temperature of 562 K. From the recently published work on isokinetic analysis on nanocrystalline Ni, *Wang et al*. [10] observed a similar result. All these experiments show that when annealing the Ni electrodeposits at 673 K, an abnormal grain growth takes place. Similar to this observation, Ni-45% Fe alloy [11] also show abnormal grain growth at annealing temperature of 673 K.

2 Texture measurement

From the texture measurements made (presented in Fig. 1) on the as-electrodeposited nanocrystalline Ni-45% Fe [11], it is clear that the matrix is composed of (100) and (111)-fibers. During annealing at different temperatures, it is observed that the growth of (111)-fiber texture over (100)-fiber texture. The Fig. 1 shows the change of measured fiber intensities obtained from their respective pole figures as a function of annealing time at 573 K. and 673 K. For Ni-45% Fe annealed at 673K, the initial pole figure intensities are 5.3 for (100)-fiber and 3.4 for (111)-fiber texture components. As these grains grow abnormally at 673 K, the (111)-fiber texture grows more rapidly than (100)-fiber. The (111)-fiber attains a maximum fiber intensity of 13 after 7 hrs of annealing. In the as-produced Ni-45% Fe nanocrystalline electrodeposits, the x-ray diffraction revealed the presence of the γ-phase only.

In the present work, an attempt is made to understand the basic mechanisms of grain growth that dictates the competitive growth of (111)-fiber over (100)-fiber in Ni-45% Fe nanocrystalline electrodeposits during annealing. Analysis of texture information obtained from experiments is also presented.

3 Texture Analysis and discussion

By using the algorithm developed by Morawiec *et al.* [12], one can compute the grain misorientation distribution function (GMDF). This calculation is carried out by computing the misorientation between an assumed orientation and a randomly created orientation in accordance with the orientation distribution function (ODF). This is repeated for 10^5 times in order to minimize the statistical error. The Fig. 3 shows the grain misorientation distribution function (GMDF) for Ni-45% Fe nanocrystalline electrodeposits. In the plot, it is clearly indicated that the grains representing (111)-fibers have a characteristic distribution in which the grain boundaries with misorientation of 45°-63° are higher in percentage than for the (100)-fiber texture and the average texture component. The GMDF for a fiber is computed by assuming the fiber orientation as the reference orientation and computing the misorientation between the fiber orientation and an orientation generated in accordance to the ODF. This computation is repeated for all the orientation and average distribution is calculated from this analysis. The GMDF of the average texture component is computed by calculating misorientation between several pairs of orientations generated in accordance with the ODF. In conventional microcrystalline materials, 15°-45° misorientation represents the highest energy and the most random grain boundary region. In order to distinguish the random boundaries from other remaining boundaries, hereafter the middle-misoriented boundaries will be called MM-type boundaries and others i.e., low (< 15°) and high misoriented (> 45°) boundaries will be called LH-type boundaries. It is evident that the (111)-fiber component has nearly 15-20% more of the LH-type boundaries than the (100)-fiber components. The average texture component has the fractions of LH-type boundaries that have the intermediate values between (111)-fiber and (100)-fiber components. The total fraction of LH-type boundary around (111)-fiber is about 53-59%. Having analyzed the GMDFs of (111) and (100)-fiber orientations in the matrix, energy and mobility associated with them have to be analyzed to understand the mechanism of grain growth and texture development.

According to Wolf and his co-researchers [7,8], grain boundary is amorphous (non-equilibrium state) in nanocrystalline materials and the energy of grain boundaries (E_{nano}) changes very little (approximately isotropic). On the contrary, the conventional polycrystalline material has definite different grain boundary energy, E_{micro} for various grain misorientation angles. During annealing, the nanocrystalline material transforms to a more stable microcrystalline structure. The difference between the nanocrystalline and microcrystalline grain boundary energies can be assumed to be a measure of the deviation of a non-equilibrium grain boundary from its equilibrium state as below:

$$\Delta E_{dev} = E_{nano} - E_{micro} \qquad (1)$$

Hereafter, ΔE_{dev} will be referred as "grain boundary energy deviation parameter". From the early research by Gertsman *et al.* [13] non-equilibrium grain boundary structure, as observed in deformed metals, results in high mobility. In a model developed based on this finding we have assumed that the LH-type boundaries in nanocrystalline materials have higher mobility than the MM-type boundaries. The grains surrounded by this type of boundaries will start growing first. During this process the length of the grain boundary segments will increase and their energy will approach that of the equilibrium state. This condition is expected to favor the growth of (111)-fiber in the Ni-45% Fe electrodeposits because the probability of encountering the grains that form LH-type misorientation is higher for (111)-fiber orientation than for the other orientations.

To have a quantitative description of mobility parameter, one has to know the deviation of nanocrystalline grain boundary energy from the similarly misoriented conventional polycrystalline grain boundary energy. There are few computational works on grain boundary energy of fcc metals. The Lennard-Jones potential [14] used for molecular dynamics calculations for Fe, Cu and Ni are similar. Thus, the shape of the relative grain boundary energy plot as a function of tilt angle for various tilt boundaries would be more or less the same for Cu and Ni and Ni-Fe alloys because they all have fcc crystal structure. Under this assumption, the "relative" boundary energy calculated from the molecular dynamics computations by Wolf *et al.* [15] for tilt boundaries of copper is assumed for Ni-45% Fe alloy. The consolidated energy (E_{micro}) as a function of misorientation is given in Fig.3. Having known the E_{micro} (equilibrium relative grain boundary energy) and assuming that a non-equilibrium relative energy E_{nano} is 1, the parameter which measures the deviation of nanocrystalline grain boundary from the equilibrium state, ΔE_{dev} is shown in Fig. 6. The grain boundaries with deviation < 5° is not considered for this calculation (<< 1% probability in all the cases) because at present, the value of energy these boundary have in nanocrystalline materials is hard to estimate. From the Fig. 6, it is however evident that the LH-type boundaries have higher ΔE_{dev} than MM-type boundaries.

For a material to experience abnormal grain growth, normal grain growth has to be hindered by pinning forces such as precipitates, solute, etc. In the classical case of Fe-Si steels, abnormal grain growth is favored only when the normally growing grains are pinned by precipitates. When it is further annealed at high temperature, the selective unpinning of certain grain boundaries take place. This activates a particular orientation to grow faster than the others [16]. As a result completely new texture and grain structure is developed. Similarly, in the case of fully dense Ni-45% Fe alloy electrodeposits at the ambient temperature does not undergo grain growth. The pinning force for this case could be offered by triple junction, vertices, excess vacancies, impurity atoms, metastability of microstructural features such as grain boundaries, etc. At temperatures greater than 573K, some grains start growing abnormally by preferable movement of grain boundaries that are highly deviating from the equilibrium states. These boundaries move by breaking free of the pinning forces that existed before the migration of that boundary. This growth would strongly favor the (111)-fiber texture because the grain boundaries that surround this fiber component are highly deviated from their equilibrium state. This speculation is tested using Monte-Carlo simulation and is described in a paper [17] in the same volume.

4 Conclusion

Grain misorientation analysis of the electrodeposited Ni-45% Fe nanocrystalline matrix predicts that (111)-fiber grains are surrounded by the highest number of grain boundaries that are highly deviated from the corresponding microcrystalline equilibrium structure. These boundaries seem to be responsible for the rapid growth of (111)-fiber texture component in nanocrystalline materials.

5 Reference

1. H.Gleiter (1981) in *Proc. Second Risø Int. Symp. On Materials Science*, edited by N.Hansen et al. Risø National Laboratory, Roskilde, Denmark. 15
2. W.Wunderlich, Y.Ishida and R.Maurer, (1990) *Scripta Metall. Mater.*, 24, 403
3. V.Y.Gertsman, R.Birringer, R.Z.Valiev and H.Gleiter (1994) *Scripta Metall. Mater*. **30**, 229
4. J.A.Eastman, M.R.Fitzsimmons and L.J.Thompson, (1992) *Phil. Mag.*, **B66**, 667
5. G.J.Thomas, R.W.Siegel and J.A.Eastman (1990)*Scripta metall.*, **24**, 201
6. C.Suryanarayana (1995) *Int. Mater. Rev.*, **40** (2), pp 41-64
7. R.W.Siegel (1992) in *Metal Interfaces: Atomic level structure and properties*, edited by D.Wolf and S.Yip, Chapman and Hall, London, 431
8. S.R.Phillpot and D.Wolf (1995) *Scripta metall. Mater.*, 33(8), 1245
9. P.Keblinski, S.R.Phillpot, D.Wolf and H.Gleiter (1997) *Acta Mater.*,**45**(3) 987
10. N.Wang, Z.Wang, K.T.Aust and U.Erb (1995) *Acta Mater.*, **45**(4),1655
11. F.Czerwinski, H.Li, M.Megret and J.A.Szpunar (1997) *Scripta Mat*, **37**(12), 1967,
12. A. Morawiec, J.A.Szpunar and D.C.Hinz, (1993) *Acta metall. Mater.*, **41**(10), 825
13. R.Z.Valiev, V.Y.Gertsman and O.A.Kaibyshev (1983) *Scripta Met.*, **17**, 853 and (1980) *Sov. Phys. Solid State*,**22** (7), 1291 (1980)
14. C.Kittel, (1986) *Introduction to solid state physics*, 6th edition, John Wiley & Sons Inc., New York, 61
15. D.Wolf (1989) *Acta Metall.*, 37(7), 1983
16. Y.Hayakawa and J.A.Szpunar, (1997) *Acta mater.*, **45**(3), 1285
17. N.Rajmohan and J.A.Szpunar (1999), *Int. Conf. Texture of Mater. (ICOTOM-12)*, Montreal. (same volume)

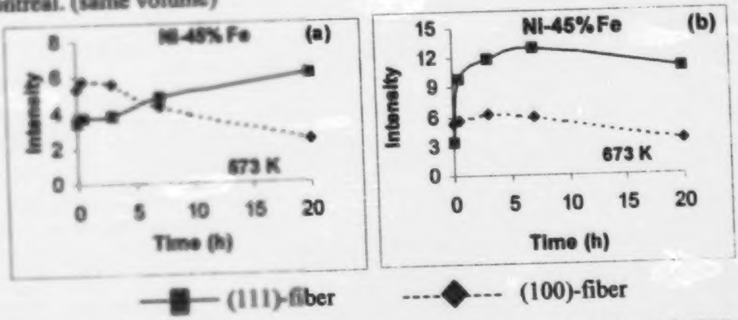

Fig. 1 **Fiber intensity observed in pole figures of (111) and (200) of Ni-45% Fe nanocrystalline electrodeposits measured after annealing at 573 K and 673 K for various annealing time**

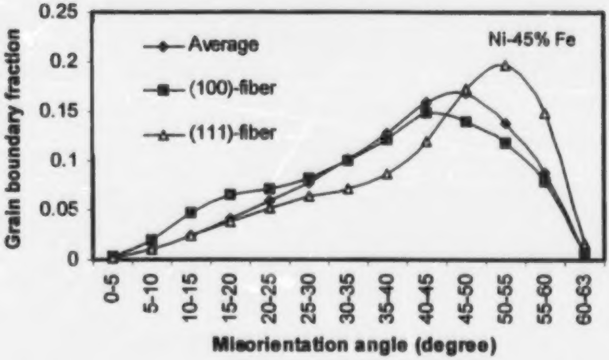

Fig. 2 Misorientation distribution calculated based on the as-electrodeposited nanocrystalline Ni-45% Fe textural information (Here curves are drawn only as a visual aid to follow the data points unambiguously)

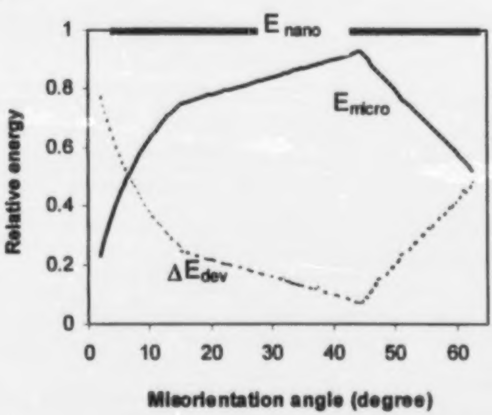

Fig. 3 Grain boundary energy deviation parameter (ΔE_{dev}) as a function of misorientation angle. The ΔE_{dev} is calculated from the assumed nanocrystalline and calculated microcrystalline grain boundary energies

TEXTURE DEVELOPMENT DURING GRAIN GROWTH IN STRONGLY TEXTURED MATERIALS

V.Yu.NOVIKOV
Treptower Str. 74d, D-22147 Hamburg, Germany

Abstract

Texture alterations accompanying grain growth have been simulated by a new statistical model taking into account the dependence of both the energy and mobility of grain boundaries on their disorientation. Model polycrystals are assumed to consist of preferably oriented grains A (the main component) and randomly oriented grains B. Therefore, there are three types of grain boundaries in these polycrystals: the high-angle A-B and B-B boundaries, and the A-A boundaries with a smaller disorientation. Abnormal grain growth leads eventually to vanishing of the main component. However the latter enhances at the incubation period of abnormal grain growth, especially in the case when the initial distribution of randomly oriented grains is displaced toward small sizes, as in materials with cube texture. Texture evolution during normal grain growth is strongly affected by the initial position of the size distribution of randomly oriented grains. If this distribution is displaced toward small sizes, the main component enhances, while it vanishes if the initial size distributions of grains A and B are identical.

Keywords: Abnormal grain growth, computer modelling, normal grain growth, texture

1 Introduction

Experimental data on texture evolution in strongly textured materials during normal grain growth (NG) are conflicting. An enhancement of the main texture component is mainly observed in materials with cube texture (e.g. Vogel et al. 1996). However a decrease of intensity of the main component is also reported (e.g. Shvindlerman et al. 1994). Abnormal grain growth (AG) results in both a complete vanishing of the initially strong component and an appearance of a scattered, multi-component texture (Grewen et al. 1958; Kronberg and Wilson 1949). It should be ascertained that the features of the initial microstructure and/or preferred orientation, affecting texture alterations, were not revealed in the known experimental investigations. At the same time, texture deve-lopment during grain growth cannot be studied theoretically because none of the existing theories takes into account the anisotropy of grain boundary properties intrinsic to textured materials (Novikov 1996). So it seems reasonable to use computer simulation to gain a better understanding of texture development during grain growth.

The first publication on computer modelling of grain growth texture evolution appeared 20 years ago (Novikov 1979). In the computer model by Abbruzzese et al. (1986) the expression for driving force in a polycrystal with grain boundaries of different energies is incorrect in terms of thermodynamics. In such a polycrystal, the driving force is determined by the energy of the growing grain's boundary as well as by the energies of the boundaries between the consumed grains (Dunn 1953) which was overlooked in the above model. Thus, this model relates to the case only when different boundaries have various mobilities, but the same energy. However, there is no physical significance in studying the effect of the boundary energy or that of the boundary mobility on grain growth separately since both the mobility and energy depend on boundary misorientation. So, we have developed a new model that for the first time takes into account the misorientation dependence of both energy and mobility of the grain boundaries. The aim of the present work is to study the effect of the initial texture on its evolution during grain growth in strongly textured polycrystals.

2 Model and method of simulation

A statistical model (Novikov 1978, 1979) is used as a basis for a new model. It was assumed that a single-component texture of a model polycrystal consists of a relatively strong main component and of a non-oriented background. In such a polycrystal there are three types of grain boundaries: between the grains of the main texture component (group A), between the grains of random orientation (group B), and between the grains A and B. It is assumed that the B-B and A-B boundaries are high-angle, and the A-A boundaries are of a smaller disorientation, Θ_{AA}, than the others. The magnitude of Θ_{AA} may be considered as a measure of the scatter of the main texture component.

According to the model, grains of different sizes and different groups are arranged randomly. A crystallite of size D_i can consume the adjacent grains of size D_j provided the driving force for growth of the former, ΔF_{ij}, is positive. A crystallite of size D_i belonging to group A (or B) when its neighbour is a grain of size D_j from group X (X=A or B) can grow if (Dunn 1953)

$$D_{iA} > D_{jA}\,\gamma_{AX}/\gamma_j, \quad \text{or} \quad D_{iB} > D_{jX}\,\gamma_{BX}/\gamma_j \tag{1}$$

Here γ_{AX} is the energy of the migrating boundary, and γ_j the energy of the disappearing boundaries of the consumed grain. The magnitude of γ_j was calculated in our model as a half-sum of the energies of the boundaries. The displacements of the boundary of the grains of sizes D_j and D_i which obey Eqn (1) are:

$$\Delta D_{iAjX} = M_{AX}\Delta F_{iAjX}\,\Delta\tau, \quad \text{and} \quad \Delta D_{iBjX} = M_{BX}\Delta F_{iBjX}\,\Delta\tau \tag{2}$$

For the other grains $\Delta D_{iAjx}=\Delta D_{iBjx}=0$. The term M in Eqn (2) is the mobility of the moving boundary, and $\Delta\tau$ the time step. It is assumed that triple junctions do not affect displacements of grain boundaries.

If we do not take into account the groups of the growing and consumed grains, an expression for the volume increment, ΔV_{ij}, of a crystallite of size D_i due to the consumption of a neighbouring grain of size D_j corresponding to Eqn (1) is:

$$\Delta V_{ij} = s_{ij}\, \Delta D_{ij}\, n_i\, n_j \tag{3}$$

where ΔD_{ij} is the grain boundary displacement from Eqn (2), s_{ij} the contact area of these grains, and n_i and n_j their current number fractions in the grain ensemble considered. The volume decrement, ΔV_{ji}, of the consumed grains of size D_j equals ΔV_{ij}. The number of grains, ΔN_j and ΔN_i, transferring into the size classes D_{j-1} and D_{i+1}, respectively, is derived from the volume decrements of the consumed grains of various sizes D_j, ΔV_{ji}, and from the volume increment of the growing crystallites of size D_i, ΔV_{ij}. Owing to this, the total volume of the ensemble remains constant with an accuracy better than 0.1% (it was assumed that the grains of size $<D_1$ disappear). Alterations in the total grain size distribution with time are computed by applying this procedure subsequently to grains of different groups and sizes.

The initial overall grain size distribution in 3-D model polycrystals was of the same, nearly log-normal shape. The relative magnitudes of the energy, γ, and mobility, M, of different boundaries were taken from the work by Humphreys (1997) and listed in Table. Groups A and B had either the same or different initial distributions in coordinates "relative frequency--grain size"; in the first case the model polycrystal was designated as PI, in the second one as PD (see Fig. 1). The evolution of microstructure and texture was traced by variation of grain size distribution with time. Texture evolution was characterized by the volume fraction of group B, V_B. Microstructure was described by the following parameters: apparent average grain diameter, d (it was calculated as if the measurements were conducted by the random section method), most probable grain diameter, d_M, and maximum grain diameter, d_{max}. The polycrystals studied had the initial microstructure with d_M=13.9 µm, d=22.5 µm, and d_{max}/d_M=3.05. The character of the grain growth process was judged from the time dependence of d_{max}/d_M. According to the experimental data (Novikov 1996), this ratio during NG is between 3 and 4. So it was assumed that AG begins at a point when d_{max}/d_M becomes >5 for the first time. The minimum size of abnormally large grains was fixed at this point which enables the calculation of the volume fraction of these grains and investigation of the AG kinetics.

Table: Grain boundary energies and mobilities used in simulations

Θ_{AA}	γ_{AA}	M_{AA}	$\gamma_{BB}=\gamma_{AB}$	$M_{BB}=M_{AB}$
2°	0.4	0.15	1.0	10.0
5°	0.7	0.55	1.0	10.0
10°	0.9	6.25	1.0	10.0

3 Results and discussion

First we studied the character of the growth process in polycrystals with different initial intensity of the main texture component, V_{A0} (from 0.99 to 0.30) as well as with different scatter of the component, Θ_{AA} (from 2 to 10°). At low Θ_{AA} a completed AG was observed at low V_{B0} (and thus at high V_{A0}), an increase of V_{B0} led to an interruption of AG, and NG was observed at high V_{B0}. An increase of Θ_{AA} from 2 to 5° resulted in a reducing of the tendency to AG at the same V_{B0}. At $\Theta_{AA}=10°$ NG only was observed. The AG incubation period in PD was much longer than in PI (Fig. 2).

As seen in Fig. 2, regardless of the character of the growth process, grain growth in PI leads eventually to an enhancement of group B. It should be, however, noted that V_B slightly decreases (and V_A, correspondingly, increases) at the AG incubation period. However, an enhancement of the main component is observed experimentally during NG in materials with cube texture. This inconsistency could be caused by the influence of some factors other than texture parameters. For instance, according to (Juul Jensen et al. 1985), during primary recrystallization cube grains grow much faster than the other grains, and, toward the end of the process, the average size of the former is greater than the size of the latter. As a result, the distribution of cube grains is displaced toward large sizes and the distribution of the others -- toward small sizes. These data were used as a starting point for further simulations on model polycrystal PD with different initial size distributions for grains A and B.

According to (Juul Jensen et al. 1985), cube grains in Al are ~2 times larger than the others at the volume fraction of the former ~0.2. It may be supposed that in the case of a greater intensity of the cube component the size advantage of cube grains should be smaller. For this reason the magnitude of $d^A_{M0}/d^B_{M0}\approx 1.2$ was used for the construction of the initial size distributions of grains A and B in polycrystal PD with $V_{A0}\geq 0.7$. It was also assumed that $d^A_{max}/d^B_{max}=1.15$, i.e., not only the peak, but also the whole distribution of grains B is displaced toward small sizes in respect to that of grains A. V_{A0} in PD

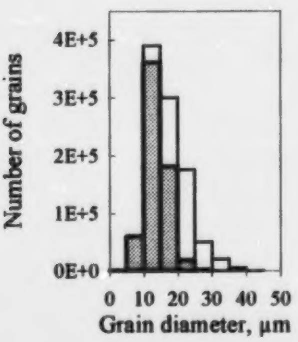

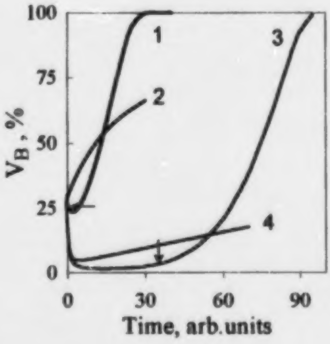

Fig. 1: Initial grain size distributions: overall distribution in PD and PI (non-shaded) and distribution of grains B in PD at $V_{B0}=0.30$ (shaded).

Fig. 2: Texture evolution in PI (curves 1 and 2) and PD (curves 3 and 4) during AG (curves 1 and 3) and NG (curves 2 and 4). Arrows show the end of AG incubation period.

was varied from ~0.7 to ~0.9, and Θ_{AA} – from 2 to 10°. AG texture in both PD and PI appears to be the same, i.e. $V_{B0} \cong 1.0$ (Fig 2). However an enhancement of the main texture component at the AG incubation period is much more significant in PD than in PI (comp. curves 1 and 3 in Fig. 2). Texture alterations during NG are in PD totally different: whereas V_B increases in PI, it decreases in PD (comp. curves 2 and 4 in Fig. 2). As shown below, distinct texture evolution is a result of an interplay of the consumption and the growth of randomly oriented grains during the growth process.

At the initial stage of the grain growth process the majority of the consumed grains are grains B. This may be explained by the following simplified model. Assume that the matrix consists exclusively of grains of a single group X and that all the grains have the same size d_X^*. (In fact, the situation is much more complicated because the matrix consists of grains of various sizes and different groups which is taken into account in the statistical model used.) Then, if they are grains B, the crystallite of size $D_B<d_B^*$ is to be consumed according to Eqn (2). If the matrix consists of grains A, the size of the crystallite B destined to be consumed is $D_B<d_A^*\gamma_{AA}/\gamma_{BB}$. Thus, grains B can be consumed by greater grains B and by both smaller and greater grains A. The latter should lead to a more significant decrease of N_B than the former, especially in the case when the initial distribution of grains B is displaced toward small sizes. As for grains A, they can be consumed by greater neighbours of any group which causes their number fraction to decrease to a lesser extent.

The rate of the growth or consumption should depend on the mobility of the boundaries of the involved grains, along with the driving force. The boundary of a crystallite of a certain group consists of portions having a different disorientation and, thus, different properties. The boundaries of grains A consist of A-A and A-B portions, and the boundaries of grains B – of A-B and B-B portions. Since it was assumed that $M_{AA}<M_{AB}$ and $M_{AB}=M_{BB}$ (see Table), grains B have boundaries with a higher "effective" mobility than grains A (Novikov 1976). The effective mobility depends on a relative magnitude of different boundary portions and, therefore, on V_A. At high V_A, grains B having a higher effective mobility of their boundaries should be consumed faster than grains A, provided the driving force for their consumption is the same. Simultaneously, the survived grains B should grow faster than the survived grains A.

A complete vanishing of the main component during AG may be explained as follows. The consumption of randomly oriented grains B belonging to low size classes gives rise to such an increase of an average size of the survived grains B that they appear larger than the survived grains A which conforms with the experimental data (Vogel et al. 1996). As a result, the highest size classes in the overall grain size distribution are occupied by grains B, apparently, due to their increased growth rate. As a consequence, all the crystallites growing during AG are grains B (Fig. 2, curves 1,3).

The texture development during NG may be explained as follows. An increase of V_B due to the contribution of the survived grains B can be either greater or smaller than a decrease of V_B due to the consumption of the other grains B. The first case is observed in PI with identical size distributions of grains A and B where V_B enhances during NG (see Fig 2, curve 2). The second case (when V_B vanishes or V_A increases) takes place in PD with the initial size distribution of grains B displaced toward small sizes (see Fig. 2, curve 4). The consumption of grains B in the second case should proceed more intensively owing to their decreased size, as shown above by the simplified model. For this reason the main component A enhances during NG. The presence of a minimum on the

$V_B(t)$ curves at the AG incubation period can also be explained by a more intensive consumption of grains B. This effect is more pronounced in polycrystal PD since on the whole grains B in this polycrystal are initially of a smaller size than in PI.

4 Conclusions

Abnormal grain growth in strongly textured polycrystals results eventually in an enhancement of initially weak texture component(s). However, the main texture component can amplify at the incubation period of abnormal grain growth, especially in the case, when the grain size distribution of the component is displaced toward large sizes, as in materials with cube texture. Normal grain growth in such a case can also result in an enhancement of the main component. In the other cases it is accompanied by a reduction of the main component.

References

Abbruzzese, G. and Lücke, K. (1986) Theory of texture controlled grain growth. Pt. 1, *Acta Metall.*, Vol. 34, No. 5, pp. 905-14.

Dunn, C.G. (1953) Secondary recrystallization texture and its origin in cold-rolled single crystals of silicon-iron, *Acta Metall.*, Vol. 1, No. 2, pp. 163-75

Grewen, J., Segmüller, A. and Wassermann, G. (1958) Walz- und Rekristallisationstexturen einer Fe-Ni Legierung mit 30% Ni, *Arch.Eisenhüttenwesen*, Vol. 29, No. 2, pp. 119-24.

Humphreys, F.J. (1997) A unified theory of recovery, recrystallization and grain growth based on the stability of cellular microstructures. Pt. 1, *Acta Mater.*, Vol. 45, No. 10, pp. 4213-20.

Juul Jensen, D., Hansen, N. and Humphreys, F.J. (1985) Texture development during recrystallization of Al containing large particles, *Acta Metall.*, Vol. 33, No.12, pp. 2155-62.

Kronberg, M.L. and Wilson, F.G. (1949) Secondary recrystallization in copper, *Trans. AIME*, Vol. 185, pp. 501-14.

Novikov, V.Yu. (1976) The structure effect on selective growth in recrystallization, *Texture*, Vol. 2, No. 1, pp. 35-44.

Novikov, V.Yu. (1978) Computer simulation of normal grain growth, *Acta Metall.*, Vol. 26, No. 11, pp. 1739-44.

Novikov, V.Yu. (1979) On computer simulation of texture development in grain growth, *Acta Metall.*, Vol. 27, No.9, pp. 1461-66.

Novikov, V. (1996) *Grain Growth and Control of Microstructure and Texture in Polycrystalline Materials.* CRC Press, Boca Raton, FL, pp. 47-74.

Shvindlerman, L.S., Sursaeva, V.G., Novikov, V.Yu. and Faulkner, R.G. (1994) Grain structure evolution during grain growth in 2-D aluminium foils, *Mater.Sci.Forum*, Vol. 157-162, pp. 1063-68.

Vogel, S., Klimanek, P., Juul Jensen, D. and Richter, H. (1996) Effect of texture on the development of grain size distribution during normal grain growth, *Scripta Mater.*, Vol. 34, No. 8, pp. 1225-30.

STUDY OF RECRYSTALLIZATION MECHANISMS IN INGOT CAST AND STRIP CAST Fe-36%Ni

F. JULLIARD, T. BAUDIN, R. PENELLE

Laboratoire de Métallurgie Structurale, URA CNRS 1107, Université Paris-Sud, Orsay, France

Abstract

A comparative study of a Fe-36%Ni alloy elaborated by either ingot casting or thin strip casting has been carried out. Cold rolling and recrystallization textures show that it is possible to obtain under specific conditions, a thin strip cast material with a strong cube texture. Cube bands develop a dislocation cell structure with an orientation gradient with respect to the cube orientation, similar to that observed in the material processed by ingot casting. So, it can be assumed that the recrystallization mechanisms are similar and hence, their study is particularly carried out after the ingot casting process. Sub-grain growth in an orientation gradient is not the only parameter for the development of cube grains as previously described, since some sub-grains having initially the critical size may develop straight into the matrix.

Keywords: Fe-36%Ni, ingot cast, nucleation, recrystallization, strip cast, TEM

1 Introduction

The Fe-36%Ni austenitic alloy is used as shadow-masks for TV and computer monitor screens or in electronics devices because of its low thermal expansion coefficient and its magnetic properties (Béranger et al. 1996). It is made classically by ingot processing route. Sheets of 250 µm thickness are obtained by hot and cold rolling of the ingot. Then a post-continuous annealing allows to develop a sharp cube texture which is in favour of a homogeneous etching for shadow-mask making.

The continuous thin strip casting is an alternative way to work out this material. The cast sheets have a small thickness and may be directly cold rolled. However, it is necessary to get the same microstructure and texture as those of the ingot.

From a fundamental viewpoint, the purpose of this study is to explain the development of the cube texture for the both processings.

2 Material and experimental techniques

Three materials have been investigated : the first (A) obtained from the hot rolled ingot, the others stemmed from the thin strip casting, the first (B) was the rough cast-product and the second (C) has been hot rolled. Then, the three samples have been cold rolled at reduction amounts comprised between 40 % and 95%.

The initial microstructures have been characterized by scanning electron microscope using channeling contrast. The initial textures have been determined by X-ray diffraction in the rolling plane for different depths from the surface, and textures of cold rolled samples at the first quarter of the thickness. The pole figures {111} {200} and {220} have been measured for each reduction amount and the component method of Helming allowed us to estimate the volume fraction of each component (Helming 1995). The local microstructure and texture of cold rolled samples (A) and (C) and lightly annealed sample (A) have been examined by transmission electron microscopy with a JEOL 2000EX microscope. In order to carry out observations on the plane perpendicular to the rolling direction, the thickness of the thin sheets had to be increased from 0,25 mm to 3 mm by electroplating nickel on the sheet. Samples were cut off , then, mechanically and electrolitically thinned.

The grain orientation was determined by an on-line indexing of the Kikuchi and spot patterns (Zaefferer and Schwarzer 1994).

3 Results and Discussion

3.1 Global Textures

Sample (A) shows a recrystallized microstructure with a grain size of about 10 µm. Its texture determined by Zaefferer et al. (1996), and already described by Park et al. (1996), is weak and almost random in the thickness of the material, except the cube component that appears only in the sheet centre. The grains of sample B are 300 µm to 1 mm long and the diameter varies from 50 µm to 300 µm. They are tilted towards the rolling direction because of the casting process. The texture is a near {100} <0vw> fiber with a 20° scattering, that is tilted in the rolling direction (figure 1a).

Sample (C) shows a heterogeneous microstructure with recrystallized grains on the surface and a recovered one in the centre. In the sheet centre (figure 1b), the main components are {522} <$4\bar{5}\bar{5}$> and {$5\bar{1}2$} <$\bar{1}\bar{2}2$> respectively close to {211} <$1\bar{1}\bar{1}$> (copper "C") and {$4\bar{1}1$} <$\bar{1}\bar{2}2$> ("C/S"), and {510} <$1\bar{5}0$> close to {100} <$0\bar{1}0$>. At the surface, the {510} <$1\bar{5}\bar{5}$> and {001} <$3\bar{4}0$> components, close to {100}<$0\bar{1}\bar{1}$> and <{001} <$1\bar{1}0$> ideal ones can be also observed (figure 1c).

During cold rolling, textures are totally modified for the three materials. The copper-type texture develops after 40% of reduction with components close to {112} <$11\bar{1}$> ("C"), {123} <$63\bar{4}$> ("S") et {011} <$21\bar{1}$> ("B"). The texture of sample (B) is more diffused than the texture of other samples and exhibits a {225} <$55\bar{4}$> main component slightly misoriented from {112} <$11\bar{1}$> whereas the orientations close to the brass component ("B") are almost absent.

For higher deformations, texture is sharper. Indeed, the components close to S, B and C increase at the detriment of the random part of the texture to give the typical texture of materials with high stacking fault energy (figure 2). However the brass-type component remains weak in the sample (B). An important feature is the retaining of cube component after cold rolling. This component already existing in the initial material remains partially stable during cold rolling and develops during annealing.

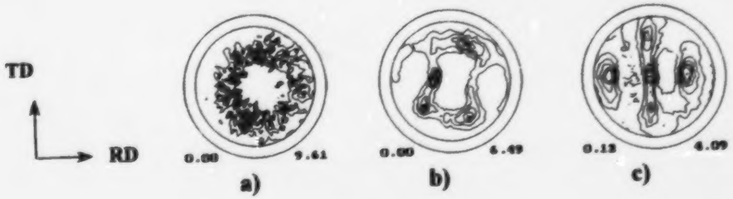

a) b) c)

Fig. 1: {111} X-ray pole figures, a) measured in the thickness quarter of sample (B), b) in the centre and c) at the surface of sample (C)

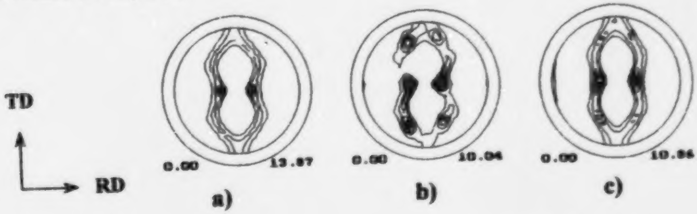

a) b) c)

Fig. 2: {111} X-ray pole figures of the 95% deformed samples, a) (A), b) (B) and c) (C)

3.2 Microstructures and local textures

TEM studies have been mainly focused on the development of cube grains. However, the matrix has been also studied.

For the highly deformed sample (A), the microstructure previously observed by Zaefferer et al. (1996), consists in many lamella bands having the rolling texture. Cube grains form bands which width ranges from 200 nm to 300 nm. They develop a structure with well recovered cells observed in the plane perpendicular to the rolling direction. The misorientation between cells is small but from one side of the band to the other, the cumulated misorientation can reach 30°, changing from a near cube orientation to the {021} <100> one.

Unlike the cube bands, the matrix does not develop a cell structure with a high accumulated misorientation but a lamellar one with a high dislocation density. By another way, no relationship between cube bands and their neighbours has been found. For the hot rolled thin strip cast material (C), cube grains develop in the same way a cell structure with an orientation gradient (figure 3), the orientation evolving from {019} <100> to {023} <100>.

From these results, it has been assumed that the development of cube nuclei occurred inside these cube bands as proposed by Zaefferer et al. (to be published).

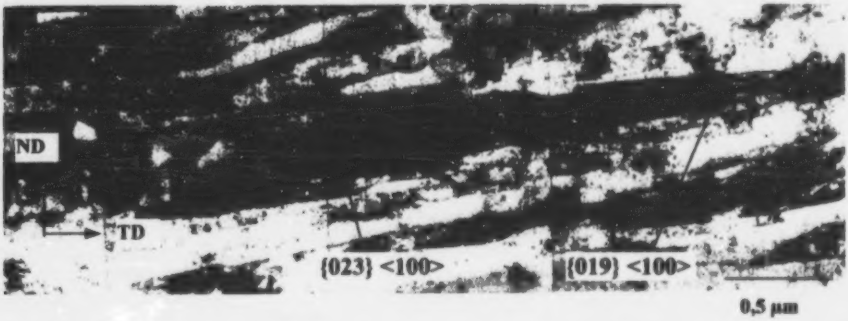

Fig. 3: TEM micrograph of sample (B) after a 95% cold rolling reduction showing a cube band with a cell structure and an orientation gradient

In the first steps of annealing, nucleation starts either by coalescence or sub-grain growth, giving a size advantage to a cube sub-grain. In spite of the small misorientation between this cube sub-grain and its neighbours, it can grow thanks to this size advantage into the cube band. Then, its cumulated misorientation increases across the band, it forms a mobile high angle grain boundary (misorientation higher than 15°) and next, develops into the matrix, the stored energy difference between cube grains and the lamella bands providing the driving force for the growth.

For thickness reductions lower than 80%, the recristallisation texture shows a weak cube component. Moreover, it has been observed that the cumulated misorientation is generally lower than 15° for these deformations amount. Zaefferer et al (to be pubished) explain the lack of cube grains in the final texture by the fact that no new high angle grain boundary can be formed and that the existing high angle grain boundaries are not sufficiently mobile to permit the development of cube grains. Short annealing time have been carried out on the material (A) in order to account for this mechanism.

Figure 4 shows a cube band with a cell structure and an orientation gradient. The orientation changes through the band from a near cube orientation to an orientation {012} <100>. In the right part of the band, a 600 nm long and 300 nm wide sub-grain develops from the band into the matrix. The misorientation between this sub-grain and the sub-grain situated on its left, inside the band, is 7°. As this misorientation is lower than 15°, the boundary is not a high angle grain boundary. However, the cube band is highly misoriented with the surrounding matrix, which means that the boundaries separating the cube sub-grains and non-cube microbands can be mobile if the cube grain size is sufficient.

As an example, Figure 5 shows a cube band with some sub-grains growing into the matrix. In the lower part of the band, an orientation gradient exists ; the orientation changes from {001} <100> to {023} <100> and a sub-grain can develop in the same way as before. However a sub-grain develops in the upper part of the band ; the misorientation with the cells standing on its left and on its right, inside the band, is respectively 1° and 2°. This small misorientation indicates that the grain does not expand into the orientation gradient but develops straight into the matrix.

From these results, it appears that the development of cube sub-grains outside the cube band is not necessarily related to the formation of a new high angle grain boundary inside the band. For high deformation amounts the cube bands are generally thin with one to three sub-grains along the normal direction.

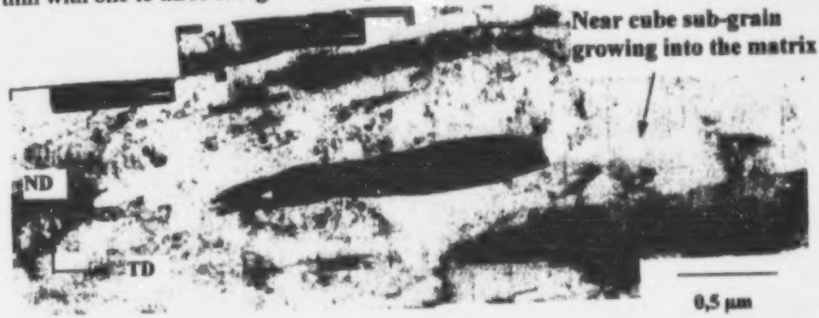

Fig. 4: TEM micrograph showing a cube band in the 95% cold rolled sample (A) and 2 min. annealed. The orientation gradient is showed by the white arrow inside the band.

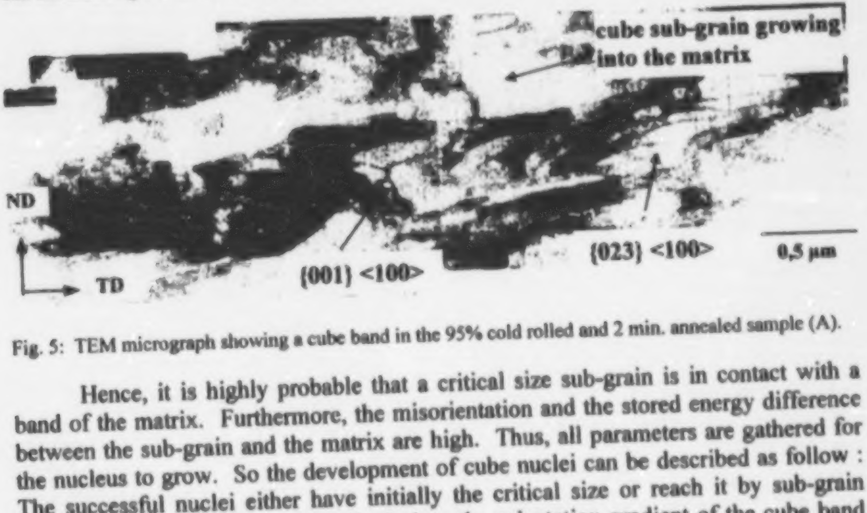

Fig. 5: TEM micrograph showing a cube band in the 95% cold rolled and 2 min. annealed sample (A).

Hence, it is highly probable that a critical size sub-grain is in contact with a band of the matrix. Furthermore, the misorientation and the stored energy difference between the sub-grain and the matrix are high. Thus, all parameters are gathered for the nucleus to grow. So the development of cube nuclei can be described as follow : The successful nuclei either have initially the critical size or reach it by sub-grain coalescence, then develop either firstly into the orientation gradient of the cube band and finally into the matrix (figure 4) or directly into the matrix thanks to the high misorientation and the difference of dislocation density (figure 5).

With regard to the intermediate deformations, the cumulated misorientation inside the band is generally lower than 15°. A sub-grain can develop also inside the band as described above, however no high angle grain boundary can be formed, hence, if the sub-grain does not reach the grain boundary with the matrix, the growth fails. It may be supposed nevertheless that with the size advantage, it will continue to develop across the band, will meet finally a high angle grain boundary and will grow into the matrix.

From these considerations, it is difficult to understand why a sharp cube recrystallization texture is not formed for intermediate rolling amounts. The incubation time necessary for the cube grain to reach a high angle grain boundary might be responsible of this lack of cube grains in the final texture. In the same time grains with other orientation may grow. However the recrystallization kinetics show that even for intermediate thickness reduction, the cube grains develop before the others. So, it is likely that the stored energy, the configuration of dislocation substructure, the rolling orientations are important parameters whose it will have to take into account to explain recrystallisation texture whatever the deformation amount.

4 Conclusion

The TEM and texture studies carried out on materials stemmed from two different processing routes showed that their behaviour is quite the same during the cold rolling. Both of them develop a copper-type texture after high thickness reductions and the cube component present at the initial state is partially retained. The cube grains appear as bands with a well recovered structure in which exists an orientation gradient.

It has been shown that the development of a cube sub-grain is not necessary related to the formation of a high angle grain boundary inside the cube band. The cube sub-grain has initially a critical size or gets it by coalescence or sub-grain growth, however a high angle grain boundary is necessary for further growth. For higher thickness reductions, the high angle grain boundary can be formed inside the band by growth of the sub-grain in the orientation gradient or the sub-grain can expand straight into the matrix thanks to the existing high angle grain boundary and the stored energy difference between the grain and the matrix. For intermediate deformation amounts, the development of cube sub-grain is more difficult because the cumulated misorientation is not large enough to form a high angle grain boundary and the bands are wide (more than five cells cells in the normal direction). If the sub-grain does not reach the matrix, the nucleation fails.

References

Béranger, G., Duffaut, F., Morlet, J., Tiers, J. F. (eds) (1996) A Hundred Years after the discovery of Invar…, The iron-nickel alloys. *Tec & Doc-Lavoisier*.

Helming, K. (1995) Texturapproximation durch Modellkomponenten. *Cuvillier Verlag Göttingen.*

Park, Y. B., Raabe, D,. Yim, T. H. (1996) Cold rolling textures of Fe-Ni soft magnetic alloys. *Scripta Materialia*, Vol.35, No 11, pp. 1277-83.

Zaefferer, S., Schwarzer, R. (1994) On line interpretation of spot and kikuchi patterns. *Materials Sciences Forum*, Vol. 157-162, pp. 247-50.

Zaefferer, S., Baudin, T., Penelle, R. (1996) The development of texture and microstructure of a Fe 36Ni (Invar) alloy during rolling : A study of the origin of the recrystallization texture. *Proceedings of the 3rd Int. Conference On Recrystallization and Related Phenomena*, Rex'96, Monterey, Ed. T. R. McNelley, pp. 347-54.

Zaefferer, S,. Baudin, T., Penelle, R. (to be published) A study on the formation mechanisms of the cube recrystallization texture in cold rolled Fe36%Ni alloys.

Texture in Steel and Aluminum

EFFECT OF PRIMARY RECRYSTALLIZATION TEXTURE ON GOSS SECONDARY RECRYSTALLIZATION TEXTURE IN Fe-3%Si ALLOY

Y.USHIGAMI, and T.KUBOTA

Electromagnetic materials, Steel Research Laboratories, Nippon Steel Corporation
20-1 Shintomi, Futtsu, Chiba 293-8511 Japan

K.MURAKAMI

Yawata Research and Development Laboratories, Nippon Steel Corporation
1-1 Tobihata, Tobata-ku, Kitakyushu 804-8501 Japan

Abstract

A strong dependence of primary recrystallization texture on Goss secondary recrystallization was demonstrated in grain oriented silicon steel produced by injected inhibitor technology. Primary recrystallization texture and structure change by grain growth and they are important parameters to control secondary recrystallization. The sharpness and anisotropy of orientation distribution of Goss secondary recrystallized grains change by grain growth of primary recrystallization structure. These features are explained by the change of the two major components of the primary recrystallization texture; {111}<112> and {411}<148>, which have a $\Sigma 9$ coincidence relationship to Goss orientation.

Keywords: silicon steel, secondary recrystallization, texture, inhibitor, coincidence boundary, grain growth

1 Introduction

Grain oriented silicon steel is a soft magnetic material widely used for transformer cores. Magnetic properties are closely related to the sharpness of {110}<001> texture, i.e. Goss texture, which is evolved by secondary recrystallization. When the preferred orientation of {110}<001> is developed, the product has a superior magnetic properties, such as low core loss, low magnetostriction and high permeability, along the rolling direction.

The principal process for developing Goss texture was invented by Goss in 1934 (Goss, 1934) and industrialized by ARMCO in the 1940's [CGO : conventional grain oriented silicon steel] (Littmann,1967). The average deviation angle of <001> axis is 7 degrees from the rolling direction. High permeability grain oriented silicon steels (average misorientation of 3 to 4 degrees) were developed by Nippon Steel in the 1960's [HI-B] (Taguchi and Sakakura,1969) and later by Kawasaki Steel in the 1970's (Goto et al.,1975). The major differences among these processes are the preparation conditions of primary recrystallization texture, which is mainly controlled by the cold rolling reduction and the contents of precipitates such as MnS, MnSe and AlN for the grain growth inhibitor of primary recrystallized matrix. In order to attain this optimum precipitates, a high temperature slab reheating technology has been applied for the solution treatment and fine precipitates are formed in the hot rolling stage and/or hot-rolled sheet annealing stage.

Recently, another technology for the preparation of the precipitate, i.e. nitrogen injection technology, was proposed by Nippon Steel (Takahashi and Harase, 1996, Arai et al.,1996, Ushigami et al.,1996a, 1996b, 1996c, Takahashi et al,1996). It was demonstrated that primary recrystallization texture and structure change by grain growth and they are important parameters to control secondary recrystallization (Ushigami et al.,1996d, Yoshitomi et al.,1996, Cicale et al.,1998).

The objective of this paper is to investigate the effect of primary recrystallization texture on Goss secondary recrystallization texture in grain oriented silicon steel produced by injected inhibitor technology and to clarify the mechanism of orientation selectivity in secondary recrystallization process.

2 Experimental Procedure

The material used in this investigation was the hot rolled Fe-3%Si sheet of 2.0mm thickness with the following chemical compositions; Si:3.3, C:0.05, Mn: 0.1, Al:0.03, N:0.007 mass%. It was processed as follows; Annealing (1120℃+900℃)→ Cold rolling (0.2mm-thickness)→Decarburization and primary recrystallization annealing ((A) 810℃, (B) 830℃, (C) 850℃, (D) 870℃, (E) 890℃ for 90s in an atmosphere of wet N_2+H_2 mixture gas)→Nitrogen-injection treatment (nitrogenized up to 0.05% by annealing at 750℃ in an atmosphere of N_2+H_2+NH_3 mixture gas) .

Then, the primary recrystallized specimens were heated up to 1075℃ and then soaked for 30h in an atmosphere of N_2+H_2 mixture gas for secondary recrystallization (Annealing Ⅰ). Among the primary recrystallized specimens, two specimens, specimen A ((810℃) and specimen C (850℃), were selected and they were heated up to 1200℃ in the temperature gradient of 0.5℃/mm in N_2+H_2 mixture gas to investigate the selective growth behavior in secondary recrystallization (Annealing Ⅱ).

Microstructure and macrostructure of the specimens were investigated by optical microscopy. Microstructures of the primary recrystallized specimens were measured on the cross section parallel to the rolling direction and macrostructures of the secondary recrystallized specimens were measured on the surface. Orientations of the secondary recrystallized grains were measured by back-reflection Laue diffraction method. Complete {100} pole figures were measured by x-ray measurement from the surface (1/5th of the thickness) and the center layer of the specimen. From the average of these data, primary recrystallization texture was determined by three dimensional texture analysis by vector method (Ruer and Baro,1977).

3 Results and Discussion

3.1 Effect of primary recrystallization structure on secondary recrystallization

Fig.1 shows the relationship between the average grain size after primary recrystallization and the sharpness of Goss secondary recrystallization texture, which is expressed by magnetic induction (B8). Fig.2 shows the macrostructures after secondary recrystallization annealing. It can be seen from Fig.1 and Fig.2 that secondary recrystallization texture becomes sharper with increasing the average grain size and magnetic induction (B8) increases until the abrupt increase of coarse grains. It was reported that abnormal grain growth, resulting in the increase of coarse grains in the primary recrystallized matrix, cause instability of secondary recrystallization (Ushigami et al.,1996d, Yoshitomi et al., 1996). In this experiment, in the course of grain growth the frequency of coarse grains with grain size more than 50 μ m, which is more than the twice of the average grain size, increases rapidly in the case of specimen E and this leads to unstable secondary recrystallization.

Taking these results into account, two specimens, specimen A and specimen C, were selected to investigate the relationship between the primary recrystallization texture and secondary recrystallization texture.

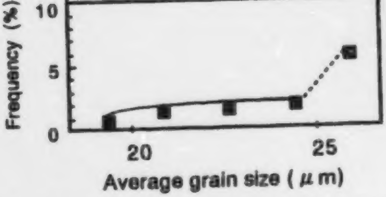

Fig.1 Effect of average grain size on the magnetic induction (B8) after secondary recrystallization and on the frequency of coarse grains (D>50 μ m)in the primary recrystallized matrix.

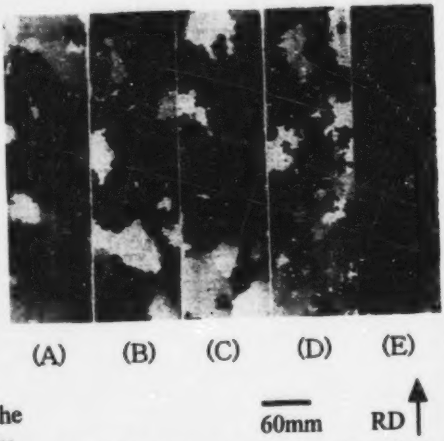

Fig.2 Macrostructures after secondary recrystallization annealing at 1075℃ .

3.2 Secondary recrystallization texture

Fig.3 illustrates the macrostructure of the secondary recrystallized grains after temperature gradient annealing (Ushigami et al.,1998). Several secondary recrystallized grains nucleate at the edge of the specimen and grow along the temperature gradient direction. In the course of grain growth, some of the grains grow preferentially to form a columnar structure. Secondary recrystallized grains are classified into two groups; stunted grains and growing grains. Orientation of individual secondary recrystallized grain was measured and represented as the deviation angles from the ideal Goss orientation around the three axes; normal direction of the sheet (ND), rolling direction (RD) , and transverse direction (TD).

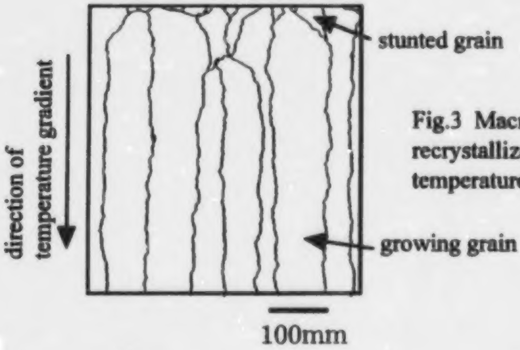

Fig.3 Macrostructure of secondary recrystallized grains of the temperature gradient annealing.

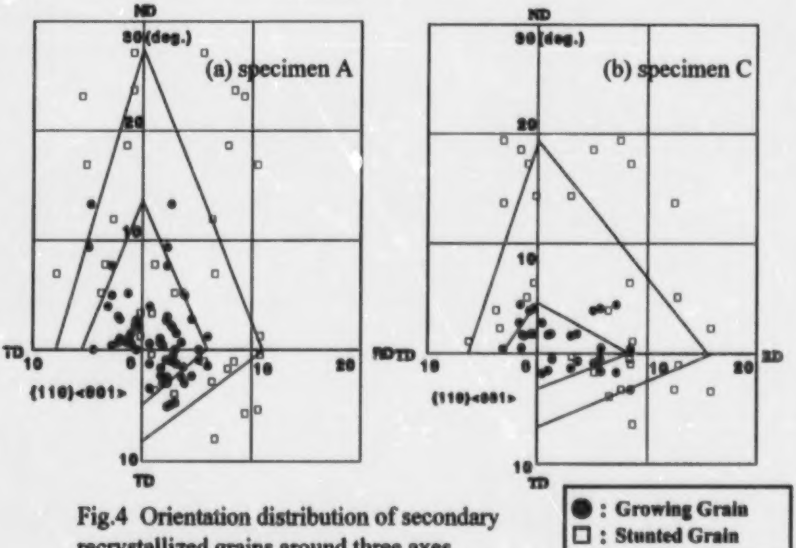

Fig.4 Orientation distribution of secondary recrystallized grains around three axes.
(a) specimen A, (b) specimen C

As shown in Fig.4, orientation distributions of secondary recrystallized grain are anisotropic and become shaper as grains grow. Especially, the orientation distributions of growing grains are different from each other. As is summarized by Table 1, the orientation distribution of specimen A is the ND-deviated type (△ND>△RD>△TD), on the other hand that of the specimen C is the RD-deviated type (△RD>△ND～△TD) . These facts suggest that selective growth during grain growth stage takes an important role in controlling the Goss secondary recrystallization texture.

Table 1: Misorientation limit angle of growing grains.

Axis of rotation	Specimen A	Specimen C
ND	13°	4°
RD	6°	8°
TD	4°	3°

3.3 Primary recrystallization texture

It has been reported that Σ9 coincidence boundary takes an important role in the selective growth behavior (Shinozaki et al,1978, Harase et al.,1986, Ushigami et al., 1991, Hutchinson and Homma,1998). Therefore, in order to figure out the role of primary recrystallization texture, primary recrystallization texture was measured and analyzed to evaluate the frequency of coincidence (Σ9) grains in the matrix. Fig.5 (a) and (b) show the three dimensional orientation distributions of the primary recrystallization texture. It can be seen that in the primary recrystallization texture the Goss orientation is a minor component and major components are classified as follows ; (a) γ-fiber with the peak of {111}<112> and (b) rotated α-fiber, which is rotated about 20 degrees around the ND axis, with the weak peak of {411}<148>. These two components, {111}<112> and {411}<148>, are calculated to have a Σ9 coincidence relationship to Goss orientation assuming the Brandon's criterion (Brandon,1966) . As shown by Fig.5 (c), {111}<112> component decreases and {411}<148> component increases with the grain growth.

Frequencies of Σ9 coincidence grains around three axes were calculated. It can be seen from Fig.6 (a) and (b) that the frequency of Σ9 coincidence grains takes a maximum value at {110}<001> orientation and the distributions of Σ9 coincidence grains in the matrix are qualitatively estimated as the ND-deviated type (△ND>△RD>△TD) for specimen A and the RD-deviated type (△RD>△TD～△ND) for specimen C, respectively, which correspond to the orientation distributions of Goss secondary recrystallized grains (Fig.4).

Thus, it can be concluded that anisotropy of orientation distribution of secondary recrystallized grains depends on the frequency of Σ9 coincidence grains in the primary recrystallized matrix.

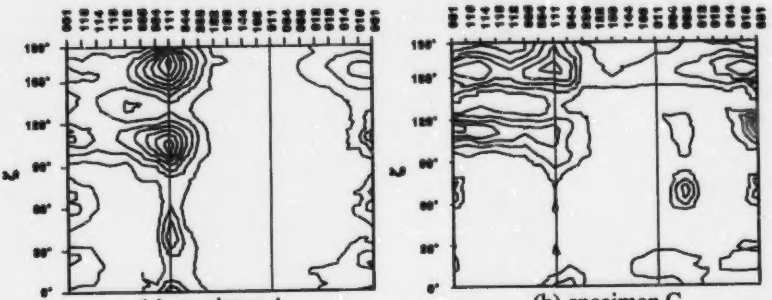

(a) specimen A (b) specimen C

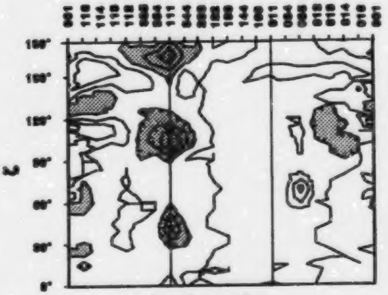

(c) subtraction

Fig. 5 Three dimensional orientation distributions of primary recrystallization texture. (x random)
(a) specimen A, (b) specimen C
(c) subtraction; specimen C-specimen A
(the hatched areas are the regions with minus sign.)

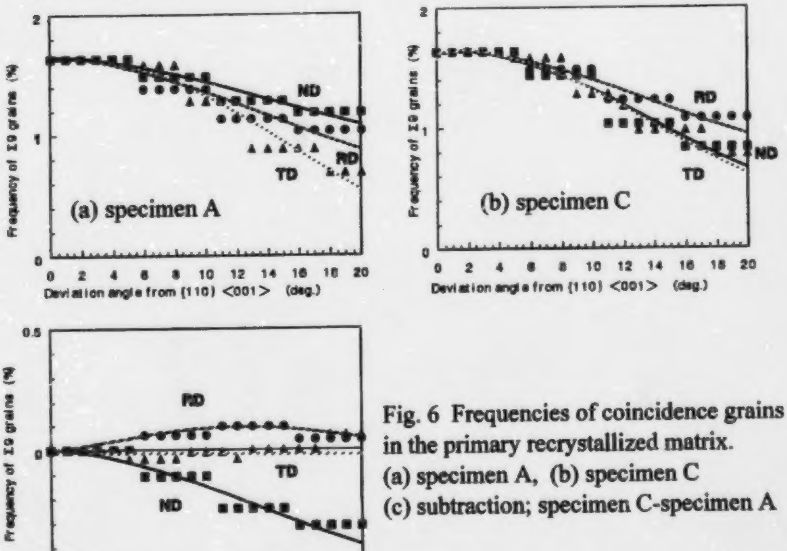

Fig. 6 Frequencies of coincidence grains in the primary recrystallized matrix.
(a) specimen A, (b) specimen C
(c) subtraction; specimen C-specimen A

3.4 Orientation selectivity behavior during grain growth

For the investigation of this selective growth mechanism, some specimens were quenched in the heating stage of the temperature gradient annealing. Fig.7 illustrates the macrostructure of the growth front of the secondary recrystallized grains. The growth front of the secondary recrystallized grain is macroscopically uniform though it has some fluctuation in microscopic point of view. It can be seen from Fig.7 that secondary recrystallization temperature, which is defined as the growth front temperature, takes a specific value depending on the orientation of the secondary recrystallized grain. The secondary recrystaliization temperatures of the secondary recrystallized grains in these specimens were in the range from 1050 to 1065℃. Secondary recrystallization temperatures of the sharper Goss grains are around 1050 ℃, which are about 10℃ lower than those of the deviated Goss grains. Depending on the difference of secondary recrystallization temperature, sharper Goss grains grow preferentially by expanding the growth front and consuming the primary matrix region earlier than the deviated Goss grains. In the end, sharper Goss grains, which have the same secondary recrystallization temperature, grow stationary along the temperature gradient direction.

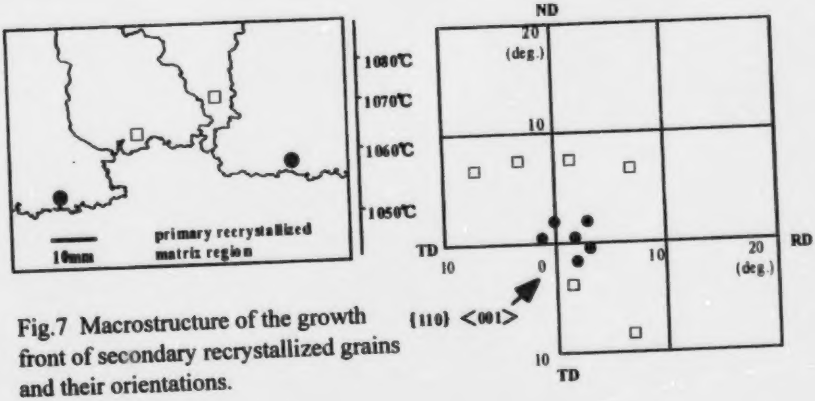

Fig.7 Macrostructure of the growth front of secondary recrystallized grains and their orientations.

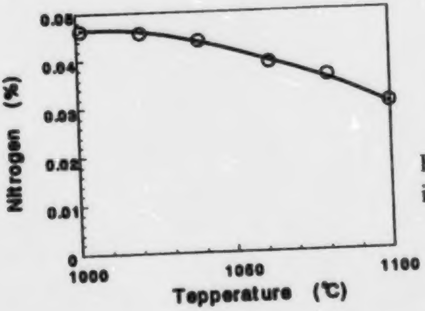

Fig.8 Change of nitrogen content in the temperature gradient annealing.

Fig.8 shows the change of nitrogen content of the specimen measured by chemical analysis. It is clear that nitrogen content which indicates inhibition intensity decreases with annealing temperature. The nitrides formed by nitrogenizing treatment are (Si,Mn)N, Si_3N_4 and they are concentrated at the surface layer. These nitrides are thermally unstable, then they dissolve in the temperature range from 750℃ to 900℃ during the heating stage of annealing and re-precipitate as (Al,Si)N through the thickness and inhibit the grain growth of the matrix grains. Above 1000℃, (Al,Si)N dissolves and nitrogen removes from the silicon iron sheet as nitrogen gas (Ushigami et al.,1996d).

It can be seen from Fig.7 and Fig.8 that secondary recrystallization proceeds during the deteriorating stage of inhibition effect and sharper Goss grains start to grow at the stage of higher inhibition level.

3.5 Mechanism of orientation selectivity

Secondary recrystallization phenomenon is described by the following Hillert's model of grain growth, which takes the textural effect into account (Hillert, 1965, Abbruzzese and Lücke,1986, Nakayama and Ushigami,1986).

$$dR/dt=MP \tag{1}$$

$$P=AE\{(1/Rc)-(K/R)-(KZ/A)\} \tag{2}$$

where R: radius of secondary recrystallized grain, Rc: critical radius of primary recrystallized matrix, M: mobility, P: total driving force of secondary recrystallized grain, A: geometrical factor, E: average grain boundary energy of primary recrystallized matrix, K: ratio of secondary recrystallized grain boundary energy to that of matrix primary recrystallized grain boundary energy (E), Z: Zener term

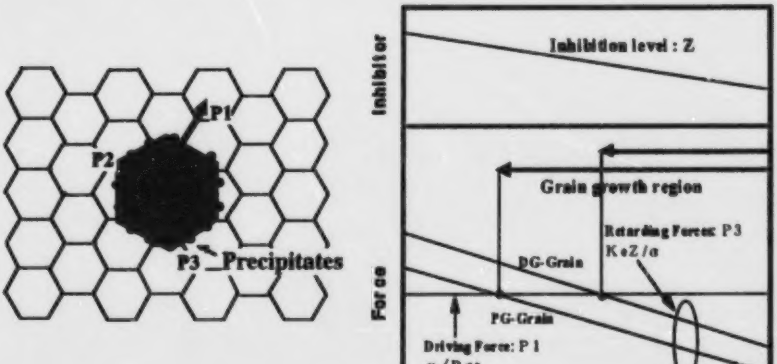

Fig.9 Schematic diagram of orientation selectivity during grain growth of secondary recrystallization. (PG-grain; precise Goss grain, DG-grain; deviated Goss grain)

As can be seen from equation (2) and the diagram (Fig.9), total driving force of secondary recrystallized grain consists of three components. The first component (P1) is the driving force derived from the tension of grain boundaries of the primary recrystallized matrix. The second (P2) is the retarding force derived from the shrinking force of the secondary recrystallized grain itself. The third (P3) is the retarding force by the pinning effect of precipitates.

To discuss the selective growth of sharper Goss grains shown by Fig.7, the grains are classified into the following two classes; (1) precise Goss grain (PG-grain) and (2) deviated Goss grain (DG-grain). It is reported that coincidence boundary has a lower grain boundary energy than the general boundary (Hasson, 1971) and thus is supposed to suffer lower pinning force from the precipitates (P3). The frequency of coincidence grains in the matrix of the precise Goss grain is evaluated to be higher than that of deviated Goss grain. Thus, the effective retarding force from the precipitates (P3) is estimated to be lower in this order. On the other hand, the driving force (P1) is independent of orientation and takes the same value for the two classes. In the growth stage, grain size of the secondary recrystallized grain is much larger than the matrix grains. Therefore, the shrinking force of the secondary recrystallized grain (P2) becomes negligible.

As a result, the intersection point of the driving force (P1) and the retarding force (P3) is estimated to be the onset of the grain growth and the growth behavior of the two classes is schematically illustrated in Fig.9. Precise Goss grain, which has higher frequency of coincidence grains in the matrix, suffers lowest retarding force from the precipitates and starts to grow at lower temperature or at the stage of higher inhibition level.

4 Conclusions

Primary recrystallization texture and structure are important parameters to control secondary recrystallization and effect of primary recrystallization texture on Goss secondary recrystallization texture was investigated in grain oriented silicon steel by injected inhibitor technology.

(1)Sharpness and anisotropy of orientation distribution of Goss secondary recrystallized grains change by the grain growth of primary recrystallization structure.

(2)These features are explained by the selective growth due to the frequency of Σ9 coincidence grains in the primary recrystallized matrix ; two major components of the primary recrystallization texture, {111}<112> and {411}<148>, which have Σ9 relationship to Goss grains, change by the grain growth and affect the orientation distribution of Σ9 coincidence grains.

(3)Sharper Goss grains which have higher frequency of Σ9 coincidence boundaries to the matrix grow at lower temperatures.

(4) Σ9 coincidence boundary is supposed to have lower grain boundary energy, thus suffers lower pinning effect from the precipitates and migrates preferentially at higher inhibition level.

References

Abbruzzese,G. and Lücke,K. (1986) Proc. 7th RISO Int. Symp. of Met. and Mat. Sci., p1

Arai,S., Ushigami,Y. and Takahashi,N. (1996) Mat. Sci. Forum, 204-206, p617

Brandon,D.G. (1966) Acta Met. 14, p1479

Cicale,S., Fortunati,G. Abbruzzese,G. and Matera,S. (1998) Proc. 3rd Int. Conf. of Grain Growth, p587

Goss,N.P. (1934) U.S.P.No.1,965,559.

Goto,I. Matoba,I, Imanaka,T. Gotoh,T. and Kan,T. (1975) Proc. Soft Mag. Mat. 2, p262

Harase,J., Shimizu,R., and Watanabe,T. (1986). Proc. 7th RISO Int. Symp. on Met. Mater. Sci., p343

Hasson,G.C. and Goux,C. (1971) Scripta Met., 5, p889

Hillert,M. (1965) Acta Met., 13, p227

Hutchinson,B. and Homma,H. (1998) Proc. 3rd Int. Conf. of Grain Growth, p387

Littmann,M.F. (1967) J.Appl.Phys., 38, p1104

Nakayama,T. and Ushigami,Y. (1986). Proc. 7th RISO Int. Symp. on Met. and Mat.Sci., p463

Ruer,D and Baro,R. (1977) J.Appl.Cryatallogr., 10, p458

Shinozaki,M., Matoba,I., Kan.T. and Gotoh,T. (1978). Trans. JIM, 19, p85

Taguchi,S. and Sakakura,A. (1969) J.Appl. Phys., 40, p1539

Takahashi,N. and Harase,J. (1996) Mat. Sci. Forum, 204-206, p143

Takahashi,N., Suga,Y. and Kobayashi,H. (1996) J.Mag. Mag. Mat., 160, p98

Ushigami,Y., Suga,Y., Takahashi,N., Kawasaki,K., Chikaura,Y and Kii,H. (1991) J.Mater. Eng. 13, p113

Ushigami,Y., Kurosawa,F., Masui,H., Suga,Y. and Takahashi,N. (1996a). Mat. Sci. Forum, 204-206, p593

Ushigami,Y., Nakayama,T., Suga,Y.and Takahashi,N. (1996b) Mat. Sci. Forum, 204-206, p599

Ushigami,Y., Nakayama,T., Suga,Y.and Takahashi,N. (1996c) Mat. Sci. Forum, 204-206, p605

Ushigami,Y., Yoshitomi,Y. and Takahashi,N. (1996d) Mat. Sci. Forum, 204-206, p623

Ushigami,Y., Kubota,T. and Takahashi,N. (1998) ISIJ International, 38, p553

Yoshitomi,Y., Ushigami,Y., Takahashi,N., Nakayama,T. Suga,Y. and Harase,J. (1996) Mat. Sci. Forum, 204-206, p629

INFLUENCE OF HEATING RATE ON RECRYSTALLIZATION IN LOW AND ULTRA-LOW CARBON STEELS

M. FERRY, D. MULJONO and D.P. DUNNE

Department of Materials Engineering, University of Wollongong, NSW, Australia

Abstract

Electrical resistance annealing using a Gleeble 3500 TMP simulator was used to study the effect of heating rate on the recrystallization kinetics, grain size and texture of a series of steels with carbon levels 0.003 - 0.05%C. The as-hot-rolled steels were cold-rolled to 70% reduction and subsequently annealed at heating rates from 50 to 1000°C/s to peak temperatures (T_p) in the range 600 to 900°C. To minimise masking effects associated with rapid isothermal recrystallization at high temperature, all samples were water-quenched within 0.05s of reaching T_p. For all steels investigated, the rate of anisothermal recrystallization and final grain size decreases with increasing heating rate. The decrease in grain size and concurrent weakening of the γ-fibre (at rates above ~200°C/s) with increased heating rate was attributed to nucleation at sites in addition to grain boundaries. The present observations are in marked contrast to previous work where it was claimed that ultra-rapid softening (which was associated with an observed decrease in recrystallization temperature at high heating rate) occurs at heating rates in excess of ~500°C/s. The present results indicate that 'ultra-rapid softening' is likely to be an artefact of these earlier experiments.

Keywords: anisothermal recrystallization, grain size, heating rate, texture

1 Introduction

It has been argued that annealing of low carbon steel at high heating rates (>500°C/s) results in *accelerated softening* (Atkinson 1993). Such terminology was used to explain a discontinuous change in annealing behaviour, that is, a sharp depression of the recrystallization start temperature and an increase in the rate of recrystallization above a critical heating rate. For a range of low carbon steels, it was reported that this high-rate annealing results in complete recrystallization in a fraction of a second over a small temperature range, producing a coarse-grained microstructure with strong recrystallization texture, that is, sharpening of the favourable {111}//ND components or γ-fibre (Atkinson 1993). The objective of the present investigation is to elucidate the effect of heating rate on annealing behaviour of cold rolled steels with carbon contents of 0.003 to 0.05wt%C. A range of heating rates (up to 1000°C/s) and peak temperatures (625 to 800°C) was studied to determine if accelerated softening, grain coarsening and texture strengthening occurs beyond a critical heating rate.

2 Experimental procedure

Steels with carbon contents 0.003, 0.02 and 0.05%C were used in this work. All steels were supplied by BHP Integrated Steel, Port Kembla in the hot rolled condition and exhibited a starting grain size of ~30μm. The steels were subsequently cold rolled to 70% reduction. Following cold rolling, 10mm x 40mm strips were annealed by resistance heating using a Gleeble 3500 TMP simulator at heating rates from 50 to 1000°C/s to peak temperatures (T_p) in the range 600 to 900°C. To study the effect of heating rate on recrystallization behaviour and to minimise masking effects associated with rapid isothermal recrystallization at high temperature, all samples were water-quenched within 0.05s of reaching T_p.

The microstructures of the cold rolled and annealed samples were examined by optical microscopy, and grain size and volume fraction recrystallized were determined by quantitative metallography. The recrystallization textures were determined using a fully automated EBSD/SEM facility using HKL™ software. The volume fraction of specific texture components (ie. <110>//RD or α-fibre, {111}//ND or γ-fibre and {110}<001> components) were determined as follows: specimens were electropolished and areas of microstructure were mapped in beam-scanning mode with a step size 1μm. For each specimen, several areas of size 200x200μm were analysed and the data processed to determined the area fraction of a particular texture component. Each grain was determined to be of a given texture component if they were within 15° of the desired orientation. Image analysis was then carried out to determine the area fraction of grains of a particular texture component. This method allows the determination of the area fraction of specific texture components as a function of heating rate and any uncertainty with calculation routines is minimised. The recrystallized grain sizes were generally greater than 10μm, such that a step scan of 1μm was found to give consistent results.

3 Results

3.1 Recrystallization Kinetics

The effect of heating rate on the recrystallization kinetics (given as the temperature corresponding to 50% recrystallization, $T_{0.5}$) is shown in Fig. 1 for all steels. It was found that $T_{0.5}$ increases with heating rate, and the temperature range of recrystallization, given as $T_{0.9}$ - $T_{0.1}$, also increases slightly (Muljono 1999).

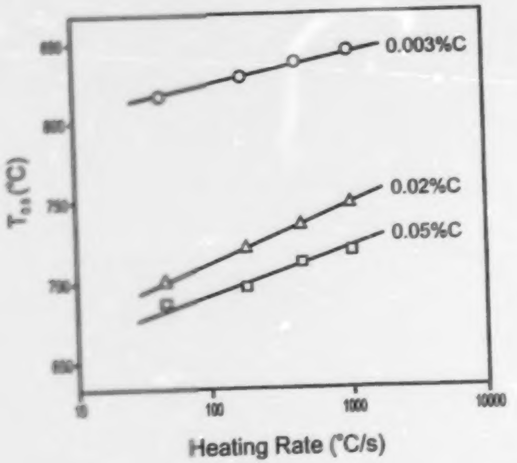

Fig. 1: Effect of heating rate on the temperature to complete 50% recrystallization ($T_{0.5}$). All samples were water quenched within 0.05s of reaching T_p.

3.2 Recrystallized Grain Size

With increasing heating rate, a decrease in the recrystallized grain size was observed in all steels (Fig. 2). Such grain refinement with increasing heating rate is in accordance with the study by Lebrun *et al*. (1981) where it was argued that increased heating rate will raise the temperature at which recrystallization starts (which is the case here), and hence increase the nucleation rate as $\dot{N} \propto \exp(-Q_N/RT)$ (Humphreys and Hatherly 1995) which will subsequently produce a finer grain size.

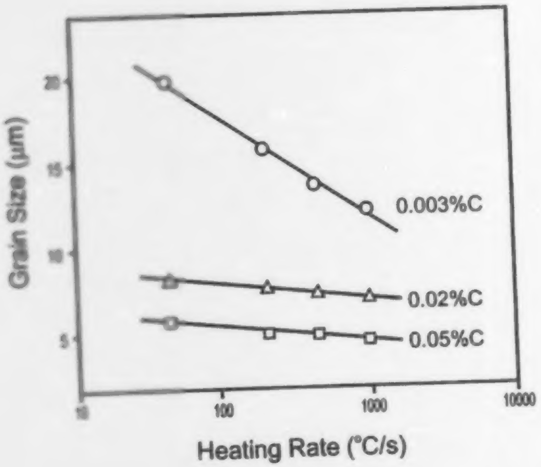

Fig. 2: Effect of heating rate on recrystallized grain size.

3.3 Recrystallization Texture

The effect of heating rate on the recrystallization texture, given as the area fraction of grains within 15° of the orientation {111}//ND or γ-fibre, is given in Fig. 3 for steels with 0.003 and 0.02%C. The area fraction of {111}//ND grains increased following heating at rates up to ~200°C/s and decreased slightly thereafter.

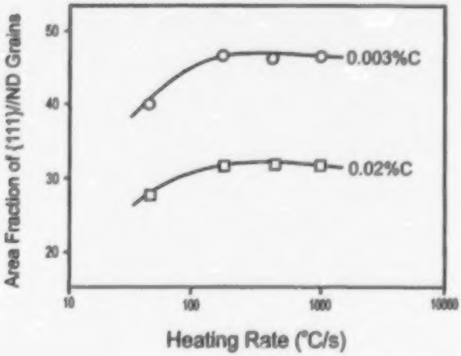

Fig. 3: Effect of heating rate on strength of recrystallization texture, given as the area fraction of grains within 15° of {111}//ND or γ-fibre.

4 DISCUSSION

4.1 Recrystallization behaviour during rapid heating

The results show that moderately cold-rolled low and ultra low carbon steels can recrystallize anisothermally by annealing at high heating rates. For steels with a range of carbon levels (0.003 - 0.05%C), an increase in heating rate resulted in an *increase* in the recrystallization start temperature and temperature range of recrystallization, and a *decrease* in final grain size and strength of the texture (at rates above ~200°C/s).

The present observations are in contrast to previous work on low carbon steel where it was claimed that ultra-rapid softening (which was associated with an observed decrease in recrystallization temperature at high heating rate) occurs at rates in excess of ~500°C/s (Atkinson 1993). This previous work reported that beyond a critical heating rate, recrystallization is accelerated, and a coarse recrystallized grain size and strong recrystallization texture is produced. In light of these observations, it was argued that ultra-rapid heating enables rapid annihilation of statistically stored dislocations rather than relaxation of the substructure into more stable arrays (ie. polygonization). It was then argued that this bifurcation of recovery processes allows easy nucleation with the associated high angle boundaries advancing rapidly into simple dislocation arrays. The term *ultra rapid softening* was used to explain this unusual type of annealing phenomenon (Atkinson 1993). In contrast to previous work, this study shows that a discontinuous change in annealing behaviour does not occur at heating rates up to 1000°C/s for steels containing a wide range of carbon levels.

4.2 The occurrence of 'ultra-rapid softening'

Detailed experiments have been carried out to clarify the effect of both overshooting of the peak temperature T_p and cooling rate from T_p on recrystallization during high-rate annealing (Muljono 1999). It was shown that extreme care must be taken to minimise overshooting at high heating rates (>500°C/s). Overshooting can, if not controlled, result in enhanced recrystallization and thus give, at high heating rates, the impression of a depression in the recrystallization temperature (Muljono 1999). Recrystallization is a thermally-activated process and the kinetics of the process such as nucleation rate and rate of grain boundary migration usually obey an Arrhenius-type relationship (Humphreys and Hatherly 1995). Subsequently, overshooting will result in rapid boundary migration to full recrystallization and possibly grain growth. Therefore, overshooting will result in a depression of the apparent recrystallization temperature and produce a coarse final grain size. Grain growth in low carbon steel is known to strengthen the {111}//ND texture components (Ray *et al.* 1994) and this may contribute to an increase in texture strength. The initial strengthening of the γ-fibre following heating at rates up to 200°C/s and a subsequent slight decrease thereafter was attributed to enhanced grain boundary nucleation, and eventually, additional nucleation of other texture components at intragranular sites (Muljono 1999).

It has been demonstrated convincingly (Muljono 1999) that the rate of cooling from the peak temperature T_p also influences the recrystallization behaviour markedly (fraction recrystallized at a given T_p). For this reason, all specimens were water quenched within 0.05s of reaching T_p to eliminate the masking effects caused by variation in cooling rate. Figure 4 shows data for the temperature range of recrystallization as a function of heating rate for immediate water quenching and delayed cooling. The peculiar results reported by Atkinson (1993) are reproduced (dashed lines) if the rate of quenching is low and/or T_p is exceeded.

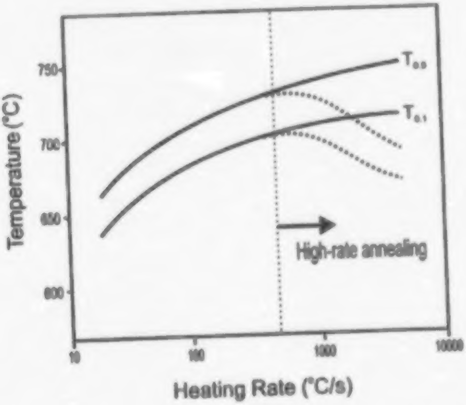

Fig. 4: Effect of delayed or slow cooling from T_p (dashed lines) on the temperature range of recrystallization, given as $T_{0.9}$ - $T_{0.1}$ for a 0.05%C steel.

The present results, whereby an increase in heating rate increases the recrystallization temperature and decreases the final grain size was reproduced for all steels. These trends are similar to work published elsewhere on an initially coarse grained low carbon steel cold rolled and induction-heated (Muljono *et al.* 1998). These results, together with careful experiments of overshooting and cooling effects, indicate that "ultra-rapid softening" is likely to be an artefact of many earlier experiments.

5 Conclusions

- For a range of cold rolled steels with carbon levels of 0.003 - 0.05%C, increasing heating rate increases the nucleation temperature and temperature range of recrystallization and produces a refinement in recrystallized grain size. The {111}//ND components of the recrystallization texture decreased at rates above ~200°C/s due to nucleation at sites in addition to grain boundaries.
- There was no evidence to suggest, for the degree of cold rolling (70%) and heating rates examined (50-1000°C/s), that accelerated softening occurs above a critical heating rate. The present results indicate that 'ultra-rapid softening' is likely to be an artefact of earlier experiments.

Acknowledgments - The authors would like to acknowledge the provision of the steels by BHP Research, Australia. One of the authors (DM) acknowledges the support of an AUSAID scholarship.

6 References

Atkinson, M. (1993) Ultra-rapid annealing of low-carbon steel, *Materials Forum*, 17, p181.

Humphreys, F.J. and Hatherly, M. (1995) Recrystallization and Related Annealing Phenomena, Pergamon Press, Oxford, UK.

Lebrun, J.J., Maeder, G. and Parniere, P. (1981) Analysis of the influence of the heating rate on the recrystallization of low carbon steel sheet, *in Proceedings of ICOTOM VI*, ed. S Nagashima, Tokyo, Japan, p787.

Muljono, D. (1999) High-rate annealing of low and ultra low carbon steel. *Ph.D Dissertation*, University of Wollongong.

Muljono, D., Ferry, M. and Dunne D.P. (1998) High-rate induction annealing of cold rolled low carbon steel sheet. *In Proceedings of 39th Mechanical Working and Steel Processing Conference*, ISS, Indianapolis, USA, 35, p667.

Obara, T., Sakata, K. and Irie, T. (1982) Effect of cooling rate in continuous annealing on tensile properties of Al-killed sheet steel, *in Metallurgy of Continuous-Annealed Steel*, eds. B.L Bramfitt and P.L. Mangonon, TMS, p84.

Ray, R.K., Jonas, J.J. and Hook, R.E. (1994) Cold rolling and annealing textures in low and ultra low carbon steels, *International Materials Reviews*, 39, p129.

OPTIMISATION OF GALVANISATION PROCESS PARAMETERS TO IMPROVE THE CRACKING RESISTANCE IN ZINC COATINGS.

S. GAIGNARD and C. ESLING
Laboratoire d'Etude des Textures et Application aux Matériaux, Metz, France
J. WEGRIA
Union Minière, Olen, Belgian
M. DUBOIS
Cockerill-Sambre, Liège, Belgian

Abstract

Galvanising steel sheet is an economic and effective process to protect steel against corrosion. This is the reason why hot-dip galvanised steel sheet has become one of the main products for automotive body panels. During forming operations of coated steels, cracking can occur and the efficiency of galvanisation drops.

In a previous study [Lazik], a clear correlation between the texture, the microstructure and the cracking resistance has been established. The higher the density of subgrains, recrystallised grains and twins is, the more the size of the domains decreases and the weaker the intensity of the (00.2) pole figure is, the better the cracking resistance will be. The sharpness of the *c*-axes peaks and its angle with the substrate surface normal determine the deformation behaviour of the coating layer. Primary zinc dendrites and recrystallised grains can hinder the crack propagation. This means that process parameters, that permit the appearance of nuclei of recrystallised grains and primary zinc dendrites, can improve the resistance to crack propagation in zinc coatings.

With this established relation, we try to modify the manufacturing process and/or bath composition to obtain optimal textures and microstructures for the best deformation behaviour. So, we choosed to test the process parameter "skin-pass reductions" to create recrystallised grains as well as "the cooling rates" to produce zinc primary dendrites. This presentation will report the first preliminary results obtained.

1 Introduction

The purpose of the present investigation was to determine the influent parameters which are able to control the texture of the galvanised coatings. It is already shown that microstructure and texture will influence coating mechanical behaviour [Lazik]. Due to the c/a ratio, basal slip is the predominant slip mode in zinc [Partridge] and so, as texture is the most important parameter as far as the anisotropy of the material properties is concerned, its influence on the deformation behaviour parameters is the most important.

Manufacture process and/or bath composition changed to obtain the most suitable texture and microstructure to obtain the best deformation behaviour. We choose to test skin-pass reductions as process parameters and the aluminium level as composition parameter.

2 Experimental procedure

The materials used in this study are hot-dip galvanised steel sheets that are industrially produced. For this study, a lot of hot-dip-galvanised steel sheets delivered by Cockerill Sambre have been studied. They differ according to their chemical compositions (Al), process parameters, mechanical treatments and thickness of the coating. To seek for the optimal parameters to optimise the cracking resistance behaviour, 5 steels have been tested before skin-pass and after respectively 1% and 5% skin-pass and with different cooling rates and processes. Some others samples have been skin-passed in an industrial line.

Incomplete (00.2) pole figures of the zinc coatings surfaces are measured in the same conditions by X-ray diffraction up to 78.5° tilt angle on samples after cutting and cleaning. The radiation used is Co - Kα, at 40 kV and 25mA. The pole figures are measured with a tilt angle step $\Delta \chi = 2.5°$ and an azimuthal step $\Delta\varphi = 5°$.

The coated surfaces of the undeformed samples have been prepared metallographically (mechanical polishing and chemical etching) and observed with an optical microscope (Zeiss Axiophot) and in some cases, with a SEM (Leica S440, Hitachi S2500). The grain size has been determined by linear analysis. The microstructure analysis is carried out after polishing, at half thickness of the coating. The cracking behaviour of the coatings was determined by bending tests and biaxial expansion, carried out in the R&D centre of Cockerill-Sambre, Belgium.

3 Result and discussion

3.1 Texture, microstructure and deformation behaviour of three samples with different aluminium contents.

Table 1 : Al content in the three studiedsamples.

	1	2	3
Aluminium content (%)	0.18	0.3	5

All the samples were characterised by texture, microstructure and deformation analysis.

In view of assessing the influence of the aluminium content, these samples were not skin – passed.

Sample 1 is a zinc alloy coating containing just a low aluminium level. The microstructure of this sample shows very big grains and it is not possible to assess the texture of this sample with one single pole figure measurement, but several pole figure have to be superimposed to increase the statistical relevance. Pole figure shows several single orientations which form a less homogeneous peak distribution, with high intensity, around the pole figure centre (figure 1). In this case, the cracking resistance is not very good ; however, when the intensity is not so high and single peaks are broadened to form a more uniform distribution, the cracking behaviour is improved.

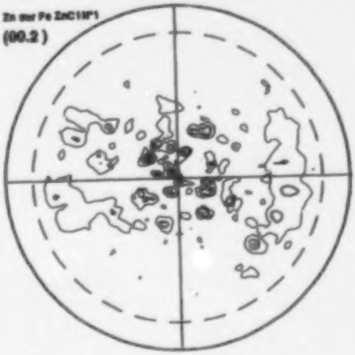

fig. 1: Superimposition of 4 measured (00.2) pole figures

Sample 2 is a zinc alloy coating containing a medium aluminium level. This sample shows a very weak basal texture and has only a few crystallites with their *c*-axis oriented parallel to the substrate normal (fig.2). There are crystallites with a more or less important tilt of the *c*-axis versus the normal direction to the substrate surface. The slip systems are preferentially active in these crystals during the deformation ; the tilted grains can accommodate the plastic deformation. Crystallites, having their *c*-axis normal to the substrate surface, remain in this stable orientation.

Sample 3 is a zinc alloy coating containing approximately 5% aluminium ; these coatings are called Galfan. In addition to the 5 % aluminium, the Galfan coating contains about 0.05% mischmetal, a naturally occurring mixture of the rare-earth elements cerium and lanthanum. This mixture improves the wettability of the samples, thus minimising uncoated spots. The microstructure of Galfan (eutectic coating) is characterised by a two-phase alloy, the zinc rich proeutectic phase being surrounded by an eutectic phase. The eutectic phase consists of alpha aluminium and zinc-rich eta-phase lamellae. The grains appear like spangles and are divided into many smaller grains. The dendrites structure of the proeutectic zinc can be observed in the grains. The effect of aluminium to minimise the intermetallic layer has been confirmed in our study. Aluminium forms an inhibition layer on the sheet surface and delays the growth of the brittle intermetallic layer between zinc and iron. The maximum diffraction intensity of the basal planes is located at the pole-figure centre, but the peak shows a broad dispersion and a weak intensity. This indicates that most basal planes are parallel or slightly tilted to the substrate surface, but no strong texture exists (fig.3). The cracking resistance of this Galfan coating is very good, confirming the results of Lazik.

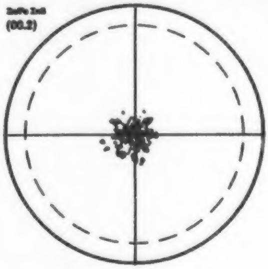

fig. 2: Very weak basal texture (I max : 5391)

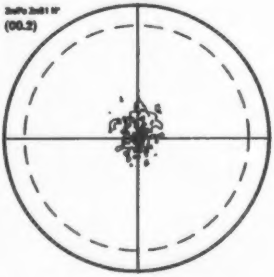

fig. 3: Galfan pole figure (I max : 5179)

To summarize, we can distinguish three groups of samples depending on aluminium content. They differ as far as microstructure, texture and cracking resistance are concerned. These samples are industrial samples ; we also studied samples obtained in a simulator, with various aluminium contents and our results confirm that with more aluminium, peak intensity and grain size decrease.

3.2 Process parameters controlling the texture of coatings

The effect of skin-pass will depend on the texture before skin-pass. If the initial texture has a major component in the pole figure centre, with weak and broadened peak intensity, a skin-pass reduces the domain sizes by producing recrystallized grains and twins (figure 4a and 4b). So the grains are divided into domains which are slightly misorientated with respect to the mean grain orientation. This leads to a drop of the intensity maximum and an increase of dispersion around the peak of reflecting grains. With a strong skin-pass (5%), even the cold rolling component can be reached (fig. 4b).

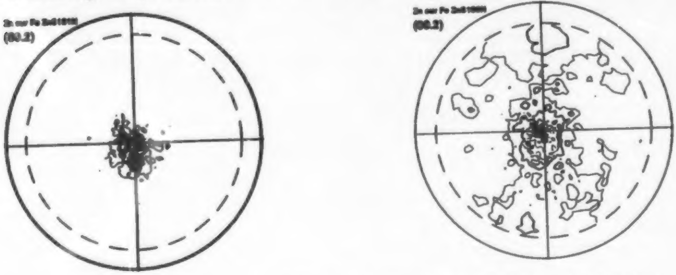

figure 4a and 4b : pole figure after 1% skin-pass (I max : 3687) and after 5% skin-pass (I max 903)

The greatest care must be taken in the assessment of the cracking resistance after the deformation test. A skin-pass may hinder the propagation of cracks by the generated small domains. But a skin-pass creates twins and recrystallised grains. These grains have different orientations which do not adapt the deformation. This is the reason why we can locally observe large cracks.

The propagation of cracks through domains is more difficult than before skin-pass because the misorientated domains impede the crack propagation.

A skin-pass improves the resistance to crack formation but a too high skin-pass induces too much of rolling and/or twinning components which are all distributed around the border of the pole figure. They lead to a lot of grains which remain undeformed during bending test, thus having a very bad influence on the cracking resistance, because they may be sources of cracking.

If the initial texture presents single orientations peaks dispersed through all the pole figures, a skin-pass has a good influence but does not lead to a major modification of the texture. Due to the plastic deformation, the grains were disturbed and divided into domains which are slightly misoriented with respect to the mean orientation. Intragranular crack propagation is more difficult than before skin-pass because the domains are smaller. But the individual orientations can still be identified ; the skin-pass does not merge all these single peaks (figure 5a and 5b).

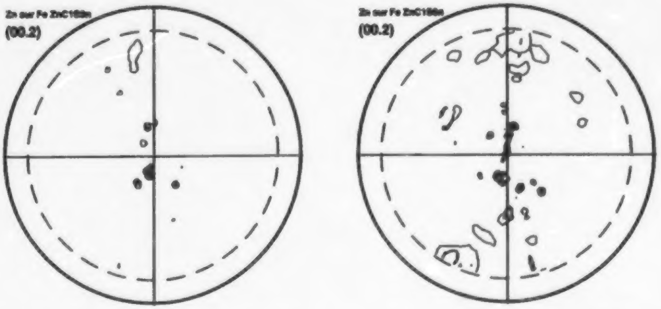

figure 5a and 5b : sample before skin-pass 1% (I max 8336) and after skin-pass 5% (I max = 2866)

4 Conclusion

Bath composition can modify to a large extent the deformation behaviour of coatings ; aluminium content is very influent. The higher aluminium content in the bath is, the better the deformation behaviour and as a consequence the cracking resistance is.

Skin-pass is an adapted process parameter to obtain a texture tailored in view of improving cracking resistance. Nevertheless skin-pass is not the only factor. The deformation degree plays the decisive role. This deformation degree depends on skin-pass reduction percentage, steel thickness, coating thickness and perhaps the work roll diameter can have an effect too. We should be careful not to go beyond a critical deformation degree. This critical value shows a disturbed microstructure and the pole figure intensity increases with the skin-pass reduction percentage. There are more and more twins, or subgrains, or recrystallised grains with the same orientation and the previous beneficial effect of skin-pass is lost.

The deformation degree is an important parameter but it is difficult to test it experimentally because there are many different parameters which are rather difficult to change on an industrial line. Thus it would be useful to develop a model to simulate all these various interdependent parameters.

5 References

Lazik, S., Esling, C., Philippe, M.J., Wégria, J., Dubois, M. : A Metallurgical Approach to the Cracking Resistance of Hot-Dip Galvanized Zinc Coatings Texture and Microstructures. Vol. 28, (1996), pp. 35-45.

Partridge, P.G. : The crystallography and deformation modes of hexagonal close-packed metals. Metallurgical Reviews. Vol. 12, (1967), pp. 169-194

EFFECT OF FINISH DEFORMATION TEMPERATURE ON TEXTURE DEVELOPMENT OF ULTRA LOW CARBON STEEL

D. YU, M. FERRY and T. CHANDRA

Department of Materials Engineering, University of Wollongong, NSW, Australia

Abstract

An ultra low carbon (ULC) steel has been deformed in plane strain compression using a Gleeble 3500 TMP simulator. Multiple-pass deformation was used to study the effect of finish deformation temperature (FDT) on microstructural development during subsequent cold rolling and annealing (CRA). It was found that a range of ferrite grain structures were produced when FDT decreased from 920 to 600°C. For FDT above 870°C, fine equiaxed ferrite was produced while a FDT of 850°C produced coarse-grained ferrite. For FDT < 800°C, as-deformed ferrite was obtained. The as-hot-deformed samples were cold rolled by 80% reduction and annealed at temperatures of 650 and 750°C. Bulk x-ray texture analyses showed that low FDT (< 800°C) produces the strongest <111>//ND texture (γ-fibre) in both hot-deformed and CRA samples. The results show that an unrecrystallized microstructure prior to cold rolling accelerates recrystallization and that the <111>//ND texture is more strongly developed.

Keywords: finish deformation temperature, recrystallization, ultra low carbon steel

1 Introduction

The development of annealing textures in low carbon (LC) and ultra low carbon (ULC) steels has been studied intensively with particular focus on the processing parameters: hot deformation temperature, cold reduction, annealing temperature and heating rate (Ray et al. 1994; Raabe 1995; Kestens and Jonas 1996; Barnett and Jonas 1997a, 1997b). Several investigations on the effect of hot-band microstructure on the annealing texture of cold-rolled strip have been undertaken in either annealed hot deformed steels (Barnett and Jonas 1997a, 1997b) or employing higher finishing rolling temperatures following high temperature coiling to get fully recrystallized hot bands (Ichiro 1998). Nevertheless, it has been found that structure prior to cold rolling could significantly affect both the rolling and annealing textures of IF steels (Nagataki and Hosoya 1996; Cui et al. 1997; He et al. 1997; Vanderschueren et al. 1997; Wang et al. 1997). It has been shown that the hot band microstructure can be influenced by pre-

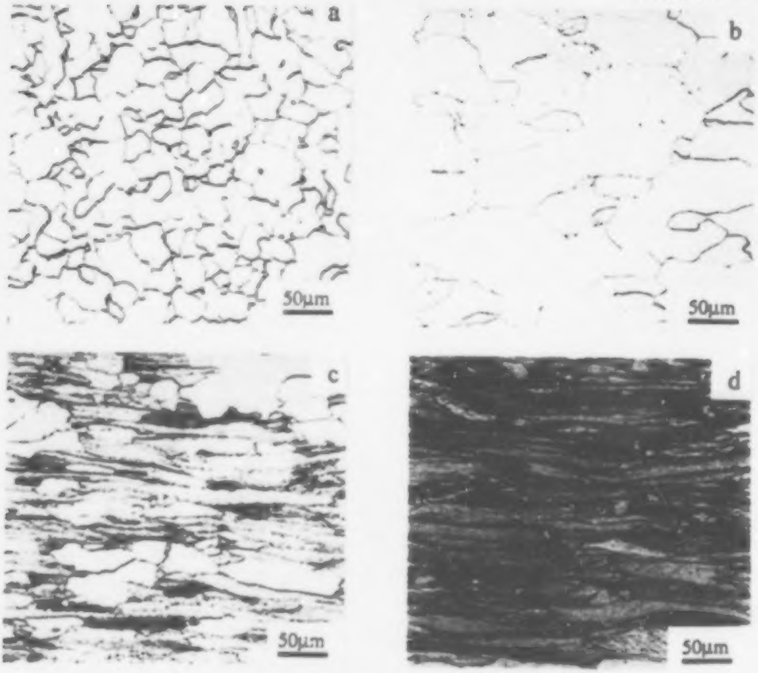
a
50µm
b
50µm
c
50µm
d
50µm

Fig. 1: Microstructures generated during multiple-pass deformation to finish deformation temperatures of a) 920, b) 850, c) 770 and d) 700°C.

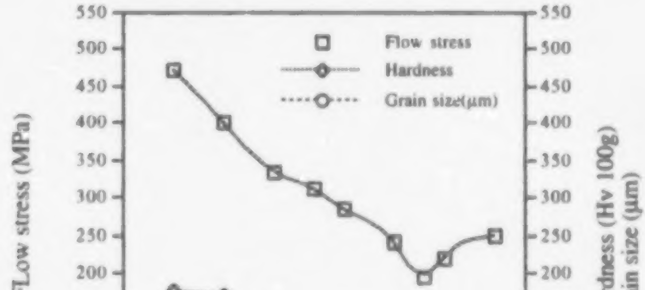

Fig. 2: Effect of FDT on flow stress, microhardness and grain size.

heating temperature, hot rolling schedule and coiling temperature. Among these, the finishing deformation temperature (FDT) has been identified as an important parameter affecting grain structure and texture of hot band (Schmickl et al. 1996). The purpose of this work is to study the development of microstructure and texture of hot deformed ULC steel, and to correlate hot and warm deformed microstructures with the microstructure and texture that develops during cold rolling and annealing.

2 Experimental procedure

An as-cast ULC steel of composition 0.0036%C, 0.019%Mn and 0.031%Al was used in this work. Rectangular samples of dimensions 10x18x20mm were cut from the slab for use in the Gleeble TMP simulator. For each sample, thin tantalum and graphite sheets were used as lubricant during plane strain compression and temperature was controlled by a thermocouple spot welded to the mid-thickness of each sample. Multiple-pass (total 5 passes) deformation schedules were carried out as described by Yu et al. (1998). Each sample was heated initially to 1200°C and held for 5min, followed by two passes at true strain rates of 10 and 20s^{-1} at temperatures above 1000°C in order to simulate rough-pass rolling. In an attempt to simulate finish rolling, three additional passes were made at true strain rates of 50, 75, and 100s^{-1} respectively at temperatures below 920°C. The as-deformed samples were subsequently cooled at a rate of 20°C/s to a 'coiling temperature' of 600°C followed by air cooling to room temperature. To study the effect of FDT on microstructural development, FDT was varied from 920°C to 600°C.

A section of each hot-deformed sample was prepared for microstructural investigation (hot *rolled* state) while other sections were cold rolled to 80% reduction and annealed at both 650°C and 750°C until fully recrystallized. This method of hot deformation and CRA of the same specimen allows the unambiguous interpretation of the effect of hot band microstructure on microstructural evolution during cold rolling and annealing. The hot-deformed and cold-rolled and annealed samples were prepared by conventional metallographic methods and grain sizes and bulk x-ray textures were determined.

3 Results

Hot deformed microstructures at various FDT are given in Fig. 1. It may be seen that deformation above 850°C produced fine, equiaxed ferrite, while at lower FDT (850°C), coarse-grained ferrite was produced. For FDT < 850°C, a deformed ferrite microstructure was observed together with a few recrystallized grains. Figure 2 shows flow stress, hardness and ferrite grain size as function of FDT. In this figure, flow stress represents the maximum stress during the last finish pass and the grain size for FDT < 850°C was measured in recrystallized regions only. It can be seen that the minimum flow stress and largest grain size was produced for FDT of 850°C whereas hardness increased continually with decreasing FDT. Figure 3 shows the recrystallization kinetics of CRA samples for three FDT conditions that produced markedly different hot-band microstructures. A FDT of 700°C resulted in faster recrystallization compared with 920°C and a FDT of 850°C resulted in sluggish recrystallization. It is pertinent to note that similar recrystallized grain sizes were produced after CRA despite the marked differences both in the hot band microstructures and recrystallization kinetics.

Figure 4 shows the maximum intensity along the <111>//ND fibre of both the hot-deformed and CRA samples as a function of FDT. It appears that a relationship exists between hot-band texture and the texture produced following cold rolling and annealing.

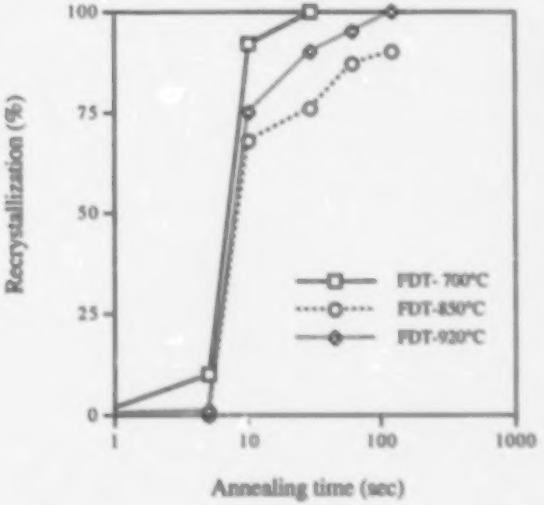

Fig. 3: Effect of FDT on recrystallization kinetics of CRA ULC steel.

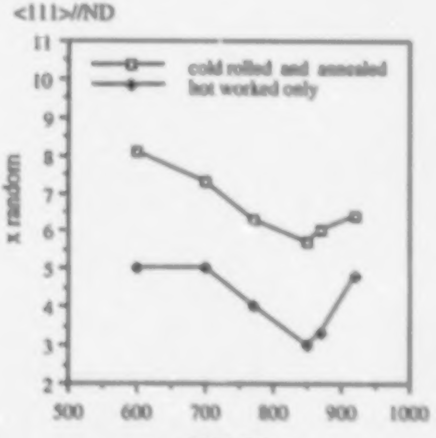

Fig. 4: Effect of FDT on maximum intensity along <111>//ND (γ-fibre) of as-hot-deformed and CRA steel.

4 Discussion

4.1 Hot deformation microstructure

The range of FDT studied in this work covers three regions: single-phase austenite (γ) above 870°C, single-phase ferrite (α) below 800°C, and two-phase γ+α (850°C). The samples deformed at high temperature (γ) produced a uniform transformed ferrite grain structure whereas samples deformed at low temperature (α) produced deformed ferrite. For final deformations carried out in the two-phase region, a mixed microstructure was produced containing both fine and coarse ferrite (Fig. 1b). It has been argued that the coarse ferrite grains form by grain boundary migration of newly transformed or recrystallized ferrite nuclei into the strained ferrite grains (Schmickl et al. 1996). For FDT < 800°C, a few strain-free ferrite grains were produced in an otherwise as-deformed microstructure. With decreasing FDT, both the flow stress and hardness increased due to the lack of recrystallization and decreasing propensity for dynamic recovery.

It has been shown previously (Inagaki 1981) that the development of coarse α during hot deformation produces an essentially random texture by the formation of ferrite grains on austenite grain boundaries during transformation. For low FDT (< 800°C), a strong rolling texture develops as a result of the generation of a preferred orientation of the deformed ferrite. It is pertinent to note that deformation at all FDT produced a relatively strong {001}<110> or *rotated cube* component which becomes more intense at low FDT (< 850°C) (Yu et al. 1998). It has been argued that deformed ferrite produces a stronger {100}<110> texture component compared with ferrite produced during transformation from austenite (Ray et al. 1994).

4.2 Cold rolled and annealed microstructure

The microstructure generated by 80% cold deformation was strongly influenced by the starting (hot-band) microstructure. It was observed that initial coarse-grained ferrite (FDT~850°C) deformed inhomogeneously compared with fine ferrite microstructures generated at higher FDT. Following low FDT, the unrecrystallized ferrite accumulated additional strain during cold rolling and this was shown to significantly increase the rate of recrystallization during subsequent annealing (Fig. 3).

Similar to the trend for the hot band texture (Fig. 4), the CRA texture was strongly dependent on FDT. It appears from initial observation that a relationship exists between the hot band texture and the texture that is produced after CRA. This phenomenon has also been reported for both LC and IF steels (Cui et al. 1997; Wang et al. 1997) where it was found that a strong {111}//ND component after hot rolling can significantly improve the annealing texture following cold rolling. It is pertinent to note, however, that accompanying the weak hot-band texture is a very coarse ferrite grain size (Fig. 2): a factor known to weaken significantly the final annealing texture following cold rolling (Hutchinson 1984). Further work is being carried out to determine if the annealing texture following cold rolling is actually related to hot band texture or if the effect is related to the hot band grain size.

5 Conclusions

- The finish deformation temperature (FDT) has a significant influence on the development of microstructure and texture of hot-deformed ULC steel. For FDT > 850°C, uniformly distributed, fine-grained ferrite is produced whereas for FDT < 800°C, deformed ferrite was retained.

- Deformation of ULC steel in the single-phase ferrite region (warm rolling) enhances the development of both {111}//ND and {001}<110> texture components.

- Warm deformation of ULC steel (low FDT) produces an unrecrystallized microstructure, and this as-strained microstructure, combined with the additional strain accumulated during cold rolling, results in accelerated recrystallization.

- The strength of the recrystallization texture of ULC steel after cold rolling and annealing correlates closely with the hot deformation microstructure and texture.

Acknowledgments - The authors wish to thank both the Australian Research Council (ARC) and BHP Integrated Steel for their financial support.

5 References

Barnett, M. R. and Jonas, J. J. (1997a) *ISIJ International*, 37, p697.
Barnett, M. R. and Jonas, J. J. (1997b) *ISIJ International*, 37, p706.
Deli, C., Jing, S. and Wang, X. (1997) *in Proceedings of ICOTOM XI*, China, p717.
He, C., Guo, D. and Shi, L. (1997) *in Proceedings of ICOTOM XI*, China, p735.
Hutchinson, W.B. (1984) *International Metals Reviews*, 29, p25.
Inagaki, H. (1981) *in Proceedings of ICOTOM VI*, p100.
Karel Eloot et al, (1998) *ISIJ International*, (1998).
Kestens, L. and Jonas, J. J. (1996) *Metall. & Mater. Transactions A*, 27, p155.
Nagataki, Y. and Hosoya, Y. (1996) *ISIJ International*, 36, p451.
Raabe, D. (1995) *Microstructural and Crystallographic Aspects of Recrystallization*. Eds. N. Hansen et al., Risϕ National Laboratory. Roskilde, Denmark, p509.
Ray, R. K., Jonas, J. J. and Hook, R. E. (1994) *International Materials Reviews*, 39, p129.
Schmickl, A., Yu, D., Killmore, C., Langley, D. and Chandra, T. (1996) *ISIJ International*, 36, p1279.
Vanderschueren, D., Bultinck, I. and De Rore, N. (1997) *in Proceedings of ICOTOM XI*, China, p879.
Wang, Z., Wang, X. and Wang, Z. (1997) *in Proceedings of ICOTOM XI*, China, p897.
Yu, D., Ferry, M. and Chandra, T. (1998) *in Proceedings of Materials 98*, 1, p179.

GRAIN BOUNDARY CHARACTER DISTRIBUTION IN A PRIMARY RECRYSTALLIZED GRAIN-ORIENTED SILICON STEEL

J.HARASE
Pohang University of Science and Technology, Pohang,Korea
R.SHIMIZU
1-19-12,Izumidai, Kokura-Kita-Ku , Kitakyusyu, Japan
J. KIM and J.S.Woo
Technical Research Laboratories, Pohang Iron & Steel Co.,Ltd. Pohang,Korea

Abstract

The probability of grains having misorientation angles 20°-45° (HE$_{20\text{-}45}$ boundary) or a $\Sigma 9$ orientation relationship($\Sigma 9$ boundary) was determined using the three dimensional orientation distribution obtained from the (100)pole figure. A primary specimen, capable of evolving a sharp Goss texture, was used. The assumption that orientations with higher intensity HE$_{20\text{-}45}$ boundaries can be nuclei for secondary recrystallization led to the prediction of secondary recrystallization not being present in the secondary recrystallization texture. However, no such contradictory prediction was made on the assumption that orientations with higher intensity $\Sigma 9$ boundaries can be nuclei for secondary recrystallization.

Keywords: coincidence boundary, primary recrystallization, secondary recrystallization,

1 Introduction

Despite remarkable progress in the technology controlling secondary recrystallization of grain–oriented silicon steel sheet, the mechanism of sharp Goss evolution is not yet fully understood. Recent publications demonstrated that Goss grain has the highest probability of coming in contact with grains, which form mobile grain boundaries (CSL-model). These mobile grain boundaries are coincidence boundaries(usually of the $\Sigma 9$ variety) (Harase et al.1990).

Quite recently a new model(HE-model) has been proposed. It indicates that mobile grain boundaries are not coincidence boundaries, but in fact high energy boundaries($HE_{20\text{-}45}$) which are formed between grains with a misorientation angle of 20°-45° (Hayakawa and Szpunar 1997a, 1997b ; Hyakawa et al. 1998). A primary recrystallized specimen , capable of evolving a sharp Goss texture, was prepared. Utilizing this specimen, distributions of $HE_{20\text{-}45}$ boundaries and CSL boundaries were investigated by the SHG method (Shimizu et al. 1990).

2 SHG method

To investigate the mechanism of grain growth, it is necessary to be familiar with the grain boundary character of grains directly or indirectly in contact with each other since new contacts are made during grain growth. The authors have investigated the use of the three-dimensional orientation distribution obtained form the pole figure using the vector method (Ruer et al. 1979). In the vector method, orientations are represented by three parameters, ω, Ψ and ζ. A unit triangle T_1 representing the plane normal is divided into 36 "boxes" of equal angular area which are numbered 1 to 36. A representative orientation (HKL) is assigned to each Box(Fig.1). Rotations (ζ) about this orientation are divided into 72 intervals of 5° each. All unit triangles are classified into one of two groups, T_1 and T_2 (T_2 being the mirror symmetry of T_1). There are a total of 5184 orientations{2(unit triangle)× 36(Box) ×72(ζ)} which represent the entire orientation space. In the SHG method, only one unit triangle T_1 and only rotations up to 180° are used. Therefore, the number of orientations decreases to 1296(36x36). This orientation group is called SO1296. Orientations are given consecutive numbers from 1 to 1296, No.1 being the

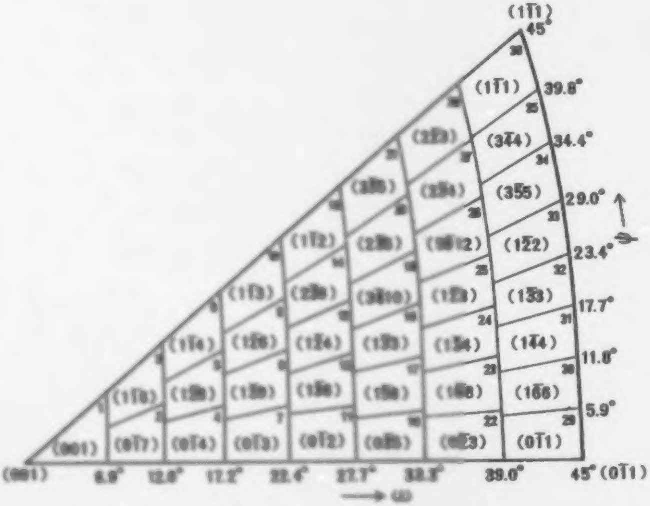

Fig. 1 : Plane orientation T_1 utilized by the vector method.

orientation of Box No. 1 at 175° and No. 1296 being the orientation of Box No.36 at 0°. The rotation matrix R, between these orientations is then calculated. The rotation axis and rotation angle α are determined form the rotation matrix R. The rotation angle α is classified by steps of 5°(e.g. 2 $5° < \alpha \leqq 30°$, $30° < \alpha \leqq 35°$). Then, orientation numbers belonging to each class are stored in memory. Coincidence orientation relationships are determined from $\Sigma 1$ up to $\Sigma 33$ using the Brandon criterion(Brandon 1966). The orientation number of coincidences found is also stored in memory. From the three dimensional orientation distribution determined by the vector method , the intensity of Σi orientations ($I_C \Sigma i$) to an arbitrary selected nucleus orientation N is obtained by calculating the sum of the orientations' intensities with respect to the Σi orientation stored in memory. A product($P_{CN} \Sigma i$) of I_N(Intensity of nucleus orientation N) and $I_C \Sigma i$ is also calculated. The intensity of orientations with a misorientation angle α(20° and 45°) to an arbitrary selected nucleus orientation N(I_{HE}20-45) is also calculated by the same procedure. The relationship between secondary recrystallization texture and I_N, $I_C \Sigma i$, $P_{CN} \Sigma i$ or I_{HE}20-45 before grain growth is then examined.

3 Experimental procedure

A cold rolled specimen of composition C:0.07,Si:3.2,Mn:0.07 ,S:0.02,Al:0.03, N:0.007wt.% and 0.22mm thickness was decarburized in a wet atmosphere. The three dimensional orientation distribution was obtained using the vector method from the (100) pole figure (obtained by X-ray measurement of the central portion of the specimen thickness). The intensity distributions of I_{HE}20-45 , $I_C \Sigma i$ and $P_{CN} \Sigma 1$ were then calculated by the SHG method. The magnetic induction B_{10} , after secondary recrystallization annealing of this specimen , was 1.94T. The average deviation angle of [001] direction from the rolling direction, was about 4°.

4 Results and discussion

4.1 Examination of the primary recrystallized texture by the SHG method

Criterions for the orientation N to be a viable nucleus for secondary recrystallization(Shimizu et al. 1990; Harase et al. 1991) in a primary recrystallized stage are

(1) $P_{CN} \Sigma 1$ of nucleus orientation N should be smaller than certain critical values.
(2) Intensity of nucleus orientation (I_N) should be larger than certain critical values.
(3) Nucleus orientation N should have a higher probability of coming in contact with mobile grain boundaries than other orientations.

In the CSL-model, the mobile boundaries are $\Sigma 9$ boundaries. Therefore, $I_C \Sigma 9$ values should be larger than a certain critical value. In the HE-model, mobile grain boundaries are alleged to be $HE_{20\text{-}45}$ boundaries. Therefore, I_{HE}20-45 should be larger than a certain critical value. Fig. 2 shows the distribution of I_{HE}20-45 of the orientations in Box No.10 and 29. Here, Goss orientation is in Box No.29, ζ at 0°

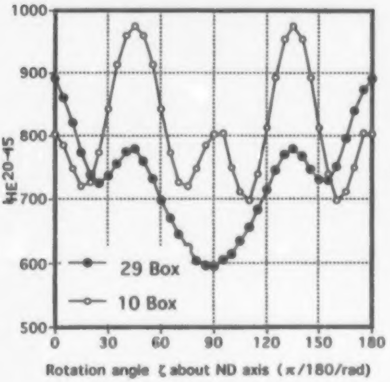

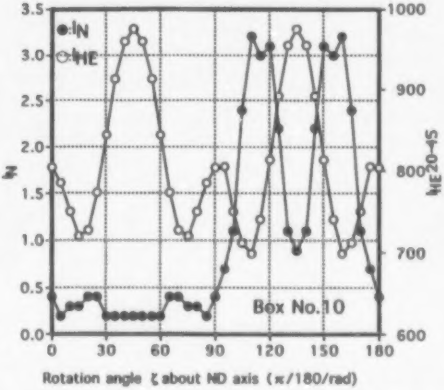

Fig. 2: Intensity distribution of I_{HE}20-45. **Fig. 3: Intensity distribution of I_{HE}20-45 and I_N.**

or 180°. It can be seen that orientations at 45° and 135° in Box No.10 have higher I_{HE}20-45 values than that of Goss orientation suggesting that these orientations support criterion (3). However, we must note here that these orientations are not present in the secondary recrystallization texture of this specimen. Fig.3 shows the distribution of I_{HE}20-45 and I_N in Box No.10. I_N at 135° is 0.9. This value supports criterion (1). Therefore , if all criterions are correct, this orientation should be included in the secondary recrystallization texture. However, the absence of this orientation is inconsistent with the HE-model. There are some other orientations,

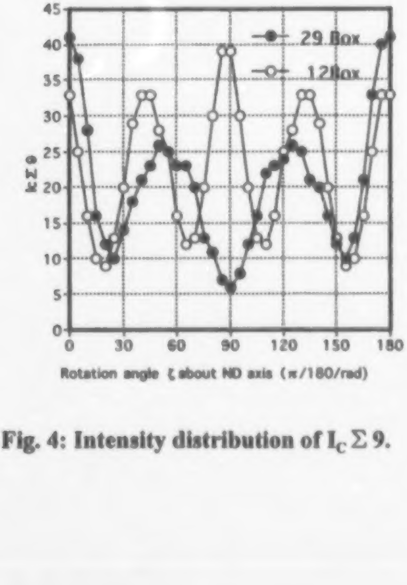

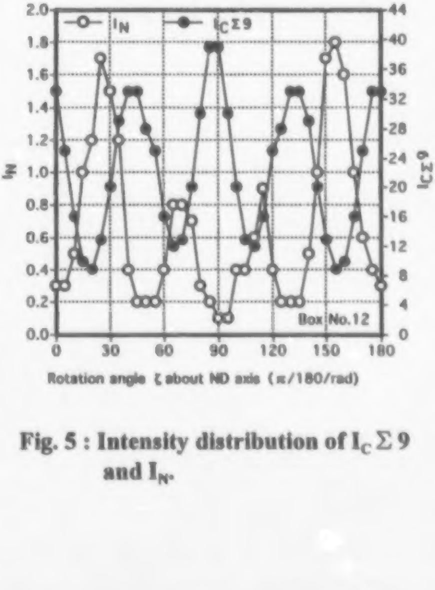

Fig. 4: Intensity distribution of $I_C \Sigma 9$. **Fig. 5 : Intensity distribution of $I_C \Sigma 9$ and I_N.**

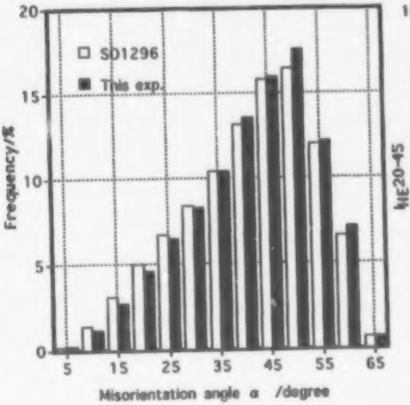

Fig. 6: Frequency of HE boundaries in SO1296 and in the primary specimen.

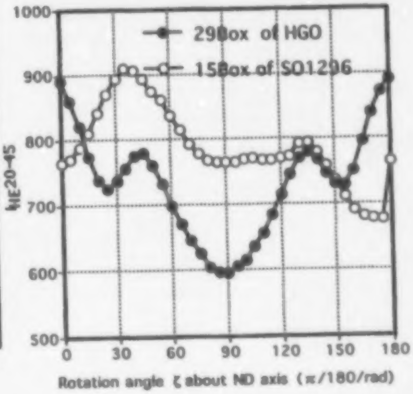

Fig. 7 : Intensity distribution of I_{HE}20-45 in 15Box of SO1296 and in the primary specimen.

which support the three criterions for secondary recrystallization, but are not present in the actual secondary recrystallization texture.

In the case of $I_C\Sigma 9$ values, no grain had a higher value than that of Goss orientation. However, as shown in Fig.4, the $I_C\Sigma 9$ value in Box No.12 at 90° is very high(39), but I_N has as a low point of 0.1 (Fig.5) suggesting this orientation doesn't support criterion (1). Therefore, the absence of this orientation in the actual secondary recrystallization texture is consistent with the CSL-model. No contradictory results occurred while examining the primary texture by these three criterions on the assumption that $\Sigma 9$ boundaries are specifically mobile. In conclusion, the assumption that $HE_{20\text{-}45}$ boundaries are specifically mobile in the secondary recrystallization process is not correct.

4.2 Distribution of I_{HE}20-45 in SO1296 and the grain oriented silicon steel

Fig.6 shows that the frequency distributions of HE boundaries are almost the same in SO1296 and in the primary texture used in this experiment. The frequency of HE boundaries in the range $20° < \alpha \leqq 45°$ are about 55% in both cases. This fact indicates that these boundaries are present everywhere regardless of the texture. In the SO1296, criterions (1) and (2) are supported since any orientation in SO1296 has the same intensity. Fig.7 shows the distribution of the I_{HE}20-45 (taken from SO1296 at Box15) together with the distribution of I_{HE}20-45 values(taken from HGO at Box No.29)of the primary texture in the present experiment. Following the HE-model, the orientations in Box No.15 at around 35° in SO1296 should be viable nuclei of secondary recrystallization as the I_{HE}20-45 of these orientations are higher than that of Goss orientation in the HGO specimen. However, no secondary recrystallization takes place in the grain-oriented silicon steel when the texture is not well developed.

5 Conclusion

The probability of grains having misorientation angles 20°-45° (HE_{20-45} boundaries) or a $\Sigma 9$ orientation relationships in a primary recrystallized specimen capable of evolving a sharp Goss texture was determined using the (100) pole figure obtained by X-ray measurement. Intensities of HE_{20-45} boundaries(I_{HE}20-45) were substantially higher around Goss grains. However, some orientations, which were not present in the secondary recrystallization texture, showed higher I_{HE}20-45 values than that of Goss orientation. Goss orientation had the highest $\Sigma 9$ boundary values in the primary texture. This investigation suggests that the newly proposed model on secondary recrystallization , based on the assumption that HE_{20-45} boundaries are specifically mobile, is not correct.

6 References

Brandon, D.G. (1966) Acta metall.,Vol.14,pp.1479.
Harase, J., Shimizu, R. and Takahashi, N. (1990) Proc.on the Inter.Conf.on Recrystallization in Metallic Materials, Recrystallization '90. pp. 459-64.
Harase,J., Nakashima, S., Kawamo ,Y. and Yoshitomi, Y. (1991) Japan Inst. Metals.Vol.56, No.6. pp.662-9.
Hayakawa, Y. and Szpunar, J.A. (1997) Acta mater.,Vol.45, No.3, pp.1285.
Hayakawa, Y. and Szpunar, J.A. (1997) Acta mater.,Vol.45, No.11,pp.4713.
Hayakawa, Y. , Kurosawa, M., Komatsubara, M. and Szpunar, J.A. (1998) Proc. Third Inter. Conf. on Grain Growth, pp.615-20.
Ruer, D., Vadon, A. and Baro, B. (1979) Texture of Cryst.Solids.,Vol.3,pp.245.
Shimizu, R., Harase, J. and Dingley, D.J. (1990) Acta metall., Vol.38,pp.973-8.

TEXTURES AND MICROSTRUCTURES OF STRIP CAST STAINLESS AND LOW-CARBON STEELS

D. RAABE and H. KRAUSE
Institut für Metallkunde und Metallphysik, RWTH Aachen, Aachen, Germany
A.D. ROLLETT and A. TEICHER
Department of Materials Science and Engineering, Carnegie Mellon University, Pittsburgh, USA

Abstract
The crystallographic textures and microstructures of strip cast austenitic stainless steels and of ferritic low carbon steels are presented and discussed. The stainless steels were produced in an unequal-diameter twin roll caster and the low carbon steels in an equal-diameter twin roll caster. The textures and microstructures are investigated in various through-thickness layers. The austenitic steels reveal weak textures with some pronounced components close to the {001}<uvw> texture fiber. In low carbon steels two types of textures are observed. While some of the low carbon strips show pronounced textures close to the {111}<uvw> fiber others reveal a weak texture with minor components close to {011}<uvw> fiber. All strip cast steel samples reveal weak through-thickness texture inhomogeneity. The austenitic steel shows martensite in the center layer. Chemical segregation is stronger in the stainless steel strips than in the low carbon steel strips.

Keywords: strip casting, stainless steel, low carbon steel, fiber texture, microstructure

1. Introduction

Steel sheet coils are industrially manufactured by continuous casting, hot rolling, hot band annealing, cold rolling, and a final annealing treatment. Recent progress in producing cast steel sheets in pilot-scale unequal-diameter or equal-diameter twin roll strip casters has stimulated efforts to convert such devices to commercial production. Strip casting technology offers the ability of bypassing the hot rolling processing stage by solidifying liquid steel on the surface of two rotating water cooled rolls and producing thin strips that are directly coilable.

Strip casting provides some main advantages compared to the conventional process. First, it can supply steel bands which have the same thickness and width as conventional hot band sheets. Second, strip cast steels exhibit weak initial crystallographic textures and weak through-thickness texture gradients, yielding favorable strength and deep drawing properties of the final sheets. Third, the high solidification rate on the roll surfaces entails a refined microstructure. Fourth, it is possible to directly cast steel sheets which are not endowed with a sufficient intrinsic ductility for rolling processes, such as certain transformer or stainless steels. The paper gives an overview of the crystallographic textures and microstructures observed in strip cast steels. The investigation includes low carbon steels and austenitic stainless steels.

2. Experimental

The austenitic stainless specimens were strip cast on a pilot-scale unequal-diameter twin roll caster (Ohno et al. 1990; Hentrich et al. 1991). The low carbon steel specimens were cast on an equal-diameter twin caster (Teicher et al 1998). The stainless steel samples were provided by former Krupp-VDM and the low carbon steel samples by Bethlehem steel. Both methods work by casting liquid steel into a preheated tundish which contacts water cooled steel rolls. Thin steel layers solidify on the roll surfaces just before reaching the bite of the rolls. The casting process is usually conducted in a way to ensure that the contact length between the liquid steel and the roll surface is equal on both rolls. The as-cast stainless steel specimens had a thickness of 2.8 *mm* and the low carbon steel strips of 0.6 *mm*.

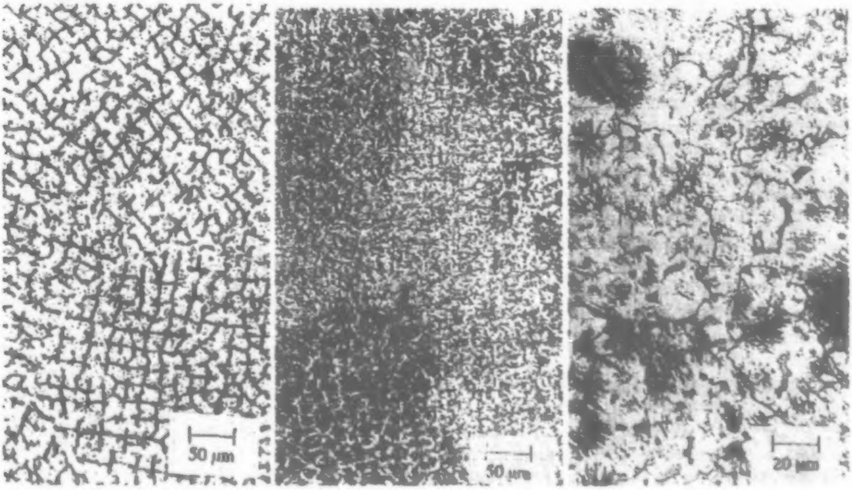

surface mid-thickness center

Fig. 1: Microstructure of a strip cast austenitic stainless steel, flat sections.

The textures of the austenitic steels were examined by measuring the {111}, {200}, {220}, and {113} pole figures and those of the low carbon steels by measuring the {110}, {200}, and {211} pole figures in the back reflection mode using CoK$_\alpha$ radiation (Schulz 1949). The specimens were descaled prior to the pole figure measurements. The orientation distribution functions were for all samples calculated by applying the iterative non-negative series expansion method to the corrected and normalized pole figures using a maximum expansion coefficient of l_{max}=22 (Dahms and Bunge 1989).

As is well known from various previous studies, the textures and microstructures of both ferritic and austenitic steels are often inhomogeneous through the sheet thickness (Raabe and Lücke 1992, 1993; Raabe 1995). This applies especially to samples which were produced by conventional hot rolling (Raabe and Lücke 1994; Raabe 1997). For this reason the textures and microstructures of both types of strip cast steels were investigated in various through-thickness layers. The low carbon steels were etched in 2% nitol. The austenitic stainless steels were prepared using concentrated HCl at 330 *K* or a solution of 50 *ml* H_2O, 50 *ml* alcohol, 50 *ml* HCl, and 2 g $CuSO_4$.

3. Strip cast austenitic stainless steels

Figs. 1 and 2 show the microstructure of a strip cast austenitic stainless steel in flat and in cross sections. Between the surface and the near-center layers uniformly oriented blocks of primary austenitic dendrites branched out up to the second generation can be observed. The dendrite blocks have an average diameter of 140 *μm* and a length of up to 500 *μm* parallel to their growth direction.

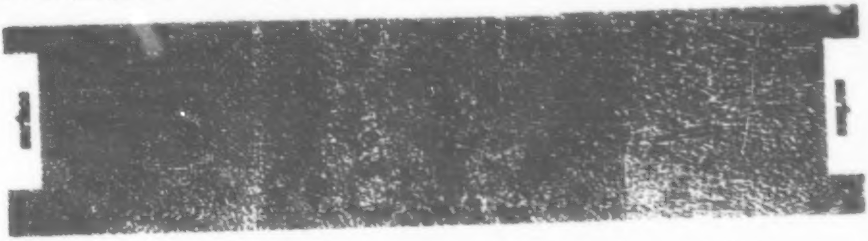

Fig. 2: Microstructure of the strip cast austenitic stainless steel, cross section.

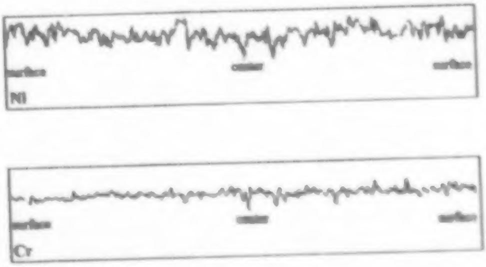

Fig. 3: Macroscopic segregation profile across the sheet thickness of the austenitic stainless steel (Teicher et al. 1998).

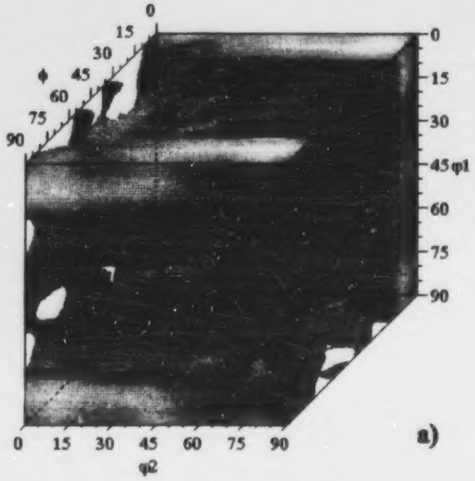

Fig. 4a: Strip casting texture of an austenitic stainless steel; the diagram shows the orientation density above $f(g) = 1$; a) surface layer, $f(g)_{max} = 2.3$.

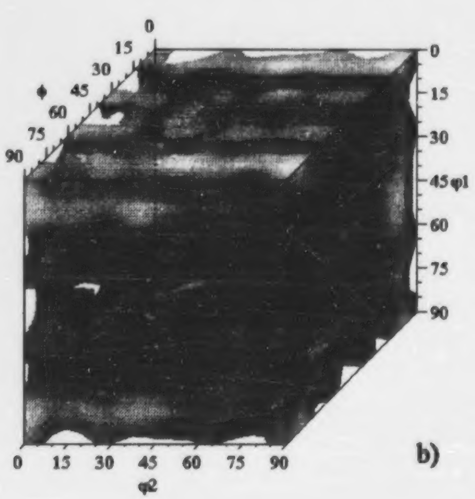

Fig. 4b: Strip casting texture of an austenitic stainless steel; the diagram shows the orientation density above $f(g) = 1$; a) mid-thickness layer, $f(g)_{max} = 2.5$.

The microsegregated interdendritic regions appear dark while the austenite appears bright. Nickel and chromium are enriched while iron is depleted between the dendrites (Siegel et al. 1986). Especially the reduction of nickel in the dendrites might destabilize the austenite with respect to strain induced martensite transformation

Fi~

(Raabe 1997). Fig. 3 shows the macrosegregation profile through the sheet thickness of the austenitic stainless steel. The analysis was performed in the scanning electron microscope using backscattered electrons. The stainless steel samples were investigated for chromium and nickel segregation. The data show that substantial macrosegregation across the strip thickness do not occur (Teicher at al 1998). While iron and chromium reveal a nearly constant distribution across the sheet thickness the nickel content reveals a slight depletion in the center layers.

Close to the center layers a blocky and nearly equiaxed morphology of the austenite is found. In this region some martensite platelets occurred as well. Further details of the initial microstructures of both ferritic and austenitic strip cast steels were reported earlier (Raabe et al. 1993; Raabe 1995, 1997).

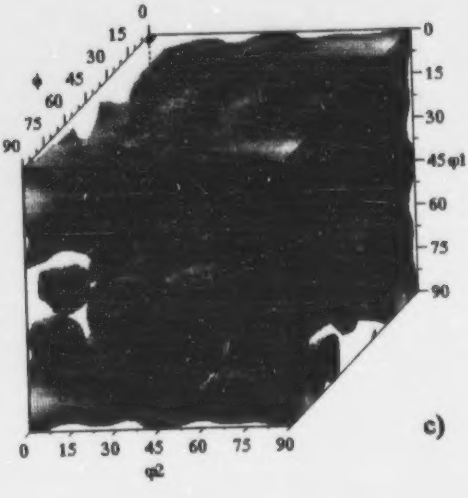

Fig. 4c: Strip casting texture of an austenitic stainless steel; the diagram shows the orientation density above $f(\mathbf{g}) = 1$; c) center layer, $f(\mathbf{g})_{\max} = 2.4$.

The texture of the strip cast material is very weak and does not show relevant through-thickness gradients. The orientation distribution function determined in the surface layer (Fig. 4a) shows a weak texture fiber {001}<uvw>.

The micrographs reveal that the layers close to the surface are not deformed or bent but appear as large blocks of austenitic dendrites. The observed texture fiber is thus attributed to growth selection among the austenitic dendrites during solidification subsequent to their nucleation on the surfaces of the casting rolls (Raabe 1997). The textures in the other layers are similar, i.e. no pronounced texture gradient as in hot rolled material is observed (Figs. 4b,c). From directional solidification experiments on other face centered cubic metals it is well established that {100}<uvw> has a larger growth rate than other orientations (Hirsch et al. 1987).

4. Strip cast low carbon steels

Fig. 5 shows the texture of the a low carbon steel. Whilst the stainless steels revealed a nearly random orientation distribution in all through-thickness layers some of the body centered cubic strip cast steels reveal a pronounced {111}<uvw> fiber texture.

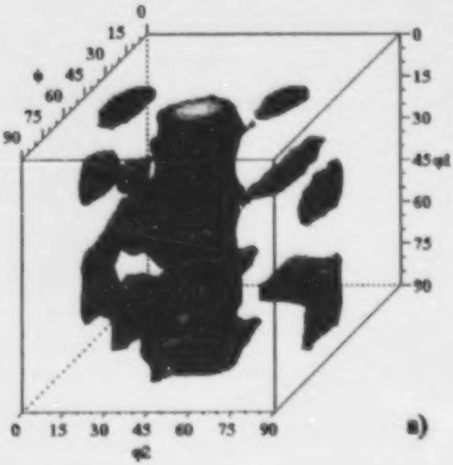

Fig. 5a: Strip casting texture of a low carbon steel with a {111}<uvw> texture; the diagram shows the orientation density above $f(\mathbf{g})$ =2.5; a) surface layer, $f(\mathbf{g})_{max}$=9.5.

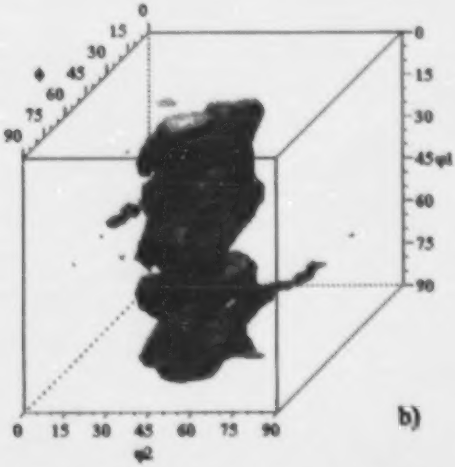

Fig. 5b: Strip casting texture of a low carbon steel with a {111}<uvw> texture; the diagram shows the orientation density above $f(\mathbf{g})$ =2.5; a) mid-thickness layer, $f(\mathbf{g})_{max}$=4.2.

The texture is stronger at the surface than in the center layer. The generation of a {111}<uvw> texture might be due to the influence of plastic deformation and recrystallization. Although exact operational details of the caster are unknown to the authors most strip casting constructions impose a certain amount of plastic deformation when the two newly solidified steel films impinge upon each other in the roll gap. This effect might entail primary recrystallization.

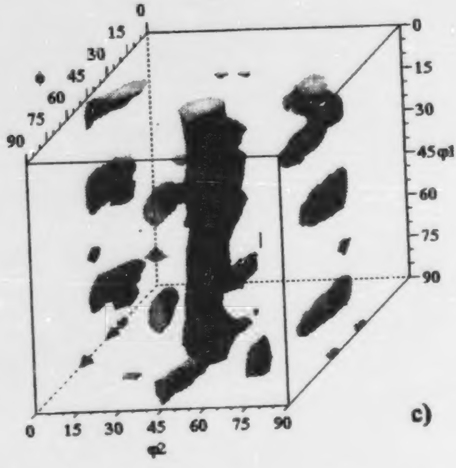

Fig. 5c: Strip casting texture of a low carbon steel with a {111}<uvw> texture; the diagram shows the orientation density above *f*(g) =2.5; a) center layer, $f(g)_{max}$=4.2.

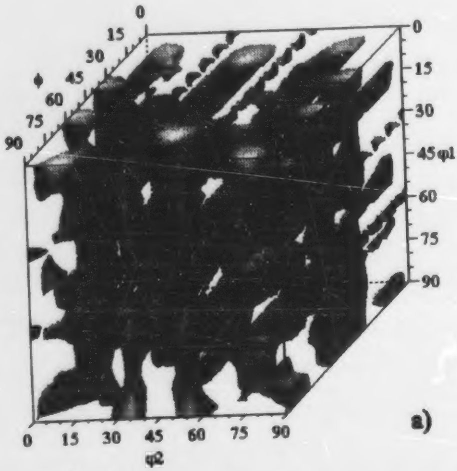

Fig. 6a: Strip casting texture of a low carbon steel with a weak {011}<uvw> texture; the diagram shows the orientation density above *f*(g) =1; a) surface layer, $f(g)_{max}$=3.2.

Producing a pronounced {111}<uvw> starting texture is very beneficial since it would most likely be further sharpened during subsequent cold rolling and thus would provide an ideal starting texture for a final heat treatment and the creation of a strong final {111}<uvw> recrystallization texture.

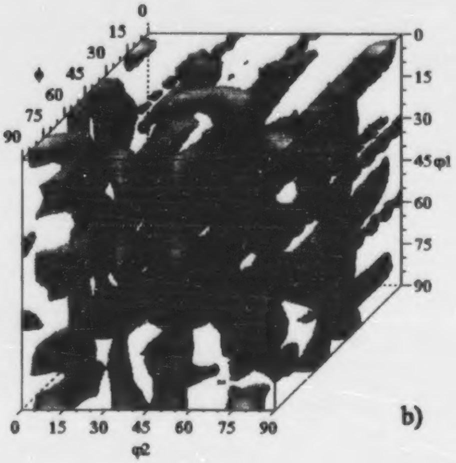

Fig. 6b: Strip casting texture of a low carbon steel with a weak {011}<uvw> texture; the diagram shows the orientation density above $f(g)$ =1; a) mid-thickness layer, $f(g)_{max}$=3.1.

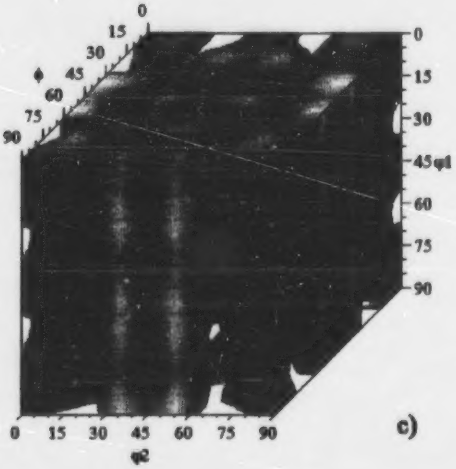

Fig. 6c: Strip casting texture of a low carbon steel with a weak {011}<uvw> texture; the diagram shows the orientation density above $f(g)$ =1; a) center layer, $f(g)_{max}$=2.5.

Another set of strip cast low carbon steel samples revealed less pronounced textures characterized by a weak fiber close to {011}<uvw>. The textures of these materials were similar to strip casting textures observed earlier in strip cast ferritic stainless steels (Raabe et al. 1993, 1994).

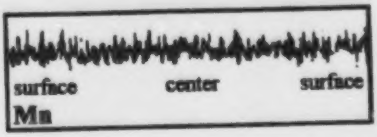

Fig. 7: Macroscopic segregation profile of manganese across the sheet thickness of a strip cast low-carbon steel.

The strip cast low carbon steel specimens were investigated for manganese segregation (Fig. 7). The experimental data show that substantial macrosegregation across the strip thickness do not occur (Teicher at al 1998).

5. Summary

The textures and microstructures of strip cast austenitic and low carbon steels were presented. The stainless steels were produced in an unequal-diameter twin roll caster and the low carbon steels in an equal-diameter twin roll caster. The textures and microstructures were investigated in various through-thickness layers. The austenitic steels revealed weak textures close to the {001}<uvw> fiber. In low carbon steels two types of textures were observed. While some of the low carbon strips showed textures close to the {111}<uvw> fiber others revealed a weak texture with minor components close to {011}<uvw> fiber. All strip cast steel samples revealed weak through-thickness texture gradients. Chemical segregation effects were stronger in the stainless steel strips than in the low carbon steel strips.

6. References

Dahms, M. and Bunge, H. J. (1989) *Journ. Appl. Cryst.* Vol. 22, pp. 439-452.

Hentrich, R., Dubke, M., Funk, H. J, Hanke, K. H., Loh, J., and Kuhlmann, S. (1991) *Stahl und Eisen* Vol. 111, pp. 51-55.

Hirsch, J., Nes, E., and Lücke, K. (1987) *Acta Metall.* Vol. 35, pp. 427-442.

Ohno, K., Tanaka, H., Sasaki, T., Dubke, M., Funk, H. J., Hanke, K. H., Pfeifer, H., and Hentrich, R. (1990) *Proceedings International Conference on New Smelting*

Reduction and Near Net Shape Casting Technologies for Steel, Pohang, Korea, pp. 14-22.

Raabe, D. (1995) *Journal of Materials Science*, Vol. 30, pp. 47–52.

Raabe, D. (1995) *Mater. Science and Technology* Vol. 11, pp. 461–468.

Raabe, D. (1995) *Metall. and Mater. Transactions A* Vol. 26, pp. 991–998.

Raabe, D. (1997) *Acta Materialia*, Vol. 45, pp. 1137–1230.

Raabe, D., and Lücke, K. (1992) *Scripta Metall.* Vol. 26, pp. 1221–1226.

Raabe, D., and Lücke, K. (1993) Mater. Science and Technology Vol. 9, pp. 302–312.

Raabe, D., and Lücke, K. (1994) Mater. Science Forum Vol. 157–162, pp. 597–610.

Raabe, D., Hölscher, M., Dubke, M., and Lücke, K. (1993) *Proceedings of International Conference on Strip Casting, Hot and Cold Working of Stainless Steels*, Quebec, Canada, ed.N.D. Ryan, A.J. Brown, H.J. McQueen, The Metallurgical Society of the Candian Institute of Materials (CIM) pp.3–17.

Raabe, D., Hölscher, M., Dubke, M., Pfeifer, H., Hanke, H., and Lücke, K. (1993) *Steel Research* Vol. 4, pp. 359–363.

Raabe, D., Hölscher, M., Dubke, M., Reher, F., and Lücke, K. (1994) *Materials Science Forum*, Vol. 157–162, pp. 1039–1044.

Schulz, L. G. (1949) *Journ. Appl. Phys.*, Vol. 20, pp. 1030-1034.

Siegel, U., Spies, H.-J., and Eckstein, H.-J. (1986) Steel Research Vol. 57, pp. 25-34.

Teicher, A., Rollett, A. D., Raabe, D. (1998) *CMU Project Report*, Department of Materials Science and Engineering, Carnegie Mellon University, Pittsburgh, USA

TORSIONAL BEHAVIOUR OF PEARLITIC WIRES ACCORDING TO THEIR CRYSTALLOGRAPHIC TEXTURE

A.TIDU
Laboratoire d'Etude des Textures et Application aux Matériaux LETAM CNRS URA 2090 / ISGMP, Ecole Nationale d'Ingénieur de METZ Ile du Saulcy 57045 METZ Cedex 01 FRANCE
B. BOLLE, Y. LIU and J.J. HEIZMANN
Laboratoire d'Etude des Textures et Application aux Matériaux LETAM CNRS URA 2090 / ISGMP,Université de METZ Ile du Saulcy 57045 METZ cedex 01 FRANCE
L. ZUO
Department of Materials Science and Engineering, Northeastern University, Shenyang, 110006 CHINA

Abstract

Pearlitic steel cords are mainly used in the tire making. During the wet or dry drawing process of steelcord, the crystallographic texture depends on the drawing conditions. Two kinds of crystallographic texture are observed inside a wire : a fiber texture and a circular texture. In this paper the influence of the dies angles is studied with the view of understanding how the grains are oriented in the wire and try to explain the behaviour of the wire. Industrial experiments according to the die angles show their influence on the homogeneity of the deformation. Torsional experiments on individual wires show that the presence of the circular texture is the reason for the weakness in the torsional behaviour of the wire.

Keywords: die angle, drawing, steel wire, torsion

1 Introduction

Pearlitic steel cords are mainly used in the tire making. The crystallographic texture depends on the drawing conditions. As iron has mechanical properties which are anisotropic, the mechanical behaviour of the steel may change according to its texture. In this paper the influence of the die angles is studied with the view of understanding how the grains are oriented in the wire and try to explain the behaviour of the wire.

2 Texture description

The components of the pearlitic wire are ferrite and cementite. A texture goniometer is used to move the sample in front of the X-ray beam and a detector measures the intensity diffracted by the (110) lattice planes of the α iron. Because of the geometrical shape of the wire, absorption correction on intensities are necessary (Langouche et al., 1989; Montesin et al., 1991). To describe the texture evolution across the radius of the wire, the diameter of the wire is reduced by successive chemical attacks. After each attack the texture is measured. The drawing process through the dies is axisymmetric consequently the wires must have an axisymmetric texture. Two kinds of texture can possess this characteristic :

1. the usual fiber texture in which the grains (crystallites) have a row [uvw] parallel to the wire axis.
2. the circular or cyclic fiber texture where the grains have also a row [uvw] parallel to the wire axis and moreover a lattice plane (hkl) tangent to the surface of the wire. This texture is named : [uvw] (hkl) according to the Grewen's notation (Langouche et al., 1989; Montesin and Heizmann, 1992).

The texture of the wires is not homogeneous ; there is a strong texture gradient inside the wires which relies strongly on the drawing conditions, particularly the die angles.

Three zones with different textures are usually observed within the wire. The first one located in the central part and very often at the surface of thin wires (wet drawing), is an usual [110] fiber texture. In the intermediate zone located between the surface and the central part of the wire a circular texture [110] (110), can be identified. The surface texture of the wire (dry drawing, and sometimes wet drawing) is a cyclic or circular texture [110] (112).

The sizes of these three zones differ according to the drawing parameters, they depend specially on the die angles (Heizmann et al., 1996).

3 Texture evolution during the torsion

In order to understand the weakness of wires drawn with large angles (Van Raemdonck et al., 1994), two wires of the same composition were drawn in the same industrial conditions from 5.5 to 1.21 mm excepted the dies angles which are respectively 10° au 16°. Among the usual mechanical tests the only difference between them is seen in the torsion test carried out with 70 cm length wires loaded with 1.2 kg. The 10° wire breaks after 183 turns while the 16° wire breaks after 171 turns. The angle γ between the spiral line and the wire generatrix observed by electron scanning microscopy corresponds to the theoretical angle $tg\gamma = r.\varphi/L$ where φ is the angle of torsion. Some wire has been overtwisted, that is to say, after a first breakage the remaining part of the wire is turned again until a new break. So the wires can reach 250 turns (for $L=0.70$ m) . On the overtwisted 16° wire appears sometimes a fracture with longitudinal splitting (delamination) .

3.1 Pole figure examination :

Texture measurements are carried out :

- at the surface of the wire for different torsion rate (0 to 150%) where 100% is the number of revolutions at the breakage.
- at the inner part of the wires. For that they are thinned down, after the torsion, until 75 % and 45 % of their initial diameter

3.1.1 Texture at the surface :

The pole figure (PF) measured at the surface of the wires (for die angle 10° and 16°) present the same evolution during the torsion. On Fig. 1 are shown the PF of the surface of the 10° wire for four torsion rates (0%, 60%, 100% and 150%). On the PF of the torsioned wires, there is a rotation of the PF around its centre. This rotation corresponds to a rotation of the crystal lattice of the grains around the radius of the wire. The rotation angle Ω (see Fig. 1) increases continuously as well as the torsion and reaches a limit value which is observable on the overtwisted wire.

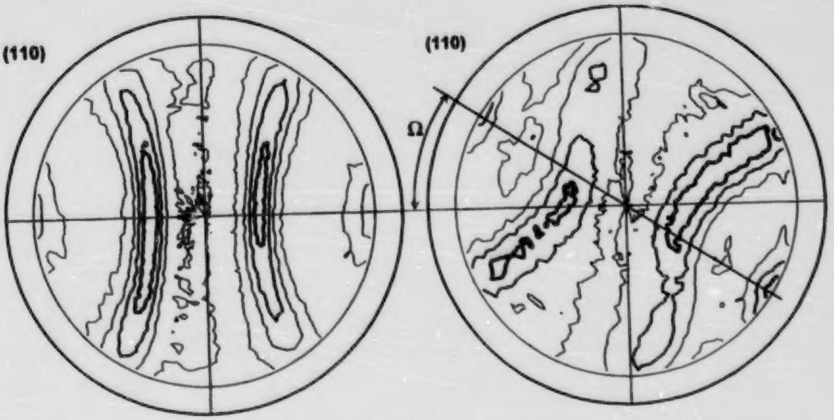

0% level : 0.8-1.2-1.6-2.0 60% level : 0.6-0.9-1.2-1.5

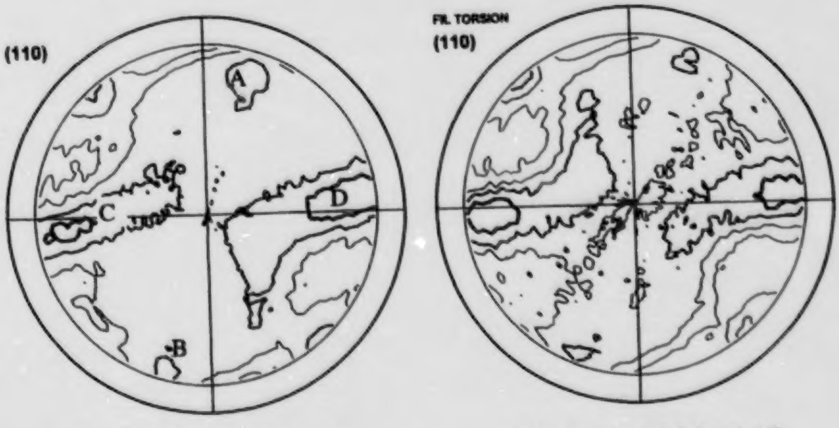

100% level : 0.6-0.8-1.1-1.5 150% level : 0.6-0.9-1.2-1.7

Fig. 1 Texture evolution of the 10° wire surface according to the torsion rate

Before torsion, the texture of the surface is mainly a fiber texture [110] with a small component of circular texture [110] (112).

At the breakage (PF 100%) and on the PF of the overtwisted wire the two maxima of the PF are very close to their limit positions which must be located on the horizontal diameter of the PF (C and D on Fig. 1). From this position there is no more rotation of the lattice of the grains. The orientations of the grains have reached a limit circular fiber texture which is close to [112](110). These orientations have already found by Montheillet on ARMCO rods (Montheillet et al., 1984) and were named "the ideal orientation D". According to the axisymmetry of the wire, this ideal orientation would be a circular texture. There is an intensity evolution within the (110) arcs on the PF. The fiber texture during its rotation Ω becomes progressively a circular texture, characteristic maximum A, B, C and D (Fig. 1) appear.

3.1.2 Texture of the intermediate area :

The intermediate area of the 10° wire presents a perfect usual fiber texture [110]. We can observe the same evolution as those observed at the surface. There is also a rotation of the PF around the radius, the rotation angle Ω is smaller than previously because the diameter of the inner part is smaller than the diameter of the wire. There is also a change of the intensity distribution on the (110) arcs towards a circular texture. At the breakage, the orientations have not reached their limit positions. The limit position is reached on the overtwisted wire. As a conclusion, it must remain in the inner part of the wire an amount of possible rotation.

The texture of the intermediate area of the 16° wire is different. It presents as expected a circular texture [110](110) before torsion. As previously, a rotation Ω of the PF is observed. At the breakage, the (110) arcs have disappeared, its remains only two maxima on the PF which are located close to the horizontal diameter of the PF. On the overtwisted wire these maxima are nearer to the diameter and their limit position will be on it. From this position, the rotation of the orientations is no more possible. This limit orientation is a circular texture [112](110).

3.1.3 Conclusion :

As a first conclusion, we could say :

- an usual fiber texture [110] evolves continuously during the torsion. There is a rotation Ω of this usual fiber texture with a transformation towards a circular texture. When the orientation reach a limit value, the wire breaks.
- on the other hand, during the torsion of a circular texture there is also a rotation Ω but the transformation usual fiber to circular texture must be less important because the wire have already this orientation. Therefore one step of the texture evolution is missing. It is probably for this reason that the wires with a circular texture may break during the torsion test before wires with a usual fiber texture.

3.2 Analysis of the results:

Three rotations are involved in the texture evolution : a rigid body rotation W, a glide rotation ω (also called plastic rotation) and the net rotation Ω of the lattice with respect to the laboratory reference. It can be written (Toth et al., 1988) : $\dot{\Omega} = \dot{W} - \dot{\omega}$. After some amount of torsion, we have: $\Omega = \int \dot{\Omega}.dt$. This quantity will represent the net rotation of the lattice which can be directly measured by texture experiments.

The rigid body rotation can be directly calculated, as during the torsion test the radius r and the length L of the wire are given. The value $W = r.\varphi/L$ is a straight line as a function of the number of turns.

At any time, the difference between Ω and W will give the integrals resultant of the plastic spin $\int \dot{\omega}.dt$. From this last value, it is not possible, without modelisation, to know how are the glides, because $\dot{\omega}$ depends on the activity of the different slip systems and on the texture.

At the surface of the two wires, at the beginning of the torsion, the two curves W and Ω (Fig. 2) are close together until 50%. One have $\dot{\Omega} = \dot{W}$ leading to $\dot{\omega} = 0$. For this condition at least four slip system are activated. At the end of the rotation, Ω becomes constant, because the limit orientation has been reached. In this case $\dot{\Omega} = 0$, leading to $\dot{W} = \dot{\omega}$, the glide rotation have to balance the rigid body rotation forced by the torsion test experiment. To obtain a great rotation rate ($\dot{\omega}$ equal to the rigid body rotation), only one or two slip systems must be activated.

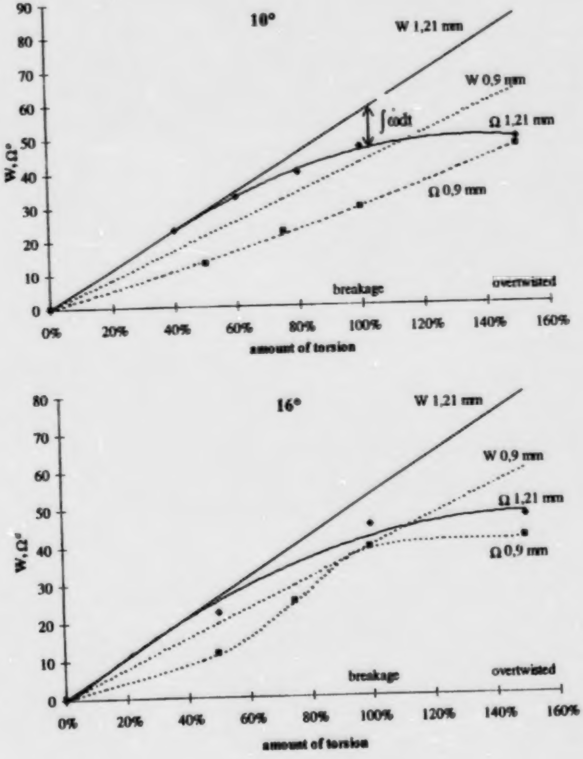

Fig. 2 Evolution of the angles W and Ω according to the torsion

At the intermediate area, the evolution of the curve Ω are very different for the two wires. Consequently, these two wires do not have the same slip systems which work in the same way because the texture of the two wires are different. At the breakage of the 16° wire, the curve Ω becomes tangent to the curve W (this leads to $\dot{\omega} = 0$). There is a shift, in the behaviour of the 10° wire with respect to the 16° one, towards a greater number of turns before reaching a limit orientation. These curves Ω confirm the assumption done after the PF examination. The shift in the mechanical behaviour of the two wires strongly depends on the presence of the circular texture.

4 Conclusion

Crystallographic texture measurement can give local informations on the deformation of the wires.

The presence of the circular texture depends on the dies angles : large dies lead to a circular texture which leads to a weakening of the torsion strength of the wire. During the torsion, the usual fiber texture is transformed into a circular one, which reaches a limit circular orientation, then the wire may break. The rotation angle measured on the pole figure can indicate if the limit of torsion is reached when the wire breaks or if it still remains a torsion capacity.

Acknowledgements : the authors acknowledge with gratitude helpful discussions with Dr Laslo Toth from Metz University.

5 References

Heizmann J.J., Abdellaoui A., Bolle B., Pelletier J.B. and Peeters L. (1996), *Metallurgy, Processing and Applications of Metal Wires* (ed. by Henry G. Paris & Dong K. Kim) TMS publication, pp. 163-173

Langouche F., Aernoudt E., and Van Houtte P. (1989), *J. Appl. cryst.*, Vol. 22, pp. 533-538

Montesin T., Heizmann J.J., and Pelletier J.B. (1991), *Wire J. Int.*, pp. 56-59

Montesin T. and Heizmann J.J. (1992), *J. Appl. cryst.*, Vol. 25, pp. 665 - 673

Montheillet F., Cohen M. and Jonas J.J. (1984), *Acta Metall.*, Vol. 32, pp.2077-2089,

Van Raemdonck W., Lefever I., and D'Haene U. (1994), *Wire Association International Technical Report*, pp. 87-98

Toth L.S., Gilormini P. and Jonas J.J. (1988), *Acta Metall.*, Vol. 36, pp. 3077-3091

TRANSFORMATION TEXTURES AND TEXTURE MEMORY IN LOW CARBON STEELS

L. RYDE, D.ARTYMOWICZ AND W.B. HUTCHINSON
Swedish Institute for Metals Research, Stockholm, Sweden

Abstract

Textures of three steels have been examined after heating to temperatures below and above Ac_3. IF steels, and notably those with Mn additions, reveal a memory of their initial textures. Present observations do not support the view that such memory is caused by stresses and an alternative hypothesis is presented in which rims of retained ferrite around titanium carbide particles act as nuclei for transformation on cooling.

Keywords: Textures, steels, phase transformation, memory, titanium, manganese

1 Introduction

When a phase transformation takes place in a metal on heating or cooling an orientation relationship frequently exists between the lattices of the parent and the daughter crystals. This means that if there is a texture in the initial structure, it will be retained in a modified form in the product. For reasons of symmetry there are usually several equivalent variants of the same orientation relationship which results in a diversification and weakening of the resulting texture. When there is a forward and a reverse transformation, as in the normalising of steel, this diversity is further increased and only a small fraction of the material is expected to return to its original orientation on a statistical basis. In some cases, however, the original texture is restored to a much greater extent than predicted on this basis (sometimes wholly restored) and this phenomenon is often referred to as 'texture memory'.

In steels, the relationship between ferrite and austenite has been described in three ways differing only slightly in their actual misorientations, e.g. Ray and Jonas (1990)

Bain	$(100)_\alpha // (100)_\gamma$, $[001]_\alpha // [011]_\gamma$	3 variants
Nishiyama-Wassermann	$(110)_\alpha // (111)_\gamma$, $[001]_\alpha // [110]_\gamma$	12 variants
Kurdjumov-Sachs	$(110)_\alpha // (111)_\gamma$, $[111]_\alpha // [110]_\gamma$	24 variants

Orientation relationships of these types apply to the transformations both on heating and on cooling; their applicability in terms of mechanisms of nucleation and/or growth has been discussed recently by Hutchinson et al.(1998a). Usually there are a multiplicity of active variants in steels with the result that the texture is greatly weakened after a normalising heat treatment, e.g. Horta et al.(1972), but in the case of manganese-alloyed IF steel Yoshinaga et al.(1994,1998) observed a perfect memory of the original texture. This was attributed to the action of residual stresses built into the austenite which caused variant-selection during the bainitic shear transformation on cooling. It was also claimed that a similar memory was possible in un-alloyed IF steel if this was quenched to bring about a shear-type of transformation. Hutchinson et al.(1998b) have raised objections to the residual stress hypothesis and we present here new results and an alternative possible explanation of the texture memory effect.

2 Experimental procedure

Three steels have been examined in the present work as summarised in Table1. Steels A and B were processed to cold rolled sheets under industrial conditions while C was laboratory produced from a 70 kg ingot. All of these have very low carbon contents but A is unstabilised whereas B and C contain titanium and C has, in addition, an increased content of manganese.

Table 1. Details of the present steels

Steel	C %	Mn %	Al %	Ti %	N %	% C/R	Ac_1-Ac_3
A	0.003	0.14	0.03	-	0.002	72%	909-927 °C
B	0.006	0.10	0.05	0.089	0.004	72%	933-949 °C
C	0.003	1.53	0.03	0.060	0.002	75%	858-901 °C

Heat treatments were carried out in a preheated laboratory furnace at various temperatures which involved a heating rate of about 20°C/s followed by holding for 1 minute at temperature. Cooling was mostly in free air (AC) with an initial rate of about 20°C/s but water quenching (WQ) and furnace cooling (1°C/min)(FC) were also used. Temperature was logged using a thermocouple spot-welded on the specimen. Samples of the same steels were also examined in a dilatometer using the same heating and cooling rates to determine the start and finish temperatures of the phase transformation from ferrite to austenite, Ac_1-Ac_3 (see Table 1). Textures were measured at 20% depth with a Siemens D5000 x-ray goniometer and CoKα radiation using (110), (200) and (211) pole figures to calculate ODFs. A simple measure of the γ-fibre strength was obtained from the average intensity in the (200) pole figure in the angular range 50–60°. Grain structures were examined using back-scattered imaging in the scanning electron microscope (SEM-BSE) and also by orientation imaging microscopy (OIM).

3 Results

It can be seen from Table 1 that steel A, which is almost unalloyed pure iron, has a transformation start temperature very close to the normal value for iron of 910 °C. Titanium in the IF steel B has raised the transformation range considerably which is probably a kinetic effect associated with solute drag as such a large effect is not expected according to the phase diagram. The presence of manganese in steel C has reduced the transformation temperature range as would be expected from the known influence of Mn as an austenite stabiliser.

Figure 1 shows the effect of the peak temperature during annealing on the γ-fibre strength of the resulting ferrite. Steels A and B both undergo a marked reduction in texture sharpness after reaching temperatures where complete transformation to austenite took place. Increasing temperature beyond this had no further influence. The texture of the IF steel B is, however, significantly stronger than that of steel A after these anneals. The manganese-alloyed steel C, in agreement with previous reports, is almost unaffected be heat treatment in the austenite range. No loss of texture sharpness could be seen even after heating to 1000°C.

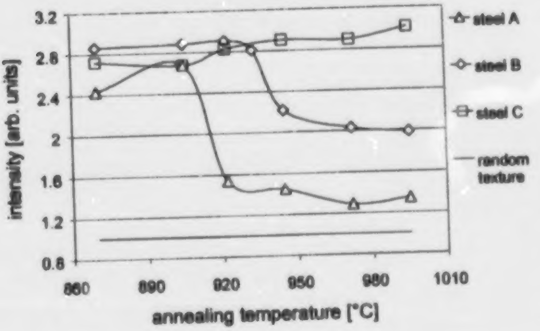

Fig. 1
Texture strength for the γ-fibre components after heating to different temperatures for the three steels investigated here.

Figure 2 shows ODF sections for the three steels after annealing at temperatures in the ferrite and in the austenite ranges. Also shown in Fig. 2 are calculated ODF sections where the initial ferrite texture has first been transformed to austenite and subsequently re-transformed back to ferrite. Random selection of variants was assumed in these calculations using the N-W orientation relationship. Calculations based on Bain or K-S produced similar textures to these although somewhat sharper or more diffuse respectively. The choice of relationship does not affect the present discussion, however. For steel A, the predicted texture after the reverse transformation is quite similar in form and intensity to the measured one. There seems to be little or no memory acting in this steel so that all variants of the transformation occur equally during both heating and cooling. The behaviour of steel B, however, cannot be predicted quantitatively using the simple model. There is a stronger retention of the original ferrite texture, indicating that some type of texture memory mechanism is operating. For steel C the calculation gives very poor agreement with experiment because texture memory is virtually perfect in this case. Some microstructures for steel C are shown in Fig.3. The initial ferrite structure has fine polygonal grains of about 10μm but after air cooling from the austenite range a bainitic structure is formed with a very fine scale internal substructure resulting from the shear transformation. From the OIM picture one can distinguish the austenite structure as composed of grains of sizes about 50-100μm. Each austenite grain has

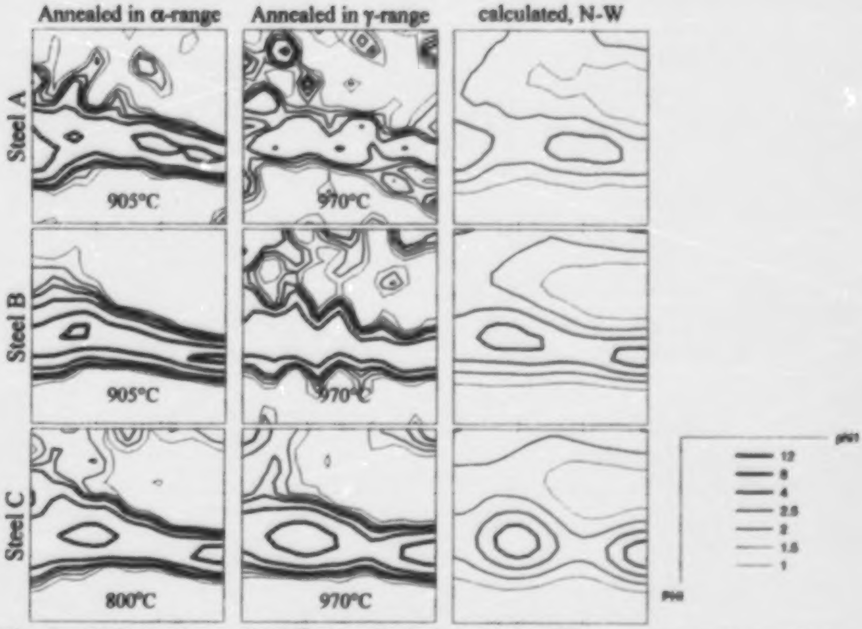

Fig. 2 ODF sections (ϕ_2=45°) for steels heated to different temperatures (see inserts) and also calculated transformation textures.

transformed to a single packet of ferrite in which the individual subgrains are misoriented by only a few degrees. Clearly, the *texture* memory in this steel is not associated with any *structure* memory since each new 'grain' has a volume equal to many of the initial ferrite grains. After slow cooling, a very different structure results. The grains are large and equi-axed with little internal substructure and had evidently formed by a diffusional transformation.

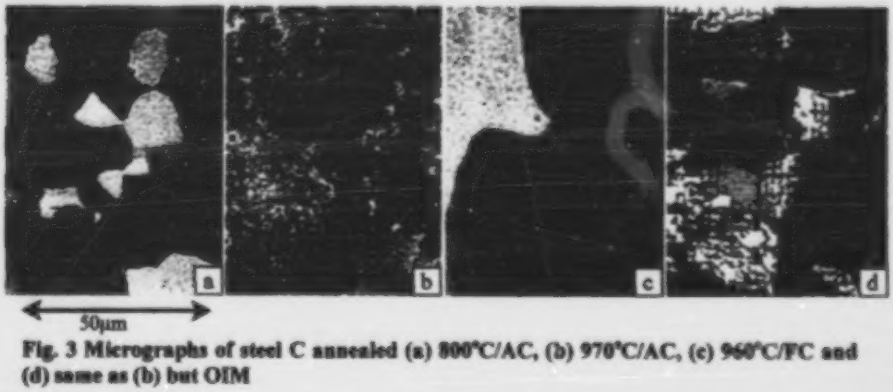

Fig. 3 Micrographs of steel C annealed (a) 800°C/AC, (b) 970°C/AC, (c) 960°C/FC and (d) same as (b) but OIM

Textures produced by cooling steels B and C at different rates from the austenite range are compared in Fig. 4. Cooling rate has little effect for steel B but slow cooling has reduced the texture strength in steel C, i.e. decreasing the memory effect in this case. This is in contrast to previous observations of Hutchinson et al (1998b) where texture in a similar steel was retained after equivalent slow cooling. Observe that the water quenched specimen is also weaker than the air cooled material.

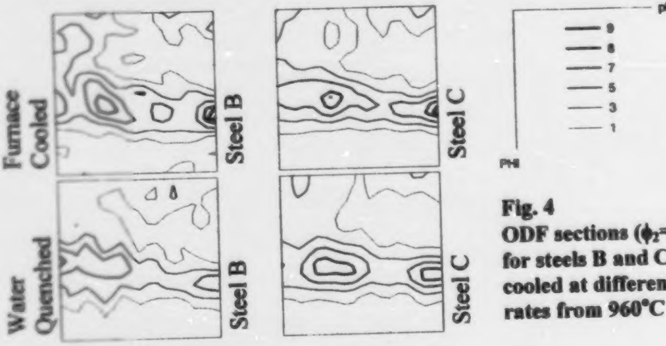

Fig. 4
ODF sections (ϕ_2=45°) for steels B and C cooled at different rates from 960°C

4 Discussion

The un-alloyed steel A seems to behave in a rational manner with all equivalent variants of the α–γ–α transformation occurring with approximately equal frequency so that there is little specific memory of the original texture after heating and cooling. The texture that results is explicable with the straightforward analysis applied here. Both the IF steels do demonstrate a memory of their initial ferrite textures and this memory is extremely pronounced in the case of steel C containing manganese.

In many ways the observations here are in agreement with those of Yoshinaga et al. (1994,1998) but there are some distinctions which lead us to a different viewpoint regarding the origin of the texture memory effect. Those workers argued that stresses built up in the austenite as a result of the α–γ transformation on heating provide a biasing effect on the reverse transformation so as to select the same variants on cooling from γ to α. Such behaviour was only expected to occur when the reverse transformation is of a shear type, which was in agreement with their observations on Mn-alloyed steel and also on a plain Ti-IF steel rapidly quenched from 930°C.

The present work suggests, however, that plain Ti-IF steels can show a texture memory, although not a perfect one, under all conditions of cooling and no special memory behaviour on quenching. It is possible that the temperature of 930°C used by Yoshinaga et al. was so close to the Ac_3 temperature of their Ti-IF steel (see the present Table 1) that not all the original ferrite had transformed to austenite in their quenching experiment. In fact, quenching the Mn-steel actually reduced the texture strength in this investigation. Another problem with the stress hypothesis is that it should not apply for diffusional transformations on slow cooling. Although slow cooling did lead to a reduction of texture memory in the present steel, there was no such effect in the previous work of Hutchinson et al (1998b) on a different Mn-alloyed IF steel. There, the texture memory was undiminished after slow cooling where polygonal ferrite resulted from a diffusional transformation mechanism. Furthermore, there is no loss of texture memory after longer holding times or higher temperatures in the austenite regime as would be expected as stresses are relaxed by creep processes.

It seems to the present authors that an alternative explanation is required which emphasises the role of titanium present in IF steels. As is well known, titanium combines with nitrogen as a very stable TiN phase and with carbon as less stable TiC particles. During heating to temperatures high in the ferrite range the TiC particles start to dissolve and carbon atoms rapidly diffuse away due to their high mobility in ferrite at such temperatures. Titanium atoms diffuse much more slowly and so a shell of Ti-enrichment remains around the particle. Since Ti is a strong ferrite-stabiliser, this enrichment can stabilise a rim of ferrite around the particles which retains its original orientation and could act as a ready-made nucleus for ferrite formation on cooling. According to the Fe-Ti phase diagram, as little as 0.8% Ti is sufficient to stabilise the ferrite phase at all temperatures and it seems quite reasonable that such a level may exist around a TiC particle which is in the process of dissolving. Alternatively, there may exist a 3-phase equilibrium of TiC, α and γ at temperatures above the nominal Ac_3.

The present explanation does not directly account for the effect of manganese in enhancing the texture memory but it is possible that this element may affect the phase equilibrium/dissolution behaviour. It may also be significant that the bainitic structure has a unique orientation within each prior austenite grain, as was shown by the OIM observations. Evidently, a single nucleus is activated in each grain and these presumably grow rapidly until the whole γ-grain is transformed. Rims of ferrite around TiC particles should act as very efficient nuclei which regenerate exactly the original ferrite orientations and should be activated more readily than other nucleation sites such as grain boundaries.

6 References

Horta, R.M.S.M., Wilson, D.V. and Roberts, W.T. (1972), Texture control in the rapid annealing of low carbon steels. *J.I.S.I.*,Vol. 210,pp.42-51.

Hutchinson, W.B., Ryde, L., Lindh, E. and Tagashira, K. (1998a), Texture in hot rolled austenite and resulting transformation products. *Mater. Sci. and Eng* Vol. A257, pp. 9-17.

Hutchinson, W.B., Ryde, L. and Artymowicz, D. (1998b), Effect of phase transformation on textures during continuous annealing. *Modern LC and ULC Sheet Steels for Cold Forming.* RWTH Aachen, Ed. W. Bleck pp.203-210.

Ray, R.K. and Jonas, J.J. (1990), Transformation textures in steels. *Int. Metall.Rev.* Vol 35, pp. 1-36.

Yoshinaga, N., Ushioda, K., Itami, A. and Akisue, O. (1994), α+γ and γ phases annealing in ultra low carbon sheet steels. *ISIJ International*, Vol 34, pp. 33-42

Yoshinaga,N., Kawasaki, K., Inoue, H., De Cooman, B.C. and Dilewijns, J.,(1998) Texture of austenite at high temperature in SULC cold-rolled sheet steels, *Modern LC and ULC Sheet Steels for Cold Forming*, RWTH Aachen Ed. W. Bleck, pp. 569-578.

INFLUENCE OF PRECIPITATES ON TEXTURE EVOLUTION OF TI-IF STEELS IN BATCH ANNEALING

JING SHI email: jshi@ecn.purdue.edu
School of Industrial Engineering, Purdue University, West Lafayette, IN 47907, USA
ZHIQIANG LI and XIANJIN WANG
University of Science and Technology Beijing, Beijing 100083, P.R.China

Abstract

The effect of precipitates on texture evolution in batch annealing of Ti-IF steels is investigated with focusing on TiC and FeTiP, because TiC usually has much denser distribution than other particles and FeTiP precipitates during batch annealing and interacts with recrystallization process. Through proper heat treatment, samples with different TiC morphology are achieved. It is found that the texture and mechanical properties of batch-annealed Ti-IF steels are hardly influenced by the different morphology of TiC particle. On the other hand, FeTiP precipitation during batch annealing is detrimental to the favorable <111>//ND recrystallization texture development, and this detrimental effect depends on FeTiP quantity and distribution. In addition, FeTiP distribution along grain boundaries is suggested to be the main cause of its detrimental effect.

Keywords: Ti-IF steels, texture, batch annealing, precipitates, mechanical properties

1 Introduction

It is well known that the interstitial-free (IF) steel can be obtained by adding Ti/Nb to stabilize interstitial atoms like C, N and S, and such process gives rise to various kinds of precipitates such as TiN, $Ti_4(CS)_2$, TiS, and TiC. Many investigations have been carried out concerning these precipitates in steelmaking, slab reheating, and hot rolling stages, and their influence behavior during cold rolling and annealing.

This paper represents the effort to investigate the effect of precipitates on texture formation and final mechanical properties of Ti-IF steels. Because TiC excels others in number and density and FeTiP can precipitate during batch annealing, they are considered the most possible ones which may have influence on the texture of IF steels. So, our focus here is on TiC and FeTiP. It is hoped that the research work will also be helpful to industrial production.

2 Experimental

Two kinds of cold rolled Ti-IF steels obtained in mass industrial production are used as the experimental materials. The chemical composition and processing parameters are listed in Table 1, in which SRT, FT, CT and CRR refer to slab reheating temperature, finish temperature, coiling temperature and cold rolling rate respectively. IF2 has similar composition and nearly identical processing parameters with IF1 except the coiling temperature.

For investigating the influence of TiC on texture and mechanical properties of Ti-IF steels, hot-rolled IF1 are divided into three parts, two of which are pretreated in gas-protected furnace before cold rolling. One part (IF1-2) is heat-treated at 710°C with a soaking time of 5 hours, and the other (IF1-3) is treated at 780°C for the same time. The purpose of pre-treatment is to coarsen TiC particles. As for the rest part of IF1 (IF1-1), it has no pre-treatment. After that, the three parts are cold rolled with a reduction of 77% and batch annealed under the same process. For studying the effect of FeTiP on Ti-IF steels, IF1-1 and IF2 are cold rolled and annealed under the same procedures so that their precipitate morphology, texture and properties can be compared. Batch annealing simulation is done a computer-controlled gas-protected furnace according to production parameters.

Table 1: Chemical composition and processing parameters of materials

Materials	C, %	N, %	S, %	Ti, %	Mn, %	P, %	RT,°C	FT,°C	CT,°C
IF1	0.0045	0.0030	0.0040	0.069	0.15	0.01	1246	892	635
IF2	0.0035	0.0028	0.0041	0.076	0.17	0.01	1227	892	690

The extracted carbon replica specimens for transmission electron microscope (TEM) are observed on JEM-200CX. The average diameter and size distribution of particles are analyzed and calculated by an image analyzer. Most precipitates in extracted replicas are identified by EDS. Optical metallurgy is conducted to study the microstructural change in samples. The texture is measured by X-ray diffraction on Rigaku 2038, and the orientation distribution function (ODF) is computed from pole figures {110}, {200}, and {112}.

3 Influence of TiC on texture and properties of Ti-IF steel

3.1 TiC morphology, microstructure, and texture before cold rolling

TiC morphologies in IF1-1, IF1-2 and IF1-3 are shown in figure 1. It is easy to find that TiC size increases as the temperature of pre-heat treatment increases, and the average TiC size in IF1-1 is smallest. In this way, the pre-heat treatment does successfully increase the average size of TiC particles. Figure 1 also shows that the density of TiC distribution is different, and IF1-1 has the highest density while IF1-3 has the lowest. It is noted here that the total mole factions of TiC in IF1-1, IF1-2 and IF1-3 are assumed to be identical because they are from the same hot band. The average TiC diameters of the three parts are 18nm, 30nm and 45nm respectively. Meanwhile, this trend remains in fully annealed samples, and the average size increases slightly in annealing for all the three groups. The average grain sizes of the three groups before cold rolling are nearly identical, which means the pre-heat treatment has no influence on the microstructure. The ODF results of the three samples before cold rolling are shown in figure 2. All of the three materials have random and weak texture. Meanwhile, α and γ-fiber textures of the IF1-1 and IF1-2 are close in tendency and intensity, while the IF1-3 has a relatively weaker γ-fiber texture and stronger {112}-{114}<110> components.

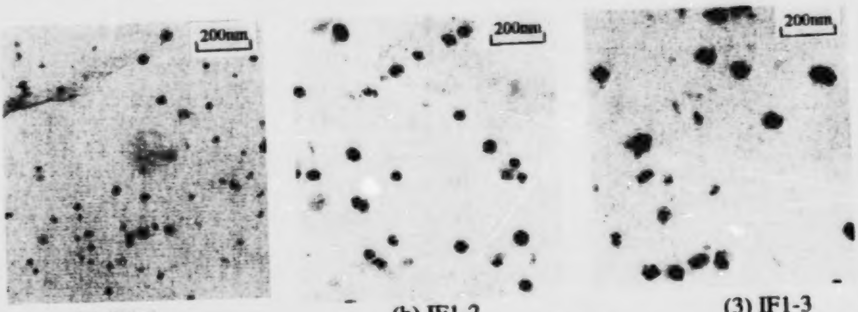

(a) IF1-1 (b) IF1-2 (3) IF1-3

Fig. 1: Different TiC morphology of IF1-1, IF1-2 and IF1-3 after pre-treatment

Therefore, IF1-1 and IF1-2 have similar texture and grain size but different TiC size before cold rolling. Also IF1-3 differs from IF1-1 and IF1-2 both in TiC morphology and texture. Thus, we can investigate the effect of TiC and texture before cold rolling on IF steel simultaneously.

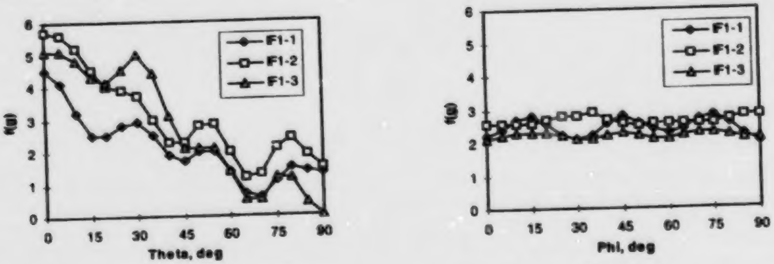

(a) α-fiber (b) γ-fiber

Fig. 2: α-fiber and γ-fiber textures of IF1-1, IF1-2 and IF1-3 after pre-treatment

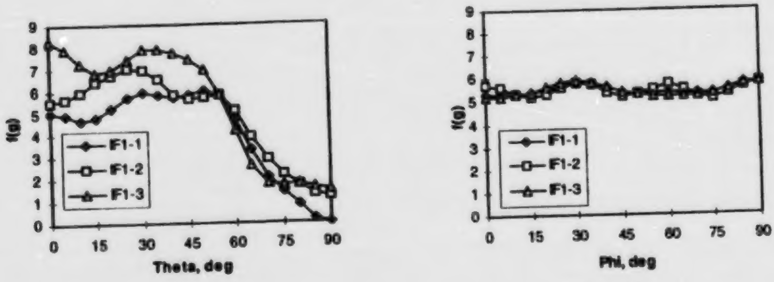

(a) α-fiber (b) γ-fiber

Fig. 3: α-fiber and γ-fiber textures of cold rolled IF1-1, IF1-2 and IF1-3

3.2 Cold rolling and annealing texture of IF1-1, IF1-2 and IF1-3

The cold rolling textures of IF1-1, IF1-2 and IF1-3 are compared in figure 3. The three have similar γ fiber texture, but they are obviously different in the α-fiber texture. IF1-3 has the strongest α fiber texture, while IF1-1 is the weakest. Figure 4 shows the batch annealing texture of the three groups. IF1-1 and IF1-2 have similar texture profiles, while IF1-3 has the weakest favorable {111} texture. Quantitative texture analysis shows that the volume percent of grains with {001} orientation in IF1-1, IF1-2 and IF1-3 are 2.63%, 1.92% and 3.77%, while the volume percent of {111} orientated grains are 43.39%, 43.97% and 41.28% respectively.

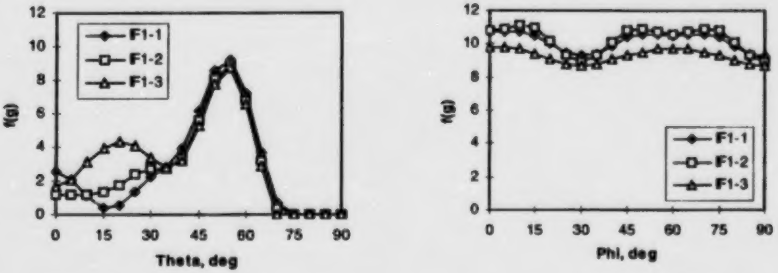

(a) α-fiber (b) γ-fiber

Fig. 4: α-fiber and γ-fiber textures of batch annealed IF1-1, IF1-2 and IF1-3

3.3 Discussion

The ranking of r_m-value from high to low is IF1-2, IF1-1 and IF1-3. The difference in TiC particle morphology causes very slight difference in texture and properties for IF1-1 and IF1-2 -- their final textures are nearly identical and the r_m-value difference is only 0.06. It is well known that the coarser and scarcer precipitates are less harmful to grain growth, and {111} annealing texture development. Because the r_m-value of IF1-2 is higher than that of IF1-1 by 0.06, so the result is still consistent with this pinning effect model. However, the favorable effect of coarser TiC is nearly negligible.

As it is shown that IF1-3 differs from IF1-1 and IF1-2 both in TiC and in texture before cold rolling, the effect of both TiC and before-cold-rolling texture can be observed here. According to the pinning effect model, the coarser and scarcer the TiC particles, the stronger the {111} annealing texture. However, IF1-3 has the weakest {111} annealing texture and the lowest r_m-value, which means the before-cold-rolling texture plays a much more important role in this case, and its deteriorating effect outweighs the favorable effect from coarser TiC particles. Meanwhile, the inheritance of texture can be observed. From figure 2, its <111>//ND texture is weaker than that of IF1-1 and IF1-2, and its <110>//RD texture is stronger than that of IF1-1 and IF1-2. This trend not only remains in cold rolling and annealing texture but also is enlarged in annealing.

4 Influence of FeTiP on annealing texture and properties of Ti-IF steels

The chemical composition, processing parameters of IF1 and IF2 are similar, and their cold rolling reduction rate and heat treatment of batch annealing simulation process are identical. In addition, the hot band grain sizes and the hot rolling texture of the two materials are also similar. But the coiling temperature of IF2 (690°C) is much higher than that of IF1 (635°C) by 55°C. According to the common knowledge about IF steels, high coiling temperature is good to high r_m-value, so IF2 should exhibit higher r_m-value than IF1-1. But the r_m-value of IF1-1 is higher than that of IF2 by 0.2 while the difference in other properties is not obvious. Meanwhile, figure 5 shows the <111>//ND texture of IF1-1 is stronger that that of IF2. IF1-1 is used here because it doesn't experience pre-heat treatment. Quantitative analysis of cold rolling and annealing texture of IF1-1 and IF2 shows that their cold rolling texture components are similar in intensity; while IF1-1 has stronger {111} annealing texture than IF2 by about 10%, and its {001} texture is weaker. Through TEM observation, it is found that both IF1-1 and IF2 have FeTiP precipitation during batch annealing process, but the amount of FeTiP of annealed IF1-1 is much less than that of IF2. It is inferred that the difference in FeTiP precipitation causes the different annealing texture and r_m-value.

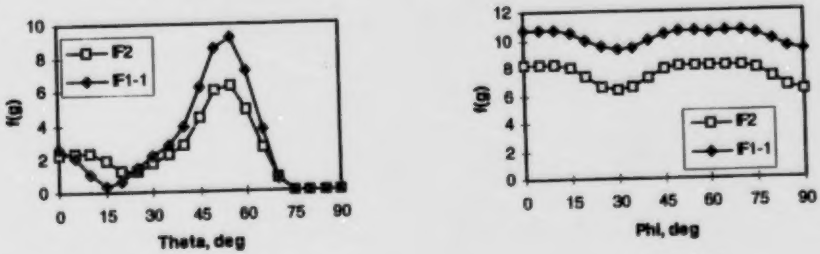

(a) α-line

(b) γ-line

Fig. 5: Comparison of α and γ fiber textures of batch annealed IF1-1 and IF2

Fig. 6: Dispersion of FeTiP along grain boundaries in batch annealed IF2

It is well known that solute P atoms exist in interstitial-free ferrite matrix substitution element and tend to concentrate on grain boundaries. From the authors' previous research about precipitate evolution during batch annealing, FeTiP only precipitates in batch annealing or annealing with long soaking time for normal ULC IF steels. Thus, FeTiP must also tend to precipitate along grain boundaries. Figure 6 shows FeTiP dispersion along grain boundaries in annealed IF2, which strongly supports our speculation. In this way, FeTiP particles retard recrystallization, cause the weaker {111} texture and lower r_m-value. For the precipitation of FeTiP in IF1 is much more than that in IF2 and its pin effect is also much stronger, a relatively more intense <111>//ND texture develops in IF2 and hence better deep drawability. In this investigation, it is obvious that coiling temperature affects the precipitation behavior of FeTiP during batch annealing. The higher the coiling temperature, the more the FeTiP precipitation in batch annealing, and then the weaker the

{111} annealing texture. From the viewpoint of FeTiP precipitation, high coiling temperature is not always helpful to obtain good deep drawability for Ti-IF steels through batch annealing.

4 Conclusions

The influence of precipitation on annealing texture development and mechanical properties of Ti-IF steels is studied with focusing on TiC and FeTiP. From the above results, the following points can be summarized.

(1) Through proper pre-treatment, the size and distribution of TiC can be altered and the grain size can be kept at the same level. However, whether the hot rolling texture will be changed depends on the pre-treatment temperature.

(2) The size of TiC particles doesn't have obviously favorable effect on the {111} annealing texture development and the increase of r_m-value. When compared with other factors like original texture before cold rolling, the TiC is far less important.

(3) The precipitating of FeTiP in batch annealing is indirectly affected by coiling temperature, that is to say, the amount of FeTiP precipitation in annealing increases with coiling temperature. The FeTiP precipitation in batch annealing hinders recrystallization, so it is harmful to obtain higher r_m-value. The more the FeTiP, the weaker the {111}//ND fiber texture and the worse the deep drawability.

References

Belyansky, A., Kapnin, V. and Larin, Y. (1994) Dispersed Particles in IF-Steels and Their Transformation in the Production Process, Proc. "International Forum for Physical Metallurgy of IF Steels", Iron and Steel Institute of Japan, pp.289-292.

Hellman, P. and Hillert, M. (1975) Effect of Second-Phase Particles on Grain Growth, Scand. J. Metall., Vol. 4, No. 5, 211-219.

Ray, R., Jonas, J., and Hook, R. (1994) Cold Rolling and Annealing Textures in Low Carbon and Extra Low carbon Steels, International Materials Reviews, Vol.39, No.4.

Satoh, S., Obara, T. and Tsunoyama, K. (1986) Effect of Precipitate Dispersion on the Recrystallization Texture of Niobium-Added Extra-Low Carbon Cold-Rolled Steel Sheet, Trans. Iron Steel Inst. Jpn., Vol. 26, No. 8, pp. 737-744.

Satoh, S., Morita, M. and Hashimoto, O. (1992) Carbide Dissolution in Interstitial Free Steels during Continuous Annealing, Proc. "Developments in the annealing of sheet steels", The Minerals, Metals & Materials Society, pp. 177-188.

Shi, J. (1998) Study on the Optimization of Batch Annealing Process and Recrystallization Texture Evolution for IF steels, Ph.D. thesis (in Chinese), University of Science and Technology Beijing.

Subramanian, S. and Gao, J.(1994) Effect of Precipitate Size and Dispersion on Lankford Values of Titanium Stabilized Interstitial-Free Steels, Proc."International Forum for Physical Metallurgy of IF Steels", Iron and Steel Institute of Japan, pp.53-56.

EFFECTS OF COMPOSITION ON ANISOTROPY AND TEXTURE OF CONTINUOUSLY ANNEALED LOW CARBON STEEL SHEETS

S.C. BAIK, and O. KWON
Technical Research Laboratories, Pohang Iron & Steel Co. Ltd., Pohang, South Korea
J. CHO and K.H. OH
Dep. Metallur. Eng., Seoul National University, Seoul, South Korea

Abstract

The effects of the nitride forming elements, B, Zr and Ti on the mechanical properties of continuously annealed low carbon steel sheet were examined. The Δr value of the Ti added low carbon steel was observed to be dependent on the annealing temperature. The r_{45} value for the Ti added low carbon steel was increased when the annealing temperature was increased, resulting in lower anisotropy of strips treated at a higher annealing temperature. The texture from {111}<110> to {110}<110> in α fibre and γ fibre was developed in the Ti added steel at annealing temperatures higher than 830°C. It can be explained by the fact that grain growth was suppressed by TiC at low temperature, and then grew selectively at high temperature so that the texture was developed.

Keywords: Anisotropy, low carbon steel, plain strain ratio, texture, Titanium

1 Introduction

Continuously annealed low carbon steels and interstitial free(IF) steels are used for large deformation parts of automobiles. In particular, IF steels have been applied to a large number of automobile parts because of excellent formability and non-aging properties. The excellent formability of IF steels is due to scavenging of the detrimental solute atoms. However, considering cost and productivity, it is advantageous to use low carbon steel instead of IF steel for automobile parts. The continuously annealed low carbon steel is a kind of bake hardening material because some of the solute C is retained after cooling and overaging (Messien and Leroy 1985). It has been reported that the bake hardening strength of low carbon steels is high and stable with small deviation of bake hardening strength according to composition and manufacturing conditions (Hayashida et al. 1994). In order to make the utmost use of the advantages of low carbon steel for automobiles, the r value of continuously annealed low carbon steel has to be increased.

The purpose of this study was to investigate the effect of nitride forming elements, B, Zr and Ti, on the texture and r value of the low carbon steels, which were continuously annealed at various temperatures. The change of planar anisotropy of low carbon steels as a function of annealing temperature, has been also studied.

2 Experiments

Table 1 shows the chemical composition of the examined steels. All the steels were vacuum melted and hot rolled to 30mm in a laboratory. These coupons were reheated at 1250°C and hot rolled. The finishing temperature of hot rolling was 910°C. Subsequently, the hot rolled sheets were soaked at 720°C for 1 hour, followed by cooling in the furnace to room temperature in order to simulate the coiling temperature process of hot coils. The hot rolled steels were pickled and cold rolled to a thickness of 0.8mm, followed by annealing at 800~880°C for 28 seconds using a continuous annealing simulator (ULVAC CCT-Y8).

ODFs were calculated by the series expansion method from the three incomplete pole figures of {110}, {112} and {200}, which were measured in the center layers of the sheets with $Mo_{K\alpha 1}$ radiation. Transformation temperatures of the examined steels were measured using differential scanning calorimeter (MAC DSC-3300) when the specimens were cooled at a cooling rate of -15°C/min from 950°C.

3 Results

3.1 *r* value measurements

Fig.1 shows values of $\bar{r}$, r_{45} and Δr for the examined steels, respectively, as a function of annealing temperature. There was a small difference between the $\bar{r}$ values of the examined steels except for the B added steel. Low $\bar{r}$ values and the high Δr values were obtained in the B added steel, because the r_{45} values were lower than those of any other steels. The addition of Zr had little effect on the anisotropy in the low carbon steel. On the contrary, the Δr values of the Ti added steel were low in comparison with those of any other steels due to high r_{45} values. The r_{45} value was increased and Δr value was decreased when the annealing temperature was increased

Table 1: Chemical composition of the examined steels. (weight %)

Steel	C	Sol. Al	Mn	P	S	N	B	Zr	Ti
LC	0.018	0.048	0.19	0.011	0.010	0.0027	-	-	-
LC-B	0.018	0.015	0.20	0.011	0.011	0.0028	0.0012	-	-
LC-Zr	0.018	0.016	0.07	0.010	0.010	0.0021	-	0.025	-
LC-Ti	0.019	0.023	0.08	0.007	0.009	0.0018	-	-	0.011

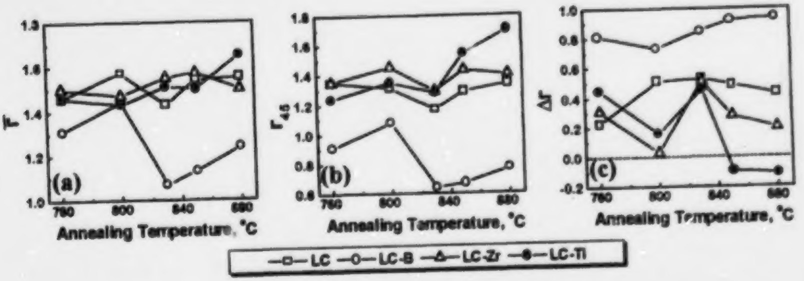

Fig.1: Plots of (a) $\bar{r}$, (b) r_{45} and (c) Δr as a function of annealing temperature.

in the Ti added steel. The Δr values were lower than 0 for the Ti added steel annealed at temperatures in the range of 850~880°C. It was reported that r values changed from pattern I ($r_{45} < r_0 < r_{90}$) to pattern II ($r_0 < r_{45} < r_{90}$) for Ti added low carbon steels annealed at 750°C for 6hours when the atomic ratio of Ti/C was increased (Matsuoka and Takahashi 1971). In this study, the result of r value measurement showed that the planar anisotropy of the Ti added low carbon steel was changed from pattern I to pattern II when temperature was increased in continuous annealing.

3.2 Texture measurements

Fig.2 shows the fibre texture in the steels annealed at various temperatures. The annealed textures were weak in the steels annealed at 800°C in comparison with those in the steels annealed at a temperature higher than 830°C. Especially, the texture of the Ti added steel annealed at 800°C was weakest. However, the texture from {111}<110> to {110}<110> in α fibre and γ fibre were increased in the Ti added steel when the annealing temperature was increased, resulting in a texture intensity of the Ti added steel higher than those of any other steels. The ODF of Ti added steel shows that the texture of steel annealed at 800°C was nearly random and the texture of the steel annealed at 850°C was similar to the cold rolled texture of steel.

The grain orientations of normal direction were measured using OIM in the Ti added steels as listed in Table.2, where the orientation in the normal direction was defined to be same when the misorientation was less than 10°. The volume percentage of the grain of {112} in the normal direction was larger than those for any direction for the steel annealed at 800°C. The volume fraction of {111} grains was increased when the annealing temperature was increased from 800°C to 850°C. This result shows that the main orientations of the grains in the normal direction were {111} and {112} in the Ti added steel annealed at 850°C.

Table 2: Volume percentages of grains of the normal directions, {111}, {112}, {110} and {100}, in steel LC-Ti annealed at 800 and 850°C measured by OIM.

Temp. (°C)	{111}	{112}	{110}	{100}
800	6.2	25.1	5.5	7.2
850	25.7	35.5	4.7	0.1

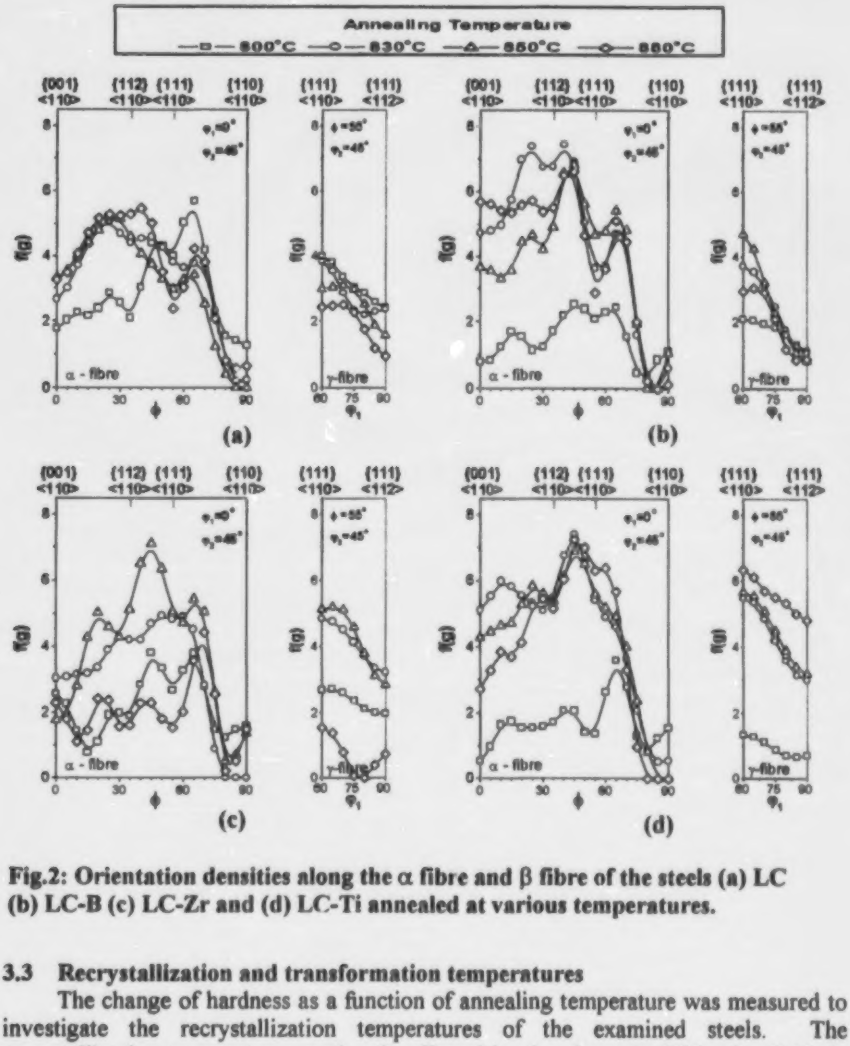

(a) (b) (c) (d)

Fig.2: Orientation densities along the α fibre and β fibre of the steels (a) LC (b) LC-B (c) LC-Zr and (d) LC-Ti annealed at various temperatures.

3.3 Recrystallization and transformation temperatures

The change of hardness as a function of annealing temperature was measured to investigate the recrystallization temperatures of the examined steels. The recrystallization temperature was barely affected by the element addition in all kinds of steel. The change of microstructures during the continuous annealing process was also observed, which illustrates that the recrystallization of steels was almost completed at about 700°C during the heating process.

The enhancement of the desired {111} recrystallization texture is attributed to two mechanisms, namely, selective grain growth of the {111} oriented grains and selective phase transformation of non-{111} grains (Klinkenberg et al. 1993). It was observed using differential scanning calorimeter that the A_{r1} temperatures of examined steels were about 880°C. Therefore, it was found that the texture evolution after recrystallization for the Ti added steels annealed at a temperature higher than 830°C, was not related to the transformation of ferrite to austenite.

As the grains in the steels annealed at 800~880°C were completely recrystallized and were not transformed, it can be explained that the development of α fibre and γ fibre is due to the selective grain growth after recrystallization.

3.4 Precipitates

Typical precipitates in the examined steels using TEM. MnS and BN were observed in the B added steel and TiS, TiN and TiC were observed in the Ti added steel. (Zr,Mn)(N,S,O) complex compounds were formed in the Zr added steel. The TiC was smaller and more abundant than any other precipitates. In order to investigate the effect of precipitate on grain growth, the precipitates on the grain boundaries were observed using TEM as shown in Fig.3. Fig.3(a) shows a grain which was prevented by TiC precipitates from growing. Many precipitates of TiC were observed on the bent grain boundaries. On the contrary, it seems that the grain growth was not influenced by a small number of large precipitates of TiN. This result indicated small and abundant precipitates, TiC, more strongly suppressed grain growth than large precipitates such as TiN, TiS, BN and MnS.

According to this result, the weakest texture in the Ti added steel annealed at 800°C can be explained by grain growth retardation by TiC. Grains then grew selectively so that the texture was developed when the driving force of grain growth was increased with increasing annealing temperature.

4 Discussion

It has been found that the r_{45} value was increased in the Ti added low carbon steel when the annealing temperature was increased, resulting in a lower anisotropy of strips treated at higher annealing temperature. A low planar anisotropic low carbon steel of $\Delta r = -0.11$ and $\bar{r} = 1.65$ could be obtained by continuous annealing. The change of r value is mainly related to the texture evolution. Though the texture of Ti added steel

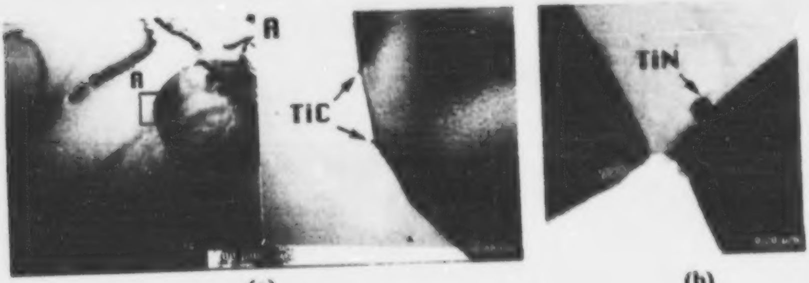

(a) (b)

Fig.3: TEMs showing the precipitates of (a) TiC and (b) TiN on the grain boundaries in steel LC-Ti annealed at 800°C.

was weakly developed in the Ti added steel annealed at 800°C, the intensity of texture became high when the Ti added steels were annealed at a temperature higher than 800°C. Fig.2(d) shows the texture from {111}<110> to {110}<110> in α fibre, and γ fibre was increased in the Ti added steel when the annealing temperature was increased. It was confirmed using OIM that the normal directions of grains were mainly {111} and {112} in the Ti added steel annealed at 850°C.

It is known that {111} <110> and {111}<112> are beneficial for high r value and that the r_{45} value is high in the {112}<110> component (Ray et al. 1994) It was reported (Zimnik et al. 1993) that the earing of deep drawn cups was dependent on the ratio of the volume fractions of {112}<110> and {111}<110>, where the earing was closely related to the planar anisotropy of materials. Considering the results of the reported papers, it can be expressed that the increase of the r_{45} value for the Ti added steel was due to the increase of the {112}<110> with {111}<110>. The difference of texture development between steels can be explained by the fact that the texture evolution is dependent on the kind of precipitate, which prevents grains from growing. The precipitate of TiC effectively suppressed grain growth at the low annealing temperature as shown in Fig.3. It was observed that a small number of large precipitates such as TiN, TiS, BN and MnS were ineffective to suppress grain growth. Therefore, it is expressed that the precipitates of TiC resulted in weak texture development in the Ti added steel annealed at 800°C. However grains grew selectively in Ti added steel so that the texture was developed, when the driving force of grain growth was increased with increasing annealing temperature.

5 Conclusions

1. The r_{45} value was increased in the Ti added low carbon steel when the annealing temperature was increased, resulting in lower anisotropy of strips treated at a higher annealing temperature.
2. The texture from {111}<110> to {110}<110> in α fibre and γ fibre was developed in the Ti added steel at an annealing temperature higher than 830°C.
3. When the annealing temperature was increased in the Ti added steel, grain growth was suppressed by TiC at low temperature, and then grew selectively at high temperature so that the texture was developed.

6 References

Hayashida,T., Oda, M., Yamda, T., Matsukawa, Y. and Tanak, J. (1994) *Proceedings of the Symposium on High-Strength Sheet Steels for the Auomotive Industry*, Iron & Steel Society, Baltimore, P.135

Klinkenberg, C., Raabe, D. and Lücke, K. (1993) Steel Research Vol.64, P.26

Matsuoka, T. and Takahashi, M. (1971) Testu-to-Hagane Vol.57, P.36

Messien, P. and Leroy, V. (1985) *Materials Technology*, Vol.56 P.385

Ray, R.K., Jonas, J.J. and Hook, R.E. (1994) *Int. Mater. Rev.*, Vol.39, P.129

Zimnik, W., Freier, K., Hssy, S. and Bunge, H. (1993) Steel Research Vol.8 P.420

THE ROLE OF IN-PLANE DISLOCATION REACTIONS DURING THE TRANSFORMATION OF HOT ROLLED AUSTENITE

J.J. JONAS and N.J. WITTRIDGE
Department of Metallurgical Engineering, McGill University,
3610 University Street, Montréal, Québec H3A 2B2, Canada

Abstract

The one-to-one correspondence between the 24 transformation variants called for by the Kurdjumov-Sachs relations and the 24 possible Bishop and Hill slip systems (including positive and negative slip) is pointed out. The slip activities associated with the plane strain rolling of fcc metals. e.g., austenite, are described. Distinctions are drawn between the burgers vectors associated with "positive" and "negative" slip and the importance of using solely the positive slip vectors is underlined. A table is introduced that can be used to establish the in-plane dislocation reactions that can take place between active (positive) slip dislocations. The table is employed to determine the reaction products that form in the case of fcc rolling. The "positive slip" and "in-plane reaction" burgers vectors are then utilized to predict the texture that is expected to form from the cooling of deformed austenite. These predictions agree very well with experimental observations.

Keywords: dislocation glide, slip systems, active slip, in-plane reactions, Kurdjumov-Sachs relations, transformation textures, variant selection, hot rolled austenite.

1 Introduction

Because of its industrial importance, the transformation of austenite following plane strain rolling is of considerable interest. Many researchers have attempted to account for this behaviour, including Bokros and Parker (1963), Haslam et al. (1973), and Davies et al. (1976). Several other approaches to this problem are reviewed in Ray and Jonas (1990). For a variety of reasons, not one of these models has turned out to be entirely satisfactory.

At the last ICOTOM meeting, Jonas et al. (1996) tried to improve the predictive accuracy of the various theories by combining three independent sub-models. However, even this more complicated approach failed to solve the problem in a truly acceptable manner. The three sub-models were based on: i) the presence of glide dislocations; ii) grain shape factors; and iii) the residual stresses remaining in grains after rolling. The third sub-model was used to eliminate some of the "unwanted" predictions of the first two, while the second was employed to provide certain texture components that were not called for by the slip model, but were nevertheless observed.

Here, a simpler approach is described, based entirely on the presence of dislocations in the deformed material. That is, neither grain shape nor residual stress considerations are involved. There are, however, two significant departures from earlier "slip activity" models: i) the first is that only "positive slip" dislocations (defined in more detail below) are employed; and ii) the second is that allowance is made for the *in-plane* reaction of glide dislocations and for the reaction products to play roles equivalent to those of the positive slip dislocations.

2 Positive Slip and Negative Slip

The present approach is based on the fact that 24 possible transformation variants are defined by the Kurdjumov-Sachs (K-S) relations (von Kurdjumov and Sachs, 1930) and that there is a one-to-one correspondence between these variants and the 24 different fcc slip systems that can be defined when allowance is made for the possible occurrence of both *positive* and *negative* slip. Here, positive slip is defined to take place in the direction of the resolved (applied) shear stress, while negative slip would involve work done *against* the applied stress and is therefore ruled out.

The first twelve slip systems are defined in Table I, where the convention first adopted by Bishop and Hill (1951 a, b) is used. Both the slip (burgers) vector and slip plane are listed here. The second twelve systems are simply the negatives of those listed in Table I. Also included in the table is the perpendicular to the burgers vector that lies in the slip plane; i.e. the <112> vector that is perpendicular to both the <110> burgers vector and the <111> direction that is perpendicular to the respective {111} slip plane. Further details regarding the correspondence between the twenty-four possible slip systems and the twenty-four K-S transformation variants are given in Butrón-Guillén et al. (1997).

The 24 <112> vectors are of importance here because they are the *rotation axes* that link a particular parent (austenite) orientation to each of the 24 K-S variants that can be formed from this orientation. This is done by means of a 90° rotation in the positive (RH) direction, as required by the K-S relationship. It should be noted that a rotation of + 90° from an arbitrary initial orientation results in a new orientation that is generally quite distinct from that produced by a – 90° rotation. Furthermore, if the + 90° rotation is identified with a particular positive slip burgers vector (and product orientation), then the – 90° rotation corresponds to the respective negative slip burgers vector (and negative slip product orientation). This important distinction was first pointed out by Sum and Jonas (1999).

Table I: Slip systems, as defined by Bishop and Hill (1951a, b) and their associated <112> axes.

Plane or Axis	**Slip System and Corresponding <112> Rotation Axis**											
	a (111)			b $(\bar{1}\bar{1}1)$			c $(\bar{1}11)$			d $(1\bar{1}1)$		
{111}	I	II	II	I	II	III	I	II	III	I	II	III
<110>	$[01\bar{1}]$	$[\bar{1}01]$	$[1\bar{1}0]$	$[0\bar{1}\bar{1}]$	$[101]$	$[\bar{1}10]$	$[01\bar{1}]$	$[101]$	$[\bar{1}\bar{1}0]$	$[0\bar{1}\bar{1}]$	$[\bar{1}01]$	$[110]$
<112>	$[2\bar{1}\bar{1}]$	$[\bar{1}2\bar{1}]$	$[\bar{1}\bar{1}2]$	$[\bar{2}1\bar{1}]$	$[1\bar{2}\bar{1}]$	$[112]$	$[211]$	$[\bar{1}\bar{2}1]$	$[\bar{1}1\bar{2}]$	$[\bar{2}\bar{1}1]$	$[121]$	$[1\bar{1}\bar{2}]$

3 Determination of the Slip Activities

Although the Taylor theory of crystal plasticity calls for the activation of *five* slip systems when a grain of arbitrary orientation is being deformed along an arbitrary strain path, such an approach calls for the selection of only 5 out of the 6 or 8 that are generally available; it therefore unavoidably involves what is known as the ambiguity problem. Because these 6 or 8 systems are identified with the respective vertices in the Bishop and Hill single crystal yield surface, a simple alternative is to specify that all six, or all eight (or a smaller number for orientations of lower symmetry) are in fact operative.

The active systems can be readily determined using an appropriate crystal plasticity computer program. If a "rate insensitive" model is employed, the six or eight can be derived by means of "averaging". Alternatively, a "rate sensitive" model can be used, in which case the 6 or 8 systems are selected directly by the computation.

The systems and slip activities (amounts of shear on each system) depend quite naturally on the strain or deformation path. Four quite distinct deformation paths can be defined: i) axisymmetric extension; ii) axisymmetric compression; iii) plane strain tension (or compression); and iv) simple shear. The first two have already been analyzed (and the predictions checked against experimental results) by: i) Wittridge et al. (1999) and ii) Sum et al. (1999), respectively. Sum and Jonas (1999) have carried out a similar investigation of plane strain compression (rolling), but only for the five single initial orientations of Liu and Bunge (1991). In all these cases, excellent agreement was obtained between the predictions and experimental observations. Finally, an investigation of the simple shear (torsion) strain path is currently under way (Wittridge and Jonas, 1999). An infinity of other modes of deformation can also be defined, consisting of arbitrary combinations of the above strain paths. These are not considered here.

Instead, we return to the case of plane strain compression (rolling) but investigate the behaviours of the seven initial orientations that constitute the fcc rolling fibre. These are the following: Cu, Cu-S, S, S-brass, brass, brass-Goss, and Goss. In this way, the analysis differs from that of Sum and Jonas (1999), who also used the dislocation reaction model, in that the starting orientations are not restricted to the cube fibre of Liu and Bunge (1991). The slip activities that apply to the above seven rolling fibre components are listed in Butron-Guillen et al. (1997). They are collected here in Table II. The present treatment differs from that of the latter workers, however, in that they employed a three component model (dislocation glide – grain shape – residual stress), while the one described below is a "positive/slip-in-plane reaction" analysis.

4 In-Plane Dislocation Reactions

In order to proceed with selection of the transformation variants, the burgers vectors that can be produced by the reaction of the glide (positive slip) dislocations of Table II must now be determined. For simplicity, only the products of *in-plane* dislocation reactions are considered here. They can be determined as follows. First, it must be recognized that when dislocations with twenty-four different burgers vectors can interact with a second set of twenty-four types of dislocations, there are 24 x 24 = 576 possible products. Fortunately, five-eighths of these are redundant, for symmetry reasons, leaving only 3/8 x 576 = 216 different cases of possible interaction.

Table II: Slip activities associated with fcc rolling (per unit von Mises strain).

Ideal Orientation	Slip Systems (Amounts of Shear)
Cu	c_{III} (1.4), - d_{III} (1.4), a_I (0.4), - a_{II} (0.4)
Cu-S	c_{III} (1.2), - d_{III} (1.6), a_I (0.4), - a_{II} (0.4)
S	c_{III} (0.9), - d_{III} (1.7), a_I (0.5), - a_{II} (0.4)
S-brass	c_{III} (0.7), - d_{III} (1.6), a_I (1.1), - a_{II} (0.2)
brass	- d_{III} (1.2), a_I (1.2), - c_I (0.4), c_{III} (0.4)
brass-Goss	- d_{III} (1.0), a_I (1.0), - c_I (0.1), c_{III} (0.1), - a_{III} (0.2), d_I (0.2)
Goss	- d_{III} (0.6), a_I (0.6), - a_{III} (0.6), d_I (0.6)

The 216 different cases are illustrated in Table III, from which the allowable products can be selected. Here, it can be seen that 6 types of interaction are possible: i) cross-slip; ii) annihilation; iii) Lomer-Cottrell lock formation; iv) energy increase (no possible reaction; v) in-plane reactions; and vi) reactions requiring cross-slip. Clearly, cross-slip and annihilation do not lead to products of interest here. Nor does lock formation or reactions that require cross-slip. (These two categories are somewhat similar and do not appear to be linked to variants that are observed experimentally). The hypothetical "energy increase" reactions can also be ruled out, leaving only the 24 possible in-plane reaction products relevant to the present discussion. Table III is a more complete version of the interaction table first proposed by Bútron-Guillén et al. (1998).

It should be noted that the lower LH half of the table represents the ½ x 12 x 12 = 72 "positive/positive" cases that correspond to the interaction of pairs of positive dislocations. (Note that "positive slip" and "positive dislocation" are not interchangeable terms. See Sum and Jonas, 1999, for the definition of "positive" dislocation that must be used when determining the reaction products that can be formed from the combination of active slip, i.e. positive slip, dislocations). Although the upper RH half of the "positive-positive" table is not presented here, it contains information that is already illustrated in the lower LH portion of the table and is therefore redundant. The twelve cases located along the underside of the diagonal correspond to "self-interaction" and are therefore excluded here. They also form part of the upper RH half of the "positive-positive" table (not shown) and so are only counted as representing ½ x 12 = 6 of the total of 72 distinct cases.

Table III: Grid of possible in-plane and other reaction products.

Reactants	-aI	-aII	-aIII	-bI	-bII	-bIII	-cI	-cII	-cIII	-dI	-dII	-dIII
aI		x 112	x 121	x 020	x 112		ANN	x 112	x 121	x 020	x 112	LC -bII -cII
aII	-aIII		x 211	x 112	x 200		x 112	x 200	LC -bI -dI	x 112	ANN	x 211
aIII	-aII	-aI				C/S	x 121	LC dI bI	x 200	LC bII cII	x 211	x 020
bI	x 200	LC cIII -dIII	x 121		x 112	x 112	x 020	x 112	LC -aII -dII	ANN	x 112	x 121
bII	LC dIII -cIII	x 002	x 211	-bIII		x 112	x 112	ANN	x 211	x 112	x 200	LC -aI -cI
bIII	x 121	x 211	ANN	-bII	-bI		LC aII dII	x 211	x 020	x 121	LC aI cI	x 200
cI	C/S			x 200		x 121		x 112	x 112	x 020	x 112	x x -bII -cI
cII		x 002	x 211		C/S		-cIII		x 112	x 112	x 200	xx -aI -cI
cIII		x 211	x 020	x 121		x 200	-cII	-cI		xx bI cI	xx bI dI	C/S
dI	x 002		x 121	C/S			x 002	LC aIII -bIII	x 112		x 112	x 112
dII		C/S			x 200	x 211	LC -aIII bIII	x 002	x 112	-dIII		x 112
dIII	x 121		x 200		x 211	x 200	x 112	x 112	ANN	-dII	-dI	
Reactants	aI	aII	aIII	bI	bII	bIII	cI	cII	cIII	dI	dII	dIII

Notes: 1) The in-plane reaction products are shown lightly shaded
2) The reaction products that could form as a result of cross-slip are heavily shaded.
3) The reactions that would lead to an energy increase are indicated with an "x'.
4) Lomer-Cottrell locks are labeled "LC".

There is an equivalent "negative/negative" table (not shown here) that can be deduced directly from the lower half of the table by simply changing the signs of the reactants as well as of the products. The classifications (e.g. cross-slip, annihilation, lock formation, energy increase, etc.) remain unchanged. This set of "negative-negative" interactions leads to a further 72 distinct cases (i.e. ½ x 12 x 12 = 72) as well as to an additional redundant 72.

Finally, there are the "positive-negative" and "negative-positive" interactions, of which there are 288. As the combination of a_I + (- c_I) leads to the same result as (- c_I) + a_I), only one set of these, e.g. the 144 "positive-negative" ones, need be considered here. Furthermore, only 72 of these are truly distinct, as the remaining 72 can be deduced from the initial 72 with the aid of symmetry arguments.

The 72 distinct "positive-negative" interactions are illustrated in the top RH half of Table III. As before, the 12 reactions represented along the diagonal are common to the 72 reactions shown as well as to the 72 not presented for symmetry reasons. It is of interest that *there are no possible in-plane reactions* when the reacting burgers vectors are of opposite sign. These hypothetical reactions are all ruled out because they involve increases in the dislocation self-energy (because dislocations with <112> or <200> type burgers vectors would be formed).

By contrast, the in-plane reaction of "positive-positive" dislocations leads to the formation of the twelve possible *negative* burgers vectors, while the equivalent "negative-negative" reactions produce the remaining twelve possible *positive* burgers vectors. It is in this way that the full complement of the twenty-four possible slip vectors is formed.

5 Classes of Dislocation-Dislocation Interaction

The frequency of occurrence of the various types of interaction listed above and illustrated in Table III can now be enumerated. In the case of the positive-positive interactions, there are 4 cross-slip, 2 annihilation, and 34 "energy increase" interactions, together with 12 in-plane reactions. In addition, there are 16 reactions requiring cross-slip and a further 4 leading to the formation of locks. By symmetry, the same numbers apply to the "negative-negative" case, leading to 4, 2, 34, 12, 16 and 4 further interactions.

By contrast, the numbers in these above six classes are quite different for both the positive-negative and the identical negative-positive cases. Under these conditions, there are 2 cross-slip, 10 annihilation, and 44 "energy increase" interactions. This is in addition to the 8 reactions that require cross-slip and the 8 further ones that lead to lock formation. The numbers applicable to all the classes of interaction reviewed above are collected and summarized in Table IV. From the table it is evident that more than half the possible reactions are ruled out because they would increase the dislocation self-energy. All but the 24 cases of in-plane reaction can be further excluded for a variety of geometric reasons.

Table IV: Numbers of each type of dislocation interaction.

Type of Interaction	Number of Cases
cross-slip	10
annihilation	14
energy increase	112
reaction	24
cross-slip reaction	40
lock formation	16
Total	216

6 Application of the In-Plane Reaction Theory to the FCC Rolling Fibre

It is now possible to investigate the reactions that can take place between the active slip systems listed in Table II for each of the 7 constituents of the fcc rolling fibre. For this purpose, the sign of the less active system must be reversed (Sum and Jonas), 1999); in the case of "balanced" slip (equal shears on two systems), products of both signs can be produced. The use of Table III leads to the following list of products in the seven cases. Note that when a product is formed (e.g. + a_{III} or – a_{III}) that can cross-slip onto an *inactive* plane, the present model calls for it to do so. Thus, + a_{III} is converted into – b_{III} and – a_{III} into + b_{III}.

Table V: Reaction products applicable to the fcc rolling fibre.

Rolling Fibre (Parent Component)	Product Before Cross-slip	Product After Cross-slip
Cu	$\pm a_{III}$	$\pm b_{III}$
Cu-S	$\pm a_{III}$	$\pm b_{III}$
S	$- a_{III}$	$+ b_{III}$
S-brass	$- a_{III}$	$+ b_{III}$
brass	$\pm c_{II}$	$\pm b_{II}$
brass-Goss	$d_{II}, - a_{II}, \pm c_{II}$	$- d_{II}, - a_{II}, \pm b_{II}$
Goss	$\pm a_{II}, \pm d_{II}$	$\pm a_{II}, \pm d_{II}$

7 Prediction of the Transformation Texture of Deformed Austenite

The transformation textures obtained from the active slip burgers vectors (positive slip only) are displayed in Fig. 1 for each of the seven initial components. Here (and in what follows), the following "weights" were assigned to each of the seven initial (austenite) orientations: Cu – 1.0; Cu-S – 0.75; S – .75; S – brass – 0.75; brass – 1.0; brass-Goss – 0.4; Goss – 0.4. These were estimated from the measurements of Hirsch and Lücke (1988) on rolled copper samples. Then, each positive slip system was further weighted according to its respective slip activity on a linear basis. (This general approach was also employed for the "negative slip" components, see below.) Those obtained from the reaction products (after cross-slip) are illustrated in Fig. 2. For the reaction products, the burgers vectors were weighted according to the lesser of the slip activities of the reactants. Finally, the two sets of predictions are combined in Fig. 3. Here, as in previous work (Wittridge and Jonas, 1999), the reaction products were given 1.5 times the weights of the positive slip components. This is again consistent with the experimental observations. This diagram should be compared with Fig. 4, in which an *experimental* transformation texture is shown. It is evident that neither the "positive slip" texture (Fig. 1) nor the "reaction" one (Fig. 2), *on its own*, gives a good match to the experimental texture. This is why *combinations* of models have been used in the past.

A further point of interest concerns the importance of variant selection. The texture components that have been excluded on the basis of negative slip are illustrated in Fig. 5. Here the presence of the cube fibre and that of a strong {116}<110> component are evident. These are not generally observed. Similarly, the components associated with the remaining rotation axes (i.e. the full 24 less positive slip, negative slip and reaction) are displayed in Figure 6. Were these to be included, they would lead to the presence of the rotated Goss, {110}<110>, and the cube fibre, which once again are not observed.

8 Conclusions

1. The transformation behaviour of deformed austenite can be predicted solely on the basis of a dislocation model. It relies on two components: i) the "positive slip" dislocations that participate in glide; and ii) the dislocations that form by in-plane reaction of the glide dislocations.
2. The possible in-plane reactions can be deduced with the aid of the table of dislocation reactions introduced here.
3. This theory has so far been applied to three strain paths: i) axisymmetric compression; ii) axisymmetric extension; and iii) plane strain rolling. In all three cases, it leads to results that are in excellent agreement with experimental observations.
4. Further work is required to explain the physical basis for the contributions of the: i) positive slip and ii) reaction dislocations.

9 Acknowledgements

The authors are indebted to the Natural Sciences and Engineering Research Council of Canada for financial support. They also acknowledge with gratitude discussions with Dr. M.P. Butrón-Guillén, who first proposed the construction of a simpler version of Table III and with M. Sum, who pointed out the importance of in-plane dislocation reactions and of using solely the burgers vectors associated with positive slip.

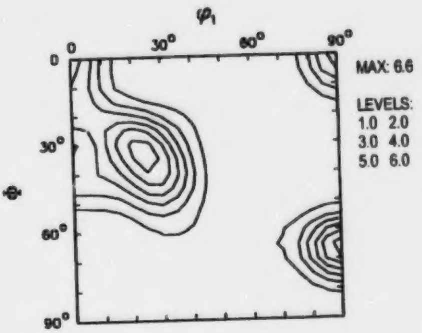

Figure 1: $\varphi_2 = 45°$ ODF section predicted via selection of the positive slip variants only.

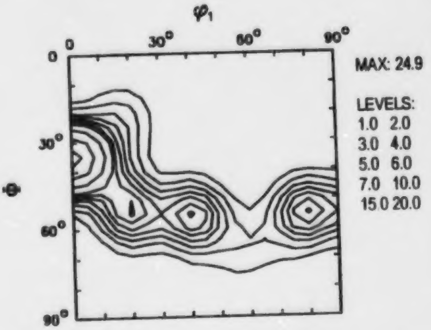

Figure 2: $\varphi_2 = 45°$ ODF section predicted via selection of the reaction products only.

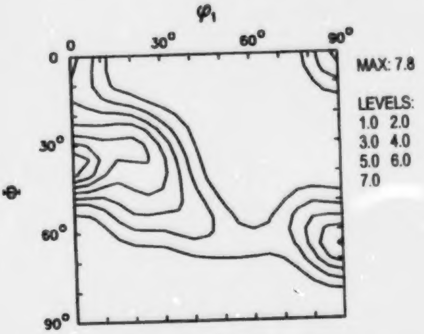

Figure 3: $\varphi_2 = 45°$ ODF section predicted using the present model (positive slip variants and reaction products).

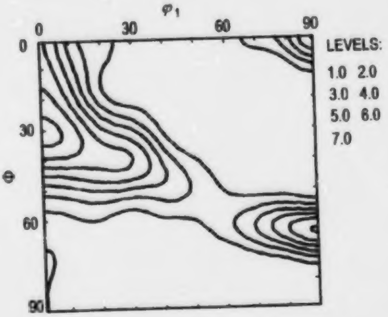

Figure 4: $\varphi_2 = 45°$ ODF section of an experimental transformation texture.

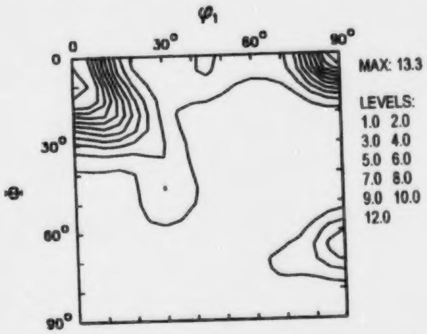

Figure 5: $\varphi_2 = 45°$ ODF section predicted via selection of the negative slip variants only.

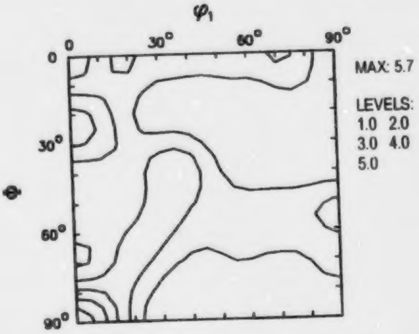

Figure 6: $\varphi_2 = 45°$ ODF section predicted via selection of all the remaining variants.

10 References

Bishop, J.F. and Hill, R. (1951a) A theory of the plastic distortion of a polycrystalline aggregate under combined stresses. *Phil. Mag.*, vol. 42, pp. 414-27.

Bishop, J.F. and Hill, R. (1951b) A theoretical derivation of the plastic properties of a polycrystalline face-centred metal. *Phil. Mag.*, vol. 42, pp. 1298-1307.

Bokros, J.C. and Parker, E.R. (1963) *Acta Metall.*, vol. 11, pp. 1291-1301.

Butrón-Guillén, M.P., da Costa Viana, C.S. and Jonas, J.J. (1997) A variant selection model for predicting the transformation texture of deformed austenite. *Metall. and Mater. Trans. A*, vol. 28A, pp. 1755-68.

Butrón-Guillén, M.P., da Costa Viana, C.S. and Jonas, J.J. (1998) Influence of slip activity and dislocation reaction on variant selection during the γ-to-α transformation. *Materials Science Forum*, vols. 273-275, pp. 151-56.

Davies, G.J., Kallend, J.S. and Morris, P.P. (1976) *Acta Metall.*, vol. 24, pp. 159-72.

Haslam, K., Coleman, T., Dulieu, D. and Dillamore, I.L. (1973) Deformation and recrystallization textures in metals and their industrial applications. *Proc. 3rd Int. Conf. on Textures of Materials, Société Française de Métallurgie*, Nancy, pp. 369-81.

Hirsch, J. and Lücke, K. (1988) Mechanism of deformation and development of rolling textures in polycrystalline fcc metals. *Acta Metall.*, vol. 36, p. 2883.

Jonas, J.J. Butrón-Guillén, M.P. and da Costa Viana, C.S. (1996) Effect of grain aspect ratio and cooling rate on variant selection during the γ-to-α transformation. *Proc. of ICOTOM 11*, Xian, China, vol. 1, pp. 575-91.

Liu, W.P. and Bunge, H.T. (1991) Variant selection in the martensitic transformation of an Fe-30% alloy with cube texture. *Materials Letters*, vol. 10, no. 7-8, p. 336.

Ray, R.K and Jonas, J.J. (1990) Transformation textures in steels. *Int. Mater. Reviews*, vol. 35, no. 1, p. 30.

Sum, M. and Jonas, J.J. (1999) A dislocation reaction model for variant selection during the austenite-to-martensite transformation. *Textures and Microstructures*, in press.

Sum, M. Jonas, J.J. and Root, J. (1999) Predicting the transformation texture of axisymmetrically compressed Fe-30% Ni using a dislocation reaction model. *Proc. of ICOTOM 12*, Montreal, Canada, in press.

von Kurdjumov, G. and Sachs, G. (1930) Üben den mechanismus det stahlhärtung. *Z. Phys.*, vol. 64, pp. 325-43.

Wittridge, N.J, Jonas, J.J. and Root, J.H. (1999) Application of the dislocation reaction model for variant selection to the transformation of an Fe-30% Ni alloy deformed in extension. *Proc. of ICOTOM 12,* Montreal, 1999, in press.

Wittridge, N.J. and Jonas, J.J. (1999) The transformation texture of an Fe-30% Ni alloy deformed in simple shear. To be published.

THROUGH-THICKNESS TEXTURE VARIATION IN PRIMRY RECRYSTALLIZED 3%SI-FE AND ITS EFFECT ON THE SHARPNESS OF (110)<001> GOSS TEXTURE

K.S. HAN, J.S. WOO and J.K. KIM
POSCO Technical Research Laboratories, Pohang, Korea
C.S. KIM
POSCO Cold Rolling Department, Pohang, Korea

Abstract

Texture variation along the thickness of primary recrystallized 3%Si-Fe sheets was studied to elucidate the sharpening of (110)<001> Goss texture after secondary recrystallization due to the temperature increase in hot band annealing. Increasing the hot band annealing temperature was found to intensify γ fiber centered around {111}[112] at the sub-surface and mid-plane of primary recrystallized sheets, whereas it showed little influence on the texture at the center. Among CSL boundaries to the Goss orientation, Σ9 and Σ5 boundaries showed a consistent trend with the temperature only at the mid-plane i.e., the frequency of Σ9 increases and that of Σ5 decreases as the temperature gets higher. Therefore it can be concluded that the increase in the frequency of Σ9 boundary at the mid-plane of primary recrystallized 3%Si-Fe results in the sharpening of the Goss texture after secondary recrystallization.

Keywords: Through-thickness texture variation, 3%Si-Fe, Goss texture

1 Introduction

Secondary recrystallization developes almost ideal (110)<001> texture, so called the Goss texture, in 3% Si-Fe when inhibition against normal grain growth and texture are properly provided in the primary recrystallized state. In spite of the many studies to clarify how the remarkably sharp (110)<001> texture is selected during the secondary recrystallization of 3%Si-Fe, it can be said that the basic mechanism has so far not been unequivocally established. However, it is generally accepted that (110)<001> oriented secondary nuclei start to develop at the subsurface and the textural inhomogeneity through thickness plays an important role for their abnomal growth behavior.

Inokuti[1] claimed that (110)[001] oriented grains with size advantage are originated from the large (110)[001] area at the subsurface of the hot bands by so called "texture memory effect" and serve as the secondary nuclei at the same location. Masuo et al[2] emphasized that the textural inhomogeneity through thickness, especially a strong presence of {111}<112> texture in the region between surface and center, provides a favorable environment for the successful development of (110)[001] secondary recrystallization. Other researchers[3,4] who examined the through-thickness variation of texture in various stages of 3%Si-Fe processing also confirmed a pronounced existence of (110)[001] texture at the subsurface and {111}<112> at the mid-plane. However, Pease et al[5] and Harase et al[6] reported that they found no conclusive evidence supporting the existence of (110)[001] oriented grains with size advantage at the subsurface. As to the selection of secondary recrystallization texture, Harase et al[6,7] propsed a role of CSL boundaries, particulary the low indexed, whereas, quite recently, Hayakawa and Szpunar[8] of High Energy boundaries.

In this study, the authors analysed the primary texture of 3%Si-Fe along the thickness direction and discussed its effect on the sharpening of (110)[001] texture after secondary recrystallization with the temperature increase in hot band annealing.

2. Experimental Procedure

A 3%Si-Fe alloy with the composition in Table I was vacuum melted and hot rolled to 2.3mm in thickness. The hot bands were annealed at the temperature range between 900 and 1150°C and then cold rolled down to 0.29mm by one stage method. The cold rolled specimens were subjected to a heat treatment for primary recrystallization and decarburization. The annealing for secondary recrystallization was carried out in a N_2+H_2 atmosphere by raising the temperature up to 1200°C at a rate of 15°C/hr.

Table 1. Chemical Composition of Experimental Material(wt%)

Si	C	Mn	S	P	Sol. Al	N
3.15	0.060	0.10	0.005	<0.01	0.026	0.008

The texture of the primary recrystallized specimens was analysed by using EBSP technique at three different locations along the thickness direction i.e., t/10(subsurface), t/4(mid-plane) and t/2(center). Magnetic induction, B_{10}, was measured after the secondary recrystallization anneal.

3. Results

Fig. 1 shows the effect of the hot band annealing temperature on magnetic induction, B_{10}. When a 3% Si-Fe alloy consists only of ideal (110)[001] orientation, its B_{10} is about 2.03T. As [001] axis of the secondary grains are not precisely aligned to the rolling direction, B_{10} of the secondary recrystallized 3%Si-Fe polycrystals is always less than the ideal value and the higher B_{10} means the better alignment of [001] to the rolling direction. Therefore it can be seen that increasing the temperature results in the sharpening of the Goss texture because all the specimens reveal 100% complete secondary recrystallization after the final anneal.

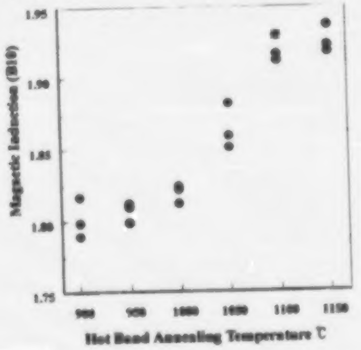

Fig. 1: Effect of hot band annealing temperature on the magnetic induction, B10 after secondary recrystallization

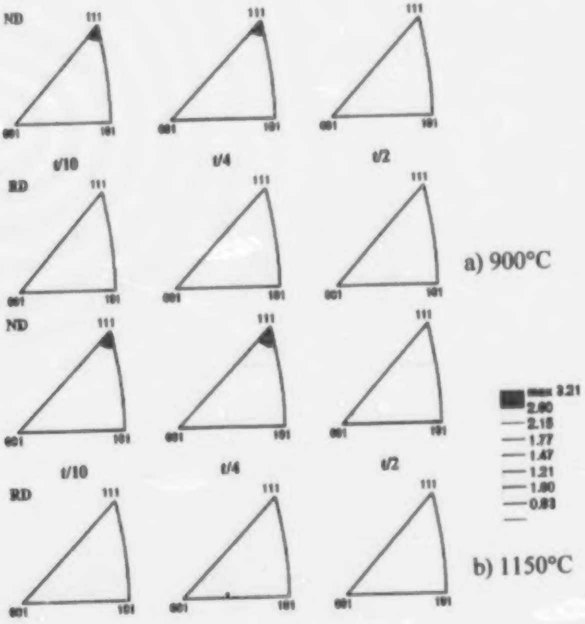

a) 900°C

b) 1150°C

Fig. 2: Inverse pole figures measured at three different locations along the thickness direction after primary recrystallization. Specimens were annealed at the temperature indicated during hot band annealing.

Inverse pole figures along the thickness of the primary recrystallized sheets are shown in Fig. 2. As the temperature becomes higher, at the subsurface and mid-plane, ND is more oriented toward [111] and RD shows more intensifying of [103]~[113] as well as [001] with somewhat lesser degree. At the center, the inverse pole figures show little influence due to the temperature rise.

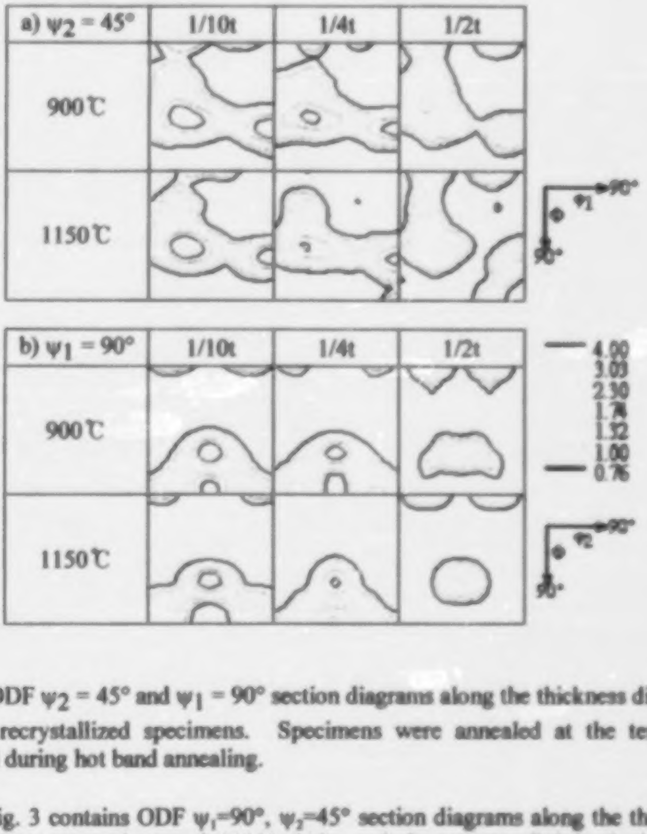

Fig. 3: ODF ψ_2 = 45° and ψ_1 = 90° section diagrams along the thickness direction of primary recrystallized specimens. Specimens were annealed at the temperature indicated during hot band annealing.

Fig. 3 contains ODF ψ_1=90°, ψ_2=45° section diagrams along the thickness. γ fiber texture centered around {111}<112> and the texture slightly deviated from (110)[001] existed the most at t/4 followed by t/10 and t/2. This trend becomes more evident due to the temperature rise especially at the subsurface and mid-plane as in the inverse pole figures.

In Fig. 4, the frequencies of low index CSL boundaries are shown with the temperature and the location. Σ9 and Σ5 are seen to be more dominant CSL boundaries than Σ7. At mid-plane, the frequencies of Σ9 and Σ5 are strongly correlated with the temperature i.e. Σ9 increases and Σ5 decreases as the temperature becomes higher.

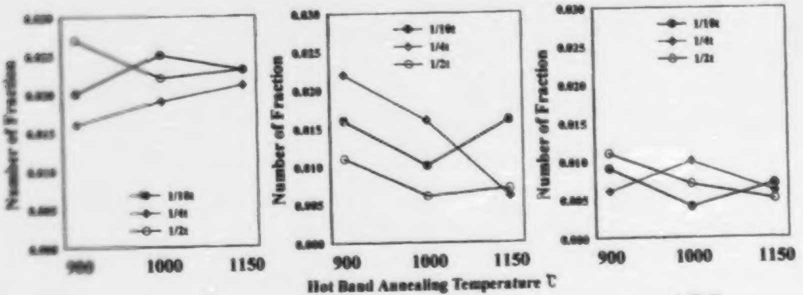

a) Σ 9 b) Σ 5 c) Σ 7

Fig. 4 Through thickness variation of low index CSL boundaries in primary recrystallized specimens

4. Dicussion

The textural inhomogeneity through the thickness of primary recrystallized 3%Si-Fe sheets has been considered a major metallurgical factor in developing a strong (110)[001] secondary recrystallization texture. Many years study has shown that such inhomogeneity is originated from the unique hot rolled microstructure of 3%Si-Fe and characterised by a presence of the Goss oriented grains at the subsurface and strong {111}<112> texture at the mid-plane. Our results in Fig.2 and 3 show the same texture variation through thickness as previous researches. Given that the Goss nuclei exist at the subsurface, it is not unreasonable to say that a strong intensity of {111}<112> texture at the mid-plane play a essential role because all the specimens in this study developed 100% complete secondary recrystallization. In addition, the sharpening of the secondary texture seems to be influenced by the texture inhomogeneity. Fig. 1~3 shows that the temperature increase in hot band annealing causes the sharpening of the Goss texture after secondary recrystallization and this phenomenon is strongly correlated with the change in the through-thickness texture variation.

Pease et al[5] compared the orientations of the secondary nuclei at the incipient stage and the secondary grains after the final anneal and concluded that some further sharpening of the Goss texture occurs during secondary recrystallization. Ushigami et al[9] also showed the same phenomenon by a directional grain growth experiment and added that the sharpening occurs as (110) plane align more to the rolling plane. Regarding the sharpening of the Goss texture after secondary recrystallization, Harase et al[7] reported that Σ9 boundary at the subsurface played an important role in single stage cold rolled 3% Si-Fe, whereas Gangli and Szpunar[10] found that increasing the frequency of Σ5 boundary sharpened the texture when the material processed by two stage cold rolling.

Fig. 4 shows the frequencies of low index CSL boundaries with the hot band annealing temperature and the location, when 3%Si-Fe is cold rolled by single stage. Σ9 boundary is seen to be the most dominant CSL boundary followed by Σ5 and Σ7. Although the temperature does not seem to influence on the frequencies of the CSL boundaries at the subsurface and the center, it is seen that raising the temperature gives rise to a consistent trend in the frequencies of Σ9 and Σ5 at the mid-plane. At the mid-plane, Σ9 boundary is found to become more frequent due the temperature rise, on the other hand the frequency of Σ5 is seen to decrease. Our results show that Σ9 boundary is more effective than Σ5 for the sharpening of the Goss texture, though both boundaries have been reported as important CSL boundaries for the successful development of secondary recrystallization in 3% Si-Fe. Furthermore, the sharpening is found to be strongly correlated with the behavior of both boundaries at the mid-plane not at the subsurface as in Harase's work[7].

5. Conclusion

Increasing the hot band annealing temperature was found to intensify γ fiber centered around {111}[112] at the sub-surface and mid-plane of primary recrystallized sheets, whereas it showed little influence on the texture at the center.

The increase in the frequency of Σ9 and the decrease of Σ5 at the mid-plane of primary recrystallized 3%Si-Fe result in the sharpening of the Goss texture after secondary recrystallization

6. References

1. Inokuti, Y. (1984) *Jounal of ISIJ,* Vol. 15, pp 2033-2040
2. Matsuo, M. (1989) *ISIJ International,* Vol. 29, No. 10, pp 809-827
3. Mishra, S., Darmann, C. and Lucke, K. (1984) *Acta Metall.* Vol. 32, No. 12, pp 2185-2201
4. Yu, Z.H., Xie, Y.F. and Gao, J. (1990) *Acta Metall. Mater.* Vol. 38, No. 6 pp 1023-1029
5. Pease, N.C., Jones, D.W., Wise, H.L. and Hutchinson, W.B. (1981) *Metal Science,* May 1981, pp203-209
6. Harase, J., Shimizu, R. and Watanabe, T (1986) *Proc. 7th RISO International Symposium* Ed. by Hansen, N. et al, pp 343-348
7. Harase, J., Shimizu, R., Yoshitomi, Y., Ushigami, Y. and Takahashi, N. (1993) *Modelling of Coasening and Grain Growth,* Ed. by Pande, C.S. and Marsh, S.P. pp 245-256
8. Hayakawa, Y. and Szpunar, J. A. (1997) *Acta Mater.* Vol. 45, No. 3, pp1285-1295
9. Ushigami, Y., Kubota, T. and Takahashi, N. (1998) *ISIJ International,* Vol. 38, No. 6, pp 553-558
10. Gangli, P. and Szpunar, J.A. (1994) *J. of Materials Processing Technology,* Vol. 47, pp 167-184

MICROSTRUCTURE AND CRYSTALLOGRAPHIC TEXTURE OF STRIP-CAST 4.3wt%Si STEEL SHEET

J. Y. PARK, K. H. OH and H. Y. RA
School of Materials Science and Engineering, Seoul National University, Seoul, Korea

Abstract

Fe-4.3wt%Silicon steel sheet was prepared by the vertical type twin roll strip casting process and then the microstructure and texture along the thickness direction of the strip were studied. The texture and microstructure through the sample thickness were inhomogeneous. Especially between subsurface layer and the midplane, Goss texture, {110}<001> component with the subgrains composed of low angle grain boundaries, was developed by the shear deformation, and rolling texture and solidification texture developed concurrently in the center layer.

Keywords : Shear deformation, Silicon steel, Twin-roll strip casting, Texture

1 Introduction

Since grain oriented silicon steel sheet was invented in 1935 by Goss (Cullity 1972), the material has been of considerable fundamental and technological interest to improve the sharpness of Goss orientation {110}<100> (Taguchi 1977). The studies have been focused on the improvement of magnetic properties. Although the manufacturing process has been well estabilished, the process is still complicated (Taguchi et al. 1966). Recently, the progress in strip-casting technology (Litterscheidt et al. 1991) provides a possibility to manufacture silicon steel sheet by a simpler processing than the conventional process, because the strip casting process can supply a silicon steel strip with the same thickness and width as that of hot rolled strip. This offers a possibility to eliminate the continuous casting and hot-rolling processes. Several researchers have reported that the texture of strip cast stainless steel strip is mainly random and homogeneous through the strip thickness (Raabe 1995). Choi reported that the texture changes were observed both in roll-with and through the thickness of the vertical type twin roll strip cast AISI430 stainless steel (Choi et al. 1996). Until recently, however, there has been a little information on the texture characterization on the strip-cast silicon steel.

In the present study, an Fe-4.3wt%Si strip was produced by the vertical type twin roll strip casting process and the microstructure and texture through the thickness direction were studied. Pole figure measurement followed by ODF analysis was used for the characterization of macroscopic texture and EBSD was used for microtexture

2 Experimental procedure

Strip casting of Fe-4.3wt%Si silicon steel were carried out by the twin-roll strip caster with internally water-cooled steel rolls of 200mm diameter and 100mm width. Hole-type nozzle was positioned at the center of a preheated tundish. Fig. 1 shows a schematic diagram of twin roll strip casting process. The thickness and width of cast-strip were 1.5mm and 100mm, respectively. Table 1 shows the chemical composition of the silicon steel used in this study. The microstructure of the specimens was observed on the plane perpendicular to the transverse direction by using an optical microscope and on the plane perpendicular to the normal direction by using a transmission electron microscope. The texture variation along the thickness direction was investigated by quantitative X-ray texture analysis and EBSD method. The position through the thickness direction can be used by a parameter s, defined as $s = 2a/d$, where a and d are the distance from the center layer of the strip and the thickness of the strip, respectively. The parameter s is called the normalized thickness. The crystallographic texture was quantitatively examined by measuring the three incomplete pole figures {110},{200},{211} in the range of the polar angle α from 0° to 70° with $CoK\alpha_1$ radiation in Seifert D3000 PTS goniometer, and Link Opal system was used to EBSD method. Samples for pole figure measurement were etched at room temperature in a solution of 90ml H_2O_2 and 10ml HF. From the measured pole figures, the orientation distribution function (ODF) was computed by the WIMV method (Matthies and Vinel 1982).

Table 1: Chemical composition of the sample in this study(wt.%).

C	Si	Al	Mn	S	N	Fe
<0.001	4.30	0.014	0.054	0.013	0.015	bal.

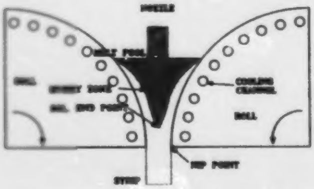

Fig. 1: Schematic diagram for twin roll strip casting process

3 Results and discussion

3.1 Microstructure

Fig. 2 shows the optical micrograph of the strip cast 4.3wt%Si steel at longitudinal section. The strip cast silicon steel sheet shows an inhomogeneous microstructure through the thickness of the strip. Near surface regions (s =1.0 ~0.6), the grains of about 200 ㎛ size are observed, which were presumably formed due to the rapid cooling (Litterscheidt et al. 1991). In the region of s = 0.6 ~0.1, the dendrites grew from the surface to the center of the strip. In the center layer (s = 0.1 ~ 0.0), the equiaxed grains of about 10 ㎛ size were observed. The microstructures of three parts are similar to those of the well known chill, dendritic and equiaxed zone in the metal mold casting. Fig. 3 shows the optical micrograph of near surface zone (s = 1.0 ~0.6), in the subsurface layer (s = 0.9 ~ 0.6), inclined lines are shown inside grains and, in the surface layer (s = 1.0 ~ 0.9), the inclined lines are not shown inside grains. Fig. 4 and Fig. 5 are the optical micrograph of the subgrains inside a grain and the TEM image of the subgrain boundary in the subsurface layer. The subgrains of 5~10 ㎛ size were observed inside a grain in the subsurface layer and the boundary of the subgrains were composed of dislocation wall (Humphreys 1995)

3.2 Texture

Fig. 6 shows the ODF from the measured pole figures at various thickness of the strip cast 4.3wt%Si steel strip. In the surface layer of s = 1.0, {100}<0vw> fiber components are evolved as shown in Fig. 6 (a). In the subsurface layer of s = 0.8, 0.6, the Goss {110}<001> component shows the maximum ODF value as shown in Fig. 6(b),(c). In the layer of s = 0.4, the intensity of {110}<001> component becomes weaker. In the center region of s = 0.2, 0.0, the {100}<0vw> fiber components, α and γ - fiber are evolved as shown in Fig. 6(e),(f).

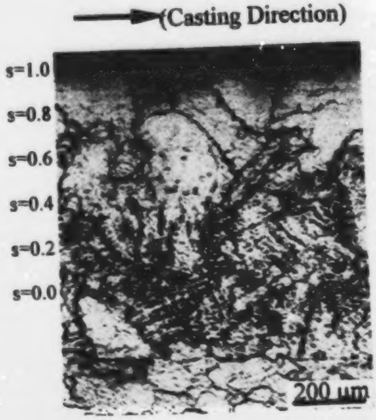

Fig. 2: Microstructure of as-cast strip longitudinal section.

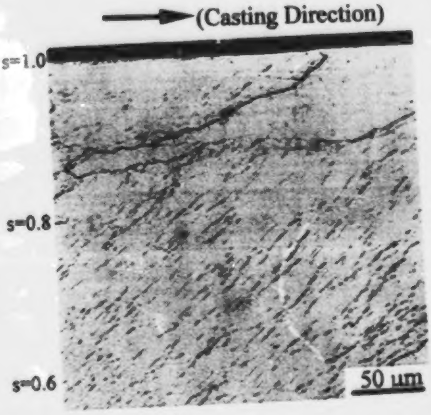

Fig. 3: Microstructure of as-cast strip near-surface laye

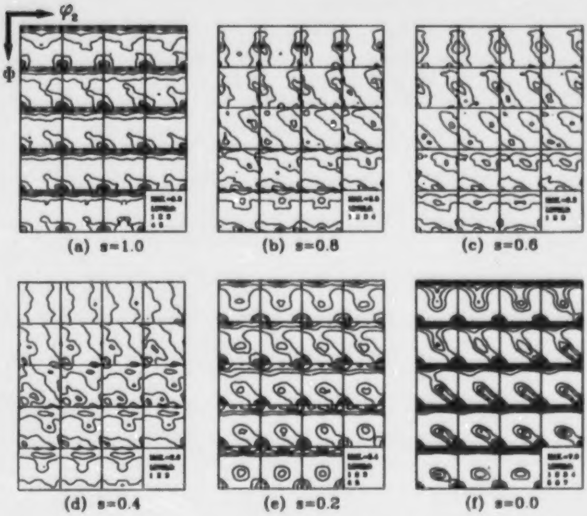

(a) s=1.0 (b) s=0.8 (c) s=0.6

(d) s=0.4 (e) s=0.2 (f) s=0.0

Fig. 6: φ_1 sections of ODF in various thickness layers of a strip cast 4.3wt%Si steel strip.

Thus, in the vertical type twin roll strip casting process, the texture of cast steel sheet composed of the solidification texture {100} fiber texture at surface, the shear {110}<001> in the subsurface and the combination of major plane strain compression texture and minor solidification texture in the center layer.

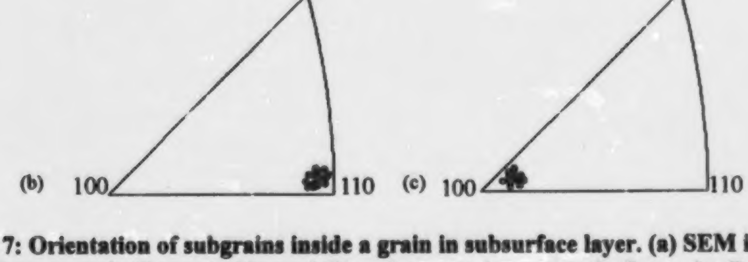

Fig. 7: Orientation of subgrains inside a grain in subsurface layer. (a) SEM image (b) Inverse pole figure in Normal Direction (c) Inverse pole figure in Casting Direction

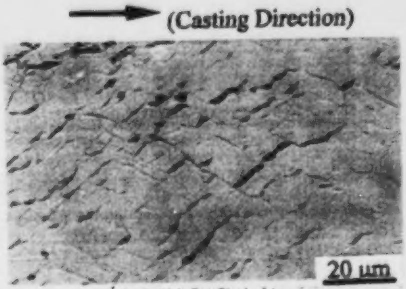

Fig. 4: Subgrains inside a grain in the subsurface layer.

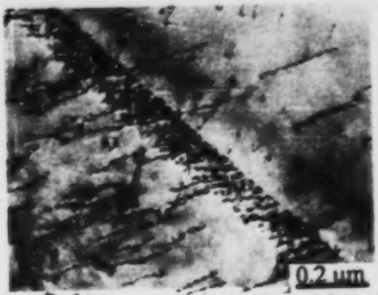

Fig. 5: TEM image showing subgrain boundary in the subsurface layer.

The orientations distributions of the subgrains inside a grain in the subsurface layer are shown in Fig. 7. Fig. 7(a) is the SEM image. Fig. 7(b), 7(c) are the inverse pole figures corresponding to numbers 1~ 15 of Fig. 7(a) by EBSD. In this grain, all of the subgrains have near ND//<110> orientation and RD//<100>, that is, the texture of this grain is Goss texture. All of the subgrain boundaries were the small angle boundaries with misorientation less than 3° in average.

The {100}<0vw> fiber components are the typical solidification texture (Choi et al. 1996). The {110}<001> component is the typical shear texture of BCC metals. α and γ - fiber are the typical rolling texture according to plane strain deformation (Raabe and Lücke 1992). In case of hot rolled steel sheets, it is well known that shear components frequently develops at s = 0.7 ~ 0.8, and the center layer deforms at the plane strain condition (Raabe 1995). During hot rolling, the inhomogenity of texture is due to the inhomogenity of deformation i.e. ; shear deformation in the subsurface layer and the plane strain compression in the center layer (Shimizu et al. 1986; Raabe and Lücke 1993). This inhomogenity of deformation results from the inhomogenity of strength due to the inhomogenity of temperature.

During the strip casting, the temperature profile is similar to that of hot rolling (Schmitz and Büchner 1991; Park et al 1999) and the temperature gradient near surface zone (s = 1.0 ~ 0.6) gives rise to the strength gradient and finally the shear deformation as shown in Fig. 3 and 4. The rapidly cooled surface layer of the strip (s = 1.0 ~ 0.9) has the larger yield strength than the inner layer (s ≤ 0.9) with the higher temperature. Because of this strength gradient between the surface layer and subsurface layer, when the strip solidified completely above the roll nip point, the surface layer maintained the solidification texture without deformation and the subsurface layer was deformed by shear for passing through the nip point (Park et al. 1999) The shear deformation in strip casting process is similar to that in hot rolling. The related shear texture component is shown in Fig. 6(b), (c) and Fig. 7. In the center layer of the strip, the major rolling fiber are due to the plane strain compression from the solidification end point to the roll nip point, which is similar to the evolution of rolling fiber during hot rolling. The minor {100}<0vw> components are the typical solidification texture.

4 Conclusion

The texture and microstructure distribution through the thickness of strip cast 4.3wt%Si steel have been examined. The inhomogenity of texture and microstructure through the sample thickness resulted from the temperature profile through the thickness during strip casting. Especially between subsurface layer (s = 0.8) and the midplane (s = 0.6), Goss texture, {110}<001> component, was developed by the shear deformation, and major rolling texture and minor solidification texture appeared in the center layer.

5 References

Choi, J.T., Kim, Y.H., Choi, C.H., Oh, K.H. and Ra, H.Y. (1996) *Melt spinning, Strip casting and slab Casting*, eds. E.F. Matthys and W.G.Truckner, The Mineral Metals and Materials Soc., Anaheim, pp. 43

Cullity, B.D. (1972) *Introduction to magnetic materials*. Addison-Wesley publishing company, Inc., Pholippines, pp. 518

Litterscheidt, H., Hammer, R., Schneider, C., Simon, R.W., Senk, D., Kopp, R. and Hehl, B. (1991) Bandgießen nach dem Zwei-Rollen-Verfahren-Stand der Entwicklung bei der Thyssen Stahl AG. *Stahl und Eisen* 111, pp. 61

Humphreys, F.J. and Hatherly, M.(1995) *Recrystallization and related annealing phenomena*. Elsevier Science Ltd, New York, pp. 145-146

Matthies, S and Vinel, G.W. (1982) On the reproduction of the orientation distribution function of texturized samples from reduced pole. *phys. stat. sol.* 112, pp. 111

Park, J.Y., Oh, K.H., and H.Y.Ra (1999) Microstructure and crystallographic texture of strip-cast 4.3wt%Si steel sheet. *Scritp. Metall.* Accepted

Raabe, D. and Lücke, K. (1992) Texture and microstructure of hot rolled steel. *Scripta Metall.* 26, pp. 1221

Raabe, D. and Lücke, K. (1993) Texture of ferritic stainless steels. *Mater. Sci. Tech.* 9, pp. 302

Raabe, D. (1995) Texture of strip cast and hot rolled ferritic and austenitic stainless steel. *Mater. Sci. Tech.* 11, pp. 461

Schmitz, J.W. and Büchner A.R. (1991) Stahl und Eisen 111(2), pp. 69

Shimizu, Y., Ito, Y. and IIDA, Y. (1986) Formation of the Goss orientation near the surface of 3 pct silicon steel during hot rolling. *Metall. Trans.* 17A, pp. 1323

Taguchi, S., Sakakura, A. and Takashima, H. (1966) Process for producing single-oriented silicon steel sheets having a high magnetic induction. *U.S.Patent* 3,287,183

Taguchi, S (1972) Review of the recent development of electrical sheet steel in Japan. *Transaction ISIJ*, Vol. 17, pp. 604-615

TEXTURE DEVELOPMENT IN COLD-ROLLED AUSTENITIC-FERRITIC DUPLEX STEEL

W. RATUSZEK, J. RYŚ, K. CHRUŚCIEL

Faculty of Metallurgy and Materials Science, University of Mining and Metallurgy, Kraków, Poland

Abstract

Duplex type austenitic-ferritic steel 00H18N6Mo3 was cold-rolled within the range up to 85% of deformation taking either low or high reductions per pass. X-ray investigations included the phase analysis, measurements of pole figures and calculation of the orientation distribution functions (ODF's) for the case of each phase. The rolling textures of ferrite and austenite were analysed within the centre layers of the sheets. Observations of deformation structures were performed by means of optical microscopy. The main feature of texture development in rolled duplex steel is the fibre character of deformation textures in both phases. The intensive development of the ferrite texture was observed in the course of deformation for both rolling variants. The rolling texture of austenite was relatively weak in the whole range of deformations. In major part the orientation relations between both phases are well described by Kurdjumow–Sachs relationship. From X–ray analysis it results that the development of ferrite and austenite rolling textures was apparently affected by strain induced ($\gamma \rightarrow \alpha$) phase transformation with a variant selection taking place during transformation.

Keywords: Austenitic-ferritic steel, deformation texture, orientation fibre, pancake structure, phase transformation, variant selection.

1. Introduction

The main advantage of duplex type steels is a favourable combination of their properties, which are much better in comparison to the properties of component phases. To a great extent this improvement is due the character of the structure and different conditions of its formation in comparison to one-phase steels (Davies, ed. 1994). In major part hithero performed investigations of austenitic-ferritic steels concerned the effect of chemical composition and thermo-mechanical treatment on the character of two-phase structures. A survey of the investigations concerning duplex steels points at the insufficient knowledge about the relation between structure and texture after deformation and recrystallization (Akdut and Foct 1995; Shek et al.1994). Especially a development of deformation textures requires further examination, since they determine the textures and structures after annealing and recrystallization affecting in consequence the mechanical properties of two-phase steels.

The aim of the present work was the analysis of texture formation in duplex type austenitic-ferritic steel subjected to cold-rolling and comparison of the results with those for bcc and fcc one-phase steels (Lucke and Holscher 1991; Donadille et al. 1989). An attempt was undertaken to explain the role of ($\gamma \rightarrow \alpha$) phase transformation induced by plastic deformation on a texture development (Butron-Guillen et al. 1996).

2. Experimental procedure

The austenitic-ferritic steel 00H18N6Mo3 in the form of ingot was homogenized and then subjected to hot forging within the temperature range 900÷1000°C. Subsequently the rectangular bars were annealed at temperature 1050°C for 3.5 hours and quenched in water. X-ray phase analysis performed after the solution treatment revealed the volume fraction of ferrite of approximately 48%, confirming a duplex character of the structure. After the preliminary treatment the steel bars were cold-rolled within the range up to 85% of deformation ($\varepsilon = 1.9$). Different reductions applied in each roll pass, which depend on the ratio of the arc of contact (L) to the mean thickness (h_m) of the sheet, resulted in different stress and strain distributions on the cross section of the sheet (Tselikov 1967). Reversed rolling was applied taking either low reductions per pass ($L/h_m \leq 0.5$) or heavy drafts ($L/h_m > 1.5$), variants A and B respectively.

Structure observations of the material after the solution treatment and the subsequent cold-rolling were carried out by means of optical microscopy on the longitudinal and cross sections of the sheets (Ratuszek et al. 1999).

X-ray investigations performed in the course of rolling included texture measurements and qualitative phase analysis using $Co_{K\alpha}$ radiation (λ=1.79 A). Measurements of pole figures were conducted by Schulz back-reflection method within the centre layers of the sheets after 40, 75 and 85% reductions. The orientation distribution functions were calculated from three incomplete pole figures following the series expansion method (Bunge 1969). The analysis of the ODFs was performed in sections of φ_2=const. for austenite and φ_1=const. for ferrite, in steps of 5° within the range 0÷90°.

3. Results and analysis

Metallographic examination revealed only small differences in development of deformation structures between both rolling variants. The initial two-phase structure after the solution treatment consisted of ferrite and austenite areas arranged parallel to the direction of hot working (Fig. 1a). In the course of cold-rolling the bands of both phases became thinner and flat, forming so-called pancake structure parallel to the rolling plane. Reductions in thickness of the ferrite and austenite bands confirmed the plastic deformation of both phases during rolling of duplex steel. At higher strains characteristic corrugated shape of banded structure was observed, with folds laying along lines at an angle 30÷40° to the rolling direction and numerous fine offsets visible at the (α/γ) phase interfaces (Fig. 1 b). Both effects seem to result from the macroscopic strain localization in the form of shears crossing the entire "pancake" structure.

Texture analysis indicates, that within both component phases the deformation textures were formed, having some typical features of the corresponding rolling textures in ferritic and austenitic one-phase steels, however certain characteristic orientations did not appear or their intensity is very different from those in one-phase steels (Lucke and Holscher 1991; Donadille et al. 1989).

The rolling texture of ferrite within the centre of the sheet for the case of variant B, i.e. high reductions per pass, is described by the limited α_1-fibre, the ε and γ orientation fibres as well as the {332}<uvw> orientations (Fig. 2b). The limited α_1-fibre extends from {001}<110> to {111}<110>. After 40% reduction two maxima appeared within that fibre, which correspond to the {001}<110> and {556}<110> orientations.

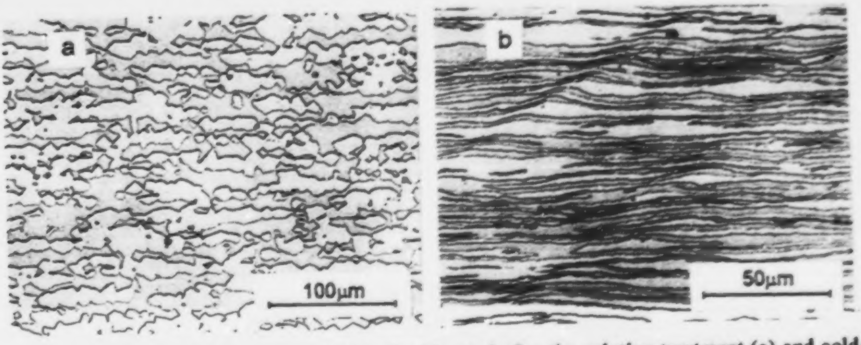

Fig. 1 Structure of duplex type austenitic-ferritic steel after the solution treatment (a) and cold-rolling up to 85% reduction (b); chemical etching.

The intensities of both maxima increased in the course of rolling. The γ-fibre, i.e. the {111}<110÷112> orientations, also appeared at 40% reduction, having the highest intensity for the {111}<110> orientation after 75% of deformation. The ε-fibre running from {001}<100> to {001}<110> has the strong {001}<100> cubic component in the whole range of deformations. Additionally the {332}<uvw> orientations appeared during rolling, having their maxima after 75% reduction for the {332}<023> and {332}<110> components. In the case of variant A (Fig. 2a), i.e. small reductions per pass, a noticeable difference in development of the ferrite texture is very weak γ-fibre within the whole range of deformations. Moreover the limited α_1-fibre, which extends from {001}<110> to {112}<110>, clearly appeared only at high strains having the maximum for the {115}<110> orientation. The ε-fibre was present in the whole range of deformations, however the intensities of the main components were considerably weaker in comparison to variant B, especially intensity of the {001}<100> orientation. Additional component, which appeared in that case, is the {332}<113> orientation.

Very important feature for development of the austenite texture in duplex steel under examination is relatively low intensity or even the absence of some components typical for the rolling textures of one-phase austenitic steels (Figs. 3 a, b).

The texture of austenite within the centre of the sheet, for the case of variant B (Fig. 3b), shows the fibre character. Within the α-fibre, which extends from {110}<001> to {110}<110>, the strongest is the Goss orientation {110}<001> in the whole range of deformations. After 85% reduction another components of that fibre attained relatively high f(g) values, namely; the {110}<112>, {110}<111> and {110}<1$\bar{1}$0> orientations. The second fibre which describes the austenite texture in the centre of the sheet is the η-fibre, which extends from {100}<001> to {110}<001> and has only one strong component, namely the Goss orientation (common for both fibres η and α). After 85% reduction, weak orientations of the {111}<uvw> type appeared additionally, namely; the {111}<110> and {111}<112>. In general the austenite texture formed in the centre of the sheet is spread (both fibres) and considerably weaker in comparison to the ferrite texture. However, still weaker and nearly random is the texture of austenite within the central layer, when rolling with small reductions per pass, i.e. for the case of variant A (Fig. 3a). Only single and spread components appeared, having very low intensities, including the {111}<110> and {772}<uvw> orientations, with the maximum for the {772}<027> orientation after 85% of deformation degree.

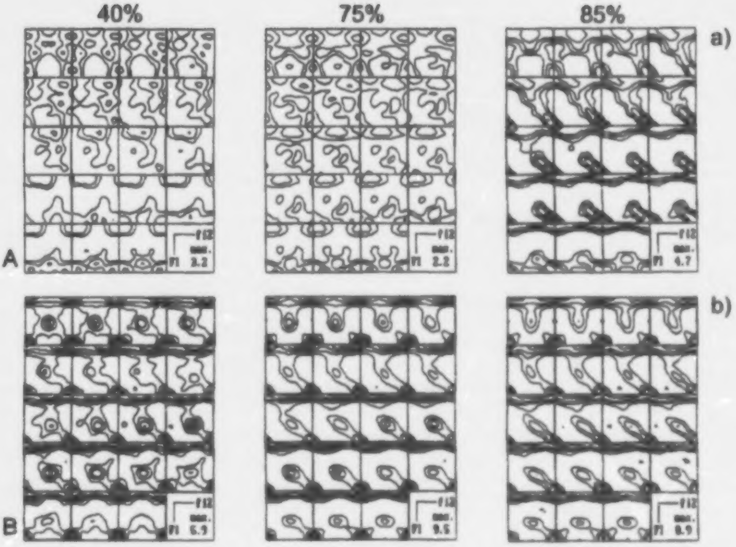

Fig. 2 Orientation distribution functions (ODF's) in sections φ_1= const. for the α-phase after 40, 75 and 85% reductions; rolling variants A and B.

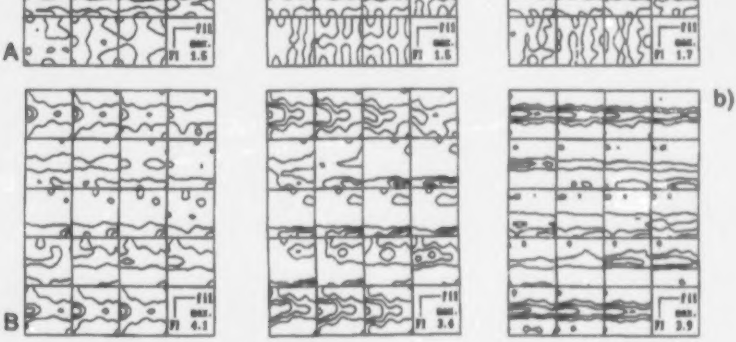

Fig. 3 Orientation distribution functions (ODF's) in sections φ_2= const. for the γ-phase after 40, 75 and 85% reductions; rolling variants A and B.

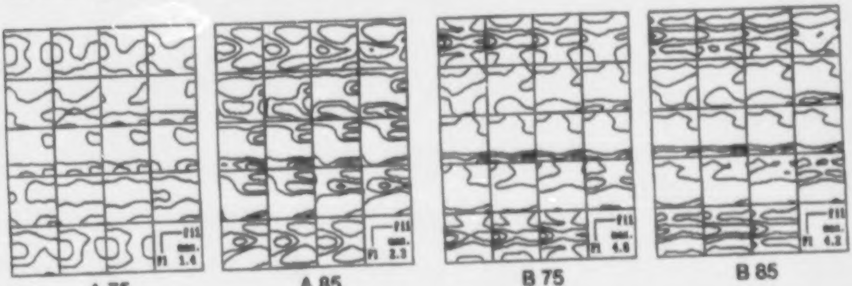

A 75 A 85 B 75 B 85

Fig. 4 Experimental ODF's after transformation of the ferrite texture according to K-S relation for specimens rolled in variants A and B up to 75 and 85% reduction (without variant selection).

Analysis of texture development during rolling of duplex steel reveals the fibrous character of ferrite and austenite deformation textures. It is worth to note a considerable difference in the texture intensities between both component phases. An intensive development of the ferrite deformation texture was observed in the course of rolling for both variants A and B, whereas in austenite the rolling texture is weak in the whole range of reductions, especially at low deformation degrees.
The explanation of weak or even random austenite texture seems to be the occurrence of strain induced (γ→ α) phase transformation, which gives rise to the enhanced texture development of ferrite at the expense of austenite, which is transformed into the α-phase. The results of texture investigations indicate that austenite behaves during deformation in various way, depending on the applied rolling variant. For the case of heavy drafts (variant B), austenite is plastically deformed and its transformation into the α-phase is limited. Such behaviour leads to the development of deformation texture, which is typical for low SFE alloys. On the other hand, in the case of rolling with small reductions per pass (variant A), the intensive (γ→ α) phase transformation proceeds during deformation. It is assumed that only fraction of austenite grains, having a preferred orientations, is transformed into the α-phase due to so-called variant selection (Butron-Guillen et al. 1996) and the rest of the austenite undergoes the plastic deformation. Hence development of the austenite texture occurs at higher strains and the deformation texture is weak due to the smaller volume fraction of austenite.

Transformations of experimental ODF's (Fig. 4) and single orientations (Ratuszek et al. 1999) of the α-phase were performed to determine the crystallographic relations between the orientations within the deformation textures of both component phases. It was found that the relationships between some orientation components of the ferrite texture and the orientations, which appear within the austenite texture are well described by the Kurdjumow-Sachs relation. Assuming the transformation of austenite into the α-phase during rolling, the presence of these orientations within the ferrite texture should be the result of the (γ→ α) phase transformation induced by the plastic deformation. In such case the development of texture and structure upon cold-rolling of duplex steel would be the result of complex deformation process, which includes plastic deformation of ferrite and austenite as well as the strain induced (γ→ α) phase transformation.

4. Concluding remarks

1. Metallographic examination of cold-rolled duplex steel confirmed the plastic deformation of both component phases, leading to the formation of ferrite-austenite pancake structure and structural effects due to the macroscopic strain localization.
2. The most important features for texture development in rolled duplex steel are the fibre character of ferrite and austenite deformation textures, very intensive development of ferrite texture in the course of deformation for both rolling variants and relatively weak rolling texture of austenite in the whole range of deformations.
3. Development of the ferrite texture within the centre layers of the sheets was more intensive during rolling with heavy drafts (variant B) in comparison to variant A i.e. small reductions per pass. Similarly the texture of austenite was a typical deformation texture for low SFE alloys for the case of variant B, however considerably weaker in comparison to the ferrite texture. Whereas in sheets rolled in variant A, the texture of austenite was nearly random.
4. X–ray investigations revealed that in major part the orientation relations between both component phases are well described by Kurdjumow–Sachs relationship. It was concluded that texture development of ferrite was apperently affected by the phase transformation (γ→ α) induced by plastic deformation.

Acknowledgements
The authors gratefully acknowledge financial support from the Polish Committee of Scientific Research (KBN).

4. References

Akdut, N., Foct, J. (1995) Phase boundaries and deformation in high nitrogen duplex stainless steels. *Scripta Metallurgica et Materialial* Vol. 32, pp. 103-8 & 109-14.

Bunge, H.J. (1969) *Mathemtische Methoden der Texturanalyse*, Akad.-Verlag, Berlin.

Butron-Guillen, M. P., da Costa Viana, C. S., Jonas, J.J. (1996) Effect of slip activity on variant selection during the γ-to-α transformation. *Proc. 11-th Int. Conf. on Textures of Materials*, China, Vol. 1, pp.604-9.

Davies, J.R., ed. (1994), *Stainless Steels*, ASM Specialty Handbook.

Donadille, A., Valle, R., Dervin, P., Penelle, R., (1989) Development of texture and microstructure during cold-rolling and annealing of fcc alloys: Example of an austenitic stainless steel. *Acta Metallurgica* Vol. 37, pp. 1547-71.

Lucke, K., Holscher, M., (1991) Rolling and recrystallization textures of bcc steels. *Textures and Microstructures*, Vol. 14-18, pp. 585-96.

Ratuszek, W., Ryś, J., Chruściel, K. (1999) Effect of deformation mode on texture development in cold-rolled duplex steel. *Archives of Metallurgy*, in print.

Shek,C.H., Shen, G.J., Lai, J.K.L., Duggan, B.J. (1994) Texture and microstructure development in a cold-rolled duplex stainless steel annealed at 800°C. *Materials Science Forum*, Vol. 157-162, pp. 853-8.

Tselikov, A. (1967) *Stress and Strain in Metal Rolling*, Mir Publishers, Moscow.

ROTATED CUBE TEXTURED SEMIFINISHED ELECTRICAL STEEL: PROCESSING AND MECHANISMS OF TEXTURE FORMATION

B. DE BOER, J. WIETING and L. SCHULTZ
Institute of Solid State and Materials Research Dresden, Institute of Metallic Materials, Dresden, Germany

Abstract

The rotated cube texture is a possibility of realizing highly permeable steel sheets for rotating machines as well as transformers. Sheets with such a texture can be obtained in unalloyed steel by a production process consisting of hot rolling and two subsequent cold rolling and recrystallisation steps. By x-ray-texture analysis, optical microscopy and scanning electron microscopy including EBSD was found that during the first recrystallisation nucleation occurs in high stored energy regions with mainly γ-fiber-orientations but also in low stored energy regions with α-fiber orientations. During the annealing after the second cold rolling with a thickness reduction of only 10% a low-energy-nucleation process is leading to a nucleation with almost only orientations near {001}<110> and accordingly to a strong final texture with its maximum near the rotated cube.

Keywords: cube texture, electrical steel, nucleation, recrystallisation, rotated-cube-texture, semifinished electrical steel, steel processing

1 Introduction

Electrical steels are acting as soft magnetic material in the core of electric devices like transformers, motors and generators. In the magnetic cores of motors and generators the magnetic flux is conducted in all directions perpendicular to the axis during each rotation. In order to minimize rotational and copper losses of these machines, a material with a high permeability in every direction in the sheet plane is favorable. Due to the magnetic anisotropy of iron, the <100>-direction exhibits the highest permeability, the lowest is measured parallel to <111>. Thus a cube texture {001}<uv0> is leading to the highest possible permeability averaged over all directions in the sheet plane (Shimanaka 1982).

In this contribution, a way to produce semifinished electrical steel that reveals a strong rotated cube texture ({001}<110>) after the final annealing treatment is presented (Mager et al. 1993). The costs of this steel is low compared to Goss textured steels and higher grades of non-oriented (NO) steels because the processing does not differ much from that of less expensive grades of NO steels. Its texture makes the material useful, especially for medium sized electrical transformers as well as motors or generators.

The recrystallisation processes which are part of the sheet fabrication were investigated in order to understand the texture formation and to optimize the production process.

2 Fabrication process

The industrial production process can be briefly outlined as follows:

- casting of an unalloyed melt with the chemical composition given in table 1.

C	Si	Mn	P	S	Cr	Al	Cu	N	
0.07	0.01	0.30	0.008	0.014	0.023	0.034	0.033	0.003	wt.%

Table1. Chemical composition of the unalloyed steel.

- hot rolling of the ingot in the temperature range between 1250°C and 840°C. Afterwards slow cooling (without waterspraying).
- cold rolling with a thickness reduction of 90% to a final thickness of 0.55 mm.
- intermediate annealing at a temperature between 550°C and 600°C for about 30 minutes in a neutral atmosphere (e.g. H_2+N_2 or H_2).
- second cold rolling with a slight reduction of 10%.
- final annealing in a decarburizing atmosphere (e.g. wet H_2).

3 Experimental

For the investigation of the texture changes due to the two static recrystallisation steps, partially recrystallised samples were prepared by varying the annealing time and temperature. Longitudinal cuts of these samples were polished mechanically and electrolytically and then etched with a solution of 2% nitride acid and ethanol. The microstructure was investigated with aid of optical microscopy and scanning electron microscopy equipped with an EBSD-device for local orientation measurements.

For texture analysis the incomplete {110}-, {200}- and {112}-pole figures were measured to calculate the orientation distribution functions (ODF) that are presented in the φ_2=45° section in which the important occurring orientations are found (fig. 1.).

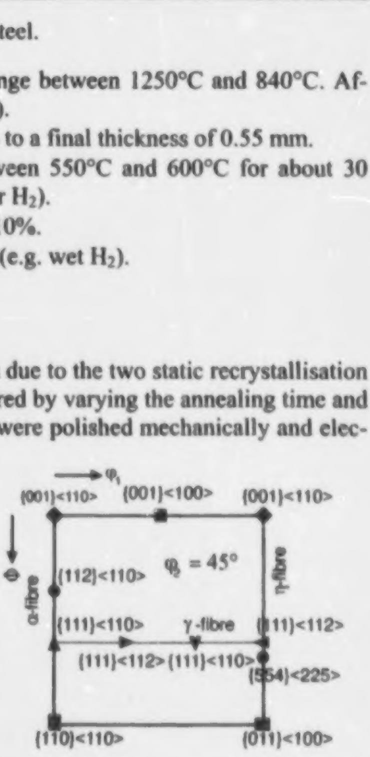

Fig. 1. φ_2=45° section of the Euler-space

4 Results

4.1 Texture Evolution

The texture after 90% cold rolling consists of γ-fiber-orientations ({111} || ND) with a maximum at {111}<112> and an even stronger α-fiber (fig. 2) that is typical of cold rolled ferrite steels. After recrystallisation by an annealing at 550°C for 30 min. this texture changes slightly. The α-fiber is weakened and its highest intensity is now at {116}<110> which is about 15° from the exact rotated cube orientation (fig. 3). The slight deformation of 10% cold rolling does not change the texture but evokes recrystallisation that occurs during annealing at temperatures above 600°C. After this recrystallisation, only orientations near the rotated cube with a maximum at {117}<110> remain (fig. 4).

4.2 Texture formation during the first recrystallisation

The longitudinal section of the recovered microstructure (after 510°C, 30 min. annealing) in fig. 5 reveals two differently structured regions elongated in rolling direction. In the first, marked with 'A', almost no subboundaries can be observed. The other regions ('B') are characterized by clearly visible subboundaries in a microstructure with subgrains of about 1 µm. Fig. 6 shows the orientation distributions of these different structures determined with EBSD. The texture of the structure 'A' consists only of α-fiber-orientations between {001}<110> and {112}<110>. Inside these regions no significant orientation differences are measured. The regions'B' have a texture with mainly γ-fiber-orientations but also others, including cube orientations. Between the subgrains of these regions large orientation differences occur.

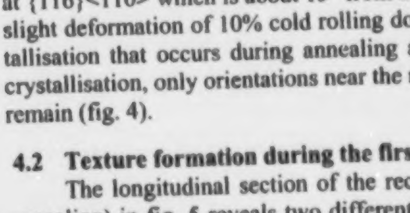

Fig. 2. ODF of the cold-rolled state, φ_2=45°-section.

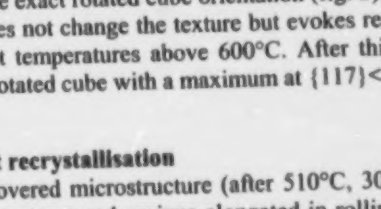

Fig. 3. ODF after first recrystallisation, φ_2=45°-section.

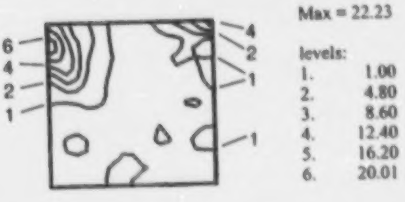

Fig. 4. ODF after second recrystallisation, φ_2=45°-section.

Another aspect in the microstructure are spherical cementite particles ('C') which are accumulated and result from perlite that has arisen during the cooling of the hot band.

After further annealing at 510°C, nucleation starts in the regions 'B' because due to the high orientation differences, the subboundaries in these regions easily develop into mobile high angle grain boundaries by mig-

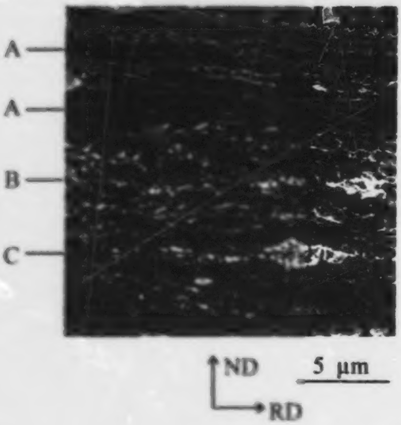

Fig. 5. SEM-micrograph of the recovered microstructure after 510°C, 30 min. annealing. A, B, C are explained in the text.

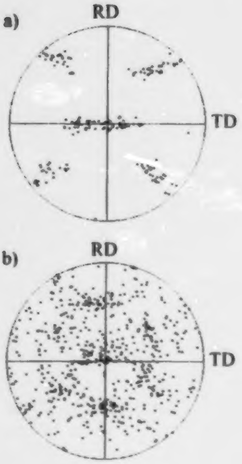

Fig. 6. Orientation distribution of the regions A (a) and B (b).

rating only over a very short distance. These nucleated grains have the variety of orientations present in the subgrain structure. This can be observed in the 50% recrystallised microstructure (fig. 7) in the area marked with '1'.

Recrystallisation continuous with the growth of the recrystallised grains but also with the nucleation of grains in the regions 'A', marked with '2' in fig.7. This nucleation can be identified with subgrains having hardly visible grain boundaries to the area out of which they are nucleated and a clearly visible mobile high angle grain boundary which migrates into the adjacent matrix. The orientations of these grains are similar to those of the 'A'-regions thus lying between {001}<110> and {112}<110>.

Particle stimulated nucleation in the way that adjacent to the cementite particles preferred nucleation takes place is not observed. But it is supposed that due to deformation inhomogeneities caused by the particles and the high degree of deformation, a high density of excess dislocations which do not disappear by recovery is introduced into the regions 'A'. For this reason a coarse subgrain structure is formed in which nucleation takes place as described above.

4.3 Texture formation during the second recrystallisation

The course of the second recrystallisation is shown in the optical micrographs of fig. 8. Due to the decarburizing atmosphere, recrystallisation propagates from the surface to the center with increasing annealing time or temperature. Almost all of the grown grains have orientations near the rotated cube. Because of the low dislocation density after the slight deformation, recrystallisation takes place by the migration of preexisting high angle grain boundaries.

The texture changes during recrystallisation can be explained by a simple model in which it is assumed that the driving force for nucleation is the difference in the

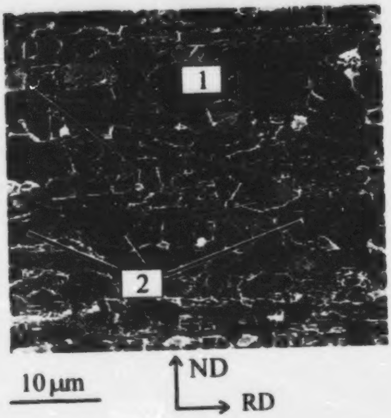

Fig.7. SEM-micrograph of the 50% recrystallised microstructure. '1' and '2' are explained in the text.

stored energy given by the dislocation and subboundary density between the two grains on each side of the grain boundary. That means, the lower the stored energy of a grain, the higher becomes its nucleation probability *P*.

According to studies of the stored energy (e. g. Dillamore et al. 1967) grains with orientations near {001}<110> exhibit the lowest stored energy after rolling and recovery. Gil Sevillano et al. 1976 found out that the stored energy $E(g)$ (g: orientation) can be expressed in terms of the Taylor-factor $M(g)$. Fig. 9 shows $M(g)$ calculated on the basis of the 'relaxed constraints' model. By this way the Taylor-factor is a quantitative orientation dependent measure for the stored energy and therefore the nucleation probability can be expressed in terms of the Taylor-factor. Also the orientation dependent nucleation probability is proportional to the quotient formed by the texture after recrystallisation divided by the texture before recrystallisation if no growth selection is assumed. Thus the recrystallisation texture should be describable as:

$$f_{Rx}(g) = C \cdot P(M(g)) \cdot f_0(g) \qquad (1)$$

$f_{Rx}(g)$: Recrystallisation texture
$f_0\,(g)$: Texture before recrystallisation

with the constant C. Fitting of $f_{Rx}(g)/f_0(g)$ to $C \cdot P(M(g))\cdot$ for the values along the α-fiber leads to a nucleation probability that can be approximately described as:

$$P\,(g) \sim \exp(-3M(g)) \qquad (2)$$

(fig. 10). The recalculation of the whole φ_2=45° section of the ODF by equation (1)

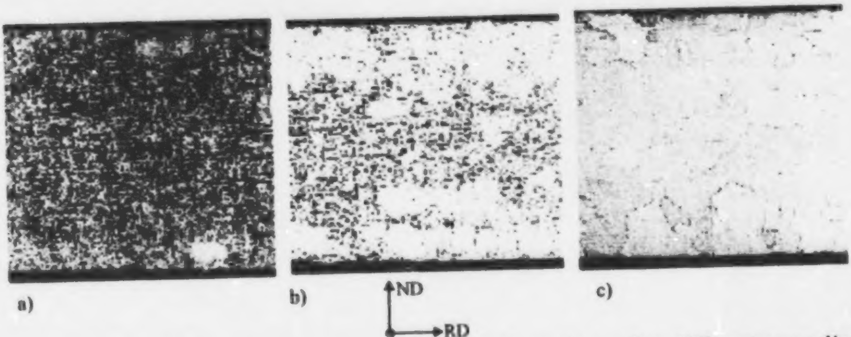

Fig. 8. Optical micrographs of longitudinal sections after different annealing times and temperatures a) 2 h at 600°C, b) 5 h at 600°C and c) 5 h at 650°C.

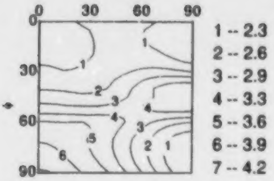

Fig. 9. φ_2=45° section of the orientation dependence of the Taylor-factor (relaxed constraints).

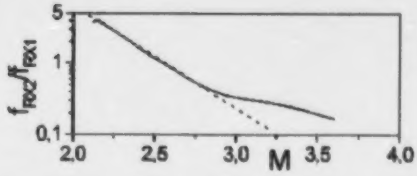

Fig. 10. Dependence of the nucleation probability on the Taylor-factor along the α-fiber. The dashed line describes the fit given by (2).

results in the texture in fig. 11 which represents well the features of the measured recrystallisation texture which are the shape of the maximum near {001}<110> and the disappearance of the γ-fiber components.

5 Summary and conclusions

A way to produce a highly textured electrical steel sheet with all orientations near the rotated cube ({001}<110>) by a process with two subsequent cold rolling and annealing steps is described. In the first step an appropriate thickness reduction and a texture with {001}<110> oriented grains is achieved. Near {001}<110> oriented grains are mainly formed by low energy nucleation that arises due to the high deformation degree and to coarse perlite particles.

By the second step a suitable coarse grained structure with the desired strong texture is developed. The small degree of deformation is leading to pure low energy nucleation in which almost only near rotated cube oriented grains nucleate. It was found that this low-energy-nucleation process is equivalent to a nucleation of grains with orientations which belong to a low Taylor-factor.

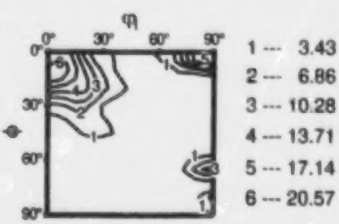

Fig.11. Recalculated recrystallisation texture.

Acknowledgements

Thanks to Ms U. Köhler for providing the Taylor data. The x-ray-texture measurements by D. Schläfer are gratefully acknowledged. The work is financially supported by the ECCS.

References

L. Dillamore, C. J. E. Smith, T. W. Watson, Metal Sci. J. **1** (1967) 49.
J. Gil Sevillano, P. van Houtte, E. Aernoudt, Scripta Met. **10** (1976) 775.
S. Mager, J. Wieting, R. Bürger, H. Kleine, Pat. No. DE4337605 (1993).
H. Shimanaka, Y. Ito, K. Matsumura, B. Fukuda, J. Magn. Magn. Mat. **26** (1982) 57.

THE TEXTURE EVOLUTION OF NON-ORIENTED SILICON STEEL

CHEN S. LEE
Research and Development Laboratories, Ispat Inland Inc., East Chicago, IN

Abstract

The influence of four different hot rolling routes on the subsequent cold rolling texture and annealing texture was studied. Although ferritic rolling produces a remarkable {001}<110> on α fiber at mid-thickness when hot rolling, it still yields a similar cold rolling texture and annealing texture as austenitic rolling. The very coarse hot band grain using hot band annealing produces an annealing texture containing a strong Gauss texture, {110}<001>, and {001}<010>. However, if the hot band grain size is (~ 46 μm) not large enough, then Gauss texture, α fiber and γ fiber co-exist when annealing.

I. INTRODUCTION:

The final texture development of non-oriented silicon steel is highly dependent on the starting hot rolled microstructure and texture. Four different processing routes can be applied in the hot rolling stage: austenitic rolling, ferritic rolling and subsequent hot band annealing (HBA) with either austenitic rolling or ferritic rolling . The purpose of this study is to explore the influence of these four processing routes on the subsequent cold rolling texture and annealing texture.

II. EXPERIMENTAL PROCEDURES:

Material containing 0.003% C, 0.6% Mn, 1.05% Si , 0.25% Al, 0.003% N, 0.006% S, was used in this study. The material was hot rolled with a finishing temperature of either 950°C or 830°C. Finishing rolling at 950°C is defined as austenitic rolling, and finishing rolling at 830°C as ferritic rolling since the Ar_3 of this material is 950°C, and Ar_1 is 900°C. After removing scale by using the hydrochloric acid, hot bands were box annealed at 820°C for 20 hours in a hydrogen atmosphere. All the hot bands were cold rolled from 0.085 inch into 0.0229 inch with a cold reduction of 73%. The cold rolled bands then were box annealed at 700°C for one hour at a heating rate of 33°C/hr in dry HN gas, containing 7% hydrogen and 93% nitrogen.

The specimens were taken at the various processing after hot rolling, cold rolling, and annealing for X-ray diffraction and microstructure examination. The specimens were scanned using X-ray diffraction at various depths between the surface and mid-thickness at 5% thickness intervals. Specimen thinning was conducted using a chemical solution. The relative intensities of reflection from the rolling planes were determined. The texture was examined by measuring the three pole figures, {110}, {200}, and {211} with the Mo-Kα radiation in the back reflection mode. The ODF was calculated from these three pole figures.

III. RESULTS AND DISCUSSIONS:

III.I. Hot Rolling Stage:

Figure 1a shows austenitic rolling produces a hot-band microstructure of nearly uniform small equiaxed grains of 13 μm. Ferritic rolling results in a mixture of fine equiaxed grains (20 μm) at subsurface and partially recrystallized structures at mid-thickness, Figure 1b. After hot-band annealing (HBA), only austenitic rolling gives a completely coarse grain structure (600-3000 μm), Figure 1c. In contrast, ferritic rolling with HBA leads to fine grains of 46 μm at mid-thickness, partially mixed with longitudinal coarse grains (~ 800 μm long) at subsurface, Figure 1d.

Figure 2a shows the case of austenitic rolling, the weak intensities of {200}, {211}, {220}, and {222} reflections remain similar with increasing depth. In general, plane textures in austenitic rolling through the thickness can be considered as a nearly random texture. In the case of ferritic rolling, the intensity of {200} substantially increases as the plane approaches from the quarter-thickness to mid-thickness, Figure 2b. The corresponding microstructure for the high intensity of {200} at mid-thickness is predominantly a partially recrystallized structure, Figure 1b.

Figure 3 presents the $\phi= 45°$ section diagram of ODF at subsurface (10% thickness below surface) and in the center of specimens. When austenitic rolling, the weak α fiber and γ fiber exist at mid-thickness. Weak shear textures of ζ fiber containing from {110}<001> to ~{110}<221> and ϵ fiber from ~{114}<221> to {112}<111> orientation exist in the subsurface. It can be considered as a nearly random texture through the thickness. Ferritic rolling presents an inhomogeneous texture through the thickness. At subsurface, weak shear textures of ζ fiber containing from {110}<112> to ~{110}<332> and ϵ fiber from {114}<221> to ~{111}<112> orientations exist. However, a substantially strong α fiber, cold rolling texture, containing major components of {001}<110>-{112}<110>, is developed at mid-thickness. This low stored energy cold rolling texture of {001}<110> is very stable, which can not develop coarse grains when hot band annealing, Figure 1d.

III.II. Cold Rolling Stage:

Both austenitic rolling and ferritic rolling yield a similar cold rolling texture after cold reduction of 73%, Figure 3a, 3b. In general, both austenitic rolling and ferritic rolling increases the intensity of α fiber and γ fiber at mid-thickness and subsurface. Ferritic rolling presents two major components of {001}<110> and {113}<110> on α fiber, and a pronounced component of {111}<110> on γ fiber. Ferritic rolling produces a stronger α fiber than austenitic rolling from the inherited hot band textures containing a high intensity of α fiber, Figure 3b. Although the major component of γ fiber in austenitic rolling is similar to ferritic rolling, the major component of α fiber at the subsurface, {223}<110>, is different.

Ferritic rolling with HBA also has the similar textures and major components as ferritic rolling without HBA. But the intensity of α fiber at mid-thickness is weaker than ferritic rolling without HBA, Figure 3d. Austenitic rolling with HBA not only produces α fiber and γ fiber, but also yields new textures of ~{110}<001>-{110}<113> on ζ fiber and

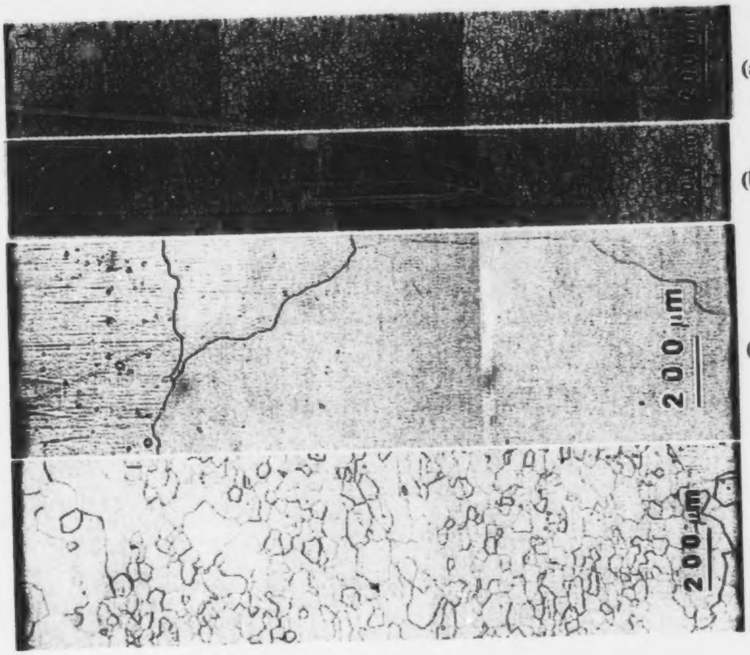

Figure 1: Hot band microstructure, (a) Austenitic rolling, (b) Ferritic rolling, (c) Austenitic rolling with HBA, (d) Ferritic rolling with HBA.

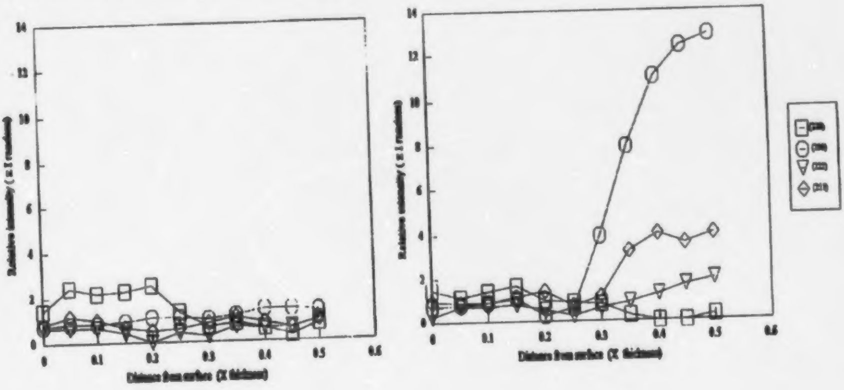

(a)

(b)

Figure 2 : Relative intensities of plane reflection as a function of position from surface to mid-thickness of hot band, finishing rolling at (a) 950°C (Austenite), (b) 830°C (Ferrite).

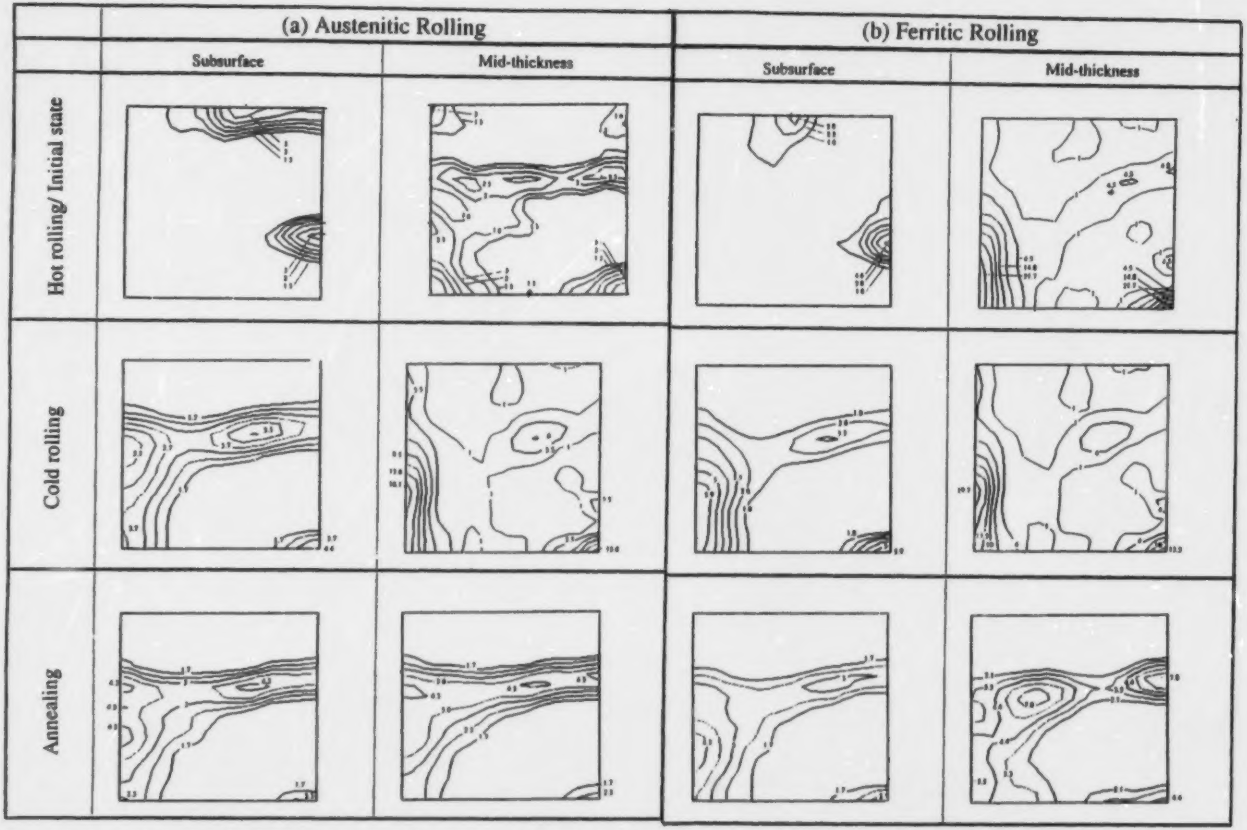

Figure 3: ϕ =45° section of ODF, (a) Austenitic rolling, (b) Ferritic rolling, (c) Austenitic rolling with HBA, (d) Ferritic rolling with HBA.

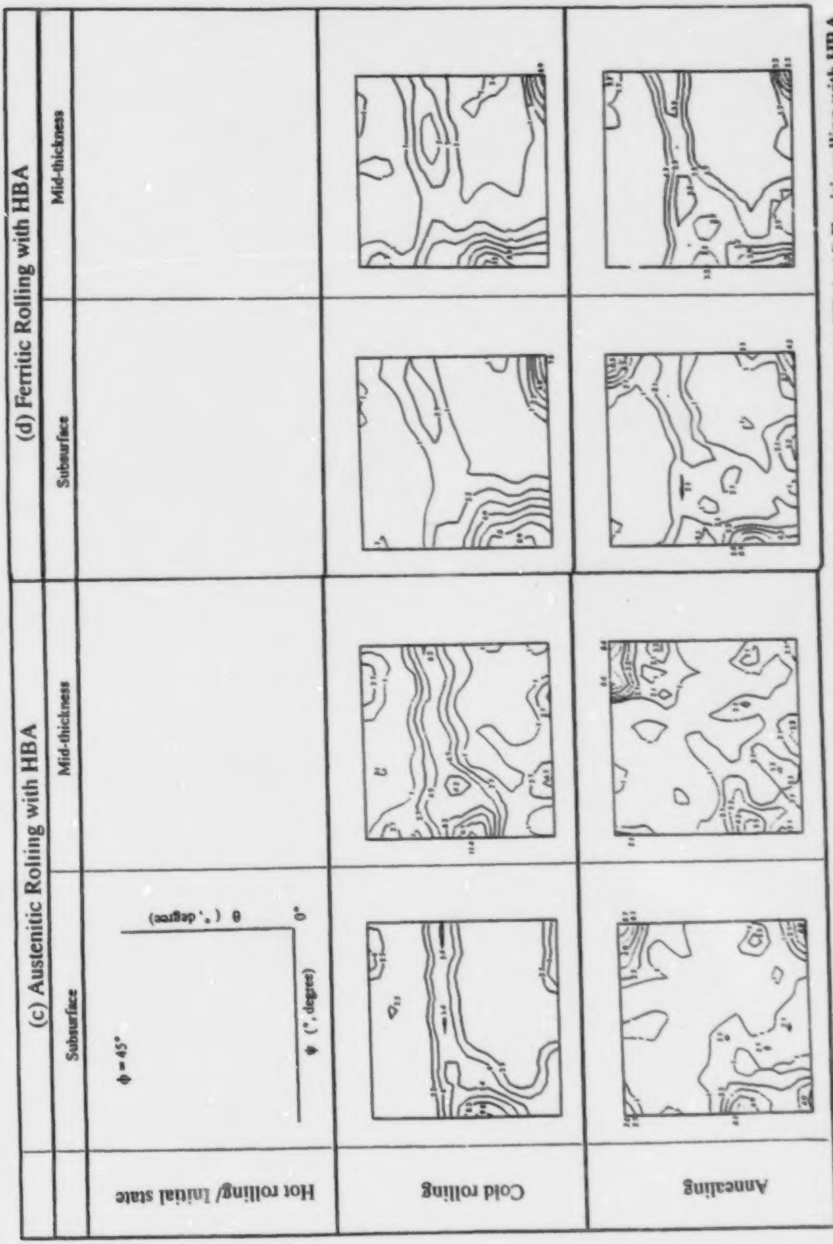

Figure 3: φ =45° section of ODF, (a) Austenitic rolling, (b) Ferritic rolling, (c) Austenitic rolling with HBA, (d) Ferritic rolling with HBA.

{001}<130> at mid-thickness, Figure 3c. The major components on α fiber and on γ fiber are also different from those in nonHBA. Austenitic rolling with HBA yields major components of ~{112}<110> on α fiber and ~{111}<112> on γ fiber at subsurface. The reason for developing this different rolling texture by HBA may be associated with a coarse initial grain structure, which then induces the large amount of shear bands when cold rolling.

III.III. Annealing Stage:

The annealing texture of both austenitic rolling and ferritic rolling without HBA is similar. In the case of nonHBA, after annealing, both austenitic rolling and ferritic rolling significantly decrease α fiber, but increase ~{111}<112> on γ fiber at mid-thickness, compared to the cold rolling textures, Figure 3a, 3b.

However, austenitic rolling with HBA develops a totally different texture, Figure 3c. It not only decreases α fiber, but also eliminates γ fiber, compared to the cold rolling texture. Another feature of austenitic rolling with HBA annealing texture is the strong occurrence of Gauss texture, {110}<100>, at both subsurface and mid-thickness, and {001}<010> at mid-thickness. Similarly to nonHBA annealing texture development, ferritic rolling with HBA also decreases α fiber, but slightly increases {111}<112> on γ fiber, compared to the cold rolling texture, Figure 3d. Besides yielding weak α fiber and γ fiber, ferritic rolling with HBA also generates some special annealing textures as austenitic rolling with HBA, such as: {110}<100> and {001}<010>. Eventually, the annealing texture of ferritic rolling with HBA is a combination of the HBA annealing texture with the nonHBA annealing texture.

In the case of nonHBA, the small hot band grain size contributes to the occurrence of grain boundary nucleation and forms a strong γ fiber during annealing[1]. In the case of austenitic rolling with HBA, the very coarse hot band grain size generates a large amount of shear bands during cold rolling, which then leads to nucleation of Gauss grains and forms a strong Gauss texture during annealing[2]. If the hot band grain size is (~ 46 μm) not large enough, then Gauss texture, α and γ fiber co-exist when annealing.

IV. CONCLUSIONS:

1. The effect of hot band grain size on the subsequent texture development is more significant than ferritic rolling. Although ferritic rolling produces a remarkable {001}<110> on α fiber at mid-thickness when hot rolling, it still yields a similar cold rolling texture and annealing texture as austenitic rolling.
2. The very coarse hot band grain using hot band annealing produces an annealing texture containing a strong Gauss texture, {110}<001>, and {001}<010>. However, if the hot band grain size is (~46 μm) not large enough, then Gauss texture, α fiber and γ fiber co-exist when annealing.

V. REFERENCES:

(1). K.Ushioda, 6th ICOTOM, p.829, 1981. (2). L. Seidei, Ph.D.Thesis, RWTH, Aachen, 1990.

APPLICATION OF THE DISLOCATION REACTION MODEL FOR VARIANT SELECTION TO THE TRANSFORMATION OF AN Fe-30%Ni ALLOY DEFORMED IN EXTENSION

N.J. WITTRIDGE and J.J. JONAS
McGill University, Department of Metallurgical Engineering, Montreal, Canada
J.H. ROOT
National Research Council, Chalk River Laboratories, Chalk River, Canada

Abstract

The dislocation reaction model of Sum and Jonas was utilised to predict the transformation texture of a Fe-30%Ni alloy deformed by axisymmetric extension prior to transformation. The model relies on two variant selection rules based on a combination of slip activity and the allowable in-plane dislocation reactions. Using the model, successful predictions of the transformation texture of a similar alloy have been made after deformation by plane strain rolling and axisymmetric compression. A cylindrical bar of Fe-30%Ni was subjected to an extension of 20%, after which the texture was measured using neutron diffraction techniques. A specimen was then quenched in liquid nitrogen to induce the transformation to martensite and again the texture was recorded. The deformation texture provided the input orientations used for the prediction of the transformation texture. Good agreement was demonstrated between the predictions and the experimental transformation textures.

Keywords: transformation texture, variant selection, γ-to-α′ transformation, Bishop and Hill, Kurdjumov-Sachs, dislocation reaction model.

1 Introduction

The evolution of texture during the austenite-to-martensite (γ-to-α′) transformation in steel is of great interest to researchers and has been well documented (Bateman and Davies, 1981, Ray and Jonas, 1990, Butrón-Guillén and Jonas, 1993). This interest is due primarily to the impact of crystallographic texture on the final properties and performance of the product. Successful models of the transformation have been proposed by Bain, Kurdjumov-Sachs (K-S), Nishiyama and Wassermann (N-W) and have been used extensively to simulate the γ-to-α′ transformation. The models provide accurate texture predictions for materials that have not undergone deformation prior to transformation; nevertheless the predictions deviate significantly from experimentally recorded textures when applied to *deformed* materials. In the latter situation, it appears that variant selection occurs during the transformation, so that only some of the crystallographically equivalent product variants contribute to the final texture of the material. As such variant selection occurs most frequently in materials that have been deformed plastically prior to transformation, the phenomenon is evidently related to the characteristics of dislocation glide.

Numerous theories, have been suggested that attempt to predict transformation textures using various selection criteria (Patel and Cohen, 1953, Bokros and Parker, 1963, Humbert et al., 1988). None of the previous models, however, has yet been able to describe the final transformation texture with accuracy. In 1999, Sum and Jonas proposed a new model for variant selection that relies on the occurrence of reactions between glide dislocations. The selection criteria are based on a combination of slip activity, where the active slip systems are defined in terms of positive shear, and allowable in-plane dislocation reactions. This model has been used successfully to predict the transformation textures produced in a Fe-30%Ni alloy after deformation along two different strain paths, namely plane strain rolling (Sum and Jonas, 1999) and axisymmetric compression (Sum et al. 1999).

In the present research, the dislocation reaction model of Sum and Jonas (1999) was utilised to predict the transformation texture produced after deformation along an additional strain path, namely axisymmetric extension. Using the same alloy for measurement of the experimental texture and the same methodology for the simulation, the objective was to evaluate the applicability of the dislocation reaction model to deformation by extension. The dislocation reaction model is briefly described below.

2 The Dislocation Reaction Model

The basis of the dislocation reaction model is the one-to-one correspondence between the 24 slip systems of the Bishop and Hill crystal plasticity model and the 24 possible variants produced according to the K-S transformation relationship. For each selected parent orientation, i.e. an orientation present in the material before transformation, the shear on each of the 24 possible slip systems is calculated. The product orientations that correspond to the various operative systems are then calculated using the appropriate <112> rotation axes of the K-S transformation. After this operation, the following two selection criteria are applied to the data:

1. Positive Shear Criterion: Only those systems that are characterised by positive or active shear are selected; concurrently those with negative shear are eliminated. For axisymmetric extension, this leads to the selection of eight positive variants for each orientation.
2. In-Plane Dislocation Reaction Criterion: The permissible in-plane reactions between the active dislocations are deduced according to Frank's Rules. In this case, four, six or eight variants are selected for each parent orientation; these are referred to as the "reaction" products. The variants that cannot be formed by reaction are labelled "no reaction" variants.

The final predicted transformation texture is obtained by combining the positive variants and the permissible reaction variants.

3 Experimental Approach

3.1 Measured Texture

The Fe-30%Ni alloy used in these experiments was selected for the stability of the austenitic phase at room temperature. In addition, it can be transformed to martensite at –196°C and this phase is retained when the material returns to room temperature. The alloy was supplied in the hot rolled condition with the chemical composition shown in Table 1.

To produce the extension textures, a circular bar of diameter 12.0 mm was machined with the axial direction aligned parallel to the rolling direction of the original plate. The bar was subjected to a swaging/extension process at a starting temperature of 300°C until a final diameter of 9.5 mm was reached. This is equivalent to a true strain of 0.48. Of the two samples cropped for texture measurement, one was quenched in liquid nitrogen at –196°C to induce the γ-to-α' transformation, while the other was preserved in the deformed condition. Neutron diffraction texture measurements were performed using the E3 neutron diffractometer at the Chalk River Laboratories of Atomic Energy of Canada Limited. The texture is displayed below in the form of inverse pole figures calculated from three complete pole figures for each of the austenite and martensite phases.

Table 1: Chemical composition of the alloy in wt%.

	C	Ni	Nb	Mn	Si	S	P	N	Fe
Wt%	0.155	30.50	<0.005	0.01	0.03	<0.001	0.002	0.0005	Bal.

3.2 Predicted Texture

For the accurate prediction of transformation textures, it is important to select the correct parent orientations to represent the deformation (parent) texture. The major orientations chosen to represent the extension texture were components of the <111> and <100> fibres; to these were added the minor components that extend along the <1vw> fibre. The parent orientations used in this calculation are listed in Table 2. They were selected after careful analysis of the measured deformation texture of the swaged bar (see Figure 1 below). To optimise the predictions, a random texture background equivalent to a volume fraction of 35% was added to each calculation.

Table 2: Parent orientations used for the predictions.

	Orientation	φ_1	ϕ	φ_2
<111> fibre	(111)[1-10]	0.00	54.74	45.00
	(111)[2-31]	19.11	54.74	45.00
	(111)[1-21]	30.00	54.74	45.00
<100> fibre	(100)[001]	0.00	0.00	0.00
	(100)[0-13]	18.43	0.00	0.00
	(100)[0-11]	45.00	0.00	0.00
<1vw> fibre	(334)	0.00	46.69	45.00
	(112)	0.00	35.26	45.00
	(113)	0.00	25.00	45.00
	(114)	0.00	19.47	45.00
	(116)	0.00	13.26	45.00

4 Comparison of the Measured and Predicted Textures

For each of the eleven parent orientations, the slip activities and 24 possible K-S transformation variants were determined. For ten of the eleven parents, all 24 variants were accounted for after application of the variant selection (and rejection) criteria. For the remaining parent, (111)[1-21], the orientation was rotated slightly off the perfect ideal orientation. This produced small shear values on additional slip systems and thus resulted in the allocation of all 24 variants.

4.1 Deformation Texture

The measured deformation texture is displayed in the form of an inverse pole figure in Figure 1; as expected the <111> and <100> fibres are dominant. Minor components can be seen to extend along the <1vw> fibre. Analysis of this inverse pole figure led to the selection and weighting of the parent orientations for use in the simulation. This resulted in the simulated inverse pole figure illustrated in Figure 2, which agrees well with the observed inverse pole figure shown in Figure 1. A gaussian half-width of 8° was applied to each discrete ideal orientation for construction of the simulated pole figures. For reference purposes, an inverse pole figure indicating the ideal orientations is shown in Figure 3.

4.2 Transformation Texture

By contrast, the <110> fibre dominates the experimental transformation texture indicated in Figure 4. The latter should be compared with Figures 5 and 6, which represent the transformation textures predicted using the positive shears and dislocation reactions, respectively. In each case, the simulated texture deviates to some extent from the measured one. After application of the present model, in which the positive slip and reaction variants are combined, the prediction more closely resembles the measured texture (Figure 7). This is evident from a comparison of Figures 4 and 7. Except for the 0.5 x random contour line in the vicinity of <100> orientation, the contours of the measured texture are closely reproduced in the predicted texture. The maximum intensity of the predicted texture (35%) is 2.5 x random using the same random background as required to fit the deformation texture. This is equivalent to the maximum intensity observed in the measured transformation texture. The reaction and positive variants were combined in a ratio of 2:1 for prediction of the final texture. This decision was motivated by analysis of the results of Liu and Bunge (1991), where the reaction variants in the measured texture appeared stronger relative to the positive variants.

The validity of the model is further strengthened by examination of the predicted texture via selection of the negative slip and no-reaction variants only (Figure 8). It is clear from the figure that choosing these two sets of variants provides a transformation texture that differs notably from the experimental one. An increase in the intensity of the <100> component to a level above one is visible, as well as a peak in the vicinity of the <210> orientation. Neither of these peaks is visible in the measured transformation texture (Figure 7). Thus the dislocation reaction model provides a more accurate representation of the transformation texture of a Fe-30%Ni alloy deformed by axisymmetric extension prior to transformation.

5 Conclusions

1. The axisymmetric extension of a Fe-30%Ni alloy produced a texture dominated by the <111> and <100> fibres. Minor components also appeared along the <1vw> fibre. Quenching induced a martensitic shear transformation and a <110> fibre texture in the alloy.
2. Transformation textures predicted using the positive slip and dislocation reaction approaches (in separate calculations) produced textures that deviated somewhat from the measured transformation texture.
3. Selection of the negative shear and the "no-reaction" variants to predict the transformation texture showed notable variations from the measured texture.
4. Combining the positive shear and reaction variants in accordance with the dislocation reaction model provided a final transformation texture that was in good agreement with the measured texture.

Acknowledgements

The authors would also like to express their gratitude to the Natural Sciences and Engineering Research Council of Canada for the financial support of this investigation and to Prof. Druce Dunne of the University of Wollongong for providing the experimental material. In addition, the authors would like to thank J. Azar and M. P. Butrón-Guillén, for providing the software programs used in the slip activity and transformation calculations, respectively.

References

Bateman, R. M. and Davies, G. J. (1981) The inheritance of texture on transformation from austenite to martensite in an Fe-30Ni alloy. *Proc. 6th Int. Conf. Textures of Materials*, ISIJ, Vol. 1, p. 690.

Bokros, J. C. and Parker, E. R. (1963) The mechanism of the martensite burst transformation in Fe-Ni Single crystals. *Acta Metall.*, Vol. 11, p. 1291.

Butrón-Guillén, M. P. and Jonas, J. J. (1993) Effect of austenite recrystallisation on ferrite transformation textures. *Materials Science Forum*, Vols. 113 – 115, p. 691.

Humbert, M., Wagner, F., Liu, W. P., Esling, C. and Bunge, H. J. (1988) Simulation of the martensitic transformation of Fe30Ni rolled sheets. *Proc. 8th Int. Conf. Textures of Materials*, Metall. Soc. of AIME, p. 743.

Liu, W. P. and Bunge, H. J. (1991) Variant selection in the martensite transformation of an Fe-30%Ni alloy with cube texture. *Materials Letters*, Vol. 10, no. 7,8, p. 336.

Patel, J. R. and Cohen, M. (1953) Criterion for the action of applied stress in the martensite transformation. *Acta Metall.*, Vol. 1, p. 531.

Ray, R. K. and Jonas, J. J. (1990) Transformation textures in steels. *Int. Materials Reviews*, Vol. 53, No. 1, p. 35.

Sum, M. and Jonas, J. J. (1999) A dislocation reaction model for variant selection during the austenite-to-martensite transformation. *Textures and Microstructures*, in press.

Sum, M., Jonas J. J. and Root J. H. (1999) Predicting the transformation texture of uniaxially compressed Fe-30%Ni using a dislocation reaction model. this proceedings.

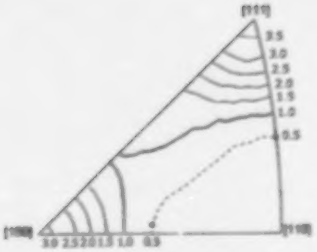

Fig. 1: Measured deformation texture.

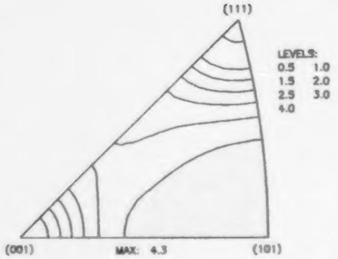

Fig. 2: Simulated deformation texture. (Shaded regions indicate <0.5 x random).

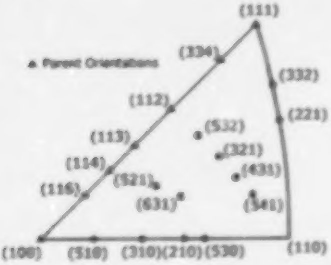
(111)
Parent Orientations
(334)
(332)
(112)
(221)
(532)
(113)
(321)
(114)
(431)
(521)
(116)
(631)
(541)
(100)
(510)
(310)
(210)
(530)
(110)

Fig. 3: Inverse pole figure of ideal orientations.

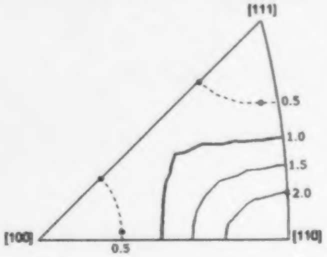

Fig. 4: Measured transformation texture.

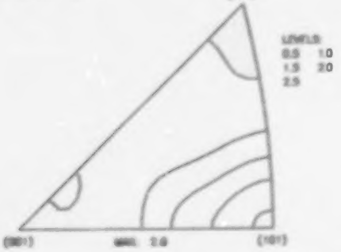

Fig. 5: Transformation texture predicted solely via selection of positive shear variants.

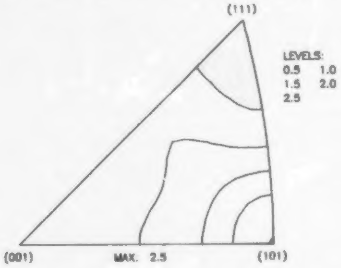

Fig. 6: Transformation texture predicted solely via selection of permissible reaction product.

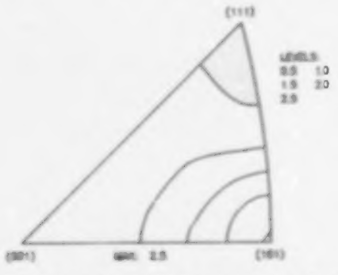

Fig. 7: Transformation texture predicted using the present model.

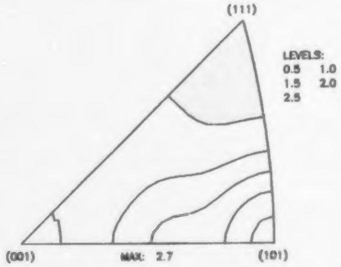

Fig. 8: Transformation texture predicted solely by selecting the negative shear and "no-reaction" variants.

INITIAL ORIENTATION DEPENDENCE OF TEXTURE EVOLUTION IN FERRITIC STAINLESS STEELS

S.H. PARK, K.Y. KIM and Y.D. Lee
Stainless Steel Research Group, Technical Research Laboratories,
Pohang Iron and Steel Co., Ltd., Pohang, Korea
C.G. PARK
Department of Materials Science and Metallurgical Engineering,
Pohang University of Science and Technology, Pohang, Korea

Abstract

The effect of initial orientation on the microstructure and texture evolution of two ferritic stainless steels was investigated. The columnar and equiaxed crystal specimens which were prepared from continuous casting slab were hot rolled, annealed, cold rolled, and annealed, respectively. The rolling and recrystallization textures at each process stage were examined by orientation distribution function (ODF) and electron back-scattered diffraction (EBSD). The observation showed that the orientation density of the α-fibre of hot rolled band of columnar crystal specimen was more pronounced than that of the equaxed one at the center layer. Nevertheless, the cold rolled textures of Type 430 steel have demonstrated a rather similar development. Compared to Type 430 steel the development of the α-fibre in the center layer of Type 409L steel was much more pronounced. The relation between texture evolution and ridging behaviour has been discussed.

Keywords: Ferritic Stainless Steel, Initial Orientation, Ridging, R-value, Texture

1 Introduction

One of the most serious defects in ferritic stainless steels is ridging, which is the form of small ridges or rope-like marks on the surface appearing after cold rolling or deep drawing process. This undesirable surface condition obliges the manufacturer to add costs in polishing operation. This phenomenon has been the subject of much published researches that connect it with the anisotropic plastic flow of mixed textures. Several theoretical models have been proposed to explain the formation of surface ridging which occurs parallel to the sheet rolling direction when the material is subjected to tensile strain in the rolling direction (Chao 1967;Takechi et al. 1967; Wright 1972). These are associated with the presence of strong texture inhomogeneity in the final product. These are based on a common hypothesis, that is, existence of grain clusters or grain colonies having large groups of grains with nearly equal orientation. There is still some contradiction over the origin and exact mechanisms of this phenomenon. Recently, the new ridging mechanisms have been proposed based on the analysis of the through-thickness texture distributions (Abbruzzese 1993;Hölscher, et al. 1991;Kim and Szpunar 1994) and microscopic local orientation measurement (Wittridge and Knutsen 1997;Brochu et al. 1997;Bethke et al. 1994). Here, these studies were mostly performed on the commercially produced cold rolled sheets with different degrees of ridging. The present study investigates the effect of initial orientation on the formation of coarse colony of cold rolled sheets and its texture evolution.

2 Experimental

The chemical compositions of type 430 and 409L stainless steels are given in Table 1. The samples used were cut from columnar (C) and equiaxed (E) zone of commercially produced continuous cast slab as shown in Fig. 1. The size of bars was 150mm long by 200mm wide and the thickness was 25mm. The bars were hot rolled to 3.5mm after a homogenization treatment. After annealing the hot bands were cold rolled to a thickness of 0.7mm by 80% reduction and finally annealed. The details of process conditions are shown in Table 2. Samples were cropped at the end of each process stage, namely hot roll (HR), hot roll-anneal (HR Ann.), cold roll (CR), and cold roll-anneal (CR Ann.).

Ridging characteristics were determined after 15% tensile elongation. Roughness profiles of the ridged samples were measured by using Mitutoyo surface measuring instrument model Surftest 501 Series 178.

Table 1: Chemical compositions (wt%).

	C	Si	Mn	Cr	Ti	N
430	0.048	0.37	0.42	16.4	-	0.037
409L	0.008	0.56	0.25	11.4	0.23	0.009

Table 2: Process conditions.

	430	409L
Reheating Temp.	1200°C	
Finishing Temp.	930°C	
Hot Roll Ann.	850°C, 5 hr	930°C, 1 min
Cold Roll Ann.	860°C, 30 sec	930°C, 30 sec

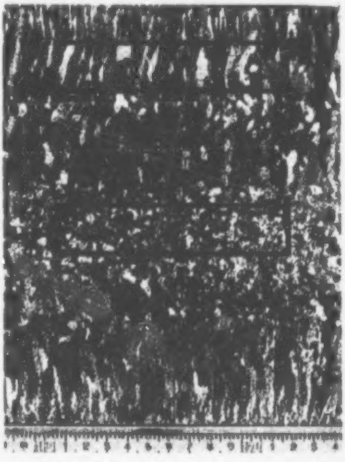

Fig. 1: Microstructure of CC Slab.

The X-ray diffraction data were obtained on three layers through the thickness at each process stage in order to ascertain the existence of through-thickness texture gradients and the texture evolution. Those internal layer positions are at the surface (Index s=1.0), at 1/4(Index s=0.5), and 1/2(Index s=0.0). Texture measurements were made on an automated pole figure goniometer using MoKα radiation. Orientation distribution function (ODF) analysis was obtained from three pole figure [(110), (200), and (211) for tilt angles up to 70°]. Microtexture analysis was performed by on-line computer interpretation of electron backscattered diffraction (EBSD) patterns using Version 2.6 of an OIM (orientation imaging microscopy) system manufactured by TSL and a scanning electron microscope model Philips XL 30.

3 Results and discussion

The evolution of the microstructure during rolling and annealing process was examined by microscope on the RD-ND (longitudinal) section. Regardless of initial orientation the microstructures of finally annealed sheets of type 430 steel have fine grains and homogeneous grain size distribution through the entire specimen thickness. In contrast, the grain size distribution of type 409L steel is inhomogeneous and much coarse band structure is formed in the middle layer for type 409L(C). The variation of the microstructures at each process stage is shown in Fig. 2, where the projected place is the middle layer of RD-TD (rolling) plane. The coarse band structures of type 409L(C) have its origin in columnar structure. Contrary to this, in the case of type 430(C), it was shown that that the coarse columnar structure had been much destroyed because of the existence of austenite phase.

The fibre intensities for the α and γ-fibres are plotted in Fig. 3, for the center layer of samples cropped at each process stage. The α-fibre density of hot band originated from the columnar structure was more pronounced than that of the equiaxed one. Here, the representative orientation was {001}<110> which was induced by columnar texture of {001}<uvw>. Fig. 4 exhibits the α and γ-fibres for three layers through thickness after final annealing. It is observed that texture inhomogeneity through thickness for type 409L(C) is rather strong, while texture gradients for the other samples are relatively weak. The α-fibre decreases and in the γ-fibre {111}<112> is dominant except type 409L(C) which exhibits strong α-fibre.

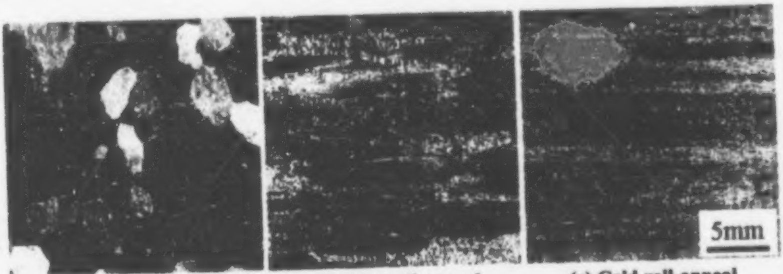

(a) Slab (b) Hot roll-anneal (c) Cold roll-anneal

Fig. 2: The microstructures at each process stage.

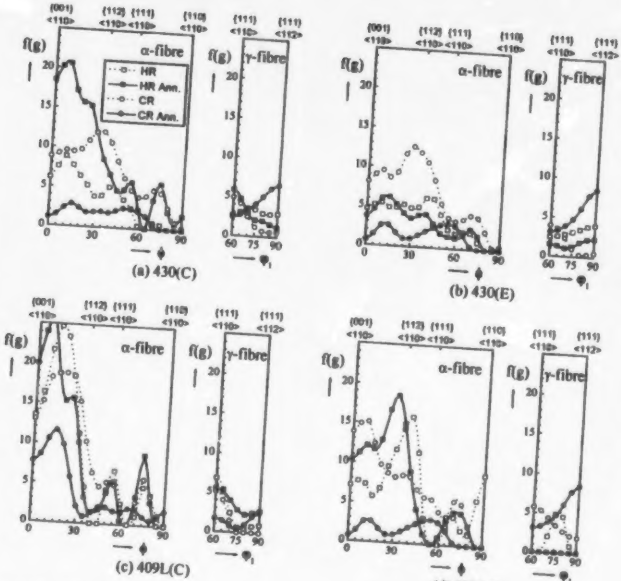

(a) 430(C)

(b) 430(E)

(c) 409L(C)

(d) 409L(E)

Fig. 3: The α and γ-fibres for the center layer at each process stage.

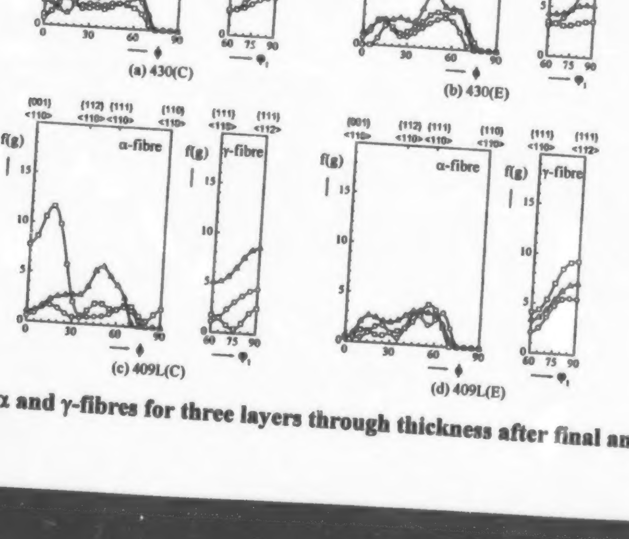

(a) 430(C)

(b) 430(E)

(c) 409L(C)

(d) 409L(E)

Fig. 4: The α and γ-fibres for three layers through thickness after final annealing.

Fig. 5 shows the ridging height of the tested samples after tensile elongation. As shown on the Fig. 5, both type 430 and 409L show higher tendency of ridging severence in the case of columnar samples. In line with this, type 409L shows 2~3 times higher ridging height than that of type 430. The ridging height of type 409L (E) is higher than that of type 430 in spite of relatively strong γ-fibre. This fact is related with the grain size inhomogeneity through thickness. It might be explained by the consideration of Wittridge that grain size banding can cause inhomogeneous plastic yielding behaviour which possibly contributes to the formation of surface ridging.

In order to ascertain the effect of such texture gradients on the ridging behaviour, the plastic strain ratios (R) were calculated from ODF by using Taylor theory as a function of the angular distance α from the RD, where three layers were measured depending on its through thickness variation. The calculated strain ratios for the angular distance α=0 from the RD are represented in Fig. 6. In the case of slight amount of ridging there is very little difference between the calculated strain ratios for the surface and interior layers. This means that all layers through thickness will deform more or less the same manner upon tensile elongation. In contrast, the severe ridging sample has R values varying with its thickness, this being the results of texture gradients in type 409L(C) as shown in Fig. 4. Therefore, the surface and center layers of these samples will not deform homogeneously under the tensile elongation. These results agree to the works of Abbruzzese and Kim et al. in which they claim that severe ridging sample exhibits strong component inhomogeneity through thickness.

The microtexture measurements were performed on the RD-ND(longitudinal) section. The microtexture analysis has not been successful in identifying the presence of coarse colonies with any certainty. In order to improve the microtexture analysis, it is thought that the section and layers of samples should be carefully prepared and analyzed. The microtexture measurements are presently ongoing.

Consequently, the mechanism generating ridging defect is connected to texture inhomogeneity, the gradient of texture through thickness, and grain size banding. Chao and Takechi et al. have suggested mechanisms based on the mixed texture, the cube-on-face and cube-on-corner components of the overall texture. Abbruzzese and Kim et al. have suggested that severe ridging is concerned with the presence of

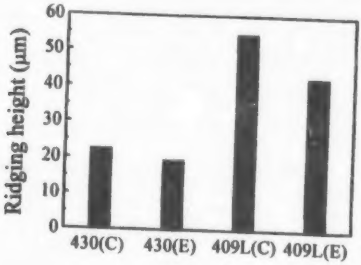

Fig. 5: The measurement of ridging height.

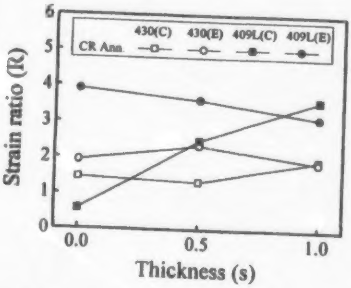

Fig. 6: Calculated strain ratio (R) as a function of the sample depth.

a texture gradient through the sheet thickness which creates layers of material with remarkably different plastic anisotropy coefficient. Wittridge et al. have suggested that grain size banding can cause inhomogeneous plastic yielding behaviour which possibly contributes to the formation of surface ridging. In general, in the case of severe ridging samples, the probability of finding these heterogeneities gose up.

4 Conclusion

Regardless of initial orientation the finally annealed sheets of type 430 steel have fine grain structures and homogeneous texture distribution through the entire thickness. Therefore, there is little difference in ridging behaviour of the two samples, columnar and equiaxed. It is because the columnar texture of {001}<uvw> originated by the crystallization in casting, which evolves grain colonies of {001}<110> texture having low anisotropy coefficient, is reduced due to the presence of austenite phase during rolling and recrystallization after annealing treatment. Type 409L steel exhibits severe ridging owing to its much coarse band structures originated by columnar structure in the middle layer and also the concomitant presence of texture and grain size inhomogeneity through thickness.

5 References

Abbruzzese, G., Fortunati, S., Campopiano, A. and Micucci, L. (1993) Relationships between microstructure, texture inhomogenities and drawing properties of 17 Cr steels:Effect of infracritical annealing. *Processes and Materials Innovation Stainless Steel*. pp.345-351.

Bethke, K., Hölscher, M. and Lücke, K. (1994) Local orientation investigation on the ridging phenomenon in Fe 17% Cr steel. *Mater. Sci. Forum*, Vol. 157-162, pp. 1137-1144.

Brochu, M., Yokota, T. and Satoh, S. (1997) Analysis of grain colonies in Type 430 ferritic stainless steels by electron back scattering diffraction(EBSD). *ISIJ Int.*, Vol. 37, No. 9, pp. 872-877.

Chao, H.C (1967) The mechanism of ridging in ferritic stainless steels. *Trans. ASM*, Vol. 60, pp. 37-50.

Hölscher, M., Raabe, D. and Lücke, K. (1991) Rolling and recrystallization textures of BCC steels. *Steel Research*, Vol. 62, No. 12, pp. 567-575.

Kim, H.M. and Szpunar, J.A. (1994) Ridging phenomena in textured ferritic stainless steel sheets. *Mater. Sci. Forum*, Vol. 157-162, pp. 753-760.

Takechi, H., Kato, H., Sunami, T. and Kakayama, T. (1967) On the mechanism of ridging phenomenon in 17%-Chromium stainless steel sheets. *J. Jpn. Inst. Met.*, Vol. 31, No. 6, pp. 717-723.

Wittridge, N.J. and Knutsen, R.D. (1997) Characterization of microstructure and texture evolution in AISI 430 ferritic stainless steel - analysis of the surface ridging phenomenon. *Thermo - Mechanical Processing in Theory, Modelling & Practice [TMP]*. pp. 390-397.

Wright, R.N. (1972) Anisotropic plastic flow in ferritic stainless steels and the roping phenomenon. *Metall. Trans.*, Vol. 3, No. 1, pp. 83-91.

RELATION BETWEEN GRAIN BOUNDARY MOBILITY AND GRAIN BOUNDARY CHARACTER IN Fe-3%Si

Y. HAYAKAWA , T. TAKAMIYA and M. KUROSAWA
Technical Research Laboratories, Kawasaki Steel Corporation
1-Kawasakidori, Mizushima, Kurashiki, Okayama, Japan, 712-8511

Abstract

A mechanism for Goss texture development in grain oriented electrical steel was proposed in our previous works based on the assumption of the high mobility of high-energy (HE) boundary during secondary recrystallization . HE boundary corresponds to the boundary which has misorientation angle between 20 and 45° following the experimental data by Dunn. The experiment to verify this assumption is designed under the presence of inhibitors. The result clearly demonstrates that HE boundary has a high mobility in the case in which the pinning force by inhibitors is in effect. The mobility of CSL boundaries is also investigated and specially high mobility is not observed .

Keywords: Electrical Steel, Secondary Recrystallization, Goss Texture, Grain Growth, Grain Boundary Energy, Inhibitor, Coincident Site Lattice Boundary

1 Introduction

The mechanism for Goss texture development during secondary recrystallization in grain oriented electrical steel has been widely discussed. Recently, much attention has been focused on the role of boundary character distribution for causing the anisotoropy of grain boundary mobility or grain boundary energy which is the essential factor for attaining secondary recrystallization (Srolovitz et al. 1984).

Shinozaki et al. (1978) and also Harase and Shimizu (1988) claimed the contribution of CSL boundary , especially that of $\Sigma 9$ boundary. CSL boundary is assumed to have high mobility and low energy, which is apparently advantageous for the grain growth. This model emphasizing the contribution of CSL boundary is called in this paper as "CSL model".

Turekawa et al. (1996) demonstrates the high mobility of $\Sigma 9$ boundary compared with near $\Sigma 19a$ boundary in certain range of temperature. This result is referred by J. S. Woo et al. (1998) as an experimental support for CSL model. We do not think the result by Turekawa et al. is in favor of CSL model. This experiment was done using bicrystal without inhibitors which is indispensable for secondary recrystallization and the difference in mobility was related to the diffusion of Si. The result may change if inhibitors are involved because the mobility is not related ro the diffusion of Si. Another point is that the orientation relationship between Goss grains and main texture component {554}<225> of primary recrystallized texture is closer to $\Sigma 19a$ which was used as a reference than to $\Sigma 9$. If the grain of main texture component is hardly consumed by the Goss grain, why it can be a secondary recrystallized grain.

Recently in CSL model (Ushigami et al. 1996), discussion on mobility is avoided, and instead the role of low energy of CSL boundary is emphasized. Ushigami et al. (1996) claimed that the pinning effect by inhibitors for CSL boundary is weak because of the low energy of CSL boundary. This assumption helps CSL boundary to be mobile in CSL model.

Hayakawa and Szpunar (1997a) argued against CSL model from the analysis of grain boundary character distribution of the primary recrystallized texture of both high permeability and conventional type of electrical steel, and another model (called here as "HE model") based on the physical property of high-energy (HE) boundary was proposed. HE boundary corresponds to the boundary which has misorientation angle between 20 and 45° following the experimental data by Dunn and Lionetti (1949). HE boundary is accepted to have a high mobility inherently, because high energy boundary has a large free volume which contributes to the boundary migration process (Valiev et al. 1986). Large free volume of HE boundary is also responsible for high grain boundary diffusion rate which facilitates the coarsening of inhibitors on HE boundary. It leads to the selective unpinning for HE boundary during the annealing, which enables the secondary recrystallization of the Goss grain. Both Monte-Carlo simulation (Hayakawa and Szpunar 1997b) and observation of grain growth behavior during the secondary recrystallization using EBSP (Hayakawa et al. 1998) supported HE model indirectly.

The measurement of boundary mobility is the direct method to test the growth models. Taoka et al.(1967) or Titorov (1973) previously investigated the mobility in Fe-3%Si by a skillful experimental technique. High mobility of HE boundary which has a misorientation angle between 20 and 45° was indicated in both works, but the experiment was carried out using the material without inhibitors. Measurement of the orientation was not so precise to detect CSL boundaries at that time.

In the present paper, experimental technique used by Titorov (1973) is performed under the presence of inhibitors to test what type of boundaries have high mobility. Also, CSL boundaries are detected precisely using Electron Back Scattering Pattern (EBSP) in order to check the high mobility of CSL boundary.

2 Experiment

Primary recrystallized specimen containing AlN and MnSe precipitates as inhibitors was annealed at 1223K for 20 hours in nitrogen atmosphere. After the annealing, secondary recrystallized portion was approximately 40%. Since the progress of secondary recrystallization is underway, pinning force by inhibitors are considered to be still in effect in the present experiment.

The specimen was pickled to remove the oxide formed on the surface and cold rolled at 5% reduction for providing the driving force for grain growth. Then, deformation by indenting was provided locally on a large Goss grain for nucleating new grains. After the subsequent annealing at 1273K for 10 minutes in nitrogen atmosphere, a lot of recrystallized grains were observed around a hole made by the indentation. Orientation relationship between the Goss matrix and newly recrystallized grains were analyzed using EBSP for the investigation of the grain boundary character of high mobility boundaries. CSL boundaries were defined using Brandon Criterion (Brandon 1966).

Although the experimental technique applied in this work is not a completely direct measurement compared with that by Turekawa et al. (1996), our experimental method enables the investigation on mobilities of much more types of grain boundaries at a time.

3 Result and Discussion

No systematic orientation change was observed after 5% cold rolling. After the subsequent annealing, newly recrystallized small grains with diameter 20 μm are observed in the region where heavy deformation was given by indentation. {100} pole figure from 408 small recrystallized grains are shown in Fig. 1. No strong texture is observed considering limited number of measured grains, therefore, nucleation can be regarded as random.

Some of the recrystallized grain elongated from the heavily deformed region by the indentation toward rolling direction. The microstructure of the elongated grain is shown in Fig.2. Subboundary structure are formed inside Goss matrix after the annealing at 1273K. It is considered that the driving force for the growth of elongated grains is subboundries remained inside the Goss matrix. Difference of the growth of elongated grain can be attributed to the difference in grain boundary mobility, because the distribution of subboundaries, or the driving force for the growth is almost uniform in Goss matrix. As nucleation can be regarded as random, boundary around elongated grain can be assumed to be highly mobile. Elongated grains over the length 20 μm is measured in order to investigate the boundary character of high mobility boundaries.

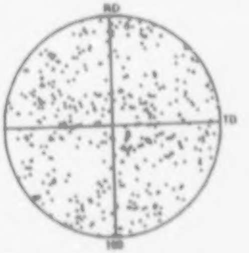

Fig. 1 {100} pole figure of newly recrystallized grains with equiaxed shape formed in heavily deformed region by indenting.

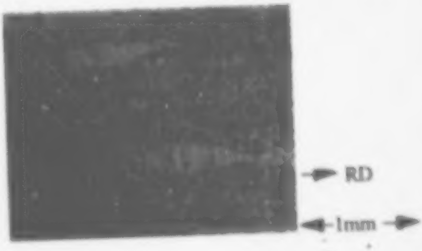

Fig. 2 Elongated recrystallized grain around a hole made by indenting.

The misorientation angle distribution for 284 elongated grain obtained from EBSP measurement is demonstrated in Fig. 3 classified by the length of the grain (L). The frequency of HE boundary is apparently enhanced compared with random distribution represented in solid line in Fig. 3. High frequency of HE boundaries demonstrates high mobility of HE boundary. Frequency of HE boundary is 90% for grains with length over 100 μm and 74% for grains with length under 100 μm.

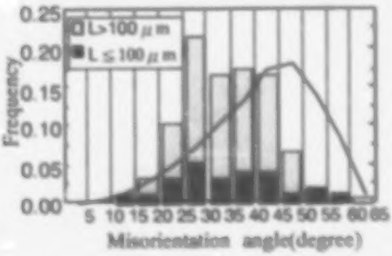

Fig. 3 Misorientation angle distribution between elongated recrystallized grain and Goss matrix. Solid line represents the distribution for random texture.

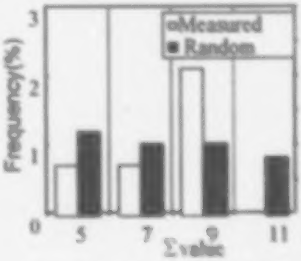

Fig. 4 The frequency of CSL boundaries between elongated recrystallized grains and Goss matrix.

Frequency of CSL boundaries were also investigated from Σ1 up to Σ19b boundary. If only CSL boundaries are mobile, they will dominate among boundaries of elongated grains. Total frequency of the CSL boundary is 9.1% of all the boundaries and this value is virtually the same with calculated value of 9.6% for random texture. This result indicates that most of high mobility boundary is non-CSL boundaries.

The frequency of Σ5 to Σ11 boundaries are shown in Fig. 4 together with calculated value for random texture. Boundary having misorientation angle with respect to <110> axis is sometimes assumed to be mobile by {110} plane matching theory (Jonas and Kestens 1996). Comparison between Σ9 and Σ11 boundary is a good example to acquire the insight about influence of grain boundary character on mobility because they have common <110> misorientation axis and similar Σ value. There found an enhancement of the frequency for Σ9 boundary, and total absence of Σ11 boundary. Σ9 boundary has 38.9° misorientation angle and should belong to HE boundary. Σ11 boundary has 50.5° misorientation angle and does not classified as HE boundary. Calculated energy of Σ11 boundary is considerably lower than Σ9 boundary (Wolf 1989). Energy cusp is found in calculation on exact position of Σ9 boundary, however the difference in boundary energy is negligibly small, so that Σ9 boundary can be assumed to be HE boundary.

Following the logic used in CSL model, Σ11 boundary should have low pinning force by inhibitors, therefore total absence of Σ11 boundary denies the assumption of weaker pinning effect for low-energy CSL boundary. It can be regarded that Σ9 boundary has high mobility, however, boundaries close to it also have high mobility as shown in Fig. 4. From the investigation above, we conclude that Σ9 boundary has a high mobility because it belongs to HE boundary.

4 Conclusion

1) HE boundary exclusively observed in boundaries for elongated recrystallized grains which grow toward Goss matrix from random nucleation by indentation. This result demonstrates that HE boundary has a high mobility even in the case in which pinning force by inhibitors is in effect.

2) Although the observed frequency is low, Σ9 boundary has also a high mobility because it belongs to HE boundary. Other CSL boundaries are not observed to have high mobility.

References

Brandon, D. G. (1966), Acta metall., Vol. 14, pp.1479.

Dunn, C. G., and Lionetti, F. (1949), AIME Trans., Vol. 185, pp.125.

Harase, J. and Shimizu, R. (1988), Trans. ISIJ, Vol. 29, pp. 388.

Hayakawa, Y., and Szpunar, J. A. (1997a), Acta mater., Vol. 45, pp. 1285.

Hayakawa, Y. and Szpunar, J. A. (1997b), Acta mater., Vol. 45, pp. 4713.

Hayakawa, Y., Muraki, M. and Szpunar, J. A. (1998), Acta meter., Vol. 46 , pp.1063.

Jonas, J. and Kestens, L. (1996), Material Science Forum, Vol. 204-206, pp. 155.

Shinozaki, M., Matoba, I., Kan, T. and Gotoh, T. (1978), Trans. JIM, Vol. 19, pp.85.

Srollovitz, D. J., Anderson, M. P., Sahni, P. and Grest, G. S. (1985), Acta metall., Vol. 33, pp.2233.

Taoka, T, Takeuchi, S., and Furubayashi, E. (1967), Trans. AIME, Vol. 239, pp.13.

Titorov, D. B. (1973) , Phys. Met. Metall., Vol. 35, pp.165.

Turekawa, S., Ueda, T., Ichikawa, T., Nakashima, H., Yoshitomi, Y. and Yoshinaga, H. (1996), Material Science Forum, Vol. 204-206, pp. 221.

Ushigami, Y., Nakayama, T., Suga, Y. and Takahashi, N. (1996), Material Science Forum, Vol. 204-206, pp. 599.

Valiev, R. Z., Gertsman, V. Yu. and Kainyshev, O. A. (1986), Phys. stat. sol(a), Vol. 97, pp.11.

Woo, J. S., Han, C. H., Hong, B. D. and Harase, J. (1998), Acta mater., Vol. 46, pp.4905.

Wolf, D (1989), Phil. Mag., Vol. B59, pp.667.

MACROTEXTURE-RELATED FATIGUE CRACK CLOSURE IN Al-Li 2090 STUDIED BY X-RAY MICROTOMOGRAPHY

R. MORANO and S.R. STOCK

School of Materials Science & Engineering and Mechanical Properties Research Laboratory, Georgia Institute of Technology, Atlanta, Georgia 30332-0245 USA

G.R. DAVIS and J.C. ELLIOTT

Dept. of Biophysics in Relation to Dentistry, Queen Mary and Westfield College, London E1 4NS, UK

Abstract

The macrotexture in the center of 12.5 mm thick plates of Al-Li 2090 T8E41 differs from that at the surface and has been held responsible for producing very low fatigue crack propagation rates in samples of this alloy. Earlier work with x-ray microtomography quantified closure as a function of position on the crack face during unloading from the maximum stress seen in a fatigue cycle; results were from two, ~ 2 mm diameter notched tensile samples. This paper reports the influence of macrotexture on fatigue crack surface geometry and crack closure for Al-Li 2090 compact tension samples; the 2 mm x 25 mm cross-sections provide larger crack areas and less influence of sample geometry than in the earlier work. Nondestructive imaging with x-ray microtomography is used to determine the three-dimensional crack position and opening associated with each position as a function of applied load. In other words, the pattern of crack closure is directly quantified and clarifies the role of various mixed mode surfaces in producing closure. The complexity of the closure processes reflects the strong macrotexture, and, if modeling the effect of closure on stress intensity range does not include this complexity, it is difficult to see how such models can accurately predict fatigue crack growth rate.

Keywords: Aluminum, crack closure, microtomography, fatigue crack growth

1. Introduction

In Al-Li 2090 T8E41, fatigue crack growth rates along certain plate orientations are unusually low compared to those of other Al alloys (Venkateswara Rao et al. 1988 and Pao et al. 1989). This is related to a characteristic macrotexture (i.e., the texture averaged over a large number of grains) in the center of the plates which produces a rough, asperity dominated crack face and significant crack deflection. One result of the crack face roughness in Al-Li 2090 is crack closure, the phenomenon where the crack faces come into contact prematurely during unloading of the sample (i.e., before the minimum stress of a fatigue cycle is reached) or where the crack faces remain in contact much longer than expected during loading (e.g., Christensen, 1963; Elber, 1971; Ritchie, 1981, 1988). Roughness-induced crack closure leads to a reduced driving "force" for crack propagation and lower fatigue crack growth rates. High-resolution x-ray computed tomography (i.e., microtomography) has been used to examine the pattern of crack face contact as a function stress level within the interior of Al-Li 2090 T8E41 samples and demonstrated that the patterns of contact were very complex (e.g., Guvenilir, 1995; Guvenilir and Stock, 1998).

2. Experimental Methods

The L-T oriented compact tension samples were from the center of 12.7 mm thick plates of Al-Li 2090 T8E41 and were 2.7 mm thick, 31.8 mm long and 30.5 mm wide (scaled according to ASTM E-399-83). Fatigue cracks in CT-35 were grown with load ratio $R=\sigma_{min}/\sigma_{max}=0.1$, and the final crack length (from the notch tip) and stress intensity range were ~5.1 mm and 12.8 MPa$\sqrt{m}$. Sample CT-41 was tested with R=0.75 and had a final crack length and stress intensity range of ~6.0 mm and 3.8 MPa$\sqrt{m}$, respectively. Laser extensometry revealed closure stress intensity $K_{cl}=9.2$ MPa$\sqrt{m}$ (0.65 K_{max}) for CT-35 and 2.5 MPa$\sqrt{m}$ (0.16 K_{max}) for CT-41 after crack growth ended. Prior to imaging with microtomography, ~4 mm was cut from the back face of CT-35 (i.e., from the original 20 mm) and ~5 mm from CT-41; this was necessary to reduce the x-ray path length.

Microtomography was performed under load using a novel time-delay integration microtomography apparatus (Davis and Elliott, 1997) and a fan-beam, filtered back-projection method to reconstruct the crack-containing volumes with isotropic 58 μm voxels (volume elements). The x-ray source was a tube with a silver target (60 kV and foreshortened spot size of 0.1 mm x 0.1mm), and the load frame (Fig. 1) was similar to that used before (Breunig et al.1993). For each of the six or more loads imaged, data collection lasted 23 hrs for CT-35 and 19 hrs for CT-41. Details, including crack opening quantification, appear elsewhere (Morano, 1998).

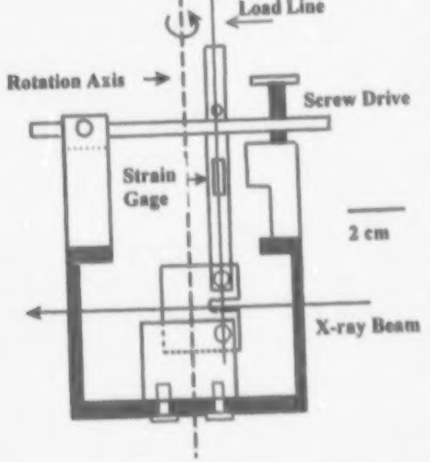

Fig. 1. Load frame. A thin-walled Al tube holds the two grips apart, a screw drive loads the sample (monitored by the strain gage. The rotation axis for collecting the different views and the x-ray beam axis also appear.

3. Results and Discussion

Figures 2 and 3 show a series of cuts through the reconstructed data for CT-35 (R=0.1) and CT-41 (R=0.75), respectively. The distance (in mm) of each cut from the tip of the notch is indicated by the number in the upper left-hand corner of each image, and the images are for the maximum load observed. The darker the pixel, the lower the attenuation coefficient and the greater the fraction of voxel occupied by the crack. The vertical direction in these figures corresponds to the load axis (parallel to L) while the horizontal axis corresponds to S (i.e., the left and right sides of each image are near the faces of the sample). Except for no more than one or two voxels on either face, the entire thickness of each sample is shown. Mixed mode I-III surfaces are clearly seen in these sections, and each sample's mode I-III surfaces are discussed separately. Note that mixed mode I-II surfaces are not obvious in these sections; but in some areas this mixed mode component is large.

For its first 2 mm, the crack in CT-35 remains roughly centered on the plane of the notch (i.e., the center of the crack in section 0.00), and asperities extend no further than 400 to 450 μm from this plane. The crack is more open on the left side of the asperities (pointing upwards in Fig. 2). The asperity just below "2" in the 0.29 mm section of Fig. 2 persists in roughly the same geometry over several hundred micrometers, and the right-most face of the asperity extends over ~2 mm without much change in geometry. After the crack was 2 mm from the notch it took an inclined geometry with quite long, uninterrupted, mixed mode I-III surfaces.

At K~6.0 MPa√m (Fig. 2), the crack in CT-35 is visible up to 4 mm from the tip of the notch: about 1 mm of the crack is invisible. This is not surprising since K is less than 0.5 K_{max} during the final increment of crack growth (14.3 MPa√m). Also, with a voxel size of 58 μm, one would not expect to distinguish between 0 and 10 μm openings. Nonetheless, one can be confident that the observations reported below accurately describe the behavior of the cracks under study.

Figure 3 of sample CT-41 (R=0.75) loaded to 40 kgf (K = 12.2 MPa√m) shows the crack begins to be indistinguishable about 5.5 mm from the end of the notch; careful inspection of the 6.09 mm section on the computer monitor reveals a hint of the crack. This is consistent with the 6.05 mm length measured optically at the sample surfaces). The first 2 mm of crack branched in the left half of the sample (as viewed in Fig. 3), and this is most clear in the 1.16 and 1.45 mm sections. Eventually, the lower branch of the crack becomes more important, and the upper branch disappears by the 2.03 mm section. The left side of the crack in the 2.03 mm section shows substantial mode I-III character which is mostly gone within the next 0.3 mm and continues to fade over the next 1 mm.

The overall impression from Fig. 2 and 3 is that the R=0.75 sample shows less tendency to form discrete asperities and has a less rough crack face, despite significant deflection, than the R=0.1 sample. Data at the other, lower loads, i.e., revealing how the crack closes, can be summarized as follows. The physical closure processes appear quite different for CT-35 and CT-41, and this appears to be related to the crack morphology. The crack in CT-35 is quite rough throughout and the primary contact at higher loads occurs on mixed mode I-III surfaces. An area of mixed mode I-II contact is found near the end of the crack, but this is probably the

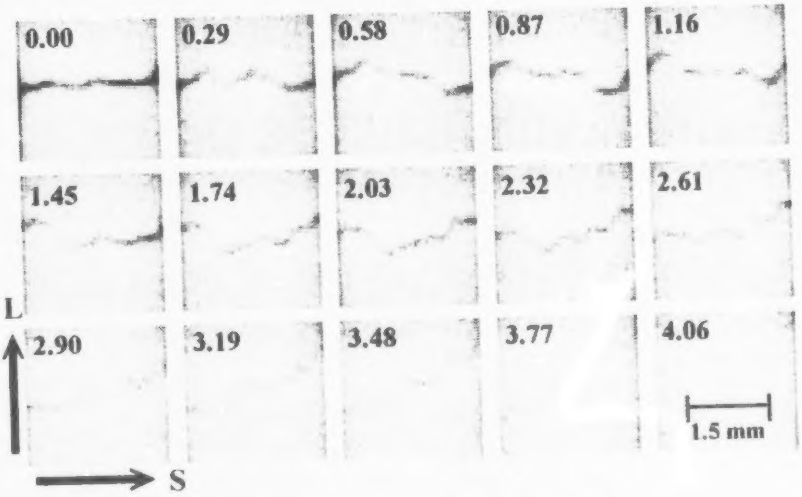
0.00
0.29
0.58
0.87
1.16
1.45
1.74
2.03
2.32
2.61
2.90
3.19
3.48
3.77
4.06
1.5 mm
L
S

Figure 2. Microtomographic sections through sample CT-35.

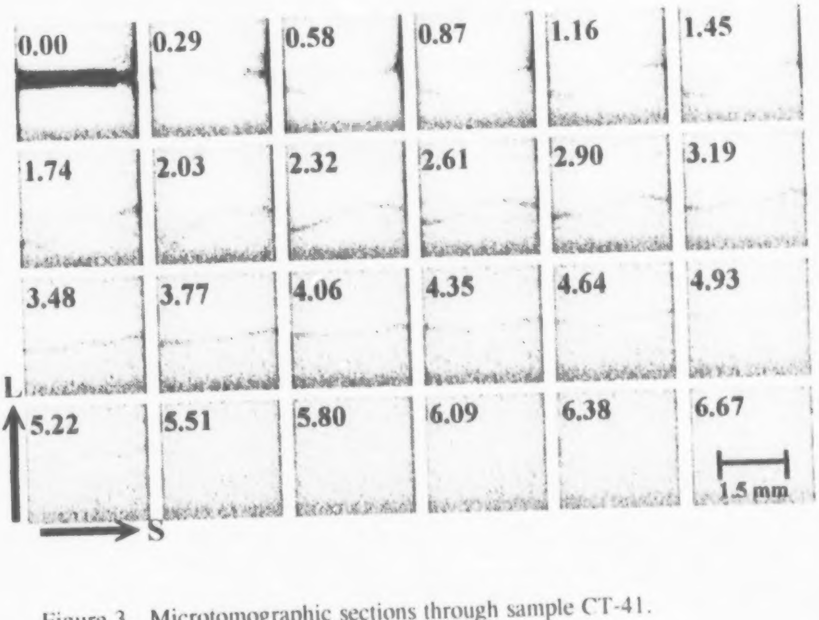
0.00
0.29
0.58
0.87
1.16
1.45
1.74
2.03
2.32
2.61
2.90
3.19
3.48
3.77
4.06
4.35
4.64
4.93
5.22
5.51
5.80
6.09
6.38
6.67
1.5 mm
L
S

Figure 3. Microtomographic sections through sample CT-41.

consequence of mixed mode I-III surface developing at one side of the sample and spreading to the second side. In CT-41, the first part of the crack is quite rough, and it was smoother over the last 2.5-3.0 mm. The point where the surface becomes smoother corresponds to the change from R=0.1 (during precracking) to R=0.75: after precracking, the crack extended 1.5 mm on one face and 2.27 mm on the other. The mixed mode components during R=0.1 crack propagation in CT-41 included I-III and I-II components while mode I-II components were most important for the R=0.75 sections of the crack.

The change of R is not the only possible reason that the crack in CT-41 transitioned from mode I-III to mode I-II geometry. Crack morphology can be quite different in adjacent 2 mm sections of samples. Mesotexture of near single-crystal volumes (see Haase et al., this volume) can vary over this length scale and can produce quite different crack face morphologies within the same sample. Thus, the origin of the change of crack morphology in CT-41 could be coincidentally due to a change in mesotexture and not to the change in R; deciding between the two alternatives must await further microbeam diffraction characterization of the samples.

4. Conclusions

X-ray microtomography of two compact tension samples revealed very different crack morphologies for R=0.1 and R=0.75. The patterns of crack closure are related to the crack morphology. In CT-35 (R=0.1), crack closure was observed on mixed mode I-III surfaces of asperities, even for the largest load/stress intensity examined, and, as load decreased, large portions of the crack closed behind a band of opening in a more planar, mixed mode I-II-III area of the crack. In CT-41 (R=0.75), a mixed mode I-II crack covered most of the surface, and crack closure appears to be spatially more uniform. The results are consistent with earlier studies of crack closure with microtomography, in which fatigue cracks in Al-Li 2090 samples were constrained via side-grooves in compact tension samples or via notches in cylindrical tensile samples. It is unclear at present whether the differences in crack morphology between CT-35 and CT-41 are related to the difference in R or to local variations in microtexture similar to those observed previously, and the resolution of this interesting question must await future microtexture characterization.

5. Acknowledgments

The US portion of the research was supported by the Office of Naval Research through grants N00014-94-1-0306, N00014-9-1-0726 and N00014-97-1-0557 and the UK portion through EPSRC Grant GR/J25628. The encouragement of Dr. George Yoder, Office of Naval Research, is gratefully acknowledged. We also thank Mr. R Brown and Mr. M.A. Langøy for their help with fatigue crack propagation and Mr. J. D. Haase, Mr. D.J. Ryan and Dr. A. Guvenilir for help with the computers used for the analysis.

6. References

Breunig, T.M., Stock, S.R., and Brown, R.C. (1993) Simple Load Frame for *in situ* Computed Tomography and X-ray Tomographic Microscopy, *Mater. Eval.* Vol. 51, pp. 596-600.

Christensen, R.H. (1963) Fatigue crack growth affected by metal fragments wedged between opening-closing crack surfaces, *Appl. Mater. Res.* Oct., pp.207-210.

Davis, G.R., and Elliott, J.C. (1997) X-ray microtomography scanner using time delay integration for elimination of ring artefacts in the reconstructed image, *Nucl. Instrum. Meth.* Vol. A394, pp. 157-162.

Elber, W. (1971) The significance of fatigue crack closure, in *Damage Tolerance in Aircraft Structures* ASTM STP 486, pp. 230-242.

Guvenilir, A. (1995) *Investigation into Asperity Induced Closure in an Al-Li Alloy Using X-ray Tomography*, PhD Thesis, Georgia Institute of Technology.

Guvenilir, A., and Stock, S.R. (1998) High Resolution Computed Tomography and Fatigue Crack Closure Modeling, *Fatigue Eng. Mater. Struct.* Vol. 21, pp. 439-450.

Morano, R. (1998) *Effect of R-ratio on Crack Closure in Al-Li 2090 T8E41, Investigated Non-destructively with X-ray Micro-Tomography*, MS Thesis, Georgia Institute of Technology.

Pao, P.S., Cooley, L.A., Imam, M.A., and Yoder, G.R. (1989) Fatigue crack growth in 2090 Al-Li alloy, *Scr. Met.* 23, pp. 1455-1460.

Ritchie, R.O. (1981) Environmental effects on near-threshold fatigue crack propagation in steels: A re-assessment, in *Fatigue Thresholds*, J. Backland, A. Blom and C.J. Beevers Eds., Eng Adv. Services, Warley, UK, pp. 503-526.

Ritchie, R.O. (1988) Mechanisms of fatigue crack propagation in metals, ceramics and composites: Role of crack tip shielding, *Mater. Sci. and Eng.* Vol. A103, pp.15-28.

Venkateswara Rao, K.T., Yu, W., and Ritchie, R.O. (1988) Fatigue crack propagation in aluminum-lithium alloy 2090: Part I. Long crack behavior and Part 2. Small crack behavior, *Met Trans.* Vol. 19A, pp. 549-569.

PREDICTING RECRYSTALLIZATION OF ALUMINUM BY APPLYING A PROBABILISTIC CELLULAR AUTOMATON TO FINITE ELEMENT DATA

D. RAABE

Institut für Metallkunde und Metallphysik, RWTH Aachen, Aachen, Germany

R. C. BECKER

Alcoa Technical Center, Alcoa Center, PA, USA

Abstract

Recrystallization is simulated by combining a crystal plasticity finite element model with a probabilistic cellular automaton. The coupling is realized by: translating the state variables used in the finite element model into the cellular automaton; mapping the finite element integration points on the automaton mesh; scaling the system; and identifying a nucleation criterion. The method is used for simulating texture and microstructure evolution in a deformed aluminum polycrystal during recrystallization.

Keywords: recrystallization, finite element, cellular automaton, aluminum

1. Introduction

Plasticity can often be described by assuming material homogeneity. This does less apply to recrystallization, where material heterogeneity determines nucleation and growth processes. For considering local effects on the development of texture and microstructure it is thus useful to apply models which take material heterogeneity into account, such as the crystal plasticity finite element and the cellular automaton method. Since the microstructure of metals is, to a large extent, inherited from the preceding process step we aim at coupling both methods for providing better input data to recrystallization simulations. For this purpose we use the results obtained from a crystal plasticity finite element simulation as starting conditions for a recrystallization simulation carried out with a probabilistic cellular automaton.

2. Crystal plasticity finite element method

The deformation of grains is determined by a crystal plasticity model which accounts for crystallographic slip and lattice rotation. Crystal kinematics follow those described by Asaro (1983), and the rate–dependent formulation follows that of Peirce *et al.* (1983). The equations are cast in an updated Lagrangian framework. The model has been implemented (Smelser and Becker 1989) in the finite element code Abaqus as used previously to simulate plastic deformation of crystals (Becker *et al.* 1991, 1995).

In the model, the velocity gradient, **L**, is decomposed into elastic and plastic parts

$$\mathbf{L} = \mathbf{L}^{*} + \mathbf{L}^{p} \tag{1}$$

each decomposed into its rate of deformation tensor, **D**, and spin tensor, $\boldsymbol{\Omega}$.

$$\mathbf{L}^{*} = \mathbf{D}^{*} + \boldsymbol{\Omega}^{*} \qquad \mathbf{L}^{p} = \mathbf{D}^{p} + \boldsymbol{\Omega}^{p} \tag{2}$$

The plastic parts, $\mathbf{D}^{p}$ and $\boldsymbol{\Omega}^{p}$, can be expressed in terms of the slip rates, $\dot{\gamma}^{\alpha}$:

$$\mathbf{D}^{p} = \frac{1}{2}\sum_{\alpha=1}^{N}\dot{\gamma}^{\alpha}\left(\mathbf{s}_{\alpha}\otimes\mathbf{m}_{\alpha} + \mathbf{m}_{\alpha}\otimes\mathbf{s}_{\alpha}\right) = \sum_{\alpha=1}^{N}\dot{\gamma}^{\alpha}\mathbf{P}_{\alpha} \tag{3}$$

$$\boldsymbol{\Omega}^{p} = \frac{1}{2}\sum_{\alpha=1}^{N}\dot{\gamma}^{\alpha}\left(\mathbf{s}_{\alpha}\otimes\mathbf{m}_{\alpha} - \mathbf{m}_{\alpha}\otimes\mathbf{s}_{\alpha}\right) = \sum_{\alpha=1}^{N}\dot{\gamma}^{\alpha}\mathbf{W}_{\alpha} \tag{4}$$

where $\mathbf{s}_{\alpha}\otimes\mathbf{m}_{\alpha}$ and $\mathbf{m}_{\alpha}\otimes\mathbf{s}_{\alpha}$ are the dyadic products of the slip vectors. The simulations on aluminum are conducted with the slip vectors $\mathbf{s}_{\alpha} = 1/\sqrt{2}(110)^{T}$ and $\mathbf{m}_{\alpha} = 1/\sqrt{3}(111)^{T}$. The elastic stretch and rotation of the lattice lead to a change of $\mathbf{s}_{\alpha}$ and $\mathbf{m}_{\alpha}$. This effect is captured by the elastic part of the velocity gradient.

$$\dot{\mathbf{s}}_{\alpha} = \mathbf{L}^{*}\cdot\mathbf{s}_{\alpha} \qquad \dot{\mathbf{m}}_{\alpha} = -\mathbf{m}_{\alpha}\cdot\mathbf{L}^{*} \tag{5}$$

By assuming a stress potential in which the stress is related to the elastic distortion of the crystal lattice, the rate of the Kirchhoff stress tensor, $\dot{\boldsymbol{\tau}}$, is given by

$$\dot{\boldsymbol{\tau}} = C:\mathbf{D}^{*} + \mathbf{D}^{*}\cdot\boldsymbol{\tau} + \boldsymbol{\tau}\cdot\mathbf{D}^{*} + \boldsymbol{\Omega}^{*}\cdot\boldsymbol{\tau} - \boldsymbol{\tau}\cdot\boldsymbol{\Omega}^{*} \tag{6}$$

where C is the fourth order elastic tensor and $\boldsymbol{\tau}$ is the Kirchhoff stress tensor. Combining the second and third terms of equation (6) with the modulus to define a fourth order tensor, $\mathcal{K}$, the Jaumann rate tensor can be written

$$\overset{\nabla}{\boldsymbol{\tau}} = \mathcal{K}:\mathbf{D}^{*} - \mathcal{K}:\mathbf{D}^{p} - \boldsymbol{\Omega}^{p}\cdot\boldsymbol{\tau} + \boldsymbol{\tau}\cdot\boldsymbol{\Omega}^{p} = \mathcal{K}:\mathbf{D}^{*} - \sum_{\alpha=1}^{N}\dot{\gamma}^{\alpha}\mathbf{R}_{\alpha} \tag{7}$$

where the last terms are expressed by the slip rates. The slip rates, $\dot{\gamma}^{\alpha}$, on system α follow a viscoplastic law. The strain rate sensitivity was $m = 0.002$. The strengths of all systems were taken to be equal. Hardening was assumed to follow macroscopic hardening as obtained from a biaxial test by fitting the experimental data to a Voce equation. Further details of the model were published by Becker *et al.* (1991, 1995).

The specimen represented by the finite element mesh was a columnar grain polycrystal of high purity aluminum (Becker, 1998). The grain size was on the order of millimeters. A rectangular specimen 30×25×10 mm^3 was excised for plane strain compression. The axis of the columnar grains is aligned with the 10 mm direction of the sample. This is also the constraint direction for the channel die experiments. The compression axis is along the 25 mm direction. The grain structure and the orientations were provided as input to the finite element analyses. Because a fine discretization is desired for coupling the deformation results with the recrystallization model a 2D finite element model was constructed. A paving algorithm was used to generate a mesh within each grain contour (MAZE 1993). The nodal locations are the same for elements on both sides of a grain boundary. The mesh used 36977 quadrilateral elements in the model plane.

3. The probabilistic cellular automaton method

The recrystallization model is designed as a cellular automaton with a probabilistic switching rule (Raabe 1998,1999). Independent variables are time and space. Space is discretized into quadratic cells. The state of each cell is described in terms of the driving force, p, and the orientation $\mathbf{g}=\mathbf{g}(\varphi_1, \phi, \varphi_2)$. The kinetics result from cell flips. The state of a cell may change due to the expansion of a recrystallizing neighbor grain which grows according to the local driving force. If an expanding grain sweeps a non–recrystallized cell the stored dislocation energy of that cell drops to zero and the orientation of the growing grain is assigned to it. The switching rule is a probabilistic analogue of Turnbull's (1951) rate equation which after linearization assumes the form

$$\dot{\mathbf{x}} = \mathbf{n}\, m p = \mathbf{n}\, m_0 \exp\left(-\frac{Q_{gb}}{k_B T}\right) p \tag{8}$$

where m is the mobility and $\dot{\mathbf{x}}$ the boundary velocity. The pre–exponential factor of the mobility $m_0 = m_0(\Delta\mathbf{g}, \mathbf{n})$ and the activation energy of grain boundary mobility $Q_{gb} = Q_{gb}(\Delta\mathbf{g}, \mathbf{n})$ may depend strongly on the misorientation $\Delta\mathbf{g}$ across the boundary and on the grain boundary normal $\mathbf{n}$. Competing flips are dealt with by replacing the rate equation by a probabilistic analogue enabling one to calculate switching probabilities.

$$\dot{\mathbf{x}} = \dot{\mathbf{x}}_0 w = \mathbf{n}\frac{k_B T m_0}{V}\frac{pV}{k_B T}\exp\left(-\frac{Q_{gb}}{k_B T}\right); \quad \dot{\mathbf{x}}_0 = \mathbf{n}\frac{k_B T m_0}{V}, \quad w = \frac{pV}{k_B T}\exp\left(-\frac{Q_{gb}}{k_B T}\right) \tag{9}$$

Mapping equation (9) on a grid with a scaling length λ_m leads to

$$\dot{\mathbf{x}} = \dot{\mathbf{x}}_0 w = \mathbf{n}(\lambda_m \nu) w \qquad \text{with} \qquad \nu = (k_B T\, m_0)/(V \lambda_m) \tag{10}$$

where ν is the eigenfrequency of the mesh characterized by λ_m. ν represents the attack frequency for *one* particular grain boundary with constant mobility. For using a *spectrum* of mobilities and driving forces it is necessary to normalize equation (10) by a common frequency ν_0. The normalized switching equation finally assumes the form

$$\hat{w}^{local} = \frac{m_0^{local} p^{local}}{\lambda_m \nu_0}\exp\left(-\frac{Q_{gb}^{local}}{k_B T}\right) = \left(\frac{m_0^{local}}{m_0^{max}}\right)\left(\frac{p^{local}}{p^{max}}\right)\exp\left(-\frac{\left(Q_{gb}^{local}-Q_{gb}^{min}\right)}{k_B T}\right) = \left(\frac{m^{local} p^{local}}{m^{max} p^{max}}\right) \tag{11}$$

i.e. the local switching probability is scaled by the ratio of the local and the maximum mobility, m^{local}/m^{max}, and by the ratio of the local and the maximum driving pressure p^{local}/p^{max}. The actual switching *decision* is made by a Monte Carlo step.

4. Coupling the finite element model with the probabilistic cellular automaton

The coupling was realized in four steps. First, the state variables of the finite element model (orientation, accumulated shear) were translated into state variables of the cellular automaton model (orientation, dislocation density). Second, the integration point locations from the finite element mesh were mapped on the quadratic automaton mesh. Third, the system was scaled by the cell size, the maximum driving force, and the maximum grain boundary mobility. Fourth, a nucleation model was defined which transforms all cells with a critical stored energy into recrystallized cells by spontaneously dropping the dislocation density in these cells to zero. When the transformed cells reveal a misorientations above 15° with respect to the neighbor cells they can expand following the local driving force as explained above.

5. Simulation of discontinuous primary static recrystallization in aluminum

Fig. 1 shows recrystallization simulations ($\varepsilon = -0.434$). The upper graphs show the orientations. The gray levels correspond to the magnitude of the Rodriguez vector. The lower graphs show the stored dislocation densities. The black areas are recrystallized, i.e. the dislocation content of the affected cells is zero. The gray lines indicate misorientations in the range 5°-15° and the white one above 15°. Nuclei were formed at $t = 0$ s in cells with a dislocation density larger than 70% of the maximum value.

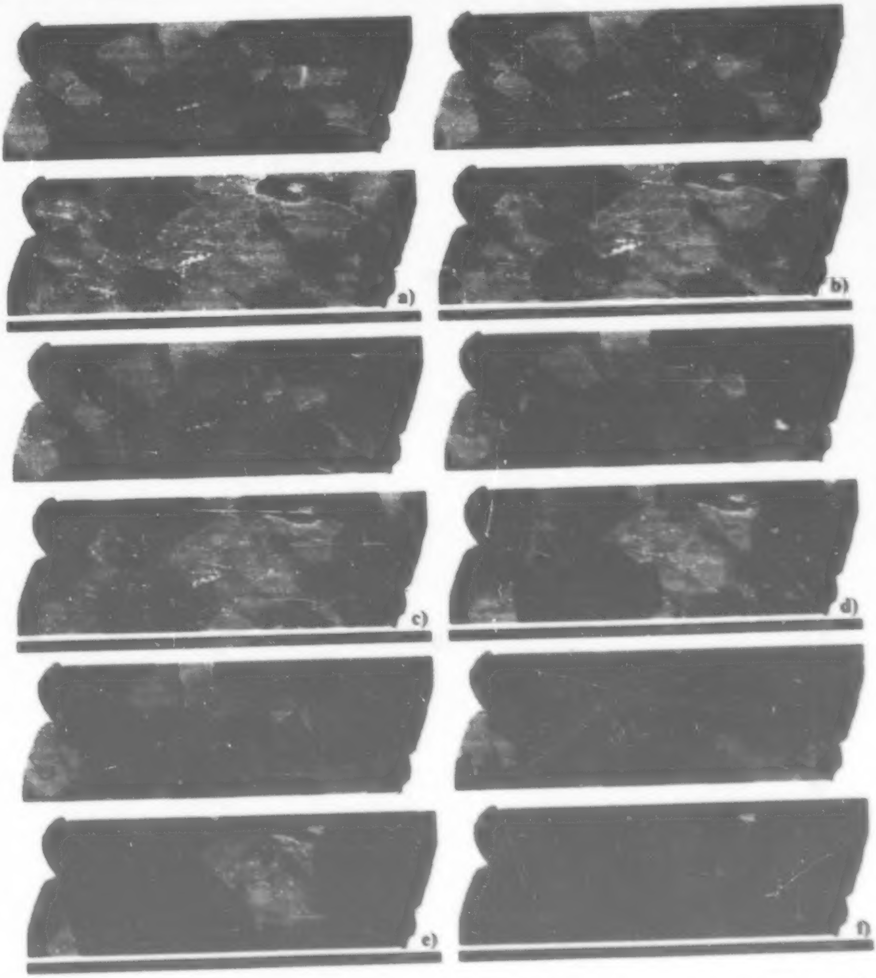

Fig. 1: Al; 800 K; site–saturated nucleation; thermodynamic nucleation criterion: cells with dislocation density above 70% of the maximum density; Q_{gb}=1.46 eV; $m_0 = 8.3\times10^{-3}$ m^3/(N s); $\lambda_m = 61.9$ μm, boundaries mobile above 15° misorientation; upper graphs: orientation map; lower graphs: dislocation density; recrystallized volume fraction: (a) 13.6 %; (b) 28.8 %; (c) 43.9 %; (d) 53.9 %; (e) 68.7 %; (f) 93.5%

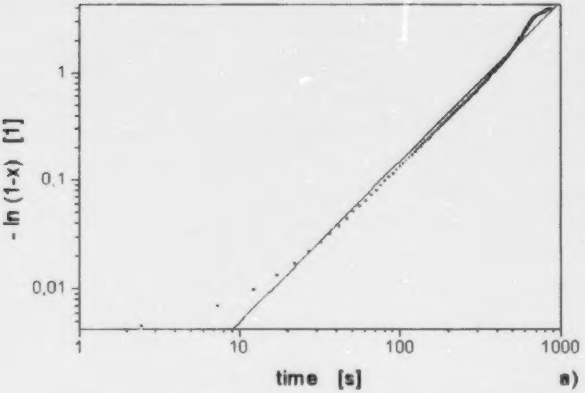

Fig. 2a: Kinetics; x: recrystallized volume fraction; Avrami-exponent=1.49.

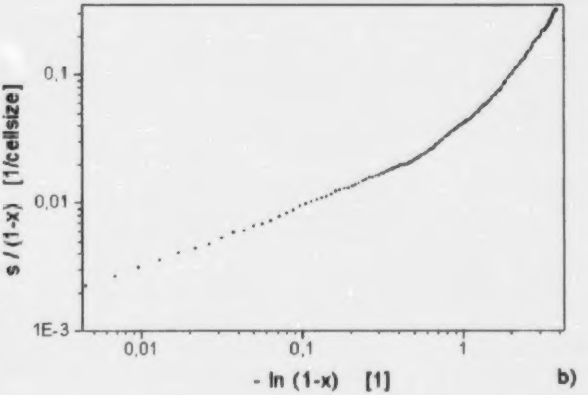

Fig. 2b: Microstructural path (Cahn-Hagel analysis); x: recrystallized volume fraction; s: interfacial area between recrystallized and deformed material.

Fig. 1a shows that nucleation occurs in areas with large accumulated local shear. Lattice curvatures above 15° promote further growth of the new grains. The distribution of the nuclei is very inhomogeneous. Deformation bands with high stored energy and large lattice curvatures reveal clusters of similarly oriented nuclei. The nuclei impinge upon each other and compete at an early stage of recrystallization. Fig. 2 shows that this leads to a substantial deviation (n=1.49) from Avrami–Johnson–Mehl–type kinetics which predicts an exponent of n_{theor}=2 in two dimensions. An important result is the partial recovery of deformed material. Fig 1 shows some areas where moving large angle grain boundaries did not sweep the deformed material. An analysis of the state variables at these coordinates and the grain boundaries involved shows that not insufficient driving forces but insufficient misorientations between the deformed and the recrystallized areas were responsible for this effect (orientation pinning).

F13

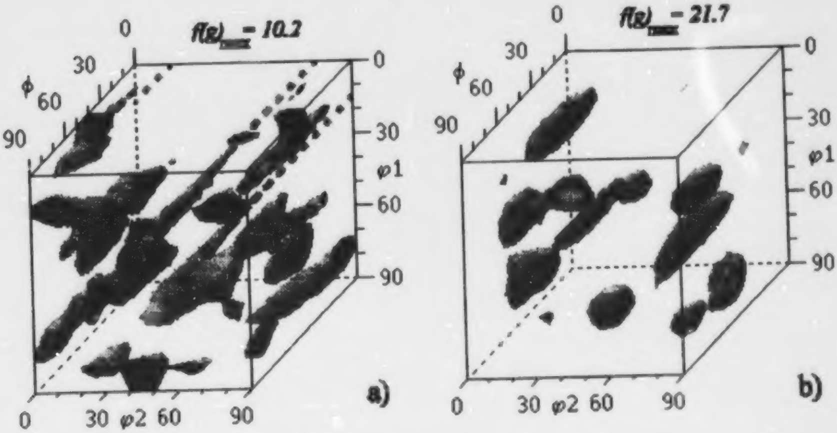

Fig. 3: Starting texture (a) and final texture (b); orientation density above (1/3) $f(\mathbf{g})_{max}$

Fig. 3 shows the textures which were calculated by replacing each orientation by a Gauss function with a scatter width of 3°. In order to emphasize the main texture components in Euler space only areas with an orientation density above (1/3) $f(\mathbf{g})_{max}$ are plotted. The initial texture is characterized by a number of smeared–out texture components, $f(\mathbf{g})_{max}$=10.2. During the annealing treatment most of the scattered components vanish and the texture becomes much sharper, $f(\mathbf{g})_{max}$=21.7. The observed texture change is due to oriented nucleation since all large angle grain boundaries were assumed to have the same mobility.

6. References

Abaqus Users' Manual (1994) Hibbitt, Karlsson and Sorensen, Pawtucket, RI.

Asaro, R. J. (1983) *Adv. appl. Mech.*, Vol. 23, pp. 1–23.

Becker, R. C. (1991) *Acta Metall. Mater.*, Vol. 39, pp. 1211–1230.

Becker, R. C. and Panchanadeeswaran, S. (1995) *Acta Metall. Mater.*, Vol. 43, pp. 2701–2719.

Becker, R. C., Butler, J., Lalli, L. A. and Hu, W. H. (1991) *Metal. Trans.*, Vol. 22A, pp. 45–58.

Becker, R. C. (1998) in: *Hot Deformation of Aluminum Alloys II*, Eds: T.R Bieler, L.A. Lalli, and S.R. MacEwen, TMS, pp. 255-266.

Maze Users Manual (1993) *LSTC Report 1005*, Livermore Software Technology Corp., Livermore, CA.

Peirce, D. Asaro, R. J. and Needleman, A. (1983) *Acta Metall.*, Vol. 31, pp. 1951–1976.

Raabe, D. (1998) in Texture and Anisotropy of Polycrystals, *Mat. Sc. Forum*, ed.: R.A. Schwarzer, Trans Tech Publications, Vol. 273-275, pp. 169–174.

Raabe, D. (1999) *Philos. Mag.*, in press.

Smelser, R. E. and Becker, R. C. (1989) Proc. *Abaqus Users' Conf.*, Strasa, Italy, Hibbitt, Karlsson and Sorensen, Inc., Providence RI, pp. 207.

Turnbull, D. (1951) *Trans. AIME*, Vol. 191, pp. 661–675.

ORIENTATION DEPENDENT STORED ENERGY IN COLD ROLLED CAN-BODY ALUMINUM ALLOY

N. RAJMOHAN and J. A. SZPUNAR
Department of Mining and Metallurgical Engineering, McGill university, Montreal, Quebec, Canada, H3A 2B2

Abstract

Information on the grain orientation dependent stored energy after cold deformation would provide great deal of understanding on the mechanism that controls the primary recrystallization in deformed metals. From the diffraction peaks that are measured using x-rays on 88% cold rolled can body aluminum alloy, stored energy as a function of crystal orientation is calculated. The obtained stored energy values are presented in the form of Stored Energy Distribution Function (SEDF) on Euler angle space similar to the Orientation Distribution Function (ODF). The scatter in the stored energy values as a function of angular deviation is discussed in detail.

Keywords: Stored energy, Deformation, Crystal orientation, SEDF, Line broadening.

1 Introduction

The stored energy is a small percentage of the energy expended in deforming a metal that remains stored in the metal and cause an increase in the internal energy. This increment in internal energy is associated with the defects mainly dislocations generated during deformation. The process of defects production and interaction between defects is expected to be different for different grain orientations. Thus, the stored energy is different for different crystallographic orientations. Various attempts have been made by numerous researchers [1-3] to evaluate the stored energy by measuring the broadening of X-ray and neutron diffraction lines. Though these methods are very useful, they are restricted to a few specific orientations. Kallend and Huang [4] and Rajmohan et al [5] proposed a more general method which can be used to determine the stored energy for a much wider range of orientations using X-ray and neutron diffraction methods respectively. The present work is focused on the determination of stored energy in a can body aluminum alloy which is cold rolled to 88%. The stored energy is also measured in the same specimen that is stress relieved after cold rolling at 200° C for 15 minutes. These measurements are undertaken, aiming to study the mechanism that governs the nucleation and growth of cube texture in this aluminum alloy. One has to understand, however, that the method used in the present work to measure only the inhomogeneous lattice strain energy, which is short-range in nature. The inhomogeneous lattice strains that are caused by the lattice defects such as dislocations and point defects tend to broaden the diffraction peaks and this broadening depends on the anisotropic deformation characteristics of the grains in the polycrystalline matrix.

2 Experimental method

A can body aluminum sheet with a final thickness of ~ 0.3 mm after a cold rolling reduction of 88% is used for the investigation. The chemical composition for AA3104 is 0.15-0.19% Cu, 0.36-0.44% Fe 1.13-1.27% Mg, 0.80-0.94% Mn, 0.17-0.23% Si, <0.03% Cr, <0.03% V and remaining Al. The grain size before the 88% cold rolling is ~20 micrometers. In order to compare the stored energy values before and after stress relieving, the cold rolled specimen is stress relieved at 200° C for 15 minutes. The reference diffraction peaks are obtained from the fully annealed and random powder specimens. In general, the reference specimen could be a fully annealed specimen. If the fully annealed specimen is highly textured, a random specimen prepared from powder is preferable. This random specimen should posses a density very close to that of the conventional polycrystalline material and should be sintered for longer time to ensure no residual stress due to compaction. The fully annealed specimen is obtained by annealing the rolled specimen at 400° C for 30 minutes. The random specimen is prepared from the aluminum powder of average size of ~10 micrometer, compacted and sintered to 550° C in argon atmosphere for over 1 hour. All the specimens were polished to the mid-section and electropolished using standard perchloric acid solution.

For the rolled, stress relieved, fully annealed and sintered specimens {111}, {200} and {220} pole figures were measured using Siemen's texture diffractometer. The orientation distribution function (ODF) (with Bunge's notation [6]) is then calculated using a discrete method proposed by Imhof [7]. The line broadening was measured at points on a polar grid having a spacing of 10° between points for {111} and {200} diffraction. The obtained diffraction curves were then fitted with Gaussian distributions to determine the full width at half-maximum values. The error in the full width at half-maximum value was high for the diffraction peaks with low signal to noise ratio. For the case of low α values, the full width half maximum (FWHM) are about 0.41° ± 0.01 for the 88% cold rolled specimen. The line broadening measurements where made up to an angle of α=80°. The instrumental broadening is corrected using reference specimens. The relevant orientation dependent Young's modulus values and Poisson's ratios are taken from Ref. [8] and [9]. The calculation of the stored energy distribution function is given elsewhere [4,5,10]

3 Results and discussion

The ODFs that are calculated for both rolled and stress relieved specimens are identical. The Fig. 1 shows the ODF of 88% cold rolled can body aluminum specimen. The Figs. 2 are the stored energy distribution functions (SEDFs) of cold rolled and stress relieved specimens. Both Fig. 1 and 2 show the ϕ_2=45°, 65° and 90° sections. The Fig.1 shows a typical Al cold rolled β-fiber texture. In the SEDFs (Fig. 2), the stored energy values are not presented for the orientations that are poorly represented, specifically for the orientations that have values below the random intensity value. These orientations have regions of zero or nearly zero intensities in a highly textured matrix and therefore calculated SEDF will be statistically unreliable. The error in the stored energy values as a function of ODF intensity is similar to the one presented in previous works [4,5,10]. As ODF intensity decreases the error in the stored energy value increases.

The Table.1 summarizes the stored energy values for the important orientations that are commonly observed in both cold rolled and stress relieved aluminum specimens. The rolling texture components of aluminum (such as S, Copper or C and Brass or B) loose part of the stored energy after stress relieving for 15 minutes at 200°C but the magnitude of stored energy reduction is more for cube texture component. The cube texture component has a stored energy of 13.5 J/g-atom after rolling and releases the energy of about 7.2 J/g-atom during stress relieving. The other recrystallization texture components such as Goss (or G) and Cube$_{RD}$ (rotated cube along the rolling direction) reach the lowest stored energy value of 0.01 to 0.1 J/g-atom after stress relieving. In the Table 1 presented above the calculated stored energy values at exact orientations in the orientation space are considered. For example, the stored energy value for the cube orientation is taken at Euler angles ϕ_1 = 0°, Φ = 0° and ϕ_2 = 0°. In practice one would prefer however to identify an ideal texture by accepting a deviation of few degrees from the ideal orientation. To understand the spread in the stored energy, the plots of stored energy (for the 88% cold rolled, $S_{cr}(g)$ and stress relieved, $S_{sr}(g)$ conditions) as a function of angular deviation from the ideal orientations of cube and rolling texture components (C, B and S) are presented in Fig. 3. In these plots the stored energy values are presented for the orientations that have the intensity values higher than 0.6 (refer Fig. 1). The method by which the points in these plots are generated can be explained by taking cube orientation as an example. The scatter plot of cold rolled stored energy for cube orientation is plotted by calculating the misorientation between the cube and any orientation in the Euler angle space (5°×5°×5° discretized) similar to the ODF space. If the calculated misorientation is less than 15° then the selected orientation in the Euler angle space is accepted and the corresponding values of stored energy and the angular deviation (in degree) from the ideal cube orientation are shown in the plot. This method is repeated until all the orientations in the Euler angle space that is discretized as 5°×5°×5° are exhausted. In the case of rolling texture components considerable number of orientations do not release noticeable stored energy during stress relieving.

In Fig. 3, the stored energy S_{cr} values are > ~5 J/mol for the case of cube. Few orientation components of the rolling texture seem to have stored energy (S_{cr}) values < 5 J/mol. The stored energy values in all these cases increase with angular deviation. After stress relieving at 150° C for 15 minutes, the average stored energy value comes down in all the cases. For the case of B and S texture components, most of the points are very close to zero after stress relieving. The spread in the plots shown in Fig. 3 is acceptable because grains undergo different rotations during deformation from the initial orientations to the final orientations. This different 'strain path history' of each grain orientation causes the spread in the stored energy and it is responsible for the highest stored energy fluctuations in the rolling texture components. At the cold rolled condition, considerable number of points for the rolling texture components have stored energies less than 5 J/g-atom, whereas the cube orientation does not show any point less than 5 J/g-atom. The cube orientations seem to have a fairly similar 'strain path history'. After stress relieving the scatter for the cube is found to be between ~2.5 and ~7.5 J/g-atom. As observed in the cold rolled state, the stress relieved state also shows a high spread as is illustrated in the plots for C, B and S-components. Unlike cube orientation, the rolling components show higher concentration of points with stored energy less than 2 J/g-atom after stress relieving.

Table 1 Stored energy values of selected orientation in 88% rolled and stress relieved (200°C, 15 minutes) can-body aluminum sheet AA3104.

Orientation	ϕ_1	Φ	ϕ_2	Intensity	Stored energy (J/g-atom)	
					after deformation	after stress relieving
Cube	0	0	0	1.14	13.6	6.4
Cube(RD)	0	20	0	2	3.6	0.01
Cube(ND)	20	0	0	0.39	7.5	3.0
Goss	0	45	0	2.48	1.9	0.1
Copper	90	30	45	11.28	6.2	5.04
S	60	35	65	9.42	4.7	2.52
R	55	35	60	6.06	4.6	2.64
Brass	35	45	90	10.65	3.2	1.16

4 Conclusion

The stored energy distribution function for the 88% cold rolled and stress relieved (at 200°C for 15 minutes) can body aluminum specimen is calculated from the measured X-ray line broadening data. Though the orientation with less than the random intensity is not presented due to high error values in the stored energy, all other abundantly represented orientations in the matrix do have reliable stored energy values. The spread in the stored energy values for rolling texture components seems to be higher than the cube component.

5 Reference

1. M. Matsuo, S. Hayami and S. Nagashima (1971) *adv. X-ray anal.*, , **14**, 214.
2. H. Takechi, H. Katoh and S. Nagashima (1968) *Trans. AIME*, , **242**, 56.
3. R. L. Every and M. Hatherly (1974) *Texture*, **1**, 183.
4. J. S. Kallend and Y. C. Huang (1984) *Met. Sci*, **18**, 381.
5. N.Rajmohan, Y.Hayakawa, J.A.Szpunar and J. H. Root (1997) *Acta mater.*,**45**, No.6.
6. H. J. Bunge: '*Texture Analysis in Materials Science - Mathematical Methods*', Translated by P. R. Morris (1982) London, Betterworths

7. J. Imhof (1982) *Textures and Microstructures*,**4**,189. *Textures and Microstructures*, (1982), **5**, 73, *Phys. Stat. Sol.* (1983), (**B**) **120**, 321.
8. W.J.M. Tegart (1966) '*Elements of Mechanical Metallurgy*', 91;, The Macmillan Company, New York.
9. C.S. Barrett (1952) '*Structure of metals, crystallographic methods principles and data*', 2^{nd} Edition, 532;, New York, McGraw-Hill.
10. N.Rajmohan, and J.A.Szpunar (1999) *Mat. Sci and Tech.* in press.

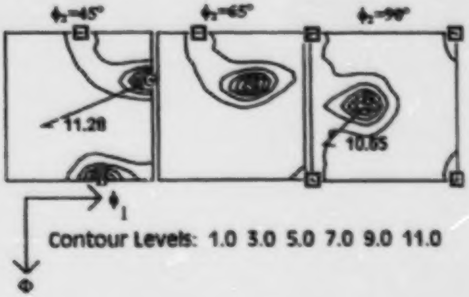

Fig. 1 **Sections of orientation distribution function (ODF) of 88% cold rolled Can-body Al alloy AA3104. The cube (□) and rolling components C,B and S are marked on the ODF sections.**

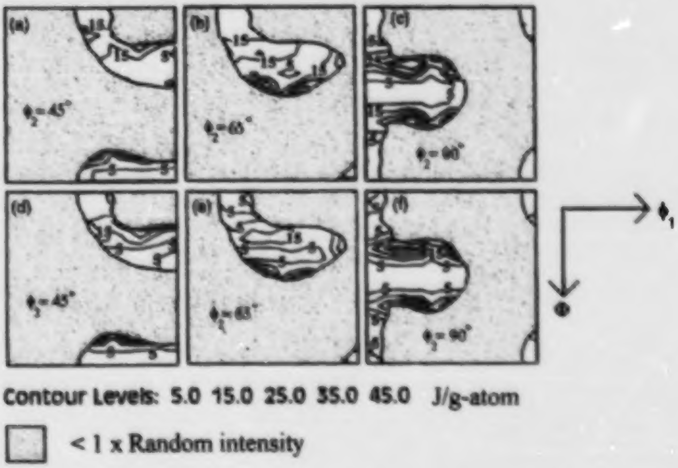

Fig. 2 **Stored energy distribution function for (a, b & c) 88% cold rolled and (d, e & f) 150° stress relieved aluminum AA3104 alloy. Here ϕ_2 = 45°, 65° and 90° sections are presented.**

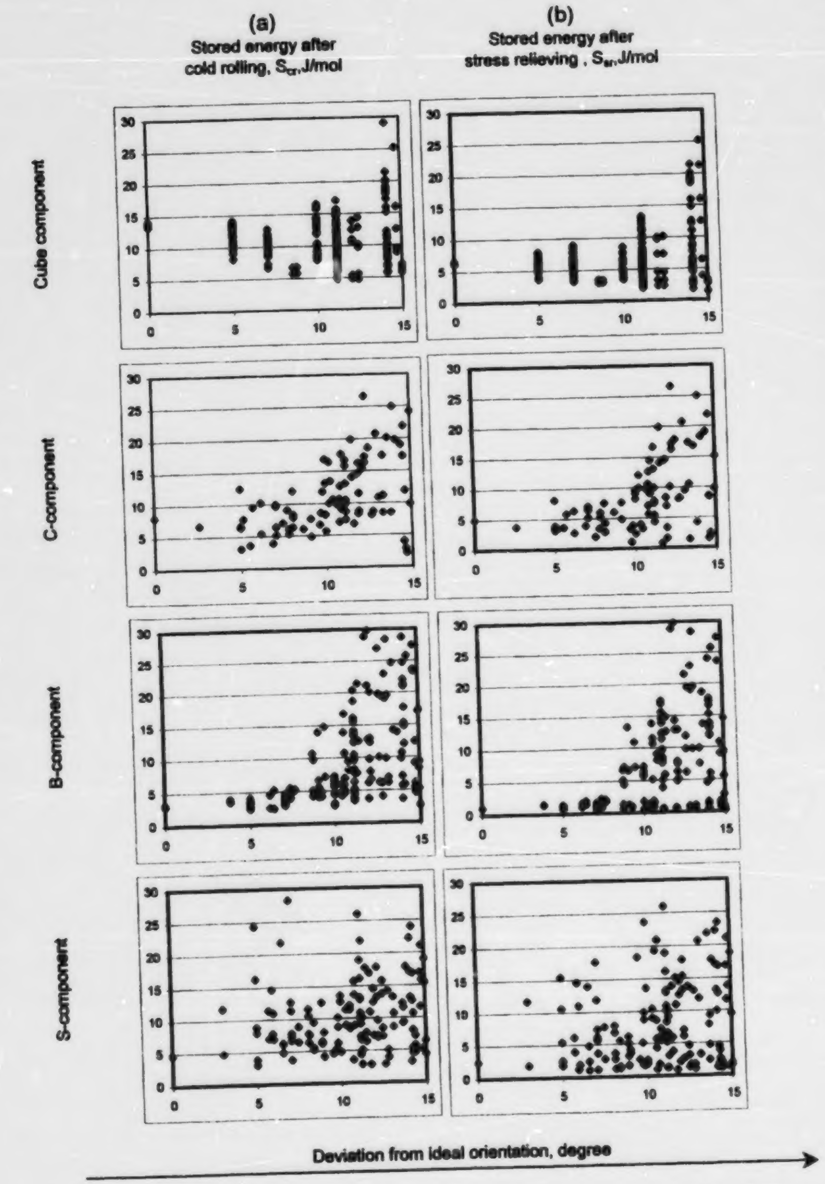

Fig. 3 Plots showing the observed spread in the measured stored energy values of Al AA3104 (a) after 88% cold rolling S_{cr} (b) after stress relieving S_{sr}

RANDOMIZATION OF THE ANNEALING TEXTURE IN ALUMINUM 5182 SHEET

M.Y. HUH and Y.H. KIM
Division of Materials Science and Engineering, Korea University, Seoul 136-701, Korea
O. ENGLER
Los Alamos National Laboratory, Center for Materials Science, Los Alamos, NM 87545, USA

Abstract

In order to obtain a randomization of the annealing texture in aluminum 5182 sheet, the normal cold rolling texture was modified by cross-rolling. The β-fiber orientations that formed through the preceding normal cold rolling are unstable under cross rolling conditions. Rather, preferred orientations with {011}//ND (α-fiber) developed. A proper control of the respective reduction degrees before and after the cross rolling led to the formation of strong orientation densities along the α-fiber. After annealing the cross-rolled samples depicted a very weak, almost random recrystallization texture. This texture randomization is explained by a suppressed nucleation and growth of the {001}<100> cube-orientation which prevails in normally rolled and recrystallized Al-sheets. Because of the resulting homogeneous planar anisotropy ($R \approx 1$) of randomly textured sheets, a better sheet formability is to be expected than in sheets with a pronounced cube-texture.

Keywords: cross rolling, recrystallization, texture randomization, AA5182

1. Introduction

Under the potential Al-alloys for substituting steel sheets in automobile body applications, 5xxx series alloys stand out by high strength, high ductility, high corrosion resistance and fairly good weldability. However, even though Al-alloys show high ductility during tensile tests, their properties during sheet forming operations, i.e. deep drawing, stamping or cupping, are generally quite poor. This is the result of an unfavorably low planar anisotropy (Takeshima et al., 1993) – i.e. a low value of the Lankford parameter R – which is attributed to the characteristic cube-recrystallization texture of annealed Al-sheets (Hirsch and Hasenclever, 1991; Engler et al., 1996a).

In this paper we report results of an ongoing study to improve the formability of sheets of the Al-alloy 5182 by realizing random annealing textures. When the texture of a metallic sheet is completely random, the sheet displays planar isotropy, i.e., R=1.0. A randomization of the recrystallization textures was accomplished by applying an additional step of cross rolling during the deformation. Cross-rolling in this work is referred to as a procedure in which the rolling direction (RD) is rotated only once by 90° during the rolling procedure (e.g. Huh et al., 1995). Thus, after the cross rolling, the new RD2 corresponds to the old transverse direction (TD). The respective reduction degrees before and after the change in rolling direction were optimized by Taylor-type simulations so as to yield optimum modification of the original rolling texture.

2. Experimental Procedure

In the present study, a hot band with a thickness of 6.5mm of the commercial aluminum alloy 5182 (Al-4.5%Mg-0.8%Mn) was used. The material had a nearly random texture and an average grain size of 30µm. The hot band was cold rolled using a laboratory mill with a roll diameter of 127mm under lubrication to a thickness of 1.625mm, corresponding to a thickness reduction of 75% and a true strain of $\varepsilon_1=1.38$. Subsequently, specimens taken from this sheet were further rolled under an angle of 90° to the former rolling direction, RD1. These specimens were deformed by an additional deformation of 20% ($\varepsilon_2=0.22$), 40% ($\varepsilon_2=0.49$), 60% ($\varepsilon_2=0.92$), or 80% ($\varepsilon_2=1.61$) to a total thickness reduction of 80% ($\varepsilon_t=1.61$), 84.5% ($\varepsilon_t=1.87$), 90% ($\varepsilon_t=2.30$), or 95% ($\varepsilon_t=3.0$), respectively, while maintaining the new RD2. After the deformation, the specimens were recrystallization annealed under hydrogen atmosphere for 1h at 400°C.

The crystallographic textures of the sheets were determined by conventional X-ray texture analysis followed by ODF calculation (Bunge, 1982). Optical microscopy and TEM were employed to characterized the development of the microstructure after deformation and recrystallization.

3. Results and Discussion

3.1 Rolling experiments

It was expected that a greater modification of the normal rolling texture by means of the cross rolling leads to a greater deviation from the normal recrystallization texture. Accordingly, the cross rolling schedule was first optimized by numerous texture simulations based on the Taylor full constraint model (Taylor, 1938). Fig. 1 shows results of the Taylor-simulations in the form of {111} pole figures; the ODFs of the corresponding experimental deformation textures are given in Fig. 2. As mentioned in Sec. 2, the rolled sample was rotated once by 90° after 75% thickness reduction. Accordingly, the rolling texture was simulated from 729 (initially random) orientations to a thickness reduction of 75% ($\varepsilon=1.38$; Fig. 1a). This resulted in a typical Al-rolling texture which is characterized by the development of preferred orientations along the β-fiber running from the Cu-orientation {112}<111> over the S-orientation {123}<634> to the Bs-orientation {011}<211> (Fig. 1a, 2a; see Hirsch and Lücke, 1988). Then, the rolling texture (Fig. 1a) was rotated by 90° around the ND and the texture evolution was further simulated up to total reductions of 80, 84.5 or 95% while maintaining the new RD2 (Fig. 1b-d).

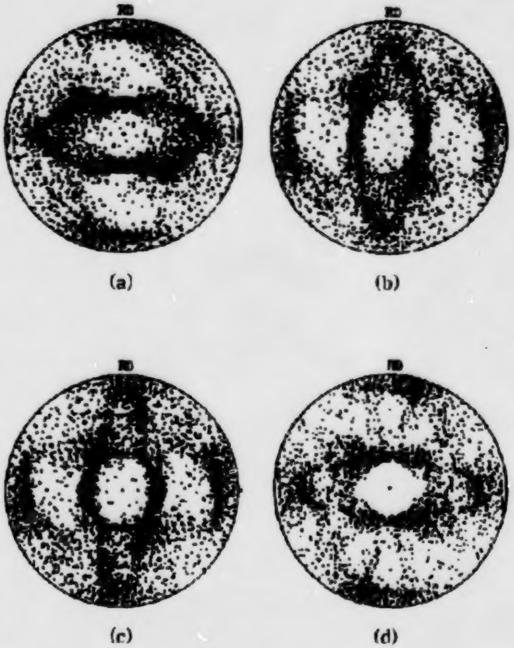

(a) (b)

(c) (d)

Fig. 1: {111} pole figures of the texture simulations according to the Taylor deformation model. (a) 75% total def. (ε_1=1.38, ε_2=0), (b) 80% total def. (ε_2=0.22), (c) 84.5% total def. (ε_2=0.49), (d) 95% total def. (ε_2=1.61).

The texture simulated for a total reduction of 80% (Figs. 1b, 2b) is similar to the (rotated) straight rolled texture (Figs. 1a, 2a). This is due to the rather small additional deformation applied after the cross rolling. After a total reduction of 84.5%, the simulated texture was entirely changed, in contrast (Figs. 1c, 2c). Here, a pronounced distribution of orientations with <110> axes parallel to the ND was observed, which means that a strong α-fiber has developed. After the change in rolling direction the Cu- and S-orientation are highly unstable in the new sample coordinate system, so that they rapidly rotate away. The Bs1-orientation, however, is only 20° away from the Bs2-orientation

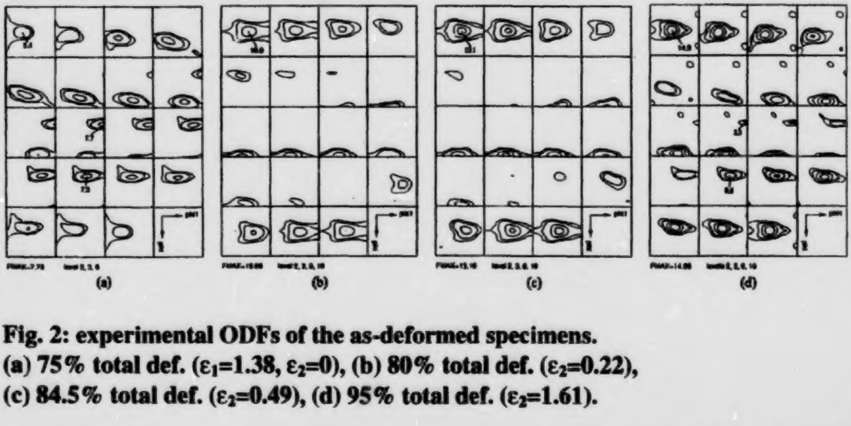
(a) (b) (c) (d)

Fig. 2: experimental ODFs of the as-deformed specimens.
(a) 75% total def. (ε_1=1.38, ε_2=0), (b) 80% total def. (ε_2=0.22),
(c) 84.5% total def. (ε_2=0.49), (d) 95% total def. (ε_2=1.61).

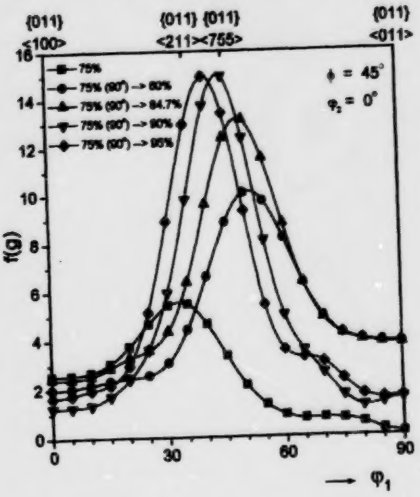

Fig. 3: α-fiber plot of the as-deformed specimens.

in the new sample frame (Engler and Lücke, 1991). Likewise, the 90°ND rotation applied through the cross rolling transforms the other orientations along the α-fiber orientation into orientations which again come to lie along the α-fiber. Upon further deformation these orientations rotate along the α-fiber towards the new Bs2-orientation before they eventually tend to rotate along the β-fiber towards the final rolling texture components S and Cu (Hirsch and Lücke, 1988). This may account for the strong intensities along the α-fiber observed in the cross rolled specimens (Fig. 2b, c).

The simulated texture after a total reduction of 95% is shown in Fig. 1d. In this case, the additional strain after the rotation (ε_2=1.61) was sufficiently large to form a texture similar to the straight rolled texture (Figs. 1a, 2a, 2d).

As evident from Fig. 2, the textures of the cross-rolled specimens can be characterized by the development of preferred orientations with {011} parallel to the ND. Fig. 3 shows the evolution of the deformation textures by plotting the orientation density along this α-fiber. The maximum in the normally rolled specimen is found at φ_1≈35°, corresponding to the Bs1-orientation {011}<211>. In the cross-rolled specimen deformed to the total reduction of 80%, 84.5%, 90% and 95%, the texture maximum is found at angles φ_1 of 52°, 49°, 44° and 41°, respectively. This decrease in φ_1 reflects the continuous rotation of the (rotated) α-fiber-orientations towards the Bs2-orientation at φ_1=35°.

3.2 Recrystallization experiments

Fig. 4 shows the evolution of the texture after recrystallization annealing at 400°C for 1h. After annealing of both the straight rolled specimen and the cross-rolled specimen that was deformed to a total reduction of 95%, the well-known copper recrystallization texture developed (Fig. 4a, d). Preferred cube-orientations with maximum texture intensities of $f(g)$≈5 were obtained. Furthermore, the textures comprised orientations along {001}//RD as well as some remainders of the rolling texture β-fiber, which are commonly summarized as R-orientation (Engler et al., 1996a). In the cross rolled specimens deformed to a total reduction of 80% or 84.5%, in contrast, much weaker, almost random recrystallization textures formed (Fig. 4b, c). Again, some intensities close to cube-orientation were observed, but the maximum orientation density did not exceed $f(g)$=2.7.

The results displayed in Fig. 4 show that the applied cross-rolling was indeed very efficient in accomplishing a randomization of the annealing texture in Al 5182 sheets.

There are two effects on how the cross-rolling can affect the recrystallization and lead to a random annealing texture, which will now be discussed.

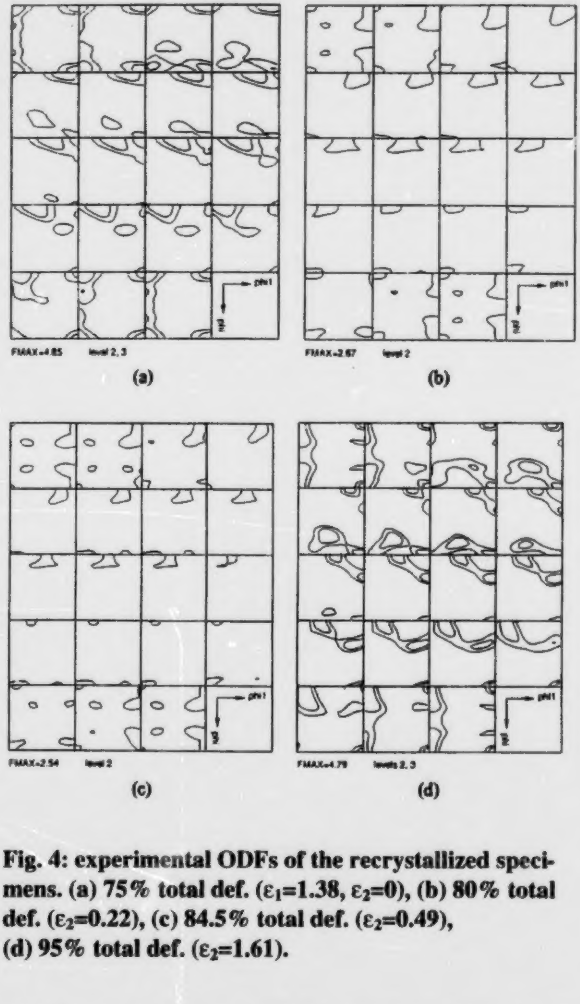

(a) (b)

(c) (d)

Fig. 4: experimental ODFs of the recrystallized specimens. (a) 75% total def. (ε_1=1.38, ε_2=0), (b) 80% total def. (ε_2=0.22), (c) 84.5% total def. (ε_2=0.49), (d) 95% total def. (ε_2=1.61).

(i) The cube-orientation, the main recrystallization texture component of many Al-alloys, is generally assumed to nucleate at the so-called cube-bands, i.e., band-like structures comprising cube-oriented subgrains which exist already in the as-deformed state (Hjelen et al., 1991; Engler et al., 1996b). After rotating the sample coordinate system by 90° around the ND, the cube-orientations within the cube-bands are principally not affected. However, examinations of the dislocation structures by TEM revealed that the microstructure in the cross-rolled specimens was quite different from that observed in the straight rolled specimen. Since the stress and the strain state before and after rotating the rolling direction are different, the cube-bands that had formed in the straight rolled specimen are microstructurally unstable under the new conditions. Accordingly, it is anticipated that the number of cube-oriented nuclei is reduced, which presumably leads to the very weak cube-textures obtained in the cross-rolled specimen (Fig. 4b, c). In the specimen with the highest total deformation, 95%, the deformation after the cross rolling was then obviously again high enough to re-build sufficient cube-nuclei so as to account for the well-defined cube-recrystallization texture found in that specimen (Fig. 4d).

(ii) Cube-oriented grains are known to have a preferable growth prospect into grains in the cold rolling texture components (Juul Jensen, 1997; Engler, 1998). However, the texture of the cross rolled specimen seems to have no preferred growth relationship with the orientations of recrystallization nuclei. Thus, it is concluded that the lack of both oriented nucleation and selected growth led to the randomization of the recrystallization texture in the cross rolled specimens.

4. Conclusions

A randomization of the annealing texture in Al 5182 sheet was obtained by a modification of the rolling procedure, viz. by cross-rolling. The rotated β-fiber orientations formed through the cross rolling are unstable upon rolling in the new rolling direction. The texture of the cross-rolled specimens was characterized by the development of preferred orientations with an ND of {011}. The evolution of an almost random texture during a subsequent recrystallization annealing was explained by a lack of both oriented nucleation and selected growth in the cross-rolled specimens.

Acknowledgments

Part of this work was supported by the Korean Ministry of Education through the Advanced Materials Program in 1997. One of the authors (O.E.) likes to acknowledge financial support given by the U.S. Department of Energy and by the Alexander von Humboldt-Foundation (Germany) through a Feodor Lynen Research Fellowship.

References

Bunge, H.J. (1982). Texture Analysis in Materials Science, Butterworths, London.
Engler, O. (1998). *Acta mater.*, vol. 46, pp. 1555-1568.
Engler, O. and Lücke, K. (1991). *Textures and Microstructures*, vol. 14-18, pp. 727-732.
Engler, O., Vatne, H.E. and Nes, E. (1996a). *Mater. Sci. Eng.*, vol. A205, pp. 187-198.
Engler, O., Yang, P. and Kong, X.W. (1996b). *Acta mater.*, vol. 44, pp. 3349-3369.
Hirsch, J. and Hasenclever, J. (1991). In *Proc. ICAA3*, ed. by L. Arnberg et al., the Norwegian Inst. of Tech, Trondheim, Norway, Vol. II, pp. 305-310.
Hirsch, J. and Lücke, K. (1988). *Acta metall.*, vol. 36, pp. 2863-2904.
Hjelen, J., Ørsund, R. and Nes, E. (1991). *Acta metall. mater.*, vol. 39, pp. 1377-1404.
Huh, M.Y., Engler, O. and Raabe, D. (1995). *Textures and Microstructures*, vol. 24, pp. 225-237.
Juul Jensen, D. (1997). *Metall. Mater. Trans.*, vol. 28A, pp. 15-25.
Takeshima, Y., Hikida, T. and Uto, H. (1993). *Sumitomo Light Metal Tech. Report*, vol. 34, pp. 59-65.
Taylor, G.I. (1938). *J. Inst. Metall.*, vol. 62, pp. 307-324.

THE EFFECT OF STRAIN PATH ON TEXTURE DEVELOPMENT IN ALUMINIUM

R.L.HIGGINSON
IMMPETUS Department of Engineering Materials, The University of Sheffield, Sheffield. UK.

Abstract

The effect of simple strain paths on the deformation behaviour, recrystallisation kinetics and texture development in an aluminium-1%manganese alloy has been investigated. The deformation was carried out using compression tests with the path change being achieved by rotating the specimen through 90° following the first deformation. It was found that there is a decrease in the flow stress on reloading compared with material deformed uniaxially. The strain path change also retarded the recrystallisation kinetics with the time for 50% recrystallisation being approximately doubled following the strain path change. The recrystallised grain size was also affected by the path change with a larger grain size seen in the material under a strain path change. The texture development was also studied after both deformation and recrystallisation. The as-received texture, which consisted mainly of rotated cube, was strengthened during deformation regardless of the strain path. During deformation the Goss component was also seen to develop and regardless of the deformation path remained stable. A third unstable component, approximately {111}<112>, was formed during uniaxial compression but diminished in strength when the strain path was changed. The recrystallised textures were similar to the deformed textures.

Keywords: Strain path, texture, aluminium, deformation, recrystallisation

1 Introduction

The effect of the strain path change on the flow stress of the material was first reported by Bauschinger (1881). When deformation was fully reversed, i.e. from tension to compression the flow stress dropped on the second deformation compared with material deformed monotonically. Similar results have been reported by other authors (Zhu and Sellars 1996). Reversals also affect the recrystallisation kinetics of the material, with material subjected to a change in strain path showing retarded recrystallisation kinetics compared with those deformed monotonically (Lindh *et al.* 1993). Cowan *et al.* (1995) found that the time for 50% recrystallisation depended not only on the extent of the strain path change, with a complete reversal giving retardation of the recrystallisation kinetics than samples deformed monotonically, but also that an increase in the strain diminished the effect. A small number of papers have also studied the effect of strain path of texture. Bacroix and Hu (1995) studied the effect of simple shearing on the texture development of low carbon steel sheet. They found that the starting texture was partially stable during deformation mainly due to the pre-existing rolling texture which is stable during simple shear.

During most industrial metal forming processes the material undergoes a complex strain history. In the relatively simple process of flat rolling, for example, the material near the surface undergoes reverse shearing due to the interaction of the metal with the rolls, which is superimposed on a plane strain compression. This leads to complex strain histories with the strain being only partially reversed. These complex strain path changes can affect the mechanical properties as well as the recrystallisation kinetics (Higginson and Sellars, 1997) and make microstructural predictions difficult, with the recrystallisation kinetics, grain size and varying across the section (*Pinna et al.* 1998). Because of the complexities involved in the study of strain path during industrial forming processes, the current paper studies the effects of simple strain path changes using partial reversals closer to those seen in rolling. Their effects on the mechanical behavior, recrystallisation behaviour and texture development have been studied in an aluminium-1%Mn alloy.

2. Experimental Procedure

The material used in this study was aluminium-1.02wt%Manganese with 0.35%Fe and trace amounts of other elements. The material was experimentally hot rolled plate with a thickness of 30mm produced by Alcan International, Banbury. Samples, approximately 8x8x8mm,were electron discharge machined from the centre of the plate where the microstructure is most homogeneous.

The samples were deformed at room temperature under compression using a servo-hydraulic machine. The machine recorded load-displacement curves which were then converted to stress-strain curves. The specimens were compressed between tool steel platens with layers of PTFE and oil used as a lubricant. The deformation tests carried out are depicted schematically in deviatonic strain space in Fig. 1.

The first uniaxial compression parallel to Z of ε_{ZZ}=0.2 gives point A in Fig. 1a. A second uniaxial compression parallel to Z to ε_{ZZ}=0.4 strain gives point B. A strain of ε_{ZZ}=0.2 followed by ε_{XX}=0.2 gives point C in Fig. 1a. This gives a strain path change of 120° in strain space. A further compression parallel to face Y was also carried out which gives a strain path back to the origin, 0 in figure 1a. Deformation structures and texture were examined and samples were annealed in a salt bath at 400°C for different times to study the recrystallisation kinetics and texture. Following deformation and/or annealing, samples were carefully cut into small slices, with special care taken to minimise any further deformation, and were prepared metallographically. The recrystallised fractions in each of the annealed samples were measured using point counting about 300 points per sample.

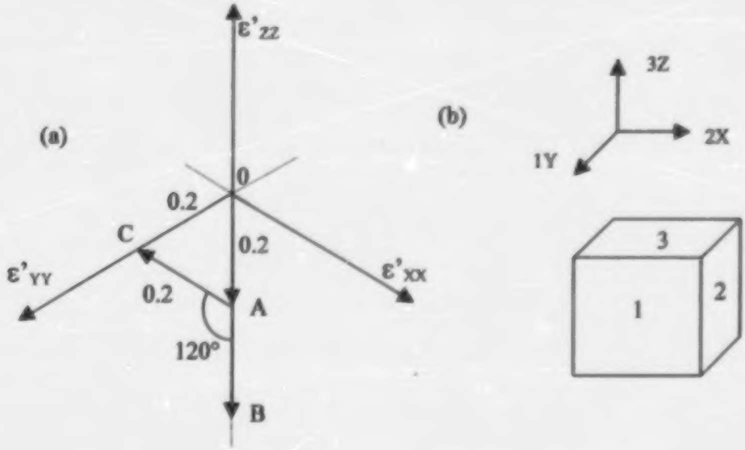

Fig. 1: A graphical representation of the strain paths used in this study (a) with the vectors represented by the cube faces in (b).

The textures of the deformed and fully recrystallised material were measured using x-ray diffraction. The textures were measured as 111, 200, 220 and 311 incomplete pole figures in a modified Siemens goniometer. The Orientation Distribution Functions (ODFs) were produced by determining the harmonic coefficients using a least squares method to a truncation of L=22. The textures are presented as constant φ_2 sections, with φ_2 equal to 0° and 45°, and with contours in multiples of random density.

3 Results and Discussion

3.1 Deformation and recrystallisation

The mechanical testing results are shown in Fig. 2 for all of the tests. The line of the test to a strain of approximately 0.2 follows that of the test to the higher strain of 0.4, indicating the degree of reproducibility. The ends of these tests are marked A and B and are equivalent to the positions in Fig. 1a. The first part of the 120° strain path test follows the path of the curves to 0.2 and 0.4. Following the unload and reload, however, there is a drop in the work hardening rate of the material and the second part of the curve is below that of the uniaxial test and the final stress is lower, indicated by point C. The strain path therefore gives a reduction in the flow stress of the material as has been seen by other authors (Zhu and Sellars 1997).

This difference also affects the recrystallisation behavior of the material. From the metallographic recrystallisation data, the times for 50% recrystallisation (t_{50}) were calculated and these, and the recrystallised grain sizes, are shown in table 1. The t_{50} value for the sample following a strain path change is more then double that of the sample deformed to the same strain uniaxially. These results are similar to those found by Lindh *et al.* (1993) for a full reversal. This effect on the recrystallisation kinetics shows that the strain path change is affecting the stored energy in the material. This reduction in the stored energy, due to the strain path change, also affects the recrystallised grain size, table 1.

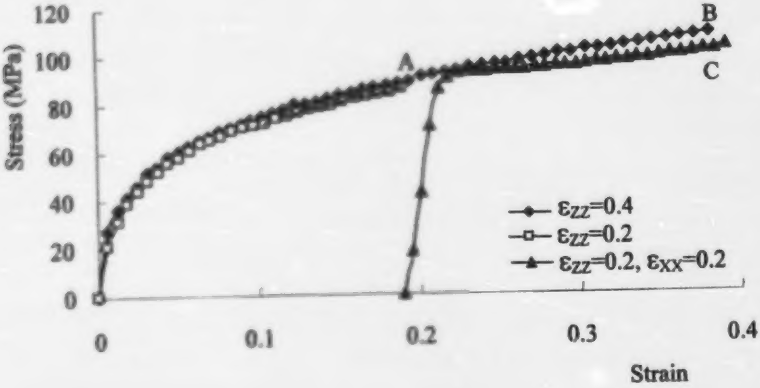

Fig. 2: Stress-strain curves for the material deformed uniaxially $\varepsilon_{ZZ}=0.4$ and $\varepsilon_{ZZ}=0.2$ followed by $\varepsilon_{XX}=0.2$ (see Fig. 1).

Table 1: Times for 50% recrystallisation and recrystallised grain sizes for samples deformed to the same equivalent strain either uniaxially or with a strain path change of 120°.

Sample	t_{50} (s)	Recrystallised grain sizes (µm)
Uniaxial	15	70
SP120°	40	144

The difference in the stored energy effects the number of nuclei operating, giving a much larger grain size in the material subjected to a strain path change than material strained to the same strain uniaxially. If site saturation is assumed, then the change in strain path reduces the local stored energy, which affects the nucleation, more than the total stored energy, which affects growth. Hargreaves *et al.* (1963) who measured the stored energy using calorimetry also reported the reduction in the stored energy on reversal. This situation is supported by the evidence found by *Hasegawa et al.* (1986) who showed that sub-structures dissolved on a strain reversal.

3.2 Texture Development

The starting texture is shown in Fig. 3a. The material shows a weak texture distribution mainly around (001) or Z rotated cube. Following a uniaxial deformation to a strain of 0.2, Fig. 3b, the texture is predominately Z rotated cube {001}<110>, Goss {110}<001> but with an extra component at approximately {111}<112>. With an increase in the strain in the same direction, this third component is strengthened, Fig. 3c. Following the change in strain path, Fig. 3d, the strength of the texture component at {111}<112> is diminished and the texture is predominately Z rotated cube. This {111}<112> component therefore appears to be 'undone' and the texture is closer to that of the starting material, though with the addition of the Goss component. This is similar to the results of Bacroix and Hu (1995) who showed that the starting texture was partially stable.

By a final compression of 0.2 parallel to Y then the strain path will return to the origin in Fig. 1. The texture at this point is shown in Fig. 3e. The main components present are rotated cube and Goss which have decreased in strength compared with those at point C, with some other minor components also present. As would be expected therefore, the initial texture is not restored when the strain path is taken back to the origin.

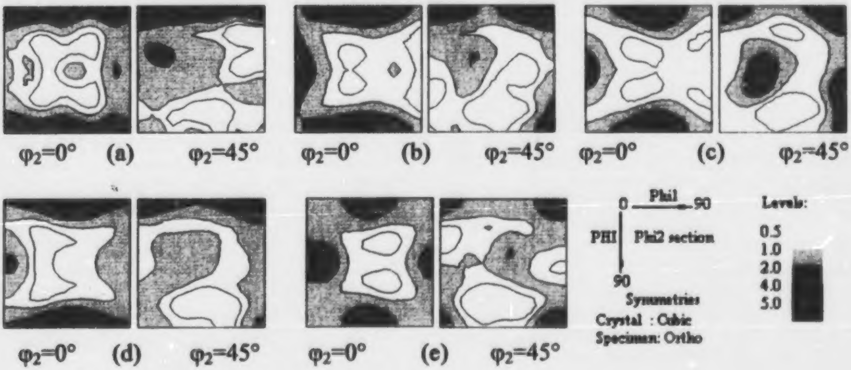
φ_2=0° (a) φ_2=45° φ_2=0° (b) φ_2=45° φ_2=0° (c) φ_2=45°

φ_2=0° (d) φ_2=45° φ_2=0° (e) φ_2=45°

Fig. 3: ODF sections φ_2 =0° and 45° for (a) the as received material (b) the material deformed parallel to Z, ε_{ZZ}=0.2, (c) to a strain of ε_{ZZ}=0.4 parallel to Z, (d) ε_{ZZ}=0.2 parallel to Z then ε_{XX}=0.2 parallel to X giving a strain path change of 120° and (e) ε_{ZZ}=0.2, ε_{XX}=0.2 followed by ε_{YY}=0.2 giving position 0 in Fig.1.

The textures of the recrystallised material were also measured and these are shown in Fig. 4. The textures are similar to those seen in the deformed material with the uniaxial sample showing Z rotated cube, Goss and the {111}<112> component. The sample subjected to a strain path has a weaker {111}<112> component with the texture consisting mainly of Z rotated cube and Goss. The recrystallisation texture in this material under these deformation conditions follows that of the deformed material, see Fig 3. The strain path is thus affecting not only the deformation texture but ultimately the recrystallised textured.

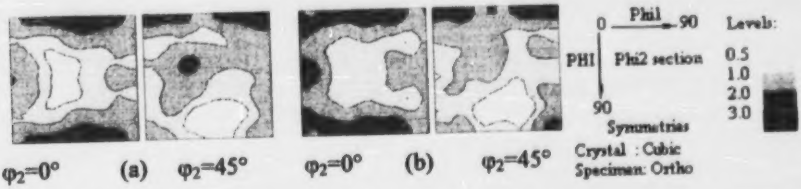

$\varphi_2=0°$ (a) $\varphi_2=45°$ $\varphi_2=0°$ (b) $\varphi_2=45°$

Fig. 4: Recrystallised textures of (a) material deformed parallel to Z to $\varepsilon_{ZZ}=0.4$ and (b) deformed parallel to Z to $\varepsilon_{ZZ}=0.2$ then deformed parallel to X to $\varepsilon_{XX}=0.2$ giving a strain path change of 120°.

Conclusions

The strain path by which the material is deformed affects the flow stress, recrystallisation kinetics, recrystallised grain size and texture. A change in the strain path by 120° leads to retarded recrystallisation kinetics and a larger recrystallised grain size compared with material deformed uniaxially. Certain texture components, Z rotated cube and Goss, are either formed or remain stable regardless of the strain path. However the other component present, {111}<112> appears to be unstable and reversible as the straining is partially reversed.

References

Bacroix, B. & Hu, Z. (1995) Texture evolution induced by strain path changes in low carbon steel sheets. *Mat.Mater Trans*. A. Vol. 26A pp. 601-613.
Bauschinger, J., (1881) *Zivilinger*. Vol. 27, pp 289-347
Cowan, J.R., Higginson, R.L., Hutchinson, W.B. & Bate, P.S., (1995) Recrystallisation following non-proportional straining in aluminium. *Mater. Sci. Tech*., Vol 11, pp.1104-1109.
Hargreaves, M.E., Loretto, L., Clarebrough, L. & Segall, R.L., (1963*) NPL Symposium No. 15 London, HMSO* pp.209-215
Hasegawa, T., Yalou, T. & Kocks, U.F., (1986) Forward and reverse re-arrangement of dislocations in tangled walls. *Mater.Sci.Eng*., Vol 81, pp. 189-199.
Higginson, R.L., & Sellars, C.M., (1997) The effect of strain path during hot rolling on the recrystallisation kinetics of 316 stainless steel. *Proc. Thermec 97 Int Conf. On Thermomechanical processing of steel and other materials, The Minerals, Metals and Materials Soc*., Warrendale, Pa,USA,Vol 1, pp.779-785.
Lindh, E., Hutchinson, B. and Ueyama, S. (1993) Effect of redundent deformation on recrystallisation behaviour of copper, *Scripta Metall. Mater*., Vol. 29, pp. 347-352.
Pinna, C., Higginson, R.L. and Beynon, J.H. (1998) Uncertainties in modelling the evolution of crystallographic texture during hot rolling. *9th Symp. Modelling of metal rolling processes, The Institute of Materials, London, UK.*
Zhu, Q. & Sellars, C.M. (1996) Effect of deformation paths on static recrystallisation behaviour in an Al-2Mg alloy. *Proc. 3rd Int. Conf. On Recrystalliation and Related Phenomena (ReX'6), California, ed T.R. McNelly et al., Monterrey Inst. Of Advanced Studies, USA, 1997*, pp. 195-202.

TEXTURE EVOLUTION DURING CONTINUOUS RECRYSTALLIZATION OF ALUMINUM ALLOYS

J. LI[*], H. JIN, F. SEKI[**], S. SAIMOTO

Department of Materials and Metallurgical Engineering, Queen's University,
Kingston, ON., K7L 3N6 CANADA
[*] Fibics Inc., 568 Booth St., Suite 224, Ottawa, ON., K1A 0G1 CANADA
[**] Department of Materials Science, Tokyo University, Bunkyo-ku, Tokyo, 113 JAPAN

Abstract

Continuous recrystallization offers grain growth studies with a large interfacial driving force since the grain size is an order of magnitude smaller than those from conventional microstructures. In this study the texture and grain size evolution have been simultaneously examined on the same specimen as function of anneal times. Depending on the specimen, the volume fraction of the texture component can vary widely but the grain growth appears to follow the same kinetics. Although monoclinic rather than orthorhombic symmetry was imposed, it appears that to quantitatively examine the subtle textural changes during annealing requires the application of triclinic symmetry.

Keyword: Continuous recrystallization, ODF, grain growth, texture components

1 Introduction

The processes of discontinuous (DCREX) and continuous recrystallization (CREX) according to quantitative textural analysis was first investigated by Hirsch and Lücke (1985). From the examination of the orientation distribution function (ODF) mapping and the volume fractions of the texture components, the mappings and pole figures of the 95 % as-rolled Al, with 0.007 wt % Fe which was the prime impurity, were correlated to those of samples recrystallized at various temperatures. The presence of similarities were taken to indicate the occurrence of CREX. Recently Saimoto et al. (1996) showed that, although heterogeneous nucleation of new grains were clearly evident during DCREX , homogeneous nucleation of very fine grains of the order less than 2 μm were found within the entire region of a deformed crystallite. Furthermore this phenomenon of fine grained CREX only occurred when the Fe impurity content was less than 1 ppm atomic. Subsequent studies showed that when the Fe impurity was reduced below 0.20 ppm atomic, dynamic recrystallization (DYREX) took place at room temperature (Jin et al. 1999). Moreover DYREX by rolling generated a very unsymmetrical texture that needs to be analyzed by triclinic symmetry.

For the present study, a more simple case was found in the industrial capacitor grade Al foil whereby the as-rolled texture correlate very well to previous studies (Hirsch and Lücke, 1985; Ito et al. 1983) although the ODF has to be treated using monoclinic symmetry to account for the asymmetry of the intensities (Saimoto et al. 1993). Moreover the grain growth characteristics has previously been studied (Seki et al. 1998). Hence aside from the deformation texture, the subtle changes during annealing can be followed due to the separation of copper and S-components to their respect Cu_1, Cu_2, S_1 and S_2 using monoclinic symmetry.

2 Experimental Procedure

The starting material was industry supplied hot mill slab 8 mm thick. The 500 mm thick Al ingot of composition in ppm wt. of 16Fe-19Si-25Cu-3Mn-13Zn was scalped, prior to homogenization at 600 °C and hot rolling followed by controlled slow cooling to precipitate out the Fe. The grain growth rate suggests that the amount of Fe content in the matrix is below 0.20 ppm atomic but above 0.02. This as-received 8 mm slab was cold rolled to 110 μm (98.6% reduction) using 320 mm dia. rolls and by reversing the entry ends (Seki et al. 1998). The four pole figures, {111}, {200}, {220} and {113}, were taken as described elsewhere and analyzed using the Van Houtte software (Saimoto et al. 1993). All the anneals were performed in a programmable hot stage (Saimoto et al. 1996) wherein the sample temperature was directly measured to ±0.2 °C. For metallographic observations the rolling surface was first electropolished and examined by electron channeling contrast (ECC) in the JEOL-840 SEM. The grain sizes, D, were measured from the ECC images using two tilt angles to eliminate ambiguities of the existence of interfaces and applying the intercept method described in ASTM E112.

3 Results

The differences between the (111) and (200) pole figures for the as-rolled surface and that after about 10 μm removed for these samples are small, this is probably due to the care exercised to insure that the rolling passes were within those recommended for homogeneous deformation. However the more diffuse nature of the as-rolled surface is attributed to the expected surface damage layer of less than 5 μm, keeping in mind that the penetration depth of the X-rays is about 30 μm and larger depending on the diffraction angle. Comparisons of the (111) and (200) plots with previous authors, Ito et al. (1983) and Hirsch and Lücke (1985) respectively, show the same general features.

The microstructure of the as-rolled surface after about 10 μm is removed is shown in Fig. 1. Note that the grain structure appears to be dynamically recrystallized. Previous work on electrical conductor grade Al with the matrix purity estimated to be 0.31 ppm atomic showed that the as-rolled structure was distinctly not recrystallized. Upon annealing for 3 min at 220 °C, however, it transformed to a structure very similar to that of Fig. 1 but the texture did not perceptibly change except to get slightly sharper. In the current case, therefore, it is surmised that incipient dynamic recrystallization did take place but the Fe content together with the initial crystallite orientations were such to retain the near orthorhombic symmetrical texture. Purer samples than these show triclinic symmetry.

As the deformed sample is annealed at 240 °C for 20 min, 1, 3 and 10 h without repolishing the surface, the sharpening of the peak profile in pole figures becomes very noticeable. Since the grain size is less than 10 μm, these measurements cannot be attributed to just surface layer effect. The corresponding grain size measurements are shown in Fig. 2 together with those on the same sheet but different specimens of Seki et al. (1998). The fact that the parabolic grain growth relation (Fig. 2 inset) did not clearly start till 1.0 h anneal at 240 °C supports the above notion that incipient DYREX was completed by CREX at this anneal temperature. The texture evolution with grain growth is summarized by plotting the volume fractions, f_V, of the components using the Gaussian spread angle, φ, of 11°. To assess the occurrence of the R recrystallized component (Hirsch and Lücke, 1985), the f_V of S were plotted as a function of φ. This examination did not show any evidence of near neighbour components.

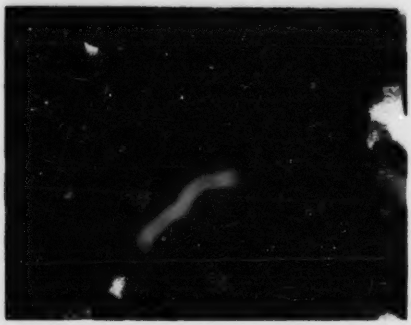

Fig. 1. ECC-SEM micrograph showing the DYREX structure of as-deformed specimen after 10 μm was removed.

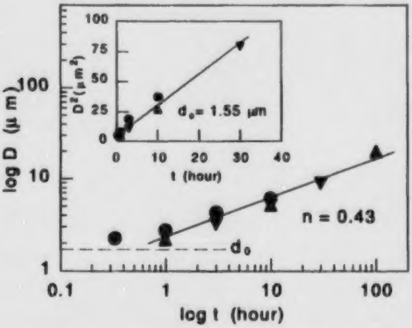

Fig. 2. Grain size vs. annealing time at 240 °C using 3 different specimens as indicated by the different symbols.

In Fig. 3a, the results for the ODF analysis in terms of volume fraction of the texture components are shown following each anneal interval. The most obvious change with grain growth is that the brass component gradually decreases. The copper increases slightly but the $S_1 + S_2$ is very stable. Another specimen from a previous work (Seki et al., 1998) in Fig. 3b shows a very asymmetric start as the guide lines indicate but with long time (almost an order of magnitude increase in grain size) the monoclinic symmetry is replaced by a near orthorhombic one. Juul-Jensen and Mehnert (1998) suggests that the minor texture component should increase at the expense of the major one. In the current example, however, the minor variant of the S texture is increasing at the expense of the symmetrically equivalent variant. Currently we are attempting to complete a triclinic analysis whereby all the variants can be quantitatively measured. The great interest here is that anneal twinning and their subsequent disappearance which has been observed for this alloy (Li et al., 1997) may contribute to the observed textural change. It is noteworthy that Hirsch et al. (1988) have shown that specific S variants upon twinning can become the symmetrical equivalent one. The large differences between the specimens from the same sheet at nearby locations in Figs. 3a and 3b demonstrate that the deformation micro-texture is highly dependent on the initial orientation of each large crystallite.

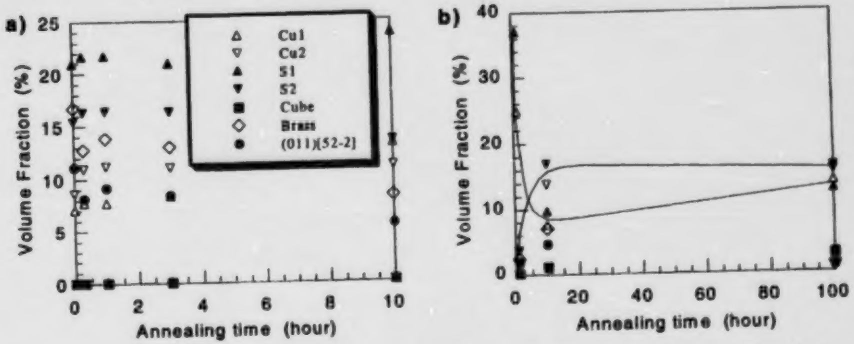

Fig. 3. **a**) From ODF analysis, the variations in volume fraction of the texture components for different annealing time at 240 °C. **b**) f_V vs anneal time for second specimen with divergent initial values due to the orientation of the large initial grains.

In the ODF analysis, we have included the (001)[52-2] component since Blicharski et al. (1993) have observed that, at the interface of two specific S variants, the lattice rotates to this orientation to decrease the boundary angle. As evident in Fig. 3a. this component decreases in a similar way as for that of the brass. Thus analytical means are required to correlate the interfacial relations from all the variant situations to the measurements such that their significance can be determined.

4 Discussion

Li and Saimoto (1998) measured initial grain size after 80 % reduction compared to that of the present case of 96 % of about 1.6 μm. Furthermore the random line electron backscattered diffraction pattern analysis shows not sub-grains but large angles. A recent study by Hughes and Hansen (1997) on crystallite subdivision by cold rolling (90%) of 99.8% pure Al shows that their effective grain size measurements for high angle boundaries (larger than 15°) were 2.1 μm. This almost exact correlation must be more than fortuitous. Similar but less quantitative study was carried out on 5 nines pure Al by Heller et al. (1977) and they found that the dislocation densities were unexpectedly low with some grains completely dislocation-free. This phenomenon was attributed to dynamic polygonization. The overall texture was very similar to that of the present work but even at this nominally high purity, static recrystallization was not initiated till over 86 °C. Thus the fine grain structure due to DYREX/CREX must evolve from the deformation process but the precise mechanisms whereby the large angle boundaries are formed in such small units are still unknown. This study illustrates however that the precise amount of Fe solute in the matrix is the prime determining factor. Since the activation energy of diffusivity of Fe in Al is more than twice that of Al self diffusion (Rummel et al. 1993), the possibility of rampant dislocation climb without the pinning effect of Fe must be the key mechanism. The climb process is enhanced by vacancy generation during deformation and by its low migration energy of 0.53 eV (Saimoto and Duesbery, 1984). This large dynamic recovery effect of dislocation annihilation, however, can not be recorded in terms of textural changes since dislocation climb without glide does not involve lattice rotation (Groves and Kelly, 1968). Hence if large dipole annihilation is envisaged during CREX, very little textural changes will be observed except for some subtle effects of diffraction due to the reduction of internal stress. This means that a dislocation annihilation process prior to dynamic polygonization exists.

The grain growth and the accompanying texture evolution reported here can not be compared easily with previous experimental studies since the matrix purity is so high and the grain size is at least an order of magnitude smaller. Moreover in the present case, the precipitates and/or their volume fractions are sufficiently large such that Zener drag is not encountered till above 20 μm. Thus the uniform grain growth with almost identical growth kinetics (Fig. 2) but quite different amounts of texture components (Fig. 3) suggests that the rapid change in the interfacial environment on both orientation and matching plane bases prevents the dominance of any one mechanism to result in a size advantage from which abnormal grain growth can result. This also means that in the micro-texture scale the usually assumed situation whereby strong texture is associated with low angle boundaries may not be valid. This observation reinforces the notion that the formation of large angle boundaries in micrometer sized blocks during deformation effectively disperses the contiguous orientations from the same parent crystallite if the effect of the pinning solute is removed.

5 Conclusion

Uniform grain growth under widely different texture component distribution is possible if the Fe content in the aluminum matrix is below 0.3 ppm atomic. The origin of the fine grain size is attributed to the formation of micrometer scale cells with high angle boundaries during deformation. This formation in three dimensions appears to be facilitated by dynamic climb mechanism which indirectly affects the micro-texture by permitting glide within such newly formed cells.

6 Acknowledgements

The authors thank the Natural Science and Engineering Council of Canada and the Materials Manufacturing Ontario (MMO) for support of this program. We are indebted to Prof. P. Van Houtte for his continued update of his software programs and invaluable advice. One of us (H.J.) is a recipient of a MMO Scholarship.

7 Reference

Blicharski, M., Becker, R. and Hu, H. (1993) Deformation texture of channel-die deformed Al bicrystals with S orientations. Acta metall. mater. 41 pp. 2007-2016.

Groves, G.W. and Kelly, A. (1968) Change in shape due to dislocation climb. Phil. mag. 19, Series 8, pp. 977-986.

Heller, H., Slakhorst, J. and Verbrak, T. (1977) The development of rolling and recrystallization textures in high purity Al. Z. Metallk., 68, pp. 31-37.

Hirsch, J. and Lücke, K. (1985) The application of quantitative texture analysis for investigating continuous and discontinuous recrystallization processes of Al-0.01 Fe. Acta metall. 33, pp. 1927-1938.

Hirsch, J., Lücke, K. and Hatherly, M. (1988) Mechanism of deformation and development of rolling texture in polycrystalline f.c.c. metals III: The influence of slip inhomogeneities and twining. Acta metall. 36, pp. 2905-2927.

Hughes, D.A., Hansen, N. (1997) High angle boundaries formed by grain subdivision mechanisms. Acta mater. 45, pp. 3871-3886.

Ito, K., Musick, R. and Lücke, K. (1983) The inflluence of iron content and annealing temperature on the recrystallization textures of high-purity aluminum-iron alloys, Acta metall. 31, pp. 2137-2149.

Jin, H., Li, J. and Saimoto, S. (1998) Thermal-mechanical processing of electrical conductor grade aluminum to induce continuous recrystallization, in Aluminum Alloys: Their Physical and Mechanical Properties. eds. Sato, T. et al., Japan Inst. Light Metals, pp. 1197-1202.

Jin, H., Li, J., Diak, B.J. and Saimoto, S. (1999) Dynamic recrystallization of nominally

pure aluminum at room temperature, ReX '99, Tsukuba, Japan. In press.

Juul-Jensen, D. and Mehnert, K. (1998) Orientation pinning during growth, in Grain Growth in Polycrystalline Materials III, eds. Weiland, H., Adams, B.L. and Rollet, A.D., TMS, pp. 251-262.

Li, J. and Saimoto, S. (1998) Texture evolution in aluminum during continuous recrystallization. Materials Sci. Forum, 273-275, pp. 459-464.

Saimoto, S. and Duesbery, M.S., (1984) Strain rate sensitivity: the role of dislocation loop and point defect recovery, Acta metall. 32, pp. 147-55.

Saimoto, S., Kamat, R.G., Clarke, P. and Van Houtte, P. (1993), A quantitative method to examine through thickness texture variation, Textures and Microstructures, 21, pp.109-120.

Saimoto, S., Li, J., Langelaan, G., Diak, B. J. and Shimizu, J., (1996) Formation of cube texture in norminally pure Al with fine particle dispersion, Textures and Microstructures, 26-27, pp. 245-262.

Seki, F., Li,J., Saimoto, S., Ito, K. and Kamijo, T. (1998) Grain growth in continuously recrystallized aluminum with fine dispersed particles, in Grain Growth in Polycrystalline Materials III, eds. Weiland, H., Adams, B. L., Rollet, A.D., TMS pp. 303-308.

Rummel, G., Zumkley,T., Erdelyi, G., Freitag, K., Hood, G.M. and Mehrer, H. (1993) Temperature and pressure dependence of the diffusion of ion-implanted transition element and ion-transition element solute diffusion in Al, Defect and Diffusion Forum, 95-98, pp.715.

SHEAR TEXTURE CONTROL AND IMPROVEMENT OF LANKFORD VALUE IN ALUMINUM ALLOY SHEET BY SINGLE-ROLL DRIVE WARM ROLLING

T.SAKAI, H.INAGAKI and Y.SAITO
Department of Materials Science and Engineering,
Graduate School of Engineering, Osaka University, Suita, Japan

Abstract

Large shear deformation was successfully introduced throughout the thickness of 5052 and 3004 aluminum alloy sheets by single-roll drive warm rolling under high friction condition. The shear texture of which main components were {111}<110>, {112}<110> and {001}<110> prevailed throughout the thickness, and typical rolling texture was not observed at any part of thickness. Shear strain was smaller and intensity of shear texture was weaker in 3004 alloy. After recrystallization annealing, shear texture became broad and nearly random texture prevailed, though weak shear texture components remained. The average r-value of annealed 5052 alloy sheet was about 1.0 which is higher than that of the sheet fabricated by conventional rolling and annealing. The planar anisotropy was also smaller than that by conventional process. The r-value of 3004 alloy also increased by single-roll drive rolling, although the rise in r-value was smaller than 5052 alloy. The single-roll drive rolling is proved to be promising process for fabricating aluminum alloy sheet having excellent formability.

Key words : 3004 alloy, 5052 alloy, r-value, shear rolling, shear texture,

1 Introduction

Improvement of formability in sheet forming of aluminum and aluminum alloys which can be accomplished by raising r-value and decreasing planar anisotropy is difficult, since cube texture and R-orientation which are detrimental to sheet formability develop during rolling and annealing of fcc metals. It is well known that the well developed <111>//ND texture is effective for improvement of r-value not only of bcc metals but also of fcc metals(Lequeu and Jonas 1988). However, <111>//ND texture can not be formed in fcc metals by conventional rolling and annealing process. The <111>//ND orientation is one of the main components of texture by shear deformation of fcc metals(Dillamore and Roberts 1963; Truszkowski et al. 1980). Accordingly, this orientation will develop in rolled aluminum sheet when shear deformation is superimposed on rolling deformation. It has been reported that shear texture is formed beneath the surface of sheet rolled under high friction condition, while the rolling texture prevails in central part of thickness(Sakai et al. 1987). Remarkable increase in r-value can not be made in such sheet of fcc metals because of cube and R-orientation resulting from typical rolling texture developed in the center layer of the rolled and annealed sheet.

The authors have proposed 2-pass single-roll drive rolling process for introducing shear deformation throughout the thickness of rolled sheet(Sakai et al. 1998). Single-roll drive rolling is a kind of asymmetric rolling which can introduce greater amount of shear deformation than conventional symmetric rolling(Hu et al. 1996). The variation of texture through the thickness of rolled sheet of 3004 and 5052 alloys was measured. The texture and mechanical property of annealed sheet was investigated and feasibility of asymmetric rolling process as a process for improving formability of aluminum and aluminum alloy sheet was proved.

2 Experimental procedure

2.1 Single-roll drive rolling

Procedure of 2-pass single-roll drive rolling is schematically shown in **Fig.1**. Single-roll drive rolling was conducted by conventional rolling mill; one roll was driven by a motor and another roll was allowed to rotate freely by disconnecting from driving shaft. By one pass single-roll drive rolling, large amount of shear deformation was introduced at the driving roll side and smaller shear deformation at the idle roll side. In the second pass, the sheet was so rolled as to introduce larger shear deformation at the side which had been faced to the idle roll in the first pass. After the second pass, almost uniform shear deformation throughout the thickness was introduced in the rolled sheet. In this study, the above mentioned process is called "unidirectional shear rolling".

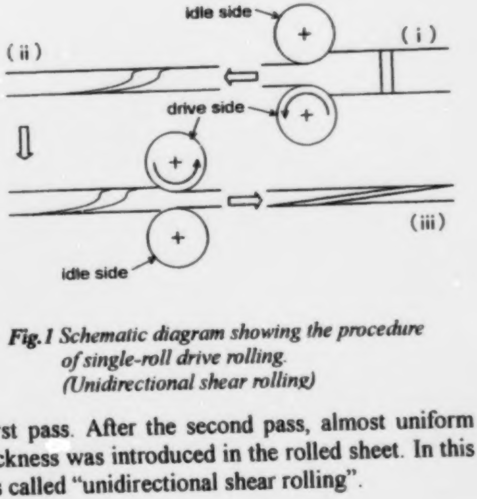

Fig.1 Schematic diagram showing the procedure of single-roll drive rolling. (Unidirectional shear rolling)

2.2 Experimental procedure

The materials used were 3004 and 5052 aluminum alloys. A sheet of 3mm in thickness was rolled by the 2-pass single-roll drive rolling, that was conducted with the mill of which roll diameter was 70mm. The 2-pass conventional (symmetric) rolling was also conducted for comparison. Rolling temperature was 310°C for 3004 and 260°C for 5052 alloy. Reduction in each pass was 50% , hence total reduction was 75%. In order to roll in high friction condition without galling, alumina powder dispersed in ethanol was applied to the roll surface. Thus, roll surface was coated with thin alumina powder after evaporation of ethanol. The rolled sheets were annealed at 310, 360, 410 and 460°C for 1.8ks. Variation of shear strain through the thickness was measured from the deformation of cylindrical pin by rolling that had been embedded in the specimen before rolling with its axis perpendicular to the rolling plane(Sakai et al. 1988). The {111} pole figure was measured at the various position of the thickness of the sheet after rolling and after annealing by Schulz's reflection and transmission method. The r-value was determined from tension test of which tensile direction was 0°, 45° and 90° from the rolling direction.

3 Results and discussions

3.1 Deformation by single-roll drive rolling

The deformation of embedded pin by unidirectional shear rolling was observed. The pin that had been perpendicular to the rolling plane inclined to one direction by shear deformation during rolling. The inclination of the pin was almost uniform through the thickness. This suggested that shear deformation was unidirectional and prevailed throughout the thickness. **Figure 2** shows the variation of shear strain through the thickness of the sheet calculated from the measurement of the inclination of the pin. In unidirectional shear rolling, definite amount of shear strain distributes throughout the thickness of both 3004 and 5052 alloy sheets, and shear strain increases near the surface. In conventional rolling, shear strain also increases near the surface, however it decreases to zero at the midthickness. Although the surface condition of rolls were same for rolling of both 3004 and 5052 alloy sheets, the amount of shear strain is larger in 5052 alloy than in 3004 alloy. It seems that the friction coefficient between the roll and the material is affected by alloy composition. The 2-pass single-roll drive rolling was proved to promising method to introduce shear strain throughout the thickness of the rolled sheet.

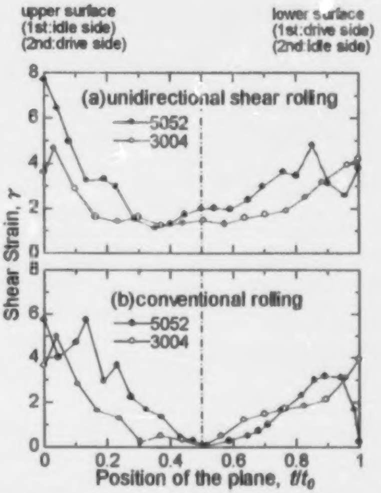

Fig.2 Effect of rolling method on variation of shear strain through the thickness.

3.2 Texture variation through the thickness

The {111} pole figures measured at various position through the thickness of the unidirectionally shear rolled sheet of 3004 and 5052 alloys are shown in **Fig.3**. In both 3004 and 5052 alloys, from the drive side in the 2nd pass to the idle side, the position of strong pole intensity were seen near {111}<110>, {112}<110> and

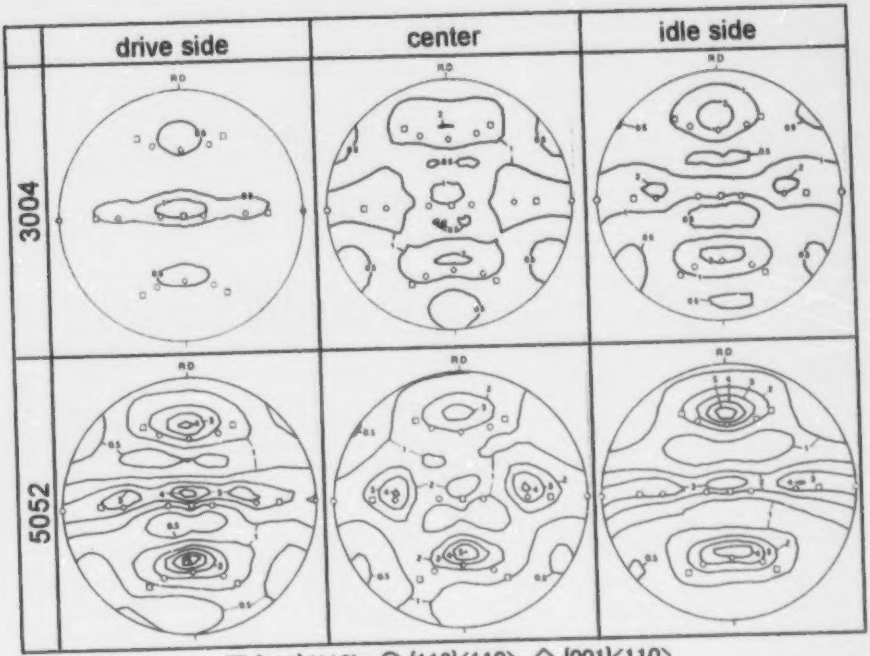

□ {111}<110> ○ {112}<110> ◇ {001}<110>

Fig.3 Variation of {111} pole figure through the thickness of the unidirectionally shear rolled sheet.

{001}<110> orientations which are main components of shear texture. The peaks of (111) pole intensity rotate about 10° around TD axis toward rolling direction. The intensity of near {001}<110> orientation is stronger than other orientations at the midthickness. The intensity ratio of {111}<110> to {001}<110> seems to be affected by the ratio of shear strain to compressive strain because shear strain at the midthickness is smaller than that near the surface (Fi.g.2), while compressive strain is constant through the thickness. Orientations of conventional rolling texture were not observed. The sheet having shear texture throughout the thickness was able to be fabricated by single-roll drive rolling. Corresponding to the difference in the amount of shear strain, the intensity of shear texture of 3004 alloy is weaker than that of 5052 alloy. The change of texture through the thickness of conventionally rolled sheet was measured. At the surface, where shear deformation was introduced, shear texture developed. At the center of the thickness, {123}<634> and {124}<112> orientations which are known as typical rolling texture of fcc metals prevailed. The intensity of {001}<110> is stronger than other orientations at a quarter from the surface, which is similar to the center of the unidirectionally shear rolled sheet.

Texture variation through the thickness of the 5052 alloy sheet annealed at 360°C for 1.8ks after unidirectional shear rolling is shown in **Fig.4**. Throughout the thickness, weak shear components remain after recrystallization. Texture spreading around shear components is very large and pole intensity is significantly weaker than that of rolled sheet. On the other hand, typical recrystallization texture of fcc metals including {001}<100> orientation developed in the center region of the thickness of

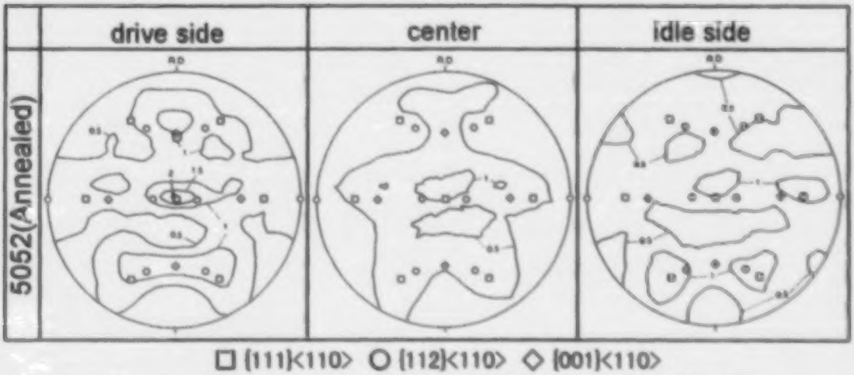

Fig.4 Variation of {111} pole figure through the thickness of the annealed 5052 sheet.

the sheet annealed after conventional rolling. However, at the surface and a quarter from the surface, where shear texture developed, textures similar to those of unidirectionally shear rolled and annealed sheet were observed. Through-the-thickness texture gradient remained after completion of recrystallization in the conventionally rolled sheet. The recrystallization texture of 3004 alloy sheet was almost similar to 5052 alloy.

3.3 r-value

The r-values of sheets of both 3004 and 5052 alloys annealed after unidirectional shear rolling and conventional rolling are shown in **Fig.5**. The average r-value of 5052 alloy is almost equal to unity, which is much superior to the conventionally rolled and annealed sheet. In 3004 alloy, r-value also increases by

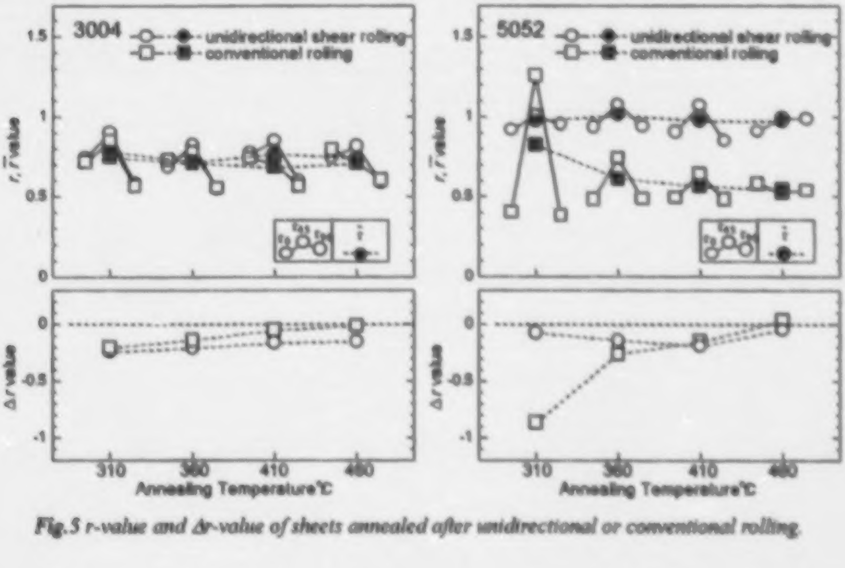

Fig.5 r-value and Δr-value of sheets annealed after unidirectional or conventional rolling.

applying unidirectional shear rolling, however rise in r-value is smaller than 5052 alloy. There were no any distinct differences between the textures of 3004 and 5052 alloy sheets annealed after unidirectional shear rolling. The slight improvement in r-value of 3004 alloy may be attributed to the dependence of the relation between texture and r-value on alloy composition, that has not been made clear now. The mechanical properties of sheets obtained in the present study are almost isotropic because nearly random recrystallization texture developed throughout the thickness of unidirectionally shear rolled sheet. Nearly random texture also developed in the greater part of the thickness of conventionally rolled sheet, therefore the conventionally rolled and annealed sheet shows isotropic mechanical properties.

4 Conclusions

1) The shear strain larger than 1.0 was introduced throughout the thickness of the sheet by unidirectional shear rolling using single-roll drive mill.
2) The shear texture developed throughout the thickness of unidirectionally shear rolled sheet. The intensity of shear texture was higher in 5052 than in 3004 alloy.
3) The sheet annealed after unidirectional shear rolling had broad texture spreading around shear texture components. This orientation develops throughout the thickness and cube texture did not observed at any part of thickness.
4) The average r-value equal to unity and planar anisotropy Δr of –0.14, which are much superior to the sheet fabricated by conventional process, are achieved in 5052 alloy sheet annealed after unidirectional shear rolling.
5) The rise in r-value of 3004 alloy by shear rolling was smaller than 5052 alloy.
6) It is proved that the 2-pases single-roll drive rolling is promising method for fabricating aluminum alloy sheet with excellent formability.

References

Dillamore, I.L. and Roberts, W.T., (1963) Crystallographic texture variation through rolled aluminum and copper sheet. *J. Inst. Metals,* Vol.92, pp.193-199

Hu, J., Ikeda, K. and Murakami, T. (1996) Effect of single roller driving cold rolling on texture and formability of pure aluminum sheet. *J. Japan Inst. Metals,* Vol.60, pp.1130-1135

Lequeu, P.H. and Jonas, J.J., (1988) Modeling of the plastic anisotropy of textured sheet. *Metall. Trans., A,* Vol.19A, pp.105-120.

Sakai, T., Saito, Y. and Kato, K. (1987) Recrystallization and texture formation in high speed hot rolling of austenitic stainless steel. *Trans. ISIJ,* Vol.27, pp.520-525

Sakai, T., Saito, Y., Hirano, K. and Kato, K. (1988) Deformation and recrystallization behavior of low carbon steel in high speed hot rolling. *Trans. ISIJ,* Vol.28, pp.1028-1035

Sakai, T., Hamada, S. and Saito, Y. (1998) Formation of shear texture in A5052 sheetr by single-roll drive warm rolling. *Proc. 6th Int. Conf. on Aluminum Alloys (ICAA-6),* Toyohashi, pp.1161-1166

Truszkowski, W., Król, J. and Major, B., (1980) Inhomogeneity of rolling texture in fcc metals. *Metall. Trans., A,* Vol.11A, pp.749-758

TEXTURE AND MICROSTRUCTURE IN DC CAST AND SC ALUMINUM ALLOYS

Y. LIU, Y. L. LIU, G. LIAO and J. G. MORRIS
Light Metals Research Laboratories
Department of Chemical and Materials Engineering, University of Kentucky
Lexington, KY , USA

Abstract

Texture and microstructure of direct chill(DC) cast and strip cast(SC) AA5XXX aluminum alloys in the annealed state were observed by electron backscattered diffraction patterns(EBSPs) and were compared. The different behaviors and features of recrystallization were identified in these two kinds of materials. Texture continuity has been observed in both DC cast AA5083 and SC AA5XXX aluminum alloys. The conditions for the formation of clusters which consist of grains with similar orientations are explained by percolation simulation. The influence of texture continuity on mechanical properties is discussed.

Keywords: aluminum alloys, percolation simulation, texture, texture continuity

1. Introduction

Textures in aluminum alloys have been investigated in the development of these alloys. Texture evolutions during deformation and recrystallization are well documented (Hirsch 1990). For a long time, aluminum alloys have been produced by the direct chill cast (DC) process and occupy a major part of industrial products. However, strip cast (SC) materials have recently received much attention due to their economical method of production. Textures are one of the important aspects in the mechanical anisotropy control of both types of aluminum materials. Investigation has been carried out in the comparison of textures of DC and SC materials by the X-ray pole figure method (Liu et al. 1998). The technique of electron backscattered diffraction patterns (EBSP) has been widely used since the early 90s. Local texture information can be detected by the EBSP technique and orientation of individual grains can be obtained . Texture continuity has been reported based on the EBSP observation in aluminum alloys (Liu et al.1999). In order to understand the mechanical anisotropy behavior of SC materials, it is necessary to make a comparison with DC materials. The present work focuses on microstructure, local texture and texture continuity of DC AA5083 and SC AA5xxx aluminum alloys. Percolation simulation has been used for an explanation of texture continuity.

2. Experiment

Commercial DC cast AA5083 and strip cast AA5XXX alloys were used for the present investigation. The state of the as received DC material is the H18 temper which utilized large cold reductions. The SC materials were industrially cold rolled to 1mm from 3mm hot band. One part of the DC materials was annealed at 343°C(650°F) for 30min and the other part was annealed at 500°C(932°F) for 30min. The SC materials were annealed at 316°C(600°F) for different times from 20min to 420min. The heat up rate used was 55°C/h(100°F/h) for both of DC and SC materials. Samples of the as received and of the annealed states were taken for microstructure observation and texture determination. Textures of deformed samples and of annealed AA5083 samples were measured by the X-ray pole figure method. Orientation distribution functions(ODF) were calculated. The EBSP technique was used to determine textures in annealed samples. Samples for the EBSP observation were prepared by electrolytic polishing.

3. Result and discussion

Figure 1 is the recalculated (200) pole figures of the initial materials in the as received condition. It shows that both DC and SC materials have very similar texture distributions. Textures are the typical cold rolling type, that is well-developed C, B and S components. ODF analysis shows that the cube component has an intensity of 1 to 2. The Goss component has an intensity of about 6 and the C, B and S have intensities over 16.

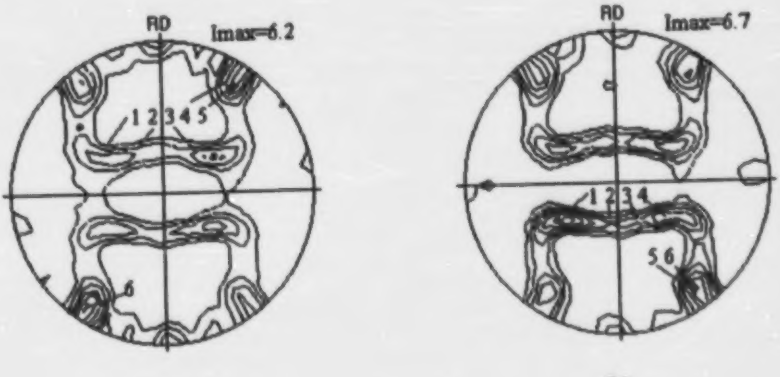

(a) (b)

Fig. 1: Recalculated (200) pole figures (a) DC cast AA5083 alloys as received H18 temper; (b) SC AA5XXX cold rolled to 1mm from 3mm hot band.

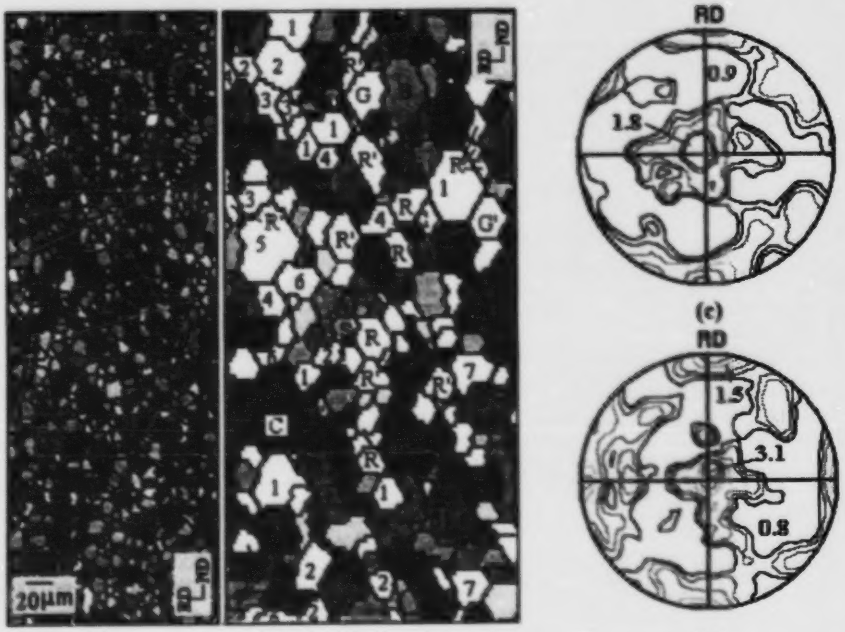

(a) (b) (d)

Fig.2: EBSP Microstructures and (200) pole figures of DC cast AA5083 aluminum alloy. (a) and (c) microstructure and (200) pole figure of samples annealed at 343°C(650°F) for 30min, respectively; (b) and (d) microstructure and (200) pole figure of samples annealed at 500°C(932°F) for 30min, respectively. White areas indicate grains with cube and rotated cube orientations. The indices of orientations in (b) are displayed in Table 1.

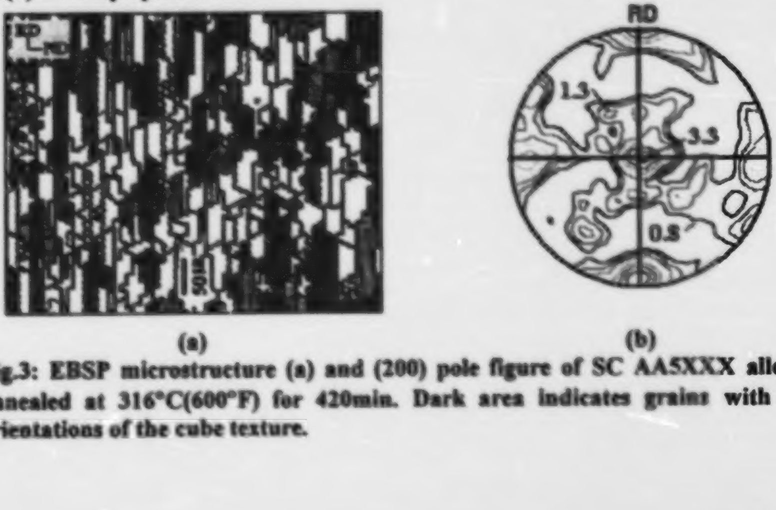

(a) (b)

Fig.3: EBSP microstructure (a) and (200) pole figure of SC AA5XXX alloy after annealed at 316°C(600°F) for 420min. Dark area indicates grains with similar orientations of the cube texture.

Table 1: Orientation indices of grains in Figure 2(b)

Index	{hkl}<uvw>	Index	{hkl}<uvw>	Index	{hkl}<uvw>
1	(0, 1, 4)[1,-4, 1]	7	(0, 0, 1)(5, 1, 0)	C	(1,-1,-2)[1, 1, 1]
1	(0, 0, 1)[1, 0, 0]	R	(0, 0, 1)[1, 1, 0]	B	(-1, 1,0)[-1,-1, 2]
3&5	(0, 1, 3)[1,-3, 1]	R'	(0, 0, 1)[2, 3, 0]	S	(2,-1, 3)[-3,6, 4]
4	(0, 1, 4)[1, 0, 0]	G	(1, 1, 0)[0, 0, 1]		
6	(0, 0, 1)[4, 1, 0]	G'	(1, 1, 0)[U,-U, 1]		

The microstructure of the DC sample shows a heavily deformed condition. The microstructure of the SC materials also presents a deformed structure, but is not as heavily deformed as that of the DC materials.

When samples were heated to an elevated temperature, the DC and SC materials gave different behaviors. The DC materials recrystallized quickly at 343°C(650°F) and 500°C(932°F) for 30min. Figure 2 displays the EBSP microstructure and (200) pole figures of the annealed DC samples. The average grain size of the sample annealed at 343°C(650°F) is about 6μm and that of the sample annealed at 500°C(932°F) is about 10μm. Textures for both conditions show a recrystallized condition. ODF analyses from the X-ray pole figure measurements indicate that the Goss component has an ODF intensity of 6.1 in the sample annealed at 343°C(650°F). The cube component and rotated components have intensities of 7.4 and 1.2 respectively. The C, B and S components have intensities of about 6.5. This indicates that the cold rolling type components remain in the recrystallization textures. With an increase of the annealing temperature to 500°C(932°F), the C, B and S components decrease to intensities of about 3. The intensity of the Goss component remains constant. The intensity of the cube and rotated cube components increase 1 level. The EBSP (200) pole figures in Figure 2 also shows an increasing trend of intensities of the cube and rotated cube components. This indicates that an increase of the annealing temperature favors the growth of the cube and rotated cube components. Figure 2 (b) gives the orientations of each individual grain. Orientation indices are listed in Table 1. The grains in the white area of the microstructure have cube or rotated cube orientations. From the top of Figure 4(b) grain 1 has an orientation of (0,1,4)[1,-4,1]; grain 2 (1,0,0)[0,0,1]. Grains 3 and 4 have orientations of (0,1,3)[1,-3,1] and (0,1,4)[4,1,0], respectively. Eight clusters with more than three grains with cube orientations are observed. They tend to bind together with each other. This condition can be defined as "texture continuity" which means that grains with similar orientations tend to connect together and form clusters of several grains . The phenomena also exists in SC materials (Liu et al. 1999). Grains with the Goss, C, B and S orientations are also marked with a corresponding letter in Figure 2(b).

In order to make a comparison of DC and SC materials, textures and microstructures of SC materials were also observed. The SC materials were heated to 316°C(600°F) and were held for different times. Partially recrystallized microstructures were observed in the SC sample annealed 80min at 316°C(600°F). Textures show deformation components for this time of annealing(80min). 100% recrystallization was confirmed in the SC samples held at 316°C(600°F) for more than 4 hours. As shown in Figure 3, the SC sample annealed at 316°C(600°F) for 7 hours has an elongated grain structure with an average grain size of about 50μm in the rolling direction and about 20μm in the

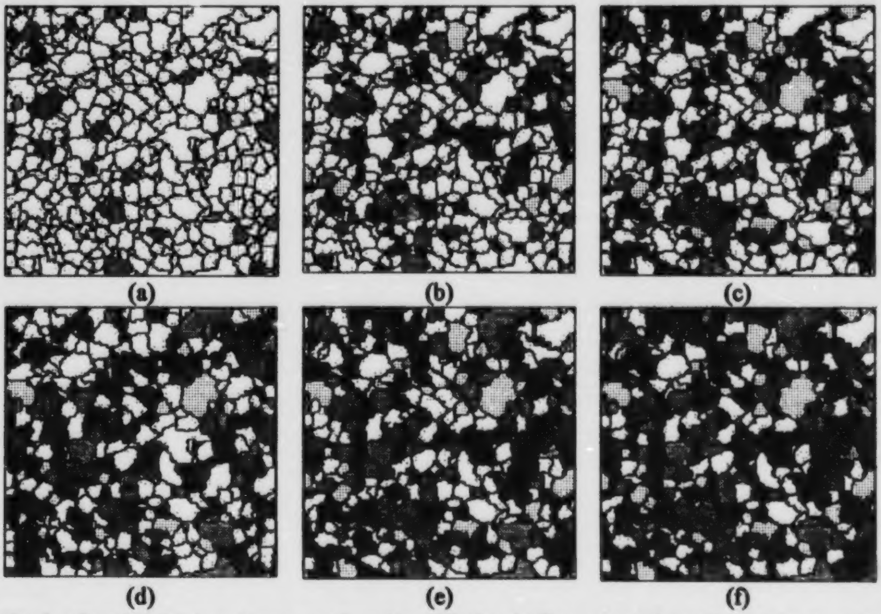
(a) (b) (c) (d) (e) (f)

Fig.4: Simulated microstructure of grains with the similar orientations (for example cube texture in the present work). (a) 9.48% volume fraction, isolated cube grains; (b) 33.75% volume fraction, several cube grains bound together; (c) 47.0%; volume fraction (d) 53.79% volume fraction; (e) 62.3% volume fraction, all cube grains in the microstructure connected together; (f) 71.56% volume fraction. The infinite cluster forms when the volume fraction approaches 62.3%. Dark areas indicate grains with cube and rotated cube orientations.

transverse direction. The cube texture is well developed. Again, texture continuity can be easily found in Figure 3(a). This sample has a relatively high intensity of the cube component. The grains with cube orientations are connected through all of the microstructure. Thus, in terms of the intensity of texture continuity a significant difference in annealing textures was observed in DC and SC AA5XXX aluminum alloys. However, for AA5XXX alloys the overall annealing textures are similar for DC and SC materials even though the grain shape and size is different.

The Taylor factor is related to the deformation behavior of materials. Grains with different orientations have different Taylor factors. The existence of texture continuity means that grains with similar orientations can form domains with the size of several grains. The domain may be an island of hard or of soft material. Whenever the sample is deformed, fracture or necking may start from the hard or soft domains. The present authors believe that inhomogeneous deformation is related to this effect.

In order to understand the behavior of texture continuity, computer simulation base on percolation theory has been used in the present investigation. The square lattice of 200 ×200 points was used. The volume fraction of a specified texture component (for example the cube texture component in the present work) is changed during the simulation. Grains on the simulated microstructure randomly take the orientations of specified textures. The simulated result is displayed in Figure 4. The dark (gray and black) grains indicate they have a cube texture. When the cube grains occupy a volume fraction less than 10%, the grains with this texture are usually isolated from each other (Fig 4 (a)). When the volume increases to 30%, grains with similar orientations tend to form a cluster with the size of several grains (Fig.4 (b)). A further increase in the volume fraction causes an increase in the size of clusters composed of grains with similar orientations (Fig 4(c), (d)). If the volume is over 60%, then the size of the cluster become infinite which means that grains with a similar orientation form a continuous network through the microstructure (Fig.4 (f). The critical transition point for an infinite cluster is close to the theoretical value of 59.275% occupation of square site percolation(Stauffer 1985).

This simulation indicates that texture continuity is a general effect which exists in materials. More grains with similar orientations tend to group together without regard to the materials. If one texture component has a volume fraction over the critical limit (59.275%) of an infinite cluster, then the property behavior of the material is mainly determined by the overwhelming texture component. DC cast materials possess this behavior and SC materials possess this behavior also to an even greater extent. The simulation is based on a random package for each grain. However, the package of grains in materials is never truly random. The initial textures in as the received samples increase the tendency to form clusters of grains with similar orientations at elevated temperatures.

4. Conclusions

Texture continuity is a general feature of crystallographic materials. For a texture component with a volume fraction over 30%, clusters of grains with similar orientations can be observed. DC cast AA5083 aluminum alloy and SC AA5XXX aluminum alloy give similar texture distributions and both possess texture continuity even though the grain shape and size in the two alloys are different.

Reference

Hirsch, J.R.(1990) Correlation of Deformation texture and microstructure. Materials. Science and Technology, Vol.6, 1990, pp.1048-1057.pp. 567-74.

Liu, Y., Liu,Y.L., Cheng., X.M. and Morris,J.G.(1998) Texture in hot rolled aluminum alloys, in Hot deformation of aluminum alloys II (ed. Bieler,T.R., Lalli,L.A. and MacEwen, S.R.), The mineal, metals & materials Society, Warrendale, Pennsylvania, pp73-84.

Liu, Y., Liu,Y.L., Liao,G. and Morris,J.G.(1999) Texture evolution of a strip cast AA5XXX aluminum alloy during annealing. in Automative alloy(III)(ed. Das, S.K., TMS 1999 meeting, San Diego (To be published).

Liu, Y.L., Liu, Y., Liao,G. and Morris,J.G.(1999) The microstructure, texture and mechanical property behavior of DC and strip cast AA3004 aluminum alloy.(to be published in) Proceeding of International Casting & Rolling Technology Conference, Aluminum Association, Baltimore, Maryland, USA, May 4-6,1999.

Stauffer, D. (1985) Introduction to percolation theory. Taylor & Francis, London and Philadelphia , pp16-18.

THE EFFECT OF ROLLING DRAUGHTS ON TEXTURE AND MICROSTRUCTURE IN ALUMINIUM

O.V. MISHIN and D. JUUL JENSEN

Materials Research Department, Risø National Laboratory, Roskilde, Denmark

B. BAY

Institute for Applied Engineering Design and Production, Technical University of Denmark, Lyngby, Denmark

Abstract

The texture gradients and microstructural variations are investigated in commercially pure aluminium plates 40% cold-rolled either with small draughts or with intermediate draughts. In these two samples, different textures are observed near the quarter-thickness layer. A pronounced shear texture is found in the sample rolled with small draughts, while a rolling texture is observed in the sample rolled with intermediate draughts. Also, significant differences were found in the rolled microstructures near the quarter thickness. After rolling with intermediate draughts, extended dislocation boundaries preferentially aligned at an angle of about 25-45° to the rolling direction are observed in the longitudinal section. After rolling with small draughts, extended dislocation boundaries are preferentially aligned closer to the rolling direction. These results are described and discussed.

Keywords: Aluminium, dislocation structures, texture inhomogeneities, rolling schedule

1. Introduction

The geometry of the roll gap is known to influence texture gradients in rolled products. Depending on the value of the l/h ratio (where l is the chordal length of the contact arc and h is the mean thickness of the plate) a distinction is made between small and large draughts (Truszkowski et al. 1980). Severe texture inhomogeneities produced by rolling are frequently associated with the shear texture. After large draughts ($l/h>5$), the shear texture has been observed at the surface of rolled sheets or plates, while small ($l/h<0.5$) draught rolling generates the shear texture in the intermediate layers (Hansen and Mecking 1975; Truszkowski et al. 1980). Rolling within the range of intermediate draughts, $0.5\leq l/h\leq 5$, has been considered to produce homogeneous rolling textures. It has been, however, shown that sufficiently high friction results in heterogeneous textures regardless of whether rolling was performed with the "homogeneous" roll gap geometry or not (Choi et al 1997).

While a large body of research into through-thickness rolling inhomogeneities deals with texture characterization, little is known about microstructural variations in different layers. In this paper, we describe both textures and microstructures produced during rolling with intermediate and small draughts.

2. Experimental

Commercially pure aluminium AA1050 was 60% cold-rolled and recrystallized at 673K for 1 hour (see Mishin et al. 1999). Two plates were ~40% rolled with different rolling schedules using kerosene as lubricant. The rolling schedules were selected either to perform intermediate (l/h=1.92) draught rolling in one pass (sample A1) or to maintain small draughts during multipass rolling (sample A2). The sample A2 was rolled in 18 passes with l/h=0.31-0.44 alternating the top and bottom sides between passes.

Textures were studied using X-ray diffraction and the EBSP technique (for details see Mishin et al. 1999). The volume fractions of different texture components were calculated from the EBSP data allowing a 15° deviation from the ideal {hkl}<uvw> orientations. When an orientation could be described as belonging to more than one component, it was ascribed to a component with the smallest deviation from that particular orientation. The volume fraction of the rolling texture was described as the summed volume fraction of the B {110}<112>, C {112}<111> and S {123}<634> orientations. Following Truszkowski et al. (1980), the shear texture was represented by the {001}<110>, {111}<112> and {111}<110> orientations.

The electron channelling contrast (ECC) technique in the scanning electron microscope was used for inspecting microstructures in the longitudinal section of bulk specimens. Thin foils cut from the same longitudinal section were investigated in the transmission electron microscope.

3. Results

Rolling textures with some minor variations in strength were produced in different layers of the sample A1. Similar textures were formed in the subsurface and in the center of the sample A2 (Mishin et al. 1999). Different textures were observed near the quarter thickness (Fig.1). The summed volume fractions of the rolling texture components and of the shear texture components at the quarter thickness were respectively 32.4% and 1.1% for the sample A1 and 5.6% and 20.5% for the sample A2. Consequently, thorough microstructural investigations were performed in the quarter thickness layer. Fig.2 shows the TEM micrographs in this layer for two samples. In the sample A1, cell blocks are delineated by sets of dense dislocation walls or microbands which preferentially form an angle of 25-45° to the rolling direction (RD). Certain grains with the near cube orientations showed less regular structures. The angles to the RD in several inspected grains are given in Table 1 along with the orientations measured in the center of grains. Here Set I and Set II indicate two sets of boundaries which form smaller and larger angles to the RD, respectively.

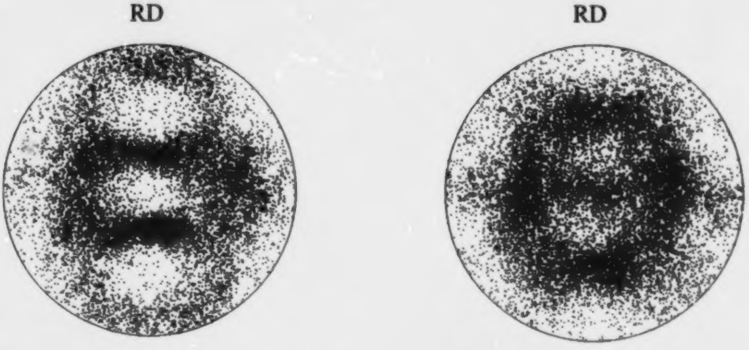

a b

Fig.1: The {111} pole figures near the quarter thickness: sample A1 (a) and sample A2 (b).

In the quarter thickness of the sample A2, different microstructures were observed. Here extended dislocation boundaries are aligned close to the rolling direction. This kind of structure was observed in the grains with the shear {001}<110> orientation (Fig.2b), cube or near cube orientations and for some "random" orientations (Table 1). Meanwhile, in some locations, the microstructures similar to those in the sample A1 were found as well.

Table 1: Alignment of dislocation boundaries to the rolling direction.

Sample	**Orientation**	**Angle to RD (°)**	
		Set I	**Set II**
A1	(0.53 -0.76 0.28) [-0.82 -0.58 -0.02]	14-24	32-42
	(-0.22 –0.97 0.13) [-0.95 0.25 0.18]	22-30	44-59
	(0.85 -0.47 0.24) [-0.52 -0.65 0.55]	20-27	38-45
	(0.87 0.02 0.49) [-0.46 -0.34 0.82]	19-35	29-33
	(0.64 -0.66 0.40) [-0.73 -0.68 0.07]	21-33	50-61
A2	(-0.98 0.19 0.07) [0.11 0.79 -0.61]	5-19	21-24
	(-0.91 -0.25 -0.33) [-0.03 0.75 -0.66]	2-15	19-24
	(-0.99 0.16 -0.00) [0.16 0.98 -0.12]	8-19	18-29
	(-0.33 –0.82 0.46) [-0.94 0.32 -0.11]	3-15	15-19
	(-0.03 -1.00 -0.06) [-0.96 0.02 0.28]	15-30	24-32

To enable observation of larger areas, the electron channeling contrast technique in the SEM was applied. Fig.3 shows the ECC images taken around the quarter thickness in both samples. The ECC technique does not resolve separate cells with very low misorientations, but extended dislocation boundaries can be observed over large sample areas. The differences in the microstructures in the two inspected samples are clearly seen. Except for some grains with S-shaped bands, the microstructure in the sample A1 is characterized by relatively large angles between dislocation boundaries and RD. Most boundaries in the sample A2 are closely aligned to the rolling direction (Fig.3b).

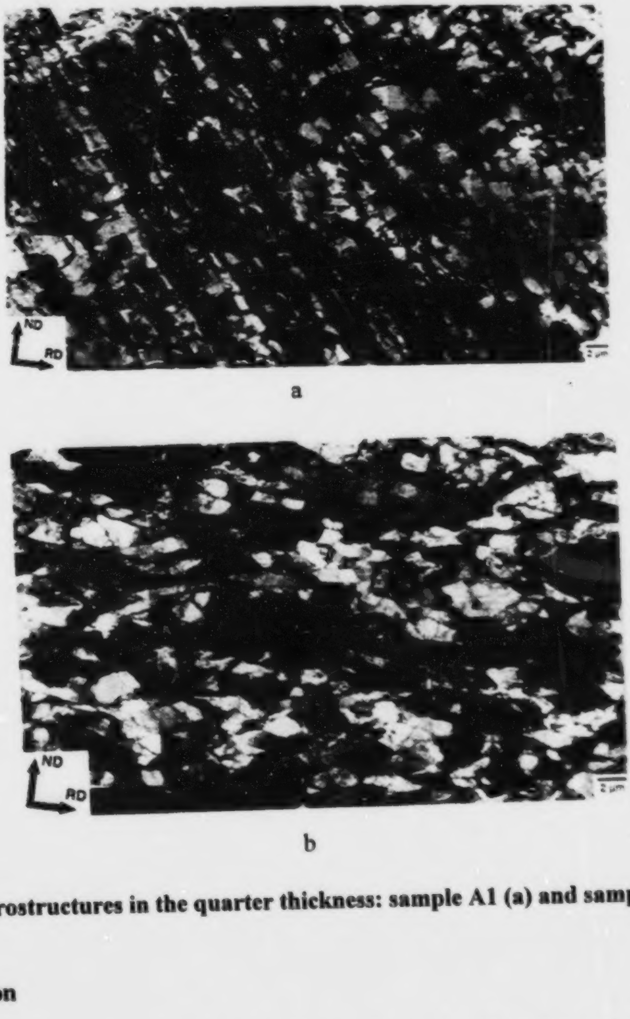

a

b

Fig.2: Microstructures in the quarter thickness: sample A1 (a) and sample A2 (b).

4. Discussion

Severe inhomogeneity associated with the shear texture observed near the quarter thickness after rolling with small draughts is in agreement with the previous experimental observations on aluminium (Hansen and Mecking 1975; Truszkowski et al. 1980) and may be attributed to a pronounced non-uniformity of metal flow. The texture development is more uniform through the thickness of the sample A1 rolled with l/h=1.92. It must be stressed, however, that the favourable geometry of the roll gap alone may not provide entirely homogeneous texture through the thickness. Texture inhomogeneities, e.g. due to friction or due to inhomogeneous texture before rolling, may be observed even after intermediate draught rolling. Indeed, some variations in the volume fractions of different texture components were found in the sample A1, but no shear texture was observed there.

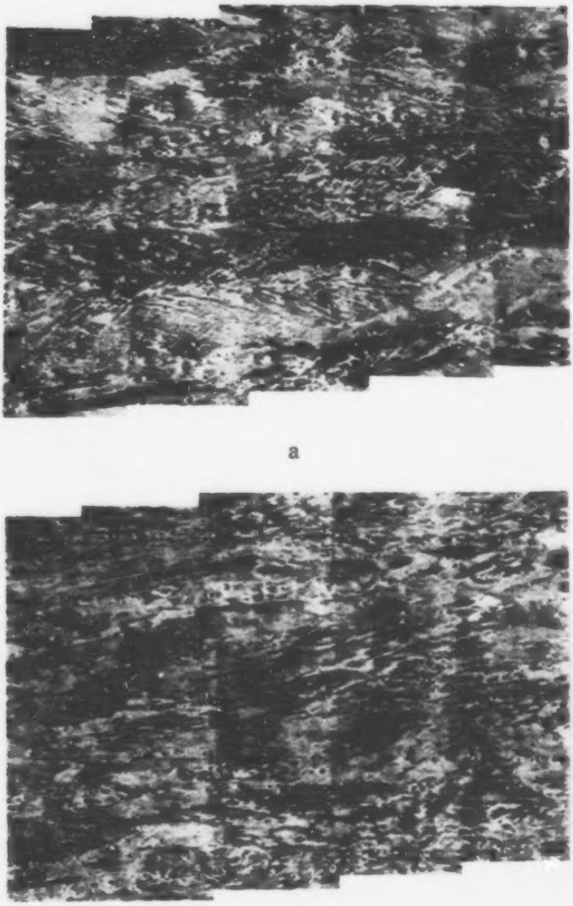

Fig.3: ECC images in the quarter thickness: sample A1 (a) and sample A2 (b).

Rolling with different roll gap geometry produces significant differences not only in texture, but also in the microstructures in the intermediate layers of the two plates. Microstructures with extended dislocation boundaries forming fairly large angles to the rolling direction have been repeatedly observed in the longitudinal section of Al cold-rolled to low and moderate strain levels (e.g. Rosen et al 1995; Hansen and Hughes 1995; Liu et al 1998). Unfortunately, in most microstructural reports, the geometry of the roll gap and the inspected depth are not specified. However, the similarity of structures found in the present study to those reported in the literature suggests that similar geometries of the roll gap were applied.

In the sample A2, 40% rolled with small draughts, extended dislocation boundaries are much closer aligned to the rolling direction than in the sample A1. To our knowledge, this kind of microstructure has never been reported for aluminium after moderate cold-rolling deformation. Since similar microstructures are observed in grains of different orientations (see Table 1), the specific structures in the quarter thickness after small draught rolling cannot explained by the orientation effect alone. It is believed that the origin of different morphology of extended dislocation boundaries can be explained through the analysis of the strain distribution. It is proposed that increasing shear strain ε_{13} leads to changes in the slip pattern which result in "non-standard" preferred macroscopic orientations of dislocation boundaries.

Conclusion

Cold rolling either with intermediate or with small draughts produces different textures and different microstructures near the quarter thickness of aluminium plates. A rolling texture is developed after intermediate draught rolling. In this sample, extended dislocation boundaries form large angles to the rolling direction. In the sample rolled with small draughts, the shear texture replaces the rolling texture in the intermediate layers. Microstructures with dislocation boundaries closely aligned to the rolling direction are observed near the quarter thickness. The results suggest that both texture and the microstructure respond to the geometry of the roll gap. Obviously, cold rolled microstructures and texture must be considered in the context of the geometry of rolling.

Acknowledgements

This work was supported by the Danish Research Council of Technical Science. Dr. G.Winther is acknowledged for useful comments.

References

Choi, C.-H., Kwon, J.-W., Oh, K. H. and Lee, D. N. (1997) *Acta Mater.* Vol.45, pp.5119-5128.

Hansen, J. and Mecking, H., (1975) *Proc. ICOTOM 4*, (eds G.J. Davies, I.L. Dillamore, R.C. Hudd and J.S. Kallend), The Metals Society, Cambridge, pp.34-46.

Hansen, N. (1990) *Mater. Sci. Techn.* Vol.6, pp.1039-1047.

Hansen, N. and Hughes, D.A. (1995) *Phys. Stat. Sol. (b)* Vol.149, pp.155-172.

Liu, Q., Juul Jensen, D. and Hansen, N., (1998) *Acta Mater.* Vol.46, pp.5819-5838.

Mishin, O.V., Lauridsen, E.M., Krieger Lassen, N.C., Poulsen, H.F., Juul Jensen, D., Brückner, G., and Bay, B. (1999) *Proc. ICOTOM 12* (this book of proceedings).

Rosen, G.I., Juul Jensen, D., Hughes, D.A. and Hansen, N. (1995) *Acta Metall. Mater.* Vol.43, pp.2563-2579.

Truszkowski, W., Krol, J. and Major, B. (1980) *Metal. Trans.*, Vol.11A, pp.749-758.

DEFORMATION BANDING AND TEXTURE DEVELOPMENT DURING COLD DRAWING OF UNIDIRECTIONALLY SOLIDIFIED POLYCRYSTALLINE ALUMINUM

Y. KANENO, H. INOUE and N. INAKAZU
Department of Metallurgy and Materials Science, College of Engineering,
Osaka Prefecture University, Sakai, Japan

Abstract

In order to investigate microstructure and texture evolution during deformation and subsequent recrystallization of a unidirectionally solidified polycrystalline material, a pure aluminum rod produced by a continuous casting with a heated mold was cold drawn and then annealed isothermally. The as-cast material had a sharp texture composed of two orientations. With increasing deformation, initial orientations moved to <111> and <100> orientations. In agreement with the orientation changes, the macroscopic banded structure as seen in drawn single crystals was formed in drawn wires. The observed deformation band was made up of differently aligned bands. The central region of the wire in which two bands were crossed each other, was harder than the other regions. Depending on such a deformed structure, recrystallization of drawn wires progressed inhomogeneously. Recrystallized grains formed in the central region did not grow during annealing, whereas these grains were quickly formed compared with those in the other regions.

Keywords: aluminum, deformation band, recrystallization, deformation texture, unidirectionally solidified polycrystal, wire drawing.

1. Introduction

Deformation bands are characteristics of drawn single crystals. It is known that they are formed in drawn copper, silver, gold and brass single crystals (Ahlborn 1966). These macroscopic banded structures have not been observed in drawn normal polycrystals. Recently, it was observed that deformed structures similar to those of drawn single crystals were formed after drawing of polycrystalline copper produced by a new continuous casting process (Kaneno et al. 1996). These copper ingots had a single orientation and consisted of unidirectionally solidified structures. The results obtained suggest that there is a possibility that deformation bands are formed in drawn polycrystalline metals. In the present study, unidirectionally solidified polycrystalline aluminum was cold drawn and subsequently annealed. The purpose of this study is to investigate microstructure and texture evolution during deformation and recrystallization of the present materials, particularly in association with formation of deformation bands.

2. Experimental

A 13 mm diameter rod of 99.99 mass% aluminum, which had been produced by the continuous casting using a heated mold (Ohno 1986), was the starting material. For comparison, an equiaxial-grained aluminum rod 12 mm in diameter with an identical chemical composition was also employed. It was prepared by extrusion and subsequent heat treatment at 773 K for 900 s. They will be denoted as samples US-Al and EG-Al, respectively. **Figure 1** shows grain structures of starting materials. The as-cast sample (US-Al) consists of unidirectionally solidified structure, that is, a structure with grain boundaries parallel to the casting direction. The extruded and heat treated sample (EG-Al) is occupied with equiaxed grains. Grain sizes in the cross section of sample EG-Al are smaller than those of sample US-Al. These materials were cold drawn to 90% reduction in area through conical dies with an average reduction per pass of 5%. The drawing speed was slow (2.7 mm/s) and final diameters of wires were 4.17 (US-Al) and 3.84 mm (EG-Al), respectively. Furthermore, drawn wires were isothermally annealed at 623 K or 473 K in a salt bath and followed by water quenching. Microstructural evolution during drawing and annealing was observed by an optical microscopy. Microhardness measurements were also carried out in cross sections of wires. For texture measurements, thin plates were cut longitudinally from the wires, and their edges of both sides were eliminated. {100} pole figures were measured by using CuKα radiation. To observe the textures at the same plane, the as-cast sample was marked with a straight line on the surface of

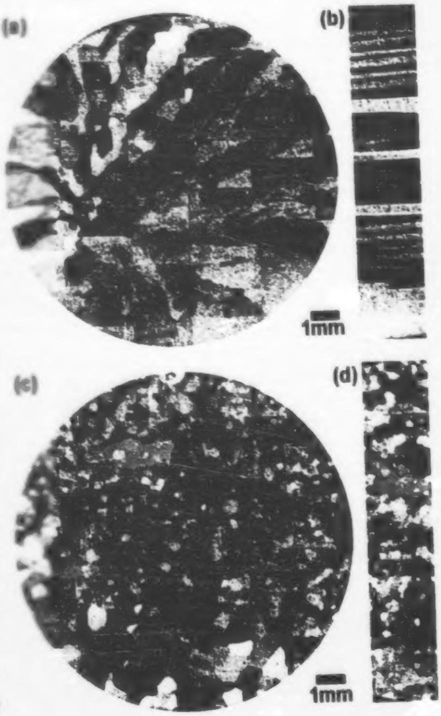

Fig.1 Optical micrographs in cross sections and longitudinal sections of starting materials. (a) and (b) Unidirectionally solidified aluminum (US-Al), (c), (d) Equiaxial-grained aluminum (EG-Al).

the rod and then specimens for measurements were cut along this line in drawn wires.

3. Results and discussion

3.1 Deformation banding

Figure 2 shows optical micrographs in cross sections of 90% drawn wires. Deformation bands can be clearly seen in the unidirectionally solidified sample (US-Al), while no banded structure is formed in the equiaxial-grained material (EG-Al). Deformation bands in sample US-Al are composed of differently aligned bands. In addition, another kind of deformation bands with appearances of ringed wrinkling, which is caused by the additional shear deformation due to the friction stresses operating between a die and a wire (Inakazu and Yamamoto 1980), are also recognized in the peripheral regions of sample US-Al.

Figure 3 shows {100} pole figures of the sample US-Al. The starting material has a sharp texture composed of only two orientations, that is, major <4 3 8> and minor <5 8 2> orientations parallel to the casting direction. The intensity of the former orientation is almost as twice as that of the latter one. With increasing drawing reduction, orientation changes accompanied by the spread of orientation occurred. From these pole figures, the changes in axial orientation during deformation of sample US-Al were determined (**Fig.4**). In Fig.4, numbers indicate drawing reductions, and solid and dashed lines show major and minor orientation changes, respectively. Obviously, the initial orientations move to <111> and <100> orientations, which are main components of drawn *fcc* metals. Therefore, the formation of deformation bands in the present material, as well as in drawn single crystals, is considered to be caused by an orientation separation due to a different lattice rotation as a result of slip. From the fact that deformation banding occurs in sample US-Al in spite of a polycrystalline material, it can be pointed out that deformation bands is not inherent in drawn single crystals. Whether deformation bands are formed or not, is considered to be mainly dependent on the initial texture and/or the grain structure of starting materials

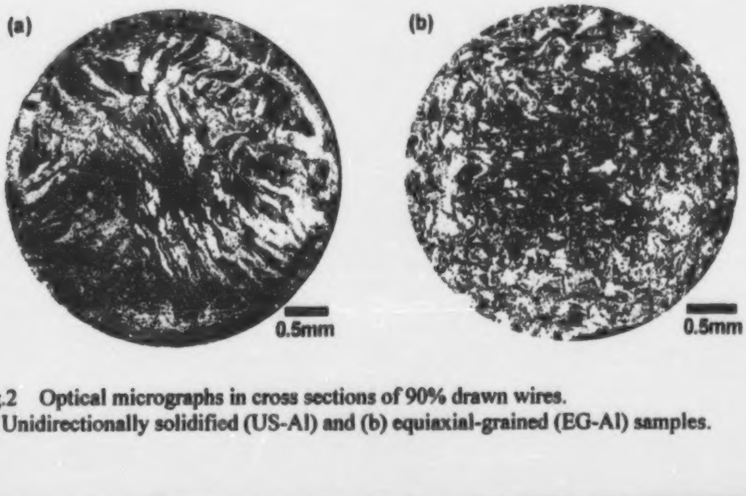

Fig.2 Optical micrographs in cross sections of 90% drawn wires.
(a) Unidirectionally solidified (US-Al) and (b) equiaxial-grained (EG-Al) samples.

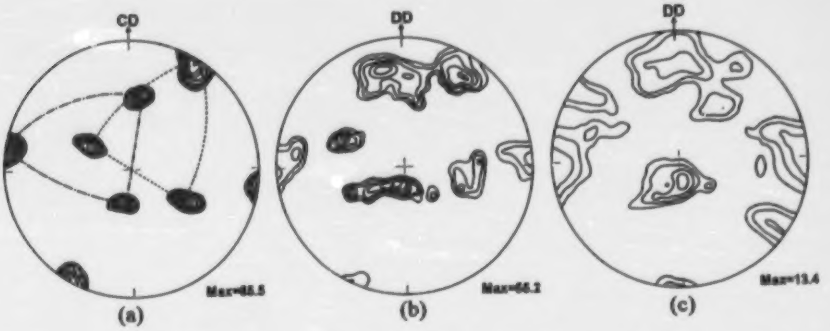

Fig.3 {100} pole figures of unidirectionally solidified aluminum, showing texture development during cold drawing. (a) As cast, (b) 50% and (c) 90% drawn wires (CD: casting direction, DD: drawing direction, Levels: 1, 2, 4, 8, 15, 30, 60, 80). Dashed and broken lines represent major <4 3 8> and minor <5 8 2> orientations, respectively.

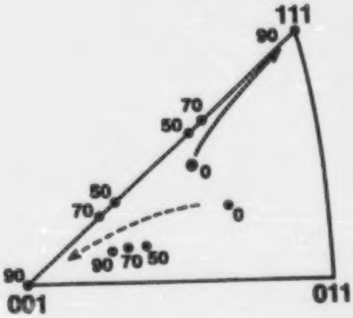

Fig. 4 Changes in axial orientation during deformation of unidirectionally solidified aluminum. Solid and dashed lines show major and minor orientation changes, respectively.

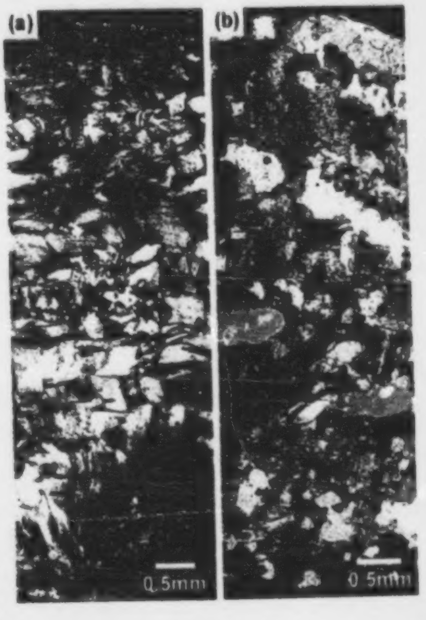

Fig.5 Optical micrographs in cross sections of annealed wires. Samples were cold drawn to 70% reduction and subsequently annealed at 623 K for 1 s. (a) Unidirectionally solidified (US-Al) and (b) equiaxial-grained (EG-Al) aluminum.

3.2 Recrystallization behavior

Drawn wires were isothermally annealed in a salt bath. **Figure 5** shows optical micrographs in cross sections of annealed wires. Both samples were drawn to 70% reduction and subsequently annealed at 623 K for 1 s. In spite of an identical annealing condition, it can be seen that there are a lot of recrystallized grains in sample EG-Al. On the contrary, in sample US-Al, new fine grains are formed only in the central position of the wire except the peripheral parts. Moreover, it is observed that recrystallization of sample US-Al progressed slower than that of

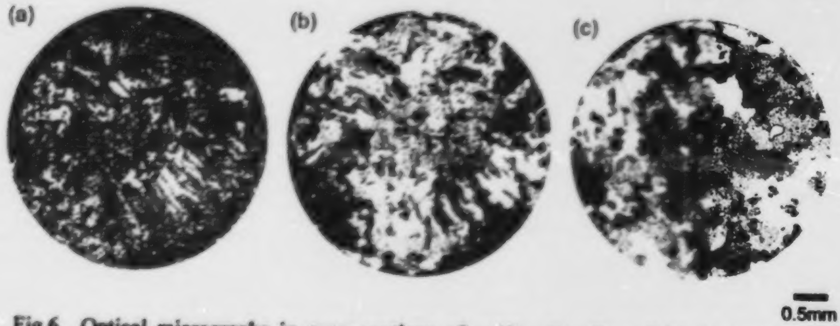

Fig.6 Optical micrographs in cross sections of unidirectionally solidified aluminum. Samples were wire drawn to 90% reduction and subsequently annealed at 623 K for (a) 1 s, (b) 20 s and (c) 50 s.

sample EG-Al. **Figure 6** shows optical micrographs in cross sections of 90% drawn and subsequently annealed wires US-Al. As well as the 70% drawn and annealed sample, the 1s annealing brings about formation of fine recrystallized grains in both center and peripheral regions (Fig.6a). As the annealing time is increased to 20s, new grains are recognized in the intermediate part between the central and the peripheral regions, and grain growth has occurred in the peripheral region (Fig.6b). After recrystallization has been complete, equiaxed grains are formed in both peripheral and intermediate regions, but fine grains formed in the central region are still small (Fig.6c). Such an inhomogeneous microstructural evolution was not observed in sample EG-Al.

Since recrystallization is affected by deformed state of materials, hardness distribution in cross sections of 90% drawn samples was measured along diameters of wires. The results are shown in **Fig.7**. In sample US-Al, the central regions are harder than other regions, while there is a small variation of hardness in sample EG-Al. In the case of sample US-Al, the central region where differently aligned bands are crossed, is divided into small parts as a consequence of formation of thinner bands.

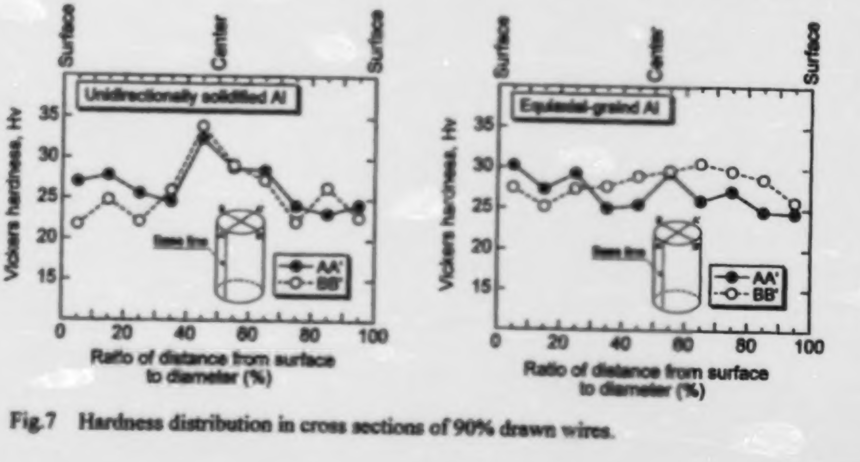

Fig.7 Hardness distribution in cross sections of 90% drawn wires.

Therefore, it may be thought that similar to the case of deformation in fine-grained metals, dislocations are easy to pile up in such a region. Consequently, increases of the dislocation density and the stored energy in the central region leads to formation of fine grains in the early stage of recrystallization. However, these grains did not grow into neighboring regions. A possible reason for this phenomena may be considered as follows: (1) From the fact that the value of hardness in neighboring regions is lower than that in the central region (*see* Fig.7), there is not sufficient strain energy for driving force of grain growth. (2) There is absence of a favorable orientation relationship for grain growth.

4. Conclusions

Microstructure and texture evolution during wire drawing and annealing of unidirectionally solidified polycrystalline aluminum was investigated. The material used had a sharp texture composed of major <4 3 8> and minor <5 8 2> orientations. With an increase of the drawing reduction, initial orientations moved to <111> and <100> with an orientation spread. In consistence with the orientation changes, deformation bands made up of differently aligned bands were formed in drawn wires. The central region of the wire was harder than the other regions. From microstructural observations after annealing, it was found that fine recrystallized grains were quickly formed in the central region, and also that these grains did not grow during annealing while growth of grains formed in other regions occurred. In summary, it is concluded that deformation and annealing behavior of the present material is single crystal-like.

Acknowledgement

The authors wish to express their appreciation to Osaka Fuji Co. for supplying materials. They also express their thanks to Miss Y. Yamagami for her assistance to experiments.

5. References

Ahlborn, H. (1966) Deformation bands in drawn fcc single crystals.: in *Recrystallization, Grain Growth and Textures* ASM, Metals Park, pp.374-85.

Inakazu, N and Yamamoto, H (1980) Deformation band developed in the periphery of drawn copper single crystals. *Journal of Japan Institute of Metals*, Vol.44, No.2, pp.1356-61.

Kaneno, Y., Inoue, H. and Inakazu, N. (1996) Texture and microstructure evolution during cold drawing and annealing of unidirectionally solidified copper: in *Proc. ICOTOM11*, Vol.2 (ed. Z. Liang, L. Zuo and Y. Chu), China, pp.1501-6

Ohno, A. (1986) Continuous casting of single crystal ingots by the O.C.C process. *Journal of Metals*, Vol.38, pp.14-6.

INFLUENCE OF STRAIN PATH ON THE FORMING LIMIT CURVE AND TEXTURE OF ALUMINUM SHEET

S. KOHARA
Department of Materials Science and Technology,
The Science University of Tokyo, Noda, Japan

Abstract

The influence of strain path on the forming limit curve and texture of aluminum sheet has been investigated. Uniaxial tensile straining followed by orthogonal uniaxial tensile straining decreased the forming limit strains. Equibiaxial tensile straining followed by uniaxial tensile straining increased the forming limit strains in the regions of plane strain and uniaxial tensile deformation. Uniaxial tensile straining followed by biaxial tensile straining increased the forming limit strains in the region of biaxial tensile deformation. The texture changes related to the strain paths were also studied.

Keywords: Aluminum, forming limit curve, sheet forming, strain path, texture

1 Introduction

In sheet metal forming processes, the forming limit curve (FLC) has been used to assess the formability of sheet material. The FLCs are usually determined with a single stage strain path, that is, monotonous straining. It is known that the FLCs are changed with the strain path. The two stage strain path may result in decreased or increased forming limit strains. In some cases, large forming limit strains without failure can be achieved with the two stage strain path. The purpose of this research is to reveal the influence of two stage strain path on the forming limit curve in aluminum sheet. To simplify the problems, three kinds of simple two stage strain paths; (1) uniaxial tensile straining followed by orthogonal uniaxial tensile straining, (2) equibiaxial tensile straining followed by uniaxial tensile straining and (3) uniaxial tensile straining followed by biaxial tensile straining were tested in the present study. The results were compared to the FLC by the single stage strain path. The texture changes related to the strain paths were also studied.

2 Experimental procedure

Aluminum sheets (A1050-O) of 1mm thickness were used as the original material in the present study. Three kinds of two stage strain paths (denoted as Strain path-1,2 and 3 hereafter) were tested as the following procedure.

Strain path-1 (Uniaxial tensile straining plus orthogonal tensile straining); Rectangular sheets of 200x400mm were stretched uniaxially with the elongation of 5-15% using a tensile testing machine. The test specimens were blanked from the central portion of stretched sheets in the orthogonal direction and uniaxially elongated.

Strain path-2 (Equibiaxial tensile straining plus uniaxial tensile straining); Circular blanks of 160 mm diameter were blanked from the original sheets and hydraulically bulged to various heights with a bulging machine. The test specimens cut from the bulged blanks were uniaxially stretched with a tensile testing machine.

Strain path-3 (Uniaxial tensile straining plus biaxial tensile straining); Rectangular sheets of 200x400mm were uniaxially stretched with the elongation of 5-12.5%. The circular test pieces were blanked from the stretched sheets and hydraulically bulged with a bulging machine and a die with a circular or elliptical opening.

The local strains were determined with a circular grid of 2.5mm diameter printed on the surface of the test specimens. The strains were represented with a

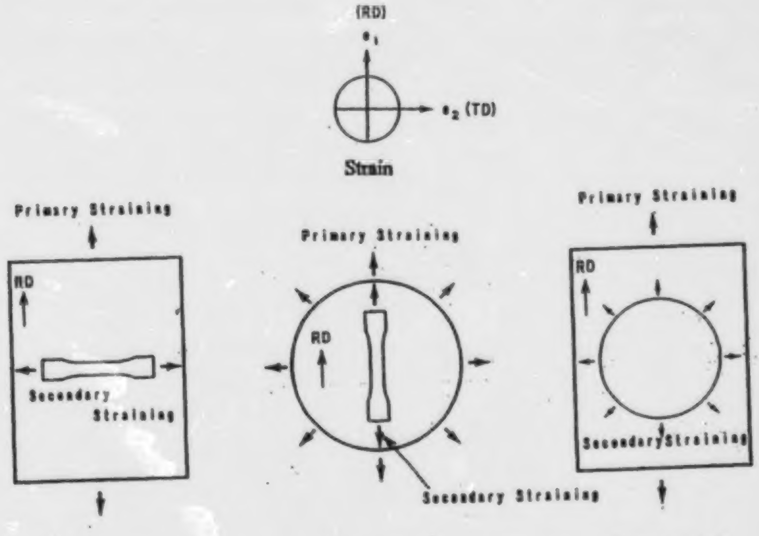

Strain path-1 Strain path-2 Strain path-3

Fig.1 Relations between directions of primary and secondary straining, and major and minor strain.

conventional strain in the text. To hold the fixed directional relation between strain path-1, 2 and 3, the longitudinal direction of the specimens for tensile test was aligned to the rolling direction of the original sheet. The strains in the forming limit diagram were defined as the following definitions. The major strain (e_1) is parallel to the rolling direction and the minor strain (e_2) is parallel to the transverse direction of the original sheet. The directional relations between the two stage strain paths and the major and the minor strains in the forming limit diagrams are illustrated in Fig.1. The details of the experimental procedures for determining the forming limit diagram with a single stage and a two stage strain path are described elsewhere.

The pole figure of the test specimens after straining were determined with the Cu k α X-ray radiation only for the specimens having large enough size for texture determination.

3 Results

The change in strain during the two stage straining along the strain path-1 (primary tensile straining + secondary orthogonal tensile straining) is shown in Fig.2 together with the forming limit curve (dotted line) determined by the monotonous deformation (single stage strain path). The forming limit strains by the two stage straining are less than those by the single stage straining. In the limit of this experiment, the larger the primary straining, the larger the decrease in the forming limit strains.

The effect of the two stage strain path-2 (primary equibiaxial tensile straining + secondary uniaxial tensile straining) on the forming limit strains is shown in Fig.2. The forming limit strains decrease in the region near to equibiaxial tensile deformation ($e_1 = e_2$), but increase in the regions near to the plane strain deformation ($e_2 = 0$) and the uniaxial tensile deformation ($e_1 > 0$, $e_2 < 0$), compared to the forming limit curve (dotted line) determined by the single stage strain path. Especially, the increase of forming limit strains in the region near to plane strain deformation is remarkable.

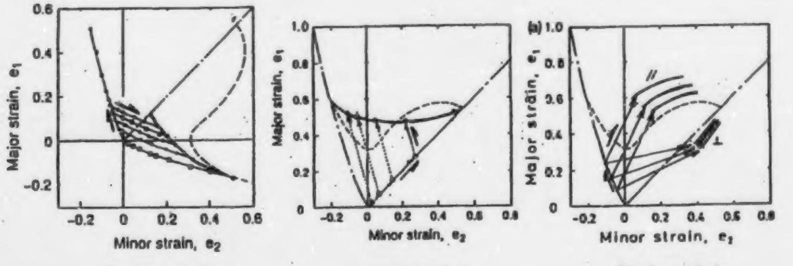

Strain path-1 Strain path-2 Strain path-3

Fig.2 Forming limit curves by Two stage sirain path.
(Dotted line: forming limit curve by single stage strain path)

The effect of the two stage strain path-3 (primary uniaxial tensile straining + secondary biaxial tensile straining) on the forming limit strains is shown in Fig.2. The forming limit strains increase in the whole regions tested in the special case. Within the limit of this experiment, the larger the primary strain, the larger the increase in the forming limit strains. However, it should be noticed that the effect of strain path depends on the directional relation between the rolling direction of the original sheet and the direction of straining. When the direction of minor axis of an elliptical die is parallel (//) to the rolling direction, the forming limit strains are increased, but is perpendicular(⊥), decreased. The direction of minor axis corresponds to the direction of maximum strain in biaxial straining with an elliptical die.

The change in texture with the strain path-1 is shown in Fig.3. The pole figure of the original sheet shows the typical annealing texture of rolled aluminum sheet which has the components of the cube and the R orientation. After the primary straining, the texture is similar to that of the original sheet, but the strong components are weakened. The components are further weakened by the secondary orthogonal straining. The texture change by the equibiaxial tensile deformation is shown in Fig.4. The texture of the original sheet changes to that having the ring like distribution of poles, which can be represented as 〈 110 〉 ⊥ rolling plane.

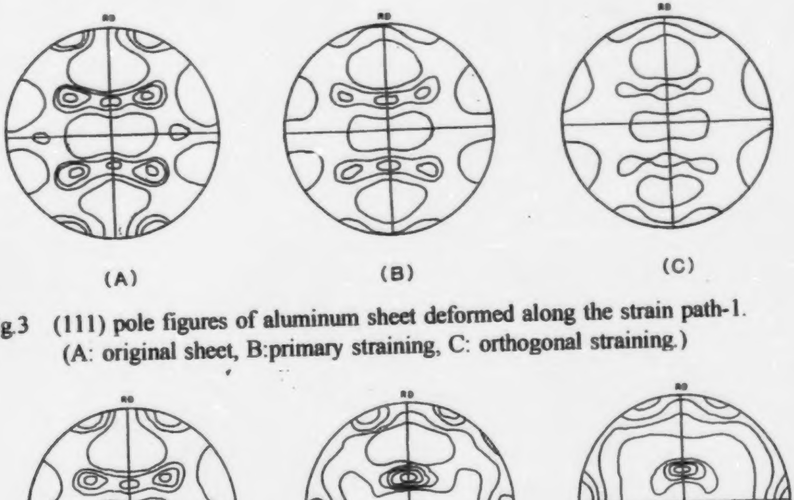

(A) (B) (C)

Fig.3 (111) pole figures of aluminum sheet deformed along the strain path-1. (A: original sheet, B:primary straining, C: orthogonal straining.)

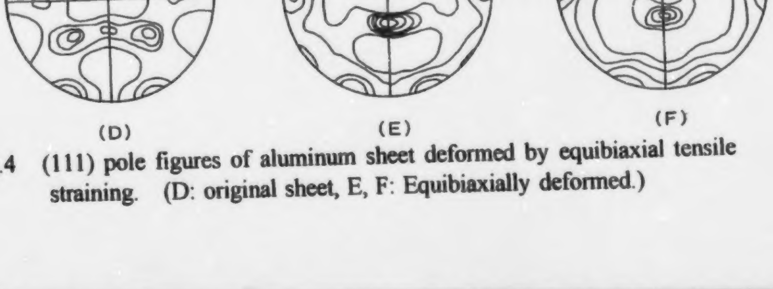

(D) (E) (F)

Fig.4 (111) pole figures of aluminum sheet deformed by equibiaxial tensile straining. (D: original sheet, E, F: Equibiaxially deformed.)

4 Discussion

It is known that the stress-strain relationship in the plastic deformation of metals is affected by the previous deformation. Therefore, the combination of two different modes of deformation may result in decreased or increased forming limit strains. By selecting a proper strain path, larger forming limit strains without failure can be achieved.

When a specimen is elongated uniaxially, the specimen is contracted in the transverse direction. It is expected that the combination of orthogonal tensile straining will yield the relaxation of a part of strain due to the preceding straining. However, the strain path-1 resulted in the decreased forming limit strains. Lloyed and Sang reported that the tensile prestraining followed by the orthogonal tensile straining resulted in the decreased ductility in aluminum and aluminum alloys. This means that the strain is accumulated in a specimen by the combination of the orthogonal tensile straining contrarily to the above mentioned expectation. So, the combination of orthogonal tensile straining should be avoided in the forming process of sheet metals.

The effect of the combination of biaxial tensile straining and uniaxial tensile straining on the forming limit strains has little been reported. Sang and Lloyed reported that the biaxial prestraining resulted in less hardening in the subsequent uniaxial tensile straining. In the strain path-2, the forming limit strains decrease in the region near to equibiaxial deformation, but increase in the regions of the plane strain deformation and uniaxial tensile deformation, compared to the forming limit curve by the single stage straining. Since the strains in highly bulged specimens are already near to the fracture limit, the secondary straining of any type will lead to the fracture of the specimen. So, the forming limit strains are lowered in the region near to equibiaxial deformation. The increase of the forming limit strains is remarkable especially in the region near to the plane strain deformation. The combination of moderate equibiaxial tensile straining and uniaxial tensile straining might have the effect of a kind of strain relaxation. The reason why the forming limit strains are increased remarkably in this region is not clear at present. In the strain path-3, the effect of the two stage strain path on the forming limit strains depends on the relation between the rolling direction and the straining direction. Though the mechanism about the effect of strain path is not clear at present, the result that increases the forming limit strains is important in the sheet metal forming processes.

The texture change in the strain path-1 shows that the strong pole concentrations in the original sheet are weakened during the two stage straining, but the texture of the original sheet seems to be retained. This shows that the strain was not released, but accumulated during the two stage straining. In the experiments of the strain path-2 and 3, the strains due to bulging should be much larger than that due to uniaxial straining. So, the texture developed by bulging will play an important role for straining. The texture change due to the equibiaxial straining shows that the pole figure has a ring like distribution of poles. The new texture has the component in which $\langle 110 \rangle$ axes are perpendicular to the rolling plane of the sheet and may be suitable for the slip deformation in a rolling plane. This new texture development in the sheet may cause the increased forming limit strains. However, the effects of the two stage strain path can not be adequately correlated with the texture changes. Especially the existence of the strong directional relation between the rolling direction and the straining direction suggests that the microstructural factors; such as grain shape, affect the forming limit strains. Further work on the microstructures in the sheet is required to reveal the mechanisms of the effect of strain path on the forming limit strains.

5 Summary

The results of the present study about the effect of two stage strain path on the forming limit curve and texture are summarized as follows. ʼ

(1) Uniaxial tensile straining followed by orthogonal uniaxial tensile straining does not increase the forming limit strains.

(2) Equibiaxial tensile straining followed by uniaxial tensile straining increases the forming limit strains in the regions of plane strain deformation and uniaxial tensile deformation, but decreases in the region near to equibiaxial tensile deformation.

(3) Uniaxial tensile straining followed by biaxial tensile straining increases the forming limit strains in the whole region in a special case. However, there is the case decreasing the forming limit strains depending on the relation between the rolling direction and the straining direction.

(4) The texture changes correspondingly to the two stage straining. However, the increase in the forming limit strains can not be adequately correlated with the texture.

6 References

Hecker, S.S. (1975) Simple technique for determining forming limit curves, *Sheet Metal Industries*, Vol.52, pp.671-76.

Hero, H. et al. (1979) Effect of strain path on the forming limit curve in metastable austenitic stainless steel, *Scandinavian J. Metallurgy*, Vol.8, pp.254-60.

Kohara, S. (1993) Forming-limit curves of aluminum and aluminum alloy sheets and effects of strain path on the curves, *J. Mater. Process. Technology*, Vol.38, pp.723-35.

Lanta-Eskola, A.J. (1980) Effect of loading path on stress-strain relationships of sheet steel and brass, *Metals Technology*, Vol.47, p.45-49.

Lloyd, D.J. and Sang, H. (1979) The influence of strain path on subsequent mechanical properties-Orthogonal tensile paths, *Met. Trans.*, Vol.10A, pp.1767-72.

Sang, H. and Lloyed, D.J. (1979) The influence of biaxial prestrain on the tensile properties of three aluminum alloys, *Met. Trans.*, Vol.10A, pp.1773-76.

TEXTURE INVESTIGATION IN THE SYSTEM AL-NB DURING PHASE TRANSITION

R. SCHNIEBER, H.J.BUNGE and H.-G. BROKMEIER
Institut für Metallkunde und –physik der Technischen Universität Clausthal, c/o GKSS-Forschungszentrum, Geesthacht, Germany

Abstract

In the current paper we describe the crystallographic texture of an Al25/Nb75 composite produced by powder metallurgy and subsequent heating 1h at different temperatures. Heating of 600°C, 800°C, 1000°C and up to 1200°C includes two phase transitions to form Al_3Nb and Nb_2Al. While Al reacts completely part of Nb is stable the whole heating cycle. The starting texture of Al was changed first by recrystallization and second by phase transformation. Texture is softer in the new intermetallic phases than in the metals. According to the similar crystal structures of Al and Al_3Nb the texture transformation will be discussed.

Keywords: Al/Nb-composite, Al_3Nb, Nb_2Al, texture transformation,

1 Introduction

Deformation, recrystallization, phase transition and a large number of variations of these three mechanisms belong to the main steps in an industrial processing line. All these steps have a high influence on the application profile as well as on mechanical and physical properties. Among others crystallographic textures are favored to explain, to understand and to optimize these processes. Longtime one was concentrated on crystallographic textures of single-phased materials. Recently composites and multi-phased systems including intermetallics are more and more of special interest (Lazik and Esling 1993, Bunge 1995, Humphreys 1996, Raabe et al. 1996, Brokmeier 1996). Improvements in all fields of quantitative texture analysis instrumentation and experimental techniques as well as calculation and simulation of crystallographic textures. This paper is focussing on the texture development of an

Al25/Nb75 composite after different annealing. The motivation of this study was to investigate the crystallographic texture during phase transition. The binary system Al-Nb is a good candidate because there are some intermetallic phases known.

Neutron diffraction was preferred because of three reasons. First is that in the case of neutron diffraction relatively sample volumes of some cm^3 can be measured. A sufficient grain statistics can be expected if in minority phases. Second is that based on previous investigation on titanium-aluminides and geological samples it was shown that a low number of complete pole figures are sufficient for a quantitative texture analysis. Only neutrons can obtain this. Third is that the samples are brittle and porous and samples for neutron diffraction has not to be prepared after annealing.

2 Sample preparation and experiment

Pure elemental powders of niobium and aluminium were mixed with volume fractions of about 75Vol. % Nb and 25Vol. % Al, respectively. Powder quality was for Nb 99.90 % purity and 100-300 µm grain size and for Al 99.94 % purity and < 100 µm grain size. Processing starts with mixing the powders under air condition using a turbular mixer followed by pre-compaction to cylindrical samples of 50 mm in diameter. Final step was cold extrusion using a rectangular die of 7x20 mm^2 to get a bar with an orthorhombic texture symmetry, which is correlated to a deformation of 93%.

The bar was cut into segments of 7x10x10mm^3, which were annealed for 1h at 600°C, 800°C, 1000°C and 1200°C 1h. At 600°C annealing no change in the phase composition was observed. First intermetallic compound was detected at 800°C annealing. The total Al reacts with part of the Nb to constitute Al_3Nb a tetragonal phase with c/a ratio of 2.24. Annealing at 1000°C shows also a two phased system of Nb and Al_3Nb. A second intermetallic compound was obtained at 1200°C annealing reacting Al_3Nb with another part of Nb to form Nb_2Al. Nb_3Al the phase with was consistent with the stoichiometry of the powder mixture of 3Nb:1Al was not obtained.

Texture measurements were carried out at the diffractometer TEX-2 (GKSS-Research Center Geesthacht, Germany). For a description of TEX-2 see Brokmeier et al. 1998. To use the whole neutron beam of 19mm cross section, two segments for each condition were glued to have a total sample volume of 1.4 cm^3. That means the average texture of the samples were get by measuring four Nb reflections (110, 200, 211, 310), four Al reflections (111, 200, 220, 311), five Al_3Nb (101, 004, 200, 204, 116) and some Nb_2Al (411, 820, 212, 331). Based on some overlappings not all of the theoretical reflections were taken into account first in the measurement and second in the data evaluation. Texture calculations were carried out by the iterative series expansion method ISEM (Dahms and Bunge 1989) with lmax=22.

3 Texture analysis

The starting texture of the cold deformed material can be described on one hand very close to pure Al and pure Nb and on the other very close to the typical texture of round extruded material. The anisotropy of the deformation is very low compared to rolling. Nevertheless all components of a rolling texture can be found in this starting textures. Figure 1 shows the inverse pole figure in deformation direction for Al and Nb.

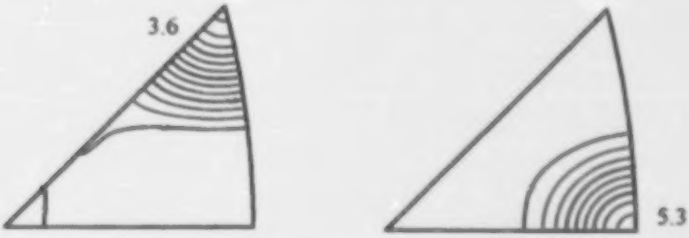

a Al in deformation direction levels 1.0, 1.2, 1.4 .... 3.4

b Nb in deformation direction levels 1.0, 1.5, 2.0 ....5.0

Fig. 1: Inverse pole figures of cold extruded Al25/Nb75 composite

Compared to pure extruded Al which shows a rather sharp texture, the typical <111> fiber texture is much weaker in the composite (Brokmeier 1994). Due to the high volume content of Nb the flow of the soft Al was turbulent around the harder Nb. For Nb the <110> fiber texture of extruded bcc metals was obtained. After 1h annealing at 600°C in both phases only small texture changes were observed. While the Nb texture was nearly constant in Al a soft decrease of the <111> texture component went parallel to a soft increase of the <100> component, see figure 2. To get a stronger recrystallization texture in Al longer annealing was necessary.

Nb was present after all annealing steps with different volume fractions depending on the phase transitions. Figure 3 shows the α-fiber of Nb for all samples one of the standard description of bcc metals (Raabe and Lücke 1994). One sees that the extruded material room temperature material (■) has developed a fiber starting with 6.2 mrd at PHI = 0° going down to 4.0 mrd at PHI = 90°. Short term annealing at 600°C (●) has made no big difference. A first phase transition at 800°C (▲) has formed Al_3Nb and an increase of the texture sharpness was observed with no difference to 1000°C annealing (▼).

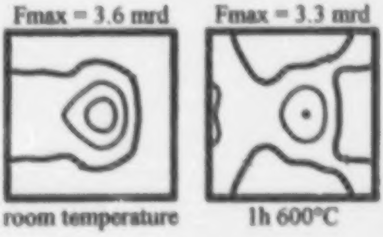
Fmax = 3.6 mrd

Fmax = 3.3 mrd

room temperature

1h 600°C

Fig. 2: ODF sections PHI/phi1 for phi2 = 0 of Al (levels 1.0, 2.0, 3.0 mrd)

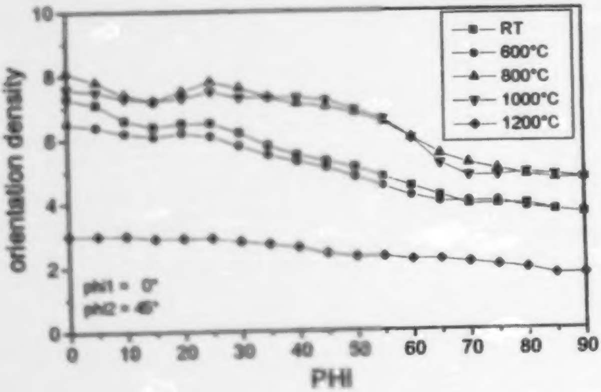

Fig. 3: Nb α- fiber at RT and annealing 1h at 600°C, 800°C, 1000°C, 1200°C

1h annealing at 1200°C has forced a second phase transition to constitute tetragonal Nb_2Al an intermetallic compound with a higher Nb content than Al_3Nb. In spite of the low volume fraction of pure Nb the texture can be measured with high accuracy. Parallel to this second phase transition a strong texture reduction was observed (◆). Looking on the γ-fiber a similar as for the α-fiber can be given. Two different phenomena, recrystallization (Raabe et al. 1994) and variant selection (Park and Bunge 1994), are influencing the texture development of niobium. During the first phase transition from Al to Al_3Nb at 600°C the temperature was relatively low that the influence of primary recrystallization was only weak. According to the presence of a second phase secondary recrystallization was hind during the second phase transition form Al_3Nb to Nb_2Al. A separation between recrystallization and variant selection can be estimated after additional investigations on pure Nb and/or doing some simulations.

Al_3Nb the new intermetallic phase formed after 800°C annealing has replaced pure Al. Depending on the crystallographic relationship between the two crystal structures one expect also a correlation between the two textures. Both crystal structures are closed packed with (111) as closed packed plane for Al and (112) as closed packed plane for Al_3Nb. The deviation of d_{111} = 2.33769 Å in the case of Al and d_{112} = 2.29796 Å in the case of Al_3Nb is only 2%. Table 1 shows a short list of corresponding lattice planes between Al and Al_3Nb.

Table 1: Corresponding lattice planes between Al and Al_3Nb

Al	Al_3Nb
(111)	(112)
(200)	(200), (004)
(220)	(220), (204)

To demonstrate the texture transition figure 4 lists the corresponding pole figures of Al and of Al_3Nb. One sees clearly the correlation between Al and Al_3Nb.

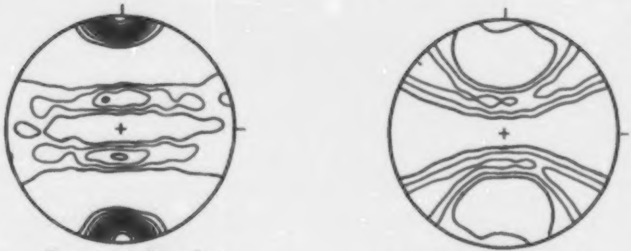

Pmax = 3.5 mrd

Al (111) RT

Pmax = 1.8 mrd

Al (200) RT

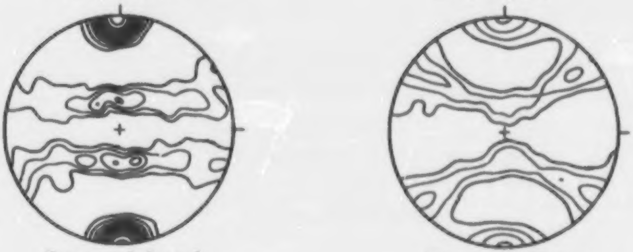

Pmax = 3.2 mrd

Al (111) 600°C

Pmax = 1.80 mrd

Al (200) 600°C

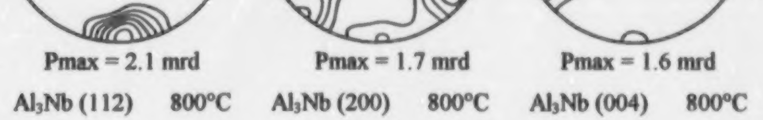

Pmax = 2.1 mrd

Al_3Nb (112) 800°C

Pmax = 1.7 mrd

Al_3Nb (200) 800°C

Pmax = 1.6 mrd

Al_3Nb (004) 800°C

Fig. 4: Al pole figures demonstrating the texture development during phase transition

It can be seen clearly that the texture is weaker in the intermetallic compound than in pure Al. Among others a geometrical effect can explain this decrease. Due to the non ideal closed packed structure of Al_3Nb the angles between equivalent <112> planes are 64.57° and 73.43°. Compared to the ideal angle in fcc structures of 70.52° splitting occurs. According to the resolution of the experiment (counting grid, beam collimation) the splitting cannot be measured and a smoothing results.

The texture of Nb_2Al is rather weak and the counting statistics is not sufficient to interpret the measured pole figures and to describe the second phase transition.

4 Conclusions

We have considered the texture development of an Al25/Nb75 extruded composite after different annealing up to 1200°C. It could be shown that the texture transition goes parallel the phase transition forming Al_3Nb. Based on the similar crystal structures of Al and Al_3Nb relatively small amounts of Nb have to replace Al-positions by diffusion. Therefor, the texture type of Al and Al_3Nb is identical but the texture strength decreases, which can be explained by a geometrical effect. Nb shows the typical bcc texture which is influenced by two phase transitions and by recrystallization. During the formation of Al_3Nb at 800°C the Nb texture increases while a strong decrease was observed after the second phase transition at 1200°C from Al_3Nb to Nb_2 Al.

This work has been funded by the Federal Ministry of Education, Science, Research and Technology (BMBF) under the contract number 03-BR4CLA-9 and the German Research Foundation (DFG).

5 References

Brokmeier, H.-G., Zink, U., Schnieber, R., Witassek, B. (1998) *Mat. Sci. Forum* Vol. 273-275, pp. 277-282.

Brokmeier, H.-G. (1994) *Mat. Sci. Engineering* Vol. A175, pp. 131-139.

Brokmeier, H.-G. (1996) Proceedings ICOTOM 11, International Academic Publishers, Beijing, China, pp. 69-74.

Bunge, H.J. (1995) *Textures Microstruc.* Vol. 24, pp. 1-12.

Dahms, M. and Bunge, H.J. (1989) *J. Appl. Cryst.* Vol. 22, pp. 439-447

Humphreys, F.J. (1996) Proceedings ICOTOM 11, International Academic Publishers, Beijing, China. Pp. 1191-1200.

Lazik, S. and Esling, C. (1993) *Textures Microstruc.* Vol 22, pp. 1-16.

Park, N.J. and Bunge, H.J. (1994) *Mat. Sci. Forum* Vol. 157-162, 563-570.

Raabe, D. and Lücke, K. (1994) *Mat. Sci. Forum* Vol. 157-162, pp. 597-610.

Raabe, D. Mülders, B., Gottstein, G. and Lücke, K (1994) *Mat. Sci. Forum* Vol. 157-162, pp. 841-846.

Raabe, D., Fischer-Bühner, J., Ball, J. and Gottstein, G. (1996) *Proceedings ICOTOM 11*, International Academic Publishers, Beijing, China pp. 941-950.

SELECTIVITY OF GOSS GRAINS DURING ABNORMAL GRAIN GROWTH IN FE-SI ELECTRICAL STEELS

N. RAJMOHAN AND J. A. SZPUNAR
Department of Mining and Metallurgical Engineering, McGill University, Montreal, Quebec, Canada H3A 2B2

Abstract

Abnormal growth of Goss grain is studied in detail by various computer experiments which uses computer specimens with imposed orientation distribution function (ODF) of primary recrystallized Fe-3%Si steel. Using these computer experiments different models for the growth of Goss grain in Fe-3%Si steel is tested. From the results, the importance of initial matrix texture and percentage of mobile boundaries around a growing grain during annealing is realized. Based on this analysis selection of Goss grain is discussed in detail.

Keywords: Abnormal grain growth, Goss texture, Fe-Si steel, Mobile boundaries.

1 Introduction

Development of Goss texture depends on the texture and microstructure of the primary recrystallized Fe-Si steel. The existence of various types and fractions of grain boundaries in the textured primary recrystallized specimen influences the secondary recrystallization. The driving force for grain growth is the reduction of GB area, and thus the total energy of the system. The kinetics of grain growth is determined by the grain boundery mobility. Among many factors such as surface energy, particle pinning, grain boundary grooving, etc., which may influence Abnormal grain growth (AGG), effect of second phase particles is considered to be of prime importance in the case of Goss texture development in Fe-Si steels. At higher temperatures, precipitate particles undergo Ostwald Ripening (OR). This causes the breakdown of GB pinning and favors certain GBs that move faster than others and are responsible for AGG. During the grain growth process, differences in the GB mobility along with the fractions of high mobile boundaries determine the final texture and grain size distribution of a material.

Use of computer models to investigate the grain growth process is observed to be inevitable, as it is possible to introduce anisotropic energy and mobility conditions along with full description of crystallographic texture and microstructure. Various research works have been already published on the computer models developed for the grain growth [1-4]. In this work, the computer experiments conducted to study the specialty of the Goss grain among the other orientations are discussed in detail. The result of the Monte-Carlo simulation, which incorporates the inherent mobility, is also discussed to explain the energy conditions for the growth of the Goss grains in the primary recrystallized matrix.

2 Random and CSL grain boundaries

Most of the works [5-9] are based on the belief that some specific Coincidence Site Lattice (CSL) boundaries such as Σ9 [7], Σ7 [8], and Σ5[9] are responsible for the abnormal grain growth. These theories assume that higher number of such boundaries, which possess low energies and high mobility, surrounds Goss grain. Though there has been some evidence that CSL boundaries move faster then the random boundaries, it was only reported on very special cases [10-11] mainly in pure material. The changes in the boundary structures at elevated temperatures have been found to destroy the special properties of CSL boundaries [12-13]. It was also reported that at high impurity levels CSL boundaries again lose their special property [11]. Previously, an experimental study on commercial purity single crystalline specimens of Fe-3%Si, using orientation measurements and grain misorientation analyses of pole figures conducted by Titorov [14-15] also concluded that GBs with middle misorientation angles (20°- 45°) were responsible for AGG of the Goss grain. Also, the experimental findings by Watanabe [16] demonstrate that the large growing grains have a high number of high-energy grain boundaries (HEGBs) (~20°-45° misoriented random boundaries). At high concentrations of alloying elements and at high processing temperatures, the HEGBs have the highest mobility and the highest precipitate coarsening rate and consequently are released for migration earlier than other boundaries in an alloy system. Based on EBSP measurements and statistical analysis of Grain Boundary Character Distribution (GBCD), Hayakawa and Szpunar [17-19] suggested that higher number of random boundaries surround the Goss grain in silicon steels than any other grain. For the high permeability steel, the fraction shows a sharp maximum that is 76% for the Goss orientation and a minimum, which is 37 % for the main texture component. A spectacular difference of ~ 40 % is seen between Goss orientation and main texture component. In the case of conventional electrical steel, though the Goss orientation has a higher fraction (~ 68 %), the peak value of 70 % fraction is found at the orientation which is deviated by 20° from Goss orientation through the *ND//<110>* axis [19]. These observations elucidate that the high-energy boundaries are considerably important for the case of Goss grains to grow in the matrix of primary recrystallized texture.

3 Computer experiments

In a polycrystalline material, various microstructural features play an important role in deciding the frequency of occurrence of a particular type of GB.

Under the assumption that a primary recrystallized specimen with equiaxed grains has very little inhomogeneity Morawiec et al [20] developed a computer procedure for calculating the frequencies of various type of GBs in Fe-3%Si steel in accordance with the ODF. In their calculation, these authors ignored the clustering and spatial relations of the grains in the matrix. The computer model developed for this work is composed of three-dimensional honeycomb grains with 12 nearest neighbors [21,22]. Each honeycomb polygonal structure is a lattice unit in this computer model and corresponds to a primary recrystallized grain. This is based on the assumption that an equiaxed grain structure of a primary recrystallized matrix can be modeled with a uniform three-dimensional polygonal structure. The algorithm developed by Morawiec et al [20] is used for the assignment of crystal orientation to the generated grains in accordance with the experimentally measured ODF. At the beginning of the computer run, the orientation, growth behavior of which is to be studied, is assigned to a grain at the center of the computer specimen. Then the grain can be allowed to grow by assuming that certain type of GBs with specific misorientation are 'allowed' and others are 'forbidden'. If the encountered GB is an allowed boundary, then the grain which makes that type of GB is assigned the same orientation as the growing grain. The detailed explanation is given in our previous work [22]. When the growing grain meets a forbidden boundary, the grain, which makes that boundary is left unaffected. The same procedure is carried out for all the nearest neighbors of the growing grain at each instant and is called a growth step. Thus, the growth step in this computer experiment corresponds to the time variable. At any particular time, GBCD of the growing grain can be computed based on orientations of its peripheral neighbors. The kinetics of the growing grain in the computer experiment can be expressed by recording the volume of the grain as a function of growth step. The volume of a grain is the number of lattice units it has. In each growth step, all the peripheral lattice units, which bound the growing grain are allowed to grow further depending on the type of the boundaries they make with the growing grain.

Several investigations [18,21,23] on the fractions of certain type of grain boundaries around the Goss grains after primary recrystallization in Fe-3%Si steels reveal that there are only 13% of highly celebrated Σ3-Σ9 CSL boundaries [23]. The next highest frequency is ~10% of Σ3-Σ9 CSL boundaries for {111}⟨112⟩ orientation component [23]. These two orientations have a difference in the probabilities of mobile boundaries (Σ3-Σ9 CSL boundaries) of only 3%. If Σ3-Σ29 CSL boundaries are considered then the Goss and {111}⟨112⟩ orientations have the probabilities of 20% and 19%, respectively. On the other hand the fraction of HEGBs around the Goss grains is approximately 70% [18,19] and difference between the Goss and that of main texture components {111}⟨112⟩ is approximately 40% in the high permeability steels. Apart from the mobility difference and energy difference between the grain boundaries, which are responsible for a particular orientation to grow abnormally during grain growth, the fraction of the mobile boundaries around that orientation is also another important factor to be considered. On various occasions [17-22], it has been proved that the fractions of CSL boundaries are too small to effect a major textural change in electrical steels. Based on these arguments, it was stated in our previous works [22] that the matrix fraction (MF) of mobile GBs is important in dealing with grain growth. The matrix fraction can be defined as the average initial fraction of mobile boundaries, the given grain would make with other grains having orientations defined by the ODF. Therefore, the MF is a constant for a given orientation in a given texture. As an example, the MF of Goss orientation in the matrix of primary recrystallized conventional Fe-Si steel, under the assumption that middle misorientation angle (20°- 45°) boundaries are 'mobile', is about 68%.

The computer experiments carried out for various MFs shows (Fig.1) that the growth of a grain is higher if the MF is higher. In Fig.1, growth behaviors of the grains, which have the MFs of 30% to 90% are given. The growth of almost all the grains is stopped when MF is 10% and 20%. On the other hand 100% mobile boundaries around the growing grain is not practical. From the observation carried out by Lin et al [23], if the allowed boundaries are $\Sigma3$-$\Sigma9$ CSL boundaries then the Goss grain would not grow as it has the MF value of only 13%. Harase and his co-workers [5-9] stressed upon the role of especially $\Sigma9$ CSL boundaries on the development of Goss texture in electrical steels. If the $\Sigma9$ CSL boundaries were the only boundaries considered as the allowed boundaries then the MF of the Goss grain would have a very low value of 3%. This extremely small percentage cannot make the Goss grains grow.

Using the growth algorithm explained previously, grains with different orientations are allowed to grow with an assumption that the middle misoriented boundaries have high mobility in a polycrystalline matrix. The grain in the polycrystalline matrix, the grains are assigned orientations that are generated from the experimentally measured ODF of conventional electrical steel using Morawiec et al. [20] algorithm. The ϕ_2=45° section of ODF of the conventional electrical Fe-3%Si steel is given in Fig.2. The main texture component here is {111}<110>. In this polycrystalline matrix, the growth of the grains with different orientations observed (using the computer experiments explained above) is given in Fig. 3. Each curve presented in the graph is an average of 10 simulations. The Fig. 3 shows that Goss orientation grows considerably faster than other orientations and the main component $\{111\}\langle110\rangle$ grows faster than the cubic $\{100\}\langle001\rangle$ orientation.

4 Conclusion

Based on the model that assumes high mobility to high-energy boundaries, the Goss grain is observed to grow much faster than the main and cubic texture components. The results of the model to analyze the importance of mobile boundary fraction shows that higher the matrix fraction of mobile boundary, higher the growth rate is. This analysis also severely questions the possible role of the CSL boundaries as they contribute only 13% to the total number of grain boundaries in the conventional electrical steel.

5 Reference

1. Anderson.M.P, Srolovitz. D.J, Grest.G.S,and Sahni.P.S, (1984) Acta metall., 32(5), 783

2. Srolovitz.D.J., Crest.G.S. and Anderson.M.P,(1985), *Acta metall.* **33**(12), 2247.
3. Srolovitz.D.J, Anderson.M.P, Crest.G.S, and Sahni.P.S,(1984) *Acta metall.* **32**(9), 1429
4. Grest. G.S, Srolovitz.D.J, and Anderson.M.P, (1985) *Acta metall.*, **33**(3), 509.
5. Harase.J, and Shimizu. R, (1988), *Trans. Iron Steel Inst. Jpn.*, **29**, 388
6. Harase.J, Shimizu. R, and Dingley. D. J, (1991), *Acta metall.*, **39**, 763
7. Shimizu. R., Harase. J., and Dingley .D.J., (1990), *Acta metall.*, **38**, 1101
8. Harase.J., Materials science Forum, (1992), **94-96**, 419
9. Yoshitomo.Y, Ushigami.Y., Harase.J., Nakayama.T., Matsui.H., and Takahashi.N., (1993) *Materials Science Forum*, **113-115**, 715.
10. Aust.K.T., and Rutter.J.W., *Trans. Metall. Soc. AIME.*, (1959) **215**, 119.
11. Gottstein.G and Shrindlerman.L.S., (1992), *Scripta Metall.*, **27**, 1515
12. Aust.K.T., and Rutter.J.W., (1963), *Recovery and Recrystallization of Metals*, ed. L. Himmel, John Wiley Sons, New York,
13. Rutter.J.W. and Aust.K.T., (1965), *Acta metall.*, **13**, 181
14. Titorov, D.B. (1973). *Fiz. Metal. Metalloved.*, **35**(6), 1299.
15. Titorov, D.B. (1994). *The physics of Metals and Metallography*,77(1), 73.
16. Watanabe, T. (1992). *Mat. Sci. Forum*, **94**, 209.
17. Hayakawa, Y., Muraki, M. and Szpunar, J.A. (1998). *Acta Mater.*,**46**(3), 1063
18. Hayakawa, Y., Szpunar, J.A., Palumbo, G. and Lin, P. (1996). *Journal of Magnetism and Magnetic Materials*, **160**, 143.
19. Hayakawa, Y. and Szpunar, J.A., (1997). *Acta mater.*, **45**(3), 1285.
20. Morawiec.A., Szpunar.J.A., and Hinz.D.C., (1993), *Acta metall.*, **41**, 2825,
21. Hinz, D. and Szpunar. J.A. (1995). *Phys Rev.*, **B52**, 9900.
22. Rajmohan. N, Szpunar.J.A, Y.Hayakawa (1998). *Mater. Sci. eng.***A259**, 8
23. Lin, P, Palumbo, G, Harase, J and Aust, K.T (1996) *Acta Mater.* **44**(12), 4677.

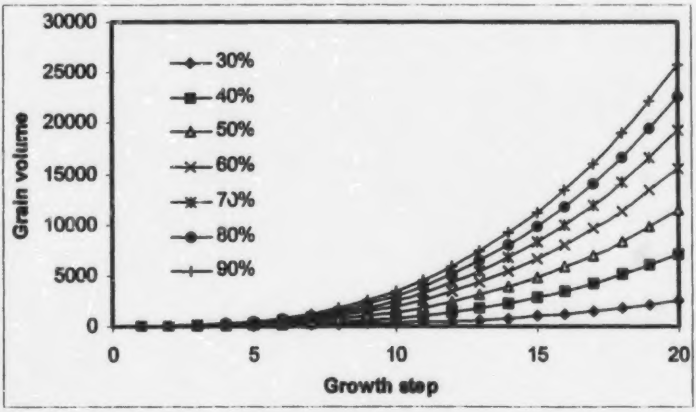

Fig. 1 **Simulated growth behavior of the grain with various percentage of mobile grain boundaries (MF) in the initial matrix**

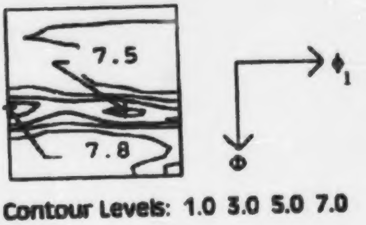

Fig. 2 ϕ_2=45° section of orientation distribution function (ODF) of conventional Fe-3% Si electrical steel

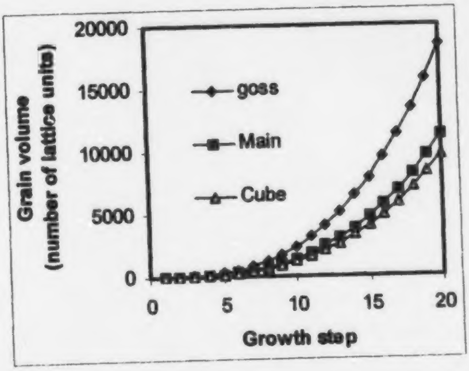

Fig. 3 Volume as a function of growth step for grains having Goss {110}<001>, main {111}<011>, and cube {001}<100> orientations obtained assuming that high energy boundaries have high mobility in the conventional Fe-3% Si steel

TEXTURE INHERITANCE IN HSLA GRADES SUBJECTED TO COMPACT STRIP PRODUCTION.

E. BOUZY, B. CARDIOLA, C. ESLING AND M. HUMBERT
Laboratoire d'Etude des Textures et Application aux Matériaux, Letam
CNRS URA 2090, ISGMP, Université de Metz, 57045 Metz Cedex 01 France.
G. FLEMMING AND K.E. HENSGER
SMS AG Postfach 230 229 40088 Duesseldorf Germany

Abstract

Textures of the ferritic phase in HSLA grades were determined after Compact Strip Production (CSP). CSP is a process for the production of hot strip from a continuously cast slab using direct charging. The conditions of the thermomechanical rolling influence the austenite to ferrite phase transformation, which modify the final microstructures and textures of the products and consequently their mechanical behaviour. By an adapted modelling of the phase transformation, the high temperature austenite textures have been evaluated, then computer simulations of the ferritic textures have been performed without variant selection. These simulated textures are compared with the experimental ones and the texture inheritances are discussed.

Keywords : Phase transformations, Variant selection, Texture.

1 Introduction

CSP (Compact Strip Production) is a process for the production of hot strip from a continuous cast thin slab (Flemming and Hensger 1996). This process allows the production of HSLA grades. Their room temperature states, inherited by phase transformation from high temperature austenitic states can be strongly influenced by the chosen hot rolling routes. For example, rolling the austenite at a temperature lower than the recrystallisation temperature (determined by adapted proportions of microalloying elements) leads to austenite with a high density of grain boundaries and deformation bands. Consequently an important grain refinement results through the γ-α transformation of the hot-worked and non-recrystallised austenite. Thus, HSLA steels, characterised by a high strength (>345MPA) and a fine grain size (=<6μm) can be produced by combining microalloying and thermomechanical rolling.

In this work, we studied the textures and microstructures of two ferritic products, inherited through the γ-α transformation but differing by their microalloying elements. The high temperature textures of the austenite just after rolling, but prior to cooling, have been evaluated in both cases thanks to a method developed in Letam. Simulating the transformation of these austenite textures into the corresponding ferritic textures allowed us to discuss the texture inheritances.

2 Experimental

Fig.1 exhibits a schematic representation of a CSP plant.

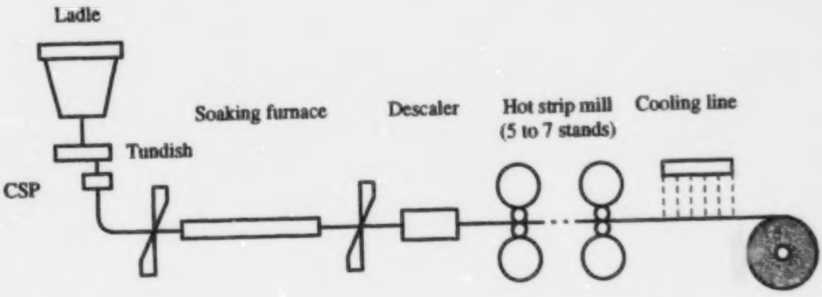

Fig. 1 Schematic representation of a CSP plant.

Using different microalloying and thermomechanical processing, two different levels of yeld strenghs were adjusted for the produced hot strip : 425 Mpa (sampleA), and 565 Mpa (sampleB).

On the hot strip mill the austenite is subjected to hot deformation. The finishing temperature is below the no-recrystallization temperature (T_{nr}). That means, a hot worked, (no or) partial recrystallized austenite leaves the mill. On the laminar cooling line this austenite (parent phase) gets transformed into ferrite (product phase).

The final thickness of samples was 6mm, obtained by the rolling of slabs of 50mm at high temperature. Particular attention has been paid to not plastically deform the products during the cooling down and in the ferritic phase.

The finishing temperature of sample A was higher than that of sample B. For sample A the ferritic microstructure, obtained through the γ-α transformation, shows equi-axed grains of about 5 to 10 µm. In sample B, a stronger work-hardening takes place during rolling, leading to a high density of grain boundaries. Consequently, the ferritic microstructure of sample B appears finer and shows more elongated grains (grain size 3.5-4.5 µm).

The ferritic textures have been determined at the surface and at the mid-section of the thickness of each sample. Three incomplete pole figures (110), (200), and (211) were measured by X ray diffraction of the K_α radiation of Cobalt. The ODFs and the recalculated pole figures were calculated with the spherical harmonic method (Bunge 1969, Wagner and Humbert 1987) up to Lmax = 30.

3 Results

3.1 Sample A

The textures at the surface and in the mid-section are quite different as shown in figures 2 and 3. The texture at the surface is likely to be linked to a shear deformation process, whereas, in the mid-section, to compression of the parent austenite. The textures are smooth, but the sharpness is more pronounced in the mid-section (texture index J = 1.81) than at the surface (texture index J = 1.64)

It is rather difficult to express the textures in terms of spatial fibres because of the smoothness and the spread of the ODF. Nevertheless, orientation (110)<111> is predominant at the surface, whereas orientation (112)<110> is more favoured in the mid-section.

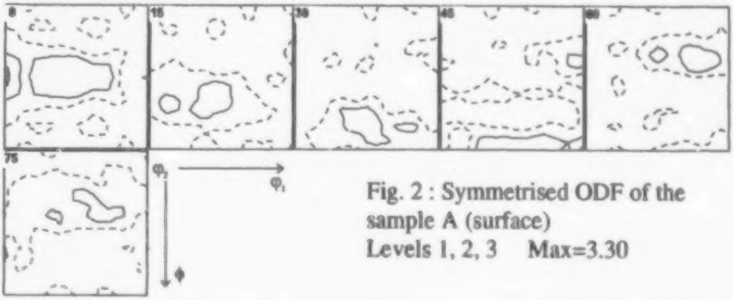

Fig. 2 : Symmetrised ODF of the sample A (surface)
Levels 1, 2, 3 Max=3.30

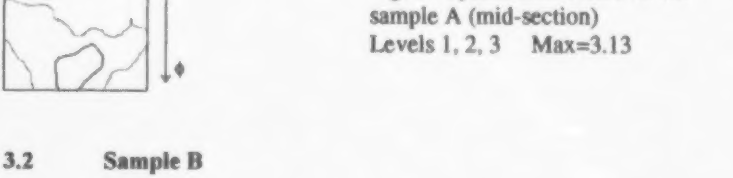

Fig. 3 : Symmetrised ODF of the sample A (mid-section)
Levels 1, 2, 3 Max=3.13

3.2 Sample B

As for sample A, the textures at the surface and in the mid-section are quite different as shown in figures 4 and 5and can be interpreted as for sample A. Globally, the texture sharpness of sample B is higher than that of sample A. As for sample A, the texture is sharper in the mid-section (J = 1.54 at the surface, J = 4,74 in the mid-section). Although more pronounced, the textures of sample B cannot be described as simple partial fibres. As for sample A, the same principal orientations in the mid-section (resp. at the surface) can be observed, but with more pronounced densities.

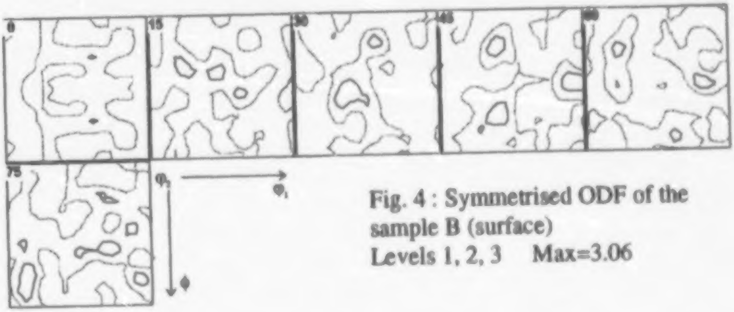

Fig. 4 : Symmetrised ODF of the sample B (surface)
Levels 1, 2, 3   Max=3.06

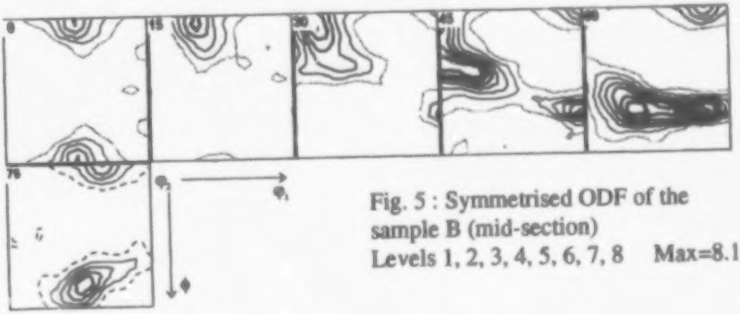

Fig. 5 : Symmetrised ODF of the sample B (mid-section)
Levels 1, 2, 3, 4, 5, 6, 7, 8   Max=8.12

4 Evaluation of the austenite texture

The ferritic phase of both samples results from the γ-α transformation of the austenite phase.

Comparison of the inherited ferritic textures clearly shows that the metallurgical states of the respective austenite phases were quite different just after rolling, prior to cooling. Nevertheless, although more widely spread for sample A, the textures are of the same type in the mid-section (resp. at the surface). Consequently, the corresponding parent textures of the autenite phase of both sample are likely to be of the same type.

At first, we calculated the texture of the austenite from the texture of the ferrite by using a method we developed (Humbert and Gey 1998). If no variant selection occurs, the transformed texture (ferrite texture) $f_2(g)$ is related to the parent texture (austenite texture) $f_1(g)$ by the convolution integral (Bunge 1982):

$$f_2(g) = \int W(g_1) \cdot f_1(g_1^{-1} \cdot g) \cdot dg_1 \qquad (1)$$

where $W(g_1)$ is the orientation transformation function taking into account the mutual orientation relation Δg_0 between both lattices. The method consists in inverting this relation using the series expansion of each function, implied in this relation. This method, tested on different materials and textures, gives the parent texture provided that no variant selection occurred and that Δg_0 be known (for example, Nishiyama-

Wassermann NW, Kurdjumov-Sachs KS , etc...). Unfortunately, in the case of samples A and B, the evaluation (by this method) of the austenite ODF failed, leading to ghost densities, for the pseudo-ODF presented high negative values, compensated by high positive ghost densities (let us remind that $\int f_1(g)\cdot dg = 1$ and $f_1(g) \ge 0$). This happens when either a strong variant selection occurred during the transformation or/and the inherited orientation were not correlated by the chosen Δg_0 . This could be related to additional effects like plastic deformations. If the negative values can be explained by the variant selection only, it is then possible to have information about the austenite texture, by calculating the correlation function R(g) (Humbert and Gey 1999). R(g) is the upper limit of the parent ODF :

$$R(g) \ge \tfrac{1}{k} f_1(g) \ge 0 \quad \text{with k=24 for KS and 12 for NW} \qquad (2)$$

Consequently, the highest densities of R(g) calculated from the ODF in the mid-section of sample B (Fig. 6) indicate the localisation of the highest densities of the parent austenite texture. But this information must be validated by additional investigations.

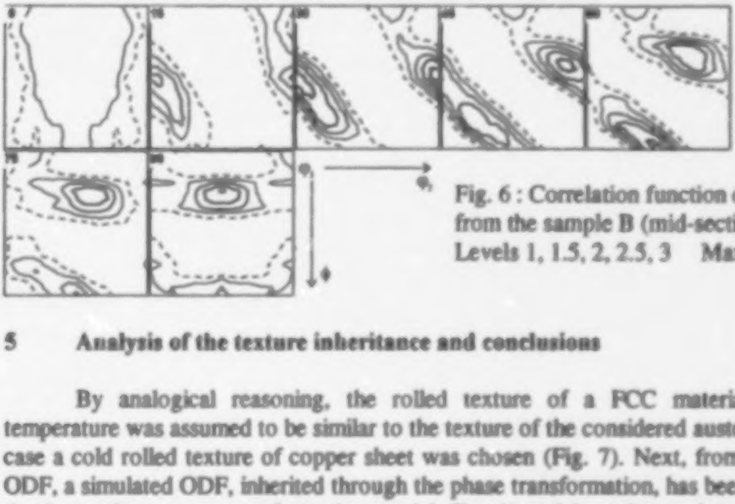

Fig. 6 : Correlation function calculated from the sample B (mid-section). Levels 1, 1.5, 2, 2.5, 3 Max=3.27

5 Analysis of the texture inheritance and conclusions

By analogical reasoning, the rolled texture of a FCC material at room temperature was assumed to be similar to the texture of the considered austenite. In this case a cold rolled texture of copper sheet was chosen (Fig. 7). Next, from this model ODF, a simulated ODF, inherited through the phase transformation, has been calculated thanks to the texture transformation model (Eq. 1) and by using various orientation relations (Nishiyama-Wassermann NW, Kurdjumov-Sachs KS). In this case no variant selection was assumed. Fig. 8 shows the sections at constant Phi1 of calculated ferrite texture, obtained with NW orientation relation :

$$(111)\gamma /\!/ (110)\alpha$$
$$<\!-211\!>\gamma /\!/ <\!-110\!>\alpha$$

The simulated ferrite ODF shows a resemblance with the experimental one, measured in the mid-section. Nevertheless, even if both ODFs present similar trends, some differences can be observed. The magnitudes of the densities are not distributed in the same manner (the simulated ferrite texture shows more peaks) and the localisations of some important peaks do not exactly correspond. These differences may be explained by the fact that :

1) the austenite model texture only presented the main trends of the real austenite texture. The rolling deformation imposed to the copper sheet differs from the austenite rolling. Moreover, copper does not behave by deformation as the austenite.
2) a variant selection occurred by the cooling. This variant selection could be varying within the 6 mm thickness of the sample.
3) additional effects like plastic deformations were imposed to the phase transformation.

In spite of this, the main features of ferrite texture are well described by the transformed copper texture, at least qualitatively.

Moreover, the correlation function R(g), calculated from the ferrite texture, and the transformed ODF of copper match very well. It may be assumed that the austenite model ODF (ODF of the copper sheet) represents the real austenite ODF, at least qualitatively.

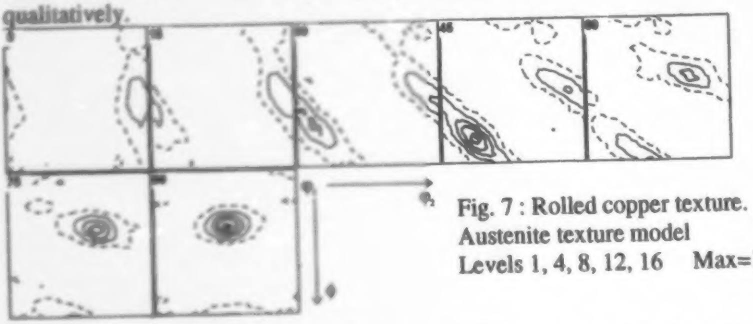

Fig. 7 : Rolled copper texture.
Austenite texture model
Levels 1, 4, 8, 12, 16 Max=18.3

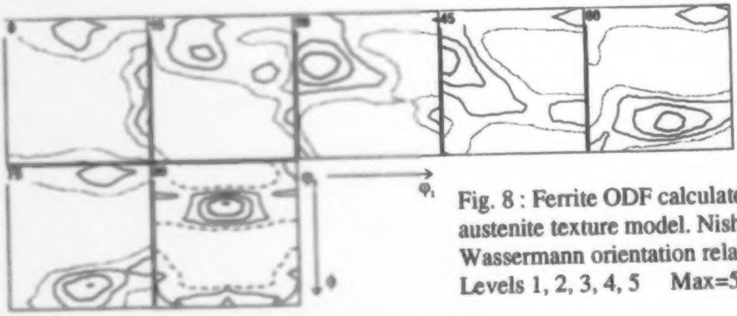

Fig. 8 : Ferrite ODF calculated from the austenite texture model. Nishiyama-Wassermann orientation relations.
Levels 1, 2, 3, 4, 5 Max=5.11

Acknowledgement : we thank Dr. J.J. Fundenberger for providing us the copper texture.

6 References

Bunge H.J. (1969) : Mathematische Methoden der Texturanalyse, Berlin, Akademie Verlag.

Bunge H.J. (1982) : Texture Analysis in Materials Science, London,Butterworths.

Flemming H.G. & Hensger K.E. Proceedings of Mech. Working and Steel Processing Conf. (1998) Pittsburgh, PA.

Humbert M. & Gey N. (1998). Material Science Forum, **273-275**, pp.163-168.

Humbert M. & Gey N. (1998). J. Appl. Cryst. **32**, pp.21-26.

Wagner F. & Humbert M.(1987) Textures and Microstructures, 7, 115-129

FORMATION OF ORIENTED LAMELLAE IN TIAL ALLOYS BY DIFFUSIONAL REACTION

H. FUKUTOMI, M. UENO and M. NAKAMURA
Department of Mechanical Engineering and Materials Science, Faculty of Engineering, Yokohama National University, Yokohama, Japan
T. SUZUKI
Department of Materials Science, Faculty of Engineering, Ibaraki University, Hitachi, Japan
S. KIKUCHI
Department of Materials Science, School of Engineering, The University of Shiga, Hikone, Japan

Abstract

The process developed on the basis of diffusional reaction between aluminum and textured titanium foils to control the alignment of lamellar microstructure in the sheet of TiAl based intermetallic compounds is experimentally analyzed. The changes in constituent phases, their volume fractions and orientations are investigated at various stages of the process by optical and scanning electron microscopy, EDX and texture measurements. It is found that about half of the lamellae is arranged in the orientations expected from the texture of the titanium foils by the process consisting of five stages. The volume fraction of the oriented lamellae can be related to the texture sharpness of the starting titanium foils and the volume fraction of α_2 (Ti_3Al) before the heating in the α single phase state.

Keywords: Diffusional reaction, oriented lamellae, textured titanium foils, TiAl alloys

1 Introduction

A series of experiments using the so-called PST crystals has shown that TiAl based intermetallic compounds with a proper alignment of lamellar microstructure have superior characteristics as a light weight-high strength material for high temperature structural applications (Inui et al. 1992; Yokoshima and Yamaguchi 1996). Thus the process development to construct the oriented lamellar microstructure in this compound was given as an important object for materials engineering.

Since the lamellar microstructure is generated by the precipitation of γ from α according to the so-called Blackburn's relationship (Blackburn 1972), how to develop a sharp texture in α single phase state is the key to construct the orientation controlled lamellar microstructure.

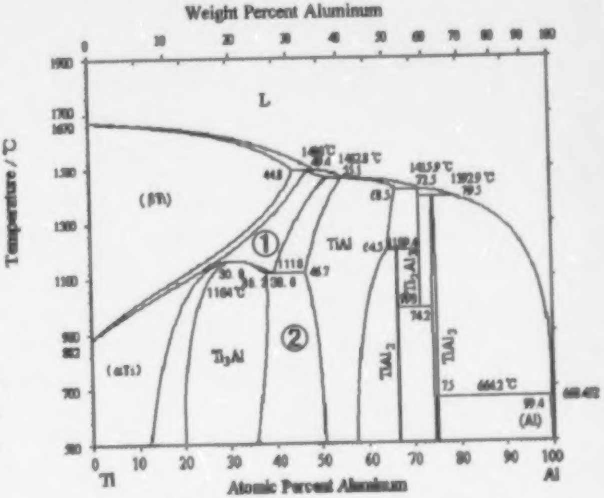

Fig. 1 Phase diagram of Ti-Al system

One of the authors proposed several methods to obtain the textured α single phase state on the basis of high temperature deformation (Fukutomi et al.1995; Nomoto and Fukutomi 1997) and the diffusional reaction of aluminum and textured titanium foils (Fukutomi et al. 1999). The process based on diffusional reaction is quite attractive in the sense that plastic forming necessary for commercial application can be easily performed in the metal state prior to the heat treatment, and no special equipments other than vacuum furnace is necessary.

In this study, phase transitions and orientation changes due to the diffusional reaction are investigated in order to develop a better process to control the arrangement of lamellar microstrucutre.

2 Principle and the process for the control of lamellar arrangement

Figure 1 shows a phase diagram for Ti-Al binary system (Masalski et al. 1990). So-called lamellar microstructure consists of α_2 (Ti_3Al) with a hexagonal structure and γ (TiAl) with a tetragonal lattice, which appear in the region denoted as ② in the diagram. The lamellae are formed during the cooling from the α single phase region denoted by ① to the two phase region denoted by ②.

As described in the introduction, the γ phase is formed by the precipitation under the so-called Blackburn's relationship; {111} and <110> of the tetragonal phase are parallel to (0001) and $\langle 11\bar{2}0\rangle$ of the hexagonal phase, respectively. This means that orientations of lamellae are dominated by the texture in the α single phase state ①.

As shown in Fig. 1, α single phase region expands from the pure titanium in the left end of the diagram to the compositions around Ti-51at%Al at 1462.8 ℃. This characteristics of the binary system enables the new process to control the orientations of lamellae proposed previously (Fukutomi et al. 1999).

If the addition of aluminum to pure titanium towards the region ① can be conducted through the α single phase region, the texture at the region ① must be dominated by the texture of titanium before the addition of aluminum. This suggests that the enrichment of aluminum in titanium having a strong texture is available as a process to produce the oriented lamellar microstructure, although the counter reaction from pure aluminum to α single phase region might reduce the texture sharpness in the α single phase state.

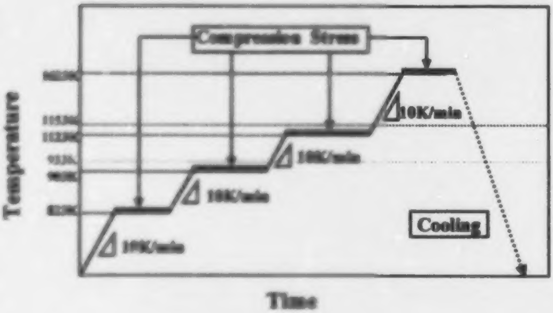

Fig. 2 Temperature-time diagram

Figure 2 is a temperature-time diagram showing the thermal process examined in this study. The process consists of five stages having different physical meanings; bonding stage of titanium and aluminum foils, transforming stage of the pure aluminum layer into Al_3Ti for avoiding the melting of aluminum in the later stages of heat treatment, enriching stage of aluminum content in the titanium layer to prevent the α-β transformation during heating up to α single phase region, the heating stage to obtain α single phase state and cooling stage from α single phase state to form the lamellar microstructure (Fukutomi et al. 1999). In this paper, these five stages are referred to as stage I, II, III, IV and V, respectively.

3 Experimental procedure

Eight titanium foils with the thickness of 100 μm and seven aluminum foils with the thickness of 80 μm were stacked alternately. Purity of the foils is 99.9 wt%. The length as well as the width of foils is 10mm. These foils were prepared by cold rolling and annealing. Texture measurements of the titanium foils by the Schulz reflection method using nickel filtered Cu K_α radiation showed that a sharp texture was constructed. The maximum pole density in (0001) pole figure was more than 15 times as high as the average pole density. The areas of high pole density situated about 35° away from the center of the pole figure towards the transverse direction (TD) at the rolling.

The nominal composition of the stacked foils is Ti-45at%Al. The surfaces of all the foils were cleaned by acid dip before heating. The distribution of lamellar orientation was estimated from TD by optical microscopy. The phases appearing at various stages of reaction were identified by SEM-EDX analysis. Heat treatments were conducted in vacuum under the compression stress of 20MPa.

4 Results and discussion

4.1 Microstructure after stage Ⅱ

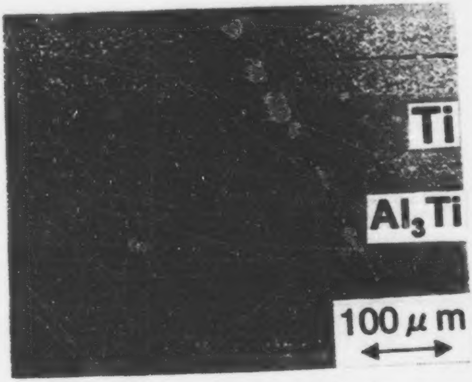

Fig. 3 Microstructure after the heating at 903K for 162ks (stage Ⅱ)

Figure 3 shows the microstructure after the heating at 903K for 162ks. Three regions are seen ; two regions with different grain sizes and a series of small pores. It was found the pores situate at the center of pure aluminum layer before stage Ⅱ, indicating that the pores are formed by Kirkendall effect (German 1996).

EDX analysis showed that the fine grained region has the composition of Ti-75at%Al, namely aluminum was transformed into Al_3Ti by the reaction with pure titanium. No pure aluminum region was observed. Although the diffusion of titanium into aluminum occurred extensively, which resulted in the vanishing of pure aluminum phase, no compositional change was detected in the coarse grained region; no elements other than titanium were detected. The volume fraction of the pure titanium region at this state was about 44%.

4.2 Microstructure after stage Ⅲ

EDX analysis after the heating at 1123K for 144ks showed that TiAl, Al_2Ti and Ti_3Al are formed. The intermetallic phase Al_3Ti which predominantly existed after the stage Ⅱ was no more observed. The volume fraction of Ti_3Al is 44%, which is the same as that of pure titanium after the stage Ⅱ. The phases and their volume percentages up to the stage Ⅲ are summarized in Table 1. It is seen that the volume fraction of the titanium based regions decreases at the stage Ⅱ and no further change occurs at the stage Ⅲ. The decrease in the stage Ⅱ probably originates from the difference between the diffusivity of titanium in aluminum and that of aluminum in titanium.

Table 1: Observed phases and their volume percentages

	Volume percentage					
Stage	**Al(%)**	**Al_3Ti(%)**	**Al_2Ti(%)**	**TiAl(%)**	**Ti_3Al(%)**	**Ti(%)**
before heating	44	–	–	–	–	56
903K for 162ks (stage Ⅱ)	–	56	–	–	–	44
1123K for 144ks (stage Ⅲ)	–	–	56(Al_2Ti+TiAl)		44	–

4.3 Microstructure and orientation distribution after stage V

It was found that many lamellae are aligned parallel to the foil surface after the stage V. In order to examine the relationship between the texture of titanium foils and the alignment of lamellae, the distribution of angles between the basal planes and the rolling direction in the starting titanium foils as well as the angles between the lamellar interfaces and the rolling directions was examined from TD. In Fig. 4 the result on lamellar interface is given.

As the areas of high pole density in (0001) pole figure of the starting titanium foils exist about 35° away from the foil normal towards TD, basal plane appears frequently at the angles between 0 to 20°. Simple estimation showed that more than 90% of the basal plane exists within this range of angles. In accordance with this distribution, high accumulation of the lamellar orientation is seen at the angles between 0 to 20° in Fig. 4. However, the volume percentage of lamellae below 20° is 50% at most which is much lower than that of basal planes expected from the (0001) pole figure for the starting titanium foils.

According to Table 1, the volume fraction of α_2 which is expected to inherit the texture of the starting titanium foils is 44%. Since almost 90% of the orientations is distributed in the angles below 20° in the titanium foil, about 90% of the α_2 exists in the same orientation range, namely about 40% of the whole specimen area. Taking the effect that some of the lamellae produced from aluminum rich phases should have orientations included in this range into account, it can be concluded that the texture of the starting titanium foils is well inherited to the lamellar microstructure via α_2 phase. At the same time, this suggests that the levels of orientation control in the two phase state can be improved by the increase in the volume fraction of titanium based phases after stage II.

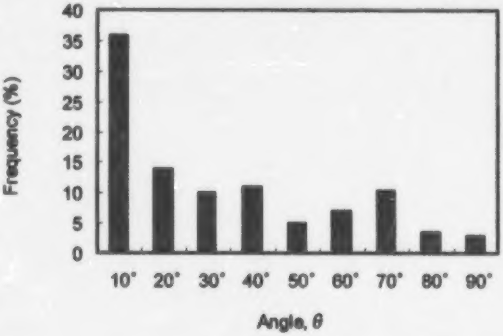

Fig. 4 Distribution of the angles between lamellar interfaces and the rolling direction

5 Conclusions

The formation process of intermetallic compound with oriented lamellar microstructure was studied by optical microscopy, SEM-EDX analysis and texture measurement. It is quantitatively shown that the texture of the starting titanium foils is transferred to the α_2 phase, resulting in the textured α single phase state. It is suggested that the increase in the volume fraction of titanium based phases before the heating up to the α single phase region is essential in order to improve the controlling level of the oriented lamellar microstructure.

Acknowledgement

The authors greatly appreciate to Mr. Unezaki in Kyoto university for his skilful analysis using SEM-EDX system. The financial supports by the Japan Society for Promotion Science and Grant-in-Aid of the Ministry of Education, Science and Culture, Japan are also appreciated.

6 References

Blackburn, M. J. (1972) *Science, Technology and Applications of Titanium,* (ed. R. T. Jaffee and N. E. Promisel), Pergamon Press, London, pp.633-643.

Fukutomi, H., Nomoto, A. and Ohta, T. (1995) Control of Lamellar Arrangement in TiAl Alloys by High-Temperature Deformation in α Single Phase and Subsequent Annealing in Two Phase Region. *Materials Transactions JIM,* Vol. 36, pp. 610-614.

Fukutomi, H., Ueno, M., Nakamura, M., Suzuki, T. and Kikuchi, S. (1999) Production of TiAl sheet with oriented lamellar microstructure by diffusional reaction of aluminum and textured titanium foils, *Materials Transactions JIM,* accepted.

German, R.M.(1996) *Sintering Theory and Practice,* John Wiley and Sons Inc., New York, pp.197-201.

Inui, H., Oh, M. H., Nakamura, A. and Yamaguchi, M. (1992) Room-temperature tensile deformation of polysythetically twinned (PST) crystals of TiAl, *Acta Mater.,* Vol.40, pp. 3095-3104.

Massalski, T. B., Okamoto, H., Subramanian, P. R. and Kacprzak, L.(1990) *Binary Alloy Phase Diagrams Second Edition CD-ROM,* ASM.

Nomoto, A. and Fukutomi, H. (1997) Orientation control of ($\alpha_2+\gamma$) lamellae in TiAl Intermetallic compounds by two-step compression at high tempereature, *J. Japan Inst. Metals,* Vol. 61, pp.378-384.

Yokoshima, S. and Yamaguchi, M. (1996) Fracture behavior and toughness of PST crystals of TiAl, *Acta Mater.,* Vol.44, pp.873-883.

TEXTURE AND MULTIPLE TWINNING IN COPPER

V. RANDLE, P. DAVIES and H. DAVIES

Department of Materials Engineering, University of Wales Swansea, Swansea, UK.

Abstract

The present work reports studies of the crystallography of Σ3 boundaries in copper, in the context of practical considerations to obtain appropriate data, the relationships between Σ3 plane indices and the deviation from exact Σ3 matching, v/v_m. It is found that it is appropriate to categorise Σ3s in terms of v/v_m and to have reasonable confidence that these low v/v_ms are associated with low energies. The boundary plane calculation is suprisingly robust to deviations in the β-angle, and a section depth of 45μm is appropriate for the procedure. The domination of high mobility boundaries during annealing can promote generation of Σ3s. Σ3 formation by these means produces boundaries having a range of v/v_m values.

Keywords: Grain boundary plane, twins, Σ3 boundaries, high mobility boundaries.

1. Introduction

Multiple twinning is known to have a complex effect on the development of texture (Gottstein 1984). Briefly, the final texture is dominated by competition between the generation of multiple twin chains and the development of a particularly high mobility boundary type. In the 'multiple twin chains' case, a random texture will develop via statistical twinning, i.e. with equal probability of all equivalent twin vaiants being chosen, up to the seventh generation. In the 'high mobility boundary' case a few fast growing orientations will develop and dominate the texture, which is more likely to happen if the propagation rate of twins is slow in comparison. Profuse annealing twinning, where twins are a subset of Σ3 boundaries in the coincidence site lattice notation, will radically alter the grain boundary geometry distribution.

The ideal characterisation of Σ3s - and indeed all interfaces - in polycrystals would include both the misorientation between the lattices of neighbouring grains and identification of macroscopic boundary plane indices. The main disadvantages of such a procedure are that it applies only to macroscopically planar boundaries (which fortunately includes many Σ3s) and is labour intensive, technically challenging and the boundary plane measurement is less accurate than the misorientation (Randle et al. 1999). These disadvantages are in contrast to measurement of misorientation alone which, using modern automated diffraction techniques, is now routine. In consequence, there is a dilemma between use of a rapid technique which allows statistically large data sets to be aquired, but only supplies part of the information, and a determination which gives all the macroscopic information but is an order of magnitude less efficient.

The viability of misorientation measurements alone, without the plane indices, can be ameliorated somewhat by considering not only the conventional generic Σ classification, but by specifying also the angular deviation of the misorientation from the exact Σ. The most widely used classification for a CSL is via the 'Brandon criterion' (Brandon 1966):

$$v_m = v_0 \Sigma^{-1/2} \tag{1}$$

where v_m is the maximum angular deviation which permits, using this scheme, a boundary to be categorised as a CSL and v_0 is a constant, the low angle boundary limit (15°), which gives $v_m = 8.67°$ for Σ3. The actual measured angular deviation from the exact CSL configuration is denoted v, and this is usually normalised as v/v_m. The free energy of the boundary correlates with v/v_m, since an increase in this parameter implies a higher density of dislocations in the boundary.

Most researchers consider categorisation of a CSL only in terms of the Brandon limit v_m and do not explore the distribution of v/v_m within that limit. There are only a very limited number of reports which discuss the variation of v/v_m particularly with respect to the boundary plane distribution. One such investigation on pure nickel shows that the the lowest v/v_ms are associated principally with {111} symmetrical tilt boundaries (STBs) and, to a lesser extent, with asymmetrical tilt boundaries (ATBs) on the 011 zone (Randle 1995). Furthermore, there is an 86% correlation between Σ3s having $v/v_m<0.2$ and the appearance of a straight trace in a section through the microstructure (Thomson and Randle 1996).

The dilemma of choosing the orientation-sampling location within neighbouring grains, with which to subsequently calculate the misorientation, has received little attention. If the traditional assumption is made that the orientation is invariant within a grain, then the sampling position is irrelevant. On the other hand the misorientation calculation will be affected if there is any lattice curvature present, e.g. that associated with compatability at boundaries. Recent work has shown that on average there are orientation perturbations of 2° in grains of well-annealed nickel, and in a few grains this figure could be higher (Randle and Davies 1999).

The purpose of the present work is to report studies of the crystallography of Σ3 boundaries in copper, in the context of practical considerations to obtain appropriate data, the relationships between Σ3 plane indices and the deviation from exact Σ3 matching, v/v_m.

2. Experimental details

The material used was 99.99+% pure copper which was annealed for 1 hour at 900°C in vacuum to give grains approximately 1mm in size. Orientation measurements were obtained by electron back scatter diffraction (EBSD) in a scanning electron microscope (SEM) using OPAL software. The measurements were then used to calculate misorientations of Σ3 boundaries.

Boundary inclinations were measured in the SEM using previously documented procedures (Randle et al. 1999) involving calibrated precision serial sectioning. As part of the present experiments the validity of the sectioning technique was explored in more detail, by performing intermediate sectioning steps in addition to one large step, ultimately limited in size by the grain size and the dimensions of the diamond indent used for calibration. Boundary plane indices were obtained, for {111}{111} Σ3s, after each intermediate sectioning step and compared.

The misorientations and Σ3 plane indices were obtained using in-house software, resulting in estimated accuracy of ±4°. The planes were categorised as being within 5° of the nearest reference set of planes, e.g. {111}{111}, or 'symmetrical' if the planes were within 5° of each other but not a twist or tilt type in the Σ3 system, and 'random' if the planes were irrational.

Three experiments were then carried out on these specimens:

- The misorientations and grain boundary plane indices for Σ3 interfaces were obtained, from the interior of the specimens. The misorientation was calculated from measurements collected at sites as close as possible to the interface.
- Additional boundary plane measurements on Σ3 interfaces were made on these specimens using three sectioning steps, rather than a single step, to obtain the boundary inclination.
- Some of the specimens were further annealed for 97h at 540°C in air. For both these and the preliminary specimens misorientations were calculated between orientations collected at sites displaced by several microns from the interface, and sites located close to the interface.

3. Results and discussion

3.1 Plane types and their relationship to v/v_m

The boundary plane analysis showed that half the Σ3s could be counted as the {111} STB reference structure and a further one-third of the Σ3s were misoriented by up to 10° from {111}. In terms of ATB descriptions, these could be designated by the reference structures {775}{23,17,17} and {332}{10,77}, which are 8° and 10° from {111} respectively on the 011 zone. The choice of these actual indices is somewhat arbitrary: for instance some of the planes in the former category could have been categorised as {554}{16,13,13}, which is 6° away from {111}. However, the pertinent point is not the exact indices but that these planes are *a few degrees*, more than the error of the measurement technique, from {111}. There was one other ATB, {211}{552}. A further group of the Σ3s either had planes within a few degrees of each other, but were not STBs or ATBs, and these will be referred to as 'symmetrical boundaries'. Finally, a small group of the Σ3s had irrational planes. The quantitative distribution of Σ3 planes according to v/v_m is shown in Figure 1 with the plane types categorised, in terms of increasing energy, according to the following: 1 - {111}{111}; 2 - {775}{23,17,17}; 3 - {332}{10,77}; 4 - other ATBs (only one {211}{552} in this case); 5 - symmetrical planes; 6 - irrational planes.

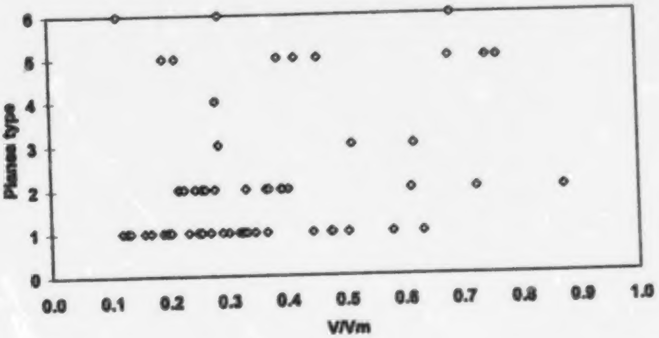

Fig. 1 v/v_m values for Σ3 boundary planes grouped according to planes type (see text)

Inspection of Figure 1 shows that most type 1 planes, {111}{111}, have $v/v_m < 0.35$ (average 0.30). Type 2 planes, near {111}{111} STBs, have v/v_m mainly 0.2-0.4 (average 0.36) and types 3,4,5 are displaced to higher average values of v/v_m (0.50 for types 3 and 5). Type 6, the irrational planes, appears to have a spread of values. This might indicate errors associated with Type 6 boundaries. Evidently, there is some correlation between the distribution of v/v_m and plane type, where plane types are designated 1-6 in terms of increasing energy, for Σ3s in these copper specimens. It is therefore feasible to categorise Σ3s in terms of v/v_m and to have reasonable confidence that these low v/v_ms are associated with low energies.

3.2 Intermediate serial sectioning

Three sequential sectioning steps were performed to assess the validity of the sectioning technique. The standard deviation of the β-angle, i.e. the inclination angle of the boundary, for the three sectioning steps, was calculated. The angular deviation from {111} reference planes for a population of Σ3 annealing twins for each of the three sections was also documented. Figure 2a shows the standard deviation of β as a function of the deviation from {111}. Interestingly, Figure 2a shows that there is no correlation between these two parameters. Figure 2b shows the angular deviation of planes from {111} as a function of section depth. Assuming that the 'best' result is the smallest deviation from {111}, it is apparent that the first section depth of 23μm introduced large errors, whereas in general the deviation converged on {111} with increasing section depth. However there was far less difference between the second section (32μm) and third section (45μm). One result out of 24 indicates an increase in the deviation from {111}. In summary, the boundary plane calculation is suprisingly robust to deviations in the β-angle, and a section depth of 45μm is appropriate for the procedure.

3.3 Near-interface and displaced-from-interface measurements

Figure 3 shows the distribution of v/v_m for orientation measurements taken both from near the interface and several microns displaced from it. It is apparent that, after 1h annealing at 900°C, there is a considerable discrepancy between misorientations calculated from near-to-boundary and displaced-from-boundary locations; the average v/v_ms are 0.18 and 0.31 respectively. After further annealing for 97h at 540°C in air this discrepancy is practically eradicated, and the average v/v_ms are 0.13 and 0.16.

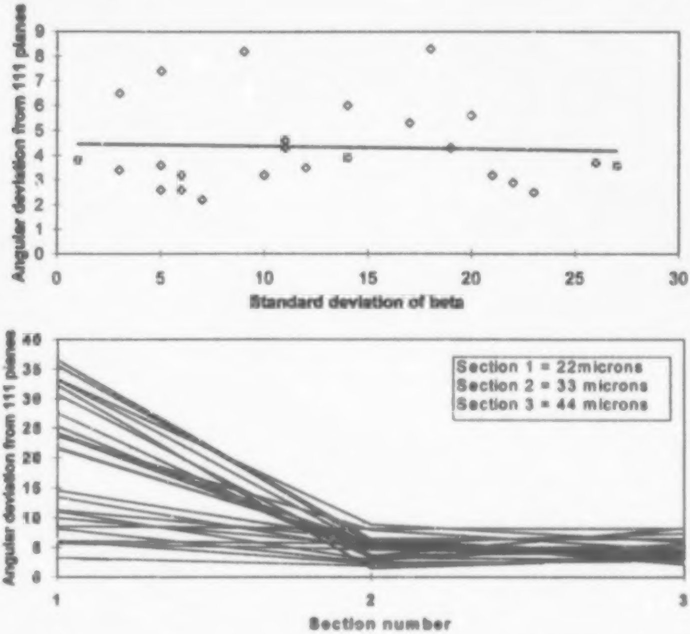

Fig. 2 (a) Plot showing that there is no correlation between the standard deviation (SD) of β and the deviation from {111}. (b) Deviation from {111} vs. increasing section depth.

3.4 The effect of twinning on v/v_m

Average reported v/v_m values for $\Sigma3$ populations can vary from 0.1 to 0.59. This is reasonable when it is remembered that the $\Sigma3$ designation encompasses interfaces ranging from newly formed annealing twins, which would have low v/v_m, to grain boundaries which have a $\Sigma3$ misorientation and can have v/v_m values up to v_m.

For the present data, the vacuum annealed specimen would (in the absence of any drag effect caused by ingress of species in an air environment) be able quickly to develop high mobility boundaries, thus allowing them to dominate and create a texture.

The domination of high mobility boundaries during annealing could, in several ways, promote generation of $\Sigma3$s, namely:

- Components of orientations which bear a $\Sigma3$ relationship to each other, such as the two components of both brass or copper texture, may impinge
- 'Back twinning' can occur by the impingment of a Σ^n boundary on to a Σ^{n-1} boundary, thus re-generating a $\Sigma3$. For example a $\Sigma81$ boundary encountering a $\Sigma27$ could re-generate a $\Sigma3$
- One variant of $\Sigma3^4$ is described as 60.41°/344 which is only 5.9° away from a $\Sigma3$ relationship, i.e. still within the Brandon criterion for a $\Sigma3$.

$\Sigma3$ formation by all of these means would produce boundaries having a range of v/v_m values. By contrast, multiple twinning alone supports the nucleation of new twins which would be characterised by low v/v_m values.

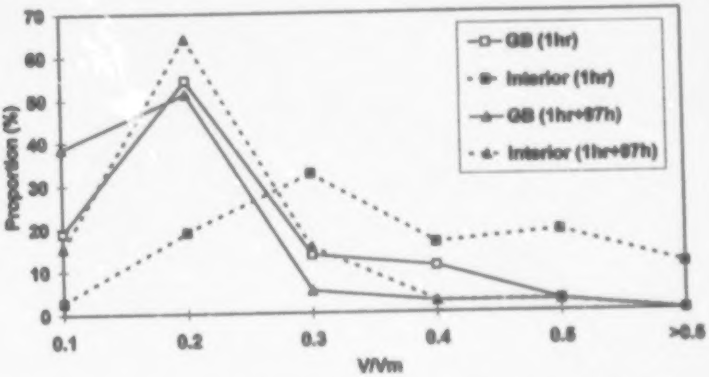

Fig. 3 Distribution of v/v_m for orientations taken both from near the interface (GB) and several microns from it (interior) for two heat treatments.

4 Conclusions

1. It is appropriate to categorise Σ3s in terms of v/v_m and to have reasonable confidence that these low v/v_ms are associated with low energies.
2. The boundary plane calculation is suprisingly robust to deviations in the β-angle, and a section depth of 45μm is appropriate for the procedure.
3. The domination of high mobility boundaries during annealing can promote generation of Σ3s. Σ3 formation by these means produces boundaries having a range of v/v_m values.

5 References

Brandon, D.G. (1966) The structure of high-angle grain boundaries. *Acta Metall.*, Vol. 14, pp. 1479-1484.

Gottstein, G. (1984) Annealing texture development by multiple twinning in F.C.C. crystals. *Acta Metall.*, Vol. 32, pp. 1117-1138.

Randle, V., Davies, P. and Hulm, B. (1999) Grain boundary plane reorientation in copper. *Philos. Mag.*, Vol. 79A, pp. 305-316.

Randle, V. and Davies, R.K. (1999) Lattice compatibility at interfaces after recrystallisation. *Mater. Sci. Tech.*, in press.

Randle, V. (1995) An investigation of grain boundary plane crystallography in bulk polycrystalline material. *J. Mater. Sci.*, Vol. 30, pp. 3983-3988.

Thomson, C.B. and Randle, V. (1996) The effect of strain annealing on grain boundary distribution and hardening in superpure nickel. *Tex. and Micros.*, Vol. 28, pp. 71-79.

MICROTEXTURE DEVELOPMENT IN HIGH STRENGTH INTERSTITIAL FREE STEELS

I. J. CROSS
Engineering and Physical Sciences Research Council Engineering Doctorate Centre - Wales, University of Wales-Swansea, Swansea, United Kingdom.
V. RANDLE
Department of Materials Engineering, University of Wales-Swansea, Swansea, United Kingdom.
S. R. DANIEL
Welsh Technology Centre, British Steel Strip Products, Port Talbot, United Kingdom.

Abstract

Electron Backscattered Diffraction (EBSD) is being used to study texture development in an High Strength Interstitial Free (HS-IF) steel throughout recrystallisation. The cold worked material is heated at a constant rate to a peak temperature from which it is quenched. Each heat treatment resulted in a different degree of recrystallisation. During the early stages of recrystallisation, typical structures were studied in the Scanning Electron Microscope (SEM) where recrystallising grains were identified within the cold worked environment. Such regions were analysed by EBSD to determine the orientation of the recrystallising fractions and the surrounding cold worked grains. Similar analyses were performed throughout the recrystallisation process. In this way an understanding of how the annealed texture develops from the cold worked structure is gained. Results are presented and discussed in the light of modern recrystallisation theories. The greater understanding allows the potential for optimization of current and future HS-IF grades.

Keywords: Electron Backscattered Diffraction, high strength interstitial free steels, recrystallisation.

1 Introduction

The inherent favourable formability of interstitial free (IF) steels has led to a large development effort in the steel community on this family of steels. The automotive industry, in particular, has an interest in their improvement, initially to allow more complex designs to be achieved in forming operations. It is well known that formability is related to crystallographic texture. Held (1965) was one of the first to show this with an empirical relationship between the {111} and {100} texture intensity ratio and the mean normal plastic strain ratio, r-bar or rm. This showed that a high proportion of material oriented such that <111> are parallel to the sheet normal direction (the gamma fibre) results in better r-bar values.

The crystallographic textures in IF steels have been studied quite extensively to gain an understanding of how favourable texture components develop so that the steel chemistry and processing can be adjusted to yield the best properties. After cold rolling, the steel strip is annealed to develop favourable properties. Annealing is one of the key processing parameters that determines the final texture and as a result has been studied extensively. The texture changes that occur during annealing have been studied in the past by conventional x-ray techniques and by the relatively new EBSD technique. Detailed studies have found that <111>//ND recrystallising grains nucleate from deformed <111>//ND grains at the grain interiors with high frequency during the early stages of recrystallisation (e.g. Vanderschueren 1994). Two general theories for the mechanism of recrystallisation texture formation have emerged from recent studies, these being oriented nucleation (e.g. Samajdar et al. 1998), or oriented growth (e.g. Park et al. 1997). Alternatively, some workers believe that the recrystallisation texture develops by a combination of the above two mechanisms (e.g. Urabe 1997).

Despite the conflicting theories, the above cited work has been carried out on 'mild' IF steels, i.e. those containing low amounts of solid solution strengthening elements such as manganese, phosphorus, silicon or boron. With the more recent incentives from the automotive industry for 'environmental friendliness' and improved driver and passenger safety, strength increases have been sought by the addition of some of these elements. Although such strengthening additions reduce the formability, an explanation for this reduction in terms of their full effects on texture development has not been reported. A typical high strength steel is, therefore, being studied as part of a doctorate program to gain more of an understanding of how the texture develops, particularly during annealing.

2 Experimental

A commercially produced high strength IF steel, with chemical composition as detailed in Table 1 was commercially hot rolled to 2.4 mm. The conditions under which it was rolled are given in Table 2. The hot band was subsequently cold rolled on a laboratory mill to a reduction of 66%.

Laboratory annealing experiments were carried out using a resistance annealing simulator. Longitudinal samples were used for all treatments. The thermal treatment involved heating the cold rolled steel at 30°C/s followed by water quenching from a range of temperatures between 740°C and 850°C, to obtain a range of partially recrystallised and fully recrystallised specimens. Water quenching, with a cooling rate of ~250°C/s, was used to freeze the condition of the steel achieved during heating. The recrystallisation phenomena were investigated using Oxford Instruments EBSD system linked to a Jeol 6100 scanning electron microscope. Through thickness samples were prepared for EBSD by electrolytic polishing in 10% perchloric + acetic acid solution. In the low fraction recrystallised specimens recrystallised grains were identified by the SEM back scattered electron image, the sharpness of the EBSD pattern and the absence

Table 1: Chemical composition of the steel studied (wt.%).

C	Si	Mn	P	S	Al(sol)	B	N	Ti	Nb
0.0065	0.01	1.22	0.050	0.012	0.068	0.0014	0.0016	0.071	trace

Table 2: Hot rolling conditions of the steel.

	Roughing	Finishing	Coiling
Temperature (°C)	1125	913	624

of fluctuation in the diffraction pattern when the beam was traversed across a small distance within an identified grain. Several grains within a fixed area of the high percentage recrystallised sample were analysed to determine their orientations. Orientations of isolated recrystallised grains from a low fraction recrystallised were determined along with the orientations of several points from the surrounding cold worked matrix from each grain.

3 Results and discussion

EBSD performed on the hot band showed a poor pattern quality and a jumping of the diffraction pattern when the beam was traversed through a grain. Pattern quality is affected by the dislocation content and hence the amount of strain in a grain. The poor pattern quality suggests that the hot band contains a degree of deformation strain which indicates that the material was unrecrystallised during hot rolling. The fluctuations in the diffraction pattern when moved only a small distance indicate a subgrain structure in this condition, further evidence of retained deformation strain. Through thickness direction and longitudinal direction measurements of the grain size were made which averaged ~8 μm and 28 μm respectively. The cold rolled structure was elongated along the rolling direction as expected, with a very fine through thickness direction grain size. Quantitative measurements could not be made due to the complexity of the structure and the inability to distinguish grain boundaries.

Figure 1 shows SEM scanning electron image micrographs of the structures during various stages of the recrystallisation process, at ~15% and 99% recrystallised. The earliest stage of recrystallisation has been detected in a sample quenched from 766°C. It was impossible to determine the positions at which these earliest grains nucleated due to the fineness and complexity of the cold worked structure. It can clearly be seen that through the progression of recrystallisation the grains grow and increase in number as they consume the cold worked structure. The sample that was 99% recrystallised had been quenched from 836°C.

Two hundred and twenty-four recrystallised grains were analysed from the ~99% recrystallised material for their orientations. Figure 2 shows the IPF representation of these grains. It can be seen that there is a clustering of orientations in the region close to <111> in the sample normal direction, which equates to the sheet ND. Analysis of these data shows that almost half of the recrystallised grains are oriented within 15° of the <111>//ND (i.e. γ-fibre type grains), which are favourable for formability requirements. The analysis results are presented in Table 3.

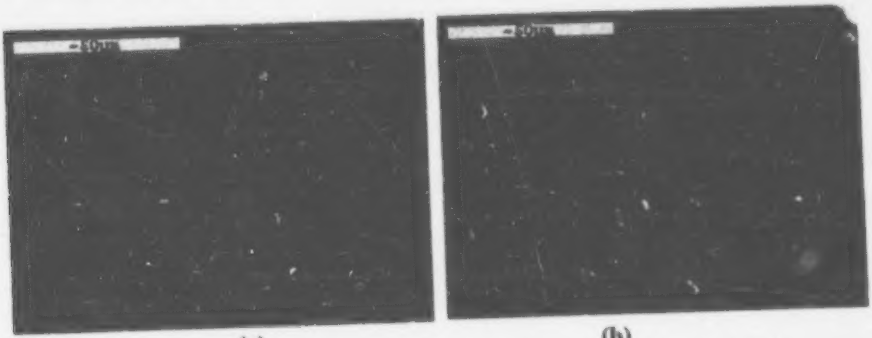
(a) (b)

Fig. 1: Micro graphs of partially recrystallised steel (a) ~15% and (b) 99%.

Initial results of the early-recrystallised grains will now be presented and discussed. 16 recrystallised grains have been analysed out of which 8 are within 15° of <111>//ND. Of the remainder 3 are within 15° of <100>//ND, 1 is within 10° of <221>, and 4 are within 15° of <113>. None were within 15° of <110>//ND, which have been reported elsewhere (Vanderschueren et al. 1996). Analysis of the misorientation angles between these recrystallised nuclei and their surroundings is presented in Figure 3. The large majority of misorientations is in the angular range 20°-50°. If the recrystallised grain types are broken down to the {111} types and other types, the misorientation angles can be seen to be spread differently, Figure 4. Again the {111} type grains have misorientations 20°-50°, whereas for the other types the misorientations are more spread in the range 10°-60°. The low angle misorientations which would surround {111} type grains nucleated from within {111} deformed grains observed in other studies (e.g. Vanderschueren et al. 1996) are not in evidence here. Either the {111} type grains have already outgrown the deformed grains from which they nucleated or they nucleated at grain boundaries to produce the high angle boundaries as observed.

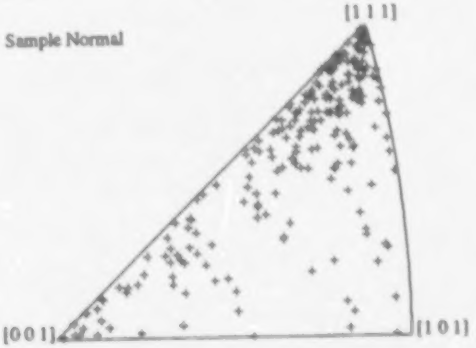

Fig. 2: IPF of the orientations of 224 recrystallised grains in the 99% recrystallised material

Table 3: Analysis of the IPF of 224 recrystallised grains

% within 15° <100>//ND	% within 15° <111>//ND	Remainder
8.5	48.6	42.9

The high incidence of grains with orientations outside {111} type may help to explain the lower r-bar values which are obtained from HS-IF steels in comparison with the mild IF steels in which {111} type grains predominate from the early stages in recrystallisation.

4 Conclusions

1. HS-IF steels have more complex microstructures than those seen in typical mild IF steels. This makes microtexture investigations more difficult by EBSD.
2. New grains nucleated during recrystallisation appear to have a larger scatter of orientations than those observed in mild IF steels. Most importantly, as an explanation for the lower r-bar values generally observed in HS-IF, there is not the clustering of orientations around the gamma fibre during the early stages of recrystallisation.
3. The trends in the orientation types observed during the early stage of recrystallisation appear to remain at completion of the process so that the microtextures exhibit a spread between the favourable and unfavourable texture components.

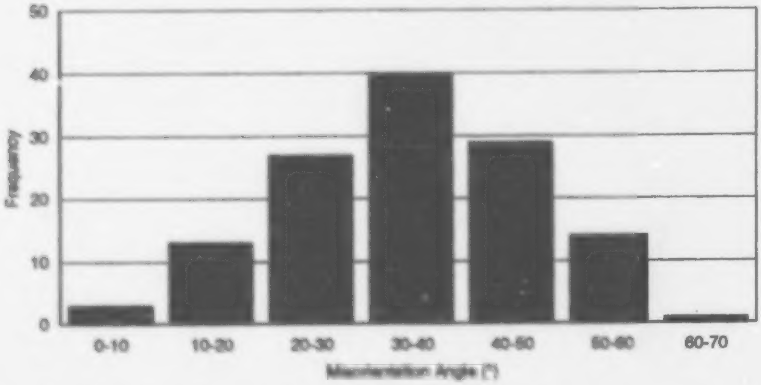

Fig. 3: Misorientation angle frequency of the deformed surroundings with recrystallised grains

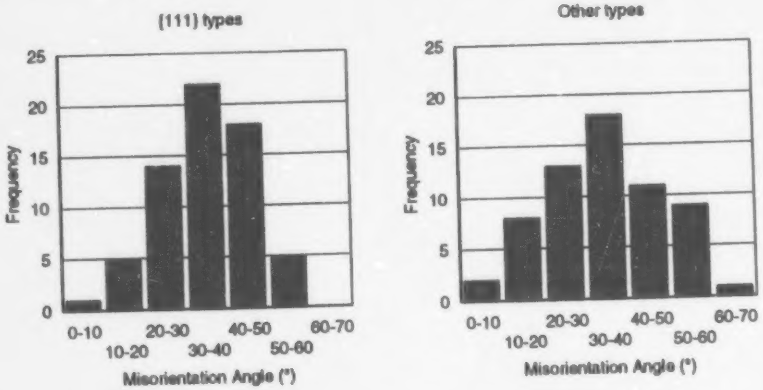

Fig. 4: Misorientation angle frequency of the deformed surroundings with recrystallised grains by grain types

5 Acknowledgements

The author would like to thank Dr B J Hewitt, Director - Technical, British Steel Strip Products and Mr E F Walker, Manager, Technical Co-ordination, Welsh Technology Centre, British Steel Strip Products for permission to publish this paper and gratefully acknowledge the support of the Engineering and Physical Sciences Research Council.

6 References

Held J.F. (1965) The Relationship Between R Values and Structure Properties of Steel Sheets, in *Mechanical Working and Steel Processing IV*, Pittsburgh, Pennsylvania, 29 November - 3 December 1965. TMS-AIME.

Park Y.B., Lee D.N. and Gottstein G. (1997) Evolution of recrystallisation textures from cold rolling textures in interstitial free steel. *Materials Science and Technology* , Vol. 13, pp. 289-298.

Samajdar I., Verlinden B. and Van Houtte P. (1998) Development of recrystallisation texture in IF-steel: An effort to explain developments in global texture from microtextural studies. *Acta Materialia*, Vol. 46, No. 8, pp. 2751-2763.

Urabe T. (1997) Modelling of the formation of recrystallisation textures in IF steel, in *THERMEC '97: Int. Conf. on Thermomechanical Processing of Steels & Other Materials*, Wollongong, Australia, 7-11 July 1997. The Minerals, Metals and Materials Society.

Vanderschueren D. (1994) The mechanism of recrystallisation of IF steel. in *Physical Metallurgy of IF Steels*, Tokyo, May 1994. ISIJ.

Vanderschueren D., Yoshinaga N. and Koyama K. (1996) Recrystallisation of Ti IF steel investigated with electron back-scattering (EBSP). *ISIJ Int.*, Vol. 36, No. 8, pp. 1046-1054.

EFFECT OF HOT BAND ANNEALING ON THE FORMATION OF SHARP {110} <001> GOSS TEXTURE IN CONVENTIONAL GRAIN ORIENTED ELECTRICAL STEELS

K. S. HAN, J. S. WOO, G. S. CHOI, and S. K. CHANG
POSCO Technical Research Laboratories, Pohang, Korea

Abstract

The effect of hot band annealing on the formation of {110}<001> texture in conventional grain-oriented electrical steels was investigated. The hot bands annealed at 900 and 1120 as well as without annealing were processed to secondary recrystallization through two-stage cold rolling and decarburization in the intermediate annealing. The intensity of {110}<001> texture in the sub-surface increases after hot band annealing. It is also found that the hot band annealing brings about the additional precipitation of fine AlN and the growth of recrystallized grains in surface layer. As the temperature increases, precipitates exist finer and more uniform in the primary recrystallized microstructure and the intensity of {110} <001> texture becomes stronger. Because of these metallurgical changes, the onset temperature of secondary recrystallization increases and, as a result, the magnetic induction is improved, as the temperature of hot band annealing becomes higher.

Keywords: Conventional Grain-Oriented, Hot Band Annealing, {110}<001> texture

1 Introduction

Grain-oriented electrical steels show excellent magnetic properties in the rolling direction due to ideal {110} <001> texture formed by secondary recrystallization. In order to obtain good magnetic properties, the distribution of fine precipitates, primary recrystallized microstructure and texture are considered to be very important [1]. Therefore, many workers have carried out the investigation of effective precipitates and optimum hot rolling condition and cold reduction rate in order to obtain excellent {110}<001> texture [2-5]. However, there have not been many studies to clarify the relation between {110}<001> texture in the primary microstructure and hot band annealing. In this study, the effect of hot band annealing on the formation of

{110}<001> texture and, consequently, the magnetic properties of conventional grain-oriented electrical steels using only AlN for a grain growth inhibitior was investigated.

2 Experimental procedure

The hot bands containing 3.1%Si, 0.05%C, 0.024% Sol.Al, and 0.0086%N were annealed at 900℃ and 1120℃ for 3min. These specimens were cold-rolled to 0.3mm in thickness by a two-stage cold rolling with intermediate annealing in a decarburizing atmosphere. And, the hot band without annealing was also treated with the same procedure as the above for comparison. The final annealing was done by heating the specimens in a dry H_2 atmosphere at 20℃/hr to 1200℃ and holding for 10hrs. The change of (110) components through the thickness of hot band and annealed hot bands were measured. And, the texture of primary recrystallized microstructures was analyzed by measuring incomplete pole figures of (110), (200), and (112) plane. AlN precipitates were observed by a Transmission Electron Microscopy (TEM). Magnetic induction at 1,000 A/m and core loss at 1.5 Tesla and 50Hz were measured by using a single strip tester.

3 Results

The microstructures of as-rolled and annealed hot bands are shown in Fig. 1. Compared to as-rolled band, those annealed at 900℃ and 1120℃ show more recrystallized and coarse microstructures. The portion of elongated grains at the center decreases due to an additional recrystallization and some grain growth is observed at the surface with increasing the temperature of hot band annealing. Fig. 2 shows the change of (110) components through the thickness of as-rolled and annealed hot bands. The intensity of (110) in as-rolled band is found to the highest at the depth of 1/5 thickness from the surface, whereas the maximum intensity appears

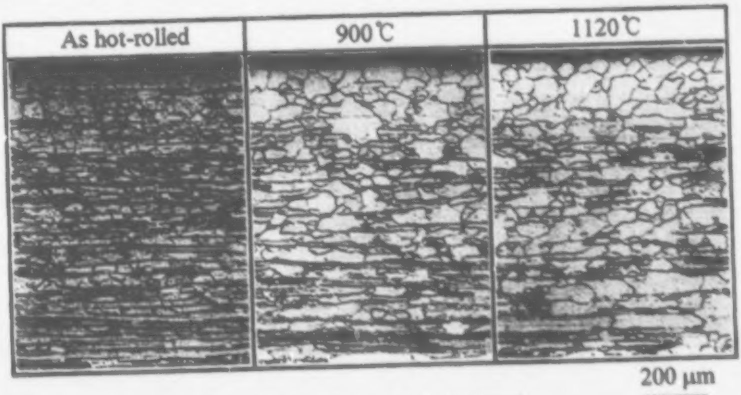

Fig. 1: Microstructures of hot band and annealed hot bands.

at 1/10 thickness depth in annealed hot bands. Fig. 3 shows precipitates at the center of the hot bands before and after annealing. In the case of the hot band before annealing, AlN precipitates are seen to exist scarcely. However, the higher the annealing temperature becomes, the more and finer AlN are precipitated. The distributions of AlN in primary recrystallized specimens are shown in Fig 4. From this figure, it is found that the number of AlN precipitates finer than 300 Å increases when the hot band is annealed at a higher temperature. In Fig. 5, it is shown that the variation of textures in the primary recrystallized specimens. The {111}<011> texture is found to be a major component, while {111}<112> and {110}<001> textures are observed as minor components. Moreover, the intensity of {110}<001> texture increases with the temperature increase in hot band annealing. The change in magnetic induction with the extracting temperature during the final annealing is shown in Fig. 6. In the case of the specimen without hot band annealing, magnetic

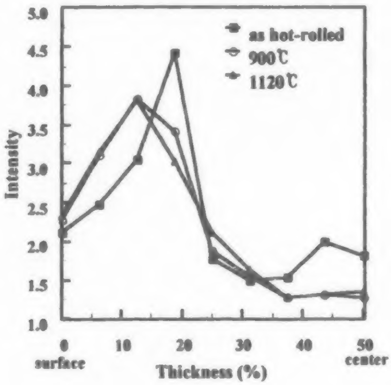

Fig. 2: Variation of (110) component through the thickness of hot bands.

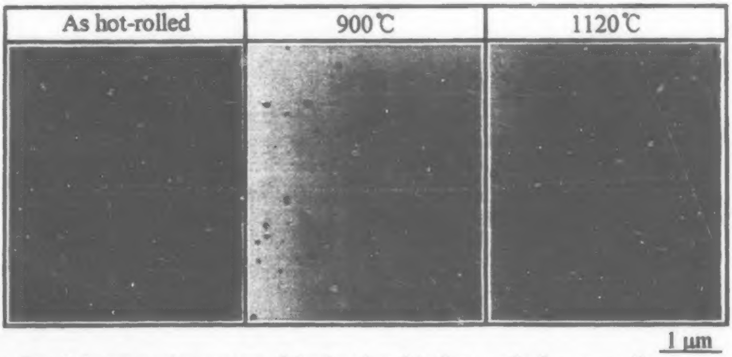
As hot-rolled | 900℃ | 1120℃

Fig. 3: Precipitates at the center of the hot band before and after annealing.

induction increases sharply up to 1.808 Tesla at 950℃, which means that secondary recrystallization already begins below that temperature. When the specimens are annealed, secondary recrystallization is found to occur at a higher temperature. In the case of the specimen annealed at 1120℃, secondary recrystallization is found to be completed at around 1100℃ and excellent magnetic properties of 1.884 Tesla and 1.248 W/kg are obtained.

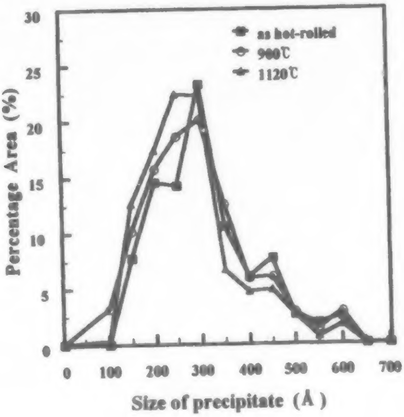

Fig. 4: Size distributions of AlN precipitates in primary recrystallized specimens.

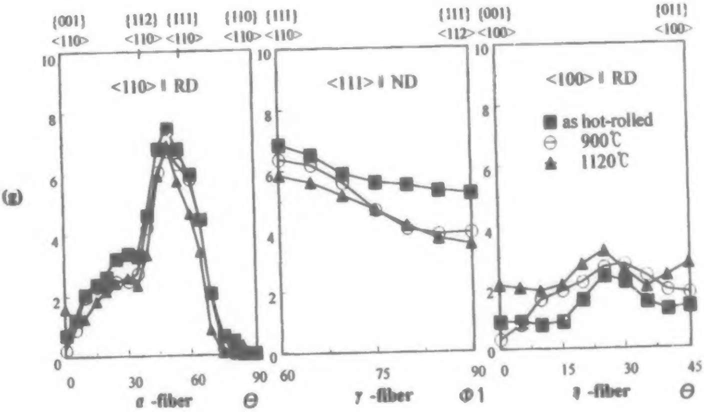

Fig. 5: Variation of textures in primary recrystallized specimens.

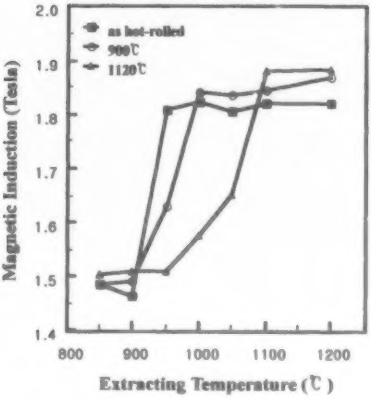

Fig. 6: Change in magnetic induction with extracting temperatures during the final annealing.

4 Disscussion

As shown in Fig. 1, when the hot band annealing temperature increases, elongated grains at the center decreases due to an additional recrystallization, and some grain growth is observed at the surface. According to the study done by H.C. Fiedler, the hot band experiences an $\alpha \rightarrow \gamma$ transformation during hot band annealing and the amount of austenite increases with the temperature [6]. M.Matsuo also reported that partial phase transformation in hot rolling and subsequent annealing produce a fine grain structure with a high dislocation density because of the transformation strain [2]. It is highly probable that recrystallization easily occurs during hot band annealing in some portion of the central layer consisting mainly of elongated grains.

The recrystallized grains at the sub-surface of hot bands are known to be formed by dynamic recrystalliaztion and recovery during hot rolling. Some of these grains are formed by heavy shear deformation and show sharp {110}<001> Goss texture. Because these Goss grains exits mainly at the sub-surface, as shown in Fig. 2, the intensity of (110) component is observed higher than at the center. During hot band annealing, the recrystallized grains at the sub-surface grow and this growth of Goss grains seems to increase the intensity of (110) component. In addition, hot band annealing is found to make the rolling plane more abundant with (110) at the sub-surface suggesting more {110}<001> oriented grains at the same location.

Fig. 3 shows AlN precipitates at the center of as-rolled and annealed hot bands. After hot band annealing, fine AlN precipitates are existed and the amount of AlN precipitates is found to increase. As mentioned above, it has been reported that hot band annealing causes $\alpha \rightarrow \gamma$ phase transformation and results in more precipitation of fine AlN. Fig. 4 shows the distributions of AlN in primary recrystallized specimens with the temperature of hot band annealing. From Fig. 4, it is found that the number of AlN precipitates finer than 300 Å increases after hot band annealing.

Haratani reported that the precipitation of fine AlN by hot band annealing in Al-killed steels increases (110)[001] component and secondary recrystallization occurs by isothermal annealing [7]. His study suggests that the precipitation of fine AlN permits the nucleation of (110)[001] oriented grains during primary recrystalliaztion. The same trend is observed by examining the textures of primary recrystallized specimens. As shown in Fig. 5, the intensity of {110}<001> texture increases with the hot band annealing temperature, while the intensities of {111}<011> and {111}<112> textures decrease. Because of low reduction rate (50%) in the second cold rolling, the intensity of {111}<011> texture is higher than that of {111}<112> texture. From the above results, it can be concluded that the increase of {110}<001> texture in primary recrystallized microstructure is caused by the grain growth at the sub-surface and the precipitation of fine AlN during the hot band annealing.

The increase of {110}<001> texture and fine AlN precipitates increase the onset temperature of secondary recrystallization and improve the magnetic properties, which means more probability of sharp (110)[001] secondary nuclei and stronger inhibition against normal grain growth. Therefore, when the hot band annealed at 1120℃, a high temperature of secondary recrystallization and good magnetic properties are obtained.

5 Conclusion

When the hot bands of conventional grain-oriented electrical steel containing only AlN as a grain growth inhibitor were annealed at 900℃ and 1120℃, the coarse growth of recrystallized grains at the sub-surface of hot bands and an additional precipitation of fine AlN are occurred. As a result of them, the intensity of {110}<001> texture increases in the primary recrystallized microstructure. Due to these metallurgical changes, the onset temperature of secondary recrystallization increases and good magnetic properties are obtained, as the temperature of hot band annealing becomes higher.

6 References

1. Y.Yoshitomi et al. (1993), *J. Japan Inst. Metals*, Vol. 57, No. 6, pp. 612-620
2. M.Matsuo et al. (1981), *Proc.6th Intern. Conf. on Textures of Materials, Ed. by Nagashima ISIJ, Tokyo, II*, pp. 918-927
3. K.Iwayama and T.Haratani (1980), *J.Magn.Mag.Mat.*, Vol. 19, pp. 15-17
4. A.Datta (1976), *IEEE Trans. on Mag., MAG-12*, No.6, pp. 867-869
5. Martin F.Littmann (1975), *Metall.Trans.A*, Vol. 6A, pp. 1041-1048
6. H.C.Fiedler (1982), *J.Appl.Phys.*, Vol. 53. No. 11, pp. 8302-8304
7. T.Haratani et al. (1981), *Trans. Japan Inst. Metals*, Vol. 22, No. 2, pp. 75-8

TEMPER ROLLING EFFECTS OF LOW-C COLD ROLLED STEELS ON TEXTURE DEVELOPMENT AND STRETCHER STRAIN PHENOMENA

Young Ho Koh, Jeong Ho Choi*, No Jin Park*, Jang Hyun Choi
R & D Center, Union Steel MFG. Co., LTD in Pusan, Korea
*Dept. of Metals and Materials Engineering, Kumoh National University in Kumi, Korea

Abstract

Stretcher strain phenomena and texture development in low-C cold rolled steels were studied to investigate the effects according to the reduction ratio of temper rolling. Cold rolling texture can be decided by the deformation criteria and slip systems. Texture components differently develop by the different deformation hysteresis in the surface and center layer.

Keywords: Stretcher strain, temper rolling, low-C cold rolled steels

1. Introduction

In the case of the press forming of low-C cold rolled steels, the anomalous surface defects appear in the dendritic or line shape on the surface of automotive body or hood that experiences a small amount of deformation. They're generally called stretcher strain or Lüders band. These surface defects are not fatal in themselves to press forming, but they remain on the final products and de-value the products quality. The defects are not concealed in the following-up plating or colour coating process, either. So manufacturers are making efforts to prevent the stretcher strain phenomena. The stretcher strain is industrially controlled by grain size, interstitial elements in steel and temper rolling, etc. By an appropriate temper rolling, stretcher strain can be suppressed effectively, but hinders press forming with the increment of mechanical properties. Hence, the amount of temper rolling should be controlled appropriately to accommodate the forming process. Cold rolled steels for an automobile require high formability and homogeneous characteristics across thickness. However, by temper rolling criteria like friction between roll and plate, tension and the contact length ratio of roll and plate, etc, steels can experience heterogeneous stress state and have its deformation hysteresis. These anomalous deformations make the texture develop heterogeneous to the direction of thickness and cause property changes across the entire thickness[1].

In this study, the optimum condition of temper rolling was set up to prevent stretcher strain. Texture heterogeneity and the changes of mechanical properties were investigated by temper rolling using low-C steels with different carbon contents.

2. Experimental Procedures

IF and AK steels are utilized as raw materials in this study, and the chemical composition is indicated in table 1. Test criteria are shown in table 2. Temper rolling to control stretcher strain was carried out with a lubricated experimental rolling machine at room temperature and then the reduction ratio was 0.5%, 1.0%, 3.0%, 5.0% and 10%, respectively. Texture was determined by the measurement of (110), (200) and (211) incomplete pole figures. ODF was calculated quantitatively using a harmonic method with a maximum series expansion degree $L_{max}=22$[2,3]. The mechanical properties of elastic modulus and lankford parameter were measured by tensile test after sampling the specimens at 0°, 45°, 90° to the roll direction. Also the elastic modulus and the lankford parameter were calculated based on the Hill model and Taylor model, respectively[4,5].

3. Results and Discussion

The average grain size after recrystallization decreases with increasing carbon contents as shown in fig. 1, and grain deformation is observed with increasing temper rolling degree. The deformation degree of surface and center layer is slightly different, as indicated in table 3, from the length ratio(grain shape factor) of long axis(roll direction) and short axis(thickness direction) in the surface and center layer.

Grains near surface are more elongated than in center because stress can't be transmitted to the center layer with heterogeneous deformation. However, in IF steel, grain shape factor is scarcely deformed in the center layer and the change is observed only in the surface layer.

Fig. 2 and 3 show texture changes in accordance with carbon contents in the surface and center layers. Before annealing, α- and γ-fibers develop nearly to the same degree in the surface and center layers of AK specimens. Since the cold rolling degree is about 60 percent, the value of maximum orientation distribution function, $f(g)_{max}$, is a low of about 5 and texture development is suppressed by increasing carbon contents. In the case of IF steels with little carbon contents, γ-fibers are more developed in the center layer, but α-fibers on the surface layer and vice versa. In general, the cold rolling texture of low-C steels is decided by the deformation criteria and slip systems being driven at the time. By the Taylor model on plastic deformation, γ-fiber is developed in a full constraints model satisfying planar deformation condition and being proceeded by {110}<111>+{112}<111>+{123}<111> slip systems. These slip systems are known to be driven by temperature higher than room temperature and high purity. If satisfied with the relaxed constraints model[6] alleviating the restraints of shear components(ε_{13}, lath model) to the rolling plane and rolling direction or shear components($\varepsilon_{13}+\varepsilon_{23}$, pancake model) to the lath model and vertical direction, ($\alpha+\gamma$)-fibers are developed with strong α-fiber. So it can be inferred that shear components have a higher activation on the surface of IF steels. After annealing, γ-fiber is developed by texture rotation to the stable orientation during recrystallization. The intensity of {001}<110> component by recrystallization is more decreased in the center layer than in the surface layer. Recrystallization textures are different according to soluted carbon contents which is the most important factor controlling the textures of cold rolled steels. Strong γ-fiber texture is well developed in IF steels as a whole and f(g) is about 10~14, but the intensity decreases with increasing carbon contents and the value is about 5 in AK steels. Since the driving force of recrystallization is lattice defects, similar to a tangle of dislocations by plastic deformation, recrystallization will be initiated preferably in the grains which have experienced a high degree of work hardening. Hence, textures having big orientation scatterings from the γ-fiber are developed in high carbon soluted steels by the recovery detention of the reaction of carbon atoms and dislocations, and in the heterogeneity of slip behavior by carbon atoms, and in plastic deformation mechanism like slip bands[7]. Strong recrystallization γ-fiber developed in IF steels develops differently in the surface and center layer, that is, {111}<112> component is developed in the center layer, but {111}<110> component in the surface layer. By temper rolling, α-fiber components are slightly increased with an increase in the reduction ratio. This results from cold rolling texture appearance by temper rolling steels having recrystallization texture. In AK containing 0.034wt.% carbon, {001}<110> component is clearly developed after 10 percent temper rolling. This trend appears in the center layer and it can be inferred that the heterogeneous texture is not formed to the thickness direction of the plate through temper rolling. As indicated in table 3, grain shape factor changes a little bit more in the surface, but it's not thought that this has a big effect on texture.

The stress-strain curves of fig. 4 are the graphed results of tensile test with annealing treated IF and AK steels in the roll direction. Before temper rolling, stretcher strain is about 0.5~1.0 percent in IF steel, but it clearly appears about 4~6 percent in AK steels. It signifies that the most important factor is soluted carbon atoms on stretcher strain phenomena. After temper rolling, the stretcher strain completely disappears with 0.5 percent temper rolling in IF steel and over 1.0 percent temper rolling the increment of yield strength is clear. In AK steels, the stretcher strain is totally controlled with a 3.0 percent temper rolling. Up until a 5.0 percent temper rolling, specimens experience relatively homogeneous deformation, but in specimens that experienced a 10 percent temper rolling the local necking happens in by far fewer tensile deformation and elongation is remarkably reduced. The reduction of yield strength is observed in the small amount of temper rolling(0.5~1.0 percent), but it tends to increase on a large scale with increasing temper rolling. It is thought that this is so because immediately after annealing the tangle of dislocations by soluted carbon atoms results in high stress concentration, however, by temper rolling the tangled dislocations escape from the atmosphere of soluted carbon atoms[8], and yield occurs at low stress from increased dislocation density by the multiplication of dislocations, and yield strength increases by work hardening as the reduction ratio goes up. Elastic modulus and lankford parameter measured from tensile tests and calculated from texture, respectively, are compared with in fig. 5 and 6. In Fe single crystal, the anisotropy of elastic modulus is about 2.2 and its value is highest in <100> direction and lowest in <111> direction. The fraction of α-fiber and γ-fiber has an effect on the formability of cold rolled steels[5]. From the results, Young's modulus changes, as shown in fig. 6, are not so big comparing the angles to the roll direction and the anisotropy of elastic modulus by texture difference in the surface and center layer is small. IF steel shows the difference between calculated and measured values and it's thought to be the result of measuring errors that happened during the measurement of elastic modulus because of the low yield strength. The calculated r values of IF steel in the surface and center layer are different because of the difference of texture development in each layer. The highest r value in the surface layer occurs at 50~60° and it's the result of the texture development of weak α-fiber and strong γ-fiber. Generally, α-fiber has an effect of increasing the intensity of r value at about 50° and γ-fiber uniformly increases the value wholly. However, in this study, the intensity of γ-fiber developed in surface layer is not homogeneous and the intensity of {111}<110> component is very high, as shown in fig. 3. This component results in high r value at around 0° and 60°. The maximum r value appears at 50~60° to the roll direction from the results. In the center layer, only strong γ-fiber develops and has a high r value on average. Contrary to the surface layer, {111}<112> components are strongly developed. In the case of AK steels, with the influence of low intensity γ-fibers homogeneously formed in plate, the r value is low and in the surface layer it's even lower. The calculated r value is similar to that of the center layer, so it's thought that the texture in the surface layer only exists in the surface. γ-fiber formation decreases with increasing carbon content and lowers the r value. Temper rolling has little effect on the texture of IF so as to Young's modulus and lankford parameter. However, in AK steel, α-fiber develops with increasing temper rolling and decreases the r value., that is, the carbon content affects the lankford parameter by temper rolling.

4. Conclusion

The effects of temper rolling on texture development and mechanical properties are investigated according to chemical composition and the reduction ratio of temper rolling, and the results are as follows;

1) Predominant γ-fiber is developed by cold rolling in center layer and ($\alpha+\gamma$)-fibers which α-fiber is strong are developed in surface layer. This is the result of the different deformation hysteresis of the surface and center layer. After recrystallization the intensity of γ-fiber is clearly developed.

2) Specimens containing higher soluted carbon atoms have a little higher stretcher strain after

recrystallization and in a temper rolling over 3.0 percent the stretcher strain is completely removed regardless of carbon contents. IF steel shows very small amount of stretcher strain and it disappeared with 0.5 percent temper rolling.

3) In specimens containing 0.034wt.% carbon the intensity of α-fiber increases with the reduction ratio of temper rolling and it lowers the r value. Also, the variation of texture and properties in the surface and center layers is thought to be the result of cold rolling and heat treatment rather than temper rolling effects.

[References]

1. C.H. Choi, J.W. Kwon, K.H. Oh, Acta Mater, 45 (1997) 5119
2. H.J. Bunge, Texture analysis in materials science (1982) Butterworth, London
3. M. Dahms, H.J. Bunge, J. Appl. Cryst., 22 (1989) 439
4. G.I. Taylor, J. Inst. metals, 82 (1938) 307
5. N.J. Park, H. Klein, E. Dahlem Klein, Program system physical properties of textured materials (1994) Cuvillier Verlag, Goettingen, Germany
6. J.L. Rahanel, P. va Houte, Acta Met, 33 (1985) 1481
7. J.P. Ahn, M.Y. Huh, B. Korea Inst. of Met. & Mat, 14 (1997) 1142
8. R.M. Rose, L.A. Shepard, J. Wulff, The structure and properties of materials, 1965

Table 1. Chemical composition of the cold rolled steels in wt.%.

Sample	C	Si	Mn	P	S	Cu	Al	Ni	Cr	Ti	Nb	Fe
IF	0.002	0.017	0.130	0.015	0.007	0.020	0.039	0.013	0.014	0.044	0.014	bal.
AK	0.034	0.019	0.232	0.015	0.012	0.031	0.029	0.017	0.010	-	0.012	bal.

Table 2. The criteria of deformation and annealing of the steels.

Sample	Carbon	Thickness	Reduction degrees	Annealing
IF	0.002%	0.45mm	77.5%	500℃ 1hr holding → 660℃ 1hr soaking
AK	0.034%	1.118mm	59.3%	680℃ 6hrs soaking

Table 3. Mean shape factor of grains(the ratio of major and minor length of grains).

Skin Pass, %		0.0	0.5	1.0	3.0	5.0	10
IF	Surface	2.077	2.176	2.206	2.259	2.558	2.609
	Center	1.956	2.023	2.025	2.047	2.065	2.212
AK	Surface	1.900	2.000	2.189	2.451	2.568	2.622
	Center	1.518	1.533	1.613	1.735	1.803	2.025

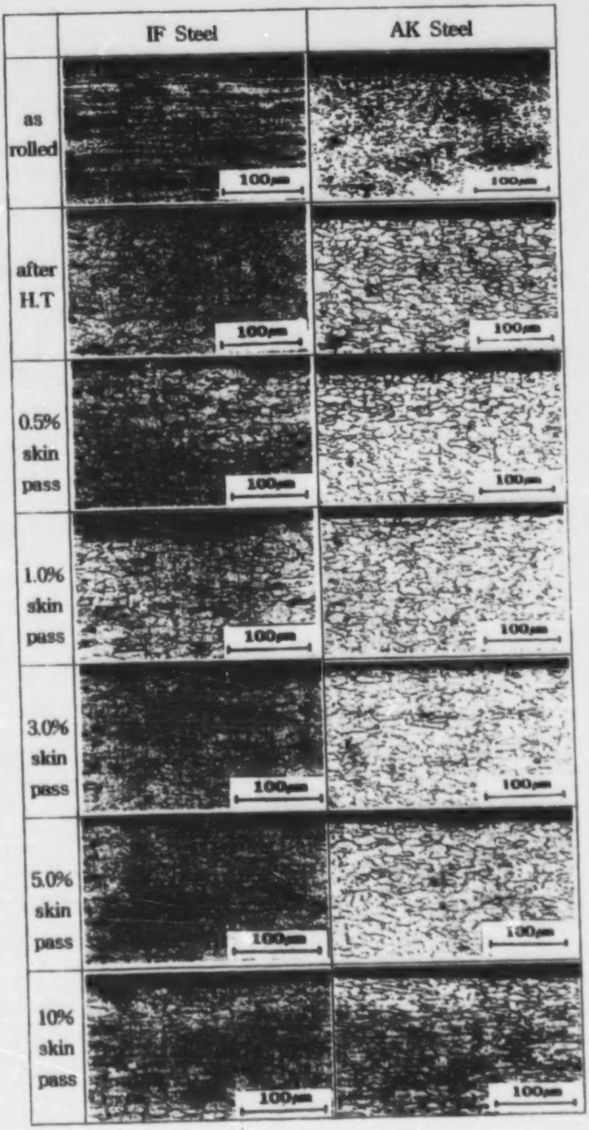
IF Steel
AK Steel
as rolled
after H.T
0.5% skin pass
1.0% skin pass
3.0% skin pass
5.0% skin pass
10% skin pass
100μm

Fig. 1 Optical micrographs in longitudinal section

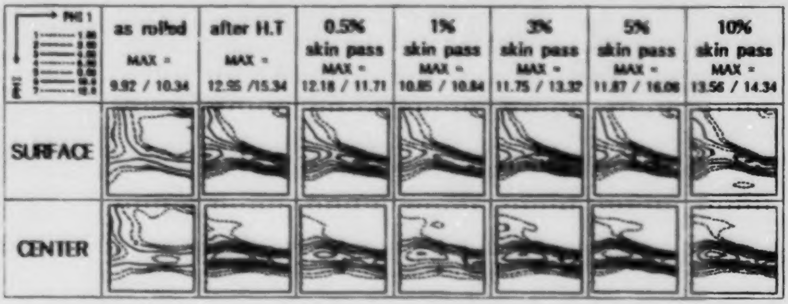

(a) IF Steel

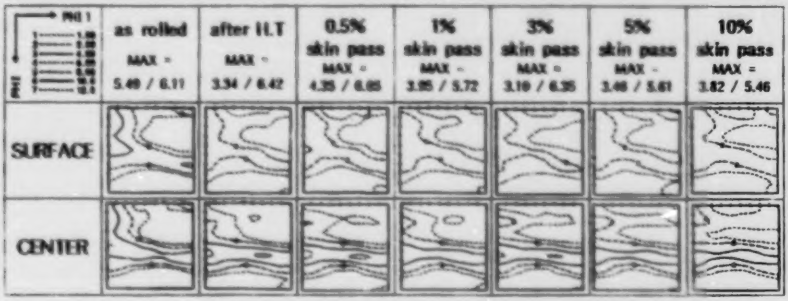

(b) AK Steel

Fig. 2 ODF in the surface and center layer after cold-rolling, heat-treatment and temper rolling. (a) IF-steel (b) AK steel (0.034%C)

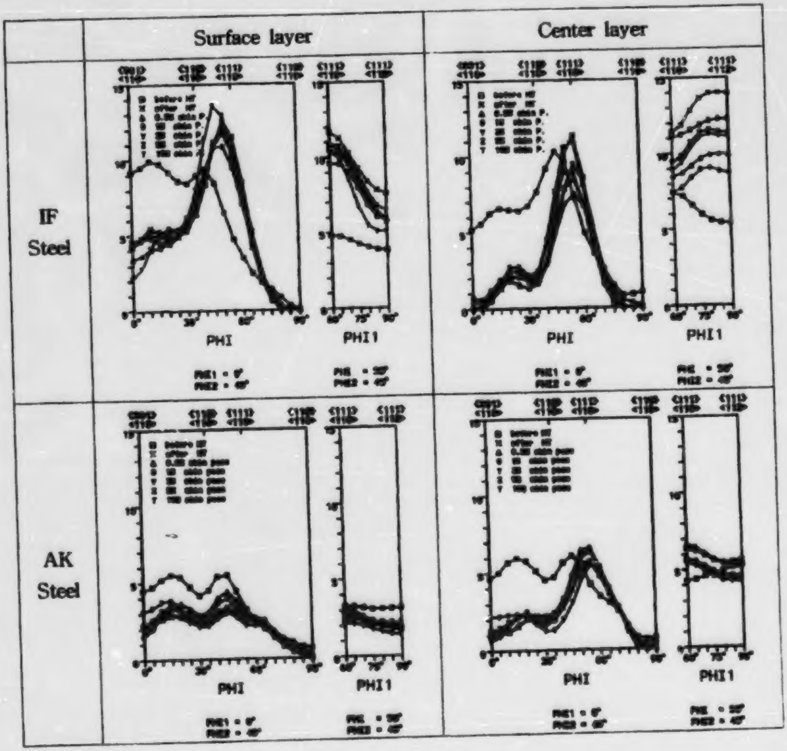

Fig. 3 Orientation density along α- and γ-fiber.

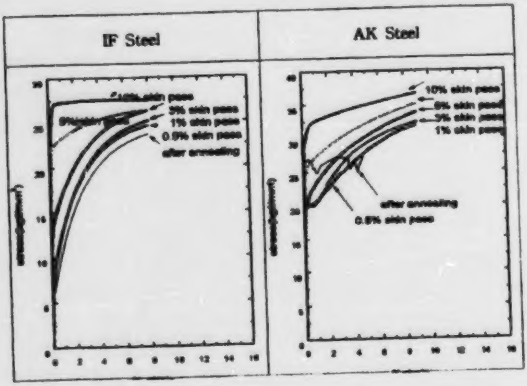

Fig.4 : Stress-strain curves of IF steel and AK steel

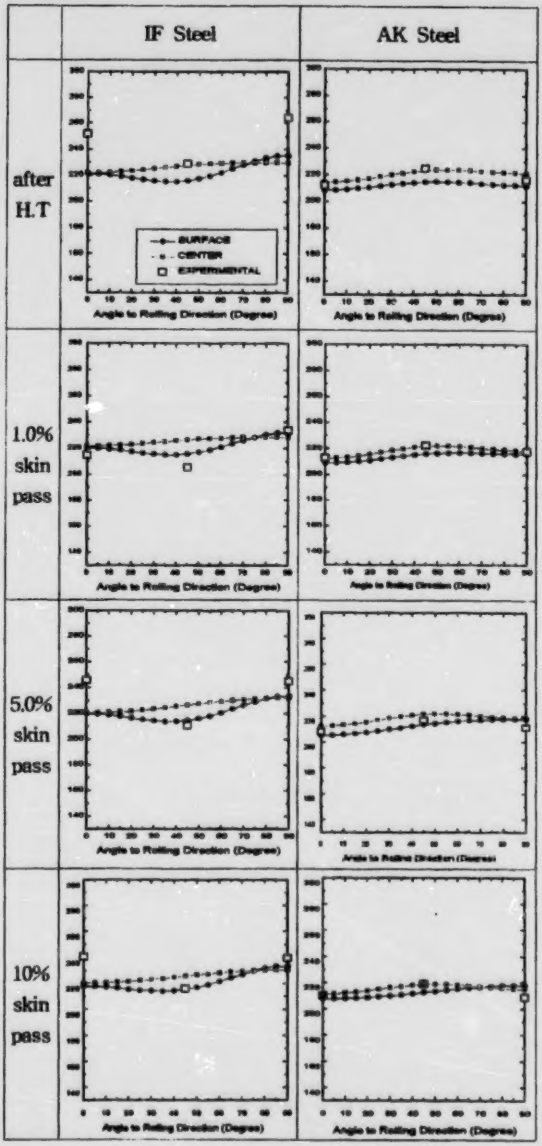

Fig. 5 Elastic modulus after heat-treatment and temper rolling.

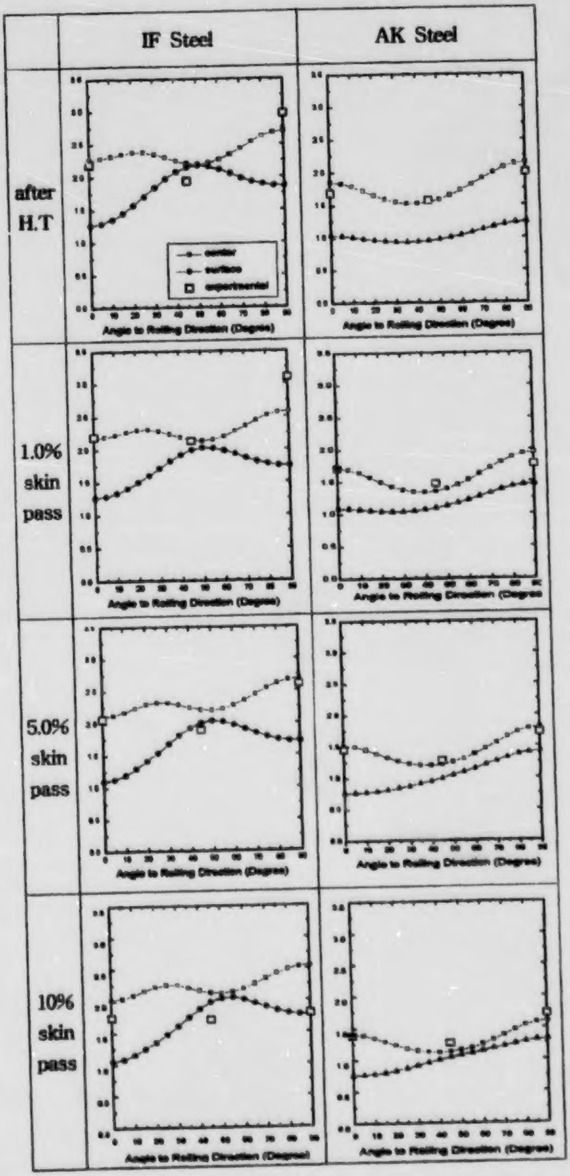

Fig. 6 r–values after heat–treatment and temper rolling.

TEXTURE EVOLUTION DURING HOT PLANE STRAIN COMPRESSION OF A HOT DEFORMED AA5182 Al-Mg ALLOY

P. RATCHEV, B. VERLINDEN and P. VAN HOUTTE
Katholieke Universiteit Leuven, Dept. of Metallurgy and Materials Engineering,
Leuven, Belgium
R. VAN DEN BROECK
Hoogovens Aluminium N.V., Duffel, Belgium
M.R. VAN DER WINDEN
Hoogovens Research and Development, IJmuiden, The Netherlands

Abstract

The texture evolution during hot deformation of a commercial AA5182 Al-Mg alloy has been studied by means of hot plane strain compression tests. The relations between the bulk texture and the deformation parameters strain, strain rate and temperature (the last two combined in the Zener-Hollomon parameter) have been revealed both after deformation and after subsequent recrystallization. The contribution of the different nucleation sources to the bulk texture has been studied by means of Orientation Imaging Microscopy.

Keywords: Al-Mg alloys, hot plane strain compression, texture evolution, OIM.

1 Introduction

In recent years the plane strain compression method has proven to be a reliable tool for simulation of commercial hot rolling (Marshal 1998). The final goal of these simulations is to model the evolution of microstructure and texture during hot rolling of aluminium, which, in spite of several interesting recent trials (Vatne 1995, 1996; Engler and Vatne 1998) has not yet been achieved.

The purpose of this work is to study the evolution of texture and microstructure as function of deformation parameters of an AA5182 Al-Mg alloy by means of plane strain compression tests. These textures and microstructures have been compared qualitatively to the results obtained by a recent model (Engler and Vatne 1998), applied until now for an AA3004 Al-Mn-Mg alloy. The contributions of different nucleation sources assumed in this model, are in agreement with the results obtained in the present AA 5182 alloy by Orientation Imaging Microscopy (OIM).

2 Experimental

The AA 5182 Al-Mg alloy was supplied by Hoogovens Aluminium N.V., Duffel in hot rolled condition with a thickness of 27 mm. Texture and microstructure studies show a fully recrystallized initial material (>95%). The Plane Strain Compression tests (PSC) have been carried out on a Thermo-Mechanical Treatment Simulator (TMTS), available within Hoogovens Research & Development. Deformations were performed at two levels of strain, namely ε=0.4 and 1, and different combinations of strain rate and temperature with a Zener-Hollomon parameter Z in the range of 3.48E9-1.2E13 s^{-1} ($Z=\dot{\varepsilon}\exp(Q/RT)$, s^{-1} where Q= 156 kJ/mol, R=8.31451 $J.mol^{-1}K^{-1}$). The temperatures used were between 350 and 550°C and the strain rates between 0.1 and 10 s^{-1}. The deformed part of the PSC samples of about 65x20 mm has been cut and used for texture and microstructure examination. Following the deformation mode, normal (ND), transverse (TD) and rolling directions (RD) have been related to the PSC samples, which make them closely comparable to hot rolled material (Baxter 1995). The textures of the investigated samples have been measured by means of bulk X-ray diffraction. Orientation Distribution Function (ODF's) and volume fractions of the texture components were calculated by means of the MTM-FHM software (with a spread of 16.5°). Grain sizes have been measured by means of the intercept method (Schücker 1968). Local textures have been measured by means of Orientation Imaging Microscopy (OIM) on surfaces containing RD and ND using the standard TSL™ OIM software. In OIM maps a thick line was used to visualize high angle grain boundaries (showing misorientation >15° and typically separating grains) and a thin line for low angle boundaries (for misorientations of 1 to 15°, typical for subgrains). Electropolishing for OIM was done with an electrolyte of perchloric acid: methanol = 1: 4 at -30°C and 11V.

3 Results and discussion

The texture of the deformed samples consists mainly of the Cube, CG (22°RD rotated Cube), CH (22°ND rotated Cube) components and the deformation components: S, Bs, Cu. The measured textures as function of the Z-value are shown in fig. 1 for the strain of 1. Since the deformation components always appear with the same approximate ratio (S: Bs: Cu = 2: 1: 1), only their sum is shown in the graphs. At the low strain (ε=0.4) the Cube, CG and CH components are almost invariable with increasing Z, but at the high strain (ε=1) they increase with decreasing Z-values, a tendency which has been already observed by Basson et al. (Basson 1998). The biggest increase with respect to the initial texture is shown by the CG texture component, followed by the Cube component. This result might be interpreted first of all in terms of rotation of unstable cube grains towards the Goss orientation, which increases the CG component, and second as Cube and near-Cube grains stabilization with decrease of Z-value (Basson 1998). The deformation components show an increase with increasing Z-value. This tendency is found for both ε=0.4 and ε=1, but the level of the volume fractions is higher at higher strains. After the deformation the samples have been annealed at the deformation temperature (simulation of inter-pass annealing during hot rolling) until recrystallization takes place. The recrystallized textures are characterised by a decrease of the deformation components close to their level prior to deformation. Compared to the deformed state, Cube, CG and CH volume fractions come very close together approximately at the level of Cube, see fig. 2. Accordingly, the change is mainly due to an increase of the volume fraction of the CH component and to a decrease of the CG component. The Cube, CH and CG textures increase with decreasing Z, a tendency that is shown also after deformation.

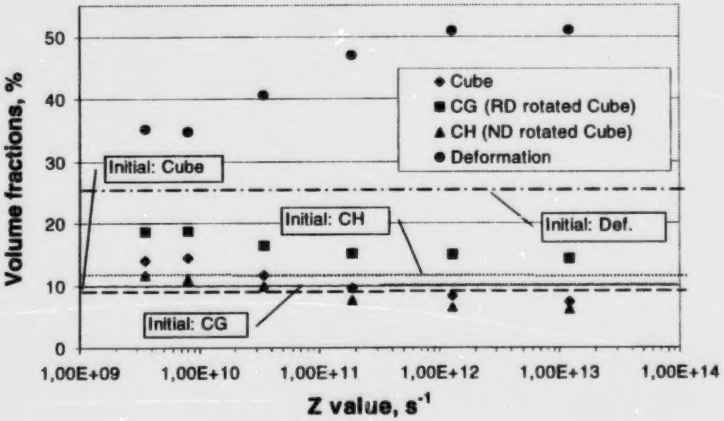

Figure 1:Textures (in volume fractions) after deformation to a strain of 1.

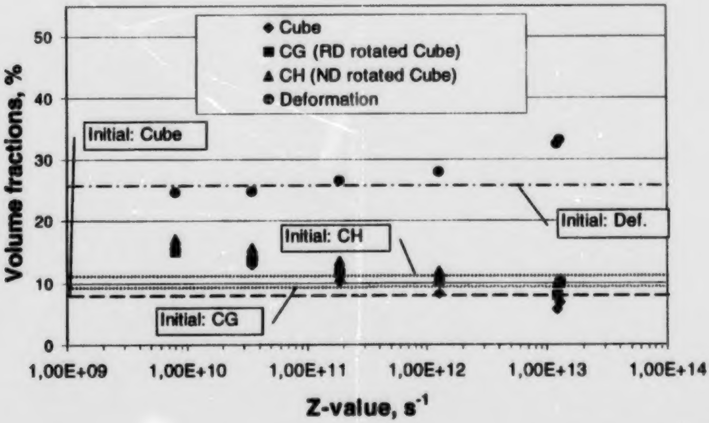

Figure 2: Recrystallized textures of samples previously deformed to a strain of 1.

This texture evolution might be understood in terms of a recent model (Engler and Vatne 1998), calculating the recrystallization texture after hot deformation. It is based on a growth selection of grains with an approximate 40°<111> orientation relationship out of a limited spectrum of preferentially formed nucleus orientation. The most important nucleation sites in rolled Al-alloys are cube bands, grain boundaries and second-phase particles. The contribution of each of these nucleation sites is determined according to an approach that calculates the number of nuclei forming at each one of them (Engler and Vatne 1998, Vatne 1995, Vatne et al. 1996). Cube bands are most active at low Z-values and they act as a nucleation site of new Cube grains. High angle grain boundaries give rise to new grains of orientations either random or close to the deformation textures, but weaker and they also act mainly at low Z. The mechanism most active at high Z-values is Particle Stimulated Nucleation (PSN). At relatively low temperatures a random texture is generated in the deformation zones around second phase particles. The decrease of the deformation texture after recrystallization, see fig. 2 vs. fig. 1 is relatively more important at high Z than at low Z (relatively, 35% vs. 28%). This can be related to the more active PSN at high Z, which is randomizing the texture, compared to the grain boundary nucleation, active at low Z, which contributes also to deformation textures. The increase of the Cube texture with decreasing Z is usually attributed to the nucleation on cube bands (Engler and Vatne 1998). On the other hand the comparison with the texture after deformation, fig. 1, shows that the volume fraction of the Cube texture does not change significantly with recrystallization. Consequently, present results do not support a Cube texture advantage with recrystallization at low Z. Actually, the Cube texture advantage at low Z appear at the deformation stage, see fig.1. Changes in recrystallization vs. deformation texture appear in the increase of the CH and decrease of the CG components. The increase of the CH component can be related to the randomizing effect of PSN nucleation, since it is relatively higher at high Z and lower at low Z according to the activity of PSN. The decrease of CG compared to the increase of CH could be due to a growth advantage of the CH component.

The role of the different nucleation mechanisms reflects the influence of deformation parameters on recrystallized grain size. In fig. 3 the recrystallized grain size is shown as function of the Z-value for the two studied levels of strain. The recrystallized grain size depends only a little on the level of the imposed deformation strain. The observed dependence on Z fits qualitatively well to the model of Engler and Vatne. The drastic increase of the grain size at low Z, according to it, has to be related to a lack of nuclei due to the inactive PSN. The activity of nucleation sites at different Z has been studied in partially recrystallized samples (10-15%) by means of Orientation Imaging Microscopy (OIM). The lack of low angle grain boundaries in a grain on the OIM scan has been used to distinguish recrystallized from as-deformed grains. The material deformed at low Z, fig. 4,a shows a lack of nuclei and consequently the new grains can grow out in the deformed matrix. Note the serrated grain boundaries developing at these deformation conditions. In fig. 4,b a sample deformed at intermediate Z is shown. At these conditions more nuclei are activated, high angle grain boundaries meet each other faster, which results in a smaller grain size. At high Z the density of nuclei is very big, see fig.4,c mainly due to PSN, which reflects in the smallest recrystallized grain size.

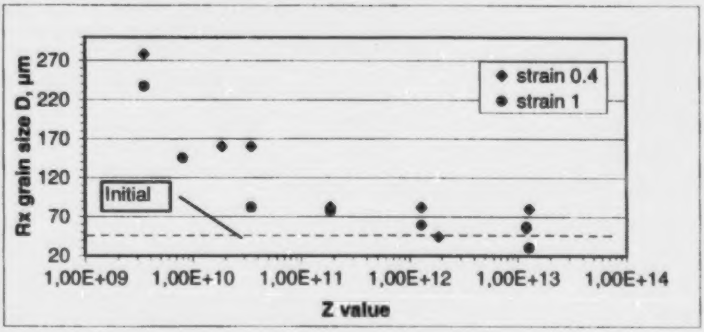

Figure 3: Recrystallized grain size as function of the deformation conditions.

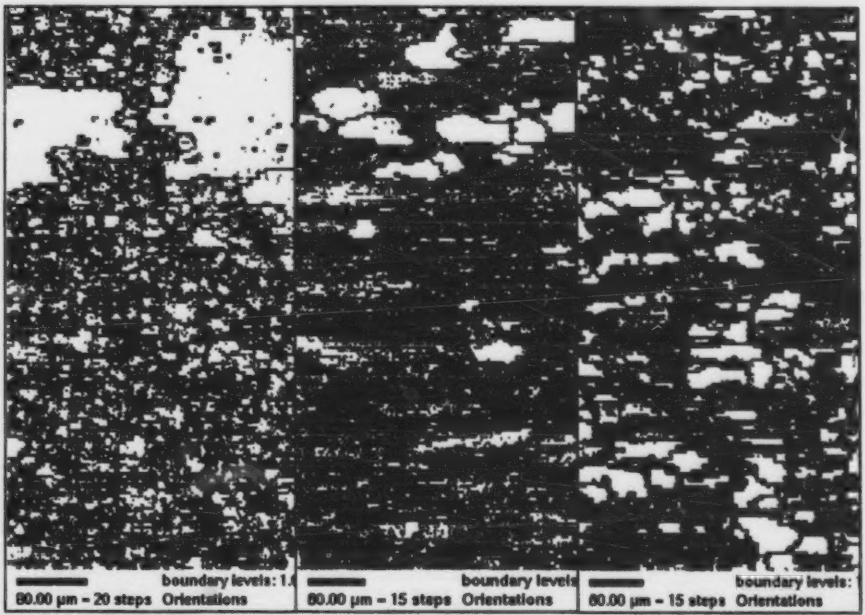
80.00 µm = 20 steps
boundary levels: 1.
Orientations
80.00 µm = 15 steps
boundary levels
Orientations
80.00 µm = 15 steps
boundary levels:
Orientations

a) Z=3.48E9 (T=500°C; $\dot{\varepsilon}$ =0.1)

b) Z=1.86E11 (T=450°C, $\dot{\varepsilon}$ =1)

c) Z=1.2E13 (T=350°C, $\dot{\varepsilon}$ =1)

Figure 4: OIM scan of partially recrystallized samples, deformed at different Z-values. The lack of nuclei at low Z results in a big recrystallized grain size. Bigger densities of nuclei at intermediate Z leads to smaller and in the case of high Z to the smallest recrystallized grain size.

4 Conclusions

- The texture of deformed samples evolves in general as follows. The deformation components increase with increasing Z-value. The level depends on the applied strain. The Cube, CG and CH textures increase with decreasing Z. The strongest texture is not the Cube, as usually reported, but the CG.
- In the recrystallized samples deformation components drop down to their initial value. The Cube, CH and CG components come close together approximately on the level of the Cube. In respect to the levels prior to recrystallization, the Cube does not change significantly, the CG decreases and the CH increases.
- The contribution of different types of nuclei to the recrystallization texture, as suggested by Engler and Vatne, has been qualitatively confirmed for AA 5182 Al-Mg alloy. In the observed range of Z-values a Cube texture advantage due to the recrystallization has not been observed. The advantage of Cube, CH and CG at low Z generated during the deformation is preserved also by the recrystallization.

5 Acknowledgements

This work was performed with the financial aid of the Flemish Government, IWT project No. 97/0332.

6 References

Baxter, G.J., Duly, D., Orsetti Rossi, P.L., Sellars, C.M., Whiteman, J.A., Shercliff, HR. and Ashby, M.F. (1995) *Microstructural evolution and recrystallization in hot worked Al-1%Mg alloy,* in Proc. of the 16th Risø Int. Symp. on Mat. Sci., (eds. N. Hansen et al.), Roskilde, Denmark, pp. 267-72.

Basson, F., Chenal, B., Necker, C.T., Embury, J.D. and Driver J.H. (1998) *Cube texture evolution during hot plane strain compression of Al-Mg alloys*, in, Proceedings of ICAA6 (eds. T. Sato et al.), Toyohashi, Japan, The Japan Inst. of Light Metals, vol. 2, pp.1167-72.

Engler, O. and Vatne, H.E. (1998) Modeling of the recrystallization textures of Al-alloys after hot deformation, in *Hot Deformation of Aluminium Alloys II*, (eds. T.R. Bieler et al.), The Minerals, Metals and Materials Society, pp. 291-302.

Marshal, G.J. (1998) Simulation of commercial hot rolling by laboratory plane strain compression and its application to aluminium industry challenges. in *Hot Deformation of Aluminium Alloys II*, (eds. T.R. Bieler, L.A. Lalli and S.R. MacEwen), The Minerals, Metals and Materials Society, pp. 367-82.

Schücker, F. (1968) Grain size. in *Quantitative microscopy*, (eds. R. De Hoff and F.H. Rhines), McGraw-Hill Book Company, New York, p. 239.

Vatne, H.E. (1995) *PhD thesis,* The Norwegian Institute of Technology, Trondheim.

Vatne, H.E., Marthinsen, K., Ørsund, R., Nes, E. (1996) Modelling recrystallization kinetics, grain sizes and textures during multipass hot rolling. *Metallurgical and Materials Transactions A*, Vol. 27A, pp. 4133-44.

THROUGH-THICKNESS INHOMOGENEITY OF THE TEXTURE DEVELOPED IN HIGH STRENGTH LINEPIPE

G. J. BACZYNSKI and J. J. JONAS
Department of Metallurgical Engineering, McGill University, Montreal, Canada
L. E. COLLINS
Research and Development, IPSCO Inc., Regina, Canada

ABSTRACT

Two X-80 steels were finish rolled at two different rolling temperatures: i) in the γ range in schedule A, and ii) in the intercritical (α+γ) region in schedule B. The final thickness of strip A was 1.53cm while that of steel B 1.03cm. Similar coiling temperatures (~578°C) and cooling rates (~13°C/s) were employed in the two cases. The final microstructures consisted of polygonal and acicular ferrite. Significant through-thickness texture gradients were observed in both cases. Typical <110>//ND shear components were identified at the surface, while the usual ND (<111>//ND) fibers were present throughout the thickness. The shear textures produced in strip B were strong but extended only to about 2.5mm below the surface. These were detected down to about 5mm below the surface in steel A, but were relatively weak. The effects of austenite (γ) and intercritical (α+γ) rolling, as well as of phase transformation, on texture development are discussed in detail.

Keywords: Bcc rolling textures, polygonal and acicular ferrite, surface shear textures

1 Introduction

Significant improvements in the strength and toughness of linepipe steels have been achieved over the past ten years. Examples can be found in the literature where new X-100 (690 MPa), Okatsu et al. (1997), and X-80 (550 MPa), Kostic et al. (1998), grades have been designed to replace the current generation of X-70 (480 MPa) high-strength-low-alloy (HSLA) pipeline steels. In general, appreciable savings in construction costs can be achieved by employing stronger materials and reducing the pipe wall thickness.

However, the final properties may vary significantly from the surface to the center of pipeline strip. This through-thickness inhomogeneity is related to the characteristics of the microstructure and crystallographic texture and, in general, fracture can occur at much lower stresses in these steels.

To control the final properties, the roles of the alloying additions and processing parameters (soaking temperature, finish rolling temperature, cooling rate and cooling interrupt temperature) have been studied extensively during the last two decades, Faucher and Dogan (1988), Baczynski et al. (1999). This has led to a better understanding of microstructural evolution and of the relation between texture and anisotropy of the mechanical properties. By contrast, much less is known about the through-thickness inhomogeneity of the microstructure and texture.

This study was therefore undertaken to analyze the through-thickness texture gradient developed during industrial rolling. An X-80 linepipe steel was selected for this purpose. Two different rolling schedules were employed; the textures were then determined and analyzed by means of ODFs.

2 Experimental material and methods

The chemical compositions of the two heats under study are given in Table 1. Two stages of controlled rolling, roughing and finishing, were performed. The roughing passes were conducted in the temperature range 1250-950°C, with total rolling reductions of 81 and 88% for schedules A and B, respectively. The finishing passes were performed in the temperature ranges 837-777°C (A, entirely in the γ phase) and 786-738°C (B, in the $\gamma+\alpha$ region). These two different rolling schedules corresponded to reductions of 60% (A) and 58% (B), respectively. Similar average coiling temperatures of 579 and 576°C and cooling rates of 13 and 14°C/s were employed for schedules A and B, respectively.

The metallographic observations were carried out just before electropolishing, i.e. before the final stage of sample preparation for texture measurement. The samples were mechanically polished on cross-sections parallel to the rolling plane; they were then chemically etched with a solution of 2% nital. As a result, the polygonal and acicular ferrite grain boundaries were revealed and the metallographic observations were recorded using a Neophot 21 optical microscope.

The texture samples (15mm x 25mm) were prepared by grinding and electropolishing and the textures were measured on the Siemens D-500 goniometer system at McGill. ODFs were calculated on the basis of cubic crystal and orthorhombic sample symmetry from {110}, {200}, and {211} incomplete pole figures. The series expansion method introduced by Bunge was employed in the present study.

Table I. Steel compositions (in weight %).

	C	Mn	Si	Mo	Nb	Ti	P	S	Ni+Cr+Cu
X80 (A)	0.038	1.77	0.27	0.25	0.090	0.022	0.009	0.002	0.59
X80 (B)	0.030	1.80	0.28	0.24	0.088	0.024	0.010	0.003	0.45

3 Experimental results

A typical microstructure of the X-80 steel processed according to schedule A is shown in Fig. 1. It is evident that both polygonal and acicular ferrite (or bainite) were formed under the present conditions. Comparable microstructures were present in the B steel. The mean grain sizes were similar in both materials. However, grains as fine as 2μm and as coarse as 20μm were present in both microstructures.

To aid in the analysis of the texture results, some important ideal orientations observed in rolling are identified in Fig. 2. These are specified in terms of texture fibers, as well as the relevant Miller indices in the standard notation. The φ_2=45° Euler space cross-section is employed here to display the experimental ODFs.

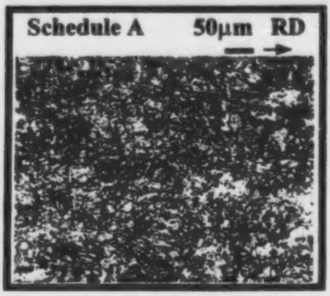

Fig. 1. Microstructure of the X-80 steel.

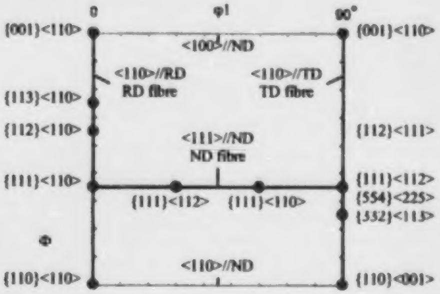

Fig. 2. φ_2=45° ODF section showing the positions of the main texture components located along the RD, TD, and ND fibers.

The through-thickness textures produced in the A and B steels are displayed in Figs. 3 and 4, respectively. The maximum intensities, isovalue-levels and distances from the surface to the cross-sections at which the textures were measured are shown as well. Note that the thickness of the A sample was 15.3mm while it was 10.3 mm for the B specimen.

Significant texture gradients are observed in both steels. The surface texture in the A steel is twice as intense as that measured at the center of the plate, see Figs. 3a and d. Typical shear components are formed at the surface. These are located mostly along the RH half of the <110>//ND fiber and are also observed at 3.8 mm below the surface, see Fig. 3b. However, the shear texture disappeared at about 5 mm below the surface and is absent at the center layer. The {111}//ND fiber is present throughout the thickness, together with the texture components located along the RD//<110> fiber.

The textures produced in the B steel change their maximum intensities from 7.1 at the surface (Fig. 4a), to 3.8 (1mm, Fig. 4b), 4.0 (2.6mm, Fig. 4c) and 6.0 (5.2mm, Fig. 4d) at the center. There is a strong <110>//ND shear component present at the surface, see Fig. 4a. However, its intensity is insignificant at about 2.5mm from the surface, see Fig. 4c. At the center, the <110>//ND shear fiber is absent. The {111}//ND rolling fiber is present throughout the thickness and some weak cube can be found as well.

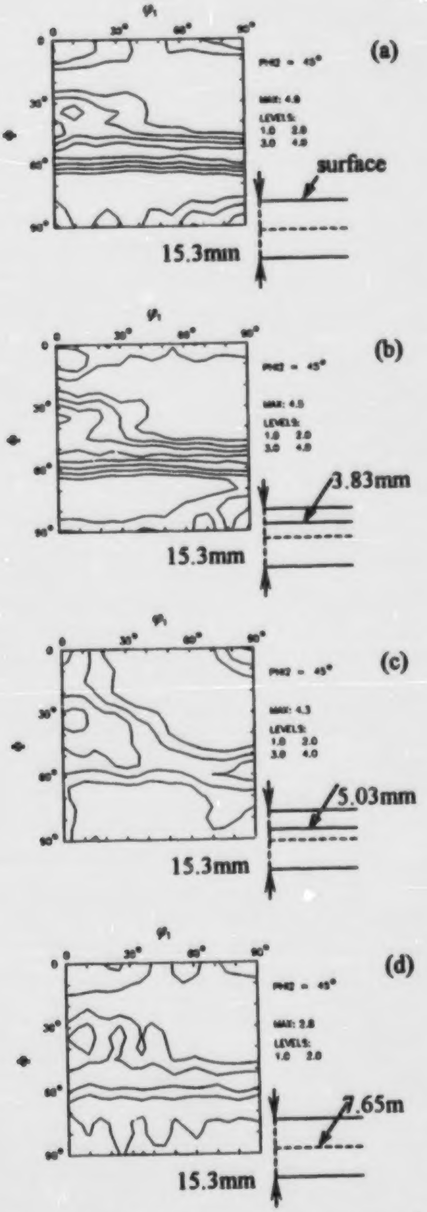

Fig. 3. Through-thickness textures measured in the X-80 A (15.3mm) plate.

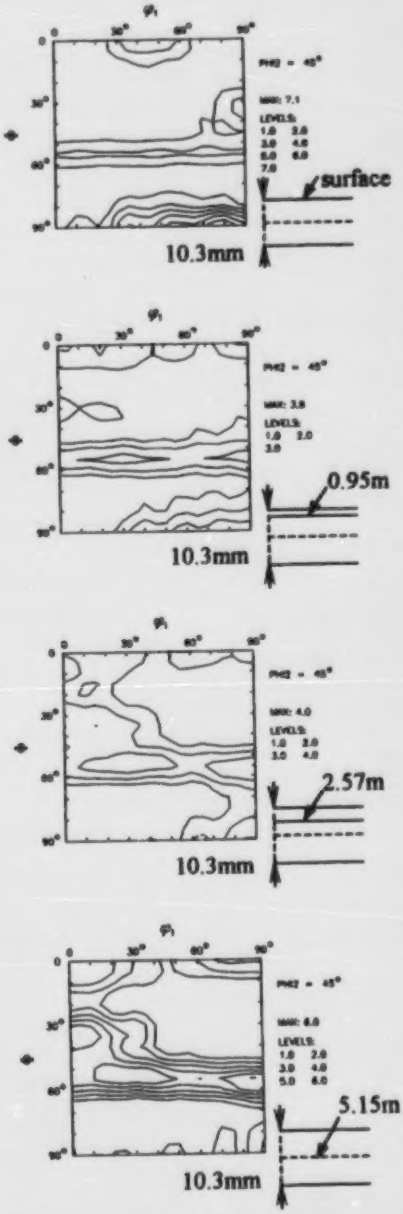

Fig. 4. Through-thickness textures measured in the X-80 B (10.3mm) plate.

4 Discussion

Textures are most commonly measured by means of the x-ray reflection technique. In this case, diffraction is produced by the crystallographic planes located close to the surface of the specimen. To obtain representative information, measurements are usually made at the quarter thickness of rolled plates and the effect of the processing conditions on texture development is deduced in this way. As a result, texture data regarding the surface and center layers are usually missing and the orientation distribution analysis is therefore incomplete. The surface texture in rolled plates reflects the fact that, close to the surface, plastic deformation takes the form of shear along the rolling direction, Regenet and Stuwe (1990). Typical bcc shear components are generally located along the <110>//ND fiber, Bleck et al. (1991).

In our study, this component was formed in both the A and B samples. However, rolling in the austenite region led to weaker shear textures than those produced by intercritical ($\alpha+\gamma$) rolling. In the latter case, the <110>//ND fiber (with intensities of seven times random) dominates the texture produced at the surface, see Fig. 4a. It appears that the majority of the surface α grains (down to a thickness of about fifty microns) in the B specimen are extensively deformed in shear. Some grains do not participate in this process and contribute instead to the {111}//ND fiber and the {112}<111> and {001}<100> components. The shear process still makes a contribution about 1mm below the surface of the B material, see Fig. 4b. However, at about 2.5mm from the surface, the shear component is relatively weak and it finally disappears completely at the center of the plate, see Fig. 4d.

The shear textures produced by torsion in fcc and bcc materials have been extensively studied during the past two decades, Montheillet et al. (1984), Baczynski and Jonas (1996). These are generally described in the shear convention (axes). When the shear axes are converted to the rolling ones, the bcc shear textures correspond to the <110>//ND fiber.

By contrast, the α grains in the A sample were formed from *deformed* austenite on cooling. The textures are therefore weaker than those observed in the B (i.e. intercritically rolled) samples. The shear component observed at the surface of the A plate was relatively weak and it disappeared completely at about 5mm from the surface.

5 Conclusions

1. Significant through-thickness texture gradients were present in the X-80 steel, whether processed in the austenite (γ) or in the intercritical ($\alpha+\gamma$) range.
2. The surface texture, as characterized by <110>//ND fiber components, was weak in the A steel and detectable down to about 5mm below the surface. By contrast, the surface texture in the B steel was stronger but remained significant only down to about 2.5mm below the surface.

6 Acknowledgements

The authors are grateful to Ipsco Inc. for supplying the X-80 steels and for financial support.

7 References

Baczynski, G.J., Jonas, J.J. and Collins, L.E. (1999) The influence of rolling practice on notch toughness and texture development in high strength linepipe. Metall. Trans. A, in press.

Baczynski, J. and Jonas, J.J. (1996) Texture development during the torsion testing of α-iron and two IF steels. Acta metall. 44, No. 11, pp. 4273-4288.

Bleck, W., Grossterlinden, R., Lotter, U. and Reip, C. (1991). Materials Technology, 62, No. 12, pp. 580-586.

Faucher, B. and Dogan, B. (1988) Evolution of the fracture toughness of hot-rolled low-alloy Ti-V plate steel. Metall. Trans., vol. 19A, pp. 505-516.

Kostic, M.M., Collins, L.E., Kapoor, A. and O'Hara, R.D. (1998) Development of heavy gauge X-80 linepipe. Proc. International Pipeline Conference, vol. 1, Calgary, June 7 - 11, ASME, New York, N.Y., pp. 665-688.

Montheillet, F., Cohen, M. and Jonas, J.J. (1984) Axial stresses and texture development during the torsion testing of Al, Cu, and α-Fe. Acta metall. 32, pp. 2077-2089.

Okatsu, M., Kawabata, F. and Amano, K. (1997) Metallurgical and mechanical features of X-100 linepipe steel. Proc. OMAE, vol. 3, ASME, New York, USA, pp. 119-124.

Regenet, P.J. and Stuwe, H.P. (1990). Z. Metallkde. 54, No. 5, pp. 273-278.

TEXTURE DEVELOPMENT DURING COLD ROLLING AND ANNEALING IN TWO 304 AUSTENITIC STAINLESS STEEL CAST STRIPS

S. TERAOKA[1,2], J. BACZYNSKI[1] and J.J. JONAS[1]

[1] Department of Metallurgical Engineering, McGill University, Montreal, Canada

[2] Hikari Technical Research Laboratories, Nippon Steel Corporation, Yamaguchi, Japan

Abstract

The textures formed in two stainless steel cast strips and a laboratory hot rolled strip (304 austenitic grade) were determined after cold rolling and annealing. The textures were characterized by a {001}<uvw> fiber in the F cast strip and a {011}<uvw> fiber in the G cast strip. The γ-to-α' deformation-induced transformation took place during cold rolling and low symmetry rolling textures were produced in sample F after 50% reduction by cold rolling. By contrast, the 80% cold rolled textures displayed orthorhombic symmetry. The recrystallization texture components changed from {001}<100> and {110}<111> to {110}<001>, {110}<112> and {112}<111> when the cold reduction was increased. The cast strips displayed weaker recrystallization textures than the H (conventionally processed) material. Moreover, sample G contained stronger $\{110\}_{ND}$ fiber components than sample F. Texture development in the rolled and annealed products is discussed in terms of the Kurdjumov-Sachs transformation relationship.

Keywords: Annealing textures, cast strip, rolling textures, transformation textures

1. Introduction

Strip casting processes have been developed by many companies and organizations. It has been reported that the type 304 stainless steel cold rolled strips produced by strip casting have low anisotropy (Ohkubo et al., 1991). Such low anisotropy is probably linked to the initial solidification microstructure and texture. Nevertheless, the texture development mechanisms operating during processing have not been fully investigated.

Type 304 stainless steel is a metastable alloy; thus austenite gradually transforms to α' during cold rolling. This occurs as a result of strain-induced transformation. The transformed α' is converted back into γ during annealing for recrystallization; thus the transformation has a significant effect on the final product texture. In this paper, the development of textures in two type 304 stainless steels that had been strip cast and then cold rolled and annealed was examined. Of particular interest was the effect of both the initial solidification and the subsequent transformation textures.

2. Experimental procedure

Two type 304 stainless steel cast strips and a laboratory hot rolled strip were prepared. The initial textures can be classified into three types, i) cast strip F contained the {001}<uvw> fiber texture, ii) cast strip G the {011}<uvw> fiber texture, and iii) the laboratory hot rolled strip H was characterized by a weak {112}<110> texture. The fiber axes of the cast strip textures were inclined by about 12° away from the horizontal towards the casting direction. Details of the preparation procedure and of the solidification textures are provided in a companion paper . The cast and hot rolled strips were annealed at 1100°C for 60 seconds, then cold rolled to reductions of 50 and 80% and subsequently annealed at 1100°C for a further 60 seconds. The rolling direction corresponded to the casting direction. The specimens for texture analysis were mechanically polished and then electrochemically polished at the quarter thickness, which contained the representative cast (columnar) structure. The textures were determined by measuring the {200}, {220} and {311} pole figures of the austenite phase, and the {200}, {211} and {220} pole figures of the martensite phase using Mo-K_α radiation. ODF's were calculated in each case using the three incomplete pole figures. The volume fractions of the α' phase were measured using a Ferrite Scope.

3. Results

The volume fractions of the α' during cold rolling are shown in Fig. 1. After 50% cold reduction, low symmetry textures were present in both phases of sample F, see Fig. 2. The γ texture contained the expected Goss {011}<100>, brass (Bs) {011}<112>, S {123}<634> and copper (Cu) {112}<111> components. On the other hand, the α' texture consisted principally of the {112}<241> component.

After 80% cold reduction, the two phases in samples F, G and H displayed almost ideal orthorhombic symmetry. The calculated ODF's are shown in Figs. 3 and 4. The γ texture included strong Goss and Bs and minor Cu and S components. This brass-type rolling texture is typical of low stacking fault energy materials. On the other hand, the α' texture contained major {112}<110>, {111}<112> and minor rotated cube {001}<110> components.

The recrystallization textures of the F, G and H samples of both the 50% as well as the 80% cold rolled materials were characterized by nearly perfect orthorhombic symmetry. The relevant ODF's are shown in Figs. 5 and 6.

The recrystallization textures of the 50% cold rolled samples contained the cube {001}<100>, {011}<111> and Cu components. By contrast, the recrystallization textures of the 80% cold rolled samples were characterized by the Goss, Bs and Cu components. When the same cold rolling reduction was employed, similar texture components were present in each sample, but the sample H material always displayed the highest maximum intensity.

4. Discussion

4.1 Rolling textures (low cold rolling reduction)

In the case of the low cold rolling reduction, the inclination of the solidification fiber texture in cast strip F produced textures that were asymmetrical with respect to the TD axis. For example, the γ texture displayed a more intense $(112)[11\bar{1}]$ than $(112)[\bar{1}\bar{1}1]$ component. The asymmetric α' texture is particularly interesting. The α' phase in the cold rolled samples was formed at increasing strains; thus the α' formed at an early stage of rolling was highly deformed during subsequent rolling, while the α' that was formed at the latest stage of rolling displays the unchanged transformation texture.

Transformation textures have been studied by various researchers and several attempts have been made to predict the textures that are produced. For example, Butrón-Guillén et al. (1998) described a model for the γ-to-α transformation in hot rolled carbon steels based on the Kurdjumov-Sachs relationship. According to this theory, the transformation texture consists of particular variants, the selection of which involves both a positive slip criterion and a dislocation reaction rule. By following their approach, the transformation texture of the present cold rolled type 304 stainless steel can also be predicted.

The parent γ texture contained Goss, Bs, S and Cu components that were not symmetrically disposed with respect to the TD axis. When these do in fact display the expected symmetry, the slip activities are themselves symmetric and the product orientations are characterized by orthorhombic symmetry. Conversely, inclination of the solidification {001}<uvw> fiber leads to asymmetric slip activity, which in turn produces the asymmetric texture. The slip activities responsible for this behavior and the variant selection that results are described in full in a separate publication.

4.2 Rolling textures (high cold rolling reduction)

After 80% cold rolling, all the sample textures displayed orthorhombic symmetry; this is consistent with the high rolling reductions. The development of γ rolling textures is related to the initial texture; thus, cast strip G with its $\{011\}_{ND}$ fiber texture developed more of the $\{011\}_{ND}$ rolling texture than cast strip F, with its initial $\{001\}_{ND}$ fiber texture. According to the deformation model that applies to fcc metals (Hirsch and Lucke, 1988), the {001}<uvw> orientation is far from the stable $\{011\}_{ND}$ rolling fiber that extends from the Bs to the Goss orientation. Thus the rolling fiber will develop more slowly in materials containing a {001} component. It should be added that the initial grain size has little effect on the alloy type of rolling texture (Öztürk et al., 1981).

The α' phase in the 80% cold rolled samples displayed the {111}<112>, {112}<110> and rotated-cube components; these correspond to typical rolling texture components in bcc metals. These transformation components can be accounted for using the previously mentioned model. However, in this case, the texture components can be calculated from the slip systems on the basis of orthorhombic symmetry. The ideal orientations predicted in this way correspond to the measured α' textures.

4.3 Recrystallization textures

During heating to 1100°C for recrystallization, the α'-to-γ reverse transformation occurs and the *deformed* γ recrystallizes. Thus the recrystallization process can be considered as a combination of the growth of transformed γ and of recrystallized γ.

In order to understand texture development under these conditions, it is useful to predict both the transformation and the recrystallization texture components using, respectively; i) the Kurdjumov-Sachs relationship (±90° rotations around the <112> axes) and the α' rolling texture; and ii) ±30-40° rotations around the <111> axes and the γ rolling texture.

The recrystallization textures include the cube, {110}<111>, Cu, Bs and Goss components. The cube is a typical fcc recrystallization texture component and forms from the copper type rolling texture; it is also one of the transformation components created from α' of the rotated-cube orientation. The {110}<111> is produced by the transformation of {111}<110> oriented α'. The Cu component is fairly close to the typical brass type recrystallization component, {236}<385>. The Goss and Bs form from the {111}<112> and {112}<110> α' orientations, which are the major texture components in the 80% cold rolled α' texture.

The major recrystallization texture changes from the cube and {011}<111> to the Goss, Bs and Cu with increasing cold rolling reduction. This appears to be related to the development of the γ and α' rolling textures and to the increase in the volume fraction of the α'. In the early stages of cold rolling, the major phase is the γ, which contains the Cu and Bs components; thus the recrystallization texture contains the cube component. By contrast, the highly cold rolled samples are characterized by high volume fractions of α'; thus the recrystallization textures displayed the Bs and Goss components.

In the case of the same cold rolling reduction, the recrystallization textures of the F samples were less intense than those of samples G and H. This seemed to arise because the G and H samples contained sharper γ rolling textures; moreover sample G consisted of a higher volume fraction of α' than sample F.

Although the initial grain size differed considerably between the cast and hot rolled strips, the effect of initial grain size on the recrystallization texture is far from clear. In the case of the brass type recrystallization texture, the effect of initial grain size seems to be negligible (Öztürk et al., 1981); nevertheless, it has been reported that the recrystallization texture weakens with increasing initial grain size in type 304 stainless steel (Ohkubo et al., 1991).

5. Conclusions

1) The 50% cold reduction textures (γ and α′) of cast strip F displayed low symmetries caused by the inclination (with respect to the horizontal) of the solidification fiber texture. By contrast, orthorhombic symmetry textures were observed after 80% cold reduction. The major α' and γ texture components are linked via the Kurdjumov-Sachs relationship.
2) The recrystallization texture components changed from the cube and {011}<111> to the Goss, Bs and Cu with increasing cold reduction. The latter evidently affected the γ rolling texture as well as the volume fraction of α', thus accounting for the different recrystallization textures.
3) The recrystallization textures of cast strips F and G were always less intense than those of sample H, the laboratory hot rolled sample. This appears to be a direct result of the initial solidification texture.

4. References

Butrón-Guillén, M. P. et al. (1998) Influence of slip activity and dislocation reaction on variant selection during the γ-to-α transformation. *Metals Science Forum* vols. 273-275, pp. 151-156.

Hirsch, J. and Lucke, K. (1988) Mechanism of deformation and development of rolling textures in polycrystalline F.C.C. metals. *Acta Metall.* vol. 36, p. 2883.

Ohkubo, N. et al. (1991) Effect of annealing conditions before cold rolling on plastic anisotropy and texture of SUS304 produced by twin-roll strip casting method. *Nisshin Steel Technical Report*, vol. 64, pp. 12-21.

Öztürk, T. et al. (1981) The effect of initial grain size on the development of rolling and annealing textures in F.C.C. metals. *Conf. Proc. of ICOTOM-6*, pp. 507-518.

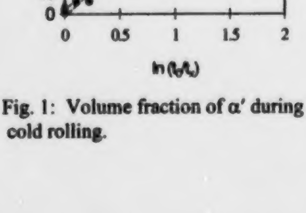

Fig. 1: Volume fraction of α′ during cold rolling.

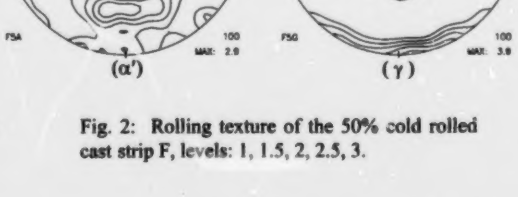

(α′) (γ)

Fig. 2: Rolling texture of the 50% cold rolled cast strip F, levels: 1, 1.5, 2, 2.5, 3.

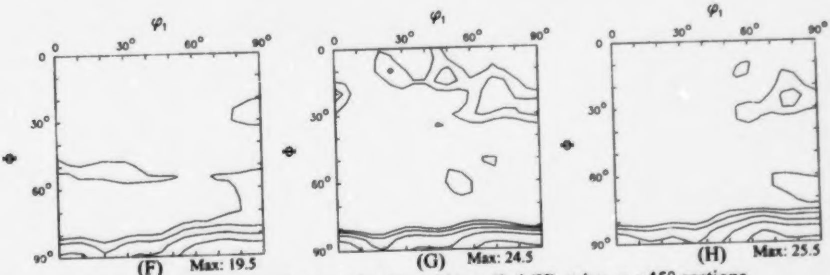

(F) Max: 19.5 (G) Max: 24.5 (H) Max: 25.5

Fig. 3: γ texture of the 80% cold-rolled cast (F, G) and hot rolled (H) strips; φ_2=45° sections, levels: 2, 4, 7, 12, 20.

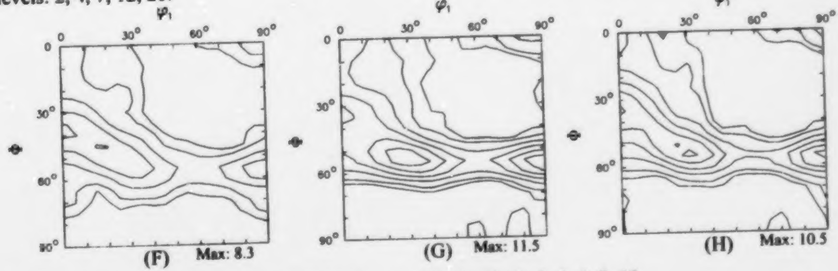

(F) Max: 8.3 (G) Max: 11.5 (H) Max: 10.5

Fig. 4: α′ texture of the 80% cold-rolled strips, φ_2=45°, levels: 1, 2, 4, 6, 8, 10.

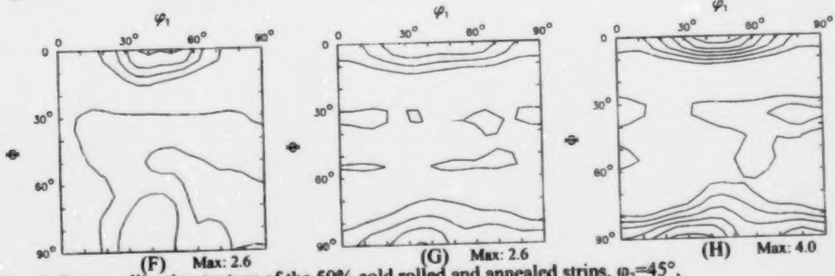

(F) Max: 2.6 (G) Max: 2.6 (H) Max: 4.0

Fig. 5: Recrystallization texture of the 50% cold rolled and annealed strips, φ_2=45°, levels: 1, 1.5, 2, 2.5, 3, 3.5.

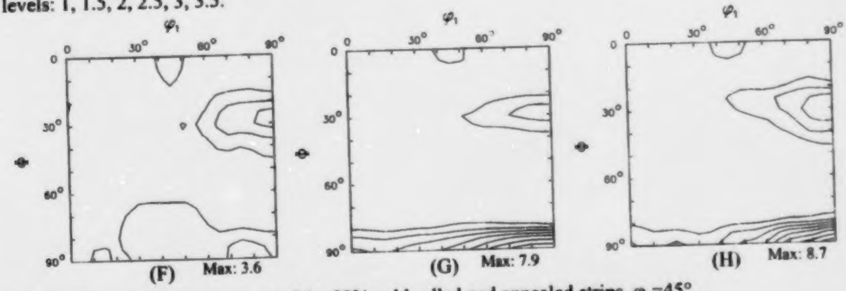

(F) Max: 3.6 (G) Max: 7.9 (H) Max: 8.7

Fig. 6: Recrystallization texture of the 80% cold rolled and annealed strips, φ_2=45°, levels: 1, 2, 3, 4, 5, 6, 7, 8.

COMPARISON OF CAST AND HOT STRIP TEXTURES AND MICROSTRUCTURES IN THREE 304 AUSTENITIC STAINLESS STEELS

S. TERAOKA [1,2], J. BACZYNSKI [1] and J.J. JONAS [1]

[1] Department of Metallurgical Engineering, McGill University, Montreal, Canada

[2] Hikari Technical Research Laboratories, Nippon Steel Corporation, Yamaguchi, Japan

Abstract

The effect of solidification mode on cast strip microstructures and textures was examined. The latter are compared to the {112}<110> + {111}<110> hot strip texture produced by laboratory hot rolling. Cast strip samples of two types were produced by solidification into the dual (δ ferrite + γ austenite) phase (F) and single (δ ferrite) phase (G) domains, respectively. During cooling, the δ ferrite transforms into austenite and columnar γ grains are produced in both samples. However, equiaxed grains are only formed in the latter case. The {001}<uvw> δ ferrite texture is converted into the {001}<uvw> γ final texture in steel F, while most of it transforms into the fcc {011}<uvw> fiber in the G samples. The results are interpreted in terms of the K-S and Bain relationships. Variant selection during transformation is considered to be an important factor in accounting for the experimental textures.

Keywords: Bcc textures, fcc textures, solidification textures, transformation textures

1. Introduction

Hot rolled steel strip is usually produced by continuous slab casting followed by conventional hot rolling. However, recent studies have shown that most of the hot rolling stage can be eliminated by replacing the conventional process with some form of strip casting technology. In the latter case, appreciable savings in production costs can be achieved and the emission of COx gases can be lowered as well. These economic and environmental benefits make strip casting attractive compared to conventional hot rolling practices. Moreover, some superior qualities, such as lower anisotropy and higher corrosion resistance, can be obtained in strip cast products without deteriorating the mechanical properties (Suehiro et al., 1990).

Nevertheless, strip casting has little flexibility for control of the final microstructure and texture. This is because of the lack of sufficient hot rolling reduction. The solidification microstructure and associated texture are therefore significant as they effect the final properties. These developments and the morphology of the solidification microstructure in austenitic stainless steel welds have been studied by several researchers (Lippold and Savage, 1980; Brooks et al., 1981, 1982). However, development of the microstructure and texture during strip casting is not fully understood. This study was undertaken to clarify these issues. Two different solidification modes ($\delta + \gamma$ and δ) were employed and the associated microstructures and textures were examined. These are compared below to the results obtained from the conventional hot rolling process. The cold rolling and annealing textures produced in these steels are discussed in a companion paper included in these proceedings.

2. Experimental procedure

The chemical compositions of the materials under study are shown in Table 1. The cast strips were produced using an equal-diameter twin drum caster (Tanaka et al., 1990). In order to analyze the effect of solidification mode, two different solidification schedules F (δ ferrite + γ austenite solidification mode) and G (δ ferrite solidification mode) were employed. A hot rolled strip (sample H) was produced as a reference material using laboratory slab casting to a thickness of 50 mm followed by reversed hot rolling. The thickness of the cast strips as well as that of the hot rolled strip after rolling was 3.7 mm.

Table 1: Chemical compositions of the cast strips and hot rolled strip (mass%).

	No.	C	Si	Mn	Ni	Cr	Mo	Cu	N	Md_{30}	Cr_{eq}/Ni_{eq}
Cast strip	F	0.057	0.5	0.9	8.6	18.2	0.1	0.4	0.036	21.3	1.60
	G	0.035	0.4	0.9	8.2	18.3	0.2	0.3	0.026	42.4	1.80
Hot rolled strip	H	0.042	0.5	1.1	8.4	18.0	0.3	0.0	0.051	26.2	1.59

Cr_{eq}=Cr+1.5Si+Mo, Ni_{eq}=Ni+0.5Mn+0.5Cu+30(C+N)

Md_{30}=413-462(C+N)-9.2Si-8.1Mn-13.7Cr-18.5Mo-9.5(Cu+Ni)

Both the cast- and hot rolled strips were annealed at 1100°C for 60 seconds to dissolve the carbides and then rapidly cooled. After that, the samples were cold rolled and annealed a second time at 1100°C for 60 seconds. The cold rolling reduction was varied from 50 to 80%. To reveal the ferrite morphology, the specimens were mechanically polished and electrolytically etched with nitric acid. Special techniques were used to reveal the austenite grain boundaries. In this case, the samples were heat treated at 1200°C for 120 seconds to homogenize the microstructure and subsequently sensitized at 650 °C for 2 hours to precipitate carbides at the grain boundaries. Then they were electrolytically etched with oxalic acid.

The texture specimens (15×25mm) were prepared by grinding and then electrolytic polishing at the quarter thickness (0.9mm from the surface) and center

The texture specimens (15×25mm) were prepared by grinding and then electrolytic polishing at the quarter thickness (0.9mm from the surface) and center thickness (1.8mm from the surface). The {200}, {220} and {311} incomplete pole figures were measured for the austenite in all samples, and the {200} for the 5% of ferrite in the G sample. For the present analysis, it was necessary to employ these two sets of pole figures because the Bragg angles of the {111}γ and the {110}δ phases are similar. Measurements were performed on the Siemens D-500 goniometer system at McGill. A molybdenum x-ray tube was run at 40 kV and 40 mamp and the reflection technique was employed for all specimens.

3. Results

3.1 Microstructures

The microstructures of the cast and hot rolled strips are shown in Fig. 1a-c. The ferrite morphology in the present materials was analyzed according to the Lippold and Brooks classification. Vermicular ferrite was formed in the F cast strip. By contrast, acicular ferrite was present in the G material. Both the F and G microstructures grew from the surface towards the center of the strip and, except for the center layer, were fairly homogenous throughout the thickness. The hot rolled strip microstructure was equiaxed and the average grain size was 35 μm, see Fig. 1c.

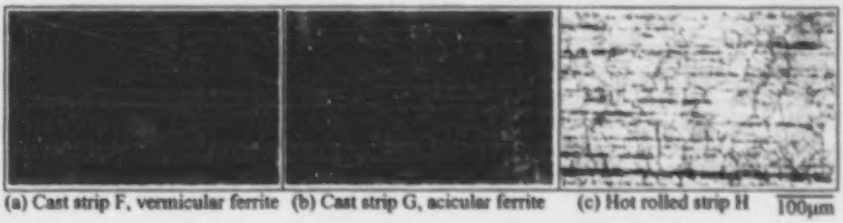
(a) Cast strip F, vermicular ferrite (b) Cast strip G, acicular ferrite (c) Hot rolled strip H

Fig. 1: Microstructures of the cast strips and the laboratory hot rolled strip.

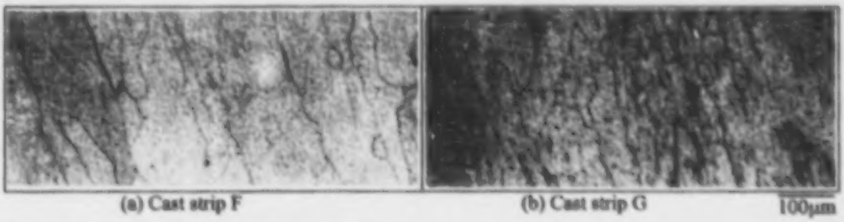
(a) Cast strip F (b) Cast strip G

Fig. 2: γ grain morphology of the cast strips.

The γ grain morphologies of the F and G cast strip materials are shown in Figs. 2a and b, respectively. It is clear that typical solidification microstructures are formed in the sample F steel, see Fig. 2a. Here, the γ grains are columnar and the solidification front is perpendicular to the long axes of the grains. The solidification microstructure in cast strip G is more equiaxed, see Fig. 2b. This is because the δ ferrite transforms progressively into austenite grains on cooling and the columnar coarser than those observed in the laboratory hot rolled strip, see Figs. 2a and b, and Fig. 1c.

3.2 Texture

The {200}γ pole figures of the cast strip F and G materials and the hot rolled strip are displayed in Figs. 3a-c. The F strip texture (Fig. 3a) displays a strong {001}<uvw>γ fiber. The quarter thickness (presented here) and half thickness (at the center of the strip) textures were qualitatively similar. However, the quarter thickness texture was somewhat stronger and the maximum intensity of the {001}<uvw>γ component is more than six times random, as indicated in Fig. 3a. This type of texture is typical of bcc and fcc materials that solidify along <001> directions. The {001} texture of Fig. 3a is inclined at about 12° with respect to the casting direction. This inclination has been previously reported in the literature and has been associated with movement of the casting "moulds" towards the casting direction (Tsukigahora et al., 1990).

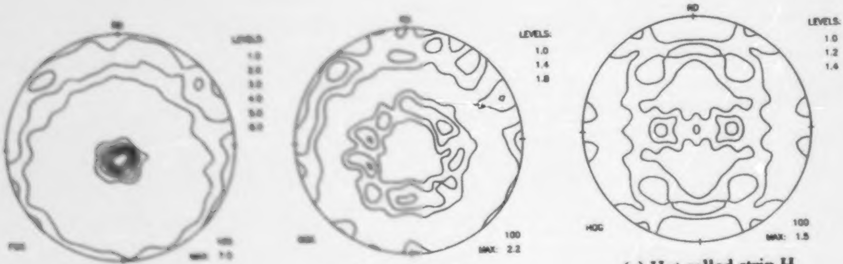

(a) Cast strip F (b) Cast strip G (c) Hot rolled strip H

Fig. 3: {200}γ pole figures of the cast and hot rolled strips.

The G strip texture (Fig. 3b) displays a {011}<uvw>γ fiber. The quarter thickness (presented here) and half thickness (at the center of the strip) textures were again qualitatively similar. However, the maximum intensity decreased slightly from about two times random in Fig. 3b (quarter thickness) towards the center.

The δ ferrite is the primary solidification phase in the strip G steel. The δ ferrite textures present in this steel were therefore estimated from the {200} incomplete pole figure. This texture consists mainly of the {001}<uvw>δ fiber. This led to the conclusion that the {011}<uvw>γ texture observed in the strip G sample (Fig. 3b) results from the transformation of the δ ferrite to austenite on cooling. This transformation texture is discussed in more detail in the next section.

The hot rolled strip H texture is weak, see Fig. 3c. It was measured at the quarter thickness of the strip and the maximum intensity here is only 1.4 times random. The texture consists of the {112}<110> and {111}<110> components, both of which are located along the <110>//RD fiber.

4. Discussion

The F cast strip texture (Fig. 3a) displayed a typical {001}<uvw>γ solidification fiber. In this case, most of the γ phase was formed from the δ ferrite on cooling. However, the transformed γ grains retained the {001}<uvw> texture. A similar orientation relationship between the δ ferrite and austenite in vermicular ferrite has been established in the literature by means of TEM diffraction techniques. In these studies, the <001> directions of the δ ferrite and austenite grains were nearly parallel along the solidification direction (Brooks et al., 1981). The relationships between the δ and γ grains were in agreement with either the Nishiyama-Wassermann (N-W) or Kurdjumov-Sachs (K-S) predictions. In the present case, the {001}<uvw> δ ferrite texture transforms into the {001}<uvw> γ fiber in the F cast strip material as well. However, if all variants of the K-S or N-W relationship were being produced, the γ texture would contain the {011}<uvw> fiber texture as well. Transformation in strip F therefore seems to proceed by the growth of eutectic γ, which has a <001> direction parallel to the solidification axis.

By contrast, the {011}<uvw>γ cast strip G texture (see Fig. 2b) results entirely from transformation of the {001}<uvw>δ ferrite texture. This is because δ ferrite is the primary solidification phase in the G strip. The N-W or K-S relationships are not satisfied in the form mentioned above. It appears that some form of variant selection rule has to be employed to account for the transformation texture produced in this steel.

Selection rules have been proposed by various authors for the austenite-to-ferrite transformation. In the G strip, the initial phase is δ ferrite. However, some of the variant selection rules proposed by earlier authors can be applied in the case of the bcc-to-fcc transformation as well.

One of the reasonable assumptions is that variant selection operates so as to reduce the residual or developed stress (Furubayashi et al., 1987). Transformation occurs both during and immediately after casting. This leads to the development of tensile stresses in the direction perpendicular to the normal direction of the strip. (These are the main sources of solidification cracks in strip cast steels). Moreover, the geometry of strip casting prevents expansion along the normal direction of the strip. The variant selection rules can therefore act so as to prevent the development of compressive stresses as a result of this expansion. In addition, reduction of the in-plane tensile stresses can result from expansion in the plane of the strip.

For simplicity, the Bain relationship, defined as a rotation of 45° around each <001> axis in turn, was adopted in this study to account for the transformation of the {001}<uvw>δ ferrite into {011}<uvw>γ austenite grains. There are three <001> rotation axes available to participate in this process. Rotation of the {001}<uvw>δ ferrite fiber by 45° around the two <001> axes perpendicular to the normal direction (ND) leads to formation of the {011}<uvw>γ austenite grains. These phase transformations cause contraction to occur along the normal direction (i.e., the solidification direction) and both expansion and contraction perpendicular to the normal direction (i.e., in the plane of the strip).

A rotation of 45° around the <001> axis parallel to the normal direction (ND) would lead to formation of the {001}<uvw>γ fiber, which is not observed experimentally. Such a transformation would produce expansion along the normal direction and contraction perpendicular to the normal direction. It is evident that the former dimension change is resisted by the rolls.

The {112}<110> and {111}<110> texture produced in the hot rolled strip material is similar to that reported in the literature for 304 hot rolled strip steels (Raabe 1995). This texture was much weaker than those of the cast strips described above. It was produced by the recrystallization process that takes place during the relatively long interpass times in laboratory hot rolling. It differs significantly from the textures produced in the two cast strips.

5. Conclusions

1) The microstructures and textures produced in the present cast strips differed significantly from those produced by conventional hot rolling.
2) The solidification mode strongly affects the development of microstructure and texture in cast strips. Columnar γ grains were present in the F sample (δ + γ solidification mode) and the {001}<uvw>γ fiber texture was produced in this case. By contrast, in the G strip (δ solidification mode), the γ grains were more equiaxed and oriented along the {011}<uvw>γ transformation fiber.
3) The transformation texture in the G strip can be reproduced by the 45° rotation of the {001}<uvw> δ ferrite fiber around the two <001> axes perpendicular to the normal direction (ND).

6. References

Brooks, J. A. et al. (1981) A fundamental study of the beneficial effects of delta ferrite in reducing weld cracking. *Welding Journal*, vol. 63, pp. 71-83.

Brooks, J. A. et al. (1982) in Trends in Welding Research. *S. A. David, Ed., American Society for Metals*, pp. 331-355.

Furubayashi, E. et al. (1987) A simple model of predicting the transformation textures in thermomechanically processed steels. *Trans. ISIJ*, vol. 27, p. 513.

Lippold, J. C. and Savage, W. F. (1980) Solidification of austenitic stainless steel weldments. *Welding journal*, vol. 59, pp. 48-58.

Raabe, D. (1995) Microstructure and crystallographic texture of strip-cast and hot-rolled austenitic stainless steel. *Metallurgical and Materials Transactions A*, vol. 26A, pp. 991-998.

Suehiro, T. et al. (1990) Properties of SUS304 stainless steel sheet by twin drum cast. *CAMP-ISIJ*, vol. 3, p. 214.

Tanaka, S. et al. (1990) Twin drum casting process for stainless steel strip. *SRNC-90, Conference Proceeding.*, RIST, Pohang / Korea, pp. 643-652.

Tsukigahora, M. et al. (1990) Inner quality of stainless steel strip cast by twin roll type. *CAMP-ISIJ*, vol. 3, p. 211.

EXPERIMENTAL APPROACH TO CONTINUUM DISLOCATION FIELDS IN <100> POLYCRYSTALLINE COLUMNAR ALUMINUM

BASSEM S. EL-DASHER, WENGE YANG and BRENT L. ADAMS
Material Science & Engineering, Carnegie Mellon University, Pittsburgh, PA, USA

Abstract

The use of fine scale orientation imaging microscopy (OIM) has been adapted to study the lattice curvature in deformed polycrystalline samples. This has allowed the observation of the interaction of geometrically necessary dislocation (GND) fields near grain boundaries. The data obtained has revealed a complex range of interactions, most interesting of which is the observation that geometrically necessary dislocations can be absorbed into or emitted from the grain boundaries in order to reduce the grain boundary surface energy.

Keywords: coincident-site lattice, dislocation, grain boundary, lattice curvature, strain

1 Introduction

Constituent grains of polycrystalline samples are observed to develop complex heterogeneous patterns upon deformation, with variations in local orientation and strain levels over a wide range of length scales. Although considerations of deformation heterogeneity are important to a more complete understanding of phenomena such as strain hardening in crystalline materials, the Hall-Petch relationship, and recrystallization and grain growth, the classical theory of crystal plasticity (Taylor 1938) does not consider them.

Heterogeneity in the stress field result from the elastic and plastic incompatibilities that develop at grain boundaries and triple junctions under mechanical loading. These stress field heterogeneities promote the observed deformation heterogeneity. The nature of the incompatibilities that arise is a complex function of the geometry and orientation of the crystals in the vicinity of the grain boundary or triple junction considered. Furthermore, these incompatibilities also depend on the atomic structure of the grain boundary or the triple junction (Sutton and Balluffi 1995).

1.1 Relating to previous work

The use of OIM (Adams et al. 1993) has allowed the examination of the field of lattice curvature down to the limiting spatial resolution of 100nm (Sun et al. 1998). Lattice curvature is considered to have two components: one from the stretching of the lattice due to elastic deformation, and the other due to plastic deformation, namely the non-zero net Burgers' vector content of dislocation fields, as expressed in the fundamental equation (Nye 1953, Kroner 1958):

$$\alpha_{ij} = e_{ikl}(\varepsilon_{jl,k} + \omega_{jl,k}) \tag{1}$$

where ε is the elastic strain, ω is the lattice rotation and α is the dislocation tensor. (Note that here the summation over repeated indices 1 to 3 is implied, that the notation $(..)_{,j}$ represents the partial derivative of (..) with respect to the spatial coordinate x_j and that e denotes the permutation tensor)

In plastically deformed samples, where dislocation based curvature predominates, the elastic component is assumed to make a small contribution and can therefore be neglected. Upon neglecting the elastic component, the fundamental equation can be simplified to relate the dislocation tensor directly to the lattice orientations g:

$$\alpha_{ij} = e_{ikl}\, g_{jl,k} \tag{2}$$

The connection therefore between experiments and theory is defined by Eqn. (2), since g is determined experimentally from OIM measurements on polished section planes of crystalline samples. However, one can also connect the dislocation tensor to the dislocation densities, $\rho^{(s)}$, Burgers' vectors, $b^{(s)}$, as well as the line directions, $\mathbf{z}^{(s)}$, of the present dislocations. This relationship is given by:

$$\alpha = \sum_{s=1}^{S} \rho^{(s)} \bar{b}^{(s)} \otimes \hat{z}^{(s)} \tag{3}$$

where s is summed over the number of types of present dislocations. Therefore, the dislocation tensor can be readily extracted given knowledge of the dislocations present.

It is important to note however that estimates of the dislocation tensor α based upon Eqn. (3) do not allow for the extraction of unique information about dislocation types and densities. Rather, what can be extracted is the lower-bound estimate of the geometrically necessary dislocation density, ρ_{GND}, that is required to explain the lattice curvature field (Sun et al. 1998).

Previous work performed to describe the observed distributions and densities of geometrically necessary dislocations at aluminum bicrystal interfaces showed interesting results (Sun et al. 1998). The bicrystal samples were deformed to two plastic strain levels (0.1 and 0.3) under channel die compression, and the ρ_{GND} distributions showed two distinct modes, one for each strain level. At the 0.1 strain level, the ρ_{GND} distributions showed a pile-up type of behavior of dislocations near the boundary, and at the 0.3 strain level a source (or sink) –like behavior, where the ρ_{GND} distribution shifted favorably to one side of the boundary. The current work is aimed at expanding the knowledge in this field by interrogating different grain boundary types. This has been done by performing similar experimental work on a columnar aluminum sample comprising of near <100> tilt boundaries, and the results of this work are described below.

2 Procedure

2.1 Sample description

The polycrystalline samples used for this experiment were of commercial purity aluminum (0.5% Cu, 0.03% Fe, 0.02% Si), and exhibited a strong <100> fiber texture parallel to the columnar axis with an average grain diameter of 3-4mm. Deformation was by means of simple uniaxial compression along the columnar axis. The sample sectioning was done perpendicular to the columnar axis; thus the grain boundaries examined were near <100> tilt boundaries. A total of 15 grain boundaries were analyzed: 7 at the 10% compression strain level and 8 at the 30% strain level.

2.2 Symmetry considerations

Indexing of electron back scatter diffraction patterns (EBSPs), which is the method used to determine the local crystal orientations, can be different for the *same* EBSP if the main constituent of the pattern is a major zone axis. In the polycrystalline samples that are examined, this holds true, since the sections observed are along near {100} type lattice planes.

To minimize the error and noise that occur when determining the orientation and dislocation tensors, and thus ensure more coherent data, it was deemed necessary to employ the 24 possible rotation tensors that represent the symmetry that occurs in the fcc lattice structure.

Two options for implementing the symmetry operators were considered: the first was to base the symmetry operator chosen such that the misorientations between neighboring data points fell within the same fundamental zone in misorientation space. The second was to choose the symmetry operator such that the angle of misorientation between neighboring points was minimized.

The second method and was selected based on the argument that minimizing the volume of misorientation space occupied by the data points allowed for more coherent data. The reason for this becomes more apparent when one considers misorientations that occur near the fundamental zone boundary.

If the first implementation method is used, then misorientations of very similar nature that occur outside the fundamental zone boundary (but close to misorientations that occur *just* inside the boundary) would be rotated by the symmetry operators into the fundamental zone. However the misorientation difference between these misorientations and the original misorientations (near the fundamental zone boundary and inside) could be large, when compared to the misorientation difference that occurs when the second method is used.

Since the data used is of a discrete nature, the smaller the misorientation spread, the more accurate the final result, as this allows for less noisy and more coherent data.

The procedure performed is as follows:

- Since the data examined is on one side of the grain boundary, and therefore in one crystal, the best indexed point is referenced as a basis point. This point is chosen based on a confidence index inherent in the scanning software that ranks the accuracy of the indexing procedure.
- Having chosen a reference orientation, the orientation data is converted using symmetry operators such that the misorientations are minimized (as described above).

3 Results

At the 10% strain level, the ρ_{GND} distributions for the 7 grain boundaries examined exhibited very similar dislocation pileup behavior, namely centered about the grain boundary as shown in Fig. 1. (Note that the cross-hatching seen in Figures 1-3 indicates the curvature present at the boundary).

Examination of boundaries at the 30% strain level yielded three different types of dislocation pileup behaviors, which we label types A, B and C for convenience. The boundaries of type A displayed a behavior identical to that shown in Fig. 1. Out of the eight boundaries examined at the 30% strain level, two displayed this type of behavior.

Four of the boundaries examined were of type B, whose ρ_{GND} distributions exhibited the type of dislocation pileup seen in Fig. 2. This type of pileup, which can be described as one sided, has a relatively flat dislocation distribution within each grain, even though the GND density on each side of the boundary can be quite different.

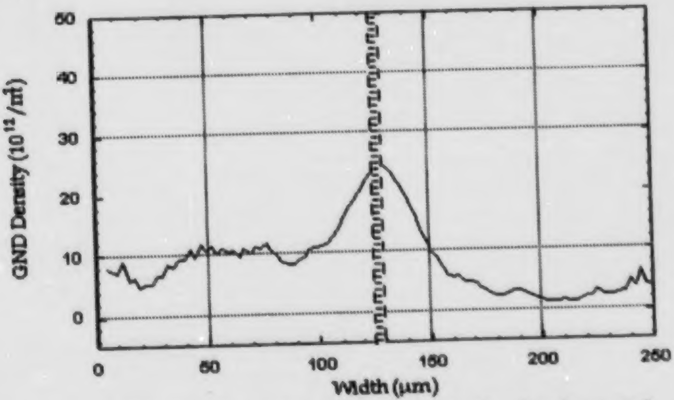

Fig. 1:Typical GND configuration in the 10% strained polycrystal

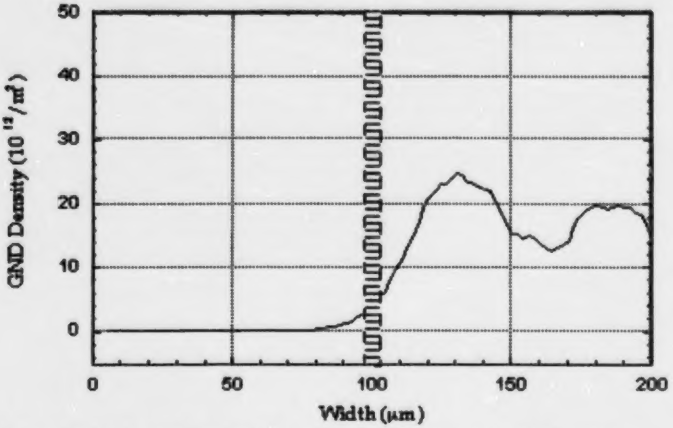

Fig. 2: Type B GND configuration in the 30% strained polycrystal

The last type of GND distributions observed, type C, show a clear, asymmetric double peak about the grain boundary, and was seen on two of the boundaries examined. Interestingly, both of these boundaries were also observed to have a CSL character. One of them was classified as Σ13a; the other Σ5.

The significance of this behavior is that it suggests that grain boundaries that exhibit type C behavior either emit or absorb dislocations in order to either reduce the free energy of the system or preserve the existing CSL character of the grain boundary.

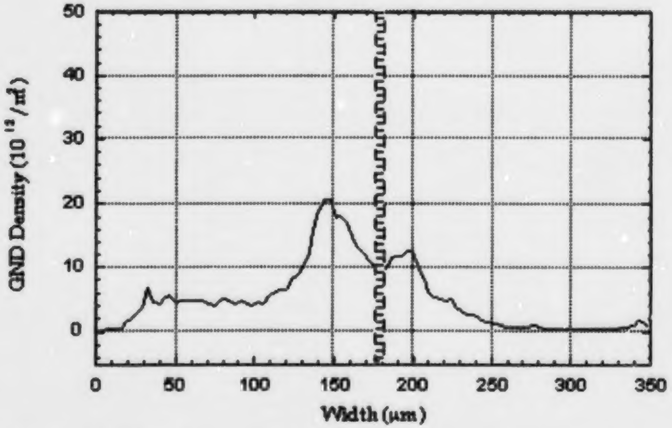

Fig. 3: Type C GND configuration in the 30% strained polycrystal

4 Conclusions

The evidence presented suggests the interactions of geometrically necessary dislocations with grain boundaries are highly sensitive to strain level as well as boundary type. This is especially true at the higher strain level of 30% compression, where a wide range of interactions occurs, as seen in Figs. 1-3.

The centered pileups, as seen in Fig. 1, seem to suggest that such pileups are the initial GND distributions that occur during the deformation process around most grain boundaries. This is in contrast to the asymmetric double pileup associated with the boundaries of CSL character, as shown in Fig. 3, which seem to indicate that boundaries with such character are stable in the deformation field.

5 **Acknowledgment**: This work was supported by MRSEC Program of NSF (DMR-9632556).

6 References:

Adams, B. L., Wright, S. I. and Kunze, K. (1993) *Metall. Trans.*, 24A, 819.

Kroner, E. (1958) *Continuum Theory of Dislocations and Self Stresses*, Springer-Verlag, Berlin.

Nye, J. F. (1953) *Acta Metall.*, 1, 153.

Sun, S., Adams, B. L., Shet, C., Saigal, S., King, W. (1998) *Scripta mater.*, 39, 501.

Taylor, G. I. (1938) J. Inst. Metals, 68, 307.

Sutton, A. and Balluffi, R. (1995) *Interfaces in Crystalline Materials*, Clarendon Press, Cambridge, UK.

EFFECT OF THROUGH THICKNESS INHOMOGENEITY OF TEXTURE ON EDGE CRACKING DURING PLANETARY HOT ROLLING OF AUSTENITIC STAINLESS STEEL

J.Y. CHO, H.T. JEONG AND J.A. SZPUNAR

Department of Metallurgical Engineering, McGill University, Montreal, Quebec, H3A 2B2, Canada

Abstract

In this paper, a possible influence of texture on edge cracking and the characterization of the through thickness inhomogeneity of texture is investigated. For this, the textural inhomogeneities in two specimens, which come from the edge and the middle part of hot rolled plate, were measured and described using the orientation distribution function (ODF). The bulk plastic anisotropies of these specimens were obtained through the calculation of the r-value. A possible correlation between inhomogeneity of texture and edge cracking during planetary hot rolling of austenitic stainless steel was suggested.

Key words: Stainless steels, Texture, R-value, Hot rolling, Edge cracking

1. Introduction

Hot rolling is a common step in the manufacturing of steel products. However, the case of planetary hot rolling is much more complex to explain than normal hot rolling. This unique and complex process may produce inhomogeneous texture distribution along the plate width and through thickness.

Several papers on through thickness inhomogeneity of texture in relation to the plastic anisotropy have been published [1-5]. It is generally agreed that rollings are highly significant for texture and texture-dependent properties. For example, friction at the roll/material interface results in significant texture difference between the surface and midplane of rolled materials. In some cases, texture gradients also exist in hot rolled materials and are influenced by the temperature distribution through the thickness of the sheet [4].

In this paper, a possible contribution of textural through-thickness inhomogeneity in edge cracking is discussed.

2. Experimental

A plate of austenitic stainless steel after hot rolling, containing edge cracks of 70 mm, was used as a research material. Specimens with a size of 20x15x5 mm and located at the edge and in the middle of the plate, were cut from hot-roll plate as shown in Figure 1a. In this investigation, specimens 1 and 4 were used. The characterization of the inhomogeneity of texture on each specimen was accomplished by measuring the texture of specimens which had their surfaces removed down to the level at which the texture was to be measured, as shown in Figure 1b. The depth is parameterized by the variable, S, the thickness parameter, which can be calculated by

$$S = \frac{t - t_0/2}{t_0/2} \qquad 1)$$

Where t is the thickness of the specimen with the surface removed, and t_0 is the specimen's original thickness. To remove any minor surface stresses remaining from the polishing, all specimens were electro-polished in a solution composed of 50 ml $HClO_4$, 750 ml ethanol and 140 ml distilled water, current limited to 3.5 Amps. The crystallographic texture of the steel was measured using a Siemens D500 x-ray goniometer. Pole figures were obtained using the reflection technique, up to maximum tilt of the specimen of 80 deg in 5 deg intervals.

3. Results

Through thickness inhomogeneity of texture of hot-rolled austenitic stainless steel

Through thickness measurements of the hot-rolled austenitic stainless steel were taken at S=1.0, -1.0, 0.75, 0.5, 0.25, and 0, for which the $\varphi_2=0°$ section of the

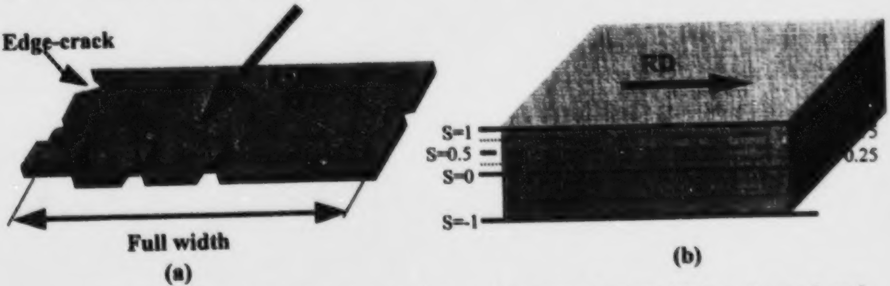

Figure 1 Schematic Diagram of the location of test specimens: (a) Specimens.1 and 4 were taken from the plate, (b) textures were measured through thickness and both surfaces.

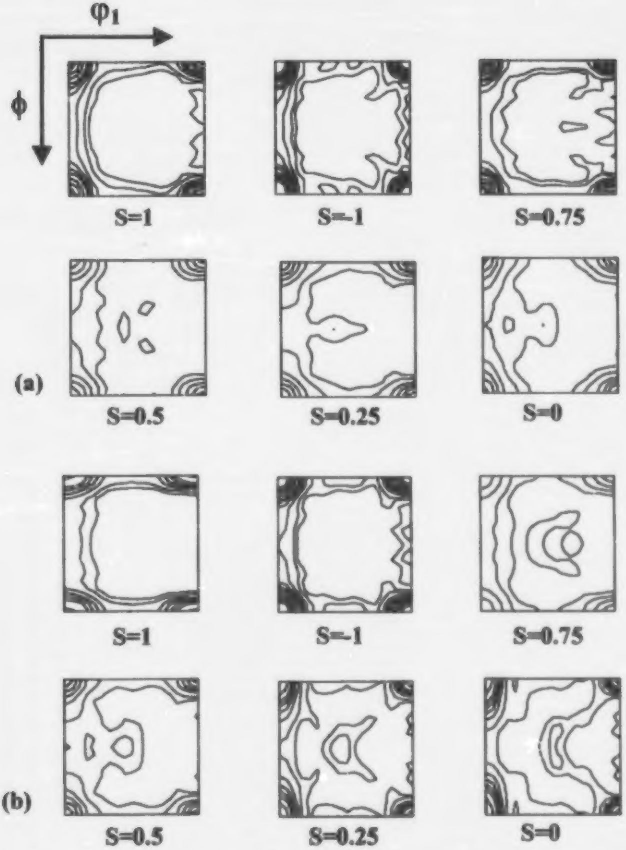

Figure 2 Φ_2=0° sections of the ODF calculated for textures of specimen, which come from the edge and middle part of the plate, measured at S=1.0, S'=1.0, S=0.75, S=0.5, S=0.25 and S=0.0. Contour Levels: =1,2,4,6,8,10,14,18,22,24: (a) the edge, (b) the middle part of the plate.

ODF are presented in Figure 2. In this figure, both specimens, which come from the edge and middle of plate, show strong cube texture ({001}<100>), and their intensities are changed through thickness. Also, weak fiber textures ({001}<uvw> and {hkl}<100>) were observed. To ease in the interpretation of the fibers in this figure, especially {hkl}<100>, Figure 3 is plotted. In spite of the presence of these fibers, it doesn't seems to be the dominant factor in this textural through thickness inhomogeneity of hot-rolled austenitic stainless steel plate, as shown in Figure 3. Comparing Figure 3a with 3b, several aspects in through thickness texture formation can be seen to exist. At first, the intensities of {001}<100> at both surfaces (S=1 and

S=-1) are different in the edge and middle of the plate. Generally, S=-1 are stronger than the other (S=1). And, the distributions of {001}<100> texture are different at both specimens. At this point, the plotting of the cube texture ({001}<100>) at $\varphi_1=0°$, $\phi=90°$ and $\varphi_2=0°$ from the edge and middle of the plate will be interesting, as shown in Figure 4. This figure shows that the maximum intensities of {001}<100> change through thickness at both specimens. In the middle of the plate, the maximum intensity is lowest at the sub-surface (S=0.75), and then it increases in the center layer of the plate (S=0). However, maximum intensities of {001}<100> in the edge of the plate are highest at the sub-surface (max. intensity = 28.7) and drops down to 9.4.

Calculation of r-value anisotropy for austenitic stainless steel

It is a well-known fact that plastic anisotropy of rolled sheet can be calculated using inputs the coefficients of the ODF. However, complications arise due to the fact

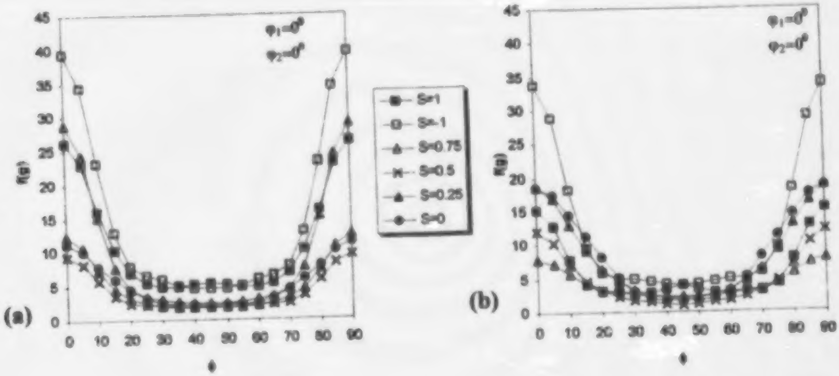

Figure 3 The distribution of {hkl}<100> texture at $\varphi_1=0°$ and $\varphi_2=0°$ section: (a) the edge, (b) the middle part of the plate.

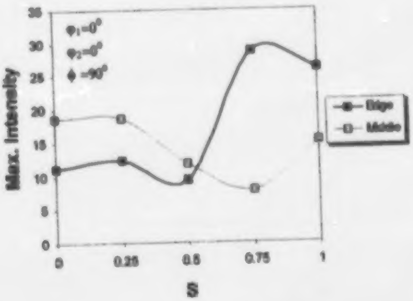

Figure 4 The plotting of the {001}<100> cube texture at $\varphi_1=0°$, $\phi=90°$ and $\varphi_2=0°$ from the edge and middle part of the plate.

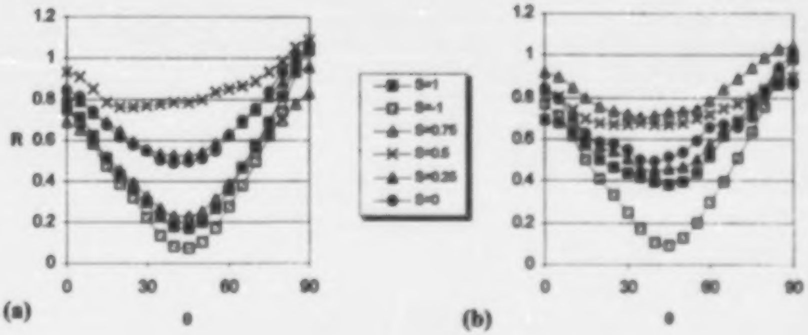

Figure 5 Calculated r-value using ODF coefficients at (a) the edge, (b) the middle part of the plate. θ is the angle with respect to the rolling direction.

that it is unclear as to what types of slip systems are active during the deformation, and so the permutations of used or possible slip systems with numerous plasticity models available, leads to plenty of choices. Because the purpose of this paper is not specifically to find the correct combination of slip system and plasticity model, r-value calculations were done based on the full constraints model and {111}<110> slip system which are nearly compatible with this case.

The r-values calculated as a result of the tests for austenitic stainless steel plate, which contains 70 mm maximum edge crack are plotted in Figure 5. Generally, the highest r-value was observed at θ=90° and the lowest r-value was observed at θ=45°. The distributions of r-value as change θ from 0 to 90° at the both specimens show the plastic anisotropy of hot-rolled plate. Comparing r-value of S=1 and 0.75 at the edge of the plate, r-values of the edge of the plate are quite lower than that of the middle, especially at θ=45°.

4. Discussion

In this investigation, the inhomogeneous texture distribution through the thickness was detected in both specimens, which come from the edge and middle part of the plate. Especially the through thickness distribution of {001}<100> cube texture at each specimen was interested. As shown in Figure 4, the maximum intensities of {001}<100> at the near surface region are quite different. Assuming shear deformation during hot rolling can depress the development of the cube recrystallization texture [5], the shear should be considered as the main reason of this inhomogeneity. At this point, rolling conditions, such as rolling geometry, lubrication and temperature, must be considered to explain the shear texture formation. Generally, high surface friction can increase shear texture and depress the cube texture. It seems that there is a correlation between the different distribution of cube texture in each specimen and the edge-crack formation in hot-rolled austenitic stainless steel plate. To support this result, r-value was calculated through the thickness, as shown in Figure 5. R-values of the near surface region (S=1 and 0.75) at θ=45° are low at the edge of the plate. This seems to relate to the results of Figure 4, which shows quite high intensities of cube texture. Another interesting result is the inhomogeneity of texture on both sides of the plate. As shown in Figures 3a and 3b, cube component at S=-1 is higher than at S=1 at each of the specimens. Comparing the edge with the middle of the plate at S=-1, the cube texture at the edge is higher than in the middle of plate. If the rolling geometry and the surface friction effect the development of the cube texture [5], it also supports a possibility that inadequate rolling condition may affect the edge-crack formation during hot rolling of austenitic stainless steel. And, the complexity of planetary hot rolling process can be another complication added to this problem.

5. Conclusions

The following conclusions are drawn from the experimental results:

1) Through thickness inhomogeneity of texture was found in hot-rolled austenitic stainless steel plate. Generally, both specimens show the strong {001}<100>cube texture and their intensities are changed through thickness.
2) The difference in the distribution of {001}<100> cube texture was found at both specimens, which comes from the edge and middle part of the plate.
3) Inhomogeneous r-value distribution was found at the different locations of the plate.
4) A relationship between the strength of cube texture and r-value was found: the higher r-value at θ=45°, the lower the maximum intensity of {001}<100> texture, especially, at surface region (S=0.75 and S=1).
5) A possible correlation between inhomogeneity of texture and edge cracking during planetary hot-rolling of austenitic stainless steel was suggested.

Acknowledgement

The authors gratefully acknowledge the financial support from Atlas Stainless Steel Inc. and from the Natural Science and Engineering Research Council of Canada.

References

1. P. Blandford and J. A. Szpunar, D. Daniel and J. Jonas (1991), *Textures and Microstructure*, Vol. 14-18, pp. 525-530.
2. J.A. Szpunar and D.C. Hinz (1990), *The Journal of The Minerals, Materials & Materials Socity*, Vol. 42, pp. 40-43.
3. D. Raabe (1997), *Acta Materialia*, Vol. 45, pp. 1137-1151.
4. O. Engler, J. Hirsch, K. Karhausen and G. Gottstein (1994), *Textures of Materials ICOTOM-10*, H.J. Bunge, de. (Switzerland: Trans. Tech. Pubs.), pp. 673-678.
5. C.S. Lee, R.E. Smallman, and B.J. Duggan (1994), *Materials Science and Technology*, Vol. 10, pp. 149-154.

RESIDUAL STRESS ANALYSIS OF RIDGED FERRITIC STAINLESS STEEL

A.P. CLARKE*, W.D. MACDONALD** and S. SAIMOTO
Materials and Metallurgical Engineering, Queen's University, Kingston, ON., K7L3N6 CANADA
* Microsoft Corp., Redmond, WA., USA
** Timinco Ltd., Carp, ON. CANADA

Abstract

Ridging in AISI430 ferritic stainless steel was examined by X-ray residual stress measurements using a 4-circle φ diffractometer. The stress tensors in two texture components were determined and for the one of low R-value a large compressive stress in the transverse direction exist. This affirms that due to the shape change modes of each grain the ones with low R undergo buckling in the transverse direction.

Keywords: AISI 430, ridging, residual stress, texture, R-value

1 Introduction

The most dramatic illustration of the phenomenon of ridging is found in ferritic stainless steel sheets whereby an apparent smooth flat surface develops unmistakable corrugations parallel to the rolling direction upon RD tensile elongation. The correlation of the ridges to the microstructure is affirmed by the fact that their manifestation became dramatically worse in sheet products derived from continuously cast slabs rather than the traditional ingot processing. The macrostructure of the corrugations and ridges are of the order of 1.0 to 1.5 mm in width and amplitudes from 10 to 50 μm with an embedded substructure of microbands in the order of 20-200 μm. These microbands are generally larger than the grain size. The cause of these ridges have been attributed to a dual texture and as pointed out by Wright (1987) in his review the rolling method of Macdonald (1986) which induced martensite formation prior to recrystallization positively shows that the elimination of this dual texture eliminates the ridging. The origin of this dual texture has also been examined and related to the dual phases which exist during hot rolling if the carbon content is too high (Macdonald and Saimoto, 1988).

In the case of a dual texture, the crystal plasticity concepts were first invoked by Chao (1967,1973) by assuming that one texture component possessed low R value, the CF, cube-on-face (100)[011], was embedded in bands of a high R texture component, the CC, cube-on-corner (111)[11-2]. This parallel band combination would result in ridging since the CF bands would prefer to reduce their thickness without strain in the transverse direction (TD) while the CC bands would do the opposite as schematically illustrated in Fig. 1a. A modified scheme was suggested by Wright (1972) whereby he recognized that the volume fraction of CF was much smaller than that of CC and it would be completely surrounded by the latter. In this situation, Euler buckling in the short (TD) direction would result due to the compressive TD stresses as depicted in Fig. 1b. In the latter model it was argued that the sheet thickness would better approach constant thickness than the former one and deliberated upon by Chao and Wright (1977).

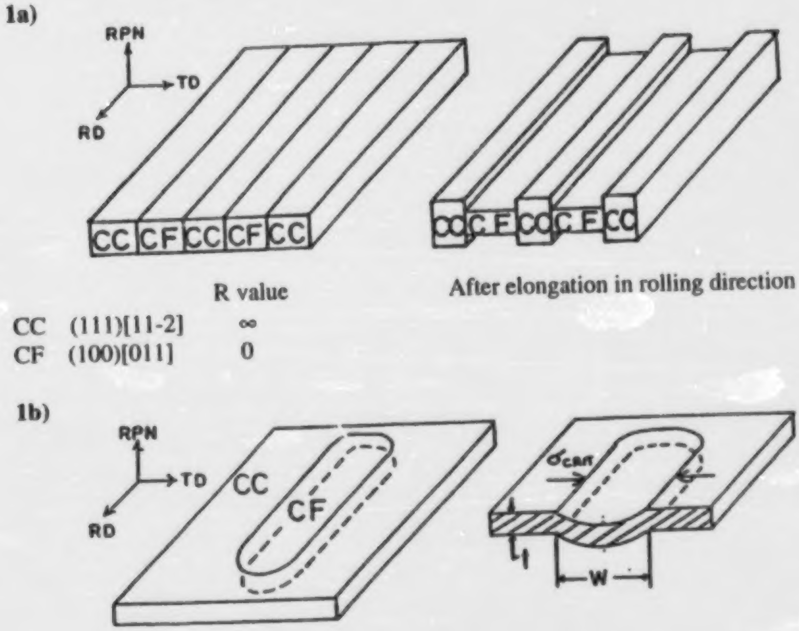

		R value
CC	(111)[11-2]	∞
CF	(100)[011]	0

Fig. 1. **a)** shows the anisotropic yielding model giving rise to ridging after Chao (1967, 1973). **b)** shows the plastic buckling model for ridging after Wright (1972).

Takeuchi et al. (1967) independently proposed a mechanism for ridging in which a [011] fibre texture parallel to the RD was required with a series of orientations between (001)[011] and (1-11)[011] as illustrated in Fig. 2. When this texture of mixed components is stretched, a discontinuity between the principal stresses is not developed between the fibres but opposite shear strains in the RPN for variants of the same components even in the case for (111)[11-2] fibres (Macdonald, 1986). From these considerations, the model which will produce the largest amount of strains in the principal sheet directions is that due to Wright (1972).

The objective of this work was to ascertain if residual stresses in the ridged sheet specimen could be measured by the standard lattice spacing, d, versus $\sin^2 \varphi$ method. Our method of using low indices peaks with high precision due to a unique primary beam alignment (Clarke, Saimoto and Ho, 1993) was adopted. Furthermore due to the strong texture components the single crystal approximation (Korhonen and Paszkiet, 1989) can be invoked whereby the texture is treated as if it were made up of a small number of single crystals which correspond to the ideal orientations. The φ–ϕ angle space of various {hkl} can located using the Euler cradle. This measurement procedure provides a composite strain versus $\sin^2 \varphi$ plot which should be linear and can be used to estimate the strain in that texture component.

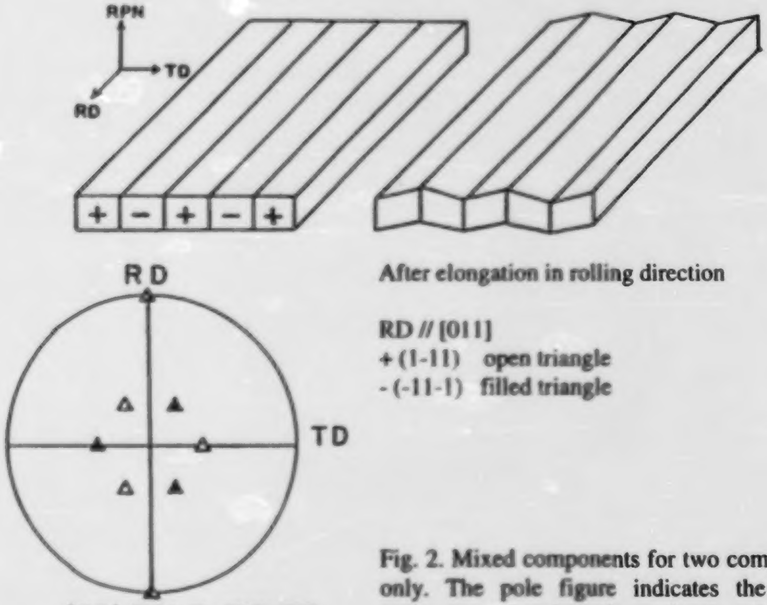

After elongation in rolling direction

RD // [011]
+ (1-11) open triangle
- (-11-1) filled triangle

Fig. 2. Mixed components for two components only. The pole figure indicates the mirror symmetry of orientations developed during rolling, after Takeuchi et. al (1967).

2 Experimental Procedure

A commercial sheet of AISI 430 ferritic stainless steel was stretched 15 % in the RD. A 1.5 × 2.5 cm^2 specimen was cut from the ridged test piece, metallographically polished and electro-polished in a perchloric solution for steel to remove residual stresses induced by the mechanical polishing. Pole figures of (110), (200), (211) and (310) were determined and the (100) [011] and (211) [01-1] ideal orientations were located (Fig. 3). The residual stress measurements have been thoroughly described elsewhere (Clarke, Saimoto and Ho, 1993; Smith et al., 1992).The latter orientation was substituted for the (111) [11-2] (CC) component since its volume fraction was too low to obtain reliable results. To determine normal strains in the RD and TD for both of the components, measurements were made along $\varphi = 0^0$ (RD) at $\sin^2 \varphi = 0$ with (200) reflection; 0.333 with (211); 0.67 with (222) for the (100) [011] component and at $\sin^2 \varphi = 0$ with (211); 0.25 with (220); 0.75 with (211) for the (211)[01-1] using copper K_α radiation.

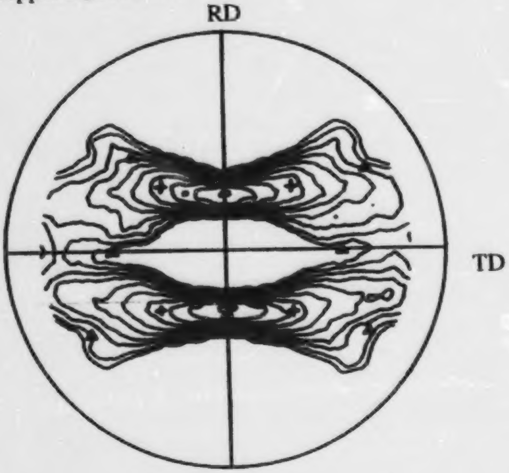

Contour: × random
0.8 1.0 1.3 1.6 2.0
2.5 3.2 4.0 5.0 6.4

Fig. 3. (110) pole figure of ridged 430 ferritic stainless steel with locations of + (100)[011] and filled triangle (211)[01-1] textures.

3 Results and Discussion

Figures 4 and 5 show the strain versus $\sin^2 \varphi$ plots with the linear regression fits. However, the error in the slopes was estimated from the uncertainty of the data points since there were so few points. The calculated slopes are:

(100) [011]
RD slope ($\varphi = 0$) $= -2.1 \pm 0.9 \times 10^{-4}$
TD slope ($\varphi = 90$) $= -10.1 \pm 1.0 \times 10^{-4}$

(211) [01-1]
RD slope $= +2.0 \pm 0.9 \times 10^{-4}$
TD slope $= +1.8 \pm 0.9 \times 10^{-4}$

Using the equations relating slopes to the elastic constants (Hauk et al., 1988), the stress tensors for the texture components were derived.

(211) [01-1]

$$\begin{matrix} 31 \pm 16 & 0 & 0 \\ 0 & 35 \pm 19 & 0 \\ 0 & 0 & 0 \end{matrix} \quad \text{MPa}$$

(100) [011]

$$\begin{matrix} 31 \pm 22 & 0 & 0 \\ 0 & -148 \pm 23 & 0 \\ 0 & 0 & 0 \end{matrix} \quad \text{MPa}$$

These results show that there exists a large compressive stress in the (100) [011] CF component in the transverse direction and much lower stresses in the rolling direction as predicted by Wright's analysis. The observed much lower tensile stresses in TD for the (2111)[01-1] component does not, at first glance, equilibrate the large compressive one for the CF component. However, this may just indicate that the volume fraction of this component in TD tension is correspondingly larger to balance the forces. Also a possibility exists that the other components not measured in these experiments contribute to maintain the equilibrium.

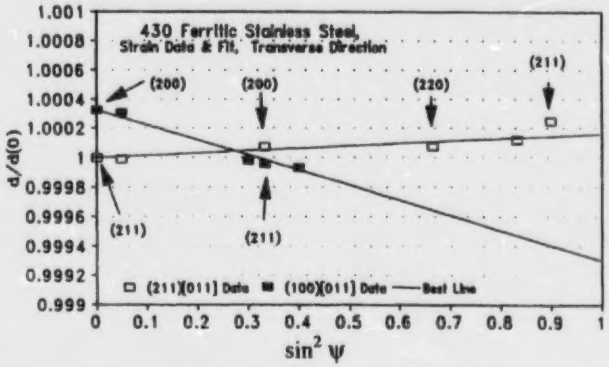

Fig. 4. Strain data for 430 ferritic stainless in transverse direction, for both (211)[01-1] and (100)[011] texture components.

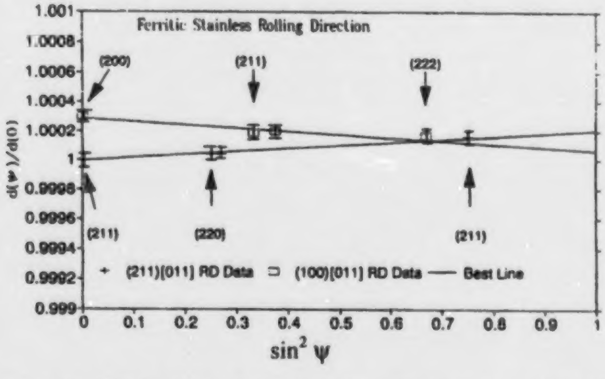

Fig. 5. Strain data for 430 ferritic stainless in rolling direction, for both (211)[01-1] and (100)[011] texture components.

4 CONCLUSION

Residual strain measurements using X-ray methods on ridged ferritic stainless steel has shown that a large compressive stress exits in the transverse direction of the low R-value texture component. This finding is consistent with the predictions of the Wright (1972) model for the occurrence of ridging in sheet where the component with the lower R is forced to buckle by the surrounding higher R grains.

5 ACKNOLEDGEMENT

The authors thank the Natural Science and Engineering Council of Canada and Natural Resources Canada for the support for this work and Atlas Specialty Steels Ltd. for the supply of the material.

6 REFERENCES

Chao, H.C. (1967) The Mechanism of Ridging in Ferritic Stainless Steels. Trans. ASM 60, p. 549

Chao, H.C. (1973) Recent Studies into the Mechanism of Ridging in Ferrite Stainless Steels. Metall. Trans. 4A, pp. 1183-1186

Chao, H.C. and Wright, R.N. (1977) Discussion of "The Direction of the Tensile Strain and "Roping" Phenomenon in Ferrite Stainless Steels". Metall. Trans. 8A, pp. 1009-1010

Clarke, A.P., Saimoto, S. and Ho, P. (1994) In-situ high temperature X-ray Stress determination in patterned, passivated Al interconnects, Proc. 2nd Intern. Workshop on Stress Induced Phenomenon in Metallization, AIP Proc. 305, eds. Ho, P.S., Li, C-Y. and Totta, P., pp 126-136.

Hauk, V., Krug, W.K, Oudelhoven, R.W.M. and Pintschovius, L. (1988) Calculation of Lattice Strains in Crystallites With an Orientation Corresponding to the Ideal Rolling Texture of Iron. Z. Metallkd. 79. pp. 159-163

Hu, H. and Goodman, S.R. (1970) Effect of Manganese on the Annealing Texture and Strain Ratio of Low-Carbon Steels. Metall. Trans. Vol. 1 No. 11. pp. 3057-3064

Korhonen, M.A. and Paszkiet, C.A. (1989) X-ray Determination of the Residual Stresses in Thin Aluminum Films Deposited on Silicon Substrates. Scripta metall. Vol 23. pp. 1449-1453

Macdonald, W.D. (1986) Process design parameters and texture development in 430 ferritic stainless steel, M.Sc. thesis, Queen's University, Kingston. Canada.

Macdonald, W.D. and Saimoto, S. (1988) Influence of texture on formability of 430 stainless steel sheet, in Proc. ICOTOM 8, eds. Kallend, J.S. and Gottstein, G. pp. 1085-1090

Smith, L. F., Kravitz, A.D., Clarke, A.P., Saimoto, S., Shi, N. and Arsenault, R. J.(1992) Residual stresses in DMMC, Mater. Sci. Eng. A159 pp. L13-L15.

Takeuchi, H., Kato, H., Sunami, T. and Nakayama, T. (1967) The Mechanism of Ridging Formation in 17% Chromium Stainless Steel Sheets. Trans. JIM 8, pp. 233-239

Wright, R.N. (1972) Anisotropic Plastic Flow in Ferrite Stainless Steels and the "Roping" Phenomenon. Metall. Trans. 3A, pp. 83-91

Wright, R.N. (1976) The Direction of Tensile Strain and the "Roping" Phenomenon in Ferrite Stainless Steels. Metall. Trans. 7A, pp. 1385-1388

Wright, R.N. (1987) A Review of the "Roping" Phenomenon in Ferritic Stainless Steels, in Formability and Metallurgical Structure, eds. Sachdev, A.K. and Embury, J.D., TMS pp. 247-260

STUDY OF TEXTURE OF ULC SHEET STEEL ROLLED IN FERRITE REGION

K. ZHAO, X.C. MI and SH.H. JIAO
Iron & Steel Research Institute of Baoshan Iron & Steel Corporation, Shanghai, China

Abstract

The effects of lubricating condition, finishing temperature and rolling reduction on texture of ULC steel rolled in ferrite region are studied. With lubricating rolling, the homogeneities of texture along the thickness direction can be improved. Moreover, the {110}<001> shear texture near the surface of sheet steel is randomized obviously and replaced by the developed <111>//ND recrystallized grains. Lower finishing temperature and higher rolling reduction are beneficial to forming preferentially <111>//ND recrystallized grains along the thickness direction of ULC sheet steel rolled in ferrite region.

Key words: Ferritic rolling, texture, ULC IF steel

1 Introduction

Conventionally controlled rolling is normally carried out in the γ phase temperature range. Since 1990, a new hot rolling process, namely "ferritic rolling", has been developed and gained more and more application (Sander et al. 1995; Parks et al. 1997). This new process has many advantages as compared with the traditional austenite rolling, such as the increase of the yield rate, the reduction of energy and improvement of surface quality and punchability of hot-rolled band. The properties of hot rolled band depend on many factors, such as the heating temperature, lubricating condition, finishing temperature, and amount of reduction during the ferritic rolling (Hashimoto et al. 1989; Senuma et al. 1990). In this study, the process of ferritic rolling was simulated in Lab to investigate the effects of lubricating condition, finishing temperature, and the amount of reduction on the texture of ULC IF steel hot rolled sheet.

2 Experiment

The material is a Ti bearing ultro-low carbon IF steel casting slab (see Table 1). It was soaked at 1100 ℃ for 1 h, and then hot-rolled in austenite region in order to refine the initial austenite grain size. The comparative experiment listed in Table 2 between the lubricating rolling and non-lubricating rolling was done in order to investigate the effect of lubrication condition on the texture of IF steel sheet. The experimental schedule of the ferritic rolling is shown in Table 3. After finish rolling, the samples were soaked at 650 ℃ for 0.5 h, and then cooled down to room temperature within soaking furnace.

Table 1: The chemical composition of the tested steel (wt%).

C	Si	Mn	P	S	N	Ti
0.003	0.04	0.20	0.02	0.005	0.004	0.06

Table 2: Experimental scheduel of the lubrication.

Sample	Reduction (%)	Lubrication	F.T. (℃)
A	75	without	750
B	75	with	750

Table 3: Experimental schedule of the ferritic rolling.

Sample	Reduction (%)	Lubrication	F.T. (℃)
C	70	with	750
	75		
	80		
D	70	without	800
	75		
	80		

The ODFs of surface, 1/4 layer, and center layer of samples were calculated from {110}, {200}, and {112} pole figures measured from XRD.

3 Results

3.1 Effect of lubrication

The variations of the TD and ND fibres through the thickness direction of both samples (A and B) were shown in Fig. 1 and Fig. 2, respectively. It can be clearly seen that the major texture components near the surface are different from that at the 1/4 layer and the center layer of both samples. The texture is weak near the surface and gradually sharpen from the 1/4 layer to the center layer. The major texture

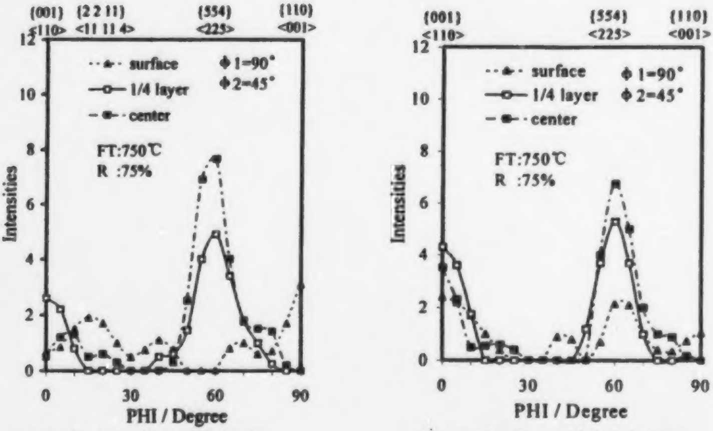

a) sample A, without lubrication b) sample B, with lubrication

Fig. 1: Effect of lubrication on the <110>//TD fibre texture in different layers.

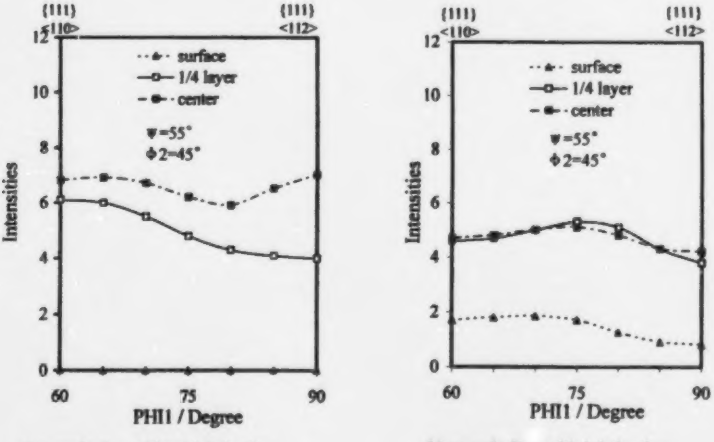

a) sample A, without lubrication b) sample B, with lubrication

Fig. 2: Effect of lubrication on the <111>//ND fibre texture in different layers.

components near the surface are {110}<001> shear texture and {2 2 11}<11 11 4> texture, which disappear at both the 1/4 layer and the center layers of the sample rolled without lubrication. The {554}<225> and {001}<110> are the relatively sharp texture under the surface. At the center layer, the major texture is the {554}<225> component, which is absent at the surface layer. In contrast, the sample B in the case of lubrication displays a relatively homogeneous textures along the thickness direction. The shear texture {110}<001> near the surface is very weak. The {001}<110>

component is almost stable. The {554}<225> is gradually sharper and finally becomes the major component at the center layer. It is apparent from Fig. 2 that in either case the major texture components in the 1/4 layer and center layer of two samples are the {111}<110> ~ <112> recrystallization textures, whereas these textures near the surface of sample B are much more intensive than those of the sample A. The intensity of the {111}<110> ~ <112> recrystallization textures goes to zero near the surface of sample A.

3.2 Effect of finishing temperature

The RD and ND fibres at the center layer are shown in Fig. 3 (a) and (b) for both samples (C and D), finishing rolled with a total reduction of 80% at the temperature of 750 ℃ and 800 ℃, respectively. From these diagrams, sample C reveals strong <110>//RD fibre texture when it is finishing rolled at 750 ℃. The major components are {001}<110> and {111}<110>. After finishing rolling at 800 ℃, the sharpness of the <110>//RD fibre texture decreases obviously. The major component is changed to {7 7 10}<110>, which diverges 10 degrees from the {111}<110>. The intensity of the <111>//ND fibre texture increases with decreasing finishing temperature [see Fig. 3 (b)].

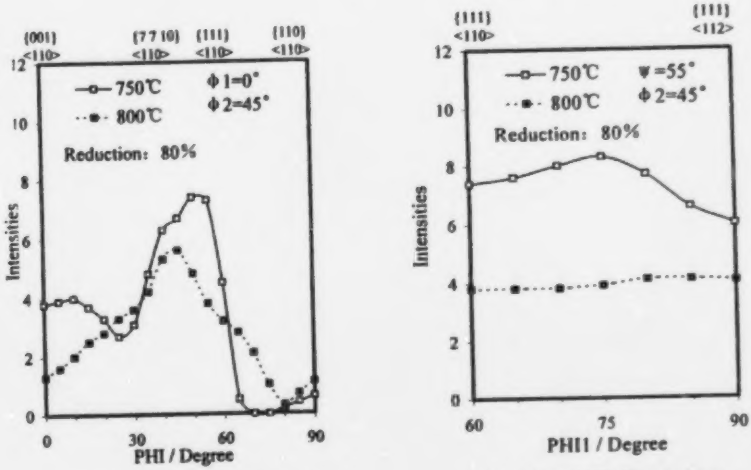

a) <110> // RD fibre texture

b) <111> // ND fibre texture

Fig. 3: Effect of the finishing temperature on the texture in center layer.

3.3 Effect of total reduction

The $\Phi_2 = 45^\circ$ ODF section for sample C is presented in Fig. 4. The sample C is finishing rolled to a total reduction of 70%, 75%, and 80%, respectively. The finishing temperature is 750 ℃. Fig. 4 shows that the textures change with different total reduction. With the total reduction of 70%, sample C is characterized by a moderately strong peak near {111}<110> and {112}<110>, in addition to the weak one

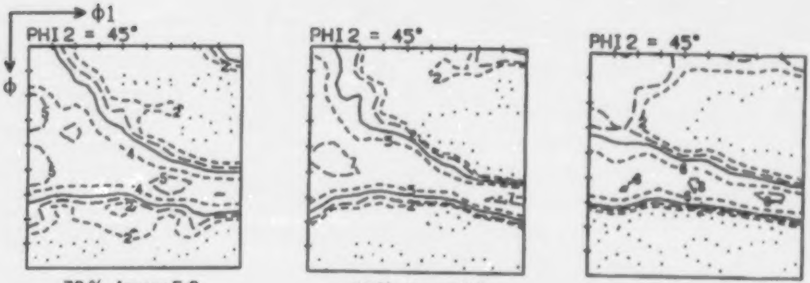

70 % , Imax=5.8 75 % , Imax=7.3 80 % , Imax=8.7

Sample C , FT : 750℃

Fig. 4: $\Phi_2 = 45°$ ODF section of the sample C rolled at different reductions.

at {001}<110>. The sharpness of the <111>//ND fibre texture consisting of the {111}<110> and {111}<112> orientations increases as the total reduction is increased, whereas the intensity of the {112}<110> and the {001}<110> finally decreases when the total reduction is increased up to 80%.

4 Discussion

As has been pointed out above, the texture reveals inhomogenous distribution along the thickness direction of the sample during the ferritic rolling without lubrication. The reason can be explained by shear deformation taking place near the surface. The severe shear deformation occurs and therefore the shear component {110}<001> is produced near the surface of the sample rolled without lubrication. It has previously been pointed out that dynamic recrystallization can take place in some particular areas, where the shear deformation strongly occurs during ferritic rolling of ULC steel (Matsuoka et al. 1997). This leads to the formation of the fine recrystallized ferrite grain with {110}<001> shear component. In contrast, both the 1/4 and the center layers are deformed by plan strain, leading to the low dislocation density. Accordingly, the recrystallization at both layers is more tardy than that on the surface during subsequent soaking process. Finally, the uniformly-distributed and fine ferrite grains with {554}<225> and {001}<110> texture are formed at both the 1/4 and the center layers. In the case of lubrication, the deformation mechanism is plan strain so that the texture is homogenously-distributed along the whole thickness direction of the sample.

As shown in Fig. 3, the texture strongly depends on the finishing temperature during ferritic rolling of the ULC IF steel. The finishing temperature in this experiment is 750 ℃ and 800 ℃. The sharpness of the <111>//ND fibre texture increases as the finishing temperature is lowered from 800 ℃ to 750 ℃, which can be explained by the dynamic recovery of the ferrite grains. During ferritic rolling at 800 ℃, the dynamic recovery occurs so that the lack of stored deformation energy could suppress primary recrystallization. Thus, the <111>//ND recrystallization texture of the sample finishing rolled at 800 ℃ is rather weak. On the other hand, the deformed ferrite grains were hardly recovered due to the lower temperature at the finishing temperature of 750 ℃. As a result, the strain of the deformed grains instantly accumulates with increasing of the reductions during ferritic rolling. In other words, the driving force for recrystallization of the sample C rolled at 750 ℃ is larger than that of the sample D rolled at 800 ℃. Therefore, the sample C rolled at 750 ℃ forms the strong <111>//ND recrystallization fibre texture during subsequent soaking at 650 ℃.

5 Conclusions

- During ferritic rolling of ultra-low carbon interstitial-free (IF) steel, the texture is very dependent on the lubrication. The distribution of the texture is inhomogeneous along the thickness direction of the sample rolled without lubrication. The grains with {110}<001> shear component can be observed at the surface. Furthermore, the grains with {554}<225> and {001}<110> orientations can be seen at both the 1/4 and the center layers of the sample. In contrast, the uniform texture along the thickness direction is formed in the sample rolled with lubrication. The shear texture {110}<001> near the surface is very weak and nearly random. The <111>//ND recrystallization fibre texture is developed along the thickness direction of the sample.
- The finishing temperature has also been found to influence the texture in ULC steel during ferritic rolling. Lower finishing temperature is the most beneficial from the point of view of developing the <111>//ND recrystallization fibre texture.
- The texture in the ULC steel is also affected by the total reductions during ferritic rolling. The <111>//ND recrystallization fibre texture is sharpened in the case of large rolling reductions.

6 References

Hashimoto, S., et al. (1989) Effect of hot rolling in ferrite phase on r-value of cold rolled and annealed extra low carbon steel sheet. *Tetsu-To-Hakane*, Vol. 12. pp. 58 - 65.

Matsuoka, S., et al. (1997) Structural variation along thickness direction of extra-low carbon sheet steels rolled in ferrite region. *Tetsu-To-Hakane*, Vol. 83. pp. 43 - 48.

Parks, W.H., et al. (1997) Ferritic rolling of interstitial-free steel. *Iron and Steel Engineer*, October, pp. 35 - 36.

Sander, A., et al. (1995) Progress in hot rolled flat product technology for demanding customers. *I&SM*, Vol. 2. pp. 21 - 23.

Senuma, T., et al. (1990) Influence of α -region hot rolling on the rolling and recrystallization texture of cold rolled Ti-bearing extra low carbon steel sheets. *ISIJ*, Vol. 54, No. 4. pp. 403 - 412.

CHARACTERIZING AND REPRESENTING TEXTURE GRADIENTS IN THICK ALUMINUM PLATE

M.P. MILLER and T.J. TURNER
Mechanical and Aerospace Engineering, Cornell University, Ithaca, N.Y.
J. SUTLIFF
General Electric Corporate Research and Development Center, Niskayuna, NY

Abstract

This paper presents a methodology for characterizing and representing a spatially-varying orientation distribution function (ODF) that can be used in processing and performance simulations for alloys containing texture gradients. We use thick AA 7050 aluminum plate, which is known to contain a through-thickness texture gradient, as a case study to demonstrate the methodology. The finite element representation of the ODF s initialized using individual lattice orientation measurements taken using the electron backscatter pattern (EBSP) technique. We investigate the optimal sample size for an accurate ODF and examine spatial interpolation of the ODF field. Finally, we employ the ODF in a polycrystal plasticity simulation of a tensile specimen taken with its axis parallel to the normal direction of the plate (ND). In the experiment, the circumference of the specimen was carefully monitored. We found that the model generally captured the strains in different zones of the specimen and correctly predicted which zone would oval most. The magnitude of the ovalling behavior was not well-predicted, however.

Keywords: Texture gradients, EBSP, ODF, Finite Elements, Polycrystal Plasticity

1 Introduction

Structural and compositional gradients arise in thick, hot-rolled aluminum plate due to inherent spatial variations in processing-related thermomechanical loading conditions. In AA 7050 plate, an aluminum alloy developed for thick plate applications, through-thickness gradients in composition, microporosity, grain morphology and crystallographic texture are known to affect material properties and alloy performance. Recent advances in high speed machining technology have made it possible to consider thick AA 7050 plate for an increasingly large number of airframe components. Because of its inherent heterogeneity, however, designing flight-critical components machined from AA 7050 plate will necessitate understanding the relevant microstructural gradients and their effect on alloy performance. We focus on crystallographic texture in this paper and present a methodology for the characterization and representation of a spatially-varying texture field as embodied by the orientation distribution function (ODF) as a field variable.

2 Experiments

The material investigated in this study is 120 mm thick AA 7050 aluminum plate. The nominal processing schedule of this material includes a series of hot rolling passes (possibly including cross rolling) reducing the cast ingot by approximately 80%. After rolling, the plate is stretched, and heat treated to develop the T7451 temper. During the heat treatment, recrystallization takes place, with the recrystallized grains typically nucleating at large secondary phase inclusions. Since the secondary phase tends to concentrate at the centerplane of the plate, the recrystallized grain fraction is highest at this location. The texture gradient in this plate arises due to the heterogeneity of the deformation imposed during hot-rolling and the non uniformity of the recrystallization that occurs during the heat treatment.

The EBSP data employed to formulate the ODF consist of individual lattice orientations along with the spatial location of the sampling point. The EBSP scan was made on an ND (normal direction) - TD (transverse direction) surface of the plate extending from the rolling surface to the centerplane. A schematic of the scan region is shown in Figure 1. The data were arbitrarily divided into 10 zones as shown, with the top of zone 1 being the rolling surface of the plate and the bottom of zone 10, the midplane.

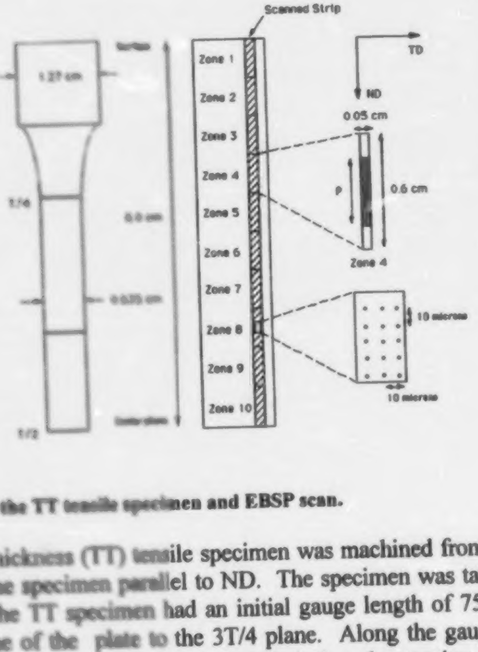

Fig. 1: Schematic of the TT tensile specimen and EBSP scan.

A through thickness (TT) tensile specimen was machined from the plate material with the axis of the specimen parallel to ND. The specimen was taken adjacent to the EBSP sample. The TT specimen had an initial gauge length of 75 mm, which spans from the T/4 plane of the plate to the 3T/4 plane. Along the gauge length, 21 cross sectional planes were marked and monitored during the tension test. The relative position of the EBSP zones and the TT specimen gage length is shown in Figure 1. The TT specimen was strained in uniaxial tension in displacement control to average axial strain increments of 1.57%, 2.18%, 3.33%, 3.94%, 4.53%, and 5.31%. After each axial strain increment had been reached, the sample was unloaded from the test machine. The circumference of the specimen at each of the marked cross sections was then measured in a precision coordinate measuring machine (CMM) to an accuracy of +/- 2 μm. Due to material anisotropy, the shape of the cross section becomes oval, with the degree of ovality varying along the axis due to the microstructural gradients. From the circumference measurements, the strains in the direction of the major and minor axes were determined and later compared to simulation.

3 Determination of the ODF

The ODF, A(**r**) is nothing more than a scalar field defined over orientation space, or a fundamental region of orientation space. In contrast to the more traditional Fourier series representation employing globally-defined spherical harmonics functions, we employ a finite element discretization of orientation space (Kumar and Dawson 1995). In the usual manner of finite elements, we represent the approximation to the ODF, $A^h(\mathbf{r})$, within a given element in orientation space as

$$A^h(\mathrm{r}) = \left[N^r(\mathrm{r})\right]\left\{A^h\right\}_{np} \tag{1}$$

where **r** is a position vector in orientation space, $[N^r(\mathbf{r})]$ is the row matrix of element interpolation or shape functions and $\{A^h\}_{np}$ is the vector of nodal point values of $A^h(\mathbf{r})$. The EBSP data enter the formulation in a manner analogous to introducing point loads in a conventional mechanical loading analysis (Kumar and Dawson 1995; Miller and Turner, 1999).

3.1 Optimal number of orientation measurements

To investigate the optimal number of lattice orientation measurements necessary to determine the ODF for each zone, we "grew" the height of the data subzone (ρ in Figure 1) and compared the resulting ODFs. The details of this analysis are reported in Miller and Turner 1999. We found that as we increase the number of orientations, the ODF quickly becomes stable but eventually starts to change under the influence of the texture gradient. The approximation to the ODF, $A^h(\mathbf{r})$, for zones 1, 3, 5, 8, and 10 employing ρ=3.5mm are shown in Figure 2. As can be seen, the texture varies significantly, transitioning from the rotated cube texture associated with shear-dominated deformation at the surface of the plate, to a more conventional rolling texture at the centerplane. The aspect ratio of the scan dictated that we add additional orientations in the direction of the texture variation (ND). Clearly, this is not optimal. We are currently conducting scans in which additional measurements are added in TD and RD and re-conducting the optimal sample size analysis. In addition to lattice orientation variations, grain size and aspect ratio as well as scanning density will affect the outcome of this study.

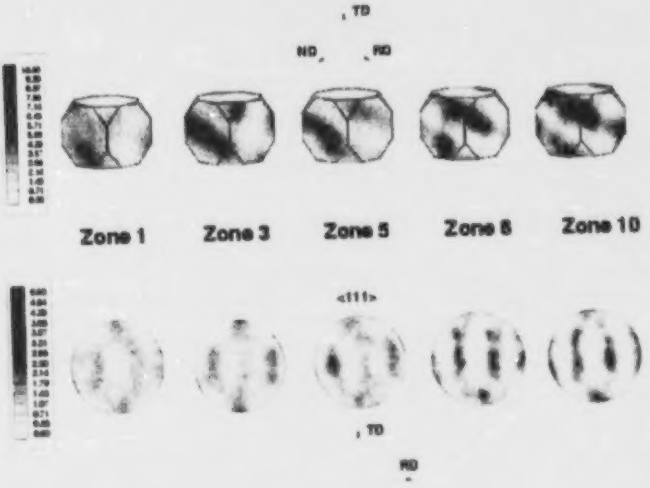

Fig. 2: The ODF for various zones of the plate depicted on the fundamental region of Rodrigues space (Top). The associated (111) pole figures (Bottom).

3.2 Interpolation

The ODF approximated with finite elements in orientation space can be merged with a conventional finite element representation in physical space in a straight-forward manner, i.e.

$$A^h(\mathbf{x},\mathbf{r}) = [N^x(\mathbf{x})][A^h]_{np}[N^r(\mathbf{r})]^T \qquad (2)$$

Here **x** is a position vector in physical space and the matrix $[A^h]_{np}$ is comprised of many $\{A^h\}_{np}$ vectors, one from each spatial nodal point (Kumar and Dawson 1995). We employed a simple one-dimensional discretization in the plate ND and interpolated between zones 1 and 3 to predict the zone 2 ODF and between zones 8 and 10 to predict the zone 9 ODF (Miller and Turner, 1999). The results for zone 9 are shown in Figure 3. We found that gradients in both physical space and orientation space affect the accuracy of the interpolation. The prediction in zone 9, where the gradient in physical space was stronger, was less accurate than that in zone 2. We also found that the regions in orientation space where the differences between the measured and interpolated textures were greatest were where the ODF was changing more rapidly(Miller and Turner 1999). As with any other finite element approximation, increased accuracy in regions of increased spatial variation can be attained by employing finer meshes in orientation space, physical space or both.

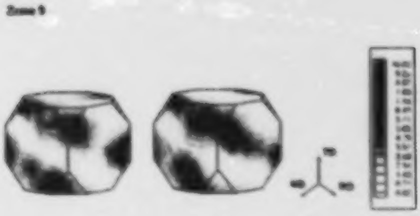

Fig. 3: Measured (Left) and interpolated (right) ODF for zone 9.

4 Simulation of tensile tests

In order to examine the texture contribution to straining anisotropy, we employed the ODF, and a polycrystal plasticity model to simulate specimen ovalling in the TT tension tests. The model (Marin and Dawson 1998) is based upon the multiplicative decomposition of the deformation gradient and takes the elastic strains, the slip system hardnesses and the crystal lattice orientations as its internal variables. The gauge section was discretized into the zones with aggregates of 256 crystals describing the constitutive behavior of each zone. The deformation is constrained to be uniform within each zone and the normal component of stress in the axial direction was assumed to be the same in each zone. The resulting zone displacement rates were constrained to add up to the experimental ram displacement rate. A single slip system hardness was evolved for each aggregate and a Taylor assumption, which equates the deformation gradient for each grain with the macroscopic deformation gradient, was employed. The slip system hardening parameters were determined by matching the overall load-displacement prediction to the experimental data.

The results of the simulation are shown along with the data in Figure 4. As can be seen, the simulation generally captured the strain levels along the major axis for each zone, correctly predicting that the specimen strained less at T/4. We see from the data that T/4 ovalled more than either T/2 or 3T/8. This ordering was accurately predicted by the model but the magnitudes were not well-predicted. We also saw (but do not depict here) that the simulation roughly predicted the correct orientation of the major axis at T/4 (within 10° of RD).

5 Summary

We examined the ND texture gradient and its effect on the mechanical response of AA 7050 plate. We employed EBSP measurements and a finite element-based ODF to quantify the texture field. The EBSP data enabled us to conduct a detailed study on optimal sample size for determination of the ODF. We found that the texture varied significantly through the thickness of the plate. Using the ODF representation, we were able to interpolate the texture field with varying degrees of accuracy. Using the ODF field and a polycrystal plasticity model, we simulated TT tension tests to quantify the crystallographic contribution to anisotropy. We found that the major axis strains at the various zones were well-predicted as was the ordering of the ovalling (T/4 ovalled more). The magnitude of the ovalling was not well-predicted, however. This may be in part due to the employment of the Taylor mean field assumption, which is least accurate in strain regimes where the elastic and plastic strain contributions are comparable. Clearly, other factors may contribute to the straining anisotropy (grain shape) and its variation along the gage length of the specimen. Understanding the inter-relationships between these factors will be the topic of future studies.

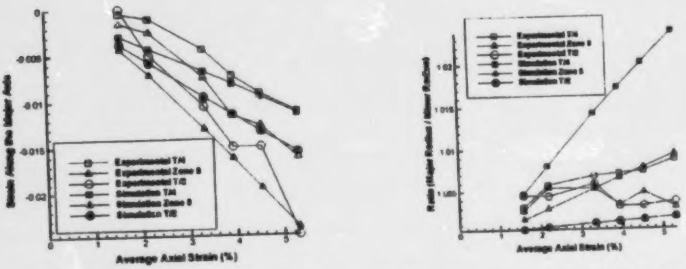

Fig. 4: Measured and predicted diametral strains along the major axis (Left) and major/minor axis ratio (Right)

6 Acknowledgements

MPM and TJT acknowledge the National Science Foundation for providing support for this work under CAREER grant CMS #9702017. Professor Armand Beaudoin of the University of Illinois and Dr. William Cassada of Reynolds Metals Inc. are gratefully acknowledged for the AA 7050 plate. Professor Paul Dawson and Mr. Nathan Barton of Cornell University are acknowledged for extensive assistance with the simulations.

7 References

Kumar, A. and Dawson, P.R. (1995) Polycrystal Plasticity Modeling of Bulk Forming with Finite Elements Over Orientation Space. *Comp. Mech.*, Vol. 17, pp.10-25.

Marin, E.B., and Dawson, P.R. (1998) On Modeling the Elasto-Viscoplastic Response of Metals Using Polycrystal Plasticity. *Comp. Methods Appl. Mech. and Eng.*, Vol. 165, pp.1-21.

Miller, M.P. and Turner, T.J. (1999) A methodology for Measuring and Modeling Crystallographic Texture Gradients in Processed Alloys. *International Journal of Plasticity, In Review.*

MICROTEXTURE INHOMOGENEITY IN HOT ROLLED TWO-PHASE STEEL

J. JURA, J. POSPIECH and J. BONARSKI
Institute of Metallurgy and Materials Science, Polish Academy of Sciences, Kraków, Polska
T. BAUDIN, C. QUESNE and R. PENELLE
Laboratoire de Métallurgie Structurale, Université de Paris Sud, Paris, France

Abstract

The paper presents an analysis of microtexture inhomogeneity in hot rolled two-phase steel with duplex-structure. Individual orientations were measured by EBSD at specific places. Then the local orientation distributions of both ferritic and austenitic phases as well as the misorientation distributions in each phase and between ferritic/austenitic grains were determined. The observed relations between these distributions and their location in the sample were analysed.

Keywords: Duplex steel, microtexture,

1 Introduction

Stainless steels with ferritic-austenitic microstructure are modern materials used in the chemical and petrochemical industries on account of their good corrosion resistance and high mechanical strength.

The important characteristics of the microstructure of a polycrystalline material are the orientation distribution and the orientation difference distribution of neighbouring grains (Bunge 1982; Vlad and Bunge 1981).

The paper analyses the local orientation distributions of grains of the ferritic and austenitic phases as well as the misorientation distributions of the neighbouring grains of both phases in the central part and in the surface layer of a duplex steel rod pass-rolled in a round -> oval -> round -> oval groove sequence.

The aim of the investigations was the description of the microstructure inhomogeneity meant as the dependence of the above mentioned distributions on the distance of the analysed area from the axis of the rolled rod.

2 Material

The investigated material was ferritic-austenitic steel of duplex structure with the following chemical composition: 23%Cr, 5.5%Ni, 3%Mo, 1.5%Mn, 0.150%N, 0.020%C, 0.4%Si. It was submitted to the following treatment: a square rod of 250x250 mm² cross-section after homogenisation annealing at the temperature 1250°C was pass-rolled at the temperature 1000°C until a round cross-section with 20mm diameter was obtained (Schubert et al. 1984; Barthel et al. 1994).

The mean grain size of austenite in the ferritic matrix was about 10μm. The fraction of the ferritic phase near the rod centre was 61%, and near the surface 63%, and that of the austenitic phase 39% and 37%, respectively. The fractions of the phases estimated using the image analysis and the estimations made on the basis of EBSD measurements gave the same results.

Figures 1 and 2 show the SEM and TEM micrographs of the duplex structure observed on the plane perpendicular to the axis of the steel rod in its central part and in its surface layer. While the SEM micrographs do not reveal any significant differences, the analysis of TEM micrographs allows to observe that the grains in both phases, in the central part of the rod, are less elongated, with less curved boundaries and lower dislocation density.

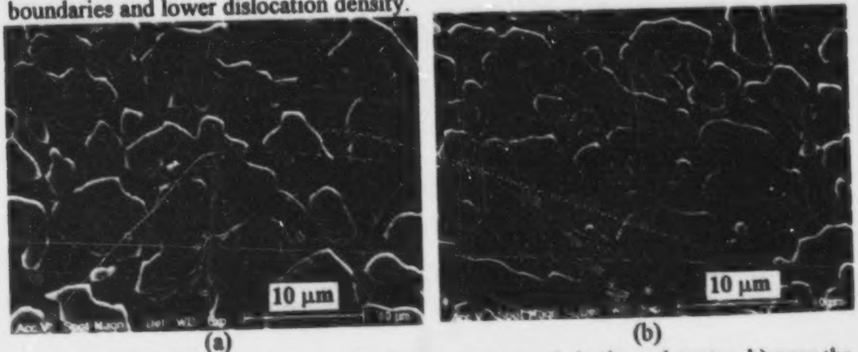

(a) (b)

Fig.1: SEM micrograph showing the duplex structure a) in the rod centre, b) near the surface.

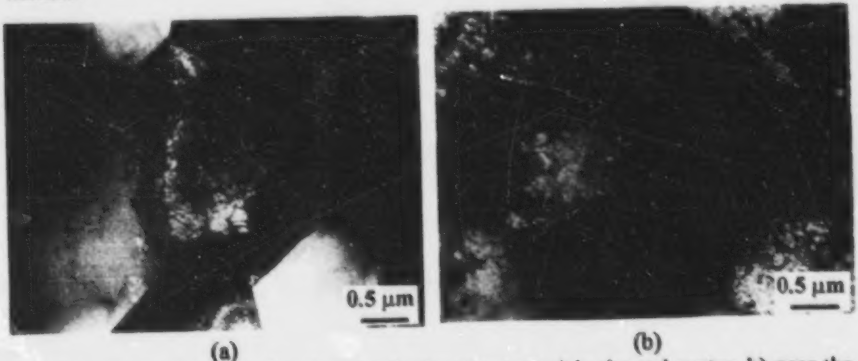

(a) (b)

Fig.2: TEM micrograph showing the duplex structure a) in the rod centre, b) near the surface.

3 Results and discussion

Measurements of single orientations made by EBSD technique inside a $100\times100\mu m^2$ area with the step equal to $0.5\mu m$.

The orientation measurements of grains of the ferritic and austenitic phases were carried out on the surface perpendicular to the rod axis, near the rod axis, as well as near the surface to observe inhomogeneity of the texture. On this basis there have been determined the orientation distributions of both phases. The orientation difference distributions of the neighbouring measured points in the areas occupied by each of the phase as well as the misorientation distributions between the neighbouring grains of both phases were also determined.

Illustrative orientation distribution functions (ODFs) for ferritic phase near the rod axis and near the surface, determined on the basis of single orientations, are shown in Figs 3a and 3b, respectively. The sample coordinate system has been defined in a such way that the rod axis is parallel to the z-axis, while the x- and y-axes are perpendicular to the symmetry planes of the deformation process. In the description of the texture components (hkl)[uvw] given below, the following conventions have been taken into consideration: the rolling direction [uvw] is parallel to the rod axis, the direction perpendicular to the plane (hkl) - i.e. the normal direction, and the transverse direction are perpendicular to the symmetry planes of the pass-rolling deformation process.

Calculation of the ODFs values was made at the assumption of a triclinic sample symmetry. Analysis of the ODFs enabled to state the absence of the orthorhombic statistical sample symmetry with reference to the analysed areas.

The orientation distribution in the ferritic phase near the rod axis comprised the following texture components:

- {233}<011> with both complementary components of this orientation well developed, {211}<011> with evident prevalence of the component $(\bar{2}\bar{1}1)[011]$.
- Near the surface there can be observed: the component $(2\bar{3}3)[011]$ (and the component $(3\bar{1}0)[001]$).

The occurence of the components of the type {hkl}<110> is interpreted as being characteristic for the development of the deformation texture, while the components {hkl}<001> for the recrystallization texture (Schubert et al. 1984). In the central part of the rod, the deformation texture has developed, and near its surface there appear the components characteristic both for the deformation and recrystallization.

In the orientation distribution in the austenitic phase near the rod axis the main component was $(2\bar{1}0)[001]$, while near the surface the component $(1\bar{3}0)[001]$ could be observed. Thus, the textures are quite similar in the central part and near the rod surface.

The analysis of the orientation difference distributions in the areas of the ferritic and the austenitic phase and between neighbouring grains of both these phases enabled to determine the characteristic features of the misorientation distributions of neighbouring grains.

Within the areas occupied by the ferritic and austenitic phases the orientation differences with low misorientation angles dominated. In the ferritic phase, forming the matrix, among the orientation differences with a high misorientation angle (ω>15°) near the rod centre Σ3 (24%), Σ11(5%) and Σ13b(3%) have been observed.

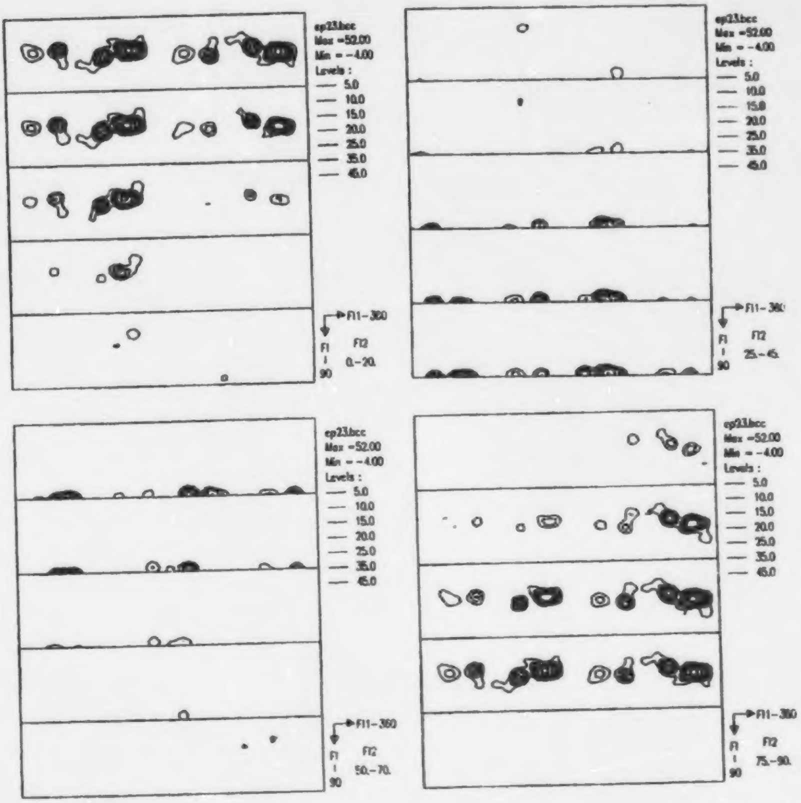

Fig. 3a: ODF for the ferritic phase, near the rod axis.

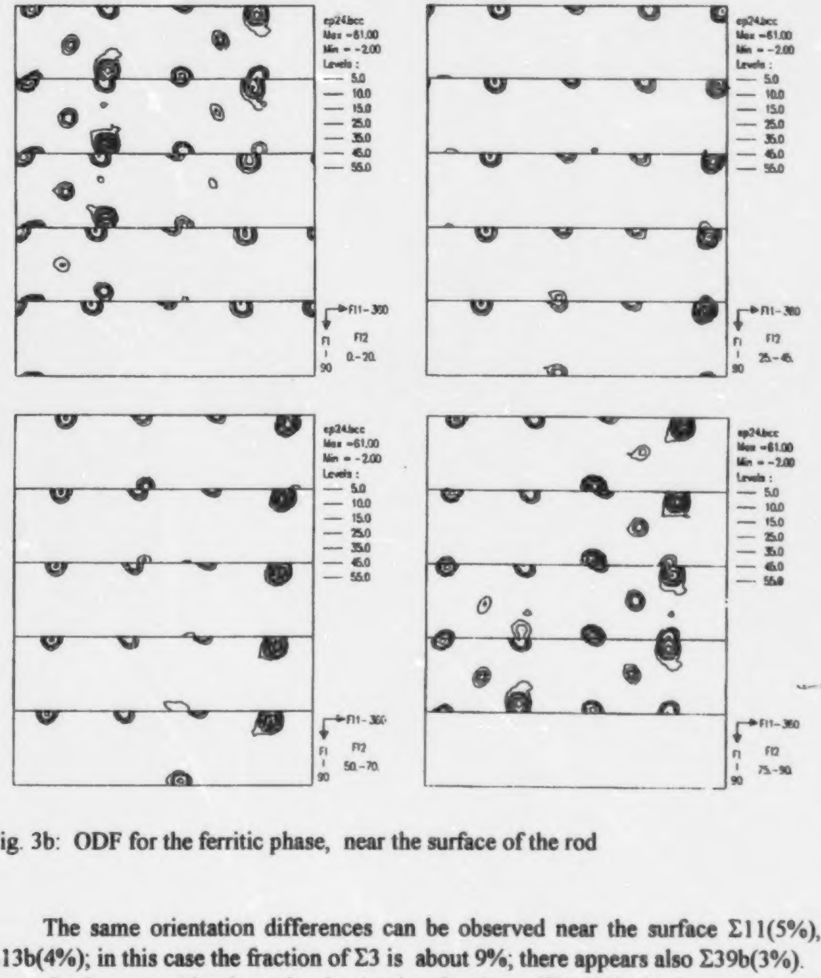

Fig. 3b: ODF for the ferritic phase, near the surface of the rod

The same orientation differences can be observed near the surface Σ11(5%), Σ13b(4%); in this case the fraction of Σ3 is about 9%; there appears also Σ39b(3%).

In the austenitic phase the dominating fraction of Σ3 (23% in the central part and 32% near the surface) can be observed. There are also present: Σ9 (4% in the central part and 6% near the surface), Σ11 (3% and 4%, respectively), and Σ13b (about 1% and about 2%, respectively).

The orientation differences between the grains of the ferritic and austenitic phases have high misorientation angles. In both cases (near the axis and at the surface of the rod) they concentrate in the area of the misorientation space, extending from the axis <001> to the axis <013> in the surroundings of the rotation angle ω=45° (The axes are defined by the spherical angles which are the same for the two phases, so the axes have pure geometrical interpretation and are not related to the atomic structure of the phases). Moreover, near the rod axis there can be distinguished the misorientations: {<110>, 35°} (4%), {<221>, 45°} (2%) and

{<221>, 60°} (about 2%). The same misorientations occur near the rod surface with the respective fractions (5%), (3%) and (1%).

4 Conclusions

Depending on the distance of the site of measurement from the axis of the steel rod pass-rolled at 1000°C, there can be observed various types of microstructure inhomogeneities, such as: shape of grains, the ferritic and austenitic phase fractions, components of local textures.

The analysed ODFs contain components forming the so called limited fibres with their axes parrallel to the steel rod axis.

Local textures (as shown by ODFs analysis) are quite similar in the austenitic phase in the central part of the rod and near the surface (<001>). On the contrary, in the ferritic phase, local textures contained components characteristic for the deformation process (<110>) (central part of the rod and near the surface), as well as for recrystallization (<001>) (near the surface).

Special boundaries represent a few percent of the detected high-angle boundaries, except Σ3 .

Within the areas occupied by the ferritic and austenitic phases the low-angle boundaries dominate, whereas between the ferritic and austenitic grains there occured, in the first place the high angle boundaries.

The types of the distinguished grain boundaries did nor undergo any essential changes dependent on the site of analysis, contrary to the local texture components.

5 References

Barthel, M., Gerth, D., Schwarzer, R.A., Klimanek, P. and Messerschmidt, U. (1994) Individual Grain Orientation Relations after high-speed hot rolling of steel rods. *Proc. of ICOTOM 10*, (ed. H.J. Bunge) Clausthal, Germany, *Materials Science Forum*, Vol. 157-162, pp.1131-1136.

Bunge, H.J. (1982) *Texture Analysis in Materials Science*, Butterworths, London.

Schubert, A., Hengser, K.-E., Klimanek, P., Matthies, S. and Mücklich A. (1984) Texture development in pass-rolling of steel rods. *Proc. ICOTOM-7*, (eds. C.M. Brakman, P. Jongenburger and E.J. Mittemeijer) Noordwijkerhout, Holland, Netherlands Society for Materials Science Zwijndrecht,The Netherlands, pp.133-138.

Vlad, C.M. and Bunge, H. J. (1981) The orientation distribution of crystallites in hot-rolled dual phase steels and its relationship to mechanical properties. *Proc of ICOTOM-6* (ed. S. Nagashima), The Iron and Steel Institute of Japan, Tokyo, Japan, pp. 649-658.

Texture in Films, Coatings and Oxides

CRYSTALLOGRAPHIC TEXTURE IN 1G DRAM REACTIVE ION ETCHED VS. DAMASCENE Al-Cu LINES

K.P. RODBELL and L.M. GIGNAC
IBM T.J. Watson Research Center, Yorktown Heights, New York 10598
J.L. HURD and YUN-YU WANG
IBM Mircoelectronics Division, Hopewell Junction, New York 12533-6531
L.A. CLEVENGER, R.C. IGGULDEN, R.F. SCHNABEL and S. WEBER
IBM/Siemens DRAM Development Alliance, Hopewell Junction, New York 12533

Keywords: polycrystalline patterned lines, EBSP, BKD, crystallographic texture

ABSTRACT

The microstructure (local texture, grain size and grain size distribution) of submicrometer wide subtractively etched versus damascene AlCu lines was investigated for use as metal interconnects in 0.18 μm ground rule 1G-bit DRAM devices. An AlCu based damascene metallurgy that both filled high aspect ratio features and had exceptional electromigration reliability was developed. The damascene films exhibited little or no texture, yet they performed substantially better in electromigration tests than highly textured subtractively etched films. The local texture was measured using electron backscatter pattern (EBSP), also known as backscatter Kikuchi diffraction (BKD. The planar metal samples exhibited either little change or a slight strengthening of their (111) fiber texture with decreasing line width, while the damascene samples showed a marked weakening in the (111) fiber texture with decreasing line width and feature size. This texture decrease occurred in all of the damascene layered thin films investigated, including AlCu/Ti/SiO_2 and AlCu/TiN/Ti/SiO_2.

INTRODUCTION

In this paper, we consider polycrystalline metal films deposited onto amorphous and polycrystalline substrates or under-layer materials, and subsequently etched into patterned lines. In these, the strength of the AlCu crystallographic grain orientation or (111) fiber texture depends on the substrate surface roughness and the presence of Ti and TiN under-layers (1-3). Recent studies of the crystallographic orientation distributions in Al and AlCu alloy interconnects have revealed a wide variety of microstructures that depend on film composition, surface roughness, and deposition parameters (1-6). Typically, sputter deposited AlCu alloy films have a strong crystallographic orientation distribution, known as a (111) fiber texture, in which (111) planes are parallel to the substrate surface. A small volume fraction of randomly oriented grains is also observed (4). It has been shown that the electromigration failure rate in subtractively etched AlCu interconnections decreases as the strength of the (111) texture increases (4, 7-9), and that electromigration failure sites (hillocks and voids) are often associated with Al grains which differ in orientation substantially from the (111) texture (10). Furthermore, the fiber texture strength is not appreciably strengthened with subsequent anneals, indicating that the film texture is defined during deposition (1) and is not altered except in those cases where the annealing temperature is close to the film's melting point, T_m (5, 6). The grain size distribution of AlCu alloys is typically monomodal, and remains monomodal during annealing to 400 °C (1), indicating normal grain growth. In addition, the line edge of patterned lines formed subtractively from a blanket film can serve as a barrier to grain growth and limit the grain size and the character of the grain to grain misorientation (8).

One method for influencing the microstructure of thin films is to deposit them onto under-layer materials with various textures or surface energies. At one extreme is epitaxy, in which a single crystal substrate determines the crystallographic orientation of the deposited single crystal film. At the other extreme is a non-wetting film/substrate combination, in which the film has minimal interaction with the substrate, and its microstructure is determined by its own surface, which may cause a specific orientation to be selected during coalescence or growth (11). More typically, there is some interaction between the film and substrate leading to a preferred crystallographic orientation or texture. For example, it has been found that remelting an Al film into a grooved substrate (trenches) alters the film grain orientation due to the large interfacial energy contribution of the trench sidewalls (6).

Recently the use of patterned substrate trenches (damascene structure), has become common (12), as both smaller line dimensions (< 0.3 μm) and process simplicity are required to form metal interconnect lines. The damascene process for defining interconnect lines typically includes patterning and etching the insulator, followed by metal deposition. Metal under-layers containing metals such as Ta, Ti or W and their nitrides are often employed to promote adhesion and/or as diffusion barriers. The microstructure of these lines is established during deposition within a patterned structure instead of on a planar surface.

Analysis through x-ray diffraction is effectively used to determine the crystallographic texture for large area thin films. In sub-micron lines, however, much less is known about the effects of under-layer materials and line width on texture. EBSP is extremely suitable and convenient for such geometries due to both its spatial resolution (0.1 μm) and the discrete orientation measurements obtained. In this paper we show that a variety of fine line textures develop as a function of metal line width for Al lines: 1) deposited onto planar substrates and subtractively etched versus 2) formed using the damascene process.

EXPERIMENTAL PROCEDURE

In this paper, two different types of Al lines were investigated (Table I). RIE lines were fabricated using subtractive metal reactive ion etch (RIE) processes and Damascene lines were formed using the damascene processes. Within the RIE sample set, Al or AlCu was deposited by either: a) partial-ion beam PIB evaporation (PIB-e) at 2 keV with 1% ions or b) physical vapor deposition sputtering (PVD-s). The PIB-e sample had 1 μm thick Al on SiO_2 and lines were fabricated ranging in width from 0.45 μm to > 10 μm (pads). The PVD-s sample had 230 nm Al-Cu on a dual underlayer of 10 nm PVD-s TiN / 10 nm PVD-s Ti on SiO_2. The metal film stack was blanket deposited at 150 °C, then patterned into lines ranging in width from 0.5 μm to > 10 μm. After patterning, both samples PIB-e and PVD-s were annealed at 400°C for 1 hour in forming gas (90% nitrogen / 10% hydrogen).

Table I. RIE and Damascene Samples.

ID #	TYPE	Film stack		Post deposition anneal
		Al Metallization	Underlayer	
PIB-e	RIE	1 μm PIB evap. Al (2 keV/ 1% ions)	None	400 °C, 1 h forming gas
PVD-s	RIE	230 nm sput. AlCu (150 °C)	10 nm sput TiN / 10 nm sput Ti	400 °C, 1 h forming gas
PVD-dam	Damascene	800 nm sput. AlCu (430 °C) / 100 nm sput AlCu (150 °C)	40 nm I-PVD Ti	None
PVD-400-CVD	Damascene	800 nm sput. AlCu (400 °C) / 50 nm CVD AlCu (265 °C)	10 nm CVD TiN (430 °C) / 30 nm I-PVD Ti	None
PVD-500-CVD	Damascene	1000 nm sput. AlCu (500 °C) / 40 nm CVD AlCu (200 °C)	5 CVD TiN (430 °C) / 24 I-PVD Ti	None

For the Damascene processed samples, trenches in SiO_2 were filled with a Ti or Ti / TiN underlayer followed by a low temperature / high temperature Al or AlCu deposition. The underlayers were used as both a diffusion barrier and adhesion promoter. Since the final layer was AlCu sputtered at high temperature (400-500 °C), the Al flowed into the damascene trenches during deposition. With this "Al reflow" damascene process, excellent fill of high aspect ratio trenches with fine line widths was achieved. There were three types of damascene processed samples. The first was an all PVD metal stack (PVD-dam) consisting of 800 nm PVD-s AlCu (430 °C) / 100 nm PVD-s AlCu (150 °C) / 40 nm ionized metal plasma (IMP) Ti, (2). The next samples were unique in that two of the metal layers were deposited by chemical vapor deposition (CVD). The first metal stack (PVD-400-CVD) consisted of 800 nm PVD-s AlCu (400 °C) / 30 nm CVD Al (265 °C) / 10 nm CVD TiN (200 °C) / 50 nm ionized metal plasma (IMP) Ti. The final sample was similar to sample PVD-400-CVD with the top AlCu layer deposited at a higher temperature (PVD-500-CVD): 1000 nm PVD-s AlCu (500 °C) / 40 nm CVD Al (200 °C) / 5 nm CVD TiN (200 °C) / 24 nm ionized metal plasma (IMP) Ti. Chemical-mechanical polishing was used to remove the metal overburden for all three damascene samples, producing lines which were 0.4 μm deep and ranged in width from 0.18-5.0 μm.

Electron backscatter patterning (EBSP) (10, 13, 14) was used to measure the individual grain orientations either in pad regions or along individual lines. A JEOL 733 Scanning Electron Microscope (SEM) microprobe utilizing a Hamamatsu integrated CCD camera was optimized for grain resolution using the results of an EBSP resolution study correlating resolution with SEM working parameters (14). An automatic Kikuchi pattern indexing procedure (< 0.5 sec cycle time) combined with automatic beam stepping allowed large grids to be scanned, typically recording 10^3 to 10^4 discrete grain orientations in each area. The orientation distribution functions, i.e., the combined Euler

Al RIE (SiO_2 underlayer, annealed at 400 °C)

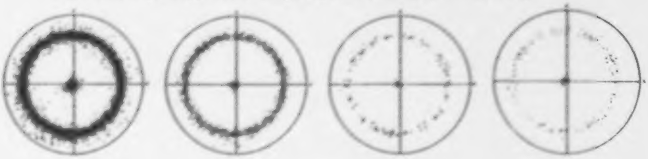

pad 10um 1um 0.45um

AlCu RIE (TiN underlayer, annealed at 400 °C)

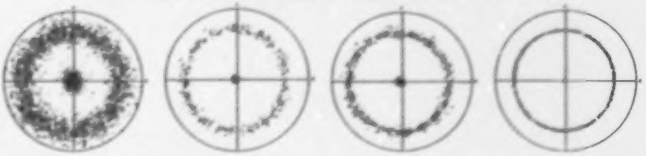

pad 6.5um 3um 0.5um

AlCu Damascene (430 °C on Ti underlayer)

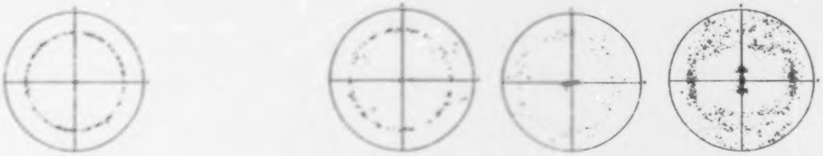

5um 1 0.5 0.3

AlCu Damascene (400 °C on CVD TiN underlayer)

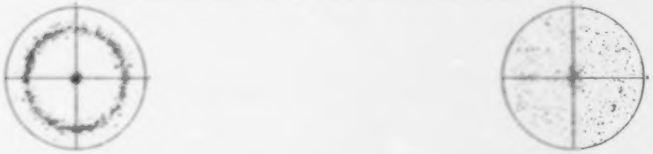

7um 0.5um

AlCu Damascene (500 °C on CVD TiN underlayer)

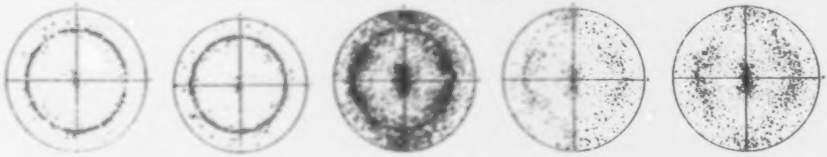

5um 2.3 1 0.5 0.4

Figure 1. (111) Pole Figures as a function of linewidth (micrometers).

angles (φ_1, ϕ and φ_2) for all orientations in a set of lines, are represented here as (111) pole figures where the (111) plane normals are plotted as discrete points in stereographic projection.

RESULTS & DISCUSSION

Figure 1 contains Al (111) pole figures for the 5 different samples. For each sample, the pole figures are shown for progressively finer lines, when viewed from left to right. It is apparent from Fig. 1 that there is a dependence of texture on the metal linewidth. The two RIE samples (samples PIB-e and PVD-s) show stronger Al (111) texture with decreasing linewidth (e.g., less scatter is noted in the pole figure for the narrow 0.45 μm wide lines than for the wider lines or pads). This effect is modest for the PIB-e sample but very pronounced for the PVD-s sample, where there is a TiN / Ti underlayer. The three damascene samples (PVD-dam, PVD-400-CVD and PVD-500-CVD), however, show the opposite behavior (15, 16).

In addition to demonstrating the linewidth effects, Fig. 1 is useful for directly comparing the Al (111) texture strength of all the film types. For wide linewidths and pads, the films with the best (111) fiber texture were the two damascene samples PVD-dam and PVD-500-CVD, with sample PVD-500-CVD more strongly (111) textured. The PVD-dam sample had a liner of IPVD Ti only while sample PVD-500-CVD had CVD TiN / IPVD Ti liner and a high temperature (500 °C) AlCu reflow. By far the worst texture of any of the films, regardless of line width, was the damascene sample PVD-400-CVD, which consisted of CVD TiN / IPVD Ti liner and a low temperature (400 °C) AlCu reflow. An earlier study on Al reflow with CVD TiN / PVD-s Ti underlayers showed that at reflow temperatures less than 430 °C, CVD TiN acts as an excellent barrier (17). However, at higher temperature Al reflow, Ti diffuses through TiN to form $TiAl_3$. Since the PVD-dam sample did not have a TiN barrier film, the Ti liner reacted with Al upon deposition. The PVD-400-CVD and PVD-500-CVD samples had a CVD TiN barrier but aluminide formed exclusively in the PVD-500-CVD sample which had a 500 °C Al reflow. Since the texture strength was better for damascene films, which formed $TiAl_3$, it appears that aluminide formation is important in determining the strength of the (111) fiber texture in Al damascene films.

When the linewidth decreases below approximately 1 μm, the damascene samples' texture strength diminishes, while the texture in the RIE samples (PIB-e and PVD-s) strengthens. It is also interesting to note, that for wide lines, sample PIB-e with Al on SiO_2 has slightly better texture than sample PVD-s with Al on TiN / Ti. The overall texture for sample PIB-e only increases slightly as the linewidth decreases while the texture of sample PVD-s improves dramatically. For very fine lines, the texture in sample PVD-s is slightly better than that for sample PIB-e.

From the (111) pole figures in Fig. 1 the fiber texture for damascene sample PVD-dam is shown to change from a strongly (111) unimodal texture for wide lines (> 1 μm) to a tri-modal (111) for fine lines (< 1 μm). The 0.5 and 0.3 μm wide lines show splitting of the (111) fiber texture into three distinct textures. This effect is most apparent in the 0.3 μm wide lines.

CONCLUSIONS

The microstructure of both RIE and damascene AlCu were measured. Two distinctly different behaviors were observed in the texture evolution of lines as a function of linewidth. In initially planar metal samples, that were subsequently patterned, no effect was seen for Al on SiO2, but an increase in the (111) fiber texture was noted for AlCu lines deposited onto Ti/TiN under layers, as a function of decreasing feature size. For damascene line samples, in which the metal was deposited into trenches, a marked decrease in the (111) fiber texture with decreasing line width was observed, and a novel tri-modal (111) texture distribution was found in 0.3 μm wide lines in which appreciable $TiAl_3$ formed. These observations are explained by considering the geometry of the dominant nucleating surfaces, and by interfacial surface energy minimization.

REFERENCES

1. D.P. Tracy, D.B. Knorr and K.P. Rodbell, *J. Appl. Phys.*, 76 2671 (1994)
2. K.P. Rodbell, V. Svilan, L.M. Gignac, P.W. DeHaven, R.J. Murphy and T.J. Licata, Mat. Res. Soc. Symp. Proc., 403 617 (1996)
3. H. Onoda, K. Touchi and K. Hashimoto, *Jpn. J. Appl. Phys.*, 34 L1037 (1995)
4. D.B. Knorr, D.P. Tracy and K.P. Rodbell, *Appl. Phys . Lett.*, 59 3241 (1991)
5. M.J.C. van den Homberg, P.F.A. Alkemade, J.L. Hurd, G.J. Leusink and S. Radelaar, Mat. Res. Soc. Symp. Proc., 391 397 (1995)
6. M.J.C. van den Homberg, P.F.A. Alkemade, S. Radelaar, J.L. Hurd and A.G. Dirks, *Appl. Phys. Lett.*, 70 318 (1997)
7. S. Vaidya and A.K. Sinha, *Thin Solid Films*, 75 253 (1981)
8. D.B. Knorr and K.P. Rodbell, *J. Appl. Phys.*, 79 2409 (1996)
9. L.M. Ting and Q-Z. Hong, Mat. Res. Soc. Symp. Pro., 428 75 (1996)
10. J.L. Hurd, K.P. Rodbell, D.B. Knorr and N.L. Koligman, Mat. Res. Soc. Symp. Proc., 343 653 (1994)
11. J.M.E. Harper and K.P. Rodbell, J. Vac. Sci. & Technol. B, 15 (1997).
12. *The National Technology Roadmap for Semiconductors* (Semiconductor Industry Association, San Jose, CA, 1997).
13. J.A. Venables, C.J. Harland, *Phil. Mag.* 27 1193 (1973)
14. J. Hjelen and E. Nes; in Proc. *XIIth Int. Cong. for Electron Microscopy*, Japan, San Francisco Press Inc., San Francisco, 1990.
15. D.P. Field, J.E. Sanchez, Jr., P.R. Besser and DJ. Dingley, J. Appl. Phys. 82 2383 (1997).
16. J.L. Hurd, K.P. Rodbell, L.M. Gignac, L.A. Clevenger, R.C. Iggulden, R.F. Schnabel, S.J. Weber and N.H. Schmidt, "Linewidth and Underlayer Influence on Texture in Sub-Micromenter Wide Al and AlCu Lines", *Appl. Phys. Lett.*, 72 (3), 326 (1998).
17. L.M. Gignac, K.P. Rodbell, L.A. Clevenger, R.C. Iggulden, R.F. Schnabel, S. Weber,C. Lavoie, C. Cabral, Jr., P.W. DeHaven, Y.-Y. Wang, S.H. Boettcher, "Thin Film Interactions Between Ti, TiN and Al During High Temperature Al Reflow For 1G DRAM Interconnects", *Advanced Metallization and Interconnect Systems for ULSI Applications, Proceedings ULSI XIII*, MRS, Pittsburgh, PA (1998).

INFLUENCE OF PROCESSING PARAMETERS ON THE TEXTURE OF PURE ZINC ELECTRODEPOSITED COATINGS ON STEEL

K. DE BLAUWE and A. DE BOECK

OCAS N.V. Research centre of the Sidmar Group, Zelzate, Belgium

J. BOLLEN and W. TIMMERMANS

Sikel N.V., Genk, Belgium

Abstract

Electrogalvanised steel is used extensively in the automotive industry. While the primary purpose is to enhance the corrosion resistance, the coating must also be compatible with the fabrication process of the car body. As the crystallographic texture of a (pure) zinc layer deposited on steel influences the application properties such as deformation and friction behaviour and corrosion resistance, it is likely to understand what the optimum texture is and which process parameters have a significant influence. This contribution focuses on the influence of the surface roughness of the substrate and electrodeposition processing parameters as current density and electrolyte speed. The zinc coatings were produced on a laboratory electroplating line as well as on an industrial line. These experiments clearly show that that a higher current density involves an increase of the percentage of high angle pyramidal and prismatic planes. On the contrary, a higher electrolyte speed results in a higher percentage of low angle pyramidal and basal planes. In these experiments no influence of the surface roughness of the substrate was observed.

Keywords: electrogalvanised steel, crystallographic texture, processing parameters

1 Introduction

Zinc coatings are increasingly used in the automotive industry to improve the corrosion resistance of steel body parts. But also a good deformation behaviour and paintability are required. Electrodeposition is very useful in order to obtain a homogeneous, smooth, defect free coating layer. However, previous research has shown that the zinc texture can have a significant influence of the application properties of the electrogalvanised steel (De Boeck 1994). Therefore it is necessary to know the influence of processing parameters on the coating characteristics. Few research work has been published in the field of the influence of processing conditions on the final texture, morphology and surface roughness of the zinc coating. Sagiyama et al. (1990) analysed the effects of both composition and electrodeposition parameters on the characteristics of the zinc layer. Ishii et al. (1998) studied the influence of some processing parameters on the press formability, the gloss and brightness of the zinc film. Martyak et al (1998) evaluated the possibility to use an Zn- MSA electrolyte in high speed electrogalvanising and its effect on morphology and roughness of the zinc deposit.

The mechanism of electrocrystallisation is also the subject of several studies. Takahashi et al. (1995) and Allely et al. (1995) have been investigated the initial stages of zinc crystallisation on graphite respectively iron from chloride and sulphate electrolytes.

In order to understand the influence of specific processing parameters on zinc layer characteristics, XRD, roughness and EPMA measurements were carried out to investigate the effect of current density, electrolyte speed and surface roughness of the steel substrate on the texture, roughness and morphology of the zinc coating.

2 Experimental

2.1 Electrodeposition

An acid sulphate based electrolyte and insoluble anodes were used in order to electrodeposit a zinc layer on a deep drawing steel grade in a laboratory vertical flow cell (De Wit 1995). Current density and electrolyte speed were varied; all other parameters were kept constant. The zinc coating was electrodeposited on shot blast and Sibetex ® steel substrates.

2.1 XRD

The texture of the zinc layer was measured with a D5000 Siemens X- Ray Diffractometer, equipped with a Cu tube. Samples of 30 by 30 mm² were measured in normal configuration, in a 2θ range of 20° to 130°, with a step of 0.02° and a counting time of 1s per step. The texture is calculated based on the 13 most important diffraction peaks. For each crystal plane, the relative texture coefficient (RTC value) is calculated which gives the percentage of this crystal plane, relative to the 12 others. It is therefore a relative measure of the presence of a specific (hkl) plane in the coating with respect to a reference standard sample with random orientation. Following equations were used:

$$RTC_{hkl} = \frac{TC_{hkl}}{\Sigma\, TC_{hkl}} 100 \quad (1)$$

with TC the texture coefficient or the ratio of the relative intensity of the plane hkl in the sample (R_{hkl}) and in the Zn powder (following ASTM 4-831) ($R_{p,hkl}$), calculated on following formulas, based on the measured peak intensities I_{hkl}:

$$TC_{hkl} = \frac{R_{hkl}}{R_{p,hkl}} 100 \qquad (2)$$

$$R_{hkl} = \frac{I_{hkl}}{\Sigma\, I_{hkl}} 100 \qquad (3)$$

$$R_{p,hkl} = \frac{I_{p,hkl}}{\Sigma\, I_{p,hkl}} 100 \qquad (4)$$

The observed influences will be correlated with the change in relative texture coefficient of the crystal planes, grouped into basal (002), prismatic ((100), (110) and (210)) and low angle ((101), (112), (201), (203) and (211)) and high angle ((102), (103), (104) and (105)) pyramidal plane orientations.

2.3 EPMA

The morphology of some zinc layers was observed by secondary electron images with a JXA- 8800L Jeol electron probe micro analysis system (EPMA).

2.4 Roughness measurements

3D- roughness measurements were carried out by means of the vertical scanning interferometry of a Wyko RST+, before and after electrodeposition in order to look for the influence of the substrate roughness on the texture of the zinc coating.

3 Results and discussion

3.1 Zinc texture

The RTC_{hkl} values for the four texture groups are presented in the graphs below as a function of the electrolyte speed and the current density for both shot blast and Sibetex ® substrate surface.

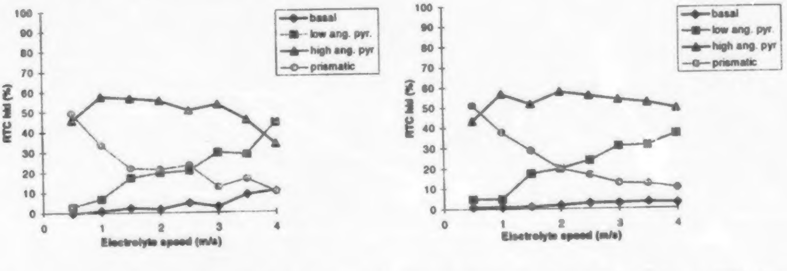

Fig. 1 and 2: Influence of the electrolyte speed on the zinc texture for a Sibetex ® (left) and a shot blast (right) surface roughness of the substrate.

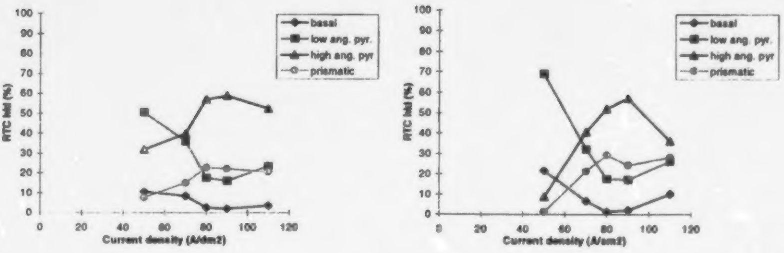

Fig. 3 and 4: Influence of the current density on the zinc texture for a Sibetex ® (left) and a shot blast (right) surface roughness of the substrate.

The graphs of the samples from the laboratory electroplating line clearly show that the increase of prismatic and high angle pyramidal planes with higher current density is compensated by the decrease of the basal and low angle pyramidal planes. A similar compensation is observed for the increasing amount of basal and low angle pyramidal planes with higher electrolyte speed. Apparently, as can be seen from figures 1 and 2, the basal and low angle pyramidal plane orientations are more pronounced in conditions that promote mass transfer of Zn^{2+} ions i.e. in case of higher electrolyte velocities. These results are in agreement with literature (Sagiyama 1990).

No significant difference has been observed between the shot blast or Sibetex ® roughness of the steel substrate. On both surfaces a similar influence of current density and electrolyte speed can be observed.

However, these tendencies revealed by the laboratory experiments are not absolute. As presented in figure 5, the industrial samples behave slightly different. Less prismatic and basal planes are present in this industrial zinc coating. Furthermore, the orientation change of the zinc planes with increasing current density is smaller than for the laboratory samples. These differences are supposed to be caused by the difference in electrolyte flow pattern in an industrial electrodeposition cell compared to a laboratory flow cell and consequently, by a different crystal growth and texture development. Further investigations are necessary in order to know the fundamental mechanism.

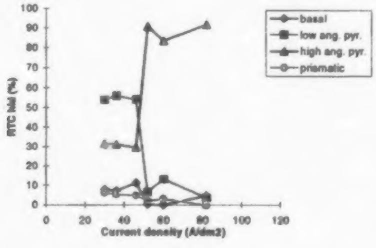

Fig. 5 : Influence of current density on the zinc texture in an industrial line.

3.2 Morphology of the zinc layer

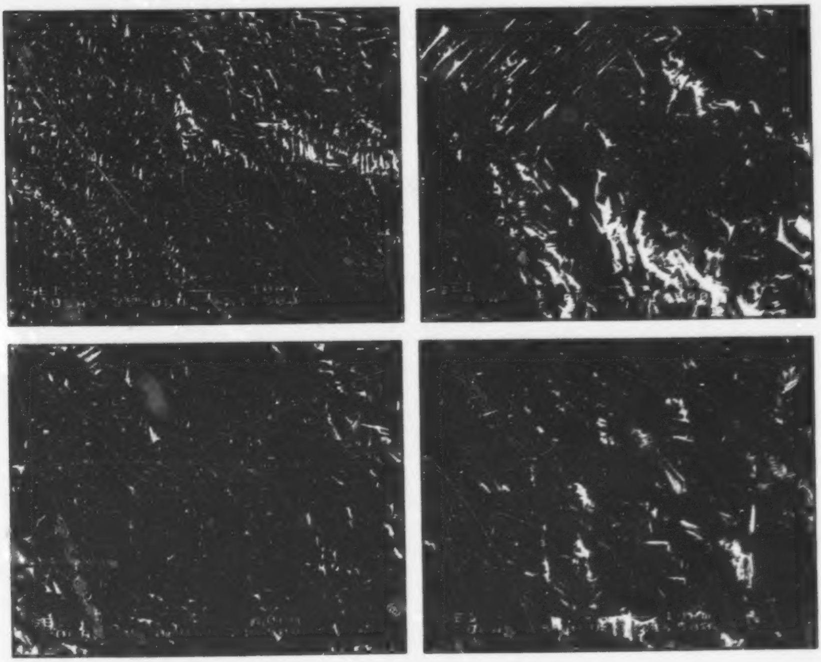

Fig. 6, 7, 8 and 9: SE - images of ELO Zn coatings with 18% (upper left), 39% (upper right), 53% (below left) and 73% (below right) basal planes.

The photographs above show some typical zinc coating morphologies. They clearly reflect the change in morphology with increasing amount of basal planes. Above about 70% basal planes, the morphology changes drastically: more hexagonal zinc crystal plates grow parallel to the steel substrate. This change in morphology also manifests in the application behaviour of the material, more specific the friction behaviour (De Boeck 1994).

3.3 Roughness of the electrodeposited layer

As figure 10 shows, the mean roughness of the laboratory samples increases by electrodepositing. This in contrary to the industrial samples where a slight decrease of the mean roughness has been observed. No significant effect has been seen between the difference in roughness before and after electrodeposition and the zinc texture. This also manifests in individual cases, where samples, coated under the same processing conditions, show a similar texture, whereas they differ significantly concerning their influence on roughness and vice versa.

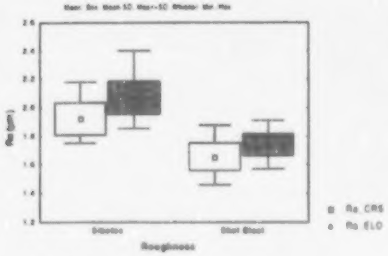

Fig. 10: Roughness measurement before and after electrodeposition of a zinc layer.

4 Conclusions

These laboratory experiments clearly show that a higher current density involves an increase of the percentage of high angle pyramidal and prismatic planes. On the contrary, a higher electrolyte speed results in a higher percentage of low angle pyramidal and basal planes. In these experiments no influence of the kind of surface roughness of the substrate was observed. No influence of the zinc texture on the final roughness of the zinc layer was seen.

In the samples of the industrial line less basal and prismatic zinc planes were present. Moreover, the change in orientation of the zinc planes with increasing current density seemed to be smaller than for the laboratory samples. These differences are supposed to be caused by the different electrolyte flow patterns in the electrogalvanizing cells and consequently, the difference in mass transfer of the Zn^{2+} ions.

Acknowledgements

The authors are grateful to J. Scheers and L. Berckmoes for their help with the roughness measurements and interpretation. We also would like to thank H. Storms for her EPMA observations.

5 References

Allély, C., Drillet, P., Charbonnier, J.C., Guttman, M., Takahashi, A., Nakazawa, M., Miyoshi, Y. (1995) Initial stages of zinc electrocrystallization on iron from sulfate and chloride baths. *Galvatech '95 Conference Proceedings*, pp. 371-75.

De Boeck, A., Vanthournout, M., Van der Hoeven, J.-M. (1994) The influence of texture on the deformation behaviour of electrodeposited zinc coatings. *IDDRG Conference Proceedings*, pp. 55-66.

De Wit, K., Dilewijns, J., De Cooman, B.C., De Boeck, A. (1995) The influence of Fe- content and phase composition on the application properties of zinc- iron electrodeposited steel sheet. *Galvatech '95 Conference Proceedings*, pp. 399-406.

Ishii, K., Kimoto, M. and Yakawa, A. (1998) Effect of crystal orientation on properties of zinc electroplated steel sheets. *Galvatech '98 Conference Proceedings*, pp. 547-552.

Martyak, N.M., Jones, A., Wormuth, R. (1998) High speed zinc galvanizing from a methanesulfonate solution. *TMS Conference Proceedings*, pp. 293-301.

Sagiyama, M., Kawabe, M. and Watanabe, T. (1990) Effects of electrolysis and bath conditions on the surface roughness, morphology and crystal orientation of zinc electrodeposit. *Tetsu-to-Hagane* 76, pp1301-1308.

Takahashi, A., Nakazawa, M., Miyoshi, Y., Allély, C., Charbonnier, J.C., Drillet, P., and Guttman, M. (1995) Initial stages of zinc electrocrystallization on graphite from sulfate and chloride baths. *Galvatech '95 Conference Proceedings*, pp. 377-81.

MICROSTRUCTURES AND TEXTURES OF COPPER ELECTRODEPOSITS ON THE WN DIFFUSION BARRIER

Insoo KIM and Sang Chul HONG
School of Advanced Materials and Systems Engineering, Kum Oh National University of Technology, Kumi, Kyung Buk, Korea, 730-701

Abstract

The microstructures and textures of copper films deposited by electroplating on the WN diffusion barrier were investigated with the variation of deposition conditions by using a copper sulfate solution.
The surface roughness of as-deposited copper film was decreased with increasing the deposition rate and increased with increasing bath temperature.
The copper electrodeposited layer develops random texture in all deposition condition,

Keywords: Electrodeposition, TiN diffusion barrier, Surface morphology, Texture

1 Introduction

Copper is being considered the material for semiconductor metallization because of its better conductivity, higher corrosion resistance in high temperature (Gewirth et al. 1998; Materials world 1998; Time 1997)
Lee et al.(1997) and Dubin et al.(1997) reported a novel method of electrodeposition of copper, producing films having a low resistivity about $2\ \mu\Omega \cdot cm$. Mak (1994) and Cho et al.(1993) reported the shortcoming of electroless deposition in copper metallization on the semiconductor. Choi et al.(1998) reported the copper metallization on the silicon wafer in copper sulfate bath.
In this study, the microstructures, textures and surface morphologies of Cu electrodeposits on the WN coated silicon wafer were investigated with the variation of deposition conditions by using copper sulfate solution.

2 Experimental procedure

A bath solution was used for copper plating, which was composed of, copper sulfate, $CuSO_4$(160 ~ 200g/l) sulfate, H_2SO_4(60 ~ 80g/l). A silicon wafer with WN CVD coated was used for copper plating.

A high purity copper plate was used as an anode. The distance between the anode and cathode was 6 cm.

The current density ranged from 2 ~ 10 A/dm^2 and the bath temperature ranged from 20℃ to 50℃. The bath was stirred and controlled to maintain a pH of 3.0.

The copper deposits of about 3 ~ 5 μm in thickness were peeled off the cathode plate.

The 2θ - plane intensity of the electrodeposits was measured by an x-ray diffractometer. The surface morphologies were observed with a scanning electron microscope.

3 Results and discussion

Figure 1 shows the surface morphologies of copper electrodeposits with the change of current density, a) 4A/dm^2, b) 8A/dm^2 and c) 12A/dm^2. The size of surface grains decreased with increasing current density.

a) b) c)

Fig 1. Surface morphologies of copper electrodeposits with the change of current density. a) 4A/dm^2, b) 8A/dm^2, c) 12A/dm^2

Figure 2 shows the surface morphologies of copper electrodeposits with the change of additives amount a) 0.1g/l b) 0.2g/l and c) 0.3g/l. The size of surface grains decreased with increasing additives.

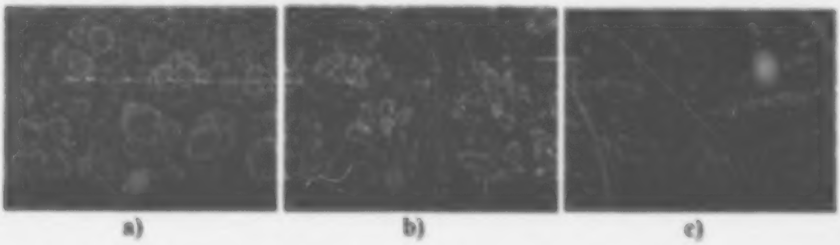
a) b) c)

Fig 2. Surface morphologies of copper electrodeposits with the change of additives amount. a) 0.1g/l, b) 0.2g/l, c) 0.3g/l

Figure 3 shows the surface morphologies of copper electrodeposits with the change of bath temperature. a) 20℃, b) 30℃ and c) 50℃. The size of surface grains increased with increasing bath temperature.

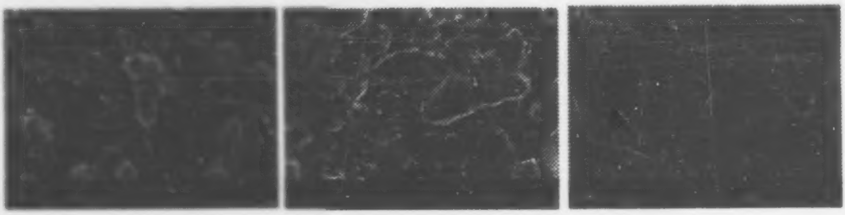

a) b) c)

Fig 3. Surface morphologies of copper electrodeposits with the change of bath temperature. a) 20℃, b) 30℃, c) 50℃

Figure 4 shows the 2θ - plane intensity with the change of electrodeposition Conditions.

Copper electrodeposits layer develops random texture in all deposition.

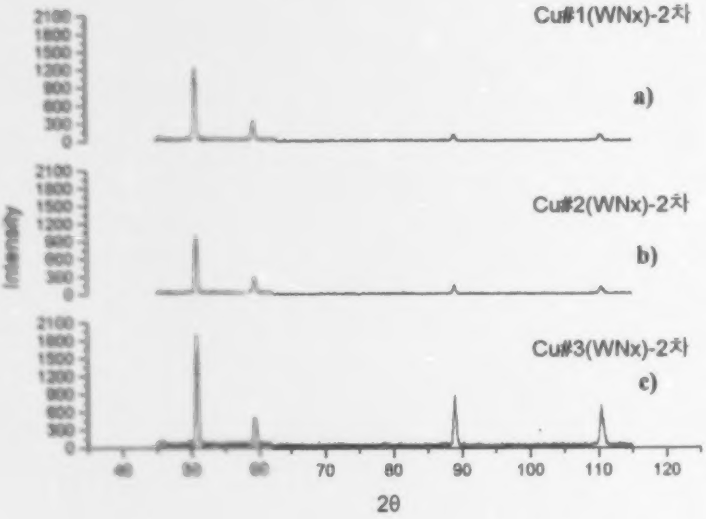

Fig 4. 2θ - plane intensity of copper electrodeposits.
($CuSO_4 \cdot 5H_2O$: 200g/l, H_2SO_4 : 80g/l, Current density : 8A/dm^2)
a) 20℃, b) 30℃, c) 50℃

4 Conclusions

1. Copper electrodeposits layer on the WN can be obtained from copper sulfate, $CuSO_4$(160 ~ 200g/l), sulfate, H_2SO_4(60 ~ 80g/l) bath.
2. Electrodeposits grains were decreased with increasing the current density and additives, increased with increasing bath temperature.
3. Copper electrodeposts layer develops random texture in all deposition conditions.

5 References

Gewith, A. A., Andricacos, P. C., Switzer, J. A. and Dukovic, J. O.(1998) *Interface(The Electrochemical Society)* Spring Vol. 22. Materials World (1998) Apr. Vol. 221.

TIME(1997) Vol. 6, P72

Lee, M. K., Wang, J. J. and Wang, H. P. (1997) *J. Electrochem Society*, Vol. 144, P 1777.

Dubin, V. M., Ting, C. H. and Cheung, R. (June, 1997) 14th *International VLSI Multilevel Interconnection Conference*, Vol. 10, P 69

Choi, C. H., Lee, H. J., Min, S. H., Kim K. B. and Lee, D. N. (1998) *J. Korean Institute of Metals and Materials*, Vol. 36, No.10, P1686

SIMULATION OF TEXTURE FORMATION IN ZrO_2 FILM GROWN ON Zr-2.5%Nb

Hualong Li, M. Glavicic and J. A. Szpunar
Dept. of Metallurgical Eng.
McGill University, Montreal, CANADA, H2X 2B2

Abstract

A computer model is developed which is capable of simulating the texture and microstructure formation. In this computer model, effects of both substrate texture and microstructure on the formation of oxide texture and microstructure are taken into account. The substrate and oxide are represented with digitized unit cells. Each unit cell has an orientation characterized by three Euler angles. In the nucleation and re-nucleation stage, the orientation of each oxide cell is determined by substrate orientation and microstructure of substrate. In the oxide grain growth stage, the orientation of each oxide cell is determined by minimizing the stress at the oxide/metal interface. In this paper, the model is applied to the simulation of the texture formation of the ZrO_2 grown on Zr-2.5%Nb substrate. Three substrates with completely different orientations and microstructures are used in the study. Good agreement between the simulated and the experimental results is obtained.

Keywords: Simulation, oxidation, ZrO_2, texture, microstructure, Zr-2.5%Nb

1 Introduction

Zr-2.5% Nb alloy pressure tubes are used in the core of CANDU nuclear power reactors. During the operation of the reactor, oxidation takes place at both the interior and exterior surfaces. The oxide film formed on the pressure tube surface is a good protective barrier against further oxidation and hydrogen ingress, both of which have a deleterious influence on the mechanical properties of the Zr-2.5% Nb alloy. The oxidation process and hydrogen ingress are both inward diffusion processes. One of the major factors that affect the diffusion process is the oxide texture, which determines the grain boundary character distribution (GBCD). Understanding of the oxide texture formation is therefore critical to the understanding of how and to what extent the oxide film can protect the alloy from further oxidation and hydrogen ingress.

In this paper, a computer model to simulate oxide texture and microstructure formation is developed. The model is applied to the simulation of the texture

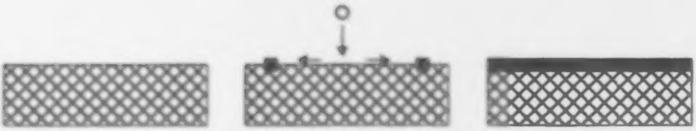

a) fresh surface b) nucleation c) first dense layer

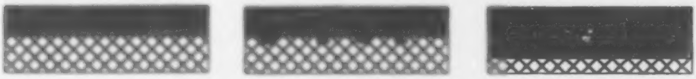

d) grain growth e) re-nucleation f) end of growth

Figure 1 - Simplified oxidation process

formation of oxide grown on the radial, tangential and longitude faces of the pressure tube, based on the previously proposed Zr oxidation mechanism [1].

2 A Cellular Model of Oxide Texture and Microstructure Formation

2.1 Brief Description of Oxidation Process

When the metal with a clean surface is exposed to oxygen, the adsorption of oxygen atoms takes place first. The adsorbed oxygen atoms diffuse on the metal surface [2]. Eventually each will find a preferable nucleation site and becomes an oxide nucleus, or it will meet an existing oxide nucleus and join it by reacting with the metal atom as shown schematically in figure 1b. The nucleus grows laterally and finally forms a continuous layer, the oxygen and metal are then separated by this layer of oxide (figure 1c). The further oxide growth will be controlled by diffusion process though this oxide layer. The oxide film grows uniformly at metal/oxide interface. During the growth, some oxide grains grow faster laterally than their neighbors and become bigger (figure 1d). This competition on growth causes the formation of the oxide texture and microstructure. Moreover, during the oxide growth stage, re-nucleation may take place and new oxide grain may be generated (figure 1e).

From this simplified oxidation process, one can see that the oxidation process consists of oxide nucleation, grain growth and re-nucleation. To simulate oxidation one has to model the oxide nucleation, grain growth and re-nucleation processes.

2.2 Cellular Model of Texture and Microstructure Formation

Before introducing the model, it is necessary to describe how to represent the two-dimensional metal substrate and oxide structures. As can be seen in figure 3, both metal substrate and oxide are represented by a number of grains. Each grain is digitized into a number of cells. The cell is defined as a small area of oxide or metal in a square lattice. Each cell is distinguished by three properties, a label indicating the type of the cell (representing metal or oxide), a pair of integers representing the position of the cell and three integers to representing the orientation in three Euler angles (φ_1,Φ,φ_2). The cells with the same labels and orientations compose the grain (metal or oxide grain). The cells with the same labels and different orientations compose the grain boundary. The cells with different labels compose the metal/oxide interface.

In the step1, a two-dimensional substrate microstructure containing Voronoi grains is generated with Monte-Carlo method. The Voronoi grain is defined as such that all the cells within this grain are closer to the center of this grain than to other grain centers. The computer-generated microstructure is called 'computer specimen' in the following section.

Step 2 is to link the experimental texture to the generated microstructure. The texture information is obtained from experimental pole figures from which the ODF can be derived. The ODF is defined as the intensities of an orientation *g* as a function of orientation *g* where orientation *g* is represented by three Euler angles, $g=(\varphi_1, \Phi, \varphi_2)$. The volume fraction of an orientation *g* has to be calculated from ODF as

$$\frac{dV}{V} = f(g)dg \tag{1}$$

where *V* is the normalized total volume of the specimen, *f(g)* represents the ODF and the *dg* is the orientation volume [3]

$$dg \equiv d(\varphi_1, \Phi, \varphi_2) = 1/8\pi^2 \sin\Phi d\Phi d\varphi_1 d\varphi_2 \tag{2}$$

where $1/8\pi^2$ is the normalization factor to ensure that the summation of all orientations is 1 when equation (2) is integrated in the range of $0 \le \varphi_1 \le 2\pi$, $0 \le \Phi \le \pi$ and $0 \le \varphi_2 \le 2\pi$.

After the ODF data are assigned to grains in the computer specimen, all three properties of the cell are defined. The labels of cells, which are range from 1 to *n* in step 1, are reset to 1, which means that the whole computer specimen is not oxidized at this stage of the simulation.

In step 3, one percent of the computer specimen is cut from the computer specimen. This piece of the computer specimen is then enlarged. The reason for this enlargement is given below. In real situation, the grain size of metal substrate is much larger than that of the oxide. Hundreds of oxide grains may be formed within one substrate grain. Large substrate grains in the computer specimen are preferred in

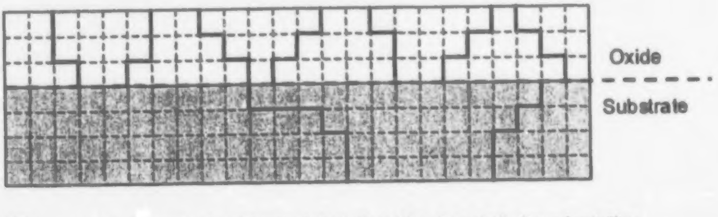

a cell characterized by its label (0-oxide, 1-metal), its orientation $(\varphi_1, \Phi, \varphi_2)$ and its coordinate (x,y)

Figure 3 - Cellular representations of oxide and substrate microstructures

order to simulate that different oxide nucleus and oxide grains can be formed within one substrate grain. Although we do not know how many cells within one substrate grain are large enough, we want the substrate grain to be able to hold as many oxide grains as possible.

In the stage 4, one percent of the computer specimen from step 3 is taken to simulate the oxidation process. The nucleation takes place if this piece of computer specimen contains the metal surface. The position of oxygen atom, which is adsorbed on the metal surface, is randomly determined. This oxygen atom is then allowed to diffuse on the surface within limited number of *n* steps where the number *n* can be arbitrarily defined. In this two-dimensional model, the direction of the surface diffusion is selected between left and right. During the diffusion process, the oxygen atom may reach a suitable nucleation location or meet an existing oxide grain. If the former case takes place first, the cell at that position becomes an oxide nucleus, its label is set to 0 and its orientation is assigned. Both the nucleation position and the oxide orientation are determined according to the specified oxidation mechanism. If the later case takes place first, the cell at that position becomes an ad-oxide and its orientation is inherited from that of the existing oxide grain. If neither of them takes place, the de-adsorption is assumed to occur and the oxygen atom disappear from the simulation. This process continues until a complete layer of oxide is formed.

In stage 5, the oxide formed in step 4 is allowed to grow. This growth process is realized in the computer by changing the substrate cells to oxide cells and assigning the oxide cells new orientations. The oxide film is assumed to grow layer by layer. As the oxide is growing, the labels of the cells in that layer are changed from 1 to 0 which represents oxide. Their orientations are the same as that of the oxide cells in previous layer if the re-nucleation positions does not take place. Otherwise, re-nucleation takes place and new orientations are assigned to the cells. After all labels of the cells in this layer are changed to 0 and the cell orientations are assigned, each cell is given *n* trials to change its orientation. The orientation of the cell can only be either that of itself or that of its neighbors, which means no re-nucleation takes place in this orientation changing process. The criterion for this process is

$$P = \left\{ \begin{array}{cc} 1 & Q_{new} \le Q_{old} \\ \exp(-\beta(Q_{new} - Q_{old})/Q_{old}) & Q_{new} > Q_{old} \end{array} \right\} \tag{4}$$

where *P* is the probability of success, β is a factor defined arbitrarily to control the difficulty of the up-hill process and *Q* is a function of oxide orientation. The Q may be the surface energy, interfacial energy, stress and so on. Step 4 and 5 are repeated until the simulation is finished.

In step 6, the qualitative oxide texture and microstructure from the simulation are generated. The number of oxide cells as a function of the three Euler angles are counted. This function, after normalization, represents the simulated qualitative ODF. The simulated ODF can be used to generate pole figures. The simulated oxide microstructure can be obtained by drawing a boundary line between the cells with different orientations and the same labels.

3 Simulation Results and Discussion

The above described computer model is used to simulate the oxide texture formation in Zr-2.5%Nb oxidation. The oxidation mechanisms proposed in [1] that are used to control the simulation are briefly summarized below.

1. The nucleation occurs at the α-Zr grain boundary region or β-Zr region. The favorable oxide nuclei orientations are those which have crystallographic directions in the oxide parallel to those of the substrate with similar atomic spacing.
2. At the oxide/metal interface region, the oxide grain orientations, which can reduce the compressive stress parallel to the metal/oxide interface, grow faster.

The simulations have been performed on three samples with different orientations. The samples are selected from the radial (RD sample), tangential (TD sample) and longitude (LD sample) faces of the pressure tube. The oxide pole figures calculated from the simulated ODF are given in figure 3(a), 4(a) and 5(a). The corresponding experimental pole figures are shown in figure 3(b), 4(b) and 5(b). It can be seen that a good agreement between the simulated and experimental results has been obtained.

4 Reference

1. Li, H., Glavicic, M., and Szpunar, J. A., (1999) *Acta. Meter.* to be published.
2. Kofstad, P., *High-Temperature Corrosion*, (1988) Elsevier, New York.
3. Bunge, H. J., (1982) *Texture Analysis in Materials Science*, Butterworth, UK.

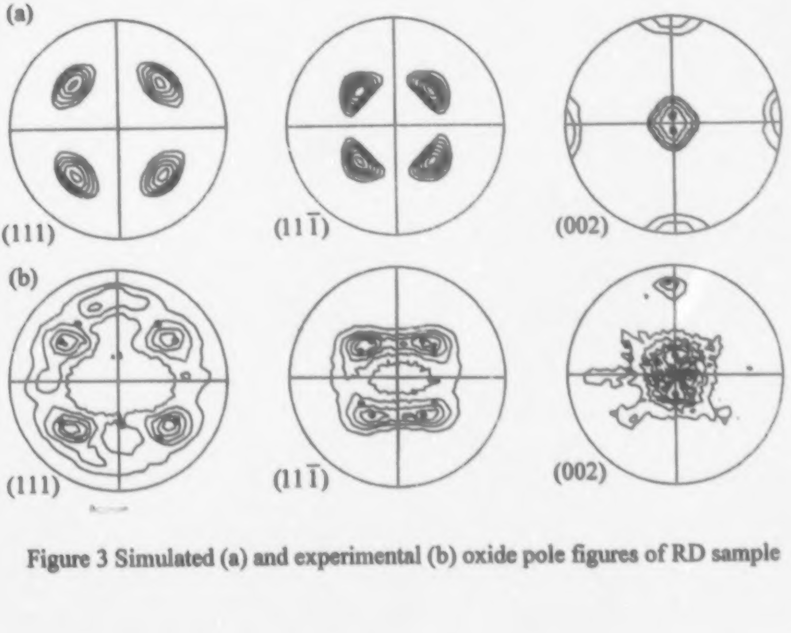

Figure 3 Simulated (a) and experimental (b) oxide pole figures of RD sample

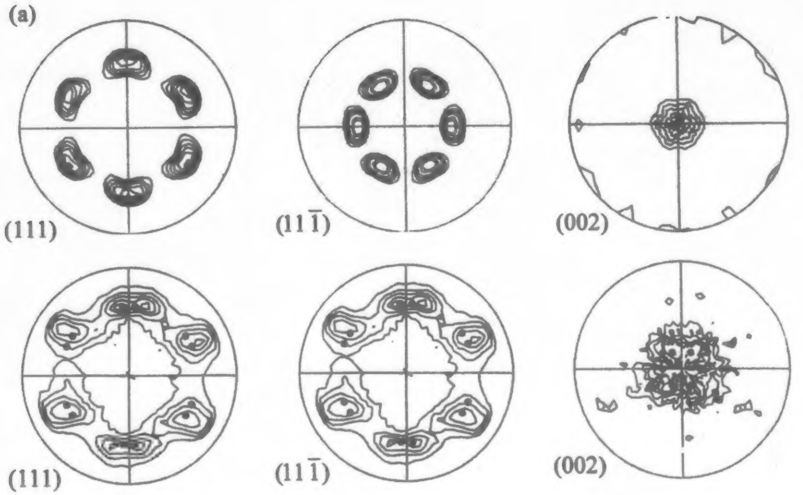

Figure 4 Simulated (a) and experimental (b) oxide pole figures of TD sample

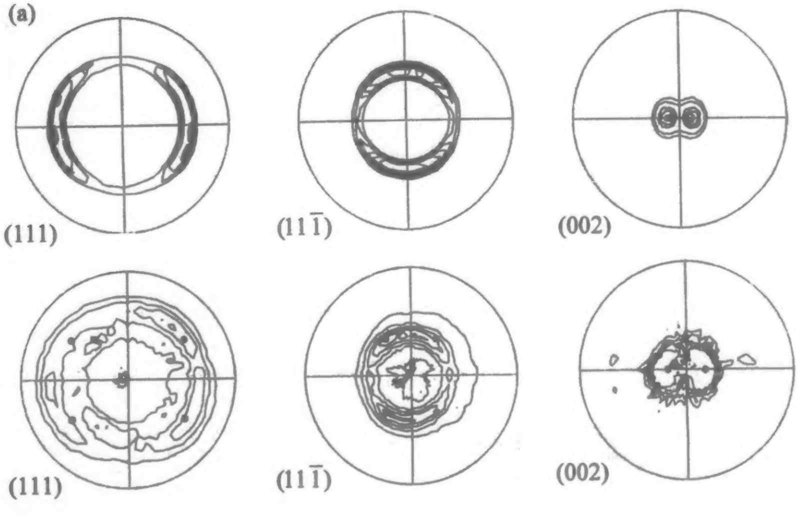

Figure 5 Simulated (a) and experimental (b) oxide pole figures of LD sample

TEXTURE EVOLUTION IN CU DAMASCENE LINES

D.P. Field
TexSEM Laboratories, Draper, Utah, USA

Abstract

The reliability of integrated circuit interconnects is dependent upon various features of the microstructure, including grain size distribution and crystallographic texture. In Al alloy lines a strong (111) texture is desirable to reduce the effects of electromigration and stress voiding and increase the time to failure. A similar relationship is expected to hold for Cu lines. This paper investigates texture and grain boundary structure evolution that occurs during elevated temperature annealing of Cu damascene fabricated interconnect lines. It is shown that the texture within the narrow lines is typically weak and inhomogeneous in nature. Structure evolution is monitored by orientation imaging subsequent to anneals at various temperatures. Texture and grain boundary structure are assumed to evolve to low energy configurations during the annealing process. The potential benefit of tailored boundary structure to IC interconnect performance is discussed in connection with the data.

Keywords: Copper, damascene, thin films, grain growth, electron back-scatter diffraction (EBSD), orientation imaging (OIM)

1 Introduction

The shift in materials selection for the fabrication of non-chip level integrated circuit interconnect lines from Al to Cu also presents a change in fabrication strategy from etching processes to a damascene based technique. The Semiconductor Industry Association's National Technology Roadmap for Semiconductors[1] indicates that future interconnect fabrication is "the technology thrust with the largest potential technology gaps." Of primary concern are fabrication procedures capable of meeting strict critical dimension tolerances. In addition, reliability of interconnects and their resistance to stress voiding and electromigration processes presents considerable challenges in future generations of ICs.

Both stress voiding and electromigration are known to depend upon the details of the interconnect line microstructure[2-6]. Reliability is a function of specific microstructural features instead of just the average properties of the interconnect line. Such features include alloy, grain size distribution, and crystallographic texture, among others. The electromigration rate is controlled by the diffusive properties of the interconnect line microstructure. Diffusion occurs through the bulk material, along grain boundaries, and along metal/oxide interfaces. Crystallographic texture has been shown to be a structural variable of primary importance in improving the reliability of IC interconnects. This relationship can be explained by the fact that a strong texture will limit the range of grain boundary and surface structures in the material. Such grain boundaries are thought to lie in stable, low energy, configurations[7]. The evolution of grain size and texture for Al, Al-Cu, and Al-Cu-Si films and interconnects in conjunction with electromigration processes has been studied extensively over the past three decades. Recent technological innovations have allowed Cu to be used as an interconnect material in place of Al alloys in non-chip level lines. Cu lines are typically fabricated using the damascene process wherein the Cu is deposited into laser-etched trenches with the excess metal being removed by chemical-mechanical planarization (CMP). It has been observed that the Cu lines recrystallize within a few days at room temperature. Various researchers have addressed the issue of the room temperature recrystallization phenomenon[6,8-10]. The subject of the present paper is an experimental investigation of elevated temperature structure evolution in Cu damascene lines, subsequent to the processes that occur at room temperature. Orientation imaging microscopy (OIM)[11-13] was used in the analysis.

2 Experimental Details

Trenches were laser-etched into TEOS SiO_2 on a (001) Si wafer to a depth of 0.5 microns. 250 angstroms of Ta were deposited as a barrier layer followed by 500 angstroms of PVD Cu and 500 angstroms of CVD Cu before electroplating to fill the trench. The structure was then polished by CMP to reveal the resulting Cu lines. Both 0.3 and 1.0 micron wide lines were analyzed. No high temperature annealing was performed, but the wafers were held at room temperature until complete room temperature recrystallization was accomplished. The lines were analyzed by standard scanning electron microscopy techniques and by orientation imaging. Structural evolution was quantified by grain size, crystallographic texture, and grain boundary character distributions. All of this information was obtained by orientation imaging techniques using a thermal source field-emission SEM at 20 kV accelerating potential and 2 nA probe current. Subsequent to the initial characterization, a one-hour anneal was performed at 310°C. The same region of the one micron wide interconnect structure as that characterized before annealing was again analyzed by orientation imaging. A new region from the 0.3 micron line was also analyzed. The process was repeated for one-hour anneals at 440 and 550°C.

Figure 1 includes secondary electron images of a small region of the Cu damascene test structure (one micron lines) after anneals at room temperature, 310°, 440°, and 550°C. The increased roughness of the specimen surface is due to an ion etching step which was performed following each OIM scan. This was done to improve the image quality of the back-scatter diffraction patterns which suffered significantly because of carbon contamination. The effects of contamination on EBSD performance is material dependent as the same experiments were performed previously on Al films with minimal detrimental effects from the prior OIM scans[14]. Several regions of the interconnect structure were analyzed by OIM subsequent to each heating cycle. The region shown in Fig. 1 was repetitively analyzed to directly observe grain structure evolution for each temperature investigated.

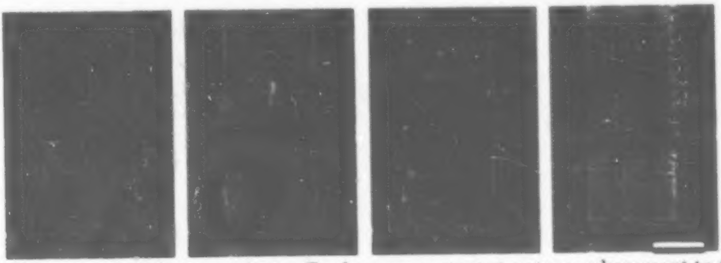

Figure 1 – SE images of the one micron Cu damascene test structure subsequent to OIM analysis at room temp, 310°, 440°, and 550°C from left to right respectively. The black and white micron bar at lower right is 2 microns.

3 Results

Orientation imaging results of analyses of the region shown in Fig. 1 are given as Fig. 2. Crystallites are colored according to pole orientation normal to the specimen surface, but since this is not a color publication, the image does not yield a one-to-one correspondence with a color key. Black regions are those which did not yield high

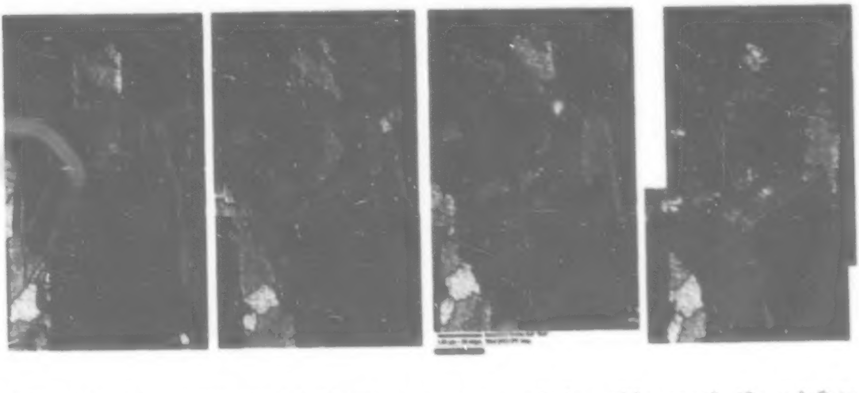

Figure 2 – Orientation images showing structure evolution with anneals (from left to right) of room temperature, 310, 440, and 550°C. The micron bar is one micron.

confidence information from the diffraction patterns. As described in the previous section, the frequency of poor quality data increases with each OIM scan over the specimen surface. The initial and final orientation distributions of the region shown are similar in nature. They both include a (111) texture component that evolves only slightly, though significant grain boundary migration is observed. This texture is not consistent across the wafer, or in the lines near the region shown. As is characteristic for Cu damascene lines, the crystallographic texture is weak and inhomogeneous across the wafer surface. It is evident by analysis of Fig. 2 that the grain which experiences the most growth is that which extends across the cross-line connecting all three interconnects. This grain is the most nearly (111)-oriented grain in the structure. Figure 3 contains $\varphi_2 = 45°$ sections of the orientation distribution function for the room temperature (left side) and 440°C anneals. The (111) oriented grains fall upon a line formed by $\varphi_2 = 45°$ and $\Phi = 54.7°$. It is apparent from this comparison that the near (111) texture strengthens slightly as the structure evolves.

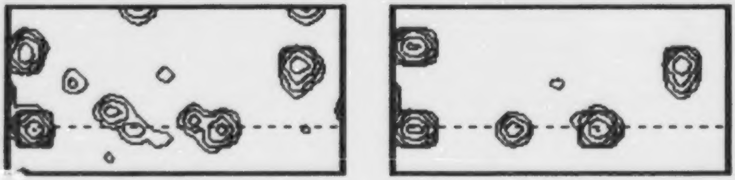

φ_2=45° φ_2=45°

Figure 3 – Comparison of ODF sections for the room temp. anneal (left) and the 440°C anneal showing the (111) fiber position (dashed line) and the evolution of orientation density towards the (111) texture. Contours are at 1, 3, 9, 29, 89, and 272 times random.

Figure 4.a, 4.b, and 4.c show the (111) pole figures for the narrow lines after the 550°C anneal, the 1.0 micron lines after the room temperature anneal, and the 1.0 micron lines after the 550°C anneal respectively. The textures were weak for all conditions analyzed. The line width dependence of texture evolution is apparent from comparison of Figs. 4.a and 4.c. A slightly preferred (111) orientation relative to the free surface is observed for the lines with a high width to height ratio. The lines with a larger height than width develop a preferred (111) orientation relative to the sidewall of the lines. The difference in preferred orientation as a function of high temperature annealing for both the wide and narrow lines is small, but the (111) texture component strengthens slightly for each.

The average grain diameter as determined by OIM analyses increased during annealing from 0.504 to 0.604 to 0.658 µm for the room temperature, 310°, and 440°C anneals respectively. Twin grains were included in the analysis as distinct grains in the distribution. The number of grains in the analysis region dropped significantly as the grain size increased, but the preferred orientation remained remarkably constant throughout. Eighty-seven percent of the grain boundaries in the initial structure were twin or twin variant boundaries as defined by crystallite lattice misorientation and coincident site lattice (CSL) theory using Brandon's criterion for specialness[15]. The fraction of Σ3 boundaries was 0.73 which is significantly higher than the two-thirds upper-bound limit given by Palumbo *et al.* for bulk materials[16]. The upper bound for narrow line structures is unity since the grain morphology is near-bamboo in nature and the triple line arguments used in determination of the 2/3 fraction are not valid for bamboo type structures. As boundary migration occurred, it became apparent that twin grains played a major role in the structure evolution. Some twins were annihilated during the process, while others propagated across the parent matrix, effectively splitting a single crystallite into two smaller grains. In isolated cases, narrow twin grains that apparently spanned the parent grain prior to annealing were annihilated. While only surface observations were made, if such a twin were destroyed, it would indicate that the coherent twin boundary is mobile under certain conditions. It is likely that the stress distribution in the line provides the driving force for motion of the coherent twin boundary. Even though the initial concentration of twin boundaries was high, the fraction of twin and twin variant boundaries increased

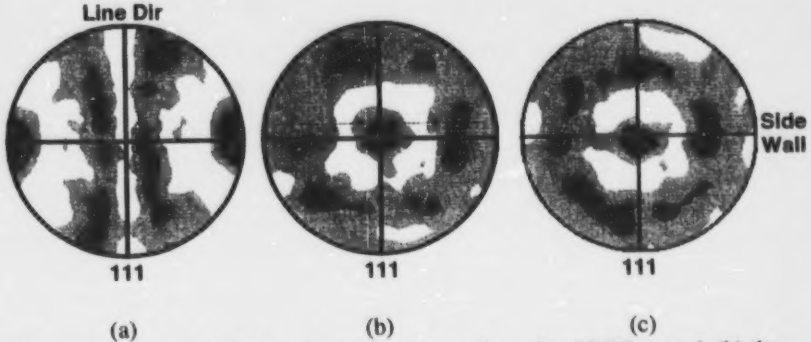

Figure 4 – (111) pole figures for (a) the 0.3 μm line after 550°C anneal, (b) the 1.0 μm line after the room temperature anneal, and (c) the 1.0 micron line after the 550°C anneal.

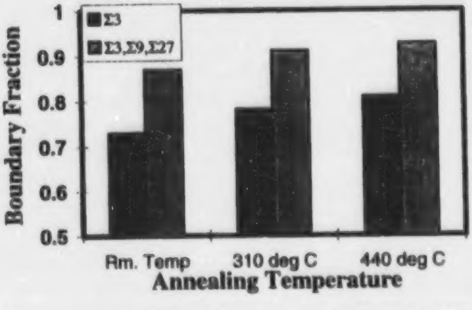

Figure 5 – Evolution of twin (Σ3) and twin variant boundaries as a function of annealing temperature.

with increased annealing temperature, as shown in Fig. 5. In all distributions, the boundaries that could not be classified as twin variants were largely low angle boundaries. A small fraction of random high angle boundaries was also present.

4 Discussion and Conclusions

The crystallographic textures were relatively weak in both the wide and narrow lines for all conditions investigated as compared with the textures typically observed in Al films. Texture evolution tends to near (111) orientations either normal to the surface or the sidewall of the interconnect line, depending upon the width to height ratio of the line. Twin grain boundaries must play a major role in structure evolution. Many twins appear to be stable, especially if they are allowed to span the line width in a near bamboo structure. Twin grains are often annihilated in favor of the single crystallite spanning the line width. In some instances, twins were observed to grow across a parent grain, splitting it in two, and effectively forming an additional grain. The fraction of twin type grain boundaries increased with annealing temperature. This is likely beneficial for avoiding electromigration failures as twin boundaries are known to be low diffusivity paths. High temperature annealing during processing of such components will form stable, non-evolving, structures in Cu damascene lines and may improve reliability of the integrated circuit.

References

1. *The National Technology Roadmap for Semiconductors* (Semiconductor Industry Association, San Jose, CA, 1997).
2. S. Vaidya and A.K. Sinha, *Thin Solid Films*, **75**, 253 (1981).
3. J.H. Rose, *Appl. Phys. Lett.*, **61**, 2170 (1992).
4. C.V. Thompson and J.R. Lloyd, *MRS Bulletin*, **Dec. 1993**, p. 19.
5. D.B. Knorr and K.P. Rodbell, *J. Appl. Phys.*, **79**, 2409 (1996).
6. J.M.E. Harper and K.P. Rodbell, *J. Vac. Sci. Technol.* B, **15**, 763-779 (1997).
7. K.T. Lee, J.A. Szpunar, A. Morawiec, D.B. Knorr, and K.P. Rodbell, *Can. Metall. Quarterly*, **34**, 287 (1995).
8. I.V. Tomov, D.S. Stoychev, and I.B. Vitanova, *J. Appl. Electrochem*, **15**, 887 (1985).
8. C. Lingk and M.E. Gross, *J. Appl. Phys.*, **84**, 5547 (1998).
10. J. M.E. Harper, C. Cabral Jr., P. Andricacos, L. Gignac, I.C. Noyan, and K.P. Rodbell, Proc. of MRS Symp., **562**,1999. To be published.
11. B.L. Adams, S.I. Wright, and K. Kunze, *Metall. Trans.*, **24**, 819 (1993).
12.. S.I. Wright, *J. Computer-Assisted Microscopy*, **5**, 207 (1993).
13. N.C. Krieger-Lassen, K. Conradsen, and D. Juul-Jensen, *Scanning Microsc.*, **6**, 115 (1992).
14. D.P. Field and J.E. Sanchez Jr., in Grain Growth in Polycrystalline Materials III, H. Weiland, B.L. Adams, and A.D. Rollett, eds, The Minerals, Metals & Materials Society, pp. 523-528, 1998.
15. D.G. Brandon, *Acta metall.*, **14**, 1479 (1966).
16. G. Palumbo, K.T. Aust, U. Erb, P.J. King, A.M. Brennenstuhl, and P.C. Lichtenberger, *Phys. Stat. Sol.* **131**, 425 (1992).

TEXTURE OF THIN LAYERS AND NANOWIRES OF ELECTRODEPOSITED THERMOELECTRIC MATERIALS SUCH AS $Bi_{1-x}Sb_x$ ALLOYS

F. BESSE, C. BOULANGER and J. M. LECUIRE
Laboratoire d'Electrochimie des Matériaux LEM CNRS UMR 7555, Université de METZ Ile de Saulcy, 57045 METZ Cedex 01 FRANCE
B. BOLLE and J. J. HEIZMANN
Laboratoire d'Etude des Textures et Application aux Matériaux LETAM CNRS URA 2090 / ISGMP, Université de METZ Ile du Saulcy 57045 METZ cedex 01 FRANCE

Abstract

Thermoelectric semi-conductors are used as converters of electric energy to thermal energy and vice versa. BiSb alloys have good thermoelectric properties, but their efficiency will depend on the crystallisation process (i.e. grain sizes, grain boundaries) and on the crystal orientation. The link between orientation and efficiency is mainly due to a strong anisotropy of the electric conductivity of these $R\bar{3}m$ materials. Thin films of $Bi_{1-x}Sb_x$ alloys are electrodeposited with different electrochemical conditions (potentiostatic and galvanostatic process, thickness of the layer, and so on). In the same way, monocrystalline nanowires of these materials can be prepared by electrodeposition using nanoporous nuclear track-etched membranes as template. The thin films and nanowires texture is studied according to the electrodeposition process parameters and their growth is described with a view to obtaining the most efficient material.

Keywords : BiSb alloys, electrodeposition, nanowires, texture, twin

1 Introduction

Bismuth - Antimony alloys are very attractive materials for thermoelectric refrigeration at low temperature (Smith and Wolfe, 1962; Yim and Amith, 1972). They present different electrical transport properties depending on antimony composition. The optimal figure of merit is obtained for $Bi_{0.9}Sb_{0.1}$ alloys (Lenoir et al., 1996). An electrochemical synthesis has been developed in order to provide an alternative process to classical methods (directional crystallisation techniques, powder metallurgy or evaporation methods). Indeed, electrodeposition has the attractive features of cost-effectiveness, simplicity in operation and production of large area thermoelements.

Our process is based on the coreduction of bismuth and antimony salts in an aqueous medium containing chloride according to (Peudon-Besse et al. 1998; Besse et al., to be published):

$$(1\text{-}x)\,BiCl_4^- + x\,SbCl_4^- + 3e^- \rightarrow Bi_{1-x}Sb_x + 4\,Cl^-$$

with coulombic efficiencies close to 100%. The electrodeposited films are polycrystalline.

However, the efficiency of $Bi_{0.9}Sb_{0.1}$ alloys applications in static coolers will depend on the crystallisation state (grain size, grain boundaries). Monocrystalline nanowires of the desired alloys can also be electrochemically synthesised within the voids of a template material (Peudon et al., 1998). In this method, the physical properties of the material can change between the bulk scale and nanoscale.

The knowledge of the relation between the crystal orientation and electrochemical conditions is important because the efficiency is due to a strong anisotropy of the electric conductivity of the $R\bar{3}m$ materials.

2 Experimental details

BiSb alloys form an homogeneous disordered solid solution at all compositions. They crystallise in a primitive trigonal system $R\bar{3}m$ with 2 atoms/cell (Pearson, 1964). Other lattices are frequently used to describe these alloys (Fig. 1) : a pseudo hexagonal one (6at/cell) or a face centred trigonal (8at/cell). In the following, all the indexes (planes and rows) are given according to the hexagonal cell.

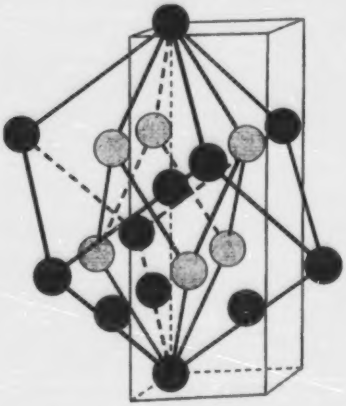

$(01.2)_h = (100)_{fct}$
$(10.4)_h = (110)_{fct}$ twin plane K_1
$(11.0)_h = (1\bar{1}0)_{fct}$
$(10.1)_h = (11\bar{1})_{fct}$

Fig. 1 : different lattices used and equivalent planes in hexagonal and face centred trigonal

The aim of this study is to promote an oriented growth of the alloy in the nanopores of the polymer, able to give well oriented BiSb nanowires. Beforehand, in order to know some parameters which govern the growth conditions, experiments are made on bulky films.

The $Bi_{0.9}Sb_{0.1}$ films were electrodeposited on vitreous carbon sheets (Carbon Lorraine) from a solution with a |Sb|/|Bi| ratio equal to 0.1. In this electrolyte, deposition was conducted either at cathodic current densities of -0.4 and -1A/dm^2 or at potentiostatic polarisation of -300 mV / SCE. The thicknesses of these polycrystalline films are between 10 and 50µm (Fig 2a surface of the bulk film 50µm -1A/dm^2).

Fig. 2 : (a) bulk films and (b) nanowires of BiSb alloys

The nanowires were electrodeposited into nanometric size cylindrical pores in polycarbonate membranes (Cyclopore) with a layer of Ag sputtered onto their bottom side. They are typically 20 µm in length and 100 nm in diameter (Fig. 2b). The pores density of the membrane is 6.10^8 wires/cm^2. The electrodeposition was performed either in a potentiostatic process (-280 and -300 mV / SCE) or in an intenstiostatic process (- 2mA for a global surface of the membrane : 0.5026 cm^2).

3 Texture determination

The pole figures (01.2), (10.4), (11.0) and (20.2) are measured to determine the texture. As the absorption coefficient is very high, only a few micrometers from the outside surface of the layer can be observed.

3.1 Texture of the bulky layers

All of the observed texture are fiber textures, so, only the plane parallel to the surface of the substrate is given.

When a potentiostatic process is used, the texture changes as the thickness of the layer increases. For layers until 10µm, no preferential orientation is detected. For 20µm, (01.2) is the dominant orientation (Fig. 3), then (10.1) orientation is the main orientation when the layers are thicker 30 to 50µm (Fig. 4). For the thicker layers (30-50µm), whatever the process which is used (intensio or potentiostatic, -0.4 and -1A/dm^2 or -300mV / SCE), the texture remains identical.

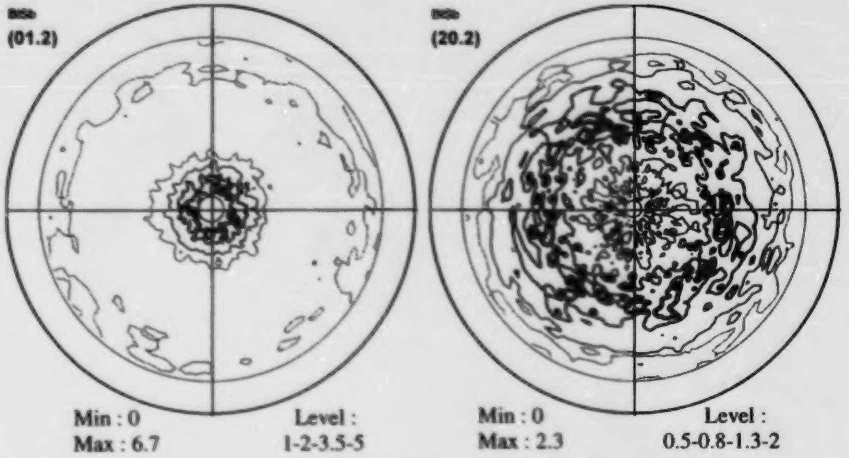

Fig. 3 : pole figures (01.2) and (20.2) of the bulky layer 20µm thick

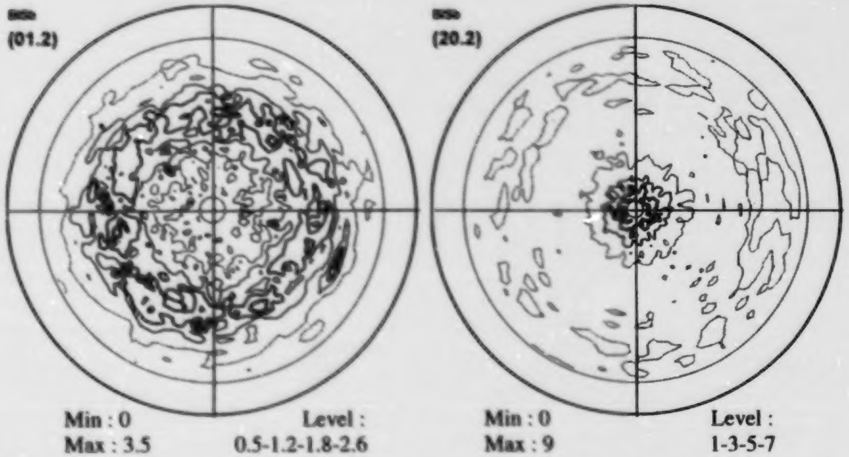

Fig. 4 : pole figures (01.2) and (20.2) of the bulky layer 50µm thick

All of the observed orientations correspond to the densest planes of the structure, either the face of the face centred trigonal or its $(11\bar{1})$ plane and their equivalents, grow parallel to the surface. This observation agrees with those of Chaouni (Chaouni et al. , 1996) or Oettel (Oettel and Klimanek, 1998) on the electrodeposition of copper. In fact, the BiSb alloys have a structure close to the fcc metals because the α angle of the face centred trigonal is 87.6°.

3.2 Nanowires texture

As the polymer is not a conducting material, one side of the membrane (20µm thick) is coated with a thin film of Ag by metallisation before the electrodeposition process. In order to know the potential influence of this metallisation, bulky films were prepared on silver metallised vitreous carbon. The same results as those observed on the uncoated substrate are found. It seems that the kind of substrate does not influence the growing process.

The texture of the nanowires is studied when they are still in the polymeric matrix ; thus the wires axes are perpendicular to the substrate. Up to now the study of only one wire shows it was a single crystal, but further investigations must be done to know if they are mono or polycrystalline.

Texture experiments on samples prepared with the same experimental conditions as the bulky layer (20µm, -300mV/SCE) show the same orientation : (01.2). When other electrodeposition conditions are used, the sample texture changes. The results are the following : -280mV/SCE (10.4) and (11.0) fiber textures (Fig. 5), -2mA (11.0) fiber texture (Fig. 6).

It can be pointed out that (10.4) orientation is never observed on the bulky layers. This orientation is probably a twinned orientation of the (11.0) one (Klassen-Neklyudova, 1964). During the growth of the wire, the walls of the pores can block the (11.0) expansion, then the (10.4) orientation takes over. On the bulky layers, several crystallites are observed at the surface (Fig. 2a). According to the orientation of this layer (10.1), the twin plane K_1 is perpendicular to the picture.

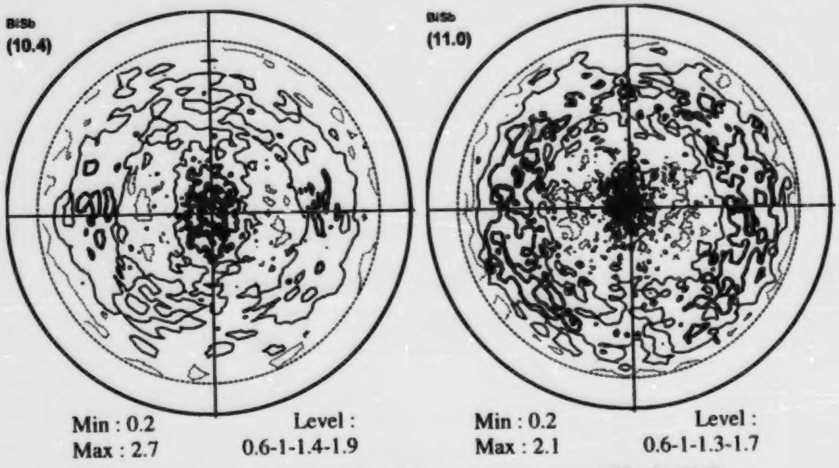

Fig. 5 : pole figures (10.4) and (11.0) of the nanowires at –280mV/SCE

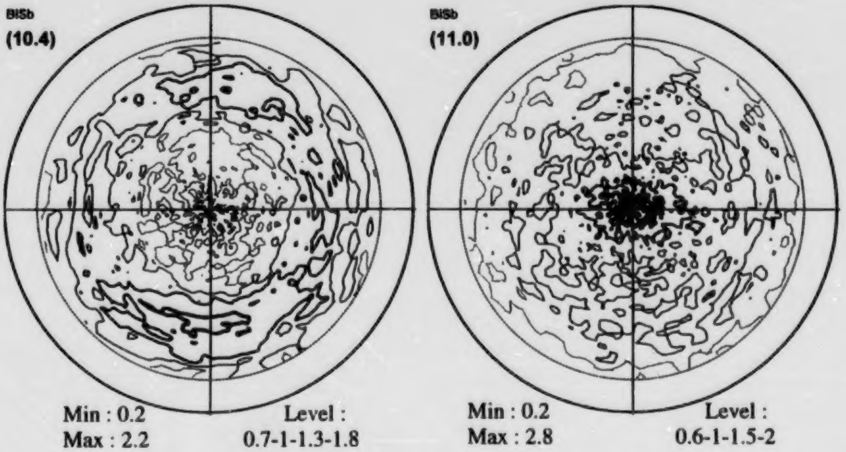

Fig. 6 : pole figures (10.4) and (11.0) of the nanowires at –2mA

4 Conclusion

Electrodeposition of bulky $Bi_{0.9}Sb_{0.1}$ alloys leads to fiber textures, the densest planes of the structure are parallel to the substrate. Nanowires also present fiber textures : (01.2) or (11.0) and (10.4) with (11.0). The simultaneity of the two last orientations can be explained by twinning which occurs during the wires growth.

5 References

Besse F., Boulanger C. and Lecuire J.M., to be published

Chaouni H., Bessieres J., Heizmann J.J. and Ech-Chaoui M. (1996) *ICOTOM 11*, (ed. by Z. Liang, L. Zuo & Y. Chu) International Academic Publishers, Vol. 2, pp. 1118-1125

Klassen-Neklyudova M.V. (1964), *Mechanical twinning of crystals*, Consultants bureau

Lenoir B., Cassart M., Michenaud J.P., Scherrer H. and Scherrer S. (1996), *J. Phys. Chem. Solids*, Vol. 57, N° 1, pp. 89-99

Oettel H. and Klimanek P. (1998), *Texture and anisotropy of polycrystals*, (ed. by R.A. Schwarzer) Trans tech publications, pp.55-59

Pearson W. B. (1964), *Handbook of lattice spacings and structures of metals and alloys*, Pergamon Press

Peudon-Besse F., Boulanger C. and Lecuire J.M. (1998), *journée ILM 98 - Matériaux Fonctionnels*, Nancy, France

Peudon F., Boulanger C. and Lecuire J.M. (1998), *journée SFC Lorraine*, Nancy, France

Smith G.E. and Wolfe R. (1962), *J. Appl. Phys.*, Vol. 33, pp. 841-846

Yim W. M. and Amith A. (1972), *Solid St. Elec.*, Vol. 15, pp. 1141-1165

BIAXIALLY ALIGNED MgO BUFFER LAYERS BY ION-BEAM ASSISTED PULSED LASER DEPOSITION

R. HÜHNE, C.-G. OERTEL and W. SKROTZKI

Institut für Kristallographie und Festkörperphysik, Technische Universität Dresden, Germany

B. HOLZAPFEL and L. SCHULTZ

Institut für Metallische Werkstoffe, Institut für Festkörper- und Werkstofforschung Dresden, Germany

Abstract

MgO thin films were deposited using pulsed laser deposition. Without an assisting ion beam strong fibre textures are observed changing from ⟨220⟩ at 25°C over ⟨200⟩ to ⟨111⟩ at 650°C. Using an ion beam under 55° with respect to the substrate normal and energies of more than 400 eV, biaxially textured films are grown with the ⟨200⟩ direction parallel to the ion beam and changing with temperature from ⟨111⟩ over ⟨220⟩ back to a tilted ⟨111⟩ parallel to the surface normal. Films with a biaxially aligned ⟨200⟩ texture and about 30° FWHM are grown by inclined substrate deposition.

Keywords: MgO, buffer layer, IBALD, biaxial texture

1 Introduction

Applications based on high temperature superconductors such as transmission cables and high field magnets require long wires with high critical currents. For Bi-based superconductors this can be achieved by the oxide-powder-in-tube process. Unfortunately this material is limited to low temperatures (<35 K) in magnetic fields due to its high anisotropy resulting in very low irreversibility fields at higher temperatures (Schmitt et al. 1991). YBCO thin films deposited on single crystals show high critical current densities (>10^6 A/cm^2 at 77 K) with a weak magnetic field dependence and a low j_c-anisotropy (Roas et al. 1990). However, YBCO films on polycrystalline metal substrates show high angle grain boundaries leading to a strong weak-link behaviour drastically reducing the critical current density in magnetic fields (Dimos et al. 1988).

Consequently, it is the main goal to grow biaxially oriented YBCO layers. Over the last few years several methods have been investigated: the preparation of biaxially oriented metal substrates (Goyal et al. 1996), the growth of biaxially textured buffer layers on polycrystalline substrates using ion-beam assisted deposition (IBAD, Iijima et al. 1992) and the deposition on inclined substrates (ISD, Hasegawa et al. 1996). IBAD has been successfully applied to the deposition of biaxially aligned YSZ (Iijima et al. 1997, Betz et al. 1997b, Wiesmann et al. 1995), Pr_6O_{11} (Betz et al. 1997a) and CeO_2 (Wiesmann et al. 1995) films. It is discussed, that the ion beam affects film growth and in this way texture formation in these materials. To obtain layers with a good in-plane texture, the films must be grown with a low deposition rate and to a thickness larger than 1 µm.

Wang et al. (1997) reported on the deposition of MgO using IBAD in an electron-beam evaporation system. They achieved an in-plane texture of 7° full-width at half maximum (FWMH) after deposition of only 10 nm thick films and assumed that the ion beam already influences the nucleation. It is the aim of the present work to study thoroughly the mechanisms of texture development in MgO buffer layers using ion-beam assisted pulsed laser deposition (IBALD).

2 Experimental

MgO buffer layers were deposited in a standard pulsed laser deposition (PLD) geometry using a KrF-excimer laser (λ = 248 nm) on amorphous substrates. Laser energy densities of 3.5 - 4 J/cm^2 and a laser pulse repetition rate of 5 Hz were used to ablate a single crystal MgO target. The distance between target and substrate was set to 55 mm. 50 nm Si_3N_4-coated as well as thermally oxidized Si-wafers were used as substrates. The films were grown to a thickness of about 600 nm. The deposition rate measured with a quartz monitor was about 2 - 3 Å/s.

An rf plasma source was used as an assisting ion beam source. A mixture of argon and oxygen (ratio 1:1) was used as ion source gas. The mean beam energy E was varied between 300 and 1000 eV with an ion flux density of about 70 - 100 µA/cm². The ion beam divergence was measured to less than 5° FWHM using a two-stage Faraday cup. The chamber pressure was $6 \cdot 10^{-4}$ mbar, due to 5 sccm Ar and 5 sccm O_2 gas flow feeding the ion source. The angle α between substrate normal and ion beam was 55°. To get another angle the substrate had to be tilted relative to the laser plume.

The preferred growth orientation was observed using X-ray Bragg-Brentano scans. The texture was determined using a four-circle X-ray goniometer. The pole figures were measured in normal Bragg-Brentano geometry and additionally under gracing incidence. The microstructure was investigated using a standard atomic force microscope (AFM) and a scanning electron microscope (SEM) Zeiss DSM 962.

3 Results and discussion

3.1. Pulsed laser deposition

A set of buffer layers was deposited at several substrate temperatures without using an ion beam. X-ray diffraction profiles show the change of preferred orientation from ⟨220⟩ at room temperature over ⟨200⟩ to ⟨111⟩ above 600°C (Fig. 1). The broad (220) peak at room temperature indicates that this film is stressed or nanocrystalline. Pole figure measurements show strong fibre textures in all cases. A rocking curve of the film showed the mosaic spread to be less than 5° FWHM. Films grown at room temperature are rough while at higher temperatures the surface is smooth with a route mean square (RMS) roughness of about 5 nm.

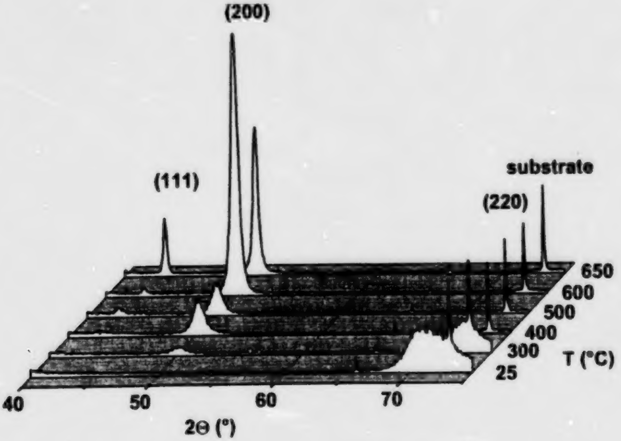

Fig. 1: X-ray diffraction profiles of PLD-MgO films showing the dependence of preferred orientation on substrate temperature

3.2. Ion-beam assisted pulsed laser deposition

According to Wang et al. (1997) the best texture develops when the ion beam is used only during the nucleation phase. Therefore MgO layers have been grown to a thickness d_i with and then up to a total thickness d of about 600 nm without ion beam. In this way, the best in-plane textures with about 20° FWHM were obtained by switching off the ion beam at d_i of about 200 nm. Further investigations are planned to understand the growth mechanism. The following results have been obtained for films grown in the described mode.

The influence of the deposition temperature on the texture of the MgO films is shown in Fig. 2. At room temperature a biaxial ⟨111⟩ texture is formed. Above 300°C the texture changes to a ⟨220⟩ biaxially aligned one. At 600°C there is again a tilted ⟨111⟩ texture. In all cases the ⟨200⟩ direction lies almost parallel to the assisting ion beam. In addition the influence of the ion beam energy on texture development was investigated at 400°C. For energies up to 400 eV the textures are not pronounced. Above 400 eV the described biaxial ⟨220⟩ textures are observed. There is no significant texture dependence on the type of substrate used.

Microstructural studies show smooth surfaces with grain sizes from 50 to 200 nm and a RMS roughness of about 10 nm (Fig. 3a).

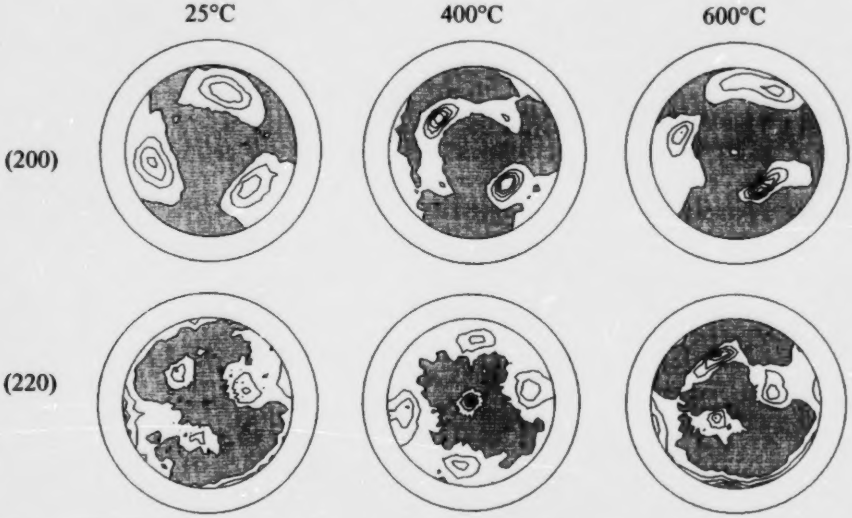

Fig. 2: Influence of the deposition temperature on the texture of MgO films deposited by IBALD (E = 600 eV, d_i = 200 nm, d = 600 nm, α = 55°)

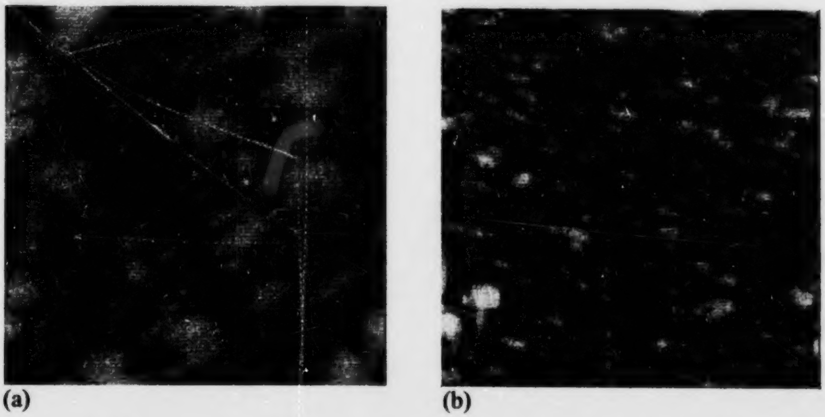
(a) (b)

Fig. 3: AFM micrographs showing the surface topography of MgO films deposited by
(a) IBALD: 1 µm x 1 µm, 400°C, α = 45°
(b) ISD: 10 µm x 10 µm, 600°C, ϕ = 45°

3.3. Inclined substrate deposition

Another possible method of obtaining in-plane textured films is by tilting the substrate relative to the laser plume. Fig. 4 shows the dependence of film texture on the inclination angle ϕ. In-plane textured ⟨200⟩ films grow by using an angle larger than 40° in a temperature range from 400 to 650°C. The best results with about 30° FWHM in-plane texture are obtained at 600°C with a tilt angle of 45°.

Microstructural investigations with AFM and SEM show surfaces with a RMS roughness of about 45 nm (Fig. 3b). The grains are aligned in the direction of the laser plume. This indicates that simultaneously with the influence of the ions in the laser plasma a preferred growth mode may play a role in texture development as has been proposed by Bauer et al. (1998).

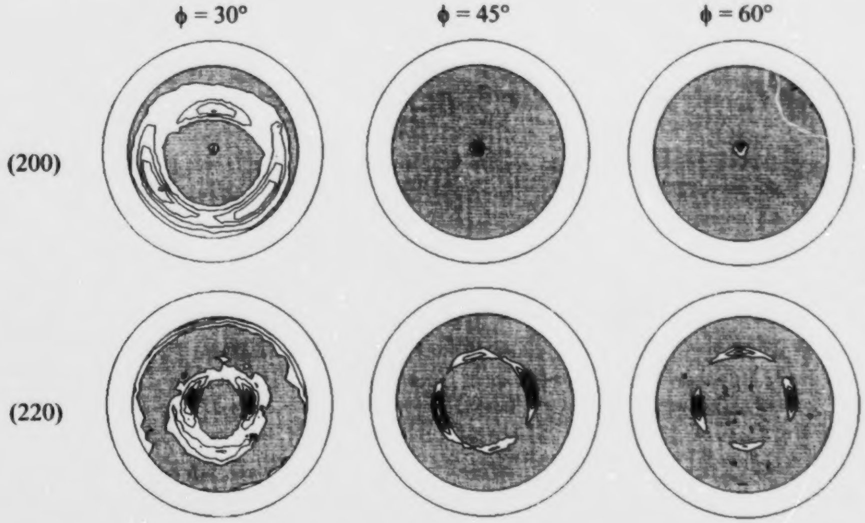

Fig. 4: Texture dependence on the inclination angle ϕ for MgO films deposited by ISD (T = 600°C)

4 Acknowledgements

This work has been supported by the Deutsche Forschungsgemeinschaft (DFG) through the Graduiertenkolleg "Structure and Correlation Effects in Solids".

5 References

Bauer, M., Schwachulla, J., Egly, J., Berberich, P. and Kinder, H. (1998) Biaxially aligned MgO buffer layers using electron beam evaporation on inclined substrates. *Advances in Superconductivity X.*, eds. K. Osamura and I. Hirabayashi, Springer, Tokyo, pp. 979ff

Betz, V., Holzapfel, B., Raouser, D. and Schultz, L. (1997a) In-plane aligned Pr_6O_{11} buffer layers by ion-beam assisted pulsed laser deposition on metal substrates. *Appl. Phys. Lett.*, Vol. 71, No. 20, pp. 2952-2954

Betz, V., Holzapfel, B., Sipos, G., Schmidt, W., Mattern, N. and Schultz, L. (1997b) Growth mechanisms for in-plane aligned YSZ buffer layers deposited on polycrystalline metallic substrates by ion-beam assisted laser deposition. *Applied Superconductivity*, IOP Conf. Series No 158, IOP Publishing, Bristol, pp. 1081-1084

Dimos, D., Chaudhari, P., Mannhart, J. and LeGoues, F.K. (1988) Orientation dependence of grain-boundary critical currents in $YBa_2Cu_3O_{7-\delta}$ bicrystals. *Phys. Rev. Lett.* Vol. 61, No. 2, pp. 219-222

Goyal, A., Norton, D. P., Budai, J. D., Paranthaman, M., Specht, E. D., Kroeger, D. M., Christen, D. K., He, Q., Saffian, B., List, F. A., Lee, D. F., Martin, P. M., Klabunde, C. E., Hartfield, E. and Sikka, V. K. (1996) High critical current density superconducting tapes by epitaxial deposition of $YBa_2Cu_3O_x$ thick films on biaxially textured metals. *Appl. Phys. Lett.*, Vol. 69, pp. 1795-1797

Hasegawa, K., Yoshida, N., Fujino, K., Mukai, H., Hayashi, K., Sato, K., Honjo, S., Sato, Y., Ohkuma,T., Ishij, H., Iwata, Y. and Hara, T. (1996) In-plane aligned YBCO thin film tape fabricated by pulsed laser deposition. *Proc. 9th Int. Symp. on Supercond.*, Sapporo

Iijima, Y., Tanabe, N., Kohno, O. and Ikeno, Y. (1992) In-plane aligned $YBa_2Cu_3O_{7-x}$ thin films deposited on polycrystalline metallic substrates. *Appl. Phys. Lett.*, Vol. 60, No. 6, pp. 769-771

Iijima, Y., Hosaka, M., Tanabe, N., Sadakata, N., Saitoh, T., Kohno, O. and Takeda, K. (1997) Biaxial alignement control of $YBa_2Cu_3O_{7-x}$ films on random Ni-based alloy with textured yttrium stabilized-zirconia films formed by ion-beam-assisted deposition. *J. Mater. Res.* Vol. 12, No. 11, pp. 2913-2923

Roas, B., Schultz, L. and Saemann-Ischenko, G. (1990) Anisotropy of the critical current density in epitaxial $YBa_2Cu_3O_x$ films. *Phys. Rev. Lett.* Vol. 64, No. 4, pp. 479-482

Schmitt, P., Kummeth, P., Schultz, L. and Saemann-Ischenko, G. (1991) Two-dimensional behavior and critical-current anisotropy in epitaxial $Bi_2Sr_2CaCu_2O_{8+x}$ thin films. *Phys. Rev. Lett.* Vol. 67, No. 2, pp. 267-270

Wang, C.P., Do, K.B., Beasley, M.R., Geballe, T.H. and Hammond, R.H. (1997) Deposition of in-plane textured MgO on amorphous Si_3N_4 substrates by ion-beam-assisted deposition and comparisons with ion-beam-assisted deposited yttria-stabilized-zirconia. *Appl. Phys. Lett.*, Vol. 71, pp. 2955-2957

Wiesmann, J., Hoffmann, J., Usoskin, A., Garcìa-Moreno, F., Heinemann, K. and Freyhardt, H.C. (1995) Biaxially textured YSZ and CeO_2 buffer layers on technical substrates for large-current HTS-applications. *Applied Superconductivity*, IOP Conf. Series No 148, IOP Publishing, Bristol, pp. 503ff

QUANTITATIVE TEXTURE OF FERROELECTRIC MODIFIED LEAD TITANATE THIN FILMS

J. RICOTE[†], D. CHATEIGNER and G. RIPAULT
Laboratoire de Physique de l'Etat Condensé, Université du Maine, Le Mans, France.
[†] Present address: Instituto de Ciencia de Materiales de Madrid, CSIC, Madrid, Spain
L. PARDO, M. ALGUERÓ[‡], J. MENDIOLA and M.L. CALZADA
Instituto de Ciencia de Materiales de Madrid, Consejo Superior de Investigaciones Científicas, Madrid, Spain
[‡] Present address: Dept. of Materials, Queen Mary and Westfield College, University of London, London, United Kingdom

Abstract

The presence of any preferred crystallographic orientation in ferroelectric thin films is a determinant factor of their behaviour. For most applications a high degree of orientation of the crystals along the polar axis is advantageous. At present the mechanisms which lead to highly textured ferroelectric thin films are under discussion. Regardless of their interest, complete quantitative texture studies, measuring diffraction pole figures with a goniometer and calculating the orientation distribution functions, have not been carried out extensively on these materials. Results show that mainly fibre textures are developed, with fibre axes perpendicular to the film plane. The texture strength can be correlated to the preparation conditions and the physical properties of the films. This information can be used to optimise the preparation methods of the films in order to obtain improved materials for specific applications.

Keywords: Ferroelectric materials, quantitative texture, thin films

1 Introduction

Thin films with a high degree of orientation are often required, overall in the case of materials like ferroelectrics. The orientation of the crystals along the polar axis should result in an improvement of the ferropiezoelectric behaviour, like for example, an increase of the net polarisation values. Therefore, the factors which lead to the production of highly textured ferroelectric thin films are under study. Regardless of the attention given to this subject, in the literature there are not many quantitative studies of the texture of ferroelectric materials, obtaining diffraction pole figures and calculating from them orientation distributions (Chateigner et al. 1998).

Among the ferroelectrics, the modified lead titanate compositions are well-known for their pyroelectric and piezoelectric properties, which make them interesting for several applications, like Surface Acoustic Wave (SAW) devices, infrared detectors and microactuators. In this work several films have been prepared, varying the processing parameters and the nature of the substrates, in order to study their influence in the resulting textures and in the final physical properties. This information will allow the optimisation of the preparation method to obtain thin films with improved properties for their use in devices.

2 Materials and experimental procedure

Thin films of two compositions are studied in this work: La modified lead titanate (PTL), $Pb_{0.88}La_{0.08}TiO_3$ with 20% excess PbO, and Ca modified (PTC), $Pb_{0.76}Ca_{0.24}TiO_3$ with 10% excess PbO. Films were obtained by spin-coating deposition of sol-gel processed solutions (Calzada et al. 1998; Sirera and Calzada 1995) and then crystallised either by rapid thermal processing, RTP, (approximate heating rate 30°C/s), direct insertion in a pre-heated furnace (>500°C/min) or by a conventional process (10°C/min). Substrates are $Pt/TiO_2/Si(100)$ for all samples, except for PTC-M, which has been deposited on Pt/MgO(100). Processing details are summarised in Table 1.

Table 1: Processing conditions of the films.

Sample	Composition	Substrate	Number of. layers	Annealing conditions Heat. rate	Annealing conditions Temp/time
PTL-1	PTL	$Pt/TiO_2/Si$ (100)	4	Conv.	650°C/12 min
PTL-2	PTL	$Pt/TiO_2/Si$ (100)	1	>500°C/min	650°C/12 min
PTL-3	PTL	$Pt/TiO_2/Si$ (100)	4	>500°C/min	650°C/12 min
PTC-S	PTC	$Pt/TiO_2/Si$ (100)	1	RTP	650°C/50 s
PTC-M	PTC	Pt/MgO (100)	2	RTP	700°C/50 s

Experimental pole figures were obtained using a Huber four-circle goniometer mounted on an INEL X-ray generator (Cu $K\overline{\alpha}$ wavelength), in the asymmetric reflection geometry. The INEL CPS-120 position sensitive detector was used to acquire a complete diffraction pattern at each position of the sample. A 5°x5° grid measurement was carried out with an incidence angle of 11°. The integrated intensities were refined and corrected using the INEL packages. The Orientation Distribution (OD) refinement was carried out following the WIMV method (Matthies and Vinel 1982). The calculation to obtain and manipulate the ODF have been carried out with the Berkeley Texture Package (BEARTEX) (Wenk et al. 1998).

The OD of the thin films have been calculated from the following experimental pole figures, taking into account the overlapped reflections: {001} pole figure contains (001) and (100); {101} contains (101) and (110); {112} contains (112) and (211); {102} contains (102), (201) and (210). For the deconvolution we assume that the relative intensities of the contributing peaks is the same as in pure lead titanate, which crystallises in the tetragonal system. In the case of the Pt layer we use the {111}, {002}, {400} and {311} experimental pole figures for the calculations, which can be affected of larger errors due to the effects of absorption occurred in the layer above it which we did not correct for, and to small contributions from reflections of the thin film.

3 Texture results

The results of the OD calculations are summarised in Table 2 and 3. The low values of the reliability factors RP0 and RP1 show the good quality of the refinement. This supports the validity of the initial assumptions of the calculations.

Table 2: Results of the orientation distribution refinement for the thin films.

Sample	Components of the texture	Texture index (m.r.d.^{2})	RP0 (%)	RP1 (%)
PTL-1	very weak <110>,<101>	1.3	14	10
PTL-2	<001>,<100>,<221>	10.5	36	16
PTL-3	<001>,<100>,<221>	4.6	18	12
PTC-S	Very weak <001>,<100>,<110>,<101>	2.4	23	12
PTC-M	<001>,<100>,<111>	5.2	22	10

Table 3: Results of the orientation distribution refinement for the Pt layer.

Sample	Component of the Pt layer texture	Texture index (m.r.d.^{2})	RP0 (%)	RP1 (%)
PTL-1	<111>	7.3	34	18
PTL-2	<111>	23.9	46	21
PTL-3	<111>	10.6	33	16
PTC-S	<111>	13.5	26	20
PTC-M	<111>	4.4	48	28

In the case of the results for the Pt layers, we have to take into account that they are affected by absorption of the film layer which is on top of them. Part of the difference found between PTL-2 and PTL-3 could be the result of the different number of film layers deposited: 1 layer for PTL-2 (130 nm) and 4 for PTL-3 (500 nm). We can assume that the Pt layer has a similar texture for all the PTL films analysed.

Both the thin films and the Pt layers show fibre textures with the fibre axes perpendicular to the film surface. Figure 1 shows interesting recalculated single pole figures as {001}, {100} and {111} for the PTL thin films (Figure 1). It is very hard to dissociate the {001} and {100} components, whose reflections appear overlapped, because of the pseudo symmetry of the crystals. But the good reproducibility of the OD refinement allows us to rely on this analysis. The less textured material PTL-1, as its low texture index indicates, shows in all the figures values close to 1 m.r.d. The other two films present maximum values of the distribution density in the centre of the {001} and {100} pole figures, which corresponds to a concentration of crystals with <001> and <100> directions perpendicular to the film plane (called $<001>_\perp$ and $<100>_\perp$ respectively).

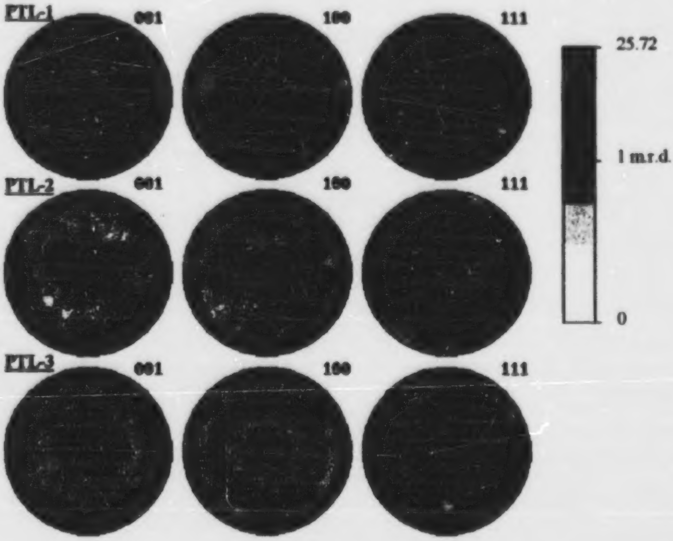

Fig. 1: {001}, {100} and {111} recalculated pole figures of PTL thin films. Equal area projection and logarithmic density scale.

Figure 2 shows the inverse pole figures for the fibre direction. Again, the less textured materials do not show any strong preferential orientation, although some weak tendencies can be observed when analysed in detail (Table II). In PTL-2 and PTL-3, apart from the <001> and $<100>_\perp$ mixed orientation, a third component appears as $<221>_\perp$, although very weak in comparison to the other. PTC-M shows as well a weak third $<111>_\perp$ component. Comparing the density levels of the $<001>_\perp$ and $<100>_\perp$ components we can say that, while for PTC-M it seems that there is a similar contribution, PTL-2 and PTL-3 have a stronger presence of crystals oriented $<100>_{\perp}$ than $<001>_{\perp}$.

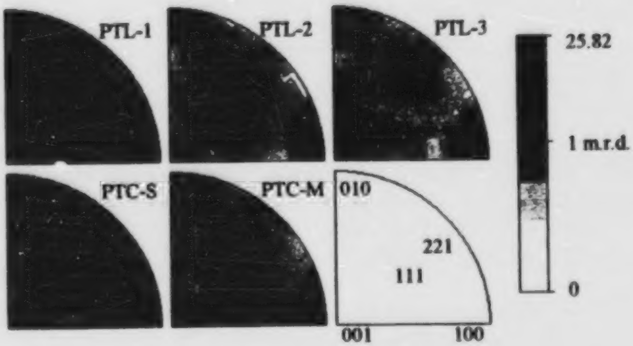

Fig. 2: Inverse pole figures for the normal direction. Equal area projection and linear density scale.

4 Discussion

The films analysed in this work present fibre textures, with fibre axes perpendicular to the film plane, like the Pt layer, on top of which they have been grown. This fact shows the large influence of the texture of the substrate on the final texture of the films.

The study reveals that the use of a different substrate, like Pt/MgO in PTC thin films, produces more textured films, and with a higher contribution of the desired $<001>_{\perp}$. The mechanisms which lead to these variations are still not clear, but it seems that the combination of several factors like the lattice matching between the films and the substrate, the texture strength of the substrate or the appearance of interlayers, among others, affect the final orientation of the film and it is under study.

Apart from the substrate, other parameters should be considered in the study of the texture of thin films. The use of a high heating rate (>500°C/min) seems to enhance the appearance of preferential orientation in PTL thin films. The film prepared with the conventional process, PTL-1, does not show any significant texture. During slow heating the formation of the ferroelectric phase is possible over a wide range of temperatures and times, which means different conditions of crystallisation, if we take into account the formation of metastable intermetallic phases observed in similar compositions (Chen and Chen 1994). Therefore, several variants of texture can be nucleated, resulting in a random film.

The differences in the texture strength found between PTL-2 and PTL-3, crystallised under the same conditions, but with a different number of layers, could be the result of a progressive loss of the texture strength with the distance to the substrate. The crystallisation habit, whose origin seems to be in the Pt layer, can relax progressively in the outer layers, which are grown on other film layers. This situation is more probable in the case of heterogeneous nucleation, i.e., when crystals nucleate in sites throughout the thickness of the film.

The preferential crystallographic orientation of the films analysed here is a mixture of $<100>_\perp$ and the desired $<001>_\perp$ directions. The latter corresponds to the polar axis, and therefore, is the responsible for the major contribution to the net polarisation in the films, as the electric field is applied perpendicular to the film surface. However, $<001>_\perp$ is not the main component of the texture, which is $<100>_\perp$. Crystals with this orientation do not contribute to the net polarisation even with the application of an electric field. This leads to a less important increase of the values of polarisation than expected for a textured film. When the ferroelectric behaviour of a film with a random orientation is compared to one with the texture of PTL-2 or PTL-3 (Algueró 1998), we observe that while in the random the polarisation reached with a high electric field is lost appreciably on removal of the field, in the textured ones this polarisation is clearly retained. This can be explained taking into account that for the textured films the orientation of dipoles due to the application of the electric field is smaller, as they are already preferentially oriented along the direction of the field.

5 Acknowledgements

First author gratefully acknowledges the financial support provided by the regional government of Pays de Loire and the French Education Ministry during his stay at Le Mans university. This work has been partially supported by the project MAT98-1068 of the Spanish CICYT, COPERNICUS CIPA-CT94-0236 and declared of technological interest by the EU COST514 action on ferroelectric ceramic thin films.

6 References

Algueró, M. (1998) *Relaciones entre la microestructura y las propiedades de láminas delgadas ferroeléctricas de $(Pb,La)TiO_3$*, Doctoral thesis, Universidad Autónoma de Madrid, Madrid, Spain.

Calzada, M.L., Algueró M. and Pardo L. (1998), *J. Sol-Gel Science and Technology*, Vol. 13, pp. 837-841.

Chateigner, D., Wenk, H.R., Patel, A., Todd, M. and Barber, D.J. (1998), *Integrated Ferroelectrics*, Vol. 19, pp. 121-140.

Chen , S:Y. and Chen, J.W. (1994), *J. Am. Ceram. Soc.*, Vol. 77, pp 2337-2344.

Matthies, S and Vinel, G.W., (1982) *Phys. Stat. Sol. B.*, Vol. 112, pp K111.

Sirera, R. and Calzada, M.L. (1995) *Mat. Res. Bull.*, Vol. 30, No. 1, pp. 11-18.

Wenk, H. R., Matthies, S., Donovan, J., and Chateigner, D (1998), *J. Appl. Cryst.*, Vol. 31, pp 262.

RESIDUAL STRESS DETERMINATION IN HIGHLY TEXTURED TITANIUM NITRIDE COATINGS

A. SAERENS[1], P. VAN HOUTTE[1] and C. QUAEYHAEGENS[2]

[1]Department of Metallurgy and Materials Engineering, Katholieke Universiteit Leuven, Belgium

[2]Institute for Materials Research, Limburgs Universitair Centrum, Belgium

Abstract

The influence of the deposition parameters and the coating thickness on the crystallographic texture and the residual stress state in TiN coatings is studied. TiN coatings of different thicknesses are deposited on tool steel substrates by Physical Vapour Deposition using two different deposition conditions, i.e. a standard deposition and a cold deposition. X-ray texture measurements reveal that the deposition conditions have a large influence on the texture. Residual stresses are determined using X-ray and synchrotron radiation. Three different approaches are used: (1) the classical d-sin$^2\psi$ method; (2) the LIBAD method and (3) the crystallite group method. In all coatings compressive stresses of the order of -4 to -8 GPa are found. Stresses are about twice as high when the cold deposition is used. The stresses only exhibit a weak dependence on coating thickness. The results also show that there is a strong influence of texture on residual stresses.

Keywords: residual stress, coatings, texture, X-ray diffraction, synchrotron radiation

1 Introduction

Titanium Nitride (TiN) coatings are of high technological importance because of their excellent resistance to wear and corrosion and their high hardness. Large residual stresses are present in these coatings. Those stresses influence the wear resistance, fatigue behaviour and the adherence of the layers to the substrate. The stresses and typical texture associated with these types of coatings strongly depend on the processing conditions and the coating thickness.

The most widespread method to measure residual stresses is X-ray diffraction. The stress tensor in a surface layer is determined in a non-destructive way. Several approaches to measure stresses in coatings will be compared.

2 Experimental

2.1 Deposition of TiN coatings

TiN coatings with thicknesses ranging from 0.9 μm to 5.5 μm are deposited on an AISI H13 steel substrate by Physical Vapour Deposition in a Balzers BAK 640 triode ion plating installation. Two different deposition procedures have been applied. A first set of samples was subjected to a *standard deposition*, in which temperatures up to 4500°C are reached. The second set was subjected to a *'cold' deposition*. This 'cold' deposition differs from the standard deposition by a lower ionisation current, a lower substrate voltage, a lower Nitrogen flow and a temperature that does not exceed 2000°C.

Texture is measured using X-ray diffraction. The coatings deposited under standard conditions all exhibit a strong (111) fibre texture. The cold deposition leads to a different and less pronounced texture. In the case of a 0.9 μm thick TiN coating the texture consists of a weak (111) fibre and a (211) fibre and in the case of a 5.5 μm coating the main texture components are a (111) fibre and a (200) fibre. The studied samples and the results of the texture measurements are summarised in table 1. As a measure for the sharpness of the texture the maxima of the poles in the inverse pole figure are used.

Table 1: Texture analysis of the studied TiN coatings.

Coating thickness (μm)	Main texture component	Texture strength
Standard deposition		
1.6	(111) fibre	6.0
3.8	(111) fibre	19.5
4.8	(111) fibre	20.5
4.9	(111) fibre	16.8
Cold deposition		
0.9	(111) + (211) fibre	1.6 (111) / 2.6 (211)
5.5	(111) + (200) fibre	4.6 (111) / 3.8 (200)

2.2 Residual stress determination

When stresses are present in a material, they cause an elastic deformation of the crystal lattice. As a result the lattice spacing of (hkl) planes is different from the spacing d_0 in a stress free material. X-ray stress measurements determine the lattice spacing d_{hkl} and compare it to the d_0 of the material. Several approaches can be used to determine the strain tensor.

2.2.1 d-$\sin^2\psi$ method

This is the classical method in x-ray stress analysis and it has been well established for bulk materials, which do not exhibit a strong texture. (Noyan and Cohen 1987)

The principle of this method is shown in figure 1. The diffraction peak of one particular high-angle lattice plane (hkl) is scanned for different orientations of the sample. The orientation of the sample is characterised by the ψ–angle, which is the angle between the normal to the surface and the diffraction vector $\bar{Q}$. The latter is defined as the normal to the diffracting lattice planes.

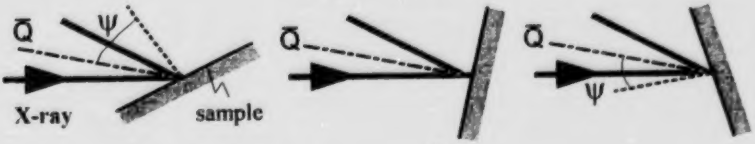

Fig. 1: Principle of the d-sin²ψ method.

The strains are linked to the stresses by equation (1) for the case of an equibiaxial stress σ in the plane of the coating (Noyan and Cohen 1987)

$$\varepsilon(0,\psi)=\frac{d_{hkl}(0,\psi)-d_0}{d_0}=\frac{1}{2}s_2^{hkl}.\sin^2\psi.\sigma+2s_1^{hkl}.\sigma \qquad (1)$$

where $d_{hkl}(0,\psi)$ are the experimental lattice plane distances, d_0 is the stress free lattice parameter and $1/2s_2^{hkl}$ and s_1^{hkl} are the X-ray elastic constants. From equation (1) it follows that the stress can be derived from the slope of the d-sin²ψ curve.

This method has several disadvantages when applying it to thin coatings: the penetration depth varies during the measurement, the X-ray beam is not kept totally within the coating and the diffracted intensity from the coating may be rather low.

2.2.2 LIBAD method (Low Incidence Beam Angle Diffraction)

In order to increase the signal from the coating the LIBAD method was developed. (De Buyser 1993, Van Acker et al. 1994) A constant low incident beam angle is used, which leads to a constant and low penetration depth of the X-ray beam. For this fixed position of the sample, the detector is moved along the goniometer circle and registers the diffraction profiles of the different (hkl) lattice planes. The principle of this method is shown in figure 2.

2.2.3 Crystallite group method

A third approach consists of idealising the texture as a set of ideal orientations. Dölle and Hauk (1979) first introduced this method. Coatings are often characterised by a strong fibre texture. This can make the measurement more difficult because diffraction peaks are only visible at few positions. In the crystallite group method the stress is measured for each set of ideal orientations separately.

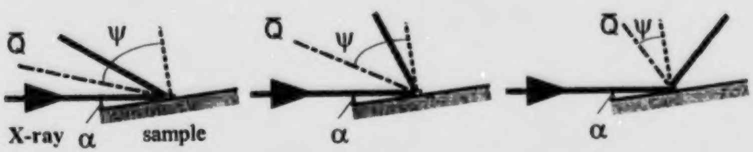

Fig. 2: Principle of the LIBAD method.

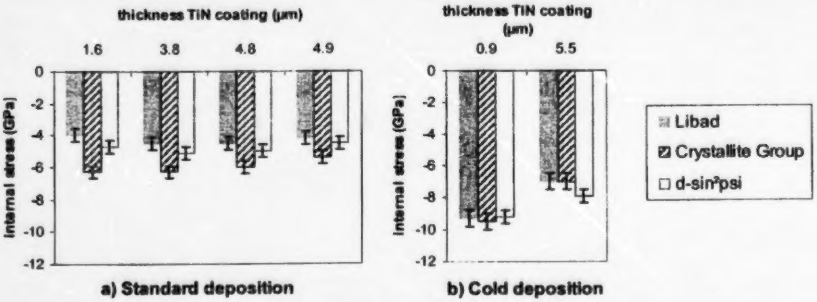

Fig. 3: Residual stresses in TiN coatings. Comparison of different measuring approaches.

3 Results

3.1 X-ray stress measurements

The residual stress measurements were performed on a Siemens D500 goniometer using Cu-Kα radiation. On all coatings listed in table 1 a d-sin$^2\psi$ measurement was performed on the (422) lattice planes, as well as a measurement using the LIBAD and the crystallite group method. Figure 3 shows the internal stress values obtained with the different methods as a function of coating thickness for both deposition conditions.

3.2 Synchrotron experiments

In order to study the influence of the preferential orientation on the stress value, some additional stress measurements were performed using synchrotron radiation at Daresbury Synchrotron Radiation Laboratory, UK. Due to the strong preferential orientation of the standard deposited coatings the intensities of the diffraction peaks are very weak in directions which deviate from the main texture component. Since the intensity is orders of magnitude higher when using synchrotron radiation, orientations deviating from the (111) fibre orientation can also be measured.

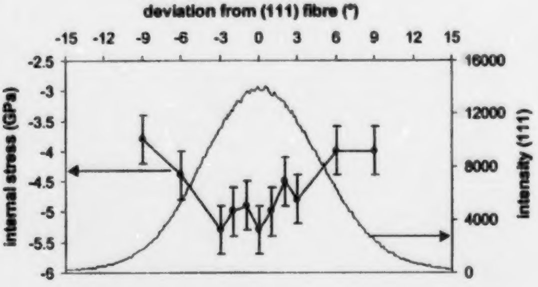

Fig. 4: Residual stresses in a 4.9 µm thick TiN coating as a function of the deviation from the (111) fibre axis.

The stresses are measured for different sets of grains. Firstly, grains oriented according to the (111) fibre are measured. A systematic deviation from this (111) orientation is studied, which results in the graph presented in figure 4.

4. Discussion

The results in figure 3 show that the deposition conditions have a large influence on the residual stress state. In all coatings stresses are highly compressive, but the stresses in standard deposited coatings are 1.5 to 2 times lower than those observed in 'cold' deposited coatings. In case of a standard deposition, stresses do not seem to be dependent on the coating thickness, whereas for the 'cold' deposition the higher stresses are observed in the thinner coating.

When the texture is rather weak and consists of more than one component, as it is the case for the 'cold' deposition, the stress values resulting from the different measuring approaches are approximately equal. In the case of a strong (111) fibre texture, there seems to be a translation of the different approaches along the stress axis. The stress values obtained with the $\sin^2\psi$ method are about 0.5 GPa higher than those obtained with the LIBAD method and about 1.5 GPa lower than those obtained with the crystallite group method. In each approach the X-ray information is generated in a different part of the coating. With the LIBAD method the X-ray information is generated in the upper part of the coating because of the low and fixed incident beam angle. During the d-$\sin^2\psi$ method and the crystallite group method the incident beam angles vary and information from the whole coating is obtained. If the stress profile across the coating is not homogeneous, different stress values are expected for the different approaches. The presence of a stress gradient across the thickness was checked using the LIBAD method under different incident beam angles, but figure 5 gives no evidence of a stress gradient being responsible for the difference in stress values.

Another distinction between the measurement approaches is the sets of grains that are measured. When the crystallite group method is used, only grains with an orientation according to (111) fibre are measured, whereas the d-$\sin^2\psi$ method and the

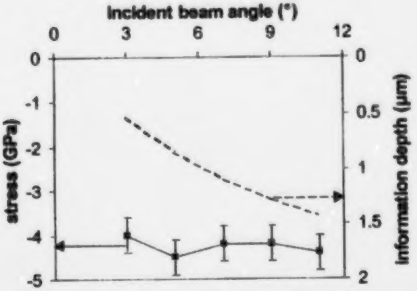

Fig. 5: Residual stresses in a 4.9 µm thick TiN coating for different information depths.

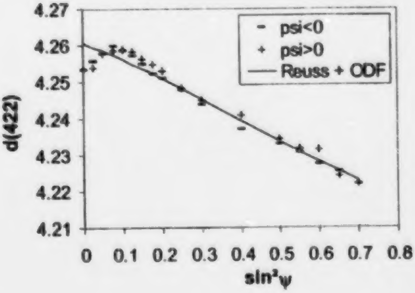

Fig. 6: Non-linear d-$\sin^2\psi$ curve of a 4.9 µm thick TiN coating.

LIBAD method measure 'at random', i.e. (111)-oriented grains as well as differently oriented grains. Figure 4 clearly indicates that stresses depend on grain orientation. The highest stresses are observed in the grains oriented according to the (111) fibre component, whereas a decrease of 30% in stress value is observed in grains deviating from this main orientation. This explains why a higher stress value is measured using the crystallite group method.

For all coatings non-linear d-$\sin^2\psi$ curves are observed. Non-linearities in d-$\sin^2\psi$ curves can be attributed to the presence of a strong texture, stress gradients, shear stresses or plastic deformation (Noyan and Cohen 1987, Hauk 1997). Texture can be taken into account by calculating the appropriate diffraction elastic constants from the orientation distribution function (Van Houtte and De Buyser 1993). As shown in figure 6 taking the texture into consideration cannot account for the observed non-linearities. As explained before, the non-linearities can't be caused by stress gradients. This leads to the conclusion that the shape of the curves cannot be explained by means of linear elastic theories.

5 Conclusions

The residual stress state and the crystallographic texture in TiN coatings strongly depend on the deposition conditions. Two types of deposition processes were studied. X-ray stress measurements were performed using three different approaches. The 'cold' deposition leads to the weakest texture and the highest compressive stresses, with no significant difference between the measurement approaches. The standard deposition gives rise to a strong (111) fibre texture in the coatings. Under these conditions stresses depend on the measurement technique. The crystallite group method leads to the highest stresses. A systematic study of the relation between stresses and grain orientation reveals that the (111) oriented grains sustain stresses which are about 30% more compressive than grains which deviate about 10° from this ideal (111) orientation.

Acknowledgements

Financial support was provided by the Federal Government of Belgium (DWTC) through the contracts NO/01/005 and IUAP P4/33; as well as by the Government of Flanders through the contract FWO G.0414.98.

References

De Buyser, L. (1993) Een nieuwe methode voor de meting van restspanningen in getextureerde deklagen, Ph.D. thesis, K.U.Leuven.

Dölle, H., Hauk, V. (1979) Röntgenographische Ermittlung von Eigenspannungen in texturierten Werkstoffen, Z. Metallkunde, Vol. 70, pp. 682-685.

Hauk, V. (1997) Structural and residual stress analysis by nondestructive methods, Elsevier Science B.V., The Netherlands.

Noyan, I.C., Cohen, J.B. (1987) Residual stress – Measurement by diffraction and interpretation, Springer-Verlag, New York.

Van Acker, K., De Buyser, L., Celis, J.P., Van Houtte, P. (1994) Characterization of thin nickel electrocoatings by the low-incident-beam-angle diffraction method. J. Appl. Cryst., Vol. 27, pp. 56-66.

Van Houtte, P., De Buyser, L. (1993) The influence of crystallographic texture on diffraction measurements of residual stress. Acta metall. mater., Vol. 41, No. 2. pp. 323-336.

INTERNAL STRESS IN TEXTURED MOLYBDENUM THIN FILMS

C.S.SHIN, J.-H.CHO and K.H. OH
School of Materials Science and Engineering, Seoul National University, Shinrim Dong, 151-742 Kwanak-Ku, Seoul, Korea

Abstract

Internal stress in sputter-deposited molybdenum thin films was studied by X-ray diffractometry with position sensitive detector(PSD) and multi-channel analyzer (MCA). The average strain tensor of the film was determined from $\sin^2\psi$ method. Measuring time could be reduced significantly using PSD and MCA. Instrumental errors due to beam optics and misalignment were corrected with a random molybdenum specimen. The internal stress measured by X-ray diffraction methods was compared with the biaxial stress evaluated by substrate curvature method. To correct defocalization in thin film texture analysis, pole figures were measured with PSD and MCA. Nonlinear profile fitting was performed to obtain integrated intensities as pole figure values and then orientation distribution function(ODF) was calculated.

Keywords: Internal stress, Position sensitive detector, Thin film, X-ray diffraction

1 Introduction

Internal stress in thin films is induced by the difference in thermal expansion between substrate and thin film and the mismatch between the lattices of film and substrate. Internal stress is usually divided into thermal stresses and intrinsic stresses. The reliability and stability of thin films are known to depend on these stresses. The texture of thin films also has a strong influence on the properties of thin film applications. X-ray diffraction(XRD) and profilometry are often used to measure internal stresses of thin films. Average strain can be evaluated by $\sin^2\psi$ method from XRD data(Noyan and Cohen 1991). The curvature of the substrate measured by profilometry gives biaxial stress using the well known Stoney's equation(Tu et al.

1992). The usage of PSD in diffraction measurements can reduce measuring time by simultaneous detection of some part of the spectrum. During pole figure measurement of thin film, it is difficult to correct defocalization, because an untextured thin compounds is practically impossible to obtain. Wenk et al proposed an analytical correction formula using the experimental bulk defocusing curves (Chateigner et al. 1994).Using integrated intensity by PSD and subsequent profile fitting, defocalization corrections in thin film texture analysis is not required(Wcislak et al. 1993).

The purpose of this study is to evaluate average internal stresses and textures of molybdenum thin films by X-ray diffraction with PSD. The results were compared with biaxial stresses of the same samples evaluated by the profilometry method and textures measured by scintillation counter.

2 Experimental procedures

Molybdenum films were sputtered onto 200μm thickness <100> silicon substrates. Before deposition, silicon was cleaned with chemical solvents. The deposition process was carried out at 10sccm argon and with a growth rate of about 7.7nm/min. Two samples were deposited with thickness of 100nm and 200nm.

Curvature measurements were conducted with Tencor P1 Surface Profiler, and XRD stress measurements and texture analyses were done with Seifert D3000 PTS X-ray diffractometer. The X-ray diffractometer contains a detection block including PSD together with the required electronics and gas controlling unit. The PSD used in this diffraction assembly was produced by M-Braun Co. The horizontal width of the radiation entrance window is 50mm, which corresponds to the stationary detector viewing angle of 6° on the 2θ circle. MCA with 4096 channels was used to get the measured data. From the three (110), (200), (211) incomplete pole figures with integrated intensity values, ODF was calculated by WIMV method(Matthies and Vinel 1982).

3 Results and discussion

3.1 Texture analysis

The texture measurements by PSD gives peak profiles at the measured position $\{\varphi,\psi\}$ in the pole figures. The peak profile was nonlinearly fitted by a model function $I_{mod}(2\theta)$:

$$I_{mod}(2\theta) = Bg + b(2\theta) \tag{1}$$

where Bg is background level and $b(2\theta)$ is a profile function. Gaussian function $b^{G}(2\theta)$, Lorentzian function $b^{L}(2\theta)$ and Pseudo-Voigt function $b^{PV}(2\theta)$ were defined as Eq. (2), where I_0 is the peak maximum intensity, $x=|2\theta-2\theta_{hkl}|$ is the local distance from Bragg-angle and σ is the full width at half maximum.

$$
\begin{aligned}
b^{G}(x) &= I_0 \cdot \exp(-k_G x^2) & k_G &= \frac{\ln 2}{(\sigma/2)^2} \\
b^{L}(x) &= \frac{I_0}{1+k_L x^2} & k_L &= \frac{1}{(\sigma/2)^2} \\
b^{PV}(x) &= m \cdot b^{G}(x) + (1-m) \cdot b^{L}(x)
\end{aligned}
\tag{2}
$$

Peak profiles were first fitted by Gaussian function for variables, Bg, I_0, σ and $2\theta_{hkl}$, which minimized Eq. (3).

$$\oint | I_{exp} - I_{mod} | \cdot I_{exp} d\theta = \min \tag{3}$$

The variables Bg, I_0, σ of Lorentzian function were nonlinearly fitted with $2\theta_{hkl}$ from the fitting result of Gaussian function. From the obtained $b^{G}(2\theta)$ and $b^{L}(2\theta)$, variable m of $b^{PV}(2\theta)$ was determined which minimized Eq. (3). Integrated intensity was calculated by integrating the model function. The integrated intensity remained practically constant with increasing sample tilt angle as shown in Fig. 1 for random molybdenum specimen. Hence, integrated intensities were used as pole figure values without defocalization corrections for molybdenum thin films. ODF was calculated by WIMV method. In WIMV method, RP-values are defined for a characterization of errors in quantitative texture analysis. To see the effectiveness of PSD-based pole figure measurement, pole figures measured by scintillation counter, then corrected by bulk random sample(called the "bulk correct"), not corrected(called the "uncorrect") and corrected by the method proposed by Wenk et al(called the "film correct") were compared with RP-values. Fig. 2 shows the RP-values for these pole figures. The RP-value of the PSD-based pole figures is lowest and that of the bulk correct data is highest. It is also seen that the RP-value of the film correct data is higher than that of the PSD data. Figs 3-a),b) show the measured (110) pole figures of the 100nm molybdenum thin film and 200nm respectively. The texture in Figs 3-a),b) shows mainly (110) fiber texture. Figs 3-c),d) show the calculated ODF of the 100nm thin film and 200nm respectively in Euler space $\{\varphi_1,\Phi,\varphi_2\}$. It is seen that both molybdenum films are (110) fiber texture and the texture of 200nm is stronger than that of 100nm.

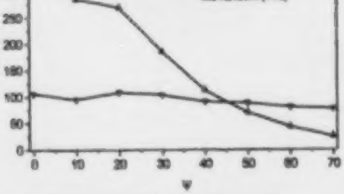

Fig. 1: Integrated intensity and max.intensity as a function of sample tilt

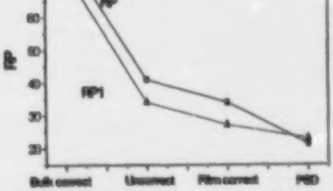

Fig. 2: RP diagram for various correction methods

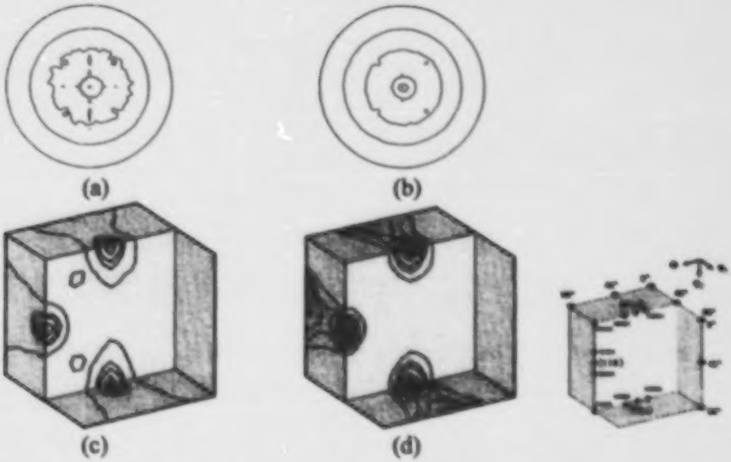

**Fig. 3: (110) pole figures of 100nm(a) and 200nm(b) (contour levels:1 3 5)
ODF in the Euler space of 100nm(c) and 200nm(d) (contour levels:1 3 5 10)**

3.2 Stress measurement

Fig. 4 shows the measured profile of Si substrates after deposition of molybdenum 100nm and 200nm. The radius of curvature, R, was calculated from the measured profile curve for each sample. Because the film thickness was much less than the substrate thickness, Stoney's equation could be used to calculate the biaxial stress of thin films:

$$\sigma = \frac{1}{6R}\frac{E_s}{1-\nu_s}\frac{t_s^2}{t_f} \qquad (4)$$

where t_s and t_f are the substrate thickness and the film thickness respectively, and $E_s/(1-\nu_s)$ is biaxial elastic constant of the silicon substrate. Before applying the equation, the measured profile of samples were corrected for previously measured profile of the uncoated substrate. All the films had tensile stress and the stress of molybdenum 100nm was about three times higher than that of molybdenum 200nm. The results are listed in Table 1. To use the $\sin^2\psi$ method, lattice spacing $d_{\varphi\psi}$ was measured for various ψ values at three φ tilts(0°,45°,90°). (110) planes were selected instead of (200),(211) planes because of the high ratio of reflected intensity to background level. Fig 5-a) shows the lattice spacings $d_{\varphi\psi}$ as a function of $\sin^2\psi$ for (110) planes of powder molybdenum specimen at φ=45°.

Table 1: Radius of curvature and biaxial stress of molybdenum films

Sample	Radius of Curvature(m)	Biaxial Stress(MPa)
Mo 100nm	15.3 ± 0.3	710.2 ± 14.1
Mo 200nm	22.6 ± 2.9	239.4 ± 27.4

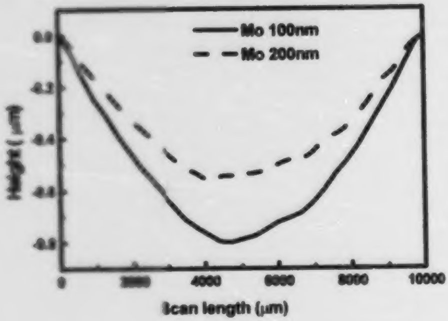

Fig. 4: Curvature of molybdenum thin film 100nm and 200nm

Assuming that the stress in powder molybdenum specimen is very low,if any,in magnitude, the decrease of $d_{\varphi\psi}$ in Fig. 5-a) could be thought to be caused by instrumental errors such as beam optics and alignment errors. Fig. 5-b) and 5-c) show the change of lattice plane spacings as a function of $\sin^2\psi$ at φ=45° for (110) planes of 100nm and 200nm molybdenum thin film, respectively.

The average internal strain could be obtained after measuring the interplanar distance $d_{\varphi\psi}$. For the plane stress state with linear elasticity assumption, the relation between average internal strain $\bar{\varepsilon}_{ij}$ and interplanar distance $d_{\varphi\psi}$ can be given as follows.

$$\varepsilon_{\varphi\psi} = \frac{d_{\varphi\psi} - d_o}{d_o} = (\bar{\varepsilon}_{11}\cos^2\varphi + \bar{\varepsilon}_{12}\sin 2\varphi + \bar{\varepsilon}_{22}\sin^2\varphi - \bar{\varepsilon}_{33})\sin^2\psi + \bar{\varepsilon}_{33} \qquad (5)$$

where d_o is the interplanar distance of the material at zero strain. The internal stress $\bar{\sigma}_{ij}$ can be evaluated with average internal strain $\bar{\varepsilon}_{ij}$ by the assumption of constant strain as follows.

$$\bar{\sigma}_{ij} = \bar{C}_{ijkl}\bar{\varepsilon}_{kl} = \int C_{ijkl} f(g) dg\, \bar{\varepsilon}_{kl} \qquad (6)$$

where $\bar{C}_{ijkl}$ is volume averaged stiffness tensor of polycrystals and calculated with orientation distribution function f(g). The average internal stress tensors of 100nm and 200nm thin films were given from Eqs (5) and (6) as follows.

Mo 100nm: $\bar{\sigma} = \begin{pmatrix} 446.2 & 20.1 \\ 20.1 & 521.5 \end{pmatrix}$(MPa)   Mo 200nm: $\bar{\sigma} = \begin{pmatrix} 156.9 & 16.9 \\ 16.9 & 171.8 \end{pmatrix}$(MPa)

The internal stress by XRD method showed tensile stress state and the magnitude of stress of molybdenum 100nm thin film was approximately three times higher than that of 200nm like the results of profilometry method. The difference between stress values of profilometry method and XRD method can be attributed to the different hypothesis of the two methods, that is, Stoney's equation assumes stress homogeneity and biaxial stress state within film, whereas XRD method assumes only plane stress state.

4 Conclusions

The internal stress in molybdenum thin films was studied by XRD method with PSD and profilometry method. The stress values by XRD method were in tension and thin film of 100nm in thickness was three times higher than that of 200nm, the ratio of the stresses of two thin films is similar to profilometry results. The pole figures of thin films measured by PSD and subsequent profile fitting was lowest in RP-values compared with scintillation-based pole figures.

5 References

Chateigner, D., Germi, P. and Pernet, M. (1994) X-ray texture analysis in films by the reflection method: principal aspects and applications. *Materials Science Forum,* Vol. 157-162. pp. 1379-1386.

Matthies, S. and Vinel, G.W. (1982) An example demonstrating a new reproduction method of the ODF of texturized samples from reduced pole figures. *Phys.Stat.Sol.(b)* Vol. 112, K115-K120

Noyan, I.C. and Cohen, J.B. (1987) Residual stress, measurement by diffraction and interpretation, Springer, New York.

Tu, K.-N., Mayer, J.W. and Feldman, L.C. (1992) Electronic thin film science for electrical engineers and materials scientists, Macmillan, New York.

Wcislak, L., Bunge,H.-J. and Nauer-Gerhardt, C.U. (1993) X-ray diffraction texture analysis with a position sensitive detector. *Z.Metallkd.* Vol.84. pp. 479-493

Acknowledgement

The authors wish to acknowledge the financial support of the Korea Research Foundation made in the Program Year 1998.

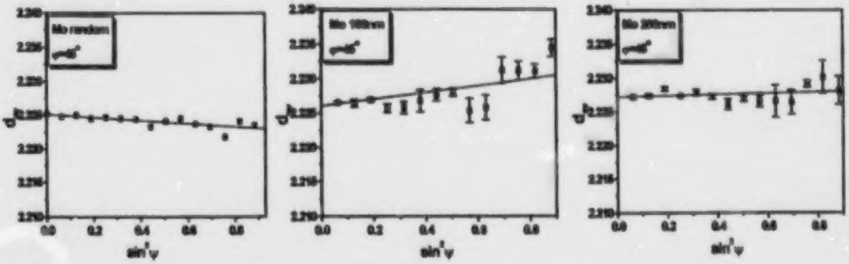

(a) (b) (c)

Fig. 5: $d_{\varphi\psi}$ vs. $\sin^2\psi$ for molybdenum random (a), 100nm film (b) and 200nm (c)

TEXTURATION INDUCED BY THE ADDITION OF SURFACTANT DURING THE SYNTHESIS OF V_2O_5 THIN FILMS.

F. ANSART, S. MEGE, A. ROUSSET

Laboratoire de Chimie des Matériaux Inorganiques et Energétiques, Université Paul Sabatier, Toulouse, France

J.M. SAVARIAULT

C.E.M.E.S., Toulouse, France

Abstract

Vanadium pentoxide xerogels were prepared by hydrolysis of vanadium alkoxide. Such shaped materials present many advantages when used as electrodes in lithium batteries or in electrochromic devices. The interface properties can be improved by increasing the porosity. The insertion of a non ionic surfactant in the gel allows to encapsulate the alkoxide molecules and intermediate hydrated species. The speed of gelification is then limited. This phenomenon may decrease the formation of bonds. The elimination of the organic chains and water molecules drive to a very porous material. FTIR analysis has shown chemical link rearrangements. By X-ray diffraction, we observed, in the material prepared with surfactant, a significant desorder in comparison to thin films elaborated without surfactant. On the contrary, the impression of diffraction shapes coupled with polarized light microscopy, exhibits texturation in the case of the surfactant addition. In this paper, we have studied why the addition of non ionic surface agent can induce such a microstructural orientation.

Keywords : texturation, surfactant, sol-gel, thin films, V_2O_5

1. Introduction

Amorphous V_2O_5 thin films are likely to play an important role in lithium batteries (Babbour et al. 1991) and electrochromic devices (Azens et al. 1992). A simple and economical method to produce such applications is to use a sol-gel process, thin film being deposited by dip-coating (in our case) or by spin-coating. Among the methods used to prepare V_2O_5 gels, the most standard is to hydrolyze vanadium alkoxides (Sanchez et al. 1988; Livage 1991). The gel obtained is deposited as a thin film on a SnO_2 sample, then it is heat treated at 290°C to eliminate a maximum amount of water (Aldebert et al. 1981). Concerning the dip-coating method, the formation of thin films is dependent on the gel viscosity. But, vanadium alkoxides are very reactive towards hydrolysis because of the high electrophilic power of the vanadium atom. This is why the hydrolysis and condensation steps are short and the gel solidification (infinite viscosity) very fast. It would be very interesting to decrease the gel solidification speed. In order to improve these physical and chemical characteristics and mainly to obtain a microporous material, a surfactant was added to the sol without the presence of an oil phase. In this work, the modifications caused by surfactant addition on the morphology were studied and, furthermore, this addition of surfactant exhibits a real texturation.

2. Experimental procedure

V_2O_5 gel was prepared by hydrolysis of a vanadium alkoxide $VO(OAm^t)_3$. This alkoxide was synthesized by reaction of tertioamyl alcohol with commercial V_2O_5 powder (Aldrich) :

$$V_2O_5 + 3\ Am^t\,OH \longrightarrow 2\ VO\,(OAm^t)_3 + H_2O.$$

Mixture was heated at 90°C under reflux system for seven days (Nabavi et al. 1991). The products were purified by distillation under argon at reduced pressure (P=4mmHg). All the preparation steps were performed under a dry atmosphere.

Alkoxide was hydrolyzed by addition of excess water (molar rate alkoxide/water = 1/80). Then, a non-ionic surfactant belonging to the nonylphenol family (named EON2) was added.

The mixture was then vigorously stirred until the required viscosity was reached (between 40 and 150 mPa/s) enabling thin films to be prepared by dip-coating.

The evolution of V_2O_5 gels viscosity was followed with a HAAK VT 181 viscosimeter. All viscosity measurements were carried out in the same conditions of water vapor pressure and at ambient temperature. At the end of the gelification reaction, FTIR spectroscopy showed if the hydrolysis reaction was complete and if the surfactant was located in particular areas of the gel. Analyses were made on dried xerogel at 80°C in KBr discs (1.2 mg of xerogel and 0.7 g of KBr) using a Perkin Elmer 1750 X apparatus. During gelification, the gel evolution was observed by polarized light microscopy using an OLYMPUS CH-2 apparatus fitted out with a camera (SONY CCD-IRIS/RGB).

3 - Results

3.1 FTIR studies and polarized light microscopy

FTIR studies were carried out on the xerogel dried at 80°C. In both types (gels with or without surfactant), no band appears at 1100 cm^{-1} which would be attributed to ν(V-OC) vibrations. So, all the $-OAm^t$ groups were eliminated during the hydrolysis meaning that the reaction was complete. An interaction was seen to occur between surfactant and V_2O_5 at the bridge bonds of V_2O_5 (Mege, 1998). In fact, the relative intensity of the characteristic band of this bond at 750 cm^{-1} clearly decreases compared to the band corresponding to chain bonds at 410cm^{-1}. During their formation, gels were observed by polarized light microscopy (see Fig. 1).

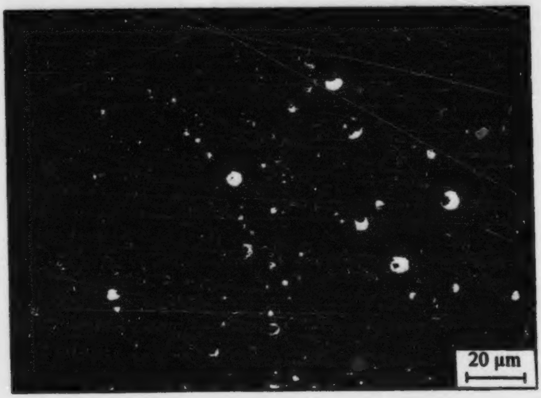

Fig. 1 : Polarized light micrography of a six hours old gel prepared with 25% molar of EON2 (X 500)

For gels without additive, a rough organization was noted after some hours (birefringent zones appear), but this was not very ordered, and was not homogeneous. Observing the same gels under normal light, their composition seemed to be homogeneous. With gels containing EON 2 (molar ratio EON/alkoxide, r = 0.25), large globules about 10µm across appeared from the start of the reaction. The distribution of the globules in the liquid was homogeneous. Order rapidly appeared both within and around the globules and with increasing time. The globule size decreased to reach a mean of 0.5µm diameter when the gel was four days old. In the xerogel too, particle distribution was completely homogeneous.

3.2- X-ray diffraction

Powder xerogels are amorphous. But, when gels are dried on a plane surface , diffractograms exhibit characteristic diffraction peaks of the 001 plane. Data were recorded at the copper Kα wavelength during 13 hours from 2° to 29° by 0.02° steps. For gels prepared with or without surfactant, the same characteristic bands according to c axis are present (Fig. 2).

The diffractogram of the xerogel, dried at 260°C, with EON2 is not so defined than the one corresponding to the gel dried at 110°C. This shows a more important structural disorder in materials after elimination of EON2.

In order to have more precise information on xerogels structure, analyses have been performed in a precession chamber with a ENRAF NONIUS device at Kα molybdenum wavelength. Thin films have been set perpendicularly to the incident beam, the device allows to heat samples in situ with a heating probe NONIUS. Results are completely different from previous ones since no 00l stripe appears.

At room temperature, xerogels with or without surfactant show a structure close to the V_2O_5 crystallized structure. 60 hours measurements confirm that reticular parameters of xerogels dried at room temperature correspond to crystallized V_2O_5.

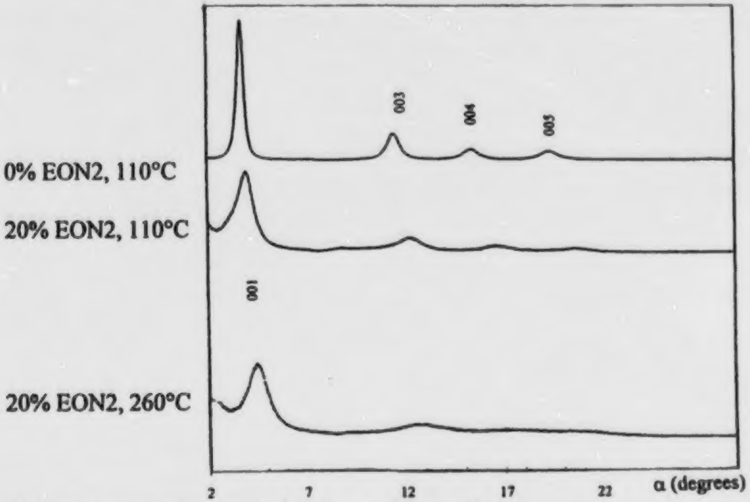

Fig. 2 : Diffractograms of xerogels dried on a plane surface

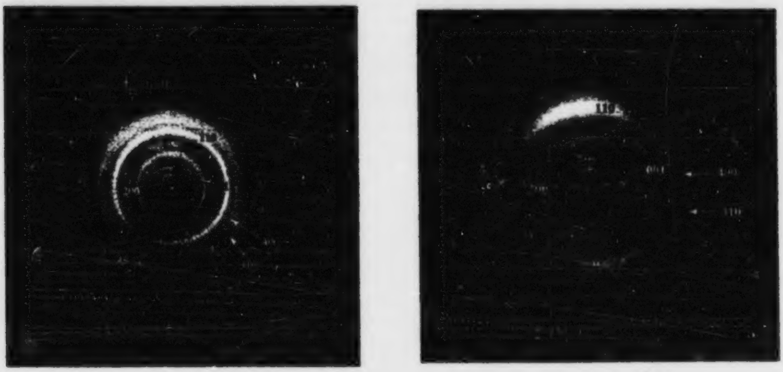

a) b)

Fig. 3 : Thin films of xerogels dried at 260°C : a) 0% EON2 b) 20% EON2

The diffraction pattern of V_2O_5, $2H_2O$ thin film prepared with surfactant only presents two printed areas. This could be evidence of a texturation caused by the addition of surfactant. After heating at 260°C, the two materials provide same feature (Fig. 3) i.e. the orthorhombic V_2O_5 type.
Only a beginning of crystallization can be observed because hkl stripes appear. The material without surfactant seems better structured than the same prepared with 20% EON2. Rings are always visible for materials with surfactant.

3-3 Transmission electronic microscopy

Photographs have been taken on a PHILIPS CM12 (120kV) device. Samples have been prepared by deposition of colloidal diluted solutions on copper grids. Films have been dried at 80°C. In the case of xerogels with 20% EON2 (Fig. 4), an orientation of fibers can be observed (50-70 Å diameter approximatively).

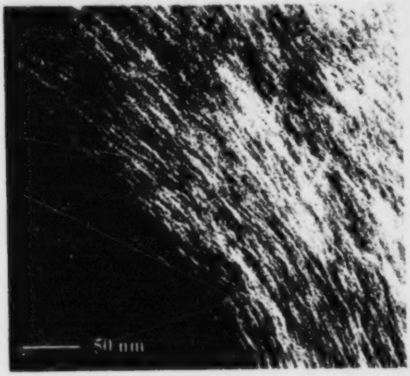

Fig. 4 : Gel of 5 hours old prepared with 20% EON2

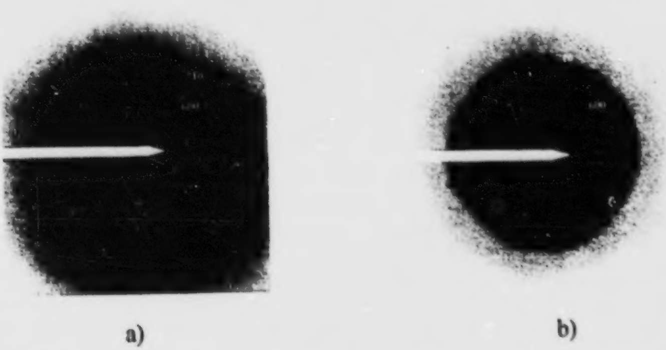
a)

b)

Fig. 5 : Electronic diffraction of gels with : a) 0% EON2 b) 20% EON2

Diffraction patterns on these samples are shown in figure 5. Gels exhibit exactly the same diffraction rings (600 and 710 planes of orthorhombic V_2O_5). In the case of sample with surfactant, diffraction is not the same in all directions. In fact, a texturation of fibers with printing of some particular areas can be noticed.

Conclusion

In this paper, the influence of adding a nonylphenol family surfactant to vanadium oxide xerogels has been studied. The method used is quite simple and presents a good reproducibility. From *a macrostructural point of view*, the kinetics clearly demonstrate that the surface active agent interacts by slowing down one of the two processes of hydrolysis and condensation without stopping it. Concerning the morphology of the layers elaborated with surfactant, better homogeneity and adherence were obtained. From *a microstructural point of view*, FTIR spectra show that some V-O bonds disappeared but these modifications were not located at the molecular scale. Roughly V_2O_5, $2H_2O$ presented the same molecular structure as crystallized V_2O_5.

Furthermore, a decrease of gelification speed have induced a preferential orientation in the materials. So, EON2 addition present many advantages : an easier control of the film thickness and the obtention of a texturation in the material.

References

Aldebert,P ,Baffier,N ,Gharbi,N ,Livage,J. (1981) *Mater . Res. Bull.*, Vol 16, pp 669-676

Azens,A ,Talledo,A ;Andersson,A.M. ,Niklasson,G.A. ,Stjerna,B ,Granqvist,C.G. (1992) *SPIE* Vol. 1728, pp.103-117

Babbour,R ,Pereira-Ramos,J.P. ;Messina,R ,Perichon,J (1991) *J. Electroanal. Chem.*, Vol. 314, pp.81-101

Livage,J .(1991) *Chem. Mater.* Vol. 3, pp. 578-593

Mege,S .(1998) *Thesis n° 3075*, Universite Toulouse III

Nabavi,M ,Sanchez,C ,Livage,J. (1991) *Eur. J Solid State Inorg. Chem.*, Vol 28 pp 1173-1192

Sanchez,C ,Nabavi,M ,Taulelle,F. (1988) *Mat. Res. Soc. Symp. Proc.* Vol. 121, pp.93-104

TEXTURE TRANSFORMATION IN NI ELECTRODEPOSITS APPLIED FOR CD-ROM STAMPERS

F. Czerwinski [1,2], A. Zielinska-Lipiec [2] and J.A. Szpunar [1]
[1] Department of Metallurgical Engineering, McGill University, Montreal, H3A 2B2 Canada
[2] Department of Metallurgy and Materials Science, University of Mining and Metallurgy, Krakow, 30-059 Poland

Abstract

Thermal evolution of the crystallographic texture in 300-μm thick Ni electrodeposits, with a specific application for replication of optical recording devices, was examined. The initially strong <100> fiber texture was unstable and transformed during annealing to the <211> fiber. The texture transformation was accompanied by grain growth and deposit softening and the temperature range for rapid changes of all parameters was between 350 and 400 °C. A numerical analysis of texture data was conducted to identify the type of Ni grain boundaries, which control grain growth and texture transformation. The microstructural observations suggest that the growth of grains with new orientation starts in fine-grained regions and controls the thermal stability of the entire deposit.

Keywords: electrodeposition, optical recording media, crystallographic texture, microstructure, Ni

1. Introduction

Electrodeposition, combined with laser lithographic patterning, is used for manufacturing optical recording devices, including computer CD-ROM drives and music CD's. The manufacturing process of CD's involves their replication from electrolytic metal templates, called stampers, with a high precision injection molding press. This is accomplished by the injection of a molten resin, made of optical grade plastic, into a mold cavity containing the stamper on one of its faces. An advantage of using the electrodeposition for the stampers production is that the surface profiles, generated primarily by laser lithography, can be easily and precisely molded. The structure of electrodeposited metals is, however, unstable and the thermal changes deteriorate the stamper hardness and wear resistance.

At present, there is no agreement in the literature on how to explain the thermal evolution of the microstructure in microcrystalline Ni electrodeposits. While some studies attribute the changes to grain growth rather than recrystallization, other supports the presence of all stages typical for recovery, recrystallization and abnormal grain growth (Jacobson and Sliwa, 1979). Our preliminary tests (Czerwinski et al., 1997,1998) revealed that the crystallographic texture seems to be very sensitive to temperature increase. Texture studies may, therefore, help to understand and improve the structural stability of the electrodeposits at elevated temperatures. The objective of this research is to assess the texture changes in the Ni electrodeposits, which take place at elevated temperatures.

2. Experimental details

The Ni stampers in the form of disks with a diameter of over 130 mm and a thickness of 0.3 mm, electrolytically deposited from a Watt's bath by Saturn Solutions Inc., were used as a research material in this study. Deposition was conducted at a temperature of 50 °C and at a current density starting from 1 and then increasing, in several consecutive steps, up to 10 A/dm^2 at the final thickness. Annealing was performed in a flowing argon atmosphere at temperatures ranging from 300 up to 800 °C for time intervals up to 20 h. The textures of Ni after deposition and annealing were measured using a D-500 Siemens x-ray goniometer and $Mo_{K\alpha}$ radiation. Pole figures data were collected using the reflection technique up to a maximum tilt of 80 deg in 5 deg polar and radial intervals. The results were corrected for absorption and defocusing based on the standard random specimen, prepared from Ni powder. The experimental pole figures were then used to calculate the orientation distribution functions of the grains (ODF) by applying the procedure described by Bunge (1982). The microstructural characterizations involved transmission electron microscopy.

3. Results and discussion

3.1. As-deposited texture and its transformation during annealing

In an as-deposited state, the orientation of Ni grains was represented by the <100> fibre texture, with the {100} planes aligned parallel to the deposit surface. As a result of annealing, the <100> texture component was getting weaker while the strength of the <211> component was growing. The evolution of the Ni texture as a function of annealing temperature is shown in Fig. 1. The intensity for <211> texture was taken from the centre of the {211} pole figures, which were recalculated from orientation distribution functions, as described later. For surfaces containing the recording pattern, the strength of the <100> component with an initial intensity of 61.5 random units, dropped drastically to the level of 4 at a temperature of 400 °C. At the same time, there was observed a fast growth of the <211> component, which reached an

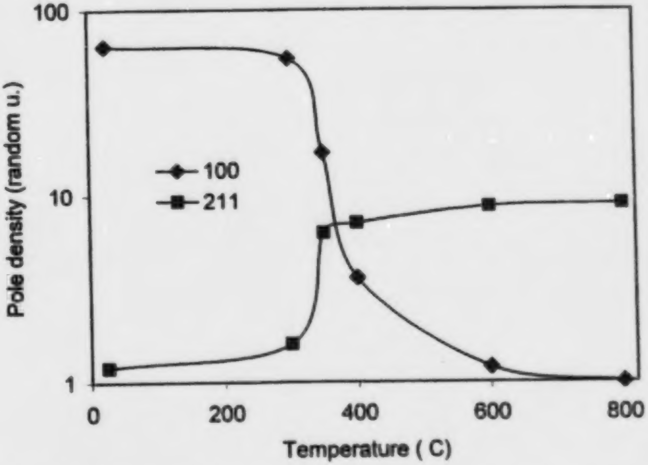

Fig.1. The evolution of texture in the Ni electrodeposit as a function of annealing temperature. The evolution of texture in the Ni electrodeposit as a function of annealing time at 300 °C.

intensity of approximately 7 at a temperature of 350 °C. The final texture, measured on this surface after annealing at 800 °C, shows exclusively the strong <211> component with an intensity of over 9 random units.

3.2. Microstructure evolution during annealing

In order to verify the finding based on x-ray technique, the deposit microstructure was analyzed by transmission electron microscopy. The typical feature of Ni microstructure after deposition is a large difference in grain size. In addition to grains with a size 4 μm, the small grains are present with a size of approximately 0.1μm (Fig. 2a). A rough estimate indicates that large and fine grain regions occupy 60% and 40%, respectively of the volume of the microstructure. While large grains exhibit the <100> axis perpendicular to the deposit surface and are surrounded by high angle grain boundaries, the orientation of fine grains is more random. The electron diffraction pattern from the fine-grain region points-out, however, a significantly lower number of orientations than could be anticipated from a number of grains visible within the diffraction area. This could suggest that some of the fine grains (subgrains, coherent domains or mosaic blocks) are separated by low angle boundaries. In general, the grains contain a higher density of structural defects, mainly pile-ups and a network of dislocations. After annealing at 300 °C for 0.5h the bimodal grain structure with large grains exhibiting <100> growth direction, is still preserved. However, fine grains contain significantly less defects and their size is larger. The chain-like colony of Ni grains with a similar orientation, shown supports the recovery process of some grains and possible coalescence of smaller subgrains. Annealing at 400 °C essentially changed the deposit microstructure. An apparent

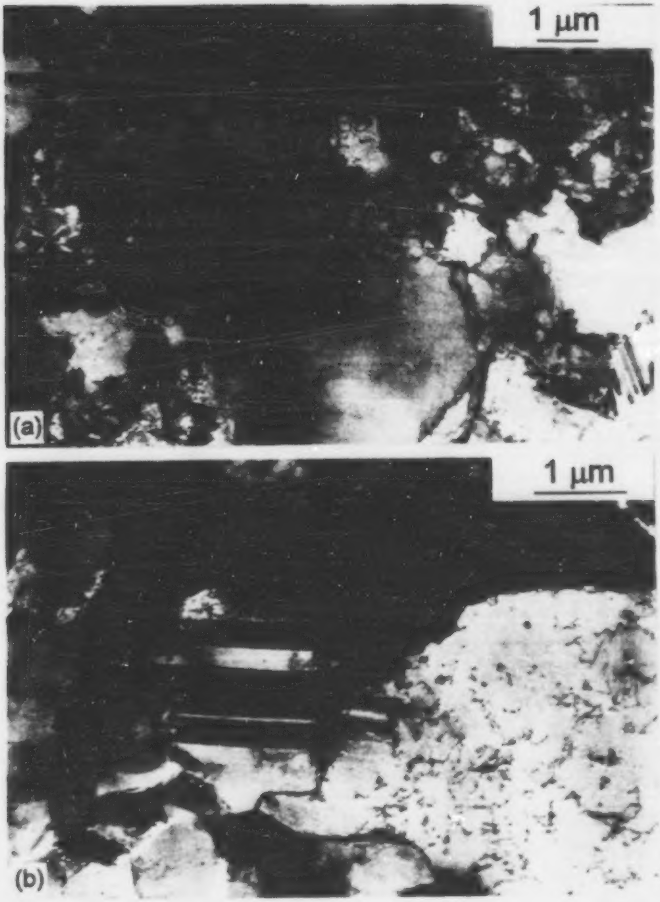

Fig. 2. TEM images of Ni after deposition and annealing: (a) general view of bimodal microstructure showing large individual grains surrounded by fine grain regions; (b) general view after annealing at 400 °C for 0.5h showing relatively uniform grains.

change after annealing is the disappearance of the bimodal grain size. Twins and stacking faults are present in regions supposedly corresponding to previous fine grain areas.

3.3. Grain boundary character distribution

The grain boundaries in the electrodeposits were classified geometrically in terms of the relative misorientation between the adjacent grains (Sutton and Baluffi, 1995). The distribution of grain boundaries as a function of misorientation represented by an axis angle pair is called grain boundary misorientation distribution (GBMD) and are calculated from experimental ODF data (Morawiec et al., 1993). The calculation is carried out by finding out the misorientation between an assumed orientation and a randomly created orientation in accordance with the measured ODF. The exemplary changes of GBMD during annealing at 600 °C are plotted in the form of histograms (Fig. 3). Here, the misorientation angles between grains were divided into four groups. It is known that the misorientations below 15 deg and above 45 deg represent grain boundaries with lower energy than misorientations between 15 and 45 deg. It is clear that annealing leads to a reduction in the percentage of grain boundaries with misorientation below 30 deg. The fractions of grain boundaries with that misorientation in both as-deposited and annealed Ni are still higher than that expected for material without texture. On the contrary, the annealing led to an increase in fractions of grain boundaries with misorientations above 45 deg. For this range, the fractions of grain boundaries in as-deposited and annealed materials were still lower than values expected for the random orientation of grains.

The energy of grain boundaries in materials with ultra fine grains is generally higher than that expected for their microcrystalline counterparts and does not essentially depend on the misorientation angle (Phillpot et al., 1995).

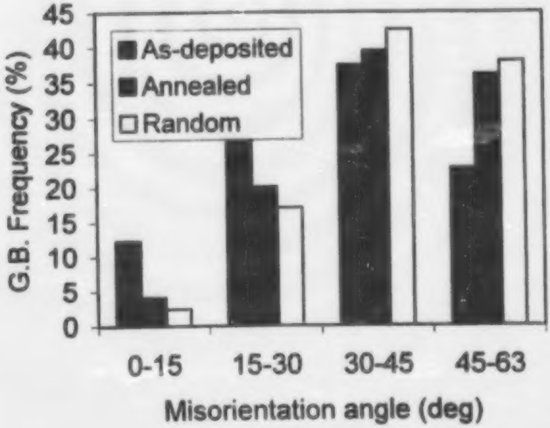

Fig. 3. Histograms of grain boundary misorientation distributions (GBMD) for as-deposited and annealed Ni. The results marked as random are calculated for a microstructure with random distribution of grain orientations.

A lack of the dependence on misorientation angle is caused by the fact that energy is stored in short segments of grain boundaries and in a dense network of the grain boundary junctions. Concurrently, the energy of grain boundaries in conventional polycrystalline material clearly depends on the grain misorientation angle (Sutton and Baluffi, 1995). This implies that low and highly misoriented boundaries, with lower energy in microcrystalline structures, will have the largest difference in energy between initial (nano) and final (micro) states. Assuming that this energy difference is a driving force for grain boundary migration, these boundaries should have a mobility advantage. The microscopic observations show that the specific microstructure of as-deposited Ni with a bimodal grain size is responsible for high thermal instability observed. While the large grains contribute mainly to the Ni texture after deposition, the fine grains control the thermal stability of the whole microstructure during annealing. Since the grain size in that areas can be smaller than 100 nm, it explains the high instability of the deposit microstructure at elevated temperatures, which is quite similar to that reported for nanocrystalline materials.

4. Conclusions

A strong <100> fibre texture in as-deposited Ni stamper is thermally unstable and transforms between 350 and 400 °C to the significantly weaker <211> fibre. The temperature range for sharp texture changes corresponds to the rapid grain growth and softening of the deposit. It is suggested that the abnormal growth of grains with <211> orientation starts in the fine (nano and submicro) grained regions of bimodal structure and controls the thermal stability of the entire deposit.

5. References

Bunge, H.J. (1982) Texture Analysis in Materials Science, Butterworth, London.

Czerwinski, F., Li, H., Megret, F., Szpunar, J.A., Clark, D.G. and Erb, U. (1997) Evolution of Texture and Grain Size during Annealing of Nanocrystalline Ni-45%Fe Electrodeposits, *Scripta Mater.*, 37, 1967-1972.

Czerwinski, F. Palumbo, G. and Szpunar, J.A. (1998) Textures of Oxide Films Grown on Nickel Electrodeposits, *Scripta Mater.*, 39, 1359-1364.

Jacobson, B.E. and Sliwa, J.W. (1979) Structure and Mechanical Properties of Electrodeposited Nickel, *Plating and Surface Finishing*, 9, 42-47.

Morawiec, A., Szpunar, J.A. and Hinz, D. (1993) Texture Influence on the Frequency of Occurrence of CSL-boundaries in Polycrystalline Materials, *Acta Metall. Mater.*, 41, 2825-2832.

Phillpot, S.R., Wolf, D. and Gleiter, H. (1995) A Structural Model for Grain Boundaries in Nanocrystalline Materials, *Scripta Metall. Mater.*, 33, 1245-1251.

Sutton, A.P. and Baluffi, R.W. (1995) Interfaces in Crystalline Materials, Clarendon, Oxford.

AFFECT OF LOCALIZED TEXTURE ON SPUTTER PERFORMANCE OF TANTALUM

C.A. MICHALUK
Cabot Performance Materials, Boyertown, PA. USA

D.B. SMATHERS
Tosoh SMD Inc., Grove City, OH. USA

D.P. FIELD
TexSEM Laboratories, Draper, UT. USA

Abstract

Tantalum has emerged as the material of choice for the barrier layer for the damascene semiconductor fabrication process. This emerging technology relies on the reactive sputtering of high-purity tantalum targets to deposit a thin-film of TaN, which then serves as the diffusion barrier between the Si substrate and the Cu conductive paths. Experiences with other materials indicate that the integrity of the deposited film is dependent on the grain size and texture of the sputtering target. This paper reports recent findings that the sputtering performance of tantalum is detrimentally influenced by the presence of localized (100) texture banding in the target. Through use of Orientation Imaging Microscopy (OIM), a means of characterizing textural bands and gradients in tantalum has been devised. Proper thermomechanical processing is shown to be instrumental for eliminating sharp (100) bands and enhancing the texture homogeneity of tantalum; these attributes are deemed to be critical for assuring the performance of tantalum sputtering targets.

Keywords: Banding, Orientation Imaging, Sputtering, Tantalum, Texture

1 Introduction

Sputtering is a physical vapor deposition technique for producing thin films and coatings. The process involves bombarding a source "target" with energetic plasma ions, which then penetrate and collide with the lattice atoms of the target. Momentum transfer produces a cascading effect within the lattice, culminating in the ejection of atoms from the surface of the target; subsequently, these sputtered atoms then deposit onto a substrate to form a thin coating.

Since practically any material can be sputtered, this low-cost deposition process is used in a vast array of commercial products. For microelectronics applications, tantalum is among the most versatile target materials. Pure tantalum serves as the thermochemical barrier in paint-jet printer heads. Compounds such as TaN, used to form the resistors in integrated circuits, are deposited by reactive sputtering of tantalum; whereas Ta_2O_5, a dielectric used in CMOS devises, integrated capacitors, and magnetic read-write heads, can be produced by reactive sputtering or by oxidization of the Ta film. Perhaps the most demanding role for tantalum targets will be its use as part of the emerging damascene process. This next-generation semiconductor fabrication technology will employ reactively sputtered TaN to serve as the diffusion barrier between Cu conductor paths and the Si substrate. In this application, optimizing the sputtering performance of the Ta target will be the most beneficial.

2 Background

For many sputtering applications it is critical that the deposited film is of uniform thickness over the entire substrate. This is especially true for microelectronics where many parts are produced from a single substrate; for example, more than 200 individual microprocessor chips can be fabricated atop a single 250mm-diameter silicon wafer. The thickness uniformity of sputter deposited films are known to be directly influenced by structural attributes of the sputtering target; specifically, the inverse relationship between the grain size of the target and the variability of film thickness has been well documented for many metals.

The affect of grain size on film quality extends from the influence of crystal orientation on sputtering yield. Magnuson and Carlston presented a simplistic model to describe the sputtering yield of a single crystal[1]:

$$S(hkl) = [K(hkl)E^{1/2}][P_c(hkl)] \tag{1}$$

The first term is the momentum transfer factor that incorporates the physical attributes of the system, such as the atomic mass of the ion and target species and the energy of the incident ions. The second term defines the probability of collision between an incident ion normal to the (hkl) plane and a lattice atom. Postulating that the probability of collisions is correlated to transparency, defined as the atomic packing efficiency of the surface atomic plane and the visibility of the atoms of underlying planes, the authors demonstrated that the sputtering yields of Cu and Ag are maximized for single crystals whose (111) planes are oriented perpendicular to the incident beam[1]. For FCC crystals, it has been confirmed that the sputtering yield varies with orientation such that *S(111) > S(100) > S(110)*[1,2], while those from BCC molybdenum indicate that *S(110) > S(100)*[3].

Other studies had revealed that the angular distribution of particles sputtered from a single crystal exhibit distinct peaks in the directions of low Miller indicies[4]. It had been theorized that momentum transfer is most efficiently directed along the close-packed rows of atoms in the crystal[5], and subsequent studies on Au, Pt, Al, and NiFe confirm that target atoms are preferentially ejected along the close pack directions in the lattice[6]. For wrought polycrystalline tungsten targets having a (001)-type texture, a spatial pattern containing five axisymmetric Warner spots was created by the sputtered particles; the central spot was formed by atoms ejected along the <100> axis, and the outer four corresponded to the <111> crystal directions in the target[7,8].

Although the sputtering characteristics of tantalum have yet to be investigated to the extent as many of the more common metals, the influence of orientation on sputter yield can be derived using the principles established from prior studies on other materials. Of the low-index atomic planes in BCC crystals, the (110) is the least transparent and would be expected to provide the highest probability for collision from an orthogonal beam of ions, while the close-packed <111> would be the preferred direction of particle ejection. Since maximum yield would occur when the incident beam is parallel to the <111> direction, one could infer that the sputter yield of BCC crystals varies with orientation as follows: *S(110) > S(111) >S(100).*

3 Analysis and Results of Rejected Tantalum Target

In 1998, a tantalum ConMag target was returned by an end-user that cited poor sputtering performance. Bulk chemical and metallurgical analysis failed to identify any abnormalities in the target material. Observations of the sputtered surfaces of the target revealed that the sputter yield over the surface of the target was inhomogeneous. The matted appearance of the surface in some regions of the target indicated that material had been sputter eroded from those areas during the process. Other portions of the target surfaces appeared smooth and lustrous, leading to the conclusion that these regions were resistant to sputtering during the process. Secondary electron images in the SEM readily revealed the difference between the two types of regions.

To investigate the dependence of crystallographic texture on target yield, these surfaces were analyzed using Orientation Imaging Microscopy (OIM) techniques[9,10,11]. In addition, cross-sections of the targets were prepared and texture gradients through the thickness of the targets were measured by OIM and quantified using values derived from the orientation distribution function. Various regions of the surface measuring about 2 mm^2 each were analyzed in an attempt to determine

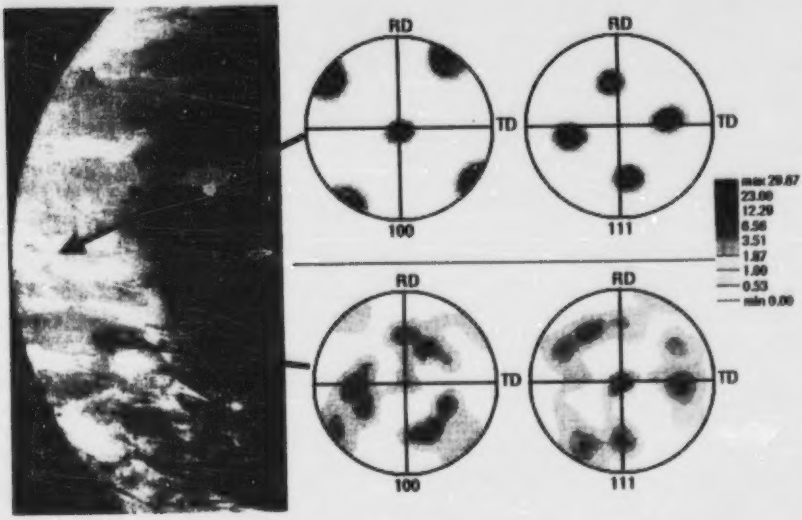

Figure 1: Pole figures from sputter-resistant (top) and sputter-eroded (bottom) surfaces of the reject tantalum target.

regions which yielded Ta during sputtering and those which did not. All measurements were performed using a 20 kV accelerating potential and 1.5 nA probe current. Figure 1 contains a comparison of representative pole figures from each region. The upper set of pole figures shows the distribution from a two square mm region of the target surface that appeared smooth, and the lower set contains pole figures from the rough surface regions. As evidenced from these pole figures, the smooth region is comprised of a colony of (100) oriented grains with grain boundaries consisting of low angle misorientations. The entire area contains grains that are the same orientation to within 15 degrees tolerance. The texture of the sputtered regions consists of both (100) and (111) texture components. No other orientations were of either primary or secondary significance in the measured distributions. In general, the preferred orientation in these regions was the (111), with the (100) component playing a secondary role.

Next, a transverse section of the target was analyzed and revealed a structure containing a series of sharp texture bands, oscillating primarily between (111) and (100) preferred orientations. Figure 2 shows an orientation map of a representative structure, nominally 1 mm wide through the target cross-section (~6mm). The darker shaded grains are near (111) while the lighter shaded grains are near (100). Combining these results with the observations from the inhomogeneous target surface reported above, it is concluded that the sputtering yield from such a structure will vary dramatically as the target is used during manufacturing. It is apparent that the poor performance of this material is due to the presence of strong, localized (100) texture bands aligned parallel to the tantalum surface; once exposed, these sputter-resistant bands acted to detract from the target's expected sputter yield.

To evaluate the severity of each texture band, the transverse orientation map was segmented into analysis areas of 300 microns depth through the plate thickness. An ODF was calculated from the data in each region assuming a five-degree half-width about each measurement. The times random value for the (111) and (100) texture components in each thickness increment was calculated by integrating the orientation distribution through Euler space to obtain the appropriate values. The average values of the (111) and (100) components of each segment are 3.0 and 3.6 times random; the maximum and minimum values of each thickness increment are 6.1 and 10.9 times random, respectively. The texture of each increment was numerically quantified as the ratio of I(111) to I(100); a plot of the log ratio versus thickness increment for the tantalum target is included in Figure 3.

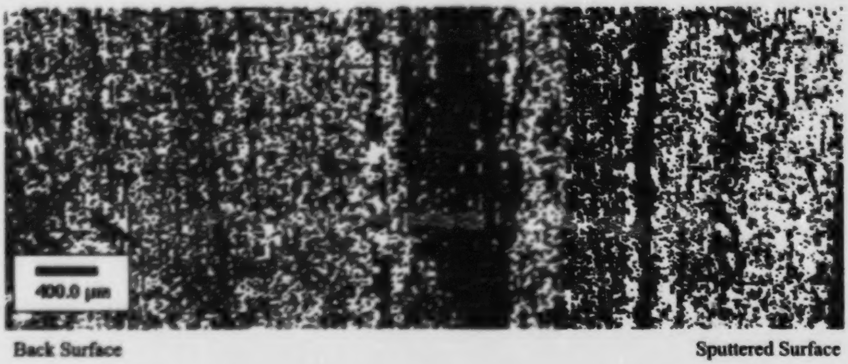

Figure 2: Inverse pole figure map along a cross section of the tantalum sputtering target. Orientations of dark bands are near (111) and of light bands are close to (100)

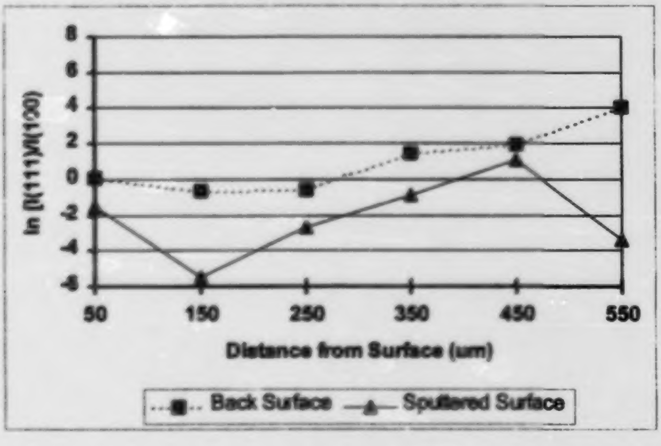

Figure 3: Texture variation versus depth from the top and bottom surfaces of the tantalum sputtering target, calculated for thickness increments of 100 μm.

4. Discussion

Several researchers have reported the existence of texture gradients and bands in recrystallized tantalum plate[12,13,14]. It is speculated that these texture bands are relics of the as-cast grain structure which remain because of improper or ineffective thermomechanical processing of the material. Tantalum mill forms are typically produced from vacuum-cast ingots: the highest purity, most consistent tantalum products are produced by multiple electron beam (EB) melting[15,16]. Unlike other refractory metals such as tungsten and molybdenum, tantalum is extremely malleable under ambient temperatures; however, the metal becomes susceptible to embrittlement in air at temperatures above about 300°C. Therefore, a proper combination of cold deformation and vacuum (or inert atmosphere) thermal treatment(s) is critical for attaining structural integrity in tantalum mill products.

Tantalum single crystal studies have demonstrated that (111) orientations readily work harden and recrystallize at a relatively low annealing temperature compared to (100) crystal orientations,

6. References

1. G.D. Magnuson and C.E. Carlston, *J. Appl. Phys.*, **34**, 11, 3267 (1963).
2. D. Onderdelinden, *Can. J. Phys.*, **46**, 739 (1968).
3. H.E. Roosendaal, Sputtering by Particle Bombardment I: Physical Sputtering of Single-element Solids, Behrisch (ed.), Springer-Verlag, Berlin, 219-256 (1981).
4. G.K. Wehner, *Phys. Rev.*, **102**, 690 (1956).
5. R.H. Silsbee, *J. Appl. Phys.*, **28**, 1246 (1957).
6. H. Tsuge and S. Esho, *J. Appl. Phys.*, **52**, 7, 4391 (1981).
7. Y.N. Zhukova, E.S. Mashkova, V.A. Molchanov, A.V. Sidorov, and W. Eckstein, *Bulletin of the Russian Academy of Sciences*, **58**, 10, 1626 (1994).
8. W. Eckstein, E.S. Mashkova, V.A. Molchanov, and A.I. Tolmachev, *Nucl. Instrom. Methods Phys. Res. B*, **115**, 482 (1996).
9. B.L. Adams, S.I. Wright, and K. Kunze, *Metall. Trans.*, **24**, 819 (1993).
10. S.I. Wright, *J. Computer-Assisted Microscopy*, **5**, 207 (1993).
11. N.C. Krieger-Lassen, K. Conradsen, and D. Juul-Jensen, *Scanning Microsc.*, **6**, 115 (1992).
12. V.I. Yushkov, V.V. Shimov, R.A. Adamesku, and V.A. Zagrebin, *Tsvetnve Metally*, **3**, 83 (1983).
13. S.I. Wright, A.J. Beaudoin, and G.T. Gray, Mat. Sci. Forum, H.J. Bunge (ed.), **157-162**, 1695 (1994).
14. H. Klein, C. Heubeck, and H.J. Bunge, Mat. Sci. Forum, H.J. Bunge (ed.), **157-162**, 1423 (1994).
15. C.A. Michaluk, Tantalum, E.Chen *et.al.* (eds.), TMS, Warrendale, PA., 205-217 (1996).
16. C.A. Michaluk and D.C. Hughes, Master File Report 789, Cabot Performance Materials, Boyertown, PA.
17. R.A. Vandermeer and W.B. Snyder, *Met. Trans. A*, **10A**, 1031 (1979).
18. T. Fujii, Y. Ohba, and Y. Yamura, *J. Less Common Metals*, **39**, 161 (1975).
19. J.B. Clark, R.K. Garrett, T.L. Jungling, R.A. Vandermeer, and C.L. Vold, *Met. Trans. A*, **22A**, 2039 (1991).
20. J.B. Clark, R.K. Garrett, T.L. Jungling, and R.I. Asfahani, *Met. Trans A*, **22A**, 2959 (1991).
21. J.B. Clark, R.K. Garrett, T.L. Jungling, and R.I. Asfahani, *Met. Trans A*, **23A**, 2183 (1992).
22. S.I. Wright, S.R. Bingert, and M.D. Johnson, Tungsten and Refractory Metals 2, A. Bose and R.J. Downing (eds.), Metal Powder Industries Federation, Princeton, 501 (1995).
23. C.A. Michaluk, Master File Report 948, Cabot Performance Materials, Boyertown, PA (1998).
24. C. Feng, T.K. Chatterjee, and L. Ting, High Strain Rate Behavior of Refractory Metals and Alloys, R. Asfahani, E. Chen, and A. Crowson (eds.), TMS, Warrendale, PA., 45 (1992).

which fail to generate new dislocation line lengths during deformation and merely polygonize at a high annealing temperature[17,18]. In polycrystalline Ta, increasing the amount of cold work prior to annealing has been shown to promote the (111) texture component, which has been deemed beneficial to enhancing microstructural homogeneity and reducing grain size in tantalum plate stock[19-22]. However, when processing a Ta EB ingot directly to plate, the cold work is not uniformly distributed though out the workpiece, but varies depending upon the orientation of the as-cast grains with respect to the directions of principle strain. Any additional cold working would not serve to improve the homogeneity of the recrystallized tantalum product. Recent findings that large, elongated grains within a heavy-gauge Ta plate had a (100) orientation and contained several small grains having low angle boundaries supports this hypothesis[23].

Aside from transverse rolling[21], the addition of an intermediate annealing operation is beneficial for improving the metallurgical and textural uniformity of tantalum. Since the recrystallization texture of tantalum lies on the (100)-(111) symmetry line[24], an in-process anneal serves to recrystallize (111) oriented grains, which then grow to partially consume unrecrystallized regions. Subsequent cold working can then be more uniformly distributed about the material due to the greater volume fraction of (111)-type grains relative to the (100)-oriented stringers. The impact of an intermediate anneal on the texture uniformity of tantalum is presented in Figure 4.

Achieving structural homogeneity in tantalum sputtering targets is contingent on several factors. First and primary, there must be sufficient cold work in the material prior to both the intermediate and final annealing operations to assure complete recrystallization of the (111)-oriented crystallites. Clearly, it is most advantageous to process the largest diameter tantalum EB ingots in order to assure the sputtering performance of the resulting target. And second, the choice of annealing temperature is critical: the temperature must be high enough that complete recrystallization and growth of the (111)-oriented grains can occur, yet not be excessive to allow (100) bands to recover or polygonize.

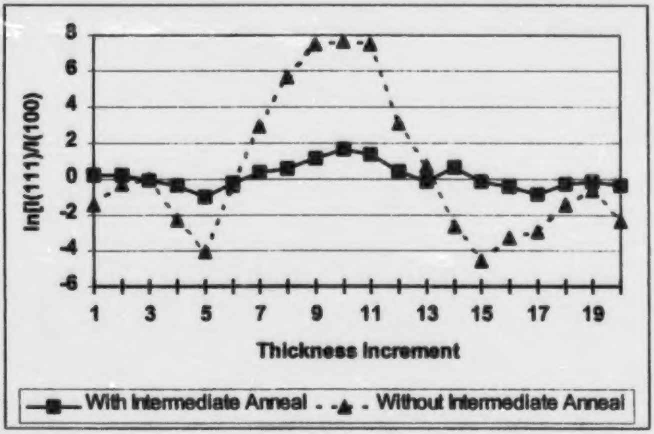

Figure 4: Effect of intermediate annealing on texture uniformity of tantalum. Each increment represents 5% of the total thickness.

5. Summary

The performance of a tantalum sputtering target is detrimentally affected by the presence of sharp (100) texture bands within the material. The consistency of the sputtering yield through the life of the target can be optimized for tantalum that contains a homogeneous (111)-type texture. The proper use of thermomechanical processing is instrumental to achieving textural uniformity in tantalum sputtering targets.

SINGULAR VALUE DECOMPOSITION OF THE ODF–PDF PROJECTION OPERATOR

K.G. v.d. BOOGAART
Graduate College "Spatial Statistics",
Freiberg University of Mining and Technology, Germany
H. SCHAEBEN
Geomathematics and Geoinformatics,
Freiberg University of Mining and Technology, Germany

Abstract

The simple relationship between harmonics for $SO(3)$ and harmonics for the unit sphere S^2 provided by the pole figure projection operator is represented as a system composed of nested matrices of simple form. This structure can be advantageously exploited to compute the singular value decomposition at small computational costs. Of the manifold applications of svd two are represented in this communication, experimental design to choose the subset of experimentally accessible pole figures imparting the most information with respect to the orientation distribution function to be reconstructed, and determination of high order harmonic coefficients from a given set of pole figures minimising the mean squared error.

Keywords: Singular value decomposition, ODF, PDF, measurement error, planning of experiments, reconstruction of high order harmonics

1 Singular value decomposition of the projection of the ODF onto a finite number of pole figures

Suppose a finite set $\{P_h : h \in H\}$ of pole figures has been measured.

$$P_h(y) = 4\pi \sum_{l=0}^{\infty} \sum_{\nu=1}^{N(l)} F_{lh}^{\nu} \dot{k}_l^{\nu}(y), \quad ODF(g) = \sum_{l=0}^{\infty} \sum_{\mu=1}^{M(l)} \sum_{\nu=1}^{N(l)} C_l^{\mu\nu} \ddot{T}_l^{\mu\nu}(g),$$

Assume the $\ddot{T}_l^{\mu\nu}(g)$ and $\dot{k}_l^{\nu}(y)$ to form a orthonormal system of functions in $L^2(SO_3)$ and $L^2(S^2)$. The structure of the projection operator in terms of C and F for $l = 1, \dots, L$ may be represented in matrix notation as

$$\begin{pmatrix} A_1 & & & & \\ & A_2 & & & \\ & & A_3 & & \\ & & & \ddots & \\ & & & & A_L \end{pmatrix} \begin{pmatrix} C_1 \\ C_2 \\ C_3 \\ \vdots \\ C_L \end{pmatrix} = \begin{pmatrix} F_1 \\ F_2 \\ F_3 \\ \vdots \\ F_L \end{pmatrix} \quad \Leftrightarrow \quad A_l C_l = F_l \ \forall l$$

These components of the system of equations have the same structure

$$\begin{pmatrix} A_l^1 & & & \\ & A_l^2 & & \\ & & \ddots & \\ & & & A_l^{N(l)} \end{pmatrix} \begin{pmatrix} C_l^{1,\cdot} \\ C_l^{2,\cdot} \\ \vdots \\ C_l^{N(l),\cdot} \end{pmatrix} = \begin{pmatrix} F_l^1 \\ F_l^2 \\ \vdots \\ F_l^{N(l)} \end{pmatrix} \Leftrightarrow A_l^\nu C_l^{\nu,\cdot} = F_l^\nu \ \forall l, \forall \nu$$

where these components are defined by

$$A_l^\nu = \tilde{A}_l = \frac{1}{\sqrt{2l+1}} \left(\dot{k}_l^\mu(h_b) \right)_{b=1,\dots,|H|\,,\,\mu=1,\dots,M(l)}$$

Thus A_l^ν is independent of ν.

$$C_l^{\cdot,\nu} = (C_l^{\mu\nu})_{\mu=1,\dots,M(l)}, \quad F_l^\nu = \left(F_{lh_b}^\nu\right)_{b=1,\dots,|H|}$$

Let $\tilde{P}_l \tilde{D}_l \tilde{Q}_l = \tilde{A}_l$ be a singular value decomposition (svd) of the small matrix $\tilde{A}_l$ with orthonormal matrices $\tilde{P}_l \in \mathbb{R}^{|H| \times r}$ and $\tilde{Q}_l \in \mathbb{R}^{r_l \times M(l)}$, and diagonal matrix $\tilde{D}_l \in \mathbb{R}^{r_l \times r_l}$ of minimal frame size $r_l = \text{rank} \tilde{A}_l$. This decomposition can be computed very fast with a computer because the frame size of $\tilde{A}$ is small (i.e. $r \leq 2l + 1 \ll 1000$). Then a singular value decomposition PDQ of A is given with matrices P, D, Q constituted of $\tilde{P}_l, \tilde{D}_l, \tilde{Q}_l$, respectively, in the form

$$P = \begin{pmatrix} \begin{bmatrix} \tilde{P}_1 & & \\ & \ddots & \\ & & \tilde{P}_1 \end{bmatrix} & & \\ & \ddots & \\ & & \begin{bmatrix} \tilde{P}_L & & \\ & \ddots & \\ & & \tilde{P}_L \end{bmatrix} \end{pmatrix}$$

$$D = \begin{pmatrix} \begin{bmatrix} \tilde{D}_1 & & \\ & \ddots & \\ & & \tilde{D}_1 \end{bmatrix} & & \\ & \ddots & \\ & & \begin{bmatrix} \tilde{D}_L & & \\ & \ddots & \\ & & \tilde{D}_L \end{bmatrix} \end{pmatrix}$$

$$Q = \begin{pmatrix} \begin{bmatrix} \tilde{Q}_1 & & \\ & \ddots & \\ & & \tilde{Q}_1 \end{bmatrix} & & \\ & \ddots & \\ & & \begin{bmatrix} \tilde{Q}_L & & \\ & \ddots & \\ & & \tilde{Q}_L \end{bmatrix} \end{pmatrix}$$

Thus, the singular value decomposition of this ODF–PDF projection can be computed at small computational cost. In the next section it will be shown how this decomposition can be applied in practical texture analysis.

2 Practical application of the SVD

The singular value decomposition immediately provides the least squared error back transformation matrix and its singular value decomposition without additional computational effort, it is the Moore–Penrose inverse of the projection matrix, and in fact of the projection operator:

$$A^- := Q^t D^{-1} P^t, \text{where } D \text{ is a diagonal matrix} \tag{1}$$

with nonzero singular values

$$\lambda_{lk} = 1/\tilde{D}_{l,kk},\ l = 1, \ldots, L, k = 1, \ldots, r_l$$

of multiplicity given by $N(l)$.

Since the inverse A^- is independent of the measured intensities, it is sufficient to compute it once and use it for all experiments with measured pole figures of the same set H of crystal forms.

Given the variance–covariance matrix Σ_F of the measurement error of the experimental coefficients $\hat{F}_{lh}^{\nu}$, the variance–covariance matrix σ_C of the measurement error of the $C_l^{\mu\nu}$ coefficients may be computed according to

$$\Sigma_C = A^- \Sigma_F A^{-t} \tag{2}$$

In the next sections it will be shown how to use this relation, but first a modified decomposition will be considered which simplifies relation (2) and yields results with smaller estimation error.

3 Taking different measurement errors into account

Some pole figures can be measured with better accuracy than others. Therefore, they have different standard errors of the experimental coefficients of their series expansion. The normalisation condition

$$\oint \left(\alpha^{-1}\, \dot{k}_l^{\nu}(y)\right)^2 dy = \alpha^{-2}$$

can be used to deal with objects of different statistical measurement errors. If the random variables F_{lh}^{ν} are replaced by $\tilde{F}_{lh}^{\mu} = \alpha_{lh}^{\nu} F_{lh}^{\nu}$ such that $\mathrm{Var}\left[\tilde{F}_{lh}^{\nu}\right] = {\alpha_{lh}^{\nu}}^2 \mathrm{Var}\left[F_{lh}^{\nu}\right] = 1,\ \forall h \in H$, using constants $\alpha_{lh}^{\nu} := (\mathrm{Var}[F_l^{\nu,h}])^{-0.5}$ to represent how well a harmonic of order l can be determined using the h pole figure, depending on the the reflex and on the sampling grid. The variances can be found by repeated measurements on appropriate test samples.

Assuming that the variance only depends on l and μ these two parameters this renormalisation does not change the structure of the singular value decomposition. But it will change the svd itself. If the variance will also depend on ν, not only on l and h the block structure of the projection matrix A will be preserved, but the $A_l^{\nu\prime}$ will then depend on ν. This will only cost more computer time, but the theory is unaffected by this:

$$(A_l^{nu\prime})_{b\mu} = (1/\alpha_{lh_b}^{\nu})(A_l^{nu})_{b\mu}$$

Applying the singular value decomposition of the operator A' projecting the $C_l^{\mu\nu}$ to these modified $\tilde{F}$ to compute its Moore–Penrose inverse using formula (1) yields $\hat{C}_l^{\mu\nu}$ with minimal measurement error variance. This follows from the theory of optimum weighted least squares regression.

4 Design of experiments

Let H be a set of experimentally accessible pole figures with independent standard measurement errors σ_{hlm} for the experimental coefficients F_{lh}^{ν} of the h pole figure. Let PDQ denote the associated singular value decomposition.

An experimental design is a subset of these crystal forms. The general idea is to look for the best subset out of some sensible subsets and measure only the pole figures belonging to this subset.

4.1 Optimality criteria

Different optimality criteria are often used in experimental design (Pukelsheim 1993):

- Determinant optimality (D-optimality): Minimize the determinant of the variance matrix.
- Average optimality (A-optimality): Minimize the mean estimation variance.
- Eigenvalue optimality (E-optimality): Minimize the largest eigenvalue of the variance matrix.
- Trace optimality (T-optimality): Maximize the trace of the information matrix (which is the inverse of the estimation variance matrix).

These entities can be calculated form the singular value decomposition by the following formulae if the stochastic errors of $\alpha_l^{h_k} F_{lh_k}^{\mu}$ are independent and every single variance is rescaled to unity

$$\mathrm{D} = \left(\prod_{l=1}^{L} (\det \tilde{D}_l)^{N(l)} \right)^{-2} \qquad \mathrm{A} = \sum_{l=1}^{L} N(l) \mathrm{trace} \tilde{D}_l^{-2}$$

$$\mathrm{E} = (\min_{l,k} \tilde{D}_{l,kk})^{-2} \qquad \mathrm{T} = \sum_{l=1}^{L} N(l) \mathrm{trace} \tilde{D}_l^{2}$$

All these formulae can be evaluated with a computer very fast. Therefore, these criteria may be evaluated for all feasible sets of pole figures which in turn may be ranked according to the amount of information they provide. The average criterion is equivalent to best approximation of the ODF in mean squared error in the space of functions $L^2(SO_3)$.

4.2 Optimality in case of dependent measurement errors

Unfortunately, the assumption of independent measurement errors may not be realistic, and they have to be treated as dependent. Therefore, the assumption is relaxed that the measurement errors of F_{lh}^{ν} are uncorrelated for different h only. Then for the average criterion the theory remains exactly true because only the diagonal elements of the matrix $(Q^t D^{-1} P^t)\Sigma_F(PD^{-1}Q)$ are relevant. These depend only on the diagonal blocks of Σ_F because of the special block structure of $PD^{-1}Q$. These diagonal blocks of Σ_F are diagonal themselves. Therefore the the non diagonal elements of Σ_F do not influent the results. For the other criteria this is only true approximately. Thus the A-optimality criterion seems favourable as it is also equivalent to optimum approximation of the ODF as already mentioned above.

This kind of dependence is e.g. also introduced in case the normalisation must be calculated from the measurements as usual.

5 Extracting information of high order

The singular value decomposition also answers a question which seems to have slipped the attention: What do pole figures tell about the harmonic terms $C_l^{\mu\nu}$ of degree $l > L = max_L \{L : N(L) \leq |H|\}$?

The conventional harmonic method reconstructs an ODF by first constraining the possible results to a subspace of functions represented by a finite harmonic series expansion of degree L, and then exactly calculates the projection of the true ODF to this subspace.

The singular value decomposition provides an orthogonal subspace of harmonic functions of any order l, for which the orthogonal projection of the ODF can be calculated. It is the subspace $\mathrm{im}Q_l^t$, where Q_l only consists of a minimum number of rows (this means the frame size of D_l is chosen to be minimum).

For these reconstructions it can be shown that

Proposition 1: If the pole figures $P_h(y)$ are compatible, then for the system

$$O\hat{D}F(g) = \sum_{l=1}^{\infty} \sum_{\nu=1}^{N(l)} \sum_{k=1}^{\mathrm{rank}\,\tilde{D}_l} \left(\tilde{D}_{l,kk}^{-1} \sum_{b=1}^{|H|} P_{l,bk} F_{lh_b}^{\nu} \right) \sum_{\mu=1}^{M(l)} Q_{l,k\mu} \dot{\ddot{T}}_l^{\mu\nu}(g)$$

it holds

$$P_h[O\hat{D}F] = P_h, \ \forall h \in H$$

which means that the pole figures are reproduced exactly. If the pole figures are not compatible, then this solution minimizes the mean squared error under all functions

$$\sum_{b \in B} \int_{S^2} \left(P_{h_b}[O\hat{D}F](y) - \tilde{P}_{h_b}(y) \right)^2 dS(y) \longrightarrow \min$$

In both cases it is the function with minimum L^2 norm that satisfies the criterion. Since it is a projection, the coefficients of all basis vectors in the image space of the reconstruction are identifiable. □

Thus, pole figures can be reproduced exactly up to any order of their harmonic series expansion.

6 References

Louis, A.K. (1986) Incomplete data problems in x-ray computerized tomography I: Singular value decomposition of the limited angle transform, *Numer. Math.* **48**, 251-262

Maaß, P. (1988) The x-ray transform: singular value decomposition and resolution, *Inverse Problems* **3**, 729-741

Friedrich Pukelsheim (1993) *Optimal Design of Experiments*, Wiley Series in Probability and Mathematical Statistics, Wiley, New York.

A ROLE OF TEXTURE AND ORIENTATION CLUSTERING IN ELECTROMIGRATION FAILURE OF ALUMINUM INTERCONNECTS

H.T. JEONG, J. A. SZPUNAR and K. LEE
Department of Mining and Metallurgical Engineering, McGill University,
3610 University Street, Montreal, Quebec, Canada H3A 2B2
D. P. FIELD
TexSEM Laboratories, Draper, UT 84020, U.S.A.

Abstract

To understand the influences of texture, special grain boundaries and orientation clustering on electromigration-induced and stress-induced failures in aluminium thin films prepared with different manufacturing conditions, the texture, the distribution of coincidence site lattice (CSL) grain boundaries and the distribution of grain size as a function of the misorientation angle were measured using orientation imaging microscopy (OIM). Stress measurement and electromigration tests were performed on all these specimens. Experimental results show that the lifetime of patterned films increases with increasing the intensity of {111} fibre texture, the orientation clustering and the frequency of CSL boundaries.

Keywords: Electromigration failure, orientation clustering, aluminium thin film, CSL boundary

1 Introduction

Thin film multilayer interconnects are becoming smaller and more complex, which induces various types of failures because of the increasing sophistication in multilayer interconnect structures of integrated circuit chips. Many factors influence the reliability of thin film interconnects including the texture, which is developed during the deposition processes and annealing (Attardo and Rosenberg 1970; Nagasawa et al. 1979; Taniguchi et al. 1993). Recent studies show that the activation energy for electromigration is dependant on the texture and that a strong {111} texture in aluminium films improve the electromigration lifetime (Li et al. 1989; Knorr and Rodbell 1992)

Coincidence site lattice (CSL) grain boundaries have special misorientations between grains. During the last few years, the research on the properties of the CSL grain boundaries has intensified, because they have been shown to be linked to special physical properties of materials (Watanabe 1989; Palumbo et al. 1991; Harase and Shimizu 1992). Specifically, the electromigration failure depends on the grain misorientation distribution and, therefore, links the grain boundary structure to the mass transport which takes place primarily along the grain boundaries. There have been few systematic studies of the effect that CSL boundaries have on electromigration failure in thin films (Fionova et al. 1993). However, it is not clearly understood what role the CSL boundaries play in electromigration failure.

Even though the influence of grain size on the reliability of thin films has been well established (Attardo and Rosenberg 1970; Cho and Thomson 1991; Genut et al. 1991), very little work has been done to determine the relationship between the morphology of thin films and their reliability.

The purpose of this study is to improve the understanding of how texture, orientation clustering and the CSL boundary distribution effect the reliability of aluminum thin film interconnects.

2 Experiments

Pure aluminium films were deposited on oxidized silicon using partially ionized beam (PIB) deposition and sputtering. Two specimens were prepared using the PIB technique with two different ion contents: PIB2/1 with 1% ion content and PIB2/2 with 2%. The other specimen, SP2, was prepared by sputtering. The samples obtained using the three different processing conditions were annealed at 400°C for an hour in forming gas (90% N_2 – 10% H_2).

The (111), (200) and (220) pole figures for each film were measured using the Schulz reflection method up to a tilting angle of 80 degrees with a Siemens D500 X-ray goniometer. The orientation distribution function was calculated using the series expansion method with L_{max}=22.

The distribution of CSL boundaries was measured using orientation imaging microscopy (OIM). The measurements using the OIM were considered to be different grain when the misorientation between two measurements was greater than 5 degrees. The numbers of total grain boundaries considered in the specimens of PIB2/1, PIB2/2 and SP2 are 13533, 15262 and 12141, respectively, and the frequency of occurrence of CSL boundaries between $\Sigma3$ and $\Sigma29$ CSL boundaries was obtained.

For the analysis of the orientation clustering, the distribution of grain size as a function of the misorientation angle that defines a grain boundary was measured using the OIM. If the misorientation between two measurements is greater than specific angle, such as 2, 5, 10, 15 or 20 degrees, the measurements are considered to be different grains. The average grain size as a function of the misorientation angle was calculated using these data.

For the electromigration failure analysis, aluminum thin films were patterned into test structures by standard silicon processing techniques. At least ten unpassivated lines 1.8μm wide were tested at a current density of 1×10^6 A/cm^2 and at the temperature of 225°C.

3 Result and Discussion

The texture of the PIB2/1, PIB2/2 and SP2 specimens are shown in Fig. 1. The specimen PIB2/1 and PIB2/2 have a strong {111} fibre texture and the specimen SP2 has a {332} fibre texture, which is inclined away from {111} fibre texture by about 10 degrees. The specimen PIB2/1 shows sharper {111} fibre texture than the specimen PIB2/2 and the specimen SP2 shows the weakest fibre texture. The maximum values of f(g) for the specimen PIB2/1, PIB2/2 and SP2 are 13.3, 7.1 and 4.9, respectively.

The results of the electromigration tests are shown as the cumulative failure distribution in Fig. 2. The median time-to-failure (t_{50} value) is illustrated as a function of the maximum intensity of the fibre texture in Fig. 3. It is clear that the lifetime of aluminum thin films increases as the strength of {111} texture increases. This result is taken from the work by Knorr and Kodbell (1992). They pointed out that a substantial improvement in reliability is possible by obtaining strong {111} fibre texture. It should be also noticed that the tilt of the predominant texture component away from the {111} fibre texture observed in SP2 has a significant effect on the failure lifetime.

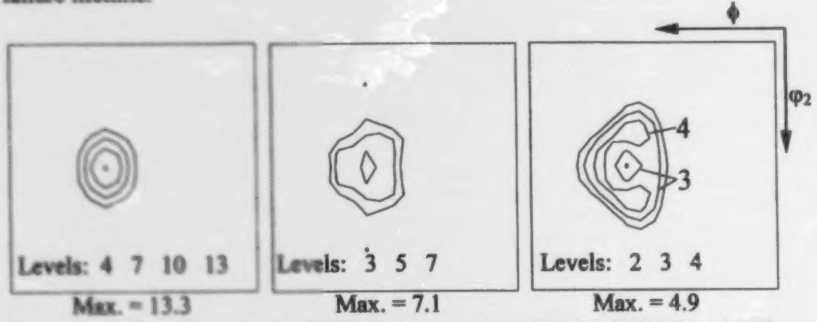

Fig. 1: $\varphi_1 = 0°$ sections in the ODF of the specimen PIB2/1, PIB2/2 and SP2.

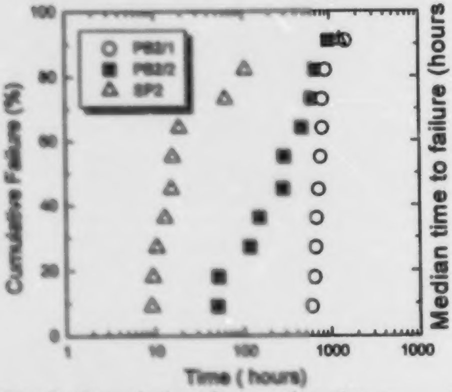

Fig. 2: Cumulative electromigration as function of time.

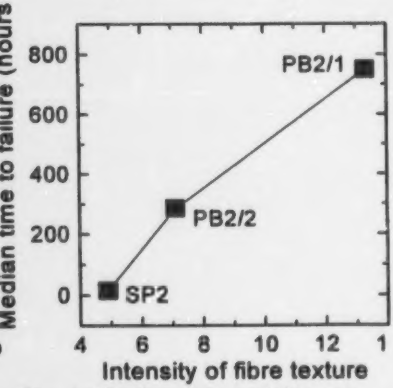

Fig. 3: Median time to failure as function of intensity of fibre texture.

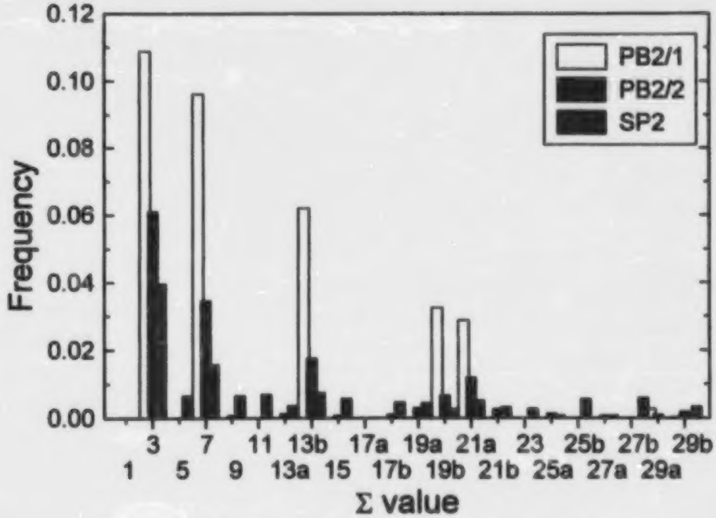

Fig. 4: Distribution of CSL boundaries from Σ3 to Σ29.

Fig. 4 shows the distribution of CSL boundaries from Σ3 to Σ29 for the three specimens. In all specimens, the frequency of occurrence of the Σ3 and Σ7 boundaries are relatively higher than other CSL boundaries. In addition the thin films deposited by partially ionized beam technique (PIB2/1, PIB2/2) have higher frequency of Σ3, Σ7, Σ13b, Σ19b and Σ21a boundaries than the sputtered film (SP2). Comparing the results for specimens PIB2/1 and PIB2/2, PIB2/1 has a higher frequency of these specific CSL boundaries than PIB2/2. These specific CSL boundaries may influence the improvement in electromigration lifetime. It is also noticeable that these boundaries are having a common <111> rotation axis. Specimen SP2 has a higher frequency of Σ3, Σ7 boundaries and relatively random distribution of CSL boundaries.

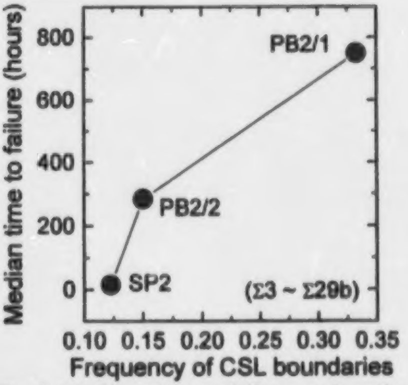

Fig. 5: Median time to failure as function of total frequency of CSL boundaries.

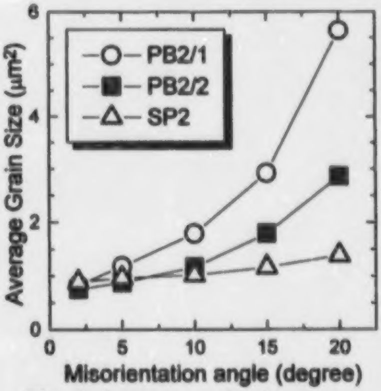

Fig. 6: Average grain size as function of misorientation angle.

The results of the electromigration test are compared to total frequency of CSL boundaries in Fig. 5. The specimen PIB2/1 has the highest percentage of CSL boundaries, 33.3%, as well as the longest median time-to-failure (t_{50} value), 772 hours. Specimen PIB2/2 had 15.0% of CSL boundaries and t_{50} value of 235 hours. Specimen SP2 had the shortest lifetime, $t_{50} = 29$ hours, and the lowest percentage of CSL boundaries, 12.3%. Several studies (Brandon 1966; Warrington and Boon 1975; Garbacz and Grabski 1993a) have calculated the frequency of CSL boundaries in materials with a random grain orientation. A total of 9.2% of the boundaries are found to be $\Sigma3$ to $\Sigma27$. This result indicates that the grain boundary texture in SP2 deviates slightly from the distribution expected in a random material. It is difficult to evaluate how important they are in controlling the electromigration lifetime of the films. Modelling of {111} fibre texture (Grabacz and Grabski 1993b) shows that the proportion of CSL boundaries continues to increase as the {111} distriubtion tightens beyond the level in PIB2/1. The trend of an increasing fraction of $\Sigma3$, $\Sigma7$, $\Sigma13$, $\Sigma19$, and $\Sigma21$ boundaries further develops.

Fig. 6 shows the average grain size as a function of the misorientation angle, which defines a grain boundary, for three specimens. For the specimen PIB2/1, the average grain size is drastically increased with increasing the misorientation angle. The specimen PIB2/2 shows similar trend with the specimen PIB2/1. However, in the case of the specimen SP2, the average grain size seems to be independent of the misorientation angle.

If the orientation of neighbour grains in textured materials were randomly distributed without any orientation clustering, the average grain size must be independent of the misorientation angle that defines a grain boundary. However, if the orientation of neighbour grains had a preference for being small angle with each other, the average grain size is increased with increasing the misorientation angle that defines a grain boundary. That is, the orientation clustering is presented by the dependency of the average grain size on the misorientation angle that defines a grain boundary. Therefore, the specimen PIB2/1 shows severe orientation clustering and the specimen PIB2/2 has less orientation clustering than the specimen PIB2/1. However, there is no orientation clustering in the specimen SP2.

It is clear from these comparisons that the frequency of occurrence of CSL boundaries and the orientation clustering are associated with the time-to-failure.; a higher percentage of CSL boundaries and more orientation clustering correlate with longer lifetime in patterned lines.

It is known that the diffusivity along the high angle grain boundaries depends on the misorientation of grains (Gleiter and Chalmers 1972; Balluffi 1982) and that the diffusivity of grain boundaries with special misorientation (CSL boundaries) is less than that for general grain boundaries by several orders of magnitude (Garbacz and Grabski 1993a). Therefore, the specimen that has more CSL boundaries may have lower diffusivity, so that the electromigration failure is retarded.

The possible reason that the orientation clustering increases the time-to-failure is also similar with the effect of the total frequency of CSL boundaries on the electromigration failure. If the orientation clustering were developed, the misorientation between grains becomes small and the total frequency of high angle grain boundaries may be reduced.

4 Conclusion

The role of texture and grain boundary character distribution on the reliability of aluminum thin films was investigated for three thin film specimens prepared with different manufacturing conditions.

1. The lifetime of aluminum thin films increases with both the strength of the {111} fibre texture and the total frequency of CSL boundaries. A strong {111} fibre texture in the films increases the total frequency of CSL boundaries. Therefore, A sharp {111} fibre texture is desirable to improve the reliability in aluminum thin films.
2. The orientation clustering can be analyzed by the measurement of the grain size distribution as a function of the misorientation angle that defines a grain boundary. The orientation clustering is presented by the dependency of the average grain size on the misorientation angle that defines a grain boundary.
3. The orientation clustering increases the time-to-failure of aluminum thin films. It may be originated from the fact that the orientation clustering reduce the total frequency of high angle grain boundaries.

5 References

Attardo, M.J. and Rosenberg, R. (1970) *J. Appl. Phys.*, Vol. 41, p.2381.

Balluffi, R.W. (1982) *Metall. Trans. A*, Vol. 13, p. 2069

Brandon, D.G. (1966) *Acta Met.*, Vol. 14, p.1479.

Cho, J. and Thompson, C.V. (1991) *J. Appl. Phys.*, Vol. 69, p.2117.

Fionova, L.K., Kononenko, O.V. and Matveev, V.N. (1993) *Thin Solid Films*, Vol. 227, p. 54.

Garbacz, A. and Grabski, M.W. (1993a) *Acta Met.*, Vol. 41 p.469.

Garbacz, A. and Grabski, M.W. (1993b) *Acta Met.*, Vol. 41 p.475.

Genut, M., Li, Z., Bauer, C.L., Mahajun, S., Tang, P.F. and Milnes, A.G. (1991) *Appl. Phys. Lett.* Vol. 58, p. 2354.

Gleiter, H. and Chalmers, B. (1972) *Prog. Mater. Sci.*, Vol. 16, p. 142.

Harase, J. and Shimizu, R. (1992) *Acta Met.*, Vol. 40, p. 1101.

Knorr, D.B. and Rodbell, K.P. (1992) *Proceedings of The Mat. Res. Soc. Symp.*, Vol. 265, p. 113.

Li, P., Yapsir, A.S., Rajan, K. and Lu, T.M. (1989) *Appl. Phys. Lett.*, Vol. 54, p. 2443.

Nagasawa, E., Okabayahsi, H., Nozaki, T. and Nikawa, K. (1979) *Proceedings of The 17th Reliability Physics Symposium(IEEE, New York)*, p.64.

Palumbo, G., King, P.J., Aust, K.T., Erb, U. and Lichtenberger, P.C. (1991) *Scripta. Metall.*, Vol. 25, p. 1775.

Taniguchi, H., Ushiro, T., Okamoto, Y., Akagi, Y. and Koba, M. (1993) *Proceedings of Mat. Res. Soc. Symp.*, Vol. 280, p. 523.

Warringtion, D.H. and Boon, M. (1975) *Acta Met.*, Vol. 23, p. 599.

Watanabe, T. (1989) *Mater. Sci. Forum*, Vol. 46, p. 25.

Al TEXTURE ON <001> W, Ti_xW_{1-x} AND TiN BARRIER LAYERS

L.D. MADSEN and E.B. SVEDBERG

Material Physics, Linköping University, Linköping, Sweden

D.B. BERGSTROM, C.-S. SHIN, I. PETROV and J.E. GREENE

Materials Science, University of Illinois, Urbana, IL USA

Abstract

TiN, TiW or a combination of Ti and TiN are often used as barrier layers in silicon technology to isolate Al metallization from the underlying Si. Tungsten, since it is used as a local interconnect and in via plugs, can also be in direct contact with the Al. Reliability, particularly electromigration continues to be an outstanding issue for Al metallization. Control of film texture is essential for the best electromigration properties of ultra-high density microelectronic device structures where epitaxy or near-epitaxy will be demanded. Using model systems of thin Al films deposited onto epitaxial buffer layers, the 'perfection' which can be achieved for the Al in terms of texture and mosaicity was investigated for buffer layers of W, Ti_xW_{1-x} and TiN. With a combination of x-ray diffraction (XRD) $\theta-2\theta$ scans, pole figure analyses, high-resolution XRD mapping, and atomic force microscopy (AFM), the texture, crystal quality and surface morphology were evaluated. Due to a large lattice misfit, Al on W developed two dominant orientations, $\langle 01\bar{6}\rangle$ and $\langle 11,3,9\rangle$ oriented grains with extensive twinning, or more simply described as tilted <001> and <101> grains. Al on TiW developed a different texture of similar complexity: $\langle 10,\bar{1},1\rangle$ and $\langle 1\overline{34}\rangle$, also with multiple placements. TiN was clearly superior as a buffer layer for Al in terms of achieving a single-domain <001> Al texture, and reducing or eliminating twins. The mismatch between Al and TiN is 3.9%. For the Al/W and Al/TiW systems, XRD mapping of asymmetric reflections allowed the average in-plane lattice parameters to be determined, indicating that the misfit is essentially identical (9.2%). It is this misfit and the resulting induced strain that plays a major factor in the texture determination.

Keywords: Aluminum, barrier layer, epitaxy, interconnect, silicon device technology, titanium nitride, titanium tungsten, tungsten

1. Introduction

Barrier layers are used to isolate Al metallization from the underlying Si, often these are TiN, TiW or a combination of Ti and TiN (Shacam-Diamand 1995). Additionally since W is used as a local interconnect and in via plugs, it can also be in direct contact with the Al depending on the overall process complexity (Shacam-Diamand 1995). Reliability, particularly electromigration continues to be an outstanding issue for Al metallization. Controlling film texture is essential for electromigration resistance of ultra-high density microelectronic device structures where epitaxy or near-epitaxy will be demanded. Using model systems of thin Al films deposited onto epitaxial buffer layers, the 'perfection' which can be achieved for the Al in terms of texture and mosaicity was investigated.

2. Experimental Details

140 nm thick <001>-oriented buffer layers of W, Ti_xW_{1-x} (referred to as TiW from herein) and TiN were grown on MgO {001} substrates by ultra-high vacuum magnetron sputtering. The W and TiW layers were deposited at a substrate temperature, T_S=600°C, whilst the TiN was deposited at $T_S \approx$720°C. The TiN and W films were grown in Ar discharges, however a heavy gas (Kr) was used for the TiW films to prevent Ti loss due to resputtering by energetic backscattered neutrals (Bergstrom et al. 1995). Without breaking vacuum, the samples were allowed to cool to room temperature and then Al films with a nominal thickness of 190 nm were grown at ambient conditions (which due to plasma heating effects made T_S~30-50°C).

Texture, crystal quality and surface morphology were determined by a combination of x-ray diffraction (XRD) $\theta-2\theta$ scans, pole figure analyses and high-resolution mapping, and atomic force microscopy (AFM). $\theta-2\theta$ XRD measurements were made on a powder diffractometer (Philips PW1820) with Bragg-Brentano geometry, a long fine line-focus Cu source with a Ni filter, 1/4° divergence slit on the primary side, and a 0.1° receiving slit and curved graphite secondary monochromator on the secondary side. $\theta-2\theta$ scans were taken at 30 kV and 30 mA over a range of 30-160° using a step size of 0.02° and a dwell time of 4 s. XRD mapping and pole figure measurements were carried out on a four-circle diffractometer (Philips MRD) operated at 40 kV and 40 mA with parallel-beam x-ray optics and a 1 x 1 mm^2 point-focus Cu x-ray source. For the mapping of the Al/TiN/MgO sample, the crystal quality was sufficient to use the 4-crystal Ge (220) Bartels monochromator on the primary side and a 1.8 mm receiving slit on the secondary side. Mapping of the MgO (200) and barrier (200) symmetric reflections were used to correct the barrier layer (222) or (024) asymmetric reflection positions for the lattice parameter calculations. Pole figures of the Al {111}, {200} and {220} reflections were taken using a reflection geometry (Schultz 1949) with tilt angles ψ from 0 to ~85° in 0.5-3° steps (depending on the accuracy required). The azimuthal direction ϕ was continuously scanned for each ψ value and integrated at 4° intervals for an 6-8 s acquisition period for every data point. Substrate intensity contributions were assessed by making similar pole figures from a reference sample of the barrier layer on MgO.

AFM measurements were performed with a NanoScope IIIa system in tapping mode, with scanning areas of 10000, 5000, and 1000 nm, and a resolution of 512 by 512 pixels. Evaluation of the root-mean-square (rms) surface height variations were carried out.

3. Results and Discussion

θ–2θ scans revealed an Al peak only for the Al/TiN sample (Fig. 1a). TiW has bcc structure (with Ti and W in solid solution) (Jin and Qiu 1993) and a larger lattice parameter than pure W and consequently its (002) reflection appears shifted to the left w.r.t. W (Fig. 1a). Pole figures revealed a simple $00l$ texture for the Al on TiN (Fig. 1b) without any hint of 111-oriented grains. Al on W developed two dominant orientations (Madsen et al. 1999), $<01\bar{6}>$ and $<11,3,9>$ oriented grains with extensive twinning, or more simply described as tilted $<00l>$ and $<l0l>$ grains. Al on TiW texture (Fig. 1c) can be explained as a $<10,\bar{1},1>$ and $<1\overline{34}>$ texture with an additional minor component, or as a texture dominated by both $0\,0\,l$ - and $0\,l\,l$-oriented film-components tilted 6-12° away from the surface normal. The atomic match at the interface between Al and TiW is such that for the $<10,\bar{1},1>$ texture, 50 TiW cells are covered by 11 Al atoms in a diamond-shaped pattern (Fig. 1d). For the $<1\overline{34}>$ texture there is a similar pattern covering 32 TiW unit cells with 8 Al atoms (Fig. 1e).

The surface of reference samples, barrier layers without Al, were examined by AFM (Fig. 2). From rms values <1.5 nm for all the barrier layers, it seems apparent that surface roughness did not play a major role in texture selection. Although the W and TiW are both rotated 45° w.r.t to the MgO unit cell, the misfit is still much larger than for the TiN case where it is sufficiently small (Table I) to promote epitaxial growth. In other metal-on-metal systems with large lattice misfits, observed tilts were believed to relieve long-range strain (Du and Flynn 1990). XRD mapping allowed the average in-plane lattice parameters to be determined (Table I), showing that the misfit is nearly identical

Table I. Comparison of lattice parameters of buffer layers to the nominal lattice parameter of 4.0494 Å for Al.

Buffer Layer	Measured Lattice Parameters [Å]		Misfit with Al	Orientation w.r.t. MgO
	Out-of-Plane	In-Plane	[%]	
W	3.18	3.15	9.2	rotated 45°
TiW	3.21	3.15	9.2	rotated 45°
TiN	4.25	4.21	3.9	no rotation

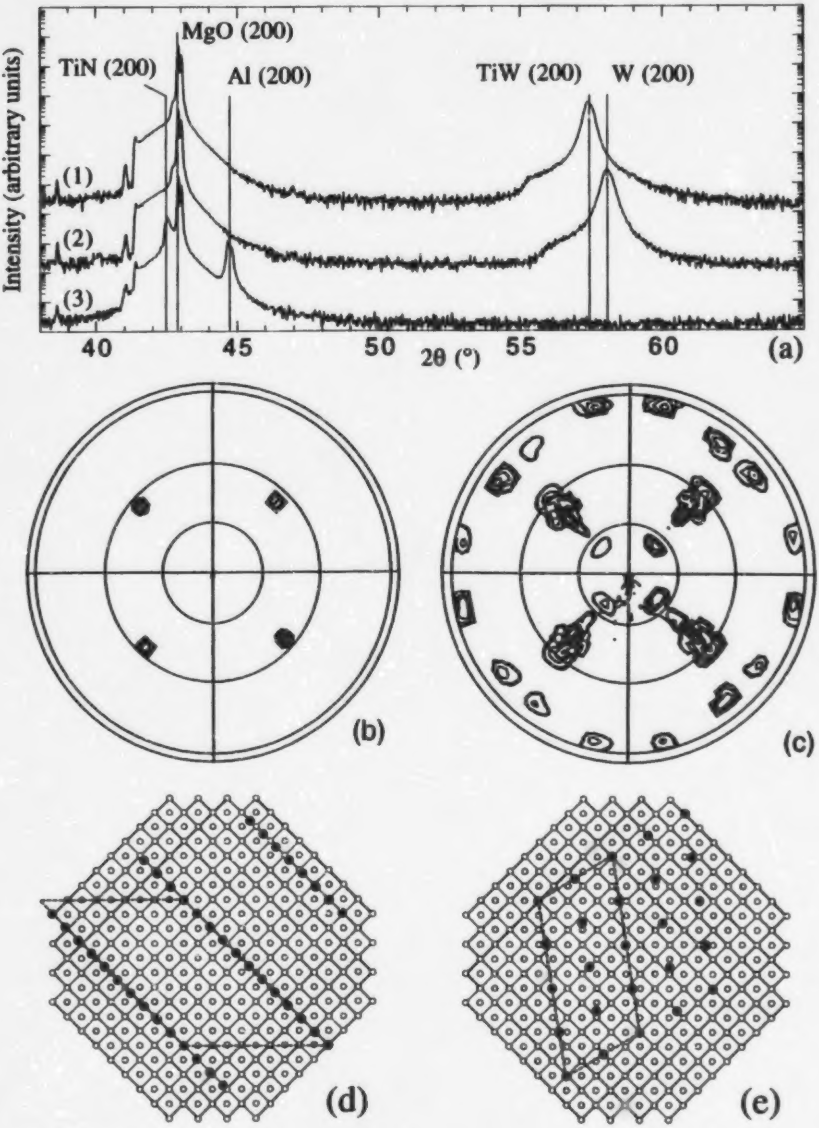

Fig. 1: (a) θ–2θ XRD scans and Al {111} pole figures are shown for (b) Al/TiN and (c) Al/TiW. Schematic representation of the Al-TiW interface for the (d) $\langle 10,\bar{1},1\rangle$ and (e) $\langle 1\overline{34}\rangle$ textures where the Al and W atom positions are represented by • and ° respectively.

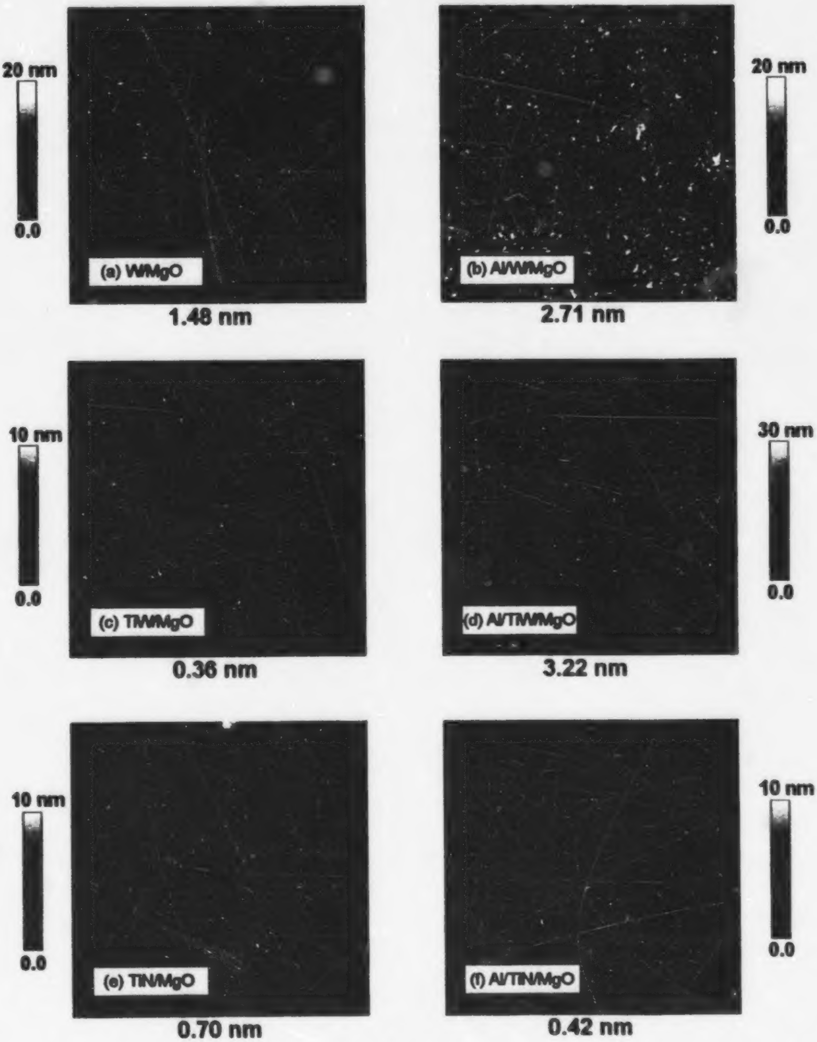
20 nm
0.0
(a) W/MgO
1.48 nm
(b) Al/W/MgO
2.71 nm
20 nm
0.0
10 nm
0.0
(c) TiW/MgO
0.36 nm
(d) Al/TiW/MgO
3.22 nm
30 nm
0.0
10 nm
0.0
(e) TiN/MgO
0.70 nm
(f) Al/TiN/MgO
0.42 nm
10 nm
0.0

Fig. 2: AFM images of barrier layers (at the left) and Al films (at the right) deposited onto W, TiW and TiN . Images are 5x5 μm^2 in area and the vertical scale varies from 10 to 30 nm as shown. Under each image, the rms roughness value is provided.

in the Al/W and Al/TiW systems. At their melting points, the bulk surface energies for Al, Ti and W are 1070, 1610 and 2670 mJ/m^2 respectively (Missol 1973). Additionally Auger spectroscopy studies of similar ones (Bergstrom et al. 1995) indicate that the surface of the TiW films are Ti-rich, due to the energy gain in having a Ti layer at the surface. Based on this, we suggest that the Ti in the TiW system in comparison to pure W significantly alters the surface energy, so that the Al mobility increases on the Ti enriched surfaces and subsequently influences the texture formation (Carel et al. 1996).

4. Conclusions

The implications for these results in terms of Al reliability are that W and TiW underlayers promote a tilted and twinned growth of two dominant Al orientations at ambient conditions and therefore should be avoided. On the other hand, Al texture formation on TiN is highly-oriented (001) suggesting its superiority as a buffer layer in terms of reducing Al grain boundaries.

5. References

Bergstrom. D.B., Tian, F., Petrov, I., Moser, J. and Greene, J.E. (1995) Origin of compositional variations in sputter-deposited TiW diffusion barrier layers. *Appl. Phys. Lett.* Vol. 67, No. 21, pp. 3102-4.

Carel, R., Thompson, C.V. and Frost, H.J. (1996) Computer simulation of strain energy effects vs surface and interface energy effects on grain growth in thin films. *Acta. Mater.* Vol. 44, No. 6. pp. 2479-94.

Du, R. and Flynn, C.P. (1990) Asymmetric coherent tilt boundaries formed by molecular beam epitaxy. *J. Phys.: Condens. Matter.* Vol. 2, pp. 1335-41.

Jin, Z.-P. and Qiu, C. (1993) Thermodynamic evaluation of the Ti-W system. Mater. Sci. Technol. Vol. 9, pp. 378-83.

Madsen, L.D., Svedberg, E.B., Bergstrom, D.B., Petrov, I and Greene, J.E. (1999) Texture of Al thin films deposited by magnetron sputtering onto epitaxial W(001). *J. Appl. Phys.* submitted.

Missol, W. (1973) Calculation of the Surface Energy of Solid Metals. *Phys. Stat. Sol. (b)* Vol. 58, pp. 767-73.

Schultz, L.G. (1949) A direct method of determining preferred orientation of a flat reflection sample using a geiger counter x-ray spectrometer. *J. Appl. Phys.* Vol. 20, pp. 1030-1032.

Shacam-Diamand, Y. (1995) The reliability of aluminum/tungsten technology for VLSI applications. *MRS Bull.* Vol. XX, No. 11. pp. 78-82.

6. Acknowledgements

Thanks are extended to the students of the New Materials course. Funding was provided through Teknikvetenskapliga forskningsrådet (TFR), Stiftelsen för Strategisk Forskning (SSF), the U.S. Department of Energy, and the joint NSF and DARPA VIP Program.

MICROSTRUCTURES AND TEXTURES OF COPPER ELECTRODEPOSITS OF TiN

Insoo KIM and Sang Chul HONG
School of Advanced Materials and Systems Engineering, Kum Oh National University of Technology, Kumi, Kyung Buk, Korea, 730-701

Abstract

Cu electrodeposition has been used for ULSI metallization on TiN diffusion barrier. The microstructures, textures and surface morphologies of Cu electrodeposits were investigated with the variation of deposition conditions by using copper sulfate solution.

The surface roughness of as-deposited copper film was decreased with increasing the current density and additives , increased with increasing bath temperature.

The copper electrodeposited layer develops random texture in all deposition conditions.

Keywords: Electrodeposition, TiN diffusion barrier, Surface morphology, Texture

1 Introduction

Copper is being considered the material for semiconductor metallization because of its better conductivity, higher corrosion resistance in high temperature.(Gewirth et al. 1998; Materials world 1998; Time 1997)

Lee et al.(1997) and Dubin et al.(1997) reported a novel method of electrodeposition of copper, producing films having a low resistivity about 2 μ Ω · cm. Mak (1994) and Cho et al.(1993) reported the shortcoming of electroless deposition in copper metallization on the semiconductor. Choi et al.(1998) reported the copper metallization on the silicon wafer in copper sulfate bath.

In this study, the microstructures and surface morphologies of Cu electrodeposits on the TiN CVD coated silicon wafer were investigated with the variation of deposition conditions by using copper sulfate solution.

2 Experimental procedure

A bath solution was used for copper plating, which was composed of, copper sulfate, $CuSO_4$(160 ~ 200g/l), sulfate, H_2SO_4(60 ~ 80g/l). A silicon wafer with TiN CVD coated was used for copper plating.

A high purity copper plate was used as an anode. The distance between the anode and cathode was 6 ㎝.

The current density ranged from 2 ~ 10 A/dm^2 and the bath temperature ranged from 20℃ to 50℃. The bath was stirred and controlled to maintain a pH of 3.0.

The copper deposits of about 3 ~ 5 ㎛ in thickness were peeled off the cathode plate.

The 2θ - plane intensity of the electrodeposits was measured by an x-ray diffractometer. The surface morphologies were observed with a scanning electron microscope.

3 Results and discussion

Figure 1 shows the surface morphologies of copper electrodeposits with the change of current density, a) 2A/dm^2, b) 4A/dm^2 and c)6A/dm^2. The size of surface grains decreased with increasing current density.

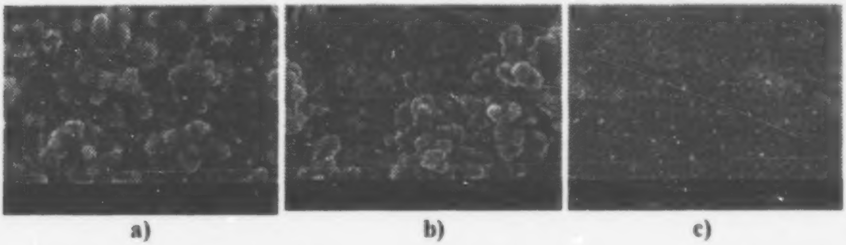
a) b) c)

Fig 1. Surface morphologies of copper electrodeposits with the change of current density. a) 2A/dm^2, b) 4A/dm^2, c) 6A/dm^2

Figure 2 shows the surface morphologies of copper electrodeposits with the change of additives amount a) 0.05g/l and b) 0.1g/l. The size of surface grains decreased with increasing additives.

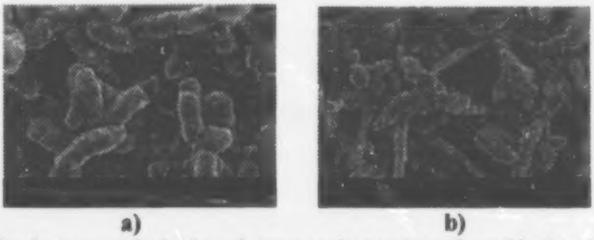
a) b)

Fig 2. Surface morphologies of copper electrodeposits with the change of additives amount. a) 0.05g/l, b) 0.1g/l

Figure 3 shows the surface morphologies of copper electrodeposits with the change of bath temperature. a) 20℃, b) 30℃ and c) 50℃. The size of surface grains increased with increasing bath temperature.

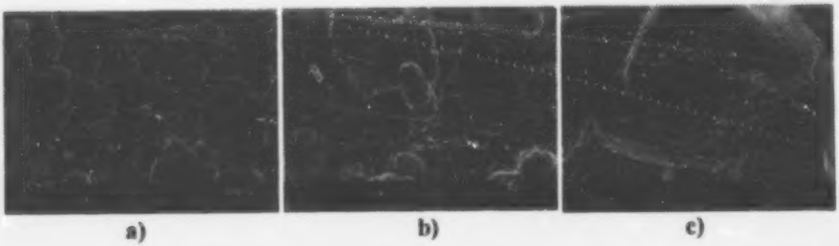

Fig 3. Surface morphologies of copper electrodeposits with the change of bath temperature. a) 20℃, b) 30℃, c) 50℃

Figure 4 shows the 2θ - plane intensity with the change of electrodeposition conditions.

Copper electrodeposits layer develops random texture in all deposition conditions.

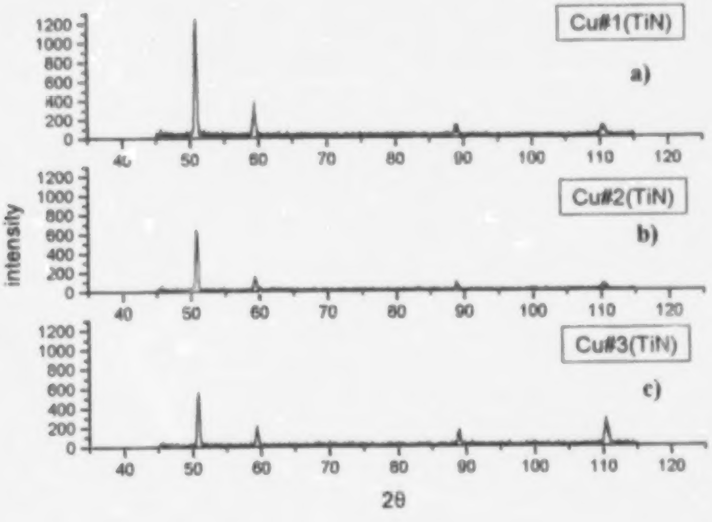

Fig 4. 2θ - plane intensity of copper electrodeposits layer.
($CuSO_4\cdot 5H_2O$: 200g/l, H_2SO_4 : 80g/l, Current density : $8A/dm^2$)
a) 20℃, b) 30℃, c) 50℃

4 Conclusion

1. Copper electrodeposits layer on the TiN can be obtained from copper sulfate, $CuSO_4$(160 ~ 200g/l), sulfate, H_2SO_4(60 ~ 80g/l) bath.
2. Electrodeposits grains were decreased with increasing the current density and additives, increased with increasing bath temperature.
3. Copper electrodeposts layer develops random texture in all deposition conditions.

5 References

Gewith, A. A., Andricacos, P. C., Switzer, J. A. and Dukovic, J. O.(1998) *Interface(The Electrochemical Society)* Spring Vol. 22. Materials World (1998) Apr. Vol. 221.

TIME(1997) Vol. 6, P72

Lee, M. K., Wang, J. J. and Wang, H. P. (1997) *J. Electrochem Society*, Vol. 144, P 1777.

Dubin, V. M., Ting, C. H. and Cheung, R. (June, 1997) 14th *International VLSI Multilevel Interconnection Conference*, Vol. 10, P 69

Choi, C. H., Lee, H. J., Min, S. H., Kim K. B. and Lee, D. N. (1998) *J. Korean Institute of Metals and Materials*, Vol. 36, No.10, P1686

COMPUTER SIMULATION OF THE EFFECT OF IMPURITIES ON DIFFUSION AT OXIDE BOUNDARIES

D.J. HARRIS and J.H. HARDING
Dept. Physics and Astronomy, University College London, London, United Kingdom

Abstract

A common method for protecting metals against corrosion is to ensure that they are covered by a thin, adherent oxide scale. The addition of suitable impurities can drastically reduce the rate at which such scales grow, leading to thinner scales of better quality. The most important process in the growth is usually considered to be diffusion down grain boundaries in the scale. We present the results of computer simulations, using a combination of a modified molecular dynamics technique and Monte Carlo, to calculate the effect of impurities on diffusion down grain boundaries in nickel oxide and alumina scales.

Keywords: atomistic simulation, correlation factors, grain boundary diffusion, Monte Carlo simulation, reactive element effect.

1 Introduction

A common method of inhibiting corrosion in metals is to grow a thin layer of oxide scale at the surface. To be effective, such scales should be impermeable, stable and adhere strongly to the metal (Schütze 1994). It is well known (Prescott and Graham 1992) that the addition of small amounts of carefully selected 'reactive' elements can have considerable beneficial effects on corrosion resistance. One of the most important effects is the slowing of the oxide growth rate, leading to dense, impermeable coatings. This result has usually been explained as the additives segregating to grain boundaries and then blocking grain boundary diffusion.

Few calculations on grain boundary diffusion have been attempted and only one (Duffy and Tasker 1986) attempted to simulate the reactive element effect. This paper considers the reactive element effect in two systems: NiO and Al_2O_3. We simulate grain boundary diffusion in two stages; first by calculating the activation energies of the various processes involved and second by using Monte Carlo methods to obtain an effective grain boundary diffusion coefficient.

2 Simulation methods

The energies of segregation of ions to the grain boundaries and of the various defect processes at the boundary are obtained by classical atomistic simulation. We assume that the ceramic consists of ions and the forces between them are the electrostatic forces between the ions and short-range pair potentials representing the Pauli repulsion and Van der Waals attraction terms. The polarisability of the ions is included using the shell model. The ion is represented as a massive core linked to a massless shell by a spring. (For a review of these models and their use see Harding (1990); for details of the potentials used see Lewis and Catlow (1985); Table 4).

We first calculate the structure of the relaxed grain boundary. We consider the crystal as a stack of planes parallel to the interface. The simulation is divided into two regions; an inner region containing the interface where the ions are relaxed to positions of zero force, and two outer regions where the ions are held fixed in relation to each other but the region is allowed to move as a whole, permitting the interface to dilate. The MIDAS code (Tasker 1979) is used for these simulations. We then calculate the energies of defects within the relaxed structure. Ions in an inner region around the defect are relaxed to positions of zero force and ions in an outer region are treated using a dielectric continuum approximation. The CHAOS code (Duffy and Tasker 1982) is used for these simulations. A major problem is finding the migration saddle points in highly asymmetric environments. A molecular dynamics approach was used (Harris et al. 1997). A small force is added to the moving ion to push it towards the vacancy while permitting it to move freely in the plane perpendicular to the direction of travel. A counter force is applied to the other ions in the simulation cell to prevent it acquiring momentum and the energies are scaled to remove energy added to the simulation by the force. This method enables us to investigate the trajectory of the moving ion and identify the saddle point and hence the migration energy. From this the hopping rate for the pathway may be estimated.

We can then use the approach of Mishin (1995) to obtain grain boundary diffusion coefficients. Monte Carlo simulations are performed of individual encounters between tracer ions and point defects. The partial correlation factors are then obtained by the usual matrix method (as discussed, for example, by Manning (1968)). From these partial correlation factors we can calculate the tracer diffusion coefficient for grain boundary diffusion and the effect of segregated 'reactive elements' on that coefficient. The method may readily be adapted to consider impurity diffusion to consider the question of the stability of the 'reactive elements' in the boundary.

3. Results

We have considered two materials; NiO and Al_2O_3. Boundaries were chosen to be representative of the types of high-angle tilt boundaries to be expected in the materials consistent with being computationally tractable. For NiO, the two boundaries chosen were the (310) and (410) symmetric tilt boundaries. Figure 1 shows the (410) boundary together with a nomenclature for the sites. Since the ion

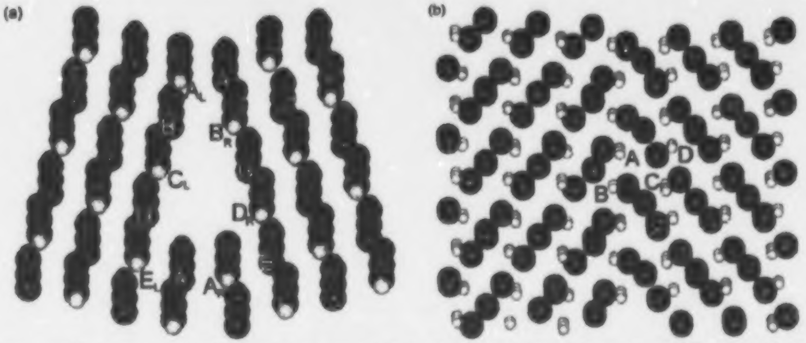

Fig. 1: Energy minimised structures of a) the (410) boundary in NiO and b) the $(10\bar{1}4)$ boundary in Al_2O_3 indicating cation sites for reactive elements.

sites for the boundary are not all equivalent, we must calculate the segregation energies for the candidate reactive elements from the bulk to each site to determine the positions of the impurities. The results are shown in Table 1. All the reactive elements segregate to the boundaries, but the energies vary from boundary to boundary and also from site to site within the boundary depending (in this example) on the ion size.

Table 1: Segregation energies (eV) for the (310) and (410) boundaries in NiO; for nomenclature of defect sites see Figure 1

Defect	(310) Boundary			(410) Boundary		
Site	Ca^{2+}	Sr^{2+}	Ba^{2+}	Ca^{2+}	Sr^{2+}	Ba^{2+}
A	-3.08	-4.14	-6.88	-0.49	-1.71	-4.77
B	-3.40	-4.83	-7.08	-1.14	-2.00	-3.33
C	-3.12	-4.80	-7.82	-1.43	-3.26	-5.96
D	-2.74	-3.03	-3.44	-1.22	-2.95	-6.02
E				-0.35	-0.53	-0.79

We then calculate the migration energies for the pathways between the sites for nickel and oxide migration. This is shown in Table 2. In the bulk, nickel migrates by a vacancy mechanism with a migration energy of 2.2eV. It is clear that the migration down the boundary has a greatly reduced migration energy. The calculated value for the bulk is significantly larger than the experimental values (1.3-1.6eV; Peterson and Wiley 1985); however, the ratio between bulk and interface values is correct (Duffy and Tasker 1986). The significant point is that in all cases, the reactive element raises the migration energy. The migration energy of the oxide vacancy in the bulk in 2.3eV; so again the presence of the boundary greatly lowers the migration energy. Here, however, the reactive elements either have little effect on the migration energy or lower it further. Matters are further complicated by the fact that oxygen migrates by

Table 2: Migration energies (eV) for vacancies in the presence of reactive elements (at their most stable sites on the right of the boundary) for the (310) and (410) boundaries in NiO: for nomenclature of pathways see Figure 1a

Defect	(310) Boundary				(410) Boundary			
	Ni^{2+} vacancy		O^{2-} vacancy		Ni^{2+} vacancy		O^{2-} vacancy	
	A_L-A_R	A_R-A_L	Fwd	Rev	A_L-A_R	A_L-A_R	Fwd	Rev
None	1.10	1.10	1.03	1.03	1.37	1.37	1.37	1.37
Ca^{2+}	1.40	1.60	1.12	0.35	0.98	1.36	1.60	1.55
Sr^{2+}	1.35	1.55	1.31	0.15	0.82	1.42	1.69	1.56
Ba^{2+}	1.85	0.50	0.90	0.73	2.54	1.02	1.15	1.26

an interstitialcy mechanism in the bulk with a migration energy of 0.9eV, but the migration energy of the interstitial mechanism in the boundary is *raised* to 1.1eV (see Table 3). This does not demonstrate that the vacancy mechanism dominates in the boundary since the activation energies are different in the two cases. Although the interstitial mechanism dominates in the boundary, it does not contribute to the oxidation of nickel as shown in the experimental study of Atkinson et al. (1985).

Table 3: Migration energies (eV) for interstitial O^{2-} down the channels in the presence of reactive elements (at their most stable sites) for the (310) and (410) boundaries in NiO.

Defect	(310) Boundary		(410) Boundary	
	Fwd	Rev	Fwd	Rev
None	1.01	1.01	1.04	1.04
Ca^{2+}	0.36	1.16	0.47	1.05
Sr^{2+}	0.58	1.26	0.22	1.00
Ba^{2+}	2.45	2.45	2.72	2.72

For Al_2O_3 we chose the $(10\bar{1}4)$ tilt boundary. There are two sites at the grain boundary that may be suitable for reactive elements (labelled A and B in Figure 1b). The calculations show that yttrium segregates to the boundary. Site B is preferred (segregation energy of –2.54 eV compared to –2.48eV for site A).

Migration energies for aluminium vacancy migration were calculated for a series of jumps around the boundary and in the bulk. Table 4 shows the migration energies at the boundary and in bulk. The energies for diffusion at the boundary are generally higher than the bulk migration energy of 1.64 eV. Le Gall et al. (1995) measured the self-diffusion of aluminium in bulk α-Al_2O_3, obtaining an *activation* energy of 5.2eV. Since their sample was contaminated by silicon, this energy represents a mixture of intrinsic and extrinsic diffusion effects and cannot easily be compared with our calculations. Vacancies migrate towards the boundary but once there they become bound. The addition of yttrium results in a decrease in the migration energy for jumps from site A to B or C and an increase for jumps from site B to D. Our results show that grain boundaries in alumina are not necessarily regions of high diffusivity.

Table 4: Migration energies (eV) for Al^{3+} vacancy migration in alumina for bulk and the $(10\bar{1}4)$ boundary: for nomenclature of pathways see Figure 1b

Jump	Undoped		Y^{3+} doped	
	Forward	Reverse	Forward	Reverse
Bulk	1.63	1.63	-	-
A-B	2.21	1.89	2.08	0.97
A-C	2.15	0.95	2.03	0.92
B-D	1.60	1.40	1.76	1.50

Initial Monte Carlo calculations have considered tracer diffusion in the (310) NiO boundary. We calculate the partial correlation factors to obtain information about the diffusion. The (isotropic) correlation factor for bulk NiO is 0.781 (Manning 1968). The boundary partial correlation factors are anisotropic, very small and vary with both temperature and Ca^{2+} dopant concentration as shown in Figure 2. The partial correlation factor increases with temperature in a series of steps. (The unrealistic temperatures are chosen simply to illustrate the effect). At low temperatures the energy required to move the vacancy away from site A is too high (1.8 eV to site B and 2.5 eV to D) and the vacancy is trapped in one diffusion path. At higher temperatures other routes are available and the correlation factor increases. (The reactive element effect breaks down above approximately 1200K; (Pint 1996). Also the reactive element effect is observed when the *bulk* dopant level is approximately 0.5 % at. (Pint 1996). From our segregation energies it is obvious that the concentration of dopants at the *boundary* will be much greater. Calculations with low concentrations of dopant in the boundary shows only a small effect of dopant concentration on the correlation coefficient. Calculations with higher dopant concentrations are in progress.

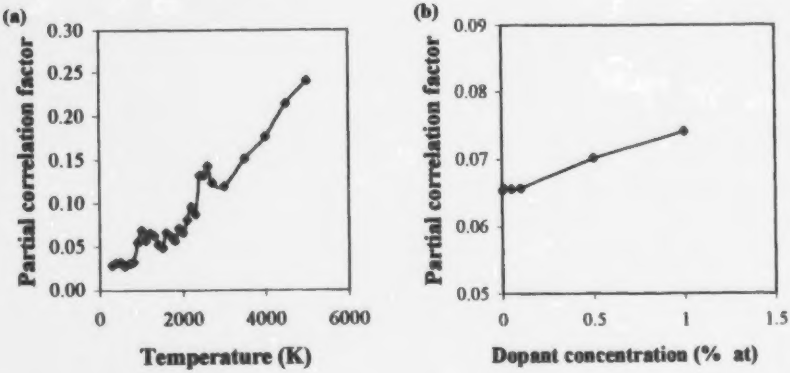

Fig. 2: Partial correlation factors for the A_L-A_R jump in the (310) boundary in NiO as a function of a) temperature, and b) dopant concentration at 1200 K. For the nomenclature of jumps see Figure 1.

4 Conclusions

Calculations on NiO support the idea that the reactive element effect works by the additives blocking diffusion down the boundaries. The simulations of the partial correlation factors show that, at temperatures where the reactive element effect is important, there is only one significant pathway for ion motion in the grain boundary and that this pathway is blocked by the reactive element. Preliminary calculations on alumina also show that reactive elements inhibit grain boundary diffusion. However, both calculations and experiments suggest that diffusion down boundaries may not dominate ion transport. We intend to investigate this case further.

5 References

Atkinson, A., Plummery, F.C.W. and Monty, C. (1985) Diffusion of O-18 tracer in NiO grain boundaries, in *Transport in Nonstoichiometric Compounds,* (ed. G. Simkovich and V.S. Stubican), Plenum, New York, pp. 359-370.

Duffy, D.M. and Tasker, P.W. (1982) *A guide to CHAOS: A program for the calculation of point defect energies near interfaces in ionic crystals.* Harwell Report AERE-R 11059.

Duffy, D.M. and Tasker, P.W., (1986) Theoretical studies of diffusion processes down coincident tilt boundaries in NiO. *Philos. Mag. A,* Vol. 54, pp. 759-771.

Harding, J.H. (1990) Computer simulation of defects in ionic solids. *Rep. Prog. Phys.,* Vol. 53 pp. 1403-1466.

Harris, D.J., Watson, G.W. and Parker, S.C. (1997) Vacancy migration at the {410}/[001] symmetric tilt boundary of MgO: An atomistic simulation study. *Phys. Rev. B,* Vol. 56, pp. 11477-11484.

Le Gall, M., Huntz, A.M., Lesage, B., Monty, C. and Bernardini, J. (1995) Self-diffusion in α-Al_2O_3 and growth rate of alumina scales formed by oxidation: effect of Y_2O_3 doping. *J. Mat. Sci.,* Vol. 30, pp. 201-211.

Lewis, G.V. and Catlow, C.R.A. (1985) Potential models for ionic oxides. *J. Phys C,* Vol. 18, pp. 1149-1161.

Manning, J. R. (1968) *Diffusion kinetics for atoms in crystals,* Van Nostrand, New York.

Mishin, Y. (1997) Calculation of diffusion coefficients and correlation factors in grain-boundary diffusion. *Philos. Mag. A,* Vol. 72, pp. 1589-1607.

Peterson, N.L. and Wiley, C.L. (1985) Point defects and diffusion in NiO. *J. Phys. Chem. Solids,* Vol. 46, pp. 43-52.

Pint, B.A. (1996) Experimental observations in support of the dynamic-segregation theory to explain the reactive element effect. *Oxid. of Metals,* Vol. 45, pp. 1-37.

Prescott, R. and Graham, M.J. (1992) The formation of aluminum oxide scales on high-temperature alloys. *Oxid. of Metals,* Vol. 38, pp. 233-254.

Schütze, M. (1994) An approach to a global model of the mechanical behaviour of oxide scales. *Materials at High Temperatures,* Vol. 12, No. 2-3. pp. 237-247.

Tasker, P.W. (1979) The surface energies, surface tensions and surface structure of the alkali halide crystals. *Philos. Mag. A,* Vol. 39, pp. 119-127.

A MODEL OF NiO TEXTURE FORMATION ON SINGLE CRYSTAL SUBSTRATE

Hualong Li, F. Czerwinski and J. A. Szpunar
Dept. of Metallurgical Eng. McGill Unversity
3610 University, Montreal, Canada, H3A 2B2

Abstract

A mechanism of NiO texture formation on Ni single crystal substrate have been proposed. In the early stage of the oxidation, it is assumed that the atomic matching between the metal and oxide lattice is the factor to determine the oxide texture. In the stages of oxide grain growth and re-nucleation, the free surface energy of oxide is the factor that determines the oxide texture. Due to the lattice matching, the oxide texture is strongly affected by the substrate texture at the beginning of the oxidation. As the oxide film become thicker, the fiber oxide texture becomes predominant. The results predicted based on the proposed oxidation mechanisms are compared with the experimental results. Good agreement has been obtained.

Keywords: Simulation, Ni, oxidation, texture, mechanism, lattice matching

1 Introduction

Although extensive studies of oxidation of Nickel have been carried out, the NiO texture was relatively unknown. Earlier studies on NiO structure mainly focused on the epitaxial relationships between the oxide and metal [1-3]. However, texture gives far more richer information than simple epitaxial relationships. Recently, Czerwinski and Szpunar have measured the NiO texture systematically [4]. Their results showed that the oxide orientation was affected strongly by the substrate orientation. In this paper, mechanisms of the oxide texture formation is proposed based on the hypothesis of crystal lattice matching and minimization of surface free energy. Oxide textures formed on $(100)_{Ni}$ and $(111)_{Ni}$ are studied.

2 Mechanisms of NiO Texture Formation

It is assumed that the orientation of oxide nuclei formed at the early stage of Ni oxidation is determined by lattice matching between oxide and metal. The oxide orientation, which has a smaller area difference with respect to the substrate, is favorable.

In figure 1, the $\{100\}_{NiO}$, $\{111\}_{NiO}$ and $\{110\}_{NiO}$ crystallographic planes are plotted on the $\{100\}_{Ni}$ plane. The $\{100\}_{NiO}$, $\{111\}_{NiO}$ and $\{110\}_{NiO}$ planes are represented with dash lines. The position of Ni atoms on the $\{100\}_{Ni}$ plane are plotted with solid lines within which contain the same number of Ni atoms as that on oxide plane and have similar atomic distribution,. The differences in surface areas occupied by Ni atoms in oxide lattice and in metal lattice for $\{100\}_{NiO}$, $\{111\}_{NiO}$ and $\{110\}_{NiO}$ matching planes are 30%, 19% and 50% respectively.

According to the assumption of the model, the $\{111\}_{NiO}$ plane is the most favorable orientation at early stage of oxidation on $\{100\}_{Ni}$ plane while $\{110\}_{NiO}$ and $\{100\}_{NiO}$ are less favorable. However, it has been experimentally observed that the expitaxial oxide orientations ($\{100\}_{NiO} \parallel \{100\}_{Ni}$) do exist at the early stage of Ni oxidation which implies that the oxide lattice can accommodate up to 30% difference in the surface area.

Therefore, the criterion used to determine oxide orientations at the nucleation stage is simplified as follows. The oxide orientations, which have area difference less than 30%, are equally favorable. All other oxide orientations are considered not favorable.

The same analysis can be applied to other low indices Ni planes, for example $\{111\}_{Ni}$. The area differences have been calculated and shown in Table 1. Using the same criteria, one can conclude that $\{111\}_{NiO}$ plane can be matched with the $\{111\}_{Ni}$.

The Table 1 gives only the crystallographic planes of the matching orientations. The crystallographic directions of the matched oxide orientations are determined by minimizing the displacement between Ni atoms in the metal lattice and the Ni ions in the oxide lattice. When the oxide orientation with *{hkl}* plane is considered favorable, its crystallographic direction *<uvw>* is determined by the best matching position.

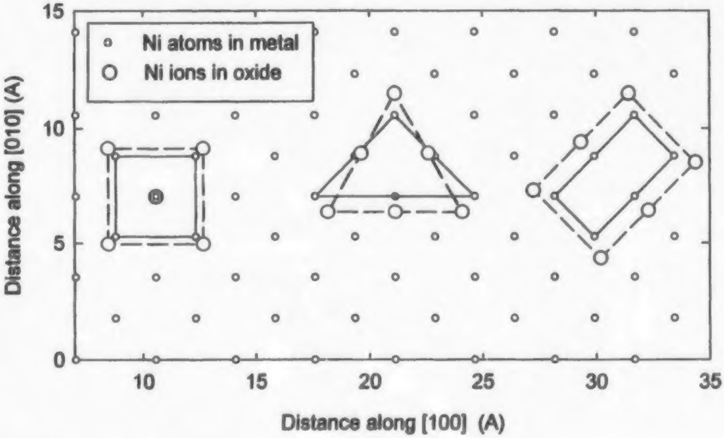

Figure 1 The lattice macthing of $\{100\}_{NiO}$, $\{111\}_{NiO}$ and $\{110\}_{NiO}$ on $\{100\}_{Ni}$

Table 1 The area difference between crystallographic planes of oxide and Ni

Substrate	Area difference		
	$(111)_{NiO}$	$(100)_{NiO}$	$(110)_{NiO}$
$(111)_{Ni}$	30% (✓)		
$(100)_{Ni}$	19% (✓)	30% (✓)	

After the first layer of oxide is formed on the Ni surface, the substrate and oxygen are separated by the oxide film. The further oxidation process is controlled by Ni outward diffusion [4]. Since the new oxide is always formed on the outer surface of the sample, it is expected that the surface free energy of NiO may be the predominant factor that controls the oxide growth. This means that oxide grains with smaller surface free energy will consume their neighbors and expand laterally.

Furthermore, during oxide growth, oxide re-nucleation may take place. Since new oxide nuclei that are formed at the stage of oxide growth are not in contact with the substrate, the matching between the oxide and the metal does not influence the orientation of the oxide nuclei. The orientation of the new oxide nuclei at the stage of oxide growth is assumed to be controlled by the surface free energy of NiO.

The NiO surface energies have been calculated using the potential of the long-range Coulomb term plus the short-range repulsive term and the results are listed in table 2.

3 Results

At the initial stage of the oxidation on $\{100\}_{Ni}$ substrate, the oxide nuclei whose orientations have their $\{100\}_{NiO}$ or $\{111\}_{NiO}$ crystallographic plane parallel to the substrate can be formed (see table 1).

In the case of $\{100\}_{NiO}$ growing on $\{100\}_{Ni}$, the crystallographic directions of the oxide orientations determined by lattice matching will follow the relationship $<001>_{NiO} \parallel <001>_{Ni}$. As a result, one should see one pole in the center of {100} oxide pole figure and four poles separated by 90° in the {111} oxide pole figure indicated by ⇨. These are observed on the experimental pole figures in figure 2(a), which confirms the prediction of the model. The samples analyzed experimentally were oxidized for 4 hours at 1073K under the oxygen pressure of 5×10^{-3} torr [4].

If {111}<*uvw*> oxide orientation forms on $\{100\}_{Ni}$ substrate, the <uvw> component of the orientation will be determined by minimizing the displacement of

Table 2 Surface energies of NiO crystallographic planes (J/m^2)

(hkl)	(100)	(111)	(110)	(210)	(211)	(221)	(311)
Surface energies	12.6	17.7	17.8	24.8	20.0	30.7	27.3

Ni atoms in the oxide and metal lattice. There are several crystallographic directions that can make the displacement of Ni atoms minimum. These directions are $<011>_{NiO} \| <001>_{Ni}$ type as shown schematically in figure 3. Due to crystal symmetry, four distinguished crystallographic directional relationships can be obtained. Therefore, four {111}<*uvw*> oxide orientations can be formed on $\{100\}_{Ni}$ substrate and they are separated by 90° to each other. Since each oxide orientation {111}<*uvw*> has three poles on {100} pole figure separated by 120° interval, one should expect to see total 12 poles appear on {100} oxide pole figure and each pole should be separated by 30°. In other words, there will be three poles in each quadrant of the {100} oxide pole figure. These four orientations should also generate one pole in the center of {111} pole figure. All these orientation maxima are observed in experiments, which are shown in figure 2(a) and are marked by→.

At early stages of the oxidation on the $\{111\}_{Ni}$ substrate, oxide orientations are relatively simple since only the {111}<uvw> epitaxial oxide orientation can be formed on $\{111\}_{Ni}$ substrate according to the results shown in table 1. The <uvw> components of the oxide orientation are parallel to the substrate <uvw> direction. It is calculated that two distinguished oxide orientations can match the substrate and they are related around <111> axes with respect to each other by 60° (or 180°). Thus, six poles can be seen on the {100} oxide pole figure separated by 60° interval and in addition one pole can be seen on the center of {111} oxide pole figure. This analysis is supported by data presented in figure 2(b). The poles are indicated by →. The ODF of the oxide grown on $\{111\}_{Ni}$ substrate is calculated and the φ_2=45° cross section is shown in figure 5 which shows that two {111}<*uvw*> orientations are separated by 60°.

As oxide grows, re-nucleation of oxide grains will eventually take place. The oxide orientations having {100} planes parallel to the sample surface will be favorable in the re-nucleation process because it has low surface energy. It will also grow faster. Since the surface energy is the same for all {100}<*uvw*> orientations, the {100} fiber texture will be formed as the oxide becomes thicker and thicker. This prediction can not be clearly observed in the experimental pole figures because the

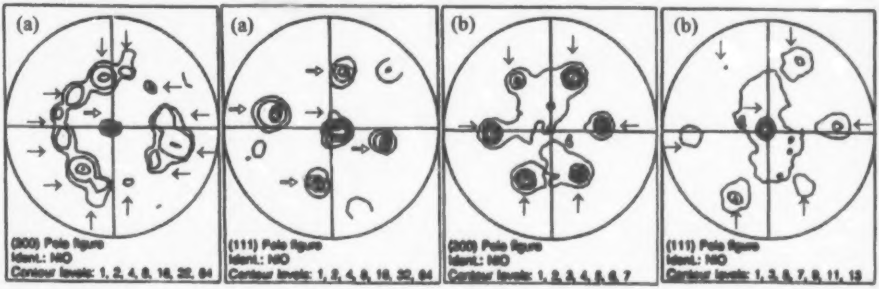

Figure 2 Experimental pole figures of NiO grown on (a) $\{100\}_{Ni}$ and (b) $\{111\}_{Ni}$
(The {100} oxide orientations are indicated by ⇾ and {111} orientations are indicated by →)

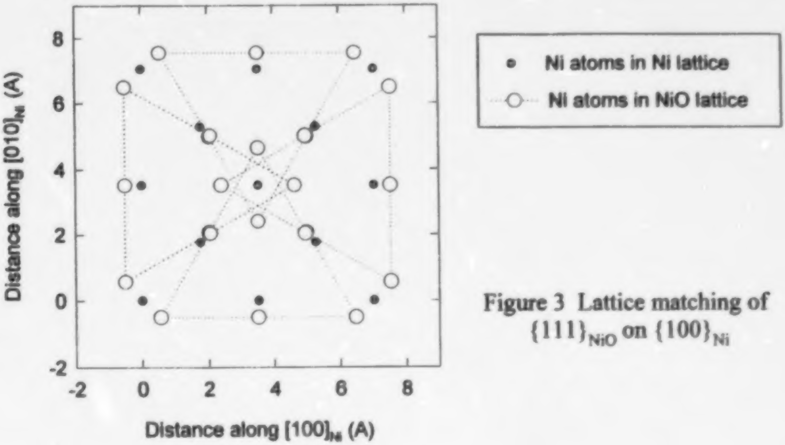

Figure 3 Lattice matching of $\{111\}_{NiO}$ on $\{100\}_{Ni}$

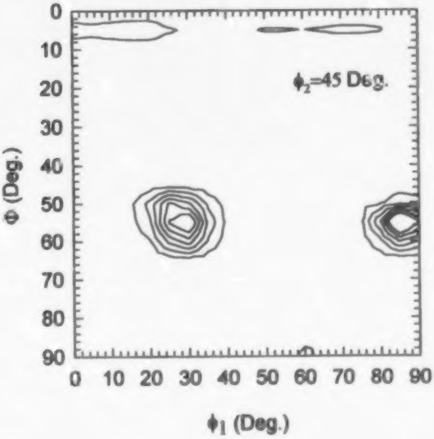

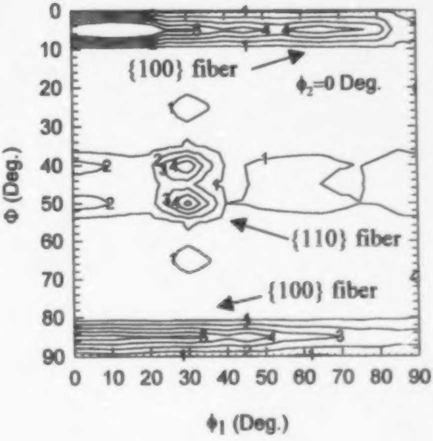

Figure 4 Calculated ϕ_2=45° cross section of the oxide ODF on $\{111\}_{Ni}$. (Contour Levels: 5,10,15,20,25,30)

Figure 5 Calculated ϕ_2=0° cross section of the oxide ODF on $\{111\}_{Ni}$. (Contour Levels: 1,2,3,4,5)

oxidation time was only 4 hours and the fiber texture component is very weak. However, in the calculated ODF for the oxide formed on $\{111\}_{Ni}$ substrate, the fiber texture component can be seen if we plot the ODF emphasizing the low intensity level. The ODF cross section view at $\varphi_2=0°$ is shown in figure 6. The {100} fiber texture component is shown at the top and bottom of figure 6. In the same figure, a weak {110} fiber texture component is also formed, which is consistent with the proposed mechanism since {110} crystallographic plane has the third lowest surface energy. Therefore, the simulation predicts that the fiber texture components will eventually out-grow the matching orientation formed at the initial stage of the oxidation and become dominant. The {100} fiber should be then the major component. The results from Christensen *et al* [5] partially support this prediction. They observed that $\{100\}_{NiO}$ faces was formed on $\{111\}_{Ni}$ substrate and concluded that it was possibly due to the low surface energy of {100} face.

Conclusions

The mechanisms of NiO texture and microstructure formation is proposed based on assumptions that the lattice matching is the main controlling factors at the nucleation stage while the surface energy is the main factor at the oxide growth and re-nucleation stages. The predicted oxide textures formed on $\{100\}_{Ni}$ and $\{111\}_{Ni}$ substrates are in agreement with experimental results.

References

1. R. N. Bloomer, Br. J. Appl. Phys., 8, 40 (1957), p.321
2. J. V. Cathcart, *Oxidation of Metals and Alloys*, (American Society for Metals, Metals Park, OH, 1971), p.17
3. J. V. Cathcart, G. F. Petersen and C. J. Sparks, J. Electrochem. Soc., 116(1969), p.664
4. F.Czerwinski, The Growth and Structure of Thin Oxide Film on Nickel Superficially Modified with Ceria and Cerium, Ph. D. thesis, McGill University (1997)
5. T. M. Christensen, C. Raoul, J. M. Blakely, Applied Surface Science, 26, n4, Oct I (1986)

THE SURFACE TEXTURING OF NICKEL FOR HIGH TEMPERATURE OXIDATION PREVENTION

F. Czerwinski [1] and J.A. Szpunar
Dept. of Metallurgical Engineering, McGill University, Montreal, H3A 2B2 Canada
[1] on leave from the University of Mining and Metallurgy, 30-059 Cracow, Poland

Abstract

Polycrystalline Ni coatings and foils with a variety of textures were manufactured using an electrodeposition technique. The initial textures and microstructures of Ni were modified using annealing in an inert atmosphere of argon. It was found that NiO grown on as-deposited Ni has a random distribution of grain orientations for all types of the substrate textures. When Ni electrodeposits were annealed prior to oxidation, there was a strong influence of substrate texture on the texture of NiO. In particular, a surface treatment composed of the electrodeposition of Ni primer with a strong <100> texture followed by annealing leads to the formation of epitaxially oriented, slow growing and highly protective NiO scales with the <111> texture.

Keywords: high-temperature oxidation, texture, electrodeposition, nickel, nickel oxide

1. Introduction

Among many factors affecting oxide growth rates at high temperatures in a corrosive environment and its resistance to spallation, the crystallographic texture of the metallic substrate plays an important role. The differences in oxidation rate constants extracted from our previous studies (Czerwinski and Smeltzer,1993; Czerwinski and Szpunar, 1998) are summarized in the form of the Arrhenius plot in Fig. 1. Polycrystalline Ni with the <111> texture and surface deformed by mechanical polishing oxidized at a rate of over one order of magnitude higher than the same material with the surface finished by chemical etching. Since the chemical etching is known to reveal the atomic structure of the grains, the differences observed indicate an importance of the crystallographic orientation of the surface exposed to the oxidizing gas. Of two crystal orientations

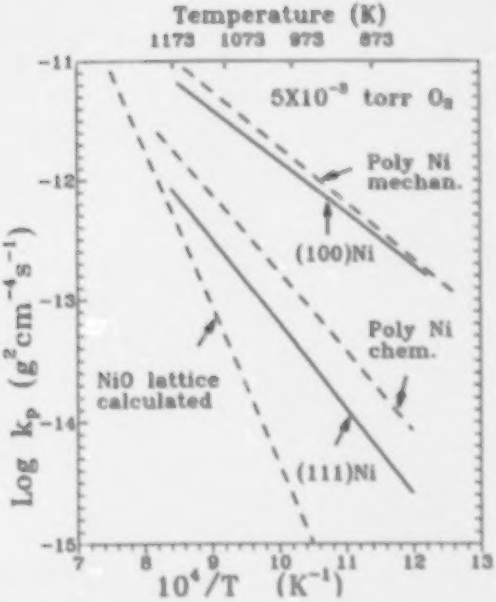

Fig. 1. Summary of oxidation kinetics data for polycrystalline Ni (99.99% purity) and two single crystals (99.999% purity). Average rate constant calculated as $k_p = w^2/t$ (w oxygen uptake, t oxidation time of 4 h).

analyzed, the higher oxidation rate exhibited the (100) face. The rate constants for NiO growth on the (100) face are very similar to that measured for polycrystalline, mechanically polished Ni. Thus oxidation kinetics measurements show clearly that in order to increase oxidation resistance at high temperatures, the surface texture should be produced with the {111} planes aligned parallel to the specimen surface.

The objective of this study is to use electrodeposition technology to manufacture the Ni electrodeposit, which leads to the growth of NiO scale with the <111> texture.

2. Experimental details

Ni electrodeposits with different textures and microstructures were manufactured as substrates for oxide growth at high temperatures. Electrodeposition was conducted in Watt's (1.07M $NiSO_4$, 0.15 M $NiCl_2$ and 2.38 M H_3BO_3) and chloride (1.22M $NiCl_2$) electrolytes (Karayannis and Patermarakis, 1995) at a temperature of 323 K. Process was carried out galvanostatically at a current density between 1 and 10 A/dm^2 and at pH value between 0.5 and 5. Some deposits were annealed at 1073 K for 0.5 h in an inert atmosphere of argon. Oxides were grown in air on both as-deposited and annealed Ni at a temperature of 1073 K and for time intervals up to 15 h. The textures of Ni substrates and NiO films were measured using a D-500 Siemens x-ray goniometer and $\mathrm{Mo}_{K\alpha}$ radiation. Pole figures were obtained using the reflection technique up to a maximum tilt of 80 deg in 5 deg polar and radial intervals. The results were corrected for absorption and defocusing using a standard random specimen prepared from Ni and NiO powder. The intensities on the pole figures are shown as multiples of intensities from a random specimen.

3. Results and discussion

3.1. The modification of Ni texture by electrodeposition

Ni electrodeposits are known for giving numerous, well-defined preferred orientations depending on electrodeposition conditions, i.e. electrolyte composition, temperature, pH, current density, stirring and organic additions. When using the chloride electrolyte and current density below about 2 A/dm^2, a <110> fibre is formed. For Watt's electrolyte, the <100> texture dominates over a wide range of current densities where deposits are compact and have good adherence to the substrate. An example of strong <100> texture in Ni foil deposited at 10 A/dm^2 is shown in Fig 2a. Both the literature data and our results reveal that a strong <111> single-component texture, which is beneficial for oxidation performance, cannot easily be obtained in as-deposited state of Ni.

3.2. Texture of NiO grown on as-deposited electrolytic Ni

During the exposure of as-deposited Ni to the oxidizing environment at high temperatures, oxide formation is superimposed on the recovery of defect structure, grain growth and texture changes of the bulk substrate. The common feature of the oxidation of as-deposited Ni is the formation of randomly oriented NiO at the beginning of the exposure to oxygen. After longer oxidation, NiO exhibits very weak <110> fibre. For example, for the Ni foil produced from Watt's bath with a strong <100> texture, NiO grown during 15 h exposure at 1073 K shows the <110> fibre with intensity of 1.8 times random units (Fig. 2b). Similar randomly oriented oxide grains were obtained on Ni with <110> and <211> textures.

3.3. Texture of NiO grown on annealed Ni electrodeposits

An annealing of the deposit with the <110> initial texture results in texture change towards <210> orientation. The strong <100> texture in Ni foil that was obtained from a Watt's electrolyte, disappears during annealing and deposit texture transforms to the <111> (Fig. 3a). On the other hand, the as-deposited <211> texture transforms after annealing to a mixture of <100> and a rough <111>. NiO grown after annealing is essentially different than that formed during the direct oxidation of as-deposited Ni. In particular, NiO formed on an annealed deposit produced from Watt's bath had the <111> texture with maximum intensity of 5 times random (Fig. 3b). The deposit with the <211> initial texture, that is transformed to a mixture of <111> and <100> after annealing, leads

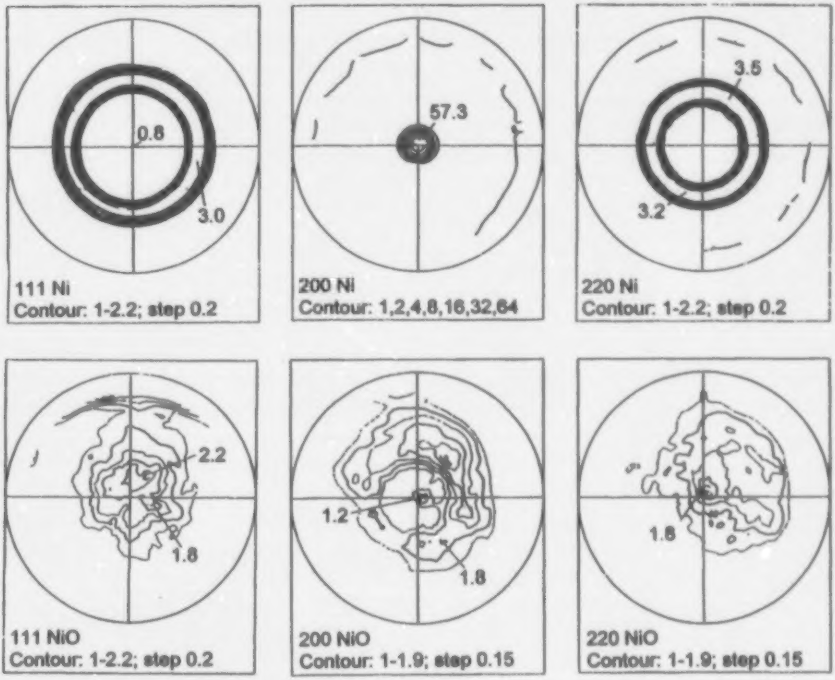

Fig. 2. The <100> texture of electrodeposited Ni (a) and roughly random texture of NiO grown at 1073 K for 0.5 h in air on as-deposited Ni (b).

to a growth of NiO having a double texture of <111> and <100> with maximum intensities of 2.8 and 1.8, respectively.

An annealing temperature of 1073 K was selected to be high enough to complete recrystallization in all deposits and to avoid substantial changes in the substrate during subsequent oxidation. Of all the specimens under investigation, the strongest <111> texture after annealing was obtained in Ni foil obtained from Watt's bath with the <100> initial texture. The strengthening of <111> texture at the expense of <100> was also observed during the recrystallization of Ni-Fe alloys. The presence of the <111> texture in annealed, i.e. free of structural defects, Ni substrate, is highly beneficial for oxidation resistance. A comparison of the pole figures of annealed substrates and corresponding oxides supports the existence of epitaxy (Figs. 3a and 3b). Epitaxial relations in many film-substrate systems can often be explained using the close-pack rule that assumes the parallel alignment of close packed directions between two phases. Such an assumption allows for the prediction of the type and number of oxide orientations formed on individual crystal phases. Some particular considerations for nickel-nickel oxide systems are published by Khoi et al. (1975). On the (111)Ni face, for example, there are two possible orientations. In the first, the oxide lattice is essentially parallel to that of the metal while in the second, the oxide lattice has been rotated 180 deg about its surface normal to produce an antiparallel orientation. In other words, the special fibre texture is made up of twin-related orientations. Such a texture is characterized by grain boundaries with low diffusivity, which makes the oxide highly protective (Li et al., 1997).

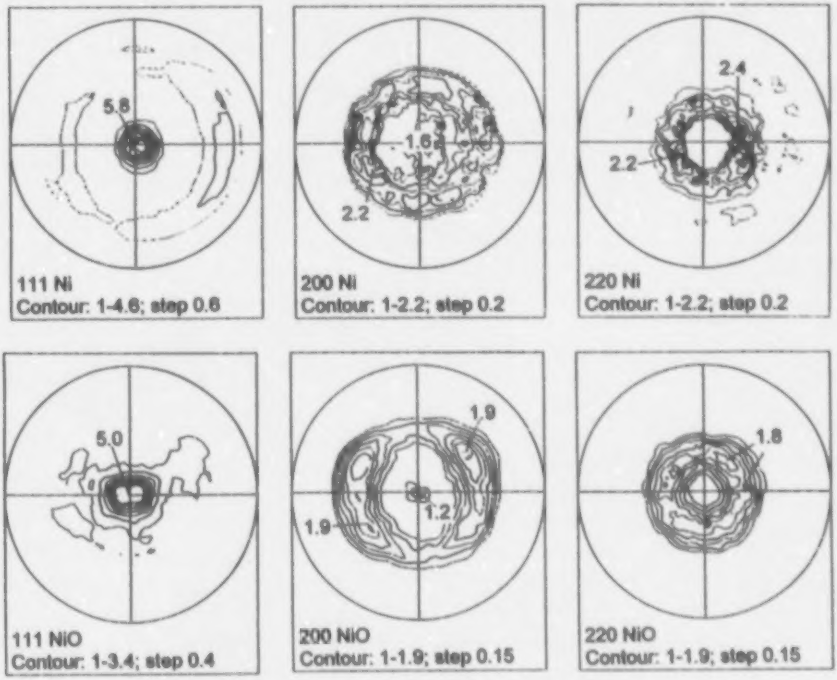

Fig. 3. The <111> texture of annealed Ni deposit (a) and the <111> texture of NiO grown at 1073 K for 0.5 h in air on annealed Ni substrate (b).

The corrosion resistance of engineering materials depends on several factors. This study discusses one of them i. e. the crystallographic orientation (texture) of the substrate. The results presented here show that a two-stage surface treatment composed of the electrodeposition of Ni with a high <100> texture followed by annealing, produces a surface with a strong <111> texture. As it was demonstrated previously (Czerwinski and Szpunar, 1998) this texture of Ni leads to the formation of highly protective and slow growing NiO scales. Moreover, the oxide having this texture also provides excellent protection against oxidation when combined with ceria ceramic coatings.

4. Conclusions

A variety of textures can be formed in Ni electrodeposits by controlling the deposition conditions. While the <100>, <110>, or <210> textures are readily obtained, the experimental efforts of this study did not permit the manufacture of deposits with the single <111> texture. The <111> texture was obtained after the annealing of Ni deposits with the <100> initial texture. The oxidation of as-deposited Ni results in the growth of randomly oriented NiO with traces of the <110> texture. The oxidation of annealed Ni electrodeposits promoted the growth of epitaxially oriented NiO. The stronger the <111> Ni substrate texture after annealing, the stronger the <111> NiO texture became after oxidation.

5. References

Czerwinski, F. and Smeltzer, W.W. (1993) The Early-Stage Oxidation Kinetics of CeO_2 Sol-Coated Nickel, *J. Electrochem. Soc.*, 140, 2606-2615.

Czerwinski, F. and. Szpunar, J.A. (1998) The Influence of Crystallographic Orientation of Nickel Surface on Oxidation Inhibition by Ceria Coatings, *Acta Mater*. 46, 1403-1417.

Karayannis, H.S. and Patermarakis, G. (1995) Effect of Cl^- and SO_4^{2-} Ions on the Selective Orientation and Structure of Ni Electrodeposits, *Electrochim. Acta*, 40, 1079-1092.

Khoi, N.N. Smeltzer, W.W. and. Embury, J.D, (1975) Growth and Structure of Nickel Oxide on Nickel Crystal Faces, *J. Electroch. Soc*., 122, 1495-1503.

Li, H., Czerwinski, F., Zhilyaev, A.P. and Szpunar, J.A. (1997) Computer Modelling the Diffusion of Ni in NiO at High Temperatures, *Corros. Sci*., 39, 1211-1219.

ON THE CALCULATION OF GRAIN BOUNDARY CHARACTER DISTRIBUTION IN TEXTURED NICKEL OXIDE LAYERS

A. P. Zhilyaev [1], F. Czerwinski [2] and J. A. Szpunar [2]
[1] Institute for Physics of Advanced Materials, USATU, Ufa, 450000 Russia
[2] Dept. of Metallurgical Engineering, McGill University, Montreal, Canada, H3A 2B2

Abstract

The calculation of grain boundary character distribution in polycrystalline oxide, grown at 1073 K on ceria-coated faces of nickel single crystals, is described. The procedure was conducted under assumption of three types of the space correlation in orientation between adjacent grains. The assumptions included: (i) the highest possibility of low angle boundaries, (ii) the highest possibility of coincidence site lattice boundaries and (iii) the highest possibility of high angle random boundaries. Using as input data the experimentally measured orientation distribution functions, substantially different types of grain boundary character distributions were obtained.

Keywords: reactive elements, texture, grain boundary, nickel oxide, ceria

1. Introduction

Grain boundaries in polycrystalline oxides act at high temperatures as short-circuit paths for diffusing species and control their protective properties (Smeltzer, 1988). In particular, for nickel oxide an increase in oxygen activity leads to an increase in the concentration of vacancies and consequently an increase in lattice diffusion coefficient for nickel. It was established that the Ni diffusion along grain boundaries and dislocations in NiO increases in a similar way (Atkinson and Taylor, 1979). This implies that the grain boundary diffusion also occurs by resembling manner and that the concentration and mobility of vacancies is greater in the boundary than in the lattice. It is known that grain boundary diffusivity is related to the grain boundary structure and energy: low activation energy for diffusion is usually associated with high interfacial energy. The control of the oxide grain boundary structure is, therefore, of primary interest for oxidation inhibition.

The size of the crystallites forming the oxide layer is frequently too small to allow direct misorientation measurements at an appreciable number of individual grain boundaries. Therefore, it is difficult to determine experimentally the grain boundary statistics or, in other words, grain boundary character distribution (GBCD) in the nickel oxide film so that it would be statistically valid. It could be done by calculation from texture data, namely from its quantitative representation, the orientation distribution function (ODF). As discussed previously (Gertsman et al. 1992; Zhilyaev et al. 1993), the relation between GBCD and texture is rather complex and ambiguous. Grain boundary statistics can be rigorously extracted from the ODF if and only if certain conditions are imposed on misorientations of nearest-neighbor grains within polycrystals. If such conditions are unknown, one can deduce them from limited microscopic and diffraction observations or from other indirect experiments (Alexandrov et al. 1995). In this paper, three types of correlation, which are possible in oxide scales formed on (100) and (111) single crystals of Ni modified by ceria gel, were assumed. The first correlation suggests that GBCD have a maximum fraction of low-angle grain boundaries. The second correlation implies that a maximum fraction of special grain boundaries is characterized by low numbers of reciprocal densities of coincidence sites, Σ. Finally, the GBCD were calculated under assumption of a lack of any correlation, which favors the high-angle random boundaries.

2. Texture of the oxides and Orientation Distribution Function

The texture of the oxide was measured by D-500 Siemens x-ray goniometer and $Mo_{K\alpha}$ radiation. Incomplete pole figure data were collected using the reflection technique up to a maximum tilt of 80 degrees in 5 degrees polar and radial intervals. The intensities were corrected for absorption and defocusing based on the standard random specimen made from NiO powder. The pole figures for nickel oxide films formed on ceria coated (100) and (111) single crystals of Ni can be found elsewhere (Czerwinski and Szpunar, 1998). Quantitative representation of texture can be calculated from the experimental pole figures using different methods (Bunge, 1982). The orientation of each grain can be described by three parameters, namely Euler angles φ_1, Φ, φ_2. The rotation matrix g (φ_1, Φ, φ_2) specifies the alignment of individual grain in the orientation space of possible rotations. According to Bunge's notation these standard co-ordinates are applied in φ_2 projection. Fig. 1 a and b show sections (φ_2 = const.) of the ODF in NiO grown on the (100) and (111) Ni modified by ceria. A comparison indicates the essential role of substrate crystallographic orientation. NiO grown on CeO_2 coated (100) Ni, showed major (100) texture (Fig. 1a). This texture described by main component of (100)[001], forms from an epitaxial relationship between nickel oxide and nickel substrate and coincides with so-called "copper recrystallization texture". Model texture of such type was presented in the earlier paper (Alexandrov et al. 1995). Orientation distribution functions have been used as input data to calculate grain boundary character distribution with three main types of space correlation.

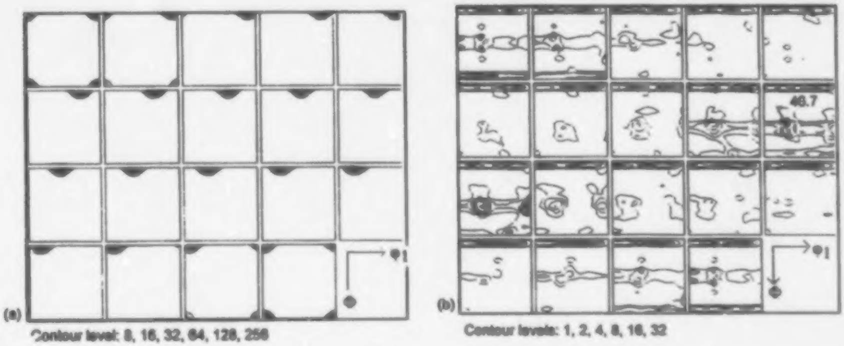

Fig. 1. Orientation distribution functions (ODF) calculated from experimental pole figure of NiO film formed on ceria coated (100) Ni (a) and (111) Ni (b).

3. Grain Boundary Character Distribution

Using ODF, obtained from experimentally measured pole figures, the GBCD for nickel oxide grown on both crystal faces of Ni were calculated. The details of the computation of GBCD have been published previously (Gertsman et al. 1992; Zhilyaev et al. 1993). The results expressed by GBCD, obtained for two crystallographic orientations of nickel substrate, are specified in Table 1.Three types of space correlation selected, represent the three GBCD which likely exist in real NiO scales. The column marked as "no" refers to GBCD calculated under assumption that there is no space correlation in orientation of neighboring grains. The column "LAB" gives results obtained while assuming the highest fraction of low angle grain boundaries. The column "Σ" refers to the assumption of the highest fraction of special grain boundaries. The Figs. 2 and 3 represent the results of the calculation, expressed by the grain boundary misorientation angle distribution (GBMD).

Table 1. CSL grain boundary statistics for NiO grown on (100)Ni and (111)Ni.

GB type	(100) Substrate			(111) Substrate		
	Type of space correlation					
	No	LAB	Σ	No	LAB	Σ
Σ1	69.1	70.0	72.0	4.5	39.0	7.6
Σ3	0.3	0.8	2.1	0.8	1.1	22.2
Other Σ	9.4	11.8	16.6	9.0	9.1	18.0
Random	21.2	10.4	9.3	85.7	50.8	52.2

It is clear that the crystallographic orientation of the substrate exerted the crucial influence on grain boundary character expressed by GBCD and GBMD. For the (100) nickel face the assumption of space correlation did not affect the GBMD

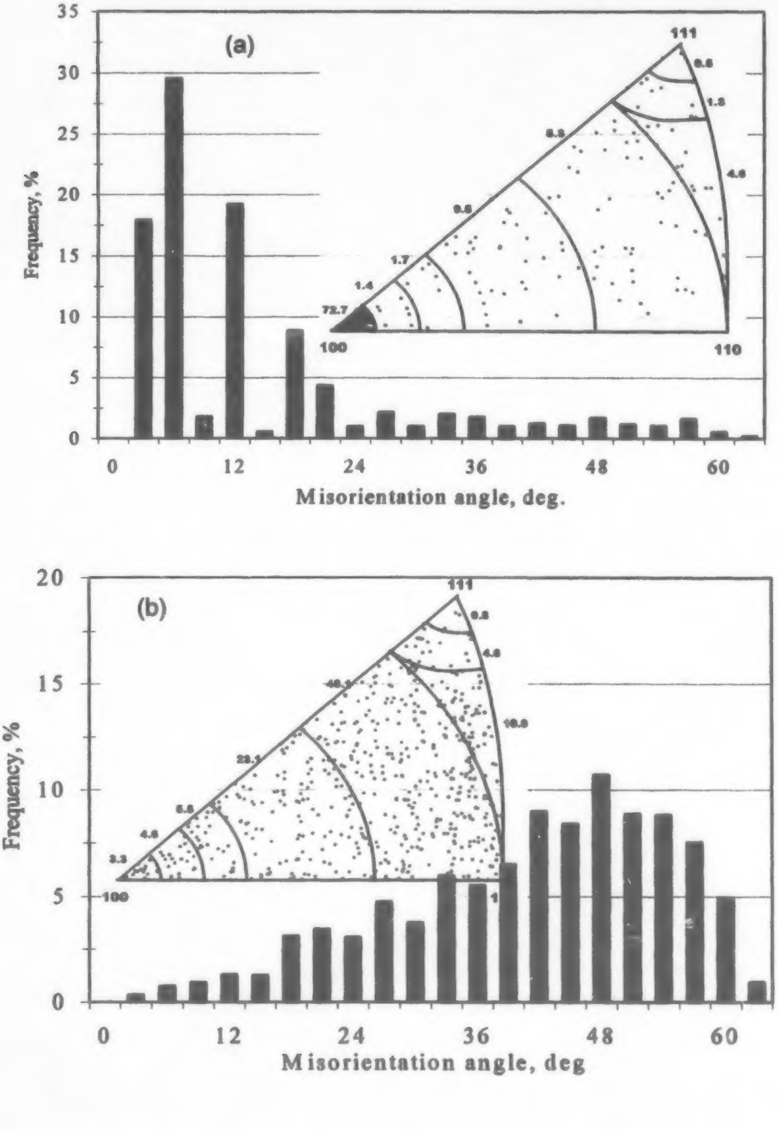

Fig. 2. Grain boundary misorientation distribution calculated from experimental texture data under assumption of the highest possibility of low-angle grain boundaries: (a) (100)Ni; (b) (111)Ni.

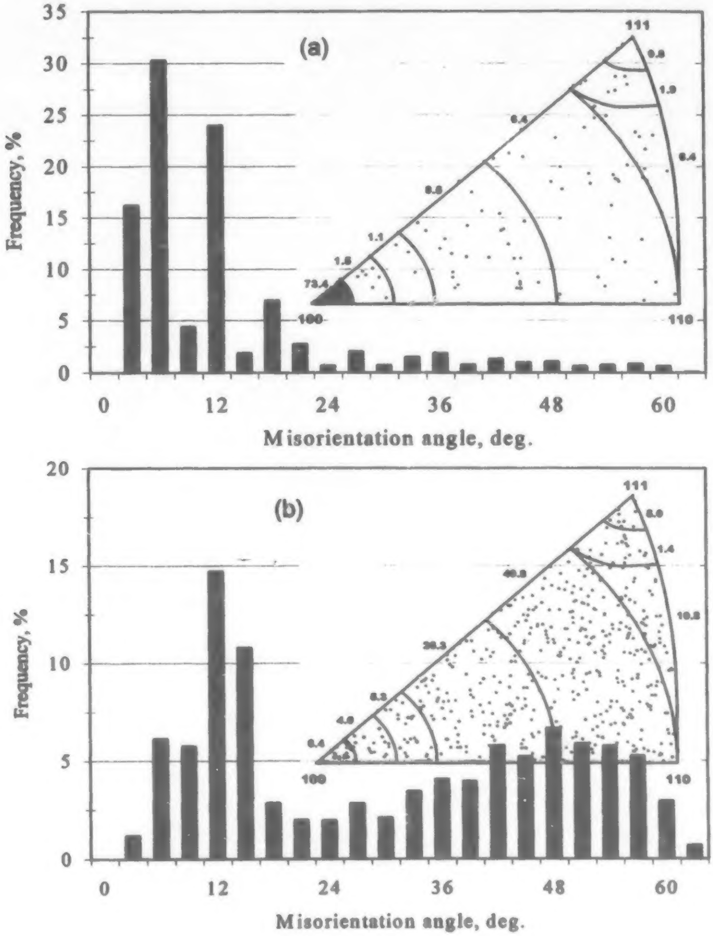

Fig. 3. Grain boundary misorientation distribution calculated from experimental texture data under assumption of the highest possibility of high-angle random grain boundaries: (a) (100)Ni; (b) (111)Ni.

and GBCD calculated from texture data (Figs. 2a and 3a). The grain boundaries in oxide formed on this face almost entirely consist of low angle grain boundaries. The (111) Ni substrate leads to the growth of the oxide with essentially different GBCD. In general it contains the higher content of high angle grain boundaries. The results calculated for this face depend strongly on the assumption of the space correlation and the specific differences are given in Table 1 and Figs. 2b and 3b.

4. Concluding remarks

The crystallographic orientation of nickel substrate coated with ceria gel exerted the essential influence on the grain boundary character distribution in oxide formed at 1073 K. For (100)Ni, a selection of the space correlation in orientation of neighboring grains did not affect the results of calculation of grain boundary character distribution based on experimentally measured texture. In contrast, for (111)Ni, the assumption of the space correlation strongly affected results of the calculations.

5. References

Alexandrov I. V., Zhilyaev A. P., Gertsman V. Yu., Pshenichnyuk A. I. (1995) A computer simulation study of the relation between grain boundary misorientation distribution and crystallographic texture, *Modelling Simul. Mater. Sci. Eng.* Vol. 3, 149-59.

Atkinson A. and Taylor R. (1979) The diffusion of Ni in the bulk and along dislocations in NiO single crystals, *Phil. Mag. A,* Vol 39, 581-595.

Bunge H. J. (1982) *Texture Analysis in Materials Science*, Berlin: Butterworth.

Czerwinski F. and Szpunar J. A. (1998) The cinfluence of crystallographic orientation of nickel surface on oxidation inhibition by ceria coatings, Acta Mater., 46, 1403-1417.

Gertsman V. Y., Zhilyaev A. P., Pschenichnyuk A. I. and Valiev R. Z. (1992) Modelling of grain boundary misorientation spectrum in polycrystals with crystallographic texture, *Acta metall. Mater.* Vol. 40, No. 6, 1433-41.

Smeltzer W. W. (1988) The influence of short-circuit grain boundary diffusion on the growth of oxide layers on metals, *Mater. Scie. Forum,* Vol. 29, 151–172.

Zhilyaev A. P., Gertsman V. Y., Mishin O. V., Pschenichnyuk A. I., Aleksandrov I. V. and Valiev R. Z. (1993) Grain boundary misorientation spectra (GBMS) determined by real ODF in F.C.C.-materials susceptible to annealing twinning, *Acta metall. mater.* Vol. 41, No. 9, 2657-65.

The Role of Oxide Texture in the Protection of Zr-2.5%Nb Alloy Pressure Tubes Against Hydrogen Ingress

M.G. Glavicic[1,2], J.A. Szpunar[2] and Y.P. Lin[3]

[1]Lambda Research, Cincinnati, Ohio, USA
[2]Dept. of Mining and Metallurgical Engineering, McGill University, Montreal, Canada
[3]Ontario Hydro Technologies, Toronto, Ontario, Canada

Abstract

Zr-2.5%Nb pressure tubes are used in the core of the CANDU nuclear reactor. One of the major difficulties encountered by these tubes during their operational life time is the uptake of hydrogen and the subsequent formation of hydrides. In this study, a series of Zr-2.5%Nb coupons were heat treated prior to oxidation. The texture of the oxides formed on these samples, in addition, to the uptake of hydrogen during their subsequent oxidation in a lithiated water environment was measured. The results of this work showed that substrate heat treatments dramatically increase the sharpness of the texture of the oxide grown. More over, a correlation between the sharpness of oxide texture, hydrogen pickup and oxide growth rates was observed.

Keywords: Hydrogen Ingress, Texture, ZrO_2, Oxidation, Heat Treatments, Zirconium

Introduction

In order for the ingress of hydrogen to occur into pressure tubes, hydrogen in either its molecular or atomic form must diffuse through the oxide to the metal surface. Several types of processes have been put forth in the past describing the migration mechanisms of the "hydrogen". Since all of these mechanisms involve an inward diffusion process, it can be seen that an improvement in the protective nature of the oxide will play a significant role in inhibiting the uptake of hydrogen. For this reason a series of experiments were conducted examining the effects of heat treatments on the oxide texture, oxidation rate and hydrogen uptake.

Experiment

A series of specimens were cut from as received pressure tubes, as shown in figure 1, such that the radial (RD//SN), transverse (TD//SN) and longitudinal (LD//SN) direction of the pressure tube were parallel to the sample normal. In addition, a fourth type of specimen was cut 120 degrees from the radial direction of the pressure towards longitudinal tube direction (LD+30//SN).

From these types of specimens three groups of heat treated samples were created. The first group were left in the As Received (AR) condition and had no additional heat treatment performed on them. The second group were heat treated for a period of 100 hours at a temperature of 673 K. The third group of specimens were heat treated for a period of 6 hours at 773K. All samples were then polished down to a 600 grit paper finish and then polished with 9 μm diamond paste. Ammonium Dichromate powder with a 0.5% HF solution was then used to give the sample their final finish. The samples were pre-oxidised in steam at 673 K for a period of 24 hours. In order to simulate reactor conditions the specimens were then placed in an autoclave which was filled with LiOH maintained at a temperature of 583 K for an initial period of 56 days. At that time a portion of the specimen was removed and the initial hydrogen pick-up of the specimens were determined by Differential Scanning Calorimetry (DSC). After a period of 168 days had elapsed all specimens were removed from the autoclave and their final hydrogen pick-ups were measured. In addition, the thickness of the oxides formed were determined by Fourier Transform Infrared Spectroscopy (FTIR).

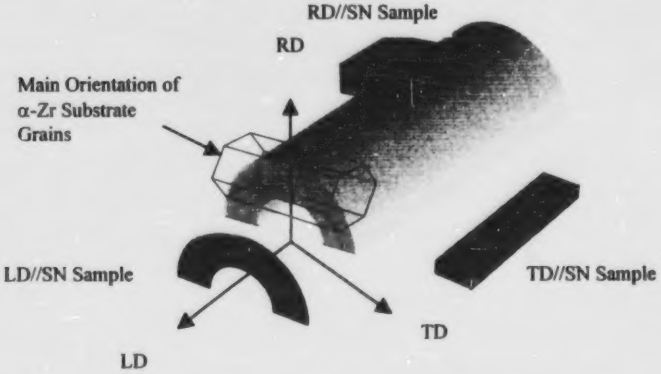

Figure 1 Schematic of how RD//SN, TD//SN and LD//SN coupons were cut from the pressure tube

The texture of the oxides formed were measured using CuKα radiation on a Siemens D500 texture goniometer. Analysis of the data and the calculation of Orientation Distribution Functions (ODF) were performed using Textools software.

Results and Discussion

All of the oxides formed in this study had a $(10\bar{4})[uvw]$ type of texture formed. In each case the maximum value in the ODF occurred along the $(10\bar{4})$ skeletal line for the monoclinic system, $\Phi = \frac{55\pi}{60}; \phi_2 = \frac{\pi}{2}; \phi_1 = 0 \rightarrow \frac{\pi}{2}$. The location of the maximums along the $(10\bar{4})$ skeletal line was dependent upon the main orientation of the underlying substrate grains upon which the oxide was grown. Complete details of the texture formed on these specimens is discussed in depth elsewhere[1].

In figure 2, a graphical representation of the effects of the heat treatments on the maximum ODF value, hydrogen pick-up measured and oxide thickness grown is displayed for the RD//SN specimens. Based upon the appearance of the graph it appears that the corrosion behaviour of the substrate is the same as the hydrogen pick-up behaviour when plotted against the maximum ODF value of the oxide grown. Very little change is observed in either parameter as a function of the applied heat treatments.

In figure 3, a graphical representation of the data for the TD//SN specimens is presented. The TD//SN specimens showed a marked improvement in the hydrogen pick-up and corrosion rate as a function of the heat treatments and oxide texture sharpness. The sharpness of the oxides formed on this specimen type were also sharper than those formed on the RD//SN specimens resulting in improved corrosion and hydrogen pick-up characteristics. In addition, it would again appear that the corrosion and hydrogen pick-up behaviour are similar in that as the resulting oxide texture became sharper both the oxide thickness grown and hydrogen pick-up decreased.

In figure 4, a graphical representation of the data for the LD//SN specimens is presented. The LD//SN specimens also showed an improvement in the hydrogen pick-up and corrosion characteristics. More over the measured oxide texture in these specimens was the sharpest of all specimens measured and again a clear correlation in the behaviour of the oxide thickness grown and hydrogen pick-up is evident.

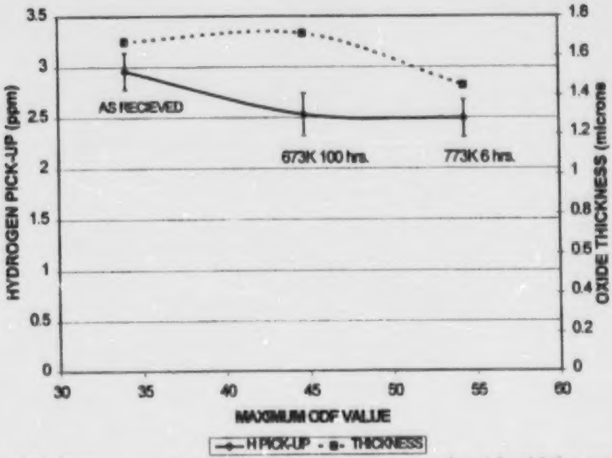

Figure 2 Graphical representation of hydrogen pick-up and oxide thickness grown as a function of sharpness of oxide texture and heat treatments applied to substrate for RD//SN specimen type

At this point it is prudent to highlight the main differences in the structure of the three Zr-2.5%Nb substrates investigated thus far. The grain shape of the α-Zr grains are asymmetrical and elongated in the LD direction of the pressure tube. In the AR condition, the β-Zr phase will surround the elongated α-Zr grains and depending upon how the sample is cut a different number of α/α and α/β type of grain boundaries will be exposed on the oxidising surface or at the metal oxide interface. As the heat treatments are applied, fragmentation of the β-Zr phase occurs so that the α-Zr grains are no longer surrounded by the β-Zr phase. This change in microstructure then changes the grain boundary network that would appear on an oxide free surface or at the metal oxide interface for any of the three specimen types; RD//SN, TD//SN and LD//SN. The oxide formed on the β-Zr phase is known to form much finer grained oxides than those formed on than the α-Zr phase. TEM photographs produced by Urbanic et al.[2] showed that the oxides formed over the β-Zr regions were typically 5-15 nm in diameter. While the oxides formed over the α-Zr regions were much larger, 20-60 nm in diameter. As a result of the smaller grain size of the oxides formed over the β-Zr regions, a higher density of grain boundaries exist in this region of the oxide in comparison to the oxide formed over the α-Zr grains. As a general rule it can be considered that the higher the number of grain boundaries present in a material, the higher the effective diffusion rate of a diffusion species will be through the material. As a result, the rate of diffusion of oxygen or hydrogen through the oxide formed over the β-Zr regions is higher than the oxide formed over the α-Zr regions. When heat treatments are applied to the substrate, the availability of β-Zr regions for consumption during oxidation is reduced. The proportion of the oxide grown by the consumption of α-Zr regions which have a definite preferred growth orientation with respect to the underlying metal substrate grains, is then increased by the application of heat treatments. As a consequence of this increase, the sharpness of the texture of the oxide as a whole is increased.

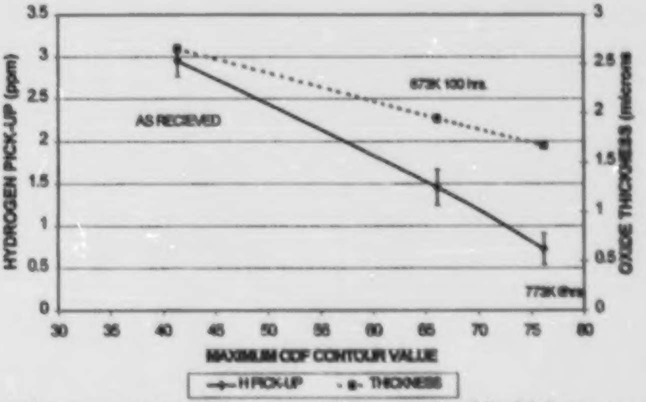

Figure 3 Graphical representation of hydrogen pick-up and oxide thickness grown as a function of sharpness of oxide texture and heat treatments applied to substrate for TD//SN specimen type

Since the sharpness of the texture reflects the number of grains of the oxide that are oriented in the same fashion with respect to one another, as the sharpness increases the distribution of the types of grain boundaries present in the oxide will change. As a result of an increase in sharpness of texture, the number of random grain boundaries present in the material will diminish and the number of low angle grain boundaries will increase. Since random grain boundaries generally have a high misorientation angle with respect to adjacent grains, they are generally considered to be easy paths for diffusion. In contrast, the diffusion rate along low angle grain boundaries is substantially less that that of a high angle grain boundary and as a result an increase in the sharpness of texture can be considered to reflect the protective nature of the oxide formed.

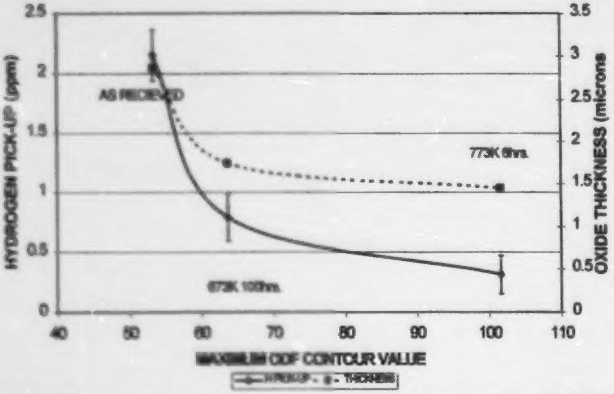

Figure 4 Graphical representation of hydrogen pick-up and oxide thickness grown as a function of sharpness of oxide texture and heat treatments applied to substrate for LD//SN specimen type

Based upon the above conclusion, it would then be logical to assume that since oxidation and hydrogen ingress are both inward diffusion processes, if the corrosion resistance is improved by the application of heat treatments the hydrogen pick-up characteristics should also be improved. This conclusion is supported by figures 2-4, since the behaviour of the specimens in terms of the thickness of the oxides grown and the hydrogen pick-up as a function of heat treatments and sharpness in texture are similar. It is then reasonable to expect that if the number of α/α type grain boundaries in a specimen is increased the protective nature of the oxide formed will improve for both corrosion hydrogen pick-up characteristics. In order to reaffirm, this hypothesis the fourth type of sample was examined LD+30//SN. In this case, the sectioning process amounts to a 120 degree rotation about the c-axis in the α-Zr substrate. The texture of the α-Zr substrate is therefore the same as the RD//SN specimen, except that the number of α/α and α/β type of grain boundaries exposed on the oxidising surface or at the metal oxide interface will be different to that of the RD//SN specimen in each of the heat treatments.

In figure 5, a graphical representation of the data for the LD+30//SN specimens is presented. In this series of specimens the hydrogen uptake is distinctively changed by the application of heat treatments. Upon comparison with the results obtained for the RD//SN specimens whose underlying texture of the α-Zr phase is the same (figure 2), dramatic changes are observed in that the hydrogen pick-up is lowered, the sharpness of the texture was increased and the thickness of the oxide grown decreased. Based upon these results a simple conclusion can be drawn, the grain boundary network of the underlying substrate plays a significant role in determining the protective nature of the oxide formed. The application of heat treatments which allows the β-Zr to α-Zr phase transformation to occur also changes the grain boundary network that will appear on an oxide free surface or at the metal/oxide interface. This change in the relative number of α/β-Zr and α/α-Zr boundaries is then responsible for the sharpening of the oxide texture which results in a more protective oxide.

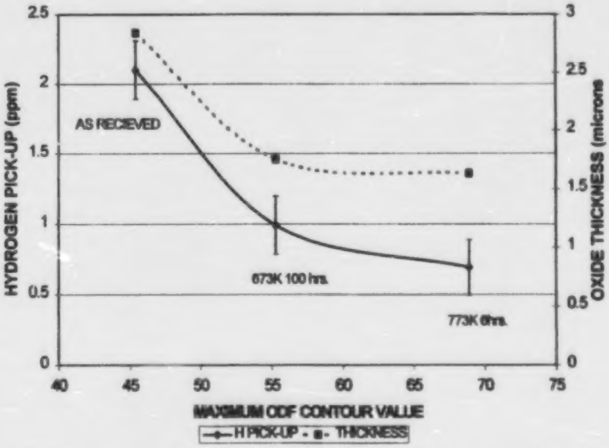

Figure 5 Graphical representation of hydrogen pick-up and oxide thickness grown as a function of sharpness of oxide texture and heat treatments applied to substrate for LD+30//SN specimen type

Conclusion

The application of heat treatments plays a significant role in determining the protective nature of oxides formed on Zr-2.5%Nb alloys. The β-Zr phase in the substrate play a significant role in determining the resulting sharpness of the oxide texture. The corrosion rate of an alloy is correlated to hydrogen ingress rate, both of which are determined by the degree of sharpness of the oxide texture.

References

[1] M.G. Glavicic, "Development and Application of Techniques for the Microstructural Characterization of Hydrogen Permeability in Zirconium Oxides", Ph.D. Thesis, McGill University, 1998

[2] V.F. Urbanic, P.K. Chan, D. Djamshid, O.T. Woo "Zirconium in the Nuclear Industry: Tenth International Symposium" ASTM STP 1245, 116 (1994)

THE INFLUENCE OF TEXTURE ON THE OXIDATION KINETICS OF COPPER

K. T. Lee and J. A. Szpunar
Department of Mining and Metallurgical Engineering, McGill University, Montreal, Canada

Abstract

To understand the oxidation kinetics of copper and the influence of substrate texture on oxide growth, copper single crystals having different orientation were oxidised in the thermogravimetric analyser at 200°C in air. The orientation of oxides was measured using the x-ray diffractometer with low glancing angle geometry. The observation of the morphology changes during the oxidation of copper was performed using atomic force microscopy (AFM). Experimental results show that the single crystal having (100) orientation oxidised much faster than other single crystals. It is observed that there is a higher number of fine oxide nuclei on the (100) single crystal than on the others in the early stage of oxidation. It may contribute to the fast oxide growth on the (100) single crystal.

Keywords: Texture, Copper oxidation, Microstructure, Oxidation kinetics

1. Introduction

Copper is being used as a new metallization material for ultra-large scale integration (ULSI) devices and electronic packaging due to its low electrical resistivity and good electromigration resistance (Murrarka et al. 1993; Gwynne 1997). One of the disadvantages of copper as an interconnect material is that copper is easily oxidised at relatively low temperature and the oxidation rate of copper is much faster than other interconnect materials such as aluminium and its alloys. It is also difficult to avoid oxygen incorporation during the copper film deposition and the further processes of integrated circuit manufacturing.

A lot of research has been carried on oxidation of copper in 50s and 60s. It has been known that copper oxidation is the outward diffusion oxidation and is strongly dependent on the oxidation temperature and oxygen partial pressure (Rönnquist and Fischmeister 1961). However, no single theory can explain the kinetics of oxidation at various temperatures.

The oxidation kinetics of copper at 200°C, which is relatively low temperature, has been studied. To understand the influence of substrate texture on oxide growth, copper single crystals having different orientation were oxidised in the thermogravimetric analyser in the atmosphere of air. It is found that the single crystal having (100) face oxidised faster than other crystals.

The study on the oxides of copper has been intensified in 90s due to the interest in using copper as an interconnection material. However, there has not been much work on the texture and the microstructure of copper oxide and its growth on the different faces of copper. The texture of oxides was measured using x-ray diffractometer with 1° of glancing angle. The observation of the morphology changes of copper oxides shows that there is a higher number of fine oxide grains on the copper single crystal having (100) face than on the others in the early stage of oxidation.

2. Experiment

Five copper single crystals having different faces were carefully selected. These single crystals were polished mechanically with metallographic polishing papers through P1200. Mechanically polished crystals were polished eletrolytically to remove strained layer. It is very important to obtain flat and clean surface before oxidation since the remaining impurities and scratches can change the oxidation pattern.

Thermogravimetric Analyser (TGA), Cahn TG-171, was used to obtain the oxidation kinetics of the single crystal specimens. The oxidation temperature is 200°C and the atmosphere is flowing air (80 ml/min). Heating rate of 20°C/min was used.

It is generally difficult to obtain a distinct diffraction pattern of thin film samples because diffracted X-rays beam is weak due to thin thickness resulting in relatively high background. Therefore, the oxide films on single crystals were characterised using x-ray diffractometer with 1° of grazing angle to increase the intensity of X-ray diffracted from the oxides. The observation of the morphology changes of oxide films during oxidation was performed by atomic force microscopy (AFM).

3. Result and discussion

The oxidation kinetics of copper single crystals having different faces is shown in Fig. 1. As shown in this figure, the order of the oxidation rate of these faces is (100), (110), (321), (413) and (311) in decreasing order. This result corresponds well with the work of Rhodin (1951) and Young (1956). Their work had been carried out at the temperature below 200°C. However, the oxidation rate of the copper faces is totally changed in case of high temperature oxidation. Bénard and Talbot (1948) oxidised several copper single crystals at 900°C and the order of rate of their oxidation was found as (210), (221), (110), (111) (100) and (123) in decreasing order. It is generally believed that Cu_2O is the only oxide formed at the temperatures below ~250°C at 1atm. in air and both Cu_2O and CuO are developed during oxidation at the temperatures above ~250°C. This should be the reason for different oxidation kinetics at low and high temperature. Low temperature oxidation is only considered in this study.

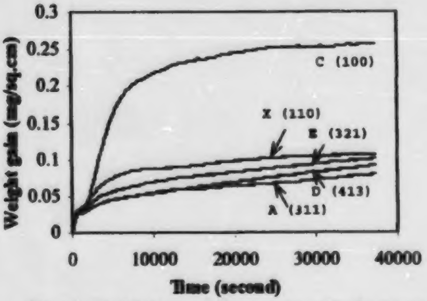

Fig. 1: Oxidation of the copper single crystals at 200°C.

No single theory of copper oxidation can explain the anisotropic oxide growth on different crystal faces although many suggestions have been made. Lawless (1956) pointed out that there are four energetically equivalent oxide orientation on (100) face, whereas there are two on the (111). The slowest oxidising (311) face has only one orientational relationship with oxide. He suggested that this might account for a large rate difference among different crystal faces. If the oxide is nucleated at many places on the surface, there is an equal probability that any of four orientational relationships will occur. As oxide grows, grain boundaries and a high concentration of structure defects develop at the place where different oxide nuclei meet one another. Therefore, the oxide on (100) face has more grain boundaries and defects than others. These grain boundaries and defects are responsible for a high rate of diffusion of copper ions towards oxide surface and hence a high oxide growth.

Fig. 2 shows the changes of the orientation of copper oxide (Cu_2O) during oxidation. The intensity of diffracted X-ray was normalised to the proportion of each orientation since the background of X-ray diffraction was different for each specimen due to the difference in their oxide thickness. The oxides on the (100) and (110) faces of the copper, single crystals having a fast oxidation rate, have only the (111) orientation in the early stage of oxidation. Other oxides also have the (200) and (220) orientation in addition to the (111) orientation parallel to faces of single crystals. The oxide on the (321) single crystal (specimen E) has all the investigated orientations from the very early stage of oxidation. All oxides of copper have all the orientation as oxidation carries on, although the (111) orientation is still dominant. It is worthy noticing the changes of the (200) orientation of the oxides. The oxides of fast oxidising specimens such as specimen C and X don't have the (200) orientation in the beginning of the oxidation. Considering the oxidation kinetics in Fig. 1, it is obvious that the rate of oxidation corresponds well with the proportion of (200) orientation as shown in Fig. 2 (b). The oxide on specimen A has a high proportion of (200) orientation after 3 hours of oxidation where the rate of oxidation of the specimen A becomes slower than that of the specimen D. It seems that the (200) oxide grains parallel to substrate may restraint the growth of oxide. The orientation of grains is related to their grain boundary character distribution. It might be interesting to analyse the influence of grain boundary characteristics of oxide films on the oxidation behaviour because the copper ions mostly diffuse through grain boundaries. There are not many differences in the orientation of these oxides at the end of the oxidation process.

The AFM morphology of Cu_2O on all the Cu specimens is shown in Fig. 3 and Fig. 4. The microstructure of Cu_2O on the specimens oxidised for 3 hours and 10 hours is not shown in this paper since their morphology is very similar. However, the grain size of Cu_2O increases as oxidation carries on. The dimension of surface area shown in Fig. 3 and Fig. 4 is 1μm by 1μm and the height (Z range) is 200nm.

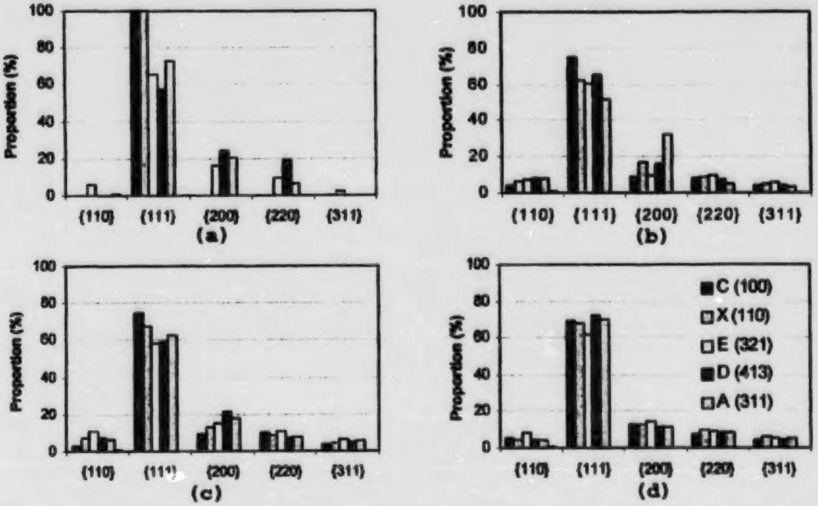

Fig. 2: Orientation of Cu_2O oxidised for (a) 1 min., (b) 30 min., (c) 3 hours and (4) 10 hours.

As shown in Fig. 3, the oxide on the specimen C, which is the copper single crystal having (100) face, is composed of tightly packed, fine homogeneous oxide grains. Unlike the oxide on specimen C, other oxides have the rough surface and their grain size is not homogeneous. It seems that the large number of fine oxide grains on specimen C contributes the fast oxidation rate of the specimen C since Cu ions diffuse mainly through grain boundaries during oxidation. The morphology of oxides has been changed after 30 minutes of oxidation as shown Fig. 4. The oxide grains grows during this period on all specimens, especially the growth of oxide grains on the specimen C is quite significant.

The oxidation kinetics of copper is rather complicated since degree of oxidation varies with pressure, temperature, atmosphere, oxide film thickness and other factors. However, it is quite clear that the early stage of oxidation is very important since most of oxidation take place in this period.

4. Conclusions

The oxidation kinetics of copper at 200°C has been studied. The order of the oxidation rate of the single crystals of copper having different faces was found to be (100), (110), (321), (413), and (311) in decreasing order. The oxides on the (100) and (110) faces of the copper, single crystals having fast oxidation rate, have only the (111) orientation in the early stage of oxidation. The oxides of copper begin all the orientation as oxidation carries on, however the (111) orientation is dominant.

There is a higher number of fine oxide grains on the copper single crystal having (100) face than on the others phases in the early stage of oxidation. This may contribute to the fast oxide growth on the (100) single crystal of copper.

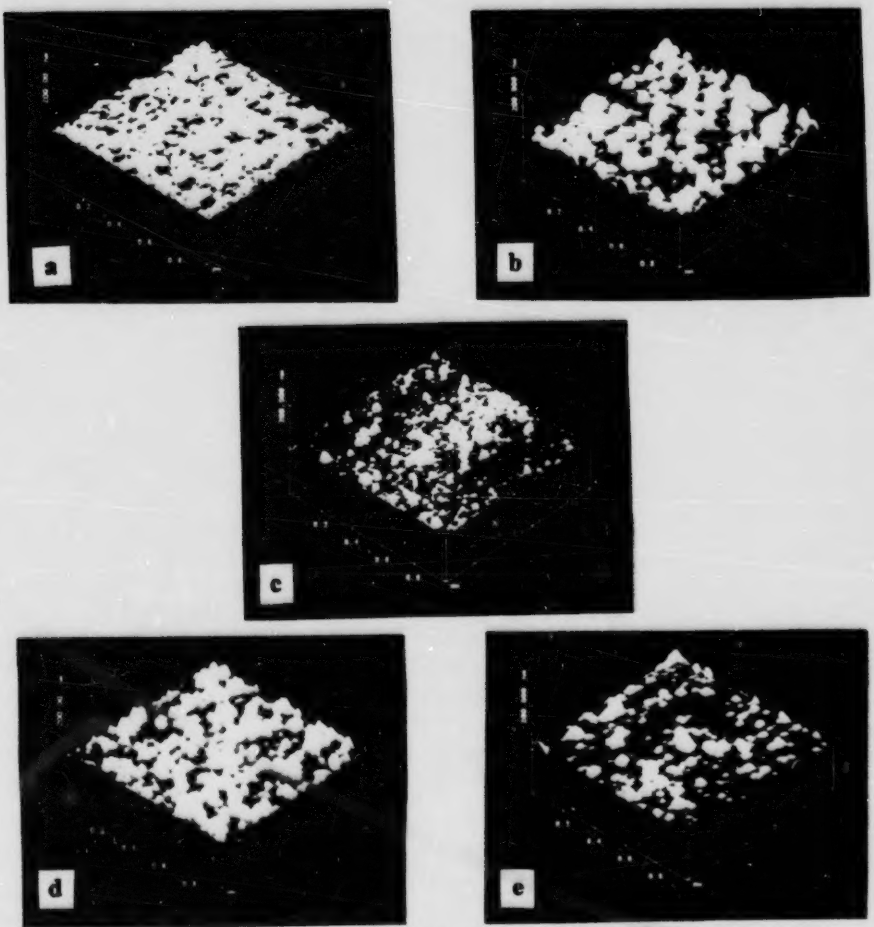

Fig. 3: The morphology of oxide films after 1 minute at 200°C on the (a) specimen C, (b) specimen X, (c) specimen E (d) specimen D and (e) specimen A.

5. References

Bénard, J. and Talbot, J. (1948) *Rev. Met.*, Vol. 45, pp. 78
Gwynne, P (1997) *IBM Research*, No. 4, pp. 17-21
Lawless, K.R. and Gwathmey, A.T. (1956) *Acta Met.*, Vol.4, pp. 153-163

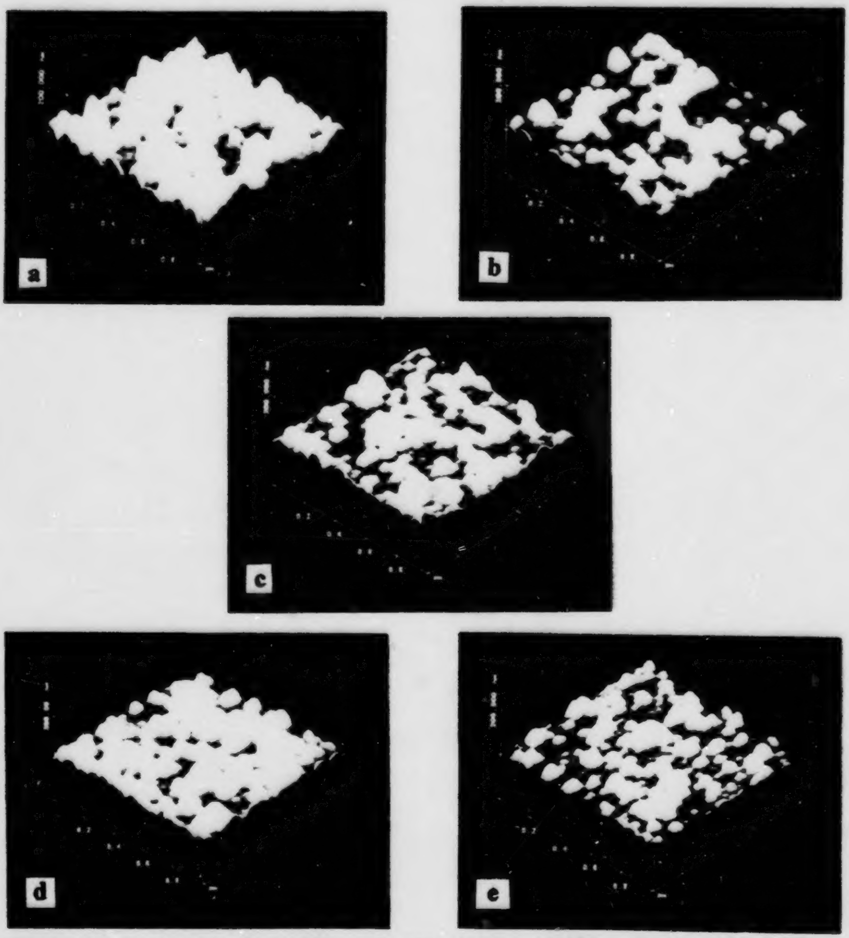

Fig. 4: The morphology of oxide films after 30 minutes at 200°C on the (a) specimen C, (b) specimen X, (c) specimen E (d) specimen D and (e) specimen A.

Murarka, S.P., Gutmann, R.J., Kaloyeros, A.E. and Lanford, W.A. (1993) *Thin Solid Films*, Vol. 236, pp. 257-266

Rhodin, Jr., T.N. (1951) *J. Amer. Chem. Soc.*, Vol. 73, pp. 3143-3146

Rönnquist, A and Fischmeister, H. (1961) *J. Inst. Met.*, Vol. 89, pp. 65-76

Young, Jr., F.W., Cathcart, J.V. and Gwathmey, A.T. (1956) *Acta Met.*, Vol.4, pp. 145-152

THE INFLUENCE OF DEPOSITION PARAMETERS ON TEXTURE IN ELECTROGALVANIZED ZINC COATINGS

H. PARK and J.A. S ZPUNAR
Department of Metallurgical Engineering, McGill University, Montreal, Canada

Abstract

The evolution of the texture and surface morphology of electrogalvanized zinc coatings has been investigated in various deposition conditions. It is found that the coatings show significant variations in texture and morphology with the change of deposition current density, pH of the bath and coating thickness. This work suggests that the transformation of texture is closely related to the evolution of coating morphology. The influence of the substrate orientation upon the coating texture is discussed. It is demonstrated that the morphology of hexagonal platelets represents the basal {0001} fiber texture. It is also demonstrated that the morphology of hexagonal ridges represents the pyramidal non-fiber texture, whereas the morphology of triangular-based pyramids represents the pyramidal {101X} fiber texture.

Keywords: Texture, surface morphology, electrogalvanized coatings, zinc, deposition parameters.

1 Introduction

Electrogalvanized zinc coatings are used to protect the automobile body steel panels because they have excellent corrosion resistance and good mechanical properties. It is well known that the coating properties are closely related to their microstructural characteristics, particularly to the texture and morphology of the deposits (Lin, 1992) By controlling the deposition parameters, the microstructure of the coatings can be significantly modified. Much research has been carried out in this field. For instance, the study of surface morphology by Lindsay et al. (1989) indicates that the primary characteristics of electrodeposited zinc coatings is the predominance of hexagonal crystal platelets of about 5 to 10 μm in diameter, whose basal plane faces are parallel or slightly tilted with respect to the substrate surface.

The microstructure of coatings evolves as a function of current density, pH, temperature of the bath, and coating thickness. High current density causes a high nucleation rate and subsequently, leads to a fine grain size and weak crystallographic anisotropy. Change of the pH value of the electrolyte can affect the coating microstructure.

The texture of the coatings tends to be related to the surface morphology of the coatings. Optimizing the texture and morphology can be a key factor in enhancing the corrosion resistance of coatings as well as other properties.

2 Experimental procedure

The specimens used for the substrate were prepared from a commercially cold rolled low carbon steel sheet with a thickness of 1 mm. Each of the specimens was sealed in the iron foil sack and annealed at 880°C for 3 hours. They were then cooled in the furnace. The specimens used as substrates were mechanically ground down to 600 μm using a SiC paper followed by polishing with diamond paste (1 μm). Prior to the electrodeposition process, the substrate specimens were electrochemically polished in the solution of 95% acetic acid and 5% perchloric acid for about 2 to 3 minutes. Subsequently, the substrate was rinsed in distilled water and ethanol, and quickly dried. An electrolytic zinc plate was used as an anode and had the same size as the cathode. The electrodeposition was carried out in a bath of the following composition

$ZnSO_4\ 7H_2O$ 350 *g/l;* $(NH_4)_2SO_4$ 30 *g/l*

The current density was varied within the range of 30 to 500 mA/cm^2. The pH value was controlled in the range between 1 to 5 by adding sulfuric acid or sodium hydroxide. The deposition time was adjusted to produce coatings with a thickness ranging from 600nm to 100μm. The bath temperature was kept constant at 50 ± 2°C. The surface morphology of the coatings was examined by Atomic Force Microscopy (AFM) and SEM.

3 The evolution of texture at different deposition parameters

3.1 The Influence of Current Density

In order to demonstrate the influence of the substrate orientation on coating texture, the texture of the substrate was measured and compared to the texture of coatings. Fig. 1 shows pole figures and ODF (Orientation Distribution Function) of an annealed steel sheet used as a substrate during the electrodeposition. It is clear from the pole figures and the ODF that the substrate has the typical annealing texture of the steel sheet. It should be noted that the poles of {110} plane are aligned towards the rolling direction, and tilted at about 35 degrees from the center of {110} pole figure. The coatings at low current density have the {0001} poles aligned towards the rolling direction with the tilted angle of 35 degrees from the center of {0001} pole figure (Fig. 2a). This tilt is also reflected by AFM images (Fig. 3). Therefore, comparing the {0001} pole figure of zinc coatings to the {110} pole figure of the steel substrate indicates a strong influence of substrate orientation upon coating texture, because zinc coatings have a specific crystallographic orientation relationship with the steel substrate.

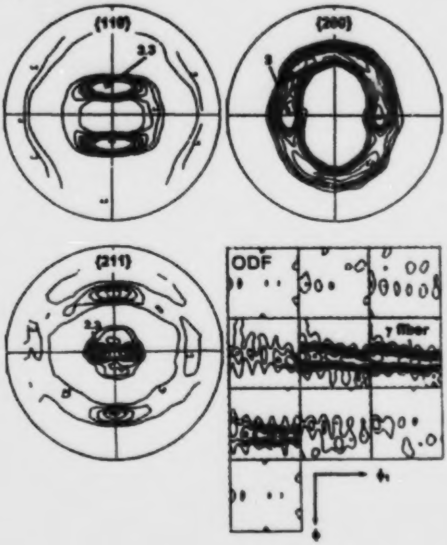

Figure 1. The pole figures and ODF of steel substrate exhibit typical annealing texture of steel sheet; The poles of {110} plane are tilted about 35 degrees from the center of {110} pole figure

It was observed that the coatings at low current densities have textures of the {0001} basal fiber component and the {1013} pyramidal non-fiber component (Fig. 2a). The basal fiber component, on the other hand, implies that the evolution of coating texture is also governed by the deposit growth mode which is closely related to the current density. The basal texture, which represents the basal plane parallel to the substrate surface is formed due to the lateral growth mode which is the predominant growth mechanism at low current densities.

At high current densities, on the other hand, the basal components disappear while the pyramidal fiber texture forms (Fig. 2c, d). The absence of basal texture implies that coating growth is no longer governed by the lateral growth mode. With increasing current density, the nucleation rate increases and the orientation of grains becomes randomized.

In the {1013} pole figures of coatings deposited at 300 to 500 mA/cm^2 , the poles are widely dispersed (fig. 2b,c,d). Thus, the coatings have the pyramidal component of the {101X} texture with higher indices, i.e. X≥3. This finding is in contrast to the sharp {1013} texture found in the coating deposited at 30 mA/cm^2 (fig. 2a). The formation of {101X} texture is an indication of the weaker substrate

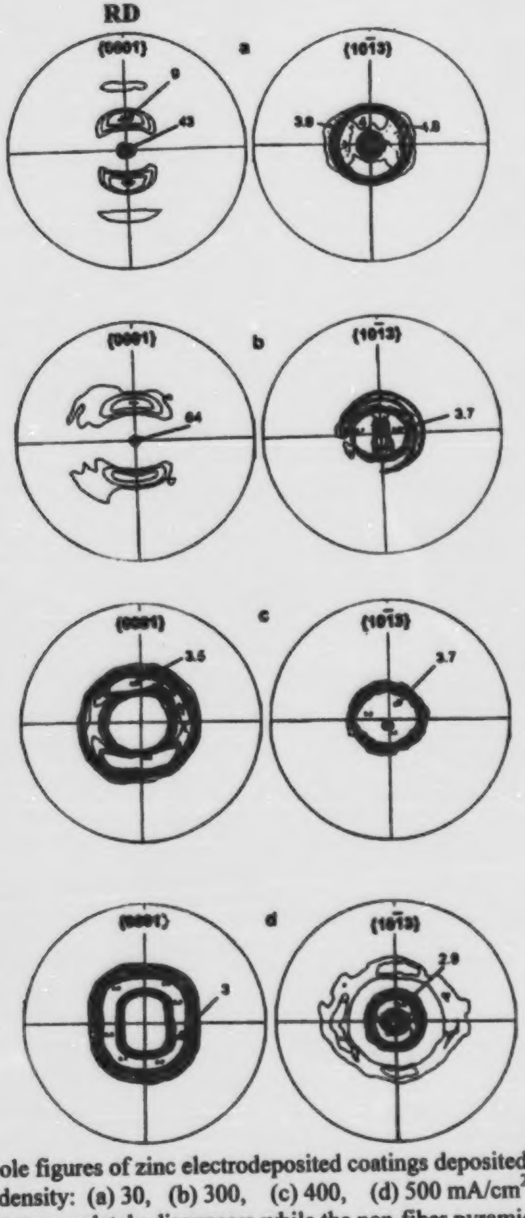

Figure 2. The pole figures of zinc electrodeposited coatings deposited at different current density: (a) 30, (b) 300, (c) 400, (d) 500 mA/cm^2; The basal component completely disappears while the non-fiber pyramidal component evolves to fiber at high current density.

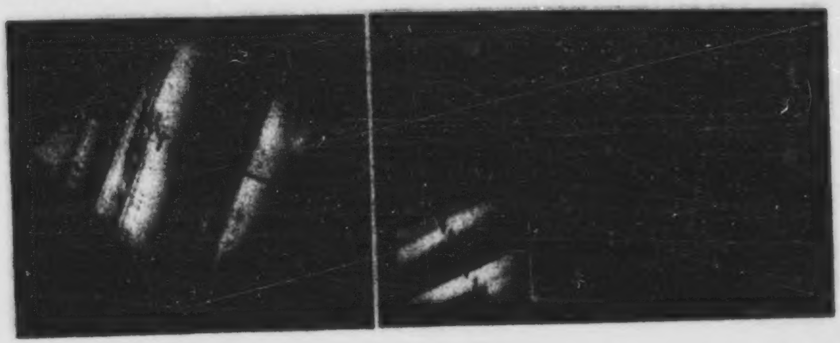

Figure 3. The AFM morphology and section profile analysis of hexagonal ridges in the zinc electrodeposited coatings; The ridges are aligned to the rolling direction and tilted about 35 degrees against the substrate surface

influence as well as the higher rate of random nucleation with increasing current densities.

3.2 The Influence of pH

In the present study, it is demonstrated also that the coating texture is sensitive to the pH of the bath. The fact that a strong basal component exists at low pH indicates that the hydrogen absorption capability is different for each of the crystallographic planes. Therefore, it can be argued that the coatings having a strong basal texture, i.e. the higher density of grains with their basal planes parallel to the substrate surface, have a higher capability of absorbing hydrogen atoms than the pyramidal texture. On the basis of the experimental results, it can be concluded that the basal texture is predominant at low pH value, whereas the pyramidal texture is the main component at high pH values.

3.3 Influence of Coating Thickness

It is observed that the pyramidal texture disappears as the coating thickness increases. It was suggested that the formation of the pyramidal non-fiber texture is due to the influence of the substrate. Based upon this suggestion, it can be inferred that the strong pyramidal texture for the thin coatings are induced by the influence of the substrate. A decrease in pyramidal texture intensity with a thickness increase indicates that the influence of the substrate is weaker.

4 Conclusions

In this paper, it has been demonstrated that the morphology and the texture of zinc coatings significantly changes with deposition parameters. A correlation is found between the texture and the morphology of zinc coatings.

As the current density increases from 30 to 300 mA/cm^2, the coating surface evolves from the morphology of hexagonal platelets and ridges to the pyramidal morphology, while the texture changes from the texture of the basal {0001} fiber and pyramidal {1013} non-fiber component to the pyramidal {101X} fiber texture. Other deposition parameters are kept constant (pH: 3.8 and coating thickness: 6μm).

As the pH of the electrolyte increases from 1 to 5, coating morphology changes from the hexagonal platelets and ridges type to the hexagonal ridge-only morphology, while the texture changes from the texture of an extremely strong and sharp basal fiber and some pyramidal non-fiber components to the major pyramidal {101X} texure. Other parameters are kept constant (current density: 300mA/cm^2 and coating thickness: 6μm).

As the coating thickness increases from 0.6 to 100 μm, the morphology evolves from the sub-micron sized particles to the thin hexagonal ridges, then to the packets of thicker hexagonal platelets and finally to the hexagonal columnar crystals. At the same time, the pyramidal texture gradually disappears, while the basal texture becomes widely dispersed. Other parameters are kept constant (current density: 30 mA/cm^2 and pH: 3.8).

Correlation is found between the morphology and texture of zinc coatings. The morphology of hexagonal ridges represents the {1013} pyramidal non-fiber texture, while the morphology of hexagonal platelets represents the {0001} basal fiber texture. The morphology of pyramidal grains represents the {101X} pyramidal fiber texture.

5 References

Lin, Y., (1992) Microstructure of Zinc-based Coatings on Steel Sheets, Ph.D. Thesis, Northwestern University, Evanston, Illinois.

Lindsay, J.H., Paluchi, R.F., Nine, H.D., Miller, V.R. and O'Keefe, T.J., (1989) *Plating and Surface Finishing*, Vol. 76, p. 62.

INFLUENCE OF HEATING RATE ON TEXTURE CHANGES IN NANOCRYSTALLINE NICKEL DURING ANNEALING

B.-K. KIM, H.-T. JEONG and J.A. SZPUNAR
Department of Metallurgical Engineering, McGill University, Montreal, H3A 2B2
Canada

Abstract

Texture changes in nanocrystalline Ni were investigated as a function of the different heating rates during annealing. Nanocrystalline Ni having (100)-fibre texture was obtained using electroplating method and annealed with different heating rates, rapid heating (RH) and slow heating (SH); around 8℃/min and 400℃/min, respectively. It is known that (100)-fibre texture of nanocrystalline Ni is changed to (111)-fibre texture after full annealing at 400℃. However, the texture of specimen annealed at 800℃ with rapid heating rate is approximated by (311)-fibre texture. The texture of a specimen annealed at 800℃ with slow heating rate is approximated by (100)-fibre texture. The recrystallization texture of nanocrystalline Ni after annealing varied with the heating rate and the annealing temperature.

Keywords: recrystallization texture, heating rate, nanocrystalline Ni

1 Introduction

Nanocrystalline (NC) materials have certain superior properties to conventional coarse-grained (CG) crystalline materials. These properties originate from a small grain size and dense grain boundary networks (Erb 1995; Suryanarayana 1995). However, NC materials rapidly transform into microcrystalline materials at elevated temperature because nanocrystalline materials have a high percentage of grain boundaries and junctions between grains. The grain boundaries and junctions between grains have higher energy and are thermodynamically unstable. Therefore, for various practical applications, is it necessary to characterize and investigate the thermal behavior and the stability of NC materials.

Among several methods used to produce nanomaterials, electrodeposition is a more convenient and efficient method than others, because it can routinely produce dense and porosity-free materials. In such electrodeposit, the grains are often textured. Since the physical and mechanical properties of electrodeposited NC materials are dependent on texture, it is important to understand the mechanisms of texture development in NC materials during heat treatment. The observation of texture change under different conditions of heat treatment facilitates the understanding of the thermal behavior of electrodeposited NC materials.

In general, electrodeposited NC Ni shows that the matrix is composed of (100) and (111)-fibre texture (El-Sherik and Erb 1995). In addition, electrodeposited NC Ni-Fe alloys have the same fibre texture components and show the same thermal behavior related to texture development (Czerwinski et al. 1997). Rajmohan et al. (1999) demonstrated how texture of NC Ni and Ni-Fe electrodeposits is transformed during the isothermal annealing at 400℃. They suggested that the reason for the fast growth of (111) fibre over (100) fibre in the NC electrodeposits is related to a higher percentage of LH-type grain boundaries surrounding (111)-fibre grains. In the LH-type grain boundaries, the misorientation is less than 15° and larger than 45°. Generally speaking, it is well accepted that the time and temperature of annealing affect texture change during grain growth (Hatherley and Hutchinson, 1979).

The purpose of the present work is to study the effects of heating rate on the texture transformation in electrodeposited NC Ni during annealing.

2 Experimental Method

NC pure Ni plates used in these experiments were prepared by using the advanced electrodeposition method (El-Sherik and Erb 1995). Electrodeposits of area 10 cm^2 were electroplated on to titanium substrate from a modified Watts bath and stripped from the substrate. In order to remove the residual surface deformation, the samples were electropolished on one side.

The annealing of NC Ni plates was conducted using the tube furnace with flowing Argon gas for preventing the oxidation of NC Ni. The heating rate was designed into two categories: rapid heating (≥400℃/min) and slow heating (≤8 ℃/min) up to 800℃. After the heating up to a specified temperature, the specimens were annealed for 4 hours or 20 hours and moved to the end of the tube furnace and cooled with flowing Argon gas. Specimens was treated according to three types of heating schedule: in one, the specimens were annealed with rapid heating (RH1) for 4 hours, the second with slow heating (SH) for 4 hours, and the third with rapid heating for 20 hours (RH2). In addition, one specimen was heat-treated with rapid heating for 4 hours at 400℃ (RHLT) in order to compare with the data of 800℃. For the texture measurement, the (111), (200) and (220) pole figures were measured using the Schulz reflection method up to a tilting angle of 80 degrees with a Siemens D-500 diffractometer and MoKα of the output of 40kV and 40mA. The inverse pole figures were calculated using the series expansion method with L_{max}=22. For observing the microstructure of annealed NC Ni, the cross-sectional area of each specimen was polished using 600 grit SiC paper and finally fine-polished by using the polishing agent of 6, 1 and 0.25 μm. The surface was etched by the solution of nitric acid 38 ml, glacial acetic acid 100 ml, distilled water 10 ml, and ethanol 10 ml.

3 Results and Discussion

The initial grain size as measured by X-ray diffraction using the Scherrer formula was 11~21 nm. Before the annealing, the texture of NC Ni shows (100)-fibre texture having the maximum pole intensity of 16.5 (Figure 1). Thus, it could be confirmed that the specimen of NC Ni prepared by the electrodeposition has a strong (100)-fibre texture.

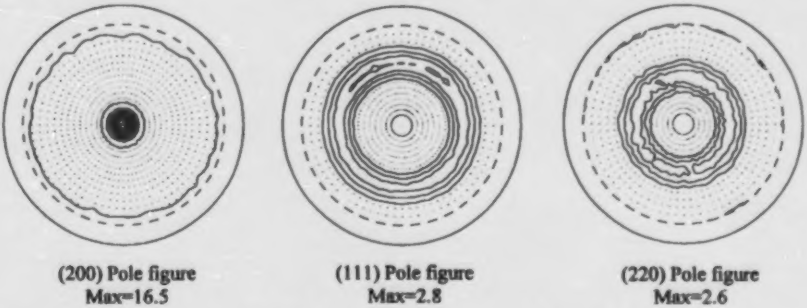

Fig. 1: Pole figures of electrodeposited nanocrystalline Ni

According to the different heating rate, the texture changes of NC Ni during annealing are compared in Table 1. In order to interpret the complex pole figures showing the texture development for annealing of NC Ni, texture data were presented as inverse pole figures showing the distribution of selected directions. Figure 2 shows inverse pole figures of the normal direction that changes according to the heating rate, annealing temperature and annealing time. Apparently, as-electrodeposited NC Ni has a strong (100) fibre texture (Figure 2a). In the case of RH1 (Figure 2b), the texture consists of a major (311) fibre texture and a minor texture (310) fibre texture. A similar pattern of texture development can be also observed in RH2 under rapid heating at 800℃ for 20 hours (Figure 2c). During the rapid heating condition for annealing at 800℃, (311) texture was developed at the initial stage of annealing and it was even observed after longer time of annealing. But, during the slow heating (Figure 2d), (100)-fibre texture is strongly developed and is accompanied by several minor texture components, (221) and (311). Here (221) represents an annealing twin of (100). An annealing twin of (311) texture has the same direction as (311) texture. Therefore, it is observed that the different heating rate of NC Ni strongly affects texture development and even though the specimen is annealed for a long time after the rapid heating to 800℃, the initial (311) texture does not change. Photo 1 shows the cross-sectional microstructure of annealed RH1, RH2 and SH specimens. Grains of RH2 are larger than RH1. This indicates that the grains of NC Ni having (311) texture grow at the initial stage of annealing and continue to grow at the grain growth stage during the rapid heating of the specimen. In the case of the slow heating, microstructure shows recrystalized grains having the size of few hundred micrometers. After annealing at 400℃ with rapid heating, RHLT has a major (100) and a minor (111) texture (Figure 2e). The microstructure of annealed RHLT shows

Table 1: Texture changes with heating rate and annealing temperature.

Samples	Annealing Condition			Major Texture		Minor Texture	
	Heating	Temp (℃)	Holding Time		Pole Intensity		Pole Intensity
N-Ni	-	-	-	(100)	11.0	-	-
RH1	Rapid	800	4 h	(311)	2.6	(310)	2.2
SH	Slow	800	4 h	(100)	6.8	(221)	3.2
						(311)	2.0
RH2	Rapid	800	20 h	(311)	2.1	(310)	1.9
RHLT	Rapid	400	4 h	(100)	6.0	(111)	2.0

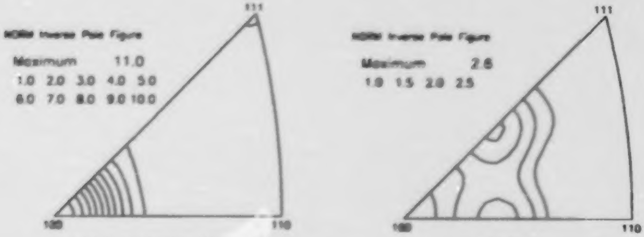

(a) As-electrodeposited (b) RH1

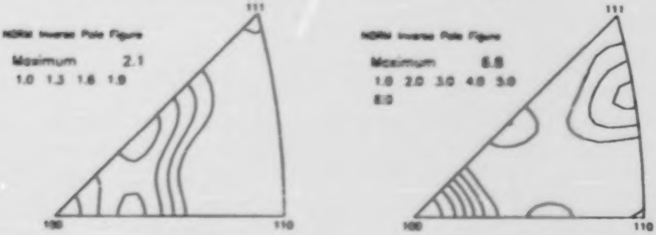

(c) RH2 (d) SH

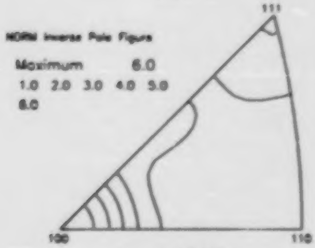

(e) RHLT

(a) As-electrodeposited NC-Ni.
(b) At 800 ℃ for 4 hours after rapid heating.
(c) At 800 ℃ for 20 hours after rapid heating.
(d) At 800 ℃ for 4 hours after slow heating.
(e) At 400 ℃ for 4 hours after rapid heating.

Fig. 2: Inverse pole figures of normal direction under different annealing condition.

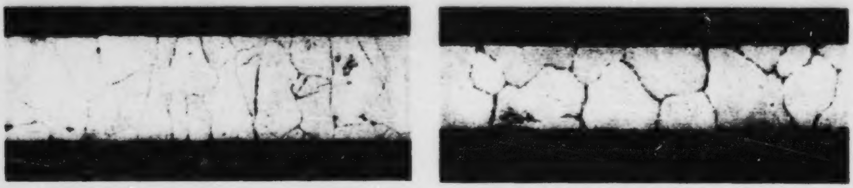

(a) Rapid heating for 4 hours (RH1)

(b) Rapid heating for 20 hours (RH2)

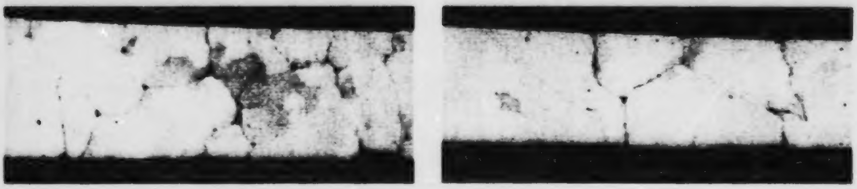

(c) Slow heating for 4 hours (SH)

100 µm

Photo 1: Microstructure of cross-sectional area of annealed RH1, RH2 and SH.

almost the same structure as NC Ni. The (111)-fibre texture is developed from initial (100)-fibre texture of NC Ni during annealing at 400℃. This result agrees with that of Rajmohan et al. (1999) and Czerwinski et al. (1997).

Boylan et al. (1991) suggested that the NC materials are transformed to the microcrystalline state at 400℃. The grain size after annealing at 400℃ is a few hundred nanometers when heating rate of 10℃ per minutes is applied (Klement et al. 1995). During annealing at temperatures that are lower than 400℃, the nanocrystalline structure is changed to the microcrystalline structure and the texture of the annealed specimen can be approximated by (111) fibre.

But the results obtained after annealing at 800℃ with different heating conditions are unlike that obtained by annealing at 400℃ under rapid heating. In the deformed metals, the rapid heating rate influences the amount of recovery before recrystallization. If a heating rate is fast, the amount of recovery occurring before recrystallization can be reduced and the driving force for recrystallization can be increased. Subsequently, this effect promotes recrystallization (Humphreys and Hatherly 1995). Similarly, the rapid heating of NC Ni may facilitate the transformation to the microcrystalline stage. The recrystallization of NC Ni could be affected by the grain boundary structure of NC materials before annealing. As a result of rapid heating, (311) texture is developed in NC Ni that has (100) texture. In polycrystalline Ni and Ni-Fe alloys, the strength of cube texture is proportionate to the temperature of annealing (Humphreys and Hatherly 1995). It is interesting to note that the recrystallization texture of NC Ni that is heated rapidly to 800℃ is different from that of the polycrystalline Ni. During slow heating, the (100) texture of RHLT is the same as texture obtained during grain growth in polycrystalline Nickel and Ni-Fe alloys. If grains of nanocrystalline materials increase in size during the slow heating before recrystallization takes place at 800℃, it is possible to speculate that the before recrystallization takes place at 800℃, it is possible to speculate that the recrystallization of NC Ni follows the same rules as in polycrystalline Ni and Ni-Fe alloys.

4 Conclusions

The heating rate affects the texture development in nanocrystalline electrodeposits. At 400℃, (111)-fibre texture is developed in nanocrystalline Ni having (100)-fibre texture. At 800℃, the texture development depends on the heating rate. Under the rapid heating, (311)-fibre texture is developed and when the specimen is maintained at this temperature for 20 hours, (311)-fibre texture still dominates. In the case of slow heating, (100)-fibre texture and its annealing twin (221) texture are developed.

Acknowledgement

The authors would like to thank G. Palumbo for providing the specimens.

5 References

Boylan, K., Ostrander, D., Erb, U., Palumbo, G., and Aust, K.T. (1991) An in-situ TEM study of the thermal stability of nanocrystalline Ni-P. *Scripta Metallurgica et Meterialia*, Vol. 25, pp. 2711-16.

Czerwinski, F., Li, H., Megret, M., Szpunar, J.A., Clark, D.G. and Erb, U. (1997) The evolution of texture and grain size during annealing of nanocrystalline Ni-45% Fe electrodeposits. *Scripta Meterialia*, Vol. 37, No. 12, pp. 1967-72.

El-Sherik, A.M. and Erb, U. (1995) Synthesis of bulk nanocrystalline nickel by pulsed electrodeposition. *Journal of Materials Science*, Vol. 30, No. 22, pp. 5743-9.

Erb, U. (1995) Electrodeposited nanocrystals: sysnthesis, properties and industrial applications. *NanoStructured Materials*, Vol. 6, pp. 533-8.

Hatherly, M and Hutchinson, W.B. (1979) *An Introduction to Textures in Metals*, Chameleon Press Ltd., London, pp. 50.

Humphrey, W.T. and Hatherly, M. (1995) *Recrystallization and Related Annealing Phenomena*, Pergamon, New York, pp. 188 & 340.

Klement, U., Erb, U. El-Sherik, A.M. and Aust, K.T. (1995) Thermal stability of nanocrystalline Ni. *Materials Science and Engineering*, Vol. A203, pp. 177-86.

Rajmohan, N., Szpunar, J.A. and Erb, U. (1999) Model for grain growth and texture transformation in nanocrystalline Ni and Ni-Fe electrodeposits during annealing. *Acta Matallurgica*, to be published.

Suryanarayana, C. (1995) Nanocrystalline materials. *International Materials Reviews*, Vol. 40, No. 2, pp. 41-64.

DEVELOPMENT OF TEXTURES AND MICROSTRUCTURES IN Fe-Ni ALLOY THIN FILMS

C.S. HA, S.S. KIM, B.I. KIM and Y.B. PARK
Department of Materials Science and Metallurgical Engineering, Sunchon National University, Sunchon, Korea

Abstract

The present study is aimed at investigating the development of textures and microstructures in Fe-Ni alloy thin films which were fabricated by physical vapour deposition and electrodeposition on low carbon steel sheets. Regardless of the coating method, the texture development of the thin films is characterized by fibre-types, whose axes depended on the processing parameters. The evolution of the microstructures of the films was examined by using the scanning electron microscope and discussed in terms of its relation with the texture development. Finally, thermomechanical properties of the coated specimens were measured to evaluate the effect of coating on them.

Keywords: Electrodeposition, Fe-Ni alloy, PVD, texture, thin films

1 Introduction

Fe-Ni alloys reveal various thermomechanical and thermochemical properties with composition (Chamberod et al., 1979). For example, Fe-36.5%Ni, which is referred to Invar, is widely used due to the thermal anomalies, whereas other Fe-Ni alloys have outstanding magnetic properties with increasing Ni content. These physical properties observed in the bulk materials are expected to basically hold but to be modified to a extent as fabricated in thin films.

In the present work, Fe-Ni alloy thin films were fabricated by physical vapor deposition (PVD) using radio frequency (RF) magnetron sputtering methods and electrodeposition on low carbon steel substrates. The development of the textures and microstructures was investigated in such thin films for various processing parameters. In order to examine the "Invar effect" of Fe-Ni film, thermal expansion of the coated specimens was estimated and compared to the bulk.

2 Experimental procedure

A conventional RF magnetron sputtering system was used for the Fe-Ni alloy thin film preparation. Typical sputtering conditions are summarized in Table 1. The target used for the current study was Fe-36.5wt-%Ni alloy with 50mm diameter and 4mm thickness. Low carbon steel was used for the substrate, whose dimension was 20mm × 20mm × 0.2mm. The substrate temperature was maintained at 200°C during sputtering. The substrate temperature was detected by a thermocouple placed just behind the substrate. The sputtering chamber was evacuated to a base pressure less than 1×10^{-6} torr. Argon gas as the sputtering gas was introduced into the chamber, keeping the flow rate constant at 5 sccm (std. cm^3/min) by a mass-flow controller. On the other hand, electrodeposition was employed to obtain the Fe-Ni alloy thin films having different compositions.

The thickness and the microstructures of the films were examined using scanning electron microscope (SEM). {111} pole figure and inverse pole figures were measured for the texture analysis of the coated layers. In order to estimate the thermal expansion behavior of the Fe-Ni alloy coated specimens, as shown in Fig. 1, the changes of the distance *L* between diamond indentations on the longitudinal sections of the specimens were measured on an image analyzer during heat cycle between room temperature and 200°C.

Table 1: Summary of sputtering conditions employed for the fabrication of Fe-Ni alloy thin films on low carbon steel substrates.

Sputtering parameters	Conditions
Target composition	Fe-36.5 wt-%Ni
Substrate material	Low-carbon steel
Substrate temperature	200°C
Deposition time	150-300 min.
Target to substrate distance	60 mm
Sputtering gas	Ar
Work pressure	5×10^{-2} torr
RF input power	120 W
Gas flow	5 sccm

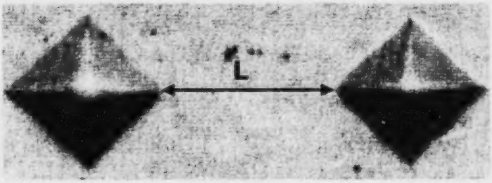

Fig. 1: Optical micrograph showing the diamond indentations on the longitudinal section of the low carbon steel substrate. The change of the distance *L* between diamond indentations was measured on a image analyzer during heat cycle between room temperature and 200°C.

3 Results and discussion

3.1 Development of microstructures

Figure 2 shows SEM microstructures of the Fe-Ni alloy thin film deposited on the low carbon steel substrate by using the RF magnetron sputtering method. The coating was carried out under the conditions as given in Table 1, and the working time was 150 min. The morphology of the grains composing the film is characterized by one dimensional growth and voided boundaries. The thickness of the deposited layer was about 3μm, and the diameter of the grains near the surface ranged between 0.5μm and 2μm. The formation of the tapered grains with dome tops is attributed to the directed incidence of the particles.

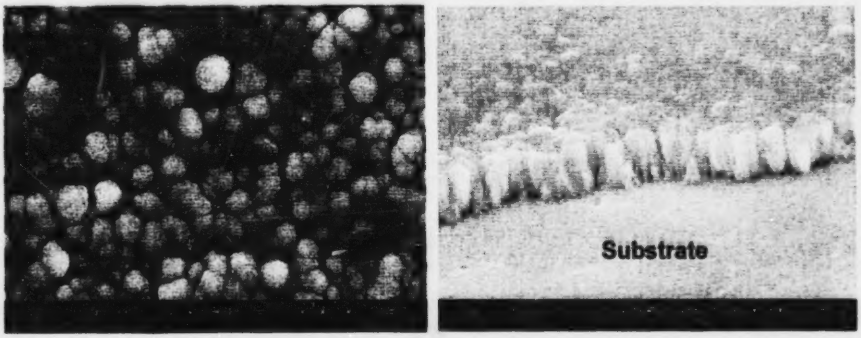

(a) (b)

Fig. 2: SEM microstructure of Fe-Ni alloy thin film sputtered for 150 min under the processing conditions as given in Table 1. (a) Top view of the specimen, (b) Morphology of the grains grown on the low carbon steel substrate.

Fig. 3: The inclination angle β of the column axes with respect to surface normal is measured to be approximately 12° in the grains observed in Fig. 2.

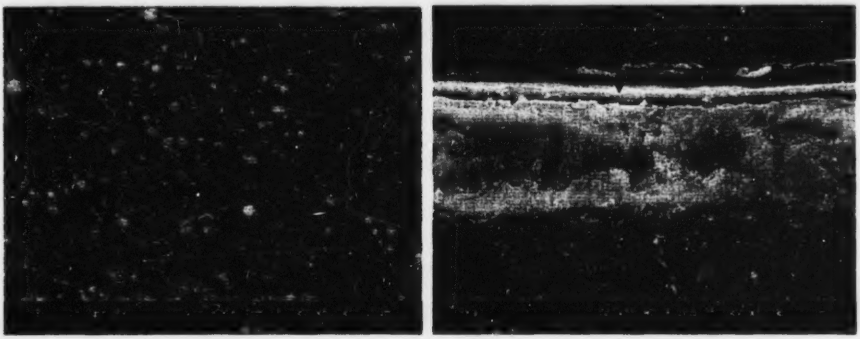

(a) (b)

Fig. 4: SEM microstructure of Fe-Ni alloy thin film sputtered for 300 min under the processing conditions as given in Table 1. (a) Top view of the specimen, (b) Morphology of the longitudinal section of the film grown on the low carbon steel substrate.

In PVD, generally, the vapour or plasma particles do not impact perpendicularly on the surface of the substrate. This is due to the geometric arrangement of the vapour sources and the substrates. In many cases, as given by Eqn (1), the empirical tangent-rule (Schulz et al. 1996) is applied to the relation between the mean angle of particle incidence α and the inclination angle β of the column axes with respect to surface normal.

$$\tan\alpha = 2\tan\beta \qquad (1)$$

Figure 3 shows an example for the inclined columnar grains of Fe-Ni alloy film as a consequence of nonperpendicular particle incidence during sputtering. In the current work, α and β were measured to be approximately 29° and 12°, respectively, reasonably satisfying Eqn (1). The microstructure development of the film depended on deposition time under the same conditions of the other processing parameters. As obviously from Fig. 4, in Fe-Ni film sputtered for 300 min, the columnar grains were rarely observed. The columnar structure developed in the early stage (*see* Fig. 2) of the deposition seems to have changed into a denser structure due to the "bombardment effect" of particles by sputtering during deposition time longer than 150 min. As a result, the voided boundaries between the columnar grains disappeared, and the frequency of the dome tops of the grains drastically decreased (Fig. 4(a)). The latter phenomena might be related to a compact thin layer which was formed in the surface section of the film (Fig. 4(b)). The thickness of this thin layer was lesser than 1 μm.

3.2 Development of textures

Figures 5 and 6 show the {111} pole figures and ND inverse pole figures in Fe-Ni alloy thin films sputtered with different deposition times. The film deposited for 150 min revealed the development of a distinct <110>//ND fibre texture (Fig. 5). Since the <111>//ND fibre dominated the textures of the steel sheet used for the current substrate, therefore, the orientation relationship between film and substrate can be expressed by $\{111\}_{\text{bcc substrate}}//\{110\}_{\text{fcc film}}$.

The texture development of the film deposited for 300 min is characterized by a mixture of the <120> and <111> fibres as shown in Fig. 6. Therefore, in comparison of Figs. 5 and 6, it is apparent that the development of the textures changes from the <110> fibre to the <120> + <111> fibres with increasing deposition time. These texture phenomena appear to be strongly related to the evolution of the microstructures as discussed above. The occurrence of the <120>//ND component might be attributed to the bombardment effect of the energetic particles on the <110>//ND oriented columnar grains which were formed in the early stage of deposition. On the other hand, the appearance of the <111>//ND component seems to correspond to the outer thin layer observed in the later stage of deposition, *see* Fig. 4. When the deposition rate decreases due to heat resulting from the collision of the incidence particles on the deposited film, the {111} plane that has the lowest surface energy can be preferred to grow.

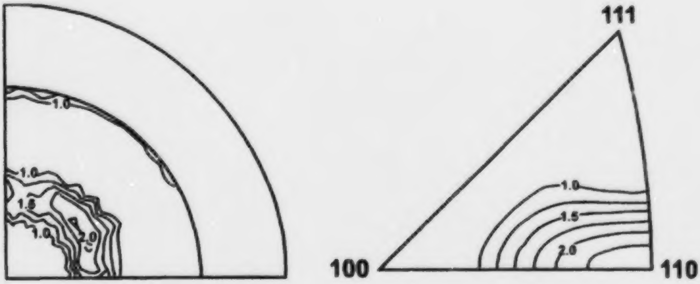

(a) (b)

Fig. 5: (a) (111)Pole figure and (b) ND inverse pole figure in Fe-Ni alloy thin film after sputtering for 150min.

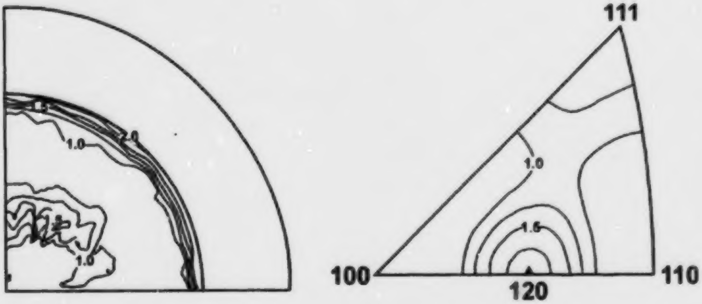

(a) (b)

Fig. 6: (a) (111)Pole figure and (b) ND inverse pole figure in Fe-Ni alloy thin film after sputtering for 300min.

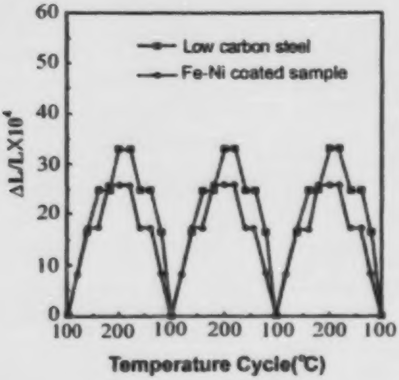

Fig. 7: Effect of Fe-Ni alloy coating on thermal expansion of low carbon steel.

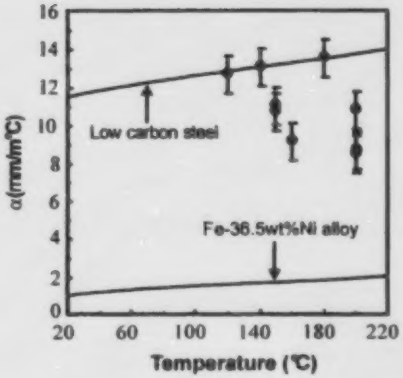

Fig. 8: Thermal expansion of the Fe-Ni alloy coated steel sheet.

3.3 Thermomechanical property

Fe-Ni alloy thin films (t=3 μm) were fabricated on low carbon steel sheet (t=0.18 mm) by electrodeposition. In order to estimate thermal expansion of the coated samples, the changes of the length *L* between the marks as shown in Fig. 1 were measured during heat cycle in the range of room temperature and 200°C. Due to Invar anomalies of Fe-Ni film, thermal expansion of the substrate material was considerably affected (Figs. 7and 8). Thus, the coefficients of thermal expansion of the specimens were estimated to be about 30 % lower than that of bulk steel.

4 Conclusions

Fe-Ni alloy thin films were fabricated by PVD and electrodeposition. The evolution of the microstructures in the thin films has been discussed in terms of the texture development for different processing parameters. Due to Invar anomalies, thermal expansion of the Fe-Ni alloy coated steel was considerably reduced when compared to bulk steel.

Acknowledgements

The authors wish to acknowledge the financial support of the Korea Research Foundation made in the program year of 1997.

References

Chamberod, A., Laugier J. and Penissen, J.M. (1979) Electron irradiation effects on iron-nickel Invar alloy. *J. Mag. Mag. Mater.*, Vol. 10, pp. 139-144.

Schulz, U., Oettel, H. and Bunk, W. (1996) Texture of EB-PVD thermal barrier coatings under variable deposition conditions. *Z. Metallk.*, Vol. 87, pp488-492.

EXAMINATION OF THE STRESS AND PHASE COMPOSITION IN TEXTURED ZIRCORNIUM OXIDES FILMS

Jianlong Lin, J. A. Szpunar
Department of Metallurgical Engineering, McGill University
Montreal, Que., Canada H3A 2B2

ABSTRACT

The studies of oxides formed on the surface of Zirconium pressure tube have confirmed that at room temperature there are tetragonal phase and monoclinic phase existing. The stress in the oxide film is believed to be the key factor that stabilizes tetragonal phase. In our study, the grazing incidence geometry was employed which allows the stress present in very thin oxides to be determined. The pole figure of oxide film and Zr-2.5%Nb and Zircaloy-4 substrates was measured using Schulz reflection method. Based on the pole figures of oxide film and substrate, the orientation distribution functions (ODF) of oxide film and substrate were calculated. The major orientation components of the oxide formed on Zr-2.5Nb substrate were $(10\bar{3})[0\bar{1}0]$ and $(10\bar{4})[401]$ while $(10\bar{4})$ fiber was formed on Zircaloy-4 substrate.

Key words: pole figure, ZrO_2, texture, ODF, X-ray, stress

1. Introduction

Zirconium alloys have been investigated over many years because of their applications in the nuclear power industry. Zirconium alloys are adopted in the nuclear power industry because they have a high corrosion resistance during exposure to hot water and stream. The performance of these alloys determines where hydrides are formed and the tube may develop crack. This happens if thermal solubility of hydrogen is exceeded and hydride plates are formed.

The oxide film that adheres to the surface can play an important role as a diffusion barrier, limiting the rate of hydrogen ingress and therefore protects against hydrogen embrittlement at high concentration. It is important that the permeation rate of hydrogen through oxide is small since this will allow minimizing the uptake rate and it will help to maximize the time of tube operation.

It is also essential to know the stresses development in the oxide for understanding the corrosion and hydrogen ingress mechanisms in Zirconium alloys.

Such stresses are different at different oxide layers and therefore should be investigated by employing grazing incidence geometry. The texture of oxide investigated in two different materials, Zr-2.5Nb and Zircaloy-4, to establish a relationship between the phase composition of oxides and the stress developed in it.

2. Experimental Procedures

The study was carried out using alloys of Zr-2.5Nb and Zircaloy-4. The materials used for this study were obtained from the Atomic Energy Research Center of Argentina. The samples were in the form of plate specimens 25mm×10mm. They were exposed to lithiated heavy water at 623K for different times. All samples have been polished carefully and have a mirror-like finish.

The x-ray reflection method proposed by Schulz was used to measure the pole figures. The specimen was mounted in a goniometer that allows tilting (ϕ) and rotation (ψ) of the specimen to cover as much of the pole figure as possible. The angle of ϕ is defined as the angle that the specimen normal is with respect to the plane containing the incident and diffracted X-ray beams. The measurements were done using Siemens D-500 texture goniometer equipped with a copper target. The $(11\bar{1})_m$,$(111)_t$,$(111)_m$ and $(002)_m$ pole figures were measured. Depending on the X-ray techniques used to determine the texture, various correction factors have to be introduced, such as defocusing correction (reflection method), due to change of measurement geometry and absorption correction. To correct the experiment data, texture free samples, chemically pure powder was measured under the same conditions as the actual textured specimens.

Stress was measured by employing a grazing incidence geometry which allows the stress present in thin film to be determined. The peak $(11\bar{1})$ was chosen to stress measurement because this is the only useful peak free from disturbing neighboring peaks, including peaks from tetragonal oxide phase and zirconium alloys substrate. A program to correct background and Lorentz polassisation factors was used to improve the accuracy of the result.

3. Results and Discussion

3. 1 Texture analysis

The pole figures presented illustrate the preferred grain orientations in the material, but they are still qualitative in nature. Orientation distribution functions (ODFs) required for quantitative analysis of texture. ODFs of oxide films were calculated using the software developed in our laboratory [1]. The ODFs were presented respectively in Figure 1 and Figure 2, with the intensity specified at constant unit intervals. The ODFs reveal that major orientation components of oxide formed on Zr-2.5Nb are $(10\bar{3})[0\bar{1}0]$ and $(10\bar{4})[401]$ while $(10\bar{4})$ fiber is formed on Zircaloy-4.

3.2 The quantitative phases and stress analysis

In this study grazing incidence geometry was employed to measure the stress present in the oxide film. Compared to the conventional X-ray measurement of stress, in this method the incident angle is kept constant. The theory behind this method is that the interplanar spacing in the material deviate from their unstressed spacing under either compressive or tensile stress. According to Bragg law, this deviation of the lattice plane spacing causes a shift of the diffraction to a new 2θ, which corresponds to the magnitude of the applied stress. The stress can be calculated by using the following equation [2]:

$$d_{\phi\psi}=\left[\frac{1+\nu}{E}\sigma_\phi d_0\sin^2\psi\right]+\left(1-\frac{\nu}{E}(\sigma_1+\sigma_2\right)$$

where ν is Poisson's ratio for the material, d_0 is the unstressed lattice spacing in the material, σ_1 and σ_2 are the principle stresses, *E* is the modulus of elasticity. The lattice spacing measured $d_{\phi\psi}$ as a function of tilt angle ψ at some angle ϕ measured with respect to one of the principal stress axis within the sample reference frame.

Figure 3 shows the measured stress on Zircaloy-4 and oxide thickness as the function of exposure time. As can be seen from the curve, the thickness of oxide increases with increaing of exposure time. However, the measured stress decreases with increasing exposure time. Previous work has shown the same result [3]. This is due to the fact that the Pilling-Bedworth ratio for Zr/ZrO$_2$ system is 1.56. This ratio will cause the compressive stress at the metal oxide interface.

The stress distribution is important because it allows understanding the phase transformation in the oxide. Based on the pole figure of oxide formed on the substrate, the tetragonal volume fraction can be calculated accurately, even in strongly textured materials. One approach to calculating the fraction of monoclinic phase is Polymorph method, which assumes that the stabilized cubic ZrO$_2$ phase can be regarded as a high-temperature polymorph of ZrO$_2$. X-ray intensity calibration in stabilized-unstabilized ZrO$_2$ system shows that [4]:

$$I_m(111)+I_m(11\bar{1})=I_H(111)$$

where I_H is the intensity of the tetragonal or cubic high-temperature ZrO$_2$ polymorph. This method provides a very useful means of phase analysis in zirconia system, however it cannot be entirely justified theoretically.

The total integrated intensities $I_t(hkl)$ of the $(11\bar{1})_m,(111)_m$ monoclinic and $(111)_t$ tetragonal pole figures are then used to determine monoclinic zirconia volume fraction with respect to the total volume of zirconia as given by the equation [4]:

$$X_m=\frac{V_m}{V_m+V_t}=\frac{C\left[I_t(11\bar{1})_m+I_t(111)_m\right]}{C\left[I_t(11\bar{1})_m+I_t(111)_m\right]+I_t(111)_t}$$

With

$$C={R(111)_t}\Big/{\left[R(11\bar{1})_m+R(111)_m\right]}$$

The theoretical intensities $R(hkl)_t$ of the considered diffraction lines and the related coefficients, C, are calculated for different radiation used. For CuKα the coefficient C is 1.381.

Figure 4 shows changes of the computed fraction of tetragonal oxide as a function of oxide thickness. It can be seen that with increasing the oxide layer thickness the fraction of tetragonal zirconia decreases. Tetragonal phase is normally stable at higher temperature is observed also at room temperature. The reason for this phenomenon is most likely the high compressive stress that exists in the oxide film. The proportion of tetragonal phase changes with the distance from the interface between metal and oxide. This is due to the fact that during inward growth of the oxide, stresses are relaxed and that lead to unstable tetragonal phase, then the tetragonal phase transforms to the monoclinic phase.

4. Conclusion

The oxide layer grown on both materials is a mixture of the tetragonal phase and monoclinic phase. Using experimental data about texture of oxide films, the phase composition of film can be determined even in oxides that are strongly textured. The results obtained show that with the increase of oxide thickness, the volume fraction of tetragonal phase decreases. The orientation distribution functions (ODFs) calculated from the pole figures show that the major orientation components of the oxide formed on Zr-2.5Nb are $(10\bar{3})[0\bar{1}0]$ and $(10\bar{4})[401]$ while $(10\bar{4})$ fiber is formed on Zircaloy-4.

By empolying grazing incidence geometry, stresses existing in oxide film were measured. With the thickness of the oxide film increasing, stresses decrease and the tetragonal phase becomes unstable. The phase transformation from tetragonal to monoclinic can be linked the thickness of oxide film.

Acknowledgement: We would like to thank Comision Nacional de Energia Atomica, Argentina for preparing samples for this work.

REFERENCES

Li, Hualong, Textools Software (1998)

Glavicic, M. G., Szpunar, J. A., Lin, Y. P. (1997) *J. Nucl. Mater.* 245 pp.147-151

Beie, Hans-Jurgen, et al. (1994) *Zirconium in the Nuclear Industry: Tenth International Symposium,* ASTM STP 1245, pp. 615-643

Garvie, R. G., Nicholson P. N., (1972) *Journal of the American Ceramic Society* 55 pp.303

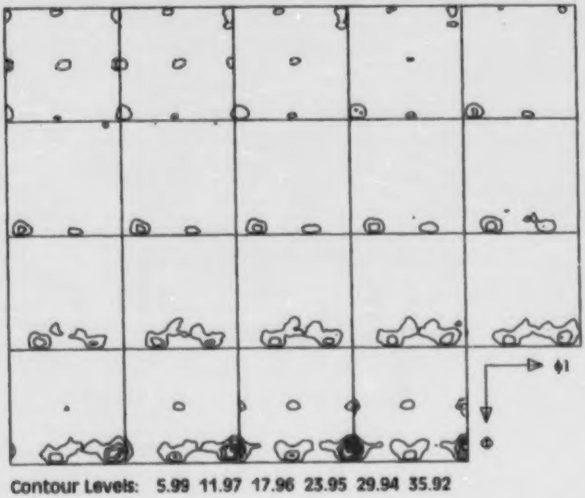

Figure 1 ODF of monoclinic phase of oxide formed on Zr-2.5Nb substrate

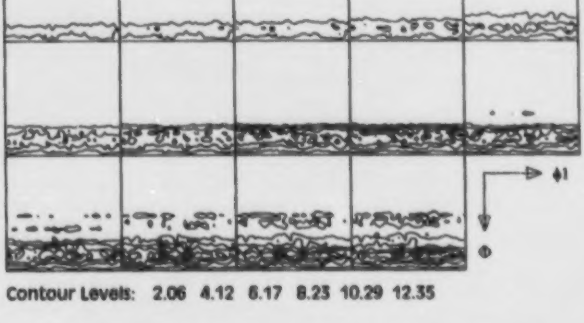

Figure 2 ODF of monoclinic phase of oxide formed on Zircaloy-4 substrate

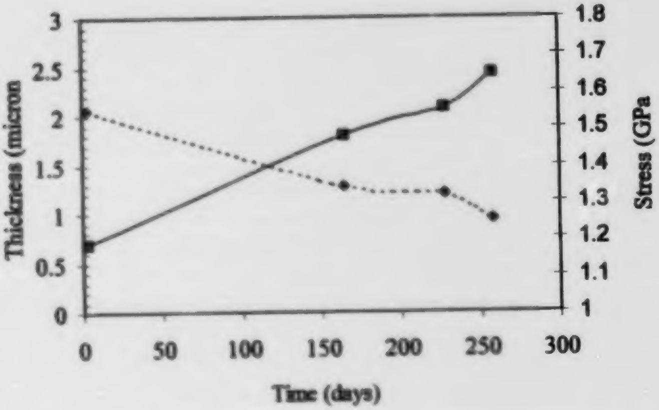

Figure 3 Measured stress and thickness of oxide film vs exposure time

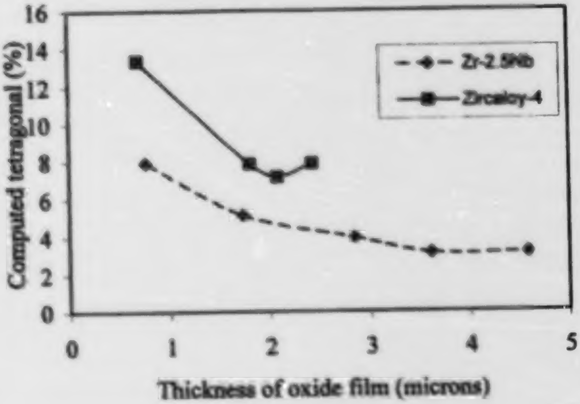

Figure 4 Computed percentage of tetragonal phase vs thickness of oxide film

TEXTURE DEVELOPMENT DURING THE ELECTROCRYSTALLIZATION OF NICKEL

Y. CAO, F. CZERWINSKI and J. A. SZPUNAR
Department of Metallurgical Engineering, McGill University, Montreal, PQ, H3A 2B2, Canada

Abstract

The microstructure and texture of nickel coatings, obtained electrolytically from a Watt's bath, were analyzed as a function of deposition parameters and coating thickness. For the wide range of current densities studied, the mixed texture composed of the <110> and <100> fibers was detected. While for low current densities the <100> component was dominant, the high current densities caused the growth of the strong <110> fiber texture. The possible mechanism, leading to the formation of the <110> and <100> textures, is discussed.

Keywords: electrodeposition, nickel, surface energy, texture

1. Introduction

Among metals of the transition group, which are electrodeposited for commercial applications, nickel is of special importance mainly due to its high resistance to corrosion, its hardness and other mechanical properties [1]. The behaviour of nickel electrodeposits depends mainly on grain size and grain orientation, which can easily be controlled by deposition conditions [2,3]. In general, the texture of electrodeposits is governed by three major factors related to the substrate, solution and processing parameters [2-6]. For thin electrodeposits, the substrate orientation plays an important role, however, this influence decreases with time and for thick deposits it is only a function of electrolyte composition and current density. Very little information is available regarding the texture of metal crystallites deposited in wide ranges of current densities. In order to control the texture of electrodeposited metals, the mechanism of its formation should be understood.

This study contains measurement of the microstructure and texture of several nickel electrodeposits, to provide more details useful in the interpretation of texture development during electrocrystallization.

2. Experimental details

The nickel electrodeposition was conducted from a Watt's bath composed of 300 g/l $NiSO_4 \times 6H_2O$, 35g/l $NiCl_2 \times 6H_2O$ and 35g/l H_3CO_3 at a temperature of 50^0C. The pH was kept constant at a level of 3. The process was carried out galvanostatically by applying current densities between 10 to 80 A/dm^2. The anode was pure nickel and the cathode substrate was low carbon steel. As a final step of substrate surface finishing, chemical polishing was applied. The thickness of deposits usually exceeded 50 μm. It is therefore assumed that there was no influence of the substrate orientation on the deposits' texture and the texture was an exclusive function of electrodeposition parameters. The nickel deposits also exerted no substrate interference during texture measurement.

The cross-sections of the nickel electrodeposits were observed with an optical microscope. Samples were mechanically polished and etched in a mixture of nitric acid and acetic acids. The texture was measured on the outer surface by the Siemens X-ray diffractometer, using a Mo target. Pole figures were obtained using the reflection technique up to a maximum tilt of 80 deg in 5 deg polar and radial intervals. The pole figures were then used to calculate the orientation distribution functions (ODF), according to the procedure described by Bunge [7].

3. Results

The cross-sectional microstructure of as-deposited nickel is shown in Fig. 1. The grains exhibit a columnar shape and are oriented perpendicular to the substrate. Their size increases with coating thickness. A visual assessment of the microstructure reveals the three zones. A very thin layer adjacent to the substrate consists of equiaxial and fine grains. Then, there is a transition zone, which gradually changes into columnar structures. Although an increase in current density significantly reduced the average grain size, the general character of the microstructure, with the three zones described above, remained the same.

The crystallographic texture of the substrate is shown in Fig. 2a. It is composed of {111}<112>/{112}<110>, which is typical for a cold rolled steel sheet. This knowledge is of importance in verifying the possible influence of the substrate orientation on the deposit texture. A simple comparison of the typical ODF of the steel substrate (Fig. 2a) and the nickel deposit (Fig. 2b) excludes the substrate contribution. Thus the measurements represent the growth texture influenced solely by the deposition parameters. A strong <100> fiber texture was clearly observed in the low current density. An analysis of the (100) pole density indicates texture strengthening with an increase in the thickness of deposits. This is especially true for low current density where an increase of coating thickness from 25 to 190 μm caused texture strengthening by one order of magnitude (Fig 3). The influence of current density on the deposit texture is shown in Fig. 4. While at low current densities the

<100> texture is a major component, at high current densities, the <110> fiber texture dominates. For the experimental conditions of this study, the region of rapid changes in intensities of the <100> and <110> texture took place between 30 and 50 A/dm^2.

4. Analysis of texture formation in nickel deposits

The nucleation stage of electrodeposits involves formation of a small embryo on the substrate. At that time, solvated ions are transferred to the cathode (substrate) by the electric field, then are hydrated and discharged into ad-atoms at the surface of the cathode and finally, after diffusing to low-energy sites, form the nuclei. The formation of a new phase requires the system to be in a metastable state. This is achieved by perturbing the equilibrium via the application of a potential field in direct electrocrystallization. The nucleation rate (I) is expressed by [6]:

$$I = J \bullet B \bullet \exp[-\Delta G^* / RT] \qquad (1)$$

where ΔG^* is the critical free energy for nucleation, which is related to the surface free energies of the electrode-solution, electrode-film and film-solution interfaces, B is a constant containing geometrical factors and J is the current density of the electrode reaction involved.

The crystal growth, which follows nucleation, is mainly controlled by the system energy and growth rate, which means the growth thermodynamics and kinetics, since during electrodepositon, the system energy is dominated by the surface energy when the depositing speed is low. This means that the grain surface with minimal energy will grow preferentially.

The surface energy ratios for some low-index crystal planes of nickel, calculated by using a Lennard-Jones potential approach, are shown in Table 1 [5,7]. It is clear that the (100) and (110) faces have lower values than that of the other faces, so nickel grows more easily on the (100) and (110) faces. This explains the experimental observation that the <100> and <110> are the most frequently observed textures in nickel electrodeposits. The especially strong <100> texture produced at low current densities results from the smaller inhibitor discharge and adsorption [5], so the surface energy plays a more important role on electrocrystallization. The (100) texture is the result of the lowest surface energy face, which grows preferentially. But the <100> texture will transfer to the <110> texture at high current densities because the inhibitor has the stronger effect. Between them, there is a mixed field of <100> and <110> texture (Fig. 4).

Table 1. Surface energies of nickel crystal planes.

$\gamma^{(100)}/\gamma^{(100)}$	$\gamma^{(110)}/\gamma^{(100)}$	$\gamma^{(111)}/\gamma^{(100)}$	$\gamma^{(311)}/\gamma^{(100)}$	Reference
1.00	1.14	1.25	----	[8]
1.00	1.06	1.12	1.21	[5]

The linear rate of electrocrystallization, v, is directly related to the current density, j, according to the expression(9)

$$v = j\,V_m / nF \qquad (2)$$

where V_m is the molar volume and F is the Faraday constant. This relationship shows that high current density will lead to a higher rate of growth. Comparing equation (1) and (2), we can find that the nucleation and growth are competitive with each other. Whit a high current density, it grows very fast shortly after the nucleation. Especially, crystal grows faster in one face than that of others. That means selective growth which usually produces the texture.

5. Summary

The nickel electrodeposits with a thickness up to 200μm exhibited columnar structure and fiber texture containing two major components, the <100> and <110>. While for low current densities, the <100> texture was dominant, the high currents caused the growth of a strong <110> fiber texture. There is a texture transition region between 30 and 50A/dm^2. The formation of the <100> and <110> texture in nickel can be explained while considering the mechanism, based on the minimization of the surface energy and inhibited growth.

Acknowledgments

One of the authors (Y. Cao) is grateful to the Natural Sciences and Engineering Research Council of Canada for the financial support in the form of a scholarship.

6. Reference

1. Parthasaradhy, N. V. (1974) *Metal Finishing*, **72** (8), pp. 36-41.
2. Weil, R. (1987) *Plating & Surface Finishing*, **74** (12), pp. 70-75.
3. Delpancke, J. L. et al. (1993) *J. Electrochem. Soc.*, **140** (10), pp. 2800-2807.
4. Sibley , P. and Brook, P. A. (1973-74) *Electrodeposition and Surface Treatment*, **2**, pp.177-190.
5. Li, D. Y. and Szpunar, J. A. (1997) *Electrotrochimeca Acta*, **42** (1), pp. 47-60.
6. Vermiyea, D. A. (1963) *Adv. Electrochemistry and Electrochemical Eng.* **3**, pp. 1254-1286
7. Bunge, H. J. (1982) *Texture Analysis in Materials Science*, Butterworths
8. Tyson, W. R. (1976) *J. Appl. Phys.* **47**, pp. 459-465
9. Walsh, F. C. and Herron, M. E. (1991) *J. Phys. D: Appl. Phys.*, 24, pp. 217-225.

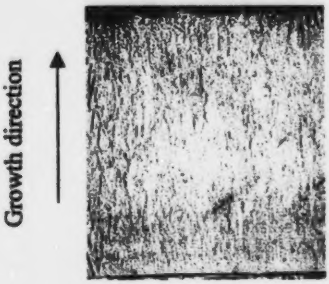

Fig 1.The cross sectional microstructure of nickel deposits

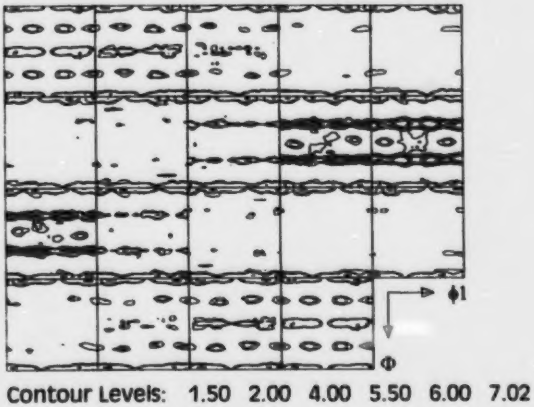

(a) low-carbon steel substrate

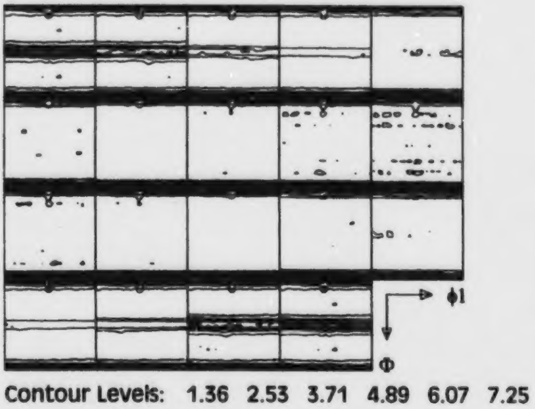

(b) nickel electrodeposit

Fig. 2. The orientation didtribution fuctions (ODF) of the steel substrate and Ni coating.

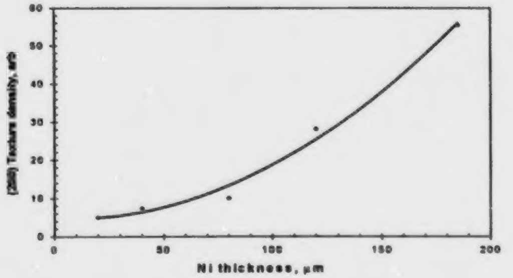

Fig. 3 The texture evolution in Ni as a function of deposit thickness at the current density of 10 A/dm^2.

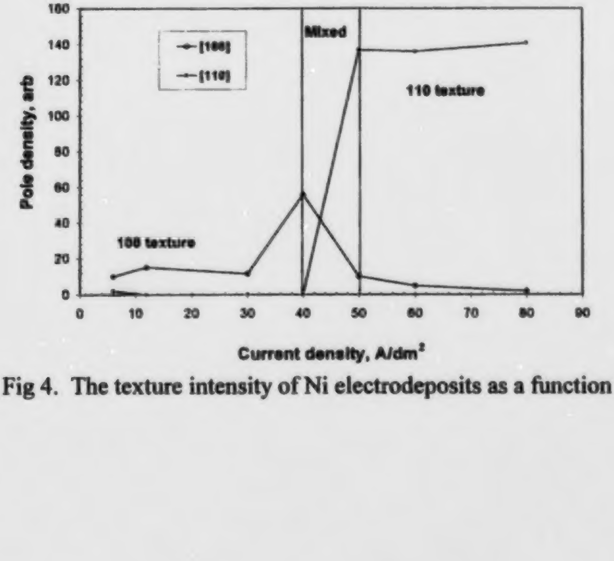

Fig 4. The texture intensity of Ni electrodeposits as a function of the current density.

Texture in Ceramics, Composites and Polymers

ORIENTATION EVOLUTION OF TEXTURED PIEZOELECTRIC CERAMICS UNDER ELECTRIC FIELDS

SHAN WAN and KEITH J. BOWMAN
School of Materials Engineering, Purdue University, IN 47907

Abstract:

The anisotropic tensors of piezoelectricity and electrostriction are inherently related to microstructure and texture. We have investigated the coupling between orientation and property anisotropy in a number of materials which possess anisotropic properties that include ferroelectricity, permittivity, piezoelectricity, fracture, elasticity and electrostriction. The flexibility and reversibility of domain structures in some of these materials afford a unique opportunity to correlate a large number of interrelated properties with microstructure and texture information. The textures in these materials can be manipulated through both mechanical and electrical stimuli. In this paper we show texture changes from poling and cross-poling to produce rolling-type textures and anisotropic properties in piezoelectric materials.

1. Introduction

Piezoelectricity in ceramics is determined by both single crystal properties and domain orientation distribution. Preferred domain orientations in piezoelectric ceramics can be changed and controlled effectively by electric field poling [1], thermal treatment [2, 3], and mechanical stress [4, 5]. Of the external stimuli that can change the domain orientation of piezoelectric ceramics, electric fields are the most effective. Poling is an essential step in manufacturing piezoelectric ceramics. Extensive research has been made on poling effectiveness by application of strong electric fields as a function of time and temperature [1, 6]. The evolution of preferred domain orientation corresponding to the applied electric field is still unclear. Our previous study has shown that the conventional poling leads to a fiber texture in which the c-axes of domains align along the poling direction [7]. Synchrotron x-ray diffraction has also been proved an effective method to measure the complete pole figures due to its extremely high intensity and adjustable wavelength. In this paper, we have used cross-poling, that is, applying an electrical field perpendicular to the original poling direction, to change and control the domain orientation. We have evaluated the resulting texture by both conventional and synchrotron-source x-rays, and explored changes in property anisotropy.

2. Experimental Procedure

Fully poled Navy-VI lead zirconate titanate (PZT) samples (Channel Industries, Santa Barbara, CA) were cut with dimensions 1.00×6.08×7.32mm. Samples were finely polished using 0.1μm alumina to eliminate the potential effects of grinding on domain orientation [8]. The samples then were cumulatively subjected to cross-poling in 1 direction from 0kV/mm to 20kV/mm at 150°C in silicone oil for 30 minutes (Fig. 1). All of the three surfaces which are normal to the 1, 2, 3 directions of cross-poled PZT samples were examined using conventional x-ray diffraction while focusing on the 002/200 peaks. The average domain sizes *l* were calculated by excluding the effect of distortion $<\Delta d/d>$ [9]:

$$\Delta 2\theta \cos\theta = \frac{\lambda}{l} + 2 < (\frac{\Delta d}{d})^2 > \sin\theta \qquad (1)$$

where θ is the Bragg angle, λ is the x-ray wavelength, $\Delta 2\theta$ *is* the half-height peak width.

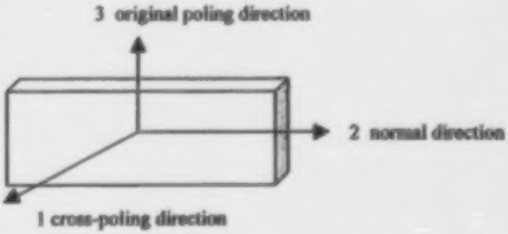

Fig. 1. Illustration of cross-poling and corresponding coordinate system.

Pole figures (χ-ϕ) have been measured using the MATRIX beam line (X18A) at the National Synchrotron Light Source of Brookhaven National Laboratory. Monochromatic x-rays of 1.908Å, a four-circle goniometer and a silicon detector were employed. Two-theta scans across (002) and (200) peaks were measured at tilts from the poling direction. The integrated area ratios were then used to calculate the magnitude of *00l* orientation.

Elastic stiffness was measured using an acoustic method and calculated by

$$C = \rho v^2 \qquad (2)$$

where ρ is the material density, v is the traveling velocity of ultrasound using a 5900PR 200Mhz pulse generator (Panametrics Co., Waltham, MA) and TDS360 oscilloscope (Tektronix Co., Wilsonville, OR).

3. Results and Discussions

Figure 2 shows XRD results for the surfaces normal to the 1, 2 and 3 directions, respectively. With increasing electric field, the intensity of the (002) peak increases and the intensity of (200) peak decreases in Fig. 2(a). The cross-poling field leads to alignment of the c-directions with the cross-poling direction. The results shown for the surface normal to the original poling direction in Fig.2(c) indicate consistent results, in that the (200) peak decreases in intensity with increased cross-poling.

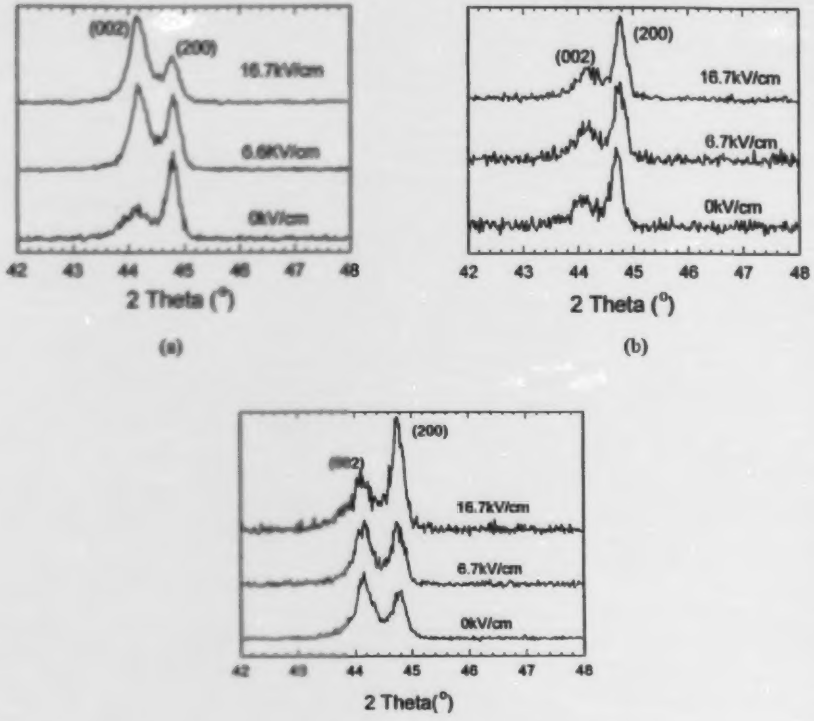

(a) (b)

(c)

Fig. 2. XRD of (a) surface normal to 1 direction (cross-poling direction), (b) surface normal to 3 direction (previous poling direction), and (c) surface normal to 2 direction (normal direction) versus various cross-poling fields.

The XRD results for the surface normal to the 2 direction undergo little or no change. Because the 2 direction is perpendicular to the cross-poling direction, it is reasonably expected that 90° domains aligned along the 2 direction would switch to the cross-poling direction, so that the (002) peak should decrease correspondingly. However, Fig. 2 (b) shows that the (002) peak intensity remains virtually unchanged. The change of intensity ratios between the (002) peaks and the (200) peaks on all three surfaces with increasing cross-poling field in Fig. 3 shows the domain motion. This figure clearly shows that under cross-poling the 90° domains mainly switch from the original poling direction 3 to the cross-poling direction 1. The contribution of 90° domain switching from 2 direction to cross-poling direction is so small that it cannot be detected. The domain switching induced by cross-poling is a two dimensional process different from the original poling process.

We have completed initial solid angle or χ scans originating from each of the three surfaces for the 3.3kV/cm cross-poled sample. The *00l* domain orientation distribution is clearly not axi-symmetric as shown in Fig. 4.

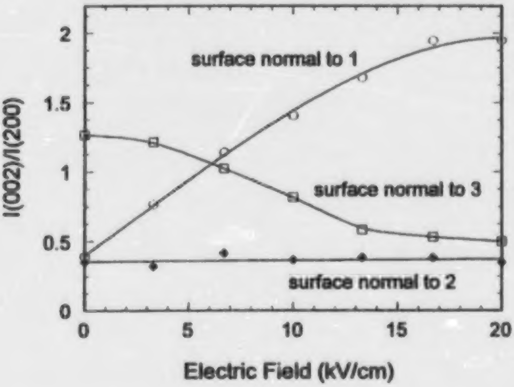

Fig. 3. Intensity ratios between (002) and (200) peaks from XRD on three surfaces versus various cross-poling fields.

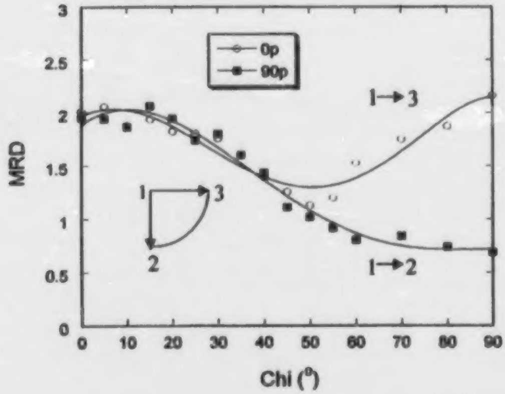

Fig.4. Pole figure of 3.3kV/cm cross-poled sample showing the orientation of 001 poles measured at angles tilting from the cross-poling plane (*P* is the rotation angle around the cross-poling direction).

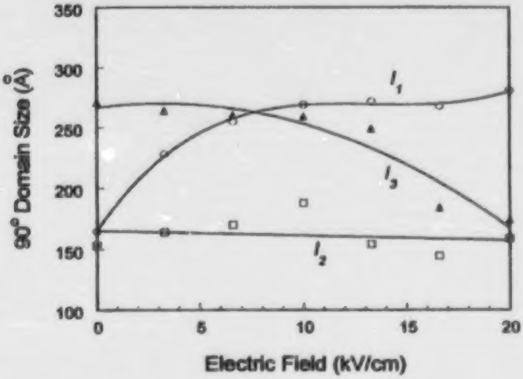

Fig.5. Domain size as a function of cross-poling field, where l_1, l_2 and l_3 represent the apparent domain size along the 1, 2 and 3 directions.

Fig. 5 indicates the change in average domain size under various cross-poling fields. The changes in domain sizes along the 1 and 3 respectively show that the domains expand in the cross-poling direction and shrink in the original poling direction. On the other hand, the domain size along the 2 direction is essentially constant with increasing electric field. These results also show the domain wall movement is accomplished by the domain switching from 3 direction to 1 direction and is irrelevant to the normal direction 2. Based on previous result, the domain switching under cross-poling is essentially a two-dimensional process as suggested by the schematic diagrams in Fig.6.[*]

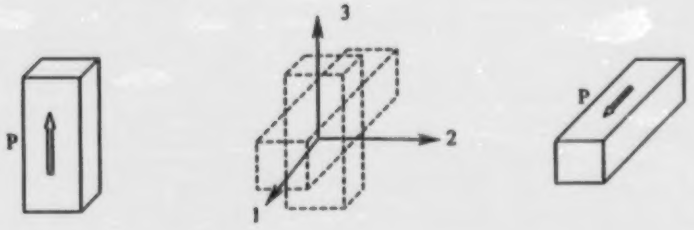

(a) Pre-poled (b) domain switching under cross-poling field (c) completely-cross poled

Fig.6. Domain switching under cross-poling field (P is the polarization).*

---

[*] It is very important to note that the actual transition is not a rotation but a distortion of the unit cell corresponding to domain motion.

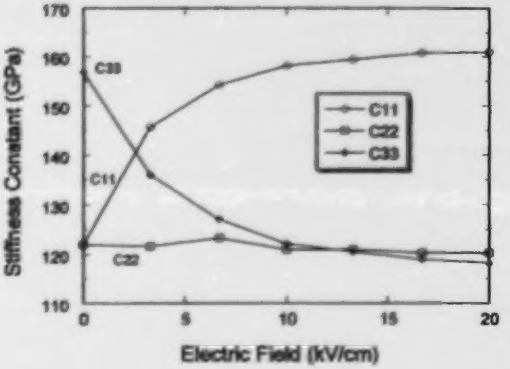

Fig.7. Stiffness constant anisotropy as a function of cross-poling field.

Fig. 7 shows the normal stiffness as a function of cross-poling field. Consistent with the orientation evolution, C_{33} decreases, C_{11} increases and C_{22} stays constant. This is consistent with the XRD results. Because the elastic constants measured by acoustic methods reflect the bulk properties this result also demonstrates that the XRD results are consistent with the bulk orientations. The obvious change of the elastic constants under various poling field demonstrate the cross-poling process is an effective way to change the preferred orientation and anisotropic properties of piezoelectric ceramics.

4. Conclusion

Preferred domain orientation has been effectively changed by applying cross-poling fields. The induced texture measured by synchrotron x-ray is similar to a rolling texture for moderate levels of cross-poling. The orientation evolution is accomplished by a two-dimensional domain switching process which is consistent with changes in domain size under cross-poling field. The mechanical anisotropy is highly dependent on the domain orientation distribution and varies with the degree of the preferred orientation induced by cross-poling field.

Acknowledgement

This research is supported by the National Science Foundation under Grant No. DMR-9528928.

References

1. B. Jaffe, W. R. Cook and H. Jaffe, Piezoelectric Ceramics, *Academic Press*, London and New York, (1971).

2. S. Wan, and K. J. Bowman, "Thermal Depoling Effects on Anisotropy of Lead Zirconate Titanate Materials", *J. Am. Ceram. Soc.* 81[10], 2717-2720 (1998).
3. H. Law, P. L. Rossiter, G. P. Simon and J. Unsworth, "A Model for the Structural Hysteresis in Poling and Thermal depoling of PZT Ceramics", *J. Mater. Sci.*, 30, 4901-4905 (1995).
4. S. Wan, W. F. Shelley II, and K. J. Bowman, "Mechanical Anisotropy of PZT Piezoelectric Ceramics", *Ceramics Transaction*, 100, (1998).
5. S. B. Kim, T. J. Chung and D. Y. Kim, "Effect of External Compressive Stress on the Domain Configuration of Barium Titanate Ceramics", *J. European Ceramics Society*, 147-151(1993).
6. M. E. Lines, and A. M. Glass, Principles and Applications of Ferroelectrics and Related Materials, *Clarendon Press*, London, 1977.
7. S. Wan, W. F. Shelley II, and K. J. Bowman, "Orientation and Anisotropy in Piezoelectric Ceramics", ", *Materials Science Forum*, 273, 581-586 (1998).
8. S. Cheng, I. K. Lloyd, and M. Kahn, "Modification of Surface Texture by Grinding and Polishing Lead Zirconate Titanate Ceramics", *J. Am. Ceram. Soc.*, 75[8], 2293-2296 (1992).
9. L. H. Schwartz, and J. B. Cohen, Diffraction From Materials, *Academic Press*, New York, (1987).

ANISOTROPY IN LAYERED AND GRADIENT CERAMICS

ROBERT MOON, WILLIAM BLANTON, F. RICHARD CICHOCKI,
JOACHIM BREHM*, KEVIN P. TRUMBLE and KEITH J. BOWMAN
Materials Engineering, Purdue University, West Lafayette, IN 47907

Abstract

Processing of layered and gradient ceramic-ceramic composites and ceramic-metal composites results in microstructure arrangements that produce anisotropic properties. Fracture anisotropy can come about from layer geometry, orientation within layers, residual stresses and matrix textures. Assessments of local and global anisotropies are critical to predict the mechanical response of these materials. In this paper, strategies for fracture assessment and elucidation of other anisotropies are given for alumina-alumina, alumina-zirconia, aluminum nitride-aluminum and alumina-copper composites. Microstructure, layer or gradient geometry and orientation effects on mechanical response are described.

Introduction

Graded and layered materials have recently received substantial attention in a wide array of applications. Our research group has been focused on developing ceramic-ceramic and ceramic-metal composites for resistance to static and dynamic fracture [1-4]. Green body processing routes that have been employed for our materials include centrifugal processing of layered and gradient materials [1,2] and a technique employing infiltration of deformed sponges [3,4]. The green bodies are then either fired to minimize porosity to produce a desired volume fraction porosity which is then filled with a metal reinforcement phase using spontaneous or low pressure infiltration [5,6]. The materials described in this paper include the composites alumina-alumina, alumina-zirconia, aluminum nitride-aluminum and alumina-copper. In each composite microstructural features vary with position in the materials. Specific microstructural features that may vary in these composites include composition, grain size, ligament size and orientation.

Materials Processing

Ceramic-Ceramic Composites

Multi-layer alumina-alumina composites and alumina-zirconia composites are produced through centrifugal sedimentation of ceramic powder suspensions using a laboratory centrifuge. The composite microstructures are tailored by controlling the ceramic powder suspension. Suspensions can be designed to produce particle size and/or composition graded sedimentation. Additionally, the properties within the composite can be varied in a stepwise manner by varying the suspension used to produce each layer. The ceramic parts are carefully removed from their containers following drying [7,8]. These ceramics are then fired for various times and temperatures to control microstructural development.

Metal-Ceramic Composites

Metal-ceramic composites were produced from porous ceramic preforms prepared via two green processing techniques. In the first technique the aluminum nitride-aluminum composites were made through the centrifuging process given above; however, sintering is carried out only to the point that necks form between particles without closing off the continuous porosity [9]. The composite was processed by first coating the porous AlN material with carbon. Al was subsequently infiltrated at 1250°C using low pressure infiltration [5,6]. The second technique, which was applied to the Al_2O_3-Cu composites, employs slip-casting into compression-molded polymer foams

---

*currently at the Technical University of Darmstadt, Darmstadt, Germany.

[3]. These polymer foams are molded to different starting pore volumes. In this way, foams with different pore volumes can be assembled to make step-wise unidirectional foams. These slurries are then infiltrated into the foams and allowed to dry. After burning out the foam and firing the final part consists of a porous body ready for infiltration by a liquid metal or polymer. The Al_2O_3-Cu composites described below were infiltrated with a Cu-8wt.% O alloy at 1250°C [5].

Table I. Effect of Layer Thickness on Fracture Toughness of Al_2O_3/Al_2O_3 Composites

Layer Thickness (μm)	K_{IC} *(MPa* $\sqrt{\mathrm{m}}$ *)*
400 μm	4.3 (0.3)
500 μm	5.0 (0.6)
800 μm	7.6 (0.6)

Results and Discussion

The results shown in Table I and Fig. 1 show the fracture response of layered composites wherein the microstructural scale varies within each layer. Unlike conventional materials there is a deviation of the crack path from the notch and also an enhancement of fracture toughness. The degree of segregation increases with increased layer thickness. This results in deviations in the crack path that increase the apparent fracture toughness.

The results shown in Fig. 2 document the influence of compositional and microstructural variations in addition to residual stresses. Because these specimens were produced with relatively modest compositional and microstructural gradients within the layers, the primary cause of the anisotropic fracture at the Vickers indents is due to residual stresses. These residual stresses come about from the larger coefficient of thermal expansion of zirconia when compared to alumina.

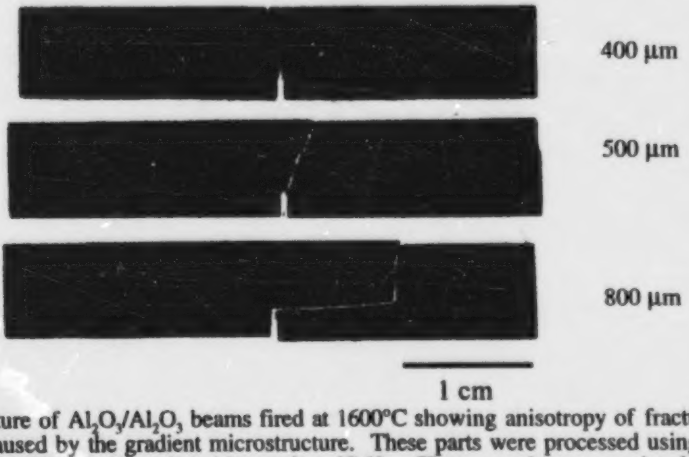

Fig. 1. Fracture of Al_2O_3/Al_2O_3 beams fired at 1600°C showing anisotropy of fracture toughness caused by the gradient microstructure. These parts were processed using a mixture of ALCOA A-10 and A-16 powders [7,8]. These specimens consisted of specimens with layer thicknesses as shown.

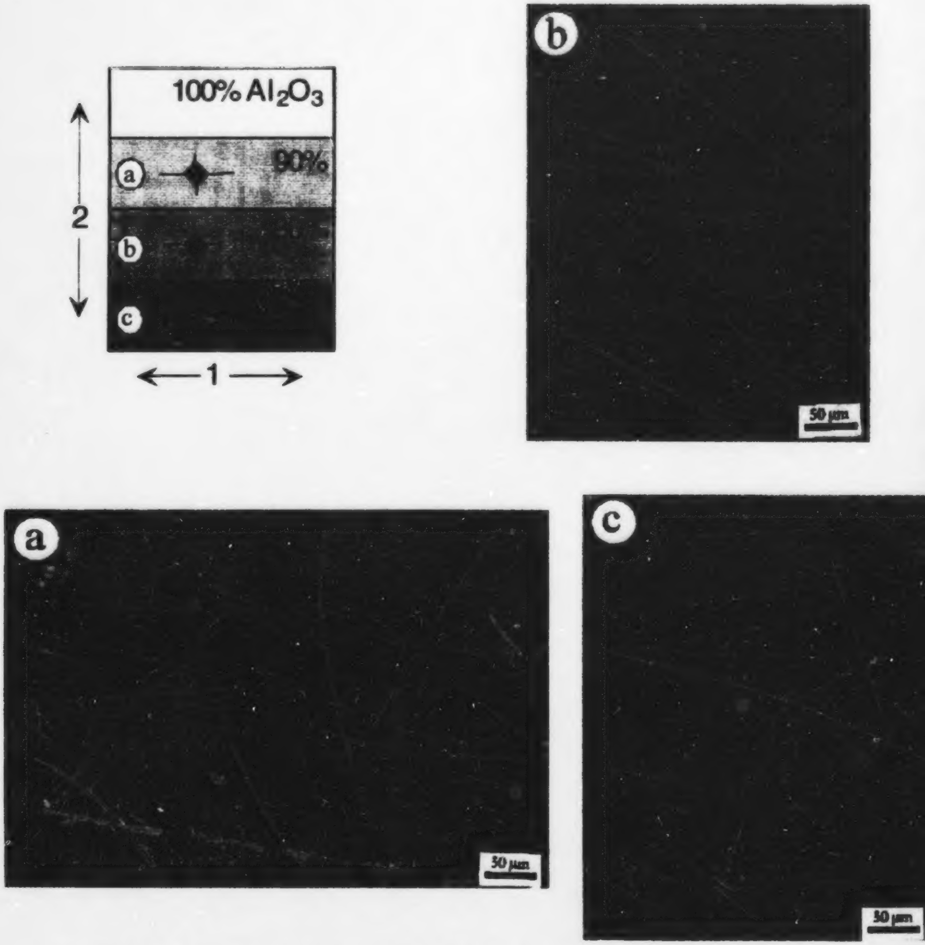

Fig. 2. Vickers indentation fracture of Al_2O_3-ZrO_2 composites showing anisotropic fracture induced by residual stresses. The schematic on the upper left shows the fraction of alumina in the layers. The anisotropy shown here is caused by the layer geometry and the residual stresses due to differences in the thermal expansion coefficient of each layer.

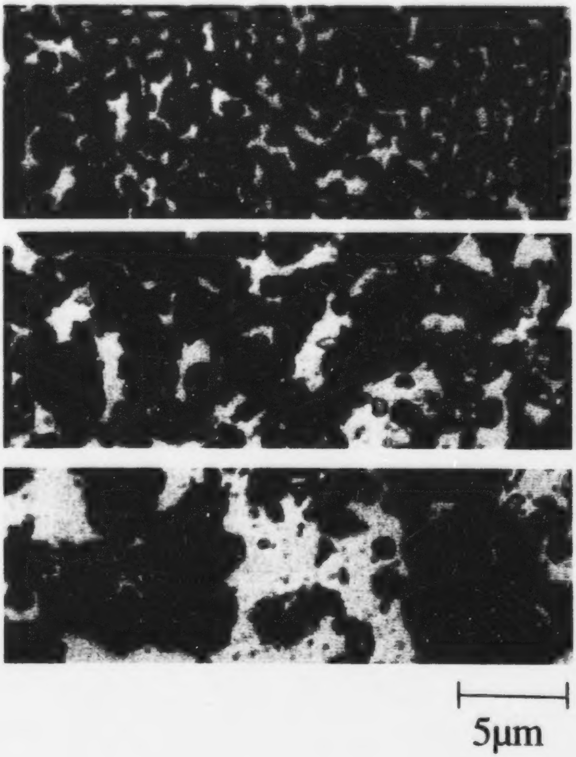

(a)

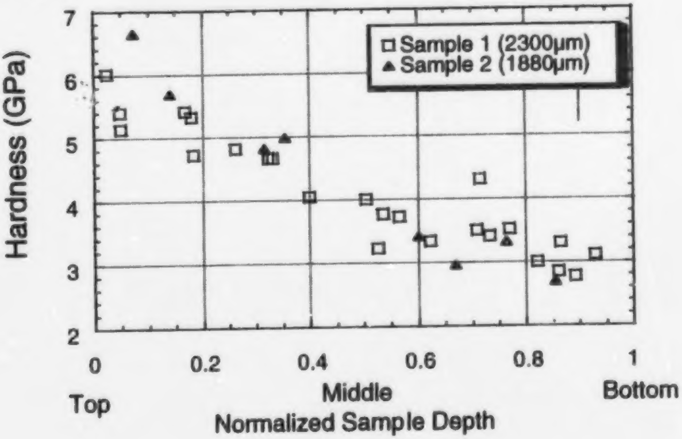

(b)

Fig. 3. For the AlN/Al composites (a) microstructures from top, middle and bottom of a specimen showing nearly constant phase fractions with varying microstructural scale. (b) Microhardness indent results showing hardness of AlN/Al composites as a function of position. Here two different thickness specimens were employed to produce different gradients. The aluminum fraction is nearly constant; however, the metal ligament size decreases from left to right.

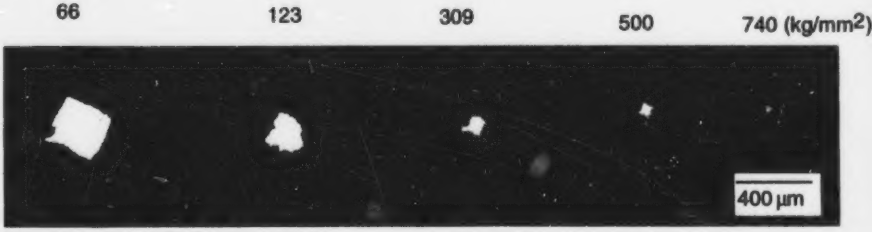

Fig. 4. Vickers indentation showing hardness gradient in layered Al_2O_3/Cu as a function of Al_2O_3 content. The alumina content increases from near 0 v/o to near 83 v/o from left to right. The average Vickers hardness numbers are given above.

Figures 3 and 4 show effects of microstructural variations for ceramics containing ductile metal reinforcements. The composites shown in Fig. 3 have almost constant compositions of aluminum (the light phase) with the only change the microstructural scale. This change in microstructural scale also results in a gradient in hardness. For Fig. 4 the microstructural scale and the composition changes leading to an increase in hardness as the volume fraction of ceramic increases. This results from the changes in the starting density of the sponge preforms.

Summary

The examples shown here document the effects on property anisotropy and properties for some ceramic-ceramic and ceramic-metal composites produced with varying microstructural scales.

Acknowledgements

This research has been supported by an Army Research Office MURI Grant No. DAAH04-96-0331.

References

1. R. K. Roeder, K. P. Trumble and K. J. Bowman, *J. Am. Ceram. Soc.*, 86, 27-36 (1997).

2. R. Moon, E. Drewry, K. J. Bowman and K. P. Trumble, 5th Functionally-Gradient Materials Conference Proceedings, Dresden, Germany, *Trans. Tech. Publications*, In Press.

3. F. R. Cichocki, Jr., K. P. Trumble, and J. R. Rödel, *J. Am. Ceram. Soc.*, 81, 1661-64 (1998).

4. F. R. Cichocki, Jr., and K. P. Trumble, 5th Functionally-Gradient Materials Conference Proceedings, Dresden, Germany, *Trans. Tech. Publications*, In Press.

5. E. J. Gonzales, K. P. Trumble, *J. Am. Ceram. Soc.*, 79, 114-119 (1996).

6. J. Hilden, Low Pressure Infiltration, Master's Thesis, Purdue University, 1998.

7. E. Drewry, Alumina Fracture Behavior of Centrifugally Cast Alumina Composites, Master's Thesis, Purdue University (1998).

8. E. N. Drewry, J. Brehm, R. J. Moon, K. J. Bowman and K. P. Trumble, Submitted to Scripta Materiala, May (1999).

9. W. Blanton, K. J. Bowman and K. P. Trumble, Unpublished Results.

TEXTURE DEVELOPMENT, RECRYSTALLIZATION, AND TRANSFERENCE OF TEXTURE BETWEEN CERAMIC MULTILAYERS EPITAXIALLY GROWN ON ROLLING ASSISTED BIAXIALLY TEXTURED SUBSTRATES (RABITS)*

A. Goyal, R. Feenstra, E. D. Specht, D. M. Kroeger, D. F. Lee, M. Paranthaman, F. A. List and D. K. Christen
Oak Ridge National Laboratory, PO Box 2008, MS 6116, Oak Ridge, TN 37831.

Abstract

It is well established that in order for many large scale bulk applications of HTS materials to be realized the cost/performance of HTS conductors needs to be optimized. In essence what is required is a flexible, near single crystal HTS conductor. A promising route to fabricate such conductors is Rolling assisted biaxially textured substrates (RABiTS). RABiTS employs simple, scaleable, thermomechanical prosessing techniques to obtain a near single crystal-like, flexible metal substrate in arbitary lengths on which epitaxial oxide buffer layers and superconductors are then deposited. High J_c's approaching 3 MA/cm^2, similar to the values obtained on single crystal ceramic substrates such as $SrTiO_3$, have been achieved on epitaxially grown YBCO films on RABiTS using thermomechanically biaxially textured Ni as the starting template. This has been made possible by modifications to the thermomechanical processing to obtain a very sharp cube texture with FWHM of the in-plane texture of 6° and out-of-plane texture of 4°. Detailed ODF and grain boundary analysis has been performed on as-rolled and annealed materials using electron backscatter Kikuchi diffrcation (EBKD). It is found that the rolling texture in the Ni substrate is highly complicated with most of the grains having orientations at and between the "B" and "S" orientations. No cube nuclei could be discerned in the etched, as-rolled sample. Upon recrystallization, a sharp, single orientation (100%), {001}<100>, cube texture is imparted to the Ni substrate. EBKD shows that the substrate is percolatively connected within 3°. Examination of epitaxial oxide layers on Ni show that excellent epitaxy is obtained. At times, undesirable orientations nucleate during growth of the oxide layer, however, these are engulfed by the growing film with the correct orientation. Orientation image micrographs of an epitaxial YBCO film on a RABiT substrate with a J_c of 1.6 MA/cm^2 at 77K, show that most of the film is percolatively connected within 2°. Comparison of spatially correlated and un-correlated grain boundary misorientation distributions (GMBD) show that local grain-to-grain correlations are present between the grains. Comparison of the data obtained for the YBCO film with those for the underlying Ni substrate shows that both the macroscopic texture and grain boundary networks are very similar in the two cases, implying excellent epitaxy of the multilayers. Furthermore, for many large scale applications, high purity Ni is not acceptable due to its magnetic nature and its low mechanical strength and modulus. This had been viewed until now as a possible fundamental limitation of this technique. We also report here on the successful fabrication of single orientation

(100%), biaxially textured, non-magnetic and strengthened Ni-Cr and Ni-V substrates. Thermomechanical processing techniques were used to obtain a single texture component with no evidence of secondary orientations including twins. In-plane and out-of-plane textures as sharp as 6° have been obtained. Orientation image microscopy was used study and highlight grain boundaries in rolled as well as annealed, cube-textured substrates. Complimentary, in-situ TEM studies were performed to study the process of recrystallization and texture evolution in both Ni and Ni-alloys. Cross-section TEM was performed to study the interface between the metal substrate and oxide buffer layers. We discuss here details of texture evolution, recrystallization, modification of GBMD's, and transference of texture through ceramic multilayers onto the HTS device layer.

Keywords: Texture, EBSP, BKD, Superconductors, Grain boundaries

1 Introduction

Numerous applications of high temperature superconductors, such as transformers, generators and motors require high current carrying, flexible conductors which can sustain magnetic fields above 0.1T . Due to the thermally activated flux flow, the critical current density of most of the highly anisotropic superconducting compunds, such as the Bi-based compounds, rapidly drops at 77K in the presence of an externally applied magnetic field. Hence, the development of a viable processing route based on (Y or Re)$Ba_2Cu_3O_x$ (YBCO) is of great interest currently and forms a central research thrust in the area of high temperature superconductivity. YBCO compounds have favorable intrinsic properties. Epitaxial YBCO thin films on single-crystal substrates yield critical current densities (J_c's) in the range of 10^6-10^7 A/cm^2 at 77K, 0T (Kormann et al., 1992). YBCO films also have a high irreversibility field of ~6T at 77K (Matsuda et al., 1992).

However, conventional ceramic fabrication methods which can be used to make a long, flexible conductor result in materials with weak, if any, macroscopic or microscopic biaxial texture. In particular, YBCO materials fabricated using conventional techniques invariably contain numerous high angle grain boundaries. High angle grain boundaries act as Josephson coupled weak-links leading to a significant field-dependent suppression of the supercurrent across the boundary. For clean stoichiometric boundaries, the grain boundary critical current density depends primarily on the grain boundary misorientation. The dependence of J_c(gb) on misorientation angle was first determined by Dimos et al. (Dimos et al., 1988, 1990) in YBCO for grain boundary types which can be formed in epitaxial films on bicrystal substrates. These include [001] tilt, [100] tilt, and [100] twist boundaries. In each case high angle boundaries were found to be weak-linked. The low J_c observed in randomly oriented polycrystalline HTS fabricated using conventional methods can be understood on the basis that the population of low angle boundaries is small and that frequent high angle boundaries impede long-range current flow. Hence, controlling the grain boundary misorientation distribution towards low angles is key to fabricating high-J_c materials. Practically speaking, this limitation entails the fabrication of biaxially textured superconductors.

Macroscopically, biaxially textured YBCO conductors have been formed by epitaxial deposition of YBCO on flexible substrates formed by two techniques - (a) A flexible, unoriented, polycrystalline metal substrate coated with an oxide buffer film(s) with a forced biaxial texture induced by ion-beam-assisted-deposition (IBAD), where an assisting noble gas beam extracted from an ion source is directed onto the growing film (Iijima et al., 1992, Reade et al., 1992, Wu et al., 1995). A similar biaxial texture is observed during oblique vapor deposition on an inclined polycrystalline substrate (Hasegawa et al., 1996) and (b) A biaxially textured, flexible metal based substrate formed by conventional thermomechanical processing followed by epitaxial deposition of buffer layer(s) (Goyal et al., 1996, 1996a, 1997; Norton et al., 1996). This technique is referred to as Rolling Assisted Biaxially Textured Substrates (RABiTS). Using both these techniques J_c's over 1 MA/cm^2 at 77K have been achieved. Fig. 1 shows a schematic of the RABiTS process along with a progression of pole figures illustrating the development and transfer of the biaxial texture to all the deposited layers.

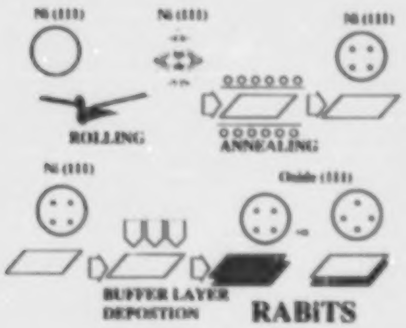

Fig. 1: Schematic of the RABiTS process with progession of texture shown using (111) pole figures. Briefly, a cube textured metal substrate is formed on which epitaxial, cube oriented device layers are grown. Since the texture is very sharp, the device layers resemble a large mosaic, single crystal.

In this manuscript, microstructural characteristics of RABiT substrates and epitaxial YBCO films on these substrates is reported. Starting from the macroscopic texture and grain boundary misorientation distributions in as-rolled Ni, a similar analysis in recrystallized, cube oriented Ni is summarized. Measurements of grain orientations and grain boundary misorientations of large, representative regions of the substrate show detailed characteristics of the well-developed biaxial texture. Orientation image micrographs constructed from tens of thousands of spatially correlated measurements show that the metal substrate is percolatively connected within 2-3°. This analysis is then extended to buffer layers and epitaxial YBCO films. It is found that in films with very high J_c's, the macroscopic texture and grain boundary misorientation distribution of the superconductor is similar to those in the starting Ni substrate. It is found that the film is percolatively connected within 2-3°. It is believed that the high-J_c observed is a direct result of this strong biaxial texture and a near complete supression of high angle grain boundaries.

2 Results and Discussion

2a As-rolled Ni Substrate

Biaxially textured Ni substrates were formed by consecutive rolling of a polycrystalline, randomly oriented high purity (99.99%) bar to total deformations greater than 90%, followed by recrystallization (Goyal et al., 1996). By controlling the surface condition of the work rolls, it was possible to obtain substrates with surfaces as smooth as those obtained by mechanical and chemical polishing. Average line scans in a 50 µm x 50 µm region indicate an rms roughness of ~ 10nm (Goyal et al., 1997). The surface condition of a substrate can greatly affect epitaxy and integrity of buffer layers and hence the J_c of the superconducting film. Obtaining substrates with surfaces adequate for film growth without the need for a cumbersome polishing step is important for scale up to long lengths. OIM data was obtained from an as rolled Ni substrate which was electropolished to remove ~ 5µm of the surface layer. Very well-formed EBKP patterns were obtained despite the sample being heavily deformed. Data was obtained on a hexagonal grid at a spacing of 1 μm from a macroscopic region of the substrate of size ~ 370 μm x 250 μm. The orientation data obtained from this region is illustrated in interpolated, log-scale, intensity (111), (100) and (110) pole figures in Fig. 2. These are also in complete agreement with X-ray diffraction determined pole figures and represent an idealized Cu-type rolling texture with intensity solely along the β-fiber. Color-coded maps of grains corresponding to the typically observed texture components in FCC metals have been drawn from this region and the statistically symmetric orientations for each texture component calculated (Goyal et al., 1999). It is found that the intensities are concentrated at and between the "B" and "S" orientations on the β-fiber. Fig. 3 shows a contour representation of an orientation distribution function calculated from the EBSP data and presented in constant sections of ϕ_2.

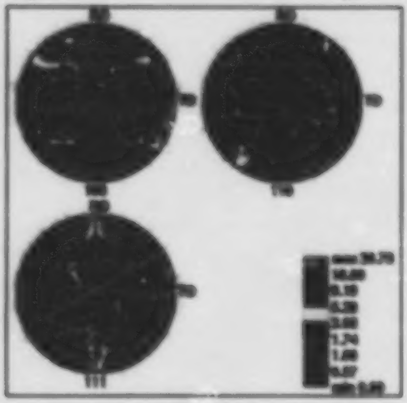

Fig. 2

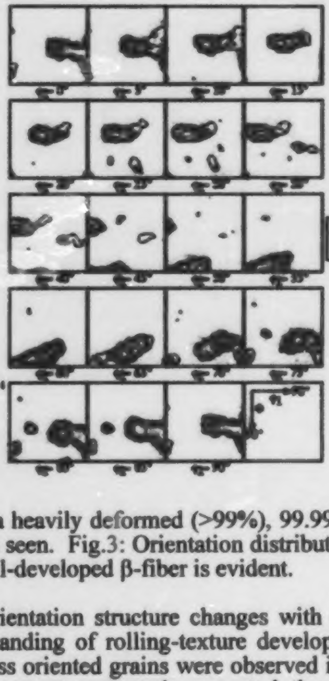

Fig. 3

Fig. 2: (111), (100) and (110) pole figures of a heavily deformed (>99%), 99.99% purity Ni sample. A well-developed cube texture can be seen. Fig.3: Orientation distribution function (ODF) of the data shown in Fig. 2a. Only a well-developed β-fiber is evident.

Studies are ongoing to see how this grain orientation structure changes with deformation conditions in an effort to get a basic understanding of rolling-texture development. It is however important to note that no Cube or Goss oriented grains were observed in the region studied. This is important since one of the most commonly accepted theories for the formation of cube texture upon annealing a FCC metal is rapid growth of prior cube nuclei. Hence, if such nuclei are present, they are of a size scale below the resolution of the EBKP technique.

2b Annealed Ni substrate

Subsequent annealing of the deformed Ni substrates in a wide temperature range in a vacuum of ~ 10^{-6} Torr results in the formation of a sharp {100}<100> cube texture. Typical samples have X-ray ω- and ϕ-scans with full-width-half-maximum (FWHM) of 6° and 7° respectively. The texture was found to be stable up to the melting point of Ni. Fig. 4a shows an orientation image micrograph of a Ni substrate annealed at 1000°C for 2hrs. Extremely well-formed EBKP patterns were obtained from the recrystallized sample. Data was obtained on a hexagonal grid at a spacing of 3 µm from a macroscopic region of the substrate of size ~ 500 µm x 500 µm. Gray level shading on the micrograph is a reflection of the pattern quality or intensity of the Kikuchi bands observed at each point. Indexing of the pattern at each location gave a unique measure of the orientation at that point. A hypothetical hexagonal lattice with a grain size of 3 µm was superimposed at each point from which a pattern was obtained and the resulting grain boundary misorientations were then calculated. Grain boundaries in Fig. 4a are color coded as shown in the figure.

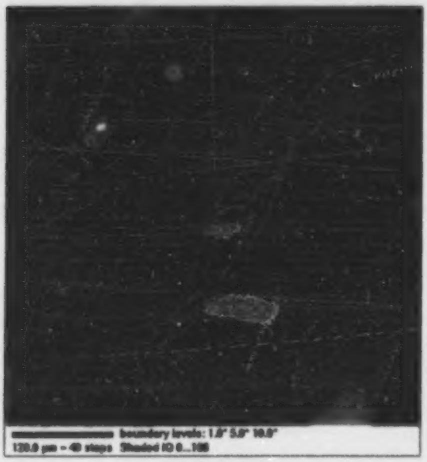
boundary levels: 1.0° 5.0° 10.0°
120.0 µm = 40 steps Shaded IQ 0...100

Fig. 4a

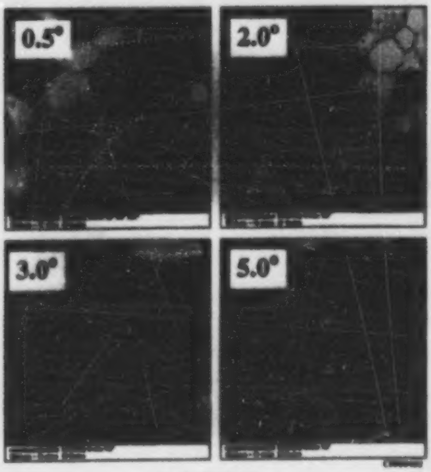

Fig. 4b

Fig. 4a: OIM micrograph from a macroscopic region of a RABiT substrate (see text for details). BKD patterns were obtained in a hexagonal grid with a step size of 3 µm. Variations in intensity is a reflection of pattern quality or intensity of the Kikuchi bands. Three types of grain boundaries are indicated in the figure, green boundaries denote boundaries with misorientations greater than 1° and less than 5°, yellow lines denote boundaries with misorientations greater than 5° and less than 10° and red boundaries denote boundaries with misorientations greater than 10°; b: Same region as in Fig. 4a, with grain coloring according to the criterion that a given color represents a percolatively connected region within 0.5°, 2°, 3° and 5° respectively.

It is clear that low angle grain boundaries less than 5° are the most prevalent. After recrystallization at 1000°C, the average grain size is approximately equal to the thickness of the substrate, which in this case was 125 µm. Thus the substrate can be thought to be comprised of a columnar structure of grains, with the columns aligned with the (100) plane parallel to the surface of the columns and the [100] direction aligned along the rolling direction. In order to visualize percolation of current flow should an epitaxial superconducting film be grown on such a substrate, Figure 4b shows coloring of the same region shown in Fig. 4a. In Fig. 4b, grains have been colored according to the criterion that a single color represents a contiguous or percolative region of orientation changes less than 0.5°, 2°, 3°, and 5° respectively. It can be seen that most of the substrate is percolatively connected within 3°.

2c Epitaxial Oxide Buffer layers

In order to grow high quality epitaxial superconducting films on the biaxially textured Ni substrate, a chemical and structural buffer layer is required. Typically, the desired buffer layers for 123 film growth are oxides. Hence the task of fabricating a suitable substrate for epitaxial deposition of the superconductor involves epitaxial deposition of oxide buffer layers on Ni. This is difficult because of the ease of surface oxide formation on Ni under the typical oxidizing conditions required for oxide film growth. Although the surface oxide on (100) Ni can be epitaxial, it typically forms a (111) textured NiO layer, the orientation of which is unsuitable for fabricating high-J_c 123 films since many high angle boundaries are present. We have found two methods that have proven successful in producing cube-on-cube epitaxial oxide buffer layer films on rolled and recrystallized Ni. The first involves epitaxial deposition of noble metal layers on Ni followed by deposition of oxides (Goyal et al, 1996, 1996a), and the second involves deposition of oxides directly on Ni under reducing conditions (Norton et al, 1996, Goyal et al., 1996). In much of the ongoing work however, the second has been the method of choice since reduction in the number of processing steps is desirable for a manufacturing process. Typically two substrate configurations are used – Ni/CeO_2/YSZ/YBCO or Ni/CeO_2/YSZ/ CeO_2/YBCO. In both cases, epitaxial layers of CeO_2 and YSZ with a single 45° rotated cube-on-cube epitaxial orientation have been successfully deposited by laser ablation (Norton et al., 1996), sputtering (List et al.,1997) or e-beam evaporation (Paranthaman et al., 1997). Fig. 5 shows x-ray phi-scans of a multilayer structure Ni/CeO_2/YSZ/CeO_2/YBCO. It can be seen that CeO_2 is 45° rotated in-plane with respect to the Ni, YSZ is cube-on-cube with respect to CeO_2 and YBCO is 45° rotated with respect to CeO_2. There is a thin layer of CeO_2 on the YSZ which is not shown as a separate scan since it is not possible to differentiate the two CeO_2 layers in X-ray diffraction.

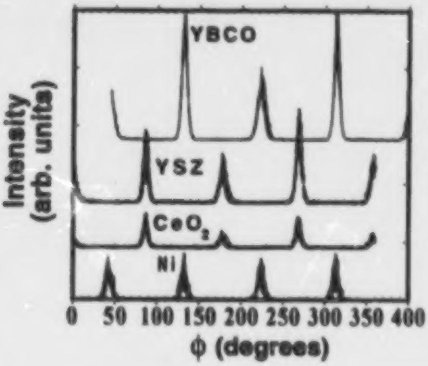

Fig. 5: X-ray phi-scans of the multilayer structure Ni/CeO_2/YSZ/CeO_2/YBCO. Ni(111), CeO_2 (111), YSZ(111) and YBCO(103) scans are shown. The full-width-half-maximum (FWHM) of the layers are 7.8°, 7.1°, 7.0° and 7.7° for Ni, CeO_2, YSZ and YBCO respectively. The out-of-plane textures for these layers are 4.7°, 4.4°, 4.3° and 3.7° respectively.

2d Epitaxial YBCO Films on RABiTS

YBCO films on RABiTS have been grown successfully using two methods. The first is *in-situ* deposition using laser ablation (Norton et al., 1996, Goyal et al, 1996, 1996a, 1997, Mathis et al., 1998) and the second is *ex-situ* formation of a BaF_2 precursor film deposited using electron beam co-evaporation (Feenstra et al., 1999). YBCO films on RABiTS have been shown to have J_c's approaching 3 MA/cm^2 (Mathis et al., 1998). EBKP data on a YBCO film fabricated using the ex-situ method are discussed here.

Fig. 6 shows orientation image micrographs of a YBCO film with a J_c of 1.6 MA/cm^2 at 77K, 0T (Feenstra et al., 1999). Data were obtained on a hexagonal grid at a spacing of 1.1 μm from a macroscopic region of the substrate of size ~ 420 μm x 260 μm. Indexing of the pattern at each location gave a unique measure of the orientation at that point. As before, a hypothetical hexagonal lattice with a grain size of 1.1 μm was superimposed at each point from which a pattern was obtained and resulting grain boundary misorientations were then calculated. In order to visualize percolation of current flow through the YBCO film, Fig. 6 shows coloring of the grains according to the criterion that a single color represents a contiguous or percolative region of orientation changes less than 1°, 1.5°, 1.8°, 2°, 5°, and 7° respectively. It can be seen that most of the film is percolatively connected within 2°. These data are in excellent agreement with similar data shown for the Ni substrate in Fig. 10, implying that the sharp biaxial texture of the Ni substrate is effectively transferred to the YBCO film. It can be further argued that the high-J_c observed in this sample is directly related to the local grain-to-grain correlations within 2° in reference to the strong dependence of J_c on misorientation angle.

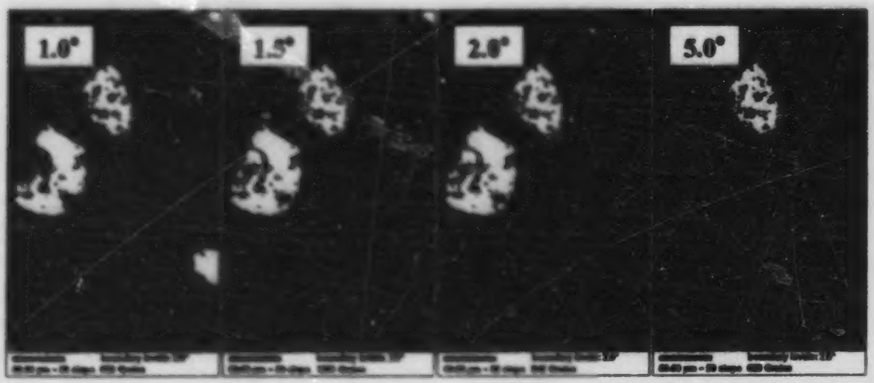

Fig. 6: OIM micrographs of a YBCO film with a J_c of 1.6 MA/cm^2 at 77K, 0T. Data was obtained on a hexagonal grid at a spacing of 1.1 μm from a macroscopic region of the substrate of size ~ 420 μm x 260 μm. In order to visualize percolation of current flow through the YBCO film, grains are colored according to the criterion that a single color represents a contiguous or percolative region of orientation changes less than 1°, 1.5°, 2° and 5° respectively. It can be seen that most of the film is percolatively connected within 2°.

3 Summary

Electron backscatter Kikuchi diffraction was used to study texture development and grain boundary networks in Rolling Assisted Biaxially Textured Substrates (RABiTS) and the transference of such a biaxial texture and preferential grain boundary network to epitaxial YBCO films grown on such substrates.

EBKP data show that the as-rolled Ni sample which upon annealing gives a sharp cube texture, has intensities predominantly at orientations corresponding to the "B" and "S" orientations. Orientation distribution functions clearly show how the texture can be characterized by localization of intensities at and between the "B" and "S" orientations. Upon recrystallization, a sharp cube texture is imparted to the Ni substrate. EBKP measurements show that grain boundary networks formed upon recrystallization are predominatly low angle with most grain boundaries having misorientations less than 5°. Point-to-point and point-to-origin misorientation line plots show how the orientation changes in a correlated and an

uncorrelated manner respectively. Maps of color coding of similarly oriented grains by plotting areas percolatively connected with a certain degree, show that the substrate is almost completely connected within 3°.

Epitaxial oxide multilayers were grown on the cube textured Ni substrate. X-ray phi-scans of the multilayer structure Ni/CeO_2/YSZ/CeO_2/YBCO indicate a full-width-half-maximum (FWHM) of the layers to be 7.8°, 7.1°, 7.0° and 7.7° for Ni, CeO_2, YSZ and YBCO respectively. The out-of-plane textures for these layers was 4.7°, 4.4°, 4.3° and 3.7° respectively. This data clearly implies that the macroscopic, mosaic single-crystal-like nature of the Ni substrate is transferred through the oxide multilayers to the superconducting device layer.

Orientation image micrographs of a YBCO film with a J_c of 1.6 MA/cm^2 at 77K, show that most of the film is percolatively connected within 2°. Comparison of the data obtained for the YBCO film with that for the underlying Ni substrate show that both the microscopic, grain boundary networks are also very similar in the two cases, implying excellent epitaxy of the multilayers.

4 Acknowledgements

Research sponsored by U.S. Department of Energy, Office of Efficiency and Renewable Energy, Office of Utility Technologies - Superconductivity Program, and the Office of Energy Research, Basic Energy Sciences, managed by Lockheed Martin Energy Research Corporation for the U.S. Department of Energy under contract DE-AC05-96OR22464.

5 References

Dimos, D., Chaudhari, P., Mannhart, J., and F. K. LeGoues, "Orientation Dependence of Grain Boundary Critical Currents in $YBa_2Cu_3O_x$ Bicrystals", Phys. Rev. Lett. , 1988, 61, 219-222; Dimos, D., Chaudhari, P., and Mannhart, J., "Superconducting Transport Properties of Grain-boundaries in in $YBa_2Cu_3O_x$ Bicrystals", Phys. Rev. B , 1990, 41, 4038-4049.

Feenstra, R., Goyal, A., Christen, D. K., Paranthaman, M., Lee, D. F., Verebelyi, D., Specht, E. D., Budai, J. D., Norton, D. P., and Kroeger, D. M., "Strong Supercurrent Transport in ex-situ Processed YBCO Films on Flexible Metal Tapes For Next-generation Superconducting Wire Technology", Submitted to Science, 1999.

Goyal, A., Norton, D. P., Christen, D. K., Specht, E. D., Paranthaman, M., Kroeger, D. M., D. P., Budai, J. D., He, Q., List, F. A., Feenstra, R., Kerchner, H. R., Lee, D. F., Hatfield, E., Martin, P. M., Mathis, J., and Park, C., "Epitaxial Superconductors on Rolling-Assisted-Biaxially-Textured-Substrates (RABiTS): A Route Towards high Critical Current Density Wire", Applied Supercond., 1996, 69, 403-427.; A. Goyal et al., US Patent No. 5, 739, 086 and US Patent No. 5, 741, 377.

Goyal, A., Norton, D. P., Kroeger, D. M., Christen, D. K., Paranthaman, M., Specht, E. D., Budai, J. D., He, Q., Saffian, B., List, F. A., Lee, D. F., Hatfield, E., Martin, P. M., Klabunde, C. E., Mathis, J., and Park, C., "Conductors With Controlled Grain Boundaries: An Approach To The Next Generation, High Temperature Superconducting Wire", J. Mater. Res., 1997, 12, 2924-2940.

Goyal, A., Norton, D. P., Budai, J. D., Paranthaman, M., Specht, E. D., Kroeger, D. M., Christen, D. K., He, Q., Saffian, B., List, F. A., Lee, D. F., Martin, P. M., Klabunde, C. E., Hatfield, E., and Sikka, V. K., "High Critical Current Density Superconducting Tapes By Epitaxial Deposition of $YBa_2Cu_3O_x$ Thick Films on Biaxially Textured Metals", Appl. Phys. Lett., 1996, 69, 1795.

Goyal, A., Ren,S. X., Specht, E. D., Kroeger, D. M., Feenstra, R., Norton, D. P., Paranthaman, M., Lee, D. F. and Christen, D. K., "Texture Formation andGrain Boundary Networks in Rolling Assisted Biaxially Textured Substrates (RABiTS) and in Epitaxial YBCO Films on such Substrates," To be published in Micron, 1999.

Hasegawa, K., Fujino, K., Mukai, H., Konishi, M., Hayashi, K., Sato, K., Honjo, S., Satao, Y., Ishii, H., and Iwata, Y., "Biaxially Aligned YBCO Film Tapes Fabricated by All Pulsed Laser Deposition", Appl. Supercond., 4, 475-486, 1996.

Iijima, Y., Tanabe, N., Kohno, O., and Ikeno, Y., "In-plane Aligned $YBa_2Cu_3O_x$ Thin-Films Deposited on Polycrystalline Metallic Substrates", Appl. Phys. Lett.., 1992, 60, 769-771.

Kormann, G., Bilde, J. B., Sorensen, K., de Reus, R., Anderson R. H., Vace, P., and Freltoft, T., "Relation between Critical Current Densities and epitaxy of Y-123 Thin Films on MgO (100) and $SrTiO_3$ (100)," J. Appl. Phys., 1992, 71, 3419-3426.

List, F. A., Goyal, A., Paranthaman, M., Norton, D. P., Specht, E. D., Lee, D. F., and Kroeger, D. M., "High-J_c YBCO Films on Biaxially Textured Ni With Oxide Buffer Layers Deposited Using Electron Beam Evaporation and Sputtering", Physica C, 302, 87-92, 1998.

Mathis, J. E., Goyal, A., Lee, D. F., List, F. A. , Paranthaman, M., Christen, D. K., Specht, E. D., Kroeger, D. M., and Martin, P. M., "Biaxially textured Y-123 Conductors on RABiTS with Critical Current Densities of 2-3 MA/cm^2," Japn. J. of Appl. Phys., 1998, 37, L1379-1382.

Matsuda, H., Soeta, A., Doi, T., Aihara, and T. Kamo, "Magnetization and Anisotropy in Single Crystals of Tl-1223 of Tl-Sr-Ca-Cu-O System,"Jpn. J. Appl. Phys., 1992, 31, L1229-31.

Norton, D. P., Goyal, A., Budai, J. D., Christen, D. K., Kroeger, D. M., Specht, E. D., He, Q., Saffian, B., Paranthaman, M., Klabunde, C. E., Lee, D. F., Sales, B. C., and List, F. A., "Epitaxial $YBa_2Cu_3O_x$ on Biaxially Textured Nickel (100): An Aproach to Superconducting Tapes with High Critical current Density", Science, 1996, 274, 755.

Paranthaman, M., Goyal, A., List, F. A., Specht, E. D., Lee, D. F., Martin, P. M., He, Q., Christen, D. K., Norton, D. P., and Budai, J. D., "Growth of Biaxially Tetxured Buffer Layers on rolled-Ni Substrates by Electron Beam Evaportaion", Physica C, 1997, 275, 266-272.

Reade, R. P., Burdahl, P., Russo, R. E., and Garrison, S. M., "Laser Deposition of Biaxially Textured Yttria-stabilized Zirconia Buffer Layers on Polycrystalline Metallic Alloys for High Critical Current Y-Ba-Cu-O Thin-films", Appl. Phys. Lett., 61, 2231-2233, 1992.

Ren, S. X., Kenik, E. A., Alexander, K. B., and Goyal, A., "Exploring Spatial Resolution in Electron Back-scattered Diffraction Experiments Via Monte Carlo Simulation", Microsc. and Microanal., 1998, 4, 15-22.

Sun, E. Y., Goyal, A., Norton, D. P., Park, C., Kroeger, D. M., Paranthaman, M., Specht, E. D., and Christen, D. K., " High Resolution TEM/AEM Characterization of Eptaxial Oxide Multilayers Fabricated By Laser Ablation on Biaxially Textured Ni", Physica C, 1999.

Wu, X. D., Foltyn, S. R., Arendt, P. N., Blumenthal, W. R., Campbell, I. H., Cotton, J. D., Coulter, J. Y., Hults, W. L., Maley, M. P., Safar, H. F., and Smith, J. L., "Properties of $YBa_2Cu_3O_x$ Thick Films on Flexible Buffered Metallic Substrates", Appl. Phys. Lett., 1995, 67, 2397.

Yang, C. Y., Babcock, S. E., Goyal, A., Paranthaman, M., List, F. A., Norton, D. P., Kroeger, D. M., and Ichinose, A., "Microstructure of Electron-beam-evaporated Epitaxial Yttria-stabilized Zirconia/CeO_2 Bilayers on Biaxially Textured Ni Tape", Physica C, 307, 87-98, 1998.

PARTICLE ORIENTATION AND TEXTURE FORMATION IN TAPE CAST CERAMIC MATERIALS

P. MARKONDEYA RAJ, F. COSANDEY and W. ROGER CANNON

Ceramic and Materials Engineering, Rutgers University, Piscataway, USA

P. MAINWARING
Oxford Instruments, Inc., Microanalysis Group, Concord, USA

Abstract

Texture in tape cast and sintered α-alumina and rutile titania was determined with Electron Backscattered Diffraction (EBSD) in a high resolution Field Emission Scanning Electron Microscope (FESEM). During tape casting, plate-like alumina aligns such that the plate-like particles are layered parallel to the tape surface resulting in strong crystallographic texture, the normal of the tape surface frequently oriented in the [0001] direction. Particle orientation is also observed in the plane parallel to the tape surface, where the major shape axis of the particles are more frequently oriented in the shearing direction. However, the inverse pole figures in the casting and transverse directions do not show any significant differences. In similar studies, tape cast titania, with relatively more equiaxed particles unlike plate-like alumina, also developed texture during sintering. Anisotropic grain growth ocurred in sintered titania along [001] direction. Texture analysis indicates that the [001] direction is most frequently oriented away from the tape normal, often lying in the plane parallel to the tape surface.

Keywords: Alumina, backscatter diffraction, particle orientation, tape casting, texture, titania

1. Introduction

Most of the ceramic forming techniques – tape casting, extrusion, injection moulding etc. involve a shearing process. Hence, nonrandom microstructures or particle packing may result in many ceramic green components. Particle orientation affects the processing in some ceramic forming systems. Orientation, resulting from shearing of anisotropic alumina powder in a high solid loading suspension, results in sintering shrinkage anisotropy in tape cast substrates in the plane of casting (Raj et al. 1999) and presumeably normal to this plane, as well. Anisotropic shrinkage, observed in injection moulded composites and ceramics made by fused deposition, is frequently attributed to the anisotropic particle packing. Injection moulded components generally have a nonuniform structure that arises from binder and particle orientation resulting in anisotropic properties. Particle shape and orientation significantly affects the macroscopic physical properties in sintered material systems. For example, the mechanical properties of a whisker-reinforced composite are strongly affected by the whisker orientation distribution.

Particle shape anisotropy generally arises from the crystallography of the material system. For example, alumina, barium hexaferrite and bismuth tianate belonging to the hexagonal system generally grow as plate-like particles. Hence, texture development that arises from particle orientation can be used to tailor and improve the final material properties. Relationships between processing conditions, particle orientation and texture can therefore guide in improving the final material properties. This report discusses texture studies in ceramic materials made from tape cast and die-pressed alumina and titania with Electron Backscatter Diffraction in a SEM. The texture is then correlated to the measured particle orientation and other microstructural characteristics. Previous texture measurements in tape cast alumina (Dimarcello et al. 1972; Huber et al. 1994) and bismuth titanate (Watanabe, 1989) were done with X-ray diffraction analysis.

2. Materials and methods

High solids loading aqueous suspensions of alumina and titania were tape cast to study the role of shearing in particle orientation and texture formation in ceramics. The particle size typically ranged from 0.3 - 0.8 microns for alumina and slighly lower for titania. The particle morphology of the starting powders is shown in Fig.s 1a, 2a and 3a. Hexagonal alumina (corundum structure) consisted of plate-like particles with some elongation even within the plane of the plate. The titania particles (rutile structure) are relatively more isotropic compared to alumina.

The tape cast samples were pyrolyzed at 425° C for one hour to remove any binder and sintered for 2 hours at 1200° C and 1500° C for TiO_2 and Al_2O_3 respectively. The processing details were discussed elsewhere (Raj et al., 1999). The sintered microstructures are shown in Figure 4a and 4b respectively. During sintering, titania tend to grow anisotropic grains unlike alumina. The microstuctures of tape cast alumina and titania in the prefired state were characterized by image analysis to detect any shear induced microstructural anisotropy. Texture development in the sintered ceramics and its relationship to particle orientation were studied the next part of this work. A high spatial resolution Electron Backscatter Diffraction (EBSD, Opal-Oxford) in Field Emission SEM (LEO-982) has been used for texture analysis and crystallographic orientation determination of the particles. Between 3000 to 4000 measurements per sample were recorded automatically to develop an orientation map. The data was then filtered to produce texture maps containing a single data point per grain.

3. Image analysis results

Particle orientation histograms were determined by identifying the orientation angle of each particle in the prefired microstructure. Orientation angle is assigned to each particle based on the angle between axis of minimum second-order moment of the particle and the casting direction. The details of the image analysis techniques were discussed in a previous publication (Raj et al. 1999). Figs. 1a and 2a show the microstructures of a top and horizontally sectioned surfaces of a tape cast alumina respectively. The shearing direction is horizontal with the page in both the micrographs. The corresponding particle orientation histograms are shown in Figs. 1b and 2b respectively. Particle orientation is stronger in the Fig. 2b because plate-like alumina tends to easily align along the surface of the tape. Some particle orientation can also be seen Fig. 1a, though plate-like alumina particles do not have such strong anisotropy within the plane of the plate (mean elongation ratio of 1.75). Similar image analysis on the tape cast TiO_2 (Fig. 3a) did not show any siginficant particle orientation.

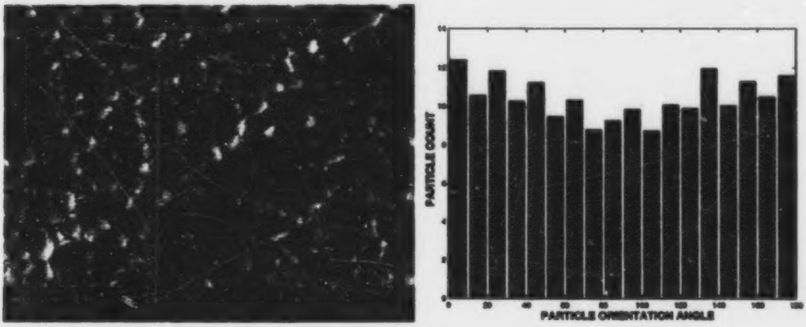

Fig. 1: FESEM image of the top surface of tape cast alumina and its particle orientation histogram.

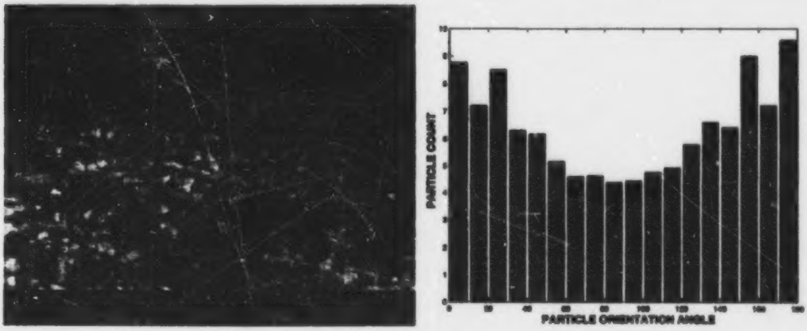

Fig. 2: FESEM image of a sectioned surface of tape cast alumina and its particle orientation histogram.

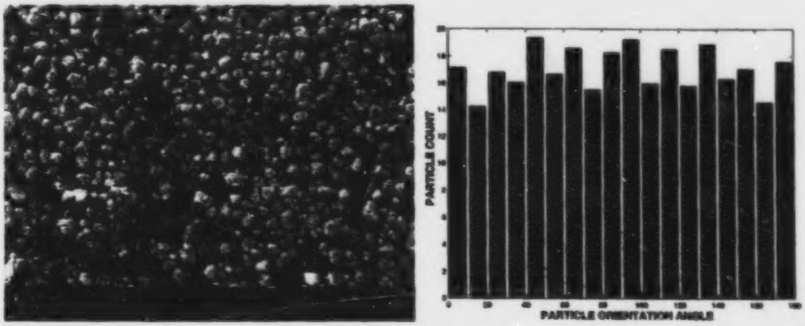

Fig. 3: FESEM image of a horizontally sectioned surface of tape cast titania and its particle orientation histogram.

4. Texture analysis results

Crystallographic texture analysis was carried out on sintered tapes. The sintered microstructures of alumina and titania are shown in Figs. 4a and 4b respectively. The inverse pole figures obtained from the EBSD analysis are shown in Fig. 5. The inverse pole figure in the normal direction reveals alignment of the (0001) basal planes which lies preferentially in the plane of the tape cast film. This correlated with the image analysis results shown in Fig. 2b since the plate-like alumina powder easily layers in the thickness direction during tape casting. The plate-like nature of the particles results from the low surface energy basal planes. The inverse pole figures in the casting and transverse directions however did not show significant differences though the major axis of the particles are frequently oriented in the casting or longitudinal direction. Orientation resulting from the particle elongation within the plane of the plate, therefore, did not result in any crystallographic texture in the tape surface. Texture analysis in a die-pressed alumina sample also showed similar texture (only in the pressing direction) as seen in the normal direction of tape cast alumina.

The FESEM image of a tape cast TiO_2 show some highly anisotropic grains with strong facets. EBSD orientation measurements taken from individual elongated particles revealed that their preferential fast growth direction is along [001]. The inverse pole figures of the sample normal and casting (longitudinal) direction are shown in Fig. 6a and Fig. 6b respectively. A pattern similar to the longitudinal direction is observed for the other in-plane (transverse) direction. The results indicate a preferred alignment of the [001] particle direction in the plane of the tape than in the plane normal to the tape. This is unexpected since the initial TiO_2 particles are relatively more isotropic compared to the plate-like alumina and no strong preferential alignment is seen in the image analysis of the prefired microstructures. Texture analysis with die-pressed TiO_2 did not show a significant difference from the tape cast samples.

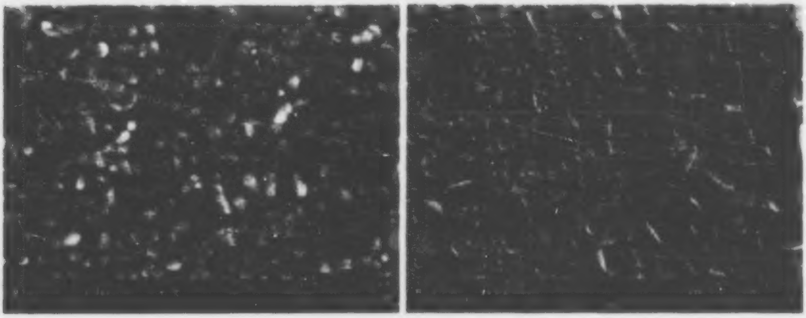

Fig. 4: FESEM image of the top surface of a sintered alumina (left) and titania (right).

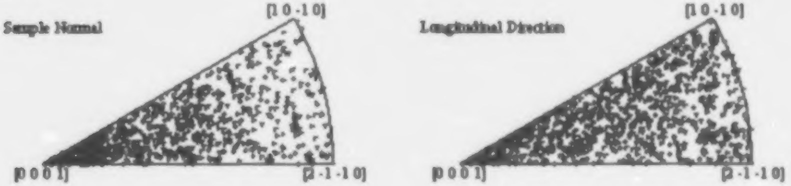

Fig. 5: Inverse pole figures in the normal and longitudinal (casting) directions obtained from tape cast alumina.

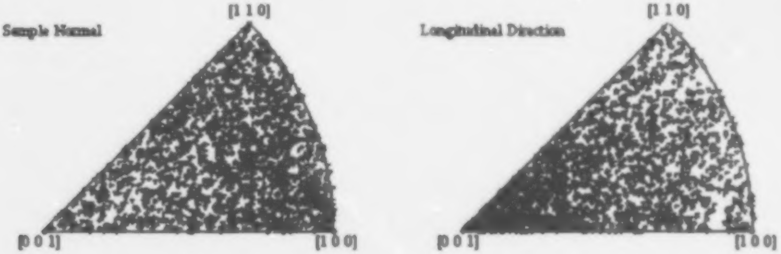

Fig. 6: Inverse pole figures in the normal and longitudinal (casting) directions obtained from tape cast titania.

5. Summary

During tape casting, plate-like alumina aligns such that the plates lay parallel to the surface of the tape resulting in strong preferred orientation. Image analysis of the top and bottom surfaces of the tape also shows some in-plane particle orientation where the major axis of the particles are frequently oriented in the shearing direction. Since the plate-like nature arises from the low energy basal planes, the particle alignment leads to strong crystallographic texture, with the grain normals frequently oriented in the [0001] direction. However, the inverse pole figures of the casting and transverse directions in the sintered tapes do not show significant differences, indicating that though the plate-like nature arises from the low energy basal planes, the elongated axis within the tape surface might not have any crystallographic significance in alumina particles.

Similar studies in rutile titania with more isotropic particles showed that the TiO_2 grains tend to grow as rods in the [001] direction laying within the plane of the tape. This behaviour is also seen in die-pressed titania.

6. References

Dimarcello F.I., Key P.L. and Williams J.C. (1972) Preferred orientation in Al_2O_3 substrates, *J. Am. Cer. Soc.*, Vol. 55, No. 10, pp. 509-514.

Huber J., Krahn W., Ernst J., Bocker A. and H. J. Bunge, (1994) Texture Formation in Al_2O_3 Substrates, *Mater. Sci. Forum*, Vol. 157-169, pp. 1411-1416.

Raj P.M. and Cannon W.R., (1999) Anisotropic shrinkage in tape cast ceramics - Role of processing parameters and particle shape, *J. Am. Ceram. Soc.*,, In Press.

Raj P.M., Dunn S.M. and Cannon W.R., (1999) Measurement of particle orientation in tape cast ceramic microstructures, *J. Comp.-Assist. Microscopy*, In Press.

Watanabe H., Kimura T. and Yamaguchi T. (1989) Particle Orientation during Tape-Casting in the Fabrication of the Grain-Oriented Bismuth titanate, *J. Am. Ceram. Soc.*, Vol. 72, No. 2, pp. 289-293.

TEXTURE OF CERAMIC REINFORCED MAGNESIUM COMPOSITES

E.M. JANSEN and H.-G. BROKMEIER
Institut für Werkstoffkunde und -technik der TU Clausthal, GKSS-Forschungszentrum, Geesthacht, Germany

K.U. KAINER
Institut für Werkstoffkunde und -technik der TU Clausthal, Clausthal-Zellerfeld, Germany

Abstract

The texture of two different series of ceramic reinforced magnesium samples was investigated in comparison to pure magnesium samples. The at different temperatures and strains extruded samples all show a double fiber texture of Mg, with both prism planes perpendicular to the extrusion direction. The intensities of the fiber components vary with temperature, strain and ceramic content.

Keywords: extrusion, ceramic reinforcement, fiber texture, magnesium, Saffil, SiC

1 Introduction

Because of the low density magnesium is an interesting material for the construction of moving engine components. In order to increase the strength and hardness of Mg, different methods of ceramic reinforcement have been tested (Kainer 1994) to reach the desired properties. The aim of the present study is to investigate the influence of different ceramic reinforcement on the texture of Mg, because the texture mainly causes the anisotropy of properties of a material.

2 Experimental methods

Two series of Mg samples were produced powder metallurgically at temperatures of 300°C and 350°C and at strains of 94.1% and 96.4%, the first series containing 10 and 20 vol.% SiC particles, the second series containing 10, 15 and 20 vol.% Al_2O_3 short fibers (Saffil). For comparison four pure Mg samples were produced at the same extrusion conditions.

The texture analyses were carried out at the TEX-2 neutron texture diffractometer, GKSS Research Center, Geesthacht. Complete pole figures of the

(10.0), (00.2) and (11.0) reflections of Mg were measured for the pure and Saffil-containig samples. The (10.1) reflection of SiC showed a total overlapping with the (00.2) reflection of Mg. Thus, for the Mg-SiC samples instead of (00.2) the (10.2) pole figures of Mg were measured, an ODF (Dahms 1992, Schaeben 1994) was calculated for each sample using the (10.0), (10.2) and (11.0) pole figure data, and the (00.1) pole figures were calculated from the ODF. The (10.0) and (11.0) pole figures were recalculated. Additionally the (11.0) and (10.9) pole figures of hexagonal (6H) SiC were measured.

3 Results and discussion

Table 1 gives the maximum intensities (m.r.d.) of the measured and ODF calculatd Mg pole figures of pure magnesium and SiC reinforced samples. The measured and calculated values are approximately identical, so that the only calculated basal plane pole figures of the SiC containing samples can be assumed to give good information.

Table 1: Maximum intensities (m.r.d.) in Mg pole figures, measured values (EXP) compared to recalculated (REC) or calculated (CAL) values.

Sample SiC content	Strain	Temperature	Imax (10.0) EXP	Imax (10.0) REC	Imax (11.0) EXP	Imax (11.0) REC	Imax (11.0) off	Imax (00.2) EXP	Imax (00.1) CAL
Mg1 pure	96.4%	300°C	6.9	6.8	2.3	2.3	21°	3.4	3.2
Mg2 pure	94.1%	300°C	6.1	6.0	2.3	2.3	18°	3.0	3.0
Mg3 pure	96.4%	350°C	7.2	7.0	2.4	2.3	21°	3.1	3.2
Mg4 pure	94.1%	350°C	5.7	5.7	2.4	2.4	21°	3.1	3.0
Mg5 10%	96.4%	300°C	4.0	3.9	2.3	2.3	12°	-	2.9
Mg6 10%	94.1%	300°C	3.7	3.9	2.4	2.2	18°	-	2.6
Mg7 10%	96.4%	350°C	3.8	3.7	2.2	2.2	15°	-	2.7
Mg8 10%	94.1%	350°C	3.3	3.4	2.3	2.2	18°	-	2.7
Mg9 20%	96.4%	300°C	2.8	3.0	2.3	2.2	12°	-	2.8
Mg10 20%	94.1%	300°C	3.0	3.0	2.3	2.2	15°	-	2.6
Mg11 20%	96.4%	350°C	2.9	3.1	2.4	2.2	12°	-	2.9
Mg12 20%	94.1%	350°C	2.6	2.7	2.2	2.2	12°	-	2.6

The pure Mg samples reveal a double fiber texture, already described by Unckel (1942). The stronger fiber component shows a distribution of (10.0) prism planes perpendicular to the extrusion direction, represented in the pole figures of this direction as central maximum with a corresponding small circle distribution 60° off the center. The weaker fiber component reveals the second prism plane (11.0) perpendicular to the extrusion direction. In the (11.0) pole figure the intensities are partially overlapped with the much stronger intensities of the <10.0> fiber, which appear in their maximum at a small circle 30° off the center, so that the maximum intensities of (11.0) also appear off the center of the pole figure (Table 1). This double planes lying nearly parallel to the extrusion direction. The <11.0> fiber is described as low temperature, the <10.0> fiber as high temperature deformation texture of magnesium (Morell and Hanawalt 1942).

As representative example, the texture development with increasing SiC particle content at 350°C and 96.4 % strain is given in Fig. 1. The central (10.0) maximum in the pole figures becomes much weaker with increasing SiC content, the small circle distribution at 60° nearly disappears. In the (11.0) pole figures the maximum intensities appear where the strong (11.0) distribution at 30°, which belongs to the <10.0> fiber, overlaps the weaker central (11.0) distribution. The maximum intensities show a tendency of moving towards the center of the pole figures with increasing SiC content (Table 1). As the maximum intensities in the (11.0) pole figures remain quite stable independent of SiC content, it can be assumed that also the <11.0> fiber texture component remains stable.

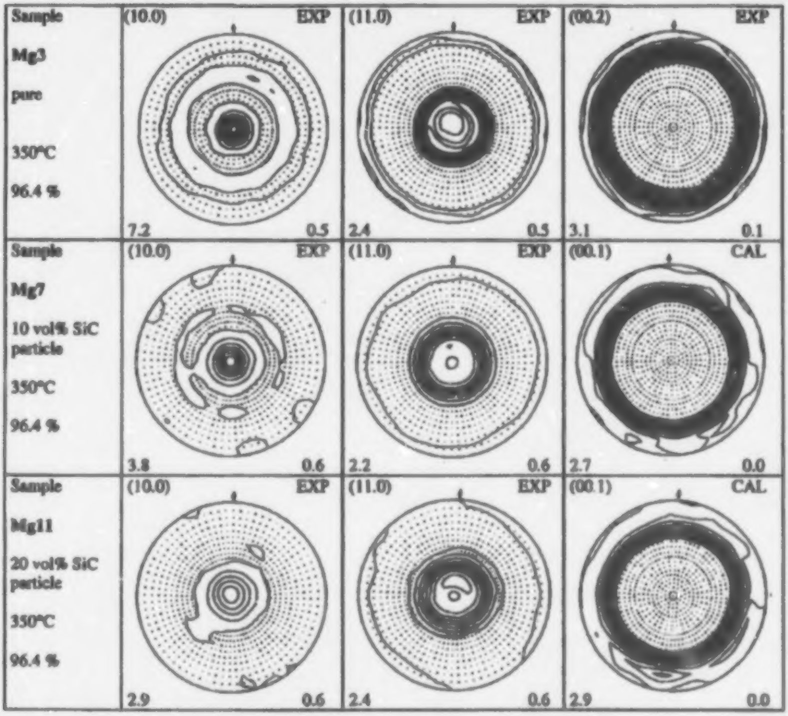

Fig. 1: Measured (EXP) and calculated (CAL) Mg pole figures. Projection plane perpendicular to extrusion direction; contour interval (10.0): 0.4, (11.0) and (00.2): 0.2; maximum intensity (m.r.d.): left, minimum: right corner; dotted area: density below 1.0 m.r.d..

The (11.0) and (10.9) pole figures of SiC, which needed a quite long measuring time, show a very weak, but distinct alignment of (11.0) perpendicular to the extrusion direction (Fig. 2). As a plastic deformation of SiC at the used extrusion conditions is very unlikely, a rotation of the particles in the Mg matrix must be responsible for the texture. An alignment is only possible, if the particles are not of a sperical shape, but show partially angular edges of a distinct crystallographic orientation. The polished sections confirm an angular shape of the particles.

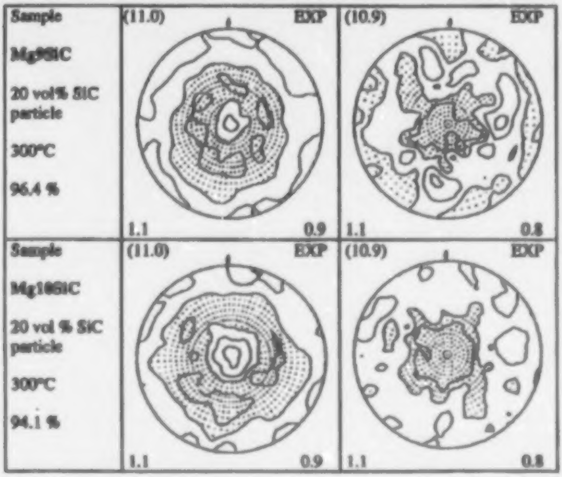

Fig. 2: Measured (EXP) SiC pole figures. Projection plane perpendicular to extrusion direction; contour interval 0.05; maximum intensity (m.r.d.): left, minimum: right corner; dotted area: density below 1.0 m.r.d..

In general, the Saffil containing samples show a similar deformation texture as the pure Mg and the SiC containing samples. Fig. 3 gives the pole figures of the samples strained 96.4 % at 350°C with increasing Saffil content. The coincidence of the measured and calculated maximum intensities (Table 2) is not as perfect as for the first series investigated (Table 1). The maximum intensities in the recalculated (10.0) pole figures, which originate from the central maximum, are lower than in the measured pole figures, whereas the maximum intensities in the calculated (001) pole figures are a little higher. The maximum intensities of (11.0) are nearly identical in the measured and calculated pole figures. The Mg <11.0> fiber component remains quite stable independent of Saffil content. The <10.0> fiber component reveals lower intensities than the pure Mg samples, but higher intensities than the corresponding Mg-SiC samples. There is no constant decrease of the <10.0> fiber intensities with increasing Saffil content, and also no constant movement of the maximum intensities of (11.0) towards the center of the pole figures (Table 2).

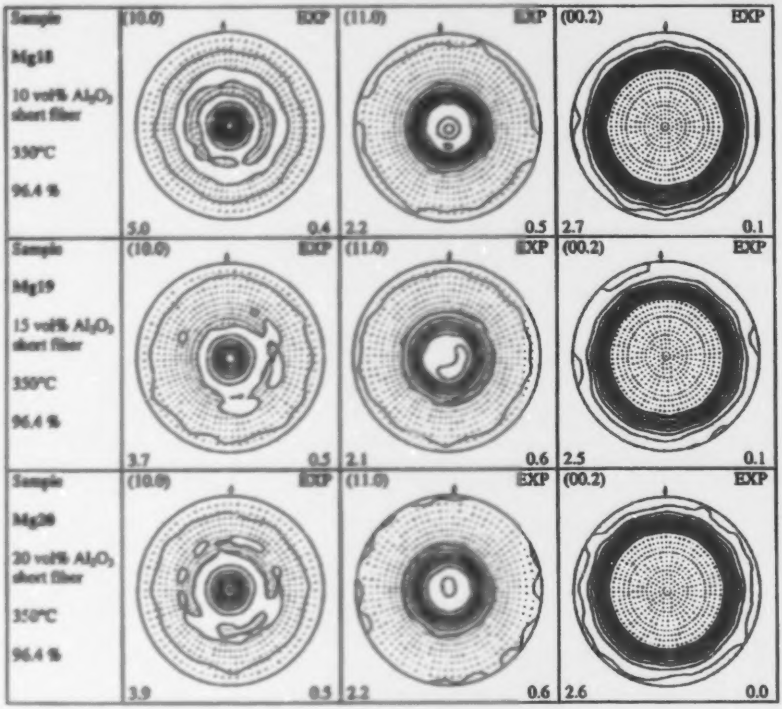

Fig. 3: Measured (EXP) Mg pole figures. Projection plane perpendicular to extrusion direction; contour interval (10.0): 0.4, (11.0) and (00.2): 0.2; maximum intensity (m.r.d.): left, minimum: right corner; dotted area: density below 1.0 m.r.d..

The texture development of SiC particle reinforced Mg is nearly foreseeable. Decreasing particle content, lower temperature and higher strain intensify the <10.0> fiber texture. The Saffil reinforced samles only show generally higher intensities of the <10.0> fiber at the higer deformation temperature. Reasons for the irregular deformation behaviour must be due to the behaviour of the fibers during the extrusion experiment. As the polished sections show, most of the fibers broke during the extrusion, and thus should behave similar to the particles. An explanation for the irregular, but higher intensities of the <10.0> fiber texture could be a possible alignment of different parts of the Saffil fibers during the preparation of powders into the later extrusion direction, so that the surface against the deformation is lower compared to the same volume of particles. All Saffil fibers show a small reaction rim against the Mg matrix. The reaction could have reduced the internal stresses. In the near future internal stress analyses of all samples will be carried out, which are exspected to clear the texture development problems.

Table 2: Maximum intensities (m.r.d.) in Mg pole figures, measured values (EXP) compared to recalculated (REC) or calculated (CAL) values

Sample Saffil content	Strain	Temperature	Imax (10.0) EXP	Imax (10.0) REC	Imax (11.0) EXP	Imax (11.0) REC	Imax (11.0) off	Imax (00.2) EXP	Imax (00.1) CAL
Mg21 10%	96.4%	300°C	4.6	3.8	2.2	2.1	18°	2.6	2.9
Mg24 10%	94.1%	300°C	3.7	3.3	2.2	2.1	9°	2.5	2.7
Mg18 10%	96.4%	350°C	5.0	3.9	2.2	2.1	18°	2.7	2.9
Mg15 10%	94.1%	350°C	4.5	4.0	2.2	2.1	18°	2.7	2.7
Mg22 15%	96.4%	300°C	3.2	3.0	2.3	2.2	15°	2.4	2.6
Mg25 15%	94.1%	300°C	3.1	2.8	2.1	2.1	12°	2.4	2.5
Mg19 15%	96.4%	350°C	3.7	3.2	2.1	2.1	15°	2.5	2.6
Mg16 15%	94.1%	350°C	4.1	3.6	2.2	2.1	15°	2.5	2.5
Mg23 20%	96.4%	300°C	3.9	3.3	2.2	2.1	15°	2.5	2.7
Mg26 20%	94.1%	300°C	3.2	3.0	2.1	2.0	18°	2.2	2.4
Mg20 20%	96.4%	350°C	3.9	3.4	2.2	2.1	15°	2.6	2.7
Mg17 20%	94.1%	350°C	3.9	3.5	2.1	2.1	18°	2.5	2.5

Acknowledgements

The authors wish to thank B. Witassek and R. Schnieber for the technical assistance at the TEX-2 equipment. K. Hirschhausen prepared the polished sections. H. Siemes kindly disposed the pole figure plot program. Financial support was given by the BMBF.

4 References

Dahms, M. (1992) The Iterative Series Expansion Method for Quantitative Texture Analysis -Part II: Applications. *J. Appl. Cryst.*, Vol. 25, pp 258-67

Kainer, K.U. (1994) Improved prediction model for time-dependent deformations of concrete. *Material and Structures,* Vol. 26, No. 194. pp. 567-74.

Morell, L.G. and Hanawald, J.D. (1932) X-Ray Study of the Plastic Working of Magnesium Alloys. *Physics,* Vol. 3, pp 161-68.

Unckel, H. (1942) Die Eigenschaften gepreßter und weiterbehandelter Stangen aus Leichtmetallen und anderen Legierungen in der Längs- und Querrichtung. *Metallwirtschaft* 21, pp 531-38.

CONTRIBUTION OF THE ORIENTATION TEXTURES IN THE AMORPHOUS AND CRYSTALLINE PHASES ON THE PLASTIC DEFORMATION OF POLYMERS

C. G'SELL, C. CABOT, A. DAHOUN, M.J. PHILIPPE and J. GRENET
Laboratoire de Physique des Matériaux (UMR CNRS 7556), Ecole des Mines, INPL, Nancy, France

According to their macromolecular structure and their fabrication process, polymers contain exhibit a more or less crystalline microstructure, typically ranging from 0% (e.g. PMMA) to 80% (e.g. PE). Even in certain cases (e.g. PET), crystallites are nucleated under the effect of stretching.

The aim of the lecture is to show, through experimental evidence, qualitative mechanisms and micro-macro models that macromolecular orientation plays a major role in the plastic hardening of polymers while they are deformed in the solid state, whatever their crystallinity. This property is intrinsically associated to the very anisotropic properties van der Waals and covalent bonds.

Traditionally, textures in amorphous and crystalline phases are assessed and modeled through very different methods and schemes, although a qualitatively similar description is possible.

The case of semi-crystalline polymers between glass-transition and melting temperatures will be analyzed more particularly. It will be shown that the hardening of mostly amorphous polymers is controlled by the statistical orientation of chains between crosslinks, the development of induced crystallites playing the role of additional junctions. Conversely, in mostly crystalline polymers, the hardening is controlled by the plastic tilt of the crystallites, the amorphous phase playing a role of strain accommodation. In the important case of nearly 50/50 semi-crystalline polymers, both mechanisms are active and the response and texture is modeled through composite self-consistent approaches.

The fine adjustment of crystallinity and texture is thus of major importance in the optimization of microstructure in view of obtaining structural materials with high performances.

APPLICATION OF ELECTRON BACKSCATTERED DIFFRACTION (EBSD) AND ATOMIC FORCE MICROSCOPY (AFM) TO DETERMINE TEXTURE, MESOTEXTURE, AND GRAIN BOUNDARY ENERGIES IN CERAMICS

S.J. GLASS and V.R. VEDULA
Sandia National Laboratories, Albuquerque, NM, USA
D.M. SAYLOR and G.S. ROHRER
Carnegie Mellon University, Pittsburgh, PA, USA

Abstract

Crystallographic orientations in alumina (Al_2O_3) and magnesium aluminate spinel ($MgAl_2O_4$) were obtained using electron backscattered diffraction (EBSD) patterns. The texture and mesotexture (grain boundary misorientations) were random and no special boundaries were observed. The relative grain boundary energies were determined by thermal groove geometries using atomic force microscopy (AFM) to identify relationships between the grain boundary energies and misorientations.

Keywords: Ceramic, texture, grain boundary energies, EBSD, AFM

1 Introduction

The microstructural evolution of materials and their properties (electrical, superconducting, optical, mechanical, thermal) depend on several factors, including the surface and grain boundary energies, orientations, and chemistry. These quantities are interdependent and the complexity of the relationships represents a serious challenge. There is mounting evidence that texture and the presence of special boundaries dominate overall material behavior (Lehockey et al. 1998).

We are interested in crack propagation in polycrystalline ceramics, in particular the influence of residual stresses that develop on cooling from the processing temperature due to thermal expansion anisotropy (see Vedula 1999). If high energy boundaries are preferentially eliminated during microstructural evolution, this may lead to a microstructure that has more fracture resistant boundaries (Gell 1967). The removal of certain misorientations may also influence the residual stresses and the onset of microcracking because textured microstructures with preferred orientations will have more small angle boundaries (Goyal 1996).

While relationships between grain size, shape, and material properties have been extensively studied, until the advent of the collection of electron backscattered diffraction (EBSD) patterns, it was not possible to characterize both the texture (lattice orientations) and mesotexture (grain boundary misorientations) and to relate them to the microstructure for a sufficient number of grains to be representative of a real material. There have been few studies on ceramics such as Al_2O_3.(Glass et al. 1998 and Mulvihill et al. 1998) It has also not been possible to determine grain misorientations/grain boundary energy relationships.

Our objective is to determine the texture and mesotexture of polycrystalline Al_2O_3 and $MgAl_2O_4$ using EBSD and to determine if and how the misorientations relate to the relative grain boundary energies. The measurements of these quantities are a starting point for structure/property simulations (see paper by Vedula) and are also useful for the validation of models of microstructural evolution that incorporate grain boundary energies and grain misorientations. In the present work, the grain boundary energy is assumed to be a function only of its misorientation.

2 Experimental procedure

2.1 Materials

The polycrystalline ceramic materials used in this study were a 99.99% pure alumina (AKP-50, Sumitomo Chemical Company) and $MgAl_2O_4$ (RCS Technologies). The complete description of the preparation of the alumina can be found elsewhere (Kovar and Readey 1994). Quantitative stereology provided mean grain sizes (d_{avg}) of 8 and 27 μm for the 99.99% alumina and the grain shape is close to equiaxed. Densities ranged from 98.6% theoretical density (TD) for the fine-grained material to 99.2% TD for the coarse grained Al_2O_3.

2.2 Sample preparation

After sintering, the samples were ground and polished flat and parallel with a diamond suspension. The final polishing step for the 27 μm Al_2O_3 used colloidal silica (pH=10), whereas for the 8 μm Al_2O_3, it was 0.25 μm diamond. The final polishing step for $MgAl_2O_4$ used colloidal silica (pH=7). The grain boundaries were thermally grooved in air at 1600°C for 1 and 100 hr for the 8 and 27 μm grain size samples respectively. The $MgAl_2O_4$ was thermally etched at 1500°C for 10 hr.

2.3 Atomic force microscopy (AFM) measurements

Surface dihedral angles were measured for the thermal grain boundary grooves on the samples using a Digital Instruments StandAlone AFM (SAA-125) positioned above the sample mounted on an X-Y translation stage (Burleigh Instruments TSE-150) with reproducible position resolution of 50 nm. Details about the imaging and error minimization can be found elsewhere (Saylor and Rohrer 1998). For the alumina and spinel samples respectively, 164 and 175 three-grain junctions were measured. The grain boundary to surface energy ratios were obtained from the simplified Herring equation $\gamma_{gb}/\gamma_s=2\cos(\psi/2)$ that assumes the torque terms are zero, the surface energies are isotropic and the grain boundary energy is a function of misorientation only.

2.4 Electron Backscattered Diffraction (EBSD) pattern collection

EBSD were collected using a Phillips SL40FEG scanning electron microscope (SEM). The same grains examined by AFM were located using fiducial marks and EBSD were obtained for each of the manually selected grains. The patterns were indexed using TSL's Orientation Imaging Microscopy Software (TexSEM Labs, Inc.) assuming cubic symmetry for spinel and hexagonal symmetry for alumina. Orientations were specified by a set of Euler angles (α, β, γ) for each grain that defines a rotation matrix with respect to the specimen coordinate system. Misorientations were defined using the Euler angles from adjoining grains and deriving the pair's common axis and the rotation angle about that axis that brings the crystallites into coincidence (so-called axis/angle pairs). The smallest positive misorientation angle from the misorientation matrix was used.

3 Results and Discussion

3.1 Surface Energies from AFM Measurements

The cumulative probability distribution of dihedral angles along with the grain boundary energy ratios is shown in Fig. 1. The mean value of the dihedral angle for the 8 μm alumina distribution and the corresponding value of $\gamma_{gb}/\gamma_s = 0.95$ are similar to those obtained for another alumina (1.1 to 1.2) using a metal reference line technique; however, the distribution is wider (Handwerker, 1990).

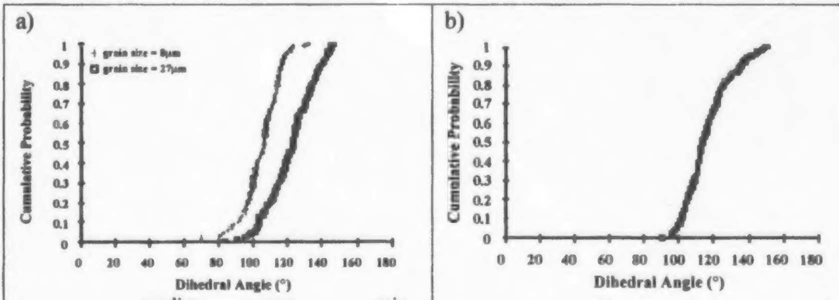

a)

	median	max	min
Ψ_s	106	132	60
γ_{gb}/γ_s	1.20	1.73	0.81

(8 μm, 1600°C, 1 hr thermal groove)

	median	max	min
Ψ_s	123	147	83
γ_{gb}/γ_s	0.95	1.50	0.57

(27 μm, 1600°C, 100 hr thermal groove)

b)

	median	max	min
Ψ_s	113	152	90
γ_{gb}/γ_s	1.10	1.41	0.48

Fig. 1: Dihedral angles and grain boundary/surface energy ratios for a) 8 and 27 μm alumina etched at 1600°C for 1 and 100 hr. respectively. b) $MgAl_2O_4$.

The higher mean dihedral angle and lower mean ratio of γ_{gb}/γ_s=1.20 for the 27 μm alumina compared to the 8 μm sample and Handwerker's results for a 99.99% pure alumina may be a result of differences in sample processing, grain size, and the difference in the surface preparation technique. The diamond polish produces more damage and may change the energies and diffusivities in the system. There is also the possibility that the colloidal silica contaminates the grain boundaries. The values for $MgAl_2O_4$ are within the range of values tabulated by Handwerker for other ceramics.

3.2 Grain Boundary Misorientations

The grain boundary misorientations and their relationships to the γ_{gb}/γ_s ratio are shown in Fig. 2 for both Al_2O_3's and the $MgAl_2O_4$. There are no low angle boundaries for either the 27 μm Al_2O_3 or $MgAl_2O_4$ samples. None of the measured boundaries are CSL boundaries with respect to Brandon's criterion. There is no clustering of the orientations and there is no apparent correlation between the misorientation and the γ_{gb}/γ_s ratio. Similar results were found for the $MgAl_2O_4$. The absence of special boundaries and a relationship between the energy and misorientation of some boundaries is in contrast to results for a MgO sample (Saylor and Rohrer 1998). Although both materials in this study have relatively high purities, the presence of glass and other grain boundary impurities may be important (Swiatnicki 1995). The grain boundary plane and atomic level faceting along the boundary may play large roles in determining the grain boundary energies, although random grain boundaries generally have higher energy and are less sensitive to the orientation of their grain boundary planes (Garbacz 1995). A TEM study of grain boundaries in alumina showed more near coincidence grain boundaries in a small grain sized homogeneous microstructure with no dense interfacial planes than in one containing abnormally large grains with boundaries with densely packed planes (Swiatnicki 1995). The materials in this study are relatively large grained.

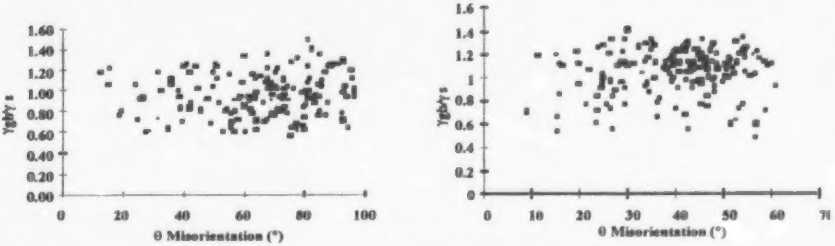

a) 27 μm Al_2O_3 b) $MgAl_2O_4$

Fig. 2: Grain boundary energy ratio vs. misorientation angle (θ).

3.3 Texture

The pole figure for the 27 μm alumina is shown in Fig. 3, where RD and TD represent the two directions parallel to the specimen axes. Each of the points represents a grain in the polycrystal for which the grain boundary energy ratios were measured. Based on these measurements and measurements for similar materials the alumina has random texture. Even in alumina materials that have been hot pressed to introduce texture,(Ma 1991) only small degrees of texture have been observed relative to the texture observed in many metal systems. In other materials systems it has been shown that the presence of grain texture has a significant effect on the grain misorientation textures (Randle 1988). Thus the absence of misorientation texture is consistent with the absence of grain texture.

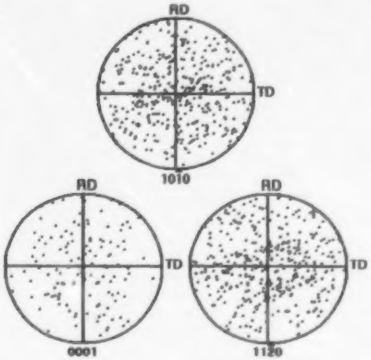

Fig. 3: Pole figures for 27 μm alumina.

4 Summary and Conclusions

Mean grain boundary to surface energy ratios were in the range of one for alumina and spinel. The differences for the two grain sizes of alumina need to be resolved to determine if they are due to intrinsic differences in the grain boundary energy distribution for different grain sizes or due to surface preparation techniques. The samples examined in this study have random texture and random misorientations and do not contain CSL boundaries. Ceramic materials that are expected to have more texture should be examined to identify effects and relationships that may be subtle.

Acknowledgments

Sandia is a multiprogram laboratory operated by Sandia Corporation, a Lockheed Martin Company, for the United States Department of Energy under Contract DE-AC04-94AL85000. This work was supported in part by the MRSEC Program of the National Science Foundation under Award Number DMR-9632556.

5 References

Garbacz, A, Ralph, B, Kurzdylowski, K.J. (1995) On the possible correlation between grain size distribution and distribution of CSL boundaries in polycrystal, *Acta metall. mater.*, Vol. 43, No. 4, pp. 1541-1547.

Gell, M., Smith, E. (1967) The propagation of cracks through grain boundaries in polycrystalline 3% silicon-iron, *Acta met*, Vol. 15, pp. 253-258.

Glass, S.J., Michael, J.R., Readey, M.J., Wright, S.I., Field, D.P., (1998) Characterization of microstructure and crack propagation in alumina using orientation imaging microscopy (OIM), pp. 803-813 in Ceramic Microstructures – Control at the Atomic Level, Edited by A.P. Tomsia and A.M. Glaeser, Plenum Press, NY.

Goyal, A., Specht, E.D., Kroeger, D.M., Mason, T.A. (1996) Effect of texture on grain boundary misorientation distributions in polycrystalline high temperature superconductors, *Appl. Phys. Lett.*, Vol. 68, No. 5, pp. 711-713.

Handwerker, C.A., Dynys, J.M., Cannon, R.M., Coble, R.L. (1990) Dihedral angles in magnesia and alumina: distributions from surface thermal grooves, *J. Am. Ceram. Soc.*, Vol. 73, No. 5, pp. 1371-77.

Kovar, D., Readey, M.J. (1994) Role of grain size in strength variability of alumina, *J. Am. Ceram. Soc.* 77:1928-38.

Lehockey, E.M., Palumbo, G., Lin, P. (1998) Improving the weldability and service performance of nickel- and iron-based superalloys by grain boundary engineering *Meta. Mat. Trans A-Phy. Meta. Mat. Sc.* 29[12] pp. 3069-3079.

Ma, Y, Bowman, K.J. (1991) Texture in hot-pressed or forged alumina, *J. Am. Ceram. Soc.*, Vol. 74, No. 11, pp. 2941-44.

Mulvihill, M.L., Gülgün, M.A., Bischoff, E., Rühle, M (1998) Orientation imaging microscopy of alpha alumina: sample preparation and texture analysis, *Z. Metallkd.*, Vol. 89, No. 8, pp. 546-550.

Randle, V., Ralph, B., Dingley, D. (1988) The relationship between microtexture and grain boundary parameters, *Acta metall.*, Vol. 36, No. 2, pp. 267-273.

Saylor, D.M. and Rohrer, G.S. (1998) Measuring the influence of grain boundary misorientation on thermal groove geometry in ceramic polycrystals. Submitted to *J. Am. Ceram. Soc.*

Swiatnicki, W., Lartigue-Korinek, S., Laval, J.Y. (1995) Grain boundary structure and intergranular segregation in alumina, *Acta metall. mater.*, Vol. 43, No. 2, pp. 795-805.

Vedula, V.R., Glass, S.J., Saylor, D.M., Rohrer, G.S., Carter, W.C., (1999) Predicting microstructural-level stresses and crack paths in ceramics, *ICOTOM-12* (1999).

QUANTITATIVE CHARACTERISATION OF MOLLUSC SHELL TEXTURES

D. CHATEIGNER
Laboratoire de Physique de l'Etat Condensé, Université Du Maine, Le Mans, France
C. HEDEGAARD
Institute of Biology, Department of Ecology and Genetics, University of Aarhus, Denmark
H.-R. WENK
Department of Geology and Geophysics, University of California, Berkeley, USA

Abstract

Textures of monoplacophora, cephalopod, bivalve and gastropod mollusc shells, composed of aragonite and calcite, vary in strength and pattern. The study emphasises textures of nacre and preferred orientation of aragonite but for some species calcite layers were analysed. Texture strength varies from random to extremely high. The aragonite texture patterns commonly have **c** axes at high angles to the shell surface. The **a** axes exhibit various patterns, from an ideal fibre texture to a perfect single crystal-like orientation, with or without presence of {110} twinning. Large texture differences are found between shells from phyllogenetically distant families, whereas textures of closely related species are more similar. A compact textural terminology is introduced to describe the various texture patterns, and to facilitate comparison between species.

Keywords: mollusc, shell, nacre, biomimetics, aragonite, calcite

1 Introduction

The formation of calcium carbonates in natural processes such as mollusc shells is of increasing interest (Urist 1965), particularly due to biomimetic relationships. For example, it has been shown that nacre from *Pinctada maxima* could be incorporated in sheep bones and stimulate bone generation by human osteoblasts (Lopez & al. 1992). Therefore a quantification of the internal microstructure and texture of shells are important. Also, since shells are the only preserved parts in fossils, their texture can become a classification criterion for paleontologists. Also, a non-trivial relationship between the crystallographic textures and shell microstructures, as seen with SEM, was revealed (Hedegaard et Wenk, 1998). Textures differ in shell structures with similar morphological patterns between distantly related molluscs, and may vary between layers within an individual (Chateigner et al. 1996). This work quantifies texture differences in shells from gastropods, bivalves, cephalopods, and monoplacophora. Wishing to explore the extent of the phylogenetic signal in textures, we undertook a systematic survey of many samples. We found it practical to use a compact notation based on the actual observations and a systematic nomenclature which helps to compare the species.

2 Samples, texture experiments

Shell specimens were provided by the University of California Museum of Paleontology, Berkeley, the Laboratoire de Biologie Animale, Le Mans and our own collections. A detailed description of the microstructural arrangements (nacre, crossed lamellar ...) can be found in Hedegaard (1990). We selected sample pairs of closely related taxa. The x-ray measurements and data corrections were detailed elsewhere (Chateigner et al., 1996). The quantitative texture analysis was done using the Berkeley Texture Package (Wenk et al. 1998). When a good reproducibility of the experimental pole figures and satisfying reliability factors were obtained, the OD was used to recalculate the {001} and {100} pole figures. Typical results for reliability are presented in a previous work (Chateigner et al. 1996). For all these experiments, the growth direction, **G**, perpendicular to the margin of the shell at the beam location is the vertical axis of our pole figures. The plane tangent to the shell at the beam location, defined by the sample holder plane, has its normal, **N**, as the normal axes of the pole figures. The third axis, **M**, direction of the growth lines is then horizontal on the pole figures. Unless specifically indicated all discussions refer to the orthorhombic mineral aragonite that composes most mollusc nacre.

3 c axis distributions

We are describing in this paragraph the orientations of the c axis component of the layers (aragonite or calcite) relative to **N**, by an angle α that makes the maximum of the distribution with **N**. A quite common feature, $c_\perp$, corresponds to α=0, like for the inner sheet nacre layer (ISN) of *Pinctada maxima* (Fig. 1a). Some species exhibit deviations from this orientation. In the inner comarginal crossed lamellar (ICCL) layer of *Nerita polita*, c axes are inclined towards **G** by α=15° (Fig. 1b).

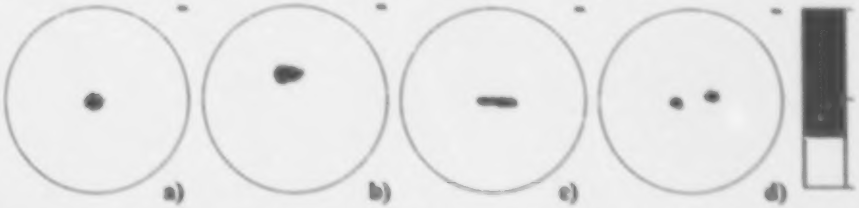
a)
b)
c)
d)

Fig. 1: recalculated {001} pole figures of *Pinctada maxima* (maximum density > 100 m.r.d.) (a), *Nerita polita* (max: 29 m.r.d.) (b), *Fragum fragum* (max: 35 m.r.d.) (c) and *Cypraea testudinaria* (max > 100 m.r.d.) (d). Linear density scale, equal area projection. Minimum densities are 0.

The ICCL layer of *Fragum fragum* shows a wide dispersion of the c axes in a plane around G, with a FWHM of α=15 (Fig. 1c). The ICCL layer of *Cypraea testudinaria* exhibits a splitting of the **c** axes into two components from N, at α=30° from each other (Fig. 1d).

4 **a** axis distribution and twinning

Many **a** axis patterns are observed. The outer comarginal crossed lamellar layer (OCCL) of *Helix pomatia* (Fig. 2a) shows a single crystal-like pattern, with **a** axes located at β=90° from G. The inner columnar nacre layer (ICN) of *Tectus niloticus* (Fig. 2b) shows a <001> fibre texture. In the case of tilted or split **c** axes, β refers to the crystalline direction located in the tangent plane (usually **a**, **b** or <110>). Between the perfect fibre and the single crystal **a** axis distributions, intermediate patterns are observed, larger distributions like in the ISN layer of *Lampsilis alatus* (not shown here) or twinning. In the context of this paper "twinning" simply means twinning-like patterns because with the methods used in this study we can not identify actual twin intergrowths. Due to the pseudosymmetry of the aragonite structure (Bragg, 1937), crystallites can share one of their (110) crystallographic planes, causing twinning. This results in domains where the **a** axes are separated by an angle close to 60°, where successive domains can rearrange in hexagonal shaped platelets like in nacre. Such hexagonal domains can then be either at random or preferably oriented to one another. On {100} pole figures, twinning in aragonite gives rise to 4 or 6 poles, 4 if one twin system ((110) or $(1\bar{1}0)$) is activated, 6 if both are, here referred to as single and double twinning, respectively. For instance, single twinning is observed in the ICCL layer of *Conus leopardus* (Fig. 2c), and double twinning in the ICN layer of *Nautilus pompilius* (Fig. 2d). We can evaluate the percentage of twinned volume from texture component intensities, V_x and V_{xx} respectively for single and double twinning, from the ratio between the {100} poles corresponding to the twinning, and all the twin components. The calculation gives V_{xx} = 61% of twinned volume for *Nautilus pompilius* (close to the maximum of 67% for this twinning type) and V_x = 46% for *Cypraea mus* (close to the maximum of 50%).

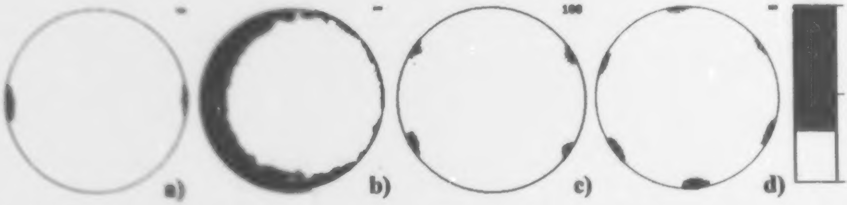

Fig. 2: recalculated {100} pole figures of *Helix pomatia* (max: 55 m.r.d.) (**a**), *Tectus niloticus* (max: 8 m.r.d.) (**b**), *Conus leopardus* (max: 49 m.r.d.) (**c**) and *Nautilus pompilius* (max: 23 m.r.d.) (**d**). Linear density scale, equal area projection. Minimum densities are 0.

In twinned patterns, β refers to the most intense component of the {100} poles or to the closest to G.

5 Textural nomenclature and discussion

A description of the microstructure (crossed lamellar, nacre) including all the important texture characteristics is necessary, particularly if several layers are present in each species. A compact description may be useful for an efficient comparison between samples. We propose, for a particular layer, L, in the shell, to specify the **c** and **a** axes dispersions, and quantify the presence of twinning and splitting. These terms may be included in $\langle c, \alpha|\mathbf{L}|P_{T}^{a,\beta}\rangle$ where L depends on the location in the shell (inner, outer, comarginal) and on its microstructure. The left hand side of the bracket describes the **c** axes pattern, ⊥ for $\mathbf{c}_{\perp}$, ∠ for one tilted component, ∨ for a split and ∀ for a dispersion. The right hand side describes the **a** axes pattern. P is ● for no texture, ⊙ stands for a fibre texture, × for a single twin, * for a double twin and | for the absence of twin. T is the percentage of twinned volume. β and α were defined previously. Using this textural description, the OCCL layer of *Helix pomatia* is described by the 'texture term' $\langle\perp|O|^{a,90}\rangle$, while the ICCL layer of *Cypraea testudinaria* and the ISN layer of *Pinctada maxima* are $\langle\vee,15|\mathrm{ICCL}|^{a}\rangle$ and $\langle\perp|\mathrm{ISN}|*_{14}^{a,90}\rangle$ respectively. Fig. 3 is a proposal for a phylogenetic tree, that includes texture results. For this work we mainly focus our discussion on the nacre inner layers and on the variation of the texture strength through the thickness, for some shells. First of all, we observe many significant deviations from the usually assumed growth relationships, with <100> and <001> respectively aligned with **G** and **N**. The **a** axes are often found at 90° from **G**, for instance in the *HELIX* or *EUGLANDINA* species. Inclined, tilt and dispersed **c** axes are observed in both bivalves and gastropods, but not in Nautiloidea, nor in Monoplacophora, though theses two latter families are only represented by four analysed species. The gastropods family exhibits the largest variability of texture patterns, from fibres to single-crystal like orientations. The inner nacre layers only show $\mathbf{c}_{\perp}$ axes except for *Haliotis cracherodi*. In bivalves, the *Neotrigonia*, *Pteria* and *Pinctada* analysed species have ISN layers with $\mathbf{c}_{\perp}$ axes and around 10% of double twinning, while other analysed branches exhibit more varied texture patterns and larger twinning ratios. For ICCL layers, 50% of single twinning occurs (except for *Paphia solanderi*) with split **c**-axes, and <110> are aligned with **G**. In gastropods, the ICN layers are <001> fibre textures, as for monoplacophoras, while ICCL or ICoCL (complex crossed lamellar) layers exhibit variable **c** and **a** axes patterns. Looking at texture variations with thickness from the interior towards the outside of the shell, we find that the outsides are generally less organised than the internal layers. For instance in the gastropod *Conus leopardus*, the ICCL layer is single twinned (with a texture index of 201 m.r.d.^{2} and an entropy S=-5.16), while the outer radial crossed lamellar (ORCL) layer is a fibre (F^2=29 m.r.d.^{2} and S=-2.65). This is also true for the bivalve *Paphia solanderi* for which both the ICCL and outer simple prismatic (OSiP) layers are fibre textures (ICCL: F^2=177 m.r.d.^{2} and S=-5.06; OSiP: F^2=44 m.r.d.^{2} and S=-3.28). Consequently it appears that fibre textures are mainly located on the outside of the shells. This feature appears to be independent of the crystalline phase, e.g. for *Viana regina*. In this species, a progressive loss of the fibre texture strength is observed, from the ICCL layer (S=-3.22), to the OCCL (S=-1.78), to the outside homogeneous calcitic (OHC) layer (S=-0.55).

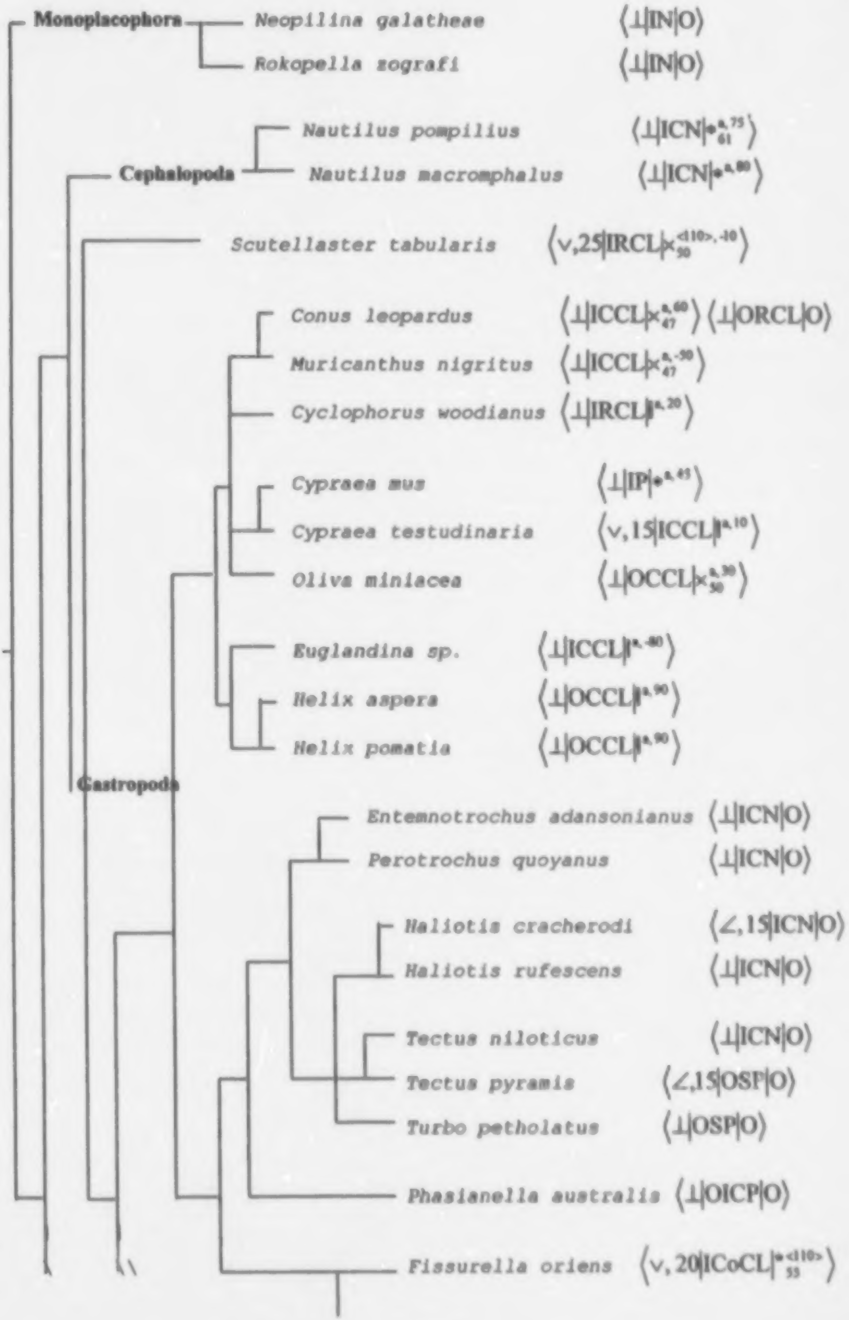
Monoplacophora
Neopilina galatheae $\langle \perp | IN | O \rangle$
Rokopella zografi $\langle \perp | IN | O \rangle$
Cephalopoda
Nautilus pompilius $\langle \perp | ICN | \bullet^{a,75}_{61} \rangle$
Nautilus macromphalus $\langle \perp | ICN | \bullet^{a,80} \rangle$
Scutellaster tabularis $\langle \vee,25 | IRCL | \times^{<110>,-10}_{90} \rangle$
Conus leopardus $\langle \perp | ICCL | \times^{a,60}_{47} \rangle$ $\langle \perp | ORCL | O \rangle$
Muricanthus nigritus $\langle \perp | ICCL | \times^{a,-50}_{47} \rangle$
Cyclophorus woodianus $\langle \perp | IRCL | \|^{a,20} \rangle$
Cypraea mus $\langle \perp | IP | \bullet^{a,45} \rangle$
Cypraea testudinaria $\langle \vee,15 | ICCL | \|^{a,10} \rangle$
Oliva miniacea $\langle \perp | OCCL | \times^{a,30}_{50} \rangle$
Euglandina sp. $\langle \perp | ICCL | \|^{a,-80} \rangle$
Helix aspera $\langle \perp | OCCL | \|^{a,90} \rangle$
Helix pomatia $\langle \perp | OCCL | \|^{a,90} \rangle$
Gastropoda
Entemnotrochus adansonianus $\langle \perp | ICN | O \rangle$
Perotrochus quoyanus $\langle \perp | ICN | O \rangle$
Haliotis cracherodi $\langle \angle,15 | ICN | O \rangle$
Haliotis rufescens $\langle \perp | ICN | O \rangle$
Tectus niloticus $\langle \perp | ICN | O \rangle$
Tectus pyramis $\langle \angle,15 | OSP | O \rangle$
Turbo petholatus $\langle \perp | OSP | O \rangle$
Phasianella australis $\langle \perp | OICP | O \rangle$
Fissurella oriens $\langle \vee,20 | ICoCL | \bullet^{<110>}_{55} \rangle$
]

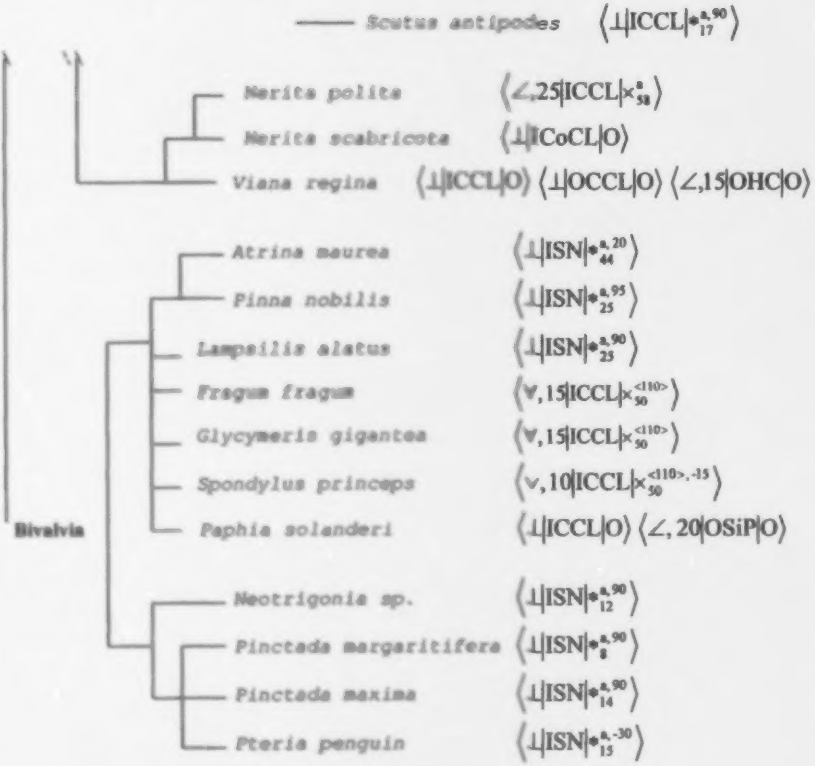
Scutus antipodes $\langle \perp | \mathrm{ICCL} | \bullet_{17}^{a,90} \rangle$
Nerita polita $\langle \angle,25 | \mathrm{ICCL} | \times_{58}^{a} \rangle$
Nerita scabricota $\langle \perp | \mathrm{ICoCL} | \mathrm{O} \rangle$
Viana regina $\langle \perp | \mathrm{ICCL} | \mathrm{O} \rangle \langle \perp | \mathrm{OCCL} | \mathrm{O} \rangle \langle \angle,15 | \mathrm{OHC} | \mathrm{O} \rangle$
Atrina maurea $\langle \perp | \mathrm{ISN} | \bullet_{44}^{a,20} \rangle$
Pinna nobilis $\langle \perp | \mathrm{ISN} | \bullet_{25}^{a,95} \rangle$
Lampsilis alatus $\langle \perp | \mathrm{ISN} | \bullet_{23}^{a,90} \rangle$
Fragum fragum $\langle \vee,15 | \mathrm{ICCL} | \times_{50}^{<110>} \rangle$
Glycymeris gigantea $\langle \vee,15 | \mathrm{ICCL} | \times_{50}^{<110>} \rangle$
Spondylus princeps $\langle \vee,10 | \mathrm{ICCL} | \times_{50}^{<110>,-15} \rangle$
Paphia solanderi $\langle \perp | \mathrm{ICCL} | \mathrm{O} \rangle \langle \angle,20 | \mathrm{OSiP} | \mathrm{O} \rangle$
Bivalvia
Neotrigonia sp. $\langle \perp | \mathrm{ISN} | \bullet_{12}^{a,90} \rangle$
Pinctada margaritifera $\langle \perp | \mathrm{ISN} | \bullet_{8}^{a,90} \rangle$
Pinctada maxima $\langle \perp | \mathrm{ISN} | \bullet_{14}^{a,90} \rangle$
Pteria penguin $\langle \perp | \mathrm{ISN} | \bullet_{15}^{a,-30} \rangle$

Fig. 3: Proposal for a phylogenetic tree, including textural patterns

These preliminary observations suggest that textural features are related to mollusc phylogeny. Pattern variations between branches are consistent are consistent with the actual mollusc phylogeny. Also, the loss of textural order or strength through the thickness of the shells is characterised by the texture entropy.

6 References

Bragg, W.-L. (1937). *Atomic Structures of Minerals*, Cornell Univ. Press, pp 114-126.

Chateigner, D., Hedegaard, C. and Wenk, H.-R. (1996). In Z. Liang, L. Zuo & Y. Chu *Textures of Materials*, vol. 2, pp 1221-1226.

Hedegaard, C. (1990). Thesis, University of Aarhus, Denmark, vol. 1 & 2.

Hedegaard, C. and Wenk, H.R. (1998). *J. Molluscan Studies*, 64, pp 133-136.

Lopez, E. & Vidal, B., Berland, S., Camprasse, S., Camprasse, G. and Silve, C. (1992), *Tissue & Cell*, 24(5), pp 667-679.

Urist M.-R. (1965), *Science*, 150, pp 893.

Wenk, H.-R., Matthies, S., Donovan, J. and Chateigner, D. (1998). *J. Appl. Cryst*. 31, pp 262-269.

MICROSTRUCTURE AND MECHANICAL PROPERTIES OF TEXTURED ALUMINA*

D. KOVAR and P.W. HALL
Texas Materials Institute and Department of Mechanical Engineering
University of Texas at Austin, Austin, TX, USA

Abstract

A method for producing a crystallographically and morphologically textured alumina has been devised using an inexpensive, solvent-based tapecasting route. A small percentage of anisometric alumina seed particles and a sintering aid are added to a conventional slurry containing solvents, a polymeric binder, and a fine α-alumina powder. The slurry is tapecast using an extended doctor blade to align the seed platelets within the tapes. After drying, the tapes are cut, stacked and compression molded to form solid billets and then the binder is removed by pyrolysis. During sintering, a grain boundary liquid phase forms that facilitates densification and results in the preferential growth of the seed platelets in directions parallel to the basal plane. X-ray measurements indicate that the sintered alumina exhibits a strong (006) fiber texture and micrographs show that the grain morphology is also elongated in the plane of tapecasting. Experiments using Vickers indentations to simulate contact damage show that resistance to cracking is significantly greater in a direction perpendicular to the plane of alignment compared to parallel to the plane of alignment.

Keywords: alumina, microstructure, texture, fracture toughness, contact damage.

1 Introduction

Because of its combination of extreme hardness, high electrical resistivity, stiffness, and strength, and low density, alumina is used as an insulator in electromagnetic railguns.(Rosenwasser 1991) In this application, the material must

---

* *This work was supported by the United States Army Research Laboratory under contract DAAA21-93-C0101.*

withstand high stresses from bending, internal pressure, and most significantly, contact stresses that arise when the projectile/sabot impacts the bore of the gun where the insulators reside. Since cracking of the insulators degrades the stiffness and resulting accuracy of the gun, designing alumina insulators with microstructures that are resistant to contact damage would significantly improve the reliability of these railguns.

Cracking that occurs in brittle ceramics as a result of contact damage is strongly dependent on the fracture toughness of the ceramic with the extent of damage decreasing as the fracture toughness is increased.(Lawn 1983) In recent years it has been shown that the fracture toughness of ceramics such as alumina can be increased by a factor of three or more by coarsening the grains, elongating the grain morphology, introducing weak grain boundary phases to promote intergranular fracture, (Bennison and Lawn 1989) and by texturing. (Lee et al. 1993; Ohji et al. 1995) These microstructures result in a highly tortuous crack path with interlocking or "bridging" grains in the crack wake. Bridging grains resist opening of the crack thereby increasing the apparent fracture toughness of the material.

Textured alumina has been produced using a number of techniques. (Ma and Bowman 1991; Carisey et al. 1995; Seabaugh et al. 1997) The existing techniques, however, either produce only modestly textured aluminas with relatively equiaxed grain morphologies, or they are not suitable for producing larger components needed for structural applications. The goal of this work is to develop a method for producing morphologically and crystallographically textured alumina for structural components and to determine whether such a microstructure is resistant to contact damage.

2 Experimental Procedure

2.1 Processing of Textured Alumina

A slurry was formed by mixing a fine alumina powder (99.995%, average particle size = 0.3 µm), and a small amount of $CaCO_3$ and SiO_2[**] with a dispersant and a blend of solvents. The slurry was ball-milled using alumina milling media for 24 hours to break agglomerates and to thoroughly mix the constituents. Anisometric alumina platelets (10-15 µm diameter by 0.5 µm thickness) were then added and the slurry was mixed for an additional 10 minutes before adding a polymeric binder and plasticizer. After mixing for an additional 24 hours, the slurries were cast onto a glass plate using a customized extended doctor blade with a gap height of 400 µm. To improve alignment of the alumina platelets within the tape during casting, the doctor blade was lengthened to 40 mm to ensure a long region of laminar flow under the blade. The shear thinning behavior of the slurry combined with rapid evaporation of

---

[**] *At the sintering temperature, 5 wt% of the material was CaO + SiO_2 sintering aid.*

the solvents ensured that the seed platelets remained aligned within the tapes during drying.

After drying, the tapes were cut, stripped from the glass, and stacked within a die. The die was heated to 130°C and the tapes were compression molded at a pressure of 30.6 MPa to form a solid billet. The polymer was removed by pyrolysis during slow heating to 600°C in flowing air. The billet was then densified by pressureless sintering in air at 1600°C for 10 hours. A nominally untextured alumina was also produced as a control material using the identical protocol used to produce the textured alumina except that alumina seed platelets were not added to the slurry and a conventional doctor blade with a length of 0.5 mm was used to cast the tapes.

2.2 Microstructural Characterization

To examine the microstructures, the samples were ground and then polished to a mirror finish using successively finer diamond suspensions. Grain boundaries were revealed by a combination of chemical (24% HF, 10 hours) and thermal etching (1500°C, 10 min) which effectively removed the grain boundary phase leaving only the Al_2O_3 grains. The microstructures were examined using optical and scanning electron microscopy. Standard (006) pole figures and fiber texture plots were performed on the surface of samples ground to a depth of at least 200 μm.

2.3 Characterization of Mechanical Properties

The response of each of the materials to contact damage was assessed using a Vickers diamond indenter at loads ranging from 50 N to 500 N. Three sets of data were obtained; 1) unseeded alumina–tensile surface parallel to the tape orientation, 2) seeded alumina–tensile surface parallel to the tape orientation, 3) seeded alumina–tensile surface perpendicular to the tape orientation.

3 Results

3.1 Microstructure

Density measurements indicate that both the seeded and unseeded aluminas have similar densities of at least 97% of the theoretical density. Optical micrographs of etched sections through the seeded and unseeded aluminas are shown in Figure 1a-b. The grain shape in both materials is tabular with an aspect ratio of 3-5 and a grain length of 10-30 μm. More significantly, in the seeded material, the grains are elongated parallel to the casting plane whereas the direction of elongation appears to be randomly distributed in the unseeded material.

Pole figures and fiber texture plots are shown in Figure 2a-b confirming that the seeded alumina exhibits a strong (006) fiber texture whereas the unseeded alumina does not exhibit significant preferred orientation. Compared to aluminas textured using deformation techniques (Ma and Bowman 1991), the magnitude of the preferred

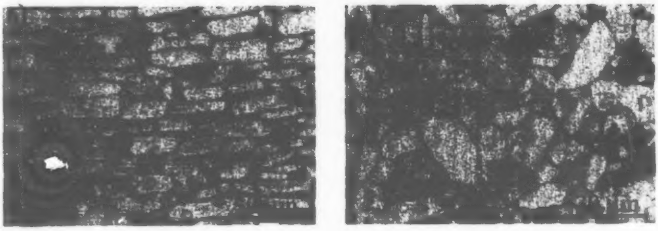

Fig. 1: Optical micrographs of polished and etched surfaces of (a) seeded alumina and b) unseeded alumina.

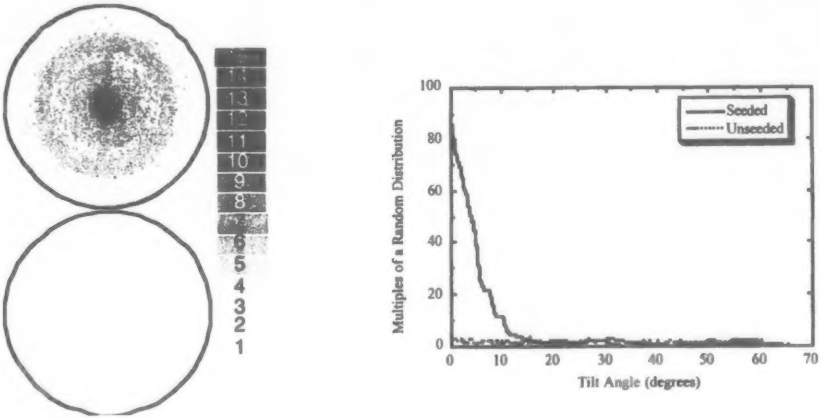

a) b)

Fig. 2: a) 006 pole figures for seeded (top) and unseeded (bottom) aluminas. b) fiber texture plot for seeded and unseeded aluminas ($\beta = 0$).

orientation in the seeded alumina is much greater. For example, a texture maximum of between 5 and 12 times random was measured in alumina textured by hot forging whereas the seeded alumina exhibits a texture maximum of more than 80 times random.

3.2 Mechanical Behavior

A summary of the strength and indentation measurements for the seeded and unseeded aluminas are shown in Table I. Although the strengths of the seeded aluminas are slightly higher than the unseeded alumina, the differences are not statistically significant given the standard deviation. The variability in strength of all of the aluminas is, however, much larger than commonly observed in commercial aluminas. (Chantikul et al. 1990)

Table I: Strength and Crack Length Measurements

Material and Orientation	Strength (MPa)	Crack Length from 500 N Indentation (μm)
Unseeded	264 ± 33	483
Seeded–Parallel	290 ± 70	479
Seeded–Perpendicular	300 ± 52	708

All of the cracks emanating from the indentations in the unseeded alumina are similar in length indicating that there is little or no fracture toughness anisotropy in this material. In contrast, the crack lengths in the seeded alumina are significantly shorter in the direction perpendicular to the alignment of the grains than in a direction parallel to the plane of alignment. The crack lengths in the seeded alumina in the direction perpendicular to the plane of alignment are similar to cracks in the unseeded alumina.

4 Discussion

4.1 Microstructure

Microstructural evolution was found to be strongly influenced by the platelets and the sintering aids that were introduced during processing. During heating, the $CaCO_3$ decomposed to CaO and subsequently reacted with the SiO_2 and some of the Al_2O_3 to form a liquid between the alumina particles. The presence of CaO-SiO_2-Al_2O_3 is known to result in faceting of alumina grains along the basal plane and also leads to anisotropy in the grain boundary mobility; (Simpson and Carter 1990) grain growth rates parallel to the basal plane are substantially faster than perpendicular to basal plane. In addition, because the aligned seed platelets are much larger than the surrounding matrix alumina, there is a thermodynamic driving force for the seed platelets to grow at the expense of the matrix alumina. The aligned seed platelets therefore facet and grow until they impinge on another growing seed platelet of similar size. Upon cooling from the sintering temperature, the liquid solidifies into an amorphous grain boundary phase occupying approximately 17 vol% of the material. In addition to being essential to the development of the observed texture in the seeded alumina, the amorphous phase is also beneficial for grain bridging in that it weakens the grain boundary.

4.2 Mechanical Behavior

Crack length measurements from Vickers indentations indicated that the fracture toughness of the seeded, textured alumina is highly anisotropic. As expected, the fracture toughness parallel to the plane of alignment is reduced compared to an untextured alumina. However, significant increases in fracture toughness for the seeded alumina were not observed perpendicular to the plane of alignment compared to an untextured alumina. Observations of the crack path indicated that cracking was primarily transgranular in this orientation and therefore improved grain bridging did not result. This suggests that improvements in fracture toughness of textured alumina could be achieved by weakening the grain boundaries further or by reducing the grain length so that intergranular cracking would be favored. Observations of the fracture surfaces also revealed the occasional presence of large (≈200 μm) bubbles originating in the glassy boundaries. The presence of these bubbles not only degraded strength but also increased strength variability. Future work will be aimed at reducing the grain length to improve fracture resistance and eliminating bubbles by reducing the fraction of glass in these materials.

5 Conclusions

A method for manufacturing alumina with a strong (006) wire texture was successfully developed using tapecasting with an extended doctor blade. This method uses seed platelets and a $CaO\text{-}SiO_2$ sintering additive to achieve preferred orientation during pressureless sintering. Compared to other methods for producing textured alumina, this technique results in a stronger crystallographic as well as morphological texture. Indentation experiments confirmed that the cracking resistance in the textured alumina is highly anisotropic.

6 References

Bennison, S. J. and B. R. Lawn (1989) *Acta. Metall.*, Vol. 37, No. 10. pp. 2659-2671.

Carisey, T., A. Laugier-Werth and D. G. Brandon (1995) *J. Eur. Ceram. Soc.*, Vol. 15, No. 1. pp. 1-8.

Chantikul, P., S. J. Bennison and B. R. Lawn (1990) *J. Am. Ceram. Soc.*, Vol. 73, No. 8. pp. 2419-2427.

Lawn, B. R. (1983) in *Surface Flaws, Statistics, and Microcracking*, (ed. R. C. Bradt, et al.), Plenum Press, New York, NY, pp. 1-25.

Lee, F., M. S. Sandin and K. J. Bowman (1993) *J. Am. Ceram. Soc.*, Vol. 76, No. 7. pp. 1793-1800.

Ma, Y. and K. J. Bowman (1991) *J. Am. Ceram. Soc.*, Vol. 74, No. 11. pp. 2941-2944.

Ohji, T., K. Hirao and S. Kanzaki (1995) *J. Am. Ceram. Soc.*, Vol. 78, No. 11. pp. 3125-3128.

Rosenwasser, S. N. (1991) *IEEE Transaction on Magnetics*, Vol. 27, No. 1. pp. 444-451.

Seabaugh, M. M., I. H. Kerscht and G. L. Messing (1997) *J. Am. Ceram. Soc.*, Vol. 80, No. 5. pp. 1181-1188.

Simpson, Y. K. and C. B. Carter (1990) *J. Am. Ceram. Soc.*, Vol. 73, No. 8. pp. 2391-2398.

PREDICTING MICROSTRUCTURAL-LEVEL RESIDUAL STRESSES AND CRACK PATHS IN CERAMICS

V.R. VEDULA, S.J. GLASS
Sandia National Laboratories, Albuquerque, NM 87185, USA
D.M. SAYLOR, G.S. ROHRER
Carnegie Mellon University, Pittsburgh, PA 15213, USA
W.C. CARTER
Massachusetts Institute of Technology, Cambridge, MA 02139, USA

Abstract

Microstructural-level residual stresses arise in ceramics due to thermal expansion anisotropy. These stresses are high enough to cause spontaneous microcracking during the processing of these materials. The orientation data obtained by backscattered electron diffraction and grain boundary energies obtained by AFM were used in conjunction with an object oriented finite element analysis package (OOF) to predict the magnitude of residual stresses in alumina. Crack initiation and propagation were also simulated based on the Griffith fracture criterion.

Keywords: Ceramics, crack paths, object oriented finite element analysis, residual stresses

1 Introduction

Residual stresses arise in ceramics during processing as a result of thermal expansion anisotropy and crystallographic misorientation across the grain boundaries. In brittle materials, the thermal strains that result during cooling from the sintering temperature can be comparable to the fracture strain of the material leading to internal cracking known as "spontaneous microcracking". Residual stresses are also critical to the R-curve behavior that occurs in ceramics.

Cubic crystals possess isotropic thermal expansion ($\alpha_{11}=\alpha_{22}=\alpha_{33}$) in that spherical regions remain spherical after a temperature change, whereas in non-cubic systems, a sphere becomes an ellipsoid. Therefore, when a polycrystalline material with non-cubic crystal symmetry is subject to a temperature change, each grain will attempt to strain differently than its neighbors, resulting in residual stresses and strains in the material. The onset of microcracking depends on the grain (crystal) size and below a critical value, no spontaneous microcracking occurs. The stresses generated in a material do not depend on the grain size, however, the strain energy does. Assuming that enough stress and potential microcrack formation sites are available, it has been shown that the formation of microcracks in ceramics is governed by the energy criterion (Kuszyk and Bradt 1973).

This paper presents a novel methodology to predict residual stresses in materials using experimentally determined crystallographic orientations and grain boundary energies. Crystallographic orientations and relative grain boundary energies were obtained using electron backscattered patterns (EBSP) and atomic force microscopy (AFM) respectively. The critical temperature for microcrack formation in alumina was calculated as a function of grain size.

2 Experimental Details

The orientations of individual grains on the surface of a polycrystalline alumina (99.99%) sample were obtained using electron backscattered diffraction (EBSD) (OIM, TSL, Inc.). The final polishing step used colloidal silica and then the samples were thermally grooved at 1550°C for 100 hours. The width and depth of the thermal grooves formed by the grain boundaries were measured by atomic force microscopy (AFM) to determine the ratio of the grain boundary free energy to the surface free energy. The details of the measurements and the orientation and grain boundary energy data are presented in an accompanying paper (Glass et al. 1999). The orientations and grain boundary energies were used to predict the residual stresses in alumina using object oriented finite element analysis (OOF).

3 Finite Element Analysis

OOF is an object oriented finite element analysis software program developed at NIST (OOF 1999). It is designed to investigate the response of microstructures to mechanical and thermal loads. The program performs thermoelastic calculations in two dimensions (plane strain or plane stress) using 3-node triangular elements. A digital image of a microstructure, either from an optical/electron microscope or a result of a computer simulation can be used for analysis. The user specifies crystallographic orientations, elastic, and thermal properties for the various regions (grains) in the microstructure. Based on this information, a finite element grid with associated properties is generated on which mechanical and/or thermal loading can be applied. A solution is then obtained for the specified boundary conditions, distortion, and temperature change.

The elements are designed to fail under the Griffith criterion, which states that a crack will propagate when the total surface energy required to propagate the crack can be supplied by the elastic energy stored in the body;

$$2l\gamma < \tfrac{1}{2}\int \sigma\varepsilon dV \qquad (1)$$

where l is the crack length and γ is the surface energy of the cracked interface. The element size is used to specify the characteristic crack length and the volume of integration is the element area (per unit depth).

The analysis involves the following steps:

(a) Thermal and mechanical loads are applied and the microstructure is equilibrated to determine stress/strain distribution.

(b) The energy balance is computed.

(c) If an element reaches the critical energy density (i.e., favorable for cracking), the direction of the maximum principle stress is found. Assuming that the crack plane is perpendicular to the maximum principal stress, C_{11} is set to 0 and all other components of the stiffness matrix C_{ij} are multiplied by a factor of 0.5 (arbitrarily chosen). The elements thus reduce their moduli anisotropically to simulate a crack.

(d) The microstructure is re-equilibrated and the stress distribution is re-calculated.

(e) The procedure is repeated until no more elements mutate or one or more cracks become unstable causing fracture into two or more fragments.

4 Results and Discussion

The orientations of grains, surface energies of grains and grain boundaries, elastic, and thermal properties were input into OOF to predict the residual stresses. The orientations obtained by EBSD were input as a set of Euler angles (α, β, γ). The elastic stiffness and coefficients of thermal expansion for α-alumina (hexagonal crystal symmetry) used in the analysis were; C_{11}=466 GPa, C_{12}=127 GPa, C_{13}=117 GPa, C_{33}=506 GPa, C_{44}=235 GPa, $\alpha_{11}=8.6\text{x}10^{-6}$ /°C, and $\alpha_{33}=9.3\text{x}10^{-6}$ /°C. The energy required for crack propagation through a grain is $2\gamma_s$ and through a grain boundary (intergranular) is $2\gamma_{ig}=(2\gamma_s - \gamma_{gb})$, where γ_s is the surface energy of grains and γ_{gb} is the grain boundary energy. γ_{gb}/γ_s values were obtained from AFM groove measurements. The surface energy of grains (γ_s) was taken as 2 J/m^2 and that of individual boundaries were calculated using $\gamma_{ig}=(4 - \gamma_{gb})/2$. γ_{ig} varied between 0.59 and 1.17 J/m^2. The grain boundary elements were assigned the elastic properties of glass (isotropic crystal symmetry), E=70 GPa and ν=0.23. The elements in the model representing grains were assigned a surface energy of 2 J/m^2 and the boundary elements were assigned their respective γ_{ig} values. The surface energy anisotropy in alumina has been reported at approx. 12% (Choi et al. 1997). However, in the present analysis the surface energy of alumina is assumed isotropic. The number of elements was 25600. The calculations were performed under plane stress and free boundary conditions.

The properties of the grain boundary glass phase are expected to influence the stress distribution and critical temperature for microcracking. Two different glass compositions were considered for grain boundary phase, namely, a high CaO and a high MgO glass. A high CaO glass has $\alpha \approx 9.5\text{x}10^{-6}$ /°C, which results in tensile residual stresses at grain boundaries, whereas for a high MgO glass ($\alpha \approx 5\text{x}10^{-6}$ /°C), compressive stresses result at the grain boundaries (Powell-Dogan and Heuer 1990). These compositions and associated properties were chosen as they represent the bounds on the type of grain boundary glass phase typically found in alumina.

The alumina microstructure shown in Fig. 1(a) is used for analysis. The maximum principal stress σ_{11} for a temperature difference of -1160°C for high CaO grain boundary glass phase is shown in Fig. 1(b). The maximum and minimum stress regions (+369 and –128 MPa) are marked * and # respectively. As can be seen, very high stresses develop at the grain boundaries due to crystallographic misorientations in conjunction with thermal expansion anisotropy in alumina. The stresses were found to drop drastically away from the boundaries. The maximum stress is comparable to typical fracture strengths of this material. The calculations assume no stress relaxation. Internal stresses in alumina (> 10 μm grain size) have been estimated at 200-300 MPa from piezospectroscopic measurements (Ma and Clark 1994).

The effect of grain size on the critical temperature for microcracking in alumina was determined using the same microstructure by varying the width of the image, i.e, different length scales were used to represent different grain sizes. The expected inverse square root grain size relationship was found (Case et al. 1980), as shown in Fig. 2. The critical grain size for microcracking for an alumina sample cooled from a 1600°C sintering temperature with high CaO glass grain boundary phase was 179 μm and with high MgO phase was 71 μm. Experimentally, grain size values have been reported between 40-400 μm. It should be noted that plane stress conditions underestimate the residual stress values, hence in reality, the critical grain size values are expected to be lower.

Microcrack propagation was simulated using the procedure described above with increasing temperature difference. Fig. 1(c) shows initiation of microcracks at the triple junctions when ΔT=-1500°C. It has been shown numerically that the largest stress intensification occurs at the triple junctions (Evans 1978). With increasing temperature difference (thermal strain), microcracks initiated at new sites and coalescence of microcracks was also observed to form large cracks. At ΔT=-2000°C, out of 1212 grain boundary elements, 266 were cracked, shown in Fig. 1(d). As can be seen, damage occurred at several regions and some of the boundaries were completely cracked. It has been shown that the inverse square root relationship seen here for microcrack initiation holds for damage evolution with increasing misfit strain and it can be described by a three parameter Weibull distribution (Zimmerman et. al. 1999).

5. Conclusions

In brittle materials such as ceramics, cooling from the sintering temperature often creates sufficiently high stresses to cause internal microcracking. The magnitude of these stresses was predicted using an object oriented finite element analysis and experimentally determined orientations and grain boundary energies. In order to determine if there is a direct correlation between the boundaries that were cracked in OOF and misorientation across the boundaries, a large number of such calculations need to be performed and data compared with experimental observations of cracks. It is important to note that besides stresses, other factors that determine the onset of microcracking include the size and location of existing flaws as these can act as nucleation sites for microcracks.

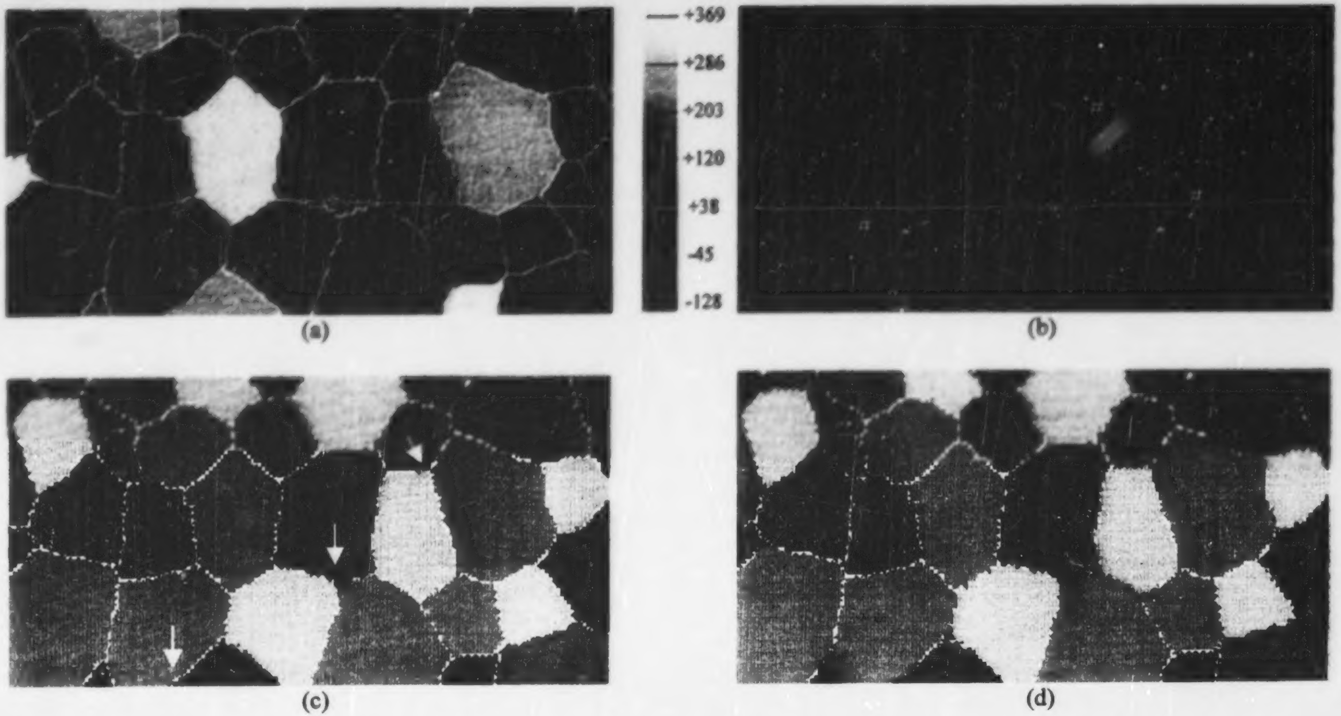

Fig.1: (a) Digital image of alumina (grain size=27μm) (b) Maximum principal stress (σ_{11}) when ΔT=-1160°C, from 369 MPa to–128 MPa (c) crack initiations at ΔT=-1500, shown by black elements along the grain boundaries (d) Damage evolution and distribution at ΔT=-2000°C.

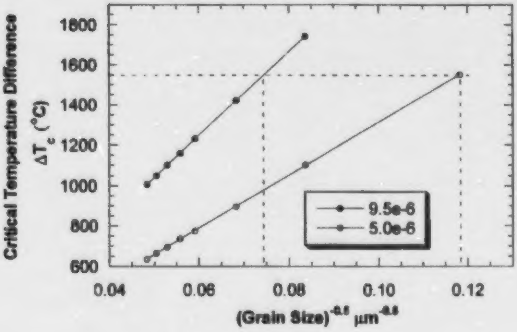

Fig. 2: Critical temperature difference vs. grain size in alumina for two different grain boundary properties (α=9.5x10^{-6} and 5x10^{-6} °/C).

References

Case, E.D., Smyth, J.R., and Hunter, O. (1980) Grain-size dependence of microcrack initiation in brittle materials, *Journal of Materials Science*, Vol. 15, pp. 149-53.

Choi, J.-H., Kim, D.-Y., Hockey, B.J., Wiederhorn, S.M., Handwerker, C.A., Blendell, J.E., Carter, W.C., and Roosen, A.R. (1997) Equilibrium shape of internal cavities in sapphire, *Journal of the American Ceramic Society*, Vol. 80, No. 1, pp. 62-8.

Evans, A.G. (1978) Microfracture from thermal expansion anisotropy – I. Single phase systems, *Acta Metallurgica*, Vol. 26, pp. 1845-53.

Glass, S.J., Vedula, V.R., Saylor, D.M., and Rohrer, G.S. (1999) Application of electron backscattered diffraction (EBSD) and atomic force microscopy (AFM) to determine texture, microtexture, and grain boundary energies in ceramics, *ICOTOM-12*, 1999.

Kuszyk, J.A. and Bradt, R. (1973) Influence of grain size on effects of thermal expansion anisotropy in $MgTi_2O_5$, *Journal of the American Ceramic Society*, Vol. 56, No. 8, pp. 420-3.

Ma, Q. and Clarke, D.R. (1994) Piezospectroscopic determination of residual stresses in polycrystalline alumina, *Journal of the American Ceramic Society*, Vol. 77, No. 2, pp. 298-302.

OOF version 1.0.7 (1999) Center for Theoretical and Computational Materials Science (CTCMS), *National Institute of Standards and Technology (NIST)*, Gaithersburg, MD.

Powell-Dogan, C.A. and Heuer, A.H. (1990) Microstructure of 96% alumina ceramics: III, Crystallization of high-calcia boundary glasses, *Journal of the American Ceramic Society*, Vol. 73, No. 12, pp. 3684-91.

Zimmerman, A., Carter, W.C., and Fuller, E.R. (1999) Damage evolution during microcrack formation in brittle solids, Submitted to *Acta Materialia*.

Sandia is a multiprogram laboratory operated by Sandia Corporation, a Lockheed Martin Company, for the United States Department of Energy under Contract DE-AC04-94AL85000. This work was supported in part by the MRSEC Program of the National Science Foundation under Award Number DMR-9632556.

Texture in Geological Research

SIGNIFICANCE OF DOMAINAL CRYSTALLOGRAPHIC FABRICS IN NATURALLY DEFORMED ROCKS

J. HIPPERTT
Departamento de Geologia, Universidade Federal de Ouro Preto
Ouro Preto, MG, Brazil
(Current address: Department of Earth and Planetary Systems Science, Hiroshima University, Higashi-Hiroshima, Japan)

Abstract

The presence of domainal crystallographic fabrics is a common feature in naturally deformed rocks. In the ductile field and at low degrees of finite strain, the first control on the development of domainal fabrics is exerted by the orientation of the host grain *(host control).* With progressive strain, the host control lose importance to the increasing *kinematic control* which progressively lead the deformed/recrystallized grain aggregate to an easy slip orientation. At low metamorphic grade conditions, heterogeneous fluid circulation may also exert an important role on the formation of domainal crystallographic fabrics in tectonites, with development of a *c*-axis *X*-maximum in domains where solution-reprecipitation creep was a dominant process. Alternatively, domainal crystallographic fabrics can also be resulted from fold transposition. In folded quartz layers, because the rate of regeneration of crystallographic fabrics is slower than the regeneration of grain shape fabrics, an alternating domainal fabric may be produced as result of inversion and subsequent transposition of microfolds. Domainal texture analysis is, therefore, an useful tool to evaluate the microstructural processes and controls operating on development of the evolving strain/deformation partitioning in naturally deformed rocks.

Keywords: Domainal fabrics, microstructure, deformation partitioning

1 Introduction

The presence of domainal crystallographic fabrics is a common feature in many deformed rocks which reflects well the heterogeneous deformation at a microscale and can be resulted from many different microstructural controls and deformation processes. The study of these domainal fabrics is, therefore, an useful tool to investigate the operative mechanisms and physical controls responsible for the microscale deformation partitioning observed in most tectonites. Previous research in this field (e.g. Fueten *et al.* 1991, Pauli *et al.* 1996) has described and interpreted some domainal crystallographic fabrics that are related to kinematic contexts with significant coaxial deformation components, where the fabric variations have been generally related to different orientations of precursor grains. As a complement to this previous investigations, I briefly describe and discuss in this paper other three types of domainal quartz *c*-axis fabrics which were produced during predominant simple shear deformation, as observed in quartz-bearing tectonites deformed in low metamorphic grade shear zones from southeastern Brazil and northwestern Argentina.

2 Description

2.1 Type 1

The coarse grained Bonfim granite was deformed in the presence of an aqueous fluid phase in the greenschist facies Moeda-Bonfim shear zone of Quadrilátero Ferrífero (southeastern Brazil). The products of deformation are mainly muscovite-rich mylonites and phyllonites derived from feldspar breakdown via mica-producing softening reactions. Quartz has deformed by crystal-plastic processes. Previous work (Hippertt 1998) has recognized overall single girdle and asymmetric cross-girdle quartz *c*-axis fabrics (Fig. 1a) where basal<*a*> and prism<*a*> were interpreted as the main operative slip systems, and rhomb glides had a secondary importance. In low to moderate strain domains of this shear zone, quartz ribbons are formed which contain partially deformed/recrystallized quartz porphyroclasts with core-and-mantle microstructures whose characteristics are clearly dependent on the original crystal orientation of the host grain. These core-and-mantle structures show a transition to the adjacent, intensely recrystallized domains which generally present contrasting *c*-axis fabrics, hence defining domainal fabrics which are restricted to the porphyroclast vicinity.

Figure 1(b,c) show cases where the porphyroclast is in an orientation for easy single slip either or basal<*a*> or prism<*a*> glides. Because of their favourable orientation, these porphyroclasts were preferentially transformed into polygonal aggregates and only relatively

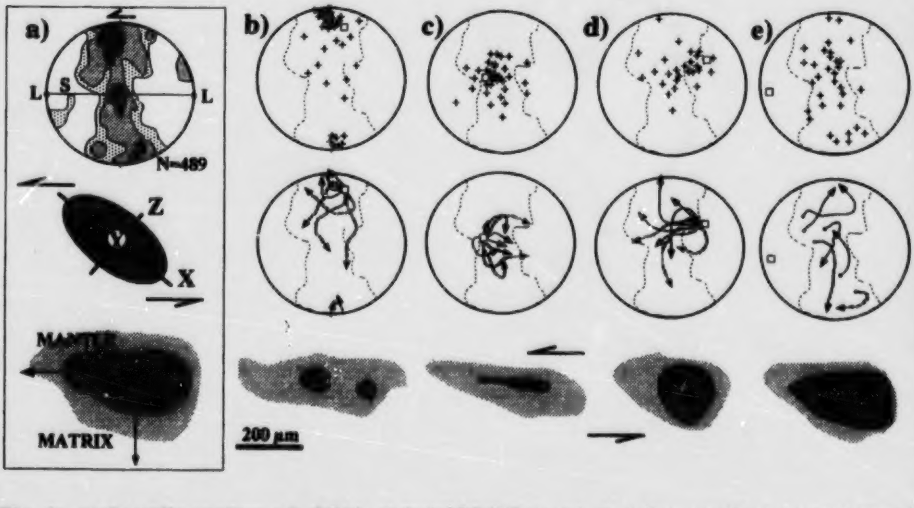

Fig. 1: a) Overall quartz *c*-axis fabric (c.I. 1.25%/1% area). b-e) New grains orientation and *c*-axis trajectory (arrows) across the recrystallized mantle around quartz porphyroclasts (squares) of different orientations. Geometries of the mantled porphyroclasts are also shown.

small relics (50-100 μm) can be found. These relics, which show well-developed deformation bands and subgrains, are surrounded by a relatively thick mantle of recrystallized grains with the same size range (35-70μm) as the adjacent subgrains, where the crystal orientation of the original grain was only smoothly changed into the orientation of the matrix aggregate. A somewhat similar situation is produced around porphyroclasts oriented for easy slip on rhomb glides (Fig. 1d). In this case, the surrounding new grains are progressively changed into the the orientation of overall fabric maxima. In contrast, porphyroclasts that were in relatively "hard" orientations of low resolved shear stress (RSS) on all basal <*a*>, prism <*a*> and rhomb glides (Fig. 1e) developed relatively thin mantles of recrystallized grains which show an abrupt, large misorientation to the host porphyroclast that, however, is consistent with the overall matrix fabric. These porphyroclasts tend to be larger (150-450μm) and more abundant than the others, and show a weak (if any) development of deformation bands and subgrains. Figure 1 also shows the corresponding *c*-axis trajectories along different profiles across the recrystallized mantles. In profiles measured perpendicular to the foliation (black arrows), the *c*-axis trajectory tend to change more regularly into the nearest easy-slip orientation than in profiles taken across strain shadow domains (gray arrows).

2.2 Type 2

Micaceous quartzites deformed in high strain domains of the greenschist facies Moeda-Bonfim shear zone (Hippertt 1994) show a conspicuously developed banded texture where three well-defined crystallographic fabric domains occur (Fig. 2). In high strain domains of the shear zone, this quartzite is totally recrystallized (quartz grain size 25-160 μm) and has a greater

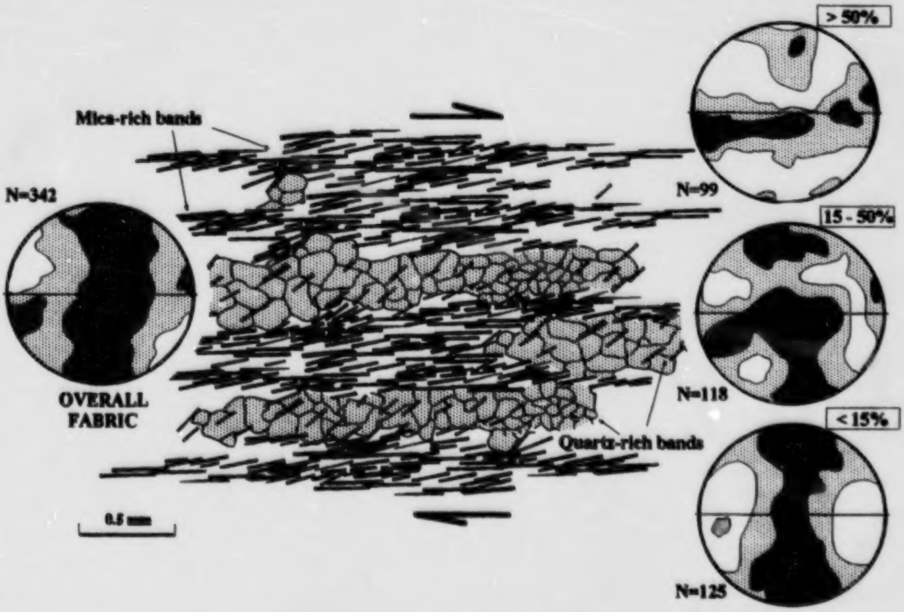

Fig. 2: Overall and domainal quartz c-axis fabrics in a micaceous quartz mylonite (c.i. 1.25%/1% area, lower hemisphere, equiarea). The plots on the right were measured in domains with different mica contents (indicated in the rectangles).

bulk phyllosilicate content (muscovite-chlorite > 15%) than the undeformed precursor (2-5%). Three compositionally distinct bands are recognized on thin section scale. Bands with a high phyllosilicate content (>70%) contain rectangular quartz grains (30 to 60 μm-long) which show a strong *c*-axis maximum at a low angle to the stretching mineral lineation defined by mica flakes (*X*-maximum) (Fig. 2a). In contrast, in the most quartzose bands (phyllosilicate content < 5%), the polygonal quartz aggregates (50-160 μm) show a pronounced *c*-axis maximum close to the mylonitic foliation pole (*Z*-maximum). In addition, a strong *Y*-maximum typically develops in bands with intermediate phyllosilicate contents (15-50%), where secondary *X*- and *Z*-maxima may also be present. Thus, the overall pattern is a micaceous quartz mylonite which is layered both compositionally and texturally.

2.3 Type 3

Granitic mylonites and ultramylonites formed in low metamorphic grade shear zones from the east border of Puna (Argentinian Andes) developed a well-defined tectonic banding with alternating pure quartz bands, pure feldspar bands and felspar-mica bands . The pure quartz bands show a strong *c*-axis preferred orientation close to the mylonitic foliation pole. These bands are composed of slightly elongated, dynamically recrystallized grains (5-25μm) defining a grain shape fabric which is 20-35 degrees oblique to the mylonitic foliation plane, consistently with the inferred shear sense. At higher strain levels, pure mica layers are also formed due to feldspar breakdown via mica-producing softening reactions. These mica layers become the main strain accommodator in the layered rock. At this stage, asymmetric intrafolial microfolding of the pure quartz layers started to occur. With continued deformation, these microfolds were progressively closed in parallel with concurrent stretching of the limbs until the complete rupture and transposition, which marks the beginning of the ultramylonitic stage of deformation (Hippertt and Hongn 1998). Thus, a complete range of microfolds with different degrees of closure and transposition can be observed in these tectonites. Domainal fabrics are progressively formed during this microfolding, as the inverted limbs of folds develop a different *c*-axis orientation with progressive fold closure (Fig. 3). The extreme case (i.e. after fold transposition) is the formation of pure quartz bands with layered *c*-axis fabrics, where the precursor fold geometry cannot be recognized anymore.

3 Discussion

3.1 Host control *vs.* crystallographic control

Type 1 domainal *c*-axis fabrics are restricted to the porphyroclast immediate vicinity and, overall, tend to show intermediate crystal orientations between the host porphyroclast and those of the recrystallized matrix aggregate. Detailed observation of this transition zone may elucidate the relative influences of the original porphyroclast crystal orientation (herein referred to as the *host control*) and of the superimposed kinematic framework (referred to as the *kinematic control*). In porphyroclasts originally oriented for easy slip on any of the operative glides, both the host control and the kinematic control aided each other leading to a comparatively fast transformation of these porphyroclasts into polygonal matrix aggregates, without any pronounced change in crystal orientation. Subgrain rotation recrystallization appears as the most suitable process to operate in this circumstances where no significant crystallographic reset is demanded. This is consistent with pronounced subgrain development and smooth transition to the recrystallized mantle as observed in these porphyroclasts.

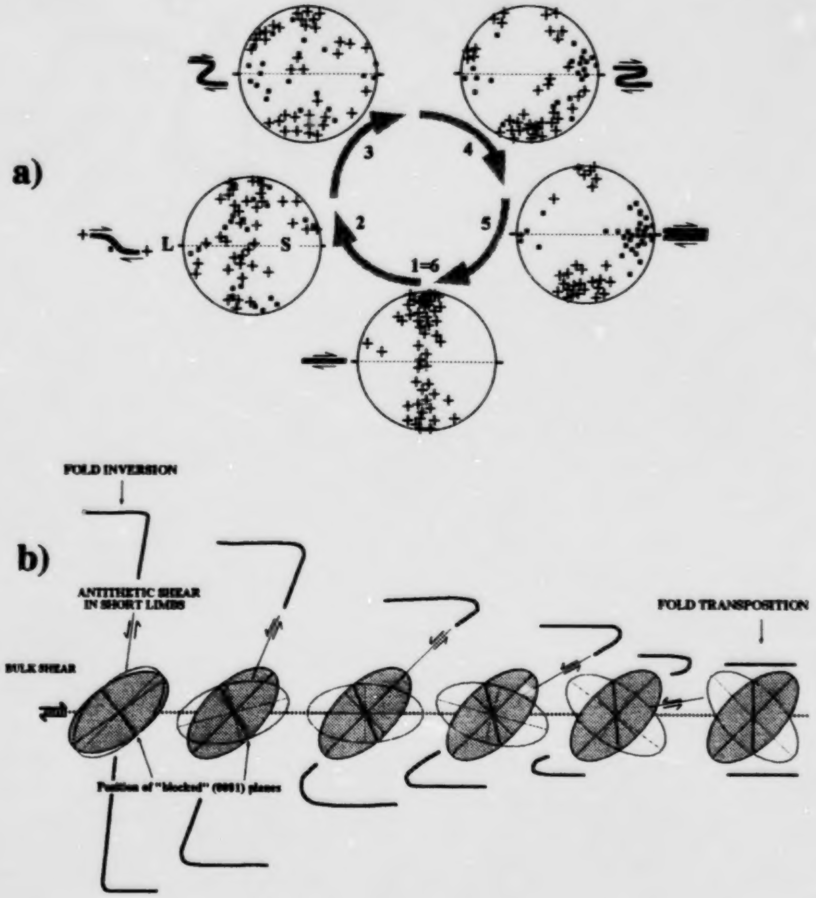
a)
3
4
2
5
1=6
L
S
b)
FOLD INVERSION
ANTITHETIC SHEAR IN SHORT LIMBS
BULK SHEAR
FOLD TRANSPOSITION
Position of "blocked" (0001) planes

Fig. 3: a) Quartz *c*-axes measured in long limbs (crosses) and short limbs (squares) of asymmetrically folded quartz bands at different degrees of fold closure (data by F. Hongn). b) Suggested mechanism for development of domainal fabrics during folding (see text).

An opposing situation occurs in porphyroclasts with 'hard' orientations (Fig. 1e). In these cases, the host control and the kinematic control acted in opposite ways, causing these porphyroclasts to be comparatively more resistent to recrystallization. The recrystallized mantle tend to be narrow, with an average thickness of only a few grains which show a large, abrupt misorientation to the host porphyroclast. This suggests that nucleation of suitably oriented new grains in the strained porphyroclast margins and subsequent grain boundary migration (due to contrasts in the stored distortional energy) was the main process of dynamic recrystallization in these porphyroclasts.

3.2 Crystal plastic *vs.* fluid processes

Type 2 domainal *c*-axis fabrics are interpreted as result of strain partitioning between crystal-plastic and fluid-assisted deformation processes. In low metamorphic grade shear zones, deformation generally occurs in the presence of an aqueous fluid phase. As the pattern of fluid circulation is expected to be highly heterogeneous in a polymineralic deforming rock (e.g. preferential fluid flow along mica-rich folia), it is reasonable to infer that different deformation processes can be activated in domains with different fluid activities. Some previous work on hydrolytic weakening of quartz (see Paterson *et al.* 1989 and references therein) has inferred that the CRSS for prism<*a*> slip may decrease in the presence of water. It can make prism<*a*> indeed 'softer' than basal<*a*> slip in some low grade shear zones with a high volumetric aqueous fluid phase (e.g. H_2O instantaneous fluid volume > 0.01%). Such a situation can explain the strong *c*-axis preferred orientation at a low angle to the *Y*-axis of finite strain (*Y*-maximum) observed in some low temperature shear zones where basal<*a*> slip would be expected to be the most operative glide. Another piece of evidence is the common occurrence of strong *Y*-maxima in phyllosilicate-rich low grade tectonites such as micaceous quartz mylonites and phyllonites, where intense fluid activity took place. In addition, in deformational contexts with intense fluid circulation (integrated fluid/rock volume ratio between 10^2 and 10^3), solution-reprecipitation creep can be a more efficient deformation process than dislocation creep, even considering the low solubility of silica at low temperatures (≈ 4-6 g/l H_2O). Solution-transfer processes typically produce *c*-axis preferred orientation at low angles to the stretching direction (*X*-maximum) (e.g. Takeshita and Hara 1998). Therefore, these crystallographic domainal fabrics in compositionally layered rocks with respect to the mica content is suggested to reflect a pattern of alternating repartitioning between different intracrystalline slip systems and also between crystal-plastic and solution-transfer processes. Thus, quartz deformation in the more impermeable mica-poor domains probably occurred at relatively dry conditions making basal<*a*> to be the dominant glide. On the other hand, in domains of moderate mica content (and moderate fluid access), hydrolytic weakening effects may have induced prism<*a*> to be the dominant slip. Finally, in domains of intense fluid circulation, quartz deformation probably occurred by solution-reprecipitation creep.

3.3 Domainal fabrics and microfolding

Development of domainal quartz *c*-axis fabrics is a common phenomenon during folding that has already been reported in the literature (e.g. Stünitz 1991). In the investigated intrafolial folds related to simple shear, the original fabric of the quartz layer was progressively obliterated in the hinge zone and inverted limb domains. The results in Fig. 3(a) show that these domainal fabrics were preserved even after stretching and rupture of the inverted limbs, with consequent fold transposition. However, the grain shape fabric that is present all over the folded domains, maintains the same obliquity which is consistent with the overall shear sense. This relationship provides information on the relative regeneration rate of the *c*-axis fabric relative to the other geometric rock fabrics such as the mylonitic foliation and the oblique grain shape fabric.

The results indicate that reset of the *c*-axis fabric is slower than that of the other rock fabrics. Initially, quartz basal planes were at low angles to mylonitic foliation. However, they do not maintain this orientation in short limbs of tight folds, and some change in the deformation conditions must have occurred in these domains. As the short limbs of folds rotate towards the shear plane after inversion, these domains are subjected to a local shearing which is opposite to the bulk shear. As a result, rotation of *c*-axis fabric is blocked and tend to be maintained in a equilibrium position where the basal planes lay in an orientation of equal extension in both the local and overall strain ellipsoids (Fig. 3b). Because the *c*-axis fabric reset is slower than the mylonitic foliation reset (through transposition), the transposed materials may conserve a domainal *c*-axis fabric even after fold transposition. Thus, the alternating domains with different orientations correspond to short and long limbs of the precursor fold. This mechanism is suggested to explain the layered textures commonly found in folded quartzose materials. Such layered domainal fabrics are also common in some sheared quartzites showing overall asymetric cross girdle *c*-axis fabrics, suggesting that folding/transposition may be a major process responsible for texture development in deformed rocks.

4 Concluding remarks

Deformed rocks are noticeably heterogeneous both microstructurally and texturally. In this paper, an attempt was made to briefly discuss different ways to form such heterogeneities in rocks subjected to predominant simple shear deformation. These heterogeneities result from coexisting deformation mechanisms operating in different microstructural domains of the deforming rock. This deformation partitioning can be related to both the domainal operation of different intracrystalline glide systems, or even the concurrent operation of crystal-plastic and fluid-assisted mass transfer processes. As the rock microstructure and their rheologic properties are continuously changing during progressive strain, and stable-state microstructures should be only 'instant microstructures' in terms of geologic time, we are left with a picture of a very dynamic deformation partitioning in tectonites. This is true principally at low metamorphic grade conditions where fluid is generally present and significantly affects deformation. Thus, the study of domainal crystallographic fabrics, associated with other common techniques of microstructural investigation, is suggested to be a useful tool to resolve the deformation partitioning history in tectonites, an important research subject that is still in early days.

5 References

Hippertt, J. (1994) Microstructures and c-axis fabrics indicative of quartz dissolution in sheared quartzites and phyllonites. *Tectonophysics*, Vol. 229, pp. 141-163.

Hippertt, J. (1998) Breakdown of feldspar, volume gain and lateral mass transfer during mylonitization of granitoid in a low metamorphic grade shear zone. *Journal of Structural Geology*, Vol. 20, pp. 175-193.

Hippertt, J. and Hongn, F. (1998) Deformation mechanisms in the mylonite/ultramylonite transition. *Journal of Structural Geology*, Vol. 20,1435-1448.

Paterson, M. (1989) The interaction of water with quartz and its influence in dislocation flow - an overview, in Rheology of Solids and of the Earth, (ed. S. Karato and M. Toriumi), Oxford University Press, pp. 171-194.

Pauli, C.; Schmid, S. and Heilbronner, R. (1996) Fabric domains in quartz mylonites: localized three dimensional analysis of microstructure and texture. *Journal of Structural Geology*, Vol. 18, 1183-1204.

Stünitz, H. (1991) Folding and shear deformation in quartzite, inferred from crystallographic preferred orientation and shape fabrics. *Journal of Structural Geology*,Vol. 12, 71-86.

Takeshita, T. and Hara, I. (1998) c-Axis fabrics and microstructures in a recrystallized quartz vein deformed under fluid-rich greenschist conditions. *Journal of Structural Geology*, Vol. 20, pp. 417-431.

TEXTURE DEVELOPMENT IN AMPHIBOLE: ORIENTED GROWTH VERSUS PASSIVE ROTATION

T. TAKESHITA
Department of Earth and Planetary Systems Science, Hiroshima University, Higashi-Hiroshima, Japan

Abstract

Although strong textures of amphibole are developed in naturally deformed amphibole-rich rocks (amphibolite and epidote-amphibolite), its origin has been an enigma. Since amphibole cannot be plastically deformed by intracrystalline slip under most of natural conditions, it is impossible to explain the texture development by the crystal lattice rotation associated with intracrystalline slip which is responsible for the texture development in deformed quartz and olivine polycrystals. The possible mechanism for the texture development of amphibole is either 'oriented growth (competitive anisotropic growth)' or 'passive rigid body rotation'. Which mechanism is relevant for the amphibole texture development has been tested in this paper through the observations of texture and microstructure of amphible from deformed epidote-amphibolite samples. Since there are both evidences which support and refute the two possible mechanisms, respectively, no conclusive answers have been given to the controversy.

Key: words: amphibole, texture, oriented growth, rigid body rotation

1 Introduction

The mechanism for texture development of amphibole in naturally deformed amphibole-rich rocks (amphibole and epidote-amphibolite) has been an enigma although strong textures of amphibole are present in these rocks. It has been known that naturally deformed amphibole does not in general show any intracrystalline deformation features such as kink bands, subgrains and recrystallized grains suggesting that dislocation creep is not the primary deformation mechanism in amphibole under natural conditions (amphibole is rheologically a very hard mineral). Natural amphibole-rich rocks may have been deformed by grain boundary diffusion creep assisted by intergranular fluid, which can be active under either lower temperature or lower differential stress conditions than those where dislocation creep is dominant. If this is true, a question arises on how the strong texture develops in grain boundary diffusion creep where texture development cannot be caused by the crystal lattice rotation associated with intracrystalline slip. There could be two possible mechanisms for texture development of amphibole in deformed amphibole-rich rocks: 'oriented growth' and 'passive rotation' of rigid rods (amphibole grains) (e.g. Shelley 1994). Both the oriented growth and passive rigid body rotation have been proposed as important mechanisms for texture development of mica (e.g. Ishii, 1988; Oertel, 1983).

In this contribution, I have evaluated the relative importance of oriented growth versus rigid body rotation for amphibole texture development by analyzing both lattice preferred orientation (LPO) and grain shape fabric in relation to LPO in deformed epidote-amphibolite from Japan. It must be mentioned however that the paper is fairly descriptive, and does not provide any conclusive answer to the controversy.

2 Sample description

Two naturally deformed epidote-amphibolite samples were collected for fabric analysis from the Sambagawa metamorphic rocks distributed in the Seba-valley district in central Shikoku, southwestern Japan (here referred to as Seba-1 and Seba-2, respectively) Both samples consist of the same mineral assemblage; amphibole, epidote, plagioclase (albite), quartz, muscovite and rutile. Amphibole and epidote are most abundant phases in the rocks, whose volume fraction together exceeds 60%. The rocks obviously originated from basaltic rocks, perhaps basaltic tuff because of a significant volume fraction of muscovite (ca. 5%). The amphibole exhibits chemical compositions of barroisite ($^{[4]}$Al=0.8-1.4 pfu, $^{[B]}$Na=0.6-1.2 pfu) with a weak retrograde compositional zoning sometimes associated with microfracturing and subsequent precipitation between the gap (Misch 1969). The peak metamorphic conditions for the epidote-amphibolite which is distributed in the albite-biotite zone in the Sambagawa metamorphic belt have been estimated as P=10 kb and T=500-550 °C (Enami et al. 1994).

The great amount of strain in the epidote-amphibolite is manifested by both the pervasive development of foliation and lineation defined by the preferred alignment of amphibole crystals, and intrafolial folds. Although the epidote-amphibolite is strongly deformed, there is no sign of intracrystalline slip in both amphibole and epidote such as kinking and strain-induced dynamic recrystallization observed under a microscope. Quartz and plagioclase are plastically deformed which is shown by the occurrence of kink bands and dynamically recrystallized grains, but exhibit an equigranular grain shape. The diameter of equivalent circle, here referred to as the equivalent diameter ($\sqrt{a \cdot b}$; a and b are the long and short axes of grain shape, respectively) varies between 50-1000 μm with the mean size of 125 μm in the XZ section of sample Seba 2, where the orientations of X- and Z-axis denote those of the lineation and foliation normal, respectively.

3 Lattice preferred orientation (LPO)

The directions of the principal axes of optical indicatrix (n_α, n_β, n_γ) which coincide with the principal vibration directions ($n_\alpha=X$, $n_\beta=Y$, $n_\gamma=Z$) in optically biaxial crystals were measured with a universal stage for amphibole grains in the epidote-amphibolite samples. Also, in the case that at least one of {110} cleavage traces was visible in amphibole, c-axis orientations were determined as the orientation of intersection of either the n_α-n_γ plane and one of {110} cleavages, or (110) and (110) plane. The angle between c-axis and n_γ in hornblende is 13-34°. Direct measurements of the angle in the amphibole of barroisite compositions show that it is ca. 20°.

Results of the LPO measurements are shown in Figures 1 and 2 for samples Seba-1 and Seba-2, respectively. In both samples, LPOs are similar with some components in common. n_α orientations are oriented at high angles to the foliation plane, and tend to form ca. 20° small circle girdles about the Z-axis in both samples, but the girdles can be better interpreted as ca. 70° incomplete small circle (cleft) girdles about the X-axis, particularly in Seba-2. n_β, [010] orientations are most concentrated in the Y-axis, and tend to form a girdle perpendicular to the X-axis in both samples. Also, a small concentration of n_β orientations parallel to the *X*-axis exists in Seba-2. n_γ orientations are most concentrated in the *X*-axis and tend to form ca. 20° small circle girdles about it. In addition, small concentrations parallel to the *XY*-plane and *Y*-axis exist in samples Seba-1 and Seba-2, respectively. *c*-Axis orientations form a strong preferred orientation parallel to the *X*-axis in both sample. While the *c*-axis orientations tend to form a girdle parallel to the *XY*-plane in Seba-1, a discrete secondary maximum parallel to the *Y*-axis exists in Seba-2. Therefore, it is clear that the 20° small circle girdles of n_γ and n_α orientations about the *X*- and *Z*-axis, respectively are crystallographically equivalent with the *c*-axis maximum parallel to the *X*-axis, and the maximum of (100) normal parallel to the *Z*-axis. Overall, it is important to note that the amphibolite textures in both sample show orthorhombic symmetry where the symmetry axes coincide with the *X*-, *Y*- and *Z*-axis of sample coordinate.

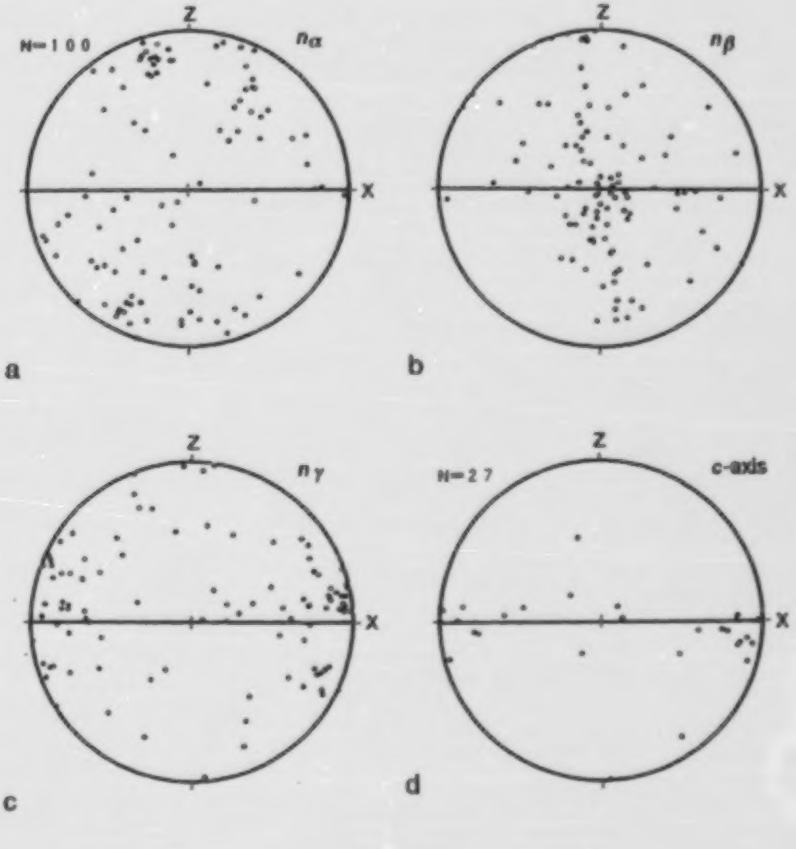

Fig. 1: LPO in sample Seba-1. Upper-hemisphere and equal-area projection.

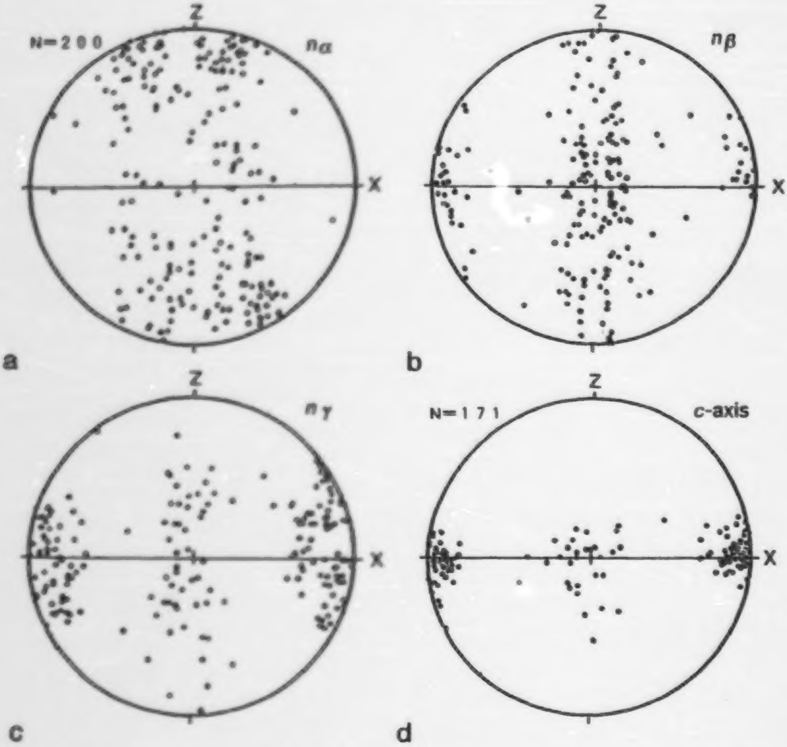

Fig. 2: LPO in sample Seba-2. Upper-hemisphere and equal-area projection.

4 Grain shape fabric in relation to LPO

We have measured the equivalent diameter and aspect ratio (*a*/*b*) of amphibole grain shape as a function of crystal orientation in the *XZ*, *YZ* and *XY* sections of sample Sb-2. First of all, there is essentially no relation between the equivalent diameter and aspect ratio in all the three mutually perpendicular sections. The aspect ratio does not increase (or decrease) at all with increasing the equivalent diameter. LPOs were separately measured for different size groups of the equivalent diameter. Based on the results, it has been shown that there is no relation between the LPO and equivalent diameter in all the three mutually perpendicular sections.

The frequency distribution of aspect ratios measured in the *XZ* and *YZ* sections, respectively is shown in Figure 3. The aspect ratios in the *XZ* and *YZ* sections vary between 1.1-10.0 and 1.0-7.6, with the mean value of 3.7 and 2.1, respectively. Since the preferred *c*-axis orientation parallel to the *X*-axis is very strong, the aspect ratios in the *XZ* and *YZ* sections mostly show the amphibole grain shape in the sections parallel and perpendicular to the *c*-axis, respectively. Therefore, it is concluded that the amphibole grains are most elongated parallel to the *c*-axis. The figure also tells us that the amphibole grains are more elongated with *c*-axes parallel to the *X*-axis than with those parallel to the *Y*-axis, because the frequency distribution of aspect ratios also represents that of grains with *c*-axes oriented parallel to the *Y*-axis.

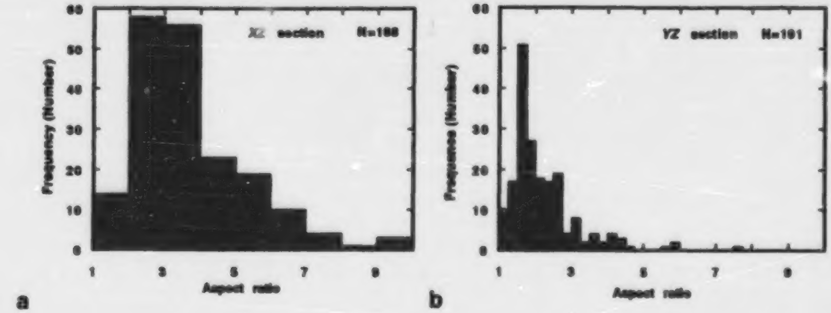

Fig. 3: Frequency distribution of aspect ratios in the (a) *XZ* and (b) *YZ* sections of sample Seba-2

5 Discussion and conclusions (origin for LPO development in amphibole: oriented growth versus passive rigid body rotation)

First of all, it is hard to conclude that the observed textures with orthorhombic symmetry were caused by the crystal lattice rotation associated with intracrystalline slip. Since a shear deformation with a top to the west sense predominated in the Sambagawa belt in central Shikoku, we should observe the textures with monoclinic symmetry as well as those with orthorhombic symmetry. This is in fact the case for the kinematically induced quartz textures in the Sambagawa belt (Tagami and Takeshita 1998). The possible mechanism to create textures with orthorhombic symmetry can be either oriented growth of crystals controlled by either stress or strain, or passive rigid body rotation controlled by strain. In this preliminary work, I have obtained both evidences which support and dispute the oriented growth and rigid body rotation for the origin of LPO development, respectively which are discussed below.

5.1 Pros and cons for the oriented growth origin

The fact that amphibole grains are more elongated with *c*-axes parallel to the *X*-axis than the *Y*-axis is certainly well explained by oriented growth. The fact that the aspect ratio does not increase at all with increasing the equivalent diameter in all the *XZ*, *YZ* and *XY* sections may suggest that the amphibole grains grew freely not strongly controlled by stress or strain state in the sample (like grain growth in contact aureole), rather than a competitive anisotropic growth.

Although it was not mentioned above, there is a very small number of grains with *c*-axes oriented in an anomalous orientation (i.e. n_α and n_γ are oriented close to the *Y*- and *Z*-axis, respectively). Such oriented grains exhibit an equigranular and ameba-like shape, and seem to have precipitated in the space surrounded by the grains with the normal orientations (i.e. *c*-axes oriented parallel to the *XY*-plane). Although these grains could have been in a hard orientation for growth, some of them grew up to fairly large sizes (equivalent diameter>200 μm in the *XZ* section). Anisotropic competitive grain growth cannot explain that such anomalously oriented grains grew perhaps with faster rate.

5.2 Pros and cons for the rigid body rotation origin

Although the preferential *c*-axis orientation parallel to the X (lineation) axis is very strong in both samples, the *c*-axis orientations tend to form a girdle parallel to the XY (foliation) plane in sample Seba-1. In fact, a well-defined XY-girdle of n_γ orientations was reported in some amphibolite (Toyoshima 1997), although *c*-axis orientations in amphibole from naturally deformed amphibolite are generally most concentrated in the X-axis. This kind of variation of *c*-axis fabric development in amphibolite could be most reasonably attributed to the passive rigid body rotation controlled by the strain geometry in rocks (i.e. a *c*-axis maximum parallel to the X-axis and a girdle parallel to the XY-plane correspond to uniaxial elongation and shortening strain, respectively), although it may be also possible to interpret the feature by anisotropic growth controlled by either stress and strain state.

Both the great circle girdle of n_β orientations and 70° small circle girdles of n_α orientations perpendicular to the X-axis observed in both samples could suggest the rigid body rotation of amphibole grains. If amphibole grains are not only elongated parallel to *c*-axis but also exhibit an elongate prism section perpendicular to the *c*-axis, the great and small circle girdles could form by the passive rotation of amphibole grains due to the shortening parallel to both the Z- and Y-axis (Shelley 1994).

The fact that there is essentially no relation between the LPO and equivalent diameter (i.e. the LPOs for different size classes are essentially the same) perhaps suggests that rigid body rotation was not an important mechanism for the LPO development in the epidote-amphibolite. If the growth and rigid body rotation of amphibole grains simultaneously occur, it is expected that coarser grains become more preferentially oriented than finer grains.

Although it was not mentioned above, there are several occurrences that microboudins separated from an amphibole grain were differentially rotated one another in the XY-plane by as much as 40°. This shows that rigid body rotation of grains in fact occurred in the samples.

It is very hard to evaluate which mechanism, oriented growth or rigid body rotation is important for the texture development in amphibolite. The theme remains to be investigated in the future.

6 References

Enami, M., Wallis, S. R. and Banno, Y. (1994) Paragenesis of sodic pyroxene-bearing quartz schist: implications for the P-T history of the Sanbagawa belt. *Contribution to Mineralogy and Petrology*, Vol. 116, pp. 182-198.

Ishii, K. (1988) Grain growth and re-orientation of phyllo-silicate minerals during the development of slaty cleavage in the South Kitakami Mountains, NE Japan. *Journal of Structural Geology*, Vol. 10, pp. 145-154.

Misch, P. (1969) Paracrystalline microboudinage of zoned grains and other criteria for synkinematic growth of metamorphic minerals. *American Journal of Science*, Vol. 267, pp. 43-63.

Oertel, G. (1983) The relationship of strain and preferred orientation of phyllosilicate grains in rocks-a review. *Tectonophysics*, Vol. 100, pp. 413-447.

Shelley, D. (1994) Spider texture and amphibole preferred orientation. *Journal of Structural Geology*, Vol. 16, pp. 709-717.

Tagami, M. and Takeshita, T. (1998) *c*-Axis fabrics and microstructures in quartz schist from the Sambagawa metamorphic belt, central Shikoku, Japan. *Journal of Structural Geology*, Vol. 20, pp. 1549-1568.

Toyoshima, T., Komatsu, M. and Shimura, T. (1997) Tectonics of the Hidaka metamorphic belt, Hokkaido, northern Japan. In: Arai, S., Maeda, J., Osanai, Y. and Niida, K. (Eds.) Magmatism in the Hidaka Crust-Mantle System, Hokkaido, Japan. *The Memoirs of Geological Society of Japan*. No. 47, pp.259-277.

CONTRASTING *C*-AXIS FABRIC PATTERNS IN LAYERS OF DIFFERENT PROPORTION OF QUARTZ AND IRON OXIDES

L. LAGOEIRO
Departamento de Geologia, Universidade Federal de Ouro Preto, Ouro Preto, MG, Brazil.

Abstract

Tectonites of banded iron formation show microfrabrics indicative of both dislocation and solution-transfer creep. These rocks, deformed under greenschist-facies conditions, have a well-developed compositional layering where pure quartz layers alternate with iron oxide-rich layers. Pure quartz layers are composed of aggregates of polygonal equant grains. In iron oxide-rich domains quartz grains are smaller and have a strong shape preferred orientation; lenticular quartz grains occur between hematite platelets and magnetite porphyroclasts. Quartz *c*-axis fabrics determined for these two different compositional domains display contrasting patterns. In pure quartz layers *c*-axes have a maximum around the intermediate shortening direction (Y-maximum). Conversely, in iron oxide-rich domains *c*-axes are concentrated around the maximum stretching direction (X-maximum). The contrasting *c*-axis patterns are interpreted as representing the operation of different deformation mechanism in these two compositional domains. Grains with *c*-axes oriented around the Y-axis are indicative of slip on prism <a> systems. Conversely, lenticular quartz grains with *c*-axis maximum at a low angle to the X-axis are interpreted as to result from syntectonic precipitation from silica-rich solutions.

Keywords: *c*-Axis fabric, dislocation creep, grain boundary migration, solution-transfer creep

1 Introduction

Quartz-iron oxide tectonites deformed in fluid-rich greenschist-facies conditions show contrasting quartz *c*-axis fabrics according to the volume proportion of quartz and iron oxide in the layers. These tectonites have a well-developed compositional layering where the volume proportion of quartz and iron oxide (magnetite and hematite) vary significantly, from pure quartz layers to iron oxide-rich layers (up to 60-70% in volume of iron oxide). The compositional banding is quite regular and its thickness varies from a few mm to a few cm. The transition between domains is quite abrupt. In pure quartz layers a *c*-axis maximum occurs around the intermediate direction (Y-maximum) of the finite strain ellipse while in iron oxide-rich layers *c*-axis fabrics are characterized by a maximum around the maximum stretching direction (X-maximum).

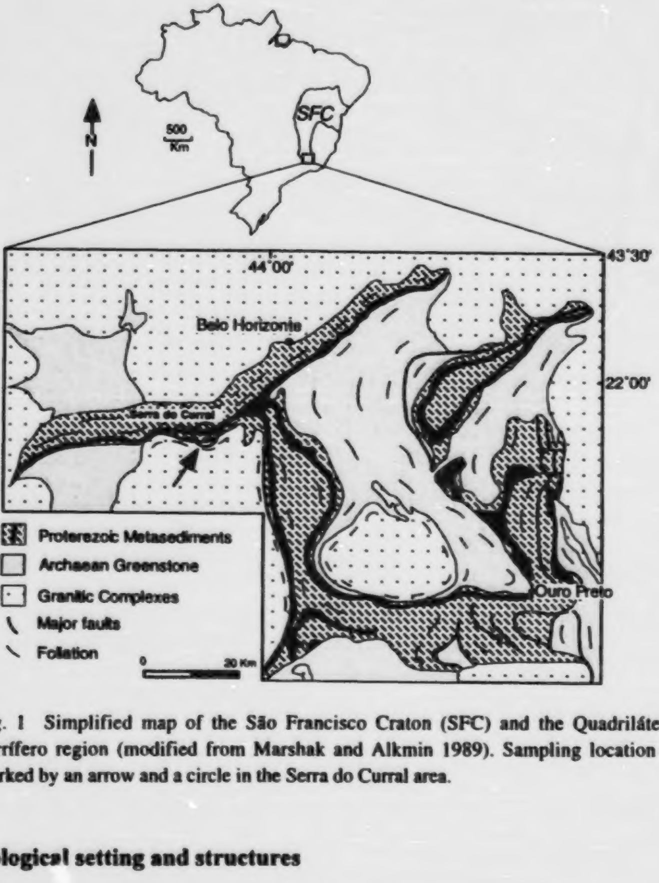
SFC
N
500 Km
44°00'
43°30'
22°00'
Belo Horizonte
Serra do Curral
Ouro Preto
Proterozoic Metasediments
Archaean Greenstone
Granitic Complexes
Major faults
Foliation
0
20 Km

Fig. 1 Simplified map of the São Francisco Craton (SFC) and the Quadrilátero Ferrífero region (modified from Marshak and Alkmin 1989). Sampling location is marked by an arrow and a circle in the Serra do Curral area.

2 Geological setting and structures

The Quadrilátero Ferrífero (QF) is a granite-greenstone terrain (Shorscher 1978), located in the southern part of the São Franscisco Craton (Fig. 1). The QF consists of an Archean metavolcanic unit covered by Paleoproterozoic clastic and chemical sediments, such as banded iron formations, which surround Archean granitic-migmatitic complexes. Major structural units are the result of polycyclic tectonic evolution with alternating extensional and compressional events (Marshak and Alkmin 1989). These events produced regional synclines and also accounted for the fold-thrust belt in the eastern margin of the QF (high-strain area). Low-grade shear zones are developed in the contacts between the Archean granitic complexes and the Proterozoic metasediments. The rocks studied in this paper came from one of these shear zones, in the western low-strain area of the QF (Serra do Curral Syncline, Fig. 1). This brittle-ductile shear zones dips 60° to 140° and all macro and microstructural kinematic indicators, such as asymmetrical folds with disrupted limbs, S-C foliation and crystallographic fabric, indicate normal dip-slip movement. Discontinuous outcrops make it difficult to estimate the total thickness of the shear zone, that affects the granitic rocks, the quartzites and the banded iron formation (BIF). The dominant mineralogy of the BIF is partially oxidized magnetite, hematite platelets and quartz grains.

Mineralogical assemblages in granitic rocks (quartz + sericite ± chlorite), the absence of crystal plastic deformation in feldspars and the dynamic recrystallization of quartz, indicate that the metamorphic conditions of deformation reached the upper greenschist facies (T ~ 400°-450° C, P~4kb). Evidence for solution transfer processes includes the presence of fibrous quartz around magnetite porphyroclasts and truncation of magnetite porphyroclast edges by concentrations of hematite platelets (Lagoeiro 1998). Thus it appears that an aqueous fluid must have been present during the deformation.

3 Microstructures and *c*-axis fabrics

3.1 Pure quartz layers

In the pure quartz layers grains are almost equant (grain size of 120μm and aspect ratio of 1.3 in average) and display a well-defined foam structure (Fig. 2a). Grain boundaries are characteristically straight and do not exhibit optically visible microstructures indicative of crystal plastic deformation, such as undulose extinction, deformation bands or subgrain boundaries.

The orientation of quartz *c*-axes of individual grains were determined in several pure quartz layers (less than 1% in volume of iron oxide minerals) using the universal stage. The *c*-axes were plotted in the lower hemisphere equal-area projection adopting the structural reference frame (X-parallel to the mineral stretching lineation, Z-normal to the foliation plane, and Y-perpendicular to the XZ plane). The *c*-axis preferred orientation patterns for all pure quartz domains (Fig. 2b) define a maximum concentration around the Y-axis (Y-maximum).

3.2 Iron oxide layers

Iron oxide-rich layers consist of hematite platelets with a strong shape preferred orientations (SPO). Their longest axes are parallel to the foliation trace and define the stretching mineral lineation. Lenticular quartz grains (Fig. 2c) occur between the hematite platelets. The quartz grains also have a strong SPO with high aspect ratios (up to 10:1). Their longest axes are also parallel to the stretching direction (X-axis of the finite strain). Some lenticular grains display oriented inclusions of hematite platelets. Large magnetite porphyroclasts (up to 5mm), with asymmetrical hook-shaped quartz pressure fringes, occur in these domains.

Although lenticular quartz grains do not show optically visible microstructures indicative of crystal plastic deformation, they have a strong *c*-axis fabric (Fig. 2d). Contrasting with the pure quartz domains, the *c*-axes in iron oxide layers define a maximum at a low angle to the maximum stretching direction (X-maximum).

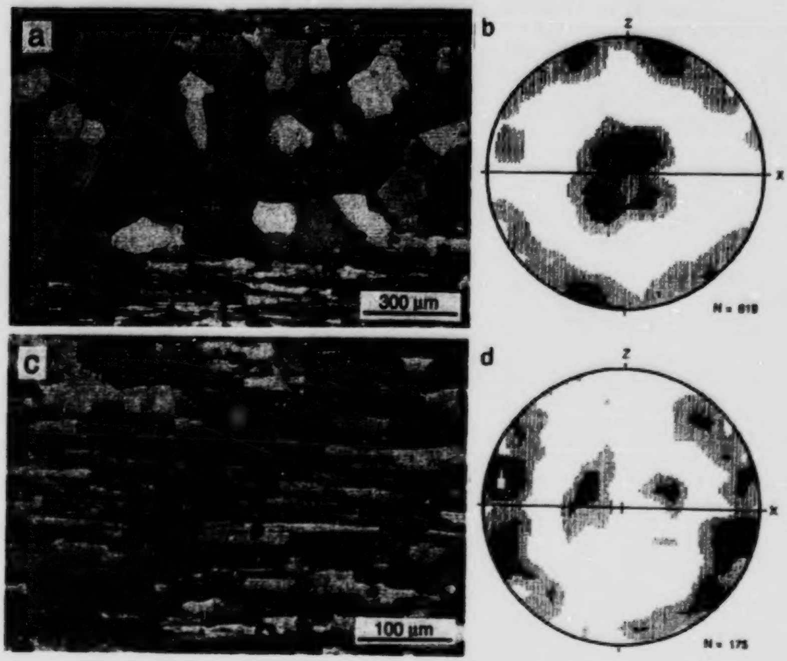

Fig. 2 Photomicrographs of quartz-iron oxide tectonites showing two different compositional domains. XZ sections taken under crossed polarizers. (a) Quartz microstructures and (b) representative *c*-axis fabric of the pure quartz domains. (c) and (d) show, respectively, lenticular quartz grains and *c*-axis fabric of the iron oxide-rich domains. Contour intervals and lowest contours, in both stereoplots, are 1% per 1% area.

4 Discussion and interpretation

4.1 *c*-Axis fabrics produced by crystal-plasticity

The contrasting quartz *c*-axis fabrics, determined for the two compositional domains, suggest a partition of the deformation between layers of different composition. Y-maximum *c*-axis fabrics, characteristic of the pure quartz domains, are attributed to the operation of prism <a> slip (Schmid and Casey 1986). However, basal (0001) slip is expected to be operative in conditions under which these tectonites were deformed (greenschist-facies conditions) and prismatic glide in quartz is generally thought to be operative in higher T metamorphic conditions (amphibolite-facies conditions). The predominance of Y-maximum *c*-axis fabrics in this domain might be in part due to the presence of water. Even small amounts of water may decrease the critical resolved shear stress (CRSS) for the activation of slip on the prism <a> system. Thus, in the presence of a high amount of aqueous fluid dislocation climb might be possible in lower T deformed rocks (Blacic 1975; Hirth and Tullis 1992) favoring slip on alternative system, such as prism <a>. Quartz microstructures with triple junctions meeting at 120°, as well as the absence of grains with optically visible microstructures indicative of crystal plastic deformation, both of which are typically found in the pure quartz domains, also indicate the importance of grain boundary migration (GBM) in the formation of the microstructures in these domains. GBM might have been co-operative with dislocation glide producing an aggregate where irregular boundaries (or subgrain boundaries) and highly strained or smaller grains were eliminated by dynamic grain growth. The intergranular fluid phase might have enhanced grain boundary diffusion thus enhancing grain boundary mobility (Urai et al. 1986). The *c*-axis fabric in this domain probably results from the operation of dislocation glide and GBM (low T regime 1, Hirth and Tullis 1992). Grains favorably oriented for slip on prism <a> are responsible for the Y-maximum while those poorly oriented for slip on this system may store high strain energy and then be consumed by GBM.

4.2 c-Axis fabric resulting from solution–transfer creep

In iron oxide-rich domains, the *c*-axis concentration around the maximum stretching direction (X-maximum) is interpreted as being indicative of solution-transfer creep. This *c*-axis pattern has also been observed in quartz aggregates deformed by solution-transfer creep at low T deformation conditions (Hippertt 1994, Takeshita and Hara 1998). Lattice preferred orientations (LPO) developed during solution-precipitation creep are attributed to the anisotropic dissolution/growth rates of minerals according to their lattice orientation (Tullis 1989). Thus, quartz grains with *c*-axes oriented at low angles to the maximum stretching direction (X-axis) are expected to grow faster than those at high angles. So, a LPO characterized by a maximum at low angles to the X-axis is produced during the development of lenticular quartz grains, precipitated directly from silica-rich aqueous solutions. Evidence for activity of an aqueous fluid is also given by the association of lenticular quartz grains with the oxidation of magnetite porphyroclasts, and consequent grain size reduction, and the formation of hematite platelets, as a result of the dissolution of magnetite grains (Lagoeiro 1998). Lenticular quartz grains show inclusions of hematite platelets with the same orientation of hematite platelets found in the matrix. Grain size reduction and the formation of hematite platelets may also have enhanced fluid circulation in the iron oxide-rich domains, as the rock permeability and the efficiency of solution-transfer generally increase in the presence of shape-oriented planar minerals and in finer grain size aggregates (Shimizu 1995).

5 Conclusions

(1) Under greenschist metamorphic conditions and in the presence of an aqueous fluid, contrasting *c*-axis fabrics observed in the quartz-iron oxide tectonites are inferred to result from the operation of different deformation mechanisms in different compositional domains.

(2) The Y-maximum *c*-axis fabrics in the pure quartz layers suggest that prism <*a*> slip was operative during the crystal plastic deformation of quartz aggregates in pure quartz domains. The microstructures in these domains also suggest that grain

boundary migration was also operative. Thus *c*-axis fabric in these domains might have resulted from the operation of dislocation creep and grain boundary migration.
(3) Conversely, in the iron oxide domains quartz *c*-axis fabrics are attributed to the anisotropic growth rates of lenticular quartz grains precipitated directly from silica-rich aqueous solutions during the deformation. The faster growth rates occurred along the crystallographic *c*-axis. Thus lenticular quartz grains might have grown with their *c*-axes at low angles to the maximum extension direction of the finite strain ellipse (the mineral stretching lineation), resulting in the development of *c*-maximum around the X-axis.

6 References

Blacic, J.D. (1975) Plastic deformation mechanisms in quartz: the effect of water. *Tectonophysics*, Vol. 27, pp. 171-194.

Hippertt, J.F. (1994) Microstructures and *c*-axis fabrics indicative of quartz dissolution in sheared quartzites and phyllonites. *Tectonophysics*, Vol. 229, pp. 141-163.

Hirth, G. and Tullis, J. (1992) Dislocation creep regimes in quartz aggregates. *Journal of Structural Geology*, Vol. 14, pp. 145-159.

Marshak, S. and Alkmin, F.F. (1989) Proterozoic contraction/extension tectonics of the southern São Francisco region, Minas Gerais, Brazil. *Tectonics*, Vol. 8, pp. 555-571.

Lagoeiro, L.E. (1998) Transformation of magnetite to hematite and its influence on the dissolution of iron oxide minerals. *Journal of Metamorphic Geology*, Vol. 16, pp. 415-423.

Schmid, S.M. and Casey, M. (1986) Complete fabric analysis of some commonly observed quartz *c*-axis patterns, in *Mineral and Rock Deformation: Laboratory Studies*, (ed. B. Hobbs and H. Heard. American Geophysical Union, Geophysical Monograph, Vol. 36, pp. 263-286.

Schorscher, H.D. (1978) Kommatiitos na estrutura 'greenstone belt'. Quadrilátero Ferrífero, Minas Gerais, *Anais do Congresso Brasileiro de Geologia*, Vol. 30, pp. 292-293.

Shimizu, I. (1995) Kinetics of pressure solution creep in quartz: theoretical considerations. *Tectonophysics*, Vol. 245, pp. 121-134.

Stallard, A. and Shelley, D. (1995) Quartz c-axes parallel to stretching directions in very low-grade metamorphic rocks. *Tectonophysics*, Vol. 249, pp. 31-40.

Takeshita, T. and Hara, I. (1998) *c*- Axis fabrics and microstructures in a recrystallized quartz vein deformed under fluid-rich greenschist conditions. *Journal of Structural Geology*, Vol. 20, pp. 417-431.

Tullis, T.E. (1989) Development of preferred orientation due to anisotropic dissolution/growth rates during solution transfer creep. *Eos, Transactions of the American Geophysical Union*, Vol., pp. 70, 457.

Urai, J.L., Means, W.D. and Lister, G.S. (1986). Dynamic recrystallization of minerals, in *Mineral and Rock Deformation: Laboratory Studies*, (ed. B. Hobbs and H. Heard), American Geophysical Union, Geophysical Monograph, Vol. 36, pp. 61-99.

COMPARISON OF NATURAL AND SIMULATED QUARTZ SHEAR TEXTURE

T. TAKESHITA
Department of Earth and Planetary Systems Science, Hiroshima University, Higashi-Hiroshima, Japan
H.-R. WENK
Department of Geology and Geophysics, University of California, Berkeley, U. S. A.
R. LEBENSOHN
Instituto de Fisica Rosario (UNR-CONICET), Rosario, Argentina

Abstract

c-Axis fabric and microstructures in a quartzite sample sheared and extensively recrystallized under greenschist facies conditions have been analyzed and compared with theoretical predictions. The *c*-axis fabric consists of four orientation components which are represented by host grain *c*-axis orientations (referred to as A, B, C and D): A and B are at high angles to the foliation plane, displaced against and with the sense of shear, respectively; C is in an intermediate direction between the *Y*- and *Z*-axis of finite strain, and D forms a subsidiary concentration around the intermediate strain (*Y*) axis. B- and C-grains are favorably oriented for basal and pyramid<a> slip, respectively and strongly deformed, while A- and D-grains are unfavorably oriented for the slip systems and little or moderately deformed. Microstructural evidence and theoretical predictions indicate that harder A-, C- and D-grains were significantly consumed by the grain boundary migration of softer recrystallized B-component. Hence, the *c*-axis maximum nearly perpendicular to the shear plane and apparently displaced with the sense of shear commonly found in naturally sheared quartzite (correlated with B-component) is presumably developed by the growth of soft orientations for basal slip by grain boundary migration at large strains.

Keywords: deformed quartzite; lattice preferred orientation; grain boundary migration

1 Introduction

A better understanding of dynamic recrystallization in quartz is necessary if LPO patterns in recrystallized quartzite are used to interpret geological processes. The LPO in quartz polycrystals resulting from intracrystalline slip is not greatly modified by rotation recrystallization, because the lattice orientations of the rotated subgrains are controlled by those of the host grains. Subgrain rotation recrystallization is important at relatively low strains. At larger strains migration recrystallization becomes dominant over subgrain rotation and this can greatly modify the LPOs (e.g. for olivine Zhang and Karato 1995; for norcamphor (quartz analogue), Herwegh and Handy 1996).

The *c*-axis fabric patterns are often significantly different between models and natural data. While asymmetric crossed girdles rotated against the sense of shear (relative to coaxial pure shear deformation) are predicted for model simple shear *c*-axis fabrics, single girdle or a maximum *c*-axis fabric rotated with the sense of shear is often developed in naturally sheared quartzite. The models are for deformation by slip, whereas the natural quartzites are generally recrystallized. In fact the shear experiments of Dell' Angelo and Tullis (1989) illustrate a *c*-axis maximum displaced against the sense of shear for low strain and a maximum displaced with the sense of shear for high strain where recrystallization occurs.

In this paper we make an attempt to reconcile the controversy about the effect of dynamic recrystallization on LPO development through a detailed analysis of microstructure and LPO in a quartzite sheared under greenschist facies conditions. The deformation and recrystallization mechanisms in this natural quartzite are then discussed by comparing the microstructures with predictions from a deformation-based model of dynamic recrystallization.

2 Deformation and recrystallization microstructures

2.1 Microstructures indicative of shear strain

In the *XZ* section of the quartzite sample analyzed in this study (Sci 490), a shear deformation is indicated by C'-type shear bands. Here, the *X*- and *Y*-axis denote the elongation (lineation) and shortening (normal to the foliation) axes of finite strain, respectively. The average trace of shear bands is rotated counterclockwise by 20° from the foliation plane about the *Y*-axis (SB in Fig. 1a). The sense of shear conforms with the shear sense inferred from the asymmetry of the quartz *c*-axis fabric.

2.2 *c*-Axis fabric components in host grains and inferred slip systems

Although recrystallization is extensive in quartz grains from the sample, the core of host grains is often preserved. The host *c*-axis fabric consists of asymmetric small circle girdles about the Z-axis, rotated by 10° with the sense of shear about the *Y*-axis (Fig. 1a). The half opening angle of the small circles is ca. 35°. The small circle *c*-axis fabric with a small half opening angle suggests that the deformation took place under greenschist facies conditions (ca. 300-400 °C) (e.g. Takeshita and Wenk 1988).

Orientation components A, B C and D are distinguished in the host *c*-axis fabric (Fig. 1a). A is a maximum at high angles to the foliation plane, displaced against the sense of shear, and B is a similar maximum displaced with the sense of shear. C represents asymmetrical concentrations in intermediate directions between the *Z*- and *Y*-axis, D is a subsidiary concentration around the *Y*-axis. Both B- and C-grains are strongly deformed, while A- and D-grains are moderately deformed as described below.

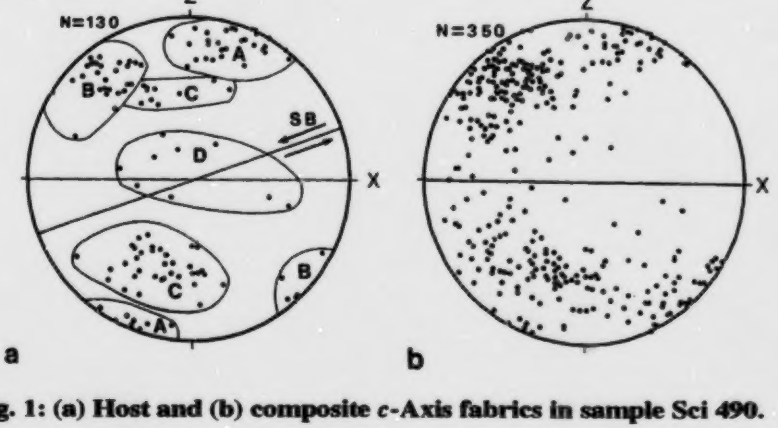

Fig. 1: (a) Host and (b) composite *c*-Axis fabrics in sample Sci 490.

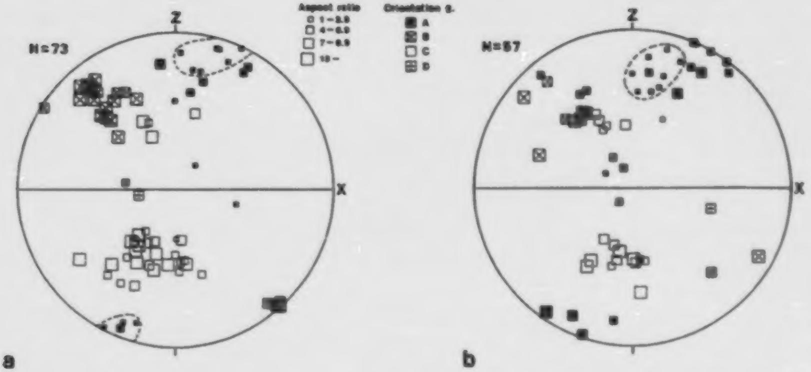

Fig. 2: Dependence of the grain aspect ratios on their *c*-axis orientations.

2.3 Microstructures of deformed host grains

We measured the length of long and short axes (denoted as *a* and *b*, respectively) and determined aspect ratio (*a*/*b*) of deformed shape of host grains both in the *XZ* and *YZ* sections. The aspect ratio has been analyzed as a function of *c*-axis orientation. The aspect ratio can be approximated as strain ratio both in the *XZ* and *YZ* sections, if the initial shape of detrital quartz grains is close to sphere. The mean aspect ratios in different orientation components vary greatly: A: 3.5, B: 12.2, C: 9.4 and D: 4.6, and A: 4.9, B: 10.6, C: 8.6 and D: 5.6 in the *XZ* and *YZ* sections, respectively. The aspect ratios of B- and C-grains are slightly but consistently higher in the *XZ* than in the *YZ* sections, and the *k*-value for these grains is inferred to be 0.01 (oblate shape). It is clear from the detailed analysis of grain aspect ratios that B- and C-grains are much more strained than A- and D-grains, in other words there was a large plastic anisotropy. The plastic anisotropy is also clearly shown in both *c*-axis fabric diagrams from the *XZ* and *YZ* sections (Fig. 2) where the size of square symbols showing individual *c*-axis orientations is proportional to the value of the aspect ratio in each grain.

2.4 *c*-Axis fabric in recrystallized grains

The composite *c*-axis fabric diagram from both host and recrystallized *c*-axis orientations in the quartzite sample is shown in Fig. 1b. Although the composite *c*-axis fabric does not differ greatly from the host *c*-axis fabric (Fig. 1a), it is more scattered. Furthermore, the density of B-component is higher in the composite than in the host *c*-axis fabric, indicating the higher density of B-component in the recrystallized *c*-axis fabric.

3 Simulation of *c*-axis fabric development in quartzite by a deformation-based model of recrystallization

3.1 Model

Based on the assumption that the stored strain energy provides the driving force for recrystallization, Wenk et al. (1997) proposed a deformation-based recrystallization model for low-symmetry materials, which has been implemented within the viscoplastic self-consistent (VPSC) formulation (e.g. Lebensohn and Tomé 1993). In the model, highly strained grains are likely to recrystallize by nucleation or to be replaced by grain boundary migration recrystallization of less deformed neighbor grains. Thus, the dynamic recrystallization texture is due to a balance between nucleation and boundary mobility that makes a grain shrink or grow. It is assumed that the crystallographic orientation of nucleated grain is same as that of the host grain.

3.2 Results: comparison of natural results and simulated data

The VPSC model is used here to assess which active slip systems are compatible with the measured natural *c*-axis fabric. In the simulations we assumed that the active slip systems during deformation were essentially basal<*a*>, pyramid<*a*> and pyramid<*a+c*> slip systems with the CRSS ratio of 1.0 : 1.5 : 2.0. The stress exponent was taken as 3 for the simulations. Simulations for deformation and dynamic recrystallization which follows the deformation were performed for an intermediate strain path between uniaxial shortening and simple shear, although the observed *oblate* deformed grain shape can never be really reproduced by the strain path (this is a best strain path which we can assume). The velocity gradient tensor (L_{ij}) for 2.5 % shear strain increment which we chose for the calculation is described as follows.

$$Lij = \begin{pmatrix} 0.025 & -0.05 & 0.0 \\ 0.0 & -0.0125 & 0.0 \\ 0.0 & 0.0 & -0.0125 \end{pmatrix} \qquad (1)$$

In all cases we started with 250 randomly oriented and equally sized orientations, and the deformation was carried out up to 1.0 shear strain (40 steps).

Figure 3 illustrates the simulated deformation *c*-axis fabric together with the overall deformation and total shear of basal slip in individual grains. As in previous simulations a broad girdle develops with a (0001) maximum near the shear plane normal but slightly rotated against the sense of shear (Wenk et al. 1989). The simulated *c*-axis fabric is more or less similar with correlative components to the natural *c*-axis fabric. While in the previous simulation (model α of Wenk et al. 1989) where the CRSS of pyramid<*a*> slip is three times as high as that of basal<*a*> slip, C-component cannot be created, it is distinct in the present simulation (Fig. 3) suggesting a significant activity of pyramid<*a*> as well as basal<*a*> slip in the quartzite sample.

It is clear from these calculations that grains with *c*-axes near the slip plane normal (corresponding to B-grains in the natural texture) are most heavily deformed with additional highly deformed grains closer to *Y*-axis (C-grains). Grains with *c*-axes rotated against the sense of shear (A-grains) are significantly harder than B-grains. Grains with *c*-axes oriented around the *Y*-axis (D-grains) are moderately deformed. Overall, "soft" highly deformed grains correspond to grains with significant basal slip.

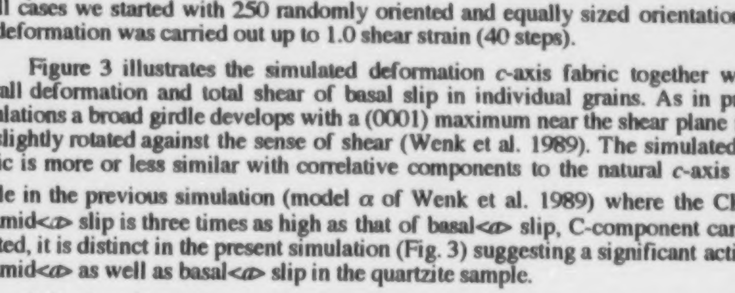

Fig. 3: Simulated *c*-axis fabric shown with (a) the overall deformation and (b) total shear of basal slip in individual grains.

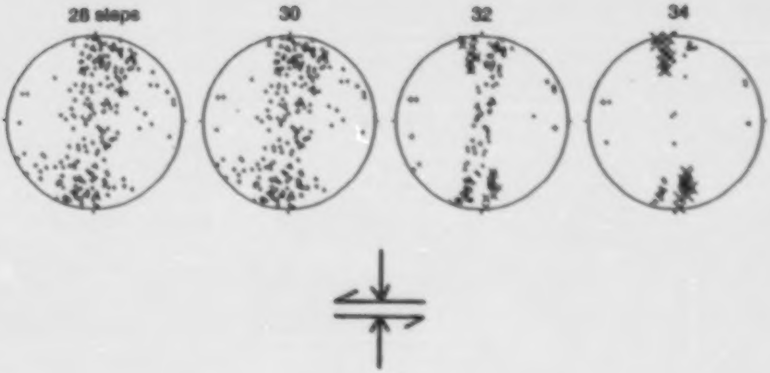

Fig. 4: Simulated *c*-axis fabric caused by concurrent deformation and recrystallization.

Dynamic recrystallization was initiated after 30 steps (shear strain of 0.75 corresponding to *c*-axis patterns illustrated in Fig. 3). Figure 4 shows the *c*-axis texture evolution for steps 28, 30, 32 and 34. In these figures + symbols identify old grains, x symbols stand for newly nucleated grains. The symbol size is proportional to the grain volume (grain size). In the model many grains disappear and the final texture is dominated by grains with *c*-axes near the shear plane normal. The final texture components correspond to "easy slip" orientations with the slip directions of the major slip system oriented parallel to the macroscopic shear direction and the slip plane parallel to the shear plane. These orientations are special for simple shear deformation in a self-consistent framework because in such a texture a single crystal deforms basically in a "single crystal" on a single slip system with no rotation.

4 Discussion and conclusions: possible effect of dynamic recrystallization on the fabric development

Compared with the host *c*-axis fabric (Fig. 1a) where the *c*-axis orientations are concentrated in the narrow zones along the fabric skeleton, the composite *c*-axis fabric from all the host and recrystallized *c*-axis orientations (Fig. 1a) is fairly scattered. The composite *c*-axis fabric skeleton is reasonably approximated as asymmetrical small circles recognizable in the host *c*-axis fabric skeleton. The diffuse nature of the *c*-axis fabric in the recrystallized grains perhaps resulted from subgrain rotation recrystallization. On the other hand, the B-component is more dominant in the composite than in the host *c*-axis fabric. The feature could be attributed to the oriented nucleation and growth of the B-component by grain boundary migration.

LPOs in polycrystals are formed by a few tens of percent of strain, and the individual crystallographic axis does not rotate much with further increasing strain relative to the fixed coordinates (i.e. the shear plane for non-coaxial deformation without spinning) (e.g. Wenk et al. 1989). Therefore, it is suggested in the present sample that A- and D-grains unfavorably oriented for basal slip (hard grains), and B-grains favorably oriented for it (soft grains) remained close to these orientations during the deformation to large strains. Hence, the hardest orientation (i.e. that of the least deformed A-grains which is circled in Fig. 2) is roughly correlated with the compression direction with respect to the shear plane at large strains.

C-grains are less favorably oriented for basal slip than B-grains, but favorably oriented for harder pyramid<a> slip in the framework of shear deformation discussed above. The fact that C-grains are slightly less deformed than B-grains suggests that these grains were mostly deformed by harder pyramid<a> slip. Microstructural evidences suggest that both C- and D-grains were significantly consumed by the recrystallized B-component which nucleated and grew in the former grains. Therefore, in the quartzite sample, softer grains for basal slip grew significantly at the expense of the harder grains by grain boundary migration. The conclusion is consistent with the result from the simple shear experiments on a quartz analogue (norcamphor) by Herwegh and Handy (1996), but opposite to deformation experiments on quartzite in regime I by Gleason et al. (1993) where the hard grains dominate the recrystallized *c*-axis fabric.

It can be inferred that the present asymmetric small circle *c*-axis fabric is ultimately transformed with increasing strain to a *c*-axis fabric dominated by orientations favorable for basal slip only (i.e. a single maximum perpendicular to the bulk shear plane). Such a single maximum *c*-axis fabric perpendicular to the shear plane (note that the *c*-axis maximum is rotated *with* the sense of shear viewed in the frame of finite strain) is observed in both experimentally sheared quartzite under low temperature conditions (Dell'Angelo and Tullis 1989) and naturally sheared quartz schist under greenschist facies conditions from the Sambagawa metamorphic belt (Tagami and Takeshita 1996), where dynamic recrystallization is extensive. Hence, it is concluded that the commonly observed *c*-axis maximum near the Z-axis rotated with the sense of shear in natural quartzite sheared under greenschist facies conditions can be attributed to the growth of soft orientations at the expense of hard orientations for basal slip at large strains.

5 References

Dell' Angelo, L. N. and Tullis, J. (1989) Fabric development in experimentally sheared quartzites. *Tectonophysics*, Vol. 169, pp. 1-21.

Gleason, G. C., Tullis, J. and Heidelbach, F. (1993) The role of dynamic recrystallization in the development of lattice preferred orientations in experimentally deformed quartz aggregates. *Journal of Structural Geology*, Vol. 15, pp. 1145-1168.

Herwegh, M. and Handy, M. R. (1996) The evolution of high-temperature mylonitic microfabrics: evidence from simple shearing of a quartz analogue (norcamphor). *Journal of Structural Geology*, Vol. 18, pp. 689-710.

Lebensohn, R. and Tomé, C. (1993) A self-consistent approach for the simulation of plastic deformation and texture development of polycrystals: application to zirconium alloys. *Acta metall. mater.*, Vol. 41, 2611-2624.

Tagami, M. and Takeshita, T. (1996) Deformation microstructures of the quartz in quartz schist from the Sambagawa metamorphic belt in central Shikoku. *The Journal of the Geological Society of Japan*, Vol. 102, pp. xi-xii.

Takeshita, T. and Wenk, H.-R. (1988) Plastic anisotropy and geometrical hardening in quartzites. *Tectonophysics*, Vol. 149, pp. 345-361.

Wenk, H.-R., Canova, G., Bréchet, Y. and Flandin, L.(1997) A deformation-based model for recrystallization of anisotropic materials. *Acta mater.*, Vol. 45, pp. 3283-3296.

Wenk, H.-R., Canova, G., Molinari, A. and Kocks, U. F. (1989) Viscoplastic modeling of texture development in quartzite. *Journal of Geophysical Research*, Vol. 94, pp. 17895-17906.

Zhang, S. and Karato, S.-I. (1995) Lattice preferred orientation of olivine aggregates deformed in simple shear. *Nature*, Vol. 375, pp. 774-777.

NEUTRON DIFFRACTION STRAIN INVESTIGATION OF SANDSTONES UNDERGOING APPLIED STRESSES

CH. SCHEFFZÜK
GeoForschungsZentrum Potsdam, Germany and
Frank Laboratory of Neutron Physics, Joint Institute for Nuclear Research,
Dubna, Russia
A. FRISCHBUTTER and K. WALTHER
GeoForschungsZentrum Potsdam, Germany

Abstract

Intracrystalline strain measurements on quartz-rich (95% SiO_2) rocks from the Elbezone (E-Germany) were carried out at the diffractometer EPSILON, which is located at beam line 7A of the pulsed reactor IBR-2 at JINR Dubna (Russia). The instrument is characterized by a good spectral resolution (better than 10^{-4}) due to a long total flight path of 102.38 m. The results underline the importance of structure-related stress studies in rocks, even if there is no detectable crystallographic preferred lattice orientation. A pressure device for a uniaxial load up to 100 kN (140 MPa at sample dimensions of $\varnothing$ = 30 mm and l = 60 mm) has been installed for diffraction experiments under load. First experiments carried out on sandstones, demonstrated a linear peak shift, indicating the dependence of strain on the applied stress. The strain values $\varepsilon = \Delta d/d_0$ are in the order of 10^{-3} at a load of about 70 MPa. The applied stress and the observed lattice contractions are consistent with HOOKE's law. Furthermore, besides the peak shift, a peak broadening was observed at increasing stress as an indicator of microstresses. A deep scanning of residual strain through the sample indicates an anisotropy within the bedding plane of the sandstone.

Keywords: deformation experiments, neutron time-of-flight diffraction, quartz, residual stress, strain measurements

1 Introduction

The spontaneous reduction of stresses inside the Earth's crust is the reason for earthquakes. Such internal stress fields are permanently present and are caused by heat transfer, plate motions and/or anomalies of gravity within the Earth's crust. Up to now their characterization has been done mainly on a macroscopic scale. A new method is to characterize the strain/stress behaviour of rocks by crystal lattice properties of minerals by means of strain measurements using diffraction methods. Such strain measurements on rocks have only been carried out by X-ray diffraction so far. For geological materials, however, neutron diffraction is a much more suitable tool because of the high penetration depth of neutrons, which allows the investigation of the stress state of bulk sample volumes of some cm^3. An especially advantageous method is the neutron time-of-flight method because several *d*-values can be determined simultaneously. The observation of many Bragg reflections increases the accuracy of the measurements, which is especially helpful for the investigation of minerals with lower crystal symmetry, of which the upper Earth's crust mainly consists of. The method allows the determination of peak shifts as an indicator of first order (macro) stress and the full width at half maximum (FWHM) as an indication of second order (micro) stress.

2 Sample description

Our first experiments were carried out on nearly monomineralic rocks (sandstones) which consist of >95% quartz (accessory minerals are white mica, feldspar, calcite). The studied samples were taken from drillings within the Elbezone (E-Germany), which is a fault structure of regional importance within the western forelands of the East European Platform. The Elbezone was represented during Cretaceous times (around 90 Ma ago) by a graben structure, which was filled with clastic sediments of several hundred metres thickness (mainly quartz-rich sandstones of Cenomanian-Turonian age).

The studied samples were prepared from drilling cores from a depth of ~250 m as cylinders with the dimensions 30 mm diameter and 60 mm length. The rocks are fine-bedded, but the quartz has no crystallographic preferred orientation. The grain size of the sandstone varies between 100 and 150 μm. The single grains are mostly edge-rounded, the cement is quarzitic or rarely limy too. Some grains are characterized by undulatory extinction, which certainly results already from the parent rock of the sediment.

The preparation of cylinders for deformation experiments was made with their axis perpendicular to the bedding plane.

3 Experimental results

3.1 Experimental procedure

Neutron strain measurements were carried out at the time-of-flight diffractometer EPSILON at the JINR Dubna (Russia). A high resolution of $\leq 10^{-4}$ is achieved by the long flight path of 102.38 m. The diffractometer is equipped with the pressure device EXSTRESS for *in situ*-stress experiments (Fig. 1). The experimental facility is described by Walther *et al.* (1999). First deformation experiments were realized at two different regimes:

1. Three steps of increasing loading perpendicular to the bedding plane of the

sample up to F = 34.2 kN, *i.e.* p = 48.38 MPa and each time keeping the load constant over 24 h during the strain measurements.

2. Stepwise unloading from a maximum load of F = 47.31 kN (p = 66.93 MPa) perpendicular to the bedding plane of the sandstone and over three steps at 24 h down to the unloaded state (Figs. 2 - 4).

3. Additionally we measured the strain differences in dependence on the depth position within a sample, after six days of cyclic deformation using EXSTRESS up to 66.38 MPa (Fig. 5).

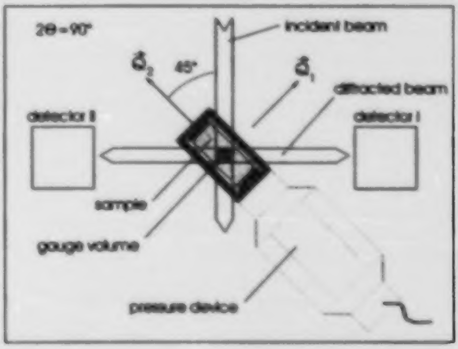

Fig. 1: Sketch of the measurement geometry at the neutron time-of-flight diffractometer EPSILON.

3.2 First and second order stress

A significant peak shift was determined for several lattice spacings of quartz by a stepwise deformation procedure. As example the peak shift of the (01-11/10-11)-reflection is shown in Fig. 2 for the regime of stepwise unloading from a primary load of 66.93 MPa down to the unloaded state. The peak position was determined using an asymmetrical fit function (Scheffzük *et al.*, 1998). The strain-stress-diagram (Fig. 3) shows a linear relation between the applied stress and the measured strain. The relationship was determined using a linear regression. A Young module of E = 66.96 GPa was calculated. This value is in good agreement with the mean value of Young moduli of a quartz single crystal ($E_{\parallel OA}$ = 103 GPa; $E_{\perp OA}$ = 79 GPa), taking into account the effects related to grain boundaries, accessory phases, the pore volume and other parameters, which may influence the Young module for the rock in comparison to this of the quartz single crystal.

Besides the macro stress, which is indicated by peak shift, the applied stress seem also to create micro, or second order stresses within the quartz phase. The effect is observed by an increasing FWHM with dependence on increasing load (Fig. 4). Because of this dependence the determined micro stresses should not be caused by the undulatory extinction of quartz, which was observed microscopically on some grains already prior to the deformation experiment.

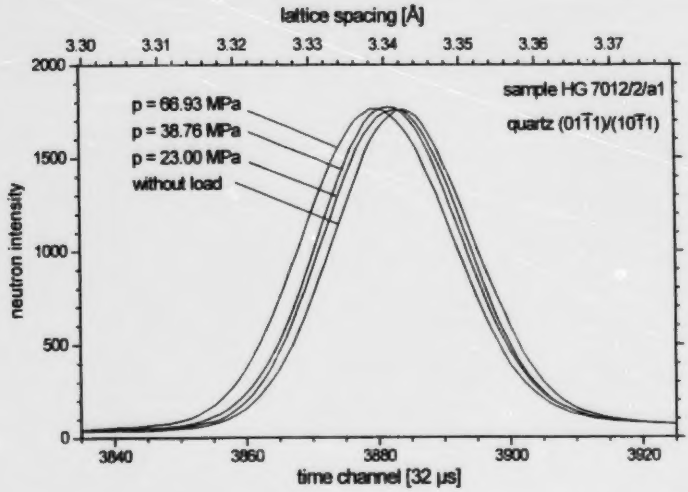

Fig. 2: The figure demonstrates the relaxation of the quartz lattice as a result of reduced load over three steps of 24 h each. The changing position of the (01-11)/(10-11)-peak is shown by the measured time of flight (in time channels) and the corresponding lattice spacing, respectively.

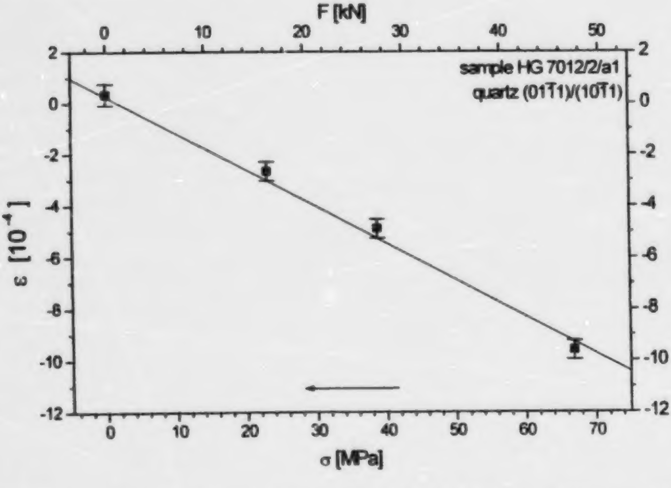

Fig. 3: The strain-stress-diagram (*c.f.* Fig. 2) indicates a linear relationship between the applied stress and the measured strain.

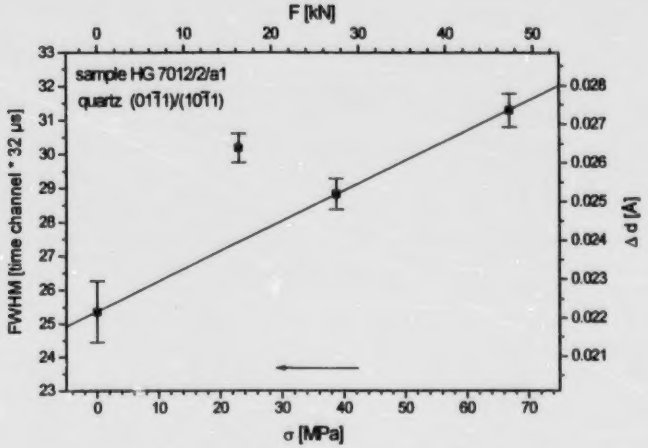

Fig. 4: Full width at half maximum (FWHM) of the quartz (01-11)/(10-11) BRAGG reflection in dependence on applied stress (*c.f.* Fig. 2) as an indication of second order stress.

3.3 Residual strain/stress

Depth dependent residual strain was measured at the same sample six days after the deformation experiment (Figs. 2-4). The measurements follow the radius, from the centre to the margin of the cylinder and were carried out in the directions [x] and [y], which are perpendicular to each other and determine the bedding plane of the sandstone.

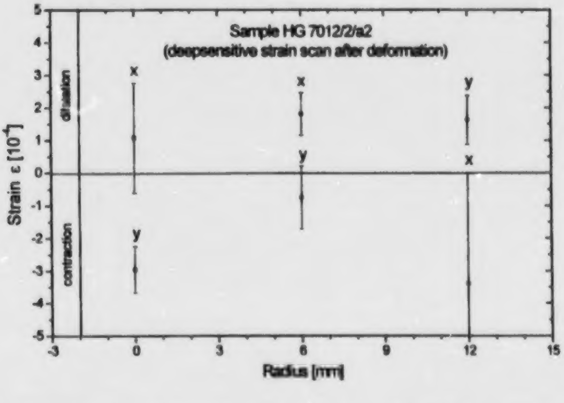

Fig. 5: Residual strain distribution within the bedding (xy)-plane of a deformed sandstone, measured six days after unloading. (Given errors are calculated as mean values from the ε-determination of five BRAGG reflections).

The results (Fig. 5) indicate an anisotropy of residual strain distributions within the bedding plane. The observation is in coincidence with earlier reported results (Scheffzük *et al.*, 1998), regarding a distinct influence of bedding on the strain/stress behaviour of a tested sandstone, even under the conditions of missing crystallographic preferred orientation.

4 Discussion and conclusions

The neutron-TOF-method is a reliable tool for intracrystalline strain/stress determinations, especially for geological materials. At the JINR Dubna there has been installed and tested an operating combination of the strain-diffractometer EPSILON with the uniaxial deformation device EXSTRESS. First combined experiments were performed by elastic deformation of sandstones. It was measured a peak shift due to first order stresses, but also peak broadening as an indicator of second order stresses. The results are consistent with HOOKE's law.

Furthermore, first residual stress measurements, carried out on previously deformed sandstone, underline the influences of rock-macrofabrics like bedding on the strain/stress behaviour of rocks, even in the absence of crystallographic preferred orientation. This may be true especially for the relaxation behaviour of rocks or their residual stress level.

Taking into account that most of the earthquakes occuring within a crustal depth of approximately 10 km, textural features of rocks as well as the mechanical characteristics of polymineralic rocks must be included into modellings of earthquake processes. Further experiments are needed from the geological point of view, mainly for the estimation of the time dependence of stress relaxation, the behaviour of polymineral systems and the effects of crystallographic preferred orientation on the anisotropy of strain and residual stress distributions in rocks.

5 Acknowledgement

The project was supported by the German Federal Ministry for Education, Research and Technology under the project number 03-DUBPOT-3. The authors thank the JINR Dubna and the GFZ Potsdam.

6 References

Scheffzük, Ch., Frischbutter, A. and Walther, K. (1998) *Intracrystalline strain measurements with neutron diffraction: Application to a Cretaceous sandstone from the Elbezone (Germany).* Schriftenr. f. Geowiss. **6**, 39-48.

Walther, K., Frischbutter, A., Lieckefett, R. and Scheffzük, Ch. (1999) *A pressure device for strain measurements of geomaterials at the neutron diffractometer "EPSILON"*. This volume.

STRESS-STRAIN DISTRIBUTION IN DEFORMED OLIVINE AGGREGATES: INFERENCE FROM MICROSTRUCTURAL OBSERVATIONS AND IMPLICATIONS FOR TEXTURE DEVELOPMENT

S. KARATO and K-H. Lee
University of Minnesota, Department of Geology and Geophysics, Minneapolis, MN, U.S.A.

Abstract

Distribution of stress and strain in deformed olivine aggregates was studied through the measurements of dislocation density and the shape of fluid inclusions. The studied specimens include synthetic olivine aggregates deformed at T(temperature)=1573 K and P(confining pressure)=300 MPa and a single crystal dynamically recrystallized at T=1923 K and P=0.1 MPa. It is found that the dislocation density and strain distribution is heterogeneous in all cases, but the degree of heterogeneity is different among the studied specimens. In a recrystallized single where deformation is nearly plane strain, a clear trend is found relating grains (or subgrains) with larger Schmid factors to larger dislocation densities. However, in deformed polycrystals where deformation is more generally three-dimensional, the correlation between Schmid factors for the active slip systems and dislocation densities is less clear. However a trend that grains with higher Schmid factors for easy slip systems tend to have higher dislocation densities and higher strains is noted.

The present results indicate that both stress (inferred from dislocation density) and strain in deformed polycrystalline olivine are highly heterogeneous, indicating that simple models of polycrystal deformation may not apply. In particular, the observed relation of dislocation density and Schmid factor is inconsistent with the Taylor model, which predicts that grains with hard orientation will have higher dislocation density. This, combined with the observed correlation between Schmid factor and strain, indicates that a constraint on deformation of a grain in polycrystalline olivine is less severe than a strict Taylor model implies. Possible models to explain these observations and its implications for texture development involving strain-induced grain boundary migration (SIGBM) and creep strength are discussed.

Keywords: dislocation density, SIGBM, dynamic recrystallization, Schmid factor

1 Introduction

Grain scale distribution of stress and strain is critical to the understanding of deformation of polycrystalline materials and resultant texture (fabric) development. In a real polycrystalline material made of anisotropic crystals, both stress and strain must be heterogeneous, but the degree of heterogeneity has not been investigated in detail. Previous models of polycrystal deformation include (i) homogeneous stress (Taylor) model, (ii) homogenous strain (Sachs) model and (iii) self-consistent model (for a review, see e.g., Kocks, 1998). These models predict different creep strengths: the Taylor model gives the upper bound, the Sachs model gives the lower bound and the self-consistent model gives a strength in between. Texture development due to strain-induced grain-boundary migration (SIGBM) would differ remarkably among these models because the density of dislocations (which provides the driving force for SIGBM) has a different dependence on the Schmid factor in each model (Karato, 1987a). When the Taylor model works, grains with high Schmid factors will survive during SIGBM and dominate the recrystallization texture. In contrast, when the Sachs model is a good approximation, then grains with low Schmid factors will survive and dominate the texture. Therefore in a more realistic intermediate situation (such as the case described by a self-consistent model), one cannot predict texture due to recrystallization even qualitatively because one does not know the dependence of stress (and strain) on the orientation of individual grains.

Thus, it is critical to investigate the stress and strain distribution from the microstructural observations of experimentally deformed polycrystals. However, the measurements of both stress (dislocation density) and strain distribution in deformed polycrystal are not straightforward. The only measurements that the authors are aware of are Kallend and Huang (1984) in which they estimated dislocation densities in individual grains in cold-rolled copper by X-ray line broadening and Azuma (1986) in which the author measured strain distribution in deformed ice polycrystals through *in situ* deformation experiments. In this paper, we will present the first results of measurements of both stress (dislocation density) and strain distribution from the same type of samples. This was possible for our samples (olivine) for the following reasons: (i) our samples contained fluid inclusions whose initial shape was nearly spherical and (ii) dislocation distribution can be investigated throughout the sample scale with high spatial resolution due to a new technique of dislocation observation (Karato, 1987b).

In this paper, the stress and the strain distribution in experimentally deformed olivine aggregates are inferred from microstructural observations. These results are combined with mechanical data and textural information (fabrics) to give some insights into the mechanisms of deformation in olivine aggregates and their effect on the associated texture development.

2 Experimental procedure

2.1. Samples

Samples used are summarized in Table 1. They include an olivine single crystal that was dynamically recrystallized at high temperature (1923 K) (Karato et al., 1980) and deformed hot-pressed olivine polycrystals (Karato et al., 1986). b-14 was an olivine single crystal that was originally oriented at the $[101]_c$ orientation in which the [100](001) and the [001](100) slip systems are activated. The sample was cut along the original (010) plane. The deformed polycrystals (4604, 4682, MIT-5) were originally hot-pressed fine-grained (~10-40 μm) aggregates deformed at P=300 MPa and T=1573 K. Samples 4604 and 4682 were hot-pressed and deformed under water-saturated conditions and contain a number of fluid inclusions. Samples 4604 and 4682 were deformed by tri-axial compression (Karato et al., 1986) whereas the sample MIT-5 was deformed by simple shear under nearly water-free conditions (Zhang et al., 1999).

Table 1: Samples used in this study.

Sample #	Water*	Temperature (K)	Pressure (MPa)	Stress (MPa)	Strain (%)
b-14	dry	1923	0.1	40	56
4604	wet	1573	300	63	13
4682	wet	1573	300	72-142	10
MIT-5	dry	1573	300	95	11

*: "Dry" indicates a water-free sample and "wet" a water-saturated sample.

2.2. Dislocation density measurement

Dislocations in these samples were observed using a backscattered electron imaging with an SEM after oxidation decoration (Karato, 1987b). With this method, dislocations in a large sample area (several $mm \times mm$) can be observed to a resolution of ~0.02 μm. Dislocation density, ρ, is defined as $\rho \equiv \sum l / V$ where $\sum l$ is the total length of dislocations and V is the volume. We use the backscattered electron image to measure the total length of dislocations $\sum l$ using the public domain NIH image analysis software. The volume V in which the total length is measured depends on the effective thickness from which the SEM image of dislocations is obtained. To estimate the effective thickness, we used a deformed single crystal of olivine in which dislocation lines are known to be straight and parallel to the [001] direction. We cut this crystal at 45° with respect to the (001) plane and observed decorated dislocations with an SEM using the same conditions as other dislocation observations. For the conditions that we used (acceleration voltage = 15 kV, current = $(2\text{-}6)\times10^{-9}$ Amp), the effective thickness turned out to be 0.9±0.1μm.

2.3. Strain measurement

Strain measurement was made for a sample (4682) that contains a number of fluid inclusions. The fluid inclusions were formed by rapid grain-boundary migration (Karato, 1989) and the initial shape is nearly spherical. After deformation, relatively large (>2 μm) fluid inclusions are deformed (**Fig. 1**), although small ones maintain nearly spherical shape due presumably to the effects of surface tension (Toriumi, 1979). Using an optical microscope we measured the shape of fluid inclusions projected to the plane of observation (**Fig. 2, 3**).

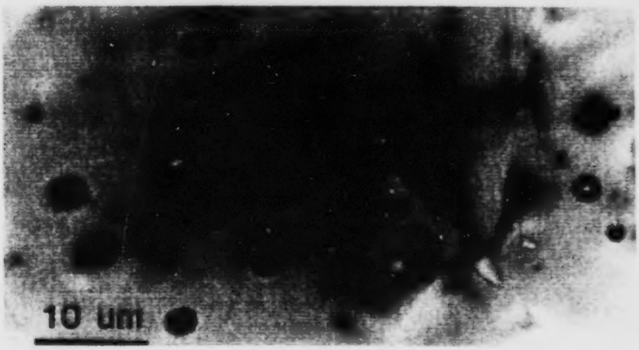

Fig. 1: Fluid inclusions in a deformed olivine (4682).

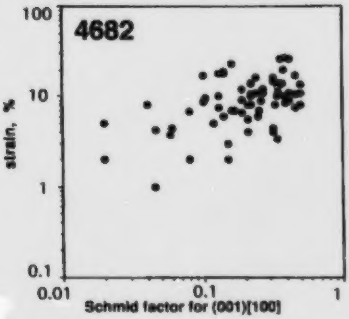

Fig. 2: Strain vs. Schmid factor relation (4682).

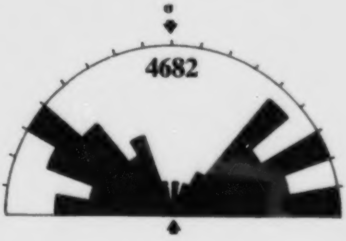

Fig. 3: Orientation of maximum elongation direction (4682).

3 Results

Fig. 4 shows an optical micrograph of sample b-14 together with the SEM images of decorated dislocations. It contains a large number of recrystallized grains (or subgrains) whose misfit angles are ~5-20°. The central portion has an orientation that is nearly the same as the original, but the outer portions show orientations that are progressively rotated away from the original one. The grain-boundaries show curvatures such that grain-boundaries bulge towards the central region. The SEM observations show that this is due to a systematic change in dislocation densities as a function of grain orientation. The dislocation density in this sample shows a strong correlation with the orientation of each grains (**Fig. 5**): dislocation density increases with the Schmid factors (S) of active slip systems as $\rho \propto S^m$ with $m \sim 2$, where the Schmid factors are defined relative to the applied stress.

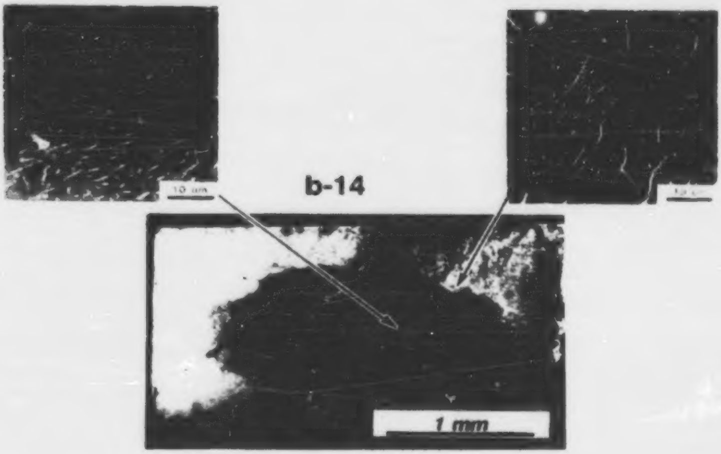

Fig. 4: Deformed and recrystallized olivine (b-14).

Fig. 6 shows the distribution of dislocations in sample 4604. As in sample b-14, dislocations are observed to influence grain-boundary migration, indicating that strain-induced grain boundary migration (SIGBM) occurred in this sample. In many cases, not only homogeneously distributed dislocations but also subboundaries appear to generate a significant driving force for grain-boundary migration (**Fig. 6**). The correlation between dislocation density and Schmid factors is investigated assuming that two slip systems, namely [100](010) and [100](001) make dominant contributions (**Fig. 7**). The correlation is much weaker in this case than in sample b-14. Nevertheless, grains with high Schmid factors tend to have higher dislocation densities than grains with low Schmid factors. A similar trend was observed in MIT-5.

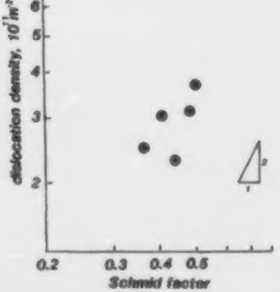

Fig. 5: Correlation of dislocation density with the Schmid factor in recrystallized olivine (b-14).

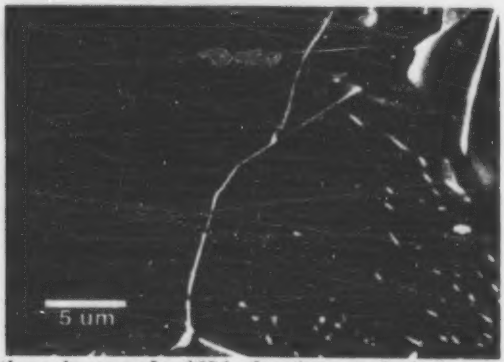

Fig. 6: Dislocations in sample 4604 showing strain-induced grain-boundary migration (SIGBM).

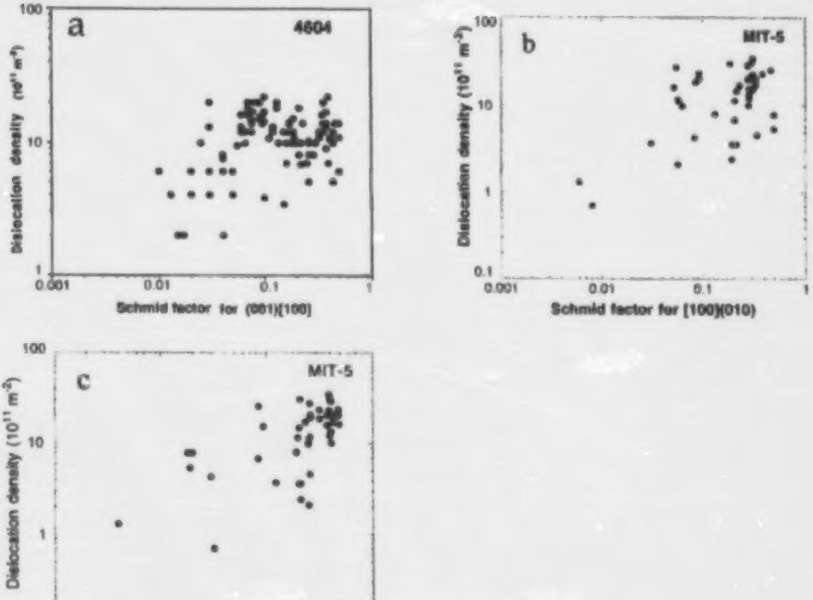

Fig. 7: Correlation of dislocation density with the Schmid factor.

Strain vs. Schmid factor correlation in sample 4682 is plotted in **Fig. 2.** The correlation is stronger than that for the dislocation density. The orientations of the main elongation axes projected to the observation plane are shown in **Fig. 3.** It is seen that the orientation is not uniformly horizontal as would be expected from the Taylor model, but has a large range of angles indicating heterogeneous strain distribution.

4 Discussion

4.1. Stress-strain distribution

Dislocation density in a given crystal is a function of *local* stress and strain. In a deformed polycrystal, each grain deforms due to local stress acting on a number of different slip systems. Dislocations for various slip systems may interact and dislocation density for each slip system could change with strain. In an ideal case where all dislocations corresponding to all possible slip systems assume steady state density, then

$$\rho \propto \sum_i S_i^2 \sigma^2 \tag{1}$$

where S_i is the Schmid factor for the i-th slip system and σ is the local stress at a grain. When all the slip systems contribute to the dislocation density, only weak dependence of dislocation density on orientation of grains is expected. However, in an anisotropic crystal such as olivine, dislocations belonging to only a small number of slip systems will actually dominate. This will occur because (i) strain is partitioned among various slip systems according to the relative easiness of slip, (ii) dislocation density for a given slip system attains the steady state value only after a certain critical strain is exceeded (~1-2%; Durham et al., 1977), and (iii) the average strain in each grain in a deforming polycrystal is small (~10%) due to continuous dynamic recrystallization. As a result, at any given time, dislocation densities for hard slip systems will be significantly smaller than those for easy ones irrespective of their orientations and the dislocation density for easy slip systems will be largely controlled by the local stress through equation (1). Consequently, significant orientation dependence of dislocation density will occur. In olivine, easy slip systems under relatively high temperature and low stress conditions are [100](010) and [100](001) (Durham and Goetze, 1977). Therefore we analyze our results assuming only these two slip systems. In doing so, we calculate the Schmid factor(s) for individual grains corresponding to the orientation of the applied stress σ_a. In reality, the local stress σ is also affected by grain interaction thus,

$$\sigma = \sigma_a + \sigma_{int} \tag{2}$$

where σ_{int} is the stress due to grain interaction. Complications in grain orientation and dislocation density relation can occur when the influence of σ_{int} is large.

Our results show significantly different distributions of dislocations between a recrystallized olivine (b-14) and polycrystals of hot-pressed samples (4604, MIT-5). The results for recrystallized crystal (**Fig. 5**) are nearly the same as an isolated crystal that has no interaction with the surrounding grains. In contrast, large deviation from such an ideal case is observed in polycrystals with more general orientation distributions (**Fig. 7**), indicating the importance of grain interactions in these cases.

This can be interpreted as due to the difference in deformation geometry. In a recrystallized olivine, deformation occurred under nearly plane strain condition and in this case deformation using two slip systems ([100](001) and [001](100)) can completely satisfy the strain compatibility conditions. In contrast, in a polycrystal with more random orientation distribution, a large number of slip systems or other modes of deformation (such as diffusion) are needed. Therefore the truncation of equation (1) with a small number of slip systems will not work, leading to a weak dependence of dislocation density on grain orientation. Also in the latter case, the role of stress due to grain interaction σ_{int} is large and it could also modify the dislocation distribution. Another complication is possible contribution from *geometrically necessary dislocations* (Ashby, 1970). Geometrically necessary dislocations are considered to be produced by *strain gradients* that is related to strain heterogeneity and their density is not a simple function of orientation of grains relative to the stress. In any case, it should be noted that there is a weak but definitive trend that density of dislocations is high for those grains with high Schmid factors for dominant slip systems, indicating that accommodation mechanisms to relax constraints at grain-boundaries are effective and σ_{int} is small for olivine polycrystals under these conditions.

The strain correlates with the Schmid factor(s) of dominant slip system(s) more strongly than dislocation density (**Fig. 2**). This is in contradiction to the Taylor model in which strain is considered to be homogeneous. In the simplest case where stress is homogeneous (the Sachs model, i.e., the case of no interaction of grains), the strain in the individual grains is related to its orientation as,

$$\varepsilon \propto \sum_i S_i^{n+1} \sigma^n t \tag{3}$$

where n is the stress exponent ($\dot{\varepsilon} \propto \sigma^n$, $\dot{\varepsilon}$: strain rate, n~3.5 for olivine (Durham and Goetze, 1977)) and t is time. Therefore, dependence of strain on the Schmid factor is expected to be stronger than that of dislocation density. Our results are consistent with this notion and clearly show that the Taylor model does not work for deformed olivine aggregates: the interaction among grains is much weaker than the Taylor model implies. A similar observation was made for polycrystalline ice deformed in the plane strain geometry (Azuma, 1986) where the relation close to (3) was found, implying a very weak grain interaction.

4.2. Implications for texture (fabric) and deformation mechanisms

Distribution of dislocations in deformed polycrystals has important implications for texture development during dynamic recrystallization. Strong orientation dependence of dislocation density provides a large driving force for SIGBM causing significant modification of texture formed by deformation (Karato, 1987a; Wenk et al., 1997). Our results suggest that such significant modification of texture by SIGBM will occur when a small number of slip systems accommodate much of the strain. Two conditions must be met for this to occur. (i) Anisotropy in the resistance for deformation among various slip systems must be large (large plastic anisotropy). (ii) Critical strain for SIGBM should not be much larger than the strain at which dislocation density assumes steady state values (otherwise dislocations in grains include those belonging to most of the slip systems and there will be little orientation dependence of dislocation density). Since these parameters are dependent upon materials and physical and chemical conditions, the nature of texture development involving SIGBM will vary from one case to the other.

Our results on dislocation density distribution in hot-pressed and deformed samples (4604, MIT-5) show that although a large number of slip systems appear to be needed for deformation, the constraints on deformation imposed by neighboring grains are largely relaxed, resulting in positive correlation between Schmid factors and dislocation density (if constraints were strong as in the Taylor model, we would have obtained negative correlation between Schmid factors and dislocation density). This is compatible with the mechanical results reported elsewhere (Zhang et al., 1999) which demonstrate that samples deformed at 1573 K do not show much geometrical hardening predicted by the self-consistent theory (Wenk et al., 1991). The degree of relaxation of constraints in these samples appears to be more significant than the self-consistent model predicts. Dynamic recrystallization may help relax these constraints by modifying the grain shape and/or by the enhancement of diffusion creep due to grain-size reduction.

This is the first work in which both stress (inferred from dislocation density) and strain distributions in deformed polycrystalline aggregates were measured as a function of orientation (Schmid factor) of individual grains. Kallend and Huang (1984) made similar studies on copper but deformation was at room temperature where recovery and recrystallization would not occur. Strain was not measured in their study. Our results confirm earlier measurements (Karato, 1987a, 1988) and are similar to the results in quartz (Gleason et al., 1993) where grains with low Schmid factors grow during dynamic recrystallization. However, these results are in contradiction to some of the early studies in other materials in which grains with low Schmid factors were inferred to grow (e.g., Urai et al., 1986). This latter case would occur when the constraints imposed by neighboring grains are strong (as implied by the Taylor model). It appears that the nature of texture caused by SIGBM (one mode of dynamic recrystallization) can vary substantially due partly to the complications in physical processes that control the distribution of driving force for recrystallization.

5 References

Ashby, M.F. (1970) The deformation of plastically non-homogeneous materials. *Philos. Mag.*, Vol. 21, pp. 399-424.

Azuma, N. (1986) *Fabric Development and Flow in Basal Ice Sheets*, Ph D thesis, Hokkaido University, pp. 230.

Durham, W.B. and Goetze, C. (1977) Plastic flow of oriented single crystals of olivine. 1. Mechanical data. *J. Geophys. Res.*, Vol. 82, pp. 5737-53.

Durham, W.B., Goetze, C. and Blake, B. (1977) Plastic flow of oriented single crystals of olivine. 2. Observations and interpretation of dislocation microstructures. *J. Geophys. Res.*, Vol. 82, pp. 5755-70.

Gleason, G.C., Tullis, J. and Heidelbach, F. (1993) The role of dynamic recrystallization in the development of lattice preferred orientation in experimentally deformed quartz aggregates. *J. Struct. Geol.*, Vol. 15, pp. 1145-68.

Kallend, J.S. and Huang, Y.C. (1984) Orientation dependence of stored energy of cold work in 50% cold rolled copper. *Metal Sci.*, Vol. 18, pp. 381-5.

Karato, S. (1987a) Seismic anisotropy due to lattice preferred orientation of minerals: Kinematic or dynamic? in *High-Pressure Research in Mineral Physics*, (eds. M.H. Manghnani and Y. Syono), Terra Sci. Pub., Tokyo, pp. 455-71.

Karato, S. (1987b) Scanning electron microscope observation of dislocations in olivine. *Phys. Chem. Mineral.*, Vol. 14, pp. 245-8.

Karato, S. (1988) The role of recrystallization in lattice preferred orientation in olivine. *Phys. Earth Planet. Inter.*, Vol. 51, pp. 107-22.

Karato, S. (1989) Grain growth kinetics in olivine aggregates. *Tectonophysics*, Vol. 168, pp. 255-73.

Karato, S., Toriumi, M. and Fujii, T. (1980) Dynamic recrystallization of olivine single crystals during high-temperature creep. *Geophys. Res. Lett.*, Vol. 7, pp. 649-52.

Karato, S., Paterson, M.S. and Fitz Gerald, J.D. (1986) Rheology of synthetic olivine aggregates: influence of grain size and water. *J. Geophys. Res.*, Vol. 86, pp. 8151-76.

Kocks, U.F. (1970) Relation between polycrystal deformation and single crystal deformation. *Metall. Trans.*, Vol. 1, pp. 1121-43.

Kocks, U.F. (1998) Kinematics and kinetics of plasticity, in *Texture and Anisotropy* (eds. U.F. Kocks, C.N. Tomé and H-R. Wenk), Cambridge University Press, Cambridge, pp. 327-89.

Toriumi, M. (1979) A mechanism of shape-transformation of quartz inclusions in albite of regional metamorphic rocks. *Lithos*, Vol. 13, pp. 1091-110.

Urai, J.W., Means, W.D. and Lister, G.S. (1986) Dynamic recrystallization in minerals, in *Mineral and Rock Deformation: Laboratory Studies*, (eds. B.E. Hobbs and H.C. Heard), Amer. Geophys. Union, Washington DC, pp. 166-99.

Wenk, H-R., Bennett, K. Canova, G. and Molinari, A. (1991) Modelling plastic deformation of peridotite with the self-consistent theory. *J. Geophys. Res.*, Vol. 96, pp. 8337-49.

Wenk, H-R., Canova, G.C., Bréchet, Y. and Flandin, L. (1997) A deformation-based model for recrystallization of anisotropic materials. *Acta Mater.*, Vol. 45, pp. 3283-96.

Zhang, S., Karato, S., Fitz Gerald, J.D., Faul, U.H. and Zhou, Y. (1999) Simple shear deformation of olivine aggregates. *Tectonophysics*, in press.

TEXTURE AND MICROSTRUCTURE OF HALITE AT A HALITE-BASALT CONTACT

CH. SCHEFFZÜK
GeoForschungsZentrum Potsdam, Germany

Abstract

This paper describes the crystallographic preferred orientations and the microstructures of halite samples taken from a basalt-halite contact zone located in the Merkers mine, Werra region (Germany). The results of preferred orientation investigation indicate a (100) cross-girdle for all samples. An isotropization of the texture for smaller distances to the basalt-halite contact was observed. That means, that the (100) cross-girdle was weakened at smaller distances to the intrusion body as a consequence of recrystallization. At a distance of 5 cm from the contact the microstructure is characterized by fluid inclusions on grain boundaries and subgrain formation with a grain size of approximately 100 µm. At a distance of 50 cm as well as fluid inclusions on grain boundaries, slip bands and subgrains with small angle grain boundaries were observed. The sample taken at a distance of 100 cm is characterized by fluid inclusions on grain boundaries, slip bands (as an indicator of slip system activations) and double grain boundaries. No subgrains were discovered at this distance. The textures and microstructures are consistent with temperature simulations across the contact zone. Maximum temperatures were calculated for the three distances with about 500°C at 5 cm after 12 hours, about 250°C at 50 cm after 2 days and about 160°C at 100 cm after 10 days. The simulations indicate that the temperature of static recrystallization, which corresponds to 50% of the melting temperature (290°C), is only reached for the sample at 5 cm distance from the contact. After a time interval of 100 days the temperature of all samples is less than 100°C.

Keywords: Basalt-halite contact, halite, microstructure, neutron diffraction, temperature simulations, texture

1 Introduction

The potassium salt deposits of the Werra region are situated at the northern margin of the Hessische Senke (Germany). The rocks were formed within a margined basin of the Zechstein sea (Zechstein 1). The salt deposits are complicated by a large number of basalt veins of Tertiary age, which form the northern parts of the Rhön volcanic edifices (Oligocene to lower Miocene).

The halite-basalt contact zone is an interesting geological subject for structure investigations, to study the temperature influence and the contact metamorphose by this intrusion. Furthermore, this structure offers the possibility to study temperature-stress induced formation of crystallographic preferred orientations, because the temperature of the intrusive body was approximately 1200°C and the melting temperature of rocksalt is about 800°C. For a better understanding of the measured texture and the observed microstructure of the halite samples, temperature simulations were carried out.

In comparison to X-ray diffraction, the neutron diffraction method is more appropriate for texture investigations of halite, because the penetration depth of neutrons is a factor 194 larger than for X-rays. Therefore, the application of neutron diffraction method allows the nondestructive determination of bulk texture.

2 Sample description

The samples were taken from the potassium salt mine near Merkers in the Werra region, near Bad Salzungen (Germany). The location of sampling was the second floor, south section 11 westward, between location 12 and 13/north, south pile, at a depth of 880 m. The samples were taken beside a basalt vein, which has a thickness of 0.5 to 0.7 m. The basalt veins are oriented in a north-south direction, they dip about 50-70°E. In the ridge region the thickness of the basalt veins increases, it demonstrates the beginning of the deposit vein. Perpendicular to the direction of cooling, shrinking cracks and gaps were observed, which are usually filled by halite and sylvinite.

The halite samples were taken at distances of 5 cm, 50 cm and 100 cm to the halite-basalt contact zone. They are characterized by their white color; the grain size varies in the range of 200 - 2500 µm.

3 Experimental results

3.1 Microstructural observations

The microstructures were revealed by a chemical polishing-etching procedure; described by Mendelson (1961) and observed by means of reflected light microscopy to get information about the deformation and the recrystallization mechanisms.

About 50% of the halite sample, which was taken from the direct contact to the basalt vein, is characterized by the development of subgrains with small angle grain boundaries, which do not show fluid inclusions (Fig. 1). The fabric does not show indications of the activation of slip systems. The old grains are partially opened, preferably in [x]-direction. They contain fluid inclusions like a pearl necklace. It can be assumed, that the grain boundaries opening in [x]-direction could be caused by the mechanical stress of the rocksalt by the intrusion body in [y]-direction. Furthermore, an anisotropy of the grain shape was observed; the long axis are preferrably oriented in NE-SW-direction, that means, parallel to the intrusion body.

Some grains of the sample at a distance of 50 cm from the contact zone show slip bands (a), which indicate the activation of slip systems (Fig. 2). It can be concluded on a very low plastic deformation because these slip bands were observed in only a few grains. However, the subgrain development with small angle grain boundaries (c) indicate a recovery of the lamellar structure of slip bands by dislocation climb. The tendency to develope subgrain boundaries was recognized as well as on old grain boundaries and intracrystalline. The size of subgrains in (b) varies from 20 to 40 µm, whereas in (c) they behave 5 to 10 µm. The fabric demonstrates an opening of the grain boundaries in [x]-direction, that means, perpendicular to main stress direction, caused by the basalt intrusion ($\sigma_1 = y$).

The sample, which was prepared at a distance of 100 cm to the basalt contact shows in some grains a weak lamellar development of slip bands, indicating the activation of slip systems (Fig. 3). However, at this distance the density of slip bands is higher, than at a distance of 50 cm (Fig. 2). At the grain boundaries were observed fluid inclusions. Grain A shows a crack, which split the old grain into two new grains. Furthermore, a double grain boundary is visible (arrow), which is comparable to a grain boundary splitting, observed by Friedman *et al.* (1984) in synthetic rocksalt, deformed at 25°C and at a strain of 10%. It can be assumed that this grain boundary splitting is a preliminary stage of a transgranular microcrack.

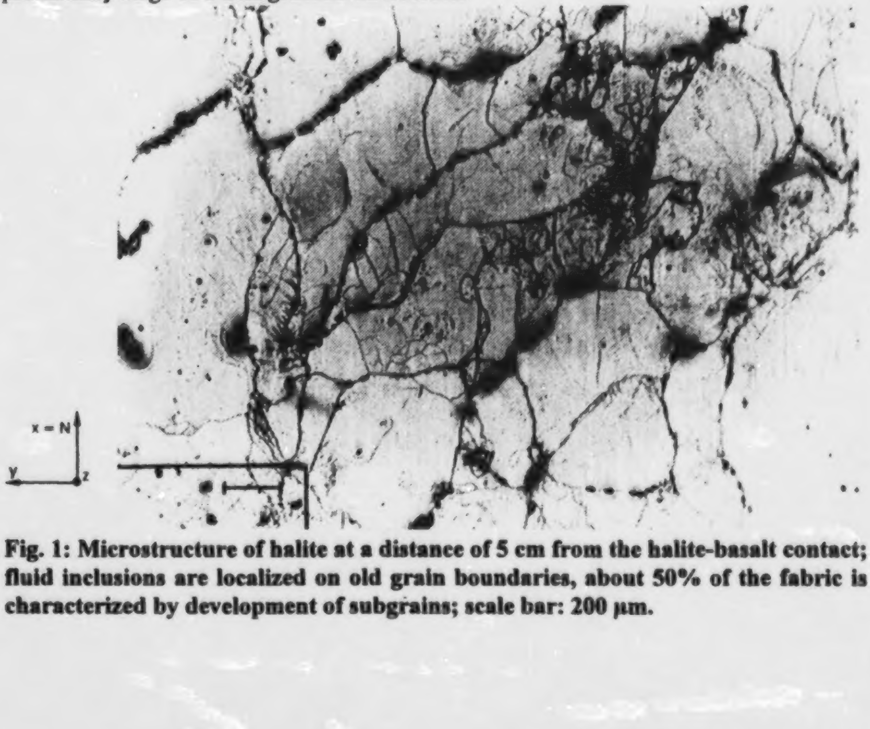

Fig. 1: Microstructure of halite at a distance of 5 cm from the halite-basalt contact; fluid inclusions are localized on old grain boundaries, about 50% of the fabric is characterized by development of subgrains; scale bar: 200 µm.

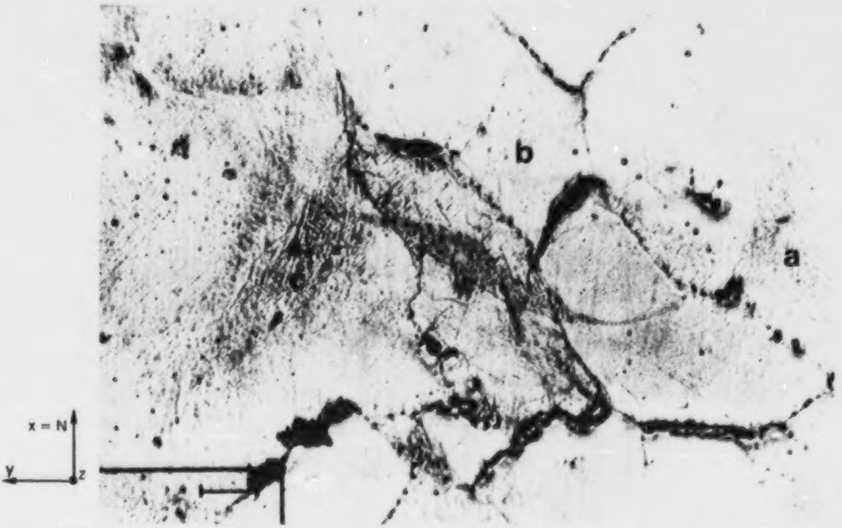

Fig. 2: Microstructure of halite at a distance of 50 cm; slip bands (a), subgrains with small angle grain boundaries: subgrains in the region of (b): 20-40 μm and (c): 5-10 μm; fluid inclusions on old grain boundaries; scale bar: 200 μm.

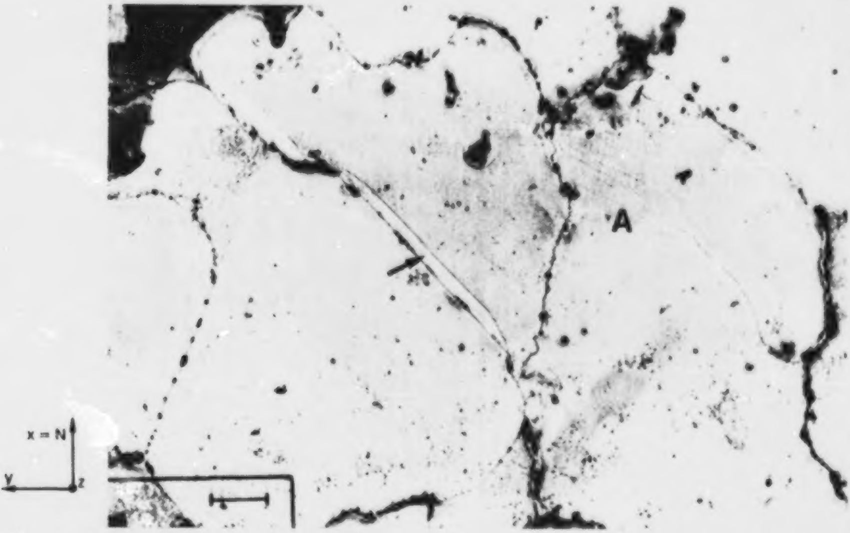

Fig. 3: Microstructural observations on halite at a distance of 100 cm; weak development of slip bands; fluid inclusions on grain boundaries, development of a double grain boundary (arrow), scale bar: 200 μm.

3.2 Texture determination

Neutron texture investigations on halite were carried out using the conventional neutron diffraction method at the texture diffractometer of the research reactor in Řež, Czech Republic, by measuring pole figures (111), (200) and (220) at a wavelength of λ = 1.4457 Å. Quantitative texture analysis was done by means of the WIMV-method (Matthies & Vinel, 1987).

All samples show very weak crystallographic preferred orientations. In all observed distances, the (100)-pole figures show a cross girdle, which was formed by (100)-planes. The position of the cross girdle is in all samples nearly comparable. Furthermore, it was detected, that the intensities of preferred orientations are decreasing at lower distances to the contact zone. The weak texture, observed at the sample C3 (Fig. 4a), can be looked upon as a nearby random distribution as a consequence of the recrystallization. The interpreted texture patterns carry any hypothetical character, because of the weak formed preferred orientation.

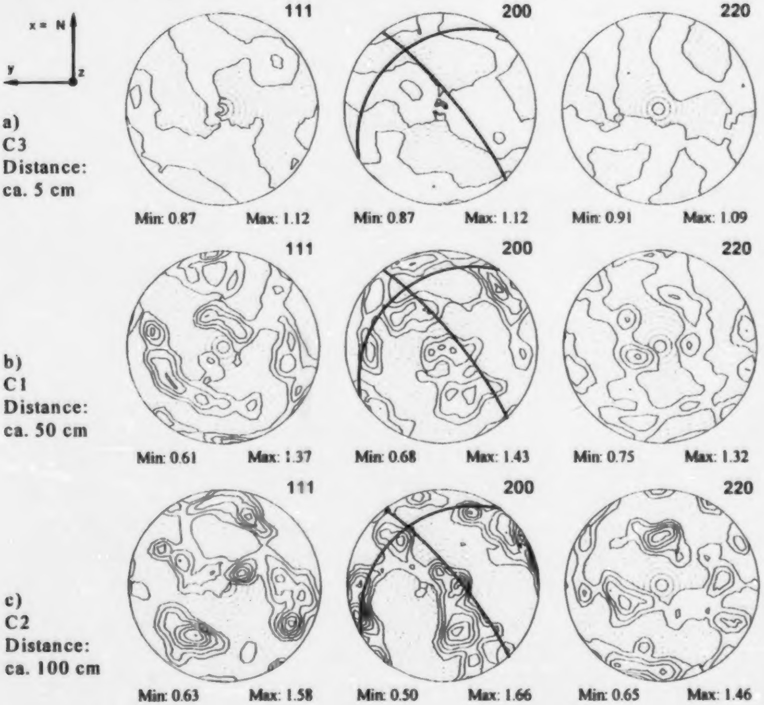

Fig. 4: Recalculated pole figures of halite, selected from the basalt-halite contact (Merkers mine), 7.5°-smoothed (Δh= 0.10 m.r.d.). Distance to the basalt contact: a) C3 about 5 cm, b) C1 about 50 cm, c) C2 about 100 cm.

4 Temperature simulations and discussion

The processes at a basalt intrusion can be understand as follows: The intrusion of the basalt vein causes a deformation of the halite with a relatively high strain rate. Furthermore, the capacity of heat of the basalt causes a slow heat flow. The strongest influence of temperature of the halite rocks exists at the direct contact to the basalt vein. Due to the convection and the conductivity of heat, the temperature wave catches the halite rocks with larger distances to the basalt vein at a later time, with a lower temperature.

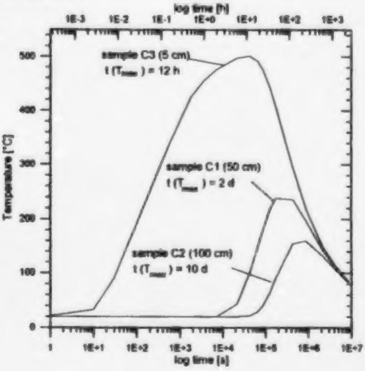

Fig. 5: Dependence of temperature on time after basalt intrusion (at $t_0 = 0$) in distances of 5 cm, 50 cm and 100 cm to the contact (thickness of the basalt vein: 60 cm).

The temperature simulations (taking into account a basalt vein with a thickness of 60 cm) show, that all investigated samples were not warmed up over a temperature of 500°C. That means, that the melting temperature of halite (800°C) was not reached at a distance of 5 cm from the basalt contact. The time-temperature-diagram indicated for the sample at 5 cm, that the maximum temperature reached after about 12 hours was 500°C. The sample at 50 cm has had a temperature of 250°C after 2 days; the sample at 100 cm was warmed up to about 160°C after 10 days (Fig. 5). As a result of the low temperatures the samples at 50 cm and 100 cm show slip bands, which are developed as a consequence of the cold deformation. The slip bands are pronouncably very weak in the 50 cm-sample, they are more pronounced in the 100 cm-sample.

5 References

Friedman, M., Dula, W.F., Gangi, A.F. and Gazonas, G.A. (1984) *Structural petrology of experimental deformed synthetic rocksalt.* In: Hardy Jr., H.R. and Langer, M. (Eds.): Proc. First Conf. on the Mechanical Behavior of Salt, 19-36.

Matthies, S. and Vinel, G.W. (1982) *On the reproduction of the orientation distribution function of texturized samples from reduced pole figures using the conception of a conditionel ghost correction.* Phys. stat. sol. (b) **112**, K111-K114.

Mendelson, S. (1961) *Dislocation etch pit formation in sodium chloride.* J. Appl. Phys. **32**, 1579-1583.

QTA AND POLARISED EXAFS CORRELATION IN SELF-SUPPORTING FILMS OF NONTRONITES

D. CHATEIGNER
Laboratoire de Physique de l'Etat Condensé, Université Du Maine, Le Mans, France
A. MANCEAU AND M. SCHLEGEL
Laboratoire de Géodynamique Interne et Tectonophysique, Université Joseph Fourier, Grenoble, France
M. PERNET
Laboratoire de Cristallographie, Centre National de la Recherche Scientifique, Grenoble, France

Abstract

This work shows the effect of the texturation of self-supporting films of nontronites on the polarised EXAFS spectra and radial structure functions. Nontronite films are stabilised with a single fibre orientation component with maximum densities from 14 m.r.d. to 39 m.r.d. approximately, the {001} planes being aligned parallel to the film planes. The {001} plane dispersions obtained by direct normalisation of pole figures provide a reasonable estimate of the orientation distribution to be used in the EXAFS analysis.

Keywords: polarised EXAFS, P-EXAFS, smectite, nontronite, self-supporting film

1 Introduction

Clay minerals are known to offer large cationic exchange capacity, specific surface area, swelling behaviour, and ability to fix interlayer cations, giving them potential capability in soil treatment. These potentialities strongly depend on their structure, which is hard to precisely investigate. Particularly, the determination of the locations of the adsorbed cations still remains a challenge, because of the low diffraction coherence of smectite crystallites which have a turbostratic stacking. Powder EXAFS spectroscopy provides a local characterisation of the atomic structure and thus can be used to study the crystallographic location of exchanged species, and the short range order of constitutive atoms. However, the quantitative interpretation of EXAFS spectra in these materials is complex due to the interference of several atomic shell contributions at close distances from the central probed atom. This difficulty can be overcome using polarised measurements (P-EXAFS), which allow the partial separation of overlapped contributions at different orientations of the sample. This technique requires the elaboration of highly textured films, then the quantitative texture characterisation becomes important to correctly interpret the P-

EXAFS signals. In this paper we show the angular variations of P-EXAFS spectra and radial structure functions (RSF) in four nontronite self-supporting films, and the corresponding quantitative texture characterisation.

2 Samples, texture experiments

Textured samples were prepared by vacuum filtration of dispersed smectites suspensions (Manceau et al, 1998a). They consist in approximately 1x1 cm^2 films, with a maximum of 2 micrometers in thickness. The idealised structure of a nontronite smectite (**a**=5.28Å; **b**=12.56Å; **c**=9.14 Å; β=99.3°, C2/m) is presented on Figure 1a, showing the octahedral sheet containing metal ions, attached to two tetrahedral sheets (with Si and Al as central atoms). X-ray texture experiments were conducted using the Cu K_α radiation (graphite monochromator) provided by a rotating anode, and using a PTS-Seifert goniometer (Manceau et al, 1998a).
Due to their turbostratic layer stacking, diffraction diagrams of such compounds show broad diffraction lines, with predominant 00ℓ and hk0 lines (Figure 1b) which occur at different tilt (ρ) angles in textured films. From such diagrams it is undoubtedly difficult to completely calculate the orientation distribution (OD), except if one allows the existence of the 11±3 lines, in the foot of {004}, as demonstrated later ({001} is not used because located at too much low Bragg angle to avoid geometrical problems). However, a quantitative estimate of the {004} density is made possible by profile integration of the lines and direct normalisation, assuming a 0-density level at high ρ values (which is reasonable from the ρ-evolutions of the peaks. Since the texture of these films is axially symmetric around their normal (Figure 3), such a normalisation provides enough information to interpret the P-EXAFS measurements.

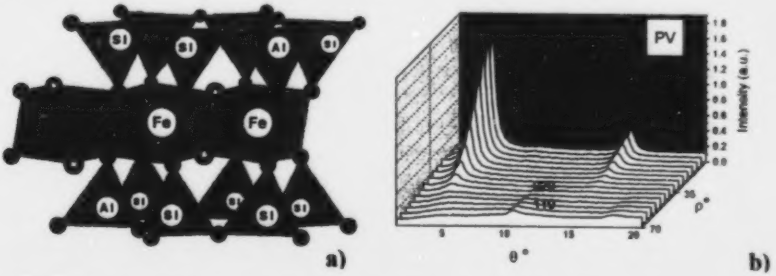

Figure 1: Idealised nontronite structure (**a**) and typical tilt evolution of the diffracted diagram for a nontronite self-supporting film (**b**).

We analysed four nontronite films coming from Garfield, Washington, Panamint Valley, California (PV), Grant County, Washington (SWa-1) and Höhen Hagen, Germany (NG1). Results for the angular distribution density of the {004} reflections are presented in Figure 2. The maximum density for the Garfield nontronite is observed much larger than in the other films, with a {004} dispersion around 20° at half maximum. Whatever the film, the dispersion is Gaussian, as revealed by a least-square fit (lines on Figure 2). On this Figure, the dashed horizontal line which indicates the 1 m.r.d. level intersects the dispersion at the ρ_l value, above which atomic pairs aligned with <001>* directions are unfavourably probed by spectroscopic measurements, comparing to a powder. Around the so-called spectroscopic "magic angle", ρ=35.3°, no anisotropic signal can be detected using P-EXAFS in such crystal systems. We can observe a small bump in the distribution around ρ=45°, that may be attributed to {11±3} reflections, giving the opportunity to solve the complete OD of the samples, using a WIMV approach (Wenk et al., 1998). Using {11±3} the recalculated pole figures compare satisfactorily with the experimental ones (Figure 3). The {001} density profile recalculated from the OD for the Garfield nontronite is presented in Figure 4.

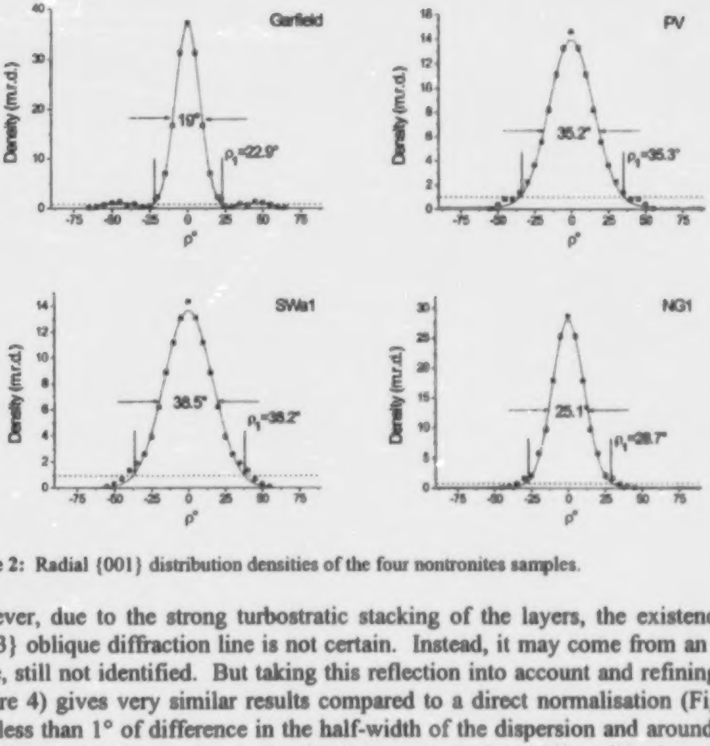

Figure 2: Radial {001} distribution densities of the four nontronites samples.

However, due to the strong turbostratic stacking of the layers, the existence of the {11±3} oblique diffraction line is not certain. Instead, it may come from an impurity phase, still not identified. But taking this reflection into account and refining the OD (Figure 4) gives very similar results compared to a direct normalisation (Figure 2a), with less than 1° of difference in the half-width of the dispersion and around 2 m.r.d. of difference in the maximum density (Manceau et al., 1998b). We then choose to neglect the potential 11±3 reflection and compare the texture of the samples using direct normalisation, which gives a slight underestimation of the strength of the achieved textures.

The maximum density, observed in the Garfield sample, reaches 38 m.r.d. for a minimum around 14 m.r.d. for SWa-1. This latter is the only one exhibiting densities above the magic angle. The observed dispersions are characteristic of strong preferred orientations for self-supporting films, and it is the purpose of the following to show how much this influences P-EXAFS spectroscopic investigations.

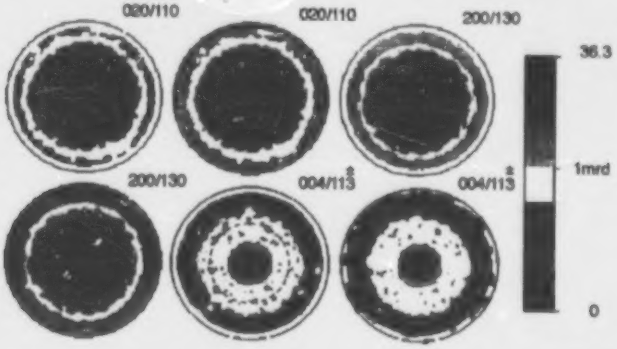

Figure 3: Experimental and recalculated normalised pole figures for the Garfield nontronite, using the {11±3} reflection. Logarithmic density scale, equal area projection.

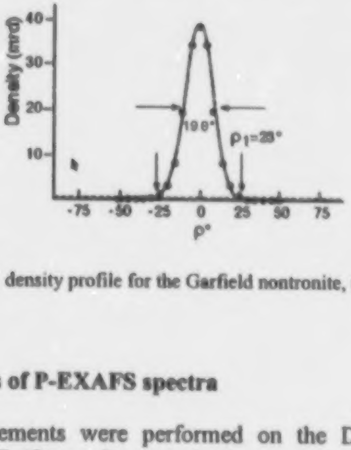

Figure 4: Recalculated {001} density profile for the Garfield nontronite, using the OD.

3 Angular variations of P-EXAFS spectra

The Fe K-edge measurements were performed on the D42 spectrometer at the synchrotron source LURE (Orsay, France), in the transmission mode. The (331)-Si reflection is used, with a divergence of 10^{-4} radians, an energy resolution of 1.5eV and a polarisation yield over 95%. For axially symmetric textures and single scattering processes in the plane-wave approximation, the angular dependence of EXAFS spectra $\chi(k,\theta)$ can be written (Stern et Heald, 1983):

$$\chi(k,\theta) = \sum_j 3 < \cos^2\theta_j > \chi^j_{iso}(k) = \sum_j \sum_{i=1}^{N_j} 3\cos^2(\theta^j_i)\chi^j_{iso}(k) \quad (1)$$

where j denotes the number of the neighbouring atomic shell, i runs over all the N_j atoms of the j^{th} shell, θ^j_i is the angle between the electric-field vector ε and the vector $\mathbf{R}_{ij}$ that binds the absorbing atom to the i^{th} atom of the j^{th} shell. χ_{iso} is the isotropic powder contribution of the j^{th} shell. It comes from Eq. 1 that P-EXAFS measurements provide directional structure information, and can be used to probe the structure of layer silicates by varying the angle between the self-supporting film and ε.

Because of the complete random distribution of crystallites around the normal to the film plane, $\cos^2\theta$ can be averaged around its normal (Bonnin et al., 1986). This allows to express the relation between the crystallographic (N_{cryst}) and the effectively probed (N_{eff}) number of neighbours (Manceau, 1990), giving the possibility to correct data:

$$N_{eff.} = 3\,N_{cryst}\,[\,\cos^2\phi\sin^2\alpha + (\sin^2\phi\cos^2\alpha)/2\,] \qquad (2)$$

Where ϕ is the angle that makes the atomic pair with the normal to the film plane, and α is the angle defined by ε and the film plane. One sees that from the knowledge of ϕ it is possible to calculate N_{eff} for every experimental α angle. Figure 5 shows the k^3-weighted P-EXAFS spectra of the Garfield sample obtained under the different polarisation configurations $0° < \alpha < 60°$. A large dependence upon polarisation is seen, consistent with the orientation measurements. The amplitude of χ decreases with increasing α at 8.5 $Å^{-1}$, and increases with α at 4 $Å^{-1}$. It is not the purpose here to discuss the structural information that one could extract from such spectra (Manceau et al., 1998b), but to evidence if it exists some correlation between P-EXAFS and texture.

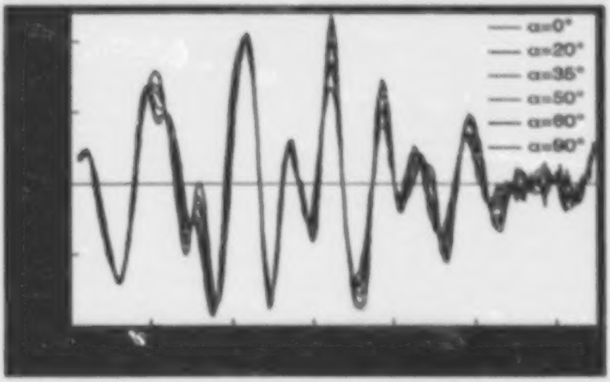

Figure 5: k^3-weighted P-EXAFS spectra taken at the Fe K-edge for Garfield nontronite at five different α angles. Spectrum for α=90° has been obtained by regression of the experimental amplitude.

Calculating the Fourier transform of the P-EXAFS spectra gives the RSF presented for the four samples on Figure 6. We clearly see the α-evolutions of RSFs, particularly for the peak around 3Å, which derives from the associated pair contributions and their orientations. This peak corresponds to the contributions of the nearest Fe,Al,Mg shell (Oct1) located in the octahedral sheet, and of the nearest tetrahedral Si,Al shell (Tet1) located apart from the octahedral sheet (Figure 1a). For the in-plane orientation (α=0), the contribution from Oct1 atoms at the crystallographic distance R=2.8Å is enhanced, while for the out-of-plane (α=90°) orientation the contribution of Oct1 is cancelled and the one of Tet1 maximised at R=3.28Å. The α-evolution of the RSF peak correspondingly shifts towards higher values with α. Other peaks of the RSFs show less α dependence (Manceau et al., 1998b). Interestingly, Garfield nontronite which shows the highest texture around 38 m.r.d. at maximum, also exhibits the largest variation of the 3Å peak. The NG1 film, for which we measured an intermediate orientation density also shows intermediate peak variation. In the case of SWa1 with densities above 1 m.r.d. at α angles larger than the magic angle, the P-EXAFS evolution is severely decreased.

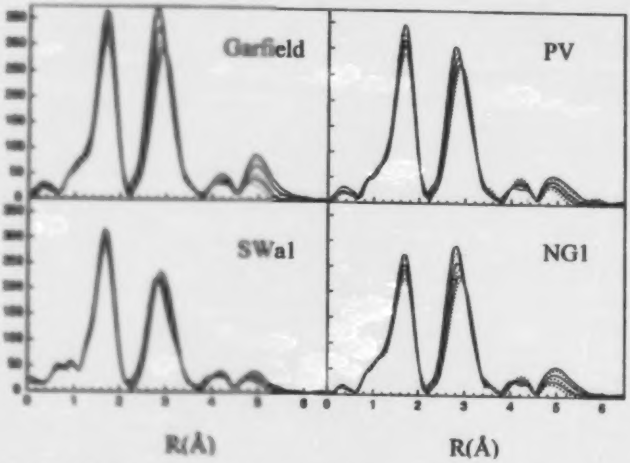

Figure 6: RSFs for the four nontronite samples. Note the strong variation for the Garfield film.

4 Conclusion

The quantitative correlation of P-EXAFS spectra and RSF with the orientation density has been shown. Polarised experiments on highly textured films give access to larger spectral range in the P-EXAFS measurements, that now need to be analysed with the incorporation of the textural information. Taking into account standard distributions of crystallites, like Gaussians, still needs to be incorporated in the EXAFS formalism.

5 References

Bonnin, D., Bouat, J., Kaiser, P., Frétigny, C. and Béguin, F. (1986). In Lagarde, P., Raoux, D. and Petiau, J. (Eds) *EXAFS and near edge structure IV, J. Phys. Paris*, pp 865-868.

Manceau, A. (1990). *Canadian Mineralogist*, 28, 321-328.

Manceau, A., Chateigner, D. and Gates, W.P. (1998a). *Physics & Chemistry Of Minerals* 25, pp 347-365.

Manceau, A., Lanson, B, Drits, V.A., Chateigner, D., Gates, W.P., Wu, J., Huo, D.F. and Stucki, J.W. (1998b). To appear *American Mineralogist*.

Stern, E.A. and Heald, S.M. (1983). In Koch, E. (Ed), *Handbook for Synchrotron Radiation*, North-Holland Amsterdam, New York pp955-1014.

Wenk, H.-R., Matthies, S., Donovan, J. and Chateigner, D. (1998). *J. Appl. Cryst*. 31, pp 262-269.

TEXTURE DEVELOPMENT OF $CaTiO_3$-FeO COMPOSITES AT HIGH-TEMPERATURE

Z.-C WANG and S. JI

Department of Geology, University of Montreal, Montreal, Canada

R. WIRTH

GeoForschungsZentrum Potsdam, Potsdam, Germany

ABSTRACT: Annealing experiments were performed to study the texture development of $CaTiO_3$-FeO (perovskite-wustite) composites. We observed two types of distinct textures: (1) homogeneous fine-grained texture at $T<1250$ °C, in which FeO distributed homogeneously along $CaTiO_3$ grain boundaries and at triple junctions; (2) heterogeneous domain texture at $T\geq1250$ °C, in which FeO is separated from the $CaTiO_3$ and forms large clusters. We interpreted this in terms of substantial change in grain boundary energy of the $CaTiO_3$ and the wetting behavior of FeO resulting from the $CaTiO_3$ phase transformation at 1250 °C.

Keywords: $CaTiO_3$, composite, FeO, perovskite, texture

1. Introduction

Texture development of composites plays an important role in modifying many material properties, such as strength of materials, elastic and electrical properties. Because of their unique properties, perovskites have been used to fabricate many types of important devices including sensors, switches, memories, capacitors, and photochemical cells. Many of these devices are sensitive to the characteristic texture of the composites. Thus, a fundamental understanding of the texture development in perovskites can lead to improved and reliable devices. We studied the texture development of $CaTiO_3$-FeO composites through annealing experiments performed at high temperatures (T) and high pressure (P). The objective goal is to characterize textures of the $CaTiO_3$-FeO and to understand the factors controlling the texture development. We demonstrated that textures of the $CaTiO_3$-FeO composites depend on the annealing conditions, and related to the changes in grain boundary energy of the $CaTiO_3$ and the wetting behavior of FeO resulting from the phase change of $CaTiO_3$.

2. Experimental Procedure

2.1. $CaTiO_3$-FeO composite samples

The $CaTiO_3$-FeO composite samples were prepared with the FeO content (V_{FeO}) varied from 0%, 1%, 3%, 6%, 10% to 20% by weight, and synthesized using hot-isostatically-pressing (HIP) techniques. To obtain samples with homogeneous initial microstructure, $CaTiO_3$ and FeO powders were prepared by mixed oxide and co-precipitation methods. The dried powders were first cold-pressed and then hot-pressed at T=1073 °C and P=300 MPa in a gas medium high-P, high-T apparatus. The synthesized composite samples were examined by scanning electron microscopy (SEM), and the initial grain sizes of $CaTiO_3$ was determined as 1.0 ± 0.5 μm. The distribution of the FeO was homogenous with maximum grain size below 1.0 μm.

2.2. Annealing experiments

Annealing experiments were performed using either a 0.1 MPa high-T apparatus or a gas-medium high-P and high-T apparatus. The temperature during an experiment was controlled within ±1 °C. Oxygen fugacity was varied by flowing continuously a mixture of CO plus CO_2 gases with different ratios and monitored with a solid electrolyte, zirconia-based sensor. We conducted the annealing experiments in either 25 °C or 50 °C steps within the range of T=1173-1350 °C. Annealing duration varied from 3 to 120 hours at an oxygen fugacity of $fO_2=10^{-11}-10^{-9}$ MPa.

2.3. Microstructural analysis

Composite samples after annealing were observed by scanning electron microscopy (SEM) and high resolution transmission electron microscopy (HR-TEM, Phillips CM 20 FEG). Samples for SEM observation was first polished with diamond lapping film, then chemically polished with 30 nm syton. To reveal grain boundaries, the sample surface was etched in acid (H_2O:HCl:HF=2:2:1) at room temperature. SEM back-scattered electron imaging (BEI) and HR-TEM were used to investigate the morphology of the FeO, the grain boundary chemistry and structures.

3. Experimental Results

To investigate the texture development of the $CaTiO_3$-FeO composites, the hot-pressed $CaTiO_3$-FeO composite samples were annealed under various (T, fO_2) conditions for sufficient long time (t>24 hours) so that grain sizes were saturated (Wang et al., 1999). We studied the grain size evolution, morphology and the grain boundary chemistry of $CaTiO_3$, and the morphology and distribution of FeO as a function of time and temperature.

3.1 Texture and morphology of $CaTiO_3$

$CaTiO_3$-FeO composites, annealed T<1523 °C, were examined by SEM, showed two typical textures of $CaTiO_3$: granoblastic polygonal texture and fine-grained polygonal texture (Table 1). A continuous increase in grain size with decreasing V_{FeO} appeared clear at a given annealing time. For example, samples with pure $CaTiO_3$ showed an average grain size of ~ 12.0 μm annealed at 1200 °C. At a comparable annealing condition, the average grain sizes were smaller than 5 μm and 4.0 μm for composite with V_{FeO}=1% and V_{FeO}=3%, respectively. The average grain sizes were even smaller than 2.0 μm for composite with $V_{FeO}\geq6\%$. Two kinds of $CaTiO_3$ grains were developed at this temperature regime: (1) For the composite with $V_{FeO}<3\%$, equilibrium granular texture was developed. Grain size showed a near log normal distribution (Wang et al., 1999). $CaTiO_3$ grains have grown to a texture in which the surface per unit volume is a minimum for the given grain size. Grain boundaries are straight and where three gains meet, they tend to do so in a symmetrical way at triple

Table 1. Textures observed in the $CaTiO_3$-FeO composites

T		$CaTiO_3$		FeO		Composites
(°C)	G* (μm)	Grain shape	Texture	Morphology	Distribution	
< 1250	<1.5	irregular, curved grain boundary.	fine-grained aggregate	1) thin film at $CaTiO_3$ grain boundary; 2) scattered distributed at triple junctions of $CaTiO_3$	homogeneous	mixed-two phase, homogeneous fine-grained aggregate.
≥ 1250	>5	regular, polygonal, equilibrium grain boundary.	granoblastic polygonal	isolated from $CaTiO_3$, forming locally large cluster	heterogeneous	separated two phase, domain aggregate.

* They are average grain sizes for composites annealed at the given temperatures.

junctions, with an interfacial or dihedral angle of about 120°. This is a type of granoblastic polygonal texture. (2) For the composites with $V_{FeO}\geq 6\%$, the textures are typical of fine-grained polygonal texture. Most of the grain boundaries are curved and grains are irregular in sharp. The texture characteristics indicated a lack of equilibrium.

The $CaTiO_3$-FeO composites, annealed at T≥1250 °C, showed different texture development. This is particularly true for composites with $V_{FeO}\geq 6\%$. Normal grain growth was dominant in samples with various V_{FeO}. Grain growth, which was substantially faster at T≥1250 °C than that observed at T<1250 °C, resulted in a granoblastic polygonal texture in $CaTiO_3$. This texture is comparable to that of $CaTiO_3$ in samples with $V_{FeO}<6\%$ annealed at T<1250 °C.

3.2 Texture and morphology of FeO

FeO, as second phase in the composite, showed a complicated texture development and distribution depending very much on the annealing temperature. A wide range of grain sizes, from nanometer size to a few microns, were observed for samples annealed at T<1250 °C. Two types of morphology of FeO were observed at this temperature regime: (1) FeO remained as fine-grained particles (~1 μm); (2) Nanometer-sized particles occurred continuously along two grain boundaries of $CaTiO_3$ (Fig. 1). The nanometer-sized FeO particles clearly pinned the $CaTiO_3$ grain boundaries. In contrast to texture and distribution of FeO in samples annealed at T<1250 °C, FeO showed a completely different morphology in samples annealed at T≥1250 °C. The most pronounced feature is that FeO tends to move away from $CaTiO_3$ boundaries. There is no longer FeO observed along $CaTiO_3$ boundaries. Instead, FeO were concentrated locally and grown into large grain (or cluster) with size of over 10 μm (Fig. 2). The redistribution of FeO formed a domain structure in the $CaTiO_3$-FeO composites.

3.3 $CaTiO_3$ grain boundary chemistry

X-ray energy dispersive analysis was performed to investigate the grain boundary chemistry. In these composite samples annealed at T≥1250 °C with granoblastic polygonal texture, no FeO has been found along the two grain boundaries. Instead high concentration of FeO was found at the $CaTiO_3$ triple junctions. In contrast, the dispersive energy spectra showed substantial concentration of FeO along most of the two grain boundaries of $CaTiO_3$ in samples with fine-grained polygonal texture.

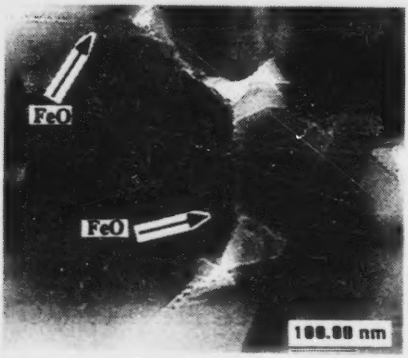

Fig. 1. HR-TEM image showing FeO particles along grain boundaries of $CaTiO_3$.

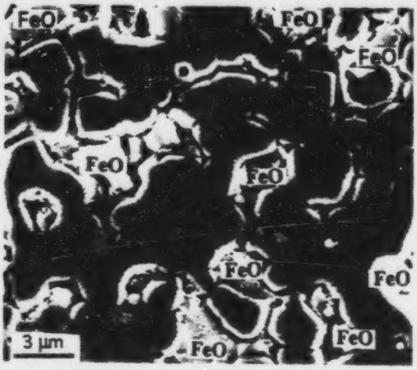

Fig. 2. BEI images showing the morphology and distribution of FeO.

4. Discussions

4.1 Formation of the textures in $CaTiO_3$-FeO composites

The texture of the $CaTiO_3$-FeO composites, annealed at T<1250 °C, is clearly controlled by grain growth of $CaTiO_3$. This is supported by the extensive presence of fine-grained FeO particles along $CaTiO_3$ grain boundaries. The rates of grain-growth were substantially lower than those of pure $CaTiO_3$ and the growth exponents were determined as high as 3.5 (Wang et al., 1999), suggesting an impurity-controlled grain growth. Why did FeO occur along $CaTiO_3$ grain-boundaries as small particles and inhibit grain growth of $CaTiO_3$ below T<1250 °C but not above T≥1250 °C? One possible interpretation would be that FeO completely wets grain boundaries of $CaTiO_3$ at T<1250 °C, but not at T≥1250 °C. The nanometer FeO particles could be the result of breakup of a continuous film of FeO during cooling. The presence of a FeO film inhibits grain growth kinetics because FeO does not dissolve $CaTiO_3$. This leads to the formation of a fine-grained texture.

$CaTiO_3$-FeO composites, annealed at T<1250 °C, shows a domain structure, in which FeO is separated from $CaTiO_3$. Two possible processes may be responsible for the separation: (1) density contrast driven melt percolation; (2) Oswald-ripening. The later is interface-energy driven due to the strong contrast in surface energies between the contacted phases. We exclude the melting of FeO based on the arguments that the experiments were performed at temperature range fairly below the melting temperature of FeO (T_m=1450 °C) and we did not observed any glass phase of FeO. Thus the separation of FeO from $CaTiO_3$ is related to the process of Oswald-ripening, which could result from a large change in interface energy of $CaTiO_3$/FeO due to the phase transformation of $CaTiO_3$.

4.2 Influence of $CaTiO_3$ crystal structure

$CaTiO_3$ perovskite may go from orthorhombic to tetragonal at T=1100-1150 °C and further to cubic at T=1250 °C (Redfern, 1996). Our grain growth experiments on $CaTiO_3$ were performed within T=1100-1350 °C, and different grain growth kinetics have been observed at T<1250 °C and T≥1250 °C. Based on the works on the similar material (Redfern, 1996), our $CaTiO_3$ samples could be of cubic structure at T≥1250 °C, but have tetragonal structure at 1100 °C<T<1250 °C. This assumption is supported

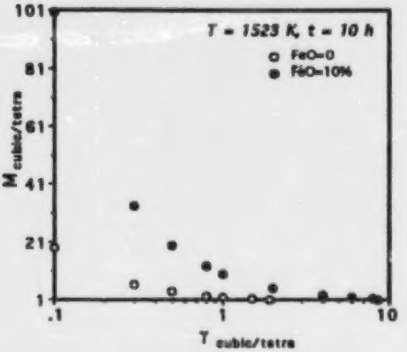

Fig. 3. Relative grain boundary mobility (M_{cubic} /M_{tetra}) is plotted as a function of the grain boundary energy ($\gamma_{cubic}/\gamma_{tetra}$).

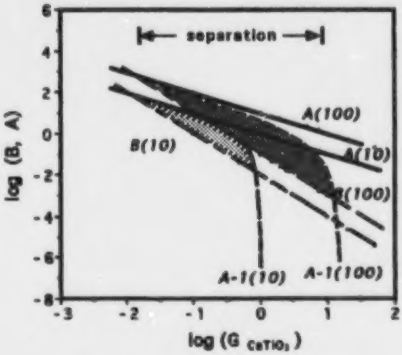

Fig. 4. The log(B) and log(A) values are plotted as a function of log(G_{CaTiO3}).

by the observed twins in $CaTiO_3$ grains. Both (112) and (110) twins were developed in the samples annealed at T≥1250 °C, but (112) twin was dominated in samples annealed at T<1250 °C. Thus, the difference in grain growth in $CaTiO_3$ may also suggest a substantial difference in grain boundary mobility between tetragonal and cubic phases.

The apparent grain-boundary mobility can be estimated from grain growth data. The grain boundary mobility, M, can be expressed as (Yan, 1980)

$$M = \frac{\kappa}{n\gamma d^{n-2}} = \frac{d^2\left[1-(d_0/d)^n\right]}{n\gamma t} \approx \frac{d^2}{n\gamma t} \tag{1}$$

where γ is the grain boundary energy. To compare the grain boundary mobility of $CaTiO_3$ in tetragonal and cubic phases, grain growth data obtained at T<1250 °C and T≥1250 °C should be extrapolated to T=1250 °C. Since there is data available for $CaTiO_3$, we can only estimate the relative grain boundary mobility with the relative grain boundary energy as a parameter. From Eq. (1), the relative mobility ($M_{relative}=M_{cubic}/M_{tetra}$) is expressed as a function of relative grain boundary energy ($\gamma_{relative}=\gamma_{cubic}/\gamma_{tetra}$):

$$M_{relative}\gamma_{relative} = c \tag{2}$$

where $c = (\frac{d_{cubic}}{d_{tetra}})^2(\frac{n_{tetra}}{n_{cubic}})$. We determined c≈1.9 for samples with FeO=0% (d_{tetra}=9.6 µm, n_{tetra}=2.2, d_{cubic}=12.6 µm, n_{cubic}=2.0) and c≈8.5 for samples with FeO=10% (d_{tetra}=1.3 µm, n_{tetra}=3.5, d_{cubic}=3.2 µm, n_{cubic}=2.5) at t=10 h. From these two values, $M_{relative}$ can be estimated as a function of $\gamma_{relative}$. In the calculations, we assume $\gamma_{relative}<1.9$ for samples with FeO=0% and $\gamma_{relative}<8.5$ for samples with FeO=10% to satisfy the observations of $M_{cubic}>M_{tetra}$. Two hints may be drawn from the calculation (Fig. 3): (1) An increase in grain boundary mobility is expected across the tetragonal/cubic phase boundary of $CaTiO_3$; (2) the increasing magnitude in grain boundary mobility is higher in $CaTiO_3$ containing 10% FeO than that in pure $CaTiO_3$.

4.3 The role of FeO and its separation from $CaTiO_3$

FeO grains at the $CaTiO_3$ grain boundaries limit grain growth in $CaTiO_3$. This is supported by HR-TEM observations: abundant nanometer-sized FeO particles were present along $CaTiO_3$ grain boundaries and/or triple junctions in samples annealed at $T<1250$ °C. FeO also inhibits the grain growth of $CaTiO_3$ at $T\geq1250$ °C. HR-TEM observations demonstrate that no FeO present along the $CaTiO_3$ grain boundaries annealed in these regimes. Thus a separation of FeO from $CaTiO_3$ grain boundaries, a process parallel to the grain growth of $CaTiO_3$, may occur at $T\geq1250$ °C. We assumed that the segregation could occur when the grain boundary velocities, V_{CaTiO3} becomes faster than V_{FeO} (Brook, 1976). In term of driving force (F) and mobility, this is when

$$V_{FeO} = F_{FeO}M_{FeO} < V_{CaTiO3} = (F_{CaTiO3} / fF_{FeO})M_{CaTiO3} \qquad (3a)$$

$$\text{or} \qquad B < A\text{-}1 \qquad (3b)$$

where $B=(M_{FeO}/fM_{CaTiO3})$, $A=(F_{CaTiO3}/fF_{FeO})$, and f was taken approximately as V_{FeO}. To estimate the conditions satisfying Eq. (3), B and A were calculated by assuming: (1) $CaTiO_3$ underwent normal grain growth, (2) the driving force for grain boundary migration was directly proportional to the grain boundary energy, (3) G_{FeO} is taken as constant (0.01 μm). From Eq. (1) and taking f=0.1, we obtained

$$A = 0.1(\frac{\gamma_{CaTiO_3}}{\gamma_{FeO}})(\frac{1}{d_{CaTiO_3}}), \quad B = 0.001(\frac{\gamma_{CaTiO_3}}{\gamma_{FeO}})(\frac{1}{d^2_{CaTiO_3}}) \qquad (4)$$

We calculated A, B and (A-1) as a function of d_{CaTiO3} with $\gamma_{CaTiO3}/\gamma_{FeO}=10$ and 100, respectively. For these two values, Eq. (3) is satisfied at $d_{CaTiO3}<1.5$ μm ($\gamma_{CaTiO3}/\gamma_{FeO}=10$) or $G_{CaTiO3}<15$ μm ($\gamma_{CaTiO3}/\gamma_{FeO}=100$), respectively (Fig. 4). Thus, the separation of FeO from $CaTiO_3$ grain boundaries is expected provided that the range of $\gamma_{CaTiO3}/\gamma_{FeO}$ is realistic.

We would interpret the separation of FeO from $CaTiO_3$ grain boundaries as a direct result from $CaTiO_3$ phase transformation, which could lead to a jump in grain boundary energy of $CaTiO_3$. Thus, the different grain growth kinetics in $CaTiO_3$ perovskite at $T<1250$ °C and $T\geq1250$ °C may reflect a combined effect from the FeO (as a second phase) and phase change in $CaTiO_3$. Grain sizes may increase by 10% to 50% across the tetragonal/cubic phase boundary, indicating the role of crystal structure. A 40% to 90% reduce in grain size is expected as FeO content increases, indicating the role of FeO. Therefore, we suggest that the presence of FeO control the texture development in $CaTiO_3$-FeO aggregates. However, the kinetics of grain growth in $CaTiO_3$ may depend on the crystal structure of $CaTiO_3$ as well, which determines the wetting behavior of the FeO and in turn the texture development of the $CaTiO_3$-perovskite composites.

References

Brook, R.J. (1976) Controlled grain growth, in *Treatise on Materials Science and Technology*: Vol. 9, Academic Press. New York, pp 331-364.

Redfern, S.A.. (1996) High-temperature structural phase transitions in perovskite ($CaTiO_3$). *J. Phys. Condens. Matter*. Vol. 8, pp. 8267-8275.

Wang, Z.C., Mei, S., Karato, S. and Wirth, R.. (1999) Grain Growth in $CaTiO_3$-Perovskite + FeO-Wüstite Aggregates. *Phys. Chem. Minerals* (in press).

Yan, M. (1980) Grain growth in Fe_3O_4 *J. Am. Ceramics Soc*. Vol. 63, pp.443-447.

QUANTITATIVE TEXTURE ANALYSIS OF EXPERIMENTALLY SHEARED ANHYDRITE AND ALBITE AGGREGATES

F. HEIDELBACH
Bayerisches Geoinstitut, Universität Bayreuth, 95440 Bayreuth, Germany

Abstract

The crystallographic preferred orientation of experimentally sheared polycrystalline aggregates of anhydrite and albite was analyzed using a synchrotron X-ray beam of 30μm diameter. In anhydrite, high shear strain ($\gamma = 8$) lead to a texture often encountered in naturally deformed samples. The preferred orientation is not related in a simple way to either the kinematic frame of the experiment or the shape preferred orientation of the sample. The textures in two albite samples ($\gamma = 7.5$ and 11) correspond to preferred orientations found in natural plagioclase deformed under low metamorphic conditions. Despite the high strains the textures are relatively weak.

Keywords: synchrotron radiation, geology, deformation, texture, shear

1 Introduction

Experimentally sheared samples often represent a challenge to standard texture analysis measurements because they are exceedingly small and/or very heterogeneous. At the same time the interpretation of shear textures is a very important and highly discussed problem in structural geology (e.g. Wenk and Christie 1991). In this work we used the focussed X-ray beam (30μm) of a synchrotron source in combination with a two dimensional CCD-detector to measure the preferred orientation with high spatial resolution in experimentally sheared aggregates of anhydrite ($CaSO_4$, orthorhombic) and albite ($NaAlSi_3O_8$, triclinic).

2 Experimental Details

The microfocus beamline (Riekel et al. 1992) at the European Synchrotron Radiation Facility (ESRF) delivers a X-ray beam produced by an undulator inserted into a straight low β section of the storage ring. A single wavelength (here: λ = 0.782 Å) between 6 and 18 keV is filtered out with a channel-cut Si (111) monochromator and the beam is subsequently focussed both horizontally and vertically with an ellipsoidal mirror to a size of about 20 (h) x 40 (v) μm^2. In the experiments presented here a final collimator of 30μm opening width was employed to define the final beamsize. Diffraction patterns were recorded with an optically coupled Princeton CCD detector cooled with liquid nitrogen. The active area of the detector was 10 by 10 cm with a pixel resolution of 96 μm.

The detector was mounted perpendicular to the incident x-ray beam (Fig. 1). Samples were prepared as doubly polished slabs of 100 μm thickness amd mounted on a rotation axis (ψ) with a rotation deviation of 1 μm. Depending on the number of reflections to be recorded and the resolution in 2Θ, the samples were placed at a distance of about 10 to 15 cm from the detector screen. The detector position (distance from the sample, tilt of the detector, center of diffraction pattern) was calibrated with a standard powder sample. The samples were rotated around ψ in steps of 5° and at each sample position a complete set of Debye rings was measured simultaneously.

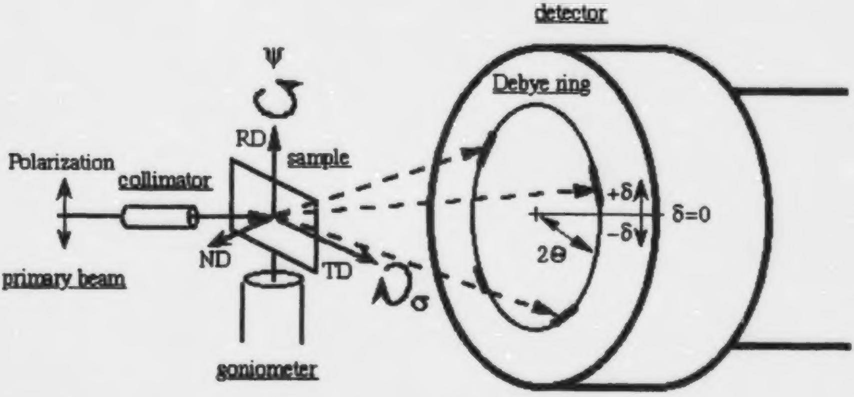

Fig. 1: Experimental setup.

The intensity variation along the diffraction rings (angle δ) yielded the orientation information for the different lattice planes. The intensities were corrected for background and polarization of the incident beam. An absorption correction was not applied due to the low absorption coefficients of the studied materials for the applied wavelength. The orientation information was then transformed into pole figure coordinates by simple spherical trigonometry (e.g. Heidelbach et al. 1999). The Debye rings represent reflections from lattice planes on small circles with an opening angle of 90-Θ around the beam axis. Sample rotations around ψ were carried out only up to ±60° in order to avoid shadowing effects of the sample. The resulting partial pole figures were sufficient to calculate the ODF with the WIMV algorithm (Matthies 1979) as it is implemented in the Berkeley texture package BEARTEX (Wenk et al. 1998). By comparison of the experimental and recalculated pole figures as well as the RP values of the ODF calculation the consistency of the data was confirmed.

3 Anhydrite

The texture development in polycrystalline anhydrite yields information about the deformation path of sedimentary sequences where anhydrite rich layers often form the weakest part and accumulate the highest strains (e.g. Jordan et al. 1990). In studies of naturally deformed anhydrite mostly symmetrical or slightly asymmetrical textures were encountered (e.g. Mainprice et al. 1993) although in some cases the strain path appeared to be non-coaxial (Jordan et al. 1990). Most experimental studies up to date have focussed on the deformation behaviour and texture development during axial compression where symmetrical textures were observed (e.g. Dell'Angelo and Olgaard 1995). In the present study we investigated the texture development in polycrystalline anhydrite deformed experimentally in torsion to very high shear strains (Stretton and Olgaard 1997). The cylindrical samples deformed in torsion display a continuous gradient of strain and strain rate from the center (0% strain) to the edge (maximum strain and strain rate) which allows to study the effect of this gradient on the texture development.

3.1 Sample

A polycrystalline aggregate of anhydrite was deformed in torsion at 700°C and a maximum strain rate of 5×10^{-3} sec^{-1} to a strain of 8.14. The stress-strain curve for this sample showed a peak strength at a shear strain of 1, followed by a softening of the material up to shear strain of 3 and a constant flow stress up to a shear strain of 8. The softening is accompanied by a reduction in grain size from 12 to 6 μm through dynamic recrystallization. From independent strain rate stepping tests, the change in rheological behaviour and stress exponent is interpreted as transition from dislocation controlled creep to diffusion controlled creep. The microstructure in the most strongly deformed part shows a recrystallized fabric with grain elongation oblique (against the shear sense) to the experimental shear plane; the angle between them is about 30°.

The crystallographic preferred orientation was measured as a function of shear strain/shear strain rate from the center to the edge of the sample. The texture of a hot pressed sample was also measured as an equivalent of the undeformed sample state for comparison; in the figure below it is displayed under $\gamma = 0$. At each point eleven partial pole figures were collected: {111}, {020}/{002}, {200}, {022}, {220}/{202}, {212}/{103}, {131}, {301}, {230}/{123}, {040}/{004} and {232}.

3.2 Results

A preferred orientation becomes discernible at shear strains of 1.5 to 2 (corresponding to strain rates of 1 and 1.3×10^{-3} sec^{-1} respectively, Fig. 2). It reaches a 'stable' position relative to the kinematic frame at a strain of about 3.7 (strain rate 2.3 $\times 10^{-3}$ sec^{-1}). The texture is marked by a maximum of {020} at 10 to 15° rotated against the shear relative to the shear direction. The formation of the stable texture coincides with the onset of the constant grain size of 6 μm, indicating that dynamic recrystallization preserves a texture that is almost independent of additional shear strain. The observed texture pattern corresponds well with preferred lattice orientations encountered in natural anhydrite mylonites (Jordan et al. 1990, Mainprice et al. 1993). However, it is clearly oblique to the kinematic reference frame (about 10 to 15°), which was not the case in the cited studies. With an angle of about 30° between the shear plane and the long axes of the ellipsoidal grains the obliquity of the shape fabric is even larger; the crystallographic orientation is therefore not in a simple way related to either the macroscopic shear plane or the grain shape fabric (foliation).

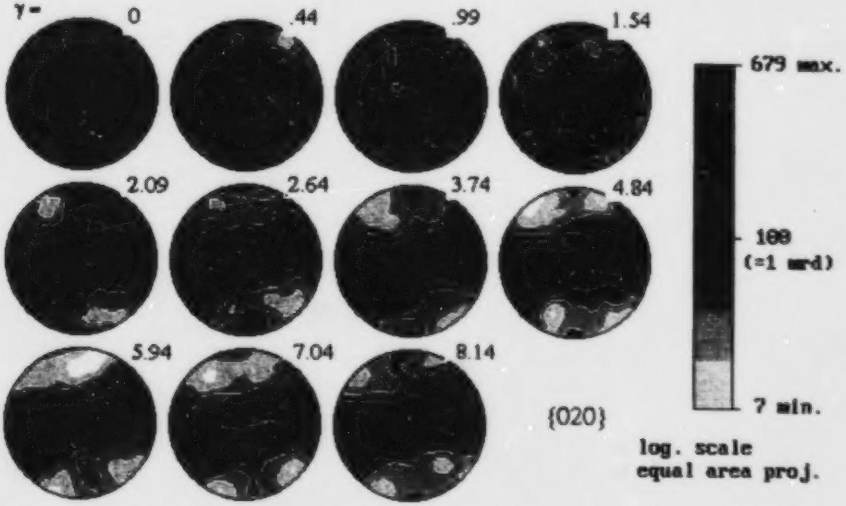

Fig. 2: Anhydrite {020} pole figures as function of shear strain γ.

4 Albite

Despite the abundance of plagioclase in the Earth's crust relatively little is known about its deformation behaviour and the development of crystallographic preferred orientation in particular. This is due to the chemical heterogeneity and the low symmetry of the plagioclase solid solution series, which causes the diffraction pattern as well as the relationship between optical indicatrix and crystal lattice to be rather complex (e.g. Wenk et al. 1986). In this study these problems were simplified by using albite, the Na rich endmember of the plagioclase series, as the sample material.

4.1 Samples

Two samples were deformed in a Griggs-type apparatus adapted for simple shear deformation (Post and Tullis 1999). In this setup, a thin layer (ca. 300μm) of the sample material was placed between two pistons cut at 30° to the cylinder axis. Axial compression of the cylinder lead to a simple shear deformation in the sample layer. The amount of shear strain was determined by the lateral displacement of the pistons after the experiment. The samples were deformed at 900°C and 15kbar confining pressure to shear strains of 7.5 (W799) and 11 (W824) respectively. The shear strain rates were 6.4×10^{-5} (W799) and 1×10^{-4} sec^{-1} (W824). The deformation lead to a grain size reduction from about 4 μm to 1 (W799) and 1.5 μm (W824). Microstructural observations indicate that both samples were dynamically recrystallized.

For the texture analysis the pole figures of the following lattice planes were measured and used in the ODF calculation: {10-1}/{001}, {01-1}/{11-1}, {1-1-1}, {20-1}, {1-11}, {1-30}/{111}, {130}/{13-1}, {11-2}, {1-1-2}, {2-20}/{040}/{20-2}, {1-31}, {04-1}/{02-2}, {131} and {1-3-2}.

4.2 Results

The textures in both samples show a similar pattern: a girdle of {001} poles perpendicular to the shear plane and maxima of the {100} poles in the shear direction as well as slightly oblique to it rotated with the shear sense (Fig. 3). Textures of this type have been found in plagioclases naturally deformed under low metamorphic conditions (e.g. Kruhl 1987, Prior and Wheeler 1999). The textures are relatively weak (maximum 2.67 m.r.d.) for the high strains. The texture of W799 (γ = 7.5) shows monoclinic symmetry which is consistent with the simple shear deformation, whereas the symmetry of the texture in sample W824 (γ = 11) is clearly triclinic, indicating that the deformation was not purely in simple shear.

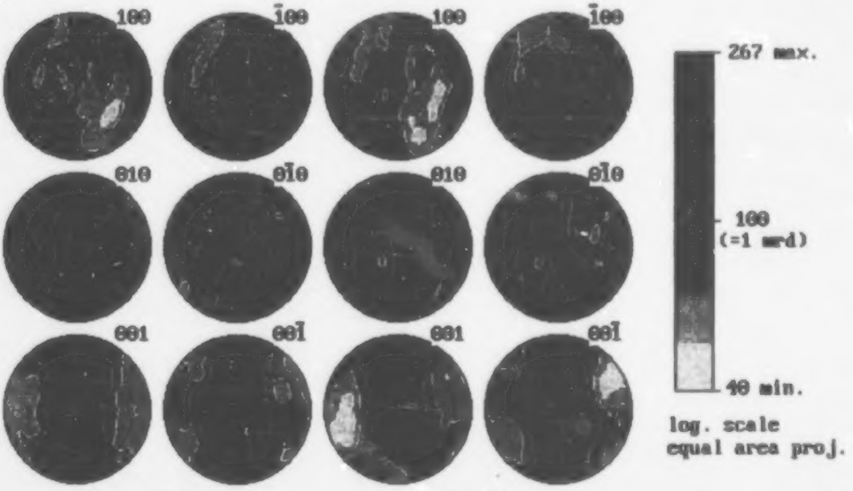

γ = 7.5 γ = 11

Fig. 3: Albite pole figures for the two samples (left W799, right W824).

5 Discussion and conclusions

The results of this study show that quantitative texture analysis can be achieved with high resolution in rather complicated samples with low crystal symmetries and heterogeneous microstructures. A lower limit for the resolution of this type of measurement is the grain size, which has to be sufficiently small to yield usable diffraction patterns. Compared to methods using single crystal diffraction in the electron microscope, this appoach only yields information about the bulk texture of the investigated volume. However, it is not limited by high amounts of strain that may cause problems for electron diffraction methods.

6 References

Dell'Angelo, L. N. and Olgaard, D. L. (1995) Experimental deformation of fine-grained anhydrite: Evidence for dislocation and diffusion creep. *Journal of Geophysical Research*, Vol. 100, No. B8, pp. 15425-40.

Heidelbach, F., Riekel, C. and Wenk, H. R. (1999) Quantitative texture analysis of small domains with synchrotron X-rays. *Journal of Applied Crystallography*, in press.

Jordan, P., Noack, T. and Widmer, T. (1990) The evaporite shear zone of the Jura Boundary Thrust - New evidence from Wisen well (Switzerland). *Eclogae Geologia Helvetiae,* Vol. 80, No. 3, pp. 525-42.

Kruhl, J. H. (1987) Preferred lattice orientations of plagioclase from amphibolite and greenschist facies rocks near the Insubric Line (Western Alps). *Tectonophysics*, Vol. 135, pp. 233-42.

Mainprice, D., Bouchez, J. L., Casey, M. and Dervin, P. (1993) Quantitative texture analysis of naturally deformed anhydrite by neutron diffraction texture goniometry. *Journal of Structural Geology*, Vol. 15, No. 6, pp.793-804.

Matthies, S. (1979) On the reproducibility of the orientation distribution function of texture samples from pole figures (ghost phenomena). *Physica Status Solidi*, Vol. B92, pp. 135-38.

Post, A. and Tullis, J. (1999) A recrystallized grain size piezometer for experimentally deformed feldspar aggregates. *Tectonophysics*, Vol. 303, No. 1-4, pp. 159-73.

Prior, D. J. and Wheeler, J. (1999) Feldspar fabrics in a greenschist facies albite-rich mylonite from electron backscatter diffraction. *Tectonophysics*, Vol. 303, No. 1-4, 29-49.

Riekel, C., Bösecke, P. and Sanchez del Rio, M. (1992) Two high brillliance beam lines at the ESRF dedicated to microdiffraction, biological crystallography, and small-angle scattering. *Review of Scientific Instrumentation*, Vol. 63, No. 1, pp. 974-981.

Stretton, I. C. & Olgaard, D. L. (1997) A transition in deformation mechanism through dynamic recrystallization - evidence from high strain, high temperature torsion. *Eos Transactions*, Vol. 78, No. 46, p. F723.

Wenk, H.-R., Bunge, H. J., Jansen, E. & Pannetier, J. (1986) Preferred orientation of plagioclase - neutron diffraction and U-stage data. *Tectonophysics,* Vol. 126, pp. 271-84.

Wenk, H.-R. and Christie, J. M. (1991) Review paper: comments on the interpretation of deformation textures in rocks. *Journal of Structural Geology*, Vol. 13, No. 10, pp. 1091-110.

Wenk, H. R., Matthies, S., Donovan, J. and Chateigner, D. (1998) BEARTEX: a Windows-based program system for quantitative texture analysis. *Journal of Applied Crystallography,* Vol. 30, pp. 262-9.

TEXTURE-RELATED ELASTIC (SEISMIC) ANISOTROPY IN CRUSTAL AND MANTLE ROCKS

H.M. KERN

Institut für Geowissenschaften, Olshausenstrasse 40, 24098 Kiel, Germany

Abstract:

The rocks constituting the Earth's crust and upper mantle have a great variety in composition and structure and contain, in general, low-symmetry mineral phases with different grain size and different physical and chemical properties. In addition, crustal and mantle rocks contain cracks and pores which can be filled with fluids. The development of pronounced fabric anisotropy is basically a result of ductile deformation, primarily controlled by intracrystalline slip and dynamic recrystallization. The generation of a deformation fabric is associated with a change of bulk physical properties from near-isotropic to largely anisotropic. This paper focuses on the directional dependence of P- and S-wave velocities in crustal and upper mantle rocks. It concentrates on elastic (seismic) anisotropy of P- and S-wave velocities, shear-wave splitting and shear-wave polarization and on their relationship to the rock fabric. Experimental and calculated data reveal details concerning seismic anisotropy and shear-wave splitting, thus providing an important basis for geophysical interpretations.

Kewords: Lattice preferred orientation (LPO), velocity anisotropy, shear wave splitting, ductile deformation, geophysical significance

Introduction

An important property of rocks constituting the Earth's crust and upper mantle is anisotropy, that is, that physical properties are different in different directions. Anisotropy in geomaterials may be due to crystallographic preferred orientation of anisotropic minerals (texture), to a layered arrangement of the components and to preferred oriented microcracks. The effectiveness of microcracks, in particular, is largely controlled by pressure and temperature. This paper focuses on elastic (seismic) anisotropy in crustal and mantle rocks and on the relation of velocity anisotropy to the rock fabric: (1) on measurements of P- and S-wave velocities (Vp and Vs) in different directions, and (2) on 3D calculations based on the lattice-preferred orientation (LPO) of the major minerals and their volume fraction together with the corresponding single-crystal stiffness coefficients of rock-forming minerals.

Experimental determination of elastic anisotropy

Experiments investigating propagation of compressional (P-waves) and shear waves (S-waves) in crustal and mantle rocks at elevated pressures and temperatures are generally carried out on dry samples using the ultrasonic pulse transmission technique (e.g. Birch, 1960). Measurements are done either on sample cylinders (e.g. Christensen, 1984) or on sample cubes (e.g. Kern, 1982). Velocities are almost measured in three perpendicular directions with the sample reference system corresponding to fabric elements (normal to foliation [Z], perpendicular to lineation [Y], and parallel to lineation [X]). Although velocity measurements along the three principal axes are generally insufficient to describe the elastic properties completely, they permit the estimate of maximum and minimum velocities and thus the coefficient of anisotropy A ($A = [(V_{max} - V_{min})/V_{mean}) * 100\%]$).

The contribution of oriented cracks and lattice-preferred orientation (LPO) to bulk velocity anisotropy at pressure and temperature

eismic wave velocities are very sensitive to the state of microfracturing, the effectiveness of which in turn is controlled by pressure and temperature (Fig. 1). In the KTB gneiss (Fig.1a) velocity anisotropy of P-waves is highest at low pressures, caused by constructive interference of the effects resulting from oriented microcracks and lattice preferred orientation (LPO). Increasing pressure reduces the effect of cracks, and the residual anisotropy is mainly due to the LPO of major minerals (e.g. Kern and Wenk, 1990; Ji and Salisbury, 1993). Vp and Vs are highest parallel to the foliation plane and lowest normal to it. The LPO-related anisotropy is largely due to the alignement of phyllosilicate minerals (biotite, muscovite) and, importantly, is not significantly affected by temperature (Fig. 1b). Shear-wave splitting is most pronounced for S- waves propagating parallel to the foliation plane (Fig. 1a, b), with the fast split shear wave polarized parallel to the foliation. Normal to the foliation plane shear wave splitting is low. The LPO-related anisotropy represents the intrinsic anisotropy, that is, the anisotropy of a rock which is almost free of effective cracks.

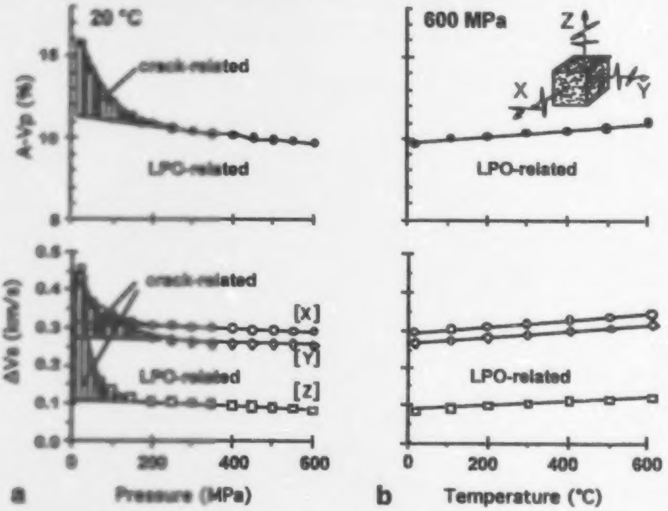

Fig. 1. Anisotropy of P-wave velocities (upper line) and shear wave splitting ΔVs (lower line) as a function of pressure (a) and temperature (b) of a KTB biotite-muscovite gneiss.

Many natural rocks exhibit more or less axial or rhombic aggregate symmetry with elastic stiffness matrices which are uniquely defined by 5 or 7 independent constants. In experiments on sample cubes the stiffness coefficients are obtained by one experiment (axial aggregate symmetry) and by two experiments (rhombic aggregate symmetry), respectively. In rocks exhibiting triclinic symmetry, the full elastic tensor has been determined on spherical samples by measuring P-wave velocities in many directions in combination with S-wave measurements on sample cylinders (Siegesmund et al, 1993).

Velocity surfaces of a KTB biotite-gneiss (axial symmetry) calculated for in-situ and intrinsic conditions, show that S-wave splitting and S-wave polarization are largely controlled by the foliation and that the effects of oriented cracks are additive to the LPO-related anisotropy (Fig. 3).

In rocks constituting the earth's crust, typical values of the intrinsic (fabric-related) anisotropy are ~11 % for quartz-mica shists, ~7 % for felsic amphibolite gneisses, ~6 % for granulite-facies metapelites, and ~5% for amphibolites (Holbrook et al., 1992). Anisotropy is largely due to the alignment of phyllosilicates and hornblende, exhibiting marked single crystal P-wave anisotropy of 85 - 116% and 31%, respectively. In olivine-dominated upper mantle rocks (dunites, lherzolite, peridotite) P-wave anisotropy is normally between 3 and 6%, but can reach 10% (Christensen, 1984). In these rocks anisotropy is basically due to the LPOs of the constituent olivine and orthopyroxene exhibiting single-crystal anisotropies of about 22 and 15 - 20%, respectively. Importantly, the variations of P- wave velocities in crustal rocks due to changes in composition are substantially greater than velocity variations due to texture-related anisotropy. The reverse is true in upper mantle rocks, where the ranges of P-wave velocities due to preferred orientation of olivine and orthopyroxene are greater than the ranges of P-wave velocities due to variability in composition.

Calculation of seismic velocities from lattice preferred orientation

The 3D-distribution of intrinsic velocities in rocks can be calculated through the Christoffel equation (Crosson and Lin, 1971) combining single-crystal densities, single crystal stiffness coefficients and LPO of the constitutive mineral phases in their modal proportions. This enables one to determine the 21 elastic coefficients (the 6x6 symmetric matrix) characterizing the aggregate intrinsic elastic behaviour and the complete anisotropic seismic velocities (Vp, Vs1, Vs2, seismic birefringence, orientation of the shear wave polarization planes). The LPO of rock-forming minerals described by an

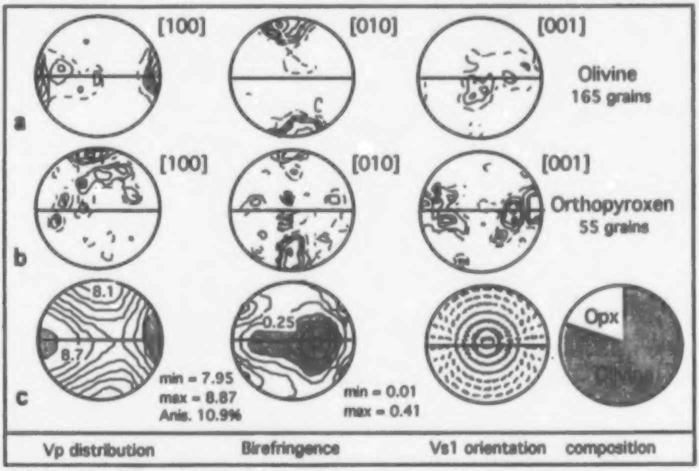

Fig. 2. Lattice preferred orientation (LPOs) of olivine (a) and orthopyroxene (b), presented on equal area projection, in the structural frame X,Y, Z. Foliation (continuous line) and lineation are east-west. Contour intervals: 1, 2, 3, 4, 6, 8, 12, 14 %). (c) 3D variations of the elastic properties: P-wave velocities (left), birefringence (middle) and orientation of the polarization plane of the fast split shear wave (right). The modal composition of the rock is displayed in the pie diagram (right) (after Barrouol and Kern, 1996).

Orientation Distribution Function (ODF) (Bunge, 1982) can be measured by volume diffraction techniques (X-rax diffraction, neutron diffraction) or by individual orientation measurements (optical microscope, electron channelling, electron backscattered patterns) (Wenk, 1998).

The spatial velocity variations of an upper mantle lherzolite from the Balmuccia peridotite massif, Italy (Fig. 2) shows a classic olivine LPO with a strong maximum of the [100]-axes parallel to lineation, whereas the [010]-axes are close to the pole of the foliation plane (a). The orthopyroxene LPO (b) is typical for upper mantle rocks (e.g. Boudier et al, 1984): *a*-axes are grouped in a maximum close to the pole of the foliation. The *c*-axes form a band in the foliation plane with a maximum close to the lineation. The whole rock seismic properties (c) are controlled by olivine, which constitutes the major volume of the rock (about 80%). The rock slow P-wave direction (7.95 km s^{-1}) is parallel to the olivine [010]-axes.The [100]-axes (fast P-wave direction in olivine single crystals) concentrated close to the lineation induces a high Vp (8.87 km s^{-1}) in this direction. The shear-wave properties are also controlled by the olivine fabric and its structural frame. The weak birefringence parallel to the [100] olivine single crystal crystallographic direction explains the very weak (less than 0.05 km s^{-1}) birefringence for shear waves propagating at high angle to the foliation. The olivine single crystal maximum birefringence is located between the [100] and [001] crystallographic axes. The band of [001]-axes parallel to the foliation with a maximum corresponding to the Y-structural axis generates a highly birefringent zone (>0.20 km s^{-1}) within the foliation with a maximum close to Y. In the foliation plane, fast split shear waves are systematically polarized parallel to foliation.

Nature of intrinsic (LPO-related) velocity anisotropy

Most crustal and mantle rocks have experienced a complex geologic history including several distinct episodes of ductile deformation. The ductile strain is primarily controlled by intracrystalline slip and dynamic recrystallization which give rise to the development of pronounced fabric anisotropy. The strong relationship between ductile strain, development of LPO and the change of seismic properties from isotropic to markedly anisotropic has been documented by Kern and Wenk (1990) in a study on granodiorite rocks from the Santa Rosa Mylonite Zone, California. During tectonism, the granodioritic protolith was progressively deformed to mylonite and ultimately to phyllonite without a change of mineral composition. Increasing strain resulted in a change of the fabric (specifically grain size and grain shape) and in the development of a strong preferred orientation of biotite. The increase of the biotite LPO (indicated by (001) pole densities) is strongly correlated with an increase of intrinsic anisotropy of P-wave velocities and S-wave splitting to 12% and 0.42 km s^{-1}, respectively. Seismic anisotropy in olivine-dominated mantle rocks (Fig. 2) is also caused by ductile deformation (Ave Lallement and Carter, 1970; Nicolas and Poirier, 1976).

Geophysical significance of LPO-related seismic anisotropy

The role of seismic anisotropy and shear-wave splitting in understanding the evolution of the Earth´s crust and upper mantle is becoming increasingly important, because the measured seismic anisotropy has a structural origin. Although shear-wave splitting observations have been made in the upper crust (e.g. Crampin and Booth, 1985), the existence of large-scale anisotropy in the lower crust is still an open question. The lack of information on lower crustal anisotropy may be due largely to the complicated pattern of deformation in the continents exhibiting smaller length scales of coherent deformation as compared with the oceanic plates. The contribution of a fabric-related (foliation-related) seimic anisotropy to the in-situ properties of an exposed lower crustal section has been demonstrated at the KTB drill site by linking velocity measurements performed on core samples to large-scale vertical seismic profiling (VSP) measurements (Rabbel, 1992; Popp and Kern, 1994; Berkhemer et al., 1997).

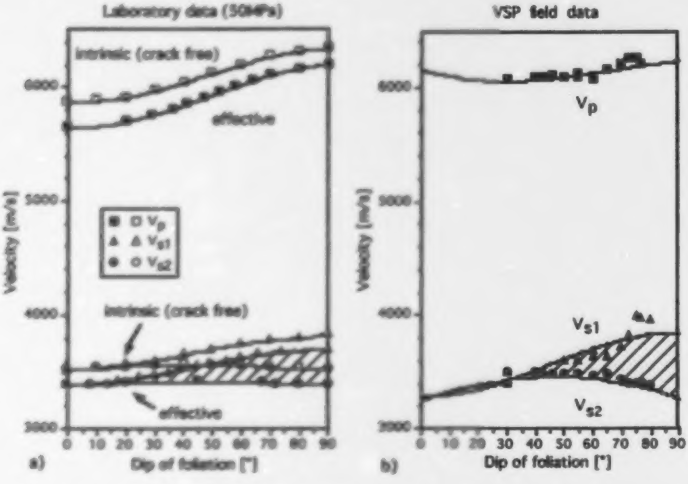

Fig. 3. Variation of Vp and S-wave splitting with the dip of the foliation plane for the depth intervall 2 - 3 km in the KTB pilot hole. (a) variation of Vp and S-wave splitting with the dip of the foliation in the biotite gneisses. Data points correspond to isolines on the respective calculated velocity surfaces of the rocks (averages of 12 samples) exhibiting axial symmetry. (b) Seismic in situ velocities as a function of the dip of the foliation. The data represent near-offset VSPs, together with model curves from least square fitting (Rabbel, 1992).

Figure 3 compares laboratory seismic data (average of 13 gneiss samples) with VSP data for the depth interval 2000 - 3000 m of the KTB pilot hole (VB), where the dip of the foliation of the biotite gneiss sequence changes slowly from 80°C to 30°. The good correspondence between the foliation-related shear-wave splitting data determined in the laboratory (dry rocks) with those obtained from the seismic experiment confirms the presence of a large scale-crustal anisotropy. The discrepancy between the anisotropies of the corresponding P-wave velocities can probably be related to in-situ intergranular fluids, which increase P-wave velocity and decrease P-wave anisotropy in the low-porosity rocks, whereas S-wave velocities and shear-wave splitting are only weakly affected (Popp and Kern, 1994).

It is widely accepted that the source of the observed large-scale azimuthal seismic anisotropy in the lithosphere (eg. Hess, 1964; Bamford, 1977) lies basically in the preferred orientation of upper mantle minerals (especially olivine). Calculated velocity surfaces of mantle xenoliths based on corresponding olivine fabrics of different geodynamic environments (subduction zone, inter-cratonic rift zone, rigid craton) are shown in Figure 4. It is most surprising that the velocity distributions mapped on the sphere show remarkably similar topologies. In the mantle peridotites, a strong relationship between maxima of P-wave velocities, shear-wave splitting and the structural frame is apparent: (1) the maximum P-wave velocity indicates the position of lineation (pointing in the direction of movement), (2) the maximum shear-wave splitting is close to the

Y-structural direction (normal to the lineation in the foliation plane), and (3) the polarization plane of the fastest shear wave is subparallel to the foliation (see Fig. 2).

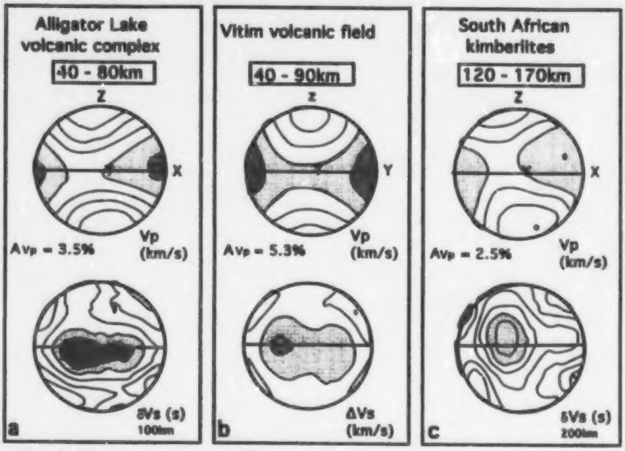

Fig. 4. Calculated velocity surfaces of Vp and S-wave splitting based on olivine LPOs from mantle xenoliths of different geodynamic environments. After (a) Ji et al. (1994); (b) Kern et al. (1996); (c) Mainprice and Silver (1993).

The close relationship between seismic anisotropy (in particular shear-wave splitting and shear wave-polarization) and strain-induced olivine LPO may provide a powerful method of studying internal deformation in the lithosphere, as well as motions in the mantle associated with plate tectonics (Silver and Chan, 1991). From seismic experiments (e.g. teleseismic SKS observations) the delay time (difference in arrival time of the split S-waves), which is a function of the thickness and anisotropy of the medium, and the orientation of the polarization planes, can be derived (Silver and Chan, 1991; Shih et al., 1991). The close association between S-wave polarization and the dominant geological fabric can thus provide information on deformation and deformed structures and finally give an answer to the question: does the anisotropic material traversed by SKS waves represent "frozen" deformation within the rigid lithosphere formed during ancient orogeney (Silver and Chan, 1991), or may the splitting be due to present-day plastic flow in the asthenosphere beneath the continental lithosphere (Vinnik et al., 1992)?

References

Bamford, D. and Crampin, S. (1977) Seismic anisotropy - the state of art. Geophys. J. R. astr. Soc., Vol. 49, pp. 1-8.

Barruol, G. and Kern, H. (1996) Seismic anisotropy and shear-wave splitting in lower-crustal and upper-mantle rocks from the Ivrea Zone - experimental and calculated data. Phys. Earth Planet. Inter., Vol. 95, pp. 175-194.

Birch, F. (1960) The velocity of compressional waves in rocks to 10 kilobars (Part 1), J. Geophys. Res. Vol. 65, 1083-1102.

Boudier, F., Jackson, M. and Nicolas, A. (1984) Structural study of the Balmuccia massif (western Alps): A transition from mantle to lower crust. Geologie en Mijnbouw, Vol. 16, pp. 179-188.

Bunge, H.J. (1982) Texture Analysis in Material Science. London, Butterworths.

Carter, N.L. and Avé Lallemant, H.G. (1970) High temperature flow of dunite and peridotite. Geol. Soc. Am. Bull., Vol. 81, pp. 2181-2202.

Christensen, N. I. (1984) The magnitude, symmetry and origin of upper mantle anisotropy based on fabric analyses of ultramafic tectonites. Geophys. J. R. astr. Soc., Vol. 76, pp. 89-111.

Crampin, S. and Booth, D.C. (1985) Shear-wave polarizations near the North Anatolian fault, II, Interpretation in terms of crack-induced anisotropy. Geophys. J. R. astr. Soc., Vol. 83, pp. 75-92.

Crosson, R.S. and Lin, J.W. (1971) Voigt and Reuss prediction of anisotropic elasticity of dunite. J. Geophys. Res., Vol. 76, pp. 570-578.

Hess, H.H. (1964) Seismic anisotropy of the uppermost mantle under oceans. Nature. Vol. 204, pp. 629-631.

Holbrook, W.S., Mooney, W.D. and Christensen, N.I. (1992) The seismic velocity structure of the deep continental crust. Continental Lower Crust. Elsevier Science Publishers.

Ji, S. and Salisbury, M.H. (1993) Shear wave velocities, anisotropy and splitting in high-grade mylonites. Tectonophysics, Vol. 221, pp. 453-473.

Ji, S., Zhao, X. and Francis, D. (1994) Calibration of shear-wave splitting in the subcontinental upper mantle beneath active orogenic belts using ultramafic xenoliths from the Canadian Cordillera and Alaska, Tectonophysics, Vol. 239, pp. 1-28.

Kern, H. (1982) P- and S-wave velocities in crustal and mantle rocks under the simultaneous action of high confining pressure and high temperature and the effect of the rock micro-structure. High Pressure Researches in Geoscience. Stuttgart, Schweizerbart'sche.

Kern, H. and Wenk, H.R. (1990) Fabric-related velocity anisotropy and shear wave splitting in rocks from Santa Rosa mylonite zone, California. J. Geophys. Res., Vol. 95, pp. 11213-11223.

Kern, H., Burlini, L. and Ashchepkov, I.V. (1996) Fabric-related seismic anisotropy in upper mantle xenoliths: evidence from measurements and calculations. Phys. Earth Planet. Inter., Vol. 95, pp. 195-209.

Mainprice, D. and Silver, P.G. (1993) Interpretation of SKS-waves using samples from the subcontinental lithosphere. Phys. Earth Planet. Inter., Vol. 78, pp. 257-280.

Nicolas, A. and Poirier, J.P. (1976) Crystalline Plasticity and Solid State Flow in Metamorphic Rocks. Wiley-Intersci. Pub.

Popp, T. and Kern, H. (1994) The influence of dry and water saturated cracks on seismic velocities of crustal rocks - A comparison of experimental data with theoretical models. Surv. Geophys., Vol. 15, pp. 443-465.

Rabbel, W. (1992) Seismic anisotropy at the KTB Drilling site. KTB-Report, Vol. 92-5, pp. 275-290.

Shih, X.R., Meyer, R.P. and Schneider, J.F. (1991) Seismic anisotropy above a subduction zone. Geology, Vol. 19, pp. 807-810.

Siegesmund, S., Vollbrecht, A., Chlupac, T., Nover, G., Dürrast, H., Müller, J. and Weber, K. (1993) Fabric-controlled anisotropy of petrophysical properties observed in KTB core samples. Scientific Drilling, Vol. 4, pp. 31-54.

Silver, P.G. and Chan, W.W. (1991) Shear wave splitting and subcontinental mantle deformation. J. Geophys. Res., Vol. 96(B10), pp. 16429-16454.

Vinnik, L.P., Farra, V. and Romanovicz, B. (1989) Azimuthal anisotropy in the earth from observations of SKS at geoscope and NARS broadband stations. Vol. 79, pp. 1542-1558.

Wenk, H.-R. (1998) Pole figure measurements with diffraction techniques, in Texture and Anisotropy. (eds. U.F. Kocks, C.N. Tomé and H.R. Wenk), Cambridge University Press, pp. 126-177

TEXTURES AND ELASTIC ANISOTROPIES OF AMPHIBOLITES FROM THE KOLA BOREHOLE

T.I. IVANKINA and A.N. NIKITIN
Frank Laboratory of Neutron Physics, Joint Institute for Nuclear Research,
Dubna, Russia
T. LOKAJICEK, Z. PROS and K. KLIMA
Geophysical Institute, Academy of Sciences, Bocni II, Prague, Czech Republic
K. ULLEMEYER
Institut für Geologie und Dynamik der Lithosphäre, Universität Göttingen, Germany

Abstract

The interpretation of the elastic properties of the earth's crust largely depends upon the knowledge of rock anisotropies of any kind, like mineralogical composition, foliations, grain shape anisotropy and mineral textures. Complete V_p patterns of five amphibolite samples from the Kola borehole were determined experimentally and modeled from the mineral textures to get insight into the elastic behaviour of this kind of rock and to discover reasons and variations of rock elastic anisotropy. It was confirmed, that in addition to the mineral textures other anisotropic factors control the elastic properties of bulk rock. Open microcracks and grain boundaries play an important role, they significantly decrease the compressional wave velocity. Additional influences cannot be excluded, nevertheless, the mineral textures and open surfaces seem to be the main controling factors. Furthermore, there is evidence, that the model assumptions for averaging require improvements.

Keywords: Amphibolite, compressional wave velocity, elastic rock properties

1 Introduction

In addition to the influence of the rock fabric, almost all physical rock properties (*e.g.* elastic, thermal, magnetic properties) are related to the textures of the rock forming minerals since they are anisotropic for the single crystal. In particular, the influence of the texture on the elastic behaviour of rocks is of interest because it affects the propagation velocity of seismic waves in rocks and therefore has consequences for the interpretation of large scale geophysical anisotropies. Five amphibolite samples from different levels of the Kola borehole (Kola peninsula, Russia) were selected to determine the spatial variation of the compressional wave velocity V_p in dependence upon the confining pressure, to model the texture related portion of V_p from the mineral textures and to discuss discrepancies between calculated and measured V_p distributions.

2 Sample description

The samples show a more or less pronounced layering in dependence upon the accumulated bulk strain, as well as a distinct elongation of the main rock-forming minerals in sections perpendicular to the foliation. Nevertheless, a lineation is hardly visible on the foliation plane, flattening seems to be the main deformation mechanism. Not in all cases the mineralogical composition corresponds to an amphibolite in the strict sense: in one case, plagioclase is completely absent, and quartz is mostly present in quite large volume fractions (refer to Table 1). The mean grain size is 300 to 500 µm, except sample 31593 which is characterized by an average grain size of about 800 µm.

Table 1: Location and composition of the samples investigated.

Sample	Depth [m]	Composition: volume fraction [%]
31593	8868	Hbl: 50, plg: 30, qtz: 15, acc: 5
31904	8945	Hbl: 50, bt: 10, plg: 20, qtz: 15, acc: 5
9665	9665	Hbl: 70, bt: 30
37172	9966	Hbl: 50, plg: 25, qtz: 20, acc: 5
43687	11379	Hbl: 45, plg: 30, qtz: 25

3 Experimental results

3.1 V_p measurements

The spatial V_P distribution was determined on spherical samples in 132 independent sample directions (corresponding to a regular 15° • 15° grid, Pros 1977) at atmospheric pressure and a confining pressure of P = 400 MPa. Subsequently, the velocity to pressure dependence $V_P = f(P)$, P = 0.1 to 400 MPa was determined for V_{Pmin} and V_{Pmax}. It is a general observation, that V_p increases with increasing confining pressure (refer to Fig. 1 and Table 2). At atmospheric pressure, the velocities range from 2 to 5 km/s with a mean value of about 3 km/s, except sample 37172 which shows considerably higher values. At 400 MPa, the velocity range is from 6 to 8 km/s, the mean value is about 7 km/s. Two more features are remarkable (1) the anisotropy of the V_p distribution which can be estimated according to $A = (V_{Pmax}-V_{Pmin})/V_{Pmax}$ is much larger at atmospheric pressure compared to the measurements at P = 400 MPa. (2) in the case of sample 43687 a clear rotation of the velocity pattern can be observed.

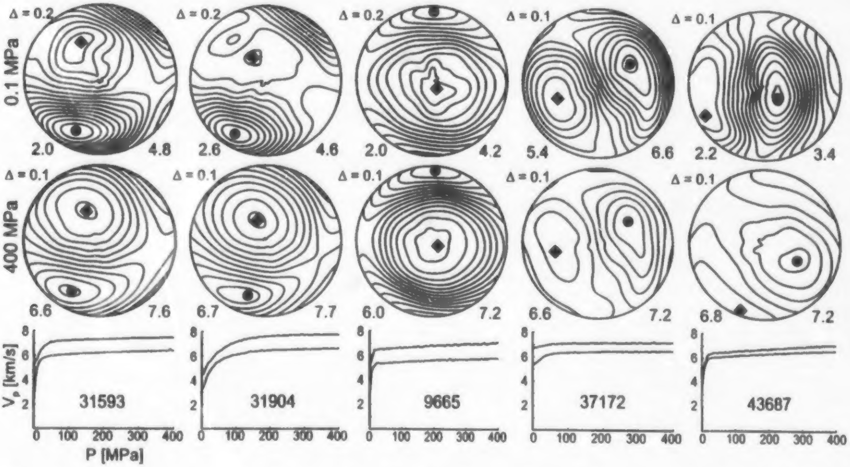

Fig. 1: Experimental V_p distributions. The directions of minimal (rhombs) and maximal (dots) velocity are indicated in the plots. The graphs V_p (P) give the interdependence for the minimum and maximum directions at P = 400 MPa. Δ: contour line step size.

Table 2: Minimum, mean, maximum compressional wave velocities and anisotropy A, estimated from $V_p = f(P)$ experiments.

Sample	P = 0.1 MPa				P = 400 MPa			
	Vp_{min}	Vp_{mean}	Vp_{max}	A[%]	Vp_{min}	Vp_{mean}	Vp_{max}	A [%]
31593	1.81	3.10	4.91	63	6.61	7.06	7.57	13
31904	2.54	3.17	4.78	47	6.72	7.21	7.72	13
9665	2.11	3.10	4.14	49	5.99	6.53	7.23	17
37172	5.29	5.93	6.62	20	6.54	6.79	7.17	9
43687	2.09	2.64	3.37	38	6.73	6.94	7.22	7

3.2 Texture determinations

Neutron texture measurements were carried out at the time-of-flight texture diffractometer at Dubna, Russia (Ullemeyer et al. 1998). The ODF of hornblende and of biotite (if present in significant amounts) was approximated by means of component deconvolution (Helming and Eschner 1990), subsequently, C-coefficients were calculated from the components because they allow easy modeling of the anisotropic rock properties by simple mathematical operations (Siegesmund and Dahms 1994). The hornblende textures show either an axial symmetrical maximum of (001) with strong preferred orientations (samples 31593, 37172 and 43687), or a more or less pronounced ellipsoidal shape of this lattice direction (samples 31904 and 9665, see Figure 2). The (100) and (010) planes form point-like or slightly ellipsoidal maxima with strong preferred orientations (samples 31593 and 31904), or girdle distributions with more or less pronounced maxima arranged on the girdle (samples 9665, 37172 and 43687). The biotite (001) pole figures (samples 31904 and 9665) are unimodal, the degree of preferred orientation is quite small in the case of sample 31904. The intensity maximum approximately parallels the foliation normal. This holds true for the (100) plane of hornblende as well, except sample 37172, which is characterized by a complete girdle with only weak submaxima. It is reported in the literature, that the (001) intensity maximum parallels the main stretching direction during rock deformation, hence, the main stretching direction usually can be estimated from the (001) pole figure if no macroscopic lineation is visible on hand specimen.

Quartz and plagioclase show only weak or even no preferred orientation (not presented here).

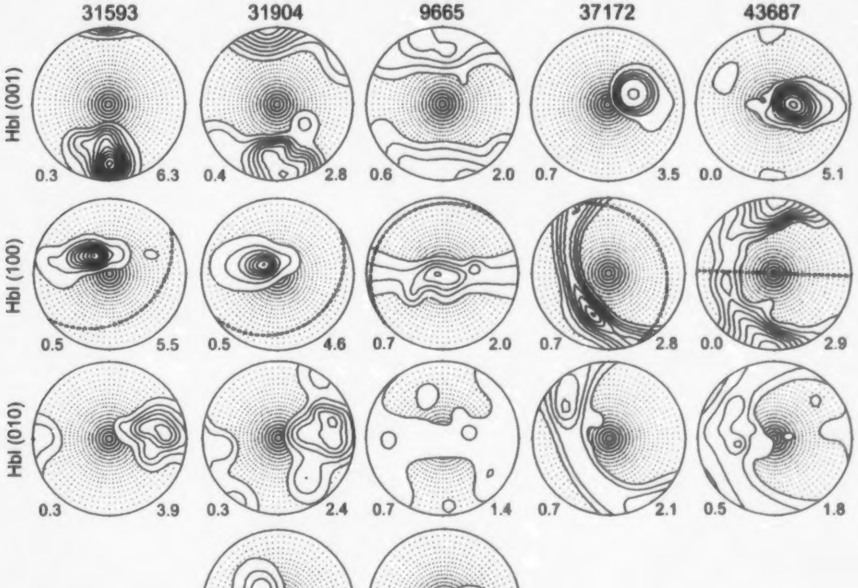

Fig. 2: Estimated textures of hornblende and biotite, recalculated from the ODF. For hornblende, the (001), (100) and (010) pole figures are given, for biotite, the (001) plane. Intensities are multiples of the random distribution, contouring starts at one time random. The great circle approximately indicates the orientation of the foliation plane.

4 Comparision of measured and modeled V_p anisotropies

Modeling of the V_p spatial distribution from the mineral textures was based on the elastic stiffness tensors compiled by Barruol (1993). Hornblende shows a monoclinic single crystal anisotropy (A = 22 %) with the maximal compressional wave velocity parallel to the [001] lattice direction and the minimal velocity parallel to [100]. For biotite, the V_p distribution is axial symmetric with the minimum velocity parallel to [001] and the maximum velocity parallel to the basal plane (A = 59 %, see Figure 3).

Quartz and plagioclase are considered to be isotropic because of a lack of pronounced preferred orientation. A mean velocity of 6.3 km/s (quartz) and 6.5 km/s (plagioclase) was used for the modeling. Accessories were neglected.

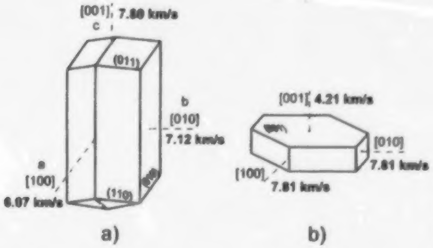

Fig. 3: Relationship between V_p and the crystal lattice of a) hornblende and b) biotite.

The averaged bulk rock velocity distributions are different from the experimental ones, this holds true for the spatial orientation of the tensors, its quantities and the degree of anisotropy as well. All modeled V_p distributions include the range from 6.1 to 6.7 km/s, the anisotropy parameter A the range from 3 to 9 % (see Fig. 4). In general, the calculated velocities much closer fit the experimental V_p distributions obtained at P = 400 MPa, nevertheless, the mean values are usually smaller. The anisotropy is highest for sample 9665 because of the well-developed biotite (001) preferred orientation and the large volume fraction of biotite in this sample (30%). Furthermore, A is larger in the experiment (refer to Table 2). Distinct orientation differences between the modeled and experimental V_p distributions are also valid, especially the samples 31904, 37172 and 43687 show clear orientation differences of the velocity patterns.

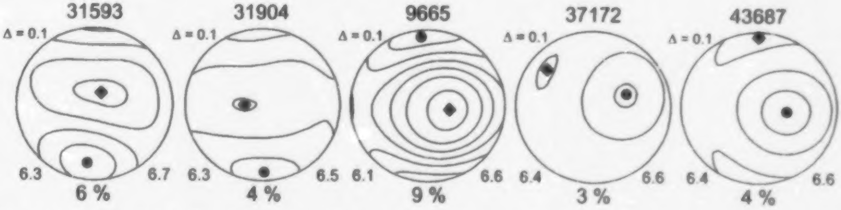

Fig. 4: Modeled V_p distributions. For explanations refer to Fig. 1.

5 Conclusions

From the above described observations the following conclusions can be drawn:

- the texture-derived (modeled) V_p anisotropy does not explain the experimentally determined bulk rock anisotropy completely. Continuous increase of the measured velocities with increasing confining pressure indicate, that open surfaces like microcracks and/or open grain boundaries are mainly responsible for velocity decrease. The $V_p = (P)$ experiments indicate, that most of them are closed at confining pressures > 100 MPa. Nevertheless, it cannot be excluded, that additional factors influence the elastic behaviour of the amphibolites.

- orientation changes of the velocity patterns at different confining pressures and orientation differences between modeled and experimental V_p distributions indicate, that one or more controling factors (beside the mineral textures) are be anisotropic as well.
- the quite small modeled rock anisotropy and the observation, that the modeled velocities are smaller as the experimental ones lead to the assumption, that the single crystal elastic constants must be varied and/or the model assumptions for averaging need improvements.

6 References

Barruol, G. (1993) Pétrophysique de la croûte inférieure. Rôle de l'anisotropie sismique sur la réflectivité et le déphasage des ondes S. *Ph.D. thesis Univ. des Sciences et Techniques du Languedoc*, Montpellier, 271 pp.

Dahms, M. and Bunge, H.-J. (1989) The Iterative Series-Expansion Method for Quantitative Texture Analysis. I. General Outline. *J. Appl. Cryst.*, Vol 22, pp. 439-447.

Helming, K. and Eschner, T. (1990) A new approach to texture analysis of multiphase materials using a texture component model. *Cryst. Res. Technol.* Vol 25, pp. K203-K208.

Pros, Z. (1977) Investigation of anisotropy of elastic properties of rocks on spherical samples at high hydrostatic pressure, in *High Pressure and Temperature Studies of Physical Properties of Rocks and Minerals*, Naukova Dumka, Kiev, pp. 56-67.

Siegesmund, S. and Dahms, M. (1994) Fabric-controlled anisotropy of elastic, magnetic and thermal properties of rocks, in *Textures of Geological Materials*, ed. H.-J. Bunge, W. Skrotzki, S. Siegesmund and K. Weber, DGM Informationsgesellschaft, Oberursel, pp. 353-380.

Ullemeyer, K., Spalthoff, P., Heinitz, J., Isakov, N.N., Nikitin, A.N. and Weber, K. (1998) The SKAT texture diffractometer at the pulsed reactor IBR-2 at Dubna: experimental layout and first measurements. *Nucl. Instr. Meth. Phys. Res.*, Vol. A 412/1, pp. 80-88.

Acknowledgements - Operation of the texture facility at FLNP/JINR is supported by the German Bundesminister für Bildung, Wissenschaft, Forschung und Technologie, operation of the Prague measuring equipment is financed by the Czech Academy of Sciences.

APPLYING EBSD TECHNIQUES TO MICROTEXTURES AND MESOTEXTURES IN ROCKS.

D.J. Prior[1], M. Bartozzi[1], A. Boyle[1], A. Day[2], D. Paden[1], D. Halliday[1] & M. Tye[3]
[1] Department of Earth Sciences, Liverpool University, UK.
[2] HKL technology, Hobro, Denmark
[3] CamScan Electron Optics Ltd, Waterbeach, Cambridgeshire, UK

Abstract

Fully automated orientation mapping using electron backscatter diffraction has become the most important technique for textural analysis of metals. The application of this technique to rocks is problematic. Charging is a genuine problem that we have overcome using a second gun induced discharge technique. A computer correctly indexes electron backscatter diffraction patterns (EBSP) of many of the low symmetry minerals that make up rocks with a success rate of only 70%. Intervention of a human operator is required for correct indexing and orientation mapping is an impractical technique for microtextural analysis. Intelligent sampling based on orientation contrast and colour orientation contrast images provide an alternative, semi automatic method for microtextural analysis.

Keywords: Electron Backscatter Diffraction, EBSD, Orientation Contrast Imaging, Rocks.

1 Introduction

Microtextures and mesotextures of hot-worked, deformed rocks, such as those exhumed from the relatively deep parts of major fault zones (like the San Andreas) or from the Earth's mantle, enable geologists to:

1. Forward model the deformation, recovery and recrystallization mechanisms responsible for the rock's microstructure.
2. Make direct, quantitative comparisons between samples and experimentally deformed rocks and rock analogues.

Such data constrain the conditions (pressure, temperature, stress, strain-rate) of natural deformation and realistic rock rheologies and have a profound impact on our understanding of the geodynamics of the Earth. This is just one application of textural analysis to the Earth sciences. This, and other applications, have been given an enormous boost by developments in electron backscatter diffraction (EBSD) systems. EBSD techniques can be applied to most rock forming minerals and have the potential to describe rock microstructures rapidly, and in a quantitative manner that was previously impossible. Application of EBSD to rocks, however, has inherent problems.

2. Charging problems

In practice, charging is a real problem in the analysis of non-conducting specimens such as rocks. The key problems associated with EBSD work on charging specimens are:

1. Image drift introduces uncertainties in the position of analysis points.
2. Image drift prevents multiple imaging of one area for noise reduction or for the production of colour orientation contrast images.
3. Point charging during analysis causes uncertainties in beam position and thus poorer spatial resolution for EBSPs.
4. Charging causes reduction of EBSP quality.
5. Charge halos around analysis points may have diameters of up to 50μm. Further EBSD analysis in charge halos is difficult or impossible

In severely charging specimens, both imaging and analysis are impossible.

Coating with a conductive material such as carbon or gold removes the charging problem but reduces the quality of EBSPs and orientation contrast (OC) images.

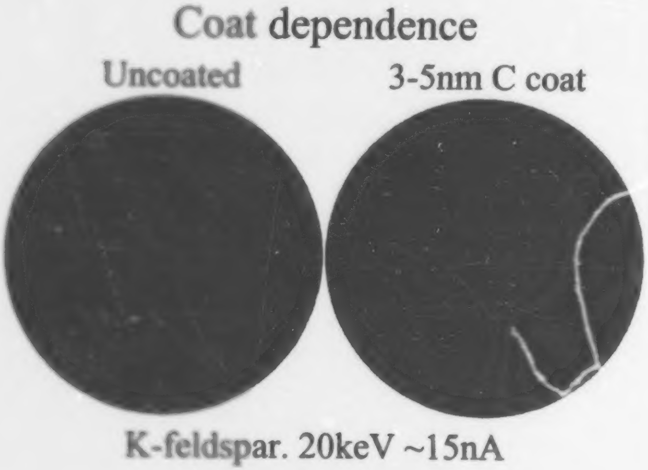

EBSP quality of coated specimens can be improved by increasing beam current and concomitant probe diameter. EBSPs, from specimens with 4-6nm of carbon coat, require one or two orders of magnitude more beam current than that required to generate EBSPs of equivalent quality in uncoated specimens. OC image quality of coated specimens never matches that of uncoated specimens, even if beam currents are increased by three orders of magnitude.

An elegant alternative to coating was reported by Morin et al., (1976). In their approach a second electron gun is placed inside the specimen chamber. The second gun operates at a high current and with an accelerating voltage close to one of the cross-over points for the material under examination. The net gain of electrons penetrating the specimen from the main beam are counterbalanced by net loss from the second beam so that no charging occurs.

We have built a second electron gun into the chamber of the Liverpool SEM and have experimented with the range of accelerating voltages and currents that give best results for a marble (pure calcite) a quartzite (pure quartz) and an albite rock. The approach is successful in all cases, but the results are most spectacular in the marble (this has the most severe charging problem). With operation of the second gun, OC images and EBSPs can be collected without image drift or point charging. If the second gun is switched off, charging becomes an immediate problem. Charging ceases within seconds of the second gun being switched on again.

Second gun induced discharge (SGID) will make work on uncoated non-conducting samples considerably easier and should give rise to better spatial resolution than employing coating techniques to reduce charging.

3. Mis-indexing

Most rocks comprise an assemblage of relatively low-symmetry minerals, many of which form chemical solid solutions. The most significant, and intractable problems of applying EBSD to rocks relate to mis-indexing. Computer algorithms typically achieve a 70% success rate in first-time correct indexing of important rock forming minerals (Prior & Wheeler, 1999) such as quartz (trigonal) and plagioclase (triclinic). In some cases misindexing relates to known psuedo-symmetries. For example, whilst quartz has trigonal symmetry many of the reflectors in quartz have hexagonal symmetry. Picking of bands with hexagonal symmetry automatically generates a 50% chance of the solution being wrong. In other minerals, such as plagioclase, misindexing relates to the similarity of angular relationships around more than one zone axis in the mineral structure. Mis-indexing means that data collected from automated orientation imaging techniques cannot be trusted. A human operator is required to check that computer indexing gives the correct solutions.

4. Intelligent sampling

Orientation contrast images (Day, 1993; Prior et al 1996) provide one of the fastest ways of constraining specimen microstructure. Colour orientation contrast images (COCI) (Day, 1993; Day & Quested, 1999) combine images with different beam-specimen-detector geometries and highlight all misorientation boundaries in a specimen. EBSD measurements from each orientation domain are all that are required to define angle-axis pairs for all misorientation boundaries (Trimby et al., 1998). The EBSD data set is much smaller than that required for orientation imaging of equivalent resolution and checking of each solution by a human operator is a manageable task. This is a potential solution for rapid semi-automated microstructural mapping in rocks and ceramics (which have similar problems). The solution to charging problems outlined above enables collection of COCI images (such as that of a marble below) of insulating specimens. These provide the best starting point for characterization of all misorientation domains from which EBSD data will be collected.

Semi automated use of imaging technology requires automated routines for picking the misorientation boundaries in OC or COCI images. While many imaging techniques exist that are able to graphically represent microscopic scale grain distribution in materials (microstructure), the problem remains of where and according to which criterion to define grain boundaries in these images. The solution should be a method characterised by reproducibility and absence of aprioristic assumptions leading to the introduction of statistically unquantifiable errors. An attempt has been made here to assess an automated grain boundary recognition procedure that minimises the number of assumptions. Being automatic, the procedure naturally matches the required characteristic of reproducibility. The procedures developed show good visual coherence with image appearance, i.e. properly defining nearly all of the objects, but several boundaries are missing, and others are drawn where perhaps none really exists. Although the method requires future refinement its application is nevertheless rigorous and repeatable and the results provide centroids for EBSD analysis.

Boundary Picking

5. Sampling efficiency

Sampling using a grid can be very inefficient. The microstructure shown in the OC image below (Trimby & Prior, 1999) would require 10,000 data points to analyse with a grid of 10µm spaced sample points. This would not give as much detail as the image. 1µm spaced sample points, requiring 1,000,000 data points are needed to approach the detail of the OC image. If analysis points are selected on the basis of the image, only 49 analysis coupled to the image will fully characterize the microtexture. With realization that some of the structures are twins only 12 analyses are needed. This example illustrates that intelligent sampling approaches may make analysis of non-problematic materials, such as metals, faster.

For many
textures
automated
analysis is very
inefficient

6. Conclusions

Microtextural studies of rocks using EBSD require a number of problems to be overcome. Charging of insulating samples can be eliminated using the SGID technique. New data collection strategies, involving the use of image based intelligent sampling, provide the best solution to mis-indexing problems. The techniques developed for rocks should be equally applicable to artificial ceramic materials and may introduce significant efficiencies into the analysis of metals.

7. References

Day, A., & Quested , T.E., 1999, A comparison of grain imaging using HOCI, COCI, EBSP and optical methods. Journal of Microscopy, in press.

Day, A., 1993, PhD thesis. University of Bristol.

Morin, P., Pitaval, M., & Vicario, E., 1976, Direct observation of insulators with a scanning electron microscope. J. Phys. E, 1017-1020.

Prior, D.J. and Wheeler, J. 1999. A study of an albite mylonite using electron backscatter diffraction. Tectonophysics, 303, 29-49.

Prior, D.J. In press. Problems in determining misorientation axis, for small angular misorientations, using electron backscatter diffraction in the SEM. Journal ofMicroscopy, in press.

Prior, D.J., Trimby, P.W., Weber, U.D., Dingley, D.J. 1996. Mineralogical Magazine., 60 859-869.

Trimby, P.W & Prior, D.J., 1999. Microstructural imaging techiques: a comparison of optical and scanning electron microscopy in the study of deformed rocks. Tectonophysics, 303, 71-81.

Trimby, P.W., Prior, D.J., and Wheeler, J.1998. Grain boundary hierarchy development in a quartz mylonite. Journal of Structural Geology, 20, 917-935

MAUD (MATERIAL ANALYSIS USING DIFFRACTION): A USER FRIENDLY JAVA PROGRAM FOR RIETVELD TEXTURE ANALYSIS AND MORE.

L. LUTTEROTTI
Dipartimento di Ingegneria dei Materiali, Università degli Studi di Trento, Italy
S. MATTHIES
Müller-Berset Strasse 3, D-01309 Dresden, Germany
H. -R. WENK
Department of Geology and Geophysics, University of California at Berkeley, USA

Abstract

Rietveld Texture Analysis (RiTA) (Wenk et al. 1994; Matthies et al. 1997) is a technique for obtaining texture, crystal structure, microstructure and the residual strain field from a multiphase material by least squares fitting of several diffraction spectra collected at different sample orientations. The technique is well suited for multi-detector systems and TOF (Time of Flight) neutron diffraction but with the increasing number of position sensitive or area detectors it will be possible to apply the methodology also in small laboratories using normal X-ray diffraction facilities. To extend the use of this powerful technique, a user friendly Java program has been built, combining a Rietveld program, the WIMV texture analysis and some line-broadening theories including the anisotropy of grain-size and line and planar defects theories. Also a model for residual strain-stress analysis has been incorporated, permitting in some cases to separate the macrostresses from the microstresses of the second kind. Amorphous structures can be analyzed as well including the possibility to easily obtain the crystalline fraction from the analysis without the need of any internal or external standard. The program benefits from an object oriented implementation, using a plug-in structure. This allows an expert user of the program with a simple knowledge of Java syntax to build his own theoretical model of analysis or introduce new kinds of instrumental geometries knowing anything of the internal structure of the program. The plug-in structure is extended also to data format, texture, line-broadening, residual stress model and many other features. The program includes a customizable database of crystal structures, diffraction instruments and can import CIF (Crystal Information Format) files including the ones exportable by the ICSD database. It run on any platform supporting Java 1.1 or later, thus including Windows (95/98/NT), Mac OS (8.0 or later), Unix (Sun, Digital, IBM, SGI etc.) and Linux. The user can run the analysis in two different modes: automatic and manual. In the automatic mode the user is requested to specify or load from the database only the basic arrangement (phases, instrument, datafiles) and which kind of analysis he wishes to perform. The rest is done automatically by the program. In the manual mode the user can specify more options and guide the analysis using his experience.

Keywords: Computer program, Diffraction, Materials, Rietveld, Stress, Texture.

1 Introduction

Stress and texture analysis is considered by most a challenge in the material research field. Even more, the presence of texture or both features will affect and in many cases limit other analyses. If a qualitative texture analysis is possible in a relatively large number of laboratories and/or research facilities, having at least a normal Bragg-Brentano diffractometer, very few of them can provide a quantification of the texture. Methods to obtain an orientation distribution function (odf) from a set of pole figure measurements have been developed from the '65 with the independent works of Bunge and Roe. From that date different methods have been followed providing better or more reliable results and also the diffraction apparatus has evolved in term of data quality, collection times, sample requirements. However, this kind of analysis has not reached the expected diffusion in spite of the greater potentiality especially in the material engineering field. One reason could be the intrinsic difficulty of applying and understanding the analysis coupled with the even more obscure science of using the results or the odf to provide insights to the application field. Only with the advent of the POPLA program and successively the one step forward BEARTEX with a user friendly interface, these texture methodologies start to be used also by people not-devoted entirely to texture and dealing also with material preparation or applications. Is opinion of the authors that a further diffusion of the texture analysis is possible only if normal users will be in condition to obtain and use the quantitative results without being a texture expert (at least for methodology). Due to the intrinsic difficulties of the subject is without doubts that this can be achieved only providing some kind of expert systems that will guide and help the user in the analysis (from the experiment to the results and application of results) avoiding as much as possible mistakes and errors. In the last few years more facilities are becoming available or are under construction (ILL-D20, Dubna-SKAT, LANL-HIPPO) in the neutron diffraction field as well as new in house X-ray instruments equipped with position sensitive detectors are increasing in number, to provide more experimental data in shorter times. Not equivalent effort has been putted in providing analysis tools capable of utilizing such a big amount of data in an efficient and friendly way. Most researchers are using fitting program and batch routines to convert the spectra collected in equivalent pole figures analyzable by the traditional methods. All this requires in any case a big effort not sustainable by occasional user and thus limiting the texture field. In this regard we are proposing a new tool to take advantage of the new facilities and instruments collecting spectra instead of pole figures. Big effort has been putted also in providing a powerful program both for expert and non-expert texture researcher. The resulting program is trying to integrate also the texture field with the crystal structure and powder diffraction users to provide more hints and reliable results to all.

2 Theory and program description

A brief description of the methodology used as basis for the program algorithms will be enlighten along with a description of the program structure and main features.

2.1 General methodology

The Maud program is based on the Rietveld method developed as a fitting methodology in the powder diffraction field to obtain a crystal structure refinement particularly efficient in the case of severe overlapping of the reflections for low symmetry compounds. The general principles for texture, stress, microstructure integration in the Rietveld method are reported elsewhere (Wenk et al. 1994; Matthies et al. 1997; Ferrari and Lutterotti, 1994). Here we will briefly notify the reader for a better understanding of the following paragraphs.

The analysis requires some spectra to be collected at different tilting angles in order to cover the significant part of the pole figure in connection with the d or 2-theta range used; larger ranges (more reflections) require less pole figure coverage. The reflection intensities are computed from the crystal structure of the different phases added to the computation corrected for the contribution of the texture trough the odf. The peak broadening is a function of some microstructural features (crystallite, microstrains, planar defect etc.) and the residual stresses coupled with the texture will determine the peak shift from the relaxed position. This will permit to compute one or more spectra as a function of the reported physical properties of the sample. These physical characteristics will become the parameters which value has to be refined trough a least squares procedure that minimises the residuals or the sum of square of the differences between the calculated and experimental diffraction points.

2.2 The Java program

The program interface and algorithms have been written in the Java language with the purpose of providing a tool independent of the underlying OS (Operative System) and capable of running easily in a network. The language also is object oriented, easy to use and thus very powerful for a large application maintaining an easy extendibility, flexibility and readability. All these features are important in the research field where nothing can be considered stable or arrived at the final state. One of the principal advantage incorporated in a plug-in structure of the program is the possibility by an expert user to write is own routines or objects that may extend some program features without the need to recompile the program or to know the internal working structure. As an example, the program will include in the final state three different texture models (plus a basic March-Dollase coming from the Rietveld field): the WIMV, a modified WIMV using tube projections like the ADC and the more classical spherical harmonic expansion theory. Anyone of these methods is a self-supporting object and different ones can be added without limitations directly by the user to test his own methodology. No help from the author is needed to do so. The plug-in structure include both the algorithm and the user interface part in an inter-related fashion but independent from the rest of the program.

Another distinguish characteristic is the wizard panel that help the user to choose the correct analysis and will drive the more appropriate strategy of refinement using an expert decision system. The essential steps that a user will follow to complete an analysis are:

- Load from the database the instrument/s used to collect the spectra.
- Create one or more set of data (one for any instrument used) and load the datafiles needed for the analysis in the appropriate dataset.
- Import from another database the phase/s he retain are present in the sample.

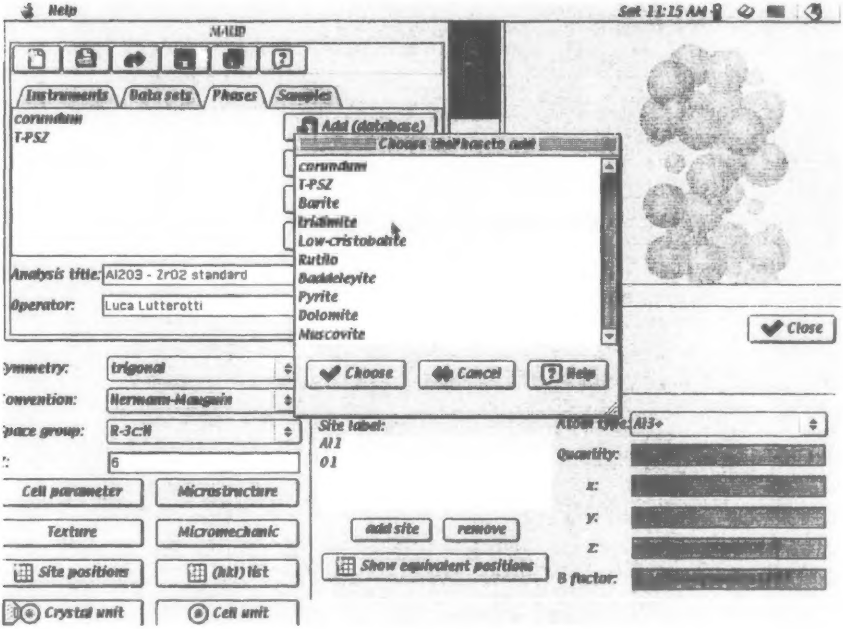

Analysis title: Al2O3 - ZrO2 standard

Operator: Luca Lutterotti

ymmetry: trigonal

onvention: Hermann-Mauguin

pace group: R-3c:H

: 6

Atom type: Al3+

Help
Sat 11:15 AM
MAUD
Instruments
Data sets
Phases
Samples
corundum
T-PSZ
Add (database)
Choose the Phase to add
corundum
T-PSZ
Barite
tridimite
Low-cristobalite
Rutilo
Baddeleyite
Pyrite
Dolomite
Muscovite
Choose
Cancel
Help
Close
Site label:
Al1
O1
Quantity:
x:
y:
z:
B factor:
Cell parameter
Microstructure
Texture
Micromechanic
Site positions
(hkl) list
Crystal unit
Cell unit
add site
remove
Show equivalent positions

Fig. 1: the Maud program interface.

- Create a new sample (more can be analysed at the same time) and specify which datasets pertain to which sample.
- Open the wizard and choose the analysis to do; for example a texture analysis and press the start button.

In figure 1 it is possible to see the program Maud in action showing the input of crystal structures, manually or from database.

3 Analysis examples

3.1 Texture of composite materials

We tested Maud and its procedure on an advanced structural material composed by a matrix of β-Si3N4 with SiC whiskers as inclusions. The material was obtained by Hot Isostatic Pressing of the powder and whiskers in order to distribute SiC randomly in the basal plane of the sample. The whiskers are growth with the (111) plane perpendicular to the longitudinal direction. This configuration of the composite will maximize the in plane fracture properties (strength, elastic modulus and toughness) high temperature applications. The goal of the analysis is to verify the distribution and angular dispersion of the whiskers from the principal plane of the sheet material resulting from the fabrication process. A cubic shape sample was obtained piling up sheets of the original material after mechanical tests. 720 spectra were collected at the D20 neutron beamline of ILL using a closed Eulerian cradle and a wavelength of 0.2413 nm. This was possible in a reasonable time using the PSD detector and the data was recorded up to 157° in 2θ, using a 10° x 10° grid on the χ and φ angles and two ω positions of the cradle. The neutron diffraction data was analyzed by Maud and it was necessary to exclude some internal ranges for few spectra due to the presence of the closed eulerian cradle masking part of diffracted beam. Due to the high abundance of data the exclusion of some range was not critical for the analysis results. Figures u and j are showing the extracted experimental pole figures compared with the reconstructed ones from the OD (Orientation Distribution) as determined by the program. The Silicon nitride resulted to be completely random, instead the SiC whiskers confirmed the in plane distribution as deducible from the figure with a acceptable angular dispersion. It was possible to obtain also the SiC volume fraction equal to 25 % and near the value used in the fabrication process.

3.2 Quantitative analysis of glassy phases

To test the accuracy of the program to analyse amorphous phases a synthetic mixture of silica-glass and crystallized corundum was prepared for different glass content ranging from the pure silica glass to the pure corundum. For any mixture of know silica amount a spectrum was collected on a Bragg-Brentano X-ray apparatus (Rigaku IIID max) equipped with a graphite curved monochromator in the diffracted beam to minimize background intensity that may correlate with the amorphous scattering. Then, the spectra were analyzed by the Maud program. First of all the nanostructure of the pure silica glass and the crystalline structure of the corundum was refined, so the structure obtained was used for the subsequent quantitative phase analyses. Both the quantitative phase analysis and the structure refinements were performed using the automatic operation mode. Quantitative phase analyses using the silica and corundum structures from the database instead of the refined ones gave not an appreciable difference respect to the use of the refined structures. Table 1 reports the result summary for the quantitative analysis by Maud compared with the known amount used to obtain the test samples. It is possible to note the high accuracy of the methodology as well as the feasibility of automatic mode of analysis by the Maud program with reduced intervention of the operator.

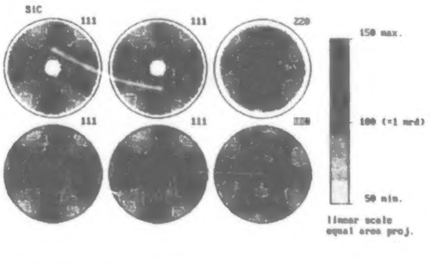

Fig. 2: Experimental (upper line) and recalculated, normalised pole figures for SiC.

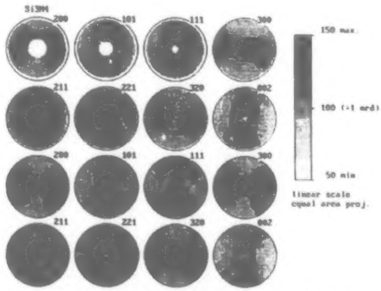

Fig. 3: Experimental (upper 2 lines) and recalculated pole figures for the silicon nitride.

Table 1: results of Maud/XRD quantitative phase analyses on synthetic silica-glass/corundum mixtures. Errors in parentheses refer to the last digit.

Sample number	1	2	3	4	5	6	7	8
Amount of silica added (wt %)	5	10	20	50	80	91	95	97
Measured amount (wt %)	3.6(7)	10(2)	20(6)	51(2)	79(1)	92(3)	96(2)	98(2)

4 Conclusions

Maud is a Java friendly program constructed to provide a powerful tool to analyzed at the same time texture, residual strain field, microstructure and crystal structure of complex materials. It has been proved, from some first test cases, that having the correct and sufficient experimental data it is possible to obtain reliable results using an automatic expert system of analysis with the minimum possible input by the user. The program has the capability to be used also by expert texture researchers and/or crystallographers who are forced to deal with both fields. Due to the friendly interface and the integration of different methodologies for material analysis the program has a natural propensity to be used in laboratories and/or research centers focused more on material applications, analysis and industrial research service.

5 Acknowledgements

The author's whish to thank other people who have contributed to the developing and testing of the program. They are not in a particular order: H. Mecking, S. Gialanella, M. Ferrari, D. Chateigner, R. W. Grosse-Kunstleve.

6 References

Wenk, H.-R., Matthies, S. and Lutterotti, L. (1994) Texture analysis from diffraction spectra. *Mater. Sci. Forum,* Vol. 157-162, pp. 473-480.

Matthies, S., Lutterotti, L. and Wenk, H.-R. (1997) Advances in Texture Analysis from Diffraction Spectra. *J. Appl. Cryst.,* Vol. 30, pp. 31-42.

Chateigner, D., Lutterotti, L. and Hansen, T. (1998) Quantitative Phase and Texture Analysis on Ceramic Matrix Composites using RTA at the D20 beamline. *ILL Annual Report 97*, pp. 28-29.

Lutterotti, L. (1999) Maud: Material Analysis Using Diffraction web downloading page, http://www.ing.unitn.it/~luttero/maud/maud.html.

Ferrari, M. and Lutterotti, L. (1994) Method for the simultaneous determination of anisotropic residual stresses and texture by X-ray diffraction, *J. Appl. Phys.*, 76 (11), pp. 7246-55.

Wenk, H.-R., Matthies, S., Donovan, J. and Chateigner, D. (1998) BEARTEX: a Windows-based program system for quantitative texture analysis, J. Appl. Cryst., 31, pp. 262-269.

A PRESSURE DEVICE FOR STRAIN MEASUREMENTS OF GEOMATERIALS AT THE NEUTRON DIFFRACTOMETER EPSILON

K. WALTHER, A. FRISCHBUTTER, R. LIECKEFETT, and C. SCHEFFZÜK[1]

Rock Mechanics and Management of Drilling Projects, GeoForschungsZentrum Potsdam, Potsdam, Germany

[1] also with the Frank Laboratory of Neutron Physics, Joint Institute for Nuclear Research, Dubna, Russia

Abstract

The neutron time-of-flight diffraction is a suitable tool for strain measurements in materials science and because of the high penetration depth of neutrons especially for geoscience but for the latter field up to now very seldom used. The principles of this method and the design of the diffractometer EPSILON, which is working on this base, are described. Furthermore, it is given a description of a device for uniaxial load of samples for *in-situ* measurements of strains (EXSTRESS). In order to reduce the afford on measuring time a concept is introduced to improve the diffractometer with a special arrangement of nine position sensitive detectors, capable to measure all information for the complete strain tensor at once. First results of applied and residual stress measurements on geological samples are given by (Scheffzük et al. 1999).

Keywords: Neutron diffraction, time-of-flight method, strain measurement, applied stress

1 Introduction

The knowledge of the strain/stress-behaviour of rocks in the Earth's crust is very important for the understanding of tectonic processes. Unfortunately, sampling from drillings, tunnels or other outcrops disturbs the original stress state of the rock. One way to investigate the stress state close to the original one is the investigation of samples undergoing applied stress.

On testing machines the strain is measured by mechanical or electrical means (micrometer screw, wire strain gauges). The results are correct only for homogeneous and pure (i.e. monophased) samples. Up to now this macroscopic technique represents the most common method for strain estimation in geological sciences. An other way is the estimation of strain by diffraction methods. Using X-ray or neutron diffraction the tension or compression of the sample can be described by measuring the net spacing of its crystallites. This method is called microscopic and offers the possibility to distinguish between the changes of net spacings concerning each mineral phase of the sample.

2 Neutron time-of-flight diffraction

The neutron diffraction technique is very similar to the X-ray diffraction. The main advantage of neutron scattering is the low - in comparison to the X-rays - absorption of the beam when passing through material. Therefore neutrons can penetrate samples with dimensions of several cm, what is of particular interest concerning geological materials. Brockmeier has compiled the values of the 'half-thickness' of some metals and minerals for both neutrons and X-rays (Brockmeier 1995).

The time-of-flight method uses a 'white' neutron beam, i.e. neutrons with a wide range of energies. Furthermore, the neutron beam must have a pulsed time structure: during most of the time there is no or even a low neutron output and only during the short time of the pulse there is generated a very high intensity of neutrons. This may be managed mechanically by choppers or a special neutron source delivers neutron beams with such time structure.

The energy of the neutrons is measured by their velocity v or by the time t they need for passing a flight path L. According to the laws of quantum physics besides mechanical quantities like velocity or momentum neutrons obey also wave properties like wave length λ. The wave length λ is proportional to the time of flight of neutrons:

$$\lambda = \frac{h}{m_n} \frac{1}{L} t \qquad (1)$$

where h is the Planck's constant, m_0 is the rest mass of the neutron. The first term is a universal constant, the second term is a constant of the experiment. More details on time-of-flight technique are given by (Buras 1975; Walther 1995).

3 The experimental setup

The neutron time-of-fligh diffractometer EPSILON (Fig. 1) is situated at the beam line 7a of the pulsed reactor IBR-2 in Dubna (Russia). The total flight path from the surface of the moderator to the sample and up to the detector is about 103 m. The most part of the flight path is consisting of a straight neutron guide with natural Ni-layer.

Two detectors are stet up at Bragg angle $2\theta = 90°$, both left and right with respect to the incident beam. The reactor has a pulse repetition rate of 5 Hz. From this fellows you can investigate the strain in a scale within a range for the lattice spacing *2d* up to 0.776 nm. Combined with a good spectral resolution, the instrument is a suitable tool for strain analysis of crystals with lower symmetry, which very often occur in rocks.

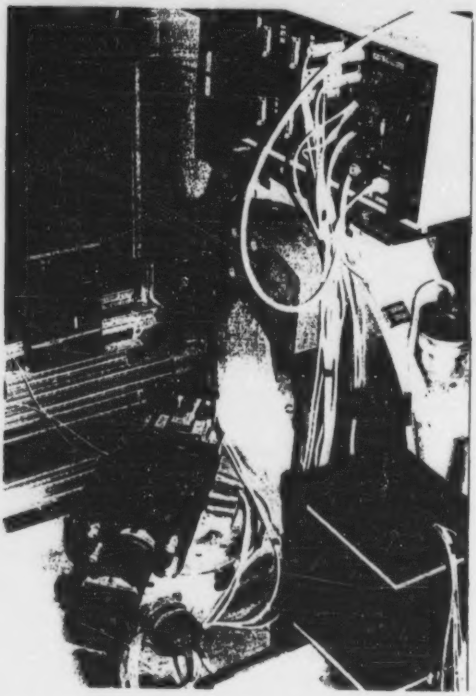

Fig. 1: The diffractometer EPSILON equipped with the pressure device EXSTRESS at beam 7A of the reactor IBR-2 in Dubna (Russian Federation).

Table 1: Characteristics of the goniometer axes

Axis	Kind of	Range of	Precision of	Unit
		motion		
χ	rotation	0 .. 360	0.0025	degree
φ	rotation	0 .. 360	0.0025	degree
x	translation	0 .. 100	0.0025	mm
y	translation	0 .. 100	0.0025	mm
z	translation	0 .. 60	0.0025	mm

The diffractometer EPSILON represents a 5-axis-goniometer: two rotation axes and three translations. The characteristics of the goniometer are compiled in table 1. This goniometer allows to scan the strain in dependence on sample dimensions, i.e. the strain in dependence on the distance from the surface or along a given direction. Usually for this kind of measurements only sample translations are needed.

An other problem is the measurement of the full strain tensor. In this case the strain $\varepsilon(\Psi,\Phi)$ is measured for several directions described by their sphere coordinates (Ψ,Φ). The six components ε_{ij} of the complete strain tensor are related to the strain values $\varepsilon(\Psi,\Phi)$ by the following relation (Noyan 1991):

$$\varepsilon(\Psi,\Phi) = \frac{d_{\Psi\Phi} - d_\eta}{d_\eta} = \begin{array}{l} \varepsilon_{\theta\theta}\cos^0\Phi\sin^0\Psi + \varepsilon_{\theta\theta}\sin2\Phi\sin^0\Psi + \varepsilon_{\theta\theta}\sin^0\Phi\sin^0\Psi \\ + \varepsilon_{II}\sin^0\Psi - \varepsilon_{II} + \varepsilon_{\theta I}\cos\Phi\sin2\Psi + \varepsilon_{\theta I}\sin\Phi\sin2\Psi \end{array} \quad (2)$$

If you measure the strain for at least six variant direction you can obtain the components of the strain tensor by solving the system of linear equations (2).

4 The pressure device

A special device for compressive uniaxial load (Fig.: 2) has been installed recently. The pressure device consists of a AC servomotor, a gear box, a thread spindle, and the sample chamber. All details of the sample chamber, wich may get into the neutron beam, are made of Ti which has a low neutron scattering length and therefore may cause only low background scattering. The pressure device can be controlled both manual or remote. The maximum force is 100 kN, i.e. 150 MPa for sample dimensions of 30 mm ⌀ and 60 mm length.

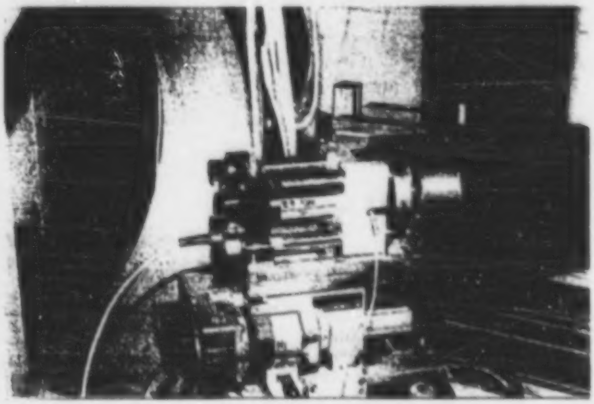

Fig. 2: The pressure device EXSTRESS installed on the diffractometer EPSILON. The dimensions of the sandstone sample are: 30 mm ⌀, 60 mm length.

During the experiment the values for the applied force, the shift of the moveable head of the press and the ambient temperature are permanently controlled. Furthermore the maximal values for deformation, deformation rate and torque can be preselected.

A usual deformation experiment is carried out with step by step deformation (increasing or decreasing load) and holding this load constant until the diffraction pattern were taken. As result of the (homogeneous) stress the peaks are shifted due to the changed size of the crystalline lattice of the sample under investigation. Besides the homogeneous strain inhomogeneous strain occurs due to grain interaction or interaction between the phases if the sample has more than one phases. Latter effect is expressed by peak broadening. First experiments were carried out on bedded sandstones of Cretaceous age from the Elbezone (E-Germany), the results of such *in-situ* experiments are reported by (Scheffzük et al. 1999).

5 Further improvement

As further improvement of the diffractometer the detectors will be replaced by nine position sensitive detectors (2d PSD). These detectors will be arranged on a ring in the plane perpendicular to the incident beam thus all detectors have the same scattering angle $2\theta = 90°$. This improvement allows the simultaneous measurement of the peak shift in nine variant directions and therefore allows the estimation of the full strain tensor without any sample rotations. On the other hand these nine detectors record the peak intensities along a certain orientation path which can be expressed as stereographic projection with the start point at the centre of a pole figure and ending at the equator of the pole figure. By this way a very rough estimate of the texture of the sample is also available.

6 Acknowledgement

The authors thank the directorate of the Frank Laboratory for Neutron Physics in Dubna, Russia, for the possibilities to carry out the experimental work. They are also grateful the GFZ Potsdam for the construction of the pressure device. The project has been supported by the German Ministry for Education, Research and Technology under the project number 03-DUBPOT-3.

7 References

Brockmeier, H.G. (1995), Thesis TU Clausthal

Buras, B. (1975) Time-of-flight diffractometry. *RCN-Report 234*, pp 307-346

Noyan, I.C. (1991) The theory of stress/strain analysis with diffraction, in Measurements of residual and applied stress using neutron diffraction, (eds. Hutching, M.T. and Krawitz, A.D.), Kluver Academic Publishers, Dordrecht/Boston/London 1992, pp. 51-65

Scheffzük, C., Frischbutter, A. and Walther, K. (1999) Neutron diffraction strain investigation of sandstones undergoing applied stresses, This volume.

Walther, K., Heinitz, J., Ullemeier, K., Betzl, M., and Wenk, H.R. (1995) Time-of-flight texture analysis of limestone standard: Dubna results. *J. Appl. Cryst.*, Vol. 28, pp. 503-7

Grain Boundaries and Misorientation Distribution

CHARACTERISTICS OF Σ3 BOUNDARIES IN STRONGLY TEXTURED COPPER

O.V. MISHIN* AND X. HUANG

Materials Research Department, Risø National Laboratory, Roskilde, Denmark

Abstract

The morphology and grain boundary planes of Σ3 boundaries are characterized in copper with a strong annealing texture. In this material, a strong cube texture was produced during recrystallization and subsequent grain growth. It is found that in this material twins form Σ3 boundaries with different deviations from the ideal Σ3 misorientation. The misorientations across straight "matrix-twin" boundaries are close to the exact twin relationship. These straight Σ3 segments are {111}/{111} boundaries, i.e. coherent twin boundaries. Grain boundaries between twins and their non-matrix neighbours of a dominant texture component may be identified as Σ3 boundaries, they are less linear and have a larger spread of deviations from the exact Σ3 misorientation.

Keywords: copper, grain boundary planes, Σ3 relationship, twin boundaries.

1. Introduction

Grain boundary (GB) engineering, i.e. manipulating GB misorientation distributions is considered to be a tool for controlling properties in polycrystals. However, the misorientation between grains is not the only parameter which can affect properties of grain boundaries. The inclination of the GB plane may control GB properties as well (Randle 1997). Despite this fact, there have been few experimental studies of GB planes in polycrystals. In most investigations, the characterization of GB ensembles is limited to classification of Σ boundaries, i.e. to measuring misorientations. It has been noted that in annealed materials with low to medium values of stacking fault energy (SFE), Σ3 boundaries usually compose the largest population in the GB distribution (Gertsman and Szpunar 1998). The fraction of these boundaries is, however, reduced during grain

---

* Also at the Institute for Metals Superplasticity, Ufa, Russia

The "neighbour-twin" Σ3 boundaries were typically not planar boundaries. For these two groups of boundaries, the values of mean angular deviations from the ideal 60° <111> misorientation are significantly different. Table 1 shows the mean Δθ deviations from the ideal Σ3 misorientation obtained using TEM and SEM methods.

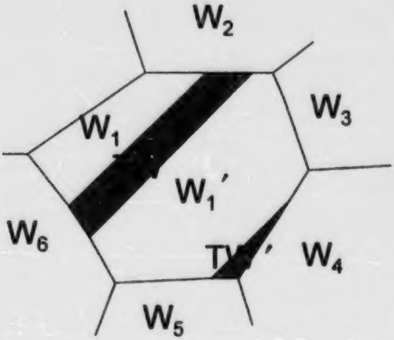

Fig. 1: Sketch illustrating possible Σ3 boundaries in strongly textured copper: boundaries W_1-TW, W_1'-TW and W_1'-TW' are "matrix-twin" (true twin) boundaries; boundaries W_2-TW, W_4-TW', W_5-TW' and W_6-TW are "neighbour-twin" grain boundaries. Symbols "W" and "TW" denote grains with the cube orientation and its twin component, respectively (Mishin 1998).

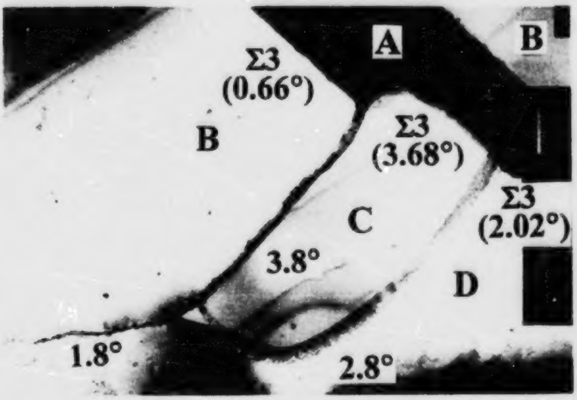

Fig.2: TEM image of Σ3 boundaries in strongly textured copper. Deviations from the ideal Σ3 misorientation (in brackets) and low-angle misorientations are indicated.

growth in the presence of a strong cube texture (Mishin and Gottstein 1998). Due to a strong texture both twin boundaries and some grain boundaries (GBs) were classified as Σ3 boundaries. While twin boundaries were always straight with or without facets, most GBs which also satisfied the Σ3 relationship appeared to be curved when inspected in the SEM. In the present work, this material is inspected in the TEM to ensure better resolution. Additionally GB planes of Σ3 boundaries are considered in this material.

2. Experimental

High purity copper was 50% cold rolled and annealed at 773K for 2h to produce a nearly random texture. This specimen was 95% cold rolled and successively annealed at 473K, 773K and 973K to develop a strong cube texture (Mishin and Gottstein 1998). Local orientations were measured in the rolling plane using both the electron backscattering pattern (EBSP) technique in the scanning electron microscope (SEM) and convergent beam electron diffraction in the transmission electron microscope (TEM). Grain boundary planes of twin segments were analyzed using a TEM method (Edington 1975, Huang and Liu 1998) that involves tilting a foil such that a boundary has the minimum image width. The angle between the traces of a twin boundary and the closest {hkl} plane indicates the angular deviation of the GB plane from the {hkl} plane. In this work, 164 boundaries classified as Σ3 using the criterion of Brandon (1964) $\Delta\theta_c = 15°\Sigma^{-1/2}$ were considered.

3. Results

The investigated material is characterized by relatively high fractions of low-angle and Σ3 boundaries (Mishin and Gottstein 1998). Large fractions of these boundaries are mandated by crystallographic texture where the major cube {001}<100> component and its twin {212}<122> orientations dominate (Mishin 1998).

Following the previous work (Mishin 1998), two groups of Σ3 boundaries are distinguished in this material. Hereafter we consider (i) "matrix-twin" boundaries, which are recognized by their straight morphology and (ii) "neighbour-twin" Σ3 boundaries between twins and their non-matrix neighbours with orientations almost identical to the orientations of the matrix grains (Fig.1). Thus it is emphasized that the "matrix-twin" boundaries are true twin boundaries between the matrix and its twin, while the "neighbour-twin" Σ3 boundaries are not produced by twinning events and are considered to be regular grain boundaries. In the TEM image shown in Fig.2, a twin plate A forms perfect straight {111}/{111} twin boundaries with the cube oriented matrix grain B. The same twin A contacts the grain C, which is only 3.8° from the grain B producing another Σ3 boundary. This boundary, however, is curved. A relatively straight morphology at this boundary is observed only over a short distance. Thus the TEM experiment confirms the previous SEM observations (Mishin 1998) of Σ3 boundaries in strongly textured copper.

In the present experiment, all long straight twin segments inspected in the TEM were identified as {111}/{111} boundaries, i.e. coherent twin boundaries. Also, {112}/{112} and {113}/{335} coarse facets were identified at certain twin boundaries.

Table 1: Mean angular deviations for two groups of Σ3 boundaries classified using Brandon's criterion ($\Delta\theta_c$=8.66°).

Σ3 boundaries	TEM	SEM
twin boundaries	1.1°	1.2°
neighbour-twin GBs	4.6°	5.5°

Both techniques give small and similar deviations from the ideal Σ3 misorientation for true twin boundaries. The "neighbour-twin" Σ3 GBs demonstrate much larger mean values of deviations. For Σ3 GBs the larger difference between mean deviations measured by two experimental techniques primarily reflects a larger spread of misorientations at these boundaries.

4. Discussion

4.1. Limitations of CSL characterization

In experimental studies of GB populations, a certain Σ value is ascribed to a boundary when the misorientation across this boundary is close to the ideal CSL relationship. The allowable deviation depends on the selected CSL criterion. Several geometrical criteria have been proposed (Brandon 1966; Ishida and McLean 1973; Pumphrey 1976; Palumbo and Aust 1990). In a general form, all of them can be written as $\Delta\theta_c = \Delta\theta_o \Sigma^{-p}$. In the different criteria, θ_o is generally taken to be 15° (some authors use θ_o=8°) and p varies from 0.5 to 1.

In Table 2, the normalized fractions of the "neighbour-twin" Σ3 grain boundaries summed from TEM and SEM data are given for several criteria with θ_o=15° and different values of p. The number of boundaries identified as Σ3 using Brandon's criterion (p=1/2) corresponds to 100%. True twin boundaries constitute 100% for all criteria and are not included in Table 2.

Table 2: Normalized fractions (%) of the "neighbour-twin" Σ3 grain boundaries classified according to different geometrical criteria.

Σ3 boundaries	p=1 $\Delta\theta_c$=5.00°	p=5/6 $\Delta\theta_c$=6.00°	p=2/3 $\Delta\theta_c$=7.21°	p=1/2 $\Delta\theta_c$=8.66°
neighbour-twin GBs	43.6	57.7	78.2	100

Considering different criteria for classifying Σ boundaries shows that all of them are excessively wide for true twin boundaries. All twin boundaries inspected in this experiment and in our previous TEM study on copper (Mishin and Huang 1999) are within 3° from the ideal Σ3 misorientation. The misorientation across the "neighbour-twin" GBs depends only on how close the orientation of the neighbour grain is to the matrix grain. Consequently, the deviation from the ideal Σ3 relationship is smaller for low "cube-cube" misorientations and large when the misorientation across the "neighbour-matrix" boundaries is relatively high. It appears that none of the CSL criteria is able to separate all of the "neighbour-twin" GBs from true twin boundaries produced by twinning events. Even a strict p=1 criterion would classify 43.6% of such boundaries as they were true twin boundaries. For instance, in Fig.2, the curved "A-C" grain boundary has a 3.7° deviation from the ideal twin relationship, which is sufficient for classification as a special boundary using any of the criteria. The fraction of the "neighbour-twin" Σ3 GBs is substantial, 19.2%, even when only a 3° deviation is allowed.

Certainly, such Σ3 GBs are less frequent in annealed materials with weaker textures. In conventional f.c.c. materials with low to medium SFE true twin boundaries dominate in the GB distribution. Some researchers have suggested that twin misorientation provides special properties. It is known, however, that twin boundaries frequently contain non-coherent facets that have a GB energy much higher than the GB energy of coherent {111}/{111} segments. According to Fullman (1951), the interfacial energy of {113}/{335} and {111}/{111} segments is 0.8 and 0.0035 of the average GB free energy, respectively. Since different facets may belong to the same boundary, CSL characterization alone may not signify any special properties for a CSL boundary.

4.2. Characterization of GB planes of twin boundaries

The TEM experiment shows that long straight segments of all inspected twin boundaries are coherent {111}/{111} boundaries. Facets may be associated with different GB planes. This result is in agreement with previous TEM experiments (Dash and Brown 1963; Sargent 1968; Sukhomlin and Andreeva 1983; Mishin and Huang 1999), however, it conflicts with some recent data obtained using SEM methods. In particular, SEM findings identify many twin boundaries as asymmetrical tilt boundaries with different grain boundary plane indices on both sides of the boundary, while it has been claimed that coherent {111}/{111} boundaries constitute only 9-40% from all twin boundaries (Randle 1994, 1995, 1997, 1999; Caul et al. 1996).

In our previous work (Mishin and Huang 1999), this discrepancy in the recognition of coherent twin boundaries when GB planes are studied by TEM and SEM methods has been discussed. It has been emphasized that the method of serial sectioning which has been used in a number of SEM studies, the inclination of the GB plane within the removed layer is only assumed. According to Randle (1999) only boundaries having a straight trace are to be considered in these experiments. However, the straight morphology in the polished section cannot guarantee that there is no change of GB plane over the distance between two sections.

It is important to note that if steps appear in the sectioning direction, the angle measured between GB traces before and after sectioning does not reflect the actual inclination of the GB plane (Mishin and Huang 1999). Therefore, different indexing results can be produced. TEM methods avoid such an ambiguous situation for the case of twin facets. Fine steps through the foil thickness can be distinguished, since in their presence, a sharp GB image may not be achieved by tilting the foil.

5. Summary

In strongly textured copper, twins form Σ3 boundaries not only with their matrix grains, but also with adjacent grains which have orientations almost identical to the matrix grains. The "matrix-twin" boundaries are characterized by small deviations from the ideal twin relationship. Long straight segments of "matrix-twin" boundaries lie on {111} on both sides of the boundary, i.e. they are coherent twin boundaries. Facets may lie on different GB planes; {112}/{112} and {113}/{335} facets were identified in the TEM. The "neighbour-twin" Σ3 GBs are not coherent boundaries, they are less linear and typically have higher deviations from the ideal twin relationship. Nevertheless, none of the applied CSL criteria is able to separate all Σ3 GBs from twin boundaries.

Acknowledgements

The authors are grateful to Dr. D. Juul Jensen, Dr. M.T. Lyttle and Dr. V.Y. Gertsman for useful comments.

References

Brandon, D.G. (1966) *Acta Metall.* Vol.14, pp.1479-1490.
Caul, M., Fiedler, J. and Randle, V. (1996) *Scripta Mater.* Vol.35, pp.831-836.
Dash, S. and Brown, N. (1963) *Acta Metall.* Vol.11, pp.1067-1075.
Edington, J.W. (1975) *Practical Electron Microscopy in Materials Science*, Philips Techn. Library.
Fullman, R.L. (1951) *J. Appl. Phys.* Vol.22, pp.456-460.
Gertsman, V.Y. and Szpunar, J.A. (1998) *Scripta Mater.* Vol.38, pp.1399-1404.
Huang, X. and Liu, Q. (1998) *Ultramicroscopy,* Vol.74, pp.123-130.
Ishida, Y. and McLean, M. (1973) *Phil. Mag.* Vol.27, pp.1125-1134.
Mishin, O.V. and Gottstein, G. (1998) in *Grain Growth in Polycrystalline Materials III*, (ed. H. Weiland, B.L. Adams and A.D. Rollett), TMS, pp.455-460.
Mishin, O.V. (1998) *J. Mater. Sci.* Vol.33, pp.5137-5143.
Mishin, O.V. and Huang, X. (1999) *Mater. Sci. Forum*, Vols.294-296, pp.401-404.
Palumbo, G. and Aust, K.T. (1990) *Acta Metall. Mater.* Vol.38, pp.2343-2352.
Pumphrey, P.H. (1976) In *Grain Boundary Structure and Properties*, Academic Press, New York, p.139.
Randle, V. (1994) *Acta Crystallogr.* A Vol.50, pp.588-595.
Randle, V. (1995) *Mater. Char.* Vol.34, pp.29-34.
Randle, V. (1997) *Acta Mater.* Vol.46, pp.1459-1480.
Randle, V. (1999) *Mater. Sci. Techn.* Vol.15, pp.246-252.
Sargent, C.M. (1968) *Trans. AIME,* Vol.242, pp.1188-1191.
Sukhomlin, G.D. and Andreeva, A.V. (1983) *Phys. Stat. Sol. (a)* Vol.78, pp.333-341.

GRAIN BOUNDARY INFLUENCE ON TEXTURE EVOLUTION DURING DEFORMATION AND RECRYSTALLISATION

S.J. LILLYWHITE and M. AINDOW
IRC in Materials for High Performance Applications and School of Metallurgy and Materials, University of Birmingham, Birmingham, UK
P.S BATE
DONCASTERS plc, Melbourne, Derbyshire, UK

Abstract

The Crystal Plasticity Finite Element Method (CPFEM) has been used in an attempt to predict the deformation behaviour of aluminium bicrystals. Of primary concern were the lattice rotations that take place during deformation and form the basis of microstructural heterogeneities such as deformation banding. In addition, controlled orientation bicrystals of aluminium were deformed by channel die compression to $\varepsilon=-0.5$ and subsequently annealed at 200°C for recrystallisation to take place. The textures and microstructures were characterised optically and by SEM(EBSD). The deformation textures and microstructures showed some agreement with the model, particularly in terms of the overall lattice rotations, but deformation heterogeneities on the subgrain scale could not be predicted. In an analysis of the recrystallisation textures the occurrence of coincident site lattice relationships between the recrystallised grains and the deformed matrix was identified.

Keywords: computer simulations, deformation texture components, grain boundaries, plane strain compression, recrystallisation texture components

1 Introduction

Prediction of recrystallisation textures is feasible provided an understanding of the deformation texture and microstructure is firstly achieved and that the orientations and viability of the nucleation sites for recrystallisation are known. The parameters that can alter texture evolution during deformation and recrystallisation include heterogeneities such as those associated with prior grain boundaries.

Computer modelling is a valuable technique for predicting microstructural development when a large number of material and deformation parameters are involved. Experimental investigations can then serve to verify the model and can be used to reveal any deviation that may result between the deformed specimens and the model predictions (Panchanadeswaran 1994). Channel die compression is a frequently used deformation mode for such investigations as plane strain conditions can be assumed and then only 2-dimensional modelling is required. The mechanical interactions of grains of differing orientation during deformation can be difficult to identify in polycrystalline material and therefore, bicrystals are favoured for such investigations (e.g. Blicharski *et al.* 1994).

Grain boundaries can play an important role in determining which nucleation sites will be viable for further growth. In some instances, the new grains that develop at prior grain boundaries can have orientations which are closely related to the grains from which they grew (Beck and Sperry 1950). In contrast, new orientations have been observed originating in the vicinity of the prior grain boundary (e.g. Inoko and Mimo 1987; Hutchinson 1989).

Before prediction of recrystallisation textures is possible, a systematic study of deformation and recrystallisation behaviour in relation to grain interactions is required. It is the purpose of this paper to report on computer modelling of, and experimental results from, aluminium bicrystals during deformation and to comment on the subsequent recrystallisation events that take place during annealing.

2 Computer simulations

It is essential that the experimental bicrystals are of orientations which minimise the anti-plane shear in the channel die plane strain compression tests. Only the extension direction (x-direction, figure 1) is free during experimental compression, all other specimen surfaces being constrained by the dies. Shearing in the x-z plane is still possible, however, depending on the crystallographic orientation of the bicrystal. A simple relaxed constraint Taylor model assuming octahedral {111}<110> slip can be used to determine which are "good" orientations, i.e., those that have little shearing in the x-z plane. Calculating a normalised quantity of the Taylor factor indicates the mechanical incentive for shear in the x-z plane. On this basis, orientations with a <110> direction parallel to the z-direction were found to produce little shearing in the x-z plane and therefore, such orientations were studied in the present investigations.

The CPFEM model used is based on constitutive equations for crystal plasticity implemented into finite element simulations. This model involves three levels of

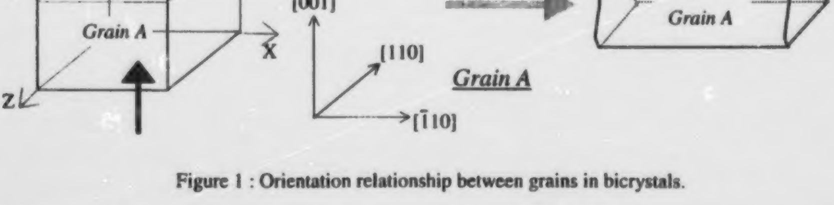

Figure 1 : Orientation relationship between grains in bicrystals.

iteration at each time step: determination of a stress state from the overall strain increment; slip increments are then calculated from this stress state; and the overall state of quasi-static equilibrium is determined (Bate 1998). The simulations discussed here involve bicrystals of various orientations (20°<θ<90°, figure 1) with simple asymmetric tilt grain boundaries. In each case, the orientation of grain A is taken as the reference with clockwise rotations away from this about [110] being defined as positive.

The CPFEM was used to simulate aluminium bicrystals deformed by plane strain compression to $\varepsilon = -0.5$ between two dies using a friction coefficient of 0.03 which is representative of oiled PTFE film lubrication. The key results are outlined in figure 2. For θ<50°, lattice rotations have taken place in opposite directions at the free surfaces of grain B, but the average rotation calculated from measurements taken over the whole grain was negative. For θ>50°, the rotations are predicted to be less severe, and resemble coarse deformation bands. For the low θ bicrystals, grain A shows a tendency to negative lattice rotation. An exception to this is near the free surface of the bicrystal at the grain boundary. For high θ bicrystals, the model predicts that the lattice rotations are greatest in the interior of grain A and reduce in magnitude as the free surfaces are approached.

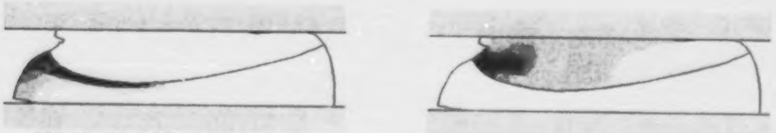

40° misoriented bicrystal, grain A

40° misoriented bicrystal, grain B

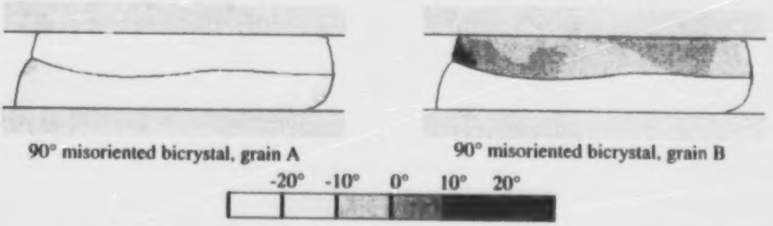

90° misoriented bicrystal, grain A

90° misoriented bicrystal, grain B

Figure 2 : Lattice rotations predicted in the x-y plane in grains A and B for low θ bicrystals (θ=40°) and high θ bicrystals (θ=90°).

Sensitivity analysis was carried out on the 90° bicrystal by varying the friction coefficient (0.02 to 0.05), the saturation value of slip resistance and the strain (-0.2 to -0.5). The amount of strain alters both the lattice rotations and the positions on the specimen where greatest orientation gradients are expected to develop and therefore, subsequent simulations were all run to $\varepsilon=-0.5$. Increasing the friction coefficient implied that the range of orientations expected in the deformed microstructure reduces. This was seen to be combined with an increased overall lattice rotation in both grains. Reducing the strain hardening however, was predicted to have the opposite effects. The position of the expected deformation banding features and the specimen shape change did not alter greatly for the range of parameters modelled.

3 Experimental procedures

Results from bicrystals of superpure aluminium that were investigated experimentally are shown in figure 1 for $\theta=40°$ and $\theta=90°$. The 40° bicrystal has a [110]/40° asymmetric tilt grain boundary with $(3\bar{3}5)\,\|\,(001)$ in the interface and the 90° bicrystal has a [110]/90° asymmetric tilt boundary with $(1\bar{1}0)\,\|\,(001)$ in the interface. Bicrystal specimens were prepared by diffusion bonding using a silver interlayer (Hauser *et al.* 1967). The specimens were channel die compressed to produce plane strain conditions and deformed to ε = -0.5. Some of this material was annealed at 200°C until recrystallisation was complete (one hour). Specimens were anodized for characterisation by optical microscopy under polarised light and electropolished for characterisation by EBSD on the SEM.

4 Results

Low magnification micrographs of each deformed bicrystal are shown in figure 3 and the coarse deformation features can be identified. In the 40° bicrystal, both grains appeared to have few coarsely banded regions implying that deformation was relatively homogeneous. However, the diffuse banding features which can be observed at this scale, are located primarily in the vicinity of the grain boundary. Higher magnification optical studies identified quite clearly deformation banding in grain B, whereas in grain A, the banding was fine, diffuse and relatively homogeneously distributed (Lillywhite *et al.* 1999). The spread of orientations measured across the banding features however was approximately equal for both grains (~20°). The average rotation of each grain from its initial orientation was seen to be negative. In figure 3b, some strong deformation banding can be observed extending from the free surfaces of grain B. In addition, finer scale deformation bands that extended across the width of the coarser bands were identified at higher magnification. This microstructure is associated with a large spread of orientations (~35°). It is interesting to note, however, that some of the initial orientation of grain B in the 90° bicrystal is retained after deformation. Grain A of the 90° bicrystal has a similar appearance optically to that of the 40° bicrystal. The resulting texture in grain A was relatively sharp and was associated with a small, negative overall lattice rotation (figure 4).

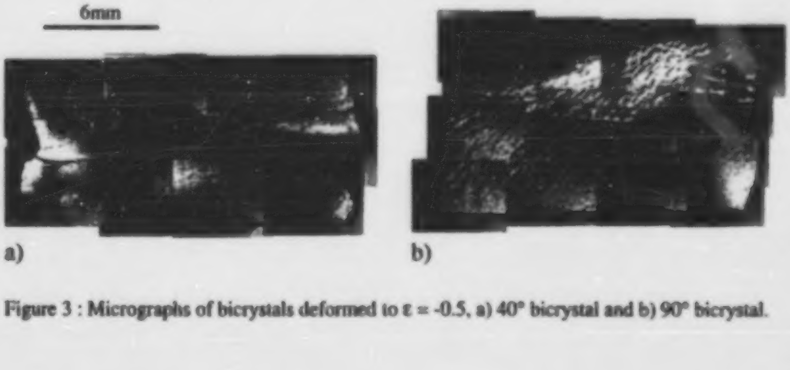

a) b)

Figure 3 : Micrographs of bicrystals deformed to ε = -0.5, a) 40° bicrystal and b) 90° bicrystal.

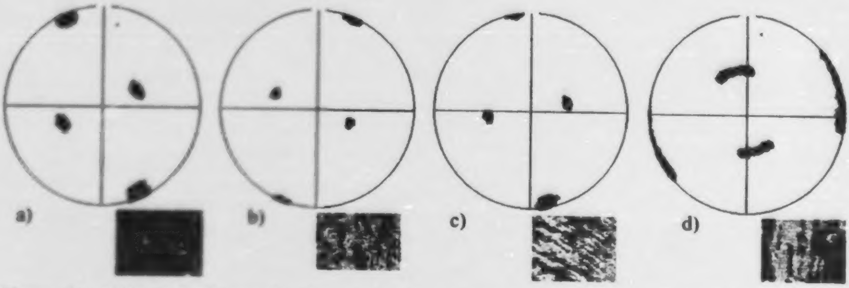

Figure 4 : (111) pole figures for deformed microstructures of each grain of each bicrystal, with orientation image of measurement region for the 40° bicrystal, a) grain A, b) grain B and the 90° bicrystal, c) grain A and d) grain B.

For the present combinations of orientations in the bicrystals, there is little evidence of recrystallisation nucleating favourably at the prior grain boundary after annealing at 200°C. Some special boundaries were identified between some of the recrystallised grains and between the recrystallising grains and the deformed microstructure. It was seen that the distribution of misorientations of the latter approximated a typical frequency distribution which would be expected for a random array of grains. Figure 5 shows that grain B of the 40° bicrystal has the majority of recrystallised grains related to the deformed matrix by ~40°<100>. For misorientations greater than ~45°, the preferred rotation axis spreads from <111> to <110>. Grain A however, has the majority of relationships clustered near 35°~50°<110>. For the 90° bicrystal, grain B has most misorientations at 30°~50° but the preferred rotation axis is not clear. Grain A of this bicrystal has mainly 20°~40°<111> relationships.

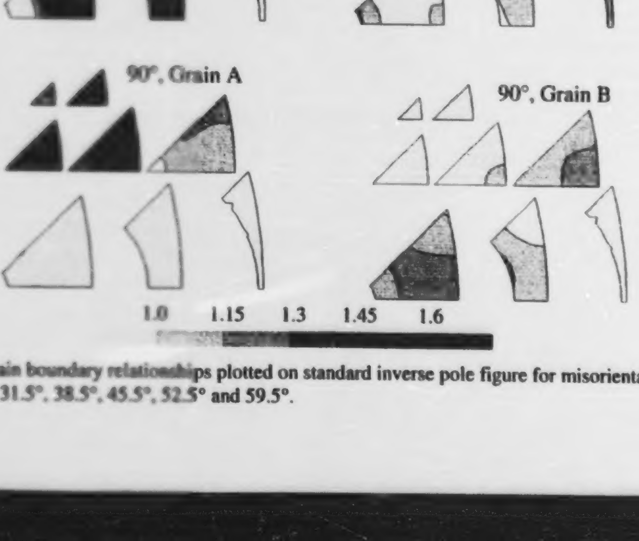

Figure 5 : Grain boundary relationships plotted on standard inverse pole figure for misorientations of 10.5°, 24.5°, 31.5°, 38.5°, 45.5°, 52.5° and 59.5°.

5 Discussion

The simulations and experiments showed some agreement, but other features expected from the simulations were not clearly demonstrated in the experiment. The simulations correctly predicted the spread of orientations measured in the deformed texture of the experimental bicrystals. The overall rotation of the lattice predicted by the model corresponded well with the texture of the deformation microstructures. The features predicted by the model in grains B could be identified in the experimental bicrystals, particularly for the 90° bicrystal, but in grains A, large lattice rotations across specific parts of the specimen were predicted that did not take place in the experiment. The fine scale banding features observed in the deformed microstructures are of the order of subgrains and are therefore, beyond the limit of the continuum model. Accumulation of dislocations during experimental deformation may form by the fine deformation banding, but in the simulation, accommodation took place by coarse banding features at specific locations of the grain.

Coincident site lattice relationships were observed between the recrystallising grains and between the recrystallising grains and the deformed matrix. This may be due to the particular deformation features in these specimens, but that further investigation is required before conclusions can be drawn. Fewer of these special boundary relationships were observed in grain B of the 90° bicrystal, where the deformation texture was well spread and the banding features were large.

6 Conclusions

The CPFEM can be useful tool for predicting lattice rotations that take place during deformation in aluminium bicrystals, although features of the order of subgrains cannot be predicted with the present model. Coincident site lattice relationships were identified between the deformed matrix and the recrystallising grains, though the significance of these is not clear at this stage.

Acknowledgements

Support is acknowledged from EPSRC and Alcan Int. (Banbury) Ltd. UK

References

Bate, P. (1998), *in press, Phil. Trans. Roy. Soc.: Deformation Processing of Metals*
Beck, P.A. and Sperry, P.R. (1950), *J. Appl. Phys.*, Vol. 21, pp150-2
Blicharski, M. Becker, R. and Hu H. (1994), *Mat. Sci. Forum*, Vol. 157, pp627-32
Hauser, D. Kammer, P.A. and Dedrick, J.H. (1967), *Welding J. Suppl.*, Vol. 46, pp11-22
Hutchinson, W.B. (1989), *Acta Metall.*, Vol. 37, pp1047-56
Inoko, F. and Mima, G. (1987), *Scripta Metall.*, Vol. 21, pp1039-44
Lillywhite, S.J. Aindow, M. and Bate, P., *to be presented at Recrystallisation'99*
Panchanadeeswaran. S., Becker, R., Doherty, R.D. and Kunze, K. (1994), *Mat. Sci. Forum*, Vol. 157, pp1277-88

THE ROLE OF TRIPLE JUNCTIONS DURING NORMAL GRAIN GROWTH UNDER HIGH PRESSURE IN 2-D STRIPS OF POLYCRYSTALLINE ALUMINIUM

V. SURSAEVA, S. PROTASOVA

Institute of Solid State Physics, Russian Academy of Sciences, Chernogolovka

W. LOJKOWSKI

UNIPRESS, High Pressure Research Centre, Polish Academy of Sciences, Warsaw, Poland

Abstract

We investigated the effect of high hydrostatic pressure up to 1.2 GPa on the normal grain growth in 2-D aluminium strips. It was shown that normal grain growth takes place both at atmospheric pressure and under high hydrostatic pressure. The activation volume for normal grain growth is 1.35 cm^3/mol. It was shown that high pressure strongly influences the final ratio of low angle boundaries to general boundaries. We investigated also the effect of high hydrostatic pressures up to 0.9 GPa on the triple junction mobility. The activation volume of Al [100] tilt triple junction motion is 4.5 cm^3/mol.

Keywords: grain growth, 2-D structure, triple junction, triple junction mobility, high hydrostatic pressure

Introduction

Recrystallization and grain growth proceed by generation and migration of grain boundaries and triple junctions. Grain boundaries and triple junctions are not alike in their properties, especially in their kinetics. To control the microstructure during grain growth it is indispensable to understand the mechanism that determines the kinetics of grain boundaries and triple junctions. Such information is difficult to be retrieved from experiments on polycrystals, since they only yield average properties of the polycrystalline assembly. Therefore experiments on the well defined grain boundaries and triple junctions are needed to elucidate the mechanisms of grain growth.

The investigation of the hydrostatic pressure effect on the kinetics of a thermally activated process permits to assess the activation volume V*. Knowledge of V* permits in turn to draw conclusions concerning the mechanism of the process investigated. V* can be expressed by the equation:

$$\partial \ln(v)/\partial p = -V^*/RT \; (2),$$

where **R** is the gas constant, **p** is high pressure, **T** is temperature and **v** is the rate of the process investigate, and the effect of pressure on the pre-exponential factor was neglected. There are only a few papers where influence of high pressure on the grain growth (Hahn and Gleiter 1979, Lojkowski et al. 1995) and migration of individual grain boundaries (Molodov et al.1984, Molodov et al. 1994) was studied.

The purposes of the present study are:

- to investigate the effect of pressure on grain growth in aluminium strips
- to investigate the effect of pressure on triple junction motion in aluminium (simple polycrystal system)

Experimental

The experiments were carried out using Al strips of thickness in the range of 0.08 - 0.1 mm. The 2-D (columnar) structure was obtained by rolling of 99.999% purity aluminium to 90% reduction in thickness and subsequent annealing at 833 K for 20 min. After annealing the grain size was larger than the thickness of the strips and the grain boundaries were perpendicular to its surface (Fig. 1). The initial mean grain area S_0 was about 0.025 mm^2. To investigate the pressure effect on grain growth, the strips were annealed at 773 K both under atmospheric pressure and under high pressure during different times t (Fig. 2).

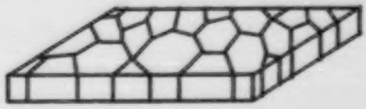

Fig. 1. The scheme of 2-D columnar structure.

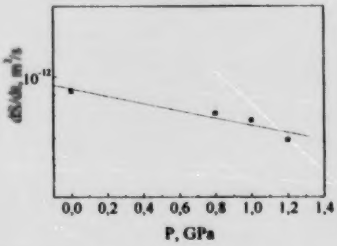

Fig. 2. The pressure dependence of the grain growth in 2-D strips.

The Al tricrystals were grown by a directed crystallization technique. A graphite crucible in high purity argon atmosphere was used. Samples with tilt and random triple junctions were specially prepared. Experiment was carried out on the triple junction with <100>,<111> tilt and random grain boundaries (Fig. 3). To investigate the pressure effect on the triple junction mobility, the samples were annealed at 733 K both under the atmospheric pressure and under the pressure of 0.3, 0.6 and 0.9 GPa.

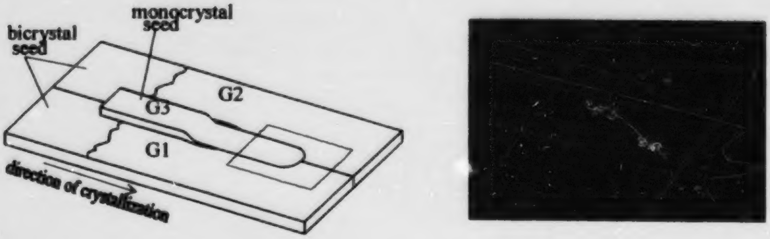

Fig. 3 The scheme of Al tricrystal (the square with thin line indicates the used triple junction) and optical micrograph of Al triple junction.

The high pressure annealings were carried out under high purity argon atmosphere. The pressure was controlled by a managing gauge with the accuracy of 2%. The temperature was controlled using three Pt 6wt.%Rh - Pt 30wt.%Rh thermocouples with an accuracy of 1K. A three zones high pressure furnace permitted to maintain a constant temperature over a plateau of 40 mm length, so that the specimens were in a uniform temperature field. The high accuracy of the temperature control was crucial to obtain meaningful results.

The mean grain size **S** was measured using optical metallography. Grain boundaries etch to a different degree depending on their energy. During metallographic investigations in the optical microscope in bright field conditions the low energy grain boundaries produce a weak contrast and it is practically impossible to reveal them. However, we performed an etching and observation procedure that permitted to reveal the low energy grain boundaries using dark field conditions, an inclined beam and a large aperture. The angle of incidence of the light beam on the specimen surface was varied by rotating the microscope stage. This caused the variation in intensity of the grain colouring and permitted to obtain data on the grain size distribution in the strips including the low energy grain boundaries.

Results and discussion

So far all the papers known to us concerning grain growth have been dealing with three dimensional (3-D) specimens (Knyazev and Titorov 1985, Rybin et al. 1984). X-ray techniques were used to obtain statistical information about the distribution of grain boundary misorientations. The data obtained in this way provided some averaged information. In contrast, the study of 2-D polycrystals permits to obtain the crystallographic data of each grain in the sample and permits a more straightforward identification of the mechanisms of grain growth (Shvindlerman et al. 1994).

In the case of our experiments we have the most important indications of the normal grain growth:

- a linear mean grain area **S** dependence on time **t** (Sursaeva et al. 1999)
- time independent topological class **n** distribution (Sursaeva et al. 1999)
- linearity of the mean topological class vs. relative grain area (Sursaeva et al. 1999)

The microstructure of 2-D strips displays (Fig.1):

- a strong texture with sharp {001}<100> component (Sursaeva et al. 1999)
- is composed of two types of regions (Sursaeva et al. 1999)
- in the region of first type the <100>axis of grains is near normal to the strip surface, the triple junctions are parallel to the <100> axis. The investigated <100> triple junctions occupy and surround this region
- the grains in the region of second type have a random axis normal to a surface, the triple junctions are of various types, the mobility of these triple junction is higher than that in the region of first type (Fig.4.)
- the fraction of low angle GBs in samples annealed 6 hours at atmospheric pressure at 773K was 25%, whereas after annealing under pressure of 1.2GPa this fraction was 55% (Sursaeva et al. 1999)

Application of high pressure in the present study of grain growth permitted to obtain new results - the activation volume for normal grain growth in 2-D aluminium strips with columnar structure (Fig. 2 and Table I).

Table 1. Experimental data concerning activation parameters and crystallography of investigated objects in Al (99.9995%).

	Misorientation				Activation enthalpy	Activation volume
	Axis	Angle				
					(eV)	(cm^3/mol)
Tilt grain boundaries in bicrystals	<100>	36.9°			1.18 [1]	12.00 [1]
	<100>	31.8°			1.93 [1]	11.90 [1]
	<111>	37.1°			1.67 [1]	11.00 [1]
	<111>	32.0°			2.02 [1]	11.90 [1]
Triple junctions		φ_{1-2}	φ_{2-3}	φ_{1-3}		
	<100>	6.0°	22.0°	28.0°	3.32	4.51
	<111>	5.0°	25.0°	20.0°	2.64 [2]	
	random				4.14	
2-D strips						1.35
Al polycrystals						2.00 [3]

[1]. Molodov, D. A., Swiderski, J., Gottstein, G., Lojkowski, W., and Shvindlerman, L. S., (1994). Acta metall, Mater., **42**, 3397.
[2]. Sursaeva, V. G. and Protasova, S. G., (1999) Materials Science Forum, Vols.294-296 pp.513-516.
[3]. Lojkowski, W., Minamino, Y., Hozumi, S. and Wyrzykowski, J., (1995) Proc. Joint XV AIRAPT& XXXIII EHPRG Intern. Conf. on High Pressure Science and Technology, Warsaw, Poland, Sept. 11-15.

As far as the activation volume is concerned, the value obtained **V*** = 1.35 cm^3/mol (Table I) is significantly less than that obtained for migration of individual grain boundaries in aluminium bicrystals with <001> and <111> tilt axis (Molodov et al. 1994). On the other hand, the present value of the activation volume matches in part with the results of Lojkowski et al. (1995) obtained for grain growth in Al 5N. Gleiter and Lisowski (1971) proposed a mechanism, where grain boundary migrates owing to movement of the contacts between atoms, involving very small movements of atoms. This mechanism can be called "atomic bonds migration mechanism". Lojkowski et al (1995) postulated that for the grain boundaries with segregated impurities transfer of atoms perpendicular to the grain boundary takes place with co-operation of vacancies, whereas at high temperatures impurities desegregate and the bond migration mechanism becomes active.

Despite the triple junctions along with grain boundaries are the main microstructural elements of polycrystals, the influence of pressure effect on triple junction motion was not treated experimentally and theoretically yet. We investigated the pressure effect on the mobility of triple junctions with two high angle and one low angle grain boundary (Fig.3). It is known such triple junction is very mobile (Czubayko et al. 1999) (Fig.4). Application of high pressure in the present study permitted to obtain a new result - the activation volume for triple junction migration.

During triple junction migration two large angle grain boundaries move and the low angle grain boundary is elongated as in the case when colony in 2-D strips is increased. Therefore, this is an experimental modelling of simple polycrystal system motion in the real case during grain growth in the 2-D columnar structure. Figure 5 shows the pressure dependence of the <100> triple junction mobility **A**. The activation volume of the migration of triple junction is 4.5 cm^3/mol. This value, similarly as the activation volume for grain growth, is less than the one for individual grain boundary motion. This means the triple junction migration is presumably not dependent on the vacancy concentration. On other hand, this value is higher than in the case of grain growth. We suppose, that during triple junction migration, two large grain boundaries move via the bond migration mechanism, whereas the extension rate of the low angle grain boundary depends on the vacancy concentration. Therefore, the activation volume of triple junction migration is intermediate between the values for the two alternative mechanisms. However, the low angle grain boundaries have presumably a higher density than the high angle ones, and are energetically favoured under high pressures.

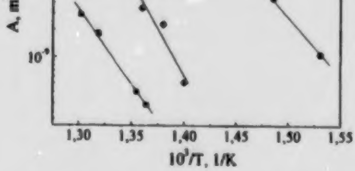

Fig.4. The temperature dependencies of triple junction mobility **A**.

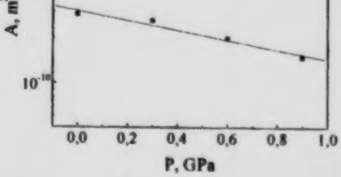

Fig.5. The pressure dependence of the <100> triple junction mobility **A**.

Conclusions

- The average activation volume for grain growth was 0.13 of the atomic volume and is compatible with grain boundary migration mechanism by movement of inter-atomic bonds.
- The activation volume for triple junction motion is 0.45 of the atomic volume. It is possible if a low angle grain boundary moves by a vacancy mechanism and the two large angle grain boundaries move by movement of inter-atomic bonds.
- The fraction of low-angle grain boundaries during normal grain growth under hydrostatic pressure is considerably higher comparing to atmospheric pressure.

Acknowledgements

The authors are grateful to Prof. Shvindlerman for fruitful discussions. The financial support of the Copernicus Network under contract no ERS ICI5CT 98 08 12 and Polish Committee for Scientific Research are acknowledged.

References

Czubayko, U., Sursaeva, V. G., Gottstein, G., Shvindlerman, L. S., (1999) Acta mater, Vol.46, No.16, 5863

Gleiter, H. and Lissowski, A., (1971), Zeitschrift fur Metallkunde **62**, 237. 12.

Hahn, H. and Gleiter, H., (1979). Scripta metall., **14**, 3-6.

Knyazev, N. M. and Titorov, D. B., (1985). Fiz. Metal. Metallov., **59**, 780.6.
Rybin, V. V., Titovetz, Yu. F. and Kozlov, A. L., (1984). Poverkhnost, **10**, 107.

Lojkowski, W., Minamino, Y., Hozumi, S. and Wyrzykowski, J., (1995). Proc. Joint XV AIRAPT& XXXIII EHPRG Intern. Conf. on High Pressure Science and Technology, Warsaw, Poland, Sept. 11-15.

Moodov, D. A., Straumal, B. B. and Shvindlerman, L. S. (1984). Sov. Phys. Solid State, **26**, 629.

Molodov, D. A., Swiderski, J., Gottstein, G., Lojkowski, W., and Shvindlerman, L. S., (1994). Acta metall, Mater., **42**, 3397.

Shvindlerman, L. S., Sursaeva, V. G., Yashnikov, V. P. and Faulkner, R. G., (1994). Interface Science. **2**, 153 - 168.

Sursaeva V., Protasova S., Lojkowski W., Jun J.,Texture and microstructure, in print 1999.

THE ORIENTATION DISTRIBUTION OF INTERFACE DETERMINED ACCORDING TO THE MAXIMUM-ENTROPY PRINCIPLE

Y.D. WANG[1], R. LIN PENG[1,2] and R. McGREEVY[1]
[1]Studsvik Neutron Research Laboratory, Uppsala University, Nyköping, Sweden
[2]Deptarment of Mechanical Engineering, Linköping University, Linköping, Sweden

B. BOLLE, A. VADON and J.J. HEIZMANN
LETAM (URA2090 CNRS)/ISGMP, Universite de Metz, Metz, France

Abstract

A method, based on the maximum entropy principle, is proposed to determinate the two-dimensional orientation distribution of planar microstructural features from their one-dimensional trace measurements. Computer simulations show that the present algorithm provides an effective method of analysis, which allows us to obtain a reliable distribution function from only several hundred individual traces of the planar microstructural features measured in two or three sections.

Keywords: Two-dimensional orientation distribution, maximum-entropy principle, interface

1 Introduction

The two-dimensional orientation distributions of planar microstructural features, such as grain-boundaries, interfaces, twin-boundaries, dislocation walls and cracks, have an important influence on the mechanical and physical properties of some polycrystalline materials. Recently there has been growing interest in the determination of the two-dimensional distributions of some planar microstructural features for the purpose of studying their roles in the properties and microstructural evolution of polycrystalline materials (Leffers and Christoffersen 1998a; 1998b). In fact, similar to the three-dimensional crystal orientation distribution, these two-dimensional orientation distributions of planar defects can be expressed and analysed using spherical surface harmonics. Usually the two-dimensional orientation distribution of planar microstructual features can be determined by direct experimental measurement using the following three methods: (1) serial sectioning through a polycrystalline material, (2) two-surface analyses and (3) transmission electron microscopy (TEM). As all of these methods require considerable experimental effort, it is difficult to perform such measurements in an automated fashion.

The stereological measurement and analysis technique provides a possible method for estimating the two-dimensional distribution function from one-dimensional trace measurements in several sections (Field and Adams 1993). The rapid development of the electron back-scattering pattern (EBSP) technique provides an effective tool for fast and automatic measurements of the one-dimensional trace distribution in various sections. It is also possible to estimate the one-dimensional trace distribution of interfaces in two-phase materials by X-ray or neutron diffraction according to the different absorption coefficients of the two phases. The key issue in the determination of the two-dimensional distribution of a planar defect lies in the method deriving the two-dimensional distribution from the one-dimensional trace measurements. Field and Adams (1993) extended the spherical surface harmonics method, widely used in texture analysis, to solve the inverse equation. It was shown that one-dimensional trace distributions measured in about 7~9 different sections could be used to obtain a reliable two-dimensional distribution. Thus, the large number of required sections limits the practical application of the stereological technique. In the present paper, the maximum entropy principle is used to determine the two-dimensional orientation distribution of planar microstructural features. Computer simulations show that the present method can produce an accurate two-dimensional distribution function from one-dimensional trace measurements in only two or three sections.

2 Analysis method

A two-dimensional orientation distribution function of certain planar features, $S_v(\vec{n})$, is defined as the area fraction of the interfaces whose normal direction parallels the observed direction $\vec{n}$ in the sample coordinate system v (OABC). This can be expanded into a spherical surface harmonic series

$$S_v(\vec{n}) = \sum_{l=0}^{\infty} \sum_{m=-l}^{l} \Gamma_{lm}^{v} \, P_l^m(\cos\chi)\exp(-im\eta) \tag{1}$$

where Γ_{lm}^{v} are the series coefficients, $p_l^m(x)$ is the associated Legendre function, and χ and η are the polar and azimuthal angles of the orientation $\vec{n}$ in the sample coordinate frame, respectively.

According to the addition theory (Bunge 1982), the two-dimensional orientation distribution function in the measurement coordinate system u (OXYZ), may be written as

$$S_u(\vec{n}) = \sum_{l=0}^{\infty} \sum_{m=-l}^{l} \sum_{n=-l}^{l} \Gamma_{ln}^{v} \, Z_{lnm}(\cos\beta) P_l^m(\cos\chi)\exp(in\alpha)\exp(im(\gamma-\eta)) \tag{2}$$

Where $\alpha\beta\gamma$ are the Euler angles to bring the coordinate system v (OABC) into the co-ordinate system u (OXYZ). $Z_{lnm}(x)$ is the augmented Jacobi function.

A one-dimensional trace distribution $\ell^u(\eta)$ of the planar microstructural feature is defined as the fraction of the line length per unit area of a given section in the measurement co-ordinate frame, u , with the line normal lying at an angle η to the reference line OX. The relationship between $\ell^u(\eta)$ and $S_u(\vec{n})$ is given by the following equation (Adams 1986)

$$\ell^u(\eta)=\frac{1}{2}\int_0^\pi S_u(\vec{n})\sin^2\chi\,d\chi \tag{3}$$

Field & Adams (1993) first expanded $\ell^u(\eta)$ into a Fourier series representation. Then a relationship between the Fourier series and Γ_{lm}^v is set up. Accordingly, if the one-dimensional distributions $\ell^u(\eta)$ in several sections are known, the Γ_{lm}^v may be determined by solving the inversion equation (3).

In fact, there are two main drawbacks in this algorithm. (1) As usually it is the directions of some traces in the sampling areas, instead of the one-dimensional trace distributions, which are directly measured, the Fourier series constructed for $\ell^u(\eta)$ contains some errors, especially for higher order terms. Those errors are introduced into Γ_{lm}^v in the following inversion, which leads to an inaccurate two-dimensional distribution. (2) The positivity condition, which is essential for all density functions, is not satisfied by both one-dimensional and two-dimensional functions. It is desribed in the following section how these two drawbacks are overcome by introducing the maximum-entropy principle into the construction of the two-dimensional orientation distribution of planar microstructual features.

According to the maximum entropy method (MEM), which is already used in texture analysis from pole figure data (Wang et al. 1996), and individual orientation measurements (Wang et al. 1999), the $S_v(\vec{n})$ can be written as

$$S_v(\vec{n}_i)=\exp(-1-\lambda_0-\sum_{l=1}^{L_{max}}\sum_{m=-l}^{l}\lambda_{lm}\sigma_{lm}^i) \tag{4}$$

with

$$\sigma_{lm}^i=p_l^m(\cos\chi_i)\exp(im\eta_i) \tag{5}$$

where $S_v(\vec{n}_i)$ is the discrete value of the two-dimensional distribution function at the orientation $\vec{n}_i$. λ_0 and λ_{lm} are the unknown Lagrangian multipliers. The advantage of equation (4) lies in that the positivity condition is automatically satisfied in both the two-dimensional function and the one-dimensional trace distribution.

By introducing (4) into (2) and (3), we obtain the following equations

$$\ell^s(\eta)=\sum_{l=0}^{\infty}\sum_{m=-l}^{l}\sum_{n=-l}^{l}\Pi_l^m\, Z_{lnm}(\cos\beta)P_l^m(\cos\chi)\exp(in\alpha)\exp(im(\gamma-\eta))$$
$$\sum_i \sigma_{ln}^i \exp(-1-\lambda_0-\sum_{l=1}^{L_{max}}\sum_{n=-l}^{l}\lambda_{ln}\sigma_{ln}^i) \tag{6}$$

with

$$\Pi_l^l=\frac{1}{2}\int_0^{\pi} p_l^l(\cos\chi)\sin^2\chi\, d\chi \tag{7}$$

If the experimental values (indicated by ^) of the one-dimensional function $\hat{\ell}^s(\eta_j)$ at some angles η_j in different sections are determined experimentally, λ_0 and λ_{lm} can be determined by the least squares equation, i.e.

$$\sum_s \sum_j \left(\hat{\ell}^s(\eta_j)-\ell^s(\eta_j)\right)\rightarrow Min \tag{8}$$

In practice, using the method previously proposed (Wang et al. 1999), $\hat{\ell}^s(\eta_j)$ may be approximately estimated from some statistical measurements of individual traces.

3 Computer simulations

The reliability of the proposed method has been tested by computer simulation. An ideal two-dimensional interface orientation distribution (Fig. 1), with a main component at $\chi = 55°$ and $\eta = 45°$ in the sample coordinate system (OABC), has been modelled on the assumption of a Gaussian peak with a full-width at half maximum (FWHM) of 15°. The sample coordinate system OABC is denoted by the typical coordinate system, which consists of the rolling direction (RD), the transverse direction (TD) and the normal direction (ND). 800 individual 'measured' unit length interfaces, 200 distributed in each of four different sections, are generated by the Monte Carlo method according to the ideal interface orientation distribution. The Euler angles (αβγ) of each section, by which OABC transforms to OXYZ, are marked in Table 1. In this simulation, some statistically 'measured' trace directions of interfaces in four sections, i.e. the angle η in the measurement coordinate system OXYZ, are used as the input files.

Table 1: Euler angles of selected sections

Number	α (°)	β (°)	γ (°)
1	0	0	0
2	90	0	0
3	90	90	0
4	35	45	0

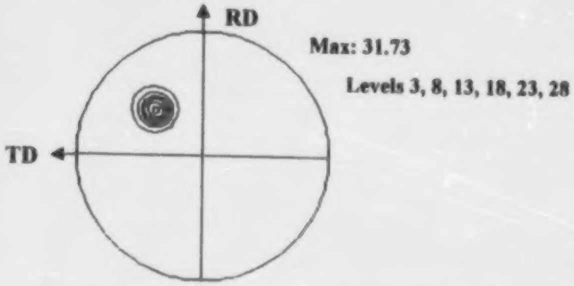

Fig. 1: The modelled two-dimensional interface orientation distribution

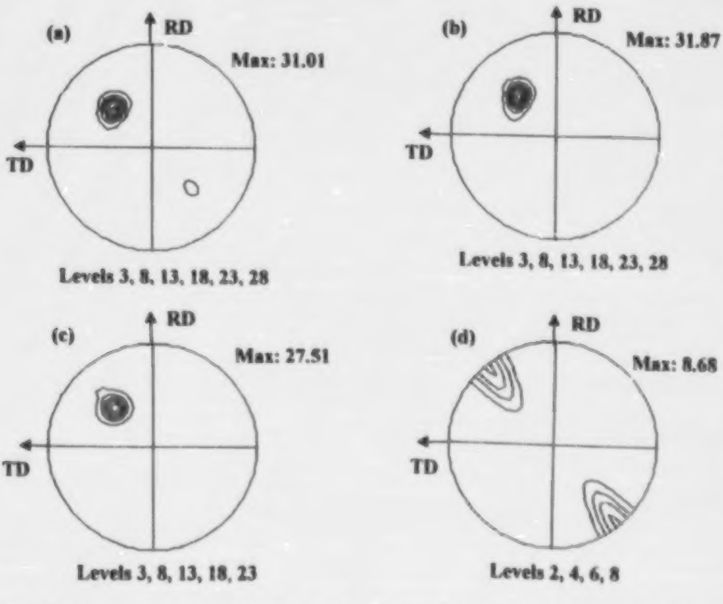

Fig. 2: Two-dimensional interface orientation distributions constructed from trace measurements in (a) four sections (1, 2, 3 and 4 in Table 1), (b) three sections (1, 2 and 3 in Table 1), (c) two sections (1 and 2 in Table 1) and (d) one section (1 in Table 1)

The interface orientation distributions constructed from trace measurements in different number of sections are shown in Fig. 2. It is shown that the interface orientation distributions, calculated from trace measurements in three or four sections, are almost the same as the original ideal distribution (Fig. 1). The values of the 'measured' and recalculated one-dimensional trace distribution densities are also similar (Fig. 3). Even the distribution calculated from some traces in only two sections (Fig. 2c), is close to the ideal one. However, the interface distribution function constructed from the trace measurement in one section only (Fig. 3d), is obviously different from the original.

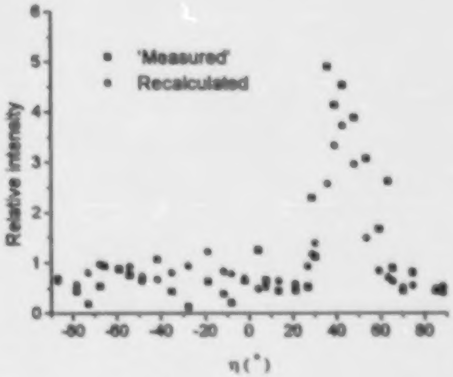

Fig. 3: 'Measured' and recalculated one-dimensional trace distribution in the section with Euler angles (0°, 0°, 0°)

Obviously we have chosen a simple test case here; for more complicated interface orientation distributions more sections will be required.

4 Conclusions

The maximum-entropy principle has been introduced for the construction of the two-dimensional distribution of planar microstructural features from one-dimensional trace measurements. The two main advantages of MEM here are: (i) the density function is constrained to be positive (i.e. physically possible) and (ii) the two-dimensional distribution is smooth (i.e. 'signal' is distinguished from 'noise'). The present algorithm allows us to determine an accurate two-dimensional orientation distribution function from fewer section measurements.

5 References

Adams B.L. (1986) *Metall. Trans.* **A17**, 2199-2207.
Bunge H.J. (1982) *Texture Analysis in Materials Science*, Butterworths, London.
Christoffersen H. & Leffers T. (1998a), *Acta Mater.* **46**, 4093-4102.
Field D.P. & Adams B.L. (1993) *Textures & Microstructures* **20**, 217-230.
Leffers T. & Christoffersen H. (1998b) *Materials Science Forum* **273-275**, 77-86.
Wang, Y.D., Xu, J.Z. & Liang, Z.D. (1996) *Textures & Microstructures* **26-27**, 103-110.
Wang, Y.D., Vadon A., Bessieres J. & Heizmann J.J. (1999) *J. Appl. Cryst.* **32**, No.3, in press.

DETERMINING SURFACE ENERGY ANISOTROPY FROM MEASUREMENTS OF THERMAL GROOVE GEOMETRY

D.M. SAYLOR and G.S. ROHRER
Carnegie Mellon University, Department of Materials Science and Engineering, Pittsburgh PA 15213-3890
D.E. MASON
Department of Materials Science and Mechanics, Michigan State University, East Lansing, MI 48864

Abstract

An experimental technique to determine the surface energy of a crystalline solid based on measurements of polycrystalline specimens has been developed. By combining geometric data obtained by atomic force microscopy with orientation data obtained from electron back scattered diffraction patterns, it is possible to index the three interfaces that meet at a thermal groove root. Observations are made at circumferential thermal grooves assumed to be in local equilibrium. Under the assumption that the grain boundary energy of such a groove is independent of its tangent plane, and that the surface energy can be parameterized as a double Fourier series, the unknown coefficients of the surface energy function can be determined by fitting the observations to the equilibrium condition.

Keywords: Surface Energy, Thermal Grooves, Atomic Force Microscopy, MgO

1 Introduction

It was demonstrated several decades ago that by characterizing the geometric and crystallographic parameters of thermal grooves, it is possible to measure the anisotropy of the surface free energy (Mykura 1961). While the method was improved and modified somewhat in the years that followed, its use remained restricted to materials that either twinned extensively or could be drawn into wires and recrystallized into a bamboo microstructure (Winterbottom and Gjostein 1966; McLean and Gale 1969). In the present paper, we describe a more general method for measuring the surface energy anisotopy. This method, which relies on experimental techniques not available to the earlier researchers, is similar in spirit but applicable to a much wider range of materials.

With reference to Fig. 1, and under the assumption that the grain boundary energy is independent of its tangent plane, the vertical components of the Herring condition for local equilibrium at a triple junctions can be written in the following way (Herring, 1951):

$$\gamma_3 \cos\alpha = \gamma_1 \cos\chi_1 - \frac{\partial\gamma_1}{\partial\chi_1}\sin\chi_1 + \gamma_2\cos\chi_2 - \frac{\partial\gamma_2}{\partial\chi_2}\sin\chi_2 \qquad (1)$$

Consider a circumferential thermal groove (see Fig. 2). If one determines the surface orientations bounding the groove root and the boundary plane inclination (α) at N points on the circumference, then one can write N local equilibrium equations that contain 2N+1 unknowns (γ_1 and γ_2 for each observation plus γ_3). The number of unknowns can be reduced below the number of observations if the surface energy is parameterized as a double Fourier series, and the number of unknown coefficients is less than N:

$$\begin{aligned}\gamma_s(\theta,\varphi) = 1 + \sum_{i=0}^{R}\sum_{j=0}^{R} \, [&a_{ij}\{\cos(2i\theta)-1\}\cos(j\varphi)\\ &+ b_{ij}\sin(2i\theta)\cos(j\varphi)\\ &+ c_{ij}\{\cos(2i\theta)-1\}\sin(j\varphi)\\ &+ d_{ij}\sin(2i\theta)\sin(j\varphi)\}]\end{aligned} \qquad (2)$$

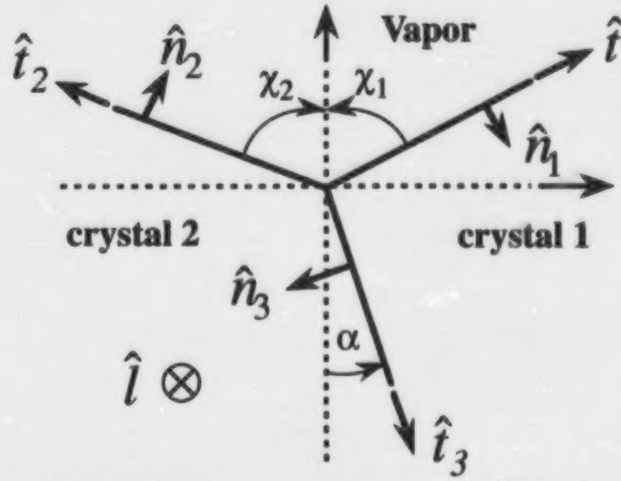

Figure 1. Definition of the terms in eqn. 1. The direction of the triple line, ($\hat{l}$), is defined by $\hat{n}_1 = \hat{t}_1 \times \hat{l}$

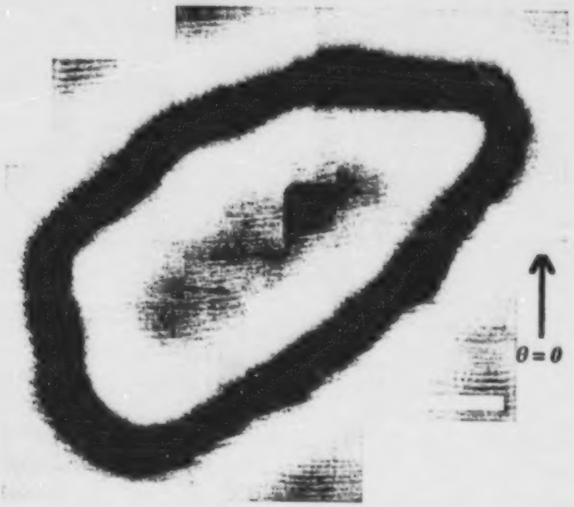

Figure 2. A montage of AFM images showing a circumferential thermal groove on the surface of a magnesia polycrystal. The black-to-white contrast is approximately 150 nm and black represents topographically lower points.

Under the assumption of local thermodynamic equilibrium, eqn. 2, which is normalized so that $\gamma_{100} = 1$, can be substituted into eqn. 1, and the unknown coefficients that parameterize the surface energy can be determined by a conventional linear least squares fit. The details of this process are described elsewhere (Saylor et al. 1999).

2 Experimental

We have applied the method described above to polycrystalline MgO, which has the rock salt structure. Magnesia powder was formed by decomposing 99.7 % pure magnesium carbonate (Fisher Scientific) at 997 °C in air. Uniaxial compaction in a hot press at 1700 °C for one hour at 61 MPa produced a disc with a diameter of 50 mm and an average thickness of 1.5 mm. Specimens cut from this disc were then packed in a magnesia crucible with the parent powder and annealed for 48 h at 1600 °C in air. Flat, parallel faces were prepared for analysis using an automatic polisher (Logitech PM5). The surface was thermally grooved by annealing it in air for 5 h at 1400 °C. The average grain size of the sample was 109 µm. At this stage, one sample was analyzed for impurities. The sample contained 0.2 % Ca, 0.02 % Al, 0.03 % Fe, 0.02 % Si, and 0.03 % Y. After thermal grooving, AFM imaging was carried out in the ambient using conventional

Si_3N_4 probes. AFM measurements were carried out in accordance with procedures described earlier (Saylor and Rohrer 1999).

The crystallite orientations were determined from electron back scattered diffraction patterns (EBSPs). The grooved samples were imaged (uncoated) in a Phillips XL40 FEG scanning electron microscope. EBSPs were obtained at a specimen tilt of 70 ° by pointing the beam at the grain of interest in the spot mode. Patterns were indexed using Orientation Imaging Microscopy Software, version 2.5 (TexSEM Laboratories, Inc.) which returns a set of Euler rotation angles (ϕ_1, Φ, ϕ_2) relating the crystal reference frame to the sample reference frame. The absolute orientation of each grain was determined from three separate diffraction patterns recorded in the same grain.

Optical micrographs of island grains, such as the one illustrated in Fig. 2, were recorded before and after a thin layer of the sample was removed by polishing. The relative lateral positions of the two images were determined by visually maximizing the overlap of all grain boundaries in the image. Based on measurements of the amount of material removed and the apparent lateral shift of the boundary between the two images, the inclination (α) at each point was determined.

The parameterized expression for the surface energy (eqn. 2) was substituted into eqn. 1 and a standard linear least squares procedure was used to determine the best fit values of the coefficients. The quality of the fit was assessed by the ratio (ρ) of the sum of the squares of the residuals to the difference between the number of observations and the number of free parameters. The results presented in the next section are based on fits to 269 observations from 5 island grains. Using a series of R = 1, $\rho = 6.76 \times 10^{-3}$. When the data set is randomly partitioned into two smaller segments, fitting to each segment leads to nearly identical results (within the standard deviation of the fit). When additional terms are added to the series (R = 2), ρ decreases slightly ($\rho = 5.47 \times 10^{-3}$). In this case, the ordering of the relative energies at the low index poles is the same as for the R = 1 fit, but the function contains additional nodes. However, when the R = 2 function is fit to the randomly partitioned data sets, the results differ from one another and from the results obtained using the complete data set. For this reason, we take the result from the R = 1 series to be the most reliable result.

3. Results

Figure 3(a) shows a plot of the values of the best fit function, for orientations obtained by a 90 ° rotation about the $[1\bar{1}0]$ axis. Figure 3(b) shows the torque ($\partial\gamma/\partial\theta$) along the same axis. The minimum energy is at (100) and the other low index poles have the following energies:

$$\frac{\gamma_{110}}{\gamma_{100}} = 1.040 \pm 0.008 \quad \frac{\gamma_{111}}{\gamma_{100}} = 1.072 \pm 0.010$$

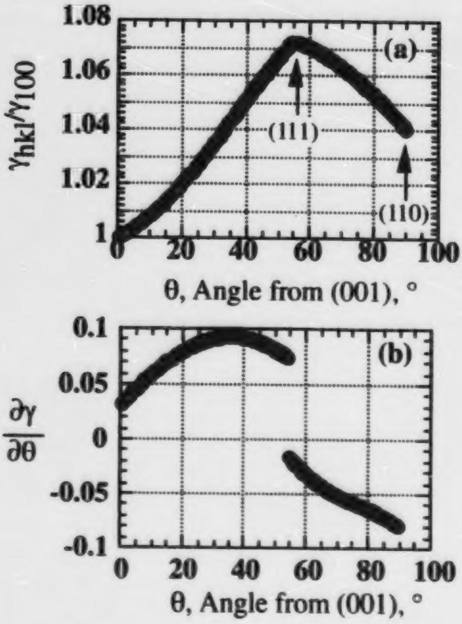

Figure 3. (a) The value of the best fit function for rotations about [1$\bar{1}$0]. In other parts of orientation space, the function varies smoothly. (b) The surface energy gradient over the same range.

4 Discussion

The magnitude of the surface energy anisotropy derived for magnesia is comparable to results from other materials. The anisotropy of Ni was determined to be 8.5 % at 1000 °C (Mykura 1961), the anisotropy of Au at 1030 °C was determined to be 6.8 % at 1030°C (Winterbottom and Gjostein 1966), and the anisotropy of sapphire at 1600°C is about 12 % (Choi et al. 1997). Because of this anisotropy, the terms in eqn. 1 containing the torques (which are plotted in Fig. 3b) can be of the same order of magnitude as the terms containing the surface tensions.

The ordering of the energies of the low index poles is in agreement with what one would anticipate on the basis of a simple nearest neighbor bond breaking model. In the bulk structure, both the Mg and O ions have six nearest neighbors. To create a (111) surface, which has the highest energy, three bonds per atom must be broken. The (110) and (100) surfaces can be formed by breaking two bonds and one bond per atom, respectively. Surface energy calculations based on an electrostatic model are consistent with the idea that as one rotates away from (100), the surface energy should increase (Duffy and Tasker 1984).

To determine absolute surface energies, one needs a fixed reference point. The only absolute surface energy data for MgO, derived from calorimetric measurements on MgO powders, places the average energy at about 1.0 J/m^2 (Jura and Garland 1952).

5 Concluding Remarks

The procedure described above should be applicable to almost any material. It is not required that the island grains be completely isolated, only that observations be accumulated from a boundary with constant misorientation and a significant degree of curvature so that many distinct orientations are exposed.

6 Acknowledgment

This work was supported by the MRSEC Program of the National Science Foundation under Award Number DMR-9632556.

7 References

Choi, J.-H., Kim, D.-Y., Hockey, B.J., Wiederhorn, S.M., Handwerker, C.A., Blendell, J.E., Carter, W.C., Roosen, A.R. (1997) *J. Amer. Ceram. Soc.*, Vol. 80. pp. 62-68.

Herring; C. (1951) in *The Physics of Powder Metallurgy*, (ed. W.E. Kingston), McGraw Hill, New York. pp. 143-79.

Jura, G. and Garland, C.W. (1952) *J. Am. Chem. Soc.*, Vol. 74. pp. 6033-4.

McLean, M. and Gale, B. (1969) *Phil. Mag.*, Vol. 20. pp 1033-45.

Mykura, H. (1961) *Acta Met.* Vol. 9. pp. 570-576.

Saylor, D.M., Mason, D.E. and Rohrer, G.S. (1999) An Experimental Method for Measuring Surface Energy Anisotropy and its Application to Magnesia, *J. Amer. Ceram. Soc.*, submitted.

Saylor, D.M. and Rohrer, G.S. (1999) Measuring the Influence of Grain Boundary Misorientation on Thermal Groove Geometry in Ceramic Polycrystals, *J. Amer. Ceram. Soc.*, Vol. 82, no. 5, in press.

Tasker, P.W. and Duffy, D.M (1984) *Surface Science*, Vol. 137. pp. 91-102.

Winterbottom, W.A.and Gjostein, N.A. (1966) *Acta Met.* Vol. 14. pp. 1041-1052.

MULTISCALE RECONSTRUCTION OF GRAIN BOUNDARY ENERGY FROM MICROSTRUCTURE

D. KINDERLEHRER, I. LIVSHITS, and S. TA'ASAN
Center for Nonlinear Analysis, Dept. of Math. Sci., CMU, Pittsburgh, USA
D.E. MASON
Dept. of Materials Science and Mechanics, MSU, East Lansing, USA

Abstract

Modeling polycrystalline materials relies on accurate knowledge of the grain boundary free energy. Assuming that triple lines in a polycrystal are in local equilibrium and that the free energy depends solely on crystallographic misorientation and grain boundary inclination, energy minimization implies that the Herring equation is valid at the triple lines. This gives rise to a large number of equations for the free energy which are inconsistent and for which direct solution techniques are unstable. We introduce a new a statistical/multiscale solution method that is robust, computationally inexpensive, and ultimately delivers an approximate grain boundary energy consistent with Herring. In an application to the surface energy of magnesia, we highlight the importance of torque terms in the reconstruction.

Keywords: grain boundary energy, reconstruction, multiscale, coarse graining

1 Introduction

Understanding the dependence of surface energy on structural properties is a fundamental problem in materials science. There are a variety of techniques employed to tackle this problem, ranging from microscopic scale methods of HRTEM and various type of molecular simulations to macroscopic scale methods. These methods are extremely valuable, but are limited by the small number and variety of interfaces that may be studied in a given experiment or simulation. The Mesoscale Interface Mapping System operates at a scale intermediate between microscopic scale and macroscopic scale and results in the harvest of large data sets containing crystallographic and geometric information from the vicinity of triple lines in a sample which is in thermal equilibrium. The Herring Condition then leads to a large system of equations that constitute an inverse problem for the grain boundary free energy σ (Adams et al., 1998; Herring, 1951). Solution of the system is achieved by a new statistical/multiscale method. The method is an iterative multiscale method and employs a Kaczmarz iterative scheme (Kaczmarz, 1937; Tanabe, 1971). The coarse graining method may be viewed as statistical in nature and it is effective in filtering unwanted coefficient noise. An application to MgO is discussed. Here we observe the surprisingly large role played by torque terms in the Herring Condition both in locating low energy surface orientations and taming the oscillations.

2 Preliminaries

In a polycrystal, grain boundaries intersect at triplelines, the cross sections of which are triplejunctions. In Figure 1 we display a typical junction, identifying the dihedral angles $\Theta^{(i)}$ and the tangent/normal pair $(\hat{\mathbf{t}}^{(i)}, \hat{\mathbf{n}}^{(i)})$ for surface $\Sigma^{(i)}$ such that the triple line direction is $\hat{\mathbf{l}} = \hat{\mathbf{n}}^{(i)} \times \hat{\mathbf{t}}^{(i)}$. Let $\mathbf{R}^{(i)}$ denote the orientation tensor for the grains $\Omega^{(i)}$, with $\mathbf{R}^{(i,j)} := \mathbf{R}^{(j)}(\mathbf{R}^{(i)})^{-1}$ the corresponding *misorientation tensor* for grain boundary $\Sigma^{(i)}$. Invoking crystal symmetry, $\mathbf{R}^{(i,j)}$ can be reduced to a unique Rodrigues vector $\boldsymbol{\rho}^{(i)} := \hat{\mathbf{n}}^{(i,j)} \tan(\omega^{(i,j)}/2)$, where $\hat{\mathbf{n}}^{(i,j)}$ and $\omega^{(i,j)}$ are respectively the axis and smallest angle of rotation for which $\Omega^{(i)}$ can be brought into coincidence with $\Omega^{(j)}$.

The energy corresponding to a grain boundary $\Sigma^{(i)}$ depends most simply on five parameters: the Rodrigues vector $\boldsymbol{\rho}^{(i)}$ and the interface normal $\hat{\mathbf{n}}^{(i)}$ that identifies the orientation of the interface $\Sigma^{(i)}$ with respect to the crystal lattice of $\Omega^{(i)}$. The total energy of the triplejunction system is then

$$\mathcal{E}_\gamma := \sum_{i=1}^{3} \int_{\Sigma^{(i)}} \sigma^{(i)}(\boldsymbol{\rho}^{(i)}, \hat{\mathbf{n}}^{(i)})\, da. \tag{1}$$

The triplejunction system is assumed to be in equilibrium. Therefore, requiring the triple line to remain a triple line under perturbation and the surfaces $\Sigma^{(i)}$ to remain smooth, the first variation condition $\delta\mathcal{E}_\gamma = 0$ for (1) yields the natural boundary condition at the triple line:

$$\sum_{i=1}^{3} \frac{\partial \sigma^{(i)}}{\partial \phi^{(i)}} \hat{\mathbf{n}}^{(i)} + \sigma^{(i)} \hat{\mathbf{t}}^{(i)} = 0. \tag{2}$$

Here, $\phi^{(i)}$ corresponds to the inclination angle of $\Sigma^{(i)}$, measured counterclockwise from the fixed line in the reference plane $\hat{\mathbf{l}}^{\perp}$, denoted by the dashed line in Figure 1. Equation (2), well known as the *Herring relation* (Herring, 1951), is the basis for the reconstruction method.

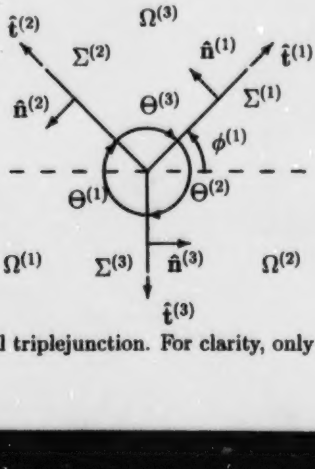

Figure 1: A typical triplejunction. For clarity, only $\phi^{(1)}$ is displayed.

3 Multiscale Energy Reconstruction

In this section we describe the reconstruction algorithm used to determine σ in Section 2. It is described for the grain boundary of a polycrystal; circumstances where less than the full number of parameters suffice, for example in the determination of surface energy, may obviously be considered as well.

Our method is iterative. It begins with setting a level of discretization for the fundamental zone $\mathcal{F}$, uniformly partitioning $\mathcal{F}$ into cells according to the level, and then forming a set of *urns* which correspond to unique triple pairings of cells from the partition. Then depending on the relative relationship between the independent variables $\{\rho^{(i)}, \hat{\mathbf{n}}^{(i)}\}_i$ at each experimentally determined triple-junction, the equations (2) are sorted into the relatively small number of *urns*, as determined by the level. Making the assumption that the energy σ can be represented by a discrete function σ^D that is piecewise constant over the partition cells, the equations in each urn are averaged with respect to their coefficients. This procedure gives rise to a linear system for σ^D with system size controlled by the discretization level. We regard each sort of an equation into an urn as an independent trial. Under this assumption, the Law of Large Numbers tells us that the average value is the most likely one. An approximate solution to the averaged system is then calculated via a Kaczmarz relaxation scheme (Kaczmarz, 1937; Tanabe, 1971). Kaczmarz is an iterative projection method that seeks in some sense the best solution to the system of equations. The level of discretization is then increased (by increasing the number of urns by a factor of two in each dimension) and the process repeated, using the solution from the previous level as the initial trial. Ultimately, a final discrete function σ^D is determined on the finest discretization level as an approximate solution to the problem. Criteria concerning when to stop the iteration are determined dynamically by tracking the variation of the solution from level to level and the statistics of the occupied urns.

The multiscale algorithm has several advantages. First, because the energy σ is reconstructed as a piecewise constant function defined over a discretization of the fundamental zone, there is no internal bias in the algorithm towards a particular representation of the surface energy. Indeed, such a bias is only introduced when one wants to *fit* a smooth representation to the discrete energy. Second, most of the work in determining the target energy approximation is performed on coarse meshes, at low levels where the system is relatively small. Third, while many iterative schemes can be highly effective introducing local, high frequency changes to solutions, they often become very slow and inefficient if smooth and slowly varying changes are needed. Contrary to this debilitating property, in our algorithm the smooth terms are already present in the solution so that very few iterative steps are required in order to obtain accurate approximations. Lastly, the method is very robust. Not only are large data sets handled efficiently, but because both averaging and the Kaczmarz technique are stabilizing to the system, the multiscale method avoids stability problems inherently associated with more traditional least-squares approaches (Saylor et al., 1999).

4 Discussion

To date we have applied the multiscale algorithm to both testbed simulation data and data from three different physical systems. In two of the physical systems, MgO and Al, triplejunction data was used to reconstruct the grain boundary free energy; this analytical formulation was described in Sections 2-3. In the third system the *surface* energy for MgO is studied; here the implementation and data structure is different (Kinderlehrer et al., 1999). We present reconstructions from the third case as an illustration of typical results.

Data from the thermal grooves of a small set of MgO island grains was gathered (Saylor and Rohrer, 1999). Because crystallography could be fixed between grain and matrix, the fundamental zone $\mathcal{F}$ was represented by two parameters (k, l) corresponding to the Miller indices of the free surface. In Figure 2 we display σ^D for both a 8×8 and 16×16 discretization of $\mathcal{F}$. To interpret the reconstruction, recall that MgO has the rocksalt structure. Therefore, due simply to correlating broken bond density with surface energy, we expect that $\sigma^D(111) > \sigma^D(110) > \sigma^D(100)$. This property is predicted by σ^D at the ultimate refinement level.

A smooth approximation σ_F to σ^D can be determined through a Fourier least-squares analysis, weighted to reflect the statistics of the data distribution in $\mathcal{F}$. It is important to point out that this selection of Fourier components is the first time that bias in representation is introduced into the reconstruction procedure. Therefore, to guide the selection of Fourier modes, correlation statistics are calculated between the discrete function σ^D and proposed Fourier representations. We considered several different modal selections through eighth order harmonics. Figure 3 displays the optimal Fourier fit σ_F, as determined from the 16×16 level reconstruction depicted in Figure 2.

The reconstructed energy σ^D predicts a general trend of increasing energy as the surface (111) is approached. However, at (111), a local minimum is predicted. Unfortunately, due to the size of the data set, the size of the minimum is a single partition cell. Therefore, depending on the modal selection for the Fourier

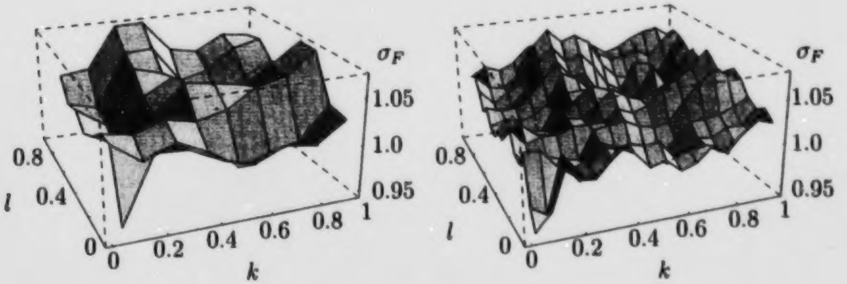

Figure 2: Reconstructions σ^D for 8×8 and 16×16 level discretizations of the fundamental zone $\mathcal{F}$. The graph has been reflected across the line $k = l$ to aid in presentation.

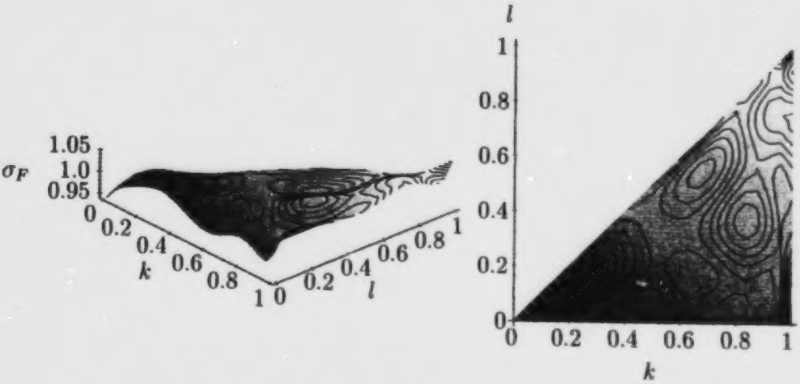

Figure 3: Fourier approximation σ_F to the reconstructed surface energy σ^D.

approximation, both local minimum and maximum can be motivated at (111). Due to the natural polarity of this surface, there is at present no clear guidance from either theory or experiment as to which trend is correct (Saylor et al., 1999). However, we believe that given a larger data set, a finer discretization of the fundamental zone would be possible, resulting in the multiscale reconstruction being able to resolve this detail with confidence. This feature illustrates that the multiscale method, when implemented on a substantial data set, provides us a glimpse of the effects of electronic structure on the material energy.

The torque terms $\partial\sigma^{(i)}/\partial\phi^{(i)}$ in (2) play an important role in the final structure of the reconstructed energy σ^D. Indeed, although the reconstruction process can be significantly simplified by ignoring the torque terms in (2), and this has often been the route chosen for expediency, this simplification is misguided. As depicted in Figure 4, removal of the torque terms leads to a significant decrease in solution regularity, and a corresponding increase in variance. Moreover, the reconstruction without torques predicts an energy decrease away from (100) and unusually large anisotropy energies, $\sigma^D(111)/\sigma^D(100) \simeq 1.4$ for the case with no torques, compared to $\sigma^D(111)/\sigma^D(100) \simeq 1.16$ for the case with torques, both features that are inconsistent with experimental evidence (Saylor et al., 1999). The multiscale method proved to be a powerful method to elucidate the necessity of torques in this computational procedure.

Acknowledgements. The authors would like to thank G. Rohrer and D. Saylor both for access to their MgO data, and enlightening discussions and advice during the course of this work. The authors further like to thank B.L. Adams, W.W. Mullins, and the entire MIMP project staff. This work was primarily supported under ARO DAAH 04 96 0060, NSF DMS-9303054, NSF DMS-9505078, and the MRSEC Program under NSF DMR-9632556.

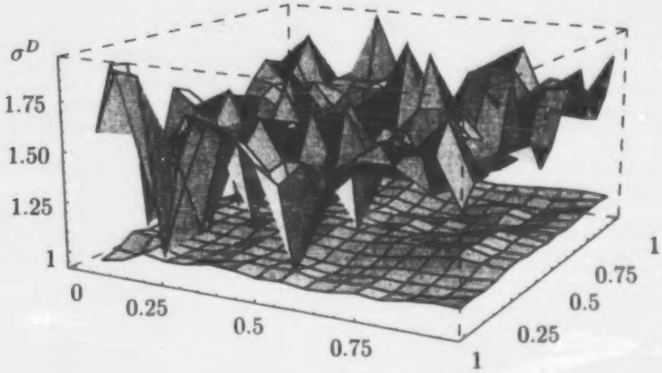

Figure 4: Reconstructed surface energies σ^D of MgO for $N_D = 16$. The top function corresponds to the case of no torques, while the lower function corresponds to the case where torque terms were included.

References

Adams, B. L., Kinderlehrer, D., Ta'asan, S., Mullins, W. W., and Costiner, S. (1998). Extracting the grain boundary free energy and mobility functions from the geometry of microstructures. *Scripta materelia*, 38(4):531–536.

Herring, C. (1951). Surface tension as a motivation for sintering. In *The Physics of Power Metallurgy*, pages 143–179, New York, NY. McGraw-Hill Book Company, Inc.

Kaczmarz, S. (1937). Angenaherte auflosung von systemen linearer gleichungen. *Bulletin of the International Acadame Polonaise des Sciences*, A:355–357.

Kinderlehrer, D., Livshits, I., Mason, D. E., and Ta'asan, S. (1999). The surface energy of magnesia; a multiscale reconstruction from microstructure. *In preparation.*

Saylor, D. M., Mason, D. E., and Rohrer, G. S. (1999). An experimental method for measuring surface energy anisotropy and its application to magnesia. *In preparation.*

Saylor, D. M. and Rohrer, G. S. (1999). Measuring the influence of grain boundary misorientation on thermal groove geometry in ceramic polycrystals. *To appear: J. Amer. Cer. Soc.*

Tanabe, K. (1971). Projection method for solving a singular system of linear equations and its applications. *Numerical Mathematics*, 17:203–214.

CORRELATION OF GRAIN BOUNDARY CHARACTER WITH WETTING BEHAVIOR

M. TAKASHIMA
Department of Materials Science and Engineering, Carnegie Mellon University, Pittsburgh, PA, USA
On leave form Kawasaki Steel Corporation, Kurashiki, Okayama, Japan
A.D. ROLLETT, P. WYNBLATT and B.L. ADAMS
Department of Materials Science and Engineering, Carnegie Mellon University, Pittsburgh, PA, USA

Abstract

Geometric criteria for grain boundary wetting have been investigated in a Fe-30wt%Mn-10wt%Cu polycrystalline alloy. Cu films were found along some grain boundaries (GB's) in the alloy after annealing above the peritectic temperature. Investigation of the three dimensional microstructure allowed determination of all five macroscopic degrees of freedom (DoF's), defined by the two GB plane normals and a twist angle, for over 900 GB's. Dry GB's often displayed one or more of the following geometric features generally associated with low GB energy: (1) low disorientation, (2) large interplanar spacing, and/or (3) low Σ ($\Sigma 3$, $\Sigma 11$) symmetrical twist. However, many dry GB's which do not belong to these low energy classes were also observed. Thus, these geometric criteria may not be sufficient to identify all wet (or dry) GB's.

Keywords: wetting, grain boundaries, grain boundary energy, iron, copper

1 Introduction

The wetting of grain boundaries (GB's) plays an important role in the embrittlement of polycrystalline solids exposed to liquids. It is therefore of technological concern in several contexts, such as the phenomenon of hot shortness which results from the accumulation of copper impurities in steel, as a consequence of

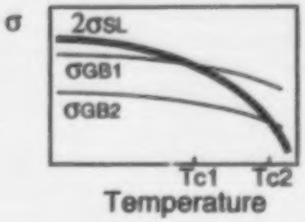

Fig. 1: Schematic illustration showing the effect of temperature on grain boundary energy and liquid-solid interfacial energy.

recycling contaminated scrap. At a more fundamental level, there is also growing interest in GB wetting as an example of two-dimensional phase transformations.

Previous work in this area has been performed mainly on controlled-orientation bicrystals (e.g., Straumal and Gust 1995). This work has shown that liquids, placed in contact with polycrystalline solids, penetrate along the GB's above a critical temperature, and that different GB's have different critical temperatures. Figure 1 illustrates the effect of temperature on GB energy and liquid-solid interfacial energy. Above a critical temperature T_C, $2\sigma_{SL}$ (where σ_{SL} is the liquid-solid interfacial energy) becomes lower than the grain boundary energy σ_{GB}, and the liquid wets the GB. Since T_C depends on the grain boundary energy, the critical temperature must depend on grain boundary character.

Therefore, in case of polycrystalline solids, at some appropriate temperature, it is expected that some GB's will be wet and others will be dry. For example, wetting of polycrystalline W by liquid Ni has been investigated (Glebovsky *et al.* 1993). Although five macroscopic degrees of freedom (DoF's) are needed to characterize a GB, that previous study of polycrystalline solids was based on specification of only one DoF.

The objective of this study was to investigate the GB wetting phase transition in the Fe-Mn-Cu system, which is of technological interest as mentioned above, and to reveal the effects of GB character on GB wetting in this system. In a previous study (Takashima *et al.* 1998), we already showed that some GB's in this system were wet after annealing above the peritectic temperature, and that small disorientation boundaries tended to be dry. In this paper, we report the effects of specifying all five DoF's.

2 Experimental procedure

10 mm in thick samples of a Fe- 30wt%Mn-10wt%Cu alloy were cold-rolled to 1mm, annealed at 1120°C in evacuated quartz tubes for 5 hours, and quenched. The GB's in the microstructure are either wet (i.e., exhibit a continuous Cu film), dry (i.e., exhibit no Cu film), or mixed (i.e. partly wet and partly dry).

To determine the five DoF's of GB's, not only adjacent grain orientations but also the GB inclinations have to be measured. These were investigated by Electron Back Scattering Patterns (EBSP) together with serial sectioning, as described below.

The GB's and the Cu-rich wetting phase in the samples were revealed by chemical polishing in 3%HF-97%H_2O_2 followed by chemical etching in 5%HNO_3-95%C_2H_5OH. The microstructure was observed in a scanning electron microscope, and grain orientations were determined by EBSP. After removing an 8μm thick surface by mechanical polishing, microstructural and EBSP observations were repeated in the same area. GB inclinations were obtained by comparing GB positions on the first and the second sections. Such data were acquired for a total of 975 GB's.

3 Theory of grain boundary representation

We begin by describing the tilt-twist decomposition method used for defining the GB DoF's (Wolf and Lutsko 1989; Rollett *et al.* 1999; Morawiec 1998).

3.1 Reduced space of the tilt-twist decomposition

We define two grains on either side of a GB as grain 1 and grain 2. The grain boundary will be specified by an orthogonal matrix g of misorientation and a unit vector **n** normal to the grain boundary. We specify the grain orientations of the two grains, g_1 and g_2, by proper rigid body rotations with respect to the reference frame. The misorientation, g, may be written as $g = g_1 g_2^{-1}$. Additionally, we specify the unit vector $\mathbf{n}_s$ normal to the grain boundary with respect to the reference frame. The grain boundary normal vectors with respect to the grain 1 and grain 2 frames, $\mathbf{n}_1$ and $\mathbf{n}_2$, are obtained by $\mathbf{n}_1 = g_1 \mathbf{n}_s$ and $\mathbf{n}_2 = g_2 \mathbf{n}_s$. Combining these equations, the grain boundary is specified by (g, $\mathbf{n}_1$) (Morawiec 1998).

A misorientation g may be decomposed according to $g = \mathbf{R}(\mathbf{n}_1, \phi)\, \mathbf{R}(\mathbf{n}_T, \varphi)$, with a tilt rotation $\mathbf{R}(\mathbf{n}_T, \varphi)$ and a twist rotation $\mathbf{R}(\mathbf{n}_1, \phi)$. **R** is a proper rigid body rotation, $\mathbf{n}_T$ and $\mathbf{n}_1$ are the tilt and the twist rotation axes, and φ and ϕ are the tilt and twist angles. Here, the tilt axis $\mathbf{n}_T$ is given by $\mathbf{n}_T = [\mathbf{n}_2 \times \mathbf{n}_1]/\|[\mathbf{n}_2 \times \mathbf{n}_1]\|$. In the tilt-twist decomposition scheme, the GB is specified by ($\mathbf{n}_1$, $\mathbf{n}_2$, ϕ) (Wolf and Lutsko 1989). As the misorientation g is a proper rigid body rotation about the rotation axis **r** by the misorientation angle θ, the twist angle ϕ is obtained by,

$$\phi = \cos^{-1}\left(2(1+\cos\theta)/(1+\cos\varphi) - 1\right), \qquad \text{when } \frac{\mathbf{m}}{|\mathbf{m}|} \bullet \mathbf{n}_1 = 1,$$

$$\phi = 2\pi - \cos^{-1}\left(2(1+\cos\theta)/(1+\cos\varphi) - 1\right), \qquad \text{when } \frac{\mathbf{m}}{|\mathbf{m}|} \bullet \mathbf{n}_1 = -1. \qquad (1)$$

$$\mathbf{m} = \begin{pmatrix} h_{32} - h_{23} \\ h_{13} - h_{31} \\ h_{21} - h_{12} \end{pmatrix}. \text{ Here, } h = \begin{pmatrix} h_{11} & h_{12} & h_{13} \\ h_{21} & h_{22} & h_{23} \\ h_{31} & h_{32} & h_{33} \end{pmatrix} = g\mathbf{R}(\mathbf{n}_T, \varphi)^{-1}.$$

The space of the tilt-twist decomposition may be reduced by noting that the GB (g, $\mathbf{n}_1$) is equivalent to the following 4×24×24 = 2304 GB's with proper symmetry operations C_1 and C_2 (Morawiec 1998):

$$(C_1\, g\, C_2^{-1},\, C_1\, \mathbf{n}_1), \qquad (C_1\, g\, C_2^{-1},\, -C_1\, \mathbf{n}_1), \tag{2.1}$$

$$(C_1\, g^{-1}\, C_2^{-1},\, C_1\, g^{-1}\, \mathbf{n}_1), \qquad (C_1\, g^{-1}\, C_2^{-1},\, -C_1\, g^{-1}\, \mathbf{n}_1). \tag{2.2}$$

In (2.1), the product of $\mathbf{n}_1$ with a particular symmetry operation C_1 or $-C_1$ will fall into a single unit triangle, such as 100-110-111. We define the product as $\mathbf{n}_1^*$. The grain boundary normal vector $\mathbf{n}_2$ may be written as $\mathbf{n}_2 = C_2\, g^{-1}\, \mathbf{n}_1^*$. Therefore, $\mathbf{n}_2$ will fall into a double unit triangle, consisting of 100-110-111 and 100-101-111. In the same way, in (2.2), the products with $\mathbf{n}_1$ or $\mathbf{n}_2$ will fall into single or double unit triangle, respectively.

3.2 Representation of grain boundary properties

We now describe a method which is useful for representing GB properties, such as energy, segregation or wetting conditions, as a function of the DoF's extracted from polycrystalline samples.

First, the reference poles **pi** for the GB normal vectors $\mathbf{n}_1$ are selected in the single unit triangle: 100-110-111. For our purposes, we selected 12 reference poles **pi** (i = 1, 2, .., 12) (Fig.2 (a)). Second, the reference poles for the grain boundary normal vector $\mathbf{n}_2$ are selected in the first unit triangle 100-110-111 and the neighboring second unit triangle 100-101-111. We selected 14 reference poles **qj** (j = 1, 2, .., 14) in the double unit triangle (Fig.2 (b)). The reference poles in the second unit triangle should lie in the interior of that triangle, because the poles along the borders of the second unit triangle are equivalent to the corresponding poles lying on the borders of the first.

After a GB is specified experimentally by $(g_1, g_2, \mathbf{n}_s)$, all equivalent descriptions in the tilt-twist decomposition scheme, $(\mathbf{n}_{1k}, \mathbf{n}_{2k}, \phi_k)$ (k = 1, 2, ..., 2304), are calculated. If the angles between $\mathbf{n}_{1k}$ and **pi**, and between $\mathbf{n}_{2k}$ and **qj**, are smaller than some tolerance angle α, the GB $(g_1, g_2, \mathbf{n}_s)$ is specified by (**pi**, **qj**, ϕ_k).

According to the above discussion on equivalent GB's, the following combinations of **pi** and **qj** may be equivalent among all the possible combinations of **pi** and **qj** (12×14=168 combinations in Fig. 2):

- $(h_1,k_1,l_1)(h_2,k_2,l_2)$ and $(h_2,k_2,l_2)(h_1,k_1,l_1)$, such as (111)(533) and (533)(111).
- $(h_1,k_1,l_1)(h_2,k_2,l_2)$ and $(h_1,k_1,l_1)(h_2,l_2,k_2)$, such as (111)(321) and (111)(312). Here, (h_1,k_1,l_1) lies on the border of the unit triangle.
- $(h_1,k_1,l_1)(h_2,k_2,l_2)$ and $(h_1,l_1,k_1)(h_2,l_2,k_2)$, such as (321)(713) and (312)(731). Here, (h_1,k_1,l_1) and (h_2,k_2,l_2) lie in the interior of the first and second unit triangle, respectively.

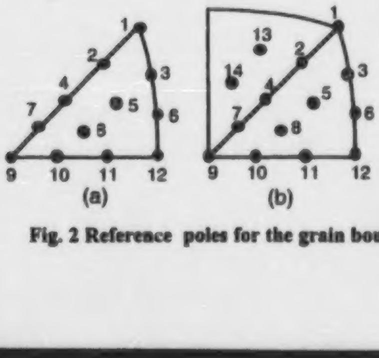

No. (hkl)	No. (hkl)
1:(1 1 1)	10:(15 4 0)
2:(5 3 3)	11:(5 3 0)
3:(7 7 4)	12:(1 1 0)
4:(3 1 1)	13:(3 1 2)
5:(3 2 1)	14:(7 1 3)
6:(7 7 2)	
7:(6 1 1)	
8:(7 3 1)	
9:(1 0 0)	

Fig. 2 Reference poles for the grain boundary normal vectors.

Considering these 87 equivalent grain boundaries, 168-87=81 combinations of pi and qj are needed to represent the properties of the whole space of the grain boundaries.

4 Results and discussion

The wetting properties of GB's described by (pi, qj, ϕ) are plotted as a function of ϕ. Although 81 figures are needed to represent the whole GB space, as discussed above, we show only four figures as examples. The tolerance angle α has been taken to be 7°. Complete analysis of the results will be published elsewhere.

Figures 3 show examples of the wetting conditions of GB's in Fe-30wt%Mn-10wt%Cu. We attempt to ratioanlize the results by means of frequently proposed geometric criteria for low GB energy: (1) low disorientation, (2) large interplanar spacing and (3) low Σ (Σ3, Σ11) symmetrical twist (Wolf 1985).

(111)(111) GB's were dry for all ϕ. The (111) plane has the largest interplanar spacing in fcc crystals, $d_{111} = 0.58\ a$. Here, *a* is the lattice parameter. At ϕ = 60°, 180° and 300°, (111)(111) GB's correspond to Σ3. For (311)(311) GB's ($d_{311} = 0.30\ a$), the wetting conditions change from dry to wet as the tilt angle (or disorientation) increases, and become dry at ϕ = 180°, which corresponds to a Σ11 symmetrical twist GB. For (533)(530) ($d_{533} = 0.15\ a$ and $d_{530} = 0.09\ a$), all grain boundaries are wet. They have large disorientations and small interplanar spacing.

However, many dry (774)(611) GB's ($d_{774} = 0.05\ a$ and $d_{611} = 0.08\ a$) are

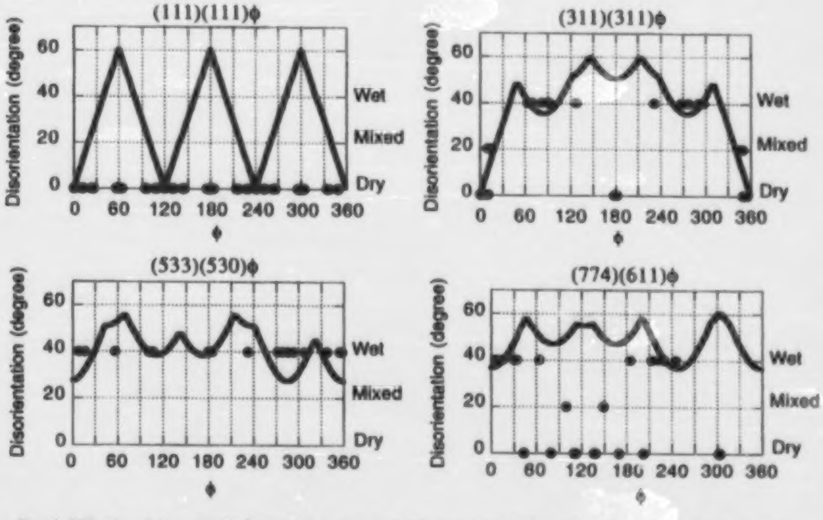

Fig.3 Effects of the grain boundary normal planes and twist angle and disorientation on wetting. Dots: Wetting conditions of grain boundaries in a Fe-Mn-Cu alloy. Solid lines: Calculated disorientation of (pi, gi, ϕ).

found. These do not conform to any of the above low energy criteria. Thus, it seems that the geometric criteria alone may not sufficient to completely identify low energy grain boundaries (Sutton and Baluffi 1987).

5 Conclusions

1. The tilt-twist decomposition method for defining GB DoF's has been used to analyze 975 GB's in a Fe-Mn-Cu polycrystalline alloy. The GB's were classified as being wet, dry or mixed.
2. The GB's which exhibited the following geometric features generally associated with low GB energy: (1) low disorientation, (2) large interplanar spacing, and (3) low Σ (Σ3, Σ11) symmetrical twist boundary, were found to be dry.
3. However, many dry grain boundaries which do not belong to these low energy criteria were observed. Thus, some factors beyond geometry may need to be considered.

6 Acknowledgement

The authors acknowledge with thanks primary support of this research by the MRSEC program of the Natural Science Foundation under grant DMR9632556. PW also wishes to acknowledge NSF support under grant DMR9802290.

7 References

Glebovsky, V., Straumal, B., Semenov, V., Suraeva, V. and Gust, W. (1993): Grain Boundary Wetting in the W-Ni System, *Proceedings of the 13th International Plansee Seminar*, H. Bildstein and R. Eck, eds., Metallwerk Plansee, Reutte,1, pp. 429-441.

Morawiec, A. (1998): Symmetries of Grain Boundary Distributions, *Grain Growth in Polycrystalline Materials III*, H. Weiland, B.L. Adams and A.D. Rollett, eds., The Minerals, Metals & Materials Society, pp. 509-514.

Rollett, A.D. Yang, C.-C. and Adams, B.L. (1999): A Five Parameter Description of Grain Boundaries, to be published.

Straumal, B.B. and Gust, W. (1995): Wetting Transition on Grain Boundaries in Al Contacting with a Sn-rich Melt, *Interface Science*, 3, pp. 127-132.

Sutton, A.P. and Balluffi, R.W. (1987): On Geometric Criteria for Low Interfacial Energy, *Acta metall.*, vol. 35, no. 9, pp. 2177-2201.

Takashima, M., Wynblatt, P. and Adams, B.L. (1998): Wetting of Fe-Mn alloy grain boundaries by liquid Cu, *Grain Growth in Polycrystalline Materials III*, H. Weiland, B.L. Adams and A.D. Rollett, eds., The Minerals, Metals & Materials Society, pp. 365-370.

Wolf. D. (1985): On the relationship between symmetrical tilt, twist, 'special,' and 'favored' grain boundaries, *J. Phys. Colloq.* (France), vol.46, no.C-4, pp. 197-211.

Wolf, D. and Lutsko, J.F. (1989): On the geometrical relationship between tilt and twist grain boundaries, *Z. Kristallographie*, vol. 189, no. 3-4, pp. 239-262.

CALCULATION OF INTRACRYSTALLINE LATTICE MISORIENTATIONS IN FACE CENTERED CUBIC POLYCRYSTALS

D. MIKA

General Electric Corporate Research and Development
Niskayuna, New York, USA

P. DAWSON

Sibley School of Mechanical and Aerospace Engineering
Cornell University, Ithaca, New York, USA

Abstract

Numerical simulations of polycrystals have been conducted to assess the ability of a crystal plasticity model to predict intracrystalline lattice misorientations. Polycrystals were constructed of dodecahedral crystals, with each crystal discretized with hundreds of finite elements. The polycrystals were subjected to uniaxial compression and plane strain compression to large strains. The single crystal anisotropy and the influence of neighboring crystals resulted in the deformations within crystals varying from one point to another. This gave rise to variations in slip system activity, and in turn, to intracrystalline lattice misorientations. The evolving misorientation distributions are presented, along with a comparison to experimental observation. Also examined is the relation of the lattice misorientation to the orientation of its associated boundary.

Key words: crystal plasticity, finite elements, lattice misorientations, boundary textures.

1. Introduction

Lattice misorientations develop within individual crystals during straining of a polycrystal due to heterogeneous deformations over crystal volumes. This heterogeneity arises in large part from the variability in the interactions with neighboring crystals. In this paper we discuss finite element simulations of lattice misorientations in face-centered cubic (fcc) polycrystals. The polycrystals consist of rhombic dodecahedral shaped crystals, each finely discretized with tetrahedral elements. Rhombic dodecahedra are twelve-sided, regular, space-filling polyhedra that are well-suited to represent a microstructure with nearly equiaxed grains. The single crystal behavior is based on rate-dependent, crystallographic slip on a restricted number of systems. Spatial variations in deformation occur in the polycrystal even under simple external loadings, and lead to grain subdivision characterized by the formation of boundaries separating regions with differing lattice orientation. Particular attention is focused on the resulting crystallographic misorientation across these boundaries and their orientations relative to the applied loads. The simulations are compared to published experimental data.

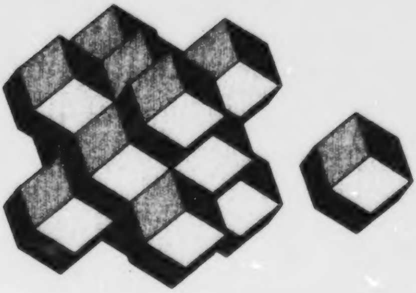

Figure 1: Rhombic Dodecahedra; Left: Dodecahedra in face-centered-cubic arrangement that fills space without voids, and Right: one rhombic dodecahedron.

2. Simulation methodology

We present here only a brief summary of the simulation methodology, which consists of the single crystal behavior, the procedure for constructing a polycrystal, and the finite element formulation for combining the single crystal relations with the balance equations to determine mechanical response. A more complete description of the simulation model is reported in (Beaudoin, Dawson, Mathur, & Kocks 1995; Mika & Dawson 1998; Mika & Dawson 1999).

The simulations focus on the inelastic behavior of polycrystals comprised only of face-centered cubic crystals under monotonic loading to large strains. As the interest is limited here to texture evolution, the elastic response has been neglected entirely. The individual crystals are permitted to slip on the twelve $\{111\}\langle 110\rangle$ systems as governed by a rate-dependent (viscoplastic) relation between resolved shear stress and the slip system shearing rate. All slip systems harden identically, according to a modefied Voce hardening model written at the slip system level. The parameters chosen for the slip system behavior are appropriate for a commercial purity aluminum.

The polycrystal is constructed by assembling individual crystals. Each crystal has a dodecahedron grain shape, as shown in Figure 1, which fits together with neighbors in a space-filling arrangement. The crystals are discretized with finite elements; there were 576 elements in each crystal for the simulations presented. Compatibility is enforced at all finite element boundaries, both of intracrystal and intercrystal type. Thus, the crystal boundaries are assumed to remain intact, although deformation certainly alters their shapes and positions. Boundary conditions are applied to the exterior surfaces to replicate the desired loading. However, of the total of 316 crystals, those on the boundary are not included in the post-simulation analyses, leaving 176 crystals that are entirely interior to the polycrystal to contribute to the lattice orientation distributions.

The polycrystals are loaded by imposing velocities at the boundaries that are consistent with an overall plane strain compression. The velocity field throughout the polycrystal is evaluated from a hybrid finite element formulation (Beaudoin, Dawson, Mathur, & Kocks 1995). In this formulation weighted residuals are formed on the tractions across element interfaces, on the equation expressing the incompressibility constraint, and on the single crystal relationship for rate-dependence of slip. Trial functions are introduced for the velocity, pressure, and deviatoric stress, with the stress trial functions chosen to satify equilibrium on the element interiors *a priori*. The formulation has been implemented to execute in a scalable parallel environment using a combination of MPI and F90.

The finite element formulation delivers the motion and stress for the polycrystal at a specific time for a given combination of geometry (coordinates of the elements comprising the crystals) and state (lattice orientations and slip system strengths). Given the velocity, stress and current state, the state is evolved over a small time step. As the individual crystals do not deform uniformly and the lattice orientations evolve according to the local kinematics, the lattices develop misorientations within the crystals. These are quantified by computing the minimum angle needed to rotate one lattice into coincidence with the other.

3. Results

The numerical model permits the direct calculation of deformation heterogeneities on the crystal level. In particular, variations in deformation rate throughout a crystal can be examined for all of the individual crystals within the polycrystal. An interesting trend that emerged from the simulations is that the level of heterogeneity is dependent on the distance from the element centroid. To see this, the dodecahedra are subdivided by tetrahedra into eighteen layers of elements with equal distance from the crystal centroid. Figure 2 is a plot of D_{11} as a function of relative centroidal distance for a typical crystal. In the figure, elements with higher neighborhood homogeneity (at the crystal center) are toward the left, while those elements with higher inhomogeneity are toward the right. The variation in deformation rate clearly increases with neighborhood inhomogeniety. In fact, it has been shown that the influence of neighborhood has a greater effect on local deformation than a crystal's own orientation (Sarma & Dawson 1996).

As the deformation proceeds, the inherent inhomogeneities over the volume of a crystal lead to segretated regions within a crystal differing in lattice orientation. These lattice misorientations can be represented with a distribution which evolves with continued straining of the polycrystal. Intracrystalline misorientation distributions obtained from experimental measurements have been shown to scale with average misorientation angle (Hughes, Liu, Chrzan, & Hansen 1997). The simulation results exhibit the same scaling law as evidenced by the collapse of the distributions from several strain levels onto one representative curve, as shown in Figure 3. The simulated behavior also has been compared to the reported experimental data in terms of the rate of growth of the average misorientation with increasing amounts of strain as shown in Figure 4. This comparison is done for the geometrically necessary dislocation distributions reported from experiments since the lattice misorientations at element boundaries would have to be accommodated by accumulations of dislocations at these boundaries.

From the simulations, it is possible also to examine the orientation of the element boundaries (with respect to the specimen and loading) relative to the magnitude of the misorientation across the element boundary. These constitute lattice-boundary textures, which are a description of the shared boundary orientation and lattice misorientation (Adams & Field 1992). Initially, all the boundaries, which

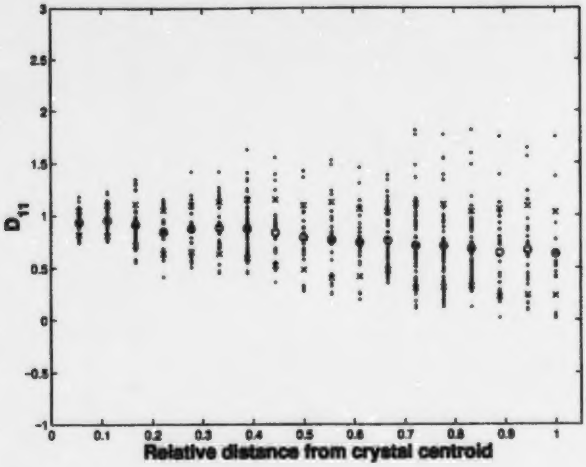

Figure 2: Variation in D_{11} at increasing relative distance from the centroid of crystal discretized with 576 elements. Individual values are designated with a '.', mean values with a 'o', and standard deviations with an 'x'.

are element interfaces, were uniformly distributed. Figure 5 shows boundary texture developed under plane-strain conditions to a strain of 0.6. At this strain, those boundaries with low misorientation are fairly randomly orientated, whereas the normals of boundaries with high misorientation are concentrated towards the compression axis.

5. Summary

Finite element simulations offer a window on the inelastic deformation processes occurring within the interior of polycrystals. Here we summarized simulations which show the influence of heterogeneous deformations of the evolution of intracrystalline lattice misorientations. The computed misorientations display a frequency distribution that scales with increasing strain in the same manner as that reported for measured values. Further, the average misorientation within all the crystals of the polycrystal evolves with strain at a rate comparable to experiment. The simulations indicate that the interfaces having greatest misorientation have normal vectors aligned with the compression direction for a plane strain deformation.

Acknowledgements

Support for this work has been provided by the Office of Naval Research under contract NOOO 14-95-I-0314. Computing resources were provided by the Cornell Theory Center.

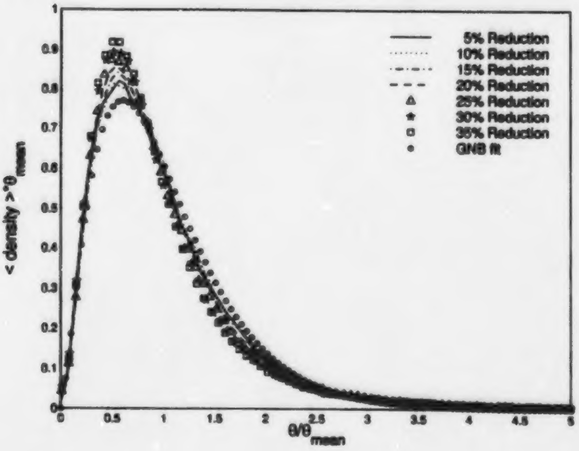

Figure 3: Scaled intra-dodecahedron misorientation distributions and fit from Hughes, et al.

References

Adams, B. L. & D. P. Field (1992). Measurement and representation of grain-boundary texture. *Metallurgical Transactions A 23A*, 2501 – 2513.

Beaudoin, A. J., P. R. Dawson, K. K. Mathur, & U. F. Kocks (1995). A hybrid finite element formulation for polycrystal plasticity with consideration of macrostructural and microstructural linking. *International Journal of Plasticity 11*, 501 – 521.

Hughes, D. A., Q. Liu, D. Chrzan, & N. Hansen (1997). Scaling of microstructural parameters: misorientations of deformation induced boundaries. *Acta Materialia 45*, 105 – 112.

Mika, D. P. & P. R. Dawson (1998). Effects of grain interaction on deformation in polycrystals. *Materials Science and Engineering A A257*, 62–76.

Mika, D. P. & P. R. Dawson (1999). Polycrystal plasticity modeling of intracrystalline boundary textures. *Acta Materialia 47*(4), 1355 – 1369.

Sarma, G. B. & P. R. Dawson (1996). Effects of interactions among crystals on the inhomogeneous deformations of polycrystals. *Acta Metallurgica et Materialia 44*, 1937 – 1953.

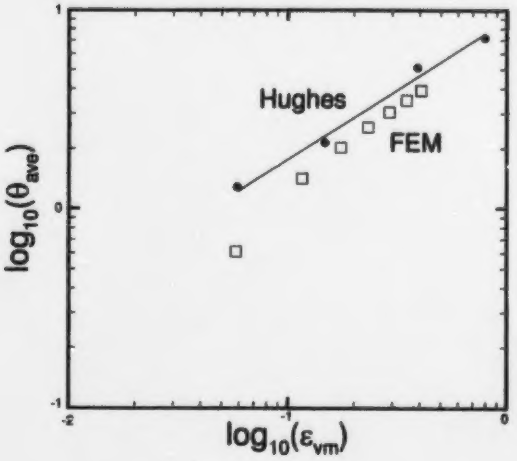

Figure 4: Power law relationship between the average misorientation angle and the von Mises strain for both simulation and measured (from Hughes, et al.) data.

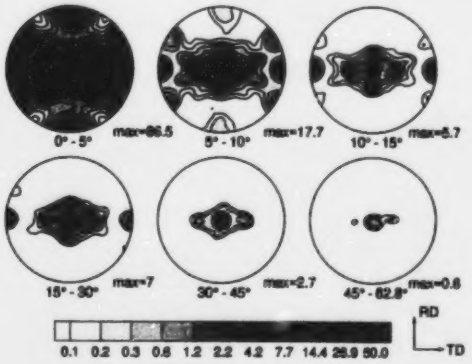

Figure 5: Stereographic plots of $f(\theta, n)$, shown at various minimum misorientation angles θ. Plane-strain compression to strain of 0.60. Maximum intensities are also shown.

ORDINARY GRAIN BOUNDARIES AND RECRYSTALLIZATION TEXTURES

D.B. TITOROV
Physical - Technical Institute, Ural Branch, Russian Academy of Sciences, Russia

Abstract

Crystallographic texture is shown to be transformed during recrystallization at the cost of the growth of recrystallization nuclei and grains, which deviate from the orientations of the principal matrix texture components on average angles, and therefore form mobile mean-angle ordinary grain boundaries with the matrix.

Keywords: ordinary grain boundary, allowed orientation, recrystallization texture

Introduction

Some orientation relations between deformation and recrystallization textures collected by Wasserman and Grewen (1962) are shown in table 1.

Table 1: Orientation relations between deformation and recrystallization textures.

Material	Deviation axes	Deviation angles	Material	Deviation axes	Deviation angles
bcc			fcc		
Fe	110	25°, 27°, 30°	Fe+Ni	111	30-40
	100	17°, 19°, 30°		100	26, 30, 38
Fe+3%Si	110	25-30°		110	18, 28
	100	17°		221	17, 28, 40
Fe+3%Si*	313	25	Cu	111	28-40
	451	38		100	15-21
W	110	17°		110	18, 28
	100	12°		random	

*** Titorov (1974)**

As seen from the table, orientation relations can be different.

Allowed orientations of primary and secondary recrystallization

The naturally located free-pole areas are shown on stereographic projections of {100} poles, fig. 1. These poles belong to the grains grown in monocrystals. The grains had been grown as a result of primary recrystallization during annealing after slight deformation or α→γ hardening.

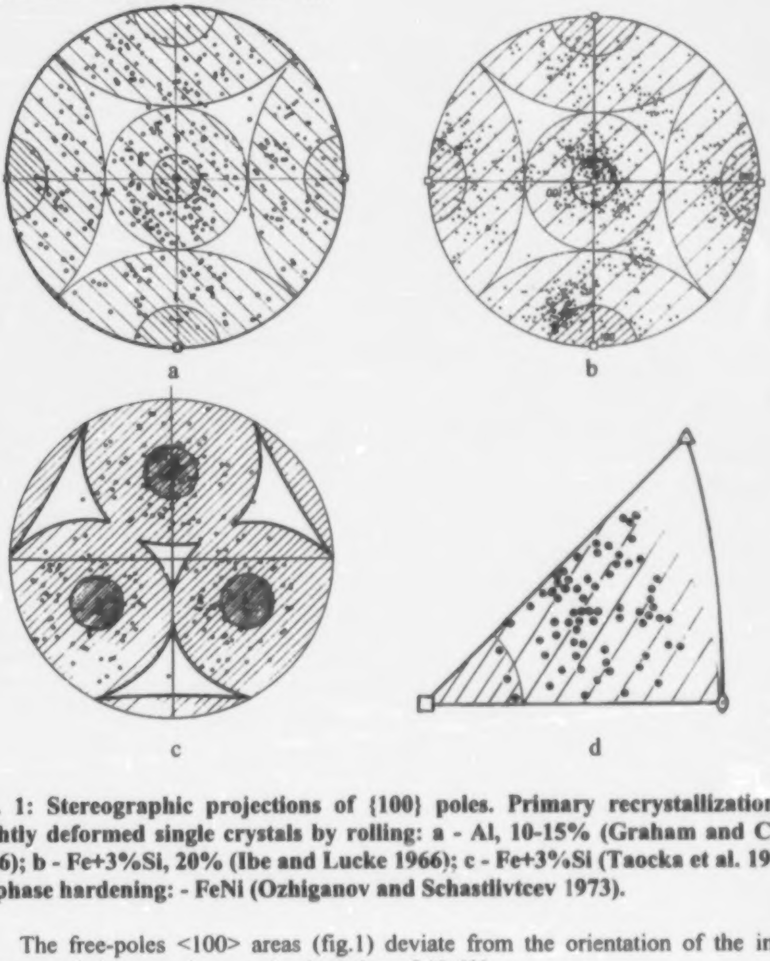

Fig. 1: Stereographic projections of {100} poles. Primary recrystallization of slightly deformed single crystals by rolling: a - Al, 10-15% (Graham and Cahn 1956); b - Fe+3%Si, 20% (Ibe and Lucke 1966); c - Fe+3%Si (Taocka et al. 1967); by phase hardening: - FeNi (Ozhiganov and Schastlivtcev 1973).

The free-poles <100> areas (fig.1) deviate from the orientation of the initial monocrystals by a maximum misorientation of 45-63°.

Analysis of experimental results carried out on Fe + 3%Si alloy plane monocrystals at the same conditions has shown that the misorientation angles between grown grains and the initial monooriented matrix can be any in the interval 10-15° to

40-45°, while the misorientation axis orientations can be essentially random. (Titorov 1974).

The same areas as for the primary free-pole naturally located areas were revealed also for the secondary recrystallization grains, fig.2.

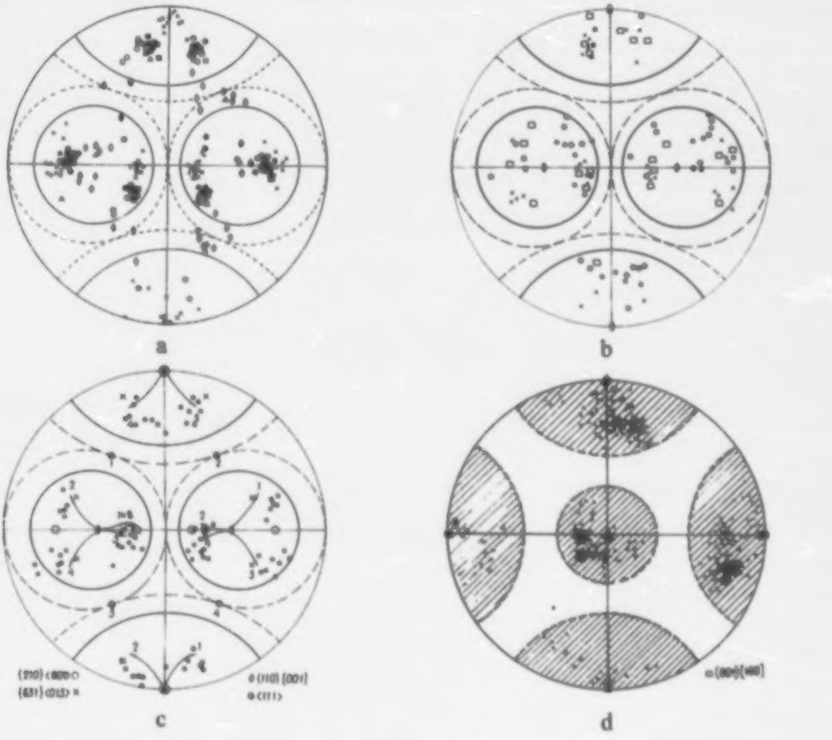

Fig. 2: Stereographic projections of {100} poles. Secondary recrystallization after severe rolling deformation: a - Fe+3%Si (Dunn 1954), b - Fe+3%Si, (Littman 1969); c - Fe+3%Si (Gokiu, Matsuo 1967); d – Cu (Bowles, Boas 1948), (× Sharp, Dunn 1952).

The authors, looking for a law in orientation relations between a matrix and evolved grains, subdivided grains into groups (poles are designated by different symbols in fig. 2a and 2b). It is visible however, that poles fall into the naturally located areas better, than correspond to orientations deviated from a matrix on the special angle and around of the special axis misorientation. In fig. 2c the arrows show turn on 25° around of axes <110> (1; 2; 3; 4).

In most cases of the above described experiments it conditions were guaranteed for origin of the recrystallization centres of any random orientations. The given data show that the grains of random orientations deviated from a matrix on average angles from 10-15° up to 40-45° grow during recrystallization processes in the monooriented matrix. It means that among ordinary grain boundaries (not special type) mean-angle grain boundaries have greater mobility in comparison with low-angle: from 0 up to 10-15° and maxi-angle: more than 40-45° and up to 63° ones.

The initial orientation (110) [001] monocrystals of Fe + 3%Si alloy were cold rolled and annealed. Their pole figures {100} are shown in fig.3.

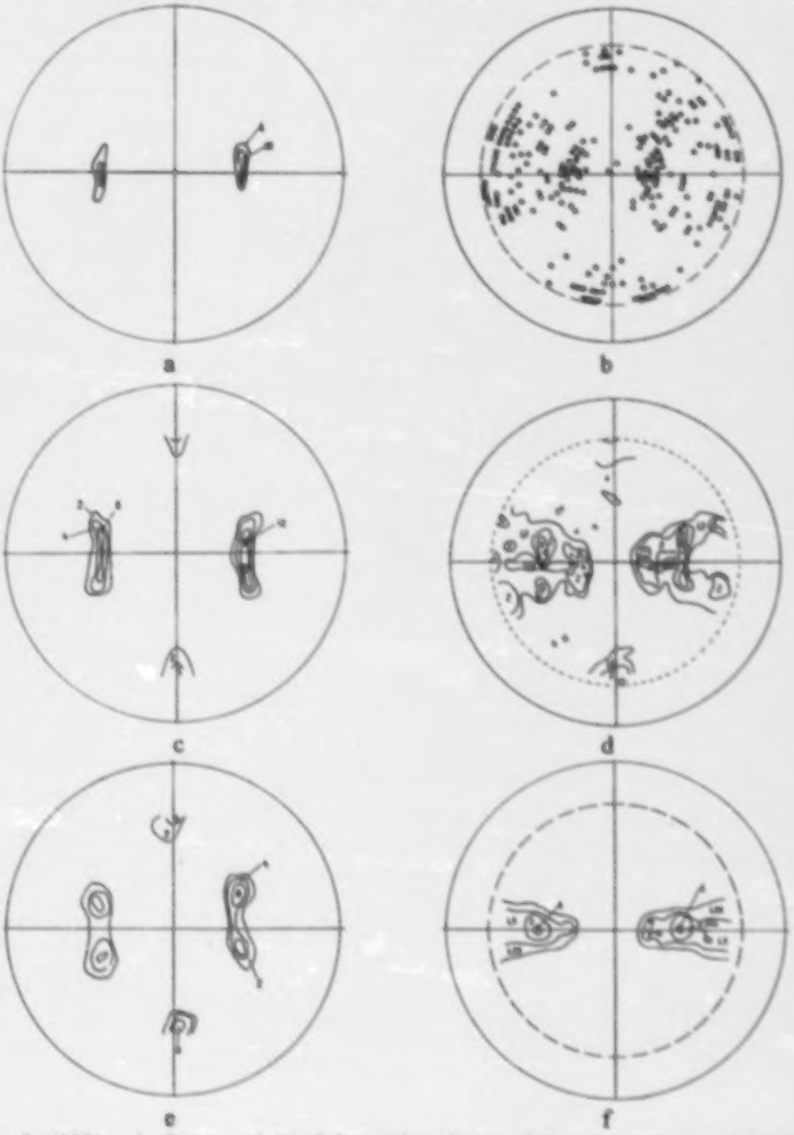

Fig. 3: {100} pole figures of the deformed and annealed monocrystals (110)[001], alloy Fe+3%Si; a – 24%, b – 1100°C, 3 min; c – 47%, 800°C, 40min ; d – 60%, 800°C, 40 min.

It can be seen, that when the single component deformation texture splinters and then transforms to two-component texture, the recrystallization texture improves.

The submitted results allow to explain the recrystallization texture formation with the help of the scheme given in fig. 4.

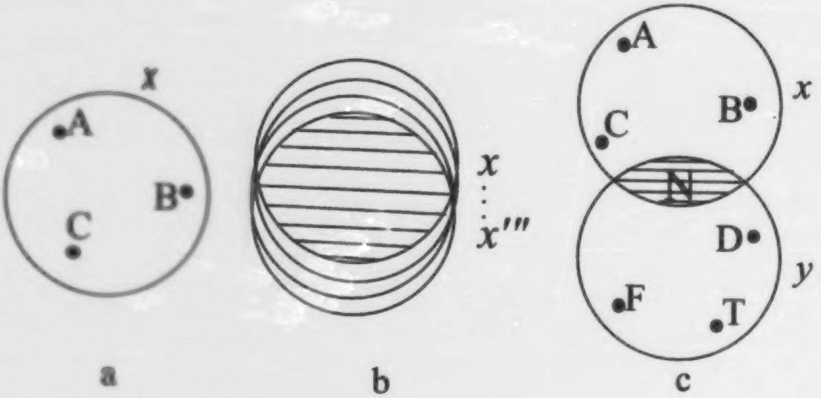

Fig. 4: Scheme of the selection of allowed recrystallization textures.

All the orientations which are deviated from an orientation of a mono-oriented matrix on average angles form a large area of allowed orientations of this matrix, fig. 4a. The recrystallization centres and grains, orientations of which correspond to a allowed orientation area (A, B, C etc.), form the mean-angle mobile grain boundaries with this matrix and consequently can grow in this matrix. The growth of the other recrystallization centres and grains is forbidden.

If a matrix mono-component texture is scattered, that consists of near x-x'-x''-x''' components, the allowed area is reduced, fig. 4b, shaded sector. Only the orientations of this sector will form mean-angle mobile grain boundaries with the all components of the scattered matrix texture.

When some different texture components are in matrix, centres and grains with the orientations of the overlapping zone of the allowed orientation areas of the most of matrix texture components grew with the maximal probability during recrystallization. For example, if the matrix consists of two texture components x and y the growth of the centres and grains with orientations of the overlapping zone, close to N (fig. 4c) will most probable during recrystallization.

The areas and zones of allowed orientations can be constructed on stereographic projections (100). Examples of forecasting recrystallization textures by construction of stereographic projections of pole areas and overlapping zones of allowed orientations are given in some author's works, Titorov (1974, 1992, 1994).

Conclusion

In conclusion, it is possible to say that recrystallization textures are not formed at the cost of special grain boundaries. The growth of recrystallization nuclei and grains, which deviate from the majority matrix texture components on average angles, form recrystallization textures. Such are recrystallization centres and grains form mean-angle ordinary grain boundaries. These centres and grains keep high mobility when meeting the greatest number of subcomponents of different matrix orientation.

References

Bowles, J.S., Boas, W. (1948) The effect of crystal arangment on secondary recrystallisation in metals. *J. Inst. Metals*, Vol. 74, pp. 501-18.

Dunn, C.G. (1953) Secondary recrystallization textures and their origin in cold rolled single crystals of silicon iron. *Acta met.*, Vol. 1, pp. 163-73.

Graham, C.D. and Cahn, R.H. (1956) Grain growth rates and orientation relationtips in the recrystallization of aluminium single crysttals. *Trans. AIME*, Vol. 206, pp. 512-17.

Gokiu, I., Matsuo, M. (1967) Rolling and recrystallization textures of of silicon-iron crystals with (110)[100] orientations. *JJJM*, Vol. 31, pp. 374-89.

Ibe, G., Lucke, K. (1996) Growth selection during recrystallization of single crystals, in *Recrystallization grain growth and textures*, ASM, Metals Park, Ohio, pp. 434-47.

Kornfeld, M.O. and Rybalko, F. (1937) Anisotropy in the linear velocity of growth of new grain in recrystallization. *Physik Z. Sowjet*, No. 12, pp. 658-63.

Littman, M.F. (1969) Effect of sulfide and carbide precipitates on the recrystallization and grain gowth behavior of 3 pct Si-Fe crystals. *Trans. AIME*, Vol. 245, pp. 2217-20.

Ozhiganov, A.V., Schastlivtsev, V.M. (1973) The features of formation of austenite structure in a critical interval of temperatures at slow heating quenched and tempered steels. *The Physics of Metals and Metallography*, Vol. 36, No. 5, pp. 1025-32

Sharp, M., Dunn, C.G. (1952) *Trans.AIME*, Vol. 94, p.1344, in *Texturen metallisher Werkstof* (Wasserman, G. and Grewen, J. 1962), Springer-Verlag, Berlin / Gottingen / Heidelberg.

Taocka, T., Takeuchi, S., Furubayashi, S. (1967) Sponteneously and artificially recrystallized textures in rolled 3 pct silicon-iron single crystals. *Trans. AIME*, Vol. 239, pp. 13-20.

Titorov, D.B. (1974) Influence of the spread of deformation texture on the recrystallization texture. *The Physics of Metals and Metallography*, Vol 37, No. 5, pp. 1026-21.

Titorov, D.B. (1991) Matrix textures that allow development of a cubic texture during recrystallization of the Fe+3%Si alloy. *The Physics of Metals and Metallography*, Vol 71, No. 3, pp. 198-200.

Titorov, D.B. (1994) Allowed cube-on-edge texture in the alloy Fe+3% Si. *The Physics of Metals and Metallography*, Vol 77, No. 1, pp. 73-6.

Wasserman, G. and Grewen, J. (1962) *Texturen metallisher Werkstof*, Springer-Verlag, Berlin / Gottingen / Heidelberg.

COMPUTER SIMULATION OF DIFFUSION PROCESS IN POLYCRYSTALLINE MATERIAL

Hualong Li and J. A. Szpunar
Dept. of Metallurgical Eng.
McGill University, Montreal, CANADA, H2X 2B2

Abstract

Understanding of diffusion processes is of great importance for understanding oxidation, precipitation, creep, annealing and other processes. In this paper, a two-dimensional computer simulation model is proposed to simulate the diffusion process in polycrystalline solids. In this model, the microstructure is described by large number of unit cells with specified orientations and the grain size and grain shape are introduced to the model using available experimental data. Each unit cell has a property defined by diffusion coefficient, which represents the lattice diffusion coefficient or the grain boundary diffusion coefficient. Grain boundary diffusion coefficient is a function of the grain boundary mis-orientation and characters. The diffusion process is simulated using the Random Walk method. The output of the simulation is presented as a normalized concentration profile and a two-dimensional contour map, which displays the distribution of diffusing species. Using this simulation model, the effects of texture, grain boundary character distribution, grain shape, grain size and the role of various structure defects on the diffusion process can be studied.

Keywords: Diffusion, texture, microstructure, grain boundaries and simulation

1 Introduction

The solid-state diffusion transport of the reactants may take place by various mechanisms: diffusion through the lattice, along grain boundaries and other easy diffusion paths. In polycrystalline materials, the diffusion along these paths are affected by the texture and microstructure of the material. In order to study such a complex process, a two-dimensional meso-scale diffusion model is introduced by assuming that the solid is continuum, that is, by ignoring the atomic structure of the solid. Effects of the texture and microstructure and also influence of various structure defects on the diffusion process can be simulated using this model.

2 Simulation Procedure

2.1 Relation between Random Walk Theory and Diffusion

The random-walk theory was initially introduced in 1905 by Smoluchowski and Einstein [1] to investigate the Brownian motion. It is a question about how far the particle will be from an arbitrary starting point after some very large number of random jumps, given the number of jumps per second and the mean jump distance.

Diffusion in the solid is a process of atom jumping from one site to another. The atomic jump frequency in solid at high temperature is known to be high. For example, near the melting point of many metals each atom has a vibrational frequency of 10^{13}-10^{14}/s and changes sites roughly 10^8 times per second. Over the period of hours or days, the number of jumps becomes astronomical. In a homogeneous solid without considering the symmetry of the actual lattice, these jumps are made in all directions and follow no particular pattern. Therefore it is reasonable to assume that the diffusion occurs by periodic jumping of atoms from one lattice site to another. If this is indeed true, the diffusion coefficient can be related to the jump frequency and jump distance. This will allow us to study the diffusion process with computer by simulating the random walk process.

The relation between the diffusion coefficient D and jump distance r and the jump frequency Γ (or the time spent on one jump Δt) can be described as [2,3]:

$$D=\frac{1}{2n}\Gamma r^2 \text{ or } \Delta t=\frac{r^2}{2nD} \tag{1}$$

where factor n is 1, 2, 3 respectively for the diffusion processes in one, two, three dimensional space.

The above equation shows that the jump frequency Γ can be calculated with a given average jump distance r and the diffusion coefficient D, and vice versa. This allows us to simulate the diffusion process by simulating the random jump process of atoms.

2.2 Description of the Cellular Model of Diffusion

In this section, a two-dimensional cellular model used to simulate the diffusion processes in a solid is described in details. In this diffusion model, the polycrystalline solid is represented by a number of grains (figure 1) and each grain is digitized into a number of cells. The cell represents a small area of solid and has a square shape. Each cell is characterized by three sets of parameters. The first one is the label of the cell which ranges from 0 to n where n is the number of different grain boundaries in the microstructure. The cell with label 0 represent the bulk of the grain and the cells with label between 1-n represent the grain boundaries. The cells with the same labels represent the regions with the same diffusion property and therefore have the same diffusion coefficient. In the simulation, the label of cell is used to control the jump frequency of the diffusing atoms. The second set of parameter of the cell is a pair of integers (X, Y) to specify its coordinate in the two dimensional space. This set of parameters is used to record positions of the diffusing atoms. The third parameter

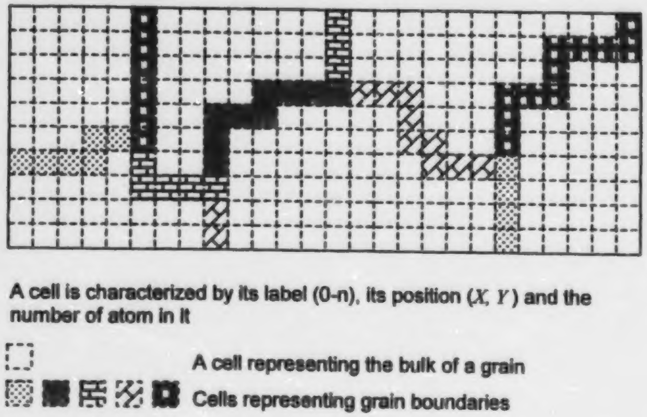
A cell is characterized by its label (0-n), its position (X, Y) and the number of atom in it
A cell representing the bulk of a grain
Cells representing grain boundaries

Figure 1 Cellular representation of the oxide microstructure in the simulation of diffusion process.

of the cell is an integer used to count the number of diffusing atoms in the cell. This microstructure is called a computer specimen in the following section.

The flow chart of the simulation procedure shown in figure 2, which illustrates the random walk process in the computer model.

The first step in the simulation module is to obtain the microstructure of the computer specimen. This microstructure can normally be generated as the Voronoi grains with Monte-Carlo method. The Voronoi grain is defined as that all the cells within this grain is closer to the center of the grain than that of others.

In the second step, the label of each cell in the computer specimen is determined randomly according to the calculated grain boundary character distribution. Each cell is labeled as 0 for the bulk and 1 to *n* for grain boundaries.

In the third step, the simulation of random walk process starts. This is the main part of the simulation. In order to describe the process clearly, the detailed description of how an atom jumps inside the bulk and along grain boundaries is given first. Then, the framework of the simulation is described. A simple computer specimen with a single grain boundary (figure 3) is used for the purpose of description. The diffusion species is called atom for convenience.

For an atom inside the bulk of a grain (region 1 in figure 3), the jump direction is randomly selected among the four possible directions since the diffusion coefficients along the four directions are the same. The time required for this jump is calculated using equation (1). If the atom is inside the grain boundary (region 2 in the figure 3), the atom may jump along the grain boundary or across the grain boundary. The diffusion coefficient along the boundary is the grain boundary diffusion coefficient D_{gb}. The diffusion coefficient across the grain boundary is the bulk diffusion coefficient D_{bulk}. The diffusion process inside the grain boundary can be considered a sum of the diffusions along and across the boundary. Both diffusions

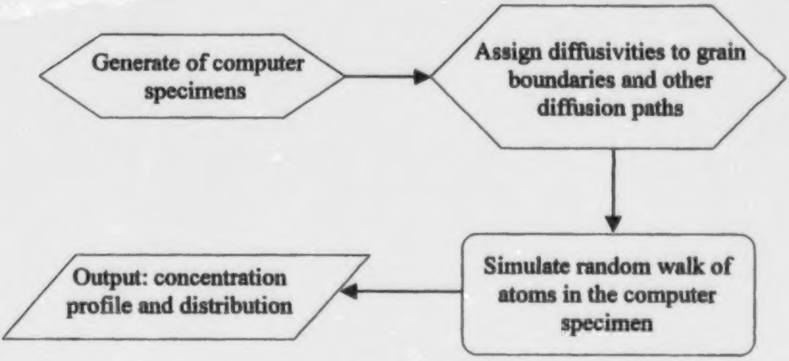
Generate of computer specimens
Assign diffusivities to grain boundaries and other diffusion paths
Simulate random walk of atoms in the computer specimen
Output: concentration profile and distribution

Figure 2 - The simulation procedure of the diffusion process in oxide.

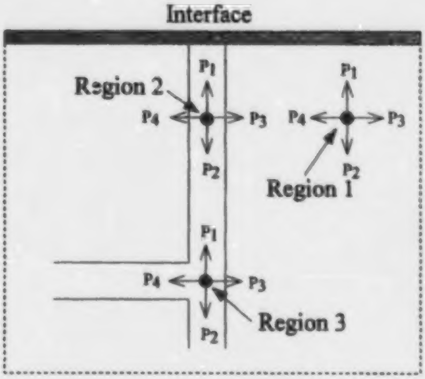
Interface
Region 2
Region 1
Region 3
P1
P2
P3
P4
P1
P2
P3
P4
P1
P2
P3
P4

Figure 3 - Illustration of the random walk process in the computer specimen

processes are one-dimensional processes. The jump frequency of the atom along and across the grain boundary can be calculated from equation (1) as

$$\Gamma_{along} = \frac{2D_{gb}}{r^2} \tag{2}$$

$$\Gamma_{across} = \frac{2D_{bulk}}{r^2} \tag{3}$$

The selection criteria of the jump direction of atoms are then assumed to be proportional to their jump frequency. $P_1=P_2=\Gamma_{across}/(\Gamma_{across} + \Gamma_{along})$ and $P_3=P_4=\Gamma_{along}/(\Gamma_{across} + \Gamma_{along})$ where P_1, P_2 are the probabilities of the jumps across the boundary and P_3, P_4 are that of the jumps along the boundary. Hence, the diffusion in the grain boundary is not a random walk process but a restricted walk. The time spent on this single restricted jump is calculated as

$$\Delta t = \frac{1}{\Gamma_{along} + \Gamma_{across}} \tag{4}$$

For the atom located in more complicated regions, for example, the junction of two grain boundaries (region 3 in figure 3), the simulation of diffusion can be realized similarly. In general, the probability of the jump toward a certain direction in the computer specimen can be calculated as follows:

$$P_n = \Gamma_n \Big/ \sum_{i=1}^{4} \Gamma_i \quad (\Gamma_n = D_n / r^2 ,\ n = 1,4) \tag{5}$$

The time spent on such a jump is then calculated as

$$\Delta t = 1 \Big/ \sum_{i=1}^{4} \Gamma_i \tag{6}$$

Once knowing how to simulate the random walk process a single atom, the diffusion process can be simulated. At the beginning of the simulation, the number of atoms contained in each cell at the first layer of the computer specimen is set to 1 million (arbitrarily defined) and kept constant which represents the constant pressure of the diffusion species at the interface. The cells in other regions of the computer specimen contain 0 atom at this stage. Then, the diffusion process starts and the atoms in the first layer are allowed to jump in the two-dimension structure by following the random walk process. The atoms jump within a small time interval Δt and the distance for one jump is r. Theoretically the time interval Δt and jump distance (r) can be of any values. In this simulation, the jump distance is equal to the width of the cell, which means that the atoms jump cell by cell. The time spent on such a jump in different cells is different and it is calculated from equation (6). The Δt is selected as the shortest time for the jump to occur within various cells.

Since within the time interval Δt the atoms in cells with the highest diffusion coefficient can jump only once, the atoms in the cells with low diffusion coefficient may not jump even once. In other words, only a fraction of the atoms in those cells jump within the time interval Δt. The fraction is determined by $\Delta t/\Delta t_i$ where Δt_i is the time it takes for the atom in the ith cells to jump once.

After the time interval Δt, the number of atoms contained in each cell of the computer specimen is counted. The number of atoms contained in the cells at the first layer is re-set to one million to keep the constant pressure at the interface. The same procedure is repeated all over again within another time interval Δt. But this time, the atoms exist in many layers in addition to the first layer. All the atoms in the computer specimen are allowed to jump. The same simulation procedure continues until the specified time is reached.

In the step 4, statistical diffusion profile is obtained. The diffusion profile is obtained by counting the number of diffusing atoms as a function of thickness of the computer specimen and normalizing it. The obtained normalized diffusion profile is quantitative.

3 Summary

A computer model of diffusion process in polycrystalline solids based on Random Walk theory is developed. The computer model is capable of simulating the effects of texture and microstructure on the diffusion process. In the simulation, the texture affects the diffusion process in the way that it changes the grain boundary character distribution. The microstructure affects the diffusion process because that it changes the network of grain boundary and the distribution of defects. This computer model has been used to simulate the oxidation kinetics of Ni [4] and the results are in agreement with experiments.

4 References

1. Einstein, A., (1956) *Investigations on the Theory of Brownian Movement*, Dover Publications, New York.
2. Shewmon, P., (1989) *Diffusion in Solids*, A Publication of The Minerals, Metals & Materials Society, p.65
3. Chandrasekhar, B.S., (1943) *Revs. Modern Phys.*, p.15
4. Li, H., Czerwinski, F., Szpunar, J. A., (1997) *Corrosion Sci.* v39, n7, p.1211

ATOMISTIC MODELLING OF INTERGRANULAR FRACTURE IN Ni_3Al

J. Lu and J.A. SZPUNAR
**Department of Mining and Metallurgical Engineering, McGill University,
Montréal, Canada**

Abstract

This paper presents the results of the intergranular fracture investigation that has been conducted using Embedded Atom Method (EAM) Molecular Dynamics (MD). At the atomistic level, the computer model is capable of treating bicrystal under the influence of external load. Exemplary results of the investigation of grain boundary structure, energy and intergranular fracture are presented. These results can be used to simulate crack propagation in textured polycrystalline Ni_3Al.

Keywords: Fracture, grain boundaries, intergranular, intermetallics, molecular dynamics

1 Introduction

The structure energetics, and free volumes associated with different types of boundaries and their statistical distribution with a textured polycrystal are expected to exert a dominant influence on macroscopic material properties such as intergranular fracture, grain boundary sliding, boundary migration, and grain boundary diffusion. Grain boundaries in pure metals represent ideal model systems for the investigation of the strictly geometrical aspects of structure-property correlations.

Despite a variety of controlled bicrystal experiments performed to date, a systematic experimental exploration of the special 3 grain boundary with the five macroscopic and three microscopic degree of freedoms has not been performed well. Because of the relative ease with which the macroscopic degree of freedoms can be manipulated in the computer, an approach utilizing the complementary capabilities of atomic-level computer simulation and experiment seems to be particularly promising. However, while a comparison between experiments and modeling results in crucial test cases is absolutely essential, the main strength of such simulations lies in their ability to provide atomic-level insights into structure-property correlations.

It should also be noted that, since real bicrystal is produced at finite temperatures, entropic and kinetic effect may also play a role in determining the properties of bicrystals. At elevated temperatures, the kinetics of all of these thermally activated processes becomes sufficiently rapid that their contributions to the overall behavior of the material are substantial. The common feature associated with all of these phenomena is thermally activated motion in a reduced coordination environment. Free volume provides a good measure of average grain boundary coordination. It is therefore logical to correlate the kinetics of these thermally activated macroscopic material properties with the boundary free volume. Free volume is useful because (a) free volume is a potentially more readily measurable quantity than grain boundary energy, and (b) in some cases it provides a direct link between structure and properties, such as grain boundary energy, grain boundary sliding, migration and fracture, etc.

2 Results of calculation

Energy minimization was performed on the grain boundary structure model, using dynamic borders, by applying the steepest descent relaxation method with a constant stress at the borders. Using the embedded-atom method potentials for Cu, Ni and Al, the correlations between energy, structure, and volume expansion for grain boundaries in Ni_3Al have been investigated. An example of 35 (120) tilt grain boundary structure for Ni_3Al is shown in Fig. 1. The results of grain boundary energy and grain boundary free volume of grain boundaries in Ni_3Al are listed in Table 1 for symmetric twist boundaries.

In these studies, it was found that both the grain boundary energy and free volume depend to a high degree on the grain boundary plane. The energy of (001) boundaries is more than twice as large as that of the (111) boundaries. The grain boundary energy and free volume are highly interrelated. A general trend of increasing grain boundary energy with increasing grain boundary expansion was observed. The 33, (111) twist and (110) 70.53° tilt coherent twin boundaries have zero expansion and zero grain boundary energy because those grain boundary configurations are identical to the perfect crystal. The results suggest that an important role is played by the grain boundary plane. The interpretation of the large differences in the grain boundary energy and free volume for different planes is offered by Yip and Wolfe (1989). Although the density in the grain boundary region has decreased due to the volume expansion at the grain boundary, and thus the average distance between atoms has increased, some atoms in a high defected environment are at separations closer than the crystalline nearest-neighbor distance. It appears that in any grain boundary unit cell there are regions of very poor match across the interface which cannot be sufficiently relaxed even when the volume increases.

It should be noted that for most of the boundaries the experimentally obtained volume expansions are about twice as large as the calculated ones, however, the volume expansion for the 33 (111) twin boundary in copper [Wood et al. 1986 [2]] found by HREM was only about 0.001±0.004nm (•a/a = 0.0028 ± 0.011) which

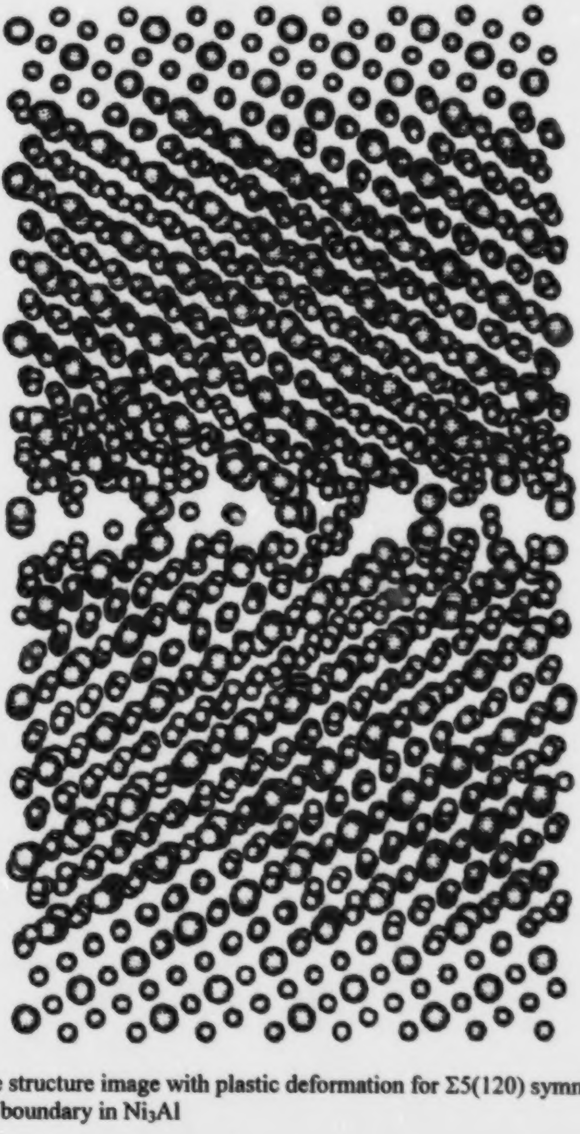

Figure 1. The structure image with plastic deformation for $\Sigma5(120)$ symmetrical tilt grain boundary in Ni_3Al

Ni – small balls; Al – large balls

agrees very well with the theoretically predicted value.

Our calculated grain boundary energy for several boundaries in Ni_3Al agrees well with the values obtained by Chen et al. (1986) and Baskes et al (1989).

A linear relationship between grain boundary energy and volume expansion was observed for Ni_3Al as shown in Figure 2. It should be noted that many material properties correlate directly or inversely with the grain boundary energy. A linear relationship between the boundary energy and volume expansion suggests that many grain boundary related material properties can be easily correlated with the average volume expansions of the boundaries constituting a polycrystal. A trend of increasing grain boundary energy and free volume with an increase in the interplanar period was observed. The grain boundary energy and volume expansion as a function of misorientation showed sharp minima (or cusps) at those values of misorientation angles which left the boundary in purely symmetric configurations. These results agree with the calculations made by Yip and Wolf [5].

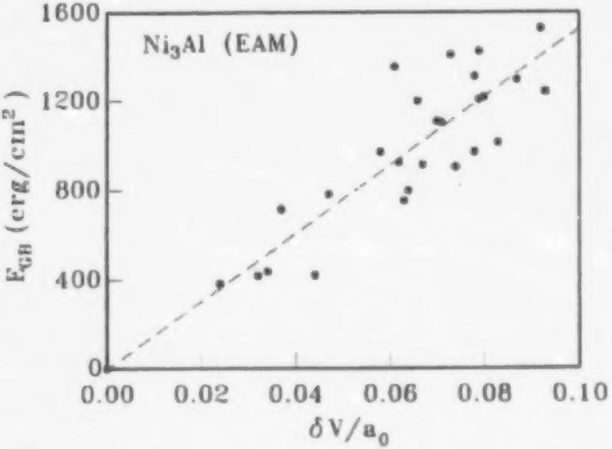

Figure 2. Relationship between grain boundary energy E_{GB} and volume expansion $\delta V/a_0$ for Ni_3Al

Because the propensity of Ni_3Al to intergranular fracture could be attributed to a low cohesive energy of the grain boundaries, it is of interest to investigate the energetics of the grain boundary for this alloy. The cohesive energy represents the energy required to cleave the boundary. It is therefore the sum of the surface energy of the two free surfaces that are created minus the energy of the grain boundary which is cleaved when the intergranular fracture occurs in the absence of plastic deformation. For the symmetric twist grain boundary, the surfaces created have the same orientation as the grain boundary plane. However, for the symmetric tilt grain boundary, the surfaces created have a different orientation from the grain boundary plane. For Ni_3Al alloy the surface energy depends on whether the exposed surface plane is the pure Ni plane, or pure Al plane, or the mixed composition plane.

3 Surface energy

In this investigation, surface energies were calculated for only three principal fcc surfaces (100), (110) and (111) using the embedded-atom method in Ni_3Al. Metal surfaces have provided a convenient proving ground for the embedded atom method. Sufficiently accurate measurements are available for some fundamental properties (for example, surface relaxations) that close comparison to experiment is possible. The EAM is seen to be capable of describing metal surfaces adequately because the effective interatomic interactions are influenced by the environment. The key here is the role of the many-body interactions incorporated in the model.

The surface energy and structure of the low-index surface (100), (110) and (111) of Ni_3Al were obtained. The calculations were performed by minimizing the total energy of thick slabs with (100), (110) and (111) surfaces. These energies are accordingly 1641, 1743, and 1676 ergs/cm^2.

In general, the surface energies are systematically lower than the experimental results [Tyson and Miller 1977], though the ordering with respect to the face is correct.

4 Summary

The results of grain boundary energy and surface energy indicate that the cohesive energy of grain boundaries in Ni_3Al alloy is not simply due to poor cohesion of the individual boundaries. Therefore, further modeling and calculations are necessary to seek the main reasons of the brittleness of Ni_3Al and to improve its fracture resistance and toughness.

5 References

Baskes, M.I., Folies, S.M. and Daw, M.S. (1989) Application of the Embedded Atom Method to Interfaces in Metals. *Interfaces in Metals, Materials Science Forum*,Vol. 46, p. 187.

Chen, S.P., Voter, A.F. and Srolovitz, D.J. (1986) Computer Simulation of Grain Boundaries in Ni_3Al: The Effect of Grain Boundary Composition. *Scripta Metallurgica*, Vol. 20, p. 1389

Wood, G.J., Stobbs, W.M. and Smith, D.J. (1986) Methods for the Measurement of Rigid-body Displacements at Edge-on Boundaries. Vol. 50, p. 375

Yip, S. and Wolf, D. (1989) Atomistic Concepts for Simulation of Grain Boundary Fracture. *Materials Science Forum*, Vol. 46, p. 77

SINGULARITY OF GRAIN BOUNDARY CHARACTER DISTRIBUTION IN ZIRCONIA FILM GROWN ON ZR-2.5%NB SUBSTRATE

A. P. Zhilyaev
Institute for Physics of Advanced Materials, USATU, Ufa, 450000 RUSSIA
V. Y. Gertsman
Pacific Northwest National Laboratory, Richland, WA, 99352, U.S.A.
J. A. Szpunar
Dept. of Metal. Engineering, McGill University, Montreal, PQ, CANADA, H3A 2B2

Abstract

TEM study has disclosed characteristic regions of the microstructure in the oxide layer grown on the surface of Zr-2.5%Nb alloys. Crystallites in those regions have dimensions on the nanometer scale. Specific texture, created in the zirconia film, reflects certain orientation relationships between the crystal lattices of α-zirconium metal and its oxide. Crystallogeometric analysis based on the constrained CSL model shows that these regions are built almost entirely of twins and appear as a mosaic pattern of rather regularly shaped crystallites with straight boundaries between them. Unlike materials with the cubic crystal lattice, several non-equivalent twin variants are possible in the monoclinic lattice of zirconia. Because of that, grain junctions consisting only of twin boundaries may exist in the monoclinic zirconia. This allows a unique situation, which manifests itself as a self-organized microstructure on the mesoscopic scale. Such a microstructure may have special properties and play important role in macroscopic properties such as diffusivity, fracture, etc. Being polycrystalline in nature, these areas may behave with regard to oxidation process almost as a single crystal. Computer modeling has been performed to evaluate possible grain boundary statistics in zirconia film. Possible implications of the results obtained are discussed.

Keywords: Zirconium alloy, crystallogeometric analysis, self-organized microstructure, twins

Introduction

In recent years, relationships between grain boundary misorientation distributions and texture have been studied both experimentally and by means of computer simulation. While there have been attempts to obtain misorientation distributions from texture data only, our studies have shown that in general the relationship between the two distributions is not straightforward but rather vague.

Experiments show that in many cases the grain boundary distributions are dominated by the correlation in the orientations of adjacent grains. For example, f.c.c. materials prone to twinning during annealing demonstrate such a correlation in orientations of crystallites that $\Sigma 3^n$ boundaries prevail (Gertsman et al. 1992, 1994; Zhilyaev et al. 1993). However, apparently only twin, $\Sigma 3$ boundaries exhibit special properties in f.c.c. materials, while other $\Sigma 3^n$ boundaries are geometrically necessary for providing connections among $\Sigma 3$ boundaries [Gertsman and Tangri, 1991; Gertsman et al. 1994]. Recently, we observed an interesting type of extremely strong tendency to creation of special regions containing only special (twins) boundaries in zirconia film formed on a zirconium alloy [Gertsman et al. 1996; 1999]. The present paper deals with such special microstructures in more details. The practical interest for this study originates from the fact that oxide film on the surface of zirconium alloys serves as a protective barrier against fast diffusion of species into the metal.

Twin Boundaries in Monoclinic Zirconia

The monoclinic unit cell parameters of ZrO_2 are close to the following values: $a = 0.5149$, $b = 0.5213$, $c = 0.5316$ nm, and $\beta = 99.23°$. Of course, the parameters actually depend on various factors, such as purity. Several non-equivalent twin variants are possible in this structure. Detailed formal analysis of them in the framework of the constrained CSL (coincidence site lattice) model can be found in (Gertsman et al. 1997; Gertsman and Szpunar, 1999). Here we give a very brief consideration of the twin crystallogeometry, which will be necessary for further discussion.

From experiments it is known that twins in monoclinic zirconia are formed on the following crystal planes: (001), (100), {110}, {011}, (101) and $(10\bar{1})$. Let us consider the corresponding misorientations. The misorientation corresponding to the (001) twin boundary is described by $180°[100]\Leftrightarrow 180°[\perp(001)]$*, and that of the (100) twin boundary is $180°[001]\Leftrightarrow 180°[\perp(100)]$. In the framework of the constrained CSL model, using the approximation $a = c$ and $\cos\beta = 1/6$, one obtains the reciprocal density of coincident sites $\Sigma=3$. Thus, these two misorientations have been designated $\Sigma 3a$ and $\Sigma 3b$, respectively [Gertsman et al. 1997]. It should be mentioned, however, that different values of Σ could be assigned to the same misorientation when different constraints of the crystal lattice are employed. Analysis of such a situation for the particular case of zirconia is published elsewhere (Gertsman and Szpunar, 1999).

The misorientation of the twin boundary on the {011} plane is

---

* *[⊥(hkl)] denotes the normal to the [*hkl*] plane*

$\theta_1[100]\Leftrightarrow 180^\circ[\perp\{011\}]$, and that on the {110} plane is $\theta_2[001]\Leftrightarrow 180^\circ[\perp\{110\}]$. Both angles θ_1 and θ_2 are close to 90°, and the deviations from a right angle depend on the actual parameters of the unit cell. When the approximation $a=b=c$ and $\cos\beta=1/6$ is employed, both misorientations are characterized by $\Sigma 71$ (in (Gertsman et al. 1996, 1997) they are denoted $\Sigma 71a$ and $\Sigma 71b$, respectively). No reasonable constraints of the lattice parameters enable obtaining a smaller Σ value. Actually, the magnitude of Σ tells nothing about the boundary singularity and, in general, the value of Σ can be high for the grain boundaries with special properties in non-cubic structures (King and Singh, 1994; Gertsman and Szpunar, 1999). The discussion of the validity of the Σ parameter is beyond the scope of the current paper, and in this paper we are using it only for nomenclature purpose, i.e. to briefly designate different boundaries.

The misorientation of the (101) symmetrical twin boundary can be described as $180^\circ[10\bar{1}]\Leftrightarrow 180^\circ[\perp(101)]$. Similarly, the misorientation of the $(10\bar{1})$ twin is $180^\circ[101]\Leftrightarrow 180^\circ[\perp(10\bar{1})]$. If the constrained CSL is constructed with the $a=c$ approximation, then both these boundaries can be formally described by $\Sigma=1$ [Gertsman et al. 1996]. Moreover, with the above approximation, the two misorientations (not to be confused with the twin planes) become equivalent: $180^\circ[101]\Leftrightarrow 180^\circ[10\bar{1}]$. We have denoted such twins as $\Sigma 1'$ so that they are not confused with low-angle boundaries sometimes also designated as $\Sigma 1$. Because in the non-constrained lattice the misorientations of the (101) and $(10\bar{1})$ twins are physically distinct, they may be symbolized as $\Sigma 1'$a and $\Sigma 1'$b, respectively. However, in reality they may be indistinguishable experimentally, and therefore we designate both as simply $\Sigma 1'$.

What is so remarkable about twin boundaries in zirconia? In the cubic structures, only one twin system exists (the one described by $\Sigma 3$ in the framework of the CSL model) and a polycrystal cannot be built entirely of twin boundaries. In the monoclinic zirconia, where there exist several non-equivalent twin variants, the situation is completely different. Junctions containing only (different) twin boundaries are possible and a polycrystalline microstructure can, in principle, be composed entirely of twins. For example, two $\Sigma 71$ and one $\Sigma 3$ boundary can form a triple junction and such junctions have been observed experimentally (Gertsman et al. 1999).

Grain Boundary Distribution

The size of the crystallites forming the oxide layer is too small (see e.g. Gertsman et al. 1999) to allow direct misorientation measurements at an appreciable number of individual grain boundaries. Therefore, at the present time it is difficult to determine experimentally the grain boundary character distribution (GBCD) in the zirconia film so that it would be statistically valid. In (Gertsman et al 1997) the GBCD was derived from preliminary texture data assuming some hypothetical types of correlation in orientations of adjacent grains. Now, when we have a better idea about both the microstructure and texture of the zirconia film, we can obtain a more realistic approximation of the GBCD in this material.

As shown earlier in (Gertsman et al. 1999), the microstructure of zirconia film grown on the surface of the Zr-2.5Nb alloy consists of the growth mode areas and fiber textured regions. Most of the crystallites in the growth mode areas have the [001] axis aligned along the oxide growth direction. Mixed [001]/[100] growth was also observed. In the regions of the microstructure with the growth mode texture in the case of the $[001]_m$ axis aligned in the growth direction, there are only two misorientations at the intercrystallite boundaries — Σ3b and Σ71b. Since most of the crystallite junctions are triple junctions, and they contain two Σ71b and one Σ3b boundary each, there are approximately twice as many Σ71b boundaries as there are Σ3b. Some of these boundaries are lying along the incoherent planes. In the regions with the mixed [001]/[100] growth, along with Σ3a, Σ3b (and, probably, Σ71a and Σ71b) twins, the following boundaries are present: incoherent twins Σ1′ and pseudo-twins Σ3c.

Thus, very few types of grain boundaries are possible in the growth mode texture, all of them being special boundaries. Their misorientations may deviate from ideal ones at the interfaces of contact between different colonies of grains with this type of texture (each colony appears by oxidation of an individual α-Zr grain). These deviations lead to the appearance of low-angle boundaries and are determined primarily by the sharpness of the growth mode texture. The latter is, in turn, determined by the texture and substructure in the α-Zr substrate.

Now we only need to analyze what types of boundaries could be present in the fiber textured regions of the microstructure and in the areas of contact between the regions with the growth mode and fiber texture components. The GBCD in the fiber texture can be calculated according to the same algorithm we have used before, see e.g. (Gertsman et al 1997). We compose a set of orientations corresponding to the fiber texture and compute the misorientations, which would be present in a polycrystal built of grains with these orientations. The following type of orientation correlation is employed in the current work: the twin misorientations are assumed to be the most favorable, and low angle (<15°) boundaries are presumably the second most favorable. The sharpness of texture is given by the half-width of the Gauss distribution describing deviations of the dominant crystallographic direction from the texture axis. We consider two variants: strong (half-width of 5°) and weak (15°) texture. The $[001]_m$ direction has been assumed as the fiber texture axis. Besides the pure [001] texture we have also calculated the 1:1 mixture of [001] and [100]. Table 1 presents possible distributions of the grain boundary types within the fiber textured regions of the microstructure. One can see that there are fair amounts of special (twin and low-angle) boundaries in the simulated misorientation sets; however, the grain boundary distributions are certainly not as special as in the growth texture mode discussed above. As expected, spreading of texture leads to an increase in the proportion of random boundaries.

All possible types of grain boundaries between the regions with the growth mode and fiber textures can be determined by the set of misorientations between the crystal orientations in the growth mode textured region on the one hand and orientations composing the fiber texture on the other hand. Thus computed frequencies of occurrence of different grain boundary types are presented in Table 2. These data show that mainly random grain boundaries occur in the areas of contact between the growth mode and fiber texture.

Table 1: Computer simulated GBCD in the regions of the microstructure with the fiber texture (numerical data — in percents)

Grain	Texture			
Boundary	$[001]_m$		$[001]_m+[100]_m$	
Type	Strong	Weak	Strong	Weak
LAB	13.7	11.4	7.6	7.0
Σ1'	0.0	0.0	8.4	4.8
Σ3a	0.8	5.2	3.5	3.1
Σ3b	14.6	6.9	5.1	3.3
Σ71a	0.0	0.0	9.3	4.4
Σ71b	24.3	13.6	11.0	3.9
Σ3c	0.0	0.0	1.0	2.9
Σ71c	0.0	0.0	2.4	3.4
Other Σ≤30	1.0	2.5	0.6	1.7
Random	45.6	60.4	51.1	65.5

Table 2: Probabilities [%] of different types of grain boundaries at the interface between the growth mode and fiber textured regions.

Grain	Main Texture Axis (Growth Mode or Fiber)			
Boundary	$[001]_m$		$[001]_m+[100]_m$	
Type	Strong	Weak	Strong	Weak
LAB	7.2	2.1	3.8	1.0
Σ1'	0.1	0.0	0.4	0.0
Σ3a	0.0	0.1	0.3	0.1
Σ3b	0.8	0.0	0.2	0.0
Σ71a	0.0	0.0	0.5	0.1
Σ71b	0.0	0.0	0.3	0.0
Σ3c	1.5	0.1	0.4	0.1
Σ71c	0.0	0.0	0.8	0.1
Other Σ≤30	2.0	2.3	2.0	2.1
Random	88.4	95.4	91.3	96.5

Closing Note

The significance of the microstructural clusters discussed in this paper is that twin boundaries may be almost as resistant to diffusion as crystallite interior. It is expected that grain boundary diffusion is the principal contributor to the diffusion properties of zirconia and it controls the oxidation kinetics and hydrogen permeation. Therefore, such clusters may be important for the protective properties of zirconia film.

References

Gertsman V. Y., Zhilyaev A. P., Pschenichnyuk A. I., and Valiev R. Z. (1992) Modelling of grain boundary misorientation spectrum in polycrystals with crystallographic texture. *Acta metall. Mater.* Vol. 40, No. 6, pp. 1433-41.

Gertsman V.Y., Tangri K. and Valiev R.Z. (1994) On the grain boundary statistics in metals and alloys susceptible to annealing twinning. *Acta Metall. Mater.*, Vol. 42, pp. 1725-1804.

Gertsman V.Y. and Tangri K. A study of grain boundary statistics in 304 and 316L stainless steels. (1991) *Phil. Mag. A*, Vol. 64, pp. 1319-1330.

Gertsman V.Y., Lin Y.P., Zhilyaev A. P. and Szpunar J. A. (1999) Special grain boundaries in zirconia corrosion films. *Phil. Mag.*, accepted.

Gertsman V.Y., Zhilyaev A.P., and J. A. Szpunar (1996) Near Coincidence Site Lattice Misorientations in Monoclinic Zirconia. *Scripta Mater.* Vol. 35, pp. 1247-1251.

Gertsman V.Y., Zhilyaev A. P., and Szpunar J. A. (1997) Grain Bounadary Misorientation in Monoclinic Zirconia. *Modelling Simul. Mater. Sci. Eng.* Vol. 5, pp. 35-52.

Gertsman V.Y. and Szpunar J. A. (1999) On the applicability of the CSL model to grain boundaries in non-cubic lattice. *Materials Science Forum*. Vol. 294-296, pp. 181-186.

King A.H. and Singh A. (1994) Generalizing the coincidence site lattice model to non-cubic materials, *J. Phys. Chem. Solids*. Vol. 55, pp. 1023-1033.

Lin Y.P., Woo O.T. and Lockwood D. J. (1994) Texture and phases in oxide films on Zr-Nb alloys,1994, *Mater. Res. Soc. Proc.* Vol. 343, pp. 487-492.

Zhilyaev A.P., Gertsman V.Y., Mishin O.V., Pshenichnyuk A.I., Aleksandrov I.V. and Valiev R.Z. (1993) Grain boundary misorientation spectra determined by real ODF in f.c.c. materials susceptible to annealing twinning. *Acta Metall. Mater.*, Vol. 41, pp. 2657-2665.

Zhilyaev A.P.,. Gertsman V.Y,, and Szpunar J.A., (1997) The Grain Boundary Diffusion Kinetics in Nanocrystalline Zirconia", Interfacial Engineering for Optimized Properties (*Proc. of MRS Fall Meeting*, Boston), Eds: Clyde L. Briant, C. Barry Carter, Ernest L. Hall, Pittsburgh, PA., Vol. 458, pp. 61-66.

MOBILITY OF TWIN GRAIN BOUNDARIES IN ZINC

V.G. SURSAEVA, A.U.TUFLIN

Institute of Solid State Physics, Russian Academy of Science, Chernogolovka, Russia

U. CZUBAYKO

Hahn-Meitner-Institut Berlin GmbH, Berlin, Germany

Abstract.

The mobility of incoherent twin $(01\bar{1}2)$ boundaries in Zn of different purity by observation *in situ* was measured. It was found that kinetic parameters of incoherent grain boundaries are varied through a definite range. The activation and activation-less motion of incoherent boundaries were observed. The surface tension of coherent grain boundary was estimated. Namely, the estimation gives that surface tension of coherent grain boundary approximately in three order of magnitude smaller than this one for high-angle grain boundary.

Keywords: Coherent (incoherent) grain boundary, mobility, enthalpy of activation.

Introduction

Twinning mechanism is an important mode of deformation in hcp metals. Atomic structure of twins was investigated much better than the kinetic parameters of them, in particular the mobility of incoherent twin grain boundaries. Deformation twins increase by the motion of twinning dislocations along the twin-matrix interface, while shrinkage of them is going by incoherent twin grain boundary motion along coherent twin grain boundaries during annealing under high temperature. The elements of the twinning mode are $K_1=(10\bar{1}2)$ and $\mu_1=[10\bar{1}\bar{1}]$. The twin grain boundary we can describe in terms of axis and angle as grain boundary generated by rotation 84° about axis $<10\bar{1}0>$.The main aim of the undertaken investigation was to measure by observation *in situ* purity (99.995 at. % and 99. 9995 at. %) in a relatively wide temperature range (275 - 410 °C).

Experimental Procedure

The study of the mobility of incoherent twin grain boundary was carried out on zinc bicrystals. Single crystals were grown by directional crystallisation, using high purity (99.995 at. % and 99,9995 at. %) zinc. By means of an applied stress twins were introduced into the single crystals (Mugschl and Stuwe 1978). Due to the distinct difference of surface tension between coherent and incoherent grain boundary the introduced twins had almost a rectangular shape (Fig. 1). The area of coherent twin boundary with high density of coincidence sites is increased with respect to the boundaries with inclination $\varphi \neq 0°$ as far as the contacting boundary becomes a straight boundary with an inclination $\varphi = 90$ (Bischop at al.1971, Hartt et al. 1974).

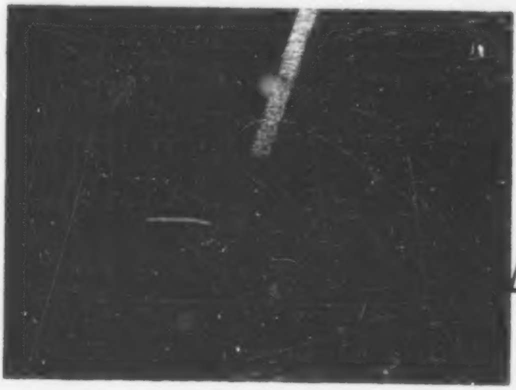

Fig. 1:Micrograph of a twin grain in zinc (99.995 at.%).

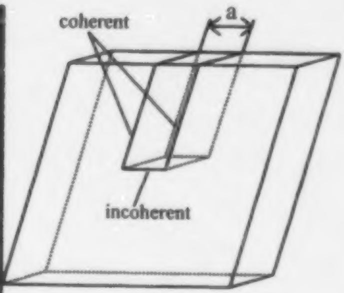

Fig. 2: Grain boundary geometry of the used zinc bicrystals.

To examine the migration of the incoherent twin grain boundary at elevated temperatures a modified optical microscope with polarised light and a hot stage was used. An additional polarisation filter applied in the reflected beam allows to distinguish the different orientations of the grains by the different intensity of the reflected light. Grain boundary motion was observed *in situ* and recorded in the course of experiment by colour video camera connected with a microscope and videocassette recorder. The samples were protected from oxidation by nitrogen atmosphere.Before measurement the sample were electropolished in the H_3PO_4-C_2H_5OH solution..

Results

The mobility of incoherent twin grain boundary under a constant driving force **p** was investigated in zinc bicrystals. Fig. 2 shows the geometry of the used bicrystals. The driving force was provided by reduction of the free energy of the coherent boundaries and reads (per unit area):

$$p = \frac{2\sigma}{a} \quad (1)$$

where σ is the surface tension of the coherent twin boundary and **a** is the width of the shrinking grain. The mobility of a grain boundary is given by the ratio of velocity **v** and driving force **p**:

$$m = \frac{v}{p} = \frac{va}{2\sigma} \quad (2)$$

In experiments we used the reduced mobility **A** (Fradkov and Shvindlerman 1982)

$$A \equiv \frac{va}{2} = m\sigma = A_0 \exp\left(-\frac{H}{kT}\right) \quad (3)$$

where **H** is the activation enthalpy and $\mathbf{A_0}$ is the preexponential factor.

The motion of individual incoherent twin boundary was investigated in the temperature interval between 275°C and 408°C. The activation enthalpy of migration was found

- to constant over the entire temperature range as obvious from the straight line Arrhenius plot (Fig. 3)
- to be equal zero for high purity Zn (99,9995 %) (Fig.4)
- change from zero over initial temperature range to constant over high temperature range (Fig.4).
- has different value for investigated twins with the same twinning mode $K_1=(10\bar{1}2)$ and $\mu_1=[10\bar{1}\,\bar{1}]$. (Fig.5).

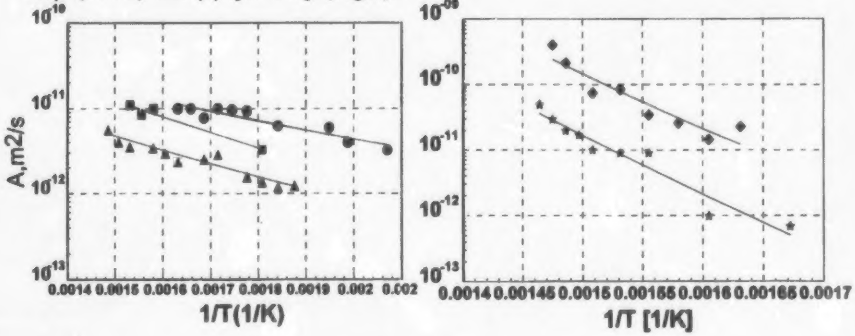

Fig.3. Temperature dependence of the mobility of incoherent twin grain boundaries in zinc (99.995 at. %): ◆ - N1, ● - N2, ■ - N3, ▲ - N4, ✪ - N5.

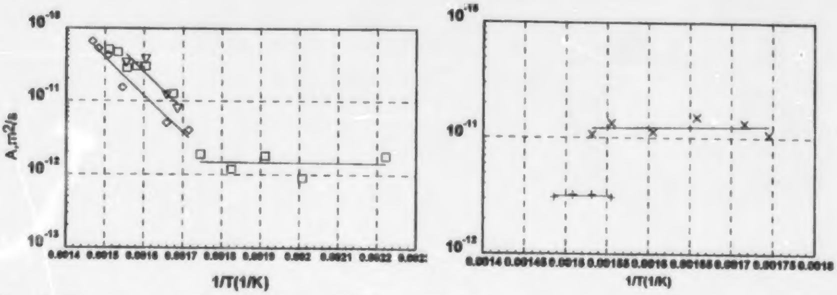

Fig.4. Temperature dependence of the mobility of incoherent twin grain boundary in zinc (99.995 at. %): □ - N6, ✧ - N7, ∇ - N8: in zinc (99.9995 at. %): + - N9, × - N10.

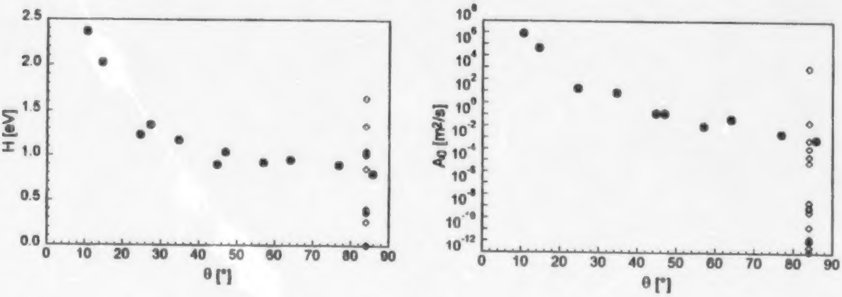

Fig.5. Misorientation dependence of the activation enthalpy and preexponential factor of grain boundary migration in zinc (99.995 at.%) for <10$\bar{1}$0>-tilt grain boundaries: ● - Kopetzkii et al.1979; for twin grain boundaries: ✧ - current investigation.

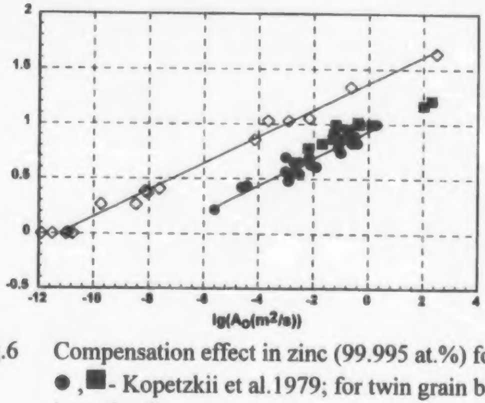

Fig.6 Compensation effect in zinc (99.995 at.%) for <10$\bar{1}$0>-tilt grain boundaries: ● ,■- Kopetzkii et al.1979; for twin grain boundaries: ✧ - current investigation

The activation enthalpy and preexponential factor of <$10\bar{1}0$> 84° tilt grain boundary with random inclination differ from the parameter of twin inclination (Fig.6). The linear dependence between the activation enthalpy and preexponential factor - compensation effect - have been observed. The compensation temperature for incoherent twin boundaries was found to be equal 350°C. (Fig.6).

Discussion

The current investigation reveals an activation enthalpy of incoherent twin boundary migration is not constant and change from 0 to 1.63 eV, less and higher (0.8 eV) than for grain boundaries in the vicinity of the exact twin misorientation (84°<$10\bar{1}0$>), (Mugschl and Stuwe 1978) (Fig. 5). Commonly it is assumed that the surface tension of high angle grain boundary varies only a little with misorientation. Therefore the misorientation dependence of the preexponential factor of the reduced mobility $\mathbf{A_0}$ is the as for the preexponential factor of the regular mobility $\mathbf{m_0}$:

$$A_0(\theta)=\sigma m_0(\theta)(4)$$

In the current case this assumption is obviously not valid. As shown by the pronounced faceting of the investigated boundary (Fig. 1) the surface tension of the coherent twin grain boundary is distinctly different from a random high angle boundary. Thus the preexponential factor in the current investigation is given by:

$$A_0(\theta)=\sigma(\theta)m_0(\theta)(5)$$

Due to the lower surface tension of the coherent twin boundary in comparison with a random high angle boundary $\mathbf{A_0}$ is not only affected by $\mathbf{m_0}$ but also by σ. In contrast to the preexponential factor the activation enthalpy does not depend on driving force. This provides a way of estimating relative value of surface tension σ of coherent twin boundaries from the compensation effect dependencies (Fig.6). The calculation shows that the surface tension of coherent twin boundary at least in 3 orders of magnitude smaller this one for high angle grain boundary.

Conclusion

- It has been found that the mobility of incoherent twin boundaries in Zn with the same twinning mode ($K_1=(10\bar{1}2)$ and $\mu_1=[10\bar{1}\bar{1}]$) varies drastically.
- The incoherent twin grain boundaries in Zn of high purity manifest activationless motion.
- The mobility of incoherent twin boundaries differs from one of high angle grain boundaries.

- The compensation effect, namely, the linear relation between the enthalpy of activation and pre-expenential factor, was observed. The compensation temperature T_c was equal to 350 °C.
- The value of surface tension of coherent twin boundaries was estimated. This value is at least in three orders of magnitude smaller than this one for high angle boundaries.

References

Bischop, G.H., Hartt, W.H. and Bruggeman, G.A. (1971) Acta Metall. **19**, 37.

Fradkov, V.E.and Shvindlerman, L.S. (1982) Phys.Chem.Mech.Surfaces, 1, 180.

Hartt, W.H., Bischop, G.H. and. Bruggeman, G.A (1974) Acta Metall. **22**, 971.

Gottstein, G., Molodov, D.A., Shvindelerman, L.S. (1998) Interface Science, 6, 7.

Kopezkii, Ch.V., Sursaeva V.G. and Shvindlerman, L.S. (1979) «Mobility of high-angle tilt grain boundaries in Zn», Reprint of the Institute of Solid State Physics, Russian Academy of Sciences, 48pp, Chernogolvka [in Russian].

Mügschl, E. and Stüwe,H.P.(1978) Z. Metallkde., 706.

Acknowledgement

The authors express their gratitude to the Deutsche Forschungsgemeinschaft for financial support.

DETERMINING RELATIVE GRAIN BOUNDARY ENERGIES FROM MEASUREMENTS OF THERMAL GROOVE GEOMETRY

D.M. SAYLOR and G.S. ROHRER
Carnegie Mellon University, Department of Materials Science and Engineering, Pittsburgh PA 15213-3890

Abstract

The misorientations of 201 adjacent pairs of grains in a magnesia polycrystal have been determined using electron back scattered diffraction patterns. The surface dihedral angles of thermal grooves at the same boundaries were measured by atomic force microscopy. Under the assumption that the surface energy is isotropic, these data can be used to calculate the relative grain boundary energy. When the relative grain boundary energy is correlated to the misorientation across the boundary, it is apparent that small misorientation boundaries have relatively lower energies. At larger misorientations, the grain boundary to surface energy ratio varies from 0.85 to 1.65 and is apparently influenced by the anisotropies of the surface energy and/or grain boundary tangent plane.

Keywords: Grain Boundary Energy, Thermal grooves, Atomic Force Microscopy, MgO

1 Introduction

A common way to probe relative grain boundary energies is to measure the surface dihedral angle at the positions where a grain boundary intersects a free surface. Assuming local equilibrium at the triple junction, isotropy of the surface energy, and that the grain boundary energy depends only on misorientation, the grain boundary to surface energy ratio (γ_{gb}/γ_s) can be written in the following way (Herring 1951).

$$\frac{\gamma_{gb}}{\gamma_s} = 2\cos\frac{\psi_s}{2} \tag{1}$$

In eqn.1, the only experimental observable is the surface dihedral angle (Ψ_s) defined in Fig. 1.

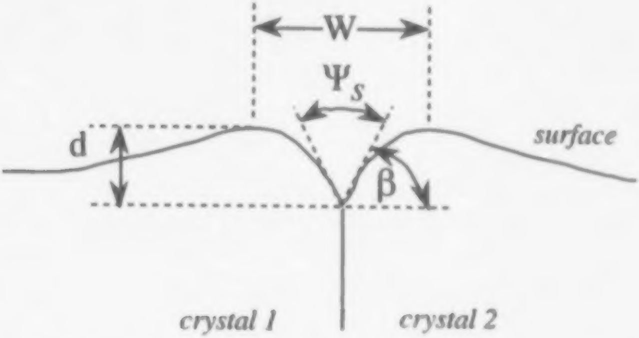

Figure 1. Schematic illustration of the macroscopic structure of a thermal groove. The aspect ratio has been exaggerated for clarity.

The atomic force microscope (AFM), which is capable of recording topographic data with sub-nanometer vertical resolution and lateral resolution on the order of 30 nm, is a facile tool for measuring the geometric parameters of thermal groove. Because sample-tip convolution errors make the direct measurement of the angle β difficult (see Fig. 1), it is more practical to measure W and d and compute β under the assumption that the groove has a quasi-static profile (Mullins 1957; Robertson 1971). It has recently been demonstrated that while the depth (d) of a groove can not be measured accurately under all circumstances, the error in the depth measurement becomes negligible for grooves that are wider than 2 µm (Saylor and Rohrer 1999).

2 Experimental

Magnesia powder was formed by decomposing 99.7% pure magnesium carbonate (Fisher Scientific) at 997 °C in air. The calcined powder was compacted uniaxially at 76 MPa and then isostatically at 276 MPa to form disc shaped pellets with a diameter of 20.0 mm and an average thickness of 2.8 mm. The discs were then packed in a magnesia crucible with the parent powder and sintered for 48 h in air at 1600 °C. After sintering, the surfaces were mechanically ground and polished with diamond suspensions down to a diamond particle size of 0.25 µm. Thermal grooves were formed by annealing the polished sample for 5 h in air at 1400 °C. The samples were enclosed in a magnesia crucible and surrounded by the parent powder. The average grain size of these samples was 40 μm, and the average width of the thermal grooves was 2.4 μm.

To minimize systematic errors in the topographic measurements, AFM data were collected in accordance with procedures described previously (Saylor and Rohrer 1999). Briefly, to make accurate quantitative measurements, it is important to precisely define the sample normal by polishing specimens to have two flat, parallel surfaces, to ensure that the AFM image plane is parallel to the surface plane, and to disable software background subtractions. To minimize the effects of the tip-surface convolution and maximize the information density, the average groove width must be at least 2μm, and a typical groove trace over this width must consist of several hundred pixels. For a typical grain boundary, the maximum systematic underestimation of Ψ_s is 2 °. By making repeated topographic measurements on straight boundaries, the standard deviation associated with random errors in the measurement procedure was determined to be 1 ° in Ψ_s for each boundary.

The crystallite orientations were determined from electron back scattered diffraction patterns (EBSPs) obtained in a Phillips XL40FEG scanning electron microscope. Fiducial marks were used to locate the same grains examined by AFM. All of the patterns were indexed using Orientation Imaging Microscopy Software, version 2.5 (TexSEM Laboratories, Inc.) which returned a set of Euler angles for each grain. The Euler angles from adjacent grain pairs were then used to define the misorientation by deriving the pair's common axis and the rotation about that axis which brings the crystallites into coincidence. The axis/angle representations of misorientation were parameterized as Rodrigues vectors, where the vector lies in the direction of the misorientation axis and has a magnitude that scales with the misorientation angle. By imposing the conditions that the rotation axis lies in the standard cubic stereographic triangle and the rotation angle is as small as possible, we obtained the symmetrically equivalent Rodrigues vectors which lie in the irreducible wedge of cubic misorientation space.

3. Results

For 201 randomly selected boundaries, the dihedral angles varied from 65 ° to 140 °; the median of the distribution was 105 ° ($\gamma_{gb}/\gamma_s = 1.2$). The agreement between the present data and that derived using the metal reference line technique indicates that the more facile AFM technique is capable of producing satisfactory results (Handwerker et al. 1990).

When the present measurements are correlated with the misorientation (see Fig. 2 and Fig. 3), a well-defined trend is observed. The relatively lower energy of boundaries with small misorientation is indicated in Fig. 2 by the presence of darker points near the origin (see Fig.

2a). According to Fig. 3, the transition to relatively lower energies occurs at a misorientation angle of approximately 10 °.

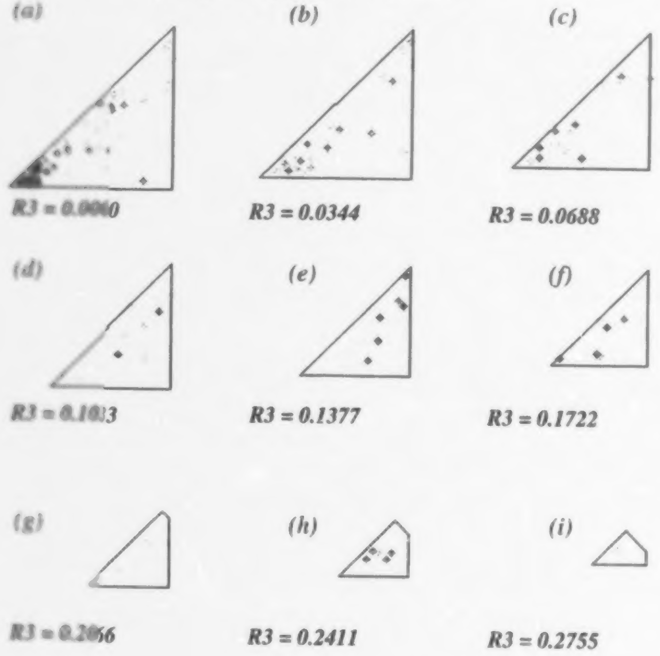

Figure 2. Distribution of observed boundaries in Rodrigues-Frank space. Progressive slices along the R3 are shown, the value of R3 listed below each slice indicates the coordinate at the lower limit. The shading of each point corresponds to the γ_{gb}/γ_s ratio for that boundary. There are 10 shades of gray with a resolution of 0.1 in γ_{gb}/γ_s, ranging from 0.7 (darkest) to 1.7 (lightest).

4 Discussion

The results indicate that the median grain boundary energy in magnesia is larger than the surface energy. At misorientations greater than 10 °, the relative energy varies between 0.85 and 1.65. To determine absolute grain boundary energies, it is necessary to know the surface energy. The only absolute surface energy data for MgO, derived from calorimetric measurements on MgO powders, places the average energy at about 1.0 J/m^2 (Jura and Garland 1952). Because the adsorption of water influenced this experiment, this value is likely to be an underestimate. However, with this noted, the measured values of (γ_{gb}/γ_s) can be taken to approximately have units of J/m^2. More recently, the anisotropy of the surface energy of magnesia was determined to be 7% at 1400 °C, with a minimum at (100) and a maximum at (111) (Saylor et al. 1999). Therefore, the isotropic surface area assumption applied in the present analysis contributes to the uncertainty in the results.

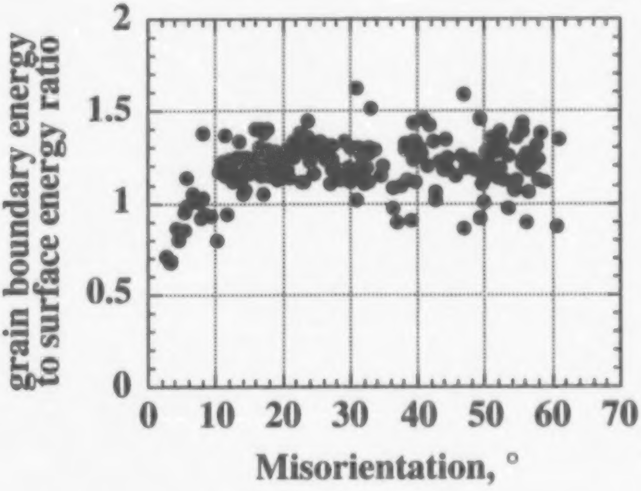

Figure 3. γ_{gb}/γ_s **as a function of the misorientation angle.**

The relative grain boundary energy of <110> symmetric tilt boundaries in an isostructural compound, NiO, were determined using the same assumptions applied here (Dhalenne et al. 1983). For angles greater than 10 °, these data vary from 0.4 (at the Σ3 misorientation) to 1.2 (for a general boundary along the same tilt axis). In addition, cusps were found at other coincident site lattice (CSL) boundaries. The present data varies over a higher range of values. However, considering the fact that a wider range of misorientation space was sampled, this is not too surprising.

In addition to the low angle boundaries in the present data set, there are a number of higher angle boundaries (misorientations ≥ 10 °) that have unusually low γ_{gb}/γ_s ratios. For example, 8 high angle boundaries in our distribution have γ_{gb}/γ_s ratios that are more than one standard deviation below the mean. We have compared these boundaries to the known 47 CSL boundaries that have values of $\Sigma \leq 49$ (Adams et al. 1990) and found that three of them have rotation axes within 3 ° and misorientation angles within 2.4 ° of a CSL misorientation. These include a Σ7, Σ17b, and Σ45a boundary. At slightly higher γ_{gb}/γ_s ratios, but still below the mean, an additional five near-CSL boundaries were detected.

However, special low Σ CSL boundaries can not explain all of the variation in the data. For example, there are two boundaries in the data set that have very nearly the same misorientation (the axes of rotation are separated by only 4.2 ° and the rotations differ by only 0.4 °), yet the values of γ_{gb}/γ_s are 1.4 and 0.9. These variations probably stem from our neglect of the torque terms that represent anisotropies of the surface and/or grain boundary tangent plane energies in the equilibrium condition.

5 Concluding Remarks

AFM is a facile method for determining the geometries of grain boundary grooves; values of γ_{gb}/γ_s determined in this manner are consistent with values derived from the metal reference line technique. When the relative grain boundary energy is correlated with the grain boundary misorientation, we find that boundaries with small or near CSL misorientations have lower relative energies. However, the data set also reveals that the groove geometry is influenced by factors other than misorientation and that through a more detailed analysis of such data, it should be possible to determine the anisotropy of the grain boundary tangent plane.

6 Acknowledgment

This work was supported by the MRSEC Program of the National Science Foundation under Award Number DMR-9632556.

7 References

Adams, B.L, Zhao, J., and Grimmer, H., (1990) *Acta Cryst.*, Vol. A46. pp. 620-2.

Dhalenne, G., Dechamps, M., and Revcolevschi, A. (1983) Advances in Ceramics, Vol. 6, *Character of Grain Boundaries*, American Ceramic Society, Columbus, OH. pp. 139-50.

Handwerker, C.A., Dynys, J.M., Cannon, R.M., and Coble, R.L. (1990) *J. Amer. Ceram. Soc.*, Vol. 73. pp. 1371-77.

Herring; C. (1951) in *The Physics of Powder Metallurgy*, (ed. W.E. Kingston), McGraw Hill, New York. pp. 143-79.

Mullins, W.W. (1957) *J. Appl. Phys.*, Vol. 28. pp. 333-39.

Robertson, W.M. (1971) *J. Appl. Phys.*, Vol. 42. pp. 463-67.

Saylor, D.M. and Rohrer, G.S. (1999) Measuring the Influence of Grain Boundary Misorientation on Thermal Groove Geometry in Ceramic Polycrystals, *J. Amer. Ceram. Soc.*, Vol. 82, no. 5, in press.

Saylor, D.M., Mason, D.E. and Rohrer, G.S. (1999) An Experimental Method for Measuring Surface Energy Anisotropy and its Application to Magnesia, *J. Amer. Ceram. Soc.*, submitted.

SIMULATION OF RECRYSTALLIZATION FROM EBSD OR TEM ORIENTATION DATA

T. BAUDIN and R. PENELLE
Laboratoire de Métallurgie Structurale, Université de Paris Sud, Orsay, France.

Abstract

Recently a new simulation procedure of primary recrystallization and grain growth has been proposed. It consists in a simulation/experimentation coupling since the input data are the experimental microstructure and microtexture characterized by OIM or by TEM. Two examples are presented to illustrate the possibilities of this approach: the simulation of the geometrical anisotropy of Goss grains during their abnormal growth in Fe3%Si sheets (grade HiB) and the simulation of the recrystallization mechanisms allowing to describe the cube texture formation in cold rolled Fe36%Ni sheets.

Keywords: Experimental input data, recrystallization, simulation.

1 Introduction

Classically, grain growth simulation is performed from a theoretical microstructure where the orientations are randomly distributed. Consequently, a such approach assumes that the experimental material presents a microstructure with an homogeneous grain size and a texture without orientation clusters. However, these assumptions are seldom verified (Baudin et al. 1999).

According this last result, a new simulation procedure (Baudin et al. 1997) has been implemented starting from a real microstructure measured by Orientation Imaging Microscopy (OIM) (Adams et al. 1993) as an input data set. The so simulation/experimentation coupling has been firstly tested to simulate the abnormal growth of Goss grains in a Fe 3% Si material. Then, Engler (1998) proposed to extend this procedure to the primary recrystallization simulation. However, as for high deformation, it is often difficult to use the OIM, this last technique must be replaced by the Transmission Electron Microscopy (TEM) one (Zaefferer 1995). In the present paper, a short review of first already published results is given.

2 Results

Several methods have been proposed in the literature to simulate the primary recrystallization and the normal or the abnormal grain growth, such as the Monte Carlo method, the cellular automata method, the Vertex method …. For all these methods, it is necessary to have an initial microstructure so as an initial microtexture currently assumed randomly distributed in the studied material. To avoid this hypothesis, it has been recently proposed to use an OIM or a TEM mapping so experimental microstructure and microtexture as input data of the simulation.

2.1 Abnormal grain growth simulation

Most of transformer cores are made of Fe 3% Si textured sheets which allow to minimize watt losses thanks to the presence of the Goss texture {110}<001> where the easiest magnetization direction <001> is parallel to the magnetic field direction. Development of such a texture occurs by abnormal growth of a minority of Goss grains present at the primary recrystallized state.

Because of the lack of data for grain boundary energy and mobility, simulations are often performed using crystallographic orientation classes (Abbruzzese et al. 1991). A calculation of misorientation allows to assign each orientation (with a spread of 15°) to one of the following "experimental" orientation classes, {111}<112>, {100}<012} and Random and then the energies and mobilities between the different orientation classes are chosen (see Paillard et al. 1994). Moreover, simulations are generally performed from a microstructure of a sample at the primary recrystallized state. However, it is not easy to compare experimental and simulated results especially from a local point of view. Indeed, to have a good resolution for drawing the OIM microstructure, the step size must be quite low and the total area remains small if the number of orientations is less than about 60.000 (this value is reasonable for the measurement time and the file size). It is then difficult to find a Goss grain that will grow in such area because the volume fraction of Goss grains is very low (Rouag and Penelle 1989). So it is easier to compare experimental and simulated results when the Goss grain has already grown knowing that the growth mechanisms are probably different at the beginning and during the abnormal growth of Goss grains. So, an experimental study where the grain boundary migration is followed after several annealings has been carried out (Amiri et al. 1998).

Figures 1a and 1b show the growth of a Goss grain after one 970°C – 5 min and two 970°C – 5 min annealings, respectively (let us note that the microstructure evolution can be affected by the surface energy and so can be different in the sample volume. Moreover, this discontinuous procedure can introduce microstructure differences in comparison with a continuous annealing). This example is interesting because it shows an anisotropic growth of the Goss grain (near the right top corner in figure 1b) that cannot be simulated by a classical 2 dimensional Monte-Carlo simulation, that is, without taking into account the experimental microstructure and microtexture as input data (Baudin et al. 1999). The geometrical growth anisotropy can be due to an impact of grains in the third dimension and/or linked to the crystallographic parameters. In the first case, because the Goss grain growth is known to begin at the fifth of the sheet thickness from the surface (Rouag and Penelle 1989; Harase et al. 1986), it can be assumed that the growth rate is higher in some parts of the Goss grain emerging at the surface due to its shape through the sheet thickness (may be related to a crystallographic effect). Under these conditions, a 3 dimensional simulation must be used from a set of experimental microstructures measured through the sheet thickness. But in this case, the Goss grain growth cannot be followed experimentally. The aim of the present study is to verify whether a 2 dimensional Monte-Carlo simulation allows one to reproduce such grain shape from an experimental texture.

Figure 1c shows, after 300 MCs, an example of the simulated microstructure obtained from the experimental one described in figure 1a. Obviously, the agreement between the experimental and simulated microstructures is not perfect (shape of the Goss grain, size of other grains larger than in the experimental microstructure, ...). However, this calculation shows that the geometrical anisotropy of the Goss grain can be simulated by only introducing the experimental crystallographic orientations.

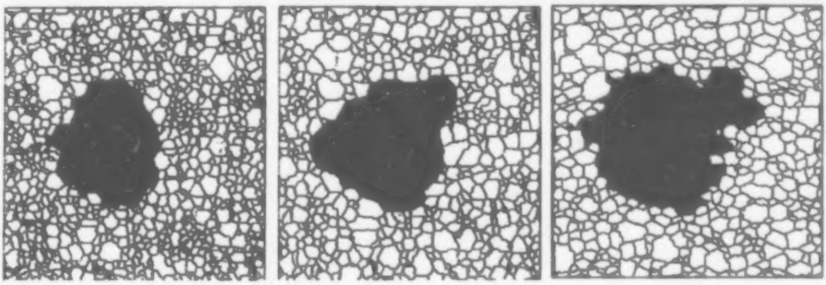

(a) (b) (c)

Fig. 1: Evolution of a Goss grain size after several annealings. (a) 970°C – 5 min., (b) (a) + two 970°C – 5 min (—— = 90μm) and (c) simulated microstructure obtained after 300 MCs from experimental OIM measurements (this figure must be compared to figure 1b).

2.2 Simulation of primary recrystallization

Engler (1998) has then tried to simulate recrystallization from OIM measurements. Each measured point is so characterized by its coordinates x and y in the microstructure and its crystallographic orientation g so as a parameter q describing the quality of the Back Kikuchi patterns (BKPs) (Wilkinson and Dingley 1991; Krieger Lassen et al. 1994) that can be linked to the stored energy. Under these conditions, Engler (1998) has shown that it is possible to simulate: recovery, taking into account a gradual increase of q and so characterizing the annihilation and the rearrangement of dislocations into more stable configurations and nucleation and growth of new recrystallized grains by growth of some specific subgrains.

The main limitation of such an approach is obviously the lack of available accurate orientation maps of the deformed microstructures. Indeed, the spatial resolution of the technique is equal to about 0.5 μm and so if the dislocation density is very large or if the size of the dislocation cells is lower than 0.5μm, the BKPs patterns are blurred and cannot be correctly indexed. This reflects that in some cases the deformed microstructure cannot be completely characterized by OIM so that some regions remain undefined. Consequently, the simulation/experimentation coupling looses a part of its interest since it is well known that the cold worked matrix plays an important role in the primary recrystallization mechanisms. Therefore, it is necessary to improve the spatial resolution of the electron beam using for example the TEM. So a novel model based on data derived by TEM orientation analysis has been recently developed (Baudin 1998; Baudin et al. to be published).

The use of maps obtained by OIM in the simulation is very easy since orientations can be measured on an hexagonal grid that can be directly used with any simulation method. With a TEM map, it is more complicated since it is first necessary to draw manually the microstructure, to color it in terms of the measured orientations using the standard triangle to define a color code (Gerth and Schwarzer 1993) and finally to transform the image in an ASCII file usable for the calculation.

This approach has been tested on a Fe 36% Ni alloy employed in the form of thin strips for the making of shadow masks used in color television tubes. After cold rolling, the strip is annealed at temperatures ranging from 600 to 1200°C. During these treatments, structure undergoes recrystallization and if the degree of cold work is sufficient (>60%) primary recrystallization produces a strong cube texture (see Julliard et al. 1999). This cube texture formation has been simulated adjusting the stored energies or more exactly the energy differences between the cube nucleus and the other first subgrains. For that, in a simplified calculation to only prove the faisability of this approach, it is assumed that the material is defined by three orientation classes: the cube one with a spreading of 5°, the near cube orientation class with a spreading of 15° and the random orientation class. Then the energy values are adjusted (Baudin et al. to be published) to reproduce the experimental observations knowing than the stored energy of the cube orientation is lower than the others.

In order to get the highest quantity of informations about the microstructure, TEM samples were prepared from the ND-TD section of a cold rolled (reduction of 94%) Fe 36% Ni sheet (see Julliard et al. 1999). Figure 2 shows an example of the microstructure where cube bands present well recovered cells. This experimental microstructure (figure 2) and its corresponding microtexture are then used as input data in the simulation (figure 3a). Figure 3b shows the simulated microstructure after 400MCs. The microstructure is here described using a grey level gradient defined as a function of the misorientation from the black cube orientation.

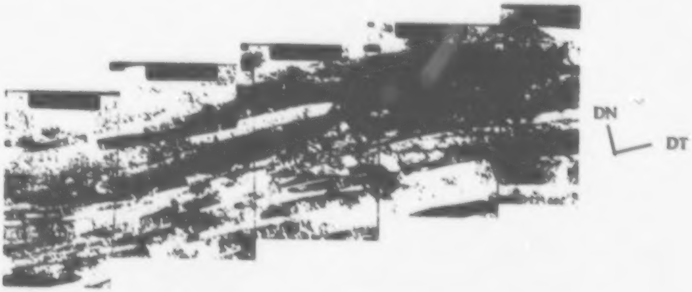

Fig. 2 : Microstructure of a cold rolled (reduction of 94%) Fe 36% Ni sheet analyzed by TEM (— = 0.1μm).

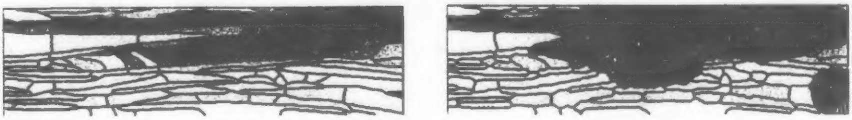
(a) (b)

Fig. 3 : Simulation of the growth of cube cells in a microstructure analyzed by TEM (figure 2) and used as input data (a)
(b) Growth of cube cells (400 MCs) (— = 0.1μm).

This example shows that the experimental observations (Julliard et al. 1999) can be reproduced with this kind of simulation. Comparing these experimental and numerical results, and adjusting the stored energy in each cell, this numerical approach can become a very important help to improve our understanding on the cube texture formation. Reciprocally, using experimental values of stored energy, the model could be validated.

3 Conclusion

The simulation that consists to use an experimental microstructure and an experimental microtexture as input data, allows one to reproduce the experimental observations and so could be used to improve our understanding of primary recrystallization and normal or abnormal grain growth.

However, it remains to improve the simulation introducing true grain boundary energy such so as stored energy to replace the adjusted energy values. Moreover, it should be also important to test this procedure with other simulation method such as the Vertex one.

It seems also very important to follow experimentally the growth of grains or of subgrains to compare with the simulated results but without to forget that this kind of simulation is performed in two dimensions knowing that experimentally the phenomena are tridimensional.

4 References

Abbruzzese, G., Campopiano, A. and Fortunati, S. (1991) Model of secondary recrystallization in silicon-iron and comparison with experiments. *Proc. of the 9th ICOTOM*, Avignon, France, Septembre 1990, ed. H.J. Bunge, *Textures and Microstructures*, Vol. 14-18, pp.775-80.

Adams, B.L., Wright, S.I. and Kunze K. (1993) Orientation imaging: the emergence of a new microscopy. *Met. Trans. A*, Vol. 24A, pp. 819-31.

Amiri, A., Baudin, T. and Penelle R. (1998) Grain boundary migration during Goss grain growth in Fe3%Si sheets (grade HiB). *Proc. of the Third Int. Conf. On Grain Growth*, ICGG III, Pittsburgh, USA, 14-19 June, Carnegie Mellon

University, Pittsburgh, PA, USA, ed. by H. Weiland, B.L. Adams and A.D. Rollet, A publication of TMS, pp. 567-572.

Baudin, T. (1998) Contribution à l'étude des relations entre la texture cristallographique et la microstructure. Mémoire d'habilitation à diriger les recherches, Orsay, France.

Baudin, T., Julliard, F. and Penelle R. (To be published) Simulation of primary recrystallization from TEM orientation data.

Baudin, T., Paillard, P. and Penelle, R. (1997) Grain growth simulation starting from experimental data. *Scripta Materialia*, Vol. 36, N°7, pp. 789-94.

Baudin, T., Paillard, P. and Penelle, R. (1999) Simulation of the anisotropic growth of Goss grains in Fe3%Si sheets (grade HiB). *Scripta Materialia*, In press.

Engler, O. (1998) A simulation of recrystallisation based on EBSD orientation microscopy data. *Proc. of the 19th Riso Int. Symp. on Materials Science*, Roskilde, Denmark, September 1998, ed. J.V. Carstensen et al., pp. 253-60.

Gerth, D. and Schwarzer, R.A. (1993) Graphical representation of grain and Hillock orientations in annealed Al-1%Si films. *Textures and Microstructures*, Vol. 21, pp. 177-93.

Harase, J., Shimizu, R. and Watanabe, T. (1986) The effects of the grain boundary character distribution on grain growth and texture formation in Fe-3%Si. *Proc. of the 7th Riso Int. Symp. on Metallurgy and Materials Science*, Roskilde, Denmark, September 1986, ed. N. Hansen et al., pp. 343-48.

Julliard, F., Baudin, T. and Penelle, R. (1999) Study of recrystallization mechanisms in ingot cast and strip cast Fe-36%Ni. *Proc. of the 12th ICOTOM*, Montreal, Canada, August 9-13, This proceedings.

Krieger Lassen, N.C., Juul Jensen, D. and Conradsen, K. (1994) Automatic recognition of deformed and recrystallized regions in partially recrystallized samples using electron back scattering paterns. *Proc. of the 10th ICOTOM*, Clausthal, Septembre 1993, ed. H.J. Bunge, Materials Science Forum, Trans. Tech. Publications, Vol. 157-162, pp. 149-58.

Paillard, P., Penelle, R. and Baudin T. (1994) Grain growth simulation by Monte Carlo method in a HiB Fe3%Si alloy. *Proc. of the 10th ICOTOM*, Clausthal, Septembre 1993, ed. H.J. Bunge, Materials Science Forum, Trans. Tech. Publications, Vol. 157-162, pp. 1847-54.

Rouag, N. and Penelle, R. (1989) Influence of grain boundary characteristics and of chemical parameters on abnormal grain growth in Fe-3%Si sheets. *Textures and Microstructures*, Vol. 11, pp. 203-17.

Wilkinson, A.J. and Dingley, D.J. (1991) Quantitative deformation studies using electron back-scatter patterns. *Acta metall. mater.*, Vol. 39, pp. 3047-3055.

Zaefferer, S. (1995) Entwicklung und Anwendungen eines elektronenmikroskopischen on-line Verfahrens zur Bestimmung von Verformungssystemen in hexxagonalen Werkstoffen, Thesis, Clausthal, Germany.

Acknowledgements

The authors thank A. Amiri and F. Julliard who measured the described microstructures and microtextures by OIM and by TEM respectively.

Author Index

Acharya, A., 547
Adams, B.L., 9, 21, 192, 724, 1248, 1649
Agnew, S.R., 575
Aindow, M., 1619
Algueró, M., 1327
An, J.K., 779, 785
Anisimova, L.I., 689
Ansart, F., 1345
Artymowicz, D., 1031
Asami, T., 405
Aus, M.J., 560
Baccino, R., 683
Bacroix, B., 328, 499
Baczynski, G.J., 635, 1230, 1236, 1242
Baghdouche, F., 611
Baik, S.C., 1043
Barlat, F., 569
Barnett, M., 910
Bartozzi, M., 1593
Bate, P.S., 34, 617, 1619
Baudin, T., 922, 973, 1278, 1696
Bauer, C.L., 4
Bay, B., 174, 1154
Beaudoin, A.J., 435, 547
Beaugnon, E., 457
Bechade, J.L., 499, 922
Becker, R.C., 1112
Bennett, K., 129
Bergstrom, D.B., 1375
Bertinetti, M.A., 334
Bertram, A., 273, 535
Besse, F., 1315
Bhattacharya, B., 824
Bieler, T.R., 529
Bingert, J., 358
Blanford, P., 487
Blanton, W., 1460
Böhlke, T., 535
Bolle, B., 98, 1025, 1315, 1631
Bollen, J., 1293
Bolmaro, R.E., 211, 316, 334, 358, 375
Bonarski, J., 1278
Bouche, G., 922
Boulanger, C., 1315
Bouzy, E., 223, 229, 1184
Bowman, K.J., 1453, 1460
Boyce, D., 505
Boyle, A., 1593
Brehm, J., 1460
Brem, J.C., 569
Brenner, R., 499
Brokmeier, H.-G., 86, 211, 334, 375, 523, 541, 1172, 1482
Brückner, G., 174, 629
Bunge, H.J., 1172
Bunsch, A., 599
Bussière, J.F., 493
Cabot, C., 1488
Calzada, M.L., 1327
Cannon, W.R., 1476
Cao, Y., 928, 1445
Cardiola, B., 1184
Carter, W.C., 1509
Casasent, D., 4
Chandra, T., 1003
Chang, S.K., 866, 1208
Chang, C.P., 694, 797
Chateigner, D., 457, 1327, 1495, 1562
Chaud, X., 457
Chen, N., 511
Cheng, X-M., 481
Cho, J., 1043
Cho, J.-H., 587, 700, 1339
Cho, J.Y, 1254
Choi, C-H., 755, 791
Choi, G.S., 1208
Choi, Jang Hyun, 1214
Choi, Jeong Ho, 298,1214
Choi, S.-H., 569, 587
Christen, D.K., 1466
Chruściel, K., 599, 1071
Cichocki, F.R., 1460
Clarke, A.P., 1260
Clausen, B., 399
Clevenger, L.A., 1287
Collins, L.E., 1230
Cooley, J., 135
Cosandey, F., 1476
Court, S., 617
Crimp, M.A., 529
Cross, I.J., 1202
Crumbach, M., 817
Czerwinski, F., 560, 1351, 1391, 1397, 1403, 1445
Czubayko, U., 1684
Da Costa Viana, C.S., 322, 671, 773

Dahoun, A., 1488
Daniel, S.R., 1202
Davies, H., 1196
Davies, P., 1196
Davis, G.R., 1106
Dawson, P.R., 3, 435, 505, 1655
Day, A.P., 217, 1593
de Boer, B., 944, 1077
De Angelis, R.J., 659
De Blauwe, K., 1293
De Broeck, A., 1293
De Graef, M., 192
Delannay, L., 340, 623, 811, 910
Diot, M., 767
Donovan, J.J., 235
Dubois, M., 493, 997
Duchene, L, 286
Duggan, B.J., 706, 805
Dunne, D.P., 991
Dzjuba, A.A., 241
Eickemeyer, J., 944
El Ghazouli, K., 98
El-Dasher, B.S., 9, 1248
Elliott, J.C., 1106
Embury, J.D., 934
Engler, O., 68, 393, 842, 1124
Erb, U., 560, 961
Esling, C., 229, 767, 997, 1184
Ferry, M., 991, 1003
Field, D.P., 1309, 1357, 1369
Fischer, A.H., 204
Flemming, G., 1184
Foct, J., 817
Fourty, A., 316, 334, 358, 375
Fragomeni, J.M., 901
Freenstra, R., 1466
Frischbutter, A., 1540, 1605
Fukushima, A., 653
Fukutomi, H., 1190
Fundenberger, J.J., 153, 223, 229, 769
G'Sell, C., 1488
Gaignard, S., 997
Gautier-Picard, P., 457
Gavard, L., 878
Gehrmann, R., 665
Gertsman, V.Y., 1678
Gervasyeva, I.V., 689, 742, 890
Gey, N., 147
Gharghouri, M.A., 677
Gignac, L.M., 1287
Glass, S.J., 1489, 1509
Glavicic, M.G., 110, 1303, 1409
Godinas, A., 286
Goryachev, S.B., 463
Gottstein, G., 292, 665, 791, 817
Goyal, A., 1466
Greene, J.E., 1375
Grenet, J., 1488
Gritsuk, A.R., 463
Grosdidier, T., 683, 694, 797, 895
Gryziecki, J., 581
Gubernatorov, V.V., 742, 890
Ha, C.S., 1433
Haase, J.D., 123
Habraken, A.M., 286
Hall, P.W., 1501
Halliday, D., 1593
Han, K.S., 866, 1059, 1208
Harasse, J., 1009
Harding, J.H., 1385
Hariz, T., 310
Harris, D.J., 1385
Hayakawa, Y, 1101
Hedegaard, C., 1495
Heidelbach, F., 1574
Heizmann, J.J., 98, 141, 1025, 1315, 1631
Helming, K., 797
Hensger, K.E., 1184
Higginson, R.L., 1130
Hippertt, J., 1515
Hoferlin, E., 249
Holzapfel, B., 944, 1321
Hong, B.D., 866
Hong, S.C., 956, 1299, 1381
Hong, S-H., 950
Houbaert, Y., 811, 910
House, J.W., 659
Hu, J., 135
Huang, H., 1613
Huang, M., 481
Huang, W.H., 694
Huang, X., 1613
Huh, M.Y., 1124
Hühne, R., 1321
Hukushima, A., 653
Humbert, M., 147, 1184
Humphreys, F.J., 74, 617
Hurd, J.L., 1287

F19

Hutchinson, W.B., 34, 1031
Iggulden, R.C., 1287
Inagaki, H., 848, 860, 1142
Inakazu, N., 168, 1160
Inoue, H., 168, 445, 884, 1160
Ishio, M., 445
Ito, K., 653
Ivankina, T.I., 1587
Jansen, E.M., 523, 1482
Jasieński, Z., 581
Jean-Prost, F., 346
Jensen, D.J., 46, 174, 605, 854, 1154
Jeong, H.T., 267, 304, 779, 785, 1254, 1369, 1427
Ji, S., 1568
Jiao, SH.H., 1266
Jin, H., 135, 1136
Johnson, G.C., 235
Jolly, L., 98, 141
Jonas, J.J., 635, 761, 910, 1049, 1089, 1230, 1236, 1242
Julliard, F., 973
Jung, V., 523
Jura, J., 68, 1278
Kadilak, J., 718
Kainer, K.U., 1482
Kaneno, Y., 1160
Kang, S.Y., 298
Kao, P.W., 694
Karato, S., 1546
Kato, H., 884
Katoh, H., 405
Keichel, J., 817
Kern, H.M., 1580
Kestens, L., 736, 811, 910
Kikuchi, S., 1190
Kim, B.I., 736, 830, 1433
Kim, B.-K., 1427
Kim, C.S., 1059
Kim, I., 956, 1299, 1381
Kim, J., 1009
Kim, J.K., 1059
Kim, K-H., 755
Kim, K.-Y., 1095
Kim, K.R., 469
Kim, S.M., 469
Kim, S.S., 1433
Kim, Y.H., 830
Kim, Y.H., 1124
Kinderlehrer, D., 9, 1643
King, W.E., 180
Klima, K., 1587
Klinkenberg, C., 475
Knutsen, R.D., 617
Kobayashi, M., 884
Kocks, U.F., 431, 934
Kogen, V.A., 241
Koh, Y.H., 1214
Kohara, S., 848, 1166
Koizumi, M., 848, 860
Kopacz, I., 417
Korzekwa, D.A., 346
Kosack, K., 80
Kovar, D., 1501
Krasilnikov, N.A., 748
Kraska, M., 273
Krause, H., 1015
Krieger Lassen, N.C., 174, 854
Kroeger, D.M., 1466
Kubota, T., 981
Kumar, M., 180
Kurosawa, M., 1101
Kusnierz, J., 517
Kwon, O., 1043
Lagoeiro, L., 1528
Langelaan, G., 135
Lauridsen, E.M., 174
Lebensohn, R., 316, 451, 1534
Leblond, C., 457
Lecomte, J.S., 223, 229, 712
Lecuire, J.M., 1315
Lee, C.S., 1083
Lee, D.F., 1466
Lee, D.N., 267, 298, 304, 755, 779, 785, 791, 950
Lee, K.-H., 1546
Lee, K.T., 1369, 1415
Lee, P.S., 21, 724
Lee, Y.D., 1095
Leffers, T., 261, 399
Lenhard, S., 683, 797
Lévesque, D., 493
Li, H., 1303, 1391, 1667
Li, J., 1136
Li, Z., 1037
Liao, G., 1148
Lieckefett, R., 1605
Lillywhite, S.J., 1619
Lin, J., 1439
Lin, Y.P., 1409

Lindh, E., 34
List, F.A., 1466
Litwora, A., 581
Liu, G.L., 706, 805
Liu, Y., 481, 1025, 1148
Liu, Y.L., 1148
Livshits, I., 9, 1643
Lloyd, D.J., 718
Lojkowski, W., 1625
Lokajicek, T., 1587
Lopes, A.M., 322, 671
Lord, M., 493
Lu, J., 1673
Lücke, K., 842
Lutterotti, L., 116, 1599
Luzin, V., 241
Lychagina, T., 541, 241
Lyttle, M.T., 46, 605
MacDonald, W.D., 1260
MacEwen, S., 505
Madsen, L.D., 1375
Mainwaring, P., 1476
Man, C-S., 481
Manceau, A., 1562
Manolache, F., 9
Mao, W., 92, 511, 629, 872, 938
Mason, D., 9
Mason, D.E., 1637, 1643
Masui, H., 279, 381, 405
Mathon, M.H., 922
Matthies, S., 40, 68, 439, 1599
McGreevy, R., 553, 1631
McQueen, H.J., 836, 878
Mecking, H. 437
Mege, S., 1345
Mehnert, K., 217
Mendiola, J., 1327
Mi, X.C., 1266
Michaluk, C.A., 1357
Mika, D., 1655
Miller, M.P., 1272
Miroux, A. 328
Mishin, O.V., 174, 1154, 1613
Monchalin, J.-P., 493
Monot, I, 457
Montheillet, F., 878
Moon, R., 1460
Morano, R., 123, 1106
Morawiec, A., 9, 62, 198
Moreau, A., 493
Morii, K., 445
Morris, J.G., 481, 1148
Muljono, D., 991
Mullins, W.W., 9
Murakami, K., 981
Nakamura, M., 1190
Necker, C.T., 346, 358
Nikitin, A.N., 1587
Nikolayev, D.I., 156, 241
Novikov, V.Y., 967
Oertel, C.-G., 730, 1321
Oh, K.H., 411, 569, 587, 700, 791, 1043, 1065, 1339
Oh, M.H., 469
Okudaira, H., 860
Opitz, R., 944
Ozdemir, S., 9
Paden, D., 1593
Padioleau, C., 493
Parathaman, M., 1466
Pardo, L., 1327
Paredes, J.C., 671
Park, C.-G., 1095
Park, H., 1421
Park, J.Y., 1065
Park, N.J., 469, 950, 1214
Park, S.-H., 1095
Park, S.-J., 587, 700
Park, Y.B., 736, 830, 1433
Peng, R.L., 553, 1631
Pennelle, R., 973, 1278, 1696
Pernet, M., 1562
Petrov, I., 1375
Philippe, M.J., 1488
Piątkowski, A., 581
Pinto, A.L., 671, 773
Pithan, C., 842
Pochettino, A.A., 451, 593
Pospiech, J., 581, 647, 1278
Poulsen, H.F., 174
Priesmeyer, H.-G., 334, 439
Prior, D.J., 1593
Pros, Z., 1587
Protasova, S., 1625
Provenzano, V., 748
Quaeyhaegens, C. 1333
Quesne, C., 1278
Ra, H.Y., 1065

Raabe, D., 1015, 1112
Radhadkrishnan, B., 352
Raj, P.M., 1476
Rajmohan, N., 255, 961, 1118, 1178
Randle, V., 1196, 1202
Ratchev, P., 1224
Ratuszek, W., 599, 1071
Rauch, E., 517
Ray, R.K., 641, 824, 916
Reger, N., 944
Ren, H., 938
Renaud, E., 560
Revol, S., 683
Rickerby, D.G., 748
Ricote, J., 457, 1327
Ripault, R., 1327
Roatta, A., 358
Rodbell, K.P., 1287
Rogan, H., 9
Rogge, R., 505
Rohrer, G.S., 9, 1489, 1509, 1637, 1690
Rollett, A.D., 9, 21, 724, 1015, 1649
Root, J., 677, 761, 1089
Rostek, T., 647
Rousset, A., 1345
Ryde, L., 1031
Ryś, J., 1071
Saerens, A., 1333
Saimoto, S., 135, 1136, 1260
Saito, Y., 1142
Saitou, T., 848
Sakai, T., 1142
Sanchez, P., 451, 593
Sarma, G.B., 352
Savariault, J.M., 1345
Saylor, D.M., 9, 198, 1489, 1509, 1637, 1690
Schaeben, H., 153, 156
Schaeben, S., 1363
Scheffzük, Ch., 1540, 1556, 1605
Schlegel, M., 1562
Schmitz, H.-P., 475
Schnabel, R.F., 1287
Schnieber, R., 523, 1172
Schraven, P., 817
Schultz, L., 944, 1077, 1321
Schwartz, A.J., 180
Schwarzer, R.A., 52, 204
Sebald, R., 292
Seki, F., 1136
Sekine, K., 423
Shi, J., 1037
Shimizu, R., 1009
Shin, C.S., 1339
Shin, C.-S., 1375
Shmayda, W., 928
Siemes, H., 153
Signorelli, J.A., 316, 334, 375
Simkin, B.A., 529
Skrotzki, W., 730, 1321
Smathers, D.B., 1357
Snegirev, M.G., 463
Sokolov, B.K., 689, 742, 890
Sokolova, T.A., 689
Solas, D.E., 369
Soubeyroux, J.-L., 457
Specht, E.D., 1466
Stepanova, I.N., 742
Stock, S.R., 123, 1106
Stüwe, H.P., 417
Sum, M., 761
Sumas, S., 641
Sun, Z., 938
Sursaeva, V., 1625
Sursaeva, V.G., 1684
Suter, R.M., 80
Sutliff, J., 1272
Suwas, S., 641, 916
Suzuki, T., 1190
Svedberg, E.B., 1375
Szpunar, B., 560
Szpunar, J.A., 6, 110, 255, 487, 560, 928, 961, 1118, 1178, 1254, 1303, 1351, 1369, 1391, 1397, 1403, 1409, 1415, 1421, 1427, 1439, 1445, 1667, 1673, 1678
Sztwiertnia, K., 647
Ta'asan, S., 9, 1643
Takamiya, T., 1101
Takashima, M., 1649
Takayama, Y., 884
Takeshita, T., 1522, 1534
Talukder, A, 9
Tamler, H., 475
Tamm, R., 730
Tang, D., 938
Tarasiuk, J., 328
Te Nijenhuis, J., 241
Teicher, A., 1015
Teraoka, S., 1236, 1242

Tidu, A., 141, 694, 1025
Timmermans, W., 1293
Titorov, D.B., 1661
Toker, E., 235
Tomé, C.N., 346, 369, 433, 677
Tóth, L.S., 310, 417
Tozawa, T., 884
Trumble, K.P., 1460
Tse, Y.Y., 805
Tsukamoto, O, 405
Tuflin, A.U., 1684
Turner, T.J., 1272
Tye, M., 1593
Ubhi, H.S., 217
Ueno, M., 1190
Ukaji, H., 405
Ullemeyer, K., 1587
Um, K.K., 267, 779, 785
Umeda, M., 445
Ushigami, Y., 981
Vadon, A., 611, 1631
Valiev, R.Z., 748
Valot, C., 98
van den Boogaart, K.G., 29, 162, 1363
van der Winden, M.R., 1224
Van den Broeck, Y., 1224
Van Bael, A., 249, 340, 811
Van Houtte, P., 249, 340, 623, 811, 910, 1224, 1333
Vatne, H.E., 393
Vaudin, M.D., 186
Vedula, V.R., 1489, 1509
Verlinden, B., 1224
Vladimirov, L.R., 689, 742, 890
Von Dreele, R.B., 129
Wagner, F., 40, 683, 694, 797, 895
Walther, K., 1540, 1605
Wan, S., 1453
Wang, X., 1037
Wang, Y.D., 553, 1631
Wang, Y.-Y., 1287
Wang, Z-C., 1568
Watt, T., 123
Weber, S., 1287
Wégria, J., 767, 997
Wells, M.A., 718
Wenk, H.-R., 3, 129, 235, 364, 1495, 1534, 1599
Wierzbanowski, K., 328
Wieting, J., 1077
Winther, G., 387, 399
Wirth, R., 1568
Wittridge, N.J., 1049, 1089
Woo, J.S., 1009, 1059, 1208
Wright, S.I., 104
Wu, C-T., 9
Wynblatt, P., 1649
Xie, Y., 235
Yang, C-C., 9
Yang, J., 298
Yang, W., 9, 192, 1248
Yu, D., 1003
Yu, Y., 92, 511, 629, 872
Zacharia, T., 352
Zao, K., 1266
Zehetbauer, M., 417
Zhao, Z., 872
Zhilyaev, A.P., 748, 1403, 1678
Zhu, G.H., 92, 629
Zielinska-Lipiec, A., 1351
Zuo, L., 1025